中国气象局气候研究开放实验室

论文汇编

第二十一卷

(2018)



LCS

气候研究开放实验室

中国气象局气候研究开放实验室

论文汇编

第二十一卷

(2018)

中国气象局气候研究开放实验室

内 容 简 介

本文集收录了2018年度中国气象局气候研究开放实验室在国内外核心期刊发表的学术论文61篇。内容涉及气候诊断、气候预测理论及方法、气候模式模拟、气候变化检测及影响评估等研究领域。

目　录

1. Sea-Effect Precipitation over the Shandong Peninsula, Northern China …… Bao B, Ren G Y (1)
2. 城市化对石家庄站近地面风速趋势的影响 …… 卞　韬　任国玉　张立霞 (19)
3. Henye-Greenstein 近似对冰云短波辐射计算的影响 …… 陈　琪　张　华 (29)
4. Scientifc basis of climate change and its response …… Chao Qingchen, Feng Aiqing (38)
5. Comparisons of observational data sets for evaluating the CMIP5 precipitation extreme simulations over Asia …… Dong S Y, Sun Y (46)
6. The changing relationship between the December North Atlantic Oscillation and the following February East Asian trough before and after the late 1980s … Feng G, Zou M, Qiao S, Zhi R, Gong Z (62)
7. Diagnosing Relationships between Mean State Biases and El Niño Shortwave Feedback in CMIP5 Models …… Samantha Ferrett and Matthew Collins, Hongli Ren (76)
8. Temporal Characteristics of Actual Evapotranspiration Over China Under Global Warming …… …… Feng Taichen, Tao Su, Fei Ji, Rong Zhi, Zixuan Han (97)
9. 东北亚地区初夏、盛夏和传统夏季降水特征及环流型的异同性研究 …… …… 胡　泊　申红艳　王晓娟　封国林 (111)
10. Multi-pentad prediction of precipitation variability over Southeast Asia during boreal summer using BCC_CSM1.2. …… Li Chengcheng, Hongli Ren, Fang Zhou, Shuanglin Li, et al (126)
11. Early summer southern China rainfall variability and its oceanic drivers …… …… Weijing Li, Hongchang Ren, Jinqing Zuo, Hongli Ren (143)
12. 中国南方夏季降水的年代际变率主模态特征及机理分析 …… 李维京　刘景鹏　任宏利　左金清 (158)
13. Concurrent droughts and hot extremes in Northwest China from 1961 to 2017 …… …… Li Xin, Qinglong You, Guoyu Ren, Suyan Wang, Yuqing Zhang, et al (176)
14. A Comparison and Evaluation of Two Centennial-scale Sea Surface Temperature Datasets in the China Seas and Their Adjacent Sea Areas …… Li Yan, Li Qingquan, Wang Qingyuan, et al (187)
15. Remarkable impacts of Indian Ocean sea surface temperature on interdecadal variability of summer rainfall in Southwestern China …… Liu Jingpeng, Hong Li Ren, Weijing Li and Jinqing Zuo (196)
16. Diagnosing the leading mode of interdecadal covariability between the Indian Ocean sea surface temperature and summer precipitation in Southern China …… …… Liu Jingpeng, Hongli Ren, Weijing Li and Jinqing Zuo (209)
17. 超强厄尔尼诺事件对中国东部春夏季极端降水频率的影响 …… 刘明竑　任宏利　张文君　任鹏飞 (221)
18. Evaluation and statistical downscaling of East Asian summer monsoon forecasting in BCC and MOHC seasonal prediction systems …… Liu Ying, Ren Hongli, et al (236)
19. 基于度-时法的哈尔滨冬季采暖强度评价 …… 刘玉莲　任国玉 (250)
20. 地面气温对微环境空间差异的响应—以漠河站为例 …… 刘玉莲　任国玉　张广英 等 (260)
21. 降水相态分离单临界气温模型建立和检验 …… 刘玉莲　任国玉　孙秀宝 (269)
22. A Coupled Dynamic Index for ENSO Periodicity …… Lu B, Jin F F, Ren H L (280)

23. An extreme negative Indian Ocean Dipole event in 2016: dynamics and predictability …… Lu B, Ren H L, Scaife A A, et al (296)
24. Indian Ocean SST modes and Their Impacts as Simulated in BCC_CSM1.1(m) and HadGEM3 …… Lu B, Ren H L, Eade R (308)
25. Multimodel detection and attribution of changes in warm and cold spell durations …… Lu C H, Y Sun, X B Zhang (322)
26. Improving representation of tropical cloud overlap in GCMs based on cloud-resolving model data …… Xianwen JING, Hua ZHANG, Masaki SATOH and Shuyun Zhao (332)
27. Climatological characteristics and long-term variation of rainy season and torrential rain over DPR Korea …… Om Kum-Chol, Guoyu Ren, Shuanglin Li, Kang-Chol O (345)
28. A new Methodology for Estimating the Surface Temperature Lapse Rate Based on Grid Data and Its Application in China …… Yun Qin, Guoyu Ren, Tianlin Zhai, Panfeng Zhang and Kangmin Wen (356)
29. Identification Standard for ENSO Events and Its Application to Climate Monitoring and Prediction in China …… Hongli Ren, Bo Lu, Jianghua Wan, Ben Tian and Peiqun Zhang (374)
30. Impact of boreal summer intraseasonal oscillation on rainfall extremes in southeastern China and its predictability in CFSv2 …… Ren Pengfei, Hongli Ren, Joshua Xiouhua Fu, Jie Wu and Liangmin Du (388)
31. Establishment of a wildfire forecasting system based on coupled weather-wildfire modeling …… Rim C B, K C Om, G Y Ren, Su Song Kim, Hyok Chol Kim, Kang Chol O (408)
32. Relationship Between Summer Low-Frequency Rainfall Over Southern China and Propagation of Tropical Intraseasonal Oscillation …… Shen Yuyang, Ren Hongli, Li Weijing, et al (413)
33. 2017年全球重大天气气候事件及其成因 …… 孙 劭 王东仟 尹宜舟 等 (423)
34. Global diurnal temperature range (DTR) changes since 1901 …… Sun X B, Guoyu Ren, Qinglong You, Yuyu Ren, Wenhui Xu, et al (432)
35. Substantial Increase in Heat Wave Risks in China in a Future Warmer World …… Sun Ying, Hu Ting, Zhang Xuebin (446)
36. 武汉城市相对湿度气候学特征与长期变化趋势 …… 索南看卓 任国玉 贾文茜 孙秀宝 (457)
37. Can CFMIP2 models reproduce the leading modes of cloud vertical structure in the CALIPSO-GOCCP observations …… Wang F and Yang S (467)
38. Representation of the ENSO Combination Mode and its Asymmetric SST Response in Different Resolutions of HadGEM3 …… Wan Jianghua, Ren Hongli (480)
39. 不同云重叠参数对全球和东亚地区模拟总云量的影响 …… 王海波 张 华 荆现文 谢 冰 (494)
40. 朝鲜中西部地区春季植被覆盖度与气候因子的关系 …… 吴刚哲 严金哲 任国玉 等 (506)
41. MJO对我国降水影响的季节调制和动力-统计降尺度预测 …… 吴 捷 任宏利 许小峰 等 (513)
42. Preliminary Assessment on the Hindcast Skill of the Arctic Oscillation with Decadal Experiment by the BCC_CSM1.1 Climate …… Wu Liquan, Li Qingquan, et al (528)

43. Impact of SST Anomaly Events over the Kuroshio-Oyashio Extension on the "Summer Prediction Barrier" …… Yujie Wu, Wansuo Duan (537)
44. Computing entropy change in synoptic-scale system …… Wu Y P, Hu Y Y, Cao H X, Fu C F, Feng G L (550)
45. Mathematical modeling of fog-Haze evolution …… Wu Yongping, Zhu Chunyangzi, Feng Guolin, Li B Larry (556)
46. 云南雨季的时空特征及与大气环流变化的关系 …… 晏红明 李清泉 王东阡 (560)
47. 中国东部季风区夏季四类雨型的水汽输送特征及差异 …… 杨 柳 赵俊虎 封国林 (571)
48. Detection of Anthropogenic Influence on Fixed Threshold Indices of Extreme Temperature …… Yin H and Y Sun (586)
49. Diagnosing changes of winter NAO in response to different climate forcings in a set of atmosphere-only timeslice experiments …… Huang Yu, Hong Li Ren, Robin Chadwick, Zhigang Cheng, Quanliang Chen (598)
50. Change in precipitation over the Asian continent from 1901—2016 based on a new multi-source dataset …… Zhan Y J, Ren G Y, Yang S (612)
51. 2016 年 10 月我国将水预测失败的原因分析 …… 章大全 陈丽娟 柳艳菊 等 (629)
52. Effective radiative forcing and climate response to short-lived climate pollutants under different scenarios …… H Zhang, B Xie and Z Wang (639)
53. Influences of the internal mixing of anthropogenic aerosols on global aridity change …… Hua Zhang, Chen Zhou and Shuyun Zhao (649)
54. Circulation System Configuration Characteristics of Four Rainfall Patterns in Summer over the East China …… Junhu Zhao, Liu Yang, Guolin Feng (660)
55. Inter-annual and inter-decadal variability of early- and late-summer precipitation over Northeast China and their background circulation …… Zhao J H, Zhou J, Yang L, Hou W, Feng G L (669)
56. 2016 年我国梅雨异常特征及成因分析 …… 赵俊虎 陈丽娟 王东阡 (678)
57. 基于新监测指标的江南入梅早晚的气候特征及影响系统分析 …… 赵俊虎 陈丽娟 熊开国 (690)
58. The Effects of El Niño-Southern Oscillation on the Winter Haze Pollution of China …… Zhao Shuyun, Zhang Hua, Xie Bing (709)
59. 北京地区大气湿度变化及城市化影响分析 …… 郑祚芳 任国玉 (724)
60. 2017 年秋季我国北方地区降水异常偏多成因分析 …… 支 蓉 陈丽娟 竺夏英 (732)
61. On effective radiative forcing of partial internally and externally mixed aerosols and their effects on global climate …… Chen Zhou, Hua Zhang, Shuyun Zhao, Jiangnan Li (742)

Sea-Effect Precipitation over the Shandong Peninsula, Northern China

BAOLEERQIMUGE BAO

Department of Atmospheric Science, School of Environmental Studies, China University of Geosciences, Wuhan, and Forestry College, Inner Mongolia Agricultural University, Hohhot, and Chinese Academy of Meteorological Sciences, Beijing, China

GUOYU REN

Department of Atmospheric Science, School of Environmental Studies, China University of Geosciences, Wuhan, and Laboratory for Climate Studies, National Climate Center, China Meteorological Administration, Beijing, China

(Manuscript received 18 July 2017, in final form 4 March 2018)

ABSTRACT

Sea-effect precipitation (SEP) over the Shandong Peninsula is a unique climatological phenomenon in mainland China, and it exerts a considerable impact on the southern shore of the Bohai Sea. From observed data from 123 stations for the period 1962–2012, the characteristics of cold-season (November–February) SEP in this area were analyzed. Results showed that SEP occurred throughout the late autumn and winter. In all, 1173 SEP days were identified during the 51 years, of which snow days accounted for 73.7% and rain and snow–rain days accounted for 16.1% and 10.1%, respectively. December had the largest number of SEP snow days, followed by January and November. November was the most productive month in terms of SEP rain and snow–rain days. Intense SEP snowfall mainly affected the inland hill area of the peninsula, whereas light SEP snowfall reached farther inland. SEP rainfall shared a similar pattern with snowfall. The SEP frequency showed a significant interannual variability and a nonsignificant upward trend over the period analyzed. SEP was most likely to occur when the temperature difference between sea surface and 850 hPa over the Bohai Sea was above 10°C, indicating a dominant influence of low-level cold-air advection over the sea on the generation and development of the weather phenomenon. A significant negative correlation was also found between the area of sea ice in the Bohai Sea and intense SEP snowfall, indicating that sea ice extent had an important effect on SEP variability over the peninsula. In the case of extremely intense SEP events, a deeper East Asian trough at the 500-hPa level developed over the southwest of the study area and temperature and geopotential height contours were orthogonal to each other, indicating strong geostrophic cold-air advection over the Bohai Sea and the Shandong Peninsula. The extremely intense SEP events were also characterized by anomalous low temperature and high relative humidity in the lower troposphere, which contributed to greater gravitational instability in the study area.

1. Introduction

Sea-effect precipitation (SEP) and lake-effect precipitation (LEP) are local or mesoscale precipitation phenomena that appear over and downwind of the sea or a lake (Laird et al. 2009a,b) when cold air flows over the relatively warmer water. They occur mostly in mid–high-latitude regions in late autumn and winter and are characterized by cloud streets, limited spatial distribution, short duration, and mostly snow (Steenburgh et al. 2000; Yu et al. 2009; Laird et al. 2009a,b). There are many studies on LEP (Braham and Dungey 1984; Burnett et al. 2003). SEP occurs independently, although it can also enhance synoptic-scale precipitation (Tardy 2000). There exist many areas of the world where SEP and LEP occur frequently, for example, northwestern Japan (Ikeda et al. 2009), easterly wind–induced snowfall in the Yeong Dong region of the Korean Peninsula (Nam et al. 2014), the Black Sea (Kindap 2010), the Great Lakes in North America (Braham and Dungey 1984; Burnett et al. 2003), and the northeastern slope of the Caucasus Mountains to the west of the Caspian Sea (Farley Nicholls and Toumi 2014). Some smaller inland lakes can also trigger LEP, such as the Great Salt Lake (Steenburgh et al. 2000), Lake Champlain (Payer et al. 2007), and the Finger Lakes (Laird et al. 2010) in the United States.

Corresponding author: G. Ren, guoyoo@cma.gov.cn

DOI: 10.1175/JAMC-D-17-0200.1

© 2018 American Meteorological Society. For information regarding reuse of this content and general copyright information, consult the AMS Copyright Policy (www.ametsoc.org/PUBSReuseLicenses).

There is much research on LEP that focuses on different sizes of water bodies (Laird et al. 2009a,b; Steenburgh et al. 2000; Payer et al. 2007). Several aspects of LEP have been analyzed, such as initial and ending time, duration time, surface temperature, lake–air temperature difference, sea–land breeze, and other atmospheric conditions. LEP mostly is initiated overnight and in the morning and dissipates in the afternoon (Laird et al. 2009a). The duration of individual LEP events varies with the size of the water bodies. The average duration is 9.4 h for the New York State Finger Lakes (six easternmost Finger Lakes, ranging in surface area from 7.6 to 175 km^2; Laird et al. 2009b), 12.1 h for Lake Champlain (1127 km^2; Laird et al. 2009a), 19.5 h for Lake Ontario (the smallest of the Great Lakes at 18 960 km^2) and the Tug Hill region (Veals and Steenburgh 2015), and even up to multiple days for larger water bodies of the Great lakes (Laird et al. 2009a). The 850-hPa temperature is an important air condition for the development of LEP and has been used as an important indicator for forecasting LEP (Laird et al. 2009a). Near-surface temperature can also be a good reference index for different LEP types, with mostly LEP as rain when the temperature is above freezing and as snow when the temperature is below freezing (Miner and Fritsch 1997).

Many studies have documented the various factors that influence LEP, such as the lake breeze (Passarelli and Braham 1981; Laird et al. 2009a; Alcott et al. 2012), upper-air troughs, surface cold fronts, wind shear, lake–air temperature differences, lake–land temperature differences (Steenburgh et al. 2000), and lake ice extent (Cordeira and Laird 2008). Burnett et al. (2003) showed that the extent of lake/sea ice has become smaller with global warming, enhancing the frequency and intensity of LEP in the Great Lakes. A comparison was given for LEP among different water areas in the studies of Lake Champlain and the Finger Lakes of New York (Laird et al. 2009a,b, 2010).

Climatological analysis on LEP has also been conducted for different lakes (Steenburgh et al. 2000; Laird et al. 2009a,b, 2010; Alcott et al. 2012; Veals and Steenburgh 2015; Laird et al. 2016). The time periods selected in these papers mostly started in the mid-1990s when WSR-88D data were available. By use of radar data, LEP days can be accurately identified and classified into different types, including pure LEP, transition type, synoptic-scale precipitation enhanced type, and enhanced precipitation of upstream water body (Laird et al. 2009a, 2010).

Numerous Chinese researchers have investigated SEP, which is also called ''cold flow precipitation'' by the authors, in the Shandong Peninsula (Zhou et al. 2008; Yang et al. 2009; Jiang et al. 2010; Zhu et al. 2010). These works encompassed such topics as mesoscale characteristics (Yang et al. 2007a; Zhang et al. 2008), diagnostic analyses (Shan et al. 2006; Li et al. 2011), possible mechanisms (Yu et al. 2009), orographic influence (X. Zhou et al. 2011), and high-level air condition (Chu and Li 2012). The first issue in the research was the segregation of SEP days. The previous studies utilized different methods to differentiate the SEP types for different purposes, but they were mostly based on the data of radar-echo maps (Yang et al. 2007a), low-level winds, and precipitation fields (Yang et al. 2007b).

Overall, the studies of SEP in the Shandong Peninsula were mostly based on case analyses of synoptic features, with little emphasis given to climatological analysis. Climatological analyses of SEP have been done only in recent years (S. Zhou et al. 2011; Yang et al. 2007b). S. Zhou et al. (2011) only analyzed SEP snow and found that the heavy SEP snowfall was mostly distributed in the eastern part of the Shandong Peninsula and that there was an annual mean of 0.9 days of heavy snowfall on the whole peninsula. Yang et al. (2007b) found that the SEP snow events generally occurred in the northeastern part of the Shandong Peninsula and that they exhibited a rapid decline from there toward the southwest of the peninsula. The two studies did not analyze snow–rain and rain, nor did they examine the long-term change in the SEP snow events. In addition, there had been less focus on the sea-effect rainfall, probably because of the relatively reduced socioeconomic effects when compared with the sea-effect snowfall.

In this paper, we differentiated SEP days from other categories of precipitation according to the daily wind field and spatial distribution of daily precipitation. Sea-effect rain, snow, and snow–rain days were identified using weather records. We then analyzed the climatology characteristics and long-term variation of frequency and intensity of the different types of SEP. The findings of this paper could contribute to in-depth understanding of the mechanisms of the cold-season SEP in the Shandong Peninsula.

2. Study area, data, and methods

Figure 1 shows the study area and the spatial coverage of the meteorological observation stations. In this investigation, we defined the Shandong Peninsula as the area east of 119°E and north of 35°N. The peninsula is located to the south of the Bohai Sea (about 77 000 km^2). Most of the peninsula area is hilly land, with the east–west-oriented Laishan Hill area (about 200–500 m high)

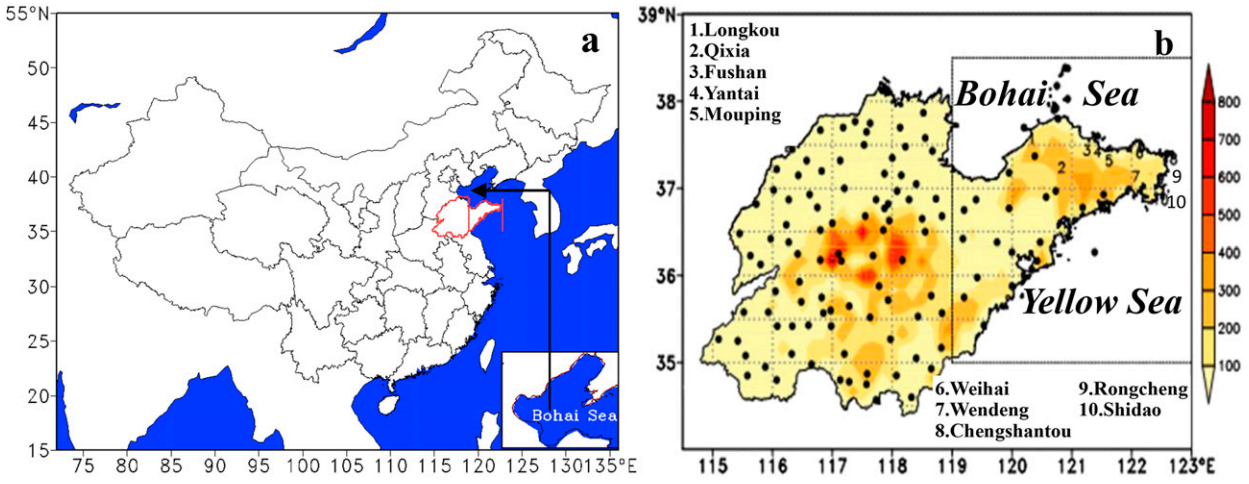

FIG. 1. (a) Study area, with the inset map showing the Bohai Sea at large, giving the locations of Shandong Province and the Shandong Peninsula. The boundary of the province is in red, with the eastern and western ends of the peninsula labeled by two vertical red lines. (b) An enlargement of the province, showing the distribution of meteorological stations. The color bar and contours are in meters, indicating height above sea level.

located at approximately 37.2°N. The northeastern coast of the peninsula is affected frequently by SEP, which sometimes causes severe snowstorms or rainstorms; for example, the heavy sea-effect snowfall of 3–21 December 2005 over the Shandong Peninsula caused severe impacts to transport and communications. Four SEP intense snow events were identified during this period (Zhou et al. 2008).

Figure 2 shows the accumulated snow cover on 19 December 2005 (Fig. 2a), and typical SEP cloud images for three days during the SEP process (Figs. 2b–d). The cumulative precipitation (water equivalent after melting) recorded at the Yantai and Weihai stations is 80.3 and 88.5 mm, respectively, being the most long-lasting and heaviest snowfall process for these two stations since precipitation began being recorded (Yantai since 1961; Weihai since 1959). This snowstorm caused significant damage to the Shandong Peninsula, resulting in the death of 13 300 poultry and the collapse of 2362 greenhouses and 73 houses in Weihai city. Also, flights were canceled, transportation was stalled, and schools were closed in the worst-hit area of the city. It brought about a 5 million yuan economic loss for Yantai and Weihai (Huang et al. 2008; Li et al. 2009). This long-lasting SEP snowfall occurrence was confirmed as one of the 10 most influential weather and climate events in mainland China in 2005. Because of the severe damage brought by the heavy SEP snowstorm, there have been case studies of this snowfall event (e.g., Jiang et al. 2010; Li et al. 2009).

The three infrared cloud photographs in Figs. 2b, 2c, and 2d show the morphology of the clouds in the typical SEP snow process. They are for 1400 Japan standard time (JST) 4 December 2005, 1400 JST 12 December 2005, and 1400 JST 17 December 2005, respectively. The satellite cloud images show that, for Shandong Peninsula SEP snow, low clouds are most frequently formed, with disorganized cells in the early stage but becoming densely arranged later over the northern coastal area (Zheng et al. 2003). Southwest–northeast-oriented cloud lines are observed that are almost vertical to the northwestern wind (Zhou et al. 2008). A cyclonic pattern is also observed for the SEP cumulus cloud (Jiang et al. 2010). Satellite images of another SEP snow day (5 December 2008) shows patterns of clouds that are similar to those of December 2005.

The National Meteorological Information Center of the China Meteorological Administration provided the data for the daily records of precipitation, temperature, and weather phenomena for November–February cold seasons for 1962–2012 (where the year indicates the end point of the cold season) for 123 stations in Shandong Province (Fig. 1b). Daily data for wind, temperature, relative humidity, and geopotential height at different pressure levels (at 2.5° × 2.5° horizontal resolution) were obtained from the U.S. National Oceanic and Atmospheric Administration/National Centers for Environmental Prediction (NOAA/NCEP). Because sea surface temperature (SST) had little variation over the course of a given week, we used weekly instead of daily mean data. The weekly SST data during 1981–2012 were obtained from the NOAA National Climatic Data Center Optimum Interpolation Sea Surface Temperature (OISST). The 24 km × 24 km daily sea ice data from the Interactive Multisensor Snow and Ice Mapping System (IMS) of the

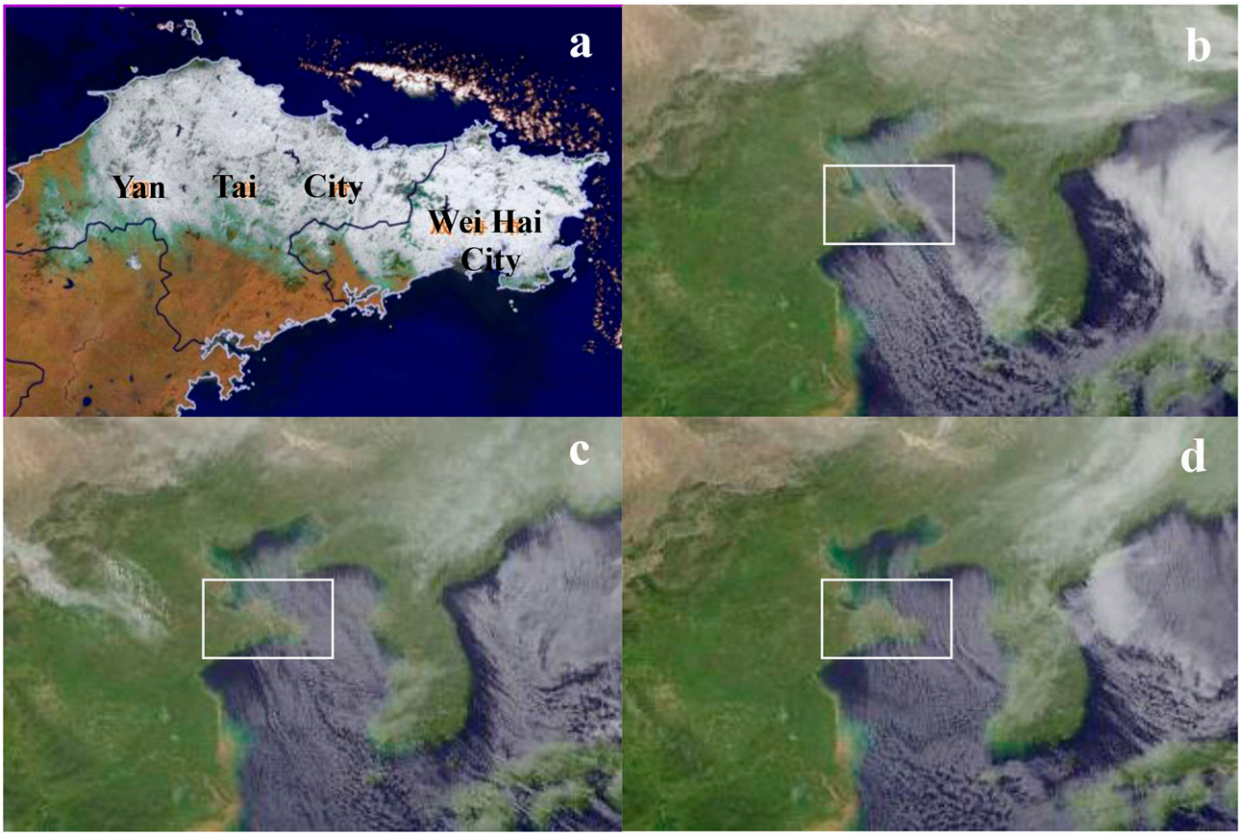

FIG. 2. (a) Snow cover on 19 Dec 2005 in the Shandong Peninsula as monitored by Earth Observing System satellite, and satellite infrared cloud images (from http://weather.is.kochi-u.ac.jp/sat/gms.fareast) at 1400 JST (b) 4, (c) 12, and (d) 17 Dec 2005. The SEP process lasted from 3 to 21 Dec 2005. The study region is indicated by the rectangle in (b), (c), and (d).

NOAA National Ice Center for the period 1997–2012 were utilized in the analysis.

Previous studies mostly used radar reflectivity maps or satellite cloud charts to separate and classify SEP and LEP from synoptic-scale precipitation (e.g., Laird et al. 2009a,b; Alcott et al. 2012). In addition, the sea/lake–air temperature difference was used as an important criterion for indicating the occurrence of SEP and LEP events, and the difference between water surface temperature and air temperature was generally applied in some studies (Sun et al. 2007; Cui et al. 2008). The daily distribution of precipitation has also been used to identify SEP and LEP (Yang et al. 2007b).

This paper was designed to examine climatological characteristics and long-term variation of SEP events using data of the last half century; the radar and satellite records were not available for the early decades. Therefore, we developed a new procedure to identify SEP days. The procedure refers to the previous studies (Yang et al. 2007b; Zhou et al. 2008; Zhu et al. 2010), taking such criteria as spatial pattern of precipitation, location of maximum precipitation, and surface wind direction or 850-hPa wind direction into consideration. These represent the most important features of a typical SEP event. To qualify as a SEP day, the daily precipitation and low-tropospheric wind had to meet the following criteria:

1) Only the Shandong Peninsula area recorded precipitation, and no precipitation was observed inland in Shandong Province. This was determined from the daily precipitation distribution maps of each day of the cold season for the period 1962–2012 in Shandong Province (precipitation amount in this paper is liquid equivalent precipitation, and the unit is millimeters).
2) The maximum precipitation center was located along the shores of the Bohai Sea, typically in the northeastern part of the peninsula.
3) The 850-hPa wind direction over the Shandong Peninsula was any of northerly, northeasterly, and northwesterly. Cold airflow supply from the Bohai Sea was a precondition for SEP formation on the peninsula.

We verify the applicability of the above criteria in identifying a SEP event in the study area by examining a

TABLE 1. Precipitation types and grades (defined in millimeters) of SEP on the Shandong Peninsula.

Precipitation types	Intensity grade	24-h amount (mm) (liquid water equivalent amount)
Snow	Light snow	<2.5
	Moderate snow	2.5–5.0
	Heavy snow	5.0–10.0
	Intense snow	>10.0
Rain	Light rain	<10.0
	Moderate rain	10.0–25.0
	Heavy rain	25.0–50.0

typical sea-effect snowfall event on 3–8 December 2005. The example shows that all of the criteria were met in the event, with the precipitation in the 6 days almost all distributed on the peninsula, the maximum precipitation occurring along the shores of the Bohai Sea (Fig. 2), and the surface and 850-hPa wind directions in the study area being northerly and northwesterly. A total of 6133 days, with 1530 days for November, 1581 days for December, 1581 days for January, and 1441 days for February, were identified as winter SEP precipitation days during 1962–2012. The SEP days were then divided into three types: snow, rain, and snow–rain (rain and snow occurred on the same day).

From the SEP days, we determined the station that had the largest precipitation amount on each of the SEP days. We then designated the weather phenomenon of the site with the maximum precipitation as the SEP type for that day. In cases in which weather-phenomenon records were unavailable, records from nearby sites and other meteorological parameters were used for the designation.

Snow and rain were categorized in terms of intensity. The SEP that generated the maximum amount of precipitation (liquid water equivalent amount) at any of the observational sites was used to determine the precipitation category. A set of specific criteria that are based on the set used by the China Meteorological Association is presented in Table 1. As shown in the table, light snow, moderate snow, heavy snow, and intense snow have an accumulated maximum precipitation amount of <2.5, 2.5–5.0, 5.0–10.0, and >10.0 mm within 24 h, respectively, and light rain, moderate rain, and heavy rain have an accumulated maximum precipitation amount of <10.0, 10.0–25.0, and 25.0–50 mm within 24 h, respectively. No intense rain was found in the study area in winter. Winter months (or the cold season) in this investigation include November and December as well as January and February of the following year.

To understand the favorable atmospheric conditions for SEP, we conducted a composite analysis on different types of SEP on the basis of NCEP reanalysis datasets of geopotential height, relative humidity, temperature, and upper wind field (Kalnay et al. 1996). Using the anomaly–standard deviation method, we selected anomalously heavy SEP days of snow, rain, and snow–rain by using the following formula:

$$k_i = (x_i - \overline{x})/\sigma_x \geq a, \quad (1)$$

where σ_x is standard deviation, x_i is annual precipitation amount, $\overline{x}$ is the long-term annual mean precipitation amount, and a is abnormal index as defined by the World Meteorological Organization, with the precipitation regarded as abnormal in cases of $a > 2$ (Tan 1992).

For SEP snow days, we defined $a = 5$, and thus four SEP snow days were determined to be anomalous SEP events (1 December 1990 with maximum snowfall of 247 mm, 4 December 2005 with maximum snowfall of 270 mm, 7 December 2005 with maximum snowfall of 244 mm, and 5 December 2008 with maximum snowfall of 265 mm). For SEP rain days, we defined $a = 3$, and four SEP rain days were determined to be anomalous or extremely intense SEP rain events (21 November 1963 with maximum rainfall of 407 mm, 7 November 1975 with maximum rainfall of 197 mm, 24 November 1999 with maximum rainfall of 245 mm, and 1 November 2004 with maximum rainfall of 269 mm). For SEP snow–rain days, we defined $a = 2.3$, and also four days were determined to be anomalous SEP events (4 November 1962 with maximum precipitation amount of 169 mm, 16 November 1983 with maximum precipitation amount of 196 mm, 11 November 1985 with maximum precipitation amount of 174 mm, and 15 November 2009 with maximum precipitation amount of 223 mm).

We used the more-extreme events in analyzing the influence of atmospheric circulation on their formation and development because they usually caused more severe damage to the local society and economy. This is also related to the normally low precipitation in the study area as compared with the other regions of the

TABLE 2. Total numbers and percentages of days with different types of SEP over the Shandong Peninsula.

	Snow				Rain			
Grade	Intense	Heavy	Moderate	Light	Heavy	Moderate	Light	Snow–rain
No. of days	50	94	126	595	2	11	176	119
Percentage (%)	4.3	8.0	10.7	50.7	0.2	0.9	15.0	10.1

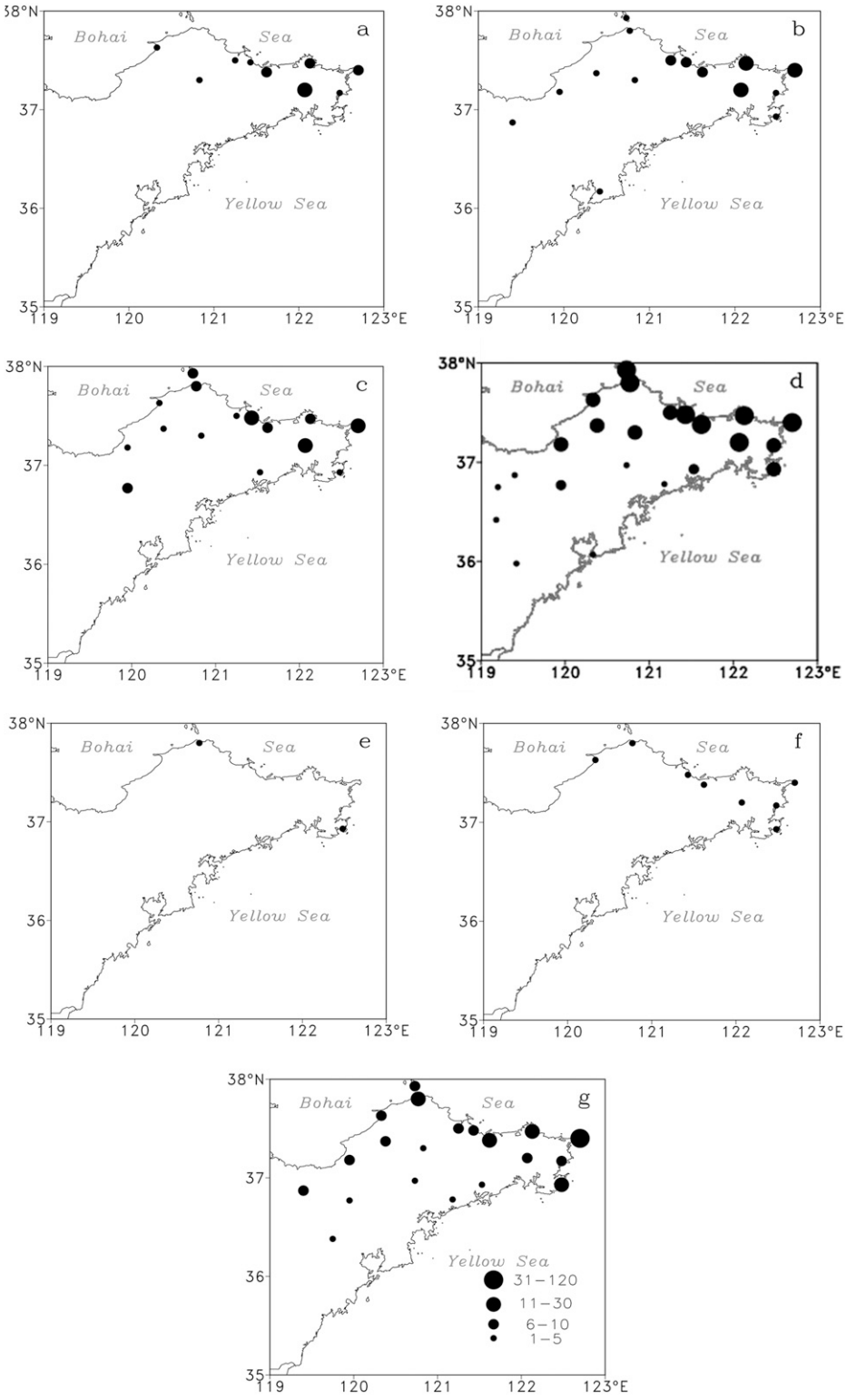

FIG. 3. Spatial distribution of number of days [see key in (g)] for different types of SEP over the Shandong Peninsula: (a) intense snow, (b) heavy snow, (c) moderate snow, (d) light snow, (e) heavy rain, (f) moderate rain, and (g) light rain.

world and the more-extreme events would be characterized by a more typical circulation field.

3. Results

a. Spatial and temporal characteristics

Table 2 shows the number of days with different types of SEP. In all, 1173 (23 days yr^{-1} on average) SEP days were identified during 1962–2012, among which 865 (73.7%, or 17 days yr^{-1}) were snow days, 189 (16.1%, or 3.7 days yr^{-1}) were rain days, and 119 (10.1%, or 2.3 days yr^{-1}) were snow–rain days. SEP was therefore predominantly snowfall events. Because snowfall was more likely to cause severe damage than rainfall, greater attention had been previously focused on snowfall, largely neglecting rain and snow–rain days. Rain days and snow–rain days accounted for 26.2% of the total SEP days, however, and they could sometimes also bring heavy precipitation; therefore, the occurrence and influence of SEP rain days and snow–rain days should not be overlooked.

Through the analysis of the amount of precipitation on snow days, the total numbers of different snowfall intensity categories were as follows: 50 (~1 day yr^{-1}) days of intense snow, 94 days of heavy snow (~2 days yr^{-1}), 126 days of moderate snow (~2.5 days yr^{-1}), and 595 days of light snow (~12 days yr^{-1}). There occurred 189 SEP rain days, with 2 days of heavy rain, 11 days of moderate rain and 176 days of light rain (about 93% of the total rain days). Figure 3 presents the spatial distributions of different types and grades of SEP. The areas of maximum precipitation for all three types were located to the east of Yantai City, along the northern coastal zone.

An examination of the spatial distribution of SEP (Figs. 2 and 3) revealed that Wendeng was the area most frequently affected by intense sea-effect snow, followed by Weihai, Chengshantou, and Mouping. Heavy snowfall was concentrated mainly in the easternmost Chengshantou and Wendeng stations, which might be partly related to the warmer SST of the eastern Bohai Sea and westernmost part of the Yellow Sea. Moderate snowfall shared the same spatial pattern as heavy snow. Overall, the northern coastal zone represented by the Yantai, Weihai, and Wendeng stations was the area most frequently affected by intense SEP events, with the moderate and stronger SEP days accounting for more than one-half of all SEP days. The extent of SEP was broader during light-SEP events, when SEP precipitation reached inland areas of the peninsula. There were 189 rain days, with the maximum rainfall of 40.7 mm recorded on 21 November 1963 and centered in the vicinity of the Shidao station in the eastern coastal zone of the peninsula. Heavy and moderate sea-effect rainfall more frequently occurred along the coastal zones as compared with the intense sea-effect snowfall, with inland regions receiving only light SEP rainfall. The prevalence of more intense snowfall farther inland when compared with rainfall might be related to the effect of higher sea surface temperature, relatively low land surface temperature, and the orographic enhancement of inland hills. In addition, 119 snow–rain days were identified, with the maximum amount of daily precipitation recorded at 22.9 mm.

TABLE 3. Monthly and annual mean number of days with different types and grades of SEP.

Category/grade	Nov	Dec	Jan	Feb	Cold season
Snow					
Intense snow	0.4	0.5	0.1	0	1.0
Heavy snow	0.2	1.1	0.5	0.1	1.8
Moderate snow	0.4	1.1	0.8	0.2	2.5
Light snow	0.8	3.5	4.8	2.6	11.7
Sum	1.7	6.3	6.2	2.8	17.0
Rain	2.6	0.6	0.3	0.3	3.7
Snow–rain	1.2	0.7	0.3	0.2	2.3

Table 3 and Fig. 4 present the seasonality of different types of SEP. The SEP was typically in the form of mixed snow and rain during November, and thereafter it was almost exclusively snow. The greatest number of snow days occurred in December, followed by in January, and the fewest snow days occurred in November. December was the month most prone to intense snow days, with November ranked second, and no intense snow days appeared in February. A similar seasonal distribution was seen for heavy and moderate snowfall. In contrast, light snowfall occurred mainly in January, followed by in December, and occurred least frequently in November.

Figure 4a displays a histogram showing the temporal variation of the total number of SEP days in 10-day bins. The total number of SEP days in the study region reached 24, 30.7, and 36.7 days for the first, second, and third 10-day bins of the month, respectively. In the first two 10-day bins of the winter, most SEP events appeared as rain; the number decreased throughout the winter, whereas SEP snow showed a significant increase afterward. SEP snow showed two maximum values during the cold season, with late December (third 10-day bin; 135 days) and late January (third 10-day bin; 115 days) seeing the maximum values. SEP snow dominated SEP from late November to the end of the cold season. Late November had the maximum SEP snow–rain value (24 days). It had a similar contribution to the total SEP as SEP rain. Sea-effect snow–rain days could occur in any month but peaked in late November and early December and decreased in frequency to the end of

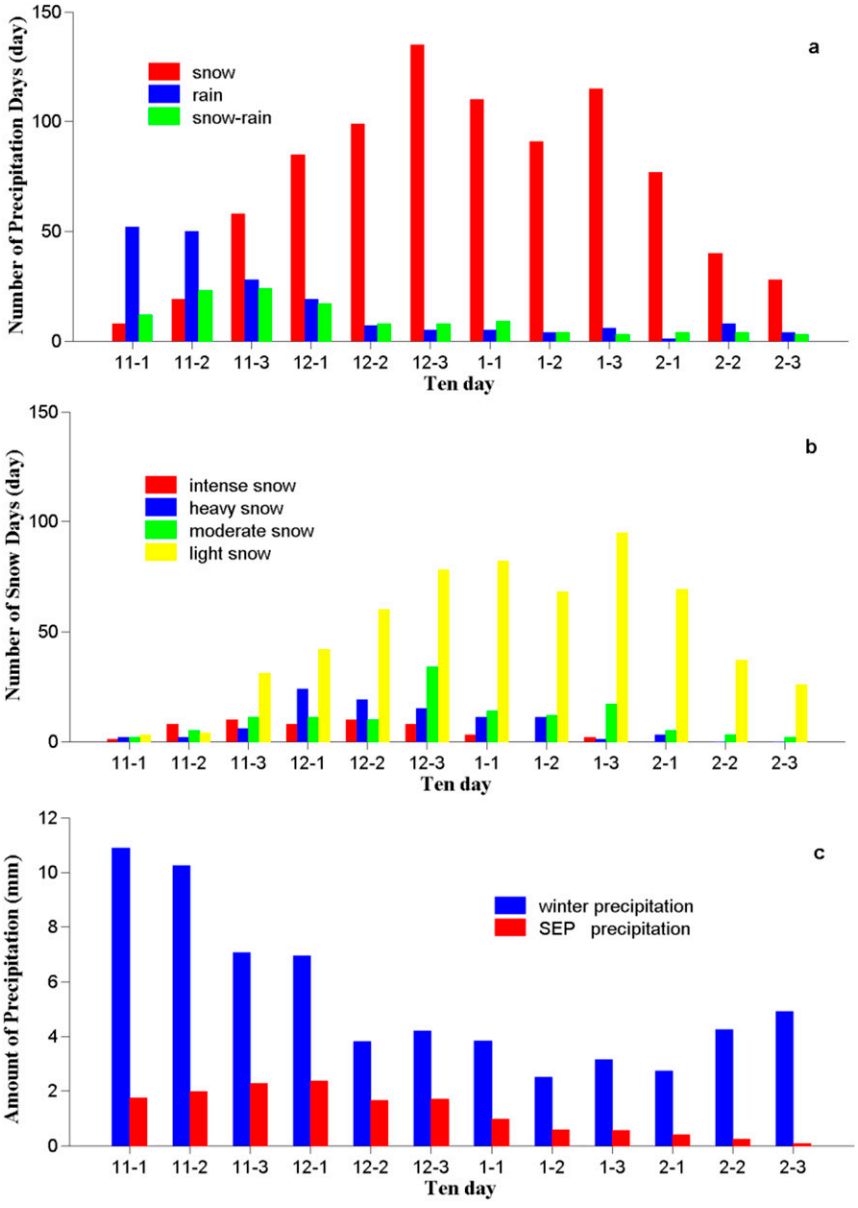

FIG. 4. Seasonal distribution of precipitation days and amount of different types in 10-day bins (e.g., 11-1 indicates the first 10-day bin for November) during 1962–2012: (a) accumulated number of days for different types of precipitation in 10-day bin during 1962–2012, (b) accumulated number of days for different ranks of snow in 10-day bin during 1962–2012, and (c) mean amount of precipitation for cold season and SEP in 10-day bins during 1962–2012.

February. This phenomenon was distributed mainly throughout November and December, with late November and early December having the peak. The intensity and frequency of snow–rain days apparently decreased from the beginning of November to the end of February. Late November was a transition period for both rain and snow. A sharp decrease of rain and an increase of snow were detected during this time. In all, SEP was mostly snowfall, and late November and early December could be regarded as a transition period for different types of SEP.

Figure 4b shows snow frequency for different grades of SEP snow. Mid-November showed an increase in snowfall of different intensities. By the end of November, there was a sharp increase in the frequency of light snow. Although there was less snowfall in November overall, it was of high intensity, and all grades of snow could occur. Snowfall of different intensities

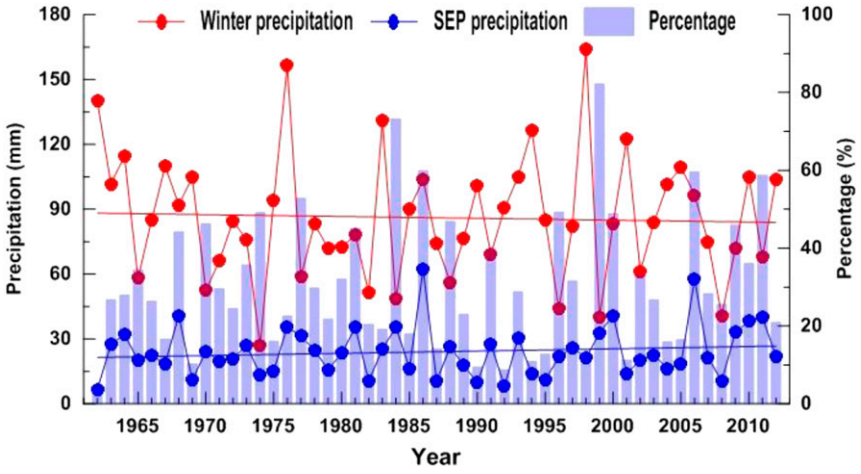

FIG. 5. Regional averaged annual cold-season total precipitation and SEP over the Shandong Peninsula during 1962–2012.

increased in December; snowfall of greater than 20 mm (intense snow) was concentrated mainly in early December. Mid-December was the peak time for the development of SEP snow. Intense snowfall was also seen in early January, although snowfall intensity decreased during the middle 10-day bins of the month. Snowfall intensity continued to weaken during the last 10-day bins, although light snowfall was still commonly seen during this time. No intense snow occurred in February, and both precipitation intensity and frequency markedly decreased. November was the peak time for rain days, accounting for 68.8% of the total SEP rains, followed by December with 16.4%, and February showed the fewest rain days. Figure 4c shows the regional average precipitation amount for SEP and winter precipitation in 10-day bins. The two curves had almost opposite patterns for the cold season.

b. *Variation of SEP*

SEP occurred every year in the Shandong Peninsula (Fig. 5) and exhibited significant interannual variability, ranging from 6.7 to 62.3 mm with an annual mean of 24.1 mm. The years 1985 and 2005 had the highest and second-highest annual amounts of SEP in the period 1962–2012. The contribution of SEP to the total precipitation of the cold season ranged from 4.8% (1992) to 82.4% (1999), once again indicating that it had a relatively large interannual variability, in particular in the 1990s. No determination could be made concerning the long-term SEP trends in these analyses because the weak upward trends as seen in Fig. 5 were not statistically significant.

Figure 6 shows the regional average change of different types of annual cold-season SEP. Annual mean SEP was 24.1 mm, with 16.4 mm or 68% occurring as snowfall. The different types of SEP showed the same characteristics of interannual variability. Snowfall accounted for 21.1%–100% of the total SEP. Annual mean rainfall of SEP was 4 mm, and the pattern of interannual variability was similar to that of SEP but with an evidently smaller magnitude, accounting for 0%–49.6% of the total SEP (17.1% yr^{-1}). Annual mean sea-effect snow–rain was 3.7 mm, accounting for 0%–67.8%, but it was not necessarily observed every year.

No significant long-term trend of the cold-season precipitation was detectable in these analyses, despite the fact that the total SEP amount for all categories and the snowfall exhibited a general upward trend over the study period, especially after the late 1980s.

c. *Relationship between surface–850-hPa temperature difference and SEP*

Sea surface–atmospheric temperature difference is an essential condition for the formation and development of SEP. Here the temperature difference between sea surface and the 850-hPa atmospheric layer, or the surface–850-hPa temperature difference, was applied as an indicator of the possible SEP-inducing factors.

Figure 7 shows that the amount and frequency of snow increased with the increase of the surface–850-hPa temperature difference. The snowfall is the equivalent precipitation amount of the station that had the largest precipitation within a SEP day. The 15°C temperature difference was an important criterion for intense snow development. Intense snow days were seen only when the temperature differences exceeded 15°C. The weaker SEP rainfall generally occurred at a temperature

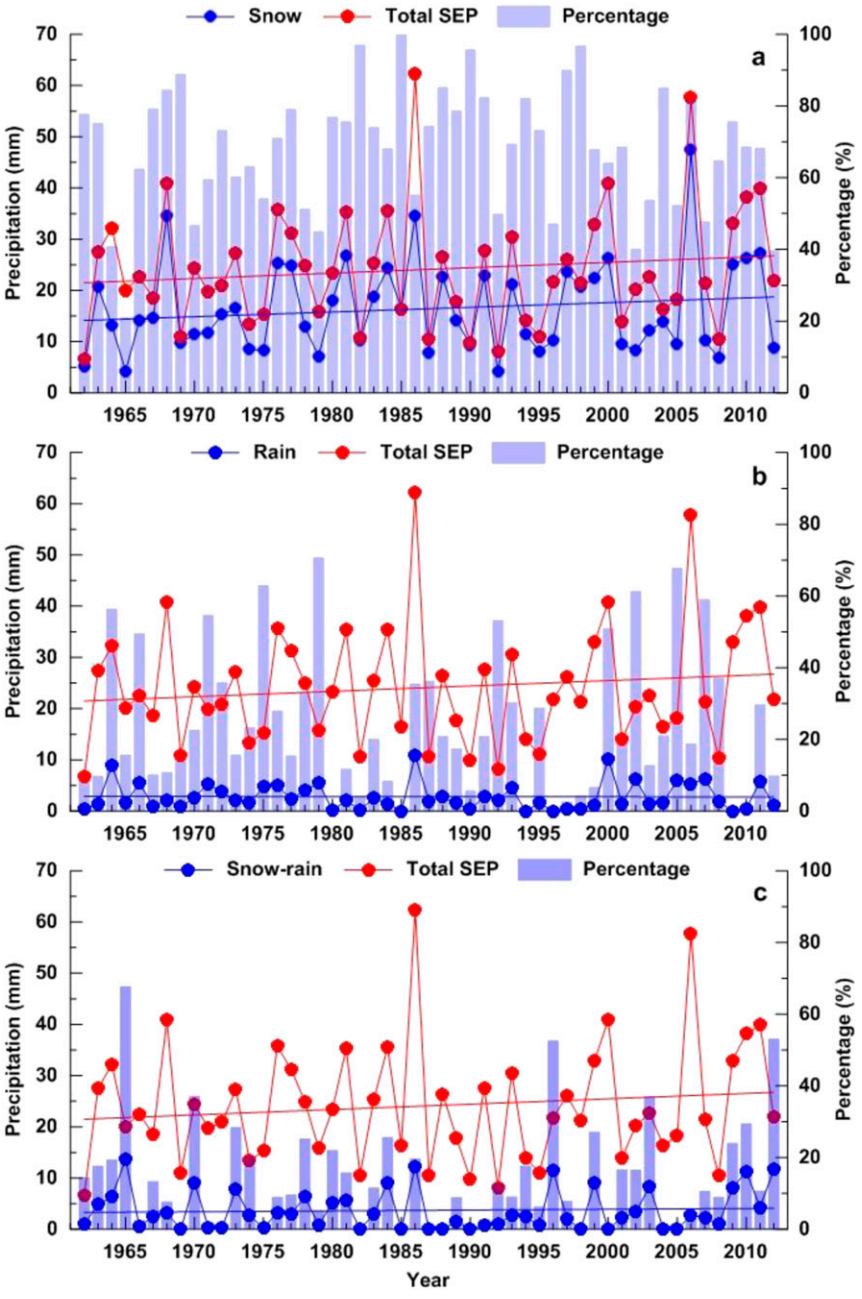

FIG. 6. Regional-averaged annual total SEP [red; identical in (a)–(c)], different types of SEP (blue), and the percentage contribution to total SEP (bars) during 1962–2012: (a) snow, (b) rain, and (c) snow–rain.

difference of 10°–20°C. Snow–rain days occurred between 10° and 25°C, with a similar distribution as snowfall. It was therefore obvious that SEP snow and snow–rain were most likely to occur with a surface–850-hPa temperature difference of 15°–20°C (see Table 4).

The positive correlation between snowfall/snow–rainfall and the surface–850-hPa temperature difference can be explained well. The larger temperature difference meant an increase of temperature lapse rate over the Bohai Sea and the northern coastal zone of the Shandong Peninsula, leading to stronger convection and instability. These would in turn promote generation and development of SEP weather on the peninsula. A previous analysis showed that approximately 80% of surface–850-hPa temperature differences for the Lake Champlain events were greater than 13°C, with a mean

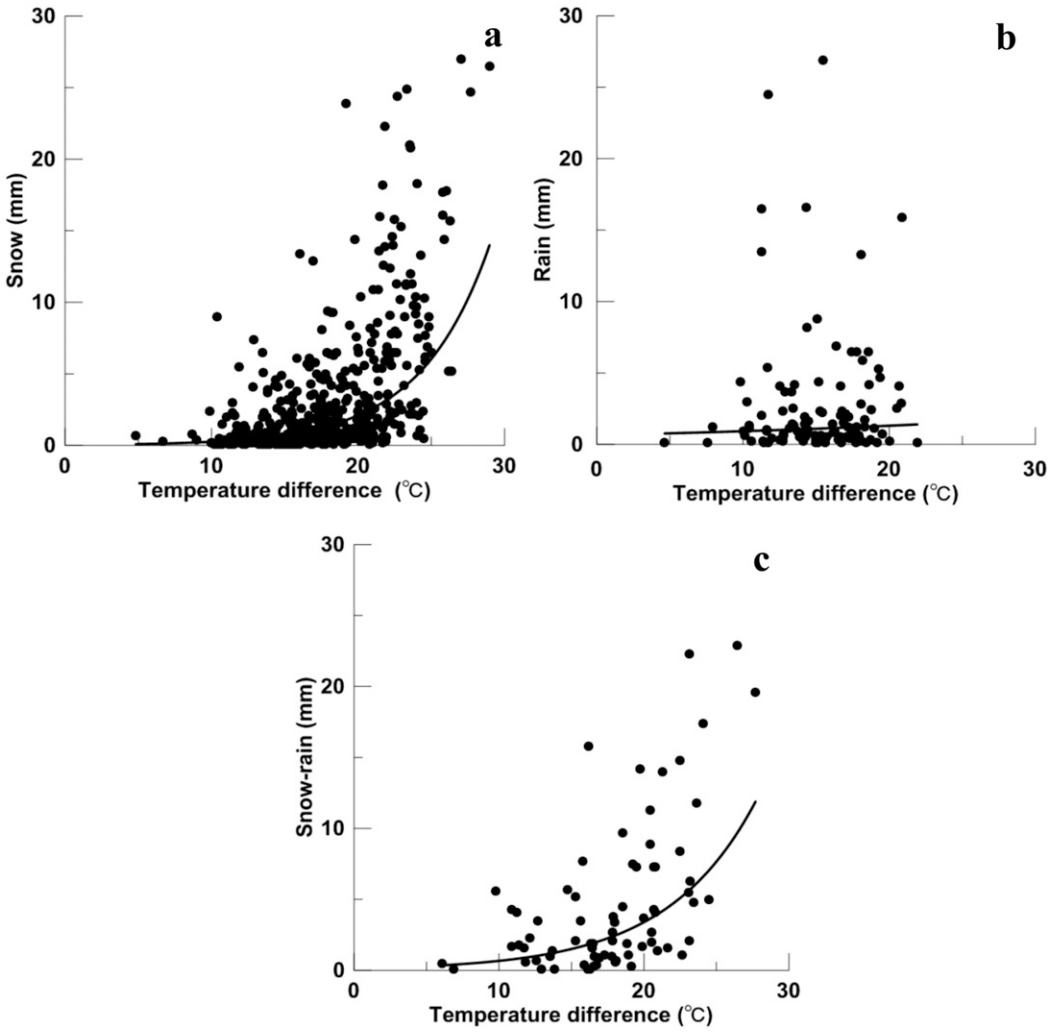

FIG. 7. Relationship between daily mean sea–850-hPa temperature difference and the maximum single-site daily SEP amount of different types and grades at stations for SEP days, 1981–2012: (a) snow (499 days), (b) rain (110 days), and (c) snow–rain (74 days).

value of 18.2°C (Laird et al. 2009a). In the Shandong Peninsula, mean surface–850-hPa temperature difference was 17.8°C for SEP snow days, 15.2°C for SEP rain days, and 17.5°C for SEP snow–rain days, with a mean of 16.8°C for all SEP days. Temperature differences of larger than 13°C accounted for 89% of the SEP snow days, 74% of SEP rain days, and 80% of SEP snow–rain days, with a mean of 86% for all SEP days. Therefore, a temperature difference of 15°C seems to be a critical criterion for intense snow development, which was similar to that reported for Great Salt Lake snowstorm events (Steenburgh et al. 2000).

Figure 8 shows that the frequency of snowfall days and the surface–850-hPa temperature difference had a good correspondence; both showed two maximum values during the cold season: one in late December and the other in late January. In late autumn and early winter, owing to the rapid decrease of the air temperature, the frequency of snowfall days exhibited a significant increase and reached the first maximum in late December, whereas at the same time a significant decrease could be seen in the frequency of rainfall and snow–rainfall days. Following the sharp increase of air temperature and slight decrease of SST, and a rapid decline of the surface–850-hPa temperature difference, the number of snow days decreased dramatically in February. The SST in the Bohai Sea displayed a continuous decreasing trend throughout the cold season, whereas air temperature first decreased until late January and then began to increase. This in turn caused the decrease in the frequency of snowfall.

TABLE 4. Significance test for the exponential fits in Fig. 7. Here, R^2 is the correlation coefficient squared and F is the F statistic.

	Sample size	R^2	F	Significance level
Snow	499	0.318	231.74	99%
Rain	110	0.006	0.65	Not significant
Snow–rain	74	0.274	27.17	99%

In addition, as Table 5 shows, sea ice extent exhibited a significant negative correlation with snowfall and snow–rainfall of SEP in the Shandong Peninsula, indicating that snowfall and snow–rainfall would generally decrease when the sea ice area in the Bohai Sea expanded and increase when it shrank. The correlation would be stronger and more significant if light snowfall and snow–rainfall events were neglected. This is understandable because, in the case of lack of sea ice, the surface–850-hPa temperature difference would be larger (Table 5), facilitating the formation and development of SEP on the peninsula.

d. Atmospheric conditions for SEP

Figure 9 gives 500-hPa mean and anomalous geopotential heights for the extremely intense SEP days selected. The main pattern for geopotential height at 500 hPa was a deep trough in the mid–high-latitude area of 110°–140°E for all of the extremely intense SEP snow and snow–rain days (Figs. 9a,e and 10e). The extremely intense SEP snow and snow–rain days shared a more similar pattern for the 500-hPa pressure level, characterized by an anomalously negative geopotential height or lower-than-normal pressure over the Shandong Peninsula and the Bohai Sea as shown by the closed center of low values. The East Asian trough (EAT) was stronger, the Shandong Peninsula was located just to the southwest of the low-value center, and the pressure gradient over this area was very large (Figs. 9a,e), allowing for strong northwesterly flow to enter the study area. In addition, the trough developed strongly on the extremely intense SEP days as compared with the day before and weakened considerably on the day after (Fig. 10). For rain days (Fig. 9c), however, the geopotential height pattern at 500 hPa was very different, the isolines were more flat in the mid–high-latitude area, and a weaker EAT moved far northeast of the study area. For the peninsula area, only a small height gradient was seen, indicating a comparatively weaker northerly airflow.

The anomalous height fields were also similar for snow and snow–rain days (Figs. 9b,f). The 500-hPa pressure had a sharp drop over the study area, with a >200-m decrease in the center, indicating the deepening of the EAT. For SEP rain days (Fig. 9d), the largest decreasing

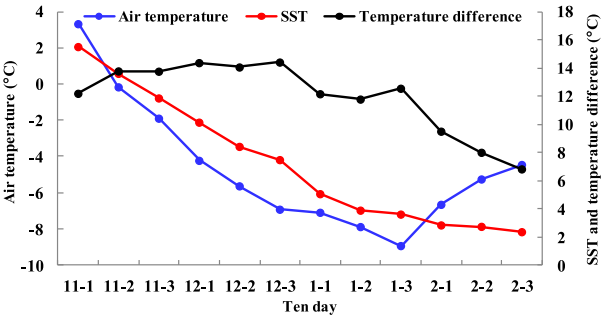

FIG. 8. Long-term mean SST, air temperature, and temperature difference in 10-day bins.

center of the geopotential height (>90 m) was located in the area of 70°–80°E, and a decrease of only approximately 30 m was seen over the study area. There was a large move of the negative anomalous geopotential height center at 500 hPa (Fig. 10) from the day before the SEP days to the day after, with the largest negative value being centered over the Shandong Peninsula and the Bohai Sea on the day before and moving eastward on the following days.

Figure 11 shows the 850-hPa mean wind field, temperature, and geopotential height of the extremely intense SEP days. Similar to the 500-hPa field, the 850-hPa geopotential height also exhibited a deep EAT over the study area during the extremely intense SEP snow days, with strong northwesterly wind affecting the peninsula. A low temperature center was also located to the north of the peninsula, and a sharp gradient in air temperature appeared over the peninsula. The steep gradients of temperature and geopotential height isolines were almost orthogonally distributed over the Shandong Peninsula, providing sufficient cold-air flow to the area. For the extremely intense SEP snow–rain days, the cold center (−20°C) was located at a higher latitude relative to the pattern for snow days and the gradient of isolines was weaker. For the extremely intense SEP rain days, temperature isolines were distributed more zonally, indicating a weaker gradient and less cold-flow supply.

Large negative temperature anomalies were seen in the whole layer below 400 hPa at 30°–40°N for the

TABLE 5. Correlation coefficient of sea ice area of the Bohai Sea with SEP over the Shandong Peninsula.

	Snow	Rain	Snow–rain
Sample size	241	68	43
Correlation coef	−0.238	−0.093	−0.339
Significance level	99%	Insignificant	95%

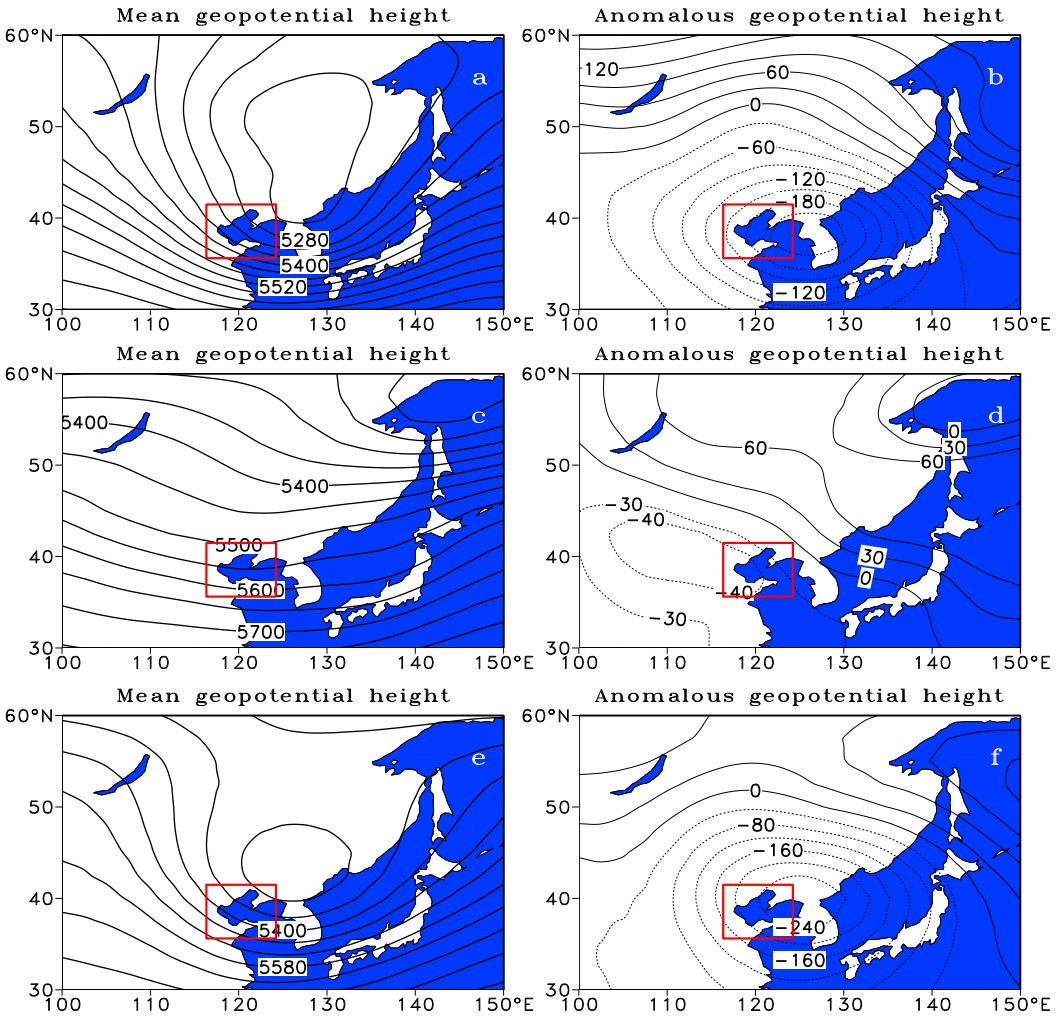

FIG. 9. The 500-hPa (left) mean and (right) anomalous geopotential height for the extremely intense SEP (a),(b) snow, (c),(d) rain, and (e),(f) snow–rain days. The study region is indicated by the red rectangle.

extreme snow (Fig. 12a) and snow–rain (Fig. 12b) cases, with an approximately 10°C decrease occurring over the study area. Conversely, temperature increases were seen above the 400-hPa layer, indicating that the cold-air transport was constrained to low levels. For the extremely intense SEP snow–rain days, the mean temperature had a pattern that was similar to that for the extremely intense SEP snow days, with a slight difference at low levels, where the air temperature was a bit higher on snow–rain days (Fig. 12). For the extremely intense SEP rain days, the temperature below 850 hPa was always above 0°C. It is obvious, therefore, that the temperature anomaly at different levels corresponded well to the precipitation types of the extremely intense SEP events in the Shandong Peninsula.

The surface air temperature plays an important role in the formation and development of the SEP events. Table 6 shows the relationship between surface air temperature and different SEP types in the study area. For 89% of SEP days, the average daily mean temperature was below freezing, and the percentage of SEP days with daily mean temperature below 0°C generally decreased with decreasing SEP intensity. In contrast, about 94% of SEP rain days registered a daily mean temperature above freezing level. This result coincided well with the analyses by Miner and Fritsch (1997) and Laird et al. (2009a). In addition, most of the SEP snow–rain days also saw a daily mean temperature above 0°C.

Relative humidity showed a unique pattern during the extremely intense SEP events (Fig. 13). High relative humidity appeared over the study area in the lower

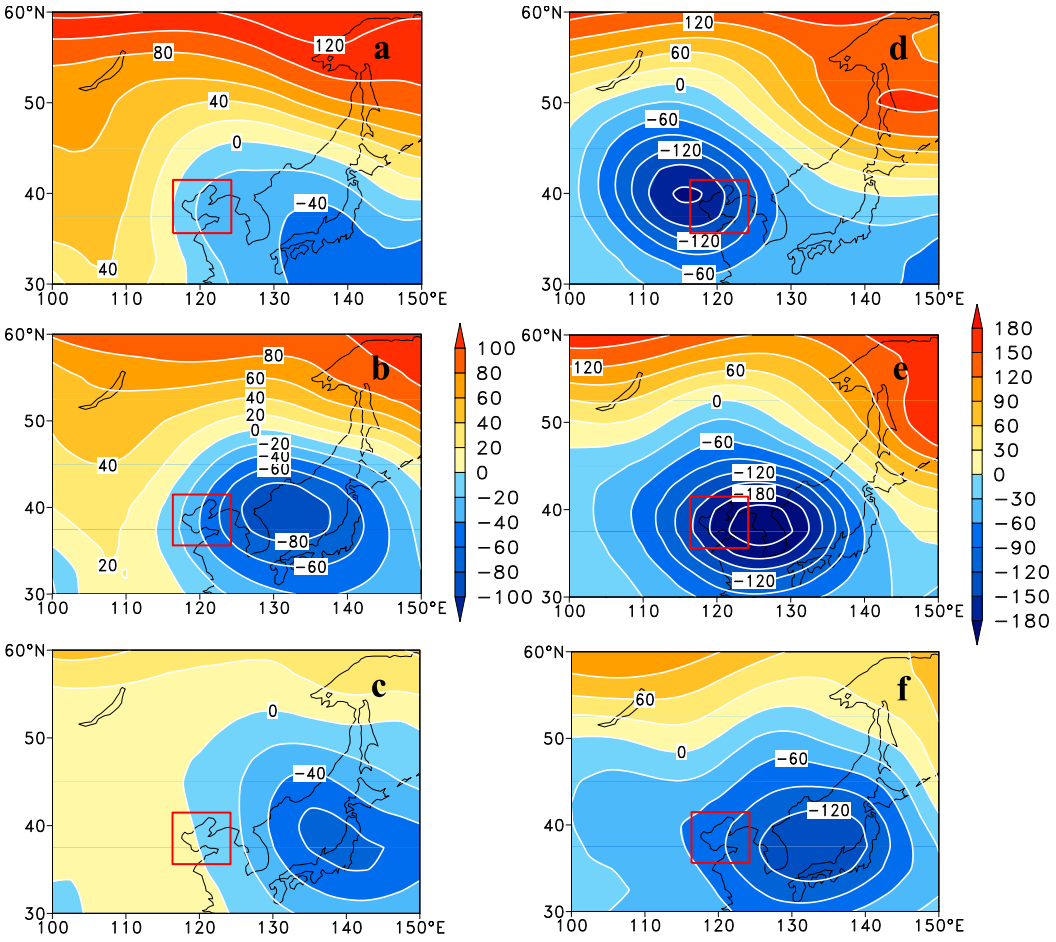

FIG. 10. Change in anomalous (left) 850- and (right) 500-hPa geopotential height of SEP snow days from −1 to +1 day [(a),(d) day before SEP snow day, (b),(e) SEP snow day, and (c),(f) day after SEP snow day]. The study region is indicated by the red rectangle.

troposphere with a value of more than 70% below the 850-hPa level for the area of 120°–125°E. SEP snow days showed the highest relative humidity, followed by the SEP snow–rain days, and the SEP rain days had the lowest relative humidity in the lower layers. In all, a high relative humidity center was generally distributed around the peninsula area and relative humidity over 70% was mostly seen at low levels during the SEP processes, indicating that the convective precipitation phenomenon occurred in a thin layer of the lower troposphere during the SEP events.

4. Discussion

In this research, a comprehensive method is developed to identify days with SEP and to examine the spatial and temporal patterns of the SEP events and their possible linkage with the atmospheric circulation anomaly.

It is obvious that the annual regional average SEP precipitation in the study area ranges generally from 10 to 50 mm (Fig. 5). The amount is small relative to those in other regions of the world. An intense snowfall event over the Shandong Peninsula is therefore largely dwarfed in comparison with that of the Great Lakes, and it would be called a moderate or even light event outside the study area. A Lake Ontario winter storm regularly produces lake-effect precipitation of more than 60 mm in merely 24 h (Campbell et al. 2016). The Shandong Peninsula, like most areas of northern China, has a climate that differs somewhat from those in other regions of the world. The climate on the peninsula is characterized by a very dry winter because of the strong prevailing winter monsoon flow from the inland Asian continent. Precipitation is extremely low in winter, that is, usually less than 60 mm from December to February, accounting for less than 10% of the annual total amount.

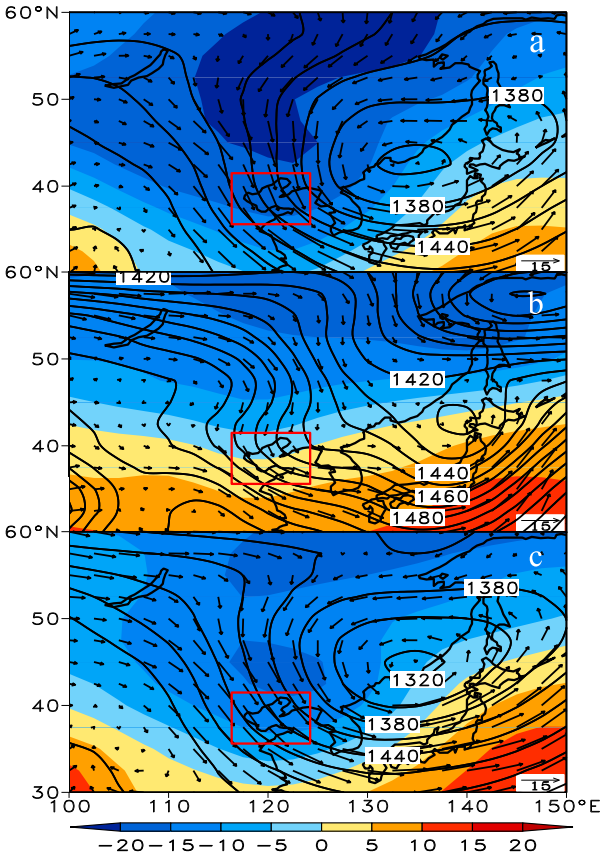

FIG. 11. The 850-hPa mean geopotential height (solid lines every 30 hPa), temperature (shaded scale, at 5°C intervals), and wind field (vectors) for extremely intense SEP (a) snow, (b) rain, and (c) snow–rain days. The study region is indicated by the red rectangle.

This is the main reason why the sea-effect events in the area produce such low accumulated precipitation in comparison with that of the other regions.

With regard to the temporal and spatial variation of the SEP snowfall, our results are generally consistent with the main characteristics as found in the previous studies (e.g., S. Zhou et al. 2011; Yu et al. 2011). The earlier studies have been focused on sea-effect snowfall, however, and none examined the SEP rainfall and snow–rainfall. We classify and analyze the three categories of the SEP events in the Shandong Peninsula. Our analysis indicates the importance of the SEP rain and snow–rain events in addition to the SEP snow days. Rain and snow–rain days account for 26.1% of the total number of SEP days, with some of the rain and snow–rain events even bringing heavy precipitation. Their incorporation in this study is a significant improvement over the previous studies.

It is also obvious that the previous works were mostly focused on the SEP characteristics merely as a weather phenomenon and its synoptic origin, and the climatological characteristics and long-term variation of different types and grades of SEP events have been overlooked to a large extent. In this work, we make a more thorough analysis of the climatological characteristics and long-term variation of the different categories and grades of SEP events over the past more than one-half of a century. The main atmospheric circulation factors for, and the indicators of, the formation and development of extremely intense SEP events are also analyzed in this paper. Although further work is needed to understand better the full spectrum of influential factors and the dynamic mechanism, the findings from this analysis—including that SEP snowfall and snow–rainfall have a significant positive correlation with the surface–850-hPa temperature difference and a negative correlation with the sea ice extent of the Bohai Sea, as well as that there is a close linkage of the extremely intense SEP events with key East Asian atmospheric circulation indices, air temperature, and humidity fields—will be helpful in understanding this unique weather and climatic phenomenon, and also in forecasting and prediction of intense SEP events in the study area and beyond. It is noteworthy that the SEP events in the Shandong Peninsula, especially the intense snowfall of the SEP, increase to a certain extent over the time period analyzed, especially after the late 1980s, despite the fact that the upward trend was not statistically significant. This might be related to the overall warming of the Bohai Sea and the decline of sea ice extent after the mid- to late 1980s, which might be caused by large-scale climate change and variability (Zhou and Ren 2011; Ren et al. 2012). The projected climate warming and the multidecadal temperature variation of East Asia in the coming decades would likely change the sea ice extents of the Bohai Sea and would therefore affect the frequency and intensity of SEP events in the study area in the decades to come.

A deficiency in this investigation is that precipitation data with higher temporal resolution are unavailable for the time being, which restricts our ability to determine the duration and hourly intensity of the SEP. Furthermore, because SEP is a mesoscale process superimposed on a synoptic-scale background, the ability to differentiate the two processes remains a most challenging problem for future research of SEP and LEP. One of the remaining issues in identifying SEP events, for example, might be related to the possible effect from the sea breeze and synoptic precipitation. The sea-breeze circulation on the northern coast of the Shandong Peninsula is the weakest in wintertime, and it generally occurs in late spring and early summer. In winter, the sea-breeze circulation, if

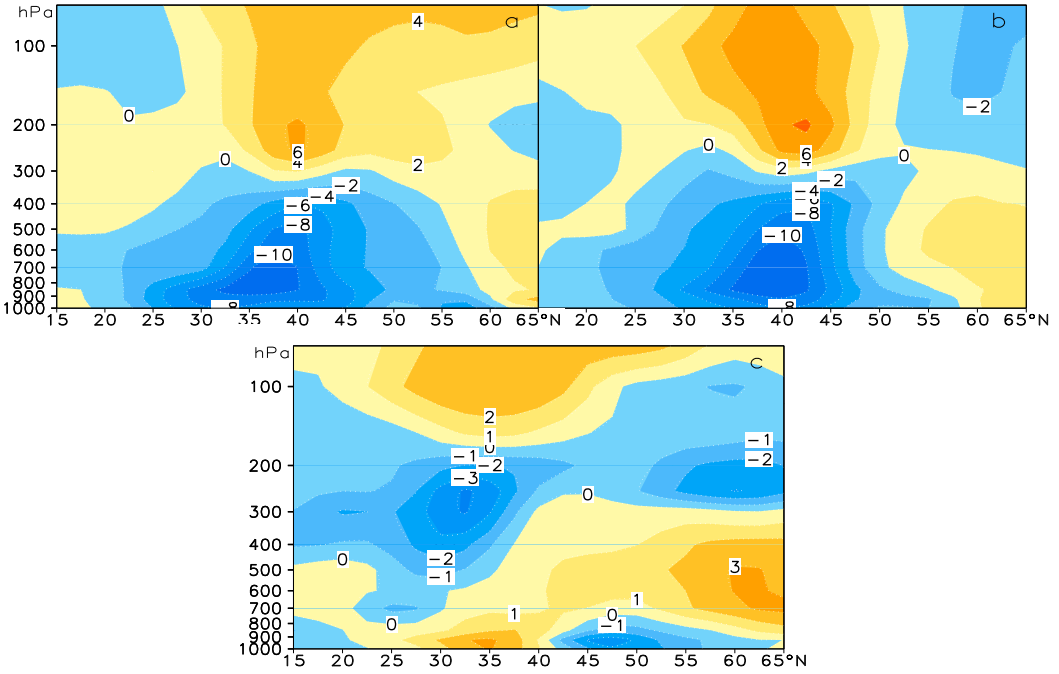

FIG. 12. Latitude–altitude profile of air temperature anomaly at 122.5°E (departure from 1981–2010 mean) for the extremely intense SEP (a) snow, (b) snow–rain, and (c) rain days.

any, is submerged by strong cold-air flow, and sea ice over the Bohai Sea is another reason for the unapparent sea-breeze circulation of the northern coastal area of the peninsula (Wang and Song 1988). In the southern Bohai Sea, where there is an area of open water, the sea surface temperature is usually higher than that of the land surface in winter, and a land breeze rather than a sea breeze will develop, even in daytime. Sea-breeze-initiated precipitation may therefore have less effect on identifying SEP days.

The criteria for identifying SEP events were developed with consideration of the specific climate condition of the study area, and they would be applicable to the analysis. Nevertheless, combined use of multivariable hourly records and satellite and radar data in future work would be helpful in differentiating the mesoscale SEP from the background synoptic process. In addition, it is also interesting to examine further the synchronous and lagged influence of planetary-scale atmosphere–ocean variability on the formation and development of SEP events in the Shandong Peninsula.

5. Conclusions

We analyzed the climatological characteristics and long-term variation of cold-season (November–February) SEP in the Shandong Peninsula using the observed daily data from 123 stations for the period 1962–2012, and also the linkage of the extremely intense SEP occurrences with a few key atmospheric circulation indices, surface–850-hPa temperature difference, sea ice area, lower-tropospheric temperature, and humidity using reanalysis data and other kinds of observations. The following conclusions were drawn:

1) A total of 1173 SEP days were identified during 1962–2012, which were further classified as snow days (73.7%), rain days (16.1%), and snow–rain days (10.1%). Together, rain days and snow–rain days

TABLE 6. Number of different types of SEP precipitation days at different surface temperatures T.

	Snow					
	Intense snow	Heavy snow	Moderate snow	Light snow	Rain	Snow–rain
Total days	50	94	126	595	189	119
$T < 0$°C	46 (92%)	87 (93%)	106 (84%)	515 (87%)	11 (6%)	31 (26%)
$T \geq 0$°C	4	7	20	80	178	88

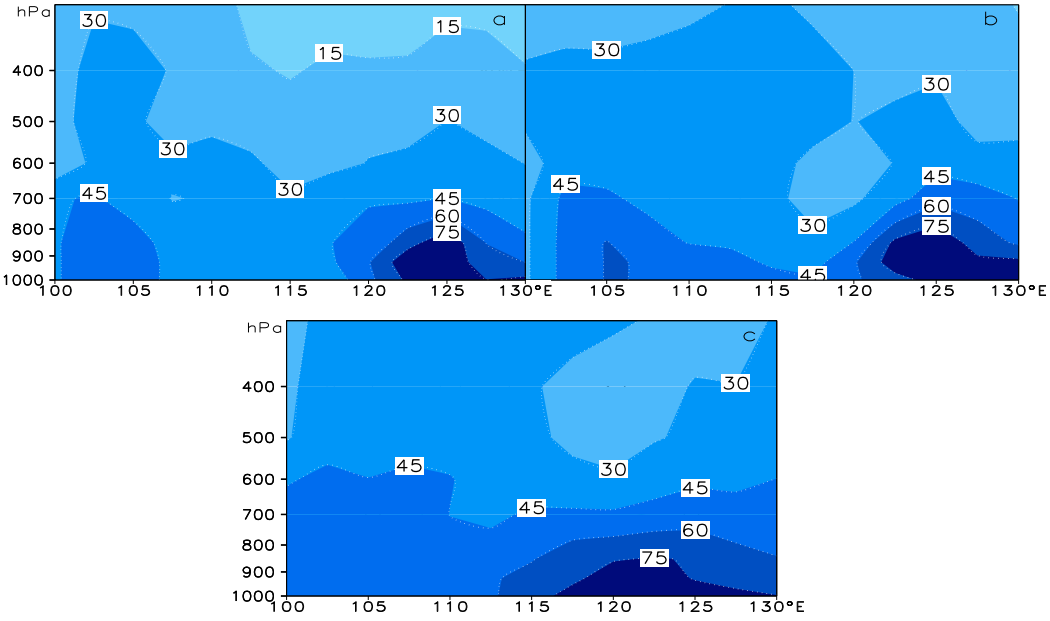

FIG. 13. Longitude–altitude profile of mean relative humidity at 37.5°N for the extremely intense SEP (a) snow, (b) snow–rain, and (c) rain days.

accounted for 26.2% of SEP days, and they occasionally brought heavy precipitation.

2) December was the month with the greatest range of intensity of SEP precipitation. November was the month when SEP rain and snow–rain days occurred most frequently. SEP snowfall was primarily distributed in the northeasternmost part of the Shandong Peninsula, whereas SEP rainfall occurred along the shoreline and islands. The maximum SEP precipitation was always located near the northeastern tip of the peninsula.
3) A temperature difference of 10°C between the sea surface and the 850-hPa level was required to trigger SEP, with a 10°–15°C temperature difference for light snow, a 15°–20°C temperature difference for moderate and heavy snow, and a temperature difference of higher than 25°C for intense snow.
4) A deeper East Asian trough at the 500-hPa level developed over the southwest of the study area on the extremely intense SEP days. The 850-hPa temperature isolines and geopotential height isolines were orthogonally distributed, indicating cold-air advection affecting the Bohai Sea and the Shandong Peninsula. Anomalously low temperature and high relative humidity also appeared in the lower troposphere during the SEP events, facilitating stronger convection in a thin layer of the lower troposphere.

Acknowledgments. This study is financed by the Ministry of Science and Technology of China (Fund 2018YFA0605603) and the China Natural Science Foundation (CNSF) (Fund 41575003).

REFERENCES

Alcott, T. I., W. J. Steenburgh, and N. F. Laird, 2012: Great Salt Lake–effect precipitation: Observed frequency, characteristics, and associated environmental factors. *Wea. Forecasting*, **27**, 954–971, https://doi.org/10.1175/WAF-D-12-00016.1.

Braham, R. R., Jr., and M. J. Dungey, 1984: Quantitative estimates of the effect of Lake Michigan on snowfall. *J. Climate Appl. Meteor.*, **23**, 940–949, https://doi.org/10.1175/1520-0450(1984)023<0940:QEOTEO>2.0.CO;2.

Burnett, A. W., M. E. Kirby, H. T. Mullins, and W. P. Patterson, 2003: Increasing Great Lake–effect snowfall during the twentieth century: A regional response to global warming? *J. Climate*, **16**, 3535–3542, https://doi.org/10.1175/1520-0442(2003)016<3535:IGLSDT>2.0.CO;2.

Campbell, L. S., W. J. Steenburgh, P. G. Veals, T. W. Letcher, and J. R. Minder, 2016: Lake-effect mode and precipitation enhancement over the Tug Hill Plateau during OWLeS IOP2b. *Mon. Wea. Rev.*, **144**, 1729–1748, https://doi.org/10.1175/MWR-D-15-0412.1.

Chu, Z., and J. H. Li, 2012: Relationship of high-altitude situation and the cold-air intense snow in the Shandong Peninsula (in Chinese with English abstract). *Meteor. Environ. Sci.*, **35**, 44–48.

Cordeira, J. M., and N. F. Laird, 2008: The influence of ice cover on two lake-effect snow events over Lake Erie. *Mon. Wea. Rev.*, **136**, 2747–2763, https://doi.org/10.1175/2007MWR2310.1.

Cui, Y., J. H. Li, F. Q. Zhang, and C. Y. Wang, 2008: Statistical analysis of cold air outbreak on Shandong Byland (in Chinese with English abstract). *Meteor. Environ. Sci.*, **31**, 22–26.

Farley Nicholls, J., and R. Toumi, 2014: On the lake effects of the Caspian Sea. *Quart. J. Roy. Meteor. Soc.*, **140**, 1399–1408, https://doi.org/10.1002/qj.2222.

Huang, C., X. Y. Shen, J. H. Sun, and L. L. Qi, 2008: Analysis of coastal front heavy snowfall in Shandong Peninsula (in Chinese with English abstract). *Climatic Environ. Res.*, **13**, 567–583.

Ikeda, S., R. Wakabayashi, K. Izumi, and K. Kawashima, 2009: Study of snow climate in the Japanese Alps: Comparison to snow climate in North America. *Cold Reg. Sci. Technol.*, **59**, 119–125, https://doi.org/10.1016/j.coldregions.2009.09.004.

Jiang, J., M. Wei, H. Kang, and X. D. Zhang, 2010: Mechanism and multi-scale characteristics if snowstorm process occurred in Shandong Peninsula in December 2005 (in Chinese with English abstract). *Trans. Atmos. Sci.*, **33**, 328–335.

Kalnay, E., and Coauthors, 1996: The NCEP/NCAR 40-Year Reanalysis Project. *Bull. Amer. Meteor. Soc.*, **77**, 437–471, https://doi.org/10.1175/1520-0477(1996)077<0437:TNYRP>2.0.CO;2.

Kindap, T., 2010: A severe sea-effect snow episode over the city of Istanbul. *Nat. Hazards*, **54**, 707–723, https://doi.org/10.1007/s11069-009-9496-7.

Laird, N. F., J. Desrochers, and M. Payer, 2009a: Climatology of lake-effect precipitation events over Lake Champlain. *J. Appl. Meteor. Climatol.*, **48**, 232–250, https://doi.org/10.1175/2008JAMC1923.1.

——, R. Sobash, and N. Hodas, 2009b: The frequency and characteristics of lake-effect precipitation events associated with the New York State Finger Lakes. *J. Appl. Meteor. Climatol.*, **48**, 873–886, https://doi.org/10.1175/2008JAMC2054.1.

——, ——, and ——, 2010: Climatological conditions of lake-effect precipitation events associated with the New York State Finger Lakes. *J. Appl. Meteor. Climatol.*, **49**, 1052–1062, https://doi.org/10.1175/2010JAMC2312.1.

——, S. A. Ganetis, A. Stieneke, and S. A. Tushaus, 2016: Climatology of lake-effect precipitation events over Lake Tahoe and Pyramid Lake. *J. Appl. Meteor. Climatol.*, **55**, 297–312, https://doi.org/10.1175/JAMC-D-14-0230.1.

Li, B., J. Li, Q. H. Wang, and K. Yang, 2011: Diagnosis analysis of one cold airflow snowfall in Shandong Peninsula. *Meteor. Environ. Res.*, **2**, 34–36.

Li, P., G. Fu, J. T. Guo, and N. Liu, 2009: An analysis and numerical modeling of a snowstorm event over Shandong Peninsula in December, 2005 (in Chinese with English abstract). *Period. Ocean Univ. China*, **39**, 173–180.

Miner, T. J., and J. M. Fritsch, 1997: Lake-effect rain events. *Mon. Wea. Rev.*, **125**, 3231–3248, https://doi.org/10.1175/1520-0493(1997)125<3231:LERE>2.0.CO;2.

Nam, H., B. G. Kim, S. O. Han, C. Lee, and S. S. Lee, 2014: Characteristics of easterly-induced snowfall in Yeongdong and its relationship to air-sea temperature difference. *Asia-Pac. J. Atmos. Sci.*, **50**, 541–552, https://doi.org/10.1007/s13143-014-0044-3.

Passarelli, R. E., and R. R. Braham, 1981: The role of the winter land breeze in the formation of Great Lake snow storms. *Bull. Amer. Meteor. Soc.*, **62**, 482–492, https://doi.org/10.1175/1520-0477(1981)062<0482:TROTWL>2.0.CO;2.

Payer, M., J. Desrochers, and N. F. Laird, 2007: A lake-effect snow band over Lake Champlain. *Mon. Wea. Rev.*, **135**, 3895–3900, https://doi.org/10.1175/2007MWR2031.1.

Ren, G., Y. H. Ding, Z. C. Zhao, J. Y. Zheng, T. W. Wu, G. L. Tang, and Y. Xu, 2012: Recent progress in studies of climate change in China. *Adv. Atmos. Sci.*, **29**, 958–977, https://doi.org/10.1007/s00376-012-1200-2.

Shan, B., C. Zhang, J. H. Li, Y. S. Cui, and C. Zhang, 2006: Diagnostic analysis of Weihai early winter first snowstorm in 2005 (in Chinese with English abstract). *J. Shandong Meteor.*, **26**, 17–18.

Steenburgh, W. J., S. F. Halvorson, and D. J. Onton, 2000: Climatology of lake-effect snowstorms of the Great Salt Lake. *Mon. Wea. Rev.*, **128**, 709–727, https://doi.org/10.1175/1520-0493(2000)128<0709:COLESO>2.0.CO;2.

Sun, X., W. Y. Wang, L. F. Yan, Y. H. Wang, and Y. Sui, 2007: Analysis of the Shandong Peninsula particularly heavy snowstorm in 2005 (in Chinese with English abstract). *Period. Ocean Univ. China*, **37**, 879–884.

Tan, L., 1992: Monthly anomalous precipitation analysis of Wuzhou. *J. Guizhou Meteor.*, **16**, 16–18.

Tardy, A., 2000: Lake-effect and lake-enhanced snow in the Champlain Valley of Vermont. NWS Eastern Region Tech. Attach. 2000-05, 27 pp., https://www.weather.gov/media/erh/ta2000-05.pdf.

Veals, P. G., and W. J. Steenburgh, 2015: Climatological characteristics and orographic enhancement of lake-effect precipitation east of Lake Ontario and over the Tug Hill Plateau. *Mon. Wea. Rev.*, **143**, 3591–3609, https://doi.org/10.1175/MWR-D-15-0009.1.

Wang, C., and X. L. Song, 1988: Sea land breezes of the northern coast of Shandong Peninsula (in Chinese). *Acta Oceanol. Sin.*, **10**, 678–686.

Yang, C., Z. C. Li, B. Zhou, Y. K. Chen, and J. J. Zhu, 2007a: Mesoscale analysis of ocean-effect snowstorms in the south coastland of Bohai Sea (in Chinese with English abstract). *J. Nanjing Inst. Meteor.*, **30**, 857–865.

——, X. S. Zhou, and Y. H. Wang, 2007b: Climatic features and previous signal of cold airflow snowfall in Shandong Peninsula (in Chinese with English abstract). *Meteor. Mon.*, **33**, 76–82.

——, Z. Y. Tao, and Z. C. Li, 2009: Overview of research on ocean (lake)-effect snow (in Chinese with English abstract). *Mar. Sci. Bull.*, **28**, 81–88.

Yu, Q., F. X. Zhou, and Q. Wang, 2009: Sea effects on local snows at Shandong Peninsula (in Chinese with English abstract). *Huadong Shifan Daxue Xuebao*, **3**, 160–169.

——, ——, Z. D. Tang, Q. Wang, and Y. Liu, 2011: Formation of the local precipitation climate in Shandong Peninsula in winter (in Chinese with English abstract). *Plateau Meteor.*, **30**, 719–726.

Zhang, Y., S. W. Shou, Y. Q. Wang, J. Zhou, and H. C. Lu, 2008: Mesoscale characteristics analysis on a snow storm in Shandong Peninsula (in Chinese with English abstract). *J. Nanjing Inst. Meteor.*, **31**, 51–60.

Zheng, L., S. Y. Shi, and S. M. Hou, 2003: Contribution of the Bohai Sea's special topography to cold vortex snow event (in Chinese with English abstract). *Meteorology*, **29**, 49–52.

Zhou, S., M. H. Cong, Z. M. Wu, S. L. Yan, C. F. Yang, and J. J. Zhu, 2008: Characteristics and maintaining mechanisms of sustained cold-air outbreak snowstorms processes in Shandong Peninsula during December 3-21, 2005 (in Chinese with English abstract). *J. Appl. Meteor. Sci.*, **19**, 444–453.

——, H. J. Li, Z. M. Wu, and Q. F. Lin, 2011: Climatic characteristics and causality of cold air-outbreak snowstorm events in Shandong Peninsula in winter (in Chinese with English abstract). *Ziran Zaihai Xuebao*, **20**, 91–98.

Zhou, X., C. F. Yang, and S. L. Zhang, 2011: Study on possible mechanism of terrain influence to cold airflow snowstorm (in Chinese with English abstract). *J. Anhui Agric. Sci.*, **39**, 19 419–19 422.

Zhou, Y., and G. Y. Ren, 2011: Change in extreme temperature events frequency over mainland China during 1961–2008. *Climate Res.*, **50**, 125–139, https://doi.org/10.3354/cr01053.

Zhu, Y., Z. M. Wu, Q. F. Lin, and S. L. Zhou, 2010: Analysis of a cold-air outbreak snowstorm event affected by Taihang Mount in Shandong Peninsula (in Chinese with English abstract). *Period. Ocean Univ. China*, **40**, 1–8.

第 14 卷 第 1 期
2018 年 1 月
气 候 变 化 研 究 进 展
CLIMATE CHANGE RESEARCH
Vol. 14 No. 1
January 2018

doi:10.12006/j.issn.1673-1719.2017.030
卞韬 , 任国玉 , 张立霞 . 城市化对石家庄站近地面风速趋势的影响 [J]. 气候变化研究进展 , 2018, 14 (1): 21-30

城市化对石家庄站近地面风速趋势的影响

卞 韬[1,2]，任国玉[2,3]，张立霞[1]

1 河北省石家庄市气象局，石家庄 050081；
2 中国地质大学（武汉）环境学院大气科学系，武汉 430074；
3 中国气象局气候研究开放实验室 /
中国气象局国家气候中心，北京 100081

摘 要：利用 1972—2012 年石家庄城市站和 4 个乡村站地面风速资料，采用城乡对比方法，对石家庄城市站地面风速序列中的城市化影响进行分析，结果表明，石家庄站年和季节平均地面风速和平均 10 min 最大风速的长期下降趋势，主要是由城市化因素引起。具体结论如下：(1) 石家庄站年和四季平均风速、平均 10 min 最大风速和大风日数均呈极显著的减少趋势，年平均减少速率分别为 −0.15 (m/s)/10a、−1.05 (m/s)/10a 和 −2.90 d/10a；乡村站年平均风速呈微弱下降趋势，年平均 10 min 最大风速减少较为明显，年大风日数减少趋势非常显著，减少速率分别为 −0.02 (m/s)/10a、−0.21 (m/s)/10a 和 −2.19 d/10a。(2) 石家庄站年平均风速下降趋势中的城市化影响为 −0.13 (m/s)/10a，城市化影响非常显著，城市化贡献率达到 86.0%。该站春、夏、秋、冬季平均风速变化的城市化影响分别为 −0.16 (m/s)/10a、−0.10 (m/s)/10a、−0.13 (m/s)/10a 和 −0.15 (m/s)/10a，城市化贡献率分别为 82.8%、87.6%、88.6% 和 85.4%。(3) 石家庄站年平均 10 min 最大风速变化趋势中的城市化影响为 −0.84 (m/s)/10a，城市化贡献率为 79.7%；春、夏、秋、冬季平均 10 min 最大风速变化趋势中的城市化影响分别为 −0.94 (m/s)/10a、−0.80 (m/s)/10a、−0.60 (m/s)/10a 和 −1.01 (m/s)/10a，城市化贡献率分别达到 90.4%、78.6%、64.9% 和 79.1%。(4) 城市化对石家庄站年大风日数减少的影响不显著，但冬季大风日数减少仍明显与城市化过程有关。

关键词：地面风速；变化趋势；城市化影响；城市化贡献率；石家庄站

引 言

风是重要的气候要素之一，是控制蒸散的关键因子，它不但可以反映大气环流的特征，也是衡量区域风能资源的基本指标。风速的变化往往对地区的环境产生较为深远的影响。作为蒸散的重要驱动因子，风速的变化将直接影响陆地水循环过程。在提倡大力发展清洁能源的今天，风能的发展潜力与风速变化也休戚相关，近年来世界大多数地区风速降低已经对风能资源的开发利用带来了挑战。此外，风速的减小不利于大气中污染物的扩散，可能是一些地区雾霾日数明显增加的原因之一。因此，探索和研究风速的变化及其原因意义重大。

关于近地面风速的变化，国内外已有不少研究成果。国内学者针对全国、区域以及单个地点风速的变化做了大量研究。国内研究[1-7]发现，中国大范围区域近地面平均风速和大风频率普遍呈现出明显的减小趋势。国内关于近地面风速变化的研究特

收稿日期：2017-02-20；**修回日期**：2017-05-15
资助项目：国家自然科学基金项目（41575003）
作者简介：卞韬，女，高级工程师，biantao0107@163.com；任国玉（通信作者），男，研究员，guoyoo@cma.gov.cn

别是早期的分析工作，对于后来提出“全球静稳”概念起到推动作用[8-9]。在国外，Pirazzoli 等[10] 通过研究意大利 1951—2000 年的年平均风速变化，发现当地风速在 20 世纪 70 年代之前为上升期，之后风速开始减小。Tuller[11] 报告了加拿大西海岸近地面风速长期下降的现象，指出 1950—1999 年期间年平均风速下降速率为 −0.17 (m/s)/10a，后来 Wang 等[12] 也注意到加拿大西部和南部的地面风速明显减小。Hobbins 等[13] 分析了 1962—1990 年美国本土 48 个州的地面风速资料，发现平均风速下降趋势为 −0.05 (m/s)/10a，Hartmann 等[14] 分析美国阿拉斯加地区 1951—2001 年期间资料得到相近似的平均下降速率；McVicar 等[9] 还发现 1979—2008 年南北半球中低纬度大部分地区风速减小明显，高纬度地区（纬度＞ 70°）风速在增大；Kousari 等[15] 的研究表明伊朗 1975—2005 年整体风速呈上升趋势，仅局部地区风速减小显著。此后，在欧洲、日本、俄罗斯、墨西哥、澳大利亚和印度等许多地区都发现近 30—50 年地面风速明显下降的现象。例如，McVicar 等[16] 发现 1975—2006 年澳大利亚全国年平均风速的减小趋势达到 0.09 (m/s)/10a。

在发现近地面平均风速普遍减小的观测事实以后，研究者对大范围风速下降的原因进行了探讨。以中国的研究为例，目前一般认为，近地面风速变化除了受大尺度气候变化影响外，还受到局地尺度城市化和观测环境变化的影响[17-20]。随着城市不断蔓延扩大及农村人口进一步向城市集中，城市化对地面风速变化的影响已引起研究者关注。彭珍等[21] 指出，随着北京城市化步伐加快，下垫面粗糙度逐年增加，其阻碍作用增加了地表对空气水平平均动能的消耗，使得近地面风速存在明显的递减趋势。刘学锋等[17] 研究表明，台站所在地城市化程度和观测场周围环境改变是风速减小趋势不可忽略的原因；张爱英等[18] 通过分析高空不同层次平均风速变化趋势剖面，认为全国平均近地面风速减弱趋势大约 2/3 是由于城市化和观测环境变化引起的；于宏敏等[20] 发现，1971—2004 年黑龙江省近地层风速呈显著减弱趋势，城市站减弱趋势较乡村站明显，城市站与乡村站的风速差值有增大趋势，表明城市化对近地面风速下降具有重要影响；Li 等[6] 分析评价了北京市城市化因素对近地面风速的影响，发现位于城市内的台站风速下降更明显，1960—2008 年间城市化对风速变化的影响约为 −0.05 (m/s)/10a，说明了总体风速下降趋势的 1/5 左右是由城市化因素造成；陶寅等[22] 利用 1981—2010 年安徽省 61 个站的逐日风速资料，结合卫星遥感台站分类法，全面分析了城市化进程对安徽省风速的影响。

石家庄站是一个典型的大陆温带城市气象观测站，过去研究表明，伴随着快速的城市化，其城市热岛强度增加趋势十分显著[23]，不仅对石家庄站地面气温均值变化趋势有显著影响，而且对极端气温事件变化趋势的影响也很明显[24]。但是，城市化对石家庄站近地面风速的长期变化趋势有什么影响，或者影响有多大，目前还不清楚。本文利用石家庄地区城市和周围 4 个乡村气象观测站 1972—2012 年的地面风速数据，对比分析城市站和乡村站地面风速的变化趋势，定量评估石家庄站地面风速序列趋势变化中的城市化影响程度。本文研究结论对于了解我国北方典型城市气象站近地面风速变化特征及其原因，更好地认识不同尺度近地面风速变化的驱动机制和评估风能资源潜力，均具有参考价值。

1 资料和方法

以石家庄气象站代表城市站，附近不同方向的藁城、元氏、平山和新乐 4 个气象站代表乡村站，观测站的基本信息详见表 1。各站月平均地面风速、月平均 10 min 最大风速和月大风日数数据来自河北省信息共享平台，数据时段为 1972—2012 年。考虑到 1969—1970 年有一次仪器更换，另外 10 min 最大风速数据 1971 年之后才有，而且石家庄站在 2013 年 1 月 1 日迁站，因此选取研究时段为 1972—2012 年。2004 年后，石家庄的测风仪器陆续由 EL 电接风型转换为 CAWS600B 自动气象观测，由于仪器测感应器原理不同，可能造成测风数据存在一定的偏差。但对各站与参考序列差值序列的统计检验，未发现明显断点，因此本文未做均一化订正。季节划分为：春季（3—5 月）、夏季（6—8 月）、秋季（9—

www.climatechange.cn

表 1　城乡气象站基本信息
Table 1　Information of the stations used in the study

站点	经纬度	海拔高度 /m	建站时间 /（年 / 月 / 日）	迁站时间 /（年 / 月 / 日）	建成区人口 / 万
石家庄	114.42°E，38.03°N	81.0	1955/01/01	2013/01/01	270
藁城	114.81°E，38.01°N	53.5	1958/08/01	1969/07, 1999/01	10
元氏	114.53°E，37.75°N	66.4	1960/01/01	1982/02, 1998/01, 2007/01	8
平山	114.02°E，38.25°N	131.0	1959/01/01	1961/09, 1964/01, 2000/01	10
新乐	114.68°E，38.35°N	70.8	1959/03/01	1961/05, 1963/12, 1989/05, 2003/01	10

11 月）、冬季（12 月至次年 2 月），其中 1972 年冬季采用 1971 年 12 月—1972 年 2 月资料。

石家庄气象站在 2012 年 12 月 31 日前未迁过站，观测站位于城市的西部。20 世纪 80 年代初以前，观测站远离城市建成区，周围环境空旷，建筑物很少；1980 年代初以来，石家庄城市化进程加速，观测站附近建筑物逐渐增多，目前已成为一个典型的城市观测站。4 个郊区气象站实际上是小城镇站，为县城所在地，分布在石家庄站东、南、西北和东北 4 个方向，平均海拔高度为 80.4 m，与城市站高度 (81.0 m) 非常接近，距离石家庄市区均在 20 km 以上；人口密度小，城镇人口在 10 万左右，经济发展相对缓慢，城镇化程度较低。这 4 个郊区站观测场周围的探测环境虽然受到一定程度的城镇化影响，但影响较弱，可以作为石家庄地区相对具有代表性的乡村站。这些站曾在以往的城市化影响分析中被当作参考站使用 [23-24]。

采用 4 个乡村站平均风速、平均 10 min 最大风速和大风日数的平均获得乡村站参考序列。采用最小二乘法 [25] 对平均风速、平均 10 min 最大风速和大风日数进行线性趋势拟合 ，即趋势倾向率，样本数为 41。

城市化是指城市人口和建成区面积不断扩大的过程。这个过程引起城市下垫面热力性质明显改变，人为热释放量和气溶胶含量逐渐增多，对市区及其附近郊区气候产生显著影响。为了定量评价城市化对地面风速变化趋势的影响，参照 Ren 等 [26] 和 Bian 等 [24] 定义如下术语：

(1) 城市化影响：指由于城市热岛效应加强等因素引起的城市附近台站地面风速、10 min 最大风速和大风日数线性趋势的变化，用 ΔX_{ur} 表示。设 X_u 为城市站地面风速（10 min 最大风速或大风日数）的变化趋势，X_r 为乡村站（平均）地面风速（10 min 最大风速或大风日数）的变化趋势，则城市化影响的表达式为：

$$\Delta X_{ur} = X_u - X_r 。 \quad (1)$$

当 $\Delta X_{ur} > 0$ 时，表示城市化影响使地面风速（10 min 最大风速或大风日数）增大或增多；当 $\Delta X_{ur} = 0$ 时，表示城市化影响为 0；当 $\Delta X_{ur} < 0$ 时，表示城市化影响使地面风速（10 min 最大风速或大风日数）减小或减少。地面风速（10 min 最大风速或大风日数）城乡差值序列的线性趋势则为城市化影响的另一种表达形式，在数值上等同于 ΔX_{ur}。

(2) 城市化贡献率：指城市化影响对城市附近台站地面风速（10 min 最大风速或大风日数）趋势变化的百分比贡献，即城市化影响在城市附近台站地面风速（10 min 最大风速或大风日数）趋势变化中所占的比率，用 E_u 表示。表达式为：

$$E_u = |\Delta X_{ur} / X_u| \times 100\% = |(X_u - X_r) / X_u| \times 100\% 。 \quad (2)$$

考虑到使城市化贡献率 $0 \leqslant E_u \leqslant 100\%$，所以取了绝对值。当 $E_u = 0$ 时，表示城市化对城市站地面风速（10 min 最大风速或大风日数）变化趋势没有贡献；当 $E_u = 100\%$ 时，表示城市站地面风速（10 min 最大风速或大风日数）变化完全是由城市化影响造成的。实际计算当中，少数情况下 E_u 可能超过 100%，说明可能存在某种尚未认识到的局地因子影响，这种情况按 100% 处理。本文只对城市化影响

通过了显著性检验的地面风速、10 min 最大风速和大风日数序列给出城市化贡献率。

2 结果分析

2.1 城乡风速的变化趋势

2.1.1 平均风速

图 1 给出了 1972—2012 年石家庄城、乡年平均风速的变化曲线及线性趋势。20 世纪 80 年代末之前，石家庄城市站年平均风速的变化趋势不明显，之后则表现为明显的减小趋势，2003 年达到最低值，仅为 1.0 m/s，之后略有增大，但均小于 1.5 m/s；近 41 年石家庄城市站年平均风速的减小趋势为 −0.15 (m/s)/10a，通过了 0.001 的显著性水平检验（表 2），减小趋势极显著。20 世纪 80 年代中期前，乡村站年平均风速呈减小趋势，之后开始缓慢增大，90 年代中后期的增大趋势较明显，2004 年后再趋向减小；整体上近 41 年石家庄乡村站年平均风速表现为微弱的减小趋势，减小趋势为 −0.02 (m/s)/10a，未通过显著性检验。

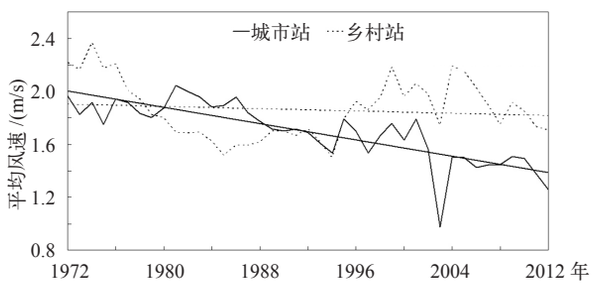

图 1 1972—2012 年石家庄城、乡年平均风速的变化曲线及线性趋势

Fig. 1 Annual mean near-surface wind speed of Shijiazhuang station and the surrounding 4 rural stations during 1972−2012

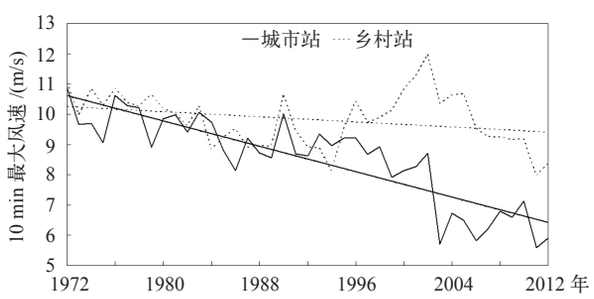

图 2 1972—2012 年石家庄城、乡年平均 10 min 最大风速的变化曲线及线性趋势

Fig. 2 Annual mean near-surface 10 min maximum wind speed of Shijiazhuang station and the surrounding 4 rural stations during 1972−2012

2.1.2 10 min 最大风速

从石家庄城、乡年平均 10 min 最大风速的变化曲线及线性趋势（图 2）可以看到，2002 年之前，石家庄城市站年平均 10 min 最大风速的减小趋势并不明显，年平均 10 min 最大风速一般在 9 m/s 以上；之后的减小趋势很明显，年平均 10 min 最大风速一般在 7 m/s 以下，2011 年最小，仅为 5.6 m/s。近 41 年石家庄城市站年平均 10 min 最大风速呈减小趋势，减小趋势为 −1.05 (m/s)/10a，通过了 0.001 的显著性检验（表 2）。20 世纪 90 年代中期前，乡村站年平均 10 min 最大风速的减小趋势不明显，之后表现为增大趋势，但 2005 年之后表现为快速减小趋势，整

表 2 1972—2012 年石家庄城、乡年和四季平均风速、10 min 最大风速及大风日数的线性趋势

Table 2 Linear trends of annual and seasonal mean near-surface wind speed, 10 min maximum wind speed and gale days of Shijiazhuang station and the surrounding 4 rural stations during 1972−2012

时间	平均风速 /((m/s)/10a)		10 min 最大风速 /((m/s)/10a)		大风日数 /(d/10a)	
	城市站	乡村站	城市站	乡村站	城市站	乡村站
年	−0.15***	−0.02	−1.05***	−0.21	−2.90***	−2.19***
春季	−0.19***	−0.03	−1.04***	−0.10	−0.72**	−0.97***
夏季	−0.12***	−0.01	−1.02***	−0.22	−0.64*	−0.41
秋季	−0.15***	−0.02	−0.92***	−0.32*	−0.71***	−0.51**
冬季	−0.17***	−0.02	−1.27***	−0.27	−0.89***	−0.32*

注：*，** 和 *** 分别表示通过 0.05、0.01 和 0.001 的显著性检验，下划线表示通过 0.1 的显著性检验，下同。

www.climatechange.cn

体上近 41 年乡村站年平均 10 min 最大风速呈现出减小趋势，减小速率为 −0.21 (m/s)/10a，但仅通过了 0.1 的显著性检验。

2.1.3　大风日数

从图 3 可以看到，20 世纪 70 年代中期到 80 年代初这段时间，石家庄城市站年大风日数呈明显的增多趋势，80 年代中期后开始表现为减少趋势，2002 年之后减少的非常明显，年大风日数都在 3 d 以下，2003 年、2007 年、2011 年和 2012 年甚至全年无大风天出现；近 41 年石家庄城市站年大风日数呈极显著的减少趋势，减少趋势达到 −2.90 d/10a（通过了 0.001 的显著性检验，表 2)。20 世纪 80 年代末之前，乡村站年大风日数减少趋势非常明显，之后到 2005 年大风日数有所增多，2005 年之后又开始减小；近 41 年乡村站年大风日数的减少趋势为 −2.19 d/10a，通过了 0.001 的显著性检验，减少趋势极显著，这与年平均风速微弱的减小趋势明显不同。

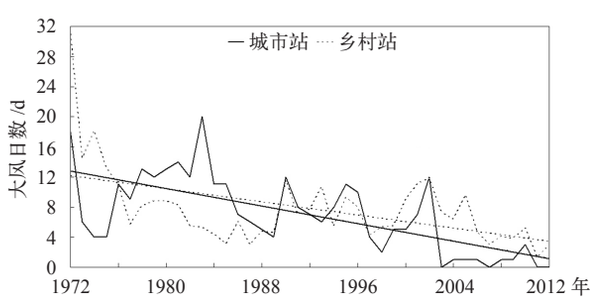

图 3　1972—2012 年石家庄城、乡年大风日数的变化曲线及线性趋势

Fig. 3　Annual gale days of Shijiazhuang station and the surrounding 4 rural stations during 1972−2012

2.2　城市化影响

2.2.1　平均风速

图 4 给出了 1972—2012 年石家庄城、乡年平均风速差值序列的变化曲线及线性趋势。1972—1978 年城、乡年平均风速差值为负值，城市站年平均风速小于乡村站，之后到 1995 年，城、乡差值均为正值，1995 年之后又转为负值，2003 年达到最低值（−0.8 m/s)。20 世纪 80 年代末之前，城、乡差值呈上升趋势，之后表现为持续的下降趋势。整体上近 41 年，石家庄城、乡年平均风速差值以 −0.13 (m/s)/10a 的速率明显下降，趋势通过了 0.01 的显著性检验（表 3)，说明石家庄城市站年平均风速减小的城市化影响非常显著；城市化贡献率达到 86.0%，表明石家

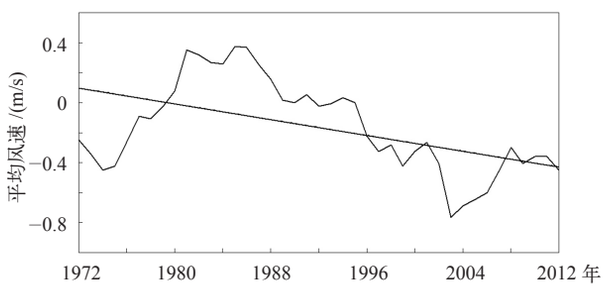

图 4　1972—2012 年石家庄城、乡年平均风速差值序列的变化曲线及线性趋势

Fig. 4　Difference series of annual mean near-surface wind speed between Shijiazhuang station and the surrounding 4 rural stations during 1972−2012

表 3　1972—2012 年石家庄城市站年和四季平均风速、10 min 最大风速及大风日数的城市化影响及其贡献率

Table 3　Urbanization effects and contributions in the annual and seasonal mean near-surface wind speed, 10 min maximum wind speed and gale days at Shijiazhuang station during 1972−2012

时间	平均风速		10 min 最大风速		大风日数	
	城市化影响 /((m/s)/10a)	城市化影响贡献率 /%	城市化影响 /((m/s)/10a)	城市化影响贡献率 /%	城市化影响 /(d/10a)	城市化影响贡献率 /%
年	−0.13**	86.0	−0.84***	79.7	−0.71	/
春季	−0.16***	82.8	−0.94***	90.4	−0.25	/
夏季	−0.10***	87.6	−0.80***	78.6	−0.23	/
秋季	−0.13***	88.6	−0.60***	64.9	−0.20	/
冬季	−0.15***	85.4	−1.01***	79.1	−0.56*	62.9

庄城市站年平均风速减小趋势主要是由城市化影响造成的。

近 41 年，石家庄城市站春、夏、秋、冬平均风速减小的城市化影响分别为 −0.16 (m/s)/10a、−0.10 (m/s)/10a、−0.13 (m/s)/10a 和 −0.15 (m/s)/10a，均通过了 0.001 的显著性检验 (表 3)，城市化影响极显著，其中春季和冬季的城市化影响相对较强，夏、秋季相对较弱；城市化贡献率分别为 82.8%、87.6%、88.6% 和 85.4%。与年平均风速一致，石家庄四季平均风速减小趋势的主要原因来自城市化影响。

2.2.2 10 min 最大风速

图 5 表明，近 41 年石家庄城、乡年平均 10 min 最大风速差值以负值为主，只有少数几年（1984 年、1987 年、1993 年和 1994 年）为正值，说明城市站年平均 10 min 最大风速一般小于乡村站；20 世纪 90 年代末之前，城、乡年平均 10 min 最大风速差值序列的变化趋势不明显，之后的下降趋势非常明显。近 41 年，石家庄城市站年平均 10 min 最大风速的城市化影响为 −0.84 (m/s)/10a，通过了 0.001 的显著性检验，城市化贡献率为 79.7%（表 3)。

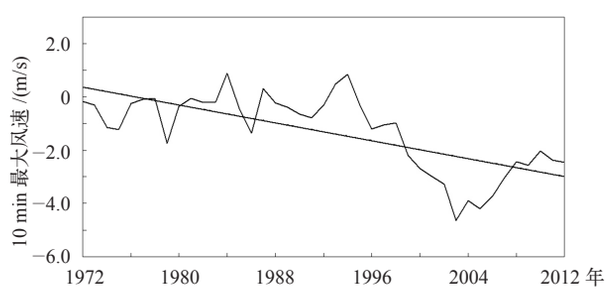

图 5 1972—2012 年石家庄城、乡年平均 10 min 最大风速差值序列的变化曲线及线性趋势

Fig. 5 Difference series of annual mean 10 min maximum wind speed between Shijiazhuang station and the surrounding 4 rural stations during 1972−2012

近 41 年，石家庄城市站春、夏、秋、冬平均 10 min 最大风速变化的城市化影响分别为 −0.94 (m/s)/10a、−0.80 (m/s)/10a、−0.60 (m/s)/10a 和 −1.01 (m/s)/10a，均通过了 0.001 的显著性检验（表 3)，其中冬季的城市化影响最强，秋季相对弱些；四季平均城市化贡献率分别为 90.4%、78.6%、64.9% 和 79.1%。

2.2.3 大风日数

从石家庄城、乡年大风日数差值序列的变化曲线及线性趋势（图 6）看，1972—1975 年城、乡年大风日数差值为负，城市站年大风日数少于乡村站；之后到 20 世纪 90 年代中期的较长时间内，城、乡年大风日数差值以正值为主，城市站年大风日数一般多于乡村站；90 年代后期之后城、乡年大风日数差值又以负值为主。近 41 年，石家庄城、乡年大风日数差值序列呈下降趋势，下降趋势为 −0.71 d/10a，未通过显著性检验。

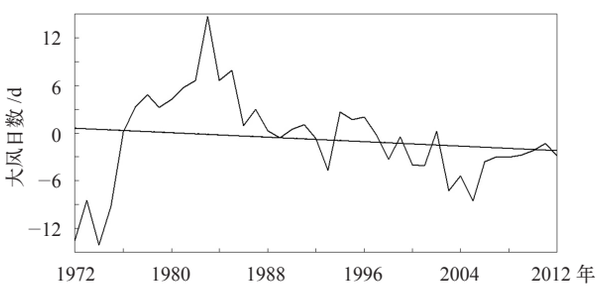

图 6 1972—2012 年石家庄城、乡年大风日数差值序列的变化曲线及线性趋势

Fig. 6 Difference series of annual mean gale days between Shijiazhuang station and the surrounding 4 rural stations during 1972−2012

近 41 年，石家庄城市站四季大风日数减少的城市化影响分别为 −0.25 d/10a、−0.23 d/10a、−0.20 d/10a 和 −0.56 d/10a，其中只有冬季通过 0.05 的显著性检验（表 3)，其他三季的城市化影响均不明显。石家庄城市站冬季大风日数减少的城市化贡献率为 62.9%。

3 讨 论

针对全国范围的早期研究表明，自 20 世纪 50 年代中期到 21 世纪初，中国近地面平均风速的减小是非常明显的，大部分线性趋势通过了显著性检验；全国年平均风速的减小趋势为 −0.11 (m/s)/10a，华北地区年平均风速的减小趋势与全国平均变化相近 [1-2]。本文结果表明，石家庄城市站年平均风速呈极显著的减小趋势，减小趋势为 −0.15 (m/s)/10a，比全国和华北地区平均下降速率略大，石家庄城市

www.climatechange.cn

站四季平均风速减小趋势一般也比全国或华北地区更强（表 4)。但是，石家庄乡村 4 个站年和四季平均风速的减小趋势比全国或华北地区弱，更比附近的石家庄城市站地面风速下降趋势弱得多，没有通过显著性检验。这说明本文所选的 4 个乡村站代表性较高，其观测记录基本上反映了不受周围人工建筑物阻挡情况下的背景风场变化。石家庄城市和乡村站冬、春季平均风速减小，可能与我国寒潮发生频率减小、强度减弱密切相关 [1]，而后者又与全球气候变暖的经向非均质性 [23] 有关。

表 4　石家庄城、乡站 (1972—2012 年) 年平均风速变化趋势与全国、华北地区 (1954—2000 年) 对比 [1]

Table 4　Linear trends of annual mean near-surface wind speed of Shijiazhuang station and the surrounding 4 rural stations during 1972−2012, and the comparison to those of mainland China and North China during 1954−2000 [1]

(m/s)/10a

时间	石家庄城市站	石家庄乡村站	全国	华北地区
年	−0.15	−0.02	−0.11	−0.12
春季	−0.19	−0.03	−0.12	−0.16
夏季	−0.12	−0.01	−0.08	−0.05
秋季	−0.15	−0.02	−0.10	−0.09
冬季	−0.17	−0.02	−0.14	−0.19

一个有趣的现象是，尽管在分析时期石家庄城市站年平均风速和平均 10 min 最大风速呈现出持续性下降，4 个乡村站年平均近地面风速和平均 10 min最大风速的减小趋势却经历了明显年代际波动，表现为在 20 世纪 90 年代中期前为下降趋势，而 20 世纪 90 年代中期以后直至 2003 年前后出现短暂上升趋势，此后发生波动性下降（图 1 和图 2)。乡村站记录的近几十年平均和极端风速的年代际波动，可能和西伯利亚高压强度和温带东亚地区冬季寒潮频率的年代尺度变异性有关，其中 20 世纪 90 年代中期以后直至 2003 年前后的短暂上升趋势对应西伯利亚高压恢复增强和温带东亚地区冬季寒潮频率再次增加 [27-28]。但是，2003 年以后西伯利亚高压和东亚冬季风强度并未减弱 [29]，冬季寒潮发生频率亦未减少，而石家庄周围 4 个乡村站的年和冬季平均风速和平均 10 min 最大风速却转而回落。这个新近下降变化与东亚冬季风年代际变异背景不协调，可能与近 10 年河北省小城镇城市化过程加快，4 个县城气象站周围观测环境变坏有联系。如果这个推论成立，则近 10 余年乡村站平均风速和极端风速的这种明显回落，在一定程度上削弱了对石家庄站城市化影响及其相对贡献的估计值，实际的城市化影响有可能更大。

即使存在参考站代表性问题，本文的分析结论表明，城市化对石家庄城市站年和四季平均风速、平均 10 min 最大风速以及冬季大风日数减小（少）的影响都非常显著，其城市化贡献率也都很高。年平均风速减小的城市化影响为 −0.13 (m/s)/10a，城市化贡献率达到 86%，各个季节平均的城市化贡献率大体一致，介于 82% ~ 89% 之间。这一结果，显然比张爱英等 [18] 根据探空资料推测得到的全国探空站近地面平均风速下降趋势 2/3 是由城市化和观测环境改变引起的估计数值来的大，也比刘学锋等 [17] 针对河北省、于宏敏等 [20] 针对黑龙江省，陶寅等 [22] 针对安徽省，以及 Li 等 [6] 针对北京市分析得到的结果大得多。刘学锋等 [17] 认为，城市化对河北省国家基准、基本站 1975—2004 年地面平均风速减小的影响程度至少达到 25%；于宏敏等 [20] 虽然未给出城市化贡献率，但根据他们的计算结果推测 1971—2004 年两个代表站的城市化贡献率为 19.4%。陶寅等 [22] 的结论是：安徽省 1981—2010 年城市站与乡村站年平均风速趋势系数之差为 −0.10 (m/s)/10a，城市化对年平均风速减弱的贡献率为 40%。同前人研究结果比较，石家庄城市站年和季节平均风速减小的城市化影响更强，主要与 20 世纪 90 年代以来的 20 多年该站处于特大城市建成区内，以及石家庄快速的城市化过程有关，可能在一定程度上也和不同研究所选区域、资料时段和乡村站不同有关。

本文分析还发现，石家庄站年和四季平均 10 min 最大风速以及冬季大风日数减小（少）的城市化贡献率也在 62.0% 以上，最高达到 90.4%。但是，石家庄站除冬季外其他季节平均大风日数的显著减小趋势中，尽管城市化影响也是负值，然而却不明显，说明春、夏、秋季平均大风日数的显著减少更主要是由大尺度环流场变化造成的，也可能和所选

乡村站多位于县城北部，或者乡村站观测场南部附近具有人工障碍物，在暖季偏南风情况下，与石家庄城市站一样感受到了城市化影响有关。但是，这个问题还需要开展进一步调查分析。

本文选取的乡村站应该为目前所获得的比较有代表性的参考站，但由于这些站都在小城镇附近，其近地面风速观测记录可能在一定程度上仍受到城市化影响。因此，本文给出的城市化对石家庄站地面风速序列趋势的影响，应看作为最低估计值，在大风日数序列中城市化影响和贡献率的估算中，这个问题可能更为突出。尽管如此，本文的分析结果清楚表明，城市发展导致下垫面改变，对石家庄站近地面风速减小产生了十分显著的影响。

4 结 论

利用 1972—2012 年石家庄城市站和 4 个乡村站地面风速资料，采用城、乡对比方法，对石家庄城市站地面风速序列中的城市化影响进行了全面分析，得到以下结论。

(1) 石家庄城市站的年和春、夏、秋、冬季平均风速均呈极显著的减小趋势，下降速率分别为 −0.15 (m/s)/10a、−0.19 (m/s)/10a、−0.12 (m/s)/10a、−0.15 (m/s)/10a 和 −0.17 (m/s)/10a，其中春季的减小趋势最强，夏季的减小趋势相对最弱；乡村站年和四季平均风速均呈微弱的减小趋势。

(2) 石家庄城市站的年和春、夏、秋、冬季平均 10 min 最大风速均呈极显著的减小趋势，减小速率分别为 −1.05 (m/s)/10a、−1.04 (m/s)/10a、−1.02 (m/s)/10a、−0.92 (m/s)/10a 和 −1.27 (m/s)/10a，其中冬季的减小趋势最强，秋季的减小趋势相对最弱。乡村站年平均 10 min 最大风速的减小趋势仅通过了 0.1 的显著性检验，且四季中只有秋季平均 10 min 最大风速减小趋势显著。

(3) 石家庄城、乡站年大风日数均呈极显著的减少趋势，下降速率分别为 −2.90 d/10a 和 −2.19 d/10a。城市站四季大风日数均表现为显著的减少趋势，其中冬季的减少趋势最强，夏季的减少趋势相对较弱；乡村站夏季以外的季节减少趋势显著或非常显著，夏季较为显著。

(4) 石家庄城市站年平均风速减小的城市化影响为 −0.13 (m/s)/10a，城市化影响非常显著，城市化贡献率达到 86.0%，表明该站年平均风速减小趋势主要是由城市化影响造成的。城市站四季平均风速减小的城市化影响均达到极显著水平，城市化贡献率在 82% 到 89% 之间。

(5) 石家庄城市站年平均 10 min 最大风速减小的城市化影响为 −0.84 (m/s)/10a，城市化影响非常明显，城市化贡献率为 79.7%。春、夏、秋、冬平均 10 min 最大风速减小的城市化影响分别为 −0.94 (m/s)/10a、−0.80 (m/s)/10a、−0.60 (m/s)/10a 和 −1.01 (m/s)/10a，均达到极显著水平，城市化贡献率在 65% 到 91% 之间。

(6) 石家庄城市站年大风日数减少的城市化影响不明显，但冬季大风日数减少的城市化影响仍然显著，城市化贡献率为 62.9%。

因此，在 1972—2012 年期间，石家庄城市站年和季节平均地面风速和平均 10 min 最大风速的长期显著下降趋势，主要是由于此期间快速城市化过程引起的。同期冬季大风日数的明显减少趋势，也主要和城市化因素有关。■

参考文献

[1] 王遵娅 , 丁一汇 , 何金海 , 等 . 近 50 年来中国气候变化特征的再分析 [J]. 气象学报 , 2004, 62 (2): 228-236

[2] 任国玉 , 郭军 , 徐铭志 , 等 . 近 50 年中国地面气温变化基本特征 [J]. 气象学报 , 2005, 63 (6): 942-956

[3] Xu M, Chang C P, Fu C B. Steady decline of east Asian monsoon winds, 1969−2000: evidence from direct ground measurements of wind speed [J]. Journal of Geophysical Research, 2006, 111: 1-8

[4] 荣艳淑 , 梁嘉颖 . 华北地区风速变化的分析 [J]. 气象科学 , 2008, 28 (6): 655-658

[5] Jiang Y, Luo Y, Zhao Z, *et al*. Changes in wind speed over China during 1956−2004 [J]. Theoretical and Applied Climatology, 2010, 99: 421-430

[6] Li Z, Yan Z W, Tu K, *et al*. Changes in wind speed and extremes in Beijing during 1960–2008 based on homogenized observations [J]. Advances in Atmospheric Sciences, 2011, 28 (2): 408-420

[7] 金巍 , 任国玉 , 曲岩 , 等 . 1971−2010 东北三省地面平均风速变化 [J]. 干旱区研究 , 2012, 29 (4): 648-653

www.climatechange.cn

[8] Vautard R, Cattiaux J, Yiou P, *et al*. Northern Hemisphere atmospheric stilling partly attributed to an increase in surface roughness [J]. Nature Geoscience, 2010, 3: 756-761

[9] McVicar T R, Roderick M L. Atmospheric science: winds of change [J]. Nature Geoscience, 2010, 3 (11): 747-748

[10] Pirazzoli P A, Tomasin A. Recent near-surface wind changes in the central Mediterranean and Adriatic areas [J]. International Journal of Climatology, 2003, 23 (8): 963-973

[11] Tuller S E. Measured wind speed trends on the west coast of Canada [J]. International Journal of Climatology, 2004, 24 (11): 1359-1374

[12] Wang H, Wang H L, Swail V R. Homogenization and trend analysis of Canadian near-surface wind speeds [J]. Journal of Climate, 2010, 23 (5): 1209-1225

[13] Hobbins M T, Ramírez J A, Brown T C. Trends in pan evaporation and actual evapotranspiration across the conterminous US: paradoxical or complementary? [J]. Geophysical Research Letters, 2004, 31 (13), L13503

[14] Hartmann B, Wendler G. The significance of the 1976 Pacific climate shift in the climatology of Alaska [J]. Journal of Climate, 2005, 18 (22): 4824-4839

[15] Kousari M R, Ahani H, Hakimelahi H. An investigation of near surface wind speed tends in arid and semiarid regions of Iran [J]. Theoretical and Applied Climatology, 2013, 114 (1−2): 153-168

[16] McVicar T R, Niel T G V, Li L T, *et al*. Wind speed climatology and trends for Australia, 1975−2006: capturing the stilling phenomenon and comparison with near-surface reanalysis output [J]. Geophysical Research Letters, 2008, 35 (20): 288-299

[17] 刘学锋 , 江滢 , 任国玉 , 等 . 河北城市化和观测环境改变对地面风速观测资料序列的影响 [J]. 高原气象 , 2009, 28 (2): 433-439

[18] 张爱英 , 任国玉 , 郭军 , 等 . 1980—2006 年我国高空风速变化趋势分析 [J]. 高原气象 , 2009, 28 (3): 680-687

[19] 赵宗慈 , 罗勇 , 江滢 . 全球大风在减少吗 [J]. 气候变化研究进展 , 2011, 7 (2): 149-151

[20] 于宏敏 , 徐永清 , 张洪玲 . 黑龙江省的城市化对近地面风速变化的影响 [J]. 太阳能学报 , 2014, 35 (9): 1797-1802

[21] 彭珍 , 胡非 . 北京城市化进程对边界层风场结构影响的研究 [J]. 地球物理学报 , 2006, 49 (6): 729-732

[22] 陶寅 , 黄勇 , 杨元建 , 等 . 城市化进程对安徽省风速的影响 [J]. 气候变化研究进展 , 2016, 12 (6): 519-526

[23] 卞韬 , 任国玉 , 张翠华 , 等 . 石家庄气象站记录的城市热岛效应及其趋势变化 [J]. 南京信息工程大学学报 : 自然科学版 , 2012, 4 (5): 402-408

[24] Bian T, Ren G Y, Zhang B X, *et al*. Urbanization effect on long-term trends of extreme temperature indices at Shijiazhuang station, North China [J]. Theoretical and Applied Climatology, 2015, 119 (3−4): 407-418

[25] 魏凤英 . 现代气候统计诊断与预测技术 [M]. 北京 : 气象出版社 , 2007: 36-41

[26] Ren G Y, Zhou Y Q. Urbanization effect on trends of extreme temperature indices of national stations over mainland China, 1961−2008 [J]. Journal of Climate, 2014, 27 (6): 2340-2360

[27] Gong D Y , Ho C H. The Siberian High and climate change over middle to high latitude Asia [J]. Theoretical and Applied Climatology, 2002, 72: 1-9

[28] Jeong J H, Ou T, Linderholm H W, *et al*. Recent recovery of the Siberian High intensity [J]. Journal of Geophysical Research Atmospheres, 2011, 116: 1-9

[29] Ding Y H, Liu Y J, Liang S J, *et al*. Interdecadal variability of the East Asian winter monsoon and its possible links to global climate change [J]. Journal of Meteorological Research, 2014, 28 (5): 693-713

Significant urbanization effect on decline of near-surface wind speed at Shijiazhuang station

BIAN Tao [1, 2], REN Guo-Yu [2, 3], ZHANG Li-Xia[1]

1 *Shijiazhuang Meteorological Bureau, Shijiazhuang* 050081*, China*; 2 *Department of Atmospheric Science, School of Environmental Studies, China University of Geosciences, Wuhan 430074, China*; 3 *Laboratory for Climate Studies of China Meteorological Administration, National Climate Center, China Meteorological Administration, Beijing* 100081*, China*

Abstract: Based on data of the surface wind speed at Shijiazhuang city meteorological station (simplified as Shijiazhuang station) and four rural meteorological stations during 1972−2012, urbanization effect on the surface wind speed series at Shijiazhuang station was analyzed using an urban−rural difference method. The results showed that: (1) In 1972−2012, there were very significant decreased trends on annual and seasonal mean wind speeds, mean maximum wind speeds of 10 min and gale days at Shijiazhuang station, and the annual mean decreased trends were −0.15 (m/s)/10a, −1.05 (m/s)/10a and −2.90 d/10a respectively. Annual mean wind speed of rural stations showed weakly decreased trend, the decreased trend on annual mean maximum wind speed of 10 min was more obvious, and the decreased trend on annual gale days was very significant. The decreased trends on annual mean wind speed, annual mean maximum wind speed of 10 min and annual gale days at rural stations were −0.02 (m/s)/10a, −0.21 (m/s)/10a, and 2.19 d/10a, respectively; (2) In the study period, urbanization effect on the annual mean wind speed at Shijiazhuang station was −0.13 (m/s)/10a, which was very significant, and the urbanization contribution reached 86.0%, indicating that the urbanization effect is large and significant. Urbanization effect on the mean wind speeds of the urban station in spring, summer, autumn and winter were −0.16 (m/s)/10a, −0.10 (m/s)/10a, −0.13 (m/s)/10a and −0.15 (m/s)/10a respectively, and the urbanization contributions were 82.8%, 87.6%, 88.6% and 85.4%, respectively; (3) Urbanization effect on the annual mean maximum wind speed of 10 min at the urban station was −0.84 (m/s)/10a, and the urbanization contribution was 79.7%. Urbanization effects on the seasonal mean maximum wind speed of 10 min were −0.94 (m/s)/10a, −0.80 (m/s)/10a, −0.60 (m/s)/10a and −1.01 (m/s)/10a, respectively for spring, summer, autumn and winter, with the urbanization contributions of 90.4%, 78.6%, 64.9% and 79.1%, respectively; (4) Urbanization effect on the annual gale days at Shijiazhuang station was not significant, but the urbanization effect on the winter gale days was large and significant.

Keywords: Surface wind speed; Trend; Urbanization effect; Urbanization contribution; Shijiazhuang

Henyey-Greenstein 近似对冰云短波辐射计算的影响

陈琪[1,2,3**], 张华[1,2,3*]

[1]中国气象科学研究院灾害天气国家重点实验室, 北京 100081

[2]南京信息工程大学气象灾害预报预警与评估协同创新中心, 江苏 南京 210044

[3]中国气象局气候研究开放实验室, 国家气候中心, 北京 100081

摘要 基于新的多形状冰云参数化方案和 BCC_RAD 辐射传输模式,详细分析了在辐射传输算法中通常使用的 HG(Henyey-Greenstein)近似对冰云短波辐射传输过程的影响。对于单个冰晶粒子光学性质,HG 近似对相函数勒让德展开式第 3 和第 4 项系数计算造成了较大误差,最大误差分别为 -0.28 和 -0.33,最大相对误差分别为 -55.7%和-73.8%。第 4 项系数的误差绝对值和相对值均高于第 3 项系数。进一步分析发现,HG 近似在可见光区造成的误差高于近红外区。对于冰云体积光学性质,HG 近似同样对第 3 和第 4 项系数造成了较大的误差,最大误差分别为 -0.18 和 -0.22,最大相对误差分别为 -27.9%和-37.1%。第 4 项系数的误差高于第 3 项系数,可见光区误差高于近红外区,与对单个冰晶粒子光学性质的影响一致。HG 近似也对有云大气的辐射传输过程计算造成了较大的误差。对短波向下辐射通量造成的最大误差为 -2.78 $W \cdot m^{-2}$,对短波向上辐射通量造成的最大误差为 -1.06 $W \cdot m^{-2}$,对短波加热率造成的最大误差为 0.27 $K \cdot d^{-1}$。HG 近似低估了短波辐射通量,高估了云内加热率。因此,在冰云辐射传输计算中需精确描述相函数。

关键词 大气光学; 大气散射; Henyey-Greenstein 近似; 辐射; 冰云

中图分类号 P422; P426.5; O435.1 **文献标识码** A **doi**: 10.3788/AOS201838.0801001

Effects of Henyey-Greenstein Approximation on Shortwave Radiative Calculations in Ice clouds

Chen Qi[1,2,3**], Zhang Hua[1,2,3*]

[1] *State Key Laboratory of Severe Weather, Chinese Academy of Meteorological Sciences, Beijing* 100081, *China*

[2] *Collaborative Innovation Center on Forecast and Evaluation of Meteorological Disasters, Nanjing University of Information Science & Technology, Nanjing, Jiangsu* 210044, *China*

[3] *National Climate Center, Laboratory for Climate Studies, China Meteological Administation, Beijing* 100081, *China*

Abstract Based on a new multi-shape ice cloud radiative parameterization scheme and the Beijing Climate Center radiative transfer mode (BCC_RAD), the effects of the Henyey-Greenstein (HG) approximation on the shortwave ice-cloud radiation are analyzed in details, in which the HG approximation is widely used in radiative calculations. To the optical properties of the single ice crystal, the HG approximation causes large errors on 3rd and 4th coefficients of the Legendre expansion of the phase function, and the maximum values of the errors are -0.28 and -0.33, respectively, while the maximum values of the relative errors are -55.7% and -73.8%, respectively. The errors of 4th coefficients are higher than those of 3rd coefficients, and the errors in near-infrared waves are higher than those in visible waves. To the bulk optical properties of the ice clouds, the HG approximation causes large errors on 3rd and 4th coefficients, and the maximum values of the errors are -0.18 and -0.22, respectively, while the maximum values of the relative errors are -27.9% and -37.1%, respectively. The errors of 4th coefficients are higher and so as in visible waves, which are same to the single ice crystal. The HG approximation also causes large errors on the radiative calculations. The maximum value of the errors on the shortwave downward fluxes is

收稿日期: 2017-12-05; **修回日期**: 2018-04-02; **录用日期**: 2018-04-09

基金项目: 国家重点研发计划(2017YFA0603502)、国家自然科学基金(41375080,91644211)、科技部公益性行业(气象)科研专项课题(GYHY201406023)

* E-mail: huazhang@cma.gov.cn; ** E-mail: chenqi1228@foxmail.com

$-2.78\ \mathrm{W\cdot m^{-2}}$, and on the shortwave upward fluxes is $-1.06\ \mathrm{W\cdot m^{-2}}$, while on the shortwave heating rates is $0.27\ \mathrm{K\cdot d^{-1}}$. The HG approximation underestimates the shortwave downward fluxes and overestimates the shortwave heating rates. Therefore, phase function accurately describing on ice clouds radiation transfer is necessary.

Key words atmospheric optics; atmospheric scattering; Henyey-Greenstein approximation; radiation; ice cloud
OCIS codes 010.1615; 010.2940; 290.4020

1 引　　言

冰云的短波辐射过程以反照率效应为主，在辐射模式中其描述精度对整个大气的辐射通量和加热率计算均有重要影响，并进而影响对天气和气候的模拟效果[1-4]。由于冰晶粒子的多形状特性，其光学性质有别于一般球形粒子，不确定性较大，需要深入研究。单个粒子的光学性质可用消光效率、单次散射比和相函数进行描述。通常通过勒让德展开式来描述相函数，然后利用勒让德展开式各项的系数对相函数的性质进行简化，如不对称因子就是相函数勒让德展开式第 1 项的系数的 1/3。

近年来，随着计算机能力的大幅提高和高精度计算对辐射传输精度的日益提高，四流近似的应用日益广泛[3-6]。由于四流近似计算中使用了第 3、4 项相函数勒让德展开式系数，Henyey-Greenstein（HG）近似必然会对四流近似计算产生一定影响。在之前的许多研究中，四流近似中使用的 3、4 项勒让德展开式系数并非精确值，而是用 HG 近似值代替[5-8]。HG 近似由 Henyey 等[9]提出，由于该近似方法算法简洁、相函数表达式简单，在辐射过程计算中应用广泛。由于 HG 近似对相函数勒让德展开式第 2～n 项均进行了近似（具体公式见章节 2），进而改变了对单个冰晶粒子的相函数勒让德展开式系数的描述，冰云体积光学性质的描述也随之改变，最终必然会对有云大气辐射过程计算产生一定的影响。Hong[10]使用该近似计算黄道尘云的散射相函数，取得了比较好的效果。Toublanc[11]比较了蒙特卡罗方法中 HG 近似与米氏散射的区别，发现对比高精度的计算 HG 近似会导致一些误差。Boucher[12]认为使用 HG 近似代替米氏散射将会影响气溶胶短波直接辐射强度的计算精度。Binzoni 等[13]发现，使用 HG 近似会对生物医学光学有一定的影响。Li 等[14]指出，在云和气溶胶辐射传输计算过程中，使用 HG 近似对四流球谐函数近似计算影响较大。与其他云和气溶胶粒子不同，冰云粒子具有明显的非球形特征，其相函数的计算方法也更复杂，因此 HG 近似对冰云辐射过程的影响值得进一步探究。

本文介绍了辐射传输和 HG 近似相关理论和公式，以及辐射模式和实验设计。详细分析了 HG 近似对整个冰云辐射过程的影响。分析了其对单个冰晶粒子光学性质的影响；基于多形状冰云参数化方案分析了 HG 近似对冰云体积光学性质的影响；然后，通过 BCC_RAD 辐射传输模式，考察了使用四流离散纵标法时，HG 近似对辐射通量和加热率的影响。

2 理论和实验方案

讨论太阳的短波辐射时，长波发射项可以被忽略，方位角平均的平面平行的辐射传输方程为[8]

$$\mu\frac{\mathrm{d}I(\tau,\mu)}{\mathrm{d}\tau}=I(\tau,\mu)-\frac{\sigma}{2}\int_{-1}^{1}I(\tau,\mu')P(\tau,\mu')\mathrm{d}\mu-\frac{\sigma}{4}F_0\exp\left(-\frac{\tau}{\mu_0}\right)P(\mu,\mu_0)\ ,\tag{1}$$

$$I(0,\mu)=0,\tag{2}$$

$$I(\tau_0,\mu)=0,\tag{3}$$

式中：$I(\tau,\mu)$为介质中光学厚度为 τ、天顶角的方向余弦为 μ 时的辐射强度；σ 为单次散射比；F_0 为大气顶垂直于太阳光方向的辐射通量；μ'为入射光的方向余弦值；P 为相函数；$P(\mu,\mu')=\sum_{n=0}^{N}\omega_n\mathrm{P}_n(\mu)\mathrm{P}_n(\mu')$，其中 $\mathrm{P}_n(\mu)$为勒让德多项式，ω_n 为相函数勒让德展开式的系数，也称为相函数的 n 阶矩量。ω_n 前两项 $\omega_0=1$、$\omega_1=3g$，其中 g 为不对称因子；其 n 次项可表示为

$$\omega_n=\frac{2n+1}{2}\int_{-1}^{1}P(\cos\Theta)P_n(\cos\Theta)\mathrm{d}\cos\Theta,\tag{4}$$

式中：$P(\cos\Theta)$为散射相函数；$P_n(\cos\Theta)$为散射相函数的勒让德展开式 n 次项；Θ 为太阳天顶角。(1)式为大气辐射传输方程，(2)式和(3)式是辐射传输方程的边界条件，表示介质的上边界和下边界无漫射入射辐射。

在二流近似中，用不对称因子 g 代替相函数代入二流近似运算中，即可得到辐射通量结果。在四流近似中，使用的系数包括 ω_1，ω_2，ω_3，ω_4。HG 近似令$\omega_n=(2n+1)g^n$，从而可由不对称因子 g 计算

得到ω_1和ω_4。此方法的优点是可以使用二流近似的相函数系数(不对称因子g)直接计算四流近似的相函数系数,从而使四流近似的使用更加广泛;缺点则是会带来一些计算误差。

对于单个冰晶的光学性质计算,本文使用了Zhang等[15]的方案,该方案综合考虑了多种形状冰晶的光学性质。按照Yang等[16]和Hong等[17]的方法将冰晶粒子分为滴晶、聚集体、子弹束、实心柱、空心柱和平板六类形状,分别计算了各类冰晶粒子在不同波长、不同最大尺度的几何性质和光学性质。几何性质包括38个尺度区间上的等效截面积和等效体积。光学性质包括38个尺度区间和65个波长的消光效率、单次散射比、不对称因子和前向峰因子。

本文使用的大气辐射传输模式为BCC_RAD[18-21]。该模式将整个长波和短波区间10～49000 cm^{-1}划分为17个波带(包括8个长波波带和9个短波波带)。气溶胶辐射方案由卫晓东等[22]、Zhang等[23]和周晨等[24]的方法给出。该模式曾参与了全球气溶胶辐射强迫模拟中的短波辐射传输方案的比较[25]。短波辐射计算采用四流离散纵标算法[26-27],累加法也选择了相应的四流累加法[27]。假定冰水含量和有效半径分别为0.0048 g/m^3和20 μm,太阳天顶角余弦值设为0.5,短波地表反射率取0.3,代表典型冰云状况[15]。热带大气的冰云云顶和云底分别设为典型值14 km和12 km,中纬度夏季大气的冰云云顶和云底分别设为典型值12 km和10 km,中纬度冬季大气的冰云云顶和云底分别设为11 km和9 km[28]。

3　结果分析

3.1　HG近似对单个冰晶粒子短波光学性质的影响

HG近似首先会对单个冰晶粒子相函数展开式系数的计算造成误差。选取$\lambda=0.46$ μm和$\lambda=1.23$ μm两个波长分别代表太阳辐射能量最集中的可见光区和近红外区。图1给出了4种形状冰晶相函数勒让德展开式第3项系数随着粒子尺度的变化,4种形状冰晶的第3项系数随粒子尺度增大主要呈增大趋势。如图1(a)所示,对于聚集体冰晶,$\lambda=0.46$ μm(可见光区)时最大误差为−0.27,相对误差可达−55.7%;$\lambda=1.23$ μm(近红外区)时最大误差为−0.19。如图1(b)所示,对于子弹束冰晶,$\lambda=0.46$ μm时最大误差为−0.22;$\lambda=1.23$ μm时最大误差为−0.20。如图1(c)所示,对于滴晶,$\lambda=0.46$ μm时最大误差为−0.28;$\lambda=1.23$ μm时最大误差为−0.18。如图1(d)所示,对于空心柱冰晶,$\lambda=0.46$ μm时最大误差为−0.14;$\lambda=1.23$ μm时最大误差为−0.12。

HG近似对各形状冰晶的相函数勒让德展开式第3项系数计算均造成了较大的负误差,所有形状均存在误差绝对值大于0.10的情况。不同形状和不同波长下,出现最大误差时的粒子尺度不同。对于聚集体和滴晶,$\lambda=0.46$ μm时,粒子尺度1000 μm以上时误差较大;$\lambda=1.23$ μm时,粒子尺度10～100 μm时误差较大。对于子弹束和空心柱,两种波长时均为粒子尺度10～100 μm时误差较大。虽然在单个冰晶粒子光学性质的模拟上确实存在较大的误差,但使用HG近似对其变化趋势影响很小。即使对较为复杂的情况(如滴晶),HG近似也能很好地反映出冰晶粒子光学性质随有效半径的趋势变化。另外,HG近似在可见光区造成的误差稍高于近红外区。

图2给出了4种形状冰晶相函数勒让德展开式第4项系数随着粒子尺度的变化,与第3项系数相同,4种形状冰晶的第4项系数随粒子尺度增大也主要呈增大趋势。如图2(a)所示,对于聚集体冰晶,$\lambda=0.46$ μm时(可见光区)最大误差为−0.33,相对误差可达−72.1%;$\lambda=1.23$ μm时(近红外区)最大误差为−0.27。如图2(b)所示,对于子弹束冰晶,$\lambda=0.46$ μm时最大误差为−0.27;$\lambda=1.23$ μm时最大误差为−0.25,相对误差甚至可达51.3%。如图2(c)所示,对于滴晶,$\lambda=0.46$ μm时最大误差为−0.30,相对误差可达−73.8%;$\lambda=1.23$ μm时最大误差为−0.21。如图2(d)所示,对于空心柱冰晶,$\lambda=0.46$ μm时最大误差为−0.20;$\lambda=1.23$ μm时最大误差为−0.18。HG近似对冰晶粒子相函数展开式第4项系数的影响比第3项系数更大,多次出现相对误差绝对值超过50%的情况,平均负误差也更大。最大误差所在粒子尺度与第3项系数基本相同,此处不再赘述。同样地,HG近似也能很好地模拟相函数展开式第4项系数随粒子尺度的趋势变化。

3.2　HG近似对冰云体积光学性质的影响

HG近似对单个冰晶光学性质计算造成的误差会进一步影响冰云体积光学性质的计算。图3给出了由Zhang方案计算得到的冰云第10、11波带展开式系数及其随有效半径的变化。如图3(a)所示,对于相函数展开式第3项系数,在第10带(近红外区)HG近似造成的误差为−0.17～−0.10,相对误

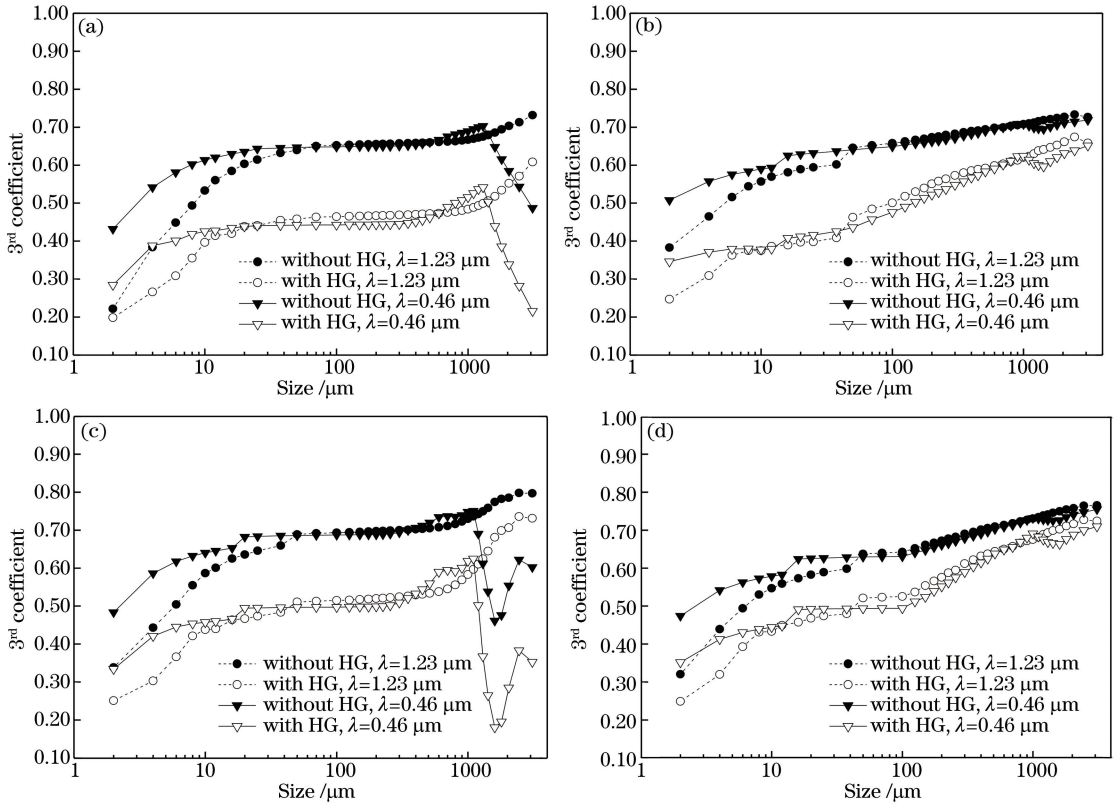

图 1　相函数第 3 项展开式系数随粒子尺度的变化。(a)聚集体；(b)子弹束；(c)滴晶；(d)空心柱

Fig. 1　Changes of 3rd coefficients of phase function expansion with crystal size.
(a) Aggregates; (b) bullet rosettes; (c) droxtals; (d) hollow columns

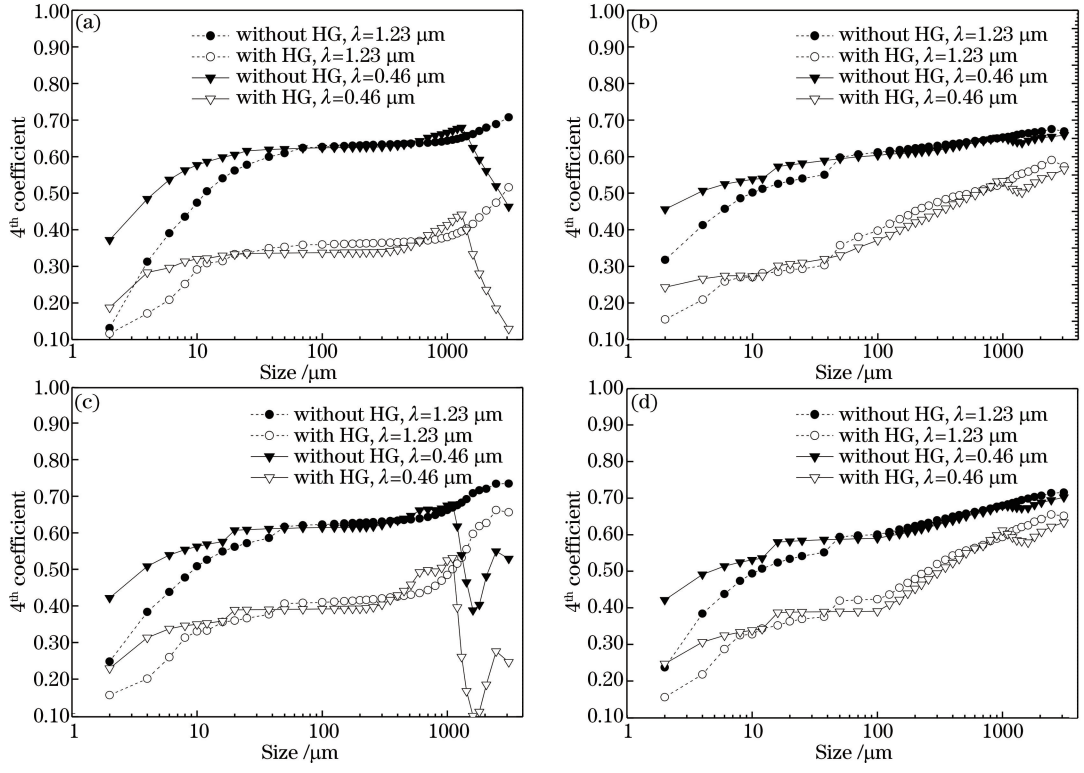

图 2　相函数第 4 项展开式系数随粒子尺度的变化。(a)聚集体；(b)子弹束；(c)滴晶；(d)空心柱

Fig. 2　Changes of 4th coefficients of phase function expansion with crystal size.
(a) Aggregates; (b) bullet rosettes; (c) droxtals; (d) hollow columns

差可达－26.3%；在第 11 带(可见光区)HG 近似造成的误差为－0.18～－0.09，相对误差可达－27.9%。如图 3(b)所示，对于相函数展开式第4 项系数，在第 10 带 HG近似造成的误差为－0.21～－0.15，相对误差可达－36.3%；在第 11 带 HG 近似造成的误差为－0.22～－0.14，相对误差可达－37.1%。HG 近似对冰云相函数展开式第 4 项系数造成的误差更大，这与单个冰晶粒子光学性质误差情况吻合。可见光区的误差稍大，这也与单个冰晶粒子光学性质误差情况一致。同样，虽然 HG 近似带来了较大的误差，但依然可以较好地反映冰云光学性质随有效半径的变化趋势。HG 近似对相函数的表达会产生一定误差，对相函数展开式第 3 项系数和第 4 项系数的误差正是来源于相函数本身的误差。图 4 给出了 HG 近似对冰云体积相函数的影响。在第 10 带和第 11 带中，在散射角接近 0°时，HG 近似造成了很大的正误差；在散射角 10°～20°、30°～40°和 50°～70°时，HG 近似造成了较大的负误差；在散射角 140°～180°时，HG 近似造成了较大的正误差。总而言之，HG 近似在很大一部分散射角范围内都无法准确地反映冰晶粒子的相函数，也无法有效体现冰晶粒子独有的前向散射峰。

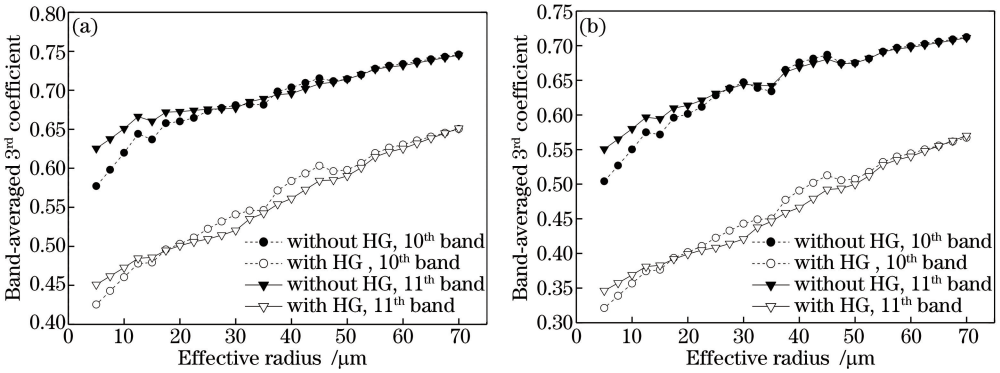

图 3　冰云体积相函数展开式系数随有效半径的变化。(a)第 3 项系数；(b)第 4 项系数

Fig. 3　Changes of the ice cloud bulk optical properties with effective radius. (a) 3rd coefficient; (b) 4th coefficient

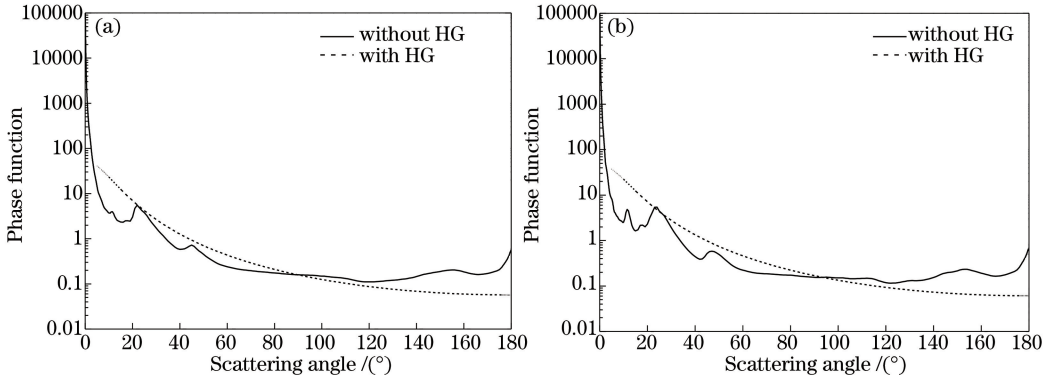

图 4　冰云体积相函数。(a)第 10 带；(b)第 11 带

Fig. 4　Bulk phase functions of ice clouds. (a) 10th band; (b) 11th band

3.3　HG 近似对有云大气短波辐射通量的影响

冰云体积光学性质描述的改变会影响有云大气辐射计算过程，进而影响辐射通量和加热率。图 5 给出了 HG 近似对热带有云大气辐射通量和加热率的影响。对于短波向下辐射通量，云顶以上高度误差很小，从云顶开始随高度下降误差绝对值逐渐增大，在云底以下高度辐射通量的误差可达－1.53 W·m^{-2}，云底以下高度，误差绝对值开始逐渐减小。对于短波向上辐射通量，云顶处的误差为－0.37 W·m^{-2}，云底处的误差为－0.47 W·m^{-2}，云层以内误差更小一些；误差在云底以下、云内和云顶以上高度的辐射通量均表现为被低估。对于短波净辐射通量，云层以外高度误差很小，云顶处的误差为 0.12 W·m^{-2}，云底处的误差为 0.16 W·m^{-2}，如表 1 所示。对于短波加热率，云层以外高度同样误差很小，云顶处的误差为 0.21 K·d^{-1}，云底处的误差为 0.18 K·d^{-1}，云顶处的误差即为云层内部的最大误差。

图 6 给出了 HG 近似对中纬度夏季有云大气辐射通量和加热率的影响。对于短波向下辐射通量，

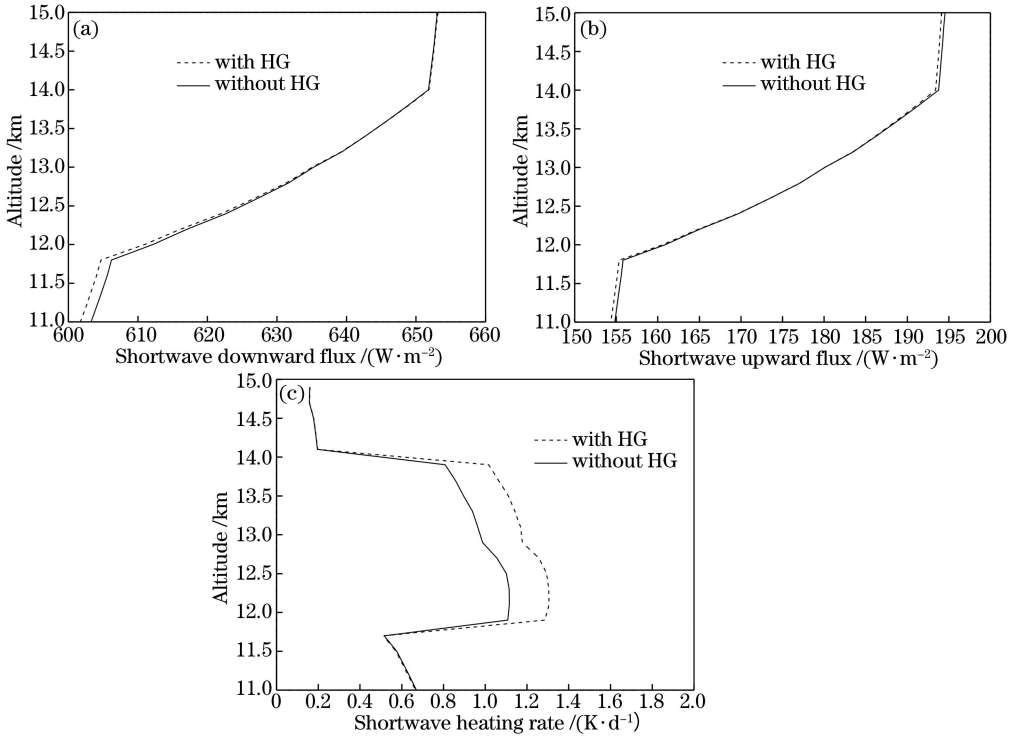

图 5　热带有云大气短波辐射通量和加热率廓线。(a)向下辐射通量;(b)向上辐射通量;(c)加热率

Fig. 5　Vertical profiles of the shortwave fluxes and the heating rates in tropical cloudy atmosphere. (a) Downward fluxes; (b) upward fluxes; (c) heating rates

表 1　不同大气条件下有云大气云顶和云底处的短波净辐射通量

Table 1　Shortwave net fluxes at cloud top and cloud base in different atmospheres

Different atmosphere	Different position	Shortwave net flux /(W·m^{-2})		
		With HG	Without HG	Error
Tropical atmosphere	Cloud top	0.61	0.49	0.12
	Cloud base	1.09	0.93	0.16
Summer mid-latitude atmosphere	Cloud top	1.44	1.22	0.22
	Cloud base	2.08	1.91	0.17
Winter mid-latitude atmosphere	Cloud top	1.28	1.05	0.23
	Cloud base	1.37	1.21	0.16

云顶以上高度误差很小,从云顶开始随高度下降误差绝对值逐渐增大,在云底处高度辐射通量的误差可达−2.43 W·m^{-2}。对于短波向上辐射通量,云顶处的误差为−0.52W·m^{-2},云底处的误差为−0.87 W·m^{-2},云层以内同样误差更小一些。对于短波净辐射通量,云层以外高度误差很小,云顶处的误差为 0.22 W·m^{-2},云底处的误差为0.17 W·m^{-2}(表 1)。对于短波加热率,云层以外高度同样误差很小,云顶处的误差为 0.26 K·d^{-1},云底处的误差为 0.16 K·d^{-1},云内最大误差为 0.27 K·d^{-1}。

图 7 给出了 HG 近似对中纬度冬季有云大气辐射通量和加热率的影响。对于短波向下辐射通量,云顶以上高度误差很小,从云顶开始随高度下降误差逐渐增大,在云底以下高度辐射通量的误差可达−2.78 W·m^{-2}。对于短波向上辐射通量,云顶处的误差为 − 0.63 W·m^{-2},云底处的误差为−1.06 W·m^{-2},云层以内误差同样更小一些。对于短波净辐射通量,云层以外高度误差很小,云顶处的误差为 0.23 W·m^{-2},云底处的误差为 0.16 W·m^{-2}(表 1)。对于短波加热率,云层以外高度同样误差很小,云顶处的误差为 0.27 K·d^{-1},云底处的误差为0.16 K·d^{-1},云顶处的误差即为云层内部的最大误差。

不同纬度、不同季节下云高不同,导致云层区域的气压和温度不同,进而影响冰云光学性质。云层高度越高,大气压越低,云层越稀薄。因此在热带大气条件下,HG 近似对辐射通量和加热率的影响较小。同样的,温度越高,云层也越稀薄。中纬度夏季

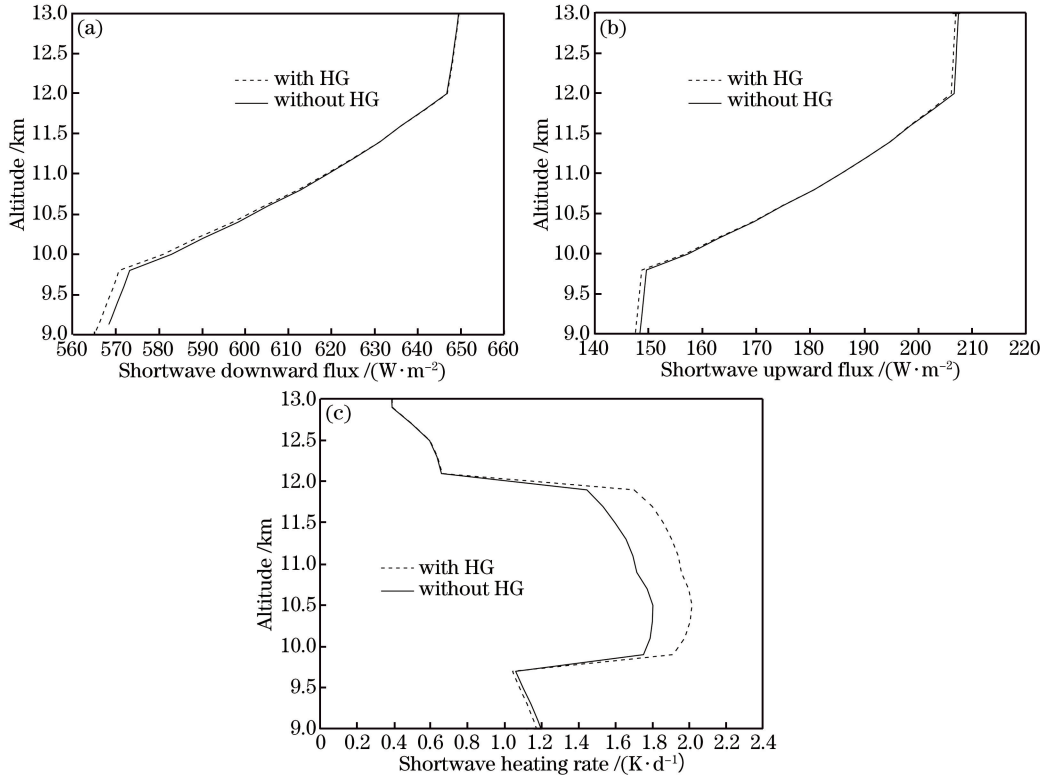

图 6　中纬度夏季有云大气短波辐射通量和加热率廓线。(a)向下辐射通量；(b)向上辐射通量；(c)加热率

Fig. 6　Vertical profiles of the shortwave fluxes and heating rates in mid-latitude summer cloudy atmosphere. (a) Downward fluxes; (b) upward fluxes; (c) heating rates

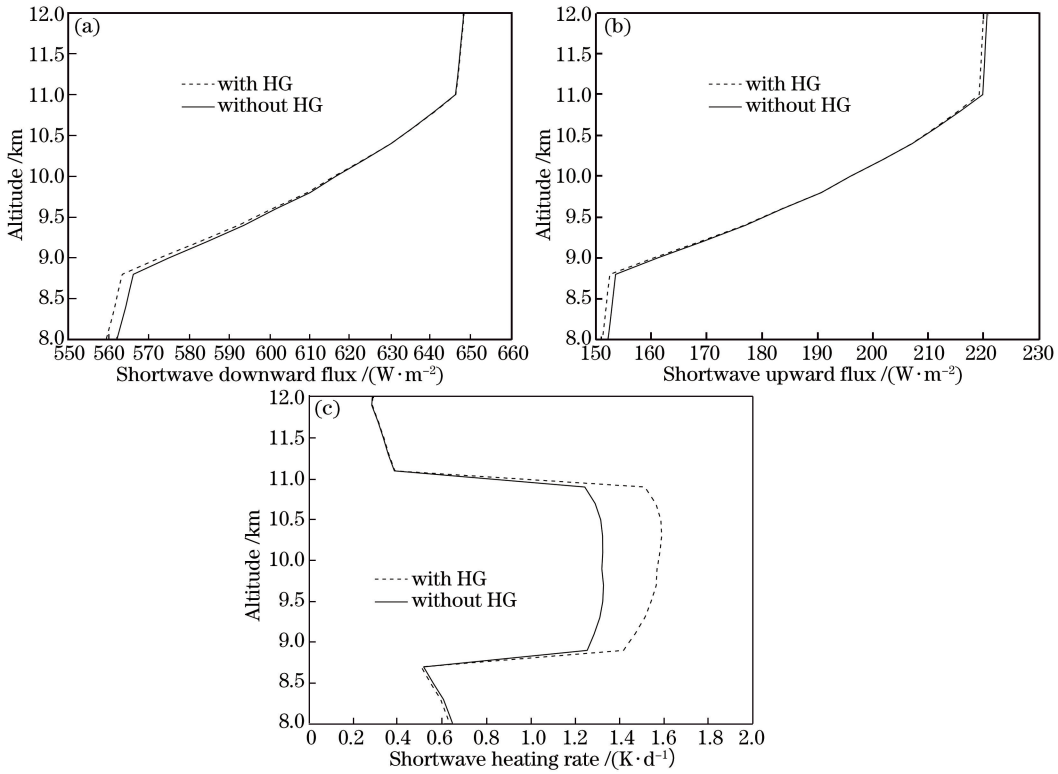

图 7　中纬度冬季有云大气短波辐射通量和加热率廓线。(a)向下辐射通量；(b)向上辐射通量；(c)加热率

Fig. 7　Vertical profiles of the shortwave fluxes and the heating rates in mid-latitude winter cloudy atmosphere. (a) Downward fluxes; (b) upward fluxes; (c) heating rates

大气云层高度更高，但大气温度也更高一些，两者相互抵消，因此中纬度夏季大气和中纬度冬季大气条件下，HG 近似对辐射和加热率的影响相差不大。一定程度上而言，纬度不同对HG近似的影响比季节不同更大。

总体上，使用 HG 近似低估了热带和中纬度有云大气云底处及云底以下高度的短波向下辐射通量，低估了包含云层在内的整层大气的短波向上辐射通量，同时高估了云内加热情况，导致了较大的误差。

4　结　论

基于多形状冰晶的新冰云参数化方案，结合 BCC_RAD 辐射传输模式，详细分析了 HG 近似对冰云短波辐射传输过程的影响。包括对单个冰晶粒子和冰云体积光学性质的影响，以及对后续的有云大气辐射通量和加热率的影响。

对于单个冰晶粒子，HG 近似对相函数勒让德展开式第 3 项系数造成了较大的负误差。波长为 0.46 μm时，最大误差为－0.28，最大相对误差为－55.7%；波长为 1.23 μm 时，最大误差为－0.18。HG 近似对第 4 项系数造成的负误差更大。波长为 0.46 μm 时，最大误差为－0.33，最大相对误差为－73.8%；波长为 1.23 μm 时，最大误差为－0.27，最大相对误差为－51.3%。第 4 项系数的相对误差绝对值频繁出现大于 50%的情况，明显高于第 3 项系数的相对误差。此外，HG 近似在可见光区的误差高于近红外区。

对于冰云体积光学性质，HG 近似对相函数勒让德展开式第 3 项造成了较大的负误差，在近红外区，最大误差为－0.17，最大相对误差为－26.3%；在可见光区，最大误差为－0.18，最大相对误差为－27.9%。HG 近似对第 4 项系数造成的负误差同样更大一些。在近红外区，最大误差为－0.21，最大相对误差为－36.3%；在可见光区，最大误差为－0.22，最大相对误差为－37.1%。HG 近似在可见光区的误差更高，与单个冰晶粒子光学性质误差情况一致。另外，HG 近似几乎无法反映冰云体积相函数前向峰，在散射角为 0°产生了大量误差。

HG 近似对有云大气短波辐射通量的计算也产生了一定的影响。热带大气条件下，对短波向下辐射通量造成的最大误差为－1.53 $W \cdot m^{-2}$，对短波向上辐射通量造成的最大误差为－0.47 $W \cdot m^{-2}$，对短波加热率造成的最大误差为 0.21 $K \cdot d^{-1}$。中纬度夏季大气条件下，对短波向下辐射通量造成的最大误差为－2.43 $W \cdot m^{-2}$，对短波向上辐射通量造成的最大误差为－0.87 $W \cdot m^{-2}$，对短波加热率造成的最大误差为 0.27 $K \cdot d^{-1}$。中纬度冬季大气条件下，对短波向下辐射通量造成的最大误差为－2.78 $W \cdot m^{-2}$，对短波向上辐射通量造成的最大误差为－1.06 $W \cdot m^{-2}$，对短波加热率造成的最大误差为 0.27 $K \cdot d^{-1}$。其中，HG 近似对中纬度冬季大气短波向下、向上辐射通量和加热率的造成的误差最大。总体上，HG 近似低估了部分高度短波向下辐射通量和整层大气的短波向上辐射通量，高估了云内加热率。

总而言之，虽然 HG 近似具有计算简单和便于应用的优点，但在冰云短波辐射计算过程中会造成明显的系统误差，并不适合高精度有云大气辐射传输计算。精确计算第 3、4 项相函数展开式系数可以提高大气辐射传输的整体计算精度，进而提高大气遥感与探测的精度；并可以减少天气预报模式和气候预测模式中物理过程描述中的不确定性。

参　考　文　献

[1] Baran A J. From the single-scattering properties of ice crystals to climate prediction: a way forward[J]. Atmospheric Research, 2012, 112: 45-69.

[2] Yang P, Liou K N, Bi L, *et al*. On the radiative properties of ice clouds: light scattering, remote sensing, and radiation parameterization[J]. Advances in Atmospheric Sciences, 2015, 32(1): 32-63.

[3] Cai Y, Liu Y L, Dai C M, *et al*. Simulation analysis of target and background contrast in condition of cirrus atmosphere[J]. Acta Optica Sinica, 2017, 37(8): 0801001.
蔡熠, 刘延利, 戴聪明, 等. 卷云大气条件下目标与背景对比度模拟分析[J]. 光学学报, 2017, 37(8): 0801001.

[4] Cao Y N, Wei H L, Bian J. Study of atmospheric radiative properties at infrared bands under ice clouds based on atmospheric infrared sounder and moderate resolution imaging spectroradiometer observation[J]. Acta Optica Sinica, 2014, 34(9): 0901003.
曹亚楠, 魏合理, 边建. 基于大气红外探空仪和中分辨率成像光谱仪观测的冰云大气红外辐射特性研究[J]. 光学学报, 2014, 34(9): 0901003.

[5] Liou K N, Fu Q, Ackerman T P. A simple formulation of the delta-four-stream approximation for radiative transfer parameterizations[J]. Journal of the Atmospheric Sciences, 1988, 45(13): 1940-1948.

[6] Chou M D. A solar radiation model for use in climate studies[J]. Journal of the Atmospheric Sciences, 1992, 49(9): 762-772.

[7] Li J, Ramaswamy V. Four-stream spherical harmonic expansion approximation for solar radiative transfer[J]. Journal of the Atmospheric Sciences, 1996, 53(8): 1174-1186.

[8] Zdunkowski W, Bott A. Radiation in the atmosphere: a course in theoretical meteorology[M]. Cambridge: Cambridge University Press, 2007.

[9] Henyey L G, Greenstein J L. Diffuse radiation in the galaxy[J]. The Astrophysical Journal, 1941, 93: 70-83.

[10] Hong S S. Henyey-Greenstein representation of the mean volume scattering phase function for zodiacal dust[J]. Astronomy and Astrophysics, 1985, 146(1): 67-75.

[11] Toublanc D. Henyey-Greenstein and Mie phase functions in Monte Carlo radiative transfer computations[J]. Applied Optics, 1996, 35(18): 3270-3274.

[12] Boucher O. On aerosol direct shortwave forcing and theHenyey-Greenstein phase function[J]. Journal of the Atmospheric Sciences, 1998, 55(1): 128-134.

[13] Binzoni T, Leung T S, Gandjbakhche A H, *et al*. The use of the Henyey-Greenstein phase function in Monte Carlo simulations in biomedical optics[J]. Physics in Medicine and Biology, 2006, 51(17): N313-N322.

[14] Li J, Barker H, Yang P, *et al*. On the aerosol and cloud phase function expansion moments for radiative transfer simulations[J]. Journal of Geophysical Research: Atmospheres, 2015, 120(23): 12128-12142.

[15] Zhang H, Chen Q, Xie B. A new parameterization for ice cloud optical properties used in BCC_RAD and its radiative impact[J]. Journal of Quantitative Spectroscopy and Radiative Transfer, 2015, 150: 76-86.

[16] Yang P, Liou K N, Wyser K, *et al*. Parameterization of the scattering and absorption properties of individual ice crystals[J]. Journal of Geophysical Research: Atmospheres, 2000, 105(D4): 4699-4718.

[17] Hong G, Yang P, Baum B A, *et al*. Scattering database in the millimeter and submillimeter wave range of 100-1000 GHz for nonspherical ice particles[J]. Journal of Geophysical Research, 2009, 114: D06201.

[18] Zhang H, Nakajima T, Shi G Y, *et al*. An optimal approach to overlapping bands with correlated *k*-distribution method and its application to radiative calculations[J]. Journal of Geophysical Research, 2003, 108(D20): 4641.

[19] Zhang H, Shi G Y, Nakajima T, *et al*. The effects of the choice of the k-interval number on radiative calculations[J]. Journal of Quantitative Spectroscopy and Radiative Transfer, 2006, 98(1): 31-43.

[20] Zhang H, Suzuki T, Nakajima T, *et al*. Effects of band division on radiative calculations[J]. Optical Engineering, 2006, 45(1): 016002.

[21] Zhang H. BCC_RAD atmosphere radiation transfer model[M]. Beijing: Meteorological Press, 2016.
张华. BCC_RAD大气辐射传输模式[M]. 北京: 气象出版社, 2016.

[22] Wei X D, Zhang H. Analysis of optical properties of nonspherical dust aerosols[J]. Acta Optica Sinica, 2011, 31(5): 0501002.
卫晓东, 张华. 非球形沙尘气溶胶光学特性的分析[J]. 光学学报, 2011, 31(5): 0501002.

[23] Zhang H, Shen Z, Wei X, *et al*. Comparison of optical properties of nitrate and sulfate aerosol and the direct radiative forcing due to nitrate in China[J]. Atmospheric Research, 2012, 113: 113-125.

[24] Zhou C, Zhang H, Wang Z L. Impact of different mixing ways of black carbon and non-absorbing aerosols on the opticalpropertise[J]. Acta Optica Sinica, 2013, 33(8): 0829001.
周晨, 张华, 王志立. 黑碳与非吸收性气溶胶的不同混合方式对其光学性质的影响[J]. 光学学报, 2013, 33(8): 0829001.

[25] Randles C A, Kinne S, Myhre G, *et al*. Intercomparison of shortwave radiative transfer schemes in global aerosol modeling: results from the AeroCom Radiative Transfer Experiment[J]. Atmospheric Chemistry and Physics, 2013, 13(5): 2347-2379.

[26] Stamnes K, Tsay S C, Wiscombe W, *et al*. Numerically stable algorithm for discrete-ordinate-method radiative transfer in multiple scattering and emitting layered media[J]. Applied Optics, 1988, 27(12): 2502-2509.

[27] Zhang F, Li J N. Doubling-adding method for delta-four-stream spherical harmonic expansion approximation in radiative transfer parameterization[J]. Journal of the Atmospheric Sciences, 2013, 70(10): 3084-3101.

[28] Sassen K, Wang Z, Liu D. Global distribution of cirrus clouds from CloudSat/Cloud-aerosol lidar and infrared pathfinder satellite observations (CALIPSO) measurements[J]. Journal of Geophysical Research, 2008, 113: D00A12.

Global Energy Interconnection
Development and Cooperation Organization

ELSEVIER
Production And Hosting By Elsevier On Behalf Of KeAi
KeAi

Volume 1 Number 4 October 2018 (420-427)
DOI: 10.14171/j.2096-5117.gei.2018.04.002

Global Energy Interconnection

Contents lists available at ScienceDirect

journal homepage: http://www.keaipublishing.com/en/journals/Global-Energy-Interconnection

Full-length article

Scientific basis of climate change and its response

Qingchen Chao[1], Aiqing Feng[1,2]

1. National Climate Center, China Meteorological Administration, Beijing 100081, P.R. China
2. Laboratory for Climate Studies, National Climate Center, China Meteorological Administration, Beijing 100081, P.R. China

Scan for more details

Abstract: The scientific understanding of climate change is based on a solid physical-theoretical foundation, and long-term observation and research. By analyzing the accelerated rise of the global climate and its wide-ranging effects on the risk of natural ecosystems and the social economy, and, particularly in view of the stringent targets of 1.5 degrees set by the Paris Agreement to limit global temperature rise, this study contends that climate security has become a new, non-traditional, security issue. The fundamental approach to implementing the objectives of the United Nations Framework Convention on Climate Change (UNFCCC) and the Paris Agreement is to develop clean energy vigorously and to accelerate energy transformation. Furthermore, building a global energy interconnection is emphasized as one of the solutions to promoting energy transformation.

Keywords: Climate Change, Scientific basis, Effects and risk, Addressing pathways, Energy transition.

1 Introduction

Climate is a most important part of nature, the basis for human survival and development, a crucial resource, and the basic condition for sustainable economic and social development. Since the industrialization of human society from ca. 1750, coupled with the marked increase in human activities, the already variable climate of the Earth has been influenced significantly by such human actions. The rise in global temperature is accelerating, with the warming climate significantly affecting natural ecosystems and the economic society globally. The progress of humankind has been marked by a relationship with and interactions among people, the economy, society, and nature. In recent years, however, the recognition has grown that climate security has become a new and non-traditional issue. Therefore, actively responding to climate change and accelerating low-carbon development have become the consensus of the international community.

By reviewing the evolution of the idea of development and the progress on the scientific cognition of climate change, this study analyzed the effects of and risk related to climate change. Particularly, in view of the stringent targets set by the Paris Agreement to limit global temperature increases, we pointed out the fundamental approach to implementing the objectives of the United Nations Framework Convention on Climate Change (UNFCCC) and the Paris Agreement. These are, namely, to develop clean energy vigorously and to accelerate energy transformation. Accordingly, building a global energy interconnection is one of the solutions to promoting energy transformation.

Received: 17 August 2018/ Accepted: 20 August 2018/ Published: 25 October 2018

✉ Qingchen Chao
chaoqc@cma.gov.cn

Aiqing Feng
fengaq@cma.gov.cn

2 Understanding evolution of the development idea and the scientific basis of climate change

2.1 Evolution of development in a philosophical sense

The development of human beings encompasses evolving from natural beings into self-conscious ones. With the increasing knowledge about the Earth and human evolution, humans have gradually come to embrace the notion that development is global and includes all mankind. The vast progress brought about by the industrial civilization has inspired a human desire to "conquer nature" and, conversely, the damage done by the environmental crisis to human interests has deepened human understanding of industrial development (Fig. 1). Air, water, and soil pollution and the degeneration of the ecology are contrary to the original targets of development and have, therefore, aroused rational thinking. Although using fossil energy has brought about substantial improvements in productivity, the excessive use of this resource has led to a significant burden on the environment and even the occurrence of natural disasters.

In the mid-20th century, people with insight proposed a more in-depth discussion of the relationship between human beings and nature, resources and environment, and development and protection. On this basis, the Norwegian Prime Minister at the time, Gro Harlem Brundtland, first proposed the concept of sustainable development in 1987. In the same year, the World Commission on Environment and Development (WCED) published a report, *Our Common Future*, which clarified further the connotation of sustainable development, i.e., development that meets the needs of the present without compromising the ability of future generations to meet their own needs. "Sustainable development" is an essential improvement in the outlook of human development [1].

2.2 Theoretical basis of climate change

Climate change has existed since ancient times but the science of "modern climate change" has come into being two hundred years ago and has been developing up to now. Several milestones in the progress of the new science include the following. In 1824, a French scientist, J. Fourier, proposed that the atmosphere of the Earth acts like a blanket or the glass of a greenhouse to increase the temperature (compared with there being no such envelope of gases), i.e., the "greenhouse effect" [2]. In 1867, the British scientist, J. Tyndall, measured the radiation characteristics of CO_2, CH_4, and other molecules, and clarified the effect of the greenhouse gases in the atmosphere on the temperature change of the earth [3]. This study on molecular physics is the core of the contemporary climate change theory. In 1896, the Swedish scientist, Svante August Arrhenius, calculated the greenhouse effect of carbon dioxide in the atmosphere [4]. In 1938, a study by British scientist, G. Callendar, linked the increase in fossil fuel combustion and the rise in the carbon dioxide concentration with the greenhouse effect. He pointed out that human actions could cause significant climate change [5]. Later, the Japanese scientist, Syukuru Manabe, and the American scientist, Jule Charney, established a relatively complete theory and

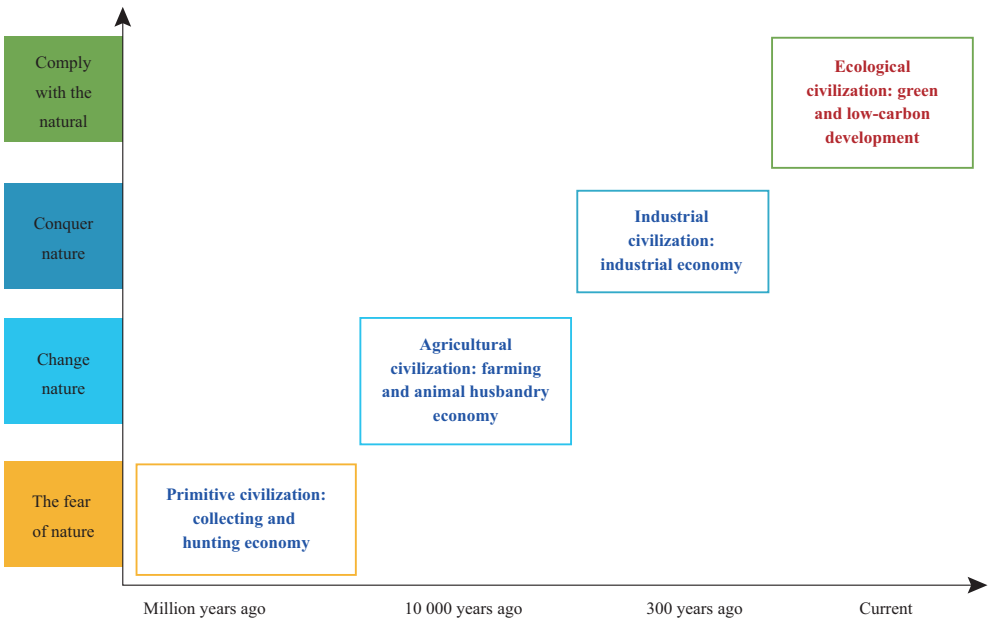

Fig. 1 Harmonious relationship between socioeconomic development and evolution of nature under different civilizations

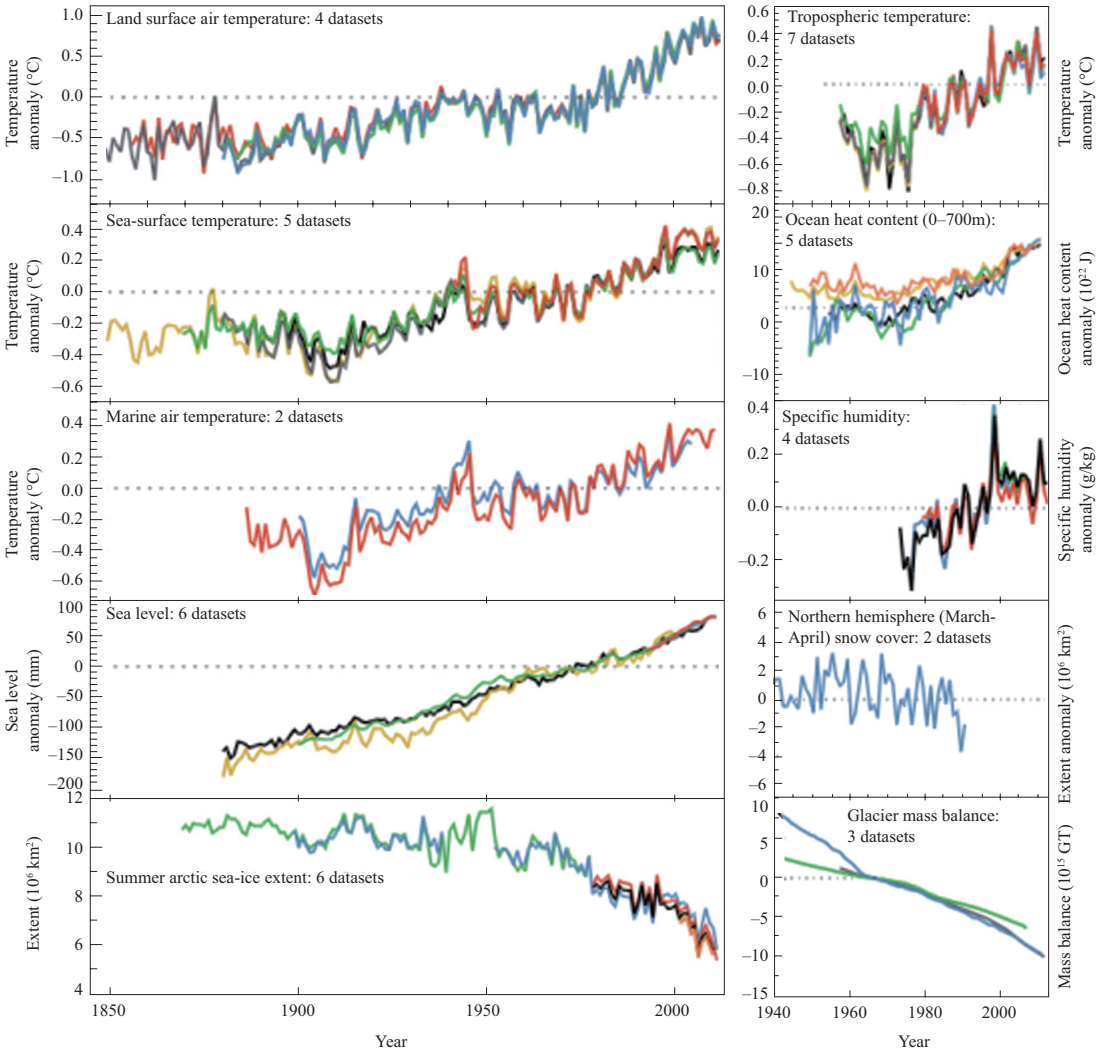

Fig. 2 Multiple independent indicators of a changing global climate. Each line represents an independently derived estimate of change in the climate element. In each panel, all data sets have been normalized to a common record period (Cited from the Fifth Assessment Report of the Intergovernmental Panel on Climate Change, IPCC AR5, WGI FAQ 2.1 Fig. 2)

evaluated the relationship (i.e., sensitivity) between the carbon dioxide concentration and climate change [6-7]. In 1958, the Mauna Loa Observatory in Hawaii, USA, started to observe the CO_2 concentration, officially unveiling the prelude to research on climate change.

2.3 Changes in the climate system

A series of actual observations of and the substantial number of studies on global climate change from the 20th century to the present [8-10] have been augmenting the scientific understanding of modern climate change. A comprehensive analysis of the latest global climate observation data confirmed that in 2017 the global surface average temperature was approximately 1.1 °C higher than was the pre-industrial level (1850–1900 annual mean). This was the second warmest year and the warmest non-El Niño year since the start of complete meteorological observation records. From 1870 to 2017, the global mean sea surface temperature (SST) showed a significant upward trend and a continued high level after 2000. In 2017, the SST in most of the global seas was higher than normal and the global average SST was the third highest since 1870. From 1958 to 2017, the global ocean heat content (upper 2000m) increased significantly, and ocean warming accelerated significantly after the 1990s. In 2017, the value of global ocean heat content was the highest since the start of modern ocean observation.

From 1979 to 2017, the extent of the Arctic sea ice decreased significantly, whereas that of the Antarctic sea ice generally showed an upward trend. However, the range of

the Antarctic sea ice was abnormally small in 2017, with a minimum value in March and the second smallest value in September since the start of satellite observation records. In addition, the global sea level has been rising consecutively for six years. In 2016, the global average sea level reached a new height, approximately 82 mm higher than when satellite recording began in 1993. Over the past 20 years, the sea level has risen at an average rate of approximately 3.4 mm per year, with the highest increases being observed in the Western Pacific and Indian oceans.

Greenhouse gas emissions continue to set new records. In 2016, the annual average global atmospheric concentration of major greenhouse gases reached a new high level, with 403.3 ppm carbon dioxide, 1853 ppb methane, and 328.9 ppb nitrous oxide, which were 145%, 257%, and 122%, respectively, of the pre-industrial (before 1750) levels. It was the first time since 800 000 years that the concentration of carbon dioxide in the atmosphere exceeded 400 ppm, an increase of 3.5 ppm compared with 2015, and the sharpest increase in 58 years. The carbon dioxide concentration of 404.4 ppm, at the Waliguan Global Almosphere Watch (GAW) station in China released by China Meteonological Administration (CMA), was slightly higher than the global average value.

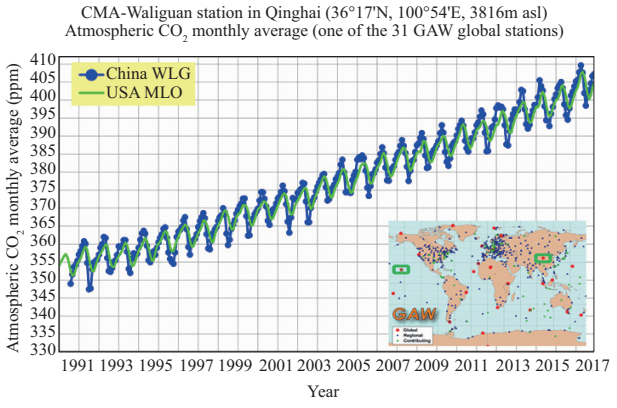

Fig. 3 The monthly CO_2 mole fractions observed at the Waliguan GAW station in Qinghai Province, China, and the Mauna Loa Observatory in Hawaii, USA

With the rise in the global temperature, extreme weather and climate events have also been increasing significantly worldwide, leading to frequently occurring disasters that have caused fatalities and substantial economic losses. Indeed, the frequency of high-temperature red alerts is rising. The extremely active hurricanes in the North Atlantic Ocean, the severe monsoon floods on the Indian subcontinent, and the continued severe droughts in Eastern Africa have contributed to economic losses totaling $320 billion in 2017, the highest annual climate-related losses since the start of records.

Studies have shown that [8] the trend of global warming is set to continue in this century. Compared with the period 1986–2005, the global average surface temperature would likely increase by 0.3–0.7 °C during the period 2016–2035, and to 0.3–4.8 °C by the end of this century. At the end of the 21st century, the sea level would have risen by 0.26–0.82 m. The Arctic Sea ice area in September would be reduced probably by 43%–94%, and the global glacial volume could probably shrink by 15%–85%. Two emission scenarios (RCP 2.6 and RCP 8.5), based on more than 20 CMIP5 (Coupled Model Intercomparison Project Phase 5) models, were used to analyze the changes in the frequency of five-consecutive-day maximum temperatures higher than 35 °C in China. The results showed that the frequency of heatwaves could increase threefold by the end of the 21st century compared with 1986–2005, if maintaining the current energy policies placed the world on the high emission pathway consistent with RCP 8.5 (Fig. 4). Overall, the uncertainty related to the high emission scenario was larger compared with the uncertainty related to the low emission scenario. Furthermore, the uncertainty was more substantial in regions with more significant warming trends compared with regions with weaker trends. Among three periods (2016–2035, 2046–2065, and 2080–2099), the projected uncertainty would be the smallest during 2016–2035.

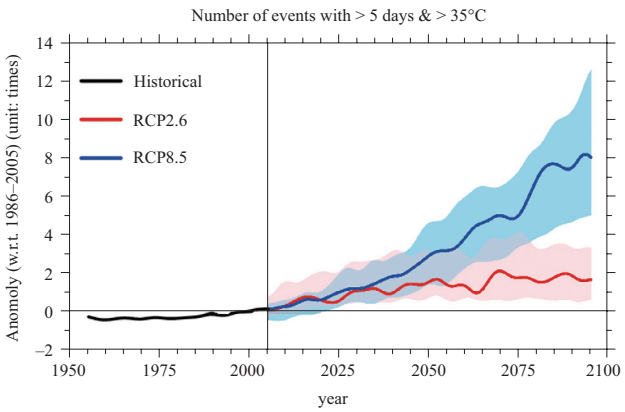

Fig. 4 Change in the number of events lasting at least five days with the daily maximum temperature exceeding 35 °C

3 Effects and Risk of Climate Change

Because of differences in natural geographical conditions and socioeconomic situations, the effects of and risk related to climate change on a global scale are heterogeneous; therefore, the responses vary as well. Furthermore, as regards the risk of future climate change to sectors, research results differ because of the difference in climate models, scenarios, data, and the like. However, the trend of the long-term climate risk is certain.

3.1 Effects on global important sectors

It indicated that adverse effects of climate change on food production are more pronounced than the beneficial effects. Globally, the average biophysical production could be reduced by 17% by 2050 compared with that under a constant climate condition [11]. By the end of this century, food production would have decreased by 0%–2% per decade, whereas the projected food demand would have increased by approximately 14% per decade by 2050. The cropland area and cropping frequency are more sensitive to climate change than crop yield [12].

Climate warming has caused precipitation changes and snowmelt in many regions, particularly in the permafrost regions of high-latitude and high-altitude mountains. Warming also affects downstream runoff and water resources. At the same time, it promotes the potential evaporation of most land areas and accelerates the hydrological cycle. Currently, approximately one billion people live in watersheds with water shortages. By 2050, there would be more than 50 million to 3.1 billion people suffering water shortages because of climate change [13]. With a global warming of 2 °C, the population at risk of serious water shortages would increase by 15% [14].

During the 21st century, ecosystems would face a substantial risk of regional-scale mutations and irreversible changes, such as the Arctic tundra and Amazon forests. The geographical distribution, seasonal activities, migration patterns, and abundance of some biological species have changed already [8]. Climate change directly affects plant physiology and ecosystem functioning, resulting in changes in global productivity and generating indirect effects on ecosystems through changes in plant composition and diversity [15]. In the 21st century and beyond, combined with other pressures, most terrestrial and freshwater species would be at a higher risk of extinction. Studies have shown that [16] between 1979 and 2013, climate change has caused an increase of 25.3% in wild forest fires worldwide, and the average length of the fire season has increased by 18.7%. This situation could worsen, thereby significantly affecting global ecosystems.

Coastal areas could be affected adversely by submergence, flooding, and erosion, caused by the rise in sea level. By 2030, the global urban area of high-frequency coastal floods would have increased from 30% in 2000 to 40% [17]. By 2100, more than half of the global delta regions would be inundated, considering the predicted sea-level rise [18]. In the absence of adaptation measures, the population of the global coastal zones at risk of flooding would reach 0.2%–4.6%, and the average GDP loss would be 0.3%–9.3% [19]. In addition, climate change would affect human health and the socioeconomic system. Moreover, it threatens the process of global sustainable development.

3.2 Climate risk under different rates in temperature rise

Generally, the global risk is medium to high compared the pre-industrial temperature with 1 °C or 2 °C rise, whereas a temperature rise of more than 4 °C or higher would indicate a high or very-high risk level. Key risks in Asia are embodied mainly in the increased flooding of rivers, oceans, and cities, where extensive damage would be caused to the infrastructure, livelihoods, and settlements.

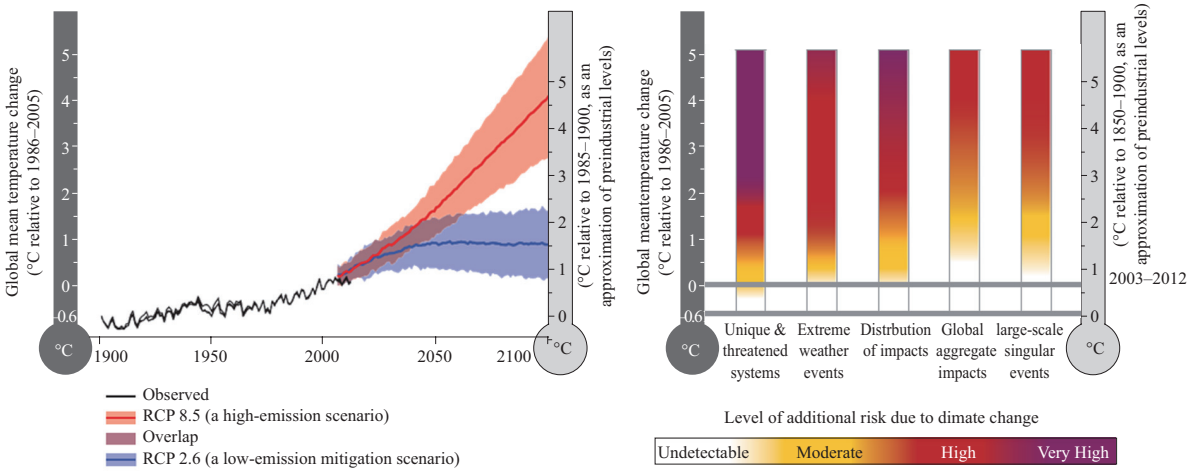

Fig. 5 Global perspective on temperature change (left) and climate-related risk (right). The color shading indicates the additional risk related to climate change when a certain temperature level is reached and subsequently sustained or exceeded

(Cited from IPCC AR5 WGII Assessment Box SPM 1 Fig. 1)

The risk of death associated with a high temperature and the risk of malnutrition resulting from drought-related water and food shortages would also rise [8].

4 Pathway to Addressing Climate Change

4.1 Evolution of long-term goals of mitigation and adaptation on climate change

The ultimate objective determined by the UNFCCC was to achieve "stabilization of greenhouse gas concentrations in the atmosphere at a level that would prevent dangerous anthropogenic interference with the climate system. Such a level should be achieved within a time-frame sufficient to allow ecosystems to adapt naturally to climate change, to ensure that food production is not threatened and to enable economic development to proceed in a sustainable manner". The UNFCCC has not elaborated on which changes were deemed dangerous, what level of human interference could lead to dangerous climate change, or how to avoid such dangerous climate changes. Starting in 1995, with the *Second Assessment* Report of the Intergovernmental Panel on Climate Change (IPCC), the international scientific community has continued to conduct research on this issue. Under the patronage of leading countries, such as the member states of the European Union, a temperature rise limit of 2 °C was put forward in the *Copenhagen Accord* in 2009 and was reconfirmed in the *Cancun Agreement* adopted in 2010. Since then, global political consensus has been reached on the 2 °C temperature rise target.

The Alliance of Small Island States (AOSIS) has appealed for a long-term goal lower than the 2 °C limit. In 2007, AOSIS submitted a detailed proposal to the UNFCCC on this long-term goal. Both the *Copenhagen Accord* in 2009 and the *Cancun Agreement* in 2010 mentioned considering the 1.5 °C target. In the final phase of the 2015 Climate Change Conference in Paris, the "High Ambition Coalition", composed of the European Union, Switzerland, the United States, Africa, the Caribbean, and the Pacific Group of States strongly promoted the global temperature rise to be controlled within the 1.5 °C limit (*Paris Agreement*). Present studies indicated that the risk to the ecosystem or the human socioeconomic system related to a temperature rise of 2 °C, compared with 1.5 °C, would obviously be higher, despite the substantial regional differences [20].

4.2 Pathway to achieving 2 °C or 1.5 °C limits

Effectively coping with the adverse effects of climate warming can only be done through adaptation and mitigation measures. Disaster risk management and enhancing the resilience of the human social systems are effective ways to adapt to climate change and reduce vulnerability and exposure, and are the only way to achieve active adaptation under sustainable development [21]. Controlling or reducing greenhouse gas emissions through climate change mitigation policies and measures is a fundamental way to address climate change, including increasing carbon sinks and employing geoengineering. The most important measures [8] to reduce greenhouse gas emissions include the reformation of the energy supply sectors and the early implementation of systematic and cross-sectoral emission reduction strategies.

Study has shown that if all the current Nationally Determined Contribution (NDC) targets were achieved punctually, global greenhouse gas emissions could be expected to reach 550 (514–573) Gt CO_2 by 2025, and 562 (520–593) Gt CO_2 [22] by 2030. As a result, the global temperature rise would be 2.2–3.4 °C by the end of 2100. To achieve the 2 °C goal, it would be necessary to reduce an additional 30%, on the basis of the current NDC targets, by 2030 [23]. The remaining carbon budget for limiting global warming to 1.5 °C is complicated because of the uncertainties in the climate response to emissions, the different sets of multi-gas and aerosol scenarios, and the use of different concepts of carbon budgets. New research has shown that the remaining carbon budget for a one-in-two chance of limiting global warming to 1.5 °C was approximately 770 Gt CO_2, and approximately 570 Gt CO_2 for a two-in-three chance using Global mean surface temperature estimation. This implies rapid reductions in the net global anthropogenic CO_2 emissions to reach net-zero around mid-century, together with the rapid reduction of other anthropogenic emissions. Limiting global warming to 1.5 °C would require rapid and far-reaching systems transitions during the coming one to two decades, in energy, land, urban, and industrial systems [24].

Currently, global energy development is showing three major trends [25, 26]. The first is to transform to clean, low-carbon, and efficient energy. In 2015, low-carbon energy (non-fossil energy and natural gas) accounted for more than 40% of the global primary energy structure and showed a growth momentum. Coal combustion accounted for 28.6% of the global energy; however, excluding China, coal combustion accounted for only 19% of the energy of the rest of the world. Second, the growth in the total global energy demand is slowing down, with growth points being mainly in emerging economies. In 2016, the total global energy consumption increased by 1%, whereas that of China increased by 1.3%, and the energy intensity decreased by 2.1%. This trend is resulted from the global economic situation and energy efficiency progress. Third, energy

technology innovation is most active and many countries are actively seizing the strategic high point of energy technology. Some of the highlights include energy storage technology, distributed energy, and intelligent technology. The fundamental way to respond actively to climate change is to accelerate the development of clean energy and to implement "two alternatives". These are developing and implementing clean energy alternatives to fossil fuels, and electricity for coal, electricity for oil, electricity from afar. Clean energy is expected to dominate in the future. The global energy interconnection would be one of the significant ways to contribute to regional or even global energy transformation in the future.

5 Conclusion

The international community has been working hard to address climate change. The *Paris Agreement* fully demonstrates the consensus of countries to cope with climate change and to promote green and low-carbon development. Advancing low-carbon development together with the energy transformation is a historical process. The nature of such change might be long-term and arduous but the direction and path are clear. Governments, enterprises, and the public need to work together to practice the concept of "innovation, coordination, green, openness, and sharing", create a new sustainable development path in China, and make a greater contribution to the progress of human civilization. The global energy interconnection can build a new pattern of energy development, stimulate new activities for economic growth, and become a new approach to addressing climate change.

Acknowledgements

This research was supported by the major project of the Ministry of Education (15JZD035), the MOST project of the 4th National Climate Change Assessment Report, and the Laboratory of Climate Studies Open Funds for Young Scholars of China Meteorological Administration in 2018.

References

[1] UNDP (2005) Human Development Report 2005. United Nations Development Programme, United University Press. Oxford

[2] Fourier J (1824) Remarques générals surles températures du globe terrestre et des espaces planétaires. Annales de Chimie et de Physique, Vol. XXVII, pp:136-167//Archer D, Pierrehumbert R (2011) The Warming Papers: The Scientific Foundation for the Climate Change Forecast. Oxford. UK: Wiley Blackwell, pp: 3-20

[3] Tyndall J (1861) On the absorption and radiation heat by gases and vapors, and on the physical connection of radiation, absorption and conduction. Philosophical Magazine Series 4, Vol. 22, pp:169-194, 273-285

[4] Arrhenius S (1896) On the influence of carbonic acid in the air upon the temperature of the ground. The London Edinburgh, and Dublin Philosophical Magazine and Journal of Science 5th Series, 465(251)//Archer D, Pierrehumbert R (2011) The Warming Papers: The Scientific Foundation for the Climate Change Forecast. Oxford. UK: Wiley Blackwell, pp: 45-77

[5] Callendar GS (1938) The artificial production of carbon dioxide and its influence on climate. Quarterly Journal of the Royal Meteorological Society, 64(275):223-240

[6] Manabe S, Wetherald R (1967) Thermal equilibrium of the atmosphere with a given distribution of relative humidity. Journal of the Atmospheric Sciences, 24(3): 242-259

[7] Charney J, Coauthors G (1979) Carbon dioxide and climate: A scientific assessment. Washington, DC: National Academy of Sciences

[8] IPCC (2014) Climate Change 2014: Synthesis Report. Contribution of Working Groups I, II and III to the Fifth Assessment Report of the Intergovernmental Panel on Climate Change [Core Writing Team, R.K. Pachauri and L.A. Meyer (eds)]. IPCC, Geneva, Switzerland, pp: 151

[9] WMO (2018) WMO Statement on the state of the global climate in 2017

[10] Climate Change Center of China Meteorological Administration (2018) Blue Book on China Climate Change. Beijing, China

[11] Nelson GC, Valin H, Sands RD et al (2014) Climate change effects on agriculture: Economic responses to biophysical shocks. Proceedings of the National Academy of Sciences, 111(9): 3274

[12] Cohn A, VanWey LK, Spera S et al (2016) Cropping frequency and area response to climate variability can exceed yield response. Nature Climate Change, 6(1): 601-604

[13] Gosling SN, Arnell NW (2016) A global assessment of the impact of climate change on water scarcity. Climatic Change, 134(3): 371-385

[14] Schewe J, Heinke J, Gerten D et al (2014) Multimodel assessment of water scarcity under climate change. Proceedings of the National Academy of Sciences, 111(9): 3245-3250

[15] Morin X, Fahse L, Jactel H et al (2018) Long-term response of forest productivity to climate change is mostly driven by change in tree species composition. Scientific Reports, 8(1): 5627

[16] Jolly WM, Cochrane MA, Freeborn PH et al (2015) Climate-induced variations in global wildfire danger from 1979 to 2013. Nature Communications, Vol. 6, pp: 7537-7547

[17] Güneralp B, Güneralp İ, Liu Y (2015) Changing global patterns of urban exposure to flood and drought hazards. Global Environmental Change, Vol. 31, pp: 217-225

[18] Syvitski J, Kettner AJ, Overeem I et al (2009) Sinking deltas due to human activities. Nature Geoscience, 2(10): 681-686

[19] Hinkel J, Lincke D, Vafeidis AT et al (2014) Coastal flood damage and adaptation costs under 21st century sea-level rise. Proceedings of the National Academy of Sciences, 111(9): 3292-3297

[20] Schleussner C, Lissner TK, Fischer EM et al (2016) Differential climate impacts for policy-relevant limits to global warming: The case of 1.5 °C and 2 °C. Earth System Dynamics, 7(2): 327-351
[21] IPCC (2014) Summary for policymakers. In: Climate Change 2014: Impacts, Adaptation, and Vulnerability. Part A: Global and Sectoral Aspects. Contribution of Working Group II to the Fifth Assessment Report of the Intergovernmental Panel on Climate Change. Cambridge University Press, Cambridge, United Kingdom and New York, NY, USA, pp: 1-32
[22] UNFCCC (2016) Updated synthesis report on the aggregate effect of INDCs. FCCC/CP/2016/2
[23] Energy Transitions Commission (2016) Pathways from Paris: Assessing the INDC opportunity. http://www.energy-transitions.org/
[24] IPCC (2018) Summary for Policymakers of the IPCC "Special Report on Global Warming of 1.5 °C, an IPCC special report on the impacts of global warming of 1.5 °C above pre-industrial levels and related global greenhouse gas emission pathways, in the context of strengthening the global response to the threat of climate change, sustainable development, and efforts to eradicate poverty". http://cache2.nmic.cn/files/304700000094E6A8/report.ipcc.ch/sr15/pdf/sr51_spm_final.pdf
[25] IEA (2017) Outlook on Energy Technology, http://www.escn.com.cn/news/show-430389.html, 13 June
[26] BP (2017) Outlook on World Energy, https://www.bp.com/zh_cn/china/reports-and-publications/_bp_2017_.html, 30 March

Biographies



Qingchen Chao received her bachelor degree in Beijing Institute of Meteorology. She received her master and Ph.D. degrees from Institute of Atmospheric Physics, Chinese Academy of Sciences. Her research areas are climate system analysis and interactions, climate risk and climate policy. She serves as the member of Global Climate Observing System Steering Committee. She currently is the deputy director general of National Climate Center of China Meteorological Administration.



Aiqing Feng received her Ph.D. degree from Institute of Geographic Sciences and Natural Resources Research (IGSNRR), Chinese Academy of Sciences (CAS). She is currently working at Meteorological Disaster Risk Management Division of National Climate Center. Her research focuses on the risk of meteorological disasters under climate change.

(Editor Chenyang Liu)

Vol. 76: 161–176, 2018
https://doi.org/10.3354/cr01534

CLIMATE RESEARCH
Clim Res

Published online October 10

OPEN ACCESS CC BY

Comparisons of observational data sets for evaluating the CMIP5 precipitation extreme simulations over Asia

Siyan Dong[1,*], Ying Sun[1,2]

[1]Laboratory for Climate Studies, National Climate Center, China Meteorological Administration, Beijing 100081, PR China
[2]Joint Center for Global Change Studies, Beijing 100081, PR China

ABSTRACT: The accurate simulation of precipitation extremes in climate models is important for the understanding of future climate change and its impacts. Due to the poor coverage and the lack of uniformity of observational precipitation extreme data in Asia, it is difficult to evaluate whether existing climate models can accurately reproduce the patterns of and changes in precipitation extremes. The present study presents a comparison between 3 observational data sets and CMIP5 models and shows that improving the data coverage in the future is of great significance for understanding precipitation extreme changes in Asia. The 3 observational data sets show good consistency with the models in the mid- and high-latitude regions of Asia, where the data generally have good coverage. Meanwhile, the differences between the observations are obvious in the low-latitude region, and the differences between the models are also large. Although these discrepancies may be related to different operational orders and interpolation methods, the spatial coverage of data can constitute an important factor leading to such differences at low latitudes. The results for the mid-latitude region show little change in the new Asian observation data set (ADEX) compared with in HadEX2, but the trend of precipitation extreme intensity indices in ADEX are closer to the simulated trend than in HadEX2 for the high-latitude region. Furthermore, the differences in the intensity indices between the observations and models are larger than those in the frequency indices, indicating that the simulated and projected values of the intensity indices are higher than those of the frequency indices. In summary, there are differences between the 3 datasets and CMIP5 models, especially for low-latitudes and the intensity indices.

KEY WORDS: Precipitation extremes · Observational data sets · CMIP5 · Model evaluation

1. INTRODUCTION

Previous studies have shown that anthropogenic influences can be identified in changes in the duration, frequency and intensity of precipitation extremes (Zhang et al. 2007, Polson et al. 2013, Zhang et al. 2013, IPCC 2014, Fischer & Knutti 2015). In addition, such influences are expected to increase the intensities and frequencies of floods and droughts, and impose negative effects on the environment, economy and society throughout Asia (IPCC 2014). Freychet et al. (2016) suggested that precipitation extremes with a greater intensity and higher frequency are likely to increase over East Asia in the future. Furthermore, some authors have attempted to evaluate precipitation extremes at the national scale over Asia (Ou et al. 2013, Sillmann et al. 2013a, Jiang et al. 2015, Freychet et al. 2016). For example, Ou et al. (2013) suggested that the Coupled Model Intercomparison Project Phase 5 (CMIP5) models overestimate precipitation extremes in western China and high-altitude regions compared with station data in China, although those models simulate the precipitation extremes in eastern China very well. Jiang et al.

*Corresponding author: dongsy@cma.gov.cn

© The authors 2018. Open Access under Creative Commons by Attribution Licence. Use, distribution and reproduction are unrestricted. Authors and original publication must be credited.

Publisher: Inter-Research · www.int-res.com

(2015) compared 4 precipitation extreme indices between different CMIP5 models; in comparison with observational station data in China, they found that the simulated data in eastern China are more reliable than those in western China. However, such evaluation studies have often focused on limited precipitation extreme indices over Asia, and focused only on the national scale (e.g. China, where the amount of daily observational data is large) or on Asia as a whole for global analysis (Sillmann et al. 2013a), the results of which are insufficient for comprehensively understanding the regional differences between models and observational precipitation extremes in different latitudinal regions across Asia.

In fact, constraining the spatial and temporal differences between various observational data sets and models can represent a major challenge for the evaluation of models across Asia. Wan et al. (2013) found that the incomplete spatial coverage of observational data records resulted in increased sampling errors of trend estimates, making it more difficult to detect statistically significant trends. The HadEX2 data set has often been used for studying precipitation extremes; however, the spatial coverage of the HadEX2 gridded product for precipitation extremes is far from ideal (Alexander et al. 2006, Sillmann et al. 2013a), and the improvements to the HadEX2 data set in the coverage of precipitation extremes are less impressive than those of temperature stations (Donat et al. 2013, Alexander 2016). Furthermore, Sillmann et al. (2013a) found that compared with HadEX2, CMIP5 models generally underestimate intensity indices (e.g. maximum 5 d precipitation [Rx5day] and Simple day intensity index [SDII], especially SDII) — for which HadEX2 lies outside of the CMIP5 model range — and overestimate the number of consecutive wet days (CWD). This situation also occurs in Asia. Some authors have even noted that HadEX2 may not be the most appropriate data set for evaluating precipitation extremes in climate models, given the order of operations used in the construction of HadEX2 (Donat et al. 2013, Alexander & Arblaster 2017). Alternatively, in recent years, the Asian Precipitation – Highly-Resolved Observational Data Integration Towards Evaluation of Water Resources (APHRODITE) project has developed daily gridded precipitation data (Yatagai et al. 2012). This observational data set currently comprises high-resolution gridded land precipitation data covering the entire Asian region, but some authors have argued that the data set exhibits obvious deviations from observational station data when describing the frequency, intensity and climatology in addition to the long-term changes in different grades of precipitation throughout China (Han & Zhou 2012, Yin et al. 2015). Additionally, the temporal coverage of APHRODITE data is shorter than that of HadEX2.

In short, there is a lack of comprehensive research focusing on climate model evaluations over Asia because of the limited amount of available observational data sets. Consequently, to improve the spatial and temporal coverage in Asia, a new daily Asian observational extreme indices data set (hereafter called ADEX) was developed in 2013 by the joint World Meteorological Organization (WMO) CCl/CLIVAR/JCOMM Expert Team on Climate Change Detection and Indices (ETCCDI) with help from scientists originating from various countries in Asia. Compared with HadEX2, this observational data set has a greater spatial coverage and provides more detailed information about climate extremes over Asia. The improvement in the spatial and temporal coverage for observations over Asia may be helpful for better understanding the changes in precipitation extremes, and for applying them to projection, detection and attribution endeavors.

Unfortunately, substantial discrepancies are likely to exist among various observational data sets (HadEX2, APHDEX and ADEX), and thus the use of various observational data sets may lead to notable uncertainties when they are used to evaluate models. Accordingly, this paper focuses on evaluating the CMIP5 multi-model ensemble with 3 observational data sets (ADEX, HadEX2 and APHDEX). We quantitatively measured the differences between the models and the 3 observational data sets with regard to the 47 yr mean climatology in precipitation extreme indices and their trends during 1961–2007. We also provide observational uncertainties using 3 independent observational data sets over Asia. Most importantly, ADEX will provide important information that will be useful for understanding climate change and its impacts throughout Asia.

2. DATA AND METHODOLOGY

2.1. Precipitation extreme indices

The 10 precipitation extremes developed by the ETCCDI (http://etccdi.pacificclimate.org/list_27_indices.shtml) and used in this study are shown in Table 1. These 10 different precipitation extreme indices include intensity indices composed of absolute intensity indices (Rx1day and Rx5day), relative intensity indices (R95p and R99p) and a simple daily inten-

sity index (SDII), in addition to frequency indices (R10mm and R20mm), duration indices (including CWD and consecutive dry days [CDD]) and annual precipitation total (PRCPTOT).

2.2. Observations

2.2.1. HadEX2

HadEX2 is a global land-based gridded climate extremes data set produced through the coordination of the joint WMO CCl/CLIVAR/JCOMM ETCCDI. It is an updated version of HadEX (Alexander et al. 2006) and contains more station data and covers a much longer period than HadEX (Donat et al. 2013, accessed at www.climdex.org/index.html). The precipitation extreme indices are based on daily observations from approximately 11 600 precipitation stations gridded on a 2.5 × 3.75° (latitude × longitude) grid from 1901 to 2010. Angular-distance weighting was used to interpolate the station data onto the required grid.

2.2.2. APHRODITE daily gridded data set

APHRODITE comprises gridded rainfall data from the APHRODITE project (Yatagai et al. 2012, accessed at www.chikyu.ac.jp/precip). This data set has been applied to climate change and water cycle research in addition to the high-resolution model results of model inspections and other fields. The present study analyses the APHRO_MA V1003R1 data set, which describes the precipitation characteristics of Monsoon Asia (MA) and mainly includes China, Japan, Mongolia, India, all countries in Southeast Asia, and some countries in Central Asia. We selected the data set with a resolution of 1 × 1° and used the period from 1961 to 2007 for analysis. The data set is also subjected to quality control processes (Yatagai et al. 2012), and in the present study, the 10 annual precipitation extreme indices were calculated from the daily precipitation gridded data and we refer to the precipitation extreme indices data as the APHDEX data set.

Table 1. Definition of the 10 extreme precipitation indices used in this study

Extreme indices	Category	Definition and calculation of index	Unit
Rx1day	Intensity indices	Monthly maximum 1 d precipitation: Let RR*ij* be the daily precipitation amount on day *i* in period *j*. The maximum 1 d value for period *j* is: Rx1day*j* = max (RR*ij*)	mm
Rx5day	Intensity indices	Monthly maximum 5 d precipitation: Let RR*kj* be the precipitation amount for the 5 d interval ending on day *k* in period *j*. Then, the maximum 5 d values for period *j* are: Rx5da*yj* = max (RR*kj*)	mm
R95p	Intensity indices	Annual total daily precipitation when RR > 95p. Let RR*wj* be the daily precipitation amount on a wet day *w* (RR ≥ 1.0 mm) in period *i*, and let RR*wn*95 be the 95th percentile of the precipitation on wet days during 1961–1990	mm
R99p	Intensity indices	Annual total PRCP when RR > 99p: Let RR*wj* be the daily precipitation amount on a wet day *w* (RR ≥ 1.0 mm) in period *i*, and let RR*wn*99 be the 99th percentile of the precipitation on wet days during 1961–1990	mm
PRCPTOT		Annual total precipitation on wet days: Let RR*ij* be the daily precipitation amount on day *i* in period *j*	mm
SDII	Intensity indices	Simple precipitation intensity index: Let RR*wj* be the daily precipitation amount on wet days *w* (RR ≥ 1 mm) in period *j*. If *W* represents the number of wet days in *j*	mm d^{-1}
R10mm	Frequency indices	Annual number of days when PRCP ≥ 10 mm: Let RR*ij* be the daily precipitation amount on day *i* in period *j*. Count the number of days where: RR*ij* ≥ 10 mm.	d
R20mm	Frequency indices	Annual number of days when PRCP ≥ 20 mm: Let RR*ij* be the daily precipitation amount on day *i* in period *j*. Count the number of days where: RR*ij* ≥ 20 mm.	d
CWD	Duration indices	Maximum length of wet spell, maximum number of consecutive days with RR ≥ 1 mm: Let RR*ij* be the daily precipitation amount on day *i* in period *j*. Count the largest number of consecutive days where: RR*ij* ≥ 1 mm	d
CDD	Duration indices	Maximum length of dry spell, maximum number of consecutive days with RR < 1 mm: Let RR*ij* be the daily precipitation amount on day *i* in period *j*. Count the largest number of consecutive days where: RR*ij* < 1 mm	d

2.2.3. The new Asian extremes indices data set

The new Asian extreme indices data set (ADEX) was developed through the joint efforts of the ETCCDI (e.g. Zhang et al. 2005, Peterson & Manton 2008). A workshop was held in Nanjing, China, in 2013 involving scientists from 15 different nations throughout Asia who computed the extreme indices using long-term daily weather observational station data (Dong et al. 2018). This data set covers the period of 1951–2012. The participants were asked to check and test the data from the best and longest climate station records in their countries of origin for homogeneity using the RHtestsV3 software package (Wang & Feng 2010), and homogenization was performed using HOMER (Mestre et al. 2013) (www.homogenisation.org/). To avoid the inclusion of erroneous observations in the analysis, the results were subjected to a second round of quality control. The Global Historical Climatology Network-Daily (GHCND) data set (Menne et al. 2012) was used to supplement additional stations or to expand the temporal completeness of the station data provided by all workshop participants, excluding those from China, for which the China National Meteorological Information Center (NMIC) was used as the data source (Cao et al. 2016).

Series that contained <15 valid years between 1961 and 1990 were excluded in ADEX. This exclusion produced an effective number of series (consisting of approximately 2300 stations) for most indices over Asia, producing more stations over some countries than both HadEX2 and APHRODITE, and enhancing the temporal coverage of grid stations over Asia. To produce the ADEX gridded precipitation extreme indices data, we gridded values on 2.5 × 3.75° (latitude × longitude) grids (i.e. the HadEX2 grid size) by averaging the stations over each grid containing ≥1 station; this procedure is different from the gridding methods used in both HadEX2 and APHDEX. The daily 1 × 1° gridded precipitation of APHRODITE was calculated to the annual precipitation extreme indices, and then the indices were regridded onto the HadEX2 grid size. Because only data from 1961 to 2007 were selected for APHRODITE, and because relatively small quantities of data are available prior to 1961 among all of the observational data sets, we used the period from 1961 to 2007 to analyze the climatology and area-averaged trends of the 3 observational data sets and CMIP5 models. HadEX2, APHDEX and ADEX were also masked in each data set grid box; therefore, all data sets had the same grids before the average trend and climatology were calculated. However, the Asian continent covers a large area from low to high latitudes, and the long-term changes and variability in precipitation extremes often vary regionally. Therefore, to conduct an in-depth analysis, Asia was divided into 3 regions (Fig. 1), namely, a low-latitude region (5–25° N, 87.5–125° E), a mid-latitude region (25–40° N, 65–143.75° E) and a high-latitude region (40–57.5° N, 50–147.5° E).

2.3. Model simulations

The ETCCDI indices from the CMIP5 simulations (Taylor et al. 2012) are based on the results of Sillmann et al. (2013a,b) for historical simulations and the simulation of representative concentration pathways (RCPs). The precipitation extreme indices, which were not available, were performed using the software used in Sillmann et al. (2013a,b). Seventeen models (with each model having at least 3 runs, a total of 82 simulations) for all historical forcing experiments were used in this study (Table 2). Because most of these simulations end at 2005, but ADEX has the longest end year at 2012, RCP4.5 (an emissions scenario for which the radiative forcing value in the year 2100 is about 4.5 W m^{-2} above the pre-industrial value) simulations were used to extend these histori-

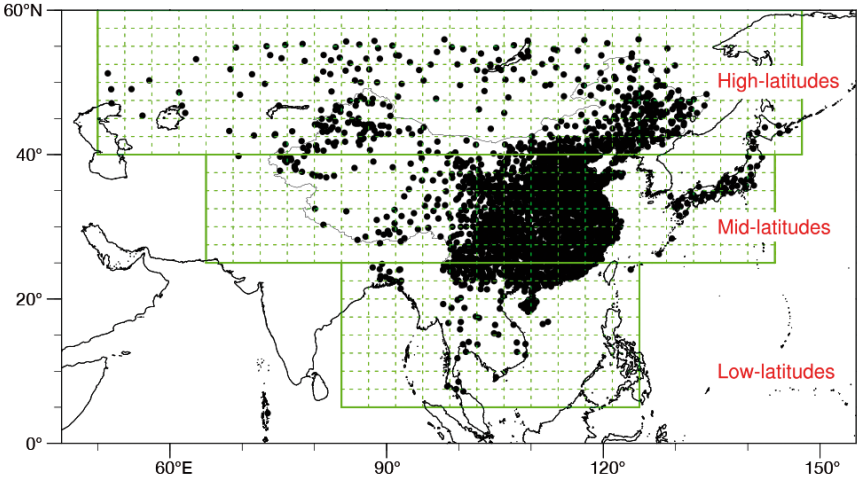

Fig. 1. Map of the station locations (black dots) and the 3 sub-regions used in the analyses. Regional boundaries are marked by green lines: low-latitude region (5–25° N, 87.5–125° E); mid-latitude region (25–40° N, 65–143.75° E); and high-latitude region (40–57.5° N, 50–147.5° E)

cal simulation data to 2012. For the purpose of evaluating the different-resolution models, all model data were interpolated onto 2.5 × 3.75° (latitude × longitude) grids (i.e. the HadEX2 grid size), and the ensemble mean multi-model values were obtained using the equally weighted arithmetic mean values of all members for each model. Table 2 depicts the institutions and the related model components of these models. Prior to regional averaging, the model simulation data were masked with 3 observational data sets to mimic the simultaneously available observational data (with each year of model data corresponding to each year of the 3 observational data sets if the 3 observational data sets all had existing values). Similar to the processing of observational data sets, the annual precipitation extreme indices were computed in each grid in the models.

2.4. Model performance metrics

We used indices of annual precipitation extremes in all 3 observational data sets and in the CMIP5 models. Accordingly, the linear least square regression method was used to analyze the corresponding trends.

To analyze the performance metrics of the various indices and models, the different model performances were assessed with the climatological root mean square errors (RMSEs) (Sheffield et al. 2013, IPCC 2013, Sillmann et al. 2013a, Dong et al. 2015), which are similar to those applied by Gleckler et al. (2008). The model simulation results and precipitation extreme indices were assessed and compared with 3 observational data sets (ADEX, HadEX2 and APHDEX). In this analysis, RMSEs were calculated for the annual mean values of the indices of precipitation extremes over all of Asia and its 3 sub-regions. The RMSE was calculated as follows:

$$\mathrm{RMSE} = \sqrt{(X-Y)^2} \quad (1)$$

where X represents the model climatology of the precipitation extreme index, and Y is the corresponding observational precipitation extreme.

All model RMSEs were then used to calculate the relative model error (RMSE′) for each model defined as:

$$\mathrm{RMSE}' = (\mathrm{RMSE} - \mathrm{RMSE}_{\mathrm{median}}) / \mathrm{RMSE}_{\mathrm{median}} \quad (2)$$

where $\mathrm{RMSE}_{\mathrm{median}}$ is the median of the RMSEs for the 17 climate models.

Table 2. Details of the 17 CMIP5 climate models

Model name	Institution (or group)	Resolution (grids in longitude by latitude unit: degree)
BCC-csm1-1	Beijing Climate Center, China Meteorological Administration	128 × 64
BCC-csm1-1-m	Beijing Climate Center, China Meteorological Administration	128 × 64
CanESM2	Canadian Centre for Climate Modelling and Analysis	128 × 64
CNRM-CM5	Centre National de Recherches Météorologiques / Centre Européen de Recherche et Formation Avancées en Calcul Scientifique	256 × 128
CSIRO-Mk3-6-0	CSIRO-QCCCE	192 × 96
FGOALS-s2	LASG-CESS	128 × 60
HadCM3	Geophysical Fluid Dynamics Laboratory	96 × 73
GISS-E2-R	NASA Goddard Institute for Space Studies	180 × 72
IPSL-CM5A-LR	L'Institut Pierre-Simon Laplace	96 × 96
IPSL-CM5A-MR	L'Institut Pierre-Simon Laplace	144 × 143
MIROC4h	Atmosphere and Ocean Research Institute (University of Tokyo), National Institute for Environmental Studies, and Japan Agency for Marine-Earth Science and Technology	640 × 320
MIROC5	Atmosphere and Ocean Research Institute (University of Tokyo), National Institute for Environmental Studies, and Japan Agency for Marine-Earth Science and Technology	256 × 128
MIROC-ESM	Japan Agency for Marine-Earth Science and Technology, Atmosphere and Ocean Research Institute (University of Tokyo), and National Institute for Environmental Studies	128 × 64
MPI-ESM-LR	Max Planck Institute for Meteorology (MPI-M)	192 × 96
MPI-ESM-MR	Max Planck Institute for Meteorology (MPI-M)	192 × 96
MRI-CGCM3	Meteorological Research Institute	320 × 160
NorESM1-M	Norwegian Climate Centre	144 × 96

The median value was chosen to avoid the influences of large model errors on the results. For example, a negative relative error indicates that the model RMSE should be smaller than $RMSE_{median}$. Similar to Gleckler et al. (2008), normalizing the RMSE results is an effective way to compare a model's performance with that of another model. Accordingly, the performance of each model was assessed with respect to the 3 observational data sets (ADEX, HadEX2 and APHDEX) in the common period of 1961–2007.

The Taylor diagram (Taylor 2001) is generally used to summarize the different indices of ensemble mean model simulations for the purpose of evaluating the performances of the extreme indices. This diagram is used to compare the simulation performances of different precipitation extreme indices in 2 regards, namely, the spatial correlation coefficient and the spatial standard deviation (SD) ratio, with observational precipitation extreme indices. Each number corresponds to the performance of each precipitation extreme index with regard to its ensemble mean simulation. Angular and radial coordinates, respectively, represent the range of the correlation and the normalized SD (Gleckler et al. 2008), allowing the model simulations among the different indices to be displayed over Asia and its different sub-regions.

3. RESULTS

3.1. Regional average climatologies

Regional climatologies were computed for the observational data sets and model simulations over the period of 1961–2007, which is available for all of the data sets. The 3 data sets and the CMIP5 models were masked, and thus we used the same grids for the analysis. The average precipitation extreme indices during 1961–2007 over Asia and its sub-regions were computed for the CMIP5 models and the 3 observational data sets. The temporal averages of these indices over Asia and its sub-regions are shown in box-and-whisker plots (Fig. 2).

Over all of Asia and its sub-regions, ADEX and HadEX2 generally have similar values, and APHDEX has lower values than both ADEX and HadEX2 except with regard to CWD. ADEX and HadEX2 generally lie within the model spread except for Rx1day, SDII and the 2 duration indices; observational Rx1day, SDII and CDD exhibit the higher end of the simulated values while CWD exhibits the lower end of the simulated values. The model simulations display an excessive number of wet days (i.e. high CWD

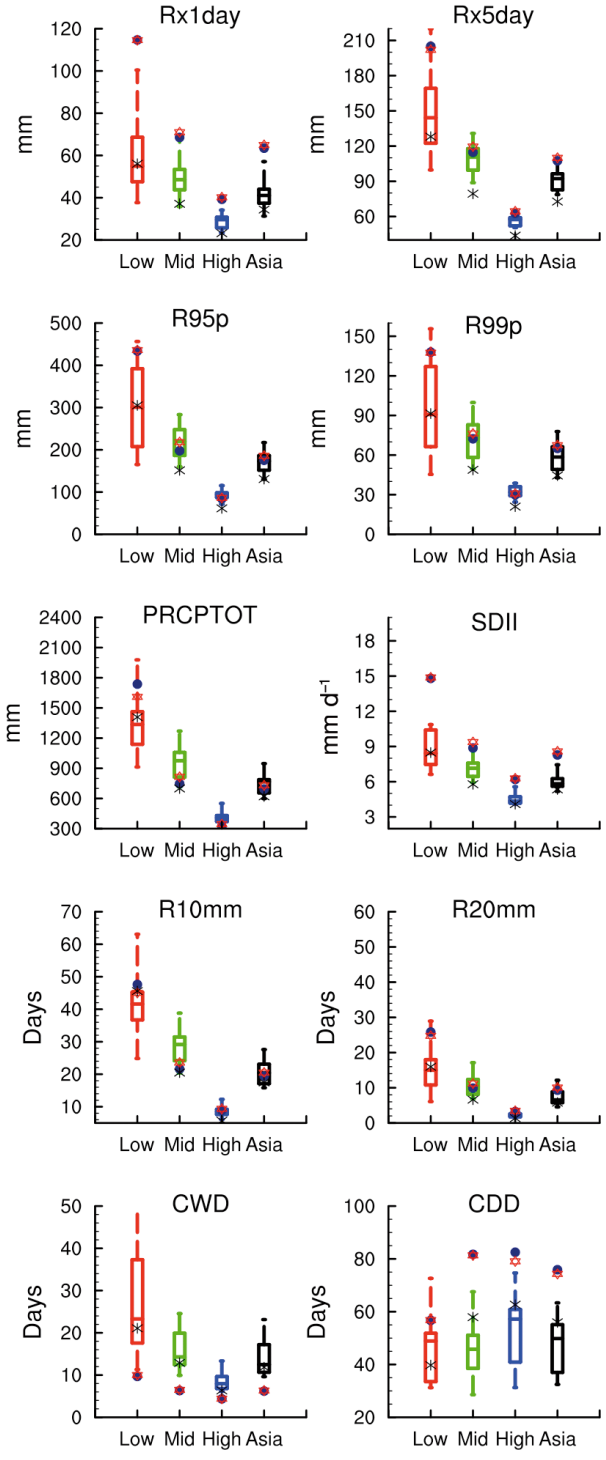

Fig. 2. Box-and-whisker plots of the extreme precipitation indices (see Table 1) calculated from the 17 CMIP5 models. Boxes: interquartile model spread (range between the 25th and 75th quantiles); midline: multi-model median; whiskers: total intermodal range during the period of 1961–2007. Black, blue, green and red: area averages over Asia and its 3 sub-regions, namely, the high-, mid- and low-latitude regions, respectively. Blue dots: ADEX; red asterisks: HadEX2; black crosses: APHDEX

values) compared with the 2 observational data sets (HadEX2 and ADEX), while the model simulations generally underestimate Rx1day, Rx5day, CDD and SDII in Asia and its sub-regions. These findings agree well with previous studies that have shown this effect on a global scale (Sillmann et al. 2013a, Alexander & Arblaster 2017). Over Asia and in the mid- and high-latitude regions, the model median values in the 2 observational data sets (ADEX and HadEX2) show slightly different performances.

The differences between the simulations and observational data sets are quite large in the low-latitude region. APHDEX shows a lower mean value than the other data sets that is closer to the median of the CMIP5 simulations, which may be associated with the low station coverage, the order of operations or the gridding method (Avila et al. 2015, Herold et al. 2016); that is, HadEX2 and ADEX calculate the indices for each station and then map them onto the grids, while APHDEX was calculated on each grid at a 1 × 1° resolution and was then interpolated on the coarser grid (2.5 × 3.75°). When the data sets are changed, the intensity indices are more sensitive to the observations in Asia and the sub-regions, and the intensity indices (e.g. Rx1day and Rx5day) are more sensitive to the change in the data sets than the frequency indices (R10mm and R20mm).

The CMIP5 models also showed large uncertainties at low latitudes, which may be explained by the large climate difference in the models at low latitudes (O'Gorman & Schneider 2009, Toreti et al. 2013). Low-intensity rainfall is simulated too frequently, while high-intensity rainfall is simulated too infrequently (Sillmann et al. 2013a). The simulated PRCPTOT, R10mm and CWD values in the mid-latitude region are all higher than those in HadEX2 and ADEX. Thus, we believe that the simulations yield a greater total precipitation in the mid-latitude region, mainly due to the contribution from low-frequency light precipitation.

The spatial patterns of CMIP5 ensemble mean and observational precipitation extreme indices (i.e. ADEX, HadEX2 and APHDEX) for the period 1961–2007 are shown in Fig. 3. The features of the spatial patterns in the 10 simulated precipitation extreme indices are similar to the observational precipitation extremes; the values for each index except for CDD are higher in Southeast China and lower in Northwest Asia. However, there are some differences between the simulations and observations, particularly for Southeast China, where the ensemble mean simulation shows lower Rx1day, Rx5day, R99p, SDII and CDD values and higher CWD values than either ADEX or HadEX2. Most of the indices in APHDEX are lower than those in the other 2 observational data sets, and the patterns of Rx1day, Rx5day, R99p and SDII are closer to the ensemble mean. Moreover, the number of grids in HadEX2 is less than that in either ADEX or APHDEX, especially for Rx1day, Rx5day, R95p and R99p. In addition, ADEX and APHDEX include many more precipitation stations in the Himalayas and Mongolia, and thus they have a greater spatial coverage than HadEX2.

The Taylor diagrams for the simulated precipitation extreme indices over Asia and its sub-regions during the period 1961–2007 are shown in Fig. 4. Generally, large index values are spread out over Asia and its different sub-regions. The correlations among the absolute intensity indices, relative intensity indices and SDII are higher than those among PRCPTOT, the frequency indices, the duration indices throughout Asia and the mid- and high-latitude regions. The ensemble mean simulation showed higher correlation values in HadEX2 than in ADEX and APHDEX that were closer to the reference values over Asia and most sub-regions for PRCPTOT and the frequency indices; thus, the simulated PRCPTOT and the frequency indices showed better performances in HadEX2 than in ADEX and APHDEX. Accordingly, the angular-distance weighting methodology may lead to a better performance and a higher correlation in HadEX2 with regard to R10mm, R20mm and PRCPTOT in the mid-latitude region. In the high-latitude region, the SDs of the ensemble mean simulations of Rx5day and R20mm show better performances in ADEX than in HadEX2. Moreover, the SDs of APHDEX for most indices except for CDD are larger than those of HadEX2 and ADEX, which are further from the reference values over all of Asia and its sub-regions.

Our results indicate that ADEX and HadEX2 are more similar, while APHDEX shows lower values than the other observational data sets in all indices except for the 2 duration indices. No substantial differences were found between the mean values of ADEX and HadEX2; most of the indices in the 2 observational data sets displayed small differences over Asia and its sub-regions. The values of Rx5day in addition to those of the relative intensity indices and frequency indices in ADEX and HADEX2 are closer to the model median values in the mid- and high-latitude regions. Large differences at low latitudes lead to larger deviations and lower APHDEX values than in the other 2 observational data sets; as a consequence, all of the indices in APHDEX are closer to the model median values at low latitudes, and the same holds for the duration indices over Asia and all

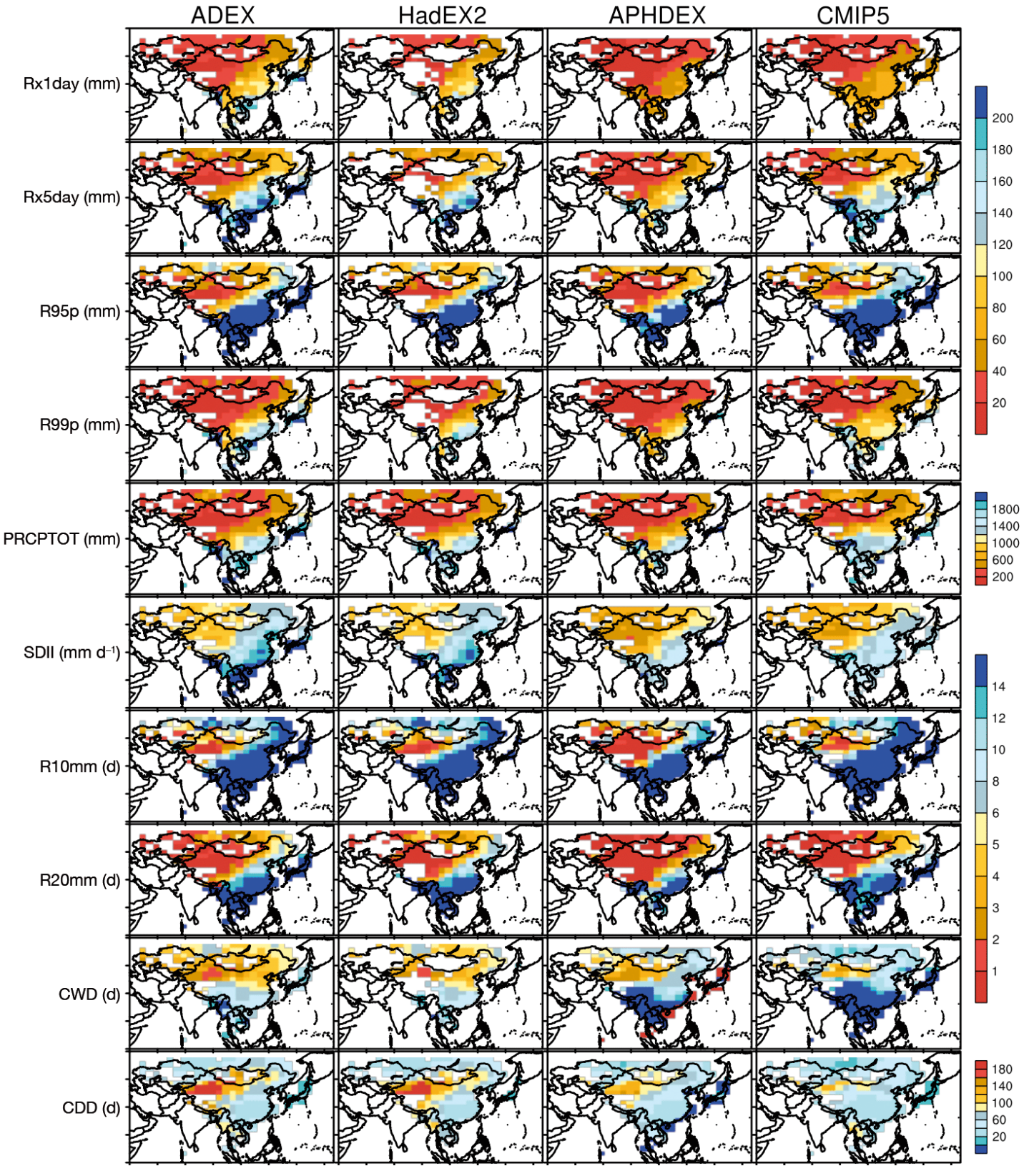

Fig. 3. Spatial distribution of the average values of the annual extreme precipitation indices (see Table 1) during 1961–2007 in the observational data sets (ADEX, HadEX2 and APHDEX) and the model-simulated ensemble mean (CMIP5). HadEX2, APHDEX and CMIP5 were masked by ADEX

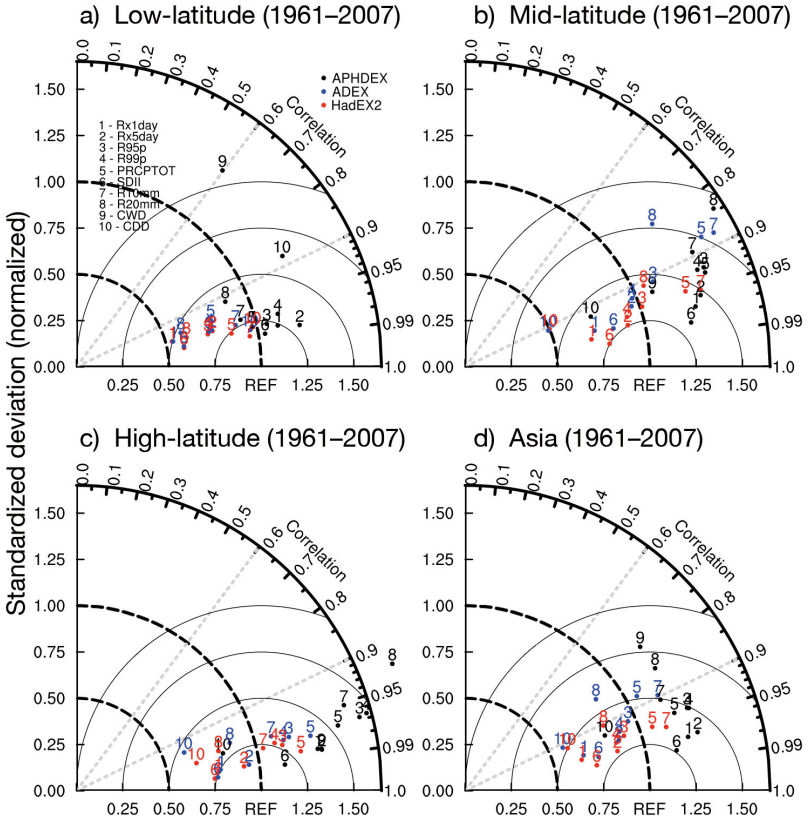

Fig. 4. Taylor diagrams of the CMIP5 ensemble mean in different regions (1961–2007): (a) low-latitude region; (b) mid-latitude region; (c) high-latitude region; and (d) all of Asia. The red dot represents the ensemble mean simulation for 10 indices compared with HadEX2, while the blue dot represents the comparison with ADEX and the black dot represents the comparison with APHDEX

of its sub-regions. The differences between the simulations and observational data sets are quite large in the low-latitude region. The intensity indices (i.e. Rx1day and Rx5day) are thus more sensitive to the data sets than the frequency indices (R10mm and R20mm).

3.2. Trends over Asia and its sub-regions

Fig. 5 shows the temporal evolution of the 10 precipitation extreme anomalies from the 3 data sets and 17 CMIP5 models (82 simulations) over all of Asia. The ADEX, HadEX2 and APHDEX data sets have different time periods of 1958–2012, 1958–2010 and 1961–2007, respectively. All of the anomalies in these data sets are relative to the base period of 1961–1990. Three of the observational data sets were masked to mimic the availability of shorter period observations over time and space when the period of one observation was shorter than another; only the CMIP5 model was masked by ADEX. Fig. 5 shows that the time series of HadEX2 and ADEX are similar, but there are some notable differences, primarily in Rx1day, Rx5day, R95p and R99p during 2001–2009, indicating that these extremes in HadEX2 have greater precipitation extremes than those in ADEX, especially at low latitudes (Figs. S1–S3 in the Supplement at www.int-res.com/articles/suppl/c076p161_supp.pdf). Observational precipitation indices generally have large variability in most cases, but CWD is an exception. The reason for this may be that the model simulations obtain higher CWD values (i.e. more wet days) than are observed, and thus the simulations output higher anomaly values. Some years of the observational range lie outside of the CMIP5 model simulations for most of the indices (Collins et al. 2013).

When the HadEX2 station data set (in which only public data were calculated, meaning that China was not included) was used to calculate each grid similar to the gridding method in ADEX, the differences between the results using this method and those in HadEX2 were small (Figs. S4–S7), except for those at low latitudes, and were large for Rx1day and Rx5day. Two approaches were used with the APHRODITE data set to calculate the annual gridded precipitation extreme indices: one interpolated the daily precipitation station data to the HadEX2 grid size before calculating the annual precipitation extreme indices at each grid; the other calculated the annual precipitation extreme indices in 1 × 1° grids and then interpolated those grids to the HadEX2 grid size. Consequently, most of the indices in APHRODITE showed large variations between the 2 approaches at low latitudes (Figs. S8–S11). Therefore, a high spread, which has been shown to increase variance (Herold et al. 2016), tends to occur in areas with a low station density, especially at low latitudes. When the station network is sparse, the availability of an insufficient spatial coverage of daily observation stations will lead to a large bias in the gridding method, and the operational order of the methodology will have the most notable impact on the high-intensity rainfall (Rx1day and Rx5day).

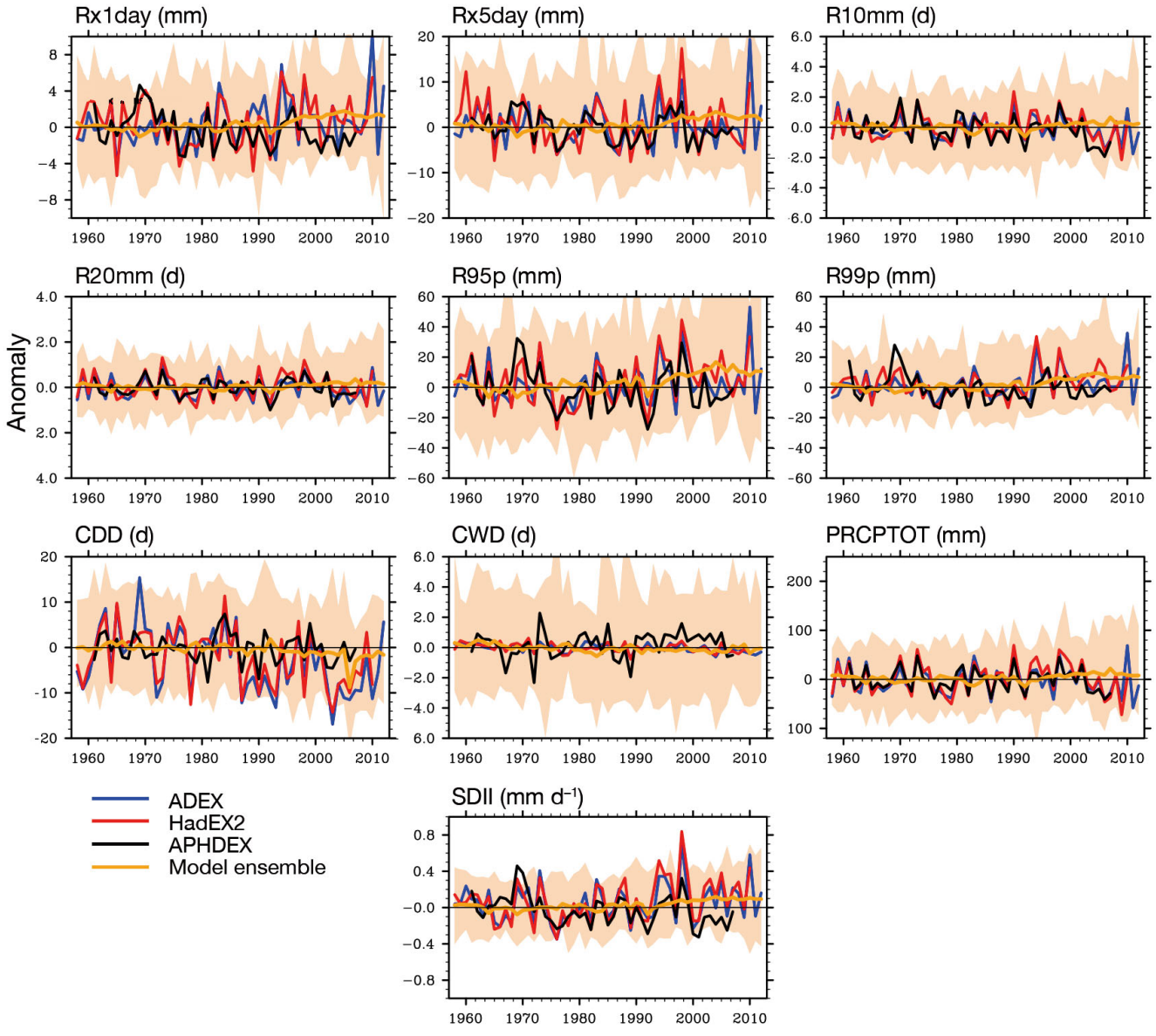

Fig. 5. Time series of mean regional average anomalies (relative to 1961–1990) for the precipitation extremes in the observations (blue lines: ADEX, 1958–2012; red lines: HadEX2, 1958–2010; black lines: APHDEX, 1961–2007) and the model simulations (1958–2012). Orange lines: multi-model ensemble means in the CMIP5 simulations

The mean linear regression slope for the model simulations and the 3 observational data sets over Asia and its sub-regions during 1961–2007 are shown in Fig. 6. The values in APHDEX are lower than those in ADEX and HadEX2 for most indices over Asia and the mid- and high-latitude regions, except for the duration indices. The results in ADEX and HadEX2 are more similar for SDII, R10mm, R20mm and CWD in the mid- and high-latitude regions. These results indicate that the simulated precipitation extreme trend is too strong in Rx5day, R95p, PRCPTOT and CDD over Asia, and the simulated SDII, R10mm, R20mm and CWD are closer to those in the 2 observational data sets (ADEX and HadEX2) in the mid- and high-latitude regions. Except for the duration indices, positive trends over Asia and its mid- and high-latitude regions were simulated by the climate models, but the absolute intensity (Rx1day and Rx5day), R10mm and PRCPTOT were significantly overestimated in most of the regions and over all of Asia.

The ADEX and APHDEX trends are generally lower than those of HadEX2 at low latitudes, where the uncertainties in the observational intensity

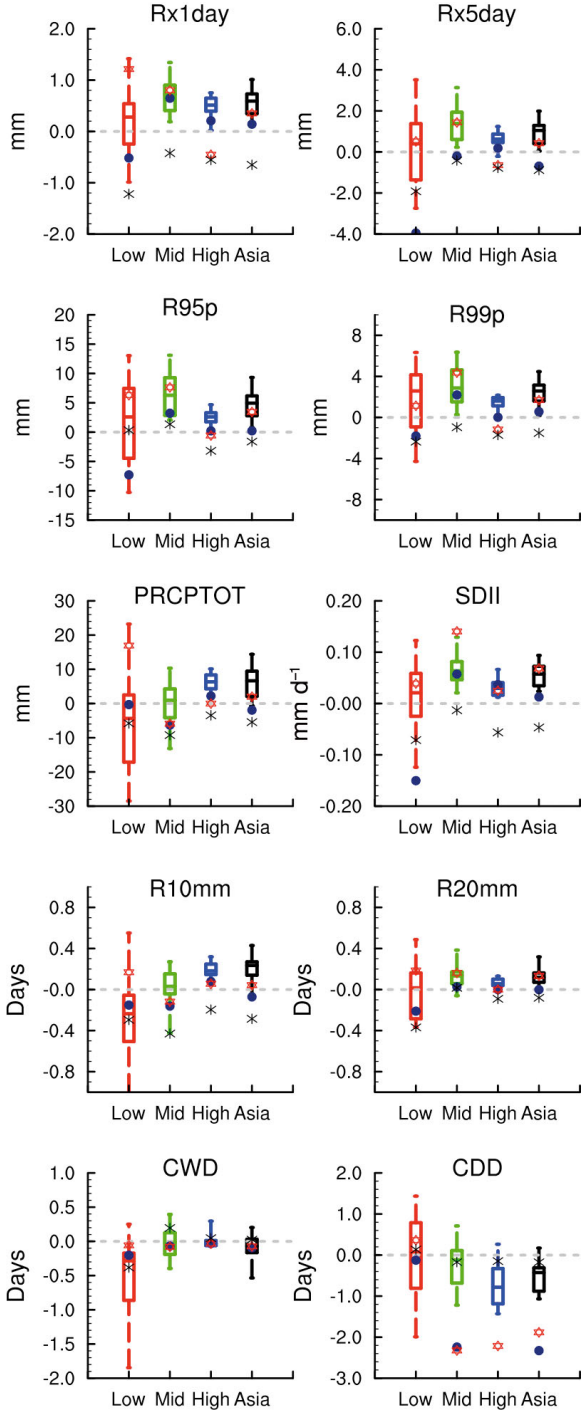

Fig. 6. Same as Fig. 2 but for the linear decadal trends in the precipitation extreme indices

indices are larger than those in the duration indices and frequency indices, and the intensity indices are more sensitive to the observational data sets. For all indices except the duration indices in the low-latitude region, a larger discrepancy is observed for the trend of the precipitation extreme indices among the 3 observational data sets, and 3 data sets do not agree on the positive/negative trends, except for CWD.

Over all of Asia, the trends of the model medians of most indices are closer to HadEX2 than either ADEX or APHDEX. The value of CDD in APHDEX is closer to the model median than that in the other 2 data sets. In the low-latitude region, ADEX is closer to the precipitation extreme of the model median than HadEX2 or APHDEX for Rx1day and CWD, and the values of R95p, PRCPTOT, R10mm and CDD are closer to the model median in APHDEX than in the other 2 observational data sets. In the mid-latitude region, the values of R99p, SDII and CDD in ADEX are closer to the model median simulation than HadEX2, while the values of Rx5day, R95p and R10mm in HadEX2 are closer to the model median value, and only CDD in APHDEX is closer to the model median value. In the high-latitude region, all of the intensity indices in ADEX are closer to the model median than HadEX2.

Fig. 7 shows the pattern of the linear regression slope for the CMIP5 model ensemble mean and the observational data sets (ADEX, HadEX2 and APHDEX) during 1961–2007. Compared with the temperature extremes, the changes in the precipitation extremes are generally more spatially complex at large scales, and their trends are largely less significant at the local scale (Donat et al. 2013). The ensemble mean showed an overestimation of the trend of most precipitation extremes compared with the observations over all of Asian and in the mid- and high-latitude regions. Most of the observational precipitation extremes are similar to the negative trends in a southwest–northeast belt from Southwest China to Northeast China, as Zhou et al. (2015) reported, and the changes in the observational precipitation extreme indices exhibit greater spatial heterogeneity than the model ensemble mean. The model mean failed to capture this characteristic in the intensity indices and did not capture the negative trends in Northeast China or the positive trend in Southeast China for PRCPTOT, R10mm, R20mm and CWD.

Our results indicate that the values of most indices (except the duration indices) in APHDEX are lower than those in ADEX and HadEX2 over Asia and the mid- and high-latitude regions. APHDEX is farther from the model median than the other 2 observational data sets, except some indices at low latitudes. The trends of ADEX and HadEX2 have some discrepancies over Asia and its sub-regions. Most of the simulated intensity index trends in ADEX show a better performance than those in HadEX2 in the high-lat-

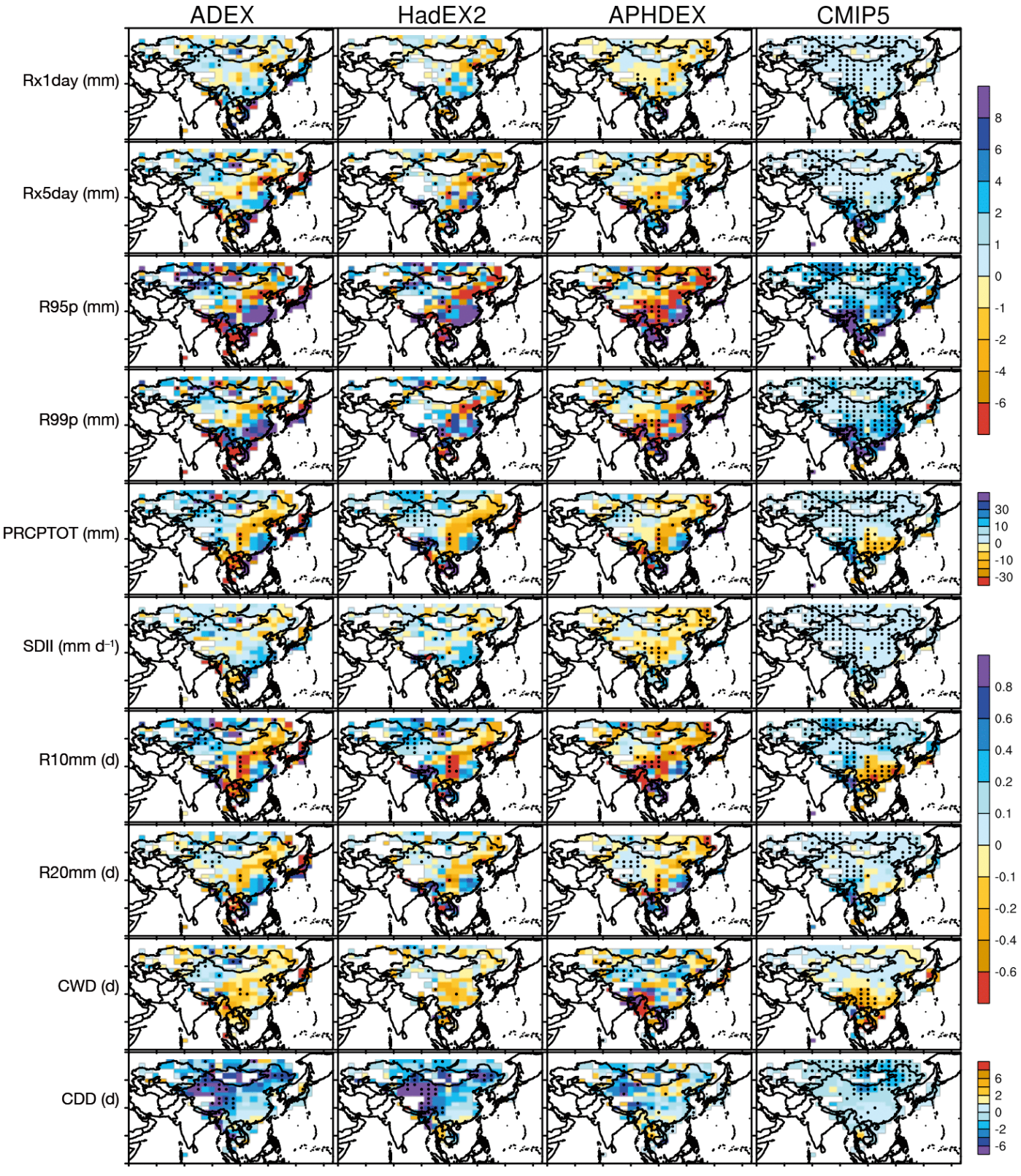

Fig. 7. Spatial distribution of the linear trend of the annual extreme precipitation indices during 1961–2007 in the observations (ADEX, HadEX2 and APHDEX) and model-simulated ensemble mean (CMIP5). Black dots indicate where the trends are significant at the 5% confidence level. HadEX2, APHDEX and CMIP5 were masked by ADEX

itude region, that is, the model simulations appear to agree better with the trends in ADEX than with those in HadEX2 with regard to the precipitation intensity indices in the high-latitude region, while the simulated trends of most indices in HadEX2 show a better performance than those in ADEX over all of Asia. Only CDD in APHDEX is closer to the model median over Asia and in the mid- and high-latitude regions. At low latitudes, the uncertainties in the intensity indices among the 3 observational data sets and the model simulations are large.

3.3. Metrics of the model performance ranking

The RMSE′ values of the different mean precipitation extreme indices in ADEX, HadEX2 and APHDEX over Asia and its sub-regions during the period of 1961–2007 are shown in Fig. 8. An obvious feature is that the ensemble mean values are generally in better agreement with the observations than the typical model due to the offset of systematic errors in the individual models in addition to a high smoothing frequency and a smaller scale (Gleckler et al. 2008). This has been noted in other multi-model comparison studies (IPCC 2013, Dong et al. 2015), but the range of the different indices and models is more pronounced for the precipitation extremes here.

However, no one model is superior or inferior to another model in every respect. For example, MROC4h obtains higher scores in the low-latitude region but does not stand out elsewhere. Most indices are effectively simulated by some models, particularly in MRI-CGCM3. Moreover, higher-resolution models generally do not show better performances with regard to precipitation extreme indices

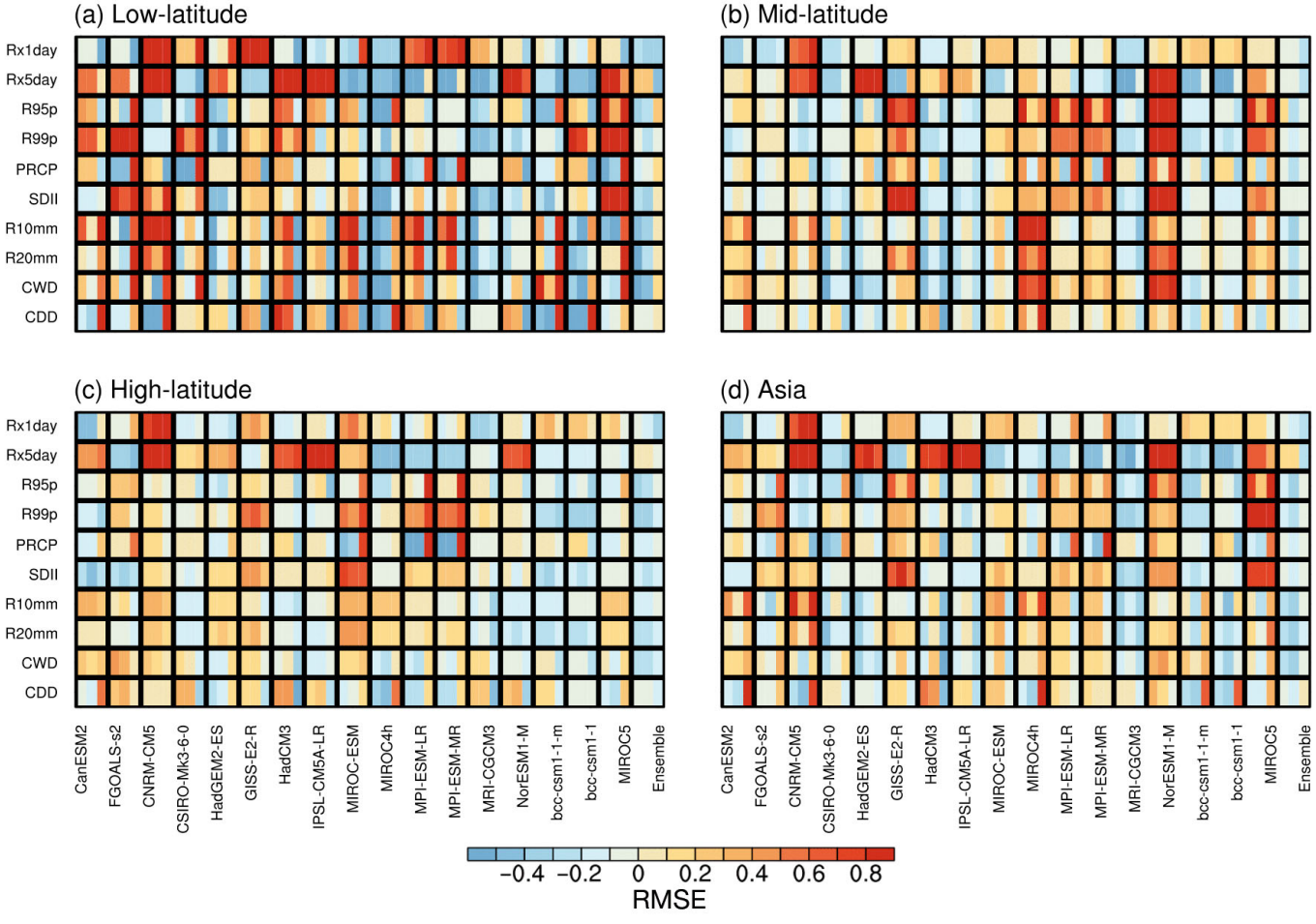

Fig. 8. Performances of the relative spatial mean root mean square errors (RMSEs) over Asia in the period of 1961–2007 in the climatologies of the extreme precipitation indices (column headings; see Table 1 for definitions) simulated by the 17 CMIP5 models (row headings; see Table 2 for further details) with respect to ADEX (left rectangle within each grid square), HadEX2 (middle rectangle) and APHDEX (right rectangle). (a) Low-latitude region; (b) mid-latitude region; (c) high-latitude region; and (d) all of Asia

than lower-resolution models (Sillmann et al. 2013a). The multi-model ensemble mean errors in ADEX and HadEX2 over Asia and its sub-regions are larger in Rx5day than in the other indices. The multi-model ensemble mean errors in most of the intensity and frequency indices exhibit small differences compared with the 3 observational data sets. The simulation ensemble mean showed better performances in ADEX and HadEX2 than in APHDEX for most of the indices over Asia and its sub-regions. For the construction of the frequency indices, the multi-model ensemble mean in ADEX and HadEX2 generally showed good performances over Asia and its sub-regions and RMSE′ values smaller than the intensity indices. The simulation mean RMSE′ in APHDEX showed the best performance among the 3 observational data sets over Asia and its sub-regions only for Rx1day and Rx5day. Meanwhile, the simulated RMSE′ in APHDEX achieved better performances at mid- and high latitudes than at low latitudes.

4. DISCUSSION AND CONCLUSIONS

This work comprehensively compared the CMIP5 models with 3 observational data sets (ADEX, HadEX2 and APHDEX) using 10 precipitation extreme indices over Asia and its different latitudinal regions. The differences in the precipitation extreme indices in the 3 observational data sets over Asia were assessed, and we also investigated whether the new observational data set (ADEX) can be utilized for extreme Asian precipitation studies.

We found that the model evaluation of extreme precipitation can be particularly affected by different data sets. Although APHDEX has a higher grid resolution than HadEX2, APHDEX may not be appropriate for evaluating Asian precipitation extremes in the CMIP5 model. Herold et al. (2017) demonstrated that the inter-product observational sensitivity is prominent at resolutions of 1 × 1° or finer; thus, differences would be amplified when evaluating precipitation extremes. Moreover, APHRODITE data have obvious deviations from HadEX2 and ADEX data in describing the climatology and the long-term changes in the precipitation frequency, intensity and duration (Han & Zhou 2012, Yin et al. 2015). In addition, ADEX and HadEX2 also exhibit higher precipitation extreme values than APHDEX, except for the duration. The *in situ* data quality, the spatial and temporal coverage of the station network, and the operational order and interpolation methods are all important factors that cause uncertainties in observational data sets (Donat et al. 2014, Avila et al. 2015). This may lead to a spread in the precipitation extremes, thereby impacting the model evaluation. We also found discrepancies between the 3 observational data sets with regard to the spatial grid coverage. The difference in the spatial grid coverage between ADEX and HadEX2 is not consistent, and it depends greatly on the selected indices. For HadEX2, the spatial station coverage is not sufficient to detect actual changes in precipitation extremes (Donat et al. 2013), particularly with regard to Rx1day and Rx5day in this study. In contrast, ADEX has higher spatial grid/station coverage and provides more detailed information about climate extremes in Asia.

The time series in various data sets become increasingly noisy (and changes are often less significant) at low latitudes, while large internal climate variability is also found in the climate model simulations at low latitudes. The differences in most observational precipitation extreme indices are large at low latitudes, which is not encouraging. Furthermore, some authors have suggested that the uncertainties in the sensitivities of precipitation extremes to warming may be higher at low latitudes (O'Gorman 2015). In addition, the uncertainties in observational precipitation extreme indices (especially for Rx1day and SDII) are generally larger in the low-latitude region than in other regions. This may be explained by the low station coverage, different operational orders and different interpolation methods that mainly lead to these large uncertainties at low latitudes; low station coverage can be an important factor that leads to large differences. This study also confirms that the intensity indices (e.g. Rx1day and Rx5day) can be very sensitive to various observational data sets, while the frequency indices (R10mm and R20mm) are relatively insensitive to the different observational data sets.

There is also a large span in the different models at low latitudes that may be associated with the larger interquartile model spread and the different climate sensitivities of the models, in addition to positive regional land–atmosphere feedback processes (Toreti et al. 2013). Although the CMIP5 ensemble mean captured most of the spatial distribution of observed precipitation extremes during 1961–2007, the CMIP5 ensemble showed lower values for some intensity indices and higher values for CWD. Therefore, CMIP5 still underestimates the precipitation intensity and overestimates wet days in ADEX over Asia, as Sillmann et al. (2013a) and Alexander & Arblaster (2017) noted in HadEX2. Furthermore, observational trends in precipitation extremes exhibit more spatial

heterogeneity than the model ensemble mean. It is difficult for the model mean to capture the negative trends in Northeast China and the positive trend in Southeast China in some indices. Patterns in precipitation extremes can vary significantly in ADEX and HadEX2 given the topography (especially in the Himalayan Plateau) and the contrast between coastal areas and in-land areas at mid-latitudes, but topographic corrections are not performed in APHDEX. Large variations in precipitation extremes occur over small spatial scales, i.e. coastal locations and mountainous areas. Therefore, the coarse resolution of CMIP5 may not be suitable for capturing observation patterns, although this situation may be improved in CMIP6.

Some researchers have shown a global increase in the precipitation extreme intensity and frequency in HadEX2 (Alexander et al. 2006, Donat et al. 2013). This study similarly showed this pattern for most of the observational intensity and frequency indices over Asia. The models generally captured some of the trends in spatial patterns of the precipitation extremes over Asia; however, local changes are spatially more variable. The large uncertainties in the observations in our paper make the evaluation of model trend rather different (Sylla et al. 2013), especially at low latitudes. Over Asia and its sub-regions, the trends of some indices in ADEX in the mid-latitude region are similar to some researchers' results in China (Zhou et al. 2016). The differences in the trends between the observational data and the simulation uncertainties can also be quite large in the low-latitude region (e.g. the mean values). HadEX2 might be more appropriate for comparing trends in Asia, but the ADEX trend appears to agree better with the model-simulated trends than HadEX2 with regard to the frequency indices in the low-latitude region and the precipitation extreme intensity indices in the high-latitude region. We found that ADEX does not show a significant change compared with HadEX2 in the mid-latitude region, which may be explained by the ADW interpolation method, which involves the spatial correlation of the station data and minimizes the impact of data quality issues at individual stations upon averaging. HadEX2, which is likely more representative of point-based estimates of extremes, has relatively few observations (Donat et al. 2013). Moreover, HadEX2 has the smallest amount of station data in China among the 3 observational data sets, and it does not improve the results a great deal compared with ADEX. APHRODITE has >700 stations in China, but this observational data set has a substantially larger bias than either ADEX or HadEX2. The trend of HadEX2 in the western mid-latitudes was higher than that of ADEX, where the low station coverage led to a positive trend in HadEX2 in the mid-latitude region. In the future, improving the station coverage in the western mid-latitudes will be very important for Asian observations.

Additionally, the ensemble mean showed good performance in reproducing the trends of the precipitation extreme indices in ADEX in the high-latitude region; nevertheless, this observational data set may be suitable for detecting and attributing precipitation extremes, especially in high-latitude regions (Wan et al. 2015). Some observational data showed opposite trends compared with the CMIP5 models; this may make it difficult to detect and attribute precipitation extreme changes in some indices. We should also ensure that uncertainties in the observations are well understood depending on the observational data set we have chosen both for the region and for the indices employed for the detection and attribution. It is also important to apply new observational data sets that have quality control processes and high temporal and spatial resolutions (e.g. ADEX) to better understand precipitation extreme variations over Asia.

Acknowledgements. The International Workshop on Climate Data Requirements and Applications held in Nanjing, China, 4–8 March 2013, was jointly funded by the World Meteorological Organization and the China Meteorological Administration. We thank the workshop participants from the different Asian countries (i.e. the Asian region) for providing daily data and computing the indices during and after the Nanjing Workshop. S.D. and Y.S. are supported by the National Key R&D Program of China (2018YFA0605604), the National Science Foundation of China (41675074) and Climate Change Project CCSF201805.

LITERATURE CITED

Alexander LV, Zhang X, Peterson TC, Caesar J and others (2006) Global observed changes in daily climate extremes of temperature and precipitation. J Geophys Res 111:D05109

Alexander LV (2016) Global observed long-term changes in temperature and precipitation extremes: a review of progress and limitations in IPCC assessments and beyond. Weather Clim Extrem 11:4–16

Alexander LV, Arblaster JM (2017) Historical and projected trends in temperature and precipitation extremes in Australia in observations and CMIP5. Weather Clim Extrem 15:34–56

Avila FB, Dong S, Menang KP, Rajczak J, Renom M, Donat MG, Alexander LV (2015) Systematic investigation of gridding-related scaling effects on annual statistics of daily temperature and precipitation maxima: a case study for south-east Australia. Weather Clim Extrem 9:6–16

Cao L, Zhu Y, Tang G, Yan Z (2016) Climatic warming in

China according to a homogenized data set from 2419 stations. Int J Climatol 36:4384–4392
Collins M, AchutaRao K, Ashok K, Bhandari S and others (2013) Observational challenges in evaluating climate models. Nat Clim Chang 3:940–941
Donat MG, Alexander LV, Yang H, Durre I and others (2013) Updated analyses of temperature and precipitation extreme indices since the beginning of the twentieth century: the HadEX2 dataset. J Geophys Res Atmos 118: 2098–2118
Donat MG, Sillmann J, Wild S, Alexander LV, Lippmann T, Zwiers F (2014) Consistency of temperature and precipitation extremes across various global gridded *in situ* and reanalysis datasets. J Clim 27:5019–5035
Dong SY, Xu Y, Zhou BT, Shi Y (2015) Assessment of indices of temperature extremes simulated by multiple CMIP5 models over China. Adv Atmos Sci 32:1077–1091
Dong S, Sun Y, Aguilar E, Zhang X, Peterson TC, Song L, Zhang Y (2018) Observed changes in temperature extremes over Asia and their attribution. Clim Dyn 51: 339–353
Fischer EM, Knutti R (2015) Anthropogenic contribution to global occurrence of heavy-precipitation and high-temperature extremes. Nat Clim Chang 5:560–564
Freychet N, Hsu HH, Wu CH (2016) Extreme precipitation events over East Asia: evaluating the CMIP5 mode atmospheric hazards. Atmospheric hazards: case studies in modeling, communication, and societal impacts. ExLi4EvA, p 87–109
Gleckler PJ, Taylor KE, Doutriaux C (2008) Performance metrics for climate models. J Geophys Res 113:D06104
Han ZY, Zhou TJ (2012) Assessing the quality of APHRODITE high-resolution daily precipitation datasets over contiguous China. Chin J Atmos Sci 36:361–373 (in Chinese)
Herold N, Alexander LV, Donat MG and others (2016) How much does it rain over land? Geophys Res Lett 43:341–348
Herold N, Behrangi A, Alexander LV (2017) Large uncertainties in observed daily precipitation extremes over land. J Geophys Res Atmos 122:668–681
IPCC (2013) Climate change 2013: the physical science basis. Contribution of Working Group I to the Fifth Assessment Report of the Intergovernmental Panel on Climate Change. Cambridge University Press, Cambridge
IPCC (2014) Climate change 2014: impacts, adaptation, and vulnerability. Part A. Global and Sectoral Aspects. Contribution of Working Group II to the Fifth Assessment Report of the Intergovernmental Panel on Climate Change. Cambridge University Press, Cambridge
Jiang Z, Li W, Xu J and others (2015) Extreme precipitation indices over China in CMIP5 models. I. Model evaluation. J Clim 28:8603–8619
Menne MJ, Durre I, Vose RS and others (2012) An overview of the global historical climatology network-daily database. J Atmos Ocean Technol 29:897–910
Mestre O, Domonkos P, Picard F and others (2013) HOMER: a homogenization software-methods and applications. Quart J Hungarian Meteorol Serv 117:47–67
O'Gorman PA (2015) Precipitation extremes under climate change. Curr Clim Change Rep 1:49–59
O'Gorman PA, Schneider T (2009) The physical basis for increases in precipitation extremes in simulations of 21st-century climate change. Proc Natl Acad Sci USA 106:14773–14777
Ou T, Chen D, Linderholm HW, Jeong JH (2013) Evaluation of global climate models in simulating extreme precipitation in China. Tellus A Dyn Meterol Oceanogr 65:1
Peterson TC, Manton MJ (2008) Monitoring changes in climate extremes: a tale of international collaboration. Bull Am Meteorol Soc 89:1266–1271
Polson D, Hegerl G, Zhang X, Osborn T (2013) Causes of robust seasonal land precipitation changes. J Clim 26: 6679–6697
Sheffield J, Barrett AP, Colle B and others (2013) North American climate in CMIP5 experiments. I. Evaluation of historical simulations of continental and regional climatology. J Clim 26:9209–9245
Sillmann J, Kharin VV, Zhang X, Zwiers FW, Bronaugh D (2013a) Climate extremes indices in the CMIP5 multimodel ensemble. 1. Model evaluation in the present climate. J Geophys Res 118:1716–1733
Sillmann J, Kharin VV, Zwiers FW, Zhang X, Bronaugh D (2013b) Climate extremes indices in the CMIP5 multimodel ensemble. 2. Future climate projections. J Geophys Res 118:2473–2493
Sylla MB, Giorgi F, Coppola E and others (2013) Uncertainties in daily rainfall over Africa: assessment of gridded observation products and evaluation of a regional climate model simulation. Int J Climatol 33:1805–1817
Taylor KE (2001) Summarizing multiple aspects of model performance in a single diagram. J Geophys Res 106: 7183–7192
Taylor KE, Stouffer RJ, Meehl GA (2012) An overview of CMIP5 and the experiment design. Bull Am Meteorol Soc 93:485–498
Toreti A, Naveau P, Zampieri M and others (2013) Projections of global changes in precipitation extremes from Coupled Model Intercomparison Project Phase 5 models. Geophys Res Lett 40:4887–4892
Wan H, Zhang X, Zwiers FW and others (2013) Effect of data coverage on the estimation of mean and variability of precipitation at global and regional scales. J Geophys Res Atmos 118:534–546
Wan H, Zhang X, Zwiers F and others (2015) Attributing northern high-latitude precipitation change over the period 1966–2005 to human influence. Clim Dyn 45: 1713–1726
Wang XL, Feng Y (2010) RHtestsV3 user manual. Climate Research Division, Science and Technology Branch, Environment Canada, Toronto
Yatagai A, Kamiguchi K, Arakawa O and others (2012) APHRODITE: Constructing a long-term daily gridded precipitation dataset for Asia based on a dense network of rain gauges. Bull Am Meteorol Soc 93:1401–1415
Yin H, Donat MG, Alexander LV and others (2015) Multidataset comparison of gridded observed temperature and precipitation extremes over China. Int J Climatol 35: 2809–2827
Zhang X, Aguilar E, Sensoy S, Melkonyan H and others (2005) Trends in Middle East climate extreme indices from 1950 to 2003. J Geophys Res Atmos 110:D22104
Zhang X, Zwiers FW, Hegerl GC, Lambert FH and others (2007) Detection of human influence on twentieth century precipitation trends. Nature 448:461–465
Zhang X, Wan H, Zwiers FW, Hegerl GC, Min SK (2013) Attributing intensification of precipitation extremes to human influence. Geophys Res Lett 40:5252–5257
Zhou B, Xu Y, Wu J, Dong SY, Shi Y (2016) Changes in temperature and precipitation extreme indices over China: analysis of a high-resolution grid dataset. Int J Climatol 36:1051–1066

Editorial responsibility: Eduardo Zorita, Geesthacht, Germany

Submitted: December 5, 2017; Accepted: August 20, 2018
Proofs received from author(s): September 23, 2018

Climate Dynamics
https://doi.org/10.1007/s00382-018-4165-8

The changing relationship between the December North Atlantic Oscillation and the following February East Asian trough before and after the late 1980s

Guolin Feng[1,2] · Meng Zou[1] · Shaobo Qiao[1,2] · Rong Zhi[2] · Zhiqiang Gong[2]

Received: 17 August 2017 / Accepted: 6 February 2018
© Springer-Verlag GmbH Germany, part of Springer Nature 2018

Abstract
This study investigates the changing relationship between the December North Atlantic Oscillation (NAO) and the following February East Asian trough (EAT) throughout the past 60 years. We found that the relationship between the December NAO and the following February EAT is significantly enhanced after the late 1980s compared with the period before the late 1980s. The changing relationship mainly results from the enhanced relationship between the December NAO and the following February North Atlantic mid-latitudes' sea surface temperature (SST) anomalies (NAMA) during the same period. During the period after the late 1980s, the persistent positive (negative) NAO pattern from December to the following January contributes to a positive (negative) NAMA, which reaches its maximum magnitude in the following February and excites an anomalous wave train along the North Atlantic and northern Eurasia, and significantly impacts the EAT. During the period before the late 1980s, the positive (negative) NAO pattern during December cannot persist into the following January, and the related positive (negative) NAMA is insignificant during the following February, causing the response of the simultaneous EAT to be insignificant as well. Moreover, there exists a significant impact of the December NAO on the December–January NAMA after the late 1980s, while the December–January NAMA is relatively less affected by the December NAO before the late 1980s. As a result, the simultaneous response of the atmospheric circulation anomalies to the December–January NAMA are evident before the late 1980s, and the positive (negative) NAMA can excite an anomalous wave train along the North Atlantic and northern Eurasia and significantly deepen (shallow) the downstream EAT. By contrast, after involving a feature of atmosphere forcing of SST, the simultaneous feedback of the December–January NAMA on EAT is significantly decreased after the 1980s.

Keywords North Atlantic Oscillation · East Asian trough · North Atlantic SST · Before and after the late 1980s · Wave train

1 Introduction

The North Atlantic Oscillation (NAO) is characterized by a meridional oscillation between the atmospheric mass of the polar low and that of the subtropical high and is the major mode of atmospheric variability over the North Atlantic (Hurrels 1995; Hurrell et al. 2003; Li et al. 2003; Jia et al. 2009), showing its strongest variability in the winter. In the wintertime, the NAO governs the large changes in the surface temperature and precipitation over Europe and North America by the modulation of the mean circulation and storm tracks. Although the NAO is a regional phenomenon, its influences can extend to East Asia via teleconnections and anomalous stationary wave activities (Chen et al. 2005; Huang et al. 2012). The influence of the NAO

This paper is a contribution to the special issue on East Asian Climate under Global Warming: Understanding and Projection, consisting of papers from the East Asian Climate (EAC) community and the 13th EAC International Workshop in Beijing, China on 24–25 March 2016, and coordinated by Jianping Li, Huang-Hsiung Hsu, Wei-Chyung Wang, Kyung-Ja Ha, Tim Li, and Akio Kitoh.

✉ Shaobo Qiao
qiaoshbokuailemore@163.com

[1] College of Physical Science and Technology, Yangzhou University, Yangzhou 225002, China

[2] Laboratory for Climate Studies, National Climate Center, China Meteorological Administration, Beijing, China

Published online: 14 March 2018

could extend to East Asia through two branches (Hoskins and Ambrizz 1993; Song et al. 2016; Zuo et al. 2015). The northern branch is oriented along the subpolar waveguide that propagates eastward into northern Eurasia, which corresponds with an enhanced Siberian High and deepened East Asian trough (EAT) during the negative NAO cases, and vice versa (Gong et al. 2001; Wu and Wang 2002; Chen et al. 2005; Wang et al. 2010; Jia and Hai 2011; Qiao and Feng 2016). The southern branch of the wave train propagates from the North Atlantic southeastward into Europe and the Arabian Gulf via the Asian jet waveguide, and this branch could exert a remote impact on the climate variability of southern China by modifying the Middle East jet stream (Yang et al. 2004; Xu et al. 2012; Wen et al. 2009; Bu et al. 2011; Zuo et al. 2015).

The relationship between the wintertime NAO and climate anomalies over East Asia also has large intraseasonal variations. Watanabe (2004) revealed that the NAO signal is relatively confined to the Euro-Atlantic sector in December, but it extends toward East Asia and the North Pacific in February. This difference is related to the NAO-induced Mediterranean convergence anomaly, which excites a Rossby wave train emanating toward East Asia along the Asian subtropical jet and is most frequently seen in February (Watanabe 2004; Hong et al. 2008). Similarly, Zuo et al. (2015) have shown that a weak in-phase relationship between the wintertime NAO and the southern China surface air temperature (SAT) occurs in December, but a significant out-of-phase relationship occurs in January–February. The different impacts of the NAO on the southern China SAT anomalies between the early and middle-to-late winter are primarily attributed to the large intraseasonal zonal migration of the Azores center of the NAO. Additional, the relationship between the wintertime NAO and the climate anomalies over East Asia also shows interdecadal variations. Corresponding to a notable abrupt change of the global climate around the late 1970s, the northern center of the NAO shifted eastward, and many links between the NAO and other parts of the climate system experienced a shift (Ding et al. 2005; Sung et al. 2006; Liu et al. 2007; Wang et al. 2009b; Wu et al. 2009; Gong et al. 2012; Wu and Zhang 2015; Zuo et al. 2016). For example, Wu and Zhang (2015) found that the wintertime NAO is significantly correlated with ENSO before the 1980s, but such correlation has broken down after the 1980s. Zuo et al. (2016) revealed that the significant out-of-phase relationship between the January NAO and the temperature over southern-central China dominants in the last two decades of the twentieth century, but a weak in-phase relationship occurs before the 1980s. Thus, a better understanding of the effects of the month-to-month variation of the wintertime NAO on the climate anomalies in East Asia and the possible interdecadal variations of their relationships are very important.

In addition to the atmospheric circulation anomalies associated with the NAO, there is substantial thermal coupling between the wintertime NAO and the North Atlantic sea surface temperature (SST) (Cayan 1992; Frankignoul et al. 1998; Qiao et al. 2017). The dominant signal shows that the NAO forces the North Atlantic SST: a positive NAO is followed by positive SST anomalies in the western subtropical North Atlantic and negative SST anomalies in the subpolar gyre as well as off the western coast of North Africa, all of which is referred to as the North Atlantic SST tripole, which has the opposite effects for a negative NAO. As a result of the NAO forcing, the tripole SST anomalies reaches its maximum amplitude in late winter, and there exists a positive feedback between the tripole and the NAO (Czaja and Frankignoul 2002). Due to the close linkage between the NAO and the North Atlantic SST in the winter, particularly the forcing of the NAO on the North Atlantic SST, the SST anomalies induced by the NAO can persist for a relatively long duration (Deser et al. 2003; He et al. 2006; Qiao et al. 2015, 2017). In the early winter, the SST anomalies may create the conditions that allow the early winter NAO to affect the late winter climate anomalies over East Asia (Czaja and Frankignoul 1999, 2002; Watanabe and Kimoto 2000; Li 2004). Among those atmospheric circulation factors related to the winter climate anomalies over East Asia, the EAT is a key factor to regulate the cold wave activities of East Asia during cold season. The deepened (shallowed) EAT corresponds to an anomalously strong (weak) EAWM (Qiu and Wang 1984; Li 1988; Wang et al. 2009a; Wu et al. 2011; Song et al. 2016). Recently, Qiao and Feng (2016) found that the December NAO has a delayed impact on the following February EAT, which is mainly realized via a wave train along the North Atlantic and northern Eurasia and effectively affect the East Asian climate. A positive (negative) December NAO induces SST tripole from December to the following January, contributing to the pronounced positive (negative) SST anomalies in the mid-latitude areas of the North Atlantic during the following February. The pronounced positive (negative) SST anomalies found during this period can excite a wave train along the North Atlantic and northern Eurasia and establish a link between the positive (negative) December NAO and the deepened (shallowed) EAT during the following February. Considering that this study merely focus on the period after the 1980s, whether these relationships are stationary throughout the 60-year period is an interesting issue, particularly whether these relationships are changing before and after the 1980s. In addition, during December–January, what the effects of the December NAO on SST anomalies over the North Atlantic and the downstream EAT, and whether their relationships experience a decadal variation remain unknown. A comprehensive comparison of the air–sea

interactions processes between the NAO, North Atlantic SST, and EAT during December, January and February is needed.

Motivated by the above questions, the changing relationship between the December NAO and the following February EAT during the past 60-year period, and the related different month-to-month air–sea interaction processes are investigated in this study. The remainder of the article is organized as follows. Section 2 introduces the data and methods employed. In Sect. 3, we present the interdecadal changes in the December NAO to the SST anomalies in the mid-latitude areas of the North Atlantic in the following February during the period from 1950 to 2013. Section 4 compares different atmospheric circulation responses to the December–January SST anomalies in the mid-latitude areas of the North Atlantic before and after the late 1980s. A summary and a brief discussions are presented in Sect. 5.

2 Data and methods

2.1 Datasets

The monthly mean geopotential heights, zonal and meridional wind components, and air temperature from the National Center for Environmental Prediction (NCEP)/National Center for Atmospheric Research (NCAR) reanalysis data were employed to analyze atmospheric circulation anomalies (Kalnay et al. 1996). This dataset is available from 1948 to the present with a 2.5° × 2.5° horizontal resolution. To support the results derived from NCEP/NCAR reanalysis, monthly mean geopotential heights from the combined datasets from the 40-year European Center for Medium-Range Weather Forecasts (ECMWF) reanalysis (ERA-40; Uppala et al. 2005) for 1958–2001 and ECMWF interim reanalysis (ERA-Interim; Dee et al. 2011) for 2002–2014 were employed. Meanwhile, the present study uses the monthly mean SST data from the Extended Reconstruction SST version 3 (ERSST3) dataset, which was provided by the National Oceanic and Atmospheric Administration (NOAA)/Oceanic and Atmospheric Research (OAR)/ Earth System Research Laboratory Physical Science Division (ERSL PSD) (Smith et al. 2003). The monthly mean NAO indices were obtained from the Climate Prediction Center (CPC) website (ftp://ftp.cpc.ncep.noaa.gov/cwlinks), and they are available from 1950 to the present. Following Qiao and Feng (2016), the East Asian trough index (EATI) is defined as the standardized value of region (35°–50°N, 120°–150°E) averaged 500 hPa geopotential height multiplied by (− 1), and a positive (negative) EATI denotes a deepened (shallowed) EAT. The standardized value of the area (30°–50°N, 20°–50°W) averaged SST is defined as North Atlantic midlatitudes' SST anomaly index (NAMAI). The data used here were mainly for the period 1950–2014.

2.2 Methods

In the middle-upper troposphere, the wave activity flux is used to diagnose the horizontal wave propagation associated with the stationary eddies on a zonally varying basic flow (Takaya and Nakamura 1997, 2001). Based on the Wentzel–Kramers–Brillouin approximation, the flux is independent of wave phase and parallel to the local group velocity of stationary Rossby waves. The divergence (convergence) of the wave activity flux further donates where the wave disturbances are emitted (absorbed). The flux in pressure (P) coordinates is defined as follows:

$$W = \frac{1}{2\left|\vec{U}\right|}\begin{pmatrix} u\left(\psi_x'^2 - \psi'\psi'_{xx}\right) + v\left(\psi'_x\psi'_y - \psi'\psi'_{xy}\right) \\ u\left(\psi'_x\psi'_y - \psi'\psi'_{xy}\right) + v\left(\psi_y'^2 - \psi'\psi'_{yy}\right) \\ \frac{f}{R\sigma/p}\left\{u\left(\psi'_x\psi'_p - \psi'\psi'_{xp}\right) + v\left(\psi'_y\psi'_p - \psi'\psi'_{yp}\right)\right\} \end{pmatrix} \quad (1)$$

where f is the Coriolis parameter, ψ is the stream function, R is the gas constant, p is the pressure, $\left|\vec{U}\right|$ is the speed of the basic state, (u, v) is the horizontal wind velocity, and $\sigma = \left(R\overline{T}/C_p p\right) - d\overline{T}/dp$ is based on temperature (T) and the specific heat at a constant pressure (C_p). In (1), the overbars and primes denote the basic-state quantities and perturbations, respectively.

To understand the storm tracks response to SST anomalies over the mid-latitudes, following the work of Hoskins and Valdes (1990), we calculated the maximum Eady growth rate at 700 hPa to determine where weather systems originate. The formula is:

$$\sigma_{BI} = 0.31\frac{f}{N}\left|\frac{\partial U}{\partial z}\right| \quad (2)$$

where f is the Coriolis parameter, N is the Brunt-Väisälä frequency, U is the horizontal wind speed, and z is the vertical height.

Over mid-latitudes, the anomalies exhibit an equivalent barotropic structure with the flow generally having the same sign at all levels. Processes generating the circulation anomalies are understood through a barotropic vorticity equation. Following Sardeshmukh and Hoskins (1988), the anomalous Rossby wave source (RWS) was computed as follows:

$$S' = -\nabla\cdot\left(V'_\chi\overline{\xi}\right) - \nabla\cdot\left(\overline{V}_\chi\xi'\right) \quad (3)$$

where ξ is the absolute vorticity, and V_χ is the divergent wind vector computed from the velocity potential. As in

(1), primes and overbars denote perturbations and basic-state quantities, respectively. The usual approximation has been to take the anomalous RWS to be:

$$S' = -fD' \tag{4}$$

where f is the Coriolis parameter, and $D' = \nabla \cdot \left(V'_{\chi}\right)$ is the divergence anomaly.

The winter months addressed in this study are December, the following January, and the following February. For example, the winter of 1950 refers to the 1950/51 winter and so on. The anomaly fields of individual variables are calculated relative to the multiyear mean climatology from 1951 to 2010 for each month. This study focuses on the variations on the interannual timescale. To obtain the component of interannual variations, we subtract the 9-year running average to all monthly mean variables, and then the linear trends were removed from these variables. This method is convenient and the results are almost the same as those from harmonic analysis (Qian et al. 2011). Correlation, composite and linear regression analyses were the main statistical techniques employed during the study. The Statistical significance tests were computed using the Student's two-tailed t-test.

3 Interdecadal changes in the December NAO and the following February NAMA from 1950 to 2013

According to the study of the Qiao and Feng (2016), the December NAO index and the following February EATI show a significant positive correlation during the period 1979–2013. We extend the time series of the EATI back to 1950s to examine the possible interdacadal variations of their relationships. Both the December NAO index and the following February EATI display obvious interannual variability, and the correlation coefficients between them is 0.33 (significant at the 95% confidence level) for the period 1950–2013 (Fig. 1a). To clearly identify the changing relationship between the December NAO index and the following February EATI for the whole period, we calculate the 25-year sliding correlations between them, and the years in Fig. 1b are labeled based on the central year of the 25-year window. The result displays a positive correlation for an insignificant period during the 1960s to the late 1980s and a significant period during the late 1980s to the 2000s, especially since the year 1989. The correlation coefficients for the periods 1950–1988 and 1989–2013 are 0.16 and 0.48 (significant at the 95% confidence level), respectively (Fig. 1b). Similar results are obtained by varying window sizes between 15 and 30 years to eliminate the sensitivity of the correlation to the length of the window. To further verify the robustness of the NAO–EATI relationship, we employ the combined ERA reanalysis to compute the February EATI for the period 1958–2014. The correlation coefficient between the two EATI exceeds 0.99, and the 25-year sliding correlations between the December NAO index and the following February EATI based on the two datasets are all the same (Fig. 1). Due to the high consistency between the two datasets in depicting the EAT, the related atmospheric circulation anomalies below are all derived from the NCAP/NCAR reanalysis for its much longer spans. In summary, the relationship between the December NAO index and the following February EATI was significantly enhanced since the late 1980s while it is not significant before the late 1980s.

Considering that the relationship between the December NAO index and the following February EATI was significantly enhanced since the late 1980s, the evolution of the following February EATI-related 500 hPa height anomalies from December to the following February for the periods before and after the year 1989 are compared in Fig. 2. For both the two periods, the deepened February EATI is associated with a wave train along the North Atlantic and northern Eurasia, with positive height anomalies over the northeastern Atlantic and northern Eurasia and negative height anomalies

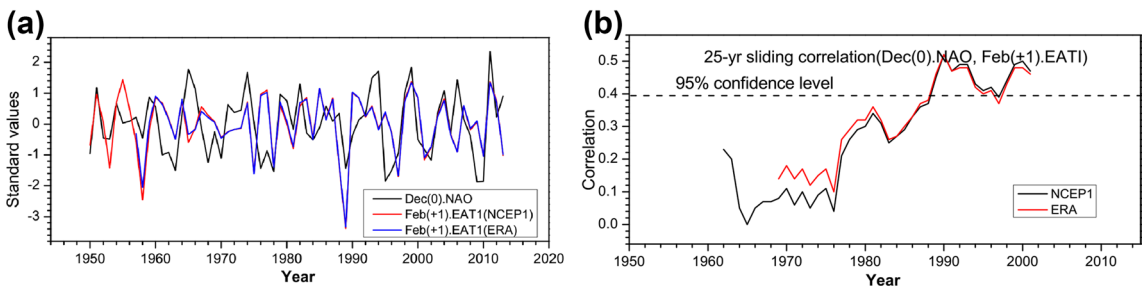

Fig. 1 **a** Time series of the standardized values of the December NAO index (black line) and the following February EATI derived from the NCEP/NCAR reanalysis for the period 1950–2013 (red line), and the following February EATI derived from the combined ERA reanalysis for the period 1957–2013 (blue line); **b** the 25-year sliding correlation between the December NAO index and the following February EATI based on the NCEP reanalysis (black line) and the combined ERA reanalysis (red line)

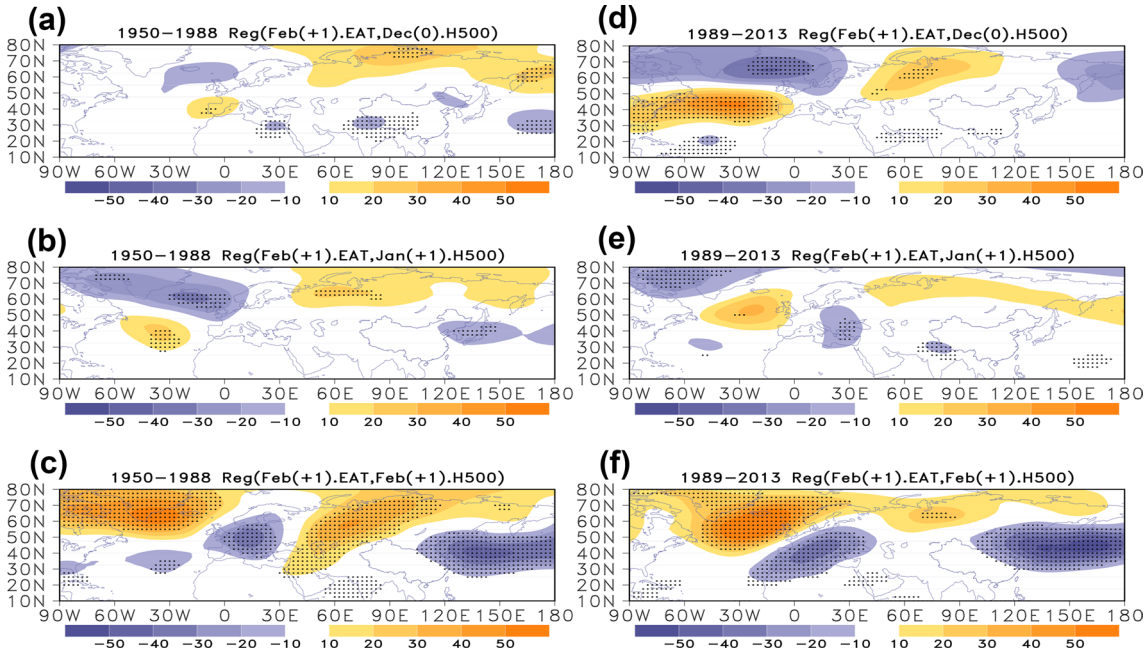

Fig. 2 Regression maps of the **a** December, **b** following January, **c** following February geopotential height anomalies (shades; gpm) at 500 hPa with regard to the following February EATI for the period 1950–1988. **d–f** are the same as **a–c**, but for the period 1989–2013. The dotted areas are significant at the 95% confidence level

over Europe and East Asia (Fig. 2c, f). During January, the wave trains are also visible but not significant for the two periods (Fig. 2b, e). However, the December height anomalies that associated with the following February EATI are obviously different before and after the late 1980s. Apparently, the regions with significant correlations are mainly located in Eurasia for the former period, with positive height anomalies over southwestern Europe and northern Asia and negative height anomalies over northwestern Europe, eastern Mediterranean, and northern India (Fig. 2a). The most pronounced height anomalies for the latter period features negative anomalies and positive anomalies over the high-latitudes and mid-latitudes of the North Atlantic, respectively, with a northeast-southwest oriented pattern that corresponds with a positive NAO phase (Fig. 2d). Moreover, the structure of the height anomalies share many similarities with the structure of NAO after the 1980s, as revealed by the previous studies (Hilmer and Jung 2000; Jung et al. 2003). Thus, in sharp contrast to the previous period, the preceding December NAO may contribute to a pronounced wave train along North Atlantic and northern Eurasia and induce EAT anomalies during February after the late 1980s.

Note that the internal dynamic processes resulting in chaotic temporal behavior of NAO persist for no longer than 2 weeks (Rodwell 2003), the sea-air interactions are useful for explaining how the December NAO leads to the EAT anomalies during the following February. As suggested by Qiao and Feng (2016), the December NAO-induced following February North Atlantic mid-latitudes' SST anomalies (NAMA) can generate feedbacks for atmospheric anomalies, establishing a link between the December NAO and the downstream EAT during following February. As such, the changing relationship between the December NAO and the following February EAT before and after the late 1980s is likely because of the changing December NAO-following February NAMA connection or the following February NAMA-following February EAT connection. Accompanied by the time series of the December NAO index and the following February EATI for the period 1950–2013 shown in Fig. 1a, the time series of the following February NAMAI is depicted in Fig. 3a. The 25-year sliding correlations between the December NAO index and the following February NAMAI and between the following February NAMAI and the following February EATI are shown in Fig. 3b. The sliding correlation between the NAMAI and the simultaneous EATI displays obvious interdecadal variability, with higher values during the period 1965–1975 and the period after the late 1980s, with lower values between the two periods. Nonetheless, the following February EATI is positively correlated with the following February NAMAI during the whole period, indicating the simultaneous impact of NAMA on the EAT during February is almost stationary throughout the 60-year period. In contrast, the sliding correlation between the December NAO index and the following February NAMAI is significant at the 95% confidence level after the 1980s and insignificant before the 1980s.

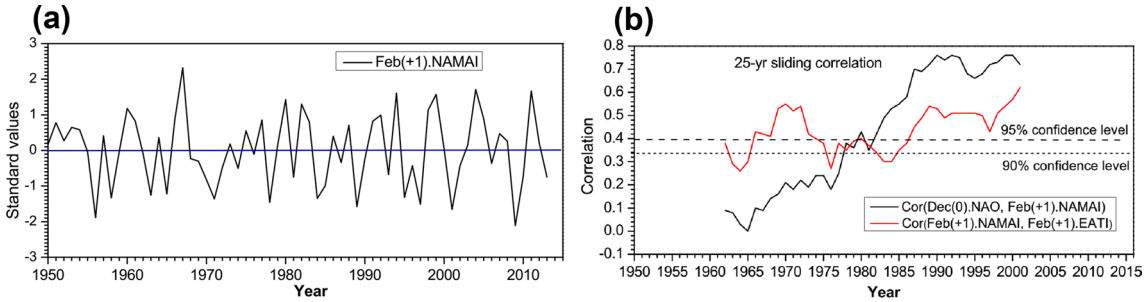

Fig. 3 **a** Time series of the standardized values of the following February NAMAI for the period 1950–2013 (black line); **b** the 25-year sliding correlation between the December NAO index and the following February NAMAI for the period 1950–2013 (black line), and the 25-year sliding correlation between the following February NAMAI and the following February EATI for the period 1950–2013 (red line)

This is consistent with the enhanced relationship between the December NAO and the following February EAT after the late 1980s (Fig. 3b). Therefore, the changing relationship between the December NAO and the following February EAT before and after the late 1980s may mainly result from the changing relationship between the December NAO and the following February NAMAI.

Note that the changing NAO–NAMA connection may explain most of the changing NAO–EAT connection in late 1980s, we will select two epochs before and after the late 1980s to compare the air–sea interaction processes associated with the changing relationship between December NAO and the following February NAMA. Due to the correlation between the NAMAI and the EATI during epoch 1958–1982 has the largest value (0.55) in all of the 25-year epochs before the late 1980s, this epoch is selected to compare with the epoch 1989–2013. This is because the impact of the NAMA on the EAT is similar during two epochs, but the NAO–NAMA connection is significantly enhanced during the latter epoch. The enhanced relationship between the NAO in December and the EAT in the following February after the late 1980s will be understood as being based on the two epochs mentioned above. Figure 4 displays maps showing the regressions of monthly mean SST and 850 hPa winds from December to the following February with regard to the December NAO index for the periods 1958–1982 and 1989–2013. During December, the NAO-related 850 hPa winds anomalies and the forcing SST anomalies are similar for both periods, and the positive NAO pattern corresponds with an anomalous anticyclone over the subtropical North Atlantic. The easterly offshore wind anomalies to the west of northern Africa increase the climatological northeasterly trade winds and promote the upwelling there, resulting in negative SST anomalies (Cayan 1992; Wu et al. 2006). The anomalous anticyclonic circulation over the mid-latitude regions corresponds to increasing solar radiation, resulting in positive SST anomalies over the mid-latitude areas of the North Atlantic. The notable difference between the two periods is that the NAO forcing the SST is more evident during the latter period (Fig. 4a, d). During the following January, the distribution of the positive SST anomalies over mid-latitude areas and the negative SST anomalies to the west of northern Africa during the period 1989–2013 are similar with those found in December, and the magnitudes of the positive SST anomalies are enhanced (Fig. 4e). This is induced by a persistent positive NAO pattern from the December to the following January. However, the positive NAO pattern and the resultant SST anomalies are much weaker in the following January during the period 1958–1982 (Fig. 4b). During the following February, the positive SST anomalies over the mid-latitudes of the North Atlantic are more significant than those in January and display an expansion toward the northeast. Meanwhile, anomalous cyclonic circulation and anomalous anticyclonic circulation patterns appear over the southwestern and northeastern areas of the positive SST anomalies, respectively (Fig. 4f). The remarkable difference between the 850 hPa winds anomalies during the following February and December–January is that the wind anomalies during February may be driven by the positive SST anomalies over the mid-latitudes of the North Atlantic via influencing transient eddy activities (Lindzen and Farrell 1980; Pan 2005). On the other hand, compared with those of the following January, the positive SST anomalies over the mid-latitudes and the related 850 hPa winds anomalies almost disappeared in the following February during the period 1958–1982 (Fig. 4c). Thus, during the period 1989–2013, the persistent positive NAO pattern in December–January contributes to the positive NAMAI, which reaches its maximum magnitude in the following February and has a feedback effect on the atmospheric circulation at this time. During the period 1958–1982, the positive NAO pattern during December cannot persist into the following January, and the resultant positive NAMAI is much weaker in the following February.

During the period 1989–2013, the December NAO pattern can persist into the following January, and induce a positive NAMAI for the whole winter with the maximum magnitude in the following February, whereas the persistent

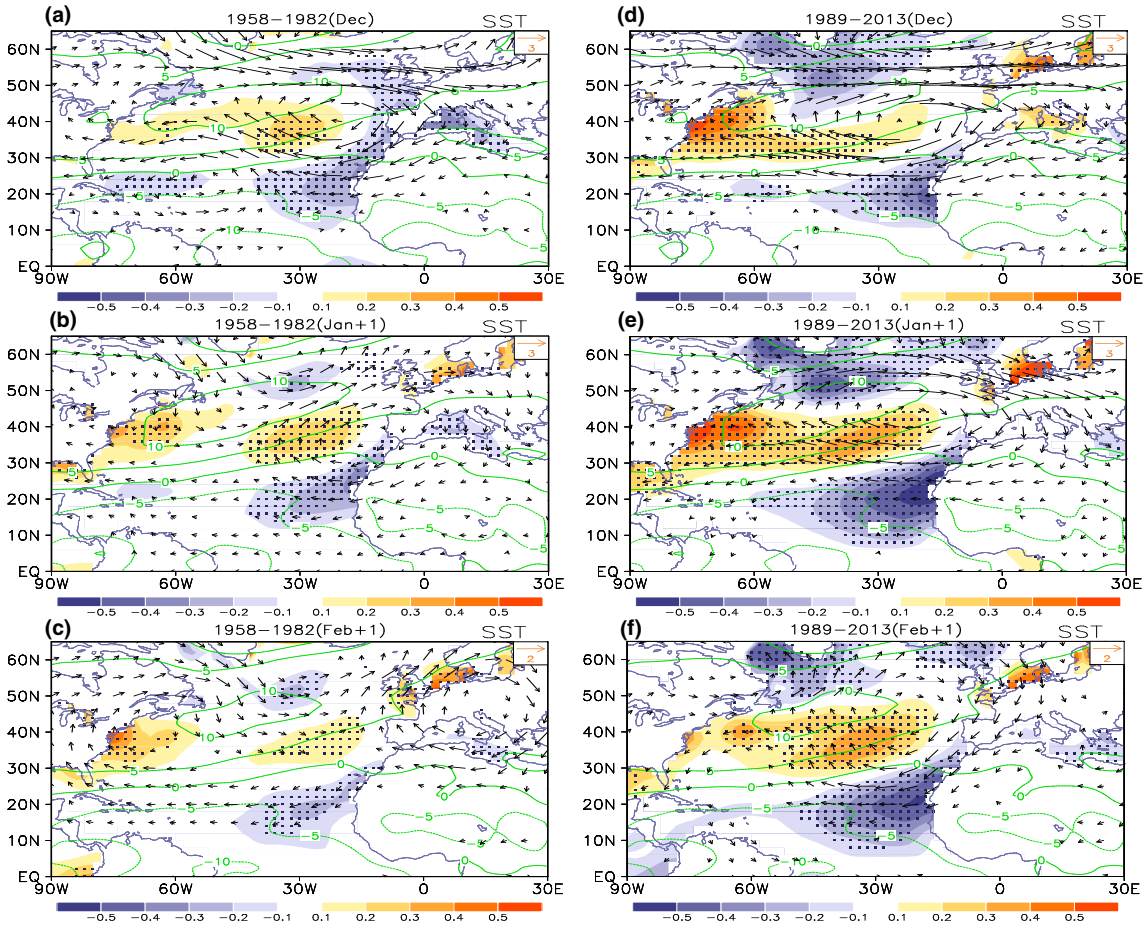

Fig. 4 Regression maps of the SST anomalies (shades; °C) and 850 hPa winds anomalies (vector; m s^{-1}; the wind speeds less than 0.5 m s^{-1} are not shown) from December to the following February with regard to the December NAO index for the period 1958–1982 (**a**–**c**) and 1989-2013 (**d**–**f**), respectively. Contours denote the climatological means of the zonal winds at 850 hPa. The dotted areas denote that the SST anomalies are significant at the 95% significance level

NAO pattern is only obvious in December during the period 1958–1982. Correspondingly, the correlation coefficient between the December NAO index and the following January NAO index is 0.32 and 0.66 for the periods 1958–1982 and 1989–2013, respectively. The correlation is insignificant in the former period and exceeds the 99% confidence level in the latter period. Previous studies have shown that the NAO is rather persistent, resulting in a significant autocorrelation at a 1-month lag, in particular when the NAO is most energetic. The month-to-month persistence primarily reflects the intrinsic atmospheric dynamics (Czaja and Frankignoul 2002). Before the late 1980s, it is shown that the 11-year running standard deviation of the December NAO index is mainly much smaller than that of the following January NAO index. After the late 1980s, the 11-year running standard deviation of the December NAO index is much larger than that of the following January NAO index (Fig. 5). This is consistent with the significant December NAO-the following February EAT relationship in the same period. The enhanced standard devivation of the December NAO index after the late 1980s may be the result of the enhanced intrinsic atmospheric variability. As a consequence, the SST tripole response and the positive feedback between the December NAO and the tripole are more evident after the late 1980s (Fig. 4b), which may effectively impact the NAO in the following January. Therefore, the December NAO can explain more of the variance of the following January NAO during the latter period, and can strengthen the NAO persistence from December to the following January.

As shown in Fig. 6, the lead-lag correlations between the monthly NAO index and the monthly NAMAI are depicted to confirm the enhanced effect of the December NAO on the following February NAMAI after the late 1980s. Following Wu and Kirtman (2007), the SST tendency of a specific month is calculated as the difference of the sea surface temperature anomaly (SSTA) between the succeeding and preceding months and is helpful for clarifying the atmospheric forcing to SST. During the period

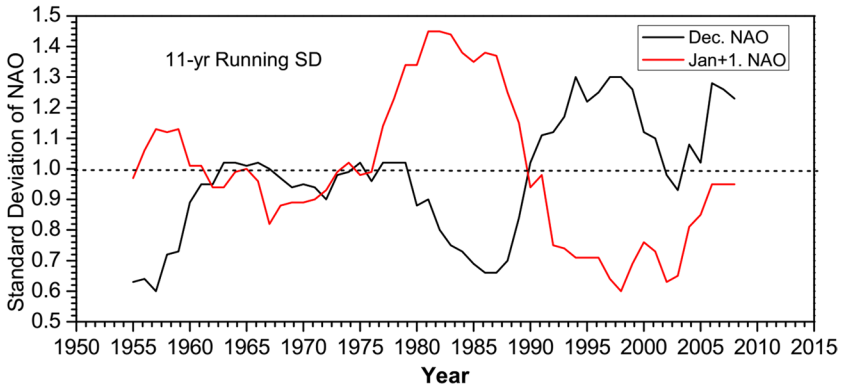

Fig. 5 The 11-year running standard deviation of the December NAO index (black line) and the following January NAO index (red line) for the period 1950–2013

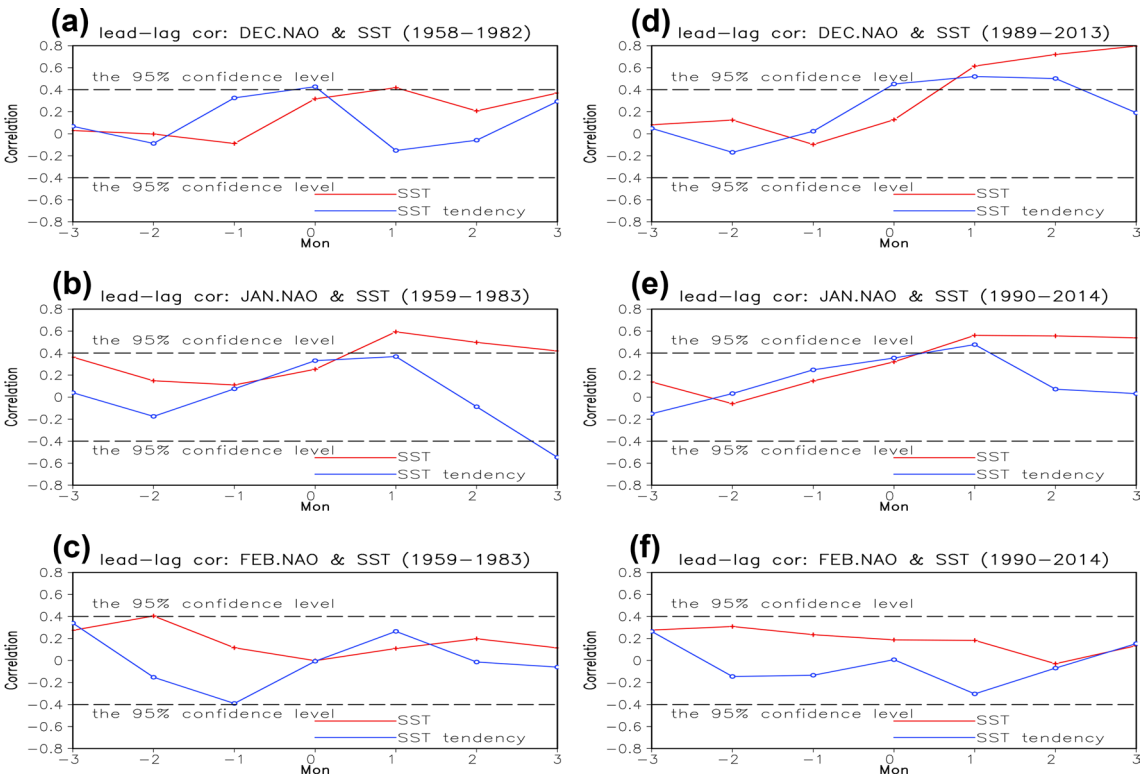

Fig. 6 **a**–**c** Lead-lag correlation of the December NAO index-monthly NAMAI for the period 1958–1982, the January NAO index-monthly NAMAI for the period 1959–1983, and the February NAO index-monthly NAMAI for the period 1959–1983, respectively. **d**–**f** are the same as **a**–**c**, but for the period 1989–2013, 1990–2014, and 1990–2014, respectively

1989–2013, a positive December NAO induces persistent increases in SST over the mid-latitude areas of the North Atlantic from December to the following February, which indicates the significant forcing effect of NAO on SST. As a result, a pronounced positive NAMA appears the following January and persists into the following February and March. The coefficient correlation between the December NAO index and the following February NAMAI can reach as high as 0.72, which exceeds the 99% confidence level (Fig. 6d). However, expect for the simultaneous impacts, the delayed impact of the December NAO on NAMA is insignificant during the period 1958–1982 (Fig. 6a). In addition, the January NAO has a delayed impact on the NAMA with a lag of 1–3 months during both the former and latter period, indicating the stationary influence of January NAO on NAMA throughout the 60-year period (Fig. 6b, e). In both of the periods 1958–1982 and 1989–2013, the February NAO index is not correlated with the simultaneous or delayed NAMAI (Fig. 6c, f). In conclusion, there exists a significant consistent influence of the December NAO on the whole wintertime NAMAI during the period 1989–2013, while the wintertime NAMAI

is relatively less affected by the December NAO during the former period.

4 The comparison of different atmospheric circulation responses to December–January NAMA before and after the late 1980s

Before and after the late 1980, the factors impacting the wintertime NAMA are significantly changed, and the influence of the December NAO on wintertime NAMA is significantly increased after the late 1980s. As a result, the feedback effects of the wintertime NAMA on atmospheric circulation may also experience a transition in the late 1980s. Hence, the 850 hPa winds and SST anomalies associated with the wintertime monthly NAMAI anomalies before and after the late 1980s are further compared in Fig. 7. After the late 1980s, it is shown that the positive NAO pattern is obvious with anticyclonic circulation anomalies over the mid-latitude areas of the North Atlantic during December, which forces the significant positive SST anomalies below (Fig. 7d). During January, a positive NAO pattern forcing the positive SST anomalies over mid-latitudes areas of the North Atlantic is rather pronounced (Fig. 7e). During February, it is evident that a positive NAMA generates feedbacks to the atmosphere, because anomalous cyclonic circulation and anomalous anticyclonic circulation patterns appear over the southwestern and northeastern areas of the positive SST anomalies, respectively (Fig. 7f). This is consistent with the results of Qiao and Feng (2016). By contrast, during December–January–February before the late 1980s, the atmospheric circulation responses to a positive NMMA is similar, with anomalous cyclonic circulation and anomalous anticyclonic circulation patterns appearing over the southwestern and northeastern areas of the positive SST

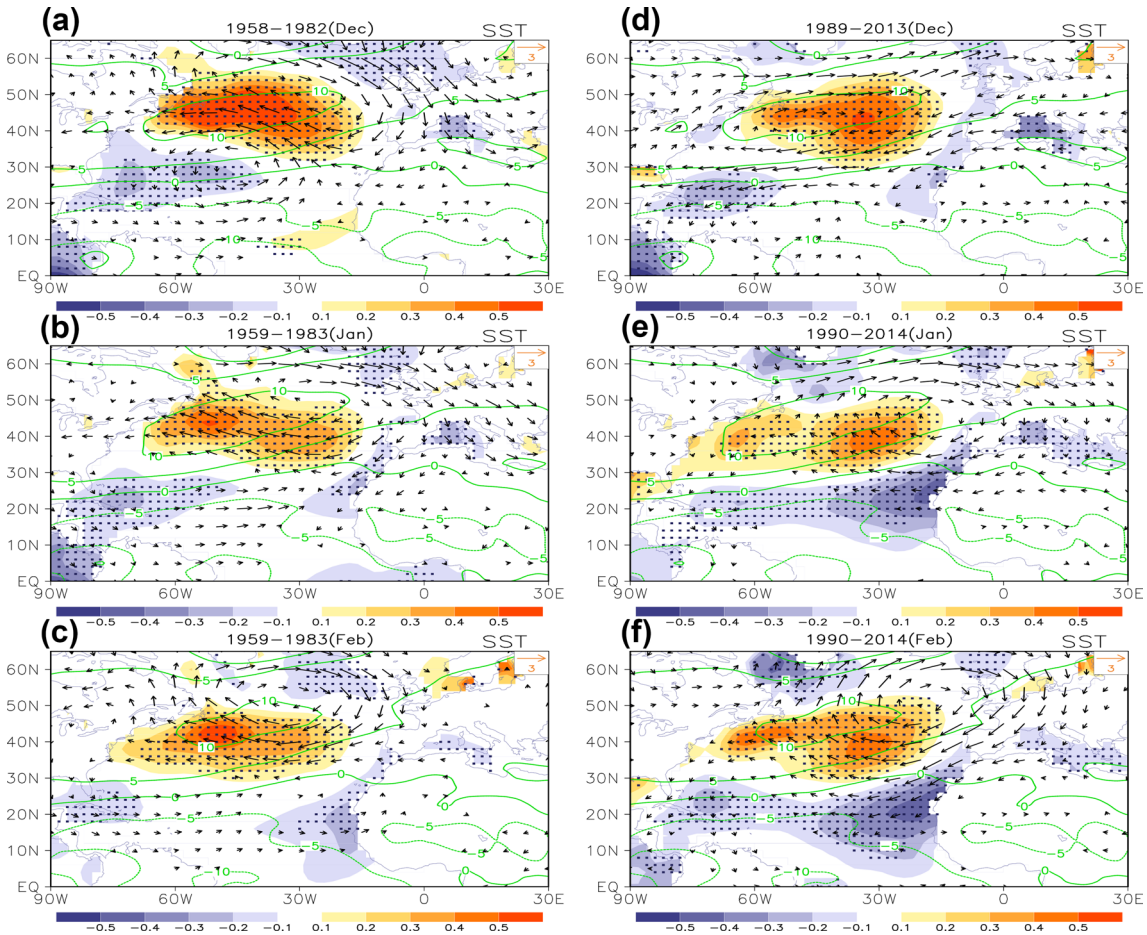

Fig. 7 **a–c** Regression maps of SST anomalies (shades; °C) and 850 hPa winds anomalies (vector; m s^{-1}, the wind speed less than 0.5 m s^{-1} are not shown) with regard to the December NAMAI for the period 1958–1982, to the January NAMAI for the period 1959–1983, and to the February NAMAI for the period 1959–1983, respectively. **d–f** are the same as **a–c**, but for the but for with regard to the December NAMAI for the period 1989–2013, to the January NAMAI for the period 1990–2014, and to the February NAMAI for the period 1990–2014, respectively. The dotted areas denote that the SST anomalies are significant at the 95% confidence level

anomalies, respectively (Fig. 7a–c). Overall, it seems that the NAMA forcing of the atmospheric circulation is evident during all 3 months before the late 1980s, while the feedback of the NAMA on the atmospheric circulation is only effective during February after the late 1980s.

Moreover, the impact of the NAMA on the simultaneous EAT is evident during all three months for the former period. When the NAMAI displays a positive anomaly, the positive and negative anomalies occur to the northeast and southwest of the mid-latitude areas of the North Atlantic respectively, with positive anomalies occurring around western Siberia and negative anomalies occurring over northeastern Asia. The anomalous wave train originates from the North Atlantic toward northern Europe and emanates to Siberia and East Asia along northern Eurasia (Fig. 8a–c). While for the latter period, the influence of the NAMA on the simultaneous EATI is only obvious during February. The atmospheric circulation anomalies and the wave trains associated with the NAMA during the December–January are relatively weak, and the forcing on the EAT is insignificant (Fig. 8d, e, f).

Before and after the late 1980s, the distinct differences between the simultaneous NAMA-EAT relationship occurs in December–January. For the former period, the NAMA forcing of the EAT is evident, as opposed to the case for the latter period. The simultaneous correlation coefficients between the NAMAI and EATI during December and January for the former period are 0.41 and 0.55, respectively, both of which exceed the 95% confidence level. The simultaneous correlation coefficients of those for the latter period are merely −0.03 and −0.30, respectively. Furthermore, the 700 hPa Eady growth rates related to the December–January NAMAI are calculated for the two periods to compare the differences of the air–sea interaction processes before and after the late 1980s. For the period before the late 1980s, it is shown that the Eady growth rates increase (decrease) to the northeast (southwest) of the mid-latitude areas of the North Atlantic and are divided at approximately 50°N, which suggests an enhanced (reduced) baroclinicity to the northeast (southwest) of the areas of positive SST anomalies during December–January, indicating the effective response of the atmospheric circulation anomalies to a positive NAMAI (Fig. 9a, b). By contrast, the positive and negative Eady growth rate anomalies over the North Atlantic displays north–south direction and are divided at approximately 40°N (Fig. 9c, d). A north–south oriented pattern may imply the changes of the mean flow induced by the NAO, and the feedback of the SST anomalies on the atmospheric circulation anomalies is significantly decreased.

Additionally, the NAMA-related upper-level positive velocity potential anomalies and positive RWS anomalies during the two periods are shown in Fig. 10. We can see that the distribution of the RWS is consistent with the wave trains depicted in Fig. 8. During December–January for the former period, the positive RWS anomalies are evident over the northeastern Atlantic, Central Asia, and northern East Asia, and the negative RWS anomalies are evident over Eastern Europe and northwestern Pacific. The distribution of the RWS anomalies indicates the wave train is to the north, and the NAMA have a significant impact on the EAT (Fig. 10a, b). However, the wave train is to the south

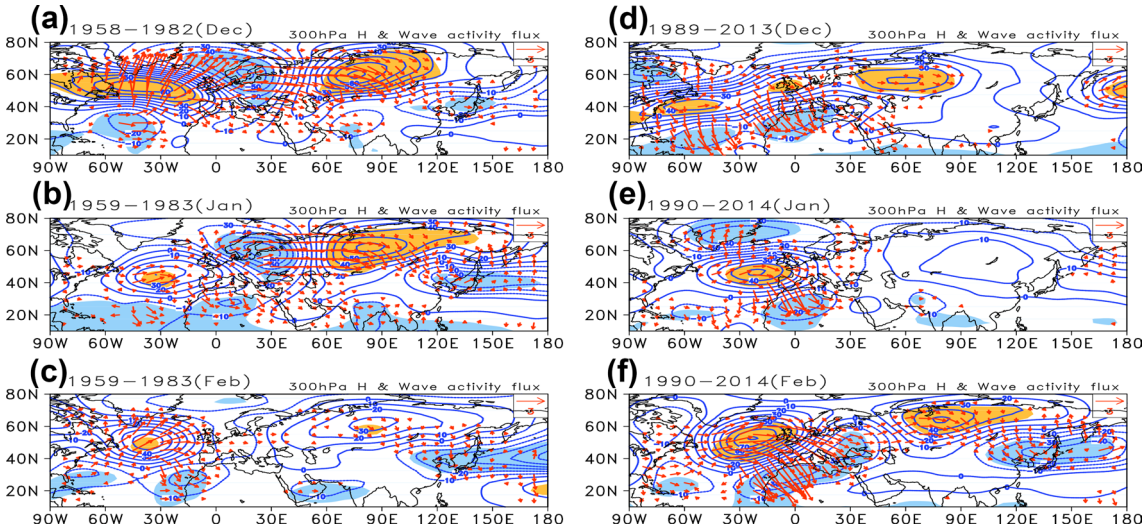

Fig. 8 **a–c** Regression maps of the simultaneous 300 hPa geopotential height (contour; gpm) and horizontal wave activity fluxes (vector; m^2 s^{-2}) with regard to the December NAMAI for the period 1958–1982, to the January NAMAI for the period 1959–1983, and to the February NAMAI for the period 1959–1983. **d–f** are the same as **a–c**, but for with regard to the December NAMAI for the period 1989–2013, to the January NAMAI for the period 1990–2014, and to the February NAMAI for the period 1990–2014, respectively. The shaded areas denotes that the height anomalies are significant at the 95% confidence level

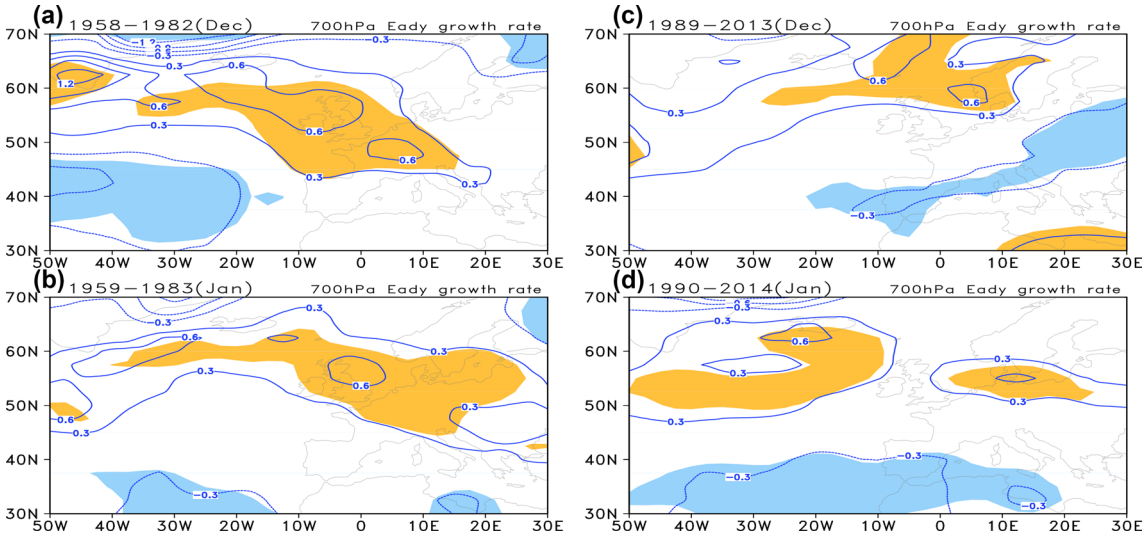

Fig. 9 **a, b** Regression maps of the simultaneous 700 hPa Eady growth rate (contour; 10^{-2} day^{-1}) with regard to the December NAMAI for the period 1958–1982, and to the January NAMAI for the period 1959–1983, respectively. **c, d** are the same as **a, b**, but for with regard to the December NAMAI for the period 1989–2013, and to the January NAMAI for the period 1990–2014, respectively. The shaded areas are significant at the 95% confidence level

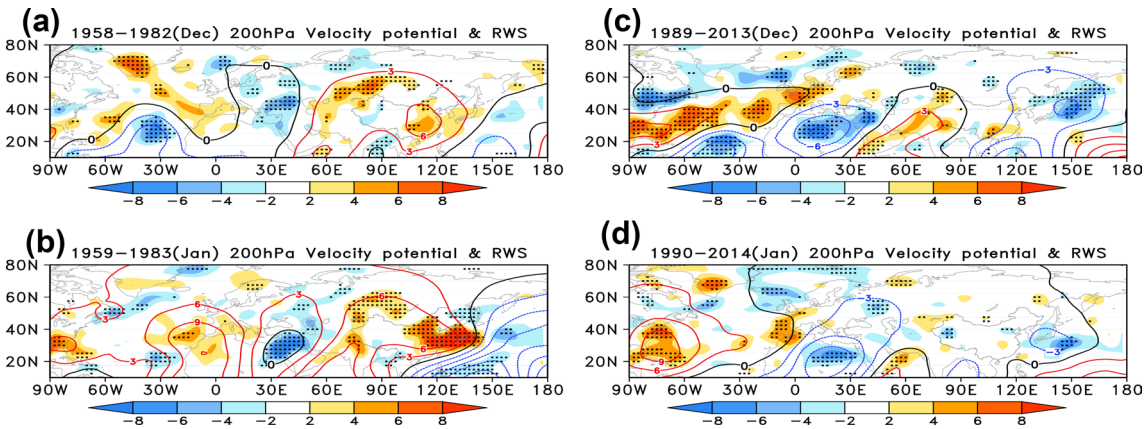

Fig. 10 **a, b** Regression maps of the simultaneous velocity potential (contour; 10^5 m^2s^{-1}) and RWS (shaded; 10^{-11} s^{-2}) at 200 hPa with regard to the December NAMAI for the period 1958–1982, and to the January NAMAI for the period 1959–1983, respectively. **c, d** are the same as **a, b**, but for with regard to the December NAMAI for the period 1989–2013, and to the January NAMAI for the period 1990–2014, respectively. The dotted areas denotes that the RWS anomalies are significant at the 95% confidence level

during the December–January for the latter period, with positive RWS anomalies over the northeastern Atlantic and northern India Peninsula, with negative RWS anomalies over North Africa. Meanwhile, the positive RWS anomalies over northern East Asia during the former period are disappeared, and the feedback of the NAMA on the simultaneous EAT is insignificant (Fig. 10c, d). The relatively southward propagation of the wave train may reflect the influence of the NAO on downstream atmospheric circulation anomalies during December–January as revealed by the results of Watanabe (2004). In summary, compared with the cases before the late 1980s, December–January NAMA are primarily forced by December NAO after the late 1980s. As such, SST anomalies over the mid-latitude areas of the North Atlantic has a feature of atmosphere forcing of SST, causing a relatively weak feedback of the NAMA on the simultaneous EAT.

5 Summary and discussions

To better understand the delayed impact of the monthly wintertime NAO on East Asian climate anomalies and the possible interdecadal variations of their relationships, this study investigates the changing relationship between the

December NAO and the following February EAT over the past 60 years. We found that the relationship between the December NAO and the following February EAT is significantly enhanced since the late 1980s, while it is not significant before the late 1980s. The enhanced relationship between the December NAO and the following February EAT after the late 1980s is mainly result from the enhanced relationship between the December NAO and the following February NAMA during this period. For the period after the late 1980s, the persistent positive (negative) NAO pattern from the December to the following January contributes to the positive (negative) NAMA, which reaches its maximum magnitude in the following February and has a feedback effect on the atmospheric circulation anomalies at this time. The atmospheric circulation response to the NAMA displays an anomalous wave train from the North Atlantic toward northern Europe, Siberia, and East Asia along northern Eurasia, and significantly impacts the EAT. During the period before the late 1980s, the positive (negative) NAO pattern during December cannot persist into the following January, and the related positive (negative) NAMA and anomalous wave train are weak in the following February. In conclusion, there exists a significant delayed influence of the December NAO on the following February EAT that depends on the pronounced December NAO-following February NAMA connection after the late 1980s, while the February NAMA affected by the simultaneous or the preceding monthly NAO are insignificant before the late 1980s.

Furthermore, the NAO–NAMA–EAT connections during December–January are compared before and after the late 1980s. Due to the December–January NAMA is relatively less affected by the December NAO before the late 1980s, so the NAMA forcing of the simultaneous EAT is evident during December–January. When the NAMAI displays a positive anomaly, it is shown that the Eady growth rates increase (decrease) to the northeast (southwest) of the mid-latitude areas of the North Atlantic and are approximately divided at 50°N, and vice versa. Correspondingly, the pathway of an anomalous wave train is to the north, which originates from the North Atlantic, extending towards northern Europe, Siberia, East Asia along northern Eurasia, and significantly influences the downstream EAT. After the late 1980s, there exists a significant impact of the December NAO on the December–January NAMA, and the SST anomalies over the mid-latitude areas of the North Atlantic has a feature of atmosphere forcing of SST, causing a relatively weak feedback of the NAMA on the simultaneous EAT.

It is noteworthy that the significant December NAO-following February NAMA connection occurs in the early 1980s, several years earlier than that of significant December NAO-following EAT connection. This result suggests the relatively weak following February NAMA-following February EAT connection may also play a role in inducing the insignificant December NAO-following February EAT connection during the early 1980s to the late 1980s (Fig. 3b). The interdecadal change of the February NAMA-February EAT connection is consistent with the 9-year mean SST anomalies over the mid-latitude areas of the North Atlantic, and the periods with higher (lower) correlation corresponds with the those with higher (lower) mean SST anomalies (figure not shown). We suppose that the atmospheric response to SST anomalies may be dependent upon the mean SST, because the atmospheric heating anomalies would be larger under a higher mean SST. Meanwhile, it is known that the NAO experiences a decadal shift from a negative phase to a positive phase in the late 1980s, the increase of the mean state of the NAO may also play a role in enhanced December NAO-following EAT connection in the late 1980s. The respective roles of the mean state of the December NAO and the following February NAMA in the resulting increased December NAO-following EAT connection should be investigated.

Additionally, the largest difference in the December NAO-following February EAT connection before and after the late 1980s depends on the enhanced persistence of the NAO from December to the following January during the latter period, which may mainly result from the increased interannal variability of the December NAO after the late 1980s, as shown in Fig. 5. On the other hand, due to the increased interannal variability of the December NAO, the forcing of the December NAO to the December–January NAMA are also increased, resulting in the decadal decrease of the impact of December–January NAMA on the simultaneous downstream EAT after the late 1980s. A better understanding of the increased variability of the December NAO and investigating the interdecadal change of the December NAO-wintertime NAMA interactions are further needed. Besides, both the NAO and NAMA exert pronounced influence on downstream East Asian climate anomalies, particularly during the late winter, so the combined effects of them and the possible decadal variation of their effects on East Asian climate also require further analysis. All these problems remain to be resolved by means of diagnostic analysis and numerical simulations in our subsequent work.

Acknowledgements This study acknowledges the support of the National Natural Science Foundation of China (41530531), Special Scientific Research Project for Public Interest (Grant no. GYHY201506001), and the National Natural Science Foundation of China (41575082, 41575074, 41475064).

References

Bueh C, Shi N, Xie Z (2011) Large-scale circulation anomalies associated with persistent low temperature over Southern China in January 2008. Atmos Sci Lett 12:273–280

Cayan DR (1992) Latent and sensible heat flux anomalies over the northern oceans: the connection to monthly atmospheric circulation. J Clim 5:354–369
Chen W, Yang S, Huang R (2005) Relationship between stationary planetary wave activity and the East Asian winter monsoon. J Geophys Res 110:D14. https://doi.org/10.1029/2004JD005669
Czaja A, Frankignoul C (1999) Influence of the North Atlantic SST on the atmospheric circulation. Geophys Res Lett 26: 2969–2972. https://doi.org/10.1029/1999GL900613
Czaja A, Frankignoul C (2002) Observed impact of Atlantic SST anomalies on the North Atlantic Oscillation. J Clim 15:606–623
Dee DP, Coauthors (2011) The ERA-Interim reanalysis: configuration and performance of the data assimilation system. Quart J Roy Meteor Soc 137:553–597. https://doi.org/10.1002/qj.828
Dese C, Alexander MA, Timlin MS (2003) Understanding the persistence of sea surface temperature anomalies in midlatitudes. J Clim 16:57–72
Ding R, Li J, Wang S, Ren F (2005) Decadal change of the spring dust storm in northwest China and the associated atmospheric circulation. Geophys Res Lett 32:L02808. https://doi.org/10.1029/2004GL021561
Frankignoul C, Czaja A, Heveder BL (1998) Air–sea feedback in the North Atlantic and surface boundary conditions for ocean models. J Clim 11:2310–2324
Gong D, Wang S, Zhu J (2001) East Asian winter monsoon and Arctic oscillation. Geophys Res Lett 28:2073–2076. https://doi.org/10.1029/2000GL012311
Gong Z, Wang X, Zhi R, Feng A (2011) Circulation system complex networks and teleconnections. Chin Phys B 20(7):079201
Gong Z, Zhi R, Hou W, Wang X, Feng G (2012) Analysis of decadal characteristics of leading teleconnections based on complex networks theory (in Chinese). Acta Phys Sin 61:029202
He W, Feng G, Gao X, Li J (2006) Amplitude death in non-feedback coupled chaotic system (in Chinese). Acta Phys Sin 55:6192–6196
Hilmer M, Jung T (2000) Evidence for a recent change in the link between the North Atlantic Oscillation and Arctic sea ice export. Geophys Res Lett 27:989–992. https://doi.org/10.1029/1999GL010944
Hong CC, Hsu HH, Chia HH, Wu CY (2008) Decadal relationship between the North Atlantic Oscillation and cold surge frequency in Taiwan. Geophys Res Lett 35:L24707. https://doi.org/10.1029/2008GL034766
Hoskins BJ, Ambrizzi T (1993) Rossby wave propagation on a realistic longitudinally varying flow. J Atmos Sci 50:1661–1671
Hoskins BJ, Valdes PJ (1990) On the existence of storm-tracks. J Atmos Sci 47:1854–1864
Huang R, Chen J, Wang L, Lin Z (2012) Characteristics, processes, and causes of the spatio-temporal variabilities of the East Asian monsoon system. Adv Atmos Sci 29:910–942
Hurrell JW (1995) Decadal trends in the North Atlantic Oscillation: regional temperatures and precipitation. Science 269:676–679
Hurrell JW, Kushnir Y, Ottersen G, Visbeck M (2003) The North Atlantic Oscillation: climatic significance and environmental impact. Geophys Monogr Amer Geophys Union 134: 279
Jia X, Lin H (2011) Influence of forced large-scale atmospheric patterns on surface air temperature in China. Mon Wea Rev 139:830–852
Jia X, Lin H, Derome J (2009) The influence of tropical Pacific forcing on the Arctic Oscillation. Clim Dyn 32:495–509
Jung T, Hilmer M, Ruprecht E, Kleppek S, Gulev SK, Zolina O (2003) Characteristics of the recent eastward shift of interannual NAO variability. J Clim 16:3371–3382
Kalnay E, Kanamitsu M, Kistler R, Collins W, Deaven D, Gandin L, Iredell M, Saha S, White G, Woolen J, Zhu Y, Chelliah M, Ebisuzaki W, Higgins W, Janowiak J, Mo KC, Ropelewski C, Wang J, Leetmaa A, Reynolds R, Jenne R, Joseph D (1996) The NCEP/NCAR 40-year reanalysis project. Bull Am Meteo Soc 77:437–471
Li C (1988) Frequent activities of stronger aero troughs in East Asia in wintertime and the occurrence of the El Niño event. Sci China Ser B 31:976–985
Li S (2004) Impact of the Northwest Atlantic SST anomaly on the circulation over the Ural Mountains. J Meteorol Soc Jpn 82:971–988
Li J, Wang JXL (2003) A new North Atlantic Oscillation index and its variability. Adv Atmos Sci 20:661–676. https://doi.org/10.1007/BF02690792
Li J, Sun C, Jin F (2013) NAO implicated as a predictor of Northern Hemisphere mean temperature multidecadal variability. Geophys Res Lett 40:5497–5502. https://doi.org/10.1002/2013GL057877
Lindzen RS, Farrell B (1980) A simple approximate result for the maximum growth rate of baroclinic instabilities. J Atmos Sci 37:1648–1654
Liu X, Ding R (2007) The relationship between the spring Asian atmospheric circulation and the previous winter northern hemisphere annular mode. Theor Appl Climatol 88:71–81
Pan L (2005) Observed positive feedback between the NAO and the North Atlantic SSTA tripole. Geophys Res Lett 32:L06707. https://doi.org/10.1029/2005GL022427
Qian W, Lu B, Liang H (2011) Changes in fossil-fuel carbon emissions in response to interannual and interdecadal temperature variability. Chin Sci Bull 56:319–324. https://doi.org/10.1007/s11434-010-4279-9
Qiao S, Feng G (2016) Impact of the December North Atlantic Oscillation on the following February East Asian trough. J Geophys Res 121:10074–10088. https://doi.org/10.1002/2016JD025007
Qiao S, Gong Z, Feng G, Qian Z (2015) Relationship between cold winters over Northern Asia and the subsequent hot summers over mid-lower reaches of the Yangtze River valley under global warming. Atmos Sci Lett 16:479–485. https://doi.org/10.1002/asl.585
Qiao S, Hu P, Feng T, Cheng J, Han Z, Gong Z, Zhi R, Feng G (2017) Enhancement of the relationship between the winter Arctic Oscillation and the following summer circulation anomalies over central East Asia since the early 1990s. Clim Dyn. https://doi.org/10.1007/s00382-017-3
Qiu Y, Wang W (1984) Progresses in the research of medium-range prediction of cold surge. In: Proceedings of Medium Range Prediction of Cold Surge. Peking University Press 1–10
Rodwell MJ (2003) On the predictability of North Atlantic climate, the North Atlantic Oscillation: climatic significance and environmental impact. 173–192. https://doi.org/10.1029/134GM08
Smith TM, Reynolds RW (2003) Extended reconstruction of global sea surface temperatures based on COADS data (1854–1997). J Clim 16:1495–1510
Song L, Wang L, Chen W, Zhang Y (2016) Intraseasonal variation of the strength of the East Asian trough and its climatic impacts in boreal winter. J Clim 29:2557–2577
Sung MK, Kwon WT, Baek HJ, Boo KO, Lim GH, Kug JS (2006) A possible impact of the North Atlantic Oscillation on the east Asian summer monsoon precipitation. Geophys Res Lett 33:L21713. https://doi.org/10.1029/2006GL027353
Takaya K, Nakamura H (1997) A formulation of a wave-activity flux for stationary Rossby waves on a zonally varying basic flow. Geophys Res Lett 24(23):2985–2988. https://doi.org/10.1029/97GL03094
Takaya K, Nakamura H (2001) A formulation of a phase-independent wave activity flux for stationary and migratory quasigeostrophic eddies on a zonally varying basic flow. J Atmos Sci 58:608–627
Uppala SM, Coauthors (2005) The ERA-40 Re-Analysis. Quart J Roy Meteor Soc 131:2961–3012. https://doi.org/10.1256/qj.04.176
Wang L, Chen W (2010) Downward Arctic Oscillation signal associated with moderate weak stratospheric polar vortex and the

cold December 2009. Geophys Res Lett 37:L09707. https://doi.org/10.1029/2010GL042659
Wang L, Chen W, Zhou W, Huang R (2009a) Interannual variations of East Asian trough axis at 500 hPa and its association with the East Asian winter monsoon pathway. J Clim 22:600–614
Wang L, Huang R, Gu L, Chen W, Kang L (2009b) Interdecadal variations of the East Asian winter monsoon and their association with quasi-stationary planetary wave activity. J Clim 22:4860–4872
Watanabe M (2004) Asian jet waveguide and a downstream extension of the North Atlantic. Oscillation J Clim 17:4674–4691
Watanabe M, Kimoto M (2000) Atmosphere–ocean thermal coupling in the North Atlantic: a positive feedback. Quart J Roy Meteor Soc 126:3343–3369. https://doi.org/10.1002/qj.49712657017
Wen M, Yang S, Kumar A, Zhang P (2009) An analysis on the large-scale climate anomalies associated with the snowstorms affecting China in January 2008. Mon Wea Rev 137:1111–1131
Wu R, Kirtman BP (2007) Regimes of seasonal air–sea interaction and implications for performance of forced simulations. Clim Dyn 29:393–410
Wu B, Wang J (2002) Winter Arctic Oscillation, Siberian High and East Asian winter monsoon. Geophys Res Lett 29:1897. https://doi.org/10.1029/2002GL015373
Wu Z, Zhang P (2015) Interdecadal variability of the mega-ENSO–NAO synchronization in Winter. Clim Dyn 45:1117–1128
Wu R, Kirtman BP, Pegion K (2006) Local air–sea relationship in observations and model simulations. J Clim 19:4914–4932
Wu Z, Wang B, Li J, Jin F (2009) An empirical seasonal prediction model of the East Asian summer monsoon using ENSO and NAO. J Geophys Res 114:D18120. https://doi.org/10.1029/2009JD011733
Wu Z, Li J, Jiang Z, He J (2011) Predictable climate dynamics of abnormal East Asian winter monsoon: once-in-a-century snowstorms in 2007/2008 winter. Clim Dyn 37:1661–1669
Xu H, Li J, Feng J, Mao J (2012) The asymmetric relationship between the winter NAO and the precipitation in Southwest China (in Chinese). Acta Meteor Sin 70:1276–1291
Yang S, Lau KM, Yoo SH, Kinter JL, Miyakoda K, Ho CH (2004) Upstream subtropical signals preceding the Asian summer monsoon circulation. J Clim 17:4213–4229
Zuo J, Ren H, Li W (2015) Contrasting impacts of the Arctic Oscillation on surface air temperature anomalies in southern China between early and middle-to-late winter. J Clim 28:4015–4026
Zuo J, Ren H, Li W, Wang L (2016) Interdecadal Variations in the relationship between the Winter North Atlantic Oscillation and Temperature in South-Central China. J Clim 29:7477–7493

Diagnosing Relationships between Mean State Biases and El Niño Shortwave Feedback in CMIP5 Models

SAMANTHA FERRETT AND MATTHEW COLLINS

College of Engineering, Mathematics and Physical Sciences, University of Exeter, Exeter, United Kingdom

HONG-LI REN

Laboratory for Climate Studies, National Climate Center, China Meteorological Administration, Beijing, and Department of Atmospheric Science, School of Environmental Studies, China University of Geoscience, Wuhan, and CMA–Nanjing University Joint Laboratory for Climate Prediction Studies, School of Atmospheric Sciences, Nanjing University, Nanjing, China

(Manuscript received 19 May 2017, in final form 15 September 2017)

ABSTRACT

The rate of damping of tropical Pacific sea surface temperature anomalies (SSTAs) associated with El Niño events by surface shortwave heat fluxes has significant biases in current coupled climate models [phase 5 of the Coupled Model Intercomparison Project (CMIP5)]. Of 33 CMIP5 models, 16 have shortwave feedbacks that are weakly negative in comparison to observations, or even positive, resulting in a tendency of amplification of SSTAs. Two biases in the cloud response to El Niño SSTAs are identified and linked to significant mean state biases in CMIP5 models. First, cool mean SST and reduced precipitation are linked to comparatively less cloud formation in the eastern equatorial Pacific during El Niño events, driven by a weakened atmospheric ascent response. Second, a spurious reduction of cloud driven by anomalous surface relative humidity during El Niño events is present in models with more stable eastern Pacific mean atmospheric conditions and more low cloud in the mean state. Both cloud response biases contribute to a weak negative shortwave feedback or a positive shortwave feedback that amplifies El Niño SSTAs. Differences between shortwave feedback in the coupled models and the corresponding atmosphere-only models (AMIP) are also linked to mean state differences, consistent with the biases found between different coupled models. Shortwave feedback bias can still persist in AMIP, as a result of persisting weak shortwave responses to anomalous cloud and weak cloud responses to atmospheric ascent. This indicates the importance of bias in the atmosphere component to coupled model feedback and mean state biases.

1. Introduction

El Niño–Southern Oscillation (ENSO) is a dominant mode of interannual variability in the equatorial Pacific that has a large impact on weather worldwide. ENSO is driven by a combination of ocean–atmosphere processes that either amplify or damp ENSO-event-related sea surface temperature anomalies (SSTAs) in the equatorial Pacific. Processes that contribute to the growth of initial positive SSTAs in the equatorial Pacific are typically related to ocean processes, such as ocean current anomalies and thermocline anomalies, as a result of decreasing surface zonal winds during El Niño events (the Bjerknes feedback; Bjerknes 1969). Conversely, surface heat fluxes damp the SSTAs (hereafter thermodynamic damping), though ocean dynamics still play a role in event damping. Positive sea surface temperature anomalies increase the vertical specific humidity gradient near the surface, hence increasing evaporation (latent heat feedback). Atmospheric circulation shifts during El Niño events also result in more cloud cover in the east, largely a response to increasing atmospheric ascent, reducing surface downward shortwave radiation (shortwave feedback). These responses have a cooling effect on the initial positive SSTA.

Methods to quantify these ENSO feedbacks are often based on simple linear models of ENSO [e.g., the Bjerknes stability index (BJ index); Jin et al. 2006; Kim and Jin 2011a]. The thermodynamic damping is one of the most dominant of these feedbacks. This is often simply defined as the regression coefficient of east

Corresponding author: Samantha Ferrett, s.ferrett@exeter.ac.uk

DOI: 10.1175/JCLI-D-17-0331.1

© 2018 American Meteorological Society. For information regarding reuse of this content and general copyright information, consult the AMS Copyright Policy (www.ametsoc.org/PUBSReuseLicenses).

equatorial Pacific area-averaged surface heat flux anomalies against east Pacific SSTAs. Thermodynamic damping consists of four components corresponding to four surface heat fluxes: latent heat flux, sensible heat flux, shortwave radiation, and longwave radiation. Ultimately, as described above, latent heat flux and shortwave radiation are the largest contributors and drive the ENSO thermodynamic damping (Lloyd et al. 2009). Coupled climate models have been found to struggle to fully capture observational estimates of ENSO characteristics, such as amplitude, spatial structure, and frequency of events (Capotondi et al. 2006; Zhang et al. 2013; Bellenger et al. 2014). Indeed, ENSO-related SSTAs show a great deal of variation in strength among coupled models (Fig. 1a). Thermodynamic damping is one of the main sources of error for ENSO in coupled climate models (Jin et al. 2006; Lloyd et al. 2009; Kim and Jin 2011a; Kim et al. 2014a).

Persistent coupled model biases in the equatorial Pacific mean climate are the cold tongue and double-ITCZ biases (Mechoso et al. 1995; AchutaRao and Sperber 2006; Lin 2007; de Szoeke and Xie 2008; Vannière et al. 2013, 2014; Li and Xie 2014; Zhang et al. 2015). Cooler temperatures along the equator, an indicator of the cold tongue bias, have been linked to the strength of thermodynamic damping during ENSO in coupled climate models (Kim et al. 2014a; Ferrett and Collins 2016). Of particular relevance to shortwave feedback is the established relationship between mean equatorial Pacific sea surface temperatures and the precipitation response during ENSO events (Sun et al. 2006, 2009; Chen et al. 2013). Despite this, a more recent study by Li et al. (2015), which decomposes shortwave feedback in a subset of the most recent generation of coupled climate models (CMIP5; Taylor et al. 2012), was unable to robustly link shortwave feedback variation to other mean climate biases. However, they did note that the vertical distribution of cloud over the equatorial Pacific is different in three CMIP5 models with the strongest negative shortwave feedbacks than those with a weaker negative shortwave feedback (see Fig. 14 of Li et al. 2015). Significant links have been identified between the mean climate in the equatorial Pacific and latent heat feedback in the CMIP5 models (Ferrett et al. 2017). As the strength of latent heat and shortwave (SW) feedback in CMIP5 tend to vary with one another (Fig. 1b), this study aims to highlight any links between the SW feedback bias and mean state bias in coupled models. The atmosphere-only runs (AMIP) are also studied in order to gain further insight into underlying causes of El Niño feedback and mean state bias.

Variation in the strength of ocean–atmosphere processes responsible for ENSO events in coupled climate

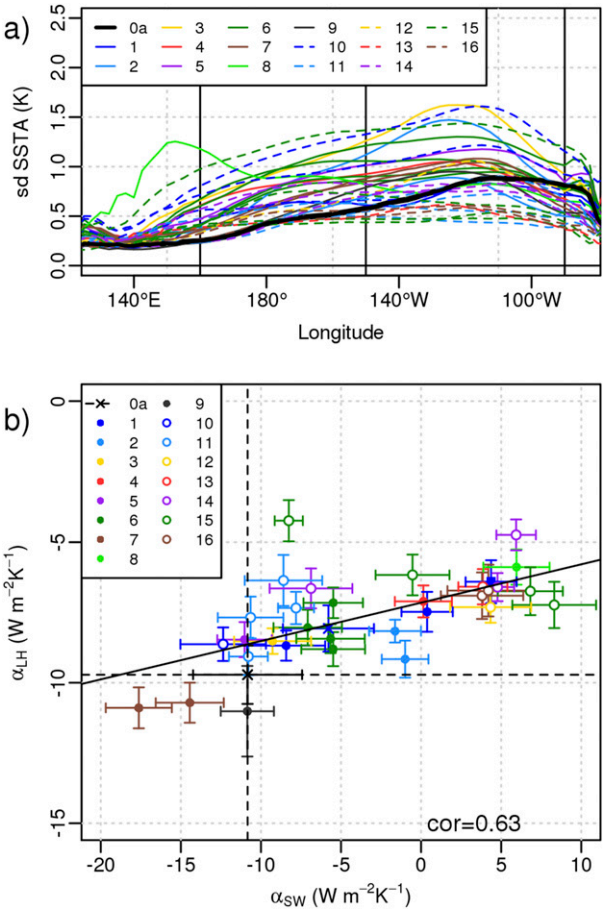

FIG. 1. CMIP5 (a) standard deviation of equatorial mean (averaged over latitude 5°S–5°N) SSTAs as a function of longitude. Niño-4 (160°E–150°W) and Niño-3 (150°–90°W) longitude bounds are shown using vertical black lines, (b) latent heat feedback α_{LH} plotted against El Niño shortwave feedback α_{SW}. Error bars indicate the 95% confidence intervals in the linear fits used in the feedback calculation. Correlations of the relationships for CMIP5 ensemble members are printed on the figure. The fitting line indicates a relationship significant at the 95% level (Student's t test). Model numbers relate to those given in Table 1, and the observational estimates are shown using dashed lines.

models are a significant source of uncertainty in ENSO projections (Sun et al. 2003, 2006; Lloyd et al. 2009, 2012; Kim and Jin 2011b; Kim et al. 2014a,b; Bellenger et al. 2014; Li et al. 2015; Chen et al. 2015, 2017). For example, Kim et al. (2014b) find that using only coupled models that best represent observed ENSO feedbacks results in more robust projections of changes in ENSO amplitude and growth rate in a warming climate. Projections of increasing frequency of extreme ENSO events (Cai et al. 2014) are also based on changes in ENSO-related precipitation anomalies, which are strongly linked to both latent heat and SW processes. Links between mean state biases and ENSO feedback biases ultimately highlight

areas to prioritize in future model development and can help improve confidence in model projections.

Here, the SW feedback decomposition proposed in previous studies (Li et al. 2014, 2015) is used to explore the possible link between common mean state biases (i.e., cold tongue and double-ITCZ biases) and the ocean–atmosphere couplings that drive SW heat flux during El Niño events in the CMIP5 ensemble. The layout of the study is as follows: Details of the CMIP5, AMIP, and observation datasets used are given in section 2. The decomposition of SW feedback used in the analysis is outlined in section 3. Section 4 describes the results of the CMIP5 and AMIP SW feedback analysis and relationships between SW feedback and the equatorial Pacific mean state. A brief summary of the results is given in section 5.

2. Data

a. CMIP5 and AMIP

This study uses historical experiments over the time period 1950–99 for 33 coupled climate models from the World Climate Research Programme (WCRP) CMIP5 multimodel ensemble (Taylor et al. 2012). Details of the models used are given in Table 1 and are chosen based on availability of monthly fields of the required variables. Three-dimensional cloud area fraction is used for a subset of the models, indicated in Table 1. Results from CMIP5 models are also compared to AMIP (Taylor et al. 2012) runs for 15 of the coupled models, indicated in Table 1 by an asterisk by the model name. AMIP analysis is over the time period 1979–2008.

b. Observations and reanalyses

A number of observation and reanalysis datasets are used in comparison to the CMIP5 models. These are ECMWF ERA-Interim (hereafter ERA-I; Dee et al. 2011), objectively analyzed air–sea heat fluxes (OAFlux; Yu and Weller 2007), International Satellite Cloud Climatology Project (ISCCP; Schiffer and Rossow 1983), NCEP–DOE AMIP-II reanalysis (NCEP2; Kanamitsu et al. 2002), Global Precipitation Climatology Project version 2.3 combined precipitation dataset (GPCP; Adler et al. 2003), and Modern-Era Retrospective Analysis for Research and Applications, version 2 (MERRA-2; Gelaro et al. 2017). Shortwave and longwave radiation for OAFlux are provided by ISCCP. Time periods for observations are given in Table 1. Cloud fraction data that may have been used for feedback calculation for Clouds and the Earth's Radiant Energy System (CERES) are not used as the analysis time period is limited enough that there is large uncertainty when linear regression is performed.

3. Methods: El Niño shortwave feedback decomposition

A number of studies highlight biases in the strength of ocean–atmosphere couplings, such as atmospheric circulation and cloud feedbacks, that can be linked to SW feedback bias and variation (Lloyd et al. 2012; Chen et al. 2013; Sun et al. 2009). The SW feedback decomposition method proposed by Li et al. (2014) enables assessment of the relative importance of these couplings to ENSO SW feedback allowing for the isolation of underlying causes of bias. This expands on a decomposition method used by Lloyd et al. (2012) that accounts only for the contribution to shortwave heat flux of processes arising from atmospheric ascent responses to SST. Li et al. (2014) build on this to include processes related to anomalous relative humidity and liquid water path.

El Niño SW feedback, α_{SW}, is calculated by linear regression of downward surface SW heat flux seasonal anomalies, Q_{SW}, averaged over the Niño-3 region (longitude 150°–90°W; latitude 5°S–5°N) on Niño-3 SSTAs, T, such that

$$\alpha_{SW} = \frac{dQ_{SW}}{dT}. \quad (1)$$

Data are detrended prior to calculation, and seasonal anomalies are calculated from monthly fields by removing the mean annual cycle. The decomposition proposed by Li et al. (2014) allows for the separation of the SW feedback into components that represent various atmospheric processes, where

$$\alpha_{SW} = \mathrm{CLDF} + \mathrm{LWPF} = \mathrm{DY} + \mathrm{RHF} + \mathrm{LWPF}. \quad (2)$$

CLDF represents the shortwave heat flux response driven by the response of cloud cover to an SST anomaly:

$$\mathrm{CLDF} = \frac{\partial Q_{SW}}{\partial \mathrm{cld}} \frac{d\mathrm{cld}}{dT}, \quad (3)$$

where $d\mathrm{cld}/dT$ is the response of total cloud cover (cld) to an SSTA, calculated using linear regression. Similarly, $\partial Q_{SW}/\partial \mathrm{cld}$ is the response of the shortwave heat flux to that cloud cover anomaly. The anomalous shortwave heat flux will then affect SST, resulting in a feedback loop. These terms calculated over Niño-3 are referred to as El Niño feedbacks; CLDF is here named the cloud feedback. CLDF can be further split into a dynamical cloud feedback (DY), representing the response of the effects of atmospheric ascent at 500 hPa, ω_{500}, on cloud cover, and therefore SW heat flux, and a surface relative humidity (rh) cloud feedback (RHF):

TABLE 1. Table of model names used in this study. Both atmosphere-only and coupled versions are analyzed. Models used in atmosphere-only analysis are indicated using an asterisk. Models with ISSCP-simulator variables are indicated in bold. Note that three-dimensional cloud was not available for models 1a, 1b, 7a, 7b, 9, 12, and 15c.

No.	Name	Modeling center/notes
0a	OAFlux/ISCCP	Provides shortwave heat flux, cloud area fraction; 1984–2007
	GPCP	Precipitation; 1980–2009
	ERA-Interim	SST, LWP, ω_{500}, relative humidity; 1984–2007
0b	NCEP2	1984–2009
0c	MERRA-2	1984–2009
1a	ACCESS1.0*	CSIRO and Bureau of Meteorology (BOM), Australia
1b	ACCESS1.3*	
2a	BCC_CSM1.1	Beijing Climate Center, China Meteorological Administration
2b	BCC_CSM1.1(m)	
3	BNU-ESM*	College of Global Change and Earth System Science, Beijing Normal University
4	**CanESM2**	Canadian Centre for Climate Modelling and Analysis
5	CCSM4*	National Center for Atmospheric Research
6a	CESM1(BGC)	Community Earth System Model contributors
6b	CESM1(CAM5)*	
6c	CESM1(FASTCHEM)	
6d	CESM1(WACCM)	
7a	CNRM-CM5*	Centre National de Recherches Météorologiques/Centre Européen de Recherche et Formation Avancée en Calcul Scientifique
7b	CNRM-CM5–2	
8	CSIRO Mk3.6.0*	Commonwealth Scientific and Industrial Research Organization in collaboration with Queensland Climate Change Centre of Excellence
9	FGOALS-g2	LASG, Institute of Atmospheric Physics, Chinese Academy of Sciences, and CESS, Tsinghua University
10a	GFDL CM3*	NOAA/Geophysical Fluid Dynamics Laboratory
10b	GFDL-ESM2G	
10c	GFDL-ESM2M	
11a	GISS-E2-H	NASA Goddard Institute for Space Studies
11b	GISS-E2-H-CC	
11c	GISS-E2-R	
11d	GISS-E2-R-CC	
12	**HadGEM2-ES***	Met Office Hadley Centre (additional realizations contributed by Instituto Nacional de Pesquisas Espaciais)
13	INM-CM4.0*	Institute for Numerical Mathematics
14a	IPSL-CM5A-LR*	L'Institut Pierre-Simon Laplace
14b	IPSL-CM5A-MR*	
14c	IPSL-CM5B-LR*	
15a	**MIROC-ESM**	Japan Agency for Marine-Earth Science and Technology, Atmosphere and Ocean Research Institute (University of Tokyo), and National Institute for Environmental Studies
15b	**MIROC-ESM-CHEM**	
15c	MIROC4h	Atmosphere and Ocean Research Institute (University of Tokyo), National Institute for Environmental Studies, and Japan Agency for Marine-Earth Science and Technology
15d	**MIROC5***	
16a	**MRI-CGCM3***	Meteorological Research Institute
16b	MRI-ESM1	

$$\mathrm{DY} = \frac{\partial Q_{\mathrm{SW}}}{\partial \mathrm{cld}} \frac{\partial \mathrm{cld}}{\partial \omega_{500}} \frac{d\omega_{500}}{dT} \quad \text{and} \tag{4}$$

$$\mathrm{RHF} = \frac{\partial Q_{\mathrm{SW}}}{\partial \mathrm{cld}} \frac{\partial \mathrm{cld}}{\partial \mathrm{rh}} \frac{d\mathrm{rh}}{dT}. \tag{5}$$

Note that the pressure tendency anomaly at 500 hPa, ω_{500}, is used; therefore, negative ω_{500} corresponds to atmospheric ascent. Shortwave heat flux is also strongly linked to cloud liquid water path, the column amount of liquid water in the cloud, as this determines cloud optical thickness. Therefore, the contribution of anomalous liquid water in clouds to shortwave heat flux feedback (LWPF) is given as

$$\mathrm{LWPF} = \frac{\partial Q_{\mathrm{SW}}}{\partial \mathrm{lwp}} \frac{d\mathrm{lwp}}{dT}. \tag{6}$$

In the text $d\omega_{500}/dT$, $\partial\mathrm{cld}/\partial\mathrm{rh}$, and $d\mathrm{lwp}/dT$ are referred to as the ω_{500}–SST coupling, the cloud–RH coupling, and the LWP–SST coupling, respectively. See also Eqs. (2) and (3) of Li et al. (2014) for the SW feedback decomposition into DY, RHF, and LWPF components. This study focuses on all components, unlike in Li et al. (2014) where the focus was mainly on total cloud, dynamical, and LWP feedbacks. This has allowed for greater insight into the SW feedback bias, in relation to the mean state bias.

Studies that quantify shortwave feedback using linear regression must account for the nonlinearity of the shortwave heat flux in response to SSTAs (Lloyd et al. 2012; Bellenger et al. 2014). The assumption of linearity is not always valid as the shortwave response during ENSO events can be asymmetric. During an El Niño, a positive SST anomaly in a region of atmospheric ascent results in an increase in convective clouds, reducing the shortwave radiation reaching the surface (Ramanathan and Collins 1991). However, during the ENSO cool phase, La Niña, a decrease in SST can increase both the static stability in the atmospheric boundary layer and the amount of stratiform clouds (Klein and Hartmann 1993; Philander et al. 1996), also decreasing the shortwave heat flux at the surface. This observed nonlinearity (i.e., less downward surface SW during both El Niño and La Niña) also tends not to be fully captured in coupled climate models (Lloyd et al. 2012; Bellenger et al. 2014). As a consequence of this nonlinear behavior, it is more appropriate to separately consider the feedback during El Niño and La Niña events (e.g., Lloyd et al. 2012; Bellenger et al. 2014; Li et al. 2015). This is opposed to assuming a linear relationship between anomalous shortwave heat flux and SSTA over both El Niño and La Niña events. Here, the focus will be only on assessing the feedback on positive SSTAs (El Niño) in CMIP5. Study of La Niña–only feedbacks gave very similar results when relating variations of SW feedbacks to the mean state, so these results have been omitted. To obtain a feedback during El Niño events only, linear regressions are calculated using positive Niño-3 SSTAs ($T > 0\,\mathrm{K}$). We note that using a different threshold for feedback calculation, such as $T > 0.5\,\mathrm{K}$, results in feedbacks not significantly different from those calculated for positive T. Similarly, results are found to be relatively insensitive to the choice of boundaries for area averaging. Feedbacks calculated using these alternatives are found to be highly correlated with those calculated using the methods in this study.

Error bars for feedbacks are based on the 95% confidence interval for the linear least squares regression fits used in the calculation of the couplings. This is calculated using the linear fit standard error and the 97.5th percentile of the Student's t distribution.

4. Results

a. *ENSO SSTAs and El Niño shortwave feedback in CMIP5*

The standard deviation of SSTAs can be used to indicate the strength and zonal location of El Niño/La Niña events along the equator (Fig. 1a). In reanalyses, SSTAs are strongest in the east equatorial Pacific. This peak in the east Pacific is present in many of the CMIP5 models but can occur at different strengths. Some models feature a larger peak in the Niño-3 region than in observations (e.g., BNU-ESM, GFDL-ESM2M, and MIROC5). However, others (e.g., MIROC4h and CSIRO Mk3.6.0) have SSTA peaks located toward the west equatorial Pacific. Generally, models used in this study display a range of SSTA variability in the east equatorial Pacific with little consistent bias in the strength. Other characteristics of ENSO, such as frequency, in CMIP5 models show similar variation (Bellenger et al. 2014).

SW feedback and the three components, DY [Eq. (4)], RHF [Eq. (5)], and LWPF [Eq. (6)], calculated for CMIP5 and two sets of observations are shown in Fig. 2. The reanalyses, ERA-I/OAFlux (marked 0a), NCEP2 (marked 0b), and MERRA-2 (marked 0c), have SW feedback during El Niño events that is negative with strengths of -10.8 ± 3.4, -6.4 ± 2.7, and $-13.6 \pm 3.8\,\mathrm{W\,m^{-2}\,K^{-1}}$, respectively (i.e., surface SW fluxes damp the positive El Niño SST anomalies). The SW feedback is also mostly driven by DY processes that have a strength of $-11.5\,\mathrm{W\,m^{-2}\,K^{-1}}$ in ERA-I/OAFlux, $-5.8\,\mathrm{W\,m^{-2}\,K^{-1}}$ in NCEP2, and $-8.0\,\mathrm{W\,m^{-2}\,K^{-1}}$ in MERRA-2 (Figs. 2a,b).

SW feedback strength tends to vary a relatively large amount throughout the CMIP5 ensemble. In comparison to ERA-I/OAFlux, 16 models have significantly weak negative SW feedback (outside of the observational 95% confidence intervals), and 8 models even have positive SW feedback. A positive SW feedback demonstrates an increase in surface downward shortwave radiation during El Niño events, increasing the initial SST anomaly. Many of the CMIP5 models have a weak negative dynamical feedback in comparison to observations. This is shown to be the most consistent source of bias with 23 CMIP5 models having DY significantly weaker than the observed (ERA-I/OAFlux) feedback (Fig. 2b). This is in agreement with previous studies that find this to be a persistent bias of coupled climate models (Lloyd et al. 2012; Chen et al. 2013; Li et al. 2015). The number of biased models is reduced when comparing CMIP5 with NCEP2 (0b) as the NCEP2 SW feedback and DY are somewhat weaker than ERA-I/OAFlux. This demonstrates the uncertainty that exists between the reanalyses.

The remaining two feedbacks are somewhat smaller in observations (ERA-I/OAFlux has -0.1 and $0.6\,\mathrm{W\,m^{-2}\,K^{-1}}$ for RHF and LWPF, respectively) though still tend to vary in strength in the CMIP5 ensemble (Figs. 2c,d). LWPF is strongly negative in 12 of the CMIP5 models. This counteracts the DY bias in these models, resulting in a SW feedback closer to the observed strength that is

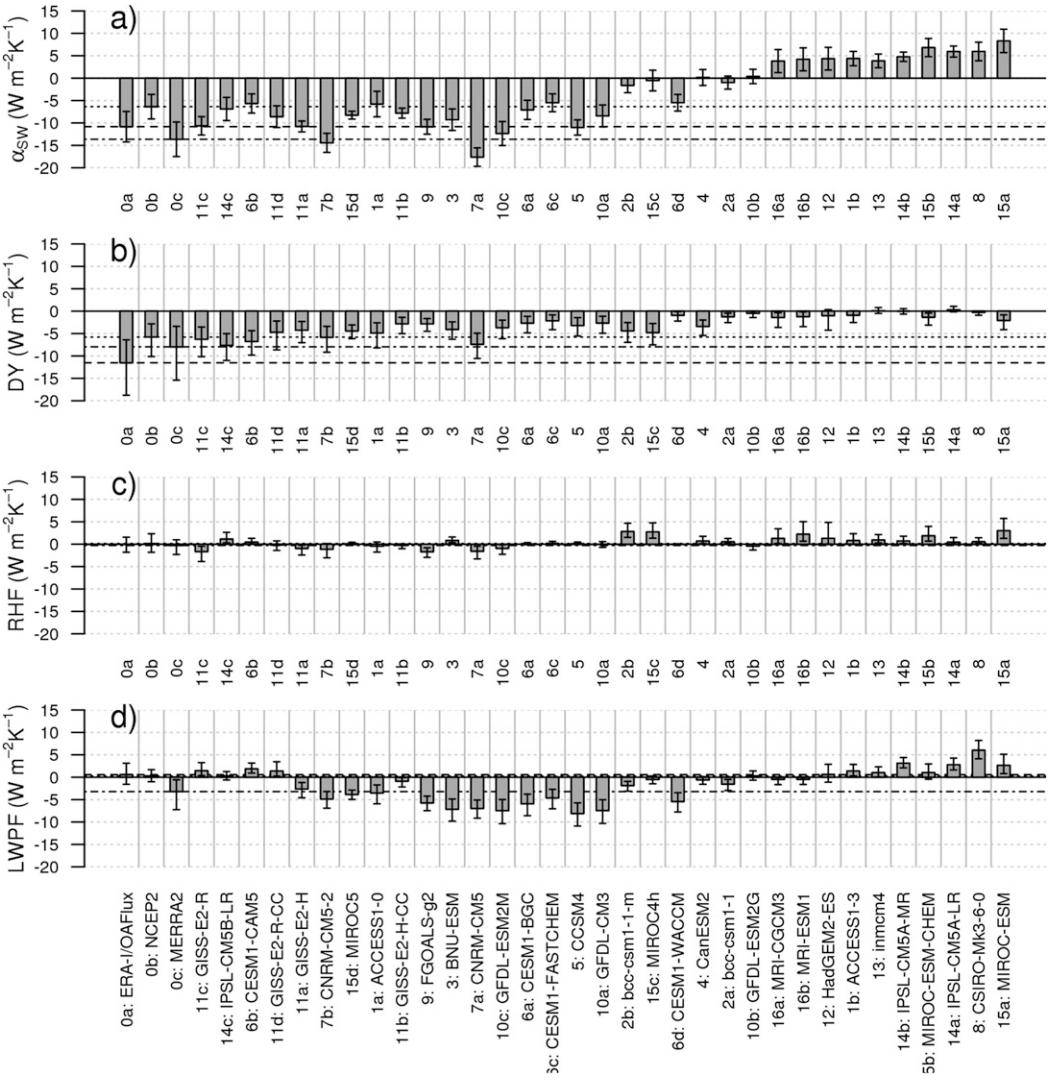

FIG. 2. CMIP5 El Niño (a) shortwave feedback (regression of Niño-3 Q_{SW} anomalies against Niño-3 SSTA for SSTA > 0), (b) DY, (c) RHF, and (d) LWPF. Error bars indicate the 95% confidence intervals in the linear fits used in the feedback calculation. CMIP5 models are ordered by the root-mean-square error of SW feedback, DY, RHF, and LWPF with the 0a feedbacks. Estimates from observations are also given and are shown by dashed (ERA-I/OAFlux), dotted (NCEP2), and dot–dashed (MERRA-2) horizontal lines.

more driven by the liquid water path response. Therefore, models that have more accurate SW feedback may still have underlying feedback errors. In the models with positive SW feedback, DY is closer to zero and both RHF and LWPF are strongly positive. The sum of the individual components can be different compared to SW damping calculated using the model shortwave heat flux field. However, SW damping given by the sum of the components is not significantly different from that calculated using the shortwave heat flux field for any of the CMIP5 models, when taking into account the 95% confidence intervals of the linear fits. As such, differences between the SW feedback and the sum of the components can be accounted for by the uncertainty in the linear regression analysis. Biases such as those shown in Fig. 2 may be indicative of spatial biases in the feedbacks. This is examined in more detail later.

Although DY dominates SW feedback in observations, the weaker feedbacks, RHF and LWPF, are still of importance when assessing model bias or the variation of SW feedback strength within an ensemble (Fig. 2). SW feedback variation among CMIP5 models is strongly related to variation in the cloud cover response to SSTAs (Fig. 3a; correlation of −0.93). SW feedback bias is largely a result of negative bias in the cloud–SST coupling. The cloud–SST coupling is important to both

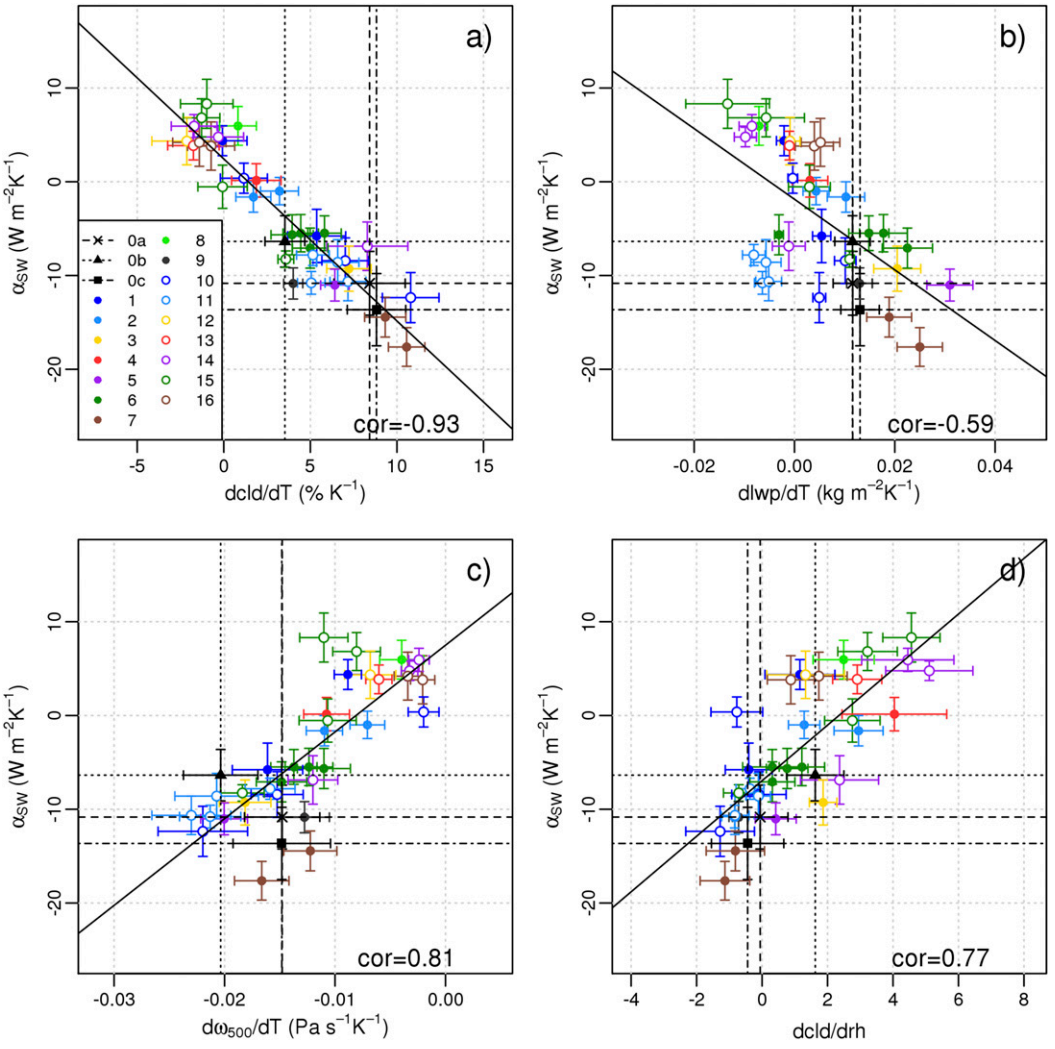

FIG. 3. CMIP5 El Niño shortwave feedback plotted against (a) cloud–SST coupling, (b) LWP–SST coupling, (c) ω_{500}– SST coupling, and (d) cloud–RH coupling. Error bars indicate the 95% confidence intervals in the linear fits used in the feedback calculation. Correlations of the relationships for CMIP5 ensemble members are printed on figures. The fitting line indicates a relationship significant at the 95% level (t test). Observational estimates are shown by dashed (ERA-I/OAFlux), dotted (NCEP2), and dot–dashed (MERRA-2) lines.

relative humidity cloud and dynamical cloud feedbacks and contains a relative humidity component and an atmospheric ascent component [Eqs. (4) and (5)].

Variations in both RHF and DY components among CMIP5 models contribute to SW feedback variation (Figs. 3c,d). Significant positive correlations are found between SW feedback and the ω_{500}–SST coupling (correlation of 0.81) and the cloud–RH coupling (correlation of 0.77). The relationship between SW feedback and the cloud–RH coupling suggests that, although RHF tends to be smaller in magnitude than DY and LWPF, it is still linked to the variation of SW feedback strength between models (see Table 2 also). It is also noted that while the total SW feedback components (DY, RHF, and LWPF) are not strongly related to one another, certain ocean–atmosphere couplings that contribute to each of the components are in fact related. The cloud–RH coupling varies with the ω_{500}–SST coupling, as well as LWPF (Table 2). Models with a strong positive cloud response to relative humidity anomalies and a positive ω_{500}–SST coupling bias tend to be models with a larger positive SW feedback bias. Finally, a component of LWPF is also related to variation in the strength of SW feedback among models. A relatively weak, but still significant, correlation of −0.59 exists between SW feedback and the LWP–SST coupling (Fig. 3b).

A study of CMIP3 models found that damping by SW flux was larger in models with weaker ENSO events

TABLE 2. Correlations between Niño-3 (N3) CMIP5 std dev of SSTA (ENSO amplitude), SW feedback, DY, RHF, LWPF, ω_{500}–SST coupling $d\omega_{500}/dT$, cloud–relative humidity coupling $\partial\text{cld}/\partial\text{rh}$, and liquid water path–SST coupling $d\text{lwp}/dT$. Correlations significant at 95% level by a Student's t test are in bold.

	Std dev N3 SSTA						
SW	**−0.48**	SW					
DY	−0.21	**0.72**	DY				
RHF	−0.22	**0.73**	0.29	RHF			
LWPF	**−0.65**	**0.74**	0.32	**0.42**	LWPF		
$\frac{d\omega_{500}}{dT}$	−0.39	**0.81**	**0.65**	**0.50**	**0.58**	$\frac{d\omega_{500}}{dT}$	
$\frac{\partial\text{cld}}{\partial\text{rh}}$	−0.27	**0.77**	**0.41**	**0.73**	**0.57**	**0.59**	$\frac{\partial\text{cld}}{\partial\text{rh}}$
$\frac{d\text{lwp}}{dT}$	**0.59**	**−0.59**	−0.27	−0.28	**−0.86**	−0.34	**−0.41**

(Lloyd et al. 2012). However, a more recent study on a subset of CMIP5 models found no obvious relationship between the two (Chen et al. 2013). Here, a slightly stronger relationship between SW feedback and ENSO amplitude is found compared with that shown by Chen et al. (2013), and is in contrast to the positive relationship found by Lloyd et al. (2012) (see Table 2). However, it is still relatively weak (correlation of −0.48) and only persists for LWPF (correlation of −0.65). The remaining two components, DY and RHF, have insignificant relationships with ENSO amplitude. This is most likely due to contributions of other feedbacks to the strength of El Niño events [e.g., as demonstrated by ENSO stability studies such as Kim and Jin (2011a,b)]. These weak relationships also suggest that significant differences can exist between modeled atmospheric responses to equivalent-strength El Niño SSTAs.

Variation in El Niño feedbacks can be a result of spatial biases, both in the mean climate and in El Niño responses. This is demonstrated by the feedbacks in Fig. 4 plotted against longitude over the equatorial Pacific. In observations, the shortwave response to Niño-3 SSTAs peaks in the central equatorial Pacific and is negative east of approximately 170°E (Fig. 4a). This demonstrates a decrease in the downward surface shortwave radiation in these regions during El Niño, cooling the SST there. Some of the CMIP5 models replicate the spatial pattern of this damping well; however, others have spatial biases. Calculating spatial correlations of α_{SW} (shortwave heat flux regressed on Niño-3 SSTA) over the tropical Pacific with the observed α_{SW} finds that 14 of the CMIP5 models have a spatial correlation less than 0.6 (not shown in figures). A correlation below this level also indicates that the CMIP5 model has a larger bias in Niño-3 SW feedback, with a value above $-1.0\,\text{W}\,\text{m}^{-2}\,\text{K}^{-1}$ (the value corresponding to BCC_CSM1.1 in Fig. 2). SW feedback in CMIP5 can be too strongly positive in the east equatorial Pacific compared with observations, indicating increasing SW flux during El Niño events, warming the SST. Some CMIP5 models also have a westward-shifted shortwave El Niño response compared with the observed response that consequently results in weaker negative, or positive, SW feedback in the east.

The CMIP5 ω_{500}–SST coupling has similar spatial biases to those of the SW feedback (Fig. 4b). This suggests this is the main driver of the westward-shifted SW feedback in Fig. 4a. It is possible this is a result of the persistent coupled climate model cold tongue bias, characterized by cool temperatures along the equator, which result in a westward shift of El Niño–related SST variance, as well as a westward shift of the ascending branch of the Walker circulation in the mean state. This means that the atmospheric response during El Niño will also tend to be shifted westward, hence weakening the ω_{500}–SST coupling in the east equatorial Pacific. This possible link between ω_{500}–SST coupling and the cold tongue bias is assessed in section 4b.

The spatial distribution of the other dominating component, cloud–RH coupling, is shown in Fig. 4c. During El Niño events, a negative RH anomaly exists in response to positive SSTA. In this case, observations have a negative cloud–RH coupling toward the west equatorial Pacific, corresponding to increasing cloud there during El Niño events, and therefore reduced SW. Conversely, there is a positive response to anomalous surface RH toward the east Pacific. Some models have a positive coupling in the east that is too strong, and this, in combination with weak ω_{500}–SST coupling (Fig. 4b), results in a significantly positive Niño-3 SW feedback for 10 CMIP5 models; both MIROC-ESM models, both IPSL-CM5A models, both MRI models, CSIRO Mk3.6.0, INM-CM4.0, ACCESS1.3, and HadGEM2-ES (Figs. 4a and 2a). CMIP5 models can also have a cloud–RH coupling spatial pattern in contrast to observations that contributes to a negative SW feedback. These models tend to have a negative coupling in the east Pacific

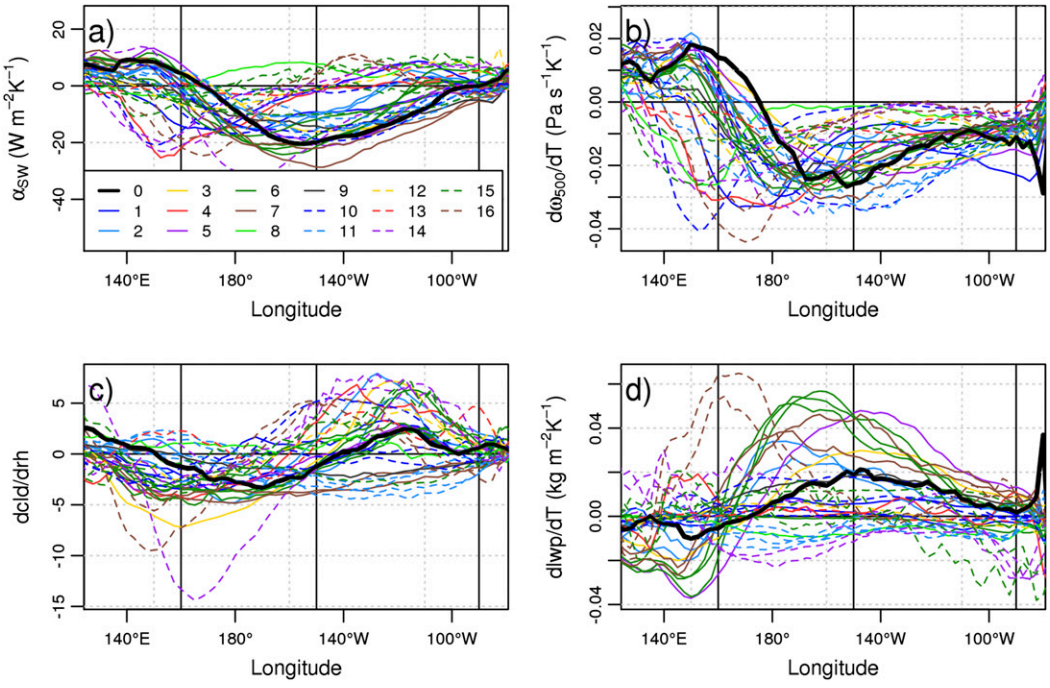

FIG. 4. (a) CMIP5 and observed SW feedback (shortwave radiation heat flux seasonal anomalies regressed on Niño-3 SSTA) as a function of longitude, averaged over latitude 5°S–5°N; (b) as in (a), but for ω_{500}–SST coupling (atmospheric ascent seasonal anomalies regressed on Niño-3 SSTA); (c) as in (a), but for cloud–RH coupling (total cloud cover seasonal anomalies regressed on Niño-3 surface relative humidity anomalies); (d) as in (a), but for LWP–SST coupling (cloud liquid water path seasonal anomalies regressed on Niño-3 SSTA). Niño-3 (longitude 150°–90°W) and Niño-4 (longitude 160°E–150°W) regions are shown using vertical black lines. CMIP5 results are shown using colored solid and dashed lines; observations (ERA-I/OAFlux) are shown using a thick solid black line. All regressions are calculated for SSTA > 0.

and a more positive coupling in the west Pacific (Fig. 4c). Twelve CMIP5 models have a negative Niño-3 cloud–RH coupling (Fig. 3d).

The observed LWP–SST coupling has a positive peak in the central equatorial Pacific, demonstrating an increased optical thickness of the clouds there during El Niño (Fig. 4d). Similar to the cloud–RH coupling, models show large variance in the sign of this coupling. There are also large positive biases in the west equatorial Pacific, with westward shifts in some models' peak LWP–SST coupling. As a result of these biases, 4 CMIP5 models have significantly strong LWP–SST coupling in Niño-3 and 20 models have significantly weak LWP–SST coupling in Niño-3. The westward shift of LWP variability in some models appears of a similar nature to the biases of both SW feedback and the ω_{500}–SST coupling, despite the weaker relationship LWP–SST coupling has with SW feedback (Fig. 3).

These coupling biases and variation are further investigated by assessing any relationship they may have with the mean state, known to be linked to ENSO-related ocean–atmosphere couplings (e.g., Guilyardi et al. 2009; Kim et al. 2014a; Ferrett and Collins 2016; Ferrett et al. 2017).

b. *Relationships between coupled model mean climate and shortwave feedback processes*

Variations in SW feedback among the CMIP5 models basically demonstrate two regimes of the SW feedback. The first is a negative regime dominated by a negative dynamical feedback and, in some CMIP5 models, negative liquid water path feedback; that is, a positive SSTA induces atmospheric ascent, and convective clouds form and reduce the downward surface SW flux (Ramanathan and Collins 1991). Models with a negative SW feedback have stronger positive cloud feedbacks at higher altitudes in the Niño-3 region (Fig. 5b). The second is a positive regime, not present in the east equatorial Pacific during observed El Niños, that is demonstrated by weak dynamical cloud feedback and positive relative humidity and liquid water path feedbacks. A positive SSTA can decrease static stability, breaking up stratiform clouds and increasing SW flux (Klein and Hartmann 1993; Philander et al. 1996). Models with positive SW feedbacks have a negative cloud feedback at lower altitudes in the Niño-3 region that is not present in models with negative SW feedbacks

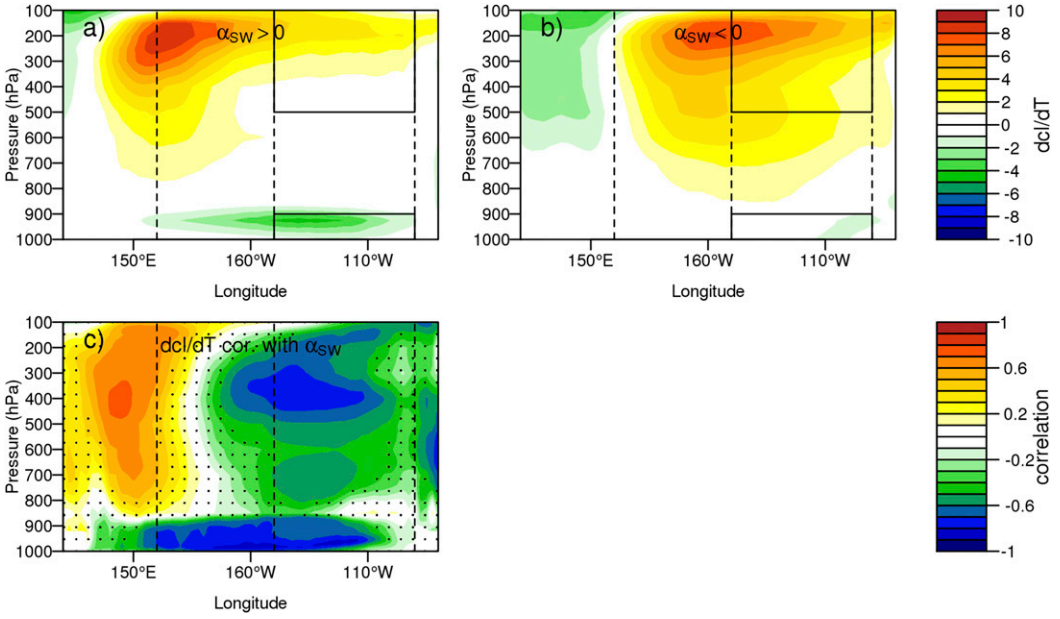

FIG. 5. (a) Cloud fraction seasonal anomalies (%; averaged over latitude 5°S–5°N) regressed onto Niño-3 SSTAs (cloud feedback) for CMIP5 models with positive Niño-3 SW feedback; (b) as in (a), but for CMIP5 models with negative SW feedback; (c) correlation of CMIP5 cloud feedback (averaged over latitude 5°S–5°N) at each grid point with CMIP5 Niño-3 SW feedback. Regions where correlation is below 95% significance (*t* test) are stippled. Niño-3 and Niño-4 regions are shown using vertical dashed lines. Boxed regions in (a) and (b) show the high (500–100 hPa) and low cloud (1000–900 hPa) regions for the high and low cloud feedback calculation.

(Fig. 5a). Furthermore, variation in the SW feedback can be significantly linked to these variations in cloud feedbacks at different altitudes (Fig. 5c) such that models with a more positive SW feedback have reduced Niño-3 high cloud feedback and more negative low cloud feedback. This is shown by significant negative correlations in these regions between Niño-3 surface SW feedback and cloud feedback. This is also confirmed by examining the relationship of the SW feedback with area-averaged Niño-3 low cloud (pressure 1000–900 hPa) feedback and Niño-3 high cloud (500–100 hPa) feedback. Correlations of −0.81 and −0.71 are found between the SW feedback and low cloud and high cloud feedbacks, respectively (Fig. 6).

The variation among the CMIP5 models between two SW feedback regimes is also supported by the link found between CMIP5 ω_{500}–SST coupling and cloud–RH coupling (Table 2; correlation of 0.59). A model with a more negative ω_{500}–SST coupling tends to also have more negative cloud–RH coupling and vice versa. SW feedback is dominated by either a negative regime or a positive regime. Both regimes are linked to background conditions, either allowing convection to occur or having more stable atmospheric conditions where stratiform clouds are present. This is shown by the relationships between SW feedbacks and the equatorial Pacific mean climate in Fig. 7. Mean states in Fig. 7 are mainly averaged over the Niño-3 region, as this is the region in which the SW feedback is calculated.

The cloud–RH coupling is linked to mean Niño-3 surface relative humidity (correlation of 0.59; Fig. 7a), such that CMIP5 models with higher mean surface relative humidity in the equatorial Pacific have a stronger positive cloud–RH coupling. This relationship also exists with Niño-4 mean relative humidity (correlation of 0.64), indicating that relative humidity across the full equatorial Pacific basin is important. Models with higher mean surface relative humidity, and the strongest positive cloud–RH couplings (Fig. 7a), may then have a positive SW feedback (Fig. 7e). Models with higher surface relative humidity demonstrate conditions associated with low cloud cover, that is, strong mean atmospheric descent, cool mean surface temperatures, and higher tropospheric static stability (assessed using potential temperature θ at 700 hPa minus θ at the surface; not shown in figures). These conditions would tend toward a positive SW feedback regime, described above and shown in Fig. 5a, and are shown here by a stronger positive cloud–RH coupling. The vertical distribution of cloud is therefore an area of interest in order to confirm that this is indeed an underlying driver of the relationships shown in Fig. 7a and Fig. 7e. This is assessed later.

Aspects of the cold tongue bias, such as mean sea surface temperature and equatorial Pacific precipitation,

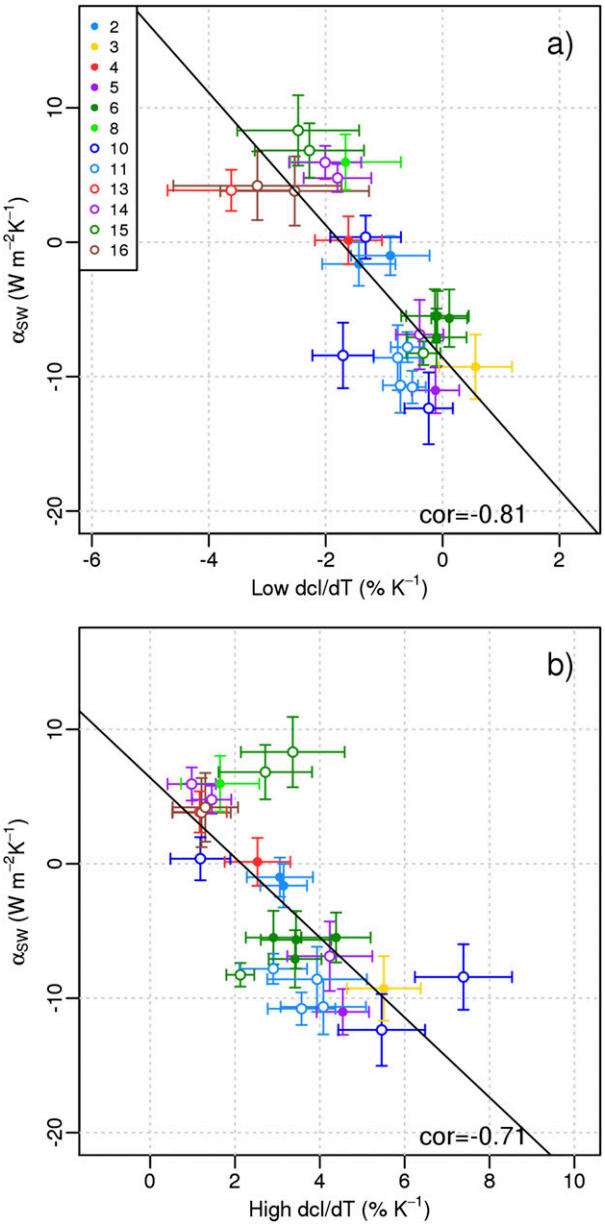

FIG. 6. (a) CMIP5 Niño-3 SW feedback plotted against CMIP5 Niño-3 low cloud (pressure 1000–900 hPa) feedback; (b) as in (a), but with CMIP5 Niño-3 high cloud (pressure 500–100 hPa) feedback on the *x* axis. Error bars indicate the 95% confidence intervals in the linear fits used in the feedback calculation. Correlations of the relationships for CMIP5 ensemble members are printed on figures. The fitting line indicates a relationship significant at the 95% level (*t* test).

can also be linked to dominant SW feedback components, as shown in Fig. 7. Figures 7b and 7c show negative correlations between the ω_{500}–SST coupling and mean Niño-3 temperature and Niño-3 precipitation with correlations of −0.61 and −0.60, respectively. The ω_{500}–SST coupling is also significantly correlated with mean Niño-4 precipitation (correlation of −0.67) and mean Niño-3 and Niño-4 atmospheric ascent (correlations of 0.55 and 0.62, respectively; not shown in figures). These relationships demonstrate that models with cooler temperatures, less precipitation, and less atmospheric ascent in the equatorial Pacific have more precipitation to the far west outside of the Niño-4 region and have weaker atmospheric ascent anomalies in response to SSTAs during El Niño events. Ultimately, the reduced atmospheric ascent anomalies mean less convective cloud cover is formed during El Niño events (via cloud–ω_{500} coupling) and so surface shortwave radiation is not as strongly reduced (via Q_{SW}–cloud coupling). As the ascending branch of the Walker circulation in the mean state tends to be shifted toward the west in models with a larger cold tongue bias, this also shifts the atmospheric ascent response westward (Fig. 4b). This then reduces the feedback in the east equatorial Pacific where damping by SW heat flux is most influential to El Niño events. Therefore, models with a larger cold tongue bias and westward-shifted precipitation tend to have reduced negative SW feedback (Figs. 7f,h). Note that the relationships between SW feedback and the cold tongue bias are somewhat less strong than that with the mean relative humidity. Despite the significant relationship between mean precipitation and the ω_{500}–SST coupling, we also note that Niño-3 precipitation is not strongly linked to the total SW feedback (Fig. 7g). It is possible this is a result of SW feedback variation being more strongly related to relative-humidity-related processes, and mean Niño-4 precipitation is linked to mean surface relative humidity (correlation of −0.83). However, Niño-3 precipitation is not. Niño-4 is also a better measure of spatial bias in the Walker circulation, given the proximity of the ascending branch of the circulation to Niño-4 compared with Niño-3.

Last, the less dominant LWP–SST coupling can be linked to Niño-3 total cloud cover (Fig. 7d). Cloud liquid water path depends on both cloud amount and in-cloud liquid water content; Li and Zhang (2008) link weak LWP–SST coupling in NCAR CAM3 to both weak cloud anomalies and weak in-cloud liquid water anomalies. Here, the relationship between LWP–SST coupling and mean Niño-3 cloud cover indicates that a higher level of mean cloud cover in the east Pacific tends to result in a more negative LWP–SST coupling. A positive relationship exists between LWP–SST coupling and cloud–SST coupling, with a correlation of 0.51 (95% significance; not shown in figures), suggesting that the more negative cloud cover responses in some models play a role in the reduced liquid water path response. Understanding negative cloud-cover responses will help to further understand LWP–SST coupling bias because

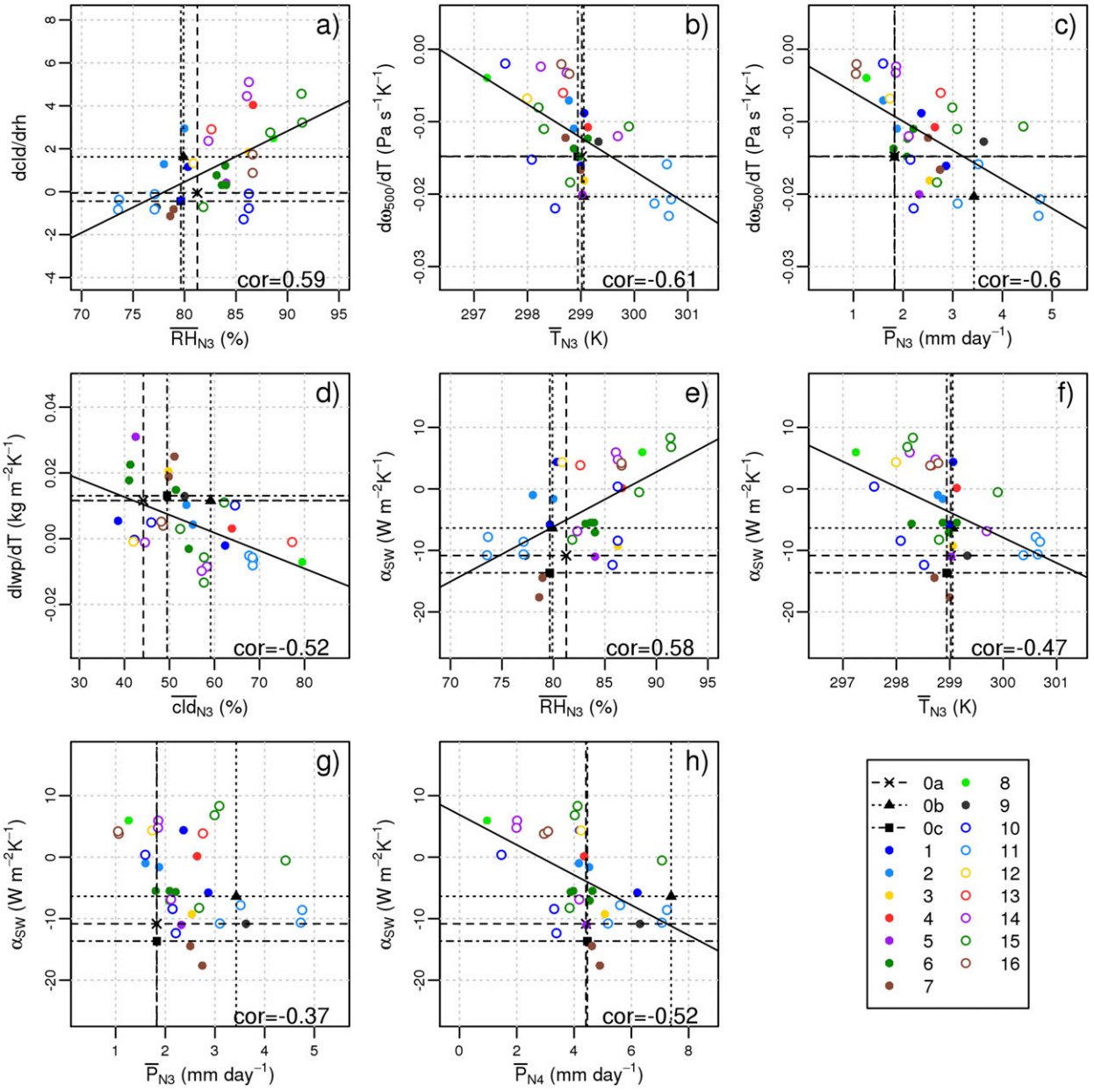

FIG. 7. (a) Cloud–RH coupling plotted against mean Niño-3 relative humidity; (b) ω_{500}–SST coupling against mean Niño-3 SST; (c) ω_{500}–SST coupling against mean Niño-3 precipitation; (d) LWP–SST coupling against mean Niño-3 cloud fraction; (e) SW feedback against mean Niño-3 relative humidity; (f) as in (e), but with mean Niño-3 SST on the *x* axis; (g) as in (e), but with mean Niño-3 precipitation on the *x* axis; (h) as in (e), but with mean Niño-4 precipitation on the *x* axis. Correlations of the relationships for CMIP5 ensemble members are printed on figures. The fitting line indicates a relationship significant at the 95% level (*t* test). Observational estimates are shown by dashed (ERA-I/OAFlux), dotted (NCEP2), and dot–dashed (MERRA-2) lines.

of this, though errors in cloud water content responses will also play a role. Note that mean total cloud cover is not strongly linked to temperature or precipitation measures of the cold tongue bias. Also, the LWP–SST coupling variation is less related to the total SW feedback than cloud–RH and ω_{500}–SST couplings. Therefore, the Niño-3 mean total cloud cover is not found to be significantly linked to the total SW feedback (not shown in figures), but rather the horizontal and vertical distribution of the clouds is of importance. For example, in two models where total cloud cover may be the same, a model with relatively more low cloud cover may have a more biased SW feedback than one with relatively more high cloud cover.

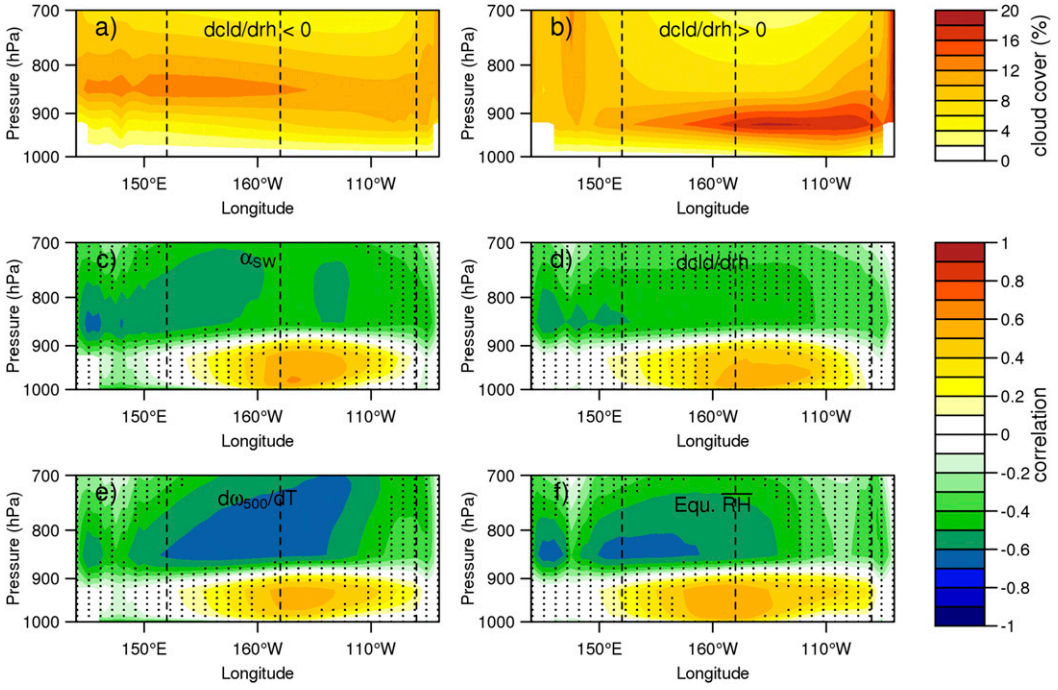

FIG. 8. (a) Mean cloud (%; averaged over latitude 5°S–5°N) for CMIP5 models with negative east Pacific cloud–RH coupling; (b) as in (a), but for CMIP5 models with positive cloud–RH coupling; (c) correlation of CMIP5 time-mean cloud (averaged over latitude 5°S–5°N) at each grid point with CMIP5 east equatorial Pacific SW feedback, α_{SW}; (d) as in (c), but correlated with CMIP5 east equatorial Pacific cloud–RH coupling; (e) as in (c), but correlated with CMIP5 east equatorial Pacific ω_{500}–SST coupling, $d\omega_{500}/dT$; (f) as in (c), but correlated with CMIP5 mean equatorial Pacific (averaged over longitude 160°E–90°W; latitude 5°S–5°N) surface relative humidity. Regions where correlation is below 95% significance (t test) are stippled. Niño-3 and Niño-4 regions are shown using vertical dashed lines.

Ultimately, these results show strong links between the mean equatorial Pacific, including persistent coupled model biases, and ENSO SW feedback processes in the CMIP5 models. In particular, links between the mean climate and cloud–RH coupling may be indicative of the variation in the vertical distribution of cloud over the equatorial Pacific. This can be confirmed by examining the vertical distribution of mean cloud cover over the equatorial Pacific for models with a negative cloud–RH coupling and models with a positive cloud–RH coupling (Figs. 8a,b). A region of more cloud cover between the surface and 900 hPa over the east and central equatorial Pacific exists for models with a positive cloud–RH coupling (Fig. 8b). By comparison, models with a negative cloud–RH coupling (Fig. 8a) have more cloud at slightly higher altitudes (900–800 hPa), farther toward the west. There is relatively less low cloud over the east equatorial Pacific, where cloud–RH coupling is important to SW feedback.

The relationship between SW feedback and the distribution of cloud is also extended in Fig. 8c, where CMIP5 Niño-3 SW feedback is correlated with mean cloud cover at each grid point. A positive correlation is found nearer the surface in the east equatorial Pacific, showing that models with more cloud in this location have a more positive SW feedback. Conversely, more cloud cover at higher altitudes toward the west is present in models with a stronger negative SW feedback. This relationship persists for both the dominant SW feedback components, cloud–RH and ω_{500}–SST couplings (Figs. 8d,e). This indicates that variation in both the vertical and the zonal distribution of cloud is linked to differences in the SW feedback regime. For example, models with more low cloud in the east equatorial Pacific tend to have weaker ω_{500}–SST coupling, reducing DY. The cloud–RH coupling also tends to be more positive, resulting in a stronger positive RHF. Therefore, the positive regime of SW feedback is more dominant; the stratiform clouds are broken up during El Niño events as a result of decreased static stability, and more shortwave radiation reaches the surface, warming the SSTs. Conversely, the negative regime of SW feedback driven by dynamical processes is more dominant in models with more cloud cover in the west and less low cloud in the east. Clouds form in the central and east equatorial Pacific during El Niño events and block the incoming shortwave radiation, cooling the SSTs.

The mean surface relative humidity in the equatorial Pacific is found to be a relatively good indicator of the distribution of clouds (Fig. 8f) and the strength of El Niño SW feedback. Models with more surface relative humidity are those with a larger amount of cloud nearer the surface in the east equatorial Pacific, as shown by the region of positive correlation, and less cloud cover in the west. This explains the relationships shown in Fig. 8a and Fig. 8e and provides a useful metric for this variation in vertical cloud distribution in CMIP5. These results provide information regarding the variation of cloud cover in relation to El Niño feedbacks in CMIP5 models but do not confirm that mean cloud and cloud responses are linked to SW feedback bias in comparison to observations.

Vertical distribution of cloud is not easily comparable to ISCCP, as observation methods complicate comparison. However, there have been efforts made as part of the Cloud Feedback Model Intercomparison Project phase 1 and phase 2 (CFMIP1 and CFMIP2; McAvaney and LeTreut 2003; Bony et al. 2011) to replicate the measurement of cloud properties in ISCCP for CMIP5 model cloud (ISCCP simulator; Klein and Jakob 1999; Webb et al. 2001). Therefore, cloud analysis is also carried out on ISCCP cloud area fraction for six of the CMIP5 models for which diagnostics are available (indicated in Table 1) to directly compare CMIP5 cloud with ISCCP observations (not shown in figures) as a means to assess cloud bias in CMIP5. It is found that, in those six models, there is a tendency for more mean cloud than observed in the Niño-3 region over 1000–800 hPa. Similarly, regressing 1000–800-hPa cloud anomalies onto Niño-3 surface relative humidity anomalies shows that the cloud–RH coupling in this region is too strong in the three models that also have a total cloud–RH coupling that is too strong: both MIROC-ESM models and CanESM2. Therefore, bias in low cloud responses is a contributor to the total cloud-cover response bias, and hence the SW damping bias, in those models. Conversely, the remaining three models, HadGEM2-ES, MIROC5, MRI-CGCM3, that do not have total cloud–RH coupling with significant biases also have no significant bias in low cloud–RH coupling.

c. *Diagnosing sources of El Niño shortwave feedback bias*

To gain greater insight into the underlying causes of SW feedback bias, the AMIP runs are also examined. In these runs, observed varying SSTs are prescribed to the atmosphere models. This means that mean-SST and El Niño–related SSTAs in the AMIP models are the same as those observed. Feedback calculation in AMIP therefore represents the atmospheric response to SSTAs but has no feedback on the SST. Figure 9 compares the CMIP and AMIP SW feedback for 15 models of the CMIP5 ensemble. SW feedback is still significantly weak in AMIP compared to the observations for a number of the models (Fig. 9a). In particular, cloud–ω_{500} coupling and SW flux–cloud coupling are significantly weak for 12 of the AMIP models (not shown). However, SW feedback can also have significant differences between CMIP and AMIP, mainly in the models that have a positive SW feedback regime in the coupled models (MRI-CGCM3, ACCESS1.3, INM-CM4.0, IPSL-CM5A-MR, IPSL-CM5A-LR, CSIRO Mk3.6.0). These models tend to show a change to a more negative SW feedback from CMIP to AMIP. This is a result of increased DY (Fig. 9b), slightly reduced RHF (Fig. 9c), and more negative LWPF (Fig. 9d) in AMIP, compared to CMIP. Feedback changes from AMIP to CMIP contribute to a more accurate SW feedback; no models have a significantly more biased SW feedback in AMIP when compared to the corresponding CMIP model feedback. It is possible that reduced bias in SW feedbacks in AMIP is a result of prescribed SSTs, following the relationships demonstrated in Fig. 7. More accurate mean SSTs may minimize mean atmospheric circulation biases and biases in atmospheric circulation responses during El Niño events (i.e., the ω_{500}–SST coupling). This can be tested by examining differences in the mean state from CMIP to AMIP and relationships they may have to the corresponding difference in SW feedback.

The differences in SW feedback from CMIP to AMIP are mainly driven by differences in the ω_{500}–SST coupling, the dominant component of the DY feedback (Fig. 10a). Models that have the largest bias reduction in SW feedback from CMIP to AMIP are those that have larger differences in the ω_{500}–SST coupling between AMIP and CMIP (correlation of 0.90). Further to this, differences between AMIP and CMIP in ω_{500}–SST coupling can be linked to mean state differences. The largest differences in ω_{500}–SST coupling coincide with more Niño-3 Pacific precipitation (Fig. 10b; correlation of -0.65) and increased atmospheric ascent (Fig. 10c; correlation of 0.77) in AMIP. These tend to be the models that have larger mean state biases in the coupled runs (Fig. 4). This implies that the models with larger feedback biases and mean state biases in the coupled runs are improved in the atmosphere-only runs, and are linked to the larger SW feedback changes in those models (Fig. 9). It is also noted that a number of the models with the largest differences between AMIP and CMIP in SW feedback and ω_{500}–SST coupling have less Niño-3.4 low cloud in the corresponding AMIP runs (Figs. 10d,h) that is linked to the positive SW feedback in the coupled runs (Fig. 8c). Niño-3.4, calculated using longitude range 170°–120°W, is

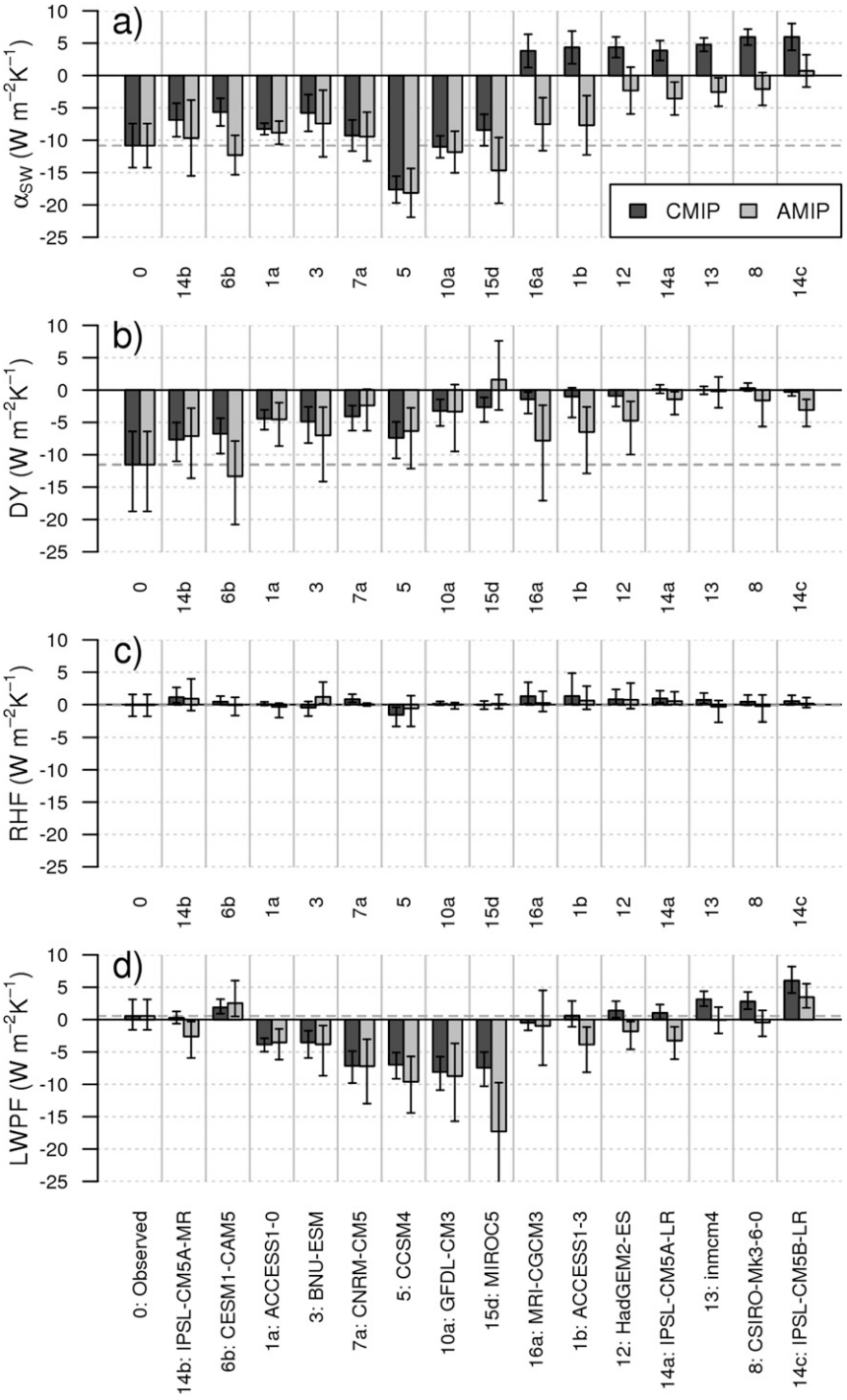

FIG. 9. CMIP5 (dark gray bars) and AMIP (light gray bars) El Niño (a) shortwave feedback (regression of Niño-3 Q_{SW} anomalies against Niño-3 SSTA for SSTA > 0), (b) DY, (c) RHF, and (d) LWPF. Error bars indicate the 95% confidence intervals in the linear fits used in the feedback calculation. Horizontal dashed line shows observational estimate using ERA-I/OAFlux.

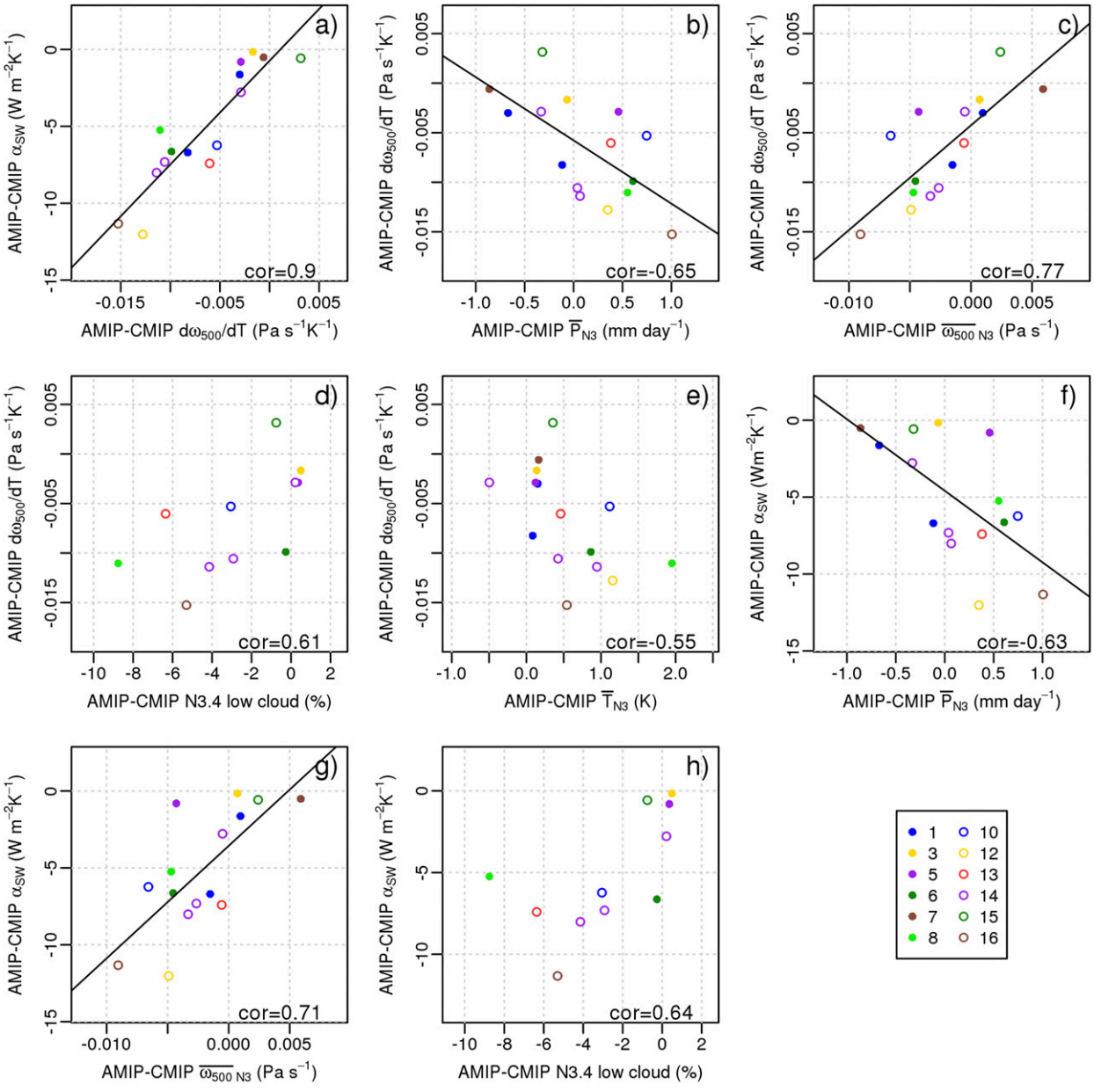

FIG. 10. (a) AMIP minus CMIP SW feedback, α_{SW}, plotted against AMIP minus CMIP ω_{500}–SST coupling; (b) AMIP minus CMIP ω_{500}–SST coupling against AMIP minus CMIP mean Niño-3 precipitation; (c) as in (b), but with mean Niño-3 ω_{500} on the x axis; (d) as in (b), but with mean Niño-3.4 low cloud fraction (cloud averaged over 1000–900 hPa) on the x axis; (e) as in (b), but with mean Niño-3 SST on the x axis; (f) as in (b), but with SW feedback on the y axis; (g) as in (c), but with SW feedback on the y axis; (h) as in (d), but with SW feedback on the y axis. Correlations of the relationships are printed on figures. The fitting line indicates a relationship significant at the 95% level (t test).

used for low cloud in Fig. 10 in order to fully capture the region of importance in Fig. 8.

There is a weaker link between the AMIP–CMIP changes in ω_{500}–SST coupling and changes in mean Niño-3 SST (Fig. 10e). This is perhaps unexpected given that the SSTs are prescribed in AMIP, eliminating SST bias; the AMIP–CMIP difference in mean Niño-3 SST is simply the CMIP5 bias. This may be expected to be linked to biases in atmospheric circulation and in the ω_{500}–SST coupling, given the strong interensemble relationship in the coupled models (Fig. 7b). However, the relationship between CMIP5 mean SST and CMIP5 ω_{500}–SST coupling for the subset of models available for AMIP analysis is less strong (correlation of −0.46) than

for the full CMIP5 ensemble. It is possible this is a cause of this weaker relationship between AMIP–CMIP ω_{500}–SST coupling and mean SST.

Note that AMIP-only feedback biases are not strongly linked to the AMIP-only mean state (not shown in figures), perhaps as a result of less variation in the mean state in AMIP models compared with CMIP5. Very accurate SSTs in AMIP, as all the models have by design, does not mean that the SW feedbacks are also as accurate, despite the link between mean SST and SW feedback when models are coupled. However, outlier INM-CM4.0 is a cause of some of the weak relationships. Removing this model from analysis significantly increases the link between mean Niño-3 precipitation and ω_{500}–SST coupling (correlation of -0.81). This is a result of this model having very excessive mean precipitation along the equator in AMIP; INM-CM4.0 has 7.22 mm day^{-1} in Niño-4 and 3.14 mm day^{-1} in Niño-3 compared to 4.41 and 1.83 mm day^{-1} in GPCP. This then means the convective response is suppressed during El Niño events in this model.

It would be very useful for model development if one could predict the magnitude of coupled model bias from some analysis of the atmosphere-only simulation. Unfortunately, no significant relationships are found between the mean state conditions and feedbacks in AMIP with the AMIP–CMIP difference in feedbacks. Nonetheless, a number of the more biased CMIP5 models are significantly biased in AMIP and showed larger differences between AMIP and CMIP runs, highlighting the importance of minimizing bias in atmosphere models. These relationships also reinforce the link between biases in equatorial Pacific mean conditions and El Niño feedback strength.

This helps to explain more significant differences for a number of the models in El Niño feedbacks between AMIP and CMIP. However, Fig. 9 does show that almost all of the models that have negative SW feedbacks in the coupled models have no significant difference in SW feedback in AMIP compared to CMIP. An exception to this is CESM1(CAM5), which has a stronger SW feedback in AMIP as a result of stronger DY. In general, difference in El Niño SW feedbacks between AMIP and CMIP is relatively small. Indeed, the AMIP and CMIP SW feedbacks are significantly related. Correlations of 0.89, 0.58, and 0.86 (95% significant) are found between CMIP and AMIP SW feedback, DY, and LWPF, respectively (not shown in figures). The relationship between CMIP and AMIP RHF is low (correlation of 0.38). However, if ACCESS1.0 is excluded this is increased to 0.71.

Results suggest that for many of these CMIP5 models, the bias in SW feedback is strongly linked to biases in the corresponding atmosphere model. In particular, biases in cloud-related processes, such as the SW–cloud coupling, the cloud–ω_{500} coupling, and the LWP–SST coupling, persist in AMIP and result in SW feedback bias (not shown in figures). It is possible these underlying feedback biases are related to convection schemes (Neale et al. 2008; Guilyardi et al. 2009; Watanabe et al. 2011; Kim et al. 2011) or atmosphere model resolution (Hack et al. 2006; Sun et al. 2006; Li and Zhang 2008) and are consequently less affected by the prescribed SSTs. However, from this study it has not been possible to attribute SW feedback bias to differences in atmospheric resolution or convection scheme, and it is not possible in a study such as this to isolate a single source of bias, as such convection schemes and atmosphere model properties are inherently linked.

5. Summary and discussion

The CMIP5 ensemble has a large range in the strength of shortwave feedback during El Niño events, with models demonstrating both positive and negative feedbacks. Here, additional insight is gained into underlying mechanisms of shortwave feedback bias by linking variations in cloud-cover responses that drive shortwave feedback variation to common CMIP5 mean state biases in the equatorial Pacific, such as cool SSTs along the equator and spatial variations in mean state atmospheric circulation and clouds.

Variation among CMIP5 models in shortwave feedback is most strongly linked to a component of the dynamical cloud feedback, the ω_{500}–SST coupling, and a component of the relative humidity cloud feedback, the cloud–RH coupling. These components are linked to one another, demonstrating two ''regimes'' of shortwave feedback, negative and positive, that are described by the idealized schematics in Fig. 11. The positive cloud–RH coupling represents a breakup of stratiform clouds during El Niño events that consequently increases surface downward shortwave heat flux (see schematics in Figs. 11c,d); the negative ω_{500}–SST coupling represents increasing atmospheric ascent during El Niño events that causes convective clouds and reduced surface shortwave heat flux (see schematic in Figs. 11a,b).

These components of the shortwave feedback, the ω_{500}–SST coupling and cloud–RH coupling, are significantly linked to biases in the mean equatorial Pacific climate in the CMIP5 models. A stronger positive cloud–RH coupling dominates in models that have higher surface relative humidity and more low cloud in the east equatorial Pacific. This low cloud is then broken up during El Niño events causing the incoming shortwave radiation to reach the surface of the ocean.

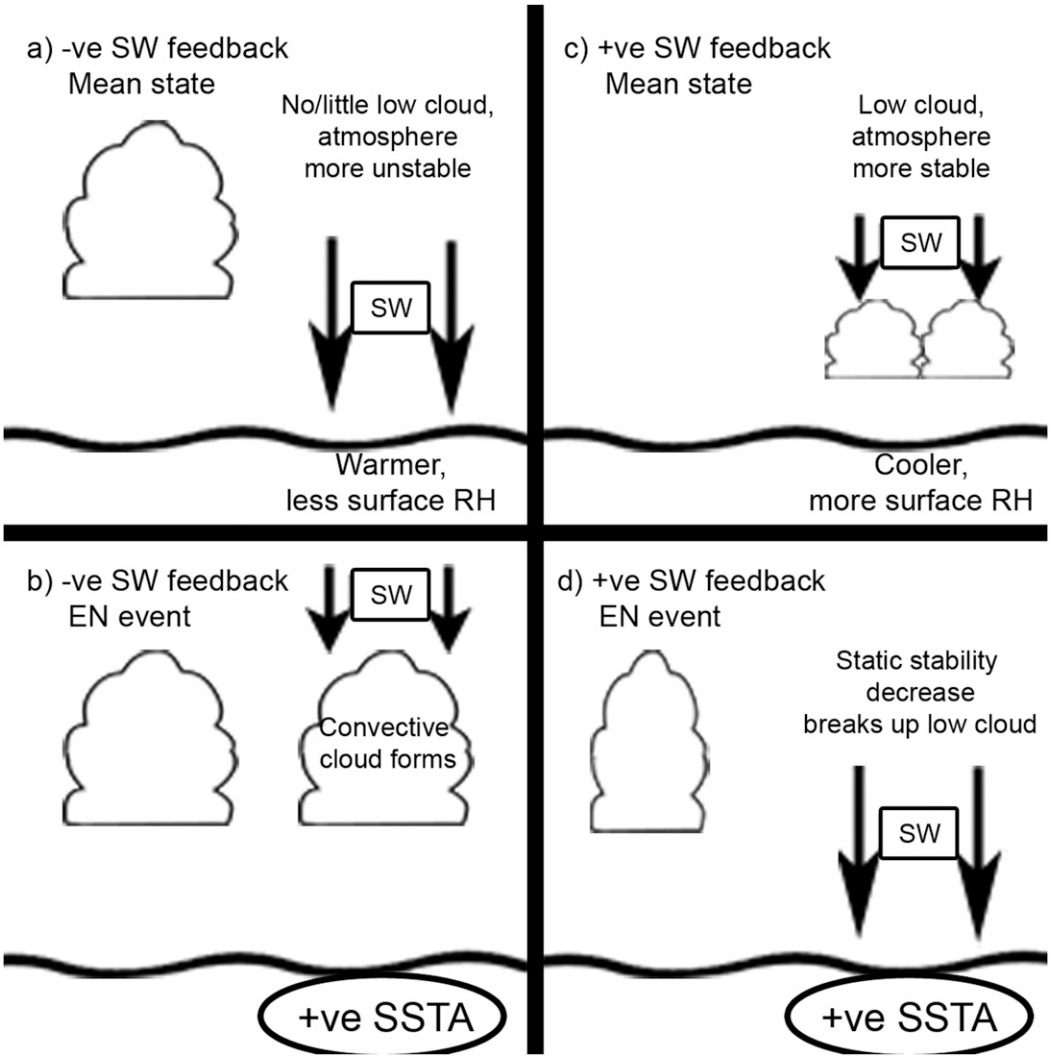

FIG. 11. Idealized schematics of the equatorial Pacific showing (a) mean state conditions for models with negative SW feedback, (b) El Niño conditions for models with negative SW feedback, (c) mean state conditions for models with positive SW feedback, and (d) El Niño conditions for models with positive SW feedback.

Conversely, those models with warmer equatorial Pacific SSTs, more equatorial precipitation, and less low cloud in Niño-3 have a stronger ω_{500}–SST coupling, and therefore a more negative shortwave feedback. While these results highlight the importance of the mean state in coupled models in relation to El Niño atmospheric feedbacks, the mean state biases discussed here are undoubtedly linked, and it is not possible to use results such as these to determine an underlying cause of mean state bias. Indeed, understanding the initial cause of such biases is a substantial ongoing area of research.

Changes in the mean state atmospheric circulation and cloud properties in the equatorial Pacific between CMIP and AMIP can also be related to changes in the ω_{500}–SST coupling that result in changes in shortwave feedback, namely a change from a positive shortwave feedback to a negative shortwave feedback in a number of models. This importance of ω_{500}–SST coupling is consistent with the interensemble relationships found and a study of previous-generation coupled models (CMIP3) by Lloyd et al. (2012). This is perhaps unsurprising as the dynamical response is driven by prescribed SSTs in AMIP but provides a feedback on the ocean in coupled models. However, AMIP analysis shows that a number of models have no significant difference in the shortwave feedback compared with CMIP5 analysis, suggesting that bias in the atmosphere model plays an important role in shortwave feedback and mean state bias.

Biases in shortwave feedback are also related to longwave feedback due to the influence of clouds on both heat fluxes. There exists a correlation of −0.89 between the two, such that bias in longwave feedback tends to compensate for bias in shortwave feedback. However, the magnitude of longwave feedback bias tends to be smaller, so a net positive thermodynamic damping bias still remains. This demonstrates how the relative contribution of El Niño atmospheric feedbacks to event damping can also be linked to the mean state.

Results found in this study can be used in combination with the study of ENSO latent heat damping by Ferrett et al. (2017) to gain a more complete understanding of El Niño thermodynamic damping in relation to the mean climate in current coupled models. Figure 1b demonstrates that latent heat feedback and shortwave feedback are related. Mean Niño-4 surface relative humidity, found here to be strongly linked to shortwave feedback, is also related to the precipitation metric for the double-ITCZ bias used by Ferrett et al. (2017); mean precipitation area averaged over longitude 150°–90°W and latitude 15°–5°S (correlation of −0.68; not shown in figures). Therefore, both the cold tongue bias and the double-ITCZ bias can be linked to errors in El Niño thermodynamic damping.

Both studies also find that errors in El Niño thermodynamic damping can be traced back to the atmosphere component of the coupled model. Furthermore, the strong links between mean state and feedback drifts introduced by coupling in some models may also be of particular importance. While no significant relationships are found between the AMIP mean state and shortwave feedbacks with the AMIP–CMIP change in shortwave feedbacks, a number of the most biased models showed larger shortwave feedback differences between AMIP and CMIP runs. These models also tend to be significantly biased in AMIP. This may indicate that modifications developed to improve the atmosphere component can be directly translated to improvements in the coupled model simulation of ENSO.

Acknowledgments. This work was supported by the U.K.–China Research and Innovation Partnership Fund through the Met Office Climate Science for Service Partnership (CSSP) China as part of the Newton Fund. MC acknowledges additional support from the Natural Environment Research Council Grant NE/N018486/1. H-L Ren is supported by the China Meteorological Administration Special Public Welfare Research Fund (GYHY201506013) and the Project for Development of Key Techniques in Meteorological Forecasting Operation (YBGJXM201705). We thank two reviewers for insightful comments and helpful suggestions on this work. We acknowledge the World Climate Research Programme's Working Group on Coupled Modelling, which is responsible for CMIP, and we thank the climate modeling groups (listed in Table 1 of this paper) for producing and making available their model output. For CMIP the U.S. Department of Energy's Program for Climate Model Diagnosis and Intercomparison provides coordinating support and led development of software infrastructure in partnership with the Global Organization for Earth System Science Portals.

REFERENCES

AchutaRao, K., and K. R. Sperber, 2006: ENSO simulation in coupled ocean-atmosphere models: Are the current models better? *Climate Dyn.*, **27**, 1–15, https://doi.org/10.1007/s00382-006-0119-7.

Adler, R. F., and Coauthors, 2003: The Version-2 Global Precipitation Climatology Project (GPCP) monthly precipitation analysis (1979–present). *J. Hydrometeor.*, **4**, 1147–1167, https://doi.org/10.1175/1525-7541(2003)004<1147:TVGPCP>2.0.CO;2.

Bellenger, H., E. Guilyardi, J. Leloup, M. Lengaigne, and J. Vialard, 2014: ENSO representation in climate models: From CMIP3 to CMIP5. *Climate Dyn.*, **42**, 1999–2018, https://doi.org/10.1007/s00382-013-1783-z.

Bjerknes, J., 1969: Atmospheric teleconnections from the equatorial Pacific. *Mon. Wea. Rev.*, **97**, 163–172, https://doi.org/10.1175/1520-0493(1969)097<0163:ATFTEP>2.3.CO;2.

Bony, S., M. Webb, C. Bretherton, S. Klein, P. Siebesma, G. Tselioudis, and M. Zhang, 2011: CFMIP: Towards a better evaluation and understanding of clouds and cloud feedbacks in CMIP5 models. *CLIVAR Exchanges*, No. 56, International CLIVAR Project Office, Southampton, United Kingdom, 20–24.

Cai, W., and Coauthors, 2014: Increasing frequency of extreme El Niño events due to greenhouse warming. *Nat. Climate Change*, **4**, 111–116, https://doi.org/10.1038/nclimate2100.

Capotondi, A., A. Wittenberg, and S. Masina, 2006: Spatial and temporal structure of tropical Pacific interannual variability in 20th century coupled simulations. *Ocean Modell.*, **15**, 274–298, https://doi.org/10.1016/j.ocemod.2006.02.004.

Chen, L., Y. Yu, and D. Sun, 2013: Cloud and water vapor feedbacks to the El Niño warming: Are they still biased in CMIP5 models? *J. Climate*, **26**, 4947–4961, https://doi.org/10.1175/JCLI-D-12-00575.1.

——, T. Li, and Y. Yu, 2015: Causes of strengthening and weakening of ENSO amplitude under global warming in four CMIP5 models. *J. Climate*, **28**, 3250–3274, https://doi.org/10.1175/JCLI-D-14-00439.1.

——, ——, ——, and S. K. Behera, 2017: A possible explanation for the divergent projection of ENSO amplitude change under global warming. *Climate Dyn.*, **49**, 3799–3811, https://doi.org/10.1007/s00382-017-3544-x.

de Szoeke, S. P., and S. Xie, 2008: The tropical eastern Pacific seasonal cycle: Assessment of errors and mechanisms in IPCC AR4 coupled ocean–atmosphere general circulation models. *J. Climate*, **21**, 2573–2590, https://doi.org/10.1175/2007JCLI1975.1.

Dee, D. P., and Coauthors, 2011: The ERA-Interim reanalysis: Configuration and performance of the data assimilation system. *Quart. J. Roy. Meteor. Soc.*, **137**, 553–597, https://doi.org/10.1002/qj.828.

Ferrett, S., and M. Collins, 2016: ENSO feedbacks and their relationships with the mean state in a flux adjusted ensemble. *Climate Dyn.*, https://doi.org/10.1007/s00382-016-3270-9, in press.

——, ——, and H.-L. Ren, 2017: Understanding bias in the evaporative damping of El Niño–Southern Oscillation events in CMIP5 models. *J. Climate*, **30**, 6351–6370, https://doi.org/10.1175/JCLI-D-16-0748.1.

Gelaro, R., and Coauthors, 2017: The Modern-Era Retrospective Analysis for Research and Applications, version 2 (MERRA-2). *J. Climate*, **30**, 5419–5454, https://doi.org/10.1175/JCLI-D-16-0758.1.

Guilyardi, E., P. Braconnot, F.-F. Jin, S. T. Kim, M. Kolasinski, T. Li, and I. Musat, 2009: Atmosphere feedbacks during ENSO in a coupled GCM with a modified atmospheric convection scheme. *J. Climate*, **22**, 5698–5718, https://doi.org/10.1175/2009JCLI2815.1.

Hack, J., J. Caron, G. Danabasoglu, K. Oleson, C. Bitz, and J. Truesdale, 2006: CCSM–CAM3 climate simulation sensitivity to changes in horizontal resolution. *J. Climate*, **19**, 2267–2289, https://doi.org/10.1175/JCLI3764.1.

Jin, F.-F., S. T. Kim, and L. Bejarano, 2006: A coupled-stability index of ENSO. *Geophys. Res. Lett.*, **33**, L23708, https://doi.org/10.1029/2006GL027221.

Kanamitsu, M., W. Ebisuzaki, J. Woollen, S.-K. Yang, J. Hnilo, M. Fiorino, and G. Potter, 2002: NCEP–DOE AMIP-II Reanalysis (R-2). *Bull. Amer. Meteor. Soc.*, **83**, 1631–1643, https://doi.org/10.1175/BAMS-83-11-1631.

Kim, D., Y.-S. Jang, D.-H. Kim, Y. H. Kim, M. Watanabe, F.-F. Jin, and J. S. Kug, 2011: El Niño–Southern Oscillation sensitivity to cumulus entrainment in a coupled general circulation model. *J. Geophys. Res.*, **116**, D22112, https://doi.org/10.1029/2011JD016526.

Kim, S. T., and F.-F. Jin, 2011a: An ENSO stability analysis. Part I: Results from a hybrid coupled model. *Climate Dyn.*, **36**, 1593–1607, https://doi.org/10.1007/s00382-010-0796-0.

——, and ——, 2011b: An ENSO stability analysis. Part II: Results from the twentieth and twenty-first century simulations of the CMIP3 models. *Climate Dyn.*, **36**, 1609–1627, https://doi.org/10.1007/s00382-010-0872-5.

——, W. Cai, F.-F. Jin, and J.-Y. Yu, 2014a: ENSO stability in coupled climate models and its association with mean state. *Climate Dyn.*, **42**, 3313–3321, https://doi.org/10.1007/s00382-013-1833-6.

——, ——, ——, A. Santoso, L. Wu, E. Guilyardi, and S.-I. An, 2014b: Response of El Niño sea surface temperature variability to greenhouse warming. *Nat. Climate Change*, **4**, 786–790, https://doi.org/10.1038/nclimate2326.

Klein, S. A., and D. L. Hartmann, 1993: The seasonal cycle of low stratiform clouds. *J. Climate*, **6**, 1587–1606, https://doi.org/10.1175/1520-0442(1993)006<1587:TSCOLS>2.0.CO;2.

——, and C. Jakob, 1999: Validation and sensitivities of frontal clouds simulated by the ECMWF model. *Mon. Wea. Rev.*, **127**, 2514–2531, https://doi.org/10.1175/1520-0493(1999)127<2514:VASOFC>2.0.CO;2.

Li, G., and G. J. Zhang, 2008: Understanding biases in shortwave cloud radiative forcing in the National Center for Atmospheric Research Community Atmosphere Model (CAM3) during El Niño. *J. Geophys. Res.*, **113**, D02103, https://doi.org/10.1029/2008JE003097.

——, and S. Xie, 2014: Tropical biases in CMIP5 multimodel ensemble: The excessive equatorial Pacific cold tongue and double ITCZ problems. *J. Climate*, **27**, 1765–1780, https://doi.org/10.1175/JCLI-D-13-00337.1.

Li, L. J., B. Wang, and G. J. Zhang, 2014: The role of nonconvective condensation processes in response of surface shortwave cloud radiative forcing to El Niño warming. *J. Climate*, **27**, 6721–6736, https://doi.org/10.1175/JCLI-D-13-00632.1.

——, ——, and ——, 2015: The role of moist processes in shortwave radiative feedback during ENSO in the CMIP5 models. *J. Climate*, **28**, 9892–9908, https://doi.org/10.1175/JCLI-D-15-0276.1.

Lin, J., 2007: The double-ITCZ problem in IPCC AR4 coupled GCMs: Ocean–atmosphere feedback analysis. *J. Climate*, **20**, 4497–4525, https://doi.org/10.1175/JCLI4272.1.

Lloyd, J., E. Guilyardi, H. Weller, and J. Slingo, 2009: The role of atmosphere feedbacks during ENSO in the CMIP3 models. *Atmos. Sci. Lett.*, **10**, 170–176, https://doi.org/10.1002/asl.227.

——, ——, and ——, 2012: The role of atmosphere feedbacks during ENSO in the CMIP3 models. Part III: The shortwave flux feedback. *J. Climate*, **25**, 4275–4293, https://doi.org/10.1175/JCLI-D-11-00178.1.

McAvaney, B. J., and H. Le Treut, 2003: The Cloud Feedback Intercomparison Project: (CFMIP). *CLIVAR Exchanges*, No. 26, International CLIVAR Project Office, Southampton, United Kingdom, 1–4.

Mechoso, C. A., and Coauthors, 1995: The seasonal cycle over the tropical Pacific in coupled ocean–atmosphere general circulation models. *Mon. Wea. Rev.*, **123**, 2825–2838, https://doi.org/10.1175/1520-0493(1995)123<2825:TSCOTT>2.0.CO;2.

Neale, R., J. Richter, and M. Jochum, 2008: The impact of convection on ENSO: From a delayed oscillator to a series of events. *J. Climate*, **21**, 5904–5924, https://doi.org/10.1175/2008JCLI2244.1.

Philander, S., D. Gu, G. Lambert, T. Li, D. Halpern, N.-C. Lau, and R. C. Pacanowski, 1996: Why the ITCZ is mostly north of the equator. *J. Climate*, **9**, 2958–2972, https://doi.org/10.1175/1520-0442(1996)009<2958:WTIIMN>2.0.CO;2.

Ramanathan, V., and W. Collins, 1991: Thermodynamic regulation of ocean warming by cirrus clouds deduced from observations of the 1987 El Niño. *Nature*, **351**, 27–32, https://doi.org/10.1038/351027a0.

Schiffer, R. A., and W. B. Rossow, 1983: The International Satellite Cloud Climatology Project (ISCCP): The first project of the World Climate Research Programme. *Bull. Amer. Meteor. Soc.*, **64**, 779–784.

Sun, D.-Z., J. Fasullo, T. Zhang, and A. Roubicek, 2003: On the radiative and dynamical feedbacks over the equatorial cold tongue. *J. Climate*, **16**, 2425–2432, https://doi.org/10.1175/2786.1.

——, and Coauthors, 2006: Radiative and dynamical feedbacks over the equatorial cold tongue: Results from nine atmospheric GCMs. *J. Climate*, **19**, 4059–4074, https://doi.org/10.1175/JCLI3835.1.

——, Y. Yu, and T. Zhang, 2009: Tropical water vapor and cloud feedbacks in climate models: A further assessment using coupled simulations. *J. Climate*, **22**, 1287–1304, https://doi.org/10.1175/2008JCLI2267.1.

Taylor, K. E., R. J. Stouffer, and G. A. Meehl, 2012: An overview of CMIP5 and the experiment design. *Bull. Amer. Meteor. Soc.*, **93**, 485–498, https://doi.org/10.1175/BAMS-D-11-00094.1.

Vannière, B., E. Guilyardi, G. Madec, F. Doblas-Reyes, and S. Woolnough, 2013: Using seasonal hindcasts to understand the origin of the equatorial cold tongue bias in CGCMs and its impact on ENSO. *Climate Dyn.*, **40**, 963–981, https://doi.org/10.1007/s00382-012-1429-6.

——, ——, T. Toniazzo, G. Madec, and S. Woolnough, 2014: A systematic approach to identify the sources of tropical SST errors in coupled models using the adjustment of initialised experiments. *Climate Dyn.*, **43**, 2261–2282, https://doi.org/10.1007/s00382-014-2051-6.

Watanabe, M., M. Chikira, Y. Imada, and M. Kimoto, 2011: Convective control of ENSO simulated in MIROC. *J. Climate*, **24**, 543–562, https://doi.org/10.1175/2010JCLI3878.1.

Webb, M., C. Senior, S. Bony, and J. J. Morcrette, 2001: Combining ERBE and ISCCP data to assess clouds in the Hadley Centre, ECMWF and LMD atmospheric climate models. *Climate Dyn.*, **17**, 905–922, https://doi.org/10.1007/s003820100157.

Yu, L., and R. A. Weller, 2007: Objectively analyzed air–sea heat fluxes for the global ice-free oceans (1981–2005). *Bull. Amer. Meteor. Soc.*, **88**, 527–539, https://doi.org/10.1175/BAMS-88-4-527.

Zhang, W., F.-F. Jin, J. Zhao, and J. Li, 2013: On the bias in simulated ENSO SSTA meridional widths of CMIP3 models. *J. Climate*, **26**, 3173–3186, https://doi.org/10.1175/JCLI-D-12-00347.1.

Zhang, X., H. Liu, and M. Zhang, 2015: Double ITCZ in coupled ocean-atmosphere models: From CMIP3 to CMIP5. *Geophys. Res. Lett.*, **42**, 8651–8659, https://doi.org/10.1002/2015GL065973.

Journal of Geophysical Research: Atmospheres

RESEARCH ARTICLE
10.1029/2017JD028227

Temporal Characteristics of Actual Evapotranspiration Over China Under Global Warming

Taichen Feng[1], Tao Su[2], Fei Ji[1], Rong Zhi[3], and Zixuan Han[1]

[1]College of Atmospheric Sciences, Lanzhou University, Lanzhou, China, [2]College of Physical Science and Technology, Yangzhou University, Yangzhou, China, [3]China Laboratory for Climate Studies, National Climate Center, China Meteorological Administration, Beijing, China

Key Points:
- An assessment is made of the trends of actual evapotranspiration (AE) over China under global warming
- Significant increasing trends in AE are found over the hyperarid, arid, and humid regions
- An increase in PET driven by global warming is the main cause of the increased AE over the humid region

Correspondence to:
T. Su and R. Zhi,
taosu@yzu.edu.cn;
z_rongphy@126.com

Citation:
Feng, T., Su, T., Ji, F., Zhi, R., & Han, Z. (2018). Temporal characteristics of actual evapotranspiration over China under global warming. *Journal of Geophysical Research: Atmospheres*, *123*, 5845–5858. https://doi.org/10.1029/2017JD028227

Received 20 DEC 2017
Accepted 14 MAY 2018
Accepted article online 22 MAY 2018
Published online 4 JUN 2018

Abstract In this study, an assessment is made of the trends of actual evapotranspiration (AE) over China under global warming from an ensemble of the following data sets: National Centers for Environmental Prediction-National Center for Atmospheric Research reanalysis I, National Centers for Environmental Prediction-Department of Energy reanalysis II, Modern-Era Retrospective Analysis for Research and Applications (MERRA), MERRA Version 2, European Centre for Medium-Range Weather Forecasts Interim Re-Analysis, and Japanese 55-year Reanalysis. For China as a whole, annual AE exhibited a significant increasing trend from 1979 to 2015, and the rate of increase was highest in autumn and lowest in summer. By subdividing China into six climatic regions using the aridity index, significant increasing trends in AE are found over the hyperarid, arid, and humid regions, but slightly decrease over the dry subhumid and subhumid regions. For the hyperarid and arid regions, the increases in potential evapotranspiration and the water supply from melting glaciers due to both climate warming and human activities might be the main contributors to the AE increases. An increase in potential evapotranspiration driven by global warming is the main cause of the increased AE over the humid region. On a seasonal basis, most AE over China occurs in summer. However, increasing AE trends have been observed mainly in autumn and winter, and the increase is statistically significant over all of China's six climatic regions in winter. In view of data availability, reanalyses are compared with the results from Mezentsev-Choudhury-Yang equation (AE_Budyko). The correlations between individual reanalyses and AE_Budyko tend to be higher over the arid region.

1. Introduction

Actual evapotranspiration (AE) changes are of great significance for water resource planning, irrigation control, and agricultural production (Douville et al., 2013; Gao et al., 2007; Sherwood & Fu, 2014). Climate change resulting from global warming could have a critical impact on AE and hence water availability (Brutsaert & Parlange, 1998; Huang et al., 2017; Ji et al., 2014; Yang et al., 2006). As the planet warms, global average rainfall increases, but so does AE. Many regions will get more rain, but it appears that few will get enough to keep pace with the growing evaporative demand (Dai, 2013; Feng & Fu, 2013; He et al., 2016; Sheffield et al., 2012). Meanwhile, changes in AE will also modulate the climate by reducing the transport of sensible heat arising from radiative energy fluxes (Wang & Dickinson, 2012). For example, the latent heat flux dominates the surface energy balance in the central and southeastern Qinghai-Tibetan Plateau and is a major energy source of the atmosphere during the summer monsoon (Zhang et al., 2007). However, as the only connecting term connecting the water balance and the energy balance, AE is perhaps the most difficult and complicated component of the hydrological cycle because of the complex interactions in the land plant-atmosphere system (Gao et al., 2007; Xu & Singh, 2005). Therefore, understanding and exploring the interannual and interdecadal/longer-term variabilities in AE is an essential part of the task of assessing climate variability and possible change (Choudhury, 1999; Douville et al., 2013).

Pan evaporation, a surrogate of potential evapotranspiration (PET), is reported to have decreased in many parts of the world since the 1950s (Cong et al., 2009; Peterson et al., 1995; Roderick & Farquhar, 2002). Pan evaporation in China is also reported to have decreased in several regions (Liu et al., 2004, 2011; Zhang et al., 2007). The contrast between expectation and observations is called the "evaporation paradox" (Cong et al., 2009). Various interpretations have been presented to explain the cause of the observed decline in pan evaporation in different regions (Cong et al., 2009; Hobbins et al., 2004; Lawrimore & Peterson, 2000). For now, however, it is still debatable whether a decreasing pan evaporation or PET rate indicates a

©2018. American Geophysical Union. All Rights Reserved.

decrease in AE (Cong et al., 2009; Hobbins et al., 2004). The key issue in determining the annual water balance at a regional scale is how to estimate AE from PET or pan evaporation (Lawrimore & Peterson, 2000).

As far as AE is concerned, only relatively few monitoring sites operate around the world and the period of record is quite short (Douville et al., 2013). Several methods can be used to evaluate AE instead (Xu & Singh, 2005). Gao et al. (2007) used a water balance model to estimate AE over China from 1962 to 2002. That study found that the estimated annual AE decreased in most areas east of 100°E and increased in the northwest of Northeast China. Wang et al. (2011) analyzed the trends of AE estimated by the advection-aridity model in the Yangtze River Basin and found that annual AE decreased in the upper and midlower Yangtze reaches. Recently, an analytical framework based on Budyko's curve has also been developed to calculate catchment-scale AE (Roderick & Farquhar, 2011; Yang et al., 2006, 2008). The existing algorithms differ in their purpose of application (Wang et al., 2011). While most of the methods were developed for specific regions, they mostly showed to be appropriate for use in similar climate conditions (Wang & Dickinson, 2012). As a result, conventional methods essentially provide point measurements, which are usually not representative of the regions because of the heterogeneity of land surfaces and the dynamic nature of heat transfer processes (Wang & Liang, 2008).

Retrospective analyses (or reanalyses) have become a valuable source of data for studying weather systems and climate variability (Lorenz & Kunstmann, 2012). One of the key benefits of reanalyses is that the output generated from the model physics provides data not easily observed, but is consistent with the analyzed observed data (Trenberth et al., 2011). Substantial attention has also been paid to AE values derived from reanalysis data sets. Su, Feng, and Feng (2015), Su, Feng, Zhou, et al. (2015) used reanalyses to examine AE variability over China with respect to climate change and found that the relationship between AE and pan evaporation was complementary with water control and proportional to energy control. Mao and Wang (2017) compared three evapotranspiration data sets for China based on surface water balance values, a modified Penman-Monteith (MPM) model, and reanalysis data and concluded that reanalysis evapotranspiration variables are consistent with MPM estimates in terms of spatial patterns, interannual variability, and temporal trends at the station scale.

Recognizing the above concerns, an attempt is made in this paper to analyze the temporal characteristics of AE over China from reanalyses so as to provide valuable information for regional hydrological studies and water resources planning and management. It should be noted that substantial uncertainties lie in the estimates of AE in reanalyses because it is seldom measured, and instead is estimated from bulk flux formulas. To avoid data dependence in the results, six reanalyses—National Centers for Environmental Prediction-National Center for Atmospheric Research (NCEP-NCAR) reanalysis I (NCEP-R1), NCEP-Department of Energy (NCEP-DOE) reanalysis II (NCEP-R2), Modern-Era Retrospective Analysis for Research and Applications (MERRA) from the National Aeronautics and Space Administration Goddard Space Flight Center, MERRA Version 2 (MERRA2), ECMWF Interim Re-Analysis (ERA-Interim, or ERA-I) from the European Centre for Medium-Range Weather Forecasts, and Japanese 55-year Reanalysis (JRA-55) from the Japan Meteorological Agency—are used. For comparison, reanalysis AE values are comprehensively evaluated with the results from the Mezentsev-Choudhury-Yang equation (AE_Budyko), which ignores the effects of the catchment characteristics on the climate elasticity (Choudhury, 1999; Roderick & Farquhar, 2011; Yang et al., 2008). Theoretically, AE is influenced by various factors related to both the both local climate and land surface conditions (Gao et al., 2007). Climate change has the potential to affect all of these factors in a combined way (Wang et al., 2011). Climate change-induced changes in AE, if fully realized, would likely vary greatly across any one continent. Thus, our results focus on recent changes and attribution of AE variability over China from a regional perspective.

2. Data and Methods

2.1. Data

The AE data used in this study are from NCEP-R1, NCEP-R2, MERRA, MERRA2, ERA-I, and JRA-55 (see Table 1 for further details on these data sets). The six reanalysis data sets have been produced using different numerical weather models or assimilation systems; thus, they are independent of each other (Trenberth et al., 2011). Our approach is to use data intercomparison to evaluate the uncertainties associated with the various estimates. Different reanalyses provide a measure of uncertainty in estimating the AE variability.

Table 1
Summary of the Six Reanalyses

Reanalysis	Horizontal resolution	Assimilation scheme	Period	Output times
NCEP-R1	T62 (~210 km)	3D VAR	1948–present	6 hr, daily, monthly
NCEP-R2	T62 (~210 km)	3D VAR	1979–present	6 hr, daily, monthly
MERRA	2/3° × 1/2°	3D VAR	1979–2016	1 hr, daily, monthly
MERRA2	2/3° × 1/2°	3D VAR	1980–present	1 hr, daily, monthly
ERA-I	T255 (~79 km)	4D VAR	1979–present	6 hr, monthly
JRA-55	T319 (~40 km)	4D VAR	1958–present	3 hr, daily, monthly

Through an intercomparison of different data sets, measurements can be regarded as more reliable by avoiding dependence on a single data set. Climatological estimates are computed by averaging all reanalyses. Uncertainties are evaluated by computing the standard error representing the deviation of various estimates from the data sets' mean.

The other physical variables used in this study include the monthly 10-m wind speed (SWS) and surface net solar radiation (NSR) from ERA-I. Monthly precipitation (PRE), PET, cloud cover (CLD), diurnal temperature range (DTR), mean temperature (TMP), and vapor pressure (VAP) were obtained from the gridded Climatic Research Unit (CRU) Time-series (TS) data version 4.00 (https://crudata.uea.ac.uk/cru/data/hrg/cru_ts_4.00/). Here PET is calculated using the Food and Agriculture Organization grass reference evapotranspiration equation. The CRU TS4.00 data set is derived from archives of climate station records that have been subject to extensive manual and semiautomated quality control measures (Harris et al., 2014).

All fields were remapped to the resolution of the CRU data set (i.e., 0.5° × 0.5°) by using a bilinear interpolation technique. Based on the original time periods covered by the six reanalysis data sets, our study mainly focuses on the time period from 1979 to 2015 (if available). The seasons are spring (March–May), summer (June–August), autumn (September–November), and winter (December–February). The nonparametric Mann-Kendall test and linear regression test were selected to establish trends in AE and related meteorological factors.

2.2. Climate Classification Using the Aridity Index

The Budyko hypothesis states that AE is primarily determined by the ratio of energy supply (PET) to water supply (PRE), which we refer to as the aridity index (AI). On a continental scale, the distribution of vegetation types is strongly controlled by climate. In turn, vegetation affects the seasonal water balance by controlling both AE and soil moisture dynamics (Wang & Dickinson, 2012; Yang et al., 2014). Of the three definitions of dryland compared by Huang et al. (2016), the AI definition is most reasonable and reliable, and the dryland coverage agrees well with the surface vegetation types.

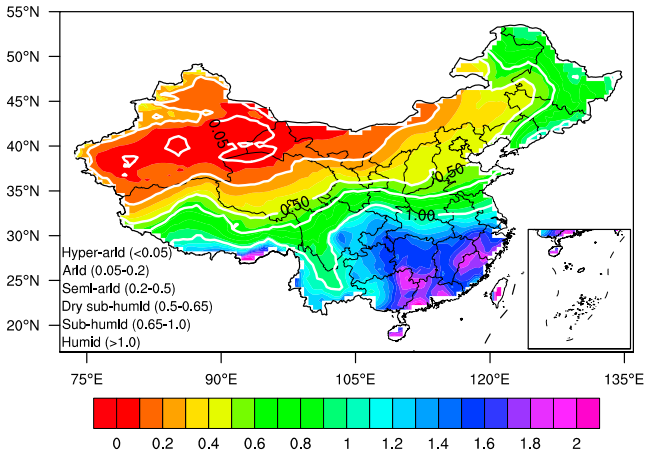

Figure 1. Six climatic regions in China and the spatial distribution of AI for 1979–2015 climatology derived from the CRU TS4.00 data set.

At the regional scale, the magnitude and spatial distribution of changes in AE remains highly uncertain. The purpose of this paper is to present a new analysis of the trends of AE over China, both on a regional basis and for the country as a whole. According to the AI, the climate in China can be roughly classified into six types from dry to moist regions: hyperarid (<0.05), arid (0.05–0.2), semiarid (0.2–0.5), dry subhumid (0.5–0.65), subhumid (0.65–1.0), and humid (>1.0; Feng & Fu, 2013). Instead of using traditional definitions, we examined the AE trends in more details by subdividing "humid" regions (AI > 0.65) into two climatic regions (i.e., subhumid and humid). As shown in Figure 1, drylands encompassing hyperarid, arid, semiarid, and dry subhumid areas are primarily distributed in northwestern China and closely match the map of the Köppen-Geiger Climate Classification. Major hyperarid areas can be found in the Taklimakan Desert, with its typical cold desert climate, while major humid areas are located in southeastern China.

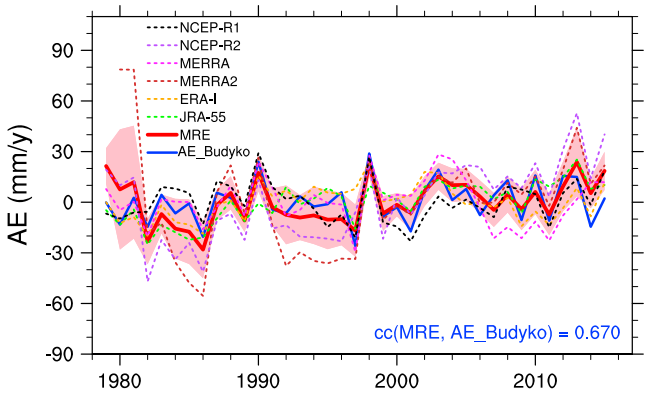

Figure 2. The variations in the regionally averaged AE over China derived from the six reanalyses and the AE_Budyko estimates (unit: mm/year). The red curve represents the multireanalysis ensemble (MRE) of the six reanalyses. The cc is the correlation between MRE and AE_Budyko for the period 1979–2015. Shading indicates 1 standard deviation of individual reanalysis departure from MRE. The anomaly was obtained from the climatology of 1979–2015.

2.3. Elasticity of AE Derived From the Mezentsev-Choudhury-Yang Equation

In general, the selection of a particular method for the determination of AE depends upon the type of meteorological data available for the given region and the accuracy desired in the computation of water needs (Wang et al., 2011; Zhang et al., 2007). With its large geographical extent, measuring AE over China for a very long time period is practically and economically impossible (Gao et al., 2007; Wang et al., 2011). Therefore, a less complex physically based approach is needed to measure AE.

By incorporating the complex effects resulting from land-surface heterogeneity, many models that are based on the coupled water-energy balance pioneered by Budyko (1974) have been successfully used for estimating the long-term water balance at the catchment scale (Yang et al., 2006). In such studies, one curve was applied to the water balance in different catchments. Yang et al. (2006) and Roderick and Farquhar (2011) derived climate elasticity theoretically based on an analytical formula for the Budyko hypothesis, that is, the Mezentsev-Choudhury-Yang equation (Choudhury, 1999; Mezentsev, 1955; Yang et al., 2008):

$$\mathrm{AE_Budyko} = \frac{\mathrm{PRE} * \mathrm{PET}}{\left(\mathrm{PRE}^{n} + \mathrm{PET}^{n}\right)^{1/n}} \tag{1}$$

with a catchment-specific parameter, n (dimensionless), that represents the integrated effects of the catchment characteristics (such as the average slope, vegetation cover, vegetation type, or land use) and climate seasonality (Yang et al., 2008, 2014). Values of n are typically in the range 0.6 to 3.6, but most are in a smaller range from 1.5 to 2.6 (Choudhury, 1999; Yang et al., 2008).

Both the climate and catchment characteristics have large spatial variations in many regions of China, which will lead to a spatial variation in the climate elasticity, and the parameter n shows a large spatial variation (ranging from 0.4 to 3.8) during 1961–2010 (Yang et al., 2014). For a given PRE and PET, higher values of n denote a higher estimate of AE (Roderick & Farquhar, 2011). Our particular interest is the temporal evolution of AE. In this paper, AE_Budyko is mainly used as the reference to evaluate the performances of the six reanalysis data sets in reproducing the interannual variation and long-term trend in AE. To maintain the simplicity of the model, we use the recommended default value for n (i.e., 1.8) across all of China (Choudhury, 1999; Su, Feng, & Feng, 2015).

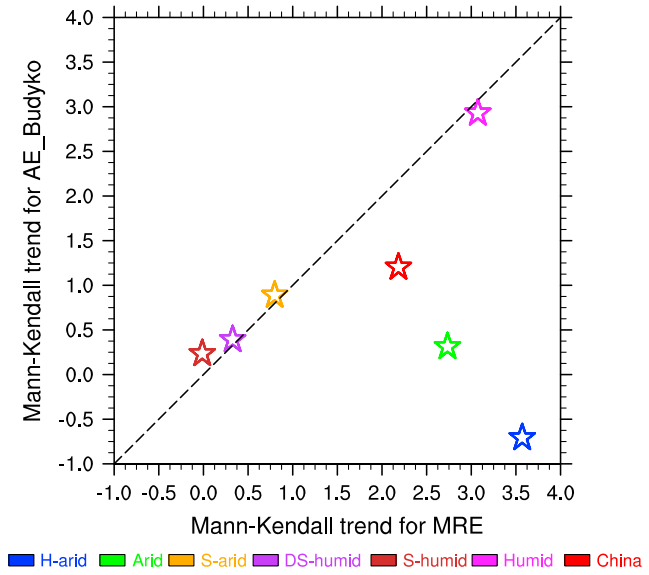

Figure 3. Mann-Kendall trends for AE_Budyko as a function of Mann-Kendall trends for MRE over the hyperarid (H-arid), arid, semiarid (S-arid), dry subhumid (DS-humid), subhumid (S-humid), and humid regions from 1979 to 2015.

3. Results and Discussion

3.1. Annual Trends of AE

AE occurs every day; thus, it can be a good indicator of regional climate change (Douville et al., 2013). The variations in the regionally averaged AE over China from reanalyses and the AE_Budyko estimates are shown in Figure 2. According to the ensemble of the six reanalyses (multireanalysis ensemble, MRE), AE variability under climate warming is characterized by substantial interdecadal variations along with strong interannual variations. In general, AE decreased from 1979 to 1986 and then rapidly increasing into the early 1990s. After that, a change point for AE series was identified around the last big El Niño event in 1998, which indicates that the long-term trend in AE is affected by climate variability. The decreasing trend in AE disappears after 1998, and there is a steady increase from 1999 to 2015 (Figure 2). From 1979

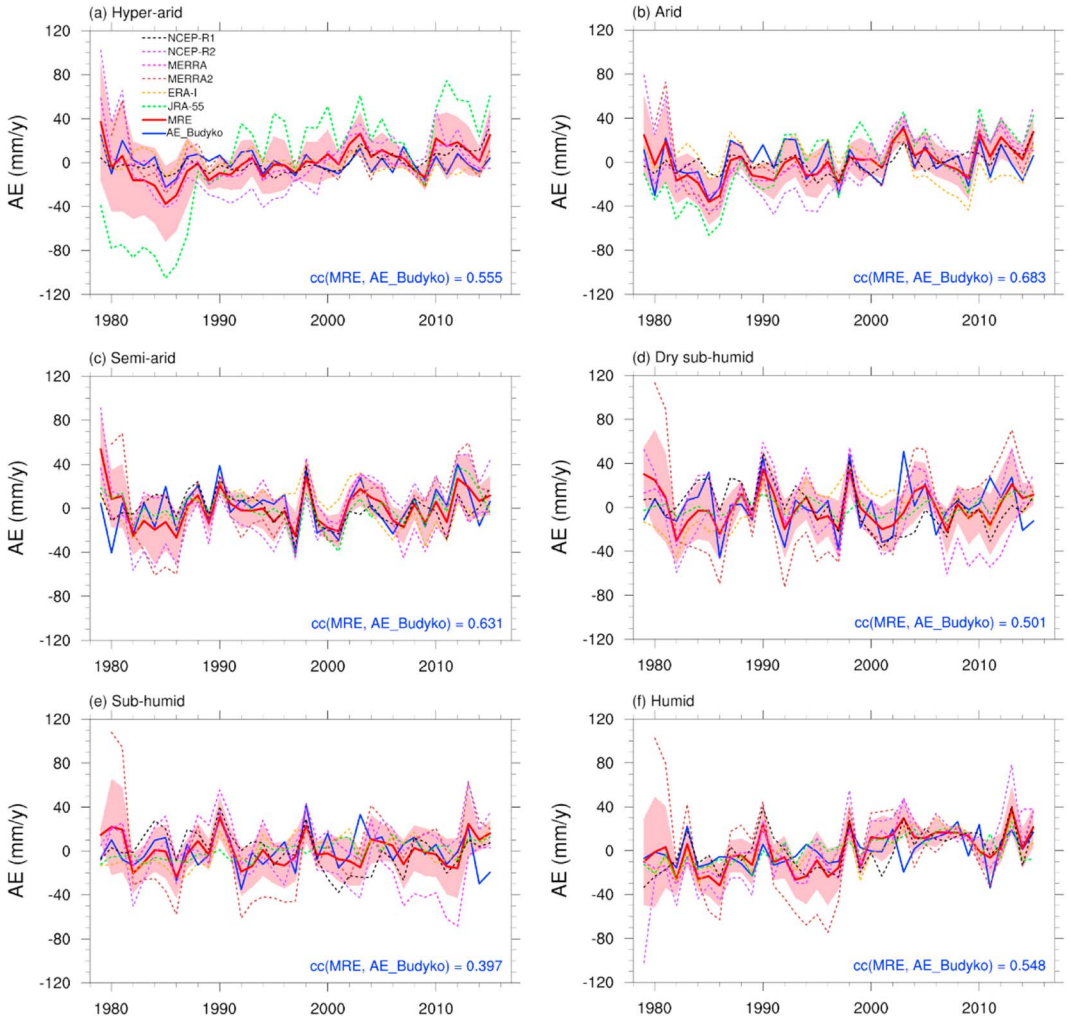

Figure 4. Same as Figure 2 but for the (a) hyperarid, (b) arid, (c) semiarid, (d) dry subhumid, (e) subhumid, and (f) humid (unit: mm/year) regions.

to 2015, MRE compared very well with the AE_Budyko, with high correlation coefficients of 0.670 and 0.651 before and after linear detrending, respectively. As presented in Figure 3, however, MRE shows a significant increasing trend ($p < 0.01$), while there is no significant trend in AE_Budyko. It is obvious that interannual fluctuations are quite consistent between MRE and AE_Budyko even though their long-term trends may differ.

To see whether there are spatial differences in the change of AE within China, we examined the AE trends of China's six climatic regions (Figure 4). At the regional level, AE shows a large regional variability. MRE are in general agreement with AE_Budyko, with correlation coefficients of 0.555, 0.683, 0.631, 0.501, 0.397, and 0.548 for each region (Figure 4), respectively, which are all statistically significant at the 95% confidence level. Long-term trends in both fields only have very limited effects on the correlation coefficients. After linear detrending, the interannual variations of MRE still show relatively high correlation coefficients (0.725, 0.716, 0.629, 0.503, 0.398, and 0.434) with AE_Budyko. It essentially reflects that the multireanalysis data can well capture the temporal variations in AE. Figure 3 presents the results of the Mann-Kendall trend test for AE. However, comparison of the long-term trends in AE reveals large differences between MRE and AE_Budyko in the hyperarid and arid regions (Figure 3). According to Yang et al. (2006), the reason is likely that the regional long-term water balance should not vary along a single Budyko curve in the nonhumid regions of China.

Moreover, glaciers play an important role in streamflow regimes over the hyperarid and arid regions, as meltwater from the ice is released when other sources such as snowmelt are depleted (Sorg et al., 2012). Climate-driven changes in glacier-fed streamflow regimes have direct implications on freshwater supply, irrigation, and hydropower potential, and all of these will affect AE potentially (Tao et al., 2011). For example, intensified glacier melt strongly affects the quantity and seasonal distribution of runoff (Sorg et al., 2012), to a large extent, such an alteration in runoff will ultimately result in a change in AE, especially in these nonhumid regions. In fact, it is difficult to use AE_Budyko to characterize variations in AE on a regional scale in view of its dependence on many local factors (Roderick & Farquhar, 2011); thus, we will examine changes in AE derived from MRE in the following sections.

For the six climatic regions, changes in AE were not uniform under climate change, with some regions experiencing increases, and others with decreases or not much change at all (Figure 4). Notably, during 1979–2015, AE shows a significant increasing trend over the hyperarid, arid, and humid regions (Figure 3). For the hyperarid region (Figure 4a), AE variability is characterized by an initial steep decrease (1979–1985) and then a progressive increase since the mid-1980s. In addition to the long-term trend, AE also shows a strong interannual variability. On the interdecadal time scale, the trends in AE over the arid region share common features as those observed over the hyperarid region, except that the amplitude of interannual variation is even greater (Figure 4b). Superimposed on the interannual variability, AE shows a substantial interdecadal variation and a positive long-term trend after the mid-2000s over the semiarid region (Figure 4c). All data sets show a roughly similar behavior, and the MRE shows a reasonable agreement with the AE_Budyko. The drylands live at the margin of sustainability, where moisture is scarce for all or part of the year. Dryness depends on PRE and on how fast water evaporates (Sherwood & Fu, 2014). Any major changes in AE may have major consequences on hydrologic processes. Such rises in AE can shift a region to a drier climate category (Sheffield et al., 2012).

Considering the entire 1979–2015 period, there are no significant AE trends over the dry subhumid (Figure 4d) and subhumid (Figure 4e) regions, and the MRE is less consistent with the AE_Budyko. Climate anomalies in China are significantly affected by the East Asian monsoon. The advance and retreat of this monsoon play a role in the weather and climate of China. The dry subhumid and subhumid regions are transitional zones between humid and arid zones, which lies along the border of the monsoon. The ecosystems in such regions are fragile and sensitive to strong interactions between human activities and climate changes and are thus highly susceptible to environmental change (Huang et al., 2016). Both the climate and catchment characteristics have large spatial variations in the dry subhumid and subhumid regions. Giving this complexity, it is difficult to quantify the AE variability with an appropriate yet simple index in AE_Budyko. As a result, the temporal evolution of AE varies significantly between MRE and AE_Budyko. Moreover, the AE fields obtained from the six reanalyses have unique characteristic. For example, there are notable inconsistencies between ERA-I and the other reanalyses when focus on the long-term trend in AE, especially in the dry subhumid region (Figure 4d). It seems that substantial uncertainty remains in how AE is responding to a warming climate because of the differences in responses among different data sets.

The concept of water-limited and energy-limited evaporation has long been used to understand the role of AE in the water balance. Assuming that PRE is the only source of water, areas where AI $>$1.0 are described as energy-limited (as AE is limited by energy, not water; McVicar et al., 2012). Not surprisingly, the analysis of long-term AE anomalies from the reanalyses and AE_Budyko consistently shows that AE increases for the entire period over the humid region (Figure 4f). Energy constraints provide insight into the source of the anomalously strong hydrologic cycle.

In view of data availability, the correlation analysis was conducted between the AE data from individual reanalyses and the AE_Budyko (Figure 5). In general, the year-by-year variations in AE derived from reanalyses are consistent with those in AE_Budyko, as most correlation coefficients are statistically significant at 95% confidence level. For China as a whole, the temporal variations in AE from the six reanalyses are remarkably similar and show relatively high correlation coefficients (0.693, 0.505, 0.535, 0.332, 0.566, and 0.553 for NCEP-R1, NCEP-R2, MERRA, MERRA2, ERA-I, and JRA-55, respectively) with the AE_Budyko. Among the six data sets, NCEP-R1 shows the highest correlation coefficient, whereas the AE time series derived from MERRA2 shows the lowest correlation coefficient with AE_Budyko mainly because the

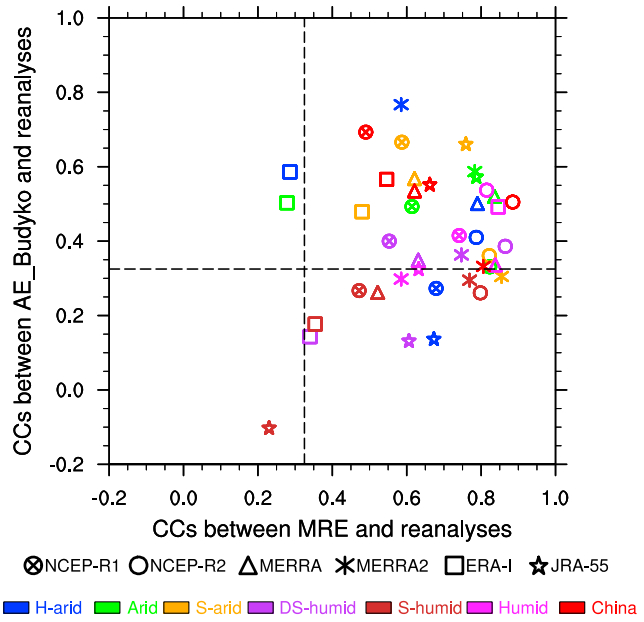

Figure 5. Temporal correlation coefficients between AE_Budyko and the six reanalyses as a function of the correlation coefficients for the ensemble (MRE) of the six reanalyses over the hyperarid (H-arid), arid, semiarid (S-arid), dry subhumid (DS-humid), subhumid (S-humid), and humid regions from 1979 to 2015. The dashed lines denote 95% confidence levels based on Student's *t* test.

amplitude of variance in MERRA2 is higher than that in the other reanalyses (Figure 2). If we remove the long-term trend, the interannual variations in AE derived from the six reanalyses are still consistent with AE_Budyko, with the correlation coefficients of 0.698, 0.491, 0.548, 0.342, 0.542, and 0.610 for NCEP-R1, NCEP-R2, MERRA, MERRA2, ERA-I, and JRA-55, respectively.

At a regional level, the correlations tend to be higher over the arid region, as evidenced by the correlation coefficients presented in Figure 5 (0.493, 0.331, 0.520, 0.587, 0.503, and 0.574 for the six reanalyses, respectively), which are all statistically significant at the 95% confidence level. Conversely, the smallest correlations occur over the subhumid region. Overall, MERRA2 and JRA-55 have substantial problems on describing the interannual variation and long-term trend in AE over China. The AE time series derived from JRA-55 show the lowest correlation coefficients with AE_Budyko in the hyperarid, dry subhumid, and subhumid regions, whereas MERRA2 has substantial uncertainties in the semiarid, subhumid, and humid regions.

In general, different reanalyses exhibit some degree of uncertainty in estimating the AE variability. The temporal variations in AE produced by the six reanalyses are not stationary and exhibit large conflicting trends. Figure 5 also shows the temporal correlations between AE from the individual reanalyses and the MRE. To some extent, the corresponding correlations reflect how well the analyzed reanalyses agree with the other reanalyses. As noted above, a significant discrepancy exists in ERA-I, which has an average correlation coefficient of 0.431.

3.2. Seasonal Trends of AE

Theoretically, AE is driven essentially by meteorological variables, mediated by vegetation and soil characteristics, and constrained by the amount of available water. The lower the liquid water content of the soil is, the lower the rate of AE of water into the air (Lawrimore & Peterson, 2000). Figure 6 shows the seasonal and annual mean AE over the six climatic regions. Obviously, AE gradually increases from drylands to humid regions, although the seasonal changes are dramatic. The annual mean AE over the hyperarid region for the period 1979–2015 is 0.3 mm/day, based on the mean of the six reanalyses, whereas the mean AE over the humid region for the same period is 2.77 mm/day.

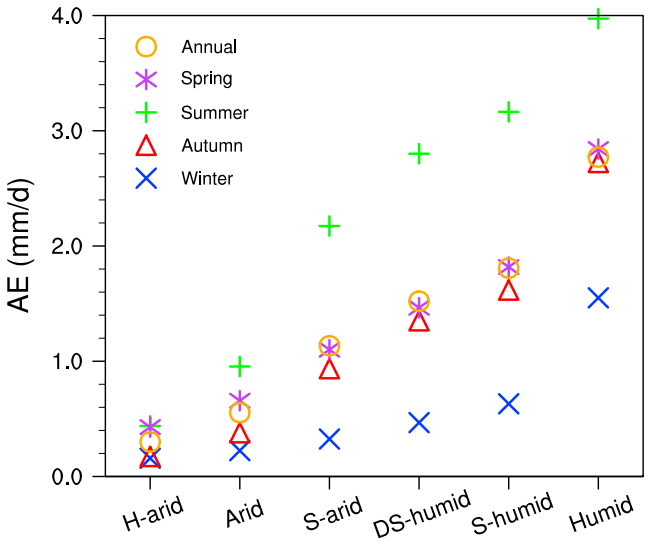

Figure 6. Annual and seasonal mean MRE for 1979–2015 climatology over the (a) hyperarid (H-arid), (b) arid, (c) semiarid (S-arid), (d) dry subhumid (DS-humid), (e) subhumid (S-humid), and (f) humid regions (unit: mm/day).

Although high PRE can lead to increasing runoff, regional increases in PRE should also be expected to lead to increasing AE (Lawrimore & Peterson, 2000). Located in a strong monsoon region, climate of China is characterized by annual reversal of prevailing surface winds and by a contrasting rainy summers and dry winters. As a result, the major controlling factors for AE and PET over China vary seasonally. The supply of moisture generally causes a reduction in AE, especially in the drylands. Furthermore, Thomas (2000) reported regionally and seasonally diverse trends in PET over China as well. For these reasons, AE is highest in summer and lowest in winter for the six climatic regions (Figure 6). The nationwide average of AE in summer is 2.25 mm/day, accounting for approximately 42.1% of the annual total AE.

The variations in the regionally averaged seasonal AE are shown in Figure 7. The result indicates that there are significant differences in the changes in seasonal AE on both interannual and interdecadal time scales. The identification of AE trends in response to changing climatic conditions could help to quantify the potential impacts of climate

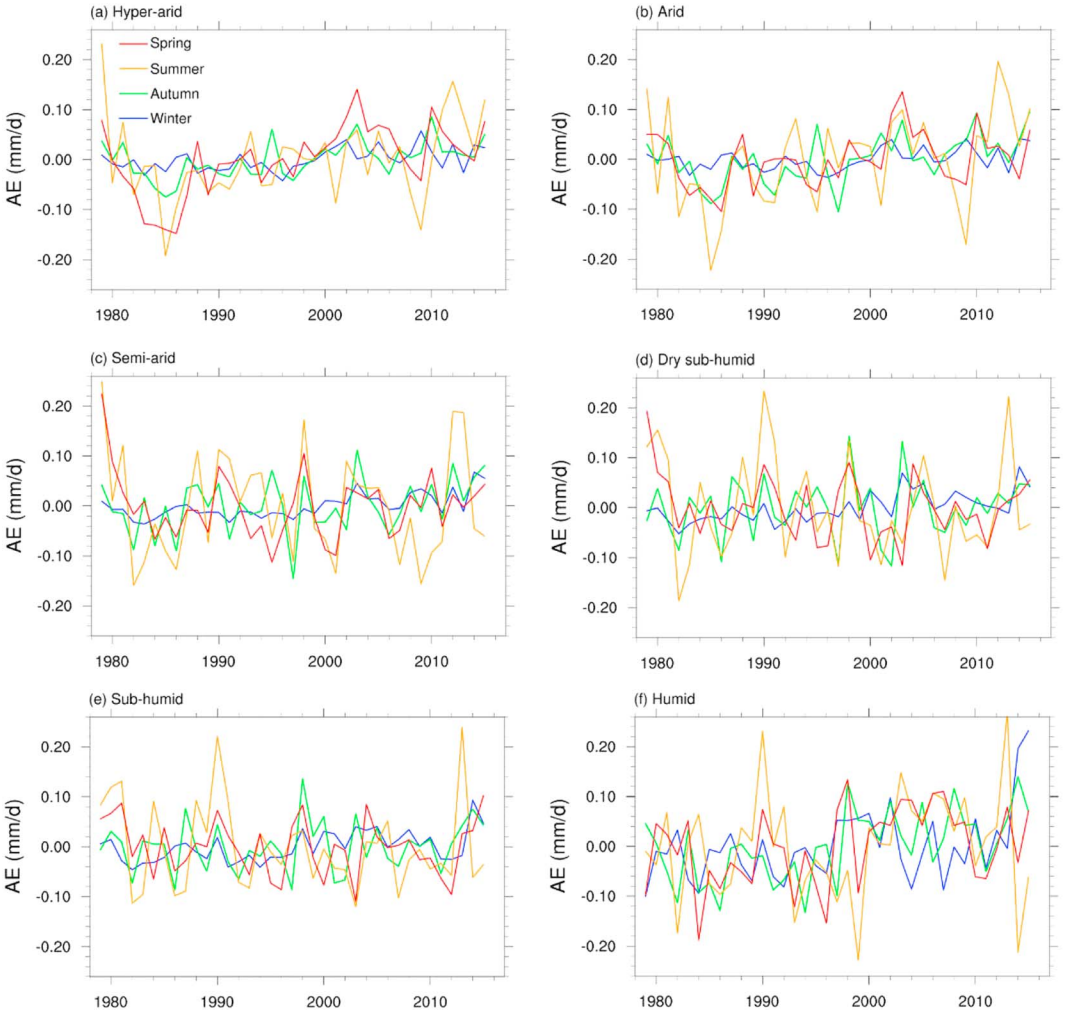

Figure 7. The variations in the regionally averaged of seasonal AE derived from MRE of the six reanalyses over the (a) hyperarid, (b) arid, (c) semiarid, (d) dry subhumid, (e) subhumid, and (f) humid regions (unit: mm/day).

change on AE. Therefore, the linear trends in annual and seasonal AE for different regions in China for the periods of 1979–2015 are listed in Table 2. For China as a whole, the annual AE shows a significant increasing trend ($p < 0.05$) from 1979 to 2015, and the rate of increase is highest in autumn and lowest in summer. At the regional scale, the annual mean AE increases over most regions except for the dry subhumid and subhumid regions, where AE slightly decreases (Table 2). Specifically, the increasing trends in AE are statistically significant at the 99% confidence level over hyperarid, arid, and humid regions, which contributes much to

Table 2
Linear Trends of Annual and Seasonal AE Over China's Six Climatic Regions for the Period of 1979–2015 Derived From MRE

Regions	Hyperarid	Arid	Semiarid	Dry subhumid	Subhumid	Humid	China
Spring	***3.191***	1.271	−0.563	−1.050	−0.593	2.417*	0.631
Summer	***1.711***	2.649*	−0.595	−1.107	−1.310	1.617	0.499
Autumn	***1.370***	***1.828***	1.317	0.672	0.698	***3.024***	***1.683***
Winter	***0.867***	0.708*	***1.275***	***1.517***	***1.241***	***2.718***	***1.542***
Annual	***6.827***	***6.192***	1.114	−0.147	−0.072	***9.245***	4.044*

Note. Units: mm/decade. According to the Mann-Kendall trend test, the bold italic values are significant at the 99% confidence level and the asterisk values are significant at the 95% confidence level.

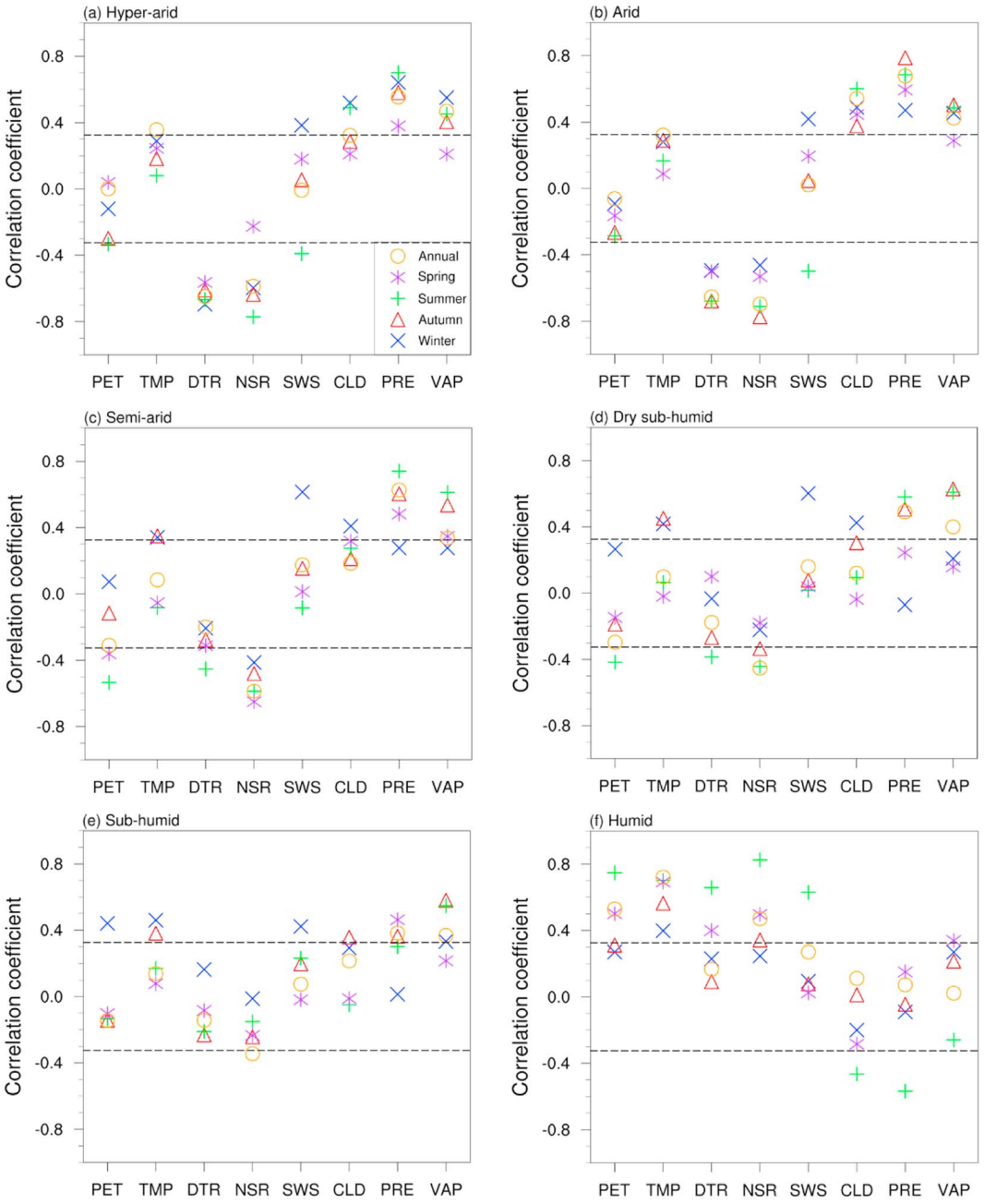

Figure 8. Temporal correlation coefficients between MRE and the major factors for each climatic region for the period of 1979–2015. The values located outside of the dotted line are significant above the 95% confidence level by Student's *t* test.

that in the whole China. Considering the magnitude and spatial distribution of long-term changes in AE, the increasing trend in the humid region is the primary contributor to the overall trend for China, followed by the arid region.

On a seasonal basis, increasing AE trends are observed mainly in autumn and winter, and the winter increase is statistically significant over all of China's six climatic regions (Table 2). For the hyperarid region, AE increases significantly all year round (Figure 7a), and the increasing trend in spring contributes most to the annual mean AE trend (Table 2). In comparison, the linear trends in AE over the arid region exhibit roughly similar behavior (Figure 7b), and only the significance levels of the nonlinear trends differ, especially in spring. Similar to the hyperarid and arid regions, the most humid regions of China feature increasing AE trends in

all seasons (Figure 7f), where the supply of moisture is relatively sufficient over the long term to produce evaporation. However, it has been demonstrated that even in the Yangtze River Basin, decreasing PRE can be one of the main contributors to decreasing AE (Wang et al., 2011). As indicated by regional mean spring PRE, it is extremely dry in the 1980s and 1990s in South China (Xin et al., 2006), and the low AE values were observed during these two dry periods in the humid region (Figure 7f). It is suggested that the influence of climate variability should be considered when quantifying the effects of global warming on AE.

The trends of seasonal AE show inconsistent behavior over the semiarid, dry subhumid, and subhumid regions. Although AE tends to increase in autumn and winter, decreasing trends are present in spring and summer. Overall, the significance of the positive trends is higher in winter than in autumn according to the Mann-Kendall trend test (Table 2). The observed change in AE for the semiarid region shows a slight increase on the annual time scale, which is dominated by the increasing trends in autumn and winter (Table 2). Furthermore, the decreasing AE trends in spring and summer lead to a slight decreasing trend in the annual AE over the dry subhumid and subhumid regions.

Under global warming, AE has increased significantly over the hyperarid, arid, and humid regions, where are the driest and wettest regions in China, respectively. When considering changes in AE (and therefore changes in the terrestrial water balance), an important consideration is the availability of water, which climatologically limits AE as illustrated in Figure 1 (McVicar et al., 2012). Nonetheless, the causal links between environmental change and AE are complex because they are often indirect, displaced in space and time, and dependent on a number of modifying forces (Liu et al., 2004). Understanding the contributions of trends and the changing patterns in the water and energy supply to changes in AE is an important issue for interpreting the AE trends.

3.3. Influence of Meteorological Variables on AE Changes

To identify the drivers of the AE trends, a correlation analysis between AE and other meteorological variables on annual and seasonal scales is performed (Figure 8). This analysis reveals that there is no universal explanation for the changes in AE over China. The major controlling factors vary from region to region and from season to season. In general, AE is most highly correlated with DTR, NSR, PRE, and VAP over the drylands, such as the hyperarid, arid, and semiarid regions, whereas AE is governed mainly by PET, TMP, and NSR over the humid region (Figure 8f).

For the hyperarid region, annual AE is mostly influenced by DTR, NSR, PRE, and VAP, with the correlation coefficients of -0.648, -0.586, 0.555, and 0.469, respectively (Figure 8a). The annual NSR, PRE, and VAP show no significant trends, whereas DTR exhibits a significant decreasing trend ($p < 0.01$; Figure 9a). It can be concluded that the main factor associated with increasing AE is DTR over the hyperarid region. Similarly, the correlation coefficient between annual DTR and AE is -0.653 ($p < 0.01$) over the arid region (Figure 8b), and the concurrent occurrences of DTR decreases and AE increases were found in all seasons (Figure 9b). This finding is in accordance with the results of Shen et al. (2010), who reported that the factor most closely related factor to decreasing pan evaporation is DTR in the arid region of China. Dai et al. (1999) also showed that the DTR is strongly affected by clouds because of their effects on surface solar radiation and, to lesser extent, by soil moisture and PRE through evaporation. Our result also suggests that DTR may integrate the effects of these factors and thus have a stronger correlation with AE than any of these individual factors.

In a region without adequate moisture, PET cannot be sustained, and as a result AE is less than PET (Lawrimore & Peterson, 2000). Although the complex relationship between factors affecting AE can produce localized differences, the moisture conditions are a limiting factor for AE over land. Overall, the amount of moisture available for AE within large regions is determined by PRE, runoff, and water storage (Budyko, 1974). Note that no statistically significant trend in any of annual and seasonal PRE is observed over the hyperarid or arid region (Figure 9). Alternatively, glaciers play a significant role in the water resource system in northwestern China and have been mostly in retreat over the past 40 years (Tao et al., 2011). Ice wastage has significantly influenced water resources (Sorg et al., 2012). Although the water supply from the mountains to the Tarim Basin is favorable, however, a quantitative assessment reveals that local human activities (such as irrigation and domestic water use) since the 1970s have led to a decrease in the water volume reaching the mainstream of the Tarim River Basin, which worsened in the 2000s (Tao et al., 2011). These changes in moisture conditions due to both climate warming and human activities can potentially affect AE. In turn, as AE increases, runoff and water storage decrease, even when the average amount of glacial meltwater

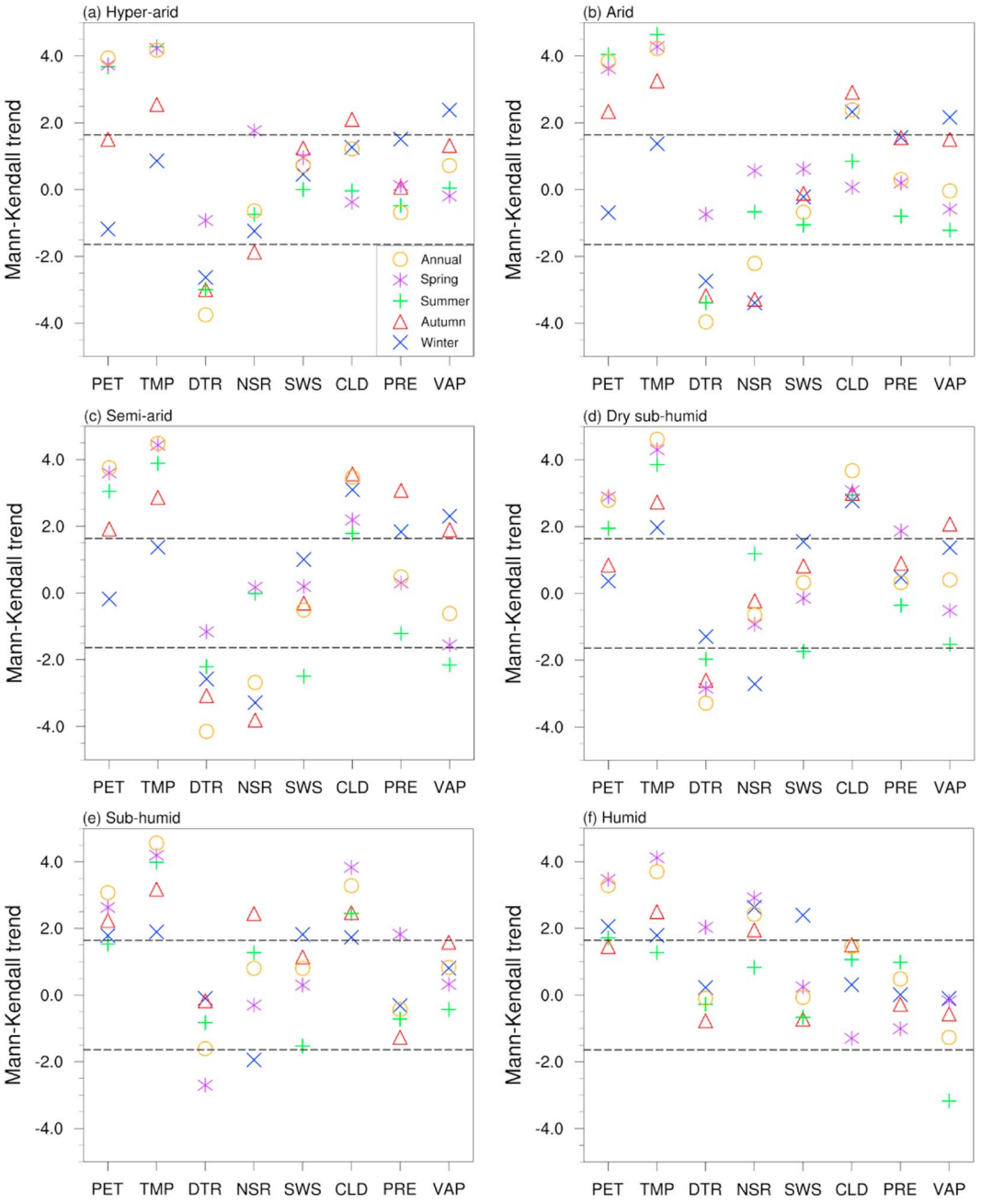

Figure 9. Mann-Kendall trends of meteorological variables for each climatic region for the period of 1979–2015. The values located outside of the dotted line are significant above the 95% confidence level.

increases during the same period. Therefore, the increase in water supply from melting glaciers might be the main contributor to increasing AE in the hyperarid and arid region. Nonetheless, the lack of observations on irrigation and water storage prevents quantitative analyses of this hypothesis at this stage.

The influence of a given climate factor can vary considerably in different seasons over the semiarid region (Figure 8c). The relationship between AE and environmental factors can become highly complicated. Above all, annual AE is most highly correlated with PRE, and the correlation coefficient is highest in summer and lowest in winter. Aside from PRE, NSR is the main contributor to changes in AE (Figure 8c), and the trend analysis shows that a concurrent occurrence of AE increases and NSR decreases in autumn and winter

(Figure 9c). This relationship may not be surprising, because terrestrial AE is largely dependent on water availability over the drylands, and the correlation of PRE with NSR is negative in theory. Therefore, increasing PRE and decreasing NSR are the main contributors to increasing AE over the semiarid region. Annual AE also correlates significantly with NSR and PRE over the dry subhumid region (Figure 8d). However, the main factors associated with AE increases in autumn and winter are TMP and CLD (Figure 9d). Moreover, TMP is also the primary contributor that causes winter AE to increase over the subhumid region (Figure 8e), and the effects of PET and SWS on AE can become more significant (Figure 9e). There is evidence that the direct impact of TMP on drying may actually be a misinterpretation of feedback between the land and the atmosphere (Sherwood & Fu, 2014; Wang et al., 2012). It is more plausible that AE actually decreases during drought because of less PRE and that drought drives increases in TMP because there is less evaporative cooling and thus a higher sensible heat flux warming the air (Sheffield et al., 2012).

For the humid region, the increase in AE is mainly caused by the increase in thermodynamic factors, such as PET, TMP, and NSR (Figure 8f). In general, as the amount of available moisture increases, AE increases, and the water limitation on the evaporative process gives way to an energy limitation. Global warming is expected to result in a higher evaporative potential of the atmosphere and an increase in the rate of evaporation from terrestrial open water bodies. Zhang et al. (2012) also suggested that positive trends in evaporation may occur in "wet" regions where energy supply limits evaporation. As a result, it can be concluded that a significant increasing AE trend over the humid region is caused by the increase in PET due to climate warming. However, this might be more complicated as increased available moisture could increase CLD and in turn decrease NSR at the surface therefore decreasing the available energy for AE.

By subdividing China into six climatic regions, we found that AE increased significantly over the hyperarid, arid, and humid regions and decreased slightly over the dry subhumid and subhumid regions. The causes of the changes in regional AE differ considerably across China. From the spatial dimension, moisture conditions were found to influence the sensitivity of AE to the changes in individual factors. Annual PET exhibits a statistically significant increasing trend everywhere in China. However, the impacts of the increased PET on AE show different characteristics depending on location and season. For the hyperarid and arid regions, increases in PET and water supply from melting glaciers might be the main contributors to the AE increases, whereas the increase in PET is the main cause of the increase in AE over the humid region.

4. Conclusions

This paper presents the results of a study on the trends of annual and seasonal AE over China under a warming climate. Based on the trend analysis of six reanalyses and AE_Budyko from 1979 to 2015 and the correlation analysis, we have reached the following conclusions:

1. For China as whole, annual AE shows a significant increasing trend from 1979 to 2015, and the rate of increase is highest in autumn and lowest in summer. At the regional scale, AE increases are statistically significant over the hyperarid, arid, and humid regions, while AE shows a slight decreasing trend in the dry subhumid and subhumid regions. Considering the magnitude and spatial distribution of long-term changes in AE, the increasing trend in the humid region is the primary contributor to the overall trend for China, followed by the arid region.
2. In the spatial dimension, annual PET portrays a statistically significant increasing trend everywhere in China. However, the impacts of the increased PET on AE vary depending on location and season. For the hyperarid and arid regions, the increases in PET and water supply from melting glaciers might be the main contributors to the increases in AE, whereas the increase in PET is the main cause of the increase in AE over the humid region.
3. In view of data availability, the correlation analysis was conducted between AE in individual reanalyses and AE_Budyko. For China as a whole, NCEP-R1 shows the highest correlation coefficient. At the regional level, the correlations tend to be higher over the arid region. Conversely, the smallest correlations occur over the subhumid. Overall, MERRA2 and JRA-55 have substantial problems on describing the interannual variation and long-term trend in AE over China.

Changing a meteorological variable in different seasons or areas will have a different effect on AE. The above findings imply that there is no single factor controlling changes in AE; instead, the AE changes are driven by regionally and seasonally differing sets of variables. The recent progress in deriving global AE from reanalyses

has allowed for basic evaluations of global trends in AE. Reanalyses provide a reference for comparison, although not without their own uncertainty. The above results provide valuable information for water resources planning and management in China and will also supply an important background and physical interpretation for climate change studies at a regional scale.

Acknowledgments
The authors would like to thank the National Centers for Environmental Prediction-National Center for Atmospheric Research (NCEP-NCAR), NCEP-Department of Energy (NCEP/DOE), National Aeronautics and Space Administration (NASA), European Centre for Medium-Range Weather Forecasts (ECMWF), Japan Meteorological Agency (JMA) (http://rda.ucar.edu/), and the Climate Research Unit (http://cdc.cma.gov.cn/) for providing data sets used in this paper. This research was supported by the National Natural Science Foundation of China (grants 41705053, 41530531, 41675050, 41505054, and 41575074) and the Fundamental Research Funds for the Central Universities (grant lzujbky-2015-253). The authors would like to express their appreciation to the anonymous reviewers, whose comments and suggestions led to significant improvements in the manuscript.

References

Brutsaert, W., & Parlange, M. B. (1998). Hydrologic cycle explains the evaporation paradox. *Nature*, *396*(6706), 30–30. https://doi.org/10.1038/23845

Budyko, M. I. (Ed.) (1974). *Climate and life*, translated from Russian by: Miller, D. H. (pp. 321–330). San Diego, CA: Academic.

Choudhury, B. (1999). Evaluation of an empirical equation for annual evaporation using field observations and results from a biophysical model. *Journal of Hydrology*, *216*(1-2), 99–110. https://doi.org/10.1016/S0022-1694(98)00293-5

Cong, Z. T., Yang, D. W., & Ni, G. H. (2009). Does evaporation paradox exist in China? *Hydrology and Earth System Sciences*, *13*(3), 357–366. https://doi.org/10.5194/hess-13-357-2009

Dai, A. (2013). Increasing drought under global warming in observations and models. *Nature Climate Change*, *3*(1), 52–58. https://doi.org/10.1038/nclimate1633

Dai, A., Trenberth, K. E., & Karl, T. R. (1999). Effects of clouds, soil moisture, precipitation, and water vapor on diurnal temperature range. *Journal of Climate*, *12*(8), 2451–2473. https://doi.org/10.1175/1520-0442(1999)012%3C2451:EOCSMP%3E2.0.CO;2

Douville, H., Ribes, A., Decharme, B., Alkama, R., & Sheffield, J. (2013). Anthropogenic influence on multidecadal changes in reconstructed global evapotranspiration. *Nature Climate Change*, *3*(1), 59–62. https://doi.org/10.1038/NCLIMATE1632

Feng, S., & Fu, Q. (2013). Expansion of global drylands under a warming climate. *Atmospheric Chemistry and Physics*, *13*(19), 10,081–10,094. https://doi.org/10.5194/acp-13-10081-2013

Gao, G., Chen, D., Xu, C., & Simelton, E. (2007). Trend of estimated actual evapotranspiration over China during 1960-2002. *Journal of Geophysical Research*, *112*, D11120. https://doi.org/10.1029/2006JD008010

Harris, I., Jones, P. D., Osborn, T. J., & Lister, D. H. (2014). Updated high-resolution grids of monthly climatic observations–the CRU TS3.10 dataset. *International Journal of Climatology*, *34*(3), 623–642. https://doi.org/10.1002/joc.3711

He, W., Zhao, S., Liu, Q., Jiang, Y., & Deng, B. (2016). Long-range correlation in the drought and flood index from 1470 to 2000 in eastern China. *International Journal of Climatology*, *36*(4), 1676–1685. https://doi.org/10.1002/joc.4450

Hobbins, M. T., Ramirez, J. A., & Brown, C. (2004). Trends in pan evaporation and actual evapotranspiration across the conterminous U.S.: Paradoxical or complementary? *Geophysical Research Letters*, *31*, L13503. https://doi.org/10.1029/2004GL019846

Huang, J., Ji, M., Xie, Y., Wang, S., He, Y., & Ran, J. (2016). Global semi-arid climate change over last 60 years. *Climate Dynamics*, *46*(3-4), 1131–1150. https://doi.org/10.1007/s00382-015-2636-8

Huang, J., Yu, H., Dai, A., Wei, Y., & Kang, L. (2017). Drylands face potential threat under 2°C global warming target. *Nature Climate Change*, *7*(6), 417–422. https://doi.org/10.1038/NCLIMATE3275

Ji, F., Wu, Z., Huang, J., & Chassignet, E. P. (2014). Evolution of land surface air temperature trend. *Nature Climate Change*, *4*(6), 462–466. https://doi.org/10.1038/nclimate2223

Lawrimore, J. H., & Peterson, T. C. (2000). Pan evaporation trends in dry and humid regions of the United States. *Journal of Hydrometeorology*, *1*(6), 543–546. https://doi.org/10.1175/1525-7541(2000)001%3C0543:PETIDA%3E2.0.CO;2

Liu, B., Xu, M., Henderson, M., & Gong, W. (2004). A spatial analysis of pan evaporation trends in China, 1955–2000. *Journal of Geophysical Research*, *109*, D15102. https://doi.org/10.1029/2004JD004511

Liu, X., Luo, Y., Zhang, D., Zhang, M., & Liu, C. (2011). Recent changes in pan-evaporation dynamics in China. *Geophysical Research Letters*, *38*, L13404. https://doi.org/10.1029/2011GL047929

Lorenz, C., & Kunstmann, H. (2012). The hydrological cycle in three state-of-the-art reanalysis: Intercomparison and performance analysis. *Journal of Hydrometeorology*, *13*(5), 1397–1420. https://doi.org/10.1175/JHM-D-11-088.1

Mao, Y., & Wang, K. (2017). Comparison of evapotranspiration estimates based on the surface water balance, modified Penman-Monteith model, and reanalysis data sets for continental China. *Journal of Geophysical Research: Atmospheres*, *122*, 3228–3244. https://doi.org/10.1002/2016JD026065

McVicar, T. R., Roderick, M. L., Donohue, R. J., Li, L. T., Van Niel, T. G., Thomas, A., et al. (2012). Global review and synthesis of trends in observed terrestrial near-surface wind speeds: Implications for evaporation. *Journal of Hydrology*, *416-417*, 182–205. https://doi.org/10.1016/j.jhydrol.2011.10.024

Mezentsev, V. (1955). More on the calculation of average total evaporation. *Meteorologiya i Gidrologiya*, *5*, 24–26.

Peterson, T. C., Golubev, V. S., & Groisman, P. Y. (1995). Evaporation losing its strength. *Nature*, *377*(6551), 687–688. https://doi.org/10.1038/377687b0

Roderick, M. L., & Farquhar, G. D. (2002). The cause of decreased pan evaporation over the past 50 years. *Science*, *298*(5597), 1410–1411. https://doi.org/10.1126/science.1075390

Roderick, M. L., & Farquhar, G. D. (2011). A simple framework for relating variations in runoff to variations in climatic conditions and catchment properties. *Water Resources Research*, *47*, W00G07. https://doi.org/10.1029/2010WR009826

Sheffield, J., Wood, E. F., & Roderick, M. L. (2012). Little change in global drought over the past 60 years. *Nature*, *491*(7424), 435–438. https://doi.org/10.1038/nature11575

Sherwood, S., & Fu, Q. (2014). A drier future? *Science*, *343*(6172), 737–739. https://doi.org/10.1126/science.%201247620

Shen, Y., Liu, C., Liu, M., Zeng, Y., & Tian, C. (2010). Change in pan evaporation over the past 50 years in the arid region of China. *International Journal of Climatology*, *24*(2), 225–231.

Sorg, A., Bolch, T., Stoffel1, M., Solomina, O., & Beniston, M. (2012). Climate change impacts on glaciers and runoff in Tien Shan (Central Asia). *Nature Climate Change*, *2*(10), 725–731. https://doi.org/10.1038/nclimate1592

Su, T., Feng, G., Zhou, J., & Ye, M. (2015). The response of actual evaporation to global warming in China based on six reanalysis datasets. *International Journal of Climatology*, *35*(11), 3238–3248. https://doi.org/10.1002/joc.%204203

Su, T., Feng, T., & Feng, G. (2015). Evaporation variability under climate warming in five reanalyses and its association with pan evaporation over China. *Journal of Geophysical Research: Atmospheres*, *120*, 8080–8098. https://doi.org/10.1002/2014JD023040

Tao, H., Gemmer, M., Bai, Y., Su, B., & Mao, W. (2011). Trends of streamflow in the Tarim River Basin during the past 50 years: Human impact or climate change? *Journal of Hydrology*, *400*(1–2), 1–9. https://doi.org/10.1016/j.jhydrol.2011.01.016

Thomas, A. (2000). Spatial and temporal characteristics of potential evapotranspiration trends over China. *International Journal of Climatology*, *20*(4), 381–396.

Trenberth, K. E., Fasullo, J. T., & Mackaro, J. (2011). Atmospheric moisture transports from ocean to land and global energy flows in reanalysis. *Journal of Climate*, *24*(18), 4907–4924. https://doi.org/10.1175/2011JCLI4171.1

Wang, K. C., & Dickinson, R. E. (2012). A review of global terrestrial evapotranspiration: Observation, modeling, climatology, and climatic variability. *Reviews of Geophysics*, *50*, RG2005. https://doi.org/10.1029/2011RG000373

Wang, K. C., Dickinson, R. E., & Liang, S. (2012). Global atmospheric evaporative demand over land from 1973 to 2008. *Journal of Climate*, *25*(23), 8353–8361. https://doi.org/10.1175/JCLI-D-11-00492.1

Wang, K. C., & Liang, S. (2008). An improved method for estimating global evapotranspiration based on satellite estimation of surface net radiation, vegetation index, temperature, and soil moisture. *Journal of Hydrometeorology*, *9*(4), 712–727. https://doi.org/10.1175/2007JHM911.1

Wang, Y., Liu, B., Su, B., Zhai, J., & Gemmer, M. (2011). Trends of calculated and simulated actual evaporation in the Yangtze River Basin. *Journal of Climate*, *24*(16), 4494–4507. https://doi.org/10.1175/2011JCLI3933.1

Xin, X., Yu, R., Zhou, T., & Wang, B. (2006). Drought in late spring of South China in recent decades. *Journal of Climate*, *19*(13), 3197–3206. https://doi.org/10.1175/JCLI3794.1

Xu, C. Y., & Singh, V. P. (2005). Evaluation of three complementary relationship evapotranspiration models by water balance approach to estimate actual regional evapotranspiration in different climatic regions. *Journal of Hydrology*, *308*(1–4), 105–121. https://doi.org/10.1016/j.jhydrol.2004.10.024

Yang, D. W., Sun, F. B., Liu, Z. Y., Cong, Z. T., & Lei, Z. D. (2006). Interpreting the complementary relationship in non-humid environments based on the Budyko and Penman hypotheses. *Geophysical Research Letters*, *33*, L18402. https://doi.org/10.1029/2006GL027657

Yang, H., Qi, J., Xu, X., Yang, D., & Lv, H. (2014). The regional variation in climate elasticity and climate contribution to runoff across China. *Journal of Hydrology*, *517*(1), 607–616. https://doi.org/10.1016/j.jhydrol.2014.05.062

Yang, H., Yang, D., Lei, Z., & Sun, F. (2008). New analytical derivation of the mean annual water-energy balance equation. *Water Resources Research*, *44*, W03410. https://doi.org/10.1029/2007WR006135

Zhang, Y., Liu, C., Tang, Y., & Yang, Y. (2007). Trends in pan evaporation and reference and actual evapotranspiration across the Tibetan Plateau. *Journal of Geophysical Research*, *112*, D12110. https://doi.org/10.1029/2006JD008161

Zhang, Y. Q., Leuning, R., Chiew, F. H. S., Wang, E. L., Zhang, L., Liu, C. M., et al. (2012). Decadal trends in evaporation from global energy and water balances. *Journal of Hydrometeorology*, *13*(1), 379–391. https://doi.org/10.1175/JHM-D-11-012.1

胡泊，申红艳，王晓娟，等. 2018. 东北亚地区初夏、盛夏和传统夏季降水特征及环流型的异同性研究 [J]. 大气科学, 42 (1): 109−123. Hu Po, Shen Hongyan, Wang Xiaojuan, et al. 2018. A study on characteristics of precipitation and circulation pattern in early summer, midsummer and conventional summer in Northeast Asia [J]. Chinese Journal of Atmospheric Sciences (in Chinese), 42 (1): 109−123, doi:10.3878/j.issn.1006-9895.1706.16290.

东北亚地区初夏、盛夏和传统夏季降水特征及环流型的异同性研究

胡泊[1] 申红艳[1] 王晓娟[3] 封国林[1, 2, 4]

1 兰州大学大气科学学院，兰州 730000
2 中国气象局国家气候中心开放实验室和预测室，北京 100081
3 常熟理工学院物理信息与工程学院，江苏常熟 215100
4 扬州大学物理科学与技术学院，江苏扬州 225002

摘 要 本文利用 1979～2015 年 GPCP（Global Precipitation Climatology Project）逐月降水资料，采用经验正交函数（EOF）分解和 Morlet 小波分析方法，对东北亚地区初夏、盛夏和传统夏季降水的时空分布特征以及环流型开展了系统性的研究，揭示了东北亚地区传统夏季降水表现为盛夏降水贡献占主导，其年际和年代际特征以及环流特征同盛夏降水特征相一致，而初夏降水和盛夏降水特征及形成机制则具有显著差异。空间分布上，初夏的降水 EOF 第一模态表现为“＋－＋”的三极型分布，而盛夏和传统夏季则表现为南北相反的偶极型特征；时间演变方面，初夏降水表现为 5～6 a 振荡周期，盛夏为 2～3 a 为主的振荡周期，传统夏季则兼具上述两类振荡周期；在年代际调整方面，在 1990 年代末，盛夏降水和传统夏季降水在华北和东北地区发生了显著的年代际转折。此外，分析降水与环流的联系发现：初夏，由于西太平洋上空异常反气旋将西太平洋等地的水汽向北方地区输送，且受欧亚 II 型（EUII）遥相关的作用，东北亚地区初夏降水异常具有明显纬向特征。盛夏，东北亚地区降水主要受到西太平洋副热带高压西伸北进、孟加拉湾和南海等地水汽加强的影响。欧亚 I 型（EUI）遥相关和亚洲太平洋型（EAP）遥相关与我国东北以西和沿海地区的降水具有显著相关性。EU 型遥相关的作用使东北亚夏季降水的异常中心存在西北—东南向的波列特征，EAP 型遥相关的作用则使夏季降水存在经向三极型或偶极型特征。

关键词 降水异常 东北亚地区 遥相关型 环流

文章编号 1006-9895(2018)01-0109-15 **中图分类号** P461 **文献标识码** A

doi:10.3878/j.issn.1006-9895.1706.16290

A Study on Characteristics of Precipitation and Circulation Pattern in Early Summer, Midsummer and Conventional Summer in Northeast Asia

HU Po[1], SHEN Hongyan[1], WANG Xiaojuan[3], and FENG Guolin[1, 2, 4]

1 *College of Atmospheric Sciences*, *Lanzhou University*, *Lanzhou* 730000
2 *Laboratory for Climate Studies*, *National Climate Center*, *China Meteorological Administration*, *Beijing* 100081
3 *College of Physical and Electronic Project*, *Changshu Institute of Technology*, *Changshu*, *Jiangsu* 215500
4 *College of Physical Science and Technology*, *Yangzhou University*, *Yangzhou*, *Jiangsu* 225002

收稿日期 2016-12-21；**网络预出版日期** 2017-06-15

作者简介 胡泊，男，1990 年出生，博士研究生，主要从事气候学研究。E-mail: 383876027@qq.com

通讯作者 王晓娟，E-mail: mouse0903@126.com

资助项目 公益性行业（气象）专项 GYHY201306021，国家自然科学基金项目 41575082、41530531、41475096、41505061

Funded by China Meteorological Administration Special Public Welfare Research Fund (Grant GYHY201306021), National Natural Science Foundation of China (Grants 41575082, 41530531, 41475096 and 41505061)

Abstract Based on monthly Global Precipitation Climatology Project (GPCP) data from 1079 to 2015, temporal and spatial characteristics of precipitation and circulation patterns in early summer, midsummer and conventional summer in Northeast Asia are systematically investigated using empirical orthogonal function (EOF) analysis and Morlet wavelet methods. Results indicate that the conventional summer precipitation is dominated by midsummer precipitation. The interannual and interdecadal circulation variations are consistent with the characteristics of midsummer precipitation, while the mechanisms for early summer and midsummer precipitation are significantly different. Looking at the spatial distribution of precipitation, it is found that the first leading mode of early summer precipitation exhibits a "＋－＋" tripole pattern along the meridional direction, while an opposite pattern is found in the first leading modes of midsummer and conventional summer precipitation. Early summer precipitation demonstrates a 5–6-a period and midsummer precipitation shows a 2–3-a period. In the late 1990s, midsummer precipitation and conventional summer precipitation experienced a significant decadal change in North China and Northeast China. Further analysis indicates that early summer precipitation anomalies are mainly zonally distributed, which is partly attributed to the water vapor transport to Northeast Asia by anomalous anticyclonic circulation over the Western Pacific and partly attributed to the effects of the Eurasian II teleconnection (EUII). In midsummer, precipitation is mainly affected by the northward extension of western Pacific subtropical high and the strengthening of water vapor transport from the Bay of Bengal and the South China Sea. Eurasia I (EUI) teleconnection pattern and East Asia-Pacific (EAP) teleconnection pattern both are significantly correlated with midsummer precipitation in western China and the coastal area of China. Summer precipitation anomalies extend from northwest to southeast due to the effects of EUII teleconnection pattern. The effect of EAP teleconnection pattern leads to the tripole or dipole patterns of summer precipitation distribution along the meridional direction.

Keywords Precipitation anomaly, Northern Asia region, Teleconnection pattern, Circulation

1 引言

东北亚地处欧亚大陆的东北部，主要包括韩国、日本、俄罗斯远东、朝鲜、蒙古东部以及我国的东北和华北大部地区，受夏季风活动强弱等因素的影响，夏季雨带的推进具有明显的阶段性特征（廉毅等，2003； Gong et al., 2006，2015；沈柏竹等，2011），且该地区夏季洪涝和干旱等气候灾害事件频发（Zhao et al., 2010; Zhu et al., 2011; Tan et al., 2014）。以往对于夏季降水预测研究，更多关注的是传统夏季（6～8 月）的降水特征，对于东北亚地区降水在其降水集中期所表现出的阶段性特征的关注度不够。事实上，沈柏竹等（2011）通过分析东北地区的降水和环流特征，已经明确指出应该对初夏和盛夏的降水特征要有区别的研究。受东亚夏季风的影响（Huang and Sun, 1992；Ding and Chan, 2005），初夏降水的主雨带主要集中在长江以南地区，盛夏降水的主雨带主要集中在华北和东北等地，而 7 月下旬和 8 月上旬后，由于夏季风的北上而带来大量低纬度的水汽，则会进一步加强东北亚地区的降水。与此同时，由于受极涡加强的影响（廉毅等，2005；沈柏竹等，2008；Zhao et al., 2015），5～6 月的东北亚地区也会出现降水量较前期明显增多的特征，其对应着与盛夏降水不同的形成机制。因此，完全有必要对东北亚地区这一农业和工业的亚洲重镇，开展相应的阶段性降水特征分析。这不仅可以加深对东北亚地区降水时空演变规律的认识，也将有助于我们更好的理解其降水形成的环流特征和外源强迫，进而为提高东北亚降水次季节—到季节尺度预报准确率提供重要的参考（封国林等，2008，2012；龚志强等，2009；Gong et al., 2016；Zheng et al., 2016）。

开展东北亚夏季降水的时空演变规律的研究，主要需要考虑其空间分布和时间演变这两方面特征。由于受东亚—太平洋遥相关型（East Asia Pacific teleconnection，简称 EAP）和欧亚遥相关（Eurasia teleconnection，简称 EU）等夏季大气遥相关的影响，东亚地区夏季降水具有典型的空间型特征，如魏凤英和张先恭（1988）都指出我国东部地区夏季降水雨带的位置可以分为三种类型。黄荣辉等（2007，2011）进一步揭示了中国东部季风区夏季降水存在两个主要模态，即从南到北的经向三极子型和偶极子型分布模态，两种模态的时空变化存在准两年周期振荡和年代际变化等。东北亚地区分别处于 EAP 型和 EU 型遥相关型影响的关键位置，因此分析其降水时空规律必然需要关注其是否具有典型的空间模态。另一方面，叶柏生等（2005）研究我国各月降水量的变化特征发现华北地区 5 月降水呈现显著增加趋势，7 月降水显著减少趋势。陆日宇（1999）对华北夏季不同月份降水年代际进行研究发现：华

北 6 月份降水较少，且年代际变化趋势不明显；7 月份降水在 1960 年代末和 1970 年代中后期均发生年代际转折。Ding et al.（2008）和黄荣辉等（2011）均指出东亚地区包括其北部地区的夏季降水在 1993～1998 年期间为从南到北的 “＋－＋”经向三极子型与“＋－”偶极子型的结合，而 1999～2009 年期间则调整为“南涝北旱”式的“＋－”经向偶极子型分布。此外，经历了 1990 年代初以来的降水偏多，东北亚地区的夏季降水距平自 1990 年代末以来出现持续偏少的特征，但 2011 年和 2012 年则又连续出现了两年的异常偏多，2013 年夏季东北及俄罗斯远东地区等降水持续增多，且东亚北部地区夏季降水的年代际特征尤为显著（龚志强等，2013）。因此，对于东北亚夏季降水演变规律的认识，必然也需要关注其是否具有年际和年代际变率，揭示其在不同时间段具有何种空间模态特征等。

分析东北亚夏季降水时空规律的同时，也需要考虑其对应的环流特征。廉毅等（2003）分析了东亚夏季风在我国东北地区的推进过程，指出东亚夏季风 7 月下旬在东北地区建立，而在 8 月中旬开始从东北地区向南撤退。沈柏竹等（2011）指出，在东北地区初夏降水偏多年时，东北地区西北部出现随高度向西倾斜的异常气旋性环流，东北地区冷涡活动频繁。盛夏，东北地区降水异常主要受到局地对流层高层的东亚高空西风急流北移以及低层的西太平洋副热带高压西伸北进的影响。随着西太平洋副热带高压西北侧西南风异常的加强，向北输送到东北地区的水汽显著增多，东北地区盛夏降水偏多。此外，陆日宇和黄荣辉（1999）也指出在北半球中高纬度地区，夏季不同月份期间，行星波表现出不同的变化特征，印证了夏季不同月份之间明显的环流调整。顾正强等（2013）和孙力等（2002）研究发现，1970～1990 年东北区域内的水汽增加，而 2000 年以后东北区域内的水汽大幅度的减少，进而对东北地区夏季降水也存在明显的年代际变化特征给出有利佐证。但我们注意到，其研究更多关注对东北区域的影响，同时对于 EAP 和 EU 等遥相关可能起到的作用也涉及较少。因此，有必要从更大的空间尺度上揭示，初夏、盛夏和传统夏季中，东北亚地区降水时空演变所对应环流的异同性特征。

综上所述，本文试图分别对东北亚地区初夏（5～6 月）、盛夏（7～8 月）以及传统夏季（6～8 月）的降水进行系统性的对比研究。分析其可能存在空间模态和时间变率特征，并联系欧亚环流系统异常，尤其是 EAP 型和 EU 型遥相关等，分析其降水年际变化对应的主要环流特征。文章第二节给出了资料和方法；第三节分析了东北亚地区初夏、盛夏降水和传统夏季降水的时空特征、异常降水的主模态、异常年的降水特征以及可能存在的年代际变化特征；第四节分析了东北亚地区初夏、盛夏和传统夏季降水对应的环流特征；第五节则给出了 EU 型和 EAP 型遥相关对东北亚夏季降水的影响；最后给出本文的总结和简要的讨论。

2 资料和方法

本文所用资料为 1979～2015 年 GPCP（The Global Precipitation Climatology Project Version 2.1）逐月降水资料（Monthly Precipitation Analysis），分辨率为 2.5°×2.5°。研究的区域为东北亚地区（30°～55°N，110°～145°E）。方法是经验正交函数（EOF）分解、合成以及相关分析。文中初夏为 5～6 月，盛夏为 7～8 月，传统夏季为 6～8 月。

文中 EAP 指数根据 Huang（2004）定义的公式为

$$I_{\mathrm{EAP}} = 0.25\times Z_{20°\mathrm{N},125°\mathrm{E}} - 0.5\times Z_{40°\mathrm{N},125°\mathrm{E}} + 0.25\times Z_{60°\mathrm{N},125°\mathrm{E}}\,. \quad (1)$$

由于影响东北亚初夏和盛夏降水的 EU 遥相关型位置有明显的不同，因此，本文中 EU 指数同时采用了 Barnston and Livezey（1987）提到的欧亚遥相关 I 型（EUI）和欧亚遥相关 II 型（EUII），其中 Barnston 定义的 EUI 遥相关的显著中心分别位于芬兰（60°～70°N，25°～50°E）、中国西北部地区（30°～45°N，80°～100°E）和日本附近地区（30°～40°N，130°～140°E）。EUII 型遥相关的三个显著中心从西往东依次为靠近英国和丹麦地区（50°～60°N，10°W～10°E）、里海北部地区（40°～50°N，50°～60°E）和中国东北地区（40°～50°N，115°～135°E）。同时采用 Wallace and Gutzler（1981）定义的 EU 指数方法，本文中 EUI 型和 EUII 型的公式为

$$I_{\mathrm{EUI}} = -0.25\times Z_{55°\mathrm{N},20°\mathrm{E}} + 0.5\times Z_{55°\mathrm{N},75°\mathrm{E}} - 0.25\times Z_{40°\mathrm{N},145°\mathrm{E}}\,, \quad (2)$$

$$I_{\mathrm{EUII}} = -0.25\times Z_{60°\mathrm{N},\,10°\mathrm{E}} + 0.5\times Z_{50°\mathrm{N},\,50°\mathrm{E}} - 0.25\times Z_{45°\mathrm{N},\,110°\mathrm{E}}\,. \quad (3)$$

公式（1）至（3）中，Z 均表示标准化后的 500

hPa 月平均高度场距平。

3 东北亚地区初夏、盛夏以及传统夏季降水时空演化规律

3.1 东北亚地区初夏、盛夏以及传统夏季降水气候特征

基于 GPCP 月平均资料来对比分析东北亚地区初夏、盛夏以及传统夏季降水时空分布的异同性。图 1 为 1981～2010 年东北亚地区逐月降水直方图。可以看出，东北亚地区降水主要呈现正态分布特征，7 月份降水最多，从 5 月份开始，降水迅速增加，5～9 月降水较其他月份而言相对较多。同时东北亚夏季降水具有显著的阶段性特征。因此，分别对东亚地区初夏（5～6 月）、盛夏（7～8 月）以及传统夏季（6～8 月）降水进行详细对比研究必然具有重要的科学意义。考虑到 9 月为东亚夏季风的南撤月份，以往的研究中多将其单独分析，所以本文未将 9 月列入对比研究的范围。

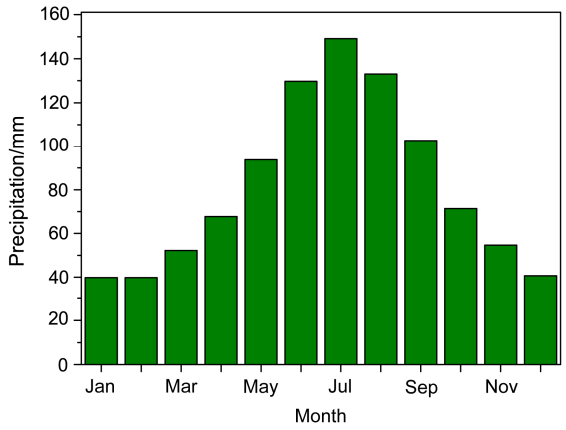

图 1 1981～2010 年东北亚地区逐月降水直方图

Fig. 1 Monthly precipitation histogram in Northeast Asia for 1981–2010

3.2 东北亚地区初夏、盛夏以及传统夏季降水时间演化特征

图 2 给出了东北亚地区初夏、盛夏和传统夏季降水标准化降水量和累积距平曲线图。从图 2a 中可以看出，东北亚地区初夏、盛夏和传统夏季降水都表现出显著的年际变化特征，其中盛夏降水和传统夏季降水的年际振幅比初夏降水强。1979～2015 年，东北亚初夏平均降水为 223 mm，而盛夏平均降水比初夏平均降水多 50 mm，且占了传统夏季降水 70%的降水。从图 2b 中累积距平曲线图可以看出，在 20 世纪 90 年代初之前，东北亚地区初夏降水呈逐渐减少趋势，之后降水量减少趋势相对减缓，直到 21 世纪初，东北亚初夏降水又呈现增多趋势。盛夏降水和初夏降水的趋势大致呈现相反特征，在 20 世纪 90 年代初之前呈现逐渐增加的趋势，到 20 世纪 90 年代末开始急剧减少。传统夏季降水与盛夏降水相比，两者的变化趋势相一致，但在 21 世纪初之后，传统夏季降水的增多趋势更显著。为了分析东北亚地区初夏、盛夏和传统夏季降水之间的相似程度，图 3 给出了东北亚地区初夏、盛夏和传统夏季降水之间的散点分布图。可以看出，初夏和盛夏降水之间的散点大致均匀分布在四个象限中，东北亚地区初夏和盛夏降水之间的相关性只有 0.02，即东北亚盛夏和初夏降水可能对应截然不同的形成机制。东北亚地区传统夏季降水由于包含了初夏和盛夏降水的信息，且盛夏的比重较大，所以东北亚传统夏季降水跟初夏降水相关性仅为 0.39，

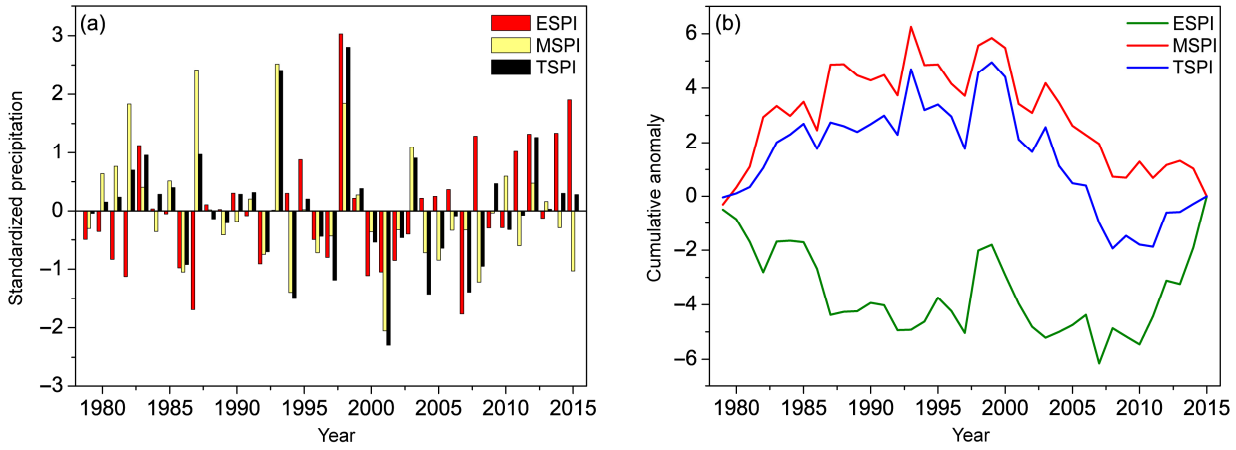

图 2 1979～2015 年东北亚地区（a）初夏（ESPI）、盛夏（MSPI）和传统夏季（TSPI）标准化降水量和（b）标准化降水量的累积距平曲线

Fig. 2 (a) Standardized precipitation in early summer (ESPI), midsummer (MSPI), and conventional summer (TSPI) and (b) cumulative anomaly curves of standardized precipitation in Northeast Asia for 1979–2015

而与盛夏降水相关高达 0.84，由此说明东北亚传统夏季降水更多的包含了东北亚盛夏降水的变化特征。从 21 世纪初之后（2005 年之后）来看，初夏与传统夏季降水相关系数为 0.53，相较 37 年的相关性高出许多，而盛夏和传统夏季降水相关系数则降低到 0.44。因此，21 世纪初之后，初夏降水对传统夏季降水的贡献有所提高。以上结果表明东北亚地区初夏、盛夏降水和传统夏季降水虽然都表现出显著的年际变化趋势，但是他们之间的振幅有明显的差异，且东北亚地区夏季降水之间的增长和减小趋势也有很大的差异。初夏和盛夏降水都对传统夏季降水有一定的影响，21 世纪初期之后传统夏季降水受到初夏降水的影响有所增强。

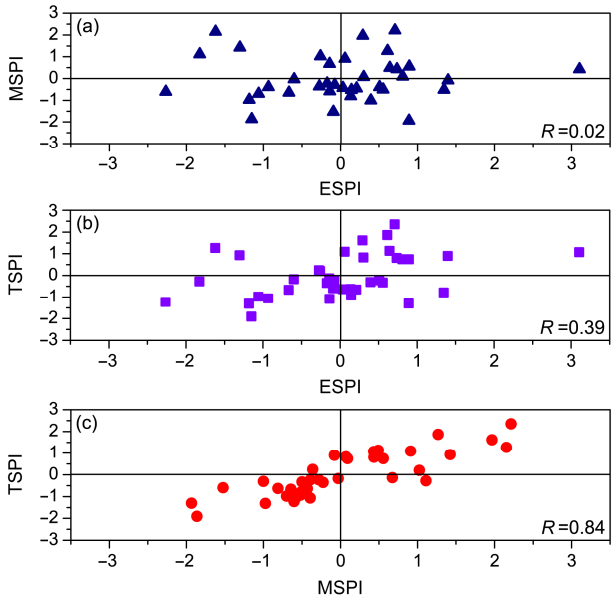

图 3　1979～2015 东北亚地区散点图分布：（a）初夏和盛夏；（b）初夏和传统夏季；（c）盛夏和传统夏季

Fig. 3　Scatter plots of (a) early summer and midsummer precipitation, (b) early summer and conventional summer precipitation, (c) midsummer and conventional summer precipitation in Northeast Asia for 1979–2015

3.3　东北亚地区初夏、盛夏以及传统夏季降水异常的空间主模态特征

图 4 给出了东北亚地区初夏、盛夏以及传统夏季降水异常的模态的空间分布图，可以看出，东北亚地区初夏降水的第一模态（EOF1）从北向南呈现“＋－＋”模态，其方差贡献为 33.29%；第二模态（EOF2）从北向南呈现正负交替的模态，其方差贡献为 16.98%。虽然两者的空间模态有类似之处，但 EOF1 多体现了西北—东南方向的三极型模态，而 EOF2 中三极型模态不明显。此外，它们的正值中心有所不同，EOF1 的正值中心主要在西太平洋地区，而 EOF2 的正值中心主要在日本南部附近。盛夏降水的第一模态（EOF1）出现从北向南的“－＋”

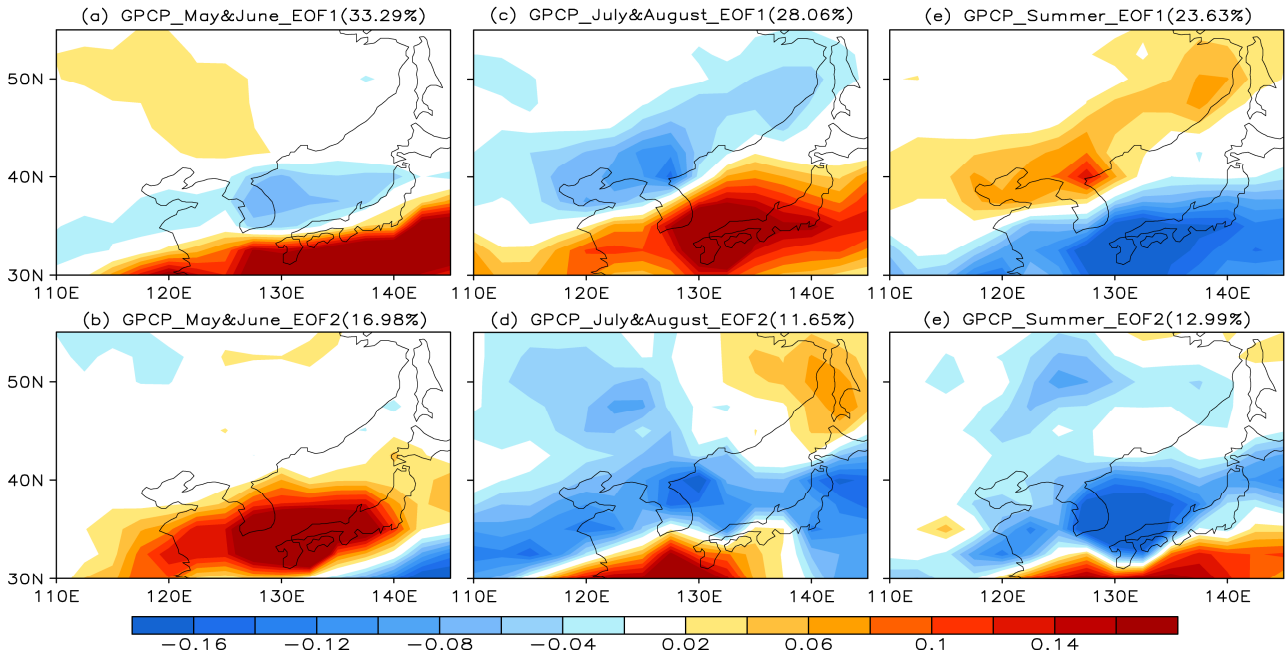

图 4　1979～2015 年东北亚地区（a、b）初夏、（c、d）盛夏以及（e、f）传统夏季降水 EOF 分析第一主模态（第一行）和第二主模态（第二行）的空间分布图

Fig. 4　Spatial patterns of the EOF1 modes (first row) and EOF2 modes (second row) of (a, b) early summer, (c, d) midsummer, and (e, f) conventional summer　precipitation in Northeast Asia for 1979–2015

海陆差异模态，其方差贡献为 28.06%；第二模态（EOF2）呈现从西南到东北的“＋－＋”模态，其方差贡献为 11.65%。东北亚地区盛夏降水沿东亚沿岸的三极子正负交替的模态跟东亚—太平洋（EAP）型（黄荣辉和李维京，1988）相类似，正负中心分别位于鄂霍次克海—东亚中纬度地区—菲律宾附近。EAP 型遥相关结构很好的反映了东亚气候与西北太平洋之间的联系（Nitta, 1987）。传统夏季降水的 EOF1 和东北亚地区盛夏降水 EOF1 空间分布特征虽然由“－＋”模态转变为“＋－”模态，但是两者的时间系数也呈现相反的特征（图 5），因此东北亚地区传统夏季降水第一模态和盛夏降水第一模态是一致的，其方差贡献为 23.63%；传统夏季降水的第二模态（EOF2）也呈现南北向的“＋－＋”模态，其方差贡献为 12.99%。综上所述，东北亚地区初夏降水的空间模态与盛夏降水和传统夏季降水的空间模态有很大的差异，盛夏降水和传统夏季降水的空间模态比较接近。

从东北亚初夏、盛夏和传统夏季降水距平经验正交展开 EOF1 和 EOF2 对应的主分量（PC1 和 PC2）的时间系数上以及时间系数的九年滑动平均（图 5）来看，东北亚地区初夏、盛夏降水和传统夏季降水空间主模态的异常分量都表现出显著的年际变化特征。东北亚地区初夏降水 EOF1 对应的主分量在 1970 年代末到 2000 年代初主要以负值为主，之后开始转变为正值，且 PC1 具有逐渐上升的

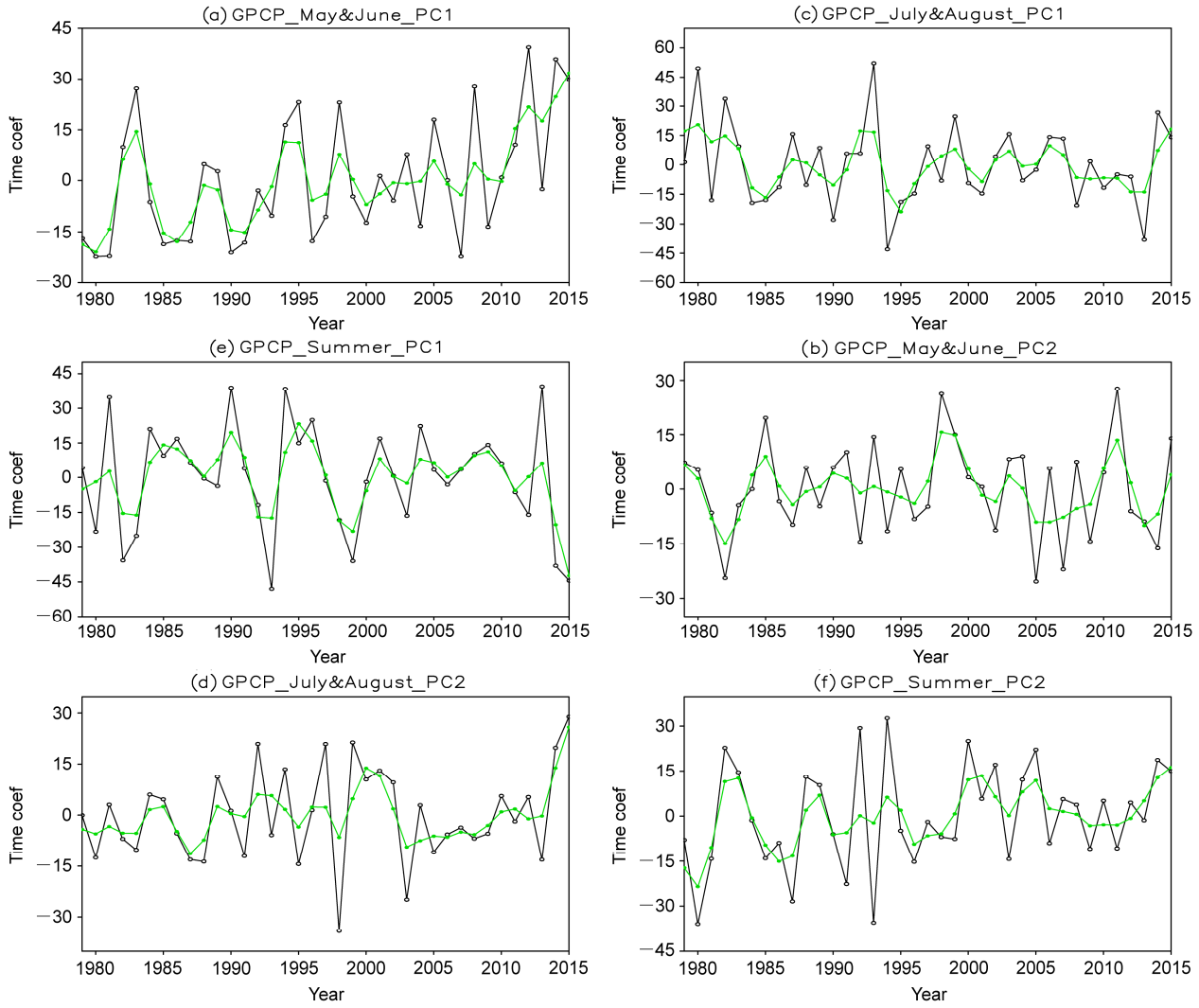

图 5　1979～2015 年东北亚地区（a、b）初夏、（c、d）盛夏以及（e、f）传统夏季降水 EOF 分析第一主分量（第一行）和第二主分量（第二行）的时间系数（绿线表示 9 年滑动平均）

Fig.5 Time coefficients of the EOF1 modes (first row) and EOF2 modes (second row) of (a, b) early summer, (c, d) midsummer and (e, f) conventional summer precipitation in Northeast Asia for 1979–2015. The green line denotes the nine-year moving average of precipitation

趋势。初夏降水 PC2 以 2～6 a 的振荡周期为主，并出现正负交替特征。盛夏降水的 PC1 具有逐渐较少的趋势，PC2 则具有与初夏 PC2 类似的趋势变化相特征，即都具有显著的年际振荡周期。表 1 中，传统夏季降水的 PC1 与盛夏降水的 PC1 呈现相反的变化特征，两者的相关系数为－0.83，通过 0.01 的显著性水平检验；两者 PC2 的相关系数为 0.43，也通过了 0.05 的显著性水平检验。东北亚初夏降水和盛夏降水的影响机制有所不同，两者降水没有直接的联系，故其相应主分量之间的相关性均不显著。由于传统夏季降水包含初夏部分降水，传统夏季降水与初夏降水的 PC1 和 PC2 的相关系数也分别通过了 0.05 和 0.01 的显著性水平检验。图 6 给出了东北亚地区初夏、盛夏以及传统夏季降水 PC1 和 PC2 的小波分析图。可以看出，初夏降水的 PC1 在 80 年代中期存在 5～6 a 为主的短期振荡周期，盛夏降水 PC2 在 1990 年代中后期存在 2～3 a 的振荡周期。传统夏季降水包含了初夏降水和盛夏降水的振荡周期，同时具有 5～6 a 和 2～3 a 的振荡周期。因此，东北亚初夏降水特征相对独立，而盛夏降水一定程度上能够反映东北亚传统夏季降水的变化的特征。

表 1 1979～2015 年东北亚地区初夏、盛夏和传统夏季降水量 EOF 分析异常主模态时间序列的相关系数

Table 1 Correlation coefficients between time series of anomalous principal EOF modes of precipitation in early summer, midsummer, and conventional summer in Northeast Asia for 1979–2015

		异常主模态时间序列的相关系数			
		初夏降水		传统夏季降水	
		PC1	PC2	PC1	PC2
盛夏降水	PC1	－0.04	－0.03	－0.83**	－0.28
	PC2	0.01	－0.15	－0.09	0.43**
传统夏季降水	PC1	－0.39*	－0.16	_	_
	PC2	0.48**	－0.44**	_	_

*表示通过 0.05 的显著性水平检验。

**表示通过 0.01 的显著性水平检验。

3.4 东北亚地区初夏、盛夏以及传统夏季降水的异常特征

本节具体分析东北亚地区初夏、盛夏和传统夏季降水的异常年对应的的空间分布特征。我们利用东北亚地区初夏、盛夏和传统夏季降水序列大于（小于）0.8 倍标准差的为降水偏多（偏少）年，降水序列大于（小于）1.3 倍标准差的为降水严重偏多（偏少）年。根据此定义，得出的东北亚地区初夏、盛夏和传统夏季异常降水存在较大的差异（表 2）。降水偏多年时，东北亚地区初夏有 8 年，盛夏为 5 年，由于受到盛夏降水的影响，传统夏季降水偏多年则减少到 6 年。从严重偏多年来看，初夏降水主要是在 1998、2012、2014 和 2015 年，盛夏降水则主要是在 1982、1987 和 1998 年，而传统夏季降水则在 1993 年和 1998 年出现严重偏多年。东北亚地区初夏降水偏少年有 10 年，盛夏降水偏少年为 6 年，而传统盛夏降水偏少年则有 7 年。从严重偏少年来看，初夏降水主要是在 1987 年和 2002 年，盛夏降水主要是在 1994 年和 2001 年，而传统夏季降水则主要是在 1994、2001 和 2007 年。同时，从表上也可以看出东北亚地区初夏、盛夏与传统夏季降水存在着相反的年份。如：1987 年，东北亚地区初夏降水为偏少年，而盛夏降水和传统夏季降水则是偏多年；2015 年，东北亚地区降水在初夏为偏多年时，而盛夏降水和传统夏季降水则属于偏少年份。还可以看出，东北亚地区初夏和盛夏降水偏多年份没有一年是相同，偏少年份则只有两年呈现相同的年份。由此说明东北亚地区初夏和盛夏降水异常存在着很大的差异性，同时传统夏季降水异常更多是由于盛夏降水异常造成。

图 7 给出了东北亚地区初夏、盛夏和传统夏季降水异常百分率偏多年和偏少年的空间分布图。东北亚地区降水为偏多年时，初夏降水大部呈现沿海地区降水相对偏少，其中降水偏多地区主要集中在华北和日本下游地区（图 7a），与初夏降水 EOF1 的空间分布型相匹配；盛夏和传统夏季降水则表现

表 2 1979～2015 年东北亚地区初夏、盛夏和传统夏季降水异常年份

Table 2 Years of precipitation anomalies in early summer, midsummer, and conventional summer in Northeast Asia for 1979–2015

	偏多年	严重偏多年	偏少年	严重偏少年
初夏降水	1983、1995、1998、2008、2011、2012、2014、2015	1998、2012、2014、2015	1981、1982、1986、1987、1992、1997、2000、2001、2002、2007	1987、2007
盛夏降水	1982、1987、1993、1998、2003	1982、1987、1993、1998	1986、1994、2001、2005、2008、2015	1994、2001
传统夏季降水	1983、1987、1993、1998、2003、2012	1993、1998	1986、1994、1997、2001、2004、2007、2008	1994、2001、2004、2007

为大部分偏多，仅在鄂霍次克海附近地区降水相对偏少（图 7b、c）。从东北亚地区降水百分率偏少年合成图上可以看出，初夏降水整体呈现一致偏少，且偏少区域主要集中在华北和东北区域（图 7d）。盛夏，日本海附近以及华北上部地区降水相对偏少（图 7e）。传统夏季降水由于初夏降水的影响，在日本海附近降水偏少率没有盛夏时期明显（图 7f）。东北亚地区夏季降水的异常年空间分布图的给出，将有利于我们在实际降水预报中更好的把握异常和严重异常降水的可能落区。

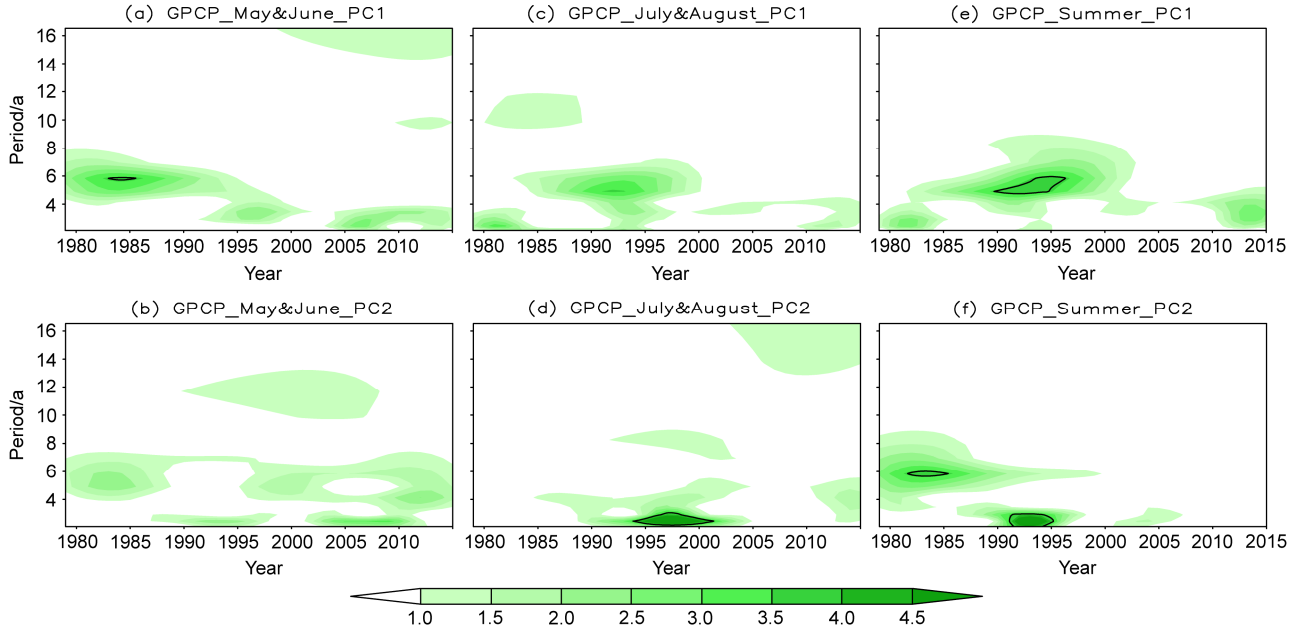

图 6 1979～2015 年东北亚地区（a、b）初夏、（c、d）盛夏以及（e、f）传统夏季降水 EOF 分析第一主分量（第一行）和第二主分量（第二行）时间系数的小波分析图

Fig. 6 Morlet wavelet transform power spectra for the time series of the EOF1 modes (first row) and EOF2 modes (second row) of (a, b) early summer, (c, d) midsummer and (e, f) conventional summer precipitation in Northeast Asia for 1979–2015

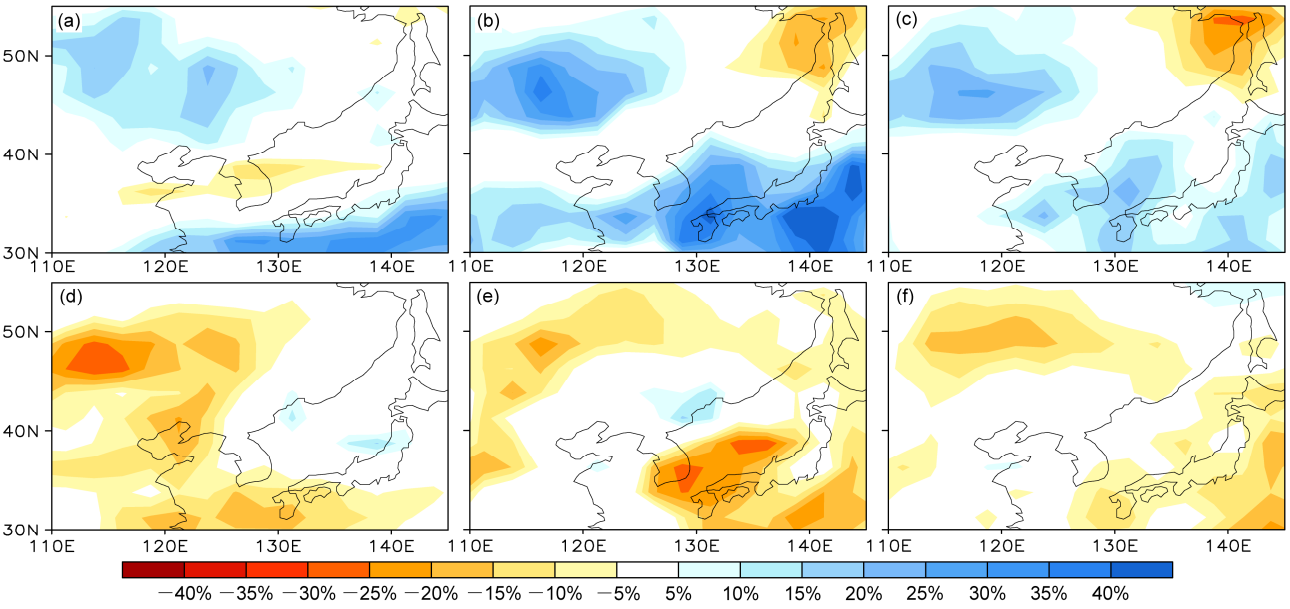

图 7 东北亚地区（a、d）初夏、（b、e）盛夏和（c、f）传统夏季降水距平百分率在降水偏多（第一行）和偏少年（第一行）合成图

Fig.7 Composite distributions of precipitation anomaly percentages in (a, d) early summer, (b, e) midsummer, and(c, f) conventional summer in Northeast Asia. (a, b, c) are for years of positive precipitation anomalies and (d, e, f) are for years of negative precipitation anomalies

3.5　东北亚地区初夏、盛夏以及传统夏季降水年代际变化特征

前人研究表明（黄荣辉等，2013；Si and Ding, 2013），东亚地区夏季降水在 20 世纪 90 年代末具有非常明显的年代际变化特征。因此，为了进一步的理解东北亚初夏、盛夏和传统夏季降水的年代际变化特征，图 8a–c 给出了东北亚地区初夏、盛夏和传统夏季降水滑动 *t* 检验（简称 MTT）（魏凤英，1999）的空间分布图。可以看出，东北亚地区在 90 年代之后的年代际变化特征不明显，只有少部分内陆地区存在通过 0.05 的显著性水平检验。而东北亚盛夏降水发生年代际变化特征的区域主要集中在华北附近和东北部分地区，且发生年代际的时间主要在集中在 1999 年前后。传统夏季降水的年代际变化特征主要受到盛夏降水的年代际特征的影响，发生年代际转折的区域与盛夏降水发生年代际转折的区域相一致。为了更清楚的了解东北亚初夏、盛夏和传统夏季降水的年代际变化特征，选取通过 0.05 显著性水平检验的区域（40°～50°N，110°～120°E），画出显著区域的初夏、盛夏和传统夏季降水距平时间序列图（图 9）。图 9 进一步证实了 20 世纪 90 年代末东北亚盛夏降水和传统夏季降水在华北等的盛夏和传统夏季降水发生了由持续偏多转为持续偏少的年代际转折特征（图 9b、c），而初夏降水更多体现年际变化特征（图 9a）。

4　大气环流变化特征对东北亚初夏、盛夏以及传统夏季降水的作用

以上的结果分析表明，东北亚地区夏季降水不仅具有年代际变化特征，还具有显著的年际变化特征。同时，东北亚地区初夏和盛夏降水也有着明显的差异。本文接下来主要探讨造成东北亚初夏、盛夏和传统夏季降水年际异常的大气环流成因。因此图 10 给出了东北亚地区初夏、盛夏和传统夏季总降水量时间序列回归的 500 hPa 高度场分布。

从图 10a 可以看出，东北亚地区初夏降水跟中亚中高纬度地区和贝加尔湖异常高压、局地异常低压和西太平洋地区异常高压有关，从空间型上具有类似 EU 型遥相关的分布特征。图 10b、c 中，盛夏和传统夏季，具有类似高度场异常的空间分布。东北亚地区降水的异常不仅跟西太平洋地区异常高压、乌拉尔山高压，东北亚局地异常低压有关，还和欧洲西部异常低压有显著的联系。EU 型遥相关存在于欧亚大陆上空从北大西洋传播至乌拉尔地

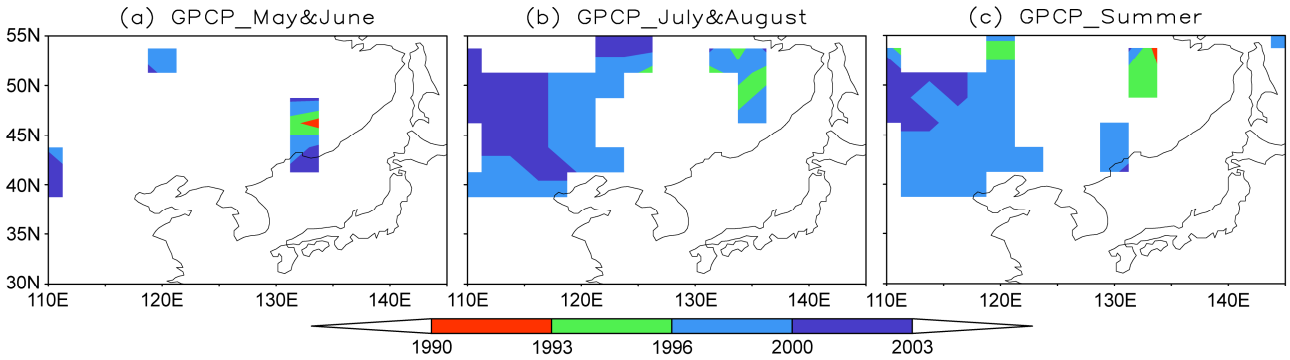

图 8　东北亚地区（a）初夏、（b）盛夏和（c）传统夏季降水 MTT 突变检验空间分布

Fig .8　Spatial distributions of moving *t*-test（MTT）of (a) early summer, (b) midsummer, and (c) conventional summer precipitation in Northeast Asia

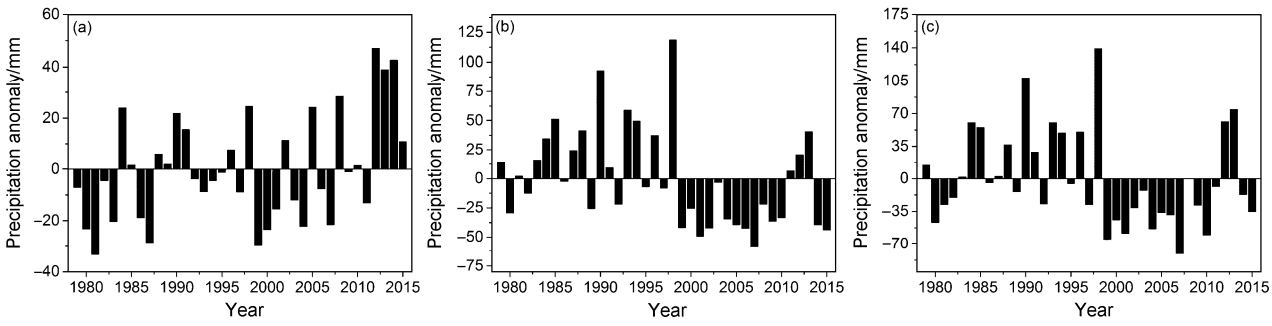

图 9　显著区域（a）初夏、（b）盛夏和（c）传统夏季降水距平时间序列（单位：mm）

Fig. 9　Time series of (a) early summer, (b) midsummer, and (c) conventional summer precipitation anomalies in the significance region (units: mm)

区以东的遥相关波列，表现为乌拉尔山地区、东亚沿岸和欧洲西部地区异常高度场的正负相间的相关关系，即纬向表现为受EU型的控制（Barnston and Livezey，1987；乔少博等，2015）。回归的500 hPa高度场在经向存在一定的正负异常中心波列分布，具有类似EAP遥相关的模态。这种经向模态在初夏表现为负异常区域在日本海附近出现了断裂，但在高纬度的正异常中心较显著，而在盛夏和传统夏季则具有更为典型的EAP型遥相关模态特征。EU型的存在对应了初夏、盛夏和传统夏季的EOF1模态的大值中心均存在一个西北—东南方向的波列特征，而EAP型的存在则决定了其经向存在的初夏的三极型分布和盛夏和传统夏季的偶极型分布。此外，虽然东北亚初夏在500 hPa上空从欧洲西部到东亚地区也出现了正负相间的波列，东北亚地区的降水与欧亚西部地区的异常低压相关性较小，即东北亚地区初夏降水更容易受到局地以及周边系统的影响。如李辑等（2014）研究发现东北冷涡是造成辽宁初夏降水异常偏多的主要影响因子。刘刚等（2017）指出东北初夏降水的62.5%为冷涡降水。

与高度场的异常分布相对应的，在西太平洋上空形成的异常反气旋（图11a），将副热带西太平洋及沿海地区等地的水汽（图12a）从韩国半岛向东北亚地区输送，同时由于贝加尔湖等地的异常高压，有利于北方的干冷气流南下，在东北亚地区与来自低纬度地区的水汽汇合，形成东北亚地区的初夏降水。同时，由于副热带地区副高带高压主要集中在20°～25°N之间，偏东偏南的副热带高压位置对东北亚地区初夏降水影响较小。图11b、c和图12b、c对应盛夏和传统夏季的风场和可降水量异常场中，来自低纬度夏季风较强，孟加拉湾和南海等地的水汽输送强盛，西太平洋上空的出现异常的反气旋偏东。同时，西太平洋副热带高压中心位置向北移动，日本、韩国、朝鲜和我国东北部分地区异常低气压处于西太平洋副热带高压的西北部，异常的水汽沿着西太平洋副热带高压西侧的南风异常向北输送到东北亚地区。盛夏和传统夏季的可降水量主要来自长江地区以及东北偏北地区。通过图11和图12的分析，更清晰给出了东北亚降水在初夏、盛夏和传统夏季降水对应的可降水量的可能源地和水汽通过风场输送的异同性特征。

对比初夏和盛夏的情况不难发现，初夏主要表现为纬向EU型遥相关，而来自低纬度地区的水汽输送相对弱，降水更多表现为与欧亚地区冷涡相联系的冷涡性降水；盛夏和传统夏季则不仅表现为受纬向的EU型影响，同时也受经向典型的EAP遥相关的影响，降水则主要表现为由于低纬度水汽输送显著加强、副高北抬而引起的季风性降水。相关结果，与廉毅等（2010）、何金海等（2006）、胡开喜等（2011）等研究结论是一致。

5 EAP型和EU型遥相关对东北亚初夏、盛夏以及传统夏季降水的影响

某个区域的气候异常与全球各个区域的环流有着一定的联系，大气遥相关型能够很好的解释某一区域的气候异常变化。夏季东亚地区气候异常与西北太平洋之间有着强力的相互作用。图10中，传统的夏季降水受到EAP型遥相关和EU型遥相关显著，因此本节主要分析EAP型遥相关和EU型遥相关对东北亚地区初夏、盛夏以及传统夏季降水的影响。

东亚—太平洋遥相关型（EAP）是北半球夏季重要的遥相关型（Huang and Li, 1987），主要是由纬度副热带西太平洋地区、东亚中纬度地区和雅库茨克及鄂霍次克海地区这三个正负相间的中心构成。因此EAP型遥相关的异常主要反映了西太平洋与东亚沿岸地区环流系统之间的相互配置。刘毓赟和陈文（2012）也指出，EU遥相关型对副热带西风急流、东亚大槽有一定的作用，并进而影响到我国的降水。从图10上可以看出影响东北亚初夏和盛夏的从欧洲西部到东亚地区的遥相关显著位置有明显的差异。Barnston and Livezey（1987）研究将欧亚遥相关型分解为欧亚遥相关I型（EUI）、欧亚遥相关II型（EUII）、东大西洋遥相关型（EA）和热带/北半球遥相关型（TNH）。因此根据Barnston定义的遥相关型可以看出，东北亚初夏降水主要受EUII遥相关型，东北亚盛夏降水则受到EUI遥相关型的影响。结合Huang（2004）定义的EAP指数和Wallace and Gutzler (1981)和Barnston and Livezey（1987）定义的EU指数，表3给出了东北亚地区初夏、盛夏和传统夏季降水分别与EAP、EUI、EUII指数的相关系数。

从表3中可以看出，东北亚地区初夏降水跟初夏EAP指数的相关系数为0.24，与初夏EUI指数相关系数是0.20，均没有通过0.05的显著性水平，而与EUII指数相关系数为0.32，通过了0.05的显著性水平检验。Hu et al（2010）对东北冷涡研究表明，初

夏东北冷涡主要在贝加尔湖及偏东地区形成，因此东北初夏降水跟东北冷涡持续日数有显著的相关性。同时，Wang et al.（2010）的研究也表明，EU 型遥相关的增强往往伴随着乌拉尔阻塞等环流异常。因此，东北亚初夏降水主要受到冷涡和局地阻塞高压等影响。东北亚地区盛夏降水和盛夏 EAP 指数、EUI 指数和 EUII 指数的相关系数分别为 0.37、0.47 和 0.08，传统夏季降水和传统夏季 EAP 指数、EUI 指数和 EUII 指数的相关系数分别为 0.50、0.49 和 0.29，盛夏和传统夏季降水均和 EUII 指数的相关系数没有通过 0.05 的显著性水平检验。因此，EAP 遥相关对东北亚盛夏和传统夏季降水有一定的作用，同时东北亚盛夏和传统夏季降水只受到 EUI 遥相关的影响。

图 13 给出了 EAP 指数、EUI 指数和 EUII 指数

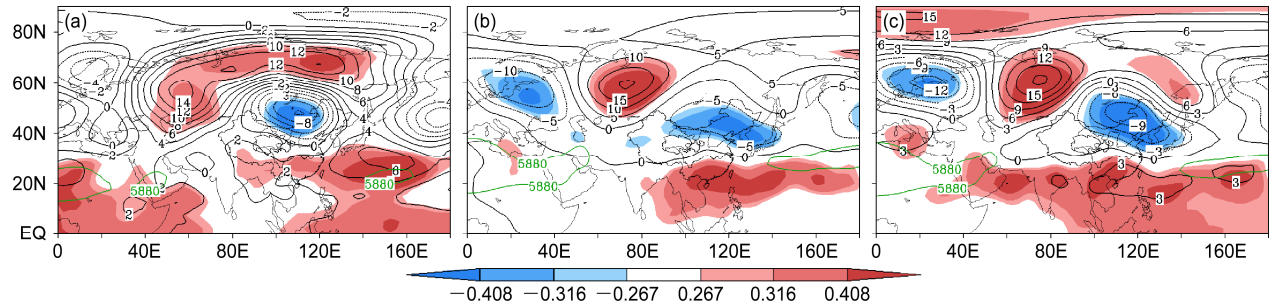

图 10　东北亚地区（a）初夏、（b）盛夏和（c）传统夏季总降水量标准化时间序列对 500 hPa 高度场的回归系数分布。绿色实线代表 500 hPa 位势高度 5880 gpm 线；图中阴影由浅到深依次表示通过 0.10、0.05 和 0.01 的显著性水平检验

Fig. 10　The spatial distribution of 500-hPa geopotential height that is regressed by the standardized precipitation in (a) early summer, (b) midsummer, and (c) conventional summer in Northeast Asia. The green line represents the 5880 geopotential meter geopotential height contour at 500 hPa; the shaded areas from shallow to deep denote the values pass test at 0.10, 0.05, 0.01 significance levels

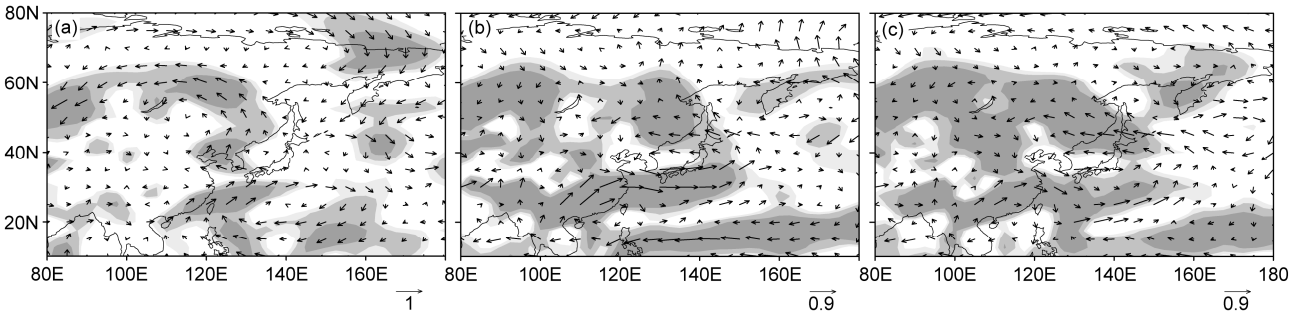

图 11　东北亚地区降水量标准化时间序列对 850 hPa 风场的回归系数分布：（a）初夏；（b）盛夏与初夏差值；（c）传统夏季与初夏差值。阴影由浅到深依次表示通过 0.1、0.05 和 0.01 的显著性水平检验

Fig. 11　The spatial distribution of 850-hPa wind field that is regressed by the standardized precipitation in Northeast Asia: (a) Early summer, (b) the difference between midsummer and early summer, (c) the difference between conventional summer and early summer. The shaded areas from shallow to deep denote the values pass test at 0.10, 0.05, 0.01 significance levels

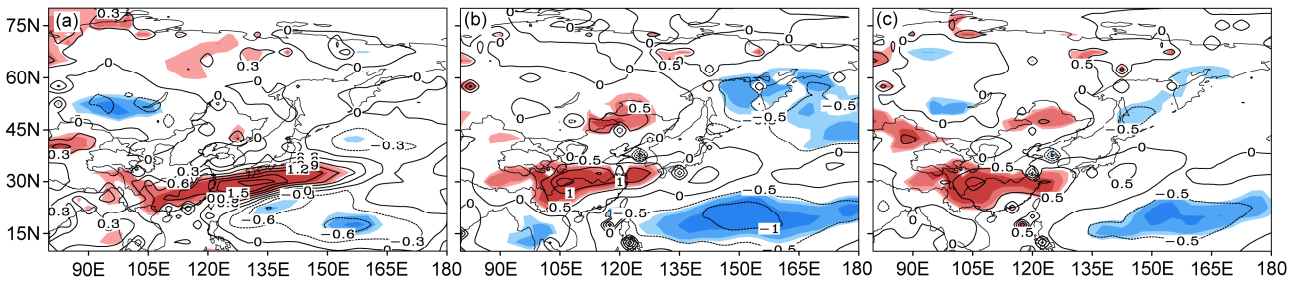

图 12　东北亚地区降水量标准化时间序列对可降水量的回归系数分布：（a）初夏；（b）盛夏与初夏差值；（c）传统夏季与初夏差值。阴影由浅到深依次表示通过 0.1、0.05 和 0.01 的显著性水平检验

Fig. 12　The spatial distribution of precipitable water that is regressed by the standardized precipitation in Northeast Asia : (a) Early summer, (b) the difference between midsummer and early summer, (c) the difference between conventional summer and early summer. The shaded areas from shallow to deep denote the values pass test at 0.10, 0.05, 0.01 significance levels

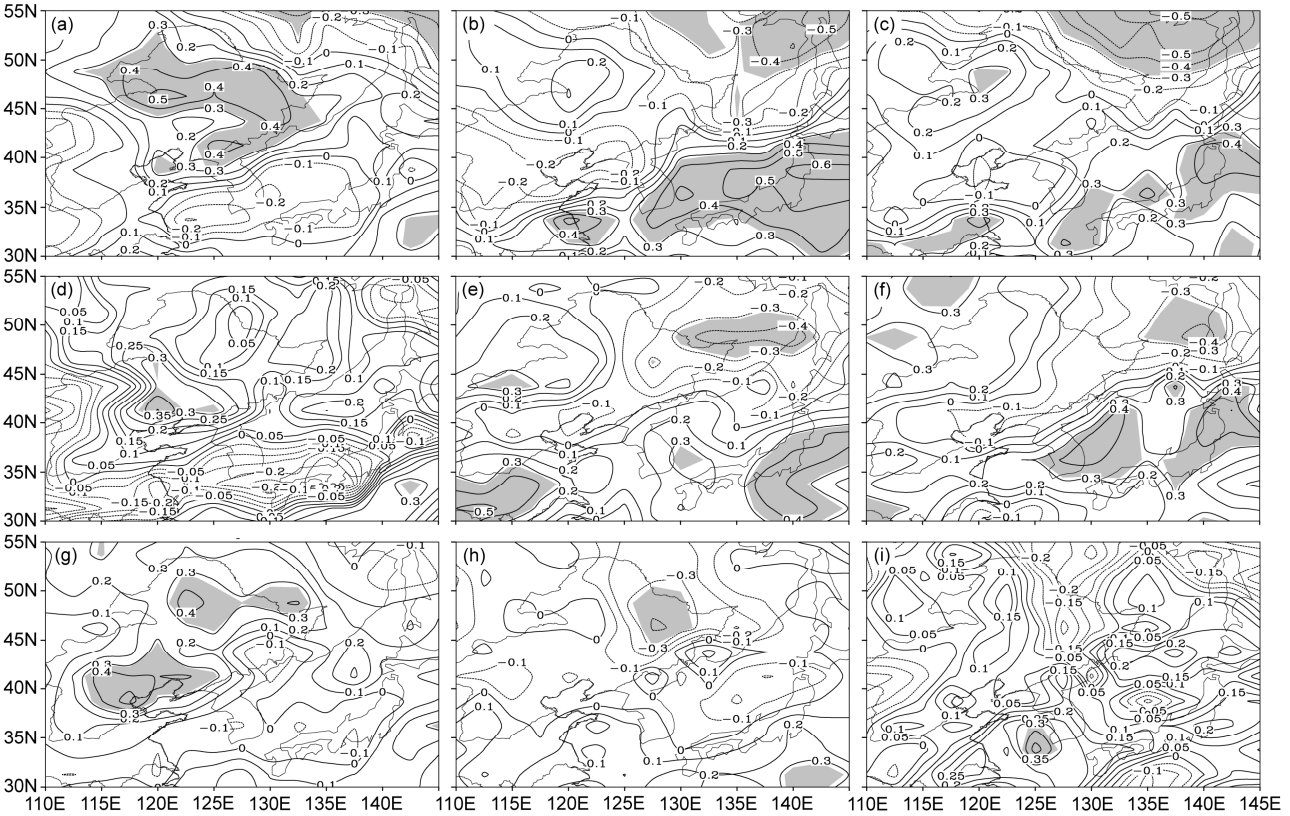

图 13 （a、b、c）EAP 指数、（d、e、f）EUI 指数和（g、h、i）EUII 指数与东北亚初夏（左列）、盛夏（中间列）以及传统夏季（右列）格点降水的相关系数

Fig. 13 Correlation coefficients between indices of (a, b, c) EAP, (d, e, f) EUI, (g, h, i) EUII and the precipitation in early summer (left column), middle summer (middle column), conventional summer (right column) in Northeast Asia

表 3 东北亚地区初夏、盛夏和传统夏季降水分别与 EAP 指数、EUI 指数、EUII 指数的相关系数

Table 3 Correlation coefficients between indices of EAP, EUI and EUII and early summer, middle summer, and conventional summer precipitation in Northeast Asia

	EAP 指数	EUI 指数	EUII 指数
初夏降水	0.24	0.20	0.32*
盛夏降水	0.37*	0.47*	0.08
传统夏季降水	0.50*	0.49*	0.29

*表示通过 0.05 的显著性水平检验。

分别与东北亚初夏、盛夏和传统夏季降水的相关系数图。从图上可以更清楚的了解 EAP 和 EU 遥相关对东北亚初夏、盛夏和传统夏季降水的影响区域。在初夏，EAP 和 EUII 型遥相关主要影响东北及华北少部分地区降水，EUI 型遥相关对东北亚地区降水没有显著相关关系（图 13a、d、g）。在盛夏，EAP 型遥相关主要影响日本、西太平洋地区以及鄂霍次克海地区降水，EUI 型遥相关对西太平洋、长江中下游以及黑龙江上游等地具有一定的作用，而 EUII 型遥相关对东北亚地区少部分地区产生一定的影响（图 13b、e、h）。传统夏季降水也是主要受到 EAP 和 EUI 遥相关型的影响，且与盛夏降水受到影响的区域相类似（图 13c、f、i）。

6 结论与讨论

本文利用 1979～2015 年 GPCP 逐月降水资料分析了东北亚地区初夏、盛夏和传统夏季降水的时空变化特征以及 EAP 和 EU 遥相关对其影响。分析结果表明：

（1）东北亚地区初夏降水表现为显著“＋－＋”模态（EOF1 和 EOF2），PC1 和 PC2 表现出显著的年际变化特征，其中 PC1 具有 5～6 a 振荡周期；盛夏降水从北向南则表现为“－＋”模态（EOF1）和“＋－＋”模态（EOF2），PC1 和 PC2 也表现出明显的年际变化特征，且 PC2 中存在 2～3 a 的振荡周期。传统夏季降水由于同时包含了初夏和盛夏的降水信息，其时间序列中既包含 5～6 a 也包含了 2～

3 a 振荡周期。东北亚地区初夏降水的空间模态与盛夏降水和传统夏季降水的空间模态有很大的差异，这可能是引起初夏降水和盛夏降水的影响因素所导致的。盛夏降水和传统夏季降水的空间模态比较接近，但第一模态的空间分布特征跟传统夏季降水第一模态的空间分布特征出现相反的模态。就年代际调整而言，东北亚地区只有在华北和东北地区在盛夏和传统夏季降水发生显著的年代际变化特征，且发生转折的时间为 20 世纪 90 年代末。对比异常年发现，无论是降水偏多年份还是降水偏少年份，东北亚地区初夏和盛夏降水分布特征都有显著的差异性。因此，我们在研究东北亚夏季降水的时候，需要对初夏和盛夏两个时期区别对待，因为其时空演化特征存在显著差异。同时，盛夏的降水时空演化特征与传统夏季基本相似，我们在研究 6～8 月夏季东北亚降水的需要将侧重点放在 7～8 月的盛夏，因为这个时间段的降水对传统夏季的降水的异常特征起到决定性作用。

（2）初夏，西太平洋上空异常反气旋将西太平洋等地的水汽向北输送，将副热带西太平洋及沿海地区等地的水汽向北输送，同时由于北方的干冷气流南下，在东北亚地区与来自低纬度地区的水汽汇合，并受到 EUII 遥相关型的影响，造成东北亚地区初夏降水。盛夏，东北亚地区降水主要受到西太平洋副热带高压西伸北进和孟加拉湾和南海等地水汽加强的影响，西太平洋上空的出现异常的反气旋偏东异常的水汽沿着西太平洋副热带高压西侧的南风异常向北输出到东北亚地区，同时受 EUI 型和 EAP 型两类遥相关型的协同作用。

参考文献（References）

Barnston A G, Livezey R E. 1987. Classification, seasonality and persistence of low-frequency atmospheric circulation patterns [J]. Mon. Wea. Rev., 115 (6): 1083–1126, doi:10.1175/1520-0493(1987)115<1083:CSAPOL>2.0.CO;2.

Ding Y H, Chan J C L. 2005. The East Asian summer monsoon: An overview [J]. Meteor. Atmos. Phys., 89 (1–4): 117–142, doi:10.1007/s00703-005-0125-z.

Ding Y H, Wang Z Y, Sun Y. 2008. Inter-decadal variation of the summer precipitation in East China and its association with decreasing Asian summer monsoon. Part I: Observed evidences [J]. Int. J. Climatol., 28 (9): 1139–1161, doi:10.1002/joc.1615.

封国林, 龚志强, 支蓉. 2008. 气候变化检测与诊断技术的若干新进展 [J]. 气象学报, 66 (6): 892–905. Feng Guolin, Gong Zhiqiang, Zhi Rong. 2008. Latest advances of climate change detecting technologies [J]. Acta Meteor. Sinica (in Chinese), 66 (6): 892–905, doi:10.11676/qxxb2008.081.

封国林, 侯威, 支蓉, 等. 2012. 极端气候事件的检测、诊断与可预测性研究 [M]. 北京: 科学出版社, 350pp. Feng Guolin, Hou Wei, Zhi Rong, et al. 2012. Detection, Diagnosis and Predictability Research of Extreme Climate Events (in Chinese) [M]. Beijing: Science Press, 350pp.

龚志强，封国林，万仕全，等. 2006. 基于启发式分割算法检测华北和全球气候变化的特征 [J]. 物理学报，55 (1): 477–484. Gong Zhiqiang, Feng Guolin, Wan Shiquan, et al. 2006. Analysis of features of climate change of Huabei area and the global climate change based on heuristic segmentation algorithm [J]. Acta Phys. Sinica, 55 (1): 477–484, doi:10.3321/j.issn:1000-3290.2006.01.084.

龚志强, 赵俊虎, 封国林. 2013. 中国东部 2012 年夏季降水及年代际转型的可能信号分析 [J]. 物理学报, 62 (9): 099205. Gong Zhiqiang, Zhao Junhu, Feng Guolin. 2013. Analysis of the summer precipitation of 2012 in East China and its possibility of decadal shift [J]. Acta Phys. Sinica (in Chinese), 62 (9): 099205, doi:10.7498/aps.62.099205.

龚志强, 王晓娟, 支蓉, 等. 2009. 中国近 58 年温度极端事件的区域特征及其与气候突变的联系 [J]. 物理学报, 58 (6): 4342–4353. Gong Zhiqiang, Wang Xiaojuan, Zhi Rong, et al. 2009. Regional characteristics of temperature changes in China during the past 58 years and its probable correlation with abrupt temperature change [J]. Acta Phys. Sinica (in Chinese), 58 (6): 4342–4353, doi:10.7498/aps.58.4342.

Gong Z Q, Feng T C, Fang Y H. 2015. Objective identification research on cold vortex and mid-summer rainy periods in Northeast China [J]. Chin. Phys. B, 24 (4): 049204, doi:10.1088/1674-1056/24/4/049204.

Gong Z Q, Hutin C, Feng G L. 2016. Methods for improving the prediction skill of summer precipitation over East Asia-West Pacific [J]. Wea. Forecasting, 31 (4): 1381–1392, doi:10.1175/WAF-D-16-0007.1.

顾正强, 巩远发, 龚强, 等. 2013. 东北区域水汽收支的变化及其与降水的关系 [J]. 程度信息工程学院学报, 28 (6): 651–658. Gu Zhengqiang, Gong Yuanfa, Gong Qiang, et al. 2013. The variation features of moisture budgets and its relationship with precipitation over the Northeast area of China [J]. J. Chengdu Univ. Inform. Technol. (in Chinese), 28 (6): 651–658, doi:10.3969/j.issn.1671-1742.2013.06.015.

何金海, 吴志伟, 祁莉, 等. 2006. 北半球环状模和东北冷涡与我国东北夏季降水关系分析 [J]. 气象与环境学报, 22 (1): 1–5. He Jinhai, Wu Zhiwei, Qi Li, et al. 2006. Relationships among the northern hemisphere annual mode, the northeast cold vortex and the summer rainfall in northeast China [J]. J. Meteor. Environ. (in Chinese), 22 (1): 1–5, doi:10.3969/j.issn.1673-503X.2006.01.001.

胡开喜, 陆日宇, 王东海. 2011. 东北冷涡及其气候影响 [J]. 大气科学, 35 (1): 179–191. Hu Kaixi, Lu Riyu, Wang Donghai. 2011. Cold vortex over Northeast China and its climate effect [J]. Chinese Journal of Atmospheric Sciences (in Chinese), 35 (1): 179–191. doi:10.3878/j.issn.1006-9895.2011.01.15.

Hu K X, Lu R Y, Wang D H. 2010. Seasonal climatology of cut-off lows and associated precipitation patterns over Northeast China [J]. Meteor. Atmos. Phys., 106 (1–2): 37–48, doi:10.1007/s00703-009-0049-0.

Huang G. 2004. An index measuring the interannual variation of the East Asian summer monsoon-the EAP index [J]. Adv. Atmos. Sci., 21 (1): 41–52, doi:10.1007/BF02915679.

黄荣辉, 李维京. 1988. 夏季热带西太平洋上空的热源异常对东亚上空副热带高压的影响及其物理机制 [J]. 大气科学, 12 (S1): 107–116. Huang Ronghui, Li Weijing. 1988. Influence of heat source anomaly over the western tropical Pacific on the subtropical high over East Asia and its physical mechanism [J]. Chinese Journal of Atmospheric Sciences (in Chinese), 12 (S1): 107–116.

黄荣辉, 陈际龙, 刘永. 2011. 我国东部夏季降水异常主模态的年代际变化及其与东亚水汽输送的关系 [J]. 大气科学, 35 (4): 589–606. Huang Ronghui, Chen Jilong, Liu Yong. 2011. Interdecadal variation of the leading modes of summertime precipitation anomalies over Eastern China and its association with water vapor transport over East Asia [J]. Chinese Journal of Atmospheric Sciences (in Chinese), 35 (4): 589–606, doi:10.3878/j.issn.1006-9895.2011.04.01.

黄荣辉, 刘永, 冯涛. 2013. 20 世纪 90 年代末中国东部夏季降水和环流的年代际变化特征及其内动力成因 [J]. 科学通报, 58 (8): 617–628. Huang Ronghui, Liu Yong, Feng Tao. 2013. Interdecadal change of summer precipitation over Eastern China around the late-1990s and associated circulation anomalies, internal dynamical causes [J]. Chin. Sci. Bull., 58 (12): 1339–1349, doi:10.1007/s11434-012-5545-9.

Huang R H, Li W J. 1987. Influence of the heat source anomaly over the tropical western Pacific on the subtropical high over East Asia [J]. Proc. International Conference on the General Circulation of East Asia. Chengdu, China, 10–15.

Huang R H, Sun F Y. 1992. Impacts of the tropical western Pacific on the East Asian summer monsoon [J]. J. Meteor. Soc. Japan, 70 (1B): 243–256, doi:10.2151/jmsj1965.70.1B_243.

李辑, 房一禾, 李菲, 等. 2014. 辽宁初夏降水大尺度环流影响因子及 2012 年初夏异常多雨成因分析 [J]. 气象, 40 (9): 1114–1122. Li Ji, Fang Yihe, Li Fei, et al. 2014. Large-scale circulation factors of early summer precipitation in Liaoning Province and causes analysis of heavy precipitation in 2012 [J]. Meteor. Mon. (in Chinese), 40 (9): 1114–1122, doi:10.7519/j.issn.1000-0526.2014.09.009.

廉毅, 沈柏竹, 高枞亭, 等. 2003. 东亚夏季风在中国东北区建立的标准、日期及其主要特征分析 [J]. 气象学报, 61 (5): 548–558. Lian Yi, Shen Baizhu, Gao Zongting, et al. 2003. The study of the on-set criterion and the date of East Asian summer monsoon in Northeast China and its main characteristic analysis [J]. Acta Meteor. Sinica (in Chinese), 61 (5): 548–558, doi:10.11676/qxxb2003.055.

廉毅, 沈柏竹, 高枞亭, 等. 2005. 中国气候过渡带干旱化发展趋势与东亚夏季风、极涡活动相关研究 [J]. 气象学报, 63 (5): 740–749. Lian Yi, Shen Baizhu, Gao Zongting, et al. 2005. Correlation of drought development tendency on China's climate transition zone and activity of East Asia summer monsoon and polar vortex [J]. Acta Meteor. Sinica (in Chinese), 63 (5): 740–749, doi:10.11676/qxxb2005.071.

廉毅, 布和朝鲁, 谢作威, 等. 2010. 初夏东北冷涡活动异常与北半球环流低频变化 [J]. 大气科学, 34 (2): 429–439. Lian Yi, Buch Cholaw, Xie Zuowei, et al. 2010. The anomalous cold vortex activity in Northeast China during the early summer and the low-frequency variability of the northern hemispheric atmosphere circulation [J]. Chinese Journal of Atmospheric Sciences (in Chinese), 34 (2): 429–439, doi:10.3878/j.issn.1006-9895.2010.02.16.

刘刚, 封国林, 秦玉琳, 等. 2017. 初夏东北地区冷涡降水“累积效应”[J]. 大气科学, 41 (1): 202–212. Liu Gang, Feng Guolin, Qin Yulin, et al. 2017. “Cumulative effect” of cold vortex precipitation in northeast China in early summer [J]. Chinese J. Atmos. Sci. (in Chinese), 41 (1): 202–212, doi:10.3878/j.issn.1006-9895.1602.15231.

刘毓赟, 陈文. 2012. 北半球冬季欧亚遥相关型的变化特征及其对我国气候的影响 [J]. 大气科学, 36 (2): 423–432. Liu Yuyun, Chen Wen. 2012. Variability of the Eurasian teleconnection pattern in the northern hemisphere winter and its influences on the climate in China [J]. Chinese Journal of Atmospheric Sciences (in Chinese), 36 (2): 423–432, doi:10.3878/j.issn.1006-9895.2011.11066.

陆日宇. 1999. 华北夏季不同月份降水的年代际变化 [J]. 高原气象, 18 (4): 509–519. Lu Riyu. 1999. Interdecadal variations of precipitations in various months of summer in North China [J]. Plateau Meteor. (in Chinese), 18 (4): 509–519, doi:10.3321/j.issn:1000-0534.1999.04.005.

陆日宇, 黄荣辉. 1999. 夏季西风带定常扰动对东北亚阻塞高压的影响 [J]. 大气科学, 23 (5): 533–542. Lu Riyu, Huang Ronghui. 1999. Influence of the stationary disturbance in the westerlies on the blocking highs over the northeastern Asia in summer [J]. Chinese Journal of Atmospheric Sciences (in Chinese), 23 (5): 533–542, doi:10.3878/j.issn.1006-9895.1999.05.03.

Nitta T. 1987. Convective activities in the tropical western Pacific and their impact on the Northern Hemisphere summer circulation [J]. J. Meteor. Soc. Japan, 65 (3): 373–390, doi:10.2151/jmsj1965.65.3_373.

乔少博, 张志森, 王晓娟, 等. 2015. 晚秋与后冬间欧亚遥相关型波列反相现象探究 [J]. 气象学报, 73 (4): 711–724. Qiao Shaobo, Zhang Zhisen, Wang Xiaojuan, et al. 2015. An investigation into the phase reversal of EU teleconnections from late autumn to the late winter [J]. Acta Meteor. Sinica (in Chinese), 73 (4): 711–724, doi:10.11676/qxxb2015.045.

沈柏竹, 李尚锋, 廉毅. 2008. 初夏东北冷涡活动的谐波分析 [J]. 吉林大学学报 (地球科学版), 38 (S): 204–208. Shen Baizhu, Li Shangfeng, Lian Yi. 2008. The harmonic analysis of cold vortex of the North-East China in early summer [J]. J. Jilin Univ. (Earth Sci. Ed.) (in Chinese), 38 (S): 204–208.

沈柏竹, 林中达, 陆日宇, 等. 2011. 影响东北初夏和盛夏降水年际变化的环流特征分析 [J]. 中国科学: 地球科学, 41 (3): 402–412. Shen Baizhu, Lin Zhongda, Lu Riyu, et al. 2011. Circulation anomalies associated with interannual variation of early- and late-summer precipitation in Northeast China [J]. Sci. China Earth Sci., 54 (7): 1095–1104, doi:10.1007/s11430-011-4173-6.

Si D, Ding Y H. 2013. Decadal Change in the correlation pattern between the Tibetan Plateau winter snow and the East Asian summer precipitation during 1979–2011 [J]. J. Climate, 26 (19): 7622–7634, doi:10.1175/JCLI-D-12-00587.1.

孙力, 安刚, 廉毅, 等. 2002. 中国东北地区夏季旱涝的大气环流异常特征 [J]. 气候与环境研究, 7 (1): 102–113. Sun Li, An Gang, Lian Yi, et al. 2002. The unusual characteristics of general circulation in drought and waterlogging years of Northeast China [J]. Climatic and Environmental Research (in Chinese), 7 (1): 102–113, doi:10.3969/j.issn.1006-9585.2002.01.010.

Tan L C, An Z S, Huh C A, et al. 2014. Cyclic precipitation variation on the western Loess Plateau of China during the past four centuries [J]. Sci. Rep., 4: 6381, doi:10.1038/srep06381.

Wallace J M, Gutzler D S. 1981. Teleconnections in the geopotential height field during the northern Hemisphere winter [J]. Mon. Wea. Rev., 109 (4): 748–812, doi:10.1175/1520-0493(1981)109<0784:TITGHF>2.0.CO;2.

Wang L, Chen W, Zhou W, et al. 2010. Effect of the climate shift around mid 1970s on the relationship between wintertime Ural blocking circulation and East Asian climate [J]. Int. J. Climatol., 30 (1): 153–158, doi:10.1002/joc.1876.

魏凤英. 1999. 现代气候统计诊断与预测技术 [M]. 北京: 气象出版社. Wei Fengying. 2007. Modern Climatic Statistical Diagnosis and Forecasting Technology (in Chinese) [M]. Beijing: China Meteorologial Press.

魏凤英, 张先恭. 1988. 我国东部夏季雨带类型的划分及预报 [J]. 气象, 14 (8): 15–19. Wei Fengying, Zhang Xiangong. 1988. The classification and forecasting of summer rain-belt in the east part of China [J]. Meteor. Mon. (in Chinese), 14 (8): 15–19, doi:10.7519/j.issn.1000-0526.1988.8.003.

叶柏生, 李翀, 杨大庆, 等. 2005. 我国过去 50 a 来降水变化趋势及其对水资源的影响 (II): 月系列 [J]. 冰川冻土, 27 (1): 100–105. Ye Baisheng, Li Chong, Yang Daqing, et al. 2005. Variation trend of precipitation and its impact on water resources in China during last 50 years (II): Monthly variation [J]. J. Glaciol. Geocryol. (in Chinese), 27 (1): 100–105, doi:10.3969/j.issn.1000-0240.2005.01.015.

Zhao J H, Yang L, Hou W, et al. 2015. Extra-seasonal prediction at summer 500 hPa height field in the area of cold vortices over East Asia with a dynamical-statistical method [J]. Chin. Phys. B, 24 (5): 059202, doi:10.1088/1674-1056/24/5/059202.

Zhao P, Yang S, Yu R C. 2010. Long-term changes in rainfall over eastern china and large-scale atmospheric circulation associated with recent global warming [J]. J. Climate, 23 (6): 1544–1562, doi:10.1175/2009JCLI2660.1.

Zheng Z H, Hu Z Z, L'Heureux M. 2016. Predictable components of ENSO evolution in real-time multi-model predictions [J]. Sci. Rep., 6: 35909, doi:10.1038/srep35909.

Zhu Y L, Wang H J, Zhou W, et al. 2011. Recent changes in the summer precipitation pattern in East China and the background circulation [J]. Climate Dyn., 36 (7–8): 1463–1473, doi:10.1007/s00382-010-0852-9.

Dynamics of Atmospheres and Oceans 82 (2018) 20–36

Contents lists available at ScienceDirect

Dynamics of Atmospheres and Oceans

journal homepage: www.elsevier.com/locate/dynatmoce

Multi-pentad prediction of precipitation variability over Southeast Asia during boreal summer using BCC_CSM1.2

Chengcheng Li[a,b], Hong-Li Ren[a,b,c,*], Fang Zhou[b], Shuanglin Li[a,c,d], Joshua-Xiouhua Fu[e], Guoping Li[a]

[a] College of Atmospheric Sciences, Chengdu University of Information Technology, Chengdu 610226, China
[b] Laboratory for Climate Studies & CMA-NJU Joint Laboratory for Climate Prediction Studies, National Climate Center, China Meteorological Administration, Beijing 100081, China
[c] Department of Atmospheric Science, School of Environmental Studies, China University of Geoscience, Wuhan 430074, China
[d] Institute of Atmospheric Physics, Chinese Academy of Sciences, Beijing 100029, China
[e] Institute of Atmospheric Sciences, Fudan University, Shanghai, China

ARTICLE INFO

Article history:
Received 8 November 2017
Received in revised form 19 January 2018
Accepted 18 February 2018
Available online 19 February 2018

Keywords:
BCC_CSM1.2 model
Pentad prediction
Intraseasonal oscillation

ABSTRACT

Precipitation is highly variable in space and discontinuous in time, which makes it challenging for models to predict on subseasonal scales (10–30 days). We analyze multi-pentad predictions from the Beijing Climate Center Climate System Model version 1.2 (BCC_CSM1.2), which are based on hindcasts from 1997 to 2014. The analysis focus on the skill of the model to predict precipitation variability over Southeast Asia from May to September, as well as its connections with intraseasonal oscillation (ISO). The effective precipitation prediction length is about two pentads (10 days), during which the skill measured by anomaly correlation is greater than 0.1. In order to further evaluate the performance of the precipitation prediction, the diagnosis results of the skills of two related circulation fields show that the prediction skills for the circulation fields exceed that of precipitation. Moreover, the prediction skills tend to be higher when the amplitude of ISO is large, especially for a boreal summer intraseasonal oscillation. The skills associated with phases 2 and 5 are higher, but that of phase 3 is relatively lower. Even so, different initial phases reflect the same spatial characteristics, which shows higher skill of precipitation prediction in the northwest Pacific Ocean. Finally, filter analysis is used on the prediction skills of total and subseasonal anomalies. The results of the two anomaly sets are comparable during the first two lead pentads, but thereafter the skill of the total anomalies is significantly higher than that of the subseasonal anomalies. This paper should help advance research in subseasonal precipitation prediction.

© 2018 Elsevier B.V. All rights reserved.

1. Introduction

Atmospheric initial conditions are the primary source of predictability for weather forecasting, but initial errors are quickly compounded as that forecast is extended for a longer lead time. As a result, the prediction of seasonal conditions relies more heavily on the slowly evolving substrate (e.g., Shukla, 2000; Ren et al., 2016). Initial and boundary conditions are

* Corresponding author at: National Climate Center, China Meteorological Administration, 46 Zhongguancun, Haidian District, Beijing 100081, China.
E-mail address: renhl@cma.gov.cn (H.-L. Ren).

https://doi.org/10.1016/j.dynatmoce.2018.02.002
0377-0265/© 2018 Elsevier B.V. All rights reserved.

equally important for subseasonal predictions, which operate on a time scale between synoptic and seasonal predictions. Predictions of weather systems between 10 days and 30 days in the future must contend with the difficulties of long-term weather prediction and short-term climate prediction. Therefore, these subseasonal predictions inhabit a "forecast desert". Improving the accuracy of subseasonal predictions is the key for advancing the field (Ren et al., 2015).

In the past few decades, subseasonal prediction has been paid increasing attention (e.g. Waliser et al., 2012; Vitart et al., 2007; Vitart and Molteni, 2010). The range of useful prediction of the dominant intraseasonal modes in dynamical models is generally three weeks (Wu et al., 2016). The use of observational data can extend this range to five weeks, suggesting ample room for improvements in dynamic model forecast systems (Ding et al., 2010, 2011).

Intraseasonal oscillations (ISO) constitute one of the most important circulation systems in the tropics. Firstly found by Madden and Julian (1971), the large-scale low-frequency oscillation, now referred to as the Madden-Julian Oscillation (MJO), is manifested in the tropical India Ocean and western Pacific Ocean (110°E–150°E) on a timescale of 40–50 d. The main period of these eastward-propagating MJO is 30–60 d. Distinct from patterns during boreal winters, boreal summer ISO (BSISO) propagation is characterised by a northward propagation. The MJO index (RMM) can directly reflect the location and propagation of MJO systems in real-time, based on a two-dimensional space phase diagram, which is composed of RMM1 and RMM2. The indices proposed by Lee et al. (2013) can depict the activity of BSISO. The BSISO1 index describes the typical northward and eastward propagation of ISO signal along the equator, and its main period is 30–60 d, while the BSISO2 index describes the northward and northwestward propagation in the pre-monsoon and monsoon periods.

Subseasonal-to-seasonal (S2S) prediction is tightly connected with ISO, which is one of the most important sources of S2S predictability. Therefore, it is important to analyze the skill of ISO as an indication of the S2S prediction skill. The connection with ISO may help model developers understand S2S predictions (Zhang, 2013; Zhao et al., 2015). Seo et al. (2009) evaluated the MJO forecast from the National Centers for Environment Prediction Climate Forecast System version 1 (CFSv1) and showed that this system provided MJO prediction skills from about 10–15 d. However, the prediction skill of this single model may be less than that of some coupled models (Fu et al., 2013). Wang et al. (2013) analyzed the prediction skill of MJO in CFSv2, and the skills were relatively low for phases 2, 3, 6 and 7, suggesting that the initial phase dependence may be consistent with variation in the skills associated with target phases. Liu and Wang (2015) followed that study by analyzing the dependence of the weekly prediction skill on the initial BSISO phase in CFSv2. The results showed higher skill in the predictions initiated from phases 1 and 5 and lower skill from phase 3.

To understand subseasonal variability and predictability, some studies have tried to obtain subseasonal signals from raw anomalies (Wheeler and Hendon, 2004; Vitart et al., 2007). For example, Seo et al. (2007) examined the influence of coupled air-sea interactions on northward and eastward propagation using a band-pass filter to retain the subseasonal components. Sperber and Annamalai (2008) tried to assess the ability of models to simulate the dominant mode of the boreal summer intraseasonal variability (BSISV) using anomalies that had been stripped of their interannual components. Liu and Wang (2015) used the Climate Forecast System version 2 (CFSv2) model to study subseasonal predictability of precipitation (PREC) in Southeast Asia by removing the 91-day running mean from the raw daily anomalies. They found that this model could capture the characteristics of precipitation anomalies in Southeast Asia: the skill of the total anomaly was still above 0.1 after 5 weeks, and the subseasonal skill was connected with the phases of BSISO1. Indeed, since these studies focused on weekly or monthly time scales, few studies have refined this time scale to pentad (5-day mean) prediction.

Low-frequency signals will weaken gradually with lead time increasing (Liu and Wang, 2015), which limits the performance of subseasonal predictions. Southeast Asia is a region in which the subseasonal variability is large and the MJO is active during its zonal propagation. The so-called boreal summer intraseasonal oscillation (BSISO) becomes the major subseasonal mode that influences PREC in Southeast Asia during boreal summertime. However, due to the differences between the initial data of sea surface temperature in models and observations, the CFSv2 has failed to capture the northeastward propagation of the enhanced convection in the northwest Pacific, which probably limits its ability to predict precipitation.

This paper will analyze the capability of the BCC_CSM1.2 model in predicting PREC and two related circulation fields: zonal wind at 850-hPa (U850) and geopotential height at 500-hPa (Z500). U850 is a representative component in the tropical circulation especially for the leading baroclinic intraseasonal modes (Lee et al., 2013). Z500 provides an integrated measure of the tropospheric general circulation. A good prediction of Z500 in the model is a prerequisite for a reliably representation of the Western Pacific Subtropical high which is a critical system affecting the weather and climate over large parts of East Asia (Liu and Wang, 2015). The model ran pentad anomalies over the target period (boreal summer) and revealed preliminary evidence of its connection with intraseasonal oscillation. This study may provide a reference and guidance for future development and improvements in S2S modeling. The rest of this paper is organized as follows. Data and methods are introduced in Section 2; in Section 3, we focus on 3 aspects: (1) mean state of PREC, U850 and Z500; (2) overall skill and subseasonal skill of forecast system in predicting pentad-mean anomalies; and (3) the connection with skill and intraseasonal activity of MJO and BSISO. Summary and further discussions are provided in Section 4.

2. Data and methods

2.1. Data

The hindcasts covering 1997–2014 with the Beijing Climate Center Climate System Model version 1.2 (BCC_CSM1.2) have been used in this study to assess the prediction skills of three important variables (PREC, U850 and Z500) associated

with Southeast Asian summer monsoon. The BCC_CSM1.2 used here is almost the same as that used for S2S prediction, but with vertical levels increased from 26 to 40. The BCC_CSM1.2 is initialized with the atmospheric conditions from NCEP FNL Operational Global Analysis for the period 2000–2014 (http://rda.ucar.edu/datasets/ds083.2/) and from NCEP reanalysis (Kalnay et al., 1996) for the period 1997–1999 because no FNL is available before 2000. The differences of these two datasets in representing tropical intraseasonal variability and possible impacts on prediction skills have been given in Wang et al. (2012) and Fu et al. (2009). The ocean component of BCC_CSM1.2 is initialized directly from the BCC global ocean data assimilation system (Ren et al., 2017). The observations used to evaluate the model hindcasts include daily precipitation (PREC) from the Global Precipitation Climatology Project and 850-mb zonal winds (U850, V850) and 500-mb geopotential height (Z500) from NECP/NCAR Reanalysis. All data are interpolated onto a $2.5^\circ \times 2.5^\circ$ grid using bilinear interpolation. The real-time multivariate MJO index (Wheeler and Hendon, 2004) and BSISO index (Lee et al., 2013) are directly downloaded from the Australian Government Bureau of Meteorology (http://www.bom.gov.au/climate/mjo/#tabs=MJO-phase) and Asia-Pacific Economic Cooperation Climate Center (http://www.apcc21.org/ser/moni.do?lang=en), respectively. Present study focuses over Southeast Asia (10°S–30°N, 60°E–150°E) during the boreal summer (May-September).

2.2. Methods

2.2.1. Climatology and anomalies

Since each BCC_CSM1.2 hindcast includes four ensemble members, we average four of them into an ensemble mean prediction. For both prediction and observation, the daily climatology is calculated as 18-year (1997–2014) means for each calendar day. The departures from daily climatology are defined as daily anomalies. Subseasonal variability is calculated first by removing the 91-day running mean of daily anomalies as

$$Anomaly = Anomaly_{TOT} - \frac{1}{91}\sum_{K-45}^{K+45} Anomaly_{TOT} \tag{1}$$

where the subscript TOT means the total anomalies. Pentad means of the derived anomalies are then taken to remove synoptic disturbances and used to assess prediction skills. Pentad-mean anomalies are calculated as the 5-day averages of *Anomaly*. Lead pentad 1 is defined as the average from lead day 2 to lead day 6, lead pentad 2 defined as the average from day 7 to day 11, and so on.

2.2.2. Measures of prediction skills

The prediction skills of the BCC_CSM1.2 model are assessed with three metrics: the anomaly correlation coefficient (ACC), temporal correlation coefficient (TCC), and root-mean-square error (RMSE). Prediction biases are defined as prediction values minus observed values.

The ACC measures the level of spatial pattern similarity between prediction and observation: a skill metrics recommended by the World Meteorological Organization since 1996. The range of the ACC is from −1.0 to 1.0, and a large positive (negative) value indicates a highly similar (opposite) spatial pattern between prediction and observation. We choose 0.12 as the threshold of ACC for 90% significance test to verifying predictions of PREC and other two circulation fields, which is same for TCC. Defining $x_{i,j}$and $y_{i,j}$ as the pentad-mean anomalies for observation and prediction in space (i) and time (j), respectively, the ACC is calculated as

$$ACC_j = \frac{\sum_{i=1}^{i=M}(\Delta x_{i,j} - \overline{\Delta x_j}) \times (\Delta y_{i,j} - \overline{\Delta y_j})}{\sqrt{\sum_{i=1}^{i=M}(\Delta x_{i,j} - \overline{\Delta x_j})^2 \times \sum_{i=1}^{i=M}(\Delta y_{i,j} - \overline{\Delta y_j})^2}} \tag{2}$$

where $\overline{x_i} = \frac{1}{N}\sum_{j=1}^{j=N} x_{i,j}$, $\overline{y_i} = \frac{1}{N}\sum_{j=1}^{j=N} y_{i,j}$, $\Delta x_{i,j} = x_{i,j} - \overline{x_i}$, $\Delta y_{i,j} = y_{i,j} - \overline{y_i}$, and M is the number of space samples over Southeast Asia and N is the number of time samples.The TCC represents the predictability of each spatial grid so that we could obtain a spatial distribution of prediction skill. It is defined as

$$TCC_i = \frac{\sum_{j=1}^{j=N}(x_{i,j} - \overline{x_i}) \times (y_{i,j} - \overline{y_i})}{\sqrt{\sum_{j=1}^{j=N}(x_{i,j} - \overline{x_i})^2 \times \sum_{j=1}^{j=N}(y_{i,j} - \overline{y_i})^2}} \tag{3}$$

The RMSE measures the degree that prediction differentiates from the observation. Small (near-zero) RMSE indicates good agreements between the prediction and observations (Chai et al., 2014). It is calculated as

$$RMSE = \sqrt{\frac{\sum_{i=1}^{i=M}(x_{i,j} - y_{i,j})^2}{M}} \tag{4}$$

The ACC and TCC values for the total and subseasonal anomalies of the PREC, U850 and Z500 are calculated during boreal summer (May–September) to assess the temporal and spatial variations of intraseasonal prediction skills of the BCC_CSM1.2. The temporally-averaged ACC and spatially- averaged TCC are also given as a summary metric of prediction skills.

2.2.3. Prediction skills of the MJO and BSISO

We further analyze the prediction skills of the MJO and BSISO indices in terms of ACC and RMSE, as shown in Eqs. (5) and (6), and the dependences of their prediction skills on the intensity and phases of subseasonal variability. The hindcasts of the BCC_CSM1.2 are also used to examine the relationship between pentad-mean ACC of PREC (the lead pentad function) and 8 BSISO1 phases (initial conditions) according to the definition of Lee et al. (2013).

$$ACC = \frac{\sum_{j=1}^{j=N}(\Delta x_j - \overline{x}) \times (\Delta y_j - \overline{y})}{\sqrt{\sum_{j=1}^{j=N}(\Delta x_j - \overline{x})^2 \times \sum_{j=1}^{j=N}(\Delta y_j - \overline{y})^2}} \tag{5}$$

$$RMSE = \sqrt{\frac{\sum_{j=1}^{N}(x_j - y_j)^2}{N}} \tag{6}$$

Where $\overline{x} = \sum_{j=1}^{j=N} x_j$, $\overline{y} = \sum_{j=1}^{j=N} y_j$, and Δx_j and Δy_j are defined as anomalies of MJO and BSISO index for observation and prediction.

3. Results

3.1. Mean state

The observed (Fig. 1a) and prediction (Fig. 1b–g) climatological mean summer PREC and wind filed, and the BCC-CMS1.2 model biases (Fig. 1h–m), reveal that the model is able to predict the basic spatial characteristics of precipitation and wind in the study region. It correctly predicts large values of PREC in the western Arabian Sea and South China Sea. Prediction biases are positive at low latitudes and negative at high latitudes, indicating a wet bias in the equatorial western Indian Ocean and a dry bias north of 10°N. In prediction, there exists convergence over the eastern Arabian Sea and equatorial western Pacific Ocean, which is consistent with wet biases of PREC. It is worth noting that the model fails to predict a precipitation center over the Bay of Bengal, but generates too strong convection over western Pacific at first lead pentad, which may be due to the biases of initial conditions and deserves further in-depth analysis.

3.2. Prediction skills

Spatial patterns of the TCCs for each lead pentad of the PREC, U850 and Z500 are shown in Figs. 2–4, respectively. The skills of both total anomalies and subseasonal anomalies decline with lead time for all three fields. Overall, the TCC skill in the tropics is generally higher than that in the subtropics. The skill distribution shows that the model performed better over oceans than over land. During the first two lead pentads, the model's PREC skills are comparable between the total (Fig. 2a–b) and subseasonal (Fig. 2g–h) anomalies, and the TCC shows relatively high skill over the part of Maritime Continent (>0.3) in pentad 2. After lead pentad 3, the TCC of the PREC rapidly drops below 0.1. Such a decline of skill with lead time is not obvious after lead pentad 2, which indicates that the model is not sensitive to the initial value of PREC. The skill of the total anomalies over the Maritime Continent is persistently higher than other regions, whereas the TCC of the subseasonal anomalies rapidly drops below 0 after lead pentad 4 (Fig. 2d). This result suggests that the prediction skill of total anomalies over the Maritime Continent could benefit from its interannual variability to some degree.

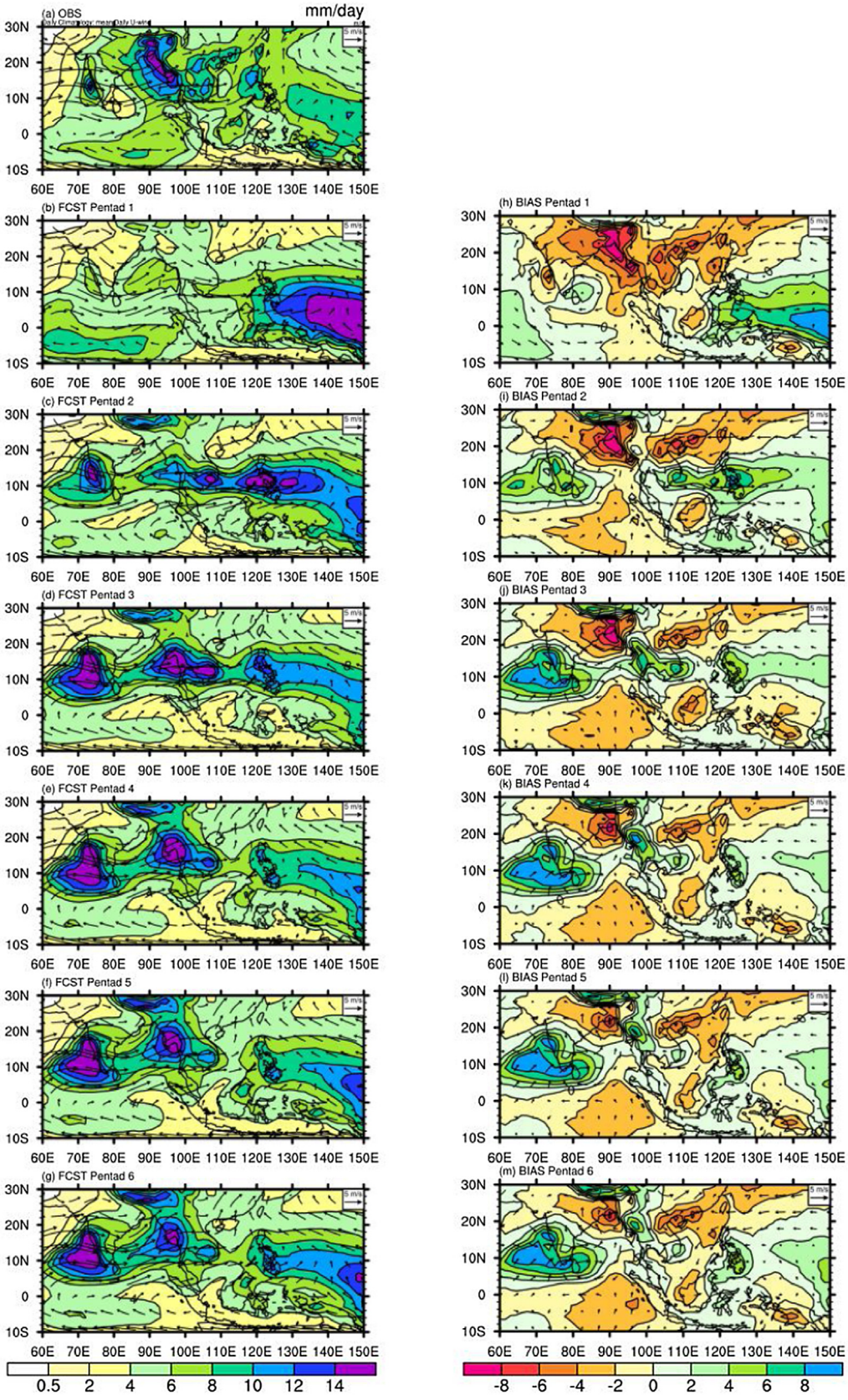

Fig. 1. Climatology from May to September for precipitation rate (mm/day) and wind (m/s) from observation (a) and BCC_CSM1.2 for lead pentads 1–6 (b–g). Forecast bias (forecast minus observation) is shown in (h-m) for lead pentads 1–6, respectively.

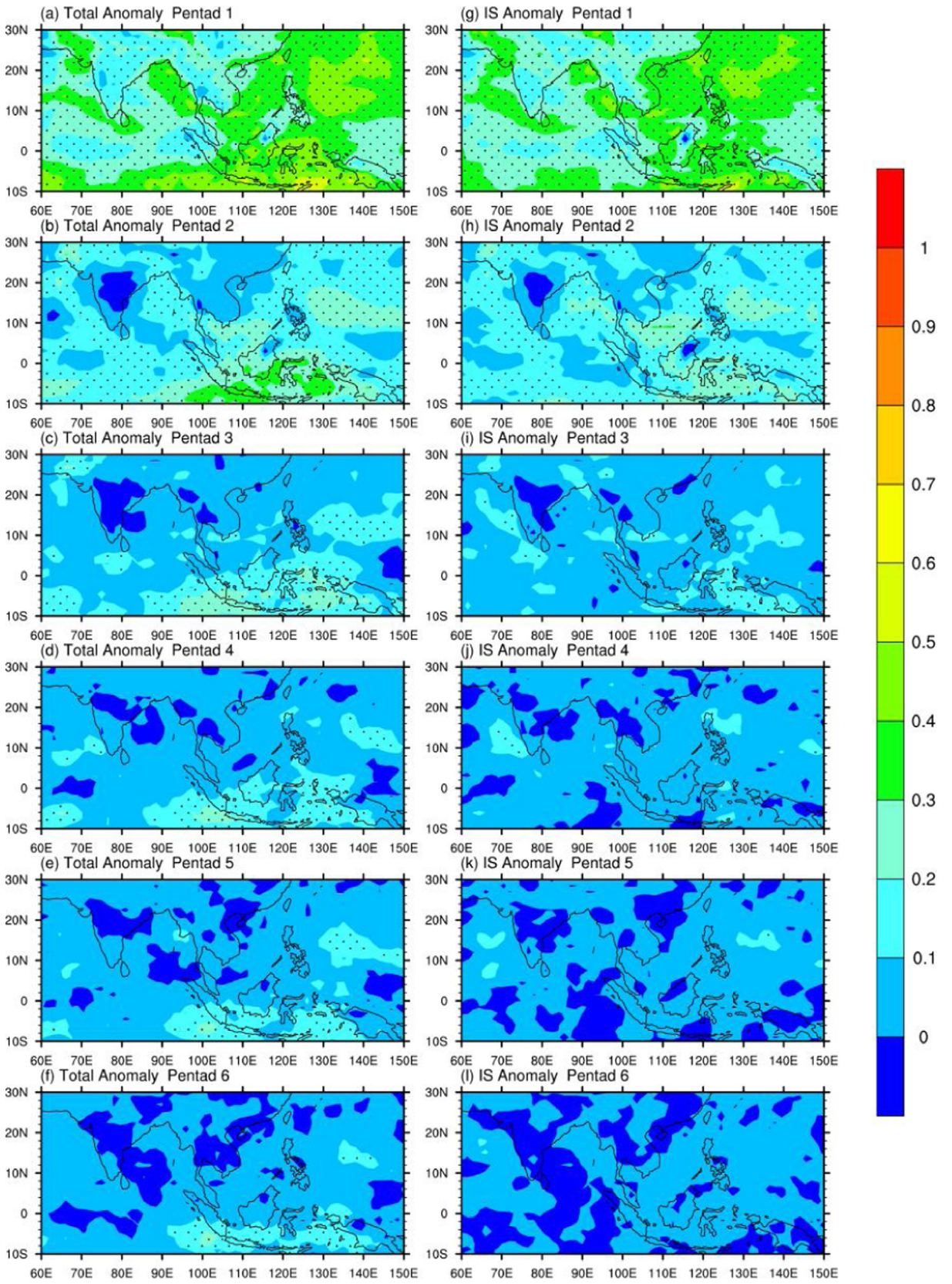

Fig. 2. TCC of predictions (Changes exceeding the 90% confidence level are dotted) for precipitation in terms of total anomalies (left panels) and subseasonal anomalies (right panels). The top, 2nd, 3rd, 4rd, 5rd, and bottom rows are for lead pentads 1–6 prediction, respectively.

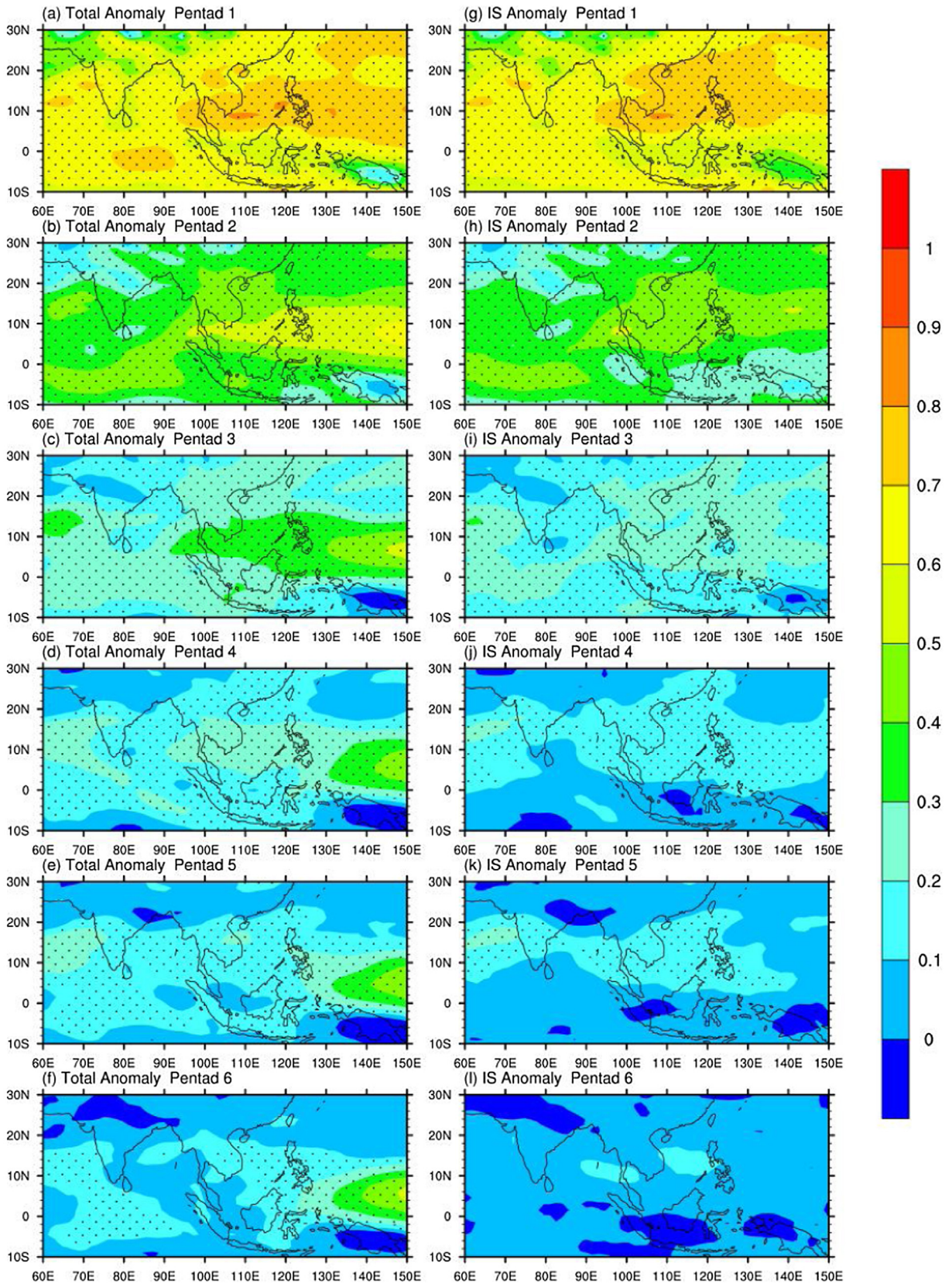

Fig. 3. As in Fig. 3, except for 850 hPa zonal wind.

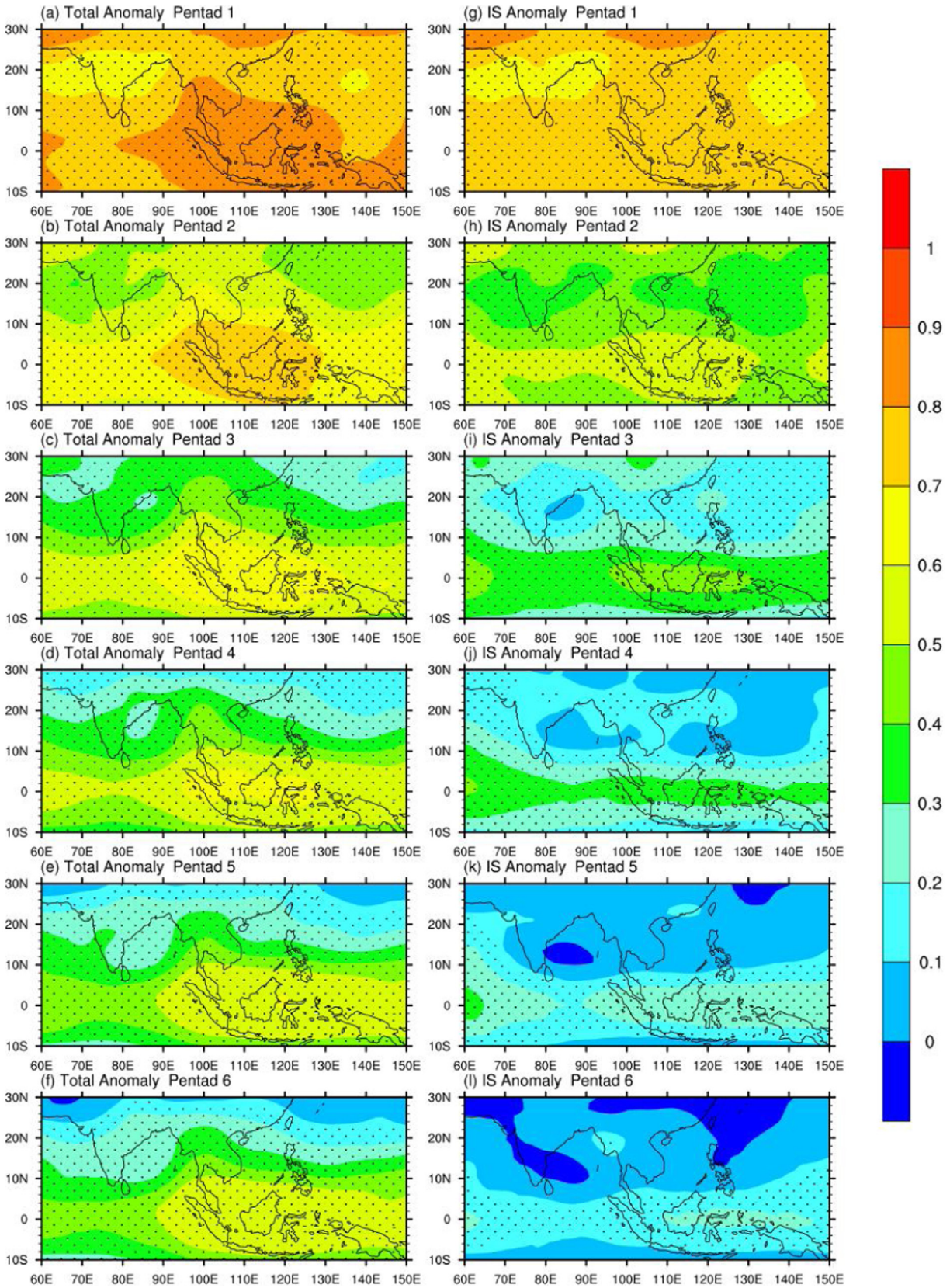

Fig. 4. As in Fig. 3, except for 500 hPa geopotential height.

Table 1
Useful prediction skills of major intraseasonal modes.

Useful prediction skill (days)	MJO	BSISO1	BSISO2
ACC	20	10	7
RMSE	21	13	9

The TCC patterns of U850 (Fig. 3) are similar to that of PREC, but with higher skills for both total and subseasonal anomalies. During the first two lead pentads, the TCC of subseasonal anomalies is comparable to that of total anomalies in most regions (Fig. 3a, b, g, h). In lead pentads 3 and 4, the TCC of total anomalies is higher than that of subseasonal anomalies in the western equatorial Pacific Ocean, where the skill of total anomalies declines slowly with a value greater than 0.3 even at lead pentad 6 (Fig. 3f).

The prediction skill of Z500 (Fig. 4) is the highest among the three variables. The TCC of subseasonal anomalies is close to that for total anomalies (Fig. 4a, b, g, h) in lead pentads 1 and 2. For longer lead times, the TCC of subseasonal anomalies is higher than 0.2 in lead pentad 3 (Fig. 4i) and higher than 0.1 in lead pentad 4 (Fig. 4i). The TCC of total anomalies maintains high skill for all lead times in the tropics, but drops quickly with lead time in the subtropics. This result indicates that initial errors grow much faster in extratropics than that in the tropics. Comparing to the PREC and U850, the TCC differences between total and subseasonal anomalies of the Z500 are much larger, in particular for longer lead times.

The ACC results (Fig. 5) are similar to those for TCC and the interpretations are also very similar. The Z500 (PREC) has highest (lowest) skill with the U850 in the middle. Although the ACC values show interannual variations, but the fluctuations are small for the PREC and U850 and the Z500, in particular at short lead times. The ACC values for the PREC, U850 and Z500 decrease with lead time for both total variability and subseasonal variability, and negative values begin appearing in lead pentad 3 or 4. High prediction skill for total anomalies always appear in El Niño–Southern Oscillation (ENSO) years (e.g., 97/98 and 09/10), especially for Z500, indicating that the model derives some of its predictive power from ENSO. However, the prediction skills of subseasonal anomalies are always lower in ENSO years, demonstrating a clear skill gap between total and subseasonal anomalies. The temporally-averaged ACC and spatially-averaged TCC (not shown) are almost the same, but the ACC is higher than the TCC. The descending order of prediction skills is always the Z500, U850 and PREC. Since meridional/zonal winds can be obtained by partial derivatives of height fields with respect to y/x through quasi-geostrophic approximation in off-equatorial regions, and PREC is proportional to vorticity (which is a partial derivative of meridional/zonal wind with respect to y/x), we can conclude that the circulation-related variables (i.e., U850, Z500) can be better predicted by this model than the convection-related variables (i.e., PREC).

Fig. 6 shows the results of RMSE for PREC (Fig. 6a), U850 (Fig. 6b) and Z500 (Fig. 6c). RMSE increases sharply for all three variables from lead pentad 1 to lead pentad 2. After lead pentad 3, the RMSE of PREC slightly declines and the error growth rates of U850 and Z500 slow down significantly. This result suggests that the model loses prediction skills quickly after lead pentad 3.

3.3. Connections between the MJO and BSISO

We calculate the ACC between the observed and predicted indices for both the MJO and BSISO. When the ACC reaches 0.5 and RMSE reaches $\sqrt{2}$, the corresponding lead time is defined as useful prediction skill in days (Table 1). The skill of the MJO is found to be better than BSISO in terms of ACC and RMSE. The former have a skill of 20-d and the 21-d. The skill of BSISO1 index (10 d) measured with ACC is slightly higher than that of BSISO2 index (7 d). On the other hand, the RMSE values give useful skills of BSISO1 and BSISO2, respectively, as 13-d and 9-d (Table 1).

Fig. 7a gives a scatter plot between the ACC skill of subseasonal PREC anomalies for lead pentad 1 and the corresponding MJO and BSISO amplitudes. The correlation between PREC skill and MJO amplitude is weakly positive ($r = 0.18$). The correlation between the U850 ACC and MJO amplitude is also similar ($r = 0.15$) (Fig. 7b). Although small, these correlations exceed 90% confidence level. In contrast, the correlation between the subseasonal ACC in lead pentad 1 and BSISO1 amplitude is apparently higher than that with the MJO, which is 0.26 and 0.31, respectively, for the PREC and U850. This result suggests that stronger BSISO intensity leads to higher prediction skills and the subseasonal predictability of precipitation over Southeast Asia mainly comes from BSISO index rather than MJO index during boreal summer.

Fig. 8 shows the impacts of BSISO1 phases on the ACC of the PREC. At first lead pentad, the ACC is higher than 0.24 in most BSISO1 phases with a maximum of 0.28 in phase 5. The ACC drops steadily with lead time no matter what are the initial phases. During lead pentads 1–6, prediction skills are higher for those initiated at phase 2 and phase 5. The phase 2 corresponds to enhanced convection in the equatorial Indian Ocean (Fig. 9a) and the phase 5 with enhanced convection extending from the Bay of Bengal to equatorial western Pacific (Fig. 10a). Skill is relatively low when initiated in phase 3 when enhanced convection is over northern Indian Ocean (Fig. 11a).

Composite patterns of observed and predicted precipitation anomalies for pentads 1–6 with initial phases 2, 5, and 3 are, respectively, given in Figs. 9–11. As shown in Fig. 8, the initial BSISO1 phases 2 and 5 (3) correspond to the highest (lowest) prediction skill among the eight initial phases. For the 6-pentad composites of initial phase 2 (Fig. 9). The observations show initial active convection over northern and eastern Indian Ocean with a tilted dry zone extending from the Bay of Bengal to equatorial western Pacific. When time increases from pentad 1–6, the convection over the Indian Ocean propagates

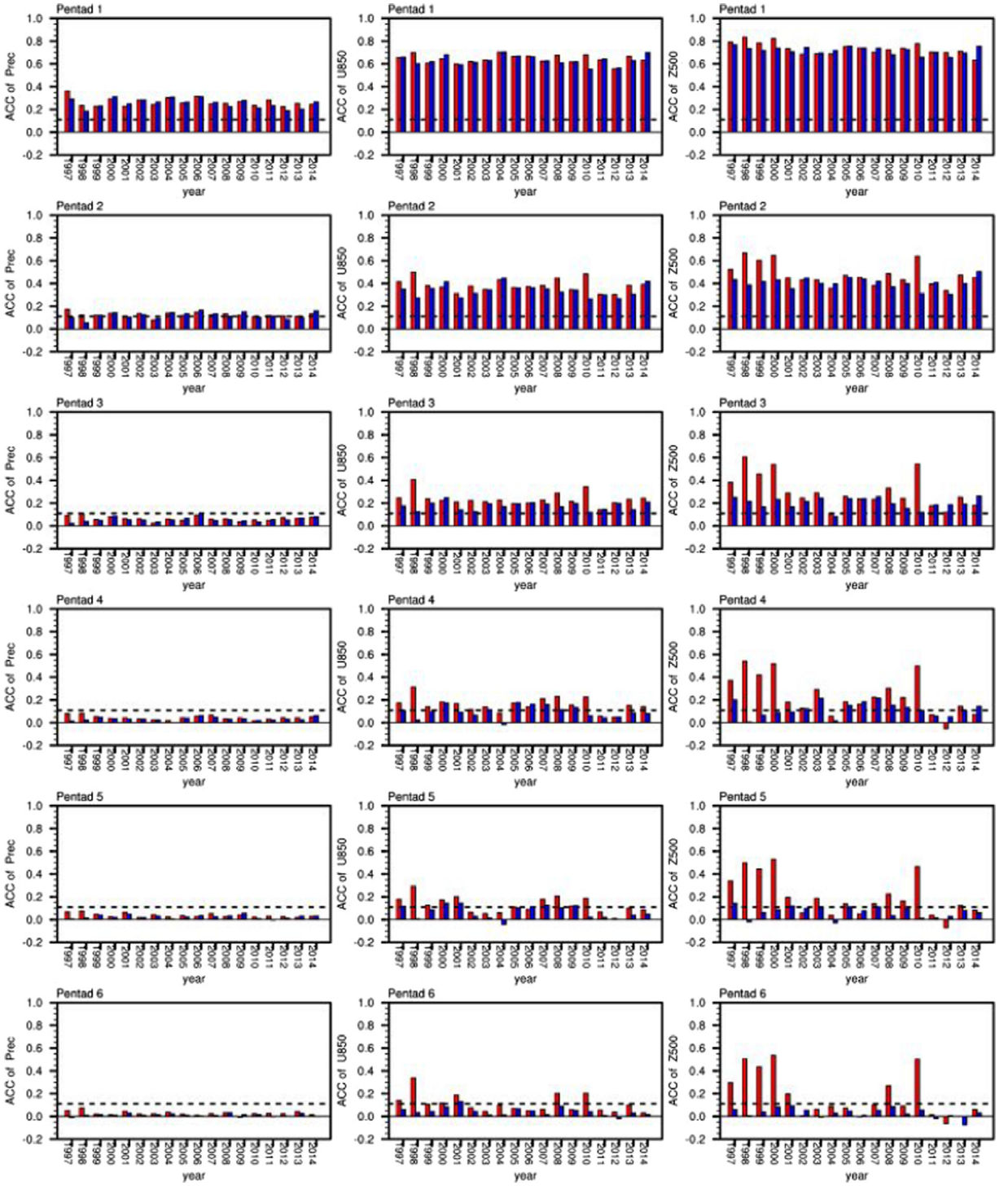

Fig. 5. Yearly Averaged (during May–September) ACC of total anomalies (blue bars) and subseasonal anomalies (red bars) for precipitation (the first column), 850 hPa zonal wind (the second column), 500 hPa geopotential height (the third column) in lead pentads 1–6 (rows 1–6). The horizontal lines are 0.12 for 90% confidence level.

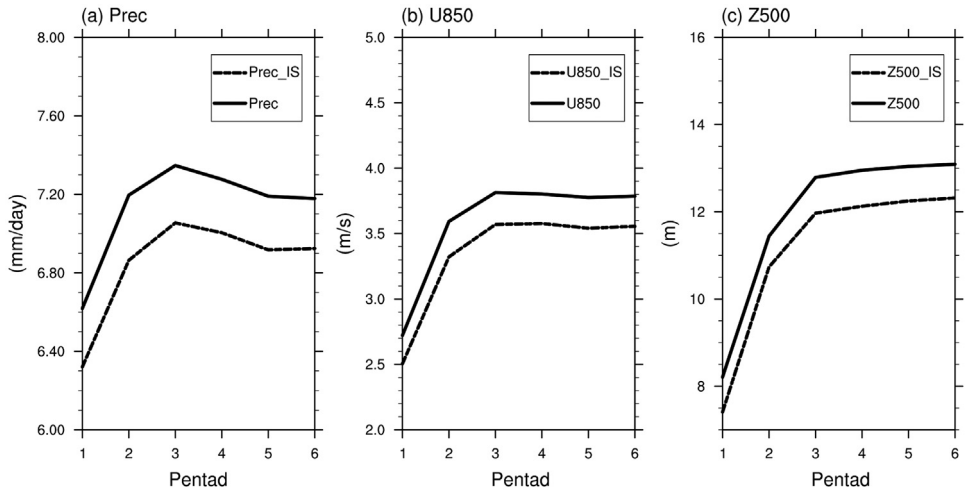

Fig. 6. RMSE of predictions in terms of total (solid curves) and subseasonal anomalies (dotted curves) for precipitation (a), 850 hPa zonal wind (b), and 500 hPa geopotential height (c), respectively.

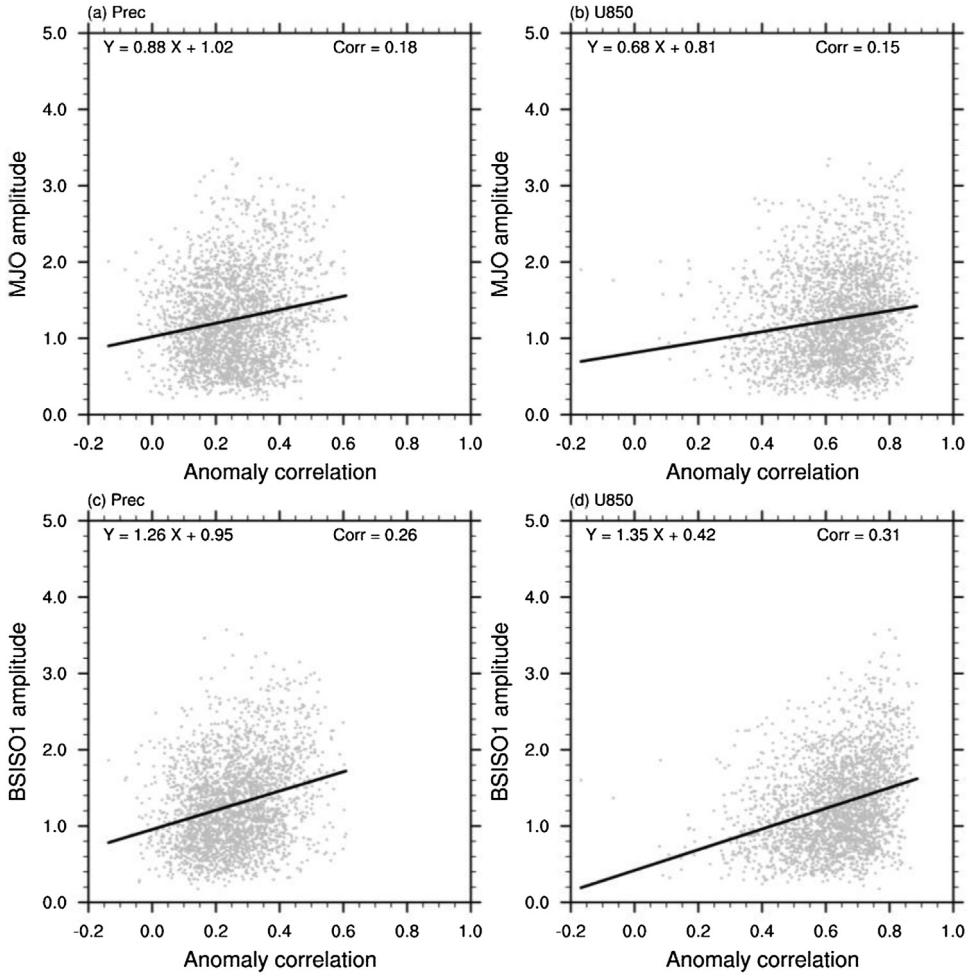

Fig. 7. Scatter plots subseasonal ACC in lead pentad 1 versus the amplitudes of MJO and BSISO1, respectively.

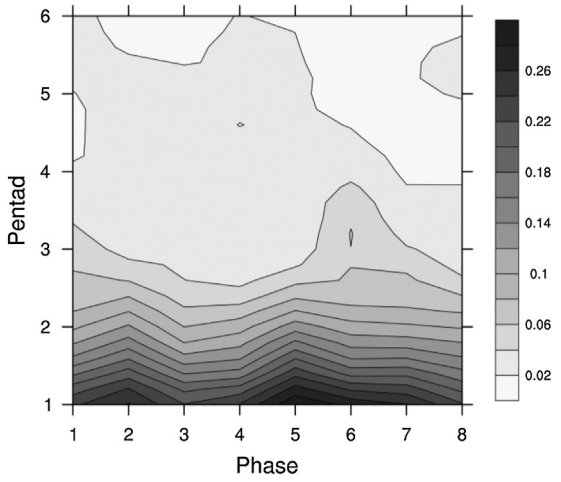

Fig. 8. Averaged ACC of precipitation as a function of lead pentad and initial BSISO1 phase.

northward and eastward to replace the tilted dry zone with active convection. At the same time, a dry phase develops over the tropical Indian Ocean. The model is able to capture the observed evolution in first two patterns and totally fails to reproduce the development of dry phase in the Indian Ocean. Similar situation occurs for the prediction initiated in phase 5 (Fig. 10). During first two pentads, the model is able to predict a rain band extending from the Bay of Bengal to the western Pacific Ocean and the associated dry zone on the equatorward. However, after pentad 2, the model has serious problem to maintain the tilted dry zone from northern Indian Ocean to western Pacific and the redevelopment of convection over the equatorial Indian Ocean. For the case initiated in phase 3 (Fig. 11), the observed convection in the Indian Ocean starts to split into north and south branches with the equatorial component over the Maritime Continent. Then, a tilted rain band along with a dry zone in the Indian Ocean forms as in the case initiated in phase 2 (Fig. 9). The model can marginally capture the convection pattern in first pentad. After that, convection anomalies in the model rapidly disappear.

Fig. 12 compares the observed and predicted northward propagations of precipitation anomalies along three longitudinal bands (eastern, western Indian Ocean and western Pacific) with initial phases 2, 5, and 3. The prediction skills are not only different among three different initial phases, but also show apparent regional differences. As shown in horizontal maps (Figs. 9–11), a major difference between the evolution from phase 3 and that from the other two phases is that the amplitude of the precipitation anomalies from phase 3 is weaker in both observation and prediction, leading to a smaller anomaly correlation compared to phases 2 and 5. The prediction skills in western Pacific are overall better than that in Indian Ocean. The model is able to predict the observed temporal evolutions very well towards 10 lead days in western Pacific. It looks that this model has better skills when initiated from wet phase than that initiated from dry phase in terms of both magnitude and propagating feature.

4. Summary and discussions

In this study, 18-year (1997–2014) hindcasts from BCC_CSM1.2 have been used to examine its subseasonal prediction skills of precipitation and associated dynamical fields in Southeast Asia during boreal summer (May to September). The skill assessments include the total and subseasonal anomalies of precipitation (PREC), 850-hPa zonal wind (U850) and 500-hPa geopotential height (Z500). In addition, we also document the prediction skills of MJO and BSISO and explore their skill connections. Our major findings are summarized in following three points:

(1) The BCC_CSM1.2 model can reasonably predict the subseasonal precipitation variability over the Southeast Asia beyond two pentads. The overall skill of Z500 is higher than U850, and both of them have higher skills than PREC. This result indicates that the precipitation usually has lower skill compared to the associated dynamical variables. In general, tropic regions have higher skill than subtropics. With the impact of ENSO, total anomalies that include interannual signals have higher skill than subseasonal anomalies. Due to the long-term persistence of interannual signals, the skill differences between the total and subseasonal anomalies increase rapidly with lead time in association with the quick drop of subseasonal forecasting skill.
(2) The model can predict MJO index better than BSISO index. The subseasonal PREC skill tends to be higher when the amplitudes of the ISO indices are large, especially for BSISO1 index. This indicates that subseasonal predictability of precipitation mainly comes from BSISO index than MJO index during boreal summer.
(3) Subseasonal prediction skill significantly fluctuates with initial BSISO1 phases. With enhanced convection over Indian Ocean, the forecasts initialized at phase 2 lead to highest skill. After evaluating the forecasts initialized at phases 2, 3 and 5, it is revealed that when initialized from phase 2, the model is able to well capture the convection propagating

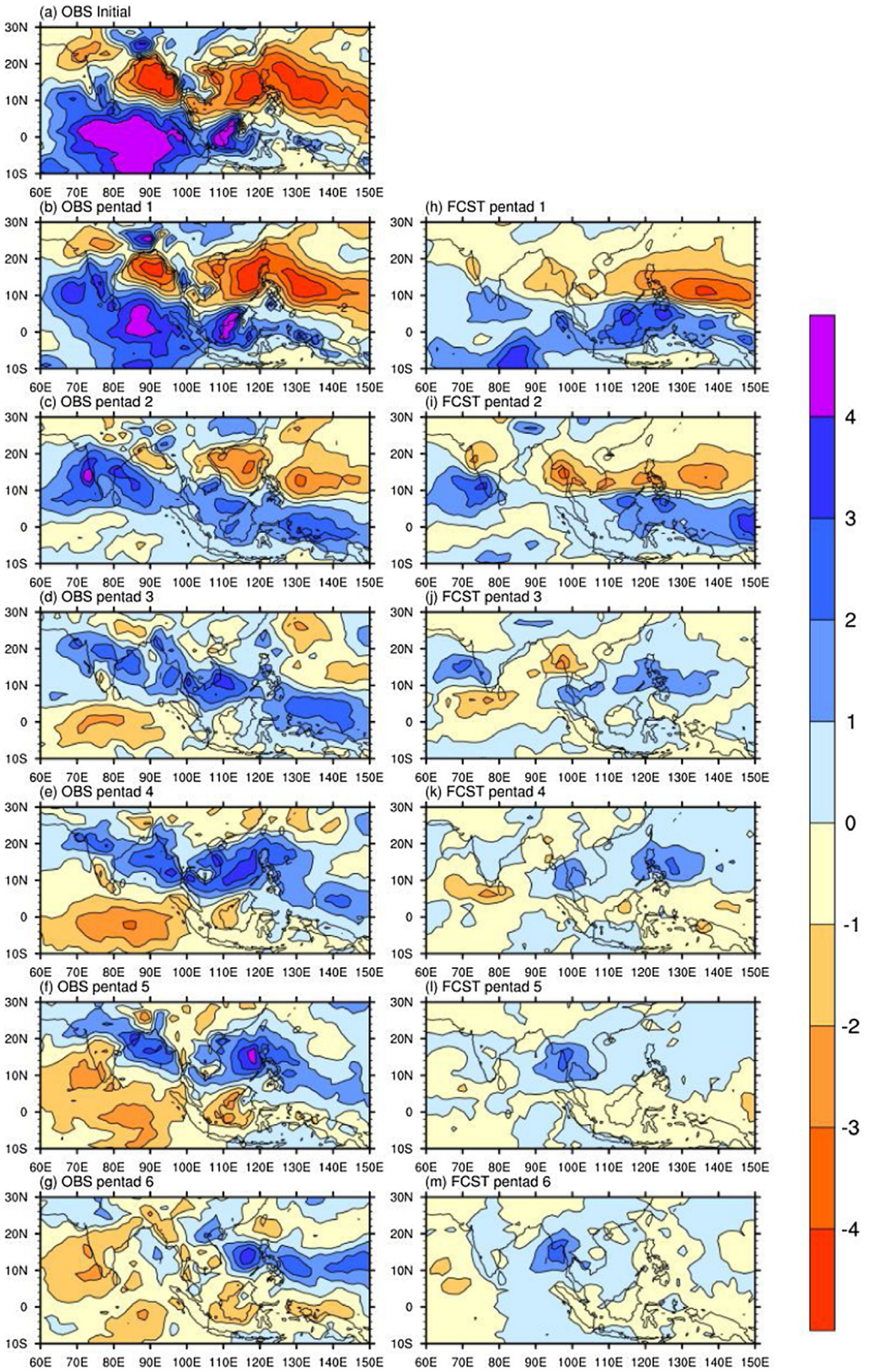

Fig. 9. Composites for observational (left panels) and predicted precipitation anomalies (mm/day) from initial conditions of BSISO1 phase 2. (a) observed initial conditions, (b–g) observed average for pentads 1–6, and (h–m) forecast average for pentads 1–6.

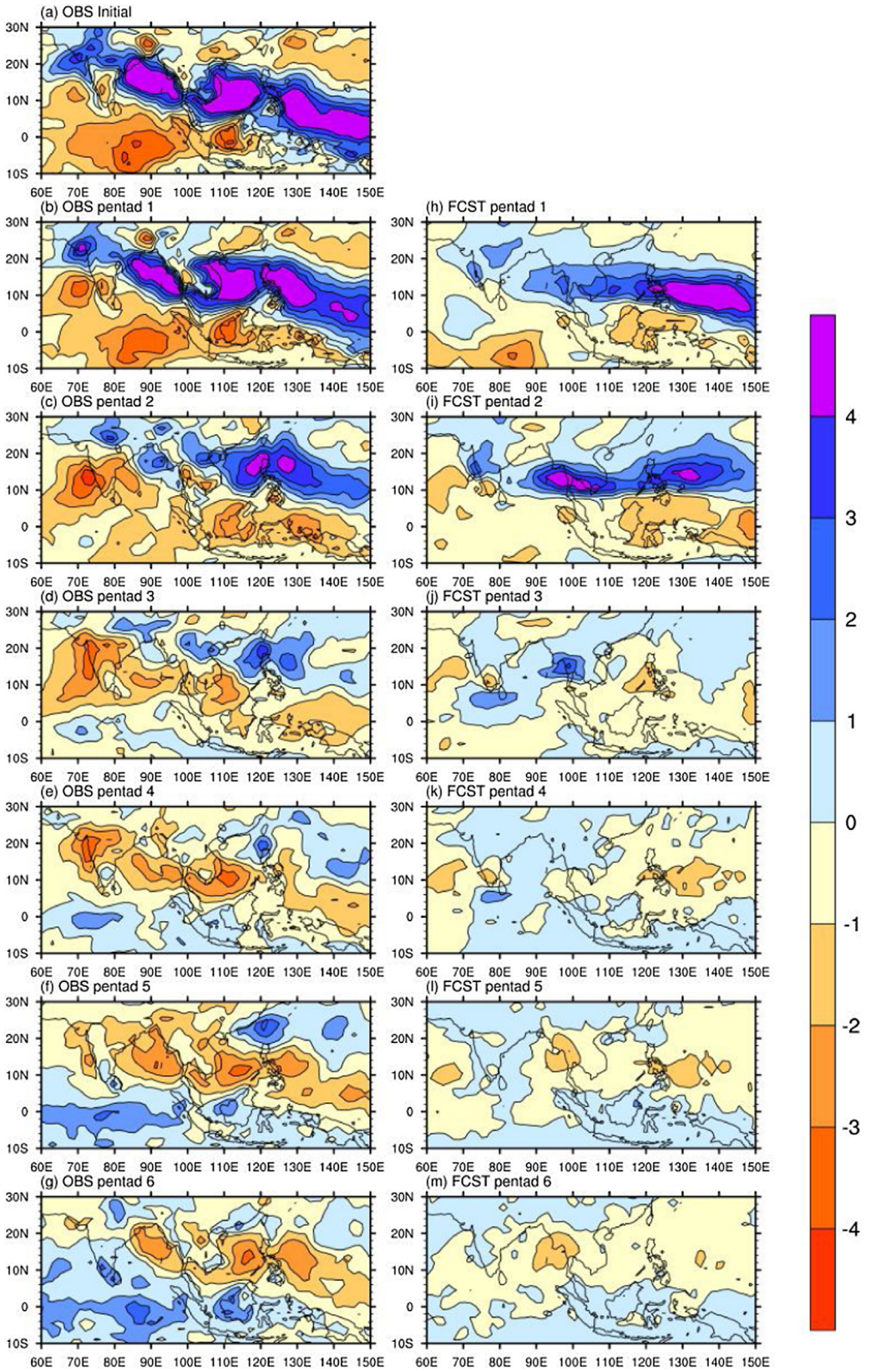

Fig. 10. As in Fig. 15, except for initial conditions of BSISO1 phase 5.

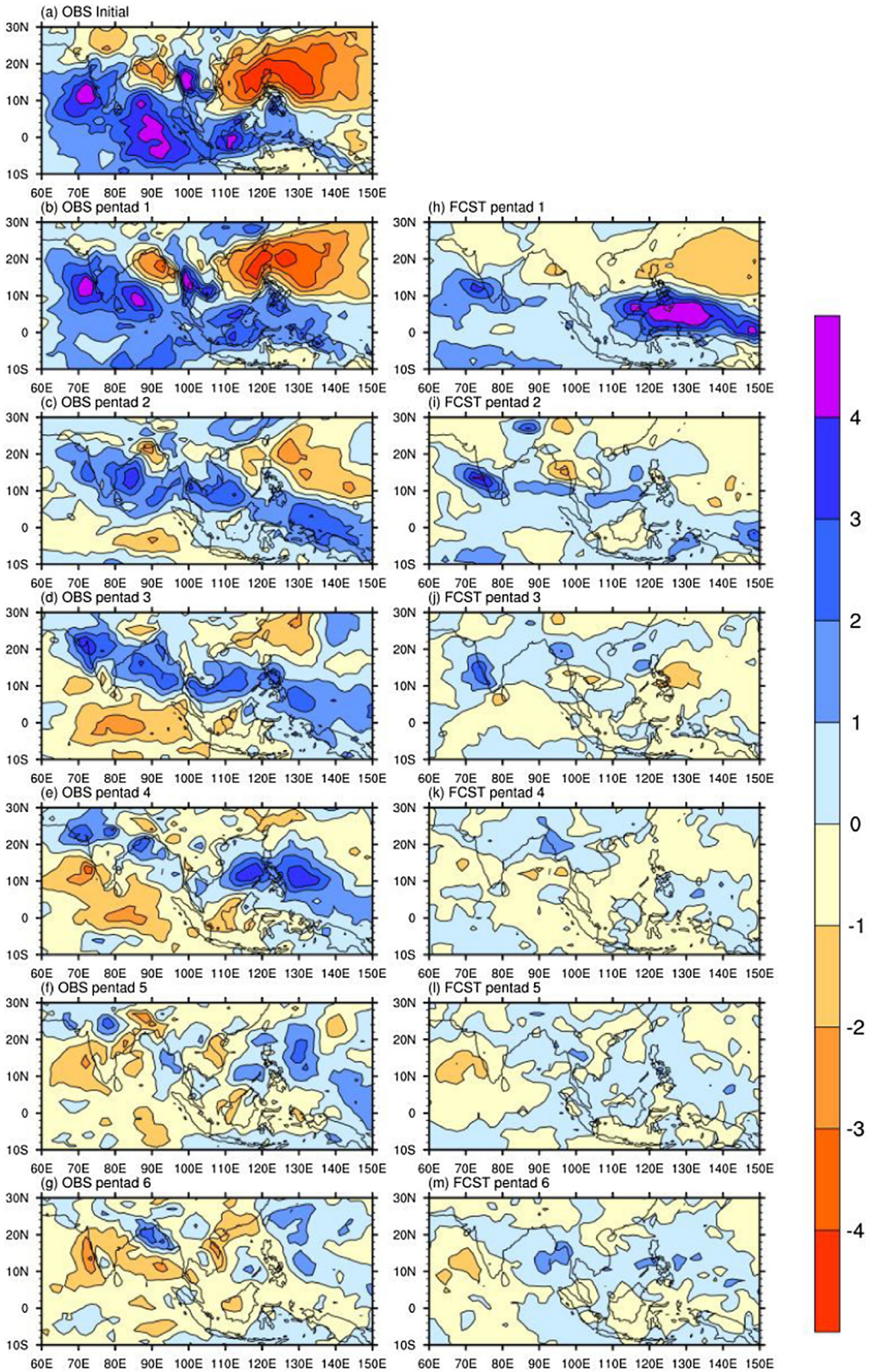

Fig. 11. As in Fig. 15, except for initial conditions of BSISO1 phase 3.

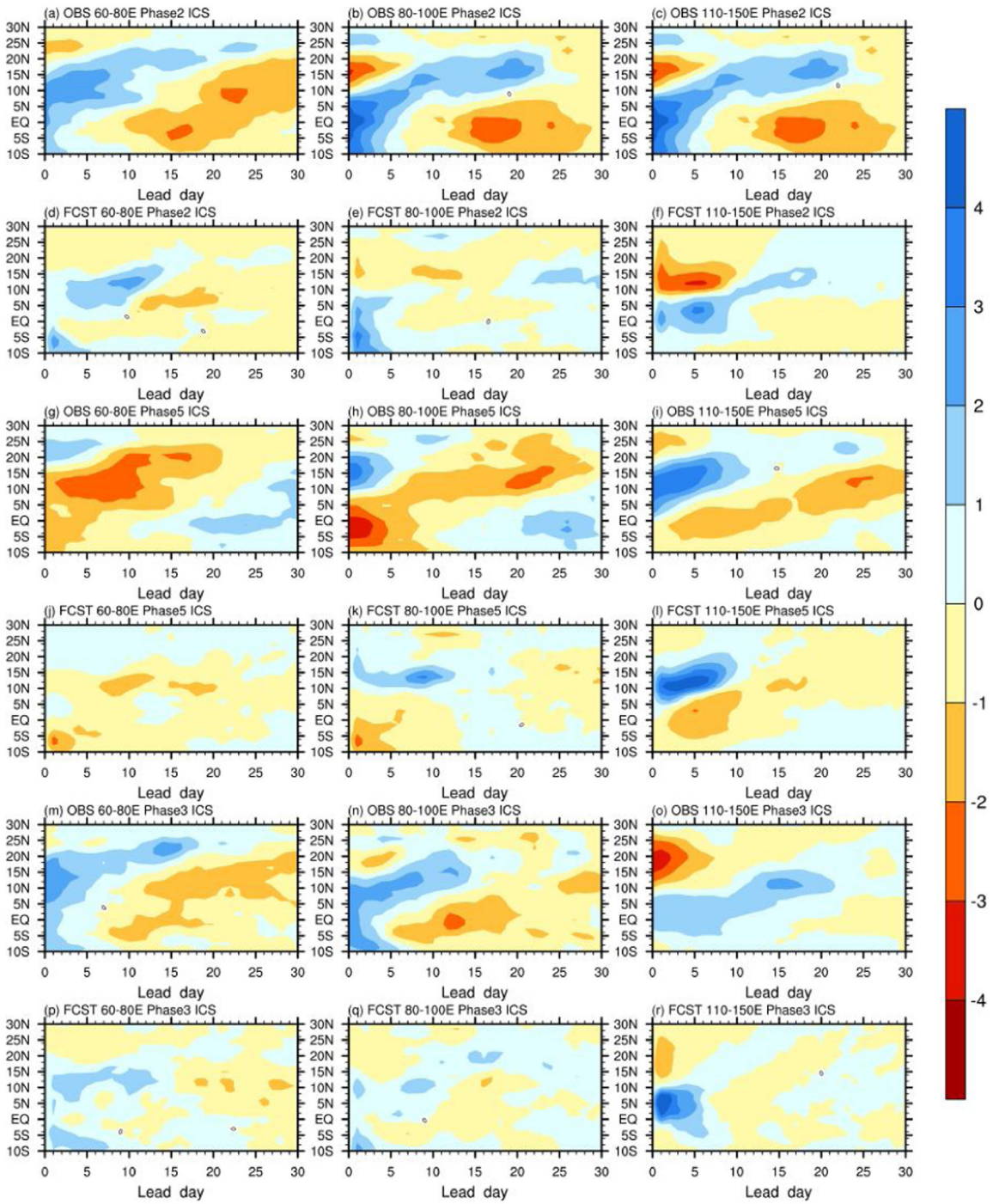

Fig. 12. Composites for observational (rows 1, 3, 5) and predicted (rows 2, 4, 6) precipitation anomalies (mm/day) zonally averaged over 60°E–80°E (left column), 80°E–100°E (center column), and 110°E–150°E (right column). Rows 1 and 2 for initial date of BSISO1 phase 2, rows 3 and 4 for initial date of BSISO1 phase 5, rows 5 and 6 for initial date of BSISO1 phase 3.

northward in Indian sector and eastward to western Pacific at lead pentads 1 and 2. When initialized at phase 5, the model also well captures the gradual decay of the rain belt during the first two lead pentads. When initialized at phase 3, the model is only able to capture the characteristics of convection in lead pentad 1. The possible reason for this lower skill from phase 3 is that, after pentad 2, the amplitude of the observation convection activity becomes weaker, which generally corresponds to a smaller predictability. The model predicts wet conditions more accurately than dry conditions in terms of both intensity and propagation. The model's ability to reproduce the observed northward propagation is much

better over western Pacific than that over the Indian sector. A deficiency of this model prediction is that the northward propagation can not be predicted well no matter it was at phases 2, 5, or 3. Even from the better prediction over the Pacific Ocean, the center of positive anomalies averaged over [110°E–150°E] from phase 2 in Fig. 12c reach near 20°N on day 13, which corresponding location at same lead time in prediction is to the south of 15°N as shown in Fig. 12f. Such a deficiency also existed in the CFSv2 and the earlier version of CFS (Wang et al., 2009; Liu and Wang, 2015). They pointed out the possible reason for such a lower north propagation in prediction is that sea surface temperature anomalies in the models are too weak compared to observation. Whether is the same reason for BCC_CSM1.2, which requires to assess the representation of upper ocean processes and their air-sea interaction, as well as its impact on the prediction of the ISO. This study has demonstrated that the BCC_CSM1.2 model can predict reasonably the Southeast Asian precipitation beyond two pentads, which is lower than the CFSv2 model (Liu and Wang, 2015). One deficiency in the BCC_CSM1.2 revealed in this paper is that the model fails to predict a precipitation center over the Bay of Bengal, but generates too strong convection over western Pacific at the first lead pentad. It may be due to the biases of initial conditions and deserves further in-depth analysis. Apparently, subseasonal prediction skills are model dependent. Further in-depth multi-model inter-comparisons are needed to understand why some models (e.g., CFSv2) have higher skill and explore the ways to further improve the subseasonal prediction skill in the BCC_CSM1.2 model.

Acknowledgements

This work was jointly supported by National Key Research Program and Development of China (2017YFC1502302), the National Basic Research (973) Program of China under Grants 2015CB453203, the China meteorological special project under Grant GYHY201406022, the China National Science Foundation under Grants 41775066 and 41375062, and the Project for Development of Key Techniques in Meteorological Operation Forecasting (YBGJXM201704).

References

Chai, T., et al., 2014. Root mean square error (RMSE) or mean absolute error (MAE)? Geosci. Model Dev. 7 (1), 1525–1534.
Ding, R., Li, J., Seo, K.H., 2010. Predictability of the Madden-Julian oscillation estimated using observational data. Mon. Weather Rev. 138, 1004–1013.
Ding, R., Li, J., Seo, K.H., 2011. Estimate of the predictability of boreal summer and winter intraseasonal oscillations from observations. Mon. Weather Rev. 139 (8), 2421–2438.
Fu, X., Wang, B., Bao, Q., Liu, P., Lee, J.-Y., 2009. Impacts of initial conditions on monsoon intraseasonal forecasting. Geophys. Res. Lett. 36, L08801, http://dx.doi.org/10.1029/2009GL037166.
Fu, X., Lee, J.Y., Hsu, P.C., et al., 2013. Multi-model MJO forecasting during DYNAMO/CINDY period. Clim. Dyn. 41 (3–4), 1067–1081.
Kalnay, E., Kanamitsu, M., Kistler, R., 1996. The NCEP/NCAR 40-Year reanalysis project. Bull. Am. Meteorol. Soc. 77 (3), 437–472.
Lee, J.Y., Wang, B., Wheeler, M.C., Fu, X., Waliser, D.E., Kang, I.S., 2013. Real?time multivariate indices for the boreal summer intraseasonal oscillation over the Asian summer monsoon region. Clim. Dyn. 40 (1–2), 493–509.
Liu, R.F., Wang, W., 2015. Multi-week prediction of South-East Asia rainfall variability during boreal summer in CFSv2. Clim. Dyn. 45 (1–2), 493–509.
Madden, R.A., Julian, P.R., 1971. Detection of a 40∼50 day oscillation in the zonal wind in the tropical Pacific. J. Atmos. Sci. 28 (5), 702–708.
Ren, H.L., Wu, J., Zhao, C., Liu, Y., Jia, X., Zhang, P., 2015. Progresses of MJO prediction researches and developments. Appl. Meteorol. Sci. 26, 658–668 (in Chinese).
Ren, H.L., Wu, J., Zhao, C., Cheng, Y., Liu, X., 2016. MJO ensemble prediction in BCC-CSM1. 1(m) using different initialization schemes. Atmos. Ocean. Sci. Lett. 9, 60–65.
Ren, H.L., Jin, F.F., Song, L., et al., 2017. Prediction of primary climate variability modes at the Beijing Climate Center. J. Meteorol. Res. 31 (1), 204–223.
Seo, K.H., Schemm, J.K.E., Wang, W., Kumar, A., 2007. The boreal summer intraseasonal oscillation simulated in the NCEP climate forecast system: the effect of sea surface temperature. Mon. Weather Rev. 135 (5), 1807–1827.
Seo, K.H., Wang, W., et al., 2009. Evaluation of MJO forecast skill from several statistical and dynamical forecast models. J. Clim. 22, 2372–2388.
Shukla, J.S., 2000. Dynamical seasonal prediction. Bull. Am. Meteorol. Soc. 81, 2593–2606.
Sperber, K.R., Annamalai, H., 2008. Coupled model simulations of borealsummer intraseasonal (30–50 day) variability, Part I: systematicerrors and caution on use of metrics. Clim. Dyn. 31, 345–372.
Vitart, F., Molteni, F., 2010. Simulation of the Madden?Julian Oscillation and its teleconnections in the ECMWF forecast system. Q. J. R. Meteorol. Soc. 136, 842–855.
Vitart, F., Woolnough, S., Balmaseda, M.A., Tompkins, A.M., 2007. Monthly forecast of the Madden–Julian oscillation using a coupled GCM. Mon. Weather Rev. 135, 2700–2715.
Waliser, D., Sperber, K., Hendon, H., Kim, D., Maloney, E., 2012. MJO simulation diagnostics. J. Clim. 22, 3006–3030.
Wang, W., Chen, M., Kumar, A., 2009. Impacts of ocean surface on the northward propagation of the boreal summer intraseasonal oscillation in the NCEP climate forecast system. J. Clim. 22, 6561–6576.
Wang, J., Wang, W., Fu, X., Seo, K.H., 2012. Tropical intraseasonal rainfall variability in the CFSR. Clim. Dyn. 38 (11–12), 2191–2207.
Wang, W., et al., 2013. MJO prediction in the NCEP climate forecast system version 2. Clim. Dyn. 42, 2509–2520.
Wheeler, M., Hendon, H., 2004. An all–season real–time multivariate MJO index: development of an index for monitoring and prediction. Mon. Weather Rev. 132, 1917–1932.
Wu, J., Ren, H.L., Zuo, J., Zhao, C., Chen, L., Li, Q., 2016. MJO prediction skill, predictability, and teleconnection impacts in the beijing climate center atmospheric general circulation model. Dyn. Atmos. Oceans 75, 78–90.
Zhang, C., 2013. Madden-Julian oscillation—bridging weather and climate. Bull. Am. Meteorol. Soc. 94, 1849–1870.
Zhao, C., Ren, H.L., Song, L., Wu, J., 2015. Madden-Julian oscillation simulated in BCC climate models. Dyn. Atmos. Oceans 72, 88–101.

Clim Dyn (2018) 50:4691–4705
DOI 10.1007/s00382-017-3898-0

Early summer southern China rainfall variability and its oceanic drivers

Weijing Li[1,2] · Hong-Chang Ren[1,3] · Jinqing Zuo[1,2] · Hong-Li Ren[2]

Received: 17 February 2017 / Accepted: 5 September 2017 / Published online: 21 September 2017
© The Author(s) 2017. This article is an open access publication

Abstract Rainfall in southern China reaches its annual peak in early summer (May–June) with strong interannual variability. Using a combination of observational analysis and numerical modeling, the present study investigates the leading modes of this variability and its dynamic drivers. A zonal dipole pattern termed the southern China Dipole (SCD) is found to be the dominant feature in early summer during 1979–2014, and is closely related to a low-level anomalous anticyclone over the Philippine Sea (PSAC) and a Eurasian wave-train pattern over the mid–high latitudes. Linear regressions based on observations and numerical experiments using the CAM5 model suggest that the associated atmospheric circulation anomalies in early summer are linked to decaying El Niño-Southern Oscillation-like sea surface temperature (SST) anomalies in the tropical Pacific, basin-scale SST anomalies in the tropical Indian Ocean, and meridional tripole-like SST anomalies in the North Atlantic in the previous winter to early summer. The tropical Pacific and Indian Ocean SST anomalies primarily exert an impact on the SCD through changing the polarity of the PSAC, while the North Atlantic tripole-like SST anomalies mainly exert a downstream impact on the SCD by inducing a Eurasian wave-train pattern. The North Atlantic tripole-like SST anomalies also make a relatively weak contribution to the variations of the PSAC and SCD through a subtropical teleconnection. Modeling results indicate that the three-basin combined forcing has a greater impact on the SCD and associated circulation anomalies than the individual influence from any single oceanic basin.

Keywords Rainfall variability · South China · SST anomalies · Teleconnections

1 Introduction

The East Asian summer monsoon plays a dominant role in setting rainfall variability over China in summer (Ding and Chan 2005). The rain band moves from low to mid–high latitudes as the summer monsoon advances northward from early to late summer. However, migration of the rain band is not gradual; it usually jumps from one relatively stationary stage to another (Wang et al. 2009; Su et al. 2014). In May–June, the rain band is located mainly in southern China, but in July it abruptly shifts northward to the Yangtze valley.

In the past few decades, a significant amount of effort has been devoted to understanding the physical processes and mechanisms governing the summer monsoon and rainfall variability over East Asia (e.g. Lau 1992; Simmonds et al. 1999; Zhang 2001; Zhou and Yu 2005). Most studies treat the summer season as the June–July–August mean. In fact, over South China there are distinct differences in the mean state, rainfall variability, and associated atmospheric circulation patterns between early and late summer (Chang et al. 2000; Wang et al. 2009; Su et al. 2014). Their controlling

Electronic supplementary material The online version of this article (doi:10.1007/s00382-017-3898-0) contains supplementary material, which is available to authorized users.

✉ Hong-Chang Ren
renhongchang921@sina.com

[1] Collaborative Innovation Center on Forecast and Evaluation of Meteorological Disasters, Nanjing University of Information Science and Technology, Nanjing, China

[2] Laboratory for Climate Studies, National Climate Center, China Meteorological Administration, Beijing 100081, China

[3] National Meteorological Center, China Meteorological Administration, Beijing 100081, China

mechanisms may also be different. Early summer rainfall anomalies in southern China are frontal and monsoonal (Chen et al. 2001; Zheng et al. 2006), while late summer rainfall comes mainly from tropical cyclones as the western Pacific subtropical high (WPSH) shifts northward (Ren et al. 2002; Lee et al. 2010).

Recent studies have examined the variability and predictability of East Asian rainfall in early summer. Ye and Lu (2011) investigated the sub-seasonal differences in ENSO-related rainfall anomalies over East Asia, revealing more (less) rainfall anomalies in early (late) summer in southern China during the decaying phase of El Niño. Mao et al. (2011) examined the general atmospheric circulation anomalies associated with the interannual variations in early summer rainfall in southern China. Yim et al. (2014) analyzed the southeast China rainfall predictability in early summer and established a physical–empirical model based on sea surface temperature (SST) tendency in the previous winter and spring. However, the associated physical mechanisms linking early summer rainfall anomalies in southern China to SST anomalies remain poorly understood.

This study aims to identify the leading mode of rainfall anomalies in southern China and the associated atmospheric circulation patterns in early summer. More importantly, we will investigate the linkage between southern China rainfall anomalies in early summer and SST anomalies in the previous winter and spring, and the physical mechanisms responsible, using observations and numerical simulations.

The remainder of this manuscript is organized as follows. Section 2 describes the datasets, model, and experiments used in this study. Section 3 presents the dominant modes of southern China rainfall anomalies and associated atmospheric circulation characteristics in May–June. Section 4 explores the linkage of southern China rainfall anomalies in early summer to SST anomalies in the previous winter and spring, as well as the physical mechanisms responsible for the linkage, and corresponding model simulations are presented in Sect. 5. Finally, Sect. 6 provides a discussion and summary.

2 Data, model, and experiments

2.1 Observational data and method

The precipitation data for the period 1979–2014 used in this study are derived from 54 meteorological stations that are well distributed throughout southern China. These datasets are provided by the National Climate Center of the China Meteorological Administration. The monthly atmospheric circulation data are obtained from the recently released ERA-Interim dataset (Dee et al. 2011) of the European Centre for Medium-Range Weather Forecasts (ECMWF) for the years 1979–2014, with a horizontal resolution of $1.5° \times 1.5°$. SST data are obtained from the Hadley Centre Sea Ice and Sea Surface Temperature (HadISST) dataset for the years 1979–2014, with a horizontal resolution of $1° \times 1°$ (Rayner et al. 2003).

The Niño3.4 and the tropical Indian Ocean (TIO) SST indices used in this study are defined as the regionally averaged SST anomalies over 5°S–5°N, 170°–120°W and 15°S–15°N, 40°E–100°E, respectively. The North Atlantic tripole (NAT) SST index is constructed as the sum of regionally averaged SST anomalies in the tropics (5°–20°N, 60°–20°W) and in the subpolar ocean (40°–55°N, 55°–30°W) minus the regionally averaged SST anomalies in the middle North Atlantic (25°–35°N, 80°–50°W). The Philippine Sea anomalous anticyclone (PSAC) index is defined as the sea level pressure anomaly averaged over the Philippine Sea (10°–20°N, 120°–150°E) following Wang et al. (2000). The intensity of the WPSH is defined following Liu et al. (2012) and is provided by the National Climate Center of the China Meteorological Administration.

To remove the impact of ENSO on atmospheric circulation, linear regression patterns of circulation anomalies against the winter Niño3.4 index are calculated, and these patterns are removed from the original circulation fields. Then the regression and correlations against other indices are recalculated using the new circulation fields. The statistical significance of the regression and correlation is determined by a two-tailed Student's *t* test.

Seasons in this work are defined as winter (December–January–February mean; DJF), spring (March–April mean; MA) and early summer (May–June mean; MJ).

2.2 Model and experimental setup

The atmospheric general circulation model (AGCM) used is the Community Atmospheric Model (CAM version 5.3) developed by the National Center for Atmospheric Research (NCAR).CAM is coupled to the Community Land Model (CLM version 4.0), and a version with 1.9° latitude by 2.5° longitude resolution with 30 vertical levels is used in this study.

Four sensitivity experiments are conducted to assess the contribution of SST anomalies in the tropical Pacific Ocean (TPO run), tropical Indian Ocean (TIO run), North Atlantic (NAT run), and the contribution of SST anomalies in all three oceanic basins (PIA run), respectively. A 10-year spin-up is run before conducting the sensitivity experiments, and integrations of 7 months (from December to June) are conducted for all experiments. Each experiment consists of 30 ensemble members with slightly varying atmospheric initial conditions, and the ensemble mean of the 30 members is used for analysis. In the control run, the model is forced with a prescribed monthly climatology of SST and sea ice

that is obtained from the monthly HadISST dataset for the period 1981–2010.

3 Leading modes of rainfall anomalies and associated circulation characteristics

3.1 Leading modes of interannual variability

Empirical orthogonal function (EOF) analysis of the MJ mean rainfall anomalies during 1979–2014 was performed in southern China (95°–125°E, 20°–30°N), and Fig. 1 shows the spatial patterns of the first two leading EOF modes and time series of the corresponding principal components (PC). The first leading EOF mode explains about 19% of the total variance and is well distinguished from the second mode according to the rule of North et al. (1982). This EOF mode features a zonal dipole pattern in rainfall anomalies over southern China (the southern China rainfall dipole; SCD) (Fig. 1a). The positive phase of the SCD is characterized by increased (decreased) rainfall anomalies in southeast (southwest) China, and vice versa.

An SCD index that represents variations of the southern China rainfall dipole is constructed as the difference in normalized rainfall anomalies between southeast China (blue dots in Fig. 1a) and southwest China (red dots in Fig. 1a). The SCD index is highly correlated with the first PC (PC1) of southern China rainfall anomalies in MJ during 1979–2014 (Fig. 1c). Their correlation coefficient (R) is about 0.83, which is statistically significant at the 99% confidence level. This suggests that the SCD is most likely a physical mode in early summer.

We present the second leading EOF mode of MJ anomalies in southern China in Fig. 1b and the corresponding PC time series in Fig. 1d. This mode is characterized by a north–south dipole in rainfall anomalies over southern China, but it explains only about 10% of the total variance. Therefore, this study mainly focuses on the atmospheric circulation and SST anomalies associated with the MJ SCD and the physical mechanisms involved. We show observed results associated with the SCD index in the following sections, but similar results can also been obtained from those associated with the PC1 of southern China rainfall anomalies (Figures not shown).

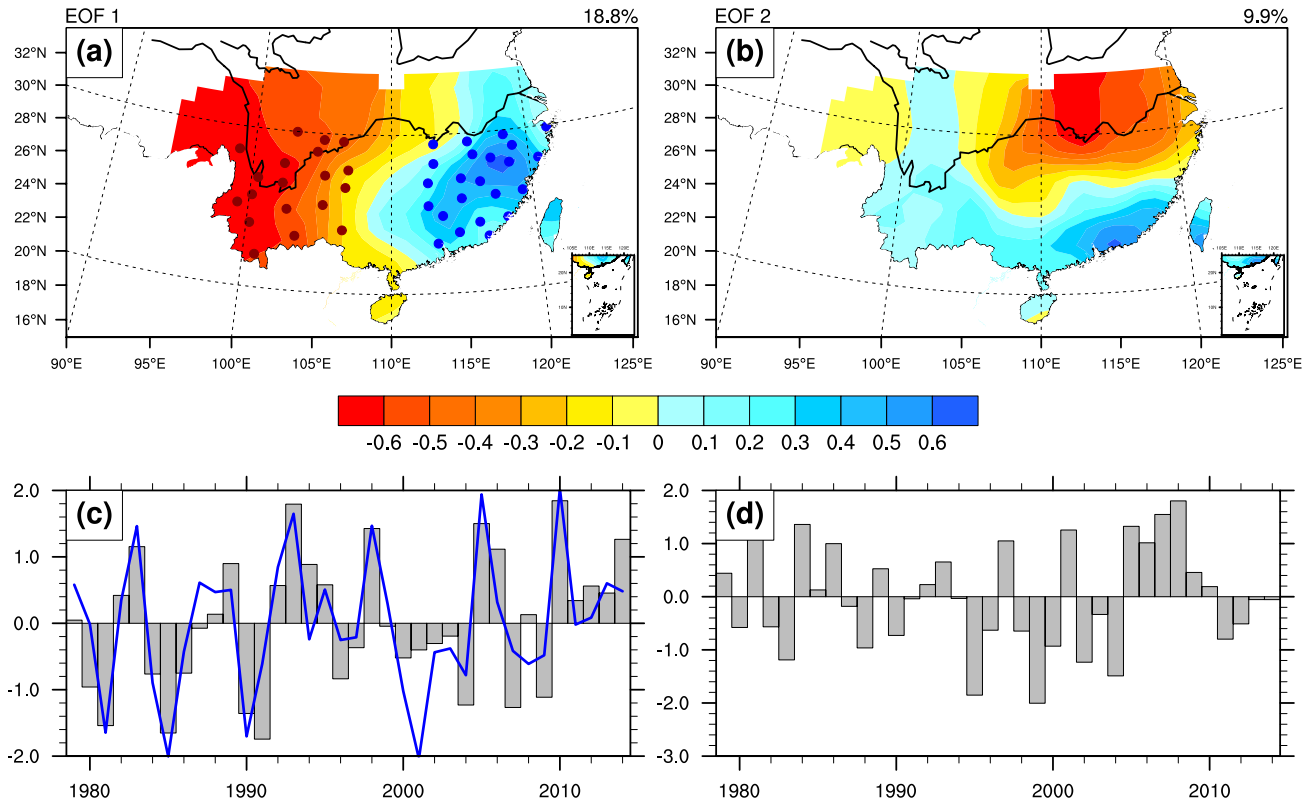

Fig. 1 The first two leading modes of MJ rainfall anomalies in southern China for the period 1979–2014. The spatial patterns show the rainfall anomalies regressed against **a** PC1 and **b** PC2, and the corresponding PCs are shown in **c** and **d**. Dots in **a** represent stations used to define the SCD index, and the blue line in **c** is the time series of the SCD index

3.2 Associated atmospheric circulation anomalies

To reveal the relationship between the SCD and atmospheric circulation anomalies, Fig. 2 shows the spatial distribution of atmospheric circulation anomalies regressed against the SCD index in MJ during 1979–2014. High values of the SCD index tend to correspond to significant and positive geopotential height anomalies over the western Pacific at 500 hPa (Fig. 2b), indicating an enhancement and westward movement of the WPSH, corresponding to an anomalous PSAC at 850 hPa (Fig. 2c). These circulation anomalies favor increased (decreased) rainfall in southeast (southwest) China. This finding is supported by the results shown in Fig. 3, which indicate that the intensified PSAC favors the convergence (divergence) of water vapor anomalies in southeast (southwest) China; the converse is also true.

Figure 4a shows time series of the SCD, WPSH, and PSAC indices in MJ during 1979–2014. The correlation coefficient between the SCD and WPSH (PSAC) indices reaches 0.53 (0.66), both statistically significant at the 99% confidence level. This confirms that the SCD is closely related to the WPSH and PSAC in MJ. In addition, there are easterly wind anomalies at lower levels over north India (Fig. 2c), which limit water vapor transport from the tropical

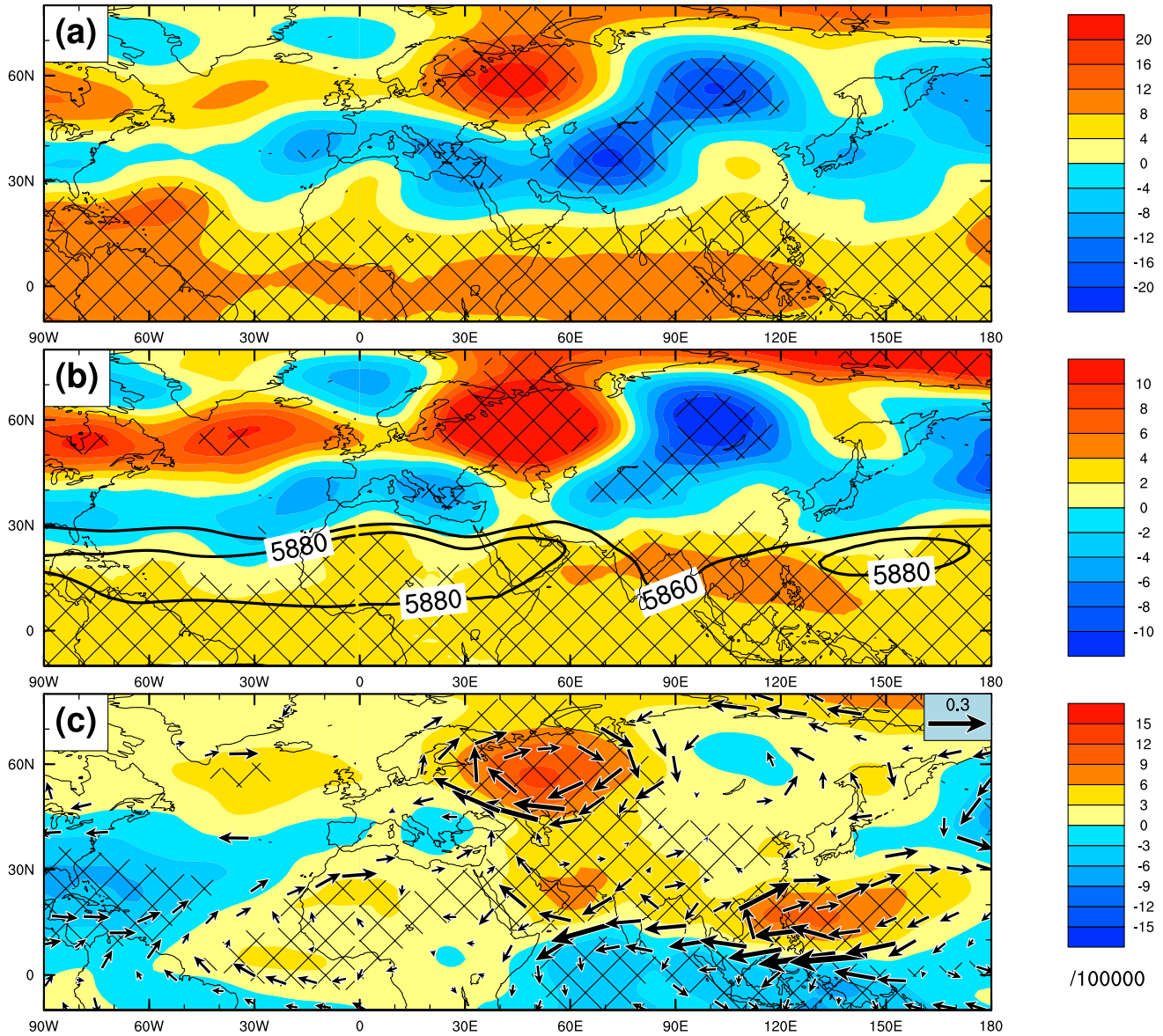

Fig. 2 Regressions against the SCD index in MJ of geopotential height anomalies (shading; gpm) at **a** 200 hPa and **b** 500 hPa. **c** Same as **a**, but for the stream function (shading; 10^5 m^2 s^{-1}) and wind vector (vectors; m s^{-1}) anomalies at 850 hPa. Black contours in **b** denote the climatological mean of the 500-hPa geopotential height (gpm). Cross-hatching denotes significance at the 95% confidence level

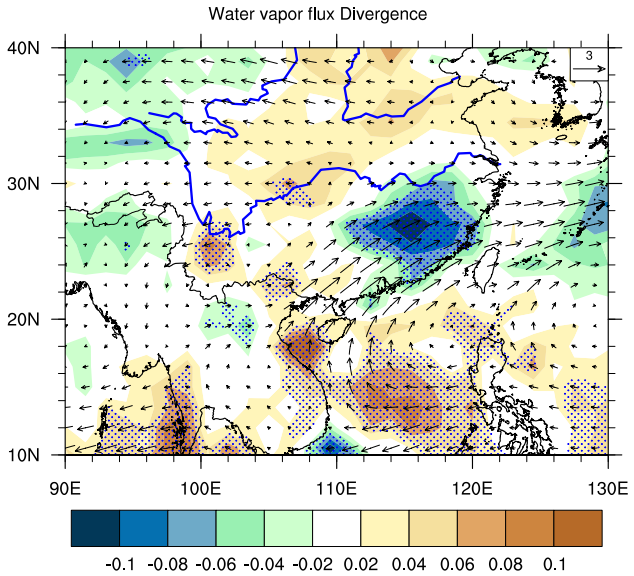

Fig. 3 Regression of vertically integrated (from the surface to 300 hPa) water vapor transport anomalies (vector; kg m^{-1} s^{-1}) against the PSAC index and corresponding divergence (shading; dots indicate significance at the 90% confidence level) in MJ

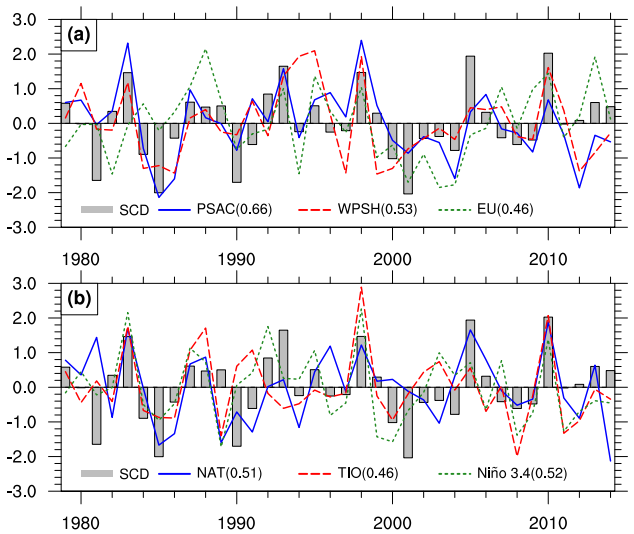

Fig. 4 **a** Time series of the normalized SCD index (bars), PSAC index (blue line), WPSH index (dashed red line), and EU index (dotted green line) in MJ, and **b** time series of the normalized SCD index (bars) in MJ, NAT index (blue line) in MA, TIO index (dashed red line) in MA, and Niño 3.4 index (dotted green line) in DJF for the period 1979–2014. Numbers in brackets denote the correlation coefficient between the SCD and corresponding indices

ocean to southwest China and thus lead to less rainfall in this region.

Another notable feature of the 500-hPa geopotential height anomalies is a wave-train pattern spanning mid- to high-latitude Eurasia (Fig. 2b). When the SCD is in its positive phase, there are positive geopotential height anomalies over Europe and the Okhotsk Sea, but negative geopotential height anomalies over Siberia, and vice versa for the negative phase. This wave-train pattern shows the same phase in the lower, middle, and upper troposphere, thereby exhibiting an equivalent barotropic structure (Fig. 2). Since such a wave-train pattern over Eurasia resembles the typical Eurasian teleconnection pattern (Wallace and Gutzler 1981), except for some differences in the center positions of the pattern, a modified Eurasia pattern (EU) index is defined as

$$[\overline{\mathrm{H500}}_{(55°-75°\mathrm{N},\,20°-60°\mathrm{E})} - 2\times\overline{\mathrm{H500}}_{(55°-65°\mathrm{N},80°-120°\mathrm{E})} + \overline{\mathrm{H500}}_{(50°-60°\mathrm{N},130°-150°\mathrm{E})}]/4,$$

where H500 represents the geopotential height at 500 hPa. Figure 4a shows that the SCD index and the modified EU index are highly in-phase in MJ during 1979–2014. Their correlation coefficient reaches 0.46, which is significant at the 99% confidence level. As revealed in the previous studies, the positive phase of the EU pattern is generally concurrent with strengthened blocking highs over mid- to high-latitude Eurasia, which favors a strengthened East Asian subtropical front and thus more rainfall anomalies in southeast China during summer (Zhang and Tao 1998; Li and Ji 2001; Li and Ding 2004; Ding and Sikka 2006).

Overall, the above results reveal that the SCD is closely related to the large-scale circulation anomalies in both lower and mid–high latitudes in MJ. In the positive phase of the SCD, the intensified WPSH and PSAC favor convergence (divergence) of water vapor in southeast (southwest) China, whereas the Eurasian wave-train pattern can lead to an enhanced East Asian subtropical front. These circulation conditions favor more rainfall anomalies in southeast China but less rainfall anomalies in southwest China. The converse is also true in the negative phase of the SCD.

4 Oceanic drivers

4.1 SST anomalies associated with the South China Dipole

SST anomalies play crucial roles in the variability of local rainfall and the associated large-scale atmospheric circulation. Figure 5 shows the SST anomalies regressed against the MJ SCD index during 1979–2014. Note that warm SST anomalies occur in the tropical central–eastern Pacific and cold SST anomalies in the northwest Pacific in the previous winter, which resembles the pattern of the El Niño mature phase. The correlation coefficient between the MJ SCD and the DJF Niño3.4 indices is 0.52 during 1979–2014, which is significant at the 99% confidence level. The El Niño-like

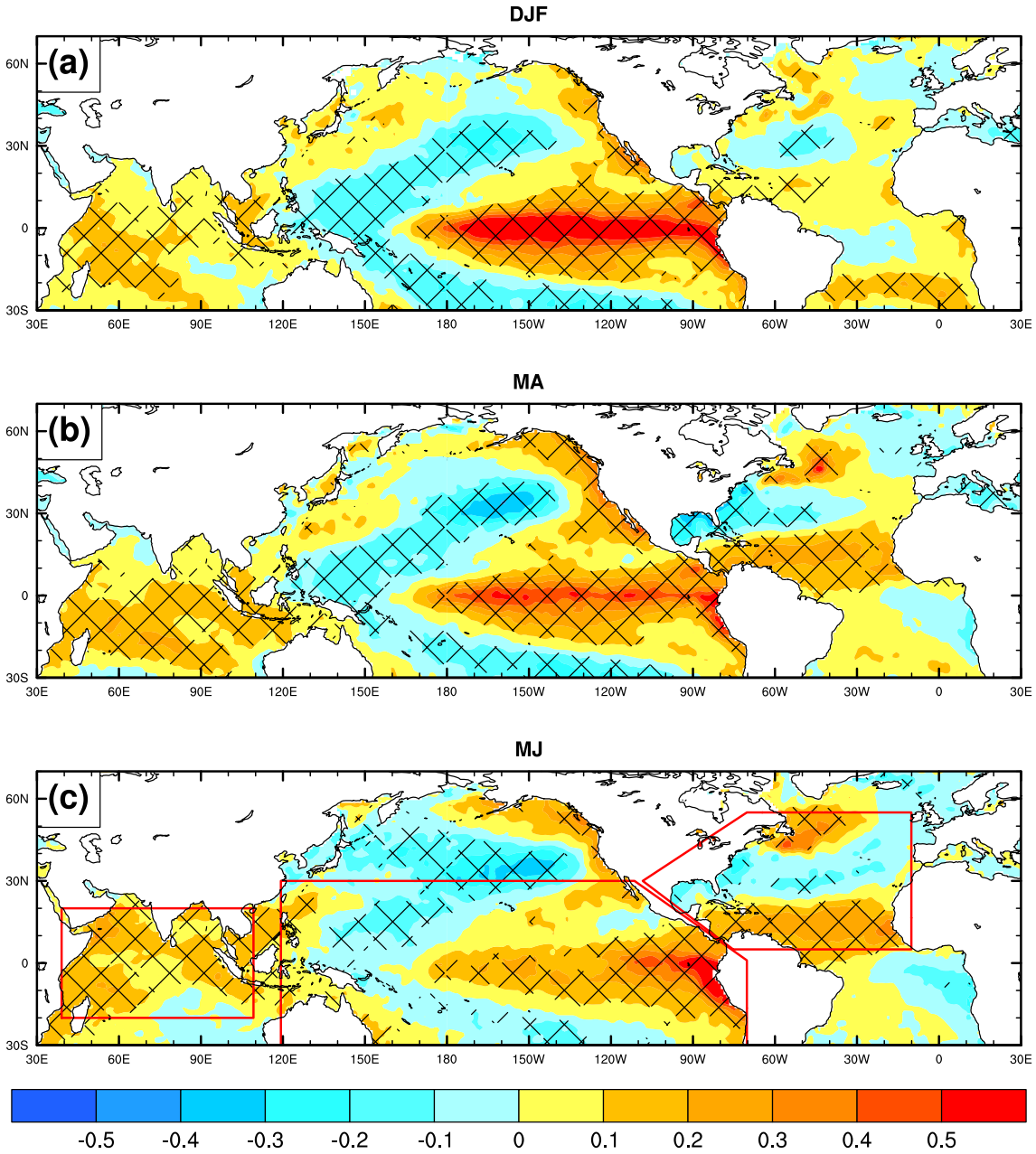

Fig. 5 Regressions of SST anomalies in DJF (**a**), MA (**b**), and MJ (**c**) against the MJ SCD index for the period 1979–2014. Areas exceeding the 95% confidence level are indicated by cross-hatching. The rectangular boxes in the tropical Indian Ocean, tropical Pacific Ocean, and North Atlantic indicate the corresponding target regions for the numerical experiments

SST anomalies in the tropical Pacific weaken from the previous winter to early summer, suggesting that the SCD tends to occur in the early summer following the mature phase of ENSO.

Figure 5 clearly shows that in the positive phase of the MJ SCD, warm SST anomalies occur in the TIO and the South China Sea in the previous winter to early summer, resembling the positive Indian Ocean basin mode. This result is consistent with previous studies, which have demonstrated that the Indian Ocean basin usually warms up (cools down) following the El Niño (La Niña) peak, reaching a maximum during spring and persisting into early summer (Klein et al. 1999; Liu and Alexander 2007). The correlation coefficient between the MJ SCD and the MA (MJ) TIO indices is 0.46 (0.50) during 1979–2014, exceeding significance at the 99% confidence level (Fig. 4b; Table 1). However, the correlation coefficient between the MJ SCD and the MA (MJ) TIO indices is only 0.07 (0.22) after removing the ENSO

Table 1 Correlations (R) of the SCD, EU and PSAC indices in MJ (May–June) with the Niño3.4 index in winter (December–January–February, DJF), and the tropical Indian Ocean (TIO) SST index and the North Atlantic tripole (NAT) SST index in MA (March–April) and MJ during 1979–2014

	MJ SCD	MJ EU	MJ PSAC
DJF Niño3.4	0.52[b]	0.21	0.52[b]
MA TIO	0.46[b]	0.23	0.50[b]
MJ TIO	0.50[b]	0.25	0.49[b]
MA NAT	0.51[b]	0.43[b]	0.59[b]
MJ NAT	0.53[b]	0.45[b]	0.59[b]
MA TIO/DJF Niño3.4	0.07	0.13	0.25
MJ TIO/DJF Niño3.4	0.22	0.16	0.19
MA NAT/DJF Niño3.4	0.38[a]	0.37[a]	0.48[b]
MJ NAT/DJF Niño3.4	0.46[b]	0.39[a]	0.50[b]

The TIO (NAT) index, from which the impact of the previous DJF Niño3.4 index has been removed linearly, is shown as MA TIO/DJF Niño3.4 (MANAT/DJF Niño3.4)

[a,b]Denote the significance at 95 and 99% confidence levels, respectively

signal from these two indices, implying that the impact of the spring–summer TIO SST anomalies on the MJ SCD is closely related to the previous winter ENSO. This finding agrees with previous studies which reported that the TIO SST anomalies act as a capacitor linking ENSO and the East Asian summer climate (Yang et al. 2007; Xie et al. 2009).

Moreover, the SST anomalies associated with the MJ SCD index are characterized by a meridional tripole pattern in the North Atlantic, which intensifies from the previous winter to spring and early summer (Fig. 5). The correlation coefficient between the MJ SCD and the MA (MJ) NAT indices is 0.51 (0.53) during 1979–2014, and both are significant at the 99% confidence level (Fig. 4b; Table 1). Previous studies have suggested that the North Atlantic tripole-like SST anomalies tend to occur during the ENSO-decaying spring and summer (Xie and Carton 2004; Wu et al. 2011). Though the MA NAT index is significantly correlated with the previous DJF Niño3.4 index ($R=0.42$), the correlation coefficient between the MA (MJ) NAT and the MJ SCD indices still reaches 0.38 (0.46) after removing the ENSO signal during 1979–2014, significant at the 95% confidence level (Table 1). This indicates that the North Atlantic tripole-like SST anomalies in MA and MJ have a significant impact on the SCD in MJ, and that this is partially independent of the ENSO impact.

From the results presented above, the MJ SCD is closely related to SST anomalies in the tropical Pacific, the tropical Indian Ocean, and the North Atlantic in the previous winter to early summer, which resemble the pattern of the El Niño (La Niña) mature phase in the positive (negative) phase of the SCD. The impact of the TIO SST anomalies on the SCD is closely related to ENSO, whereas the impact of the North Atlantic tripole-like SST anomalies only partially depends on ENSO. In fact, the North Atlantic tripole-like SST anomalies are also closely coupled with the North Atlantic Oscillation (NAO; Cayan 1992; Czaja and Frankignoul 2002; Zuo et al. 2013). As proposed in Chang et al. (2016), the tropical warm (cold) SST anomalies in the North Atlantic may result in a warming (cooling) in the northern Indian Ocean in summer. We find that the NAT index in MA has a correlation coefficient of 0.52 (0.33) with the TIO index in MA (MJ) during 1979–2014, both exceeding significance at the 95% confidence level. This suggests that the TIO SST anomalies in MJ may be also related to the North Atlantic tripole-like SST anomalies in MA, but the associated physical mechanism still needs further examination, which is beyond the scope of present study.

4.2 Impact of SST anomalies on the atmospheric circulation

To further demonstrate the impact of SST anomalies on the MJ SCD and the associated large-scale atmospheric circulation anomalies, Fig. 6 presents the 500-hPa geopotential height and 850-hPa stream function anomalies in MJ regressed against the previous DJF Niño3.4, MA TIO, and MA NAT indices during 1979–2014. A zonal wave-train pattern over the Eurasian continent and a low-level anomalous anticyclone in the northwest Pacific are clearly seen in all circulation anomaly fields associated with the SST index, despite some differences in the amplitude of the circulation anomalies (Fig. 6). These patterns of circulation anomalies resemble that associated with the MJ SCD index shown in Fig. 2b.

Moreover, the correlation coefficients of the PSAC index in MJ with the Niño3.4 index in DJF and the TIO and NAT in MA and MJ are all significant at the 99% confidence level during 1979–2014 (Table 1). This indicates that the MJ SCD-associated circulation anomalies over the middle–low latitudes are associated with SST anomalies in the tropical Pacific and Indian Ocean, and in the North Atlantic in the previous winter to early summer. However, the modified EU index in MJ, which is closely related to the SCD index in MJ, is only significantly correlated with the NAT index in MA and MJ (Table 1), implying that the MJ SCD-related circulation anomalies over the Eurasian middle–high latitudes are likely associated with the North Atlantic tripole-like SST anomalies rather than the tropical Indo–Pacific SST anomalies in the previous winter to early summer.

We have shown that the basin-scale SST anomalies in the TIO and tripole-like SST anomalies in the North Atlantic are influenced in part by ENSO variability. Thus, we further examine the circulation anomalies in MJ regressed against the TIO and NAT indices in MA and MJ after linearly removing the previous winter ENSO signal. The high

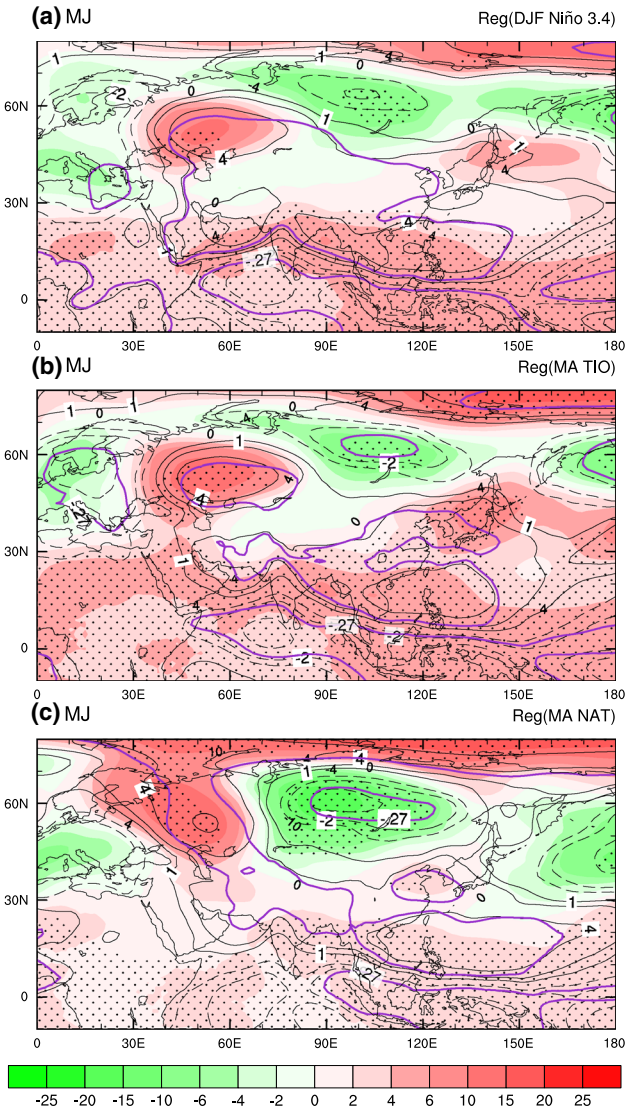

Fig. 6 Regressions of geopotential height (shading; gpm) anomalies at 500 hPa and stream function (contours at ±1, ±2, ±4, ±8, and $\pm 16 \times 10^5$ m^2 s^{-1}; negative values are shown as dashed lines) anomalies at 850 hPa in MJ against the **a** DJF Niño3.4 index, **b** MA TIO index, and **c** MA NAT index. Dots (purple contours) represent significance at the 90% confidence level for geopotential height (stream function) anomalies

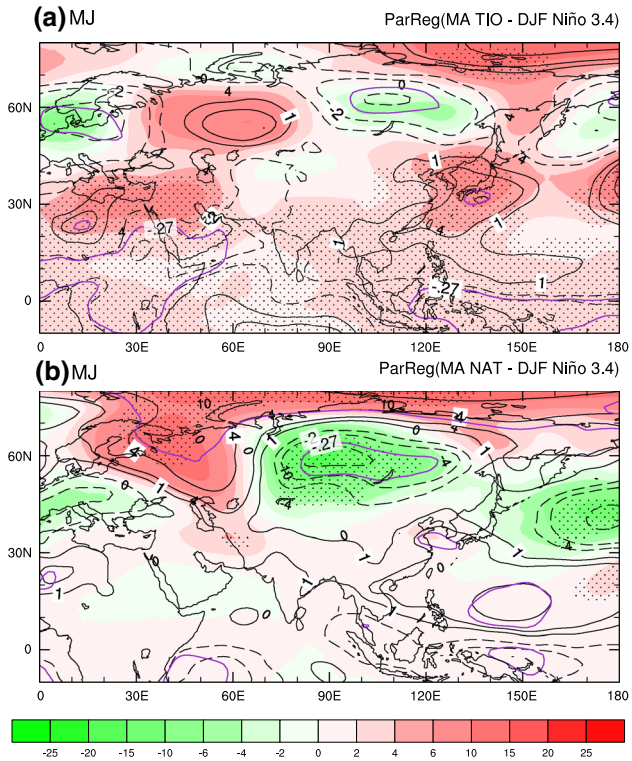

Fig. 7 Same as Fig. 6b, c, but for the regressions after removing the ENSO signal in the previous DJF season

correlation between the MA TIO and DJF Niño3.4 indices means that after removing the ENSO signal, the MJ geopotential height anomalies associated with the MA TIO index are weakened in the northwest Pacific and, in particular, the low-level anomalous anticyclone over the Philippine Sea almost vanishes (Fig. 7a). The correlation coefficients between the MA (MJ) TIO and MJ PSAC indices also decrease sharply and become insignificant after removing the ENSO signal. In contrast, the Eurasian wave-train pattern associated with the MA NAT index remains strong and significant after removing the ENSO signal (Fig. 7b). Though the positive geopotential height anomalies in the northwest Pacific are much weaker at 500 hPa, anticyclonic circulation anomalies are still observed over a smaller region to the east of the Philippines at 850 hPa. This is consistent with the correlation coefficient between the MA (MJ) NAT and MJ PSAC indices remaining as high as 0.48 (0.50) after removing the ENSO signal during 1979–2014 (Table 1).

From the above analysis, it can be concluded that the MJ SCD and associated circulation anomalies are closely related to SST anomalies in the tropical Pacific and Indian Ocean, and in the North Atlantic in the previous winter to early summer. The decaying ENSO-like SST anomalies in the tropical Pacific and Indian Ocean primarily affect the MJ SCD through changing the variability of the WPSH and PSAC, whereas the North Atlantic tripole-like SST anomalies mainly exert a downstream impact on the SCD by inducing a wave-train pattern over the Eurasian middle–high latitudes. The North Atlantic tripole-like SST anomalies also play a relatively weak role in modulating the PSAC variability.

5 Simulations of the forcing mechanism by the CAM5 model

Analysis of the observations has revealed the possible mechanisms responsible for the linkage between the early

summer SCD and the previous winter–spring SST anomalies in the tropical Pacific, the tropical Indian Ocean, and the North Atlantic. To confirm the possible mechanisms and assess the contribution of SST anomalies in different ocean basins to the MJ SCD variability, we perform numerical experiments using the CAM5 model forced by SST anomalies regressed against the MJ SCD index. The spatial correlation of geopotential height at 850 hPa between the control runs and observations is above 0.93, and is higher in the middle and upper troposphere. The root mean square errors are less than 0.5 gpm, and the ratios of standard deviation are between 0.88 and 1.09, indicating that CAM5 is capable of reproducing realistic climatology and variations of geopotential height for a given climatological SST distribution. The CAM5 model can also capture the key features of the major seasonal variation of rainfall arising from the onset and advance of the Asian monsoon (Li et al. 2015).

For the sensitivity experiments (TPO, TIO, NAT and PIA), the monthly SST anomalies are obtained by regression against the MJ SCD index during 1979–2014. The monthly SST anomalies are added to the climatological SSTs for the corresponding months. Target domains for these experiments are illustrated in Fig. 5c.

In the PIA runs, SST forcings from the tropical Pacific, the TIO, and the North Atlantic are all taken into consideration. The simulated geopotential height anomalies (Fig. 8a) are very close to those regressed against the SCD index in MJ (Fig. 2). In the northwest Pacific, there are significant positive geopotential height anomalies, indicating an enhancement and westward extension of the WPSH. The enhanced WPSH is concurrent with an intensified PSAC at 850 hPa. In addition, there is a wave train extending from the tropical northwest Pacific to the Okhotsk Sea, which resembles the East Asia–Pacific teleconnection pattern (EAP; Huang and Sun 1994). Also, there exists a wave-train pattern accompanying wave activity flux (Takaya and Nakamura 2001) transport from the North Atlantic to the Eurasian mid–high latitudes, which resembles the observed EU-like pattern shown in Fig. 7b. Note that wave activity flux anomalies are transported from Europe to the Middle East and South Asia, concurrent with negative geopotential height anomalies over the Middle East and positive anomalies over and adjacent to north Indian. Therefore, the key

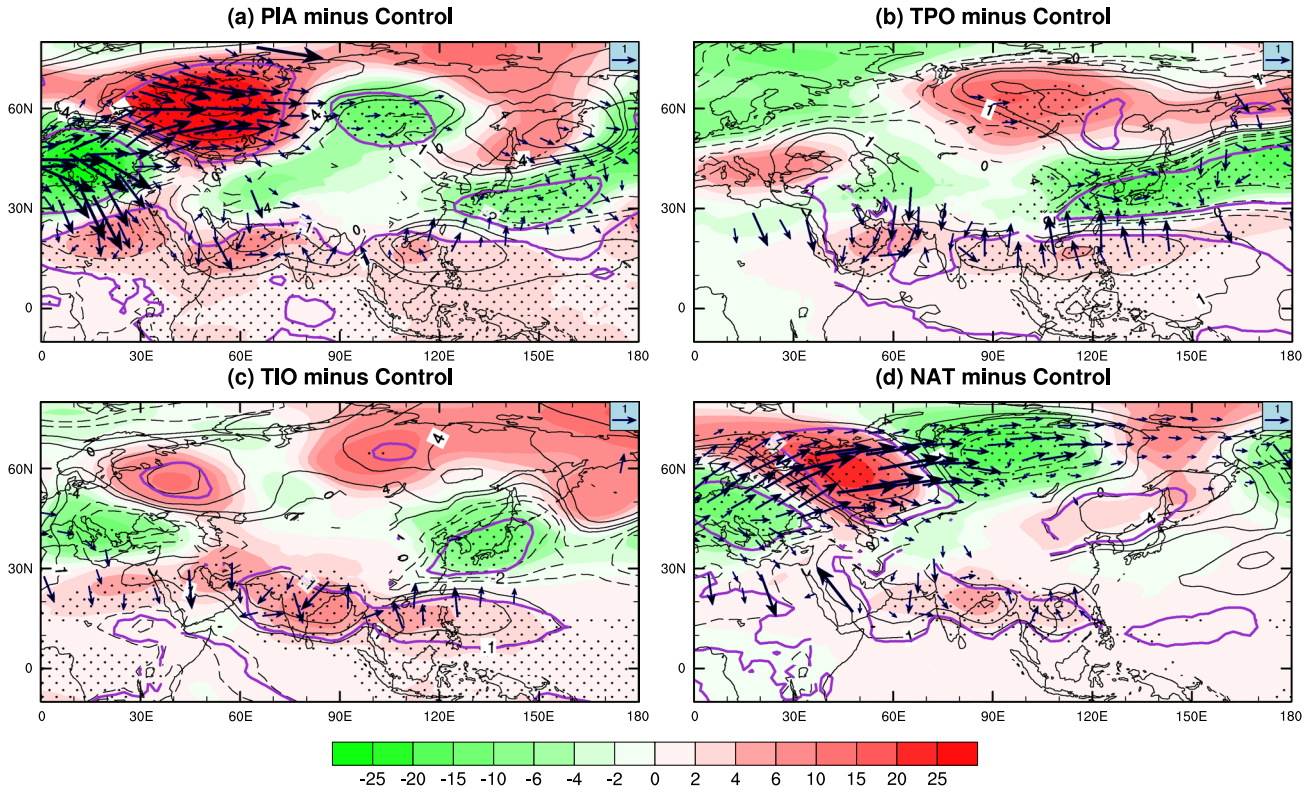

Fig. 8 **a** Differences in geopotential height (shading; gpm) and associated wave activity flux ($m^2\ s^{-2}$) at 500 hPa, and stream function anomalies (contours at ±1, ±2, ±4, ±8, and $\pm 16\times10^5\ m^2\ s^{-1}$; negative values are shown as dashed lines) at 850 hPa in response to the **a** PIA, **b** TPO, **c** TIO, and **d** NAT SST forcing as obtained with the CAM5 model. Dots represent significance at the 90% confidence level for geopotential height anomalies, and regions inside the purple contours indicate significance at the 90% confidence level for the stream function anomalies

anomalous circulation systems associated with the MJ SCD are well captured in the PIA runs.

The EAP pattern is also well captured when only SST anomalies in the tropical Pacific or TIO are imposed as the boundary forcing (Fig. 8b, c), which is consistent with previous modeling studies (e.g. Wu et al. 2010; Kosaka et al. 2013). The simulated WPSH is intensified and extends westward, concurrent with an anomalous PSAC at 850 hPa in MJ. Although an anomalous PSAC is clearly seen in both the TPO and TIO runs, the mechanisms responsible for its formation and maintenance are different. The basin-scale warming in the TIO can generate easterly wind anomalies extending into the western tropical Pacific by inducing an atmospheric Kelvin wave, and therefore leads to a low-level anomalous PSAC in the western Pacific (Xie et al. 2009, 2010). In contrast, the anomalous PSAC in the TPO runs is primarily excited and maintained by local cold SST anomalies in the tropical northwestern Pacific (Wang et al. 2000, 2003; Lau and Nath 2003; Xie and Carton 2004). The remote eastern–central Pacific warming also has a contribution to the PSAC variability (Zhang et al. 1996, 2017; Wang et al. 2000).

In the NAT runs (Fig. 8d), the atmospheric circulation response to the North Atlantic tripole-like SST forcing features a notable wave activity flux accompanying the wave train pattern from the North Atlantic to the Eurasian mid–high latitudes in MJ, which resembles the observed Eurasian wave-train pattern shown in Fig. 7b. This wave-train pattern is triggered primarily by diabatic heating associated with the tropical North Atlantic SST anomalies (shown in supplementary material: Fig. S1) and is enhanced by synoptic eddy-vorticity forcing related to the North Atlantic storm track activity (Zuo et al. 2013). Furthermore, an anomalous PSAC is observed over the western Pacificin the NAT runs, though its amplitude is much weaker than those in the TPO and TIO runs. This is in agreement with the observational data shown in Figs. 6 and 7. As noted in the previous studies (Ham et al. 2013; Hong et al. 2014; Chang et al. 2016), the impact of the North Atlantic SST anomalies on the PSAC is likely related to a westward atmospheric teleconnection. In the positive phase of the North Atlantic SST tripole, warm SST anomalies in the tropical North Atlantic favor an active convection over this region. (Figure not shown). This is concurrent with convergent (divergent) anomalies in the lower (upper) troposphere over the tropical Atlantic (Fig. 9a, b), as well as an anomalous low-level cyclone over the tropical North Atlantic and eastern Pacific (Fig. 9c), which resemble the Gill-type Rossby-wave response. Moreover, convergent (divergent) anomalies occur in the upper (lower) troposphere over the central Pacific, leading to suppressed convection and descending anomalies in the central Pacific and in turn producing an anomalous low-level anticyclone over the western Pacific.

Furthermore, comparison between Fig. 8a–c indicates that the atmospheric response is strong in East Asia and the northwest Pacific but relatively weak over the Eurasian mid–high latitudes in the TPO and TIO runs. In contrast, the atmospheric response is strong in the Eurasian mid–high latitudes but relatively weak in the northwest Pacific in the NAT run. This result is consistent with the observations, confirming that the Eurasian wave-train pattern is caused primarily by tripole-like SST anomalies in the North Atlantic, and the anomalous PSAC is related mainly to SST anomalies in the tropical Pacific and Indian Ocean. Moreover, a dipole pattern with increased (decreased) rainfall anomalies over southeast (southwest) China in MJ is captured well in all four sensitivity experiments (Fig. 10). In particularly, the PIA run has a high skill in simulating the SCD mode, with the spatial correlation coefficient reaches about 0.8. Also, the dipole pattern in the model runs resembles that regressed against the SST index (shown in supplementary material: Fig. S2). Consistency between model simulations and observations further supports the important role of SST anomalies in inducing the SCD in early summer.

Therefore, the resemblance between the simulations and observations confirms the impact of SST anomalies in the tropical Pacific and Indian oceans and the North Atlantic on atmospheric circulation over Eurasia and the western Pacific that links directly to the MJ SCD variability. The North Atlantic tripole-like SST anomalies appear to play a more important role in inducing the EU-like pattern over Eurasian mid–high latitudes, whereas the tropical Pacific and Indian Ocean SST anomalies tend to contribute more to the variations of the WPSH and PSAC. Based on the results found herein and related findings from the previous studies, Fig. 11 shows a schematic diagram of the mechanisms responsible for the linkage between the SCD in early summer and SST anomalies in the previous winter to early summer.

6 Summary and discussion

The leading mode of rainfall variability in southern China and the associated changes in atmospheric circulation in early summer (May–Jun) were analyzed. The results show that during 1979–2014 the first leading mode of southern China rainfall anomalies features a zonal dipole pattern (SCD) in early summer. The positive phase of the SCD is characterized by increased (decreased) rainfall anomalies in southeast (southwest) China, and vice versa in the negative phase. When the SCD is in its positive phase, the WPSH tends to be intensified and shifted westward, concurrent with an anomalous PSAC in the lower troposphere. The intensified WPSH and PSAC favor the convergence (divergence) of water vapor over southeast (southwest) China, leading to increased (decreased) rainfall over this region. Moreover,

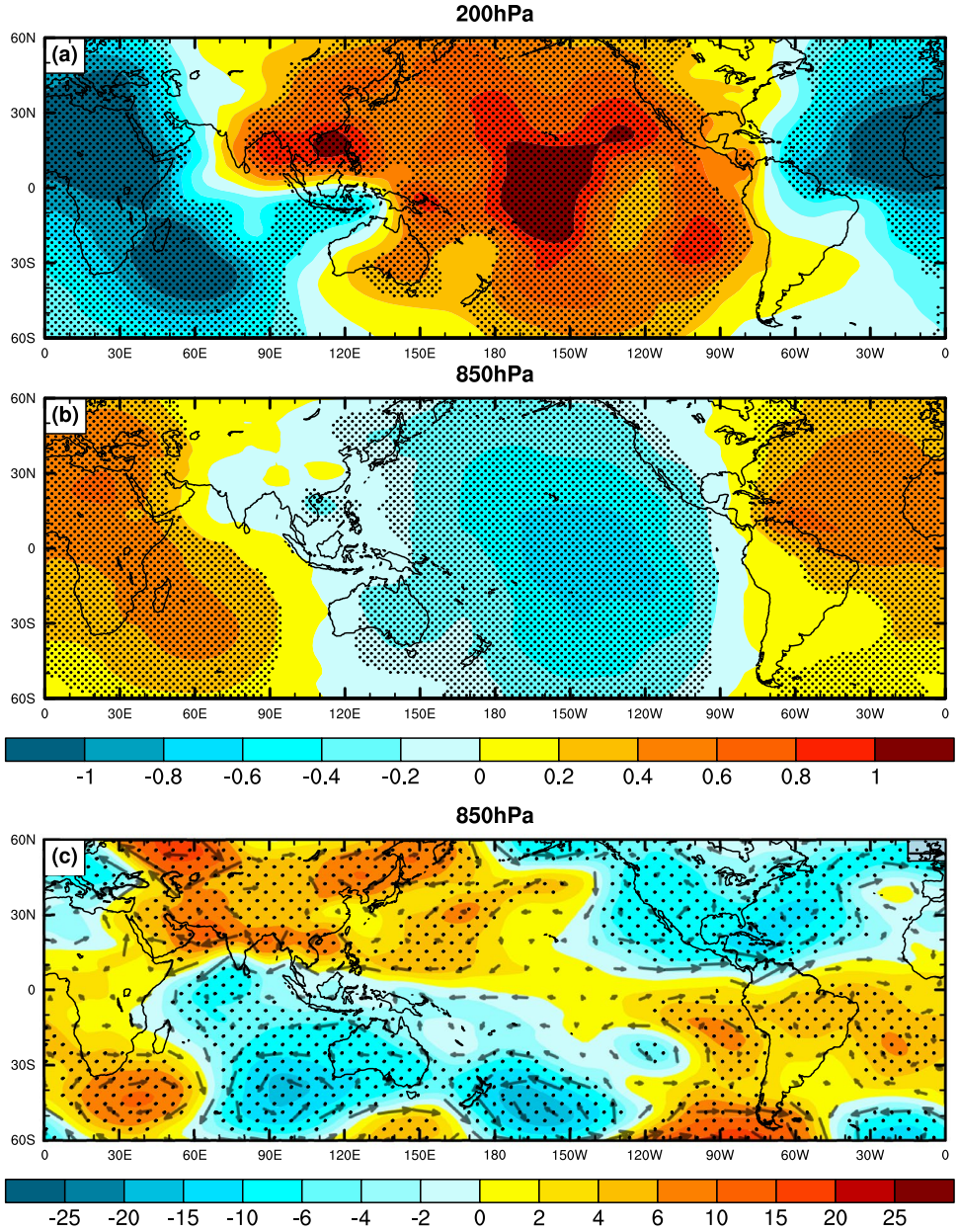

Fig. 9 Differences in velocity potential (unit: 10^{-6} m^2 s^{-1}) at **a** 850 hPa and **b** 200 hPa and **c** stream function (shading; unit: 10^5 m^2 s^{-1}) and wind (vector; m s^{-1}) at 850 hPa in MJ in response to the NAT SST forcing as obtained with the CAM5 model. Dots represent stream function anomalies that are significant at the 90% confidence level

there are low-level easterly wind anomalies over north India, which reduce the transport of water vapor from the tropical ocean to southwest China and thus lead to less rainfall over this region. Additionally, a wave-train pattern with positive geopotential height anomalies over the Ural Mountains is clearly observed in the mid–high latitudes of Eurasia. Such a pattern favors an enhancement of the East Asian subtropical front, and thus leads to increased (decreased) rainfall anomalies in southeast (southwest) China (Zhang and Tao 1998; Li and Ji 2001; Li and Ding 2004; Ding and Sikka 2006).

We found that the early summer SCD and associated atmospheric circulation anomalies are closely related to decaying ENSO-like SST anomalies in the tropical Indo-Pacific Ocean and tripole-like SST anomalies in the North Atlantic in the previous winter to early summer. When the SCD is in its positive phase in early summer, warm (cold) SST anomalies are observed in the tropical central–eastern Pacific and Indian Ocean (western Pacific) in the previous winter to early summer, and vice versa for the negative phase. Correlations between the SCD in early summer and SST anomalies in the previous winter to early summer show a tripole pattern in the North Atlantic, with positive correlations in the tropical and subpolar ocean, and negative correlations in the northwestern North Atlantic. The SCD-related SST anomalies in the tropical central–eastern Pacific are stronger in winter than in spring and early summer, whereas the SCD-associated SST anomalies in the TIO and the North Atlantic are most significant in

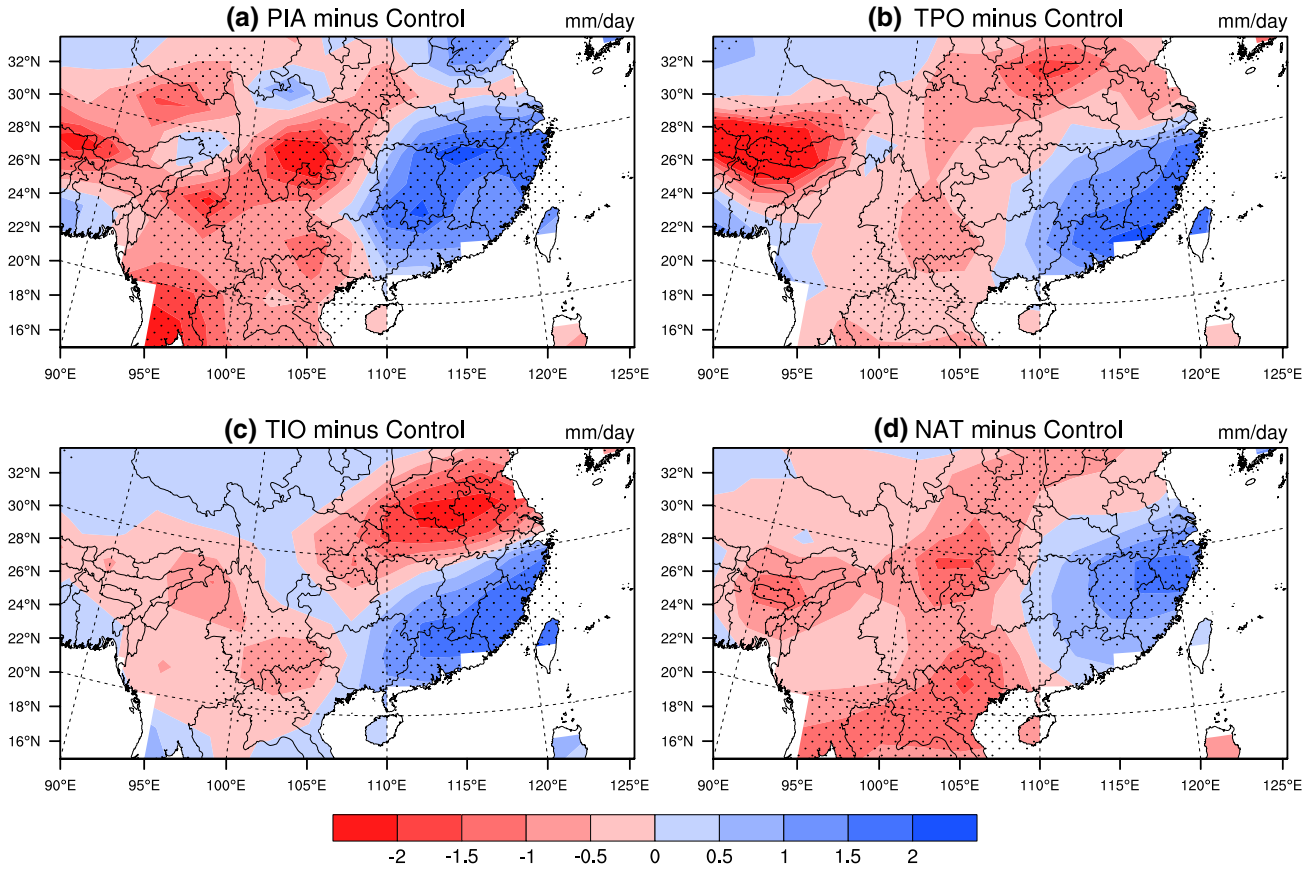

Fig. 10 Same as Fig. 8, but for rainfall anomalies (mm day^{-1}). Dots denote significance at the 90% confidence level

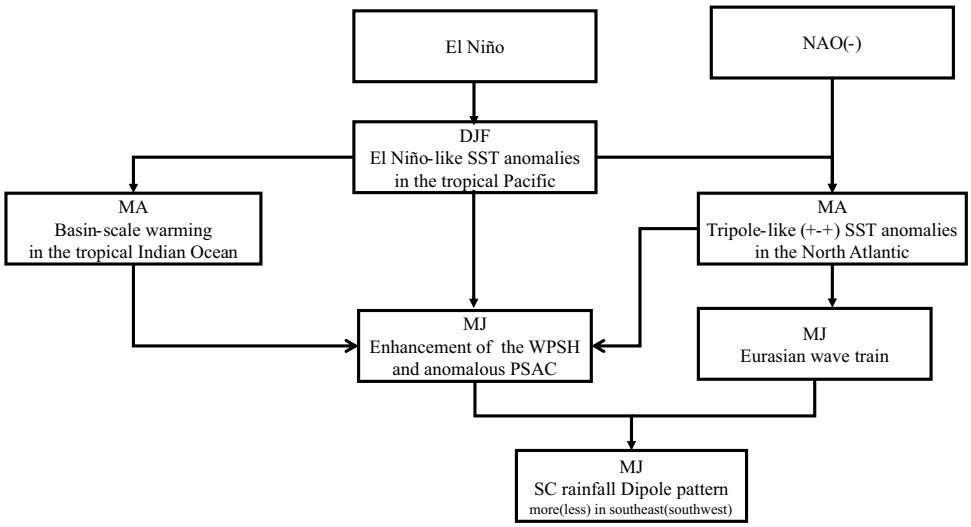

Fig. 11 Schematic summarizing the possible mechanisms responsible for the linkage between the early summer SCD and SST anomalies in the previous winter to early summer

spring and early summer. The spring–summer SST anomalies in the TIO are closely related to the previous winter ENSO, indicating that the TIO acts as a capacitor linking the winter ENSO to the following early summer SCD (Yang et al. 2007; Xie et al. 2009). Although the North Atlantic tripole-like SST anomalies in spring and summer are partly related to the previous winter ENSO, their relationship with the SCD in early summer is still statistically significant after removing the ENSO signal. This is reasonable, given that the North Atlantic tripole-like SST

anomalies are also closely coupled with the NAO (Cayan 1992; Czaja and Frankignoul 2002; Zuo et al. 2013).

The physical mechanisms that establish the linkage between the SCD in early summer and SST anomalies in the previous winter to early summer were further explored by analyzing observations and a set of numerical experiments run on the CAM5 model. The decaying El Niño (La Niña)-like SST anomalies in the tropical Pacific that peak in winter primarily exert an impact on the following early summer SCD by inducing an anomalous low-level anticyclone (cyclone) over the Philippine Sea. The formation and maintenance of the PSAC are attributed to both in situ and remote eastern–central Pacific SST anomalies through an atmospheric Rossby wave response and wind–evaporation feedback (Wang et al. 2000; Zhang et al. 2017). In addition, warm (cold) SST anomalies are observed in the TIO in the spring following an El Niño (La Niña) peak, which can persist into early summer and thus generate easterly wind anomalies extending into the western equatorial Pacific (Xie et al. 2009, 2010). Therefore, the basin-scale SST anomalies in the TIO can give rise to and prolong the anomalous PSAC, leading to changes in the SCD in early summer.

Observational and numerical results suggest that the tripole-like SST anomalies in the North Atlantic can persist from spring to early summer and exert a downstream impact on the SCD by inducing a Eurasian wave-train pattern. Such a pattern is triggered primarily by diabatic heating associated with the tropical North Atlantic SST anomalies and is enhanced by synoptic eddy-vorticity forcing related to North Atlantic storm track activity (Zuo et al. 2013). In addition, the North Atlantic tripole-like SST anomalies in spring have a delayed impact on the variability of the PSAC and SCD in early summer through a westward atmospheric teleconnection (Hong et al. 2014; Chang et al. 2016), though this effect is weaker than that of SST anomalies in the tropical Pacific and Indian Ocean.

Moreover, the SCD in early summer is well captured in the sensitivity experiment with SST forcing in different ocean basins. It is important to note that the patterns of the response of atmospheric circulation and southern China rainfall anomalies to SST anomalies in all three ocean basins bear most similarity to the observations in early summer. In other words, the combined effect of SST anomalies has more effect on the SCD and associated circulation anomalies than the individual effect of SST anomalies in any single oceanic basin.

This work mainly focused on the impact of SST anomalies in winter and spring on the following early summer SCD and associated circulation anomalies. However, other factors, such as Arctic sea ice (e.g., Zhao et al. 2004; Wu et al. 2009a) and snow anomalies in the Eurasia and the Tibetan Plateau (e.g., Wu and Qian 2003; Wu et al. 2009b; Ren et al. 2016), could also influence early summer southern China rainfall anomalies, but these factors are outside the scope of this work.

Acknowledgements The authors are indebted to Dr. Peili Wu of the Hadley Centre for Climate Prediction and Research for carefully reading and helpful comments on the original manuscript. This research was jointly supported by the National Basic Research Program of China (Grant 2013CB430203), the China Meteorological Special Programs (Grants GYHY201506013), the National Key Research and Development Program of China (during the 13th Five-year Plan) (Grants 2016YFA0601501). The authors are grateful to two anonymous reviewers for their insightful comments to improve the quality of the paper.

Open Access This article is distributed under the terms of the Creative Commons Attribution 4.0 International License (http://creativecommons.org/licenses/by/4.0/), which permits unrestricted use, distribution, and reproduction in any medium, provided you give appropriate credit to the original author(s) and the source, provide a link to the Creative Commons license, and indicate if changes were made.

References

Cayan DR (1992) Latent and sensible heat flux anomalies over the northern oceans: driving the sea surface temperature. J Phys Oceanogr 22(8):859–881. doi:10.1175/1520-0485(1992)022<0859:LASHFA>2.0.CO;2

Chang CP, Zhang Y, Li T (2000) Interannual and interdecadal variations of the East Asian Summer Monsoon and tropical Pacific SSTs. Part I: roles of the subtropical ridge. J Clim 13:4310–4325. doi:10.1175/1520-0442(2000)013<4310:IAIVOT>2.0.CO;2

Chang TC, Hsu HH, Hong CC (2016) Enhanced influences of tropical Atlantic SST on WNP-NIO atmosphere–ocean coupling since the Early 1980s. J Clim 29:6509–6525. doi:10.1175/JCLI-D-15-0807.1

Chen LX, Li W, Zhao P, Tao SY (2001) On the process of summer monsoon onset over East Asia. J Meteorol Res 15:436–449

Czaja A, Frankignoul C (2002) Observed impact of Atlantic SST anomalies on the North Atlantic oscillation. J Clim 15:606–623. doi: 10.1175/1520-0442(2002)015<0606:OIOASA>2.0.CO;2

Dee DP et al (2011) The ERA-Interim reanalysis: configuration and performance of the data assimilation system. Q J Roy Meteorol Soc 137:553–597. doi:10.1002/qj.828

Ding YH, Chan JCL (2005) The East Asian summer monsoon: an overview. Meteorol Atmos Phys 89:117–142. doi:10.1007/s00703-005-0125-z

Ding YH, Sikka DR (2006) Synoptic systems and weather. In: Wang B (ed) The Asian monsoon, vol 201. Springer, New York, p 131

Ham YG, Kug JS, Park JY, Jin FF (2013) Sea surface temperature in the north tropical Atlantic as a trigger for El Niño/Southern Oscillation events. Nat Geosci 6:112–116. doi:10.1038/NEGO1686

Hong CC, Chang TC, Hsu HH (2014) Enhanced relationship between the tropical Atlantic SST and the summertime western North Pacific subtropical high after the early 1980s. J Geophys Res Atmos 119:3715–3722. doi:10.1002/2013JD021394

Huang RH, Sun FY (1994) The impact of thermal state in the western Pacific warm pool and the convective activity above the warm pool on the east Asian climate anomalies (in Chinese). Chin J Atmos Sci 18:141–151

Klein SA, Soden BJ, Lau NC (1999) Remote sea surface temperature variations during ENSO: evidence for a tropical atmospheric bridge. J Clim 12:917–932. doi:10.1175/1520-0442(1999)012<0917:RSSTVD>2.0.CO;2

Kosaka Y, Xie SP, Lau NC, Vecchi GA (2013) Origin of seasonal predictability for summer climate over the Northwestern Pacific. Proc Natl Acad Sci USA 110:7574–7579. doi:10.1073/pnas.1215582110

Lau KM (1992) East Asian summer monsoon rainfall variability and climate teleconnection. J Meteorol Soc Jpn 70:211–242

Lau NC, Nath MJ (2003) Atmosphere–ocean variations in the Indo-Pacific sector during ENSO episodes. J Clim 16:3–20. doi:10.1175/1520-0442(2003)016<0003:AOVITI>2.0.CO;2

Lee MH, Ho CH, Kim JH(2010) Influence of tropical cyclone landfalls on spatiotemporal variations in typhoon season rainfall over South China. Adv Atmos Sci 27:443–454. doi:10.1007/s00376-009-9106-3

Li F, Ding YH (2004) A statistical study of blocking highs in Eurasia in summer by using 30-year NCEP datasets (in Chinese). Acta Meteorol Sin 62:347–354

Li S, Ji L((2001) Background circulation characteristics of the persistent anomalies of the summertime circulation over the Ural Mountains (in Chinese). Acta Meteorol Sin (in Chinese) 59:280–293

Li J, Yu R, Yuan W, Chen H, Sun W, Zhang Y (2015) Precipitation over East Asia simulated by NCAR CAM5 at different horizontal resolutions. J Adv Model Earth Syst 7:774–790. doi:10.1002/2014MS000414

Liu Z, Alexander M (2007) Atmospheric bridge, oceanictunnel, and global climatic teleconnections. Rev Geophys. doi:10.1029/2005RG000172

Liu Y, Li W, Ai W, Li Q (2012) Reconstruction and application of the monthly western Pacific subtropical high indices. J Appl Meteor 23:414–423 **(in Chinese)**

Mao JY, Chan JCL, Wu GX (2011) Interannual variations of early summer monsoon rainfall over South China under different PDO backgrounds. Int J Climatol 31:847–862. doi:10.1002/joc.2129

North GR, Bell TL, Cahalan RF, Moeng FJ (1982) Sampling errors in the estimation of empirical orthogonal functions. Mon Weather Rev 110:699–706

Rayner NA, Parker DE, Horton EB, Folland CK, Alexander LV, Rowell DP, Kent EC, Kaplan A (2003) Global analyses of sea surface temperature, sea ice, and night marine air temperature since the late nineteenth century. J Geophys Res 108:4407. doi:10.1029/2002JD002670

Ren FM, Gleason B, Easterling D(2002) Typhoon impacts on China's precipitation during 1957–1996. Adv Atmos Sci 19:943–952. doi:10.1007/s00376-002-0057-1

Ren HC, Li W, Ren HL, Zuo J((2016) Distinct linkage between winter Tibetan Plateau snow depth and early summer Philippine Sea anomalous anticyclone. Atmos Sci Lett 17:223–229. doi:10.1002/asl.646

Simmonds I, Bi D, Hope P (1999) Atmospheric water vapor flux and its association with rainfall over China in summer. J Clim 12:1353–1367. doi:10.1175/1520-0442(1999)012<1353:AWVFAI>2.0.CO;2

Su Q, Lu R, Li C(2014) Large-scale circulation anomalies associated with interannual variation in monthly rainfall over South China from May to August. Adv Atmos Sci 31:273–282. doi:10.1007/s00376-013-3051-x

Takaya K, Nakamura H (2001) A formulation of a phase-independent wave-activity flux for stationary and migratory quasigeostrophic eddies on a zonally varying basic flow. J Atmos Sci 58:608–627. doi:10.1175/1520-0469(2001)058<0608:AFOAPI>2.0.CO;2

Wallace JM, Gutzler DS (1981) Teleconnections in the geopotential height field during the Northern Hemisphere winter. Mon Weather Rev 109:784–812. doi:10.1175/1520-0493(1981)109<0784:TITGHF>2.0.CO;2

Wang B, Wu R, Fu X (2000) Pacific-East Asia teleconnection: how does ENSO affect East Asian climate? J Clim 13:1517–1536. doi:10.1175/1520-0442(2000)013<1517:PEATHD>2.0.CO;2

Wang B, Wu R, Li T (2003) Atmosphere–warm ocean interaction and its impact on Asian–Australian monsoon variability. J Clim 16:1195–1211. doi:10.1175/1520-0442(2003)16<1195:AOIAII>2.0.CO;2

Wang B, Liu J, Yang J, Zhou T, Wu Z (2009) Distinct principal modes of early and late summer rainfall anomalies in East Asia. J Clim 22:3864–3875. doi:10.1175/2009JCLI2850.1

Wu TW, Qian ZA (2003) The relation between the Tibetan winter snow and the Asian summer monsoon and rainfall: an observational investigation. J Clim 16:2038–2051. doi:10.1175/1520-0442(2003)016<2038:TRBTTW>2.0.CO;2

Wu B, Zhang R, Wang B, D'Arrigo R (2009a) On the association between spring Arctic sea ice concentration and Chinese summer rainfall. Geophys Res Lett. doi:10.1029/2009GL037299

Wu B, Yang K, Zhang R (2009b) Eurasian snow cover variability and its association with summer rainfall in China. Adv Atmos Sci 26:31–44.doi:10.1007/s00376-009-0031-2

Wu B, Li T, Zhou T (2010) Relative contributions of the Indian Ocean and local SST anomalies to the maintenance of the western north Pacific anomalous anticyclone during the El Niño Decaying Summer. J Clim 23:2974–2986. doi:10.1175/2010JCLI3300.1

Wu R, Yang S, Liu S, Lian Y, Gao Z(2011) Northeast China summer temperature and North Atlantic SST. J Geophys Res. doi:10.1029/2011JD015779

Xie SP, Carton JA(2004) Tropical Atlantic variability: patterns, mechanisms, and impacts. Earth climate: the ocean–atmosphere interaction. Geophys Monogr. doi:10.1029/147GM07

Xie SP, Hu K, Hafner J, Tokinaga H, Du Y, Huang G, Sampe T (2009) Indian Ocean capacitor effect on Indo-western Pacific climate during the summer following El Niño. J Clim 22:730–747. doi:10.1175/2008JCLI2544.1

Xie SP, Du Y, Huang G, Zheng XT, Tokinaga H, Hu KM, Liu QY (2010) Decadal shift in El Niño influences on Indo-Western Pacific and East Asian climate in the 1970s. J Clim 23:3352–3368. doi:10.1175/2010JCLI3429.1

Yang J, Liu Q, Xie SP, Liu Z, Wu L (2007) Impact of the Indian Ocean SST basin mode on the Asian summer monsoon. Geophys Res Lett 34:L02708. doi:10.1029/2006GL028571

Ye H, Lu R (2011) Subseasonal variation in ENSO-related East Asian rainfall anomalies during summer and its role in weakening the relationship between the ENSO and summer rainfall in eastern China since the late 1970s. J Clim 24:2271–2284. doi:10.1175/2010JCLI3747.1

Yim SY, Wang B, Xing W (2014) Prediction of early summer rainfall over South China by a physical-empirical model. Clim Dyn 43:1883–1891. doi:10.1007/s00382-013-2014-3

Zhang RH(2001) Relations of water vapor transport from Indian monsoon with that over east Asia and the summer rainfall in China. Adv Atmos Sci 18:1005–1017

Zhang QY, Tao SY (1998) Influence of Asian mid-high latitude circulation on East Asian summer rainfall. Acta Meteorol Sin (in Chinese) 56:199–211

Zhang RH, Sumi A, Kimoto M (1996) Impact of El Niño on the East Asian Monsoon: a diagnostic study of the '86/87 and '91/92 events. J Meteor Soc Japan 74:49–62. doi:10.2151/jmsj1965.74.1_49

Zhang RH, Min QY, Su JZ (2017) Impact of El Niño on atmospheric circulations over East Asia and rainfall in China: role of the anomalous western North Pacific anticyclone. J Sci China Earth Sci. doi:10.1007/s11430-016-9026-x

Zhao P, Zhang X, Zhou X, Ikeda M, Yin Y (2004) The sea ice extent anomaly in the North Pacific and its impact on the East Asian summer monsoon rainfall. J Clim 17:3434–3447. doi:10.1175/1520-0442(2004)017<3434:TSIEAI>2.0.CO;2

Zheng B, Liang JY, Lin AL, Li CH, Gu DJ (2006) Frontal rain and summer monsoon rain during pre-rainy season in South China.

Part I: determination of the division dates. Chin J Atmos Sci (in Chinese) 30:1207–1216

Zhou TJ, Yu RC (2005) Atmospheric water vapor transport associated with typical anomalous summer rainfall patterns in China. J Geophys Res. doi:10.1029/2004JD005413

Zuo JQ, Li WJ, Sun CH, Xu L, Ren HL (2013) Impact of the North Atlantic sea surface temperature tripole on the East Asian summer monsoon. Adv Atmos Sci 30:1173–1186. doi:10.1007/s00376-012-2125-5

李维京，刘景鹏，任宏利，等. 2018. 中国南方夏季降水的年代际变率主模态特征及机理研究 [J]. 大气科学, 42 (4): 859−876. Li Weijing, Liu Jingpeng, Ren Hongli, et al. 2018. Characteristics and corresponding mechanisms of the leading modes of interdecadal variability of summer rainfall in southern China [J]. Chinese Journal of Atmospheric Sciences (in Chinese), 42 (4): 859−876, doi:10.3878/j.issn.1006-9895.1802.17283.

中国南方夏季降水的年代际变率主模态特征及机理研究

李维京 [1, 2, 3] 刘景鹏 [1, 2, 3] 任宏利 [3] 左金清 [3]

1 中国气象科学研究院，北京 100081
2 中国科学院大学，北京 100049
3 中国气象局国家气候中心气候研究开放实验室，北京 100081

摘 要 在气候变暖背景下，中国南方夏季降水存在明显的年代际变化特征。本文利用 1920～2014 年的逐月降水，以分析南方夏季降水年代际变率主模态为切入点，以研究南方夏季降水年代际变率空间分布型的年代际变化特征为重点，进一步研究了印度洋、北太平洋及北大西洋海温的年代际变率对南方夏季降水主模态年代际变率的可能影响机制。得到的主要结论包括：（1）指出中国南方夏季降水年代际变率的两个主模态为全区一致型和东西反相型降水模态。两个主导模态在 1971/1972 年发生了显著的年代际转变，在 1925～1971 年的第一主模态为东西反相型降水；在 1972～2009 年的第一主模态为一致型降水。不同主模态对应的海温异常关键区也在 1971/1972 年发生了相应的年代际变化。（2）揭示了全区一致型和东西反相型降水模态对应的环流场异常特征。一致多（少）型降水对应着中国南海及西北太平洋低空的反气旋（气旋）性异常，有（不）利于水汽自南海向南方地区输送。而贝加尔湖东侧低空的反气旋（气旋）性异常，有（不）利于冷空气向南方输送，并与来自南海地区的水汽在南方地区辐合，有利于南方地区降水一致偏多（少）。东多西少（西多东少）型降水对应着中国东南地区高空的正（负）异常中心，有利于高空辐散（辐合）及异常的上升（下沉）运动，其与南方地区东部低空的气旋（反气旋）性异常共同作用，有利于东部降水偏多（偏少）。与此同时，低空中南半岛反气旋（气旋）性异常及菲律宾地区反气旋（气旋）性异常，不（有）利于水汽自孟加拉湾及南海地区输送向南方地区西部，有利于形成东多西少（西多东少）的降水型。（3）揭示了印度洋海温、北太平洋海温和北大西洋海温协同影响南方地区东西反相型降水和一致型降水的机制。

关键词 中国南方夏季降水 海温 年代际变率 主模态 影响机制
文章编号 1006-9895(2018)04-0859-18 **中图分类号** P461 **文献标识码** A
doi:10.3878/j.issn.1006-9895.1802.17283

Characteristics and Corresponding Mechanisms of the Leading Modes of Interdecadal Variability of Summer Rainfall in Southern China

LI Weijing[1, 2, 3], LIU Jingpeng[1, 2, 3], REN HongLi[3], and ZUO Jinqing[3]

1 *Chinese Academy of Meteorological Sciences*, *Beijing* 100081

收稿日期 2017-11-16；**网络预出版日期** 2018-02-12
作者简介 李维京，男，1955 年出生，博士，研究员，主要从事短期气候预测及气候动力学研究。E-mail: liwj@cma.cn
资助项目 国家重点基础研究发展计划（973 计划）项目 2013CB430203，“十三五”国家重点研发计划项目 2016YFA0601501，中国气象科学研究院基本科研业务费专项资金项目 2017Y005
Funded by National Basic Research Program of China (973 Program) (Grant 2013CB430203), the National Key Research and Development Program of China (during the 13th Five-year Plan) (Grant 2016YFA0601501), Fundamental Research Funds of CAMS (Chinese Academy of Meteorological Sciences) (Grant 2017Y005)

2 *University of Chinese Academy of Sciences*, *Beijing* 100049
3 *Laboratory for Climate Studies*, *National Climate Center*, *China Meteorological Administration*, *Beijing* 100081

Abstract In the background of global warming, rainfall in southern China during boreal summer (June to August) shows distinct interdecadal variability. Using monthly rainfall data for the period of 1920-2014, the leading modes of the interdecadal variability of Southern China Summer Rainfall (SCSR) are revealed. Meanwhile, the interdecadal changes of spatial pattern of SCSR are uncovered. Finally, the underlying possible mechanisms connecting the sea surface temperature in the Indian Ocean, the North Pacific Ocean and the North Atlantic Ocean and the leading modes of SCSR on interdecadal timescale are analyzed. The main results are as follows. (1) The first two leading modes of the interdecadal variability of SCSR, i.e., the monopole pattern and the zonal dipole pattern, are uncovered. The dominance of these two modes experienced an obvious decadal change around 1971/1972. During 1925–1971, the dominant pattern of the interdecadal variability of SCSR is the zonal dipole pattern, while the monopole pattern prevailed during 1972–2009. The key regions of sea surface temperature associated with the first two leading modes also changed around 1971/1972. (2) The atmospheric circulation anomalies associated with the monopole pattern and the zonal dipole pattern of SCSR are uncovered. Corresponding to the positive (negative) phase of the monopole pattern, an anticyclonic (cyclonic) anomaly is located over the South China Sea and northwestern Pacific, which is (not) in favor of moisture transport from the South China Sea to southern China. The lower-level anticyclonic (cyclonic) anomaly over Lake Baikal may lead to more southward transport of cold air, which can converge with the moisture transported from the South China Sea and is favorable for the formation of positive (negative) phase of the monopole pattern. Corresponding to the positive (negative) phase of the zonal dipole pattern, a positive (negative) center is located over the eastern part of southern China, which is favorable for upper-level divergence (convergence) and anomalous ascending (descending) motion. When combined with the lower-level cyclonic (anticyclonic) anomaly, it may result in increased (decreased) rainfall in eastern part of southern China. Meanwhile, the anticyclonic (cyclonic) anomaly over Indo-china peninsula and the Philippines is favorable (unfavorable) for moisture transport from the Bay of Bengal to western part of southern China, which is in favor of generating the positive (negative) phase of the zonal dipole pattern. (3) The combined impacts of sea surface temperature in the Indian Ocean, the North Pacific Ocean and the North Atlantic Ocean on the monopole pattern and the zonal dipole pattern of SCSR are revealed.

Keywords Southern China summer rainfall, Sea surface temperature, Interdecadal variability, Leading mode, Impact mechanism

1 引言

中国东部夏季降水受东亚夏季风影响，其年际和年代际变率均十分显著（Kwon et al., 2007；Xu et al., 2015）。20 世纪中期以来，东亚夏季风发生了明显的年代际变化，其强度在 20 世纪 70 年代末期显著减弱（Wang, 2001; Ding et al., 2008），其夏季环流场在 1990 年代初期发生了进一步的年代际变化，表现为东亚副热带地区高空急流强度显著减弱（Kwon et al., 2007; Zhang et al., 2017）。与之相对应，中国东部夏季降水在 1970 年代末期、1990 年代初期及 1990 年代末期相继发生了明显的年代际变化（Ding et al., 2008；黄荣辉等，2011；Zhu et al., 2011；李维京等，2015；Xu et al., 2015）。在 1970 年代末之前，中国东部降水型由长江中下游少雨，华北和华南多雨的经向“＋－＋”型，之后转换为长江中下游多雨，华南和华北少雨的经向“－＋－”型降水（黄荣辉等，2011）。在 1990 年代初期，长江流域及其以南地区夏季降水显著增加（Wu et al., 2010）。在 2000 年以后，中国东部夏季雨带开始北移，表现为长江中下游和华北地区夏季降水减少，淮河流域降水增多，主雨带北移至淮河流域（黄荣辉等，2011；Zhu et al., 2011；Xu et al., 2015）。因此，伴随着东亚夏季风的年代际变化，中国东部夏季主雨带也具有明显的年代际经向南北移动特征（Ding et al., 2008；黄荣辉等，2011；李维京等，2016）。整体而言，东亚夏季风经历了 20 世纪 70 年代以来的两次年代际突变之后，中国东部的夏季降水空间分布型由 1970 年代末期之前的“北涝南旱”型转变为 1990 年代初期之后的“南涝北旱”型（Ding et al., 2008; Zhang and Zhou, 2015）。Ding et al.（2008）及黄荣辉等（2011）的研究表明，中国东部夏季降水的年代际变率主要包含两种空间模态，其一是由南到北的经向三极子模态（长江多雨，

华北和华南少雨）；其二是经向偶极子模态（南方多雨，北方少雨），中国东部夏季降水年代际变率的空间分布主要由这两种降水模态的叠加效应所决定（黄荣辉等，2011）。20 世纪中期以来，中国南方地区夏季降水也经历了显著的年代际变化，在 1992/1993 年前后开始年代际增强（Wu et al., 2010），并在 2003 年后发生年代际的减弱（Xu et al., 2015）。

研究表明（Ding et al., 2009；黄荣辉等，2011；Xu et al., 2015；Wu et al., 2016）太平洋、北大西洋及印度洋海表温度（Sea Surface Temperature，简称 SST）的年代际变率对中国东部及南方夏季降水年代际变率有重要影响。太平洋年代际振荡（Pacific Decadal Oscillation，简称 PDO）是太平洋海温年代际尺度上最显著的变率模态（Mantua et al., 1997）。PDO 可通过影响东亚地区大气环流系统进而影响中国东部夏季降水的年代际变率，对中国东部夏季主雨带的年代际经向南北移动有重要作用。PDO 处于正位相时，可以引起海洋大陆区域与华南地区之间的 Hadley 环流异常增强，进而使得华南地区 6 月份的降水偏少（Wu and Mao, 2017），与此同时，PDO 还可在东亚地区对流层低空激发太平洋—日本（Pacific–Japan，简称 PJ）型遥相关波列，进而使得 1970 年代末期以后长江流域夏季降水偏多，中国华北地区降水偏少，中国东部夏季主雨带位于长江流域（张庆云等，2007；Si and Ding, 2016；Yang et al., 2017）。当 PDO 处于负位相时，环流的响应基本是反相的，此时东亚副热带西风急流减弱，这是引起 2000 年以后黄淮流域降水增多，长江流域降水减少的主要原因，中国东部夏季主雨带北移至淮河流域（Zhu et al., 2015）。因此在 PDO 影响下，东亚地区低纬度和中高纬度环流的异常变化是协调一致的，其位相变化对中国东部夏季主雨带的年代际经向南北移动有重要影响。

北大西洋多年代际涛动（Atlantic Multidecadal Oscillation，简称 AMO）是北大西洋海温最显著的年代际变率模态（Knight et al., 2006; Sutton and Hodson, 2007）。研究表明，AMO 主要通过大气遥相关作用影响东亚地区大气环流，进而调制中国东部夏季降水（Lu et al., 2006; Li et al., 2008; Wu et al., 2016; Si and Ding, 2016）。AMO 暖位相对应着欧亚大陆大部分地区的增暖，增强了夏季欧亚大陆与太平洋之间的海陆热力差异，使得东亚夏季风增强（Lu et al., 2006; Wang et al., 2009）。与此同时，AMO 暖位相在北半球夏季可以激发中高纬度的欧亚遥相关波列及中纬度沿东亚副热带西风急流传播的遥相关波列（Si and Ding, 2016; Wu et al., 2016）。欧亚遥相关波列使得中国黄淮流域上空产生气旋性异常，长江流域上空产生反气旋性异常，从而使得黄淮流域多雨，长江中下游地区少雨。而中纬度的遥相关波列通过引起中国东南地区低空气旋性环流异常，造成中国东南地区降水增多。最近的研究表明，AMO 还可通过大气遥相关作用，调制热带西太平洋海温的多年代际变率（Sun et al., 2017）。由于热带西太平洋是东亚最重要的热源和水汽源地，对东亚气候有重要影响，因此 AMO 还可实现对东亚夏季风及中国南方地区夏季降水年代际变率的间接影响。

近十年来，印度洋海温对中国夏季降水年代际变率的影响受到越来越多的关注（Wu et al., 2010; Cao et al., 2014; Zhang et al., 2017）。热带印度洋在 1990 年代初以后的年代际增暖增加了印太地区东西方向的海温梯度，由其引起的垂直环流异常上升支在热带印度洋，下沉支在中国南海地区，对应着低空的反气旋性环流异常，有利于中国南方地区夏季降水在 1990 年代初以后显著增多（Wu et al., 2010）。南印度洋海温在 1970 年代末期显著增暖，并在 1990 年代初期开始变冷，对东亚夏季风在 1970 年代末期及 1990 年代初期的两次年代际转折均有影响，造成南方地区夏季降水在 1970 年代偏少，在 1990 年代初期后偏多（Zhang et al., 2017）。

综上所述，前人研究大多集中关注整个中国东部夏季降水的时空变化特征及其机理，而本文则重点研究中国南方地区夏季降水年代际变率的时空变化特征，以及不同海区海温异常对中国南方夏季降水年代际变化的协同影响。本文拟首先分析中国南方地区夏季降水年代际变率的主模态，其次揭示这些主模态在气候变暖背景下的年代际变化特征，然后重点研究不同海域海温年代际变率与南方夏季降水主模态之间的关系及其可能影响机制。此外，最新研究表明，中国南方初夏（5～6 月）降水的年际变率主模态是三大洋海温年际变率协同影响的结果（Li et al., 2017a）。在年代际尺度上，三大洋海温是如何协同影响中国南方夏季降水年代际变率的呢？本文将进一步尝试通过多因子回归拟合南方夏季降水指数的方式，对该问题加以初步

探讨。

2 资料和方法

2.1 资料

本文主要研究对象是中国南方夏季（6～8 月）降水的年代际变率。采用了东英吉利大学提供的 1901～2014 年 0.5°×0.5°的逐月降水资料 CRU（Climatic Research Unit；New et al., 2000）及国家气象信息中心提供的 5°×5°的中国区域 1900～2014 年逐月降水资料（NMIC；Li et al., 2012）。将 CRU 降水资料平均到 1°×1°的网格，并做了 3°×3°的空间平滑，以消除空间噪音。海温资料采用英国气象局哈德来中心提供的 1870～2014 年 1°×1°的逐月海温资料（HadISST；Rayner et al., 2003）。大气环流资料采用 NOAA–CIRES 提供的 1851～2014 年 2°×2°的 20CR（20th Century Reanalysis；Compo et al., 2011）。由于 1920 年以前的热带海洋观测资料十分稀疏（Dai, 2013），本文中研究时段统一取为 1920～2014 年。

2.2 方法

为了重点分析中国南方夏季降水年代际变率及其机理，去除了夏季降水和海温资料的线性趋势，并采用 Lanczos 滤波方法（Duchon, 1979）进行了 11 年的低通滤波以去除年际尺度的变率。各变量的距平值均为相对于 1920～2014 年的平均值计算得到。对降水进行经验正交函数（Empirical Orthogonal Function，简称 EOF；Lorenz, 1956）分解前，将降水距平做了标准化处理。

对相关系数及回归系数的显著性检验，文中均采用非参数化的蒙特卡洛检验（Livezey and Chen, 1983）。对 A 和 B 两个序列的相关系数检验方法如下：若 A 的样本数为 N，则将 A 中的 N 个样本随机排列后，与 B 求相关。如此重复 1000 次，将所得 1000 个相关系数从小到大排序。若 A 和 B 的相关系数超过了该组相关系数的 95%分位数，则认为 A 和 B 的相关系数通过了信度为 95%的显著性检验。回归系数的显著性检验与此类似。

西太平洋副热带高压（西太副高）脊线指数参照刘芸芸等（2012）的定义，具体定义为在 500 hPa 等压面上，将北半球西太副高范围内（10°N～60°N，110°E～150°E）东西风分量的零线所在纬度的平均值作为脊线位置。1900～2015 年逐月的 PDO 指数定义为北太平洋逐月海温距平第一主模态对应的标准化时间系数（Zhang et al., 1997；http://jisao.washington.edu/pdo/PDO.latest [2018-02-08]），取 6～8 月的平均作为夏季 PDO 指数。

3 中国南方地区夏季降水年代际变率及对应大气环流的主要特征

3.1 中国南方地区夏季降水主要模态及其年代际变化

中国南方夏季降水的年代际变率十分显著，在南方地区西部和东部的大部分地区，降水的年代际变率的方差占降水总方差的比率超过了 40%（图略）。为得到南方夏季降水年代际变率的典型模态，将 CRU 降水的年代际变率进行 EOF 分解，得到了中国南方夏季降水年代际变率的前两个主模态（图 1a1 和 a2）。根据 North 检验（North et al., 1982），前两个主模态是相互独立的。图 1a1 表明，南方夏季降水年代际变率的第一模态为全区一致型降水，解释方差为 34.6%；第二模态为东西反相型降水，解释方差为 15.2%。前两个主模态累积解释方差约为 50%（图 1a2）。

为进一步验证前两个主模态的真实性，采用 NMIC 降水资料，将（20°N～30°N，100°E～120°E）区域平均的降水记为南方一致型降水指数（Southern China Rainfall Index，简称 SCRI；图 1b1 的黑色实线），其与 PC1 的相关系数为 0.96，达到 99%的信度水平，表明了南方一致型降水主模态在南方夏季降水年代际变率中的真实性。为计算东西反相型降水指数，将（25°N～30°N，110°E～120°E）区域平均的降水记为南方地区东部降水，将（25°N～30°N，99°E～108°E）区域平均的降水记为南方地区西部降水，将东部降水减去西部降水的差值记为东西反相型降水指数（Southern China Zonal Dipole Index，简称 SCZDI；图 1b2 的黑色实线）。SCZDI 与 PC2 的相关系数为 0.84，达到了 95%的信度水平，表明了东西反相型降水主模态在中国夏季降水年代际变率中的真实性。下文将第一主模态记为一致型降水，将第二主模态记为东西反相型降水，将 SCRI 和 SCZDI 分别作为一致型降水指数和东西反相型降水指数。

图 1a 和 b 是对 1925～2009 年中国南方夏季降水年代际变率进行 EOF 分解的主模态及对应的时间系数。由图 1b1 和 b2 可知，PC1 的振幅在 1971/1972 年以前相对较弱，在 1971/1972 以后明显

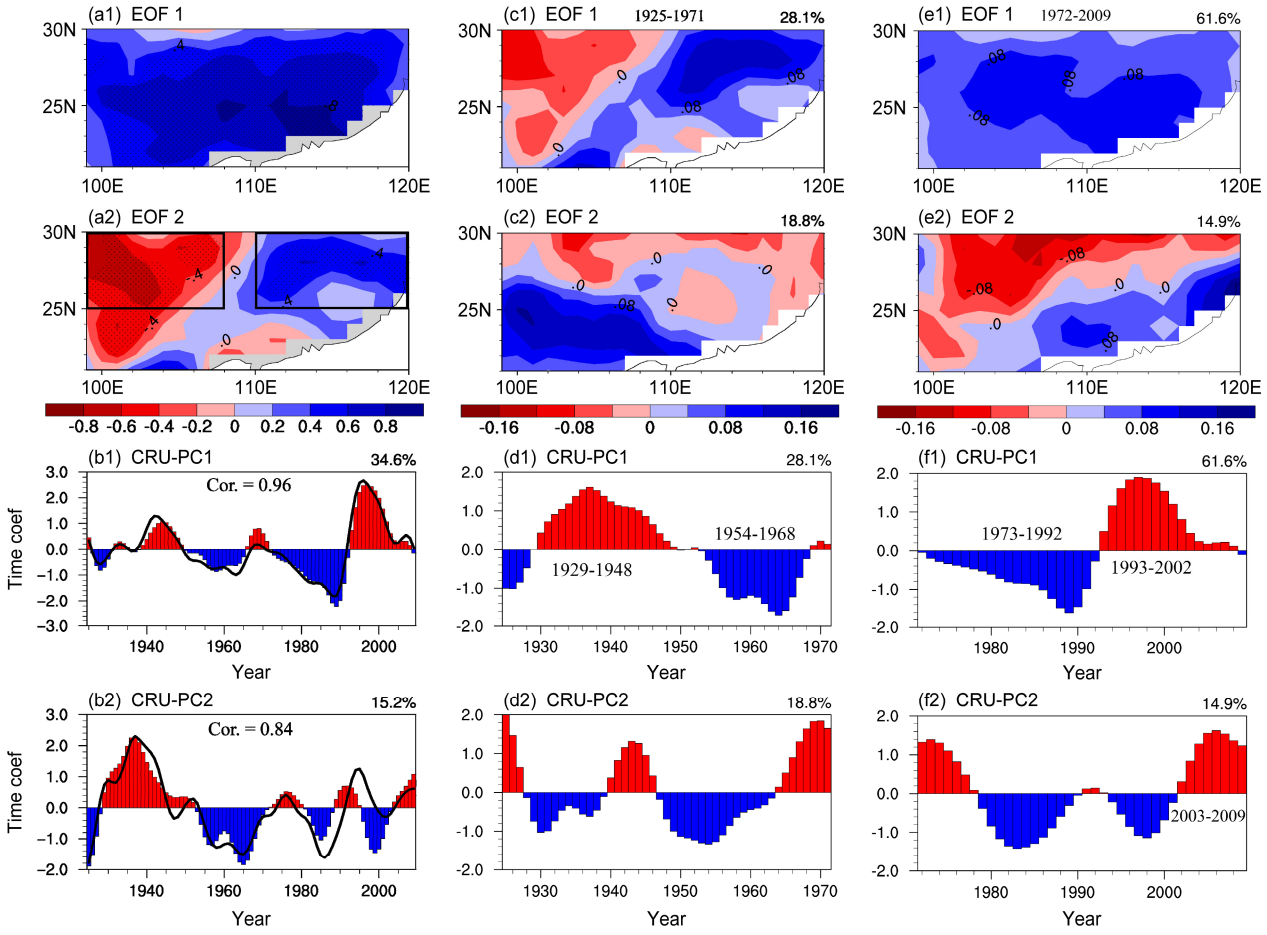

图 1　采用 EOF 分解方法得到的南方夏季降水年代际变率的前两个主模态及对应的时间系数：(a, b) 1925～2009 年；(c, d) 1925～1971 年；(e, f) 1972～2009 年。(b) 中的黑色实线为采用 NMIC（国家气象信息中心）降水数据得到的一致型降水指数（上图）和东西反相型降水指数（下图）

Fig. 1　The first two leading EOF modes of the interdecadal variability of southern China summer rainfall and corresponding principal components (PCs) for (a, b) the period of 1925–2009, (c, d) the period of 1925–1971, and (e, f) the period of 1972–2009. The black lines in (b) denote the SCR index (upper panel) and SCZD index (lower panel) by using NMIC (National Meteorological Information Center) rainfall data, respectively

增强，PC2 的振幅在 1971/1972 以前相对较强，在 1971/1972 以后明显减弱。表明南方降水年代际变率的第一主模态在 1970 年代初发生了年代际的变化。为此，分别对 1925～1971 年及 1972～2009 年的降水进行 EOF 分解，得到图 1c 和 e。图 1c1 和 c2 表明，1925～1971 年，南方降水的第一主模态为东西反相型降水，解释方差达到了 28.1%；第二模态为一致型降水，解释方差达到了 18.8%。图 1e1 和 e2 显示，1972～2009 年，南方降水的第一主模态为一致型降水，解释方差达到了 61.6%；第二模态为东西反相型降水，解释方差仅有 14.9%。由此可知，中国南方夏季降水年代际变率的第一主模态在 1971/1972 年发生了明显的年代际变化，由 1925～1971 年的东西反相型降水转变为 1972～2009 年的一致型降水。进一步对 1925～1971 年和 1972～2009 年两个时期降水第一主模态对应的时间系数分析发现：由图 1d1 和 d2 中的 PC1 可以看出，在 1925～1971 年期间，1929～1948 年（Period one，简称 P1）为东多西少型降水，1954～1968 年（Period two，简称 P2）为西多东少型降水。由图 1f1 和 f2 中的 PC1 可以看出，在 1972～2009 年期间，1973～1992 年（Period three，简称 P3）为一致偏少型降水，1993～2002 年（Period four，简称 P4）为一致偏多型降水。

由图 1f 还可发现，1972～2009 年期间，降水第一主模态时间系数在 2002/2003 年之后明显减弱，而第二模态时间系数在 2002/2003 年之后开始增强。这表明，2002/2003 年之后，一致型降水振

幅开始减弱，而东西反相型降水振幅开始增强。由于第二模态的空间分布型在 2003～2009 年（Period five，简称 P5）期间也是东部偏多，西部偏少，后面的分析将 P5 的降水型也归入东多西少型降水。因此在 1925～2009 年期间，中国南方夏季降水的年代际变率存在两种主模态，分别是东西反相型降水及一致型降水；这两种主模态进而产生四种降水型，分别是东多西少型降水（P1、P5）、西多东少型降水（P2）、一致偏少型降水（P3）和一致偏多型降水（P4）。

为进一步分析中国南方夏季降水的年代际变化特征，将 P1 至 P5 这五个时期的夏季降水分别进行了合成（图 2）。图 2a、b 表明，在 1929～1948 年期间，降水空间分布型为东多西少型。东部每年降水距平值为 15～20 mm，西部每年降水距平值为－10～－15 mm；在 1953～1968 年期间，降水空间分布型为西多东少型，东部每年降水距平值为－10～－20 mm，西部每年降水距平值为 5～15 mm。而在 1970 年代初期以后，南方降水的第一主模态由东西反相型转变为全区一致型,其中 1972～1992 年期间，降水空间分布型为一致偏少型，每年降水距平值为－5～－20 mm（图 2c）。在 1993～2002 年期间，降水空间分布型为一致偏多型，每年降水距平值为 10～25 mm（图 2d）。在 2002/2003 年以后，南方地区夏季降水空间分布型又重新转变为东多西少型，东部每年降水距平值为 10～25 mm，西部每年降水距平值为－5～－15 mm（图 2e）。

由于采用合成分析可以凸显出各时期降水变率的第一主模态，图 2 进一步证明了在 1925～2009 年期间，中国南方夏季降水的年代际变率存在两种主模态，分别是一致型和东西反相型，并且南方地区夏季降水的主导模态在 1970 年代初发生了年代际变化，由东西反相型转变为一致型降水模态。

3.2 欧亚大气环流异常与主要降水模态年代际变化的关系

降水的年代际变率与大气环流异常密切相关（Zhu et al., 2011; Xu et al., 2015）。采用合成分析方法揭示东西反相型降水和一致型降水分别对应的高低空环流异常特征（图 3）。东西反相型降水对应的环流场异常取为 P1 与 P2 对应环流场异常的差值

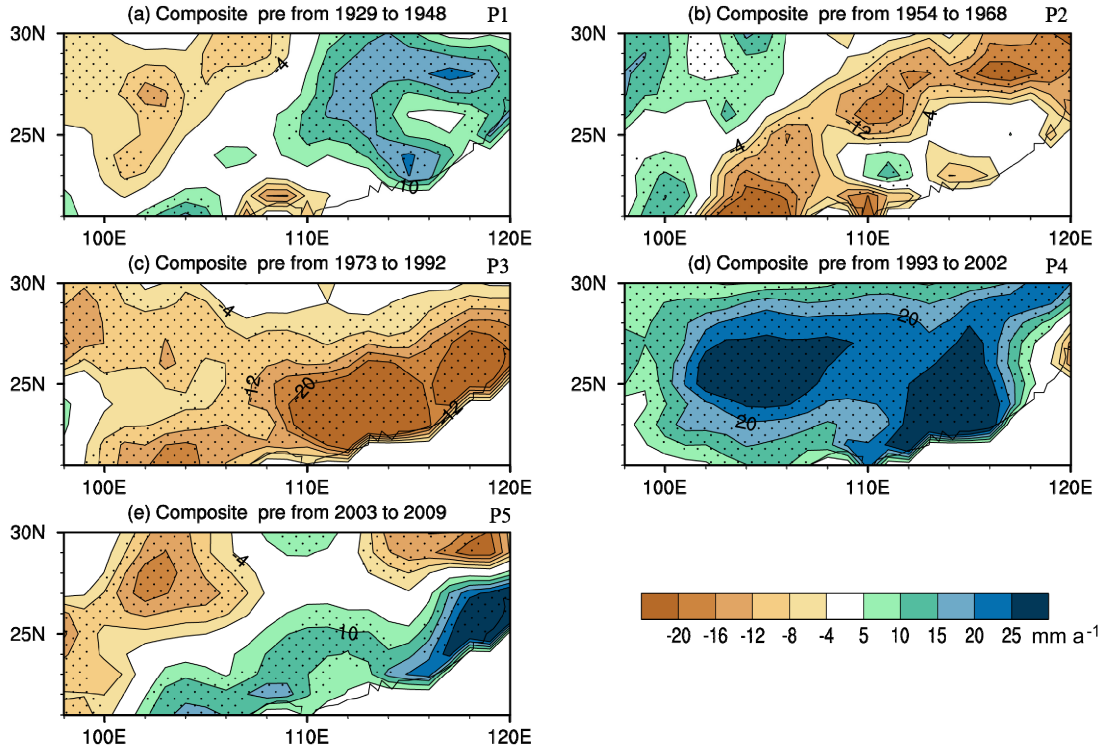

图 2 中国南方夏季降水年代际变率的空间分布（填色，单位：mm a^{-1}）：（a）1929～1948 年；（b）1954～1968 年；（c）1973～1992 年；（d）1993～2002 年；（e）2003～2009 年。打点区域表示达到了 95%的信度水平

Fig. 2 Composition of the interdecadal variability of southern China summer rainfall for (a) the period of 1929–1948, (b) the period of 1954–1968, (c) the period of 1973–1992, (d) the period of 1993–2002, and (e) the period of 2003–2009. Units: mm a^{-1}. Black dots denote areas significant at the 95% confidence level

场；一致型降水对应的环流场异常取为 P4 与 P3 对应环流场异常的差值场。

图 3a–c 是东西反相型降水（以下为东多西少型降水）对应的环流场异常特征。在高层（200 hPa）流函数异常最显著的特征为北半球沿中纬度的波列结构（图 3a），正异常中心分别位于北大西洋热带地区、里海和中国东部地区，负异常中心位于地中海和贝加尔湖以南。其中里海和贝加尔湖以南的异常中心位于亚洲副热带西风急流带上，这可能为该波列向下游的传播起到波导作用（Ambrizzi et al., 1995）。另外自南亚到中南半岛存在一个显著的负异常中心。图 3b 显示中层（500 hPa）环流异常的主要特征是位于中南半岛上空的正异常中心及位于中国东部上空的负异常中心，即中国南方地区上空 500 hPa 的流函数场为西高东低的特征，这有利于南方西部的下沉运动及东部的上升运动，从而有利于南方西部降水偏少，东部降水偏多。图 3c 是低层（850 hPa）的流函数场和风场异常图，在中南半岛为反气旋性环流异常，不利于孟加拉湾水汽向西南地区输送，从而不利于南方地区西部降水；南方地区东部上空为气旋性环流异常，有利于水汽自东海向东南地区输送，有利于南方地区东部降水偏多。上述分析也适用于西多东少型降水，只是环流场异常特征完全相反。

图 3d–f 是一致型降水（以下为一致偏多型降水）对应的环流场异常特征。在高层（200 hPa）流函数异常最显著的特征为北半球中高纬度的波列结构（图 3d），正异常中心分别位于东欧地区及贝加尔湖以东，负异常中心位于北大西洋副热带地区、西伯利亚及日本海。该波列相较于图 3a 中的

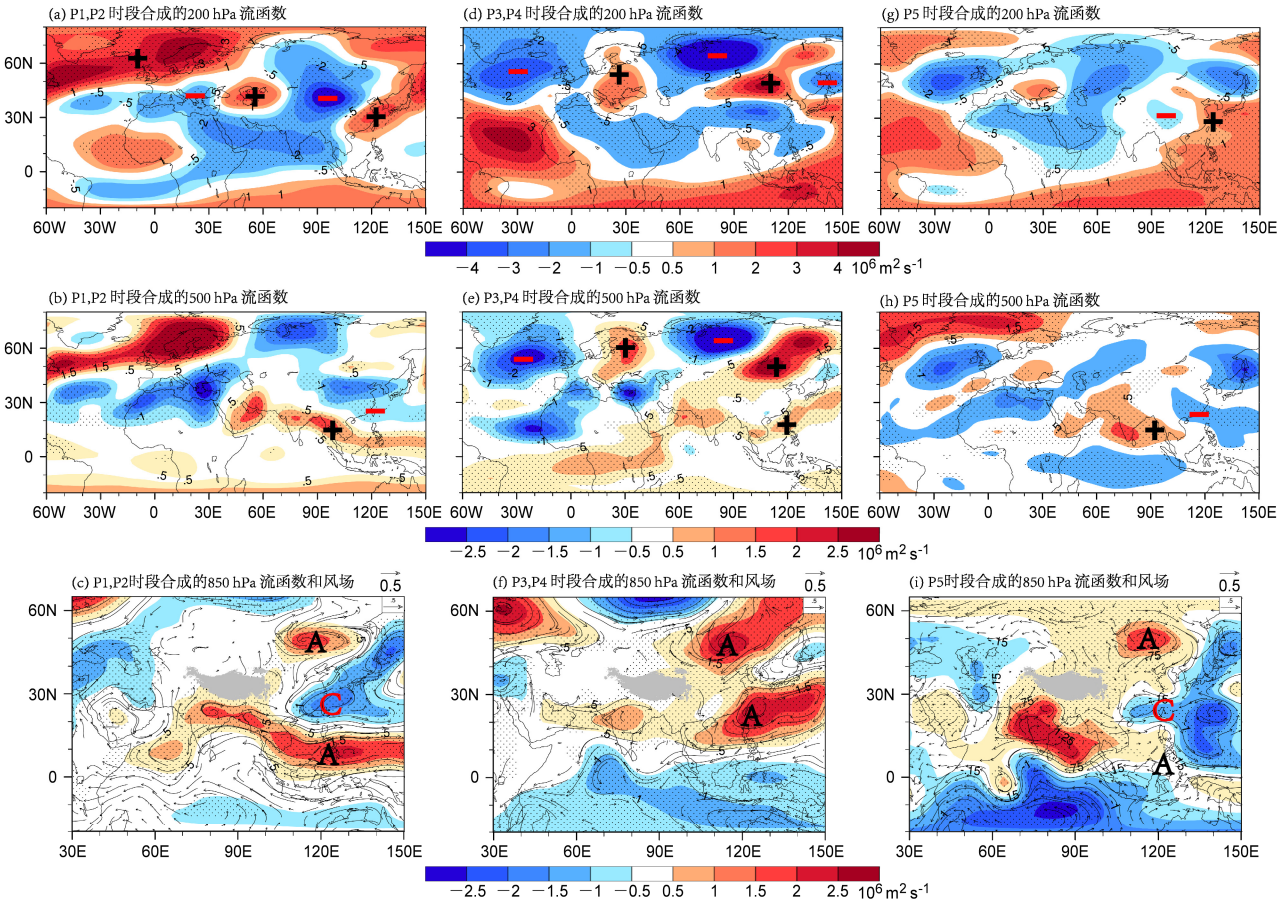

图 3　南方夏季不同时期环流异常差值分布：P1 与 P2 的差值，对应东西反相型降水（左列）；P4 与 P3 的差值，对应一致型降水（中间列）；P5 的合成，对应东多西少型降水（右列）。（a、d、g）分时段合成的 200 hPa 流函数场（填色，单位：10^6 m^2 s^{-1}）；（b、e、h）500 hPa 流函数场（填色，单位：10^6 m^2 s^{-1}）；（c、f、i）850 hPa 的风场（矢量，单位：m s^{-1}）和流函数场（填色，单位：10^6 m^2 s^{-1}）。打点区域表示达到了 90%的信度水平

Fig. 3　Composition of stream function (shading, units: 10^6 m^2 s^{-1}) at (a, d, g) 200 hPa, (b, e, h) 500 hPa, and (c, f, i) stream function (shading, units: 10^6 m^2 s^{-1}) and wind (vectors, units: m s^{-1}) anomalies at 850 hPa in JJA. The left column are the difference between the means of Period one and Period two; the middle column are the difference between the means of Period four and Period three; the right column are the composition of Period five. Black dots denote areas significant at the 90% confidence level

中纬度波列，位置更为偏北，且位相完全相反，这种环流型的变化对应着南方地区降水型的变化。最近的研究表明，当 AMO 处于暖位相的时候，北大西洋热带地区（Li et al., 2017b）和中高纬度地区（Lin et al., 2016）海温异常均可强迫出向下游传播的遥相关波列。因此，北大西洋海温异常可能对图 3a 和图 3d 中波列结构的形成有直接影响。图 3e 显示中层的流函数异常最明显的特征也是中高纬度的波列结构，其正负异常中心与高层波列完全一致，表明该波列具有准正压的特征。在图 3e 中 500 hPa 环流异常场另一个明显特征为西北太平洋的正值中心，表明西太平洋副热带高压异常偏西偏强，这对应着图 3f 中 850 hPa 中国南海及菲律宾地区显著的反气旋性环流异常，有利于将更多的水汽输送到中国南方地区。850 hPa 流函数场的一个正异常中心位于贝加尔湖东南部，对应着风场上显著的反气旋性环流异常，有利于冷空气向南方地区输送。来自北方的冷空气和来自南海及西北太平洋地区的水汽在南方地区辐合，有利于南方地区降水一致偏多。上述分析也适用于一致偏少型降水，只是环流场异常特征完全相反。

对应于 2003～2009 年期间中国南方夏季降水的东西反相型分布特征，图 3g–i 给出了该时段合成的环流场异常特征。在图 3g 中 200 hPa 流函数异常在中国南方上空为西低东高的形势，与图 3a 中的较为类似。图 3h 显示 500 hPa 流函数异常在东亚中低纬度为西高东低的形势，与图 3b 中的较为类似，这种环流形势有利于中国南方西部的下沉运动和东部的上升运动，从而有利于西部降水偏少，东部降水偏多。850 hPa 环流场异常在东亚地区主要表现为由南到北的反气旋—气旋—反气旋的经向三极子结构，与图 3c 中的较为类似。图 3g–i 显示 2003～2009 年期间东多西少型降水与图 3a–c 中东西反相型降水对应的高低空环流场异常特征较为相似，有利于形成南方地区东多西少型降水。

4 南方夏季降水年代际变率主导模态的可能形成机制

为了分析南方东西反相型降水和一致型降水模态形成机理，对两种降水模态对应的海温异常特征进行深入分析，图 4 分别给出了两种降水型对应的合成海温异常图。

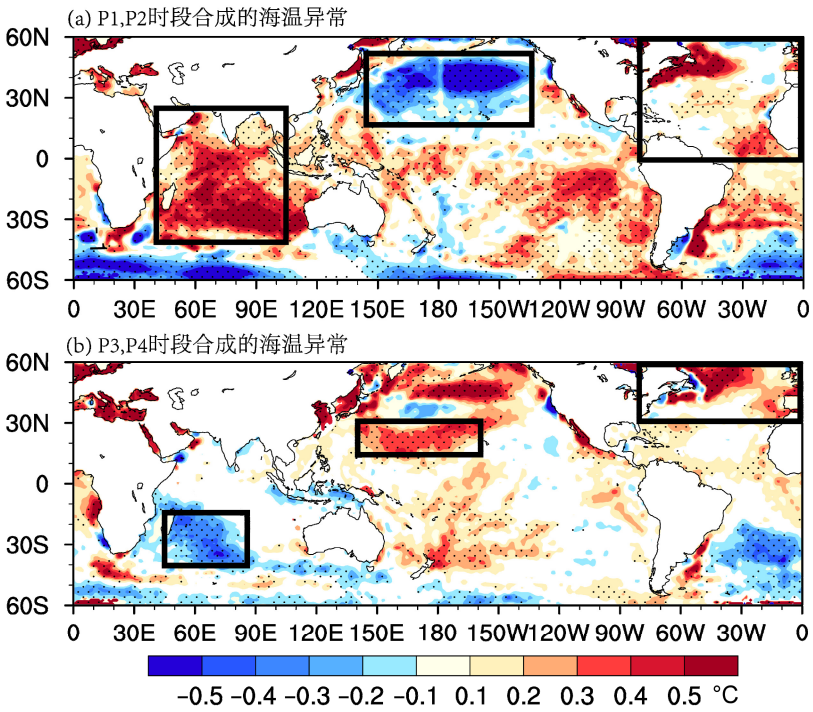

图 4 南方夏季不同时期海表温度异常差值图（填色，单位：°C）：（a）东西反相型降水在 P1 与 P2 的异常海温差值；（b）一致型降水在 P4 与 P3 的异常海温差值。各框图区为各海区对应的海温关键区；打点区域表示达到了 95%的信度水平

Fig. 4 Composites of sea surface temperature anomaly differences (shading, units: °C): (a) The difference between the means of Period one and Period two; (b) the difference between the means of Period four and Period three. Black rectangle boxes denote the key SST region in each ocean. Black dots denote areas significant at the 90% confidence level

图 4a 显示，与东多西少型降水相关的海温异常特征体现为印度洋海温和北大西洋海温一致偏暖及北太平洋海温异常偏冷的特征。西多东少型降水对应的海温异常特征与上述海温异常特征完全相反。Dong et al.（2016）的研究表明，印度洋海温一致偏暖模态是印度洋海温年代际变率的第一主模态，可以通过引起异常的纬向垂直环流影响东亚夏季风及中国南方地区夏季降水的年代际变化（Wu et al., 2010; Zhang et al., 2017）。北太平洋的异常海温区与 PDO 的活跃区域较为一致（Mantua et al., 1997），因此该区域异常海温可能主要体现 PDO 年代际变率对东西反相型降水的影响。而北大西洋一致偏暖可能通过激发向下游传播的遥相关波列，进而影响到中国夏季的降水（Lin et al., 2016; Li et al., 2017b）。根据海温显著异常的区域，分别选取（40°S～25°N，40°E～105°E）作为印度洋海温关键区，（20°N～50°N，140°E～220°E）作为北太平洋海温关键区，（0°～60°N，0°～80°W）作为北大西洋的海温关键区。北太平洋海温关键区平均的海温异常与 Zhang et al.（1997）定义的 PDO 指数在 1925～2009 年的相关系数为－0.94，达到了 99%的信度水平（图略），因此北太平洋海温关键区海温异常的年代际变率主要反映 PDO 信号。下文中将采用根据 Zhang et al.（1997）的定义计算得到的 PDO 指数作为图 4a 中北太平洋海温关键区海温指数，将图 4a 中印度洋及北大西洋海温关键区平均的海温距平记为 IO（Indian Ocean SST anomaly，简称 IO）及 AMO，进一步探讨不同海区海温变化对东西反相型降水的影响。

图 4b 显示，一致型降水对应的海温型与东西反相型对应的海温型特征显著不同。一致偏多型降水对应的海温异常特征在印度洋主要表现为南印度洋海温的异常偏冷，热带印度洋和北印度洋的海温异常并不显著。而北太平洋海区最显著特征是西北太平洋海温的异常偏暖，该区域是西太副高的活动中心，因此该海区的海温异常可能通过影响西太副高进而影响南方地区的降水异常。相比之下，北大西洋热带地区的海温异常并不显著，而中高纬度的海温异常则十分明显。一致偏少型降水对应的海温异常特征与上述海温异常特征完全相反。为了深入分析不同海区海温异常与南方夏季一致型降水的关系，分别选取（40°S～15°S，45°E～85°E）作为南印度洋海温关键区，（15°N～30°N，140°E～200°E）作为西北太平洋海温关键区，（30°N～60°N，0～80°W）作为北大西洋北部海温关键区。下文中分别将图 4b 中各关键区平均的海温距平记为 SIO（Southern Indian Ocean SST anomaly）、NWPO（Northwestern Pacific Ocean SST anomaly）及 NA（Northern Atlantic SST anomaly），进一步探讨不同海区海温变化对一致型降水的影响。由图 4 还可发现，无论是一致型降水还是东西反相型降水，印度洋海温距平与北太平洋海温距平符号均相反。而印度洋海温与北大西洋海温距平则在一致型时符号相反，在东西反相型时符号相同。这强烈地反映出三大洋各海温关键区对中国南方夏季降水的两种主要模态可能存在着显著的协同影响。

对应于 2003～2009 年期间中国南方夏季降水的东西反相型分布特征，该时段合成的海温场异常特征与图 4a 中的海温场异常特征较为类似（图略），表明相似的海温异常分布型可导致相似的降水分布型。

图 4 中确定了可能影响南方地区东西反相型及一致型降水的海温关键区，下面进一步从时间演变的角度分析各海温关键区与降水型之间的对应关系。将各海温关键区平均的海温距平标准化后作为各海温关键区的海温指数。由于东西反相型降水在 1925～1971 年为南方地区夏季降水的第一主模态，因此分别计算了 IO 指数、PDO 指数及 AMO 指数与 SCZDI 在 1925～1971 年及 1972～2009 年的相关系数。由图 5a 可知 IO 指数、PDO 指数及 AMO 指数与 SCZDI 在 1925～1971 年的相关系数分别为 0.86、0.78 及 0.76，均达到了 90%的信度水平，表明印度洋一致型海温、北太平洋海温及北大西洋海温的年代际变率均可能对东西反相型降水有较显著的影响；并且东西反相型降水与 IO、PDO 及 AMO 均为正相关关系。另外，IO 指数、PDO 指数及 AMO 指数与 SCZDI 在 1972～2009 年的相关系数分别为 0.04、－0.36 及 0.24，均未通过显著性检验，表明在 1971/1972 年之后，三个海温关键区的海温对东西反相型降水的影响均显著减弱了。

由于一致型降水在 1972～2009 年为南方地区夏季降水的第一主模态，因此分别计算了 SIO 指数、NWPO 指数及 NA 指数与 SCRI 在 1925～1971 年及 1972～2009 年的相关系数。由图 5b 可知，SIO 指数、NWPO 指数及 NA 指数与 SCRI 在 1972～2009

年的相关系数分别为−0.85、0.75 及 0.70，均达到了 90%的信度水平，这表明南印度洋海温，西北太平洋海温及北大西洋北部海温的年代际变率均可能对一致型降水有一定影响。另外 SIO 指数、NWPO 指数及 NA 指数与 SCRI 在 1925～1971 年的相关系数分别为 0.84、0.03 及 0.24，只有 SIO 指数与 SCRI 的相关系数达到了 95%的信度水平。即 SIO 与 SCR 的关系在 1925～1971 年为显著的正相关，而在 1972～2009 年为显著的负相关，因此 SIO 与 SCR 的关系在 1971/1972 年前后发生了年代际的变化，具体原因将在 4.2 节中加以讨论。

4.1 南方夏季东西反相型降水的可能形成机制

印度洋海温、北太平洋海温及北大西洋海温在 1925～1971 年期间，是如何影响南方东西反相型降水的呢？已有的研究表明，印度洋海温正（负）异常主要通过引起异常的低空（高空）辐合（辐散），及对应的垂直环流异常来影响东亚夏季风（Wu et al., 2010; Zhang et al., 2017）。因此，这里分别合成了东西反相型降水所对应的高层和低层的速度势和辐散风（图 6a、b）。图 6a、b 对应东多西少型降水的情形，下面的分析也适用于西多东少型降水，只是符号完全相反。由图 6a、b 可知，由于印度洋是一致的异常偏暖的海温分布，在赤道印度洋中部低空为辐合中心，高空为辐散中心；中南半岛高空为辐合中心，低层为辐散中心，形成了一个跨越赤道的异常垂直环流圈，其下沉支位于中南半岛，引起了中南半岛低空 850 hPa 的反气旋性异常（图 3c），这不利于水汽向西南地区输送。当印度洋处于暖（冷）位相时，通过引起垂直环流异常，不（有）利于向西南地区的水汽输送，不（有）利于西南地

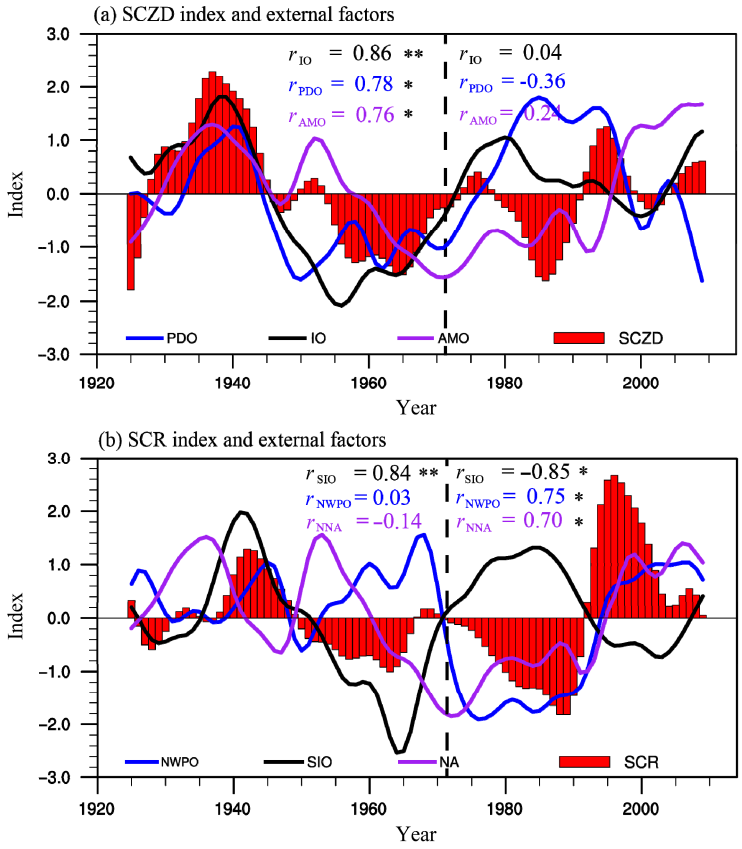

图 5 主要模态降水指数与各关键区海温指数的对应关系：（a）SCZDI（红色柱状图）与 IO 指数（黑色实线），PDO 指数（蓝色实线）及 AMO 指数（紫色实线）；（b）SCRI（红色柱状图）与 SIO 指数（黑色实线），NWPO 指数（蓝色实线）及 NA 指数（紫色实线）。“*”和“**”表示相关系数分别达到了 90%和 95%的信度水平。黑色虚线为 1971/1972 年的分界线

Fig. 5 Indices of the SCZD and SCR and indices of averaged SST anomalies in each region associated with the SCZD (Southern China Zonal Dipole) and SCR (Southern China Rainfall). The red bars in (a) and (b) denote the SCZD index and the SCR index, respectively. The black lines in (a) and (b) denote the IO index and the SIO index, respectively. The blue lines in (a) and (b) denote the PDO index and the NWPO index, respectively. The purple lines in (a) and (b) denote the AMO index and the NA index, respectively. “*” and “**” denote correlation coefficients significant at the 90% and 95% confidence levels, respectively. The black dashed lines denote the year of 1971/1972

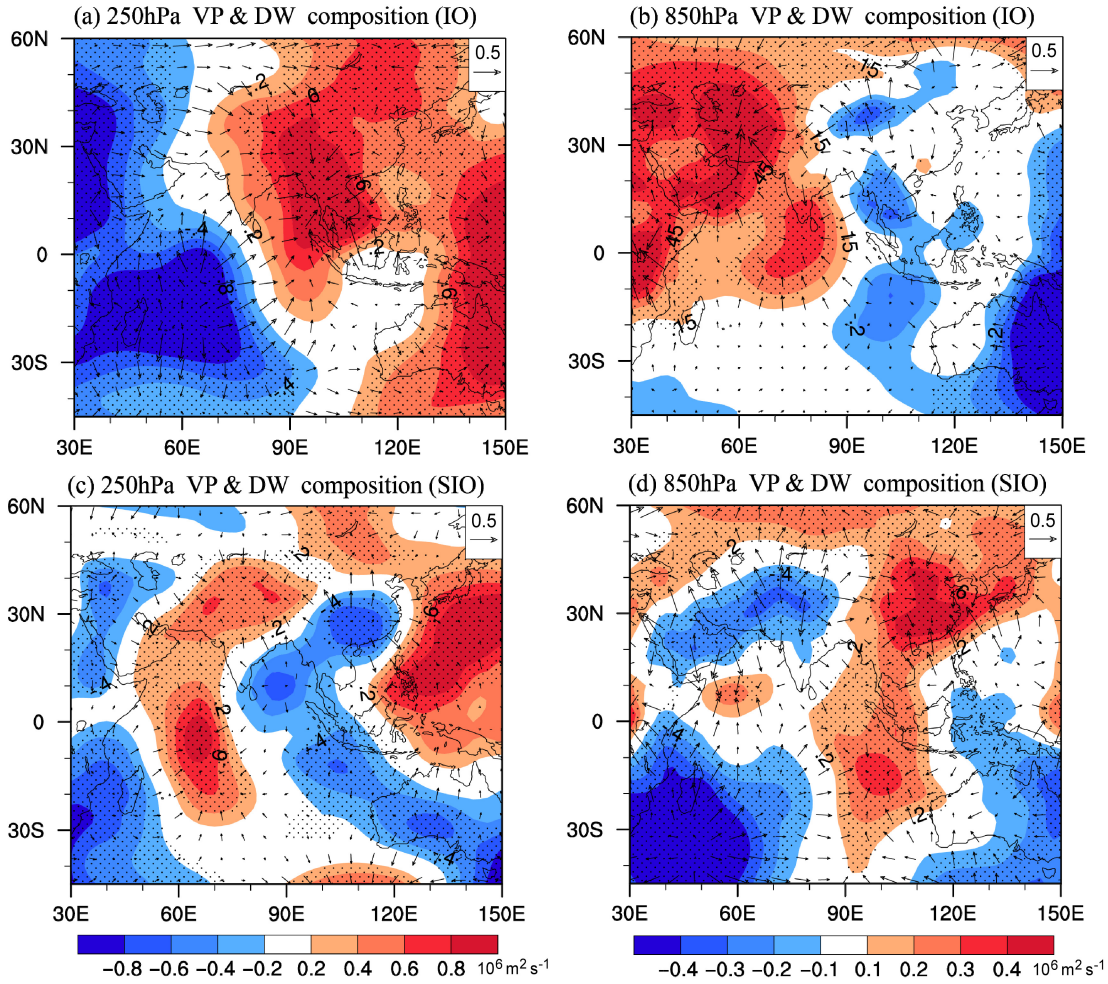

图 6　（a、b）东西反相型降水（P1 与 P2 的差值）及（c、d）一致型降水（P4 与 P3 的差值）对应的夏季速度势及辐散风的差值场：（a、c）250 hPa 的速度势（填色图，单位：10^6 m^2 s^{-1}）及辐散风（矢量，单位：m s^{-1}）；（b、d）850 hPa 的速度势（填色图，单位：10^6 m^2 s^{-1}）及辐散风（矢量，单位：m s^{-1}）。打点区域表示达到了 90%的信度水平

Fig. 6　The JJA divergent winds (vectors, units: m s^{-1}) and velocity potentials (shading, units: 10^6 m^2 s^{-1}) at 250 hPa (left column) and 850 hPa (right column) corresponding to the (a, b) zonal dipole pattern and (c, d) monopole pattern of SCSR. (a, b) show the differences between the means of Period one and Period two; (c, d) show the differences between the means of Period four and Period three. Black dots denote areas significant at the 90% confidence level

区的夏季降水，南方地区容易形成东多西少（西多东少）型降水。

分析发现，PDO 也对南方夏季东西反相型降水有显著的影响。图 7 为 1925～1971 年的 PDO 指数回归的 850 hPa 位势高度场和风场，在东亚上空由南向北为反气旋—气旋—反气旋的异常环流型，反气旋性环流异常位于菲律宾以东及贝加尔湖以东，气旋性环流异常位于中国东南地区。东亚地区这种经向的三极子波列结构，与 PJ 型遥相关波列较为类似（Kosaka and Nakamura, 2006）。研究表明（Zhang et al., 1997；张庆云等，2007），当 PDO 处于正位相时，北太平洋中高纬度海温为负异常，热带中东太平洋海温为正异常，有利于异常的上升运动及热带西太平洋异常的下沉运动，从而有利于菲律宾异常反气旋的形成，抑制该地区的对流活动（Wang and Zhang, 2002; Xie et al., 2009）。菲律宾地区异常的对流活动可以激发东亚地区低空经向的 PJ 型遥相关波列，气旋性异常中心位于中国东南地区，有利于东南地区降水增多（Kosaka and Nakamura, 2006; Wu et al., 2016; Si and Ding, 2016），这与本文的研究结果较为一致。因此，PDO 的暖（冷）位相可以通过引起东亚低空的 PJ 型遥相关波列，在中国东南地区低空引起气旋（反气旋）性异常，增强（减弱）了自中国东海向南方地区东部的水汽输送，从而有（不）利于南方地区东部降水。

为分析 1925～1971 年 AMO 对东西反相型降水的影响，图 8a 合成了 1925～1971 年 AMO 正负位相下 300 hPa 的流函数与波活动通量。可以看到，与 AMO 相关的准静止遥相关波列由中纬度及高纬度两条路径向下游传播。其中中纬度的传播路径与亚洲西风急流的位置十分契合，呈现出清晰的五波结构。因此，1925～1971 年北大西洋海温是通过中纬度沿西风急流传播的遥相关波列来影响东西反

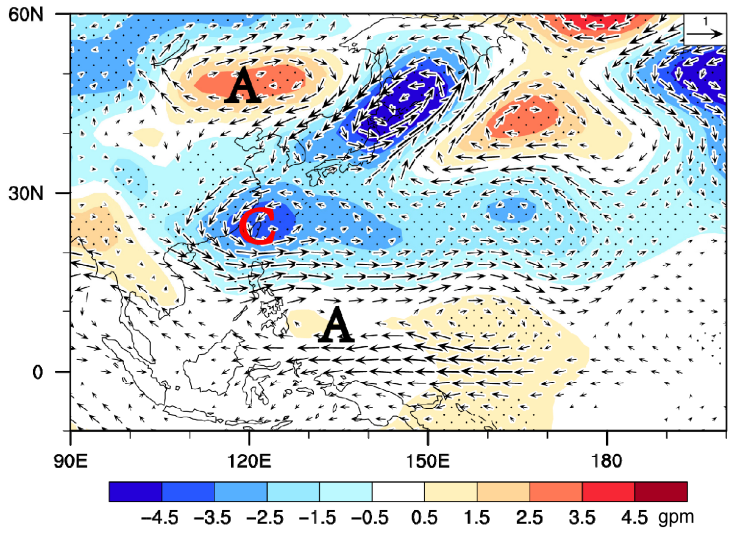

图 7　1925～1971 年的 PDO 指数回归的 850 hPa 位势高度场（填色，单位：gpm）和风场（矢量，单位：m s^{-1}）。打点区域表示达到了 95%的信度水平

Fig. 7　Regression of geopotential height (shading, units: gpm) and wind (vectors, units: m s^{-1}) against the PDO index for the period of 1925–1971. Black dots indicate areas significant at the 95% confidence level

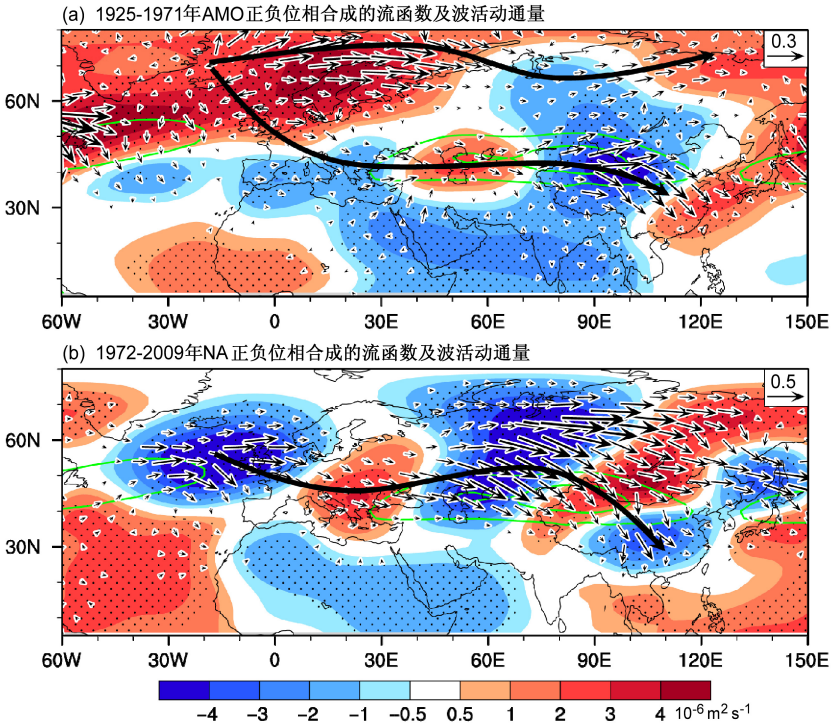

图 8　（a）1925～1971 年 AMO 正负位相下合成的 300 hPa 流函数场（填色，单位：10^6 m^2 s^{-1}）和波活动通量场（矢量，单位：10^{-6} m^2 s^{-2}）；（b）1972～2009 年 NA 正负位相下合成的 300 hPa 流函数场（填色，单位：10^6 m^2 s^{-1}）和波活动通量场（矢量，单位：10^{-6} m^2 s^{-2}）。(a, b）中绿色实线为气候态 200 hPa 的 20 m s^{-1} 和 25 m s^{-1} 纬向风等值线

Fig. 8　(a) Composites of stream function (shading, units: 10^6 m^2 s^{-1}) and wave activity flux (vectors, units: 10^{-6} m^2 s^{-2}) at 300 hPa according to the phases of AMO for the period of 1925–1971; (b) composites of stream function (shading, units: 10^6 m^2 s^{-1}) and wave activity flux (vectors, units: 10^{-6} m^2 s^{-2}) at 300 hPa according to the phases of NA for the period of 1972–2009. Green contours in (a, b) denote the climatological zonal wind isolines of 20 m s^{-1} and 25 m s^{-1} at 200 hPa

相型降水的。位于中国东部上空正的活动中心有利于高空辐散和伴随的低空辐合，使得南方地区东部上空易于形成异常的上升运动，这有利于该地区降水增多。

4.2 南方夏季一致型降水的可能形成机制

图 5a 表明，在 1971/1972 年之后，IO、PDO 及 AMO 对东西反相型降水的影响均明显减弱了。并且在 1971/1972 年之后，南方地区夏季降水的第一主模态转变为一致型降水。与之对应的，在 1972～2009 年期间，热带印度洋和北印度洋海温的年代际变率变得不再显著，而南印度洋海温距平（SIO）异常比较明显。并且西北太平洋地区海温距平（NWPO）异常偏暖，而北大西洋北部海温距平（NA）异常偏暖。因此进一步分析 SIO、NWPO 和 NA 在 1972～2009 年期间对南方一致型降水的协同影响。

为分析 SIO 对南方一致型降水的影响，分别合成了对应的高层和低层的速度势和辐散风（图 6c、d）。图 6c、d 对应一致偏多型降水的情形，下面的分析也适用于一致偏少型降水，只是符号完全相反。图 6c、d 显示，SIO 处于冷位相时，可以引起南印度洋低空辐散及高空辐合，在东印度洋引起高空辐散和低空辐合，进而导致中国南海及西北太平洋地区的高空辐合和低空辐散，这有利于在中国南海及西北太平洋地区低空形成异常的反气旋（图 3f），增加向南方地区的水汽输送，从而有利于南方地区降水一致偏多，这与 Zhang et al.（2017）的研究较为一致。因此，南印度洋的冷（暖）海温异常有利于南方地区降水一致偏多（少）。图 5b 指出，SIO 与 SCR 的关系在 1971/1972 年前后发生了年代际的变化。由 1971/1972 年之前的正相关变为之后的负相关。可能原因是 1971/1972 年之前，热带印度洋和北印度洋海温起到了更显著的作用，暖海温异常引起的垂直环流异常上升支位于赤道中印度洋，下沉支位于中南半岛。在这样的背景之下，南印度洋暖海温异常通过单圈的垂直环流异常，对一致型降水的作用主要体现为东南地区降水偏多。也即 SIO 与 SCR 在 1925～1971 年期间为同位相变化关系。但该时段一致型降水并非南方降水的主导模态，因此，在 1925～1971 年南印度洋海温在印度洋海温一致增暖中可能扮演了相对次要的角色。而当 1972～2009 年印度洋海温最显著的年代际变率出现在南印度洋时，大气环流对南印度洋海温异常的响应与 1925～1971 年期间有较大差异（图 6c、d），SIO 与 SCR 的关系也相应转变为显著的负相关关系。

NWPO 位于西太副高的活动中心，可能通过影响西太副高进而影响南方地区一致型降水。在 1972～2009 年期间，由 NWPO 正负位相下 500 hPa 西太副高脊线位置及 5870 gpm 等值线位置可以发现（图 9a），当 NWPO 处于正（负）位相时，西太副高脊线偏南（北），位置偏西（东）。从图 9b 可以看到，当 NWPO 处于正（负）位相时，无论高层还是低层，西太副高脊线整体偏南（偏北），这对应着西北太平洋低空的反气旋（气旋）性异常（图 3f）。由此可见 NWPO 异常偏暖可与 SIO 异常偏冷协同影响中国南海及西北太平洋低空的反气旋性异常，进而有利于南方地区降水一致偏多。

为分析 1972～2009 年 NA 对一致型降水的影响，合成了 1972～2009 年 NA 正负位相下 300 hPa 流函数与波活动通量（图 8b）。图 8b 表明，与 NA 相关的准静止遥相关波列由高纬度路径向下游传播。其中正异常中心位于东欧及贝加尔湖，负异常中心位于北大西洋北部、西伯利亚及日本海，呈现出清晰的五波结构。因此 1972～2009 年北大西洋北部海温异常可能是通过欧亚遥相关波列来影响一致型降水的。

5 不同关键区海温异常对南方夏季降水主模态的协同影响

通过分析 IO、PDO 和 AMO 对东西反相型降水的影响发现，三大洋海温可以协同影响南方地区 1925～1971 年的东西反相型降水。由 IO 暖（冷）位相引起的中南半岛低空反气旋（气旋）性异常减弱（增强）了从孟加拉湾及南海地区输送向南方地区西部的水汽，有利于西部降水偏少（偏多）。由 AMO 暖（冷）位相引起的中国东南地区高空正（负）异常中心有利于高空辐散（辐合）及南方地区异常的上升（下沉）运动，其与 PDO 暖（冷）位相引起的南方东部低空的气旋（反气旋）性异常共同作用，有利于东部降水偏多（少），从而有利于东多西少（西多东少）型降水的形成。而 SIO、NWPO 和 NA 可以协同影响东亚地区低空的大气环流异常，进而影响 1972～2009 年南方地区的一致型降水。SIO 冷（暖）位相可与 NWPO 暖（冷）位相协同作用，引起中国南海及西北太平洋低空的反气旋

（气旋）性异常，有（不）利于水汽自中国南海向南方地区输送。而 NA 暖（冷）位相则通过引起贝加尔湖东侧低空的反气旋（气旋）性异常，有（不）利于冷空气向南方地区输送并与来自南海地区的水汽在南方地区辐合，有利于南方地区降水一致偏多（少）。

为进一步研究多种外部因子对南方主要降水型的协同影响，分别利用各海温关键区对应的海温指数，对 1925～1971 年的南方东西反相型降水指数 SCZDI 和 1972～2009 年南方地区的一致型降水指数 SCRI 进行多因子回归拟合分析。

图 10a、b、c 为分别采用单因子（IO）、双因子（IO 和 PDO）及三因子（IO、PDO 及 AMO）回归拟合的 1925～1971 年的 SCZDI。由图 10a 和表 1 可知，采用 IO 单一因子可以较好地拟合 SCZDI，解释方差为 66.1%，拟合曲线与 SCZDI 指数相关系数为 0.813，符号一致率为 85.1%。当采用 IO 和 PDO 两个因子时（图 10b 和表 1），解释方差为 68.2%，相关系数为 0.830，均有一定的提高。由于 IO 和 PDO 在 1925～1971 年为近似的同位相变化（图 5a），由 IO 和 PDO 两个因子来拟合时，解释方差与采用单一因子时差别不太显著。当采用 IO、PDO 及 AMO 三个因子拟合 SCZDI 时（图 10c 和表 1），拟合曲线和 SCZDI 较为一致，位相转折点及振幅大小均拟合的较好。此时采用三因子拟合的解释方差显著提高，达到 86.3%，拟合曲线与 SCZDI 指数相关系数为 0.929，符号一致率为 97.9%。相较采用单一因子或者双因子拟合的结果，采用三个因子拟合的效果最好。这也进一步表明，IO、PDO 和 AMO 的协同作用是影响南方地区东西反相型降水的主要原因。

图 10d、e、f 为分别采用单因子（SIO）、双因子（SIO 和 NWPO）及三因子（SIO、NWPO 及 NA）回归拟合的 1972～2009 年的 SCRI。由图 10d 和表 1 可知，采用 SIO 单一因子拟合 SCRI 的解释方差为 72%，拟合曲线与 SCRI 的相关系数为 0.853，符号一致率为 92%。当采用 SIO 和 NWPO 两个因子时（图 10e 和表 1），解释方差为 72.8%，相关系数为 0.860，符号一致率为 93.5%，相较采用单一因子的拟合结果均有一定的提高。由于 SIO 和 NWPO 在 1972～2009 年为近似的反位相变化（图 5b），由 SIO 和 NWPO 两个因子来拟合时，解释方差与采用单一因子时差别不太显著。当采用 SIO、NWPO 及

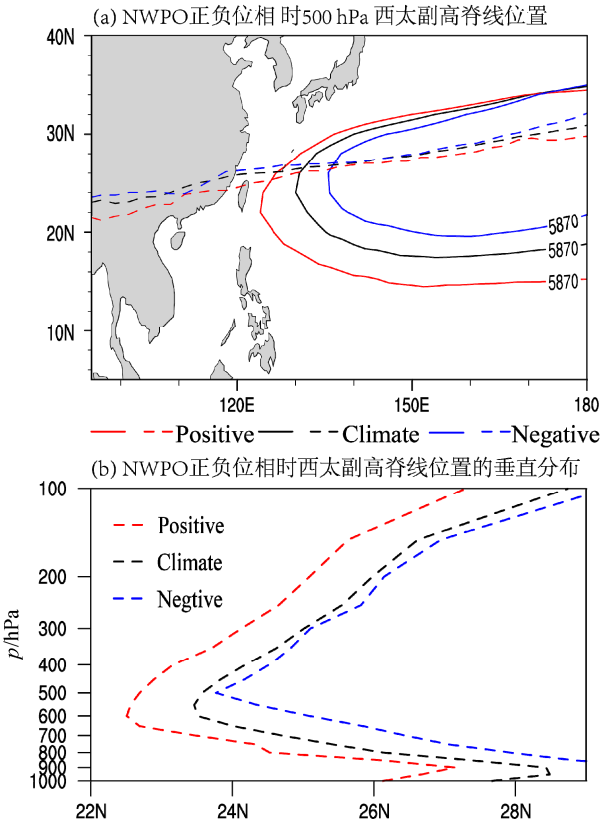

图 9 基于 1972～2009 年的（a）NWPO 指数合成的 500 hPa 西太副高脊线位置和（b）120°E～140°E 平均的西太副高脊线位置的垂直分布。黑色、红色和蓝色虚线（实线）分别代表 1972～2009 年气候态、NWPO 正位相、NWPO 负位相下西太副高脊线的位置（5870 gpm 等值线位置）

Fig. 9 (a) Composites of the ridge position of WPSH (Western Pacific Subtropical High) at 500 hPa according to the phases of NWPO index for the period of 1972–2009. (b) As in (a), but for the vertical distribution of ridge position averaged between 120°E and 140°E. The black solid (dotted) lines denote the climatological 5870 gpm isolines (the ridge positions of WPSH). The red and blue solid (dotted) lines denote the 5870 gpm isoline (the ridge position of WPSH) in the positive and negative phases of NWPO index, respectively

NA 三个因子拟合 SCRI 时（图 10f 和表 1），拟合曲线和 SCRI 较为一致，位相转折点及振幅大小均拟合的较好。此时采用三个因子拟合的解释方差显著提高，达到 79.0%，拟合曲线与 SCRI 指数相关系数为 0.894，符号一致率为 95.0%。相比较采用单一因子或者双因子拟合的结果，采用三个因子拟合的效果最好。这也进一步表明，SIO、NWPO 和 NA 的协同作用是影响南方地区一致型降水的重要原因。

我们也分别采用单因子（IO）、双因子（IO 和 PDO）及三因子（IO、PDO 及 AMO）回归拟合了 1925～2009 年的 SCZDI （图略），但其效果均不如

表 1　采用各海区海温指数回归拟合东西反相型及一致型降水指数的效果检验

Table 1　The validity of fitted SCZD index and SCR index using the indices of averaged SST anomalies in each sea region

时间段	回归模型	解释方差	回归结果检验	
			相关系数	符号一致率
1925～1971 年	SCZD＝0.81IO	66.1%	0.813	85.1%
1925～1971 年	SCZD＝0.70IO＋0.15PDO＋0.31	68.2%	0.830	83.0%
1925～1971 年	SCZD＝0.66IO＋0.12PDO＋0.41AMO	86.3%	0.929	97.9%
1972～2009 年	SCR＝－0.85SIO	72.0%	0.853	92.0%
1972～2009 年	SCR＝－0.88SIO＋0.04NWPO	72.8%	0.860	93.5%
1972～2009 年	SCR＝－0.80SIO＋0.14NWPO＋0.13NA	79.0%	0.894	95.0%

仅拟合 1925～1971 年这一时段的 SCZDI。分别采用单因子（SIO）、双因子（SIO 和 NWPO）及三因子（SIO、NWPO 及 NA）回归拟合 1925～2009 年的 SCRI 的效果也均不如仅拟合 1972～2009 年这一时段的 SCRI（图略）。这表明在不同时期，多因子协同影响南方降水的机制也有所差异，因此分时段拟合的效果优于全时段拟合的效果。

6　结论与讨论

通过分析 1925～2009 年中国南方夏季降水的年代际变率特征及形成机制，揭示了中国南方夏季降水年代际变率的主模态，并采用诊断分析的方法系统研究了印度洋、北太平洋及北大西洋海温的年代际变率对南方夏季降水年代际变率主模态的协

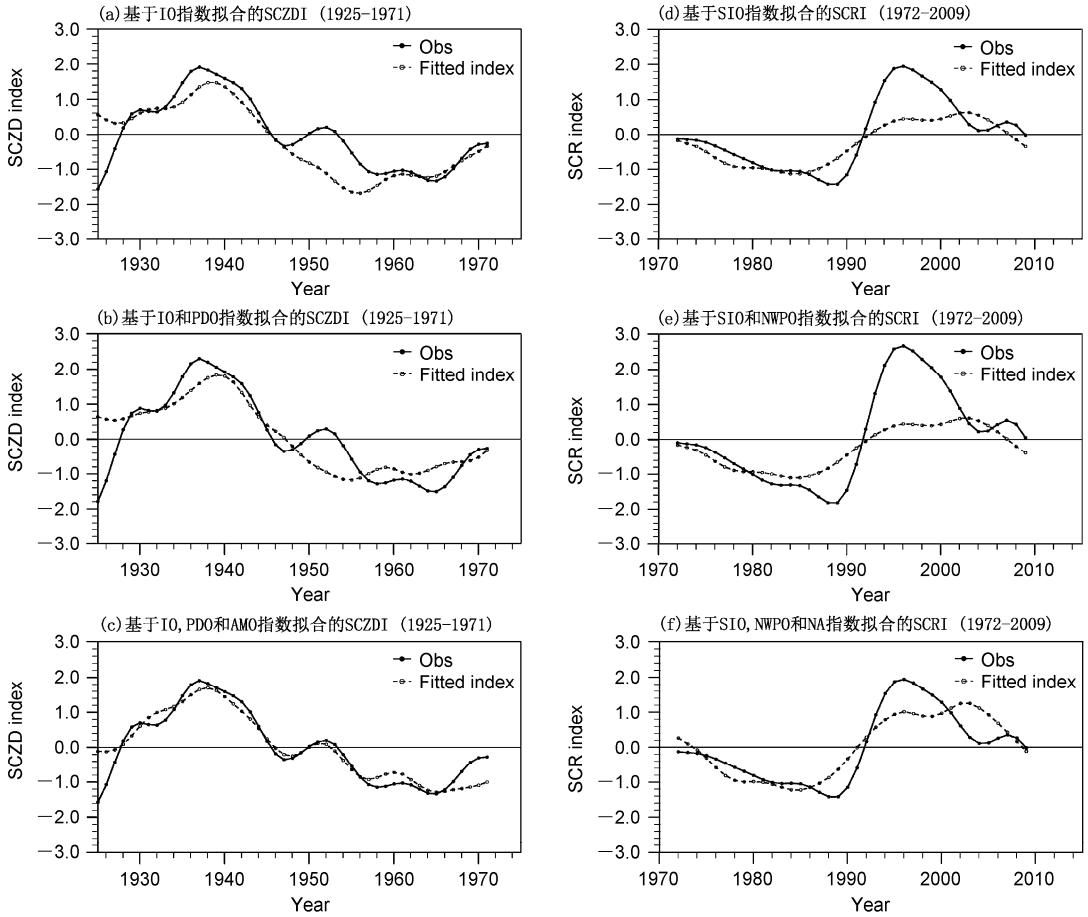

图 10　采用各海区海温指数回归拟合的东西反相型及一致型降水指数：（a、b、c）分别为采用单因子（IO）、双因子（IO、PDO）及三因子（IO、PDO 和 AMO）回归拟合的 1925～1971 年的 SCZD 指数；（d、e、f）分别为采用单因子（SIO）、双因子（SIO、NWPO）及三因子（SIO、NWPO 和 NA）回归拟合的 1972～2009 年的 SCR 指数。虚线为拟合的降水指数，加粗实线为对应时段的降水指数

Fig. 10　The fitted SCZD (Southern China Zonal Dipole) index and SCR (Southern China Rainfall) index using the indices of averaged SST anomalies in each sea region. (a, b, c) are the fitted SCZD indexes using one index (the IO index), two indices (the IO index and the PDO index), and three indices (the IO index, the PDO index and the AMO index) , respectively, for the period of 1925–1971. (d, e, f) are the fitted SCR indexes using one index (the SIO index), two indices (the SIO index and the NWPO index), and three indices (the SIO index, the NWPO index and the NA index) , respectively, for the period of 1972–2009. The dashed curves denote the fitted indices, and the bold solid curves denote the corresponding rainfall indices for the same period

同影响机制。

首先采用 1920～2014 年中国南方夏季逐月降水资料及经验正交分解的方法得到了南方夏季降水年代际变率的主模态。1925～2009 年，南方夏季降水年代际变率的主模态为一致型降水和东西反相型降水，两个模态累积解释方差约为 50%。中国南方夏季降水的第一主模态在 1971/1972 年发生了明显的年代际变化，由 1925～1971 年的东西反相型降水转变为 1972～2009 年的一致型降水。这两种主模态又可进一步分为四种降水型，分别是东多西少型降水（1929～1948 年及 2003～2009 年）、西多东少型降水（1954～1968 年）、一致偏少型降水（1973～1992 年）和一致偏多型降水（1993～2002 年）。因此，中国南方夏季降水年代际变率的主要年代际变化特点可以归纳为上述的“两模四型”，即两种降水主模态及对应的四类降水空间分布型。

揭示了印度洋海温距平（IO）、北太平洋海温距平（PDO）和北大西洋海温距平（AMO）协同影响南方地区东西反相型降水的机制。对于东多西少（西多东少）型降水的形成机制来说，当印度洋海温处于暖（冷）位相时，主要通过引起垂直环流异常来影响东西反相型降水，该环流的下沉支（上升支）位于中南半岛，在中南半岛低空形成异常的反气旋（气旋），不（有）利于向西南地区的水汽输送，从而不（有）利于西南地区降水；PDO 的暖（冷）位相则通过引起东亚低空的 PJ 型遥相关波列，在中国东南地区低空引起气旋（反气旋）性异常，增强（减弱）了自中国东海向南方地区东部的水汽输送，从而有（不）利于南方地区东部降水；而 AMO 暖（冷）位相则是通过引起北半球沿亚洲副热带西风急流传播的遥相关波列，在中国东南地区高层形成异常的正（负）活动中心，有（不）利于高空辐散，进而有（不）利于南方地区东部异常的上升运动，从而有（不）利于南方地区东部降水。IO，PDO 和 AMO 可以通过协同影响东亚地区的环流异常从而有利于东多西少（西多东少）型降水的形成。

揭示了南印度洋海温距平（SIO）、西北太平洋海温距平（NWPO）和北大西洋北部海温距平（NA）协同影响南方地区全区一致型降水的机制。对于全区一致偏多（偏少）型降水的形成机理来说，当南印度洋海温处于冷（暖）位相时，可以引起南印度洋低空辐散（辐合）及高空辐合（辐散），在东印度洋引起高空辐散（辐合）和低空辐合（辐散），进而有利于中国南海及西北太平洋地区的高空辐合（辐散）和低空辐散（辐合），在中国南海及西北太平洋地区低空形成异常的反气旋（气旋），有利于南方降水偏多（偏少）；当西北太平洋海温处于暖（冷）位相时，可以引起西太副高偏西偏强（偏东偏弱），也有利于西北太平洋低空形成反气旋（气旋）性异常，有（不）利于水汽自中国南海向南方地区输送，也有利于南方降水偏多（偏少）；而北大西洋北部海温暖（冷）位相通过引起欧亚大陆高纬度地区准正压的遥相关波列，在贝加尔湖东南侧低空形成反气旋（气旋）性异常，有（不）利于将冷空气向南方地区输送，并与来自南海的水汽在南方地区辐合，有利于南方地区形成一致偏多（偏少）型降水。SIO、NWPO 和 NA 可以通过协同影响东亚地区的环流异常从而有利于一致偏多（偏少）型降水的形成。

通过本文的研究，对中国南方夏季降水年代际变率特征及其形成机理有了更全面的认识。然而，仍有科学问题值得进一步讨论。除了海温年代际变率的影响，青藏高原热力因素等陆面外强迫因子对降水年代际变率也有一定影响（Ding et al., 2009），这值得进一步加以分析。北极海冰的异常对中高纬度环流及气候要素的年代际变化也有重要影响（Wu et al., 2009a, 2009b），其与中国南方夏季降水年代际变化的关系值得深入研究。另外，下一步需要采用数值模式模拟试验的方式进行南方夏季一致型降水及东西反相型降水特征和机制的深入研究。

参考文献（References）

Ambrizzi T, Hoskins B J, Hsu H H. 1995. Rossby wave propagation and teleconnection patterns in the austral winter [J]. J. Atmos. Sci., 52 (21): 3661–3672, doi:10.1175/1520-0469(1995)052<3661:RWPATP>2.0.CO;2.

Cao J, Yao P, Wang L, et al. 2014. Summer rainfall variability in low-latitude highlands of China and subtropical Indian Ocean dipole [J]. J. Climate, 27 (2): 880–892, doi:10.1175/JCLI-D-13-00121.1.

Compo G P, Whitaker J S, Sardeshmukh P D, et al. 2011. The twentieth century reanalysis project [J]. Quart. J. Roy. Meteor. Soc., 137 (654): 1–28, doi:10.1002/qj.776.

Dai A G. 2013. The influence of the inter-decadal Pacific oscillation on US precipitation during 1923–2010 [J]. Climate Dyn., 41 (3–4): 633–646, doi:10.1007/s00382-012-1446-5.

Ding Y H, Wang Z Y, Sun Y. 2008. Inter-decadal variation of the summer precipitation in East China and its association with decreasing Asian summer monsoon. Part I: Observed evidences [J]. Int. J. Climatol., 28 (9): 1139–1161, doi:10.1002/joc.1615.

Ding Y H, Sun Y, Wang Z Y, et al. 2009. Inter-decadal variation of the summer precipitation in China and its association with decreasing Asian summer monsoon Part II: Possible causes [J]. Int. J. Climatol., 29(13): 1926–1944, doi:10.1002/joc.1759.

Dong L, Zhou T J, Dai A G, et al. 2016. The footprint of the inter-decadal Pacific oscillation in Indian Ocean sea surface temperatures [J]. Sci. Rep., 6: 21251, doi:10.1038/srep21251.

Duchon C E. 1979. Lanczos filtering in one and two dimensions [J]. J. Appl. Meteor., 18 (8): 1016–1022, doi:10.1175/1520-0450(1979)018<1016:LFIOAT>2.0.CO;2.

黄荣辉, 陈际龙, 刘永. 2011. 我国东部夏季降水异常主模态的年代际变化及其与东亚水汽输送的关系 [J]. 大气科学, 35 (4): 589–606. Huang Ronghui, Chen Jilong, Liu Yong. 2011. Interdecadal variation of the leading modes of summertime precipitation anomalies over eastern China and its association with water vapor transport over East Asia [J]. Chinese Journal of Atmospheric Sciences (in Chinese), 35 (4): 589–606, doi:10.3878/j.issn.1006-9895.2011.04.01.

Knight J R, Folland C K, Scaife A A. 2006. Climate impacts of the Atlantic multidecadal oscillation [J]. Geophys. Res. Lett., 33 (17): L17706, doi:10.1029/2006GL026242.

Kosaka Y, Nakamura H. 2006. Structure and dynamics of the summertime Pacific–Japan teleconnection pattern [J]. Quart. J. Roy. Meteor. Soc., 132 (619): 2009–2030, doi:10.1256/qj.05.204.

Kwon M, Jhun J G, Ha K J. 2007. Decadal change in East Asian summer monsoon circulation in the mid-1990s [J]. Geophys. Res. Lett., 34 (21): L21706, doi:10.1029/2007GL031977.

Li Q X, Peng J D, Shen Y. 2012. Development of China homogenized monthly precipitation dataset during 1900–2009 [J]. J. Geogr. Sci., 22 (4): 579–593, doi:10.1007/s11442-012-0948-8.

Li S L, Perlwitz J, Quan X W, et al. 2008. Modelling the influence of North Atlantic multidecadal warmth on the Indian summer rainfall [J]. Geophys. Res. Lett., 35 (5): L05804, doi:10.1029/2007GL032901.

李维京, 张若楠, 孙丞虎, 等. 2016. 中国南方旱涝年际年代际变化及成因研究进展 [J]. 应用气象学报, 27 (5): 577–591. Li Weijing, Zhang Ruonan, Sun Chenghu, et al. 2016. Recent research advances on the interannual-interdecadal variations of drought/flood in South China and associated causes [J]. J. Appl. Meteor. Sci. (in Chinese), 27 (5): 577–591, doi:10.11898/1001-7313.20160507.

李维京, 左金清, 宋艳玲, 等. 2015. 气候变暖背景下我国南方旱涝灾害时空格局变化 [J]. 气象, 41 (3): 261–271. Li Weijing, Zuo Jinqing, Song Yanling, et al. 2015. Changes in spatio–temporal distribution of drought/flood disaster in southern China under global climate warming [J]. Meteor. Mon. (in Chinese), 41 (3): 261–271, doi:10.7519/j.issn.1000-0526.2015.03.001.

Li W J, Ren H C, Zuo J Q, et al. 2017a. Early summer southern China rainfall variability and its oceanic drivers [J]. Climate Dyn., doi:10.1007/s00382-017-3898-0. (in Press)

Li Y, Ding Y H, Li W J. 2017b. Interdecadal variability of the Afro-Asian summer monsoon system [J]. Adv. Atmos. Sci., 34 (7): 833–846, doi:10.1007/s00376-017-6247-7.

Lin J S, Wu B, Zhou T J. 2016. Is the interdecadal circumglobal teleconnection pattern excited by the Atlantic multidecadal oscillation? [J]. Atmos. Oceanic Sci. Lett., 9 (6): 451–457, doi:10.1080/16742834.2016.1233800.

刘芸芸, 李维京, 艾税秀, 等. 2012. 月尺度西太平洋副热带高压指数的重建与应用 [J]. 应用气象学报, 23 (4): 414–423. Liu Yunyun, Li Weijing, Ai Wanxiu, et al. 2012. Reconstruction and application of the monthly western Pacific subtropical high indices [J]. J. Appl. Meteor. Sci. (in Chinese), 23 (4): 414–423, doi:10.3969/j.issn.1001-7313.2012.04.004.

Livezey R E, Chen W Y. 1983. Statistical field significance and its determination by Monte Carlo techniques [J]. Mon. Wea. Rev., 111 (1): 46–59, doi:10.1175/1520-0493(1983)111<0046:SFSAID>2.0.CO;2.

Lorenz E N. 1956. Statistical forecasting program: Empirical orthogonal functions and statistical weather prediction [J]. Sci. Rep., 409 (2): 997–999.

Lu R Y, Dong B W, Ding H. 2006. Impact of the Atlantic multidecadal oscillation on the Asian summer monsoon [J]. Geophys. Res. Lett., 33 (24): L24701, doi:10.1029/2006GL027655.

Mantua N J, Hare S R, Zhang Y. 1997. A Pacific interdecadal climate oscillation with impacts on salmon production [J]. Bull. Amer. Meteor. Soc., 78 (6): 1069–1080, doi:10.1175/1520-0477(1997)078<1069:APICOW>2.0.CO;2.

New M, Hulme M, Jones P. 2000. Representing twentieth-century space–time climate variability. Part II: Development of 1901–96 monthly grids of terrestrial surface climate [J]. J. Climate, 13 (13): 2217–2238, doi:10.1175/1520-0442(2000)013<2217:RTCSTC>2.0.CO;2.

North G R, Bell T L, Cahalan R F, et al. 1982. Sampling errors in the estimation of empirical orthogonal functions [J]. Mon. Wea. Rev., 110 (7): 699–706, doi:10.1175/1520-0493(1982)110<0699:SEITEO>2.0.CO;2.

Rayner N A, Parker D E, Horton E B, et al. 2003. Global analyses of sea surface temperature, sea ice, and night marine air temperature since the late nineteenth century [J]. J. Geophys. Res., 108 (D14): 4407, doi:10.1029/2002JD002670.

Si D, Ding Y H. 2016. Oceanic forcings of the interdecadal variability in East Asian summer rainfall [J]. J. Climate, 29 (21): 7633–7649, doi:10.1175/JCLI-D-15-0792.1.

Sun C, Kucharski F, Li J P, et al. 2017. Western tropical Pacific multidecadal variability forced by the Atlantic multidecadal oscillation [J]. Nat. Commun., 8: 15998, doi:10.1038/ncomms15998.

Sutton R T, Hodson D L R. 2007. Climate response to basin-scale warming and cooling of the North Atlantic Ocean [J]. J. Climate, 20 (5): 891–907, doi:10.1175/JCLI4038.1.

Wang B, Zhang Q. 2002. Pacific–East Asian teleconnection. Part II: How the Philippine Sea anomalous anticyclone is established during El Niño development [J]. J. Climate, 15 (22): 3252−3265, doi:10.1175/1520-0442(2002)015<3252:PEATPI>2.0.CO;2.

Wang H J. 2001. The weakening of the Asian monsoon circulation after the end of 1970's [J]. Adv. Atmos. Sci., 18 (3): 376–386, doi:10.1007/BF02919316.

Wang Y M, Li S L, Luo D H. 2009. Seasonal response of Asian monsoonal climate to the Atlantic multidecadal oscillation [J]. J. Geophys. Res., 114 (D2): D02112, doi:10.1029/2008JD010929.

Wu B, Zhou T J, Li T. 2016. Impacts of the Pacific–Japan and circumglobal teleconnection patterns on the interdecadal variability of the East Asian

summer monsoon [J]. J. Climate, 29 (9): 3253–3271, doi:10.1175/JCLI-D-15-0105.1.

Wu B Y, Yang K, Zhang R H. 2009a. Eurasian snow cover variability and its association with summer rainfall in China [J]. Adv. Atmos. Sci., 26 (1): 31–44, doi:10.1007/s00376-009-0031-2.

Wu B Y, Zhang R H, Wang B, et al. 2009b. On the association between spring Arctic sea ice concentration and Chinese summer rainfall [J]. Geophy. Res. Lett, 36 (9): L09501, doi:10.1029/2009GL037299.

Wu R G, Wen Z P, Yang S, et al. 2010. An interdecadal change in southern China summer rainfall around 1992/93 [J]. J. Climate, 23 (9): 2389–2403, doi:10.1175/2009JCLI3336.1.

Wu X F, Mao J Y. 2017. Interdecadal variability of early summer monsoon rainfall over South China in association with the Pacific decadal oscillation [J]. Int. J. Climatol., 37 (2): 706–721, doi:10.1002/joc.4734.

Xie S P, Hu K M, Hafner J, et al. 2009. Indian Ocean capacitor effect on Indo-western Pacific climate during the summer following El Niño [J]. J. Climate, 22 (3): 730–747, doi:10.1175/2008JCLI2544.1.

Xu Z Q, Fan K, Wang H J. 2015. Decadal variation of summer precipitation over China and associated atmospheric circulation after the late 1990s [J]. J. Climate, 28 (10): 4086–4106, doi:10.1175/JCLI-D-14-00464.1.

Yang Q, Ma Z G, Fan X G, et al. 2017. Decadal modulation of precipitation patterns over eastern China by sea surface temperature anomalies [J]. J. Climate, 30 (17): 7017–7033, doi:10.1175/JCLI-D-16-0793.1.

Zhang H Y, Wen Z P, Wu R G, et al. 2017. Inter-decadal changes in the East Asian summer monsoon and associations with sea surface temperature anomaly in the South Indian Ocean [J]. Climate Dyn., 48 (3–4): 1125–1139, doi:10.1007/s00382-016-3131-6.

Zhang L X, Zhou T J. 2015. Drought over East Asia: A review [J]. J. Climate, 28 (8): 3375–3399, doi:10.1175/JCLI-D-14-00259.1.

张庆云, 吕俊梅, 杨莲梅, 等. 2007. 夏季中国降水型的年代际变化与大气内部动力过程及外强迫因子关系 [J]. 大气科学, 31 (6): 1290–1300. Zhang Qingyun, Lü Junmei, Yang Lianmei, et al. 2007. The interdecadal variation of precipitation pattern over China during summer and its relationship with the atmospheric internal dynamic processes and extra-forcing factors [J]. Chinese Journal of Atmospheric Sciences (in Chinese), 31 (6): 1290–1300, doi:10.3878/j.issn.1006-9895.2007.06.23.

Zhang Y, Wallace J M, Battisti D S. 1997. ENSO-like interdecadal variability: 1900–93 [J]. J. Climate, 10 (5): 1004–1020, doi:10.1175/1520-0442(1997)010<1004:ELIV>2.0.CO;2.

Zhu Y L, Wang H J, Ma J H, et al. 2015. Contribution of the phase transition of Pacific decadal oscillation to the late 1990s' shift in East China summer rainfall [J]. J. Geophys. Res., 120 (17): 8817–8827, doi:10.1002/2015JD023545.

Zhu Y L, Wang H J, Zhou W, et al. 2011. Recent changes in the summer precipitation pattern in East China and the background circulation [J]. Climate Dyn., 36 (7–8): 1463–1473, doi:10.1007/s00382-010-0852-9.

Received: 8 March 2018 | Revised: 18 November 2018 | Accepted: 20 November 2018

DOI: 10.1002/joc.5944

International Journal of Climatology RMetS

RESEARCH ARTICLE

Concurrent droughts and hot extremes in northwest China from 1961 to 2017

Xin Li[1,2] | Qinglong You[1,4] | Guoyu Ren[3] | Suyan Wang[2] | Yuqing Zhang[1] | Jianling Yang[2] | Guangfen Zheng[2]

[1]Key Laboratory of Meteorological Disaster, Ministry of Education/Joint International Research Laboratory of Climate and Environmental Change/Collaborative Innovation Center on Forecast and Evaluation of Meteorological Disasters/Earth System Modeling Center, Nanjing University of Information Science and Technology, Nanjing, China

[2]Key Laboratory of Meteorological Disaster Monitoring and Early Warning and Risk Management of Characteristic Agriculture in Arid Regions, CMA, Yinchuan, China

[3]Laboratory for Climate Studies, National Climate Center, CMA, Beijing, China

[4]Department of Atmospheric and Oceanic Sciences & Institute of Atmospheric Sciences, Fudan University, Shanghai, China

Correspondence
Qinglong You, Key Laboratory of Meteorological Disaster, Ministry of Education/Joint International Research Laboratory of Climate and Environmental Change/Collaborative Innovation Center on Forecast and Evaluation of Meteorological Disasters/Earth System Modeling Center, Nanjing University of Information Science and Technology, Nanjing, China.
Email: yqingl@126.com

Funding information
China Meteorological PublicWelfare Scientific Research Project, Grant/Award Number: GYHY201306027GYHY201506001; National Key R&D Program of China, Grant/Award Number: 2016YFA0601702; National Natural Science Foundation of China, Grant/Award Number: 41771069; the Priority Academic Program Development of Jiangsu Higher Education Institutions(PAPD)

Northwest China forms the main part of the arid and semiarid areas in China, and even includes some extremely arid areas. This zone of interaction is affected by the westerlies and monsoons making it sensitive to global climate change. Drought is the main type of natural disaster affecting northwest China. Global warming has caused a gradual strengthening of the frequency and intensity of hot extremes, when dry conditions and heatwaves occur simultaneously or successively; as a result, that socio-economic risks can increase considerably. The present study examined changes in concurrent droughts and hot extremes in northwest China during 1961–2017 based on data from 119 meteorological stations. The result shows that the frequency of concurrent droughts and hot extremes exhibited an increasing trend over most parts of northwest China, while a negative trend occurred in western Xinjiang and at some sites in Qinghai. Concurrent droughts and hot extremes appeared more often in May in western Xinjiang, and in summer in other parts of northwest China. Overall, the trends of such concurrent events, regardless of different definitions, increased from 1961–2017 over northwest China. In particular, from 1981–2017, the trend rose more significantly than in other decades, and reached an abrupt point of change in 1996. Although the trend changed from a positive significant signal to a negative one from 2001–2017, the trend grew 2–3 times from 1997–2017. Changes in large-scale atmospheric circulation show that an anticyclonic circulation strengthened, increasing in geopotential height over the midhigh latitudes of Eurasia and was centred on Mongolia and Lake Baikal. This enhanced relative humidity in western Xinjiang and eastern Qinghai, and weakened it elsewhere from 1997–2017. These changes have contributed to the changes in the spatial distribution and trends in concurrent droughts and hot extremes in northwest China.

KEYWORDS
concurrent droughts and hot extremes, northwest China, SPEI, threshold

1 | INTRODUCTION

Extreme climatic events, such as hot extremes and droughts both lead to serious environmental and economic problems. Droughts are considered among the most costly type of natural disasters because of their effects on crop yield, infrastructure, industry, and tourism (Mishra and Singh, 2010). Droughts develop more slowly than other types of extreme weather and climate phenomena, such as floods, hurricanes, and tornadoes (Nasrollahi *et al.,* 2015). Droughts are projected to increase in frequency and severity in the future as a result of climate change, mainly as a consequence of decreases in regional

 © 2018 Royal Meteorological Society

precipitation but also because of increasing evaporation driven by global warming (Dai, 2011; Trenberth, 2011; Sheffield *et al.,* 2012; Greve *et al.,* 2018; Samaniego *et al.,* 2018). The relationship between droughts and hot extremes is widely acknowledged (Vautard *et al.,* 2007; Zampieri *et al.,* 2009; Mueller and Seneviratne, 2012). High temperatures lead to accelerated soil evaporation, reduced soil moisture, and plant water loss. A lack of soil moisture strongly reduces latent cooling and thereby has a crucial effect on the spatial extent and amplitude of hot extremes. The occurrence probability of hot extremes is increasing under global warming (Perkins *et al.,* 2012; Donat *et al.,* 2013; Seneviratne *et al.,* 2014; Chen and Zhai, 2017). Soil moisture deficits are likely to enhance the frequency and duration of hot extremes (Hirschi *et al.,* 2010). In some regions, hot extremes have been shown to be induced by surface moisture deficits (Seneviratne *et al.,* 2010; Mueller and Seneviratne, 2012).

Northwest China lies in the centre of the innermost part (31°–50°N, 73°–111°E) of the Eurasian continent, where isolation from any nearby oceans results in a dry climate (Shi *et al.,* 2006) (Figure 1). This region forms the main part of the arid and semiarid areas in China, and even includes some extremely arid areas. Droughts are the main type of natural disasters occurring in this region, although observations show that precipitation rates have experienced an increasing trend over the past 50 years in the western part of northwest China (Shi *et al.,* 2006; Li *et al.,* 2016; Ren *et al.,* 2016; Peng and Zhou, 2017). The frequency and intensity of hot extremes are increasing in a warming climate, trend that is predicted to increase in the future as a result of climate change in northwest China (Ding *et al.,* 2010; Li *et al.,* 2012; Chen *et al.,* 2018; Chen and Sun, 2018; Xu *et al.,* 2018; Zhu *et al.,* 2018). As one of the most sensitive areas in the world in terms of responding to global climate change, when dry conditions and heatwaves occur simultaneously or successively, the combined effects often have severe additional impacts while socioeconomic risks increase (Mishra and Singh, 2010; AghaKouchak *et al.,* 2014; Leonard *et al.,* 2014; Mazdiyasni and AghaKouchak, 2015; Zhang *et al.,* 2018). In this study, we focused on changes in events involving concurrent droughts and hot extremes in northwest China using the standardized precipitation evapotranspiration index (SPEI) (Vicente-Serrano *et al.,* 2010; Beguería *et al.,* 2014; Yu *et al.,* 2014). Moreover, we investigate the change of climate extremes caused by both individual and joint occurrence of droughts and hot extremes while focusing on additional information related to an analysis of how concurrent extreme events differ from the variables individually.

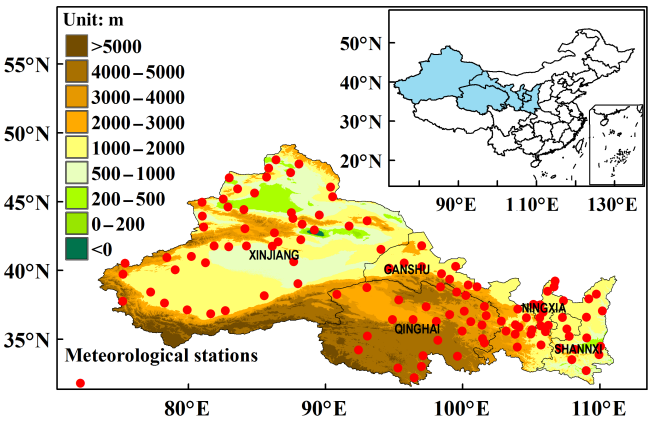

FIGURE 1 The distribution of the meteorological stations in northwest China [Colour figure can be viewed at wileyonlinelibrary.com]

2 | METHODS

2.1 | Data

The monthly precipitation (mm), air temperature (°C), and daily maximum temperature data (°C) acquired during 1961–2017 from 119 meteorological stations in northwest China were collected from the National Meteorological Information Centre of the China Meteorological Administration, available from http://data.cma.cn/ (Figure 1). Daily maximum temperatures have been adjusted for homogeneity and abrupt discontinuities have been corrected. Missing data of one or 2 days were filled in by average values of day −1 and day +1. Monthly data have been verified by quality control and homogeneity assessment, and availability of various weather elements is generally above 99%. Monthly average data were used to compute the SPEI to represent meteorological drought. Daily maximum temperature data were used to compute the hot extremes as described in Section 2.3 below.

In addition to observational data, monthly National Centers for Environmental Prediction/National Center for Atmospheric Research (NCEP/NCAR) Reanalysis 1 dataset with a grid resolution of 2.5° × 2.5° from 1961 to 2017 are used to investigate the atmospheric circulation changes controlling concurrent of droughts and hot extremes in northwest China, including geopotential height at 500 hPa and relative humidity at 700 hPa.

2.2 | Droughts

In this work, the SPEI was employed for defining drought events. The SPEI was developed by combining the sensitivity of the Palmer Drought Severity Index (Palmer, 1965) to the changes in evaporative demand (caused by air temperature fluctuations and trends) with fairly simple calculation methods; however, the SPEI also has the robustness of the multitemporal nature of evaporative demand, such as the Standardized Precipitation Index (McKee *et al.,* 1993). The multiscalar characteristics of the main formula are as follows (Vicente-Serrano *et al.,* 2010; Yang *et al.,* 2017):

$$D_n^k = \sum_{i=0}^{k-1} (P_{n-i} - \mathrm{PET}_{n-i}), \quad (1)$$

where D_n^k is the aggregate of the difference between the precipitation (P) and potential evapotranspiration (PET) from month ($n - k + 1$) to month (n) on a timescale (k). For example, when

k is 12, D_n^{12} is the sum of the moisture anomalies for the antecedent 11 months plus that of the current month.

Different methods have been proposed to indirectly estimate PET from meteorological parameters measured at weather stations. Therefore, we followed the simplest approach to calculate PET (Thornthwaite, 1948), which has the advantage of only requiring data on the mean monthly temperature. Following this method, the monthly PET (Breshears *et al.,* 2005) is obtained by Equation (2):

$$PET = 16d\left(\frac{10T}{I}\right)^a, \tag{2}$$

where T is the monthly-mean temperature (°C); I is a heat index, which is calculated as the sum of 12 monthly index values i, the latter being derived from mean-monthly temperature using Equation (3):

$$i = \left(\frac{T}{5}\right)^{1.514}, \tag{3}$$

where a is a coefficient depending on I:

$$a = 6.75\times10^{-7}I^3 - 7.71\times10^{-5}I^2 + 1.79\times10^{-2}I + 0.492, \tag{4}$$

where d is a correction coefficient that depends on the latitude and month. Next, the water balance is normalized into a log-logistic probability distribution to obtain the SPEI index series. The log-logistic distribution was selected for standardizing the D series to obtain the SPEI. The probability density function of log-logistic distributed variable is expressed as (Yu *et al.,* 2014):

$$f(x) = \frac{\beta}{\alpha}\left(\frac{x-\gamma}{\alpha}\right)\left[1+\left(\frac{x-\gamma}{\alpha}\right)\right]^{-2}, \tag{5}$$

where α, β, and γ are the scale, shape, and origin parameters, respectively, for D values in the range of ($\gamma > D < \infty$). The three parameters of the Pearson III distribution can be obtained following Singh *et al.,* 1993.

Thus, the probability distribution function of the D series is given by Equation (6):

$$F(x) = \left[1+\left(\frac{\alpha}{x-\gamma}\right)^{\beta}\right]^{-1}. \tag{6}$$

Then with $F(x)$, the SPEI can easily be obtained as the standardized values of $F(x)$ (Abramowitz and Stegun, 1964):

$$\mathrm{SPEI} = W - \frac{C_0 + C_1W + C_2W^2}{1 + d_1W + d_2W^2 + d_3W^3}, \tag{7}$$

where $W = \sqrt{-2ln(P)}$ for $p \le 0.5$ and P is the probability of exceeding a determination D value, $P = 1 - F(x)$. If $p > 0.05$, then P is replaced by 1–P and the sign of the resultant SPEI is reversed. The constants are $C_0 = 2.515517$, $C_1 = 0.802853$, $C_2 = 0.010328$, $d_1 = 1.432788$, $d_2 = 0.189269$, and $d_2 = 0.001308$.

In the present study, the SPEI was calculated over 12-month (for drought trends and analysis) and 3-month (for concurrent droughts and hot extremes analysis) time scales using monthly air temperature and precipitation data for the period of 1961–2017 from 119 stations covering northwest China. A drought is defined as an event that has an SPEI of <-1.0.

2.3 | Hot extremes

A hot extreme event was defined as a period of ≥3 consecutive days with maximum temperatures above the daily threshold for each month of the period 1961–2017. The threshold is defined as the 85th and 90th percentile levels of daily maxima for a given location (Meehl and Tebaldi, 2004; Perkins and Alexander, 2013; Russo *et al.,* 2014), to capture a relatively large number of events. There is a consensus that the 85th and 90th percentiles can be defined as extreme (Easterling *et al.,* 2000; Perkins and Alexander, 2013).

We only considered events that occurred during a 6-month warm season (May–October) for hot extremes using the following two conditions: the daily maximum temperature above the 85th or 90th percentile for at least three consecutive days for H_{85} or H_{90}, respectively.

2.4 | Concurrent droughts and hot extremes

We derived concurrent droughts and hot extremes in northwest China by summing the number of concurrent events occurring during May–October for each year. When a month 3-month SPEI < -1.0, we respectively summed the number of different conditions of hot extremes for each month (Mazdiyasni and AghaKouchak, 2015). Here, the number of concurrent droughts and hot extremes was defined as follows: simultaneous a month 3-month SPEI < -1.0 and hot extremes for a fixed H_{85} (DH_{85}) or H_{90} (DH_{90}).

2.5 | Trend analysis methods

The linear trend over time was assessed using Pearson's Correlation Tests (Pearson, 1895). The statistical significance of the linear trend was assessed at the 95% level.

A Mann–Kendall (MK) test for abrupt change of time series was employed (Mann, 1945; Kendall, 1975). The MK test for monotonic trends is a nonparametric method that can reveal the changing trend in a time series, and has been widely applied in climatology. It calculates two standardized statistic series, UF and UB as defined below, for a data series and plots them with confidence lines. The null hypothesis is rejected and a significant abrupt change occurred if the UF curve and the UB curve intersect within the confidence zone. The present study used the confidence level of 95% (1.96 and −1.96) as the boundary lines of the confidence zone (Du *et al.,* 2015).

Given a time series of $X = (x_1, x_2, x_3, \ldots, x_n)$,the statistical parameter f_k was given using Equation (8):

$$f_k = \sum_{i=1}^{k} \sum_{j=1}^{i} \text{log}istic(x_i > x_j), \quad k = 2,3,\ldots,n, \tag{8}$$

when $x_i > x_j$, logistic $(x_i > x_j)$ is 1, and 0 otherwise. The mean and variance of f_k were defined using Equations (9) and (10):

$$E[f_k] = \frac{k(k-1)}{4} \text{ and } \text{var}(f_k) = k(k-1)(2k+5)/72 \tag{9}$$

$$UF(k) = \frac{[f_k - E(f_k)]}{\sqrt{var(f_k)}}, \quad (k = 2,3,\ldots,n). \tag{10}$$

A reversed data series $X' = (x'_1, x'_2, x'_3, \ldots, x'_n) = (x_n, x_{n-1}, x_{n-2}, \ldots, x_1)$ was used in the calculation for UB.

$$UB(k) = -\frac{[f_k - E(f_k)]}{\sqrt{var(f_k)}}, \quad (k = 2,3,\ldots.n), \tag{11}$$

where f_k, $E(f_k)$, and var(f_k) were calculated using the same equations used for UF(k).

3 | RESULTS

3.1 | Characteristics of drought in northwest China

In general, from 1961 to 2017 the frequency of annual droughts over northwest China has been between 0.30 and 0.40 year^{-1} (Figure 2a), where a drought is defined as a 12-month period during which the SPEI < -1.0 in December. The annual drought frequency in western northwest China, Ningxia, and in some parts of Gansu and Shaanxi Provinces was higher than other areas of northwest China. In particular, droughts in the Tarim and Turpan basins occurred most often because the regions experience a warm temperate continental climate in this area of extremely arid desert (Yang and Scuderi, 2017).

Annual SPEI trends in northwest China for the period 1961–2017 showed a strongly different pattern of distribution. Droughts occurred with increasing frequency mainly in eastern Xinjiang, the northern area of Golmud in the Qinghai Province, the Hexi Corridor, Ningxia to Longnan, and north Shaanxi; the trends of the annual SPEI in these areas were less than -0.20 decade^{-1}. In western Xinjiang and some areas of Qinghai, a decrease in drought occurrence was detected (Figure 2b). The spatial changes in the water vapour flux in northwest China were similar to the spatial distribution of SPEI (Wei *et al.,* 2010; Ren *et al.,* 2016).

The surface-sensible heat flux in northwest China was the strongest on the Eurasian continent; however, the corresponding surface latent heat flux in the present study area was very weak (Bueh *et al.,* 2002). Conversely, the heat flux reflected the lack of a water source in this region, leading to the deficiency in annual precipitation.

Although previous research has shown that northwest China has generally become wetter (Zou *et al.,* 2005), the decadal probability of a monthly drought event (3-month SPEI < -1.0) between May and October shows other and different characteristics. The probability of a monthly drought in the southwest of Xinjiang, the Hexi Corridor, and Ningxia was below 10%; meanwhile, in northwest Xinjiang and east Qinghai, it was between 20 and 40%, and in other parts of the region fell between 10 and 20% in the 1960s and 1970s (Figure 3a,b). The area with a less than 10% probability of a monthly drought in the 1980s increased when compared with that of the 1960s and 1970 (Figure 3c). However, from 1990 through to 2017, this probability increased to greater than 20% in most parts of northwest China while the area with the probability of drought at below 10% shrank in spatial extent. The probability of a monthly drought in southwest Xinjiang, the Hexi Corridor, and in Northern Ningxia increased to greater than 30%, and even to as much as 50%, but decreased in east Qinghai and Shaanxi (Figure 3d,e,f)). Our result shows that although the frequency of droughts declined in the 1980s, the threat of drought in the above area continued to exist.

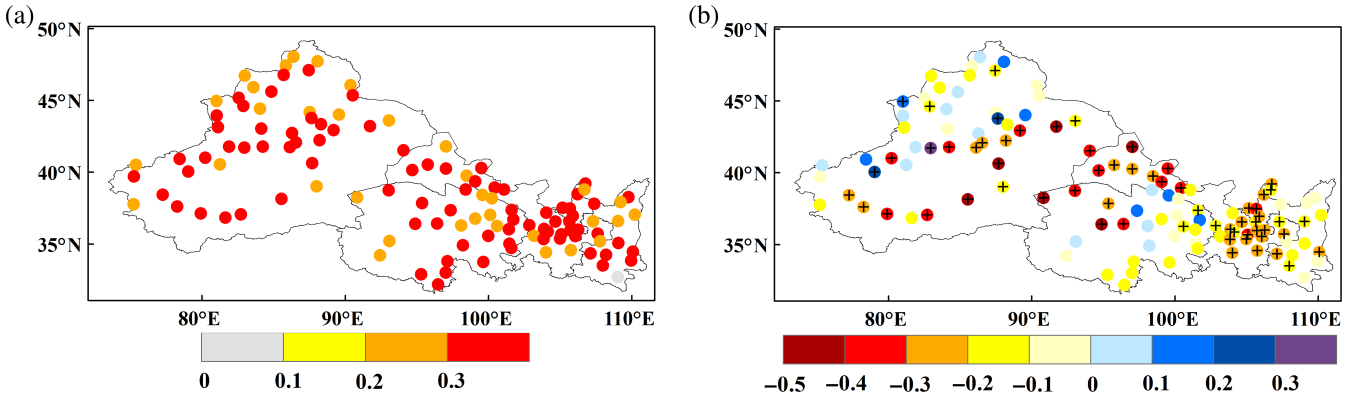

FIGURE 2 (a) Spatial distribution of drought, which is defined as a 12-month standardized precipitation evapotranspiration index (SPEI) < -1.0 between 1961–2017 over northwest China (unit: Year^{-1}) and (b) trend in the variation of the 12-month SPEI over northwest China for 1961–2017 (unit: Decade^{-1}); + indicates statistical significance at the 95% confidence level) [Colour figure can be viewed at wileyonlinelibrary.com]

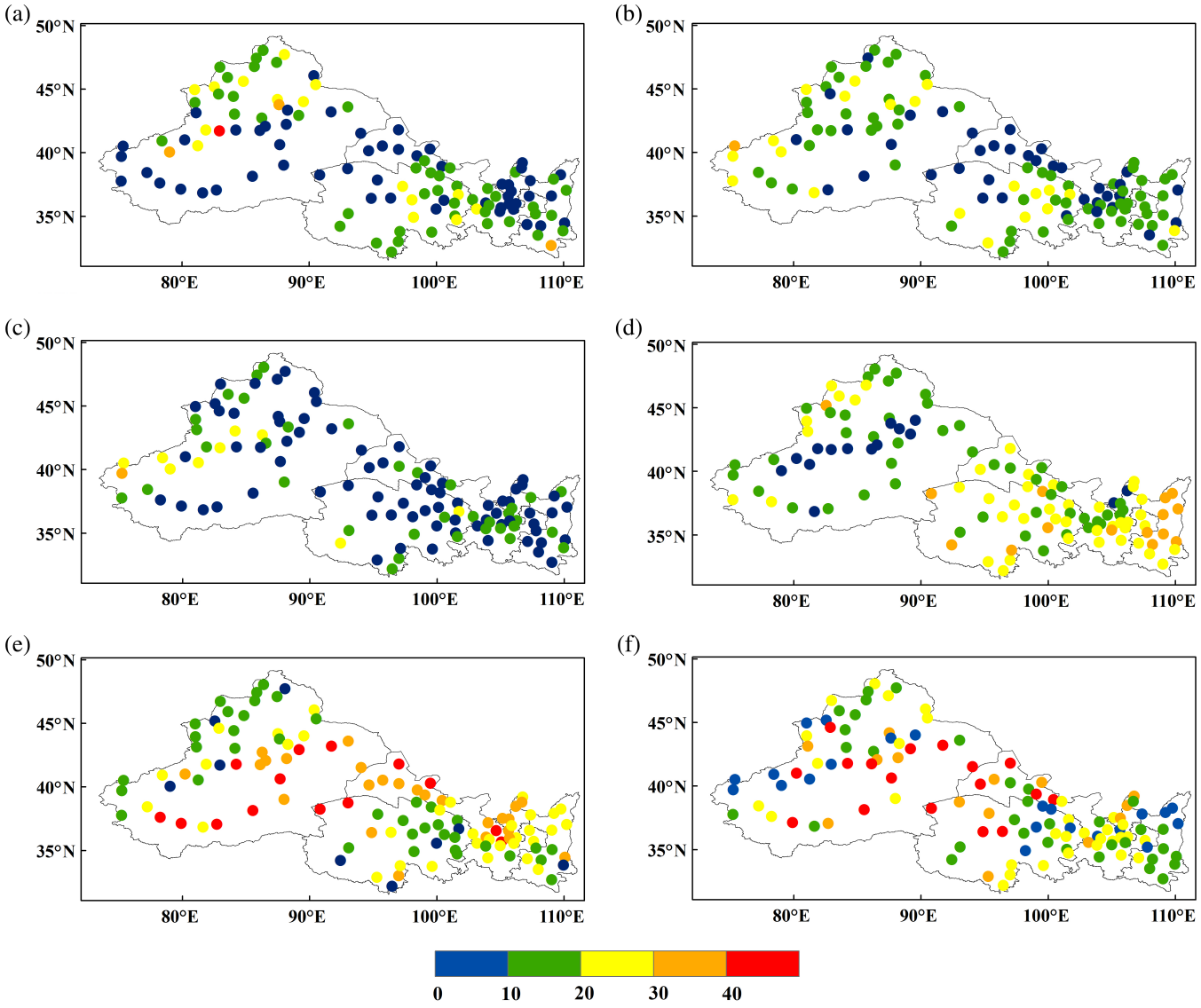

FIGURE 3 Decadal probability of a monthly drought event (3-month SPEI < −1.0) between May and October over northwest China (unit: %): (a) 1960s, (b) 1970s, (c) 1980s, (d) 1990s, (e) 2000s, and (f) 2011–2017 [Colour figure can be viewed at wileyonlinelibrary.com]

3.2 | Characteristics of hot extremes in northwest China

Clear increasing trends were observed for hot extreme events in most parts of northwest China for the period of 1961–2017 (Figure 4). Regardless of the thresholds and duration, the trends of hot extreme events showed a similar spatial distribution across the study area. An increasing trend was mainly observed in southern Xinjiang, the Hexi Corridor, and Ningxia; the trends of H_{85} included increases of greater than 0.60 decade^{-1}. The trends of H_{90} in the above areas were initially smaller, but also showed significant increasing trends at the 95% confidence level.

3.3 | Characteristics of concurrent droughts and hot extremes in northwest China

The time series of annual concurrent droughts and hot extremes over northwest China were calculated based on the average of 119 stations from 1961–2017. The number of concurrent droughts and hot extremes increased sharply in the 1990s and the rate of change remained stable in other years, regardless of different definitions (Figure 5). Figure 6 shows the result of the MK abrupt change test for the number of concurrent of droughts and hot extremes and was used to detect potential abrupt changes over the period of 1961–2017. An intersection point between UF and UB curves was detected in 1996 and was significant at the confidence level of 95%. Before the abrupt change point, the number of concurrent droughts and hot extremes did not increase significantly at the confidence level of 95% (UF statistic < 1.96); since 1996, however, the UF statistic exceeded 1.96, which marks the 95% confidence level for a significant increasing trend. The mean annual numbers of DH_{85} and DH_{90} from 1961–1996 were 0.6 and 0.4; later, the numbers increased to 1.7 and 1.2 during 1997–2017 by growing by 2.8 and 3.2 times, respectively.

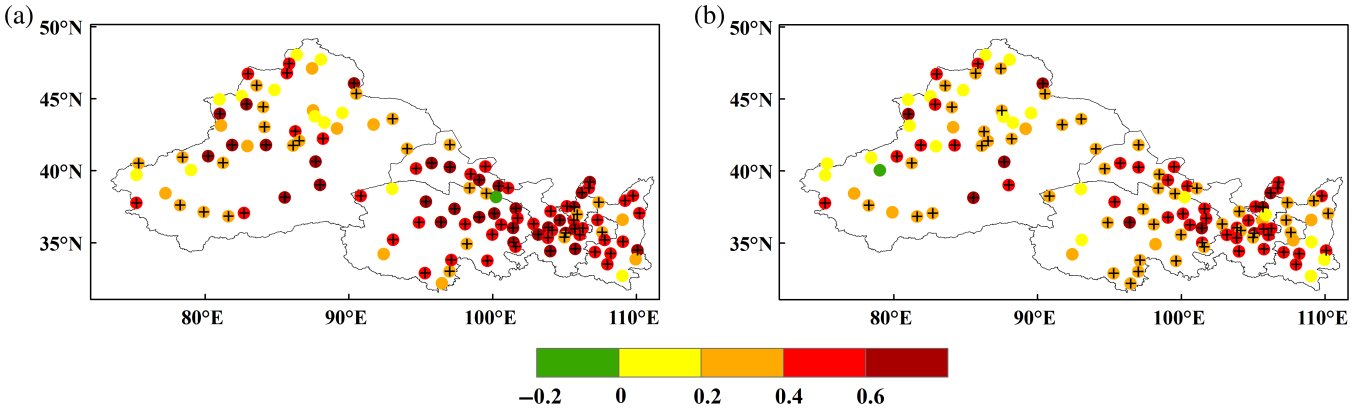

FIGURE 4 Trend variations of the number of hot extremes for the period of 1961–2017 in northwest China (unit: Decade^{-1}), (a) H_{85}, (b) H_{90} (+ represents statistical significance at the 95% confidence level). H_{85} and H_{90} indicate the daily maximum temperature exceeded the 85th and 90th percentile for at least three consecutive days, respectively [Colour figure can be viewed at wileyonlinelibrary.com]

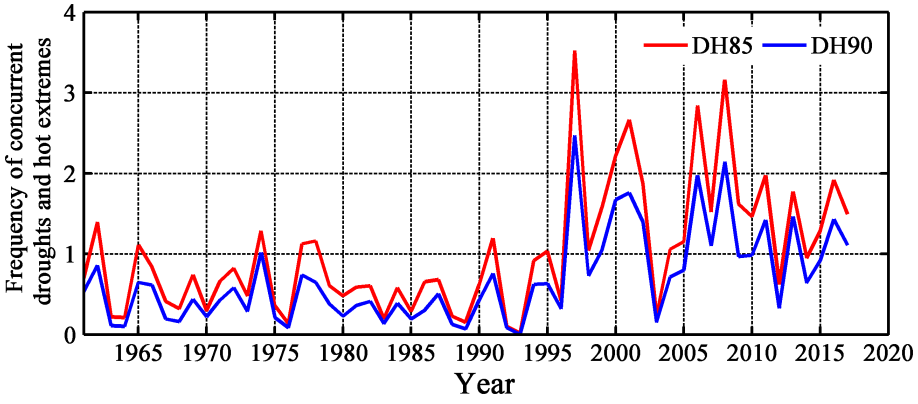

FIGURE 5 Variations in the number of concurrent droughts and hot extremes for the period of 1961–2017 in northwest China. Red line for DH_{85}, blue line for DH_{90}. DH_{85} and DH_{90} indicate simultaneous a month 3-month SPEI < −1.0 and hot extremes during which the daily maximum temperature exceeded the 85th and 90th percentiles for at least three consecutive days, respectively [Colour figure can be viewed at wileyonlinelibrary.com]

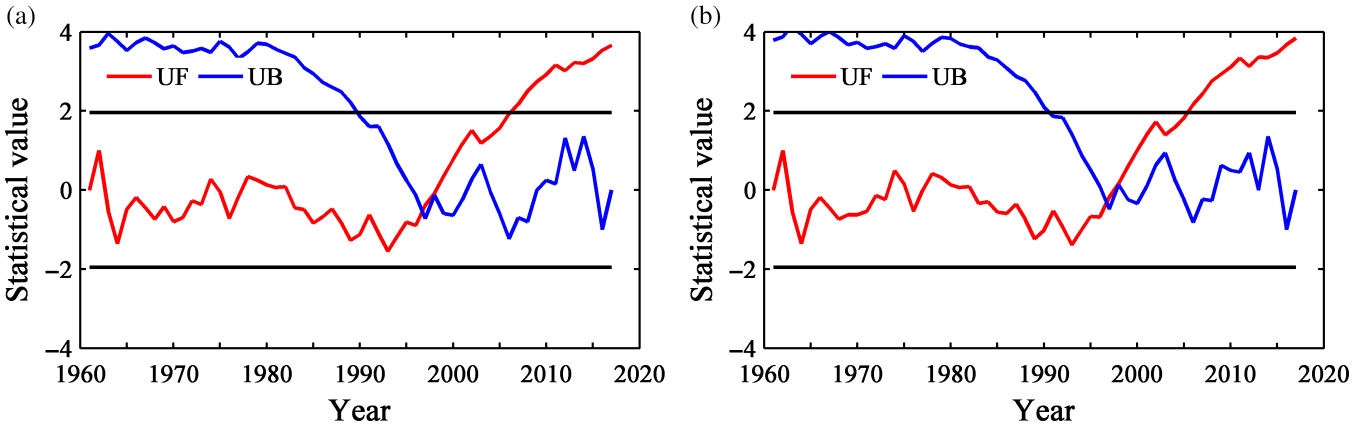

FIGURE 6 Mann–Kendall test for the number of concurrent droughts and hot extremes for the period of 1961–2017 in northwest China, (a) DH_{85}, (b) DH_{90}. DH_{85} and DH_{90} indicate simultaneous a month 3-month SPEI < −1.0 and hot extremes during which the daily maximum temperature exceeded the 85th and 90th percentiles for at least three consecutive days, respectively [Colour figure can be viewed at wileyonlinelibrary.com]

We applied a running trend analysis to determine whether the trend signal was persistent in concurrent droughts and hot extremes, which entailed estimating trends over time windows of variable width starting in 1961 for the five selected stations; the running annual averages for each decade were calculated to the end of the time series (Table 1). For the entire period, the value of DH_{85} showed increasing rates of 0.24 decade^{-1}, while the trend of DH_{90} was 0.18 decade^{-1}. Significant trends were observed during 1961–2017. From the 1970s to 1980s, the trend of concurrent droughts and hot extremes increased more quickly than during the other periods. Even the trends of DH_{85} and DH_{90}

TABLE 1 Comparison of trends in concurrent droughts and hot extremes (unit: Decade^{-1})

	DH_{85}	DH_{90}
1961–2017	0.24[a]	0.18[a]
1971–2017	0.31[a]	0.23[a]
1981–2017	0.42[a]	0.31[a]
1991–2017	0.26	0.21
2001–2017	−0.20	−0.09
2011–2017	0.24	0.26

[a] Indicates statistical significance at the 95% confidence level. DH_{85} and DH_{90} indicate simultaneous a month 3-month SPEI < −1.0 and hot extremes during which the daily maximum temperature exceeded the 85th and 90th percentiles for at least three consecutive days, respectively.

rose to 0.42 decade^{-1} and 0.31 decade^{-1}, and it was mainly significant from 1981 to 2017. The trend changed from a positive significant signal to a negative signal from 2001 to 2017, then, the trends changed again to a positive signal.

Although the regional average number of concurrent droughts and hot extremes increased between 1961 and 2017 over northwest China, the spatial distributions of the trend of the number of concurrent droughts and hot extremes varied with different thresholds and durations over time.

In fact, the number of DH_{85} events exhibited an increasing trend over most parts of northwest China, especially in eastern Xinjiang, north of Golmud in the Qinghai Province, and in the Hexi Corridor, Ningxia to Longnan, and north Shaanxi where the rates were greater than 0.30 decade^{-1} and were significant at the 95% confidence level (Figure 7a). Even in eastern Xinjiang and in north of Golmud in Qinghai, the trends exceeded 0.60 decade^{-1}. This spatial distribution was similar to the annual SPEI trends in northwest China for the period 1961–2017 (Figure 2b). In western Xinjiang and at some individual sites, the trends were negative.

The trend and distribution of the number of DH_{90} events was similar to the trends for DH_{85} events. The DH_{90} events exhibited increasing trends in most parts of the region; in particular, the trends were greater than 0.30 decade^{-1} in eastern Xinjiang, north of Golmud in the Qinghai Province, and in the Hexi Corridor, Ningxia to Longnan, and north Shaanxi. Moreover, the trends in the southern Taklamakan Desert and a small part of northern Qinghai were above 0.50–0.60 decade^{-1} (Figure 7b). Here, we also found that the area with a downward trend for DH_{90} events in western Xinjiang was larger than those for DH_{85}; the same area had a downward trend for the incidence of drought. This means the occurrence of DH_{90} events in this area was determined by the existence of drought. However, the trends of DH_{90} events in north Qinghai were different, with the incidence of drought decreasing, and the incidence of both H_{90} and DH_{90} increasing. These findings indicate that the characteristics of concurrent droughts and hot extreme events can be distinguished from the incidence of droughts or extreme hot events when considered alone.

Western Xinjiang and southern Qinghai experienced their greatest number of DH_{85} events in May (Figure 8a). The greatest number of DH_{85} events in the Tarim basin and Hexi Corridor appeared in June, and these occurred most frequently in July in Ningxia, eastern Xinjiang, western Gansu, and northern Shaanxi. The areas with the greatest number of DH_{85} events occurring in August–October were smaller than that in May–July, and the stations with this pattern were scattered. Areas with the greatest number of DH_{85} events occurring in October only included part of the transition area between southern Ningxia and Gansu. Months when the greatest number of DH_{90} events occurred in most areas of northwest China and were different areas than those with DH_{85} events (Figure 8b). The areas of western Xinjiang and south Qinghai had the greatest number of DH_{90} that occurred in May, and it decreased over time as well as the greatest number that occurred in June–August and the number of these increased over time. The month of greatest number of DH_{90} events was July in part of the Hexi Corridor and in northern Qinghai. In part of the transition area between south Ningxia and Gansu, the greatest number of DH_{85}

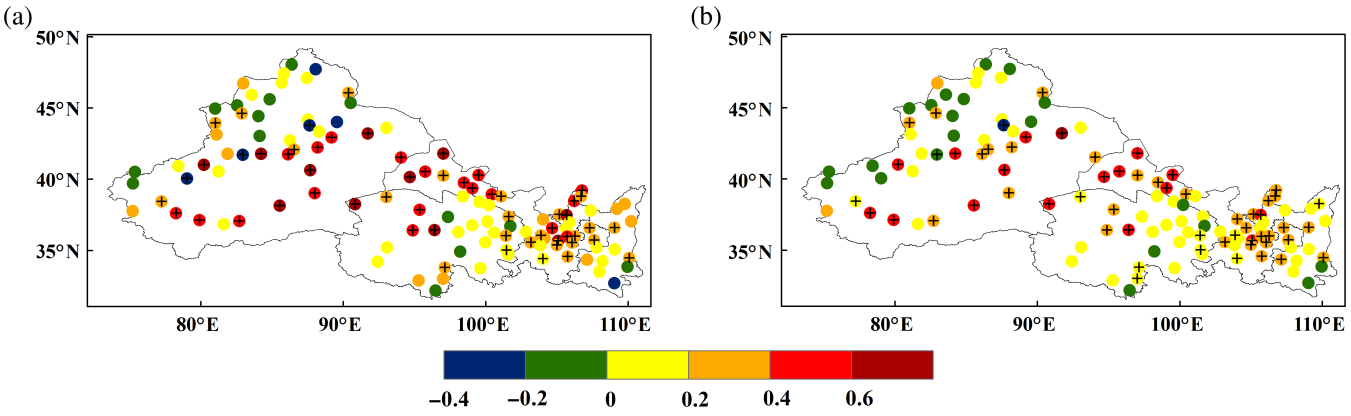

FIGURE 7 Trend variations of the number of concurrent droughts and hot extremes for the period of 1961–2017 in northwest China (unit: Decade^{-1}), (a) DH_{85}, (b) DH_{90} (+ represents statistical significance at the 95% confidence level). DH_{85} and DH_{90} indicate simultaneous month 3-month SPEI < −1.0 and hot extremes during which the daily maximum temperature exceeded the 85th and 90th percentiles for at least three consecutive days, respectively [Colour figure can be viewed at wileyonlinelibrary.com]

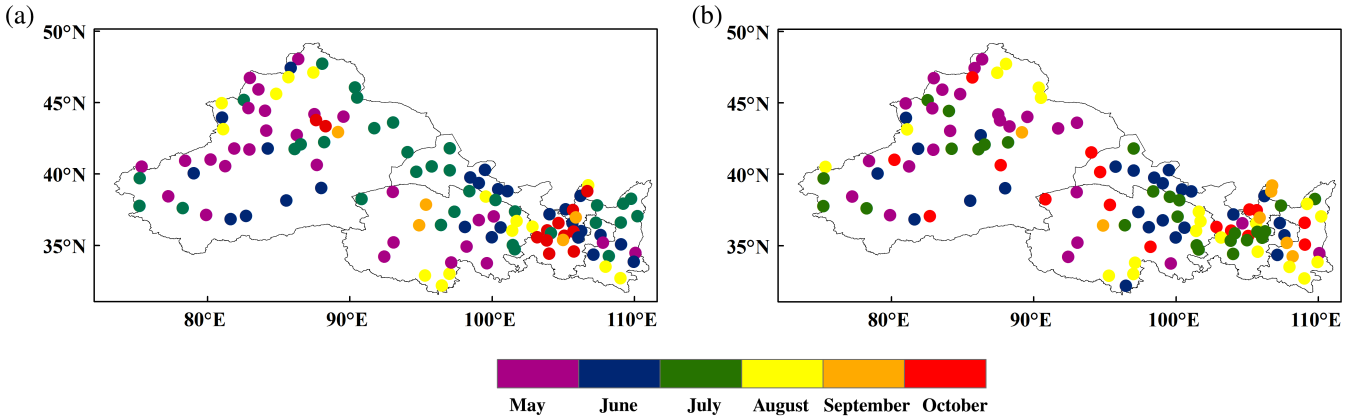

FIGURE 8 Months when the greatest number of concurrent droughts and hot extremes occurred during 1961–2017 in northwest China, (a) DH_{85}, (b) DH_{90}. DH_{85} and DH_{90} indicate simultaneous a month 3-month SPEI < -1.0 and hot extremes during which the daily maximum temperature exceeded the 85th and 90th percentiles for at least three consecutive days, respectively [Colour figure can be viewed at wileyonlinelibrary.com]

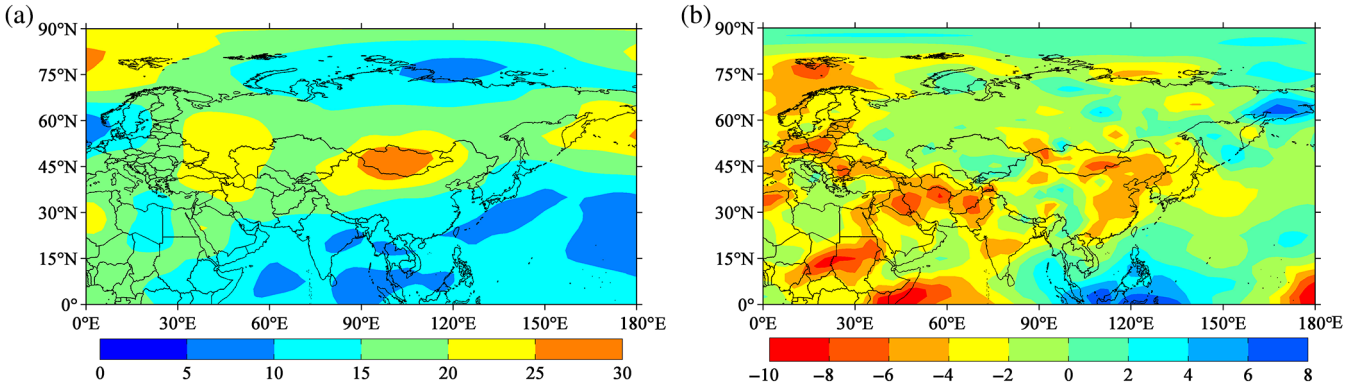

FIGURE 9 Difference of geopotential height (unit: m) at 500 hPa (a) and relative humidity (unit: %) at 700 hPa (b) in May–October between 1997–2017 and 1961–1996 [Colour figure can be viewed at wileyonlinelibrary.com]

events occurred from October to July. In much of the eastern part of northwest China, the greatest number of DH_{90} events occurred in August. By comparing the months with the greatest number of DH_{85} and DH_{90} events that occurred in northwest China, we found that in Xinjiang, DH_{85} events are more likely to appear in May, and in eastern Xinjiang, extreme DH_{85} events occurred more frequently in summer.

3.4 | Changes in large scale atmospheric circulation (geopotential height, relative humidity)

Anomalies in large-scale circulation should play a role in change in trends of concurrent droughts and hot extremes in northwest China. Therefore, we created composite circulation maps from the National Centres for Environmental Prediction and the National Centre for Atmospheric Research reanalysis data in May–October for the two halves of the data period (1961–1996 and 1997–2017), and subtract one from the other. Opposite distributions of the 500 hPa geopotential height and the 700 hPa relative humidity are obvious between the means found in 1997–2017 and 1961–1996 (Figure 9). This distribution suggests that positive anomalies of the 500 hPa height were centred over the midhigh latitudes of Eurasia, centred on Mongolia and Lake Baikal. At the 500 hPa geopotential height, the largest differences (more than 25 m) occur near Lake Baikal; this causes cold air from high latitudes in the west less likely to spread south; therefore, the frequency and intensity of hot extremes are increasing in northwest China (Figure 9a). The enhanced relative humidity at 700 hPa in western Xinjiang and eastern Qinghai, and weakened in other regions during 1997–2017 may explain the decreasing trend in drought in western Xinjiang and eastern Qinghai with a concurrent increasing trend in other areas (Figure 9b). This finding indicated that most of northwest China is under warm-dry conditions, but conditions across western Xinjiang and eastern Qinghai were relatively warm-wet from 1997 to 2017.

4 | CONCLUSIONS

The combined analysis of different types of climate extremes may reveal information that is not apparent from the analysis of individual extremes (Hao *et al.*, 2013). In this study, we have examined the spatial and temporal distribution of droughts and hot extremes based on individual and joint

viewpoints for 119 stations in northwest China over the period 1961–2017.

The frequency of drought appeared to be higher in western northwest China, Ningxia, and in some parts of Gansu and Shaanxi Provinces than in other parts of northwest China. In western Xinjiang and some areas of Qinghai, decreases in drought trends were detected. Most areas in eastern Xinjiang experienced their highest probability of a monthly drought from 1990–2017. The minimum probability of a monthly drought was in northwest China in the 1980s. This may be caused by an increase in annual precipitation in western northwest China over the past 50 years (Ren *et al.,* 2016).

Hot extreme events in most parts of northwest China are clearly increasing regardless of the threshold applied and drought duration, even in the areas where the trend of drought occurrence decreased, such as western Xinjiang and some areas of Qinghai. The frequency of concurrent droughts and hot extremes exhibited an increasing trend over most parts of northwest China, especially in eastern Xinjiang, north of Golmud in the Qinghai Province, the Hexi Corridor, Ningxia to Longnan, and north Shaanxi, but negative trend in western Xinjiang and at some individual sites in Qinghai. Concurrent droughts and hot extremes appeared more often in May in western Xinjiang, and in summer in other parts of northwest China. Overall, the trends of concurrent droughts and hot extremes, regardless of different definitions, increased from 1961–2017 over northwest China, especially from 1981–2017. The trend rose more significantly at this time than in other decades, and reached an abrupt point of change in 1996, which is similar to time points of abrupt change for spring and summer temperature in most of northwest China (Ding and Zhang, 2008). Although the trend changed from a positive significant signal to a negative one from 2001–2017, the trend grew 2–3 times from 1997–2017. However, longer-term changes in concurrent droughts and hot extremes should be related to changes in large-scale atmospheric circulation. In the Northern Hemisphere, positive anomalies of the 500 hPa height centred over the midhigh latitudes of Eurasia, centred on Mongolia and Lake Baikal; simultaneously, the relative humidity increased at 700 hPa in western Xinjiang and eastern Qinghai, and weakened elsewhere from 1997–2017. This pattern may explain the changes in spatial distribution and trends in concurrent droughts and hot extremes in northwest China.

5 | DISCUSSION

The contributions of droughts and hot extremes individually in concurrent droughts and hot extremes varied in diverse areas. Our analysis shows that concurrent droughts and hot extremes appeared more often in May in western Xinjiang, and in summer in other parts of northwest China. This is consistent with the most frequent occurrence of seasonal drought and hot extremes in the region (Qian *et al.,* 2011), leading to the occurrence of concurrent droughts and hot extremes more easily during this season. The water deficit serves as the dominant driver for most droughts, because the supply of terrestrial moisture is limited and sparse vegetation occurs in most parts of northwest China. As a result, evapotranspiration decreases with the decrease in soil moisture (Wang and Yuan, 2018), coupled with the appearance of extreme temperatures, leading to the concurrent occurrence of droughts and hot extremes. In addition, observations indicate that during the last 20 years, most of the increase in the number of drought events happened under warm-dry conditions that coincided with relatively high temperature anomalies but without large anomalies in annual precipitation, implying the number of hot drought events increased (Chen and Sun, 2017). However, in areas such as western Xinjiang and some areas of Qinghai where individual areas experienced increased precipitation with a concurrent warming trend, the trends of concurrent droughts and hot extremes decreased in western Xinjiang, while increasing in Qinghai. This would explain why the change of concurrent droughts and hot extremes was mainly affected by the occurrence of drought in western Xinjiang, and affected by hot extremes in north Qinghai. Changes in the relationship between precipitation and temperature may be more important than changes in one or the other individually (Nicholls, 2004). This indicates that the characteristics of concurrent droughts and hot extreme events can be distinguished from individual drought or hot extreme events when these are considered alone.

The trends of concurrent droughts and hot extremes reached an abrupt point of change in 1996 that may be associated with changes in atmospheric circulation patterns, but are also caused by other changes in natural variability. The snow cover of the Tibetan Plateau can affect regional (eastern Asia in particular) climate change (Zhang *et al.,* 2004; Wu and Kirtman, 2007; Wang *et al.,* 2008; Lin and Wu, 2011). Previous studies have found that snow cover in the Tibetan Plateau declined significantly after 1995, passing the 99% significance test (Wu *et al.,* 2012b). A reduced snow anomaly in the Tibetan Plateau can enhance the climatological high-pressure ridge over Mongolia and the adjacent regions. The subsidence associated with the high-pressure anomalies tends to suppress local cloud formation, which increases the net radiation budget, heats the surface, and favours the occurrence of more frequent heatwaves (Wu *et al.,* 2012a). Moreover, reduced sea ice coverage in the Arctic Ocean, phase change of the Pacific Decadal Oscillation, and other external forcing factors will cause changes of synoptic systems and circulation anomalies associated with droughts and hot extremes (Zhang *et al.,* 2005; Wang *et al.,* 2014; You *et al.,* 2016). Anthropogenic warming has increased the occurrence of hot droughts, and the impact will be amplified in the future (Samaniego *et al.,* 2018). Further

studies of mechanism are needed to explain these "discrepancies" between individual and combinations of extreme climate events.

ACKNOWLEDGEMENTS

This study was supported by the National Key R&D Program of China (grant no. 2016YFA0601702), the China Meteorological Public Welfare Scientific Research Project (grant nos. GYHY201506001, GYHY201306027), the National Natural Science Foundation of China (grant no. 41771069), and the Priority Academic Program Development of Jiangsu Higher Education Institutions. We would like to thank LetPub for providing linguistic assistance during the preparation of this manuscript.

ORCID

Xin Li https://orcid.org/0000-0002-3381-1059

Qinglong You https://orcid.org/0000-0002-5329-9697

REFERENCES

Abramowitz, M. and Stegun, I.A. (1964) *Handbook of Mathematical Functions, with Formulas, Graphs, and Mathematical Tables*. New York, NY: Dover.

AghaKouchak, A., Cheng, L., Mazdiyasni, O. and Farahmand, A. (2014) Global warming and changes in risk of concurrent climate extremes: insights from the 2014 California drought. *Geophysical Research Letters*, 41, 8847–8852.

Beguería, S., Vicente-Serrano, S.M., Reig, F. and Latorre, B. (2014) Standardized precipitation evapotranspiration index (SPEI) revisited: parameter fitting, evapotranspiration models, tools, datasets and drought monitoring. *International Journal of Climatology*, 34, 3001–3023.

Breshears, D.D., Cobb, N.S., Rich, P.M., Price, K.P., Allen, C.D., Balice, R.G., Romme, W.H., Kastens, J.H., Floyd, M.L., Belnap, J., Anderson, J.J., Myers, O.B. and Meyer, C.W. (2005) Regional vegetation die-off in response to global-change-type drought. *Proceedings of the National Academy of Sciences*, 102, 15144–15148.

Bueh, C., Ji, L. and Cui, M. (2002) Energy balance of land surface process in the arid and semi-arid regions of China and its relation to the regional atmospheric circulation in summer. *Climatic and Environmental Research*, 7, 61–73.

Chen, H. and Sun, J. (2017) Anthropogenic warming has caused hot droughts more frequently in China. *Journal of Hydrology*, 544, 306–318.

Chen, H. and Sun, J. (2018) Projected changes in climate extremes in China in a 1.5 °C warmer world. *International Journal of Climatology*, 38, 3607–3617.

Chen, Y. and Zhai, P. (2017) Revisiting summertime hot extremes in China during 1961-2015: overlooked compound extremes and significant changes. *Geophysical Research Letters*, 44, 5096–5103.

Chen, Y., Zhai, P. and Zhou, B. (2018) Detectable impacts of the past half-degree global warming on summertime hot extremes in China. *Geophysical Research Letters*, 45, 7130–7139.

Dai, A. (2011) Drought under global warming: a review. *Wiley Interdisciplinary Reviews: Climate Change*, 2, 45–65.

Ding, Y. and Zhang, L. (2008) Intercomparison of the time for climate abrupt change between the Tibetan Plateau and other regions in China. *Chinese Journal of Atmospheric Sciences*, 32, 794–805.

Ding, T., Qian, W. and Yan, Z. (2010) Changes in hot days and heat waves in China during 1961-2007. *International Journal of Climatology*, 30, 1452–1462.

Donat, M.G., Alexander, L.V., Yang, H., Durre, I., Vose, R., Dunn, R.J.H., Willett, K.M., Aguilar, E., Brunet, M., Caesar, J., Hewitson, B., Jack, C., Klein Tank, A.M.G., Kruger, A.C., Marengo, J., Peterson, T.C., Renom, M., Oria Rojas, C., Rusticucci, M., Salinger, J., Elrayah, A.S., Sekele, S.S., Srivastava, A.K., Trewin, B., Villarroel, C., Vincent, L.A., Zhai, P., Zhang, X. and Kitching, S. (2013) Updated analyses of temperature and precipitation extreme indices since the beginning of the twentieth century: the HadEX2 dataset. *Journal of Geophysical Research-Atmospheres*, 118, 2098–2118.

Du, S., Gu, H., Wen, J., Chen, K. and Van Rompaey, A. (2015) Detecting flood variations in Shanghai over 1949–2009 with Mann-Kendall tests and a newspaper-based database. *Water*, 7, 1808–1824.

Easterling, D.R., Evans, J.L., Groisman, P.Y., Karl, T.R., Kunkel, K.E. and Ambenje, P. (2000) Observed variability and trends in extreme climate events: a brief review. *Bulletin of the American Meteorological Society*, 81, 417–426.

Greve, P., Gudmundsson, L. and Seneviratne, S.I. (2018) Regional scaling of annual mean precipitation and water availability with global temperature change. *Earth System Dynamics*, 9, 227–240.

Hao, Z., AghaKouchak, A. and Phillips, T.J. (2013) Changes in concurrent monthly precipitation and temperature extremes. *Environmental Research Letters*, 8, 034014.

Hirschi, M., Seneviratne, S.I., Alexandrov, V., Boberg, F., Boroneant, C., Christensen, O.B., Formayer, H., Orlowsky, B. and Stepanek, P. (2010) Observational evidence for soil-moisture impact on hot extremes in southeastern Europe. *Nature Geoscience*, 4, 17–21.

Kendall, M.G. (1975) *Rank Correlation Measures*. London: Charles Griffin.

Leonard, M., Westra, S., Phatak, A., Lambert, M., van den Hurk, B., McInnes, K., Risbey, J., Schuster, S., Jakob, D. and Stafford-Smith, M. (2014) A compound event framework for understanding extreme impacts. *Wiley Interdisciplinary Reviews: Climate Change*, 5, 113–128.

Li, B., Chen, Y. and Shi, X. (2012) Why does the temperature rise faster in the arid region of northwest China? *Journal of Geophysical Research-Atmospheres*, 117, D16115.

Li, B., Chen, Y., Chen, Z., Xiong, H. and Lian, L. (2016) Why does precipitation in northwest China show a significant increasing trend from 1960 to 2010? *Atmospheric Research*, 167, 275–284.

Lin, H. and Wu, Z. (2011) Contribution of the autumn Tibetan Plateau snow cover to seasonal prediction of north American winter temperature. *Journal of Climate*, 24, 2801–2813.

Mann, H.B. (1945) Nonparametric tests against trend. *Econometrica*, 13, 245–259.

Mazdiyasni, O. and AghaKouchak, A. (2015) Substantial increase in concurrent droughts and heatwaves in the United States. *Proceedings of the National Academy of Sciences*, 112, 11484–11489.

McKee, T.B., Doesken, N.J. and Kleist, J. (1993) The relationship of drought frequency and duration to time scales. In: *Proceedings of the 8th Conference on Applied Climatology*. Boston, MA: American Meteorological Society, pp. 179–183.

Meehl, G.A. and Tebaldi, C. (2004) More intense, more frequent, and longer lasting heat waves in the 21st century. *Science*, 305, 994–997.

Mishra, A.K. and Singh, V.P. (2010) A review of drought concepts. *Journal of Hydrology*, 391, 202–216.

Mueller, B. and Seneviratne, S.I. (2012) Hot days induced by precipitation deficits at the global scale. *Proceedings of the National Academy of Sciences*, 109, 12398–12403.

Nasrollahi, N., AghaKouchak, A. and Cheng, L. (2015) How well do CMIP5 climate simulations replicate historical trends and patterns of meteorological droughts? *Water Resources Research*, 51, 2847–2864.

Nicholls, N. (2004) The changing nature of Australian droughts. *Climatic Change*, 63, 323–336.

Palmer, W.C. (1965) *Meteorological Drought*. Washington, DC: US Department of Commerce, Weather Bureau.

Pearson, K. (1895) Mathematical contributions to the theory of evolution. III. Regression, heredity and panmixia. *Proceedings of the Royal Society of London*, 59, 353–358.

Peng, D. and Zhou, T. (2017) Why was the arid and semiarid northwest China getting wetter in the recent decades? *Journal of Geophysical Research-Atmospheres*, 122, 9060–9075.

Perkins, S.E. and Alexander, L.V. (2013) On the measurement of heat waves. *Journal of Climate*, 26, 4500–4517.

Perkins, S.E., Alexander, L.V. and Nairn, J.R. (2012) Increasing frequency, intensity and duration of observed global heatwaves and warm spells. *Geophysical Research Letters*, 39, L20714.

Qian, W., Shan, X. and Zhu, Y. (2011) Ranking regional drought events in China for 1960–2009. *Advances in Atmospheric Sciences*, 28, 310–321.

Ren, G., Yuan, Y., Liu, Y., Ren, Y., Wang, T. and Ren, X. (2016) Changes in precipitation over northwest China. *Arid Zone Research*, 33, 1–19.

Russo, S., Dosio, A., Graversen, R.G., Sillmann, J., Carrao, H., Dunbar, M. B., Singleton, A., Montagna, P., Barbola, P. and Vogt, J.V. (2014) Magnitude of extreme heat waves in present climate and their projection in a warming world. *Journal of Geophysical Research-Atmospheres*, 119, 12,500–12,512.

Samaniego, L., Thober, S., Kumar, R., Wanders, N., Rakovec, O., Pan, M., Zink, M., Sheffield, J., Wood, E.F. and Marx, A. (2018) Anthropogenic warming exacerbates European soil moisture droughts. *Nature Climate Change*, 8, 421–426.

Seneviratne, S.I., Corti, T., Davin, E.L., Hirschi, M., Jaeger, E.B., Lehner, I., Orlowsky, B. and Teuling, A.J. (2010) Investigating soil moisture–climate interactions in a changing climate: a review. *Earth-Science Reviews*, 99, 125–161.

Seneviratne, S.I., Donat, M.G., Mueller, B. and Alexander, L.V. (2014) No pause in the increase of hot temperature extremes. *Nature Climate Change*, 4, 161–163.

Sheffield, J., Wood, E.F. and Roderick, M.L. (2012) Little change in global drought over the past 60 years. *Nature*, 491, 435–438.

Shi, Y., Shen, Y., Kang, E., Li, D., Ding, Y., Zhang, G. and Hu, R. (2006) Recent and future climate change in northwest China. *Climatic Change*, 80, 379–393.

Singh, V.P., Guo, H. and Yu, F.X. (1993) Parameter estimation for 3-parameter log-logistic distribution (LLD3) by pome. *Stochastic Hydrology and Hydraulics*, 7, 163–177.

Thornthwaite, C.W. (1948) An approach toward a rational classi- fication of climate. *Geographical Review*, 38, 55–94.

Trenberth, K.E. (2011) Changes in precipitation with climate change. *Climate Research*, 47, 123–138.

Vautard, R., Yiou, P., D'Andrea, F., de Noblet, N., Viovy, N., Cassou, C., Polcher, J., Ciais, P., Kageyama, M. and Fan, Y. (2007) Summertime European heat and drought waves induced by wintertime Mediterranean rainfall deficit. *Geophysical Research Letters*, 34, 1–5.

Vicente-Serrano, S.M., Beguería, S. and López-Moreno, J.I. (2010) A multiscalar drought index sensitive to global warming: the standardized precipitation evapotranspiration index. *Journal of Climate*, 23, 1696–1718.

Wang, L. and Yuan, X. (2018) Two types of flash drought and their connections with seasonal drought. *Advances in Atmospheric Sciences*, 35, 1478–1490.

Wang, B., Bao, Q., Hoskins, B., Wu, G. and Liu, Y. (2008) Tibetan Plateau warming and precipitation changes in East Asia. *Geophysical Research Letters*, 35, 1–5.

Wang, W., Zhou, W. and Chen, D. (2014) Summer high temperature extremes in Southeast China: bonding with the El Niño–southern oscillation and east Asian summer monsoon coupled system. *Journal of Climate*, 27, 4122–4138.

Wei, N., Gong, Y., Sun, X. and Fang, J. (2010) Variation of precipitation and water vapor transport over the northwest China from 1959 to 2005. *Journal of Desert Research*, 30, 1450–1457.

Wu, R. and Kirtman, B.P. (2007) Observed relationship of spring and summer east Asian rainfall with winter and spring Eurasian snow. *Journal of Climate*, 20, 1285–1304.

Wu, Z., Jiang, Z., Li, J., Zhong, S. and Wang, L. (2012a) Possible association of the western Tibetan plateau snow cover with the decadal to interdecadal variations of northern China heatwave frequency. *Climate Dynamics*, 39, 2393–2402.

Wu, Z., Li, J., Jiang, Z. and Ma, T. (2012b) Modulation of the Tibetan Plateau snow cover on the ENSO teleconnections: from the east Asian summer monsoon perspective. *Journal of Climate*, 25, 2481–2489.

Xu, Y., Gao, X., Giorgi, F., Zhou, B., Shi, Y., Wu, J. and Zhang, Y. (2018) Projected changes in temperature and precipitation extremes over China as measured by 50-yr return values and periods based on a CMIP5 ensemble. *Advances in Atmospheric Sciences*, 35, 376–388.

Yang, X. and Scuderi, L.A. (2017) Hydrological and climatic changes in deserts of China since the late Pleistocene. *Quaternary Research*, 73, 1–9.

Yang, Q., Li, M., Zheng, Z. and Ma, Z. (2017) Regional applicability of seven meteorological drought indices in China. *Science China Earth Sciences*, 60, 745–760.

You, Q., Jiang, Z., Kong, L., Wu, Z., Bao, Y., Kang, S. and Pepin, N. (2016) A comparison of heat wave climatologies and trends in China based on multiple definitions. *Climate Dynamics*, 48, 3975–3989.

Yu, M., Li, Q., Hayes, M.J., Svoboda, M.D. and Heim, R.R. (2014) Are droughts becoming more frequent or severe in China based on the standardized precipitation evapotranspiration index: 1951-2010? *International Journal of Climatology*, 34, 545–558.

Zampieri, M., D'Andrea, F., Vautard, R., Ciais, P., de Noblet-Ducoudré, N. and Yiou, P. (2009) Hot European summers and the role of soil moisture in the propagation of Mediterranean drought. *Journal of Climate*, 22, 4747–4758.

Zhang, Y., Tim, L. and Bin, W. (2004) Decadal change of the spring snow depth over the Tibetan plateau: the associated circulation and influence on the east Asian summer monsoon. *Journal of Climate*, 17, 2780–2793.

Zhang, P., Yang, S. and Kousky, V.E. (2005) South Asian high and Asian-Pacific-American climate teleconnection. *Advances in Atmospheric Sciences*, 22, 915–923.

Zhang, Y., You, Q., Mao, G., Chen, C. and Ye, Z. (2018) Short-term concurrent drought and heatwave frequency with 1.5 and 2.0 °C global warming in humid subtropical basins: a case study in the Gan River basin, China. *Climate Dynamics*, 1–21. https://doi.org/10.1007/s00382-018-4398-6.

Zhu, J., Huang, G., Baetz, B., Wang, X. and Cheng, G. (2018) Climate warming will not decrease perceived low-temperature extremes in China. *Climate Dynamics*, 1–16. https://doi.org/10.1007/s00382-018-4469-8

Zou, X., Zhai, P. and Zhang, Q. (2005) Variations in droughts over China: 1951-2003. *Geophysical Research Letters*, 32, 1–4.

How to cite this article: Li X, You Q, Ren G, *et al.* Concurrent droughts and hot extremes in northwest China from 1961 to 2017. *Int J Climatol*. 2018;1–11. https://doi.org/10.1002/joc.5944

Article ID: 1006-8775(2018) 04-0448-09

A COMPARISON AND EVALUATION OF TWO CENTENNIAL–SCALE SEA SURFACE TEMPERATURE DATASETS IN THE CHINA SEAS AND THEIR ADJACENT SEA AREAS

WANG Qing-yuan (王庆元)[1, 2], LI Yan (李 琰)[3], LI Qing-quan (李清泉)[1, 4], WANG Ya-nan (王亚男)[2]
(1. Collaborative Innovation Center on Forecast and Evaluation of Meteorological Disasters (CIC-FEMD), Nanjing University of Information Science & Technology, Nanjing 210044 China; 2. Tianjin Meteorological Observatory, Tianjin 300074 China; 3. National Marine Data and Information Service, Tianjin 300171 China; 4. Laboratory for Climate Studies, National Climate Center, China Meteorological Administration, Beijing 100081 China))

Abstract: Two reconstructed sea surface temperature (SST) datasets (HadISST1 and COBE SST2) with centennial-scale are compared on the SST climate change over the China Seas and their adjacent sea areas. Two independent datasets show consistency in statistically significant trends, with a warming trend of 0.07—0.08 ℃ per decade from 1890 to 2013. However, in shorter epochs (such as 1961—2013 and 1981—2013), HadISST1 exhibits stronger warming rates than those of COBE SST2. Both datasets experienced a sudden decrease in the global hiatus period (1998—2013), but the cooling rate of HadISST1 is lower than that of COBE SST2. These differences are possibly caused by the different observations sources which are incorporated to fill with data-sparse regions since 1982. Different data sources may lead to higher values in HadISST1 from 1981 to 2013 than that in COBE SST2. Meanwhile, the different data sources and bias adjustment before the World War II may also cause the large divergence between COBE SST2 and HadISST1, leading to lower SST from 1891 to 1930. These findings illustrate that the long-term linear trends are broadly similar in the centennial-scale in the China Seas using different datasets. However, there are large uncertainties in the estimate of warming or cooling tendency in the shorter epochs, because there are different data sources, different bias adjustment and interpolation method in different datasets.

Key words: sea surface temperature; regional climate change; comparison; linear trend; Taylor diagram
CLC number: P467 **Document code:** A
doi: 10.16555/j.1006-8775.2018.04.004

1 INTRODUCTION

The knowledge of sea surface temperature (SST) is a key factor for a wide set of social activities and an important indicator of climate change. The China Seas, consisting of the Bohai Sea, the Yellow Sea, the East China Sea (ECS), and the South China Sea (SCS), are important marginal seas. Marine ecosystems within the coastal boundary systems, including coastal China Seas and adjacent seas, are sensitive to sea temperature increase. Thus, there are many studies and discussions on the SST effect with the background of global warming (Zhang et al.[1]; Zhang et al.[2]; Xie et al.[3]; Wu et al.[4]).

A number of extended historical observed SST products have been used in the global climatological community (Boehme et al. [5]), as well as in regional climate change, such as the China Seas (Jin and Wang[6]; Liu and Zhang [7]; Wang et al. [8]; Hirahara et al. [9]). However, historical SST datasets have large uncertainties in long-term trend patterns in some regions. For example, observed SST changes in the tropical Pacific are still controversial, depending on different datasets and study period (Bunge and Clarke[10]). Vecchi et al. indicated that the equatorial zonal SST gradient in the Pacific intensified in Hadley Centre Sea Ice and Sea Surface Temperature (HadISST) but weakened in Extended Reconstructed SST (ERSST) from the nineteenth to twentieth centuries [11]. Scientists utilized several different datasets, including the reconstructed and un-interpolated datasets, to study the SST variability in tropical area and the China Seas (Xie et al.[3]; Liu and Zhang[7]; Tokinaga et al.[12]). They found that there were larger uncertainties in the estimate of SST warming patterns using HadISST version 1 (HadISST1) (Rayner et al.[13]) and HadISST version 3 (HadISST3). Thus, it is also necessary to compare different SST products over the China Seas in detail. There are a variety of global gridded SST datasets that have been independently created through historical "reconstruction" techniques. In the current study, we focus on two centennial-scale SST reconstructions, that is, the HadISST1 and the Centennial Observation-Based Estimates of SST version 2 (COBE SST2)(Hirahara et al.[9];

Received 2018-02-07; **Revised** 2018-09-11; **Accepted** 2018-11-15
Foundation item: National Key Basic Research Program of China (2016YFA0602200, 2012CB955203, 2013CB430202)
Biography: WANG Qing-yuan, associate research fellow, primarily under taking research on regional marine meteorology.
Corresponding author: LI Qing-quan, e-mail: liqq@cma.gov.cn

Ishii et al.[14]). The major goal of this work is to analyze SST linear trends over the China Seas and adjacent sea areas in different periods using the two independent SST datasets. Then the discrepancy between HadISST1 and COBE SST2 is investigated and possible causes will be discussed.

Following the introduction, Section 2 presents the study region, data and methods. Section 3 describes the results and comparisons. Further discussion and a summary are given in Section 4 and 5.

2 STUDY REGION, DATA AND METHODS

2.1 *Study region*

In this study, the China Seas and their adjacent sea areas are considered. The areas are defined as the region of 15—45°N and 105—135°E. Stations A-M used in this paper are coastal hydrological stations (Fig.1).

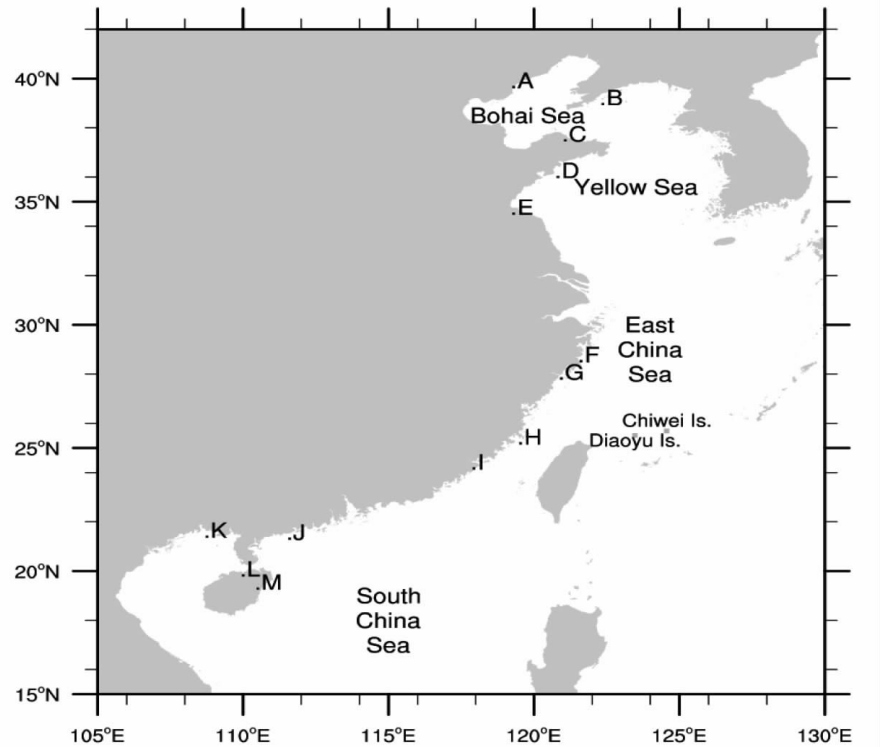

Figure 1. The study region in this paper. Stations A-M coastal hydrological stations are used.

2.2 *Data*

The two centennial-scale SST datasets are used in this study.

(1) Monthly mean HadISST data are taken from the Met Office Hadley Centre (http://www.metoffice.gov.uk/hadobs/hadisst/data/download.html), which has 1° spatial resolution from January 1870 to December 2013[13].

(2) Monthly mean COBE SST2 data also have a spatial resolution of 1° latitude by 1° longitude for the period of January 1891 to December 2013 and are obtained from Japan Meteorology Agency (http://www.ds.data.jma.go.jp/tcc/products/elnino/cobesst/cobe-sst.html).

2.3 *Methods*

Regional mean value of SST is calculated by area-weighted averaging the grid data using latitude cosine as weights (Jones and Hulme [15]). To understand the trend of SST series, we conducted linear regression analyses and calculation of climate trend coefficients (r). This method has been successfully applied to several previous studies (Chen et al.[16]). The linear regression equation is expressed as:

$$y=a+bx$$

where y represents meteorological elements SST, and x represents year.

The statistical significance of the linear trends has been estimated by using the modified Mann-Kendall nonparametric test (Hamed and Rao [17]; Von Storch and Zwiers [18]), with a significance level defined as p_value <0.05.

To obtain comparable time series, we selected the data from 1891 to 2013 for analysis. Climatology represents the mean value for a grid cell over an extended period (usually 30 years according to the WMO), whereas an anomaly is the deviation from that mean. Here, we calculated a monthly climatology for each grid cell based on the period of 1960—1990.

3 RESULTS AND COMPARISONS

Annually averaged SST anomalies (SSTAs) over the China Seas and their adjacent sea areas are shown in Fig.

2. SSTAs exhibit a clear warming tendency from 1891 to 2013 in the two-time series and reflect a similar interannual variability in the centennial scale. In the decadal means, there are a general cool period from 1890s to 1930s and a significant warm period from 1980s to 2000s in both centennial-scale SST datasets (Table 1). Bao and Ren also reported the same decadal variations appearing in the HadISST1 series[19]. However, the differences are much noticeable in 1910s and 1920s, when the HadISST1 exhibits a much lower SSTA, with values of –0.10 ℃ and –0.19 ℃. The differences are also significant in 1990s and 2000s, when the HadISST1 data exhibits higher SSTAs, with values of 0.11 ℃ and 0.17 ℃. Clearly, there are some discrepancies in the two datasets around 1910s—1920s and 1990s—2000s.

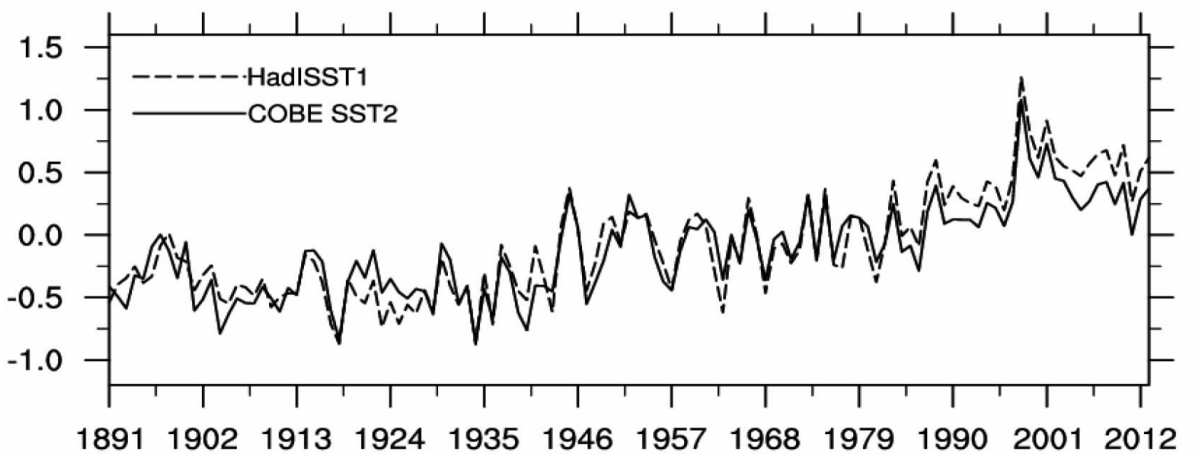

Figure 2. Time series of regional mean annual SST anomalies for the China Seas and their adjacent sea areas during 1891—2013 relative to 1961—1990 (solid line: COBE SST2, dashed line: HadISST1).

Table 1. 10-year averaged annual SST anomalies during 1891—2013 (℃) (larger difference is marked in bold).

Period	HadISST1	COBE SST2	difference
1890s	–0.19	–0.14	**–0.05**
1900s	–0.34	–0.41	**0.07**
1910s	–0.38	–0.28	**–0.10**
1920s	–0.44	–0.25	**–0.19**
1930s	–0.37	–0.38	0.01
1940s	–0.03	–0.07	0.04
1950s	0.08	0.08	0
1960s	0.06	0.06	0
1970s	0.18	0.16	0.02
1980s	0.22	0.14	**0.08**
1990s	0.56	0.45	**0.11**
2000s	0.69	0.52	**0.17**

Table 2. Linear trends of annual SST anomalies over the study region during 1891—1930, 1910—1930, 1891—2013, 1961—2013, 1981—2013, and 1998—2013 (Unit: ℃ per decade).

	1891—1930	1910—1930	1891—2013	1961—2013	1981—2013	1981—2013	1998—2013
HadISST1	–0.07	–0.04	0.08	0.19	0.20	0.29	–0.27
COBE SST2	–0.01	0.02	0.07	0.11	0.14	0.20	–0.34
Trend difference	–0.06	–0.06	0.01	0.08	0.06	0.09	0.07

This research focuses on the linear trends of the two SST datasets and linear trends are computed. Except for the long-term period of 1891 to 2013, we also analyze the linear trends of several shorter epochs: 1891—1930, 1910—1930, 1961—2013, 1981—2013, 1981—1997, and 1998—2013. These period divisions are based on the following reasons. (1) As mentioned above, the differences of the two datasets are notable in 1910s—1920s and 1990s—2000s. (2) The number of SST observations increased greatly with time, and 100—1,000 times more observations were available after 1950s than in the earlier time (for example 1890s), especially since 1960s [9]. (3) Since 1980s, satellite observations from the advanced very high-resolution radiometer (AVHRR) have been incorporated in the HadISST1. (4) Before the World War II (1891—1930), which is also called observational data sparse period, HadISST1 were often lower than COBE SST2 (Fig. 3). (5) The Intergovernmental Panel on Climate Change Fifth Assessment Report (IPCC AR5) pointed out that during the recent years (1998—2013), the global warming rate has slowed down. This period has been discussed in a number of papers (Kosaka and Xie[20]; Smith[21]) and has been known as a "hiatus" (Fyfe et al.[22]) or "global slowdown" (Guemas et al. [23]). This phenomenon has aroused wide attention of scientists all over the world and needs to be examined.

SST trends of these shorter epochs and the period of 1891—2013 over the study region are calculated and results are shown in Table 2. From Fig.2 and Table 2, we can find that the two series are very close, with HadISST1's warming trend of 0.08 ℃ per decade and COBE SST2's warming trend of 0.07 ℃ per decade from 1891 to 2013. The trends are significant at the 95% confidence level. However, trends of annual mean HadISST1 in the shorter epochs (0.19 ℃ per decade for 1961—2013, 0.20 ℃ per decade for 1981—2013, 0.29 ℃ per decade for 1981—1997, and −0.27 ℃ per decade for 1998—2013) are generally much higher than those of annual mean COBE SST2 (0.11℃ per decade for 1961—2013, 0.14 ℃ per decade for 1981—2013, 0.20℃ per decade for 1981—1997, and −0.34 ℃ per decade for 1998—2013) (Table 2). The two largest trend differences are in the two decadal time scale, that is, the accelerated warming period of 1981—1997 and 1961—2013, with the difference values of 0.09 ℃ per decade and 0.08 ℃ per decade. Another interesting issue can be found in the time series from 1981 to 2013 (including the accelerated warming period and hiatus period) (Fig.4). Obviously, values in HadISST1 time series are higher than those in COBE SST2 series since 1981, contrary to these before the World War II. We calculate the trends in the period of 1891—1930 and 1910—1930. The trends of annual mean HadISST1 in the above two epochs (−0.07 ℃ per decade and −0.04 ℃ per decade) are different from these of annual mean COBE SST2 in the same area (−0.01 ℃ per decade and 0.02 ℃ per decade). Results indicate that the trends of the two datasets in the shorter epochs are very different, especially on the fifty-year scale or shorter (Table 2). The differences of data sources may have a significant impact on the trend of short period, but they have little effect on the trend of the centennial. The SST trends having uncertainties in the shorter epochs and readers need to be cautious in using the SST trend rate at short time period.

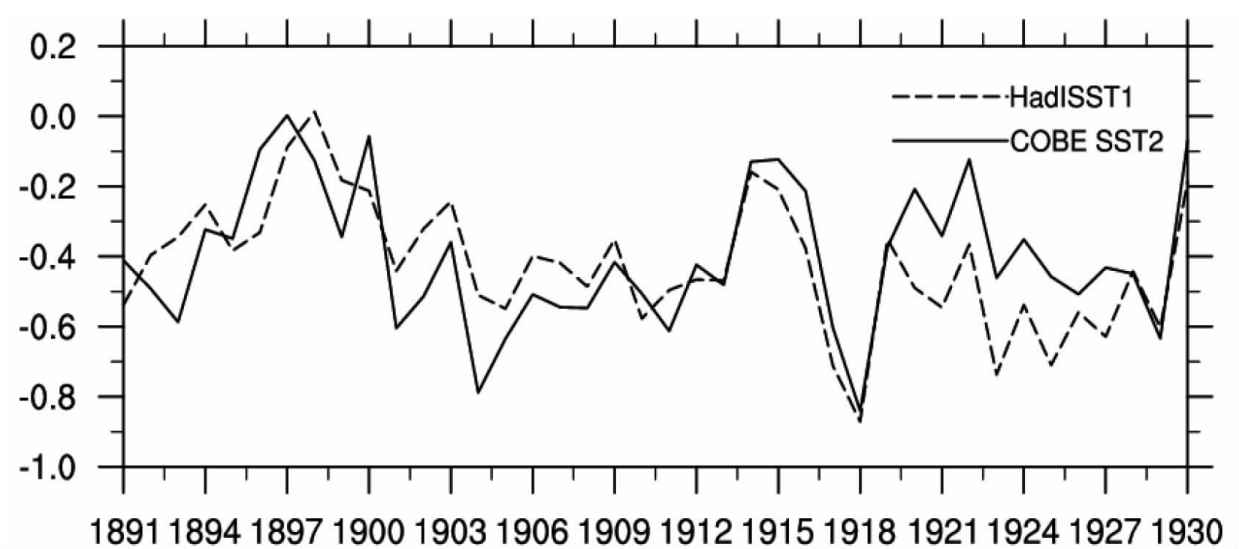

Figure 3. Time series of regional mean annual SSTAs for the China Seas and their adjacent sea areas during 1891—1930 relative to 1961—1990 (solid line: COBE SST2, dashed line: HadISST1).

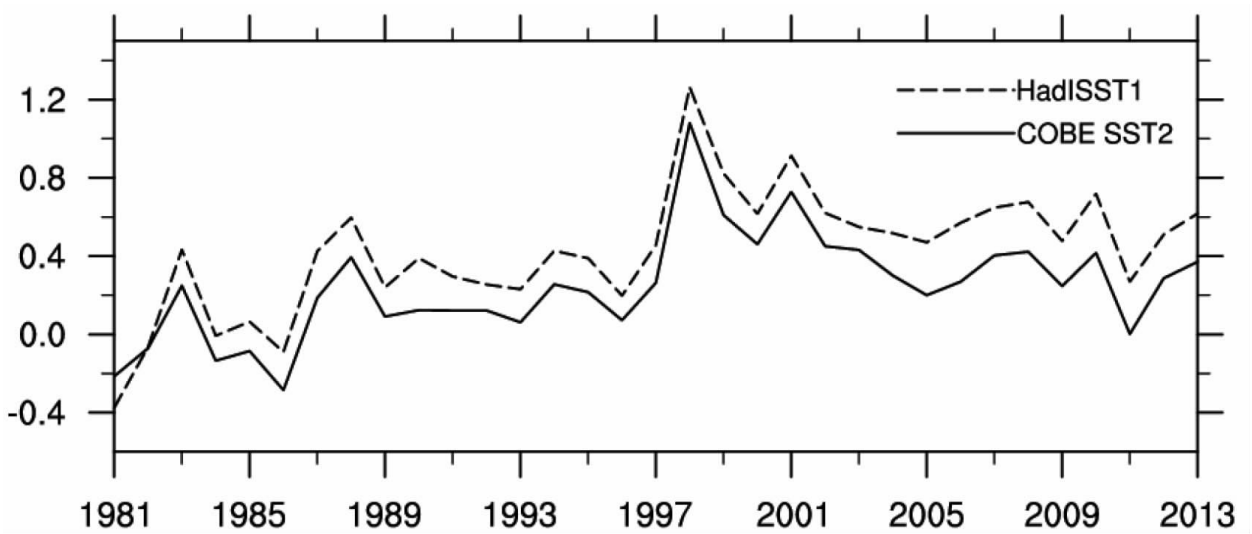

Figure 4. Time series of regional mean annual SST anomalies for the China Seas and their adjacent sea areas during 1981—2013 relative to 1961—1990 (solid line: COBE SST2, dashed line: HadISST1).

Spatial distributions of annual SSTAs' trends from HadISST1 and COBE SST2 during three shorter epochs, 1961—2013, 1981—2013 and 1998—2013, which are widely discussed in climate literatures in China, are shown in Fig.5. The two SST datasets show the consistent warming pattern during 1961—2013 and 1981—2013. The largest warming trend almost appears at the same area, south of the Yellow Sea and East China Seas (Fig. 5a, b, c, and d). However, the rates estimated from HadISST1 are larger than those from COBE SST2 during 1961—2013 and 1981—2013, especially in the East China Sea and the east of Taiwan Island. During the hiatus period (1998—2013), the rates from HadISST1 during 1998—2013 are lower than those from COBE SST2 (Fig.5e and f). The maximum cooling rate from HadISST1 exceeding −0.4℃ per decade appears in the Yangtze River and the offshore region of the East China Sea. While the maximum cooling rate from COBE SST2 exceeding −0.4℃ per decade is in the Yellow Sea, the trends from HadISST1 and COBE SST2 have much difference in spatial distributions and values which indicates some uncertainties involved in the regional climate change trend.

4 DISCUSSIONS

From Table 1, larger discrepancies are pronounced around the 1920s and 1980s. In the period of 1981—2013, HadISST1 is higher than that of COBE SST2 (Fig. 4). The annual SST trends from HadISST1 and COBE SST2 also have differences, especially in the short period (fifty-year or shorter time scale) (Table 2). To find out the causes for the discrepancies, we check the data sources, bias adjustment, and reconstruction method of HadISST1 and COBE SST2 over the China Seas and their adjacent sea areas. HadISST1 dataset is composed of the SST data from Marine Data Bank in the United Kingdom (mainly ship tracks) and ICOADS. From 1982 onward, HadISST1 also consists of adjusted satellite-derived SST data from the AVHRR. Though data gaps in HadISST1 have been interpolated, the performance of HadISST1 in describing the SST variability in the China Seas, particularly in the offshore areas, is still questionable, because of the data sparseness and limitations of the interpolation techniques (Zhang et al.[1]; Liu et al.[7]; Rayner et al.[13]; Cai et al.[24];). COBE SST2 also composes the ICOADS, U.K. Marine Data Bank, and U.S. Marine Meteorological Journals[9]. To construct unobserved variability in data-sparse regions, we incorporate satellite observations into the present objective analysis scheme. However, the satellite observations are used only for constructing empirical orthogonal functions (EOF) that represent interannual-to-decadal SST variations; they are not used in the final COBE SST2 to preserve the homogeneity of the SST analysis for more than 100 years. Hirahara et al. (2014) pointed out that this was because the use of satellite data for the whole analysis makes the grid wise variability of SST analysis larger by 10% —20% , compared with that without the data (Huang et al.[25]). Different data sources may lead to the phenomenon that HadISST1 is higher than COBE SST2 from 1981 to 2013 (Fig.4). The differences of data sources may cause different trends in the two datasets from 1961 to 2013, 1981 to 2013, 1981 to 1997, and 1998 to 2013 (Table 2). Meanwhile, we note that trends over short periods are inherently more uncertain because the period is short-term (such as from 1981 to 1997 and from 1998 to 2013), and both random and shorter-term systematic effects will not be cancelled as they would in longer-term periods[25].

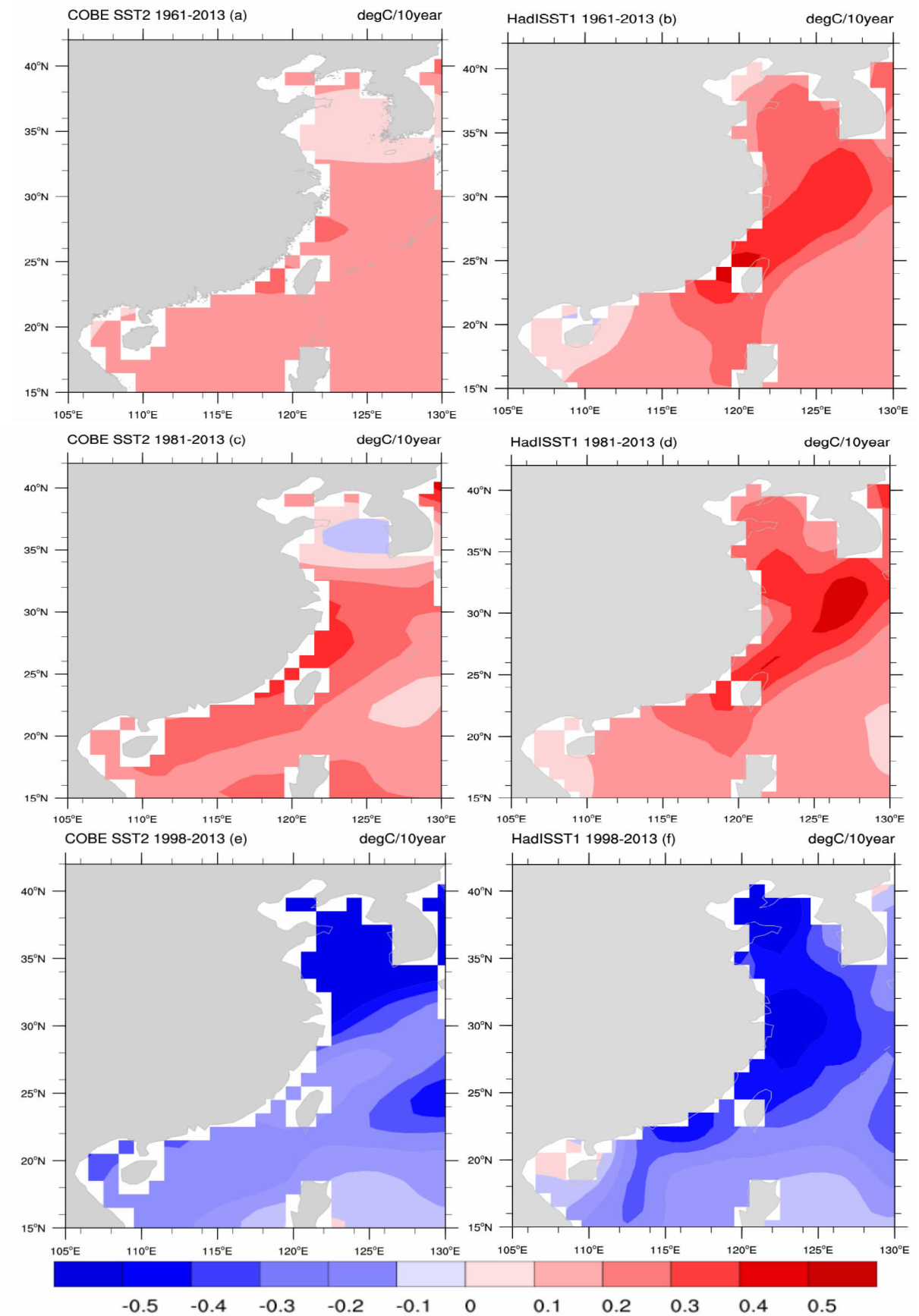

Figure 5. Linear trends spatial distribution of annual SSTAs over the study area during 1961—2013, 1981—2013 and 1998—2013 (Left panel: COBE SST2; right panel: HadISST1) (Unit: ℃ per decade).

Furthermore, the SST trend of HadISST1 is much lower than that of COBE SST2 from 1891 to 1930 (Fig.3 and Table 2). It is well known that observations in the early years are sparse and unevenly distributed. Given this, a set of extra SST observations for the area around Japan before the World War II is merged with ICOADS to construct COBE SST2. This dataset is archived by the Japanese Fishery Agency (Kubo et al.[26]) and has not been included or merged in HadISST1. Besides, bucket observations compose most observations before the World War II [9]. For COBE SST2, cold inherent biases in uninsulated-bucket observations are eliminated to obtain SST series of homogeneous quality (Folland and Parker[27]). However, for HadISST1, it does not apply any bias adjustments to the earlier period. Thus, the different data sources and different bias adjustment before the World War II may cause a large divergence between COBE SST2 and HadISST1 from 1891 to 1930.

As mentioned above, several factors can explain the discrepancies in the two datasets. However, we still are not clear which product is appropriate for the regional climate studies in the China Seas. The hydrological observing network has been established around 1960 in China. 27 coastal hydrological stations at the coastline of China have been taking routine observations since 1960, with few missing data. All these data are provided by the National Marine Data and Information Service (NMDIS) in Tianjin and have been quality controlled and homogenized (Li et al.[28]). These SSTs data from coastal hydrological stations are not merged into HadISST1 or COBE SST2. Therefore, long-term SST observations of 13 coastal hydrological stations which are randomly selected are used for comparison and evaluation of the two SST datasets from January 1960 to December 2011. To do the work, HadISST1 and COBE SST2 are interpolated to the stations' locations. The correlation and standard deviation on the annual basis are computed and shown in a Taylor diagram (Taylor[29]; You et al.[30]).

The Taylor diagram (Fig.6) can provide a statistical summary of how well the HadISST1 and COBE SST2 match the stations-based observations. As seen in Fig.6, SSTs of COBE SST2 are more clustered around each other. Most of them have positive correlations with observations within the range of 0.6—0.7, except for the thirteenth station (only 0.45) (the 99% confidence level is 0.35). But, the correlations between HadISST1 and observations are smaller, within the range of 0.3—0.5. Taylor diagram analysis also reveals that COBE SST2 has the lower standard deviations (most of the values are no more than 0.5), comparing to the HadISST1 (Fig.6). It indicates that COBE SST2 can capture observations better than HadISST1 in the coast area of China.

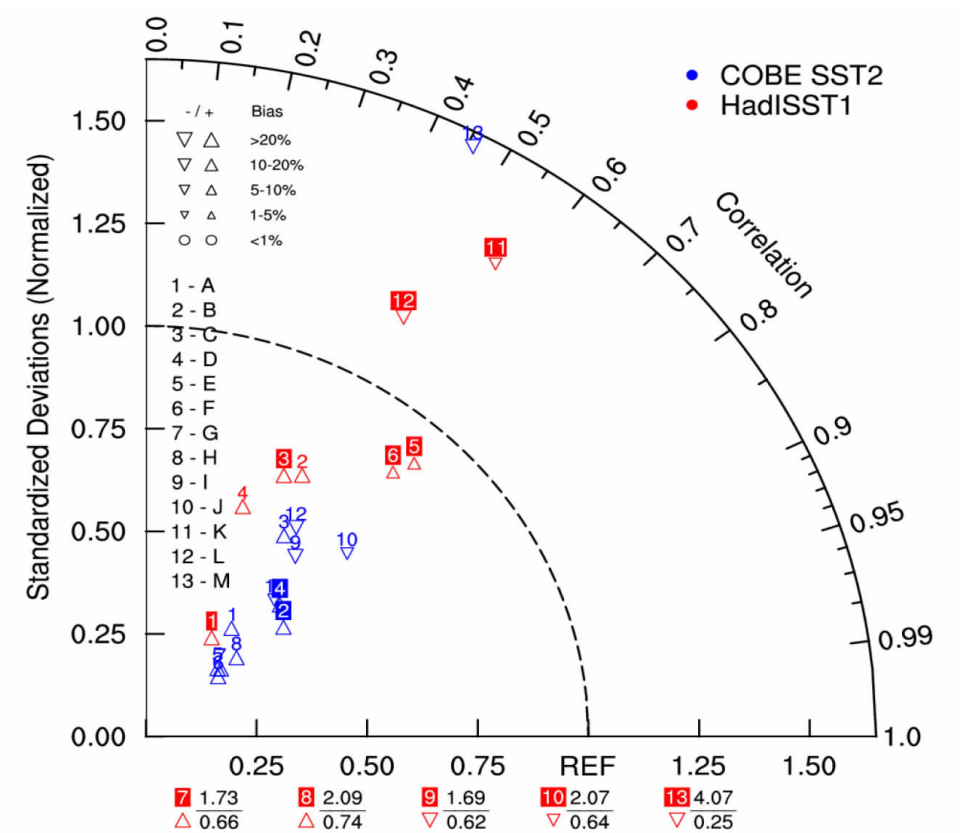

Figure 6. Taylor diagram of the annual mean SST from HadISST1 and COBE SST2 compared with those SST from stations observations. Further, it also plots negative correlations and standard deviations > 1.65 as text at the bottom of the figure (REF: Reference value). The radial distance from the origin is proportional to the standard deviation ratio. The triangles and circle mean the bias between HadISST1 (COBE SST2) and stations observations).

5 CONCLUSIONS

Historical SST data have played an important role in climate simulations, assessment and monitoring. In this study, we compute the linear trends of two centennial-scale SST datasets in the China Seas and their adjacent sea areas at several different epochs. Meanwhile we explore the causes of the discrepancies in the two datasets. Results show that the two SST series from HadISST1 and COBE SST2 from 1891 to 2013 have a similar warming trend. However, the trends of annual mean HadISST1 are generally much higher than those of annual mean COBE SST2 in the periods of 1961—2013, 1981—2013, 1981—1997 and 1998—2013. In the periods of 1891—1930 and 1910—1930 (before the World War II), the trends of annual mean HadISST1 are lower than these of COBE SST2. The maximum warming rates of 1961—2013 and 1981—2013 from HadISST1 and COBE SST2 are both located at the East China Sea and Taiwan Strait as shown in Fig.5, while the rates are much different. The maximum cooling rate of HadISST1 appears in the Yangtze River and the offshore region of the East China Sea, while the maximum cooling rate of COBE SST2 is in the Yellow Sea. The differences between the two datasets may arise from the different data sources, bias adjustment, reconstruction technique or the incorporation of satellite observations since 1980s. Results show that the differences in the two SST datasets do not change the inter-decadal trends significantly at much long-time scales. However, there are many uncertainties in the short-time scales such as fifty-year scale or shorter.

The Taylor diagram shows that the spatial correlation coefficients between station observations and COBE SST2 range from 0.6 to 0.7, and most of the standard deviations are lower than 0.5. It means that in the coast areas of the China Seas, COBE SST can capture station observations better than HadISST1 in the period of 1960 to 2011. Further studies are evidently needed to verify the reliability of the two datasets by more long-term observations over the China Seas and their adjacent sea areas instead of just at the Chinese coast.

Acknowledgement: We are truly grateful to the two anonymous reviewers for their professional comments and suggestions to this study.

REFERENCES:

[1] ZHANG Xiu-zhi, QIU Yue-fang, WU Xun-ying. The long-term change for sea surface temperature in the lasts in 100 years in the offshore sea of China [J]. Clim Environ Res, 2005, 10(4): 799-807 (in Chinese).

[2] ZHANG L, WU L, LIN X, et al. Modes and mechanisms of sea surface temperature low-frequency variations over the coastal China seas [J]. J Geophys Res Oceans, 2010, 115 (C8): 396-413.

[3] XIE S P, MA J, DESER C, et al. Global warming pattern formation: sea surface temperature and rainfall [J]. J Climate, 2010, 23(4): 966-986.

[4] WU L X, CAI W J, ZHANG L P, et al. Enhanced warming over the global subtropical west boundary currents [J]. Nature Climate Change, 2012, 2(3): 161-166.

[5] BOEHME L, LONERGAN M, TODD C D. Comparison of gridded sea surface temperature datasets for marine ecosystem studies [J]. Mar Ecol Prog Ser, 2014, 516, 7-22, doi:10.3354/meps11023.

[6] JIN Qi Hua, WANG Hui. Multi-time scale variations of sea surface temperature in the China Seas based on the HadISST dataset [J]. Acta Oceanol Sinica, 2011, 30(4): 14-23.

[7] LIU Qin-yu, ZHANG Qi. Analysis on long-term change of sea surface temperature in the China Seas [J]. J Ocean Univ China, 2013, 12(2): 295-300.

[8] WANG Fan, MENG Qing-hua, TANG Xiao-hui, et al. The long-term variability of sea surface temperature in the seas east of China in the past 40 a [J]. Acta Oceanol Sinica, 2013, 32(3): 48-53.

[9] HIRAHARA S, ISHII M, FUKUDA Y. Centennial-scale sea surface temperature analysis and its uncertainty [J]. J Climate, 2012, 27(1): 57-75.

[10] BUNGE L, CLARKE A J. A verified estimation of the El Niño index Niño-3.4 since 1877 [J]. J Climate, 2009, 22 (14): 3979-3992.

[11] VECCHI G A, CLEMENT A, SODEN B J. Examining the tropical Pacific's response to global warming [J]. Eos Trans Amer Geophys Union, 2008, 89(9): 81-83.

[12] TOKINAGA H, XIE S P, DESER C, et al. Slowdown of the Walker circulation driven by tropical Indo-Pacific warming [J]. Nature, 2012, 491(7424): 439-43.

[13] RAYNER N A, PARKER D E, HORTON E B, et al. Global analyses of sea surface temperature, sea ice, and night marine air temperature since the late nineteenth century [J]. J Geophys Res Atmos, 2003, 108 (D14): 1063-1082.

[14] ISHII M, SHOUJI A, SUGIMOTO S, et al. Objective analyses of sea-surface temperature and marine meteorological variables for the 20th century using ICOADS and the Kobe Collection [J]. Int J Climatol, 2005, 25(7): 865-879.

[15] JONES P D, HULME M. Calculating regional climatic time series for temperature and precipitation: methods and illustrations [J]. Int J Climatol, 1996, 16(4): 361-377.

[16] CHEN J, LI Q, NIU J, et al. Regional climate change and local urbanization effects on weather variables in southeast China [J]. Stoch Environ Res Risk Assess, 2011, 25(4): 555-565.

[17] HAMED K H, RAO A R. A modified Mann-Kendall trend test for autocorrelated data [J]. J Hydrol, 1998, 204(1-4): 182-196.

[18] VON STORCH H, ZWIERS F W. Statistical analysis in climate research [J]. J Amer Statist Assoc, 1999, 27(3): 3-10.

[19] BAO B, REN G Y. Climatological characteristics and long-term change of SST over the marginal seas of China [J]. Contin Shelf Res, 2014, 77(1): 96-106.

[20] KOSAKA Y, XIE S P. Recent global-warming hiatus tied to equatorial Pacific surface cooling [J]. Nature, 2013, 501 (7467): 403-407.

[21] SMITH D. Oceanography: Has global warming stalled? [J].

Nature Climate Change, 2013, 3(7): 618-619.
[22] FYFE J C, GILLETT N P, ZWIERS F W. Overestimated global warming over the past 20 years [J]. Nature Climate Change, 2013, 3(9): 767-769.
[23] GUEMAS V, DOBLAS-REYES F J, ANDREW-BURILLO I, et al. Retrospective prediction of the global warming slowdown in the past decade [J]. Nature Climate Change, 2013, 3(7): 649-653.
[24] CAI R S, TAN H J, QI Q H. Impacts and adaptation to inter-decadal marine climate in coastal China Seas [J]. Int J Climatol, 2015, doi: 10.1002/joc.4591.
[25] HUANG B, THORNE P W, SMITH T M. Further exploring and quantifying uncertainties for extended reconstructed Sea Surface Temperature (ERSST) Version 4 (v4) [J]. J Climate, 2015, 29(9): 151211135749001.
[26] KUBO H, TOMOSADA A, NISHIHATA I, et al. Oceanography of Kashima-nada, off the east coast of Honshu. III. Water characteristics of Joban to Boso Sea area [J]. Bull Tokai Reg Fish Res Lab, 1982, 96: 11-28.
[27] FOLLAND C K, PARKER D E. Correction of instrumental biases in historical sea surface temperature data [J]. Quart J Roy Meteor Soc, 1995, 121(522): 319-367.
[28] LI Y, WANG G S, FAN W J, et al. The homogeneity study of the sea surface temperature data along the coast of the China Seas [J]. Acta Oceanol Sinica, 2018, 40(1): 17-28.
[29] TAYLOR K E. Summarizing multiple aspects of model performance in a single diagram [J]. J Geophys Res Atmos, 2001, 106 (D7): 7183-7192.
[30] YOU Q L, JIAO Y, LIN H B, et al. Comparison of NCEP/NCAR and ERA-40 total cloud cover with surface observations over the Tibetan Plateau [J]. Int J Climatol, 2013, DOI: 10.1002/joc.3852.

Citation: WANG Qing-yuan, LI Yan, LI Qing-quan, et al. A comparison and evaluation of two centennial-scale sea surface temperature datasets in the China Seas and their adjacent sea areas [J]. J Trop Meteor, 2018, 24(4): 448-456.

atmosphere

MDPI

Article

Remarkable Impacts of Indian Ocean Sea Surface Temperature on Interdecadal Variability of Summer Rainfall in Southwestern China

Jingpeng Liu [1,2,3], Hong-Li Ren [3,4,*], Weijing Li [3] and Jinqing Zuo [3]

1 Chinese Academy of Meteorological Sciences, Beijing 100081, China; liujingpeng@cma.gov.cn
2 University of Chinese Academy of Sciences, Beijing 100049, China
3 Laboratory for Climate Studies & CMA-NJU Joint Laboratory for Climate Prediction Studies, National Climate Center, CMA, Beijing 100081, China; liwj@cma.gov.cn (W.L.); jqzuo425@126.com (J.Z.)
4 Department of Atmospheric Science, School of Environmental Studies, China University of Geoscience, Wuhan 430074, China
* Correspondence: renhl@cma.gov.cn; Tel.: +86-10-6840-9514

Received: 2 February 2018; Accepted: 5 March 2018; Published: 13 March 2018

Abstract: During the boreal summer from June to August, rainfall in Southwestern China shows substantial interdecadal variabilities on timescales longer than 10 years. Based on observational analyses and numerical modeling, we investigated the characteristics of interdecadal Southwestern China summer rainfall (SWCSR) and its dynamic drivers. We find that the SWCSR is markedly impacted by the interdecadal Indian Ocean basin mode (ID-IOBM) of the sea surface temperature (SST), which may induce anomalous inter-hemispheric vertical circulation. During the cold phase of the ID-IOBM, an enhanced lower-level divergence and upper-level convergence exist over the tropical Indian Ocean. The simultaneous lower-level outflow anomalies further converge over the Indo-China peninsula, resulting in an anomalous ascending motion and a lower-level cyclone that contribute to strengthening the eastward moisture transport from the Bay of Bengal to Southwestern China. The joint effects of the anomalous ascending motion and the above-normal moisture transport play a key role in increasing the SWCSR. In summers during the warm phase of the ID-IOBM, the situation is approximately the same, but with opposite polarity. After the beginning of the 1970s, the impacts of interdecadal Indian Ocean dipole (ID-IOD) on SWCSR is strengthening. The anomalous vertical circulation associated with the positive (negative) phase of ID-IOD is in favor of decreased (increased) rainfall in SWC. However, the impacts of ID-IOD on SWCSR is relatively weak before the 1970s, indicating that the ID-IOD is the secondary driver of the interdecadal variability of SWCSR. Modeling results also indicate that the ID-IOBM of SST anomalies is the main driver of interdecadal variability of SWCSR.

Keywords: Southwestern China; summer rainfall; Indian Ocean; sea surface temperature; interdecadal variability

1. Introduction

Southwestern China (SWC) is one of the most populated agricultural regions in China, providing approximately 16% of the national food supply [1]. It contains the headwaters of many important rivers, including the Yangtze, Lancang, and Nujiang rivers, which provide as much as 46% of China's available water resources [1]. The terrain in this area is very complex. The average altitude in SWC (about 23–30° N and 99–105° E) exceeds 1500 m above sea level, shown in the rectangle in Figure 1. The climatological summer rainfall in SWC gradually decreases from southeast to northwest, with values ranging between 5 mm day^{-1} and 8 mm day^{-1} (Figure 1). Unlike flatlands, agriculture and ecosystems in this region are quite vulnerable to summer rainfall variability in low-latitude highlands [2,3].

Southwestern China summer rainfall (SWCSR) exhibits variability on a broad range of timescales. Large interannual variability often causes rainfall to vary from year to year [4], whereas the interdecadal variability always results in persistent droughts and floods, which considerably impact the socio-economic development and the natural environment [5]. Since 2006, the frequency of extreme droughts increased significantly in SWC. Record-breaking droughts hit SWC in the summer of 2006 [6], the autumn of 2009 [7], and the late summer of 2011 [8], which have caused concern among the Chinese government, the public, and the academic sector. Most previous studies focused on the characteristics and the physical causes of SWCSR on interannual timescale [2,7–10]. Therefore, understanding the primary features of the interdecadal variability of SWCSR and the associated mechanisms is both urgent and valuable.

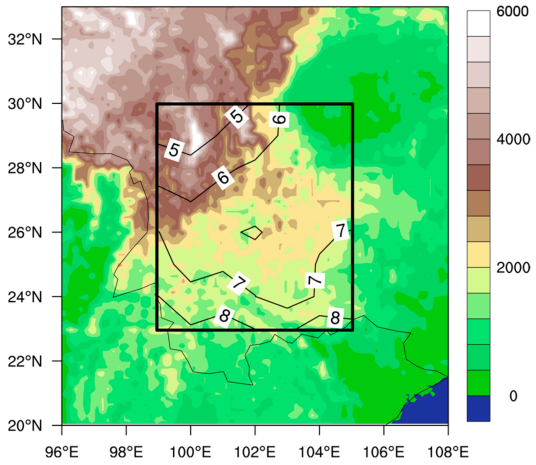

Figure 1. Climatological mean of summer precipitation (contour; mm day^{-1}) for the period of 1921–2016 and the terrain (shading; m) of Southwestern China. The rectangle denotes the studied region for Southwestern China.

With the Indian Ocean (IO) located southwest of SWC, some studies emphasized the strong influence of the IO on the decadal variability in East Asian summer climate, especially the Southeastern China summer rainfall (SECSR) [11,12]. The climatological SECSR is different from that in SWC. It gradually decreases from south to north with more abundant rainfall ranging between 6 mm day^{-1} and 11 mm day^{-1}. Wu et al. [11] revealed that the equatorial IO sea surface temperature (SST) had been increasing since the early 1990s, which led to the development of an anomalous lower-level anticyclone over the South China Sea and the Philippines. As a result, the SECSR increased. Zhang et al. [12] revealed that the southern IO SST considerably impacted the interdecadal changes of the East Asian summer monsoon, which was featured by a decrease in the late 1970s and an increase in the early 1990s. An interdecadal cooling in the south IO triggered anomalous vertical overturning circulation, which led to a lower-level anticyclonic anomaly over the tropical northwestern Pacific. This pattern of circulation anomalies resulted in additional moisture transport into Southeastern China and subsequent rainfall increase. Cao et al. [2] revealed that the subtropical Indian Ocean dipole was the main driver of the interannual variability of SWCSR. To date, the impacts of the IO on the interdecadal variability of SECSR have been extensively studied, whereas the impacts of the IO on the interdecadal variability of SWCSR are less understood. Therefore, the present study focused on the characteristics of interdecadal variability of SWCSR and their connections with the IO SST.

The rest of this paper is organized as follows: Section 2 describes the datasets, methods, and model used in this study. Section 3 investigates the relationship between interdecadal variability of SWCSR and the IO SST. Section 4 describes the mechanisms used to connect the SST anomalies (SSTA) in the IO with the SWCSR. Finally, the discussionand summary are presented.

2. Datasets, Model, and Experiments

2.1. Datasets and Methods

In this study, 116 years of monthly rainfall data (1901–2016) were used to examine the interdecadal variability of summer (June to August, JJA) rainfall in SWC. The monthly rainfall data include monthly mean rainfall from the Global Rainfall Climatology Centre (GPCC) [13] with a spatial resolution of 1.0° × 1.0°, and monthly rainfall in China provided by the National Meteorological Information Center (NMIC) of the China Meteorological Administration on a grid of 2.0° × 2.0° for the period of 1901 to 2016 [14]. Monthly mean sea surface temperature data was provided by the Hadley Centre of the U.K. Met Office (HadISST) [15] for the period of 1847 to 2016. Monthly mean atmospheric fields were extracted from the NOAA-CIRES 20th Century Reanalysis products (20CR) [16] for the period of 1851 to 2014. The spatial resolutions of the 20CR datasets and the HadISST datasets were 2° × 2° and 1° × 1°, respectively. As SST observations in the tropical ocean are sparse prior to 1920 [17], analyses of the present study focused on the period of 1921 to 2016.

To extract interdecadal signal, linear trends were first removed from all the data. Variabilities on timescales shorter than 11 years were then filtered out using the Lanczos filter method [18]. As the most updated 20CR ends in 2014, thereafter, the anomalies of each dataset were calculated relative to the climatology for the period of 1921 to 2014.

The significance test of the correlation coefficient uses the Monte Carlo method [19]. Considering time series A and B, the original time series A was randomly rearranged to obtain a new time series at each grid point. The correlation between this new time series and time series B was then calculated. This process was repeated 1000 times and a distribution of the correlation values at each grid point was finally obtained. The quoted significance level of the correlation between time series A and B indicates the percentage of randomized correlation coefficients that exceed the value being tested. The significance of the regression coefficient was tested using the same method.

2.2. Model and Experimental Setup

The atmospheric general circulation model (AGCM) used was the Community Atmospheric Model version 5.3 (CAM5) developed by the National Center for Atmospheric Research (NCAR, Boulder, CO, USA). CAM5 is coupled to the Community Land Model (CLM version 4.0), and a version with 1.9° latitude by 2.5° longitude resolution and 30 vertical levels was used in this study. Li et al. [20] showed that CAM5 model could effectively capture the spatial features of the summer climate over the IO and East Asia. We conducted three experiments using the CAM5 model. In the control experiment (CTRL run), the model was forced with the climatological mean seasonal cycle of SST (1921–2014). Parallel to the control experiment, two sensitivity experiments were performed with an imposed JJA IO SST anomalous pattern, which we refer to here as the ID-IOBM in the region of 30° S–25° N and 40° E–105° E. One experiment was imposed with the climatological seasonal cycle of SST plus the cold phase of the ID-IOBM (CIO run), and the other with the climatological seasonal cycle of SST minus the cold phase of the ID-IOBM (WIO).

3. Association of Interdecadal Variability of SWCSR with IO SST

The longitude-time cross-section of observed SWCSR averaged between 23° N and 30° N is provided to reveal the temporal evolution characteristics of interdecadal SWCSR. As shown in Figure 2, the SWCSR displays apparent drought and flood periods during 1926 to 2011, which indicates an evident interdecadal signal in the SWCSR. Flood periods occurred from 1944 to 1971 and 1994 to 2003, whereas drought periods occurred from 1926–1943, 1972–1993, and 2004–2011. The positive (negative) phase of the SWCSR is characterized by increased (decreased) rainfall in SWC. Notably, since the beginning of the 2000s, SWCSR transitioned into a negative phase, which could be considered the interdecadal background of frequent extreme droughts during the past decade [8]. Hereafter, the average rainfall anomalies in SWC, highlighted by the rectangle in Figure 1, is defined as the SWCSR

index for further analyses. We aimed to determine the mechanisms responsible for the interdecadal variability of SWCSR.

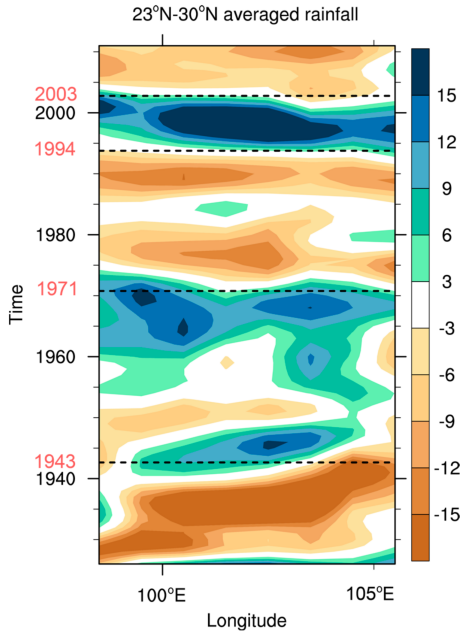

Figure 2. Longitude-time cross-section of the anomalous Southwestern China summer rainfall (SWCSR) for the period of 1926 to 2011 averaged between 23° N and 30° N using the Global Rainfall Climatology Centre (GPCC) datasets. An 11-year filter was applied. Dashed lines denote the transition years between drought and flood periods.

SSTA play crucial roles in the interdecadal variability in rainfall and the associated large-scale atmospheric circulation over East Asia [21,22]. Figure 3a shows the correlation coefficients between SSTA and the SWCSR index for the period of 1926 to 2011. The most significant correlation is found in the IO, which exhibits a basin-wide monopole pattern, whereas an only limited significant correlation area was observed in the Pacific and the Atlantic. This SST pattern in the IO is similar to the conventional IO basin mode (IOBM) that was defined on interannual timescale [23,24]. Given this resemblance, the interdecadal basin-wide mode of IO SST is termed the ID-IOBM in this study. The warm (cold) phase of the ID-IOBM is characterized by warming (cooling) in the entire IO. The average SST anomaliesin the IO is calculated, which is defined as the ID-IOBM index, shown by the red bars in Figure 3b.

Figure 3b also shows the SWCSR and the ID-IOBM indices. The correlation coefficient between the SWCSR index derived from GPCC data (the black line in Figure 3b) and the ID-IOBM index is –0.78 for the period of 1926 to 2011, which is significant at the 95% confidence level, suggesting that the ID-IOBM is closely negatively correlated with the SWCSR. When the ID-IOBM is in its cold phase with below-normal SST over the entire IO, summer rainfall tends to be abundant in SWC. To further confirm the results, the SWCSR index was also calculated using the NMIC observed grid data, shown by the blue line in Figure 3b. The correlation coefficient between the two SWCSR indices, derived from GPCC and NMIC data, is 0.90 for the period of 1926 to 2011, which is significant at the 99% confidence level, indicating that the interdecadal variability of SWCSR is robust in observational rainfall data. The correlation coefficient between the SWCSR index derived from the NMIC data and the ID-IOBM index is −0.77, which is significant at the 95% confidence level, showing a steady relationship between the ID-IOBM and the SWCSR, irrespective of the rainfall data used. Hereafter, the SWCSR index derived from the NMIC data is used for further analyses.

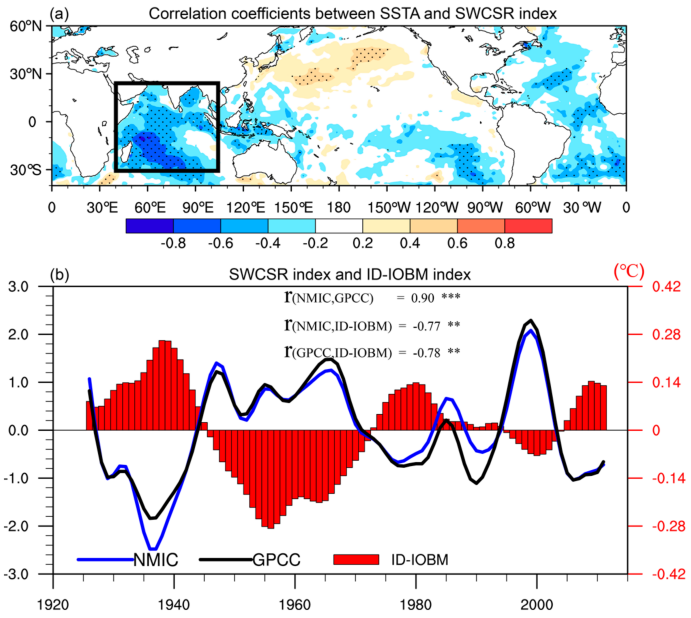

Figure 3. (**a**) Correlation coefficients between sea surface temperature anomalies and the SWCSR index. Black dots indicate areas significant at the 95% confidence level. The rectangle denotes the studied region for Indian Ocean; (**b**) the SWCSR index (lines) and the interdecadal Indian Ocean basin mode (ID-IOBM) index (red bars). Blue (black) line denotes the SWCSR index derived from the National Meteorological Information Center (NMIC) (GPCC) data. ** and *** indicate correlation coefficients significant at the 95% and 99% confidence level, respectively.

Previous studies demonstrated that the interdecadal variation of rainfall is always accompanied by atmospheric circulation variability [25,26]. Therefore, summer atmospheric circulation patterns associated with the SWCSR and the ID-IOBM indices were investigated to verify the interdecadal connection between the SWCSR and the ID-IOBM (Figure 4). Note that the sign of the ID-IOBM index is reversed during regression analyses to represent the impacts of the cold phase of the ID-IOBM.

The stream function patterns regressed against the SWCSR index and the ID-IOBM index at 200 hPa are shown in Figure 4a,b, respectively. From Figure 4a, the most distinct signal associated with the SWCSR was the positive action center (above-normal center of stream function) located over the Indo-China peninsula, which is favorable for upper-level divergence and the accompanying ascending motion. The highly similar features are outlined in Figure 4b. Figure 4c,d show the regressed stream function patterns at 500 hPa. The common characteristics between Figure 4c,d are the significant positive action center located over the Indo-China peninsula and the negative action center over IO, indicating an anomalous ascending motion over the Indo-China peninsula and a descending motion over the tropical IO. The lower-level circulation anomalies associated with the SWCSR index, as shown in Figure 4e, exhibit opposite patterns to the upper level, including prevailing westerly wind anomalies over the entire tropical IO and an anomalous cyclone over the Indo-China peninsula. Significant westerly anomalies are observed at the west flank of the cyclone, which may strengthen the moisture transport from the Bay of Bengal (BOB) to SWC. The lower-level circulation anomalies associated with the ID-IOBM index (Figure 4f) have a similar pattern to that shown in Figure 4e.

Based on these circulation results, we inferred that the anomalous cyclone over the Indo-China peninsula at 850 hPa may impact the SWCSR by strengthening the moisture transport from the BOB to SWC. The anomalous negative action center at 500 hPa and the positive action center at 200 hPa favor the anomalous ascending motion over the Indo-China peninsula, corresponding well with the anomalous cyclone at 850 hPa. The combined effects of the anomalous ascending motion and the above-normal moisture transport are favorable for above-normal SWCSR. Notably, the anomalous

circulation patterns associated with the cold phase of the ID-IOBM (Figure 4b,d,f) and the positive phase of the SWCSR (Figure 4a,c,e) are very similar. Therefore, these circulation anomalies may act as the bridge connecting the SWCSR with the ID-IOBM.

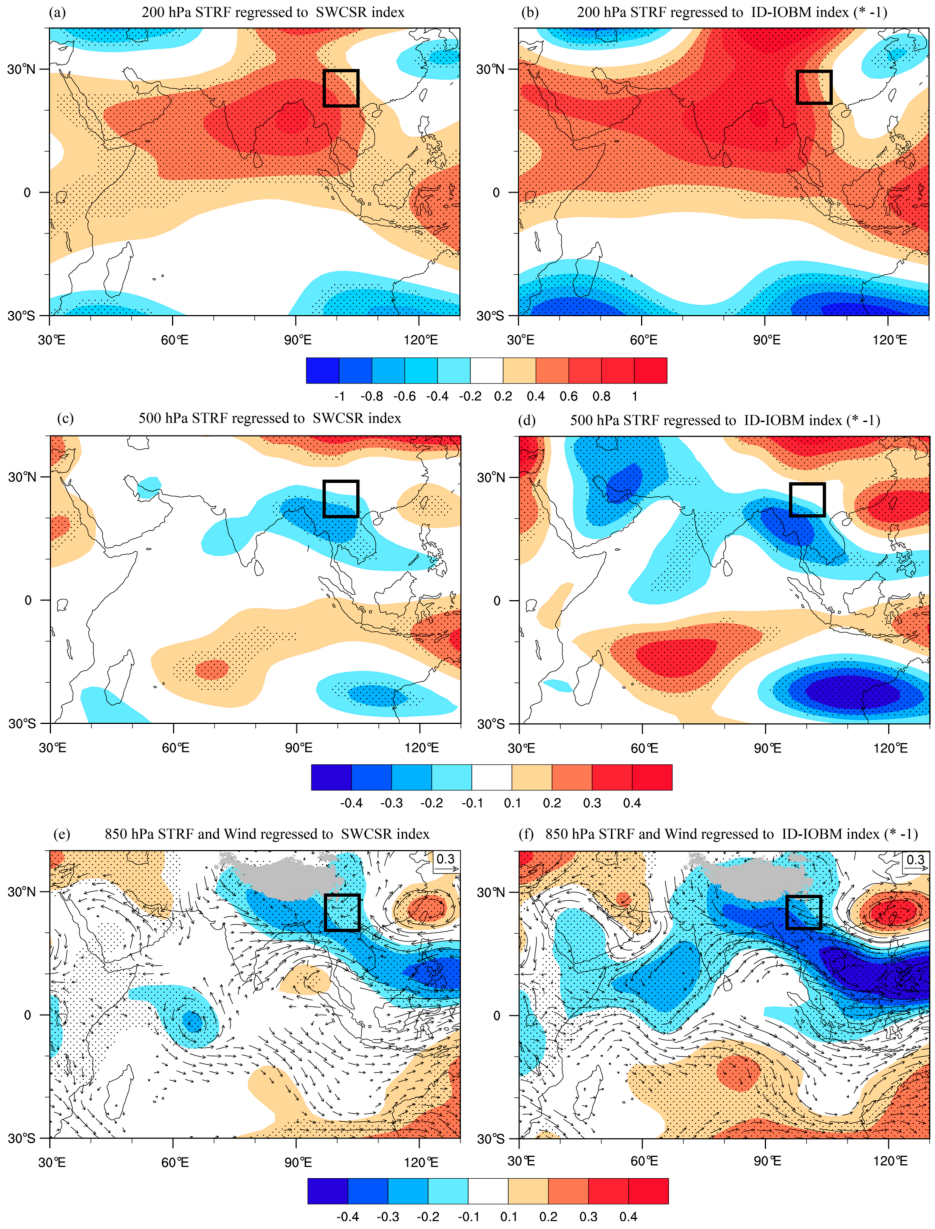

Figure 4. Stream function (STRF, shading; 10^6 m^2/s) regressed against the SWCSR index and the ID-IOBM index at (**a**,**b**) 200 hPa and (**c**,**d**) 500 hPa; and (**e**,**f**) regressed STRF (shading; 10^6 m^2/s) and wind field (vectors; m/s) anomalies at 850 hPa in June, July, and August (JJA). "*" denotes "multiply by". Black dots denote areas significant at the 95% confidence level.

4. Possible Mechanisms of the Impacts of IO SST on SWCSR

To further confirm the above-mentioned physical processes of the impacts of the ID-IOBM on the SWCSR, observational diagnoses and model simulation experiments were performed. The results are shown in terms of the positive phase of the SWCSR and the cold phase of the ID-IOBM.

4.1. Observational Analyses

First, Figure 5 shows the regressed divergent wind and velocity potential against the SWCSR index and the ID-IOBM index. A notable lower-level divergence and upper-level convergence associated with the cold phase of the ID-IOBM is found over the tropical IO, as seen in Figure 5b,d. At the lower level, anomalous outflows from the tropical IO converge over SWC, corresponding to a regional ascending motion. An accompanying upper-level divergence center is located over SWC, and the corresponding outflows converge over the tropical IO. Therefore, an inter-hemispheric anomalous vertical circulation cell emerges between the tropical IO and SWC. Figure 5b,d show that the regressed divergent wind patterns associated with the ID-IOBM index are highly consistent with those associated with the SWCSR index, indicating that the anomalous inter-hemispheric vertical circulation cell, induced by the ID-IOBM in its cold phase, may be an important driver that increases SWCSR. Such a mechanism shares some similarity with that presented by Krishnamurthy and Goswami [27], who showed that the anomalous vertical circulation also acted as the bridge connecting the interdecadal variability of Indian summer monsoon rainfall and tropical eastern Pacific SST.

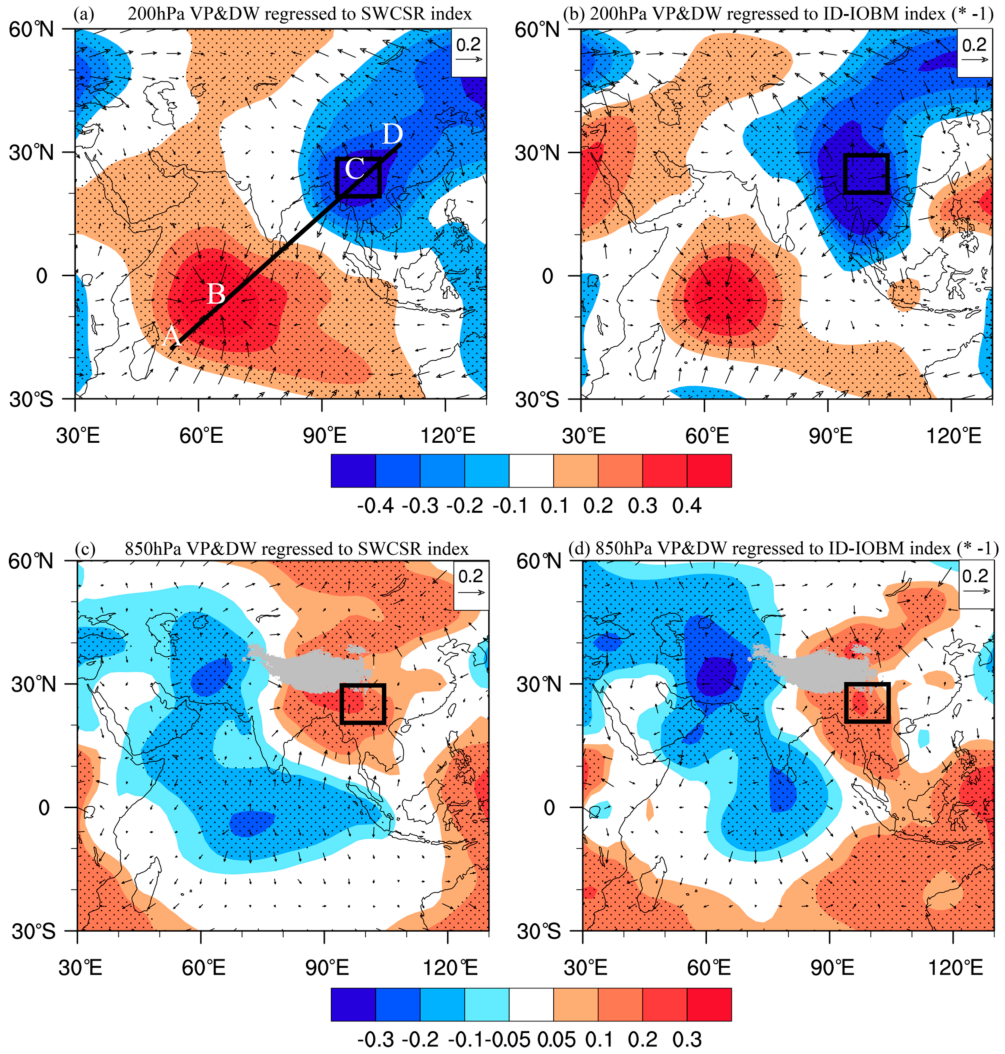

Figure 5. Regressed divergent winds (vectors; m/s) and velocity potentials (shading; 10^6 m^2/s) at (**a**,**b**) 200 hPa and (**c**,**d**) 850 hPa against (**a**,**c**) the SWCSR index and (**b**,**d**) the ID-IOBM index. Line ABCD in (**a**) is the location for slice in height analysis hereafter. The rectangles indicate Southwestern China. "*" denotes "multiply by". Black dots denote areas significant at the 95% confidence level.

To further verify the linkage between the ID-IOBM and the SWCSR, Figure 6 displays the two highly similar vertical circulation patterns associated with the two indices along the chosen cross-section, shown by the black line in Figure 5a. The most significant feature is the anomalous vertical circulation located between B (around 5° S, 65° E) and C (around 25° N, 100° E). The ascending motions over C (SWC) are accompanied by lower-level southwestern moisture transport from the BOB, both of which favor increased rainfall in SWC. The descending motions over B (tropical IO) are associated with the underlying cold phase of the ID-IOBM. The similar pattern in Figure 6b further confirms that the anomalous inter-hemispheric vertical circulation cell induced by the ID-IOBM in its cold phase is an important factor that leads to increased SWCSR.

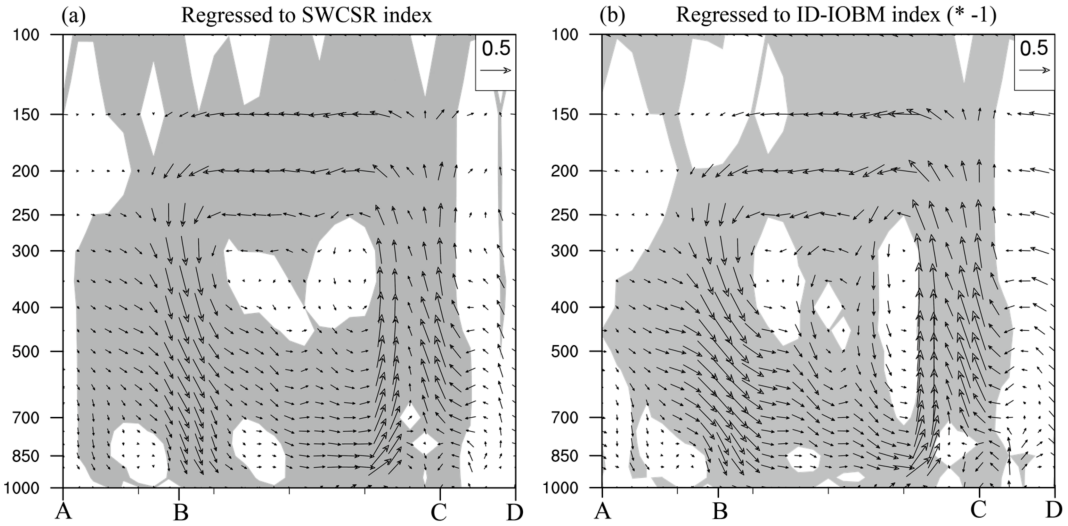

Figure 6. Regressed vertical circulation against (**a**) the SWCSR index and (**b**) the ID-IOBM index along line ABCD (m/s, vertical speeds are multiplied by 50 for visual clarity). "*" denotes "multiply by". Shading indicates the areas significant at the 90% confidence level.

4.2. Model Simulation

To demonstrate the possible driving effect of IO SST on the circulation anomalies associated with the SWCSR, three numerical experiments described in Section 2 were completed with CAM5: the CTRL run, the CIO run, and the WIO run. The CTRL run used the climatological seasonal cycle of SST. The CIO (WIO) run was completed with the climatological seasonal cycle of SST plus (minus) JJA SSTA regressed against the SWCSR index, which we refer to here as the cold phase of the ID-IOBM in the region of 30° S–25° N and 40° E–105° E (Figure 7a,b). The ID-IOBM pattern was scaled by a factor of four and used to drive the model. For each experiment, the model was integrated for 50 years. The first 10 years of output were discarded to exclude any possible transient spin-up effects. A time mean was then calculated by averaging the output for the remaining 40 years for each JJA season. The linear response to the SST forcing was defined as the difference between the time means for the CIO (WIO) run and the CTRL run. The response was scaled by a factor of 0.25 to allow a comparison with the observed results.

The difference of atmospheric response between the CIO and CTRL experiments is shown in Figure 7c,e. In response to the cold phase of the ID-IOBM, the descending motion over the tropical IO tends to intensify, whereas the ascending motion developments were observed over the Indo-China peninsula, accompanied by outflows to the tropical IO at the upper level (Figure 7c). The consequent increase in the divergence at 200 hPa over the Indo-China peninsula was accompanied by an anomalous lower-level convergence (Figure 7e). The difference in atmospheric response between the WIO and CTRL experiments is shown in Figure 7d,f. The atmospheric responses

were approximately the same, but with opposite polarity, highlighting the symmetric impacts of the ID-IOBM on the SWCSR. These atmospheric responses are similar to the observational regressions in Figure 5, though the location of atmospheric circulation anomalies over the IO displays some small differences from observations. We can see that the model results confirm our hypothesis that the circulation anomalies induced by the ID-IOBM connect the SWCSR with the ID-IOBM.

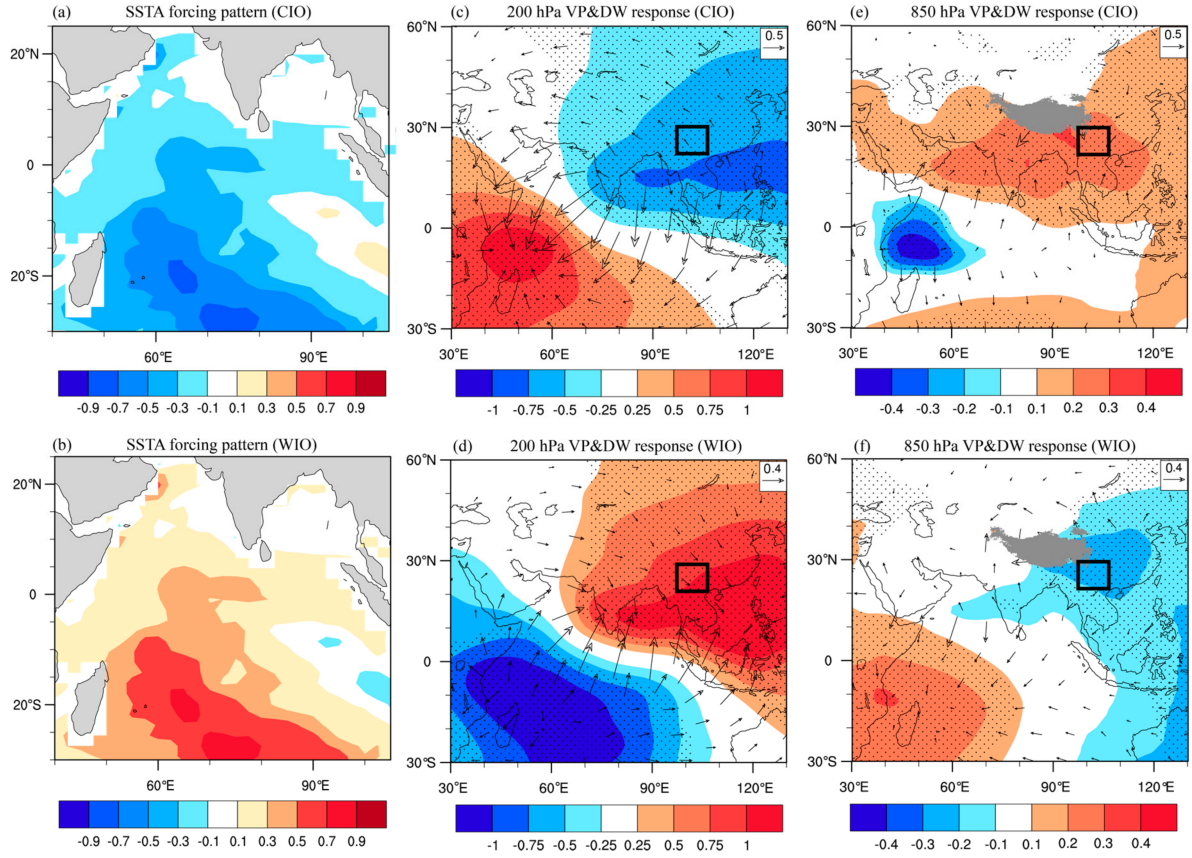

Figure 7. The SSTA specified in (**a**) the cold phase of the ID-IOBM (CIO) run and (**b**) the warm phase of the ID-IOBM (WIO) run; divergent winds (vectors; m/s) and velocity potentials (shading; 10^6 m^2/s) responses to (**c**,**e**) the CIO run and (**d**,**f**) the WIO run in JJA. The rectangle indicates Southwestern China. Black dots denote areas significant at the 95% confidence level.

5. Discussion

In Figure 3b, it is interesting to note that the amplitude of ID-IOBM is gradually decreasing after the beginning of 1970s, while the variability of SWCSR does not show such a change. Are there any other potential factors that can have impacts on the SWCSR?

To explain such a phenomenon, we calculate the correlation coefficients between the IO SSTA and the SWCSR index after remove the ID-IOBM from the IO SSTA, which displays a significant dipole pattern (Figure 8a). The SSTA in the southwestern (southeastern) Indian Ocean is negatively (positively) correlated with the SWCSR index. This pattern is termed the interdecadal Indian Ocean dipole (ID-IOD) hereafter. The positive phase of the ID-IOD is characterized by above-normal (below-normal) SSTA in the southwestern (southeastern) IO, and vice versa. The ID-IOD is quite different from the conventional IOD, which is active mainly in the tropical IO on interannual timescale in boreal autumn [28,29]. The difference between the average SSTA in 28° S–10° S, 55° E–83° E and 20° S–10° S, 95° E–110° E (rectangles in Figure 8a) is defined as the ID-IOD index (Figure 8b). The amplitude of ID-IOD is

increasing after the beginning of 1970s, which may be responsible for the decreasing amplitude of ID-IOBM in the recent past decades.

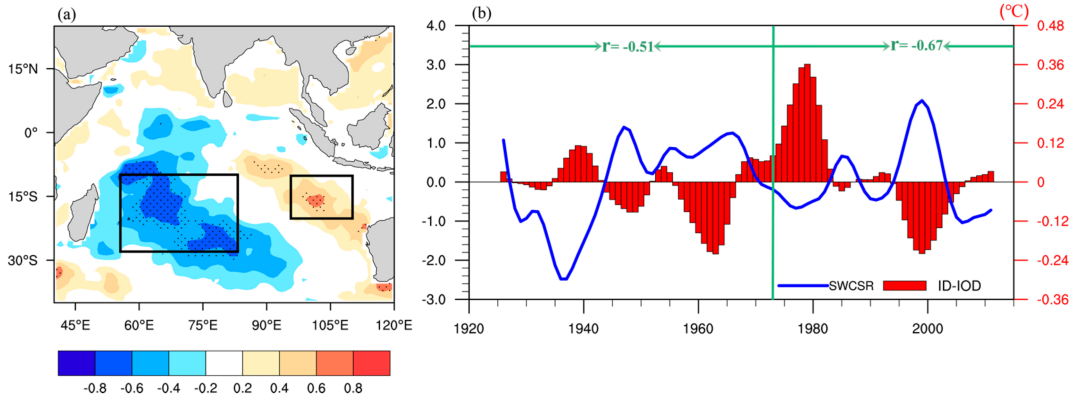

Figure 8. (**a**) Correlation coefficients between the IO SSTA and the SWCSR index. The average SSTA in the Indian Ocean were removed from SSTA before calculation. The rectangles indicate the key region used to calculate the ID-IOD index. Black dots indicate areas significant at the 95% confidence level; (**b**) the SWCSR index (blue line) and the interdecadal Indian Ocean dipole (ID-IOD) index (red bars). The green line denotes the transition year after which the amplitude of ID-IOBM is gradually decreasing. The correlation coefficient between the SWCSR index and the ID-IOD index is −0.51 (r = −0.51, not significant) for the period of 1926–1972 and is −0.67 (r = −0.67, significant at the 90% confidence level) for the period of 1973–2011.

To investigate the possible relationship between ID-IOD and SWCSR, the correlation coefficient between the SWCSR index and the ID-IOD index is calculated, which is −0.51 (not significant) for the period of 1926–1972 and is −0.67 (significant at the 90% confidence level) for the period of 1973–2011, indicating that the SWCSR is more closely associated with the ID-IOD after the beginning of 1970s. The relatively low correlation between the SWCSR index and the ID-IOD index before 1970s is possibly due to the weak amplitude of simultaneous ID-IOD.

To further investigate the possible influence of the ID-IOD on the SWCSR and associated physical processes, we analyzed SSTA and circulation anomalies associated with the ID-IOD. Figure 9a shows that the regressed SSTA against the ID-IOD index in the IO displays an apparent dipole pattern in the southern IO, which is similar to the conventional subtropical Indian Ocean dipole defined on interannual timescale [30]. The anomalous easterlies prevail over the subtropical south IO, resulting in anomalous convergence over the southwestern IO and the central tropical IO, corresponding to a regional ascending motion. Figure 9b shows that the anomalous ascending motion over the central tropical IO is accompanied with anomalous upper-level divergence. One branch of the corresponding upper-level outflows converges over the Indo-China peninsula, which is favorable for anomalous descending motion and lower-level northeasterly anomalies, both of which favor decreased rainfall in SWC. This is consistent with the results revealed by Cao et al. [2], who showed that the summer rainfall in SWC is negatively connected with the subtropical Indian Ocean dipole on interannual timescale. The positive subtropical Indian Ocean dipole facilitated easterly anomalies off the eastern coast of BOB and weakened climatological water vapor flux to the northern BOB. As a result, anomalous water vapor divergence and less rainfall was observed over the SWC.

Therefore, the decreasing amplitude of ID-IOBM in the recent past may be related to the increasing amplitude of ID-IOD. After the beginning of 1970s, the impacts of ID-IOD on SWCSR is strengthening. The combined impacts of ID-IOBM and ID-IOD sustained the variability of SWCSR. The ID-IOBM is closely associated with the SWCSR for the whole period of 1926–2011. However, the impacts of ID-IOD on SWCSR is relatively weak before 1970s, indicating that the ID-IOD is the secondary driver of the interdecadal variability of SWCSR.

Though the SECSR and SWCSR are neighboring regions, the relationship between ID-IOBM and SECSR are quite different from the ID-IOBM and SWCSR relationship. We studied the relationship between ID-IOBM and SECSR separately [31], which is beyond the scope of this work.

These results provide an efficient prediction potential for summer rainfall variations, especially for extreme droughts and floods over SWC. With the Tibetan Plateau to the northwest of the SWC, the influence on the interdecadal variability of SWCSR is worth studying in the future. Our efforts in this study were dedicated to studying the historical changes and causes of SWC; however, the future changes in drought risk in SWC under global warming need to be further studied. This information is crucial to advance planning for agricultural adaptation and water resource management. Therefore, a multimodel projection of future rainfall in SWC will be completed in the future.

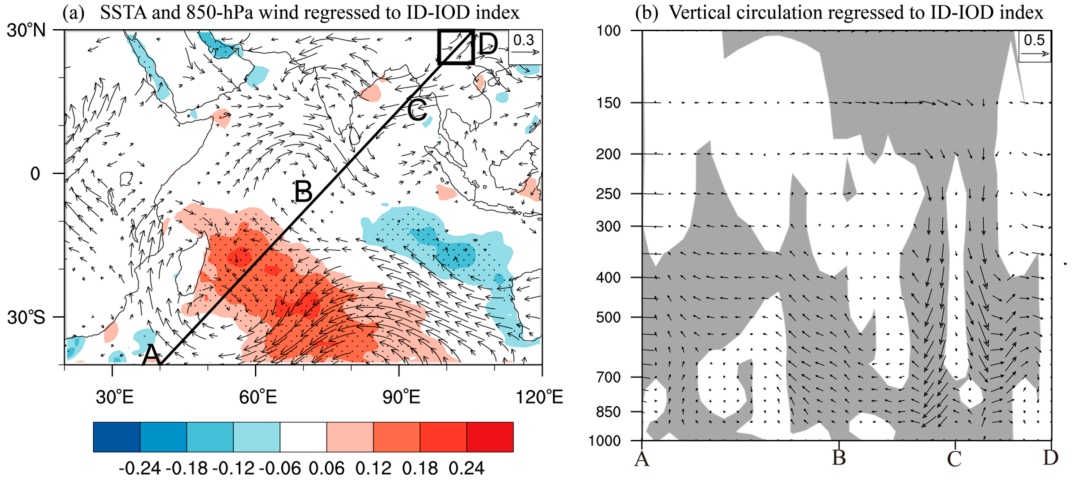

Figure 9. (**a**) Regressions of SSTA (shading; °C) and wind anomalies (vectors; m/s) against the ID-IOD index at 850 hPa in JJA for the period of 1926–2009. Line ABCD is the location for slice in height analysis hereafter. Black dots indicate areas significant at the 95% confidence level; (**b**) regressed vertical circulation against the ID-IOD index along line ABCD (m/s, vertical speeds are multiplied by 50 for visual clarity). Shading indicates the areas significant at the 90% confidence level.

6. Summary

In this study, we focused on the characteristics of the intedecadal variability of SWCSR and its relationship with the IO SST through observational analyses and model simulation experiments. We found a remarkable negative correlation between the SWCSR and the ID-IOBM in summer. The dynamic processes linking the SWCSR to the ID-IOBM were then examined.

The SWCSR displays apparent drought and flood periods during 1926–2011, which indicates an evident interdecadal signal in the SWCSR. Flood periods were 1944–1971 and 1994–2003, whereas drought periods were 1926–1943, 1972–1993, and 2004–2011. The SWCSR was negatively correlated with the ID-IOBM, which induced the anomalous inter-hemispheric vertical circulation between the tropical IO and the Indo-China peninsula. During the cold phase of the ID-IOBM, an enhanced lower-level divergence and an upper-level convergence occurred over the tropical IO. The corresponding lower-level outflow anomalies from the tropical IO converged over the Indo-China peninsula, corresponding to a lower-level anomalous cyclone that contributed to the increase in the eastward moisture transport from the BOB into SWC. Therefore, the increased moisture transport, and the anomalous ascending motion associated with the inter-hemispheric vertical circulation over SWC, increased SWCSR. In summer during the warm phase of the ID-IOBM, the situation is approximately the same, but with opposite polarity.

After the beginning of 1970s, the impacts of ID-IOD on SWCSR is strengthening. During the warm (cold) phase of the ID-IOD, an anomalous vertical circulation located between the tropical central

IOand Indo-China peninsula is in favor of decreased (increased) rainfall in SWC. However, the impacts of ID-IOD on SWCSR is relatively weak before the 1970s, indicating that the ID-IOD is the secondary driver of the interdecadal variability of SWCSR.

The impacts of the ID-IOBM on the circulation anomalies associated with the interdecadal variability of SWCSR were further verified using numerical modeling experiments. The results of the sensitivity experiments showed an apparent anomalous inter-hemispheric circulation response to both the cold and warm phases of the ID-IOBM pattern, though the location of the anomalies over the IO displayed small differences from observations, and the amplitude of the response was somewhat greater than that found in the observations.

Acknowledgments: The authors are grateful to the anonymous reviewers for their insightful comments, which helped improve the quality of this paper. We also acknowledge the supports from the National (Key) Basic Research and Development (973) Program of China (no. 2013CB430203), China Meteorological Special Project (no. GYHY201506013) and the National Key Research Program and Development of China (no. 2017YFC1502302).).

Author Contributions: J.L. and W.L. conceived and designed the experiments; J.L. performed the experiments; J.L. and H.-L.R. analyzed the data and wrote this paper; W.L. and J.Z. provided the instructions to this article. All authors have read and approved the final manuscript.

Conflicts of Interest: The authors declare no conflict of interest.

References

1. Wang, L.; Chen, W.; Zhou, W.; Huang, G. Drought in Southwest China: A review. *Atmos. Ocean. Sci. Lett.* **2015**, *8*, 339–344. [CrossRef]
2. Cao, J.; Yao, P.; Wang, L.; Liu, K. Summer rainfall variability in low-latitude highlands of China and subtropical Indian Ocean dipole. *J. Clim.* **2014**, *27*, 880–892. [CrossRef]
3. Tao, Y.; Cao, J.; Hu, J.; Dai, Z. A cusp catastrophe model of mid–long-term landslide evolution over low latitude highlands of China. *Geomorphology* **2013**, *187*, 80–85. [CrossRef]
4. Yao, S.X.; Huang, Q.; Zhao, C. Variation characteristics of rainfall in the pre-flood season of South China and its correlation with sea surface temperature of Pacific. *Atmosphere* **2016**, *7*, 5. [CrossRef]
5. Liu, Y.; Huang, G.; Huang, R.H. Inter-decadal variability of summer rainfall in Eastern China detected by the Lepage test. *Theor. Appl. Climatol.* **2011**, *106*, 481–488. [CrossRef]
6. Peng, J.B.; Zhang, Q.Y.; Bueh, C. On the characteristics and possible causes of a severe drought and heat wave in the Sichuan-Chongqing region in 2006. *Clim. Environ. Res.* **2007**, *12*, 464–474.
7. Yang, J.; Gong, D.; Wang, W.; Hu, M.; Mao, R. Extreme drought event of 2009/2010 over Southwestern China. *Meteorol. Atmos. Phys.* **2012**, *115*, 173–184. [CrossRef]
8. Wang, L.; Chen, W.; Zhou, W.; Huang, G. Understanding and detecting super-extreme droughts in Southwest China through an integrated approach and index. *Q. J. R. Meteorol. Soc.* **2016**, *142*, 529–535. [CrossRef]
9. Feng, L.; Li, T.; Yu, W. Cause of severe droughts in Southwest China during 1951–2010. *Clim. Dyn.* **2014**, *43*, 2033–2042. [CrossRef]
10. Wang, L.; Chen, W.; Zhou, W.; Huang, G. Teleconnected influence of tropical Northwest Pacific sea surface temperature on interannual variability of autumn precipitation in Southwest China. *Clim. Dyn.* **2015**, *45*, 2527–2539. [CrossRef]
11. Wu, R.; Wen, Z.; Yang, S.; Li, Y. An interdecadal change in Southern China summer rainfall around 1992/93. *J. Clim.* **2010**, *23*, 2389–2403. [CrossRef]
12. Zhang, H.; Wen, Z.; Wu, R.; Chen, Z.; Guo, Y. Inter-decadal changes in the East Asian summer monsoon and associations with sea surface temperature anomaly in the South Indian Ocean. *Clim. Dyn.* **2017**, *48*, 1125–1139. [CrossRef]
13. Schneider, U.; Becker, A.; Finger, P.; Meyer-Christoffer, A.; Rudolf, B.; Ziese, M. *GPCC Full Data Reanalysis Version 6.0 at 1.0: Monthly Land-Surface Precipitation from Rain-Gauges Built on GTS-Based and Historic Data*; Global Precipitation Climatology Centre: Offenbach, Germany, 2011.
14. Li, Q.X.; Peng, J.; Shen, Y. Development of China homogenized monthly precipitation dataset during 1900–2009. *J. Geogr. Sci.* **2012**, *22*, 579–593. [CrossRef]

15. Rayner, N.; Parker, D.E.; Horton, E.; Folland, C.; Alexander, L.; Rowell, D.; Kent, E.; Kaplan, A. Global analyses of sea surface temperature, sea ice, and night marine air temperature since the late nineteenth century. *J. Geophys. Res. Atmos.* **2003**, *108*. [CrossRef]
16. Compo, G.P.; Whitaker, J.S.; Sardeshmukh, P.D.; Matsui, N.; Allan, R.J.; Yin, X.; Gleason, B.E.; Vose, R.; Rutledge, G.; Bessemoulin, P. The twentieth century reanalysis project. *Q. J. R. Meteorol. Soc.* **2011**, *137*, 1–28. [CrossRef]
17. Dai, A. The influence of the inter-decadal Pacific oscillation on US precipitation during 1923–2010. *Clim. Dyn.* **2013**, *41*, 633–646. [CrossRef]
18. Duchon, C.E. Lanczos filtering in one and two dimensions. *J. Appl. Meteorol.* **1979**, *18*, 1016–1022. [CrossRef]
19. Livezey, R.E.; Chen, W. Statistical field significance and its determination by Monte Carlo techniques. *Mon. Weather Rev.* **1983**, *111*, 46–59. [CrossRef]
20. Li, W.J.; Ren, H.C.; Zuo, J.Q.; Ren, H.L. Early summer Southern China rainfall variability and its oceanic drivers. *Clim. Dyn.* **2017**, 1–15. [CrossRef]
21. Ding, Y.; Wang, Z.; Sun, Y. Inter-decadal variation of the summer precipitation in East China and its association with decreasing Asian summer monsoon. Part I: Observed evidences. *Int. J. Climatol.* **2008**, *28*, 1139–1161. [CrossRef]
22. Si, D.; Ding, Y. Oceanic forcings of the interdecadal variability in East Asian summer rainfall. *J. Clim.* **2016**, *29*, 7633–7649. [CrossRef]
23. Yang, J.; Liu, Q.; Xie, S.P.; Liu, Z.; Wu, L. Impact of the Indian Ocean SST basin mode on the Asian summer monsoon. *Geophys. Res. Lett.* **2007**, *34*. [CrossRef]
24. Yang, J.; Liu, Q.; Liu, Z.; Wu, L.; Huang, F. Basin mode of Indian Ocean sea surface temperature and Northern Hemisphere circumglobal teleconnection. *Geophys. Res. Lett.* **2009**, *36*. [CrossRef]
25. Xu, Z.; Fan, K.; Wang, H. Decadal variation of summer precipitation over China and associated atmospheric circulation after the late 1990s. *J. Clim.* **2015**, *28*, 4086–4106. [CrossRef]
26. Zhu, Y.; Wang, H.J.; Zhou, W.; Ma, J.H. Recent changes in the summer precipitation pattern in East China and the background circulation. *Clim. Dyn.* **2011**, *36*, 1463–1473. [CrossRef]
27. Krishnamurthy, V.; Goswami, B.N. Indian monsoon-ENSO relationship on interdecadal timescale. *J. Clim.* **2000**, *13*, 579–595. [CrossRef]
28. Saji, N.H.; Goswami, B.N.; Vinayachandran, P.N.; Yamagata, T. A dipole mode in the tropical Indian Ocean. *Nature* **1999**, *401*, 360–363. [CrossRef] [PubMed]
29. Wu, R.G.; Yeh, S.W. A further study of the tropical Indian Ocean asymmetric mode in boreal spring. Subtropical SST dipole events in the southern Indian Ocean. *J. Geophys. Res.* **2010**, *115*, D08101. [CrossRef]
30. Behera, S.K.; Yamagata, T. Subtropical SST dipole events in the southern Indian Ocean. *Geophys. Res. Lett.* **2001**, *28*, 327–330. [CrossRef]
31. Liu, J.; Ren, H.; Li, W.; Zuo, J. Diagnosing the leading mode of interdecadal covariability between the Indian Ocean sea surface temperature and summer precipitation in Southern China. *Theor. Appl. Climatol.* **2018**. [CrossRef]



© 2018 by the authors. Licensee MDPI, Basel, Switzerland. This article is an open access article distributed under the terms and conditions of the Creative Commons Attribution (CC BY) license (http://creativecommons.org/licenses/by/4.0/).

Theoretical and Applied Climatology
https://doi.org/10.1007/s00704-018-2430-8

ORIGINAL PAPER

Diagnosing the leading mode of interdecadal covariability between the Indian Ocean sea surface temperature and summer precipitation in southern China

Jingpeng Liu[1,2,3] · Hong-Li Ren[3,4] · Weijing Li[3] · Jinqing Zuo[3]

Received: 16 October 2017 / Accepted: 14 February 2018
© Springer-Verlag GmbH Austria, part of Springer Nature 2018

Abstract
Precipitation in southern China during boreal summer (June to August) shows a substantial interdecadal variability on the timescale longer than 8 years. In this study, based on the analysis of singular value decomposition, we diagnose the leading mode of interdecadal covariability between the observational precipitation in southern China and the sea surface temperature (SST) in the Indian Ocean. Results indicate that there exist a remarkable southern China zonal dipole (SCZD) pattern of interdecadal variability of summer precipitation and an interdecadal Indian Ocean basin mode (ID-IOBM) of SST. It is found that the SCZD is evidently covaried with the ID-IOBM, which may induce anomalous inter-hemispheric vertical circulation and atmospheric Kelvin waves. During the warm phase of the ID-IOBM, an enhanced lower-level convergence and upper-level divergence exist over the tropical Indian Ocean, which is a typical Gill-Matsuno-type response to the SST warming. Meanwhile, the accompanied upper-level outflow anomalies further converge over the Indo-China peninsula, resulting in a lower-level anticyclone that contributes to reduction of the eastward moisture transport from the Bay of Bengal to the west part of southern China. In addition, the Kelvin wave-like pattern, as a response of the warm ID-IOBM phase, further induces the lower-level anticyclonic anomaly over the South China Sea–Philippines. Such an anticyclonic circulation is favorable for more water vapor transport from the East China Sea into the east part of southern China. Therefore, the joint effects of the anomalous inter-hemispheric vertical circulation and the Kelvin wave-like pattern associated with the ID-IOBM may eventually play a key role in generating the SCZD pattern.

1 Introduction

Southern China is one of the most populated agricultural regions in the world. The economy and the whole society in general are quite vulnerable to the variability in summer precipitation. Southern China summer precipitation (SCSP) exhibits variability on a broad range of timescales. Large interannual variability often causes precipitation to vary from year to year (e.g., Fu et al. 2017; Yuan et al. 2017), while the interdecadal variability always brings about persistent droughts and floods, which have great impacts on the societal and economic development (Liu et al. 2011). Thereby, studying the interdecadal variability of SCSP and understanding the underlying mechanisms are of great importance.

On the interdecadal timescale, many people have focused on summer precipitation over eastern and southern China in the recent two decades (Huang et al. 1999; Huang et al. 2006; Ding et al. 2008; Ding et al. 2009; Huang et al. 2011; Si and Ding 2016; Yang et al. 2017). Previous studies showed that there are two dominant meridional modes of interdecadal variability of summer precipitation in eastern China during the period of 1951–2004 (e.g., Ding et al. 2008; Huang et al. 2011). One is the meridional tripole pattern, with more precipitation over the middle and lower reaches of the Yangtze River but less precipitation over South and North China, and the other is the meridional

✉ Hong-Li Ren
renhl@cma.gov.cn

[1] Chinese Academy of Meteorological Sciences, Beijing 100081, China

[2] University of Chinese Academy of Sciences, Beijing 100049, China

[3] Laboratory for Climate Studies and CMA-NJU Joint Laboratory for Climate Prediction Studies, National Climate Center, CMA, Beijing 100081, China

[4] Department of Atmospheric Science, School of Environmental Studies, China University of Geoscience, Wuhan 430074, China

Published online: 07 March 2018

dipole pattern, which is usually referred to as the "southern flooding and northern drought" pattern (Ding et al. 2008; Huang et al. 2011; Yang et al. 2017). A further study of Ding et al. (2009) indicated that these two dominant modes could be attributed to the combined effects of abrupt increase in winter–spring snow cover over the Tibetan Plateau since around 1977 and significant interdecadal warming of SST in the tropical central and eastern Pacific Ocean that occurred in the mid-1960s, the late 1970s, and the early 1990s. Since the middle of the twentieth century, summer precipitation over eastern China has experienced three decadal variations, which occurred in the mid and late 1970s, early 1990s, and late 1990s, respectively (Xu et al. 2015). The abrupt shift of summer precipitation pattern over eastern China in the late 1970s is associated with the weakening of the East Asian summer monsoon (Wang 2001; Huang et al. 2006; Huang et al. 2011). In the early 1990s, summer precipitation over South China increased remarkably (Kwon et al. 2007; Ding et al. 2008), which could possibly be caused by the warming of the tropical Indian Ocean (IO) SST in summer and the increase in snow cover over the Tibetan Plateau in winter and spring (Wu et al. 2010). In the late 1990s, the decadal variation of summer precipitation over eastern China was probably associated with the shift of the Pacific Decadal Oscillation (PDO) from positive to negative phase.

The PDO is well known as the leading mode of decadal variability of Pacific SST (Mantua et al. 1997). Previous studies have revealed the impacts of the PDO on summer precipitation in China (Zhu and Yang 2003; Chan and Zhou 2005; Zhu et al. 2011; Qian and Zhou 2014; Yu et al. 2015). Qian and Zhou (2014) found that the drought index in North China is significantly negatively correlated with the PDO index during 1900–2010. Zhu et al. (2011) attributed the increased precipitation in the Huang-Huai River region and decreased precipitation in the Yangtze River region in the late 1990s to the phase shift of the PDO from warm to cold around 1999. Wu and Mao (2017) found that the wintertime PDO contributed to the interdecadal variability of South China monsoon rainfall in early summer via atmospheric and oceanic teleconnections during 1926–2013. Several recent studies also showed that the PDO contributed to the decadal variability of the meridional dipole pattern of summer precipitation in eastern China (Si and Ding 2016; Yang et al. 2017).

In addition, SST in the North Atlantic may also affect precipitation over eastern China on decadal timescale (Lu et al. 2006; Wang et al. 2009; Si and Ding 2016). The positive phase of Atlantic Multidecadal Oscillation (AMO) can lead to strengthened East Asian summer monsoon (Lu et al. 2006; Wang et al. 2009). Li et al. (2008) found that anomalous southerly winds in southeastern China are favorable for abnormally high precipitation in this region in the positive phase of AMO. The mid-high-latitude precipitation in eastern China is also sensitive to the North Atlantic SST forcing. The abrupt decrease in North China precipitation in the 1960s was proposed to be connected to the cooling of extra-tropical North Atlantic Ocean based on an AGCM simulation (Liu and Chiang 2012). Si and Ding (2016) revealed that AMO might lead to the decadal variability of East China summer precipitation by causing negative (positive) precipitation anomalies over the Yangtze River valley (Huanghe-Huaihe River valley) through a stationary circumglobal baroclinic wave train. Most of the previous studies by far have focused on the decadal variability of summer precipitation over the whole southern and eastern China. However, there has been relatively limited research focusing on precipitation variability in the west part of southern China (Cao et al. 2014). Thereby, it is quite important to focus on the interdecadal variability of precipitation in southern China by considering the summer precipitation over both the west and east parts of southern China, and to further discuss the primary features of the interdecadal variability of summer precipitation and the associated mechanisms.

Furthermore, AMO and PDO have been regarded as the two principal drivers for the interdecadal variability of summer precipitation over East China. However, some studies also emphasized the role of the IO in the interdecadal variability of SCSP (Wu et al. 2010; Zhang et al. 2016). Zhang et al. (2016) revealed that the South IO SST influenced the interdecadal changes of the East Asian summer monsoon, which was featured by a decrease in the late 1970s and an increase in the early 1990s of SCSP. An interdecadal cooling in the South IO could trigger anomalous vertical overturning circulation, which led to abnormal descending motion and a lower-level anticyclonic anomaly over the South China Sea–Philippines. Such a pattern of circulation anomaly would result in additional moist air transport into southern China and subsequent precipitation increase there. Wu et al. (2010) revealed that the equatorial IO SST had increased since the early 1990s, which led to the development of an anomalous lower-level anticyclone over the South China Sea and the Philippines, and as a result, the SCSP increased. So far, the impacts of PDO and AMO on summer precipitation in eastern and southern China have been well studied, whereas the impacts of the IO on southern China have been less investigated. Particularly, little study has been conducted to explore the characteristic responses of SCSP to the IO SST forcing and the associated mechanisms behind. Thus, the present study is focused on the interdecadal variability characteristics of SCSP and their connections with the IO SST.

The rest of this paper is organized as follows. Section 2 describes the datasets and methods used in this study. Section 3 investigates the leading mode of the interdecadal covariability between SCSP and IO SST. Section 4 describes the possible mechanisms through which SST anomalies in the IO can be physically connected with SCSP. Finally, the summary and discussion are presented in Section 5.

2 Datasets and methods

2.1 Datasets

In this study, 114 years of monthly precipitation data (1901–2014) are used to examine the interdecadal variability of summer (June to August, JJA) precipitation in southern China. The monthly precipitation data include monthly mean precipitation from the Climatic Research Unit (CRU, New et al. 2000) with a spatial resolution of 0.5° × 0.5° and monthly precipitation in China provided by National Meteorological Information Center of China Meteorological Administration on a grid of 5° × 5° for the period of 1901–2014 (NMIC, Li et al. 2012). Monthly mean sea surface temperature is provided by the Hadley Centre of the UK Met Office (HadISST, Rayner et al. 2003) for the period of 1847–2014. Monthly mean atmospheric fields are extracted from the NOAA-CIRES twentieth Century Reanalysis products (20CR, Compo et al. 2011) for the period of 1851–2014. The spatial resolutions of the HadISST datasets and the 20CR datasets are 2° × 2° and 1° × 1°, respectively. As SST observations in the tropical ocean are very sparse before 1920 (Dai 2013), analyses of the present study are focused on the period of 1920–2014.

2.2 Methods

2.2.1 Extracting interdecadal signal

Linear trends are removed first from all the data. Variabilities on the timescales shorter than 11 years are then filtered out using the Lanczos filter method (Duchon 1979). The anomalies relative to the climatology for the period of 1920–2014 are calculated. The anomalous precipitation and SST are normalized before analysis.

2.2.2 Significance tests

The significance test uses the Monte Carlo method (Livezey and Chen 1983). Considering time series A and B, the original time series A is randomly rearranged to obtain a new time series at each grid point. The correlation between this new atmospheric time series and time series B is then calculated. This progress is repeated for 1000 times and a distribution of correlation values at each grid point is finally obtained. The quoted significance level of the correlation between time series A and B indicates the percentage of randomized correlation coefficients that exceed the value being tested. The significance of regression coefficient is tested in the same way.

2.2.3 Singular value decomposition

The singular value decomposition (SVD) method (Bretherton et al. 1992) is used to identify major linear covariation modes between interdecadal variability of SCSP and SST anomalies in the IO. SVD is an algebraic technique to decompose arbitrary matrices in orthogonal matrices. It is easy to perform and requires no user-supplied parameters. To identify statistically significant modes from random noise, experiments with Gaussian-distributed random data are repeated 100 times, and variance contribution rates of the singular values at a significance level of 95% are obtained via the Monte Carlo method (Shen and Lau 1995).

3 Interdecadal covariation of SCSP with IO SST

First of all, the SVD analysis is implemented to reveal the spatially and temporally covariated mode between interdecadal SCSP and IO SST. Figure 1 shows the climatology and standard deviation of SCSP based on the original CRU precipitation data. It can be found that climatological summer precipitation is mainly distributed to the south of 30° N, where there are also relatively high values of standard deviation. The climatological precipitation gradually decreases from south to north, with values ranging between 5 and 10 mm day^{-1}.

For the interdecadal variability, the ratio of the interdecadal variance to the total variance of summer precipitation (Fig. 1(b)) is also calculated using spectrum analysis method (Thomson 1982). The ratio is as high as 40% in the west and east parts of southern China, which indicates the important role of the interdecadal variability in these areas. In contrast, the ratio in the Yangtze River basin is less than 20%, indicating that the interannual variation of summer precipitation is probably dominant there. Given the climatology of summer precipitation and the high ratio of its interdecadal variability to total variability, the region of southern China over the area (20° N–30° N, 99° E–120° E) is selected for the present study (see the black rectangle box in Fig. 2(a)).

In the SVD analysis, the left field is the normalized interdecadal SCSP, and the right field is the normalized IO SST anomalies (30° S–25° N, 40° E–105° E). The precipitation and SST are normalized by their area-averaged standard deviation. Results show that the first pair of SVD modes exceeds the noise level (not shown) and explains 61.3% of the total covariance. It is significantly larger than, and separated from, other SVD modes. Thereby, analyses will be focused on the first pair of SVD modes in the following sections.

As shown in Fig. 2(a), the first SVD mode of interdecadal SCSP displays an apparent zonal dipole pattern, which is termed as the southern China zonal dipole (SCZD) hereafter. The positive center with values larger than 0.6 is mainly

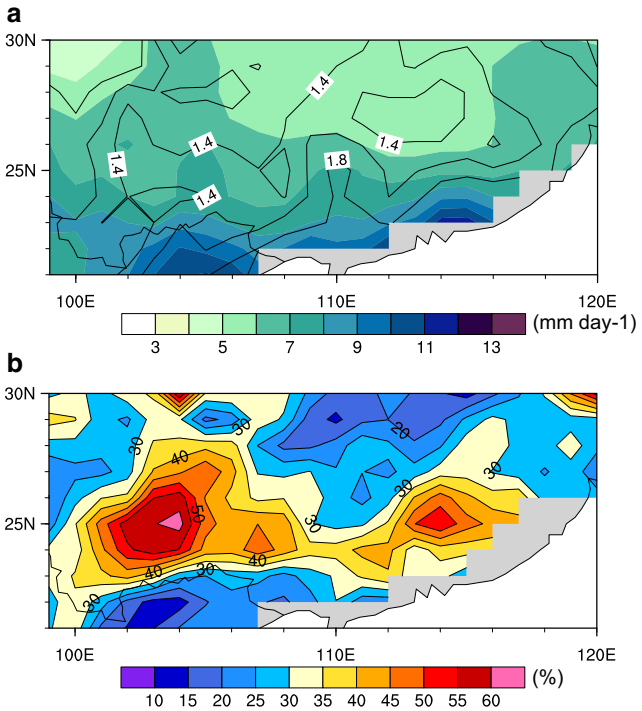

Fig. 1 (a) Climatological mean of summer precipitation (shading; mm day^{-1}) and corresponding standard deviations (contour; mm) based on the original CRU precipitation data for the period of 1920–2014, and (b) the ratio of interdecadal variance to total variance of precipitation (%) using CRU precipitation data. All plots were generated using NCL

located in the east part of southern China (ESC, 25° N–30° N, 110° E–120° E), and the negative center with values less than − 0.5 is mainly located in the west part of southern China (WSC, 25° N–30° N, 99° E–108° E). Thus, the positive phase of SCZD is characterized by increased (decreased) precipitation anomalies in the ESC (WSC), and vice versa. Such a spatial pattern is different from the well-known meridional dipole or tripole pattern in East China (Ding et al. 2008). The question is, what is the mechanism responsible for the SCZD?

The associated simultaneous SST field exhibits a basin-wide monopole pattern in the IO as shown in Fig. 2(b). This pattern is consistent with that revealed in the study by Dong et al. (2016), who showed that a basin-wide SST anomaly pattern was the dominant mode of IO decadal variability. The basin-wide monopole pattern revealed in the present study is similar to the conventional Indian Ocean basin mode (IOBM) defined on the interannual timescale (Yang et al. 2007; Yang et al. 2009; Zhu et al. 2015). Given this resemblance, the interdecadal basin-wide mode of Indian Ocean SST is termed as ID-IOBM. The warm (cold) phase of ID-IOBM is characterized by the warming (cooling) in the entire IO.

The correlation coefficient between the time series of SCZD (Fig. 2(c)) and ID-IOBM (Fig. 2(d)) is 0.79, which is significant at the 99% confidence level, suggesting that the interdecadal basin-wide mode in the IO is closely associated with the SCZD. When the ID-IOBM is in positive phase with above-normal SST over the entire IO, summer precipitation tends to be abundant in the ESC and deficient in the WSC.

To further confirm the SVD results, the NMIC data is used to calculate the average precipitation in the ESC and WSC (denoted by right and left green rectangle boxes in Fig. 2(a)). The difference between the normalized average precipitation in the ESC and WSC is defined as the SCZD index (the green line in Fig. 2(c)). The correlation coefficient between the SCZD index and Pre_TS1 is 0.87, which is significant at the 99% confidence level, indicating that the SCZD mode is robust in observational precipitation data. Meanwhile, the average SST anomaly in the IO is also calculated, which is defined as the ID-IOBM index (the black line in Fig. 2(d)). The correlation coefficient between the ID-IOBM index and the SST_TS1 is 0.99 (significant at the 99% confidence level).

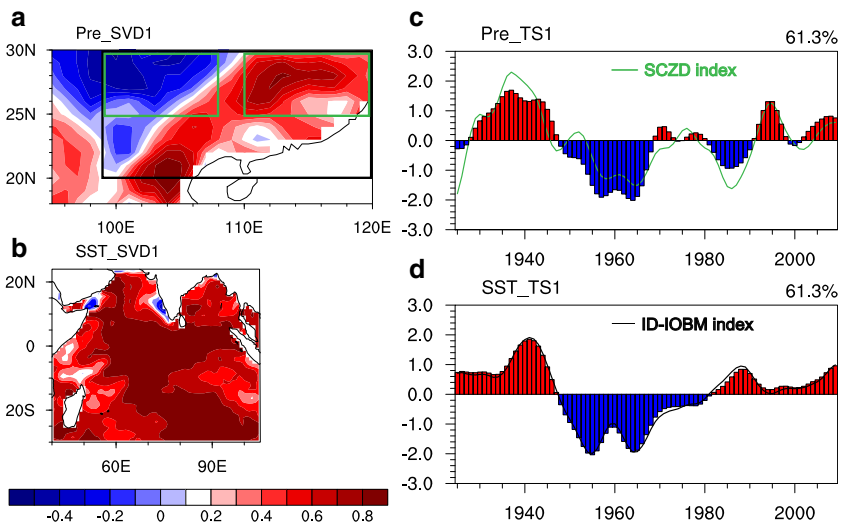

Fig. 2 First leading modes of SVD for JJA 11-year low-pass filtered CRU precipitation anomalies in southern China (a), SST anomalies in the IO (b) for the period of 1925–2009, and normalized time series of first SVD modes (c, d, bars). The green line in (c) denotes the SCZD index. The black line in (d) denotes the ID-IOBM index. The black rectangle box in (a) denotes the region of southern China. The left (right) green rectangle box in (a) denotes the region of west (east) part of southern China. All plots were generated using NCL

Moreover, the SCZD index and ID-IOBM index are significantly correlated with the correlation coefficient of 0.69. Hereafter, these two indices are used for further analyses.

Previous studies have demonstrated that the interdecadal variation of precipitation is always accompanied by atmospheric circulation variability (Zhu 2011; Xu et al. 2015). Therefore, summer atmospheric circulation patterns associated with the SCZD index are examined in the present study, and the upper-level and lower-level circulation patterns associated with the ID-IOBM index are investigated to verify the interdecadal connection between the SCZD and ID-IOBM.

The lower-level circulation anomalies associated with the SCZD index and the ID-IOBM index are shown in Fig. 3(c, d), respectively. In Fig. 3c, easterly wind anomalies prevail over the entire tropical IO and the Maritime Continent area, while an anomalous anticyclone exists over the Indo-China peninsula. At the west flank of the anticyclone are the significant easterlies, which may suppress moisture transport from the Bay of Bengal (BOB) to southern China. Figure 3(c) also shows a Pacific–Japan (PJ) wave-like pattern over East Asia. Moreover, an obvious anticyclonic anomaly is located over the tropical western North Pacific Ocean. To the north of the anticyclonic anomaly, there is a cyclonic anomaly appearing over southeastern China, which is favorable for the enhanced moisture transport from the East China Sea to southern China. Such a wave-like pattern resembles the PJ pattern initially defined on the interannual or intraseasonal timescales (Nitta 1987; Huang and Sun 1992). A recent study revealed that the interdecadal PJ pattern could be driven by negative convective heating anomalies over the tropical western North Pacific (Wu et al. 2016). They showed that the anomalous meridional circulation centers are distributed along 120° E, which was consistent with the result in the present study. Figure 3(d) shows that the PJ-like pattern is also visible over East Asia in the lower-level circulation anomalies associated with the ID-IOBM, indicating that such a circulation pattern is likely induced by the latter. The link between the PJ-like pattern and the ID-IOBM will be further discussed in Section 4.

The stream function pattern regressed against the SCZD index at 200 hPa is shown in Fig. 3(a). The most distinct signal in this field is the wave-like pattern along the Asian Westerly Jet Stream (AWJS), where two positive centers are located over west-central Asia and East China, respectively, and one negative center is located over Northwest China. Kuang et al. (2007) argued that the AWJS could act as the waveguide, and the Rossby wave energy propagated along the waveguide to downstream regions (Ambrizzi et al. 1995). The positive center over eastern China is favorable for upper-level divergence and accompanying ascending motion. Considering the upper-level circulation anomalies associated with the ID-IOBM, the most significant feature is the Rossby wave-like pattern along the AWJS at 200 hPa (Fig. 3(b)), which is similar to the wave-like pattern shown in Fig. 3(a). To verify this, we calculate the spatial correlation coefficient between regressed 200-hPa stream function patterns against the SCZD index and the ID-IOBM index, which is 0.92. Meanwhile, the spatial correlation coefficient between regressed 850-hPa wind patterns against the two indices reaches 0.93 (see Table 1), which validate the hypothesis to some degree that the ID-IOBM may be the main factor that leads to the SCZD.

In summary, the lower-level anomalous anticyclone over Indo-China peninsula may have an impact on the SCZD via suppressing the moisture transport from the BOB to southern China. Moreover, the anomalous cyclone over eastern China is favorable for more westward moist air transport from the ocean into southern China. Indeed, such lower-level circulation anomalies are closely connected with the ID-IOBM.

4 Possible mechanisms of interdecadal covariability between SCSP and IO SST

To further investigate the possible influence of the ID-IOBM on the SCZD and associated physical processes, regression and correlation analyses are performed in the present study. The results are shown in terms of a positive phase of the SCZD and a warm phase of the ID-IOBM, which also apply to a negative phase of SCZD and a cold phase of the ID-IOBM.

Figure 4(a) shows the regressed pattern of SST anomalies and wind anomalies at 850 hPa against the ID-IOBM index. It is clear that the entire IO experiences an apparent warming in the warm phase of the ID-IOBM. According to the study of Xie et al. (2009), such a warming pattern tends to trigger a Kelvin wave-like pattern, which subsequently induces northeasterly surface wind anomalies. The resultant subtropical divergence and suppressed deep convection favor to form an anomalous anticyclonic pattern in the northwest Pacific. In Fig. 4(a), it can be seen that an anomalous anticyclone is located over the South China Sea and to the east of the Philippines. To the north of the anticyclone, there is an anomalous cyclonic pattern appearing over southeastern China. To verify the existence of such a PJ-like pattern, we calculate the wave activity fluxes (Takaya and Nakamura 1997) associated with the ID-IOBM index for the lower troposphere. It is found in Fig. 4(b) that the poleward energy transport from the subtropical northwestern Pacific to East Asia is evident at 850 hPa, which is a typical property of the conventional PJ pattern, consistent with the results showed by Wu et al. (2016). To investigate the mechanism responsible for the PJ-like pattern, we show precipitation anomalies associated with the ID-IOBM in Fig. 4(c). As noted by Kosaka and Nakamura (2006), the anomalous convective heating to the east of the Philippines would induce the conventional PJ pattern, where the perturbation associated with the convective heating is able to propagate into the mid-latitudes in the form of Rossby waves in the lower troposphere. As shown in Fig. 4(c), a suppressed

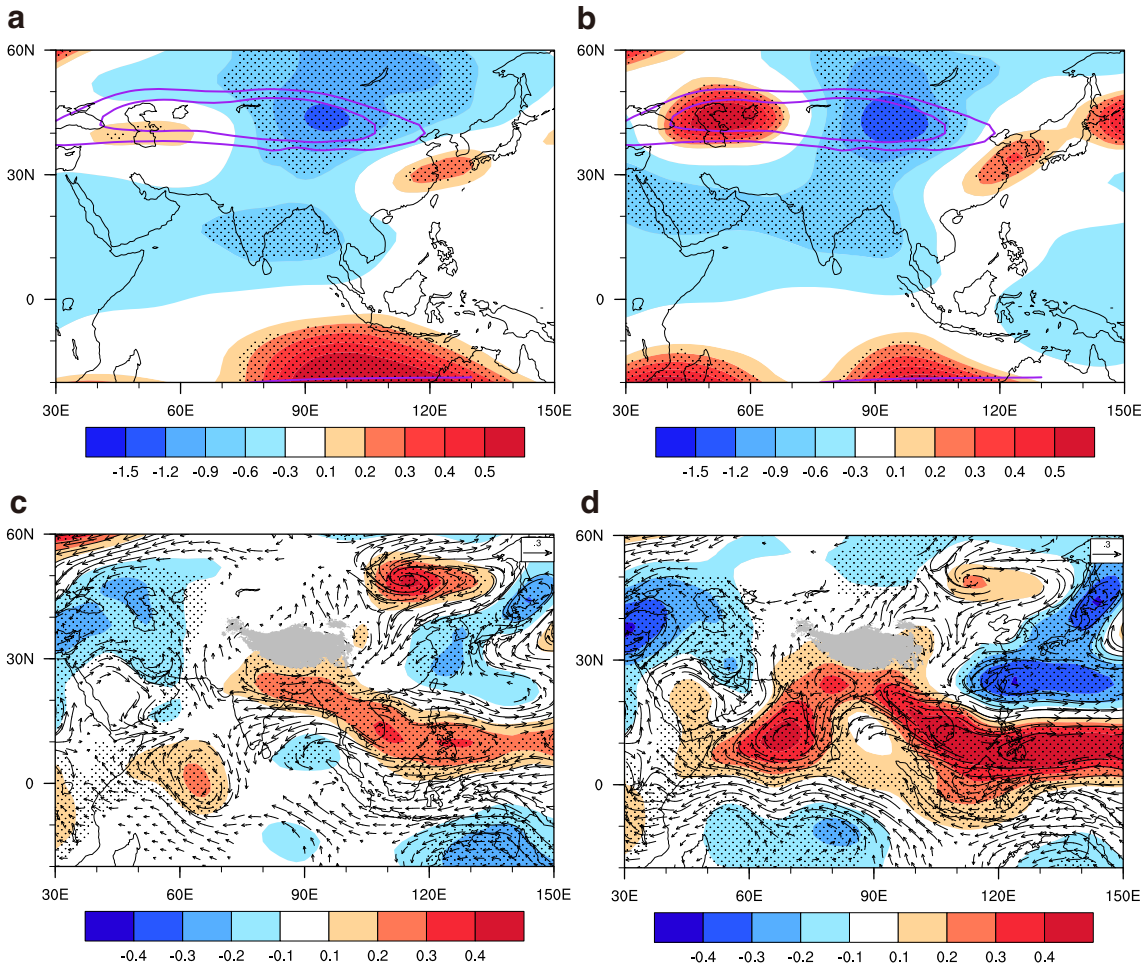

Fig. 3 Stream function (shading; 10^6 m^2 s^{-1}) at 200 hPa regressed against the SCZD index and the ID-IOBM index (a, b), and stream function (shading; 10^6 m^2 s^{-1}) and wind field (vectors; m s^{-1}) anomalies at 850 hPa in JJA (c, d). Purple contours in (a) and (b) denote the climatological means of 20 and 25 m s^{-1} zonal wind isoline at 200 hPa. Black dots denote areas significant at the 95% confidence level. All plots were generated using NCL

heating pattern that corresponds to the negative precipitation anomalies is located to the east of the Philippines, which may contribute to generation of the PJ-like pattern through the poleward propagation of perturbation as Rossby waves. Meanwhile, as we can see in Fig. 4(c), an enhanced precipitation center is located over southeastern China, which is probably associated with the abnormal cyclone center of the PJ-like pattern. Such a cyclonic circulation contributes to the increased westward moisture transport and subsequent moisture convergence in the east part of southern China. Therefore, the PJ-like pattern might be connected with the ID-IOBM through its Kelvin wave-like response pattern. Evidently, the cyclonic anomaly over southeastern China associated with the PJ-like pattern is favorable for higher than normal moisture transport into southern China.

Furthermore, Fig. 5 shows the regressed divergent wind and velocity potential against the SCZD index and the ID-IOBM index. Anomalous easterlies associated with the Kelvin wave are found over the entire tropical IO and the Maritime Continent region. The anomalous easterlies and northeasterlies from the BOB converge at the central tropical IO. A notable lower-level convergence and upper-level divergence in association with the ID-IOBM can be found over the central tropical IO (Fig. 5(b, d)). At the upper levels, outflows

Table 1 Spatial correlations between the patterns regressed against the SCZD index and the ID-IOBM index, respectively

200 hPa divergent wind	200 hPa stream function	850 hPa divergent wind	850 hPa stream function	850 hPa wind	Water vapor flux/ corresponding divergence
0.85	0.92	0.84	0.71	0.93	0.80/0.82

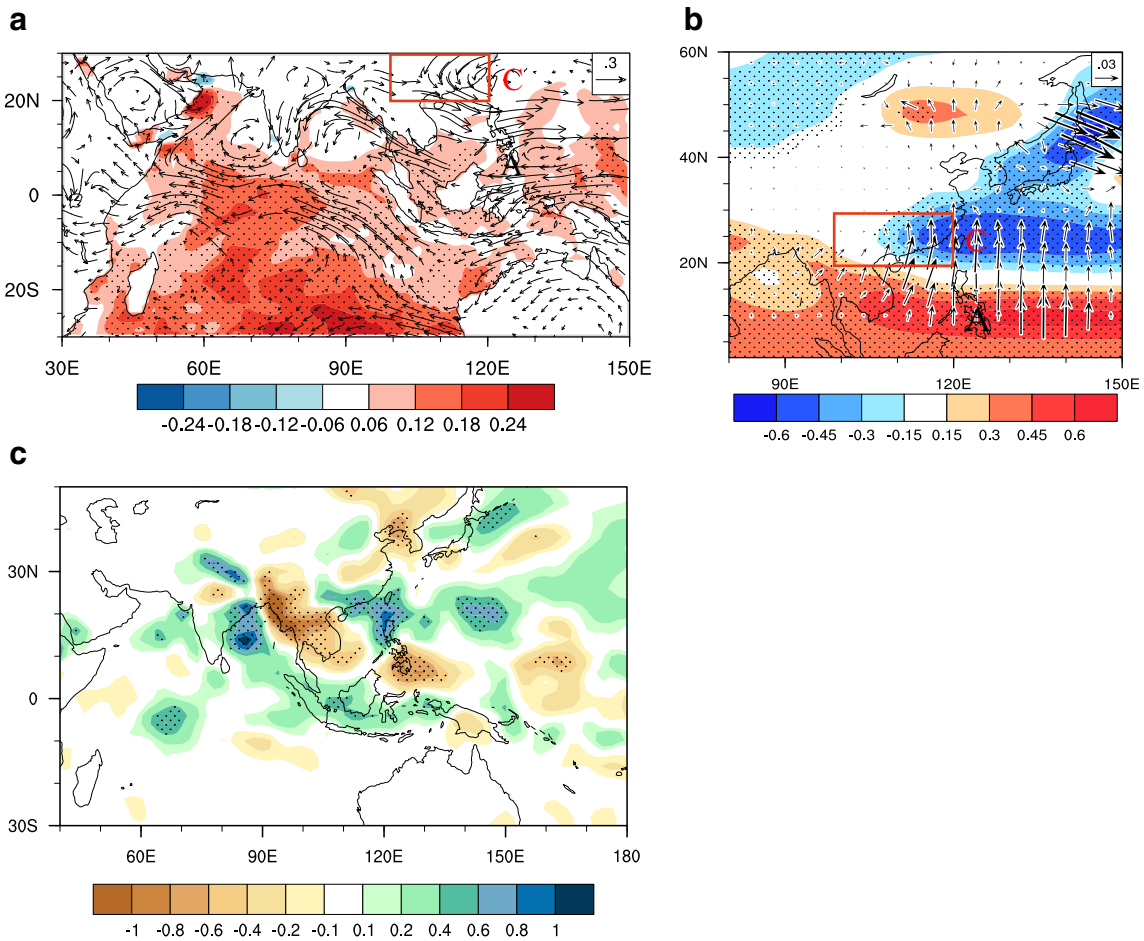

Fig. 4 (a) Regressions of SST anomalies (shading; °C) and wind anomalies (vectors; m s^{-1}) against the ID-IOBM index at 850 hPa in JJA for the period of 1925–2009. (b) Same as (a) but for stream function (shading; 10^{-6} m^2 s^{-1}) and wave activity flux (vectors; 10^{-6} m^2 s^{-2}). (c) Same as (a) but for precipitation (shading; 10^{-2} Pa s^{-1}). Black dots denote areas significant at the 95% confidence level. The rectangular box indicates southern China. "A" and "C" denote anticyclone and cyclone, respectively. All plots were generated using NCL

from the central tropical IO converge over the Indo-China peninsula, corresponding to a regional descending motion. Accompanying with such a descending motion, an anomalous anticyclone appears at 850 hPa over the Indo-China peninsula while abnormal easterlies occur in the northern BOB, both of which behave to decrease the moisture transport from the BOB to southern China (Fig. 3(c, d)). Thus, such an inter-hemispheric anomalous vertical circulation emerging between the central tropical IO and the Indo-China peninsula is likely responsible for forming the SCZD by reducing the moisture transport from the BOB to the west part of southern China. Figure 5 shows that the regressed divergent wind patterns associated with the ID-IOBM index exhibit patterns that are highly similar to those associated with the SCZD index. The spatial correlation coefficient between the divergent wind patterns regressed against the ID-IOBM index and the SCZD index is 0.85 at 200 hPa. Meanwhile, the spatial correlation coefficient between the divergent wind patterns regressed against the two indices is 0.84 at 850 hPa (see Table 1), indicating that the anomalous inter-hemispheric vertical circulation induced by the ID-IOBM in its warm phase may be an important factor that leads to the SCZD pattern.

To further verify the linkage between the inter-hemispheric vertical circulation and the lower-level PJ-like pattern on the SCZD, Fig. 6 shows the vertical and zonal wind patterns associated with the SCZD index and the ID-IOBM index, respectively. The descending motions over the west part of southern China are associated with the vertical circulation, which corresponds to the lower-level moisture divergence. Such a divergence is in favor of decreased precipitation in the west part of southern China. Meanwhile, the ascending motions over the east part of southern China are associated with the PJ-like pattern, which contributes to the increased precipitation there.

Figure 7 further gives patterns of the vertically integrated moisture flux anomaly and its divergence regressed against the two indices, respectively. We can see that the convergence is centered over the ESC and the divergence over the WSC.

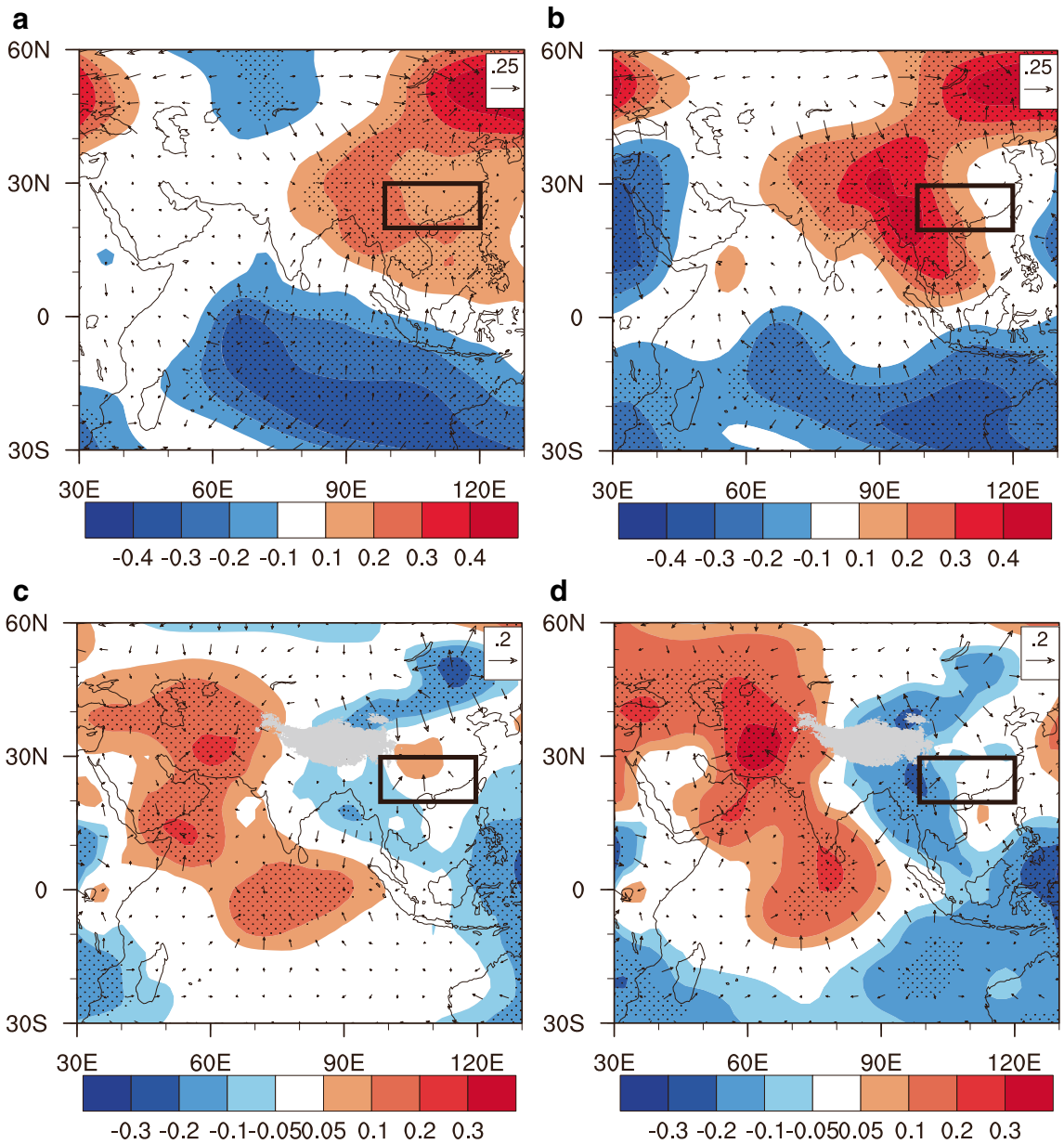

Fig. 5 Regressed divergent winds (vectors; m s^{-1}) and velocity potentials (shading; 10^6 m^2 s^{-1}) at 200 hPa (a, b) and 850 hPa (c, d) against the SCZD index (a, c) and the ID-IOBM index (b, d). The rectangular box indicates southern China. Black dots denote areas significant at the 95% confidence level. All plots were generated using NCL

Both the anomalous descending motion and corresponding lower-level divergence contribute to a decreased transport of moisture into the WSC and thus are unfavorable for precipitation there. The enhanced moisture flux from the East China Sea can transport additional moisture into the ESC and is favorable for precipitation increase there. The spatial correlation coefficients between the vertically integrated moisture flux and its divergence patterns regressed against the two indices are 0.80 and 0.82, respectively, indicating that the SCZD is well covariated with the ID-IOBM.

The SCZD is significantly related to the ID-IOBM through two ways: the inter-hemispheric vertical circulation and the lower-level Kevin wave-like pattern. The divergence at lower level associated with the descending branch of the vertical circulation could impact the SCZD through reducing the moisture transport into the WSC. The lower-level Kelvin wave-like pattern could mainly impact on the SCZD through enhancing the moisture supply to the ESC.

5 Summary and discussion

In this study, we focus on diagnosing the leading mode of the interdecadal covariability between the SCSP and the IO SST

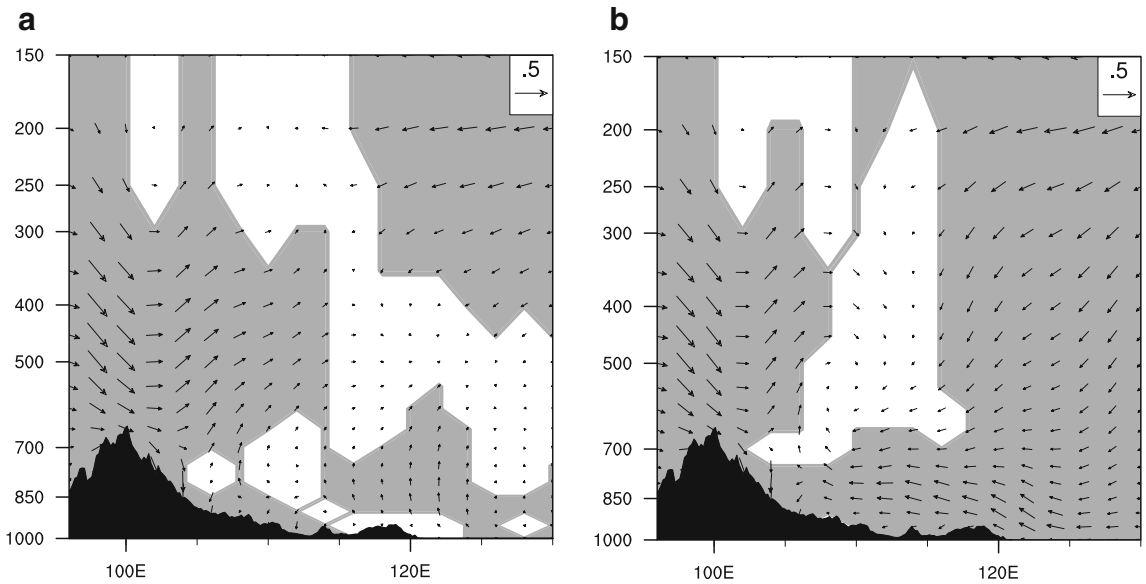

Fig. 6 Patterns of vertical velocity (hPa day^{-1}) and zonal wind (m s^{-1}) averaged between 25° N and 30° N regressed against the SCZD index (a) and the ID-IOBM index (b) (shading indicates the areas significant at the 90% confidence level). All plots were generated using NCL

through conducting the SVD analysis of the precipitation and SST data. We found a remarkable zonal dipole mode of interdecadal SCSP termed the SCZD, and an ID-IOBM. This leading mode, as represented by the first pair of SVD modes derived from 11-year low-frequency-pass filtered summer precipitation and simultaneous SST anomalies, had an increased (decreased) precipitation in the ESC (WSC) and a basin-wide warming in the IO. Our diagnosis results showed that the SCZD had a positive covariation with the ID-IOBM in summer and the dynamical processes linking the SCZD to the ID-IOBM were then examined.

Figure 8 shows the schematic diagram of the physical picture of the key anomalous circulation patterns associated with the SCZD in response to the ID-IOBM. The SCZD is related to the ID-IOBM which may induce the anomalous interhemispheric vertical circulation and the Kelvin wave-like pattern. During the warm phase of the ID-IOBM, an enhanced lower-level convergence and upper-level divergence occur over the tropical IO, which is a typical Gill-Matsuno-type response to the warm phase of the ID-IOBM. The corresponding upper-level outflow anomalies from the tropical IO converge over the Indo-China peninsula, corresponding to a

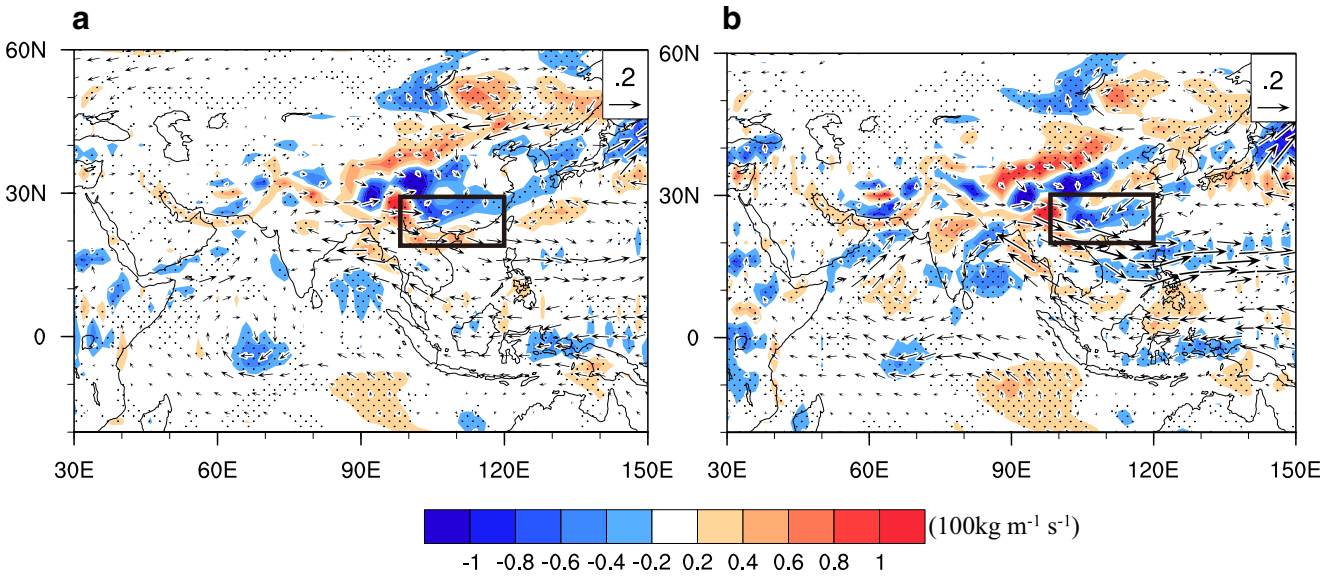

Fig. 7 Regression of vertically integrated (from the surface to 300 hPa) water vapor flux (vector; 100 kg m^{-1} s^{-1}) against the SCZD index (a) and the ID-IOBM index (b), and corresponding divergence in JJA (shading; 100 kg m^{-2} s^{-1} dots indicate areas significant at the 95% confidence level). The rectangular box indicates southern China. All plots were generated using NCL

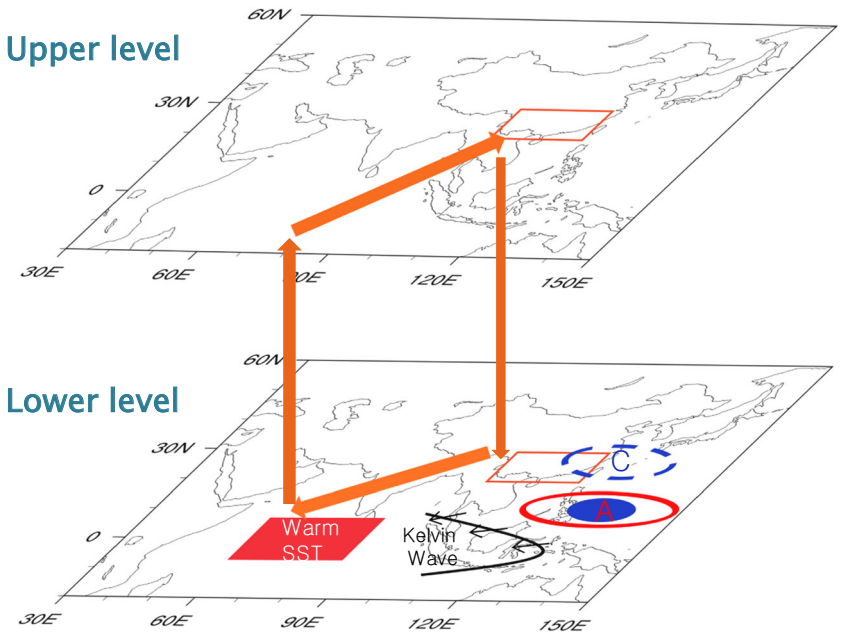

Fig. 8 Schematic diagram of the response of atmospheric circulation to SST anomalies in the IO. The red rectangle box denotes anomalous SST in the IO. The blue round box denotes negative convective heating. The brown rectangle box denotes southern China. The brown vectors denote the abnormal inter-hemispheric vertical circulation. Black curve and vectors denote Kelvin wave and corresponding divergence around the South China Sea and the Philippines in lower level. "A" and "C" denote abnormal anticyclone and cyclone, respectively. This plot was generated using NCL and licensed Microsoft PowerPoint

lower-level anomalous anticyclone that contributes to the reduction of the eastward moisture transport from the BOB into the west part of southern China. Meanwhile, the ID-IOBM in its warm phase tends to form the Kelvin wave-like pattern over the equatorial western Pacific, which acts to induce northeasterly surface wind anomalies. The resultant subtropical divergence and suppressed deep convection lead to an anomalous anticyclonic pattern to the east of the Philippines. The anomalous anticyclone in turn tends to suppress the precipitation, where such a suppressed pattern to the east of the Philippines can further lead to the PJ-like pattern. Meanwhile, the enhanced precipitation center is located over southeastern China, which is probably associated with the anomalous cyclone center of the PJ-like pattern. Such a cyclone contributes to the increased westward moisture transport which converges into the east part of southern China. Therefore, the above-normal moisture transport associated with the Kevin wave-like pattern is favorable for the increased precipitation in the east part of southern China. Besides, the suppressed moisture transport associated with the inter-hemispheric vertical circulation in the west part of southern China brings about the decreased precipitation there. The joint effects of the anomalous inter-hemispheric vertical circulation and the Kevin wave-like pattern associated with the ID-IOBM may eventually lead to the formation of the SCZD pattern.

It is well-known that some mid-high-latitude circulation factors can influence the SCSP. Figure 3(a) shows clearly that a Rossby wave-like pattern exists over the middle latitudes, which may have impacts on the SCZD through an upper-level divergence and an anomalous ascending motion over southeastern China. The active centers of the wave-like pattern are the same as the interdecadal circumglobal teleconnection pattern over the Asian continent, which is linked to the AMO (Lin et al. 2016). Thus, the mechanisms for such a wave-like pattern may be related to upstream factors, which are beyond the scope of this study and would be considered in the future.

In Fig. 2(c), it is interesting to note that the positive phase of SCZD has become active after the 2000s, which may indicate that summer precipitation in the WSC tends to become subnormal during the 2000s. This is consistent with the fact that frequency of severe droughts increased in Southwest China in the last decade. Record-breaking droughts hit Southwest China in the summer of 2006 (Peng et al. 2007), the autumn of 2009 (Wang et al. 2015) and the late summer of 2011 (Wang et al. 2015). Thus, this study will help us improve our understanding of the interdecadal modulation of severe droughts in Southwest China.

Although the possible impacts of ID-IOBM on the interdecadal variability of SCSP have been revealed in this diagnostic paper, the corresponding mechanisms of such an interdecadal covariability still need to be further verified by numerical experiments, which will be addressed in future study.

Funding information The authors are grateful to the anonymous reviewers for their insightful comments, which helped improve the quality of this paper. We also acknowledge the supports from the National Key Research Program and Development of China (No. 2017YFC1502302) and the National (Key) Basic Research and Development (973) Program of China (Nos. 2013CB430203 and 2010CB950404).

References

Ambrizzi T, Hoskins BJ, Hsu H (1995) Rossby wave propagation and teleconnection patterns in the austral winter. J Atmos Sci 52:3661–3672. https://doi.org/10.1175/1520-0469(1995)052<3661:RWPATP>2.0.CO;2

Bretherton CS, Smith C, Wallace JM (1992) An intercomparison of methods for finding coupled patterns in climate data. J Clim 5:

541–560. https://doi.org/10.1175/1520-0442(1992)005<0541:AIOMFF>2.0.CO;2
Cao J, Yao P, Wang L (2014) Summer rainfall variability in low-latitude highlands of China and subtropical Indian Ocean dipole. J Clim 27: 880–892. https://doi.org/10.1175/JCLI-D-13-00121.1
Chan JCL, Zhou W (2005) PDO, ENSO and the early summer monsoon rainfall over south China. Geophys Res Lett 32:L08810. https://doi.org/10.1029/2004GL022015
Compo GP, Whitaker JS, Sardeshmukh PD (2011) The twentieth century reanalysis project. Quart J Roy Meteor Soc 137:1–28. https://doi.org/10.1002/qj.776
Dai A (2013) The influence of the inter-decadal Pacific oscillation on US precipitation during 1923–2010. Climate Dyn 41:633–646. https://doi.org/10.1007/s00382-012-1446-5
Ding Y, Wang Z, Sun Y (2008) Inter-decadal variation of the summer precipitation in East China and its association with decreasing Asian summer monsoon part I: observed evidences. Int J Climatol 28: 1139–1161. https://doi.org/10.1002/joc.1615
Ding Y, Sun Y, Wang Z (2009) Inter-decadal variation of the summer precipitation in China and its association with decreasing Asian summer monsoon part II: possible causes. Int J Climatol 29:1926–1944. https://doi.org/10.1002/joc.1759
Dong L, Zhou T, Dai A (2016) The footprint of the inter-decadal Pacific oscillation in Indian Ocean sea surface temperatures. Sci Rep 6: 21251. https://doi.org/10.1038/srep21251
Duchon CE (1979) Lanczos filtering in one and two dimensions. J Appl Meteorol 18:1016–1022. https://doi.org/10.1175/1520-0450(1979)018<1016:LFIOAT>2.0.CO;2
Fu YF, Pan X, Yang YJ, Chen F, Liu P (2017) Climatological characteristics of summer precipitation over East Asia measured by TRMM PR: a review. J Meteor Res 31:142–159. https://doi.org/10.1007/s13351-017-6156-9
Huang R, Sun F (1992) Impacts of the tropical western Pacific on the East Asian summer monsoon. J Meteor Soc Japan 70:243–256. https://doi.org/10.2151/jmsj1965.70.1B_243
Huang R, Xu Y, Zhou L (1999) The interdecadal variation of summer precipitations in China and the drought trend in north China. Plateau Meteor 18:465–476 (in Chinese)
Huang R, Cai RS, Chen JL, Lian-Tong AZ (2006) Interdecadal variations of drought and flooding disasters in China and their association with the East Asian climate system. Chinese J Atmos Sci 30:730–743 (in Chinese)
Huang R, Chen J, Liu Y (2011) Interdecadal variation of the leading modes of summertime precipitation anomalies over Eastern China and its association with water vapor transport over East Asia. Chinese J Atmos Sci 35:589–606 (in Chinese)
Kuang X, Zhang Y, Liu J (2007) Seasonal variations of the East Asian subtropical westerly jet and the thermal mechanism. J Meteor Res 21:192–203
Kosaka Y, Nakamura H (2006) Structure and dynamics of the summertime Pacific-Japan teleconnection pattern. Q J R Meteorol Soc 132: 2009–2030. https://doi.org/10.1256/qj.05.204
Kwon MH, Jhun JG, Ha KJ (2007) Decadal change in East Asian summer monsoon circulation in the mid-1990s. Geophys Res Lett 34: L21706. https://doi.org/10.1029/2007GL031977
Li Q, Peng J, Shen Y (2012) Development of China homogenized monthly precipitation dataset during 1900–2009. J Geogr Sci 22:579–593. https://doi.org/10.1007/s11442-012-0948-8
Li SL, Perlwitz J, Quan X, Hoerling MP (2008) Modelling the influence of North Atlantic multidecadal warmth on the Indian summer rainfall. Geophys Res Lett 35:L05804. https://doi.org/10.1029/2007GL032901
Lin JS, Wu B, Zhou TJ (2016) Is the interdecadal circumglobal teleconnection pattern excited by the Atlantic multidecadal Oscillation? Atmospheric and Oceanic Science Letters 9(6):451–457. https://doi.org/10.1080/16742834.2016.1233800
Liu Y, Huang G, Huang R (2011) Inter-decadal variability of summer rainfall in Eastern China detected by the Lepage test. Theor Appl Climatol 106:481–488. https://doi.org/10.1007/s00704-011-0442-8
Liu Y, Chiang J (2012) Coordinated abrupt weakening of the Eurasian and North African monsoons in the 1960s and links to extratropical North Atlantic cooling. J Clim 25:3532–3548. https://doi.org/10.1175/JCLI-D-11-00219.1
Livezey R, Chen W (1983) Statistical field significance and its determination by Monte Carlo techniques. Mon Wea Rev 111:46–59. https://doi.org/10.1175/1520-0493(1983)111<0046:SFSAID>2.0.CO;2
Lu R, Dong B, Ding H (2006) Impact of the Atlantic Multidecadal Oscillation on the Asian summer monsoon. Geophys Res Lett 33: L24701. https://doi.org/10.1029/2006GL027655
Mantua NJ, Hare SR, Zhang Y, Wallace JM, Francis RC (1997) A Pacific interdecadal climate oscillation with impacts on salmon production. Bull Amer Meteor Soc 78:1069–1079. https://doi.org/10.1175/1520-0477(1997)078,1069:APICOW.2.0.CO;2
New M, Hulme M, Jones P (2000) Representing twentieth-century space-time climate variability. Part II: development of 1901–96 monthly grids of terrestrial surface climate. J Clim 13:2217–2238. https://doi.org/10.1175/1520-0442(2000)013<2217:RTCSTC>2.0.CO;2
Nitta T (1987) Convective activities in the tropical western Pacific and their impact on the northern hemisphere summer circulation. J Meteor Soc Japan 65:373–390. https://doi.org/10.2151/jmsj1965.65.3_373
Peng J, Zhang Y, Bueh C (2007) On the characteristics and possible causes of a severe drought and heat wave in the Sichuan-Chongqing region in 2006. Climatic Environ Res 12:464–474 (in Chinese)
Qian C, Zhou T (2014) Multidecadal variability of north China aridity and its relationship to PDO during 1900–2010. J Clim 27:1210–1222. https://doi.org/10.1175/JCLI-D-13-00235.1
Rayner N, Parker D, Horton E (2003) Global analyses of sea surface temperature, sea ice, and night marine air temperature since the late nineteenth century. J Geophys Res 108:1063–1082. https://doi.org/10.1029/2002JD002670
Shen S, Lau K (1995) Biennial oscillation associated with the East Asian summer monsoon and tropical sea surface temperatures. J Meteor Soc Japan 73:105–124. https://doi.org/10.2151/jmsj1965.73.1_105
Si D, Ding Y (2016) Oceanic forcings of the interdecadal variability in East Asian summer rainfall. J Clim 29:7633–7649. https://doi.org/10.1175/JCLI-D-15-0792.1
Takaya K, Nakamura H (1997) A formulation of a wave-activity flux for stationary Rossby waves on a zonally varying basic flow. Geophys Res Lett 24:2985–2988. https://doi.org/10.1029/97GL03094
Thomson D (1982) Spectrum estimation and harmonic analysis. Proc IEEEs 70:1055–1096. https://doi.org/10.1109/PROC.1982.12433
Wang H (2001) The weakening of the Asian monsoon circulation after the end of 1970's. Adv Atmos Sci 18:376–386. https://doi.org/10.1007/BF02919316
Wang L, Chen W, Zhou W (2015) Understanding and detecting super-extreme droughts in Southwest China through an integrated approach and index. Quart J Roy Meteor Soc 142:529–535. https://doi.org/10.1002/qj.2593
Wang Y, Li S, Luo D (2009) Seasonal response of Asian monsoonal climate to the Atlantic Multidecadal Oscillation. J Geophys Res 11:356–360. https://doi.org/10.1029/2008JD010929
Wu B, Zhou T, Li T (2016) Impacts of the Pacific–Japan and circumglobal teleconnection patterns on the interdecadal variability of the East Asian summer monsoon. J Clim 29:3253–3271. https://doi.org/10.1175/JCLI-D-15-0105.1
Wu R, Wen Z, Yang S (2010) An interdecadal change in southern China summer rainfall around 1992/93. J Clim 23:2389–2403. https://doi.org/10.1175/2009JCLI3336.1

Wu X, Mao J (2017) Interdecadal variability of early summer monsoon rainfall over South China in association with the Pacific Decadal Oscillation. Int J Climatol 37:706–721. https://doi.org/10.1002/joc.4734

Xie S, Hu K, Hafner J (2009) Indian Ocean capacitor effect on Indo-western Pacific climate during the summer following El Niño. J Clim 22:730–747. https://doi.org/10.1175/2008JCLI2544.1

Xu Z, Fan K, Wang H (2015) Decadal variation of summer precipitation over China and associated atmospheric circulation after the late 1990s. J Clim 28:4086–4106. https://doi.org/10.1175/JCLI-D-14-00464.1

Yang J, Liu Q, Xie S (2007) Impact of the Indian Ocean SST basin mode on the Asian summer monsoon. Geophys Res Lett 34:155–164. https://doi.org/10.1029/2006GL028571

Yang J, Liu Q, Liu Z (2009) Basin mode of Indian Ocean sea surface temperature and Northern Hemisphere circumglobal teleconnection. Geophys Res Lett 36:L19705. https://doi.org/10.1029/2009GL039559

Yang Q, Ma Z, Fan X (2017) Decadal modulation of precipitation patterns over East China by sea surface temperature anomalies. J Clim 30:7017–7033. https://doi.org/10.1175/JCLI-D-16-0793.1

Yu L, Furevik T, Ottera OH, Gao Y (2015) Modulation of the Pacific Decadal Oscillation on the summer precipitation over East China: a comparison of observations to 600-years control run of Bergen climate model. Clim Dyn 44:475–494. https://doi.org/10.1007/s00382-014-2141-5

Yuan Y, Gao H, Li WJ, Liu YJ, Chen LJ, Zhou B, Ding YH (2017) The 2016 summer floods in China and associated physical mechanisms: a comparison with 1998. J Meteor Res 31:261–277. https://doi.org/10.1007/s13351-017-6192-5

Zhang H, Wen Z, Wu R, Chen Z, Guo Y (2016) Inter-decadal changes in the East Asian summer monsoon and associations with sea surface temperature anomaly in the South Indian Ocean. Climate Dyn 48:1–15. https://doi.org/10.1007/s00382-016-3131-6

Zhu J, Huang B, Kumar A, Kinter JL III (2015) Seasonality in predictive skill and predictable patterns of tropical Indian Ocean SST. J Clim 28:7962–7984. https://doi.org/10.1175/JCLI-D-15-0067.1

Zhu Y, Yang X (2003) Relationships between Pacific decadal oscillation (PDO) and climate variabilities in China. Acta Meteor Sin 61:641–654 (in Chinese)

Zhu Y, Wang H, Zhou W, Ma J (2011) Recent changes in the summer precipitation pattern in East China and the background circulation. Climate Dyn 36:1463–1473. https://doi.org/10.1007/s00382-010-0852-9

doi:10.11676/qxxb2018.021

超强厄尔尼诺事件对中国东部春夏季极端降水频率的影响*

刘明竑[1,2]　任宏利[2,3]　张文君[1]　任鹏飞[2,4]

LIU Minghong[1,2]　REN Hongli[2,3]　ZHANG Wenjun[1]　REN Pengfei[2,4]

1. 南京信息工程大学气象灾害教育部重点实验室/气候与环境变化国际合作联合实验室/气象灾害预报预警与评估协同创新中心,南京,210044
2. 中国气象局国家气候中心气候研究开放实验室,北京,100081
3. 中国气象局-南京大学气候预测研究联合实验室,南京,210023
4. 中国气象科学研究院,北京,100081

1. *Key Laboratory of Meteorological Disaster, Ministry of Education/International Joint Laboratory on Climate and Environment Change/Collaborative Innovation Center on Forecast and Evaluation of Meteorological Disasters, Nanjing University of Information Science and Technology, Nanjing* 210044, *China*
2. *Laboratory for Climate Studies, National Climate Center, China Meteorological Administration, Beijing* 100081, *China*
3. *CMA-NJU Joint Laboratory for Climate Prediction Studies, Nanjing* 210023, *China*
4. *Chinese Academy of Meteorological Sciences, Beijing* 100081, *China*

2017-11-16 收稿,2018-03-21 改回.

刘明竑,任宏利,张文君,任鹏飞. 2018. 超强厄尔尼诺事件对中国东部春夏季极端降水频率的影响. 气象学报, 76(4):539-553

Liu Minghong, Ren Hongli, Zhang Wenjun, Ren Pengfei. 2018. Influence of super El Niño events on the frequency of spring and summer extreme precipitation over eastern China. *Acta Meteorologica Sinica*, 76(4):539-553

Abstract Features and mechanisms of the probability changes of spring and summer extreme precipitation during super El Niño events are investigated using the 0.5°×0.5° resolution China daily precipitation data from the National Meteorological Information Center. Through analyzing the water vapor transport and vertical motion characteristics contributed by the super El Niño and its derived mode, the mechanism of super El Niño impacts on extreme precipitation over eastern China are discussed. The results show that during the decaying phase of the super El Niño event, the occurrence probability of spring extreme precipitation increases significantly over the whole eastern China, especially to the north of the Yangtze-Huai River Valley. In summer, the probability is almost doubled that in regular years over the Yangtze River Valley, whereas it decreases sharply over southern and northern China. Physical analysis indicates that in spring, the super El Niño itself and the combination mode (C-mode) derived from its nonlinear interaction with the tropical Pacific annual cycle both have significant impacts on the anomalous circulation background, i.e., the strong anti-cyclonic circulation anomaly over the northwestern Pacific leads to abundant moisture convergence and ascending motion over eastern China, which is conducive to the occurrence of the observed extreme precipitation. In the subsequent summer, the super El Niño event has disappeared, but the anomalous Northwest Pacific anti-cyclonic circulation associated with the C-mode still exists, and the favorable condition for extreme precipitation maintains over the Yangtze

* 资助课题:公益性(气象)行业专项项目(GYHY201506013)、全球变化与海气相互作用专项(GASI-IPOVAI-03)、国家自然科学基金项目(41675073)。

作者简介:刘明竑,从事 ENSO 机理及气候影响研究。E-mail: lmh_nuist@126.com

通讯作者:张文君,主要从事 ENSO 机理及海气相互作用等方面研究。E-mail: zhangwj@nuist.edu.cn

River Valley. Additionally, in spring and summer, daily meridional wind anomalies in the mid-upper troposphere over eastern China are exceptionally active during the super El Niño events, and the frequent meridional convergence of cold air from north and warm moisture from south could lead to enhanced convective events, which may also contribute to the increased occurrence of extreme precipitation.

Key words Super El Niño event, Extreme precipitation, ENSO derived mode, C-mode, Eastern China

摘 要 利用中国国家气象信息中心提供的中国地面逐日降水 0.5°×0.5°格点数据集,研究了超强厄尔尼诺事件衰减年春、夏季中国东部极端降水发生概率的变化,并通过诊断超强厄尔尼诺自身及其衍生模态各自的水汽输送和垂直运动特征,探讨了超强厄尔尼诺事件对中国东部极端降水的影响机制。结果表明,超强厄尔尼诺事件衰减年春季,整个中国东部尤其是江淮以北地区,极端降水事件发生概率显著增大。同年夏季,长江流域极端降水发生概率比常规年份高出近 1 倍,而在华南和华北地区则相对减小。诊断分析显示,春季超强厄尔尼诺自身及其与热带太平洋地区年循环相互作用衍生出的组合模态(C-mode)均对降水的环流背景影响显著,热带太平洋西北部低空存在强盛的反气旋性异常环流,导致大量水汽在中国东部汇聚并上升,有利于该地区极端降水事件的发生。夏季,厄尔尼诺事件已经消亡,但与 C-mode 影响相关联的西北太平洋异常反气旋环流仍然存在,长江流域维持极端降水事件发生的有利条件。此外,研究也显示,超强厄尔尼诺事件衰减年春、夏季中国东部对流层中上层持续有异常经向风活动,频繁的南北冷暖气流交汇可能导致强对流事件发生次数增多,这也为该区域极端降水的频发提供了支持。

关键词 超强厄尔尼诺, 极端降水, ENSO 衍生模态, C-mode, 中国东部

中图法分类号 P47

1 引 言

厄尔尼诺-南方涛动(ENSO, El Niño-Southern Oscillation)是热带太平洋地区海-气耦合系统中最强的年际变化信号,其发生、发展往往引起全球范围的天气、气候异常(Rasmusson, et al, 1982; Philander, 1983; Trenberth, et al, 1998; Wallace, et al, 1998)。中国地处亚洲东部,受东亚季风影响深远,其气候异常与 ENSO 密切相关(Huang, et al, 1989; 陶诗言等, 1998; Wang, et al, 2000; Zhang, et al, 1996)。因此,深入认识 ENSO 相关的气候影响及其机理问题,对中国短期气候预测工作具有重要的指导意义。

长期以来,ENSO 与中国降水异常的关系一直受到人们关注。研究表明,ENSO 一般通过影响东亚季风的强、弱进而调控中国的降水,不同阶段对中国降水异常的影响有所不同(符淙斌等, 1988; Zhang, et al, 1996, 2002; Gong, et al, 1999)。例如,在厄尔尼诺衰减年春季,从中国华南延伸至日本南部降水均异常增多;夏季,主要表现为江淮流域降水偏多、华南和华北地区相对偏少的异常分布特征(刘永强等, 1995; 赵振国, 1996; Zhang, et al, 1999; 金祖辉等, 1999)。伴随着季节平均降水变率的增大,极端降水事件的发生也会相应受到影响。中国极端降水时、空变化复杂,具有明显的区域性和季节性特征(翟盘茂等, 2003; Zhai, et al, 2005; 陈海山等, 2009)。李威等(2009)研究发现,在厄尔尼诺年冬、春季和拉尼娜年夏、秋季,中国极端降水事件频发,多数地区更易发生在 ENSO 暖位相出现后半年左右。王苗等(2013)的研究则表明,空间上,厄尔尼诺衰减年春、夏季北方多极端降水事件,而南方分布形势较为复杂。Xiao 等(2017)也指出,厄尔尼诺发展年中国中部地区极端降水事件通常较少,而次年中国东部地区则更易发生极端降水事件。目前对极端降水与厄尔尼诺事件之间联系的研究仍然很少,多以统计厄尔尼诺年极端降水分布为主且缺少定论,其特征与机理成因均需进一步深入研究。

2015/2016 年发生了继 1982/1983 和 1997/1998 年之后又一次超强厄尔尼诺事件,引起广泛关注。此次事件持续时间长、强度大,相应的气候响应非常显著(翟盘茂等, 2016; 邵勰等, 2016; 袁媛等, 2016)。毕宝贵等(2017)指出,在超强厄尔尼诺衰减年,极端降水和强对流天气发生的频次明显较常规年份多,而其他厄尔尼诺事件期间极端降水的多发特征并不明显。因此,按照厄尔尼诺事件强度加以区分,可能是研究其对极端天气影响的一个关键点。对于超强厄尔尼诺事件的典型特征及其影响,前人已经有了一些认识(Latif, et al, 2015; Chen, et al, 2016; 张文君等, 2016; 任宏利等, 2017)。最近的研

究发现,ENSO 除了自身的直接影响外,还能通过与其他信号相互作用产生新的衍生模态。例如,ENSO 与热带太平洋地区年循环信号发生非线性相互作用,会衍生出一种经向非对称的海-气异常模态(图 1),被称为 ENSO-年循环组合模态(ENSO-AC combination mode,简称 C-mode)(Stuecker,et al,2013),该模态峰值出现在厄尔尼诺衰减年冬末春初,一般在强厄尔尼诺事件中较为显著。在强厄尔尼诺衰减年的春、夏季,C-mode 对中国东部地区降水异常有显著的贡献(李海燕等,2016;Zhang,et al,2016a, 2016b)。目前对超强厄尔尼诺事件以及 C-mode 影响的研究主要关注季节平均降水异常,对更易引发灾害的极端降水的影响还知之甚少。因此,本研究在考虑 C-mode 作用的基础上,专注于超强厄尔尼诺事件气候影响,探讨其衰减年春、夏季中国极端降水事件发生概率的变化以及可能成因,以期进一步加深对超强厄尔尼诺气候影响的认识,为中国极端降水事件的预测提供一些新的思路和参考。

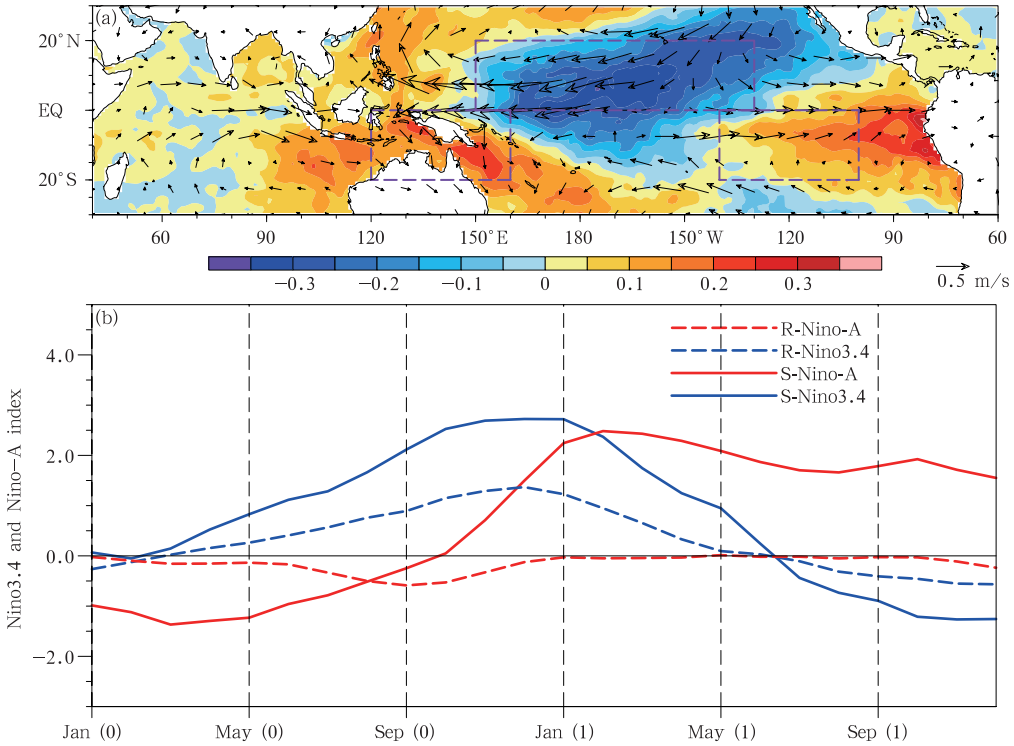

图 1 (a)热带印度-太平洋区域 Nino-A 指数(基于紫色框内海表温度定义)回归的海表温度异常(色阶,单位:℃)以及 850 hPa 风场异常(矢线),(b)超强厄尔尼诺事件(实线)、普通厄尔尼诺事件(虚线)分别合成的标准化 Nino3.4 指数(蓝线)和 Nino-A 指数(红线)时间序列演变((0)表示厄尔尼诺发展年,(1)表示衰减年)

Fig. 1 (a) SST anomalies (shadings, unit: ℃) and 850 hPa wind anomalies (vectors) in the Indo-Pacific regressed onto the normalized Nino-A index (defined based on the SST anomalies in the regions highlighted in the purple boxes). (b) Normalized Nino3.4 index (blue) and Nino-A index (red) composited from the super El Niño events (solid lines) or the regular El Niño events (dashed lines) ((0) indicates the El Niño developing year and (1) indicates the decaying year)

2 资料和方法

所使用的降水资料来自中国国家气象信息中心提供的中国地面降水日值格点数据集(V2.0),该数据集基于中国国家气象信息中心基础资料专项最新整编的中国地面高密度台站(2472 个中国国家级气

象观测站)降水资料空间插值所得,水平分辨率为0.5°×0.5°;其他气象要素来自美国国家环境预测中心/国家大气研究中心(NCEP/NCAR)的逐日以及月平均再分析资料集(Kalnay,et al,1996),水平分辨率为2.5°×2.5°,同时也使用了欧洲中期天气预报中心(ECMWF)提供的ERA-Interim再分析资料集(Dee,et al,2011)对比验证;所用海表温度资料为英国哈得来中心提供的月平均海表温度(HadISST)资料(Rayner,et al,2003),水平分辨率为1°×1°。所用资料的时段除ERA-Interim以外,统一取为1961年1月—2016年12月。

依据刚颁布的国家标准《厄尔尼诺/拉尼娜事件判别方法》(国家质量监督检验检疫总局,2017),定义峰值达到或超过2.5℃,即3倍标准差的事件为超强厄尔尼诺事件,共计1982/1983、1997/1998、2015/2016年3次,剩余事件(1963/1964、1965/1966、1969/1970、1972/1973、1976/1977、1977/1978、1979/1980、1986/1987、1991/1992、1994/1995、2002/2003、2004/2005、2006/2007、2009/2010年)归为普通厄尔尼诺事件。对于极端降水事件,参考已有的研究(翟盘茂等,2003;任国玉等,2010),定义各季节雨日95百分位降水量为该季节极端降水阈值,当日降水量超过阈值即定义该日发生极端降水事件。传统的ENSO指数一般只能用来表征厄尔尼诺本身的强弱而无法描述其衍生模态,为此,采用Zhang等(2016a)定义的Nino-A指数来衡量C-mode的时间变化

$$\text{Nino-A} = 0.5[\text{SSTA}]_{\text{SW}} + 0.5[\text{SSTA}]_{\text{SE}} - [\text{SSTA}]_{\text{NC}} \quad (1)$$

式中,方括号[ ]代表所示范围海表温度异常的区域平均,SW、SE和NC分别表示赤道太平洋西南(EQ—20°S,120°—160°E)、东南(EQ—20°S,100°—140°W)和中北部(EQ—20°N,150°E—130°W)3个区域(图1a紫色框区)。

该指数同时刻画了ENSO海温响应在纬向和经向分布上的不对称性,能够非常好地表征C-mode的时间演变,并且与Nino3.4指数有很好的独立关系,无论是用来描述ENSO局地海-气特征还是刻画ENSO气候影响,都是对传统ENSO指数(即Nino3.4指数)有力的补充(Zhang,et al,2016a)。由图1b也可以看到,Nino-A指数在超强厄尔尼诺事件中振幅非常明显,而在普通厄尔尼诺事件中很弱。

3 衰减年春、夏季中国东部极端降水发生概率变化特征

中国东部降水主要集中在东亚季风盛行的春、夏季,不同季节雨带存在明显的南北移动。图2给出了该区域春、夏季气候态降水和极端降水阈值的分布,春季气候态降水主要集中在长江以南,极端降水阈值也呈现出由东南往西北递减的趋势,长江以南雨强基本超过大雨标准(25 mm/d)(图2a、c)。夏季,随着气候态降水整体增多,极端降水大值区也向北向西扩张,在长江流域形成一条高值中心带,同时南方沿海地区也有一片大值区存在(图2b、d)。

总体而言,极端降水阈值的分布与气候态降水基本一致。然而,在超强厄尔尼诺事件衰减年,ENSO信号对中国东部降水有着明显的调控作用。从3次超强厄尔尼诺事件异常降水的合成结果来看,衰减年春季,几乎整个东部地区的降水都显著增多,大值区域主要在江淮流域以及华南部分地区(图3a);而普通厄尔尼诺事件中春季异常降水无论是振幅还是覆盖范围都要差很多(图3c)。夏季,超强厄尔尼诺事件中北方降水仍旧偏多,而华南已经转为较弱的负异常;在长江流域沿线,则存在着一条显著的降水正异常大值带(图3b),而普通厄尔尼诺事件长江中下游降水已经变成负异常(图3d)。可见中国东部季节平均降水对超强厄尔尼诺事件的响应基本以增多为主,并且,长江流域的降水正异常最为显著且持久。那么,基于这样的季节趋势,单日极端降水事件分布是否也会有类似的变化呢?为了直观地考察其发生概率的变化特征,参考前人的方法(Xavier,et al,2014;Hsu,et al,2016;Ren,et al,2017),计算了超强厄尔尼诺事件衰减年春、夏季极端降水发生概率的百分比变化ΔP_{SE}。它反映了在超强厄尔尼诺影响背景下,极端降水发生概率相对于正常年份的变化

$$\Delta P_{\text{SE}} = \frac{P_{\text{SE}}(x \geqslant x_{\text{t}}) - P_{\text{cli}}(x \geqslant x_{\text{t}})}{P_{\text{cli}}(x \geqslant x_{\text{t}})} \times 100\% \quad (2)$$

式中,P_{SE}为超强厄尔尼诺年极端降水事件发生的概率,实际计算时使用所挑选超强厄尔尼诺衰减年各

季节逐日降水量 x 超过极端降水阈值 x_t(即前述各季节雨日 95 百分位降水量)的频率代替。同样 P_{cli} 为在气候态常规情况下极端降水发生的概率,使用所有年份逐日降水量值超过极端降水阈值的频率代替。

对每一年极端降水事件发生情况计算百分比变化之后,给出了超强厄尔尼诺年合成的概率变化分布(图 4),以分析超强厄尔尼诺事件对极端降水产生的共性影响。衰减年春季,中国东部绝大部分地区极端降水发生概率均有所提升(图 4a)。与季节平均降水变化规律类似,极端降水变化最显著的区域也主要在黄河流域和东北地区,这些地区春季气候态降水量基数小,降水稍有增加就可以达到极端水平。极端降水阈值较高的长江中下游沿海以及华南部分地区,最高也提升了接近100%。夏季

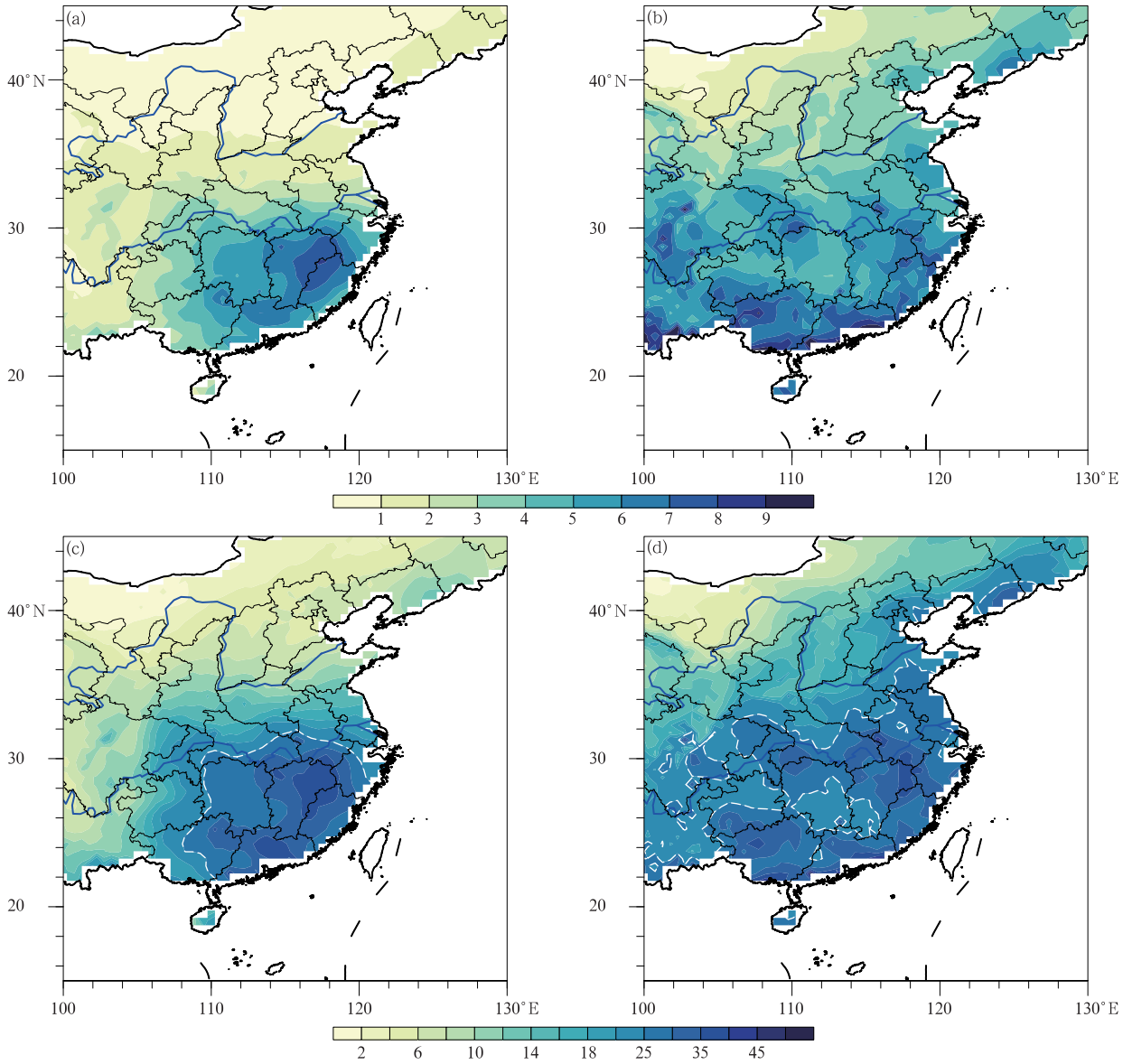

图 2 中国东部(a)春季、(b)夏季气候态(1961—2010 年)降水分布(单位:mm/d);(c、d)同(a、b),但为极端降水阈值分布

(白色虚线表示 25 mm/d 等降水量线)

Fig. 2 Distributions of (a) spring and (b) summer climatological mean precipitation (1961-2010) over eastern China (unit: mm/d). (c, d) Same as (a, b) but for extreme precipitation thresholds

(the white dashed contours indicate the 25 mm/d precipitation lines)

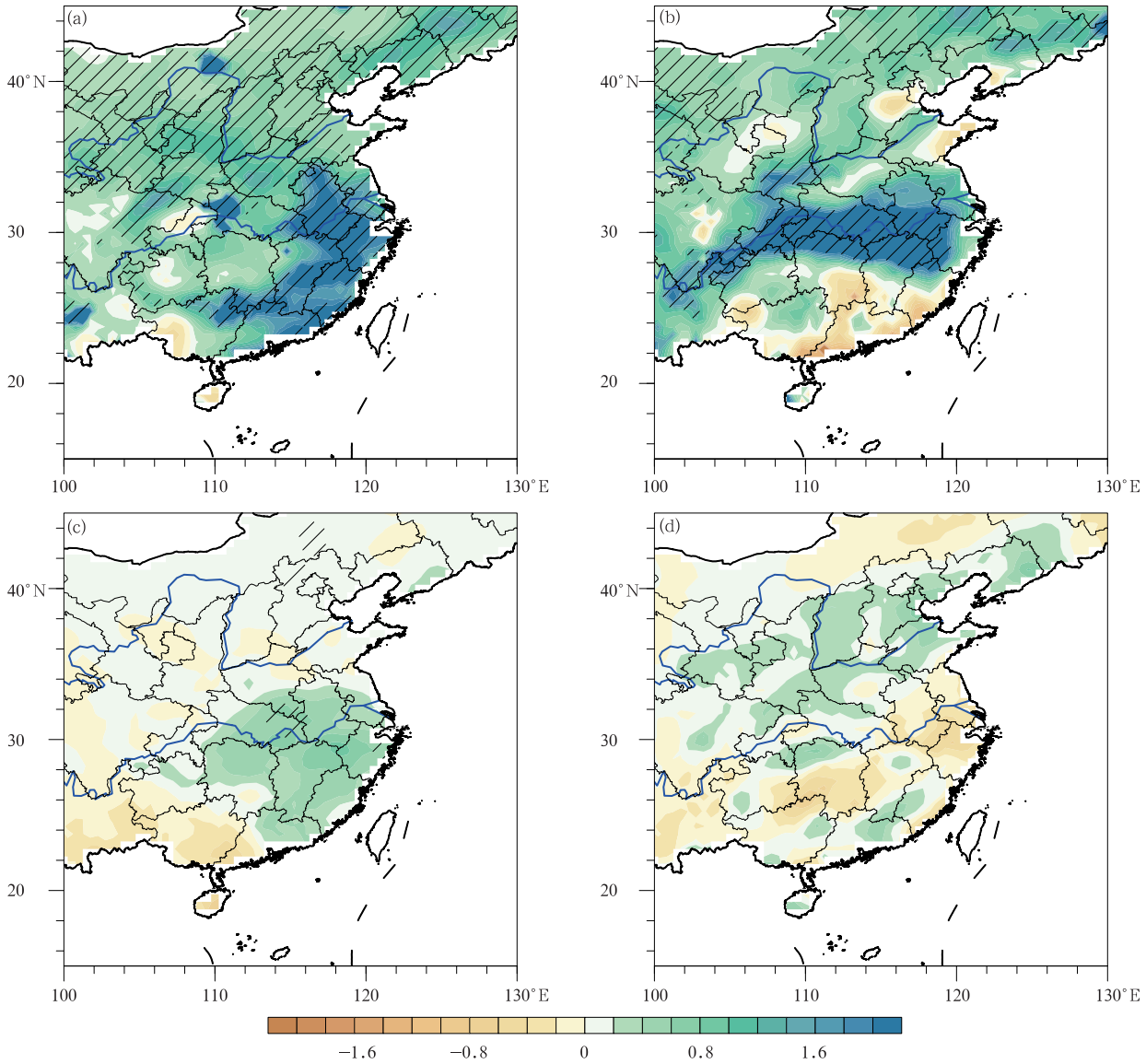

图 3 超强厄尔尼诺事件衰减年(a)春季、(b)夏季合成的中国东部降水异常(单位:mm/d,划线区域为通过 0.05 水平显著性 t 检验);(c、d)同(a、b),但为普通厄尔尼诺事件合成结果

Fig. 3 Composite seasonal precipitation anomalies (unit: mm/d, the slashed areas indicate the anomalies exceed 0.05 significance level of t-test) over eastern China during the decaying phase of super El Niño events (a. spring, b. summer; c, d. same as a, b, except for regular El Niño events)

(图 4b),北方随着整体极端降水阈值的提高以及 ENSO 影响的减弱,极端降水事件发生概率迅速减小,但长江流域仍然高出常年约 1 倍,并且高概率区域向内陆延伸。整体呈现出长江流域偏高,而其两侧的华北与华南相对偏低的纬向带状分布特征。这也是超强厄尔尼诺衰减年夏季长江流域容易发生洪涝灾害的原因之一。

作为比较,给出了 20 世纪 60 年代之后普通厄尔尼诺事件对应季节的极端降水发生概率百分比变化(图 4c、d)。合成结果几乎没有区域通过显著性 t 检验,说明普通厄尔尼诺事件对极端降水影响弱且不稳定。对比而言,衰减年春季,不同强度厄尔尼诺事件的影响在中国北方分布还有些相似;而夏季则差异明显,普通厄尔尼诺事件长江流域极端降水发生概率反而减小,与其季节平均降水偏少的特征相符,这体现了超强事件影响的独特性。综上所述,超强厄尔尼诺衰减年春、夏季,中国东部极端降水发生概率相比常年变化明显,特别是长江流域灾害性天

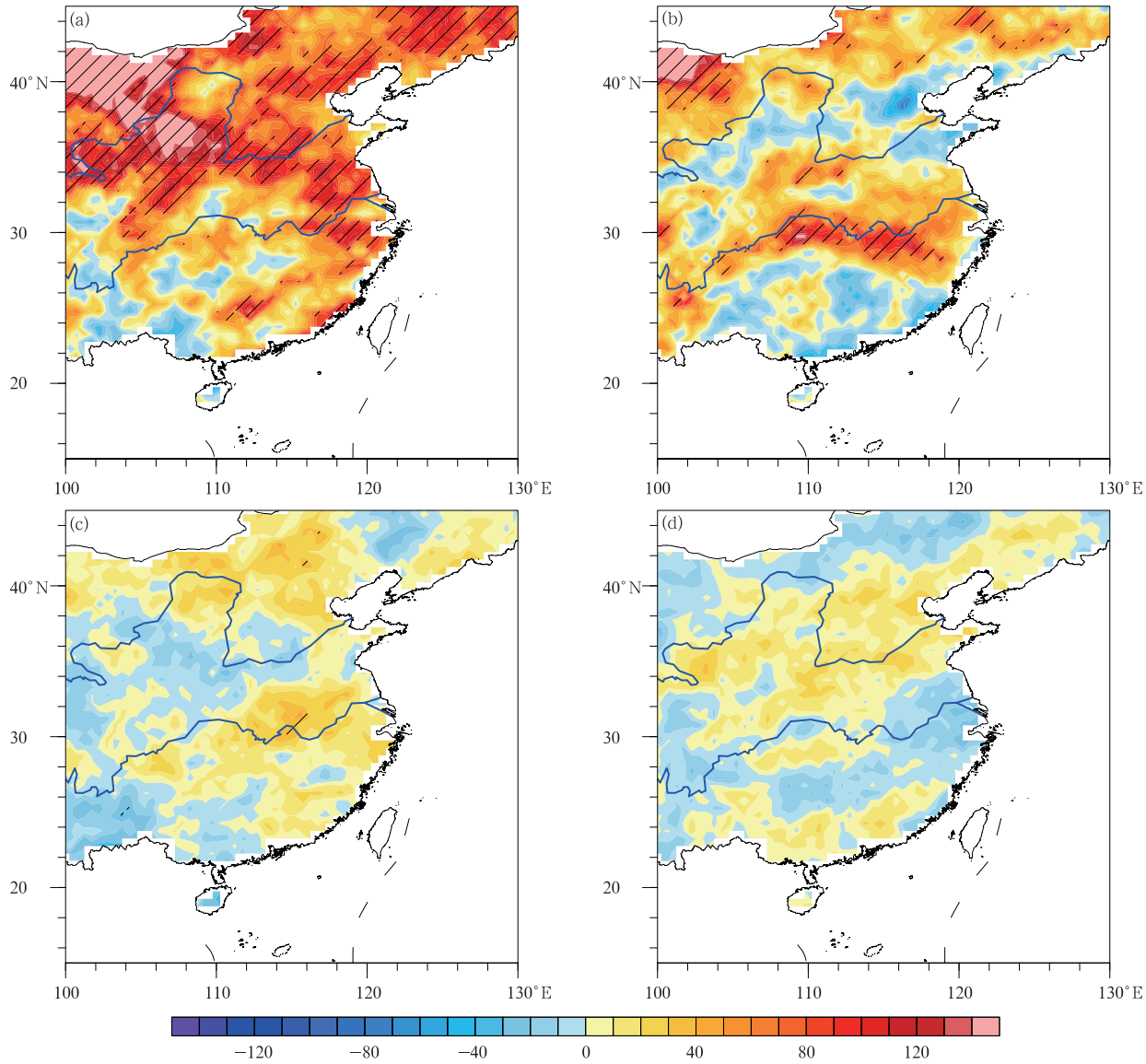

图 4 超强厄尔尼诺事件衰减年(a)春季、(b)夏季合成的中国东部极端降水发生概率百分比变化(单位:%,划线区域表示通过 0.05 水平显著性 t 检验);(c、d)同(a、b),但为普通厄尔尼诺事件合成结果

Fig. 4 Composite seasonal percentage changes in probability of extreme precipitation over eastern China during the decaying phase of super El Niño events (unit: %, the slashed areas indicate the anomalies exceed 0.05 significance level of t-test)
(a. spring, b. summer; c, d. same as a, b, except for regular El Niño events)

气发生的可能性显著增大,这种变化的可能成因尚需进一步探讨。

4 超强厄尔尼诺事件影响极端降水的可能机制

强降水事件的频繁发生依赖大尺度环流背景的支持(O'Gorman, et al, 2009),图 5 给出了合成的整层积分水汽通量异常及其散度的水平分布。超强厄尔尼诺事件衰减年春季,西北太平洋海面上有明显的异常反气旋存在,在其西北侧来自中国南海和西太平洋的异常水汽向北输送,使得从华南延伸至日本海南部均有大量水汽汇聚(图 5a)。除了水汽条件之外,剧烈的上升运动也是强降水过程不可或缺的要素。从衰减年春季 110°—120°E 平均的垂直方

向水汽通量异常环流可以看到(图 6a),EQ—10°N 表现为强下沉运动,对应西北太平洋的强反气旋活动,通过它大量水汽被输送到赤道外,在 20°—35°N 存在显著的异常上升。这种水汽丰沛、对流强盛的背景条件为中国东部极端降水的发生、发展提供了有力支持。相对而言,普通厄尔尼诺事件衰减年春季中国东部地区水汽通量异常辐合与上升都不明显(图 5c、6c)。夏季,虽然中东太平洋的厄尔尼诺响应已经消失,但是西北太平洋反气旋仍然存在并略向西扩张,同时在其东北侧日本岛上空产生了一个异常气旋,呈现类似东亚-太平洋型(EAP)遥相关分布(黄荣辉等,2006)。这样的异常环流结构使得水汽输送异常沿长江流域呈现纬向带状辐合,而在华南、华北呈偏辐散的特征(图 5b)。从图 6b 的垂直环流上亦可看出,在长江流域上空仍然保持着较强的上升运动趋势,因此,超强厄尔尼诺衰减年夏季该区域上空环流背景仍然有利于极端降水事件发生。普通厄尔尼诺事件衰减年夏季尽管西北太平洋有微弱的反气旋存在但是位置相对偏东偏南(图 5d),这个反气旋可能是厄尔尼诺转相后中东太平洋的冷异常海温或者局地海-气相互作用带来的(Stuecker, et al,2015b),垂直方向长江流域上空水汽输送表现为异常下沉(图 6d),对极端降水事件的发生并无明显影响。

以往研究已经表明,ENSO 除了自身的直接影响,其衍生的 C-mode 也对东亚地区气候异常有着非常重要的影响。为了深入分析超强厄尔尼诺事件对中国东部极端降水影响的可能机制,需要分析 C-mode 在其中所起的作用及其与 ENSO 自身影响的联系。为此,使用 1961—2010 年各季节平均的标准

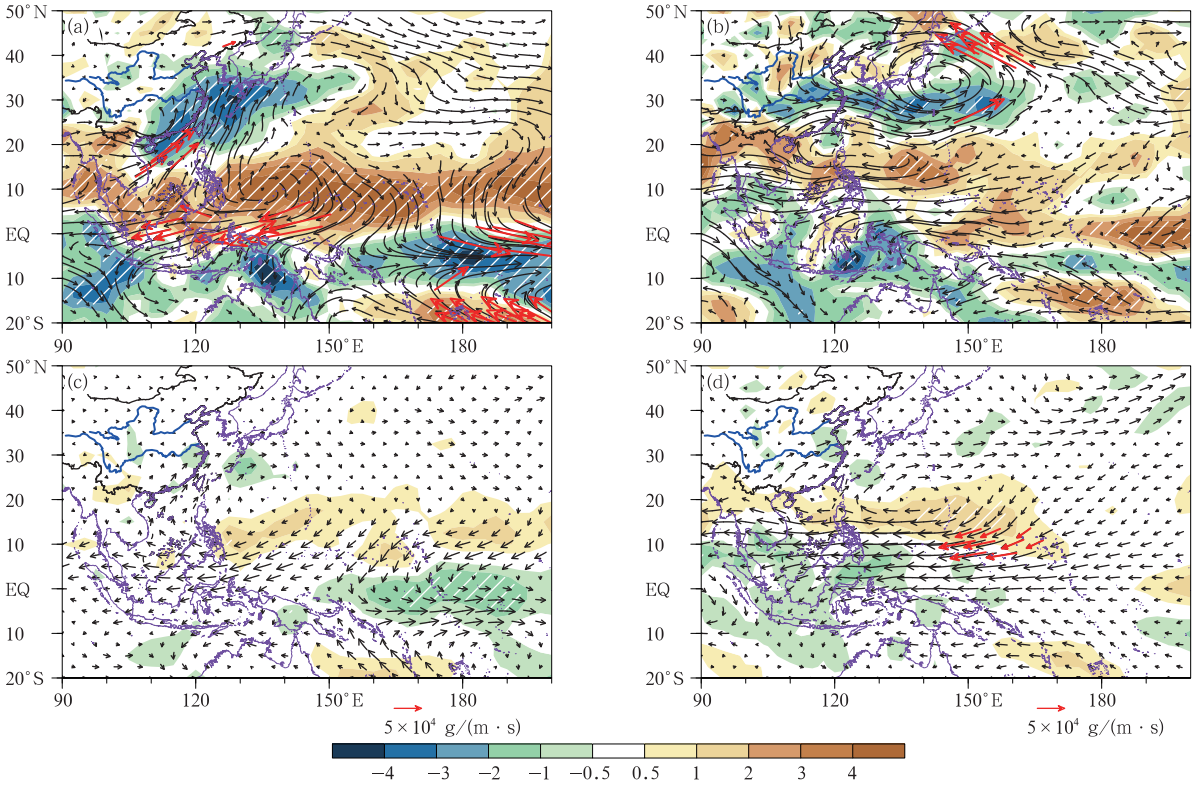

图 5 超强厄尔尼诺事件衰减年(a)春季、(b)夏季合成的整层水汽通量距平(矢线)及其散度(色阶,单位:10^{-2} g/(m²·s))分布

(红色矢量及划线区域表示通过 0.05 水平显著性 t 检验);(c、d)同(a、b),但为普通厄尔尼诺事件合成结果

Fig. 5 Composite seasonal vertically integrated moisture transport anomalies (vectors) and their divergences (shadings, unit: 10^{-2} g/(m²·s)) during the decaying phase of super El Niño events

(a. spring, b. summer; the slashed areas and red vectors indicate the anomalies exceed 0.05 significance level of t-test); c, d. same as a, b, except for regular El Niño events)

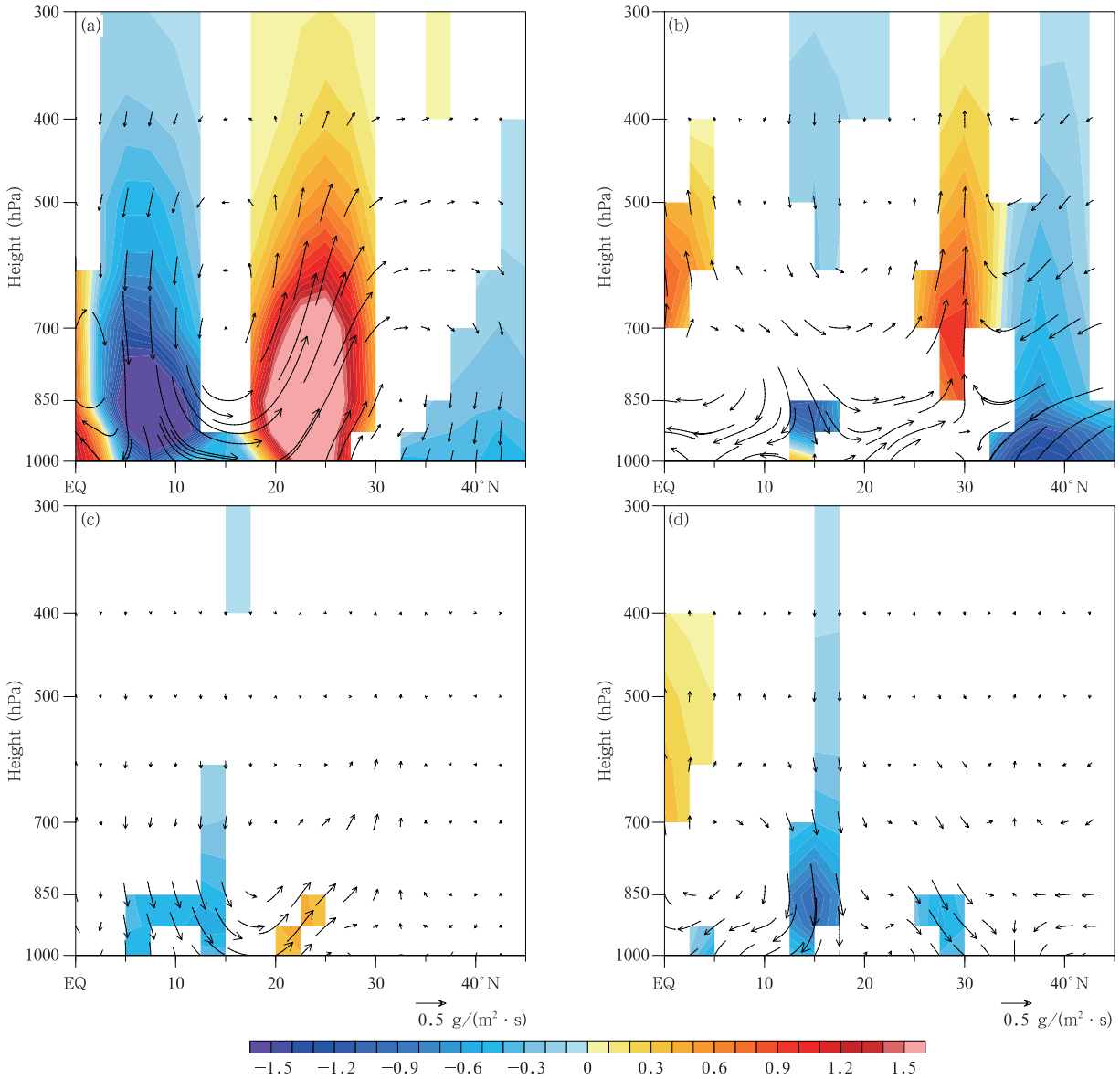

图 6 超强厄尔尼诺事件衰减年(a)春季、(b)夏季 110°—120°E 平均的垂向水汽通量异常环流(矢线,其中垂直分量已扩大 100 倍并用色阶(单位:g/(m² · s))标出其通过 0.05 水平显著性 t 检验部分);(c、d)同(a、b),但为普通厄尔尼诺事件合成结果

Fig. 6 Composite seasonal vertical moisture transport anomalies averaged over 110° − 120°E during the decaying phase of super El Niño events (vectors, the vertical components have been multiplied by a factor of 100, and those exceeding 0.05 significance level of t-test are highlighted by the shadings (unit: g/(m² · s)))
(a. spring, b. summer; c, d. Same as a, b, except for regular El Niño events)

化 Nino3.4 和 Nino-A 两个指数序列多元回归同期的异常水汽通量场,再将对应的回归系数乘上各自指数序列得到每年的重构结果,然后将超强厄尔尼诺年的结果合成,得到超强厄尔尼诺事件期间 ENSO 自身影响以及 C-mode 各自对水汽通量的贡献。

由图 7 可知,超强厄尔尼诺事件衰减年春季,ENSO 自身影响与 C-mode 的影响都为中国东部地区贡献了大量的水汽。其中 ENSO 自身的响应在赤道太平洋地区向东水汽输送明显,表现为经典的 ENSO 影响结构,在西北太平洋地区有反气旋结构存在,使

得大量水汽被输送到中国东部和南部(图 7a)。而 C-mode 的响应在赤道地区表现为向西水汽输送异常,然而,在西北太平洋却与 ENSO 自身直接影响类似地表现为显著的反气旋异常,得以将赤道地区的水汽向东亚地区输送(图 7c)。垂向水汽通量异常的响应同样可以分解为两个部分(图 8),衰减年春季,ENSO 自身影响在热带地区主要以下沉气流为主,向北输送后在亚洲东部上空出现明显的上升运动(图 8a);而 C-mode 影响在整个中低纬度地区都呈现上升运动,以中国华南地区对应的 20°N 左右为最强(图 8c)。夏季,厄尔尼诺事件对应的东太平洋正海温异常已经消失,ENSO 自身对东亚的影响基本可以忽略(图 7b、8b);而 C-mode 通过局地海-气相互作用可以将异常信号存储到海洋中,引起 Nino-A 相关区域海温持续异常,从而将其影响延续到厄尔尼诺衰减年的夏季(Stuecker, et al, 2015b)。与其相联系的大气环流场中,西北太平洋反气旋结构仍然存在,源自太平洋和中国南海的水汽最终输送到长江流域及其东部海面(图 7d)。在垂直环流场上,与 C-mode 相关的大气场在长江流域对应的 30°N 左右维持了较强的上升运动(图 8d)。综上所述,超强厄尔尼诺事件对衰减年春、夏季降水背景的影响可以分为 ENSO 自身直接影响和衍生的 C-mode 影响两个部分,春季两个部分都对中国东部地区的水汽累积和上升运动倾向做出了贡献;夏季,则主要是 C-mode 的作用使得长江流域仍然维持着有利于极端降水事件发生的水汽和环流条件。在对普通厄尔尼诺事件的水汽背景做类似分解时,发现只有衰减年春季 Nino3.4 指数的重构结果比较显著(图略),说明普通厄尔尼诺事件中只有 ENSO 自身影响发挥了一定的作用。

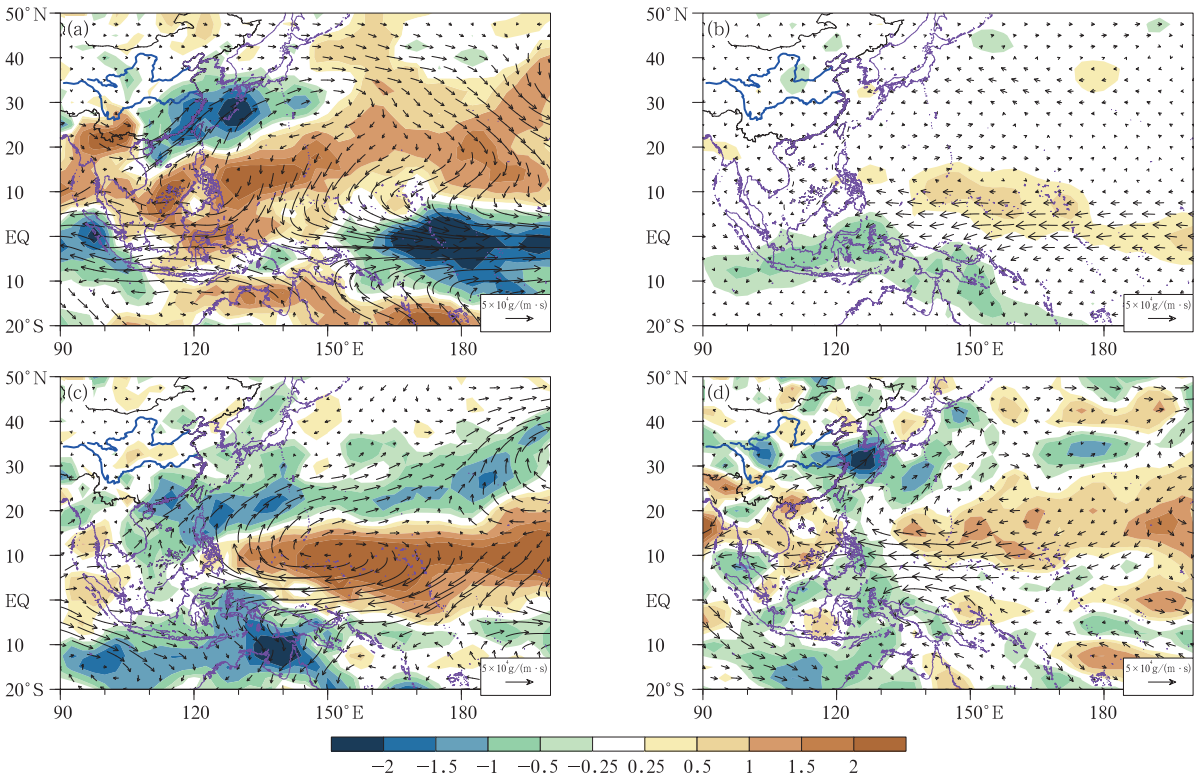

图 7 超强厄尔尼诺事件衰减年(a)春季、(b)夏季平均的 Nino3.4 指数偏回归重构的水汽通量距平(矢线)及其散度(色阶,单位:10^{-2} g/(m^2 · s))分布;(c、d)同(a、b),但为 Nino-A 指数偏回归重构的结果

Fig. 7 Reconstruction of vertically integrated moisture transport (vectors) and its divergence anomalies (shadings, unit: 10^{-2} g/(m^2 · s)) during the decaying phase of super El Niño events using partial regression with only Nino3.4 index (a. spring, b. summer; c, d. same as a, b, except with only Nino-A index)

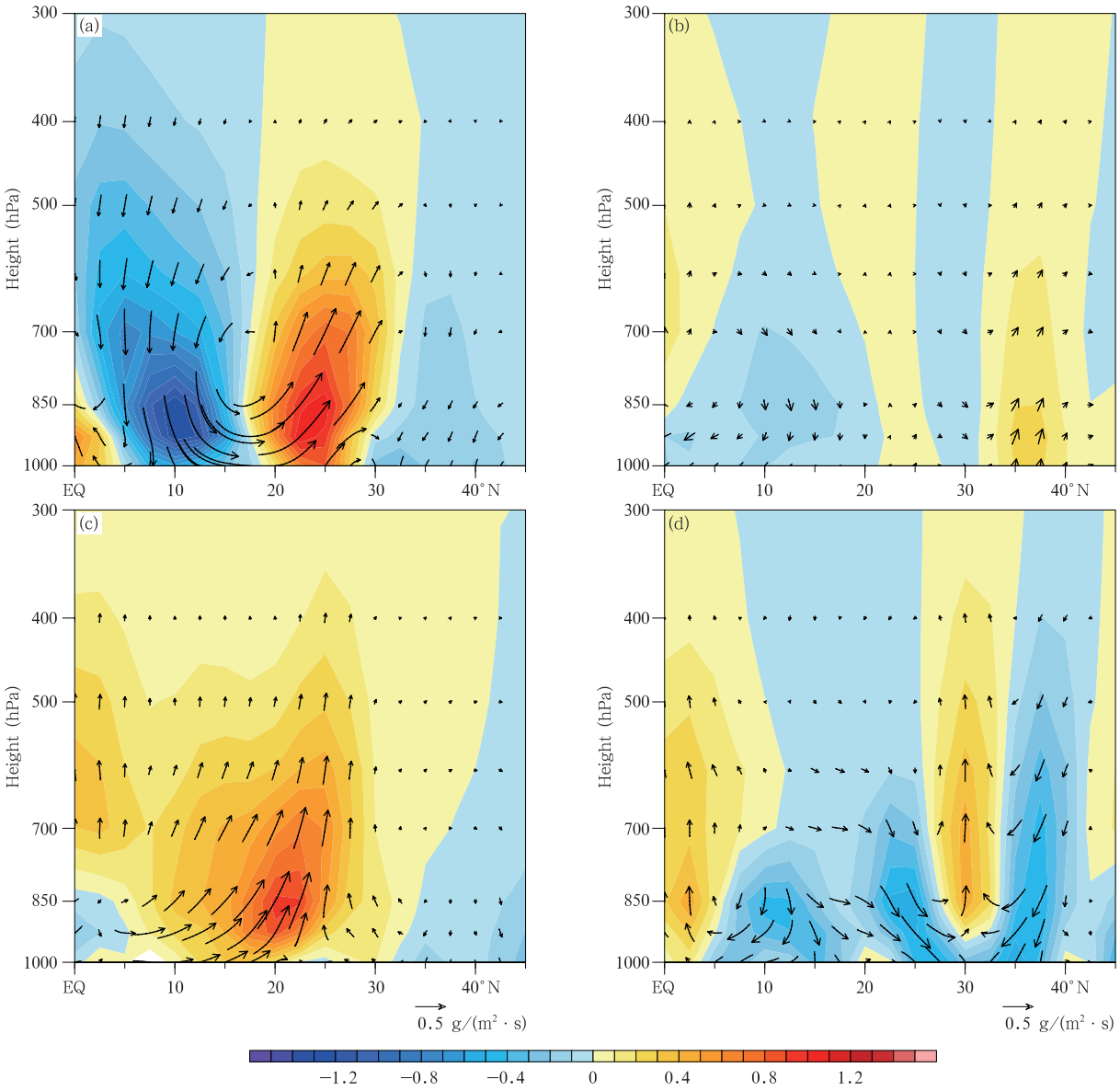

图 8　超强厄尔尼诺事件衰减年(a)春季、(b)夏季平均的 Nino3.4 指数偏回归重构的 110°—120°E 平均的垂向水汽通量异常环流(矢线,其中垂直分量已扩大 100 倍并用色阶(单位:g/(m² · s))标出);(c、d)同(a、b),但为 Nino-A 指数偏回归重构的结果

Fig. 8　Reconstruction of vertical moisture transport anomalies averaged over 110° − 120°E during the decaying phase of super El Niño events using partial regression with only Nino3.4 index (the vertical components have been multiplied by a factor of 100 and highlighted by the shadings (unit: g/(m² · s))) (a. spring, b. summer; c, d. same as a, b, except with only Niño-A index)

从上述分析可知,超强厄尔尼诺事件衰减年中国东部地区有充沛的水汽向北输送。在此基础上,每当有来自北方的冷空气向南活动时,便可能引发一次强对流甚至极端降水事件。为此,诊断了衰减年对流层中上层逐日经向风场相比于气候态风场的方差异常变化(图 9)。春季,东部沿海地区方差比常年明显增大,对流层中上层高频经向风异常活跃,这意味着低层冷空气将被频繁地引导南下,出现极端降水事件的几率随之上升(图 9a)。夏季,长江流域也处于经向风变化最剧烈的区域之内,同时这里还是水汽输送的大值区,频繁的冷、暖空气交汇很可能导致强对流事件大幅度增多(图 9b)。相对的,在

普通厄尔尼诺事件中,南方地区对流层中上层异常经向风的活动反而是偏少的(图 9c、d)。因此,超强厄尔尼诺事件引发的经向风场异常活跃也为极端降水频繁发生提供了支持。当然,进一步的机理问题尚待深入研究。

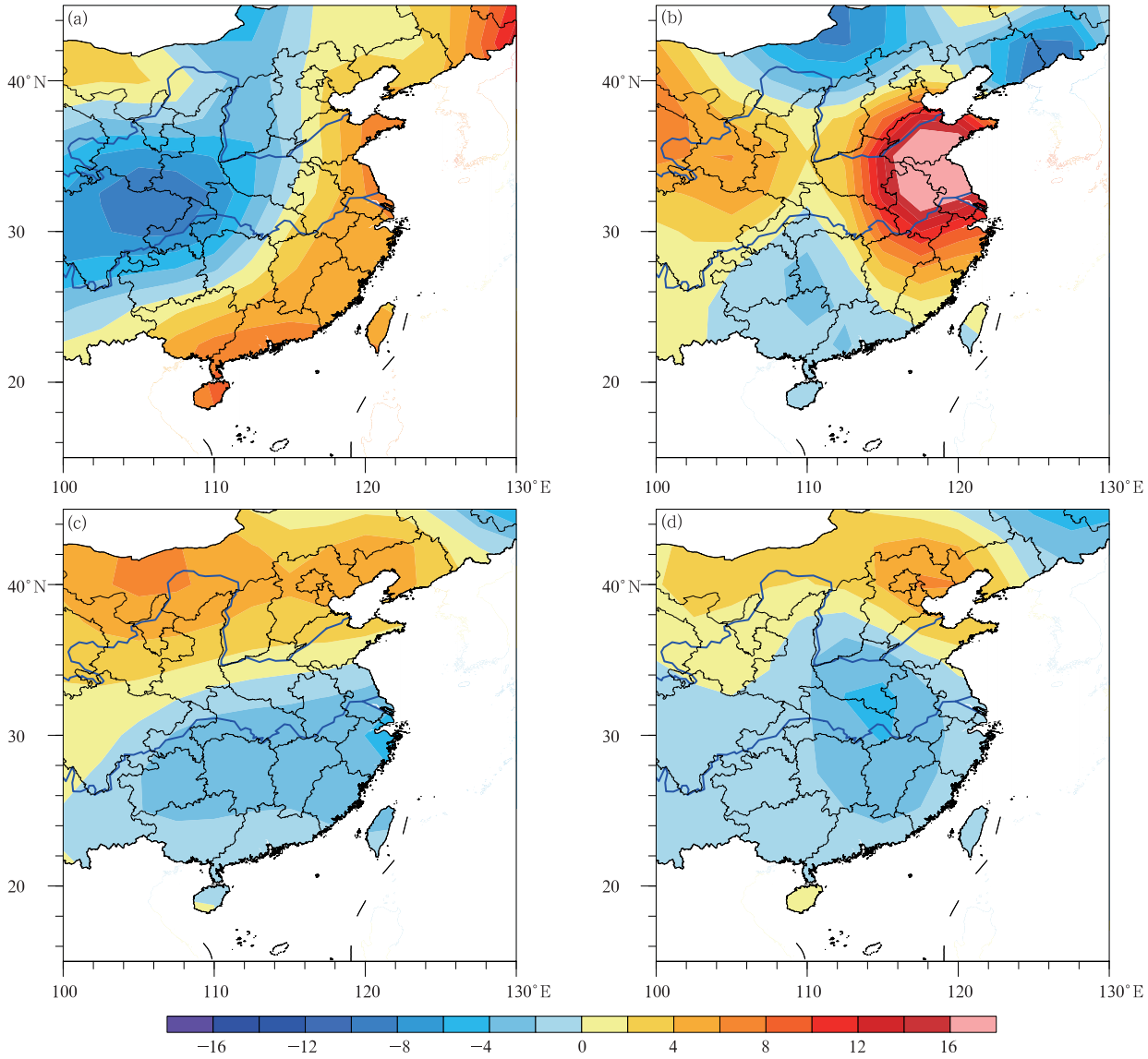

图 9 超强厄尔尼诺事件衰减年(a)春季、(b)夏季中国东部 500—200 hPa 逐日经向风方差与对应季节气候态经向风方差的差值(单位:m^2/s^2)分布;(c、d)同(a、b),但为普通厄尔尼诺事件合成结果

Fig. 9 Difference (unit: m^2/s^2) of 500 − 200 hPa daily meridional wind variance between during the decaying phase of super El Niño events and in climatology over eastern China (a, spring, b, summer; c, d, same as a, b, except for regular El Niño events)

5 结论与讨论

利用中国逐日降水格点资料,考察了超强厄尔尼诺事件影响下中国东部春、夏季极端降水发生概率的变化特征,并结合超强事件自身及其衍生模态(C-mode)的影响深入分析了这些特征的可能成因。主要结论如下:

(1) 超强厄尔尼诺事件衰减年春季,整个中国

东部尤其是江淮以北地区,极端降水事件发生概率均显著增大,南方地区相比正常年份最高也有接近100%的提升;同年夏季,华北、华南地区极端降水事件发生概率降低,而长江流域发生极端降水的概率依然比正常年份高出约1倍。

(2) 超强厄尔尼诺事件可以通过调控亚洲东部地区衰减年春、夏季环流背景为极端降水事件的发生提供有利条件。春季,ENSO自身直接影响使得暖湿气流在亚洲东部大量汇聚并上升,同时其衍生的C-mode也通过西北太平洋反气旋促进赤道地区的水汽向东亚地区输送;夏季,ENSO自身影响减弱甚至消失,但C-mode的影响依旧显著,长江流域上空仍然表现出水汽汇聚、上升运动较强的特征。

(3) 超强厄尔尼诺事件还能通过某种途径引起春、夏季中国东部对流层中上层经向风场的异常活动,引起北方冷空气频繁南下与背景场丰沛的北上暖湿气流相互作用,可能导致强对流事件发生次数增多,从而为极端降水事件的频发提供有利支持。

极端降水事件的物理成因十分复杂,超强厄尔尼诺事件通过影响月、季尺度环流背景可以为其创造非常有利的发生条件,但最终决定其发生频次的还是天气尺度要素的变化。ENSO对这些高频变化的激发机制还需要进一步研究。例如,衰减年东亚地区高频经向风的异常活跃,可能与强厄尔尼诺事件对大气加热强迫促进高、低纬度间的经向热力交换(Lee,2012)有关,可能是通过引发如太平洋北美型遥相关等大气环流型异常间接导致的(Renwick, et al,1996;Chan,et al,2005),也可能与副热带"丝绸之路"波列的异常活动存在联系(Lu, et al, 2002)。

ENSO作为具有全球影响的年际信号,可以与局地气候变率相互作用产生出不同频率的衍生模态(Stuecker,et al,2015a),这些衍生模态对上述天气要素的影响也需要继续探索。另外,文中采用合成分析强调了ENSO的强度对极端降水产生的共性影响,但即便同样是超强厄尔尼诺事件,不同个例太平洋异常海温时、空演变特征的细微偏差也可能导致其在外赤道地区的气候影响不同(Rao, et al, 2017;Liu, et al, 2018)。鉴于有可靠记录以来发生的超强厄尔尼诺事件较少,未来还需要利用能够同时较好地模拟ENSO事件和C-mode的模式(Ren, et al,2016),来进一步模拟超强厄尔尼诺及其衍生模态对极端事件的影响,从而加深对超强厄尔尼诺事件气候影响问题的认识。

参考文献

毕宝贵,张小玲,代刊. 2017. 2016年超强厄尔尼诺背景下的强对流和极端降水天气特点. 科学通报,62(9):928-937. Bi B G, Zhang X L, Dai K. 2017. Characteristics of 2016 severe convective weather and extreme rainfalls under the background of super El Niño. Chinese Sci Bull, 62(9): 928-937 (in Chinese)

陈海山,范苏丹,张新华. 2009. 中国近50 a极端降水事件变化特征的季节性差异. 大气科学学报,32(6):744-751. Chen H S, Fan S D, Zhang X H. 2009. Seasonal differences of variation characteristics of extreme precipitation events over China in the last 50 years. Trans Atmos Sci, 32(6): 744-751 (in Chinese)

符淙斌,滕星林. 1988. 我国夏季的气候异常与埃尔尼诺/南方涛动现象的关系. 大气科学,12(S1):133-141. Fu C B, Teng X L. 1988. Climate anomalies in China associated with El Niño/Southern Oscillation. Chinese J Atmos Sci, 12(S1): 133-141 (in Chinese)

国家质量监督检验检疫总局. 2017. 厄尔尼诺/拉尼娜事件判别方法,GB/T 33666-2017. 北京:中国标准出版社,1-6. General Administration of Quality Supervision, Inspection and Quarantine of the People's Republic of China. 2017. Identification Method for El Niño/La Niña Events, GB/T 33666-2017. Beijing: Standards Press of China, 1-6 (in Chinese)

黄荣辉,蔡榕硕,陈际龙等. 2006. 我国旱涝气候灾害的年代际变化及其与东亚气候系统变化的关系. 大气科学,30(5):730-743. Huang R H, Cai R S, Chen J L, et al. 2006. Interdecadal variations of drought and flooding disasters in China and their association with the East Asian climate system. Chinese J Atmos Sci, 30(5): 730-743 (in Chinese)

金祖辉,陶诗言. 1999. ENSO循环与中国东部地区夏季和冬季降水关系的研究. 大气科学,23(6):663-672. Jin Z H, Tao S Y. 1999. A study on the relationships between ENSO cycle and rainfalls during summer and winter in Eastern China. Chinese J Atmos Sci, 23(6): 663-672 (in Chinese)

李海燕,张文君,何金海. 2016. ENSO及其组合模态对中国东部各季节降水的影响. 气象学报,74(3):322-334. Li H Y, Zhang W J, He J H. 2016. Influences of ENSO and its combination mode on seasonal precipitation over eastern China. Acta Meteor Sinica, 74(3): 322-334 (in Chinese)

李威,翟盘茂. 2009. 中国极端强降水日数与ENSO的关系. 气候变化研究进展,5(6):336-342. Li W, Zhai P M. 2009. Relationship between ENSO and frequency of extreme precipitation days in China. Adv Climate Change Res, 5(6): 336-342 (in Chinese)

刘永强,丁一汇. 1995. ENSO事件对我国季节降水和温度的影响. 大气科学,19(2):200-208. Liu Y Q, Ding Y H. 1995. Reappraisal of the influence of ENSO events on seasonal precipitation

and temperature in China. Chinese J Atmos Sci, 19(2): 200-208 (in Chinese)

任国玉，封国林，严中伟. 2010. 中国极端气候变化观测研究回顾与展望. 气候与环境研究，15(4)：337-353. Ren G Y, Feng G L, Yan Z W. 2010. Progresses in observation studies of climate extremes and changes in mainland China. Climatic Environ Res, 15(4): 337-353 (in Chinese)

任宏利，王润，翟盘茂等. 2017. 超强厄尔尼诺事件海洋学特征分析与预测回顾. 气象学报，75(1)：1-18. Ren H L, Wang R, Zhai P M, et al. 2017. Upper-ocean dynamical features and prediction of the super El Niño in 2015/2016: A comparison with 1982/1983 and 1997/1998. Acta Meteor Sinica, 75(1): 1-18 (in Chinese)

邵勰，周兵. 2016. 2015/2016 年超强厄尔尼诺事件气候监测及诊断分析. 气象，42(5)：540-547. Shao X, Zhou B. 2016. Monitoring and diagnosis of the 2015/2016 super El Niño event. Meteor Mon, 42(5): 540-547 (in Chinese)

陶诗言，张庆云. 1998. 亚洲冬夏季风对 ENSO 事件的响应. 大气科学，22(4)：399-407. Tao S Y, Zhang Q Y. 1998. Response of the Asian winter and summer monsoon to ENSO events. Sci Atmos Sinica, 22(4): 399-407 (in Chinese)

王苗，郭品文，邬昀. 2013. ENSO 对我国东部极端降水的季节影响. 长江流域资源与环境，22(6)：808-816. Wang M, Guo P W, Wu Y. 2013. Impact of ENSO on the seasonal extreme rainfall over eastern China. Resour Environ Yangtze Basin, 22(6): 808-816 (in Chinese)

袁媛，高辉，贾小龙等. 2016. 2014—2016 年超强厄尔尼诺事件的气候影响. 气象，42(5)：532-539. Yuan Y, Gao H, Jia X L, et al. 2016. Influences of the 2014－2016 super El Niño event on climate. Meteor Mon, 42(5): 532-539 (in Chinese)

翟盘茂，潘晓华. 2003. 中国北方近 50 年温度和降水极端事件变化. 地理学报，58(S1)：1-10. Zhai P M, Pan X H. 2003. Change in extreme temperature and precipitation over northern China during the second half of the 20th century. Acta Geogr Sinica, 58(S1): 1-10 (in Chinese)

翟盘茂，余荣，郭艳君等. 2016. 2015/2016 年强厄尔尼诺过程及其对全球和中国气候的主要影响. 气象学报，74(3)：309-321. Zhai P M, Yu R, Guo Y J, et al. 2016. The strong El Niño in 2015/2016 and its dominant impacts on global and China's climate. Acta Meteor Sinica, 74(3): 309-321 (in Chinese)

张文君，耿新. 2016. 2015/2016 年超强 El Niño 局地海气特征及其特殊性. 大气科学学报，39(6)：778-787. Zhang W J, Geng X. 2016. Characteristics and particularity of local air-sea processes for the 2015/2016 super El Niño event. Trans Atmos Sci, 39(6): 778-787 (in Chinese)

赵振国. 1996. 厄尔尼诺现象对北半球大气环流和中国降水的影响. 大气科学，20(4)：422-428. Zhao Z G. 1996. Impact of El Niño events on atmospheric circulations in the northern hemisphere and precipitation in China. Sci Atmos Sinica, 20(4): 422-428 (in Chinese)

Chan J C L, Zhou W. 2005. PDO, ENSO and the early summer monsoon rainfall over south China. Geophys Res Lett, 32(8): L08810

Chen L, Li T, Behera S K, et al. 2016. Distinctive precursory air-sea signals between regular and super El Niños. Adv Atmos Sci, 33(8): 996-1004

Dee D P, Uppala S M, Simmons A J, et al. 2011. The ERA-Interim reanalysis: Configuration and performance of the data assimilation system. Quart J Roy Meteor Soc, 137(656): 553-597

Gong D Y, Wang S W. 1999. Impacts of ENSO on rainfall of global land and China. Chin Sci Bull, 44(9): 852-857

Hsu P C, Lee J Y, Ha K J. 2016. Influence of boreal summer intraseasonal oscillation on rainfall extremes in southern China. Int J Climatol, 36(3): 1403-1412

Huang R H, Wu Y F. 1989. The influence of ENSO on the summer climate change in China and its mechanism. Adv Atmos Sci, 6(1): 21-32

Kalnay E, Kanamitsu M, Kistler R, et al. 1996. The NCEP/NCAR 40-year reanalysis project. Bull Amer Meteor Soc, 77(3): 437-472

Latif M, Semenov V A, Park W. 2015. Super El Niños in response to global warming in a climate model. Climatic Change, 132(4): 489-500

Lee S. 2012. Testing of the tropically excited arctic warming mechanism (TEAM) with traditional El Niño and La Niña. J Climate, 25(12): 4015-4022

Liu B Q, Zhu C W, Su J Z, et al. 2018. Why was the western Pacific subtropical anticyclone weaker in late summer after the 2015/2016 super El Niño? . Int J Climatol, 38(1): 55-65

Lu R Y, Oh J H, Kim B J. 2002. A teleconnection pattern in upper-level meridional wind over the North African and Eurasian continent in summer. Tellus A, 54(1): 44-55

O'Gorman P A, Schneider T. 2009. The physical basis for increases in precipitation extremes in simulations of 21st-century climate change. Proc Natl Acad Sci USA, 106(35): 14773-14777

Philander S G H. 1983. El Niño southern oscillation phenomena. Nature, 302(5906): 295-301

Rao J, Ren R. 2017. Parallel comparison of the 1982/83, 1997/98 and 2015/16 super El Niños and their effects on the extratropical stratosphere. Adv Atmos Sci, 34(9): 1121-1133

Rasmusson E M, Carpenter T H. 1982. Variations in tropical sea surface temperature and surface wind fields associated with the Southern Oscillation/El Niño. Mon Wea Rev, 110(5): 354-384

Rayner N A, Parker D E, Horton E B, et al. 2003. Global analyses of sea surface temperature, sea ice, and night marine air temperature since the late nineteenth century. J Geophys Res Atmos, 108(D14): 4407

Ren H L, Zuo J Q, Jin F F, et al. 2016. ENSO and annual cycle interaction: The combination mode representation in CMIP5 models. Climate Dyn, 46(11-12): 3753-3765

Ren H L, Ren P F. 2017. Impact of Madden-Julian Oscillation upon winter extreme rainfall in southern China: Observations and predictability in CFSv2. Atmosphere, 8(10): 192

Renwick J A, Wallace J M. 1996. Relationships between North Pacific wintertime blocking, El Niño, and the PNA pattern. Mon Wea Rev, 124(9): 2071-2076

Stuecker M F, Timmermann A, Jin F F, et al. 2013. A combination mode of the annual cycle and the El Niño/Southern Oscillation. Nat Geosci, 6(7): 540-544

Stuecker M F, Jin F F, Timmermann A. 2015a. El Niño-Southern Oscillation frequency cascade. Proc Natl Acad Sci USA, 112(44): 13490-13495

Stuecker M F, Jin F F, Timmermann A, et al. 2015b. Combination mode dynamics of the anomalous Northwest Pacific anticyclone. J Climate, 28(3): 1093-1111

Trenberth K E, Branstator G W, Karoly D, et al. 1998. Progress during TOGA in understanding and modeling global teleconnections associated with tropical sea surface temperatures. J Geophys Res, 103(C7): 14291-14324

Wallace J M, Rasmusson E M, Mitchell T P, et al. 1998. On the structure and evolution of ENSO-related climate variability in the tropical Pacific: Lessons from TOGA. J Geophys Res, 103(C7): 14241-14260

Wang B, Wu R G, Fu X H. 2000. Pacific-East Asian teleconnection: How does ENSO affect East Asian climate?. J Climate, 13(9): 1517-1536

Xavier P, Rahmat R, Cheong W K, et al. 2014. Influence of Madden-Julian Oscillation on Southeast Asia rainfall extremes: Observations and predictability. Geophys Res Lett, 41(12): 4406-4412

Xiao M Z, Zhang Q, Singh V P. 2017. Spatiotemporal variations of extreme precipitation regimes during 1961 – 2010 and possible teleconnections with climate indices across China. Int J Climatol, 37(1): 468-479

Zhai P M, Zhang X B, Wan H, et al. 2005. Trends in total precipitation and frequency of daily precipitation extremes over China. J Climate, 18(7): 1096-1108

Zhang R H, Sumi A, Kimoto M. 1996. Impact of El Niño on the East Asian monsoon: A diagnostic study of the '86/87 and '91/92 events. J Meteor Soc Japan, 74(1): 49-62

Zhang R H, Sumi A, Kimoto M. 1999. A diagnostic study of the impact of El Niño on the precipitation in China. Adv Atmos Sci, 16(2): 229-241

Zhang R H, Sumi A. 2002. Moisture circulation over East Asia during El Niño episode in northern winter, spring and autumn. J Meteor Soc Japan, 80(2): 213-227

Zhang W J, Jin F F, Stuecker M F, et al. 2016a. Unraveling El Niño's impact on the East Asian monsoon and Yangtze River summer flooding. Geophys Res Lett, 43(21): 11375-11382

Zhang W J, Li H Y, Stuecker M F, et al. 2016b. A new understanding of El Niño's impact over East Asia: Dominance of the ENSO combination mode. J Climate, 29(12): 4347-4359

Received: 8 January 2018 | Revised: 28 August 2018 | Accepted: 16 September 2018 | Published on: 12 November 2018

DOI: 10.1002/qj.3405

RESEARCH ARTICLE

Quarterly Journal of the Royal Meteorological Society RMetS

Evaluation and statistical downscaling of East Asian summer monsoon forecasting in BCC and MOHC seasonal prediction systems

Ying Liu[1,2] | Hong-Li Ren[1,3] | Adam A. Scaife[4,5] | Chaofan Li[6]

[1]Laboratory for Climate Studies and CMA-NJU Joint Laboratory for Climate Prediction Studies, National Climate Center, China Meteorological Administration, Beijing, China
[2]Collaborative Innovation Center on Forecast and Evaluation of Meteorological Disasters, Nanjing University of Information Science and Technology, Nanjing, China
[3]Department of Atmospheric Science, School of Environmental Studies, China University of Geoscience, Wuhan, China
[4]Met Office Hadley Centre, Exeter, UK
[5]College of Engineering, Mathematics and Physical Sciences, Exeter University, Devon, UK
[6]Center for Monsoon System Research, Institute of Atmospheric Physics, Chinese Academy of Sciences, Beijing, China

Correspondence
Hong-Li Ren, Laboratory for Climate Studies, National Climate Center, China Meteorological Administration, Beijing 100081, China.
Email: renhl@cma.gov.cn

Funding information
National Key Research and Development Program on monitoring, Early Warning and Prevention of Major Natural Disaster, 2017YFC1502302. National Natural Science Foundation grant of China, 41730964, 41405080. UK–China Research & Innovation Partnership Fund through the Met Office Climate Science for Service Partnership (CSSP) China.

In seasonal climate predictions, the East Asian summer monsoon (EASM) is still a challenge, in spite of the wide usage of coupled climate models. Therefore, in this article the predictability of the monsoon including the atmospheric circulation and precipitation anomalies is investigated, based on the reforecast data during 1992–2011 in two coupled prediction systems: GloSea5 from the Met Office Hadley Centre (MOHC) and BCC_CSM1.1m from the Beijing Climate Center (BCC). The results show that the interannual variability of 850 hPa zonal wind over East Asia and the northwest Pacific can be well reproduced, and the prediction skill is significant in both systems. The Philippine anticyclone is highly predictable over the tropical northwest Pacific, and it transfers the predictable signals from the winter El Niño-Southern Oscillation (ENSO) into the climate prediction in East Asia and rainfall prediction in the Yangtze River basin. Two dynamical indices of the EASM show that the prediction skills in these two systems are comparable. BCC_CSM1.1m tends to overestimate the coupling between the monsoon and ENSO, while GloSea5 shows a similar magnitude to the observations. Besides, a simple statistical downscaling method is adopted in this article based on the predictable circulation data, which provides an efficient tool to improve the raw rainfall forecast skill over China.

KEYWORDS
BCC_CSM1.1m, East Asian summer monsoon, GloSea5, model evaluation, seasonal forecast, statistical downscaling

1 | INTRODUCTION

As an important component of the climate, the East Asian summer monsoon (EASM) has a major impact on the climate and weather in East Asia and even around the globe (e.g. Lau and Li, 1984; Huang and Sun, 1992; Lau, 1992; Wang, 2001). EASM is often associated with extreme events in East Asia, such as floods, droughts and heatwaves. As persistent heavy rainfall events often occur after the onset and advance of the EASM, it is important to better understand the seasonal predictability of the EASM climate, particularly the precipitation.

In recent decades, climate prediction systems have been much improved in many aspects, such as the resolution, initial condition, ensemble size and model physics, as well as ensemble size. These improvements are mainly attributed to the improved computing resources, and they have facilitated coupled general circulation models (CGCMs) to be a standard tool for seasonal climate prediction (Yang *et al.,* 2008; Weisheimer *et al.,* 2009; Zhu and Shukla, 2013; Ma and Wang, 2014; Tompkins *et al.,* 2017; Zhu *et al.,* 2017). However, the prediction skill of the EASM climate depends on the models and monsoon index selections. For example, the ENSEMBLES, DEMETER, BCC_CSM1.1m, CFS and

 © 2018 Royal Meteorological Society

POAMA have relatively similar skill (e.g. Wang *et al.,* 2009; Li *et al.,* 2012; Liu *et al.,* 2015) when the interannual EASM index defined by Wang and Fan (1999) is employed. But, the prediction skill for summer precipitation over East Asia and the northwest Pacific shows differences in different models (Lee *et al.,* 2011; Li *et al.,* 2012), and has only recently been demonstrated in any system (Li *et al.,* 2016). Indeed, a large number of climate model prediction systems from the Climate Prediction and its Application to Society (CliPAS) project showed relatively low skill in predicting summer rainfall anomalies in the East Asian monsoon area (Wang *et al.,* 2009). Li *et al.* (2012) investigated the interannual temporal correlation coefficients (TCCs) of summer rainfall and 850 hPa zonal wind anomalies from ensemble prediction during 1960–2005. They showed a positive anomaly correlation of 850 hPa zonal wind over south China, but had limited skill in showing rainfall and large intermodal differences. Similarly, the multi-model ensemble (MME) mean of CFS and POAMA exhibited positive correlation coefficients of 850 hPa zonal wind over most of east China (Lee *et al.,* 2011).

The prediction of EASM climate attracts special concern in China every year, because of its potentially serious impact on agriculture, industry and lives. Although the current dynamical climate prediction models have advanced from the uncoupled two-tier prediction approach (Zeng *et al.,* 1990; Zhou *et al.,* 1998; Zhang *et al.,* 2006) to the coupled one-tier approach (Ding *et al.,* 2004; Li *et al.*, 2005; Liu and Wang, 2015), the prediction skill of Asian climate remains a big challenge due to the low predictability in dynamical models. Alternative methods, such as statistical modelling and statistical downscaling, have proved to be useful in recent years (Ding *et al.,* 1998; Ren and Chou, 2006; 2007; Fan *et al.,* 2008; Sun and Chen, 2012; Liu and Ren, 2015). Meanwhile, dynamical prediction methods have also been improved in initialization schemes, model formulation and parametrization, ensemble methods, assimilation and so on (Zhang, 2011; Vecchi *et al.,* 2013; Wu *et al.*, 2013; Zhu *et al.,* 2013; Yang *et al.,* 2015).

BCC_CSM1.1m is the 1.1 version of the Beijing Climate Center (BCC) Climate System Model, which products the operational seasonal climate predictions in China (Wu *et al.*, 2013). BCC_CSM1.1m shows reasonable skill in Asian summer monsoon predictions (Ren *et al.,* 2017), but the correlation of rainfall is positive only in the Yangtze River Valley and north China, even at 0 month lead time (i.e. started on 1 June) (Liu *et al.,* 2015). The prediction skill of winter precipitation over south China is also limited (Lu *et al.,* 2017). The GloSea5 forecast system of the Met Office (MacLachlan *et al.,* 2015) has demonstrated some skill in predicting the EASM rainfall and winter rainfall (Li *et al.,* 2016; Johnson *et al.,* 2017; Lu *et al.,* 2018; Wan *et al.,* 2018).

In the present study, the prediction skill of the East Asian summer monsoon in GloSea5 is determined, and a comparison with BCC_CSM1.1m predictions is made. An attempt has also been made to improve the precipitation prediction skill in China based on statistical downscaling. The remainder of the article is organized as follows. Data and verification methods are introduced in section 2. Results are presented in sections 3 and 4. Statistical downscaling is applied to model predictions in section 5. Summary and discussions are given in section 6.

2 | DATA AND METHODS

2.1 | Observational and hindcast datasets

GloSea5 uses the HadGEM3 model that couples the Met Office Unified Model atmosphere component, the Nucleus for European Modelling of the Ocean (NEMO) model and the Los Alamos sea ice model (CICE) with the Ocean Atmosphere Sea Ice Soil (OASIS) coupler. GloSea5 has a horizontal resolution of 0.56° latitude by 0.83° longitude with 85 vertical levels, and NEMO is used on a tripolar grid with a nominal resolution of 0.25° and 75 vertical levels (MacLachlan *et al.,* 2015). The European Centre for Medium-range Weather Forecasts (ECMWF) reanalysis Interim data is used to initialize the atmosphere and land surface (Rawlins *et al.,* 2007; Weedon *et al.,* 2011). The Global Forecast Ocean Assimilation Model (Blockley *et al.,* 2013), which supplied a 23-year (1989–2011) reanalysis, is used to initialize the ocean and sea ice components of GloSea5. The June–August (JJA)-mean predictions used here are initialized on 25 April, 1 May and 9 May with 24 members (eight members per start date) for each summer during 1992–2011.

The BCC_CSM1.1m is the 1.1 version of a seasonal climate prediction system developed at the BCC, China Meteorological Administration (CMA). The atmospheric component of the model is the BCC Atmospheric General Model with a T106 horizontal resolution and 26 levels in a hybrid sigma/pressure vertical direction (Wu *et al.,* 2010). The land component is the 1.0 version of the BCC Atmosphere and Vegetation Interaction Model. The ocean and sea ice components are z-coordinate Modular Ocean Models version 4 and Sea Ice Simulator, respectively, which are developed by the Geophysical Fluid Dynamics Laboratory (Wu *et al.*, 2013). The hindcasts are started on the 10th day of each calendar month from 1991 to 2013 and end after a 9-month forecast integration with 24 members. For the JJA prediction, 15 members are produced by a combination of lagged average forecasting on five atmospheric (i.e. 27 April, 28 April, 29 April, 30 April and 1 May) and three oceanic (i.e. 29 April, 30 April and 1 May) initial starts, and nine members are produced by singular vector perturbation of sea-surface temperature (SST). The National Centers for Environmental Prediction (NCEP) Reanalysis is utilized as the atmospheric initial condition, and sea temperature and salinity from the NCEP Global Oceanic Data Assimilation System is used to initiate the oceanic conditions (Liu *et al.,* 2015). All the data from the above two models are interpolated to the same resolution (i.e. 2.5° × 2.5°) as the NCEP Reanalysis 1.

Atmospheric circulation of observation/analysis is obtained from the NCEP/NCAR Reanalysis 1 (Kalnay *et al.,* 1996), and the monthly precipitation data are obtained from Global Precipitation Climatology Project (GPCP) Version 2.2 (Adler *et al.,* 2003) and a dataset of 160 standard stations in China from BCC/CMA. The monthly average SST, composed of a 1° latitude by 1° longitude grid in a globally complete dataset, is obtained from the NOAA Optimum Interpolation SST V2 (OISST.V2: Reynolds *et al.,* 2002).

The data analysed here cover 1992–2011. The forecasts of the JJA-mean initialized in early May are defined as 1-month lead forecasts. The MME mean is calculated through a simple composite by applying equal weight to each individual member of GloSea5 and BCC_CSM1.1m.

2.2 | Methods

The prediction skill score used in this study is the TCC obtained by calculating correlation coefficients between observed and predicted values during 1992–2011.

With a chaotic nature, the intrinsic variability of atmospheric circulation inherently limits seasonal climate predictability. Therefore, the signal-to-noise ratio is used in the dynamical ensemble prediction to assess the potential for predicting seasonal climate (Rowell, 1998; Kumar and Shukla, 2006; Kumar *et al.,* 2007). The estimated total variance (σ^2_{TOT}) of one variable is divided into two parts: signal variance (σ^2_{S}) and noise variance (σ^2_{N}) (Rowell *et al.,* 1995; Rowell, 1998; Siegert *et al.,* 2016). The noise variance can be expressed as

$$\sigma^2_{\mathrm{N}} = \frac{1}{N(n-1)} \sum_{i=1}^{N} \sum_{j=1}^{n} (x_{ij} - \overline{x}_i)^2,$$

where x is the variable, i is the individual year, and j is the ensemble member. N and n indicate the total number of years and ensemble members respectively. $\overline{x_i}$ is the ensemble mean. Signal (external) variance is obtained from the mean square of the deviation of each year's ensemble mean from the model climatological mean. The formulae are as follows:

$$\sigma^2_{\mathrm{S}} = \sigma^2_{\mathrm{EN}} - \frac{1}{n}\sigma^2_{\mathrm{N}},$$

$$\text{and } \sigma^2_{\mathrm{EN}} = \frac{1}{N-1} \sum_{i=1}^{N} (\overline{x_i} - \overline{\overline{x}})^2,$$

where $\overline{\overline{x}}$ is the climatological mean and $\overline{\overline{x}} = \frac{1}{Nn} \sum_{i=1}^{N} \sum_{j=1}^{n} x_{ij}$ (Lee *et al.,* 2011; Li *et al.,* 2014). The potential predictability of one variable can be defined as the ratio of signal variance to total variance ($\sigma^2_{\mathrm{S}}/(\sigma^2_{\mathrm{S}}+\sigma^2_{\mathrm{N}})$) (e.g. Eade *et al.,* 2014; Kumar *et al.,* 2014), which is a little different from that defined by Johnson *et al.* (2017).

3 | EVALUATIONS OF PREDICTION SKILL IN JJA 850 HPA ZONAL WIND AND EASM

The pattern of significant correlation skill in 850 hPa zonal wind shows a northeast–southwest distribution (Figure 1). Other CGCMs have similar results (Li *et al.,* 2012), and regions exceeding the 1% confidence level extend from the tropical Pacific to the northwest Pacific and East Asia (Figure 1). In detail, GloSea5 and the MME have higher interannual correlation skill than the BCC_CSM1.1m. High correlations can be found mainly over the tropical northwest and southeast Pacific, where the TCC exceeds 0.8.

Then, the interannual variability of 850 hPa zonal wind was examined, which was large over the northwest Pacific both in observations and models. The model ensemble members have comparable interannual variability to observations over East Asia (figure not shown). Figure 2 shows that the potential predictability (i.e. ratio of signal variance to total variance) of 850 hPa zonal wind in GloSea5 and BCC_CSM1.1m could reach ∼0.9 over the tropical region. A large prediction signal is centred over the tropical regions in both models, which is consistent with the signal-to-noise ratio of zonal vertical wind shear in Johnson *et al.* (2017), indicating that the main source of predictability of 850 hPa zonal wind is located there. On the other hand, the potential predictability of the lower-tropospheric zonal wind over East Asia and the northwest Pacific is ∼0.4 or less, which suggests that the prediction skill is lower over land.

Next, the EASM indices (EASMI) from Wang and Fan (1999) (EASMI-W99) and Zhang *et al.* (2003) (EASMI-Z03) are calculated. The EASMI-W99 is defined as the difference of the 850 hPa zonal wind averaged between (5–15°N, 90–130°E) and (22.5–32.5°N, 110–140°E). A positive (negative) EASMI-W99 represents an anomalous cyclonic (anticyclonic) circulation over the northwest Pacific. Thus it has a close relationship with East Asian climate. The EASMI-Z03, which represents the interannual variability of low-level wind over East Asia, is defined as the difference of the 850 hPa zonal wind averaged between the East Asian tropical monsoon trough region (10–20°N, 100–150°E) and the East Asian subtropical region (25–35°N, 110–150°E). A positive (negative) EASMI-Z03 means a strong (weak) monsoon year. The region where EASMI-Z03 has been defined is farther north than that in EASMI-W99.

Figure 3 shows the time series for the JJA-mean normalized EASMI-W99 and EASMI-Z03 obtained from observations, GloSea5, BCC_CSM1.1m, and their MME predictions. It is found that the models and MME can well predict the interannual variation of the EASMI-W99 and EASMI-Z03. The correlation coefficients between MME means (GloSea5; BCC_CSM1.1m) and observations are 0.86 (0.85; 0.68) and 0.83 (0.79; 0.76) for EASMI-W99 and EASMI-Z03 respectively. Especially in 1998, following the El Niño peak, the weak EASM indices resulted in the above-normal precipitation in the Yangtze River Valley of China (Zhang and Tao, 1998; Gao *et al.,* 2014), and individual models and MME both reproduced the significant anomaly seen in observations. It is well known that the EASM and associated climate are affected by ENSO with a time lag, which is significant in the ENSO decaying phase (Wang *et al.,* 2000). Thus,

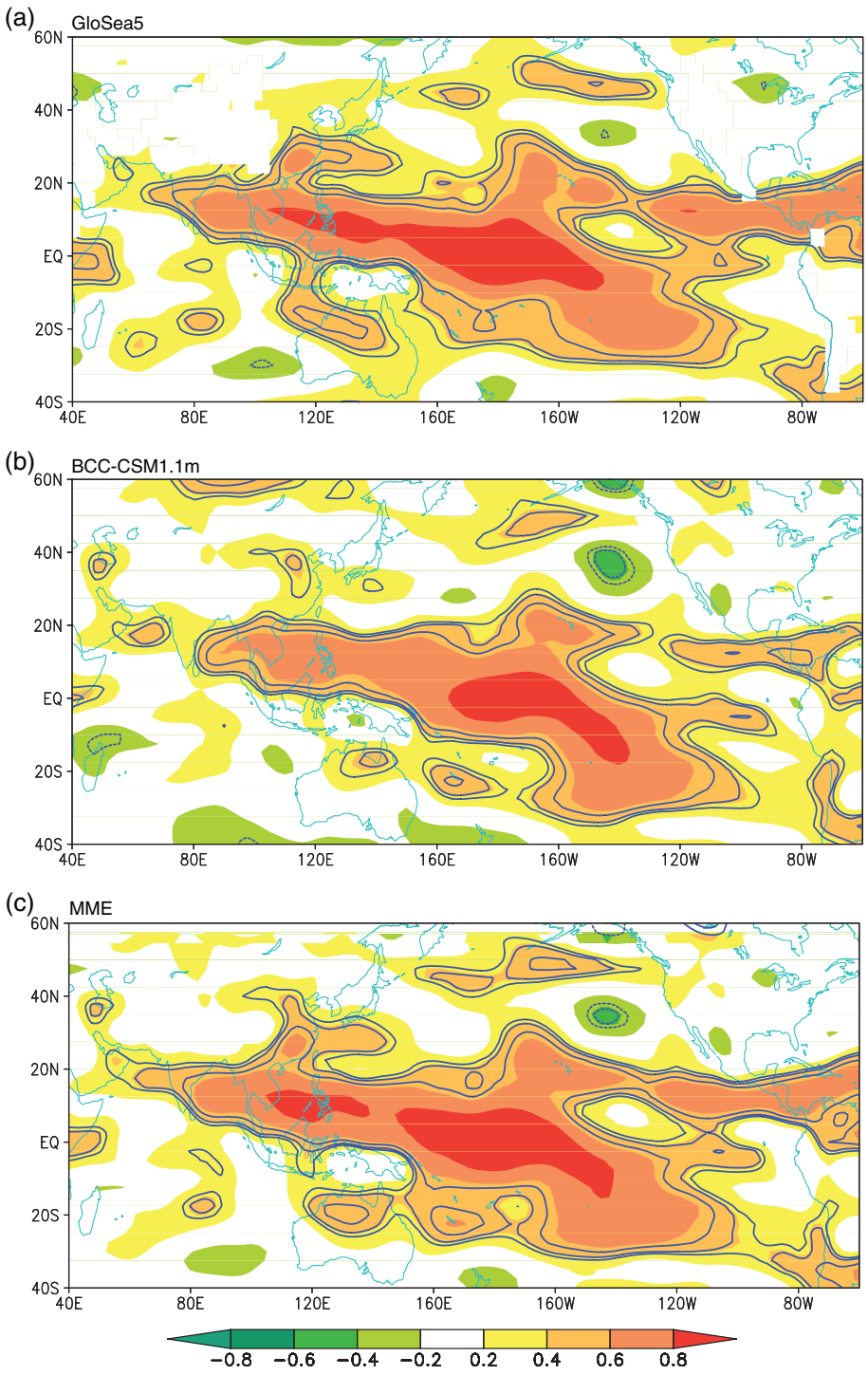

FIGURE 1 Temporal correlation coefficients for 1992–2011 JJA-mean U850 between observation and (a) GloSea5, (b) BCC_CSM1.1 m, (c) the ensemble mean (MME). The blue contours represent the correlation coefficients at 90, 95 and 99% significance level, respectively

the lagged relationship between EASMIs and the preceding Niño3.4 index for observations and model predictions are briefly investigated in longer-range forecasts. In GloSea5, winter forecasts were initialized on 25 October, 1 November and 9 November with 24 members (eight members per start date). In BCC_CSM1.1m, winter forecasts were initialized by a combination of lagged average of five atmospheric initializations on 28 October, 29 October, 30 October, 31 October and 1 November, and three oceanic initializations on 30 October, 31 October and 1 November to give 15 members. The winter Niño3.4 SST index for the MME was computed based on the ensemble mean of all the members from GloSea5 and BCC_CSM1.1m.

As shown in Figure 4, the observational JJA EASM indices (i.e. EASMI-W99 and EASMI-Z03) have significant negative correlations with the preceding winter Niño3.4 index. For the model ensemble members, almost all the correlations are significantly negative and the average correlations are beyond

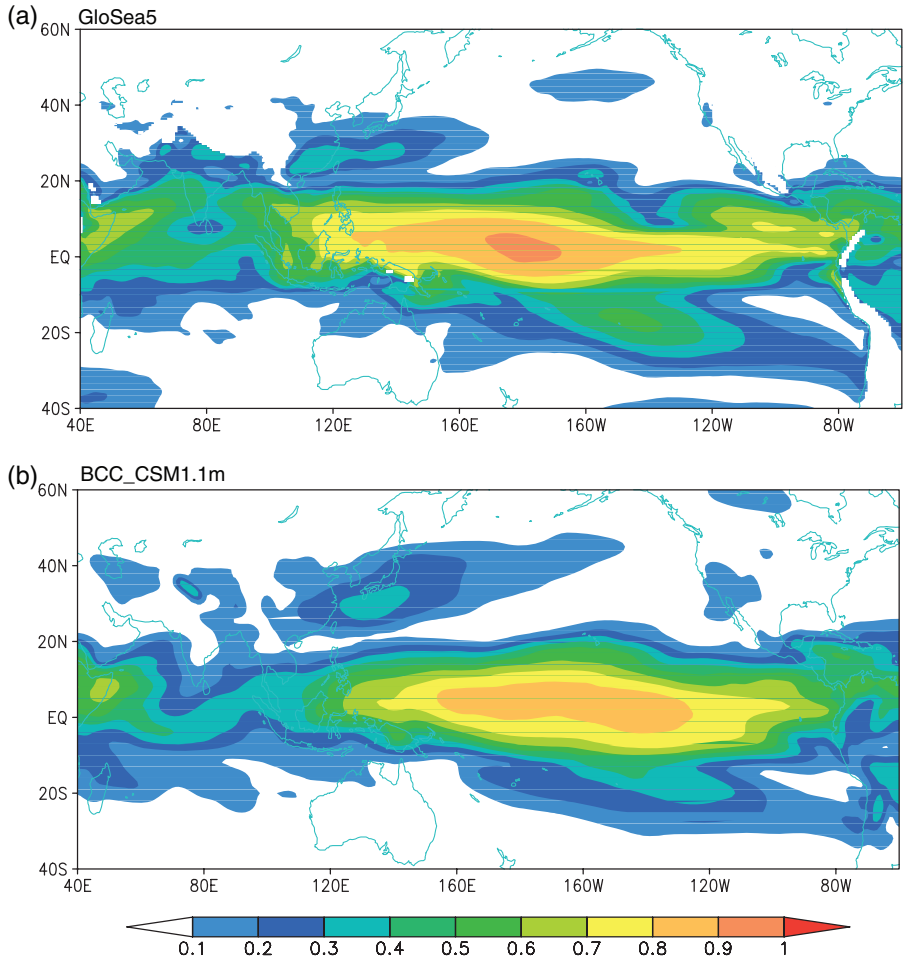

FIGURE 2 Potential predictability of JJA-mean 850 hPa zonal wind between (a) GloSea5 (24 members) or (b) BCC_CSM1.1m (24 members) and observations

the 95% confidence level (−0.42). It implies that the previous winter ENSO and following EASM for the two indices can be well captured by GloSea5 and BCC_CSM1.1m as well as their ensemble mean at 1-month lead. Compared with the observations, BCC_CSM1.1m does overestimate as shown by Liu *et al.* (2015).

The patterns of SST anomalies regressed onto the EASMIs, for both the observation and predictions, are shown in Figure 5. It can be seen that for EASMI-W99 and EASMI-Z03, the regressed patterns in the eastern tropical Pacific are quite similar to the typical eastern Pacific (EP) ENSO prediction (e.g. Ren and Jin, 2011), but the sign is reversed. The significantly negative regression values are located in the tropical central-eastern Pacific and the western Indian Ocean, and the positive regressions are located in the northwest and South Pacific (Figures 5a,b). Both models and their ensemble at 1-month lead appear to be capable of reproducing the observed regression patterns between the predicted EASM indices and the predicted surface temperature initialized in November (Figure 5), and similar results could be found in Lee *et al.* (2011). GloSea5 reproduces the significant regression regions except in the South Pacific (Figure 5c,d), whereas BCC_CSM1.1m overestimates the relationship between EASM and ENSO over the tropical Pacific. This result is consistent with Figure 4, in which BCC_CSM1.1m tends to exaggerate the negative relationship between the Niño3.4 index and EASMIs. And there is a horseshoe pattern in the extratropical Pacific (Figure 5e,f).

In general, El Niño tends to cause a weak EASM, while La Niña always leads to a strong EASM (Wang *et al.,* 1999). For example, when the super-El Niño occurred in 1997/1998, the observed negative correlation between ENSO and EASM is well predicted in GloSea5 and BCC_CSM1.1m. The ENSEMBLES data also present a good prediction of dynamical EASM indices in 1998 (Li *et al.,* 2014). The EASM can be affected by the central and eastern Pacific SST anomalies through the anomalous anticyclone over the Philippine Sea (the Philippine anticyclone), which can maintain itself for two or three seasons from winter to summer due to a positive feedback between atmospheric Rossby waves and the west Pacific warm pool (Wang *et al.,* 2000; Wu and Wang, 2002). Moreover, the anomalous high SST in the eastern tropical Pacific acts to suppress convective activity in the western tropical Pacific, directly influencing the monsoonal circulation over the northwest Pacific and East Asia (Zhang *et al.,* 1996; Chang *et al.,* 2000). In summary, the preceding winter ENSO signal is a major source in predicting the EASM indices, and the two forecast systems used here can reproduce

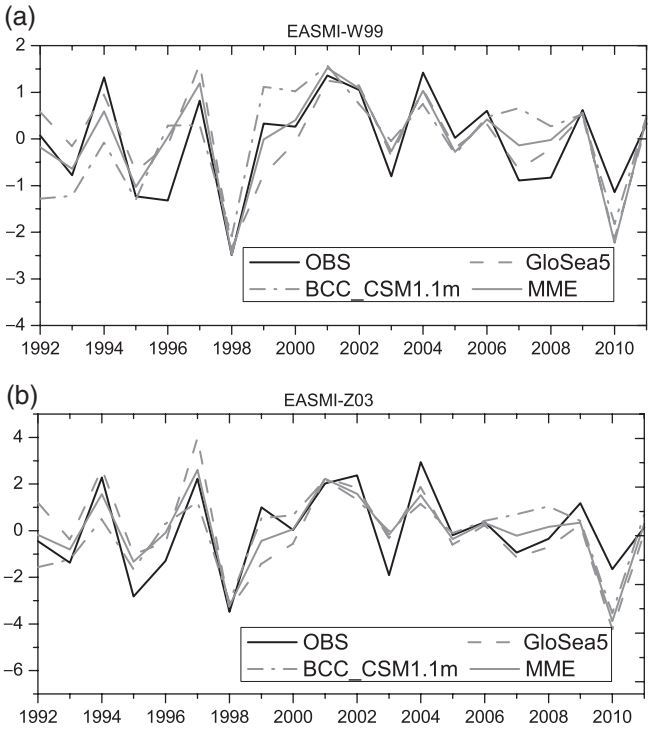

FIGURE 3 Time series of summer-mean East Asian summer monsoon indices during 1992–2011. (a) EASMI-W99, (b) EASMI-Z03.The CGCM data initiates from May for the JJA prediction. Correlation coefficients for EASMI-W99 and EASMI-Z03 are 0.86 (0.85; 0.68) and 0.83 (0.79; 0.76) in MME (GloSea5; BCC_CSM1.1 m)

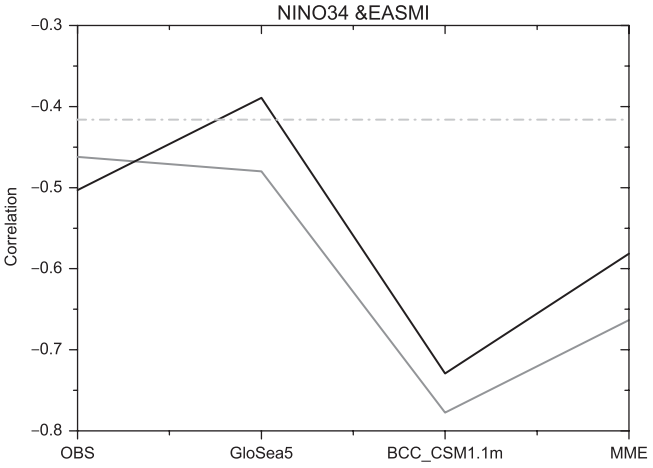

FIGURE 4 Correlation coefficients of previous winter Niño3.4 SST index with the JJA EASMI. Black and grey lines are correlation coefficients between Niño3.4 SST index in previous winter and JJA EASMI-Z03 or EASMI-W99. The grey dash-dot line represents statistical correlation at 95% significance level

this mechanism, and can give comparable prediction skill and dynamical measures of the EASM.

The Western Pacific Subtropical High (WPSH) has been identified as an important component of the EASM system (Lau and Li, 1984; Tao and Chen, 1987; Huang and Wu, 1989; Ding, 1994). The seasonal variation of WPSH is closely related to the onset and withdrawal of the EASM (Yang *et al.,* 2017). The interannual variability of large-scale EASM frontal zones is dominated by the position, shape and strength of the WPSH (Zhou and Yu, 2005). The observed 850 hPa zonal wind has large interannual anomalies that overlap with the equatorial Pacific, and the standard deviation could reach around 1.4 m/s over the west North Pacific and the coast of East Asia. The general features of observed interannual variability are well captured by the models, except for lower standard deviation over East Asia and the northwest Pacific, but the deficiency is less than 0.5 m/s (figure not shown). It implies that GloSea5, BCC_CSM1.1m and the MME are skilled in predicting the WPSH to some extent. Zhou *et al.* (2009) have demonstrated that the SST anomalies in the Indian Ocean–west Pacific (IWP) have a significant impact on the zonal movement of the WPSH. They found that the IWP SST could influence the Walker circulation, with reduced convection in the tropical central and eastern Pacific modulating the WPSH. In Figure 5, the models could reproduce the significant response of EASM to the IWP SST, with relatively higher regressions in GloSea5 and lower ones in BCC_CSM1.1m. This indicates that both models could predict the WPSH well, and it is another important source of predictability in predicting the EASM indices.

4 | EVALUATION OF PREDICTION SKILL IN JJA PRECIPITATION

In East Asia, precipitation is directly influenced by the EASM. The patterns of correlation skill between observations and model predictions of precipitation are shown in Figure 6. Overall, over the tropical Pacific and Maritime Continent, GloSea5, BCC_CSM1.1m and the MME have similar patterns of significant positive correlations. It is consistent with results of other models (e.g. Lee *et al.,* 2011). In GloSea5, the significant positive correlations extend westwards over land. The JJA precipitation prediction skill over most parts of the East Asian continent, including China, is relatively low in spite of the good performance in 850 hPa zonal wind and EASM (Figures 1 and 3). In contrast, the TCC prediction skill of precipitation over the regions with defined EASM indices are relatively high, indicating that the precipitation directly influenced by EASM can be well captured by the models. The correlations are mostly negative over north China in both models, although GloSea5 has larger areas of positive correlation than BCC_CSM1.1m. The latter performs better in both northeast and northwest China. Note that, compared with the two models, MME has modest correlation skill (Figure 6).

We also checked the interannual variability of the JJA precipitation in terms of ensemble mean standard deviations (figure not shown), and found that the interannual variability in two models over East Asia was at least 1.0 mm/day less than observations, due to the limited predictability of the ensemble mean. Presumably, the relatively small amplitude of JJA precipitation predictions in the models had reduced prediction skill in East Asia, especially in China. As the EASM governs summer rainfall in summer, only variations in the

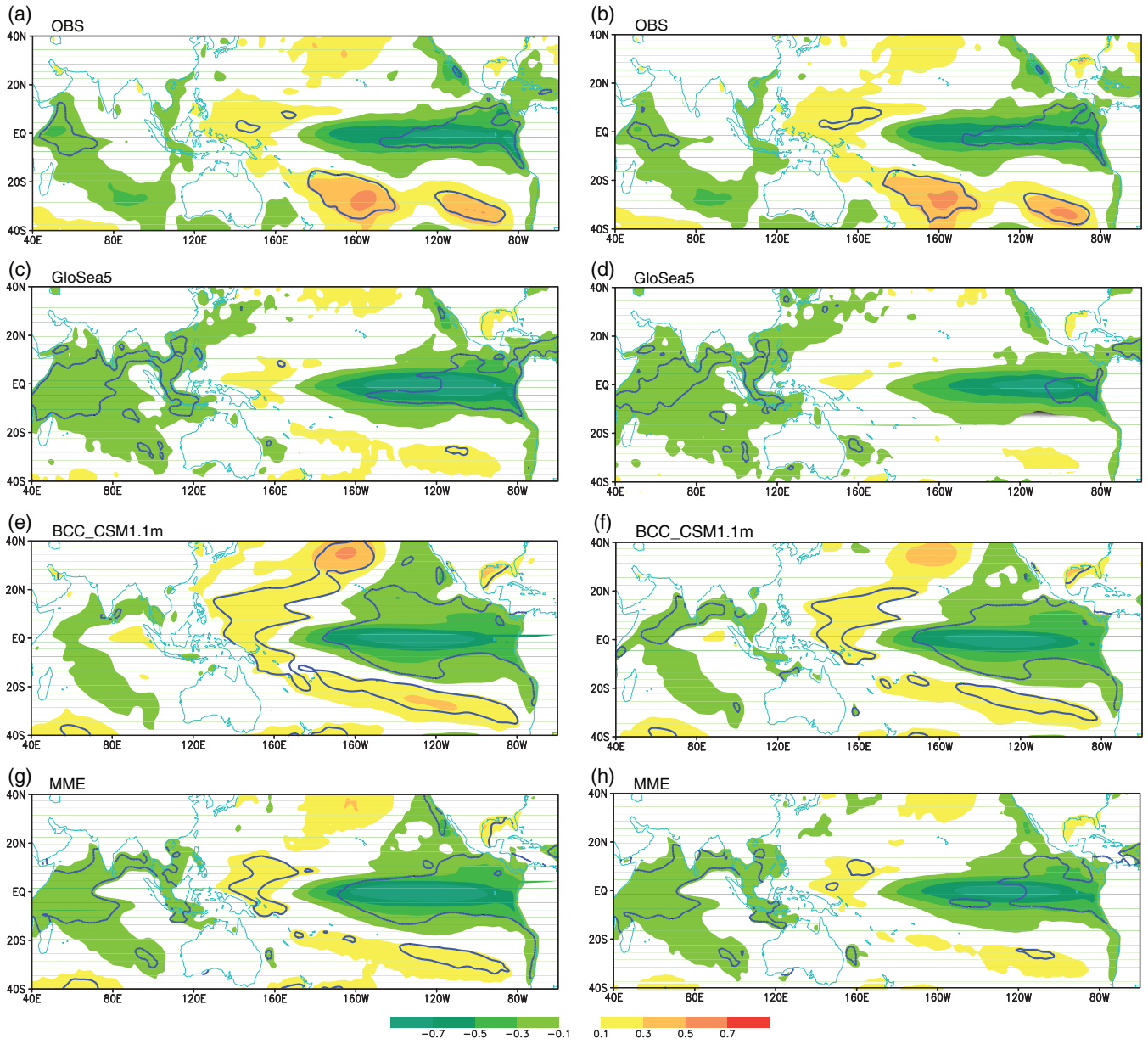

FIGURE 5 Regression of previous DJF surface temperature on JJA EASMI-W99 (a,c,e,g) and EASMI-Z03 (b,d,f,h). Blue lines show the 95% significance level. Unit: °C

EASM–ENSO teleconnection on a decadal time-scale would limit the prediction capability on the East Asian summer rainfall (Wu and Wang, 2002).

Then we investigated the spatial patterns of the JJA-mean precipitation anomalies associated with the dynamical EASM indexes, as shown in Figure 7. Between EASMI-W99 and EASMI-Z03, similar regressed spatial patterns can be found in observations. The signs in the Yangtze River Basin and south China are opposite, indicating that the EASM has a negative influence on summer precipitation over the Yangtze River Basin and a positive one over south China (Zang and Wang, 1984; Zhang and Tao, 1998; Zhao *et al.,* 2006). GloSea5, BCC_CSM1.1m and MME have similar patterns to observations in China, and the negative values located in the Yangtze River basin can be well simulated, which shows the relatively high prediction skill over the Yangtze River basin. However, the prediction skill is low over other regions (Figure 6), and the models tend to underestimate the positive anomaly over south China, which is even completely missed in BCC_CSM1.1m. Clearly, models can better predict dynamical monsoon metrics than the EASM precipitation in China. So how can we correct this deficiency to improve the seasonal rainfall prediction over China?

5 | IMPROVEMENT IN SUMMER PRECIPITATION PREDICTION BY USING STATISTICAL DOWNSCALING

Due to the intrinsic complexity of climate variability and the uncertainty of climate model deficiencies, improving the accuracy of model predictions of the EASM rainfall

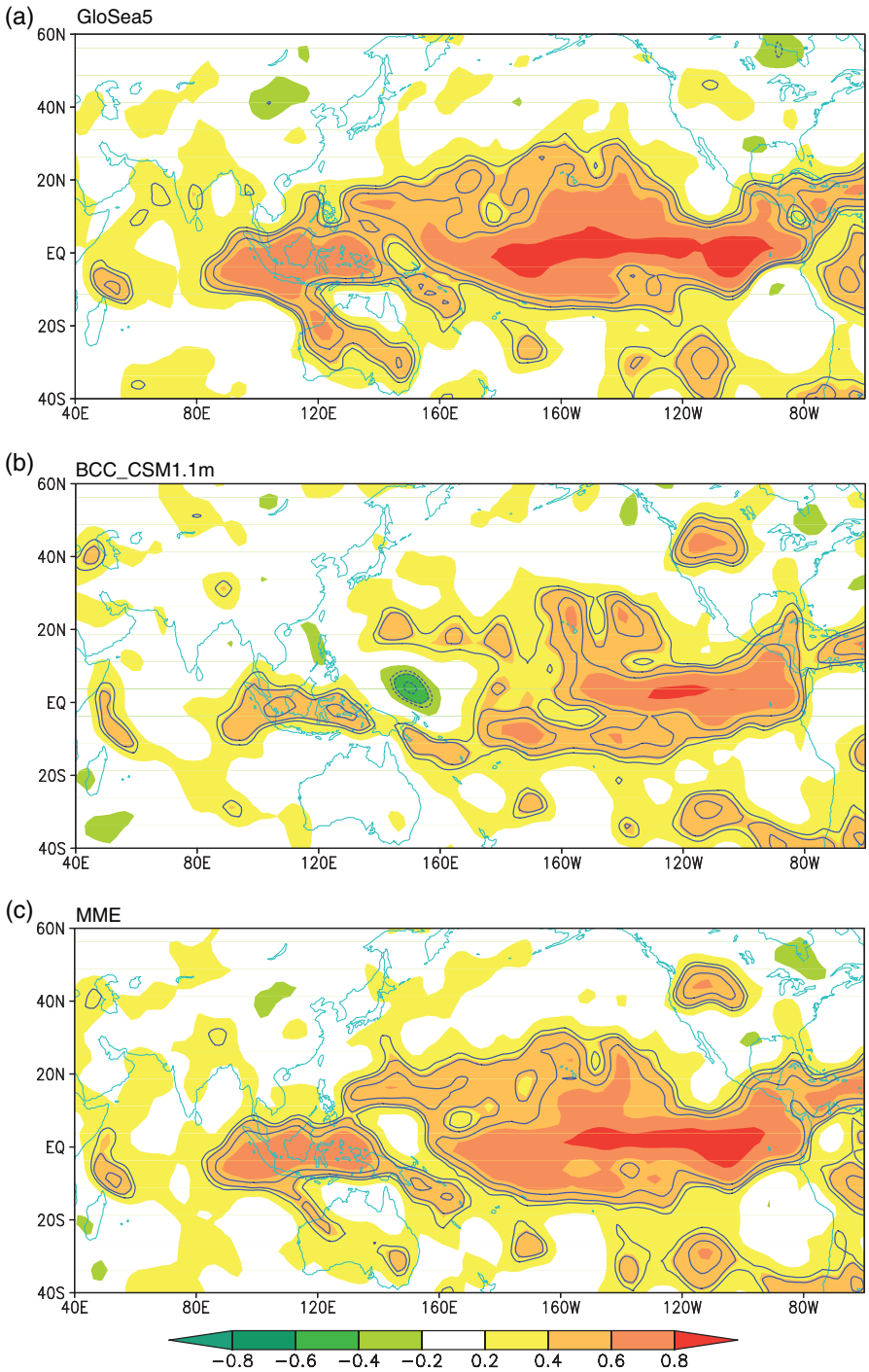

FIGURE 6 (a–c) Same as Figure 1, but for JJA-mean precipitation

is still a challenging issue. Taking advantage of model skill in dynamical indices and their relationship with observed rainfall, statistical downscaling of model predictions is a potentially effective tool for improving prediction skill.

Due to the limited available model datasets from 1992 to 2011, the leave-one-year-out cross-validation (Michaelsen, 1987) is adopted to set up a statistical model of the year in question by using the data from the other years. Both the predictor and the predictand are first reconstructed by using their respective empirical orthogonal functions (EOF) and the principal components to filter out small-scale noise during the training period. Then, the singular value decomposition (SVD: Bretherton *et al.,* 1992), which statistically describes the link between the predictand and its predictors, is applied to extract the coupled patterns between observed precipitation and model prediction of large-scale circulation. Finally, the downscaled precipitation prediction is obtained by utilizing the circulation anomaly forecast and the statistical link between circulation and rainfall. More detailed information regarding this statistical downscaling method can be found in the paper of Liu and Fan (2012; 2013).

The spatial domain selected for defining a predictor should be large enough to resolve the relevant large-scale patterns (Feddersen and Andersen, 2005). Here, the JJA sea-level

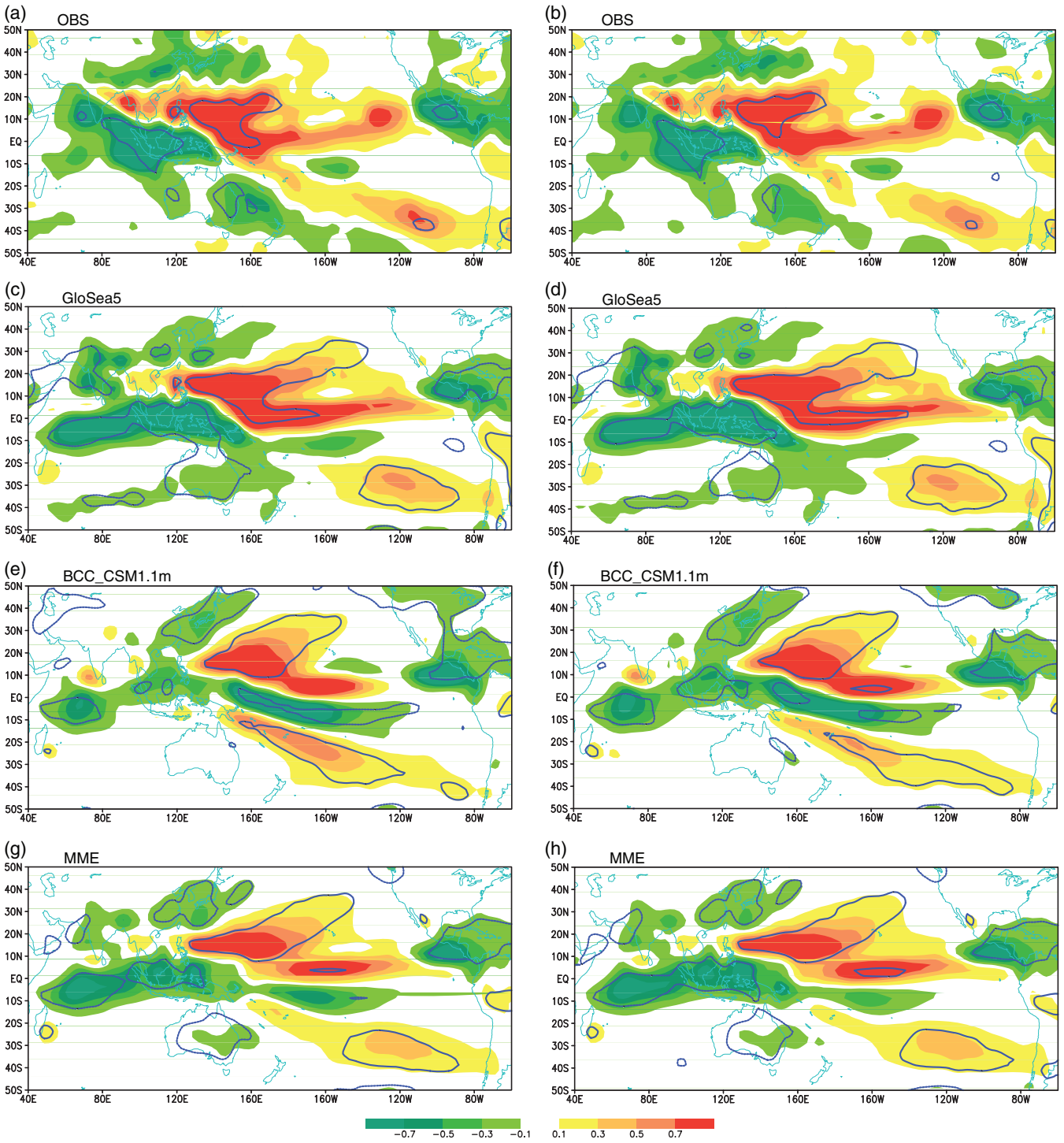

FIGURE 7 Regression of JJA precipitation on JJA EASMI-W99 (a,c,e,g) and EASMI-Z03 (b,d,f,h). Blue lines show the 95% significance level. Unit: m/s

pressure (SLP) over East Asia (i.e. 5–55°N, 60–150°E) is used as the predictor (Shi *et al.,* 1996). As seen in Figure 8, significant predictive skill covers most parts of this domain, indicating that the two models can represent the spatial distribution of the large-scale interannual variability.

The prediction skill of the downscaled predictions is shown in Figure 9d–f. Positive correlation skill now can be found in most parts of China except for small regions in the upper reaches of the Yellow River. It is clearly seen that the correlations in north China have changed from negative values (around −0.3) of the raw model data (Figure 9a–c) (Li *et al.,* 2016) to positive values (around 0.3) (Figure 9d–f). The positive increments of the correlations are much larger over northern and southeastern China than over the regions between them. The skill of the climate models over south China is relatively high without too much room for improvement, while those over north China are relatively low and could be easily improved. The dynamical predictor from climate models with significant positive prediction skill over East Asia has provided effective information on the large-scale circulation

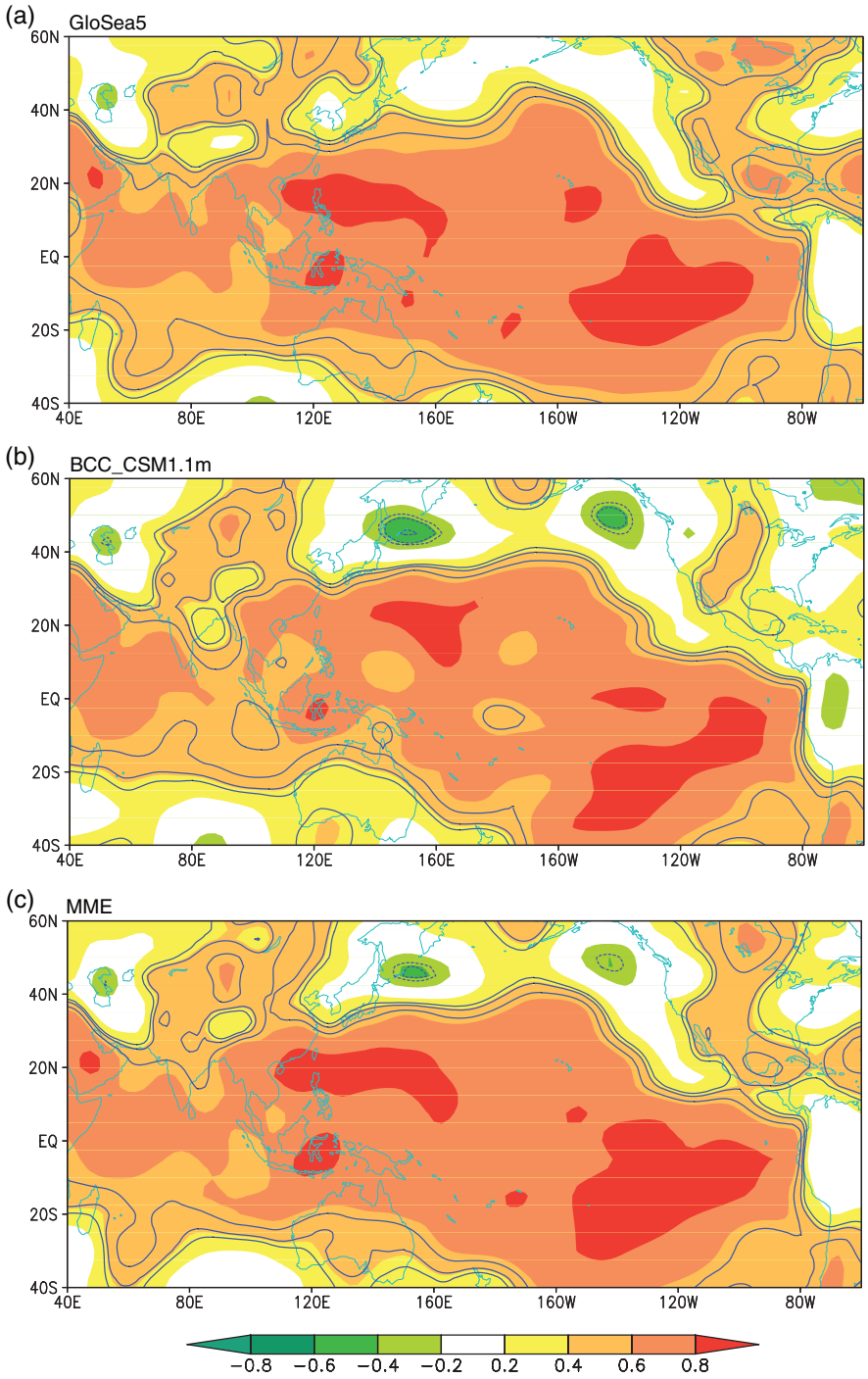

FIGURE 8 (a–c) Same as Figure 1, but for sea-level pressure

and the precipitation anomaly over China via the statistical downscaling model. In summary, the statistical downscaling method is an effective tool to improve the prediction skill over the regions where the raw climate model data have low prediction skill of rainfall anomalies.

6 | SUMMARY AND DISCUSSION

In this study, the prediction skills of two coupled prediction systems have been investigated by using hindcast data initialized in early May during 1992–2011. The prediction skill of large-scale lower tropospheric variables and the EASM have been evaluated. The prediction of summer rainfall over the Yangtze River is skilful (Li *et al.,* 2016), but skill is relatively low over other regions in China. Therefore, a statistical downscaling method is used to improve the prediction of summer precipitation.

For the 850 hPa zonal wind, GloSea5 and BCC_CSM1.1m show significant skill over the tropical Pacific and East Asia. While the predictable interannual variability in East Asia is much lower than observations, the large observed interannual variability over the tropical Pacific can be well reproduced. The predictable signal in GloSea5 and BCC_CSM1.1m

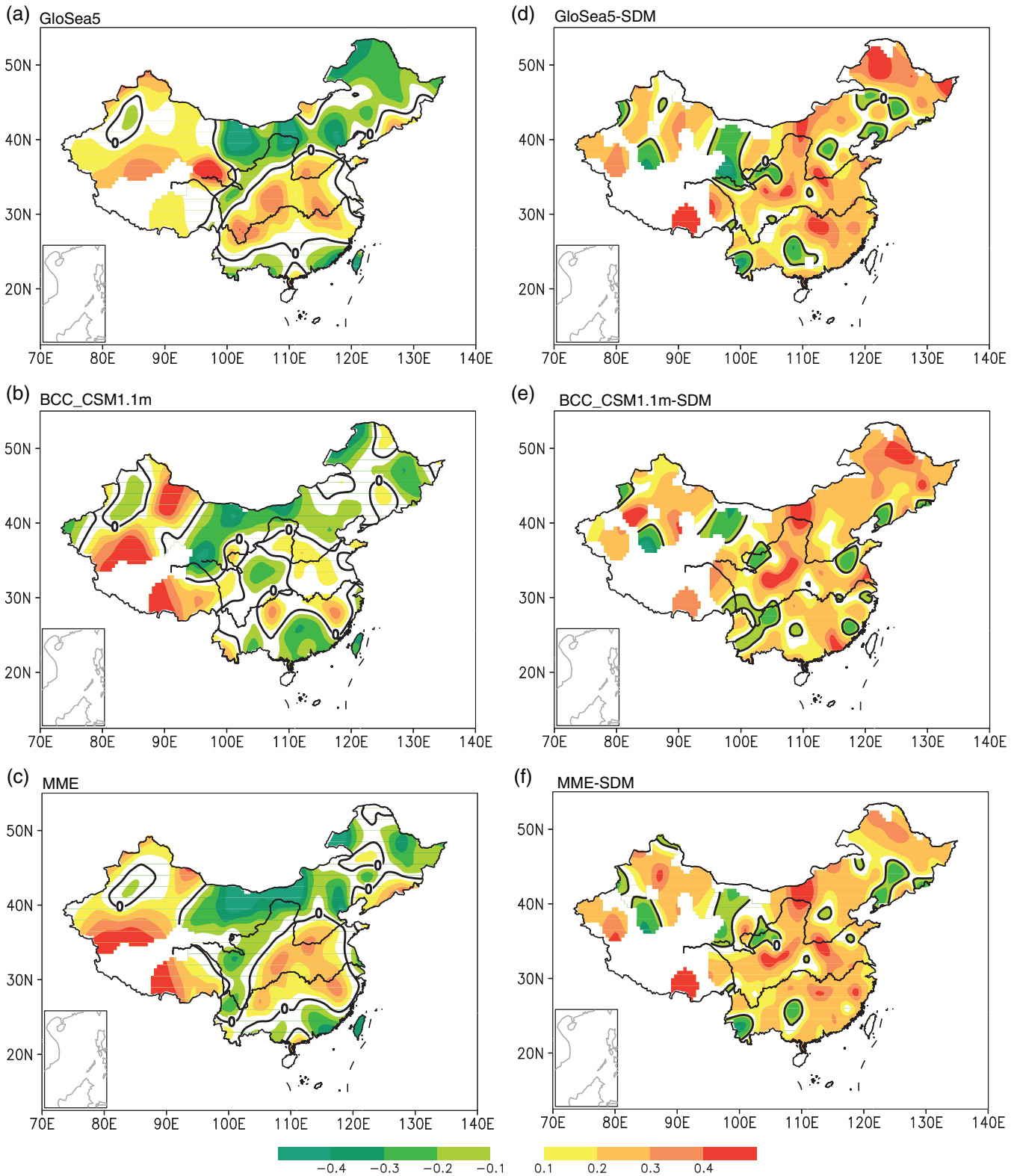

FIGURE 9 Temporal correlation coefficients for 1992–2011 JJA-mean precipitation between observation and dynamical models or the corresponding statistical downscaling model results based on station dataset in China. (a,d) GloSea5, (b,e) BCC_CSM1.1m, (c,f) MME

in the northwest Pacific and East Asia reaches a value around 0.4.

The GloSea5 and BCC_CSM1.1m can predict the 850 hPa zonal wind and EASM well. The main sources of predictability in EASM in both models, which were checked in this study, are the atmosphere–ocean interactions between ENSO and the WPSH. Indeed, the effective response of the EASM to the previous winter SST over the tropical Pacific and Indian Oceans plays an essential role in both models. It is notable that early summer EASM has different relationships with ENSO in its developing and decaying phases. The JJA EASM has a significant negative relationship with the previous winter

ENSO signal. Additionally, the predictability of early summer EASMI in both models is relatively low compared with that of JJA EASMI. The predictability of EASMI-W99 is higher than that of EASMI-Z03, and GloSea5 performs better than BCC_CSM1.1m in predicting early summer EASM indices.

The models have relatively high prediction skill in large-scale circulation, but they exhibit less skill in predicting JJA precipitation over most parts of East Asia, including China. Therefore, a statistical downscaling method is proposed to improve the prediction of JJA precipitation in China based on the large-scale dynamical predictor from the coupled models. First, SLP, which acts as a large-scale variable in the lower troposphere, is considered as an important predictor for summer precipitation in China. Second, both models are able to predict climate anomaly variation. The interannual variability of the SLP predictor over East Asia in both models is comparable to that in observations.

While the rainfall prediction skill can be improved by statistical downscaling, the prediction skill of East Asian monsoon climate and the predictability sources in coupled models should be further analysed. Among these, snow cover on the Tibetan Plateau may be another contributing factor to EASM activity, thus further analyses and discussions may be needed in the future.

ACKNOWLEDGEMENTS

This work was jointly supported by the National Key Research and Development Program on monitoring, Early Warning and Prevention of Major Natural Disaster (2017YFC1502302), National Natural Science Foundation of China (Key Program) (41730964), National Natural Science Foundation grant of China (41405080), and the UK–China Research and Innovation Partnership Fund through the Met Office Climate Science for Service Partnership (CSSP) China, as part of the Newton Fund.

ORCID

Ying Liu https://orcid.org/0000-0001-8037-5125

REFERENCES

Adler, R.F., Huffman, G.J., Chang, A., Ferraro, R., Xie, P.P., Janowiak, J., Rudolf, B., Schneider, U., Curtis, S., Bolvin, D., Gruber, A., Susskind, J., Arkin, P. and Nelkin, E. (2003) The version-2 global precipitation climatology project (GPCP) monthly precipitation analysis (1979–present). *Journal of Hydrometeorology*, 4, 1147–1167.

Blockley, E.W., Martin, M.J., McLaren, A.J., Ryan, A.G., Waters, J., Lea, D.J., Mirouze, I., Peterson, K.A., Sellar, A. and Storkey, D. (2013) Recent development of the Met Office operational ocean forecasting system: an overview and assessment of the new global FOAM forecasts. *Geoscientific Model Development*, 7, 2613–2638.

Bretherton, C.S., Smith, C. and Wallace, J.M. (1992) An intercomparison of methods for finding coupled patterns on climate data. *Journal of Climate*, 5, 541–560.

Chang, C.P., Zhang, Y. and Li, T. (2000) Interannual and interdecadal variations of the East Asian summer monsoon and tropical Pacific SSTs. Part I: Roles of the subtropical ridge. *Journal of Climate*, 13, 4310–4325.

Ding, Y.H. (1994) The summer monsoon in East Asia. In: *Monsoons over China*. Netherlands: Kluwer Academic, pp. 1–9.

Ding, Y.G., Jiang, Z.H. and Zhu, Y.F. (1998) Experiment on short-term climate prediction models on SSTA over the Niño oceanic region. *Journal of Tropical Meteorology*, 5, 1–8 in Chinese.

Ding, Y.H., Li, Q.Q., Li, W.J., Luo, Y., Zhang, P.Q., Zhang, Z.Q., Shi, X.L., Liu, Y.M. and Wang, L. (2004) Advance in seasonal dynamical prediction operation in China. *Acta Meteorologica Sinica*, 62, 598–612 in Chinese.

Eade, R., Smith, D., Scaife, A.A. and Wallace, E. (2014) Do seasonal to decadal climate predictions underestimate the predictability of the real world? *Geophysical Research Letters*, 41, 5620–5628.

Fan, K., Wang, H.J. and Choi, Y.J. (2008) A physically-based statistical forecast model for the middle-lower reaches of the Yangtze River valley summer rainfall. *Chinese Science Bulletin*, 53, 602–609.

Feddersen, H. and Andersen, U. (2005) A method for statistical downscaling of seasonal ensemble predictions. *Tellus A*, 57, 398–408.

Gao, H., Jiang, W. and Li, W. (2014) Changed relationship between the East Asian summer monsoon circulation and the summer rainfall in eastern China. *Journal of Meteorological Research*, 28, 1075–1084.

Huang, R. and Sun, F. (1992) Impacts of the tropical western Pacific on the East Asian summer monsoon. *Journal of the Meteorological Society of Japan*, 70, 243–256.

Huang, R. and Wu, Y. (1989) The influence of ENSO on the summer climate change in China and its mechanism. *Advances in Atmospheric Sciences*, 6, 21–32.

Johnson, S.J., Turner, A., Woolnough, S., Martin, G. and MacLachlan, C. (2017) An assessment of Indian monsoon seasonal forecasts and mechanisms underlying monsoon interannual variability in the Met Office GloSea5-GC2 system. *Climate Dynamics*, 48, 1447–1465. https://doi.org/10.1007/s00382-016-3151-2.

Kalnay, E., Kanamitsu, M., Kistler, R., Collins, W., Deaven, D., Gandin, L., Iredell, M., Saha, S., White, G., Woollen, J., Zhu, Y., Leetmaa, A., Reynolds, R., Chelliah, M., Ebisuzaki, W., Higgins, W., Janowiak, J., Mo, K.C., Ropelewski, C., Wang, J., Jenne, R. and Joseph, D. (1996) The NCEP/NCAR 40-year reanalysis project. *Bulletin of the American Meteorological Society*, 77, 437–471.

Kumar, A., Jha, B., Zhang, Q. and Bounoua, L. (2007) Methodology for estimating the unpredictable component of seasonal atmospheric variability. *Journal of Climate*, 20, 3888–3901.

Kumar, A., Peng, P. and Chen, M. (2014) Is there a relationship between potential and actual skill? *Monthly Weather Review*, 142, 2220–2227.

Lau, K.M. (1992) The East Asian summer monsoon rainfall variability and climate teleconnection. *Journal of the Meteorological Society of Japan*, 70, 211–241.

Lau, K.M. and Li, M. (1984) The monsoon of East Asia and its global association – a survey. *Bulletin of the American Meteorological Society*, 65, 114–125.

Lee, S.S., Lee, J.Y., Ha, K.J., Wang, B. and Schemm, J. (2011) Deficiencies and possibilities for long-lead coupled climate prediction of the western North Pacific–East Asian summer monsoon. *Climate Dynamics*, 36, 1173–1188.

Li, C., Lu, R. and Dong, B. (2012) Predictability of the western North Pacific summer climate demonstrated by the coupled models of ENSEMBLES. *Climate Dynamics*, 39, 329–346.

Li, C., Lu, R. and Dong, B. (2014) Predictability of the western North Pacific summer climate associated with different ENSO phases by ENSEMBLES multi-model seasonal forecasts. *Climate Dynamics*, 43, 1829–1845.

Li, C., Scaife, A.A., Lu, R., Arribas, A., Brookshaw, A., Comer, R.E., Li, J., MacLachlan, C. and Wu, P. (2016) Skillful seasonal prediction of Yangtze river valley summer rainfall. *Environmental Research Letters*, 11, 094002. https://doi.org/10.1088/1748-9326/11/9/094002.

Liu, Y. and Fan, K. (2012) Prediction of spring precipitation in China using a downscaling approach. *Meteorology and Atmospheric Physics*, 118, 79–93.

Liu, Y. and Fan, K. (2013) A new statistical downscaling model for autumn precipitation in China. *International Journal of Climatology*, 33, 1321–1336.

Liu, Y. and Ren, H. (2015) A hybrid statistical downscaling model for prediction of winter precipitation in China. *International Journal of Climatology*, 35, 1309–1321.

Liu, S. and Wang, H.J. (2015) Extra-seasonal short-term prediction systems based on CCSM3 and their evaluation. *International Journal of Climatology*, 35, 4681–4694.

Liu, X.W., Wu, T., Yang, S., Jie, W., Nie, S., Li, Q., Cheng, Y. and Liang, X. (2015) Performance of the seasonal forecasting of the Asian summer monsoon by BCC_CSM1.1(m). *Advances in Atmospheric Sciences*, 32, 1156–1172.

Lu, B., Scaife, A.A., Dunstone, N., Smith, D., Ren, H.-L., Liu, Y. and Eade, R. (2017) Skillful seasonal predictions of winter precipitation over southern China. *Environmental Research Letters*, 12, 074021. https://doi.org/10.1088/1748-9326/aa739a.

Lu B, Ren H, Eade R, Andrews M. (2018) Indian Ocean SST modes and Their Impacts as Simulated in BCC_CSM1.1(m) and HadGEM3. *Advances in Atmospheric Sciences*, 35(8), 1035–1048. https://doi.org/10.1007/s00376-018-7279-3.

Ma, J.H. and Wang, H.J. (2014) Design and testing of a global climate prediction system based on a coupled climate model. *Science China Earth Sciences*, 57, 2417–2427.

MacLachlan, C., Arribas, A., Peterson, K.A., Maidens, A., Fereday, D., Scaife, A.A., Gordon, M., Velling, M., Williams, A., Comer, R.E., Camp, J., Xaviera, P. and Madec, G. (2015) Global seasonal forecast system version 5 (GloSea5): a high-resolution seasonal forecast system. *Quarterly Journal of the Royal Meteorological Society*, 141, 1072–1084.

Michaelsen, J. (1987) Cross-validation in statistical climate forecast models. *Journal of Applied Meteorology and Climatology*, 26, 1589–1600.

Rawlins, F., Ballard, S.P., Bovis, K.J., Clayton, A.M., Li, D., Inverarity, G.W., Lorenc, A.C. and Payne, T.J. (2007) The Met Office global four-dimensional variational data assimilation scheme. *Quarterly Journal of the Royal Meteorological Society*, 133, 347–362. https://doi.org/10.1002/qj.32.

Ren, H. and Chou, J. (2006) Analogue correction method of errors by combining statistical and dynamical methods. *Acta Meteorologica Sinica*, 20, 367–373.

Ren, H. and Chou, J. (2007) Strategy and methodology of dynamical analogue prediction. *Science in China, Series D: Earth Sciences*, 50, 1589–1599.

Ren, H.-L. and Jin, F.-F. (2011) Niño indices for two types of ENSO. *Geophysical Research Letters*, 38, L04704. https://doi.org/10.1029/2010GL046031.

Ren, H.-L., Jin, F.-F., Song, L., Lu, B., Tian, B., Zuo, J., Liu, Y., Wu, J., Zhao, C., Nie, Y., Zhang, P., Ba, J., Wu, Y., Wan, J., Yan, Y. and Zhou, F. (2017) Prediction of primary climate variability modes in Beijing Climate Center. *Journal of Meteorological Research*, 31(1), 204–223.

Reynolds, R.W., Rayner, N.A., Smith, T.M., Stokes, D.C. and Wang, W. (2002) An improved *in situ* and satellite SST analysis for climate. *Journal of Climate*, 15, 1609–1625.

Rowell, D.P. (1998) Assessing potential seasonal predictability with an ensemble of multidecadal GCM simulations. *Journal of Climate*, 11, 109–120.

Rowell, D.P., Folland, C.K., Maskell, K.M. and Ward, M.N. (1995) Variability of summer rainfall over tropical North Africa (1906–92): observations and modelling. *Quarterly Journal of the Royal Meteorological Society*, 121, 669–704.

Shi, N., Zhu, Q.G. and BG, W. (1996) The East Asian Monsoon in relation to summer large scale weather–climate anomaly in China for last 40 years. *Chinese Journal of Atmospheric Sciences*, 20, 575–583 in Chinese.

Siegert, S., Stephenson, D., Scaife, A.A., Eade, R. and Arribas, A. (2016) A Bayesian framework for verification and recalibration of ensemble forecasts: how uncertain is NAO predictability? *Journal of Climate*, 29, 995–1012.

Sun, J.Q. and Chen, H.P. (2012) A statistical downscaling scheme to improve global precipitation forecasting. *Meteorology and Atmospheric Physics*, 117, 87–102.

Tao, S.Y. and Chen, L.X. (1987) A review of recent research on the East Asian summer monsoon in China. In *Monsoon meteorology*. In: *Oxford Monogr. on Geology and Geophysics*, Vol. 7. New York: Oxford University Press, pp. 60–92.

Tompkins, A., Zárate, M.I.O.D., Saurral, R.I., Vera, C., Saulo, C., Merryfield, W.J., Sigmond, M., Lee, W.S., Baehr, J., Braun, A., Butler, A., Déqué, M., Doblas-Reyes, F.J., Gordon, M., Scaife, A.A., Imada, Y., Ishii, M., Ose, T., Kirtman, B., Kumar, A., Müller, W.A., Pirani, A., Stockdale, T., Rixen, M. and Yasuda, T. (2017) The climate-system historical forecast project: providing open access to seasonal forecast ensembles from centers around the globe. *Bulletin of the American Meteorological Society*, 98, 2293–2301.

Vecchi, G.A., Msadek, R., Anderson, W., Chang, Y.S., Delworth, T., Dixon, K., Gudgel, R., Rosati, A., Stern, B., Villarini, G., Wittenberg, A., Yang, X., Zeng, F., Zhang, R. and Zhang, S. (2013) Multiyear predictions of North Atlantic hurricane frequency: promise and limitations. *Journal of Climate*, 26, 5337–5357.

Wan, J., Ren, H.-L. and Wu, P. (2018) Representation of the ENSO combination mode and its asymmetric SST response in different resolutions of HadGEM3. *Advances in Atmospheric Sciences*, 35, 1063–1076. https://doi.org/10.1007/s00376-018-7285-5.

Wang, H.J. (2001) The weakening of the Asian monsoon circulation after the end of 1970s. *Advances in Atmospheric Sciences*, 18, 376–386.

Wang, B. and Fan, Z. (1999) Choice of South Asian summer monsoon indices. *Bulletin of the American Meteorological Society*, 80, 629–638.

Wang, H.J., Zhang, R.H., Julie, C. and Chavez, F. (1999) El Niño and the related phenomenon Southern Oscillation (ENSO): the largest signal in interannual climate variation. *Proceedings of the National Academy of Sciences of the United States of America*, 96, 11071–11072.

Wang, B., Wu, R. and Fu, X. (2000) Pacific–East Asian teleconnection: how does ENSO affect East Asian climate? *Journal of Climate*, 13, 1517–1536.

Wang, B., Lee, J.Y., Kang, I.S., Shukla, J., Park, C.K., Kumar, A., Schemm, J., Cocke, S., Kug, J.S., Luo, J.J., Zhou, T., Wang, B., Fu, X., Yun, W.T. and Alves, O. (2009) Advance and prospectus of seasonal prediction: assessment of the APCC/CliPAS 14-model ensemble retrospective seasonal prediction (1980–2004). *Climate Dynamics*, 33, 93–117.

Weedon, G.P., Gomes, S., Viterbo, P., Shuttleworth, W.J., Blyth, E., Ö, s.H., Adam, J.C., Bellouin, N., Boucher, O. and Best, M. (2011) Creation of the WATCH forcing data and its use to assess global and regional reference crop evaporation over land during the twentieth century. *Journal of Hydrometeorology*, 12, 823–848. https://doi.org/10.1175/2011JHM1369.1.

Weisheimer, A., Doblas-Reyes, F.J., Palmer, T.N., Alessandri, A., Arribas, A., Déqué, M., Keenlyside, N., MacVean, M., Navarra, A. and Rogel, P. (2009) ENSEMBLES: a new multi-model ensemble for seasonal-to-annual predictions-skill and progress beyond DEMETER in forecasting tropical Pacific SSTs. *Geophysical Research Letters*, 36, L21711. https://doi.org/10.1029/2009GL040896.

Wu, R. and Wang, B. (2002) A contrast of the East Asian summer monsoon and ENSO relationship between 1962–1977 and 1978–1993. *Journal of Climate*, 15, 3266–3279.

Wu, T.W., Yu, R., Zhang, F., Wang, Z., Dong, M., Wang, L., Jin, X., Chen, D. and Li, L. (2010) The Beijing Climate Center atmospheric general circulation model: description and its performance for the present-day climate. *Climate Dynamics*, 34, 123–147.

Yang, S., Zhang, Z., Kousky, V.E., Higgins, R.W., Yoo, S.H., Liang, J. and Fan, Y. (2008) Simulations and seasonal prediction of the Asian summer monsoon in the NCEP Climate Forecast System. *Journal of Climate*, 21, 3755–3775.

Yang, X., Vecchi, G.A., Gudgel, R.G., Delworth, T., Zhang, S., Rosati, A., Ji, L., Stern, W.F., Wittenberg, A.T., Kapnick, S., Msadek, R., Underwood, S.D., Zeng, F., Anderson, W. and Balaji, V. (2015) Seasonal predictability of extra-tropical storm tracks in GFDL's high-resolution climate prediction model. *Journal of Climate*, 28, 3592–3611.

Yang, R., Xie, Z. and Cao, J. (2017) A dynamic index for the westward ridge point variability of the western Pacific subtropical high during summer. *Journal of Climate*, 30, 3325–3341.

Zang, H.F. and Wang, S.W. (1984) The impact on atmospheric circulation at low latitude by sea surface temperature over tropical eastern Pacific. *Acta Oceanologica Sinica*, 6, 16–24 in Chinese.

Zeng, Q.C., Yuan, C.G., Wang, W.Q. and Zhang, R.H. (1990) Numerical extra-seasonal prediction experiment for climate anomalies. *Scientia Atmospherica Sinica*, 14, 10–25 in Chinese.

Zhang, S. (2011) A study of impacts of coupled model initial shocks and state-parameter optimization on climate predictions using a simple pycnocline prediction model. *Journal of Climate*, 24, 6210–6226.

Zhang, Q. and Tao, S. (1998) Tropical and subtropical monsoon over East Asia and its influence on the rainfall over eastern China in summer. *Journal of Applied Meteorological Science*, 8, 16–23 in Chinese.

Zhang, R., Sumi, A. and Kimoto, M. (1996) Impact of El Niño on the East Asian monsoon: a diagnostic study of the '86/87 and '91/92 events. *Journal of the Meteorological Society of Japan*, 74, 49–62.

Zhang, Q., Tao, S. and Chen, L. (2003) The inter-annual variability of East Asian summer monsoon indices and its association with the pattern of general circulation over East Asia. *Acta Mathematica Sinica*, 61, 559–568 in Chinese.

Zhang, R.H., Yin, Y.H., Li, Q.Q., Liu, Y.M. and Niu, T. (2006) Utilizing ARGO data to improve the prediction of ENSO and short-term climate prediction of summer rainfall in China. *Journal of Applied Meteorological Science*, 17, 538–547 in Chinese.

Zhao, L., Zou, L., Wang, C.L. and Yin, H.B. (2006) Impacts of the East Asian summer monsoon anomaly during the ENSO event period on the summer precipitation in the lower-middle reaches of the Yangtze River and Huaihe River Valley. *Journal of Tropical Meteorology*, 22, 360–366 in Chinese.

Zhou, T. and Yu, R. (2005) Atmospheric water vapor transport associated with typical anomalous summer rainfall patterns in China. *Journal of Geophysical Research*, 110, D08104. https://doi.org/10.1029/2004JD005413.

Zhou, G.Q., Li, X. and Zeng, Q.C. (1998) A coupled ocean–atmosphere general circulation model for ENSO prediction and 1997/1998 ENSO forecast. *Climatic Environmental Research*, 3, 349–357 in Chinese.

Zhou, T., Yu, R., Zhang, J., Drange, H., Cassou, C., Deser, C., Hodson, D.L.R., Sanchez-Gomez, E., Li, J., Keenlyside, N., Xin, X. and Okumura, Y. (2009) Why the western Pacific subtropical high has extended westward since the late 1970s. *Journal of Climate*, 22, 2199–2215.

Zhu, J. and Shukla, J. (2013) The role of air–sea coupling in seasonal prediction of Asia–Pacific summer monsoon rainfall. *Journal of Climate*, 26, 5689–5697.

Zhu, J., Huang, B., Hu, Z.-Z., Kinter, I.I.J.L. and Marx, L. (2013) Predicting US summer precipitation using NCEP Climate Forecast System version 2 initialized by multiple ocean analyses. *Climate Dynamics*, 41, 1941–1954.

Zhu, J., Kumar, A., Lee, H.-C. and Wang, H. (2017) Seasonal predictions using a simple ocean initialization scheme. *Climate Dynamics*, 49, 3989–4007.

How to cite this article: Liu Y, Ren H-L, Scaife AA, Li C. Evaluation and statistical downscaling of East Asian summer monsoon forecasting in BCC and MOHC seasonal prediction systems. *Q J R Meteorol Soc* 2018;144:2798–2811. https://doi.org/10.1002/qj.3405

自然资源学报, 2018, 33(1): 139-148
Journal of Natural Resources
http://www.jnr.ac.cn
DOI: 10.11849/zrzyxb.20161270

基于度-时法的哈尔滨冬季采暖强度评价

刘玉莲[1,2],任国玉[2,3*]

(1. 黑龙江省气候中心,哈尔滨 150030; 2. 中国地质大学(武汉)环境学院大气科学系,武汉 430074;
3. 中国气象局国家气候中心气候研究开放实验室,北京 100081)

摘要:采用度时法比度日法更能细致地反映采暖和制冷强度时间分布特征。论文应用度时法分析了哈尔滨采暖期内采暖强度的时间变化特征,获得如下结论:1)哈尔滨集中供暖时间为183 d,近10 a采暖期平均气温-7.7 ℃,平均气温距平最高值2.6 ℃(2007、2008年)、最低值-2.0 ℃(2013年)。采暖期小时平均气温最高在14:00(-3.6 ℃),最低在06:00(-11.3 ℃)。2)2005—2014年,哈尔滨年平均采暖强度1.1×10^5 ℃·h,最大1.2×10^5 ℃·h(2013年),最小1.0×10^5 ℃·h(2007年)。3)哈尔滨采暖期小时平均采暖强度为25.7 ℃·h,日内呈单峰分布,06:00采暖强度最大,为29.3 ℃·h,14:00采暖强度最小,为21.6 ℃·h。晚上21:00到次日上午9:00,采暖强度大于日平均值,而上午9:00到晚上21:00采暖强度则明显低于日平均水平。4)采暖期各月平均的小时采暖强度1月最大,为35.4 ℃·h,从大到小依次减少顺序是1、12、2、11、3、10、4,4月小时采暖强度仅为12.0 ℃·h。5)日内小时采暖强度最小值3、4月出现在15:00,其余月份在14:00;最大值1、2、12月出现在07:00,3、10、11月在06:00,4月在05:00。在每年1月中旬06:00~08:00,出现整个采暖期采暖强度极大值。

关 键 词:度日;度时;气温;采暖强度;哈尔滨
中图分类号:TU832 **文献标志码**:A **文章编号**:1000-3037(2018)01-0139-10

我国用于建筑供暖、通风和空调等的建筑能耗占总能耗的20%~25%,东北地区由于室外温度低,采暖能耗占建筑能耗达到50%以上,通常也是这部分能耗浪费最多,节能潜力巨大[1]。准确估算采暖耗能需求,以便在保证人们正常生产、生活的前提下,根据实际需求合理利用能源供暖,可以节约大量能源,对于节能减排、缓解城市空气污染和应对气候变化,均具有重要的实际意义。

国内外利用度日方法对全球不同气候带的采暖和制冷能源强度进行了大量研究。20世纪90年代,张家诚等[2]指出采暖气候条件包括采暖期长度与采暖强度两个指标;陈峪等[3]探讨气候变化对能源需求的影响,计算分析了中国北方地区采暖度日变化;白美兰[4]、轩春怡等[5]、李丽光等[6]、曹洁等[7]、胡轶鑫等[8]分别评估了内蒙古、北京、辽宁中部城市群、山东省及长白山区采暖度日分布及变化特征;陈莉等[9-11]、李明财等[12]评估了度日与采暖能耗关系,并对气候变化背景下基于采暖度日的能源消耗需求变化进行了分析。这

收稿日期:2016-11-21;**修订日期**:2017-01-04。
资助项目:中国气象局气候变化专项(CCSF201842);黑龙江省气象局自立项目(HQ2016026)。[**Foundation items:** The Special Project in Climate Change of China Meteorological Administration, No. CCSF201842; Self-reliance Project of Heilongjiang Province Meteorological Bureau, No. HQ2016026.]
第一作者简介:刘玉莲(1974-),女,黑龙江兰西人,硕士,高工,主要从事气候变化研究。E-mail: liuyl74@qq.com
***通信作者简介**:任国玉(1958-),男,辽宁康平人,研究员,研究方向为气候变化与古气候研究。E-mail: guoyoo@cma.gov.cn

些研究都是基于日平均气温和度日方法计算分析采暖强度，具有计算方法简便、资料容易获取等优点。但是，基于度日方法和日平均气温资料的分析评价，难以捕捉能源需求的日内变化规律，对于日间和月间能源需求变化特征的描述有时也会出现误差[13]。

Satman 等[14]采用度时方法和不同基础温度评估了土耳其的采暖和制冷强度；Papakostas 等[15]利用度时方法分析评价了希腊两个主要城市（Athens 和 Thessaloniki）的采暖和制冷能源需求。Bolattürk[16]利用度时方法计算分析了土耳其最暖气候带的采暖和制冷强度，并进一步评价了建筑物墙壁理想绝缘厚度，提出暖热气候条件下针对制冷情况的绝缘墙体采用具有显著节能效果，理想墙体厚度介于3.2 ~ 3.8 cm之间，而针对采暖节能的理想墙体厚度介于1.6 ~ 2.7 cm之间。

长期以来，由于缺少高分辨率气温观测资料，国内采用度时方法开展相关研究极为罕见。本文利用哈尔滨地面气象观测站2005—2014年的小时气温观测数据，基于度时法计算并分析哈尔滨的采暖强度时间变化特征，其结果可以为政府和供热部门采暖精细化决策服务提供科学依据，并为能源需求与消耗研究提供参考。

1 方法和资料

度日是一个基本的设计参数，最初是用来反映农作物生长中所需热量水平的物理单位，现已广泛应用在居民生活、能源规划、电力、军事、保险等领域[17-18]。1952年，美国Thom首次用度日分析法研究能源消费与温度变化的关系[19]，1954年他进一步解释了平均温度和基础温度与平均度日数的关系[20]，1962年研究了通过月平均温度及其标准差得到月平均度日数的方程[21]。近年来，度日已经被发展为一个能够反映采暖和制冷所需能源的时间温度指数，把度日分析法作为研究温度和能源关系的基本方法。

所谓某一天的度日就是指日平均温度与规定的基础温度的实际离差。为研究方便，度日又分为两种：采暖度日和降温度日。1 a的采暖度日数计算公式为

$$HDD=\sum_{i=1}^{N_d}(1-\gamma_d)(T_b-T_i) \tag{1}$$

式中：N_d 为某一年的天数；T_i 为日平均温度；T_b 为基础温度；γ_d 为采暖判别参数，当日平均温度高于基础温度时为1，否则为0。采暖期的采暖度日即为采暖强度。

《采暖通风与空气调节设计规范（GB50019—2003）》[22]规定：当室内日平均气温在18 ℃以下，人们开始有采暖的要求，中国建筑热工通常采用的计算采暖强度的基础温度为18 ℃，于是采暖期采暖强度计算公式为：

$$HD=\sum_{i=1}^{N_d}(1-\gamma_d)(18-T_i) \tag{2}$$

式中：N_d 为采暖期天数；T_i 为采暖期日平均气温；HD 为某一年的采暖强度（℃·d）。

在国内，使用日平均气温计算度日存在两个问题。第一个问题是不同方法计算的日平均气温及其度日数值不同。地面气象观测网日平均气温的计算常用有3种：第一种是日内4次定时观测值算术平均（T_4：02:00、08:00、14:00、20:00实际观测气温值的算术平均）；第二种是3次加权平均（T_3：适用于夜间02:00无观测台站，08:00、14:00、20:00气温实际观测得到，02:00气温由当日最低气温与前一天20:00气温之和的算术平均值代替）；第三种是用日内最高、最低气温算术平均（T_{mn}）。显然，如果24次定时观测

值算术平均（T_{24}）准确表达1 d气温的平均状态，那么这3种计算方法都较24次观测值平均有差异。例如，受地方平均太阳时差及纬度影响，我国北方地区3次加权平均值较4次平均值偏高[23]；西部地区由于地方平均太阳时差，北方地区夏季由于日落时间偏晚，3次加权平均值均将加大20:00观测气温（温度值较高）的权重，导致计算的日平均气温值偏高。

第二个问题是日平均气温小于基础温度时，并不是日内每个时次的气温都小于基础温度。在这种情况下，用日平均气温计算的采暖强度值，可能并不与用实际小时气温计算的累积值相等。日内温度具有明显的周期性变化。例如，初冬或暮春，白天温度会高于18 ℃，此时不需耗能供暖，按照日平均气温计算采暖强度就会有误差。在哈尔滨市，4月中旬日平均气温可能高于18 ℃，根据度日法计算的采暖强度为0，但如果采用小时气温资料估算采暖强度则可能大于0。

早期国家地面气象观测站网中只有基准站是每天24次观测，其他都是8次、4次或3次观测。2005年以来，随着气象自动站的使用，使得各地面气象台站都有24 h气温观测资料，这就为计算采暖强度使用更精准的度时法提供了可能性。

度时法是在度日法计算基础上，使用小时气温数据，计算规定基础温度与日内每个小时平均气温的离差累积值，单位为度时（℃·h）。度时法的采暖期采暖强度计算公式为：

$$HH=\sum_{i=1}^{N_d}\sum_{j=0}^{23}\left(1-\gamma_d\right)\left(18-T_{ij}\right) \tag{3}$$

式中：j为日内时次；T_{ij}为采暖期日内小时平均气温；HH为某一年的采暖强度（℃·h）。

文中所用资料来自于黑龙江省地面气象观测站网2005—2014年哈尔滨站地面小时气温数据。

哈尔滨市政府规定的采暖期为每年10月20日至次年4月20日。2005—2014年间，有两个润年（2008、2012年），为统一比较，上半年的采暖期采用儒略日计数法，取每年的前110 d，即平年的1月1日至4月20日，润年的1月1日至4月19日，则每年哈尔滨采暖期为183 d。

2005—2014年采暖期间缺测气温记录有7个（缺测率0.2‰），用前后两个相邻时次的气温观测值算术平均插补。由于地面气象台站日资料记录是从前一天的21:00到当天的20:00，资料中2014年12月31日无当天21:00、22:00、23:00记录，取2014年12月26—30日，这5天21:00、22:00、23:00气温与20:00气温的距平平均，加31日当天20:00气温值代替。

2　采暖期气温特征

2005—2014年哈尔滨采暖期平均气温为-7.7 ℃，近10 a中2007、2008年采暖期气温最高，高于平均值2.6 ℃，2013年最低，低于平均值2.0 ℃ [图1(a)]。

采暖期间各月平均气温（月内实有日数的平均）4月最高，1月最低 [图1(b)]。近10 a哈尔滨采暖期间4月的平均气温为6.0 ℃，最高较平均值高5.7 ℃（出现在2007年），最低较平均值低4.6 ℃（出现在2013年）；1月平均气温-17.4 ℃，最高较平均值高6.0 ℃（出现在2008年），最低较平均值低3.6 ℃（出现在2013年）。

哈尔滨每年采暖时间为183 d。近10 a采暖期间每日的平均气温如图2。可见，采暖

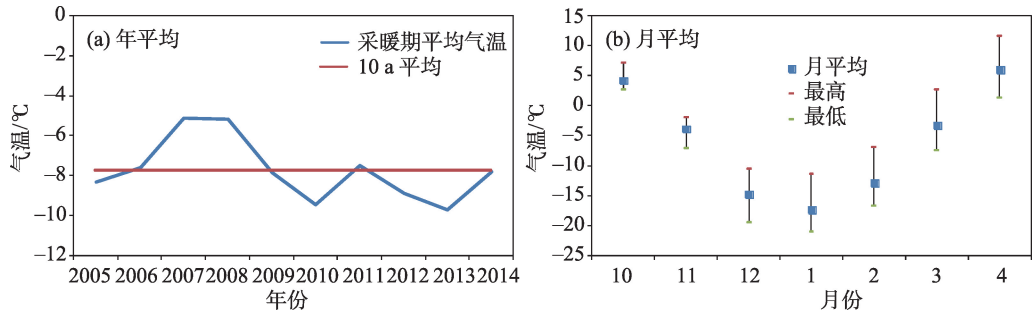

图1 哈尔滨采暖期年平均气温（a）及各月平均气温（b）

Fig. 1 Average temperature of heating period during 2005−2014 (a) and monthly mean temperature of heating period (b) in Harbin City

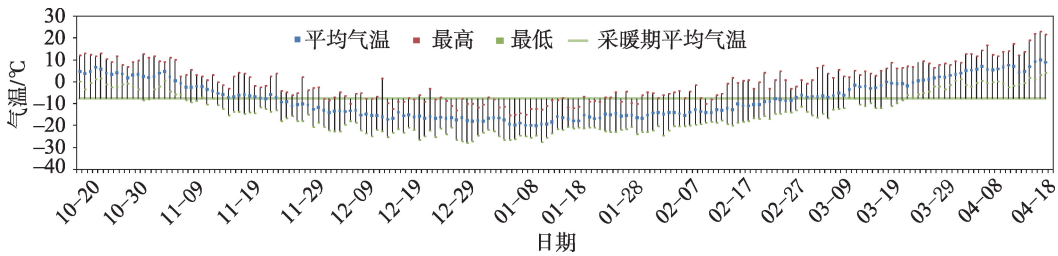

图2 哈尔滨采暖期日平均气温

Fig. 2 Average daily temperature of heating period in Harbin City

期日平均气温最高10.2 ℃（4月19日），最低−20.1 ℃（1月13日）；日平均气温极端最高23.1 ℃（2008年4月19日），极端最低−27.9 ℃（2013年1月1日）。采暖期结束阶段的4月16—20日平均气温比开始阶段的10月16—20日平均大约高出2.0~3.0 ℃，但采暖期开始阶段的年际波动也比较大。

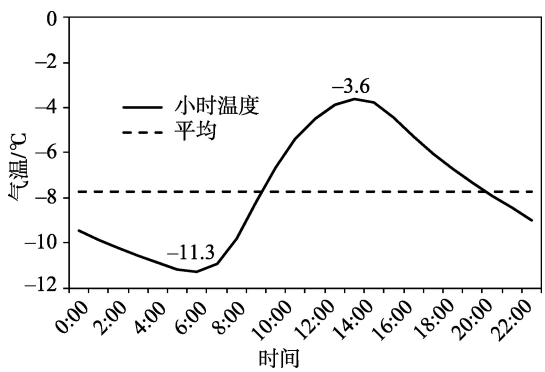

图3 哈尔滨采暖期间日内小时平均气温分布

Fig. 3 Distribution of hourly temperature in a day of heating period in Harbin

采暖期间小时平均气温分布如图3。日内24 h平均气温呈准正弦曲线分布，最高在午后14:00（−3.6 ℃），最低在清晨6:00（−11.3 ℃）。采暖期间的日内气温分布与年平均的日内气温分布略有差异，这是因为哈尔滨地处北半球45°N，采暖期太阳直射点大部分时间在南半球，日照时间短，日最高气温出现时间与全年平均接近，而最低气温出现时次较全年平均晚约1 h，出现在北京时间早晨6:00~7:00之间。

3 采暖强度

按式（3）计算采暖期平均及期间各月采暖强度。2005—2014年，哈尔滨采暖期平均每年累积采暖强度为1.1×10^5 ℃·h，最大1.2×10^5 ℃·h（2013年），最小1.0×10^5 ℃·h（2007年）（图4）。2007和2008年采暖期气温较高，采暖强度最小；2013和2010年气温

偏低，采暖强度最大。采暖强度分布与采暖期平均气温呈高度负相关，相关系数达到-0.99。

2005—2014年期间哈尔滨采暖期各月平均采暖强度如图5。各月平均累积采暖强度1月最大，为2.63×10^4 ℃·h，按数值从大到小顺序排列依次为1、12、2、11、3、4、10月，10月最小，仅为0.40×10^4 ℃·h。

采暖期平均的日内小时平均采暖强度分布与日内气温分布呈反位相关系（图6）。在2005—2014年期间，哈尔滨采暖期间平均每小时采暖强度为25.7 ℃·h；采暖强度日内呈现单峰分布形态，高值出现在清晨，06:00采暖强度最大，为29.3 ℃·h；低值发生在午后，14:00采暖强度最小，平均为21.6 ℃·h。图6还表明，北京时间每天晚上21:00到次日上午09:00，小时平均采暖强度大于日平均值，而上午09:00到晚上21:00采暖强度则明显低于日平均水平。

图7给出2005—2014年哈尔滨采暖期各月平均的日内小时平均采暖强度分布。各月平均小时采暖强度1月最大，为35.4 ℃·h，从大到小排列顺序与月累积采暖强度相同，依次为1、12、2、11、3、10、4月，4月最小，仅有12.0 ℃·h。10—4月，随着太阳高度角和日照时间的变化，日内各小时平均采暖强度分布存在明显差异。日内小时平均采暖强度最小值，3月和4月发生在午后15:00，其余月份出现在午后14:00；小时平均采暖强度最大值，1、2、12月出现在清晨07:00，3、10、11月在清晨06:00，4月在05:00。图7还表明，在隆冬时节小时平均采暖强度高时（1月和12月），昼夜采暖强度变化不大；但在小时平均采暖强度比较小的采暖期开

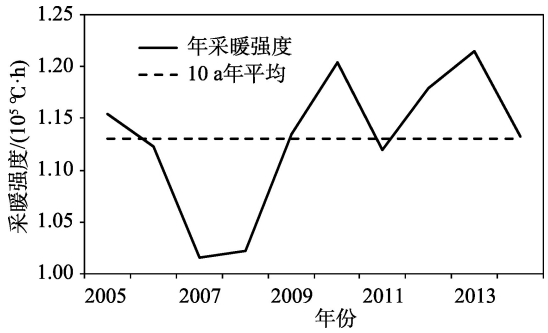

图4　哈尔滨市采暖期每年累积采暖强度（2005—2014年）

Fig. 4　The annual accumulated heating intensity of heating period in Herbin during 2005-2014

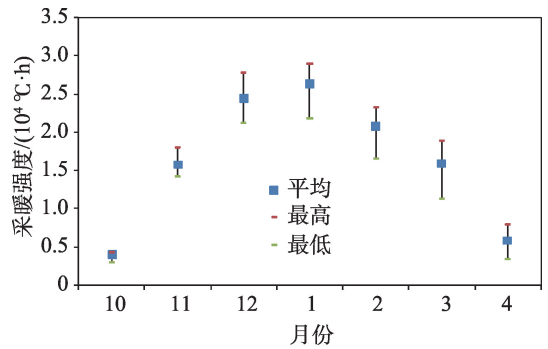

图5　哈尔滨市采暖期各月累积采暖强度（2005—2014年）

Fig. 5　The monthly accumulated heating intensity in Harbin City during 2005-2014

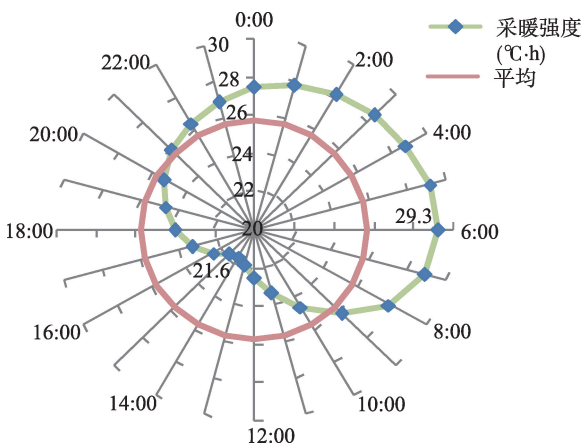

图6　哈尔滨市采暖期小时平均采暖强度分布（2005—2014年）

Fig. 6　Diurnal distribution of hourly mean heating intensity of heating period in Harbin during 2005-2014

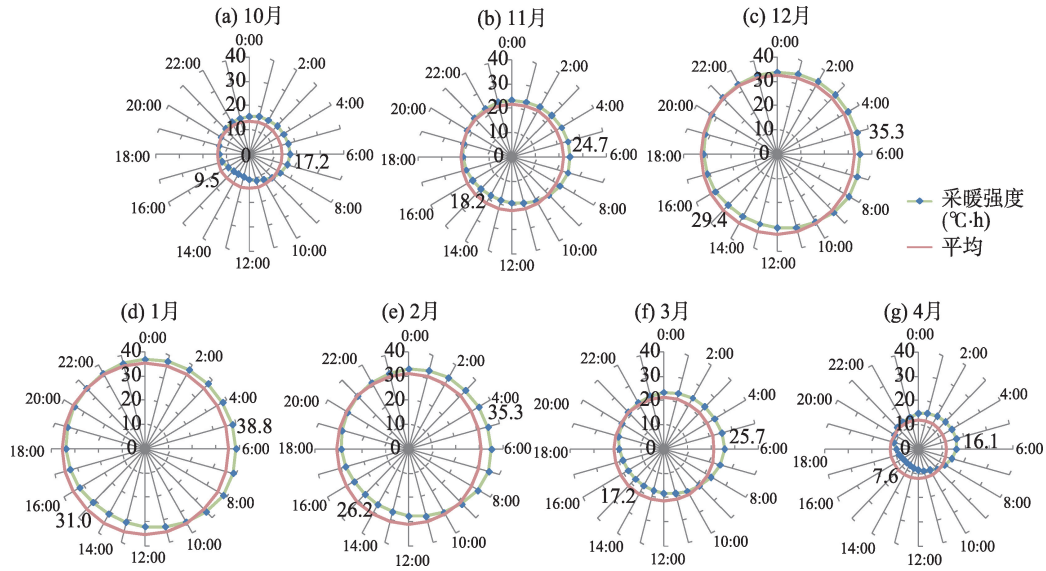

图7 哈尔滨市采暖期各月小时平均采暖强度分布（2005—2014年）

Fig. 7 Hourly mean heating intensity in each month of heating period in Harbin during 2005–2014

始阶段（10月20—31日）和结束前阶段（4月1—20日），昼夜小时平均采暖强度差异愈发明显。

图8表示哈尔滨采暖期小时平均采暖强度的时–日剖面，可以更清楚地看出采暖强度不同时间尺度上的分布规律。小时平均采暖强度最大值为42.4 ℃·h，出现在第87天（1月14日）清晨07:00、08:00，最小值为4.8 ℃·h，出现在采暖期末端4月18日下午14:00。在采暖期的两端（10月和4月）以及每天的中午到午后前期，是小时平均采暖强度较小时段；采暖期第60～120天间（12月中旬到2月下旬）采暖强度大，清晨北京时间05:00～08:00尤甚，在第83～93天（1月10—20日）的清晨06:00～08:00，出现整个采暖期的极大值，是采暖强度最高时刻。

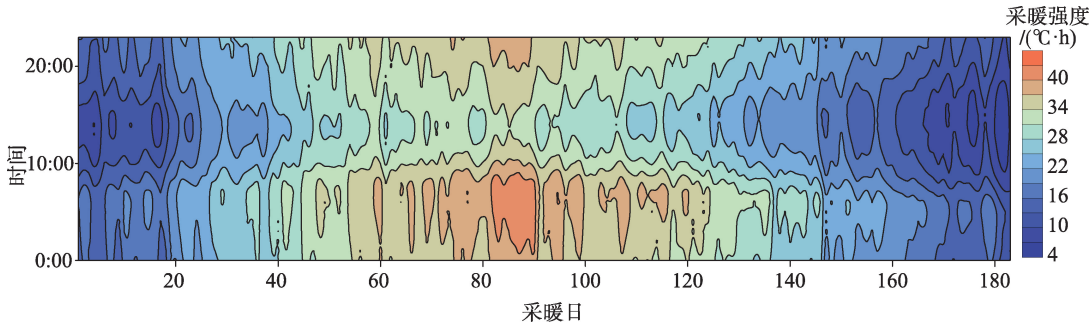

注：横坐标日期按下半年采暖初日（10月20日）为第1天，次年上半年采暖终日（4月20日）为第183天。

图8 哈尔滨市小时平均采暖强度时–日剖面图

Fig. 8 Hour-day profile of hourly mean heating intensity in Harbin

4 讨论

哈尔滨是我国地理位置最北的特大城市，每年的采暖耗能较高，采暖燃煤排放导致

的污染较严重。在提高燃煤质量及加强排放过滤的同时，提高能源利用率是很重要的节能减排、防治空气污染措施。本文分析获得的采暖期间各月及其日内采暖强度分布数据，对于合理有效供暖、提高能源利用率和节能减排、防治空气污染，具有实际参考价值。采暖部门可以根据采暖强度小时分布以及时-日剖面分布规律，结合考虑加热到户的滞后延时时间，精准规划给热供暖时间。

本文评价的依据是国标，以室内气温18 ℃作为采暖与否的标准。然而，实际上室内气温多数时候高于室外大气温度，同时由于建筑使用的材料不同，以及房屋结构等因素，这个室内外气温差异并不相同。因此，在采暖强度计算中，其结果相对真实的采暖需求会存在一个偏大的误差。文中计算没有对这个误差进行考虑处理。此外，集中供热的加热时间与不同距离建筑节点升温的时间差，本文也没有考虑。在实践中参考本文结果，这些问题还需要加以注意。

哈尔滨位于45°N，属中温带大陆性季风气候区。依据气象行业标准《气候季节划分》（QA/T152—2012）方法[24]和1981—2010年基准气候期数据，哈尔滨的冬季（日平均气温稳定低于10 ℃）持续时间为204 d[25]，始于10月2日，终于次年4月23日。但目前我国实际采暖起讫时间确定基本是以日平均气温稳定低于5 ℃为标准，这样哈尔滨采暖开始时间是10月20日，终结日期为4月20日，采暖期长度短于气候上的冬季。借助建筑物的绝热和蓄热性质，在采暖开始前和结束后的数日里，室外平均气温接近5 ℃时，室内气温一般可以保持在10 ℃左右。10 ℃左右的室内气温人体会感到不舒适，对健康与工作效率都有一定影响，简陋的房屋室内外温差更小，愈发感觉不舒适，严格来说也是存在采暖需求的。随着经济实力增强和人民生活水平提高，在大幅度提高建筑能效的基础上，未来哈尔滨也可能将调整采暖期标准，以提高居民的生活质量和工作效率。但是，本文分析评价的基本结论，对于未来延长采暖期后的供热计划和管理仍然具有参考价值。

观测资料的不确定性主要和观测点位置及其迁站有关。本文使用的10 a小时资料，其中2005—2012年是在旧址的观测记录，2013—2014年则是西北城外新址的观测记录。由于分析评价的采暖期平均小时气温和平均采暖强度变化，迁站引起的资料非均一性对于分析结果的影响应该很小。但平均气温和采暖强度最终应主要反映城市近郊附近的情况，而不是城市中心地区，城市热岛强度空间分布非均质性[26]的影响需要给予关注。由于城市热岛效应存在明显的空间差异，作为一个特大型城市，哈尔滨市中心区域平均气温无疑将比本文给出的结果略偏高，平均采暖强度略偏低；而且城市中心区域小时气温和采暖强度的日内变化也将与现在的计算分析结果略有差异，表现为夜间气温略偏高，采暖强度略偏低。今后，随着城市气象观测网密度加大，这种城市区域内部的气温和采暖强度差异也应该给予进一步分析评价。

5　结论

本文应用度时法和小时气温资料，计算分析了哈尔滨采暖期气温及其采暖强度的时间特征。得到以下主要结论：

1）哈尔滨集中供暖时间183 d，2005—2014年采暖期平均气温-7.7 ℃，其中2007和2008年采暖期平均气温最高，距平值均为2.6 ℃，2013年平均气温最低，距平值为-2.0 ℃。采暖期间平均的日内小时平均气温最高出现在午后14:00（-3.6 ℃），最低在清

晨06:00（−11.3 ℃）。

2）2005—2014年，哈尔滨平均年采暖强度1.1×10^5 ℃·h，最大1.2×10^5 ℃·h（2013年），最小1.0×10^5 ℃·h（2007年）。

3）哈尔滨采暖期间小时平均采暖强度为25.7 ℃·h，日内呈单峰分布，06:00采暖强度最大，为29.3 ℃·h，14:00采暖强度最小，为21.6 ℃·h；晚上21:00到次日上午09:00，小时平均采暖强度大于日平均值，而上午09:00到晚上21:00采暖强度则明显低于日平均水平。

4）采暖期各月平均的小时采暖强度1月最大，为35.4 ℃·h，从大到小按减少顺序依次是1、12、2、11、3、10、4月，4月小时采暖强度仅为12.0 ℃·h。

5）日内小时平均采暖强度最小值3、4月出现在午后15:00，其余月份在午后14:00；最大值1、2、12月发生在清晨07:00，3、10、11月在清晨06:00，4月在05:00。在每年1月中旬清晨06:00～08:00，出现整个采暖期采暖强度极大值。

参考文献(References)：

[1] 贺平, 孙刚, 王飞, 等. 供热工程 [M]. 北京: 中国建筑工业出版社, 2009: 9-34. [HE P, SUN G, WANG F, et al. Heating Engineering. Beijing: China Architecture & Building Press, 2009: 9-34.]

[2] 张家诚, 高素华, 潘亚茹. 我国温度变化与冬季采暖气候条件的探讨 [J]. 应用气象学报, 1992, 3(1): 70-75. [ZHANG J C, GAO S H, PAN Y R. Investigation on the relationship between temperature change and winter heating in China. Journal of Applied Meteorological Science, 1992, 3(1): 70-75.]

[3] 陈峪, 黄朝迎. 气候变化对能源需求的影响 [J]. 地理学报, 2000, 55(S1): 11-19. [CHEN Y, HUANG C Y. Impact of climate change on energy demand. Acta Geographica Sinica, 2000, 55(S1): 11-19.]

[4] 白美兰. 内蒙古地区冬季持续变暖对采暖的影响 [J]. 内蒙古气象, 2001(1): 26-27. [BAI M L. Impacts of winter continuous warming on heaing in Inner Mongolia. Mongolia Meteorology, 2001(1): 26-27.]

[5] 轩春怡, 高燕虎, 李慧君. 北京市冬季采暖气候条件分析 [J]. 气象科技, 2003, 31(6): 373-375. [XUAN C Y, GAO Y H, LI H J. Analysis of heating climatic condition in winter in Beijing. Meteorological Science and Technology, 2003, 31 (6): 373-375.]

[6] 李丽光, 王宏博, 赵先丽, 等. 辽宁中部城市群度日的变化特征 [J]. 气象科学, 2010, 30(3): 387-392. [LI L G, WANG H B, ZHAO X L, et al. Degree-day characteristics in the city group of middle Liaoning Province. Scientia Meteorologica Sinica, 2010, 30(3): 387-392.]

[7] 曹洁, 邱粲, 刘烯彬, 等. 山东省采暖与降温度日数的时空分布规律研究 [J]. 气象, 2013, 39(1): 94-100. [CAO J, QIU C, LIU H B, et al. Study on the temporal and spatial distribution of heating and cooling temperature days in Shandong Province. Meteorological Monthly, 2013, 39(1): 94-100.]

[8] 胡轶鑫, 刘玉英, 张晨琛, 等. 长白山地区采暖度日特征分析 [J]. 气象与环境学报, 2016, 32(4): 144-149. [HU Y X, LIU Y Y, ZHANG C C, et al. Characteristics of heating degree daya in the Changbai Mountains. Jorunal of Mereorology and Environment, 2016, 32(4): 144-149.]

[9] 陈莉, 李帅, 方修琦, 等. 中国严寒和寒冷地区城镇住宅采暖耗能影响因素分析——以吉林省为例 [J]. 地理科学, 2009, 29(2): 212-216. [CHEN L, LI S, FANG X Q, et al. Influence factor analysis of urban residential heating energy consumption in severe cold and cold regionsin China—A case of Jilin Province. Scientia Geographica Sinica, 2009, 29 (2): 212-216.]

[10] 陈莉, 方修睦, 方修琦, 等. 过去20年气候变暖对我国冬季供暖气候条件与能源需求的影响 [J]. 自然资源学报, 2006, 21(4): 590-597. [CHEN L, FANG X M, FANG X Q, et al. Impacts of climate warming on heating climatic conditions and energy requirements over China in the past 20 years. Journal of Natural Resources, 2006, 21(4): 590-597.]

[11] 陈莉, 李帅, 覃雪, 等. 东北地区采暖气候条件变化特征及预测 [J]. 自然资源学报, 2014, 29(7): 1185-1195. [CHEN L, LI S, QIN X, et al. Change characteristics and prediction of climatic conditions of heating in Northeast China. Journal of Natural Resources, 2014, 29(7): 1185-1195.]

[12] 李明财, 郭军, 史珺, 等. 利用采暖/制冷度日分析建筑能耗变化的适用性评估 [J]. 气候变化研究进展, 2013, 9(1): 43-48. [LI M C, GUO J, SHI J, et al. Applicability evaluation of cooling/heating degree-days in analyzing building energy consumption changes. Advances in Climate Change Research, 2013, 9(1): 43-48.]

[13] ROSENTHAL D H, GRUENSPECHT H K, MORANET E A. Effects of global warming on energy use for space heating and cooling in the United States [J]. Energy Journal, 1995, 16(2): 77-96.

[14] SATMAN A, YALCINKAYA N. Heating and cooling degree-hours for Turkey [J]. Energy, 1999, 20(10): 833-840.

[15] PAPAKOSTAS K, KYRIAKIS N. Heating and cooling degree-hours for Athens and Thessaloniki, Greece [J]. Renewable Energy, 2005, 30(12): 1873-1880.

[16] BOLATTÜRK A. Optimum insulation thicknesses for building walls with respect to cooling and heating degree-hours in the warmest zone of Turkey [J]. Build and Environment, 2008, 43(6): 1055-1064.

[17] KADIOGLU M, ZEKAI S. Degree-day formulations and application in Turkey [J]. Journal of Applied Meteorology and Climatology, 1999, 38(6): 837-846.

[18] 张海东. 气候变化对我国取暖和降温耗能的影响及优化研究 [D]. 南京: 南京信息工程大学, 2007. [ZHANG H D. Influence of Climate Change on Warming/Cooling Energy Consumption and Optimization. Nanjing: Nanjing University of Information Science and Technology, 2007.]

[19] THOM H C S. Seasonal degree day statistics for the United States [J]. Monthly Weather Review, 1952, 80(9): 143-147.

[20] THOM H C S. The rational relationship between hearing degree days and temperature [J]. Monthly Weather Review, 1954, 82(1): 1-6.

[21] THOM H C S. Normal degree days above any base by the universal truncation coefficient [J]. Monthly Weather Review, 1962, 94(7): 461-465.

[22] 中华人民共和国建设部. 采暖通风与空气调节设计规范 (GB50019—2003) [S]. 北京: 中国计划出版社, 2003: 25-350. [Ministry of Construction, P R china. Code for design of heating, ventilation and air conditioning (GB50019–2003). Beijing: China Planning Press, 2003: 25-350.]

[23] 刘小宁, 张洪政, 李庆祥. 不同方法计算的气候平均值差异分析 [J]. 应用气象学报, 2005, 16(3): 345-356. [LIU X N, ZHANG H Z, LI Q X. Analyses on average temperature difference resulted from different calculation methods. Journal of Applied Meteorological Science, 2005, 16(3): 345-356.]

[24] 中国气象局. 气候季节划分QX/T152—2012 [S]. 北京: 气象出版社, 2012. [China Meteorological Administration. Climatic Seasons QX/T152–2012. Beijing: China Meteorological Press, 2012.]

[25] 刘玉莲. 1961—2010年黑龙江省气候季节时空分布及其变化特征 [J]. 气象与环境学报, 2015, 21(2): 89-96. [LIU Y L. Temporal and spatial distribution of climatic season and its variation from 1961 to 2010 in Heilongjiang Province. Journal of Meteorology and Environment, 2015, 21(2): 89-96.]

[26] YANG P, REN G Y, LIU W D. Spatial and temporal characteristics of Beijing urban heat island intensity [J]. Journal of Applied Meteorology and Climatology, 2013, 52: 1803-1816.

Analysis of Heating Intensity in Harbin Based on Degree-hours Method

LIU Yu-lian[1,3], REN Guo-yu[2,3]
(1. Heilongjiang Climate Center, Harbin 150030, China; 2. Department of Atmospheric Science, School of Environmental Science, China University of Geosciences, Wuhan 430074, China; 3. Laboratory for Climate Studies, National Climate Center, CMA, Beijing 100081, China)

Abstract: Compared to degree- day, degree- hour is more realistic to indicate the heating intensity. Using the degree- hour method and hourly temperature data of 2005– 2014, the characteristics of temperature and heating intensity of the heating period in Harbin City were analyzed. The main conclusions include: 1) During the 183 days of Harbin heating period, the average temperature was −7.7 ℃. Higher temperatures appeared in 2007 and 2008, which were 2.6 ℃ higher than the average, and the lower temperature occured in 2013, which was 2.0 ℃ lower than the average. 2) During the period of 2005– 2014, the average annual heating intensity was 1.1×10^5 ℃·h, with the maximum value 1.2×10^5 ℃·h (2013), and the minimum value 1.0×10^5 ℃·h (2007). The highest heating intensity was in January, and the lowest was in April; the maximum hourly mean heating intensity appeared in the early morning, and the minimum hourly mean heating intensity appeared in the early afternoon. 3) The hourly mean heating intensity of Harbin heating period was 25.7 ℃·h, and the diurnal distribution of hourly mean heating intensity was opposite to the temperature. The maximum hourly mean heating intensity, 29.3 ℃·h, was at 06:00 am, while the minimum value, 21.6 ℃·h, was at 14:00 pm. The heating intensity was generally higher than the average during the period from 21:00 pm to 09:00 am, and was lower than the average during the period from 09:00 am to 21:00 pm. 4) January has the maximum hourly mean heating intensity of 35.4 ℃·h, followed by December, February, November, March, October, and April had the minimum of only 12.0 ℃·h. 5) The minimum hourly mean heating intensity was at 15:00 pm in March and April, and was at 14:00 pm in other months of the heating period; the maximum hourly mean heating intensity was generally at 07:00 am in January, February and December, and happened at 06:00 am in March, October and November, and 05:00 am in April. The highest hourly mean heating intensity happened from 06:00 am to 08:00 am in mid-January.

Key words: degree-days; degree-hours; temperature; heating intensity; Harbin

地面气温对微环境空间差异的响应——以漠河站为例

刘玉莲[1,2] 任国玉[2,3*] 张广英[4] 于宏敏[5]

(1 黑龙江省气候中心,哈尔滨 150030; 2 中国地质大学环境学院大气科学系,武汉 430074; 3 中国气象局气候研究开放实验室 国家气候中心,北京 100081; 4 黑龙江省大兴安岭地区气象局,加格达奇 165000; 5 黑龙江省公共气象服务中心,哈尔滨 150002)

摘要 测站附近微环境条件对地面气温观测记录的影响目前还不清楚。本文对 2010 年漠河国家基准气候站地面观测对比试验数据进行了分析,得到如下结论:①年平均地面气温近障碍物点低于标准观测场内,但 1、6 月的月平均气温近障碍物点偏高;②06:00—17:00 和 21:00,近障碍物地点的气温偏低;18:00 至次日 05:00(除 21:00),近障碍物点气温偏高;③春季各时次近障碍物点地面气温均偏低;夏季 06:00—17:00 近障碍物点气温偏低,18:00 至次日 05:00 相反;秋季仅 01:00、03:00、19:00、23:00 近障碍物点气温偏高,其他时次相反;冬季 07:00—19:00 近障碍物点气温偏低,20:00 至次日 06:00 相反。冷季近障碍物点气温偏低;暖季昼间近障碍物点气温偏低,夜间相反;④日最高、最低气温出现时间不同地点大体相同,最高气温近障碍物点偏低,最低气温近障碍物点偏高,但最高气温偏低绝对值大于最低气温偏高绝对值;⑤有雾情况下近障碍物地点的气温偏高几率大;雨雪多云天气近障碍物地点气温均偏低;晴朗的白天近障碍物地点的气温偏低,有风天气更明显;而晴朗的夜间近障碍物地点气温偏高,无风天气更明显;晴朗天气条件下,无风时近障碍物地点与观测场内气温差值大于有风时。结果表明,地面气温观测记录对台站观测场附近微环境改变十分敏感,微环境条件的变化将导致地面气温观测出现明显不连续性,对气候变化分析产生影响。

关键词 微环境;地面观测;对比试验;障碍物;气温;偏差

中图分类号: P461 **DOI**: 10.19517/j.1671-6345.20170200 **文献标识码**: A

引言

气候变化分析需要均一性地面气温观测资料序列。但是,很多因素可以导致地面气温观测资料的非均一性,致使长序列资料在气候变化研究中的应用价值大打折扣。长期以来,研究者对站址迁移、观测仪器变更、观测时次变化和计算日平均值方法的改变等引起的气温观测资料非均一性给予很多关注,并采用多种方法进行订正[1-4],而对于观测场内部和附近由于各种原因引起的微环境变化重视不多。如何评价和消除这些由于微环境改变造成的资料非均一性,对于气候和气候变化研究同样是重要的理论基础并具有实际意义。

气象观测环境是指为避开各种干扰保证气象观测设施准确获得气象信息所必需的最小距离构成的环境空间。地面气象观测场是取得地面气象资料的主要场所,根据《地面气象观测规范》[5]和《气象探测环境和设施保护办法》[6]规定,地面气象观测场必须符合探测环境的技术要求。气象观测是在自然条件下进行的,观测资料是具有区域代表性的真实气象记录。这里的观测环境在很大程度上指测站附近的微环境,如果遭受破坏,观测资料序列可能会出现非均一性。

许多研究者分析了地面气象观测环境变化对气温观测的影响[7-8]。这些工作包括对迁站前后气温观测对比的分析[9-10],多站或单站台站环境自身变

国家自然科学基金项目(41575003)、国家公益性行业(气象)科研专项(GYHY201206012、GYHY201106013)资助

作者简介:刘玉莲,女,1974 年生,高级工程师,主要从事区域气候变化研究,Email: Liuyl74@qq.com

收稿日期:2017 年 4 月 6 日;定稿日期:2017 年 8 月 4 日

* 通信作者,Email: guoyoo@cma.gov.cn

化对气象要素观测影响分析[11-13]，处于不同位置环境的多站气温观测对比分析[14-16]，仪器和环境引起的观测误差对气温变化趋势的影响评估等[17-19]。总体上看，已有文献针对观测场附近微环境变化可能影响的研究比较少。

2009 年，中国气象局国家气候中心在黑龙江省漠河国家观象台（简称漠河站）开展了观测场附近地面气温对比观测试验。试验设置 2 个对比气温探测仪，1 个在地面气象观测场内，1 个在地面气象观测场外，靠近场外人工建筑物（值班室）。2 个仪器具有相同探测高度，相同仪器型号，同时对地面气温进行连续探测，同一收集系统获取对比观测数据。本文利用漠河站 2010 年 1 年的对比观测数据，分析观测场周边障碍物等微环境条件对地面气温观测记录的影响。

1 台站位置、环境及对比观测试验

黑龙江省漠河县位于大兴安岭北部，是我国纬度最高的县，其南面和西面为大兴安岭主脉，境内属于低山丘陵，四面隆起，中部为山间盆地。冬季漫长寒冷，夏季短暂温热，属于寒温带大陆性季风气候。

漠河站建于漠河县西林吉镇西北城郊，52°58′N，122°31′E，观测场海拔高度 433.0 m。观测场东面为林区和居民（0.5 km 外），南方 20 km 内均为林区，西为林区和居民点（1 km 外），北为林区和居民点（图 1a）。观测场周围地势较平坦，地表为植被覆盖，视野开阔，人为障碍物较少，仅正北面有业务办公楼，其地平圈遮蔽情况和人为障碍物仰角见图 1b。观测场北边的业务办公楼高 4.5 m，距离观测场北边缘 52 m。

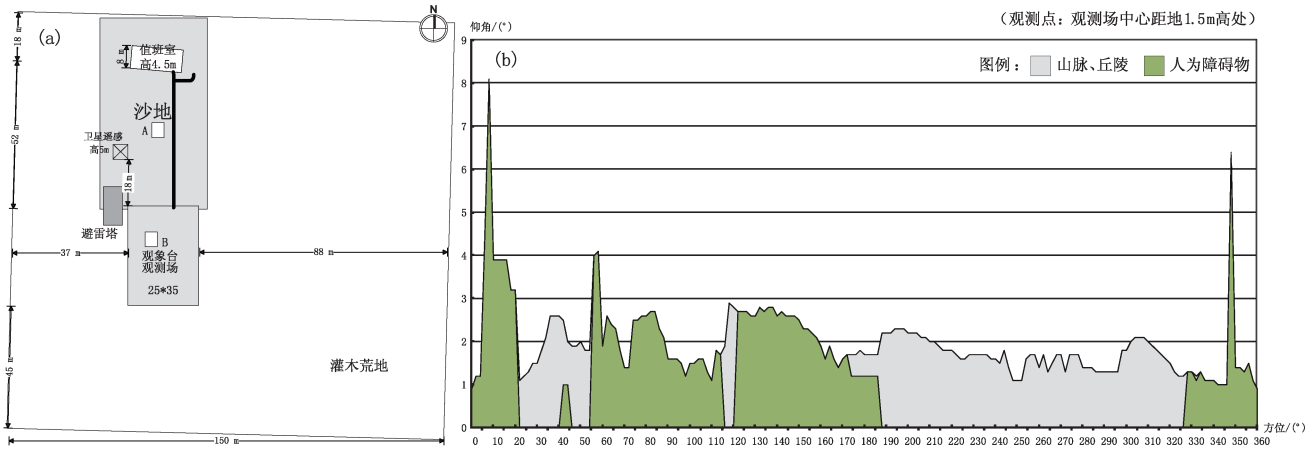

图 1 漠河站址平面示意图（a）及地平圈遮蔽和人为障碍物仰角图（b）

对比观测的 2 个气温探测仪 1 个位于值班室与观测场之间（地点 A），距离观测场 25 m 的百叶箱内（近障碍物）；另 1 个置于观测场内百叶箱中（地点 B），型号都是 RCY-1A，河北高碑店厂家生产。气温对比观测资料是 2010 年 1 月 1 日至 12 月 31 日 1 年的数据，分别以地点 A 气温和地点 B 气温指代。两地点气温差是指地点 A 气温减地点 B 气温的差值。

2 资料质量

本文使用漠河对比观测试验收集的观测数据进行分析，原始观测为每分钟观测 1 次，每个时次内 60 个分钟观测记录的平均为时观测数据，如果时次内有观测数据缺失，按实有观测数据取平均，时次内无记录则记为缺测。

观测使用的 RCY-1A 型数字测温仪最小分辨率为 0.01 ℃，基本误差±0.03 ℃。由于本文旨在检测不同微环境条件下的气温微小差异，所以保留小数点后 2 位数据，以对观测差异有更细致地了解。分析结果中可能存在误差范围内的偏差，为减小这种偏差影响，使用数据最小时间单元为小时平均（时次内 60 个分钟数据记录的平均值），这种处理可对随机误差进行平滑。

由于仪器、采集故障等偶发原因，观测记录基本完整但也偶有缺失。年内时观测数据缺测率不到 4‰，考虑缺测数据出现的月份和时次较为均匀，本文对其未做更多处理，不做统计。

分析有记录数据，9 月存在 1 个时次的观测明

显偏差,查对国家观象台地面观测记录,期间无特殊天气现象记录,排除天气影响,确认为仪器故障;12 月存在连续 4 个时次明显偏差,且有 1 组记录连续 3 h 没有变化,期间无特殊天气现象记录,认为是仪器故障。计算前后 4 d 同一时次差值平均为基准差,参照记录正确的另 1 组观测数据进行订正。

3　结果分析

3.1　年、月、候平均气温差值

2010 年,地点 A 年平均气温为－4.37 ℃,地点 B 为－4.30 ℃,其差值为－0.07 ℃,即近障碍物地点年平均气温比观测场内约低 0.07 ℃。

A、B 两点各月平均气温差值仅 1、6 月为正,且 1 月差值大于 6 月,其余各月均为负值,即 1 年大部分时间地点 A 气温低于地点 B;差值绝对值最大为 5 月,地点 A 平均气温低于地点 B 约 0.15 ℃;其次为 12、3、10、11、4 月,其地点 A 的平均气温值低于地点 B 超过 0.1 ℃(表 1)。

从候平均气温看,1 年中地点 A 气温偏高有 19 候,1—10、32、34—36、39、44、46、48、50 候,偏高最多为第 3 候(0.14 ℃,1 月 11 日—15 日),其他各候地点 A 气温都偏低,偏低最多为第 12 候(－0.25 ℃,2 月 26—28 日),持续偏低时段为 11—31 候(2 月 21 日—6 月 5 日)和 51—72 候(9 月 11 日—12 月 31 日)。因此,1 年大部分候 A 点气温比 B 点来的低,但夏季几乎没有差异,冬季 1 月和 2 月上中旬则 A 点气温比 B 点平均气温明显高(图 2)。

表 1　2010 年漠河站近障碍物地点 A 与观测场内地点 B 月、年平均气温差值　℃

1 月	2 月	3 月	4 月	5 月	6 月	7 月	8 月	9 月	10 月	11 月	12 月	年
0.07	－0.01	－0.14	－0.12	－0.15	0.01	－0.02	－0.01	－0.05	－0.12	－0.12	－0.14	－0.07

注:差值为地点 A 气温减地点 B 气温的差值,下同。

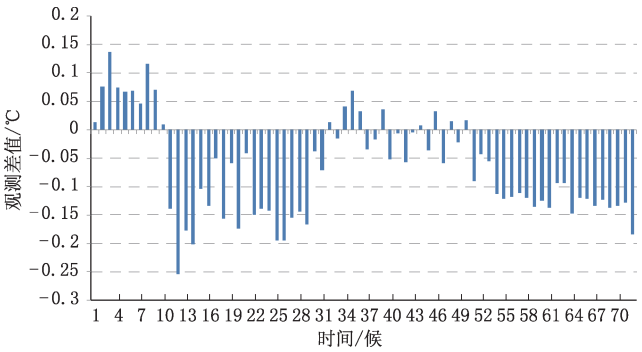

图 2　2010 年漠河站近障碍物地点 A 与观测场内地点 B 候平均气温差值
(差值为地点 A 气温减地点 B 气温,下同)

3.2　小时平均气温差值

图 3 给出 2010 年全年中每天 24 个时次地点 A 与地点 B 平均气温差值。可见,各时次中,06:00—17:00,地点 A 的观测气温较地点 B 低,其差值为明显负值;18:00 至次日 05:00(除 21:00),地点 A 的气温较地点 B 略高,差值为正;11:00 负差值的绝对值最大,地点 A 的气温较地点 B 低 0.23 ℃;23:00,正差值的绝对值最大,但地点 A 的气温较地点 B 仅高出 0.05 ℃。因此,白天近障碍物点地面平均气温较观测场内点明显低,而夜晚一般相反,近障碍物点地面平均气温较观测场内点略高,但差异很小。

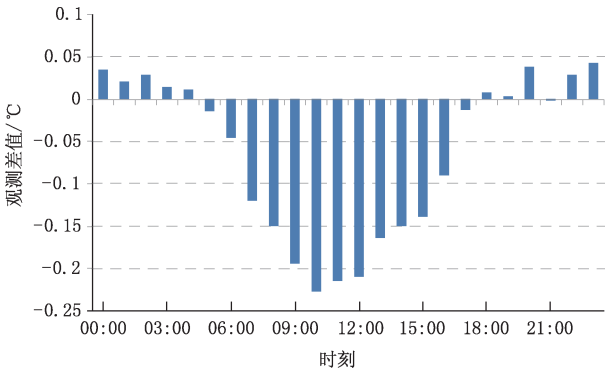

图 3　2010 年漠河站近障碍物地点 A 与观测场内地点 B 每时次平均气温差值

图 4 表示地点 A 和地点 B 各月每 1 天不同时次地面平均气温差值。可见,不同月份各时次地点 A 气温偏高于地点 B 的有:1 月 18 个时次(15:00—16:00、18:00 至次日 09:00)、2 月 11 个时次(19:00 至次日 07:00)、4 月 5 个时次(00:00—04:00)、5 月 2 个时次(20:00 和 23:00)、6 月 15 个时次(15:00 至次日 05:00)、7 月 11 个时次(18:00 至次日 04:00)、8 月 12 个时次(18:00 至次日 05:00)、9 月 13 个时次(18:00 至次日 06:00)、10 月 1 个时次(19:00)。上述各月其他时次,以及 3 月、11 月和 12 月全部时次,地点 A 气温一般明显低于地点 B。

地点 A 与地点 B 气温差值绝对值最大的时次，正值在 7 月的 20:00(0.23 ℃)，负值在 4 月的 10:00(−0.37 ℃)。

不同时次间波动较大的月份是 2 月、6 月和 7 月，均为 0.44 ℃，波动较小月份是 3 月、11 月和 12 月，均在 0.28 ℃以下；不同月份间波动较大的时次是 19:00(0.45 ℃)、22:00(0.40 ℃)和 08:00(0.39 ℃)，波动较小时次是 17:00、12:00 和 18:00，一般在 0.24 ℃以下。

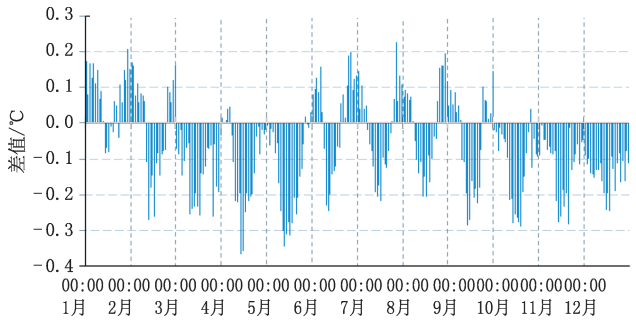

图 4 2010 年漠河站近障碍物地点 A 与观测场内地点 B 各月不同时次平均气温差值

图 5(彩页)表示漠河站地点 A 与地点 B 平均气温差值的小时-候时间剖面。地点 A 与地点 B 平均气温差值正值集中分布在第 10 候(2 月 20 日)前的 08:00 前和 18:00 后(即隆冬时节的夜间)，以及第 30—50 候(5 月 25 日至 9 月 10 日)的 06:00 前和 18:00 后(即盛夏时节的夜间)；负值集中出现在各候的 08:00—16:00 之间，其中第 10—30 候的白天的负值绝对值最大。

按不同季节，分别统计不同时次地点 A 与地点 B 平均气温差值。季节划分采用 2 种方法：①气象学上的划分季节方法，3—5 月为春季，6—8 月为夏季，9—11 月为秋季，12 月至次年 2 月为冬季；②按冷暖半年来分，10 月至次年 3 月为冷季，4—9 月为暖季。为了对比日间与夜间气温差异，记 08:00—19:00 为昼，20:00 至次日 07:00 为夜。

春季各个时次地点 A 与地点 B 平均气温差值均为负，即地点 A 气温低于地点 B 气温；夏季日间 06:00—17:00 气温差值为负，地点 A 气温低于地点 B 气温，夜间 18:00 至次日 05:00 差值为正，地点 A 气温高于地点 B 气温；秋季仅 01:00、03:00、19:00、23:00 差值为正，其他时次均为负；冬季日间 07:00—19:00 差值为负，夜间 20:00 至次日 06:00 差值为正(图 6，彩页)。

地点 A 与地点 B 平均气温正差值最大为夏季的 20:00，为 0.20 ℃；负差值绝对值最大出现在春季的 10:00，为−0.29 ℃；四季日间气温差值平均都为负，夏季绝对值最小(−0.01 ℃)，冬季次小(−0.03 ℃)，秋季再次(−0.10 ℃)，春季最大(−0.13 ℃)。

春、秋季昼、夜间地点 A 与地点 B 平均气温差值都为负，夏、冬季昼为负，夜为正；四季气温差值昼间都低于夜间。

按冷暖季划分，冷季地点 A 与地点 B 平均气温差值昼、夜平均都为负，即地点 A 低于地点 B 观测气温，日间平均差值(−0.13 ℃)比夜间(−0.02 ℃)低；暖季地点 A 与地点 B 平均气温差值昼为负(−0.14 ℃)、夜为正(0.03 ℃)，即日间地点 A 气温低于地点 B，夜间则相反(表略)。

3.3 最高和最低气温

地点 A 与地点 B 每日最高、最低气温出现时间基本一致(图 7，彩页)。最高气温出现在下午 15:00 的频次最多，其次是 14:00、16:00；最低气温出现频次最多时间在午夜 23:00，其次是 06:00 和 04:00、05:00。地点 A 年平均最高气温为 3.96 ℃，地点 B 为 4.10 ℃，差值为−0.14 ℃；地点 A 年平均最低气温是−12.63 ℃，地点 B 是−12.66 ℃，差值为 0.03 ℃。最高气温地点 A 较地点 B 偏低，差异较明显；最低气温地点 A 较地点 B 偏高，但差异较小。

地点 A 与地点 B 各月日较差除 3 月地点 A 较大外，其他月份都是地点 B 较大(表 2)。9 月这个差值最大，这个月份地点 B 的日较差较地点 A 大的最多，其次是 5、4、2、11 月份。

1、6 月最高气温地点 A 偏高，1 月最高；其他月份地点 A 偏低，5 月最低，其次为 10、11 月；1、2、4、6、7、8、9 月最低气温地点 A 偏高，1 月最高，其次是 6 月，其他月份地点 A 偏低，10 月最低，其次为 12、3 月。

3.4 不同天气条件观测对比分析

结合本站基准观象台地面观测记录，按照天气条件，分别统计分析 2 地点观测的差异。天气类型分为雾天、雨雪多云、晴朗有风与晴朗静稳无风 4 种。

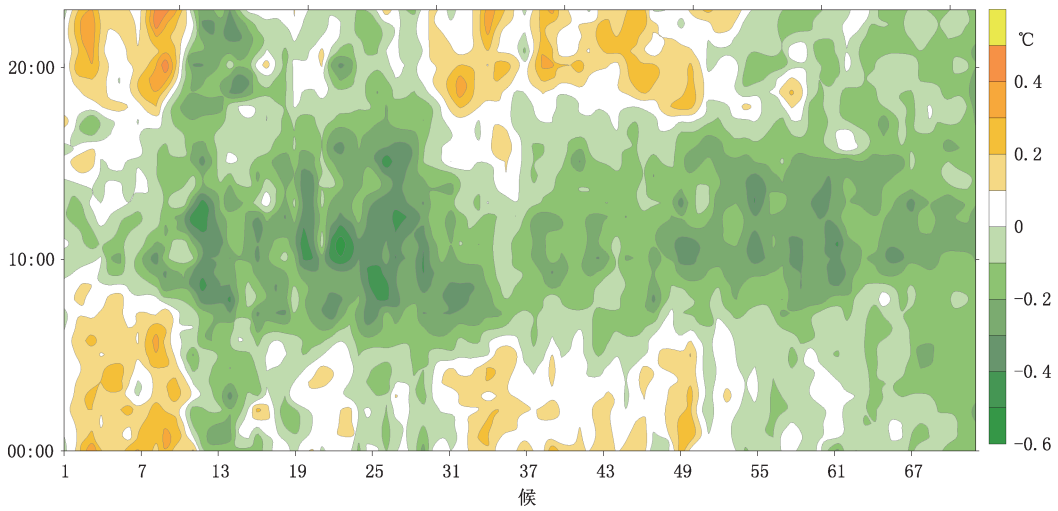

图 5　2010 年漠河站近障碍物地点 A 与观测场内地点 B 平均气温差值小时-候时间剖面图

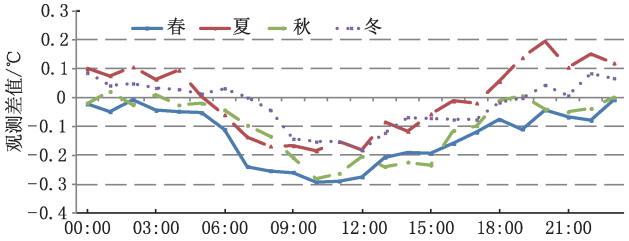

图 6　2010 年漠河站近障碍物地点 A 与观测场内地点 B 各季节平均小时气温差值

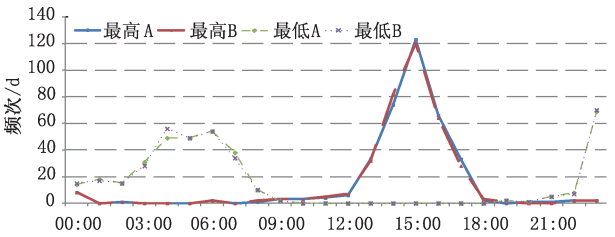

图 7　2010 年漠河站近障碍物地点 A 与观测场内地点 B 每日不同时刻最高、最低气温出现频次

表 2　2010 年漠河站近障碍物地点 A 与观测场内地点 B 各月最高、最低观测气温的差值及日较差的差值　℃

	1 月	2 月	3 月	4 月	5 月	6 月	7 月	8 月	9 月	10 月	11 月	12 月
最高气温	0.06	−0.12	−0.06	−0.22	−0.28	0.02	−0.11	−0.08	−0.23	−0.25	−0.24	−0.11
最低气温	0.17	0.096	−0.08	0.01	−0.04	0.15	0.10	0.09	0.10	−0.13	−0.02	−0.10
日较差差值	−0.11	−0.22	0.02	−0.23	−0.25	−0.13	−0.21	−0.17	−0.33	−0.12	−0.21	−0.01

统计漠河国家观象台每日的地面天气现象观测记录,2010 年漠河出现雾的天数为 61 d,占全年天数比例 16.71%(2010 年 365 d),分钟观测记录为 14886 个,占实有观测记录比例 2.85%(实有观测记录 521421 个);雨雪多云出现的天数为 148 d,占全年天数比例 40.54%,分钟观测记录 61515 个,占实有观测记录比例 11.8%。

结合漠河国家观测台每日 4 次(02:00、08:00、14:00、20:00)的定时风速观测资料,分析在不同风速条件下 A、B 点对比观测气温。观测定时风为 2 min 风速平均,每日 4 次定时观测、每定时 2 min 平均,则年实有记录 2904 次,去除雨雪多云还有 2561 个记录,比例为 88.19%。

3.4.1　雾天

图 8 给出有雾和全天气条件下两观测点气温差值变化及其比较。图 8a 是有雾出现时次两点气温差值、全天气现象时两点气温差值,图 8b 表示有雾与全天气现象两观测点气温差值的差。

漠河雾出现最多的季节是夏季,其次是冬季,初秋和晚春少有发生;1 天内雾出现在夜里 22:00 后,最晚可持续到下午 13:00。除 05:00、06:00、07:00 和 12:00,有雾与全天气现象两观测点气温差值为负(负值最小在 06:00),其余时次均为正(正值最大是 22:00)。正值表示有雾时两观测点气温差值高于全天气现象时两观测点气温差值,负值表示有雾时两观测点气温差值低于全天气现象时两观测点气

温差值。有雾和全天气现象的气温差值符号一致，而其差值却为正，可见，尽管有雾出现时两观测点气温差值与全天气现象时具有一致的日变化（均在05:00到13:00之间为负值，23:00至次日清晨05:00为正值），但雾天条件下两观测点气温差值负值的绝对值比在全天气现象来的小，而正值比在全天气现象来的大。这说明，雾天情况下，白天障碍物对空气温度的降温作用较全天气现象小，而夜间的增温作用较全天气现象大。

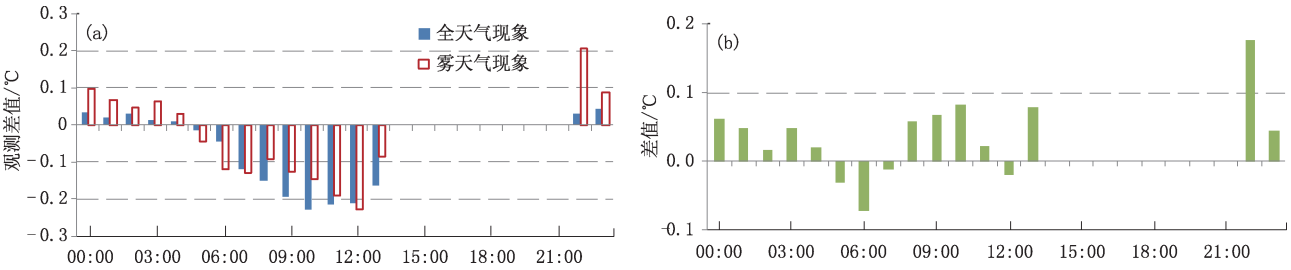

图 8 2010 年漠河站近障碍物地点 A 与观测场内地点 B 雾天与全天气现象分时平均差值(a)和有雾与全天气象现象两观测点观测差的差值(b)

3.4.2 雨雪多云

统计 2010 年漠河雨雪多云天气出现的时间，计算分析两观测地点气温差值与全天气现象观测差值的不同（雨雪多云天气包括雷暴、雨、阵雨、雨夹雪、雪、阵雪、阵性雨夹雪）。

雨雪多云天气各时次平均地点 A 与地点 B 观测气温差值都是负值（图 9），即地点 A 的观测气温较地点 B 的观测气温低。与全天气现象各时次平均差值相比，07:00—15:00 雨雪多云天气平均差值大于全天气现象差值（雨雪多云天气 07:00—15:00 地点 A 气温观测值与地点 B 观测值差值绝对值低于全天气现象差值绝对值），16:00 至次日 06:00 雨雪天气平均差值低于全天气现象差值。这说明，雨雪多云天气条件下，无论白天还是夜间，障碍物对观测空气温度的影响都表现为降温，白天的降温幅度高于夜间，而低于全天气现象时的障碍物降温效果。

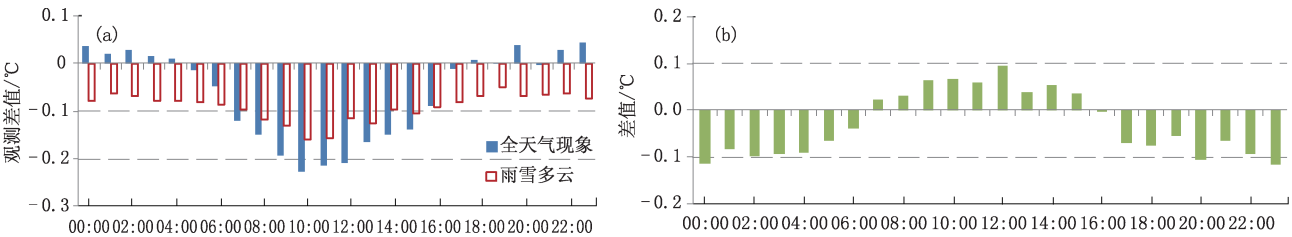

图 9 2010 年漠河站近障碍物地点 A 与观测场内地点 B 雨雪多云天气与全天气现象分时平均差值(a)和雨雪多云天气与全天气象现象两点观测差的差值(b)

3.4.3 晴朗有风和晴朗静稳无风

不同风速条件下的对比观测差值见图 10。风速小于 2.0 m/s 时取 0.1 m/s 间隔平均，2.0～3.0 m/s 之间取 0.5 m/s 间隔平均，3.0～5.0 m/s 之间取 1.0 m/s 间隔平均，5.0 m/s 风速以上平均，并统计小于 1.0 m/s 风速（无风）和大于等于 1.0 m/s 风速（有风）时的平均差值。可见，当风速为 0 m/s、0.1 m/s 和 0.9 m/s 时，地点 A 与地点 B 的差为正，即地点 A 的观测气温大于地点 B；当风速在 1.0 m/s 以上时，地点 A 与地点 B 的差都为负，其中风速为 1.6 m/s 时差值绝对值最小。

参考天气现象观测记录，以 1.0 m/s 风速为界，风速大于等于 1.0 m/s 为有风，风速小于 1.0 m/s 为无风，无雨、雪、霜、露现象为晴朗，提取全年漠河每日 4 次观测时晴朗有风和晴朗静稳无风天气条件分析对比观测气温。

表 3 说明，晴朗静稳无风时观测差值大于晴朗有风时观测差值。晴朗天气，白天地点 A 观测气温低于地点 B，夜间地点 A 观测气温高于地点 B；晴朗的白天，有风天气地点 A 的观测气温更低于地点 B

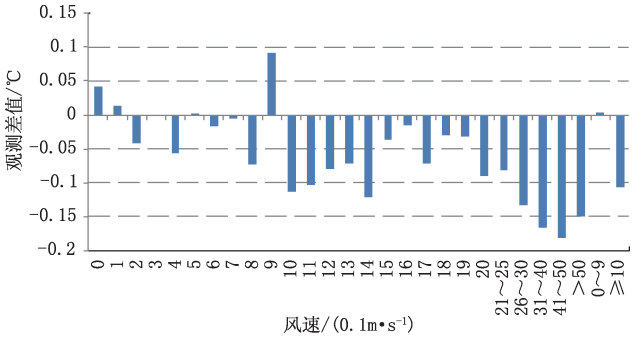

图 10　2010 年漠河站不同风速条件下 A、B 观测点观测差值

观测气温,晴朗的夜间,无风天气地点 A 的观测气温更高于地点 B 的观测气温。晴朗天气里,无论白天还是夜间,地点 A 与地点 B 的观测差值都是无风天气大于有风天气。

晴朗天气,夜晚近建筑物处接收建筑物辐射热减缓气温下降速率,远离建筑物空旷处气温更低,无风天气更明显;白天近建筑物处气温较远离建筑物空旷处气温低,有风天气更明显。

表 3　晴朗有风和晴朗静稳无风每日 4 次定时观测气温差值　　℃

时次	无风	有风	无风-有风
02:00	0.07	0.00	0.07
08:00	−0.11	−0.24	0.14
14:00	−0.08	−0.17	0.09
20:00	0.08	0.02	0.06

4　结论与讨论

(1)近障碍物观测点与标准地面气象观测场内观测点对比差值年平均为−0.07 ℃,即近障碍物点年平均气温低于标准观测场内气温;各月平均观测差值 1、6 月为正,地点 A 气温高于地点 B,其余各月观测差值均为负,地点 A 气温低于地点 B;地点 A 气温偏高的候仅有 1—10、32、34—36、39、44、46、48、50 候。

(2)各时次中,06:00—17:00 和 21:00,地点 A 的观测气温较地点 B 低;18:00—05:00(除 21:00),地点 A 的观测气温较地点 B 高;11:00,差值负的绝对值最大,地点 A 的气温较地点 B 低的最多;23:00,差值正的绝对值最大,地点 A 的气温较地点 B 高的最多。

(3)春季(3—5 月)各时次地点 A 观测气温都低于地点 B;夏季(6—8 月)日间 06:00—17:00 地点 A 观测气温低于地点 B,其他时次地点 A 高于地点 B;秋季(9—11 月)仅 01:00、03:00、19:00、23:00 地点 A 高于地点 B;冬季(12 月至次年 2 月)日间 07:00—19:00 地点 A 低于地点 B。总体看,冷季(10 月至次年 3 月)地点 A 低于地点 B 观测气温;暖季(4—9 月)昼间地点 A 观测气温低于地点 B,夜间相反。

(4)地点 A 和地点 B 日最高、最低气温出现时间大体相同,最高气温 A 点较 B 点偏低,最低气温 A 点较 B 点偏高,最高气温偏低绝对值大于最低气温偏高绝对值。

(5)有雾情况下两观测点对比观测差值,在全天气现象时为正的时次段里,正值更大,即地点 A 的观测气温更高于地点 B,在全天气现象为负的时次段时,负值减小,即地点 A 的观测气温偏低程度减小;雨雪多云天气各时次地点 A 的观测气温均较地点 B 的低;晴朗的白天,地点 A 的观测气温低于地点 B,有风情况下更明显;晴朗的夜间,地点 A 的观测气温高于地点 B,无风时更明显。

本文使用的气温对比观测数据,地点 A 在观测场外,距建筑物(值班室)较近,同时其偏西南方还有卫星接收设备和避雷塔;地点 B 在观测场内,四周比较开阔。年平均气温 A 点低于 B 点,白天尤为明显。白天建筑物的遮挡作用可能使建筑物附近的空气温度平均低于远离建筑物的观测场内空气温度平均。夜晚地点 A 偏高,可以归因为办公室房子白天吸收太阳辐射,夜晚会以长波辐射方式发射,还有人为热辐射释放。晴朗天气,夜晚近建筑物处接收建筑物辐射热减缓气温下降速率,远离建筑物空旷处气温更低,无风天气更明显;白天近建筑物处 A 地点气温较远离建筑物空旷处气温低,有风天气更明显,可能同靠近值班室、西南方向设有卫星接收天线和避雷塔等人工障壁物对阳光的遮挡有关。对比观测试验最高气温地点 A 也较地点 B 偏低,最低气温地点 A 较地点 B 偏高。但是,2 个地点地面气温均值及其季节和日内变化差异的具体原因,还需要开展进一步研究。

气象观测环境变化对气温观测的影响是多方面的,最常见的变化是城市发展,观测场周边建筑物的不断增多。以往关于城市化对气象观测影响的研究多认为,建筑物数目增加、高度提升、与台站的距离

缩短，都是造成观测场气温升高的重要因素，白天建筑物受阳光直接照射、因为热容量小能够强烈吸收太阳短波辐射而迅速升温，其午后和夜晚放射出的长波辐射就会加热周围空气，使观测场上空气温升高；夜间这些建筑物内部的人类活动导致其本身也是1个热源，其放出的额外长波辐射也会造成观测场上空气温偏高。同时建筑物数量增多和高度增加会阻挡空气的自然流动、造成观测场附近的风速变小[20]，也会导致局地气温上升。

本文分析结果表明，观测场附近微环境变化对气温观测的影响与城市化发展的大环境背景产生的“热岛效应”等存在不同，探测仪器附近的建筑物对观测值的影响实际表现为年平均是降温的作用(各月平均也以降温为主)。同时也进一步证明地面气温观测记录对台站观测场附近微环境改变十分敏感。微环境条件的变化如附近办公楼加高加长、仪器安装地点地面特性改变、附近绿地面积变化或养护方式改变等，都可能影响气温观测结果，导致地面气温观测出现明显不连续性，对单点和小区域平均长期气候变化分析结果产生影响。随着城镇建设规模迅速扩大，一些原本位于城郊、探测环境优良的气象探测场所，目前已经处于当地城区范围甚至是中心城区，观测场四周的各种障碍物和干扰源严重影响气象探测，受人为因素影响较大，如汽车尾气排放、家庭空调、燃气燃烧等，影响气象观测资料的准确性、连续性和代表性。

上述情况使得对地面观测气温代表性和均一性的研究变得更加复杂。城市化和社会发展以及观测场周边微环境改变对地面观测记录的影响，需要做更深入和系统的研究。

参考文献

[1] 任国玉，郭军，徐铭志，等. 近50年中国地面气候变化基本特征[J]. 气象学报，2005，63(6)：948-952.

[2] 丁一汇，任国玉. 中国气候变化科学概论[M]. 北京：气象出版社，2008.

[3] 郭守生，闫蓉，李进虎，等. 互助站迁站前后气温序列均一性检验及订正[J]. 气象科技，2016，44(1)：31-35.

[4] 李亚丽，薛春芳，卓静. 利用台站元数据及卫星遥感资料分析影响气温序列均一性的原因[J]. 气象科技，2016，44(1)：23-30.

[5] 中国气象局. 地面气象观测规范[M]. 北京：气象出版社，2003.

[6] 中国气象局. 气象探测环境和设施保护办法[M]. 北京：气象出版社，2004.

[7] Davey C A，Pielke R A. Microclimate exposures of surface-based weather stations：implications for the assessment of long-term temperature trends [J]. Bulletin American Meteorological Society，2005，86(4)：497-504. doi. org/10.1175/BAMS-86-4-497

[8] Runnalls K E，Oke T R. A technique to detect microclimatic inhomogeneities in historical records of screen-level air temperature [J]. Journal of Climate，2006，19(6)：959-978.

[9] 庞成，阙龙凯，王伏村. 张掖气象站新旧站址对比观测资料分析[J]. 气象水文海洋仪器，2013，(3)：93-97.

[10] 周晓倩，李又君，李雪源，等. 气象台站迁址历史观测资料三性分析[J]. 中国农学通报，2015，31(8)：223-228.

[11] 梁琼芳，肖盛，凌莉，等. 靖西县气象观测场环境变化对气象要素的影响[J]. 气象研究与应用，2009，30(3)：108-109.

[12] 赵艳兰. 试论气象观测环境的改变对气象要素的影响[J]. 科技创新导报，2010，22：118-119.

[13] Peterson T C. Examination of potential biases in air temperature caused by poor station locations [J]. Bull Amer Meteor Soc，2006，87(8)：1073-1089.

[14] 刘勇，王东勇，田红，等. 气象观测环境的变化对气温序列的影响分析[J]. 气象科学，2003，26(4)：436-441.

[15] Souleymone F，Anthany W，Nielsengammon J，et al. Analysis of theimpacts of station exposure on the U. S. Historical Climatology Network temperatures and temperature trends [J]. J Geophys Res，2011，116(D14)：120.

[16] Trewin B. Exposure，instrumentation，and observing practice effects on land temperature measurements [J]. WIREs Clim. Change，2010，1(4)：490-506.

[17] Mahmood R，Foster S A，Logan D. The geoprofile metadata，exposure of instruments，and measurement bias in climatic record revisited [J]. Int J Climatol，2006，26(8)：1091-1124.

[18] Pielke R A，Nielsengammon J，Davey c，et al. Documentation of uncertainties and biases associated with surface temperature measurement sites for climate change assessment [J]. Bull Amer Meteor Soc，2007，88(6)：913-928.

[19] Pielke R A，Davey C A，Niyogi D，et al. Unresolved issues with the assessment of multidecadal global land surface temperature trends [J]. J Geophys Res，2007，112(D24)：177-180.

[20] 陈燕，蒋维楣. 城市建筑物对边界层结构影响的数据试验研究[J]. 高原气象，2003，25(5)：824-831.

Response of Surface Air Temperature to Micro-Environmental Change: Results from Mohe Parallel Observation Experiment

Liu Yulian[1,2]　Ren Guoyu[2,3]　Zhang Guangying[4]　Yu Hongmin[5]

(1 Heilongjiang Climate Center, Harbin 150030; 2 Department of Atmospheric Science, School of Environmental Science, China University of Geosciences, Wuhan 430074; 3 Laboratory for Climate Studies, National Climate Center, CMA, Beijing 100081; 4 Daxinganling Meteorological Service, Jiagedaqi 165000; 5 Heilongjiang Public Meteorological Service Center, Harbin 150002)

Abstract: The effects of micro-environmental conditions on the observations of surface air temperature within a standard observational field are unclear. In this paper, the surface observation data of a parallel observational experiment at Mohe Station in 2010 are analyzed. The conclusions are as follows: (1) The annual mean temperature at Site A (close to a house) was lower than that of the standard observational field (Site B), but the monthly mean temperature in January and June at Site A was higher than that of Site B. (2) Between 06:00 and 17:00 (BJT), and at 21:00, lower temperature occurred at Site A; between 18:00 and 05:00 (except 21:00), however, mean temperature at Site A was higher. (3) Lower temperature was recorded at the near-obstacle site for all times in spring (March to May); summer (June to August) also saw the relatively lower temperature at Site A from 06:00 to 17:00; autumn (September to November) mean temperature at Site A was higher than that of the observational field only at 01:00, 03:00, 19:00, 23:00, and it was lower for other times; winter (December to February) mean temperature at Site A was generally lower from 07:00 to 19:00, but higher from 20:00 to 06:00 at night. In cold season (October to March), the mean temperature at Site A was lower than that of the observation field in both daytime and nighttime; but in the warm season (April to September) mean temperature at Site A was lower only during daytime, and higher during nighttime. (4) Minimum and maximum temperatures were recorded at approximately the same time at points A and B, but the maximum temperature was lower, and the minimum temperature is higher at Site A. (5) In the fog weather condition, the temperature at Site A was mostly higher than that at Site B; snow and rain weathers were generally characterized by a lower temperature at Site A; sunny days were more likely to experience lower temperature at Site A; and fair nights were more likely to see a higher temperature at Site A; fair and calm weather conditions were more often accompanied by higher temperature at Site A relative to Site B. It is therefore obvious that the surface air temperature observations are very sensitive to the micro-environmental change at Mohe Station.

Keywords: Micro environment; ground observation; parallel observational experiment; obstacle; surface air temperature; deviation; Mohe station.

刘玉莲,任国玉,孙秀宝. 降水相态分离单临界气温模型建立和检验. 应用气象学报,2018,29(4):449-459.
DOI: 10.11898/1001-7313.20180406

降水相态分离单临界气温模型建立和检验

刘玉莲[1)2)]　任国玉[2)3)*]　孙秀宝[3)]

[1)](黑龙江省气候中心, 哈尔滨 150030)

[2)](中国地质大学(武汉)环境学院大气科学系, 武汉 430074)

[3)](中国气象局国家气候中心气候研究开放实验室, 北京 100081)

摘　　要

使用雪日直接界定法,建立了中国大陆长江以北地区(30°N 以北)降水相态分离单临界气温统计模型,分东部季风区、西北干燥区和青藏高原区 3 个不同气候区独立样本建模,检验模型外推使用的可能性,并对单临界气温分离的雨夹雪偏差进行分析。结果表明:所有地区独立样本建立模型估算的单临界气温与根据天气现象记录确定的单临界气温相关性均达到 0.05 显著性水平,3 个气候区独立建模能够估算出降水相态单临界气温的范围及区域特性;以东部季风区和青藏高原区为样本独立建模的估算结果好于西北干燥区;3 个独立模型估算的单临界气温偏差绝对值不大于 1℃的气象站都多于 74%,估算的标准差偏差在−0.5～0.5℃之间的气象站数量占比 77%,在−1.0～1.0℃之间的气象站数量占比 90%;日平均气温低于单临界气温的雨夹雪日数和降水量与实际降雪日和降雪量的比率北部略小、南部较大,东部季风区的南部雨夹雪界定的雪日和雪量比率均超过 100%;使用统计模型确定不同区域雨夹雪中界定的雪日和雪量比率分布也具有可行性。

关键词: 降水; 相态; 分离; 单临界气温; 统计模型

引　言

降水是表征一个地区气候特征和气候变化的重要参数,是地球水循环和能量循环的关键环节之一[1-3]。1992—2001 年全球水文气象灾害事件约占各类灾害的 90%,经济损失约占所有自然灾害损失的 65%[4]。干旱、热带气旋和洪水是造成生命损失和经济损失的主要原因[5]。在降水量相同的条件下,不同相态的降水在地球表层系统中的作用明显不同,其所产生的社会经济影响有着显著差异,区分并认识降雪特征和异常及其成因具有重要理论和实际意义。此外,在监测和研究全球气候变化背景下次大陆以上空间尺度极端降水事件长期变化时,同样需要区分历史降水资料中的降雨和降雪信息。当前针对全球及亚洲区域固态降水的研究较少,对国内固液态降水研究较多[6-18],主要是由于国内的地面观测网有固态降水观测,而全球交换资料只有总降水量,没有降水相态说明,无法分离液态降水(降雨)与固态降水(降雪);即使在国内气象观测资料相对丰富的情况下,由于专业领域限制和工作量考虑等因素,不少研究常常也需要采用客观方法分离历史降水资料中的不同相态降水。

2008 年冬季中国南方大范围冰冻雨雪灾害发生之后,出于灾害性天气预报的需要,国内学者进行了较多降水相态判别辨识研究[19-21]。这些降水相态判别方法运用地面气温、露点温度、高空气温、相对湿度等,开展国内范围的相关研究,是可行的。在更大尺度研究中,全球交换资料中只有地面气温(平均气温、最高气温、最低气温),没有完善的相对湿度、露点温度、高空气温等观测数据,上述资料和方法难以采用。

2017-12-20 收到, 2018-05-11 收到再改稿。

资助项目: 国家自然科学基金项目(41771067),中国气象局气候变化专项(CCSF201842),中央引导地方科技发展专项(ZY18C12),公益性行业(气象)科研专项(GYHY201206012, GYHY201106013)

* 通信作者, 邮箱: guoyoo@cma.gov.cn

在水文循环过程中，降雨径流过程和融雪过程是完全不同的水文过程。因而在一些水文模型中，固液态降水分离多采用自定义的双临界气温法[22-25]、单临界气温法[26-27]，或者依靠降水雷达监测资料[28]。韩春坛等[29]论述了应用双临界气温法的困难，并利用1961—1979年中国气象局国家基本气象站和基准气象站数据，绘制了中国大陆地区的单临界气温等值线图，同时，结合月降雪比率分离法，判断流域内某月是否有降雪，降雪量是多少，对降水相态进行分离。Chen等[30]补充了中国固液态降水分离的临界日平均露点温度。这些研究使用资料为1979年以前观测数据，且以月降雪比率分离法作为辅助手段，而在各月雨雪状况并不掌握时，辅助方法无法使用；同时许多共享气象资料中也没有露点温度数据，在资料难于获得的情况下，该方法也无法应用。

本文基于雪日直接界定法确定的中国长江以北地区雨雪气温单临界值，使用经度、纬度、海拔高度、年降水量、年平均气温等地理、气候信息建立单临界气温统计模型，分别以不同气候区独立建模、检验，并分析该单临界气温界定的雨夹雪偏差，以了解不同地理和气候单元之间的估算模型外推的可行性及固态降水分离的偏差范围。

1 资料与方法

1.1 资 料

本研究主要目的是检验对固态、液态降水分离单临界气温法建模的外推可能性，并分析单临界气温分离的雨夹雪偏差(为方便叙述，以下均称临界气温)。

资料来源于国家气象信息中心气象资料室，其中气温、降水、相对湿度来源于《中国地面气候资料日值数据集(V3.0)》，降水天气现象来源于《中国地面气候资料天气现象日值数据集》，原始数据均经过质量控制。其中《中国地面气候资料日值数据集(V3.0)》包含了中国基准气象站、基本气象站1951年1月以来本站气压、气温(日平均、日最高、日最低)、降水量、蒸发量、相对湿度、风向风速、日照时数和0 cm地温要素的逐日资料。《中国地面气候资料天气现象日值数据集》为中国基本气象站、基准气象站1951年以来天气现象编码日值数据。交叉比对两套资料记录及气象站信息，剔除气温、降水、相对湿度、天气现象数据不完整的记录，同时对气象站经纬度及海拔高度校对检验订正，保留气象站信息完整、序列连续性较好、气候基准期(1981—2010年)内有20年以上记录的气象站。建模选取1981—2010年的同站年平均气温和降水量值，迁站等因素造成的资料序列非均一性对分析结果无明显影响，未对气象站资料进行均一化订正。

研究对象为中国大陆1月平均气温3℃等值线(大约30°N附近)以北，且1961年以来历史降雪记录不低于100个的长江以北地区324个气象站(图1)，为避免极端事件对临界气温确定的影响，各相态日平均气温的最大、最小极值事件不参与统计。有效降水为去除雾、露、霜等及微量降水，且不低于1 mm的降水。文中分析的降雨指气象站当日发生的降水仅为液态，降雪指当日降水仅为固态，雨夹雪指当日的降水为固态、液态混合。每个气象站雨夹雪发生时的最高、最低气温作为雨雪气温临界值的参考检验阈值。对气象站雨雪极值数据进行当日天气现象及气温、降水比对检验，保证降雨、降雪事件发生日最低、最高气温的正确。雨夹雪出现时，日平均气温范围较大。确定临界气温只针对降雨、降雪，雨夹雪仅作为界定时的气温阈值参考。

文中临界气温的界定及检验所用数据序列长度为1961—2013年，建立临界气温模型时所用的年平均气温、年降水量因子为气候基准期(1981—2010年)多年平均值。为与国外交换资料统一，平均气温采用最高、最低气温平均的极值平均方法计算得到。

参考中国自然地理区划方法，将中国大陆划分为东部季风区(231个站)、西北干燥区(67个站)和青藏高原区(26个站)(图1)。

定义降雪日数(降雪量)偏差百分率为用估算的临界气温确定的降雪日数(降雪量)与实际降雪日数(降雪量)差值占实际降雪日数(降雪量)的百分比，表达估算界定的效果。

文中气温单位为℃，降水量单位为mm，降雨量和降雪量单位均为mm，相对湿度单位为%，经纬度单位为(°)，海拔高度单位为m。

1.2 方 法

估算模型的建立使用SPSS 17.0的逐步回归分

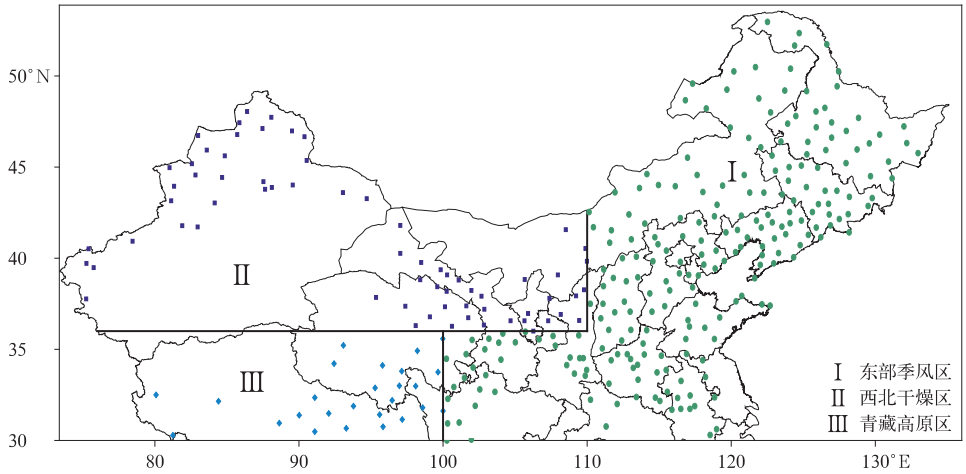

图 1　中国长江以北地区分区及气象站分布

Fig. 1　Division and station distribution in northern China

析方法实现。将变量逐个引入,引入变量的条件是偏回归平方和经检验是显著的,同时每引入一个新变量后,对已选入的变量进行逐个检验,将不显著变量剔除,保证最后所得的变量子集中所有变量均显著,最终得到最优变量子集。回归方程中所含自变量个数较少,便于应用;剩余标准差较小,方程稳定性好;由于每一步都进行检验,因此保证了方程中所有自变量均显著。文中建立的模型均达到 0.05 显著性水平。

定义气象站降雪发生时的日平均气温最大值为 T_{sm},降雨发生时的日平均气温最小值为 T_{rn};T_{rn} 和 T_{sm} 间降雪日数为 S_n,降雨日数为 R_n,T_{rn} 和 T_{sm} 间的全部雨雪日数为 $N_{sr}=S_n+R_n$;根据天气现象记录确定的雨日、雪日临界气温为 T_d,即当日平均气温低于 T_d 时发生的降水事件认为是降雪事件,否则认为是降雨事件;统计模型估算的临界气温为 T_p。

雪日直接界定法界定降水相态分离单临界气温,首先找出各气象站 T_{rn} 和 T_{sm},统计 S_n 和 R_n,计算 N_{sr};然后计算 N_{sr} 的日平均气温,并将其按升序排序;最后计算排序后第 S_n 日的日平均气温和第 S_{n+1} 日的日平均气温的平均值,作为 T_d,对于雨雪不交叉地区(降雪发生时的日平均气温最大值 T_{sm},低于降雨发生时的日平均气温最小值 T_{rn},即降雪和降雨事件在排序后的日平均气温序列中不交叉),取雪日最高日平均气温与雨日最低日平均气温的平均值为 T_d。当 T_d 不在雨夹雪日平均气温区间时,令 T_d 与雨夹雪日平均气温平均值的算术平均为 T_d,本项工作中的 T_d 在雨夹雪的日平均气温范围内,因此,未做此运算。

2　临界气温统计模型

2.1　东部季风区降水相态分离临界气温

使用雪日直接界定方法界定中国大陆长江以北地区(30°N 以北)雨、雪临界气温,图 2 为东部季风区临界气温空间分布。东部季风区 T_d 最高为 5.55℃(四川新龙、四川马尔康),最低为 −1.20℃(黑龙江肇州),温度范围 6.75℃,平均为 2.30℃。自西向东 T_d 渐减,高值区在四川、青海,大于 4℃;低值区在东北东部、华北和淮河流域,低于 2℃。

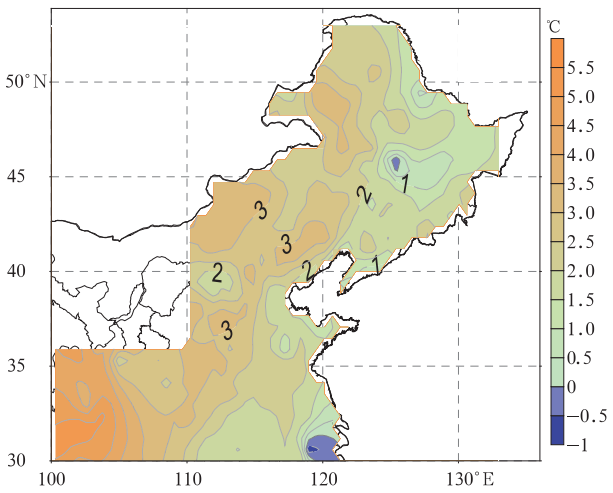

图 2　东部季风区降水相态 T_d 分布

Fig. 2　Spatial distribution of precipitation phase temperature T_d in Eastern Monsoon Region

2.2 东部季风区临界气温统计模型

为大尺度降雪气候学，特别是次大陆以上尺度降雪气候变化研究，建立以气象站地理及气候信息为因子的降水相态分离临界气温的估算模型。本文旨在检验模型外推的偏差，建模时选用 3 个气候区都能够获取的地理信息数据（经度、纬度、海拔高度）、气候信息数据（年降水量和年平均气温）为因子。

利用 SPSS 软件逐步回归分析方法，建立东部季风区（231 个站）临界气温统计模型（F 值的进入值为 0.05，删除值为 0.10，R=0.815）：

$$T_{p1} = -1.557 - 0.049M + 0.181Z + 0.001H - 0.0001R_p + 0.206T_{mn}。 \quad (1)$$

式(1)中，T_{p1} 为东部季风区估算的临界气温，M 为气象站经度，Z 为气象站纬度，H 为气象站海拔高度，R_p 为气象站年降水量，T_{mn} 为年平均气温。T_{p1} 与 T_d 相关系数为 0.78。T_{p1} 最高为 4.83℃，最低为 −0.20℃，温度范围 5.03℃，平均为 2.30℃。T_{p1} 与 T_d 的最大正偏差是 2.90℃，最大负偏差是 −1.38℃（图 3）。

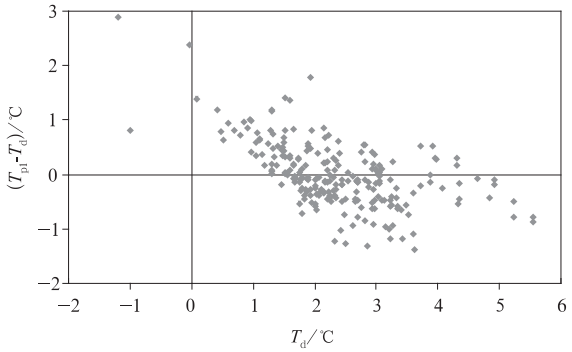

图 3 东部季风区 T_{p1} 与 T_d 差值和 T_d 关系

Fig. 3 The relationship of difference between T_{p1} and T_d to T_d in Eastern Monsoon Region

利用 T_{p1} 计算得到降雪日数和降雪量偏差百分率小于 10%的气象站分别为 95%和 90%。

图 4 为东部季风区采用 T_{p1} 确定的气象站降雪日数（图 4a）和降雪量（图 4b）相对气象站实际降雪偏差百分率空间分布。估算降雪日数与实际降雪日数的标准差和中位数偏差整体较小，中位数在降雪较多的东北地区偏差略大，而在安徽黄山存在异常值。东部季风区各气象站估算降雪日数与实际降雪日数标准差差值在−0.5～0.5℃的气象站数量占比为 83.5%，在−1.0～1.0℃的气象站数量占比为 94.8%。东部季风区降雪日数偏差范围为−14.02%～14.50%，平均值为−0.12%；降雪量的偏差范围为−15.50%～27.07%，平均值为1.09%，空间分布与雪日偏差图基本一致。冬季东部季风区北部受西伯利亚冷高压影响，寒冷干燥；南部虽有日本海和黄渤海带来的少量水汽，但气温较高，只有降雪天气现象的降雪日数和降雪量相对较少，年际间波动较大。雪日偏差百分率的均方根误差为 4.06%，雪量偏差的均方根误差为 5.43%，雪量的估算偏差百分率波动较大。

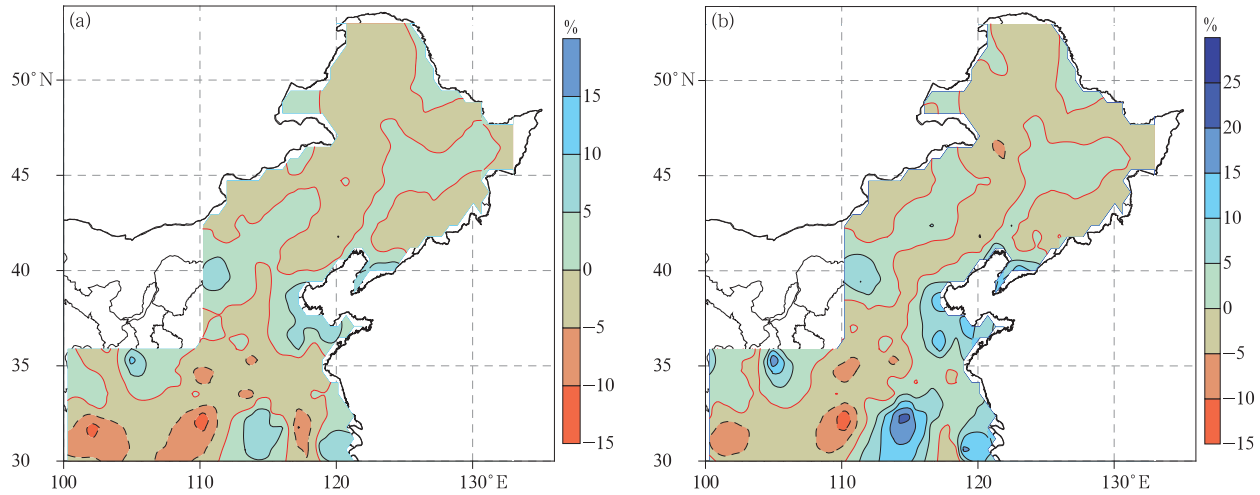

图 4 东部季风区根据 T_{p1} 界定的降雪日数(a)和降雪量(b)偏差百分率分布

Fig. 4 Deviation distribution of snow day number(a) and snowfall(b) according to T_{p1} in Eastern Monsoon Region

2.3　分区临界气温统计估算检验

以西北干燥区 67 个站、青藏高原区 26 个站独立建模,并利用 T_d 对 3 个气候区的独立模型在中国长江以北地区的偏差进行检验,以了解不同地理和气候单元之间的估算模型外推的可能性。

模型因子与前面相同(经度、纬度、海拔、年降水量、年平均气温),临界气温统计估算方程如下:

$$T_{p2} = -1.339 + 0.023M + 0.009Z + 0.001H - 0.003R_p + 0.123T_{mn}, \quad (2)$$

$$T_{p3} = 4.534 - 0.054M + 0.053Z + 0.001H - 0.0005R_p + 0.214T_{mn}。 \quad (3)$$

其中,T_{p2},T_{p3} 为西北干燥区、青藏高原区估算的临界气温。

中国长江以北地区降水相态分离临界气温估算及检验结果见表 1 和表 2。根据式(1)、式(2)、式(3)估算的临界气温 T_{p1},T_{p2},T_{p3},与中国长江以北(30°N 以北)临界气温的相关系数分别为0.78,0.86,0.75,均达到 0.05 显著性水平(表 1)。

不同气候区样本建模得到的估算临界气温(T_{p1},T_{p2},T_{p3})与 T_d 差值平均东部季风区和青藏高原区偏高(分别偏高 0.22℃和 0.18℃),西北干燥区偏低(偏低0.33℃)。以东部季风区和青藏高原区模型估算的临界气温偏差($T_p - T_d$)与 T_d 负相关(达到 0.05 显著性水平),即 T_d 较高的气象站其估算临界气温易偏低,而 T_d 较低气象站其估算临界气温易偏高,因此,其估算的雪日与雪量也与 T_d 呈负相关(表 2)。

图5为以不同气候区为样本建模得到的估算临界气温(T_{p1},T_{p2},T_{p3})与 T_d 差值的空间分布。3 个气候区为独立样本建立的模型能很好地估算出中国地区降水相态临界温度的范围及区域特性。由图 5 可见,以东部季风区和青藏高原区为独立样本建立的模型,对西北干燥区的估算偏差略大,而以西北干燥区为独立样本建立的模型对其他两个气候区的估算,对东部季风区的估算临界气温整体偏低,对青藏高原区的估算临界气温整体偏高,东部季风区个别区域估算临界气温偏低较大。

表 1　分区独立样本估算临界气温

Table 1　The estimated temperature threshold of the partitioned independent sample fitting

区域	要素项	最小值/℃	最大值/℃	平均值/℃	偏差绝对值低于 0.5℃气象站占比/%	偏差绝对值低于 1℃气象站占比/%	与 T_d 相关系数
东部季风区	T_{p1}	−0.20	6.34				0.78
	$T_{p1}-T_d$	−1.38	4.34	0.22	61	86	−0.31
西北干燥区	T_{p2}	−3.90	6.59				0.86
	$T_{p2}-T_d$	−2.90	2.57	−0.33	43	74	0.05
青藏高原区	T_{p3}	0.19	6.43				0.75
	$T_{p3}-T_d$	−2.53	4.16	0.18	44	76	−0.23

表 2　分区独立样本估算偏差检验

Table 2　The estimated snowfall day number and snowfall deviation of the partitioned independent sample fitting

区域	要素项	最小值/%	最大值/%	平均值/%	偏差绝对值低于 10% 气象站占比/%	偏差绝对值低于 20% 气象站占比/%	与 T_d 相关系数
东部季风区	雪日偏差	−14	15	1	95	100	−0.34
	雪量偏差	−15	27	2	90	99	−0.28
西北干燥区	雪日偏差	−61	22	−3	85	94	0.18
	雪量偏差	−65	46	−2	84	94	0.23
青藏高原区	雪日偏差	−8	39	3	86	94	−0.29
	雪量偏差	−13	57	5	78	90	−0.24

以 3 个气候区为独立样本建立模型的拟合检验,估算临界气温偏差绝对值不大于 1℃的气象站均多于 74%,估算的雪日偏差和雪量偏差小于 10% 气象站也超过 78%(图 6,表 1,表 2)。

不同气候区估算的各气象站降雪日数与实际降雪日数标准差差值为−0.5～0.5℃的气象站数量占比 77%,标准差差值为−1.0～1.0℃的气象站数量占比 90%。东部季风区和青藏高原区建模的估算降雪日数与实际降雪日数的标准差和中位数相差整

体较小，标准差平均偏差为－0.18℃，中位数平均偏差为－0.35～－0.38℃。中位数和标准差偏小较多气象站多在青藏高原区或其东部海拔较高的东部季风区气象站，这是由于高海拔气象站年际间降雪日数波动较大，估算易偏小。

图7为不同气候区建模的估算临界气温确定的气象站降雪量偏差百分率空间分布。由图 7 及表 2 可知，东部季风区的独立建模外推到整个研究区，其雪日和雪量偏差百分率范围多为－10%～10%，效果最佳，几乎接近于整个区域建模的效果。青藏高原区气象站独立建模，对东北地区估算偏少，新疆西部和江淮偏多。西北干燥区独立建模，对江淮流域估算偏小，高原北部估算偏多，这可能是因为西北干燥区临界气温的分布特征与青藏高原区和东部季风区表现反相，所以其建立的模型表达也与这两个气候区不同，估算结果也出现了较大差异。

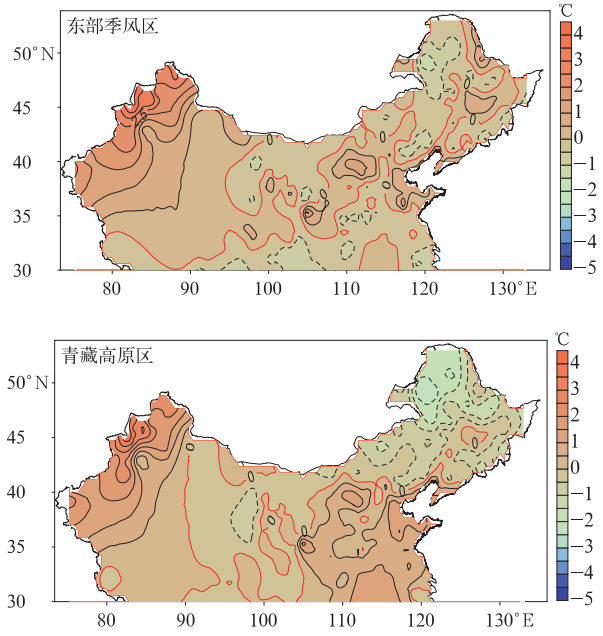

图 5 3 个气候区独立样本估算临界气温与 T_d 差值空间分布

Fig. 5 Spatial distribution of difference between the estimated temperature threshold of three climatic zones with independent sample fitting and T_d

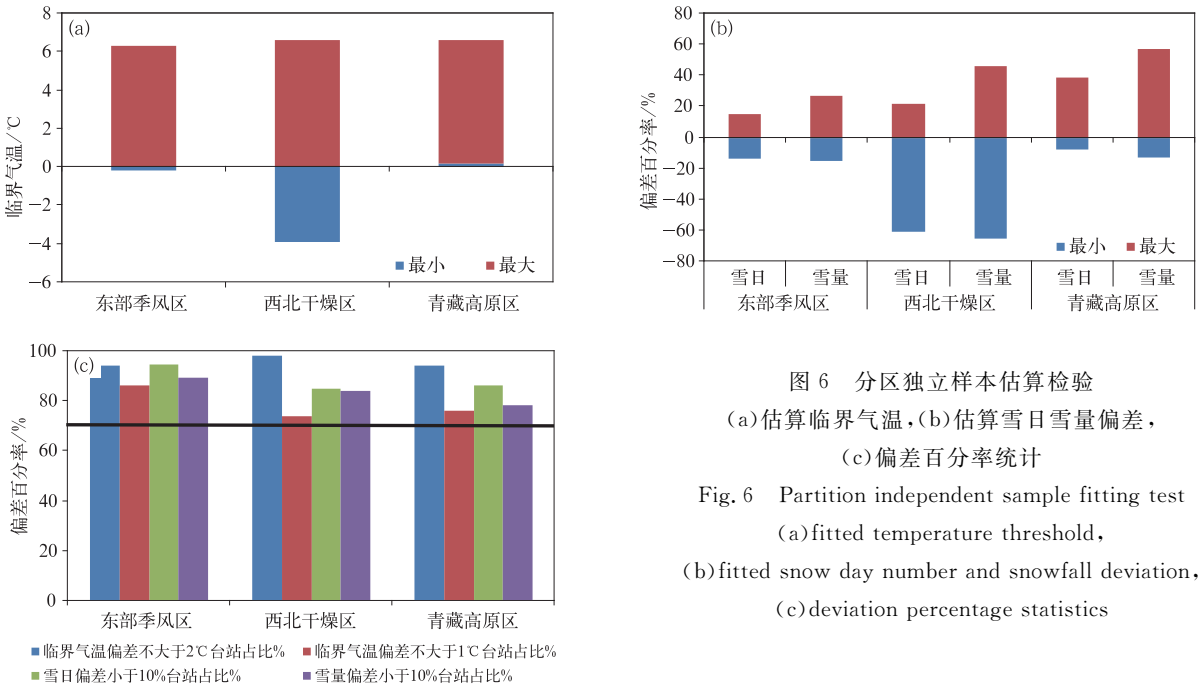

图 6 分区独立样本估算检验

(a)估算临界气温，(b)估算雪日雪量偏差，(c)偏差百分率统计

Fig. 6 Partition independent sample fitting test

(a)fitted temperature threshold, (b)fitted snow day number and snowfall deviation, (c)deviation percentage statistics

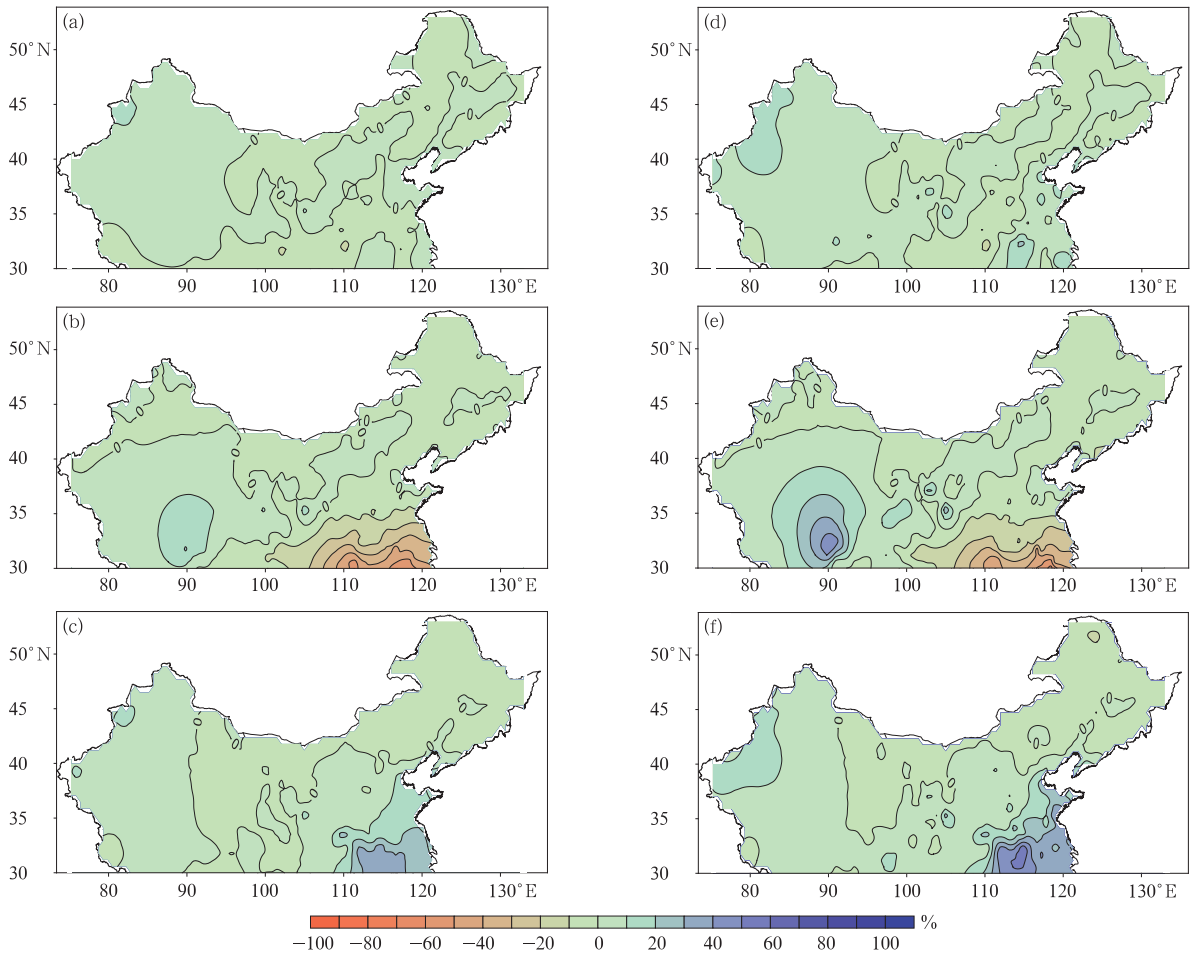

图 7　分区样本估算临界气温界定的雪日和雪量偏差百分率分布

(a)东部季风区估算雪日偏差,(b)西北干燥区估算雪日偏差,(c)青藏高原区估算雪日偏差,(d)东部季风区估算雪量偏差,(e)西北干燥区估算雪量偏差,(f)青藏高原区估算雪量偏差

Fig. 7　Distribution of the deviation percentage of snow day number and snowfall defined by the temperature threshold of partition sample estimation

(a)estimated snow day number deviation in Eastern Monsoon Region, (b)estimated snow day number deviation in Northwest Arid Area, (c)estimated snow day number deviation in the Tibetan Plateau Region, (d)estimated snowfall deviation in Eastern Monsoon Region, (e)estimated snowfall deviation in Northwest Arid Region, (f)estimated snowfall deviation in the Qinghai-Tibet Plateau

根据东部季风区和青藏高原区的估算检验,认为外推方法可以使用;而由西北干燥区建立的模型,虽然其与实际临界气温相关较好,雪日和雪量的偏差小于 10%气象站超过 90%,但其临界气温偏差绝对值不大于 1℃气象站仅大于 74%,由于该区与其他区域气候特征差异明显,部分气象站估算结果有较大偏差;不过也可以看到,估算偏多和偏少的区域正是降雪较多和较少的区域,所以对降雪空间分布的界定还是合理的,只是强度有加强,多雪区更多,少雪区更少。3 个气候区独立样本估算界定的中国长江以北地区降雪日数和降雪量偏差低于 20%气象站都超过 90%,由西北干燥区和青藏高原区气象站建模外推时,偏差较大气象站分布在海拔较高的高原区和年降水量较多的江淮区。

通过分区估算临界气温,推到整个研究区试用检验,可见由少水区域或者海拔较高区域气象站建

模外推时，易在海拔较高区域或年降水量较多区域产生较大偏差；而长江以北包含有多水（东部季风区）、少水（西北干燥区）和高海拔（青藏高原区）3 种气候类型区，对于该项工作拟外推的亚洲区域，其极少降水区域大部分在中国境内 30°N 以北地区的塔克拉玛干沙漠，海拔最高处是在青藏高原区。因此，如果该模型外推到亚洲 30°N 以北地区，其偏差范围接近东部季风区独立样本建模外推的范围，在降水较少的亚洲 30°N 以北地区的东北部气象站考虑可能会出现较大估算偏差。

2.4 低于临界气温的雨夹雪分析

在确定降水相态临界气温时，由于已知降水相态（雪、雨、雨夹雪），只考虑区分雪和雨，没有统计雨夹雪现象。而在应用临界气温对未知相态的降水进行界定时，无法分离出雨夹雪。但相态分离必然会将雨夹雪界定为雪或雨，了解这部分雨夹雪量值及其相对降雪占比，有助于增进对降水相态转换过程和临界气温模型可靠性的认识。

统计中国大陆长江以北地区各气象站日平均气温低于 T_d 的雨夹雪日数和降水量与实际降雪日和降雪量的百分比值见图 8。由图 8 可见，日平均气温低于 T_d 的雨夹雪日与雪日比率分布北部少，南部多，东部季风区的南部，雪日和雪量比率超过 100%。这是因为江淮一带由于平均气温较高，降雪日数较少，而雨夹雪事件相对较多；西部的青藏高原地区其固态降水主要发生在冬春和秋冬转换季节，真正冬季固态降水较少，也是雨夹雪事件较多。

日平均气温低于T_d的雨夹雪日数相对总降雪

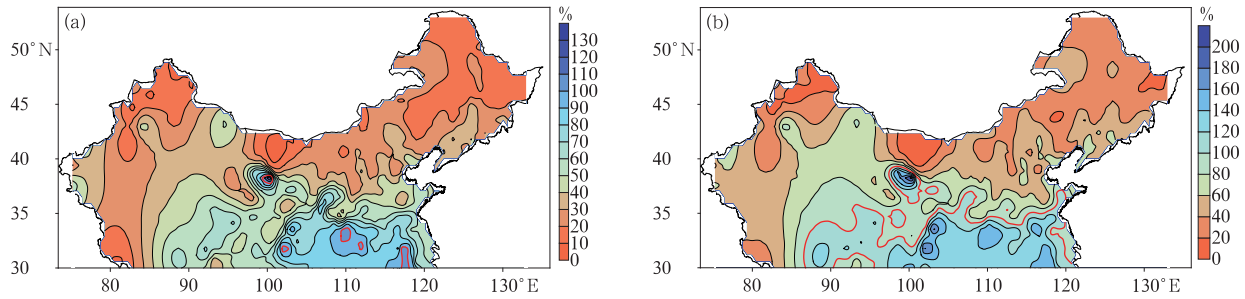

图 8 低于 T_d 的雨夹雪日数(a)和降水量(b)与实际降雪日数和降雪量的比率空间分布

（图中红粗线为 100%等值线）

Fig. 8 Spatial distribution of the ratio of sleet day number(a) and sleet-fall(b) below T_d in the actual snow day number and snowfall

(the red thick line denotes 100%)

日数比率，最大为 141.6%（青海祁连，38°11′N，100°15′E，2787 m），最小为 5.4%（新疆阿勒泰，47°44′N，88°05′E，735 m），中国长江以北地区所有站平均为 39.6%，高值集中区在东部季风区江淮流域，低值区在新疆北部、河套和东北；日平均气温低于 T_d 的雨夹雪降水量与总降雪量比率，最大为 224.0%（青海祁连，38°11′N，100°15′E，2787 m），最小为 4.9%（新疆精河，44°34′N，82°49′E，329 m），所有站平均为 66.8%，高值区在青藏高原北部、江淮流域，低值区在新疆北部和河套地区。这部分的雨夹雪日和降水量与年平均气温、年降水量均为明显正相关关系，与年平均气温相关系数为 0.36 和 0.25，与年降水量相关系数为 0.47 和 0.44，可见，年平均气温高和年降水多的地方低于 T_d 的雨夹雪事件更多。这个比率的空间分布与前面的 T_d 空间分布格局有较高的一致性。

为大致了解中国长江以北地区低于临界气温的雨夹雪事件，对上面分析的各气象站低于 T_d 的雨夹雪与实际降雪比率建立统计模型：

$$P_{sd} = 166.74 - 0.177M - 2.928Z - 0.002H + 0.023R_P - 0.298T_{mn}, \quad (4)$$

$$P_{sf} = 164.97 - 0.023M - 3.379Z + 0.009H + 0.045R_p + 0.598T_{mn}。 \quad (5)$$

其中，P_{sd} 为日平均气温低于 T_d 的雨夹雪日数与实际降雪日比率（单位：%）统计模型估算值，P_{sf} 为日平均气温低于 T_d 的雨夹雪量占实际降雪量比率（单位：%）统计模型估算值。中国地区 P_{sd} 和 P_{sf} 与实际日平均气温低于 T_d 的雨夹雪日与实际降雪日比率和降雪量比率相关系数为 0.75 和 0.77，空间分布一致。

3　结论与讨论

对中国大陆长江以北地区(30°N 以北)降水相态分离的临界气温建立统计模型,以不同气候区为独立样本建模,检验模型外推使用的可能性,并对临界气温分离的雨夹雪偏差进行分析。本文主要结论如下:

1) 分别以东部季风区、西北干燥区、青藏高原区独立建模对中国长江以北气象站临界气温进行估算检验,得到的估算临界气温与根据天气现象记录确定的临界气温相关性均达到 0.05 显著性水平,3 个气候区独立建模能很好地估算出整个研究区降水相态临界气温的范围及区域特性。

2) 以东部季风区和高原区独立建模,对西北干燥区的估算偏差略大;而以西北干燥区独立建模,对东部季风区的估算临界气温整体偏低(个别区域偏低较大),对青藏高原区的估算临界气温整体偏高。3 个独立模型都与根据天气现象记录确定的临界气温明显高相关,且估算临界气温偏差绝对值不大于 1℃气象站多于 74%,雪日和雪量的偏差小于 10% 气象站超过 78%,不同气候区估算的气象站降雪日数与实际降雪日数标准差差值在−0.5～0.5℃的气象站数量占比 77%,在−1.0～1.0℃的气象站数量占比 90%。以此模型外推到更大区域可行,但在使用时需要注意个别气象站存在估算偏差较大的可能。

3) 日平均气温低于临界气温的雨夹雪日数和降水量与降雪日和降雪量的比率北部略少,南部较多,东部季风区的南部雪日和雪量偏差比率都超过 100%,可以使用统计模型确定不同区域雨夹雪事件界定的雪日与雪量占实际雪日与雪量的比率分布。

中国地域辽阔,降水呈南多北少、东多西少分布特征,长江以北地区(30°N 以北,30°～54°N,73°～136°E),气候类型包括了温带季风气候、温带大陆性气候、高寒气候。3 个气候区独立样本试验的检验结果表明:西北干燥区建模结果外推到青藏高原区和东部季风区的模型估算值会有小范围的较大偏差,但极端干燥区范围较小,气候类型较单一,总体上模型外推次大陆降雪丰富区域(30°N 以北)降水相态临界气温估算,尽管仍存在一定局限性,但是可行的。

单临界气温只界定了降雪和降雨两种相态,未对雨夹雪进行界定。在雨夹雪情况下,一天内气温变化大,既有雨夹雪,也有降雨和降雪,实际临界气温波动较大,难以准确模拟。由于没有界定雨夹雪,所以对气象站降水进行固、液态分离时,会将低于临界气温的雨夹雪日界定为雪日,高于临界气温的雨夹雪日界定为雨日,本文对这部分雨夹雪界定的雪日和雪量占实际降雪比率分布进行分析,并建立模型对其进行估算,在应用时可以使用模型对雨夹雪事件界定为雪日和雪量的比率进行大致确定。

参 考 文 献

[1] 丁一汇,王绍武,郑景云,等. 中国气候. 北京:科学出版社,2013:327-391.

[2] 刘国纬. 水文循环的大气过程. 北京:科学出版社,1997:1-245.

[3] 夏军,刘春蓁,任国玉. 气候变化对我国水资源影响研究面临的机遇与挑战. 地球科学进展,2011,26(1):1-12.

[4] WMO. Reducing and managing risks of disasters in a changing climate. *WMO Bulletin*,2013,62(Special Issue):23-31.

[5] 王昂生. 中国减灾与可持续发展. 北京:科学出版社,2007.

[6] 刘玉莲,任国玉,于宏敏. 中国降雪气候学特征. 地理科学,2012,32(10):1176-1185.

[7] 刘玉莲,任国玉,于宏敏,等. 我国强降雪气候特征及其变化. 应用气象学报,2013,24(3):304-313.

[8] 任国玉,战云健,任玉玉,等. 中国大陆降水时空变异规律——Ⅰ. 气候学特征. 水科学进展,2015,26(3):299-310.

[9] 任国玉,任玉玉,战云健,等. 中国大陆降水时空变异规律——Ⅱ. 现代变化趋势. 水科学进展,2015,26(4):451-465.

[10] 任国玉,柳艳菊,孙秀宝,等. 中国大陆降水时空变异规律——Ⅲ. 趋势变化原因. 水科学进展,2016,27(3):327-348.

[11] 除多,洛桑曲珍,杨志刚,等. 1981—2010 年青藏高原降雪日数时空变化特征. 应用气象学报,2017,28(3):292-305.

[12] 袁杰,魏凤英,巩远发,等. 关键区海温年代际异常对我国东部夏季降水影响. 应用气象学报,2013,24(3):268-277.

[13] 邓汗青,罗勇. 近年长江中下游春季和梅雨期降水变化特征. 应用气象学报,2013,24(1):23-31.

[14] 何立富,陈涛,孔期. 华南暖区暴雨研究进展. 应用气象学报,2016,27(5):559-569.

[15] 魏维,张人禾,温敏. 南亚高压的南北偏移与我国夏季降水的关系. 应用气象学报,2012,23(6):650-659.

[16] 陈春艳,王建捷,唐冶,等. 新疆夏季降水日变化特征. 应用气象学报,2017,28(1):72-85.

[17] 张人禾,张若楠,左志燕. 中国冬季积雪特征及欧亚大陆积雪对中国气候影响. 应用气象学报,2016,27(5):513-526.

[18] 王冀,何丽烨,张雪梅. 华北农牧交错带冬季降雪时空变化特征. 地理学报,2015,70(9):1363-1374.

[19] 刘原峰,朱国锋,赵军,等. 黄土高原区不同降水相态的时空变化. 地理科学,2016,36(8):1227-1233.

[20] 张琳娜,郭锐,曾剑,等. 北京地区冬季降水相态的识别判据研

究. 高原气象,2013,32(6):1780-1786.

[21] 尤凤春,郭丽霞,史印山,等. 北京降水相态判别指标及检验. 气象与环境学报,2013,29(5):49-54.

[22] Wigmosta M S, Vail L, Lettenmaier D P. A distributed hydrology-vegetation model for complex terrain. *Wat Resour Res*,1994,30:1665-1679.

[23] Kang E S,Cheng G D,Lan Y C,et al. A model for simulating the response of run off from the mountainous watershed of inland river basins in the arid area of northwest China to climatic changes. *Science in China*(*Series D*),1999,42(Suppl):52-63.

[24] 康尔泗,程国栋,蓝永超,等. 西线南水北调雅砻江调水坝址径流模拟. 冰川冻土,2001,23(2):139-148.

[25] Chen R S,Kang E S,Lu S H,et al. A distributed water-heat coupled model for mountainous watershed of an inland river basin in Northwest China (I) model structure and equations. *Environmental Geology*,2008,53:1299-1309.

[26] Arnold J G, Srinivasan R, Muttiah R S, et al. Large area hydrologic modeling and assessment part Ⅰ: Model development. *Journal of the American Water Resources Association*, 1998,34(1):73-89.

[27] Refsgaard A,Seth S M,Bathurst J C,et al. Application of the SHE to catchments in India. Part Ⅰ:General results. *Journal of Hydrology*,1992,140:1-23.

[28] Edwin P M,Clifford M. Using radar data to partition precipitation into rain and snow in a hydrologic model. *Hydrologic Engrg*,2006,11:214-221.

[29] 韩春坛,陈仁升,刘俊峰,等. 固液态降水分离方法探讨. 冰川冻土,2010,32(2):249-256.

[30] Chen R S,Liu J F,Song Y X. Precipitation type estimation and validation in China. *Journal of Mountain Science*,2014, 11(4):917-925.

Establishment and Verification of Single Threshold Temperature Model for Partition Precipitation Phase Separation

Liu Yulian[1)2)]　Ren Guoyu[2)3)]　Sun Xiubao[3)]

[1)] (*Heilongjiang Provincial Climate Center*, *Harbin* 150030)

[2)] (*Department of Atmospheric Science*, *School of Environmental Science*, *China University of Geosciences*, *Wuhan* 430074)

[3)] (*Laboratory for Climate Studies*, *National Climate Center*, *CMA*, *Beijing* 100081)

Abstract

Precipitation is an important parameter to characterize climate characteristics and climate change in a region. It is a key link in global water cycle and energy cycle. Under the same rainfall conditions, effects of different-phase precipitation in the earth's surface system are significantly different. The social and economic impacts produced by them also have significant differences. It is of great theoretical and practical significance to distinguish and recognize snowfall characteristics, their anomalies and causes. In addition, when monitoring and studying the global climate change background and long-term changes of the extreme precipitation events above the sub-continental scale, it is also necessary to distinguish rainfall and snowfall information from historical precipitation data.

A statistical model with single temperature thresholds is established for separating cold season rainfall and snowfall with independent samples of different climate zones to the north of the Yangtze River in mainland China (north of 30°N). The applicability of the model is tested, and the deviation of the model on sleet recognizing is analyzed.

Results show that correlations between estimated temperature thresholds and actual thresholds pass the significance level test for three areas, i. e., Eastern Monsoon Region, Northwest Arid Region and Qinghai-Tibet Plateau. Models for three areas can well simulate the temperature thresholds, the range and regional characteristics. Simulations in East Monsoon Region and Qinghai-Tibet Plateau are better than those in Northwest Arid Region. Among all of the stations in three regions, stations with absolute bias of the simulated threshold temperature less than 1 ℃ account for more than 74%, and stations with standard deviation biases between −0.5−0.5 ℃ account for 77%, and those between −1.0−1.0℃ account for 90%. When the daily mean temperature gets lower than thresholds, ratios of sleet days and precipitation compared to snow days and actual precipitation are slightly smaller in the north and larger in the south. In the south of Eastern Monsoon Region, ratios are more than 1. Statistical models can also be used to determine the distribution of the ratio in different areas.

Climate types to north of the Yangtze River include temperate monsoon climate, temperate continental climate, and high-cold climate. Results of the independent sample test in three climatic zones indicate that applying this model to estimate the threshold temperature of precipitation phase in sub-continental snow-rich areas, although still limited, is basically feasible.

Key words: precipitation; phase; separation; single threshold temperature; statistical mode

A Coupled Dynamic Index for ENSO Periodicity

BO LU

Laboratory for Climate Studies, National Climate Center, China Meteorological Administration, Beijing, and CMA–NJU Joint Laboratory for Climate Prediction Studies, School of Atmospheric Sciences, Nanjing University, Nanjing, China

FEI-FEI JIN

Department of Atmospheric Sciences, University of Hawai'i at Mānoa, Honolulu, Hawaii, and Laboratory for Climate Studies, National Climate Center, China Meteorological Administration, Beijing, China

HONG-LI REN

Laboratory for Climate Studies, National Climate Center, China Meteorological Administration, Beijing, and CMA–NJU Joint Laboratory for Climate Prediction Studies, School of Atmospheric Sciences, Nanjing University, Nanjing, and Department of Atmospheric Science, School of Environmental Studies, China University of Geosciences, Wuhan, China

(Manuscript received 14 July 2017, in final form 20 November 2017)

ABSTRACT

El Niño–Southern Oscillation (ENSO) is the most active interannual climatic mode, with great global impacts. The state-of-the-art climate models can simulate this dominant mode variability to a large extent. Nevertheless, some of ENSO's fundamental time–space characteristics still have a large spread in the simulations across the array of recent climate models. For example, the large biases of ENSO periodicity still exist among model simulations from phase 5 of the Coupled Model Intercomparison Project (CMIP5). Based on the recharge oscillator framework, a coupled dynamic index for ENSO periodicity is proposed in this study, referred to as the Wyrtki index, in parallel to the Bjerknes index for ENSO instability. The Wyrtki index provides an approximate dynamic measure for ENSO linear periodicity. It has two main contribution terms: the thermocline and zonal advective feedbacks (or F factor) multiplied by the efficiency factor B of discharging–recharging of the equatorial heat content driven by ENSO wind stress anomalies. It is demonstrated that the diversity of simulated ENSO periodicity in CMIP5 models results from the biases in mean state and several key parameters that control ENSO dynamics. A larger F factor would result in a shorter ENSO period [e.g., BCC_CSM1.1(m)], whereas a smaller B factor would lead to a longer ENSO period (e.g., HadGEM2-ES). The Wyrtki index serves as a useful tool for a quantitative assessment of the sources for ENSO periodicity in reanalysis data and its biases in CMIP5 model simulations.

1. Introduction

The El Niño–Southern Oscillation (ENSO) phenomenon dominates the climate fluctuations on the interannual time scale, with its period varying from 2 to 7 yr. It has been recognized as a result of the ocean–atmosphere interaction over the tropical Pacific. Since Bjerknes' recognition of a new coupled ocean–atmosphere instability for ENSO (Bjerknes 1969), theoretical studies have made great progress in understanding the dynamics of ENSO in terms of coupled instability of the tropical climate system (McCreary 1983; Philander et al. 1984; Suarez and Schopf 1988; Battisti and Hirst 1989; Cane at al 1990; Neelin 1991; Neelin and Jin 1993; Jin and Neelin 1993a,b; Jin 1997a,b; An and Jin 2000, 2001; Fedorov and Philander 2000, 2001; Bejarano and Jin 2008). Based on the simple recharge oscillator (RO) model, an approximate coupled instability index, referred to as the Bjerknes instability index, was formulated by Jin et al. (2006). This instability index has been found to be a useful tool for assessing ENSO stability and its control on ENSO amplitude in the climate models (Kim and Jin 2011; Kim et al. 2014).

Supplemental information related to this paper is available at the Journals Online website: https://doi.org/10.1175/JCLI-D-17-0466.s1.

Corresponding author: Fei-Fei Jin, jff@hawaii.edu

DOI: 10.1175/JCLI-D-17-0466.1

© 2018 American Meteorological Society. For information regarding reuse of this content and general copyright information, consult the AMS Copyright Policy (www.ametsoc.org/PUBSReuseLicenses).

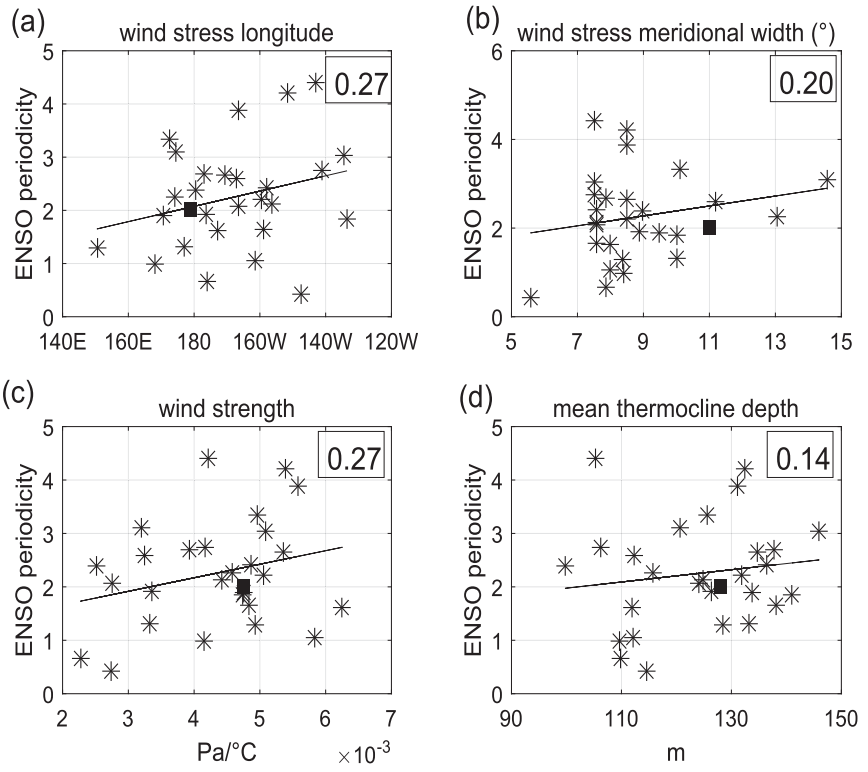

FIG. 1. Scatterplots of ENSO periodicity against (a) the longitude of ENSO-induced zonal wind stress, (b) the meridional width of ENSO-induced zonal wind stress, (c) the air–sea coupling strength, and (d) the mean thermocline depth over the eastern equatorial Pacific in each CMIP5 model (stars) and the GODAS reanalysis (black-filled squares). The regression fitting is indicated by the straight lines. Numbers in the top right denote the correlation coefficients. We adopted the metric suggested by Bellenger et al. (2014) for ENSO periodicity evaluation. First, the wavelet analysis (Morlet et al. 1982) is applied to the eastern Pacific SST. Second, ENSO spectra characteristics are further analyzed by computing the ratio between the spectral energy in the 3–8-yr band and that in the 1–3-yr band. This ratio metric serves as a more robust measure than the classic spectrum peak metric, especially when multiple peaks appear in the ENSO spectrum.

The periodicity of ENSO modes in linear stability studies has been found to be sensitively dependent on various factors, including the ENSO meridional width, longitudinal location, ocean–atmosphere coupling, and climate mean states (Cane et al. 1990; Jin and Neelin 1993a; Jin 1997b; Kirtman 1997; Kang and An 1998; Timmermann et al. 1999; Fedorov and Philander 2000; An and Wang 2000; Syu and Neelin 2000; Bejarano and Jin 2008; MacMynowski and Tziperman 2008; Stuecker et al. 2013). The linear stability analysis is able to retrieve the eigenmodes that control the broad range of simulated ENSO periodicity, although nonlinearity has been shown to alter ENSO's linear periodicity (Jin 1997b; Eccles and Tziperman 2004). Recent studies (Bellenger et al. 2014; Dommenget et al. 2014; Wang et al. 2015) have shown that the biases of feedback processes still exist in the state-of-the-art climate models that participated in phase 5 of the Coupled Model Intercomparison Project (CMIP5; Taylor et al. 2012). As a result, large spread is evident in the simulations of ENSO periodicity (Bellenger et al. 2014). The diversity of ENSO periodicity in the CMIP5 models is not only due to statistical uncertainties, but it also reflects the inherent differences in model physics. Thus, it is important to understand the sources of ENSO periodicity biases in climate models.

As shown in Fig. 1, simulated diverse ENSO periodicity is not dominantly controlled by any known factors, such as the zonal position of zonal wind stress (An and Wang 2000), the meridional width of zonal wind stress (Kirtman 1997; Capotondi et al. 2006), the air–sea coupling strength (MacMynowski and Tziperman 2008), and the mean thermocline depth (Timmermann et al. 1999). What controls the range of periodicity of ENSO in these state-of-the-art models remains unknown and is worthy of further investigation. In this study, following

TABLE 1. Detailed information about the CMIP5 models used in this paper. The southern and northern edges of the boxes are selected with the largest ENSO-related wind stress curl in each CMIP5 model. The southern and northern boundaries are 6°S and 4.5°N in the GODAS reanalysis. (Expansions of acronyms are available online at http://www.ametsoc.org/PubsAcronymList.)

Modeling center	Model name	Simulation length	Southern edge	Northern edge
Commonwealth Scientific and Industrial Research Organisation and Bureau of Meteorology, Australia	ACCESS1.0	1850–2005	7.5°S	2.5°N
	ACCESS1.3	1850–2005	5°S	2.5°N
Beijing Climate Center, China	BCC_CSM1.1	1850–2012	4.2°S	1.4°N
	BCC_CSM1.1(m)	1850–2012	6.2°S	1.7°N
Canadian Centre for Climate Modelling and Analysis, Canada	CanESM2	1850–2005	7°S	1.4°N
National Center for Atmospheric Research, United States	CCSM4	1850–2005	5.2°S	3.3°N
Community Earth System Model contributors (NSF–DOE–NCAR), United States	CESM1(BGC)	1850–2005	5.2°S	3.3°N
	CESM1(CAM5)	1850–2005	5.2°S	3.3°N
	CESM1(FASTCHEM)	1850–2005	5.2°S	3.3°N
	CESM1(WACCM)	1850–2005	4.7°S	2.8°N
Centro Euro-Mediterraneo sui Cambiamenti Climatici, Italy	CMCC-CESM	1850–2005	9°S	5.6°N
	CMCC-CM	1850–2005	7.1°S	1.9°N
	CMCC-CMS	1850–2005	8.4°S	4.7°N
Centre National de Recherches Météorologiques/ Centre Européen de Recherche et de Formation Avancée en Calcul Scientifique, France	CNRM-CM5.2	1850–2005	4.9°S	3.5°N
NOAA/Geophysical Fluid Dynamics Laboratory, United States	GFDL CM3	1860–2005	7°S	3°N
	GFDL-ESM2M	1861–2005	7.1°S	3°N
NASA Goddard Institute for Space Studies, United States	GISS-E2-R	1850–2005	5°S	3°N
	GISS-E2-R-CC	1850–2010	5°S	3°N
Met Office Hadley Centre, United Kingdom	HadGEM2-CC	1860–2005	5°S	2.5°N
	HadGEM2-ES	1860–2005	5°S	2.5°N
L' Institut Pierre-Simon Laplace, France	IPSL-CM5A-LR	1850–2005	4.7°S	2.8°N
	IPSL-CM5A-MR	1850–2005	5.1°S	3.8°N
	IPSL-CM5B-LR	1850–2005	6.6°S	2.8°N
Max Planck Institute for Meteorology, Germany	MPI-ESM-MR	1850–2005	8.4°S	2.8°N
Meteorological Research Institute, Japan	MRI-CGCM3	1850–2005	5°S	2.8°N
Norwegian Climate Centre, Norway	NorESM1-M	1850–2005	4.7°S	2.8°N
	NorESM1-ME	1850–2005	4.7°S	2.8°N

the approach using the formulation of the Bjerknes instability index based on the RO framework, we propose an approximate measure for ENSO linear periodicity. Moreover, we will utilize this new dynamic index to gain insights into the main causes of ENSO periodicity in the reanalysis data, as well as in the simulations of CMIP5 models.

This paper is organized as follows. Observational datasets and CMIP5 experiments are briefly introduced in section 2. The formulation of the coupled dynamic index for ENSO periodicity is derived in section 3. Section 4 further investigates the dynamic approximation of the coupled periodicity index. A summary and conclusions are presented in section 5.

2. Data and methodology

NCEP Global Ocean Data Assimilation System (GODAS) data (Behringer et al. 1998) are used to represent the objective estimations of the observational monthly three-dimensional current and temperature in the ocean, as well as the momentum and heat flux at the surface since 1980. The monthly mean output from CMIP5 models are also analyzed in this study. (All these data are available at http://pcmdi9.llnl.gov/.) Table 1 summarizes the model information, including the model names, their associated modeling centers, and their simulation lengths.

In this paper, we consider the models that provide output of three-dimensional ocean current, temperature and surface momentum, and heat flux data of historical simulations. The historical simulations use initial conditions taken from the preindustrial control experiment under full historical forcing (e.g., greenhouse gases, aerosols, ozone, volcanic aerosols, and land use). To remove decadal and longer variability, an 8-yr running average is removed from the anomalous quantities.

3. Measuring periodicity of ENSO

Following recharge–discharge oscillation framework (Jin 1997a), two prognostic equations for SST and thermocline depth anomalies can be written as

$$\frac{d}{dt}T_E = RT_E + Fh \quad \text{and} \tag{1}$$

$$\frac{d}{dt}h = -\varepsilon h - BT_E, \tag{2}$$

where T_E represents the SST anomalies averaged over the eastern equatorial Pacific (170°–90°W; meridional boundaries shown in Table 1), and h represents the thermocline depth anomalies averaged over the entire equatorial Pacific (140°E–90°W; meridional boundaries shown in Table 1). The parameter R indicates the damping rate of eastern Pacific SST and is often referred to as the Bjerknes instability index (Jin et al. 2006). The parameter ε denotes the damping rate of thermocline depth resulting from the energy leak at the western boundary and mixing. The parameter F represents the impact of the discharged–recharged state of ocean heat content onto SST, and the parameter B indicates the efficiency of the discharging–recharging of the equatorial heat content driven by ENSO SST anomalies induced by the equatorial wind stress curl anomalies. The noise forcing and nonlinear terms are omitted here for brevity.

We first examine the effectiveness of the above simple set of equations in capturing ENSO slow dynamics using the reanalysis and CMIP5 simulation data. Here, the parameters R, F, ε, and B are calculated by linear regressions. It should be noted that this recharge oscillator model only captures essential slow and linear processes of ENSO. Various quasi-balance assumptions adopted in deriving the recharge oscillator (Jin et al. 2006) have implicitly filtered out the fast variability associated with ENSO. Therefore, as shown in Fig. 2, the tendencies of SST and thermocline depth anomalies can be well explained by this simple RO model when the high-frequency variability is filtered, for instance, by even using a simple running average. In CMIP5 simulations, the total variance of SST (thermocline depth) tendency can be explained by only 43% (30%) without smoothing; however, the explained variance increases to 60% (54%) if a 9-month running mean is applied. The variance of SST (thermocline depth) tendency can be explained by 47% (60%) when a 9-month running mean is applied to GODAS data. It should be noted that the simulation length is about 150 years in CMIP5 historical simulations and 36 years in GODAS data, which may result in the some differences in the explained variance between the CMIP5 multimodel mean (MME) and the reanalysis data. Overall, the simple RO model indeed captures a significant portion of the slow variation of the SST and thermocline depth, even though other terms, such as nonlinearity and subgrid processes, are omitted. Hereafter, a 9-month running average will be utilized for the analysis in this paper.

Assuming a simple linear solution as $T = Ae^{i\omega t}$, the ENSO period of the RO model can be obtained as $4\pi[4BF - (R + \varepsilon)^2]^{-1/2}$. As shown in Table 2, the term $(R + \varepsilon)^2$ is small in both the GODAS reanalysis and the CMIP5 models and, thus, can be neglected. Then, the period solution is simplified as

$$I_{\text{Wyrtki}} = \frac{4\pi}{\sqrt{4BF}}. \tag{3}$$

Here, we refer to I_{Wyrtki} as the Wyrtki index (yr) because Wyrtki (1985) first recognized ENSO phase turn as a result of equatorial heat content recharge and discharge.

Figure 3 shows the scatterplot of ENSO periodicity versus the Wyrtki index in the CMIP5 historical simulations and the GODAS reanalysis. Consistent with previous findings (Bellenger et al. 2014), there is a large spread in the simulated ENSO periods. Some models [BCC_CSM1.1, BCC_CSM1.1(m), and CNRM-CM5.2] produce ENSO with a too-short period. Other models [CCSM4, CESM1(BGC), HadGEM2-ES, and MPI-ESM-MR] tend to have a spectral peak displaced toward relatively longer periods. The periodicity measured by the spectrum pattern (Bellenger et al. 2014; see also the caption of Fig. 1) varies from 0.5 to 4.3 in CMIP5 historical simulations. The multimodel mean periodicity ratio is 2.2, which is very close to the observed ratio of 2.1; both roughly correspond to a periodicity of about 3.5 yr, as measured by Wyrtki index. As shown in Fig. 3, the period diversity can be well explained by the Wyrtki index. The correlation coefficient reaches 0.86, which is significant at the 99% level (using the Student's t test). In other words, a longer (shorter) period generally corresponds to a large (smaller) Wyrtki index. Thus, the Wyrtki index can be considered a reasonable indicator for the ENSO period. Here, the Wyrtki index is fitted from the data using a simple RO model. In the next section, we will derive an approximate formulation for this index.

4. An approximate formulation of the Wyrtki index

As shown in Eq. (3), the ENSO periodicity index is determined by two factors: B and F. Adopting the approach for the Bjerknes index of ENSO growth rate (Jin et al. 2006), we can derive their approximate representations.

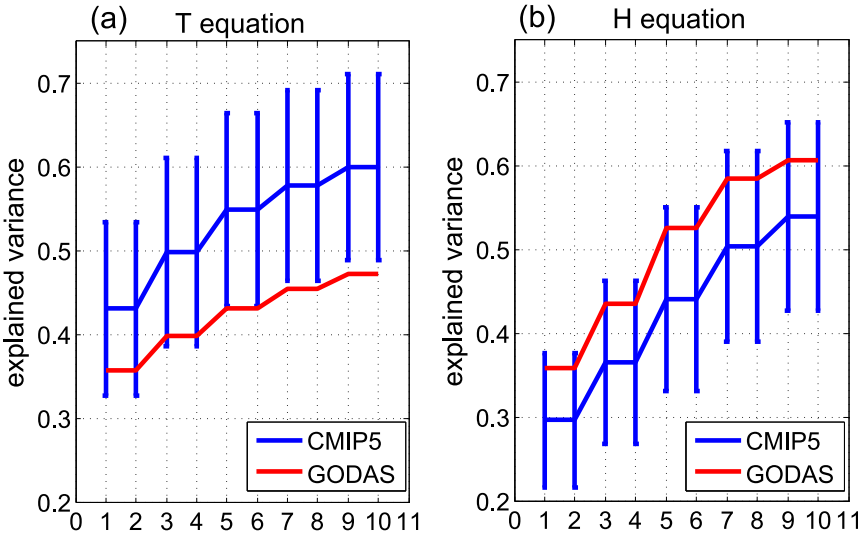

FIG. 2. The variances of the (a) SST tendency and (b) thermocline depth tendency explained by the simple RO model in Eqs. (1) and (2) as the function of smooth time (months) in the CMIP5 models (blue) and GODAS (red). The error bars indicate the standard deviations of explained variances among different CMIP5 models.

a. Response of SST tendencies to the thermocline

The F factor in Eq. (1) originated from the response of SST owing to the feedback processes. We can derive an approximate representation of the parameter F from the following linearized SST equation of the mixed layer:

$$\frac{\partial T}{\partial t} = -\left(\overline{u}\frac{\partial T}{\partial x} + \overline{v}\frac{\partial T}{\partial y} + \overline{w}\frac{\partial T}{\partial z} + u\frac{\partial \overline{T}}{\partial x} + v\frac{\partial \overline{T}}{\partial y} + w\frac{\partial \overline{T}}{\partial z}\right) + Q, \tag{4}$$

where T, Q, u, v, and w denote the mixed layer ocean temperature, net anomalous heat flux at sea surface, and three-dimensional ocean current anomalies. The overbars represent the climatologic mean states. We apply the box average on Eq. (4) over the equatorial central–eastern Pacific. The longitude range of this eastern Pacific box is 170°–90°W, and the mixed layer depth is fixed at 50 m for simplicity. The meridional range of the box is listed in Table 1, which will be discussed later. Following Jin et al. (2006), the box-averaged SST anomaly equation can be written as follows:

TABLE 2. The contribution terms of the Wyrtki index in the CMIP5 models and the observation.

	CMIP5 (yr^{-2})	GODAS (yr^{-2})
$4BF$	12.9 ± 3.5	13.1
$(R+\varepsilon)^2$	0.4 ± 0.4	1.8

$$\frac{\partial \langle T\rangle}{\partial t} = -\left(\frac{\langle \overline{u}\rangle}{L_x} + \frac{\langle -2y\overline{v}\rangle}{L_y} + \frac{\langle H(\overline{w})\overline{w}\rangle}{H_m}\right)\langle T\rangle - \langle u\rangle\left\langle\frac{\partial \overline{T}}{\partial x}\right\rangle + \gamma\langle H(\overline{w})\overline{w}\rangle\frac{\langle T_{\rm sub}\rangle}{H_m} - \langle w\rangle\left\langle H(\overline{w})\frac{\partial \overline{T}}{\partial z}\right\rangle + \langle Q\rangle, \tag{5}$$

where L_x and L_y are the zonal and meridional extents of the box. The y in the second term on the rhs denotes the meridional coordinate, which comes from the assumption that the SST anomalies have a Gaussian-like meridional pattern with an e-folding decay (Jin et al. 2006). The H_m is the effective depth for the vertical advection, which is fixed at 75 m in this paper, and $T_{\rm sub}$ is the subsurface temperature anomaly. The $H(x)$ is a step function that only considers the regions with upward vertical advection. The angle brackets denote the average of quantities over the eastern box (170°–90°W; varying meridional range in Table 1). The square brackets denote the average of quantities over the entire equatorial Pacific (140°E–90°W; varying meridional range in Table 1). Following the Zebiak–Cane model (Zebiak and Cane 1987), parameter γ measures the effectiveness of the vertical entrainment. The term $v\partial\overline{T}/\partial y$ in Eq. (4) has been omitted, as in Jin et al. (2006), because the advection of the mean temperature by the anomalous meridional current is small. The nonlinear terms have also been omitted.

The terms on the rhs of Eq. (5) represent the dynamical damping process, zonal advective feedback, thermocline

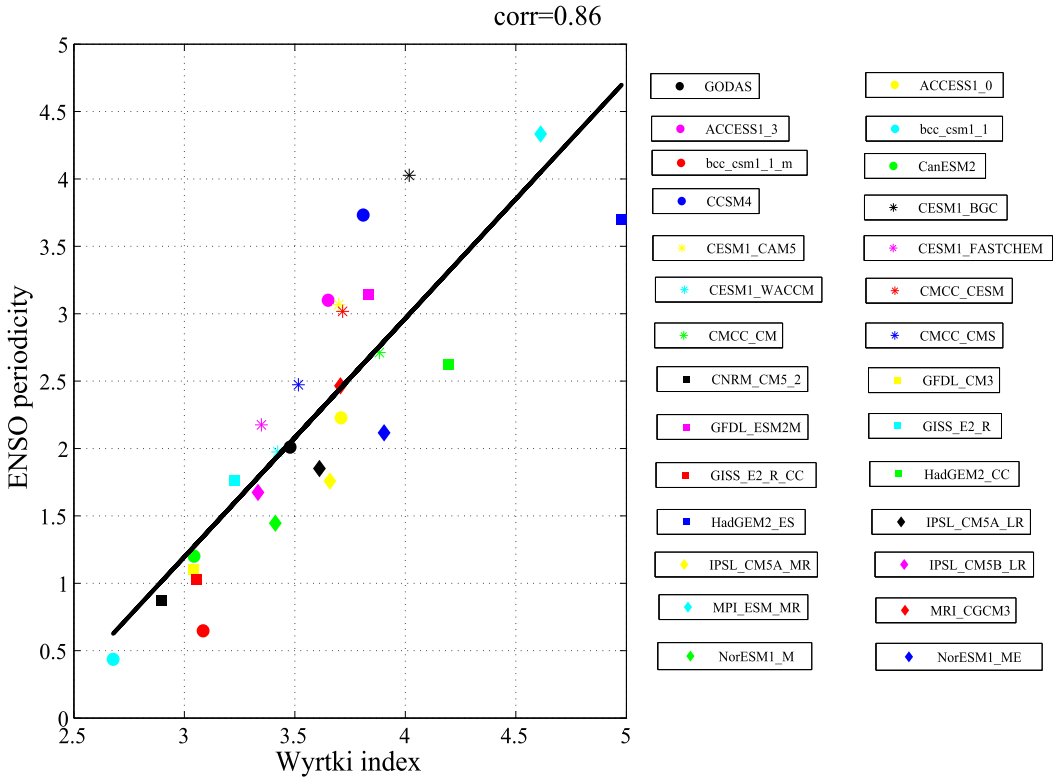

FIG. 3. Scatterplot of ENSO periodicity against the Wyrtki index (yr) in the CMIP5 historical simulations and the GODAS reanalysis. ENSO periodicity (y axis) following Bellenger et al. (2014) is nondimensional and measures the ratio of power in the 3–7-yr band over the1–3-yr band. The Wyrtki index (x axis) measures the theoretical ENSO period. The linear regression fitting is indicated by the straight line. The number at the top right denotes the correlation coefficient.

feedback, Ekman feedback, and thermal damping processes, respectively. The five terms on the rhs can be expressed as a linear function of the thermocline depth anomalies and SST anomalies. Following the quasi-balance approximations proposed in Jin et al. (2006), Eq. (5) can be recast in the form of a standard RO model.

First, the SST warming over the eastern Pacific will induce a westerly wind stress anomaly. We can have

$$[\tau_x] = \mu_a \langle T \rangle. \tag{6}$$

Here, $[\tau_x]$ denotes the zonal mean surface wind stress averaged over 140°E–90°W. The coefficient μ_a is often referred to as the air–sea coupling strength. This balance equation holds very well for both CMIP5 simulations and the reanalysis data (Fig. S1 in the supplemental material). Based on the Student's t test, the linear regressions are all significant at the 99% level. Although CMIP5 models tend to underestimate the wind stress response in the central Pacific (Bellenger et al. 2014), the MME coupling coefficient ($0.0048\,\mathrm{Pa\,°C^{-1}}$) is close to the observed value of $0.0042\,\mathrm{Pa\,°C^{-1}}$ in the GODAS reanalysis.

Second, we assume that the heat flux anomalies depend on the local SST anomalies:

$$\langle Q \rangle = -\alpha \langle T \rangle. \tag{7}$$

This linear equation is often used to estimate the thermal damping rate α. This linear relationship is robust in the models and the reanalysis data (Fig. S1). However, the MME damping rate α is $7.0\,\mathrm{W\,m^{-2}\,°C^{-1}}$, which is only half of the observed thermal damping of $13.7\,\mathrm{W\,m^{-2}\,°C^{-1}}$. This weak thermal damping is largely due to the biases in the SST–cloud–shortwave radiation feedbacks (Lloyd et al. 2011). However, we will show that the biases in thermal damping processes contribute little to the periodicity biases.

Third, the westerly wind stress $[\tau_x]$ reduces the upwelling in the eastern equatorial Pacific. We can obtain the following balance relationship:

$$\langle w \rangle = -\beta_w [\tau_x]. \tag{8}$$

As shown in Fig. S3 of the supplemental material, the correlation between the upwelling and the wind stress

anomalies is weaker than the wind–SST relationship in Eq. (5). The correlation coefficient is only 0.3 in the reanalysis data. The parameter β_w also exhibits large spread among the CMIP5 models. However, we will also show that this spread has little impact on the Wyrtki index, although it does impact the Bjerknes index for ENSO stability.

Fourth, following the arguments of Jin and An (1999) and Jin et al. (2006), the surface ocean current may be related to both the zonal wind stress and the upper-ocean pressure anomalies as follows:

$$\langle u\rangle = \beta_u[\tau_x] + \beta_{\rm uh}[h]. \tag{9}$$

Here, $[h]$ denotes the zonal mean thermocline depth over 140°E–90°W. The coefficient β_u represents the wind-driven effect, which contributes to the ENSO growth rate (Jin et al. 2006). The term $\beta_{\rm uh}[h]$ represents the geostrophic zonal current associated with the zonal mean of the equatorial heat content. Thus, $\beta_{\rm uh}$ will be a part of the F factor related to ENSO periodicity. This balance relationship is quite robust in both the models and the reanalysis data (Fig. S4 in the supplemental material).

Fifth, based on the Sverdrup balance, the zonal pressure gradient induced by the tilt of thermocline is balanced by the surface wind stress on the ENSO time scale, and we obtain

$$\langle h\rangle - [h] = \beta_h[\tau_x]. \tag{10}$$

Finally, the subsurface temperature anomalies are well correlated with local thermocline depth anomalies. Without loss of generality, we have

$$\langle T_{\rm sub}\rangle = a_h\langle h\rangle. \tag{11}$$

The balanced Eqs. (10) and (11) are also robust in terms of the significant correlations for both the CMIP5 simulations and the GODAS reanalysis (Figs. S5 and S6 in the supplemental material).

After applying the approximate Eqs. (6)–(11), we can reformulate Eq. (5) into a standard RO model, as in Eq. (1). The dynamic contributors of the R and F factors are obtained as follows:

$$\begin{aligned} R = &-\left(\frac{\langle\overline{u}\rangle}{L_x} + \frac{\langle -2y\overline{v}\rangle}{L_y} + \frac{\langle H(\overline{w})\overline{w}\rangle}{H_m}\right) \\ &+ \mu_a\beta_u\left\langle -\frac{\partial\overline{T}}{\partial x}\right\rangle + \gamma\mu_a\beta_h a_h\left\langle\frac{H(\overline{w})\overline{w}}{H_m}\right\rangle \\ &+ \mu_a\beta_w\left\langle H(\overline{w})\frac{\partial\overline{T}}{\partial z}\right\rangle - \alpha \quad \text{and} \end{aligned} \tag{12}$$

TABLE 3. The partial correlation coefficients between the processes on the rhs of Eq. (5) and the thermocline depth anomalies with the impact from ENSO SST removed in the CMIP5 models MME.

	DD	ZA	TH	EK	TD
CMIP5	0	0.69	0.86	0	0.06

$$F = F_{\rm adv} + F_{\rm th} = \beta_{\rm uh}\left\langle -\frac{\partial\overline{T}}{\partial x}\right\rangle + \gamma a_h\left\langle\frac{H(\overline{w})\overline{w}}{H_m}\right\rangle. \tag{13}$$

The parameter R is related to the Bjerknes index for the growth rate of ENSO. Jin et al. (2006) suggested that the dynamical damping process (DD), zonal advective feedback (ZA), thermocline feedback (TH), Ekman feedback (EK), and thermal damping processes (TD) all contribute to the Bjerknes ENSO instability. Here, it becomes clear in Eq. (13) that zonal advective and thermocline feedbacks are the main contributing processes to the F factor for ENSO periodicity.

It should be noted that a two-box model here cannot explicitly take into account the zonal SST phase propagations, which may contribute to ENSO periodicity. Thus, the thermal (heat flux) damping, Ekman feedback, and dynamical damping (zonal advection by mean zonal currents) may contribute to ENSO periodicity because these processes may all contribute to zonal SST phase propagations. Nevertheless, as shown in Table 3, the dynamical damping, Ekman feedback, and thermal damping are, to a large extent, uncorrelated with the thermocline depth anomaly that has a near-90° phase difference from SST. All three processes have small phase lags with SST and, thus, have small contributions to ENSO periodicity, which supports the robustness in the formulation of Eq. (13). The dominance of the zonal advective and thermocline feedbacks in the F factor is consistent with previous studies (An et al. 1999; Jin and An 1999) using the Zebiak–Cane model.

As shown in Eq. (13), the F factor is controlled by the mean zonal SST gradient, mean upwelling in the climate mean state, and the coefficients of $\beta_{\rm uh}$ and a_h. The biases in the CMIP5 models are further investigated by performing intermodel correlations between the F factor and its contributing terms. As shown in Fig. 4, the biases of $F_{\rm adv}$ in the CMIP5 models are mainly due to the spread of the parameter $\beta_{\rm uh}$. Further studies show that models with weaker tropical Pacific trade winds over the central to western Pacific tend to simulate a larger $\beta_{\rm uh}$ and, thus, a stronger zonal advective feedback (Fig. 5). For the intermodel thermocline feedback $F_{\rm th}$ biases, the contributions from the

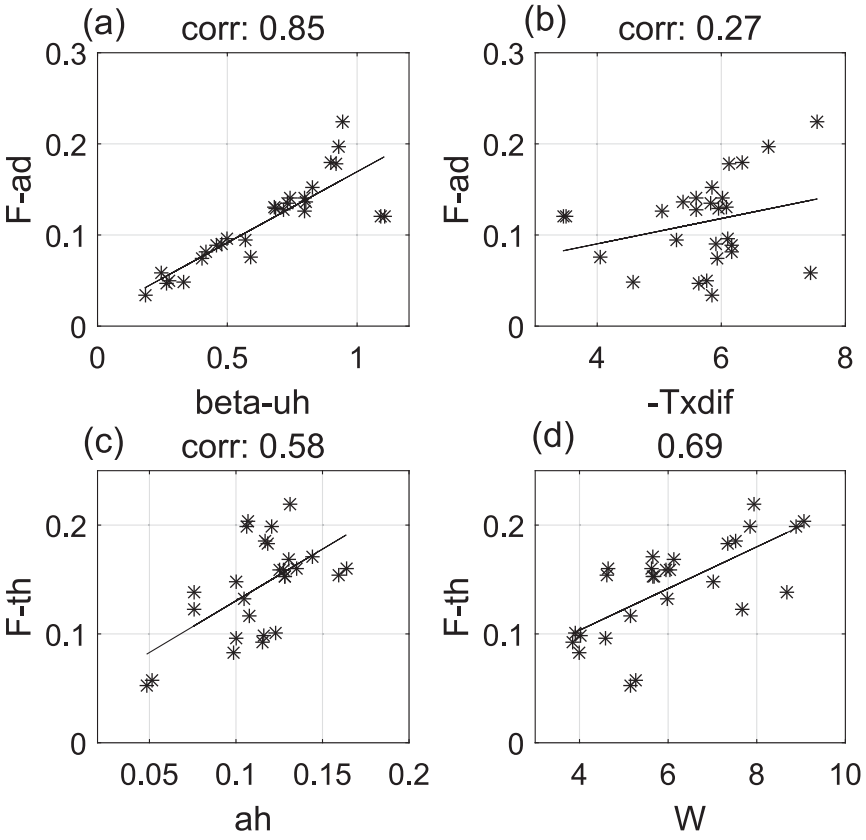

FIG. 4. Scatterplots for the zonal advective feedback F_{adv} (°C yr^{-1} m^{-1}) against (a) the parameter β_{uh} (10^{-2} s^{-1}) and (b) zonal SST gradient (10^{-7} °C m^{-1}) and scatterplots for F_{th} (°C yr^{-1} m^{-1}) against (c) the parameter a_h (°C m^{-1}) and (d) mean upwelling (10^{-6} m s^{-1}) in CMIP5 models. The numbers at the top of each panel denote the correlation coefficients.

parameter a_h and the mean upwelling are generally comparable (Figs. 4c,d). The models with shallower thermocline in the eastern Pacific tend to simulate a larger F_{th} (Fig. 6). We further validate this dynamical approximate formulation of the F factor, as expressed by Eq. (13), by the comparison with the empirically derived F values from the RO model [Eq. (1)]. As shown in Fig. 7a, the correlation coefficient between the dynamically and empirically derived F values reaches 0.71, which is significant at the 99% level using the Student's t test. In other words, Eq. (13) serves as a reasonable approximate estimation for the F factor. For instance, the empirically derived F factor in ACCESS1.0 by the parameter fitting method is about 0.18°C m^{-1} yr^{-1}, which is the smallest among all the CMIP5 models. The dynamically derived F value by Eq. (13) is also the smallest. The model BCC_CSM1.1(m) has the largest empirically derived F value of 0.47°C m^{-1} yr^{-1} among CMIP5 models, and its dynamic derived value is also the largest. The larger the F value, the smaller the Wyrtki index and the shorter the ENSO period. Thus, the short ENSO periodicity bias in BCC_CSM1.1(m) partly results from the F factor being too large.

b. *Response of thermocline tendencies to the SST*

The zonal mean thermocline depth changes, as expressed in Eq. (2), come from the recharge and discharge of warm water in the upper ocean. The wind stress curl associated with SST anomalies plays a fundamental role in this thermocline change (Jin 1997a,b; Clarke et al. 2007). As an effort to obtain an approximate estimation for the parameter B, we take two steps. First, we relate wind stress curl along the south and north of the equator to SST anomalies, which was taken into consideration implicitly through the meridional wind stress structure in Jin (1997a,b). Second, we follow the approach by Clarke et al. (2007) to relate the meridional mass convergence/divergence and, thus, heat content recharging and discharging, to the difference of the wind stress curl anomalies between the north and south sides of the equatorial Pacific. These two steps

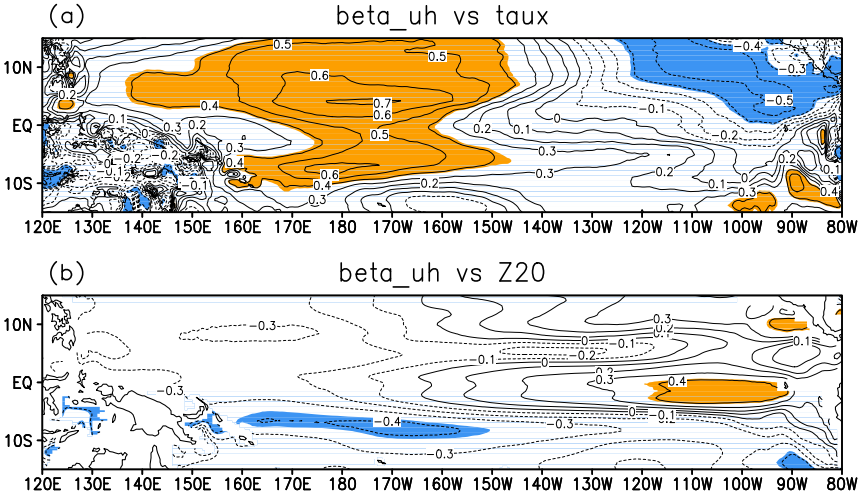

FIG. 5. Spatial patterns of intermodel correlation coefficients between the parameter β_{uh} and the (a) mean wind stress and (b) mean thermocline depth. Correlation coefficients that are significant at the 95% confidence level from the Student's t test are shaded.

can be described by the following two equations, respectively:

$$\overline{\mathrm{curl}\boldsymbol{\tau}'}|_{L_N} - \overline{\mathrm{curl}\boldsymbol{\tau}'}|_{L_S} = B_1\langle T\rangle \quad \text{and} \tag{14}$$

$$\frac{\partial[h]}{\partial t} = -B_2(\overline{\mathrm{curl}\boldsymbol{\tau}'}|_{L_N} - \overline{\mathrm{curl}\boldsymbol{\tau}'}|_{L_S}). \tag{15}$$

Here, L_S and L_N denote the southern and northern boundaries where the wind stress curl is averaged, $[h]$ represents the box-averaged thermocline depth anomalies over the entire equatorial Pacific (140°E–90°W), and $\overline{\mathrm{curl}\boldsymbol{\tau}'}|_{L_N}$ indicates the mean wind stress curl along the northern boundary. The detailed meridional ranges for the CMIP5 models are presented in Table 1. Given that the ENSO-induced wind stress curl pattern shows remarkable spread among the CMIP5 models (Fig. S7 in the supplemental material), the meridional range is model dependent based on the maximum ENSO-induced wind stress pattern in each model. If wind stress curl is averaged at the fixed boundaries at 5°S–5°N, its relations with SST anomalies [Eq. (14)] and the tendency of thermocline changes [Eq. (15)] will be very weak in some models (Fig. S8 in the supplemental material). Here, the model-dependent meridional ranges lead to more robust correlations in Eqs. (14) and (15) (Fig. S9 in the supplemental material).

As shown in Fig. 8, the wind stress curl is significantly correlated with the SST anomalies in the CMIP5 models, which gives rise to the robust estimation of the B_1 factor. In addition, the impact of wind stress curl on the thermocline tendency is pronounced among the

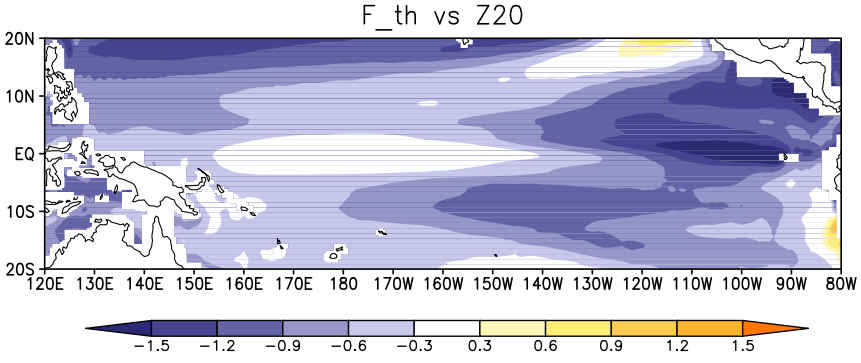

FIG. 6. The spatial pattern of the differences of mean thermocline depth (m) between the four models with the strongest thermocline feedbacks (HadGEM2-ES, NorESM1-ME, HadGEM2-CC, and NorESM1-M) and the four models with the weakest thermocline depths (ACCESS1.0, ACCESS1.3, CanESM2, and CMCC-CMS).

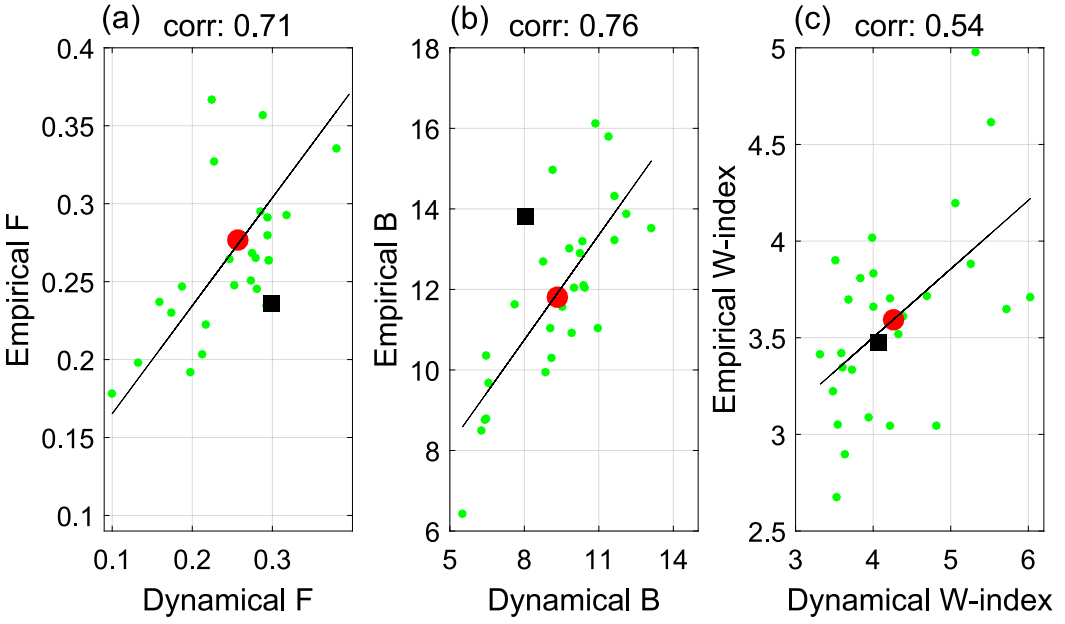

FIG. 7. (a) Scatterplot of the empirically derived F factor by linear fitting in the simple RO model [Eqs. (1) and (2)] against the dynamically derived F factor in Eq. (13) (°C m^{-1} yr^{-1}). (b) Scatterplot of the empirically derived B factor by linear fitting in the simple RO model [Eqs. (1) and (2)] against the dynamically derived B factor in Eq. (16) (unit: m °C^{-1} yr^{-1}). (c) Scatterplot of the empirically derived Wyrtki index (yr) using the empirical F and B factors against the dynamically derived Wyrtki index (yr) using the dynamical F and B factors in the CMIP5 historical simulations (green dots) and GODAS reanalysis (black-filled squares). The multimodel mean is indicated by the red-filled circles. The linear regression fitting is indicated by the straight lines.

CMIP5 models (Fig. 9). Thus, the estimation of the B_2 factor is also robust. Combining Eqs. (14) and (15), we can easily obtain the dynamics for the parameter B in Eq. (2):

$$B = B_1 B_2 . \tag{16}$$

This two-step estimation of the B factor is well correlated with direct empirical parameter fitting using the RO estimation for the B factor [Eq. (2)], with the correlation coefficient reaching 0.76 (Fig. 7b). The empirically derived B factor is the smallest in HadGEM2-ES, and its dynamically derived B factor is also the smallest, which explains its long ENSO period (Fig. 3). This result confirms the central role of the wind stress curl in bridging the SST anomalies and the thermocline changes (Jin 1997b). It is also evident in Fig. 7b that the CMIP5 MME underestimates the B factor, which suggests the underestimation of the efficiency of ENSO SST anomaly-induced equatorial heat content recharging–discharging. This lower efficiency is compensated by higher values in the simulated F factor (Fig. 7a), which represents the strong SST response to the zonal mean equatorial thermocline depth. These two biases largely cancel out and lead to the rather realistic ENSO period in the CMIP5 MME (Fig. 7c). Because biases in both B_1 and B_2 contribute to the B factor in a compounding way, the relative contributions of the biases of B_1 and B_2 are examined by a log–linear relationship. It is clear that intermodel biases in both B_1 and B_2 contribute significantly to the intermodel spread of the B factor (Fig. 10).

As shown in Fig. 11, the B_1 factor is closely related to the ENSO-induced wind stress pattern. The larger B_1 factor in the coupled model corresponds to the stronger westerly wind stress response to ENSO along the equator and the stronger easterly wind stress response to ENSO off the equator. Thus, both the air–sea coupling strength μ_a and the meridional width of the wind stress L_y are of great importance to the B_1 factor. Figure 12a shows that the intermodel B_1 is highly correlated with intermodel μ_a, with the correlation coefficient reaching 0.65. The linear combination of μ_a and L_y can explain about 58% of the total variance of the B_1 factor (Fig. 12c). Recent studies suggested that the B_1 factor is also correlated with β_h among the CMIP5 models, indicating the importance of the B_1 factor in determining ENSO dynamics (An et al. 2017).

Following Clarke et al. (2007), the coefficient B_2 can be derived from the horizontal momentum equations

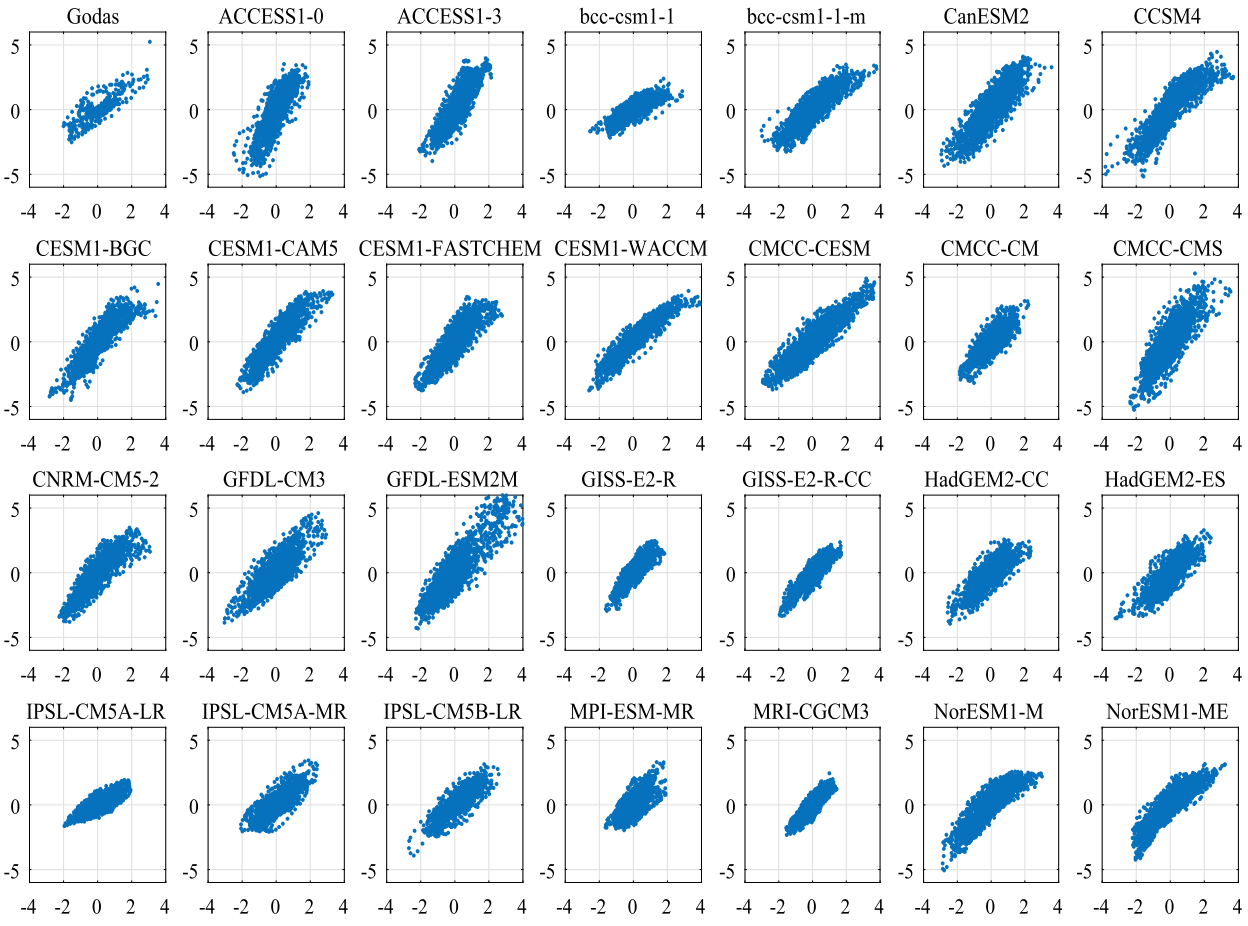

FIG. 8. Scatterplots for Eq. (14) in the CMIP5 models and GODAS reanalysis. The unit for the x axis is degrees Celsius, and the unit for the y axis is 10^{-8} Pa m^{-1}.

$$-fv = -\frac{1}{\rho}\frac{\partial p}{\partial x} + \frac{\tau_x}{\rho} \quad \text{and} \tag{17}$$

$$fu = -\frac{1}{\rho}\frac{\partial p}{\partial y} + \frac{\tau_y}{\rho}, \tag{18}$$

where τ_x and τ_y denote the zonal and meridional components of wind stress, respectively, ρ denotes the density, and p represents the pressure. Differentiating Eq. (17) with respect to y and Eq. (18) with respect to x, we obtain

$$f\left(\frac{\partial u}{\partial x} + \frac{\partial v}{\partial y}\right) + \beta v = \frac{1}{\rho}\left(\frac{\partial \tau_y}{\partial x} - \frac{\partial \tau_x}{\partial y}\right). \tag{19}$$

Applying the continuity relationship, we can further have

$$\beta v = f\frac{\partial w}{\partial z} + \frac{\text{curl}\boldsymbol{\tau}}{\rho}. \tag{20}$$

Integrating Eq. (20) from the thermocline depth h to the surface, we obtain

$$V = \frac{f}{\beta}\frac{\partial h}{\partial t} + \frac{\text{curl}\boldsymbol{\tau}}{\beta\rho}. \tag{21}$$

Neglecting the water transport at the zonal and lower boundaries, the mean thermocline changes can be expressed as

$$\int_A \frac{\partial h}{\partial t} dA = \int_0^{L_S} V_S\, dx - \int_0^{L_N} V_N\, dx, \tag{22}$$

where V_S and V_N denote the meridional current at the southern and northern edges, respectively. Applying Eq. (21) to Eq. (22), we obtain

$$\int_A \frac{\partial h}{\partial t} dA + \left(\frac{f_N}{\beta}\int_0^{L_N} \frac{\partial h}{\partial t} dx - \frac{f_S}{\beta}\int_0^{L_S} \frac{\partial h}{\partial t} dx\right) = \frac{1}{\beta\rho}\left(\int_0^{L_N} \text{curl}\boldsymbol{\tau}'\, dx - \int_0^{L_S} \text{curl}\boldsymbol{\tau}'\, dx\right). \tag{23}$$

Clarke et al. (2007) found that the thermocline depth changes at the meridional boundaries are significantly

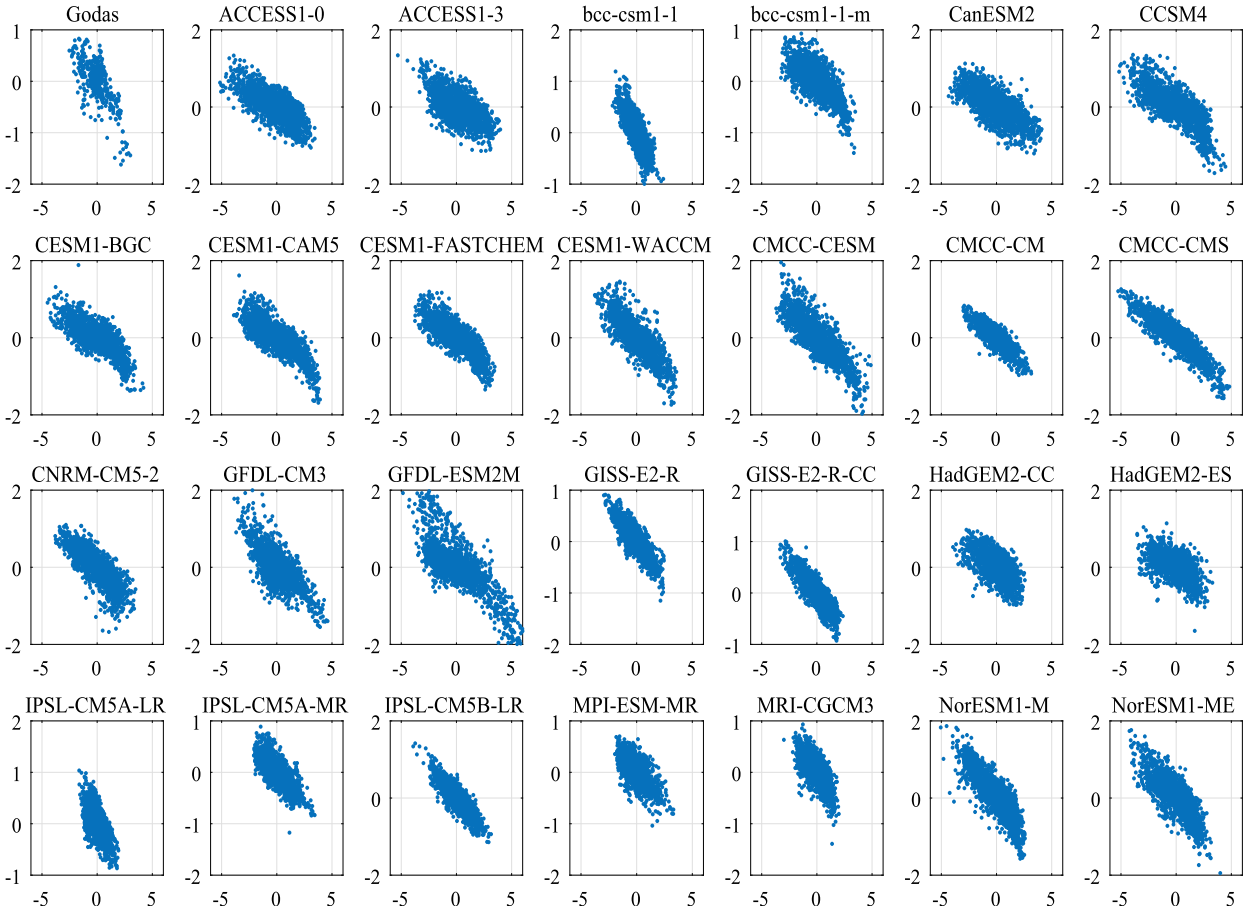

FIG. 9. Scatterplots for Eq. (15) in the CMIP5 models and GODAS reanalysis. The unit for the x axis is 10^{-8} Pa m^{-1}, and the unit for the y axis is 10^{-6} m s^{-1}.

correlated with the mean thermocline depth changes in the equatorial region

$$\frac{f_N}{\beta}\int_0^{L_N}\frac{\partial h}{\partial t}dx-\frac{f_S}{\beta}\int_0^{L_S}\frac{\partial h}{\partial t}dx=a\int\frac{\partial h}{\partial t}dA. \qquad (24)$$

Thus, Eq. (23) can be written as

$$(1+a)\frac{\partial[h]}{\partial t}=\frac{(\overline{\mathrm{curl}\boldsymbol{\tau}'}|_{L_N}-\overline{\mathrm{curl}\boldsymbol{\tau}'}|_{L_S})}{\beta\rho L_y}, \qquad (25)$$

where $[h]$ represents the box-averaged thermocline depth anomalies over the entire equatorial Pacific, L_y denotes the meridional range, and $\overline{\mathrm{curl}\boldsymbol{\tau}'}|_{L_N}$ indicates the mean wind stress curl along the northern boundary. Then, we can obtain the formulation of B_2 as

$$B_2=\frac{1}{(1+a)\beta\rho L_y}. \qquad (26)$$

Equation (26) indicates that the parameter B_2 is affected by the meridional range of wind stress curl and the parameter a. If the volume of discharge–recharge water transport induced by wind stress curl is fixed, the wider meridional range will lead to the smaller thermocline changes and, thus, the longer ENSO period. The parameter a is about 1 in the CMIP5 MME, which is consistent with previous findings by Clarke et al. (2007), although it varies substantially among the models.

5. Summary and discussion

As an effort toward understanding ENSO periodicity and its biases in climate simulations, we formulated a coupled dynamic index, referred to as the Wyrtki index, to investigate the contributing dynamical factors to ENSO periodicity. We demonstrate that this dynamically derived, semianalytical index provides a reasonable approximate estimation for ENSO main periodicity, simulated by CMIP5 models and in the reanalysis data.

The formulation of the Wyrtki index shows that ENSO periodicity mainly depends on two key factors, F

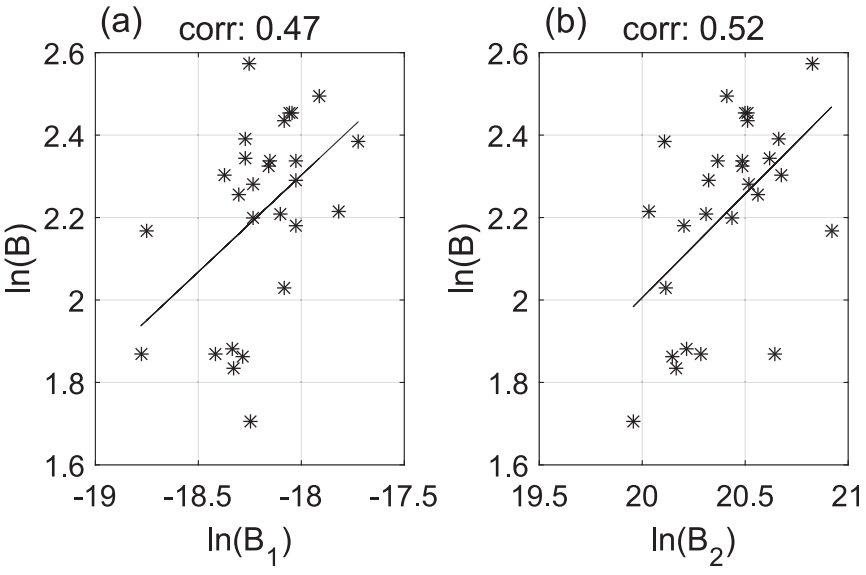

FIG. 10. Scatterplots for the natural logarithm of the B factor against the natural logarithm of (a) B_1 and (b) B_2 among the CMIP5 models, with the linear fitting lines indicated. The numbers at the top of each panel denote the correlation coefficients.

and B, that measure the efficiency of the SST changes in response to the equatorial zonal mean thermocline anomaly and the efficiency of the recharge–discharge of the equatorial thermocline changes in response to the SST anomalies induced off-equatorial wind stress anomaly, respectively. We further delineate that the F factor mainly comes from zonal advective feedback and thermocline feedback, and it can be semianalytically related to the zonal SST gradient and upwelling in the mean state with compounding effects from the ocean–atmosphere coupling and thermocline sharpness. In particular, the approximate formulation of the F factor combines the multiple effects from both mean state and coupling processes into a succinct measure that controls ENSO periodicity. The B factor comes from the compounding effect of the two processes that relate the ENSO-induced wind stress curl difference along the north and south of the equator and the further induced recharge–discharge of the equatorial heat content.

As an approximate dynamic quantification of ENSO periodicity, the Wyrtki index roughly captures the observed main periodicity of ENSO and the wide range of ENSO periodicity in the climate model simulations, with the intermodel correlation reaching 0.86. The sources for ENSO periodicity biases can also

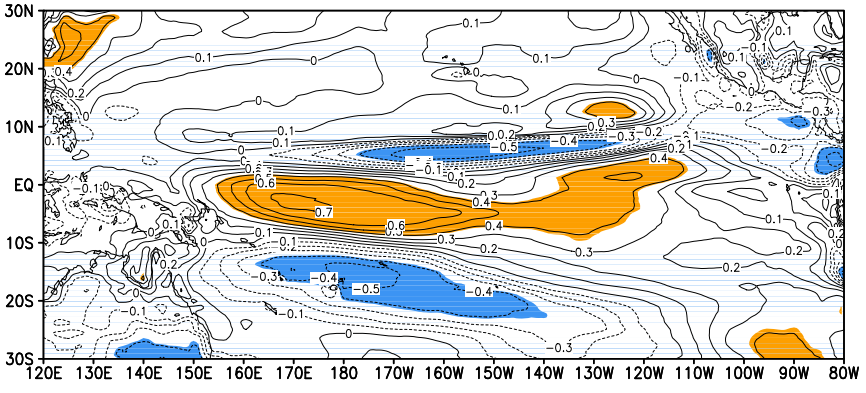

FIG. 11. The pattern of correlation coefficients (nondimensional) between the intermodel B_1 factor (Pa m^{-1} °C^{-1}) and intermodel ENSO-induced wind stress (Pa °C^{-1}). Correlation coefficients that are significant at the 95% confidence level from the Student's t test are shaded.

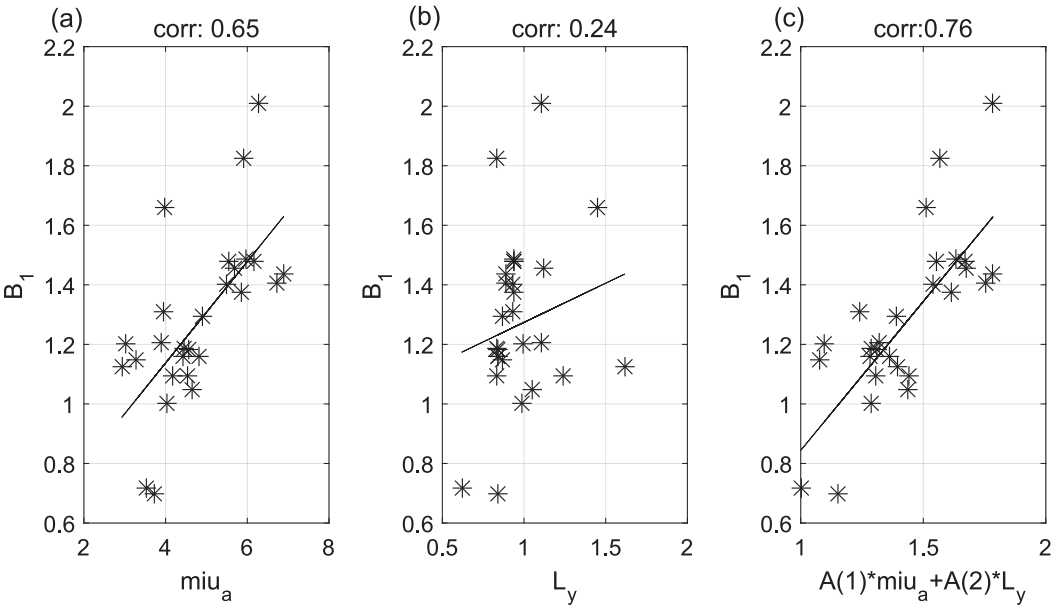

FIG. 12. Scatterplots for the intermodel B_1 factor (10^{-8} Pa m^{-1} °C^{-1}) against (a) the intermodel parameter μ_a (10^{-3} m s^{-1} Pa^{-1}), (b) the intermodel meridional width of wind stress curl (10^6 m), and (c) their linear combination (10^{-8} Pa m^{-1} °C^{-1}), with the linear fitting lines indicated. The numbers at the top of each panel denote the correlation coefficients.

be analyzed using the Wyrtki index. For example, the short ENSO period in BCC_CSM1.1(m) can be attributed to the larger F; the long ENSO period in HadGEM2-ES is caused by the small B factor. It is shown that the spread of simulated ENSO periodicity in the CMIP5 models results from the biases in mean state and several key parameters. Specifically, the intermodel zonal advective feedback F_{adv} is mainly caused by the intermodel biases in the parameter β_{uh}, while the intermodel biases in thermocline feedback F_{th} mainly result from both the intermodel spread of the parameter a_h and the mean upwelling. The intermodel B factor comes from both the biases in the ENSO-induced wind stress curl and the further induced thermocline tendency.

Our current formulation of the Wyrtki index did not take into consideration the contribution of nonlinear processes to ENSO periodicity, which may be significant (Jin 1997b; Eccles and Tziperman 2004). The nonlinear effect on ENSO periodicity in principle can be taken into consideration by examining the contributions of the nonlinear dynamic heating and other nonlinearity in the coupled system to ENSO periodicity. We have also ignored the impact of the background annual cycle on ENSO periodicity, although its impact may be limited, as noted in Jin et al. (1996). Despite these limitations, the linear Wyrtki index may thus serve as a useful tool for studying ENSO periodicity and its changes under different climate conditions in the past and future.

Acknowledgments. This work is jointly supported by China Meteorological Special Program (GYHY201506013), National Key R&D Program of China (2016YFA0602100), U.S. National Science Foundation (NSF) Grant AGS-1406601, U.S. Department of Energy (DOE) Grant DE-SC000511, and National Science Foundation of China (41605116). The authors declare no conflicts of interest. We thank Dietmar Dommenget and other two anonymous reviewers who helped to improve this paper.

REFERENCES

An, S.-I., and F.-F. Jin, 2000: An eigen analysis of the interdecadal changes in the structure and frequency of ENSO mode. *Geophys. Res. Lett.*, **27**, 2573–2576, https://doi.org/10.1029/1999GL011090.

——, and B. Wang, 2000: Interdecadal change of the structure of the ENSO mode and its impact on the ENSO frequency. *J. Climate*, **13**, 2044–2055, https://doi.org/10.1175/1520-0442(2000)013<2044:ICOTSO>2.0.CO;2.

——, and F.-F. Jin, 2001: Collective role of thermocline and zonal advective feedbacks in the ENSO mode. *J. Climate*, **14**, 3421–3432, https://doi.org/10.1175/1520-0442(2001)014<3421:CROTAZ>2.0.CO;2.

——, ——, and I.-S. Kang, 1999: The role of zonal advection feedback in phase transition and growth of ENSO in the Cane-Zebiak model. *J. Meteor. Soc. Japan*, **77**, 1151–1160, https://doi.org/10.2151/jmsj1965.77.6_1151.

——, E. S. Heo, and S. T. Kim, 2017: Feedback process responsible for intermodel diversity of ENSO variability. *Geophys. Res. Lett.*, **44**, 4272–4279, https://doi.org/10.1002/2017GL073203.

Battisti, D. S., and A. C. Hirst, 1989: Interannual variability in a tropical atmosphere–ocean model: Influence of the basic state, ocean geometry and nonlinearity. *J. Atmos. Sci.*, **46**, 1687–1712, https://doi.org/10.1175/1520-0469(1989)046<1687:IVIATA>2.0.CO;2.

Behringer, D. W., M. Ji, and A. Leetmaa, 1998: An improved coupled model for ENSO prediction and implications for ocean initialization. Part I: The ocean data assimilation system. *Mon. Wea. Rev.*, **126**, 1013–1021, https://doi.org/10.1175/1520-0493(1998)126<1013:AICMFE>2.0.CO;2.

Bejarano, L., and F.-F. Jin, 2008: Coexistence of equatorial coupled modes of ENSO. *J. Climate*, **21**, 3051–3067, https://doi.org/10.1175/2007JCLI1679.1.

Bellenger, H., E. Guilyardi, J. Leloup, M. Lengaigne, and J. Vialard, 2014: ENSO representation in climate models: From CMIP3 to CMIP5. *Climate Dyn.*, **42**, 1999–2018, https://doi.org/10.1007/s00382-013-1783-z.

Bjerknes, J., 1969: Atmospheric teleconnections from the equatorial Pacific. *Mon. Wea. Rev.*, **97**, 163–172, https://doi.org/10.1175/1520-0493(1969)097<0163:ATFTEP>2.3.CO;2.

Cane, M. A., M. Münnich, and S. E. Zebiak, 1990: A study of self-excited oscillations of the tropical ocean–atmosphere system. Part I: Linear analysis. *J. Atmos. Sci.*, **47**, 1562–1577, https://doi.org/10.1175/1520-0469(1990)047<1562:ASOSEO>2.0.CO;2.

Capotondi, A., A. Wittenberg, and S. Masina, 2006: Spatial and temporal structure of tropical Pacific interannual variability in 20th century coupled simulations. *Ocean Modell.*, **15**, 274–298, https://doi.org/10.1016/j.ocemod.2006.02.004.

Clarke, A. J., S. Van Gorder, and G. Colantuono, 2007: Wind stress curl and ENSO discharge/recharge in the equatorial Pacific. *J. Phys. Oceanogr.*, **37**, 1077–1091, https://doi.org/10.1175/JPO3035.1.

Dommenget, D., S. Haase, T. Bayr, and C. Frauen, 2014: Analysis of the Slab Ocean El Niño atmospheric feedbacks in observed and simulated ENSO dynamics. *Climate Dyn.*, **42**, 3187–3205, https://doi.org/10.1007/s00382-014-2057-0.

Eccles, F., and E. Tziperman, 2004: Nonlinear effects on ENSO's period. *J. Atmos. Sci.*, **61**, 474–482, https://doi.org/10.1175/1520-0469(2004)061<0474:NEOEP>2.0.CO;2.

Fedorov, A. V., and S. G. Philander, 2000: Is El Niño changing? *Science*, **288**, 1997–2002, https://doi.org/10.1126/science.288.5473.1997.

——, and ——, 2001: A stability analysis of tropical ocean–atmosphere interactions: Bridging measurements and theory for El Niño. *J. Climate*, **14**, 3086–3101, https://doi.org/10.1175/1520-0442(2001)014<3086:ASAOTO>2.0.CO;2.

Jin, F.-F., 1997a: An equatorial ocean recharge paradigm for ENSO. Part I: Conceptual model. *J. Atmos. Sci.*, **54**, 811–829, https://doi.org/10.1175/1520-0469(1997)054<0811:AEORPF>2.0.CO;2.

——, 1997b: An equatorial ocean recharge paradigm for ENSO. Part II: A stripped-down coupled model. *J. Atmos. Sci.*, **54**, 830–847, https://doi.org/10.1175/1520-0469(1997)054<0830:AEORPF>2.0.CO;2.

——, and J. D. Neelin, 1993a: Modes of interannual tropical ocean–atmosphere interaction—A unified view. Part I: Numerical results. *J. Atmos. Sci.*, **50**, 3477–3503, https://doi.org/10.1175/1520-0469(1993)050<3477:MOITOI>2.0.CO;2.

——, and ——, 1993b: Modes of interannual tropical ocean–atmosphere interaction—A unified view. Part III: Analytical results in fully coupled cases. *J. Atmos. Sci.*, **50**, 3523–3540, https://doi.org/10.1175/1520-0469(1993)050<3523:MOITOI>2.0.CO;2.

——, and S.-I. An, 1999: Thermocline and zonal advective feedbacks within the equatorial ocean recharge oscillator model for ENSO. *Geophys. Res. Lett.*, **26**, 2989–2992, https://doi.org/10.1029/1999GL002297.

——, J. D. Neelin, and M. Ghil, 1996: El Niño/Southern Oscillation and the annual cycle: Subharmonic frequency-locking and aperiodicity. *Physica D*, **98**, 442–465, https://doi.org/10.1016/0167-2789(96)00111-X.

——, S. T. Kim, and L. Bejarano, 2006: A coupled-stability index of ENSO. *Geophys. Res. Lett.*, **33**, L23708, https://doi.org/10.1029/2006GL027221.

Kang, I.-S., and S.-I. An, 1998: Kelvin and Rossby wave contributions to the SST oscillation of ENSO. *J. Climate*, **11**, 2461–2469, https://doi.org/10.1175/1520-0442(1998)011<2461:KARWCT>2.0.CO;2.

Kim, S.-T., and F.-F. Jin, 2011: An ENSO stability analysis. Part II: Results from the twentieth and twenty-first century simulations of the CMIP3 models. *Climate Dyn.*, **36**, 1609–1627, https://doi.org/10.1007/s00382-010-0872-5.

——, W. Cai, F.-F. Jin, and J.-Y. Yu, 2014: ENSO stability in coupled climate models and its association with mean state. *Climate Dyn.*, **42**, 3313–3321, https://doi.org/10.1007/s00382-013-1833-6.

Kirtman, B. P., 1997: Oceanic Rossby wave dynamics and the ENSO period in a coupled model. *J. Climate*, **10**, 1690–1704, https://doi.org/10.1175/1520-0442(1997)010<1690:ORWDAT>2.0.CO;2.

Lloyd, J., E. Guilyardi, and H. Weller, 2011: The role of atmosphere feedbacks during ENSO in the CMIP3 models. Part II: Using AMIP runs to understand the heat flux feedback mechanisms. *Climate Dyn.*, **37**, 1271–1292, https://doi.org/10.1007/s00382-010-0895-y.

MacMynowski, D. G., and E. Tziperman, 2008: Factors affecting ENSO's period. *J. Atmos. Sci.*, **65**, 1570–1586, https://doi.org/10.1175/2007JAS2520.1.

McCreary, J. P., 1983: A model of tropical ocean–atmosphere interaction. *Mon. Wea. Rev.*, **111**, 370–387, https://doi.org/10.1175/1520-0493(1983)111<0370:AMOTOA>2.0.CO;2.

Morlet, J., G. Arens, E. Fourgeau, and D. Glard, 1982: Wave propagation and sampling theory—Part I: Complex signal and scattering in multilayered media. *Geophysics*, **47**, 203–221, https://doi.org/10.1190/1.1441328.

Neelin, J. D., 1991: The slow sea surface temperature mode and the fast-wave limit: Analytic theory for tropical interannual oscillations and experiments in a hybrid coupled model. *J. Atmos. Sci.*, **48**, 584–606, https://doi.org/10.1175/1520-0469(1991)048<0584:TSSSTM>2.0.CO;2.

——, and F.-F. Jin, 1993: Modes of interannual tropical ocean–atmosphere interaction—A unified view. Part II: Analytical results in the weak-coupling limit. *J. Atmos. Sci.*, **50**, 3504–3522, https://doi.org/10.1175/1520-0469(1993)050<3504:MOITOI>2.0.CO;2.

Philander, S. G., T. Yamagata, and R. C. Pacanowski, 1984: Unstable air–sea interactions in the tropics. *J. Atmos. Sci.*, **41**, 604–613, https://doi.org/10.1175/1520-0469(1984)041<0604:UASIIT>2.0.CO;2.

Stuecker, M. F., A. Timmermann, F.-F. Jin, S. McGregor, and H.-L. Ren, 2013: A combination mode of the annual cycle and the El Niño/Southern Oscillation. *Nat. Geosci.*, **6**, 540–544, https://doi.org/10.1038/ngeo1826.

Suarez, M. J., and P. S. Schopf, 1988: A delayed action oscillator for ENSO. *J. Atmos. Sci.*, **45**, 3283–3287, https://doi.org/10.1175/1520-0469(1988)045<3283:ADAOFE>2.0.CO;2.

Syu, H. H., and J. D. Neelin, 2000: ENSO in a hybrid coupled model. Part I: Sensitivity to physical parameterizations. *Climate Dyn.*, **16**, 19–34, https://doi.org/10.1007/PL00007920.

Taylor, K. E., R. J. Stouffer, and G. A. Meehl, 2012: An overview of CMIP5 and the experiment design. *Bull. Amer. Meteor. Soc.*, **93**, 485–498, https://doi.org/10.1175/BAMS-D-11-00094.1.

Timmermann, A., J. Oberhuber, A. Bacher, M. Esch, M. Latif, and E. Roeckner, 1999: Increased El Niño frequency in a climate model forced by future greenhouse warming. *Nature*, **398**, 694–697, https://doi.org/10.1038/19505.

Wang, G., D. Dommenget, and C. Frauen, 2015: An evaluation of the CMIP3 and CMIP5 simulations in their skill of simulating the spatial structure of SST variability. *Climate Dyn.*, **44**, 95–114, https://doi.org/10.1007/s00382-014-2154-0.

Wyrtki, K., 1985: Water displacements in the Pacific and the genesis of El Niño cycles. *J. Geophys. Res.*, **90**, 7129–7132, https://doi.org/10.1029/JC090iC04p07129.

Zebiak, S. E., and M. A. Cane, 1987: A model El Niño–Southern Oscillation. *Mon. Wea. Rev.*, **115**, 2262–2278, https://doi.org/10.1175/1520-0493(1987)115<2262:AMENO>2.0.CO;2.

Clim Dyn (2018) 51:89–100
DOI 10.1007/s00382-017-3908-2

An extreme negative Indian Ocean Dipole event in 2016: dynamics and predictability

Bo Lu[1,2] · Hong-Li Ren[1,2,4] · Adam A. Scaife[3,5] · Jie Wu[1,2] · Nick Dunstone[3] · Doug Smith[3] · Jianghua Wan[1,2] · Rosie Eade[3] · Craig MacLachlan[3] · Margaret Gordon[3]

Received: 10 April 2017 / Accepted: 9 September 2017 / Published online: 14 September 2017
© The Author(s) 2017. This article is an open access publication

Abstract During 2016 boreal summer and fall, a strong negative Indian Ocean Dipole (IOD) event occurred, which led to large climate impacts such as the drought over East Africa. In this study, efforts are made to understand the dynamics of this IOD event and to evaluate real-time IOD predictions from current operational seasonal forecast systems. We show that both the wind-evaporation-SST and thermocline feedback lead to fast IOD growth in boreal summer 2016. Anomalous westerlies over the tropical Indian Ocean warmed the sea surface temperature (SST) over the tropical southeastern Indian Ocean (TSEIO) by reducing local evaporation; and wind induced thermocline deepening increased TSEIO SST by vertical advection. The intraseasonal disturbances in May induced the early subsurface warming and initiated the 2016 IOD. Due to negative cloud-radiation-SST feedback, the 2016 IOD event decayed quickly after October. We also demonstrate the successful real-time IOD predictions by the operational Hadley Center Global seasonal forecasting system version 5 (GloSea5) and the Beijing Climate Center Climate System Model (BCC-CSM1.1m). Resulting from the realistic representation of observed air–sea interactions, both models successfully predicted the evolution of the 2016 IOD up to 2 seasons ahead. The skillful prediction is also due to the precursor of the early subsurface warming in the eastern Indian Ocean, which increases intrinsic predictability of the 2016 IOD event. It is also demonstrated that IOD amplitude biases can be reduced by the joint-model prediction. The successful prediction of the 2016 IOD event allowed the East African drought to be predicted 4–6 months ahead. Our study reveals that current operational climate models can give useful warning of impending IOD events and impending climate extremes.

Keywords Indian Ocean Dipole · Air–sea interaction · East African drought · Seasonal prediction

1 Introduction

The Indian Ocean dipole (IOD) is a zonal dipole in the tropical Indian Ocean sea surface temperature (SST) varying on the interannual timescale (Saji et al. 1999; Webster et al. 1999). A positive (negative) IOD is associated with a cooling (warming) off the Sumatran coast and a warming (cooling) over the western equatorial Indian Ocean. The IOD has attracted much attention since the extreme 1997 positive IOD event which brought severe floods to East Africa and droughts to Indonesia (Webster et al. 1999). The interaction of the IOD with the Asian monsoon and the El Niño/Southern Oscillation (ENSO) has also been extensively studied (Ashok et al. 2001, 2003, 2004; Yu et al. 2002; Behera and Yamagata 2003; Gadgil et al. 2004; Kug and Kang 2006; Ashok and Saji 2007; Yuan et al. 2008; Izumo et al. 2010; Luo et al. 2010). By exciting atmospheric planetary waves,

✉ Hong-Li Ren
renhl@cma.gov.cn

1 Laboratory for Climate Studies, National Climate Center, China Meteorological Administration, Beijing, China

2 CMA-NJU Joint Laboratory for Climate Prediction Studies, Institute for Climate and Global Change Research, School of Atmospheric Sciences, Nanjing University, Nanjing, China

3 Met Office Hadley Center, Exeter, UK

4 Department of Atmospheric Science, School of Environmental Studies, China University of Geoscience, Wuhan 430074, China

5 College of Engineering, Mathematics and Physical Sciences, University of Exeter, Exeter, UK

IOD influences can even reach remote regions (e.g. Saji and Yamagata 2003).

In 2016, an extreme negative IOD event occurred, it is the strongest negative IOD in the period since 1980 according to NOAA Optimum Interpolation Sea Surface Temperature V2 dataset (OISSTv2; Reynolds et al. 2002), with the peak Indian Ocean Dipole Mode index (DMI; Saji et al. 1999) reaching −1.5 °C (see Fig. 1a). As shown in Fig. 2a, the 2016 boreal fall SST anomalies feature a strong warming off the coast of Sumatra (>1 °C), and a moderate cooling over the equatorial western Indian Ocean (<−0.5 °C). This strong IOD led to large climate influences such as the East African drought in 2016. During the East African short rain season (from October to December), the rainfall was reduced by

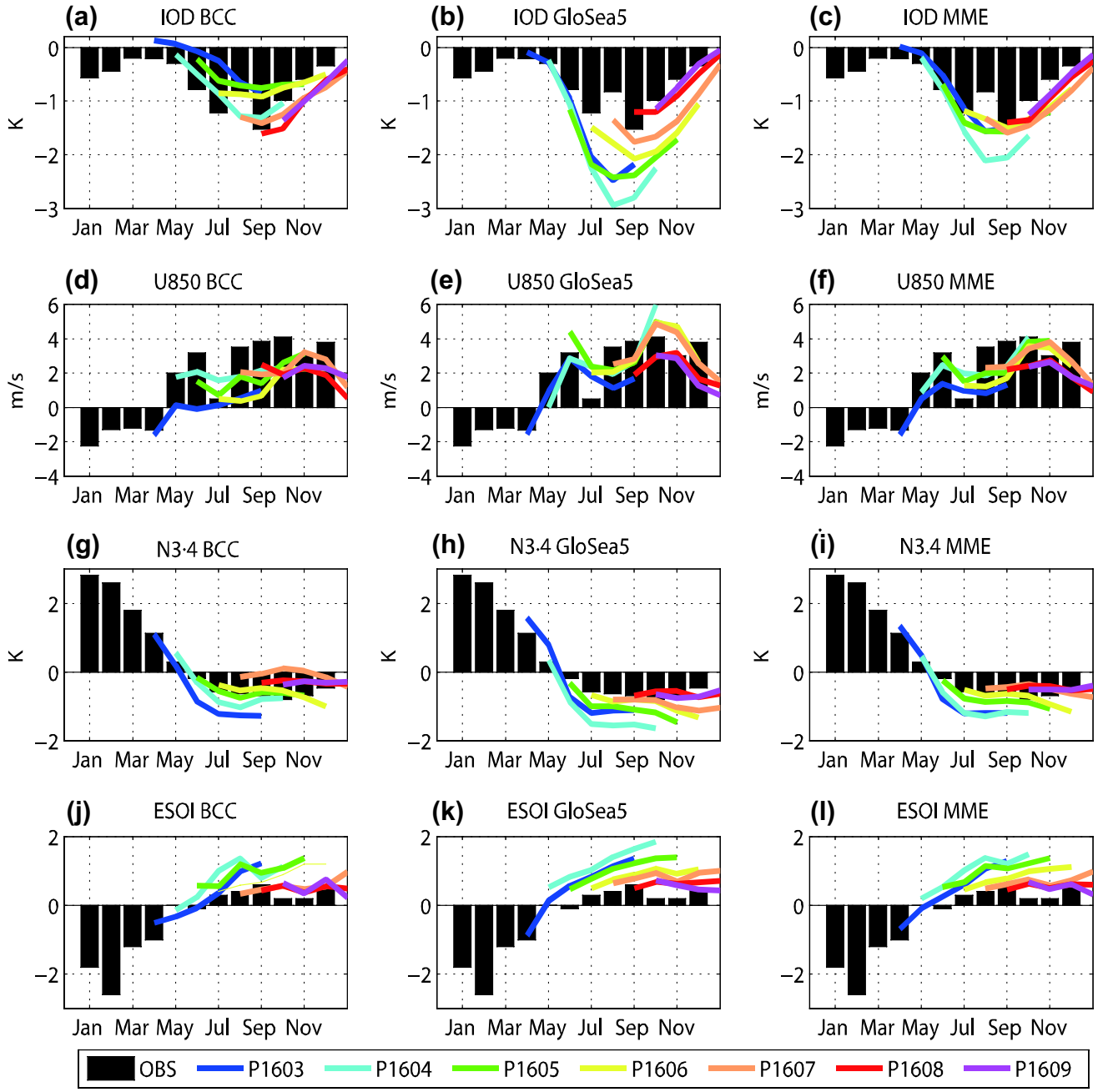

Fig. 1 Observed (bars) and predicted (curves) IOD index (**a**–**c**), equatorial zonal wind anomaly (**d**–**f**), Niño3.4 anomaly (**g**–**i**) and equatorial Southern Oscillation index (**j**–**l**) by BCC-CSM1.1m (left panel), GloSea5 (middle panel) and their average (right panel) in 2016. The real-time predictions were initialized in March (blue), April (light blue), May (green), June (yellow), July (orange), August (red) and September (purple), respectively

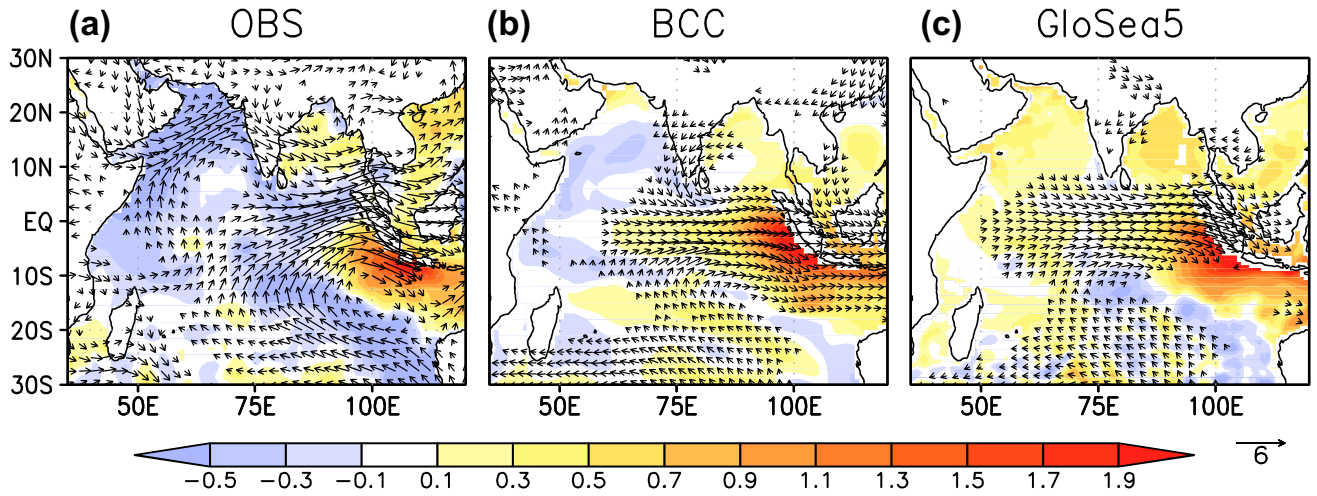

Fig. 2 The patterns of SST and 850 hPa wind anomalies during boreal fall 2016 in the observations (**a**) and the real-time predictions by BCC-CSM1.1m (**b**) and GloSea5 (**c**) initialized in August. Wind anomalies less than 0.6 m/s have been omitted for clarity

1 mm/day (Fig. 3a), with some regions recording below 50% of normal rainfall. As reported by the Inter-Agency Working Group (IAWG) in December 2016, over 15 million people in Somalia, Ethiopia and Kenya were experiencing devastating drought, food insecurity and unsafe drinking water. Thus, it is important to investigate the dynamics and predictability of this 2016 extreme negative IOD event.

The dynamics of IOD events are not completely understood. Dommenget (2011) argued that IOD cannot be distinguished from red noise based on a null hypothesis. A number of studies have pointed out the dependence of IOD on ENSO (e.g., Allan et al. 2001; Dommenget and Latif 2002; Baquero-Bernal et al. 2002; Yu and Lau 2004; Wang and Wang 2014), emphasizing the El Niño induced anomalous

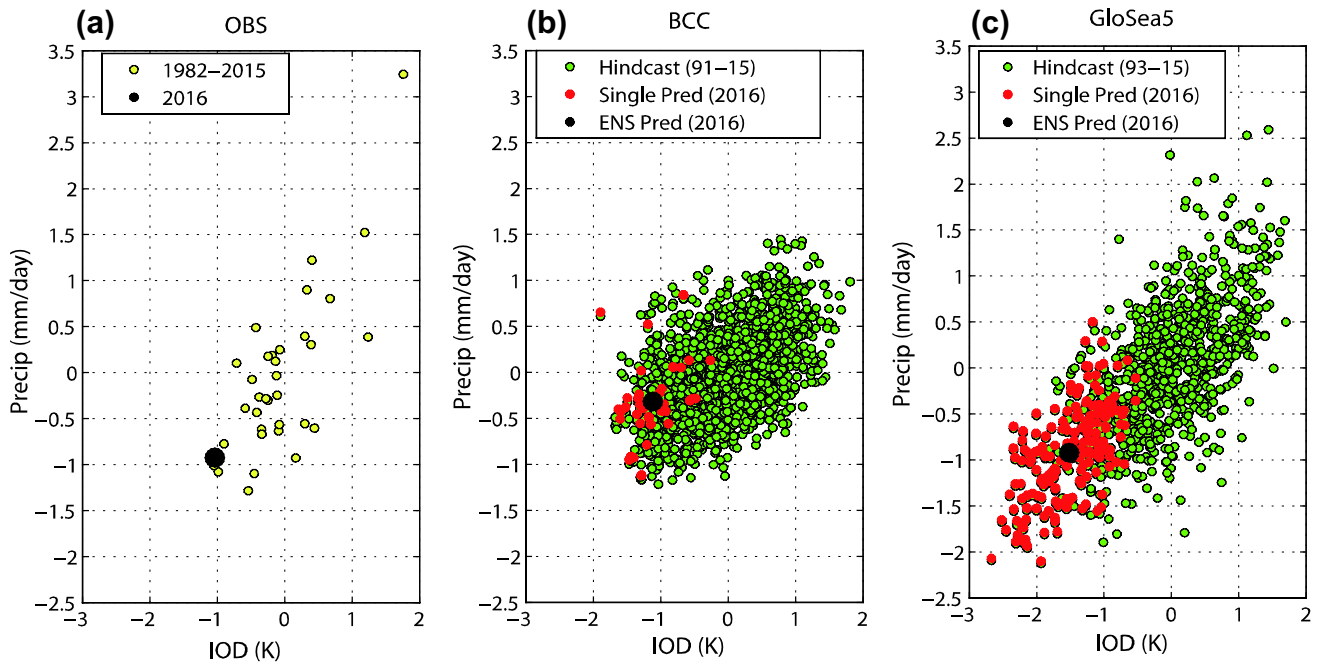

Fig. 3 Scatter plots of East African precipitation anomalies (land portion within 10°S–10°N; 30°E–45°E) during the short rain season (October, November and December) against the IOD index during boreal fall in the observations (**a**) and predictions by BCC-CSM1.1m (**b**) and GloSea5 (**c**) initialized in boreal summer (June, July and August). The hindcast experiments and the 2016 real-time prediction are shown in green and red circles, respectively. The black circle in **a** represents the observation for the 2016 negative IOD case. The black circles in **b, c** indicate the ensemble mean prediction for the 2016 negative IOD case by BCC-CSM1.1m and GloSea5, respectively

easterly wind off Sumatran coast during ENSO development in boreal summer. However, given the fact that several IOD events occurred in the absence of ENSO forcing, other studies suggest IOD as an inherent mode of internal variability within the Indian Ocean basin (Behera et al. 1999; Webster et al. 1999; Ashok et al. 2003; Yamagata et al. 2003). In a recent modeling study, one-third of the total IOD variance was due to ENSO forcing and the remaining arose from internal variability in the absence of ENSO (Yang et al. 2015). Coincident with the extreme negative IOD in 2016, the large 2015/2016 joint record El Niño decayed quickly and transited into a weak La Niña state over the tropical Pacific. Hence it is necessary to investigate the potential roles of internal variability in the Indian Ocean and the weak La Niña to explain the evolution of the 2016 IOD. In addition to ENSO, other possible triggers have also been proposed for initiating IOD events, such as the Indonesian Throughflow (Annamalai et al. 2003), the severe cyclone over the Bay of Bengal (Francis et al. 2007), the Hadley circulation over the western Pacific (Kajikawa et al. 2003), the subtropical IOD (Feng et al. 2014) and springtime Indonesian rainfall (Wang et al. 2016). The key role of wind-evaporation-SST (WES) and thermocline feedbacks are suggested to be fundamental to IOD growth (Li et al. 2003; Liu et al. 2011). However, not all the historical IOD events were accompanied by the WES and thermocline feedbacks. For example, WES feedback was inactive during 1997 IOD event. Therefore, the extreme negative IOD event in 2016 offers a good opportunity to further validate the dynamics of IOD formation.

The predictability of IOD events has been assessed for several coupled climate models (Luo et al. 2005, 2007; Song et al. 2008; Zhao and Hendon 2009; Shi et al. 2012; Liu et al. 2017). The lead time for skillful SST prediction is 5–6 months for the western Indian Ocean (IODW; 10°S–10N°, 50°E–70°E) and 3–4 months for the eastern Indian Ocean (IODE; 10°S–0°, 90°E–110°E). In general, skillful predictions of Dipole Mode Index (DMI) can only be made one season ahead (Shi et al. 2012; Liu et al. 2017). There is a winter predictability barrier (Luo et al. 2007), with a rapid drop of skill for IOD predictions across boreal winter. Although the prediction skill by dynamical coupled models is comparable to simple linear statistical models (Dommenget and Jansen 2009), higher skill can be achieved for larger IOD events. For example, the strong 2006 and 2007 positive IOD events were successfully predicted by SINTEX-F 3 seasons ahead owing to the oceanic subsurface memory in the South Indian Ocean (Luo et al. 2008). Considering the severe societal impacts of the strong 2016 negative IOD event (IAWG 2016), it is important to evaluate its real-time operational prediction by current operational seasonal prediction models. It is also interesting to study whether the prediction of impending extremes, such as the East African drought, can benefit from successful IOD predictions.

The remainder of the paper is organized as follows. Section 2 describes the observational, hindcast and real-time forecast datasets used in the study. In Sect. 3, we study the dynamics of the evolution of the 2016 IOD event. Real-time prediction of the 2016 IOD and its climate impacts are evaluated in Sect. 4. Finally, a summary and discussion of the results is given in Sect. 5.

2 Data and methodology

SST observations are taken from OISSTv2 (Reynolds et al. 2002), and the NCEP Global Ocean Data Assimilation System (GODAS; Behringer et al. 1998) is analyzed for the heat budget of the upper ocean. Monthly precipitation over land and ocean are obtained from the CPC Merged Analysis of Precipitation (CMAP; Xie and Arkin 1997) covering the period since 1979, while the Global Precipitation Climatology Centre monthly precipitation dataset (GPCC; Schneider et al. 2011) is utilized to study the precipitation only over land. Observed atmospheric circulation is obtained from the National Centers for Environmental Prediction/Department of Energy (NCEP/DOE) Reanalysis 1 (Kalnay et al. 1996).

In this study, we assess the IOD prediction by two operational seasonal prediction models, namely Global seasonal forecasting system version 5 (GloSea5) and the Beijing Climate Center Climate System Model (BCC-CSM1.1m). BCC-CSM1.1m is employed as the current operational model for seasonal prediction in Beijing Climate Center (Wu et al. 2010). Its ocean component is developed by modifying MOM4 from Geophysical Fluid Dynamics Laboratory (Griffies et al. 2004). Its horizontal resolution is $1° \times 1°$ poleward of 30°N and 30°S, incrementally increasing to 1/3° latitude within 30°N and 30°S. This ocean model has 40 vertical layers and includes dynamic and thermodynamic Sea Ice Simulator (Winton 2000). The atmospheric component is the BCC_AGCM2.2 at T106 horizontal resolution and 26 vertical layers (Wu et al. 2008), and the land model is BCC_AVIM (Ji et al. 2008) with a same horizontal resolution as the atmospheric model. The real-time forecast is performed at the beginning of every month, with 24 members per prediction by lagged initial dates (15 members) and singular vector perturbation method (9 members; Kleeman et al. 2003). BCC-Godas ocean reanalysis is used to initialize the ocean (Liu et al. 2005), while initial atmosphere and sea ice conditions are nudged toward NCEP reanalysis (Kalnay et al. 1996) and NOAA Optimum Interpolation Ice Concentration data (Reynolds et al. 2002), respectively. A monthly hindcast set covers the period from 1991 to 2014, with the same experimental design as the real-time forecast.

GloSea5 is the operational seasonal forecasting system of the Met Office (MacLachlan et al. 2015). The coupled HadGEM3 model is used in GloSea5. The atmosphere component uses Met Office Unified Model (Brown et al. 2012) atmosphere, and the ocean component uses NEMO (Nucleus for European Modelling of the Ocean; Madec 2008). GloSea5 uses the N216 resolution (0.8° in latitude and 0.5° in longitude) for the atmosphere, and the ORCA0.25 grid (0.25°) for the ocean. There are 85 vertical levels for the atmosphere and 75 levels for the ocean. The model contains no flux corrections or relaxation to climatology. GloSea5 produces 210-day long real-time seasonal forecasts initialized every day with two members. The initial atmospheric conditions are obtained from the Met Office 4D-Var data assimilation system (Rawlins et al. 2007), and the ocean and sea ice conditions are initialized from the short-range ocean forecasting and data assimilation system (MacLachlan et al. 2015). As an effort to obtain the model climatology and correct the mean state bias, a hindcast set initialized on the 1st, 9th, 17th and 25th days every month is completed from 1993 to 2015. Following the weighting strategy described in Arribas et al. (2011), the daily climatology is weighted average of the closest hindcast initialization dates. More details can be found in MacLachlan et al. (2015). Additional hindcast experiments with 24 members were performed for boreal summer, initialized on 25 April, 1 May and 9 May from 1992 to 2011. Each start date has eight ensemble members with different stochastic parameterization of model physics (Tennant et al. 2011), thus totaling 24 ensemble members per year. The GloSea5 Ocean and Sea Ice Analysis (1989–2011) supplies initial conditions for the ocean and sea ice, and ERA-Interim reanalysis data is used to initialize the atmosphere and land surface in the hindcast members. This extra hindcast dataset with a larger ensemble size is utilized to evaluate the historical IOD prediction skill by GloSea5.

3 Dynamics of the 2016 IOD event

Figure 1a shows the evolution of the 2016 IOD event (Saji et al. 1999). At the beginning of 2016, the Indian Ocean SST was passively modulated by the 2015/2016 super El Niño. It is well known that the Indian Ocean often warms following El Niño (Weare 1979) due to suppressed atmospheric convection and intensified surface energy flux. This basin wide warming was observed from January to April 2016, with the positive SST anomalies in both poles of the IOD (Figure not shown). Following the rapid decay of the 2015/2016 El Niño in boreal spring (Fig. 1g), SST over the western Indian Ocean dropped to 0.5 °C below normal. However, IODE SST remained warmer than normal throughout 2016, which is similar to the persistent IODE warming in 1998 and 2010 after the 1997/1998 and 2009/2010 El Niño events, respectively. The southeastern Indian ocean warmed up again during boreal summer 2016, and reached 1 °C above normal in September 2016, forming the strongest negative IOD event occurred since the 1980s (Fig. 1a). Thus, IODE played a more important role in the 2016 IOD than the western pole, and we focus on the dynamics of SST evolution in the tropical southeastern Indian Ocean.

A negative (positive) IOD event is often accompanied by a westerly (easterly) wind anomalies over the equatorial Indian Ocean, suggesting a role for local air–sea interaction (Saji et al. 1999; Yamagata et al. 2004). Consistent with this, a strong westerly wind anomaly was evident over the equatorial central to eastern Indian Ocean in 2016 (Fig. 2a). This westerly wind anomaly was pronounced from May to December 2016 (Fig. 1d). The northwesterly wind anomaly off the coast of Sumatra (Fig. 2a) reduced the local climatologic southeasterly during boreal summer, resulting in reduced local evaporation and a warmer IODE. According to Gill's solution (1980), the warming in IODE also induced an anomalous cyclone over the southeastern Indian Ocean (Fig. 2a), leading to a stronger northwesterly wind anomaly and further warming off Sumatran coast. We quantitatively evaluate the latent heat flux changes over IODE. As shown in Fig. 4, the weakening of local wind speed led to a reduction of latent heat loss which warmed IODE during boreal summer. The above wind-evaporation-SST feedback was suggested to be important for IOD growth (Li et al. 2003;

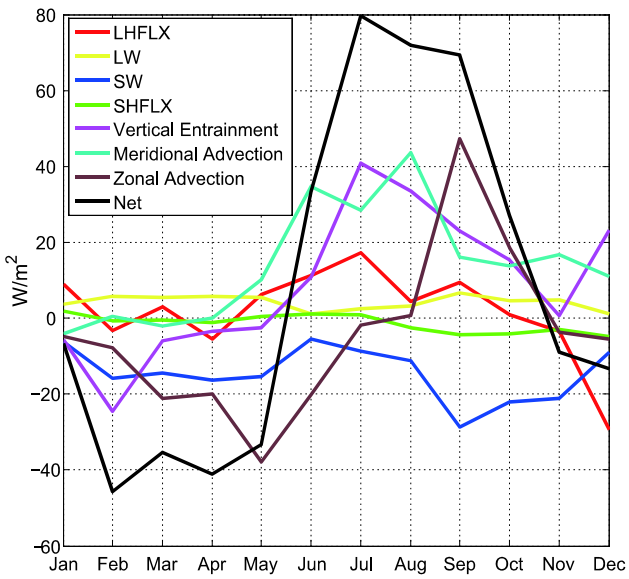

Fig. 4 The observed anomalies of latent heat flux (red), net downward long wave radiation at surface (yellow), net downward short wave radiation at surface (blue), sensible heat flux (green), vertical entrainment (purple), meridional advection (cyan), zonal advection (brown) and the net energy flux (black) over tropical southeastern Indian Ocean (90°E–110°E, 10°S–Equator) in 2016

Liu et al. 2011). Here, the fast growth of 2016 IOD event validates this hypothesis and also confirms IOD as a natural climate mode. It should be noted that WES feedback is positive only when the climatological southeasterly wind is pronounced in boreal summer and early fall. Although the equatorial westerly wind anomaly remained strong even in December 2016, the WES feedback became negative (Fig. 4) since the climatological wind turns northwesterly during boreal winter.

Along with the thermodynamic WES feedback, the anomalous equatorial westerly can also warm IODE by inducing a thermocline deepening and ocean warming. This thermocline feedback was first proposed in the eastern equatorial Pacific (EEP), where the easterly trade wind is strong and the thermocline is shallow. However, the thermocline in the Indian Ocean is relatively flat and deep due to the annual mean westerly wind. Thus, thermocline feedback is generally weaker in the Indian than the Pacific Ocean. However, the thermocline feedback is active from July to November (e.g. reviewed by Schott et al. 2009), when the mean upwelling is strong and the mean thermocline is shallow in the tropical eastern Indian Ocean. As shown in Fig. 4, the vertical advection of the anomalous subsurface warm water by the mean upwelling was pronounced from July to October, contributing to the peak phase of 2016 IOD. It is demonstrated that the impact of thermocline feedback on the 2016 IOD event is larger than WES feedback, which is consistent with previous studies (Murtugudde et al. 2000). We also note that the downward solar radiation is reduced with the IODE warming throughout 2016 (Fig. 4), indicating negative cloud-SST feedback. During boreal winter, this cloud-SST feedback and negative WES feedback terminated the IODE warming quickly, explaining the fast decay of 2016 negative IOD event (Fig. 1a).

Besides the WES and thermocline feedbacks during boreal summer and fall, the precursor of the 2016 extreme IOD event in late spring is also investigated. Prior to the IOD SST development, the tropical westerly wind anomaly occurred in May and June over the Indian Ocean basin (Fig. 1d), which initiated the early subsurface warming in the tropical southeastern Indian Ocean (Fig. 5). We further investigate the early zonal wind anomaly among historical IOD events. As shown in Fig. 6a, the significant correlation (0.62) is evident between the zonal wind and subsurface heat content anomalies in May and June at the 99% confidence level using a student-t test. Also, the early subsurface heat content anomaly in May and June is well correlated (0.50) with the SST in the tropical southeastern Pacific during the mature phase in boreal fall (Fig. 6b), implying the ocean memory and the effective thermocline feedback during IOD growth. It should be noted that the early westerly wind anomaly acted as an precursor for the strong negative IOD events in 1998 and 2016. However, the activation of

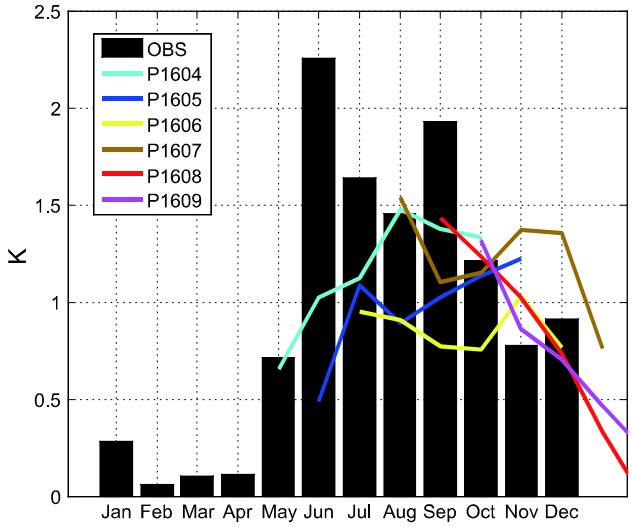

Fig. 5 Heat content anomalies of the upper ocean (0–200 m) over the tropical southeastern Indian Ocean in the observations (bars) and the real-time predictions by BCC-CSM1.1m (curves) in 2016. The predictions initialized in April, May, June, July, August and September are indicated by the light blue, blue, yellow, orange, red and purple curves, respectively

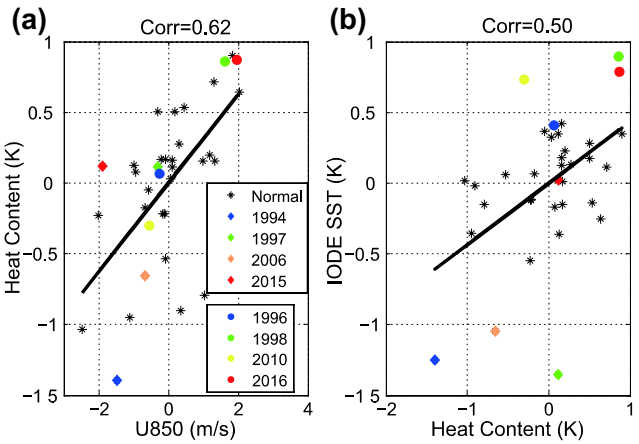

Fig. 6 The scatter plots of the heat content anomaly (0–200 m) against the zonal wind anomaly at 850 hPa (**a**) and the SST anomaly against the heat content anomaly (**b**) over [90°E–110°E; 10°S–Equator]. Note that the heat content and zonal wind anomalies are averaged in May and June, while the IODE SST anomaly is averaged from September to November. Four strongest positive IOD years (1994, 1997, 2006, 2015) and four strongest negative IOD years (1996, 1998, 2010 and 2016) since 1980s are indicated by the colorful symbols based on the IOD index (Saji et al. 1999) averaged from September to November. The straight lines represent the linear fitting line. The correlation coefficients are denotes by the numbers on the top of each figure

the negative IOD events in 1996 and 2010 cannot be attributed to early westerly wind or early subsurface warming, implying the existence of other precursors, such as oceanic

equatorial Kelvin waves and the variations of ITCZ rainfall (Rao et al. 2009).

We now investigate the origin of the early westerly wind in May. ENSO has been suggested to trigger IOD by modulating zonal winds off the Sumatran coast (e.g. Dommenget and Latif 2002). A weak La Niña coincided with the 2016 IOD (Fig. 1g). The atmospheric response to La Niña is characterised by the equatorial Southern Oscillation index (ESOI; http://www.cpc.ncep.noaa.gov/data/indices/), which measures the standardized anomaly of the difference between the area-average sea level pressure in an area of the eastern equatorial Pacific (80°W–130°W, 5°N–5°S) and an area over Indonesia (90°E–140°E, 5°N–5°S). As shown in Fig. 1j, the ESOI index remained negative from January to April, indicating a slowing of the Walker Circulation induced by the previous 2015/2016 El Niño. As the eastern Pacific developed into a weak La Niña state in July (Fig. 1g), ESOI turned positive and reached a peak in September. The resulting strengthening of the Walker Circulation helped to reinforce the anomalous westerly wind over the equatorial Indian Ocean during boreal fall. However, the La Niña induced atmospheric changes were moderate, with ESOI only reaching 0.6 standard deviation during boreal fall 2016. Furthermore, the westerly wind was evident as early as May and June (Fig. 1d) when ESOI was neutral (Fig. 1j), implying that the initiation of westerly wind in May and June was independent of the La Niña forcing. The westerly wind anomaly in 2016 may simply result from internal variability within the Indian Ocean, with the weak La Niña playing a secondary role.

Since the initiation of 2016 negative IOD was unrelated to ENSO forcing, we investigate other possible triggers. Wang et al. (2016) suggested that positive (negative) IOD can be initiated by springtime Indonesian rainfall deficit (surplus) in the absence of ENSO. Figure 7b, d show the intraseasonal evolution of zonal wind at 850 hPa and outgoing longwave radiation (OLR) in 2016. The above normal convection over Indonesian was observed during late spring, which induced the westerly wind anomaly that is important for IOD dynamics. Furthermore, the Indonesian rainfall anomaly was found to be originated from the western Indian Ocean. The eastward propagation of Madden-Julian oscillation (MJO) was clearly evident in May (Fig. 7). Similar feature was also evident in the extreme 1998 IOD event (Fig. 7a, c). In fact, the amplitude of MJO (Wheeler and Hendon 2004) in May 1998 and 2016 reached 3.6 and 1.6, respectively, indicating strong MJO activities. Although IOD and MJO have different time scales, the IOD-MJO interaction has been documented by many studies. Shinoda and Han (2005) found that MJO activity is strongly reduced during positive IOD years. The termination of 2003 and 2007 positive IOD events was suggested to be a result from convection-enhancing MJOs which deepen the thermocline in the southeastern equatorial Indian Ocean (Rao et al. 2009). Also, easterlies associated with the convection-suppressing phase of of MJO initiated the positive IOD event in 2006 (Rao et al. 2009). Here, we suggested that the active phase of MJO could induce strong westerly wind in late spring, which might activate the negative IOD events in 1998 and 2016 by initiating the early subsurface warming.

4 Evaluations of real-time predictions of the 2016 IOD

It has been shown the air–sea interaction is key for the 2016 negative IOD event. Now we demonstrate to what extent our operational coupled models can capture the IOD dynamics and predict the 2016 negative IOD event. Figure 2b, c show the real-time predictions of boreal fall SST and wind anomalies by BCC-CSM1.1m and GloSea5, respectively. The strong warming off the Sumatran coast was well predicted by both models, and BCC-CSM1.1m also captured the weak cooling over the western Indian Ocean. The strong anomalous westerly wind along the equator was successfully predicted by both models, indicating the realistic air–sea interaction. Similar to the observation, the IODE SST warming induced the northwesterly wind off the Sumatran coast as a part of the associated cyclone over southeastern Indian Ocean, which further warmed IODE SST by reducing the local surface wind speed. This implies that the observed WES feedback was also well reproduced by both models, which helped to drive the successful 2016 IOD predictions.

Both models also predicted remote factors, such as the 2016 weak La Niña. As shown in Fig. 1g, although the Pacific cooling was overestimated when initialized in March and April, the weak La Niña is well predicted after May. Furthermore, the La Niña induced weak atmospheric response was also well reproduced. The predicted strengthening of the Walker Circulation, as indicated by a positive ESOI (Fig. 1j, k, l), reinforced the westerly wind over the Indian Ocean in agreement with the observations. Consistent with the Niño 3.4 predictions, the atmospheric responses are overestimated by both models when initialized in boreal spring. However, the observed moderate positive ESOI is well reproduced when initialized in boreal summer and fall. Thus, a secondary role of the 2016 La Niña is well represented in the predicted 2016 IOD growth, consistent with observations.

Observational evidence shows that the 2016 IOD event was triggered by active MJOs in May. The intraseasonal perturbation is usually difficult to be captured by seasonal prediction models. The MJO-induced westerly wind anomaly in May 2016 was underestimated by GloSea5 (Fig. 1e). However, BCC-CSM1.1m correctly predicted the initiation of westerly wind anomaly 1 month ahead (light blue curve

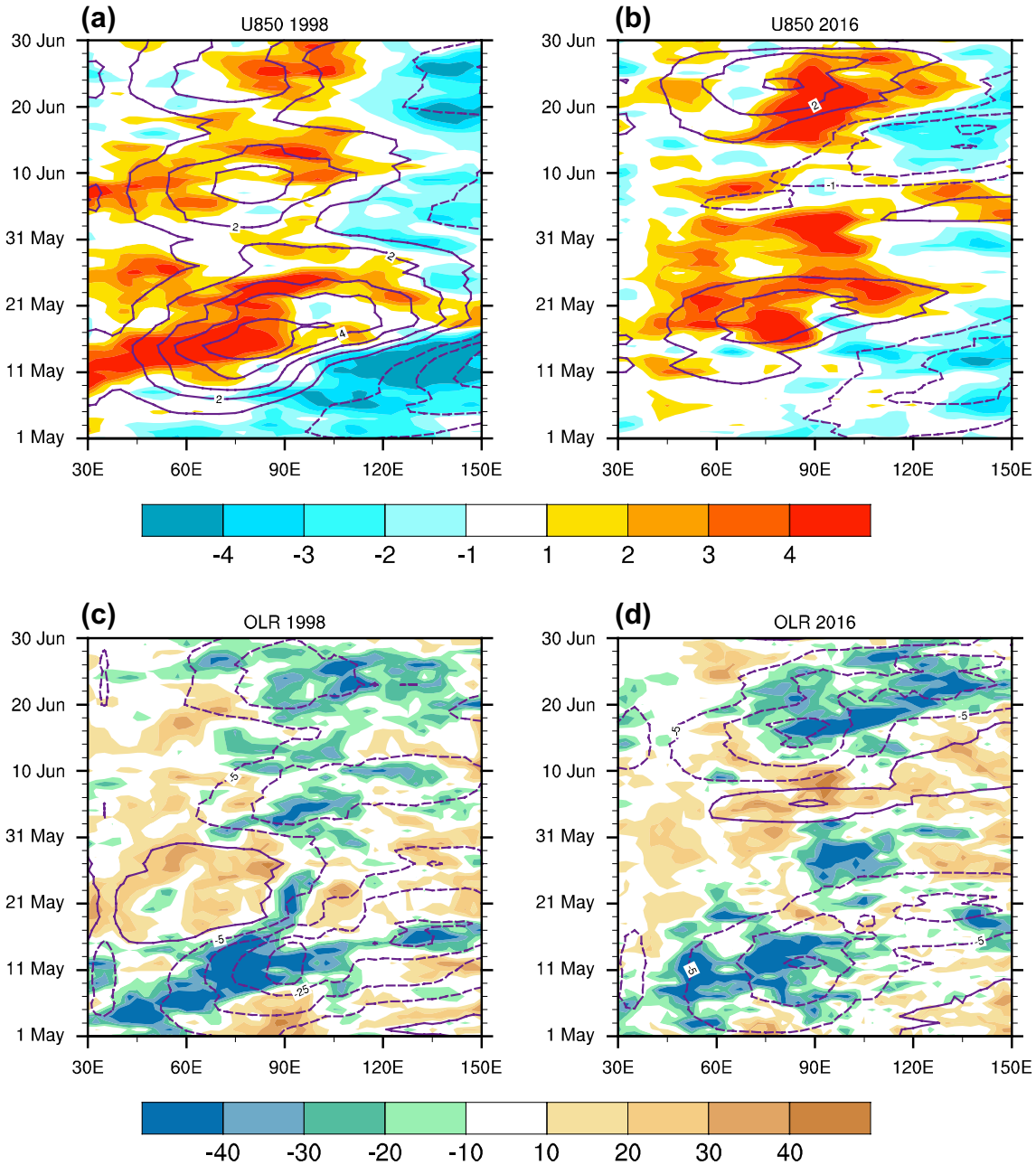

Fig. 7 Time-longitude plots of observed zonal wind anomalies (upper panel; m/s) and outgoing longwave radiation (lower panel; W/m^2) along the equator (10°S–10°N) during the strong negative IOD years of 1998 (**a, c**) and 2016 (**b, d**). The contours indicate the reconstructions by Real-time Multivariate MJO Indices (Wheeler and Hendon 2004)

in Fig. 1d). Similar to observations, the predicted westerly wind onset in BCC-CSM1.1m is unrelated to the concurrent 2016 La Niña, because the predicted atmospheric response was unclear in May (light blue curve in Fig. 1j). This implies a possible impact of internal intraseasonal processes on IOD initiation in predictions by BCC-CSM1.1m.

The real-time prediction plumes of DMI are given in Fig. 1b, c. It is interesting that early warning of the extreme 2016 negative IOD can be predicted as early as March 2016. Both models correctly predicted the quick onset, fast decay and peak season of the 2016 negative IOD. However, amplitude biases are evident in both models. BCC-CSM1.1m underestimated the 2016 negative IOD amplitude, while GloSea5 over-predicted it, especially when initialized in spring. Similar amplitude biases are also seen during other years in the 24 members hindcast experiments by both models (Fig. 8). We suggest that IOD amplitude bias is due to the mean state bias in tropical Indian Ocean. For GloSea5,

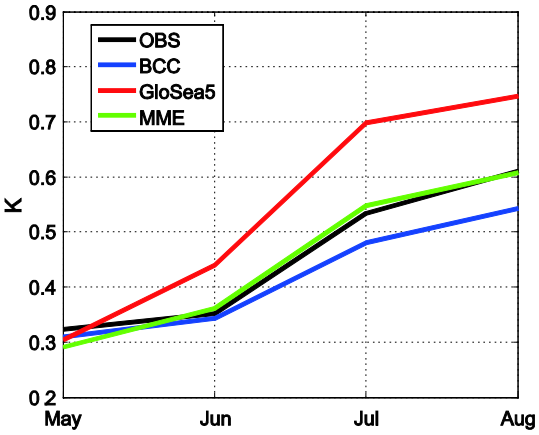

Fig. 8 Standard deviation of IOD index in the observations (black curve) and hindcast experiments initialized in May by BCC-CSM1.1m (blue), GloSea5 (red) and their average (green)

the mean thermocline is too shallow in the eastern equatorial Indian Ocean (Johnson et al. 2017), leading to an overestimation of thermocline feedback and the resultant IOD amplitude. In contrast, for BCC-CSM1.1m, the mean thermocline is too deep in the eastern equatorial Indian Ocean (Fig. 9) and hence the SST response is too weak. The IOD amplitude bias is reduced in the joint-model mean (Figs. 1c, 8), because the mean state biases in the two models cancel.

The IOD prediction skill is quite low at current level, with correlation of 0.5 around 3–4 months for most models (Shi et al. 2012; Liu et al. 2017). The overall IOD prediction skill by BCC-CSM1.1m is not significantly higher than other models, with the ACC skill quickly dropping under 0.5 after 3 months (not shown). Thus, the successful prediction of 2016 IOD event is partly due to the intrinsic predictable components inherent to this event. Figure 10 demonstrates the hindcast of IOD initialized in May and November by

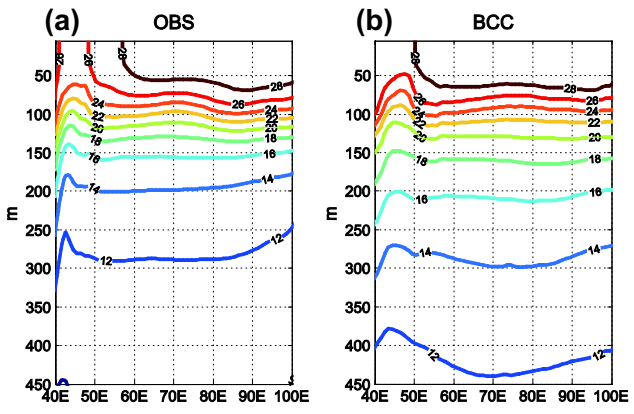

Fig. 9 Vertical profiles of climatologic Indian Ocean temperature along equator (5°S–5°N) during boreal summer in the observation (**a**) and the simulation by BCC-CSM1.1m (**b**)

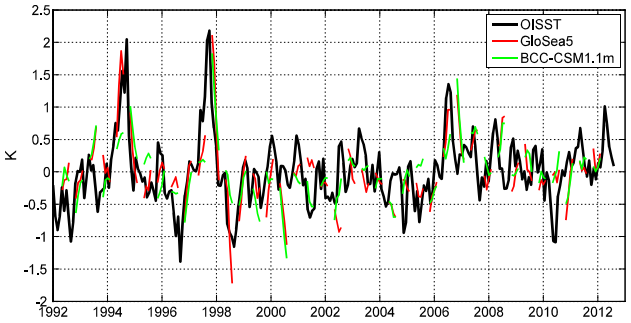

Fig. 10 The IOD index in the observation (black curve), and in the hindcast experiment initialized in May and November by GloSea5 (red curves) and BCC-CSM1.1m (green curve)

BCC-CSM1.1m and GloSea5. As previously discussed, the early westerly wind and subsurface warming acted as precursors in the negative IOD events in 1998 and 2016. As a result, the prediction of the strong negative IOD in 1998 and 2016 is successful although the amplitude is underestimated (overestimated) by BCC-CSM1.1m (GloSea5) due to the biases in mean thermocline depth (Fig. 9). However, the strong negative IOD events in 1996 and 2010 is not predicted by two models (Fig. 10) due to the unclear precursors (Fig. 6).

Previous studies have shown important climate impacts of IOD (Saji and Yamagata 2003), including the severe East African flood during the two strongest positive IOD years in 1994 (Behera et al. 1999) and 1997 (Birkett et al. 1999; Webster et al. 1999). Figure 11 shows the rainfall pattern during the short rain season from October to December (Clark et al. 2003). The precipitation anomalies were clearly anchored by 2016 IOD forcing, with above normal rainfall over the tropical eastern Indian Ocean and the below normal rainfall over the western Indian Ocean and East Africa. The observed pattern is well predicted by BCC-CSM1.1m and GloSea5 (Fig. 11c, d). These successful rainfall predictions result from both the correct 2016 negative IOD prediction and also a realistic IOD-rainfall relationship in both models. Consistent with previous studies (Black et al. 2003; Clark et al. 2003), the correlation of DMI index with East African short rainfall reaches 0.77 in the observations (Fig. 3a). The modulation of IOD on East African rainfall has been studied with atmospheric model simulations (Latif et al. 1999; Ummenhofer et al. 2009). Although other forcings, such as Arctic Oscillation (Gong et al. 2016), can also modulate East African short rain, IOD plays a dominant role (Bahaga et al. 2015). Here we demonstrate that coupled seasonal predictions also capture the observed connection between East African rainfall and IOD. As shown in Fig. 3, the correlation coefficients reach 0.54 and 0.72 for BCC-CSM1.1m and GloSea5, respectively. Given the successful 2016 negative IOD prediction, the East African drought is well predicted

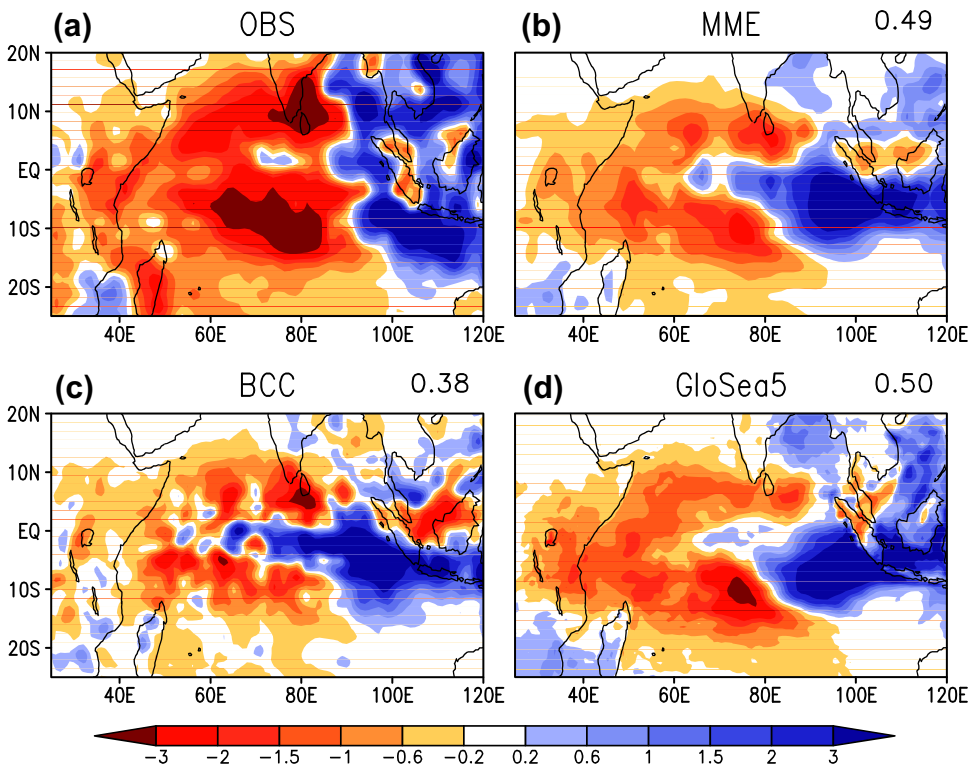

Fig. 11 Patterns of precipitation anomalies during the East African short rain season (from October to December 2016) in the observations (**a**) and the real-time prediction initialized in August 2016 by BCC-CSM1.1m (**c**), GloSea5 (**d**) and their average (**d**). Numbers denote the spatial correlation coefficients between the observation and real-time predictions

by BCC-CSM1.1m, although the ensemble mean amplitude is smaller than the observations due to the large ensemble spread (Fig. 3b). GloSea5 predicted a reduction of East African short rain by 1 mm/day 4–6 months ahead (Fig. 3c), which is very close to the observation.

5 Summary and conclusion

An extreme negative IOD event in 2016 caused major climate impacts such as severe East African drought as reported by IAWG. We investigated the dynamics and predictability of the 2016 IOD evolution. We found that the internal variability, involving the WES and thermocline feedbacks, played an important role in 2016 IOD growth during boreal summer. The strong westerly wind anomaly over the equatorial Indian Ocean deepened the thermocline and reduced the wind speed off the Sumatran coast. As a result, increased IODE SST during boreal summer was influenced by the vertical advection and reduced evaporation. Thus, the 2016 IOD event developed quickly in boreal summer and reached a peak of −1.5 °C in September 2016, the largest in the period since 1980s. Due to the negative cloud-SST-radiation feedback, the 2016 negative IOD decayed rapidly.

Besides internal variability, possible impact from remote forcing was also studied. A weak La Niña developed in the tropical Pacific during 2016. A moderate atmospheric response was evident, which intensified the Walker circulation and reinforced the westerly wind anomaly over the tropical Indian Ocean during boreal fall. Since the La Niña induced atmospheric response was very weak before July, we suggest that the early westerly wind in May was triggered by active MJOs in May. The subsurface warming immediately followed the MJO induced westerlies in late May. The ocean memory sustained the subsurface warming, and increased the SST off the Sumatran coast when the mean thermocline became shallow after July.

Real-time predictions of the 2016 IOD event were assessed in two prediction systems. Both models successfully predicted the evolution of the 2016 IOD up to 2 seasons ahead. The quick onset, fast decay and peak season of the 2016 negative IOD are all well captured. However, the amplitude is overestimated (underestimated) by GloSea5 (BCC-CSM1.1m). Hindcast experiments confirm the IOD amplitude biases due to the mean state errors in both models. Joint model predictions by BCC-CSM1.1m and GloSea5 give more realistic IOD amplitudes. The successful 2016 IOD predictions result from correct representations of atmosphere–ocean feedback. The reduction of wind speed over eastern Indian Ocean is predicted by both models (Fig. 2), implying realistic WES feedback. Although the subsurface ocean data is unavailable for GloSea5, we show that the observed wind-driven subsurface ocean warming was captured by BCC-CSM1.1m (Fig. 5), indicating a good representation of thermocline feedback in real-time predictions. The 2016 weak La Niña is also

predicted by both models, offering realistic external forcing for further IOD development. The skillful prediction is also due to the precursor of the early subsurface warming in the eastern Indian Ocean, which increases intrinsic predictability of the 2016 IOD event. Consistent with the successful prediction of the 2016 negative IOD event, the observed East African drought was also be well predicted. Early warning of deficient short rains was obtained 4–6 months ahead, providing potentially important societal benefits from current real-time seasonal prediction systems.

Acknowledgements This work is jointly supported by National Key Research Program and Development of China (2016YFA0602104), National Basic Research (973) Program of China under Grant 2015CB453203, China Meteorological Special Program (GYHY201506013), National Science Foundation (41605116), and the UK-China Research & Innovation Partnership Fund through the Met Office Climate Science for Service Partnership (CSSP) China as part of the Newton Fund.

Open Access This article is distributed under the terms of the Creative Commons Attribution 4.0 International License (http://creativecommons.org/licenses/by/4.0/), which permits unrestricted use, distribution, and reproduction in any medium, provided you give appropriate credit to the original author(s) and the source, provide a link to the Creative Commons license, and indicate if changes were made.

References

Allan R, Chambers D, Drosdowsky W et al (2001) Is there an Indian Ocean dipole and is it independent of the El Niño-Southern Oscillation. CLIVAR Exch 21:18–22

Annamalai H, Murttugudde R, Potema J, Xie S-P, Wang B (2003) Coupled dynamics over the Indian Ocean: spring initiation of the zonal mode. Deep Sea Res Part II Top Stud Oceanogr 50:2305–2330

Arribas A, Glover M, Maidens A et al (2011) The GloSea4 ensemble prediction system for seasonal forecasting. Mon Wea Rev 139:1891–1910. doi:10.1175/2010MWR3615.1

Ashok K, Saji NH (2007) On the impacts of ENSO and Indian Ocean dipole events on sub-regional Indian summer monsoon rainfall. Nat Hazards 42(2):273–285

Ashok K, Guan Z, Yamagata T (2001) Impact of the Indian Ocean dipole on the relationship between the Indian monsoon rainfall and ENSO. Geophys Res Lett 28(23):4499–4502

Ashok K, Guan Z, Yamagata T (2003) A look at the relationship between the ENSO and the Indian Ocean dipole. J Meteorol Soc Jpn 81(1):41–56

Ashok K, Guan Z, Saji NH et al (2004) Individual and combined influences of ENSO and the Indian Ocean dipole on the Indian summer monsoon. J Clim 17(16):3141–3155

Bahaga TK, Mengistu Tsidu G, Kucharski F, Diro GT (2015) Potential predictability of the sea-surface temperature forced equatorial East African short rains interannual variability in the 20th century. Q J R Meteorol Soc 141(686):16–26

Baquero-Bernal A, Latif M, Legutke S (2002) On dipolelike variability of sea surface temperature in the tropical. Indian OceanJ Clim 15(11):1358–1368

Behera SK, Yamagata T (2003) Influence of the Indian Ocean dipole on the Southern oscillation. J Meteorol Soc Jpn 81:169–177

Behera SK, Krishnan R, Yamagata T (1999) Unusual ocean–atmosphere conditions in the tropical Indian Ocean during 1994. Geophys Res Lett 26:3001–3004

Behringer DW, Ji M, Leetmaa A (1998) An improved coupled model for ENSO prediction and implications for ocean initialization. Part I: The ocean data assimilation system. Mon Wea Rev 126:1013–1021

Birkett C, Murtugudde R, Allan R (1999) Indian Ocean climate event brings floods to East Africa's lakes and the Sudd Marsh. Geophys Res Lett 26:1031–1034

Black E, Slingo J, Sperber KR (2003) An observational study of the relationship between excessively strong short rains in coastal East Africa and Indian Ocean SST. Mon Wea Rev 131:74–94

Brown A et al (2012) Unified modeling and prediction of weather and climate: a 25-year journey. Bull Am Meteorol Soc 93:1865–1877

Clark CO, Webster PJ, Cole JE (2003) Interdecadal variability of the relationship between the Indian Ocean zonal mode and East African coastal rainfall anomalies. J Clim 16:548–554

Dommenget D (2011) An objective analysis of the observed spatial structure of the Tropical Indian Ocean SST variability. Clim Dyn 36:2129–2145

Dommenget D, Jansen M (2009) Predictions of Indian Ocean SST indices with a simple statistical model: a null hypothesis. J Clim 22(18):4930–4938

Dommenget D, Latif M (2002) A cautionary note on the interpretation of EOFs. J Clim 15(2):216–225

Feng J, Hu D, Yu L (2014) How does the Indian Ocean subtropical dipole trigger the tropical Indian Ocean dipole via the Mascarene high? Acta Oceanolog Sin 33(1):64–76

Francis PA, Gadgil S, Vinayachandran PN (2007) Triggering of the positive Indian Ocean dipole events by severe cyclones over the Bay of Bengal. Tellus A 59(4):461–475

Gadgil S, Vinayachandran PN, Francis PA et al (2004) Extremes of the Indian summer monsoon rainfall, ENSO and equatorial Indian Ocean oscillation. Geophys Res Lett 31(12), doi:10.1029/2004GL019733

Gill AE (1980) Some simple solutions for heat-induced tropical circulation. Q J R Meteorol Soc 106:447–462

Gong DY, Guo D, Mao R, Yang J, Gao Y, Kim SJ (2016) Interannual modulation of East African early short rains by the winter Arctic Oscillation. J Geophys Res 121:9441–9457

Griffies SM, Harrison MJ, Pacanowski RC, Rosati A (2004) A technical guide to MOM4. NOAA/Geophysical Fluid Dynamics Laboratory, Princeton, p 337

IAWG (2016) Call to action: horn of Africa drought crisis. http://reliefweb.int/report/ethiopia/call-action-horn-africa-drought-crisis-hornofafricadrought-december-2016. Accessed 09 Dec 2016

Izumo T, Vialard J, Lengaigne M et al (2010) Influence of the state of the Indian Ocean Dipole on the following year's El Niño. Nature Geosci 3(3):168–172

Ji J, Huang M, Li K (2008) Prediction of carbon exchanges between China terrestrial ecosystem and atmosphere in 21st century. Sci China (Ser D) 51(6):885–898

Johnson SJ, Turner A, Woolnough S et al (2017) An assessment of Indian monsoon seasonal forecasts and mechanisms underlying monsoon interannual variability in the Met Office GloSea5-GC2 system. Clim Dyn 48(5):1447–1465

Kajikawa Y, Yasunari T, Kawamura R (2003) The role of the local hadley circulation over the Western Pacific on the zonally asymmetric anomalies over the Indian Ocean. J Meteorol Soc Jpn 81(2):259–276

Kalnay et al (1996) The NCEP/NCAR 40-year reanalysis project. Bull Am Meteorol Soc 77:437–470

Kleeman R, Tang Y, Moore A (2003) The calculation of climatically relevant singular vectors in the presence of weather noise. J Atmos Sci 60:2856–2867
Kug JS, Kang IS (2006) Interactive feedback between ENSO and the Indian Ocean. J Clim 19(9):1784–1801
Latif M, Dommenget D, Dima M, Grötzner A (1999) The role of Indian Ocean sea surface temperature in forcing East African rainfall anomalies during December–January 1997/98. J Clim 12(12):3497–3504
Li T, Wang B, Chang CP, Zhang YS (2003) A theory for the Indian Ocean dipole–zonal mode. J Atmos Sci 60:2119–2135
Liu Y, Zhang R, Yin Y, Niu T (2005) The application of ARGO data to the global ocean data assimilation operational system of NCC. Acta Meteorol Sinica 19:355–365
Liu L, Yu W, Li T (2011) Dynamic and thermodynamic air–sea coupling associated with the Indian Ocean dipole diagnosed from 23 WCRP CMIP3 models. J Clim 24:4941–4958
Liu H, Tang Y, Chen D et al (2017) Predictability of the Indian Ocean Dipole in the coupled models. Clim Dyn 48:2005–2024
Luo JJ, Masson S, Behera S et al (2005) Seasonal climate predictability in a coupled OAGCM using a different approach for ensemble forecasts. J Clim 18(21):4474–4497
Luo JJ, Masson S, Behera S et al (2007) Experimental forecasts of the Indian Ocean dipole using a coupled OAGCM. J Clim 20(10):2178–2190
Luo JJ, Behera S, Masumoto Y et al (2008) Successful prediction of the consecutive IOD in 2006 and 2007. Geophys Res Lett 35(14), doi: 10.1029/2007GL032793
Luo JJ, Zhang R, Behera SK et al (2010) Interaction between El Nino and extreme Indian ocean dipole. J Clim 23(3):726–742
MacLachlan C et al (2015) Global Seasonal forecast system version 5 (GloSea5): a high-resolution seasonal forecast system. Q J R Meteorol Soc 141(689):1072–1084
Madec G (2008) NEMO Ocean Engine, Note du Pole de Modelisation. Institut Pierre-Simon Laplace (IPSL), Paris
Murtugudde R, McCreary JP, Busalacchi AJ (2000) Oceanic processes associated with anomalous events in the Indian Ocean with relevance to 1997–1998. J Geophys Res 105:3295–3306
Rao SA, Luo JJ, Behera SK, Yamagata T (2009) Generation and termination of Indian Ocean Dipole events in 2003, 2006 and 2007. Clim Dyn 33:751–767
Rawlins F, Ballard SP, Bovis KJ et al (2007) The Met Office global four-dimensional variational data assimilation scheme. Q J R Meteorol Soc 133:347–362
Reynolds RW, Rayner NA, Smith TM et al (2002) An improved in situ and satellite SST analysis for climate. J Clim 15:1609–1625
Saji NH, Yamagata T (2003) Possible impacts of Indian Ocean dipole mode events on global climate. Clim Res 25(2):151–169
Saji NH, Goswami BN, Vinayachandran PN et al (1999) A dipole mode in the tropical Indian Ocean. Nature 401:360–363
Schneider U, Becker A, Finger P et al (2011) GPCC Full Data Reanalysis Version 6.0 at 1.0°: Monthly Land-Surface Precipitation from Rain-Gauges built on GTS-based and Historic Data. doi:10.5676/DWD_GPCC/FD_M_V7_100
Schott FA, Xie SP, McCreary JP (2009) Indian Ocean circulation and climate variability. Rev Geophys 47:RG1002. doi:10.1029/2007RG000245
Shi L, Hendon HH, Alves O et al (2012) How predictable is the Indian Ocean dipole? Mon Wea Rev 140(12):3867–3884
Shinoda T, Han W (2005) Influence of the Indian Ocean dipole on atmospheric subseasonal variability. J Clim 18:3891–3909
Song Q, Vecchi GA, Rosati AJ (2008) Predictability of the Indian Ocean sea surface temperature anomalies in the GFDL coupled model. Geophys Res Lett 35(2), doi: 10.1029/2007GL031966
Tennant WJ, Shutts GJ, Arribas A, Thompson SA (2011) Using a stochastic kinetic energy backscatter scheme to improve MOGREPS probabilistic forecast skill. Mon Wea Rev 139:1190–1206. doi:10.1175/2010MWR3430.1
Ummenhofer CC, Gupta AS, England MH, Reason CJC (2009) Contributions of Indian Ocean sea surface temperatures to enhanced East African rainfall. J Clim 22:993–1013
Wang X, Wang C (2014) Different impacts of various El Niño events on the Indian Ocean Dipole. Clim Dyn 42:991–1005
Wang H, Murtugudde R, Kumar A (2016) Evolution of Indian Ocean dipole and its forcing mechanisms in the absence of ENSO. Clim Dyn 47:2481–2500
Weare BC (1979) A statistical study of the relationships between ocean surface temperatures and the Indian monsoon. J Atmos Sci 36:2279–2291
Webster PJ, Moore AM, Loschnigg JP, Leben RR (1999) Coupled ocean–atmosphere dynamics in the Indian Ocean during 1997–98. Nature 401:356–360
Wheeler MC, Hendon HH (2004) An all season real-time multivariate MJO index: development of an index for monitoring and prediction. Mon Wea Rev 132:1917–1932
Winton M (2000) A reformulated three-layer sea ice model. J Atmos Ocean Technol 17:525–531
Wu T, Yu R, Zhang F (2008) A modified dynamic framework for the atmospheric spectral model and its application. J Atmos Sci 65:2235–2253
Wu T, Yu R, Zhang F (2010) The Beijing Climate Center atmospheric general circulation model: description and its performance for the present-day climate. Clim Dyn 34:123–147
Xie P, Arkin PA (1997) Global precipitation: A 17-year monthly analysis based on gauge observations, satellite estimates, and numerical model outputs. Bull Am Meteorol Soc 78:2539–2558
Yamagata T, Behera SK, Rao SA et al (2003) Comments on "Dipoles, temperature gradients, and tropical climate anomalies". Bull Am Meteorol Soc 84:1418–1422. doi:10.1175/BAMS-84-10-1418
Yamagata T, Behera SK, Luo JJ et al (2004) Coupled ocean–atmosphere variability in the tropical Indian Ocean. Earth climate: the ocean–atmosphere interaction. Geophys Monogr 147:189–212
Yang Y, Xie SP, Wu L et al (2015) Seasonality and predictability of the Indian Ocean Dipole mode: ENSO forcing and internal variability. J Clim 28(20):8021–8036
Yu JY, Lau KM (2004) Contrasting Indian Ocean SST variability with and without ENSO influence: a coupled atmosphere-ocean GCM study. Meteorol Atmos Phys. doi:10.1007/s00703-004-0094-7
Yu JY, Mechoso CR, McWilliams JC et al (2002) Impacts of the Indian Ocean on the ENSO cycle. Geophys Res Lett 29(8), doi: 10.1029/2001GL014098
Yuan Y, Yang H, Zhou W, Li CY (2008) Influences of the Indian Ocean dipole on the Asian summer monsoon in the following year. Int J Climatol 28:1849–1859
Zhao M, Hendon HH (2009) Representation and prediction of the Indian Ocean dipole in the POAMA seasonal forecast model. Q J R Meteorol Soc 135(639):337–352

ADVANCES IN ATMOSPHERIC SCIENCES, VOL. 35, AUGUST 2018, 1035–1048

• **Original Paper** •

Indian Ocean SST modes and Their Impacts as Simulated in BCC_CSM1.1(m) and HadGEM3

Bo LU[1,2,3], Hong-Li REN*[1,2,4], Rosie EADE[5], and Martin ANDREWS[5]

[1]*Laboratory for Climate Studies, National Climate Center, China Meteorological Administration, Beijing* 100081 *China*
[2]*CMA-NJU Joint Laboratory for Climate Prediction Studies, Institute for Climate and Global Change Research, School of Atmospheric Sciences, Nanjing University, Nanjing* 210023*, China*
[3]*Xin Jiang Climate Center, Ürümqi* 830002*, China*
[4]*Department of Atmospheric Science, School of Environmental Studies, China University of Geoscience, Wuhan* 430074*, China*
[5]*Met Office Hadley Center, Exeter* EX1 3PB*, UK*

(Received 6 November 2017; revised 24 February 2018; accepted 4 March 2018)

ABSTRACT

The sea surface temperature anomalies (SSTAs) in the tropical Indian Ocean (TIO) show two dominant modes at interannual time scales, referred to as the Indian Ocean basin mode (IOBM) and dipole mode (IOD). Recent studies have shown that the IOBM and IOD not only affect the local climate, but also induce remarkable influences in East Asia via teleconnections. In this study, we assess simulations of the IOBM and IOD, as well as their teleconnections, using the operational seasonal prediction models from the Met Office (HadGEM3) and Beijing Climate Center [BCC_CSM1.1(m)]. It is demonstrated that the spatial patterns and seasonal cycles are generally reproduced by the control simulations of BCC_CSM1.1(m) and HadGEM3, although spectra biases exist. The relationship between the TIO SSTA and El Niño is successfully simulated by both models, including the persistent IOBM warming following El Niño and the IOD–El Niño interactions. BCC_CSM1.1(m) and HadGEM3 are capable of simulating the observed local impact of the IOBM, such as the strengthening of the South Asian high. The influences of the IOBM on Yangtze River rainfall are also captured well by both models, although this teleconnection is slightly weaker in BCC_CSM1.1(m) due to the underestimation of the northwestern Pacific subtropical high. The local effect of the IOD on East African rainfall is reproduced by both models. However, the remote control of the IOD on rainfall over southwestern China is not clear in either model. It is shown that the realistic simulations of TIO SST modes and their teleconnections give rise to the source of skillful seasonal predictions over China.

Key words: Indian Ocean SST, teleconnection, simulation, seasonal prediction

Citation: Lu, B., H.-L. Ren, R. Eade, and M. Andrews, 2018: Indian Ocean SST modes and their impacts as simulated in BCC_CSM1.1(m) and HadGEM3. *Adv. Atmos. Sci.*, **35**(8), 1035–1048, https://doi.org/10.1007/s00376-018-7279-3.

1. Introduction

Sea surface temperature anomalies (SSTAs) in the tropical Indian Ocean (TIO) exhibit two dominant modes on interannual time scales. The first empirical orthogonal function (EOF) mode shows a uniform SSTA over the entire TIO basin, which is referred to as the Indian Ocean basin mode (IOBM). The second EOF mode—namely, the Indian Ocean dipole mode (IOD)—exhibits a cooling (warming) off the Sumatran coast and a warming (cooling) over the western equatorial Indian Ocean. The IOBM accounts for about 39% of the total variance of the TIO SSTA, while the IOD explains about 11%.

The IOBM is believed to be controlled by the El Niño–Southern Oscillation (ENSO) (Wallace et al., 1998). During El Niño, atmospheric convection is suppressed over the Indian Ocean, and the resultant increase in solar radiation contributes to the basin-wide warming over the TIO (Chiang and Sobel, 2002). Forced by the heat flux changes, the warming of the TIO often occurs during El Niño development and persists after the mature phase of El Niño events (Klein et al., 1999; Liu and Alexander, 2007). This basin-wide warming plays an important role in modulating the local and remote climate. The interannual variability of the South Asian high (SAH) has been found to be forced by the IOBM (Yang et al., 2007; Yang and Liu, 2008). When the TIO warms up, the SAH strengthens and exhibits a southward extension due to the heating in the boundary layer (Huang et al., 2011). The basin-wide warming over the TIO also induces an eastward propagating Kelvin wave, which strengthens the anticyclone over the subtropical northwestern Pacific and then increases

* Corresponding author: Hong-Li REN
Email: renhl@cma.gov.cn

© Copyright [2018], British Crown (administered by Met Office); Bo LU, and Hong-Li REN.

the summer rainfall over the Yangtze River valley (Xie et al., 2009).

The dynamics of IOD events is still unsolved, especially for its relationship with ENSO. A number of studies have argued its dependence on ENSO (Allan et al., 2001; Baquero-Bernal et al., 2002; Dommenget and Latif, 2002; Dommenget and Jansen, 2009). However, other studies point out the importance of the internal air–sea interaction within the Indian Ocean basin (Behera et al., 1999; Webster et al., 1999; Ashok et al., 2003; Yamagata et al., 2003). The IOD not only affects the local rainfall around the Indian Ocean, such as Australia (Ashok et al., 2003) and East Africa (Black et al., 2003), but also influences global climate variability (Saji and Yamagata, 2003) via atmospheric teleconnection with regions, such as East Asia (Yuan et al., 2008; Qiu et al., 2014) and South America (Chan et al., 2008).

Considering the remarkable climatic impacts of Indian Ocean SST modes, they could serve as sources for skillful seasonal predictions if our operational models can reproduce a realistic IOBM and IOD and their teleconnections. In this study, we assess simulations of Indian Ocean SST by two operational seasonal prediction models, from the Beijing Climate Center and the UK Met Office respectively. We also explore how well our models can capture the TIO SST teleconnections and whether the simulations of TIO SST modes can influence the seasonal rainfall predictions over China. The remainder of the paper is organized as follows:

Section 2 describes the observations, control experiment and hindcast datasets used in the study. In section 3 we evaluate the control simulations of the IOBM and IOD in the operational models. Local and remote climate impacts of TIO SST in the models are investigated in section 4, with a comparison to seasonal forecasting systems. Finally, a summary and discussion of the results is given in section 5.

2. Data and methods

2.1. *Observational data*

This study utilizes HadISST (Rayner et al., 2006) for the observed monthly mean SST, CRU TS Version 4.01 (Harris et al., 2014) for the observed grid precipitation over land, and NCEP–DOE Reanalysis-1 (Kalnay et al., 1996) for the horizontal wind and geopotential height. The horizontal grid resolutions of these datasets are $1^\circ \times 1^\circ$, $1^\circ \times 1^\circ$ and $2.5^\circ \times 2.5^\circ$, respectively. For consistency with the period of the Reanalysis-1 data, the common period of 1948–2016 is analyzed for the observation.

2.2. *Operational climate model at the Beijing Climate Center*

Version 1.1 (moderate resolution) of the Beijing Climate Center's Climate System Model, i.e., BCC_CSM1.1(m), is currently employed as the operational model for seasonal prediction at the Beijing Climate Center. The model details are described in Wu et al. (2010). The output from a 400-year pre-industrial control experiment is analyzed to obtain a robust assessment of the Indian Ocean SST modes and their impacts in BCC_CSM1.1(m). A set of seasonal hindcasts, performed at the beginning of every month, with 24 members per prediction, from 1991 to 2014, are also assessed. The hindcast design of BCC_CSM1.1(m) is described in detail in Lu et al. (2017).

2.3. *Operational climate model at the UK Met Office*

Version 5 of the Global Seasonal Forecasting System (GloSea5) is the current operational seasonal forecasting system of the UK Met Office. The HadGEM3 coupled model is used in GloSea5. The model details are introduced by MacLachlan et al. (2015). In an effort to obtain the robust features of Indian Ocean SST and associated teleconnections in HadGEM3, a 100-year pre-industrial control experiment is utilized. Seasonal hindcast experiments of GloSea5 are also assessed; 24 members are performed for boreal summer (winter), initialized on 25 April (October), 1 May (November) and 9 May (November) from 1992 to 2011. The hindcast design of Glosea5 is described by MacLachlan et al. (2015).

3. Simulations of the IOBM and IOD

Figure 1 illustrates the climatological SST and horizontal wind at 850 hPa over the TIO domain. Winds over the northern Indian Ocean reverse direction from northeasterly (Fig. 1a) during boreal winter to southwesterly during boreal summer (Fig. 1d), which exhibits a typical monsoon climate. As a result, the trade wind over the TIO is very weak compared with that over the tropical Pacific, and the annual mean westerly wind is evident. Thus, the upwelling is stronger and the SST is cooler in the western Indian Ocean than in the eastern side.

The seasonal reversal of low-level wind is generally reproduced well by BCC_CSM1.1(m) and HadGEM3, with a realistic northeasterly wind in boreal winter and southwesterly wind in boreal summer. For BCC_CSM1.1(m), the westerly wind between the equator and 10°S in January is slightly stronger than in the observations, and the northwesterly wind off the Sumatran coast is overestimated (Fig. 1b). Thus, the thermocline in the eastern Indian Ocean is deeper in BCC_CSM1.1(m) than that observed (Lu et al., 2017), which implies an underestimation of the air–sea interaction in the eastern TIO. For HadGEM3, the tropical SST is warmer than in the observations (Figs. 1c and f). In January, the observed equatorial westerly wind is missed in HadGEM3 (Fig. 1c), leading to the underestimation of the zonal SST gradient along the equator in boreal winter. In July, the southeastern wind off the Sumatran coast is too strong and an unrealistic cross-equator wind over the eastern TIO is evident in HadGEM3. As a result, the thermocline is shallower (Johnson et al., 2017) than observed and the air–sea interaction in the southeastern TIO is too active in HadGEM3.

We further evaluate the leading modes of the TIO SST in BCC_CSM1.1(m) and HadGEM3 at interannual time scales. EOF analysis is performed on the monthly mean SST in the

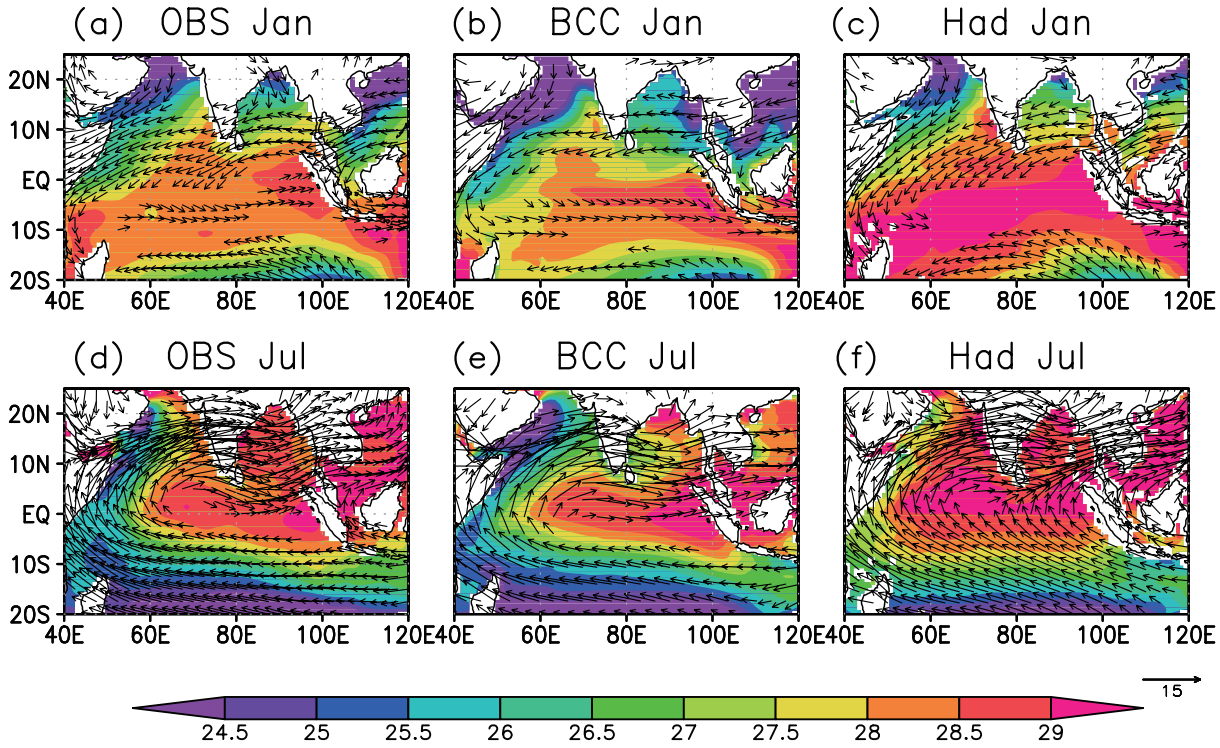

Fig. 1. Climatological patterns of SST (units: °C) and horizontal wind at 850 hPa (units: m s^{-1}) over the TIO during (a–c) January and (d–f) July, in the (a, d) observation and the simulations by (b, e) BCC_CSM1.1(m) and (c, f) HadGEM3 (c, f).

TIO (15°S–30°N, 25°–120°E) for all calendar months. To focus on the interannual variability, the remarkable warming trend in TIO SST (Du and Xie, 2008) has been removed linearly. As shown in Fig. 2, the two leading modes in BCC_CSM1.1(m) and HadGEM3 show similar features to the observations. The first EOF mode shows the basin-wide warming in the observations, which is generally simulated well by both models (Figs. 2b and c). The first EOF mode in BCC_CSM1.1(m) (HadGEM3) explains 25% (24%) of the total variance, which is smaller than that in the observation. Du et al. (2013) investigated the leading EOF modes of TIO SST among CMIP5 models and showed similar results that the explained variance of this basin mode is underestimated by many state-of-the art models that participating in CMIP5. The observed second EOF mode shows a zonal dipole feature, with reverse SST changes between the western and southeastern TIO. Both models generally capture the zonal dipole pattern in the second EOF mode (Figs. 2e and f). The second EOF mode in BCC_CSM1.1(m) (HadGEM3) explains 15% (10%) of the total variance, which is comparable to that in the observation.

Although both models capture the general features of the observed leading modes, some distinct biases still exist. For the first mode, the positive signal in BCC_CSM1.1(m) locates in the western TIO, while a weak negative signal occurs in the eastern basin. As indicated by Du et al. (2013), this bias pattern is also evident in several CMIP5 models, such as ACCESS1.0, HadGEM2-ES, and MPI-ESM-LR. On the other hand, the pronounced positive signal in HadGEM3 is constrained in the central TIO. For the second mode, the negative signal in BCC_CSM1.1(m) locates in the northeastern TIO, while the observed negative signal locates in the southeastern TIO. In addition, the distribution of the negative signal is constrained to the east of 80°E; however, the simulated patterns show a westward extension of the negative signal in both models. Efforts have been made to understand the causes of this cold-tongue-type distribution bias in the simulated EOF2 (IOD).

Previous studies have shown that the wind–evaporation–SST (WES) feedback is crucial to IOD growth (Li et al., 2003; Liu et al., 2011). The cooling over the eastern TIO will induce an easterly wind anomaly, which may then cool the local SST by increasing the evaporation if the climatological wind is also easterly. Figure 3 demonstrates the mean state of the zonal wind at 850 hPa along the TIO during boreal fall, when IOD events often reach their mature phase. In the observation, the easterly trade wind is pronounced in the eastern TIO; however, westerly wind is evident in the central TIO. As a result of the inactive WES feedback in the central TIO, the negative node of the observed IOD mode is constrained in the eastern TIO. In HadGEM3, the climatological easterly wind is pronounced over the entire TIO. Thus, the simulated WES feedback is also active in the central TIO, which gives rise to the cold tongue distribution in the simulated EOF2 in HadGEM3. The climatological zonal wind in BCC_CSM1.1(m) is consistent with the observation overall. However, in the central TIO, an easterly wind bias is also evident, which may extend the eastern node of the

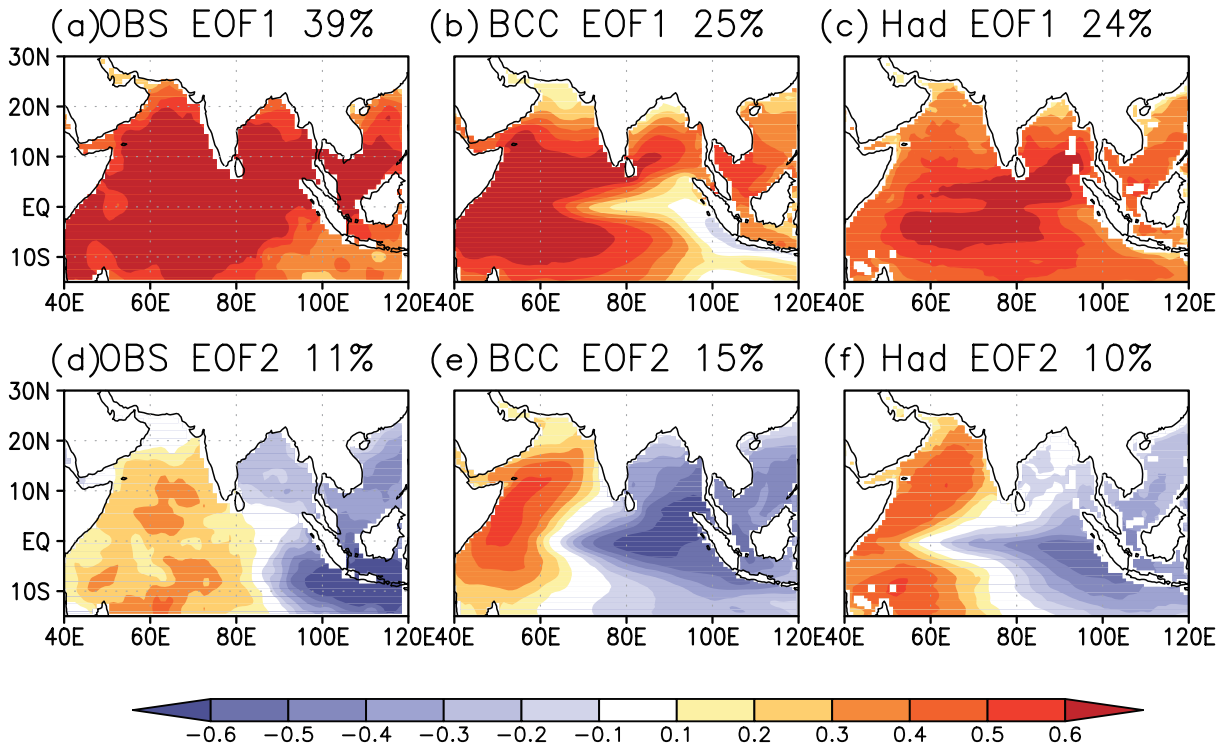

Fig. 2. Spatial patterns of the leading two EOF modes for TIO SST in the (a, d) observations and the simulations by (b, e) BCC_CSM1.1(m) and (c, f) HadGEM3. The explained variances are indicated.

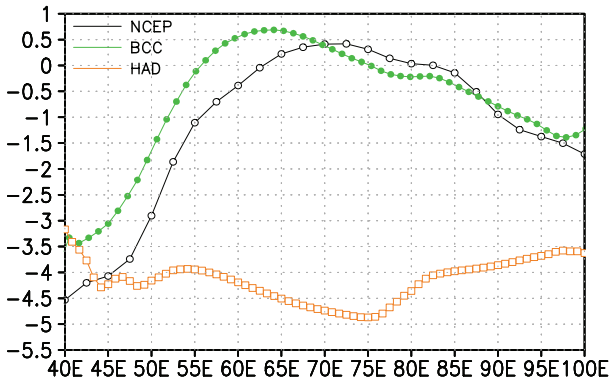

Fig. 3. Climatological zonal wind at 850 hPa averaged over the TIO (10°S–10°N) during November in NCEP Reanalysis-1 (black), BCC_CSM1.1(m) (green), and HadGEM3 (orange).

simulated IOD in BCC_CSM1.1(m). It should be noted that the mean state biases in zonal wind might also affect the ocean-current advection. Due to the lack of availability of three-dimensional ocean data, this effect is not discussed here.

This strong easterly wind bias in the TIO as shown above is a common problem for most CMIP5 models (Li et al., 2015). Their analyses show that such bias can be traced back to errors in the South Asian summer monsoon (SASM). The simulated SASM is generally too weak in most models, which leads to weakened cross-equatorial low-level wind over the western basin and further generates a warm SST bias over the western equatorial Indian Ocean. This warm bias over the western equatorial Indian Ocean is prolonged to the boreal autumn, when Bjerknes feedback helps amplify the error into the equatorial easterly bias over the TIO. Following the above argument by Li et al. (2015), we further explore the causes of the equatorial easterly bias in HadGEM3. The simulated summer [June–July–August (JJA)] rainfall over South Asia (10°–25°N, 70°–90°E) is 4.3 mm d^{-1}, which is much weaker than the observed rainfall of 8.8 mm d^{-1}. As a result of the underestimation of the SASM, the climatological SST over the western TIO (10°S–10°N, 40°–60°E) is remarkably warmer in HadGEM3 (28.1°C) than in the observation (26.4°C) during boreal summer (JJA). This warm bias is prolonged to boreal autumn [September–October–November (SON)], with the mean SST over the western TIO staying 0.7°C warmer than in the observation. Thus, the equatorial easterly bias in HadGEM3 is generated by this warm SST bias over western TIO when Bjerknes feedback becomes active during boreal autumn (Li et al., 2015).

Figure 4 illustrates the seasonal cycle of the principle component (PC) for the two leading modes. The basin-wide warming mode is strong in boreal winter and spring but weak in boreal summer and fall, which is simulated well by both BCC_CSM1.1(m) and HadGEM3 (Fig. 4a). The dipole mode is active during boreal summer and fall in the observation (Fig. 4b), when the mean upwelling becomes strong and the mean thermocline is shallow in the eastern TIO [e.g., as reviewed by Schott et al. (2009)]. HadGEM3 reproduces the observed seasonal cycle of the dipole mode. However,

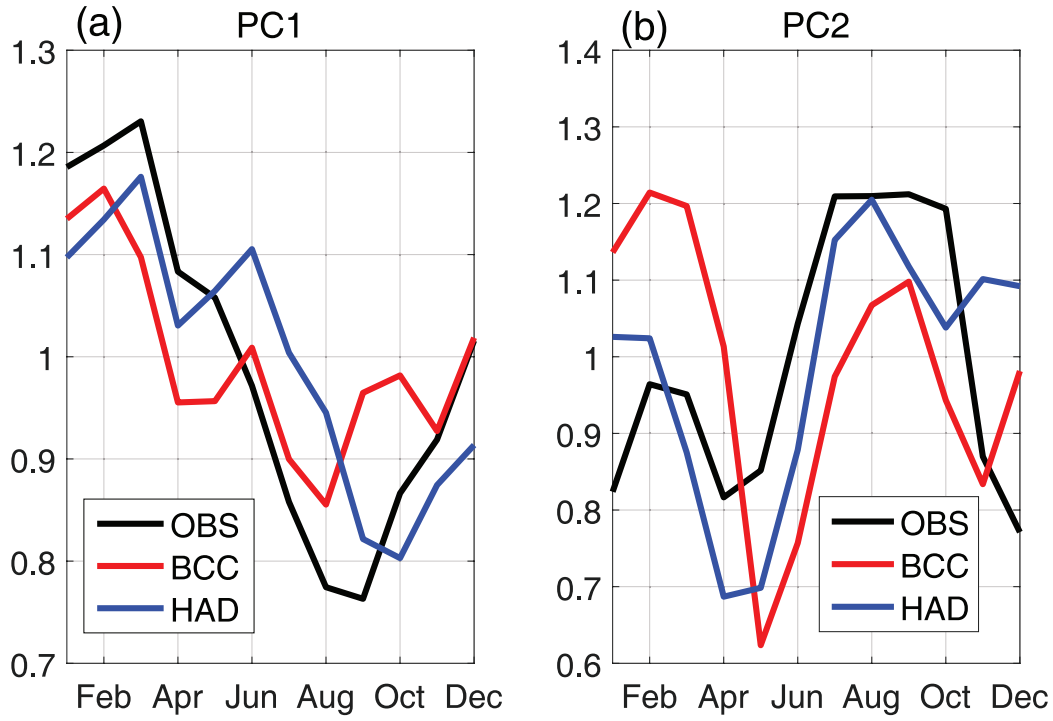

Fig. 4. Seasonal cycles of the standard deviation of (a) EOF PC1 and (b) EOF PC2 in the observation (black) and the simulations by BCC_CSM1.1(m) (red) and HadGEM3 (blue).

BCC_CSM1.1(m) overestimates its amplitude in late winter and early spring. We further investigate their periodicity features by applying wavelet analysis (Fig. 5). To ensure statistical robustness for the computation of spectra (Wittenberg, 2009; Stevenson et al., 2010), simulations with long lengths are necessary. As a result, the wavelet analysis is performed upon the whole period for the model simulations. The spectrum of the first PC peaks from three years to five years, which is consistent with the periodicity of ENSO. However, BCC_CSM1.1(m) tends to simulate a quasi-two-year period for the IOBM, which is much shorter than in the observation (Fig. 5g). The reason for this periodicity bias is related to the simulation of ENSO in BCC_CSM1.1(m). Due to the underestimated air–sea interaction over the tropical Pacific, the period of ENSO in BCC_CSM1.1(m) is about two years (Lu and Ren, 2016a). As a result of the dominant control of ENSO forcing on the IOBM, the short period bias is also evident here. On the contrary, HadGEM3 has a peak spectrum at seven years, which is longer than in the observation. For the IOD spectrum, a sharp peak of five years is observed (Fig. 5h). However, the simulated IOD spectrum is relatively too broad in both models. Overall, both BCC_CSM1.1(m) and HadGEM3 are able to simulate the observed IOBM and IOD as their two leading modes. The spatial patterns and seasonal cycles are generally captured well by both models, although biases in the spectra are evident.

We adopt an IOBM index definition as the average of the SSTAs over (20°S–20°N, 40°–110°E). We also follow the definition of the IOD index given by Saji et al. (1999) by taking the SSTA difference between the western (10°S–10°N, 60°–80°E) and eastern (10°S–0°, 90°–110°E) Indian Ocean regions. As shown in Table 1, these two indices are very good representations of the two leading modes. Hereafter, these simplified indices are used to indicate the IOBM and IOD events in the observations and model simulations.

Table 1. Correlation coefficients between the IOBM (IOD) indices and the PC of the first (second) EOF mode in the observation and the simulations by BCC_CSM1.1(m) and HadGEM3.

	OBS	BCC_CSM1.1(m)	HadGEM3
PC1 vs IOBM	0.98	0.95	0.98
PC2 vs IOD	0.87	0.70	0.89

4. Simulated teleconnections of Indian Ocean SST modes

4.1. *Relationship with ENSO*

ENSO is the strongest climatic variability on interannual time scales, and controls the TIO SSTA via an atmospheric bridge (Klein et al., 1999; Alexander et al., 2002). Figure 6 illustrates the lag correlation between the Niño3.4 and IOBM indices. The El Niño-induced surface flux change leads to a positive phase of the IOBM in boreal winter. The air–sea interaction over Indo-Pacific oceans sustain the IOBM warming to boreal summer (Du et al., 2009; Fig. 6a). This so-called "Indian Ocean capacitor effect" stores the ENSO forcing during the previous winter, and further affects the East Asian cli-

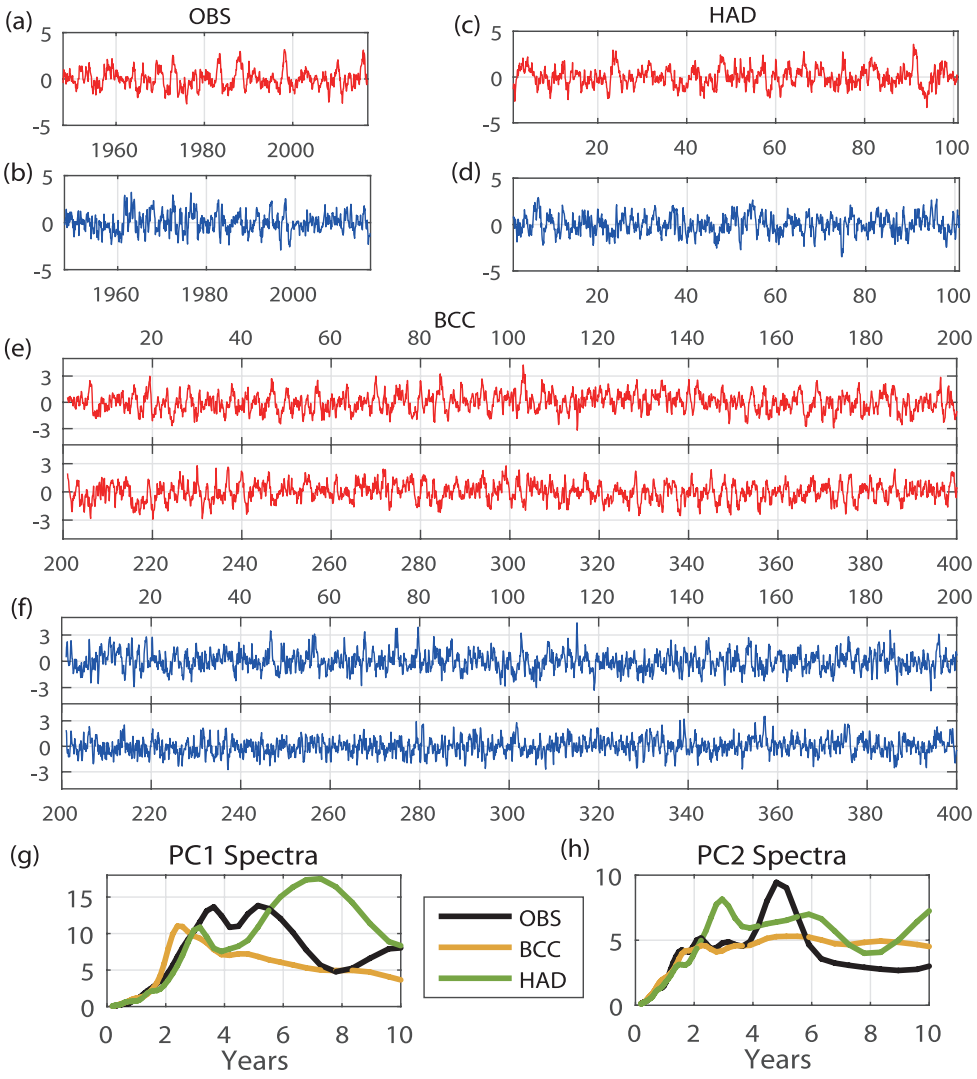

Fig. 5. Interannual variation of the first (red) and second (blue) EOF component in the (a, b) observation and the simulations by (c, d) HadGEM3 and (e, f) BCC_CSM1.1(m). (g, h) Spectra of (g) EOF PC1 and (h) EOF PC2 in the observations (black) and the simulations by BCC_CSM1.1(m) (yellow) and HadGEM3 (green).

mate in boreal summer (Xie et al., 2009). A previous study showed that this ENSO–IOBM relationship is simulated well by CMIP5 models (Du et al., 2013). As demonstrated in Figs. 6b and c, both BCC_CSM1.1(m) and HadGEM3 capture the TIO warming following El Niño. This simulated warming persists during boreal summer as observed, implying realistic Indo- Pacific air–sea interaction in both models.

The relationship between the IOD and ENSO is still a matter of debate. Some studies emphasize the dependence of the IOD on ENSO (e.g., Dommenget and Latif, 2002; Dommenget, 2011). As shown in Fig. 6, the IOD leads Niño3.4 by one season in the observation, with a significant lag correlation reaching 0.5 at the 99% confidence level (based on the Student's *t*-test). BCC_CSM1.1(m) is able to simulate this lag correlation, while the IOD–ENSO relationship is weak in HadGEM3. Given the fact that several IOD events have occurred without coinciding with ENSO, other studies have suggested the IOD as an inherent mode of internal variability within the TIO (Behera et al., 1999; Webster et al., 1999; Ashok et al., 2003; Yamagata et al., 2003). The WES and thermocline feedbacks have been suggested as fundamental to IOD growth (Li et al., 2003; Liu et al., 2011). A recent modeling study suggested that only one-third of the total IOD variance is forced by ENSO (Yang et al., 2015). Here, we find that 43% of all IOD events in the observation are accompanied by ENSO events. In the simulations by BCC_CSM1.1(m) and HadGEM3, 45% and 35% of all IOD events co-occur with ENSO events, respectively. Thus, the dependence of the IOD on ENSO is simulated well.

Recent studies have found that the IOD is not only a passive response to ENSO, but it can also affect ENSO properties. Coupled modeling experiments suggest that the ENSO amplitude is larger with than without IOD forcing (Yu et al., 2002). As shown in Fig. 7, El Niño events accompanied

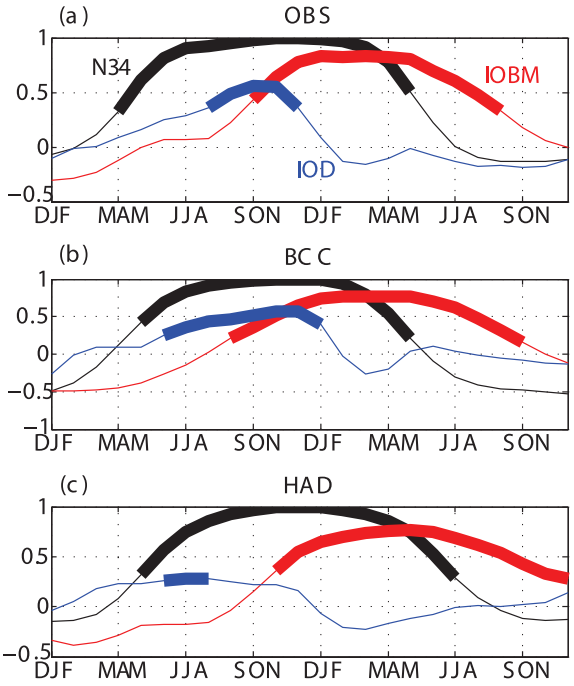

Fig. 6. Lag correlation of the November–January Niño3.4 anomaly with Niño3.4 (black), IOBM (red) and IOD (blue) anomalies in the (a) observation and the simulations by (b) BCC_CSM1.1(m) and (c) HadGEM3. Thick curves represent significant correlations at the >99% confidence level based on the Student's *t*-test.

by positive IOD events are generally stronger than pure El Niño, which is simulated well by BCC_CSM1.1(m) (Fig. 7b). However, La Niña events exhibit similar amplitudes with or without negative IOD forcing, which is successfully captured by HadGEM3 (Fig. 7f). Annamalai et al. (2005) pointed out that El Niño grows faster during boreal fall when coinciding with an IOD, as opposed to without (also see Fig. 7a), which is reproduced by BCC_CSM1.1(m). There is also evidence for a more rapid decay of El Niño when associated with an IOD event than without (Fig. 7a), due to the IOD-induced easterly wind over the tropical Pacific (Kug and Kang, 2006). As shown in Figs. 7b and c, this rapid decay of El Niño with a positive IOD is captured well by both BCC_CSM1.1(m) and HadGEM3. Given the remarkable impact of the IOD on ENSO, it is often used as a key factor in statistical ENSO prediction models (Ren et al., 2017).

4.2. *Local and remote impacts of the IOBM*

Figure 8 compares the geopotential height changes in the upper troposphere for different phases of the IOBM. The SAH is evident around the Tibetan Plateau during boreal summer. The variations and displacements of the SAH lead to rainfall anomalies over East Asia (Zhang et al., 2002). Huang et al. (2011) pointed out that IOBM warming results in a strengthening and southward extension of the SAH (also see Fig. 8a) via changing the equivalent potential temperature in the boundary layer. Although the model biases appear in the specific SAH value, a bigger (smaller) and stronger

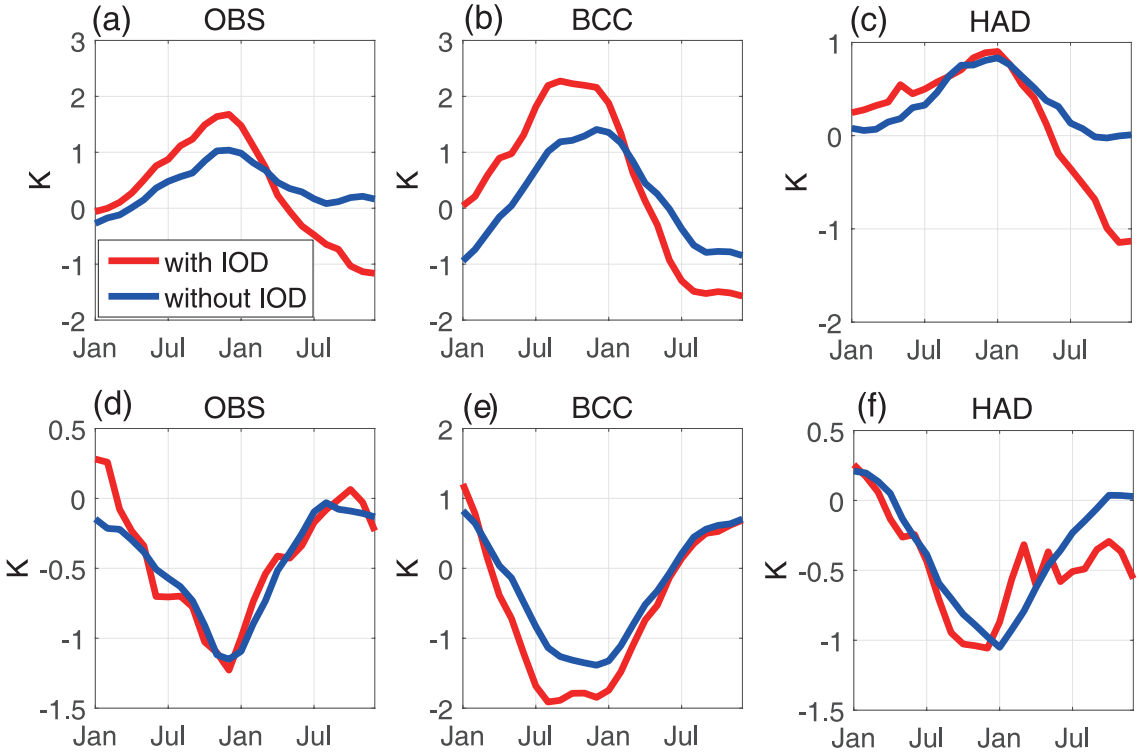

Fig. 7. Composites of the evolution of the Niño3.4 anomaly (units: °C) for the (a–c) El Niño and (d–f) La Niña years with (red) or without (blue) the coexistence of IOD years, from the (a, d) observations and the simulations by (b, e) BCC_CSM1.1(m) and (c, f) HadGEM3. The El Niño (La Niña) years are defined when the Niño3.4 anomaly reaches 0.5°C (−0.5°C). The IOBM (IOD) years are defined when the IOBM (IOD) index reaches one standard deviation.

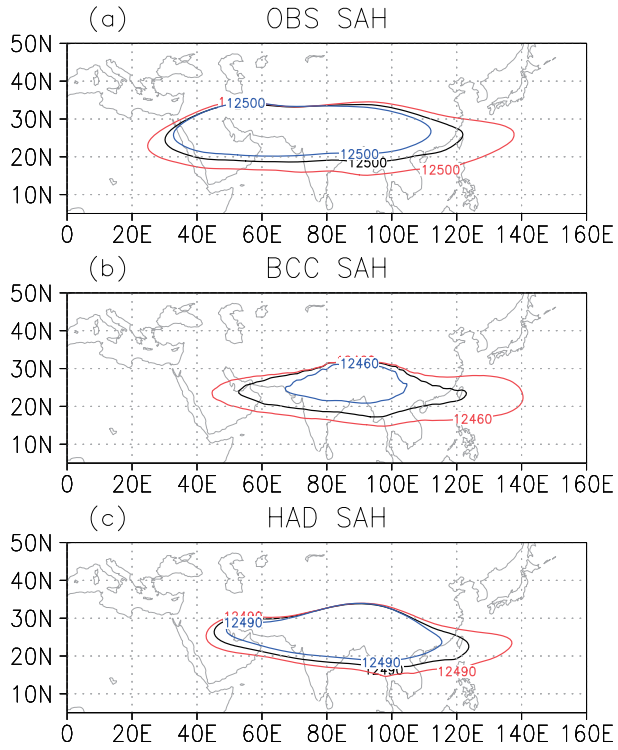

Fig. 8. Composites of the JJA SAH (units: gpm) in the climatology (black), warm IOBM years (red) and cold IOBM years (blue), from the (a) observations and the simulations by (b) BCC_CSM1.1(m) and (c) HadGEM3.

(weaker) SAH is reproduced when the TIO warms up (cools down) in both BCC_CSM1.1(m) and HadGEM3. This realistic IOBM–SAH relationship helps to give reasonable IOBM teleconnections over East Asia.

It is now well known that the IOBM acts as a capacitor that anchors the impact of ENSO in the previous winter (Xie et al., 2009). El Niño-induced TIO warming persists to boreal summer (Fig. 6) and excites a baroclinic Kelvin wave into the Pacific, which leads to the strengthening of the anomalous anticyclone over the northwestern Pacific (Fig. 9a). The resultant southwesterly wind anomaly brings water vapor from the ocean and enhances the rainfall over the Yangtze River valley (Fig. 9a). It is interesting that the cooling of the TIO induces the cyclonic wind anomalies over the northwestern Pacific, which is not as pronounced as that in the warming cases (Fig. 9b). This IOBM teleconnection is captured by half of the CMIP5 models (Du et al., 2013). As shown in Fig. 9, the atmospheric response to IOBM forcing is successfully simulated by HadGEM3, with realistic ACC changes over the northwestern Pacific and reasonable summer rainfall changes over the Yangtze River valley. In the simulations by BCC_CSM1.1(m), although the TIO warming (cooling) induces realistic easterly (westerly) wind anomalies over the TIO, the anomalous anticyclone (cyclone) over the northwestern Pacific is not as strong as in the observation (Figs. 9c and d). Consequently, the summer rainfall over the Yangtze River valley increases (decreases) following TIO warming (cooling); however, the changes are small compared with the observation. Since the northwestern Pacific subtropical high (NWPSH) is important for Yangtze River rainfall, it is very helpful to understand the causes of this weakened teleconnection between the IOBM and NWPSH in BCC_CSM1.1(m).

In a recent review paper, Xie et al. (2016) revealed that the air–sea coupling over the Indo-western Pacific Ocean plays an important role in the IOBM–NWPSH teleconnection. Following a Gill-type solution, the TIO warming can induce an easterly wind anomaly from the western Pacific to the northern TIO. On the one hand, this easterly wind anomaly further warms the TIO SST by reducing the local evaporation over the northern TIO, because the climatological wind is westerly due to a strong South Asian monsoon. On the other hand, this easterly wind anomaly increases the evaporation and cools the SST over the tropical northwestern Pacific due to the strong climatological trade wind. In turn, the warming over the TIO and cooling over the northwestern Pacific amplify the easterly wind anomaly, which then stimulates the strengthening of the NWPSH (Du et al., 2011). Thus, the IOBM-induced easterly wind anomaly is an indicator of the air–sea coupling over the Indo-western Pacific Ocean. Because of the asymmetric responses of the NWPSH to TIO warming and cooling phases, Fig. 10 focuses on the TIO warming cases. In the observation, the easterly wind anomaly over the Indo-western Pacific Ocean is significantly correlated (99% confidence level; Student's *t*-test) with the TIO SSTA. HadGEM3 basically captures this relationship, but it is not so robust in BCC_CSM1.1(m). This weak air–sea coupling over the Indo-western Pacific Ocean explains the underestimation of the NWPSH response to TIO warming in BCC_CSM1.1(m).

Next, the IOBM-induced circulation changes in the middle troposphere are investigated. Figure 11 demonstrates the configuration of the geopotential height at 500 hPa during warm and cold phases of the IOBM. In the observation, two dominant circulation patterns are evident during warm IOBM events. In the meridional direction over East Asia, the geopotential height anomalies show a high–low–high pattern from the tropics to the midlatitudes, which resembles the so-called "East Asia–Pacific" pattern (Huang and Sun, 1992). In the zonal direction, a stronger Urals blocking high (UL) and Okhotsk blocking high (OB) are observed when the TIO warms up. Previous studies have suggested that the "high–low–high EAP" pattern and strengthening of the UL and OB lead to the convergence of cold and warm air over Yangtze River valley (Zhang and Tao, 1998; Zhao et al., 2016). As a result, the configuration of the circulation induced by TIO warming is conducive to abundant rainfall over the valley. In the simulations by BCC_CSM1.1(m) and HadGEM3, the "high–low–high" tripole EAP pattern is not captured well. Instead, a "high–low" dipole pattern occurs under TIO warming. Thus, the strengthening of the OB is not simulated by both models. The stronger OB is simulated by HadGEM3, but the amplitude is largely underestimated. In BCC_CSM1.1(m), the OB remains unchanged. For the negative phases of the IOBM, the observed configuration of the

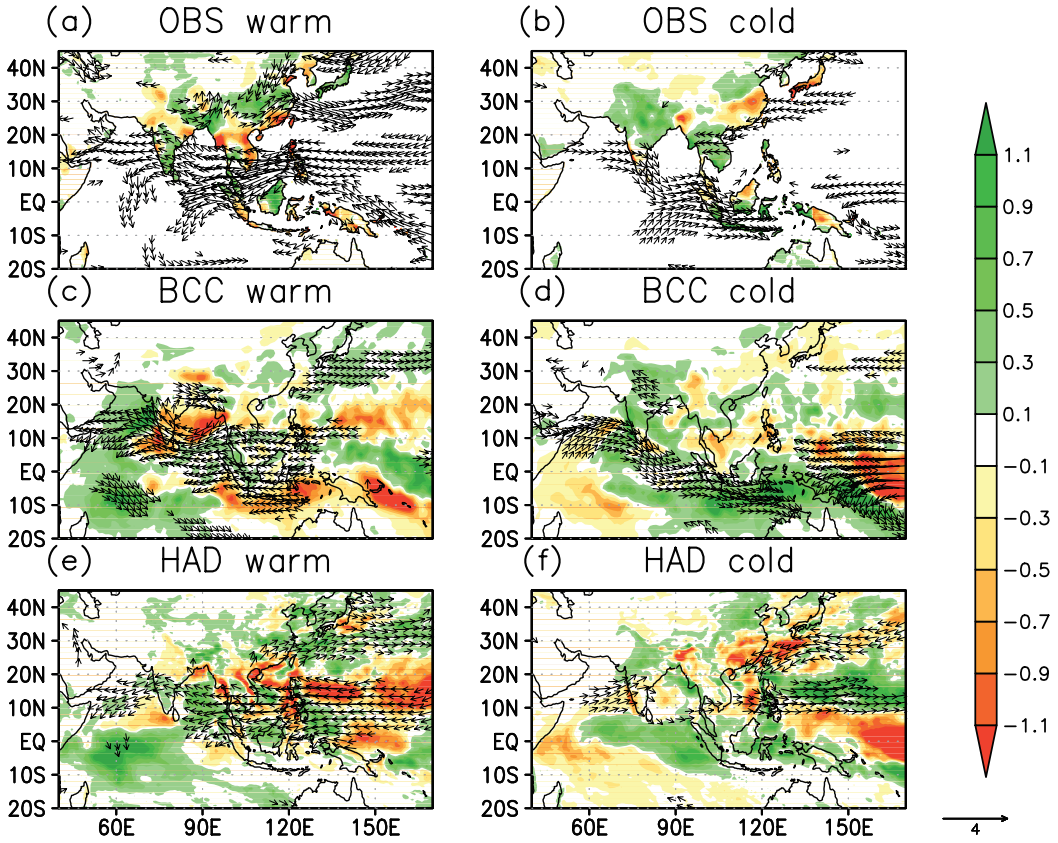

Fig. 9. Composites of JJA rainfall (units: mm month^{-1}) and horizontal wind at 850 hPa (units: m s^{-1}) during (a, c, e) warm IOBM years and (b, d, f) cold IOBM years, from the (a, b) observations (land only) and the simulations by (c, d) BCC_CSM1.1(m) and (e, f) HadGEM3.

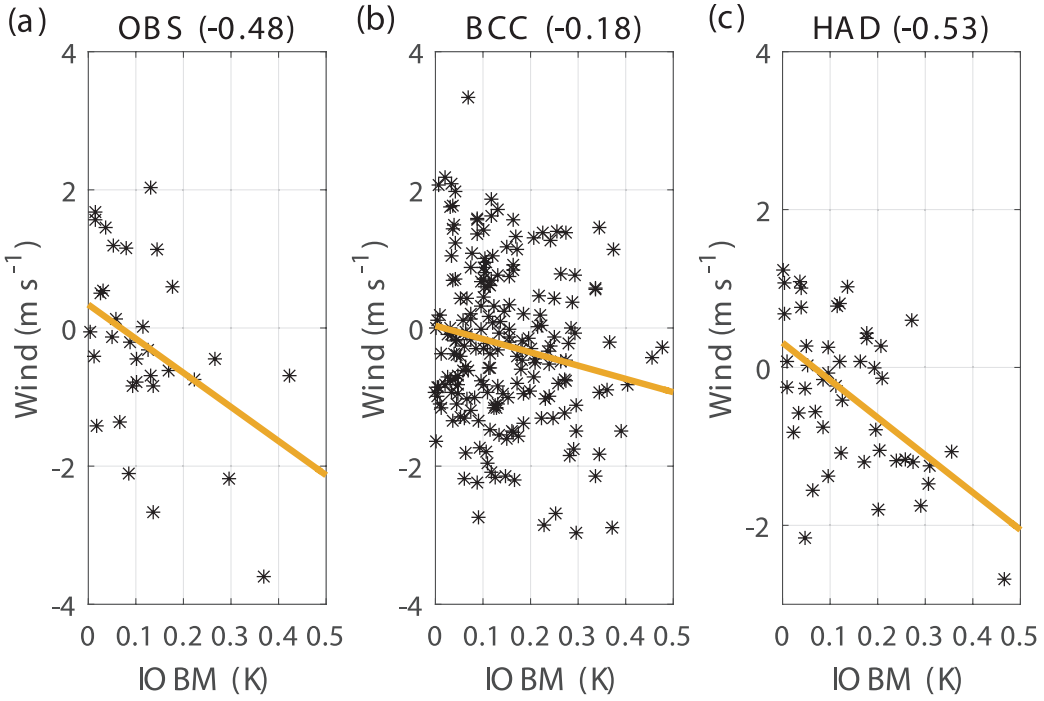

Fig. 10. Scatterplot of the zonal wind anomaly at 850 hPa averaged over the Indo-western Pacific Ocean (5°–15°N, 80°–130°E) against the IOBM indices in the (a) observation and the simulations by (b) BCC_CSM1.1(m) and (c) HadGEM3. The straight lines indicate the linear trend. The correlation coefficients are given in parentheses. It should be noted that only the warm phases of the IOBM are shown here, due to the asymmetric responses of the East Asian climate to the cold and warm TIO forcing.

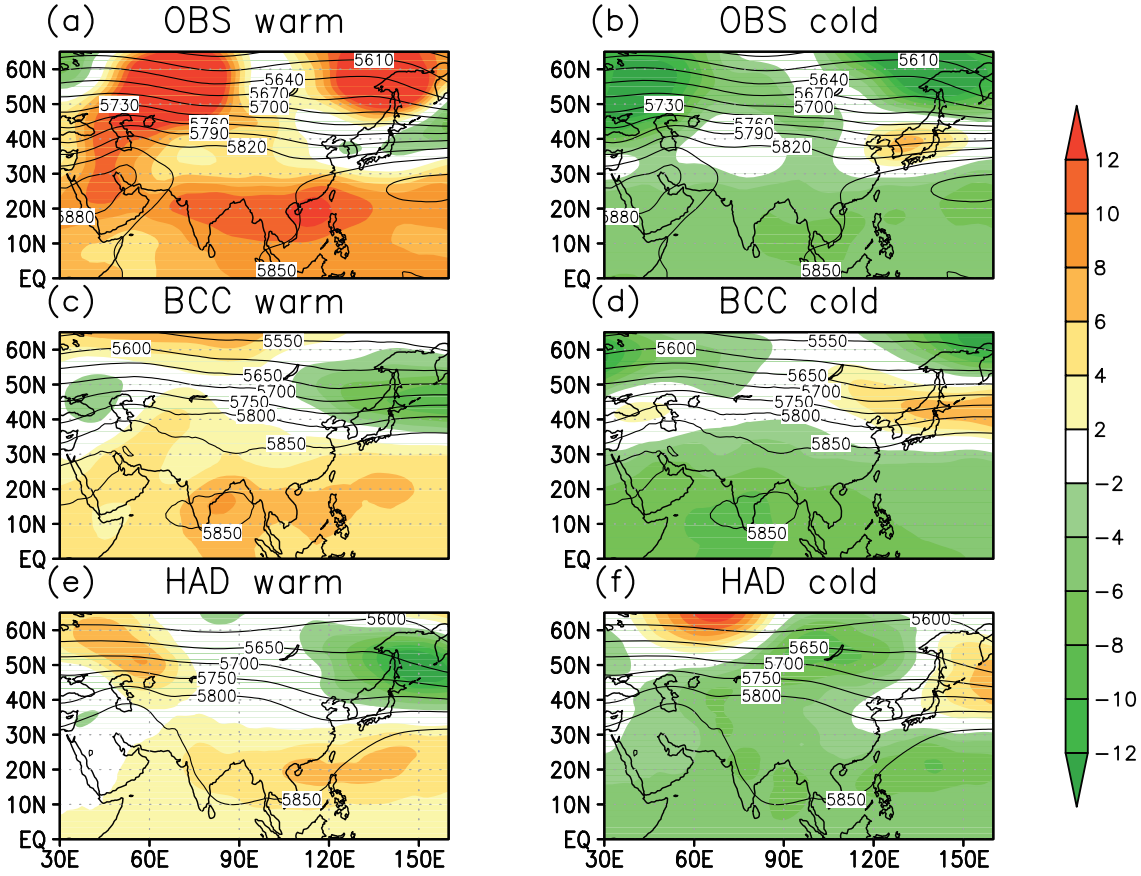

Fig. 11. Composites of JJA climatological (contours) and anomalous (shading) geopotential height at 500 hPa during (a, c, e) warm IOBM years and (b, d, f) cold IOBM years, from the (a, b) observations and the simulations by (c, d) BCC_CSM1.1(m) and (e, f) HadGEM3.

circulation at 500 hPa is simulated well by BCC_CSM1.1(m).

The realistic simulations of the IOBM and its teleconnections enable skillful seasonal predictions of the East Asian climate during boreal summer by the seasonal prediction systems of BCC_CSM1.1(m) and GloSea5 (the operational system at the UK Met Office using HadGEM3). As illustrated by Table 2, when initialized in May, the correlation skill of the IOBM is as high as 0.9 for both models. The variation of the NWPSH is predicted well by GloSea5, with the correlation skill reaching 0.9. Due to the weak biases of the IOBM-induced ACC over the northwestern Pacific, the prediction skill of the NWPSH is slightly lower than that of GloSea5. However, the correlation skill still reaches 0.7, which is significant at the 99% confidence level using the Student's *t*-test. The successful prediction of the NWPSH offers realistic water vapor transport. Thus, GloSea5 and BCC_CSM1.1(m) are capable of predicting the variation in summer rainfall over Yangtze River valley (Li et al., 2016), with the correlation skill reaching 0.54 and 0.47, respectively.

4.3. *Local and remote impacts of the IOD*

Previous studies have shown important climatic impacts of the IOD (Saji and Yamagata, 2003), including the severe East African flood during the two strongest positive IOD years in 1994 (Behera et al., 1999) and 1997

Table 2. Correlation skill of the IOBM, SLP over the northwestern Pacific (10°–20°N, 130°–155°E), and the Yangtze River rainfall (25°–35°N, 91°–122°E) during boreal summer from the BCC_CSM1.1(m) and GloSea5 seasonal forecasts when initialized in May.

	IOBM	SLP over northwestern Pacific	Precipitation over the Yangtze River
BCC_CSM1.1(m)	0.86	0.73	0.47
GloSea5	0.90	0.89	0.54

(Birkett et al., 1999; Webster et al., 1999), and the drought in 2016 (Lu et al., 2017). Figure 12 illustrates the rainfall and wind anomalies during boreal fall during IOD events. The impact from ENSO has first been removed by linear regression. It is clear that a positive (negative) IOD induces easterly (westerly) wind anomalies over the equatorial Indian Ocean, which brings above-normal (below-normal) rainfall over East Africa during boreal fall. The influence of the IOD on East African rainfall has been reproduced in some model simulations (Latif et al., 1999; Ummenhofer et al., 2009). Here, it is demonstrated that this IOD–East Africa rainfall relationship is reproduced well by BCC_CSM1.1(m) and HadGEM3 (Fig. 12). As a result, real-time predictions based on these

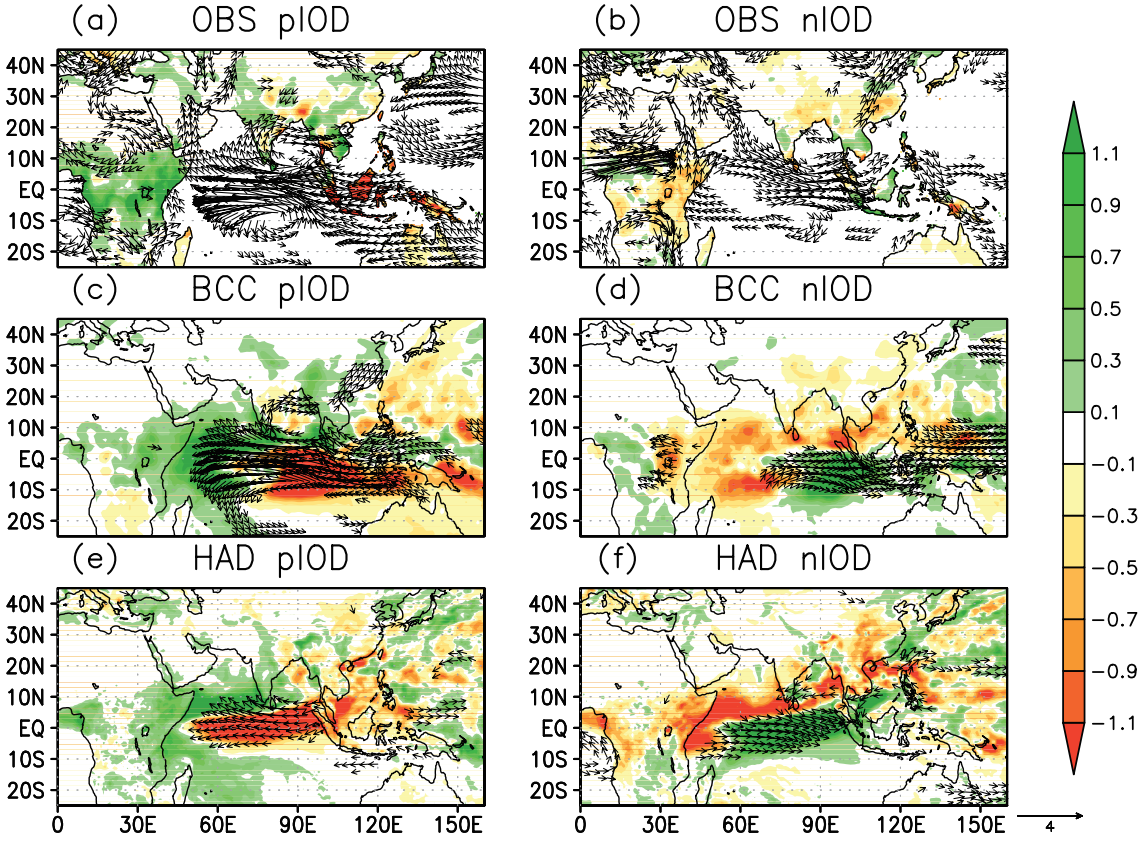

Fig. 12. Composites of SON rainfall (units: mm month^{-1}) and horizontal wind at 850 hPa (units: m s^{-1}) during (a, c, e) positive IOD years and (b, d, f) negative IOD years, in the (a, b) observation (precipitation over land only) and the simulations by (c, d) BCC_CSM1.1(m) and (e, f) HadGEM3. The influence of ENSO has first been removed by linear regression.

two models captured the 2016 East African drought two seasons ahead (Lu et al., 2017).

During positive IOD events, the cooling in the eastern TIO induces equatorial easterly wind and excites cyclonic wind anomalies over the Bay of Bengal (BOB) following a Gill-type response (Gill, 1980). As a result, the northern BOB is controlled by westerly wind anomalies (Fig. 12a), which intensify the India–Burma trough and increase the rainfall over the eastern Indochina Peninsula and southwestern China (Qiu et al., 2014; Lu and Ren, 2016b). As shown in Fig. 13, the observed southwestern China rainfall during boreal fall is significantly correlated with the IOD index. However, this relationship is not simulated by either BCC_CSM1.1(m) or HadGEM3 (Figs. 13b and c). Consequently, the southwestern China rainfall during boreal fall is not predicted well by the seasonal prediction systems using these two models. The prediction skill is as low as 0.35 in the hindcast by BCC_CSM1.1(m), which is insignificant even at the 90% confidence level.

5. Summary and discussion

The SST variations in the TIO not only affect the local climate around the Indian Ocean region, but also induce global impacts, including East Asia. Given the important role of the TIO SSTA in modulating the climate anomalies, it is necessary to assess how well the major TIO SST modes, as well as their teleconnections, are simulated by our operational models. In this study, the control experiments of BCC_CSM1.1(m) and HadGEM3 are evaluated.

It is demonstrated that the climatological monsoonal wind and SST patterns are generally simulated well by BCC_CSM1.1(m) and HadGEM3. The leading two modes at interannual time scales, the IOBM and IOD, are also reproduced well by both models. Similar to the observations and most CMIP5 models (Du et al., 2013), the simulated first EOF mode shows a basin-wide pattern, while the simulated second mode exhibits a zonal dipole pattern. The explained variances of the simulated first EOFs are smaller than in the observations, which is a common bias for many CMIP5 models (Du et al., 2013). The explained variances of the simulated second EOFs are comparable to the observations. The seasonal cycles of the IOBM and IOD variability are captured well by both models, except that BCC_CSM1.1(m) overestimates the IOD variability in boreal winter and early spring. Following the periodicity biases in ENSO simulations (Lu and Ren, 2016a), the periodicity of the IOBM is also too short compared with the observation. The spectrum of IOD variability is not captured by either model.

The SST variation in the TIO is tightly connected to

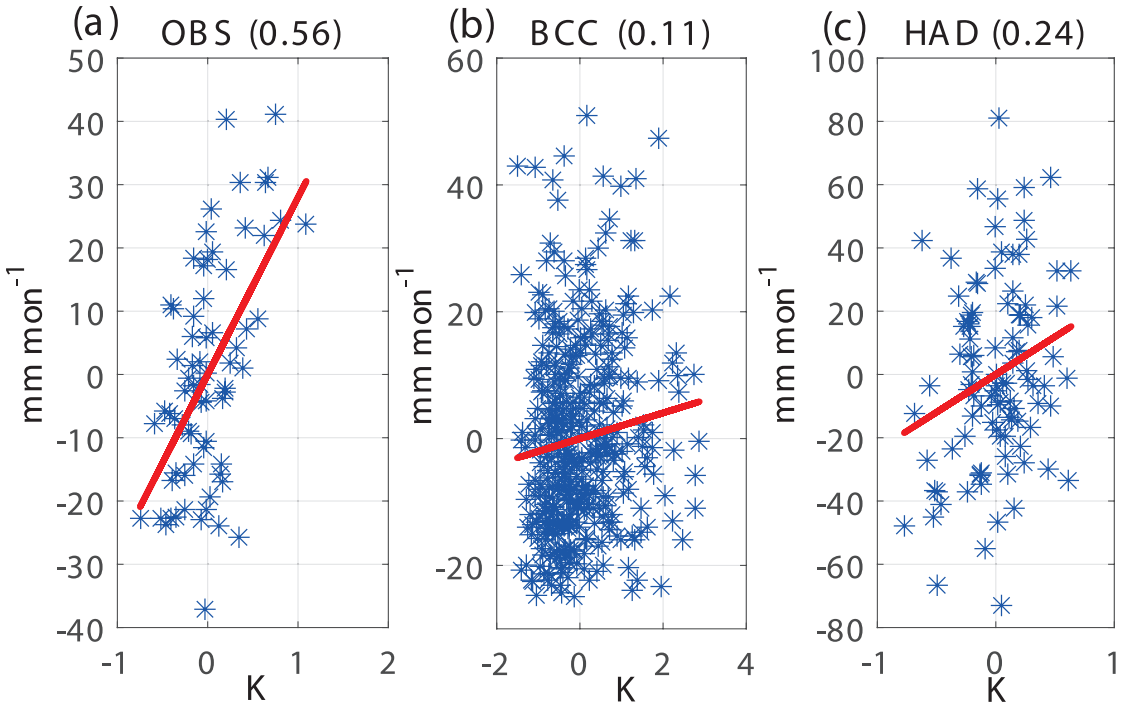

Fig. 13. Scatterplots of the precipitation over southwestern China (24°–28°N, 103°–109°E) against the IOD indices in the (a) observation and the simulations by (b) BCC_CSM1.1(m) and (c) HadGEM3. The linear fitting line is indicated.

ENSO. Like most CMIP5 models (Du et al., 2013), the persistent IOBM warming following El Niño is successfully simulated by both models. The dependence of the IOD on ENSO is reproduced by BCC_CSM1.1(m), implying the presence of realistic IOD dynamics. IOD events in HadGEM3 are more independent of ENSO forcing, indicating strong air–sea interaction within the Indian Ocean basin (Johnson et al., 2017). The IOD can also feed back to ENSO. The faster decay of El Niño with the coexistence of the IOD (Kug and Kang, 2006) is reproduced by both models. BCC_CSM1.1(m) also captures the relationship of a stronger El Niño when coinciding with an IOD event rather than without (Yu et al., 2002). The realistic TIO SST–ENSO relationships indicate the successful representation of TIO–Pacific feedbacks in BCC_CSM1.1(m) and HadGEM3.

Observational evidence shows that IOBM warming can affect local impacts, such as a strengthening of the SAH, which is simulated well by both models. The IOBM warming induces easterly wind anomalies over the TIO and northwestern Pacific, which intensifies the NWPSH and increases the summer rainfall over the Yangtze River valley (Xie et al., 2009). Like half of the CMIP5 models (Du et al., 2013), this so-called "Indian Ocean capacitor" effect is simulated well by HadGEM3. As a result, the Met Office seasonal prediction system (GloSea5) based on this model shows high skill in predicting the NWPSH and Yangtze River summer rainfall. In BCC_CSM1.1(m), the response of the NWPSH to IOBM forcing is weaker than observed, and thus the prediction skill of Yangtze River summer rainfall is slightly lower than that in GloSea5. For the impact of the IOD, both models successfully capture the response of East African rainfall to IOD forcings. However, the control by the IOD of the precipitation over southwestern China during boreal fall is not clear in either model. Consequently, the prediction skill of precipitation over southwestern China during boreal fall is relatively low. Our results suggest that realistic simulations of the TIO SSTA and its impact are the foundation of skillful seasonal predictions.

Acknowledgements. This work is jointly supported by the National Key Research and Development Program of China (Grant No. 2016YFA0602104), the China Meteorological Special Program (Grant No. GYHY201506013), and the National Science Foundation (Grant No. 41605116). This work and its contributors (Bo LU, Hong-Li REN, Rosie EADE, and Martin ANDREWS) were supported by the UK–China Research & Innovation Partnership Fund through the Met Office Climate Science for Service Partnership (CSSP) China as part of the Newton Fund.

REFERENCES

Alexander, M. A., I. Bladé, M. Newman, J. R. Lanzante, N. C. Lau, and J. D. Scott, 2002: The atmospheric bridge: The influence of ENSO teleconnections on air-sea interaction over the global oceans. *J. Climate*, **15**, 2205–2231, https://doi.org/10.1175/1520-0442(2002)015<2205:TABTIO>2.0.CO;2.

Allan, R., and Coauthors, 2001: Is there an Indian Ocean dipole, and is it independent of the El Niño-Southern Oscillation? *CLIVAR Exchanges*, **6**, 18–22.

Annamalai, H., S.-P. Xie, J.-P. McCreary, and R. Murtugudde, 2005: Impact of Indian Ocean sea surface temperature on de-

veloping El Niño. *J. Climate*, **18**, 302–319, https://doi.org/10.1175/JCLI-3268.1.

Ashok, K., Z. Y. Guan, and T. Yamagata, 2003: Influence of the Indian Ocean Dipole on the Australian winter rainfall. *Geophys. Res. Lett.*, **30**(15), 1821, https://doi.org/10.1029/2003GL017926.

Baquero-Bernal, A., M. Latif, and S. Legutke, 2002: On dipole-like variability of sea surface temperature in the tropical Indian Ocean. *J. Climate*, **15**(11), 1358–1368, https://doi.org/10.1175/1520-0442(2002)015<1358:ODVOSS>2.0.CO;2.

Behera, S. K., R. Krishnan, and T. Yamagata, 1999: Unusual ocean-atmosphere conditions in the tropical Indian Ocean during 1994. *Geophys. Res. Lett.*, **26**, 3001–3004, https://doi.org/10.1029/1999GL010434.

Birkett, C., R. Murtugudde, and R. Allan, 1999: Indian Ocean climate event brings floods to East Africa's lakes and the Sudd Marsh. *Geophys. Res. Lett.*, **26**, 1031–1034, https://doi.org/10.1029/1999GL900165.

Black, E, J. Slingo, and K. R. Sperber, 2003: An observational study of the relationship between excessively strong short rains in coastal East Africa and Indian Ocean SST. *Mon. Wea. Rev.*, **131**, 74–94, https://doi.org/10.1175/1520-0493(2003)131<0074:AOSOTR>2.0.CO;2.

Chan, S. C., S. K. Behera, and T. Yamagata, 2008: Indian Ocean Dipole influence on South American rainfall. *Geophys. Res. Lett.*, **35**, L14S12, https://doi.org/10.1029/2008GL034204.

Chiang, J. C. H., and A. H. Sobel, 2002: Tropical tropospheric temperature variations caused by ENSO and their influence on the remote tropical climate. *J. Climate*, **15**, 2616–2631, https://doi.org/10.1175/1520-0442(2002)015<2616:TTTVCB>2.0.CO;2.

Dommenget, D., and M. Jansen, 2009: Predictions of Indian Ocean SST indices with a simple statistical model: A null hypothesis. *J. Climate*, **22**(18), 4930–4938, https://doi.org/10.1175/2009JCLI2846.1.

Dommenget, D., and M. Latif, 2002: A cautionary note on the interpretation of EOFs. *J. Climate* **15**(2), 216–225, https://doi.org/10.1175/1520-0442(2002)015<0216:ACNOTI>2.0.CO;2.

Dommenget, D., 2011: An objective analysis of the observed spatial structure of the Tropical Indian Ocean SST variability. *Climate Dyn.*, **36**, 2129–2145, https://doi.org/10.1007/s00382-010-0787-1.

Du, Y., and S.-P. Xie, 2008: Role of atmospheric adjustments in the tropical Indian Ocean warming during the 20th century in climate models. *Geophys. Res. Lett.*, **35**, L08712, https://doi.org/10.1029/2008GL033631.

Du, Y., S.-P. Xie, G. Huang, and K. M. Hu, 2009: Role of air–sea interaction in the long persistence of El Niño–induced North Indian Ocean warming. *J. Climate*, **22**, 2023–2038, https://doi.org/10.1175/2008JCLI2590.1.

Du, Y., L. Yang, and S.-P. Xie, 2011: Tropical Indian Ocean influence on Northwest Pacific tropical cyclones in summer following strong El Niño. *J. Climate*, **24**, 315–322, https://doi.org/10.1175/2010JCLI3890.1.

Du, Y., S.-P. Xie, Y. L. Yang, X. T. Zheng, L. Liu, and G. Huang, 2013: Indian Ocean variability in the CMIP5 multimodel ensemble: The Basin mode. *J. Climate*, **26**, 7240–7266, https://doi.org/10.1175/JCLI-D-12-00678.1.

Gill, A. E., 1980: Some simple solutions for heat-induced tropical circulation. *Quart. J. Roy. Meteor. Soc.*, **106**, 447–462, https://doi.org/10.1002/qj.49710644905.

Harris, I., P. D. Jones, T. J. Osborn, and D. H. Lister, 2014: Updated high-resolution grids of monthly climatic observations—The CRU TS3.10 Dataset. *Int. J. Climatol.*, **34**, 623–642, https://doi.org/10.1002/joc.3711.

Huang, G., X. Qu, and K. M. Hu, 2011: The impact of the tropical Indian Ocean on South Asian high in boreal summer. *Adv. Atmos. Sci.*, **28**, 421–432, https://doi.org/10.1007/s00376-010-9224-y.

Huang, R. H., and F. Y. Sun, 1992: Impacts of the tropical western Pacific on the East Asian summer monsoon. *J. Meteor. Soc. Japan*, **70**, 243–256, https://doi.org/10.2151/jmsj1965.70.1B_243.

Johnson, S. J., A. Turner, S. Woolnough, G. Martin, and C. MacLachlan, 2017: An assessment of Indian monsoon seasonal forecasts and mechanisms underlying monsoon interannual variability in the Met Office GloSea5-GC2 system. *Climate Dyn.*, **48**(5), 1447–1465, https://doi.org/10.1007/s00382-016-3151-2.

Kalnay, E., and Coauthors, 1996: The NCEP/NCAR 40-year reanalysis project. *Bull. Amer. Meteor. Soc.*, **77**, 437–472, https://doi.org/10.1175/1520-0477(1996)077<0437:TNYRP>2.0.CO;2.

Klein, S. A., B. J. Soden, and N. C. Lau, 1999: Remote Sea surface temperature variations during ENSO: Evidence for a tropical atmospheric bridge. *J. Climate*, **12**, 917–932, https://doi.org/10.1175/1520-0442(1999)012<0917:RSSTVD>2.0.CO;2.

Kug, J.-S., and I.-S. Kang, 2006: Interactive feedback between ENSO and the Indian Ocean. *J. Climate*, **19**, 1784–1801, https://doi.org/10.1175/JCLI3660.1.

Latif, M., D. Dommenget, M. Dima, and A. Grötzner, 1999: The role of Indian Ocean sea surface temperature in forcing East African rainfall anomalies during December–January 1997/98. *J. Climate*, **12**(12), 3497–3504, https://doi.org/10.1175/1520-0442(1999)012<3497:TROIOS>2.0.CO;2.

Li, C. F., and Coauthors, 2016: Skillful seasonal prediction of Yangtze river valley summer rainfall. *Environmental Research Letters*, **11**, 094002, https://doi.org/10.1088/1748-9326/11/9/094002.

Li, G., S.-P. Xie, and Y. Du, 2015: Monsoon-induced biases of climate models over the tropical Indian Ocean. *J. Climate*, **28**, 3058–3072, https://doi.org/10.1175/JCLI-D-14-00740.1.

Li, T., B. Wang, C. P. Chang, and Y. S. Zhang, 2003: A theory for the Indian Ocean dipole–zonal mode. *J. Atmos. Sci.*, **60**, 2119–2135, https://doi.org/10.1175/1520-0469(2003)060<2119:ATFTIO>2.0.CO;2.

Liu, L., W. D. Yu, and T. Li, 2011: Dynamic and thermodynamic air–sea coupling associated with the Indian Ocean dipole diagnosed from 23 WCRP CMIP3 models. *J. Climate*, **24**, 4941–4958, https://doi.org/10.1175/2011JCLI4041.1.

Liu, Z. Y., and M. Alexander, 2007: Atmospheric bridge, oceanic tunnel, and global climatic teleconnections. *Rev. Geophys.*, **45**, RG2005, https://doi.org/10.1029/2005RG000172.

Lu, B., and H.-L. Ren, 2016a: Improving ENSO periodicity simulation by adjusting cumulus entrainment in BCC_CSMs. *Dyn. Atmos. Oceans*, **76**, 127–140, https://doi.org/10.1016/j.dynatmoce.2016.10.005.

Lu, B., and H.-L. Ren, 2016b: SST-forced interdecadal deepening of the winter India–Burma trough since the 1950s. *J. Geophys. Res.*, **121**(6), 2719–2731, https://doi.org/10.1002/2015JD024393.

Lu, B., and Coauthors, 2017: An extreme negative Indian Ocean Dipole event in 2016: Dynamics and predictability. *Climate*

Dyn., https://doi.org/10.1007/s00382-017-3908-2. (in Press)

MacLachlan, C., and Coauthors, 2015: Global Seasonal forecast system version 5 (GloSea5): A high-resolution seasonal forecast system. *Quart. J. Roy. Meteor. Soc*., **141**(689), 1072–1084, https://doi.org/10.1002/qj.2396.

Qiu, Y., W. J. Cai, X. G. Guo, and B. Ng, 2014: The asymmetric influence of the positive and negative IOD events on China's rainfall. *Scientific Reports*, **4**, 4943, https://doi.org/10.1038/srep04943.

Rayner, N. A., P. Brohan, D. E. Parker, C. K. Folland, J. J. Kennedy, M. Vanicek, T. J. Ansell, and S. F. B. Tett, 2006: Improved analyses of changes and uncertainties in sea surface temperature measured in situ since the mid-nineteenth century: The HadSST2 dataset. *J. Climate*, **19**, 446–469, https://doi.org/10.1175/JCLI3637.1.

Ren, H. L., and Coauthors, 2017: Prediction of primary climate variability modes at the Beijing Climate Center. *J. Meteor. Res*., **31**, 204–223, https://doi.org/10.1007/s13351-017-6097-3.

Saji, N. H., and T. Yamagata, 2003: Possible impacts of Indian Ocean Dipole mode events on global climate. *Climate Res*., **25**, 151–169, https://doi.org/10.3354/cr025151.

Saji, N. H., B. N. Goswami, P. N. Vinayachandran, and T. Yamagata, 1999: A dipole mode in the tropical Indian Ocean. *Nature*, **401**, 360–363, https://doi.org/10.1038/43854.

Schott, F. A., S.-P. Xie, and J. P. McCreary Jr., 2009: Indian Ocean circulation and climate variability. *Rev. Geophys*., **47**, RG1002, https://doi.org/10.1029/2007RG000245.

Stevenson, S., B. Fox-Kemper, M. Jochum, B. Rajagopalan, and S. G. Yeager, 2010: ENSO model validation using wavelet probability analysis. *J. Climate*, **23**(20), 5540–5547, https://doi.org/10.1175/2010JCLI3609.1.

Ummenhofer, C. C., A. S. Gupta, M. H. England, and C. J. C. Reason, 2009: Contributions of Indian Ocean sea surface temperatures to enhanced East African rainfall. *J. Climate*, **22**, 993–1013, https://doi.org/10.1175/2008JCLI2493.1.

Wallace, J. M., E. M. Rasmusson, T. P. Mitchell, V. E. Kousky, E. S. Sarachik, and H. von Storch, 1998: On the structure and evolution of ENSO-related climate variability in the tropical Pacific: Lessons from TOGA. *J. Geophys. Res*., **103**, 14241–14259, https://doi.org/10.1029/97JC02905.

Webster, P. J., A. M. Moore, J. P. Loschnigg, and R. R. Leben, 1999: Coupled ocean–atmosphere dynamics in the Indian Ocean during 1997-98. *Nature*, **401**, 356–360, https://doi.org/10.1038/43848.

Wittenberg, A. T., 2009: Are historical records sufficient to constrain ENSO simulations? *Geophys. Res. Lett*., **36**, L12702, https://doi.org/10.1029/2009GL038710.

Wu, T. W., and Coauthors, 2010: The Beijing Climate Center atmospheric general circulation model: Description and its performance for the present-day climate. *Climate Dyn*., **34**, 123–147, https://doi.org/10.1007/s00382-008-0487-2.

Xie, S.-P., K. M. Hu, J. Hafner, H. Tokinaga, Y. Du, G. Huang, and T. Sampe, 2009: Indian Ocean capacitor effect on Indo-western Pacific climate during the summer following El Niño. *J. Climate*, **22**, 730–747, https://doi.org/10.1175/2008JCLI2544.1.

Xie, S.-P., Y. Kosaka, Y. Du, K. M. Hu, J. S. Chowdary, and G. Huang, 2016: Indo-western Pacific ocean capacitor and coherent climate anomalies in post-ENSO summer: A review. *Adv. Atmos. Sci*., **33**(4), 411–432, https://doi.org/10.1007/s00376-015-5192-6.

Yamagata, T., S. K. Behera, S. A. Rao, and H. N. Sall, 2003: Comments on "Dipoles, temperature gradients, and tropical climate anomalies". *Bull. Amer. Meteor. Soc*., **84**, 1418–1422, https://doi.org/10.1175/BAMS-84-10-1418.

Yang, J. L., and Q. Y. Liu, 2008: The "charge/discharge" roles of the basin-wide mode of the Indian Ocean SST anomaly——influence on the South Asian High in summer. *Acta Oceanologica Sinica*, **30**, 12–19, https://doi.org/10.3321/j.issn:0253-4193.2008.02.002. (in Chinese with English abstract)

Yang, J. L., Q. Y. Liu, S. P. Xie, Z. Y. Liu, and L. X. Wu, 2007: Impact of the Indian Ocean SST basin mode on the Asian summer monsoon. *Geophys. Res. Lett*., **34**, L02708, https://doi.org/10.1029/2006GL028571.

Yang, Y., S.-P. Xie, L. X. Wu, Y. Kosaka, N. C. Lau, and G. A. Vecchi, 2015: Seasonality and predictability of the Indian Ocean Dipole mode: ENSO forcing and internal variability. *J. Climate*, **28**(20), 8021–8036, https://doi.org/10.1175/JCLI-D-15-0078.1.

Yu, J.-Y., C. R. Mechoso, J. C. McWilliams, and A. Arakawa, 2002: Impacts of the Indian Ocean on the ENSO cycle. *Geophys. Res. Lett*., **29**(8), 46-1–46-4, https://doi.org/10.1029/2001GL014098.

Yuan, Y., H. Yang, W. Zhou, and C. Y. Li, 2008: Influences of the Indian Ocean Dipole on the Asian summer monsoon in the following year. *Int. J. Climatol*., **28**, 1849–1859, https://doi.org/10.1002/joc.1678.

Zhang, Q., G. X. Wu, and Y. F. Qian, 2002: The bimodality of the 100 hPa South Asia high and its relationship to the climate anomaly over East Asia in summer. *J. Meteor. Soc. Japan*, **80**, 733–744, https://doi.org/10.2151/jmsj.80.733.

Zhang, Q. Y., and S. Y. Tao, 1998: Influence of Asian mid-high latitude circulation on East Asian summer rainfall. *Acta Meteorologica Sinica*, **56**, 199–211, https://doi.org/10.11676/qxxb1998.019. (in Chinese with English abstract)

Zhao, J. H., L. Yang, Y. X. Zeng, and G. L. Feng, 2016: Analysis of atmospheric circulation and prediction signals for summer rainfall patterns in southern China. *Chinese Journal of Atmospheric Sciences*, **40**(6), 1182–1198, https://doi.org/10.3878/j.issn.1006-9895.1601.15249. (in Chinese with English abstract)

Environmental Research Letters

LETTER

Multimodel detection and attribution of changes in warm and cold spell durations

Chunhui Lu[1], Ying Sun[1,2] and Xuebin Zhang[3]

[1] National Climate Center, Laboratory for Climate Studies, China Meteorological Administration, Beijing 100081, People's Republic of China

[2] Collaborative Innovation Center on Forecast and Evaluation of Meteorological Disasters, Nanjing University of Information Science and Technology, Nanjing, 210044, People's Republic of China

[3] Climate Research Division, Climate Change and Environment Canada, Toronto, ON M3H 5T4, Canada

E-mail: sunying@cma.gov.cn

OPEN ACCESS

RECEIVED
18 August 2017

REVISED
5 June 2018

ACCEPTED FOR PUBLICATION
8 June 2018

PUBLISHED
2 July 2018

Keywords: detection and attribution, warm and cold spell duration, human influence

Supplementary material for this article is available online

Original content from this work may be used under the terms of the Creative Commons Attribution 3.0 licence.

Any further distribution of this work must maintain attribution to the author(s) and the title of the work, journal citation and DOI.

Abstract

The duration of warm and cold spells is measured by the persistence of instances when daily temperatures are greatly above or below their normal values. These spells represent a prolonged period of times when daily temperatures are extreme and can potentially be connected to climate impacts in the agricultural, health, energy and other sectors. This study aims to determine evidence of responses in the durations of warm (WSDI) and cold (CSDI) spells to forcings external to the climate system. We consider the globe, the six continents and China during the period from 1958–2010 in this analysis. Here we compare the observed duration indices with those derived from simulated daily temperature by climate models participating in the Coupled Model Intercomparison Project Phase 5 (CMIP5), using an optimal fingerprint method. The results show that, averaged over the global lands, the WSDI has substantially increased by 15 days while the CSDI has decreased by 3 days over the 53 year period. The simulated changes are generally consistent with the observations; models, however, overestimate the observed changes in the WSDI in five of the six continental regions. We consider a signal is detected if it is significant at the 10% level. At the global scale, human influences on both warm and cold spell durations are detected. At the continental scale, an anthropogenic signal is detected in the warm spell durations of most continents. The human influence on cold spell duration is detectable only in the Asian and European continents. In China, human influence can clearly be detected in both the warm and cold spell durations. Responses to natural forcings are generally not detected at the continental or smaller spatial scales.

1. Introduction

Accumulating evidence from observational records has shown remarkable changes in warm and cold extremes at the global and regional scales (Alexander *et al* 2006, Brown *et al* 2008, Hartmann *et al* 2013). The frequency, intensity and duration of extreme temperatures all show clear changes that are consistent with global warming (Donat *et al* 2013, Sillmann *et al* 2013a). These changes exert considerable impacts on human society and natural systems. The possible causes of these changes have been explored. Some authors have investigated the effects of external forcings on these changes from the viewpoint of detection and attribution and have found that changes in mean temperatures can be attributed to anthropogenic forcing at global and regional scales (Tett *et al* 2002, Stott *et al* 2006, Zwiers and Zhang 2003, Zhang *et al* 2005, Zhang *et al* 2006, Bindoff *et al* 2013, Donat *et al* 2014, Donat *et al* 2016). Christidis *et al* (2005) was the first study presenting a formal detection and attribution analysis of extreme temperatures and found clear anthropogenic influences on the intensity of warm nights and cold days and nights. Subsequent papers have examined possible anthropogenic influences on the intensity (e.g. Zwiers *et al* 2011, Min *et al* 2013,

© 2018 The Author(s). Published by IOP Publishing Ltd

Kim *et al* 2015, Wen *et al* 2013) and frequency (e.g. Morak *et al* 2013, Lu *et al* 2016) of daily temperature extremes at the global and regional scales. These analyses show that anthropogenic signals can be robustly detected in observed changes in the intensity and frequency of warm and cold extremes (Christidis *et al* 2011, Zwiers *et al* 2011, Min *et al* 2013, Christidis *et al* 2014, Kim *et al* 2015) in various regions and in China (Lu *et al* 2016, Yin *et al* 2016). Moreover, human activities may also have increased the probability of individual high-impact extreme high temperature events, such as the 2003 European heat wave (Stott *et al* 2004) and the extreme hot summer in 2013 in eastern China (Sun *et al* 2014).

The understanding of anthropogenic influence on the duration or persistence of daily temperature extremes has been very limited. Christidis and Stott (2016) studied the duration or persistence of daily temperature extremes around the globe and in Europe. The authors compared a set of 16 observed extreme temperature indices, including those duration indices with those computed from the output of HadGEM3-A simulations. They found that anthropogenic forcings have affected most indices in recent decades with only a few exceptions for a few extreme temperature indices in Europe. In particular, they detected human influence in duration indices in European but not in the global series. As anthropogenic induced warming is everywhere, it is reasonable to assume that most of the changes in these duration indices are also thermal dynamic rather than changes in circulation; one would expect stronger signal-to-noise ratio in the global series than in the European series. Thus the related results reported in Christidis and Stott (2016) do not seem to be robust. This and the fact that the study was based on simulation by one climate model, and the work focused only on the globe and Europe, suggests a need for a more comprehensive analysis with simulations by multiple climate models and for different continents of the earth to determine the robustness of results from the earlier study and evidence of human influence in other continents as well.

This paper attempts to fill in this gap. Here, we compare changes in the observed warm spell duration (as measured by the warm spell duration index, WSDI) and cold spell duration (as measured by the cold spell duration index, CSDI) with those simulated by multiple models participating in the Coupled Model Inter-comparison Project Phase 5 (Taylor *et al* 2012) at both the global and continental scales. These two indices were defined by the ETCCDI (Zhang *et al* 2011). The WSDI is defined as the annual number of days with at least six consecutive days when the daily maximum temperature is above the 90th percentile. The CSDI is similarly defined as the annual number of days with at least six consecutive days when the daily minimum temperature is below the 10th percentile. The structure of this paper is as follows: section 2 describes the data and detection methods, including the data processing. Section 3 presents the main results. The conclusions of this research and some discussions are given in section 4.

2. Data and methods

2.1. Observations

We consider the WSDI and CSDI over the global land and six continental regions where observation histories are sufficiently long. The six regions are based on the Giorgi regions (Giorgi and Francisco 2000, see figure S1). Additionally, we include China (CN) as a separate region due to our strong interest in this country.

The observational data for the global, continental and China analyses come from the HadEX2 dataset (Donat *et al* 2013). HadEX2 provides a global gridded land-based dataset at a resolution of 3.75° longitude × 2.5° latitude. The data are based on station observations and cover the period from 1901–2010. Compared with the earlier version of the dataset, HadEX (Alexander *et al* 2006), HadEX2 provides a better quality global dataset with more stations and a longer observational period. We include only the data after 1958 in our analysis as data coverage was poor prior to this period (Donat *et al* 2013).

Daily maximum and daily minimum temperatures for 2419 Chinese stations were also used to analyze changes in the WSDI and CSDI in China. These data have been quality controlled and homogeneity adjusted (Xu *et al* 2013, Wang and Feng 2014) by the China National Meteorological Information Center (NMIC). The station data were aggregated to produce gridded datasets at the HadEX2 grid resolution by averaging indices from all available stations within a grid box. Compared with the Chinese station observations, the HadEX2 dataset can capture the essential features of the observed changes as this is a more comprehensive dataset; however, there are some problems. The Chinese station data show weaker warming in western China than the HadEX2 dataset, though this feature does not lead to clear differences in national averaged extreme temperatures between these two datasets. Additionally, the region with the strongest warming over the western part of the Tibetan Plateau in the HadEX2 dataset does not have underlying station data, even in the 2419 station network (figure S2, lower panel).

2.2. Model simulations

We use indices computed from daily outputs of simulations by the climate models in the Coupled Model Inter-comparison Project Phase 5 (CMIP5; Taylor *et al* 2012) to estimate climate responses to external forcings and natural internal climate variability. The indices computed by Sillmann *et al* (2013a, 2013b) are used in this study. We also computed indices for

the model runs for which daily outputs are available but were not used in Sillmann *et al* (2013a, 2013b). The computational codes that generated the indices in Sillmann *et al* (2013a, 2013b) are used in these cases. Table S1 lists the model simulations used in this study. Altogether, 96 simulations were conducted with 21 climate models driven by the combined effects of historical natural and anthropogenic forcings (ALL). These simulations ended in 2005, and we used the RCP4.5 simulations for the years 2006–2010 to extend the data to 2010. In total, 32 historical greenhouse gas (GHG) simulations were conducted with nine climate models. Additionally, 36 natural forcing-driven (NAT) simulations were conducted with nine climate models. Both the GHG and NAT simulations ended in 2012. We estimate the response to anthropogenic forcing (ANT) as the differences between the model responses to ALL and NAT forcings assuming linear additivity. Linearly additivity holds for large-scale temperature changes (Meehl *et al* 2003, Gillett *et al* 2004). However, non-additive approaches have not been widely adopted. To estimate the natural internal climate variability, we also use index data computed from preindustrial control simulations (CTL) from 28 models. These data consist of 230 pieces of 53 year chunks. The model data are set as missing if the corresponding observation data for the time and space is missing prior to the calculations of the global and regional mean series.

2.3. Detection methods

We perform two types of detection analysis. For the first, we simply ask whether the long-term change in the indices can be expected by chance by performing a simple trend analysis. Here, we compute linear trends in the index series using a least-squares fit. This detection analysis is called a trend analysis in the remaining of the paper. In the second case, we ask a more refined detection and attribution question. Here, we ask whether the expected response to external forcing as simulated by the climate models can be detected in the observations. If the answer is yes, we further ask whether the results are consistent, which allows for the attribution of observed changes to causes.

The detection and attribution analysis is conducted by comparing the time evolutions of the extreme indices in the observations and modeled responses using a standard optimal fingerprinting technique (Allen and Stott 2003). A brief introduction is given in the supporting information available at stacks.iop.org/ERL/13/074013/mmedia. Because of the limited data availability for the estimation of natural internal variability, the fingerprinting method can operate only at relatively small dimensions. Christidis and Stott (2016) used spherical harmonics at a T8 truncation to reduce the dimensionality of the 16 extreme indices at the global scale. Here, we average the data over space and time and conduct the detection and attribution analysis based on global or regional 5 year mean series to reduce the data dimensionality. The optimal fingerprinting method assumes a Gaussian distribution for the residuals. Different methods have been used when the residuals do not follow a Gaussian distribution (Christidis *et al* 2011, Zwiers *et al* 2011). As our analyses are performed on space-time averages, we expect the regression residuals to approach a Gaussian distribution. We also use two methods to transform the data such that the distribution of residuals is very close to a Gaussian to examine the sensitivities of the results to the Gaussian assumption.

Two regression analyses are performed, namely, single-signal and two-signal analyses. In the single-signal analysis, the observations are regressed against the multimodel mean responses to an external forcing or combined effect of different forcing (in the case for ALL). This approach provides a quick and simple overview to determine whether the model-simulated response to a specific forcing can be detected in the observed changes. This approach is particularly useful in the case of the ALL signal as it includes the expected response to the combined effect of all known external forcings. In the two-signal analyses, we aim to partition the observed changes into responses to two known external forcings, namely, NAT and ANT, including greenhouse gases and anthropogenic aerosols. The objective is to determine whether the two major external forcings can be detected separately in the presence of the other signal. However, there is a caveat when ALL and NAT are estimated from the different sets of models. The difference between ALL and NAT can also reflect the fact that the models that are used to estimate the signals are different. For this reason, we repeated the detection and attribution analysis using the eight models that provide both ALL and NAT simulations. We found that the detection results were quite similar (figure S7).

The analysis requires two independent estimates of the covariance of natural internal variability. These estimates are achieved by using data from preindustrial control simulations and the residuals of each model member after the removal of the model ensemble mean. We split the control run data and intra-ensemble differences equally into two independent sets with 272 fifty-three-year chunks of noise data in each set. We use these two sets for optimization to obtain the best estimate of scaling factor β, for estimating the uncertainty range of β and for conducting the residual consistency test. The reliability of the detection and attribution analyses depends critically on the model performance in simulating natural internal climate variability. To determine whether model-simulated variability is sufficiently large, we compare the power spectra of the modeled and observed indices. We also conduct a residual consistency test using the implementation of Ribes and Terray (2013).

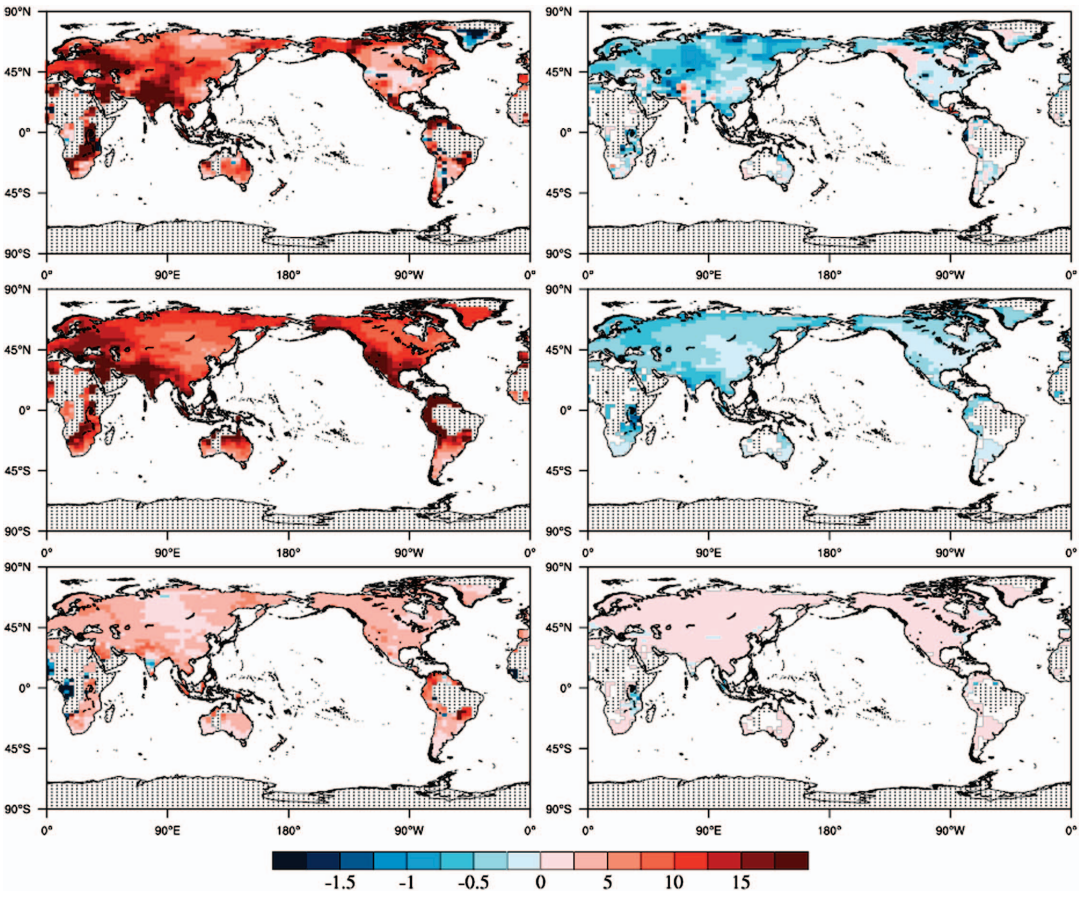

Figure 1. Trends (days over 53 years) in the annual values of the WSDI (left panel) and CSDI (right panel) during 1958–2010 in the observations (top panel) and in the model-simulated responses to ALL forcing (middle panel) and NAT forcing (lower panel). Black dots denote grid boxes without observations. Blank areas over the land indicate that no warm or cold spells are observed.

3. Results

Figure 1 shows the trends in the observed and modeled WSDI and CSDI series. The top panel presents the observed trend based on the HadEX2 data. The trends are characterized by an increase in the duration of warm spells and a decrease in the duration of cold spells, both of which are consistent with global warming. However, regional differences are present in the trends for both indices. WSDI shows the largest increasing trend over India, Southeast Asia and Central Europe and a much weaker positive trend in North and South America. In parts of India, the increase can be as large as 20 days during 1958–2010. There appears to be a negative trend in Greenland, which may be an artifact of data processing as the availability of station data in this region is very limited. A decrease can also be found in South America. CSDI exhibits a strong negative trend for much of Eurasia and a weaker negative trend in eastern Asia and North and South America. The decrease in parts of Eurasia can be as large as 5 days during the 53 year period. A positive trend can be observed in India and some areas in North America. In some areas along the tropics and in South America, a cold spell as defined by ETCCDI is not usually observed (blank areas in the land).

The middle panel of figure 1 shows the trend in the multimodel ensemble mean under ALL forcing. WSDI increases almost everywhere. The spatial pattern of trends is in generally consistent with the observed trend pattern. The magnitude over Europe and South America is reasonably consistent with that of the observed trend, while the small observed trend in North America, Australia and Africa could not be well simulated in the models. The models also underestimate the observed changes in Asia. CSDI decreases everywhere, which is largely consistent with the observations. The lower panel of figure 1 shows the trends in the multimodel ensemble mean under NAT forcing. The NAT trends are generally weak, much weaker than the observations for WSDI, suggesting that NAT forcing alone cannot contribute to the observed changes in warm spell duration. The NAT trend in the CSDI is also very weak and of opposite sign to that of the observations, indicating a negligible role of natural forcing in the CSDI decrease.

Table 1 shows trends in the global and regional averages of the WSDI and CSDI during 1958–2010 in the observations and the model simulations. Averaged over the globe, WSDI increased by approximately 15 days, while CSDI decreased by approximately 3 days. As shown in figure 1, the observed WSDI trend

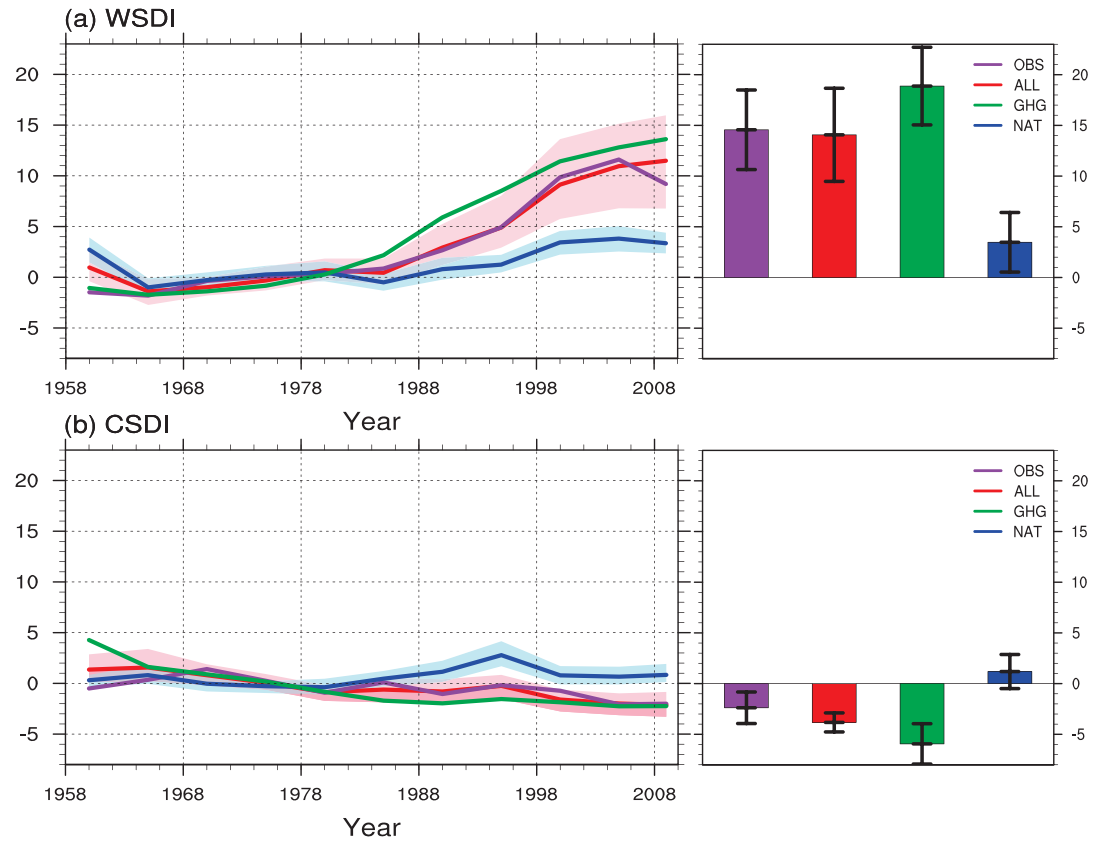

Figure 2. Observed and simulated global mean WSDI (*a*) and CSDI (*b*) series (left panel) and their long-term trends (right panel). The time series are plotted as five-year mean anomalies (in days) relative to the 1961–1990 average. The solid lines show the observation or ensemble means of the model simulations, while the shaded areas show the 5%–95% ranges of model simulations. Red, green and blue denote model simulations under ALL, GHG, and NAT forcings, respectively. The black error bars on the right panel indicate the 95% confidence intervals of the linear trends.

Table 1. Trends (days over 53 years) in the WSDI and CSDI during 1958–2010 computed with observations and the multimodel ensemble simulations.

	WSDI							
	GLB	ASI	EUR	NAM	SAM	AUS	AFR	CN
OBS	14.62	16.48	10.33	5.94	15.42	7.74	7.16	11.61
ALL	13.72	11.82	11.89	13.13	17.4	11.42	12.87	12.71
NAT	3.33	3.12	3.23	3.44	3.39	2.80	3.28	3.02
	CSDI							
	GLB	ASI	EUR	NAM	SAM	AUS	AFR	CN
OBS	−2.81	−3.18	−2.97	−1.48	−2.07	−1.17	−0.80	−3.34
ALL	−3.86	−3.99	−3.50	−3.14	−3.11	−2.08	−1.88	−3.49
NAT	1.21	1.43	1.32	1.16	0.90	0.79	0.79	1.16

is of a similar magnitude to the modeled trend under ALL forcing, but the modeled trend under NAT forcing is much weaker. The modeled CSDI trend under ALL forcing is of the same sign as the observed trend but of a larger magnitude. However, the modeled CSDI trend under NAT forcing is of the opposite sign as that observed.

Figure 2 displays the 5 year mean anomaly (relative to 1961–1990 mean) of the WSDI and CSDI at the global scale from the observations and model simulations. We consider 5 year mean values as a compromise between removing natural inter-annual variability and maintaining responses to natural external forcing such as volcanic activity. The trends in the global mean series are also shown. The observed WSDI is characterized by little change in the early period and an obvious increase after the late 1970s. This feature is successfully reproduced by the ALL simulations: the observed series match the ensemble mean series and fall within the range of the model simulations. The response to GHG displays similar temporal variations but has a larger trend, greater than that of ALL and the observations, reflecting a stronger warming response to GHG forcing. The observations are not consistent with the NAT simulations and are well above the range of the NAT simulations starting in the early 1980s. CSDI is characterized by a small decreasing trend. Again, the observations are consistent with the model simulations under ALL and GHG forcing but are not consistent with the model simulations under NAT forcing. As the period 1961–1990, in which temperature is lower, is used as base period, and as the value of the CSDI cannot be smaller than zero, there is very little room for CSDI to decrease. However, there is no such constraint for an increase in the WSDI. This characteristic may explain the large difference in the magnitudes of the trends of the WSDI and CSDI series in both the observations and model simulations under ALL forcing. This difference may also explain the larger variability in the WSDI compared to that in

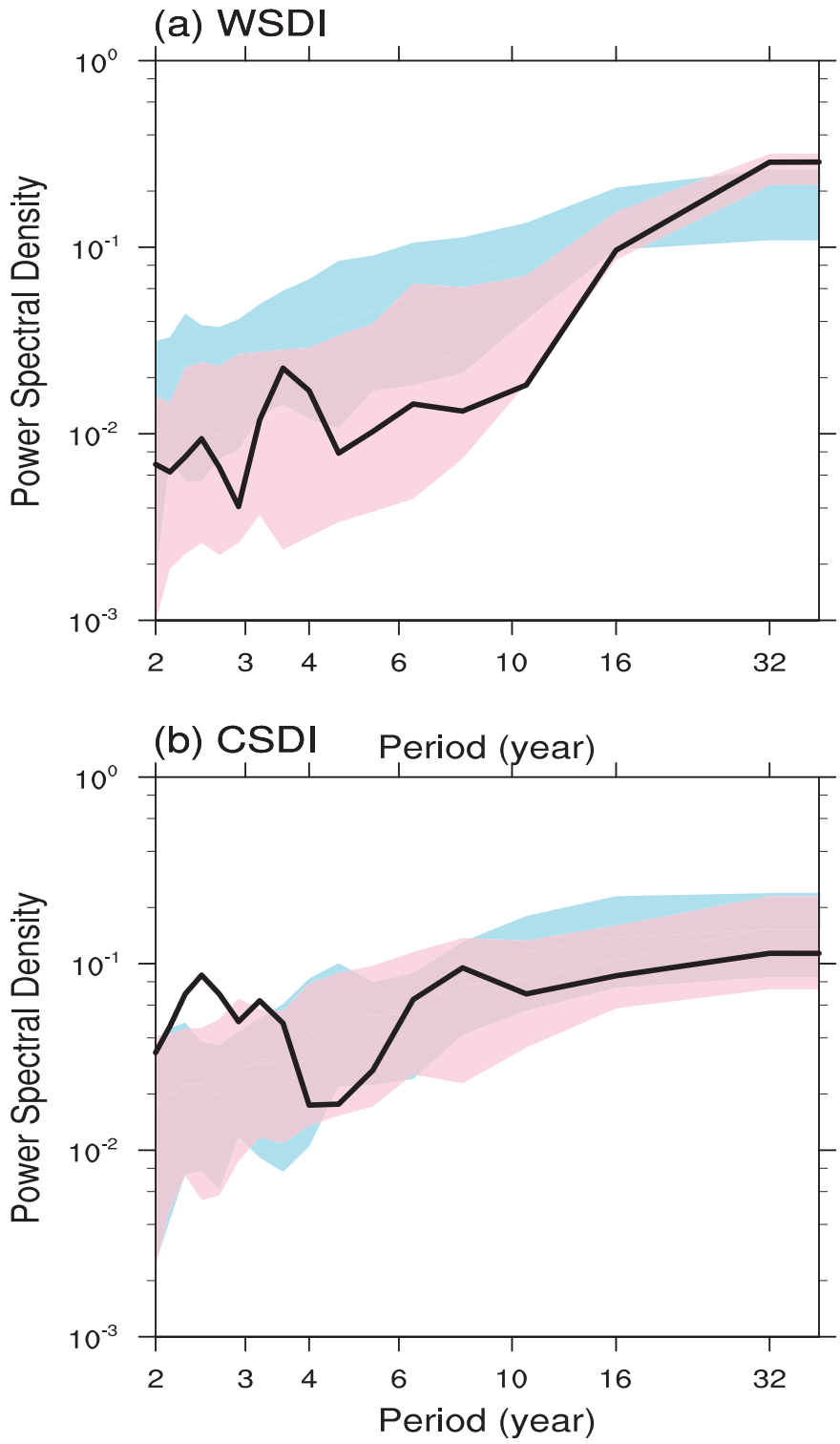

Figure 3. Power spectral density (PSD) of the WSDI (*a*) and CSDI (*b*) computed from relevant global mean values from 1958 to 2005 for the observations (black) and model simulations. The pink and blue shadings show the 5%–95% ranges of the PSD computed from individual members of ensemble runs forced with historical ALL and historical NAT.

the CSDI (table S2). Despite the smaller variability in the CSDI, the signal-to-noise ratio (see supporting information) in the CSDI is lower than that in the WSDI. Thus, detecting the influence from external forcing in the CSDI is more difficult than in the WSDI. For the six continents and China, the regional results are similar to the global results (figures S3 and S4).

The power spectra of the observed and model-simulated global indices are shown in figure 3. The power spectra for the modeled indices are computed using time series from individual model runs. The power spectra of the observed WSDI lie within the range of the ALL simulations on all the time scales examined. This result suggests that the model-simulated

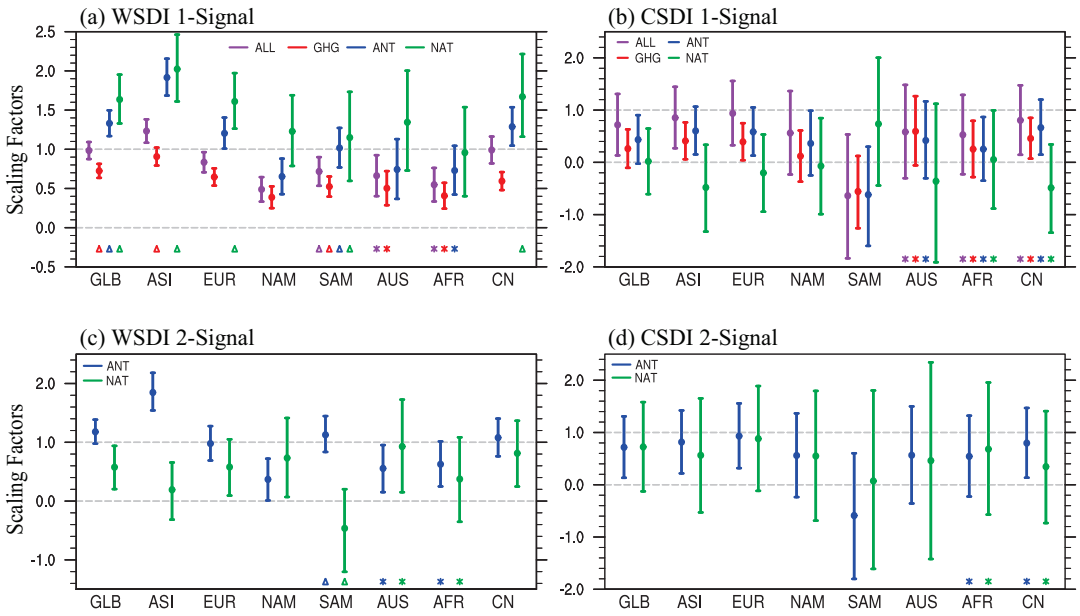

Figure 4. Scaling factors and their 5%–95% confidence intervals from the single-signal and two-signal analyses for the globe, Asia, Europe, North America, South America, Australia, Africa and China series and for different forcings. An asterisk indicates that the model-simulated variability is too low (and thus, the confidence interval of the scaling factor may be too narrow for the detection to be valid), while a triangle indicates that the model-simulated variability is too high (and thus, the detection result is conservative).

variability is also consistent with that of the observations, which indicates that detection and attribution analyses based on these model simulations should be credible. The power spectra of the NAT series are more evenly distributed compared with those of the ALL series and are larger at higher frequencies but smaller at low frequencies, corresponding to a lack of a long-term trend in the NAT responses. The power spectra of the observed CSDI are generally consistent with those of the ALL simulations but are at the lower edge of the modeled power spectra at low frequencies. This result means that the modeled variability at low frequency, which is the most relevant to detection and attribution, may be too large. The implication for detection and attribution analysis is that the confidence interval of the scaling factor could be too large, making it harder to detect the signal. The observed power spectra are larger than those of the model simulations at high frequencies, but this relation has little effect on detection and attribution analysis because high frequency variability is filtered out in the 5 year mean series. The comparisons of the power spectra for the six continents and China yield similar results (figures S5 and S6). We therefore conclude that the modeled variabilities relevant to the detection and attribution analyses in both the WSDI and CSDI are generally sufficient for credible detection analyses.

The best estimates and the 90% confidence intervals of the scaling factors from the single-signal analyses including ALL, GHG, ANT and NAT signals are summarized in figures 4(*a*) and (*b*) for the globe, continents and China. For the global (GLB) mean series, ALL is robustly detected in both the WSDI and CSDI. The 90% confidence interval of their scaling factors include 1, indicating that the observed changes in the WSDI and CSDI are generally consistent with the expected response to the combined effect of anthropogenic and natural external forcings as simulated by the CMIP5 models. The scaling factors of GHG, ANT, and NAT for the WSDI are significantly greater than zero at the 5% level; however, the residual consistency tests failed, meaning that the regression fit was poor. For the CSDI, the GHG, ANT and NAT signals are not detected individually, indicating that responses to these individual forcings alone are not sufficient to explain the observed changes.

At the continental scale, the detection results for the WSDI series are generally similar to those of the global scale, but the consistency between the modeled responses and the observed changes are poor. For example, the modeled response to ALL forcing is too large compared with the observed changes in most regions except Asia and China. This difference may have some relevance for climate model evaluation. The modeled response to external forcing is not detected in the CSDI for most of the regions, except in Asia and Europe. In fact, even in the perfect model world, the signal-to-noise ratios for the CSDI in these regions are low (table S2). These results highlight the challenge of detecting and attributing changes in the CSDI.

The best estimates and the 90% confidence intervals of the scaling factors from the two-signal analysis are summarized in figures 4(*c*) and (*d*). For the WSDI, ANT and NAT are separately detected in the observed series for global land (GLB), the continents of Europe (EUR), North America (NAM), Australia (AUS) and China (CN), while ANT is additionally detected in the continents of Asia (ASI), South America (SAM),

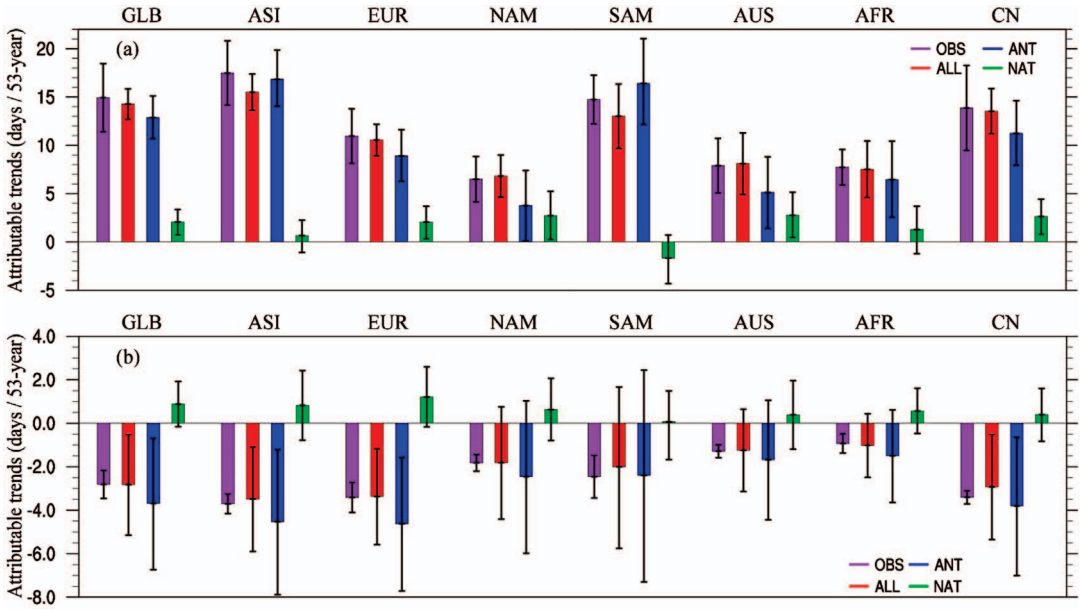

Figure 5. Observed trends and trends attributable to external forcings in the WSDI (top panel) and CSDI (lower panel). The attributable trends are estimated as the linear least-squares trends of the relevant time series multiplied by the corresponding scaling factors.

and Africa (AFR) when the effect of NAT is taken into account. These results indicate that both anthropogenic forcing and natural external forcing have detectable responses in the observations at the global and continental scales. As NAT has a very small long-term trend, it follows that the ANT response dominates the observed increase in the WSDI. For the CSDI, ANT is detected in the presence of NAT in the GLB, ASI, EUR, and CN series but is not detected in the other regions. NAT is not detected for the globe or for all the continents. These results indicate that anthropogenic forcing has contributed to the observed changes in the CSDI at the global and some regional scales.

We also conducted detection and attribution analyses over China based on the HadEX2 dataset (figure S8). The results are very similar to those of analyses based on more comprehensive datasets that contain more than 2000 stations. While HadEX2 may have missed important regional details over China, this dataset is able to capture essential large-scale information, at least for the WSDI and CSDI.

Figure 5 shows the observed trends in the WSDI and CSDI and those attributable to various external forcings. The global averaged WSDI increased by approximately 15 days over 1958–2010. The best estimate of the increase attributable to all external forcing is approximately 14 days (with a 90% confidence interval of 12–16 days). The best estimate of the attributable increase due to anthropogenic forcing (ANT) is approximately 13 days (with a 90% confidence interval of 11 to 15 days). For the CSDI, the observed decrease attributable to all external forcing is approximately 3 days (with a 90% confidence interval of 1–5 days). The decrease that is attributable to anthropogenic forcing is approximately 4 days (with a 90% confidence interval of 1–7 days).

Because the WSDI and CSDI are both bounded by zero, the time series for the WSDI and CSDI are unlikely to follow Gaussian distributions. This property may have an effect on the estimation of the confidence intervals of the scaling factors as the regression procedure for the detection and attribution analysis assumes a Gaussian distribution. We examined the robustness of our results to this potential violation of the distributional assumption by taking the cubic root for both the observational series and the modeled series and repeating the detection and attribution analysis. The results are very similar to those reported above. We also applied a natural logarithm transformation to the data, and the detection and attribution results are also similar. We therefore conclude that our detection results are robust to this particular assumption.

4. Conclusions and discussion

In this study, we focused on possible causes for the observed long-term changes in the duration of warm spells and cold spells. We found a substantial increase in warm spell duration and a decrease in cold spell duration, both of which are consistent with warming. The climate models generally successfully reproduce the observed changes in the WSDI and CSDI at the global scale. However, the models overestimate the observed changes in the WSDI for five continents and exhibit poor performance in simulating the CSDI in American regions. We also found that much of the observed changes in the WSDI and CSDI can be attributed to external forcing and anthropogenic forcing at the

global scale and for many continents. Christidis and Stott (2016) also analyzed the WSDI and CSDI along with many other temperature indices using simulations conducted with one global model. The authors detected anthropogenic influences in the WSDI and CSDI over Europe but not in the global series. Their results are difficult to interpret as one would generally expect more robust detection at the global scale than over a continent for temperature-related indicators. Our analysis must have benefited from the use of multimodel ensemble data. The larger datasets enabled us to produce more robust estimates for the modeled responses to external forcings and the natural internal variability, both of which are important for robust detection and attribution analyses. The results from our study show strong consistencies between trends in the observations and the model simulations as well as a strong consistency of the detection results under different analysis settings.

Anthropogenic influence has resulted in hotter annual hottest daily temperatures and warmer annual coldest daily temperatures (Zwiers *et al* 2011, Min *et al* 2013). This influence has also contributed to more frequent moderate hot temperature extremes and less frequent cold temperature extremes (Morak *et al* 2013, Lu *et al* 2016). Here, we found that anthropogenic influence contributes to longer warm spells and shorter cold spells. Together, these findings provide clear evidence of anthropogenic influences on extreme temperature and show that anthropogenic forcing has altered different aspects of temperature extremes, including their magnitude, frequency, and duration. Extreme hot temperatures have clearly become hotter, more frequent, and longer lasting, while extreme cold temperatures have become less cold, less frequent and more short-lived. Because extreme temperature has impacts on both human society and natural systems, and because warming is projected to continue, rapid action is required to adapt to the new climate.

Acknowledgments

We appreciate the constructive comments from John Mitchell, an anonymous reviewer and an ERL board member. We acknowledge the Program for Climate Model Diagnosis and Intercomparison and the World Climate Research Programme's Working Group on Coupled Modeling for their roles in making the WCRP CMIP multimodel datasets available. This study was supported by the National Key R&D Program of China (2018YFA0605604), the National Natural Science Foundation of China (41675074 and 41775082) and two Climate Change Projects (CCSF201704 and CCSF201805).

ORCID iDs

Chunhui Lu https://orcid.org/0000-0003-0335-8465

References

Alexander L V *et al* 2006 Global observed changes in daily climate extremes of temperature and precipitation *J. Geophys. Res.* **111** D05109

Allen M R and Stott P A 2003 Estimating signal amplitudes in optimal fingerprinting part I: theory *Clim. Dyn.* **21** 477–91

Brown S J, Caesar J and Ferro C A 2008 Global changes in extreme daily temperature since 1950 *J. Geophys. Res.* **113** D05115

Bindoff N L *et al* 2013 Detection and attribution of climate change: from global to regional *Climate Change 2013: The Physical Science Basis* ed T F Stocker *et al* (Cambridge: Cambridge University Press) pp 867–952

Christidis N, Stott P A, Brown S, Hegerl G C and Caesar J 2005 Detection of changes in temperature extremes during the second half of the 20th century *Geophys. Res. Lett.* **32** L20716

Christidis N, Stott P A and Brown S J 2011 The role of human activity in the recent warming of extremely warm daytime temperatures *J. Clim.* **24** 1922–30

Christidis N, Stott P A and Zwiers F W 2014 Fast-track attribution assessments based on pre-computed estimates of changes in the odds of warm extremes *Clim. Dyn.* **45** 1547–64

Christidis N and Stott P A 2016 Attribution analyses of temperature extremes using a set of 16 indices *Weather Clim. Extremes* **14** 24–35

Donat M G *et al* 2013 Updated analyses of temperature and precipitation extreme indices since the beginning of the twentieth century: the HadEX2 dataset *J. Geophys. Res. Atmos.* **118** 2098–118

Donat M G *et al* 2014 Changes in extreme temperature and precipitation in the Arab region: long-term trends and variability related to ENSO and NAO *Int. J. Climatol.* **34** 581–92

Donat M G, Alexander L V, Herold N and Dittus A J 2016 Temperature and precipitation extremes in century-long gridded observations, re-analyses, and atmospheric model simulations *J. Geophys. Res. Atmos.* **121** 11174–89

Giorgi F and Francisco R 2000 Uncertainties in regional climate change prediction: a regional analysis of ensemble simulations with the HADCM2 coupled AOGCM *Clim. Dyn.* **16** 169–82

Gillett N P, Wehner M F, Tett S F B and Weaver A J 2004 Testing the linearity of the response to combined greenhouse and sulfate aerosol forcing *Geophys. Res. Lett.* **31** L14201

Hartmann D L *et al* 2013 Observations: atmosphere and surface *Climate Change 2013: The Physical Science Basis. Contribution of Working Group I to the Fifth Assessment Report of the Intergovernmental Panel on Climate Change* ed T F Stocker *et al* (Cambridge: Cambridge University Press)

Kim Y H, Min S K, Zhang X, Zwiers F, Alexander L V, Donat M G and Tung Y S 2015 Attribution of extreme temperature changes during 1951–2010 *Clim. Dyn.* **46** 1769–82

Lu C, Sun Y, Wan H, Zhang X and Yin H 2016 Anthropogenic influence on the frequency of extreme temperatures in China *Geophys. Res. Lett.* **43** 6511–18

Meehl G A, Washington W M, Wigley T M L, Arblaster J M and Dai A 2003 Solar and greenhouse gas forcing and climate response in the 20th century *J. Clim.* **16** 426

Min S K, Zhang X, Zwiers F W, Shiogama H, Tung Y S and Wehner M 2013 Multi-model detection and attribution of extreme temperature changes *J. Clim.* **26** 7430–51

Morak S, Hegerl G C and Christidis N 2013 Detectable changes in the frequency of temperature extremes *J. Clim.* **26** 1561–74

Ribes A and Terray L 2013 Application of regularised optimal fingerprint to attribution. Part II: application to global near-surface temperature *Clim. Dyn.* **41** 2837–53

Stott P A, Stone D A and Allen M R 2004 Human contribution to the European heat wave of 2003 *Science* **432** 610–4

Stott P A, Mitchell J F B, Allen M R, Delworth T L, Gregory J M, Meehl G A and Santer B D 2006 Observational constraints on past attributable warming and predictions of future global warming *J. Clim.* **19** 3055–69

Sillmann J, Kharin V V, Zhang X, Zwiers F W and Bronaugh D 2013a Climate extremes indices in the CMIP5 multimodel ensemble: part 1, model evaluation in the present climate *J. Geophys. Res.* **118** 1716–33

Sillmann J, Kharin V V, Zwiers F W, Zhang X and Bronaugh D 2013b Climate extremes indices in the CMIP5 multimodel ensemble: part 2, future climate projection *J. Geophys. Res.* **118** 2473–93

Sun Y, Zhang X, Zwiers F W, Song L, Wan H, Hu T, Yin H and Ren G 2014 Rapid increase in the risk of extreme summer heat in Eastern China *Nat. Clim. Change* **4** 1082–5

Tett S F B *et al* 2002 Estimation of natural and anthropogenic contributions to twentieth century temperature change *J. Geophys. Res.* **107** D164306

Taylor K E, Stouffer R J and Meehl G A 2012 An overview of CMIP5 and the experiment design *Bull. Am. Meteorol. Soc.* **93** 485–98

Wang X L and Feng Y 2014 RHtests V4 User Manual. P26, (Climate Research Division, Science and Technology Branch, Environment Canada) (http://etccdi.pacificclimate.org/RHtest/RHtestsV4_UserManual_10Dec2014.pdf)

Wen H Q, Zhang X, Xu Y and Wang B 2013 Detecting human influence on extreme temperatures in China *Geophys. Res. Lett.* **40** 1171–6

Xu W H, Li Q X, Wang X L, Yang S, Cao L and Feng Y 2013 Homogenization of Chinese daily surface air temperatures and analysis of trends in the extreme temperature indices *J. Geophys. Res. Atmos.* **118** 9708–20

Yin H, Sun Y, Wan H, Zhang X and Lu C 2016 Detection of anthropogenic influences on the intensity of extreme temperatures in China *Int. J. Climatol.* **37** 1229–37

Zwiers F W and Zhang X 2003 Toward regional-scale climate change detection *J. Clim.* **16** 793–7

Zwiers F W, Zhang X and Feng Y 2011 Anthropogenic influence on long return period daily temperature extremes at regional scales *J. Clim.* **24** 881–92

Zhang X *et al* 2005 Trends in Middle East climate extreme indices from 1950 to 2003 *J. Geophys. Res.:* A **110** D22104

Zhang X, Zwiers F W and Stott P 2006 Multi-model multi-signal climate change detection at regional scale *J. Clim.* **19** 4294–307

Zhang X, Alexander L V, Hegerl G C, Jones P, Tank A K, Peterson T C, Trewin B and Zwiers F W 2011 Indices for monitoring changes in extremes based on daily temperature and precipitation data *WIREs Clim. Change* **2** 851–70

Improving Representation of Tropical Cloud Overlap in GCMs Based on Cloud-Resolving Model Data

Xianwen JING[1], Hua ZHANG[1,2*], Masaki SATOH[3], and Shuyun ZHAO[1,4]

1 *Collaborative Innovation Center on Forecast and Evaluation of Meteorological Disasters, Nanjing University of Information Science &Technology, Nanjing* 210044, *China*
2 *State Key Laboratory of Severe Weather, Chinese Academy of Meteorological Sciences, Beijing* 100081, *China*
3 *Atmosphere and Ocean Research Institute, The University of Tokyo, Kashiwa* 2778564, *Japan*
4 *Laboratory for Climate Studies, National Climate Center, China Meteorological Administration, Beijing* 100081, *China*

(Received June 26, 2017; in final form November 15, 2017)

ABSTRACT

The decorrelation length (L_{cf}) has been widely used to describe the behavior of vertical overlap of clouds in general circulation models (GCMs); however, it has been a challenge to associate L_{cf} with the large-scale meteorological conditions during cloud evolution. This study explored the relationship between L_{cf} and the strength of atmospheric convection in the tropics based on output from a global cloud-resolving model. L_{cf} tends to increase with vertical velocity in the mid-troposphere (w_{500}) at locations of ascent, but shows little or no dependency on w_{500} at locations of descent. A representation of L_{cf} as a function of vertical velocity is obtained, with a linear regression in ascending regions and a constant value in descending regions. This simple and dynamic-related representation of L_{cf} leads to a significant improvement in simulation of both cloud cover and radiation fields compared with traditional overlap treatments. This work presents a physically justifiable approach to depicting cloud overlap in the tropics in GCMs.

Key words: cloud overlap, decorrelation length, cloud-resolving model, Nonhydrostatic Icosahedral Atmospheric Model (NICAM)

Citation: Jing, X. W., H. Zhang, M. Satoh, et al., 2018: Improving representation of tropical cloud overlap in GCMs based on cloud-resolving model data. *J. Meteor. Res.*, **32**(2), 233–245, doi: 10.1007/s13351-018-7095-9.

1. Introduction

The simulation of clouds has been a major source of uncertainty in projections of future climate using general circulation models (GCMs) (Stephens, 2005; Li et al., 2009; Bony et al., 2015). One limitation of cloud simulation is the coarse spatial resolution of GCMs (tens of kilometers to 100–200 km), which leaves clouds smaller than grid size unresolved (Barker et al., 2003; Randall et al., 2003). Consequently, clouds in GCMs usually cover only part of a grid layer and the overlap of fractional clouds in the vertical layers has to be addressed artificially in radiation calculations by imposing overlap assumptions (Tompkins and Di Giuseppe, 2015; Zhang and Jing, 2016). For a given vertical distribution of cloud fractions, the assumption of cloud overlap determines the total cloud cover or total cloud fraction (C_{tot}), which has a considerable influence on solar and terrestrial radiative transfer (Wang et al., 2016).

The cloud overlap assumption most widely used in recent decades is the maximum random overlap (MRO) assumption (Morcrette and Fouquart, 1986; Tian and Curry, 1989), in which clouds within layers that are vertically continuous are assumed to have a maximum overlap, whereas those that are separated by cloud-free layers are considered to overlap randomly. Such treatment is insufficient to represent the realistic features of cloud overlap as observed by ground-based radar (Hogan and Illingworth, 2000; Mace and Benson-Troth, 2002) and depends largely on the vertical resolution of the host

Supported by the National Key Research and Development Program of China (2017YFA0603502), (Key) National Natural Science Foundation of China (91644211 and 41375080), and China Meteorological Administration Special Public Welfare Research Fund (GYHY201406023).

*Corresponding author: huazhang@cma.gov.cn.

©The Chinese Meteorological Society and Springer-Verlag Berlin Heidelberg 2018

model (Bergman and Rasch, 2002).

In contrast with the simple, crude cloud overlap treatments such as the MRO assumption, Liang and Wang (1997) were among the first to explicitly depict the subgrid distribution of clouds of distinct physical types and to apply different treatments of vertical overlap for different types of clouds. This sophisticated, physically based treatment of cloud overlap (termed "mosaic") has been demonstrated to improve cloud radiative forcing and radiative heating in both cloud-resolving model (CRM) domains (Liang and Wu, 2005; Wu and Liang, 2005a, b) and climate simulations (Zhang F. et al., 2013).

Another ingenious approach is the analytical representation of cloud overlap proposed by Hogan and Illingworth (2000) and Mace and Benson-Troth (2002) based on radar observations. This method is called general overlap (GenO). In GenO, for two layers of clouds at heights of Z_k and Z_l with cloud fractions of C_k and C_l, respectively, $C_{\rm tot}$ is defined as

$$C_{\rm tot} = \alpha_{k,l} C_{k,l}^{\rm max} + (1-\alpha_{k,l}) C_{k,l}^{\rm ran}, \tag{1}$$

where $C_{k,l}^{\rm max} = \max(C_k, C_l)$ and $C_{k,l}^{\rm ran} = C_k + C_l - C_k C_l$ are the total cloud fractions calculated using the maximum overlap and random overlap assumption, respectively, and $\alpha_{k,l}$ is the overlap coefficient derived from

$$\alpha_{k,l} = \exp\left(-\int_{z_k}^{z_l} \frac{1}{L_{\rm cf}} {\rm d}Z\right). \tag{2}$$

$L_{\rm cf}$ is the decorrelation length (in km) representing the distance at which $\alpha_{k,l}$ decreases to the value of e^{-1}. With Eqs. (1) and (2), the extent of overlap degrades exponentially from maximum overlap to random overlap as the vertical separation of clouds increases. This relationship of decreasing overlap with increasing distance has been reported from both radar observations and simulations by CRMs (Oreopoulos and Khairoutdinov, 2003). The merits of GenO are two-fold: (1) it realistically depicts the distance-related feature of cloud overlap and (2) it is independent of the vertical resolution of the host model and thus more widely applicable among models with various vertical configurations.

In GenO, the extent of cloud overlap is determined by $L_{\rm cf}$. For given fractional clouds in a vertical column, the use of larger values of $L_{\rm cf}$ results in smaller values of $C_{\rm tot}$ (prone to maximum overlap) and smaller values of $L_{\rm cf}$ result in larger values of $C_{\rm tot}$ (prone to random overlap). The parameter $L_{\rm cf}$ is highly variable both spatially and temporally because of variations in the shapes and formation processes of clouds. Therefore, when applying GenO, one challenge is to determine an optimum value of $L_{\rm cf}$ for each GCM grid point. Various attempts have been made to obtain detailed information about $L_{\rm cf}$ (e.g., Di Giuseppe, 2005; Kato et al., 2010; Shonk et al., 2010; Oreopoulos et al., 2012; Peng et al., 2013; Zhang H. et al., 2013). It has been demonstrated that $L_{\rm cf}$ is related to the cloud type and atmospheric dynamics (Naud et al., 2008; Di Giuseppe and Tompkins, 2015; Li et al., 2015) and that it has a global median value of approximately 2 km (Barker, 2008). Simplified expressions have also been extracted to represent $L_{\rm cf}$ in GCMs, either as a function of latitude and/or season without interannual variations (Shonk et al., 2010, Oreopoulos et al., 2012; Jing et al., 2016) or as a function of cloud type, which is affected by the limited cloud classification schemes of the host models (Zhang et al., 2014). These approaches either lack a direct link between $L_{\rm cf}$ and the instant large-scale meteorological conditions that foster the clouds or address the dynamic (e.g., wind shear) impact on cloud overlap over the globe without considering the very different circulation conditions in different regions.

The formation and evolution of clouds are essentially associated with large-scale circulation (Bony et al., 1997). Therefore one physically robust approach to describe $L_{\rm cf}$ is to establish a direct connection between $L_{\rm cf}$ and large-scale circulation conditions. CRMs, because of their ability to simulate cloud micro- and macro-physical structures as well as meteorological conditions in detail, have long been used as a tool to explore cloud physics and to obtain parameterizations applicable in GCMs (GEWEX Cloud System Science Team, 1993; Randall et al., 2003; Wu and Li, 2008). This study uses simulation results from a global CRM to explore the relationship between $L_{\rm cf}$ and atmospheric circulation. Unlike previous studies that attempted to explore such a relationship over the whole globe, we focus on the tropical region and vertical motion only, considering that there are large uncertainties in cloud radiative forcing due to vertical overlap treatment in the intertropical convective zone (ITCZ) (Barker and Räisänen, 2005; Zhang and Jing, 2010; Lauer and Hamilton, 2013) and that the formation and maintenance of clouds in this particular region are closely related to vertical convection. We will attempt to establish a statistical, mathematical description of the $L_{\rm cf}$–convection connection, which is a novel application in GCMs, and then evaluate its effectiveness in improving the GCM-scale cloud cover and radiation calculations.

The CRM data and the method used to derive $L_{\rm cf}$ are described in Section 2. Section 3 presents the analysis of $L_{\rm cf}$ versus atmospheric convection and evaluates the established representation of $L_{\rm cf}$. The discussion and conclusions are presented in Section 4.

2. Data and methods

2.1 *CRM data*

The global CRM data are from a simulation of the Nonhydrostatic Icosahedral Atmospheric Model (NICAM) developed at Japan Agency for Marine–Earth Science and Technology and the University of Tokyo (Tomita and Satoh, 2004; Satoh et al., 2008, 2014). The cloud microphysics scheme of Grabowski (1998) is adopted and no convective scheme is used. This scheme is simpler than other cloud microphysics schemes, but convective circulation is explicitly calculated so that the associations between convection and large-scale atmospheric states are consistently represented. The boundary layer scheme with moist processes is implemented (Nakanishi and Niino, 2006). The vertical resolution of the model is 40 levels with Lorenz grids (Satoh et al., 2008, 2014) stretching from the surface up to about 40 km. The vertical interval of the half-level (ΔZ) increases with height from about 170 m at the bottom to about 3 km near the top ($\Delta Z < 1$ km below 10 km).

NICAM can be run using different horizontal resolutions depending on the grid division level used. In this study, data from a simulation using a grid division level of 11 (corresponding to a grid size of about 3.5 km) (Miura et al., 2007) are adopted; the cloud characteristics of this dataset have been extensively analyzed by Inoue et al. (2008, 2010), Masunaga et al. (2008), Sato et al. (2009), and Satoh et al. (2010). The simulation was started from 0000 UTC 25 December 2006 and integrated for 7 days. The results were stored as instantaneous snapshots at 0000 UTC on each day. Figures 1 and 2 show the simulated total cloud fraction and the zonal mean vertical cloud fraction profile, respectively, compared with those from the 2B-GEOPROF product of CloudSat observations (Marchand et al., 2008) during the same period. The NICAM simulation captures both the geographical distribution of cloud systems in the deep convective regions (Fig. 1) and the vertical cloud profiles in the tropics (Fig. 2). The cloud top height of NICAM in Fig. 2 is slightly higher than the CloudSat observations, which is because CloudSat does not detect optically thin clouds in the topmost layers (Stephens et al., 2008).

The variables used in this study are the mass mixing ratios of liquid and ice water condensates (q_c and q_i, respectively), in-cloud precipitation (q_r) and snow (q_s), and vertical velocity (w).

2.2 *Derivation of L_{cf}*

To obtain L_{cf} at the resolution of the GCM and to establish the GCM-oriented relationship between L_{cf} and atmospheric convection, the original NICAM output is averaged based on a 2.8° × 2.8° (latitude × longitude) grid division, which is close to a T42 GCM resolution. The grid mean fields are then used to obtain L_{cf} using a stochastic cloud generator (Räisänen et al., 2004) as follows.

1) Diagnose the occurrence of cloud from q_c, q_i, q_r, and q_s. If $q_c + q_i + q_r + q_s > 0.01$ g kg^{-1} in a CRM grid cell, then this grid cell is regarded as cloudy (i.e., cloud fraction = 1), otherwise the grid cell is regarded as clear (i.e., cloud fraction = 0). This criterion was also used in Grabowski (1998).

2) Average the original CRM fields to the 2.8° × 2.8°

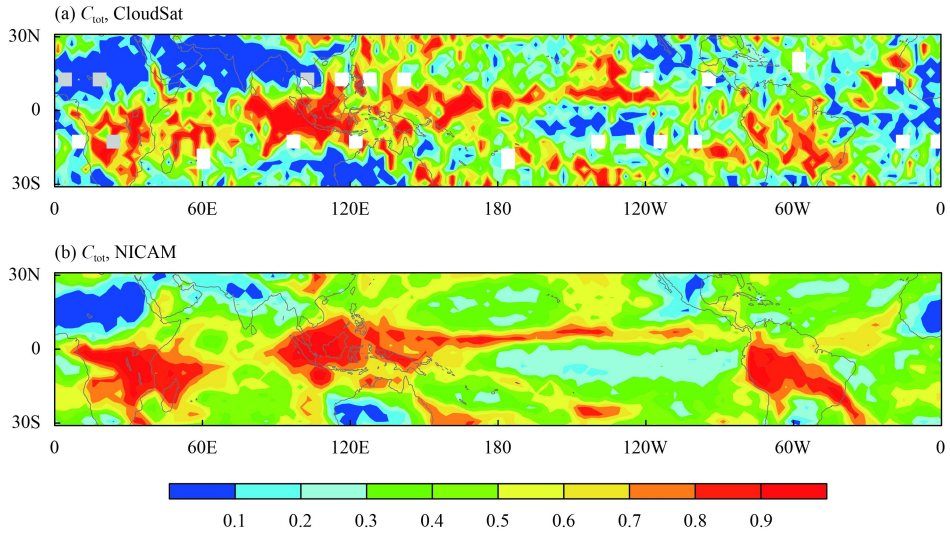

Fig. 1. Comparison of total cloud fraction (C_{tot}) between (a) CloudSat observations and (b) the NICAM simulation during the 7-day period starting from 0000 UTC 25 December 2006.

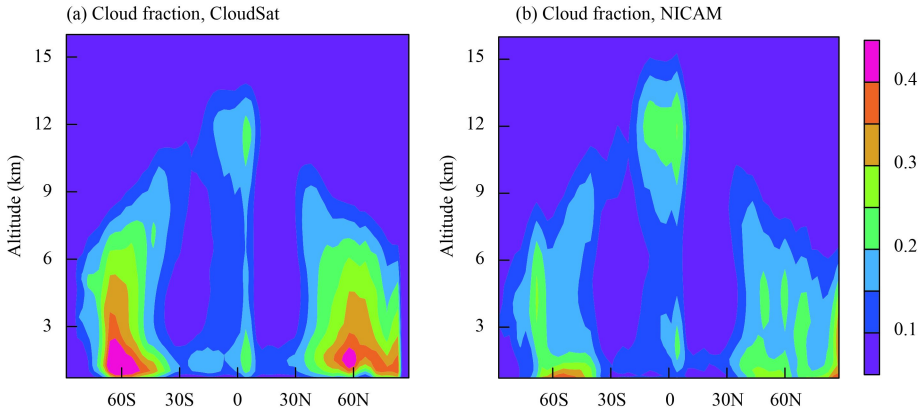

Fig. 2. Comparison of zonal mean vertical cloud fraction profile between (a) CloudSat observations and (b) the NICAM simulation during the 7-day period starting from 0000 UTC 25 December 2006.

grid division. The cloud fraction and the vertical velocity at 500 hPa (w_{500}) are averaged within each GCM grid. These yield vertical distributions of cloud fractions and w_{500} for each GCM grid. In addition, the vertically projected cloud fraction (i.e., $C_{\rm tot}$) for each GCM grid is derived by dividing the number of cloudy CRM columns by the total number of CRM columns within the grid.

3) Obtain $L_{\rm cf}$. The vertical cloud fraction profile and $C_{\rm tot}$ in each GCM grid are supplied to the stochastic cloud generator with GenO incorporated to obtain $L_{\rm cf}$. $L_{\rm cf}$ is defined as the value that gives the same $C_{\rm tot}$ as the original CRM cloud field when used in Eqs. (1) and (2). To demonstrate the effectiveness of using this procedure to capture the cloud overlap characteristics, a GCM grid with a typical cloud profile often seen in the tropical deep convective region is chosen as an example and the generated and original cloud structures are examined. The properties examined include the vertical cloud fraction profile, the downward cumulative cloud fraction, and the cloud fraction exposed to space at different heights (Fig. 3). It is suggested that, by applying the achieved $L_{\rm cf}$ in GenO, the generated cloud structures (dotted lines) resemble those of the original CRM field (solid lines). The characteristics of clouds shown in Fig. 3 are important to both solar reflectance and upward longwave emissivity. Therefore, the cloud structures generated by GenO with an accurate value of $L_{\rm cf}$ potentially facilitate the computation of radiation fields.

3. Results

3.1 *Dynamic representation of L_{cf}*

The vertical velocity in the mid-troposphere (w_{500}) has been shown to be a representative indicator of tropical convection and cloud radiative forcing (Ichikawa et al., 2012). The relationship between $L_{\rm cf}$ and w_{500} is assessed in this subsection. As the overlap of clouds with very large or very small cloud fractions is of secondary importance for $C_{\rm tot}$ and radiation calculations, grids with maximum layer cloud fractions > 0.9 or < 0.1 are discarded.

Figure 4 shows the distributions of $L_{\rm cf}$ and w_{500} for

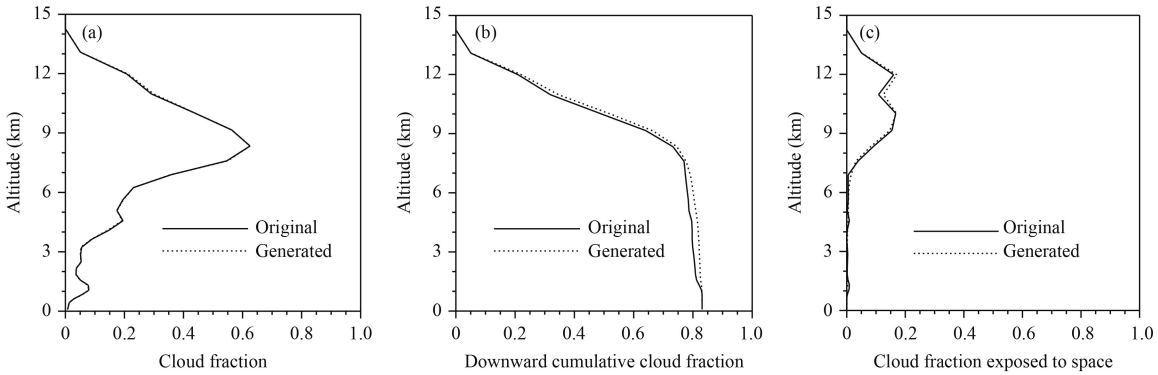

Fig. 3. Comparison of cloud features in a selected domain for the original CRM cloud field and that generated based on GenO with the true value of $L_{\rm cf}$. (a) Cloud fraction at different altitudes, (b) downward cumulative cloud fraction, and (c) cloud fraction exposed to space at different altitudes.

each model day. Domains with a large and positive w_{500} (e.g., the western Pacific and South America) mostly have a large value of L_{cf} (typically 4–7 km and up to 10 km in extreme cases). By contrast, in domains with a small or negative w_{500}, L_{cf} is mostly about or below 2 km. Figure 5 shows the pattern correlation between the geographical distributions of L_{cf} and w_{500} for each snapshot. The pattern correlation stays at a moderate, but notable and constant level (from 0.61 to 0.66), implying a physically close association between L_{cf} and w_{500}.

Based on pattern similarity and the clear difference between areas of ascent ($w_{500} > 0$) and descent ($w_{500} < 0$), the relationship between L_{cf} and w_{500} will be explored separately for areas of ascent and descent.

Figure 6 shows the statistics for L_{cf} and w_{500} and their relationships in the ascending areas. A total of 4926 samples were used to derive these statistics. The gray lines in Fig. 6a show the median and the first and third quartiles of L_{cf} for each bin of L_{cf}. These lines clearly show a positive relationship between L_{cf} and w_{500} for areas of ascent: when $w_{500} < 0.02$ m s^{-1}, the most frequent occurrence of L_{cf} is around 2 km; as w_{500} increases

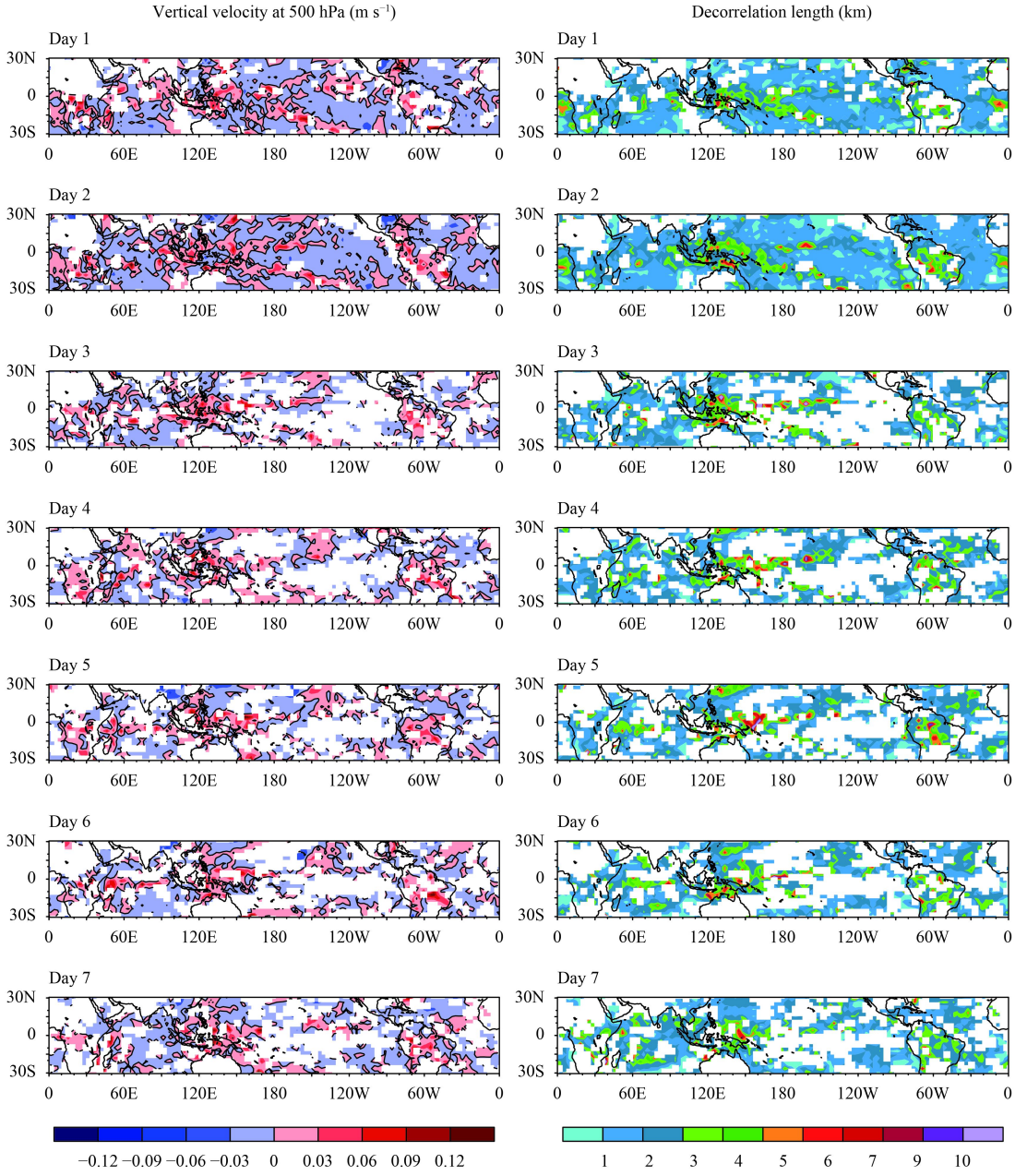

Fig. 4. Distributions of w_{500} (left-hand panels) and L_{cf} (right-hand panels) in the tropics for each model day. Masked grids are those with maximum cloud fraction in the vertical direction of > 0.9 or < 0.1 and were thus eliminated from the analysis.

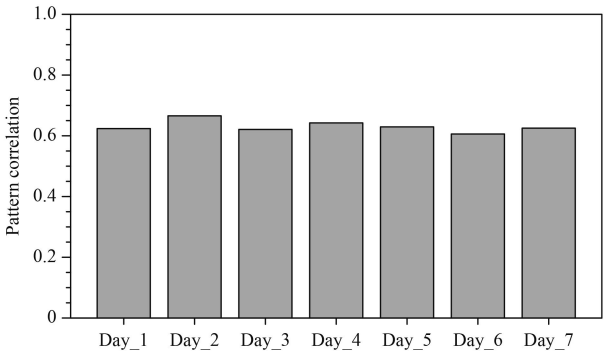

Fig. 5. Pattern correlation between L_{cf} and w_{500} for each snapshot shown in Fig. 4.

to 0.08 m s^{-1}, the corresponding value of L_{cf} increases to as much as 6–8 km, although the occurrence probability of w_{500} > 0.08 m s^{-1} is very small (Fig. 6b). Linear regression is conducted (as shown by the black solid line and the regression equation in Fig. 6a) for L_{cf} as a function of w_{500}. The regression line captures very well the relationship illustrated by the yellow shaded area in Fig. 6a. The 95% confidence interval (blue dotted lines) and 95% prediction interval (red dashed lines) for this regression are also shown in Fig. 6a. The small 95% confidence interval (the mean of L_{cf} is 95% likely to fall into this interval for a given value of w_{500}) suggests that the linear regression is an excellent representation of the average relationship between L_{cf} and w_{500}; however, it should also be noted that the dispersion of the L_{cf} and w_{500} relationship is relatively large, as indicated by the 95% prediction interval (an individual L_{cf} for a given w_{500} falls into this interval with probability of 95%). The large dispersion of the L_{cf} and w_{500} relationship may stem primarily from the effect of other meteorological conditions on cloud overlap, which cannot be captured by a simple linear regression. Nevertheless, these results demonstrate that, in the statistical sense, L_{cf} and w_{500} are linearly related in the ascending regions of the tropics. The analysis in the following sections shows that addressing this statistical relationship will benefit the calculation of the cloud fraction and radiation fields.

The same analysis for areas of descent shows that L_{cf} changes very little with w_{500} (data not shown) and that a value of 2 km is a good representation for these areas regardless of the specific w_{500}. Consequently, L_{cf} can be approximated in the region 30°S–30°N depending on w_{500} as:

$$L_{cf} = \begin{cases} 56.054 \times w_{500} + 1.951, & \text{for } w_{500} \geqslant 0.0, \\ 2.0, & \text{for } w_{500} < 0.0. \end{cases} \quad (3)$$

It should be noted that although GenO is independent of the vertical resolution, Eq. (3) may be affected by the vertical resolution of the NICAM data. Thus we should be cautious when applying Eq. (3) in a model with a notably different vertical resolution from that of NICAM, especially in the troposphere.

3.2 *Evaluation in terms of cloud fraction*

The better representation of L_{cf} is primarily expected to be capable of generating a realistic C_{tot} for given cloud fraction profiles. We evaluate here the generated C_{tot} by using the L_{cf} parameterized from Eq. (3) (denoted as

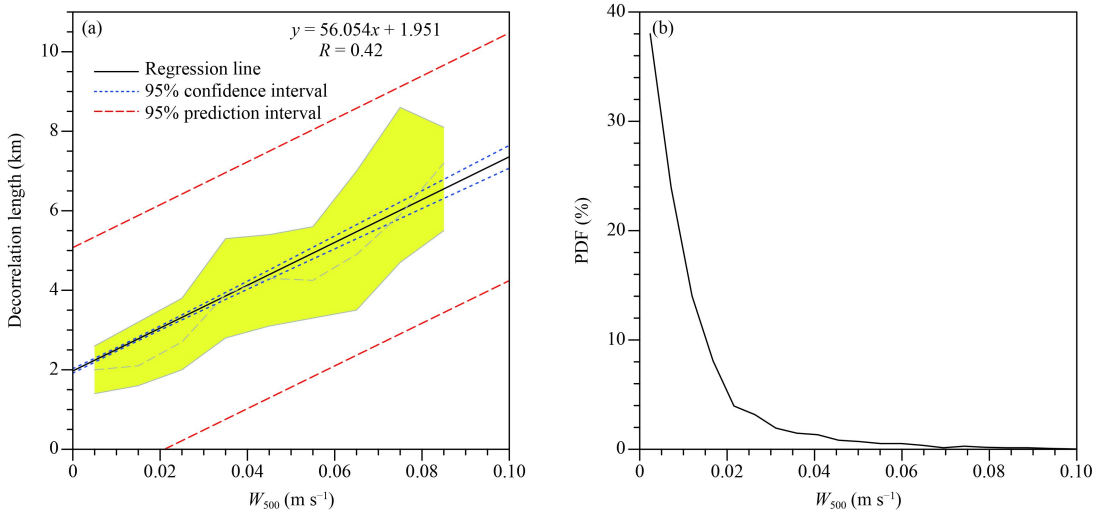

Fig. 6. Statistics of L_{cf} and w_{500} constructed for the whole 7-day period. (a) The median (gray dashed line) and first and third quartiles (gray solid lines) of L_{cf} for each w_{500} bin (bin width 0.01 m s^{-1}) and the linear regression of L_{cf} as a function of w_{500} (black solid line) (the linear regression equation and correlation coefficient are also shown). The yellow shaded area is the interquartile range of L_{cf}; the blue dotted line and red dashed line are the 95% confidence interval and 95% prediction interval of the regression, respectively. (b) Probability distribution function of w_{500}.

PARA). Two other cloud overlap treatments are also included to compare with PARA: the traditional MRO assumption, which has been widely used not only in GCMs (Räisänen, 1998; Collins, 2001), but also in model assessment tools such as the CFMIP Observation Simulator Package (Bodas-Salcedo et al., 2011); and the simplified GenO using a constant L_{cf} (2 km) (denoted as G2KM), which applies the framework of GenO, but with a constant L_{cf} suggested as a global mean value (Barker, 2008). These cloud overlap treatments are used to generate sub-grid cloud fields from the cloud fraction profiles of the CRM and the values of C_{tot} of the generated fields are then compared with those of the original CRM fields.

Figure 7 shows the 7-day mean biases of C_{tot} generated from the three cloud overlap representations relative to the reference value. It can be seen that the widely used MRO assumption remarkably underestimates C_{tot} in most regions. This is because there are few clear layers to separate the cloud layers in the vertical columns and therefore there is a maximum overlap of clouds in most cases. This demonstrates one drawback of the MRO technique: it depends greatly on the vertical resolution of the host model and is therefore usually non-equivalent among models.

The use of GenO significantly reduces the negative biases compared with the MRO assumption, even when a constant L_{cf} of 2 km is used (Fig. 7b). However, G2KM leads to notable C_{tot} biases in the ITCZ, especially in the western Pacific and Amazon regions, where clouds are generally more vertically organized because of systematic large-scale upward motion. When the dynamic representation of L_{cf} for regions of ascent is used, the cloud fraction errors in the ITCZ are remarkably reduced (Fig. 7c).

3.3 *Evaluation in terms of radiation effects*

Radiation calculations are performed for the generated cloud fields and the original CRM cloud fields in the evaluation using the BCC–RAD correlated-k distribution radiation model (Zhang et al., 2003, 2006a, b), which has been implemented in the GCM of the Beijing Climate Center (BCC_AGCM2.0.1) (Zhang et al., 2014). For both the generated and original cloud fields, the cloud water/ice content in each GCM grid is obtained as a grid mean value to eliminate the effect of the horizontal distributions of cloud water/ice. Because only the cloud and dynamic output from NICAM are stored (due to the large amount of data), we apply in the radiation calculation the atmospheric pressures, temperatures, and gas concentrations from the tropical atmosphere of the US Air Force Geophysics Laboratory atmospheric models (Anderson et al., 1986) and the broadband surface albedos for the ocean (0.08, Jin et al., 2004) and solid surfaces (0.28, Liang, 2001), respectively.

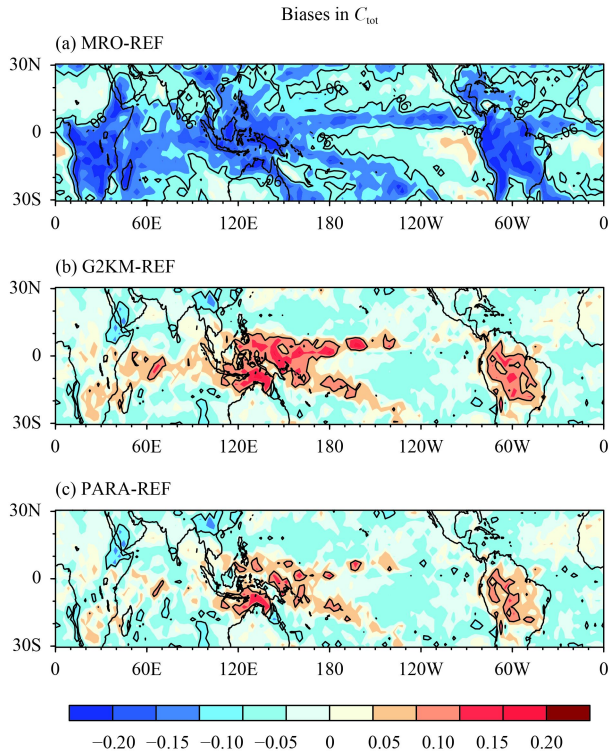

Fig. 7. Biases of generated C_{tot} using (a) the MRO assumption, (b) GenO with universal L_{cf} = 2 km (G2KM), and (c) GenO with dynamic representation of L_{cf} (PARA) relative to the true C_{tot} from the CRM (REF). Contour lines are shown for ±0.06.

Figure 8 shows the biases in the generated net longwave (LWTOA) and shortwave (SWTOA) radiative fluxes at the top of the atmosphere relative to the CRM results. The largest radiation biases occur in the ITCZ, where the largest C_{tot} biases are also seen. The MRO assumption shows significant negative biases for LWTOA and positive biases for SWTOA (mostly > 10 and > 25 W m^{-2}, respectively) (Figs. 8a, b) due to the underestimation of C_{tot}. Figures 8c and 8d show that the use of GenO with a constant L_{cf} of 2 km reduces the biases in subtropical regions, but also introduces notable biases in the ITCZ with opposite signs to the biases of the MRO assumption. The dynamic representation of L_{cf} largely reduces the negative biases in the ITCZ (Figs. 8e, f), with considerably fewer regions having absolute biases > 10 and > 25 W m^{-2} for LWTOA and SWTOA, respectively.

Figure 9 shows the biases in the net longwave (LWSFC) and shortwave (SWSFC) radiative fluxes at the surface. By comparing Fig. 9 with Fig. 8, it is seen that the main features of the biases at the surface are similar to those at the TOA, except that G2KM and PARA have much smaller (larger) biases in LWSFC over (outside) the ITCZ. PARA has the smallest errors among the three

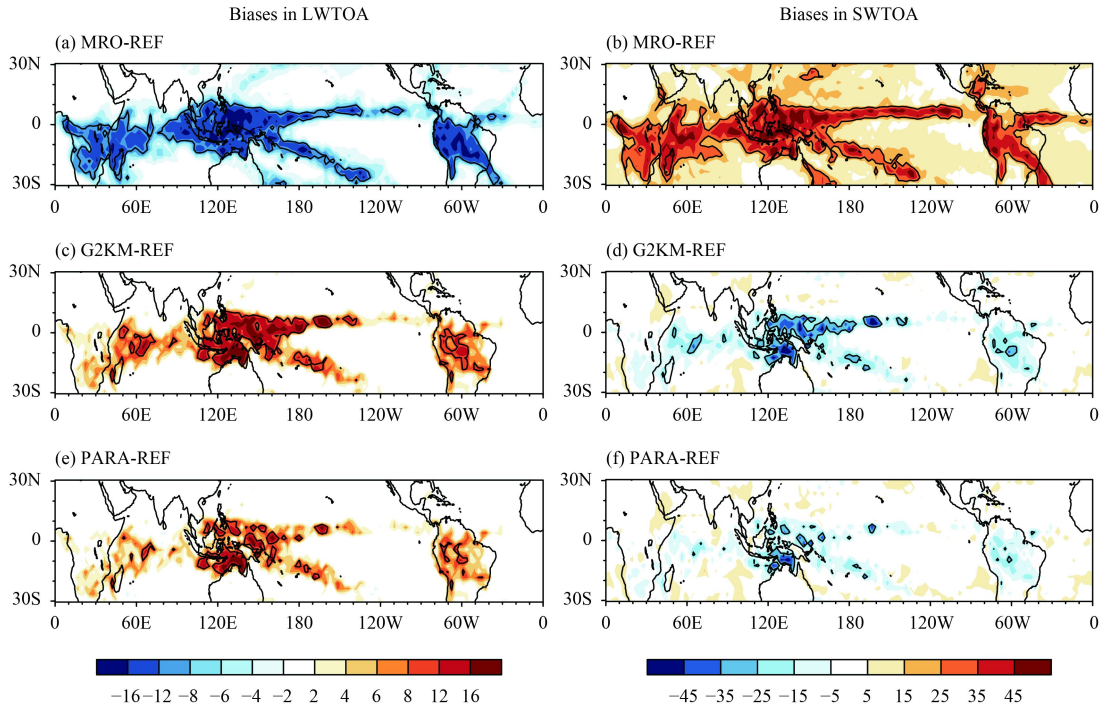

Fig. 8. Biases of generated LWTOA (left-hand panels) and SWTOA (right-hand panels) using (a, b) the MRO assumption, (c, d) GenO with L_{cf} = 2 km universally, and (e, f) GenO with dynamic representation of L_{cf}, relative to those calculated directly from the CRM fields. The downward direction is defined as positive. The contour lines for ±10 and ±25 W m^{-2} are shown for LWTOA and SWTOA, respectively.

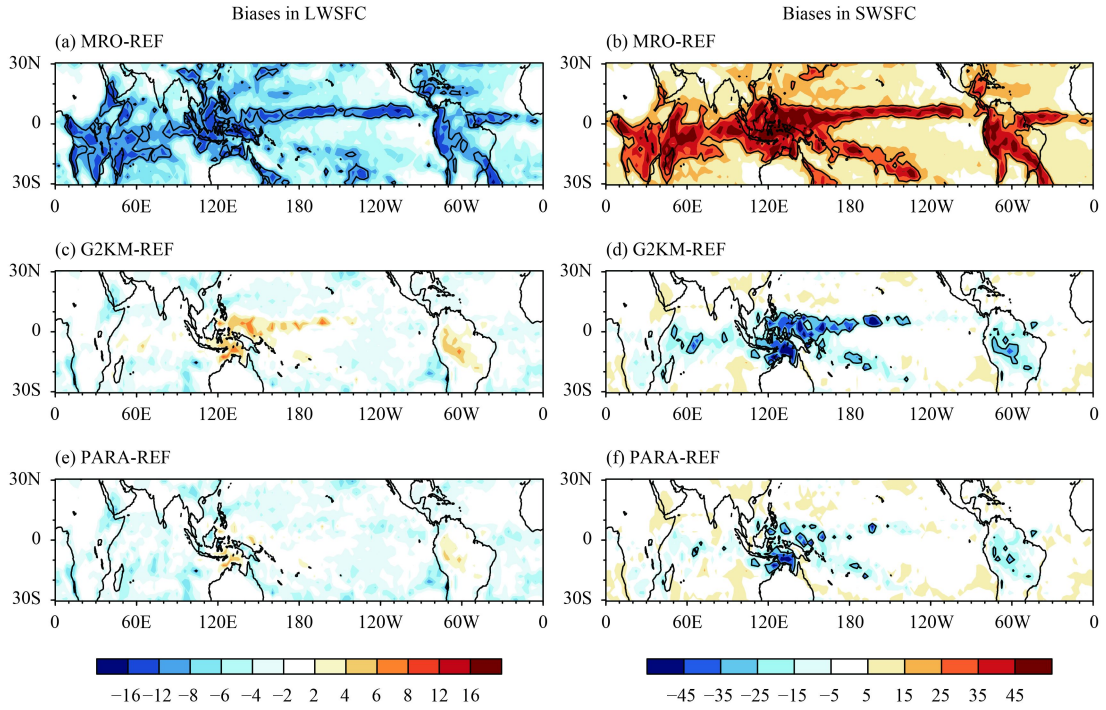

Fig. 9. As in Fig. 8, but for (a, c, e) LWSFC and (b, d, f) SWSFC.

treatments of cloud overlap over the ITCZ for both LWSFC and SWSFC. It is therefore evident that the dynamic representation of L_{cf} yields the best spatial patterns of the radiation fields.

Figures 10 and 11 are scatter diagrams comparing the generated and reference radiation fields at the TOA and surface, respectively. Systematically negative biases in LWTOA and positive biases in SWTOA are shown for

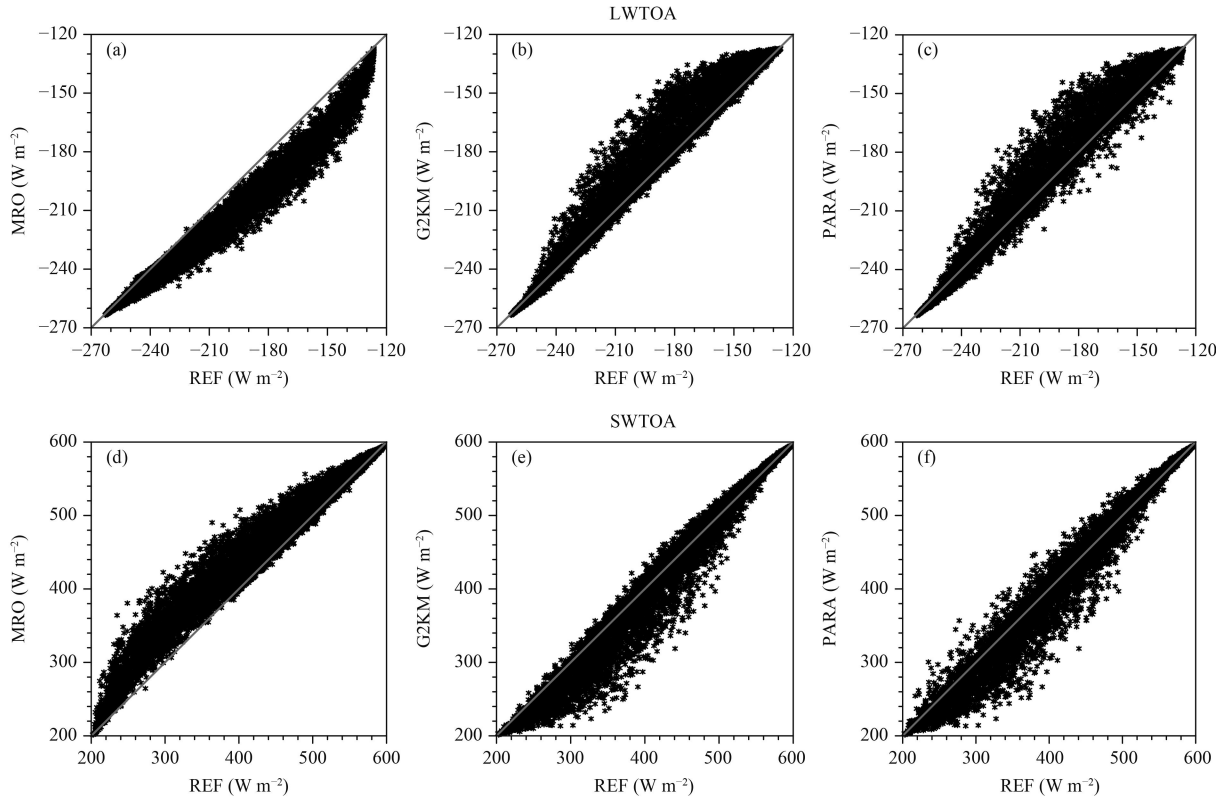

Fig. 10. Comparisons between LWTOA and SWTOA calculated from generated cloud fields with different cloud overlap treatments (MRO, G2KM, and PARA) and the values calculated directly from the CRM fields (REF) for the tropical areas.

the MRO assumption (Figs. 10a, d) and the opposite for G2KM (Figs. 10b, e). PARA shows little systematic bias in LWTOA and SWTOA—that is, the points are distributed more symmetrically around the reference lines (Figs. 10c, f). Similar features are also shown at the surface (Fig. 11), except that G2KM and PARA resemble each other for the LWSFC (Figs. 11b, c), consistent with their similarity in Fig. 9.

Figure 12 shows the tropical-averaged radiation biases for all areas (solid fill) and areas of ascent only (hatched fill). As expected, the MRO assumption shows the largest errors relative to the reference, especially for the shortwave fluxes (about 16 W m^{-2} at both the TOA and the surface). G2KM performs much better than the MRO assumption, with absolute errors of approximately 2 W m^{-2} for LWTOA and SWTOA. PARA reduces the errors more significantly, especially for shortwave fluxes. The error in LWSFC of PARA is more negative than that of G2KM (Fig. 12c); this is because PARA reduces the positive errors in the ITCZ (as shown in Fig. 9) that compensate for negative errors in other regions. It should be stressed that, for most of these variables, PARA reduces the all-area mean errors as effectively as it does in the areas of ascent only, implying that unrealistic cloud overlap treatment in areas of ascent is a major source of radiation error in tropical areas. Considering that these areas typically have large radiation biases in GCM simulations (Lauer and Hamilton, 2013), the introduction of PARA-like overlap treatment could possibly reduce the uncertainty in tropical radiation calculations.

The treatment of vertical cloud overlap also influences the radiative heating rate in the atmosphere, a property important for atmospheric stability and circulation. Figure 13 compares the effects of different overlap treatments on the ascending area mean longwave (LWHTR) and shortwave (SWHTR) heating rates. The LWHTRs of different overlap treatments are similar to each other in the middle to higher troposphere, but near the surface the MRO assumption shows remarkable longwave cooling (Fig. 13b) and G2KM and PARA show overestimated longwave heating. This is probably due to the underestimated (overestimated) cloud fraction of the MRO assumption (G2KM and PARA) over these regions (as shown in Fig. 7). For the SWHTR, the MRO assumption underestimates heating around altitudes of 2 and 10 km, whereas G2KM overestimates heating around 10 km height and underestimates heating in the lower troposphere. PARA has a similar SWHTR to G2KM, but the bias in the upper troposphere is remarkably reduced and the bias in the lower troposphere is also reduced to some

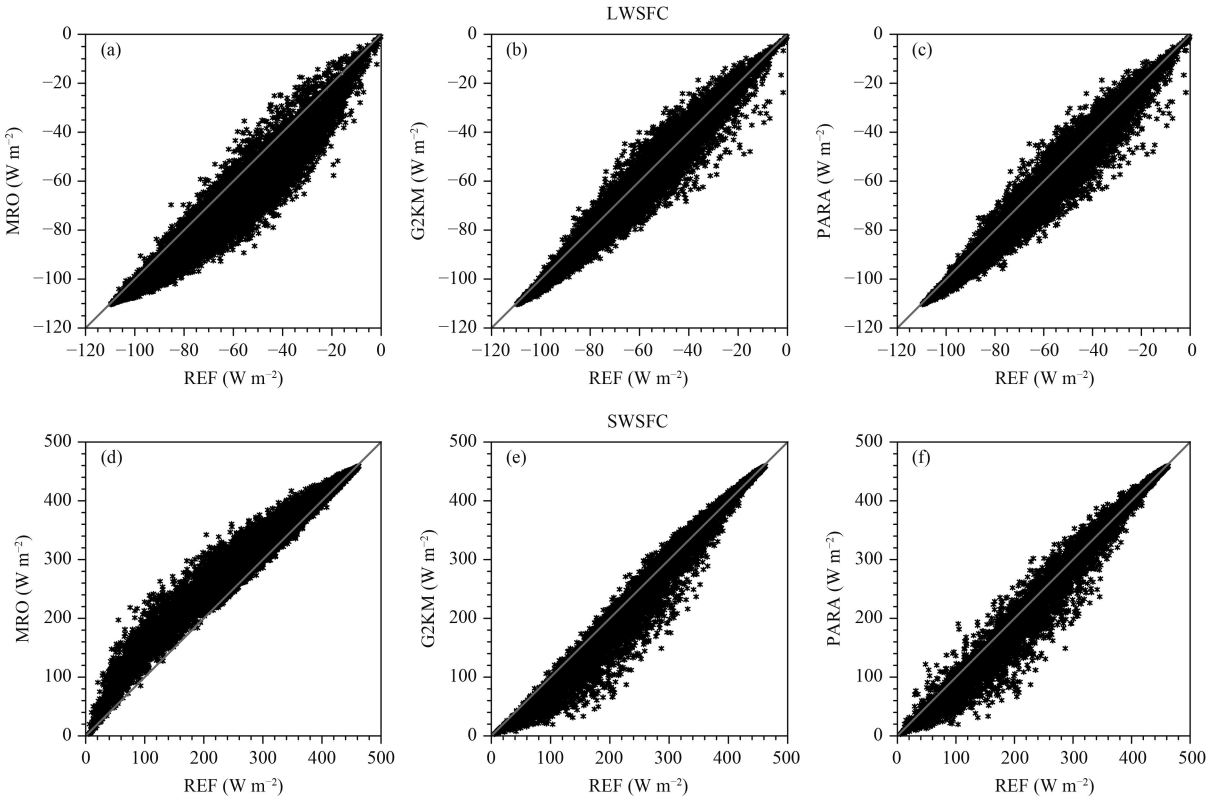

Fig. 11. As in Fig. 10, but for (a, b, c) LWSFC and (d, e, f) SWSFC.

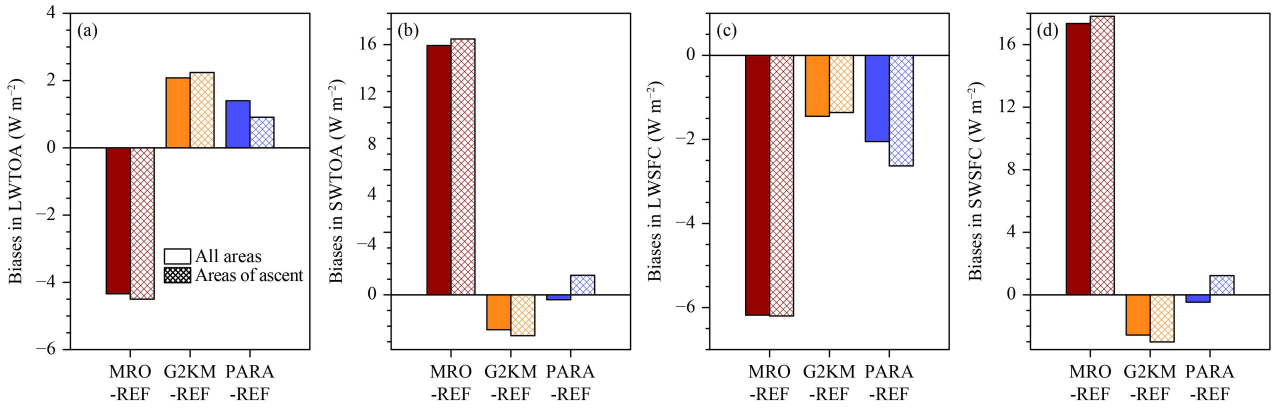

Fig. 12. Tropical mean biases in (a) LWTOA, (b) SWTOA, (c) LWSFC, and (d) SWSFC for generated clouds fields with different cloud overlap treatments (MRO, G2KM, and PARA) compared with those for the CRM fields (REF) over all areas (solid fill) and areas of ascent only (hatched fill).

extent. These changes in the radiative heating rates caused by applying PARA, when coupled with a circulation model, will exert an influence on atmospheric stability in the vertical direction and consequently change the dynamic circulation. These aspects will be explored in future studies.

4. Discussion and conclusions

The treatment of cloud overlap plays a crucial part in radiation calculations in GCMs. However, it is difficult to achieve a unified description of this highly variable (both spatially and temporally) property of clouds. By using the simulation of a CRM isolated to the tropical region, a statistical relationship between cloud overlap and convective strength was found and a dynamic representation of L_{cf} (which determines the extent of cloud overlap) was established. A simple linear regression of L_{cf} as a function of vertical velocity in the mid-troposphere is capable of partly capturing the cloud overlap dynamic

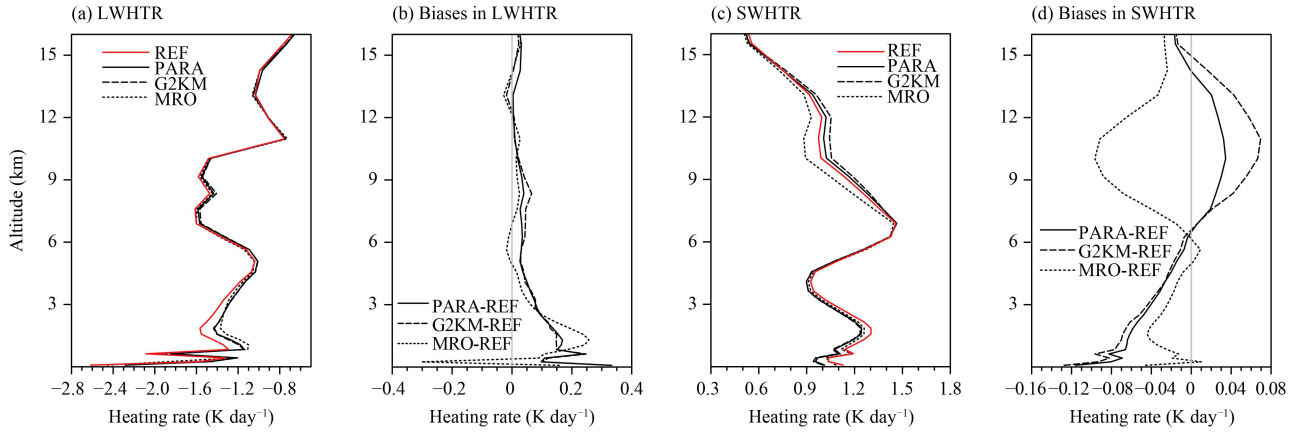

Fig. 13. (a) Longwave and (c) shortwave heating rates for the three cloud overlap treatments (MRO, G2KM, and PARA) and REF over the tropical ascending area and the differences between the three overlap treatments and REF (b and d, respectively).

connection and thus remarkably reduces biases in the cloud fraction and radiation fields in tropical convective regions. These regions are where major cloud fraction and radiation biases exist and therefore a reduction in these biases would make a significant contribution to the reduction of the overall bias in the tropics.

In spite of the improvement in cloud fraction and radiation fields by implementing the convection-dependent overlap treatment, the results rely on the fidelity of the intrinsic physical and dynamic properties of the CRM. Cloud overlap characteristics also depend on other meteorological conditions in addition to convection, such as wind shear and atmospheric instability (Naud et al., 2008; Di Giuseppe and Tompkins, 2015), even in the tropical deep convection region. Thus the method derived here should not be regarded as a perfect deterministic relationship between cloud overlap and convection, but an empirical, statistical approximation of the contribution of convection to cloud overlap. Other meteorological conditions are virtually ignored in the overlap treatment in this study. The treatment of cloud overlap in extratropical areas was not addressed in this work because the overlap of clouds in such areas relates to large-scale meteorological conditions in a more complex manner than in the tropics. Another aspect of sub-grid cloud structures, i.e., the horizontally inhomogeneous distribution of cloud water, is also highly important in radiation calculations (Barker et al., 1996; Wu and Liang, 2005a); this aspect was excluded in the overlap treatment of this study.

The results of this study do, however, provide modelers with a simple and effective approach to more realistically address cloud overlap in tropical regions. This approach acts as another, although not perfect, constraint of cloud–radiation interactions, an aspect of GCMs that contributes greatly to uncertainties in simulations. The form of the L_{cf}–convection relationship is open to further improvement and the application of this method to extended CRM and observational datasets (e.g., datasets from the multi-sensor A-Train constellation) will provide essential evidence of the L_{cf}–convection relationship from the points of view of both simulation and observation, and produce more robust treatments of L_{cf} in future studies.

REFERENCES

Anderson, G. P., S. A. Clough, F. X. Kneizys, et al., 1986: AFGL atmospheric constituent profiles (0.120 km). AFGL Tech. Rep., AFGL-TR-86-0110, Bedford, MA, Air Force Geophys. Lab., 1–43.

Barker, H. W., 2008: Representing cloud overlap with an effective decorrelation length: An assessment using CloudSat and CALIPSO data. *J. Geophys. Res.*, **113**, D24205, doi: 10.1029/2008JD010391.

Barker, H. W., and P. Räisänen, 2005: Radiative sensitivities for cloud structural properties that are unresolved by conventional GCMs. *Quart. J. Roy. Meteor. Soc.*, **131** , 3103–3122, doi: 10.1256/qj.04.174.

Barker, H. W., B. A. Wiellicki, and L. Parker, 1996: A parameterization for computing grid-averaged solar fluxes for inhomogeneous marine boundary layer clouds. Part II: Validation using satellite data. *J. Atmos. Sci.*, **53**, 2304–2316, doi: 10.1175/1520-0469(1996)053<2304:APFCGA>2.0.CO;2.

Barker, H. W., G. L. Stephens, P. Partain, et al., 2003: Assessing 1D atmospheric solar radiative transfer models: Interpretation and handling of unresolved clouds. *J. Climate*, **16**, 2676–2699, doi: 10.1175/1520-0442(2003)016<2676:ADASRT>2.0.CO;2.

Bergman, J. W., and P. J. Rasch, 2002: Parameterizing vertically coherent cloud distributions. *J. Atmos. Sci.*, **59** , 2165–2182, doi: 10.1175/1520-0469(2002)059<2165:PVCCD>2.0.CO;2.

Bodas-Salcedo, A., M. J. Webb, S. Bony, et al., 2011: COSP: Satellite simulation software for model assessment. *Bull. Am.*

Meteor. Soc., **92**, 1023–1043, doi: 10.1175/2011BAMS2856.1.

Bony, S., K.-M. Lau, and Y. C. Sud, 1997: Sea surface temperature and large-scale circulation influences on tropical greenhouse effect and cloud radiative forcing. *J. Climate*, **10**, 2055–2077, doi: 10.1175/1520-0442(1997)010<2055:SSTALS>2.0.CO;2.

Bony, S., B. Stevens, D. M. W. Frierson, et al., 2015: Clouds, circulation and climate sensitivity. *Nature Geosci.*, **8**, 261–268, doi: 10.1038/ngeo2398.

Collins, W. D., 2001: Parameterization of generalized cloud overlap for radiative calculations in general circulation models. *J. Atmos. Sci.*, **58** , 3224–3242, doi: 10.1175/1520-0469(2001)058<3224:POGCOF>2.0.CO;2.

Di Giuseppe, F., 2005: Sensitivity of one-dimensional radiative biases to vertical cloud-structure assumptions: Validation with aircraft data. *Quart. J. Roy. Meteor. Soc.*, **131** , 1655–1676, doi: 10.1256/qj.03.129.

Di Giuseppe, F., and A. M. Tompkins, 2015: Generalizing cloud overlap treatment to include the effect of wind shear. *J. Atmos. Sci.*, **72**, 2865–2876, doi: 10.1175/JAS-D-14-0277.1.

GEWEX Cloud System Science Team, 1993: The GEWEX cloud system study (GCSS). *Bull. Amer. Meteor. Soc.*, **74**, 387–400, doi: 10.1175/1520-0477(1993)074<0387:TGCSS>2.0.CO;2.

Grabowski, W. W., 1998: Toward cloud resolving modeling of large-scale tropical circulations: A simple cloud microphysics parameterization. *J. Atmos. Sci.*, **55**, 3283–3298, doi: 10.1175/1520-0469(1998)055<3283:TCRMOL>2.0.CO;2.

Hogan, R. J., and A. J. Illingworth, 2000: Deriving cloud overlap statistics from radar. *Quart. J. Roy. Meteor. Soc.*, **126**, 2903–2909, doi: 10.1002/qj.49712656914.

Ichikawa, H., H. Masunaga, Y. Tsushima, et al., 2012: Reproducibility by climate models of cloud radiative forcing associated with tropical convection. *J. Climate*, **25**, 1247–1262, doi: 10.1175/JCLI-D-11-00114.1.

Inoue, T., M. Satoh, H. Miura, et al., 2008: Characteristics of cloud size of deep convection simulated by a global cloud resolving model over the western tropical Pacific. *J. Meteor. Soc. Japan*, **86A**, 1–15, doi: 10.2151/jmsj.86A.1.

Inoue, T., M. Satoh, Y. Hagihara, et al., 2010: Comparison of high-level clouds represented in a global cloud system-resolving model with CALIPSO/CloudSat and geostationary satellite observations. *J. Geophys. Res.*, **115** , D00H22, doi: 10.1029/2009JD012371.

Jin, Z. H., T. P. Charlock, W. L. Jr. Smith, et al., 2004: A parameterization of ocean surface albedo. *Geophys. Res. Lett.*, **31**, L22301, doi: 10.1029/2004GL021180.

Jing, X. W., H. Zhang, J. Peng, et al., 2016: Cloud overlapping parameter obtained from CloudSat/CALIPSO dataset and its application in AGCM with McICA scheme. *Atmos. Res.*, **170**, 52–65, doi: 10.1016/j.atmosres.2015.11.007.

Kato, S., S. Sun-Mack, M. F. Miller, et al., 2010: Relationships among cloud occurrence frequency, overlap, and effective thickness derived from CALIPSO and CloudSat merged cloud vertical profiles. *J. Geophys. Res.*, **115**, D00H28, doi: 10.1029/2009JD012277.

Lauer, A., and K. Hamilton, 2013: Simulating clouds with global climate models: A comparison of CMIP5 results with CMIP3 and satellite data. *J. Climate*, **26** , 3823–3845, doi: 10.1175/JCLI-D-12-00451.1.

Li, J., J. Huang, K. Stamnes, et al., 2015: A global survey of cloud overlap based on CALIPSO and CloudSat measurements. *Atmos. Chem. Phys.*, **15** , 519–536, doi: 10.5194/acp-15-519-2015.

Li, J. D., Y. M. Liu, and G. X. Wu, 2009: Cloud radiative forcing in Asian monsoon region simulated by IPCC AR4 AMIP models. *Adv. Atmos. Sci.*, **26**, 923–939, doi: 10.1007/s00376-009-8111-x.

Liang, S. L., 2001: Narrowband to broadband conversions of land surface albedo. I: Algorithms. *Remote Sens. Environ.*, **76**, 213–238, doi: 10.1016/S0034-4257(00)00205-4.

Liang, X. Z., and W. C. Wang, 1997: Cloud overlap effects on general circulation model climate simulations. *J. Geophys. Res.*, **102**, 11039–11047, doi: 10.1029/97JD00630.

Liang, X. Z., and X. Q. Wu, 2005: Evaluation of a GCM subgrid cloud-radiation interaction parameterization using cloud-resolving model simulations. *Geophys. Res. Lett.*, **32**, L06801, doi: 10.1029/2004GL022301.

Mace, G. G., and S. Benson-Troth, 2002: Cloud-layer overlap characteristics derived from long-term cloud radar data. *J. Climate*, **15** , 2505–2515, doi: 10.1175/1520-0442(2002)015<2505:CLOCDF>2.0.CO;2.

Marchand, R., G. G. Mace, T. Ackerman, et al., 2008: Hydrometeor detection using *CloudSat* —An earth-orbiting 94-GHz cloud radar. *J. Atmos. Oceanic Technol.*, **25** , 519–533, doi: 10.1175/2007JTECHA1006.1.

Masunaga, H., M. Satoh, and H. Miura, 2008: A joint satellite and global cloud-resolving model analysis of a Madden–Julian Oscillation event: Model diagnosis.. *J. Geophys. Res.*, **113**, D17210, doi: 10.1029/2008JD009986.

Miura, H., M. Satoh, T. Nasuno, et al., 2007: A Madden–Julian oscillation event realistically simulated by a global cloud-resolving model. *Science*, **318** , 1763–1765, doi: 10.1126/science.1148443.

Morcrette, J. J., and Y. Fouquart, 1986: The overlapping of cloud layers in shortwave radiation parameterizations. *J. Atmos. Sci.*, **43** , 321–328, doi: 10.1175/1520-0469(1986)043<0321:TOOCLI>2.0.CO;2.

Nakanishi, M., and H. Niino, 2006: An improved Mellor-Yamada level-3 model: Its numerical stability and application to a regional prediction of advection fog. *Bound.-Layer Meteor.*, **119**, 397–407, doi: 10.1007/s10546-005-9030-8.

Naud, C. M., A. Del Genio, G. G. Mace, et al., 2008: Impact of dynamics and atmospheric state on cloud vertical overlap. *J. Climate*, **21**, 1758–1770, doi: 10.1175/2007JCLI1828.1.

Oreopoulos, L., and M. Khairoutdinov, 2003: Overlap properties of clouds generated by a cloud-resolving model. *J. Geophys. Res.*, **108**, 4479, doi: 10.1029/2002JD003329.

Oreopoulos, L., D. Lee, Y. C. Sud, et al., 2012: Radiative impacts of cloud heterogeneity and overlap in an atmospheric general circulation model. *Atmos. Chem. Phys.*, **12** , 9097–9111, doi: 10.5194/acp-12-9097-2012.

Peng, J., H. Zhang, and X. Y. Shen, 2013: Analysis of vertical structure of clouds in East Asia with CloudSat data. *Chinese J. Atmos. Sci.*, **37** , 91–100, doi: 10.3878/j.issn.1006-9895.2012.11188. (in Chinese)

Räisänen, P., 1998: Effective longwave cloud fraction and maximum-random overlap of clouds: A problem and a solution. *Mon. Wea. Rev.*, **126** , 3336–3340, doi: 10.1175/1520-0493(1998)

126<3336:ELCFAM>2.0.CO;2.

Räisänen, P., H. W. Barker, M. F. Khairoutdinov, et al., 2004: Stochastic generation of subgrid-scale cloudy columns for large-scale models. *Quart. J. Roy. Meteor. Soc.*, **130**, 2047–2067, doi: 10.1256/qj.03.99.

Randall, D., M. Khairoutdinov, A. Arakawa, et al., 2003: Breaking the cloud parameterization deadlock. *Bull. Amer. Meteor. Soc.*, **84**, 1547–1564, doi: 10.1175/BAMS-84-11-1547.

Sato, T., H. Miura, M. Satoh, et al., 2009: Diurnal cycle of precipitation in the tropics simulated in a global cloud-resolving model. *J. Climate*, **22** , 4809–4826, doi: 10.1175/2009JCLI2890.1.

Satoh, M., T. Matsuno, H. Tomita, et al., 2008: Nonhydrostatic icosahedral atmospheric model (NICAM) for global cloud resolving simulations. *J. Comput. Phys.*, **227** , 3486–3514, doi: 10.1016/j.jcp.2007.02.006.

Satoh, M., T. Inoue, and H. Miura, 2010: Evaluations of cloud properties of global and local cloud system resolving models using CALIPSO and CloudSat simulators. *J. Geophys. Res.*, **115**, D00H14, doi: 10.1029/2009JD012247.

Satoh, M., H. Tomita, H. Yashiro, et al., 2014: The non-hydrostatic icosahedral atmospheric model: Description and development. *Progress in Earth and Planetary Science*, **1** , 18, doi: 10.1186/s40645-014-0018-1.

Shonk, J. K. P., R. J. Hogan, J. M. Edwards, et al., 2010: Effect of improving representation of horizontal and vertical cloud structure on the Earth's global radiation budget. Part I: Review and parametrization. *Quart. J. Roy. Meteor. Soc.*, **136**, 1191–1204, doi: 10.1002/qj.647.

Stephens, G. L., 2005: Cloud feedbacks in the climate system: A critical review. *J. Climate*, **18** , 237–273, doi: 10.1175/JCLI-3243.1.

Stephens, G. L., D. G. Vane, S. Tanelli, et al., 2008: CloudSat mission: Performance and early science after the first year of operation. *J. Geophys. Res.*, **113** , D00A18, doi: 10.1029/2008JD009982.

Tian, L., and J. A. Curry, 1989: Cloud overlap statistics. *J. Geophys. Res.*, **94**, 9925–9935, doi: 10.1029/JD094iD07p09925.

Tomita, H., and M. Satoh, 2004: A new dynamical framework of nonhydrostatic global model using the icosahedral grid. *Fluid Dyn. Res.*, **34**, 357–400, doi: 10.1016/j.fluiddyn.2004.03.003.

Tompkins, A. M., and F. Di Giuseppe, 2015: An interpretation of cloud overlap statistics. *J. Atmos. Sci.*, **72** , 2877–2889, doi: 10.1175/JAS-D-14-0278.1.

Wang, X. C., Y. M. Liu, and Q. Bao, 2016: Impacts of cloud overlap assumptions on radiative budgets and heating fields in convective regions. *Atmos. Res.*, **167** , 89–99, doi: 10.1016/j.atmosres.2015.07.017.

Wu, X. Q., and X.-Z. Liang, 2005a: Radiative effects of cloud horizontal inhomogeneity and vertical overlap identified from a monthlong cloud-resolving model simulation. *J. Atmos. Sci.*, **62**, 4105–4112, doi: 10.1175/JAS3565.1.

Wu, X. Q., and X.-Z. Liang, 2005b: Effect of subgrid cloud-radiation interaction on climate simulations. *Geophys. Res. Lett.*, **32**, L24806, doi: 10.1029/2005GL024432.

Wu, X. Q., and X. F. Li, 2008: A review of cloud-resolving model studies of convective processes. *Adv. Atmos. Sci.*, **25**, 202–212, doi: 10.1007/s00376-008-0202-6.

Zhang, F., X.-Z. Liang, J. N. Li, et al., 2013: Dominant roles of subgrid-scale cloud structures in model diversity of cloud radiative effects. *J. Geophys. Res. Atmos.*, **118**, 7733–7749, doi: 10.1002/jgrd.50604.

Zhang, H., and X. W. Jing, 2010: Effect of cloud overlap assumptions in climate models on modeled earth–atmosphere radiative fields. *Chinese J. Atmos. Sci.*, **34**, 520–532, doi: 10.3878/j.issn.1006-9895.2010.03.06. (in Chinese)

Zhang, H., and X. W. Jing, 2016: Advances in studies of cloud overlap and its radiative transfer in climate models. *J. Meteor. Res.*, **30**, 156–168, doi: 10.1007/s13351-016-5164-5.

Zhang, H., T. Nakajima, G. Y. Shi, et al., 2003: An optimal approach to overlapping bands with correlated k distribution method and its application to radiative calculations. *J. Geophys. Res.*, **108**, 4641, doi: 10.1029/2002JD003358.

Zhang, H., G. Y. Shi, T. Nakajima, et al., 2006a: The effects of the choice of the k-interval number on radiative calculations. *J. Quant. Spectro. Rad. Trans.*, **98**, 31–43, doi: 10.1016/j.jqsrt.2005.05.090.

Zhang, H., T. Suzuki, T. Nakajima, et al., 2006b: Effects of band division on radiative calculations. *Opt. Eng.*, **45**, 016002, doi: 10.1117/1.2160521.

Zhang, H., J. Peng, X. W. Jing, et al., 2013: The features of cloud overlapping in eastern Asia and their effect on cloud radiative forcing. *Sci. China Earth Sci.*, **56**, 737–747, doi: 10.1007/s11430-012-4489-x.

Zhang, H., X. Jing, and J. Li, 2014: Application and evaluation of a new radiation code under McICA scheme in BCC_AGCM2.0.1. *Geosci. Model Dev.*, **7**, 737–754, doi: 10.5194/gmd-7-737-2014.

Tech & Copy Editor: Hongqun ZHANG

Weather and Climate Extremes xxx (xxxx) xxx–xxx

Contents lists available at ScienceDirect

Weather and Climate Extremes

journal homepage: www.elsevier.com/locate/wace

Climatological characteristics and long-term variation of rainy season and torrential rain over DPR Korea

Kum-Chol Om[a,b], Guoyu Ren[a,c,*], Shuanglin Li[a], Kang-Chol O.[a,d]

[a] Department of Atmospheric Science, School of Environmental Studies, China University of Geosciences, 388 Lumo Road, Wuhan, 430074, China
[b] Department of Meteorology, Faculty of Global Environmental Science, Kim Il Sung University, Daesong District, Pyongyang, North Korea
[c] Laboratory for Climate Studies, National Climate Center, China Meteorological Administration, Beijing, 100081, China
[d] Department of Meteorology, Faculty of Agricultural Science, Wonsan Agriculture University, Wonsan, l Science, Wonsan, AgKangwon Province, North Korea

ARTICLE INFO

Keywords:
Onset
Retreat
Rainy season
Jangma/Changma
Torrential rain
El Niño/La Niña
Orographic effect
Climate change

ABSTRACT

Understanding extreme precipitation variability in Democratic People's Republic of Korea (DPRK) is important for monitoring and predicting droughts and floods, which is crucial for agricultural activities and water resources management in the country. Observed daily (hourly) precipitation data from 181 stations in DPR Korea during 1960–2007 (1969–2007) was used to analyze the onset, retreat and length of the rainy season (called Jangma in DPRK, Changma in South Korea, and Meiyu in the Yangtze basin of China), and to examine the climatological features and long-term change of torrential rains. The results showed: (1) The Onset, Retreat and Length of Rainy Season (O-RS, R-RS and L-RS) experienced an obvious inter annual and decadal variability, and they also had a good correlation with El Niño (La Niña), with some differences from those found in South Korea; (2) The linear trend of O-RS was 1.9day/decade during 1960–2007, indicating a gradually delayed O-RS, and the R-RS were getting earlier with a rate of −2.7day/decade, leading to a shortening L-RS at a rate of −4.7day/decade; (3) Regional differences of the numbers of Torrential Rain (TR) were obvious, which was related to the orographic effect, with the south and northwest of the study area registering the most frequent TR events; We also found that the frequency, intensity and amount of annual TR events generally increased during the last 4 decades; (4) The annual number of TR events with amount of precipitation more than 100 mm/6 h increased from 4.2 times (1974–1983) to 7.4 times (2003–2012), and the annual number of extremely intense TR more than 200mm/12 h also increased from 0.6 times to 1.2 times over the same two time periods.

1. Introduction

The Democratic People's Republic of Korea (DPRK) is located in Northeast Asia. It is affected largely by the East Asian monsoon in summer and Torrential Rain (TR) events are highly concentrated in the Rainy Season (RS). Because of the significant inter annual variability of the East Asian monsoon and the relationship between the intensity of summer monsoon and rainfall amount during RS, droughts and floods frequently occur over DPRK, resulting in the frequent occurrences of disastrous floods and agricultural failure.

Onset and Retreat of Rainy Season (O-RS and R-RS) are important parameters in the agricultural calendar in countries. Each country defined O-RS by different criteria because influence of synoptic systems on beginning, end and duration of RS is different in various regions. In addition, many regions over the world are expected to suffer from substantial climate modifications as a result of global warming (IPCC, 2013). These changes will affect the O-RS and R-RS which has become more irregular over the years for the past decades (Salack et al., 2011), making it difficult for farmers to plan for the seed planting, adjust to the length of the growing season and determine the harvesting period (Mugalavai et al., 2008). The immediate consequences would be the decrease of agricultural production and an increasing risk of hunger in developing countries. Therefore, the determinations of the O-RS and R-RS dates in various regions in particular in the developing countries of Asian Monsoon zone have become a focus for research.

O-RS is the beginning time of a rainy period of a year, when rainfall has become adequate for crop and vegetation growth; R-RS means the end of the rainy period, and Length of Rainy Season (L-RS) is the time period between the O-RS and the R-RS. In order to define quantitatively RS in mainland China, researchers used the climatologically pentad rainfall amounts, or the percentage (%) of total annual rainfall amounts, to determine the onset dates, ending dates, peak rainfall dates

* Corresponding author. Department of Atmospheric Science, School of Environmental Studies, China University of Geosciences, 388 Lumo Road, Wuhan, 430074, China.
E-mail address: guoyoo@cma.gov.cn (G. Ren).

https://doi.org/10.1016/j.wace.2018.09.003
Received 11 July 2017; Received in revised form 6 September 2018; Accepted 6 September 2018
2212-0947/ © 2018 The Authors. Published by Elsevier B.V. This is an open access article under the CC BY license (http://creativecommons.org/licenses/BY/4.0/).

Please cite this article as: Om, K.-C., Weather and Climate Extremes, https://doi.org/10.1016/j.wace.2018.09.003

and lengths of the major RSs, (e.g. Wang and Ding, 2008; Zhan and Ren, 2016). Overall, the methods for determining O-RS and R-RS dates were classified into several categories according to Odekunle (2006) and others: (1) Intertropical Discontinuity (ITD)-rainfall model, (2) rainfall-evapotranspiration relation model, (3) percentage cumulative average rainfall model, based on rainfall data alone (Adejuwon, 2006), (4) wind shear model, (5) the Available Water Resources Index (AWRI), (6) model by using the daily rainfall data (Reiser and Kutiel, 2008), and (7) model based on outgoing longwave radiation (OLR) data (Garcia and Kayano, 2009).

Reiser and Kutiel (2008) conducted an in-depth research on definition of RS using accumulative precipitation from and till a day on which 10% and 90% of annual total precipitation is accumulated for determining O-RS and R-RS. Garcia and Kayano (2009) used the anti-symmetric feature in relation to equator outgoing long wave radiation (AOLR) to define rainy season and suggested a method of determining the O-RS date based on scale of spatial averages of the AOLR. Guenang and Mkankam (2012) studied O-RS, R-RS and L-RS by using observed precipitation in Cameroon during 1962–1993 and compared results to control simulations by four IPCC AR4 AOGCMs. Qiang and Yang (2008) made demarcations on O-RS and R-RS, and they found that the averaged O-RS date is in pentad 19 (the 1st pentad of April), while the R-RS is in pentad 34 (the 4th pentad of June) in south China. Laux et al. (2008) applied Fuzzy-logic method and daily precipitation data to determine the regional onset date of RS using linear discriminant analysis and linear regression analysis. These methods are potentially useful to judge whether the current onset of RS has already begun.

Researchers explained characteristics of RS and TR events over East Asia. Lau and Yang (1997) defined the RS standard as an average daily precipitation of 6.0 mm a day, but other researches showed that analysis of pentad rainfall is adequate to define beginning of RS (Hachigonta et al., 2007; Thomas, 1993; Qiang et al., 2008; Wang et al., 2010). Zhan and Ren (2016) analyzed climatological characteristics and temporal variation of O-RS and R-RS over East Asia during 1951–2009. They defined the RS by a pentad rainfall standard, constructed the regional average temporal series by using the weighted-average method, and analyzed the latitude–pentad profile of RS in East Asia including the Korean Peninsula. The work showed that the rainy belt slowly moves northward from 33°N to 36°N on the Korean Peninsula and the most rapid propagation of the onset time occurs around 36th pentad (25–29 June) in eastern China, followed by that in the Korean Peninsula.

Yao et al. (2008) showed that the summer precipitation has declined over the past 30 years in the Russian Far East and the northern part of DPRK. Lu et al. (2001) analyzed O-RS and R-RS of the Korean Peninsula, and the results showed that later O-RS onset is associated with the significantly weakened Asian monsoon, the lower-level westerlies are weakened and the atmospheric convection is suppressed, and the surface temperature is higher due to more net solar radiation flux and less latent heat flux at the surface. Jiang et al. (2008) indicated that, because of the East Asian summer monsoon begins later, summer precipitation decrease after the late 1970s in East China except for the Yangtze River basin. During the same period, Korean summer monsoon rainfall peak has delayed as well (Lee et al., 2010), though the second peak has advanced (Ho et al., 2003). Ding and Chan (2005) showed that the moisture transport coming from the Indochina Peninsula and the South China Sea plays an important role in supplying moisture for precipitation in East Asia after the onset of the Asian summer monsoon. Fang et al. (2017) analyzed the changing contribution rate of heavy rainfall to the rainy season precipitation in Northeast China, and they found that, although the contribution rate of heavy rainfall to the total rainy season rainfall showed a decrease during 1961–1979, it exhibited no significant trend during 1981–2013.

Recently, Ohba et al. (2015), Ma and Zhou (2015), Awan et al. (2015), Kim et al. (2016) and Liu and Wu (2016) also examined the long-term variation in rainy season and intense precipitation in East Asia Monsoon region over the past decades, and they all showed a complicated spatial and temporal pattern of summer extreme precipitation changes in the region.

Most studies on O-RS and R-RS in a few of countries or regions were performed on a limited number of stations or on relatively short time periods because of the lack of complete data series. Some researchers made detailed analyses of RS and intense precipitation individually for East Asian countries, but made no effort to investigate in details the long-term change in RS and TR over DPRK.

This paper made a first attempt to analyze O-RS, R-RS and L-RS over DPRK, and the synoptic circulation background at the beginning of RS. It also examined the climatological characteristics and long-term variation of TR over the country. The study will be help in deepening our understanding of the summer monsoon precipitation variability of the East Asia, and in coping with meteorological disaster risks under the changing climate condition.

2. Data, study area and methods

2.1. Observational data and definitions

Four observational data sets were used in the study: daily rainfall data from 181 stations during 1960–2007 (48 years), weather maps for RS in DPRK during 1960–2007 (44 years), El Niño (La Niña) records from TCC (Tokyo Climate Center), and daily precipitation and hourly maximum precipitation records for period 1969–2012. Station precipitation, typhoon data, TR data and weather maps were all provided by the HMBK (Hydro-Meteorological Bureau of DPRK). The TCC El Niño (La Niña) data are a little different from those by the Climate Prediction Center (CPC) of the United States National Ocean and Atmospheric Administration (NOAA) due to the different definitions of the NINO regions, with the TCC definition applying NINO 3 (5 N - 5 S and 150 W - 90 W) SST anomalies for El Niño (La Niña) events. All the precipitation data have been quality-controlled by the HMBK; however, in-homogeneities of the daily precipitation data probably caused by station relocations and instrumentations have not been examined and adjusted. Compared to those in other developing countries of Asia, the data inhomogeneities related to the station relocations may have not so serious in DPRK due to the relatively slow urbanization processes in the country. TR indicates much amount and heavy intensity of rainfall for a specified period. In DPRK, rainfall with an amount larger than 30 mm (50 mm, 100 mm and 200 mm) for an hour (3 h, 6 h and 12 h) was defined as TR. This definition is different from those in other countries. For example, China Meteorological Administration (CMA) defined the heavy rain event with precipitation amount larger than 16 mm (30 mm and 50 mm) for an hour (12 h and 24 h) as TR or rainstorm. The accumulated precipitation in RS events is almost equivalent to about 60 percent of amount of annual total precipitation in DPRK, and TR frequency during Jul–Aug accounts for 95 percent of total number of annual TR. In RS precipitation, the share of TR varies from region to region, with some regions like the Chongchon River basin reaching more than 80%. In South Korea, more than half of the annual precipitation occurs during summer, and more than 40% of the summer precipitation occurs during the Changma (Jangma) (Kripalani et al., 2002; Lu et al., 2001; Lu, 2002).

RS is regarded in DPRK as a sustained period of time when the rain frequently occurs within a year; In South Korea, however, RS is defined as “the rainy period with rain keeping falling for many days in summer” (Ryoo, 2001).

In this paper, O-RS is defined as the beginning time of RS when daily rainfall amount is over 50 mm for three continuous days, and it rains (rainfall > 0.1 mm/day) again within four days without clear weather. At the same time, the equivalent potential temperature at 850 hPa height keeps up more than 330 K over the area of more than two provinces of the country. If these conditions are met, RS in DPRK is considered to begin. Here, the two provinces are represented by two

ARTICLE IN PRESS

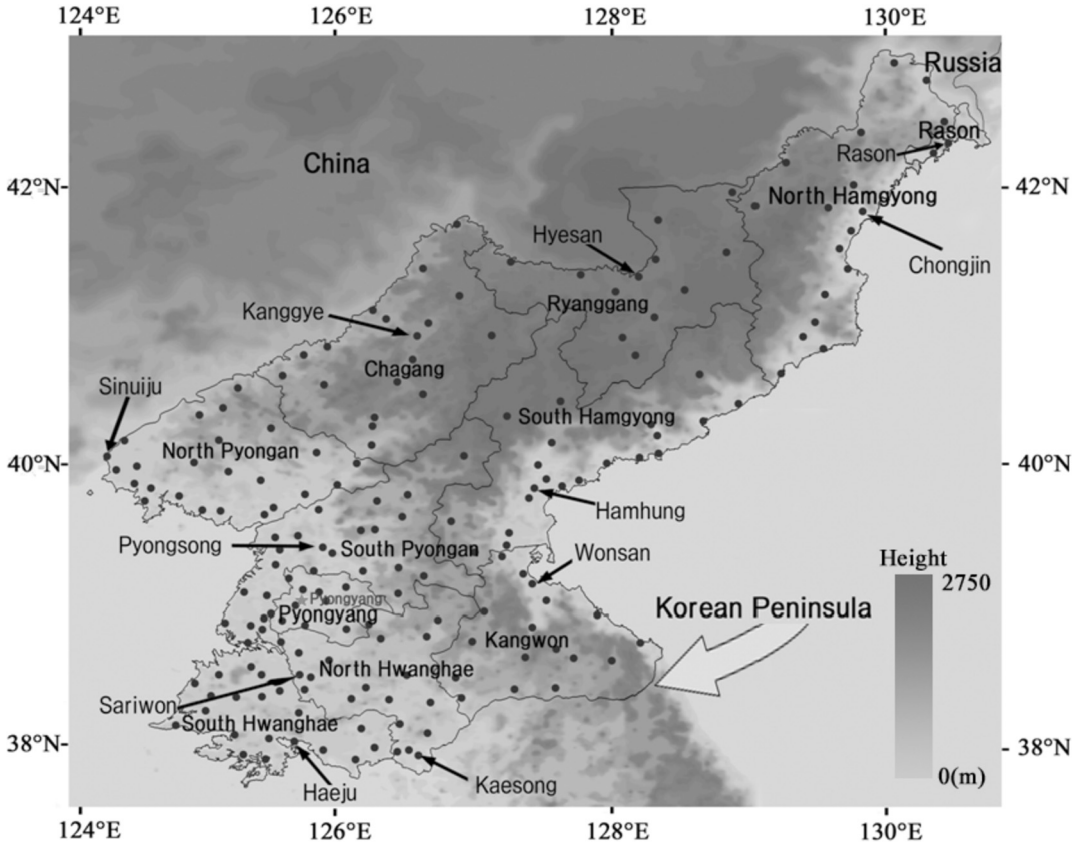

Fig. 1. Study area and the geographical locations of 181 surface observation stations in DPR Korea (37–43°N and 124–131°E). Boundaries between provinces are shown. The sites indicated by names and arrows are the eleven representative observational stations of the provinces.

respective typical stations which were chosen for use in PDRK weather operation (Fig. 1). R-RS, on the other hand, is defined as the end time of RS when daily rainfall more than 50 mm is no longer observed in the overall study area for three consecutive days, and the equivalent potential temperature at 850 hPa height is lower than 330 K over the area of more than two provinces. In this case, RS of DPRK is considered to be over. L-RS is the days from the O-RS to the R-RS.

2.2. Study area

The study domain, DPRK, is located in northern Korean Peninsula, between 37.7°N and 43°N and 124°E − 131°E (Fig. 1). It is encompassed by the Korean East and West Seas. Climate in the country is characterized by rainy and hot summer, and dry and cold winter, due to the influence of East Asian Monsoon. Wet and warm southerly airflows moves northward during summertime, bring moisture and heat to the study area.

The geographical location of the stations and terrain conditions of the study area are shown in Fig. 1. Most of the study area is mountainous, usually are characterized by a series of horn gates opening to the southwest and south, which benefiting occurrences of TR events (e.g. northern South Pyongan and southern North Pyongan). Representative stations highlighted in Fig. 1 are generally belonging to the provincial capitals or municipality cities, which have the best data quality and the longest records of observation. Though most of the rest stations also keep a very good precipitation record during the study period, some of them have missing values. The missing daily records, however, account for less than 2% of total observations, and will not have a significant impact on the analysis results.

The average distance between stations in the study area is less than 30 km. The densest distributions are seen in Pyongyang and South Pyongan, and the density of stations is the lowest in Ryanggang and North Hamgyong.

2.3. Circulation patterns of RS

The O-RS is characterized by a typically abnormal circulation fields. Due to the expansion of ridgeline of the West Pacific Subtropical High (WPSH), the warm and moist air flows from the Indian Ocean and the South China Sea to the Korean Peninsula and Japan through southern China and the Yangtze basin, forming a front in boundary with air from high latitude, which is called as “Jangma (DPRK)/Changma (South Korea) Front”. The summer RS in DPRK is generally consistent with “Jangma/Changma”.

To understand the circulation patterns for O-RS, we analyzed annual mean-500 hPa geopotential height in upper level and mean-850 hPa barometric distribution in low level for five days before the beginning time of Jangma/Changma or RS, respectively. All 5-day mean weather maps for 1960–2007 were used to analyze the circulation patterns. Circulation types of the five days before the beginning of Jangma over DPRK were divided into two patterns. The first pattern begins with the condition that the WPSH moves northward and westward significantly. These cases accounts for 80 percent of the total (Fig. 2a). This pattern is characterized by the strengthened northwestward expansion of the upper-layer WPSH, a large cyclone area over the western Bay of Bengal and the Indo-China Peninsula, a blocking high over the west of Ural and the Far East of Russia, and a long-wave trough line in the central Siberia and cold air coming down continuously southward from the west of the Baikal Lake (E 104°–109°, N 51°–55°). On the other hand, along the western boundary of the strengthened WPSH, warm and moist marine tropical air mass flows toward northeast, forming Jangma-Front and the summer RS begins over study area. At the surface, a cyclone strongly develops in North China and the western Yellow Sea, forming a pressure distribution with east high-west low pattern.

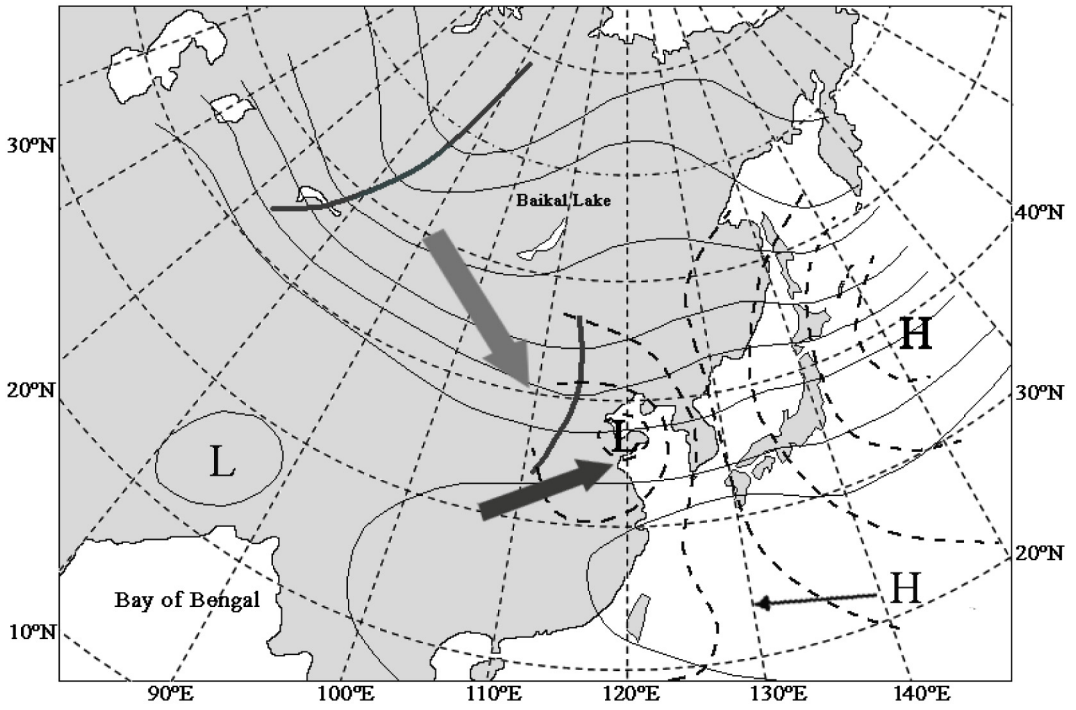

(a)

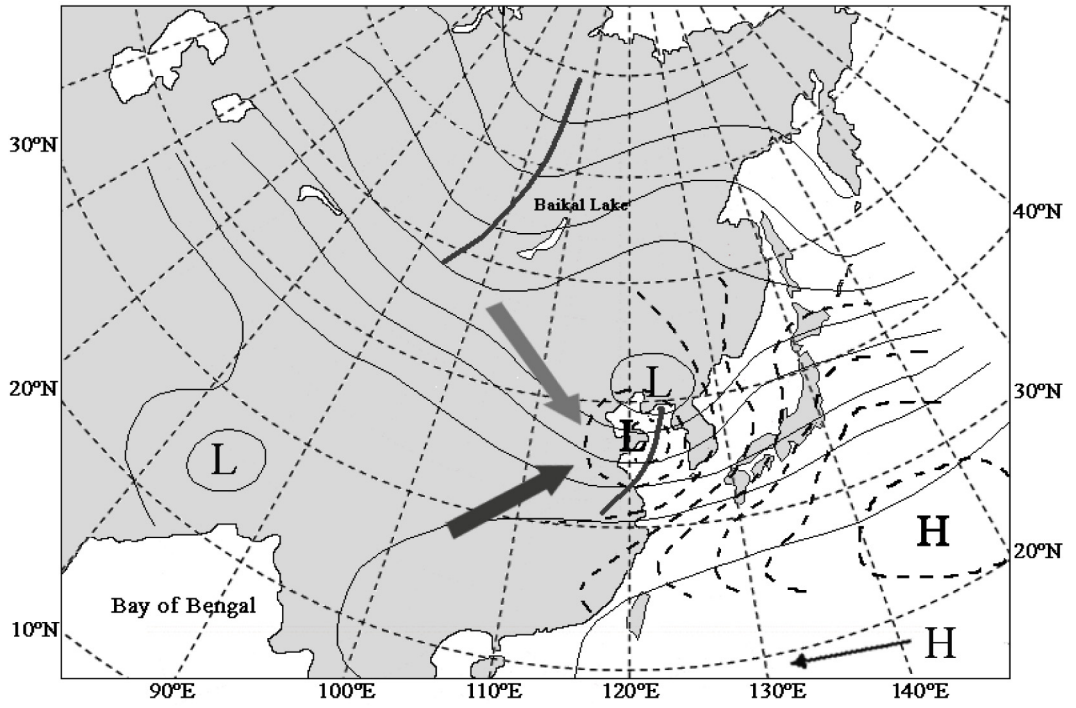

(b)

Fig. 2. Two circulation patterns for onset of rainy season (O-RS). a: first pattern, b: second pattern, solid line: 500 hPa geopotential height (unit: 8gpdkm), dash line: 850 hPa geopotential height (unit: 8gpdkm); thick and light grey arrow: cold air, thick and dark grey arrow: warm air, thin arrow: moving direction of the Western North Pacific High ridge.

The second pattern develops without the characters as mentioned above, and these account for 20 percent of the total cases (Fig. 2b). In this pattern, the WPSH is weaker than the first pattern, and it is located on south of 25°N with no closed center. It extends slightly northward compared to the first pattern, but expands to the west a little bit further. The local cyclone is located over the western Bay of Bengal and the Indo-China Peninsula, the blocking high over the west of the Ural leans to more eastward than the first pattern, and the long-wave trough is located over the west of the Baikal Lake. At the surface, the cyclone in North China strengthens relatively. In the second pattern, the further expansion of WPSH makes the northeastward movement of warm and humid airflow to be weaker, and the rainfall during RS in the study area is lower and L-RS is shorter than those in the first pattern.

Therefore, the synoptic characteristics at O-RS are an obvious movement of WPSH northward to the north of 25°N and westward to the west 150°E, with the ridgeline swing between 25°N and 27°N; at the same time, jet stream axis of high level over the longitude zone near DPRK moves to the north of 35°N-37°N.

With the same procedure, we also analyzed annual mean-500 hPa geopotential high in upper level and mean-850 hPa barometric distribution in low level for five days after the end of Jangma respectively, and identified the dominant patterns of the DPRK R-RS.

In the following sections of this paper, we analyzed the temporal variations of the RS indicators and TR events over the study area, including the decadal means and the long-term trends of the indicators, in addition to their climatological characteristics for the entire periods of observations available. Statistical significance of the trends of all climatic elements and indicators were tentatively examined using T-test method.

3. Results

3.1. Characteristics and variation of O-RS and R-RS

RS usually lasts from June to August in the study area. When the first rain of RS occurs, the Yangtze River cyclone usually lies over the north of central DPRK, and the Yellow River cyclone moves northeastward. In view of characteristics of air masses, the equatorial air mass is widely distributed over south of the Yangtze River and the subtropical air mass occupies up to 40°N. Table 1 shows the statistical values of RS during 1960–2007. Regarding the O-RS dates, it is 18th of June (1990) in the earliest case, 29th of July (2000) in the latest, and 5th of July in average. If it began within one week of the average date, then O-RS was considered as normal.

The mean R-RS is on 25th August, however, the earliest date (1972) is in early July and the latest one (1964) appears in the mid of September. 1972 witnesses the earliest retreat date on 6th July, and it is an extremely anomalous case. Usually, the retreat date occurs in the end of August or early September, though the Typhoon processes passing through East Asia including DPRK occasionally can delay the retreat date to early or even mid-September. If the RS began within June, it could be called an early RS; if it ended in September, it could be called a late RS. The longest L-RS occurred in 1966 and 1990, both reaching 76 days, and the two shortest L-RS were in 1972 (3 days) and in 1991 (16 days) (Fig. 3). The average L-RS is 54 days.

Table 1
Statistical values in O-RS and R-RS.

Statistical indicator	Value
Mean of O-RS	5 July
Mean of R-RS	25 August
Standard deviation of O-RS	8.89 d
Standard deviation of R-RS	13.06 d
Correlation coefficient between O-RS and L-RS	−0.60 (99.9%)
Correlation coefficient between R-RS and L-RS	0.84 (99.9%)

Years 1966 and 1990 are the cases of early O-RS. The ridgeline of WPSH is located on north of 25°N well before July. The circulation belongs to the first pattern of O-RS. In 1991, when a late O-RS was observed, WPSH hadn't developed into a closed center and it hadn't moved northward. The high stayed between 20°N and 25°N for almost 50 days. The O-RS in 1972 was normal, when the weakened WPSH hadn't had a closed center as well but it extended northwestward more than normal; however, WPSH retreated to the east of 150°E on July 6, leading to an unusual early end of RS. In the study, we considered these cases as the second pattern of air circulation.

Table 2 shows the decadal mean values of O-RS, R-RS and L-RS from 1960 to 2007. It is clear that the decadal mean of O-RS delays gradually, R-RS becomes earlier in some extent and the L-RS has an overall downward trend. Therefore, the characteristics of RS have changed obviously over DPRK during the past decades. The linear trend of O-RS was 1.9day/decade, indicating a tendency for the O-RS dates to be gradually delayed during the study period. On the contrary, R-RS dates are getting earlier with a decreasing rate of −2.7day/decade. As a result, L-RS is getting shorter with a trend −4.7day/decade. All the above trends are statistically significant at the 0.10 confidence level, but only the trend for L-RS is significant at the 0.05 confidence level.

3.2. TR events in RS

We analyzed the spatial and temporal characteristics of TR events, and their relations with different weather processes in the study periods. The most frequent weather processes accompanying TR events are cyclonic weather (~35% of the total TR events), followed by typhoon processes (~30%) and frontal weather (~22%), with the others only accounting for less than 13%.

3.2.1. Change in number of TR events

Annual mean number of TR events more than 100mm/6 h and more than 200mm/12 h for 181 stations over DPRK during 1969–2012 is shown in Fig. 4. The annual mean number of TR events less than 6 times accounts for a much proportion before 1993, and most of the years have more than 6 times after that year. Therefore, more frequent TR events occurred after 1993. Fig. 5 shows decadal mean of TR frequencies (R_{6h}≥100 mm, and R_{12h}≥200 mm) for the period 1974–2012. It can be seen that the annual mean of TR events (R_{6h}≥100 mm) is 6.2 times, and it increased from 4.2 times for 1974–1983 to 7.4 times for 2003–2012 (Fig. 5a and Table 3). Fig. 5b shows that the annual mean of TR (R_{12h}≥200 mm) is 0.9, and it also significantly increases since 1974, with 0.6 for the first decade to 1.2 for the last decade. Hence the extremely intense rainfall for R_{12h}≥200 mm almost doubles from the first decade to the last decade during the period 1974–2012. Linear trends of R_{6h}≥100 mm and R_{12h}≥200 mm are 0.67/decade and 0.2/decade, respectively, and the trends are all significant at the 0.05 confidence level.

The extremely TR event with precipitation above 300mm/18 h occurred only once (2012/07/30); and TR events with precipitation beyond 200mm/12 h and 100 mm/6 h occurred more frequently, reaching 38 times and 271 times respectively. The annual mean of TR events ranges from 0.1 (beyond 270mm/18 h) to 6.2 (beyond 100 mm/6 h). Monthly mean TR (R_{6h}≥100 mm and R_{12h}≥200 mm) frequencies and percentages during the study period are shown in Table 3. It is obvious that all TR events occurred during summertime (June to September), and they appeared most frequently in August especially for TR (R_{12h}≥200 mm) which amounts to 47.4% of total. Table 4 also shows that the months with high frequency of TR events, in descending order, are August, July, September and June, which is consistent with the fact that precipitation amount and rain frequencies are mostly concentrated in mid-summer of July and August.

Typhoon processes across East Asian region including the Korean Peninsula are the main reason why many TR occur more often in September than in June. In 2002, Typhoon Rusa produced a record

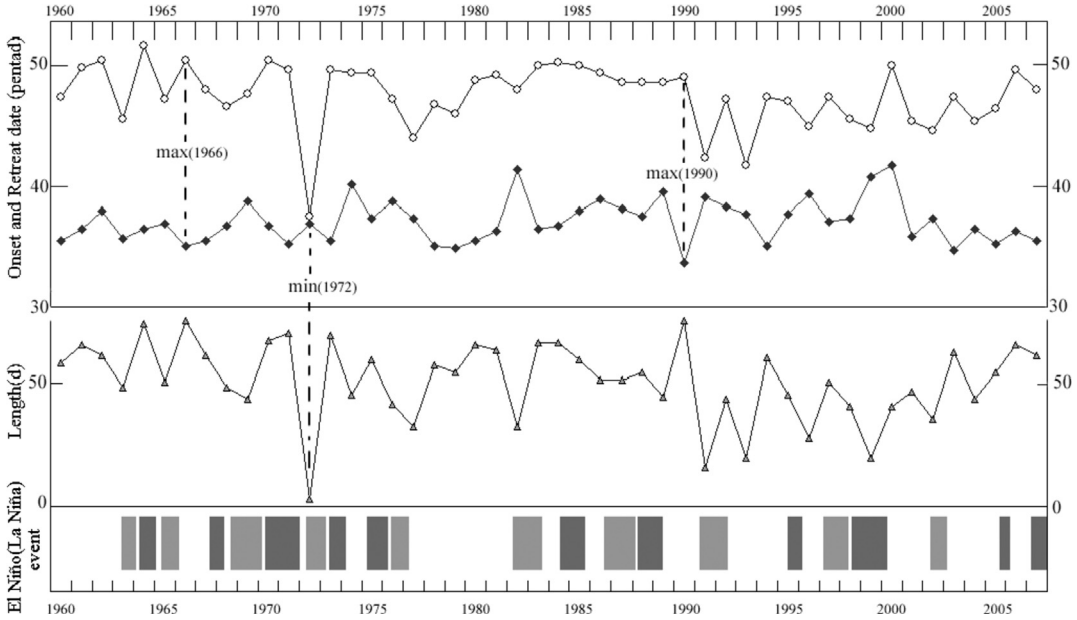

Fig. 3. Onset date, retreat date and the length of rainy season (O-RS, R-RS and L-RS) over the study area. Solid square: O-RS date; open circle: R-RS date; triangle: L-RS. Light grey: El Niño event, and dark grey: La Niña event, at the bottom.

Table 2
Decadal mean values of O-RS, R-RS and L-RS in the study area.

Decade	Onset date	Retreat date	Length (d)
1960–1969	7/02	8/30	59
1970–1979	7/05	8/23	49
1980–1989	7/06	9/03	59
1990–1999	7/07	8/20	44
2000–2007	7/07	8/23	47

rainfall (870.5mm/d) in Gangneung at the foot of the Taebaek Mountain range over South Korea; this was the maximum record of precipitation in the country (Lee and Choi, 2010). According to the analysis of pressure systems over the study area, the TR events of Jul–Aug are mostly related with the temperate cyclones and front, but those in the end of Aug and early Sept occur mainly due to influence of typhoons or tropical cyclones.

It is worth noting that TR frequencies have a low correlation with the O-RS, R-RS and L-RS. The shortest L-RS is in 1972, and TR (R_{6h}≥100 mm) occurred 6 times, and TR (R_{6h}≥100 mm) occurred 10 times during the longest L-RS of 1990. The TR occurrences are therefore irregular in some extent. The correlation between L-RS and TR (R_{6h}≥100 mm) frequency is the highest, but it reaches only 0.18, showing the possibility that the longer L-RS somewhat benefits the more frequent occurrence of the low-grade TR events.

3.2.2. Spatial difference of TR events

Fig. 6 shows that the frequent TR events and large TR amount are generally in the northwest or the mid-basin of the River Taeryong and the River Kuryong, including North Pyongan Province, and the southernmost parts of the study region. The most frequent occurrences of TR (R_{6h}≧100 mm) are in Pyonggang, Kosong, Kumkang, Taechon, Unsan, Kusong, Tokchon, Maengsan, Jangpung, Chorwon and Tongchang, and most frequent occurrences of TR (R_{12h}≧200 mm) are in Chorwon, Unsan, Tosan, Huichon and Kosong. The distribution of the several TR centers and their topographic conditions are shown in Fig. 6a.

DPRK belongs to monsoon climate, with the direction of summer prevailing flows being southwest and southeast. The three main rainfall centers with high frequent TR all lie to the windward slopes of mountain range for the summer southwesterly and southeasterly. Particularly, regions with most frequent TR are usually surrounded by high mountains on three sides, and other side is 'V-shaped' terrain just like a horn gate. Upper stream and midstream of the River Taeryong and the River Kuryong have a couple of such 'V-shaped' terrains. These rivers are tributaries of the River Chongchen, flowing through south of

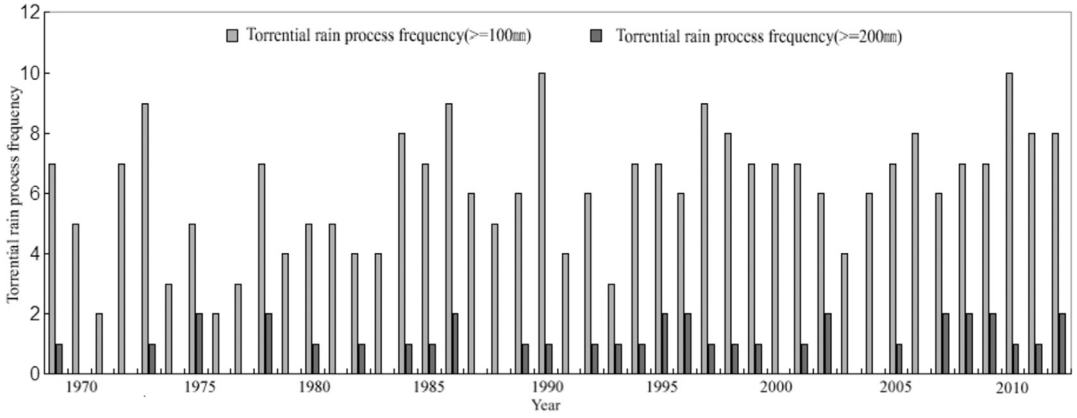

Fig. 4. Annual mean frequencies (occurrences) of torrential rain (TR) events (> =100 mm/6 h and ≥ 200mm/12 h) during 1969–2012 in the study area.

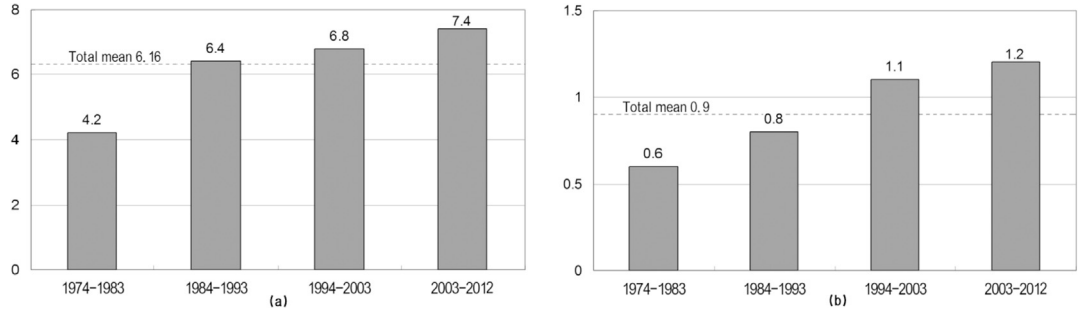

Fig. 5. Decadal mean numbers of occurrences of torrential rain (TR) events for the last 4 decades in the study area (a): R_{6h}≧100 mm, (b): R_{12h}≧200 mm.

Table 3
The number of different categories of TR events in DPR Korea during 1969–2012.

Temporal scale (hours)	Classification (mm)	Process number	Annual mean
6	R≧100	271	6.2
12	R≧200	38	0.9
18	R≧200	36	0.7
	R≧220	17	0.4
	R≧270	4	0.1
	R≧300	1	

Table 4
Monthly TR event frequencies and percentages in DPR Korea during 1969–2012.

Temporal scale	Classification (mm)	Jun	Jul	Aug	Sept	Total
6 h	R≧100	14	101	114	42	271
		5.2%	37.3%	42.1%	15.5%	100%
12 h	R≧200	2	12	18	6	38
		5.3%	31.6%	47.4%	15.8%	100%

TR frequent regions (Taechon, Unsan, Kusong and Tongchang) in North Pyongan Province, and the high-frequent TR regions lie to the southern slope of the Jekyuryeng Mountain range. The Tokchon and Maengsan regions also lie to the upper stream of the Taedong River, and the Pukdaebong and the Myohyangsan Mountain ranges seat respectively east and north of these regions, with southwest being opened horn gate terrain, benefiting occurrences of summer TR. Chorwon, Pyonggang, Kumkang and Kosong of Kangwon Province also became known as habitual TR regions, with the Ahobiryong Mountain range stretching to the west, the Chorryong Mountain range on east, and the southwest opened to the Ganghua Bay. In addition, TR events caused by typhoons occur more frequently in Kangwon region than those in other regions. In this case, WPSH often expands to southern DPRK, low level jet stream axis lies north of 35°N, and the moist and warm air flows can easily enter the study area, making TR events more frequently to occur.

4. Discussion

4.1. Differences between this study and that reported in South Korea

In many case, the long-term variations of O-RS and R-RS in DPRK are consistent with the previous studies for East Asian region (e.g. Kitoh and Uchiyama, 2006; Endo, 2011; Zhan and Ren, 2016). However, Choi et al. (2008) showed that R-RS in South Korea was delayed from early September to mid-September for 1973–2007, which is somewhat different from our result for the study area. The possible cause for the difference may mainly result from the different definitions of O-RS and R-RS. Ryoo (2001) analyzed the results of the prior studies on RS in South Korea and found that the definitions for RS are different among researchers. However, a unified definition does not exist. A

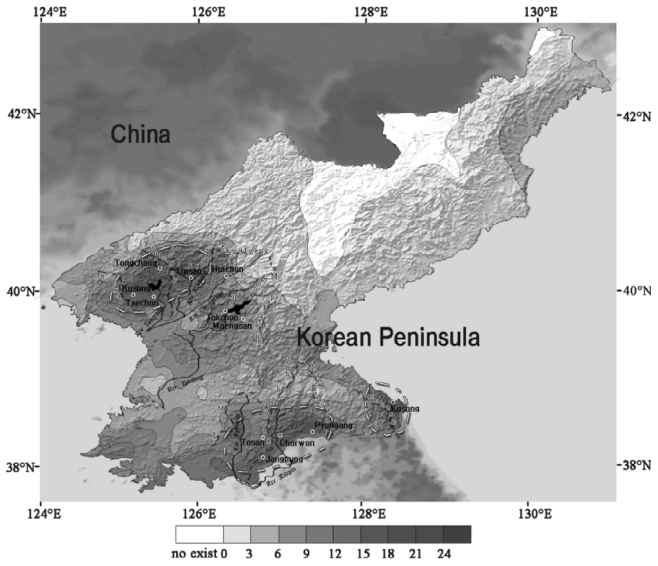

(a)

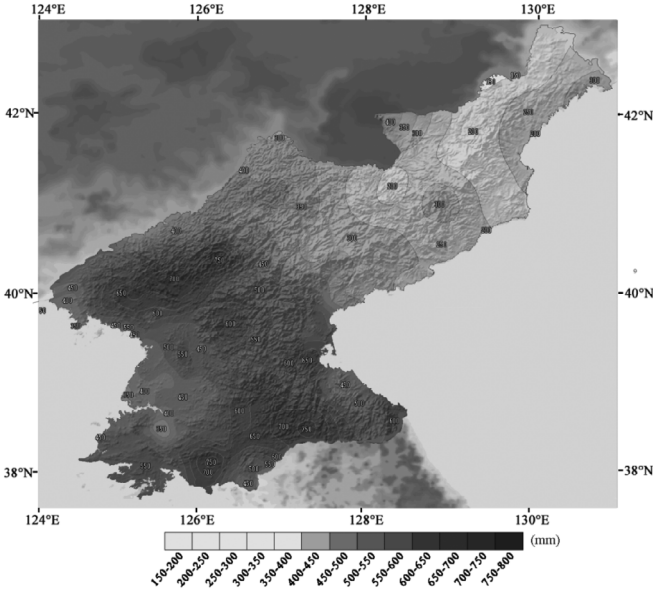

(b)

Fig. 6. High-frequency TR regions in major river basins (a), and annual mean frequencies (occurrences) of TR events and precipitation distribution (b), over DPR Korea for period 1969–2012. Solid line: river; dash line: watershed.

ARTICLE IN PRESS

representative definition of RS recommended by Korean Meteorological Administration (KMA) is as follow.

Onset date: At a specified region, (a) the duration of rainfall is more than 3 days, and (b) the quasi-stationary (Changma) front is located over the whole South Korea; Retreat date: the duration of non-precipitation exceeds three days and the quasi-stationary fronts leave northward.

Based on this and the one given in this paper, we found three main differences in the definitions and meanings of RS in the study area and South Korea.

(1) Regional classification: KMA announces O-RS and R-RS dates by region (Jeju, Mokpo and Seoul) (Ryoo, 2001). However, this study considers the first day of RS in any area as the onset date of the national RS, and the latest day as the retreat date. These are the most notable difference. Some researchers (e.g., Lee and Kim, 1983) from South Korea have also suggested considering the country RS to begin (end) when any area of Jeju, Mokpo and Seoul witness the beginning (retreat) of RS.
(2) Circulation pattern: KMA regards the non-precipitation (the mid-break of RS) due to WPSH expansion to cover the whole South Korea as R-RS. In this study, although Jangma Front moves to north of 45°N in the early August to mid-August, resulting in a mid-break of RS, we probably still consider the period (it is called “late Jangma” in DPRK) as RS because the weakened Jangma Front may move southward and precipitation may be observed again. The length of the mid-break in the study area is also much shorter than that in South Korea due to the differentiated time periods controlled by WPSH, and this may be the reason why the period from late-August to mid-September is not considered as part of RS in South Korea.
(3) Precipitation indicators: In the definition of O-RS, we used cumulative precipitation amount of more than 50 mm for 3 days in study. However, three consecutive days with precipitation are used in defining the beginning of O-RS in South Korea.

We compared the results of the study with those by using the criteria in South Korea (Ryoo, 2001) for the period 1961–2000 (Fig. 7). It is clear that the R-RS dates in this study are usually 16 days later than those obtained by KMA. In the study, the precipitation condition for O-RS date is similar to that in South Korea, and the difference of O-RS between DPRK and South Korea is not so large.

In other words, under the same atmospheric circulation, the difference between this study and KMA is caused by the northward migration of Jangma Front from Jeju Island in South Korea to the southern region of the study area. The almost same onset dates between regions in 1990 mean that Jangma Front moved very rapidly to the north. In addition, the difference of retreat dates, 33 days on average, reflects the usual time period taken for the Jangma Front to move southward again through the study area after it leaves South Korea. Mean L-RS in this study is 17 days longer than that reported in KMA, in spite of the fact that it was much shorter in 1972, 1991 and 1993 (Fig. 7b), when Jangma Front had been stagnant for a longer period in south of 25°N, and had shifted to the southeast without any northward jump of WPSH. On contrary, the difference of L-RS between the two regions is beyond 60 days in 1973, with the mid-break of RS in the study area relatively longer because Jangma Front stays in Northeast China for an unusually long time after it crosses the Korean Peninsula.

It should be pointed out that different definitions of climatological terms are usually applied for different countries and regions. This would be mainly related to the varied climatic and geographical conditions, and also to the relatively independent studies by researchers in different countries. This may result a difference among the analysis results of climatological features. However, the long-term climatic change and variability of rainy season and torrential rain events as analyzed in this paper would not be affected by the different definitions used in the two countries. What is important is that we have used consistent terms throughout the study, and this would guarantee the reliability of the analysis results of the long-term rainy season and terrestrial rain variation.

4.2. Mechanisms of TR and RS variations

As shown in Fig. 4, the annual extreme precipitation events significantly increased during the analysis period, with the mid-1990s as a shift point. Especially, TR (R_{6h}≧100 mm) has grown sharply by about 1.5 times since 1984, compared with the pre-period (1974–1983) (Fig. 5). These results are consistent with the results of Choi et al. (2008) and Jung et al. (2002, 2011). Sun et al. (2006) showed that the precipitation amount and intensity of annual rainstorms had a detectable upward trend in Northeast China for four decades of last century. The similar changes in extreme precipitation over the past decades in eastern China were also observed (e.g. Zhai et al., 2005; Zhang et al., 2009; Ren et al., 2010).

The monthly frequencies of TR (R_{6h}≧100 mm and R_{12h}≧200 mm) in August are bigger than July, as shown in Table 4. This result is also comparable to the analysis by In et al. (2014). They also found an increasing trend of precipitation amount and precipitation frequency in August from 1973 to 2010 over South Korea, which may have caused the average frequencies of TR to rise in the last two decades.

The main cause of the regional difference in distribution of TR events over DPRK is related to the orographic effect. In particular, Kosong, Taechon, Unsan, Tokchon, Maengsan and Chorwon regions (Fig. 6) are located on the windward side of the southwest or southeast wind during the summer monsoon season. The spatial characteristics of TR due to the orographic effect in the Taebaek Mountain Range was also seen in South Korea (Lee et al., 2012), where the most frequent occurrences of the monthly maximum precipitation in the Gangneung area could be caused by orographic effects. Choi et al. (2008) further showed that the statistically significant increasing trend of TR for 1973–2007 was centered on the Taebaek Mountain Range, which include Kosong and Kumkang regions of DPRK.

The long-term changes in RS and TR in DPRK may be related to the following factors and mechanisms. We analyzed the correlation coefficient between O-RS and R-RS dates over DPRK and El Niño events. Results show that the correlation coefficients of O-RS and R-RS dates with El Niño events of preceding winter are −0.31 and 0.23, respectively, indicating that mean SST anomalies in the equatorial Pacific significantly influences RS in DPRK, with the stronger El Niño event followed by the longer RS of next summer in DPRK. A strong La Niña event appeared during spring 1970-winter 1971/72, and the L-RS of 1972 in DPRK was the shortest (3 days).

Different El Niño events may have different effects on the location and strength of WPSH in summer (Wang et al., 2012; Li and Wang, 2012). It is possible that the upward movement of the air by rising SST in the eastern equatorial Pacific due to the strongly maintained EP-El Niño event during preceding winter not only changes the normal Walker Circulation but also weakens Hadley Circulation which otherwise transports enormous thermal energy from the equator to the subtropical region in the western Pacific. The suppressed circulation forms a pattern with Sea Level Pressure (SLP) higher in the east than that in the west in zones around 30°N, a dynamical condition which makes WPSH to strengthen and its ridgeline to expand northwestward, benefiting the northward move of warm and moist airflow to invade into northeastern Asia along the western boundary of the WPSH. In the case of CP-El Niño, a different pattern appears, in which SLP in the central part is higher than that of the west in subtropical area, and the pressure gradient is steeper than that in the first pattern, which gives the possibility that WPSH ridge more shifts to the north. As a result, RS in the study area begins usually earlier and lasts longer than that in case of EP-El Niño event.

In La Niña, the atmospheric circulation system is reversed, and it

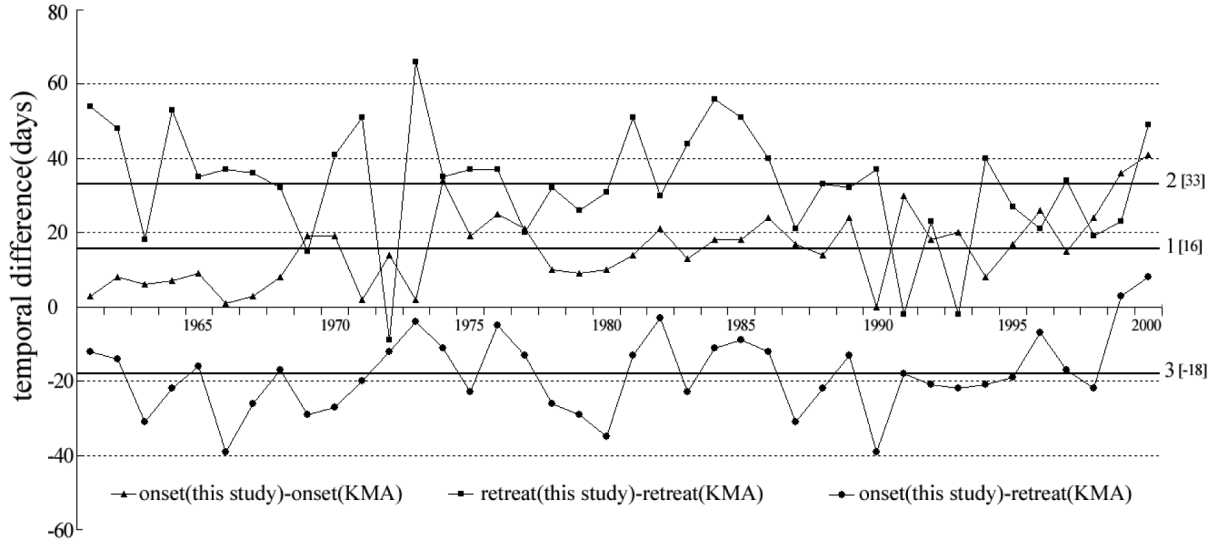

(a)

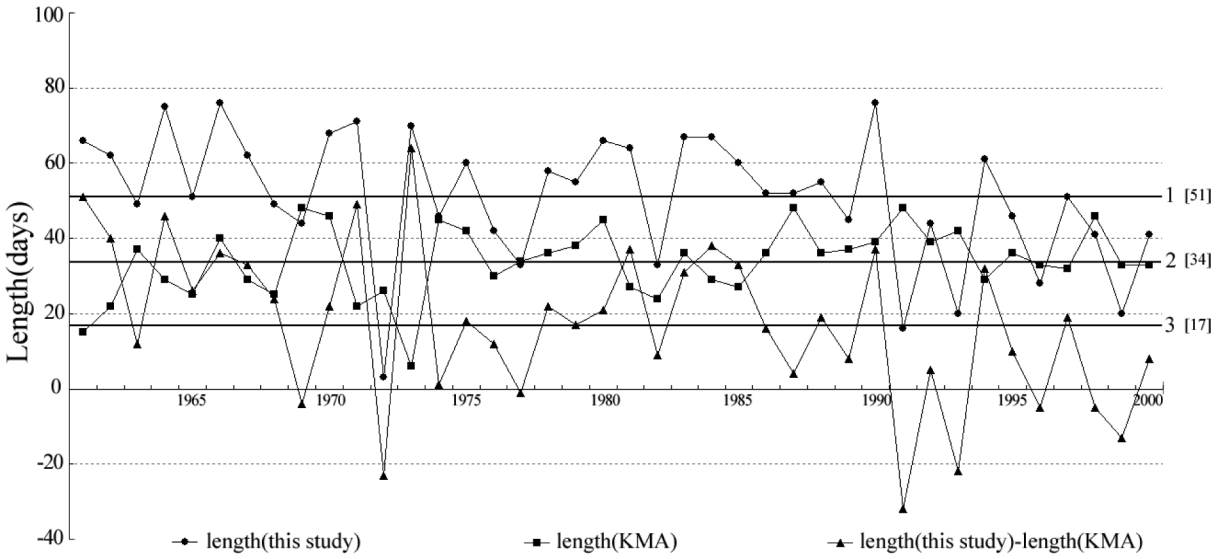

(b)

Fig. 7. Differences of onset, retreat and length of rainy season (O-RS, R-RS and L-RS) between this study and KMA. a-1 (triangle): onset (this study) - onset (KMA), a-2 (square): retreat (this study) - retreat (KMA), a-3 (circle): onset (this study) - retreat (KMA)); b-1 (circle): average for L-RS of this study, b-2 (square): average for L-RS of KMA, b-3 (triangle): average difference of L-RS between this study and KMA. Values in square brackets on rights of the curves are mean order number of pentads. KMA: Korean Meteorological Administration.

therefore benefits a later and shorter RS in the study area. This mechanism also satisfactorily explains the anomalously short RS (3 days) in DPRK in 1972 summer after a strong La Niña in 1970/71. We found that, on average, O-RS was 4.4 days earlier and L-RS 5.5 days longer after the CP-El Niño event than they were after the EP-El Niño, and O-RS with La Niña was delayed by 5.6 days and L-RS decreased by about 7 days.

Cai et al. (2003), Jin et al. (2005), Li et al. (2010), Wang et al. (2012), and Li and Wang (2012) all reported the changes of WPSH and East Asian climate under different patterns of El Niño events, but they had not discussed about the conceptual relationship of the patterns with O-RS and L-RS variations in East Asia in particular in DPRK. Other factors and processes may also affect the RS and TR over the country. Among others, mid-latitude trough and western Pacific typhoon would be important, and they deserve serious consideration in the future studies.

In addition, TR may be also associated with aerosol emission in eastern Asia. During RS, the study area is often affected by the Yangtze River cyclone and Yellow River cyclone. These cyclones occur 8–9 times a year in the Yangtze River and Yellow River basins and the Bohai Sea in mainland China, and move eastward to the study area. The currents and clouds in the cyclones contain high concentration of aerosols with their generation and development, which may play an important role in formation and development of TR as cloud condensation nuclei (CCN), facilitating or weakening the rainstorms in the Korean Peninsula when combined with water vapor. The microphysical mechanism of aerosol in clouds and precipitation is complex. However, it may act to suppress precipitation in shallow clouds, and to encourage precipitation of rain

ARTICLE IN PRESS

clouds by the vigorous convection and the nucleating process of large water droplets in warm and moist thick clouds (Qian et al., 2003; Rosenfeld et al., 2008; Stevens and Feingold, 2009). The extremely intense rainfall of RS in the study area may be affected in some extents by these eastward-moving cyclones. During the study period, the annual precipitation caused by the temperate cyclones indeed shows an increase at a rate of 22.5mm/decade (90% confidence level), which may be in certain extent related to the aerosols effect, in spite of the fact that there is a large uncertainty in our understanding of this issue.

The rapid regional warming should also be considered (Alexander et al., 2012). The upward trend of TRs in DPRK may be the response of regional climate to the strengthening of the hydro-cycle induced by climate warming. Our analysis (not shown in this paper) showed that the rate of temperature increase in DPRK since the late-1970s reached 0.35 °C/decade, which was higher than global (0.17 °C/decade), northern Hemispheric (0.30 °C/decade) and Asian (0.28 °C/decade) (Jones and Moberg, 2003) and mainland China (about 0.25 °C/decade) (Ren et al., 2012) averages during same period. The increasing rate of mean temperature during RS period (7/5–8/25) in DPRK is about 0.25 °C/decade. The more rapid warming generally occurred in the lower atmosphere, leading to a steeper temperature lapse rate and a more intense air convection motion, which may in some regions cause an increasing TR.

The increasing difference of warming between the oceans and the continents in summer should cause the stronger East Asian summer monsoon, leading to more frequent and intense TRs in DPRK. However, many studies showed a weakening summer monsoon during the past decades, in particular in the period since late 1970s (e.g. Wang, 2001; Wang and Ding, 2008; Jiang et al., 2008; Ren et al., 2015). The weakening East Asian summer monsoon actually decreased the precipitation and intense rainfall of summer in northern China (Ren et al., 2000; 2015; Zhai et al., 2005; Ding et al., 2008). The causes of the change in East Asian summer monsoon have not been well understood, but it has been related to the increase in the atmospheric aerosols in East Asia in particular in eastern China (Rosenfeld et al., 2008; Ding and Ren, 2008). If so, the observed change in occurrence of TR events in the study area and northern China may not rule out the possibility of influence of global and regional warming on summer monsoon of East Asian and intense precipitation of DPRK. Further studies of attribution using climate models may help on this regard.

Whatever the causes of the observed change in RS and TR events, it would be important for evaluating the risks of the climate change and variability to agriculture and economic development in DPRK. As seen above, annual TR events showed a significant increasing trend, in spite of the fact that L-RS was getting shorter. This implies that the agriculture and water resources management are facing a larger risk of severe floods during summer, and effective measures have to be taken to copy with the potential disasters.

The results reported here are also relevant to researchers who have long focused on observed and modeled studies of precipitation change and variability in East Asia including mainland China and Japan with DPRK left blank due to the availability of high-quality data. However, there are still a couple of issues which need to be tackled in the future. These include, among others, the difference between DPRK and neighboring countries in definition of TR, the studies of change of the other extreme precipitation events in DPRK, the investigation of the possible causes and mechanisms of the observed decadal variation and long-term trends of RS and TR events in the country, and the modeling and projection of the DPRK precipitation and torrential rain processes in decades to come under the anthropogenic global and regional climate change.

5. Conclusions

There is a relatively dense observational network consisting of 181 meteorological stations with at least 44 year records in DPRK. Daily precipitation data of these stations were used to analyze onset, retreat and length of rainy season. Also analyzed were the climatological characteristics and long-term variations of torrential rain events over the past decades. The following conclusions can be drawn from the analysis:

(1) Onset, retreat and length of rainy season in DPRK showed obvious inter annual and decadal variability. Onset of rainy season was associated with the northwestward move of western Pacific Subtropical High to the area north of 25°N and west of 150°E, with the high ridgeline vibrating between 25°N and 27°N.
(2) The linear trend of onset of rainy season was 1.9d/decade during 1960–2007, indicating a tendency for onset of rainy season to be gradually delayed, and retreat of rainy season was getting earlier with a downward trend of −2.7d/decade. This had led to a shortening length of rainy season at a rate of −4.7d/decade.
(3) Torrential rain events and rainy season precipitation amount had clear regional differences. In the southwest and northwestern regions of the study area, torrential rain events were the most frequent and precipitation also was the highest, and these were attributed to the orographic influence benefiting occurrences of summer torrential rain.
(4) Annual frequency, intensity and amount of torrential rain kept increasing over DPRK during the last four decades. The annual number of torrential rain events with amount of precipitation more than 100 mm/6 h linearly increased from 4.2 times to 7.4 times in the period 1974–2012, and the annual number of extremely intense torrential rain events more than 200mm/12 h also significantly increased during the same period.
(5) Influences of El Niño (La Niña) on rainy season might not so straight, with the rainy season after Central-Pacific El Niño events beginning earlier and lasting longer than that in case of Eastern-Pacific El Niño event. After La Niña of preceding winter, a later and shorter rainy season usually resulted. The possible impacts of large scale anthropogenic emissions of aerosols and greenhouse gas on onset and length of rainy season had not yet been determined.

Acknowledgements

This study is financially supported by the National Key R&D Program (Fund No. 2018YFA0605603) and the Natural Science Foundation of China (NSFC) (Fund No: 41575003). We would thank to the State Hydro-Meteorological Administration (SHMA), DPRK, for providing the observed daily precipitation data of the study region.

References

Adejuwon, J.O., 2006. Variability and the severity of the little dry season in Southwestern Nigeria. J. Clim. 19, 483–493.
Alexander, L.V., Zhang, X., Peterson, T.C., et al., 2012. Global observed changes in daily climate extremes of temperature and precipitation. J. Geophys. Res. Atmos. 111 (D5), 1042–1063.
Awan, J.A., Bae, D.-H., Kim, K.-J., 2015. Identification and trend analysis of homogeneous rainfall zones over the East Asia monsoon region. Int. J. Climatol. 35, 1422–1433. https://doi.org/10.1002/joc.4066.
Cai, Xue-zhan, Wen, Zhen-Zhi, Wu, Bin, 2003. Relationship between West Pacific subtropical high and ENSO and its influence on rainfall distribution of rainy season in Fujian. J. Trop. Meteorol. 19 (1), 36–42. https://doi.org/10.16032/j.issn.1004-4965.2003.01.005. (In Chinese).
Choi, G., Kwon, W.T., Boo, K.O., et al., 2008. Recent spatial and temporal changes in means and extreme events of temperature and precipitation across the Republic of Korea. J. Kor. Geogr. Soc. 43, 681–700 (in Korean).
Ding, Yihui, Chan, Johnny C.L., 2005. The East Asian summer monsoon: an overview. Meteorol. Atmos. Phys. 89, 117–142. https://doi.org/10.1007/s00703-005-0125-z.
Ding, Yihui, Ren, Guoyu, 2008. Introduction of China Climate Change Science. China Meteorological Press, Beijing (in Chinese).
Ding, Y., Wang, Z., Sun, Y., 2008. Inter-decadal variation of the summer precipitation in East China and its association with decreasing Asian summer monsoon. Part I: observed evidences. Int. J. Climatol. 28, 1139–1161.
Endo, H., 2011. Long-term changes of seasonal progress in Baiu rainfall using 109 years (1901-2009) daily station data. SOLA 7, 5–8.

ARTICLE IN PRESS

Fang, Yi-He, Chen, Hai-Shan, Teng, Fang-Da, Wang, Xiao-Juan, Wang, Ji, Zhao, Chun-Yu, 2017. Changing contribution rate of heavy rainfall to the rainy season precipitation in Northeast China and its possible causes. Atmos. Res. 197 (15), 437–445.
Garcia, S.R., Kayano, M.T., 2009. Determination of the onset dates of the rainy season in central Amazon with equatorially antisymmetric outgoing longwave radiation. Theor. Appl. Climatol. 97 (3), 361–372.
Guenang, G.M., Mkankam Kamga, F., 2012. Onset, retreat and length of the rainy season over Cameroon. Atmos. Sci. Lett. 13, 120–127.
Hachigonta, S., Reason, C.J.C., Tadross, M., 2007. An analysis of onset date and rainy season duration over Zambia. Theor. Appl. Climatol. 91, 229–243. https://doi.org/10.1007/s00704-007-0306-4.
Ho, C.-H., Lee, J.-Y., Ahn, M.-H., Lee, H.-S., 2003. A sudden change in summer rainfall characteristics in Korea during the late 1970s. Int. J. Climatol. 23, 117–128.
In, S.R., Han, S.O., Im, E.S., et al., 2014. Study on temporal and spatial characteristics of summertime precipitation over Korean Peninsula. Sci-Tech Inf. Dev. Econ. 24 (2), 159–171.
IPCC, 2013. Climate change 2013: the physical science basis. In: Solomon, S., Qin, D. (Eds.), Contribution of Working Group I to the Fourth Assessment Report of the Intergovernmental Panel on Climate Change. Cambridge University Press, Cambridge, United Kingdom and New York, NY, USA.
Jiang, Z., Yang, S., He, J., Li, J., Liang, J., 2008. Interdecadal variations of East Asian summer monsoon northward propagation and influences on summer precipitation over East China. Meteorol. Atmos. Phys. 100, 101–119.
Jin, Y.H., Kawamura, A., Jinno, K., Berndtsson, R., 2005. Detection of ENSO-influence on the monthly precipitation in South Korea. Hydrol. Process. 19, 4081–4092.
Jones, P.D., Moberg, A., 2003. Hemispheric and large-scale surface air temperature variations: an extensive revision and an update to 2001. J. Clim. 16, 206–223.
Jung, H.S., Choi, Y., Oh, J.H., et al., 2002. Recent trends in temperature and precipitation over South Korea. Int. J. Climatol. 22 (11), 1327–1337.
Jung, I.W., Bae, D.H., Kim, G., 2011. Recent trends of mean and extreme precipitation in Korea. Int. J. Climatol. 31 (3), 359–370.
Kim, H.S., Chung, Y.S., Tans, P.P., Yoon, M.B., 2016. Climatological variability of air temperature and precipitation observed in South Korea for the last 50 years. Air Qual. Atmos. Health 9 (6), 645–651.
Kitoh, A., Uchiyama, T., 2006. Changes in onset and withdrawal of the East Asian summer rainy season by multi-model global warming experiments. J. Meteorol. Soc. Jpn. 84, 247–258.
Kripalani, R.H., Kim, B.-J., Oh, J.-H., Moon, S.-E., 2002. Relationship between Soviet snow and Korean rainfall. Int. J. Climatol. 22, 1313–1325. https://doi.org/10.1002/joc.809.
Laux, P., Kunstmann, H., Bardossy, A., 2008. Predicting the regional onset of the rainy season in West Africa. Int. J. Climatol. 28, 329–342. https://doi.org/10.1002/joc.1542.
Lau, K.-M., Yang, S., 1997. Climatology and interannual variability of the southeast Asian summer monsoon. Adv. Atmos. Sci. 14, 141–162.
Lee, D.K., Choi, S.J., 2010. Observation and numerical prediction of torrential rainfall over Korea caused by Typhoon Rusa (2002). J. Geophys. Res. 115 (115), 1256–1268.
Lee, B.-S., Kim, S.-S., 1983. Climatological characteristics of the Changma season. J. of Korea Meteor. Soc 19 (1), 1–11.
Lee, S.-S., Vinayachandran, P.N., Ha, K.-J., Jhun, J.G., 2010. Shift of peak in summer monsoon rainfall over Korea and its association with El Nino–Southern oscillation. J. Geophys. Res. 115, 355–365.
Lee, J.J., Kwon, H.H., Kim, T.W., 2012. Spatio-temporal analysis of extreme precipitation regimes across South Korea and its application to regionalization. J. Hydro-Environ. Res. 6 (6), 101–110.
Li, S.L., Wang, Q., 2012. A new approach for classifying two types of El Niño events. Atmos. Oceanic Sci. Lett. 5 (5), 414–419.
Li, Y., Yang, X.Q., Xie, Q., 2010. Selective interaction between interannual variability of North Pacific subtropical high and ENSO cycle. Chin. J. Geophys. 53 (7), 1543–1553. https://doi.org/10.3969/j.issn.0001-5733. 2010.07.005. (in Chinese).
Liu, G., Wu, R., 2016. Spatial and temporal characteristics of summer precipitation events spanning different numbers of days over Asia. Int. J. Climatol. 36, 2288–2302. https://doi.org/10.1002/joc.4495.
Lu, R., 2002. Association between the surface temperature in Eurasia and the Changma withdrawals. Korean Journal of the Atmospheric Sciences 5, 63–70.
Lu, Riyu, Oh, Jai-Ho, Kim, Baek-Jo, Back, Hee-Jeong, Huang, Ronghui, 2001. Associations with the interannual variations of onset and withdrawal of the Changma. Adv. Atmos. Sci. 18 (6), 1066–1079.
Ma, S., Zhou, T., 2015. Observed trends in the timing of wet and dry season in China and the associated changes in frequency and duration of daily precipitation. Int. J. Climatol. 35, 4631–4641. https://doi.org/10.1002/joc.4312.
Mugalavai, E.M., Kipkorir, E.C., Raes, D., Rao, M.S., 2008. Analysis of rainfall onset, cessation and length of growing season for western Kenya. Agric. For. Meteorol. 148, 1123–1135.
Odekunle, T.O., 2006. Determining rainy season onset and retreat over Nigeria from precipitation amount and number of rainy days. Theor. Appl. Climatol. 83, 193–201.
Ohba, M., Kadokura, S., Yoshida, Y., Nohara, D., Toyoda, Y., 2015. Anomalous weather patterns in relation to heavy precipitation events in Japan during the baiu season. J. Hydrometeorol. 16, 688–701. https://doi.org/10.1175/JHM-D-14-0124.1.
Qian, Y., Ruby, L.L., Ghan, S.J., et al., 2003. Regional climate effects of aerosols over China: modeling and observation. Tellus B 55 (4), 914–934.
Qiang, Xue-Min, Yang, Xiu-Qun, 2008. Onset and end of the first rainy season in south China. Chin. J. Geophys. 51 (5), 944–957.
Reiser, H., Kutiel, H., 2008. Rainfall uncertainty in the Mediterranean: definition of the rainy season – a methodological approach. Theor. Appl. Climatol. 94 (1), 35–49.
Ren, Guoyu, Feng, Guolin, Yan, Zhongwei, 2010. Progresses in observation studies of climate extremes and changes in mainland China. Clim. Environ. Res. 15 (4), 337–353 (in Chinese).
Ren, Guoyu, Ding, Yihui, Zhao, Zongci, 2012. Recent progress in studies of climate change in China. Adv. Atmos. Sci. 29 (5), 958–977.
Ren, Guoyu, Ren, Yuyu, Zhang, Yunjian, et al., 2015. Spatial and temporal patterns of precipitation variability over mainland China: II: recent trends. Adv. Water Sci. 26 (4), 451–465 (in Chinese).
Ren, G.Y., Wu, H., Chen, Z.H., 2000. Spatial characteristics of precipitation change over China. J. Appl. Meteorol. Sci. 11, 322–330.
Rosenfeld, D., lohmann, U., Raga, G.B., et al., 2008. Flood or drought: how do aerosols affect precipitation? Science 321 (5894), 1309–1313.
Ryoo, S.B., 2001. On the etymology and definition of Changma. Atmos. Korean Meteorol. Soc. 11 (2), 6–12 (in Koreat).
Salack, S., Muller, B., Gaye, A.T., 2011. Rain-based factors of high agricultural impacts over Senegal. Part I. Integration of local to subregional trends. Theor. Appl. Climatol. 106, 1–22. https://doi.org/10.1007/s00704-011-0414-z.
Stevens, B., Feingold, G., 2009. Untangling aerosol effects on clouds and precipitation in a buffered system. Nature 461 (7264), 607–613.
Sun, F., Zhijian, W.U., Yang, S., 2006. Temporal and spatial variations of extreme precipitation and dryness events in Northeast China in last 50 years. Chin. J. Ecol. 25 (7), 779–784.
Thomas, Axel, 1993. The onset of the rainy season in Yunnan province, PR China and its significance for agricultural operations. Int. J. Biometeorol. 37, 170–176.
Wang, H., 2001. The weakening of the Asian monsoon circulation after the end of 1970s. Adv. Atmos. Sci. 18, 376–386.
Wang, Z.Y., Ding, Y.H., 2008. Climatic Characteristics of rainy seasons in China. Chin. J. Atmos. Sci. 32 (1), 1–13 (in Chinese).
Wang, B., Jhun, J.G., Moon, B.K., 2010. Variability and singularity of Seoul, South Korea, rainy season (1778 -2004). J. Clim. 20 (11), 2572–2580.
Wang, Q., Li, S.L., Fu, J.J., Li, G.P., 2012. On the formation of anomalous summer precipitation in the years of 2010 and 1998: a comparison of the El Nino's impact between Modoki and typical El Nino cases. Acta Meteorol. Sin. 70 (6), 1207–1222 (in Chinese).
Yao, C., Yang, S., Qian, W., Lin, Z., Wen, M., 2008. Regional summer precipitation events in Asia and their changes in the past decades. J. Geophys. Res. 113, 1161–1165.
Zhai, P.M., Zhang, X.B., Wan, H., et al., 2005. Trends in total precipitation and frequency of daily precipitation extremes over China. J. Clim. 18, 1096–1108.
Zhan, Yunjian, Ren, Guoyu, 2016. Start and end dates of rainy season and their temporal change in recent decades over East Asia. J. Meteorol. Soc. Jpn. 94 (1), 41–53. https://doi.org/10.2151/jmsj.2016-003.
Zhang, Q., Xu, C.Y., Zhang, Z., et al., 2009. Spatial and temporal variability of precipitation over China, 1951–2005. Theor. Appl. Climatol. 95, 53–68.

remote sensing

MDPI

Article

A New Methodology for Estimating the Surface Temperature Lapse Rate Based on Grid Data and Its Application in China

Yun Qin [1], Guoyu Ren [1,2,*], Tianlin Zhai [3], Panfeng Zhang [1] and Kangmin Wen [1]

[1] Department of Atmospheric Science, School of Environmental Studies, China University of Geosciences, Wuhan 430074, China; shuyunchenyun@163.com (Y.Q.); zhangpanfeng@cug.edu.cn (P.Z.); wenkangmin@126.com (K.W.)
[2] Laboratory for Climate Studies, National Climate Center, China Meteorological Administration, Beijing 100081, China
[3] School of Resource and Environmental Sciences, Wuhan University, Wuhan 430079, China; tianlinzhai@whu.edu.cn
* Correspondence: guoyoo@cma.gov.cn or gyren@cug.edu.cn; Tel.: +86-10-6840-6408

Received: 6 July 2018; Accepted: 9 October 2018; Published: 11 October 2018



Abstract: Land surface temperature (LST) is an important parameter in the study of the physical processes of land surface. Understanding the surface temperature lapse rate (TLR) can help to reveal the characteristics of mountainous climates and regional climate change. A methodology was developed to calculate and analyze land-surface TLR in China based on grid datasets of MODIS LST and digital elevation model (DEM), with a formula derived on the basis of the analysis of the temperature field and the height field, an image enhancement technique used to calculate gradient, and the fuzzy c-means (FCM) clustering applied to identify the seasonal pattern of the TLR. The results of the analysis through the methodology showed that surface temperature vertical gradient inversion widely occurred in Northeast, Northwest, and North China in winter, especially in the Xinjiang Autonomous Region, the northern and the western parts of the Greater Khingan Mountains, the Lesser Khingan Mountains, and the northern area of Northwest and North China. Summer generally witnessed the steepest TLR among the four seasons. The eastern Tibetan Plateau showed a distinctive seasonal pattern, where the steepest TLR happened in winter and spring, with a shallower TLR in summer. Large seasonal variations of TLR could be seen in Northeast China, where there was a steep TLR in spring and summer and a strong surface temperature vertical gradient inversion in winter. The smallest seasonal variation of TLR happened in Central and Southwest China, especially in the Ta-pa Mountains and the Qinling Mountains. The TLR at very high altitudes (>5 km) was usually steeper than at low altitudes, in all months of the year.

Keywords: temperature lapse rate; MODIS; seasonal pattern; Sobel; FCM

1. Introduction

Temperature lapse rate (TLR) is the rate at which temperature decreases with altitude. Generally, there are two kinds of TLRs, dynamic and static TLR. The former describes the temperature change of the air parcel when it rises (e.g., dry adiabatic lapse rate); the latter indicates the temperature changes with space, which may be vertical (e.g., tropospheric free-air TLR) or along the earth's surface with different altitudes. The focus of this article is the TLR along the earth's surface, or lapse rate of land surface temperatures (LST).

LST is an important parameter in the study of the physical processes of land surface, which is frequently used in the fields of hydrological and meteorological models [1,2], agricultural and

ecological monitoring [3–5], and urban heat island analyses [6–8]. Remote sensing technology provides a spatial continually-distributed LST, which is of benefit to the analysis of spatial variation when compared to the limited ground meteorological stations [9]. The lapse rate of LST reflects the spatiotemporal variation of the thermal processes of land surface and the difference of regional climate, which can be used for the study of mountainous climates and probably for regional climate change, especially in remote mountainous areas where observations from ground meteorological stations are lacking. For example, different land-surface TLR at different sides of a mountain may be related to the vertical zoning of vegetation, and a steep TLR may cause a rapid vegetational change in the vertical [10,11]. In addition, elevation-dependent warming in mountainous areas may result in a temporal change in the TLR, and the more rapid warming at high altitude may be related to the shallower land surface and near-surface air TLR [12].

Some studies have found that there is a strong relationship between the mean LST and mean near-surface air temperature [13–16], and the seasonal pattern of monthly mean land-surface TLR is very similar to that of the near-surface air TLR [17]. However, as the LST is influenced by the surface regime [18,19], the relationship between them is not always stable. However, many previous studies have focused on the near-surface air TLR, and studies of the land-surface TLR are rare. Therefore, it is necessary to examine the land-surface TLR as a complement in the study of climatology and climate change. To avoid confusion, a negative TLR has usually been designated when the temperature decreases with the increase of elevation, and a positive TLR has been regarded as the temperature vertical gradient inversion in a substantial body of literature [11,20–24].

Atmospheric temperature decreases with the increase of elevation in the troposphere, and the global average annual mean atmospheric TLR is about $-6.5\ ^{\circ}C/km$ [25], which is generally used as a reference for near-surface air TLR. However, varied values of annual mean near-surface air TLRs have been reported for different areas [21,22,26,27]. Pepin and Losleben [28] found that TLR was steeper at higher elevations, and Mokhov and Akperov [29] pointed out that TLR became shallower from a low latitude to the polar regions. In addition, the atmospheric temperature sometimes remains constant or even increases with elevation [30]. A temperature inversion is frequently found in winter [23,31,32]. The annual cycle of the TLR shows different seasonal patterns, with some steeper in summer and shallower in winter [21,23,33,34], some steeper in winter and shallower in summer [11], and others that are steeper in spring and shallower in later summer or autumn [35,36].

Linear regression is widely used to calculate the TLR of a small region based on observational data of meteorological stations [24,37]. For a large region, stations are usually divided into several groups and the TLR in each group is calculated separately [22,34,38], or aggregated through a moving spatial window, thus each station has a local TLR [39,40]. Regarding the grid data, linear regression [41,42] and moving window regression [20] have also been adopted, based on grid values. However, as the TLR calculated through linear regression depends strongly on the stations being considered, and the station distribution is usually denser at low altitude than at high altitude, the results obtained may represent the TLR of a low altitude than of the whole mountainous area. It is also notable that as the grouping methods are different, the stations being considered in a group are different, which may reduce the comparability of the research results. Due to the heterogeneous spatial distribution of stations, a moving window regression cannot avoid the statistical errors caused by different sampling size or scales [43]. Though a linear regression, based on the grid data, eliminates the influence of heterogeneity, low correlation coefficients may be obtained, especially for the case of winter with enhanced temperature-inversion effects [21]. As for the identification of the seasonal pattern of a TLR, a line chart can tell the seasonal variation in a mountainous area or large scope, but cannot describe the details of a small scope with the effect of microclimate.

In this paper, we developed a methodology to calculate and analyze the TLR based on grid data, and used China as a case study for the application of the methodology by using grid datasets of moderate-resolution imaging spectroradiometer (MODIS) LST and digital elevation model (DEM). To be specific, we derived a formula on the basis of the analysis of the relationship of the temperature

field and the height field, applied the image enhancement technique to calculate the gradient, and used the fuzzy c-means (FCM) clustering method to identify the seasonal pattern of the TLR. The analysis results were broadly in accordance with previous studies based on meteorological stations, which would form a reference to the study and application of both land-surface TLR and near-surface air TLR, in a large region with complex topography.

2. A Conceptual Framework

For a continuous, spatially-distributed height field and temperature field, the gradient of the height points to the direction that the variables increase at the greatest rate [44–46], i.e., the steepest terrain slope. However, the direction may not be the same as the direction in which the temperature decreases at the greatest rate (the gradient of temperature). Generally, there is an angle between them; an angle greater than $\pi/2$ indicates that temperature decreases with the increase in height, and less than $\pi/2$ indicating that temperature increases with the increase in height, i.e., the temperature vertical gradient inversion, and an angle equal to $\pi/2$ indicates an unchanged temperature, with the increase in height. In a small region (compared with the average area covered by one meteorological station), the rate of change of height or temperature along a given direction can be considered to be constant, approximately, due to the continuously-varied terrain and the same atmospheric factors affecting the climate. Hence, the increase in temperature along the direction of the steepest topographical slope is the directional derivative of temperature, along the direction of the gradient of height at a site, i.e., the increase of temperature within a small region is the length of the gradient of temperature in the direction of the gradient of height.

For example, the angle between the gradient of height and the gradient of temperature, $\theta > \pi/2$, shows a negative correlation between height and temperature (Figure 1). Within a given small scope of a distance between P_A and P_B (denoted as $d_{P_AP_B}$), the TLR is the difference of temperature, divided by the difference of height, i.e., TLR $= \frac{t_1 - t_5}{h_4 - h_1}$. The length of the gradient of height at this scope is $h_4 - h_1$, and the length of the gradient of temperature is $t_6 - t_1$. In a homogeneous field, the difference of temperature between P_A and P_E, $t_5 - t_1$, is equal to $\frac{d_{P_AP_E}}{d_{P_AP_D}} \cdot (t_6 - t_1)$, where $d_{P_AP_E} = d_{P_AP_B} \cdot \cos(\pi - \theta)$. As $d_{P_AP_B}$ is equal to $d_{P_AP_D}$, the TLR can be written as $\frac{(t_6 - t_1) \cdot \cos\theta}{h_4 - h_1}$, which is the length of the gradient of temperature divided by the length of the gradient of height, in the direction of the gradient of height.

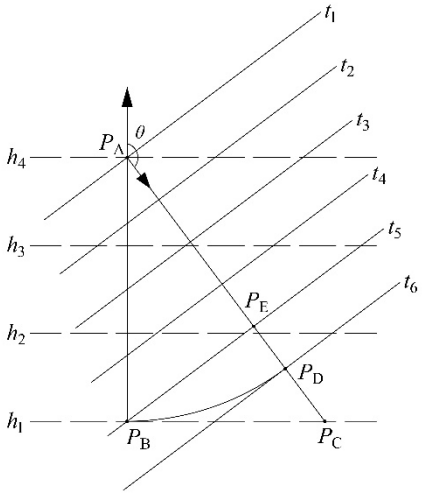

Figure 1. Contour of homogeneous height field (dashed line) and temperature field (solid line). Contour lines of the height field and the temperature field are given as h and t, respectively ($h_1 < h_2 < h_3 < h_4$, $t_1 < t_2 < t_3 < t_4 < t_5 < t_6$). The northward and southeastward arrow show the direction of the gradient of height and temperature, respectively. P_A, P_B, $\cdots$, P_E represent the geographical positions on a two-dimensional map. The arc between P_B and P_D is part of a circle centered on P_A.

In digital image processing, height field and temperature field are both discrete, and the gradient can be obtained through image enhancement techniques [47]. Three of the most common operators, Roberts, Prewitt, and Sobel, are used in edge-detection (a kind of image enhancement), and the Prewitt and Sobel operators are generally preferred to the Roberts [48]. As the Sobel operators implement differentiation in one direction and Gaussian averaging in the other, it makes for a smoother gradient and reduces the influence of noise.

Theoretically, temperature changes in a given cycle period. Hence, the TLR, which is decided by the gradient of temperature, also changes in the same cycle period as temperature. Hence, how the TLR changes with the seasons can be translated into two issues: (1) when the steepest (or shallowest) TLR occurs, i.e., where the wave trough (or crest) is, and (2) how much the magnitude of variability is within a year. To identify the variability model of TLR, four kinds of seasonal pattern were assumed, which were the steepest in spring, summer, autumn, and winter, respectively. However, the actual variability of TLR is usually characterized by more than one pattern. In order to identify which pattern it most likely belonged to and how much of it belonged to the pattern, the FCM clustering algorithm [49] was used. Furthermore, four standard samples generated artificially were added as a reference, which represented the typical seasonal patterns (the steepest in April, July, October, and January) in each season.

3. Materials and Methods

3.1. Data

The LST datasets were provided by the International Scientific & Technical Data Mirror Site, Computer Network Information Center, Chinese Academy of Sciences (http://www.gscloud.cn). The monthly mean LST was the average of the daily mean LST (average of diurnal and nocturnal LST) in each month, which was retrieved from MODIS data obtained by the satellite Terra and Aqua [9]. To avoid confusion, the mean LST above-mentioned is expressed as "LST" below. As there were a few missing values on the images, linear interpolation was used to fill the blank patches. These MODIS images were based on the geographic coordinate system of WGS-1984, at a spatial resolution of 0.0059° × 0.0059°. The range of the study area covered the whole of China, located from 4°00′N to 53°31′N latitude and from 73°40′E to 135°05′E longitude (Figure 2). The observed time ranged from January 2001 to December 2015. Monthly average LST was the average of the monthly LSTs of each month, from 2001 to 2015. Annual average LST was the average of the monthly average LST.

The dataset of DEM (GMTED2010) was provided by Natural Earth (https://www.naturalearthdata.com). The elevation data came from the DEM images, which were based on the geographic coordinate system of WGS-1984, at a spatial resolution of 30′ × 30′.

As the calculation of the TLR was based on both MODIS LST and DEM, they must have the same resolution. Hence, it was necessary to carry out resampling. When original images with a relatively high resolution were applied to a large-scale region, noise would seriously interfere with the accuracy of the judgment of the results, which might drown out the main information. In order to keep a balance between the denoising and maintaining the feature of the microclimate, resampling to a new spatial resolution of 10 km × 10 km (after projection) was undertaken in this case study.

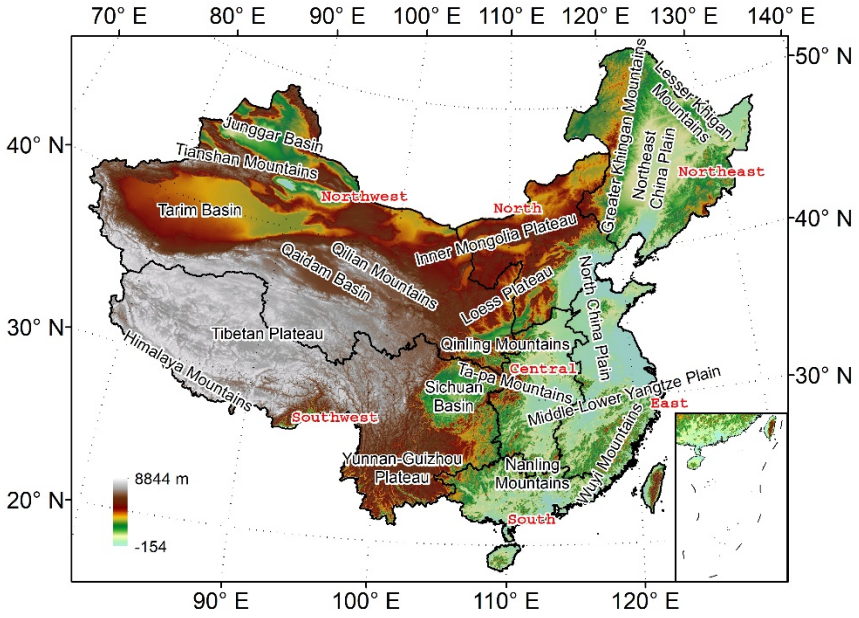

Figure 2. Topography of the study area (China) and seven geographical divisions.

3.2. Calculation of TLR

As LST is a function of space at a given time, its distribution throughout space is a scalar field (i.e., temperature field T), and so is elevation (i.e., height field H). The gradient of H at a site, denoted as ∇H, is a vector pointing in the direction of the steepest slope at that site. Along this direction, the increase of temperature per unit of height is supposed to be the TLR. Hence, the TLR can be expressed as follows:

$$\Gamma = \frac{|\nabla T| \cdot \cos\langle \nabla H, \nabla T \rangle}{|\nabla H|}, \tag{1}$$

where ∇T is the gradient of T and $\langle \nabla H, \nabla T \rangle$ is the angle between ∇H and ∇T. When the numerator and the denominator are both multiplied by $|\nabla H|$, Equation (1) can be written as follows:

$$\Gamma = \frac{\nabla T \cdot \nabla H}{|\nabla H|^2}, \tag{2}$$

As MODIS images are based on the geographic coordinate system of WGS-1984, the distribution throughout space was on the surface of an ellipsoid, so the gradient could not be directly calculated through a computer. Equidistant cylindrical projection [50] was used to transform the surface of an ellipsoid into a plane, which simplified the complexity of calculation. Through this transformation, the pixels of the new image, denoted as T_0, had the same distance along the longitudinal and latitudinal direction (10 km × 10 km). An extensional Sobel operator [51,52] of two 5 × 5 kernels,

$$O_1 = \begin{pmatrix} 1 & 2 & 0 & -2 & -1 \\ 4 & 8 & 0 & -8 & -4 \\ 6 & 12 & 0 & -12 & -6 \\ 4 & 8 & 0 & -8 & -4 \\ 1 & 2 & 0 & -2 & -1 \end{pmatrix}, O_2 = \begin{pmatrix} -1 & -4 & -6 & -4 & -1 \\ -2 & -8 & -12 & -8 & -2 \\ 0 & 0 & 0 & 0 & 0 \\ 2 & 8 & 12 & 8 & 2 \\ 1 & 4 & 6 & 4 & 1 \end{pmatrix},$$

were convolved with the image to calculate the gradient,

$$|\nabla T| = \sqrt{T_x^2 + T_y^2}, \tag{3}$$

$$\alpha = a\tan(\frac{T_y}{T_x}), \tag{4}$$

where $|\nabla T|$ and α are the length and the direction of ∇T, respectively. T_x and T_y are the derivatives for x changes (longitudinal direction) and for y changes (latitudinal direction), which are calculated by

$$T_x = T_0 \otimes \mathrm{O}_1/960, \tag{5}$$

$$T_y = T_0 \otimes \mathrm{O}_2/960, \tag{6}$$

where $\otimes$ denotes the two-dimensional signal processing convolution operation. The outside weights ([1,1,4,4,6] or [−1,−4,−6,−4,−1]) of each kernel are based on Pascal's triangle, the coefficients of which are subject to a Gaussian distribution, and the inside ones ([2,2,8,8,12] or [−2,−8,−12,−8,−2]) are twice as much as them. As the center parts are given greater weights than the edge parts, the spatial relationship is a kind of impedance or a distance decay. The farther away a pixel is from the center, the smaller the impact it has on the TLR of the center pixel. Note that 960 is the product of the sum of the absolute of each element of a kernel ($\sum_{i=1}^{5}\sum_{j=1}^{5}|\mathrm{o}_{i,j}|$) and the size of each pixel (10 km), and the unit of gradient is °C/km. ∇H, H_x, and H_y are calculated the same as ∇T, T_x, and T_y.

3.3. Analysis of Seasonal TLR Variation

First, the standard score normalization, then unity-based normalization were carried out, based on the TLR. Four artificially generated standard samples, which shared the same cycle period (12 months) and held different phases ($\{0, \pi, \pm\frac{\pi}{2}\}$ indicating that the wave trough occurred in April, July, October, and January, respectively), were added to make the clustering. FCM was based on the minimization of the following objective function:

$$J_M = \sum_{i=1}^{n}\sum_{j=1}^{c} u_{ij}^M \|\boldsymbol{r}_i - \boldsymbol{c}_j\|^2, \tag{7}$$

where M is the fuzzifier (= 1.01 here); n is the number of samples (including all non-void image pixels and four standard samples); c is the number of clusters (= 4 here); $\boldsymbol{r}_i$ is the normalized TLR at the ith sample (which is a vector of 12 elements); $\boldsymbol{c}_j$ is the center of the jth cluster; and u_{ij} is the degree of membership of $\boldsymbol{r}_i$ in the jth cluster. Note that $\|\boldsymbol{r}_i - \boldsymbol{c}_j\|$ is the norm expressing the similarity between $\boldsymbol{r}_i$ and $\boldsymbol{c}_j$. Fuzzy partitioning is carried out through an iterative optimization of Equation (7), with the update of u_{ij} and $\boldsymbol{c}_j$, which are expressed as follows:

$$u_{ij} = \frac{1}{\sum_{k=1}^{c}\left(\frac{\|\boldsymbol{r}_i - \boldsymbol{c}_j\|}{\|\boldsymbol{r}_i - \boldsymbol{c}_k\|}\right)^{\frac{2}{M-1}}}, \tag{8}$$

$$\boldsymbol{c}_j = \frac{\sum_{i=1}^{n} u_{ij}^M \boldsymbol{r}_i}{\sum_{i=1}^{n} u_{ij}^M}, \tag{9}$$

The sample i would be classified into the cluster with the largest u_{ij}. The image pixels that shared the same cluster as any one standard sample, would hold a similar seasonal pattern to it. The magnitude of variability was measured by the range of the TLR, within a year.

4. Results of Case Analysis

4.1. Spatial Variation of TLR

There were some areas with extremely small or large values of TLR ($\Gamma \leq -15$ or $\Gamma > 10$ °C/km), which were mainly located in the North China Plain, Northeast China Plain, and Tarim Basin (Figure 3).

When leaving these areas out of consideration, the annual average TLR of $\Gamma \leq 0$ °C/km accounted for 86.3%, indicating that the LST decreased with the increase of altitude, in most parts of China. The steep annual average TLR ($-15 < \Gamma \leq -7$ °C/km) mainly took place in the Tibetan Plateau. Temperature vertical gradient inversion ($0 < \Gamma \leq 10$ °C/km) could be seen in some regions of Northeast, Northwest, and North China.

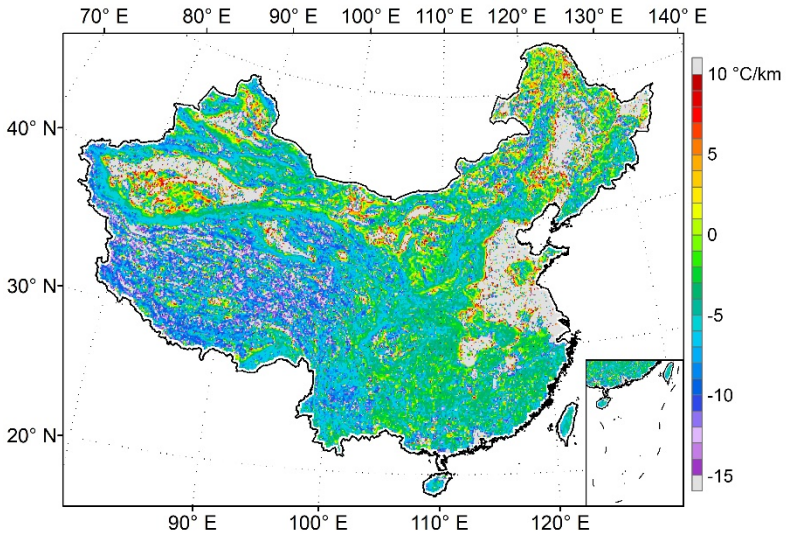

Figure 3. Spatial distribution of the annual average TLR during 2001–2015. The spatial resolution is 10 km × 10 km. The color bar shows twenty-seven levels of the TLR.

A big difference was found in the seasonal distribution (Figures 4 and 5). The steep monthly average TLR mainly occurred in the Southwest (the percentage of image pixels with $-15 < \Gamma \leq -7$ °C/km was greater than 20%, in all four seasons), Northwest (spring, summer, and early autumn), Northeast, and North China (summer and later spring) (Figure 5). The TLR of the mountainous and the hilly areas in Central, South, and East China became steeper (the percentage of image pixels with $-15 < \Gamma \leq -7$ °C/km increased) in summer, and at the same time, the TLR of the Eastern Tibetan Plateau became shallower. The TLR of Eastern Tibetan Plateau became the steepest in later autumn and winter, but that of the western part of the plateau began to become shallow (Figure 4). The region-wide monthly average TLR of the Eastern Tibetan Plateau was shallower than the western part by about 1.6 °C/km, from June to September (Figure 6a,c). In winter, the temperature vertical gradient inversion was widely distributed in Northeast, Northwest, and North China (the percentage of image pixels with $0 < \Gamma \leq 10$ °C/km was greater than 20%) (Figure 5). It is notable that there was a temperature vertical gradient inversion in the western and northern parts of the Greater Khingan Mountains in Northeast China, in winter and in early spring, but a steep TLR occurred in some parts of the eastern slope of the mountains (Figure 4). The region-wide monthly average TLR of the Western and Northern Greater Khingan Mountains could be greater than 0 °C/km, in December and January, but those of the eastern slope of the mountains were much less than 0 °C/km, in the two months (Figure 6b,d).

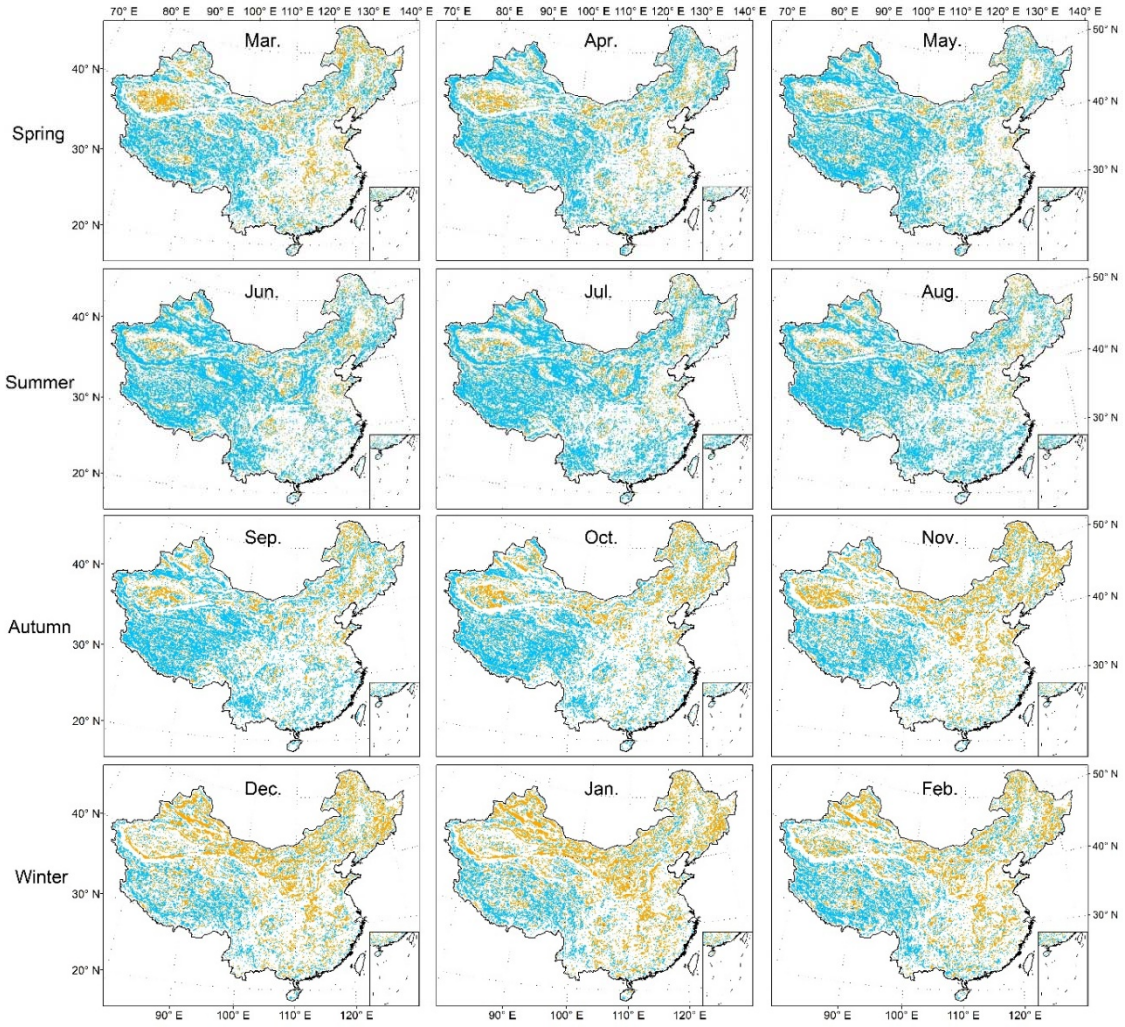

Figure 4. As Figure 3 but of the monthly average TLR. The blue and orange color indicate the image pixels with $-15 < \Gamma \leq -7$ and $0 < \Gamma \leq 10$ °C/km, respectively. The white color indicates the other TLR values.

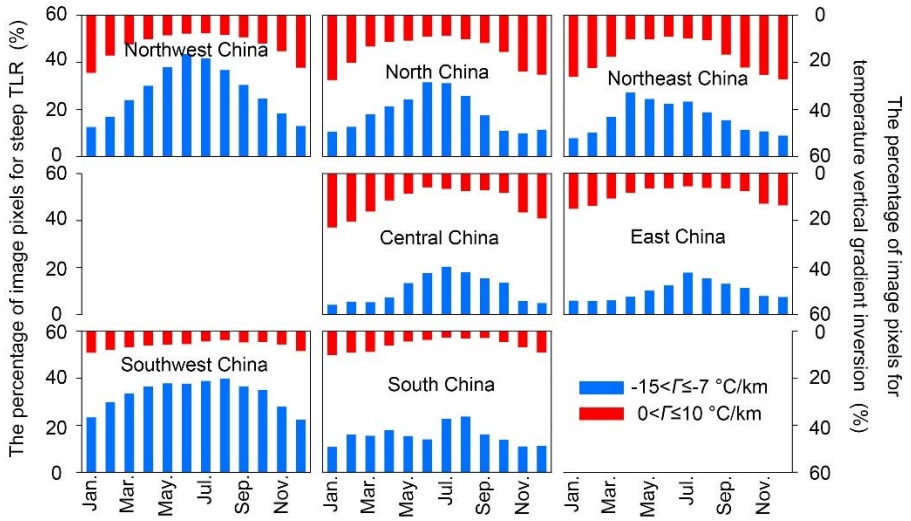

Figure 5. Bar chart of the percentage of image pixels for the steep TLR (blue) and the temperature vertical gradient inversion (red) in each region. The primary and secondary Y-axis represent the percentages for the steep TLR and the temperature vertical gradient inversion, respectively.

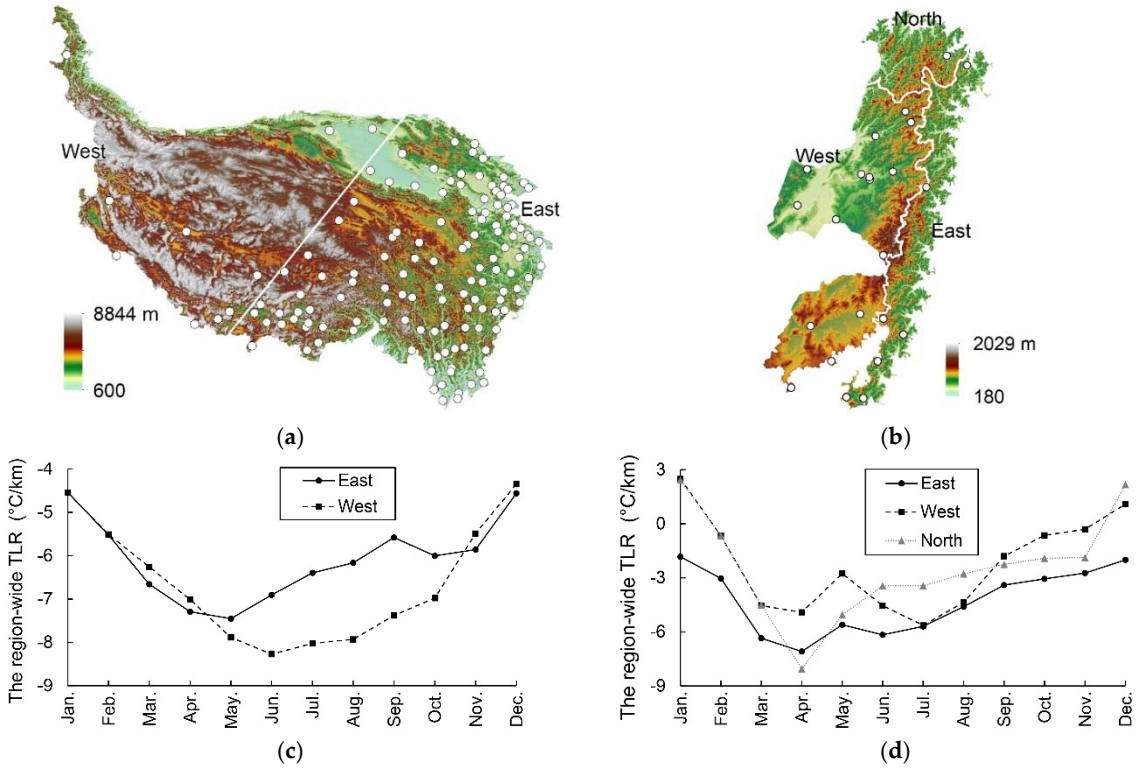

Figure 6. The region-wide monthly average TLR of the Tibetan Plateau (**a** and **c**) and the Greater Khingan Mountains (**b** and **d**). The white circles in the patches (**a**) and (**b**) represent the ground meteorological stations. The dividing line in patch (**a**) indicates east and west of the plateau with much more stations in the east, and patch (**b**) indicates the mountain ridgeline. The TLR in patches (**c**) and (**d**) are the average of the TLR values of image pixels with $-15 < \Gamma \leq 10$ °C/km in every month.

4.2. Temporal Variation of TLR

TLR is changeable in the areas of plains and basins with extremely small values of $|\nabla H|$ (Figures 3 and 4). However, the percentage of these areas ($\Gamma \leq -15$ or $\Gamma > 10$ °C/km) in each month was relatively stable (accounting for about 10%, respectively) (Figure 7). Based on this, this research focused on the other twenty-five levels of $-15 < \Gamma \leq 10$ °C/km.

The country-wide monthly average TLR was steeper in summer than in winter (Figure 7). The spatial variability was larger in winter than in summer (standard deviation was 5.0 °C/km in winter and 4.5 °C/km in summer, data not shown). The percentage of predominant levels of $\Gamma \leq 0$ °C/km was larger in summer than in winter. Meanwhile, there was an increased percentage of temperature vertical gradient inversion in winter, when compared to that in summer.

The monthly average TLR was roughly steeper at a higher altitude than at a lower one (Figure 8a), and was also generally steeper in summer than in winter, at a given elevation. Temperature vertical gradient inversion mostly happened at low altitudes, in winter. Though the monthly average TLR showed complex changes with an increase in LST, shallow TLR or temperature vertical gradient inversion also happened in winter (Figure 8b). Furthermore, strong temperature vertical gradient inversion could be found in winter, especially in December and January, at low elevations less than 0.2 km above sea level.

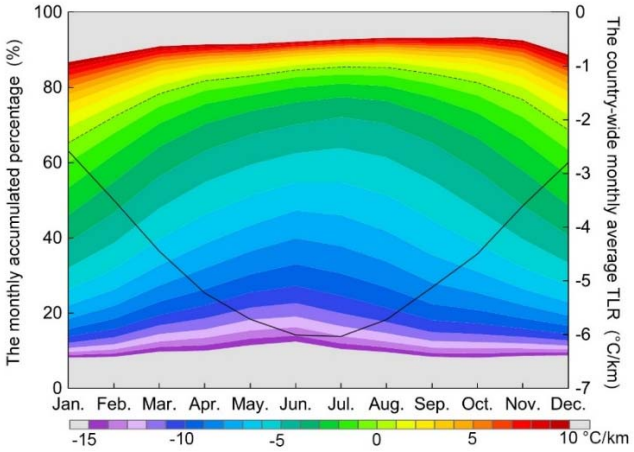

Figure 7. Variation of monthly accumulated percentage at each level of the TLR and the country-wide monthly average TLR. The primary Y-axis represents the accumulated percentage of image pixels at each level; the secondary Y-axis represents the country-averaged monthly average TLR. The dashed line is the dividing line between levels of $\Gamma \leq 0$ and $\Gamma > 0$ °C/km. The solid line is the mean of the monthly average TLR of the image pixels, where $-15 < \Gamma \leq 10$ °C/km.

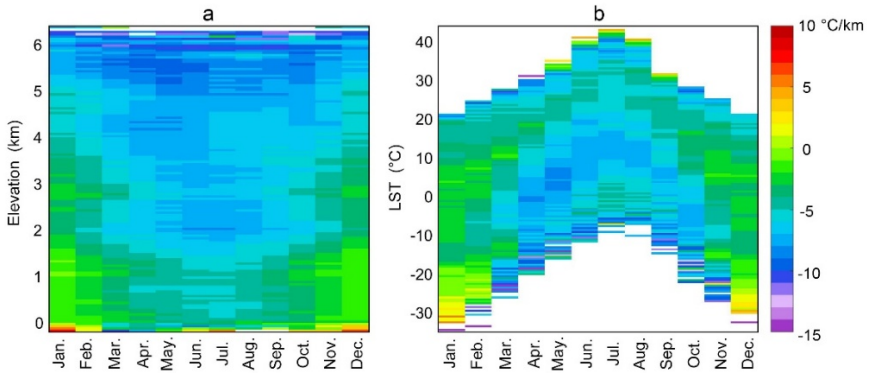

Figure 8. Profile of the monthly average TLR with elevation (**a**) and LST (**b**). The color bar shows twenty-five levels of TLR with $-15 < \Gamma \leq 10$ °C/km. The spacing of elevation was 50 m (**a**) and that of LST was 1 °C (**b**). The value of a grid was the mean of the TLR of the image pixels where the TLRs ranged within the grid bound. If the number of above-mentioned image pixels was less than two, the value was assigned as null

4.3. The Relationship of TLR with Elevation and LST

As a whole, the annual average LST decreased with the increase in elevation (Figure 9a). Steep annual average TLR ($\Gamma \leq -7$ °C/km) occurred frequently at elevations of $h > 1.5$ km, especially at $h > 4$ km. In contrast, temperature vertical gradient inversion occurred frequently at $h < 1.5$ km. The annual average TLR also showed less variability (average standard deviation $\sigma = 2.8 \pm 0.1$ °C/km at 95% significant level) at $1.5 < h < 4$ km than those at other elevations ($\sigma = 3.7 \pm 0.1$ °C/km) (Figure 9b).

The monthly average LST also showed a remarkable decreasing trend with elevation in warm months (summer, later spring, and early autumn) (Figure 10). However, as the LST at low altitude could reach the same low as at high altitude in cold months (winter, early spring, and later autumn), the relationship between elevation and LST was complex, especially at $h < 2$ km. The TLR at $h > 5$ km was steeper than that at low altitude, in all months. Temperature vertical gradient inversion mostly happened in winter, in cases of low LST and low altitude ($h < 2$ km), and also in some grids at middle altitude ($2 < h < 4$ km). The former was represented by Northeast China, and the latter shown by Northwest China. Interestingly, the monthly average TLR was often steeper at higher LST than at low LST, at $2 < h < 6$ km, in summer.

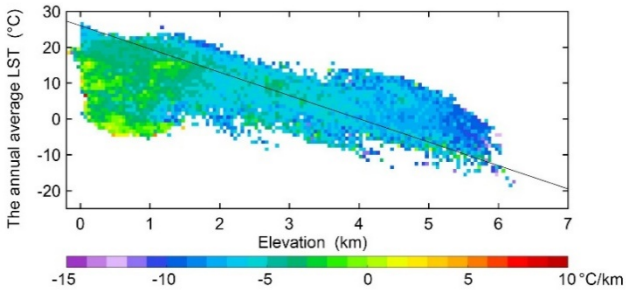

(**a**) The mean of the annual average TLR

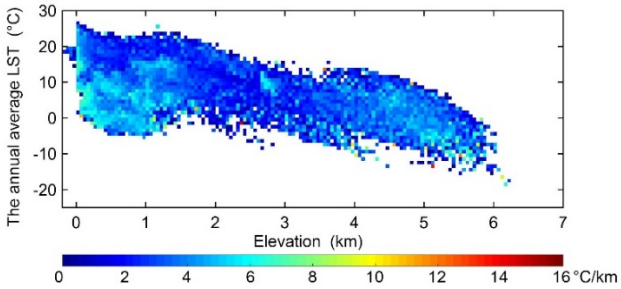

(**b**) The standard deviation of the annual average TLR

Figure 9. The relationship of the mean (**a**) and standard deviation (**b**) of the annual average TLR with elevation and the annual average LST. The spacing of elevation was 50 m and that of LST was 1 °C. The value of a grid in patch **a** (**b**) was the mean (standard deviation) of the TLRs of the image pixels, where TLRs ranged within the grid bound. If the number of above-mentioned image pixels was less than two, the value was assigned as null. The slope of the solid line in patch (**a**) represents a reference TLR of −6.5 °C/km. The color bar in patch (**a**) is the same as that in Figure 8.

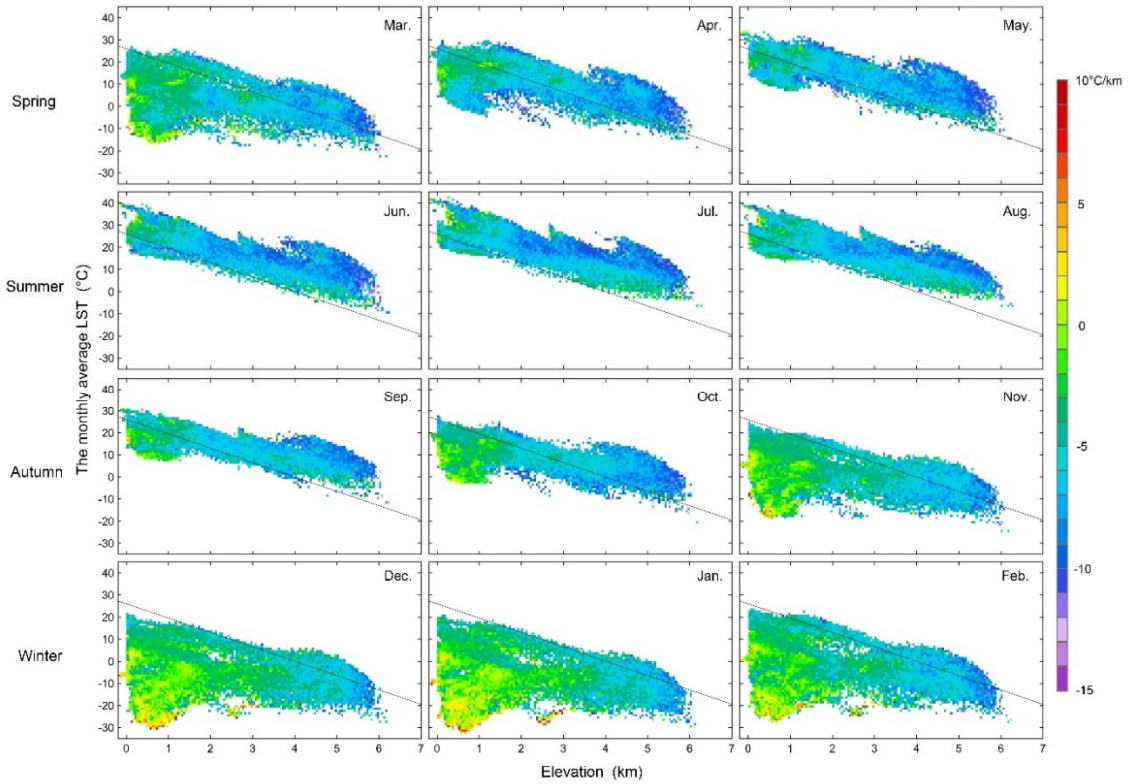

Figure 10. As Figure 9a but of the monthly average TLR with elevation and the monthly average LST. The color bar is the same as that in Figure 9a.

4.4. Seasonal Pattern and Magnitude of Variability

The summer pattern, or the patches with the steepest TLR in summer, was widely distributed across most of China; the spring pattern and winter pattern mainly happened in the eastern parts of the Tibetan Plateau, and the autumn pattern mainly took place in the North China Plain (Figure 11a). As the areas with extremely large magnitudes of variability are well matched with the areas of plains and basins with a small terrain slope and a low confidence of the calculating results, focus was given to the rest of the areas. What was different from the previous analyses [22,38,40] was that not all parts of the Tibetan Plateau showed a distinct seasonal pattern, but the eastern region of the plateau did exhibit a winter and spring pattern. Moreover, the winter pattern was mainly distributed in the northern slopes of the Eastern Himalayan Mountains. The smallest magnitude of variability occurred in Central and Southwest China, especially in the Ta-pa Mountains and the Qinling Mountains, and the large magnitude of variability was mostly distributed in the hills and mountainous areas of Northeast China (Figure 11b), where the magnitude of variability could reach more than 15 °C/km.

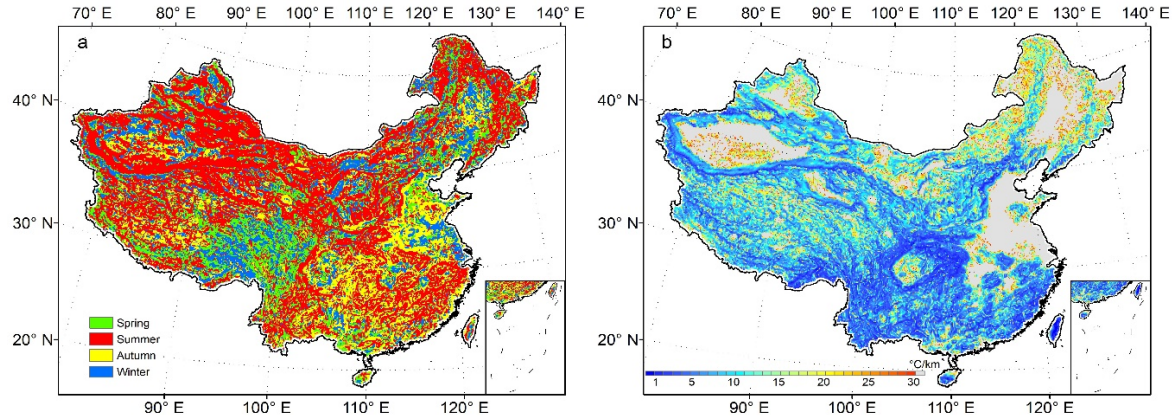

Figure 11. Seasonal pattern (**a**) and magnitude of variability (**b**) of the TLR. The type of seasonal pattern in patch (**a**) indicates in which season the steepest TLR took place. The magnitude of variability in patch (**b**) represents how much the TLR changed within a year. The grey color indicates the patches where the confidence of the calculating results was low due to the flat topography.

5. Discussion

LST is an important parameter in the study of the physical processes of land surface. The land-surface TLR could reflect the spatiotemporal variation of thermal processes and the difference of the regional climate. The traditional ways to calculate surface TLR and identify the seasonal pattern are linear regression and line charts, respectively. However, strong spatial heterogeneity led to a large uncertainty, in the TLR estimated through linear regression, for a large region. Generally, stations or grids were divided into several groups and the TLR in each group was calculated separately when the study area was large. Although grouping could improve the accuracy to a certain extent, the grouping results would directly affect the value of the TLR, and sparse meteorological stations in high altitude would result in statistical bias. Meanwhile, as the station grouping was uncertain, different seasonal patterns among small regions could not be distinguished clearly.

Therefore, a methodology was developed in this paper that was composed of a formula which was derived on the basis of the analysis of the temperature field and the height field, an image enhancement technique which was used to calculate the gradient, and FCM clustering which was applied to identify the seasonal pattern of the TLR. Furthermore, the spatiotemporal variation of land-surface TLR in China was analyzed by applying this methodology. The analysis results were broadly in accordance with previous studies. The spatial variability in winter was larger than in summer, which has also been found in previous studies [24,53]. Previous analysis results also showed that the summer pattern is a dominant mode [21,27,33,35,54], which was consistent with the result of this work.

Nevertheless, some previous studies have found that the Tibetan Plateau had a different seasonal pattern when compared to other regions in the world, with the TLR steeper in winter than in summer [22,38,40]. Unlike the previous analyses, however, not all parts of the Tibetan Plateau showed such a distinct seasonal pattern, and this only occurred in the eastern region of the plateau (Figure 11a). Moreover, the TLR of the Eastern Tibetan Plateau was steep, not only in winter, but also in spring, and the winter pattern was mainly distributed in the northern slopes of the Eastern Himalayan Mountains. A major reason for the difference of this analysis from previous ones could be related to the uneven distribution of meteorological stations in the plateau. There are few meteorological stations in the Western Tibetan Plateau (Figure 6a), and the seasonal pattern of TLR, which has been based on linear regressions and meteorological observational data, in previous studies, actually represented only the eastern region. As seasonal pattern could usually be identified by checking the trend of the line chart, which strongly depended on the results of the station grouping, detailed seasonal features based on the small scope have not been researched in the Eastern Tibetan Plateau. Kattel et al. [11] found that the TLR in the northern slopes of the eastern Himalayan Mountains was steep in winter and shallow in summer, which was consistent with our results.

The distinctive seasonal pattern of the TLR in the Eastern Tibetan Plateau was due to the unique climatic regimes, dry and cold in winter, and moist and warm in summer [22]. On one hand, the intense latent heat released at the upper atmosphere (water vapor condensation from moist convection of southwest currents from the Bay of Bengal) and decreasing sensible heat at the surface (heavier rainfall and denser cloudiness) produced the shallowest TLRs in summer in this region; on the other hand, strong sunshine and the resulting sensible heat at the surface in the non-monsoon seasons (November to April) produced the steepest TLR, in winter or spring [37].

As for the Xinjiang Autonomous Region located in Northwest China, temperature vertical gradient inversion has also been observed, in winter, in previous studies [34,38,53]. In Northeast China, however, the results of our analysis were different from some of the previous studies [38,40], which did not observe the phenomenon of temperature vertical gradient inversion, but found a steep TLR in winter. In order to reproduce their results as much as possible, the dataset from the National Meteorological Information Center, China Meteorological Administration (CMA), was used to conduct the linear regression. As shown in Figure 12, a steep monthly average TLR (−9.3 °C/km) was indeed found in the northeastern parts of China (mostly in the northern part of Northeast China). However, though the linear regression was significant, the goodness of fit was low ($R^2 = 0.312$). More than 70% of these stations were located in low altitude (<400 m), which accounted for less than 50% of the explained sum of squares (ESS), and most residuals through linear regression came from those in high altitude.

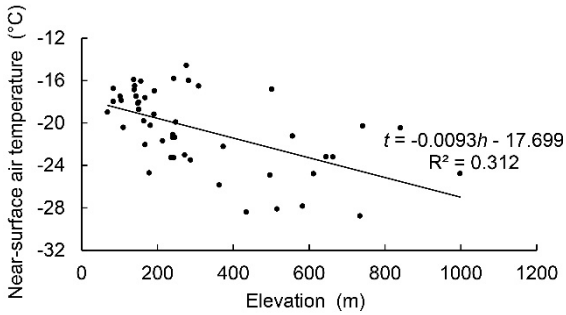

Figure 12. Scatter of elevation and near-surface air temperature in the northeastern parts of China in January, during 1981–2010. Elevation and near-surface air temperature are denoted by h and t in the equation of linear regression, respectively. A total of forty-nine meteorological stations were selected by using the same division standard as Li et al. [38], and the stations were located in the north at 45°N and in the east at 115°E.

The meteorological stations were mostly distributed in and around the Northeast Plain with low altitude (not shown), but there were a few in the Greater Khingan Mountains and Lesser Khingan

Mountains, at higher altitudes. As there were only a few stations in the mountainous and the hilly areas, the temperature vertical gradient inversion could not be seen clearly. The magnitude of variability of the TLR could reach more than 15 °C/km, in Northeast China (Figure 11b), which revealed a greatly different TLR, within a year. There was a temperature vertical gradient inversion in the Lesser Khingan Mountains and in the western and northern parts of the Greater Khingan Mountains, in winter and early spring, but a steep TLR in some places of the Eastern Greater Khingan Mountains was also notable (Figure 4). The temperature vertical gradient inversion, in the Greater Khingan Mountains and Lesser Khingan Mountains, has also been reported in some other previous studies [55,56].

The widely distributed temperature vertical gradient inversion in the Northeast, Northwest, and North China, in winter, may be related to the complex topography, including the cold air lake effect, in the cold months, in the basins and lowlands of the northern parts of China [57,58]. It is also interesting to note that the temperature vertical gradient inversion was distributed in the western and northern parts of the Greater Khingan Mountains, in winter and in early spring, while a steep TLR has been found in the eastern parts of the mountains. The former may be related to a persistent snow cover, while the latter might have been caused by the unique Foehn effect, during these seasons. On one hand, persistent snow cover and the inherent geomorphology might have been the main factors for the formation of temperature vertical gradient inversion. The winter snow cover in the mountains and plateau caused strong cooling near the surface and an obvious temperature vertical gradient inversion; the plateau west of the Greater Khingan Mountains acted as a quasi-basin where cold air masses from the northwest were more easily kept, at the surface, benefiting the formation and development of the temperature vertical gradient inversion. On the other hand, as the Greater Khingan Mountains are located west of the Northeast Plain, when the northwest wind passed by in winter, the relatively warm air currents above the cool air masses in the Western and Northern Greater Khingan Mountains descended along the leeward slopes, which led to a steep TLR in the eastern parts of the mountains [59].

In addition, the smallest magnitude of variability occurred in the Central and Southwest China, especially in the Ta-pa Mountains and the Qinling Mountains. This was due to the relatively large cloudiness and rainfall in the subtropical monsoon climate, which is characterized by not so high temperature in summer and not so cold temperature in winter, as the cold currents of the northwest winds are blocked away from the southern slopes of the Qinling Mountains. Hence, the small intra-seasonal variability of temperature produced a relatively stable TLR.

The TLR at very high altitudes (>5 km) was steeper than at low altitudes, in all months. It was also found that the TLR generally increased with altitude [28]. This might be the result of low air humidity at high altitude. As water vapor holds larger latent heat than dry air, when air with little vapor arises, the temperature decreases quickly. Meanwhile, compared with high altitude, the temperature vertical gradient inversion was more likely to happen in low altitude, in winter.

With the prevalence of satellite remote-sensing technology, the development of the methodology for calculating and analyzing TLR, based on the grid data, is necessary, therefore, especially for the studies of TLR in a large region with a complex topography. In this research, a formula derived on the basis of the analysis of the temperature field and the height field could provide a new procedure to calculate and analyze the TLR, which is beneficial to the study of mountainous microclimates. Moreover, an image enhancement technique was used for the calculation of TLR and the FCM clustering method was applied to the identification of seasonal patterns, the combination of which made it possible to analyze the TLR, on a large spatial scale. In addition, as the methodology was based on grid data, it was also applicable for estimating and analyzing the near-surface air TLR of a large region when the datasets had been transformed into grid data, and further in the studies of mountainous climate and regional climate change.

As LST is related to land use and vegetation cover, which might change with anthropogenic influences [60,61], the gradient of the LST might also change, correspondingly. Depending on the gradient of the LST, the land-surface TLR becomes changeable, especially in regions with denser

populations. These changes might increase the spatial heterogeneity of land-surface TLR, which would increase the noises of land-surface TLR images and reduce the accuracy of the methodology. Considering this deficiency, stratifying the results with land use maps or vegetation index data might be another promising way to analyze the variation of the land-surface TLR and to find the relationship between the land-surface TLR and land cover.

6. Conclusions

A new methodology was developed in this paper to calculate and analyze the land-surface TLR. With this methodology, the spatial and temporal pattern of the TLR in China was analyzed, and some new findings were reported and discussed.

Surface temperature vertical gradient inversion widely occurred in Northeast, Northwest, and North China, in winter, especially in the Xinjiang Autonomous Region, northern and western parts of the Greater Khingan Mountains, the Lesser Khingan Mountains, and the northern area of Northwest and North China. The summer pattern, which was characterized by the steepest TLR during summertime, was distributed more widely throughout China. The Eastern Tibetan Plateau held a distinct seasonal pattern, when compared to other regions in the world, with a steep TLR in winter and spring, and a shallow TLR in summer. The temperature vertical gradient inversion phenomenon occurred widely in Northeast China, in winter and early spring, with a strong temperature vertical gradient inversion in western and northern parts of the Greater Khingan Mountains, but a steep TLR appeared in some parts of the eastern slopes of the mountains. A large magnitude of variability of TLR was found in Northeast China, where there was a steep TLR in spring and summer, and a strong temperature vertical gradient inversion in winter. The smallest magnitude of variability occurred in Central and Southwest China, especially in the Ta-pa Mountains and the Qinling Mountains. The TLR at high altitude was generally steeper than at low altitude, and was usually steeper at very high altitude (>5 km) than at low altitude, in all months of the year.

The methodology developed in this study has the potential to be applied for estimating grid near-surface air TLR of a large region with complex topographical and geographical conditions, and further in the studies of mountainous climates and regional climate change, in the future. However, as only one case was used for the application of this methodology in this paper, the choice of the spatial resolution was not discussed. Furthermore, the treatment of the near-zero gradient of height was somehow rough. These two issues of the methodology, developed in this article, should be improved in future studies. The spatial resolution can be adjusted to meet the different needs of studies in diverse spatial scales. In order to shrink the influence of noise and obtain detailed information on TLR, as much as possible, high-resolution data are suggested for the study of a smaller region. Mid-low resolution data are suitable for the study of a larger region. In consideration of the relationship between the LST and the land-use and vegetation cover, it would be a promising procedure to analyze the land-surface TLR, by stratifying the results with the land-use maps or vegetation index data.

Author Contributions: Y.Q. developed the methodology, performed the calculations, and wrote the manuscript. G.R. conducted the study, contributed to the interpretation of the results, and reviewed the manuscript. T.Z. provided technical support, made the geographical divisions, and reviewed the manuscript. P.Z. and K.W. validated and reviewed the manuscript.

Funding: This work was supported by the Chinese Ministry of Science and Technology (MOST) National Key R&D Program (No. 2018YFA0605603) and the Natural Science Foundation of China (NSFC) (No. 41575003).

Acknowledgments: We thank two anonymous reviewers for providing constructive comments, which greatly improved this manuscript.

Conflicts of Interest: The authors declare no conflict of interest.

References

1. Noilhan, J.; Planton, S. A simple parameterization of land surface processes for meteorological models. *Mon. Weather Rev.* **1989**, *117*, 536–549. [CrossRef]
2. Wang, L.; Sun, L.; Shrestha, M.; Li, X.; Liu, W.; Zhou, J.; Yang, K.; Lu, H.; Chen, D. Improving snow process modeling with satellite-based estimation of near-surface-air-temperature lapse rate. *J. Geophys. Res. Atmos.* **2016**, *12*, 5–30. [CrossRef]
3. Wan, Z.; Wang, P.; Li, X. Using MODIS land surface temperature and normalized difference vegetation index products for monitoring drought in the southern Great Plains, USA. *Int. J. Remote Sens.* **2004**, *25*, 61–72. [CrossRef]
4. Sow, M.; Mbow, C.; Hély, C.; Fensholt, R.; Sambou, B. Estimation of herbaceous fuel moisture content using vegetation indices and land surface temperature from MODIS data. *Remote Sens.* **2013**, *5*, 2617–2638. [CrossRef]
5. Zhang, D.; Tang, R.; Zhao, W.; Tang, B.; Wu, H.; Shao, K.; Li, Z. Surface soil water content estimation from themal remote sensing based on the temporal variation of land surface temperature. *Remote Sens.* **2014**, *6*, 3170–3187. [CrossRef]
6. Clinton, N.; Gong, P. MODIS detected surface urban heat islands and sinks: Global locations and controls. *Remote Sens. Environ.* **2013**, *134*, 294–304. [CrossRef]
7. Schwarz, N.; Lautenbach, S.; Seppelt, R. Exploring indicators for quantifying surface urban heat islands of European cities with MODIS land surface temperatures. *Remote Sens. Environ.* **2011**, *115*, 3175–3186. [CrossRef]
8. Tomlinson, C.J.; Chapman, L.; Thornes, J.E.; Baker, C.J. Derivation of Birmingham's summer surface urban heat island from MODIS satellite images. *Int. J. Climatol.* **2012**, *32*, 214–224. [CrossRef]
9. Justice, C.O.; Townshend, J.R.G.; Vermote, E.F.; Masuoka, E.; Wolfe, R.E.; Saleous, N.; Roy, D.P.; Morisette, J.T. An overview of MODIS land data processing and product status. *Remote Sens. Environ.* **2002**, *83*, 3–15. [CrossRef]
10. Tang, C.Q. Forest vegetation as related to climate and soil conditions at varying altitudes on a humid subtropical mountain, Mount Emei, Sichuan, China. *Ecol. Res.* **2006**, *21*, 174–180. [CrossRef]
11. Kattel, D.B.; Yao, T.; Yang, W.; Gao, Y.; Tian, L. Comparison of temperature lapse rates from the northern to the southern slopes of the Himalayas. *Int. J. Climatol.* **2015**, *35*, 4431–4443. [CrossRef]
12. Mountain Research Initiative EDW Working Group. Elevation-dependent warming in mountain regions of the world. *Nat. Clim. Chang.* **2015**, *5*, 424–430. [CrossRef]
13. Zhu, W.; Lü, A.; Jia, S. Estimation of daily maximum and minimum air temperature using MODIS land surface temperature products. *Remote Sens. Environ.* **2013**, *130*, 62–73. [CrossRef]
14. Neteler, M. Estimating daily land surface temperatures in mountainous environments by reconstructed MODIS LST data. *Remote Sens.* **2010**, *2*, 333–351. [CrossRef]
15. Williamson, S.N.; Hik, D.S.; Gamon, J.A.; Kavanaugh, J.L.; Flowers, G.E. Estimating temperature fields from MODIS land surface temperature and air temperature observations in a sub-Arctic Alpine environment. *Remote Sens.* **2014**, *6*, 946–963. [CrossRef]
16. Benali, A.; Carvalho, A.C.; Nunes, J.P.; Carvalhais, N.; Santos, A. Estimating air surface temperature in Portugal using MODIS LST data. *Remote Sens. Environ.* **2012**, *124*, 108–121. [CrossRef]
17. Zhang, H.; Zhang, F.; Zhang, G.; Che, T.; Yan, W. How accurately can the air temperature lapse rate over the Tibetan Plateau be estimated from MODIS LSTs? *J. Geophys. Res. Atmos.* **2018**, *123*, 3943–3960. [CrossRef]
18. Jin, M.; Dickinson, R.E. Land surface skin temperature climatology: Benefitting from the strengths of satellite observations. *Environ. Res. Lett.* **2010**, *5*, 044004. [CrossRef]
19. Good, E.J.; Ghent, D.J.; Bulgin, C.E.; Remedios, J.J. A spatiotemporal analysis of the relationship between near-surface air temperature and satellite land surface temperatures using 17 years of data from the ATSR series. *J. Geophys. Res. Atmos.* **2017**, *122*, 9185–9210. [CrossRef]
20. Wang, Y.; Wang, L.; Li, X.; Chen, D. Temporal and spatial changes in estimated near-surface air temperature lapse rates on Tibetan Plateau. *Int. J. Climatol.* **2018**, *D24*, 1–15. [CrossRef]
21. Rolland, C. Spatial and seasonal variations of air temperature lapse rates in Alpine Regions. *J. Clim.* **2003**, *16*, 1032–1046. [CrossRef]

22. Guo, X.; Wang, L.; Tian, L. Spatio-temporal variability of vertical gradients of major meteorological observations around the Tibetan Plateau. *Int. J. Climatol.* **2016**, *36*, 1901–1916. [CrossRef]
23. Chiu, C.A.; Lin, P.H.; Tsai, C.Y. Spatio-temporal variation and monsoon effect on the temperature lapse rate of a subtropical island. *Terr. Atmos. Ocean. Sci.* **2014**, *25*, 203–217. [CrossRef]
24. Blandford, T.R.; Humes, K.S.; Harshburger, B.J.; Moore, B.C.; Walden, V.P.; Ye, H. Seasonal and synoptic variations in near-surface air temperature lapse rates in a mountainous basin. *Theor. Appl. Climatol.* **2008**, *47*, 249–261. [CrossRef]
25. Hartmann, D.L. *Global Physical Climatology*, 2nd ed.; Elsevier: Waltham, MA, USA, 2016; ISBN 9780123285317.
26. Harlow, R.C.; Burke, E.J.; Scott, R.L.; Shuttleworth, W.J.; Brown, C.M.; Petti, J.R. Research note: Derivation of temperature lapse rates in semi-arid south-eastern Arizona. *Hydrol. Earth Syst. Sci.* **2004**, *8*, 1179–1185. [CrossRef]
27. Marshall, S.J.; Sharp, M.J.; Burgess, D.O.; Anslow, F.S. Near-surface-temperature lapse rates on the Prince of Wales Icefield, Ellesmere Island, Canada: Implications for regional downscaling of temperature. *Int. J. Climatol.* **2007**, *27*, 385–398. [CrossRef]
28. Pepin, N.; Losleben, M. Climate change in the Colorado Rocky Mountains: Free air versus surface temperature trends. *Int. J. Climatol.* **2002**, *22*, 311–329. [CrossRef]
29. Mokhov, I.I.; Akperov, M.G. Tropospheric lapse rate and its relation to surface temperature from reanalysis data. *Izv. Atmos. Ocean. Phys.* **2006**, *42*, 430–438. [CrossRef]
30. Whiteman, C.D. *Mountain Meteorology Fundamentals and Applications*; Oxford University Press: New York, NY, USA, 2000; ISBN 0195132718.
31. Whiteman, C.D.; Bian, X.; Zhong, S. Wintertime evolution of the temperature inversion in the Colorado Plateau Basin. *J. Appl. Meteorol.* **1999**, *38*, 1103–1117. [CrossRef]
32. Kirchner, M.; Faus-Kessler, T.; Jakobi, G.; Leuchner, M.; Ries, L.; Scheel, H.E.; Suppan, P. Altitudinal temperature lapse rates in an Alpine valley: Trends and the influence of season and weather patterns. *Int. J. Climatol.* **2013**, *33*, 539–555. [CrossRef]
33. Tang, Z.; Fang, J. Temperature variation along the northern and southern slopes of Mt. Taibai, China. *Agric. For. Meteorol.* **2006**, *139*, 200–207. [CrossRef]
34. Du, M.; Zhang, M.; Wang, S.; Zhu, X.; Che, Y. Near-surface air temperature lapse rates in Xinjiang, northwestern China. *Theor. Appl. Climatol.* **2018**, *131*, 1221–1234. [CrossRef]
35. Minder, J.R.; Philip, W.M.; Lundquist, J.D. Surface temperature lapse rates over complex terrain: Lessons from the Cascade Mountains. *J. Geophys. Res.* **2010**, *115*, D14122. [CrossRef]
36. Pepin, N.; Kidd, D. Spatial temperature variation in the Eastern Pyrenees. *Weather* **2006**, *61*, 300–310. [CrossRef]
37. Kattel, D.B.; Yao, T.; Panday, P.K. Near-surface air temperature lapse rate in a humid mountainous terrain on the southern slopes of the eastern Himalayas. *Theor. Appl. Climatol.* **2018**, *132*, 1129–1141. [CrossRef]
38. Li, X.; Wang, L.; Chen, D.; Yang, K.; Xue, B.; Sun, L. Near-surface air temperature lapse rates in the mainland China during 1962–2011. *J. Geophys. Res. Atmos.* **2013**, *118*, 7505–7515. [CrossRef]
39. Dodson, R.; Marks, D. Daily air temperature interpolated at high spatial resolution over a large mountainous region. *Clim. Res.* **1997**, *8*, 1–20. [CrossRef]
40. Li, Y.; Zeng, Z.; Zhao, L.; Piao, S. Spatial patterns of climatological temperature lapse rate in mainland China: A multi–time scale investigation. *J. Geophys. Res. Atmos.* **2015**, *120*, 2661–2675. [CrossRef]
41. Jain, S.K.; Goswami, A.; Saraf, A.K. Determination of land surface temperature and its lapse rate in the Satluj River basin using NOAA data. *Int. J. Remote Sens.* **2008**, *29*, 3091–3103. [CrossRef]
42. Liu, Y.; Li, F. *A Preliminary Approach on the Land Surface Temperature (LST) Lapse Rate of Mountain Area Using MODIS Data*; Remote Sensing and Space Technology for Multidisciplinary Research and Applications, International Society for Optics and Photonics: Beijing, China, 2006; Volume 619907.
43. Fischer, M.M.; Getis, A. *Handbook of Applied Spatial Analysis: Software Tools, Methods and Applications*; Springer: New York, NY, USA, 2010; ISBN 9783642036460.
44. Dubrovin, B.A.; Fomenko, A.T.; Novikov, S.P. *Modern Geometry-Methods and Applications, Part I, The Geometry of Surfaces, Transformation Groups, and Fields*, 2nd ed.; Springer: New York, NY, USA, 1992; ISBN 0387976639.
45. Schey, H.M. *Div, Grad, Curl, and All That: An Informal Text on Vector Calculus*, 4th ed.; W.W. Norton & Company, Inc.: New York, NY, USA, 2005; ISBN 0393925161.

46. Korn, G.A.; Korn, T.M. *Mathematical Handbook for Scientists and Engineers: Definitions, Theorems, and Formulas for Reference and Review*; Mc. Graw. Dover: New York, NY, USA, 1961; ISBN 0486411478.
47. Solomon, C.J.; Breckon, T.P. *Fundamentals of Digital Image Processing: A Practical Approach with Examples in Matlab*; Wiley Blackwell: New York, NY, USA, 2011; ISBN 0470844728.
48. Gonzalez, R.C.; Woods, R.E.; Eddins, S.L. *Digital Image Processing Using Matlab*, 2nd ed.; Gatesmark Publishing: Knoxville, TN, USA, 2009; ISBN 9780982085400.
49. Bezdek, J.C. *Pattern Recognition with Fuzzy Objective Function Algorithms*; Springer: New York, NY, USA; 1981; ISBN 1475704526.
50. Snyder, J.P. *Flattening the Earth: Two Thousand Years of Map Projections*; The University of Chicago Press: Chicago, IL, USA, 1997; ISBN 0226767477.
51. Sobel, I. History and Definition of the Sobel Operator. 2014. Available online: https://www.researchgate.net/publication/239398674_An_Isotropic_3_3_Image_Gradient_Operator (accessed on 14 June 2015).
52. Nixon, M.S.; Aguado, A.S. *Feature Extraction and Image Processing*, 3rd ed.; Academic Press: London, UK, 2012; ISBN 0123965497.
53. Shen, Y.-J.; Shen, Y.; Goetz, J.; Brenning, A. Spatial-temporal variation of near-surface temperature lapse rates over the Tianshan Mountains, central Asia. *J. Geophys. Res. Atmos.* **2016**, *121*, 14006–14017. [CrossRef]
54. Gardner, A.S.; Sharp, M.J.; Koerner, R.M.; Labine, C.; Boon, S.; Marshall, S.J.; Burgess, D.O.; Lewis, D. Near-surface temperature lapse rates over Arctic Glaciers and their implications for temperature downscaling. *J. Clim.* **2009**, *22*, 4281–4298. [CrossRef]
55. Zhao, J.; Lu, Z.; Meng, Y. Influence of the temperature inversion to the weather in Daxinganling Region. *J. Anhui Agric. Sci.* **2014**, *42*, 6741–6756. (In Chinese)
56. Lollino, G.; Manconi, A.; Clague, J.; Shan, W.; Chiarle, M. *Engineering Geology for Society and Territory—Volume 1: Climate Change and Engineering Geology*; Springer: New York, NY, USA, 2015; pp. 271–277, 285–290, ISBN 9783319092997.
57. Petkovšek, Z. Turbulent dissipation of cold air lake in a basin. *Meteorol. Atmos. Phys.* **1992**, *47*, 237–245. [CrossRef]
58. Zhong, S.; Whiteman, C.D.; Bian, X.; Shaw, W.J.; Hubbe, J.M. Meteorological processes affecting the evolution of a wintertime cold air pool in the Columbia Basin. *Mon. Weather Rev.* **2001**, *129*, 2600–2613. [CrossRef]
59. Weng, D.; Sun, Z. A preliminary study of the lapse rate of surface air temperature over mountainous regions of China. *Geogr. Res.* **1984**, *3*, 24–34. (In Chinese)
60. Amiri, R.; Weng, Q.; Alimohammadi, A.; Alavipanah, S.K. Spatial-temporal dynamics of land surface temperature in relation to fractional vegetation cover and land use/cover in the Tabriz urban area, Iran. *Remote Sens. Environ.* **2009**, *113*, 2606–2617. [CrossRef]
61. Ahmed, B.; Kamruzzaman, M.; Zhu, X.; Rahman, M.S.; Choi, K. Simulating land cover changes and their impacts on land surface temperature in Dhaka, Bangladesh. *Remote Sens.* **2013**, *5*, 5969–5998. [CrossRef]



© 2018 by the authors. Licensee MDPI, Basel, Switzerland. This article is an open access article distributed under the terms and conditions of the Creative Commons Attribution (CC BY) license (http://creativecommons.org/licenses/by/4.0/).

Identification Standard for ENSO Events and Its Application to Climate Monitoring and Prediction in China

Hong-Li REN[1,2*], Bo LU[1], Jianghua WAN[1], Ben TIAN[1], and Peiqun ZHANG[1]

1 *Laboratory for Climate Studies &China Meteorological Administration–Nanjing University Joint Laboratory for Climate Prediction Studies, National Climate Center, China Meteorological Administration, Beijing* 100081

2 *Department of Atmospheric Science, School of Environmental Studies, China University of Geoscience, Wuhan* 430074

(Received May 8, 2018; in final form October 9, 2018)

ABSTRACT

The El Niño–Southern Oscillation (ENSO) reflects anomalous variations in the sea surface temperature (SST) and atmospheric circulation over the tropical central–eastern Pacific. It remarkably impacts on weather and climate worldwide, so monitoring and prediction of ENSO draw intensive research. However, there is not yet a unique standard internationally for identifying the timing, intensity, and type of ENSO events. The National Climate Center of China Meteorological Administration (NCC/CMA) has led the effort to establish a national identification standard of ENSO events, which was officially endorsed by the National Standardization Administration of China and implemented operationally in NCC/CMA in 2017. In this paper, two key aspects of this standard are introduced. First, the Niño3.4 SST anomaly index, which is well-recognized in the international ENSO research community and used operationally in the US, has replaced the previous Niño Z index and been used to identify the start, end, and peak times, and intensity of ENSO events. Second, two new indices—the eastern Pacific ENSO (EP) index and the central Pacific ENSO (CP) index, based on the SST conditions in Niño3 and Niño4 region respectively, are calculated to first determine the ENSO type before monitoring and assessing the impacts of ENSO on China's climate. With this standard, all historical ENSO events since 1950 are consistently re-identified; their distinct properties are diagnosed and presented; and the impacts of ENSO events under different types on China's climate are re-assessed. This standard is also employed to validate the intensity, grade, and type of the ENSO events predicted by the NCC/CMA operational ENSO prediction system. The new standard and the thus derived unified set of re-analyzed historical ENSO events and associated information provide a good reference for better monitoring and prediction of future ENSO events.

Key words: El Niño–Southern Oscillation, identification standard, monitoring, prediction

Citation: Ren, H.-L., B. Lu, J. H. Wan, et al., 2018: Identification standard of ENSO events and its application to climate monitoring and prediction in China. *J. Meteor. Res.*, **32**(6), 923–936, doi: 10.1007/s13351-018-8078-6.

1. Introduction

The terms "El Niño" and "La Niña" originate from Spanish and mean "the little boy" and "the little girl, " respectively. El Niño (La Niña) is associated with a band of warm (cold) water, occurring every few years over central to eastern equatorial Pacific. The recurrence of El Niño and La Niña events is the biggest fluctuation in the earth's climate system and can not only affect the local climate near the eastern Pacific but also induce global climatic impacts via teleconnection (e.g., Bjerknes, 1969; Horel and Wallace, 1981; Rasmusson and Carpenter, 1982; Trenberth et al., 1998). For example, the super strong El Niño in 1997/98 and 2014–16 led to severe climatic disasters, including flooding in the Yangtze River basin (Huang et al., 2000; Zhang et al., 2016). Therefore, the monitoring and prediction of El Niño and La Niña events are extremely important.

Although much attention has been paid to El Niño and La Niña events, their identification methods differ in different countries (Wang, 1991; Trenberth, 1997; Guo et al., 1998; Li and Zhai, 2000; Trenberth and Stepaniak, 2001; Hanley et al., 2003; Li et al., 2005), which may

Supported by the National Key Research and Development Program (2018YFC1506005), State Oceanic Administration International Cooperation Program (GASI-IPOVAI-03), China Meteorological Administration Special Public Welfare Research Fund (GYHY201506013), and National Natural Science Foundation of China (41606019 and 41605116).

*Corresponding author: renhl@cma.gov.cn.

©The Chinese Meteorological Society and Springer-Verlag Berlin Heidelberg 2018

cause discrepancies. For example, the beginning and end of the 2014–16 El Niño event were not the same in China, the US, Australia, and Japan. After studying previous identification methods, the research team at the National Climate Center (NCC) of China Meteorological Administration (CMA) has formulated a standard for identification of ENSO events (Ren et al., 2017a). This new standard adopts the latest research results concerning ENSO events and helps improve the operational monitoring and prediction of these events. The standard was officially endorsed by the National Standardization Administration of China as GB/T 33666-2017 and implemented operationally in NCC/CMA in 2017.

Prior to that, the Niño Z index was used in operational monitoring of ENSO in NCC/CMA. It is defined as an area-weighted average of sea surface temperature (SST) over the Niño1+2, Niño3, and Niño4 regions (Li and Zhai, 2000). The advantage of this index is that the overall states of the tropical Pacific are reflected. A number of studies have pointed out the existence of different types of El Niño events due to varied zonal positions of the warming center (Fu and Fletcher, 1985; Ashok et al., 2007; Kao and Yu, 2009; Kug et al., 2009; Ren et al., 2013, 2016a). The climatic impacts induced by different types of El Niño events are very distinct (e.g., Weng et al., 2007; Zhang et al., 2011, 2012, 2016; Yuan and Yang, 2012; Yuan and Yan, 2013). But the Niño Z index cannot distinguish different types of El Niño, which limits its capability for El Niño monitoring.

Given the limitation of the Niño Z index, the new national standard (GB/T 33666-2017) uses the Niño3.4 index to describe the beginning, end, and amplitude of El Niño/La Niña events. In addition, it adopts the eastern Pacific (EP) and central Pacific (CP) type ENSO indices to verify the types of ENSO events (Ren and Jin, 2011, 2013). This paper intends to describe the rational, methods, and results associated with establishment of the new ENSO identification standard in NCC/CMA. We begin (in Section 2) by describing the details of the standard for identification of ENSO events. Then, in Section 3, the characteristics of historical ENSO events are summarized by using this national standard. The use of the national standard in ENSO prediction is discussed in Section 4. In Section 5, impacts of different types of ENSO events on China's climate are investigated. Finally, a summary and discussion are provided in Section 6.

2. Identification standard for ENSO events

2.1 *Data and index definition*

We use the Hadley Centre Sea Ice and Sea Surface Temperature dataset (HadISST) to calculate the SST anomaly during the period 1950–81 (Rayner et al., 2003), and the Optimum Interpolation SST dataset, version 2 (OISSTv2) (Reynolds et al., 2002), with a 0.25° resolution, provided by the Climate Prediction Center (CPC) of NOAA from 1982 to 2017. Monthly 2-m temperature and precipitation data from 160 standard meteorological stations in China, collected since 1951, were obtained from NCC/CMA.

The study domain includes the Niño1+2 sector (10°S–0°, 90°–80°W), the Niño3 sector (5°S–5°N, 150°–90°W), the Niño4 sector (5°S–5°N, 160°E–150°W), and the Niño3.4 sector (5°S–5°N, 170°–120°W).

Observationally, the Niño3 and Niño4 SST indices are highly correlated. Two independent indices from Ren and Jin (2011)—the piecewise linear combination of the Niño3 and Niño4 indices conditioned by the ENSO phase—are used here to describe the EP-type and CP-type of ENSO events.

The EP-type ENSO index, N_{EP}, is defined as

$$N_{EP} = N_3 - \alpha \times N_4, \tag{1}$$

where N_3 is the Niño3 index (°C), N_4 is the Niño4 index (°C), and α is 0.4 if $N_3 \times N_4 > 0$ and 0 if $N_3 \times N_4 \leqslant 0$.

The CP-type ENSO index, N_{CP}, is defined as

$$N_{CP} = N_4 - \alpha \times N_3. \tag{2}$$

The parameter α is determined by a minimization procedure to produce two independent indices out of the Niño3 and Niño4 indices. To make the national standard easy to use, here, a fixed value of 0.4 is applied. The running correlation between the CP and EP El Niño indices is much weaker than that between the Niño3 and Niño4 indices for any given period (figure omitted), implying that the fixed value of 0.4 for α is robust.

All the Niño indices are calculated with respect to a 30-yr running average climatology (see footnote in Table 2). Though a fixed climatology is reasonable for research purposes, a changing climatology is more suitable for operational monitoring, because the dataset is constantly updated and previously defined events cannot be revised even if the climatology changes in the future. A changing climatology is hence recommended by the World Meteorological Organization (WMO) and adopted by CPC/NOAA and Japan Meteorological Agency (JMA) in ENSO operational monitoring.

2.2 *Identification method*

2.2.1 *Event definition*

An ENSO event can be identified if the absolute value of the 3-month running mean Niño3.4 index (to one decimal point) reaches or exceeds 0.5°C and lasts for at least 5 months (El Niño event if the Niño3.4 index ⩾

0.5°C; La Niña event if the Niño3.4 index ⩽ –0.5°C). We use the Niño3.4 index instead of the Niño3 index used by the JMA, because the Niño3.4 index measures a part of both the Niño3 sector and the Niño4 sector, meaning that it can be used to capture the general features of ENSO.

2.2.2 *Event duration*

The start month is defined as the earliest month during which the Niño3.4 index meets the criterion of an ENSO event. The end month is defined as the latest month when the Niño3.4 index meets the criterion of an ENSO event. The duration of an event is the number of months from the start month to the end month.

2.2.3 *Event strength*

The event peak includes the peak time and the peak value, and can be defined as when the absolute value of the 3-month running mean Niño3.4 index reaches its maximum during the event. If there is more than one peak with the same value, the first one is chosen as the event peak.

The event strength is defined by the peak value of the event. The strength grade (intensity rank) of an ENSO event is identified as weak if the absolute value of the event peak is ⩾ 0.5°C but < 1.3°C; a medium event has an event peak between 1.3 and 2.0°C; a strong event has an event peak between 2.0 and 2.5°C; and a super strong event has an event peak > 2.5°C.

Note that the criteria of 1.3, 2.0, and 2.5°C are approximately 1.5, 2.5, and 3 times the standard deviation of the Niño3.4 index, respectively.

2.2.4 *Event type*

An EP-type event is identified if the absolute value of the N_{EP} index is ⩾ 0.5 and lasts for at least 3 months. A CP-type event is identified if the absolute value of the N_{CP} index is ⩾ 0.5 and lasts for at least 3 months.

If both of the above conditions are satisfied in one event with a transition between the two types, the type when the event reaches its peak time is considered to be the primary type and the other one is the secondary type. Such a primary type is used as the type for the entire ENSO event.

2.3 *Comparison with the standards of other operational centers*

The CMA national standard for identification of ENSO events is compared with the operational standards used in other countries such the US, Australia, and Japan (Table 1). It is seen that JMA uses the Niño3 index and Australian Bureau of Meteorology (BoM) uses the Southern Oscillation index (SOI) to define ENSO events, while both CPC/NOAA and NCC/CMA use the Niño3.4 index. It should be noted that only the NCC/CMA standard adopts additional type identification for EP- or CP-type ENSO events to obtain more accurate climate impact assessment.

3. Re-identification of historical ENSO events

We re-compile the basic information of all the El Niño/La Niña events since 1950 according to the ENSO identification standard of NCC/CMA (Table 2). Furthermore, all the ENSO events identified by the national meteorological operation centers of the US, Australia, and Japan are also listed in Table 3, in comaprison with those identified by China. The performances of different ENSO identification standards are mostly similar, but with quite some discrepancies, in terms of event number, occurrence time, duration, and so on, for both El Niño/La Niña events. It should be noted that the difference between the events defined by China and the US results from different SST datasets used by the two countries. CPC/NOAA utilizes ERSSTv5 (Extended Reconstructed SST, version 5) data (Huang et al., 2017), while NCC/CMA uses HadISST (Titchner and Rayner, 2014) during 1950–81 and OISSTv2 after 1982 (Reynolds et al., 2002).

As shown in Table 2, there are 19 El Niño events and 14 La Niña events since 1950, including 13 EP El Niños, 6 CP El Niños, 10 EP La Niñas, and 4 CP La Niñas. Most of the events identified here are quite consistent with those found in previous studies (Kao and Yu, 2009; Kug et al., 2009; McPhaden et al., 2011; Zhang et al., 2015). Notably, a few so-called mixed-type events found in the record have been mandatorily determined as either EP- or CP-type events in view of the China national standard, such as the 2016/17 event. To further examine the variations of ENSO phases based on these events, Table 4 shows the transitions of the ENSO events. Most of the EP El Niño events develop into EP La Niña events or a neutral state, while most of the EP La Niña events develop into EP El Niño events within two years. The de-

Table 1. Identification standards for ENSO events used by different meteorological operation centers (countries)

	NCC/CMA (China)	CPC/NOAA (USA)	BoM (Australia)	JMA (Japan)
EP-type: $\|N_{EP}\| \geqslant 0.5$ CP-type: $\|N_{CP}\| \geqslant 0.5$	3-month running mean Niño3.4 index continues at 0.5°C (–0.5°C) or higher (lower) for 5 consecutive months or longer	3-month running mean Niño3.4 index continues at 0.5°C (–0.5°C) or higher (lower) for 5 consecutive months or longer	Sustained negative (positive) SOI values below –7 (+7) for El Niño (La Niña)	5-month running mean Niño3 index continues at 0.5°C (–0.5°C) or higher (lower) for 6 consecutive months or longer

Table 2. El Niño and La Niña events since the 1950s, as identified by the NCC/CMA standard

	Number	Time span	Duration (month)	Peak month	Amplitude (°C)	Grade	Type
El Niño events	1	1951.08–1952.01	6	1951.11	0.8	Weak	EP
	2	1957.04–1958.07	16	1958.01	1.7	Medium	EP
	3	1963.07–1964.01	7	1963.11	1.1	Weak	EP
	4	1965.05–1966.05	14	1965.11	1.7	Medium	EP
	5	1968.10–1970.02	17	1969.02	1.1	Weak	CP
	6	1972.05–1973.03	11	1972.11	2.1	Strong	EP
	7	1976.09–1977.02	6	1976.10	0.9	Weak	EP
	8	1977.09–1978.02	6	1977.11	0.8	Weak	CP
	9	1979.09–1980.01	5	1980.01	0.6	Weak	EP
	10	1982.04–1983.06	15	1983.01	2.7	Extreme	EP
	11	1986.08–1988.02	19	1987.08	1.9	Medium	EP
	12	1991.05–1992.06	14	1992.01	1.9	Medium	EP
	13	1994.09–1995.03	7	1994.12	1.3	Medium	CP
	14	1997.04–1998.04	13	1997.11	2.7	Extreme	EP
	15	2002.05–2003.03	11	2002.11	1.6	Medium	CP
	16	2004.07–2005.01	7	2004.09	0.8	Weak	CP
	17	2006.08–2007.01	6	2006.11	1.1	Weak	EP
	18	2009.06–2010.04	11	2009.12	1.7	Medium	CP
	19	2014.10–2016.04	19	2015.12	2.8	Extreme	EP
La Niña events	1	1950.01–1951.02	12	1950.01	–1.4	Medium	EP
	2	1954.07–1956.04	22	1955.10	–1.7	Medium	EP
	3	1964.05–1965.01	9	1964.11	–1.0	Weak	EP
	4	1970.07–1972.01	19	1971.01	–1.6	Medium	EP
	5	1973.06–1974.06	13	1973.12	–1.8	Medium	CP
	6	1975.04–1976.04	13	1975.12	–1.5	Medium	CP
	7	1984.10–1985.06	9	1985.01	–1.2	Weak	EP
	8	1988.05–1989.05	13	1988.12	–2.1	Strong	EP
	9	1995.09–1996.03	7	1995.11	–0.9	Weak	EP
	10	1998.07–2000.06	24	2000.01	–1.6	Medium	EP
	11	2000.10–2001.02	5	2000.12	–0.8	Weak	CP
	12	2007.08–2008.05	10	2008.01	–1.7	Medium	EP
	13	2010.06–2011.05	12	2010.12	–1.6	Medium	EP
	14	2011.08–2012.03	8	2011.12	–1.1	Weak	CP

NOTE 1: The climatology adopts a 30-yr running average, as suggested by the WMO. The anomalies during 1950–90 are relative to the climatology of 1951–80. The anomalies during 1991–2000 are relative to the climatology of 1961–90. The anomalies since 2011 are relative to the climatology of 1981–2010. The SST during 1950–81 is HadISST (Titchner and Rayner, 2014). The SST after 1982 is NOAA's 1/4° daily OISSTv2 (Reynolds et al., 2002). NOTE 2: Because the SST dataset used here starts in January 1950, the beginning of the 1950/51 La Niña event cannot be traced back to before 1950.

velopment of CP El Niño/La Niña events is rather uncertain, which may cause difficulties for the prediction of ENSO type.

The three strongest El Niño events are 1982/83, 1997/98, and 2014–16, which are super strong El Niño events because their peak strength exceeds 2.5°C in all three cases (Fig. 1). The La Niña events are relatively weak, with no super strong events since 1950. Figure 2 exhibits the life cycle of different types of El Niño events. The EP El Niño events are generally stronger than the CP El Niño events. Figure 3 exhibits the temporal evolution of different types of La Niña events. The EP- and CP-type La Niña events are similar in their evolutionary features and strengths. With regard to the duration of El Niño events, as shown in Fig. 4, the two EP-type El Niño events of 1986–88 and 2014–16 have the longest life span, lasting for 19 months (Table 2), while the longest CP El Niño event occurs during 1968–80, lasting for 17 months (Table 2). Overall, La Niña events have a relatively longer lifetime compared to El Niño events, and the EP-type events are evidently longer than the CP type, with an earlier start month and later end month. Figure 5 further illustrates the probability density function of the Niño3.4 index and shows a strong asymmetry between the El Niño and La Niña phases, with a greater number of strong El Niño events. For the strong and super strong events especially, there are notably fewer La Niña events than El Niño events.

4. Application of the China standard

Based on the above-mentioned standard, 20-yr ENSO hindcasts with a multi-method ensemble (MME) provided by the NCC's System of ENSO Monitoring, Analysis, and Prediction (SEMAP 2.0; Ren et al., 2016b, 2017b) are used here to evaluate the accuracy in predicting the strength grades and types of ENSO events (Table 5). It can be seen that the SEMAP 2.0 MME can predict approximately 80% of the El Niño/La Niña events begin-

Table 3. El Niño and La Niña events identified by different meteorological operation centers

		CMA (China)	CPC (USA)	BoM (Australia)	JMA (Japan)
El Niño	1	1951.08–1952.01	1951.06–1952.01	1951.03–1952.02	Spring 1951 to winter 1951/52
Events	2	/	1953.02–1954.02	/	Spring 1953 to autumn 1953
	3	1957.04–1958.07	1957.04–1959.03	1957.03–1957.11	Spring 1957 to spring 1958
	4	1963.07–1964.01	1963.06–1964.02	1963.09–1964.03	Summer 1963 to winter 1963/64
	5	1965.05–1966.05	1965.05–1966.04	1965.03–1965.11	Spring 1965 to winter 1965/66
	6	1968.10–1970.02	1968.10–1969.05; 1969.08–1970.01	1969.06–1970.02	Autumn 1968 to winter 1969/70
	7	1972.05–1973.03	1972.05–1973.03	1972.03–1972.12	Spring 1972 to spring 1973
	8	1976.09–1977.02	1976.10–1977.02	/	Summer 1976 to spring 1977
	9	1977.09–1978.02	1977.10–1978.01	1977.06–1978.02	/
	10	1979.09–1980.01	1979.10–1980.02	/	/
	11	1982.04–1983.06	1982.04–1983.06	1982.04–1983.02	Spring 1982 to summer 1983
	12	1986.08–1988.02	1986.10–1988.02	1987.05–1988.01	Autumn 1986 to winter 1987/88
	13	1991.05–1992.06	1991.05–1992.06	1991.03–1992.04	Spring 1991 to summer 1992
	14	/	/	1993.07–1994.02	/
	15	1994.09–1995.03	1994.10–1995.03	1994.03–1995.04	/
	16	1997.04–1998.04	1997.05–1998.05	1997.04–1998.03	Spring 1997 to spring 1998
	17	2002.05–2003.03	2002.06–2003.02	2002.03–2003.01	Summer 2002 to winter 2002/03
	18	2004.07–2005.01	2004.07–2005.02	/	/
	19	2006.08–2007.01	2006.10–2007.01	2006.05–2007.05	/
	20	2009.06–2010.04	2009.07–2010.03	2009.05–2010.03	Summer 2009 to spring 2010
	21	2014.10–2016.04	2014.11–2016.05	2015.04–2016.04	Summer 2014 to spring 2016
	Sum	19	21	17	15
La Niña	1	1950.01–1951.02	1950.01–1950.07	1949.12–1951.02	Summer 1949 to summer 1950
Events	2	1954.07–1956.04	1954.05–1956.09	1954.04–1957.01	Spring 1954 to winter 1955/56
	3	1964.05–1965.01	1964.05–1965.01	1964.04–1964.10	Spring 1964 to winter 1964/65
	4	/	/	/	Autumn 1967 to spring 1968
	5	1970.07–1972.01	1970.07–1972.01	1970.06–1972.03	Spring 1970 to winter 1971/72
	6	1973.06–1974.06; 1975.04–1976.04	1973.05–1974.07; 1974.10–1976.04	1973.06–1976.03	Summer 1973 to spring 1974 Spring 1975 to spring 1976
	7	/	1983.09–1984.01	/	/
	8	1984.10–1985.06	1984.10–1985.08	/	Summer 1984 to autumn 1985
	9	1988.05–1989.05	1988.05–1989.05	1988.04–1989.07	Spring 1988 to spring 1989
	10	1995.09–1996.03	1995.08–1996.03	/	Summer 1995 to winter 1995/96
	11	1998.07–2000.06; 2000.10–2001.02	1998.07–2001.02	1998.05–2001.03	Summer 1998 to spring 2000
	12	/	2005.11–2006.03	/	Autumn 2005 to spring 2006
	13	2007.08–2008.05	2007.07–2008.06	2007.06–2008.02	Spring 2007 to spring 2008
	14	/	/	2008.08–2009.04	/
	15	2010.06–2011.05; 2011.08–2012.03	2010.06–2011.05; 2011.07–2012.03	2010.04–2012.03	Summer 2010 to spring 2011
	16	/	2016.08–2016.12	/	/
	Sum	14	16	10	14

NOTE: The CPC (USA) results are from http://origin.cpc.ncep.noaa.gov/products/analysis_monitoring/ensostuff/ONI_v5.php; the Bureau of Meteorology (BoM; Australia) results are from http://www.bom.gov.au/climate/enso/enlist/; and the JMA (Japan) results are from http://ds.data.jma.go.jp/tcc/tcc/products/elnino/ensoevents.html. SOI denotes Southern Oscillation index.

Table 4. Number of transition between different types of El Niño and La Niña events from 1950 to 2016

		Transition to				
		EP El Niño	CP El Niño	Neutral	EP La Niña	CP La Niña
Transition from	EP El Niño	0	1	6	5	1
	CP El Niño	1	1	1	3	0
	Neutral	5	2	**	2	0
	EP La Niña	6	1	1	0	2
	CP La Niña	1	1	1	0	1

NOTE: A transition is counted if the succeeding event happened within two years of the peak month of the preceding event. Because the neutral state is not an event, the summary here does not take the neutral–neutral transition (denoted by **) into account.

ning from July; meanwhile, the system can also successfully distinguish the types of most El Niño events, which provides a very good background for the forecasting of the location of summer rainfall belt in China. It is clear that the SEMAP 2.0 prediction of ENSO amplitude is generally one grade weaker than observed. This may be related to the use of MME mean forecasting in SEMAP 2.0. How to further correct the predicted strength of ENSO within the SEMAP 2.0 system needs to be addressed in future work.

The new ENSO standard was also employed to assess the performance of the ENSO hindcasts. An example of the predictions beginning from July in each year is shown here. As indicated in Fig. 6, for the El Niño events

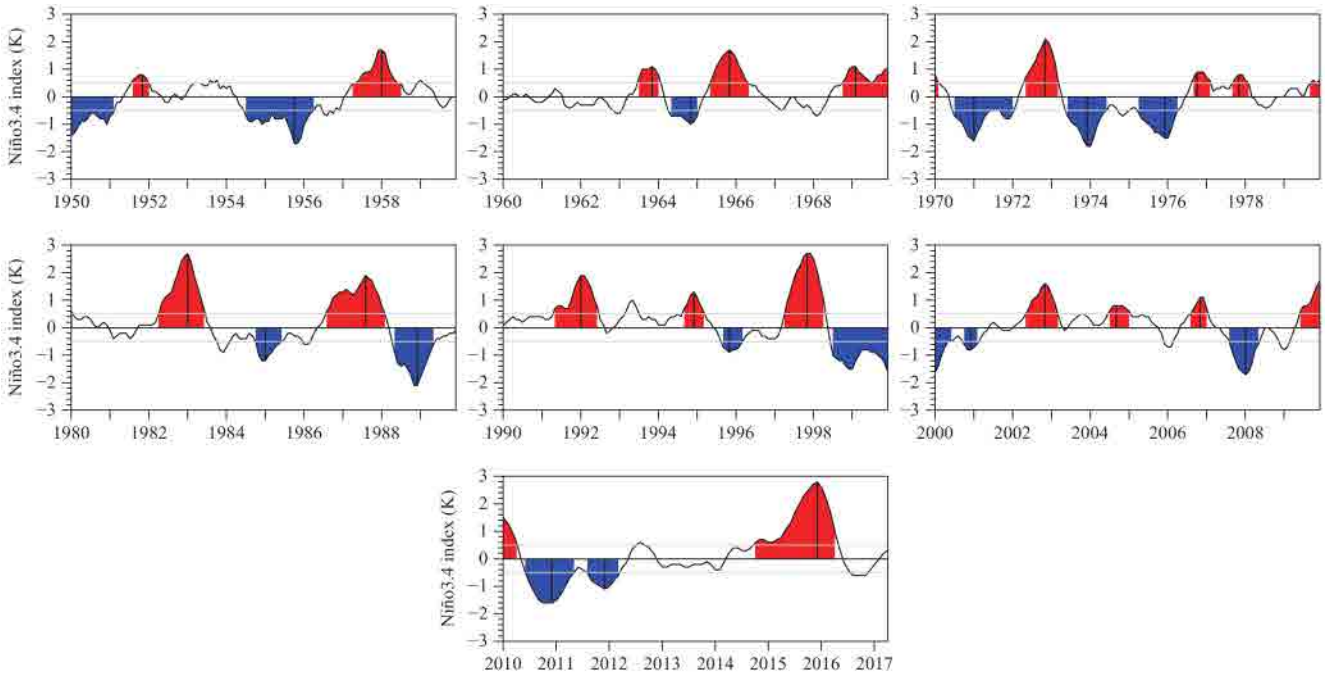

Fig. 1. Distribution of all ENSO events since 1950. Black curves represent the Niño3.4 index (based on a moving climatology). The red and blue filled areas represent the El Niño and La Niña events, respectively. The black vertical line indicates the peak month of the event.

that have occurred since 1996, the Niño3.4 index predicted by SEMAP 2.0 can represent the observed peak strength well, and the correlation coefficient between the predicted and the observed peak strength is as high as 0.96. However, the correlation coefficient itself does not fully reflect the prediction bias of the ENSO intensity level. Instead, the new ENSO standard can be used to visually reflect this information. According to the standard for classification of different grades of ENSO events, the 2-D value domain in Fig. 6 is divided into several boxes. The boxes on the diagonals indicate that the predicted ENSO event grade is perfectly consistent with the actual observation level. We can see that, out of the 11 incidents, only 2 events fall into the diagonal boxes. As shown in Fig. 7a, SEMAP 2.0 tends to underestimate the intensity of both El Niño and La Niña events. Specifically, with the exception of the weak El Niño event in 2004/05 and the medium La Niña event in 2010/11, the predicted grades of all other ENSO events tend to be one level lower than the actual level (Fig. 7b). Therefore, ENSO predictions by SEMAP2.0 are generally weaker than observed.

The new ENSO standard can also be applied to evaluating the predicted ENSO type in addition to its strength. As shown in Fig. 8, the type predictions of 8 events out of the 11 ENSO events since 1996 are generally correct (the percentage is 73%). Of these, 4 out of 6 El Niño events are accurate, but the 2006/07 EP El Niño event is misrepresented as a CP El Niño event. For 2009/10, the CP El Niño event is misreported as an EP event. Four out of five La Niña events are accurate, and only the 2000/01 CP La Niña event is misrepresented as an EP La Niña event. Overall, the SEMAP2.0 MME performs reasonably well for predicting ENSO intensity grades and types. Indeed, the difficulty in distinguishing the two types of ENSO, even at a short lead time, is considerable (Ren et al., 2018a). The skillful forecast in the current case of SEMAP2.0 indicates a substantial positive contribution from the multi-method ensemble of the dynamical model prediction and its empirical error correction (Liu and Ren, 2017), as well as the physics-based statistical prediction (Ren et al., 2018b). This is a promising topic in need of further examination.

5. Revisiting the impacts of different types of ENSO events on China's climate

As Fig. 8 shows, if we can make a more accurate judgment on the ENSO event type, important indications will be derived concerning regional climate (temperature and precipitation) predictions in China. As for ENSO's impacts on China's climate, many studies have been conducted and evident differences have been found existing between the impacts of the two types of events (Weng et al., 2007; Feng et al., 2010; Feng and Li, 2011; Zhang et al., 2011, 2012; Yuan and Yang, 2012; Yuan and Yan,

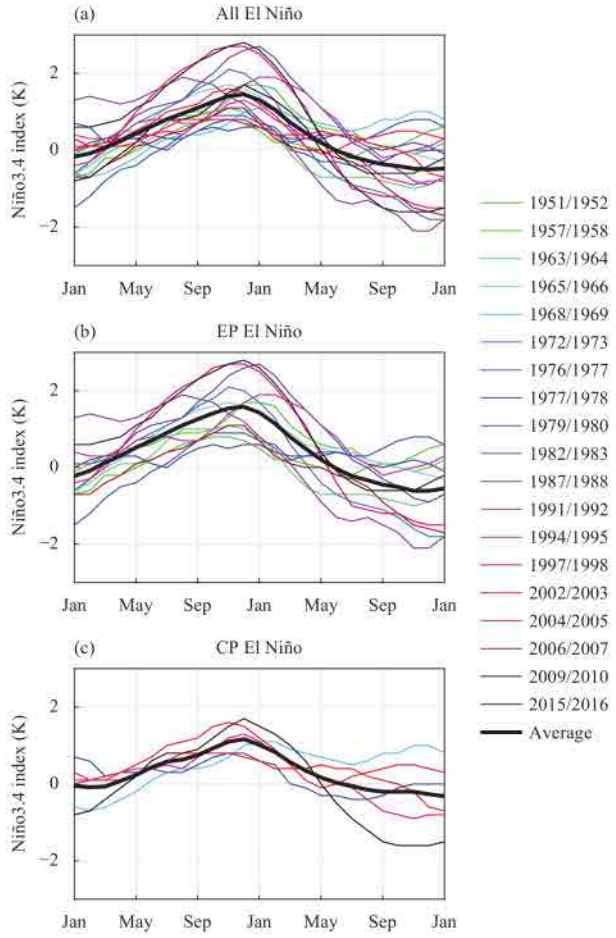

Fig. 2. Evolutions of the Niño3.4 index for El Niño events since 1950: (a) all El Niño events, (b) EP El Niño events, and (c) CP El Niño events.

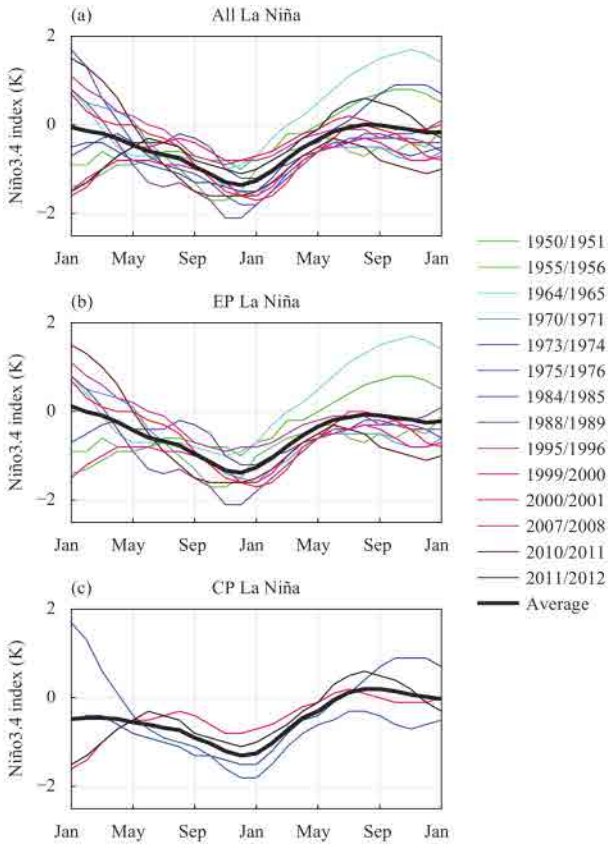

Fig. 3. Evolutions of the Niño3.4 index for La Niña events since 1950: (a) all La Niña events, (b) EP La Niña events, and (c) CP La Niña events.

2013). However, the conclusions in these studies regarding the impacts of the two ENSO types have not yet been systematically reviewed. Here, we use the information on the ENSO events shown in Figs. 2, 3 to comprehensively demonstrate significant differences in the impacts of the different types of ENSO events on precipitation and air temperature in China in the summers of ENSO development, the winters of ENSO peaks, and the following summers of ENSO decay (Figs. 9, 10). Here, the climatology of temperature and precipitation is defined by using all the data, and the linear trend is removed.

Figure 9 shows the composite maps of precipitation anomalies in summer and winter in China based on all and different types of ENSO events. For the summers of the El Niño developing years, the precipitation in North China and the south part of northeastern China during the EP El Niño events is significantly low; the locations where rainfall is relatively less abundant can also be detected corresponding to the CP type events, which primarily occur southward in the lower reaches of the Yellow River and the upper-to-middle reaches of the Yangtze River. Meanwhile, precipitation in most of northeastern China is much less abundant compared to southern China. During summer (JJA1) of the decaying phase of EP-type El Niño, positive anomalies appear in northern China as well as south of the Yangtze River; whereas in the same stage for CP-type El Niño, increased precipitation is mainly located in the Yellow–Huaihe River valley and negative anomalies are present to the south of the Yangtze River, consistent with previous studies (Feng et al., 2010; Yuan et al., 2012). Furthermore, significant positive rainfall anomalies are observed in South China for EP-type El Niño during its mature phase (DJF0), as also demonstrated in some previous works (Feng et al., 2010; Yuan and Yang, 2012). Meanwhile, several inconsistent features of precipitation exist, relating to CP-type El Niño. Our study shows that, during the mature phase of CP-type El Niño, positive rainfall anomalies are significant over Southeast China, which is usually absent in other studies (Feng et al., 2010; Yuan and Yang, 2012). Several factors may lead to the differences with regard to this point. Firstly, some

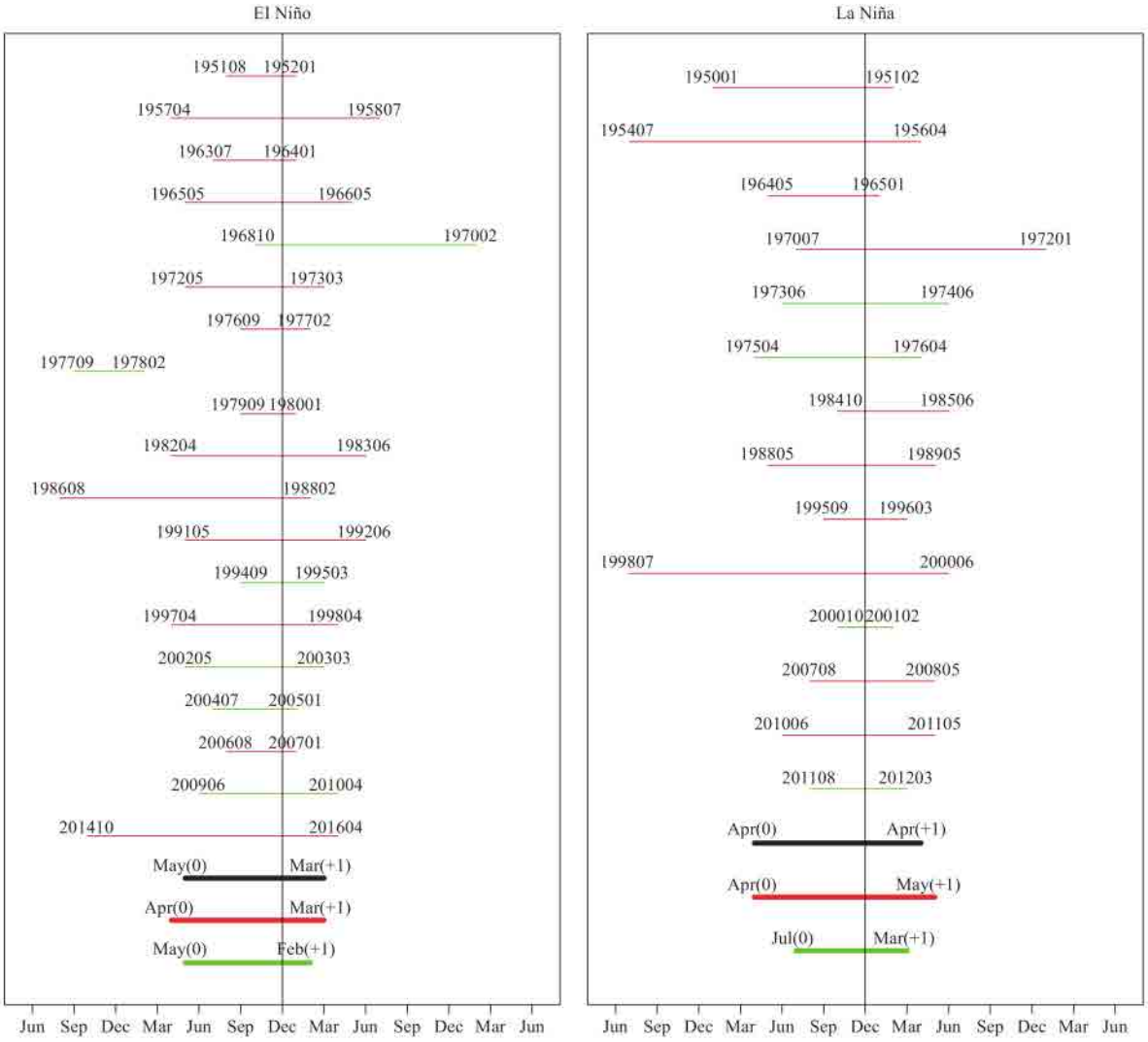

Fig. 4. Timespan of all EP (red) and CP (green) ENSO events. The three thick lines at the bottom are the averages of all events (black), EP events (red), and CP events (green). The left-hand panel is under the El Niño condition, and the right-hand panel is under the La Niña condition.

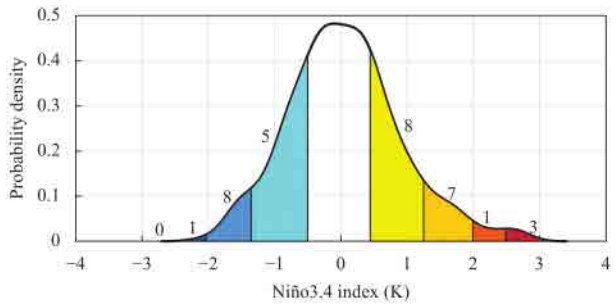

Fig. 5. Probability density function of the Niño3.4 index. The intervals are –2.5, –2.0, –1.3, –0.5, 0.5, 1.3, 2.0, and 2.5 K. The numbers indicate the number of events within each grade.

previous studies focused on a different and often shorter research period, thus adopting different ENSO events (even in the same period). Specifically, the event in 2009, which is a strong CP-type El Niño and generally absent in previous research, has been shown to seriously influence summer rainfall in Southeast China (Wang et al., 2012). Furthermore, most previous studies utilized the Niño3 and El Niño Modoki indices to compare the potential effects of the two types of ENSO, so varied definitions of ENSO types may also explain how these differences arise. Also, the precipitation from station rainfall data used here could differ from that obtained from some of the analysis data employed in other works, which may also make a difference to these results.

For the La Niña events, the differences between the two types of events are generally obvious in the three typical seasons. The differences in the summers of ENSO development are primarily in southwestern China, western Inner Mongolia, and so on, where an EP-type La Niña event corresponds to relatively humid conditions, while significantly less precipitation takes place during

Table 5. El Niño/La Niña predictions by the NCC SEMAP2.0 from 1996 to 2016. OBS and PRED indicate observations and predictions made from July of each year, respectively. The ENSO intensity grades SS, S, M, W, and N are abbreviations for super strong, strong, medium, weak, and neutral events, respectively

Number	Event	Peak amplitude (OBS/PRED)	Grade (OBS/PRED)	Type (OBS/PRED)
1	1997–1998	2.7/2.3	SS/S	EP/EP
2	2002–2003	1.6/0.9	M/W	CP/CP
3	2004–2005	0.8/0.6	W/W	CP/CP
4	2006–2007	1.1/0.3	W/N	EP/CP
5	2009–2010	1.7/1.0	M/W	CP/EP
6	2014–2016	2.8/2.2	SS/S	EP/EP
1	1998–2000	–1.6/–1.1	M/W	EP/EP
2	2000–2001	–0.8/–0.4	W/N	CP/EP
3	2007–2008	–1.7/–0.8	M/W	EP/EP
4	2010–2011	–1.6/–1.6	M/M	EP/EP
5	2011–2012	–1.1/–0.2	W/N	CP/CP

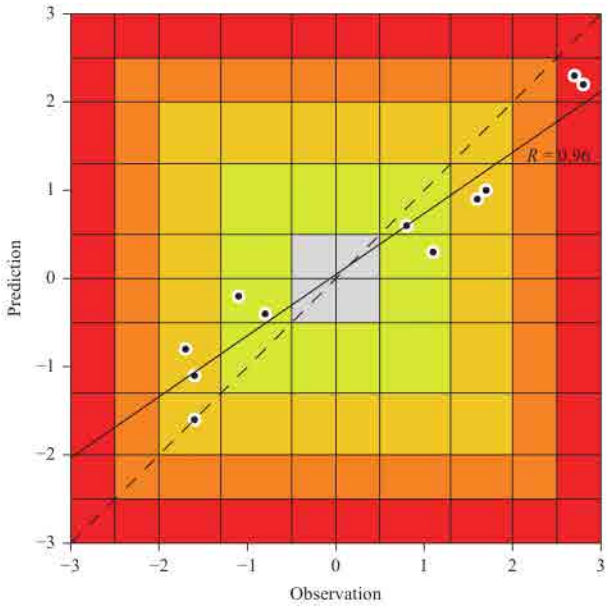

Fig. 6. Scatterplot of the ENSO intensities between the observations (*x*-axis) and the predictions (*y*-axis) made from July of the ENSO developing year. Colors are used according to the ENSO intensity, where gray, yellow, orange, and red indicate values < 0.5, < 1.3, < 2.5, and > 2.5, respectively. The correlation coefficient between the predictions and the observations is 0.96.

CP-type events. In the winters of the two types of La Niña events, more precipitation appears in central China, and the difference lies in the obvious drought in the lower reaches of the Yangtze River corresponding to EP La Niña events. For the summers of the ENSO decaying years, larger deviations are found in central–eastern China, South China, Northeast China, and especially, South–central China. The EP La Niña events correspond to a "wet north–dry south" distribution, while the precipitation pattern during CP La Niña is nearly opposite.

Figure 10 further shows the distributions of air temperature anomalies in China for the two types of ENSO events. In the summers of the El Niño developing years, the 2-m temperature characteristics during the EP El Niño events and all El Niño events are more consistent, showing low temperatures over the whole of China, as compared to the CP events, in which high temperatures across the northern part of the country form in significant contrast.

In the summers of the developing years for both types of La Niña events, northeastern China is notably warmer, especially so during CP El Niño events; and in the following winters of the CP warm events, the warm pattern remains while low temperatures mostly dominate across the whole of China corresponding to CP La Niña events, which are most significant in South China. In addition, note that, during the summers when the La Niña events decay, despite the fact that most of the central–southern parts of China tend to be cold, the colder areas during the CP La Niña events are close to the coastal areas and tend to move southward.

The above-mentioned results suggest significant differences exist between the influences of the two types of ENSO events on precipitation and temperature anomalies in China. Therefore, when considering the impacts of ENSO on climate anomalies, it is fairly necessary to further classify the types of events to obtain effective signals to predict climate anomalies in China.

6. Summary and discussion

The monitoring and prediction of El Niño/La Niña events are important topics in global climate studies. Even though great improvements have been achieved toward understanding El Niño/La Niña events, there is no unique method/standard to identify the start time, end time, duration, intensity grade, and type of these events. As a consequence, the operational monitoring of ENSO events often differs across institutions and countries. Recently, the research team in NCC/CMA formulated the national standard for the identification of El Niño/La Niña events (GB/T 33666-2017), which was officially

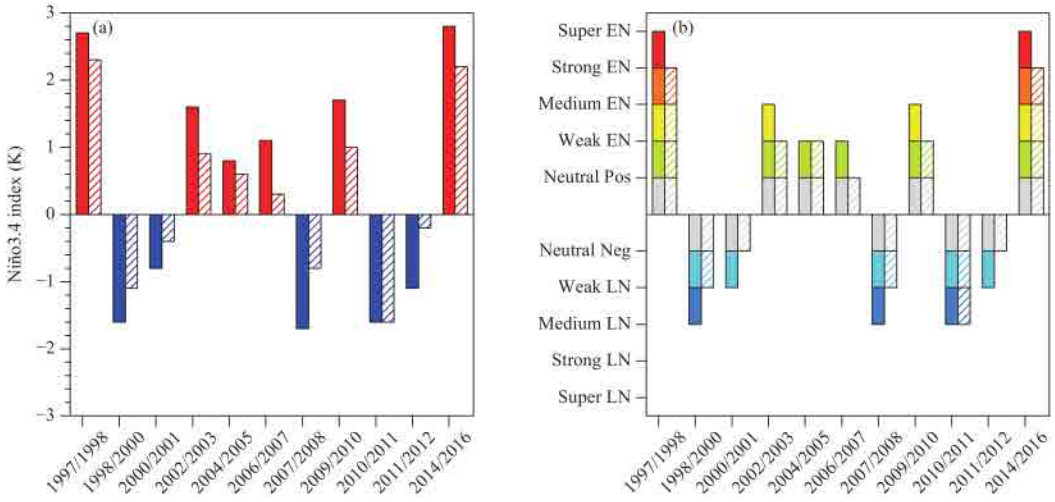

Fig. 7. ENSO (a) intensity and (b) grade from the observations (shaded bars) and the predictions (striped bars) of SEMAP2.0.

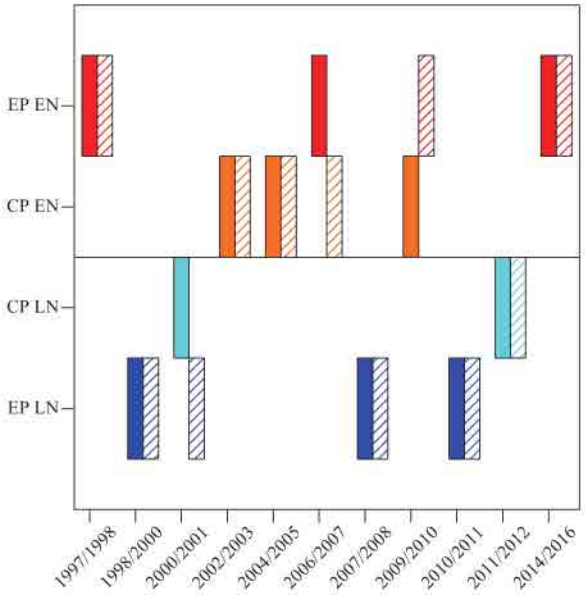

Fig. 8. ENSO types based on observations (shaded bars) and SEMAP2.0 predictions (striped bars). The shaded (striped) bars in red and orange represent EP El Niño and CP El Niño events, respectively, while the shaded (striped) bars in blue and green indicate EP La Niña and CP La Niña events, respectively.

endorsed by the National Standardization Administration of China in March 2017 and operationally implemented in NCC/CMA at the end of that year.

In this paper, this national standard is introduced in detail and applied to climate monitoring and prediction. In this standard, the Niño3.4 index is used to describe the properties of the start time, end time, duration, and intensity of El Niño/La Niña events. Given that the Niño3.4 region is a key dynamical region for El Niño/La Niña dynamics, the Niño3.4 index is also widely used by international communications. In addition, the new national standard adopts two further Niño indices to quantitatively verify the types of El Niño/La Niña events, which is a distinguishing feature of this identification method. In light of the various impacts of the different types of El Niño/La Niña events on the climate over China, the identification of EP- and CP-type El Niño/La Niña events could improve the operational capability of ENSO monitoring.

According to this national standard, the characteristics of historical El Niño/La Niña events are comprehensively re-investigated, including the start time, end time, duration, intensity grade, and type of these events. As an application of this national standard, the operational prediction ability of El Niño/La Niña events by the NCC/CMA ENSO prediction system SEMAP2.0 is also assessed, by using the information on these events. It is demonstrated that most of the occurrences of El Niño/La Niña events can be predicted well at a six-month lead, even though the event amplitude is often underestimated with a relatively lower grade of intensity. The type of El Niño/La Niña event is also captured, at an accuracy rate of 73%. Overall, the ENSO prediction system of the NCC/CMA is capable of successfully predicting the key characteristics (intensity grade and classification) of El Niño/La Niña events.

As a recommended standard, it provides a reliable identification method for operational El Niño/La Niña monitoring. Our paper demonstrates, via a summary of historical events, an evaluation of operational predictions, and an assessment of different climatic impacts, that this national standard is a capable one. Particularly, the impacts of the ENSO events under different types on the precipitation and air temperature in China are revisited, and some new conclusions have been obtained. This

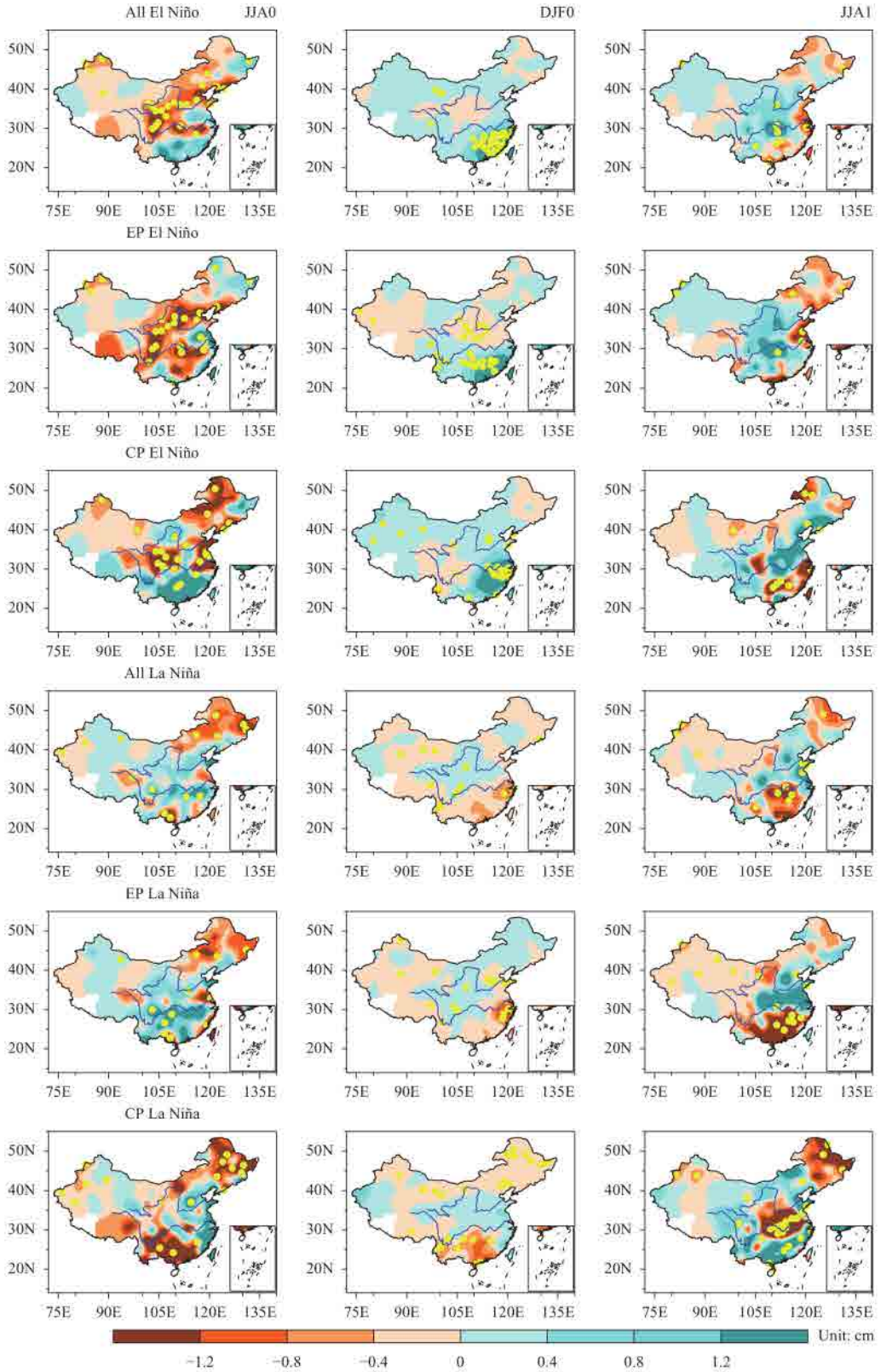

Fig. 9. Composites of precipitation for all ENSO events and the two types of ENSO events. The six rows from top to bottom represent the composites of all El Niño, EP El Niño, CP El Niño, all La Niña, EP La Niña, and CP La Niña events, respectively. The three columns correspond to the boreal summer (JJA0) and winter (DJF0) in the ENSO developing year, and the summer (JJA1) in the ENSO decaying year. The yellow dotted areas are statistically significant at the 90% confidence level.

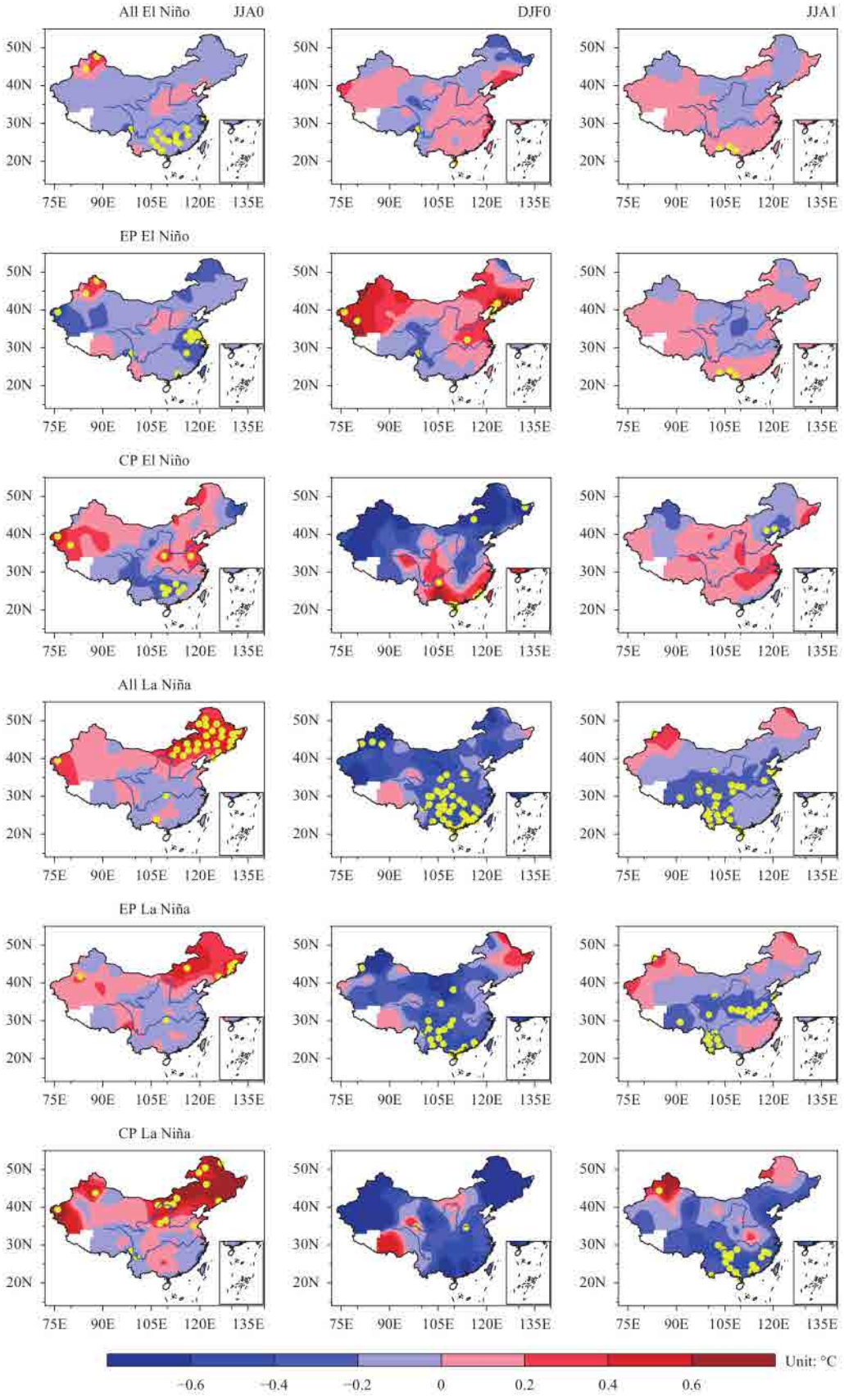

Fig. 10. As in Fig. 9, but for the composites of 2-m temperature.

new national standard will help improve our understanding and ability to predict El Niño/La Niña in terms of their different intensity grades and types.

REFERENCES

Ashok, K., S. K. Behera, S. A. Rao, et al., 2007: El Niño Modoki and its possible teleconnection. *J. Geophys. Res. Oceans*, **112**, C11007, doi: 10.1029/2006JC003798.

Bjerknes, J., 1969: Atmospheric teleconnections from the equatorial Pacific. *Mon. Wea. Rev.*, **97**, 163–172, doi: 10.1175/1520-0493(1969)097<0163:ATFTEP>2.3.CO;2.

Feng, J., and J. P. Li, 2011: Influence of El Niño Modoki on spring rainfall over South China. *J. Geophys. Res. Atmos.*, **116**, D13102, doi: 10.1029/2010JD015160.

Feng, J., L. Wang, W. Chen, et al., 2010: Different impacts of two types of Pacific Ocean warming on Southeast Asian rainfall during boreal winter. *J. Geophys. Res. Atmos.*, **115**, D24122, doi: 10.1029/2010JD014761.

Feng, J., W. Chen, C. Y. Tam, et al., 2011: Different impacts of El Niño and El Niño Modoki on China rainfall in the decaying phases. *Int. J. Climatol.*, **31**, 2091–2101, doi: 10.1002/Joc.2217.

Fu, Z. B., and J. Fletcher, 1985: Two patterns of equatorial warming associated with El Niño. *Chinese Sci. Bull.*, **30**, 1360–1364.

Guo, Y. J., P. M. Zhai, and Y. Q. Ni, 1998: A new index for ENSO monitoring. *Quart. J. Appl. Meteor.*, **9**, 169–177. (in Chinese)

Hanley, D. E., M. A. Bourassa, J. J. O'Brien, et al., 2003: A quantitative evaluation of ENSO indices. *J. Climate*, **16**, 1249–1258, doi: 10.1175/1520-0442(2003)16<1249:AQEOEI>2.0.CO;2.

Horel, J. D., and J. M. Wallace, 1981: Planetary-scale atmospheric phenomena associated with the Southern Oscillation. *Mon. Wea. Rev.*, **109**, 813–829, doi: 10.1175/1520-0493(1981)109<0813:PSAPAW>2.0.CO;2.

Huang, B. Y., P. W. Thorne, V. F. Banzon, et al., 2017: Extended reconstructed sea surface temperature, version 5 (ERSSTv5): Upgrades, validations, and intercomparisons. *J. Climate*, **30**, 8179–8205, doi: 10.1175/JCLI-D-16-0836.1.

Huang, R. H., R. H. Zhang, and Q. Y. Zhang, 2000: The 1997/98 ENSO cycle and its impact on summer climate anomalies in East Asia. *Adv. Atmos. Sci.*, **17**, 348–362, doi: 10.1007/s00376-000-0028-3.

Kao, H. Y., and J. Y. Yu, 2009: Contrasting eastern-Pacific and central-Pacific types of ENSO. *J. Climate*, **22**, 615–632, doi: 10.1175/2008JCLI2309.1.

Kug, J. S., F. F. Jin, and S. I. An, 2009: Two types of El Niño events: Cold tongue El Niño and warm pool El Niño. *J. Climate*, **22**, 1499–1515, doi: 10.1175/2008JCLI2624.1.

Li, X. Y., and P. M. Zhai, 2000: On indices and indicators of ENSO episodes. *Acta Meteor. Sinica*, **58**, 102–109, doi: 10.11676/qxxb2000.010. (in Chinese)

Li, X. Y., P. M. Zhai, and F. M. Ren, 2005: Redefining ENSO episodes based on changed climate references. *J. Trop. Meteor.*, **21**, 97–103. (in Chinese)

Liu, Y., and H.-L. Ren, 2017: Improving ENSO prediction in CFSv2 with an analogue-based correction method. *Int. J. Climatol.*, **37**, 5035–5046, doi: 10.1002/joc.5142.

McPhaden, M. J., T. Lee, and D. McClurg, 2011: El Niño and its relationship to changing background conditions in the tropical Pacific Ocean. *Geophys. Res. Lett.*, **38**, L15709, doi: 10.1029/2011GL048275.

Rasmusson, E. M., and T. H. Carpenter, 1982: Variations in tropical sea surface temperature and surface wind fields associated with the Southern Oscillation/El Niño. *Mon. Wea. Rev.*, **110**, 354–384, doi: 10.1175/1520-0493(1982)110<0354:VITSST>2.0.CO;2.

Rayner, N. A., D. E. Parker, E. B. Horton, et al., 2003: Global analyses of sea surface temperature, sea ice, and night marine air temperature since the late nineteenth century. *J. Geophys. Res. Atmos.*, **108**, 4407, doi: 10.1029/2002JD002670.

Ren, H.-L., and F. F. Jin, 2011: Niño indices for two types of ENSO. *Geophys. Res. Lett.*, **38**, L04704, doi: 10.1029/2010GL046031.

Ren, H.-L., and F. F. Jin, 2013: Recharge oscillator mechanisms in two types of ENSO. *J. Climate*, **26**, 6506–6523, doi: 10.1175/JCLI-D-12-00601.1.

Ren, H.-L., F. F. Jin, M. F. Stuecker, et al., 2013: ENSO regime change since the late 1970s as manifested by two types of ENSO. *J. Meteor. Soc. Japan*, **91**, 835–842, doi: 10.2151/jmsj.2013-608.

Ren, H.-L., F. F. Jin, B. Tian, et al., 2016a: Distinct persistence barriers in two types of ENSO. *Geophys. Res. Lett.*, **43**, 10,973–10,979, doi: 10.1002/2016GL071015.

Ren, H.-L., Y. Liu, J. Q. Zuo, et al., 2016b: The new generation of ENSO prediction system in Beijing Climate Center and its prediction for the 2014/16 super El Niño event. *Meteor. Mon.*, **42**, 521–531, doi: 10.7519/j.issn.1000-0526.2016.05.001. (in Chinese)

Ren, H.-L., C. H. Sun, F. M. Ren, et al., 2017a: GB/T 33666-2017 Identification method for El Niño/La Niña events. Standards Press of China, Beijing, 1–6. (in Chinese)

Ren, H.-L., F. F. Jin, L. C. Song, et al., 2017b: Prediction of primary climate variability modes at the Beijing Climate Center. *J. Meteor. Res.*, **31**, 204–223, doi: 10.1007/s13351-017-6097-3.

Ren, H.-L., A. A. Scaife, N. Dunstone, et al., 2018a: Seasonal predictability of winter ENSO types in operational dynamical model predictions. *Climate Dyn.,* doi: 10.1007/s00382-018-4366-1.

Ren, H.-L., J. Q. Zuo, and Y. Deng, 2018b: Statistical predictability of Niño indices for two types of ENSO. *Climate Dyn.,* doi: 10.1007/s00382-018-4453-3.

Reynolds, R. W., N. A. Rayner, T. M. Smith, et al., 2002: An improved in situ and satellite SST analysis for climate. *J. Climate*, **15**, 1609–1625, doi: 10.1175/1520-0442(2002)015<1609:AIISAS>2.0.CO;2.

Titchner, H. A., and N. A. Rayner, 2014: The Met Office Hadley Centre sea ice and sea surface temperature data set, version 2: 1. Sea ice concentrations. *J. Geophys. Res. Atmos.*, **119**, 2864–2889, doi: 10.1002/2013JD020316.

Trenberth, K. E., 1997: The definition of El Niño. *Bull. Amer. Meteor. Soc.*, **78**, 2771–2778, doi: 10.1175/1520-0477(1997)078<2771:TDOENO>2.0.CO;2.

Trenberth, K. E., and D. P. Stepaniak, 2001: LETTERS: Indices of

El Niño evolution. *J. Climate*, **14**, 1697–1701, doi: 10.1175/1520-0442(2001)014<1697:LIOENO>2.0.CO;2.

Trenberth, K. E., G. W. Branstator, D. Karoly, et al., 1998: Progress during TOGA in understanding and modeling global teleconnections associated with tropical sea surface temperatures. *J. Geophys. Res. Oceans*, **103**, 14291–14324, doi: 10.1029/97JC01444.

Wang, Q., S. L. Li, J. J. Fu, et al., 2012: On the formation of anomalous summer precipitation in the years of 2010 and 1998: A comparison of the El Niño's impact between Modoki and typical El Niño cases. *Acta Meteor. Sinica*, **70**, 1207–1222, doi: 10.11676/qxxb2012.102. (in Chinese)

Wang, S. P., 1991: The criteria, classification and characteristics of El Niño episodes. *Acta Oceanol. Sinica*, **13**, 611–620. (in Chinese)

Weng, H. Y., K. Ashok, S. K. Behera, et al., 2007: Impacts of recent El Niño Modoki on dry/wet conditions in the Pacific rim during boreal summer. *Climate Dyn.*, **29**, 113–129, doi: 10.1007/s00382-007-0234-0.

Yuan, Y., and S. Yang, 2012: Impacts of different types of El Niño on the East Asian climate: Focus on ENSO cycles. *J. Climate*, **25**, 7702–7722, doi: 10.1175/JCLI-D-11-00576.1.

Yuan, Y., and H. M. Yan, 2013: Different types of La Niña events and different responses of the tropical atmosphere. *Chinese Sci. Bull.*, **58**, 406–415.

Yuan, Y., H. Yang, and C. Y. Li, 2012: Study of El Niño events of different types and their potential impact on the following summer precipitation in China. *Acta Meteor. Sinica*, **70**, 467–478, doi: 10.11676/qxxb2012.039. (in Chinese)

Zhang, W. J., F. F. Jin, J. P. Li, et al., 2011: Contrasting impacts of two types of El Niño over the western North Pacific during boreal autumn. *J. Meteor. Soc. Japan*, **89**, 563–569, doi: 10.2151/jmsj.2011-510.

Zhang, W. J., F. F. Jin, H.-L. Ren, et al., 2012: Differences in teleconnection over North Pacific and the rainfall shift over the USA associated with two types of El Niño during boreal autumn. *J. Meteor. Soc. Japan*, **90**, 535–552, doi: 10.2151/jmsj.2012-407.

Zhang, W. J., L. Wang, B. Q. Xiang, et al., 2015: Impacts of two types of La Niña on the NAO during boreal winter. *Climate Dyn.*, **44**, 1351–1366, doi: 10.1007/s00382-014-2155-z.

Zhang, W. J., F. F. Jin, M. F. Stuecker, et al., 2016: Unraveling El Niño's impact on the East Asian Monsoon and Yangtze River summer flooding. *Geophys. Res. Lett.*, **43**, 11,375–11,382, doi: 10.1002/2016GL071190.

Tech & Copy Editor: Lan YI

Journal of Geophysical Research: Atmospheres

RESEARCH ARTICLE
10.1029/2017JD028043

Key Points:
- BSISO significantly influences probability of extreme rainfall in southeastern China, showing an evident regional dependence
- Intensified moisture convergence and upward moisture transport during BSISO active phases favor the occurrence of extreme rainfall
- CFSv2 can well reproduce the impact of BSISO on extreme rainfall and show considerable predictability

Correspondence to:
H.-L. Ren,
renhl@cma.gov.cn

Citation:
Ren, P., Ren, H.-L., Fu, J.-X., Wu, J., & Du, L. (2018). Impact of boreal summer intraseasonal oscillation on rainfall extremes in southeastern China and its predictability in CFSv2. *Journal of Geophysical Research: Atmospheres*, *123*, 4423–4442. https://doi.org/10.1029/2017JD028043

Received 10 NOV 2017
Accepted 27 MAR 2018
Accepted article online 12 APR 2018
Published online 2 MAY 2018

©2018. American Geophysical Union. All Rights Reserved.

Impact of Boreal Summer Intraseasonal Oscillation on Rainfall Extremes in Southeastern China and its Predictability in CFSv2

Pengfei Ren[1,2], Hong-Li Ren[2,3], Joshua-Xiouhua Fu[4], Jie Wu[2], and Liangmin Du[5]

[1]Chinese Academy of Meteorological Sciences, Beijing, China, [2]Laboratory for Climate Studies, CMA-NJU Joint Laboratory for Climate Prediction Studies, National Climate Center, China Meteorological Administration, Beijing, China, [3]Department of Atmospheric Sciences, School of Environment Studies University of Geoscience, Wuhan, China, [4]Institute of Atmospheric Sciences, Fudan University, Shanghai, China, [5]Wuhan Regional Climate Center, Hubei, China

Abstract The boreal summer intraseasonal oscillation (BSISO) is one of the dominant modes of intraseasonal variability of the tropical climate system, which has prominent northward propagation extending much further from the equator. The impacts of BSISO on extreme rainfall in eastern China were studied using the BSISO indices and daily rainfall data in China. We revealed that the responses of extreme rainfall to BSISO activity in eastern China are not spatially uniform. Under the influences of BSISO1, the probability-distribution functions of rainfall in two southeastern China subregions: South China and Yangtze River Valley significantly skew toward larger values, respectively, in phases 4 and 8, and phases 3 and 4 with the probability of 90th extremes increased by 35–45% relative to May–August rainfall probability-distribution function, showing southward propagation with the speed of 1.96°/phase. Under the BSISO2, the probability of the 90th extremes increased more than 40% in South China and Yangtze River Valley, respectively, during phases 4–5 and phases 6–7, showing northward propagation with a speed of 2.75°/phase. Physical analysis showed that the increased probability of extreme rainfall is associated with intensifying moisture convergence and upward moisture transport during BSISO active phases. The hindcasts from the Climate Forecast System version 2 have been used to evaluate the modulations of BSISO on extreme rainfall and associated predictability. It was shown that the Climate Forecast System version well reproduces the modulations of BSISO on extreme rainfall within 2 weeks. These results demonstrate the feasibility to develop medium-to-extended-range probabilistic forecasts of extreme rainfall for southeastern China.

1. Introduction

Extreme rainfall is one of the most prominent extreme weather and climate events. Its sudden and destructive characteristics can lead to flood, landslide, and mudflow with the potential to cause catastrophic losses of property, agriculture, and even threaten the human lives. In the summer of 1998, a major flood that occurred in Yangtze River Valley (YRV) claimed over 3,000 lives and resulted in $45 billion economic loss (Huang et al., 1998). In May–June of 2008, the persistent heavy rainfall over South China (SC) caused 168 people dead (Wang et al., 2011). In June of 2010, 15 consecutive days of heavy rain in Fujian Province affected more than 2.95 million people's lives and caused direct economic losses up to $1.6 billion (Gao et al., 2013). Due to high vulnerability to rainfall extremes in eastern China (EC), better understanding the physical processes inducing prolonged heavy rainfall and improving prediction skill for such extreme events are needed to establish an extended-range (10–30 days) flood forecast system and provide improved meteorological services for this region (Hsu et al., 2016; Lee et al., 2017; Webster et al., 2010).

One major source of predictability at the subseasonal-to-seasonal time range comes from the intraseasonal oscillation (ISO), especially the Madden-Julian Oscillation (MJO) characterized by a zonal planetary scale with eastward propagation occurs at a rate of about 5 m/s (Madden & Julian, 1971, 1972). As the leading mode of subseasonal variability in the tropical climate system, MJO can exert a significant impact on precipitation and temperature in different parts of the globe (Alvarez et al., 2016; Barlow et al., 2005; Bond & Vecchi, 2003; Jeong et al., 2005; Jia et al., 2011; Jones, 2000; Jones et al., 2004; Xavier et al., 2014; Zhang et al., 2009). However, the tropical ISO exhibits remarkable seasonal variations (Madden & Julian, 1994; Wang & Rui, 1990; Zhang & Dong, 2004). During boreal winter, MJO tends to be more active with stronger amplitude and more eastward-propagating events than other seasons, whereas it tends to be weaker during boreal summer. Compared to the equatorial-trapped eastward propagating MJO, the boreal summer ISO (BSISO) is more complex in nature with dominant northward propagation confined to the Indian and western

Pacific monsoon regions (Jiang et al., 2004; Lee et al., 2012). The BSISO is one of the key factors modulating the rainfall variability and flooding in the Asian monsoon regions (Chen et al., 2015; Hsu et al., 2016; Lee et al., 2017; Mao & Wu, 2006; Yang et al., 2010; Zhu et al., 2003).

In order to facilitate detection, monitoring, and prediction of the BSISO activity, Lee et al. (2012) proposed two BSISO indices based on multivariate empirical orthogonal function (EOF) analysis of daily anomalies of outgoing longwave radiation and 850-hPa zonal wind (U850) over the Asian monsoon sector (10°S–40°N, 40°E–160°E). The first two leading EOF modes, which together represent the canonical northward/northeastward propagating variability with quasi-oscillating periods of 30–60 days, are referred to as BSISO1. The other component referred to as BSISO2 is defined by the third and fourth EOF modes, which identify the 10 to 30-day northward/northwestward propagating variability. Recently, Hsu et al. (2016) used the BSISO indices to examine the influences of BSISO modes on the spatial distribution of extreme rainfall in southern China. Their results showed that the probability of extreme-rainfall events exceeding the 75th and 90th percentile can be significantly increased during the phases 2–4 of BSISO1 and the phases 5–7 of BSISO2 compared to the non-BSISO mode. However, the response of extreme rainfall to BSISO activity is not spatially uniform in the EC. What are the regional differences in the impact of BSISO on extreme rainfall in the EC and what are the underlying causes? This study will address these two questions.

As an important factor modulating weather activity, the predictability and prediction skill of BSISO is one of the key issues for extended-range forecasting. Fu et al. (2013) used four state-of-the-art models to evaluate the BSISO forecast skill. Their results showed that the intraseasonal forecast skills of the BSISO-related rainfall and zonal wind are, respectively, about 1–2 and 3 weeks measured with the spatial anomaly correlation coefficient (ACC). Zhao et al. (2014) assessed the performance of four Chinese AGCMs participating in the Coupled Model Intercomparison Project Phase 5 in the simulation of BSISO, and the results showed that the four models can reproduce boreal summer intraseasonal signals of precipitation. Lee et al. (2015) used six coupled models in the Intraseasonal Variability Hindcast Experiment project to examine the predictability and prediction skill of BSISO. They found that the multimodel-mean BSISO predictability and prediction skill with strong initial amplitude are about 45 and 22 days, respectively. Skillful prediction of BSISO offers an opportunity for probabilistic prediction of extreme rainfall in southeastern China (SEC) where BSISO has a significant impact. And from a prediction perspective, it would be useful to provide the probability information of extreme-rainfall events based on BSISO activity. Xavier et al. (2014) presented one method to evaluate the predictability of extreme-rainfall probability in Southeast Asia based on hindcasts from the operational GloSea5 forecasting system in the Met Office's Hadley Center. Their results demonstrated that it is feasible to derive probabilistic information about extreme-rainfall events at medium range during the passage of MJO. In the present study, we have also worked to explore the performance of one state-of-the-art operational Climate Forecast System version 2 (CFSv2) for forecasting the relationship between the BSISO and extreme rainfall, with the aim of assessing predictability of the extended-range probability of extreme-rainfall events in SEC.

The remainder of this paper is organized as follows: The data and methodology are given in section 2; section 3 presents the influences of BSISO on summer extreme rainfall in EC; furthermore, the physical basis for modulations of BSISO on rainfall extremes is briefly analyzed in order to illustrate the potential indicators of extreme events; then, evaluation of CFSv2's ability to forecast the relationship between the BSISO and extreme rainfall is presented in section 4; and summary and discussion are presented in section 5.

2. Data and Methods

2.1. Observational Data

The observational data used in this study include (1) daily rainfall from 2,400 stations in China covering the period from 1 January 1981 to 31 December 2013, as collected and compiled by the National Meteorological Information Center of the China Meteorological Administration; (2) NCEP-NCAR daily reanalysis (Kalnay et al., 1996), including wind, vertical velocity, and specific humidity covering the same period as the rainfall data; and (3) the BSISO index proposed by Lee et al. (2012), which was downloaded from http://www.apcc21.org/ser/moni.do?lang=en. Lee et al. (2012) demonstrated that the two

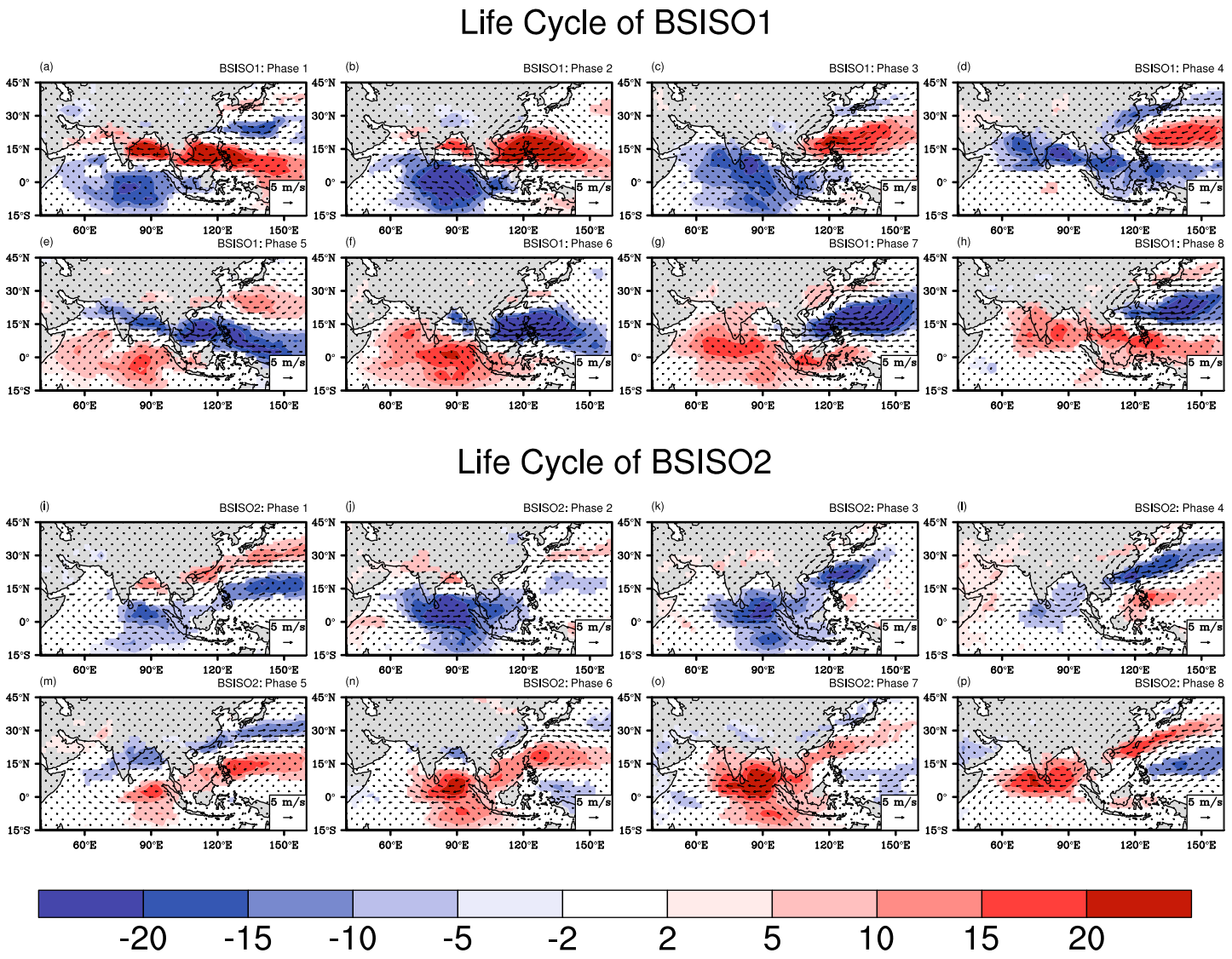

Figure 1. Life cycle composite of outgoing longwave radiation (OLR; shading) and 850-hPa wind (vector) anomaly based on eight phases of (a)–(h) boreal summer intraseasonal oscillation 1 and (i)–(p) boreal summer intraseasonal oscillation 2. Only 95% significant values are shaded for the OLR anomaly.

BSISO indices are capable of describing a large fraction of the total intraseasonal variability in Asia and better represent the northward propagation than the real-time multivariate MJO index (Wheeler & Hendon, 2004).

2.2. Forecast Data

Our analysis is based on the hindcasts from CFSv2 (Saha et al., 2010, 2014), which consists of fully coupled components of ocean, atmosphere and land. The atmospheric component is the NCEP Global Forecast System operational with a horizontal resolution of T126 (~100 km) and 64 vertical levels extending from the surface to 0.26 hPa. The oceanic component is the Geophysical Fluid Dynamics Laboratory Modular Ocean Model version 4, which uses 40 levels in the vertical direction, a zonal resolution of 0.5°, and a meridional resolution of 0.25° between 10°S and 10°N, gradually increasing through the tropics until becoming fixed at 0.5° poleward of 30°S and 30°N. Ren and Ren (2017) examined the model-based predictability for extreme rainfall in winter using hindcasts from CFSv2, and the results showed that the modulations of MJO on extreme rainfall are captured and forecasted well in the CFSv2 system. Adopting a similar approach, we

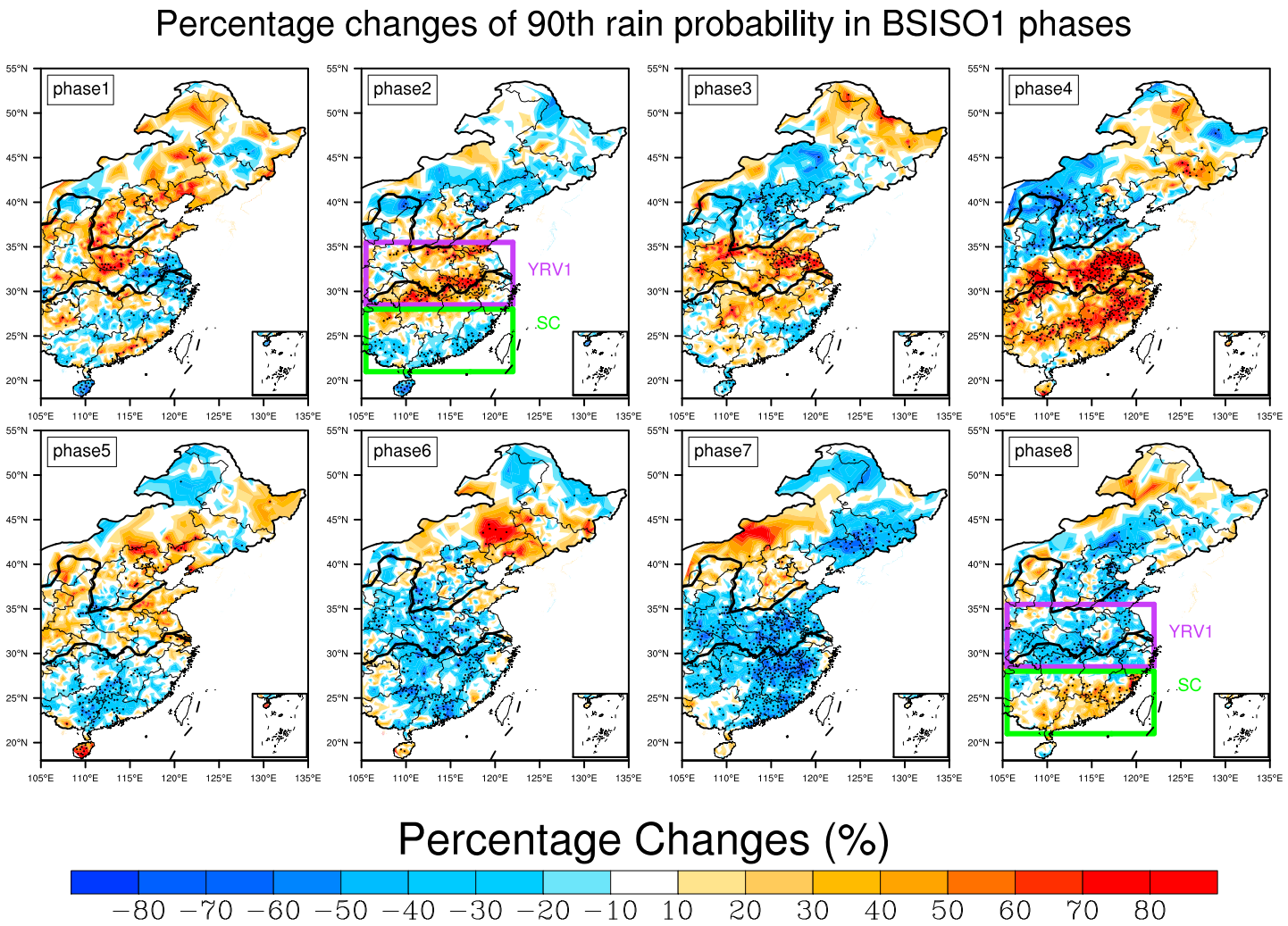

Figure 2. Percentage changes in the probability of rainfall at 90th extremes for each of eight phases of boreal summer intraseasonal oscillation 1. The dots represent stations that exceed the 95% confidence level. The Yangtze River Valley 1 and South China were selected by the purple and green boxes, respectively.

analyzed the 45-day hindcasts of CFSv2 initialized daily from 1 January 1999 to 31 December 2010. For each initial day, four forecasts were made every 6 hr at 00Z, 06Z, 12Z, and 18Z, forming a daily four-member ensemble mean.

2.3. Methods

The eight phases of BSISO1 (or BSISO2) were defined based on the signs and amplitudes of PC1 (PC3) and PC2 (PC4) (Lee et al., 2012) to show the evolutions and propagation features of BSISO. BSISO composites are constructed for BSISO1 and BSISO2 phases 1–8 with normalized amplitude greater than 1. General features of BSISO evolution are as follows (Figure 1): Convection anomaly associated with BSISO1 appears over the equatorial Indian Ocean in phase 1, and then propagates northeastward reaching the Indian subcontinent in phase 3 and the Bay of Bengal in phases 4 and 5. Then, convection anomaly over the Maritime Continent and equatorial western Pacific propagates northward and reaches the SC Sea in phase 7 and the WNP in phase 8. For BSISO2, the convection anomaly is located in the equatorial Indian Ocean and Philippine Sea in phase 1. Then, it propagates northwestward over the Indian Ocean and WNP-East Asian regions. For further details of the BSISO indices, the readers can referred to Lee et al. (2012).

Besides, following the percentile-based threshold method of Zhang et al. (2011), an extreme event was defined by a daily rainfall amount greater than the 90th (95th) percentile of the rainy days, which is

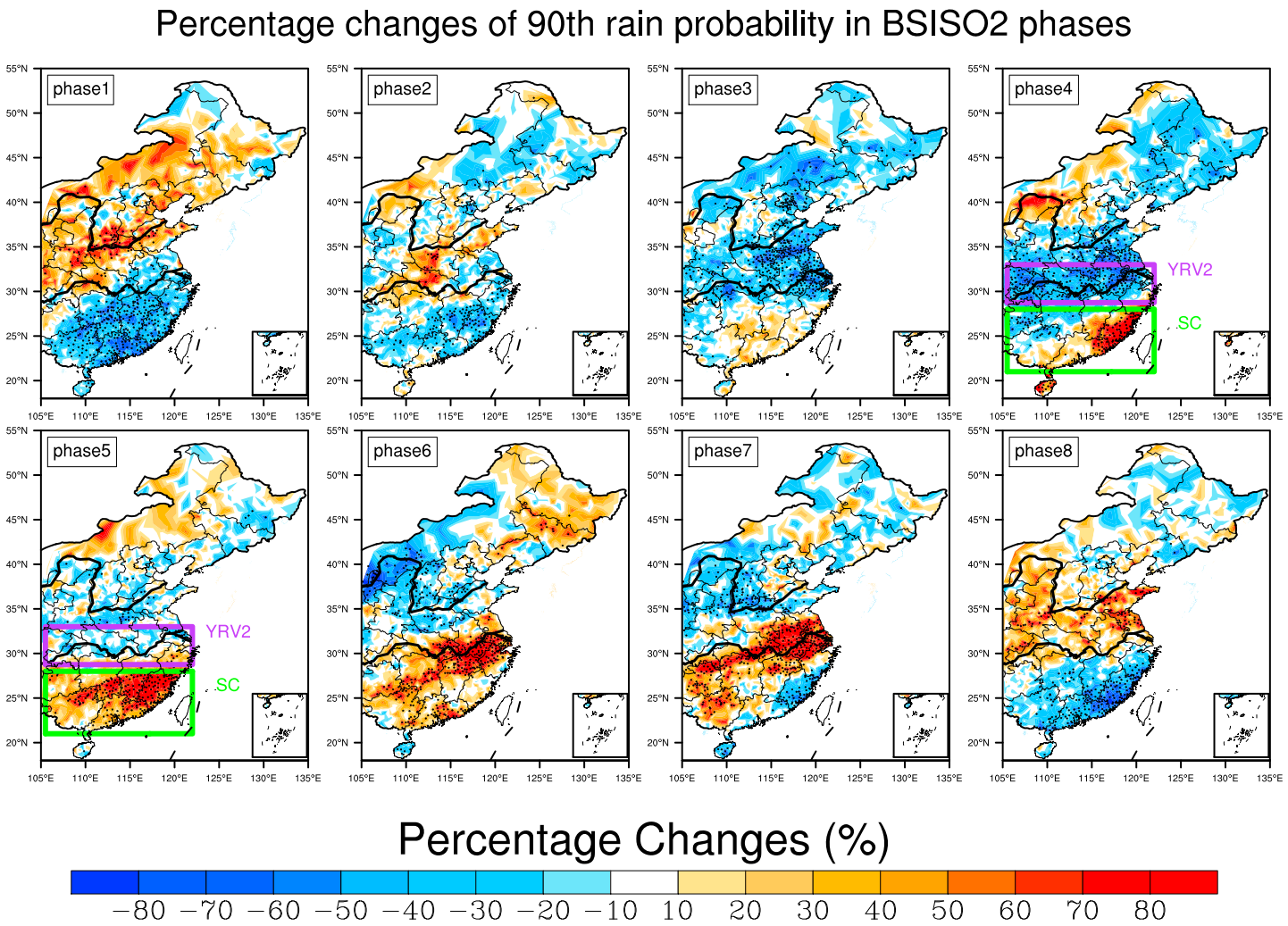

Figure 3. Same as Figure 2 but for each of eight phases of BSISO2.

referred to as the 90th (95th) extremes. Moreover, the percentage changes in probability-distribution functions (PDFs) of rainfall are calculated as follows:

$$\Delta P_{BSISO} = \frac{P_{BSISO}(x \geq x_c) - P_{all}(x \geq x_c)}{p_{all}(x \geq x_c)} \times 100\% \quad (1)$$

Here ΔP_{BSISO} is the percentage change in the cumulative probability of rainfall (x) exceeding a given threshold (x_c) due to the BSISO. P_{BSISO} is the cumulative probability that the rainfall exceeding the threshold calculated for only the days of the given BSISO1 (or BSISO2) phase, and P_{all} is for all days during the summer season.

The common period for all data sets (except for CFSv2 model) mentioned above covers the period from 1981 to 2013. Due to the data availability of CFSv2, the predictability of extreme rainfall was assessed only for the period from 1999 to 2010. The summer season in this paper was defined as the period from 1 May to 31 August (MJJA).

3. The Influences of BSISO on Extreme Rainfall

3.1. Modulations of BSISO on Rainfall Extremes

The composites of percentage change in the probability of rainfall at 90th extremes during BSISO1 phases 1–8 are shown in Figure 2. In order to better illustrate the regional differences in the impact

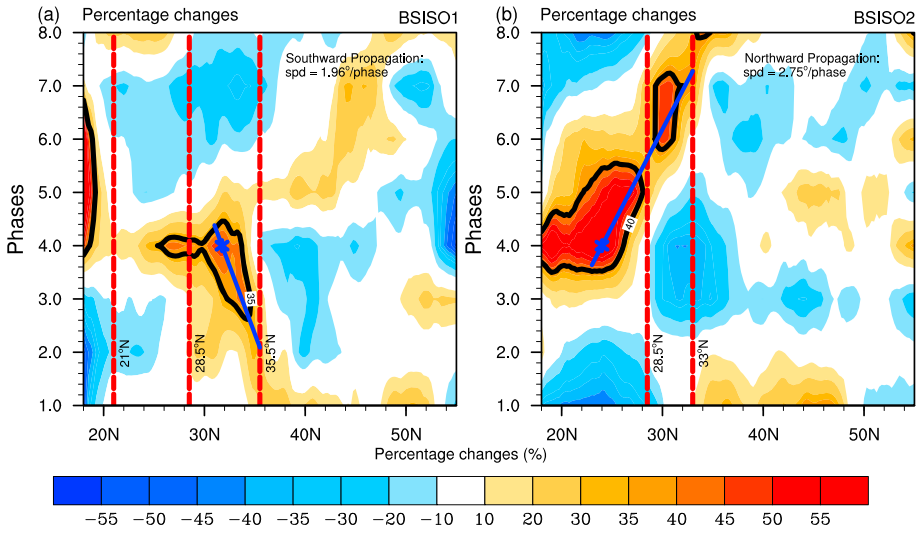

Figure 4. Zonal mean percentage changes in the probability of 90th extremes as a function of the eight phases of (a) boreal summer intraseasonal oscillation 1 and (b) boreal summer intraseasonal oscillation 2. The black-thick contours represent the increased probability of (a) 35% and (b) 40%. The blue-thick lines represent the percentage changes track and the slopes are defined as their (a) southward and (b) northward propagation speed.

of BSISO1 on extreme rainfall, we have shown the results in the entire EC region (e.g., east of 105°E). From Figure 2, we can clearly see that the probabilities of extreme rainfall in EC show systemic variations with the changes of BSISO1 phases. In general, significant changes in the probability of extreme rainfall are concentrated in the SEC. Given that the impact of BSISO1 on extreme rainfall is more significant in the SEC, we are going to focus on this region in the next research on the modulation of BSISO1 on extreme rainfall. The results of Figure 2 show that during the BSISO1 phases 2 and 3, the probabilities of 90th extremes increase in the YRV with a magnitude of more than 60% but decrease in northern and southern China. Only at the BSISO1 phase 4, the increases in probability of 90th extremes extend southward to cover almost the entire SEC region. Thus, the response of extreme rainfall to BSISO1 in the EC region is not always uniform. In fact, a dipole pattern between SC and YRV can be clearly seen in the BSISO1 phase 2 and phase 8. Due to the regional differences in the impact of BSISO1 on extreme rainfall, the SEC can be divided into two parts, namely, the SC (21°N–29.5°N) and YRV1 (29.5°N–35°N) regions (box in the Figure 2). Like BSISO1, we also investigated the impacts of BSISO2 on extreme rainfall in EC. Figure 3 shows the composite analysis similar to Figure 2, but for the phases 1–8 of BSISO2. In general, the modifications of BSISO2 on extreme rainfall are vigorous and the significant changes of 90th extremes are also concentrated in the SEC region. Similarly, the impacts of BSISO2 on extreme rainfall also show regional differences. For example, at BSISO2 phase 4 and phase 5, the frequency of extreme occurrence is significantly increased in the SC but reduced in the YRV. Moreover, it is interesting to note that the regional increases of extreme rainfall have steady northward propagation from southeastern coast to the north of the YRV during phases 4–8 (Hsu et al., 2016) and further toward northern China at phase 1. Similarly, the SEC can be divided into two parts, namely, SC (21°N -28.5°N) and the YRV2 (28.5°N–33°N; box in the Figure 3), based on the differences in the regional influences of BSISO2.

The regional differences mentioned above remind us that the spatial variations should be considered when investigating the impacts of BSISO on extreme rainfall in the EC. In order to better illustrate the meridional differences of BSISO modulations on rainfall extremes, the zonal mean percentage changes (calculated by east of 105°E) as a function of BSISO1 (or BSISO2) phases are given in Figure 4. From Figure 4a, we can clearly see that the typical active phases for the 90th extreme occurrences are phases 4 and 8 and phases 3 and 4, respectively, in SC and YRV1. During the typical active phases, the probabilities increase by more than 35% of 90th extremes. Besides, the regional increases of 90th extremes have a southward progression tendency during the BSISO1 phases 2–4. Following the approach of Ling et al. (2014), we can obtain the southward propagation speed of the modulations of BSISO1 on extreme rainfall based on this phase-latitude diagram

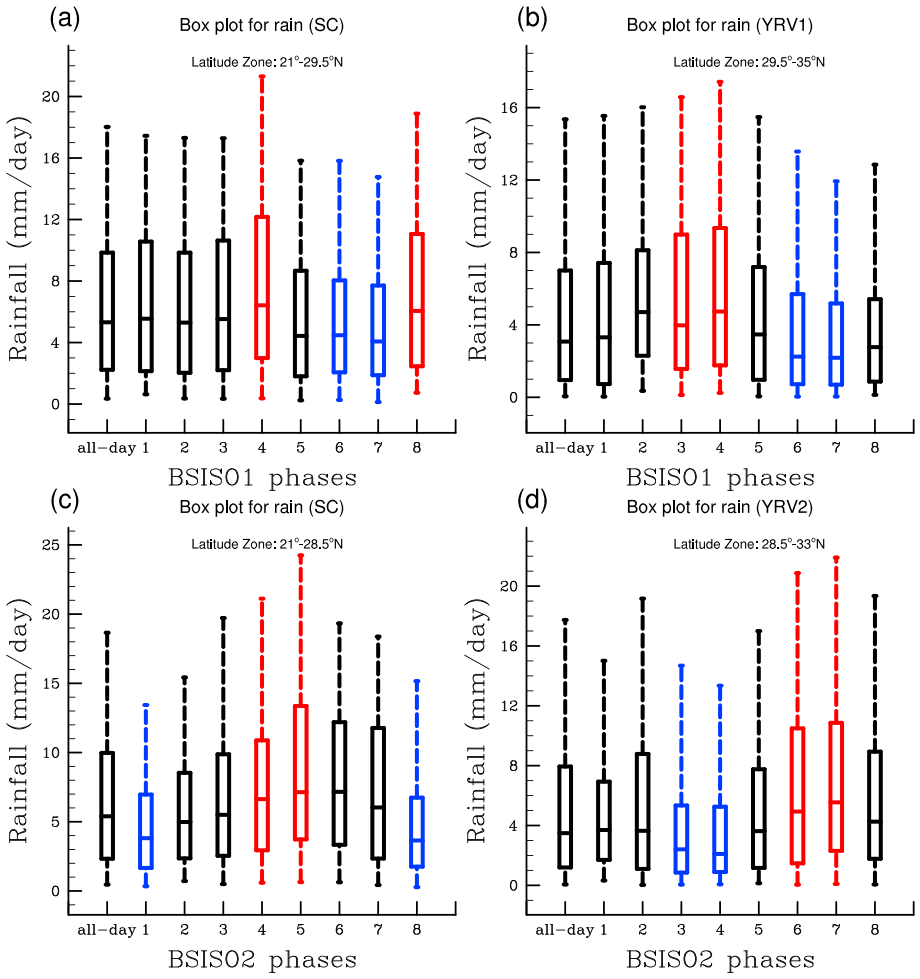

Figure 5. (a and b) Probability-distribution functions of rainfall averaged in a given area during boreal summer intraseasonal oscillation 1 phases 1–8 and all days (MJJA). (c and d) The same as (a) and (b) but for boreal summer intraseasonal oscillation 2 phases 1–8. The phases with a more positively (negatively) skewed distribution are in red (blue).

(Figure 4a). During the phases 2–4 of BSISO1, the typical speed for the southward propagation is about 1.96°/phase. Figure 4b shows the zonal mean percentage changes in the probability of 90th extremes as a function of the eight phases of BSISO2. From Figure 4b, we can see that the favorable phases for the 90th occurrence are phases 4–7 of BSISO2. Moreover, during these phases, the impacts of BSISO2 on 90th extremes have an obvious northward propagation with a speed of 2.75°/phase. This northward impact is closely related to the northwestward-propagating feature of BSISO2 mode in EC (Figure 9). On its course northward, the BSISO2 induces a dipole response of extreme rainfall in SC and YRV2. During phases 4–5 (6–7) of BSISO2, the probabilities of 90th extremes increase more than 40% (decrease) in SC and decrease (increase more than 40%) in the YRV2.

The changes in PDF of rainfall during BSISO1 and BSISO2 phases 1–8 with respect to the climatological PDF (with all days in MJJA included) are shown in Figure 5. The PDFs are obtained by selecting a given percentile for average rainfall over SC and YRV regions and represented as box plots with values for the 5th (lower bound), 25th (lower quartile), 50th (median), 75th (upper quartile), and 95th (upper bound) percentiles of the regional mean. We can define a selection criterion that separates more positively (negatively) skewed distributions and others by picking the top (lowest) two rainfall bins in the BSISOs' eight phases based on the 95th percentile rainfall. From Figures 5a and 5b, it can be seen that BSISO1 phases 4 and 8 and phases 3 and 4 tend to have a more positively skewed distribution compared to the climatological PDF in the SC and YRV1, respectively. In addition, BSISO1 phases 6 and 7 have a lower skewness of the PDF in SEC. The PDFs of rainfall during the phases 1–8 of BSISO2 are shown in Figures 5c and 5d. As mentioned above,

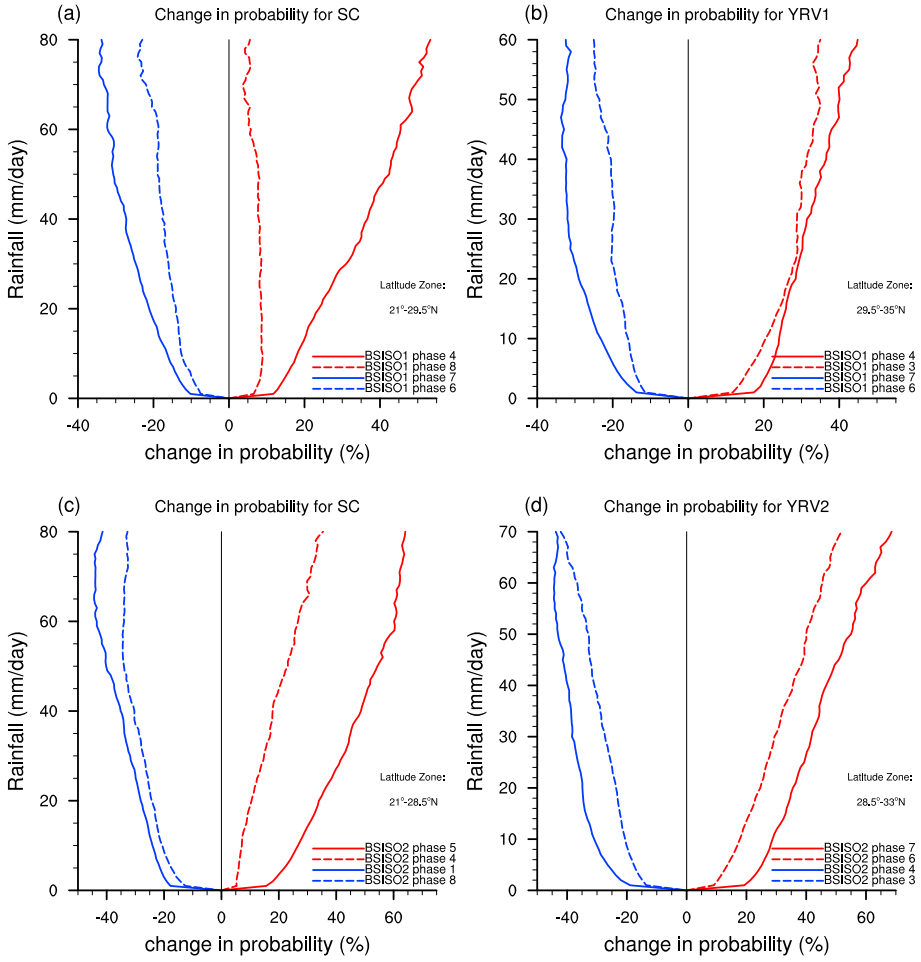

Figure 6. (a and b) Percentage changes in the probability of rainfall for typical active phases (red lines) and typical suppressed phases (blue lines) of boreal summer intraseasonal oscillation 1 with respect to the probability-distribution function of all May–August days. (c and d) The same as (a) and (b) but for boreal summer intraseasonal oscillation 2 phases.

there is a northward propagation in the impacts of BSISO2 on extreme rainfall. Phases 4 and 5 of BSISO2 have a more positively distribution relative to the PDFs for all MJJA days in SC. Along with the northward propagation of BSISO2, the rainfall becomes more positively skewed in YRV2 during phases 6 and 7. In a brief summary, during phases 4 and 8 and phases 3 and 4 of BSISO1, the extreme rainfall is in active phases, respectively, for SC and YRV1, whereas phases 6 and 7 are suppressed phases of extreme rainfall for SEC region. Similarly, the BSISO2 phases 4 and 5 and phases 6 and 7 are typical active phases of extreme rainfall for SC and YRV2, respectively. The corresponding suppressed phases for SC and YRV2 are phases 1 and 8 and phases 3 and 4, respectively.

These differences are further illustrated in Figure 6 as percentage changes in rainfall PDFs averaged in specific areas during the typical active phases (red lines) and typical suppressed phases (blue lines). It can be clearly seen that the probabilities of rainfall are substantially higher during typical active phases than during typical suppressed phases for both BSISO1 (Figures 6a and 6b) and BSISO2 (Figures 6c and 6d). Moreover, we can see that the more extreme the rainfall is, the more the probability increases due to the modulations of typical phases of the BSISO. From Figures 6a and 6b, the probability of rainfall over 60 mm/d increases more than 40% during the phase 4 of BSISO1 in SC. Phases 3 and 4 of BSISO1, as typical active phases for the occurrence of extreme rainfall in YRV1, can increase the probabilities of rainfall exceeding 50 mm/d by about 35%. From Figures 6c and 6d, we can see that the probabilities of rainfall exceeding 60 mm/d increase more than 60% during the phase 5 of BSISO2 in SC and the phase 7 of BSISO2 in YRV2.

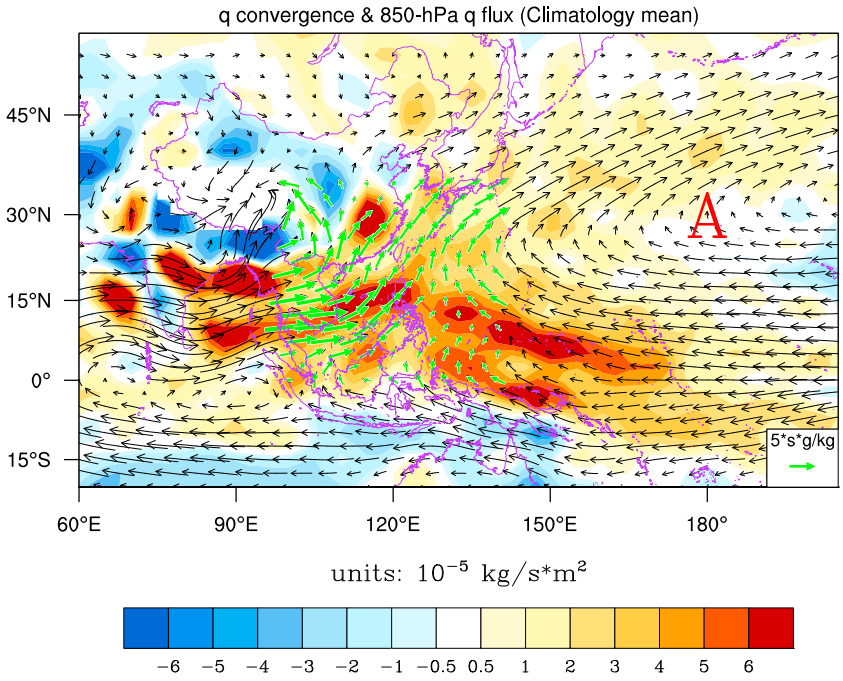

Figure 7. Climatological mean of column-integrated moisture convergence (shading, positive is convergence and negative is divergence, unit: 10^{-5} kg/s * m^2) and 850-hPa moisture flux (vector, unit: 5 * s * g/kg) for May–August. Letter "A" represents the anticyclonic circulation.

3.2. Physical Basis of Extreme Rainfall Changes

Several studies have suggested that the changes in upward motion and moisture are directly related to extreme rainfall changes (Loriaux et al., 2016; O'Gorman & Schneider, 2009). To better understand the moisture processes with the occurrence of the extreme rainfall, we have examined the moisture flux divergence ($\frac{1}{g}\nabla\cdot\left(q\vec{V}\right)$), which is considered as an important factor of heavy rainfall during BSISO1 phases and BSISO2 phases. The complete equation of moisture flux divergence is listed as follows:

$$\frac{1}{g}\nabla\cdot\left(q\vec{V}\right)=\frac{1}{g}\vec{V}\cdot\nabla q+\frac{1}{g}q\nabla\cdot\vec{V} \tag{2}$$

Moisture flux divergence includes two items, one is the moisture advection and the other is the moisture convergence. The moisture advection was not considered in our study because its contribution to extreme rainfall is negligible (Hsu et al., 2016; Ren & Ren, 2017).

First, the climatological mean moisture convergence and 850-hPa moisture flux are shown in Figure 7. In boreal summer, there are three major water vapor channels that transport moisture to SEC. They are the southwesterly moisture transport from the Bay of Bengal, the southerly moisture transport from the SC Sea, and the southeasterly moisture transport from the Western North Pacific (WNP). Rich moisture supply makes abundant rainfall in the SEC possible.

Then, the composites of moisture anomalies during BSISO1 phases 1–8 with respect to the seasonal mean are given in Figure 8. It can be seen that the spatial distribution of moisture convergence anomalies in the SEC is considerably modulated by BSISO1 life cycle. In phases 1–2 of BSISO1 (Figures 8a and 8b), corresponding to anticyclonic anomaly over the Philippine Sea and SC Sea, abnormal moisture divergence at western part of anticyclone induces an unfavorable condition for the occurrence of extreme events in Hainan Island. In the following two phases (Figures 8c and 8d), the anticyclonic anomalies move to the WNP and change to be northeast-southwest oriented, and the YRV is dominated by westerly anomalies located in the northwest side of the anomalous anticyclone. This configuration of circulation facilitates the transport of moisture to the YRV and induces significant moisture convergence there. Meanwhile, the BSISO1-related cyclonic anomalies propagate northeastward into Bay of Bengal and Indian Subcontinent in phases 4 and 5 (Figures 8d and 8e),

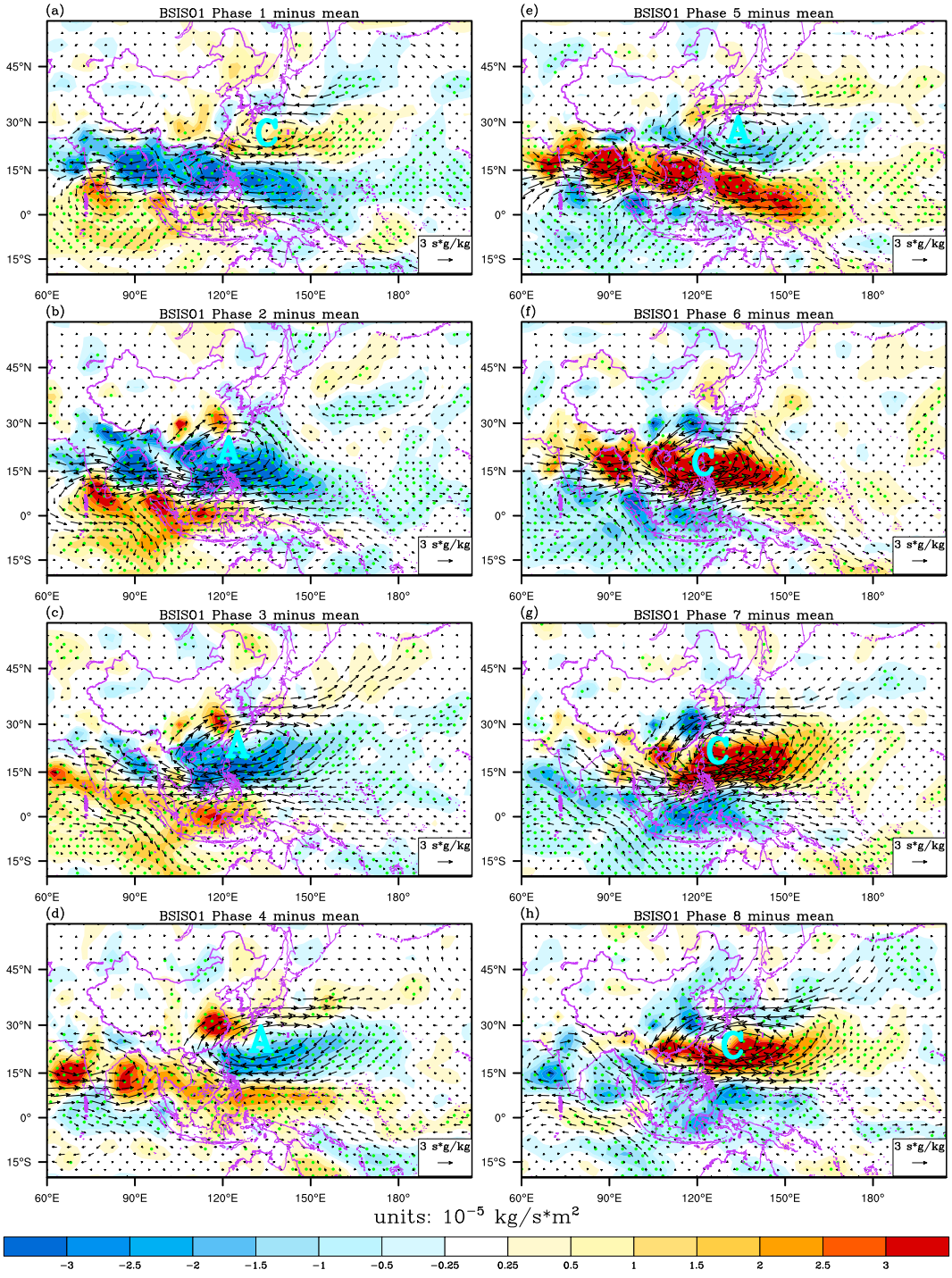

Figure 8. Changes of moisture convergence (shading) and 850-hPa moisture flux (vector) in boreal summer intraseasonal oscillation 1 phases 1–8 relative to climatological mean (Figure 7). Changes in moisture convergence exceeding the 95% confidence level based on a Student's *t* test are dotted in green. Letters "A" and "C" represent the anticyclonic anomalies and cyclonic anomalies, respectively.

which induce significant moisture convergence in Hainan. When the cyclonic anomalies propagate northeastward into the Philippine Sea and SC Sea during phases 6 and 7 of BSISO1 (Figures 8f and 8g), anomalous northeasterly is unfavorable for moisture convergence in the SEC region. As BSISO1 further moves to the northeast during phase 8 (Figure 8h), the associated westerly induces significant moisture convergence in SC.

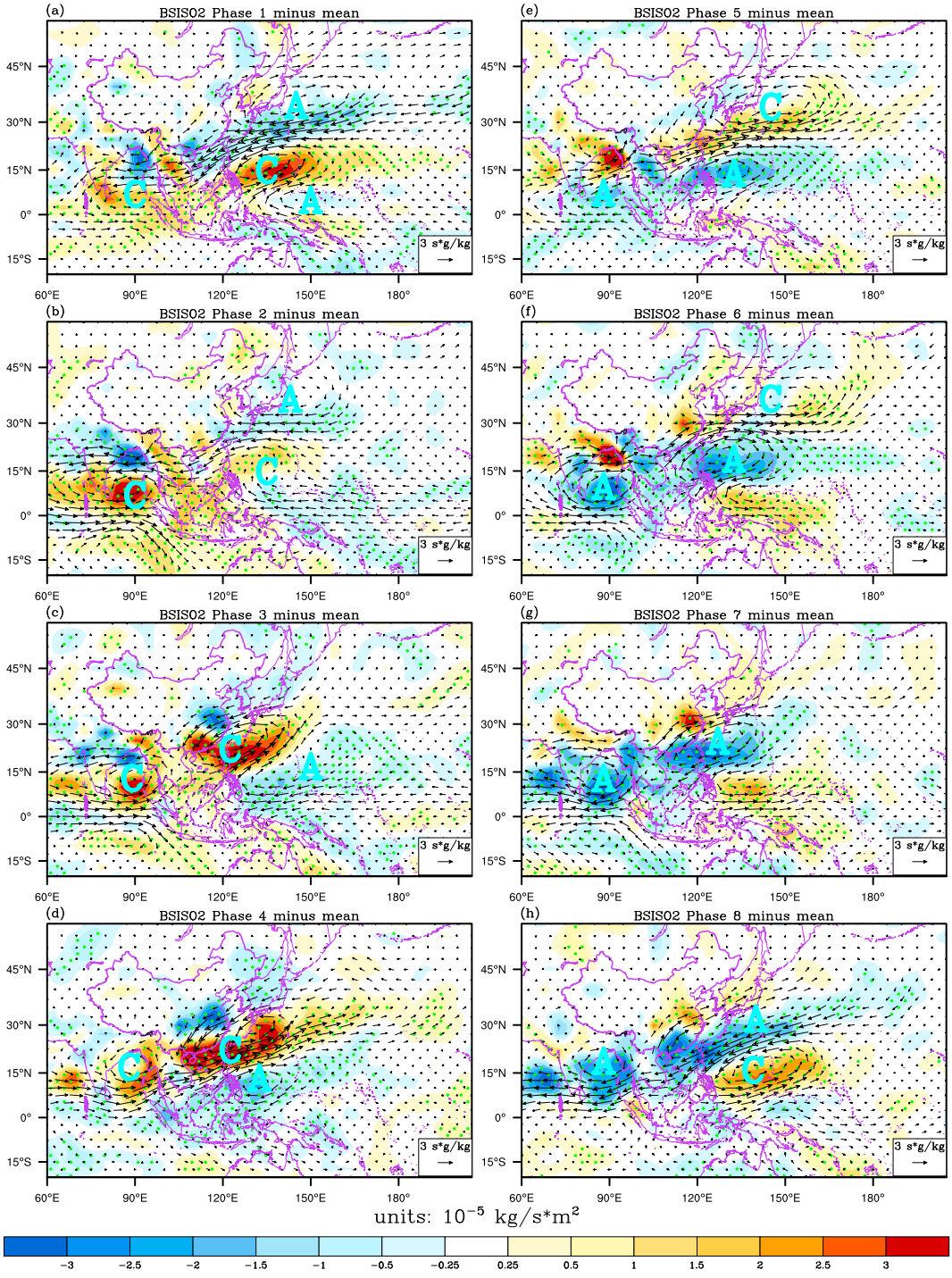

Figure 9. Same as Figure 8 but for phases 1–8 of boreal summer intraseasonal oscillation 2, respectively.

Boreal summer intraseasonal oscillation 2 variability also exerts significant influences on extreme rainfall in the SEC region via modulating the atmospheric moisture convergence. During phases 1 and 8 of BSISO2 (Figures 9h and 9a), corresponding to a strong anomalous anticyclone near Japan and a strong anomalous cyclone over the Philippine Sea, associated northeasterly induces significant moisture divergence in the SC. As BSISO2 propagates northwestward, the associated anomalous cyclone moves slowly close to the coastal areas of SEC during phases 3–5 (Figures 9c–9e); this is beneficial to the moisture convergence in

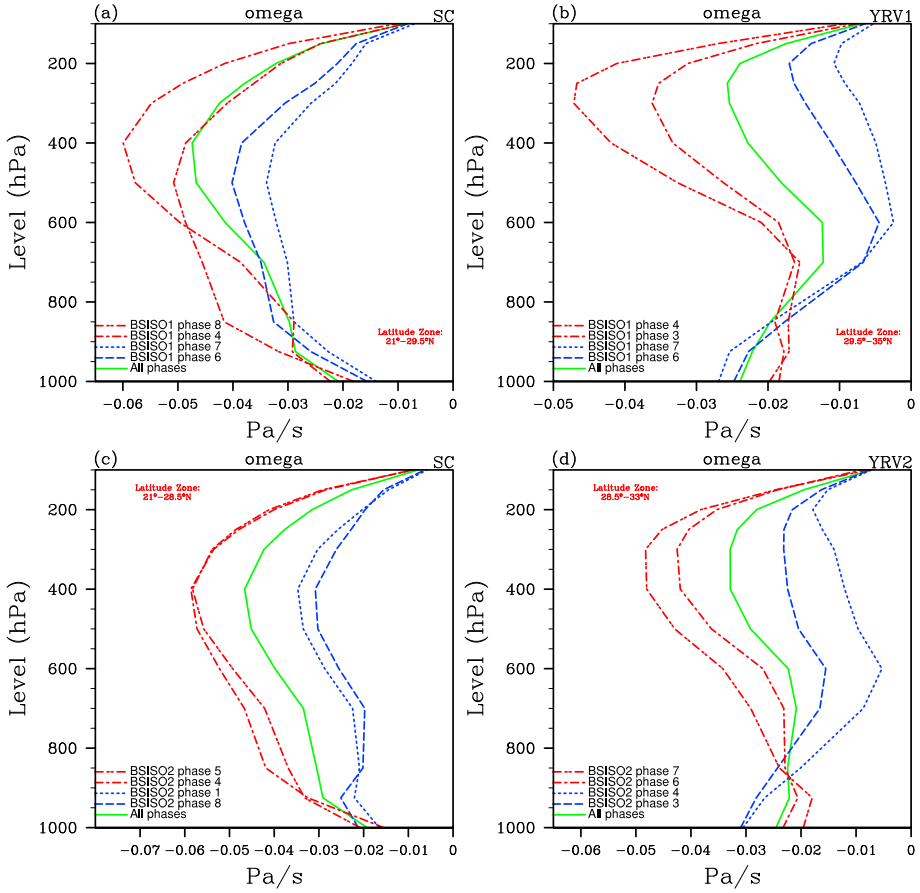

Figure 10. Composite profiles of vertical pressure velocity. Climatological values are shown in green, typical active phases of boreal summer intraseasonal oscillation 1 (or boreal summer intraseasonal oscillation 2) in red, and typical suppressed phases in blue.

the SC. At the same time, the YRV is still controlled by the northeasterly. Therefore, the BSISO2 phases 3–5 provide a favorable condition for the occurrence of extreme rainfall in SC but not in the YRV. As BSISO2 further moves to the northwest, the SEC region is gradually controlled by an anticyclone. The associated southwesterly transports abundant water vapor to YRV, which favors the occurrence of extreme rainfall there during phases 6 and 7 (Figures 9f and 9g). On the northward course of BSISO2 (phases 4–8), the associated anomalous anticyclone also moves northwestward from Philippine Sea to the Japan Sea, which results in a northward progression of moisture convergence (Figures 9d–9h) and regions with increased extreme rainfall (Figure 4).

In order to further demonstrate the contributions of upward motion and vertical moisture transport to rainfall extremes, Figures 10 and 11 show the mean profiles of vertical pressure velocity (ω) and vertical moisture advection ($-\omega\frac{\partial q}{\partial p}$), which are supposed to be related to extreme rainfall (Loriaux et al., 2016). Figure 10 shows the vertical velocity profiles, which are closely related to large-scale convergence. For the BSISO1, the upward motions in SC and YRV1 are systematically intensified during phases 4 and 8 and phases 3 and 4, respectively. For the BSISO2, the ascending motions in the SC and YRV2 are much stronger during phases 4 and 5 and phases 6 and 7, respectively. On the contrary, the upward motions at a specific area are consistently reduced during the typical suppressed phases of BSISO1 (or BSISO2). Similarly, the profiles of vertical moisture advection are given in Figure 11. Along with the changes in vertical motion, we can clearly see that the vertical moisture advection at middle and upper levels is substantially enhanced during typical active phases of BSISO1 (or BSISO2). It is expected that the associated moisture detrainment at midlevels makes the environment more favorable for further convection development. The clear separations of large-scale vertical velocity and moisture advection profiles between typical active and suppressed phases further testify the

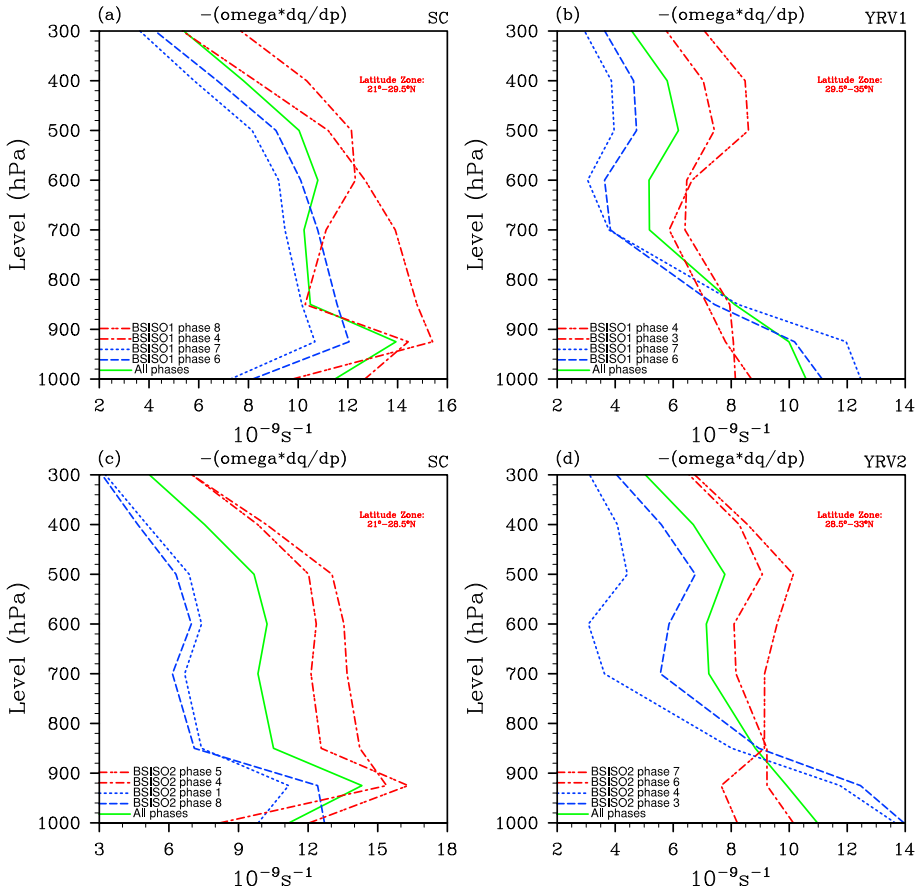

Figure 11. Same as Figure 10 but for the composite of vertical moisture advection.

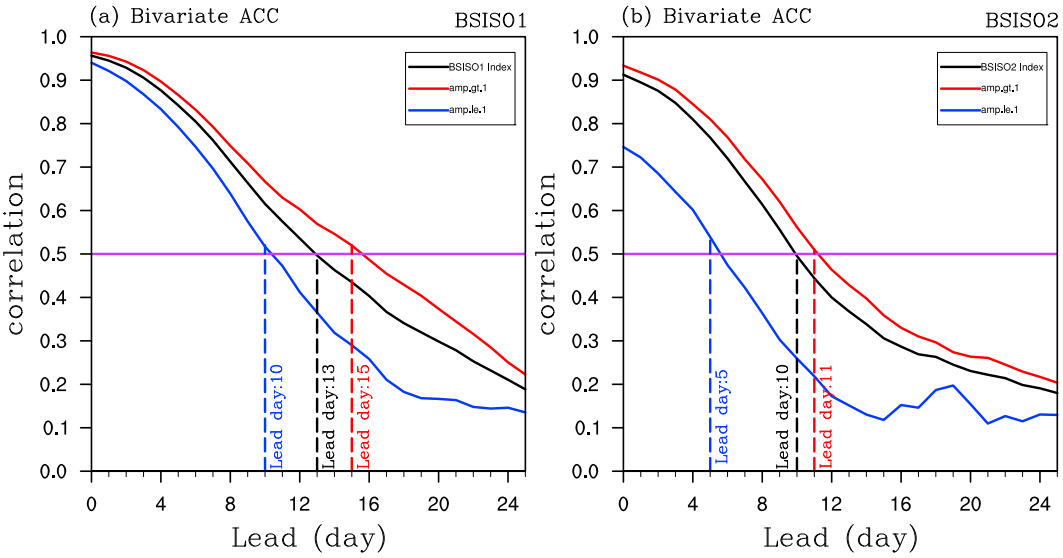

Figure 12. Correlation skill for the bivariate (a) BSISO1 and (b) BSISO2 indices between Climate Forecast System version 2 and observation's counterpart as a function of lead days. The black curves, the red curves, and the blue curves represent boreal summer intraseasonal oscillation (BSISO) indices, strong BSISOs, and weak BSISOs, respectively.

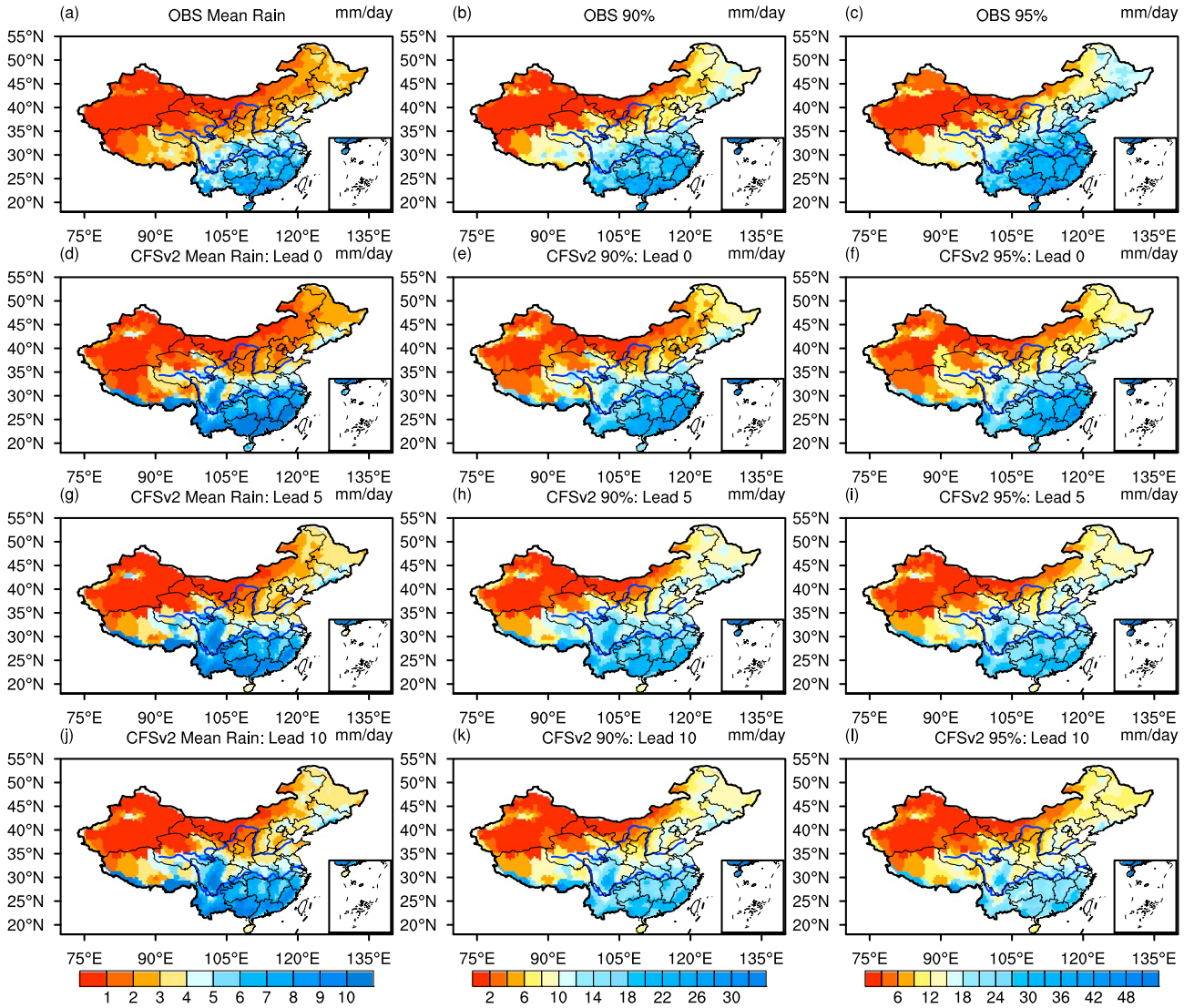

Figure 13. (a–c) Mean rainfall and 90th and 95th percentile values of rainfall (mm/d) in observations are compared with (d–f) those from Climate Forecast System version 2forecasts at lead day 0, (g–i) for lead day 5, and (j–l) for lead day 10.

strong modulations of BSISO on extreme rainfall. During the active (suppressed) phases, the intensified (weakened) large-scale upward motion and moisture advection apparently favors the increased (decreased) probability of the extreme rainfall.

4. Predictability of Extreme Rainfall in CFSv2

Another goal of this study is to evaluate CFSv2's capability of reproducing the BSISO's influences on extreme rainfall probability. Liu and Wang (2015) have shown that the intraseasonal forecast skill of rainfall in CFSv2 tends to be higher when the amplitudes of the MJO and BSISO are lager, especially for the BSISO. Figure 12 shows the bivariate ACC of the CFSv2 BSISO1 (Figure 12a) and BSISO2 (Figure 12b) with the observationally based counterpart. Taken 0.5 as the threshold of useful ACC skill, the BSISO1 (BSISO2) can be predicted out to 13-day (10-day) lead time. The dependence of the forecast skill on the BSISOs amplitude suggests that the useful forecast skill of BSISO1 reaches about 15 (10) days when the BSISO1 amplitude was large (small). Similarly, the useful skill of BSISO2 reaches 11 (5) days for strong (weak) BSISO2 events. Present evaluation will further derive probabilistic information of extreme rainfall during the passage of BSISO. After

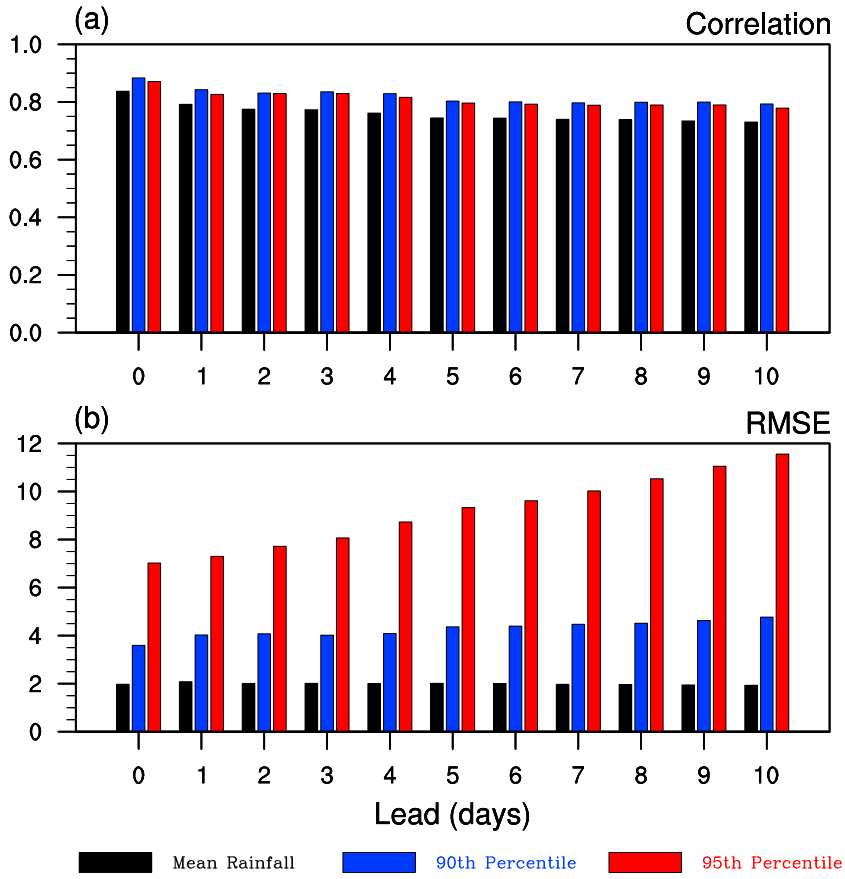

Figure 14. (a) Pattern correlation and b root-mean-square error of the rainfall in Figure 13 between observations and Climate Forecast System version 2 forecasts from lead day 0 to day 10.

interpolating onto the observational stations, the hindcast data of the CFSv2 during the period 1999–2010 are used for evaluation. The observational data during the same period have been used to verify the rainfall forecasts.

Figure 13 shows the spatial distributions of observational mean rainfall and the 90th and 95th percentile values and compares them with the CFSv2 forecasts at lead day 0, lead day 5, and lead day 10. We can see that the model strongly damps the amplitude of rainfall amounts, particularly for extreme rainfall, with the increase of lead time (e.g., lead day 10). Furthermore, the pattern correlation and root-mean-square error (RMSE) between observations and CFSv2 forecasts from lead day 0 to day 10 are shown in Figure 14. We can see that regardless of the average rainfall and the 90th and 95th percentile value, the correlation coefficient does not change much with the lead time and stays above 0.7. Which means the spatial patterns, center locations, and the decreasing trend from southeastern to northwestern China of average rainfall and extreme values can be well captured and represented with high skill by the model. However, we all know that correlation analysis only reflects the correlation between two variables, which is insensitive to the amplitude error between variables. The RMSE can take into account errors in amplitude, which is also shown in Figure 14. We can clearly see that RMSE increases with the increase of the lead time and the amount of rainfall. This proved in another way that the amplitude of rainfall, especially extreme rainfall, decreases with the increase of the CFSv2 lead time. Therefore, in order to avoid the weakening of the amplitude of extreme rainfall in the CFSv2, we used the respective percentile values of the observation and model in the subsequent study. The ability of the model in forecasting the probability changes of regional extremes is further examined in Figures 15 and 16, which show the percentage changes in the probability of percentile rainfall with the forecasts initialized from phases 1–8 of BSISO1 and BSISO2, respectively. We can see that, within 2 weeks, the CFSv2 is able to capture the observed probability increases of extreme rainfall in the SC and YRV1 during phases 1 and 8 and the phases 2 and 3 as well as the suppression of extreme rainfall in SC and YRV1

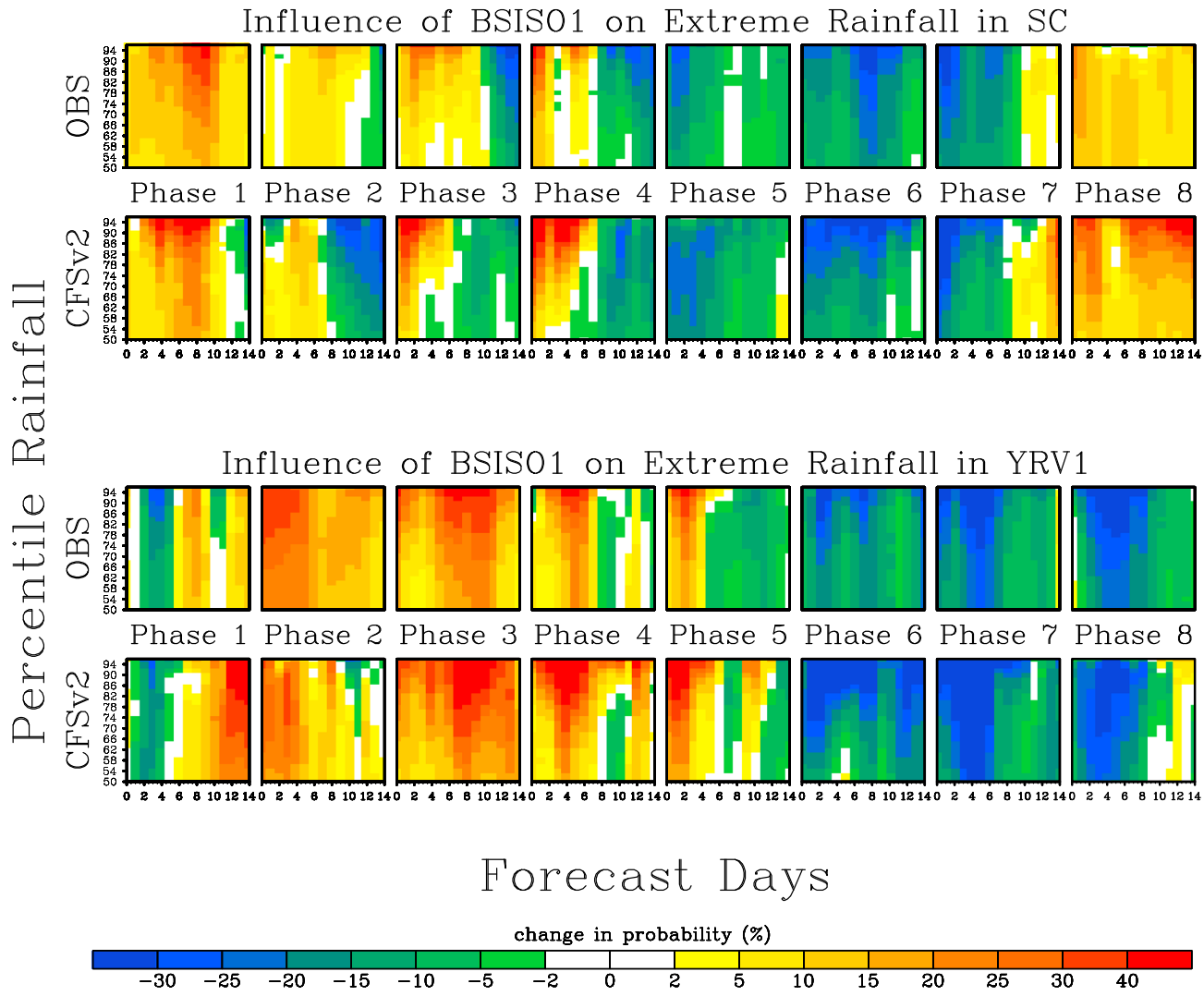

Figure 15. Percentage changes in the probability of rainfall as a function of forecast time (day) when initialized from phases 1–8 of boreal summer intraseasonal oscillation 1 with respect to a climatological probability-distribution function, where the upper two rows represent South China and bottom two rows for Yangtze River Valley 1.

during phases 5 and 6 and phases 6 and 7 of BSISO1, respectively. General agreements between model forecasts and observations indicate that the CFSv2 is able to reproduce the modulations of BSISO1 on extreme rainfall at least for lead time of 2 weeks. Similarly, the CFSv2 system's ability for reproducing the influences of BSISO2 on extreme rainfall is also examined in Figure 16. The results from Figure 16 show that the CFSv2 model has good skill to predict the BSISO2's impacts on extreme rainfall in 2 weeks. We also notice that the predictability of extreme rainfall in the SC is better than YRV2, which may be due to the YRV2 being away from the main convection region of BSISO2. When the modulations of the BSISO2 weaken, the CFSv2's forecasting skill of extreme rainfall is also reduced. Furthermore, in order to quantitatively evaluate the predictability of CFSv2 for forecasting extreme rainfall, we have calculated the pattern correlation (Figure 17) of percentage change between the CFSv2 and observations in Figures 15 and 16. From the results of correlation analysis, we can see that the CFSv2 model has a good predictive ability for the continuous change of extreme rainfall probability. Except for the individual phases (such as BSISO2 phase 5 relative to YRV2) that did not pass the significance test, CFSv2 can effectively predict the probability anomalies of rainfall in SEC within 2 weeks. The above encouraging results show that the CFSv2 system can be used to make extended-range predictions for the probabilistic information of extreme rainfall based on the BSISO's impacts in SEC region.

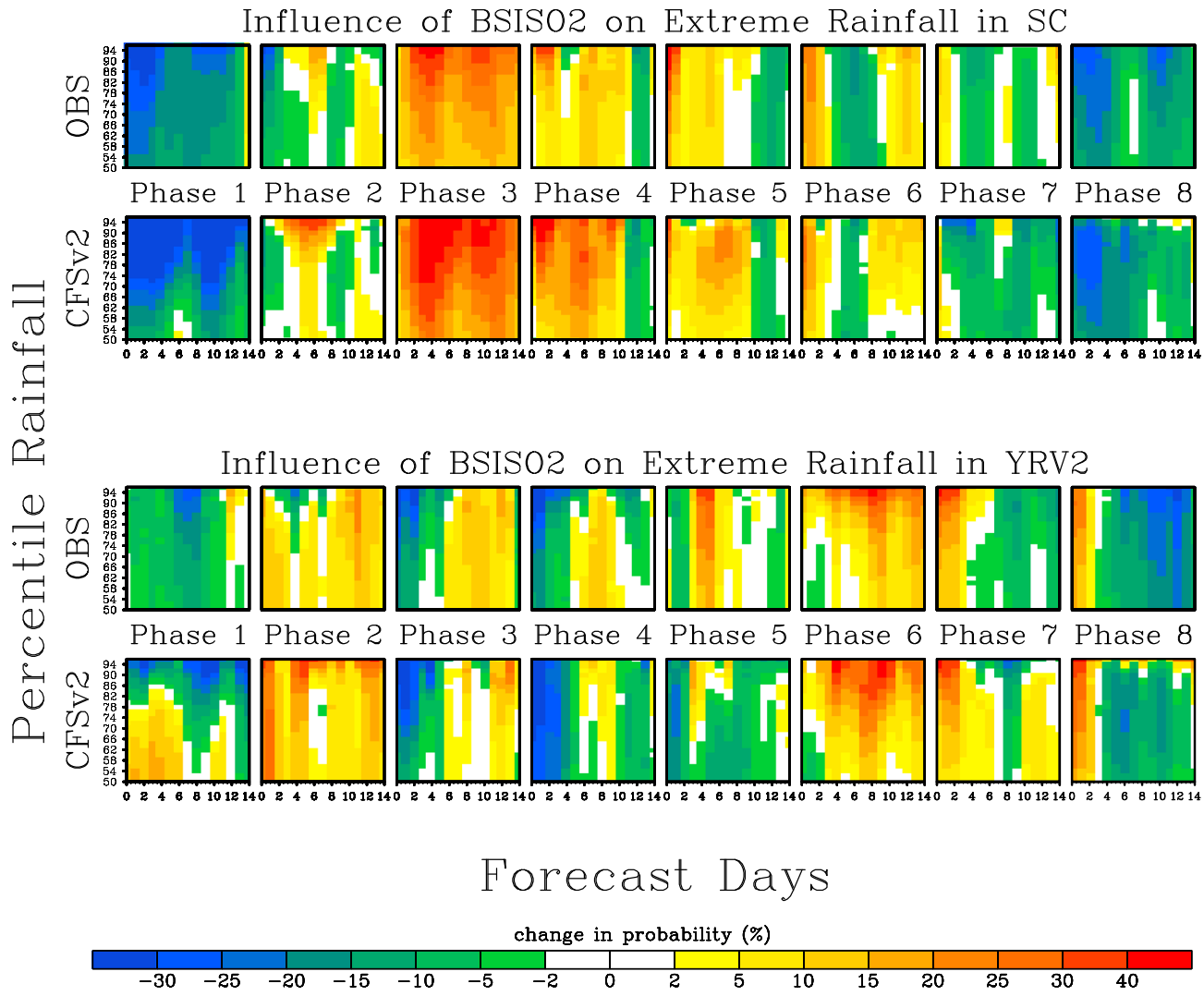

Figure 16. Same as Figure 15 but initialized from phases 1–8 of boreal summer intraseasonal oscillation 2, where the upper two rows represent South China and bottom two rows for Yangtze River Valley 2.

5. Summary and Discussion

This study documented the statistical relationships between the BSISO and the probabilities and spatial distributions of extreme rainfall in the EC, particularly in the SEC region. The associated atmospheric circulations and moisture processes were analyzed to reveal the physical mechanisms through which the BSISO modulates the occurrence of extreme rainfall. Finally, the CFSv2's ability to capture the observed relationships was evaluated, and its probabilistic predictability of extreme rainfall in the SEC at medium-to-extended range was assessed.

We found that the responses of extreme rainfall to BSISO activity in the EC are not uniform. Based on the distinctive impacts of BSISO1 on extreme rainfall, the SEC can be divided into two subregions: SC (21°N–29.5°N) and YRV1 (29.5°N–35°N). Similarly, the SEC can be divided into two subregions: SC (21°N–28.5°N) and YRV2 (28.5°N–33°N) based on the impacts of BSISO2. The BSISO1 significantly increases the probabilities of extreme rainfall by about 35–45% for SC and YRV1, respectively, during phases 4 and 8, and phases 3–4, showing a southward propagation with the speed of 1.96°/phase. The BSISO2, however, increases the probability of rainfall extremes by more than 40% in the SC and YRV2, respectively, during phases 4 and 5 and phases 6 and 7. This is due to the changes in skewness of rainfall PDF along with the life cycle of BSISO. During the typical active phases, regional rainfall PDF skews toward larger values compared

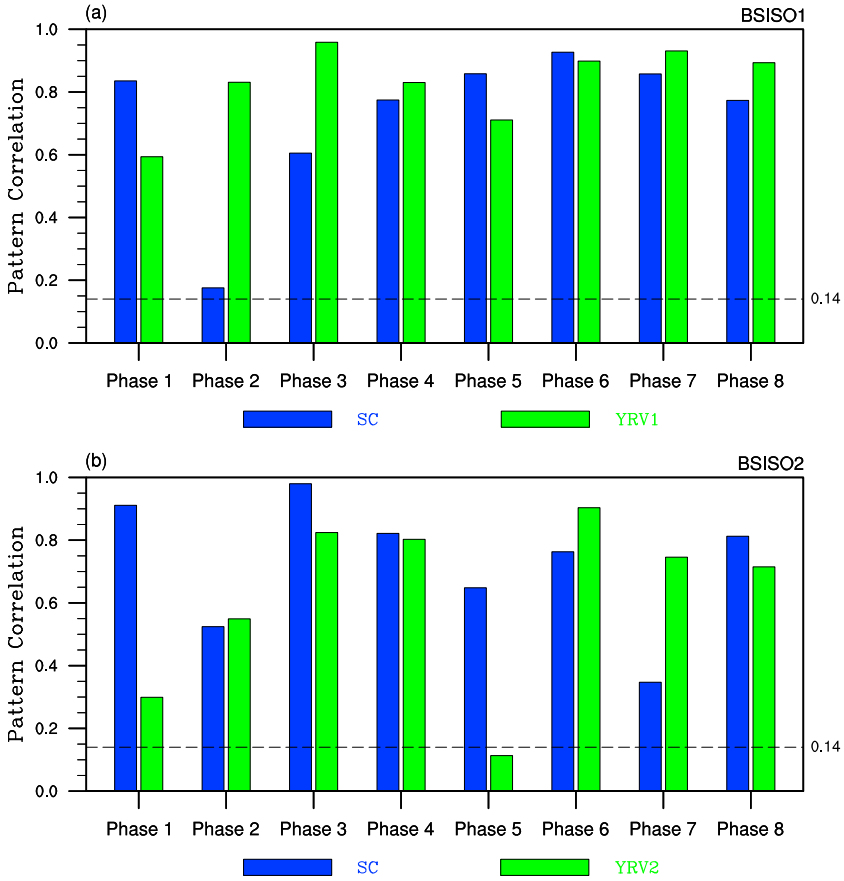

Figure 17. (a) Pattern correlations of percentage change between the Climate Forecast System version 2 and observations in Figure 15, during the phases 1–8 of boreal summer intraseasonal oscillation 1. B is the same as a but for the pattern correlations in Figure 16, during the phases 1–8 of boreal summer intraseasonal oscillation 2. The black dotted line corresponds to the correlation of 99% confidence level.

with all-day PDF. It is further noticed that, as a response to the 10 to 30-day northwestward-propagating BSISO mode (Figure 9), the region with significant increases in 90th extremes during phases 4–7 of BSISO2 also exhibits a steady northward progression with a speed of 2.75°/phase (Figure 4).

The BSISO influences the extreme rainfall in the SEC mainly through changing the large-scale atmospheric circulations and moisture supplies from the Bay of Bengal, the SC Sea, and WNP. During its life cycle, the associated circulation and moisture changes will induce large-scale moisture convergence in a specific area of SEC. The moisture convergence further leads to intensified upward motion and vertical moisture advection, thus providing a more favorable condition for the occurrence of extreme rainfall. Our analyses corroborate that both horizontal moisture convergence and vertical moisture advection can serve as key factors of extreme-rainfall events.

Extended-range hindcasts of CFSv2 during 1999–2010 have been used to evaluate the model's capability in representing the BSISO's impacts on rainfall extremes. It is revealed that the BSISO1 (BSISO2) can be predicted out to 13-day (10-day) lead time by CFSv2. Besides, the model is able to capture the observed spatial patterns of climatological rainfall, extreme values at 90th and 95th percentiles in the SEC. Within 2 weeks, CFSv2 can largely reproduce the observed impacts of BSISO on extreme rainfall. This result suggests that CFSv2 has great potential for monitoring and forecasting the probabilistic information of extreme rainfall in the SEC based on real-time BSISO indices.

Current study focused on the effects of BSISO on extreme rainfall in the SEC. Other studies (e.g., Jeong et al., 2005) also found that the spatial pattern and magnitude of surface air temperature anomalies over East Asia vary significantly with MJO phases in boreal winter. Whether and how the BSISO modes influence the surface air temperature extremes in the EC deserve further study. Besides, current study shows that both horizontal

moisture convergence and vertical moisture advection can provide more favorable conditions for the occurrence of extreme rainfall under the influence of BSISOs. However, it should be noted that the local vertical velocity and vertical moisture advection can also be caused by rainfall extremes themselves since rainfall-caused diabatic heating will have a feedback on the atmospheric circulations (Lu & Lin, 2009). Therefore, the physical mechanism of BSISOs increasing the probability of extreme rainfall remains to be further studied.

Acknowledgments
The daily rainfall from 2,400 stations in China was provided by the National Meteorological Information Center of the China Meteorological Administration (http://data.cma.cn/). The atmospheric circulation data used in this work came from NCEP/NCAR Reanalysis data (https://www.esrl.noaa.gov/psd/data/gridded/data.ncep.reanalysis.pressure.html). The CFSv2 hindcasts are available at the National Oceanic and Atmospheric Administration (https://www.ncdc.noaa.gov/data-access/model-data/model-datasets/climate-forecast-system-version2-cfsv2). This work was jointly supported by the National Basic Research (973) Program of China under grant 2015CB453203; the National Key Research Program and Development of China (2017YFC1502302); the China Meteorological Special Project under grant GHY201406022; the China National Sciences Foundation under grants 41505065, 41375062, and 41775066; and the 973 Program of China under grant 2010CB950404.

References

Alvarez, M. S., Vera, C. S., Kiladis, G. N., & Liebmann, B. (2016). Influence of the Madden Julian Oscillation on precipitation and surface air temperature in South America. *Climate Dynamics*, *46*(1–2), 245–262. https://doi.org/10.1007/s00382-015-2581-6

Barlow, M., Wheeler, M., Lyon, B., & Cullen, H. (2005). Modulation of daily precipitation over southwest Asia by the Madden-Julian oscillation. *Monthly Weather Review*, *133*(12), 3579–3594. https://doi.org/10.1175/Mwr3026.1

Bond, N. A., & Vecchi, G. A. (2003). The influence of the Madden-Julian Oscillation on precipitation in Oregon and Washington. *Weather and Forecasting*, *18*(4), 600–613. https://doi.org/10.1175/1520-0434(2003)018%3C0600:tiotmo%3E2.0.co;2

Chen, J., Wen, Z., Wu, R., Chen, Z., & Zhao, P. (2015). Influences of northward propagating 25–90-day and quasi-biweekly oscillations on eastern China summer rainfall. *Climate Dynamics*, *45*(1–2), 105–124. https://doi.org/10.1007/s00382-014-2334-y

Fu, X., Lee, J. Y., Wang, B., Wang, W., & Vitart, F. (2013). Intraseasonal forecasting of the Asian summer monsoon in four operational and research models. *Journal of Climate*, *26*(12), 4186–4203. https://doi.org/10.1175/jcli-d-12-00252.1

Gao, J., Chen, C., Zhou, X., & You, L. (2013). Analysis of low-frequency features on typical persistent heavy rainfall during pre-flood season in Fujian Province in 2010 (in Chinese). *Advances in Meteorological Science and Technology*, *3*(1), 39–45. https://doi.org/10.3969/j.issn.2095-1973.2013.01.006

Hsu, P. C., Lee, J. Y., & Ha, K. J. (2016). Influence of boreal summer intraseasonal oscillation on rainfall extremes in southern China. *International Journal of Climatology*, *36*(3), 1403–1412. https://doi.org/10.1002/joc.4433

Huang, R., Xu, Y., Wang, P., & Zhou, L. (1998). The features of the catastrophic flood over the Changjiang River basin during the summer of 1998 and cause exploration (in Chinese). *Climatic and Environmental Research*, *3*(04), 300–313. https://doi.org/10.3878/j.issn.1006-9585.1998.04.02

Jeong, J. H., Ho, C. H., Kim, B. M., & Kwon, W. T. (2005). Influence of the Madden-Julian Oscillation on wintertime surface air temperature and cold surges in East Asia. *Journal of Geophysical Research*, *110*, D11104. https://doi.org/10.1029/2004JD005408

Jia, X., Chen, L., Ren, F., & Li, C. (2011). Impacts of the MJO on winter rainfall and circulation in China. *Advances in Atmosphere Sciences*, *28*(3), 521–533. https://doi.org/10.1007/s00376-010-9118-z

Jiang, X., Li, T., & Wang, B. (2004). Structures and mechanisms of the northward propagating boreal summer intraseasonal oscillation. *Journal of Climate*, *17*(5), 1022–1039. https://doi.org/10.1175/1520-0442(2004)017%3C1022:samotn%3E2.0.co;2

Jones, C. (2000). Occurrence of extreme precipitation events in California and relationships with the Madden-Julian Oscillation. *Journal of Climate*, *13*(20), 3576–3587. https://doi.org/10.1175/1520-0442(2000)013%3C3576:ooepei%3E2.0.co;2

Jones, C., Waliser, D. E., Lau, K. M., & Stern, W. (2004). Global occurrences of extreme precipitation and the Madden-Julian Oscillation: Observations and predictability. *Journal of Climate*, *17*(23), 4575–4589. https://doi.org/10.1175/3238.1

Kalnay, E., Kanamitsu, M., Kistler, R., Collins, W., Deaven, D., Gandin, L., et al. (1996). NCEP/NCAR 40-year reanalysis project. *Bulletin of the American Meteorological Society*, *77*(3), 437–472. https://doi.org/10.1175/1520-0477(1996)077%3C0437:TNYRP%3E2.0.CO;2

Lee, J.-Y., Wang, B., Wheeler, M. C., Fu, X., Waliser, D. E., & Kang, I.-S. (2012). Real-time multivariate indices for the boreal summer intraseasonal oscillation over the Asian summer monsoon region. *Climate Dynamics*, *40*(1–2), 493–509. https://doi.org/10.1007/s00382-012-1544-4

Lee, S.-S., Moon, J.-Y., Wang, B., & Kim, H.-J. (2017). Subseasonal prediction of extreme precipitation over Asia: Boreal summer intraseasonal oscillation perspective. *Journal of Climate*, *30*(8), 2849–2865. https://doi.org/10.1175/jcli-d-16-0206.1

Lee, S.-S., Wang, B., Waliser, D. E., Neena, J. M., & Lee, J. Y. (2015). Predictability and prediction skill of the boreal summer intraseasonal oscillation in the Intraseasonal Variability Hindcast Experiment. *Climate Dynamics*, *45*(7–8), 2123–2135. https://doi.org/10.1007/s00382-014-2461-5

Ling, J., Bauer, P., Bechtold, P., Beljaars, A., Forbes, R., Vitart, F., et al. (2014). Global versus local MJO forecast skill of the ECMWF model during DYNAMO. *Monthly Weather Review*, *142*(6), 2228–2247. https://doi.org/10.1175/mwr-d-13-00292.1

Liu, R.-F., & Wang, W. (2015). Multi-week prediction of South-East Asia rainfall variability during boreal summer in CFSv2. *Climate Dynamics*, *45*(1–2), 493–509. https://doi.org/10.1007/s00382-014-2401-4

Loriaux, J., Lenderink, G., & Siebesma, A. P. (2016). Peak precipitation intensity in relation to atmospheric conditions and large-scale forcing at midlatitudes. *Journal of Geophysical Research: Atmospheres*, *121*, 5471–5487. https://doi.org/10.1002/2015jd024274

Lu, R. Y., & Lin, Z. D. (2009). Role of subtropical precipitation anomalies in maintaining summertime meridional teleconnections over the western North Pacific and East Asia. *Journal of Climate*, *22*(8), 2058–2072. https://doi.org/10.1175/2008JCLI2444.1

Madden, R. A., & Julian, P. R. (1971). Detection of a 40–50 day oscillation in the zonal wind in the tropical Pacific. *Journal of the Atmosphere Sciences*, *28*(5), 702–708. https://doi.org/10.1175/1520-0469(1971)028%3C0702:doadoi%3E2.0.co;2

Madden, R. A., & Julian, P. R. (1972). Description of global-scale circulation cells in the tropics with a 40–50 day period. *Journal of the Atmosphere Sciences*, *29*(6), 1109–1123. https://doi.org/10.1175/1520-0469(1972)029%3C1109:dogscc%3E2.0.co;2

Madden, R. A., & Julian, P. R. (1994). Observations of the 40–50-day tropical oscillation—A review. *Monthly Weather Review*, *122*(5), 814–837. https://doi.org/10.1175/1520-0493(1994)122%3C0814:ootdto%3E2.0.co;2

Mao, J., & Wu, G. (2006). Intraseasonal variations of the Yangtze rainfall and its related atmospheric circulation features during the 1991 summer. *Climate Dynamics*, *27*(7–8), 815–830. https://doi.org/10.1007/s00382-006-0164-2

O'Gorman, P. A., & Schneider, T. (2009). The physical basis for increases in precipitation extremes in simulations of 21st-century climate change. *Proceedings of the National Academy of Sciences of the United States of America*, *106*(35), 14,773–14,777. https://doi.org/10.1073/pnas.0907610106

Ren, H.-L., & Ren, P. (2017). Impact of Madden-Julian Oscillation upon winter extreme rainfall in Southern China: Observations and predictability in CFSv2. *Atmosphere*, *8*(12), 192. https://doi.org/10.3390/atmos8100192

Saha, S., Moorthi, S., Pan, H. L., Wu, X. R., Wang, J. D., Nadiga, S., et al. (2010). The NCEP climate forecast system reanalysis. *Bulletin of the American Meteorological Society*, *91*(8), 1015–1058. https://doi.org/10.1175/2010BAMS3001.1

Saha, S., Moorthi, S., Wu, X. R., Wang, J., Nadiga, S., Tripp, P., et al. (2014). The NCEP climate forecast system version 2. *Journal of Climate*, *27*(6), 2185–2208. https://doi.org/10.1175/Jcli-D-12-00823.1

Wang, B., & Rui, H. (1990). Synoptic climatology of transient tropical intraseasonal convection anomalies: 1975–1985. *Meteorology and Atmospheric Physics*, *44*(1–4), 43–61. https://doi.org/10.1007/bf01026810

Wang, D., Xia, R., & Liu, Y. (2011). A preliminary study of the flood causing rainstorm during the first rainy season in South China in 2008 (in Chinese). *Acta Meteorologica Sinica*, *69*(1), 137–148. https://doi.org/10.11676/qxxb2011.012

Webster, P. J., Jian, J., Hopson, T. M., Hoyos, C. D., Agudelo, P. A., Chang, H. R., et al. (2010). Extended-range probabilistic forecasts of Ganges and Brahmaputra floods in Bangladesh. *Bulletin of the American Meteorological Society*, *91*(11), 1493–1514. https://doi.org/10.1175/2010BAMS2911.1

Wheeler, M. C., & Hendon, H. H. (2004). An all-season real-time multivariate MJO index: Development of an index for monitoring and prediction. *Monthly Weather Review*, *132*, 1917–1932. https://doi.org/10.1175/1520-0493(2004)132%3C1917:Aarmmi%3E2.0.Co;2

Xavier, P., Rahmat, R., Cheong, W. K., & Wallace, E. (2014). Influence of Madden-Julian Oscillation on Southeast Asia rainfall extremes: Observations and predictability. *Geophysical Research Letters*, *41*, 4406–4412. https://doi.org/10.1002/2014gl060241

Yang, J., Wang, B., & Bao, Q. (2010). Biweekly and 21–30-day variations of the subtropical summer monsoon rainfall over the lower reach of the Yangtze River basin. *Journal of Climate*, *23*(5), 1146–1159. https://doi.org/10.1175/2009jcli3005.1

Zhang, C. D., & Dong, M. (2004). Seasonality in the Madden-Julian Oscillation. *Journal of Climate*, *17*(16), 3169–3180. https://doi.org/10.1175/1520-0442(2004)017%3C3169:Sitmo%3E2.0.Co;2

Zhang, L., Wang, B., & Zeng, Q. (2009). Impact of the Madden-Julian Oscillation on summer rainfall in Southeast China. *Journal of Climate*, *22*(2), 201–216. https://doi.org/10.1175/2008jcli1959.1

Zhang, X. B., Alexander, L., Hegerl, G. C., Jones, P., Tank, A. K., Peterson, T. C., et al. (2011). Indices for monitoring changes in extremes based on daily temperature and precipitation data. *Wiley Interdisciplinary Reviews: Climate Change*, *2*(6), 851–870. https://doi.org/10.1002/wcc.147

Zhao, C., Zhou, T., Song, L., & Ren, H. (2014). The boreal summer intraseasonal oscillation simulated by four Chinese AGCMs participating in the CMIP5 project. *Advances in Atmospheric Sciences*, *31*(5), 1167–1180. https://doi.org/10.1007/s00376-014-3211-7

Zhu, C. W., Nakazawa, T., Li, J. P., & Chen, L. X. (2003). The 30–60 day intraseasonal oscillation over the western North Pacific Ocean and its impacts on summer flooding in China during 1998. *Geophysical Research Letters*, *30*(18), 1952. https://doi.org/10.1029/2003GL017817

Applied Geography 90 (2018) 224–228

Contents lists available at ScienceDirect

Applied Geography

journal homepage: www.elsevier.com/locate/apgeog

Establishment of a wildfire forecasting system based on coupled weather–Wildfire modeling

Chang-Bok Rim[a], Kum-Chol Om[a,b], Guoyu Ren[b,c,*], Su-Song Kim[a], Hyok-Chol Kim[a], Kang-Chol O.[d]

[a] Department of Meteorology, Faculty of Global Environmental Science, Kim Il Sung University, Daesong District, Pyongyang, North Korea
[b] Department of Atmospheric Science, School of Environmental Studies, China University of Geosciences, 388 Lumo Road, Wuhan, 430074, China
[c] Laboratory for Climate Studies, National Climate Center, China Meteorological Administration, Beijing, 100081, China
[d] Department of Meteorology, Faculty of Agricultural Science, Wonsan Agriculture University, Wonsan, Kangwon Province, North Korea

ARTICLE INFO

Keywords:
Wildland fire
WRF
Atmosphere-fire model
Monitoring
DPRK

ABSTRACT

The Weather Research and Forecasting model (WRF) includes a wildland fire-behavior module, WRF-Fire, which simulates wildland fire interactions with the atmosphere. Combining the WRF model with the coupled weather–wildland fire model allows simulations of wildland fire propagation. In this paper, we have chosen the method that performs simulation of wildfire spread progress coupled with prepared weather data as soon as a wildfire is found. In simulation of the weather field data, a one-way nest model is used with a grid resolution of 1 km. The high-resolution Digital Elevation Model (DEM) data (0.002° × 0.002°) and fuel distribution maps based on forest type data were used. We demonstrated the potential for establishing a real-time wildland fire forecasting system using WRF-Fire model based on the existing conditions and computing resources for weather condition at fire monitoring stations, which can be applied in monitoring and forecasting of the wildland fire disasters in the area of the country.

1. Introduction

Accurate forecasts of wildfire propagation are vitally important for wildfire management, including the emergent response to the wildfire through setting wildfire warning system and evacuation buffers (Larsen, Dennison, Cova, & Jones, 2011). Wildfire forecast models typically evaluate the possibility of fire reaction with various fuels (vegetation) on a landscape and analyze fire interactions with atmospheric and climate factors to guide firefighting operations (Anderson, 1982).

A number of wildfire forecasting and fire simulation studies have been developed based on work in different areas of the world (Balia, Serra, & Modugno, 2011; Coen, 2005; Dobrinkova, Jordanov, & Mandel, 2010; Finney, 1998; Peace & Mills, 2012; Peace, Mattner, & Mills, 2011). Many of these studies have evaluated the effectiveness of the wildfire module (SFIRE) in the Weather Research and Forecasting model (WRF) (NCAR, 2012). SFIRE is a non-static, compressible model consisting of a continuity equation, thermodynamic equation, and water vapor equation, which anticipate wind speed, temperature, water vapor, cloud water, rain, and ice water, etc. in a three-dimensional grid. SFIRE uses an Arakawa C-grid in the horizontal direction and a dynamic vertical coordinate with topography in the vertical direction. This model has multiple nested functions, enabling to establish various finer grids within coarse grid spacing. Thus, it can well simulate how a three-dimensional atmospheric flow structure varying in time influences a wildfire.

Wildland fire modeling can simulate the development, spread, and suppression of a wildfire, and also describe the rate of wildfire spread as well as the heat released in the burning of fuel in two dimensions. Wildland fire modeling deals with three physical processes: the rate of spread of the wildfire perimeter (boundary between burning fuel and unburned fuel), the release of heat in a wildfire area, and scale extension to convert released heat into the atmospheric model. Because physical processes occur on much smaller scales than is captured by the grid and time step of the atmospheric model, semi-empirical formulas are used for parameterization of the sub-grid scale in wildfire simulations (Mandel, Beezley, & Kochanski, 2011b). The wildfire perimeter advances for each time step as unburned fuel ignites and more fuel is consumed in areas that have already ignited. Atmospheric models are relatively coarse, with high-resolution only for the actual wildfire area. Release of heat is determined as a function of time of ignition, fuel properties, and atmospheric conditions.

Using WRF-Fire, coupled weather–wildland fire modeling with

* Corresponding author. Department of Atmospheric Science, School of Environmental Studies, China University of Geosciences, 388 Lumo Road, Wuhan, 430074, China.
E-mail address: guoyoo@cma.gov.cn (G. Ren).

https://doi.org/10.1016/j.apgeog.2017.12.011
Received 26 March 2017; Received in revised form 11 December 2017; Accepted 11 December 2017
0143-6228/ © 2017 Elsevier Ltd. All rights reserved.

WRF, and the wildfire behavior module for predicting wildfire, the influences of a wildfire on the atmosphere and the influence of atmospheric conditions on the wildfire can be simulated. In WRF-Fire, characteristics of the atmosphere and wildfire modules are exchanged in each time step. In the atmosphere module, the influence of the wind field on the wildfire rate of spread is calculated (Coen et al., 2013). Clark, Coen, and Latham (2003) showed a detailed interpretation of the WRF-Fire model through various experiments. They diagrammatically examined the propagation direction and the rate of fire spread, focusing specifically both on the uncoupled model, which did not consider the ambient wind effect. The results demonstrated that uncoupling was possible in a relatively simple fire simulation. They also concluded that more meteorological fire simulations can be realized using a coupled atmosphere-fire model. Kochanski et al. (2010) simulated fire plumes using a coupled atmosphere–fire model based on the ARW atmospheric core and the Rothermel fire model (Rothermel, 1972). Their results showed that the background flow characteristics were not well simulated at higher elevations where flows were away from the surface and did not affect the fire. Beezley, Kochanski, Kondratenko, Mandel, and Sousedik (2010) found that simulated results showed more rapid propagation and fire spread than actual observations in fire spread, and more detailed fuels models and moisture component data were needed to overcome these errors. Clark et al. (1996a,b) provided a more detailed description of the coupled atmosphere–fire model. Coen (2005) also reported an experiment for simulating fire using the Big Elk Fire as an example.

Clark et al. (1996a,b) used the coupled atmosphere–fire model to conduct a more in-depth study of fire spread simulations. Their results showed that if the wind speed was relatively low, the coupling between the atmosphere and the fire was strengthened and the rate of fire spread increased with wind speed; however, if the wind speed was high, the coupling between atmosphere and fire was rather weakened. This was especially true when the wind speed was more than 10 m/s. In contrast, the coupling between the fire and its induced motion weakened and decoupling between the fire and atmosphere occurred. Another study found that turbulence in the atmospheric boundary layer, which is highly affected by the ground surface, plays an important role in fire spread (Sun, Krueger, Jenkins, Zulauf, & Charney, 2009). A simulation of the effect of ambient wind on the fire spread speed by Beer (1991) showed that the fire propagation speed was more than 50% faster in wind conditions of 2–6 m/s when atmospheric conditions were unstable. Other results have shown that the background wind profile is very important for simulating fire propagation, which is dependent on low pressure associated with the development of vortices (Kochanski, Jenkins, Mandel, & Beezley, 2012b).

Near-surface wind is input from the atmosphere module to the wildfire module, which determines spread rate and direction as well as fuel conditions and topographic gradient. A simulated wildfire consumes fuels, including living and dead plants, and releases heat and water vapor to the air. Wind blown into the flame is changed under wildfire conditions. The wildfire module calculates fuel consumed and energy released by the wildfire and transfers this information to the atmospheric variable. On the lowest layer of the atmospheric model, energy released during the wildfire is transferred to the sensible and latent heat variables of the atmospheric model equations. Simpson, Sharples, Evans, and McCabe (2013, 2014) used the WRF-Fire model to investigate vorticity-driven lateral fire spread (VLS) and reported that both high spatial resolution for simulating fire spread and the two-way coupled atmosphere-fire model are important components for modeling VLS using the atmosphere–fire model.

There have been a series of studies aimed at numerically simulating the development of fire under specific conditions using the WRF-SFIRE model, which consists of the Weather Research and Forecasting (WRF) model coupled with the fire-spread model (SFIRE) (Kochanski, Beezley, Mandel, & Kim, 2012a, 2012b; Mandel, Beezley, & Kochanski, 2011a; Mandel et al., 2014a,b; Vejmelka, Kochanski , & Mandel, 2013). Vejmelka et al. (2013) suggested a method for obtaining a moisture map of various flammable substances by assimilating data on the state of the atmosphere from remote automatic weather stations (RAWS) into WRF-SFIRE. Kochanski et al. (2012a) described a newly added WRF-Chem coupling model for fire simulation, and this model reveals that fire behavior can be treated as the dynamic flow of various gas combustion materials.

Mandel et al. (2014a) provided a more detailed study of the WRF-SFIRE model. They showed that the coupling between the fire model and atmospheric chemistry was effective in improving simulations of fire and air quality, and also emphasized the possibility of using the model in other studies of atmospheric chemistry. Another study described a new assimilation method for active detection of fire based on the modification of fire arrival time using a Bayesian inverse problem technique (Mandel et al., 2014a,b).

Our study evaluated the potential for application of WRF-fire over an area in the DPRK based on prior theoretical research and numerous simulations for managing fire.

2. Atmospheric model settings and implementation

Wildfires are affected by complex and multi-scale weather and climate processes (Fox et al., 2015; Mandel et al., 2011b). Wildfire spread simulation requires meteorological fields with high-resolution. However, the higher the resolution is, the more time it requires. The purpose of wildfire forecasts is to provide rapid assistance to fire managers by predicting the direction of fire evolution. However, this requires too much computational time to use the optional run. Therefore, it is important to set the nesting domain and scale of resolution.

2.1. Nesting domains and resolution in the atmospheric model

WRF supports a multi-grid nesting configuration, and the standard coarse-to-fine grid ratio is 3. The coupled atmosphere–fire model is run in only the finest mesh. Four nested domains are required to scale the simulation down from atmospheric initialization (25 km) to the fire grid resolution (about 1 km) (Table 1). In this case, it required a great deal of time to generate a 24-h forecast. Thus, we used a one–way nesting run configuration. In one-way nesting, the parent-to-child grid ratio is 5. The construction of nested grid domains was as follows.

Model run outputs were obtained by running WRF in every analysis time step for the two domains shown in Fig. 1. The fire spread simulation was started from the time the fire was discovered in a satellite image. Mandel et al. (2014a) proposed a method of assimilating satellite data into wildfire simulations to provide fire updates using satellite image data.

We ran the WRF-SFIRE model with a grid resolution of 1 km and the domain determined in a given grid dimension with fire position as the center. The fire grid refinement was 10. A two-dimensional fire propagation model was run in finer mesh with grid spacing of 100 m subdivided by 10 times based on the 1 km-resolution atmosphere–fire model.

2.2. Calculating meteorological data using one-way nesting

First, geogrid and metgrid were run for two domains as two-way

Table 1
The resolution of atmospheric model for fire spread simulation.

Domain	Grid spacing (km)	x-grid dimension	y-grid dimension	Vertical dimension
d01	25	80	80	35
d02	5	141	141	35
d03	1	40	40	69

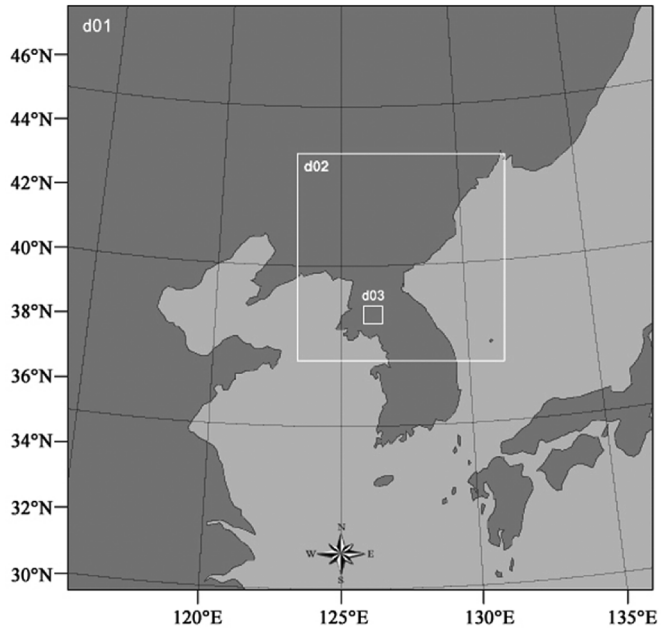

Fig. 1. Domains chosen for obtaining meteorological data. D01: Domain One; d02: Domain Two; do3: Domain Three.

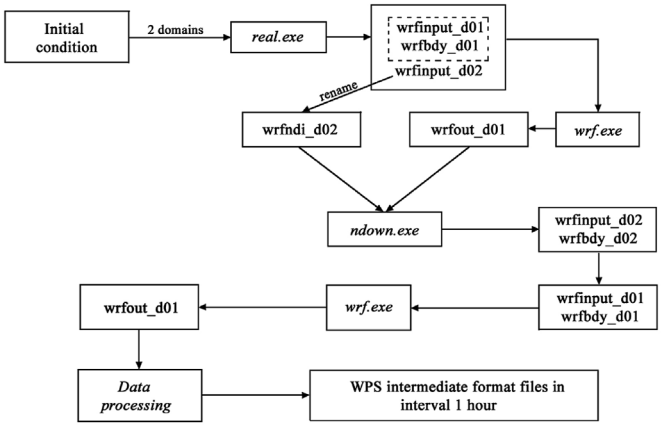

Fig. 2. One-way-nested configuration of multi domains.

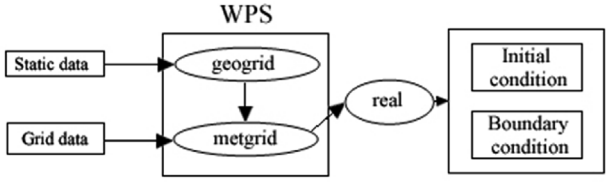

Fig. 3. Schematic diagram of WRF preprocessing system.

nesting with *namelist.wps* and *namelist.input* edited with horizontal grid spacing of 25 km and 5, respectively. Then, the two initial and boundary condition files were obtained from a *real.exe* run.

Second, we ran the model (wrf.exe) in the outer nest (parent's nest) for 24 h and obtained the WRF output of domain 1 (wrfout_d01). Then, we used the model output and the initial condition (wrfinput_d02) in the second domain to run *ndown.exe* to get a new initial condition for the second domain. A 24-h forecast output file for the second domain was obtained using the initial condition. The output interval time was one hour. The parameter file (*namelist.input*) must be edited in every step. In cases in which the fire position, size, and ignition time are known, simulations must be carried out from the time of ignition (result

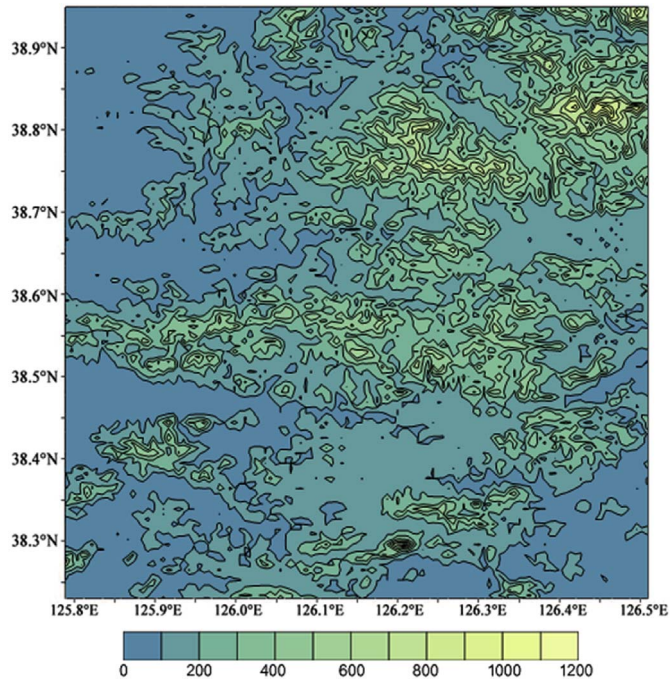

Fig. 4. The topographical conditions of the simulated area (Domain Three in Fig. 1). Unit of elevation: m above sea level.

of sufficient model stabilization step) so that the amount of calculations can be reduced.

In the operational run, there are two analysis processes per day (00UTC, 12UTC). So, when the analysis data is obtained, the NWP model run produces output at intervals of one hour, meaning the fire can be simulated using any starting time for fire ignition. The WRF meteorological output is then converted to WPS intermediate files.

Fig. 2 shows the process of obtaining the meteorological data (with 5 km horizontal grid spacing) necessary to run the coupled WRF-Fire model.

3. WRF-fire model settings and implementation

3.1. Building a static database (high resolution topography and fuel data)

The wildfire simulation is carried out considering topographical and fuel factors. Therefore, it is necessary to build static databases for the high-resolution topographic and the fuel data that can be used in the WRF model. In wildfire simulations, topographical conditions have as much significance as atmospheric conditions. In particular, simulations of the paths of spread for a wildfire require sufficient coupled conditions of atmospheric conditions and terrain (Sharples, Mcrae, & Wilkes, 2012). The static database is read when *geogrid.exe* is executed in the WRF Preprocessing System (WPS) to generate static data for the wildfire forecast area (Fig. 3).

We created the topography and fuel databases using a series of steps. We made a binary file written as a geogrid format using DEM data for the DPRK area with 0.0002° spacing (20–30 m grid spacing). A 5000 × 5000 array (dataset of 1° × 1° domain) was written for each data file. The fuel database consisted of five classes of fuel data from the National Forest Survey, which was numerically coded according to tree species. The classes of fuel data from the National Forest Survey include Grass, Chaparral, Brush and Litter. In some areas of DPRK, Slash in Anderson fuel categories (Anderson, 1982) can hardly be seen. Therefore, we set the corresponding relation between Anderson 14 fuel categories and the fuel categories, considering fuel weights and total fuel loads. The 5 fuel categories used are: 1-Grass (Anderson categories 1-3average), 2- Chaparral (Anderson category 4), 3- Brush (Anderson

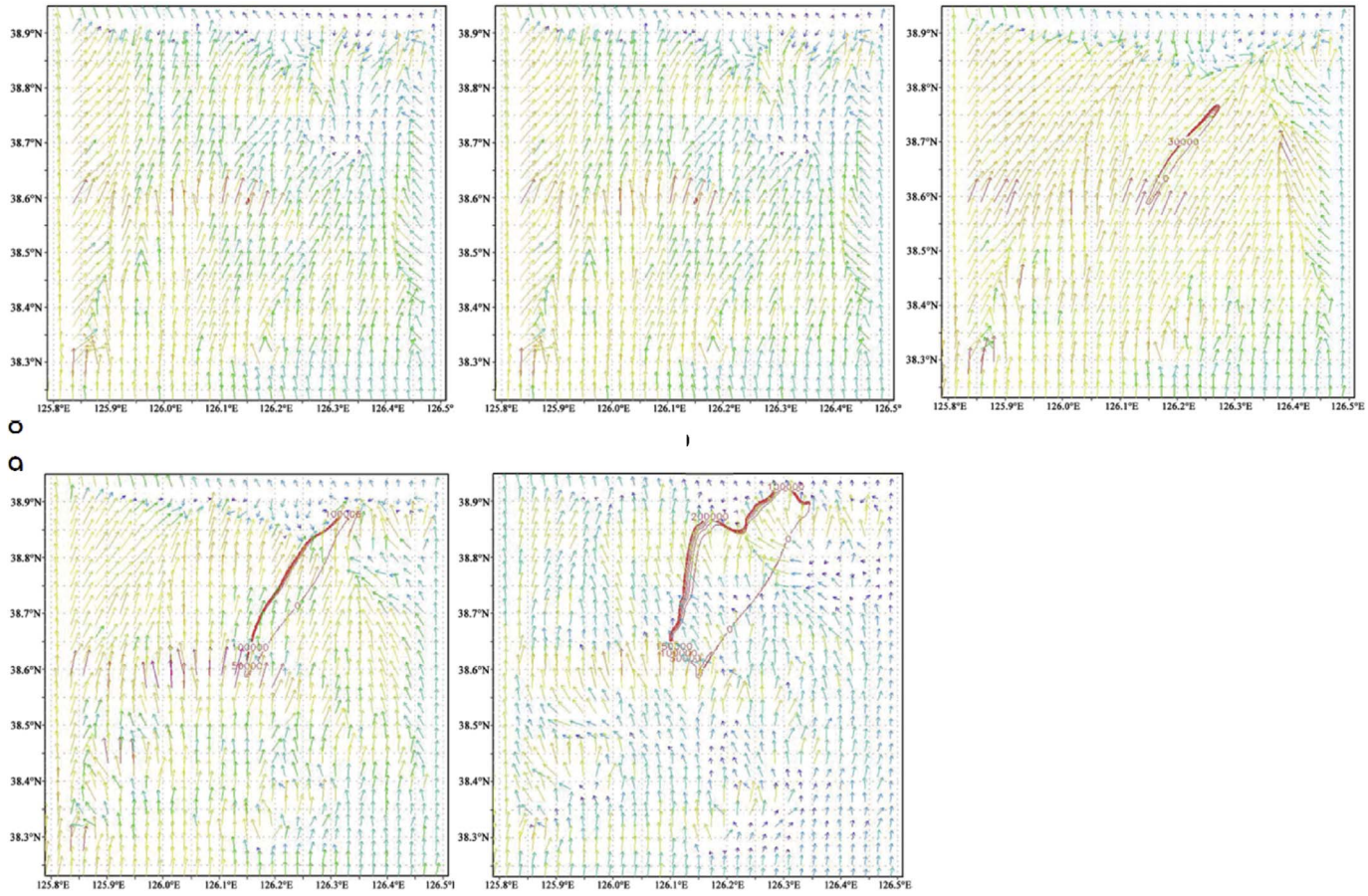

Fig. 5. Fire spread after different time periods in the simulated area (Domain Three of Fig. 1). a, b, c, d, e denote the simulated fire spread after 150s, 300s, 450s, 540s and 600s of the fire ignition.

category 5), 4- litter (Anderson categories 8-10average), 5- no fuel (Anderson category 14).

Besides the binary data files, the geogrid requires an extra metadata file (named "index") for each data set. The geogrid produces static data based on the list of the *GEOGRID.TBL* file. Therefore, we edited the list of topographic and fuel data (*ZSF* and *NFUEL_CAT*) in the *GEOGRID.TBL* file.

3.2. Implementation of the fire-model

The fire-model was executed according to the following steps:

Step 1. We edited the fire mesh domain information in *namelist.wps* based on the fire-center position (longitude and latitude coordinates), fire size (the radius of fire area, m), ignition time (yy/mm/dd/hh) obtained from the fire guard. As mentioned above, we defined 1 km of meteorological calculating domain grid spacing and 40 × 40 of horizontal dimensions in the coupled atmosphere–fire model. We recommend using a fire mesh refinement ratio of 10 (subgrid_ratio_x = 10, subgrid_ratio_y = 10); fire mesh grid spacing was 100 m.

Step 2. We ran geogrid and metgrid, and generated metgrid files combined with meteorological data and static data.

Step 3. We edited *namelist.input* and executed it for generating the initial and boundary files necessary to run the model. We recommend setting vertical layer numbers to 50 (vert = 50) to keep the difference between the lowest layers small. If the difference is large, the wind field for calculating fire propagation will be interpolated too large than the actual case.

Because the fire model is 2-dimensional based on the effects of wind and topographic factors, the effect of physical processes on fire propagation is relatively small. However, calculation of physical processes in the model run takes a lot of time. Therefore, we disabled options for physical processes (microphysics processes and longwave and shortwave radiation processes). We recommend the option *isfflx = 1*, which makes WRF use a surface model to compute the surface fluxes. Other options for constant heat fluxes and drag are not well suited for fire simulations. Out of all surface exchange parameterizations, only the classic Monin-Obukhov theory (sf_sfclay physics = 1) is recommended for the LES cases. We defined time_step = 6 in order to satisfy CFL conditions because the fire mesh grid spacing is 1 km.

4. Simulation results and discussions

The fire forecast system was run immediately after the location of fire ignition was confirmed from an information source such as satellite data. We simulated the spread progression of the perimeter of the fire with a 1000 m radius that occurred at 38.53°N, 125.75°E at 12:50, Mar 28, 2016. The topographical conditions of the simulated area are shown in Fig. 4, and the fire spread area and wind vectors are shown in Fig. 5.

In the optional run, a model run for obtaining meteorological data with 1 km mesh grid is carried out twice every day (requires 20min using a PC-i7). When a fire occurs, a fire model is run in 40 × 40 km domains centered on the fire position. It takes about 15 min to generate a 24-h forecast.

The meteorological field can be obtained optionally by using a one-way nested configuration in every analysis process. Then, whenever a fire occurs, the WRF-Fire model is run. In this case, the fire propagation process is simulated in relatively short time using only one PC-i7

computer.

The standard program of the WRF-ARW model does not support coordinate and terrain gradient data in making an initial condition file. Therefore, we inserted codes for calculating coordinates of fire mesh and terrain gradient data in the *real_em* module and fire calculation modules. The results from several simulations showed that fire ignition time was related to fire area size. The larger the fire area, the later the fire ignition time was. For example, fire-burning time was 2 min after time of ignition in the case of a fire radius of 100 m, but about 25min in the case of a fire radius of 1000 m.

In the optional fire guard system, it is possible to monitor a fire with a radius of more than 1000 m because of satellite resolution. Therefore, the fire model was run from an earlier initial condition (before 30min) to simulate fire spread based on the start time.

In the simulations, fire spread behavior was faster than the on-the-ground situation, which was consistent with Beezley et al. (2010). This is because the atmosphere–fire model was run over a coarser mesh. Clark el al. (1996b) found that the simulated fire spread was faster than observation in case of lower resolution. In our simulation, the resolution of atmospheric model was 1 km and the resolution of fire model was 100 m. These resolutions were coarser than the 400 m-resolution atmospheric model and 30 m-resolution fire model in Mandel et al. (2011a). When the simulated spread speed and direction of wildfire and burned area were compared with observation images by the stationary satellite GMS (every 15min) and HIMAWARI (every 10min), and polar orbital satellite NOAA (every 12 h), the previous researches were qualitatively confirmed. However, establishment of a fire spread forecast system that simulates fire spread direction using the low capacity computers available at all fire guard stations is a large contribution in preventing and managing wildfires.

5. Conclusions

The weather field was calculated first for a grid of 1 km, and the calculation was carried out as soon as the wildfire was detected, based on the one-way nested method. The ratio between the atmospheric model and the fire-model grid was 1:10. DEM data of 0.0002° (20–30 m) intervals in both longitude and latitude coordinates were used as high-resolution topographic data.

We showed that the simulated fire spread behavior was faster than the observed spread, probably because the atmosphere–fire model was run over an inadequate mesh condition. Consequently, we explained the influence of the results on establishing a real-time wildland fire forecasting system using WRF-Fire based modeling and the existing computing resources.

We concluded that numerical simulations of fire spread, even under normal facility conditions, have some significance in current fire monitoring conditions. In the future, however, the high-resolution data processing required in the meteorological fire modeling fields should be considered. It would be also interesting to further examine the long-term change in wildfire events and the future risks under the background of global and regional climate change (Fox et al., 2015), and the applicability of the WRF-Fire model in the changing climate condition the study area.

References

Anderson, H. E. (1982). Aids to determining fuel models for estimating fire behavior. *Bark Beetles, 122*.

Balia, A., Serra, P., & Modugno, S. (2011). Identifying dynamics of fire ignition probabilities in two representative Mediterranean wildland-urban interface areas. *Applied Geography, 31*, 930–940.

Beer, T. (1991). The interaction of wind and fire. *Boundary-Layer Meteorology, 54*(3), 287–308.

Beezley, J. D., Kochanski, A., Kondratenko, V. Y., Mandel, J., & Sousedik, B. (2010). Simulation of the meadow creek fire using WRF-Fire. Agu Fall Meeting Abstracts http://ccm.ucdenver.edu/w/images/a/ae/Agu10_jb.pdf.

Clark, T. L., Coen, J., & Latham, D. (2003). Description of a coupled atmosphere–fire model. *International Journal of Wildland Fire, 13*(1), 49–63.

Clark, T. L., Jenkins, M. A., Coen, J., & Packham, D. (1996b). A coupled atmospheric-fire Model: Convective feedback on fire line dynamics. *Journal of Applied Meteorology, 35*, 875–901.

Clark, T. L., Jenkins, M. A., Coen, J. L., Packham, D. R., Clark, T. L., Jenkins, M. A., et al. (1996a). A coupled atmosphere-fire model: Role of the convective Froude number and dynamic fingering at the fireline. *International Journal of Wildland Fire, 6*(4), 177–190.

Coen, J. L. (2005). Simulation of the big elk fire using coupled atmosphere–fire modeling. *International Journal of Wildland Fire, 14*(1), 49–59.

Coen, J. L., Cameron, M., Michalakes, J., Patton, E. G., Riggan, P. J., & Yedinak, K. M. (2013). WRF-fire: Coupled weather-wildland fire modeling with the weather research and forecasting model. *Journal of Applied Meteorology & Climatology, 52*(1), 16–38.

Dobrinkova, N., Jordanov, G., & Mandel, J. (2010). *WRF-fire applied in Bulgaria. international conference on numerical methods and applications*Springer-Verlaghttp://ccm.ucdenver.edu/reports/rep290.pdf.

Finney, M. A. (1998). Farsite: Fire area simulator-model development and evaluation. *USDA Forest Service - Research Papers RMRS, 18*(RP-4)https://www.fs.fed.us/rm/pubs/rmrsrp004.pdf.

Fox, D. M., Martin, N., Carrega, P., Andrieu, J., Adnes, C., Emsellem, K., et al. (2015). Increases in fire risk due to warmer summer temperatures and wildland urban interface changes do not necessarily lead to more fires. *Applied Geography, 56*, 1–12.

Kochanski, A. K., Beezley, J. D., Mandel, J., & Kim, M. (2012a). WRF fire simulation coupled with a fuel moisture model and smoke transport by WRF-Chem. *2012 WRF Users Workshop, Boulder, CO, 25-29 June 2012, paper P51* (pp. 5). . http://www.openwfm.org/w/images/c/c6/WRF_workshop_2012_poster.pdf.

Kochanski, A., Jenkins, M., Krueger, S. K., Mandel, J., Beezley, J. D., & Clements, C. B. (2010). Evaluation of the fire plume dynamics simulated by WRF-Fire. http://www.openwfm.org/w/images/1/16/AGU.2010.kochanski.key.pdf.

Kochanski, A. K., Jenkins, M. A., Mandel, J., & Beezley, J. D. (2012b). Evaluation of WRF-SFIRE performance with field observations from the fireflux experiment. *Geoscientific Model Development, 6*(4), 1109–1126.

Larsen, J. C., Dennison, P. E., Cova, T. J., & Jones, C. (2011). Evaluating dynamic wildfire evacuation trigger buffers using the 2003 Cedar Fire. *Applied Geography, 31*, 12–19.

Mandel, J., Amram, S., Beezley, J. D., Kelman, G., Kochanski, A. K., Kondratenko, V. Y., et al. (2014a). Recent advances and applications of WRF-SFIRE. *Natural Hazards and Earth System Sciences, 14*(10), 2829–2845.

Mandel, J., Beezley, J. D., & Kochanski, A. K. (2011a). Coupled atmosphere-wildland fire modeling with WRF 3.3 and SFIRE 2011. *Geoscientific Model Development, 4*(3), 591–610.

Mandel, J., Beezley, J. D., & Kochanski, A. K. (2011b). Coupled atmosphere-wildland fire modeling with WRF-FIRE. *Geoscientific Model Development Discussions, 4*(1), 691–695.

Mandel, J., Kochanski, A. K., Vejmelka, M., & Beezley, J. D. (2014b). Data assimilation of satellite fire detection in coupled atmosphere-fire simulation by WRF-SFIRE. *Physics*. http://dx.doi.org/10.14195/978-989-26-0884-6_80.

NCAR (2012). Weather research and forecasting version3 modeling system user's guide. *NCAR*, 12–97.

Peace, M., Mattner, T. W., & Mills, G. (2011). The Kangaroo island bushfires of 2007: A meteorological case study and WRF-FIRE simulation. Modelling & Simulation Society of Australia & Nz http://mssanz.org.au/modsim2011/A2/peace.pdf.

Peace, M., & Mills, G. (2012). *A case study of the 2007 Kangaroo Island bushfires* Report, CAWCR Technical Report No. 053, Bureau of Meteorology, Melbourne, Victoria, Australia.

Rothermel, R. C. (1972). Usda Forest Service General Technical Report*A mathematical model for predicting fire spread in wildland fuels*, *115*US forest Servicehttps://www.treesearch.fs.fed.us/pubs/32533.

Sharples, J. J., Mcrae, R. H. D., & Wilkes, S. R. (2012). Wind–terrain effects on the propagation of wildfires in rugged terrain: Fire channelling. *International Journal of Wildland Fire, 21*(3), 282–296.

Simpson, C. C., Sharples, J. J., & Evans, J. P. (2014). Resolving vorticity-driven lateral fire spread using the WRF-FIRE coupled atmosphere-fire numerical model. *Natural Hazards and Earth System Sciences, 14*(9) 2359–2237.

Simpson, C. C., Sharples, J. J., Evans, J. P., & McCabe, M. F. (2013). Large eddy simulation of atypical wildland fire spread on leeward slopes. *International Journal of Wildland Fire, 22*(5), 599–614.

Sun, R. Y., Krueger, S. K., Jenkins, M. A., Zulauf, M. A., & Charney, J. J. (2009). The importance of fire-atmosphere coupling and boundary-layer turbulence to wildfire spread. *International Journal of Wildland Fire, 18*(1), 50–60.

Vejmelka, M., Kochanski, A. K., & Mandel, J. (2013). Data assimilation of fuel moisture in WRF-SFIRE. *Proceedings of 4th fire behavior and fuels conference, feb 18-22, 2013, Raleigh, North Carolina, USA*.

Article ID: 1006-8775(2018) 01-0092-10

RELATIONSHIP BETWEEN SUMMER LOW-FREQUENCY RAINFALL OVER SOUTHERN CHINA AND PROPAGATION OF TROPICAL INTRASEASONAL OSCILLATION

SHEN Yu-yang (沈雨旸)[1], REN Hong-li (任宏利)[2,3], LI Wei-jing (李维京)[2], ZHANG Yu-jie (张玉洁)[4], ZUO Jin-qing (左金清)[2]

(1. Public Meteorological Service Centre, China Meteorological Administration, Beijing 100081 China; 2. Laboratory for Climate Studies & CMA-NJU Joint Laboratory for Climate Prediction Studies, National Climate Center, China Meteorological Administration, Beijing 100081 China; 3. Department of Atmospheric Science, School of Environmental Studies, China University of Geoscience, Wuhan 430074 China; 4. Beijing Meteorological Bureau, Beijing 100089 China)

Abstract: This study investigates the relationship between summer low-frequency rainfall over southern China and tropical intraseasonal oscillation (ISO) in the atmosphere by examining systematically the propagation features of the tropical ISO in terms of focusing on five large-scale low-frequency rainfall regimes in summer over southern China. It is demonstrated that there is a close linkage between the five rainfall regimes over southern China and the northward propagation of the tropical ISO. The moist ISO signals, which influence the low-frequency rainfall events in different regions of southern China, mainly propagate northwestward from the tropical ocean to the southeast of China. The southeast China rainfall regime is intimately associated with the moist ISO signals propagating northwestward from the equatorial mid-western Pacific Ocean. For both the Yangtze River regime and South of Yangtze River regime, the moist ISO signals over the northern South China Sea show an evident northward propagation towards the Yangtze River region, and then propagate westward. It is further found that the interaction between the northward propagation of low-latitude ISO signals and the southward propagation of high-latitude ISO signals can also make a clear influence on the low-frequency rainfall in southern China. For the Southern China regime, the moist ISO signals show a significant northward propagation from the Philippines. Moreover, for the rainless regime, southern China is under dry ISO signals' control, and the latter shows no clear propagation to southern China. This study may provide insights for the extended-range forecasting of summer rainfall in southern China.

Key words: summer low-frequency rainfall; intraseasonal oscillation propagation; composite analysis

CLC number: P466 **Document code:** A

doi: 10.16555/j.1006-8775.2018.01.009

1 INTRODUCTION

Intraseasonal oscillation (ISO) is an important component of atmospheric circulation, and many studies have investigated the structures, propagation, and mechanisms of ISO (Madden and Julian[1], Li[2-4], Huang et al.[5]; Yang [6]; Hsu and Li [7]). It is generally accepted that ISO propagation includes zonal and meridional propagation with significant seasonal and regional differences (He et al.[8]; Ju et al.[9]; He and Yang[10]; Lin et al.[11]; Wang and Rui [12]; Lawrence and Webster[13]). While ISO undergoes predominantly eastward propagation along the equator, especially during boreal winter, it also undergoes westward propagation, most obviously in off-equatorial regions (Yang and Li[14]). The ISO meridional propagation is much more complicated than its zonal counterpart (Lin et al.[11]). Importantly, the boreal summer ISO undergoes significant northward propagation, primarily south of 30°N (Wang and Rui[12]; Li et al.[15]; Teng and Wang [16]). Two dominant periods of ISO have been identified: the 30–60d (MJO) and 10–20d (QBWO) modes. Their activity characteristics and mechanisms are both subjects of ongoing research (Wen and Zhang[17]; Wen et al.[18]; Annamalai and Slingo[19]).

China is located in the East Asia monsoon region. In summer, increased precipitation in Southern China heightens the risk of flooding, at great cost to human life and property. Thus, summer precipitation variability in Southern China is an important area of research aimed at disaster prevention. Summer precipitation in this region exhibits significant low-frequency characteristics (Miao and Lau[20]; Yang[21]). Analyses of summer drought and flooding events in various areas in Southern China have shown a close link between

Received 2017-06-26; **Revised** 2017-12-20; **Accepted** 2018-02-15

Foundation item: 973 Program of China (2015CB453203,2013CB430203); China Meteorological Special Project (GYHY201406022); China National Science Foundation (41505065, 41375062)

Biography: SHEN Yu-yang, M. S., Research Assistant, primarily undertaking research on short-term climate prediction

Corresponding author: REN Hong-li, e-mail: renhl@cma.gov.cn

precipitation anomalies and ISO propagation (Ju et al.[9]; Ju and Zhao[22]; Lu and Ding[23]; He et al.[24]; Chen et al.[25]). For example, He et al.[24] reported that in wet years, ISO undergoes significant northward propagation over the Yangtze-Huaihe Rivers (Jiang-Huai) basin, and southward propagation in drought years. Lu et al.[23] analyzed the relationship between ISO activity and anomalously heavy rain in the Jiang-Huai basin in summer 1991. They noted that warm moist air was transported by low-frequency oscillation to Jiang-Huai where it interacted with cold air and made an important contribution to the observed heavy rain. Low-frequency precipitation is an important component of summer rainfall; however, previous research has focused mainly on drought and flooding years, with few studies of summer low-frequency rainfall in Southern China and its relationship to ISO variability and propagation. Therefore, an investigation into the relationship between low-frequency precipitation and ISO propagation is necessary to improve our understanding of rainfall distribution and variability in Southern China.

Zhang et al.[26] divided summer low-frequency rainfall in Southern China into five regimes (RRs; Southeast China, Yangtze River, South of the Yangtze River, Southern China, and a rainless regime) to describe the intraseasonal temporal and spatial variability of large-scale rainfall anomalies in Southern China.

Following from the work of Zhang et al.[26], this study presents an analysis of ISO evolution and propagation corresponding to the various RRs. The aim is to reveal the relationship between summer low-frequency rainfall in Southern China and ISO propagation. Thus, results presented here may be used to improve extended-range forecasting of summer rainfall in Southern China.

2 DATA AND METHODS

The primary datasets include (1) 1981–2011 daily precipitation data from 756 stations in China, although only 603 stations are used in the analysis due to missing data; (2) the 1997–2011 GPCP global precipitation dataset with 1°×1° horizontal resolution (Adler et al.[27]); (3) daily outgoing longwave radiation (OLR) from NOAA (Gruber and Krueger [28]); and (4) daily zonal wind at 850 hPa from NECP/NCAR (Kalnay et al.[29]). OLR and 850 hPa zonal wind both have a 2.5°×2.5° horizontal resolution.

We also employ the BSISO index proposed by Lee et al.[30], which can be used to accurately describe the characteristics of BSISO northward propagation in non-equatorial areas. Unless otherwise noted, the time period used in this work is May to September 1981–2011.

The primary methods used here are common diagnostic analysis techniques used in climate research, including band-pass filters, composite analysis, and regression analysis. A Butterworth filter is used to isolate the 10–90d ISO signal. A statistical *t*-test is applied to the composite results, and ISO signals are divided into wet-phase and dry-phase categories. Hereafter, the negative (positive) anomaly is used to represent the wet (dry) phase of the ISO.

3 FIVE LOW-FREQUENCY RAINFALL REGIMES AND CONTRIBUTION OF ISO TO SUMMER RAINFALL VARIANCE

3.1 *Spatial features of the five summer low-frequency rainfall regimes in Southern China*

Large-scale low-frequency rainfall can be divided into several regimes using phase space and applying cluster analysis techniques (Zhang et al.[26]). Letting the state point in phase space represent the daily rainfall observation field, the long-term evolution of rainfall can form the main state point, which can represent the large-scale low-frequency rainfall regime with higher probability of occurrence.

Using this method, the dimensionality of phase space is decreased using the empirical orthogonal function (EOF) and the state point classified using rainfall samples and a *k*-means clustering analysis to compile composite maps of the five RRs [Southeast (R1), Rainless (R2), Yangtze River (R3), South of Yangtze River (R4), and Southern China (R5)]. Each regime persists in time and appears by turn in season, reflecting the low-frequency evolution of large-scale anomalous rainfall in Southern China.

Table 1 lists the five RRs (Zhang et al.[26]) and Fig. 1 presents the spatial features of the rainfall anomalies. Regime R1 includes a positive anomaly centered in Southeast China near Taiwan Island, while the remaining regions of Southern China lack rainfall. Regime R2 shows lower precipitation in Southern China. Regime R3 includes a positive anomaly centered in the Yangtze River Valley, and negative rainfall anomalies in Southern China and the South China Sea. In contrast to R2, more precipitation appears south of the Yangtze River Valley in R4. In R5, the positive rainfall anomaly is centered in Southern China and the northern South China Sea, while the negative anomaly center lies in the Yangtze River Valley, in contrast to R3.

Figure 1. Composite patterns of the five RRs over Southern China in summer (a. Southeast regime; b. Rainless regime; c. Yangtze River regime; d. South of Yangtze River regime; e. Southern China regime, unit: mm/day, the domains enclosed by green contours are significant at the 95% confidence level).

3.2 *Contribution of ISO to summer low-frequency rainfall*

Low-frequency rainfall is an important component of summer rainfall. The five RRs can explain 25%–30% of the variance in total summer rainfall in Southern China. The meridional propagation of the ISO is an

important factor influencing summer low-frequency rainfall in Southern China. Using BSISO indices (Lee et al.[30]) to represent the ISO, the contribution to variance in low-frequency rainfall in Southern China can be calculated. Fig.2 shows the contribution of the variance captured by the BSISO indices to variances in total summer rainfall anomalies and low-frequency rainfall anomalies. ISO contributes 4%—10% of the variance in summer rainfall. The highest contributions to variance are located in the Yangtze River Valley and Southern China, notably in Southeast China, where the contribution to variance exceeds 8% . For summer low-frequency rainfall, ISO contributes over 25% of the variance, increasing to 30%—35% in the Yangtze River Valley and Southern China. Thus, ISO makes a significant contribution to the low-frequency variability in Southern China summer rainfall.

Table 1. The catalog of the low-frequency rainfall regimes (May-September, 1951–2011) (Zhang et al.[26]).

RRs	Sample number	Event number	Number of the events given duration (d)					Mean duration (d)	Maximum duration (d)	Mean interval between events
			(0,5]	(5,10]	(10,15]	(15,20]	(20,∞]			
R1	1011	366	326	39	1	0	0	2.8	11	11
R2	2325	520	371	116	27	5	1	4.5	21	21
R3	924	266	230	34	1	1	0	3.5	18	18
R4	713	224	201	20	3	0	0	3.2	15	15
R5	1089	315	275	38	2	0	0	3.5	12	12

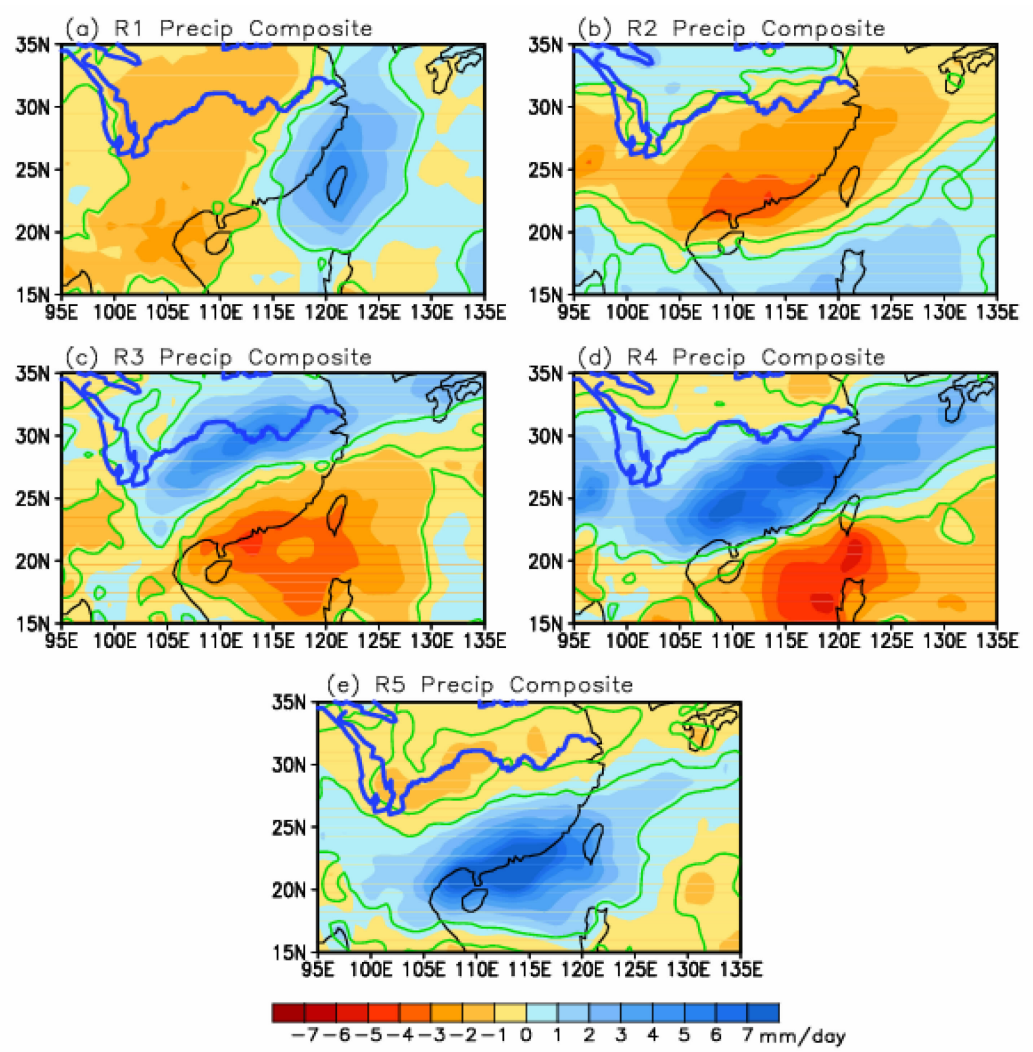

Figure 1. Composite patterns of the five RRs over Southern China in summer (a. Southeast regime; b. Rainless regime; c. Yangtze River regime; d. South of Yangtze River regime; e. Southern China regime, unit: mm/day, the domains enclosed by green contours are significant at the 95% confidence level).

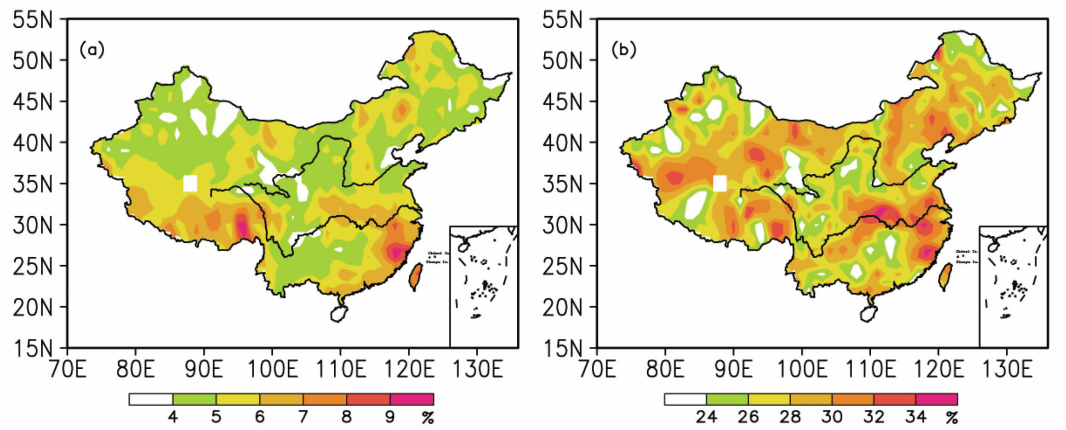

Figure 2. Percentages of the variance explained by BSISO indices in variances of (a) total rainfall (b) low-frequency (10-90d filtered) rainfall of stations during summer (June-August).

4 PROPAGATION OF ISO CORRESPONDING TO FIVE LOW-FREQUENCY RAINFALL REGIMES

To further study the ISO signal and propagation features for each low-frequency RR in summer in Southern China, individual rainfall events are characterized. The first day of each rainfall event is defined as d0, and 2d intervals are used to investigate OLR propagation during −12 to 2d for the five RRs to reveal ISO propagation features during low-frequency rainfall events. The longitude and latitude that show ISO propagation most clearly are used as an ancillary analysis. The OLR signal correlates to that of the ISO best at low latitudes, while errors exist in areas north of 30°N. For these areas, U850 (zonal wind on 850hPa) is used to analyze ISO propagation, as the distribution is similar to measured convection when U850 is used to represent ISO meridional propagation (Lin et al.[31]).

Figure 3 shows the OLR propagation for R1. Moist ISO signals (negative OLR anomalies) propagate northwestward from the equatorial mid-western Pacific Ocean, with gradually increasing strength. The moist ISO signal passes the Philippines and finally reaches Taiwan Island and the southeast coast of China. The ISO propagation closely follows the time-longitude profile and time-latitude profile of the OLR and U850 anomalies. The time-longitude profile at 20° N (Fig.4a) shows that moist ISO signals propagate westward from 160° E, with a center that lies near 120° E during the rainfall event. Fig.4b shows the time-latitude profile at 125°E, which indicates that moist ISO signals propagate northward from the equator to 20°–25°N.

Figure 5 shows ISO propagation for R3 events. In contrast to R1, the moist ISO signals of R3 originate north of the South China Sea, propagate northward along the east coast of China towards the Yangtze River Valley and then propagate westward. The time-longitude profile at 27.5° N (Fig.4c) shows that moist ISO signals propagate westward from 130° E to 110° E. The time-latitude profile at 120° E shows two moist ISO signals that propagate northward from 15° N and southward from 40° N, then converge and are reinforced near 30° N. The U850 signals primarily indicate northward propagation. Both easterlies and westerlies propagate northward from the equator to 25°–30° N, with a convective center in the Yangtze River Valley.

Similar to R3, the moist ISO signal of R4 originates north of the South China Sea and the sea near Taiwan Island. The ISO propagates northward to 25°N, then westward to Southern China, with enhancing strength during westward propagation (Fig.6). Fig.4e shows the time-longitude profile at 27.5°N, in which the moist ISO signals propagate westward from 130°E, with enhancing strength in the region 110° −120° E. The time-latitude profile at 120° E (Fig.4f) indicates that moist ISO signals propagate northward from 20° N. Additionally, on day −6, moist ISO signals propagate southward from ~40°N, after which the two branches of ISO converge and are reinforced near 30°N. The U850 fields indicate primarily northward propagation, and easterlies and westerlies both propagate northward from low latitudes to ~25°N.

The moist ISO signals of R5 propagate northwestward from the Philippines and east of the Philippines to the South China Sea and Taiwan Island, then propagate northward to Southern China (Fig.7). The time-longitude profile at 20° N (Fig.4g) indicates that moist ISO signals propagate westward from 135° E to 110°–120° E with increasing strength. In Fig. 4h, the time-latitude profile at 115° E shows both OLR and U850 signals that indicate significant northward propagation from the equator to 20° −25° N. The convective center lies in Southern China.

Figure 8 shows that ISO signals of R2 events undergo weak, indistinct propagation. The time-latitude profile at 120° E indicates that weak moist ISO signals

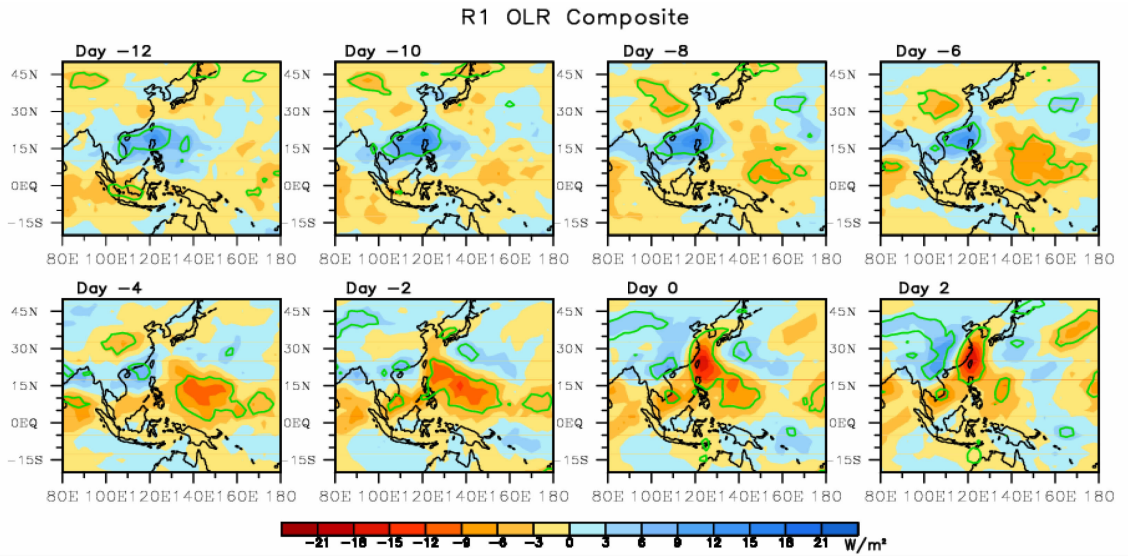

Figure 3. The composite maps of OLR anomalies corresponding to R1 (47 events), lead 12d-lag 2d (units: W/m^2, the domains enclosed by green contours are significant at the 95% confidence level).

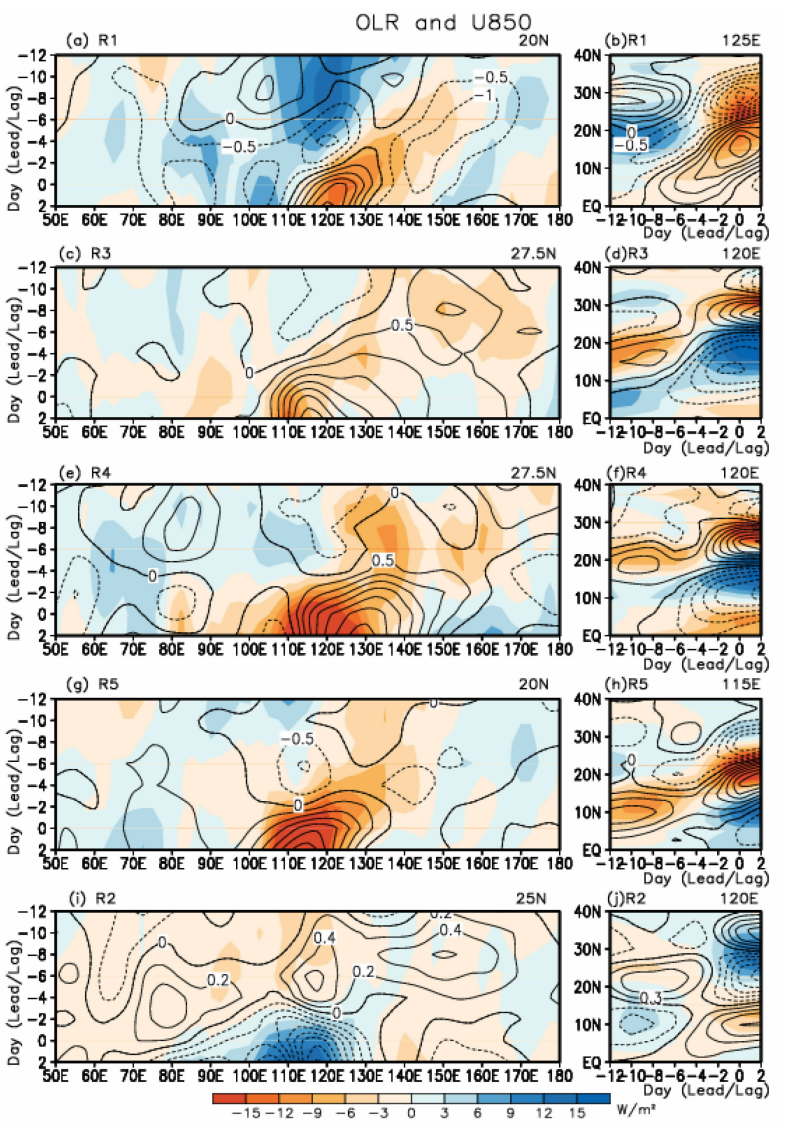

Figure 4. The time-longitude and time-latitude cross sections of OLR anomalies (shaded, units: W/m^2) and U850 anomalies (contour, units: m/s) corresponding to the five RRs. (a-b: R1; c-d: R3; e-f: R4; g-h: R5; i-j: R2). The latitude (longitude) corresponding to time-longitude (time-latitude) profile on the top right corner.

propagate from the equator and extratropical region on day −12. The moist ISO signals converge around 10°–15°N on day −4. During this period, Southern China is dominated by a dry ISO phase and undergoes convective inhibition, which leads to decreased precipitation. The U850 field does not suggest significant southward propagation from the extratropical region; however, this may be caused by errors arising from the use of OLR to represent ISO signals. The moist ISO signal does not suggest significant zonal propagation at 25°N (Fig.4i).

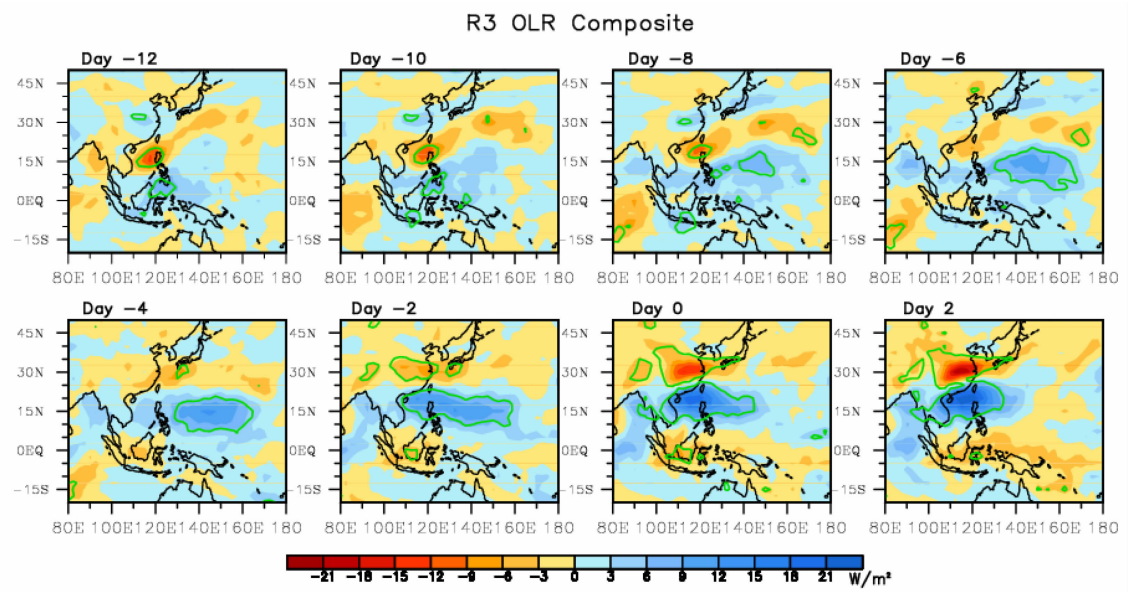

Figure 5. Same as Fig.3, but for R3 (39 events).

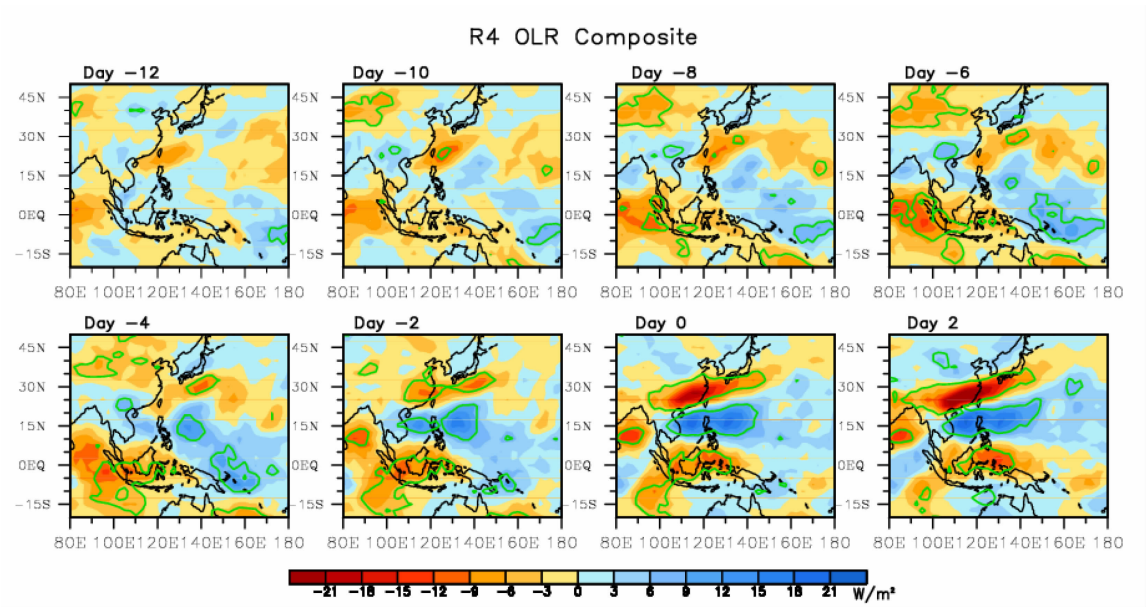

Figure 6. Same as Fig.3, but for R4 (25 events).

Previous studies have shown that the northwestward propagation of OLR follows low-frequency cyclone/anticyclone propagation (Cao et al.[32]) in the same direction. An additional analysis of relative vorticity propagation for each rainfall regime was performed with OLR and U850 field data as part of this work, yielding a similar conclusion (data not shown).

Based on the above analyses, with the exception of the R2 regime, moist ISO signals generally travel from tropical marine areas to the southeast of China, with increasing strength during northwestward propagation, and then arrive at various regions of Southern China where they influence low-frequency precipitation. However, the origin of the ISO signals differs among the various rainfall regimes. Moist ISO signals of R1 come from the mid-western equatorial Pacific Ocean, while both R3 and R4 moist ISO signals originate from

north of the South China Sea, although there is a slight difference in the propagation path. For R5, the ISO originates in the Philippines and the region east of the Philippines. The ISO signal for R2 is weak, and from day −4 Southern China is dominated by a dry ISO pattern and undergoes depressive convection, which leads to low precipitation. Therefore, these results indicate that the generation of low-frequency rainfall in Southern China is closely linked to early moist ISO propagation.

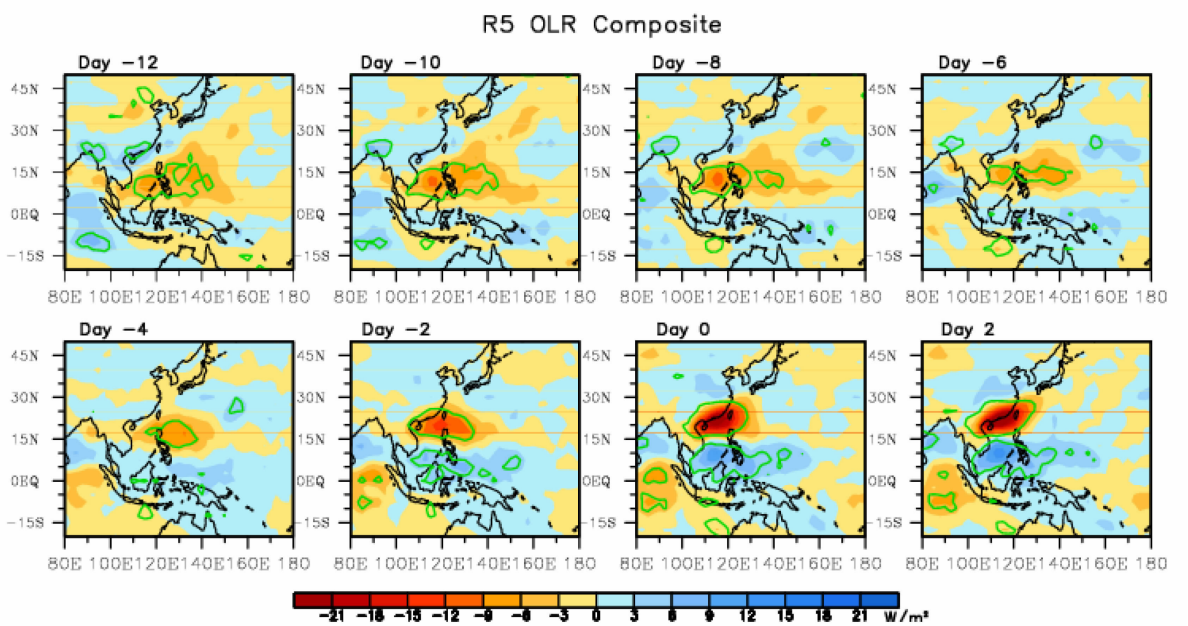

Figure 7. Same as Fig.3, but for R5 (56 events).

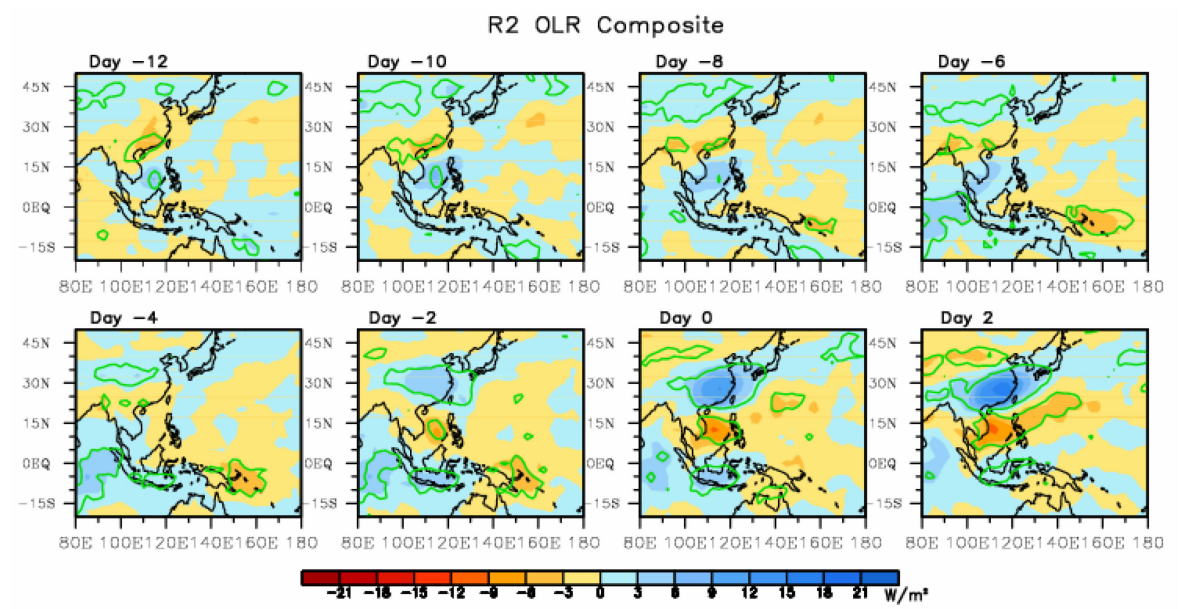

Figure 8. Same as Fig.3, but for R2 (123 events).

5 ISO SIGNAL PROPAGATION PRIOR TO LOW–FREQUENCY RAINFALL EVENTS

As shown above, there is a strong correlation between summer low-frequency rainfall in Southern China and moist ISO northward and westward propagation. To confirm the relationship between different RRs and ISO propagation, typical low-frequency rainfall events are identified in which (1) the duration exceeds five days, and (2) total precipitation exceeds 30 mm (See Fig.9). Early stage propagation of ISO signals is investigated for these events using the same data and methods as described in Section 4. Results demonstrate that the propagation path of typical rainfall events is similar to common events, although with greater strength (data not shown). The time-latitude and time-longitude profiles of typical rainfall events show a clearer westward and northward propagation of moist ISO than common events.

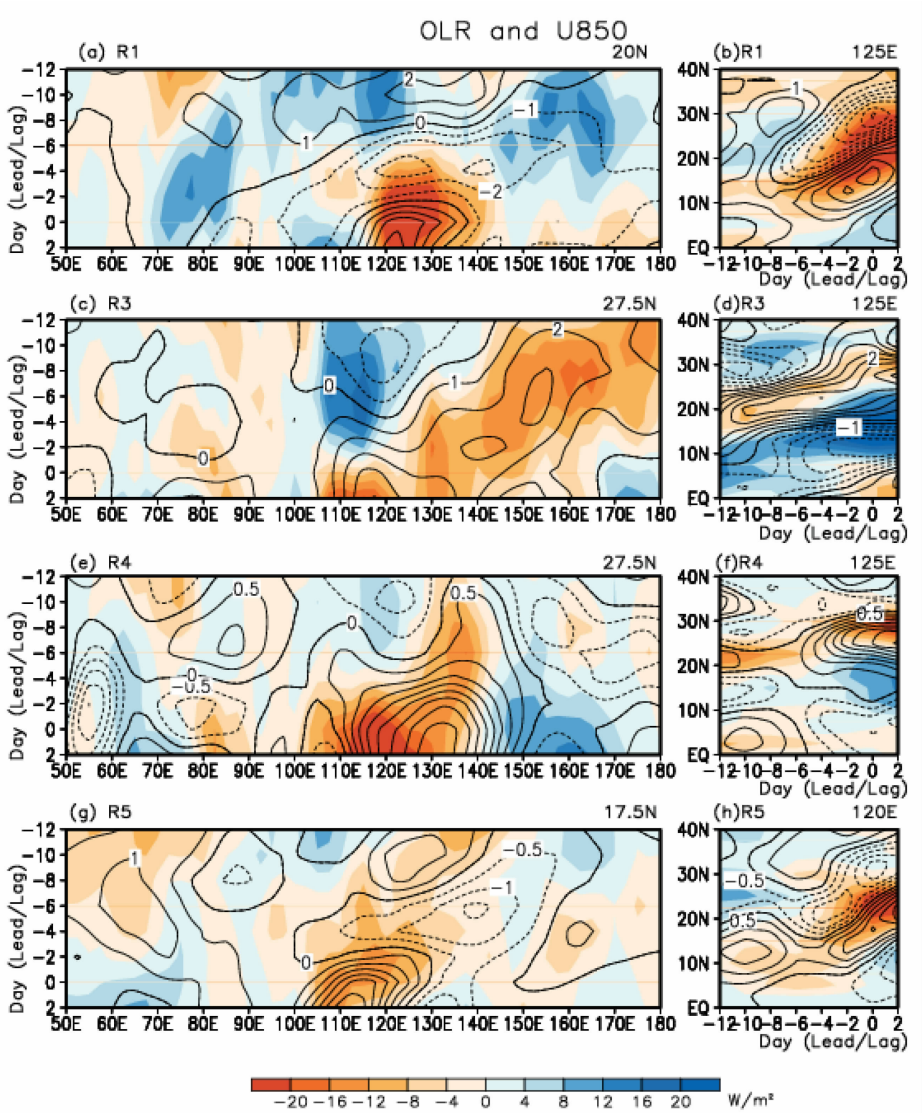

Figure 9. Same as Fig.4, but for the typical low-frequency events of the five RRs: a-b: R1(9); c-d: R3(7); e-f: R4(9); g-h: R5(19), where the numbers of events are included in the brackets.

Typical low-frequency rainfall events in each RR can be correlated with regional persistent heavy precipitation to some extent. Previous studies have shown that in summer, regional persistent heavy rainfall undergoes significant low-frequency oscillation, and is usually associated with the moist phase of ISO (Yang et al.[33]). During persistent heavy rainfall, low-frequency signals originate primarily in the northwest Pacific Ocean and Philippine Sea, and undergo westward and northward propagation during the earlier stages of rainfall events (Cao et al.[32]; Wen et al.[34]). The analysis described in this section also demonstrates that persistent heavy rainfall is closely related to the westward and northward propagation of low-frequency signals.

6 SUMMARY

This study investigated the relationship between summer low-frequency rainfall in Southern China and ISO signal propagation by using five summer low-frequency rainfall regimes (RRs). The contribution of ISO to summer low-frequency rainfall variance in China was explored, with a focus on the preceding and concurrent ISO propagation features of the five low-frequency RRs. The highest contribution of ISO to summer low-frequency rainfall variance (30%–35%) occurs in the Southern China regime. It is shown that ISO originating at low latitudes plays an important role in low-frequency variations in summer rainfall in Southern China.

The moist ISO signals corresponding to each low-frequency rainfall regime generally originate in the tropical marine area to the southeast of China, although the exact originating positions differ among regimes. The Southeast China regime is closely associated with moist ISO signals from the equatorial mid-western Pacific Ocean. For both the Yangtze River and South of Yangtze River regimes, the moist ISO signals originate

in the northern South China Sea, while in the Southern China regime the signals originate in the Philippines. Moist ISO signals that influence low-frequency rainfall events in Southern China generally propagate northwestward with increasing strength. The generation of summer low-frequency rainfall events in Southern China is closely related to the northward propagation of moist ISO signals. Furthermore, the interaction between zonal and meridional ISO propagation, and the latitude at which ISO signals can reach, can both influence rainfall events.

The influence of ISO signals on summer precipitation in Southern China has been the focus of many recent studies (e.g., Ren et al.[35]; Zuo et al.[36]). In this study, we analyzed the relationship between summer low-frequency rainfall in Southern China and the propagation of ISO. Results confirm that ISO meridional propagation has a significant impact on the distribution of summer low-frequency rainfall in Southern China. The mechanism by which ISO northward propagation influences summer rainfall in Southern China is beyond the scope of this work, but warrants future investigation. This study also generally explored low-frequency summer rainfall; however, seasonal differences in the ISO signal, which influences low-frequency rainfall, occur between early summer (May to June) and late summer (July to August). Future research could focus on these periods separately (Que and Li [37]). Finally, the ISO signals discussed in this paper originate mainly in the South China Sea and western Pacific Ocean; however, rainfall data indicate a relationship between ISO originating in the India Ocean and summer low-frequency rainfall in Southern China, and this warrants future exploration.

REFERENCES:

[1] MADDEN R, JULIAN P R. Detection of a 40- 50 day oscillation in the zonal wind in the Tropical Pacific [J]. J Atmos Sci, 1971, 28(5): 702-708.

[2] LI Chong-yin. Intraseasonal oscillation in the atmosphere [J]. Chin J Atmos Sci, 1990, 14(1): 32-45 (in Chinese).

[3] LI C Y. Actions of summer monsoon troughs (ridges) and tropical cyclone over South Asia and moving CISK mode [J]. Sci Sinica (B), 1985, 28(11): 1197-1206.

[4] LI Chong-yin. New advances of the research on the atmospheric intraseasonal oscillation [J]. Progr Nat Sci, 2004, 14(7): 734-741 (in Chinese).

[5] HUANG Hai-yan, HE Jin-hai, ZHU Zhi-wei. Advances in research on atmospheric intraseasonal oscillation and its application to extended range forecast [J]. Meteor Disast Reduct Res, 2011, 34(3): 1-8 (in Chinese).

[6] YANG Qiu-ming. Interannual Variations of Intraseasonal Oscillation Pattern of OLR in Rainy Seasons in East Asia [J]. Sci Technol Rev, 2010, 28(6): 83-87.

[7] HSU P C, LI T. Role of the boundary layer moisture asymmetry in causing the eastward propagation of the Madden-Julian Oscillation [J]. J Climate, 2012, 25 (14): 4914-4931.

[8] HE Jie-lin, WAN Qi-lin, GUAN Zhao-yong, et al. The observation research on intraseasonal oscillation propagating characteristics associated with tropical synoptic waves in Asia-western Pacific region in boreal summer [J]. J Trop Meteor, 2010, 26 (6): 724-732 (in Chinese).

[9] JU Jian-hua, SUN Dan, LV Jun-mei. The Relay Character Analysis of the Zonal and Longitudinal Propagations of the Atmospheric Intraseasonal Oscillation in the East Asian Monsoon Region [J]. J Atmos Sci, 2008, 32 (3): 523-529 (in Chinese).

[10] HE Jin-hai, YANG Song. Meridional propagation of east Asian low-frequency mode and midlatitude low-frequency waves [J]. Acta Meteor Sinica, 1992, 50 (2): 190-198 (in Chinese).

[11] LIN Ai-lan, LIANG Jian-yin, GU De-jun. Review of impacts of tropical atmospheric intraseasonal oscillation on east Asia monsoon and multiple time scales variation of tropical atmospheric intraseasonal oscillation [J]. J Trop Meteor, 2008, 24(1): 11-19 (in Chinese).

[12] WANG B, RUI H. Synoptic climatology of transient tropical intraseasonal convection anomalies: 1975-1985 [J]. Meteor Atmos Phys, 1990, 44(1): 43-61.

[13] LAWRENCE D M, WEBSTER P J. The boreal summer intraseasonal oscillation: relationship between northward and eastward movement of convection [J]. J Atmos Sci, 2002, 59(9): 1593-1606.

[14] YANG Hui, LI Chong-yin. A Study of Propagation of Tropical Intraseasonal Oscillation and Its Influence Mechanism [J]. Clim Environ Res, 2005, 10(2): 145-156 (in Chinese).

[15] LI Chong-yin, LONG Zhen-xia, MU Ming-quan. Atmospheric Intraseasonal Oscillation and Its Important Effect [J]. Chin J Atmos Sci, 2003, 27 (4): 518-535 (in Chinese).

[16] TENG H Y, WANG B. Interannual Variations of the Boreal Summer Intraseasonal Oscillation in the Asian - Pacific Region [J]. J Climate, 2003, 16(22), 3572-3584.

[17] WEN M, ZHANG R H. Quasi-Biweekly Oscillation of the Convection around Sumatra and Low-Level Tropical Circulation in Boreal Spring [J]. Mon Wea Rev, 2008, 136(1): 189-205.

[18] WEN M, YANG S, KUMAR A, et al. Structure and origin of the Quasi-Biweekly Oscillation over the Tropical Indian ocean in boreal spring [J]. J Atmos Sci, 2010, 67(6): 1965-1982.

[19] ANNAMALAI H, SLINGO J M. Active/break cycles: diagnosis of the intraseasonal variability of the Asian Summer Monsoon [J]. Clim Dyn, 2001, 18(1-2): 85-102.

[20] MIAO Jin-hai, LAU K M. Low frequency oscillation (30-60 day) of summer monsoon rainfall over east Asia [J]. Chin J Atmos Sci, 1991, 5(5): 65-71 (in Chinese).

[21] YANG Guang-ji. The Characteristics of Low Frequency Oscillation about Rainfall and Wind Disturbances over Eastern China [J]. Chin J Atmos Sci, 1992, 16 (1): 103-110 (in Chinese).

[22] JU Jian-hua, ZHAO Er-xu. Impacts of the low frequency oscillation in east Asian summer monsoon on the drought and flooding in the middle and lower valley of the Yangtze River [J]. Chin J Atmos Sci, 2005, 21 (2): 163-171 (in Chinese).

[23] LU Er, DING Yi-hui. Low frequency oscillation in east Asia during the 1991 excessively heavy rain over

Changjiang-Huaihe river basin [J]. Acta Meteor Sinica, 1996, 54(6): 730-736 (in Chinese).
[24] HE Yi-hua, WANG Xiao-ling, JIN Qi. The preliminary analysis for the impact of intraseasonal oscillation of the tropical convection over South China Sea on the droughts and floods of Changjiang and Huaihe river basin [J]. J Trop Meteor, 2006, 22(3): 259-264 (in Chinese).
[25] CHEN L X, ZHU C W, WANG B, et al. Analysis of the characteristics of 30-60 day Low-frequency Oscillation over Asia during 1998 SCSMEX [J]. Adv Atmos Sci, 2001, 18(4): 623-638.
[26] ZHANG Yu-jie, LIU Shou-dong, REN Hong-li, et al. Characteristics and the inter-decadal variation of the low-frequency rainfall regimes over southern China in summer[J]. Acta Meteor Sinica, 2014, 72(6): 1205-1217 (in Chinese).
[27] ADLER R F, KIDD C, PETTY G, et al. Intercomparison of global precipitation products: The third precipitation intercomparison project (PIP-3) [J]. Bull Amer Meteor Soc, 2001, 82(7): 1377-1396.
[28] GRUBER A, KRUEGER A F. The status of the NOAA outgoing lonwave radiation data set [J]. Bull Amer Meteor Soc, 1984,65(9): 958-962.
[29] KAINAY E, KANAMITUS M, KISTLER R, et al. The NCEP/NCAR 40-year reanalysis project [J]. Bull Amer Meteor Soc, 1996, 77(3): 437-471.
[30] LEE J Y, WANG B, WHEELER M C, et al. Real-time multivariate indices for the boreal summer intraseasonal oscillation over the Asian summer monsoon region [J]. Clim Dyn, 2013, 40(1-2): 493-509.
[31] LIN Ai-lan, TIM L, Li Chun-hui. Comparison of propagating boreal summer intraseasonal oscillation over tropics represented by wind and convection fields [J].J Appl Meteor Sci, 2010, 21(5): 545-555 (in Chinese).
[32] CAO Xin, REN Xue-juan, YANG Xiu-qun, et al. The quasi-biweekly oscillation characteristics of persistent severe rain and its general circulation anomaly over southeast China from May to August [J]. Acta Meteor Sinica, 2012, 70(4): 766-778 (in Chinese).
[33] YANG J, WANG B, BAO Q. Biweekly and 21-30 Day Variations of the Subtropical Summer Monsoon Rainfall over the Lower Reach of the Yangtze River Basin [J]. J Climate, 2010, 23(5): 1146-1159.
[34] WEN Zhi-ping, DONG Ling-ying, WU Li-ji, et al. The Characteristics of 30-60 Day Oscillation and its Relation to the Durative Rainstorm in Guangdong [J]. Acta Sci Nat Univ Sunyatseni, 2007, 46(5): 98-103 (in Chinese).
[35] REN Hong-li, ZHANG Pei-qun, CHOU Ji-fan, et al. Large-scale low-frequency rainfall regimes and their transition modes in summertime over China [J]. Chin Sci Bull, 2006, 51(11): 1355-1367.
[36] ZUO Jin-qing, REN Hong-li, LI Wei-jing, et al. Intraseasonal characteristics of the water vapor transport associated with the low-frequency rainfall regimes over Southern China in summer [J]. Chin J Geophys, 2009, 52 (5): 922-935.
[37] QUE Zhi-ping, LI Chong-yin. Impacts of the monthly anomalies of intraseasonal oscillation over South China Sea and south Asia on the activity of the summer monsoon and the rainfall in eastern China [J]. J Trop Meteor, 2004, 30(5): 811-824 (in Chinese).

Citation: SHEN Yu-yang, REN Hong-li, LI Wei-jing et al. Relationship between summer low-frequency rainfall over southern China and propagation of tropical intraseasonal oscillation [J]. J Trop Meteor, 2018, 24(1): 92-101.

孙劭，王东阡，尹宜舟，等，2018. 2017 年全球重大天气气候事件及其成因[J]. 气象，44(4)：556-564.

2017 年全球重大天气气候事件及其成因*

孙 劭[1,2] 王东阡[1] 尹宜舟[1] 王国复[1] 柯宗建[1]

1. 中国气象局国家气候中心，北京 100081
2. 中国气象局气候研究开放实验室，北京 100081

提 要：2017 年全球主要温室气体浓度继续攀升，地表温度相比工业化前水平高出 1.1℃，位列 2016 年之后，为有气象观测记录以来的历史第二高值，也是有记录以来最暖的非厄尔尼诺年份。全球冰冻圈持续萎缩，冬季北极最大海冰范围创历史新低，南极海冰范围全年处于历史低位。全球海表面温度显著高于常年，海平面持续上升，海洋热含量创历史新高，海洋酸化的影响持续加剧。世界各地发生了许多重大天气气候事件，包括异常活跃的北大西洋飓风、印度次大陆的季风洪水、东非部分地区的持续干旱，以及全球多地的暴雨洪涝、高温热浪、低温寒流和强对流天气，2017 年成为有记录以来气象灾害造成经济损失最大的年份。本文总结了 2017 年全球重大天气气候事件及其影响，并重点分析了大西洋飓风季异常活跃和美国西海岸高温热浪天气两个典型事件的形成原因。分析表明，8 月底至 10 月初，加勒比海和热带西大西洋海温偏高，对流活动旺盛，风速垂直切变偏小，为飓风的发展加强提供了有利的背景条件，加之北美副热带高压出现阶段性减弱，导致 4 个强飓风接连登陆美国和加勒比海地区；7 月上旬，受副热带西风急流加强东伸，东北太平洋切断低压维持影响，北美副热带高压持续控制美国西南部地区，是当地高温热浪事件发生的主要原因。

关键词：表面温度，降水量，极端事件，气象灾害

中图分类号：P461 **文献标志码**：A **DOI**：10.7519/j.issn.1000-0526.2018.04.009

Global Major Weather and Climate Events in 2017 and the Possible Causes

SUN Shao[1,2] WANG Dongqian[1] YIN Yizhou[1] WANG Guofu[1] KE Zongjian[1]

1. National Climate Centre, Beijing 100081
2. Laboratory for Climate Studies, CMA, Beijing 100081

Abstract: The concentration of greenhouse gases continued to increase in 2017, and the global mean temperature was 1.1℃ above the pre-industrial levels, making the year 2017 become the second warmest year on record and the warmest year not influenced by El Niño event. The cryosphere continued its contraction. The maximum sea-ice extent of Arctic sea in winter broke the lowest record while the sea-ice extent of Antarctic was near the record low level throughout the year. Global sea surface temperatures were significantly above the 1981－2010 average, and the global mean sea level kept rising steadily. The ocean heat content reached new record highs due to the intensified impact of ocean acidification. Many significant weather and climate events occurred in 2017, including a very active North Atlantic hurricane season, major monsoon floods in the Indian subcontinent, severe droughts in East Africa as well as some torrential rains, heat waves, cold waves and severe convective weather at regional or local scale worldwide. Economic losses from the weather and climate related disasters set a new record in 2017. This paper summarizes the major events and its impact in 2017, and analyzes the formation causes of typical events including the exceptionally destructive hurricanes that occurred in rapid succession in the North Atlantic and the

* 国家自然科学基金项目(41701103)和公益性行业(气象)科研专项(GYHY201506002)共同资助
2018 年 3 月 27 日收稿； 2018 年 4 月 3 日收修定稿
第一作者：孙劭，主要从事气候变化与灾害风险研究. Email：sunshao@cma.gov.cn

significant summer heat waves in the United States. Analysis of atmospheric circulation and external forcing shows that the positive SST anomalies of Caribbean and western tropical Atlantic enhanced the convective activity and decreased the vertical shear of wind speed, providing favorable background conditions for the development of hurricanes. In addition, the stage weakening of North American subtropical high caused four destructive hurricanes to make landfall successively in southern United States and the Caribbean region. In early July, the North American subtropical high that was influenced by the eastward extension and enhancement of subtropical westerly jet and the maintaining of Northeast Pacific cut-off low continued controlling the southwestern United States. This was the major reason for the summer heat wave on the west coast of the United States.

Key words: surface temperature, precipitation, extreme events, meteorological disaster

引　言

世界气象组织发布的《全球气候状况声明》显示,2017 年全球温度相比常年(以 1981—2010 年为基准期)偏高 0.46℃(±0.10℃),超过工业化时代之前的全球温度 1.1℃(±0.10℃),仅次于 2016 年,成为有气象记录以来第二暖的年份(WMO,2018)。全球主要温室气体浓度持续上升,二氧化碳、甲烷和一氧化二氮浓度分别创历史新高。2017 年全球海洋表面温度略低于受厄尔尼诺事件影响的 2016 和 2015 年,位列有记录以来的历史第三高,海洋上层 0～700 和 0～2000 m 热含量同创历史新高,全球海平面继续保持上升趋势。2017 年全球冰冻圈持续萎缩,冬季北极海冰最大范围创历史新低,南极海冰则全年处于历史低位,格陵兰冰盖和北半球积雪范围接近或略高于常年平均水平(NOAA,2018b)。

2017 年世界各地发生了许多重大天气气候事件,例如异常活跃的北大西洋飓风、印度次大陆的季风洪水、东非部分地区的持续干旱等,给公众生命财产安全和经济社会可持续发展带来严重影响和损失。年内,美国和加勒比海地区连续遭遇多个飓风袭击,南亚、中国、塞拉利昂、秘鲁等地遭受严重暴雨洪涝及其引发的地质灾害,非洲东部、欧洲西部和南部受持续性干旱影响,美国西海岸和欧洲南部发生多起森林大火,中国、菲律宾、印度等地遭受热带气旋袭击。据德国慕尼黑再保险公司统计,2017 年全球气象灾害导致经济损失达 3200 亿美元,成为有记录以来气象灾害造成损失最大的年份,气象灾害占全年自然灾害总损失的 93%(Munich, 2018)。

极端天气气候事件不仅是国际社会应对气候变化的重要领域,也是所有国家应对气候变化的当务之急和优先重点(秦大河,2015)。在 1997—2016 年,全球范围内发生了约 11000 次极端天气气候事件,由此引发的气象灾害共导致 52.4 万人丧生,经济损失(购买力评价)高达 3.2 万亿美元(Eckstein et al,2018)。近年来,国家气候中心持续关注全球范围内发生的重大天气气候事件,并分析典型气候事件的形成原因,为全球变化背景下极端天气气候事件和气象灾害风险管理的研究工作提供科学参考。本文系统性回顾了 2017 年全球气候概况和年内发生的重大天气气候事件,并重点分析了典型事件的形成原因。所用资料包括 GPCC 全球降水量观测资料集、NCEP/NCAR 再分析资料集和 OISST 海温资料集。

1　全球重大天气气候事件概述

1.1　地表温度列历史第二位

2017 年全球温度相比常年(1981—2010 年)偏高 0.46℃(±0.10℃),超过工业化时代之前(1850—1900 年)的温度 1.1℃(±0.10℃),低于受厄尔尼诺事件影响的 2016 年,成为有完整气象观测记录以来第二高值(图 1)。厄尔尼诺事件通常会导致全球温度异常偏高 0.1～0.2℃,尤其在厄尔尼诺结束年这种影响最为明显(例如 2016 年)。2017 年由于前期厄尔尼诺事件造成的额外增温效应消退,年内地表温度并没有再创历史新高,但全球变暖的大趋势仍在持续,2017 年也是有记录以来最暖的非厄尔尼诺年份。

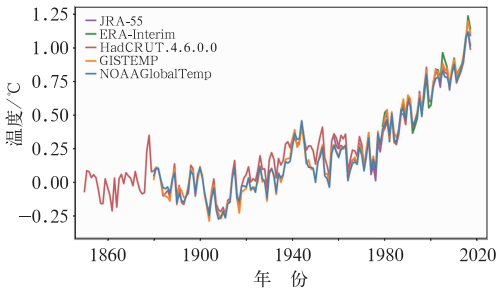

图 1 全球平均温度距平(相对 1850—1900 年平均值)时间序列(WMO, 2018)

Fig. 1 Global average temperature anomalies (compared to the 1850—1900 average) (WMO, 2018)

观测资料表明,有气象记录以来最暖的 9 个年份均出现在2005年以后,2013—2017年也是历史上最暖的 5 年期,全球平均温度高出常年 0.4℃,超过工业化时代之前的温度 1.0℃。2017 年内,1—3 月全球地表温度偏高最为明显,温度距平值分别高于常年 0.5℃以上,其中 3 月温度距平值最高,为 0.64℃;4—12 月温度距平维持在 0.3～0.5℃,其中 6 月距平值最低,为 0.34℃。

从全球温度距平值的空间分布来看(以 1981—2010 年为基准期),俄罗斯、蒙古、中国北部等亚洲中高纬度地区,以及加拿大东北部、美国大部、墨西哥北部、澳大利亚东部等地温度高于常年值 1℃以上,其中北半球高纬度部分区域偏高 2℃以上;加拿大西部、非洲利比亚和南非等地温度低于常年平均水平;全球其余地区的温度与常年相比偏高幅度在 1℃以内。在国家尺度上,阿根廷、毛里求斯、墨西哥、西班牙和乌拉圭地表温度创历史新高(图 2)。

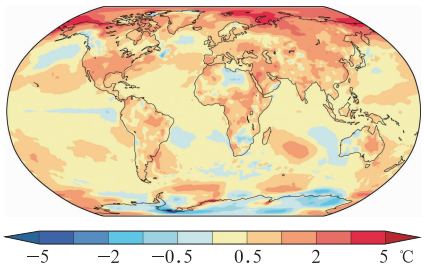

图 2 2017 年全球平均温度距平(相对 1981—2010 年平均值)空间分布(WMO, 2018)

Fig. 2 Global temperature anomalies in 2017 (compared to the 1981—2010 average) (WMO, 2018)

1.2 海冰范围创历史新低,海洋热容量突破纪录

在全球暖化的大背景下,2017 年冰冻圈进一步萎缩。冬季北极海冰最大范围 1442 万 km^2,创历史新低;随后春季和夏季北极海冰消融速度偏慢,夏季海冰最小范围 464 万 km^2,位列历史第八低。南极海冰面积全年处于历史低位,冬季海冰最大范围 1803 万 km^2,位列历史第二低,夏季海冰最小范围 211 万 km^2,创历史新低。

格陵兰冰原从 2016 年秋季开始降雪量异常偏多,冰层总量在 2016 年 9 月至 2017 年 8 月期间明显高于常年(1981—2010 年),随后 9—12 月与常年基本持平。从 2017 年全年来看虽然冰量有所上升,但多年来冰量逐渐减少的大趋势并未发生改变,从 2002 年起格陵兰冰原已经累计减少了约 3.6 万亿吨冰量。北半球积雪覆盖范围略多于常年,其中 5 月积雪范围达 9%,为近 20 年来同期最高值,特别是俄罗斯西北部和斯堪的那维亚半岛地区偏多最为明显,夏季积雪逐渐融化后回到常年平均水平。

2017 年全球海表温度低于 2016 和 2015 年,位列历史第三高值。海洋热容量突破历史纪录,海洋上层 0～700 和 0～2000 m 的热容量分别达 1.6×10^{23} 和 2.3×10^{23} J,同创历史新高。在海洋热膨胀和海冰融化的共同作用下,2017 年全球海平面继续保持上升趋势。

在海洋升温的影响下,海洋的理化特征发生了显著变化,从而直接影响了海洋食物链和生态系统。调查表明,澳大利亚东岸的大堡礁地区已连续 2 年温度明显偏高,珊瑚白化现象日益加剧;密克罗尼西亚和关岛等热带西太平洋地区也发生了珊瑚白化现象;大洋洲塔斯马尼亚岛南部海域和新西兰附近海域的鱼类资源分布特征出现了明显改变(NOAA, 2018a)。此外,由于二氧化碳的排放量持续增加,海洋酸化的程度也在加剧,有研究表明夏威夷北部海域的海水 PH 值已经从 1980 年的 8.10 下降到近 5 年的 8.04～8.09,海洋酸化将进一步加大暖化对海洋生态系统的影响(WMO, 2018)。

1.3 全球多地遭遇暴雨洪涝侵袭

相对于受厄尔尼诺事件影响的 2015—2016 年而言,2017 年全球大范围降水异常偏多的区域明显减少。从全球降水量距平的空间分布来看(以 1951—2000 年为基准期),只有欧洲东北部、青藏高原、澳洲西部、阿拉斯加北部、加拿大北极群岛、格陵

兰东部及东南亚的部分地区降水量偏多 25%以上(图 3)。

尽管全球累计降水量整体平稳,但区域性极端降水事件频发,在世界各地造成了严重人员伤亡和财产损失,其中南亚地区受灾最为严重。印度北部、孟加拉国北部和尼泊尔东部等地在雨季期间(6—9月)频繁遭遇严重洪水,8 月中旬印度和尼泊尔边境地区的单日降水量一度超过 400 mm;季风洪水导致印度、尼泊尔和孟加拉国超过 1200 人丧生,4000 万人受灾,并且出现了不同程度的大范围传染病事件。

夏季,中国南方持续性暴雨引发了流域汛情和区域性洪涝灾害。6 月下旬,中国南方大部连续遭受 2 次大范围强降水过程,湖南、江西和广西的局地累计雨量超过 500 mm,导致长江中下游地区发生区域性大洪水,西南、江南及华南多条河流发生超历史洪水,造成湖南、江西、广西、四川等省(区)发生严重洪涝及地质灾害,56 人因灾死亡,直接经济损失高达 50 亿美元。

在欧洲地区,1 月上旬德国东北部海岸遭遇 2006 年以来最大规模的洪水袭击,波罗的海水位比平时高 1.7 m,导致多个沿岸城市受灾,造成大量交通事故和财产损失。

在南美洲地区,3 月秘鲁遭遇持续性强降水天气,引发特大洪水及山体滑坡,许多道路、桥梁被毁,全国半数以上地区宣布进入紧急状态,75 人因灾死亡,63 万人受灾,7 万余人流离失所;4 月 1 日,哥伦比亚南部地区由于连日暴雨导致多个区域发生泥石流,造成 320 人死亡,100 余人失踪。

在非洲地区,8 月 1—14 日塞拉利昂遭遇强降水过程,累计降水量达 1459.2 mm,超过历史同期 4 倍以上,首都弗里敦及周边地区因强降雨引发洪水和泥石流灾害,造成 500 余人死亡,超过 2000 人无家可归。

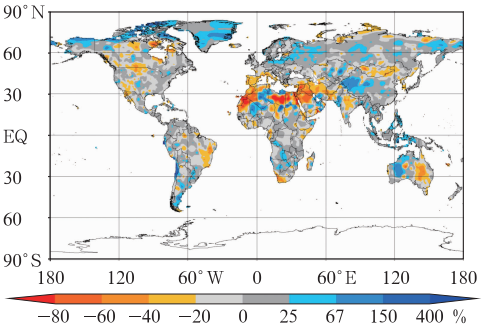

图 3　2017 年全球降水量距平百分率(相对于 1951—2000 年平均值)分布

Fig. 3　Percentages of total precipitation anomaly in 2017 (compared to the 1951−2000 average)

1.4　非洲和地中海沿岸多国受干旱影响

非洲是世界范围内受干旱影响最严重的地区。2 月,苏丹北达尔富尔省旱情严重,莱索托、津巴布韦和南非大多数省份宣布进入灾害状态。由于过去两年降雨急剧减少,干旱天气导致非洲多国的粮食歉收,水库干涸,大批牲畜死亡,约 3200 万人面临饥荒。3—5 月,索马里、肯尼亚和埃塞俄比亚南部地区降水量比常年同期(1981—2010 年)偏少 20%以上,其中肯尼亚北部和索马里局部地区偏少 50%以上。索马里南部持续干旱引发饥荒和霍乱,仅 2 天就有 110 人死亡。索马里半数人口面临粮食短缺,约有 670 万人急需粮食援助,每天有超过 3000 人因干旱逃离家园。埃塞俄比亚和肯尼亚分别有 560 万和 270 万人急需救助。

2017 年地中海地区降水量普遍偏少,其中意大利全年降水量比常年偏少 26%,创历史新低。西班牙、葡萄牙、摩洛哥、法国、土耳其和以色列等其他地中海沿岸国家的降水量也远低于历史同期,分别遭受了不同程度的干旱影响。此外,北美洲中部地区(美加边境地带)在下半年经历了严重旱情,引发了多起森林大火;南美洲的巴西、智利等地延续了多年来的干旱状态;亚太地区的朝鲜半岛在上半年也出现了异常旱情,下半年逐渐得到缓解。

1.5　超强飓风重创北美和加勒比海

2017 年,全球范围内共生成 84 个热带气旋,与常年基本持平;北大西洋飓风异常活跃,9 月累积气旋能量指数(accumulated cyclone energy, ACE)创历史新高;太平洋地区气旋数量接近常年,但气旋能量偏低;南半球气旋数量和能量都低于常年,其中西南印度洋和西南太平洋气旋数量明显偏少,南半球累积气旋能量指数创历史新低。

8 月底至 10 月初,相继有 4 个极具破坏力的飓风登陆美国及加勒比海地区,其中飓风厄玛和玛丽亚都是最高等级的 5 级飓风,给当地造成巨大损失。8 月 25 日至 9 月 1 日,美国遭遇超强飓风哈维袭击,飓风在美国得克萨斯州停留数天,狂风暴雨造成 44 人死亡,130 万人受灾,10 万间房屋被损毁,直接经济损失高达 1250 亿美元,位列美国飓风史第三位(仅次于 2005 年飓风卡特里娜和 2012 年飓风桑迪);9 月 6—10 日,5 级飓风厄玛横扫美国和加勒比

海地区，共造成100多人死亡，直接经济损失500亿美元，其中美国580万户家庭断电，700万人紧急撤离，加勒比海地区巴布达岛受灾最为严重，创纪录的强降水和3 m高的风暴潮摧毁了当地90%以上的财产，整座岛屿几乎沦为废墟；9月19—23日，飓风玛丽亚袭击加勒比海地区，造成60多人死亡，直接经济损失900亿美元，其中多米尼克和波多黎各受灾最为严重，数十万群众被疏散撤离；10月初，飓风纳特在中美洲地区引发局地洪涝，造成30人死亡，随后分别于7和8日在美国路易斯安那州和密西西比州两次登陆，造成美国超过10万户断电。

在东亚地区，8月23日台风天鸽在中国广东沿海登陆，最大风力达45 m·s^{-1}，广东、广西、云南、贵州、香港和澳门等地出现强风暴雨，造成246万人受灾，40人死亡失踪，直接经济损失60亿美元。在东南亚地区，12月下旬台风天秤穿越菲律宾东南部，引发洪水导致当地129人死亡。在南亚地区，5月29日气旋风暴莫拉在孟加拉国登陆，暴雨洪涝导致当地177人死亡，109人失踪；12月上旬气旋风暴奥奇袭击印度西南部，25人因灾死亡，86人失踪，失踪人员多为出海作业的渔民。在非洲地区，3月中旬南印度洋热带气旋爱娜沃袭击了马达加斯加，引发暴雨洪涝导致81人丧生，给当地基础设施和农业生产造成重大损失。在大洋洲地区，3月下旬飓风黛比袭击了澳大利亚东海岸，昆士兰州2.5万人被紧急疏散，飓风带来的强风暴雨导致码头设施被损坏和电力供应中断，直接经济损失达13亿美元。

1.6 世界各地经受高温热浪天气，北美和欧洲林火频发

在全球变暖的大背景下，2017年北美洲、欧洲、西南亚、东亚、大洋洲、南美洲等多个地区都遭受到高温热浪天气的影响。在北美洲地区，美国西南部经受了异常炎热的夏季，7月加州死亡谷地区月均气温达到41.9℃，突破历史极值；7月7日凤凰城最高气温达47℃，创造历史同日最高气温纪录（1905年7月7日凤凰城的日最高气温是46℃）；7月8日洛杉矶好莱坞受高温影响出现大面积断电，约14万人受影响；由于连续高温，7月上旬美国西部多个州山火频发，加拿大西部的不列颠哥伦比亚省也发生多起森林火灾；9月初加州海岸带地区气温再次刷新历史同期纪录，其中旧金山最高温度达到41.1℃；10月上中旬，美国加州北部再次遭遇山火，过火面积达750 km^2，导致5700栋房屋被烧毁，44人因灾死亡，直接经济损失超过94亿美元。

在欧洲地区，6月上旬至7月上旬土耳其和塞浦路斯经受高温热浪天气，其中7月1日土耳其安塔利亚最高气温达45.4℃；6月17—18日，葡萄牙中部地区发生森林大火，造成64人死亡，160多人受伤；6月27日，西班牙南部发生大规模森林火灾，高温和强风天气加剧火势；7月8—15日，欧洲南部遭遇罕见热浪袭击，意大利、西班牙和希腊等国多地的日最高气温超过40℃，西班牙科尔多瓦、格拉纳达、巴尔霍斯等多个城市的最高气温突破历史极值（其中科尔多瓦7月13日最高气温达到46.9℃），意大利南部地区及西西里岛由于大风、干燥等因素频繁发生林火；8月上旬，意大利及巴尔干半岛地区再次出现高温热浪天气，意大利佩斯卡拉、坎波巴索等多个气象站观测到创纪录的极端高温事件；10月17—18日，葡萄牙北部和中部以及西班牙北部发生森林大火，造成45人死亡。

在西南亚地区，5月下旬巴基斯坦、伊朗、阿曼、阿联酋等国家遭遇极端高温天气，上述国家的局部地区日最高温度均突破50℃，其中5月28日巴基斯坦西南部城市图尔伯德最高气温达到54.0℃，刷新历史纪录。在东亚，7月中下旬中国南方地区出现大范围持续高温天气，浙江、江苏、安徽、重庆、陕西、湖北、湖南的部分地区日最高气温超过40℃，7月21日上海徐家汇最高气温达40.9℃，打破了徐家汇1873年以来的历史纪录。

在大洋洲地区，澳大利亚新南威尔士州北部的莫里市从2016年12月28日至2017年2月19日连续54天气温高于35℃，创造该州历史最高纪录；其中2月11—12日，新南威尔士州的多个城市刷新了历史单日最高温度纪录，持续性高温导致该州东部地区发生森林大火。

在南美洲地区，2016年12月至2017年2月智利经历了持续性干燥和高温天气，引发史上最严重的森林大火，过火面积达61.4万hm^2，11人因灾死亡；与此同时，1月下旬智利和阿根廷的多个气象站观测到突破历史极值的最高气温，其中1月27日阿根廷玛德琳港气温一度达到43.4℃。

1.7 北美和欧洲遭受寒流和暴风雪袭击

1月上旬美国加州大部分地区出现暴风雪天气，高速公路部分路段封闭。1月6—7日，美国东海岸受到暴雪天气影响，导致交通事故多发、电力中断、航班取消，5人因灾死亡。2月9日，美国东北部

地区遭遇暴雪,约 6000 万人生活受到影响。3 月 14 日,暴风雪再次肆虐美国东北部,5000 多万人生活受到严重影响,6500 余次航班被取消。此外,2017 年年底至 2018 年年初,美国东部和加拿大遭遇被称为“炸弹气旋”的大范围持续性寒潮过程,大部地区气温连续两周以上低于冰点;多地迎来创纪录的低温,纽约、费城等地最低气温达-13℃,波士顿则连续 7 天最高温度低于-7℃,刷新历史纪录;严寒天气导致美国 22 人死亡。

在欧洲中部和东南部地区,许多国家经历了近 30 年来最寒冷的 1 月。其中,1 月 6—11 日意大利、捷克、波兰、罗马尼亚、塞尔维亚、保加利亚、克罗地亚、希腊、土耳其、拉脱维亚和俄罗斯等多国遭遇低温寒流和暴风雪袭击,在塞尔维亚南部,一些地区的积雪高达 2 m。导致交通瘫痪,学校停课,居民日常生活受到严重影响,60 人在寒流中丧生。此外,4 月下旬瑞士、奥地利、乌克兰、罗马尼亚、斯洛文尼亚等国家遭遇了“倒春寒”天气,霜冻导致农业生产严重受损,直接经济损失达 33 亿美元。

在全球其他地区,1 月中旬日本多地连降暴雪,部分地区积雪达到 2 m 以上,6 人因灾死亡,300 人受伤。这次过程导致日本交通出现严重混乱,全日空和日航两家航空公司两天内取消约 130 次航班,东海道新干线严重延误。2 月上旬阿富汗各地连降大雪,中部和北部省份发生多起雪崩事件,摧毁众多民宅,造成超过 100 人死亡,有两座村庄被掩埋。阿富汗邻国巴基斯坦也因气候恶劣造成灾情,西北部地区有 13 人死于雪崩或暴风雪。

1.8　强对流天气袭击美国、欧洲等地

美国是世界上遭受龙卷风侵袭最为频繁的国家之一。1 月 1—3 日,美国东南部地区遭遇风暴袭击,暴雨、冰雹和龙卷风导致 5 人死亡,数万住宅停电。1 月 19—23 日,美国南部多个州遭遇致命龙卷风和强风暴,造成广泛破坏,有 19 人在风灾中丧生。2 月 7 日,美国路易斯安那州东南部遭龙卷风袭击,风灾造成约 20 人受伤,当地约 1 万户民居停电。

春、夏季,欧洲中部和东部地区强对流天气多发。3 月 6—7 日,法国西北部地区遭遇 2010 年以来最强风暴宙斯袭击,最大风速达 54 $m \cdot s^{-1}$;5 月 29 日,莫斯科遭遇雷暴天气,风速超过 30 $m \cdot s^{-1}$,造成 11 人丧生;7 月 10 日,维也纳南部地区遭遇龙卷风和冰雹袭击;7 月 27—30 日,伊斯坦布尔多次遭遇强风和冰雹袭击,风速高达 46 $m \cdot s^{-1}$,冰雹最大直径超过 9 cm;8 月 12 日,芬兰遭遇大范围雷暴天气,超过 5 万间房屋电力中断;9 月 11 日,克罗地亚突发暴雨山洪,12 h 内降水量达 283 mm,突破历史极值;10 月下旬,奥地利和捷克遭遇暴风雨袭击,最大风速 47 $m \cdot s^{-1}$,共计 11 人丧生。

2017 年全球重大天气气候事件如图 4 所示。

2　典型重大气候事件可能成因分析

2.1　飓风接连重创北美和加勒比海

2017 年大西洋飓风异常活跃,8 月底至 10 月初,强飓风哈维、厄玛、玛丽亚和纳特相继登陆美国和加勒比海地区,造成上述地区人员伤亡和重大经济损失。

这一时段内,大西洋暖池区海表温度(sea surface temperature,SST)偏高、对流活动活跃及垂直风切变偏弱,为飓风的活跃提供了有利的背景条件。SST 对飓风的发生频次及其所能达到的强度有显著的影响,SST 越高,飓风发展的潜在强度(empirical potential intensity,EPI)越强。前人研究发现,飓风发生的基本条件是 SST 必须在 26℃以上,而飓风强度发展到四级以上则需要 SST 超过 28℃(Merrill, 1988; Lighthill et al, 1994);此外,对长期变化趋势的研究也表明,SST 升高是导致飓风活动增加的重要原因(Emanuel, 2005; Webster et al, 2005; Mark et al, 2012; Varotsos et al, 2015)。分析 8 月 21 日至 10 月 10 日平均的海表温度和距平分布可以发现(图 5),大西洋暖池中心区海温超过 30℃,加勒比海及热带西大西洋 SST 较常年同期偏高 0.5～1℃左右,区域平均(10°～20°N、85°～60°W)的 SST 较气候均值(1982—2010 年平均)偏高 0.7℃,为 1982 年以来第三高值(仅次于 2005 和 2010 年同期)。受海温偏高的影响,加勒比海地区向外长波辐射较常年同期偏低 10～20 $W \cdot m^{-2}$(图 6),表明这一区域对流活动相对活跃,而大西洋飓风前期云团活动区附近,如果低空辐合运动(对流活动)发展强烈,则有利于强飓风的发展。风速垂直切变是热带气旋能否发展的另一个重要条件,较小的风速垂直切变有利于飓风生成时暖心结构的维持,使飓风容易进一步发展为强飓风(Gallina and Velden, 2002; Wong and Chan, 2004)。从 2017 年飓风异常活跃期高、低空风切变异常的分布特征看(图 7),在加勒比海及热带西大西洋地区高低空

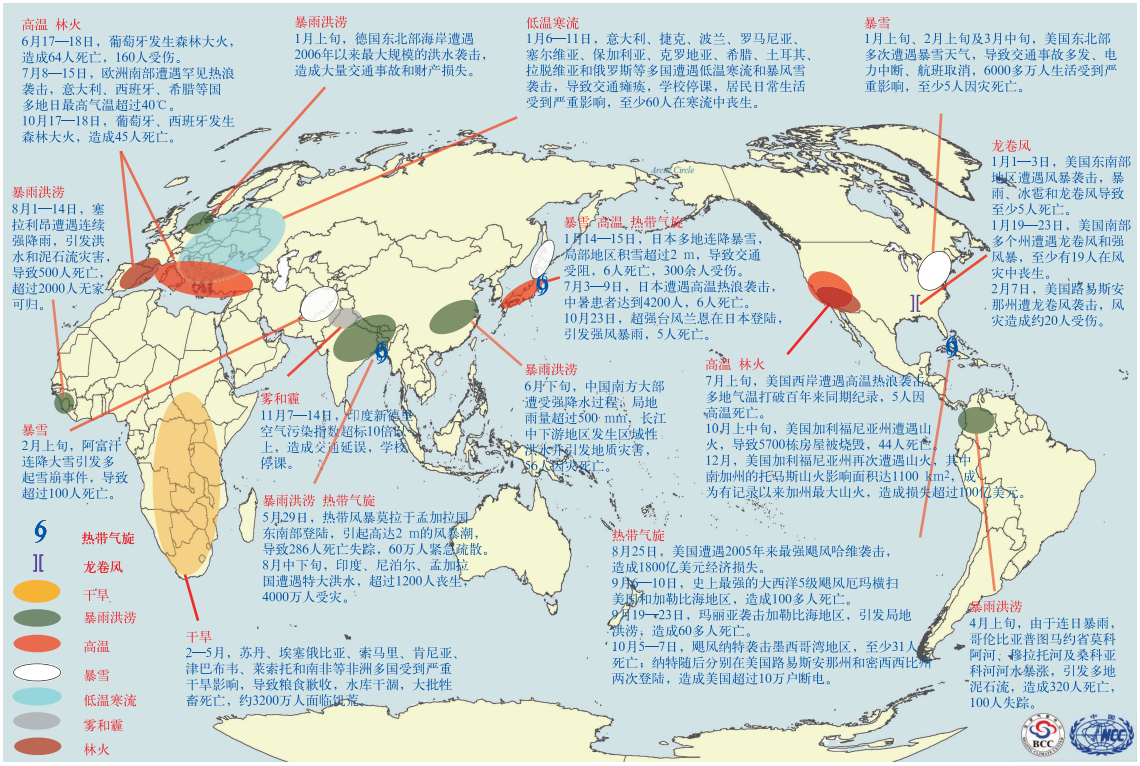

图 4 2017 年全球重大天气气候事件示意图

Fig. 4 Diagram of global major weather and climate events in 2017

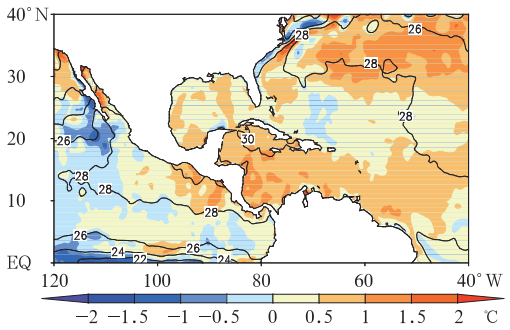

图 5 2017 年 8 月 21 日至 10 月 10 日海表面温度(等值线)及其距平(阴影)分布

Fig. 5 Sea surface temperature (contour) and its anomalies (shadow) from 21 August to 10 October 2017

风切变与常年同期相比明显偏弱，这样的切变动力条件更加有利于飓风暖心结构的维持和发展。

2017 年夏季以来，北美副热带高压(以下简称副高)面积总体偏大、强度偏强，加勒比海及热带西大西洋地区受北美副高影响，对流层中层大部分时段内为下沉气流控制，不利于深对流的发展加强；但北美副高强度逐日演变表明(图 8)，8 月下旬开始，北美副高出现 4 次明显的阶段性减弱。北美副高阶段性减弱期内，受有利的下垫面及动力学环境影响，飓风发展加强并沿副高外围的引导气流移动，给美国和加勒比海地区造成重大损失。

2.2 美国西岸遭受高温热浪袭击

2017 年 7 月上旬，美国西岸遭受“地狱热浪”袭击，凤凰城和洛杉矶市区日最高气温打破一百多年来同期纪录，并导致美国西部多个州山火频发。

IPCC 第五次评估报告指出(IPCC，2013)，

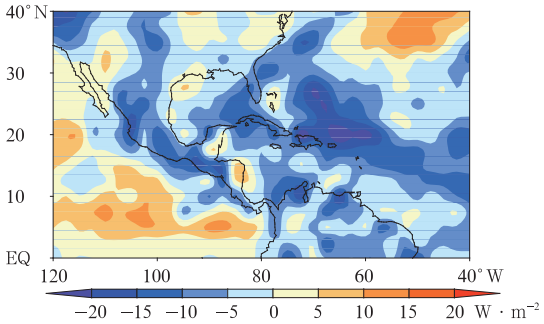

图 6 2017 年 8 月 21 日至 10 月 10 日向外长波辐射距平分布

Fig. 6 Outgoing long-wave radiation anomalies from 21 August to 10 October 2017

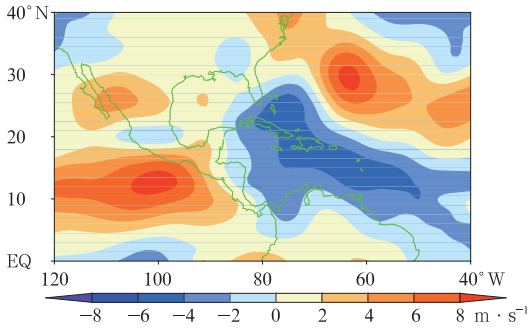

图 7　2017 年 8 月 21 日至 10 月 10 日
200 与 850 hPa 风速差异分布
Fig. 7　Difference of wind velocity
at 200 hPa and 850 hPa from 21 August
to 10 October 2017

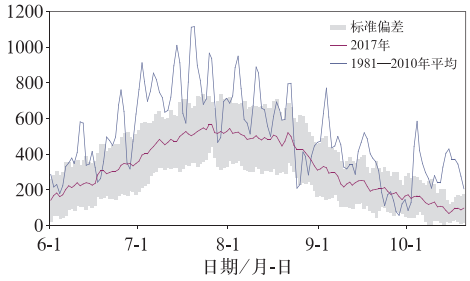

图 8　2017 年 6 月 1 日至 10 月 20 日
北美副高强度指数逐日演变
Fig. 8　Daily variation of North American
subtropical high intensity index from
1 June to 20 October 2017

1880—2012 年,全球地表平均温度约升高 0.85℃;WMO发布的 2017 年全球气候报告显示(WMO,2018),2013—2017 年平均全球平均气温是有记录以来的 5 年平均气温最高值,较 1850—1900 年偏高约 1℃。全球变暖是近年来高温热浪事件频发的大气候背景。近期的研究也表明,受全球变暖影响,尽管处于 ENSO 循环的不同位相,近年来北美和欧洲等地夏季均出现严重的高温热浪事件(王东阡等,2013;王艳姣等,2014;孙劭等,2017)。

2017 年 7 月上旬,北美副高加强西伸(图 8),副高强度持续较常年同期偏高 1.5～2 倍标准差,7 月 1—10 日平均的副高强度较气候均值(1981—2010 年平均)偏高 80%,为 1951 年以来第二位(仅次于 2016 年同期);500 hPa 位势高度及其异常分布显示(图 9),受副高持续偏强影响,位势高度正距平控制美国西部大部分地区。北美西部地区盛行下沉气流,以晴好天气为主,太阳短波辐射加热及下沉增温效应共同作用下,出现高温热浪。这一时段内,西北太平洋上空形成准静止的切断低压,阻挡上游波动向下游传播,导致北美大陆经向型环流维持,有利于北美副高稳定控制美国西南部地区。进一步分析发现,7 月 1—10 日,北太平洋区域副热带西风急流显著加强东伸(图 10),其激发的次级环流有利于急流出口左前侧上升运动的发展,为切断低压的形成和维持提供了有利的动力条件。

3　结　论

2017年全球主要温室气体浓度继续攀升,地表温度相比工业化前水平高出 1.1℃,位列 2016 年之后,为有气象观测记录以来第二暖的年份,也是有记录以来最暖的非厄尔尼诺年份。全球冰冻圈继续萎

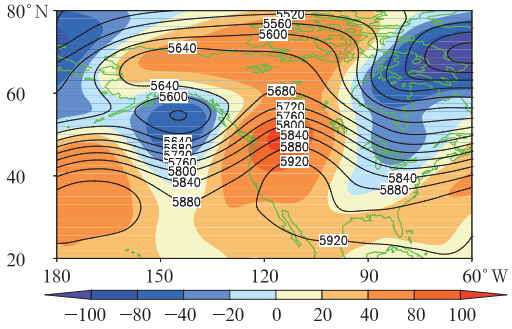

图 9　2017 年 7 月 1—10 日 500 hPa
位势高度(等值线)及其距平
(阴影)分布(单位:gpm)
Fig. 9　Geopotential height at 500 hPa
(contour) and its anomalies (shadow)
from 1 to 10 July 2017 (unit: gpm)

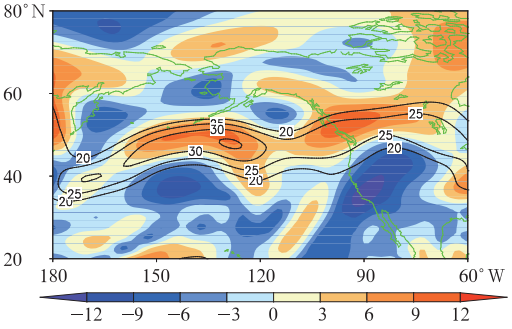

图 10　2017 年 7 月 1—10 日 200 hPa
风速(等值线)及其距平(阴影)
分布(单位:m·s⁻¹)
Fig. 10　Wind speed at 200 hPa (contour)
and its anomalies (shadow) from 1 to
10 July 2017 (unit: m·s⁻¹)

缩，冬季北极海冰最大范围创历史新低，南极海冰则全年处于历史低位。全球海洋表面温度略低于受厄尔尼诺事件影响的2016和2015年，位列有记录以来的历史第三高，海洋上层0～700和0～2000 m热含量创历史新高，全球海平面继续保持上升趋势。在海洋升温的影响下，海洋的理化特征发生了显著变化，从而直接影响了海洋食物链和生态系统，澳大利亚东岸的大堡礁地区和热带西太平洋部分地区的珊瑚白化现象日益加剧，新西兰附近海域的鱼类资源分布特征也出现了明显改变。

在全球变暖的大背景下，年内北美洲、欧洲、西南亚、东亚、大洋洲、南美洲等地遭受高温热浪天气的影响，许多地区观测到突破历史极值的极端高温，美国、加拿大、西班牙、葡萄牙、智利等地由于高温干燥引发森林大火；全球区域性极端降水事件频发，暴雨洪涝及其引发的地质灾害在南亚、中国、南美、非洲等地造成了严重人员伤亡和财产损失，其中南亚东北部地区受灾最重；非洲和地中海沿岸国家遭受干旱影响，非洲索马里、肯尼亚、埃塞俄比亚、苏丹等多个国家连年干旱导致粮食短缺，约3200万人面临饥荒；北大西洋飓风异常活跃，8月底至10月初，相继有4个极具破坏力的飓风登陆美国及加勒比海地区，累计造成200余人死亡，直接经济损失高达2650亿美元；年初，美国东部及欧洲中部和东南部地区遭受寒流和暴风雪袭击，导致部分地区交通瘫痪、电力中断、航班取消，数千万居民日常生活受到严重影响；年内，美国南部及欧洲中部和东部地区强对流天气多发，龙卷风、强风暴、雷暴、冰雹等天气造成局部地区一定人员伤亡和财产损失。

对环流和外强迫的进一步分析表明，8月底至10月初，加勒比海和热带西大西洋海温偏高，有利于对流活动活跃，风速垂直切变偏小，有利于飓风发展时暖心结构的维持，为飓风的形成和发展加强提供了有利的下垫面和动力学环境。这一时段内，北美副高出现4次明显的阶段性减弱，导致强飓风哈维、厄玛、玛丽亚和纳特相继重创美国和加勒比海地区。2017年7月上旬，北太平洋区域副热带西风急流显著偏强，东北太平洋出现切断低压，有利于北美地区维持经向环流，加之北美副高加强西伸，导致位势高度正异常持续控制美国西部地区，致使当地遭受高温热浪袭击。

参考文献

秦大河，2015. 中国极端天气气候事件和灾害风险管理与适应国家评估报告[M]. 北京：科学出版社.

孙劭，李多，刘绿柳，等，2017. 2016年全球重大天气气候事件及其成因[J]. 气象，43(4)：477-485.

王东阡，王腾飞，任福民，等，2013. 2012年全球重大天气气候事件及其成因[J]. 气象，39(4)：516-525.

王艳姣，高蓓，周兵，等，2014. 2013年全球重大天气气候事件及其成因[J]. 气象，40(6)：759-768.

Eckstein D，Künze V，Schäfer L，2018. Global Climate Risk Index 2018[R/OL]. http://germanwatch.org/en/cri.

Emanuel K A，2005. Increasing destructiveness of tropical cyclones over the past 30 years[J]. Nature，436：686-688.

Gallina G M，Velden C S，2002. Environmental vertical wind shear and tropical cyclone intensity change utilizing enhanced satellite derived wind information[R]. San Diego：Extended Abstracts，25th Conf on Hurricanes and Tropical Meteorology，Amer Meteor Soc：172-173.

IPCC，2013. Climate Change 2013：The Physical Science Basis[M]. Contribution of Working Group I to the Fifth Assessment Report of the Intergovernmental Panel on Climate Change. Cambridge：Cambridge University Press.

Lighthill J，Holland G，Gray W，et al，1994. Global climate change and tropical cyclones[J]. Bull Am Meterol Soc，75(11)：2147-2157.

Mark R J，Rosimar R B，Eduardo G，2012. Caribbean hurricanes：changes of intensity and track prediction[J]. Theor Appl Climatol，107(1/2)：297-311.

Merrill R T，1988. Environmental influences on hurricane intensification[J]. J Atmos Sci，45(11)：1678-1687.

Munich Re，2018. Natural catastrophe review 2017[R/OL]. https://www.munichre.com/en/media-relations/publications.

NOAA，2018a. Coral Reef Watch Satellite Monitoring and Modeled Outlooks[R/OL]. https://coralreefwatch.noaa.gov/satellite/index.php.

NOAA，2018b. Global Climate Report Annual 2017[R/OL]. https://www.ncdc.noaa.gov/sotc/global/201713.

Varotsos C A，Efstathiou M N，Cracknell A P，2015. Sharp rise in hurricane and cyclone count during the last century[J]. Theor Appl Climatol，119(3/4)：629-638.

Webster P J，Holland G J，Curry J A，et al，2005. Changes in tropical cyclone number，duration，and intensity in a warming environment[J]. Science，309：1844-1846.

WMO，2018. WMO statement on the status of the global climate in 2017[R/OL]. https://library.wmo.int/opac/doc_num.php?explnum_id=4453.

Wong M L M，Chan J C L，2004. Tropical cyclone intensity in vertical wind shear[J]. J Atmos Sci，61：1859-1876.

Climate Dynamics
https://doi.org/10.1007/s00382-018-4329-6

Global diurnal temperature range (DTR) changes since 1901

Xiubao Sun[1,2,3] · Guoyu Ren[2,3] · Qinglong You[1] · Yuyu Ren[3] · Wenhui Xu[4] · Xiaoying Xue[2,3] · Yunjian Zhan[4] · Siqi Zhang[3] · Panfeng Zhang[2]

Received: 7 January 2018 / Accepted: 24 June 2018
© Springer-Verlag GmbH Germany, part of Springer Nature 2018

Abstract
Previous observational analyses show that the land-surface diurnal temperature range (DTR) has decreased in the past 6 decades worldwide. Based on a newly developed China Meteorological Administration–Land Surface Air Temperature (CMA-LSAT) dataset, we analyzed the DTR changes between 1901 and 2014. Results indicate that the global land surface DTR significantly decreased at a rate of −0.036 °C decade^{-1} over the 1901–2014 period, mainly due to the large decrease in DTR from 1951 to 2014. For the first half of the twentieth century, most grid boxes (spatial resolution 5° × 5°) show a positive DTR trend, with the positive trends of 32.4% grid boxes being statistically significant, leading to a large and significant increase of 0.048 °C decade^{-1} in DTR. However, a dramatic reversal in DTR change occurred in early 1950s, with most parts of global lands exhibiting a shift from increasing to decreasing trends. The global land average DTR decrease during 1951–2014 was −0.054 °C decade^{-1}, with 45.0% grid boxes showing significant negative trends. The reverse phenomenon is more obvious in the Northern Hemisphere than that in the Southern Hemisphere. For the periods 1979–2014 and 1998–2014, the decreasing trends in DTR mainly occur in the Northern Hemisphere. The DTR in the Southern Hemisphere experienced much larger increases during the two recent periods than during the period 1951–2014. Asia, Eastern North America, and Australia exhibited widespread decreases in DTR, although the trend pattern for global DTR is generally mixed during 1979–2014 and 1998–2014. There is a good negative correlation between DTR and precipitation in the Northern Hemisphere from 1901 to 2014, with a correlation coefficient of −0.61. The change in precipitation and number of volcanic eruptions, and the "early brightening" of Europe (Stockholm) all benefit the increase of DTR at global and regional scales in the first half of the twentieth century.

Keywords DTR · Trends · Maximum temperature · Minimum temperature · Global lands

1 Introduction

Diurnal temperature range (DTR) is an important indicator of climate change in the past century and can provide more information than mean temperature alone (Braganza et al. 2004). The changes in DTR can directly reflect the consistency of the maximum and minimum temperature changes. The Fifth Assessment Report of the Intergovernmental Panel on Climate Change (IPCC AR5) indicated a much smaller warming rate of maximum temperature (T_{max}) than minimum temperature (T_{min}), but mean temperature (T_{mean}) has almost certainly shown a significant increasing trend since 1950, at a warming rate of more than 0.1 °C decade^{-1} (IPCC 2013). On the global scale, previous studies have indicated a warming rate of T_{min} approximately twice that of T_{max} since 1950, which has directly caused the significant large-scale decreasing trends in the global and hemispheric mean

✉ Guoyu Ren
guoyoo@cma.gov.cn

1 College of Atmospheric Science, Nanjing University of Information Science and Technology (NUIST), Nanjing 210044, China

2 Department of Atmospheric Science, School of Environmental Studies, China University of Geosciences (CUG), Wuhan 430074, China

3 Laboratory for Climate Studies, National Climate Center, China Meteorological Administration (CMA), Beijing 100081, China

4 National Meteorological Information Center, China Meteorological Administration (CMA), Beijing 100081, China

Published online: 28 June 2018

DTR (e.g. Karl et al. 1993; Easterling et al. 1997; Alexander et al. 2006; Vose et al. 2005; Wang et al. 2014; Thorne et al. 2016).

On the regional scale, the DTR in some countries and regions, including America (Karl et al. 1993; Powell and Keim 2014), Europe (Klein Tank and Können 2003; Hundecha and Bárdossy 2005; Makowski et al. 2009; Jaagus et al. 2014; Río et al. 2012), China (Zhai and Pan 2003), Canada (Zhang et al. 2000), and Hindu Kush-Himalaya region (Sun et al. 2017a), has also shown a significant decreasing trend. In contrast, both T_{max} and T_{min} have shown synchronous variations in some other countries and regions, resulting in no significant change in DTR in these countries and regions, including India (Kumar et al. 1994), New Zealand (Salinger and Griffiths 2001), and parts of Africa (Samba and Nganga 2014). On the seasonal scale, Vose et al. (2005) found that the DTR has decreased in all seasons on the global and hemispheric scales, especially in December–February and September–November. Besides these interdecadal variations, previous studies have also found that the global DTR shows a remarkable reversal phenomenon, but with different reversal periods. Makowski et al. (2008) found that the long-term decreasing trend of the DTR in Western Europe began to reverse in the 1970s, while the reversal phenomenon in Eastern Europe occurred in the 1980s. Based on a climate model, Easterling et al. (2006) found that the global DTR will decrease until 2035, but will change to no real trend from 2035 to 2100. Zhou et al. (2009) investigated DTR as simulated by 11 AOGCMs models since 1900 and indicated that the global DTR will decrease by 0.30 °C from 1900 to 2099. However, climate models cannot simulate the actual DTR changes very well.

Overall, despite the different study periods and scales, most previous studies concur in finding a decrease in the global DTR over the past few decades. Furthermore, the trend of global and regional DTR simulated by climate models is obviously smaller than the trend detected from observation.

Dai et al. (1997, 1999) investigated the causes of the decreasing DTR and found that clouds, soil moisture, and precipitation can reduce DTR by 25–50% compared with clear-sky days over most land areas, while atmospheric water vapor has a small effect on DTR. Stone and Weaver (2002) also found that decreasing DTR in model simulations tends to be associated with changes in cloud cover and soil moisture. Zhou et al. (2008, 2009) analyzed the reasons for the obvious DTR reduction in dry regions and found that vegetation removal and reduced soil radiation can reduce DTR during periods of drought in semi-arid regions. Furthermore, long-term variations in solar radiation reaching the surface cause much of the observed decadal DTR variability (Wild et al. 2005, 2007; Shen et al. 2015; Wang et al. 2013). Easterling et al. (1997) indicated that atmospheric aerosol levels in the Southern Hemisphere (SH) were lower than those in the Northern Hemisphere (NH), which contributed to the different decreasing rates in hemispheric DTR. In addition, urbanization effects are also considered to be another major reason for decreasing global and regional DTR (e.g. Ren et al. 2006, 2014; Wang et al. 2012; Zhou and Hansen 2004; Zhou and Ren 2011).

Owing to the poor spatial coverage of daily observation data, most previous research into the characteristics of DTR changes begin in 1951 (e.g. Karl et al. 1993; Easterling et al. 1997; Vose et al. 2005). Recent studies have increased the global coverage rates of the last decades from 54% (Easterling et al. 1997) to 71% (Vose et al. 2005).

However, there are a few outstanding problems in global T_{max}, T_{min}, and DTR research that need to be addressed. These include: (1) what is real change in first half of the twentieth century, and what is the overall DTR trend of the whole twentieth century? These questions have not yet been understood due to the poor quality of the observations; (2) what are the possible reasons for the different changes in early and late twentieth century? And what is the main reason for the 1950s reversal phenomenon? (3) do T_{max} and T_{min} have 'diurnal asymmetry' changes in the first half of twentieth century, and what is the possible reason of the diurnal asymmetry?

To address these issues, we use the newly developed, global-scale, China Meteorological Administration–Land Surface Air Temperature (CMA-LSAT) dataset (Sun et al. 2017b; Xu et al. 2017) in the present study to analyze the characteristics of DTR change since 1901, and we are able to obtain a few of interesting results with emphasis on the early 1950s reversal phenomenon.

2 Data and methods

The source of the monthly mean temperature used in the current analysis is the CMA-LSAT dataset, which includes 10,240 stations with a record length of 114 years (1901–2014) and a quality control and homogenization procedure reported previously in the literatures (Sun et al. 2017b; Xu et al. 2017). Compared with the other existing global land surface air temperature datasets, this new dataset shows similar ability in describing global temperature changes, despite there are some differences when describing regional temperature changes (Xu et al. 2017). Nonetheless, this problem is considered to have little influence on the results. The complete dataset contains monthly T_{max} and T_{min} values for 7999 and 7381 stations, respectively (Sun et al. 2017b; Xu et al. 2017).

In this study, we select only those stations that have at least 15 years of records in the base period 1961–1990, and at least 2 years of records in every 10 years during the base

period. We also consider the problem of missing data by discarding the annual value with monthly records of less than 6 months in calculating the annual temperature anomalies. Ultimately, we obtain a dataset consisting of monthly T_{max}, T_{min}, and DTR for 4664, 4447, and 4399 stations, respectively, for use in our analysis. The spatial distribution and record lengths of the stations are shown in Fig. 1a. Clearly, there is better spatial coverage of stations and grid boxes in the Northern Hemisphere (NH) than in the Southern Hemisphere (SH). Stations with record lengths of more than 100 years are mainly concentrated in Europe, North America, Japan, and Australia. Areas with low spatial coverage are Africa, South America, Antarctica, and high latitudes in the NH. The spatial distribution of stations is generally consistent with that used in the study by Vose et al. (2005).

China Meteorological Administration- Global Historic Precipitation dataset (CMA-GHP) (Yang et al. 2016) is used to calculate the changes in the precipitation in the NH from 1901 to 2014. The local and discontinuous properties of precipitation data are taken into account, and we select only those stations that have at least 60 years of records. Finally, 412 NH precipitation grid boxes (5°×5°) corresponding to those of the DTR data are selected to calculate the NH precipitation series.

We construct both the NH and SH time series using the method of Jones et al. (2001). First, each hemisphere is divided into grid boxes with a spatial resolution of 5°×5°, and each grid box has at least one station. The grid boxes used for the estimation of regional average are shown in Fig. 1b (the purple areas). Then, gridding of the temperature anomalies is carried out by averaging all values within the 5°×5° grid boxes. Finally, the time series are constructed by area-weight averaging all the grid boxes with data using the cosines of the central latitudes of the grid boxes as weight coefficients. A global annual anomaly time series is obtained by combining the Southern and Northern Hemisphere time series with a weighting coefficient of 1:2 (Jones and Moberg 2003).

The double-end (Start and end year) moving linear trend (DEMLT) refers to the moving linear trend with a fixed step but with double ends of the sub-series displayed backwards over time. In this study, the DEMLT is calculated for 30- and 50-year steps. Such a moving linear trend analysis method has also been used in previous studies (Ren et al. 2015; Fyfe et al. 2016).

Annual mean values are those from January to December. The linear trends of the anomaly series are obtained using the least-squares method to calculate the linear regression coefficients between temperature and ordinal numbers of time (e.g. $i = 1, 2, 3 \ldots 114$ for 1901–2014). The significance of the linear trends of the temperature series is judged using the two-tailed Student's t test. In this study, a trend is considered statistically significant if it is significant at the 5% ($P < 0.05$) confidence level. The MK test and polynomial fitting are used to detect the trend change and abrupt point of the global DTR series.

3 Changes in global DTR

3.1 Long-term time series

Global and hemispheric annual T_{max}, T_{min}, and DTR anomaly long-term time series from 1901 to 2014 are shown in Fig. 2a–c, respectively. It can be seen that the warming rate of global and hemispheric T_{min} was larger than that of T_{max} during 1901–2014, which suggests that the decreasing trend of DTR for the entire study period can be attributed to stronger increases in T_{min} (Fig. 2a, b). Global DTR showed obvious decreasing trends after the 1950s (Fig. 2c). During

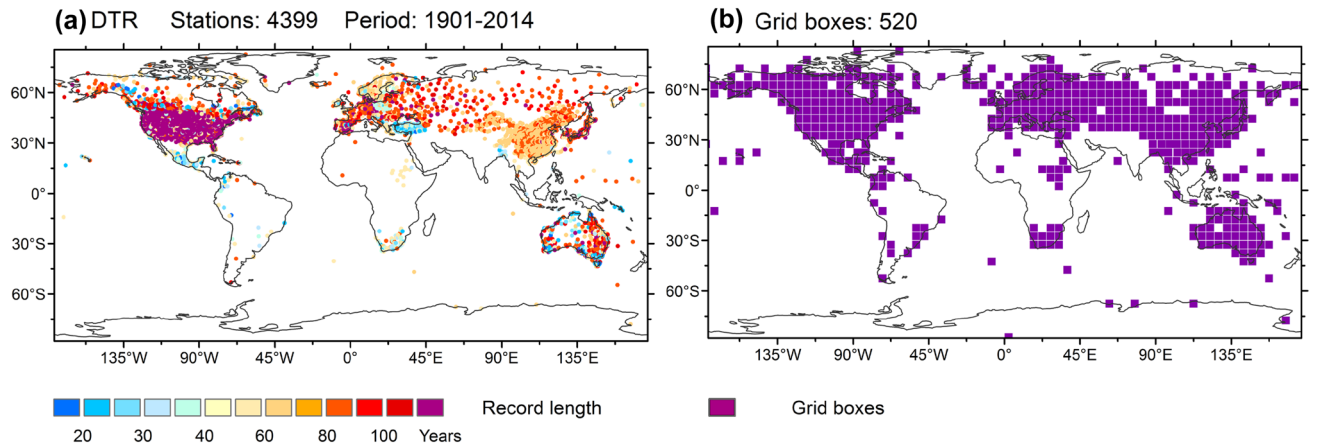

Fig. 1 Distribution of global observation stations from 1901 to 2014 (**a**) and the grid boxes at a spatial resolution of 5°×5° used in this work (**b**). Color points in **a** indicate the different record length of the data

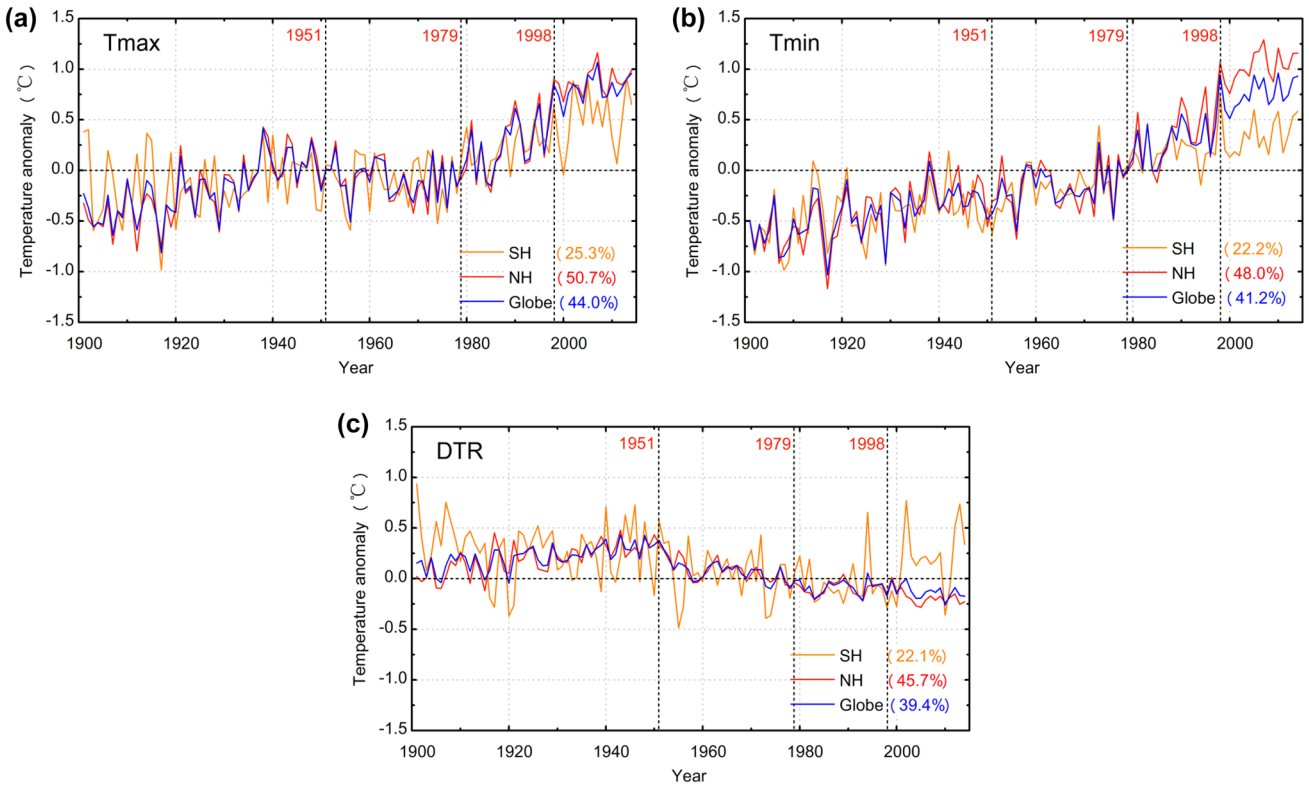

Fig. 2 Annual mean **a** T_{max}, **b** T_{min}, and **c** DTR anomaly series for the global (blue curves) and NH and SH (red and orange curves, respectively) between 1901 and 2014 relative to 1961–1990. Percentages in parentheses indicate station coverage

the late 1970s to 2000, T_{max} and T_{min} exhibited a similar variation pattern with the change of T_{mean}, and showed a dramatic increasing trend. Furthermore, we find that both T_{max} and T_{min} consistently showed a warming slowdown from 1998 (2000), which is also in agreement with the recently reported regional and global warming hiatus phenomenon (e.g. Sun et al. 2017b, c; Kerr 2009; Fyfe and Gillett 2014; Li et al. 2015).

Figure 2c shows the global and hemispheric DTR anomaly series. During 1901–1951, the global DTR series shows an increasing trend with positive anomalies in most years. In the early 1950s, a remarkable reversal phenomenon occurred in DTR, when it changed from increasing to decreasing in most parts of the world. After 1951, in general, DTR showed a decreasing trend. However, there were also slight reversal phenomena between 1951 and 2014. DTR shows an obvious and consistent decreasing trend in 1951–1983 and 2000–2014, but a slight increasing or stable trend during 1984–2000. The pattern of changes during 1951 to the 2000s agrees with previous studies by Easterling et al. (1997), Vose et al. (2005) and Thorne et al. (2016). All of the above analyses reveal that three reversal phenomena occurred in the past century. A remarkable reversal phenomenon occurred in the early 1950s, while slightly weaker reversal phenomena occurred in the 1980s and 2000s.

3.2 Heterogeneity of change rates

The change rates of T_{max} and T_{min} for the globe and the two hemispheres in different periods are shown in Fig. 3a, b. For the entire study period, the results clearly reveal that both global T_{max} and T_{min} decreased by nearly 1.1 and 1.6 °C between 1901 and 2014, respectively. The warming rate of T_{min} (0.142 °C decade^{-1}) is approximately 1.5 times that of T_{max} (0.1 °C decade^{-1}). T_{max} and T_{min} showed a more obvious warming trend during 1979–2014, and the global T_{max} and T_{min} increases occurred at rates of 0.284 °C decade^{-1} and 0.301 °C decade^{-1}, respectively. The warming rates of T_{max} and T_{min} in the first half of the twentieth century were obviously lower than those in the second half of the twentieth century. The warming rates in the NH are larger than those in the global and SH for different periods. For 1998–2014, the change rates of global T_{max} and T_{min} were 0.098 °C decade^{-1} and 0.119 °C decade^{-1}, respectively. Remarkably, all of the trends in the period 1998–2014 are not significant ($P < 0.05$), with a higher level of uncertainty (black error bars in Fig. 3a, b), probably because of the sensitivity of trend estimates to the length of a series.

The changes rates of DTR for the globe and the two hemispheres in different periods are shown in Fig. 3c. The DTR in the NH, SH, and globe consistently decreased by nearly

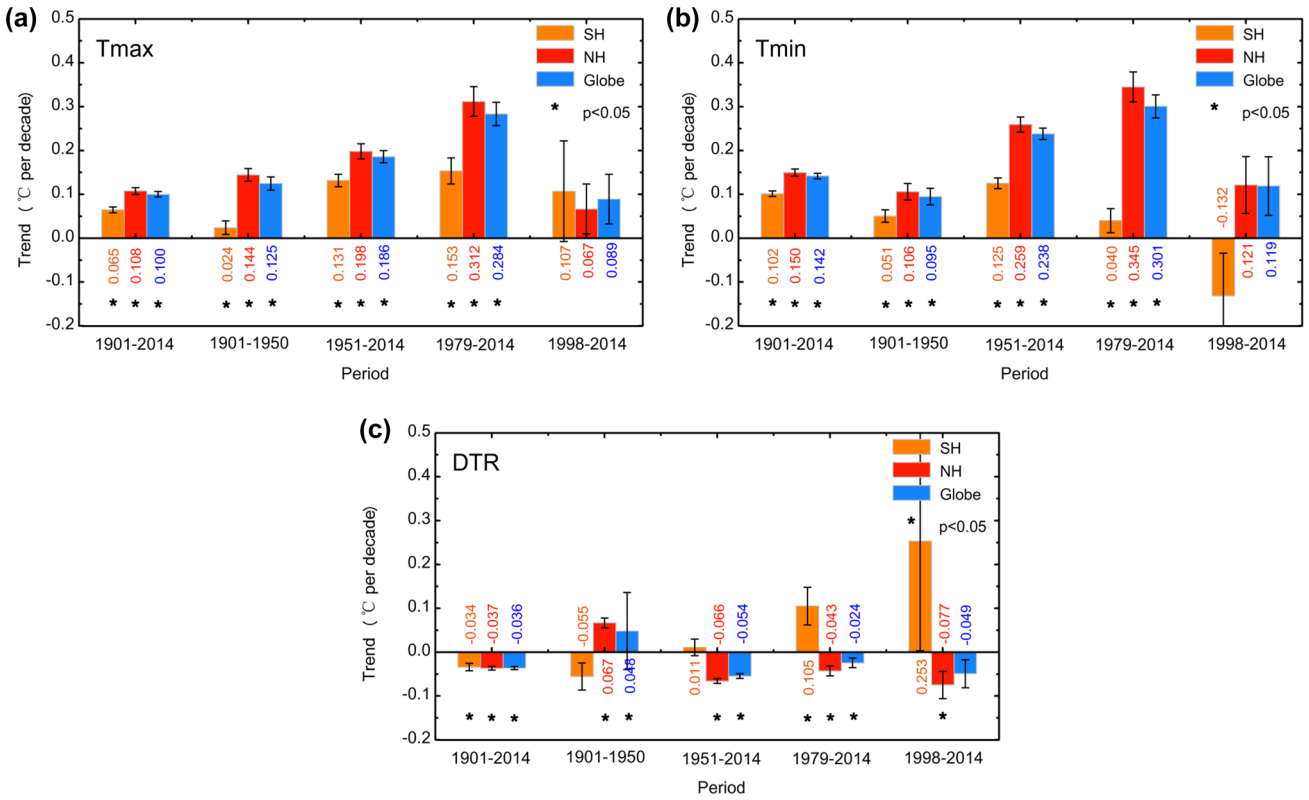

Fig. 3 Hemispheric and global **a** T_{max}, **b** T_{min}, and **c** DTR trends in different periods [1901–2014, 1901–1950, 1951–2014, 1979–2014, and 1998–2014]. Numbers in different colors indicate the rates of change. Error bars indicate 2 times the standard deviation. Statistically significant ($P < 0.05$) trends are marked with asterisks

0.4 °C between 1901 and 2014. The decreasing trend of DTR was slightly larger in the NH (−0.37 °C decade^{-1}) than in the SH (−0.34 °C decade^{-1}). In the first half of the twentieth century, global DTR showed a significant increasing trend (0.046 °C decade^{-1}), NH DTR showed a dramatic increasing pattern (0.067 °C decade^{-1}), and SH DTR shows a statistically insignificant decreasing trend (−0.055 °C decade^{-1}). In the second half of the study period, the trend of DTR showed obvious reversal phenomenon, and the trends of global, NH, and SH DTR were −0.054, −0.066, and 0.011 °C decade^{-1}, respectively. Therefore, the downward trend of DTR between 1901 and 2014 was mainly due to the large decreased DTR from 1951 to 2014. For 1979–2014 and 1998–2014, the global (−0.049 °C decade^{-1}) and NH (−0.077 °C decade^{-1}) DTR showed an obvious decreasing trend, while the SH showed a statistically insignificant ($P < 0.05$) increasing trend with a high level of uncertainty.

The double-end moving linear trends (DEMLTs) with 30- and 50-year fixed steps more clearly display the temporal evolution of the long-term temperature trends. The 30-year DEMLT for the annual mean T_{max}, T_{min}, and DTR for the globe are shown in Fig. 4a. A negative DTR DEMLT appears in the stage with start years between 1930 and 1960. It is clear that the DEMLT differences between T_{max} and T_{min} have two major stages. In the first stage, the T_{max} warming rate is larger than that for T_{min} between the DEMLTs of 1901–1930 and 1930–1960. In the second stage, the T_{max} warming rate is lower than that of T_{min} between the DEMLTs of 1930–1960 and 1974–2014. Therefore, the global DTR shows an increasing trend in the first stage and a decreasing trend in the second stage. Figure 4a also reveals that the global DTR trend changed from dramatically decreasing to slightly decreasing around 1940–1969 in the second stage. The DTR DEMLT shows almost no change in the most recent 40 years. Similar to the 30-year DEMLT, the 50-year DEMLT for the globe also shows two major stages for T_{max} and T_{min}. A negative DEMLT appeared in the stage with start years between 1915 and 1965. In general, the 30- and 50-year DTR DEMLTs show that the DTR trend has changed from increasing to decreasing and that the change rate of DTR slightly decreased in the past 5 decades.

3.3 Spatial variation patterns for different periods

The percentage of grid boxes with positive (red bars) and negative (blue bars) DTR trends are shown in Fig. 5a. It can be seen that the percentage of grid boxes with a negative DTR trend is above 50% on most of the timescales

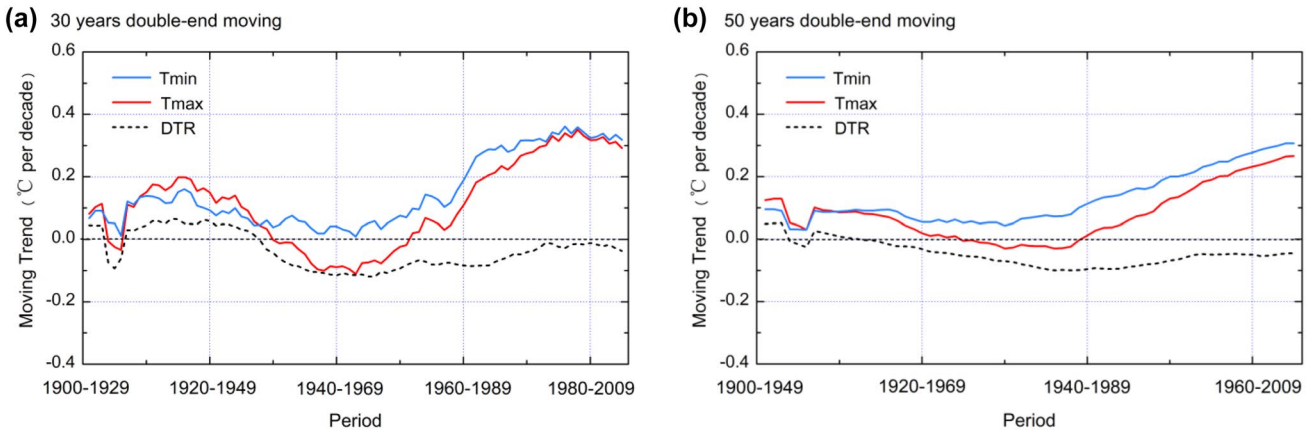

Fig. 4 **a** 30-year and **b** 50-year DEMLTs of annual mean T_{max} (red curves), T_{min} (blue curves), and DTR (black dotted curves) for the globe. Values above zero indicate an increasing trend; values below zero indicate a decreasing trend. For example, the first value of the 30-year DEMLT **a** indicates the linear trend in the period 1901–1930

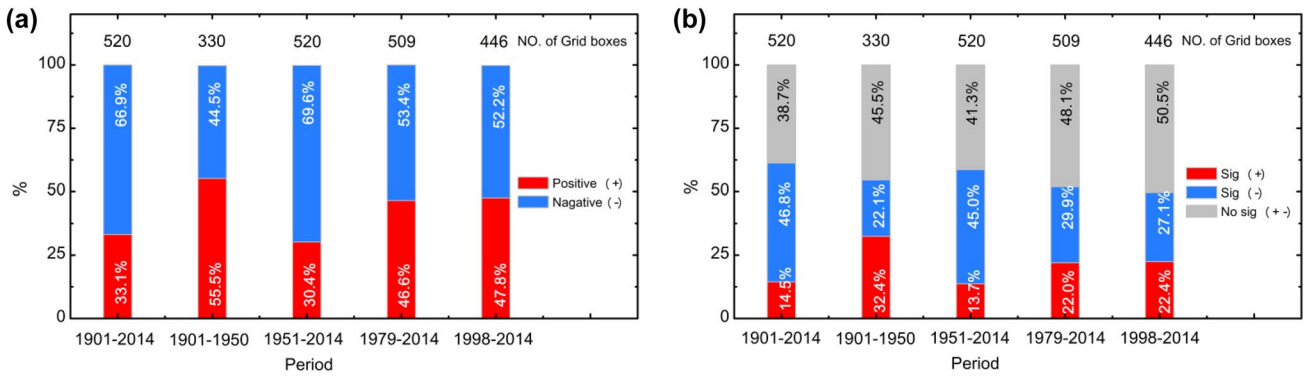

Fig. 5 **a** Percentage of grid boxes with positive (red bars) and negative (blue bars) DTR trends. **b** Percentage of grid boxes with significant positive trends (red bars), significant negative trends (blue bars), and no significant trends (gray bars) in DTR at a confidence level of 95% ($P<0.05$). Numbers in bars with different colors indicate the percentages. Numbers above the bars indicate the number of grid boxes with a spatial resolution of 5°×5°

analyzed, except the period 1901–1950. For 1901–2014 and 1951–2014, the percentage of grid boxes with a negative DTR trend is more than 65%. For 1901–1950, the percentage of grid boxes with a negative DTR trend is 44.5%. Remarkably, there are only 330 grid boxes in the period 1901–1950, which means that the results for this period are more uncertain than those for other periods. For 1979–2014, the percentage of grid boxes with a negative DTR trend (46.6%) is slightly lower than those with a positive DTR trend (53.4%). For the period 1998–2014, the percentages of grid boxes with negative or positive trends exhibit similar rates as in the period 1979–2014.

The percentages of grid boxes with significant positive and negative trends and no significant trends in DTR at a confidence level of 95% are shown in Fig. 5b. Over time, 50% of the grid boxes show statistically significant increasing and decreasing trends in all of the different periods. For the entire study period, 46.8% of the grid boxes show a significant negative trend, while only 14.5% of the grid boxes show a significant increasing trend. For the period 1901–1950, 32.4% of the grid boxes show a significant positive trend, and only 22.1% show a significant negative trend. The percentages of grid boxes with significant negative and positive trends during 1951–2014 are consistent with those for the entire study period. For 1979–2014 and 1998–2014, the percentage of grid boxes with significant trends totals approximately 50%, while there are approximately 22% of grid boxes with significant positive trends.

Overall, the decreasing DTR over the entire study period is mainly due to the obvious decrease in DTR from 1951 to 2014. In 1901–1950, more grid boxes show a positive trend (55.5%), and most of the positive trends are statistically significant (32.4%), which leads to a significant increase in DTR before 1950.

The spatial distribution of annual mean DTR trends during 1901–2014 is shown in Fig. 6a. For the entire study

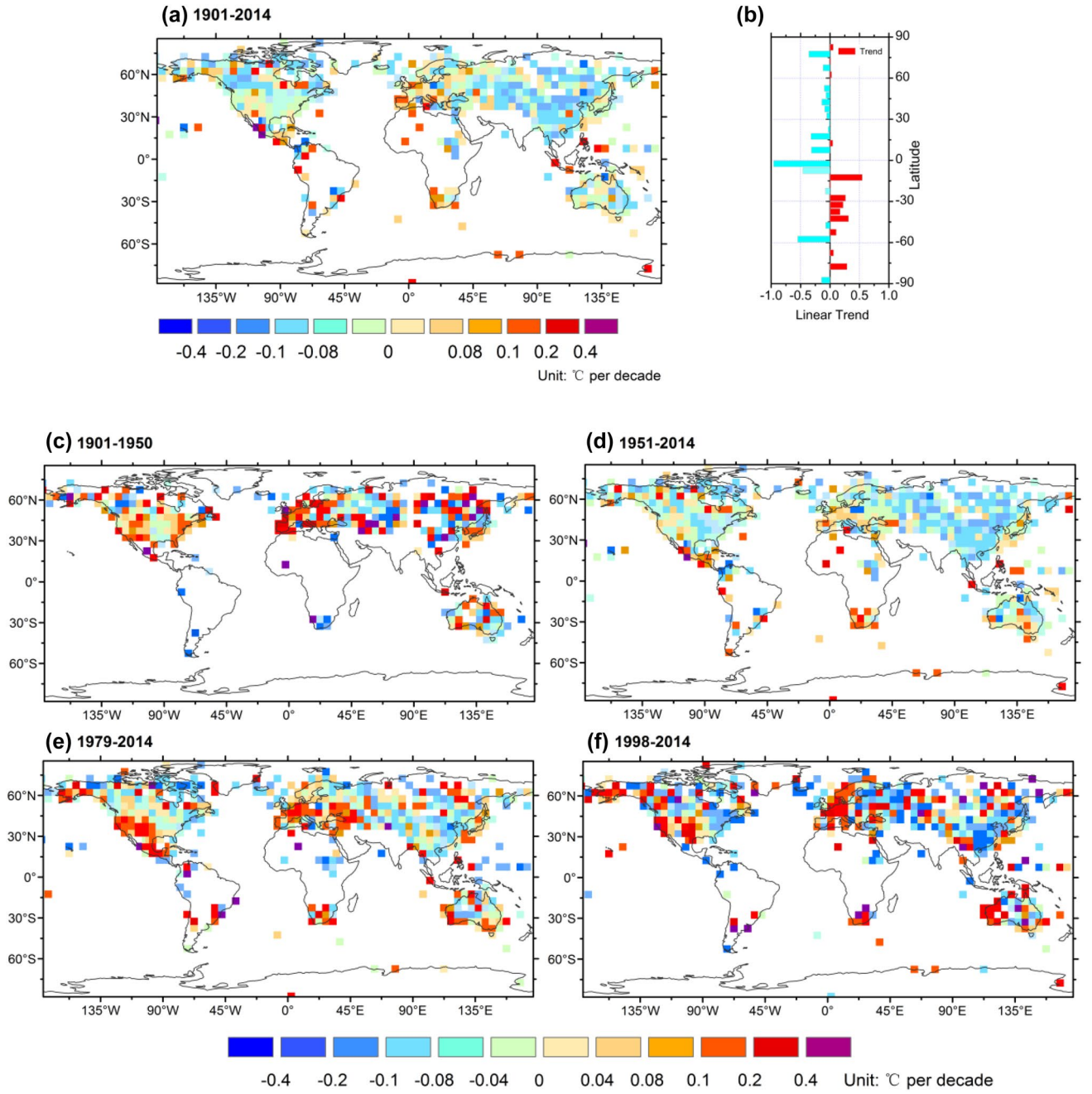

Fig. 6 Global DTR trends in specific periods: **a** 1901–2014, **c** 1901–1950, **d** 1951–2014, **e** 1979–2014, and **f** 1998–2014. **b** The zonal average trends for every 5° of latitude from 1901 to 2014

period, DTR decreased over most areas of the world, with notable dramatic decreases in Asia, North America, and Australia. In most parts of Europe, DTR shows an increasing trend. The zonal average trends for every 5° of latitude are shown in Fig. 6b. The largest annual change corresponding to a decrease in DTR is around the Equator. The decreased areas in DTR are mainly distributed in the NH, while the obvious increasing trends are mainly distributed in the SH. Additionally larger uncertainties are seen in the SH zonal average trends than those in the NH, and the reason can be mainly attributed to fewer grid boxes in the SH than in the NH.

For the period 1901–1950 (Fig. 6c), the DTR in the Northern Hemisphere shows a significant increasing trend, especially in East Asia and Europe. Africa and South America show a downward trend, while Central and Northern Australia shows an increasing trend. For the period 1951–2014, major changes in global DTR show decreasing

trends (Fig. 6d). In this period, most of the grid boxes show a decreasing trend, especially in the NH. Antarctica shows an increasing trend, but it has few grid boxes. Therefore, the global DTR shows an increasing trend in the first half of the last century and a decreasing trend in the second half, once again indicating that an obvious reversal phenomenon occurred around the early 1950s. In 1979–2014, most grid boxes in North America, Europe, Africa, South America, Antarctic, and Western Australia show an obvious increasing trend (Fig. 6e). Asia and Eastern North America exhibit widespread decreases in DTR, although the trend pattern for global DTR is generally mixed. The trends during 1998–2014 exhibit a similar pattern for the period 1979–2014 (Fig. 6f). However, the trend of increasing or decreasing DTR at grid scale is more obvious.

In general, for global DTR, most grid boxes show an obvious decreasing trend during 1901–2014, and an obvious reversal phenomenon around the early 1950s. In addition, the trends of increasing and decreasing global DTR in 1979–2014 and 1998–2014 were more obvious than in other periods.

4 Discussion

4.1 Long-term changes in global DTR

Because of poor observational data, there are few studies focused on the change of DTR on the century scale. Our analysis indicates that global DTR showed a decreasing trend in the 1900–2014 period based on more than 4,000 stations around the World, with a decreasing rate of − 0.036 °C decade^{-1}. Based on data from 524 stations, which were mainly concentrated in North America, Europe, and Australia, Wang and Dickinson (2013) concluded that global and hemispheric DTR showed a downward trend in the period 1900–2010. They also indicated that the main reason for long-term variations is the change of solar radiation reaching the surface, and the impact of solar radiation was − 0.011 °C decade^{-1} from 1900 to 2010.

For the past 6 decades, the quality of global data has been greatly improved, and the changes in DTR have attracted increased attention from researchers. The results in our study are generally consistent with the results achieved by previous studies made over past 6 decades (e.g. Karl et al. 1993; Vose et al. 2005; Easterling et al. 1997; IPCC 2013). These studies used different data sets and base periods, but they consistently show significant decreasing trends in global DTR since the early 1950s, but with different decrease rates. Based on multiple global temperature datasets, Thorne et al. (2016) recently indicated that globally averaged annual mean DTR had decreased since the 1950s or 1960s but that this decrease had not been linear.

The research periods in the studies of Easterling et al. (1997) and Karl and Steurer (1990) are concentrated from the early 1950s to the early 1990s. We choose the results of the Vose et al. (2005) to compare with our results (Sect. 3.1) (Table 1). In general, different results consistently show significant decreasing trends in global DTR since the early 1950s. In the results of Vose et al. (2005), however, global and NH DTR showed more obvious decreasing trends. The major reason is that T_{max} and T_{min} temperature changes tend to be consistent after 2000, resulting in the value of global DTR change to gradually become smaller. The data coverage in the SH is poor, so the results there always have more uncertainty than those in the NH.

In addition to the trend features, a reversal phenomenon was found around 1979 in the studies of Easterling et al. (1997) and Vose et al. (2005) for the period 1951–2004. Owing to the short observation period, the reversal phenomenon did not attract much attention. Makowski et al. (2008) analyzed the changes in DTR in Europe and found that the long-term decreasing trend of DTR in Western Europe began to reverse in the 1970s, while the reversal phenomenon in Eastern Europe occurred in the 1980s. Furthermore, Makowski et al. (2008) also indicated that the reversal phenomenon in Europe occurred in summer and autumn. Based on the new observational dataset, we analyze the changes in DTR for a longer period, 1901–2014, and we find an obvious reversal phenomenon in DTR around the early 1950s, when the trend changes from increasing to decreasing in most parts of the World. The MK test and polynomial fitting are used to detect the trend change and abrupt point of the global DTR series (Fig. 7a, b). Figure 7a shows that global DTR shows a significant increasing trend from the 1930s to the end of the 1950s, and turns to a significant downward trend after the 1970s. Figure 7a also shows that a significant abrupt point occurred in 1978. The MK test could not detect the trend-reversal phenomenon around the early 1950s, but this reversal phenomenon also can be clearly found from the polynomial fitting of the global DTR series (Fig. 7b). Figure 7b shows that the reversal phenomenon around the early 1950s is more obvious than those at other times. This phenomenon is also demonstrated in the series of 30- and

Table 1 Comparison of global DTR changes of the globe, NH, and SH between Vose et al. (2005) and the present paper

References	Data set	Period	Trend (°C decade^{-1})		
			Global	NH	SH
Vose et al. (2005)	GHCN[a]	1950–2004	− 0.066	− 0.076	− 0.033
This paper	CMA-LSAT	1951–2014	− 0.054	− 0.066	0.011

[a]Global Historical Climatology Network data set (Peterson and Vose 1997)

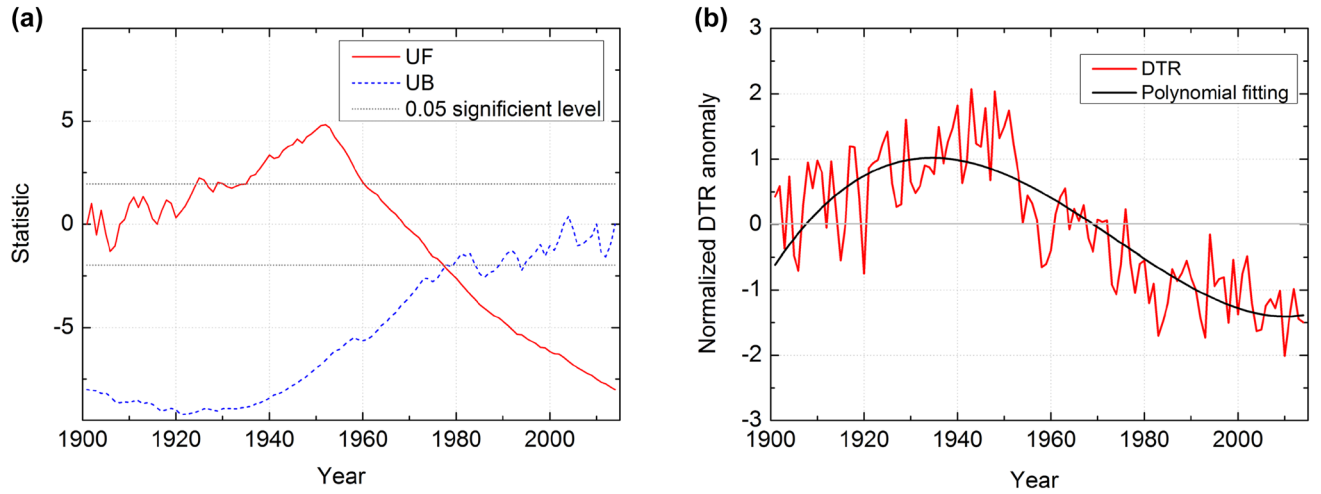

Fig. 7 **a** MK test and **b** polynomial fitting results of global annual mean normalized DTR anomaly series from 1901 to 2014

50-year moving trends. The reversal phenomenon in the NH is consistent with the global DTR pattern and it is statistically significant. In contrast, the reversal phenomenon does not occur in the SH.

4.2 Causes of the long-term changes in global DTR

Previous studies indicated that the long-term changes in cloudiness, precipitation, soil moisture, aerosols, terrestrial vegetation, and local urbanization processes would all play a role in decreasing global DTR since 1951 (e.g. Dai et al. 1999; Zhou and Hansen 2004, 2008; Wild et al. 2005, 2007; Ren et al. 2014). In the recent time periods of 1951–2014 and 1979–2014, southern Europe, northern Africa, the western Middle East, as well as the southwestern United States exhibit obvious increasing DTR trends, which are rather different from the global average. The positive trends have been related to the decrease in cloudiness and precipitation and the increasing drought frequency in these regions (IPCC 2013). The significant decrease in DTR over mainland China and other Asian developing countries might have been mainly caused by the regional dimming resulting from increasing aerosols (Wang and Dickinson 2013; Shen et al. 2015) and rapid urbanization around the observational stations (e.g. Zhou and Ren 2011; Wang et al. 2012; Ren et al. 2006, 2014).

However, due to the lack of observational data and the poor credibility of the observations in the first half of the twentieth century, there are only very few studies focused on the cause of the decreasing trend of global DTR, and few reports are available to analyze the possible causes of the reversal phenomenon around the early 1950s. Table 2 summarizes the previous observational studies reporting trends of the influential factors of DTR in the first half of the twentieth century.

Surface solar radiation (SSR) is considered to play a prominent role in influencing global and regional DTR (Makowski et al. 2009). Since SSR is only present during the day, it could affect T_{max} more than T_{min} (Wild et al. 2007; Makowski et al. 2009). A large number of studies on global and regional "brightening" and "dimming" after 1951 demonstrated that changes in global and regional DTR mainly depend on changes in SSR (e.g. Wild 2009; Makowski et al. 2009; Wild et al. 2008; Long et al. 2009; Che et al. 2005; Qian et al. 2007). However, because of the poor early SSR observational data, there are only a very few studies focused on time series of directly observed SSR for the first half of the twentieth century. Romanou et al. (2007) simulated global SSR in the twentieth century using nine models and found that global SSR showed a decreasing trend over the entire twentieth century. Wild (2009) investigated the SSR data from the longest observational record in Stockholm (Europe) and indicated that there were two "global brightening" periods in the twentieth century, one at the end of the century, and a second one before the 1940s ("early brightening") (Table 2). This can effectively support the DTR reversal phenomenon in Europe that occurred around the early 1950s.

In addition to the most direct SSR factor, another major factor affecting DTR variation is generally recognized to be precipitation. Dai et al. (1997) investigated the relationship between precipitation and DTR and indicated that increased precipitation may have contributed to a DTR decrease by increased evaporative cooling. A more obvious correlation between DTR and precipitation in Europe, North America, and Australia from 1901 to 1990 was also indicated, with the correlation coefficients all above 0.55 in these areas.

Table 2 Summary of the previous studies reporting trends of the influential factors of DTR in the first half of the twentieth century

References	Region	Data sources	Trend increase or decrease (period)		
SSR					
Wild et al. (2009)	Europe(Stockholm)	GEBA[a]	**Increase** (1923–1940 s)	**Decrease** (1950–2002)	n/a
Precipitation					
Present paper	Northern Hemisphere	CMA-GHP[b]	Decrease (1901–1950)	**Increase** (1951–2014)	**Increase** (1901–2014)
TCC					
Henderson-Sellers (1989, 1992), Croke et al. (1999), Sanchez-Lorenzo et al. (2012), Dai et al. (1999, 2006)	North America	Surface-based observations	**Increase** (1901–1950 s)	**Increase** (1960s–1999)	**Increase** (1900–1999)
Lough et al. (1983), Henderson-Sellers (1992)	Europe	Surface-based observations	**Increase** (1901–1940 s)	**Decrease** (1950s–1987)	**Increase** (1900–1987)
Jones and Henderson-Sellers (1992)	Australia	Historical records of Australia	Decrease (1910–1930 s)	**Increase** (1930s–1989)	**Increase** (1910–1989)
Warren et al. (2007)	South America	EECRA[c]	n/a	**Decrease** (1971–1996)	**Decrease** (1971–1996)
	Africa		n/a	Decrease (1971–1996)	Decrease (1971–1996)
Xia (2010)	China	CMA-Monthly TCC	n/a	**Decrease** (1955–2005)	
Volcanic					
Wang et al. (2014)	Global	SIGVP[d]	Increase (1901–1950)	**Increase** (1950–2010)	**Increase** (1901–2010)

All of the following studies are based on observational data

Black bold fonts represent a statistically significant trend

[a]Global energy balance archive

[b]China Meteorological Administration—Global Historic Monthly Mean Precipitation Dataset

[c]Extended edited cloud reports archive

[d]Smithsonian Institution Global Volcanic Program

The changes of total cloud cover (TCC) are the main reason for the variability of long- and short-wave radiation at land surfaces (Sanchez-Lorenzo et al. 2012). The TCC and DTR have been proved to have a good correlation in some parts of the World after the 1950s (Dai et al. 1999), except for some regions such as South America, Africa (Warren et al. 2007), China (Xia 2010), and Italy (Maugeri et al. 2001). Observational TCC records mainly began being recorded in the mid-eighteenth century in Europe, North America, and Australia. Table 2 shows the TCC changes in different regions, including some details of the reviewed publications. In Europe, the TCC trend showed a significant increase before the 1940s, decreased significantly after the 1950s and became increasing after the 1970s (Lough et al. 1983; Henderson-Sellers 1989). These studies therefore could not support the global and regional DTR changes since 1901. Dai et al. (1999) found that the correlation coefficient between total cloud cover and DTR was very low in Europe, and the correlation coefficient was lower than 0.35 from 1900 to 1990. In Australia, TCC also showed a general increasing trend from 1910 to 1989, with the main increase having occurred in the 1930s to the 1980s (Jones and Henderson-Sellers 1992). In North America, previous studies confirmed that TCC has increased in a fluctuating way from 1900 to the 1980s, as the major increase occurred around the 1930s–1950s and 1960s–1980s (Henderson-Sellers 1989, 1992; Croke et al. 1999; Sanchez-Lorenzo et al. 2012). These studies could not support the reversal DTR phenomenon in North America around the early 1950s. However, Karl and Steurer (1990) indicated that the period of increasing TCC in the 1930s–1950s in North America can be mainly attributed to biases in observation methodology and observational environments, although the increasing trend after the 1950s has higher reliability. Sanchez-Lorenzo et al. (2012) indicated that traditional TCC observations lack objectivity. Changes in observational environment, observational experience, observation times, and observers can cause TCC series inhomogeneity. Therefore, due to the low credibility of early TCC observations, the changes in

DTR before the early 1950s cannot be explained by the changes in total cloud coverage.

Volcanic eruption can affect land-surface air temperature by reducing solar radiation (Robock 2000). Robock (2000) indicated that five kinds of volcanic eruption indexes showed increasing trends from 1901 to 2000, although the change was not significant. It was also found that the volcanic intensity showed a significant decreasing trend from the 1960s to 2000. Based on Smithsonian Institution global volcanic program data, Wang et al. (2014) also indicated that the large volcanic eruption events showed an increasing trend during 1901–2010. These previous studies indicated that the increase of both volcanic eruption frequency and volcanic eruption intensity could partly explain the long-term decrease of global DTR since 1901.

In addition to the above factors that affect changes in DTR, aerosol, water vapor, and land use changes would be also important. Huang et al. (2006) simulated the interaction between aerosols and clouds and indicated that aerosols led to the decrease of DTR in East Asia since 1950. Makowski et al. (2008) confirmed that there is a significant correlation between SO_2 levels and DTR change in European countries. By analyzing the meteorological data observed after 1950, Kalnay and Cai (2003) pointed out that 50% of the DTR decrease in America in the second half of the twentieth century was caused by changes in land use (including local urbanization). Dai et al. (1999) analyzed the relationship between water vapor and DTR and indicated that water vapor does not have a significant effect on DTR change relative to cloud cover and other factors. None of above factors has credible observational records since 1901, so it is very difficult to analyze the effect of these factors on DTR trends in the first half of the twentieth century.

In general, due to the lack of observational data and the poor credibility of observations in the first half of the twentieth century, it is difficult to assess the causes for the increase in DTR before the early 1950s. Based on the CMA–GHP dataset, we analyzed the relationship between precipitation series and long-term DTR variation in the NH (Fig. 8). Because DTR reversal occurs mainly in the NH, we only calculated the correspondence between the normalized DTR series and normalized precipitation series in the NH (a total of 412 5° × 5° grid boxes). Figure 8 shows that there is a significant negative correlation between precipitation and DTR in the NH, with a correlation coefficient of − 0.61. Precipitation in the NH decreased before the early 1950s, while the trend after the early 1950s has increased. Overall, precipitation data could strongly support the DTR reversal phenomenon occurring around the 1950s. Because precipitation is generally accompanied by clouds, the TCC over the global lands may have also increased, which, together with precipitation, may have contributed to the decline of the global and regional DTR. The larger increasing trend

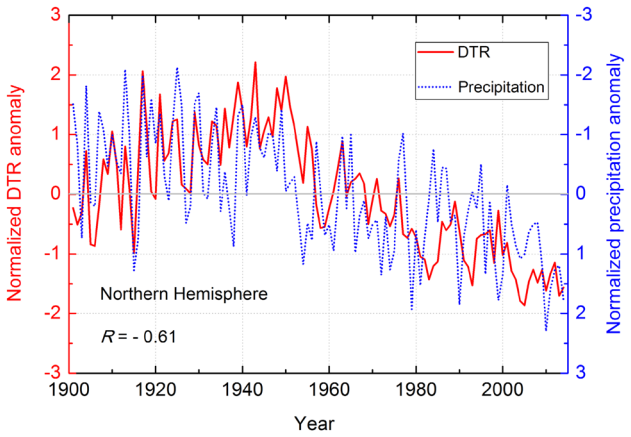

Fig. 8 Variations of normalized anomaly of NH DTR series (red solid line) and precipitation series (blue dashed line) from 1901 to 2014 (relative to 1961–1990). The number represents the correlation coefficient *R*. To compare the two normalized series more easily, the *Y* axis of the precipitation series is placed upside down

Table 3 Trend in DTR for stations with long-term records and all the stations in different periods, along with percentage errors

Period	1901–1950	1951–2014	1901–2014
DTR			
≥ 100 years stations (°C decade^{-1})	0.059	− 0.034	−0.024
All stations (°C decade^{-1})	0.048	− 0.054	−0.036
Percentage errors (%)	23.403	37.421	35.187

of annual precipitation based on the CMA–GHP dataset, as compared to those based on other global precipitation data, needs to be confirmed in the following works, but it is partly supported by a recent analysis of Asian continent, the largest continent of the world (Zhan et al. 2018).

4.3 Uncertainties

Our results are limited by several uncertainties. The major uncertainty is related to DTR calculated using the monthly temperature data. If there are no missing data, the results would be similar to those using daily data. Most observational data used in this study have a relatively long and high-quality record history, especially after 1960. However, the station spatial coverage is poor for the period 1901–1950, which results in the uncertainty of the calculated results. Table 3 shows the DTR trend for stations with long-term records and all stations in three different periods along with the percentage errors. The DTR trends based on the different station networks show consistent patterns of change, but with different magnitudes. The results also clearly show that the differences in DTR trends between long-term record

stations and all stations are at the same level of magnitude. The percentage error for the entire study period is approximately 35%, which is lower than that for 1951–2014 (37%). Before the 1950s, stations with long-term records account for a larger proportion of all stations, which reduces the percentage error to approximately 23%. Therefore, the findings of the DTR reversal phenomenon and the continued decreasing trend of DTR in the past century still have a larger reliability, in spite of the uncertainty.

5 Conclusions

Previous studies indicated that global DTR has been greatly reduced since 1951, and that an obvious reversal phenomenon in DTR occurred around the 1970s. At the same time, it is considered that the change of SSR and precipitation is significantly related to the change of DTR after the 1950s. Changes in factors such as land use, cloud cover, and water vapor can explain the change of DTR after the 1950s. Based on the newly developed CMA-LSAT datasets, in this paper we indicate that global DTR has shown a significant decreasing trend since 1901, and obvious reversal phenomena occurred in global and NH DTR in the early 1950s. Furthermore, precipitation, the number of volcanic eruptions, and the "early brightening" of Europe all support the increase of DTR in the first half of the twentieth century. The results of previous studies on total global cloud cover could not, however, support the increase of DTR in the first half of the twentieth century. Main conclusions of our analysis are as follows.

Observations reported in the present study show changes in annual mean T_{max} and T_{min} to be asymmetrical from 1901. Global T_{max} and T_{min} decreased by nearly 1.1 and 1.6 °C between 1901 and 2014, respectively. The warming rate of T_{min} (0.142 °C decade^{-1}) is approximately 1.5 times that of T_{max} (0.100 °C decade^{-1}), which results in a significant decreasing trend in global DTR (– 0.036 °C decade^{-1}). However, DTR shows obvious interdecadal changes. For the first half of the twentieth century, most grid boxes show a positive DTR trend, with the positive trends of 32.4% grid boxes being statistically significant, leading to a large and significant increase of 0.048 °C decade^{-1} in DTR. However, a dramatic reversal in DTR change occurs around the 1950s, with most parts of global lands seeing a shift from increasing to decreasing trends. The change rate of global land mean DTR is − 0.054 °C decade^{-1} in the second half of the twentieth century. There are 45.0% grid boxes during 1951–2014 showing negative trends of statistical significance.

Spatial distribution shows that DTR has decreased over most areas of the World, with notable dramatic decreases in Asia, North America, and Australia between 1901 and 2014. In most parts of Europe, the DTR shows an increasing trend. However, the global DTR change shows a different spatial distribution in different periods. For the period 1901–1950, annual mean DTR in the NH shows a significant increasing trend, especially in East Asia and Europe. For the period 1951–2014, major changes in global DTR show decreasing trends. Therefore, global DTR shows an increasing trend in the first half of the twentieth century and a decreasing trend in the second half, again indicating that an obvious reversal phenomenon occurred around the 1950s. In the periods 1979–2014 and 1998–2014, most grid boxes in North America, Europe, Africa, South America, Antarctica, and Western Australia show obvious increasing trends, but Asia and Eastern North America still exhibit widespread decreases in DTR.

We also find that the reversal phenomenon that occurred around the 1950s, on global and grid scales, is more obvious than those that occurred at other times. This phenomenon is also demonstrated in the series of 30- and 50-year moving trends. The reversal phenomenon in the NH is consistent with the global DTR pattern and is of statistical significance. In contrast, the reversal phenomenon does not occur in the SH. Owing to the lack of observational data and the poor credibility of the observations in the first half of the twentieth century, it is difficult to assess the causes for the increase in DTR before 1951. However, there is a good negative correlation between DTR and precipitation in the NH from 1901 to 2014, with a correlation coefficient of − 0.61. The number of volcanic eruptions can also support the increase of global DTR before 1951. The Stockholm long-term SSR series and the "early brightening" claim based on the data series are also consistent with the European DTR increase before 1951. The robust reasons for the long-term DTR changes obviously require further study.

Acknowledgements This study is financed by the National Key R&D Program of China (Fund No: 2018YFA0605603), China Natural Science Foundation (CNSF) (Fund No: 41575003) and the MOST (Fund No: GYHY201206012).

References

Alexander LV, Zhang X, Peterson TC, Caesar J, Gleason B, Tank AMGK, Haylock M, Collins D, Trewin B, Rahimzadeh F (2006) Global observed changes in daily climate extremes of temperature and precipitation. J Geophys Res 111(D5):1042–1063

Braganza K, Karoly DJ, Arblaster JM (2004) Diurnal temperature range as an index of global climate change during the twentieth century. Geophys Res Lett 31(13):405–407

Che HZ, Shi GY, Zhang XY, Arimoto R, Zhao JQ, Xu L, Wang B, Chen ZH (2005) Analysis of 40 years of solar radiation data from China, 1961–2000. Geophys Res Lett 32:L06803. https://doi.org/10.1029/2004GL022322

Croke MS, Cess RD, Hameed S (1999) Regional cloud cover change associated with 15 global climate change: case studies for three regions of the United States. J Clim 12:2128–2134

Dai A, Genio ADD, Fung IY (1997) Clouds, precipitation and temperature range. Nature 386(6626):665–666
Dai A, Trenberth KE, Karl TR (1999) Effects of clouds, soil moisture, precipitation, and water vapor on diurnal temperature range. J Clim 12(8):2451–2473
Dai A, Karl TR, Sun B, Trenberth KE (2006) Recent trends in cloudiness over the United States: a tale of monitoring inadequacies. Bull Am Meteor Soc 87(5):597–606
Easterling DR, Horton B, Jones PD, Peterson TC, Karl TR, Parker DE, Salinger MJ, Razuvayev V, Plummer N, Jamason P (1997) Maximum and minimum temperature trends for the globe. Science 277(5324):364–367
Easterling DR, Gleason B, Vose RS, Stouffer R (2006) A comparison of model produced maximum and minimum temperature trends with observed trends for the 20th and 21st centuries. In: 18th conference on climate variability and change, Session 5, January 27–February, 2006, Atlanta, USA
Fyfe JC, Gillett NP (2014) Recent observed and simulated warming. Nat Clim Change 4(3):150–151
Fyfe JC, Meehl GA, England MH, Mann ME, Santer BD, Flato GM, Hawkins E, Gillett NP, Xie SP, Yu K (2016) Making sense of the early-2000s warming slowdown. Nat Clim Change 6(3):224–228
Henderson-Sellers A (1989) North American total cloud amount variations this century. Global Planet Change 1:175–194
Henderson-Sellers A (1992) Continental cloudiness changes this century. Geo J 27:255–262
Huang Y, Dickinson R, ChameidesWL (2006) Impact of aerosol indirect effect on surface temperature over East Asia. Proc Natl Acad Sci USA 103(12):4371–4376
Hundecha Y, Bárdossy A (2005) Trends in daily precipitation and temperature extremes across western Germany in the second half of the 20th century. Int J Climatol 25(9):1189–1202
IPCC (2013) Climate change 2013: the physical science basis. In: Stocker TF, Qin D, Plattner G-K, Tignor M, Allen SK, Boschung J, Nauels A, Xia Y, Bex V, Midgley PM (eds) Contribution of Working Group I to the fifth assessment report of the intergovernmental panel on climate change. Cambridge University Press, Cambridge, p 1535. https://doi.org/10.1017/CBO9781107415324
Jaagus J, Briede A, Rimkus E, Remm K (2014) Variability and trends in daily minimum and maximum temperatures and in the diurnal temperature range in Lithuania, Latvia and Estonia in 1951–2010. Theor Appl Climatol 118(1–2):57–68
Jones PA, Hendersonsellers A (1992) Historical records of cloudiness and sunshine in Australia. J Clim 5(3):260–270
Jones PD, Moberg A (2003) Hemispheric and large-scale surface air temperature variations: an extensive revision and an update to 2001. J Clim 16(2):206–223
Jones PD, Osborn TJ, Briffa KR, Folland CK, Horton EB, Alexander LV, Parker DE, Rayner NA (2001) Adjusting for sampling density in grid box land and ocean surface temperature time series. J Geophys Res 106(D4):3371–3380
Kalnay E, Cai M (2003) Impact of urbanization and land-use change on climate. Nature 423(6939):528–531
Karl TR, Steurer PM (1990) Increased cloudiness in the United States during the first half of nthe twentieth century: fact or fiction? Geophys Res Lett 17:1925–1928
Karl TR, Knight RW, Gallo KP, Peterson TC, Jones PD, Kukla G, Plummer N, Razuvayev V, Lindseay J, Charlson RJ (1993) A new perspective on recent global warming: asymmetric trends of daily maximum and minimum temperature. Bull Am Meteor Soc 74(6):1007–1024
Kerr RA (2009) What happened to global warming? Scientists say just wait a bit. Science 326(5949):28–29
Klein Tank AMG, Können GP (2003) Trends in indices of daily temperature and precipitation extremes in Europe, 1946–1999. J Clim 16(22):3665–3680
Kumar KR, Kumar KK, Pant GB (1994) Diurnal asymmetry of surface temperature trends over India. Geophys Res Lett 21(8):677–680
Li Q, Yang S, Xu W, Wang XL, Jones P, Parker D, Zhou L, Feng Y, Gao Y (2015) China experiencing the recent warming hiatus. Geophys Res Lett 42(3):889–898
Long CN, Dutton EG, Augustine JA, Wiscombe W, Wild M, McFarlane SA, Flynn CJ (2009) Significant decadal brightening of down welling shortwave in the continental United States. J Geophys Res 114:D00D06. https://doi.org/10.1029/2008JD011263
Lough JM, Wigley TML, Palutikof JP (1983) Climate and climate impact scenarios for Europe in a warmer world. J Appl Meteorol 22(22):1673–1684
Makowski K, Wild M, Ohmura A (2008) Diurnal temperature range over Europe between 1950 and 2005. Atmos Chem Phys 8(21):6483–6498
Makowski K, Jaeger EB, Chiacchio M, Wild M, Ewen T, Ohmura A (2009) On the relationship between diurnal temperature range and surface solar radiation in Europe. J Geophys Res 114(D10):1–16. https://doi.org/10.1029/2008JD011104
Maugeri M, Bagnati Z, Brunetti M, Nanni T (2001) Trends in Italian total cloud amount, 1951–1996. Geophys Res Lett 28:4551–4554. https://doi.org/10.1029/2001GL013754
Peterson TC, Vose RS (1997) An overview of the global historical climatology network temperature database. Bull Am Meteorol Soc 78(12):2837–2849
Powell EJ, Keim BD (2014) Trends in daily temperature and precipitation extremes for the southeastern United States: 1948–2012. J Clim 28(4):1592–1612
Qian Y, Wang L, Leung LR, Kaiser DP (2007) Variability of solar radiation under cloud-free skies in China: The role of aerosols. Geophys Res Lett 34(12):2111–2121. https://doi.org/10.1029/2006GL028800
Ren G, Zhou Y, Chu Z, Zhou J, Zhang A, Guo J, Liu X (2006) Urbanization effects on observed surface air temperature trends in North China. J Clim 21(6):1333–1348
Ren G, Ren Y, Li Q, Xu W (2014) An overview on global land surface air temperature change. Adv Earth Sci 29(8):934–946 **(in Chinese)**
Ren G, Ren Y, Zhan Y, Sun X, Liu Y, Chen Y, Wang T (2015) Spatial and temporal patterns of precipitation variability over mainland China: II: recent trends. Adv Water Sci 26(4):451–465 **(in Chinese)**
Río SD, Cano-Ortiz A, Herrero L, Penas A (2012) Recent trends in mean maximum and minimum air temperatures over Spain (1961–2006). Theor Appl Climatol 109(3–4):605–626
Robock A (2000) Volcanic eruptions and climate. Rev Geophys 38(2):191–219
Romanou AB, Liepert B, Schmidt GA, Rossow WB, Ruedy RA, Zhang Y (2007) 20th century changes in surface solar irradiance in simulations and observations. Geophys Res Lett 34(5):89–103. https://doi.org/10.1029/2006GL028356
Salinger MJ, Griffiths GM (2001) Trends in New Zealand daily temperature and rainfall extremes. Int J Climatol 21(12):1437–1452
Samba G, Nganga D (2014) Minimum and maximum temperature trends in Congo-Brazzaville: 1932–2010. Atmos Clim Sci 04(3):404–430
Sanchez-Lorenzo A, Calbó J, Wild M (2012) Increasing cloud cover in the 20th century: review and new findings in Spain. Clim Past 8(4):1199–1212
Shen X, Liu B, Li G, Wu Z, Jin Y, Yu P, Zhou D (2015) Spatiotemporal change of diurnal temperature range and its relationship with sunshine duration and precipitation in China. J Geophys Res 119(23):13163–13179
Stone DA, Weaver AJ (2002) Daily maximum and minimum temperature trends in a climate model. Geophys Res Lett 29(9):70-1–70-4

Sun X, Ren G, Bhaka SA, Ren Y, You Q, Zhan Y, Xu Y, Rajbhandari R (2017a) Changes in extreme temperature events over the Hindu Kush Himalaya during 1961–2015. Adv Clim Change Res 8(3):157–165

Sun X, Ren G, Xu W, Li Q, Ren Y (2017b) Global land-surface air temperature change based on the new CMA GLSAT data set. Sci Bull 62(4):236–238

Sun X, Ren G, Ren Y, Fang Y, Liu Y, Xue X, Zhang P (2017c) A remarkable climate warming hiatus over Northeast China since 1998. Theor Appl Climatol. https://doi.org/10.1007/s00704-017-2205-7

Thorne PW, Donat MG, Dunn RJH, Dunn H, Williams CN, Alexander LV, Caesar J, Durre I, Harris I, Hausfather Z, Jones PD, Menne MJ, Rohde R, Vose RS, Davy R, Klein-Tank AMG, Lawrimore JH, Peterson TC, Rennie JJ (2016) Reassessing changes in diurnal temperature range: intercomparison and evaluation of existing global data set estimates. J Geophys Res. https://doi.org/10.1002/2015JD024584

Vose RS, Easterling DR, Gyron G (2005) Maximum and minimum temperature trends for the globe: an update through 2004. Geophys Res Lett. https://doi.org/10.1029/2005GL024379

Wang K, Dickinson RE (2013) Contribution of solar radiation to decadal temperature variability over land. Proc Natl Acad Sci USA 110(37):14877–14882

Wang K, Ye H, Chen F, Xiong Y, Wang C (2012) Urbanization effect on the diurnal temperature range: different roles under solar dimming and brightening. J Clim 25(3):1022–1027

Wang H, Hao Z, Zheng J (2014) Temporal and spatial distribution characteristics of strong volcanic eruption in 1750–2010. Acta Geogr Sin 69(1):134–140 **(in Chinese)**

Warren SG, Eastman RM, Hahn CJ (2007) A survey of changes in cloud cover and cloud types over land from surface. J Clim 20:717–738

Wild M (2008) Decadal changes in surface radiative fluxes and their importance in the context of global climate change. In: Climate Variability and Extremes During the Past 100 Years. Adv. Global Change Res. Ser. Springer, New York

Wild M (2009) How well do IPCC-AR4/CMIP3 climate models simulate global dimming/brightening and twentieth-century daytime and nighttime warming? J Geophys Res 114:D00D11. https://doi.org/10.1029/2008JD011372

Wild M, Gilgen H, Roesch A, Ohmura A, Long CN, Dutton EG, Forgan B, Kallis A, Russak V, Tsvetkov A (2005) From dimming to brightening: decadal changes in solar radiation at Earth's surface. Science 308(5723):847–850

Wild M, Ohmura A, Makowski K (2007) Impact of global dimming and brightening on global warming. Geophys Res Lett 34(4):545–559

Xia X (2010) Spatiotemporal changes in sunshine duration and cloud amount as well as their relationship in China during 1954–2005. J Geophys Res Atmos 115:D00K06. https://doi.org/10.1029/2009JD012879

Xu W, Li Q, Jones P, Wang X, Trewin B, Yang S, Zhu C, Zhai P, Wang J, Vincent L (2017) A new integrated and homogenized global monthly land surface air temperature dataset for the period since 1900. Clim Dyn. https://doi.org/10.1007/s00382-017-3755-1

Yang S, Xu W, Xu Y, Li Q (2016) Development of a global historic monthly mean precipitation dataset. J Meteorol Res 30(2):217–231

Zhai P, Pan X (2003) Trends in temperature extremes during 1951–1999 in China. Geophys Res Lett 30(17):169–172

Zhan YJ, Ren GY, Yang S (2018) Change in precipitation over Asian continent from 1901 to 2016 based on a new multi-source dataset. Clim Res. https://doi.org/10.3354/cr01523

Zhang X, Vincent L, Hogg W, AinNiitsoo (2000) Temperature and precipitation trends in Canada during the 20th century. Atmosphere 38(3):395–429

Zhou L, Hansen JE (2004) Evidence for a significant urbanization effect on climate in China. Proc Natl Acad Sci USA 101(26):9540–9544

Zhou Y, Ren G (2011) Change in extreme temperature event frequency over mainland China, 1961–2008. Clim Res 50(1–2):125–139

Zhou L, Dickinson R, Dirmeyer P, Chen H, Dai Y, Tian Y (2008) Asymmetric response of maximum and minimum temperatures to soil emissivity change over the Northern African Sahel in a GCM. Geophys Res Lett 35(5):1–6. https://doi.org/10.1029/2007GL032953

Zhou L, Dickinson RE, Dirmeyer P, Dai A, Min SK (2009) Spatiotemporal patterns of changes in maximum and minimum temperatures in multi-model simulations. Geophys Res Lett 36:L02702. https://doi.org/10.1029/2008GL036141

Earth's Future

RESEARCH ARTICLE
10.1029/2018EF000963

Key Points:
- Higher global warmings correspond to more heat wave days, longer heat wave seasons, and hotter hottest day temperature in China
- The frequencies of extremes in the heat wave metrics increases rapidly with warming while the magnitudes increase more linearly
- Risk ratio is larger for rarer extreme heat waves at the same global warming level

Correspondence to:
Y. Sun,
sunying@cma.gov.cn

Citation:
Sun, Y., Hu, T., & Zhang, X. (2018). Substantial increase in heat wave risks in China in a future warmer world. *Earth's Future*, *6*, 1528–1538. https://doi.org/10.1029/2018EF000963

Received 15 JUN 2018
Accepted 17 OCT 2018
Accepted article online 19 OCT 2018
Published online 5 NOV 2018

©2018. The Authors.
This is an open access article under the terms of the Creative Commons Attribution-NonCommercial-NoDerivs License, which permits use and distribution in any medium, provided the original work is properly cited, the use is non-commercial and no modifications or adaptations are made.

Substantial Increase in Heat Wave Risks in China in a Future Warmer World

Ying Sun[1,2], Ting Hu[1], and Xuebin Zhang[3]

[1]National Climate Center, Laboratory for Climate Studies, China Meteorological Administration, Beijing, China, [2]Collaborative Innovation Center on Forecast and Evaluation of Meteorological Disasters, Nanjing University of Information Science and Technology, Nanjing, China, [3]Climate Research Division, Environment and Climate Change Canada, Toronto, Ontario, Canada

Abstract Increases in the frequency and intensity of heat waves have serious impacts on human health, agriculture, energy and infrastructure. Here we use three simple metrics including the number of heat wave days, the length of heat wave season, and the annual hottest day temperature to characterize future changes in heat wave severity in China, based on large ensemble simulations conducted with the Canadian Earth System Model Version 2 (CanESM2) in the context of emergency preparedness. A heat wave day is defined as a day with daily maximum temperature reaching heat alert level (35 °C). We find that global warming is associated with more severe heat waves including more heat wave days, longer heat wave season and higher hottest day temperature, and expansion of regions impacted by heat waves. While the increase in the magnitude of extremes in heat wave metrics with global warming level is close to linear, the increase in the frequency of extremes is much faster. For example, the historically hottest summer in 2013 in Eastern China, which occurs about one in 5 years in the 2013 climate, is projected to become more frequent than one in 2 years under 1.5 °C global warming and almost every year would be worse than 2013 under 2 °C warming. Additionally, the increase in the frequency of the extreme events is larger for rarer extremes. The frequencies for once-in-5-year, once-in-10-year, and once-in-50-year events increase by 2.5, 3.5, and 5.5 times under 1.5 °C global warming, respectively.

Plain Language Summary Heat waves have serious impacts on human health, agriculture, energy, and infrastructure. Though a few studies have investigated the future changes in heat waves in China, the heat waves defined in those studies are seldom of direct relevance to emergency preparedness. Here we study changes in heat wave days that are defined as daily maximum temperature above 35 °C, a threshold for issuing a heat alert according to China's national Standards. We examine three simple metrics including the annual number of heat wave days, the length of heat wave season, and the annual hottest day temperature based on large ensemble simulations of CanESM2. We find that global warming is associated with more severe heat waves including more heat wave days, longer heat wave season, higher hottest day temperature, and expansion of regions impacted by heat waves. The increase in the heat wave metrics with global warming level is close to linear, while the increase in the frequency of extremes in these metrics is much faster. For example, the once-in-5-year event in the current climate, with a magnitude of the historically hottest summer in 2013 in Eastern China, is projected to become more frequent, to become a once-in-2-year event under 1.5 °C global warming and every year event under 2 °C global warming.

1. Introduction

Extreme heat can have significant adverse effect in many aspects of human and natural systems. It affects human health, reduces labor capacity and productivity of exposed workers, damages infrastructures, and decreases crop yields (Steffen et al., 2014). For example, heat waves are associated with excess deaths in many Chinese cities (Gao et al., 2015; Ma et al., 2015; Zhang et al., 2016). Mortality increases shortly after temperature exceeds a certain level (Gao et al., 2015). During the record-breaking 2013 heat wave in Eastern China, many cities reported excess deaths, especially in the female and elderly people (Bai et al., 2014; X. Sun, Sun, et al., 2014). The 2013 heat wave also caused substantial economic and societal impacts. The estimated direct economic losses from the accompanying drought are 59 billion RMB (Hou et al., 2014).

Because of warming, the hottest summers appear to have clustered in recent years. The five hottest summers in Eastern China between 1950s (when a systematic meteorological observing system was established) and

2013 had all occurred after 2000 and in 2013, 2007, 2000, 2010, and 2011 (Y. Sun, Zhang, et al., 2014). Record daily maximum temperature broke successively in 2013 and then in 2016 and 2017 at many stations in Eastern China (China Meteorological Administration, 2017, 2018). As of writing, the summer of 2018 seems to be another very hot summer (though the observations are still incomplete). The warming observed in China can be attributed to human-induced emission of greenhouse gases (Lu et al., 2016; Y. Sun et al., 2016; Yin et al., 2017), exacerbated by urbanization (Y. Sun et al., 2016). As warming is projected to continue (Stocker et al., 2013) and irreversible (Solomon et al., 2009), it is important to understand how heat waves may change in the future. Q. Sun et al. (2017) examined anthropogenic influence on the probability of extreme heat waves in China. They found that the likelihood of the strongest heat wave in observational record recurring across more than half China would increase by tenfold in the late 21st century under the moderate Representative Concentration Pathway 4.5 scenario (Stocker et al., 2013). They used the Heat Wave Magnitude Index (Russo et al., 2014) to characterize the severity of heat waves. The Heat Wave Magnitude Index is defined based on number of days in which daily maximum temperature exceeds a relative threshold (90th percentile over a base period). While heat wave defined based on relative threshold has its own utility and importance in characterizing hot events across all seasons (see also Perkins & Alexander, 2013; Zhang et al., 2011), its link to impact is difficult to decipher because of difficulties in relating the relative temperature thresholds to impacts.

Like in many countries, China's meteorological services issue heat alerts if daily maximum temperature is predicted to exceed certain high values. China National Standards GB/T 27962-2011 uses criteria for heat alert based on maximum daily temperature. A yellow heat alert is issued if maximum daily temperature is predicted to be above 35 °C over three consecutive days. An orange or a red heat alert is issued respectively if maximum daily temperature is predicted to be above 37 °C or above 40 °C within 24 hr. Here we examine how some simple metrics of severity of heat waves that are relevant to impacts and emergency preparedness might change under different global warming levels. We consider the number of days when daily maximum temperature exceeds 35 °C within a year and the time period in the year when those days occur. We believe such knowledge is useful when assessing future climate change impacts and when developing mitigation measures.

2. Data and Method

2.1. Observational and Model Data

We use the gridded daily maximum temperature available from the China National Meteorological Information Center (http://data.cma.cn/). This data set has a 0.5° × 0.5° resolution. It is based on the homogenized daily temperature data at 2,419 stations (Cao et al., 2016) interpolated using inverse distance weighting. The observing stations are sparse in the northwest and the Tibetan plateau, to avoid possible artifact due to interpolation in data sparse regions, we retain the 0.5° × 0.5° grid if there exists at least one observing station within the grid and mask the grids as missing otherwise. To make those data more comparable with climate model simulations, they are converted to 2.5° × 2.5° resolution by averaging all available 0.5° × 0.5° data within the 2.5° × 2.5° grid.

We also use daily outputs of a large ensemble simulations conducted with the Canadian Earth System Model Version 2 (CanESM2, Arora et al., 2011). This large ensemble consists of 50 simulations, each driven by historical forcing including both anthropogenic and natural external forcings for 1950–2005 and then the Representative Concentration Pathway 8.5 scenario for 2006–2100 with different initial conditions (Fyfe et al., 2017). The CanESM2 is a coupled model including four main components: an atmospheric model (CanAM4, Von Salzen et al., 2013), an ocean model (CanOM4), a terrestrial carbon model (CTEM), and an ocean carbon model (CMOC; Arora & Boer, 2010). The outputs of the CanESM2 runs are on the T63 triangular truncation (about 2.81° resolution) and are converted to 2.5° × 2.5° using inverse distance weighting. The maximum daily temperatures are used to project future heat waves. As a part of contribution to the international coupled model intercomparison project phase 5 (CMIP5), the Canadian Centre for Climate Modelling and Analysis also produced historical simulations of a five-member ensemble for 1850–2005 with the CanESM2, forced with observed anthropogenic and natural external forcings. Surface temperature data from this set of simulations for the period 1850–1900 is used to estimate CanESM2-simulated temperature for preindustrial era.

2.2. Metrics of Heat Wave Severity

We define a day as a heat wave day when daily maximum temperature is above 35 °C, as there is a potential need for issuing a heat alarm. The first instance when a heat wave day occurs in a year is said to have started a heat wave season of the year, and the last heat wave day of the year concludes the heat wave season. The total number of days spanning from the start to the end of a heat wave season is the length of heat wave season (HWL). We use HWL and the total number of heat wave days (HWD) within a heat wave season, and the annual highest maximum temperature (TXx) as three metrics to characterize severity of heat waves in a year as these can be useful parameters for emergency preparedness. To put the future projection in a historical context, we present future projection in terms of occurrence probability of the extremes of the heat wave metrics.

2.3. Bias Correction for Model Data

Model simulated temperature has bias at regional and local scales. Flato et al. (2013) reported large bias in the simulations of the GCMs participating in the CMIP5. The median biases in the seasonal and annual mean temperatures range from −3 to 1.5 °C in 26 global land areas relative to the Climate Research Unit high-resolution gridded data set (CRU TS3.10). As a heat wave day is defined based on the fixed threshold of 35 °C, this model bias hinders the proper calculation of HWD for the past and for the future. To reduce the impact of model bias on heat wave projection, we use a simple bias correction procedure by replacing the model climatological values of daily temperature with the observed climatology. We first compute the seasonal cycle of daily maximum temperature, that is, climatological values of the temperature for each calendar day, by averaging daily values over the 30-year period 1986–2015 for a window of 15 days centered on that day for every no-missing 2.5° × 2.5° grids separately. This calculation is performed for the observational data. The similar calculation is performed for each of the CanESM2 simulations, but using a 30-year period for which the modeled global mean temperature has increased the same amount as the observed global mean temperature during 1986–2015, as described in the following subsection. We then remove the modeled seasonal cycle from individual model runs and add the observed seasonal cycle to the model data to produce the bias-corrected model data for 1950–2100. The procedure only adjusts bias in the mean, not in the variability. Thus, any mismatch between the observed and simulated variabilities will remain. This bias-corrected data set is used in the subsequent heat wave estimation.

2.4. Global Warming Levels

Extremes in the current climate are fresh in people's memory and can easily be associated with impacts one is familiar with. They can serve as useful reference for impacts of future extremes. On the other hand, preindustrial climate, when human influence on the climate is negligible, is often used as a reference point for global warming in the international climate policy discussion such as the Paris agreement. For these reasons, we are interested in projected changes of current-climate extreme heat waves in the future at various global warming levels. This necessarily introduces two different reference points: the current climate and the preindustrial climate.

The CanESM2 warms slightly faster than median response by CMIP5 models (Stocker et al., 2013), with a climate sensitivity of 3 °C. Its temperature increases more rapidly than the observed warming. The modeled global mean temperature for the period 1986–2015 is 0.986 °C above its preindustrial (1850–1990) value, while the observed global mean temperature for the period 1986–2015 is only 0.686 °C above 1850–1900 average based on updated global historical gridded dataset of surface temperature HadCRUT4 (Morice et al., 2012; available at https://www.metoffice.gov.uk/hadobs/hadcrut4/). The 30-year period for which the modeled global warming is the closest to the observed warming during 1986–2015 is 1977–2006; the modeled warming is 0.685 °C. For this reason, we consider the 30-year period 1977–2006 in the simulation to be equivalent to the observed 30-year period 1986–2015 and use modeled annual cycle during 1977–2006 for bias correction described in the previous subsection. Figure 1 displays the observed and simulated annual cycles of daily maximum temperatures averaged across China. It appears that the model overestimate summer temperature and, at the same time, underestimate winter temperature. This can have implications in the characterization of heat waves defined with a fixed threshold.

We consider different global warming levels including 1.0, 1.5, 2, 3, 4, and 5 °C above the preindustrial. The 10-year periods in the simulations corresponding to these warming levels are 1995–2004 (0.983 °C), 2007–2016 (1.454 °C), 2021–2030 (1.981 °C), 2042–2051 (2.958 °C), 2061–2070 (3.978 °C), and 2079–2088 (4.980 °C),

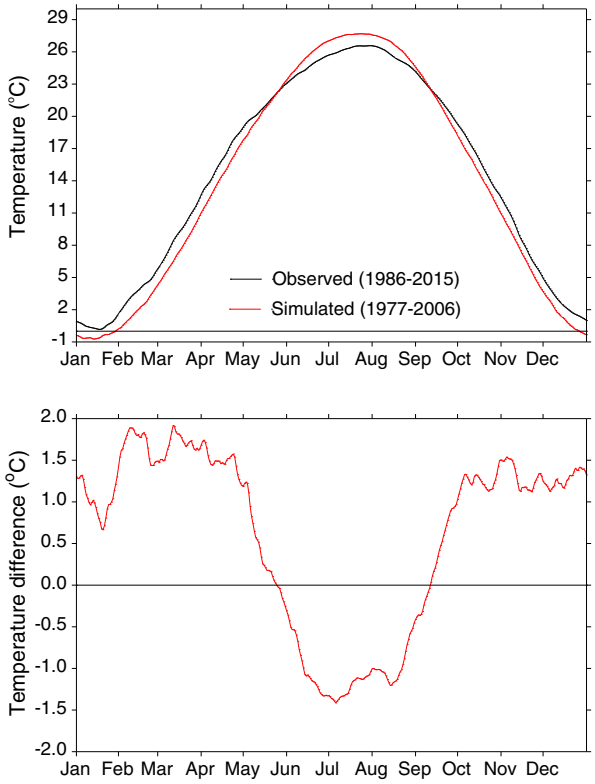

Figure 1. The observed and simulated annual cycles of daily maximum temperatures averaged over China. (upper) Observed (black line) and simulated (red line) annual cycles. (lower) The difference between the observed and simulated annual cycles; this represents the effect of bias correction on the annual cycle of modeled data.

respectively. The biased corrected daily maximum temperature data from the 50 members of the ensemble for the specific periods are pooled to estimate heat wave metrics at these warming levels. The 1 °C warming is used to represent the current climate since the annual temperature of 2016 is about 1.1 °C above preindustrial level (World Meteorological Organization, 2017).

2.5. Risk Ratio

We consider changes in the absolute values in heat wave metrics including HWD, HWL, and TXx. We also consider changes in the probability of extremes in the heat wave metrics. The changes in the probability are expressed as relative risk or risk ratio (RR) defined as $RR = p_1/p_0$. Here p_0 is the event probability in the current climate, while p_1 is the event probability in the future climate. RR is an established concept in statistics and epidemiology to describe the ratio of (low) probabilities of an event occurring (for example, developing a disease) in an exposed group to the event occurring in a nonexposed group. It is also used in the event attribution literature (National Academies of Sciences, Engineering, and Medicine, 2016). In the context of the Intergovernmental Panel on Climate Change assessment reports, risk is often associated with weather and climate events (hazard), exposure, and vulnerability (Field et al., 2012). Assuming all else is equal, that is, there is no change in the exposure and vulnerability, RR represents change in the risk due to weather and climate events.

For the purpose of illustration, we consider three arbitrary chosen levels of rarity of extremes, including events that occur once in 5, 10, and 50 years. Thus, p_0 is fixed to be 0.2, 0.1, and 0.02. To provide a perspective for such events, the 2013 summer mean temperature in Eastern China was the historical record at the time. Y. Sun, Zhang, et al. (2014) estimated that this particular event has a return period of about 5 years in the climate of 2013. That is, the once-in-5-year event in the current climate is about the historically worst event in the region.

Different methods may be used to estimate probabilities. A probability distribution is often used to fit the data if a particular form of the distribution can be assumed. For example, a generalized extreme value distribution is routinely used to fit extreme values such as annual maximum daily temperatures (Kharin et al., 2013, 2018). While TXx may follow an extreme value distribution, there is no a known form of distribution for other two metrics HWD and HWL. For simplicity and consistency among all three metrics, we use an empirical quantile to estimate probability. This is justified as the probabilities of the events with a maximum of 50-year return period we estimate are well constrained by the relatively large data sample (of a size of 500). The empirical quantile uses the formula $P = (m - 0.31)/(N + 0.38)$. This was introduced by Beard (1943) and detailed in Jenkinson (1977). See also Bonsal et al. (2001) for an example of its application. Here N is the sample size, and the P is the probability that a random value is less than or equal to the value ranked m in ascending order. The return levels of number of HWD, the HWL, and the highest temperature for 5-, 10-, and 50-year return periods in the current climate are estimated based on 500 years of data from the 50 simulations at 1 °C warming level, that is, for the 1995–2004 period. The probabilities of these return levels in a future climate at different warming levels, p_1, are estimated based on the data corresponding to the particular warming level. Uncertainty in RR estimates is determined using a bootstrap procedure. Here we first draw fifty 10-year samples from the 50 runs for the current climate, with replacement. We then estimate a set of return levels. This process is repeated for 500 times, obtaining 500 sets of return levels for the current climate. We then draw fifty 10-year samples from the 50 runs at a future warming level. We then obtain a set of p_1 corresponding to each of the 500 sets of the current-climate return levels. This produces 500 sets of RR values. This process is repeated for 500 times, resulting a 500 × 500 sets of RR values, from which the 5–95% uncertainty range for the future warming level is determined.

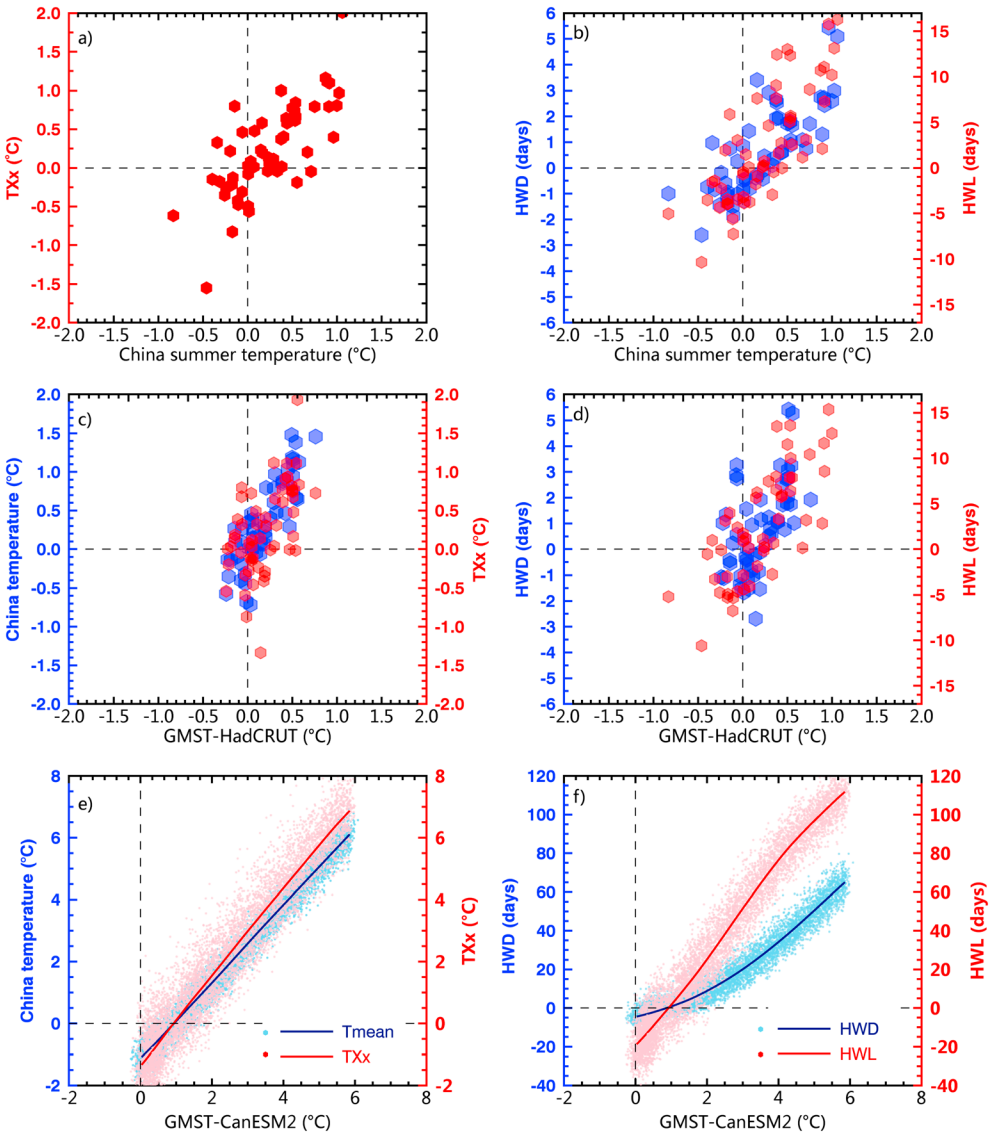

Figure 2. Relationship between heat wave metrics and China or global annual mean near-surface temperatures (GMST). (a) Scatter plot of the observed mean maximum temperature (TXx) and summer mean temperature in China. (b) Scatter plot of observed heat wave days (HWD), the length of heat wave season (HWL) and summer mean temperature in China. (c) Relationship between China annual mean temperature, TXx and GMST in observations. (d) Relationship between China annual mean HWD and HWL and GMST in observations. In panels (a)−(d), heat wave metrics TXx, HWD, and HWL are averaged over grids with at least five heat wave days during 2006–2015 in the observations. All values are anomalies relative to 1961–1990 mean. (e) Relationship between China annual mean temperature, TXx and GMST in Canadian Earth System Model Version 2 (CanESM2) simulations. (f) Relationship between China annual mean HWD and HWL and GMST in CanESM2 simulations. In panels (e) and (f), heat wave metrics TXx, HWD, and HWL are averaged over grids with at least 250 heat wave days in the 50 runs for the current climate. China annual mean temperature and heat wave metrics are anomalies relative to the current climate while GMST is relative to the preindustrial level. Small dots represent values from individual simulations, while solid lines are Lowess smoothing lines.

3. Results

3.1. Global Warming Affects Heat Wave Metrics

National average values for TXx, HWD, and HWL in the observations are computed by averaging available values over a region with heat wave days observed. The region consists of grid boxes that have at least five HWD in the last 10-year of the observational data (2006–2015). Mean temperature over China is the average across all 2.5 × 2.5 grid boxes covering China. As shown in Figures 2a and 2b, there is a clear, near-linear

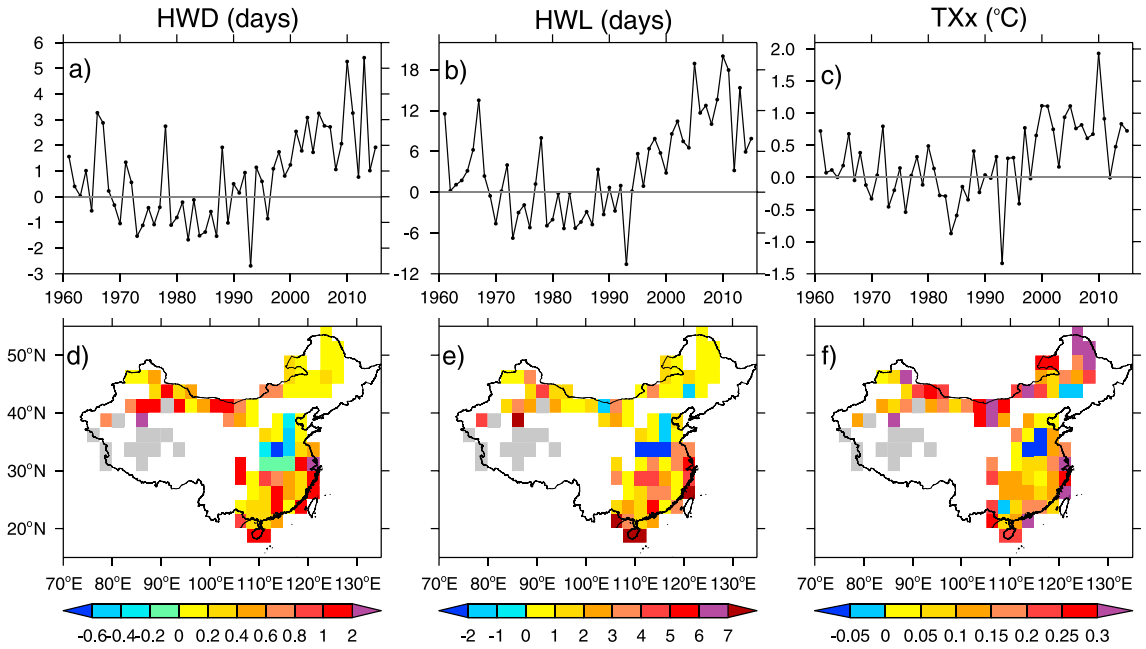

Figure 3. Observed heat wave days (HWD), heat wave season (HWL), and maximum temperature (TXx) anomalies (relative to 1961–1990 mean) and their long-term trends. The top panel shows time series of HWD, HWL, and TXx for China national averages. The lower panel displays the linear trends of HWD, HWL, and TXx anomalies during 1961–2015. Grids without observational data to bias correct model simulations are marked gray. White areas indicate regions with less than five heat wave days in the 2006–2015 climate. Time series are computed over the colored regions, their units are in days for HWD and HWL and in degrees Celsius for TXx. Units for the linear trends are in days per decade for HWD and HWL and in degrees Celsius per decade for TXx.

relationship between summer average temperature and average TXx, HWD, and HWL in China. The correlation coefficients between China summer mean temperature and HWD, HWL, and TXx are 0.78, 0.78, and 0.74, respectively. Higher summer mean temperature is associated with hotter TXx, and higher number of HWD and longer HWL. This is consistent with findings of Y. Sun, Zhang, et al. (2014) for Eastern China. Warming since 1960s in China (Y. Sun et al., 2016) is associated with more frequent HWD, longer heat wave seasons, and higher TXx and over most areas in Eastern China and Northwestern China (Figures 3d−3f). The changes in HWD, HWL, and TXx during 1961–2015 are about 2.7 days, 12.0 days, and 0.9 °C, respectively (Figures 3a−3c). Observed increase of annual mean temperature over China tracks well with the increase of global temperature albeit at a higher rate (Figure 2c), perhaps due to different land-sea thermal heating and the amplification of various local feedback processes. Changes in the observed heat wave metrics also track well with the observed global temperature change (Figures 2c and 2d).

As model grid boxes with HWD are not identical to those in the observations or among 50 simulations and as area with heat wave expands in the future, national average values for TXx, HWD, and HWL in the bias-corrected model data are computed over a fixed region for all warming levels. This region consists of grid boxes with at least 250 HWD in the 50 runs at 1 °C warming level (i.e., 1995–2004). As in the observations, simulated increase of annual mean temperature over China and changes in heat wave metrics tracks well with the simulated global temperature increase (Figures 2e and 2f). A 1 °C increase in GMST corresponds to 1.6 °C increase in China mean temperature. It is thus clear that global warming is associated with more HWD, longer heat wave seasons, and hotter hottest summer temperatures in China. It is noted that, in the simulations, both HWD and HWL increases with GMST at a rate faster than a linear increase, indicating accelerated worsening of heat wave at higher warming levels.

3.2. Warming Results in Expansion of Heat Wave-Affected Areas

As a large country with diverse climates, China does not experience heat wave everywhere. In fact, a large portion of the country has never experienced a heat wave day (Figures 3d−3f). Warming will result in an expansion of areas being affected by heat wave, with larger expansion corresponding to higher global warming levels (Figure 4). Regions that experienced heat wave will see more HWD, longer heat wave seasons with

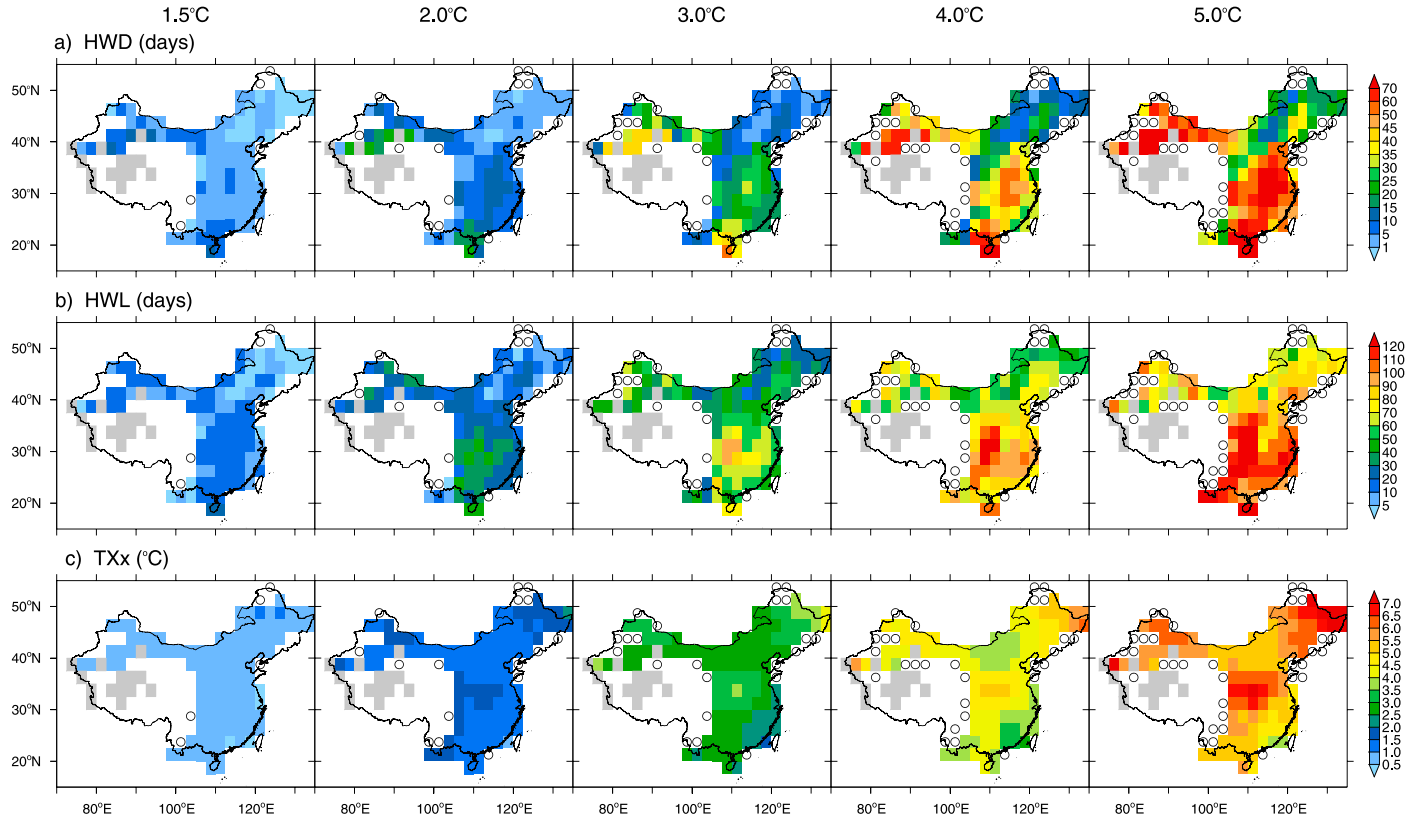

Figure 4. Projected changes in three heat wave metrics under the 1.5, 2, 3, 4, and 5 °C global warming levels. The top (a), middle (b), and lower (c) panels display results for heat wave days (HWD), heat wave season (HWL), and maximum temperature (TXx), respectively. The projected changes are relative to the current climate. Grids without sufficient observational data are marked gray. White areas indicate regions with less than one heat wave day per 2 years in the current climate. Circles mark grid boxes where a heat wave day emerges in the warmer climates.

earlier start and later end dates (Figure 5), and hotter extreme temperatures. For example, in Eastern China, as much as 10 additional HWD can be expected in Eastern China even under 1.5 °C global warming. In the same region and under the same warming level, heat wave season can also extend by as many as 20 days, with the start date as early as 10 days and end date as late as 10 days. Higher global warming levels will obviously make heat wave much worse, bringing significant challenges to emergency preparedness. Additionally, what used to be a seasonal phenomenon can become a year around event. In the current climate, no parts of China experience a heat wave year around. In the future warmer climates, heat wave can occur in most of time in the year. Some regions in Eastern China are projected to have as many as 232 HWD and as long as 365 days of heat wave season or effectively a year-long heat wave season when the global mean temperature rises by 5.5 °C.

3.3. Probability Distributions of Heat Wave Metrics Change in the Future

Figure 6 displays the histograms (with kernel smoothing) of heat wave metrics under different global warming levels. The metrics are national averages over the regions experiencing heat waves in the current climate (i.e., there are at least 250 HWD in the 50 runs for 1995–2004). The distribution of HWD shifts toward right and also spreads wider, indicating an increase in both the mean and variability of the number of HWD with warming. The estimated median values and their corresponding 5–95% range of HWD are 9.2 days (5.2–15.6 days), 12.6 days (8.0–19.9 days), 17.4 days (10.4–25.8 days), 28.0 days (20.2–38.1 days), 42.6 days (31.8–53.7 days), and 58.4 days (49.1–70.2 days) for the current climate and under the 1.5, 2, 3, 4, and 5 °C global warming levels. Changes in the probability distribution of HWL has similar pattern, shifting rightward and also spreading wider with global warming. There is an exception, however. As global temperature increase reaches to 4 °C, the probability distribution in HWL becomes narrower, indicating a saturation of heat wave season in parts of the country, that is, heat wave can occur any day of the year once global warming level reaches

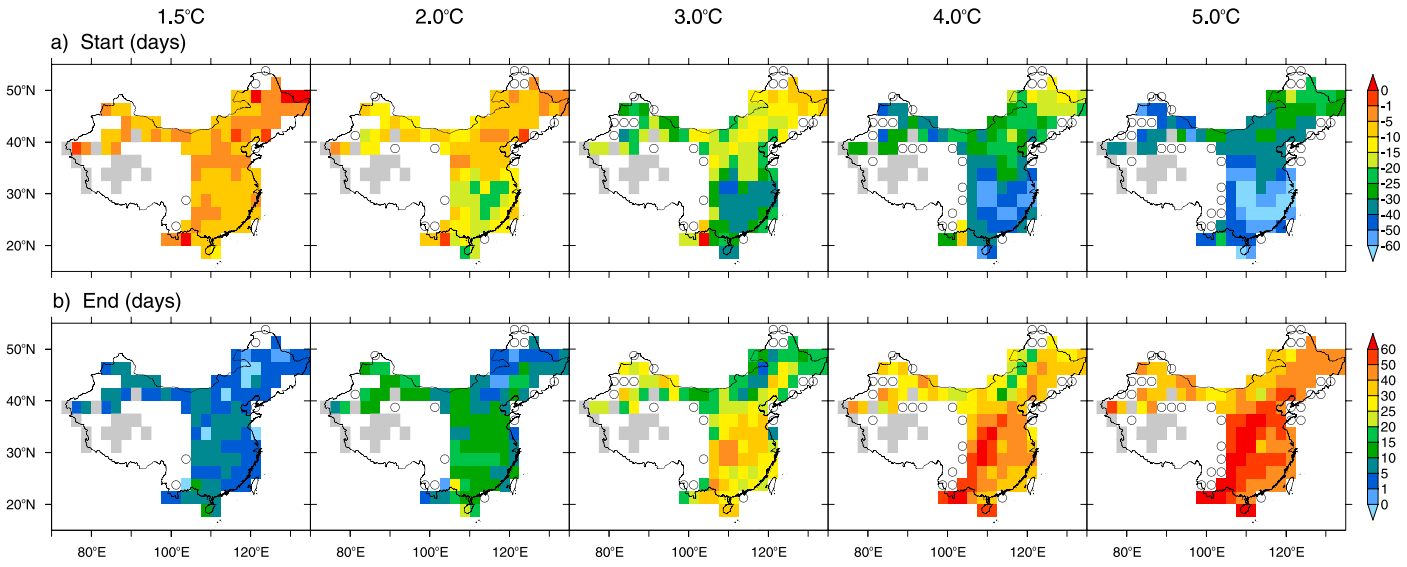

Figure 5. Same as Figure 4 but for the changes in the starting (a) and ending (b) dates of heat wave season.

4 °C. The estimated median values and their corresponding 5–95% range of HWL are 42.0 days (25.5–59.1 days), 53.0 days (36.1–69.7 days), 65.6 days (45.0–83.3 days), 92.3 days (74.3–109.7 days), 117.2 days (101.8–132.7 days), and 137.9 days (125.2–149.4 days) for the current climate and under the 1.5, 2, 3, 4, and 5 °C global warming levels. The main feature of changes in the probability distribution of TXx is the shift toward right; there is also small change in the variability. The estimated median values and their corresponding 5–95% range of TXx are 36.9 °C (35.6–38.3 °C), 37.7 °C (36.5–39.1 °C), 38.3 °C (37.0–39.6 °C), 39.8 °C (38.6–41.1 °C), 41.2 °C (40.1–42.5 °C), and 42.6 °C (41.6–43.7 °C) for the current climate and under the 1.5, 2, 3, 4, and 5 °C global warming levels. The median values of TXx increase almost linearly with global warming level, although at a faster rate. It should be noted that while the median values of TXx increases with global warming linearly, changes in the probabilities of extreme TXx does not. As it is known that a small change in the mean can result in large changes in the occurrence of extremes (Katz & Brown, 1992), RRs associated with these shifts are large, with a much larger RR for rarer events as discussed in Kharin et al. (2018) and as we will see in the next subsection.

3.4. Rarer Events are Associated With Larger RR

Figure 7 shows the RR of three heat wave metrics under different global warming levels for events at three rarity levels with return periods of 5, 10, and 50 years in the current climate. Substantial increase in the

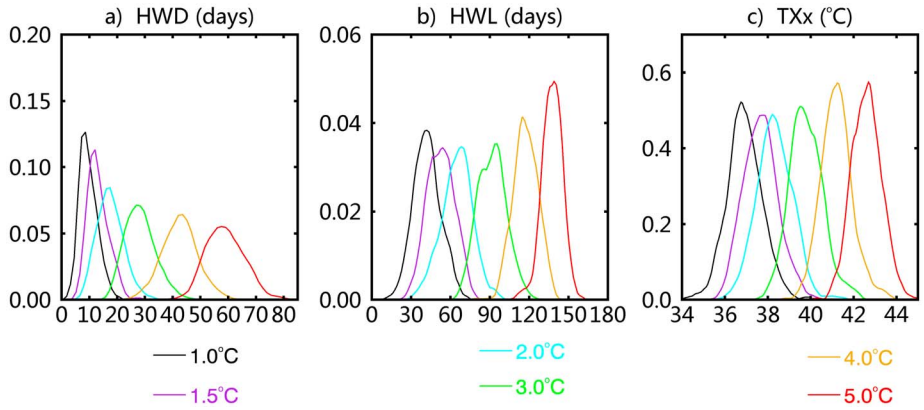

Figure 6. Smoothed histogram for (a) heat wave days (HWD; days), (b) length of heat wave season (HWL; days), and (c) maximum temperature (TXx; °C) as simulated by Canadian Earth System Model Version 2 large ensemble. Values are computed and averaged over the grids in which there was at least one heat wave day per 2 years in the current climate.

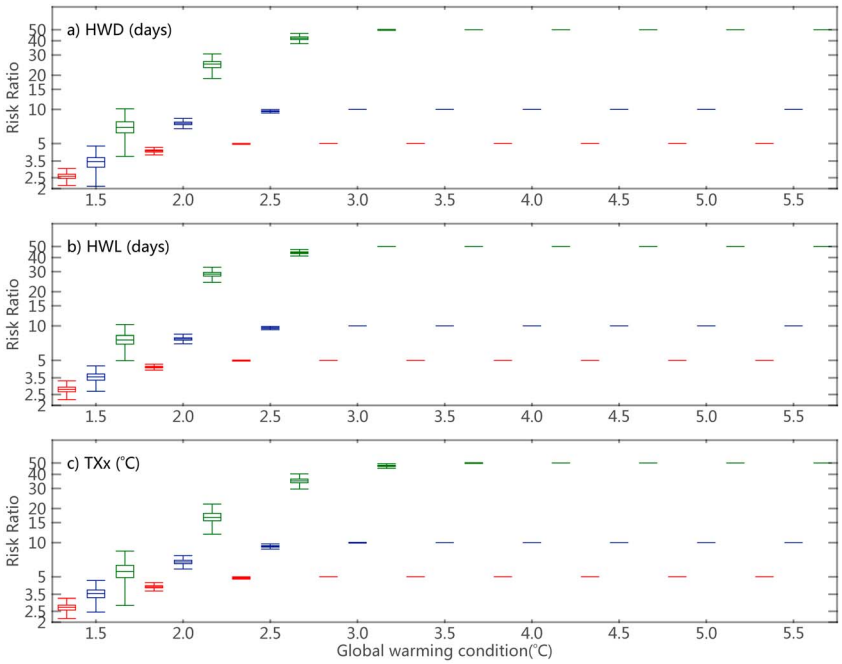

Figure 7. Box plots of risk ratio for extremes of heat wave metrics with 5-year (red), 10-year (blue), and 50-year (green) return periods in the 1995–2004 climate under different global warming levels for (a) heat wave days (HWD; upper panel), (b) length of heat wave season (HWL; middle panel), and (c) maximum temperature (TXx; bottom panel). Values are computed and averaged over the grids in which there is at least one heat wave day per 2 years in the current climate.

probability of occurrence of extreme heat wave metrics is projected. For example, the RR for current climate 5-year HWD under 1.5 °C global warming level is about 2.5. This means that the historically worst heat wave season such as the summer 2013 in Eastern China (Y. Sun, Zhang, et al., 2014) would have a probability of 0.5 to occur in a given year that such an event would become a usual event (every other year). Larger increase in the probabilities is associated with more extreme events. RR is about 3.5 for the 10-year HWD event and is larger than 5.5 for the 50-year HWD event. Similar pattern of change is observed for both HWL and TXx. Larger magnitude of warming is obviously associated with larger RR. The RR is saturated at 5 and 10 for the 5-year and 10-year events at the 3 °C global warming level. This means that heat wave metrics including the number of HWD, the HWLs, and the hottest day temperature in almost every year would be worse than the worst in the 1995–2004 climate (1 °C warming), when global temperature increases above 3 °C. At the 4 °C warming level, almost every year would be worse than the current 50-year event.

4. Conclusion and Discussions

We have examined projected changes in three simple heat wave metrics representing the frequency and intensity of heat wave in China under different global warming levels in the large ensemble simulations conducted with CanESM2. We define a day as a heat wave day when daily maximum temperature is above 35 °C as this situation would potentially call for issuing a heat wave alert in China. The metrics we consider include the number of HWD in a year, the HWL, and the highest temperature of the year. We find that warming is associated with more HWD, longer heat wave seasons, and hotter hottest day temperature, with larger changes associated with stronger warming. Additionally, warming will also result in HWD to appear in regions or in the part of year where a heat wave day never occurred before. While the numerical values of the heat wave metrics increase more linearly with the increase in global mean temperature, the increase in the probability of extreme heat wave metrics is much faster, consistent with the understanding that a small change in the mean can result in a large change in (the occurrence of) extreme events. Each additional degree global warming is associated with an accelerated increase in extreme heat wave risks. Event of 5-year return period such as the historically hottest summer in 2013 in Eastern China is projected to become norm under 1.5 °C global warming. Under the 2 °C global warming, heat waves in almost every year would be worse

than the worst in the current climate. A larger RR is associated with rarer extreme heat waves. For example, the risk of the current climate 5-year event is projected to increase by 2.5 times under 1.5 °C global warming, it increases by more than 3.5 times for the 10-year event and about 5.5 times for the 50-year event. Heat wave occurrence is projected to be a year-around event in some regions of Eastern China when the global temperature rises by 5.5 °C.

Our study also suggests that any level of less warming would make a difference especially for extreme heat waves, indicating that any mitigation effort would make a difference. The imminent danger of severe heat waves due to warming is not sufficiently appreciated and calls for rapid adaptation action.

Acknowledgments
We thank two anonymous reviewers for their helpful suggestions and comments. This study was supported by the National Key R&D Program of China (2018YFA0605604), the National Science Foundation of China (41675074), and Climate Change Project CCSF201805. We thank the China National Meteorological Information Center for archiving the observational data (available at http://data.cma.cn/). The CanESM2 data are available from government of Canada's open data portal https://open.canada.ca/data/en/dataset/aa7b6823-fd1e-49ff-a6fb-68076a4a477c.

References

Arora, V. K., & Boer, G. J. (2010). Uncertainties in the 20th century carbon budget associated with land use change. *Global Change Biology*, *16*(12), 3327–3348. https://doi.org/10.1111/j.1365-2486.2010.02202.x

Arora, V. K., Scinocca, J. F., Boer, G. J., Christian, J. R., Denman, K. L., Flato, G. M., et al. (2011). Carbon emission limits required to satisfy future representative concentration pathways of greenhouse gases. *Geophysical Research Letters*, *38*, L05805. https://doi.org/10.1029/2010GL046270

Bai, L., Ding, G., Gu, S., Bi, P., Su, B., Qin, D., et al. (2014). The effects of summer temperature and heat waves on heat-related illness in a coastal city of China, 2011–2013. *Environmental Research*, *132*, 212–219. https://doi.org/10.1016/j.envres.2014.04.002

Beard, L. R. (1943). Statistical analysis in hydrology. *Transactions of the American Society of Civil Engineers*, *108*, 1110–1160.

Bonsal, B. R., Zhang, X., Vincent, L. A., & Hogg, W. D. (2001). Characteristics of daily and extreme temperatures over Canada. *Journal of Climate*, *14*(9), 1959–1976.

Cao, L., Zhu, Y., Tang, G., Yuan, F., & Yan, Z. (2016). Climatic warming in China according to a homogenized data set from 2419 stations. *International Journal of Climatology*, *36*(13), 4384–4392. https://doi.org/10.1002/joc.4639

China National Standards (2011). Graphical symbols for meteorological disaster warning signal icon, GB/T 27962–2011.

China Meteorological Administration (2017). *China climate bulletin 2016* (p. 50). Beijing, China: China Meteorological Administration.

China Meteorological Administration (2018). *China climate bulletin 2017* (p. 50). Beijing, China: China Meteorological Administration.

Field, C. B., Barros, V., Stocker, T. F., Qin, D., Dokken, D. J., Ebi, K. L., et al. (Eds.). (2012). Managing the risks of extreme events and disasters to advance climate change adaptation. A special report of Working Groups I and II of the Intergovernmental Panel on Climate Change. Cambridge, United Kingdom and New York, NY: Cambridge University Press.

Flato, G., Marotzke, J., Abiodun, B., Braconnot, P., Chou, S. C., Collins, W., et al. (2013). Evaluation of climate models. In T. F. Stocker, D. Qin, G. K. Plattner, M. Tignor, S. K. Allen, J. Boschung, et al. (Eds.), *Climate change 2013: The physical science basis. Contribution of Working Group I to the Fifth Assessment Report of the Intergovernmental Panel on Climate Change* (pp. 741–866). Cambridge, United Kingdom and New York, NY: Cambridge University Press.

Fyfe, J. C., Derksen, C., Mudryk, L., Flato, G. M., Santer, B. D., Swart, N. C., et al. (2017). Large near-term projected snowpack loss over the western United States. *Nature Communications*, *8*, 14996. https://doi.org/10.1038/ncomms14996

Gao, J., Sun, Y., Liu, Q., Zhou, M., Lu, Y., & Li, L. (2015). Impact of extreme high temperature on mortality and regional level definition of heat wave: A multi-city study in China. *Science of the Total Environment*, *505*, 535–544. https://doi.org/10.1016/j.scitotenv.2014.10.028

Hou, W., Chen, Y., Li, Y., Wang, Y., Wang, Z., Zhu, X., et al. (2014). Climatic characteristics over China in 2013. *Meteorological Monthly*, *40*, 491–501.

Jenkinson, A. F. (1977). The analysis of meteorological and other geophysical extremes. *Synoptic Climatology Branch Memo*. 58, the U.K. Met. Office, Bracknell, Berkshire, United Kingdom, 41 pp.

Katz, R. W., & Brown, B. G. (1992). Extreme events in a changing climate: Variability is more important than averages. *Climatic Change*, *21*, 289–302.

Kharin, V. V., Flato, G. M., Zhang, X., Gillett, N. P., Zwiers, F., & Anderson, K. J. (2018). Risks from climate extremes change differently from 1.5 °C to 2.0 °C depending on rarity. *Earths Future*, *6*, 704–715. https://doi.org/10.1002/2018EF000813

Kharin, V. V., Zwiers, F. W., Zhang, X. B., & Hegerl, G. C. (2013). Changes in temperature and precipitation extremes in the IPCC ensemble of global coupled model simulations. *Climatic Change*, *119*(2), 345–357. https://doi.org/10.1175/JCLI4066.1

Lu, C., Sun, Y., Wan, H., Zhang, X., & Yin, H. (2016). Anthropogenic influence on the frequency of extreme temperatures in China. *Geophysical Research Letters*, *43*, 6511–6518. https://doi.org/10.1002/2016GL069296

Ma, W., Zeng, W., Zhou, M., Wang, L., Rutherford, S., Lin, H., et al. (2015). The short-term effect of heat waves on mortality and its modifiers in China: An analysis from 66 communities. *Environment International*, *75*, 103–109. https://doi.org/10.1016/j.envint.2014.11.004

Morice, C. P., Kennedy, J. J., Rayner, N. A., & Jones, P. D. (2012). Quantifying uncertainties in global and regional temperature change using an ensemble of observational estimates: The HadCRUT4 dataset. *Journal of Geophysical Research*, *117*, D08101. https://doi.org/10.1029/2011JD017187

National Academies of Sciences, Engineering, and Medicine (2016). *Attribution of extreme weather events in the context of climate change*. Washington, DC: The National Academies Press. https://doi.org/10.17226/21852

Perkins, S. E., & Alexander, L. V. (2013). On the measurement of heat waves. *Journal of Climate*, *26*(13), 4500–4517. https://doi.org/10.1175/JCLI-D-12-00383.1

Russo, S., Dosio, A., Graversen, R. G., Sillmann, J., Carrao, H., Dunbar, M. B., et al. (2014). Magnitude of extreme heat waves in present climate and their projection in a warming world. *Journal of Geophysical Research: Atmospheres*, *119*, 12,500–12,512. https://doi.org/10.1002/2014JD022098

Solomon, S., Plattner, G. K., Knutti, R., & Friedlingstein, P. (2009). Irreversible climate change due to carbon dioxide emissions. *Proceedings of the National Academy of Sciences of the United States of America*, *106*(6), 1704–1709. https://doi.org/10.1073/pnas.0812721106

Steffen, W., Hughes, L., & Perkins, S. (2014). Heatwaves: Hotter, longer, more often. The Climate Council of Australia. Retrieved from http://climatecouncil.org.au

Stocker, T. F., Qin, D., Plattner, G. K., Tignor, M., Allen, S. K., Boschung, J., et al. (Eds.) (2013). *Climate change 2013: The physical science basis. Contribution of Working Group I to the Fifth Assessment Report of the Intergovernmental Panel on Climate Change*. Cambridge, United Kingdom and New York, NY: Cambridge University Press.

Sun, Q., Miao, C., AghaKouchak, A., & Duan, Q. (2017). Unraveling anthropogenic influence on the changing risk of heat waves in China. *Geophysical Research Letters*, *44*, 5078–5085. https://doi.org/10.1002/2017GL073531

Sun, X., Sun, Q., Zhou, X., Li, X., Yang, M., Yu, A., et al. (2014). Heat wave impact on mortality in Pudong New Area, China in 2013. *Science of the Total Environment*, *493*, 789–794. https://doi.org/10.1016/j.scitotenv.2014.06.042

Sun, Y., Zhang, X., Ren, G., Zwiers, F. W., & Hu, T. (2016). Contribution of urbanization to warming in China. *Nature Climate Change*, *4*, 1082–1085. https://doi.org/10.1038/nclimate2956

Sun, Y., Zhang, X., Zwiers, F. W., Song, L., Wan, H., Hu, T., et al. (2014). Rapid increase in the risk of extreme summer heat in Eastern China. *Nature Climate Change*, *4*, 1082–1085. https://doi.org/10.1038/nclimate2410

Von Salzen, K., Scinocca, J. F., McFarlane, N. A., Li, J., Cole, J. N., Plummer, D., et al. (2013). The Canadian Fourth generation atmospheric global climate model (CanAM4)—Part I: Representation of physical processes. *Atmosphere-Ocean*, *51*(1), 104–125. https://doi.org/10.1080/07055900.2012.755610

World Meteorlogical Organization (2017). WMO statement on the state of the global climare in 2016. WMO-No. 1189, 1–28.

Yin, H., Sun, Y., Wan, H., Zhang, X., & Lu, C. (2017). Detection of anthropogenic influences on the intensity of extreme temperatures in China. *International Journal of Climatology*, *37*, 1229–1237. https://doi.org/10.1002/joc.4771

Zhang, J., Liu, S., Han, J., Zhou, L., Liu, Y., Yang, L., et al. (2016). Impact of heat waves on nonaccidental deaths in Jinan, China, and associated risk factors. *International Journal of Biometeorology*, *60*(9), 1367–1375. https://doi.org/10.1007/s00484-015-1130-7

Zhang, X., Alexander, L., Hegerl, G. C., Jones, P., Klein Tank, A., Peterson, T. C., et al. (2011). Indices for monitoring changes in extremes based on daily temperature and precipitation data. *Wiley Interdisciplinary Reviews: Climate Change*, *2*(6), 851–870. https://doi.org/10.1002/wcc.147

索南看卓, 任国玉, 贾文茜, 等. 2018. 武汉城市相对湿度气候学特征与长期变化趋势 [J]. 气候与环境研究, 23 (6): 715−724. Suonan Kanzhuo, Ren Guoyu, Jia Wenqian, et al. 2018. Climatological characteristics and long-term trend of relative humidity in Wuhan [J]. Climatic and Environmental Research (in Chinese), 23 (6): 715−724, doi:10.3878/j.issn.1006-9585.2017.17122.

武汉城市相对湿度气候学特征与长期变化趋势

索南看卓[1] 任国玉[1, 2] 贾文茜[1] 孙秀宝[3]

1 中国地质大学（武汉）大气科学系，武汉 430070
2 中国气象局国家气候中心气候研究开放实验室，北京 100081
3 南京信息工程大学大气科学学院，南京 210044

摘 要 在对相对湿度（RH）序列进行均一性检验和订正的基础上，分析了武汉 4 个城市站 RH 的气候学特征和长期变化趋势。结果表明：（1）迁站对 RH 序列引起较大非均一性偏差，其中武汉站 2010 年迁站引起的偏差达到 8%；（2）城区年平均 RH 较高，介于 75%～85%，武汉站最高；（3）每年 1～6 月城区 RH 逐渐增加，6 月达到峰值，之后缓慢减少，但季节内变化一般很小，月际间差异仅有 0.1%～2.5%，存在夏季 RH 最高，春、秋次之，冬季最低的季节性特征；（4）武汉城市区域 1961～2015 年平均 RH 总体呈长期减少趋势，线性变化趋势−0.81%/10 a，20 世纪 90 年代之后下降趋势加剧；（5）近 55 年城区春、秋、冬 3 个季节平均 RH 均呈不同程度的下降，以春季最为明显，夏季存在较为显著的上升趋势，但 1991 后年及四季均呈现显著的下降趋势。

关键词 相对湿度 资料非均一性 武汉 城市化 气候特征 长期趋势
文章编号 1006-9585（2018）06-0715-10 **中图分类号** P463.3 **文献标识码** A
doi:10.3878/j.issn.1006-9585.2017.17122

Climatological Characteristics and Long-Term Trend of Relative Humidity in Wuhan

SUONAN Kanzhuo[1], REN Guoyu[1, 2], JIA Wenqian[1], and SUN Xiubao[3]

1 *Department of Atmospheric Sciences*, *China University of Geosciences (Wuhan)*, *Wuhan* 430070
2 *Laboratory for Climate Studies*, *China Meteorological Administration, National Climate Center*, *Beijing* 100081
3 *College of Atmospheric Science*, *Nanjing University of Information Science and Technology*, *Nanjing* 210044

Abstract Based on the homogeneity test and correction of the relative humidity series, climatological characteristics and long-term trend of relative humidity in the urban area of Wuhan are analyzed. The results showed that: (1) The non-homogeneity deviation caused by relocated stations in the relative humidity series is prodigious, and the deviation caused by relocation of Wuhan station in 2010 is 8%. (2) Annual average relative humidity in the urban area of Wuhan remains high, and the values vary between 75%−85% with the highest value occurring at Wuhan station. (3) The relative humidity gradually increases from January to June, and then begins to decrease slowly after reaching its peak value in June. Monthly differences are pretty small with the values within 0.1%−2.5%. Seasonal characteristics of relative humidity in the urban area of Wuhan show that the RH is the highest in the summer and lowest in the winter during the whole year. (4) From 1961 to 2015, the average relative humidity in the urban area of Wuhan urban area exhibited a

收稿日期 2017-08-14；**网络预出版日期** 2017-11-16
作者简介 索南看卓，女，1993 年出生，硕士研究生，主要从事城市气候研究。E-mail: 1138223859@qq.com
通讯作者 任国玉，E-mail: guoyoo@cma.gov.cn
资助项目 国家自然科学基金项目 41575003
Funded by National Natural Science Foundation of China (Grant 41575003)

long-term decreasing trend, and the linear trend was accelerated after the 1990s. (5) In the past 55 years, time series of average relative humidity in the spring, autumn, and winter all show declining trends in varied degrees, of which the trend in the spring is more obvious, and a significant rising trend is found in the summer. However, the annual and seasonal means are showing a significant downward trend after 1991.

Keywords Relative humidity, Data non-uniformity, Wuhan, Urbanization, Climate characteristics, Long-term trend

1 引言

气象学中通常用空气中的实际水汽压与饱和水汽压的百分比值来表征大气的相对湿度（RH）。不同于其他大气水分参数，RH 除受到大气中实际水汽含量影响外，还受到空气的水汽潜在容纳能力影响（Peixoto and Oort，1996；盛裴轩等，2003），而后者主要取决于空气温度。RH 的高低对人体的健康和生活的舒适程度等均有较大影响，并且是降水、气温预报以及紫外线和舒适度等专业预报的主要影响因子，其大小是衡量一个地区干湿程度的标志之一（刘明春等，2012）。空气 RH 也是影响大气颗粒物浓度的主要气象因子，从而间接影响到空气质量和大气能见度（白永清等，2016）。因此，RH 的研究对城市气候和应用气候研究，以及对于水资源管理和空气污染预报预警都有重要的科学意义。

湖北省武汉市地处长江中游江汉平原，境内横贯长江和汉江两条河流，河网密布，湖泊众多，水域面积占全市土地总面积的 1/4，是我国典型的亚热带内陆湿地型特大城市。城市内湿地有利于空气 RH 增加（Saaroni and Ziv，2003），改变局地气候环境条件（汪光焘等，2005；轩春怡等，2010）。朱春阳（2015）在对武汉市三环内主城区 14 块湖泊湿地的温湿研究中发现，城市 RH 与湿地面积大小和距离湿地远近呈显著正相关关系；杨凯等（2004）研究上海市城区河流及水体周边小气候效应发现，湖泊下风向的 RH 较上风向增幅达到 10%，指出水体的面积和布局是影响小气候效应的重要因素；轩春怡等（2010）研究发现，城市水体在夏季具有降温、增湿、缓解城市热岛效应的功能，并能使其周边地区的气温和地表温度降低。目前，对武汉城区内相对湿度的气候特征，关注极少。

此外，有研究分析了半干燥区气象站的 RH 长期变化，发现近 50 年年平均和四季平均 RH 在波动中下降（靳英华等，2009）；Um et al.（2007）发现，作为韩国大城市代表观测点的首尔站，其年平均 RH 自 1905 年以后呈明显下降趋势，而选取的中等规模城镇站和乡村站 RH 减少趋势低于首尔站；城市的快速发展和城市化进程的加快也同样影响北京城市气候变化，其中城区年平均 RH 总体呈明显下降趋势，而郊区则略有上升（郑思轶和刘树华，2008；Liu et al.，2009），Yang et al.（2017）也发现，北京城区年平均相对湿度比郊区低得多，呈现出明显的所谓“干岛效应”，中心城区年平均 RH 可比郊区站低 7%～10%；甘肃武威市年平均 RH 总体呈减少趋势，并存在 6～8 a 的周期波动（刘明春等，2012）。

20 世纪 90 年代以来武汉经济发展加速，城区面积迅速扩大，不但占用了很多耕地，而且大量围湖建房，使市区湖泊面积急剧减少（余程鹏，2008）。快速城市发展及其相伴随的城区湖泊面积减小，对于城区 RH 产生了什么影响，目前还不清楚。但有研究表明，城市化致使武汉城区气候发生了显著变化，主要表现为年和四季城市热岛强度持续增强，近地面气温显著上升（陈正洪等，2005a，2007；王苗等，2015）。研究还显示，武汉市最低气温表征的热岛强度和相对湿度呈正相关，而最高气温和平均气温表征的热岛强度则与相对湿度呈现负相关（王苗等，2015），说明武汉市相对湿度年际和长期变化表现出较为复杂的特征。武汉市作为我国典型的亚热带内陆湿地型特大城市，研究其相对湿度序列变化趋势特征及其可能原因，对于深入理解城市气候不同要素之间的相互作用机理，进一步研究和评估城市气候变化对人体健康和生态系统的影响，均具有重要意义。

本文对武汉城市气象站 RH 观测资料进行了均一化处理，并利用均一化资料分析了 1961～2015 年期间年、季节 RH 的气候学特征和长期变化趋势，结果有助于加深认识武汉城市 RH 的季节变化和长期变化规律。

2 资料与方法

2.1 资料与研究区域

研究区域为武汉城区，经纬度范围为（29°58′N～

31°22′N，113°41′E～115°05′E）。1961～2015 年武汉地区逐月平均 RH 数据来自于国家气象信息中心。数据已进行了人工转自动观测的非均一性误差订正。蔡甸站的 1968 年 6、7、8 月缺测，分别以 55 年月均值补偿。为使分析结果更加可靠，选取了具有长序列观测资料，并且能够代表武汉城市的 4 个气象站，对各站点的 RH 序列重新进行非均一性检验和订正。

2.2　城市站确定

由于城市热岛效应（UHI）的影响，城市和郊区的地表温度（LST）分布通常显示为围绕城市中心的封闭等温线。因此，理论上讲可以根据具有适当间隔的等温线分布来确定 UHI 影响区域。Ren and Ren（2011）利用 MODIS（Moderate Resolution Imaging Spectroradiometer）资料在国家基本、基准站中选出不受 UHI 影响的 113 个乡村站。本文采用 Ren and Ren（2011）的方法，利用卫星遥感（RS）资料获取气象台站周围的地表亮度温度等值线，确定城市气象站的相对位置。

利用 8 d 合成的 2016 年 7 月 28 日 MOD11A2 地表亮度温度/发射率产品，其空间分辨率为 1 km，以 0.5 ℃ 等温线间隔绘制武汉地区地表亮度温度等值线分布图（图 1）。LST 的等温线间隔应反映出受 UHI 影响的城市中心到郊区的温度梯度，而且受到诸如微观形态学等局部因素的影响较小。城市环境温度场中最外圈闭合等温线可用以代表受城市热岛影响区域的边界（Winkler et al.，1981；Ren and Ren.，2011）。本文确定该日最外圈闭合等值线为

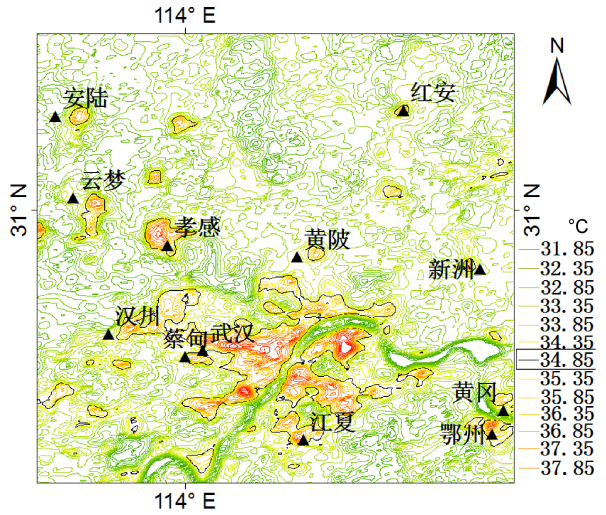

图 1　2016 年 7 月 28 日武汉地区地表亮度温度分布（单位：℃）

Fig.1　Land surface brightness temperature (℃) distribution in Wuhan area in 28 July 2016

34.85 ℃，将其作为武汉市城市地表热岛效应的界限。图 1 中，在城市地表热岛中心存在很明显的低值区，将温度高值区域分为两个部分，结合谷歌地图（Google Earth）大比例尺地图可知，长江干流和市区湖泊是影响武汉城市地表热岛空间分布的重要因素。

城市代表站的选取参照以下标准：（1）研究期间迁站次数最多 3 次（包括 1961 年），以便尽可能保证站史的简洁性（图 2）。（2）与武汉站的海拔高度差小于 50 m，避免由于高度差异带来的气温直减率影响；距离少于 30 km，保证与武汉站处于相同的大尺度环流和气候背景下。（3）在迁站过程中站点位置至少有一次包含在最外层等温闭合线以内，以保证受到城市化气候效应的影响。（4）利用 Google Earth 或土地利用资料证实站点周围微环境，排除周围水体等特殊环境的影响。其中，武汉站新旧站址受到不同微气候环境的影响，但均在上述温度闭合等值线之内，是受到城市化影响明显的一个城市代表站。

据此选择 4 个武汉城市的代表站点，即武汉站（站号 57494）、江夏站（站号 57493）、蔡甸站（站号 57489）和新洲站（站号 57492）。具体站点信息见表 1。

表 1　武汉城市站站点信息

Table 1　Information of urban stations in Wuhan

站点（站号）	站点位置		观测场海拔	1960 年后	
	经度	纬度	高度/m	迁站次数	迁站年月
武汉（57494）	114°03′E	30°36′N	23.6	2	1994 年 4 月
					2010 年 1 月
江夏（57493）	114°20′E	30°20′N	73.5	1	2006 年 1 月
蔡甸（57489）	114°00′E	30°35′N	38.4	1	1965 年 4 月
新洲（57492）	114°50′E	30°50′N	40.7	3	1976 年 9 月
					1995 年 1 月
					2014 年 1 月

2.3　非均一性订正

气候资料序列中由于迁站、更换仪器等非自然原因造成的观测记录不连续点称之为非均一性。使用未订正的数据会模糊气候变化信号，分析某地区实际发生的气候变化，应该首先检验和订正其非均一性，即均一化。

本文通过构建参考资料序列，参考 Peterson-Easterling 方法（Peterson and Easterling，1994），订正所选站点相对湿度数据序列的非均一性。年均值序列较小受到季节变率的影响，为最大程度上去除

序列中自回归过程的影响（曹丽娟和严中伟，2011），本文对武汉城市站 RH 年值序列进行非均一性检验和订正（Li et al.，2004；周雅清和任国玉，2005）。具体步骤和方法如下：

建立参考序列：为了提高对台站相对湿度序列不连续点检测的能力，构建步长为 1 的逐年差值序列，这样可以剔除序列趋势和周期影响，使其比待检原始序列变率减小。因此建立 12 个单站的年均 RH 序列之后，计算其逐年差值时间序列 D：

$$D_i = \varphi_{i+1} - \varphi_i , \quad (1)$$

其中，φ 表示 RH，i 为年份序号。

计算武汉地区待检城市站与候选参考站逐年差值序列之间的相关系数，选取相关系数最大的 5 个站作为参考站。然后利用各自相关系数的平方作为权重计算出参考时间序列：

$$D_{\text{new}} = \sum_{j=1}^{5} r_j^2 D_j , \quad (2)$$

其中，r_j^2 为第 j 个站与待检站之间的相关系数，j 为站号标记，使用逐年差值时间序列的加权方法得到的参考序列，其标准偏差接近待检站的标准偏差。最后，反算得到相对湿度参考序列。

待检序列断点确定：结合滑动 t 检验法和 M−K 检验法，对待检序列和参考序列的差值序列确定最终的不连续点，并通过台站迁站历史资料确定其合理性。如果突变点附近年份存在台站迁移，认为该突变点是属于人为影响，进行下一步的订正；否则保留原始记录。1961 年后武汉各城市站的迁站次数，时间与位置见图 2。

城市站数据订正：计算待检站序列与参考序列差值序列断点前后各五年的平均值的差值，并将其作为订正值。订正顺序是从后向前进行的，最近断点之后序列保持不变。最后得到 4 个武汉城市站的均一化 RH 序列。表 2 是对各站相对湿度序列的订正次数，对应的迁站时间和订正值。

2.4 统计方法

本文使用 4 个城市站的逐月 RH 数据，统计 1961～2015 年武汉城市区域平均逐月和四季平均相对湿度，在此基础上分析多年平均气候学特征。以 3、4、5 月的均值代表春季，6、7、8 月的均值代表夏季，9、10、11 月的均值代表秋季，12、1、2 月的均值代表冬季。计算订正后各个站和 4 站平均的逐年逐月、季节平均 RH 距平及距平百分率。以 1981～2010 年（30 年）作为参考期计算距平值和距平百分率。线性趋势通过最小二乘法获得，用 t 检验方法确认线性趋势的显著性水平。

表 2 各站检测出的人为不连续点及其对应的迁站时间、订正次数和订正值

Table 2 Detected man-made discontinuities in the RH series for each station, and corresponding relocation time and numbers of revision and revised values

站点	t 检验断点年份	M−K 检验断点年份	对应迁站时间	订正次数	订正值
武汉	无	2013 年*、1969 年	2010 年 1 月	1	8.60%
江夏	1965 年、1975 年、2007 年*	1983 年	2006 年 1 月	1	−1.13%
蔡甸	无	1993 年	无	0	无
新洲	1965 年、1975 年*、2010 年	1985 年	1976 年 9 月	1	−5.34%

* 表示合理断点年份。

3 结果与分析

3.1 相对湿度的气候学特征

近 55 年武汉市 RH 的逐月多年平均（图 3）显示，武汉市各月平均 RH 均大于 75%。RH 在 1～6 月逐渐增加，并且在 6 月达到峰值，可达 80%以上，随后缓慢减小，于 12 月下降至全年最低值。各月间的差异并不明显，仅在 0.1%～2.5%，这与武汉市雨季的进退有着密切的联系。各月 RH 的分布带有季节性特征，即春秋低于夏季，但高于冬季。

55 年武汉年均 RH 为 84.73%，新洲为 75.98%，江夏为 76.19%，蔡甸为 78.01%，武汉站年平均 RH 值明显高于其余 3 个城市站。图 4 给出了 1961～2015 年不同时间段 4 个武汉城市站各季节 RH 的多年平均值。1961～2015 年内（图 4c）总体上呈现出夏季 RH 最高，春、秋次之，冬季最低的季节性特征，与逐月多年平均 RH 分布相似（图 3）。此外，武汉站各个季节的 RH 也明显高于其余 3 个站，以 1961～1989 年期间最为明显，而近 35 年的武汉站与 3 个站的差异变小。对于各站各季节之间 RH 的差异，理论上可以用理想气体状态方程 $PV=nRT$ 解释。以夏季为例，在气体分子数 n、理想气体常数 R 和气体体积 V 不变的条件下，夏季温度 T 高，饱和水汽压 P 随温度的升高而增大，由于夏季降水量充沛，水分蒸发强，水汽容易达到饱和，导致实际水汽压的增大，进而使得夏季的 RH 值偏高。

1961～2015 年不同时间段的 RH 平均值显示

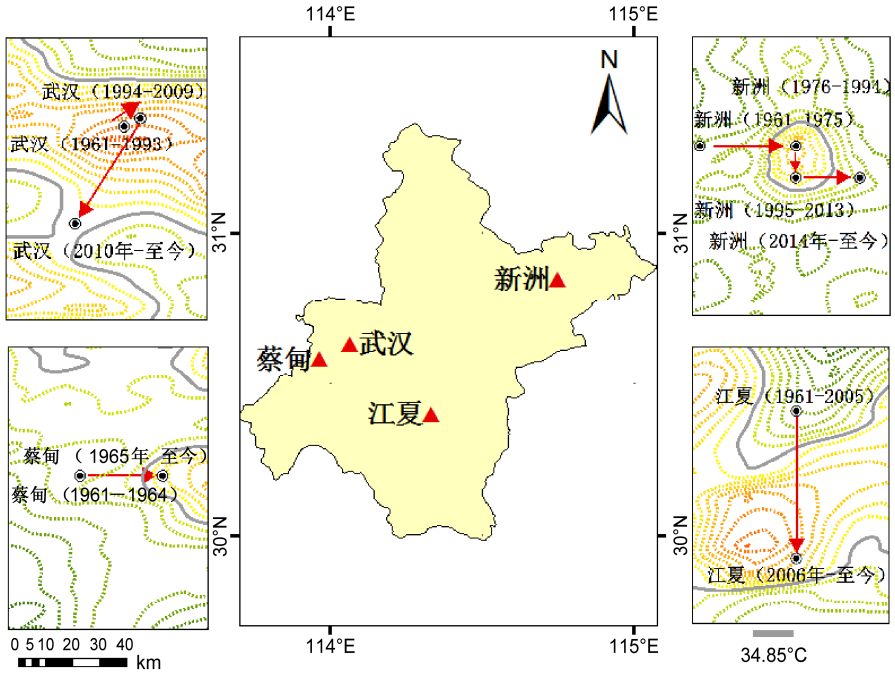

图 2 武汉各城市站的迁站过程（等值线：地表亮度温度，单位：°C，等值线间隔：0.5 °C）

Fig. 2 Relocation processes of each urban station in Wuhan area (contour stands for land surface brightness temperature, units: °C, isoline interval: 0.5 °C)

（表 3），各季节 RH 从高到低依次为夏季（80.53%）、春季（79.10%）、秋季（78.33%）和冬季（76.98%）。无论在 1990 年以前还是以后以及整个研究时段，各季节 RH 之间的差距并不大，差异都在 4%以内。从 1990 年前后时期比较来看，1990 年以前春秋冬三季 RH 均高于 1990 年以后 RH 的平均值，而夏季 1990 年前后时期基本保持一致。

表 3 1961～2015 年不同时间段武汉城市四季 RH 均值

Table 3 Seasonal mean RH at urban stations in Wuhan during different periods of 1961−2015

年份	RH 均值			
	春季	夏季	秋季	冬季
1961～1989 年	80.94%	80.45%	79.39%	77.28%
1990～2015 年	76.88%	80.62%	77.16%	76.64%
1961～2015 年	79.10%	80.53%	78.34%	76.98%

对于武汉年平均 RH 及其不同季节、月份之间差异的解释，已经有一些研究。受武汉地理位置的影响，武汉地处地势低洼的长江中游河谷中，类似盆地的地势加之充足的水系使得水汽集易散难，所以全年和四季都维持着高的相对湿度（吴敏，1999）。同时，武汉具有亚热带季风性湿润气候特点，6 月进入梅雨季，大气中低层的西南暖湿气流带来充沛的水汽（朱乾根等，2007），近地表空气相对湿度达到全年最高，雨量和暴雨频次也多（陈正洪等，2005b）。12 月 RH 出现低值，可能和冬季风南侵带来的干冷空气有关。

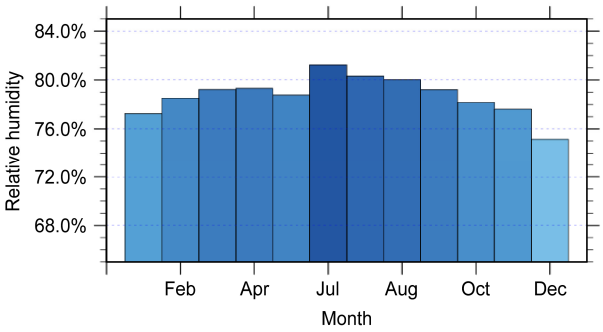

图 3 1961～2015 年武汉城市各月 RH 均值

Fig. 3 Monthly mean RH (Relative Humidity) in urban area of Wuhan during 1961−2015

3.2 相对湿度的长期变化

图 5a 给出了武汉城市站年平均 RH 距平的时间序列，可以看出 1961～2015 年武汉城市的平均 RH 总体呈减少趋势，下降趋势为-0.83%/10 a。长期序列显示，RH 出现两个变化阶段，第一个阶段是 1990 年代以前，RH 大部分年份都为正距平，并且变化趋势并不明显；第二个阶段是 1990 年代以后，RH 大部分年份都为负距平，并且呈现显著下降的趋势。在 1980 年代末期，RH 出现了几个高值年，最

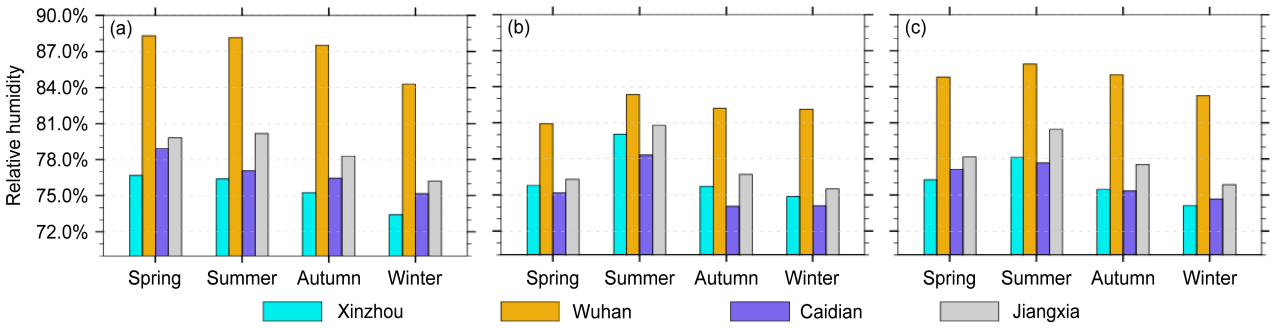

图 4 （a）1961～1989 年、（b）1990～2015 年、（c）1961～2015 年时间段 4 个武汉城市站四季 RH 均值

Fig. 4 Seasonal mean RH at the four urban stations in Wuhan during (a) 1961−1989, (b) 1990−2015, and (c) 1961−2015

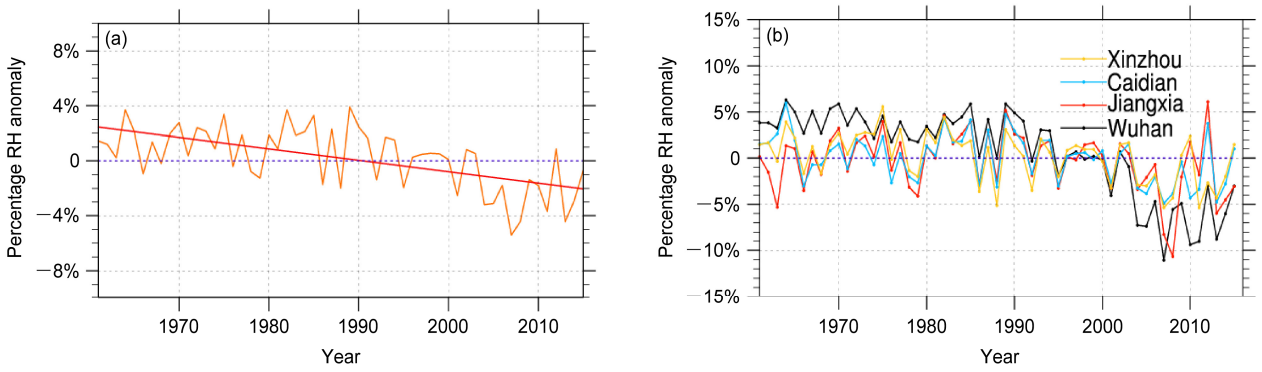

图 5 1961～2015 年（a）武汉城市 RH 距平序列和（b）武汉城市各站 RH 距平百分率年代序列

Fig. 5 Time series of (a) RH anomaly in urban area of Wuhan and (b) percentage RH anomaly series at four urban stations in Wuhan from 1961 to 2015

高年份达到了 82.6%；2000 年代以后，武汉城市 RH 出现了最低的 15 年，最低值出现在 2007 年，年均 RH 仅为 73.2%。因此，根据以上观测事实可以发现，武汉市气候逐渐向干化发展，特别是在 1990 年代以后干化趋势更为明显，这种现象与针对北京市、武威市等地的研究发现基本一致（郑思轶和刘树华，2008；刘明春等，2012）。

图 6 为对武汉城市各站平均季节 RH 距平序列和线性趋势。春、秋、冬 3 个季节的 RH 都显示出一致的下降趋势，这与年平均 RH 的变化趋势相同，但下降速率不同，分别是−1.410%/10 a、−0.540%/10 a、−0.507%/10 a，其中春季下降趋势最明显；夏季的 RH 存在较为显著的上升趋势，可达 0.214%/10 a。年平均 RH 的下降主要是春秋冬三季下降引起的，春季的下降贡献最大。

1961～2015 年和 1990～2015 年武汉城市年及各季节 RH 距平变化趋势（表 4）显示，RH 距平年代变化从 1961 年以来呈现显著下降趋势，而 1990 年以后这种下降趋势更加明显，下降速率几乎是 1961 年以来变化的两倍。1961～2015 和 1990～2015 两个时段除了夏季，各季节均在 1990 年以后下降更显著；夏季 1961～2015 时期显示显著上升趋势，而 1990～2015 时期则显示出显著的下降趋势。

表 4 1961～2015 年和 1990～2015 年武汉城市四季及年平均 RH 距平变化趋势

Table 4 Changing trends of annual and seasonal mean RH in urban area of Wuhan for the periods 1961−2015 and 1990− 2015

	RH 距平变化趋势/% (10 a)$^{-1}$				
	年	春季	夏季	秋季	冬季
1961～2015 年	−0.83	−1.41	0.21	−0.54	−0.51
1990～2015 年	−1.61	−2.46	−1.14	−1.44	−1.38

注：均通过了 0.01 的显著性检验。

研究发现，1961～2012 年期间武汉降水量变化最大的季节是夏季，趋势为 22.96 mm/10 a，夏季降水在 20 世纪 60 年代到 70 年代偏少，70 年代中期以后逐渐上升，于 20 世纪 90 年代达到最高，此后呈现微弱的下降趋势（张意林等，2008；曹小雪，2015），这与本文研究得到的夏季 RH 变化趋势有明显的相似性。春季是平均气温上升速率最大的季

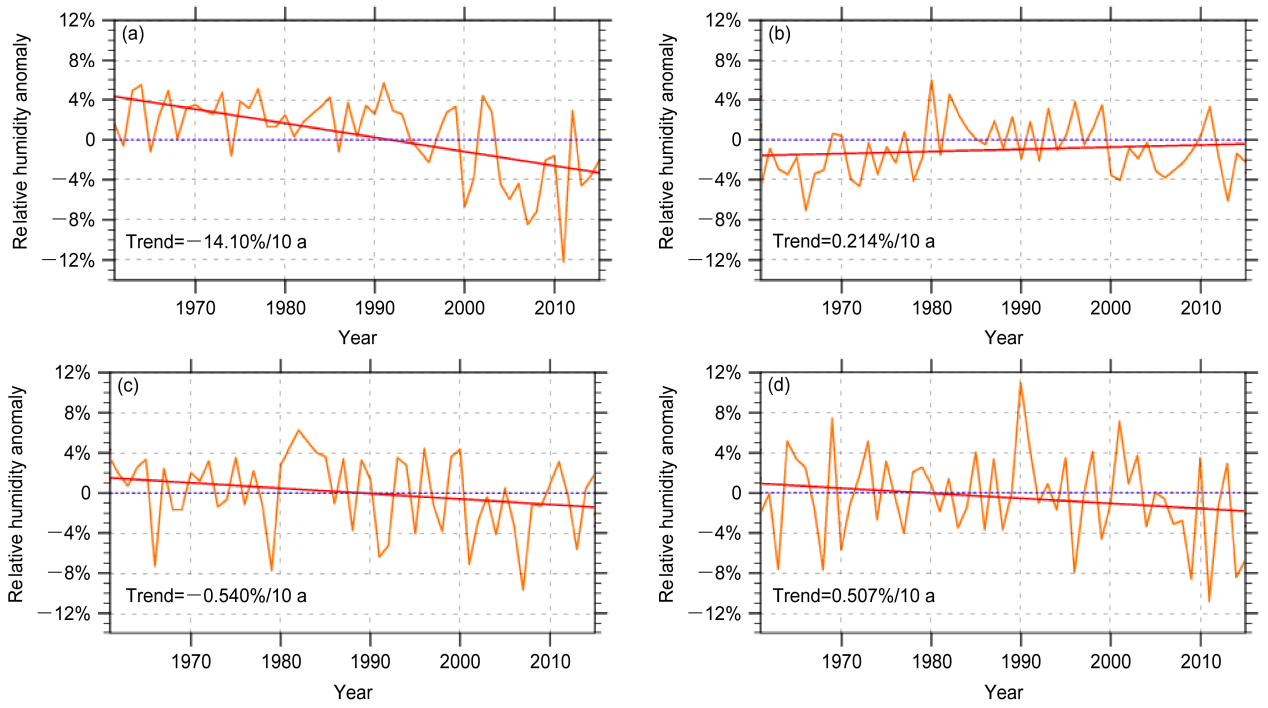

图 6　1961～2015 年武汉城市（a）春季、（b）夏季、（c）秋季、（d）冬季 RH 的距平序列（红色直线表示线性趋势，蓝色虚线表示零线）

Fig. 6　Time series of RH anomalies (black curves) in urban area of Wuhan averaged in the (a) spring, (b) summer, (c) autumn, and (d) winter and their linear trends (red lines) from 1961 to 2015 (blue lines denote the zero line)

节，为 0.47 ℃/10 a，在 20 世纪 90 年代初之后上升趋势更为明显（曹小雪，2015），这可能是影响武汉春季 RH 变化趋势最大的一个因素。因此 RH 在春、夏两季具有完全不同的变化趋势，可能与降水量和温度在这两个季节的长期变化有一定联系。

4　讨论

观测数据序列中的非均一性，对于单站气候要素长期趋势分析结果有明显影响。本文对 RH 数据的非均一性进行了检验和订正。非均一性数据订正的可信度及合理性，可以从 E-P 方法检测序列断点的能力进行评价。从表 2 来看，此方法检测出了序列中由于台站迁址所造成的断点，并检测出非台站迁站所造成的断点信息。对武汉城市站 RH 序列均一化后，订正绝对值均值大约为 5.03%。武汉站在 2010 年迁站至城郊之后有 RH 突然升高现象，站史资料显示这种上升并非真实的自然变化，而是迁站引起的非均一性误差。这种虚假的 RH 升高使得以线性回归得到的变化趋势由−0.83%/10 a 上升到−0.65%/10 a。由此可见，RH 序列因迁站引起的的非均一性影响较为明显，开展 RH 序列变化研究时，对其进行合理的订正是有必要的。当然，本文的非均一性订正以剔除迁站影响为主，没有考虑观测时间变化等可能引起的误差，有待今后进一步完善。

李灿和陈正洪（2010）的分析表明，1951～2007 年武汉市平均相对湿度的气候倾向率为−1.248%/10 a；曹小雪（2015）研究则得出 1961～2012 年 RH 的下降速率是−1.36%/10 a。本文在均一性数据和客观选择城市站的基础上，得到 1961～2015 年期间年平均 RH 的变化趋势为−0.83%/10 a。可见，三者分析结果基本相近，RH 都呈下降趋势，但年平均趋势大小有差别（表 5）。本文获得的年平均 RH 下降趋势明显小于其他两项研究结果，但本文结果指出武汉市平均RH变化主要是在1990年之后的急速下降造成的，这段时间变化趋势可达−1.62%/10 a；各个季节平均 RH 下降趋势均小于前人研究结果，夏季本文结果为弱上升趋势。这些差异可能与不同的研究时段、站点选择方法、有无对资料序列做均一性检验和订正、以及城市台站数量差异等诸多因素有关。

武汉市城市发展在 20 世纪 80 年代末 90 年代初明显加速，到 2009 年后城区面积增加了 2.25 倍；五环线内水体面积由 1987 年的 509.94 km^2 减少至

表 5 武汉市 RH 长期变化趋势不同研究结果之间的对比

Table 5 Comparison of different research results of long-term trends of RH in Wuhan

参考文献	研究时段	研究区域/站点	有无非均一化检验与订正	气候倾向率/%(10 a)$^{-1}$				
				年	春	夏	秋	冬
李灿和陈正洪（2010）	1951～2007 年	武汉市	无	−1.25*	无	无	无	无
曹小雪（2012）	1961～2012 年	武汉站	无	−1.36*	−2.32*	−1.05*	−1.41*	−0.57
本文	1961～2015 年	武汉城市（武汉站、江夏站、蔡甸站、新洲站）	有	−0.83*（注：1990～2015 年：−1.61*）	−1.41*	0.21*	−0.54*	−0.51*

*代表通过 0.001 的显著性检验。

2009 年的 298.51 km^2，主要是城市发展过程中大量的土地用于住房建设，导致水体区域被填埋（王宁涛等，2012）。1990 年之后武汉城市化加速很有可能是 RH 急剧下降的一个主要因素。

RH 的变化也同样受到气象因素的直接影响。有研究显示 RH 与气温和风速呈负相关，与降水量呈正相关（靳英华等，2009），1953～2002 年半干燥地区三者与相对湿度的相关系数分别为：−0.384、0.351、0.072，即其中气温对其影响最大。在上海，城市干岛效应（UDI）总是伴随着城市热岛效应（UHI）现象（周淑贞，1994）；北京城市干岛强度（UDII）与城市热岛强度（UHII）的空间结构也具有相似的分布，强度均在秋季和冬季的夜晚大于春季和夏季的白天，但 UHII 和 UDII 最大值和最小值出现的季节略有差异（Yang et al.，2017）。在 1961～2000 年，武汉城市的年均气温在 20 世纪 80 年代末期开始明显增加，其热岛效应影响存在着显著的随时间增大趋势，年平均、最低、最高气温的热岛增温速率分别为 0.2、0.37、0 ℃/10 a（陈正洪等，2005a，2006）。曹小雪（2015）指出，虽然 2007～2012 年气温呈现下降趋势，但这一阶段的气温平均值高于近 52 年平均值 0.5 ℃，即仍然处于温暖期。这可能是城市热岛效应加强和全球气候变暖共同作用的结果。本文计算表明，武汉城市站年平均气温与 RH 序列的相关系数为−0.65，这与靳英华等（2009）的研究结果相类似，说明武汉城区气温的明显上升可能是导致相对湿度不断下降的直接气象因素。

武汉城市暖干化的结论，和其他处于沿海季风区城市相关研究结论基本一致。例如，1959～2005 年城市化进程对长江三角洲城市 RH 变化的影响也较为突出，尤其是在上海、宁波、杭州、常州等城市，RH 出现了显著下降，城市干岛效应愈发突出（史军等，2008）；随着城市规模的扩大，南京市的城市干岛效应总体也呈现增强趋势（顾丽华等，2009）。

本文研究结果对天气和气候预报、城市水资源研究、城市气候以及城市规划有实际借鉴意义。总体上看，在一个相对湿度很高的城市，城市化导致的气候暖干化趋势，对于缓解高温热浪影响、提高制冷和取暖能源利用效率具有一定正面影响，但对于湿地保护和城市园林生态系统功能维护，可能具有不利影响。

5 结论

运用武汉市 4 个气象站资料，分析了城市 RH 的气候学和长期变化特征，得到以下主要结论：

（1）武汉城市站由于迁站引起的非均一性对 RH 序列造成约 5%的误差，这种虚假的 RH 升高使得以线性回归得到的变化趋势由－0.83%/10 a 上升至－0.65%/10 a。

（2）城区各月平均 RH 均大于 75%。RH 在 1～6 月逐渐增加，6 月达到峰值，可达 80%以上，随后缓慢减小，于 12 月下降至全年最低值，月际间保护范围为 0.1%～2.5%。

（3）城区夏季平均 RH 为 80.53%，春季 79.10%，秋季 78.33%，冬季为 76.98%；春秋冬三季平均 RH，1990 年以前高于 1990 年以后，夏季 1990 年前后基本保持一致；武汉站年均 RH 为 84.73%，其各个季节的 RH 均明显高于其余 3 站。

（4）1961～2015 年期间，城市区域年平均 RH 在 1990s 以前以正距平为主，下降趋势并不明显，1990s 以后大部分为负距平，并且呈现显著下降的趋势；4 个城市站中，武汉站下降趋势最明显。

（5）1961～2015 年武汉城市在春、秋、冬三个季节平均 RH 都呈现显著下降趋势，但夏季平均 RH 存在较为显著的上升趋势；除了夏季，各季节趋势

均在 1991 年以后出现加速下降现象，夏季在 1991 年以后也表现出下降趋势。

参考文献（References）

白永清, 祁海霞, 刘琳, 等. 2016. 武汉大气能见度与 PM2.5 浓度及相对湿度关系的非线性分析及能见度预报 [J]. 气象学报, 74 (2): 189–199. Bai Yongqing, Qi Haixia, Liu Lin, et al. 2016. Study on the nonlinear relationship among the visibility, PM2.5 concentration and relative humidity in Wuhan and the visibility prediction [J]. Acta Meteorologica Sinica (in Chinese), 74 (2): 189–199, doi:10.11676/qxxb2016.013.

曹丽娟, 严中伟. 2011. 地面气候资料均一性研究进展 [J]. 气候变化研究进展, 7 (2): 129–135. Cao Lijuan, Yan Zhongwei. 2011. Progresses in research of homogenization of climate data [J]. Advances in Climate Change Research (in Chinese), 7 (2): 129–135, doi:10.3969/j.issn.1673-1719.2011.02.009.

曹小雪. 2015. 1961～2012 年武汉市气候变化特征分析 [D]. 武汉: 华中师范大学硕士学位论文, 11−19. Cao Xiaoxue. 2015. Analysis of characteristics climate change in Wuhan city from 1961–2012 [D]. M.S. thesis (in Chinese), Wuhan: Central China Normal University, 11−19.

陈正洪, 王海军, 任国玉, 等. 2005a. 湖北省城市热岛强度变化对区域气温序列的影响 [J]. 气候与环境研究, 10 (4): 771–779. Chen Zhenghong, Wang Haijun, Ren Guoyu, et al. 2005a. Change of urban heat island intensity and its effect on regional temperature series: A case study in Hubei province [J]. Climatic and Environmental Research (in Chinese), 10 (4): 771–779, doi:10.3969/j.issn.1006-9585.2005.04.008.

陈正洪, 杨宏青, 任国玉, 等. 2005b. 长江流域面雨量变化趋势及对干流流量影响 [J]. 人民长江, 36 (1): 22–23, 30. Chen Zhenghong, Yang Hongqing, Ren Guoyu, et al. 2005b. Area rainfall variation tendency in the Yangtze River basin and its influence on runoff of the main stream [J]. Yangtze River (in Chinese), 36 (1): 22–23, 30, doi:10.3969/j.issn.1001-4179.2005.01.010.

陈正洪, 王海军, 任国玉. 2006. 武汉城市热岛强度非对称变化及对气温序列的影响 [C]// 中国气象学会 2006 年年会“大气成分与气候、环境变化”分会场论文集. 成都: 中国气象学会, 63–767. Chen Zhenghong, Wang Haijun, Ren Guoyu. 2006. Asymmetrical change of urban heat island intensity and its impact on temperature series in Wuhan [C]//Proceedings of China Meteorological Society 2006 Annual Meeting "Atmospheric Composition and Climate, Environmental Change" Sub-Venues Proceedings (in Chinese). Chengdu: Chinese Meteorological Society, 763–767.

陈正洪, 王海军, 任国玉. 2007. 武汉市城市热岛强度非对称性变化 [J]. 气候变化研究进展, 3 (5): 282–286. Chen Zhenghong, Wang Haijun, Ren Guoyu. 2007. Asymmetrical change of urban heat island intensity in Wuhan, China [J]. Advances in Climate Change Research (in Chinese), 3 (5): 282–286, doi:10.3969/j.issn.1673-1719.2007.05.007.

顾丽华, 邱新法, 曾燕. 2009. 南京市城市干岛和湿岛效应研究[C]//第 26 届中国气象学会年会气候环境变化与人体健康分会场论文集. 杭州: 中国气象学会, 606–612. Gu Lihua, Qiu Xinfa, Zeng Yan. 2009. Study on the effects of urban Dry Island and Wet Island in Nanjing [C]//Proceedings of the 26th Annual Meeting of Climate Meteorology and Human Health in China (in Chinese). Hangzhou: Chinese Meteorological Society, 606–612.

靳英华, 廉士欢, 周道玮, 等. 2009. 全球气候变化下的半干旱区相对湿度变化研究 [J]. 东北师范大学报 (自然科学版), 41 (4): 134–138. Jin Yinghua, Lian Shihuan, Zhou Daowei, et al. 2009. Study on change of relative humidity in semiarid region under global climate change [J]. Journal of Northeast Normal University (Natural Science Edition) (in Chinese), 41 (4): 134–138, doi:10.3321/j.issn:1000-1832.2009.04.030.

李灿, 陈正洪. 2010. 武汉市主要年气候要素及其极值变化趋势 [J]. 长江流域资源与环境, 19 (1): 37–41. Li Can, Chen Zhenghong. 2010. Trend of main climatic factors and its extreme values in Wuhan [J]. Resources and Environment in the Yangtze Basin (in Chinese), 19 (1): 37–41.

Li Q X, Liu X N, Zhang H Z, et al. 2004. Detecting and adjusting temporal inhomogeneity in Chinese mean surface air temperature data [J]. Advances in Atmospheric Sciences, 21 (2): 260–268, doi: 10.1007/BF02915712.

刘明春, 杨晓玲, 殷玉春, 等. 2012. 武威市相对湿度气候特征及预报 [J]. 干旱区研究, 29 (4): 654–659. Liu Mingchun, Yang Xiaoling, Yin Yuchun, et al. 2012. Climate characteristics and forecast of relative humidity in Wuwei City [J]. Arid Zone Research (in Chinese), 29 (4): 654–659, doi:10.13866/j.azr.2012.04.020.

Liu W D, You H L, Dou J X. 2009. Urban-rural humidity and temperature differences in the Beijing area [J]. Theor. Appl. Climatol., 96 (3–4): 201–207, doi:10.1007/s00704-008-0024-6.

Peixoto J P, Oort A H. 1996. The climatology of relative humidity in the atmosphere [J]. J. Climate, 9 (12):3443–3463, doi:10.1175/1520-0442(1996)009<3443:TCORHI>2.0.CO;2.

Peterson T C, Easterling D R. 1994. Creation of homogeneous composite climatological reference series [J]. International Journal of Climatology, 14 (6): 671–679, doi:10.1002/joc.3370140606.

Ren Y Y, Ren G Y. 2011. A remote-sensing method of selecting reference stations for evaluating urbanization effect on surface air temperature trends [J]. J. Climate, 24 (13): 3179–3189, doi:10.1175/2010JCLI3658.1.

Saaroni H, Ziv B. 2003. The impact of a small lake on heat stress in a Mediterranean urban park: The case of Tel Aviv, Israel [J]. International Journal of Biometeorology, 47 (3): 156–165, doi:10.1007/s00484-003-0161-7.

盛裴轩, 毛节泰, 李建国, 等. 2003. 大气物理学 [M]. 北京: 北京大学出版社, 19–22. Sheng Peixuan, Mao Jietai, Li Jianguo, et al. 2003. Eastrophysics (in Chinese) [M]. Beijing: Peking University Press, 19–22.

史军, 周伟东, 崔林丽. 2008. 1959 年～2005 年长江三角洲气候要素变化趋势分析 [J]. 资源科学, 30 (12): 1803–1810. Shi Jun, Zhou Weidong, Cui Linli. 2008. Change trend of climatic factors in the Yangtze River delta from 1959 to 2005 [J]. Resources Science (in Chinese), 30 (12): 1803–1810.

Um H H, Ha K J, Lee S S. 2007. Evaluation of the urban effect of long-term relative humidity and the separation of temperature and water vapor effects [J]. International Journal of Climatology, 27 (11): 1531–1542, doi:10.1002/joc.1483.

汪光焘, 王晓云, 苗世光, 等. 2005. 城市规划大气环境影响多尺度评估技术体系的研究与应用 [J]. 中国科学 (D 辑), 35 (S1): 145–155. Wang Guangtao, Wang Xiaoyun, Miao Shiguang, et al. 2005. Research and

application on the technology system of multi-scale assessment of the impact on the atmospheric environment by urban planning [J]. Science in China (Series D) (in Chinese), 35 (S1): 145–155, doi:10.3969/j.issn.1674-7240.2005.z1.014.

王苗, 邬昀, 任永建, 等. 2015. 武汉地区城市热岛效应及影响要素分析 [C]//中国气象学会 2015 年年会论文集. 天津: 中国气象学会, 232–245. Wang Miao, Wu Yun, Ren Yongjian, et al. 2015. An analysis of the features of the urban heat island in Wuhan and the influence elements[C]//Proceedings of Chinese Meteorological Society 2015 Annual Conference Proceedings (in Chinese). Tianjin: Chinese Meteorological Society, 232–245.

王宁涛, 崔放, 陈植华, 等. 2012. 武汉市 1987～2009 年城市发展及其驱动力分析 [J]. 安全与环境工程, 19 (4): 1–7. Wang Ningtao, Cui Fang, Chen Zhihua, et al. 2012. Analysis on the urban development and driving force in Wuhan City during 1987–2009 [J]. Safety and Environmental Engineering (in Chinese), 19 (4): 1–7, doi:10.3969/j.issn.1671-1556.2012.04.001.

Winkler J A, Skaggs R H, Baker D G. 1981. Effect of temperature adjustments on the Minneapolis-St. Paul urban heat island [J]. J. Appl. Meteor., 20 (11): 1295–1300, doi:10.1175/1520-0450(1981)020<1295:EOTAOT>2.0.CO;2.

吴敏. 1999. 武汉的地形、洪灾及成因 [J]. 湖北档案, (2): 41. Wu Min. 1999. Terrain, flood and cause of Wuhan [J]. Hubei Archives (in Chinese), (2): 41.

轩春怡, 王晓云, 蒋维楣, 等. 2010. 城市中水体布局对大气环境的影响 [J]. 气象, 36 (12): 94–101. Xuan Chunyi, Wang Xiaoyun, Jiang Weimei, et al. 2010. Impacts of water layout on the atmospheric environment in urban areas [J]. Meteorology (in Chinese), 36 (12): 94–101, doi:10.7519/j.issn.1000-0526.2010.12.014.

杨凯, 唐敏, 刘源, 等. 2004. 上海中心城区河流及水体周边小气候效应分析 [J]. 华东师范大学报 (自然科学版), (3): 105–114. Yang Kai, Tang Min, Liu Yuan, et al. 2004. Analysis of microclimate effects around river and waterbody in Shanghai urban district [J]. Journal of East China Normal University (Natural Science) (in Chinese), (3): 105–114, doi:10.3969/j.issn.1000-5641.2004.03.019.

Yang P, Ren G Y, Hou W. 2017. Tempo–spatial patterns of relative humidity and the Urban dryness Island effect in Beijing City [J]. Journal of Applied Meteorology and Climatology, 56 (8): 2221–2237, doi:10.1175/JAMC-D-16-0338.1.

余程鹏. 2008. 武汉市土地利用变化及其对水环境的影响 [D]. 武汉: 华中师范大学硕士学位论文, 65–66. Yu Chengpeng. 2008. Land-use change of Wuhan city and its environmental impact on water [D]. M.S. thesis (in Chinese), Wuhan: Central China Normal University, 65–66.

张意林, 覃军, 陈正洪. 2008. 近 56 a 武汉市降水气候变化特征分析 [J]. 暴雨灾害, 27 (3): 253–257. Zhang Yilin, Qin Jun, Chen Zhenghong. 2008. Analysis on the change characteristics of precipitation in the latest 56 years in Wuhan [J]. Torrential Rain and Disasters (in Chinese), 27 (3): 253–257, doi:10.3969/j.issn.1004-9045.2008.03.010.

郑思轶, 刘树华. 2008. 北京城市化发展对温度、相对湿度和降水的影响 [J]. 气候与环境研究, 13 (2): 123–133. Zheng Siyi, Liu Shuhua. 2008. Urbanization effect on climate in Beijing[J]. Climatic and Environmental Research (in Chinese), 13 (2): 123–133, doi:10.3878/j.issn.1006-9585.2008.02.02.

周淑贞. 1994. 上海大气湿度的城、郊对比分析 [J]. 海洋湖沼通报, (2): 13-25. Zhou Shuzhen. 1994. Discussion of the urban-rural differences in atmospheric humidity of Shanghai area [J]. Transaction of Oceanology and Limnology, (2): 13–25, doi:10.13984/j.cnki.cn37-1141.1994.02.002.

周雅清, 任国玉. 2005. 华北地区地表气温观测中城镇化影响的检测和订正 [J]. 气候与环境研究, 10 (4): 743–753. Zhou Yaqing, Ren Guoyu. 2005. Identifying and correcting urban bias for regional surface air temperature series of North China over period of 1961−2000 [J]. Climatic and Environmental Research (in Chinese), 10 (4): 743–753, doi:10.3969/j.issn.1006-9585.2005.04.005.

朱春阳. 2015. 城市湖泊湿地温湿效应—以武汉市为例 [J]. 生态学报, 35(16): 5518–5527. Zhu Chunyang. 2015. Effects of urban lake wetland on temperature and humidity: A case study of Wuhan City [J]. Acta Ecologica Sinica (in Chinese), 35 (16): 5518–5527, doi:10.5846/stxb201312132951.

朱乾根, 林锦瑞, 寿绍文, 等. 2007. 天气学原理和方法 [M]. 4 版. 北京: 气象出版社, 354–355. Zhu Qian'gen, Lin Jinrui, Shou Shaowen, et al. 2007. Principles and methods of weather science (in Chinese) [M]. 4th ed. Beijing: China Meteorological Press, 354–355.

Theor Appl Climatol (2018) 131:1465–1477
DOI 10.1007/s00704-017-2051-7

ORIGINAL PAPER

Can CFMIP2 models reproduce the leading modes of cloud vertical structure in the CALIPSO-GOCCP observations?

Fang Wang[1,2,3] · **Song Yang**[4,5]

Received: 28 September 2015 / Accepted: 18 January 2017 / Published online: 13 February 2017
© The Author(s) 2017. This article is published with open access at Springerlink.com

Abstract Using principal component (PC) analysis, three leading modes of cloud vertical structure (CVS) are revealed by the GCM-Oriented CALIPSO Cloud Product (GOCCP), i.e. tropical high, subtropical anticyclonic and extratropical cyclonic cloud modes (THCM, SACM and ECCM, respectively). THCM mainly reflect the contrast between tropical high clouds and clouds in middle/high latitudes. SACM is closely associated with middle-high clouds in tropical convective cores, few-cloud regimes in subtropical anticyclonic clouds and stratocumulus over subtropical eastern oceans. ECCM mainly corresponds to clouds along extratropical cyclonic regions. Models of phase 2 of Cloud Feedback Model Intercomparison Project (CFMIP2) well reproduce the THCM, but SACM and ECCM are generally poorly simulated compared to GOCCP. Standardized PCs corresponding to CVS modes are generally captured, whereas original PCs (OPCs) are consistently underestimated (overestimated) for THCM (SACM and ECCM) by CFMIP2 models. The effects of CVS modes on relative cloud radiative forcing (RSCRF/RLCRF) (RSCRF being calculated at the surface while RLCRF at the top of atmosphere) are studied in terms of principal component regression method. Results show that CFMIP2 models tend to overestimate (underestimated or simulate the opposite sign) RSCRF/RLCRF radiative effects (REs) of ECCM (THCM and SACM) in unit global mean OPC compared to observations. These RE biases may be attributed to two factors, one of which is underestimation (overestimation) of low/middle clouds (high clouds) (also known as stronger (weaker) REs in unit low/middle (high) clouds) in simulated global mean cloud profiles, the other is eigenvector biases in CVS modes (especially for SACM and ECCM). It is suggested that much more attention should be paid on improvement of CVS, especially cloud parameterization associated with particular physical processes (e.g. downwelling regimes with the Hadley circulation, extratropical storm tracks and others), which may be crucial to reduce the CRF biases in current climate models.

1 Introduction

Cloud is the primary uncertainty source of climate sensitivity among climate models (e.g. Stephens 2005). This uncertainty mainly originates from the diverse representations of cloud properties and their radiative effects (REs) in climate models, as well as the feedbacks between them and large-scale ambient fields (Wang et al. 2014a). It should also be noted that cloud tuning, a common approach in climate models to achieve a desired radiation balance at the top of atmosphere (TOA) with observations on the global and annual scale, can make the models to neglect some deficiencies in simulating cloud's spatial variability, especially in the vertical dimension (Golaz et al. 2013; Mauritsen et al. 2012). Indeed, cloud vertical structure (CVS) has important effects on radiation and has been long concerned in climate analysis and modelling

✉ Fang Wang
fangwang@cma.gov.cn

[1] Laboratory for Climate Studies, National Climate Center, China Meteorological Administration, Beijing, China

[2] Collaborative Innovation Center on Forecast and Evaluation of Meteorological Disasters, Nanjing University of Information Science & Technology, Nanjing, China

[3] Joint Center for Global Change Studies, Beijing, China

[4] School of Environmental Science and Engineering, Sun Yat-sen University, Guangzhou, China

[5] Institute of Earth Climate and Environment System, Sun Yat-sen University, Guangzhou, China

studies (Cesana and Chepfer 2012; Rossow and Zhang 2010; Rossow et al. 2005; Wang et al. 2014b).

Before the revolutionary progress in detecting CVS through satellites with active remote sensors, the CVS was traditionally obtained through ways such as surface weather observations (e.g. Hahn et al. 2001; Warren et al. 1988), passive sensor satellites (e.g. International Satellite Cloud Climatology Project (ISCCP) (Rossow and Schiffer 1999)), analysis of vertical profiles of relative humidity from radiosondes (Wang et al. 2000), observations from the sites of the Atmospheric Radiation Measurement (ARM) (Ackerman and Stokes 2003) and others. However, the CVS information from most of these observations is incomplete for analysis of CVS climatology from the global scale. Although ISCCP dataset has complete spatial and temporal representation, it provides information from a 'top down' viewpoint and only see the uppermost cloud top in each vertical column other than CVS (Rossow and Zhang 2010). Meanwhile, the evaluation of CVS in climate models has mainly focused on the distribution of high, middle and low clouds as defined by ISCCP (Zhang et al. 2005) or cloud vertical profiles constrained in the limited ARM sites (Qian et al. 2012).

The CVS has been actively detected since the launching of CloudSat and CALIPSO (the Cloud-Aerosol Lidar and Infrared Pathfinder Satellite Observation) satellites in the A-Train constellation (Stephens et al. 2002); both of which can provide a global survey of CVS. The CALIPSO, carrying the active Cloud-Aerosol Lidar with Orthogonal Polarization (CALIOP), has a distinct advantage in profiling the clouds with optical depth lower than 3 in the troposphere and lower stratosphere although some limitations still exist (Cesana and Chepfer 2012; Winker et al. 2009). Based on CALIPSO, the GCM-Oriented CALIPSO Cloud Product (CALIPSO-GOCCP, hereafter GOCCP) has been developed for cloud evaluation in climate models (Chepfer et al. 2010). GOCCP provides a global 3D viewpoint of cloud cover, among others, which has been used for cloud evaluation in climate models, focusing mainly on the vertical profile of cloud cover averaged over latitudes or along some cross section (Cesana and Chepfer 2012; Cesana et al. 2012; Chepfer et al. 2008; Kay et al. 2012).

Considering clouds' complex horizontal and vertical structures, principal components analysis (PCA) (or empirical orthogonal function analysis) has been proved an effective method to explore the cloud vertical structure by transforming the multi-level clouds into limited but physically significant CVS modes, which has been applied in GOCCP and two BCC AGCMs recently (Wang et al. 2014b). Under the framework of phase 2 of Cloud Feedback Model Intercomparison Project (CFMIP) (CFMIP2), a part of the CMIP5 (the fifth phase of the Climate Model Intercomparison Project) (Taylor et al. 2012), more standard CFMIP cloud output in GOCCP vertical levels, using the lidar simulator (Chepfer et al. 2008), has been available for a further evaluation of CVS and its REs among CFMIP2 models. In view of this, the work in Wang et al. (2014b) has been extended to multiple CFMIP2 models but with updated physical interpretations to answer how CFMIP2 models reproduce the leading CVS modes and what radiative effects can be made by the simulation deficiencies in CVS modes.

The remainder of this study is arranged as follows. The data and methodology used for comparisons between CFMIP2 models and GOCCP are described in Sect. 2. Results are shown in Sect. 3, including evaluation on CVS and its REs in CFMIP2 modes, as well as related discussions. Finally, a summary is given in Sect. 4.

2 Data and methodology

2.1 Data

GOCCP was developed from the CALIPSO level 1 products for special purpose in cloudiness evaluation in climate models under the CFMIP framework (Chepfer et al. 2010). The GOCCP monthly cloud cover used in this study has a vertical resolution of 480 m (40 vertical levels) and a horizontal resolution of 2° × 2°, from June 2006 to December 2010. The data are available at the website of CALIPSO-GOCCP (http://climserv.ipsl.polytechnique.fr/cfmip-obs/Calipso_goccp.html).

Monthly cloud covers (1979–2008) from 11 CFMIP2 models (Table 1) are also selected for our study. These data came from the AMIP experiment of CMIP5 and only the r1i1p1 ensemble was used. Unlike other AMIP variables, the CFMIP2 clouds are additional output of a lidar simulator embedded in those models. The lidar simulator is one of the simulators of CFMIP Observational Simulator Package (COSP) (Bodas-Salcedo et al. 2011), being specially used to simulate the cloud cover in model atmosphere just as observed by the CALIPSO. Cloud cover output from lidar simulator in CFMIP2 models is consistent with that in GOCCP in both physics and resolution, facilitating direct comparisons between them.

The corresponding radiative fluxes from 11 CFMIP2 models are used to derive the cloud REs. The monthly CERES Energy Balanced and Filled (EBAF) surface and TOA L3B Ed2.6r data products (Kato et al. 2013), specially designed for the intercomparison of radiative fluxes between satellite-based estimates and model simulations, are used as the reference data. The CERES data sets have a spatial resolution of 1° × 1° latitude/longitude and time periods from March 2000 to February 2010 for surface data and from March 2000 to June 2012 for TOA data.

Table 1 Description of CFMIP2 models and cloud cover schemes

No.	Model ID	Country	Atmospheric model resolution	Cloud cover scheme
1	BCC-CSM1.1	China	T42, L26	Diagnostic scheme treating marine stratocumulus, convective, and layered clouds separately (Wang et al. 2014b).
2	BCC-CSM1.1(m)	China	T106, L26	Same as BCC-CSM1.1
3	CanAM4	Canada	T63, L35	Statistical cloud scheme (von Salzen et al. 2013).
4	GFDL-CM3	USA	C48, L48	Prognostic cloud scheme (Donner et al. 2011).
5	HadGEM2-A	Britain	N96, L38	Parameterized RH-crit and vertical gradient area cloud scheme (Martin et al. 2006).
6	IPSL-CM5A-LR	France	3.75° × 1.875°, L39	Statistical cloud scheme based on a PDF of total water content (Dufresne et al. 2013).
7	IPSL-CM5A-MR	France	2.5° × 1.25°, L39	Same as IPSL-CM5A-LR
8	IPSL-CM5B-LR	France	3.75° × 1.875°, L39	Statistical cloud scheme coupled to convection scheme and boundary scheme with different PDFs (Dufresne et al. 2013).
9	MIROC5	Japan	T85, L40	PDF-based hybrid prognostic cloud scheme (Watanabe et al. 2009).
10	MPI-ESM-LR	Germany	T63, L47	Diagnosed as a function of RH (Stevens et al. 2013).
11	MRI-CGCM3	Japan	TL159 (1.125° × 1.12-5°), L48	PDF-based and Tiedtke cloud scheme (Yukimoto et al. 2011).

2.2 Methods

2.2.1 Data processing and definitions

The annual mean cloud cover in GOCCP is computed from the period of January 2007 to December 2010, and the period of January 2001 to December 2008 is used to calculate the annual means of cloud cover in CFMIP2 models and radiative fluxes in both CERES and models. The multi-model ensemble (MME) is the equal-weighted average of individual models. In order to compare easily, both the GOCCP and the model output are linearly interpolated to the same horizontal resolution of 1° × 1° latitude/longitude as the CERES radiative fluxes.

The cloud REs in this study are represented by relative shortwave (SW)/longwave (LW) radiative forcing (RSCRF/RLCRF) (Wang et al. 2014b), RSCRF being calculated at the surface while RLCRF at the TOA, that is:

$$\mathrm{RSCRF} = \frac{SW_{dn,all} - SW_{dn,clr}}{SW_{dn,clr}} * 100 \quad (1)$$

$$\mathrm{RLCRF} = \frac{LW_{up,all} - LW_{up,clr}}{LW_{up,clr}} * 100 \quad (2)$$

where $SW_{dn,all}$ and $SW_{dn,clr}$ ($LW_{up,all}$ and $LW_{up,clr}$) indicate the all-sky and clear-sky surface (TOA) downwelling SW (upwelling LW) radiation fluxes respectively.

2.2.2 Principal component analysis (PCA)

The central idea of PCA is to reduce the dimensionality of a data set with a large number of interrelated variables while retaining maximum variation of the data set. In this study, PCA is used to transform the 40-level cloud cover to limited vertical modes (i.e. eigenvectors, EVs hereafter) and horizontal projections of these modes (i.e. principal components, PCs hereafter).

Let X_{mn} be the cloud cover matrix with m vertical levels and n horizontal grid points, by linear transformation, the PCs can be expressed as

$$P_{mn} = V'_{mm} \times X_{mn} \quad (3)$$

where V'_{mm} is the transpose of eigenvector matrix V_{mm}. V_{mm} is composed of m eigenvectors, $v_k = (v_{1k}\ v_{2k} \ldots v_{mk})'$, $k = 1, 2, \ldots, m$. The corresponding eigenvalues, $\lambda_k, k = 1, 2, \ldots, m$, satisfy $\lambda_1 \geq \lambda_2 \geq \ldots \geq \lambda_m$ and can be obtained by solving the following polynomial equation:

$$|A - \lambda I| = 0 \quad (4)$$

where A and I denote the covariance matrix of X_{mn} and identity matrix, respectively.

The derived PCs are uncorrelated and are ordered based on λ_k so that the first few ones contain most of the variation in

original variables. In this study, PCs are first calculated from standardized cloud cover field (hereafter SPC), and then the corresponding original PCs (hereafter OPC) are recovered by reversing the standardization formula. The SPC and OPC reflect the relative and actual horizontal distribution patterns of CVS mode, respectively.

2.2.3 Principal component regression (PCR)

PCR is further used to investigate the effects of independent PCs on radiation to eliminate the impacts of collinearity between cloud vertical levels on regression. PCR is basically identical to a standard linear regression model but using PCs as explanatory variables, which can be formulated as

$$Y = b_0 + \sum_{k=1}^{m} b_k P_k \quad (5)$$

where Y is a dependent variable (RSCRF or RLCRF in this study), P denotes explanatory variables (i.e. PCs in the previous section), b_0 is the regression constant, b_k indicates regression coefficients and m is the number of explanatory variables.

The standardized regression coefficients ($b_k^{'}$) can also be obtained through above regression model with standardized dependent and explanatory variables, which is related to b_k as

$$b_k^{'} = b_k \frac{S_{P_k}}{S_Y} \quad (6)$$

where S denotes the standard deviation of a given variable.

3 Results

3.1 CVS modes in GOCCP

The first three EVs and their SPCs in GOCCP and CFMIP2 models are shown in Figs. 1 and 2. All the CVS modes are statistically significant based on the North Test (North et al. 1982). First three GOCCP EVs explain 80.6% of the total variance and well represent the original cloud cover field. The CVS modes are basically consistent with those in Wang et al. (2014b), but with much more detailed description in this study to further understand the physics of these modes.

The leading CVS mode (EV1 42.3%) depicts a vertical pattern with opposite-sign eigenvectors divided by the height around 10 km (Fig. 1a). The negative values of PC1 (corresponding to the negative phase of EV1) are mainly located in the latitudes between 30° S and 30° N, characterized by high clouds in the tropical deep convective regions along the Inter-Tropical Convergence Zone (ITCZ). The positive SPC1 values (corresponding to the positive phase of EV1) in the middle and high latitudes (Fig. 2 (m1)) are linked to the deep and continuous clouds around 60° latitudes, extending from the PBL to about 10 km. EV1 also reflects the descending of maximum cloud-top height corresponding to the decrease in troposphere height from around 17 km in the tropics to about 10 km in the middle-high latitudes (Dessler et al. 2006).

The second CVS mode (EV2 26.2%) is characterized by strong negative eigenvectors through levels above 3 km and with the peak around 7 km (Fig. 1b), corresponding to the middle-high clouds in the tropical convective cores (Fig. 2 (m2)). On the contrast, the positive eigenvectors are much weaker and are located in the planetary boundary layer (PBL) (Fig. 1b), corresponding to the main subtropical anticyclonic regions in SPC2 (Fig. 2 (m2)), where the formation of middle to high clouds are depressed. In addition, positive eigenvectors are also indicative of the PBL marine stratocumulus clouds over the subtropical eastern oceans (Wood 2012). It is also found that the high-SPC-value regions correspond well to the main strong upwelling/downwelling regimes over oceans (Dolinar et al. 2015).

The third CVS mode (EV3, 12.1%) portraits a two-peak structure for both the positive and negative eigenvectors (Fig. 1c). One of the positive (negative) peaks is located at about 10 km (16–17) and the other at around 1 km (2–3), corresponding to upper-level clouds and low-level clouds, respectively. The relevant positive values in SPC3 are typically located in extratropical cyclonic regions (Fig. 2 (m3)), implying a close linkage between EV3 and extratropical cyclonic

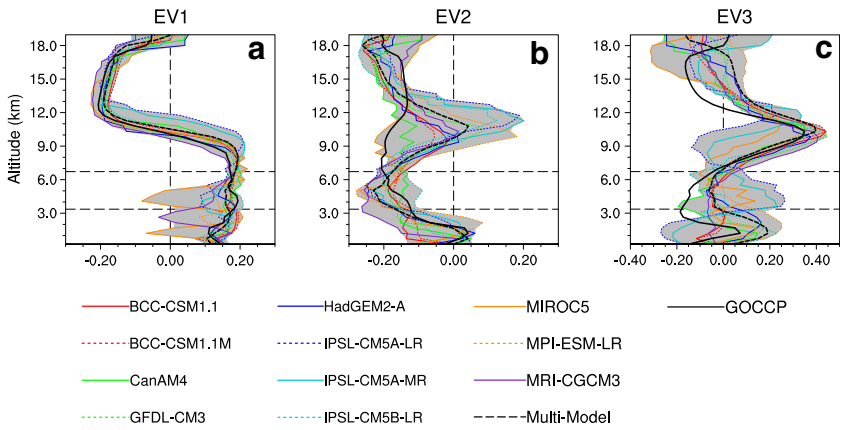

Fig. 1 First three leading modes of cloud cover vertical structure simulated by 11 CFMIP2 models and their MME, and observed by GOCCP. *Horizontal axis* denotes values of eigenvector. *Horizontal dashed lines* indicate boundaries of ISCCP high, middle and low clouds at 3.36 and 6.72 km, respectively. *Grey shadings* denote EV spread among models at a given level

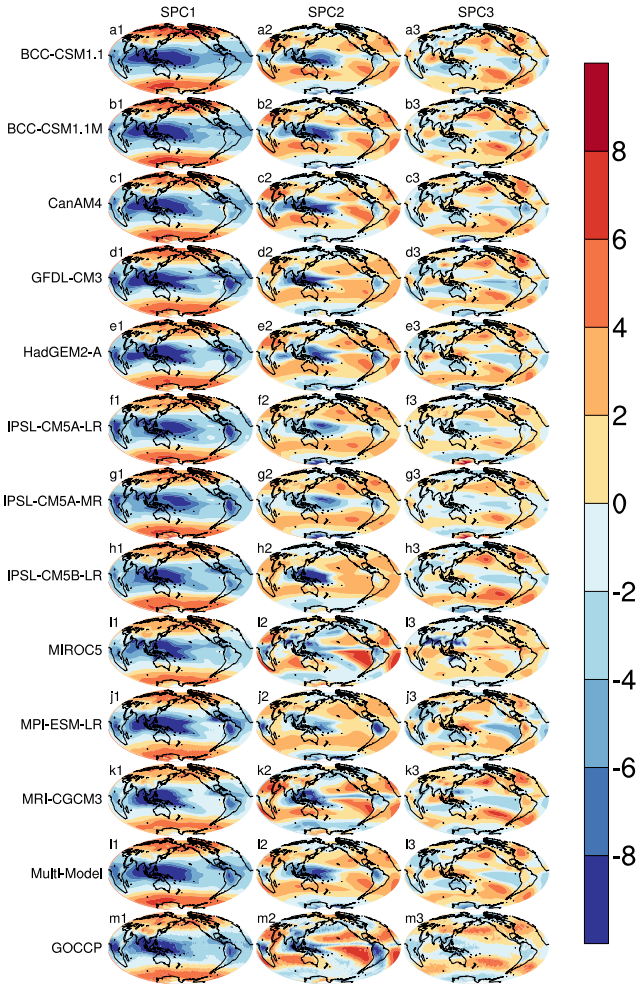

Fig. 2 First three SPCs simulated by 11 CFMIP2 models and the MME, and observed by GOCCP

clouds, whereas negative values are in tropical deep convective regions and polar regions. The positive two-peak structure is consistent with the asymmetric dipole structure of midlatitude storm-track cloud systems revealed by A-Train observations (Huang et al. 2014).

Given the close association of the first three EVs with tropical high, subtropical anticyclonic and extratropical cyclonic clouds, we introduce the term of tropical high cloud mode (THCM), subtropical anticyclonic cloud mode (SACM) and extratropical cyclonic cloud mode (ECCM), respectively.

3.2 Evaluation on CVS modes in CFMIP2 models

The total variances explained by the first three EVs in CFMIP2 models vary from 69.6 to 86.7%, most of which exceed 80.0% except for two IPSL-CM5A models, MIROC5 and MRI-CGCM3 (Table 2). For individual EV, most models (except for MIROC5 and MRI-CGCM3) overestimate the explained variances in THCM, whereas all models underestimate those of SACM remarkably.

Table 2 Percentages of variance explained by the first three EVs in CFMIP2 models and CALIPSO-GOCCP

Model	EV1 (%)	EV2 (%)	EV3 (%)	Total (%)
BCC-CSM1.1	55.0	19.9	11.9	86.7
BCC-CSM1.1M	54.4	20.9	11.3	86.6
CanAM4	47.5	18.8	13.7	80.0
GFDL-CM3	56.6	17.0	12.1	85.7
HadGEM2-A	48.3	19.0	13.7	81.0
IPSL-CM5A-LR	44.3	20.6	10.7	75.5
IPSL-CM5A-MR	45.2	21.0	9.8	76.0
IPSL-CM5B-LR	45.4	20.2	14.4	80.0
MIROC5	36.1	20.3	13.3	69.6
MPI-ESM-LR	51.0	17.6	11.6	80.1
MRI-CGCM3	38.1	23.8	13.7	75.7
MME	52.6	18.4	12.8	83.7
GOCCP	42.3	26.2	12.1	80.6

All the models have excellent skills in capturing the CVS features of THCM (Fig. 1a), except that two models (IPSL-CM5A-LR and IPSL-CM5A-MR) seem to simulate a slightly higher cloud top height at middle to high latitudes. In addition, the positive eigenvectors in THCM exhibit obvious discontinuity in two models, i.e. MRI-CGCM3 and MIROC5. SPCs are generally successfully reproduced by all the models, especially the deep convective cores along the ITCZ (Fig. 2).

With respect to SACM, most models successfully simulate the basic features: few-cloud regimes over the subtropical anticyclonic regions, PBL stratocumulus clouds over the subtropical eastern oceans and the negative SPC pattern in tropical convective cores (Figs. 1b and 2). However, most models produce lower peaks of negative eigenvectors (between 3 and 6 km) than that around 7 km in GOCCP, as well as much weaker negative eigenvectors around 9–12 km. Some models (e.g. three IPSL models and MPI-ESM-LR) even simulate a false peak of positive eigenvectors around 9 to 12 km.

The basic two-peak structure of positive eigenvectors in ECCM is captured by most of models except five models (two BCC models, two IPSL-CM5A models and the MRI-CGCM3), failing to simulate the peak in PBL (Fig. 1c). In addition, remarkable insufficiencies are found in simulations of the two negative-eigenvector peaks (Fig. 1c). SPCs corresponding to the positive EV3 phase are generally captured along extratropical cyclonic regions, whereas those relative to the negative phase are not well simulated in most of models especially along ITCZ convective cores (Fig. 2).

Taylor diagrams (Taylor 2001) are further applied to provide a quantitative evaluation of the simulated SPCs in CFMIP2 models and GOCCP. As expected, models have the best performance in simulating THCM SPCs, with spatial correlation coefficients above 0.90 between GOCCP and models and with less spread among models (Fig. 3a). The

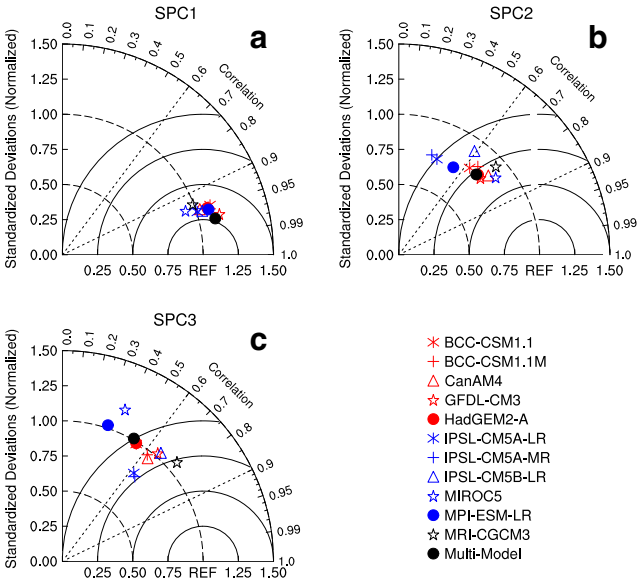

Fig. 3 Taylor diagram for the first three SPCs simulated by 11 CFMIP2 models and the MME, where the reference fields are from GOCCP. The *abscissa* denotes the pattern standard deviation ratio, and the *azimuthal angle* indicates the pattern correlation coefficient

inter-model spread becomes larger and spatial correlations decrease remarkably in SACM and ECCM (Fig. 3b, c), being closely associated with the large divergence in simulating SACM and ECCM among models (Fig. 1b, c).

Similar analysis is also made on OPCs (Figs. 4 and 5). It is found that spatial patterns are basically consistent between OPCs and SPCs (Figs. 2 and 4), whereas the magnitude, pattern standard deviation ratio and centred root-mean-square error of OPCs diverge greatly compared to SPCs, indicating large differences in both OPC mean bias and spatial dispersion in models relative to GOCCP. In addition, pattern standard deviations of all three OPCs in most CFMIP2 models are simulated larger than that in GOCCP. It also noted that global mean OPC1 (OPC2 and OPC3) are consistently underestimated (overestimated) by all models (most of models) compared to the observed value(s) of 9.5% (−25.7 and 3.2%) (Table 3), which may contribute greatly to simulated RSCRF/RLCRF biases in the following sections.

3.3 Radiative effects of CVS modes in CFMIP2 models

Both the ordinary and standardized linear equations are constructed between OPCs and RSCRF/RLCRF for CFMIP2 models and GOCCP data, producing ordinary and standardized regression coefficients (RCs and SRCs), respectively. RCs depend on the dispersion of dependent and explanatory variables, denoting the SW extinction efficiency (mainly determined by extinction optical depth (EOD)) for RSCRF or LW emission efficiency (mainly depending on cloud top temperature or cloud top height) for RLCRF by unit OPC, whereas standardized PCR removes the effects of variables' average

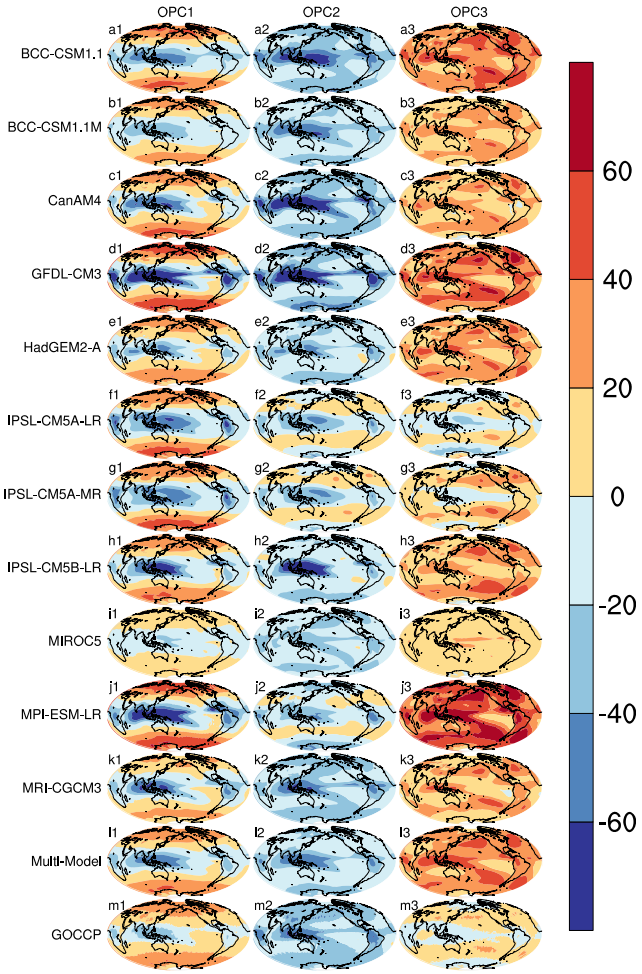

Fig. 4 First three OPCs simulated by 11 CFMIP2 models and the MME, and observed by GOCCP

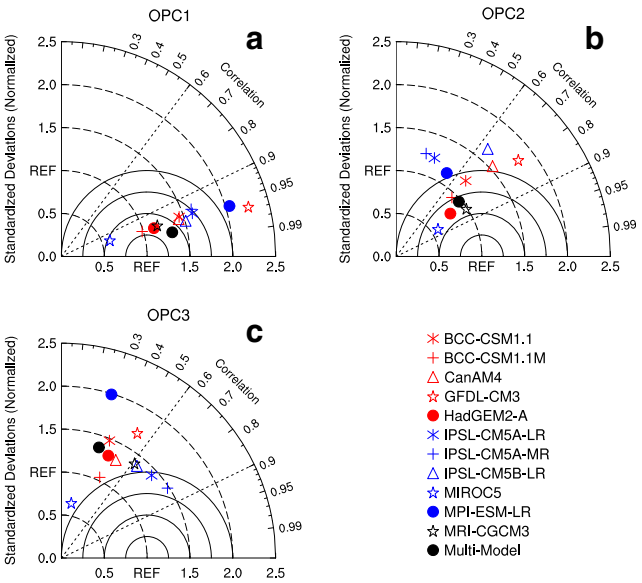

Fig. 5 Taylor diagram for the first three OPCs simulated by 11 CFMIP2 models and the MME, where the reference fields are from GOCCP. The *abscissa* denotes the pattern standard deviation ratio, and the *azimuthal angle* indicates the pattern correlation coefficient

Table 3 Global mean of relative SW/LW cloud radiative forcing (RSCRF/RLCRF) (%) and original principal component (OPC) (%)

Model	RSCRF	RLCRF	OPC1	OPC2	OPC3
BCC-CSM1.1	−30.4	11.2	2.9	−27.4	33.4
BCC-CSM1.1M	−28.7	10.8	1.7	−20.0	19.5
CanAM4	−25.8	9.7	5.2	−28.9	18.9
GFDL-CM3	−26.0	10.1	0.6	−29.7	34.8
HadGEM2-A	−23.9	9.4	6.6	−16.4	24.9
IPSL-CM5A-LR	−26.3	11.3	0.4	−5.7	−2.5
IPSL-CM5A-MR	−26.3	11.7	1.7	−4.3	10.3
IPSL-CM5B-LR	−26.8	10.2	2.8	−18.0	23.4
MIROC5	−27.3	9.7	1.5	−17.1	10.6
MPI-ESM-LR	−25.0	9.6	1.1	−10.3	47.2
MRI-CGCM3	−25.1	8.9	−2.0	−23.6	19.4
MME	−25.1	9.5	3.8	−18.2	31.1
OBS	−24.9	9.9	9.5	−25.7	3.2

value and standard deviation on SRCs, whose absolute values directly reflect the relative importance of OPCs in determining RSCRF/RLCRF, the relation between which are given in Eq. (7). All the regression equations (*F*-test) and PCs (Student *t* test) pass the significance test at the 99% confidence level.

3.3.1 Dependence of RSCRF/RLCRF on CVS modes (SRCs and RCs)

The absolute values of SRCs (Fig. 6a, b) directly reflect the influencing degree of SPCs on RSCRF/RLCRF, and signs of them denote positive or negative dependent relation of RSCRF/RLCRF to SPCs. It is found that the largest relative contribution to RSCRF is from SPC1, then from SPC2, and the least from SPC3 (Fig. 6a), whereas SPC2 contributes the largest to RLCRF, and then SPC3 and SPC1 as shown in observations (Fig. 6b). In most cases, CFMIP2 models simulate the sign-consistent dependence of RSCRF/RLCRF to SPCs, except for that of RLCRF to SPC1, where only half of the models give the right sign. Overall, CFMIP2 models tend to overestimate the relative contributions of SPC1 (10/12 models) and SPC3 (9/12 models) to RSCRF, whereas underestimate that of SPC2 (10/12 models) compared to observations (Fig. 6a). In contrast, CFMIP2 models tend to underestimate the relative contribution of SPC1 (9/12 models) and SPC2 (12/12 models) to RLCRF, whereas overestimate that of SPC3 (12/12 models) compared to observations (Fig. 6b).

RCs (Fig. 6c, d) are completely sign consistent with SRCs, implying coherent dependent relation of RSCRF/RLCRF to them. Considering that Eq. (5) is strictly established if global mean RSCRF/RLCRF and OPCs are substituted, RCs may represent the SW extinction efficiency for RSCRF (i.e. absorbing and scattering ability to SW radiation) or LW emission efficiency for RLCRF corresponding to unit global mean OPC (hereafter unit OPC). RCs may also be interpreted to a large extent as the difference in SW EOD for RSCRF or cloud top height for RLCRF between positive and negative phase clouds in CVS modes (Fig. 1) in unit OPC. According to Eq. (3), unit OPC depends on two factors: One is eigenvectors (i.e. CVS modes in Fig. 1), and the other is global mean vertical profiles of cloud cover (Fig. 7). CVS modes have been discussed in detail in Sects. 3.1 and 3.2, and here, we focus on the mean cloud vertical profiles. Two peaks are observed in GOCCP cloud profile, one of which is located below 3 km, corresponding to abundant optically-thick stratocumulus cloud over the oceans, and the other is around 8 km, mainly contributed by mi-latitude high clouds (Wang et al. 2014b). The most notable difference in global mean cloud vertical profiles is that high clouds are markedly overestimated with the peak at 9–12 km, whereas middle and low clouds are typically underestimated in most CFMIP2 models compared GOCCP (Fig. 7b). This feature may imply compensation between cloud cover and cloud REs in climate models to obtain a better match between simulated and observed TOA radiation balance, that is, models tend to overestimate (underestimate) the REs of low (high) clouds, which may be associated with the overestimation of liquid cloud water contents and possible underestimation of ice cloud water contents in most climate models (Jiang et al. 2012; Wang et al. 2014a). The overestimation of REs in low clouds is also known as the 'too few, too bright' low-cloud problem (Karlsson et al. 2008; Nam et al. 2012).

OPC1 acts to intensify RSCRF corresponding to its unit change as given in observations, indicating in unit OPC1 that the REs of positive phase clouds (mainly low/middle clouds) dominate those of negative phase clouds (high clouds) in THCM. Eight out of 12 models (except two BCC-CSM models, IPSL-CM5B-LR and MIROC5) are found to slightly underestimate the SW REs in unit OPC1, which may be mainly caused by more high clouds (corresponding to negative phase) and fewer low clouds (corresponding to positive phase) in unit OPC1 simulated by these models (Fig. 7b), in view of basically consistent eigenvectors in THCM (Fig. 1a) and the known possible underestimation (overestimation) of REs in high (low) clouds. It is noted that MIROC5 simulated less mid/high clouds and more low clouds (Fig. 7), resulting in obvious overestimation of SW REs in unit OPC1. OPC2 acts to weaken RSCRF in observations, meaning that REs of negative phase clouds in SACM (Fig. 1b) are predominant over those of positive phase clouds (Fig. 6c). Most models, except two (i.e. BCC_CSM1.1 (m) and MRI_CGCM3), underestimate the RSCRF contribution by unit OPC2 or even simulate the opposite sign, contributing to damp the weakening of RSCRF as observed. This feature may be qualitatively explained from three aspects. First, biases in most models tend to increase the proportion of high clouds and decrease that in

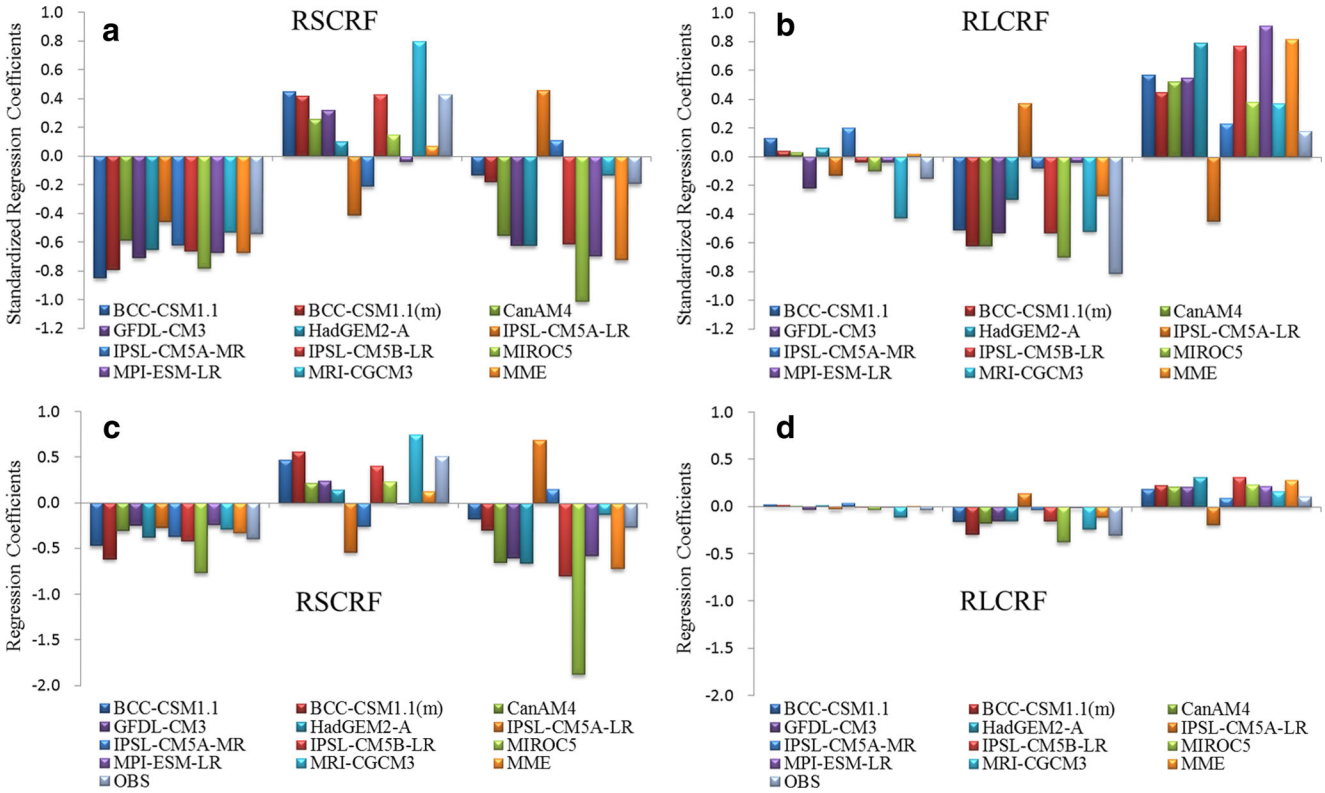

Fig. 6 **a**, **b** Standardized and **c**, **d** ordinary regression coefficients as calculated from the multiple linear regression of RSCRF/RLCRF on the first three PCs

lower levels in negative phase (Fig. 7), which contribute to decrease the REs difference between the two phases in SACM. Second, the fact of underestimation (overestimation) of REs in high (low) clouds further reduces the REs difference. Thirdly, remarkable biases in SACM eigenvectors around 9–12 km may greatly weaken the REs corresponding to negative phase clouds in SACM (acting to reduce RCs) or even produce positive clouds at 9–12 km, producing RCs with the opposite sign in some models (e.g. MPI-ESM-LR and two IPSL-CM5A models). OPC3 acts to intensify RSCRF with its

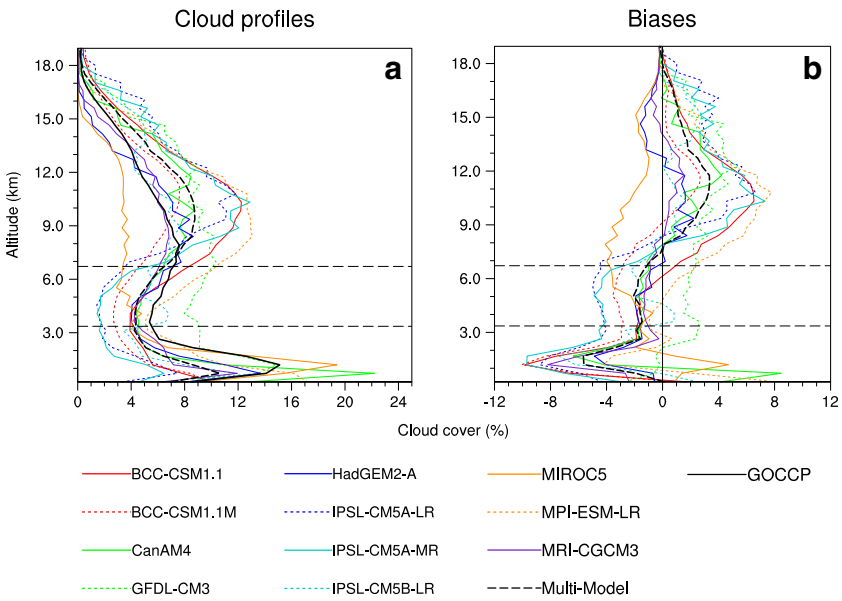

Fig. 7 Global mean vertical profiles of **a** cloud cover in CFMIP2 models and GOCCP, and **b** cloud cover biases compared to GOCCP in CFMIP2 models (units: %). *Horizontal dashed lines* indicate boundaries of ISCCP high, middle and low clouds at 3.36 and 6.72 km, respectively

unit change in observations, indicating the domination of REs in positive phase clouds on those in negative phase clouds. The RSCRF corresponding to unit OPC3 is markedly overestimated by seven models (CanAM4, GFDL-CM3, HadGEM2-A, IPSL-CM5B-LR, MIROC5, MPI-ESM-LR and MME), which commonly feature stronger positive peak in low/middle cloud levels (Fig. 1c), together with REs overestimation in low clouds, resulting in larger REs in positive phase clouds and then stronger RSCRF in unit OPC3 compared to observations.

The RLCRF from OPCs mainly depends on the difference in cloud top temperature (the lower the temperature, the stronger the RLCRF) as well as the absolute weight of top-level clouds between the two phases in CVS modes (Fig. 1). As a result, OPC3 acts to intensify the RLCRF in observations, opposite to OPC1 and OPC2, although its cloud top height decreases with unit increase in OPC1, due mainly to the larger weight of positive eigenvectors associated with top-level clouds. Overall, CFMIP2 models tend to underestimate or simulate the opposite sign of RLCRF RCs by OPC1 and OPC2 compared to observations, except MRI-CGCM3 for OPC1 and MIROC5 for OPC2, whereas overestimate the relative RLCRF contribution by OPC3 except two IPSL-CM5A models (Fig. 6b). Biases of RLCRF RCs also depend on biases in CVS modes (Fig. 1) as well as those in global mean cloud vertical profiles (Fig. 7). Different from RSCRF, high cloud cover biases in cloud profiles may play dominant roles in determining RLCRF biases compared to low/middle cloud cover biases. Considering these features, above-mentioned RSCRF RCs biases may be mainly resulted from overestimated high clouds especially around 9–12 km (Fig. 7b) as well as the abnormal peaks of eigenvectors at 9–12 km in SACM and ECCM (Fig. 1b, c).

3.3.2 Global mean RSCRF/RLCRF biases from CVS modes

Compared to CERES observations on global mean RSCRF and RLCRF (−24.9 and 9.9%), CFMIP2 models tend to overestimate the RSCRF intensity except HadGEM2-A, while one half of the models simulate opposite biases to the other half regarding RLCRF compared to CERES (Table 3). By substituting the global mean of OPCs into the original regression equations, the global mean RSCRF/RLCRF contribution from each OPC is calculated for both models and observations. The signs of global mean RSCRF contributed by OPCs are correctly simulated by 11/12 (except MRI-CGCM3), 9/12 (except IPSL-CM5A-LR, IPSL-CM5A-MR and MPI-ESM-LR) and 11/12 (except IPSL-CM5A-MR) CFMIP2 models for OPC1, OPC2 and OPC3, respectively. Only 5/12 models capture the correct signs of global mean RLCRF contributions from OPC1, whereas 11/12 (except IPSL-CM5A-LR) and all models simulate the correct signs of those from OPC2 and OPC3, respectively (data not shown).

The global mean biases of RSCRF/RLCRF contributed by OPCs are shown in Fig. 8a b, from which remarkable biases are found for RSCRF (RLCRF) compared to observations, i.e. −3.7% (−0.3%) for OPC1, −13.2% (7.8%) for OPC2 and −0.9% (0.4%) for OPC3, respectively. RSCRF intensity contributed by OPC3 are markedly overestimated by 11/12 models (except IPSL-CM5A-MR), whereas those from OPC1 and OPC2 are underestimated except one model (MRI-CGCM3) in the case of OPC2 compared to observations (Fig. 8a). RSCRF intensity underestimation from OPC2 may also reflect that cloud radiative forcing biases in downwelling regimes (with biases weakening RSCRF) are much larger than those in upwelling regimes (with biases strengthening RSCRF) (Dolinar et al. 2015), which also applies to the RLCRF biases from OPC2 below. Overall, contribution from OPC3 predominates over contributions from OPC1 and OPC2 in most models. This indicates that ESCM, with the least explained variance, may play an essential role in the overestimation of RSCRF intensity among CFMIP2 models (Table 3).

Although no system RLCRF bias relative to observations is simulated globally among CFMIP2 models (Table 3), biases from three OPCs show remarkable consistency among models (Fig. 8b). That is, RLCRF intensity contributed by OPCs are consistently overestimated (underestimated) in OPC3 (OPC1 and OPC2) by all models compared to observations. It is noted that the RLCRF biases from OPC1 are very small (generally lower than 0.5%) although obvious overestimation of high clouds observed in both the tropics and the middle-high latitudes (data not shown). This is due mainly to the opposite roles that high clouds play in RLCRF in the two regions and the cancellation between them. The RLCRF biases from OPC2 and OPC3 are obviously larger than those from OPC1. However, these biases have opposite signs and offset each other to a large extent, resulting in reduced contributions to RLCRF in CFMIP2 models.

3.3.3 Decomposition of RSCRF/RLCRF biases

Based on Eq. (7), RSCRF and RLCRF biases from different OPCs are further decomposed into three parts, that is, RC bias term, OPC bias term and their joint effect, which are shown in Fig. 8c–h. RC bias term denotes the biases from difference in REs corresponding to unit OPC between models and observations, while OPC bias term mainly refers to biases from cloud cover differences between models and observations.

Similar features are found in bias decomposition between RSCRF and RLCRF. Underestimation of RSCRF/RLCRF intensity from OPC1 (Fig. 6c, d) is mainly from OPC biases (Fig. 8e, f), featured by consistent underestimation of global mean OPC1 (Table 3), which mainly come from the overestimated high clouds in the tropics in most of the models (Fig. 4). In contrast, RSCRF biases from RCs and the joint

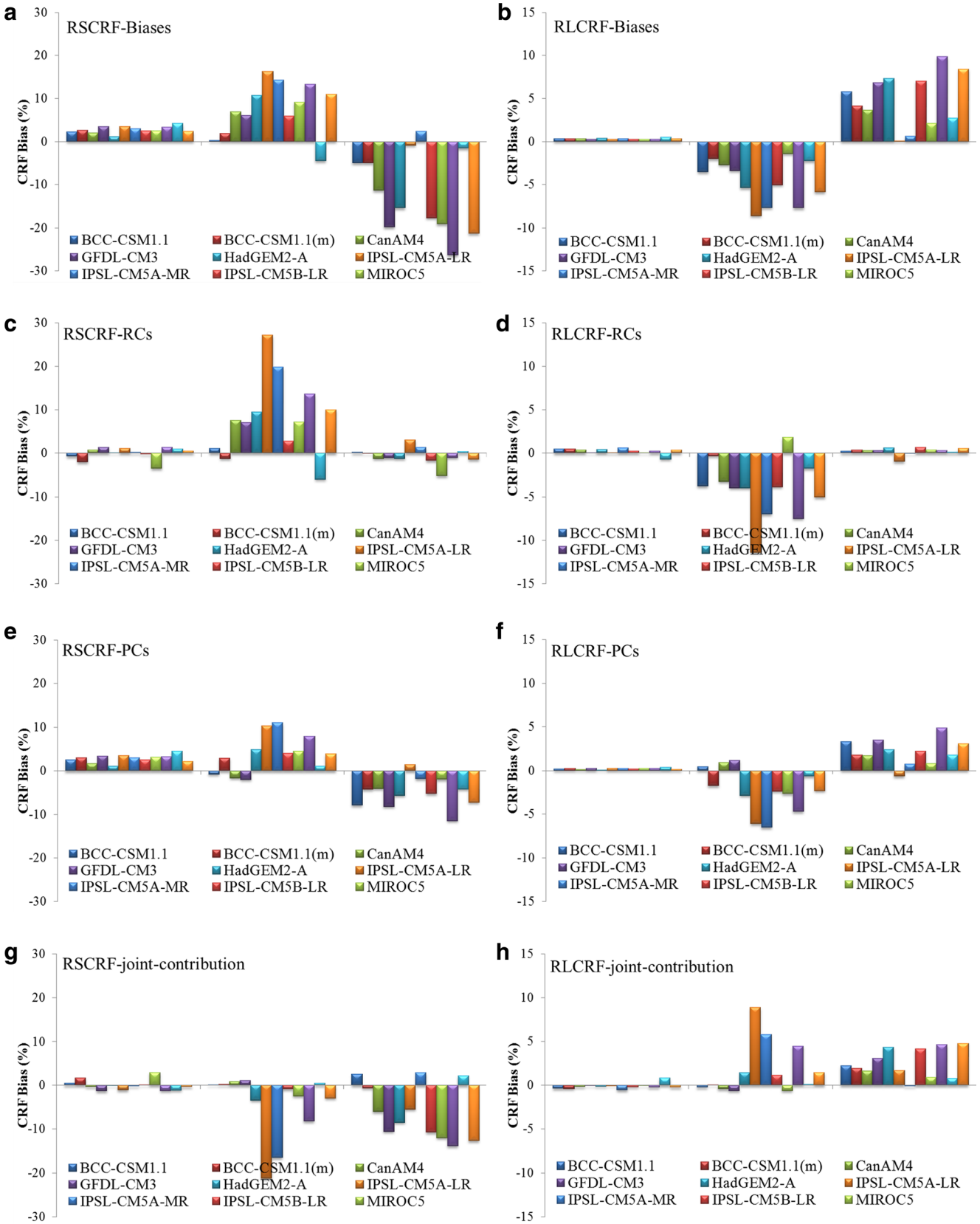

Fig. 8 Global mean **a** RSCRF and **b** RLCRF biases compared to observations. **c**, **e**, **g** RSCRF and **d**, **f**, **h** RLCRF biases contributed by regression coefficient biases (*upper row*), principal component biases (*middle row*) and both of them (units: %)

contribution of RC and OPC cancel each other greatly, due to the opposite sign between global mean OPC1 and OPC1 bias in CFMIP2 models (Table 3). For OPC2, underestimation of RSCRF/RLCRF intensity mainly arises from RC biases (Fig. 8c, d) as well as OPC biases (Fig. 8e, f), corresponding to smaller absolute coefficients (means underestimation of REs by unit OPC2, see Fig. 6c, d) and larger global mean OPC2 in most models (Table 3 and Fig. 4), whereas the joint contribution tends to take the opposite effect (Fig. 8g, h). Overestimation of RSCRF/RLCRF intensity from OPC3 is contributed by overestimated OPC3 (Table 3 and Fig. 4), also added up by the joint contribution from RC and OPC.

3.4 Discussion

A question that needs to be addressed here is why the CVS biases and their REs have been produced by CFMIP2 models? The answer may lie on two aspects, cloud/radiation parameterizations and the relevant large-scale environmental fields simulated by those models, between which complex feedback processes exist but cannot be separated from each other in the present study. However, we notice the remarkable improvement in the simulation of CVS modes and their REs in IPSL-CM5B-LR (Figs. 1 and 6), wherein the convective boundary layer and cumulus clouds are better represented compared to IPSL-CM5A models (Hourdin et al. 2013).

Data uncertainty is still an inevitable problem in the GOCCP and CERES datasets, which may come from multiple sources, e.g. spatial and temporal sampling, retrieving algorithm and even accuracy of satellite sensors (Stubenrauch et al. 2013; Young et al. 2013). In addition, not all information for certain identified cloud type is constrained in the relevant CVS mode, although they may be physically associated. For example, tropical deep convective clouds are mainly explained by THCM; however, part of information is also included in other two CVS modes. As a final note, the physical explanations on RCs are more qualitative rather than quantitative, which may be not exactly but do contribute to a better understanding of RCs.

4 Summary

In this paper, the leading CVS modes simulated by 11 CFMIP2 models and the MME are evaluated using PCA method against the GOCCP data set. The REs of these modes are further accessed in terms of PCR based on CERES radiative fluxes. Main conclusions are listed as follows.

1. The GOCCP data set reveals three leading CVS modes, i.e. tropical high cloud mode (THCM), subtropical anticyclonic cloud mode (SACM) and extratropical cyclonic cloud mode (ECCM). THCM mainly reflect the contrast between tropical high clouds and clouds from PBL to about 10 km in middle and high latitudes. SACM is closely associated with middle-high clouds in tropical convective cores, few-cloud regimes in subtropical anticyclonic regions and stratocumulus over subtropical eastern oceans. ECCM mainly corresponds to clouds along extratropical cyclonic regions, generally characterized by an asymmetric dipole structure. CFMIP2 models consistently reproduce the THCM and corresponding SPCs quite well, depicting the fundamental latitude-altitude structure of cloud cover. SACM and ECCM are generally poorly simulated mainly in vertical structure relative to their standardized horizontal loadings (i.e. SPCs) compared to GOCCP. In addition, pattern standard deviations of all three OPCs are simulated larger than that in GOCCP by most CFMIP2 models, and OPCs are consistently underestimated (overestimated) for THCM (SACM and ECCM) by CFMIP2 models.
2. Using standardized PCR, the relative importance of OPCs in determining RSCRF/RLCRF (i.e. absolute values of SRCs) is evaluated for CFMIP2 models compared to observations. It is shown that the largest relative contribution to RSCRF is from SPC1, then from SPC2, and the least is from SPC3, whereas SPC2 contributes the largest to RLCRF, and then SPC1 and SPC3, as seen from observations.
3. Ordinary regression coefficients (RCs) denote the SW extinction efficiency for RSCRF (i.e. absorbing and scattering ability to SW radiation) or LW emission efficiency for RLCRF corresponding to unit global mean OPC. It is difficult to provide exact explanations on RCs but qualitative ones in the present studies, mainly due to their dependence on multiple factors, e.g. global mean cloud vertical profiles (features by underestimation of low/middle clouds and overestimation of high clouds) and CVS modes (featured by remarkable differences in SACM and ECCM).

   OPC1 and OPC3 (OPC3) act to intensify RSCRF (RLCRF), whereas OPC2 (OPC1 and OPC2) takes the opposite effect corresponding to its unit change as given in observations. CFMIP2 models tend to overestimate (underestimated or simulate the opposite sign) RSCRF/RLCRF radiative effects (REs) of ECCM (THCM and SACM) in unit global mean OPC compared to observations. These RE biases may be attributed to two factors, one of which is underestimation (overestimation) of low/middle clouds (high clouds) (also known as stronger (weaker) REs in unit low/middle (high) clouds) in simulated global mean cloud profiles, the other is eigenvector biases in CVS modes (especially for SACM and ECCM).
4. The global mean RSCRF and RLCRF biases caused by three CVS modes are calculated based on the ordinary PCR equations and global mean OPCs. The majority of

CFMIP2 models tend to underestimate global mean RSCRF/RLCRF intensity from OPC1 and OPC2, whereas to overestimate them by OPC3 as compared to observations. Further examination shows that RSCRF/RLCRF biases from OPC1 mainly caused by OPC biases, that is, consistent underestimation of OPC1 by CFMIP2 models. RC biases as well as OPC overestimation jointly contribute to global mean RSCRF/RLCRF biases contributed by OPC2. In addition, RSCRF/RLCRF biases from OPC3 are mainly contributed by OPC3 overestimation as well as the joint contribution from RC and OPC.

Our results have shown that the THCM and its REs has been better reproduced in most CFMIP2 models compared to SACM and ECCM. Although the SACM and ECCM are poorly simulated in most models, their standardized horizontal loadings are overall reasonably captured (Fig. 2), indicating that the improvement on CVS, especially cloud parameterization associated with particular physical processes (e.g. downwelling regimes with the Hadley circulation, extratropical storm tracks and others), may be crucial to reduce the CRF biases simulated by climate models.

Acknowledgements This work was supported by the National Natural Science Foundation of China (grants 41275077 and 41475069). We are grateful to the World Climate Research Programme's Working Group on Coupled Modelling, which is responsible for the CMIP. We thank the Climate Modelling Groups (listed in Table of this paper) for producing their model output and making it available.

Open Access This article is distributed under the terms of the Creative Commons Attribution 4.0 International License (http://creativecommons.org/licenses/by/4.0/), which permits unrestricted use, distribution, and reproduction in any medium, provided you give appropriate credit to the original author(s) and the source, provide a link to the Creative Commons license, and indicate if changes were made.

References

Ackerman TP, Stokes GM (2003) The atmospheric radiation measurement program. Phys Today 56:38–44

Bodas-Salcedo A, Webb MJ, Bony S, Chepfer H, Dufresne J-L, Klein SA, Zhang Y, Marchand R, Haynes JM, Pincus R (2011) COSP: satellite simulation software for model assessment. Bull Am Meteorol Soc 92:1023–1043

Cesana G, Chepfer H (2012) How well do climate models simulate cloud vertical structure? A comparison between CALIPSO? GOCCP satellite observations and CMIP5 models. Geophys Res Lett 39: L20803

Cesana G, Kay JE, Chepfer H, English JM, de Boer G (2012) Ubiquitous low-level liquid-containing Arctic clouds: new observations and climate model constraints from CALIPSO-GOCCP. Geophys Res Lett 39:L20804

Chepfer H, Bony S, Winker D, Chiriaco M, Dufresne J-L, Sèze G (2008) Use of CALIPSO lidar observations to evaluate the cloudiness simulated by a climate model. Geophys Res Lett 35:L15704

Chepfer H, Bony S, Winker D, Cesana G, Dufresne J, Minnis P, Stubenrauch C, Zeng S (2010) The GCM-oriented CALIPSO cloud product (CALIPSO-GOCCP). J Geophys Res 115:D00H16

Dessler A, Palm S, Spinhirne J (2006) Tropical cloud-top height distributions revealed by the ice, cloud, and land elevation satellite (ICESat)/geoscience laser altimeter system (GLAS). Journal of Geophysical Research: Atmospheres (1984–2012) 111:D12215

Dolinar E, Dong X, Xi B, Jiang J, Su H (2015) Evaluation of CMIP5 simulated clouds and TOA radiation budgets using NASA satellite observations. Clim Dyn 44:2229–2247

Donner LJ, Wyman BL, Hemler RS, Horowitz LW, Ming Y, Zhao M, Golaz J-C, Ginoux P, Lin SJ, Schwarzkopf MD, Austin J, Alaka G, Cooke WF, Delworth TL, Freidenreich SM, Gordon CT, Griffies SM, Held IM, Hurlin WJ, Klein SA, Knutson TR, Langenhorst AR, Lee H-C, Lin Y, Magi BI, Malyshev SL, Milly PCD, Naik V, Nath MJ, Pincus R, Ploshay JJ, Ramaswamy V, Seman CJ, Shevliakova E, Sirutis JJ, Stern WF, Stouffer RJ, Wilson RJ, Winton M, Wittenberg AT, Zeng F (2011) The dynamical Core, physical parameterizations, and basic simulation characteristics of the atmospheric component AM3 of the GFDL global coupled model CM3. J Clim 24:3484–3519

Dufresne JL, Foujols MA, Denvil S, Caubel A, Marti O, Aumont O, Balkanski Y, Bekki S, Bellenger H, Benshila R, Bony S, Bopp L, Braconnot P, Brockmann P, Cadule P, Cheruy F, Codron F, Cozic A, Cugnet D, de Noblet N, Duvel JP, Ethé C, Fairhead L, Fichefet T, Flavoni S, Friedlingstein P, Grandpeix JY, Guez L, Guilyardi E, Hauglustaine D, Hourdin F, Idelkadi A, Ghattas J, Joussaume S, Kageyama M, Krinner G, Labetoulle S, Lahellec A, Lefebvre MP, Lefevre F, Levy C, Li ZX, Lloyd J, Lott F, Madec G, Mancip M, Marchand M, Masson S, Meurdesoif Y, Mignot J, Musat I, Parouty S, Polcher J, Rio C, Schulz M, Swingedouw D, Szopa S, Talandier C, Terray P, Viovy N, Vuichard N (2013) Climate change projections using the IPSL-CM5 earth system model: from CMIP3 to CMIP5. Clim Dyn 40:2123–2165

Golaz J-C, Horowitz LW, Levy H II (2013) Cloud tuning in a coupled climate model: impact on twentieth century warming. Geophys Res Lett 40:2246–2251

Hahn CJ, Rossow WB, Warren SG (2001) ISCCP cloud properties associated with standard cloud types identified in individual surface observations. J Clim 14:11–28

Hourdin F, Grandpeix J-Y, Rio C, Bony S, Jam A, Cheruy F, Rochetin N, Fairhead L, Idelkadi A, Musat I, Dufresne J-L, Lahellec A, Lefebvre M-P, Roehrig R (2013) LMDZ5B: the atmospheric component of the IPSL climate model with revisited parameterizations for clouds and convection. Clim Dyn 40:2193–2222

Huang Y, Protat A, Siems ST, Manton MJ (2014) A-train observations of maritime midlatitude storm-track cloud systems: comparing the Southern Ocean against the North Atlantic. J Clim 28:1920–1939

Jiang JH, Su H, Zhai C, Perun VS, Del Genio A, Nazarenko LS, Donner LJ, Horowitz L, Seman C, Cole J (2012) Evaluation of cloud and water vapor simulations in CMIP5 climate models using NASA "A-train" satellite observations. J Geophys Res 117:D14105

Karlsson J, Svensson G, Rodhe H (2008) Cloud radiative forcing of subtropical low level clouds in global models. Clim Dyn 30:779–788

Kato S, Loeb NG, Rose FG, Doelling DR, Rutan DA, Caldwell TE, Yu L, Weller RA (2013) Surface irradiances consistent with CERES-derived top-of-atmosphere shortwave and longwave irradiances. J Clim 26:2719–2740

Kay JE, Hillman BR, Klein SA, Zhang Y, Medeiros B, Pincus R, Gettelman A, Eaton B, Boyle J, Marchand R (2012) Exposing global cloud biases in the community atmosphere model (CAM) using satellite observations and their corresponding instrument simulators. J Clim 25:5190–5207

Martin GM, Ringer MA, Pope VD, Jones A, Dearden C, Hinton TJ (2006) The physical properties of the atmosphere in the new

Hadley Centre global environmental model (HadGEM1). Part I: Model Description and Global Climatology J Clim 19:1274–1301

Mauritsen T, Stevens B, Roeckner E, Crueger T, Esch M, Giorgetta M, Haak H, Jungclaus J, Klocke D, Matei D (2012) Tuning the climate of a global model. J Adv Model Earth Syst 4:M00A01

Nam C, Bony S, Dufresne JL, Chepfer H (2012) The 'too few, too bright' tropical low-cloud problem in CMIP5 models. Geophys Res Lett 39: L21801

North GR, Bell TL, Cahalan RF, Moeng FJ (1982) Sampling errors in the estimation of empirical orthogonal functions. Mon. Wea. Rev. 110: 699–706

Qian Y, Long CN, Wang H, Comstock JM, McFarlane SA, Xie S (2012) Evaluation of cloud fraction and its radiative effect simulated by IPCC AR4 global models against ARM surface observations. Atmos Chem Phys 12:1785–1810

Rossow WB, Schiffer RA (1999) Advances in understanding clouds from ISCCP. Bull Am Meteorol Soc 80:2261–2287

Rossow WB, Zhang Y (2010) Evaluation of a statistical model of cloud vertical structure using combined CloudSat and CALIPSO cloud layer profiles. J Clim 23:6641–6653

Rossow WB, Zhang Y, Wang J (2005) A statistical model of cloud vertical structure based on reconciling cloud layer amounts inferred from satellites and radiosonde humidity profiles. J Clim 18:3587–3605

Stephens GL (2005) Cloud feedbacks in the climate system: a critical review. J Clim 18:237–273

Stephens GL, Vane DG, Boain RJ, Mace GG, Sassen K, Wang Z, Illingworth AJ, O'Connor EJ, Rossow WB, Durden SL (2002) The CloudSat mission and the A-train. Bull Am Meteorol Soc 83: 1771–1790

Stevens B, Giorgetta M, Esch M, Mauritsen T, Crueger T, Rast S, Salzmann M, Schmidt H, Bader J, Block K, Brokopf R, Fast I, Kinne S, Kornblueh L, Lohmann U, Pincus R, Reichler T, Roeckner E (2013) Atmospheric component of the MPI-M earth system model: ECHAM6. J Adv Model Earth Syst 5:1–27

Stubenrauch C, Rossow W, Kinne S, Ackerman S, Cesana G, Chepfer H, Di Girolamo L, Getzewich B, Guignard A, Heidinger A (2013) Assessment of global cloud datasets from satellites: project and database initiated by the GEWEX radiation panel. Bull Am Meteorol Soc 94:1031–1049

Taylor KE (2001) Summarizing multiple aspects of model performance in a single diagram. J Geophys Res 106:7183–7192

Taylor KE, Stouffer RJ, Meehl GA (2012) An overview of CMIP5 and the experiment design. Bull Am Meteorol Soc 93:485–498

von Salzen K, Scinocca JF, McFarlane NA, Li J, Cole JNS, Plummer D, Verseghy D, Reader MC, Ma X, Lazare M, Solheim L (2013) The Canadian fourth generation atmospheric global climate model (CanAM4). Part I: Representation of Physical Processes Atmosphere-Ocean 51:104–125

Wang J, Rossow WB, Zhang Y (2000) Cloud vertical structure and its variations from a 20-yr global rawinsonde dataset. J Clim 13:3041–3056

Wang F, Yang S, Wu T (2014a) Radiation budget biases in AMIP5 models over the east Asian monsoon region. Journal of Geophysical Research: Atmospheres 119:13400–13426

Wang F, Xin X, Wang Z, Cheng Y, Zhang J, Yang S (2014b) Evaluation of cloud vertical structure simulated by recent BCC_AGCM versions through comparison with CALIPSO-GOCCP data. Adv Atmos Sci 31:721–733

Warren SG, Hahn CJ, London J, Chervin RM, Jenne RL, 1988: Global distribution of total cloud cover and cloud type amounts over the ocean. NCAR Tech. Note NCAR/TN-31 7 + STR, 212 pp

Watanabe M, Emori S, Satoh M, Miura H (2009) A PDF-based hybrid prognostic cloud scheme for general circulation models. Clim Dyn 33:795–816

Winker DM, Vaughan MA, Omar A, Hu Y, Powell KA, Liu Z, Hunt WH, Young SA (2009) Overview of the CALIPSO mission and CALIOP data processing algorithms. J Atmos Ocean Technol 26:2310–2323

Wood R (2012) Stratocumulus Clouds. Mon Wea Rev 140:2373–2423

Young SA, Vaughan MA, Kuehn RE, Winker DM (2013) The retrieval of profiles of particulate extinction from cloud–aerosol Lidar and infrared pathfinder satellite observations (CALIPSO) data: uncertainty and error sensitivity analyses. J Atmos Ocean Technol 30:395–428

Yukimoto S, Yoshimura H, Hosaka M, Sakami T, Tsujino H, Hirabara M, Tanaka TY, Deushi M, Obata A, Nakano H, Adachi Y, Shindo E, Yabu S, Ose T, Kitoh A (2011) Meteorological Research Institute-Earth System Model Version 1 (MRI-ESM1): Model Description. Technical Reports of the Meteorological Research Institute No.64**:** 83 pp

Zhang MH, Lin WY, Klein SA, Bacmeister JT, Bony S, Cederwall RT, Del Genio AD, Hack JJ, Loeb NG, Lohmann U, Minnis P, Musat I, Pincus R, Stier P, Suarez MJ, Webb MJ, Wu JB, Xie SC, Yao MS, Zhang JH (2005) Comparing clouds and their seasonal variations in 10 atmospheric general circulation models with satellite measurements. Journal of Geophysical Research: Atmospheres 110:D15S02

ADVANCES IN ATMOSPHERIC SCIENCES, VOL. 35, AUGUST 2018, 1063–1076

• **Original Paper** •

Representation of the ENSO Combination Mode and its Asymmetric SST Response in Different Resolutions of HadGEM3

Jianghua WAN[1], Hongli REN*[1,2], and Peili WU[3]

[1]*Laboratory for Climate Studies, and CMA-NJU Joint Laboratory for Climate Prediction Studies, National Climate Center, China Meteorological Administration, Beijing* 100081*, China*

[2]*Department of Atmospheric Sciences, School of Environment Studies University of Geoscience, Wuhan* 430074*, China*

[3]*Met Office Hadley Center, Exeter* EX1 3PB*, UK*

(Received 15 November 2017; revised 27 April 2018; accepted 2 May 2018)

ABSTRACT

Previous studies have revealed a combination mode (C-mode) occurring in the Indo-Pacific region, arising from nonlinear interactions between ENSO and the western Pacific warm pool annual cycle. This paper evaluates the simulation of this C-mode and its asymmetric SST response in HadGEM3 and its resolution sensitivity using three sets of simulations at horizontal resolutions of N96, N216 and N512. The results show that HadGEM3 can capture well the spatial pattern of the C-mode associated surface wind anomalies, as well as the asymmetric response of SST in the tropical Pacific, but it strongly overestimates the explained variability of the C-mode compared to the ENSO mode. The model with the three resolutions is able to reproduce the distinct spectral peaks of the C-mode at the near annual combination frequencies, but the performance in simulating the longer periods is not satisfactory, presumably due to the unrealistic simulation of the ENSO mode. Increasing the horizontal resolution can improve the consistency between atmospheric and oceanic representations of the C-mode, but not necessarily enhance the accuracy of C-mode simulation compared with observation.

Key words: ENSO combination mode, asymmetric response, Niño-A index, HadGEM3, horizontal resolution

Citation: Wan, J. H., H. L. Ren, and P. L. Wu, 2018: Representation of the ENSO combination mode and its asymmetric SST response in different resolutions of HadGEM3. *Adv. Atmos. Sci.*, **35**(8), 1063–1076, https://doi.org/10.1007/s00376-018-7285-5.

1. Introduction

The El Niño–Southern Oscillation (ENSO) is a dominant mode of interannual climate variability and has pronounced impacts on global climate (Ropelewski and Halpert, 1987; Trenberth et al., 1998; Wallace et al., 1998; Trenberth and Caron, 2000). Recent studies have shown that nonlinear interactions between ENSO and the background western Pacific warm pool annual cycle can generate an ENSO/annual cycle combination mode (C-mode) (Stuecker et al., 2013), which exhibits pronounced variability of near-annual combination tone periods at ~10 and ~15 months. Besides, it demonstrates distinct meridionally asymmetric patterns related to the equator in atmospheric variables (Stuecker et al., 2013, 2015a, 2015b), as well as SST anomalies (Zhang et al., 2016b).

This C-mode over the Pacific warm pool plays an important role in the ENSO life cycle by contributing to the southward shift of anomalous central Pacific low-level zonal winds during the rapid termination of El Niño events (Harrison and Vecchi, 1999; Vecchi, 2006; McGregor et al., 2012; Stuecker et al., 2013). In addition, it plays a considerable part in the developing and maintaining processes of the anomalous low-level Northwest Pacific anticyclone (Stuecker et al., 2015b). A distinguished annual-cycle modulation of the meridional asymmetry in the atmospheric response to Eastern Pacific El Niño events has been detected, which does not emerge in Central Pacific El Niño or La Niña events (Zhang et al., 2015; Zhang et al., 2016b). Moreover, the C-mode may significantly affect East Asian precipitation anomalies and remarkably improve the predictability of Yangtze River basin summer rainfall (Li et al., 2016a; Zhang et al., 2016a, 2016b).

Considering the C-mode is crucial for both ENSO seasonally modulated dynamics and the ENSO climatic influence in the tropical Pacific to the western North Pacific, it is of great importance to evaluate the performances of models in simulating the C-mode. Li et al. (2016b) found the southward shift of the anomalous westerly over the central Pacific might only occur with the annual cycle background in an AGCM. Zhang et al. (2016b) evaluated the predictive skill of the oceanic C-mode in five dynamical models that participated in Weisheimer et al. (2009), and found it to be lower

* Corresponding author: Hongli REN
Email: renhl@cma.gov.cn

© Copyright [2018], British Crown (administered by Met Office); Jianghua WAN and Hongli REN.

than that for the Niño3.4 index. Ren et al. (2016) assessed the performance of capturing the observed C-mode characteristics in 27 CGCMs from CMIP5. Most of the coupled climate models in CMIP5 are able to reproduce the spatial pattern of the C-mode well in terms of the surface wind variability, and about half can reproduce the spectral power at the combination tone periodicities. In this study, both the atmospheric aspect and the oceanic response of the combination mode were examined in a model simulation, and the sensitivity to model resolution was discussed.

2. Data and methods

The climate model used in this study is HadGEM3-GC2, which is the latest version of the UK Met Office Hadley Centre's coupled climate modeling system. It consists of the Met Office's Unified Model as the atmospheric component, JULES as the land-surface component, NEMO as the ocean component, and CICE as the sea-ice model. More details of the model can be found in Hewitt et al. (2011), Williams et al. (2015) and Senior et al. (2016). We utilized three different horizontal resolution configurations to look at the sensitivity of the C-mode simulation to the resolution. The N96 horizontal resolution is 1.25° latitude ×1.875° longitude, which is approximately 130 km at the surface. N216 is 0.8° latitude ×0.5° longitude (approximately 60 km at the surface), and N512 is approximately 25 km. The fully coupled model was integrated for 61 years at each resolution.

For comparison, we utilized the monthly 10-m wind data from the NCEP–NCAR reanalysis dataset (1961–2015) (Kalnay et al., 1996), NCEP–DOE data, ERA-40 data, and 20CR data. The SST anomalies (1961–2011) associated with ENSO and the C-mode are examined using the HadISST1 dataset, provided by the UK Met Office (Rayner et al., 2003), as well as the OISST and ERSST datasets. The precipitation data are from CMAP.

The ENSO C-mode was derived following the same approach as in Stuecker et al. (2013). We first conduct a combined empirical orthogonal function (EOF) analysis on the anomalous zonal and meridional wind anomalies over the tropical Pacific region (10°S–10°N, 100°E–60°W), and then regress the horizontal wind anomalies onto the first two normalized principal components (PCs), respectively. The oceanic aspect of the C-mode can be represented by the Niño-Asymmetry SST index (Niño-A index), which can comprehensively capture both the meridional asymmetry and the zonal SST asymmetry (Zhang et al., 2016b). The Niño-A index is defined as

$$\text{Niño} - \text{A} = 0.5[\text{SSTA}]_{\text{sw}} + 0.5[\text{SSTA}]_{\text{SE}} - [\text{SSTA}]_{\text{NC}} ,$$

where the brackets denote the area-averaged SST anomalies over the regions SW (0°–20°S, 120°–160°E), SE (0°–20°S, 100°–140°W), and NC (0°–20°N, 150°E–130°W). The Niño3.4 index is defined as the SST anomalies averaged over the region (5°S–5°N, 120°–170°W).

3. Results

3.1. *Characteristics of the C-mode in the reanalysis data*

3.1.1. *Atmospheric features of the C-mode*

Figure 1 displays the first two leading EOF patterns of tropical Pacific surface wind anomalies in different reanalysis products. The datasets show considerable agreement with one another. The first EOF pattern (EOF1) is characterized by a meridionally quasi-symmetric wind distribution with equatorial westerly anomalies over the western-central Pacific, which describes the anomalous Walker circulation associated with ENSO (Figs. 1a, c, e and g). The second EOF mode (EOF2) exhibits a meridionally antisymmetric circulation with a distinct anomalous Northwest Pacific anticyclone and southward shift of the equatorial central-Pacific westerly wind anomalies (Figs. 1b, d, f and h), which is the characteristic atmospheric response to the C-mode (Stuecker et al., 2013, 2015b).

The PC time series are also highly correlated among the different reanalysis datasets (Fig. 2). The correlation coefficient of the PCs between each dataset and the NCEP–NCAR data is higher than 0.9, except for the PC2 between ERA-40 and NCEP–NCAR, which still reaches 0.84. Hereinafter, we use the NCEP–NCAR reanalysis data to validate the model simulation of the C-mode atmospheric variability.

The PC1 time series is highly correlated ($r = 0.85$) with the Niño3.4 index (Fig. 3a), further verifying that EOF1 captures the main ENSO mode in the reanalysis. To better understand the relationship between the ENSO mode and the combination mode, we followed Stuecker et al. (2013) to utilize a theoretical approximation to the C-mode time series by multiplying PC1 by a sinusoidal function with the annual cycle; that is,

$$\text{PC1cos} = \text{PC1}_{\text{obs}}(t) \times \cos(\omega_a t - \varphi) .$$

The ω_a in this equation denotes the angular frequency of the annual cycle, t denotes time and φ represents a one-month shift. This time series represents the combination tones of the ENSO signal and the annual cycle by its mathematical nature. In the reanalysis, PC1cos shows remarkable agreement with the observed PC2 (Fig. 3b). The correlation coefficient is 0.63.

To further understand the combination tones, we calculate the power density spectra for both the PC1 and PC2 time series in the reanalysis (Fig. 4a). The spectrum for PC1 exhibits pronounced levels of variability, mostly in the interannual period band of 2–8 years, while PC2 exhibits a significant spectral peak at a period of ~15 months and a weaker one at ~10 months. Actually, these two peaks align well with the two shifted frequency bands of ENSO-annual cycle combination tones, which is the sum tone as $1 + f_{\text{E}}$ and the difference tone as $1 - f_{\text{E}}$, where f_{E} denotes the ENSO characteristic interannual frequency band.

3.1.2. *Asymmetric SST response of the C-mode*

Besides the surface atmospheric response of the C-mode, the nonlinear processes in the ocean–atmosphere coupled

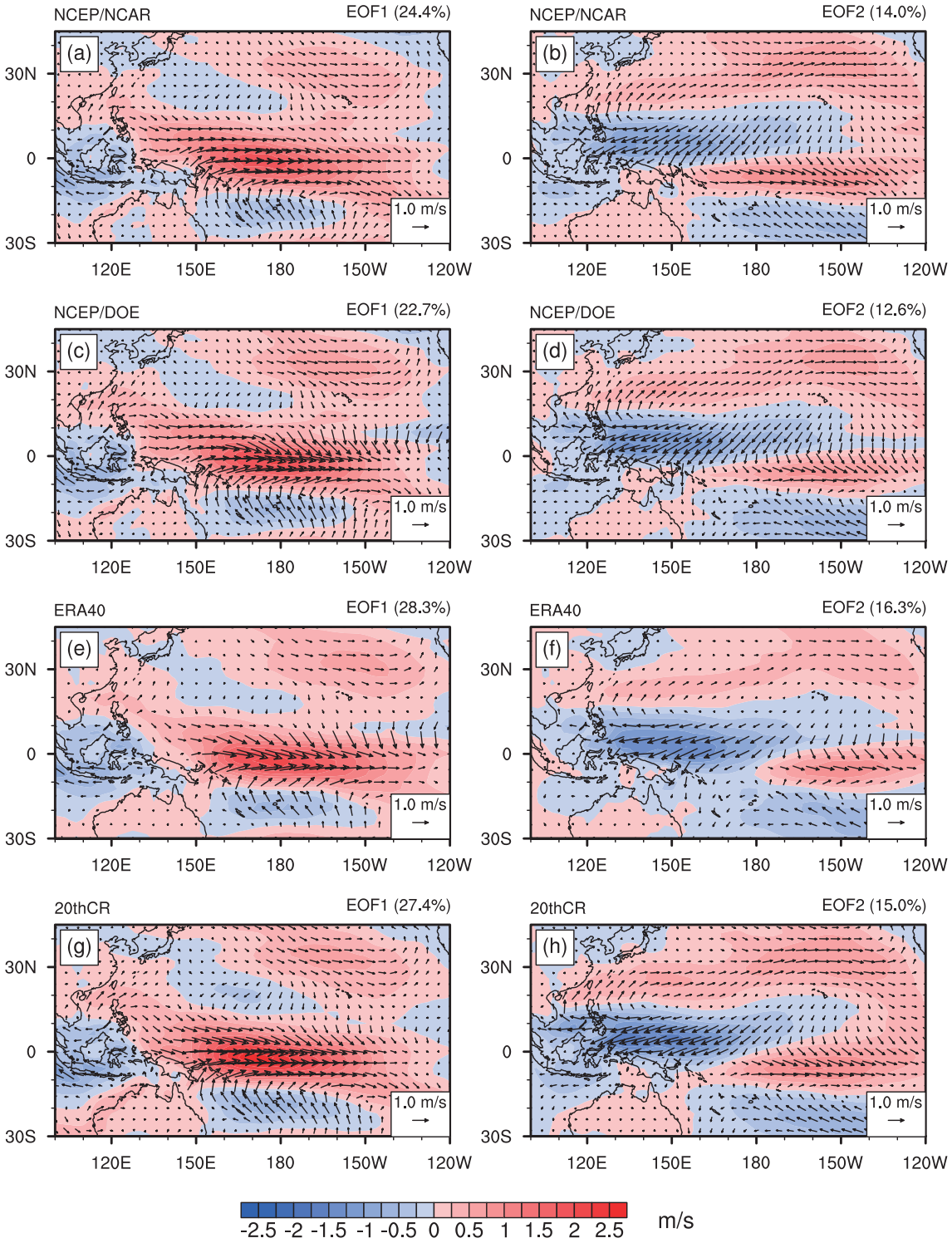

Fig. 1. The leading two EOF spatial patterns of tropical Pacific surface wind anomalies (units: m s^{-1}) for (a, b) NCEP–NCAR, (c, d) NCEP–DOE, (e, f) ERA-40 and (g, h) 20CR. Shading indicates the regressed zonal wind anomalies. Percentages of variance explained by the EOF patterns are given in parentheses.

system may also result in combination tones in oceanic variables (Jin et al., 1994; Stein et al., 2014). Zhang et al. (2016b) pointed out the Niño-A index can capture the SST response to the C-mode very well. Figure 5 demonstrates the SST anomalies and 850-hPa horizontal wind anomalies regressed onto the Niño3.4 and Niño-A indices in different observational datasets. The spatial SST distribution related to ENSO is characterized as a meridionally symmetrical SSTA pattern (Figs. 5a, c and e). Also, the Niño-A index–associated SST anomaly pattern exhibits negative SST anomalies over

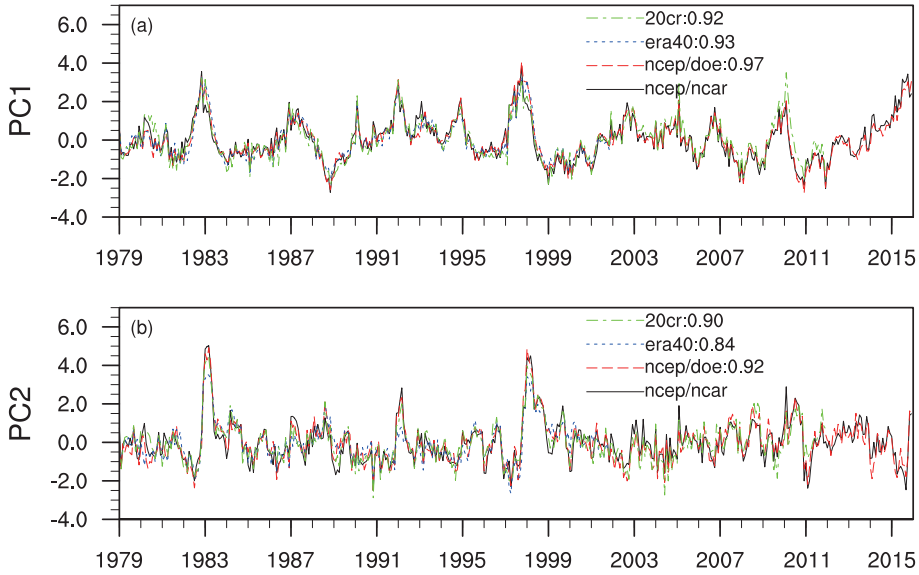

Fig. 2. (a) PC1 and (b) PC2 in different reanalysis datasets. Numbers after the colon are the correlation coefficients between each dataset and the NCEP–NCAR reanalysis.

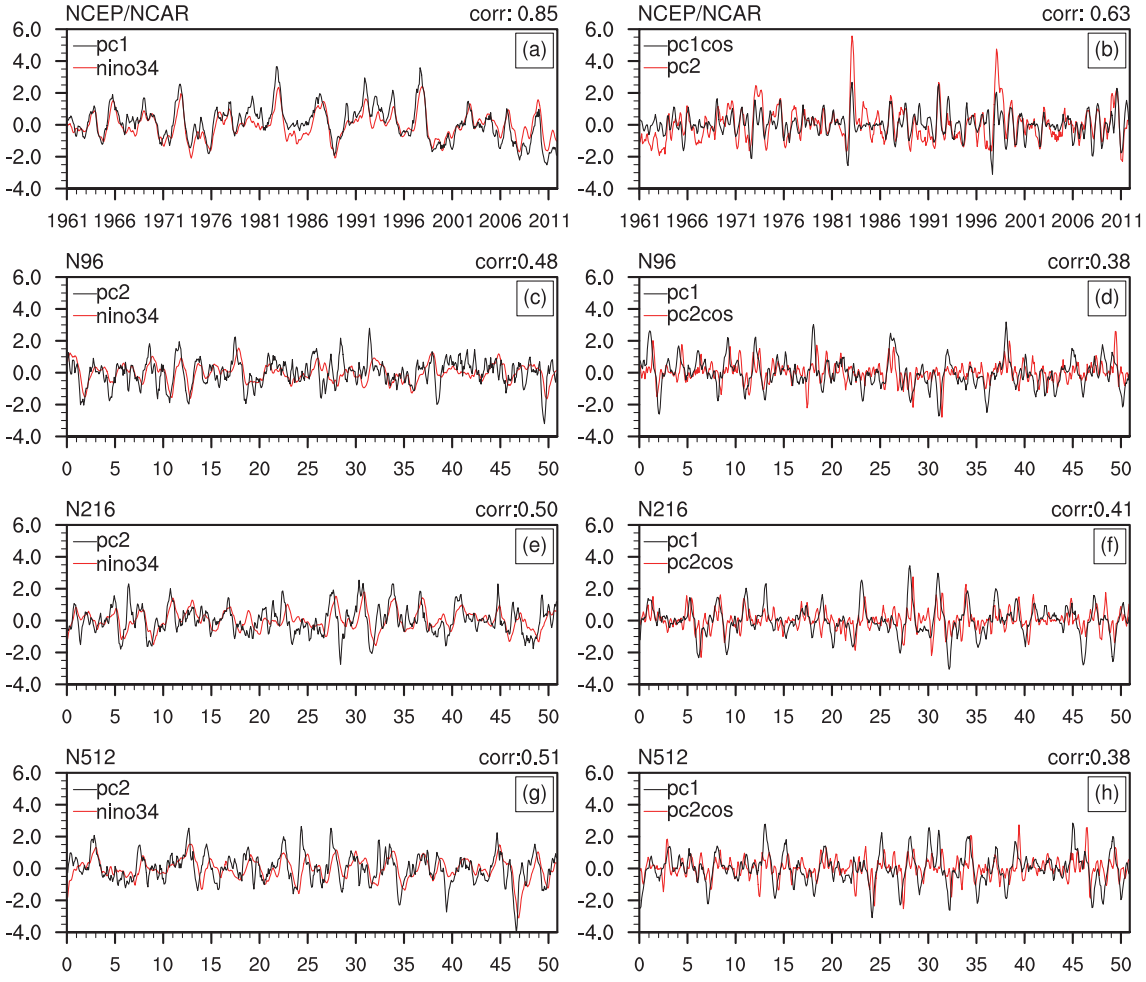

Fig. 3. (a) PC1 and Niño3.4 index for the reanalysis; (b) PC1cos and PC2 for the reanalysis. PC2 and Niño3.4 indices for models at (c) N96, (e) N216 and (g) N512. PC1 and PC2cos for models at (d) N96, (f) N216 and (h) N512. Correlation coefficients between two curves are given in the top right.

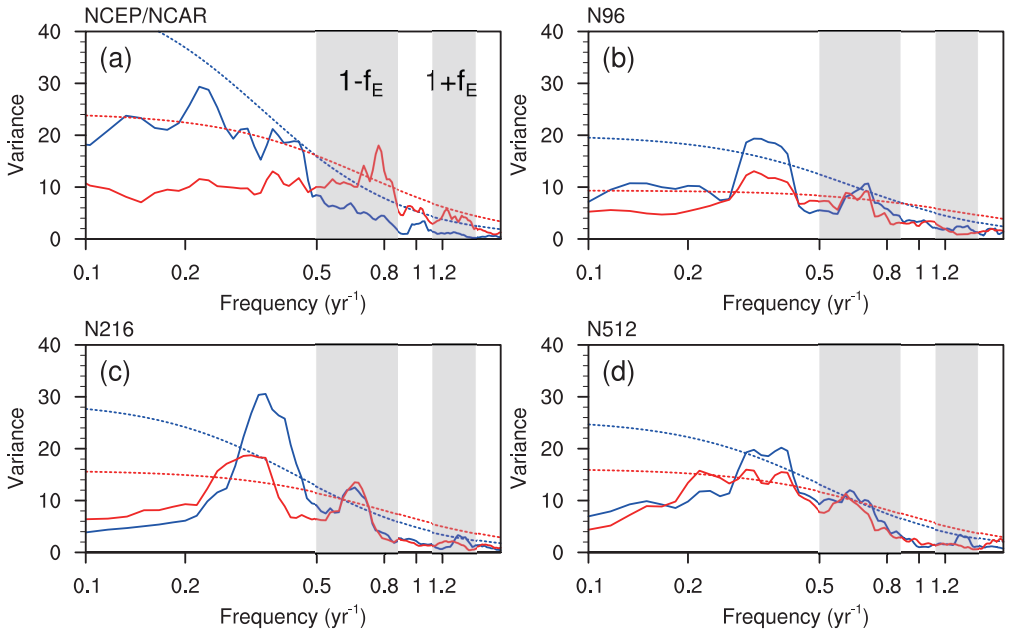

Fig. 4. Spectra curves of PC1 (blue) and PC2 (red), where the dashed lines indicate the statistical significance at the 95% confidence level. Grey rectangles indicate the near-annual combination tone frequency bands.

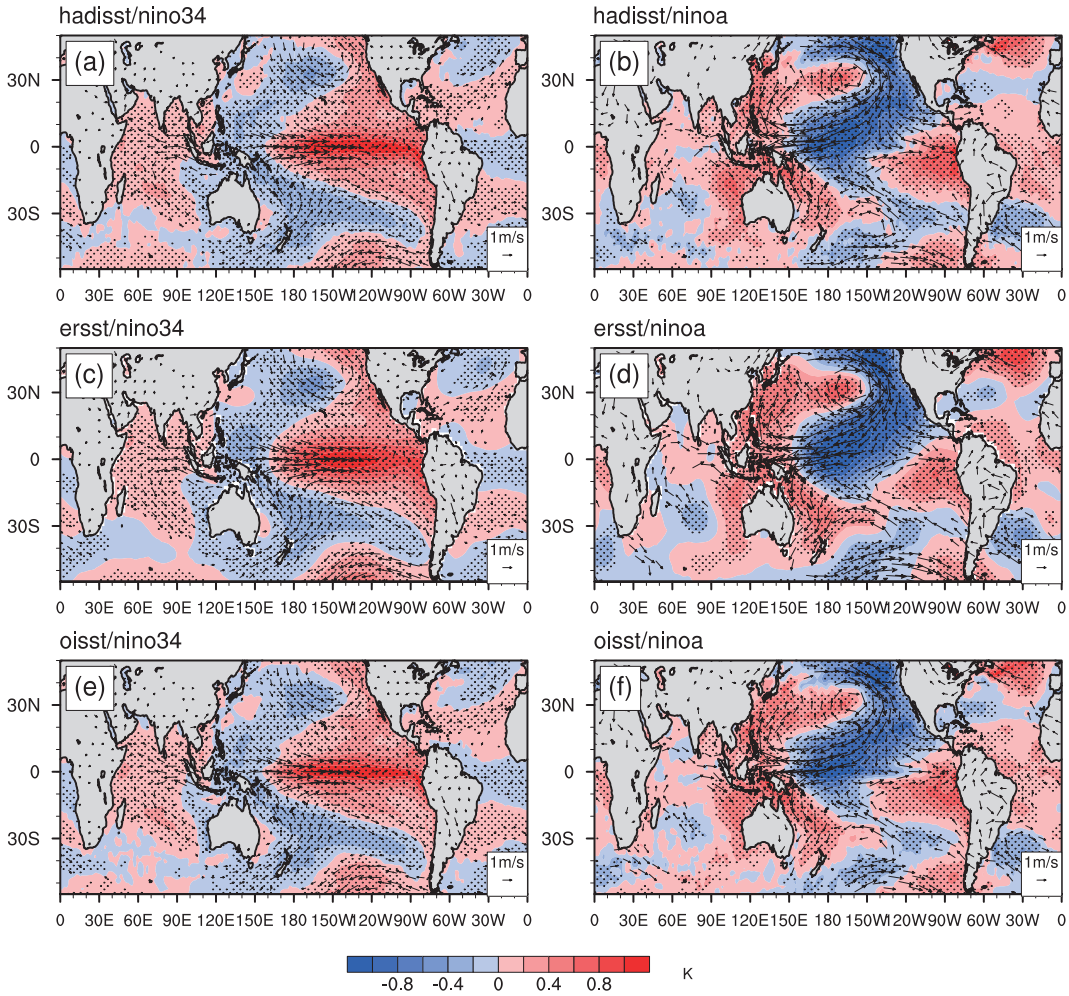

Fig. 5. SST (contours; units: K) and 850-hPa wind (vectors; units: m s^{-1}) anomalies regressed onto the Niño3.4 (left panels) and Niño-A (right panels) indices for (a, b) HadISST, (c, d) ERSST and (e, f) OISST data. Black dots represent the 99% confidence level of the SST. Only regions with at least either of the two components of wind at the 95% confidence level are shown.

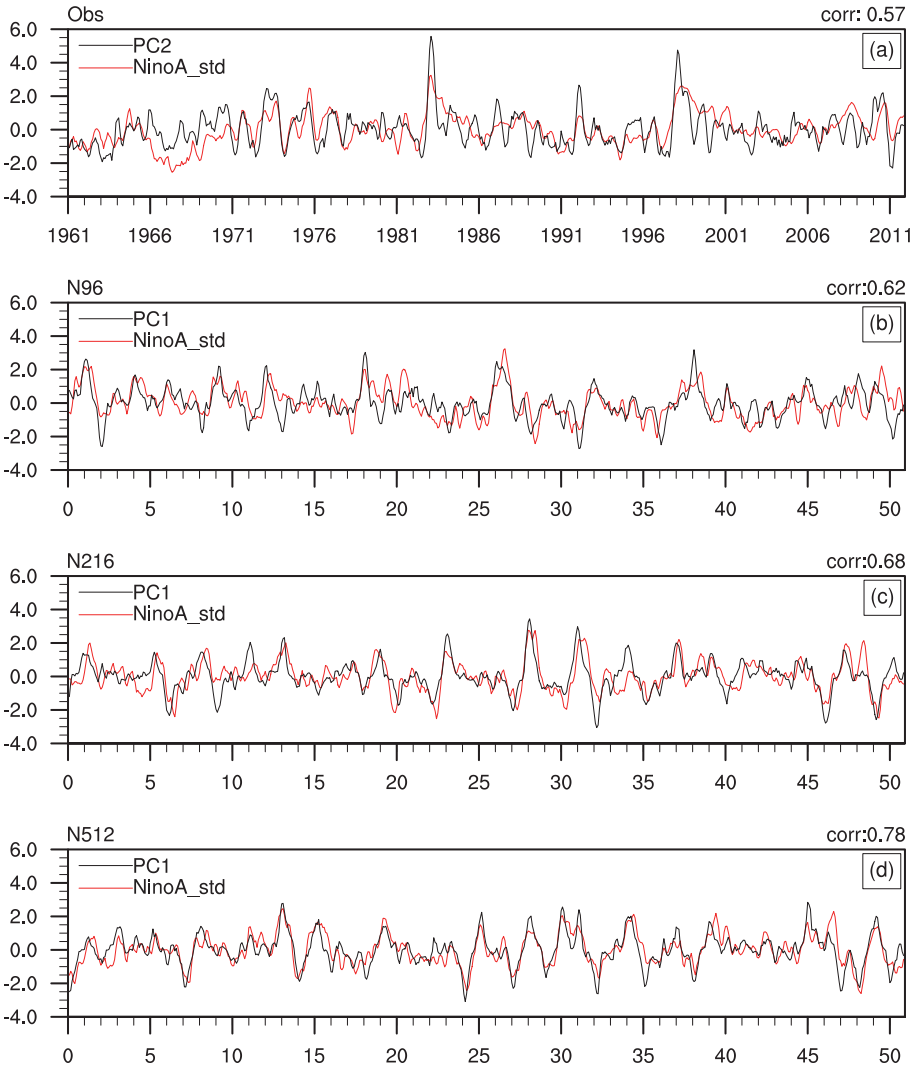

Fig. 6. (a) PC2 (NCEP–NCAR dataset) and standardized Niño-A (HadISST dataset) indices for the observation. (b–d) PC1 and standardized Niño-A indices for model outputs. Correlation coefficients between two curves are given in the top right.

the northern central tropical Pacific and positive SST anomalies over the southwestern and southeastern tropical Pacific (Figs. 5b, d and f), which exhibits a very similar structure to the forced C-mode SST pattern (Zhang et al., 2016b). The anomalous anticyclone over northwestern Pacific can be seen more clearly in the 850-hPa wind field. The results of different observational datasets also show great similarity. We use the HadISST dataset to validate the model simulation of the C-mode oceanic variability afterwards.

The Niño-A index is highly correlated with the PC2 in the reanalysis data (Fig. 6a), verifying it represents the oceanic features of the C-mode. The spectral analysis indicates that the Niño3.4 index spectrum shows a significant 2–8-year peak, and the Niño-A index peaks at combination tone periods of ~10 months and ~15 months (Fig. 7a), which is in agreement with Fig. 4. This implies the Niño-A index also exhibits the combination tone frequency based on the ENSO period and the annual cycle.

3.2. *Simulated C-mode in different model resolutions*

3.2.1. *Simulated spatial patterns of the C-mode*

If we compare the first two leading EOFs simulated by HadGEM3 (Fig. 8) with the corresponding patterns in the reanalysis (Fig. 1), they show significantly different spatial distributions. Unlike the equatorially symmetric EOF1 in the reanalysis, the EOF1 patterns in all three versions of the model exhibit remarkable meridionally antisymmetric structures, with strong shear of anomalous zonal wind across the equator, which bears great resemblance to the EOF2 pattern in the reanalysis, although the anomalous Philippine anticyclones in the models are weaker than in the reanalysis. Meanwhile, the EOF2 patterns in the models show a meridionally symmetric feature, resembling the EOF1 rather than the EOF2 pattern in the reanalysis.

This reversed similarity relationship can be more directly seen in Table 1. The pattern correlation coefficients of the

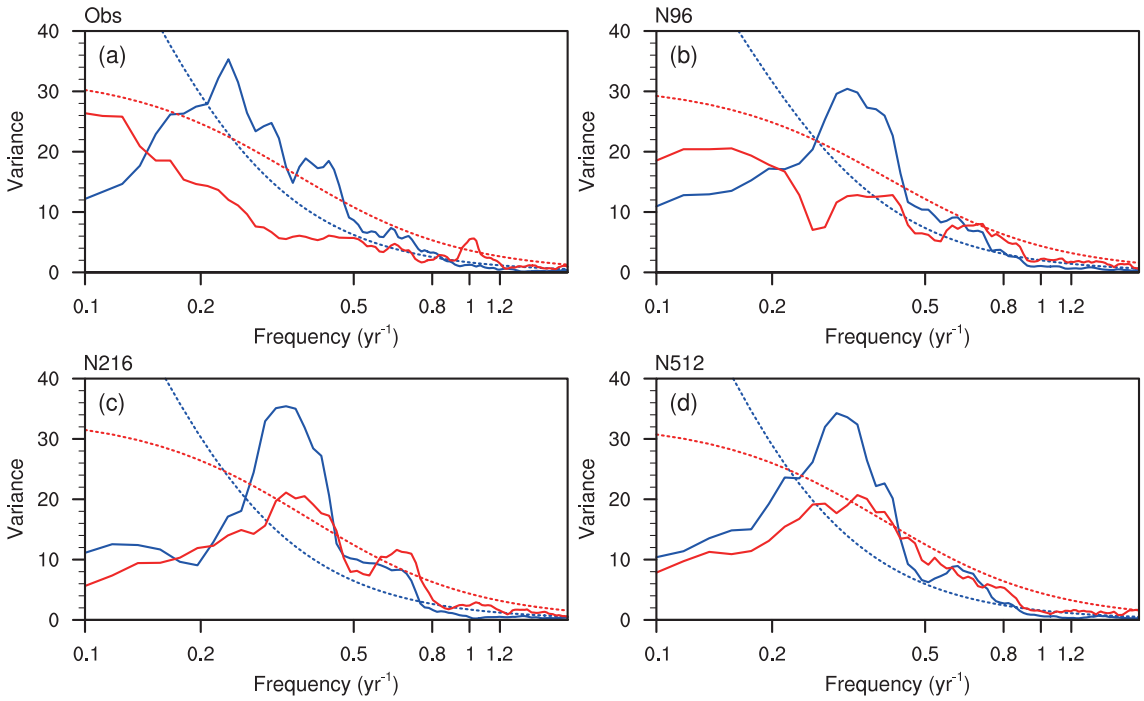

Fig. 7. Spectra curves of standardized Niño3.4 (blue) and Niño-A (red) for the observation and model results. Dashed lines indicate the statistical significance at the 95% confidence level.

same EOF patterns between the models and the NCEP–NCAR reanalysis are very low, with an absolute value of ~0.25 in the case of EOF2. On the other hand, they get much higher when we switch the order of the compared observed EOF. The correlation coefficient between the N96-simulated EOF2 and the observed EOF1 can reach 0.79, and it becomes slightly lower as the resolution gets higher. Moreover, models with better ability to reproduce the ENSO mode can also simulate the C-mode spatial pattern more realistically, which is in accordance with the CMIP5 results (Ren et al., 2016). The results indicate that HadGEM3 can capture the spatial structures of the ENSO mode and the C-mode in the surface wind field. However, it tends to emphasize the C-mode component too much, such that the C-mode turns into the dominant pattern in the tropical Pacific surface wind variability, instead of the ENSO mode as in the reanalysis.

3.2.2. *Simulated combination tone features*

As mentioned above, the ENSO mode in the simulation is represented by EOF2 instead of EOF1; thus, we compare the PC2 in the simulation with the Niño3.4 indices. They agree with each other well, with correlation coefficients around 0.5 in all three simulations (Figs. 3c, e and g). The correlation coefficients grow slightly higher as the model resolution gets higher, which is opposite to the spatial pattern trend (Table 1).

Table 1. Pattern correlation coefficients between the first two leading EOF patterns in the models and reanalysis. The letter "m" in parentheses denotes the EOF of models, and "r" stands for the reanalysis, which is the NCEP–NCAR dataset in this table.

Resolution	EOF1(m)–EOF1(r)	EOF2(m)–EOF2(r)	EOF1(m)–EOF2(r)	EOF2(m)–EOF1(r)
N96	0.44	−0.25	0.66	0.79
N216	0.51	−0.28	0.64	0.75
N512	0.48	−0.24	0.62	0.74

For the model theoretical approximation to the C-mode time series, a similar method was applied, except we used PC2 as the ENSO signal and the theoretical C-mode signal was PC2cos. The PC1s are also well correlated with the theoretical C-mode time series (Figs. 3d, f and h). The middle resolution (N216) model shows the best performance, with the correlation coefficient reaching 0.41. However, the spectra of the first two leading PCs in the model simulation are difficult to distinguish from each other (Figs. 4b, c and d). The ENSO signal (PC2) peaks around the 2–8-year period bands, but also exhibits high-frequency signals, especially at the $1 - f_E$ frequency band. This is notable in the left-hand panel of Fig. 3, in which the PC2s contain detectable high-frequency variability compared with either the PC1 in the reanalysis or the Niño3.4 indices in the simulation. The combination tones (PC1) can capture the $1 - f_E$ and $1 + f_E$ frequency peaks well, but they also show a significant peak in the ENSO mode characteristic low-frequency band, which is not the case in the reanalysis (Fig. 4a).

3.2.3. *Asymmetric SST response of the C-mode in the simulation*

Figure 9 demonstrates the SST anomalies and 850-hPa horizontal wind anomalies regressed onto the Niño3.4 and Niño-A indices in the simulations. All three configurations

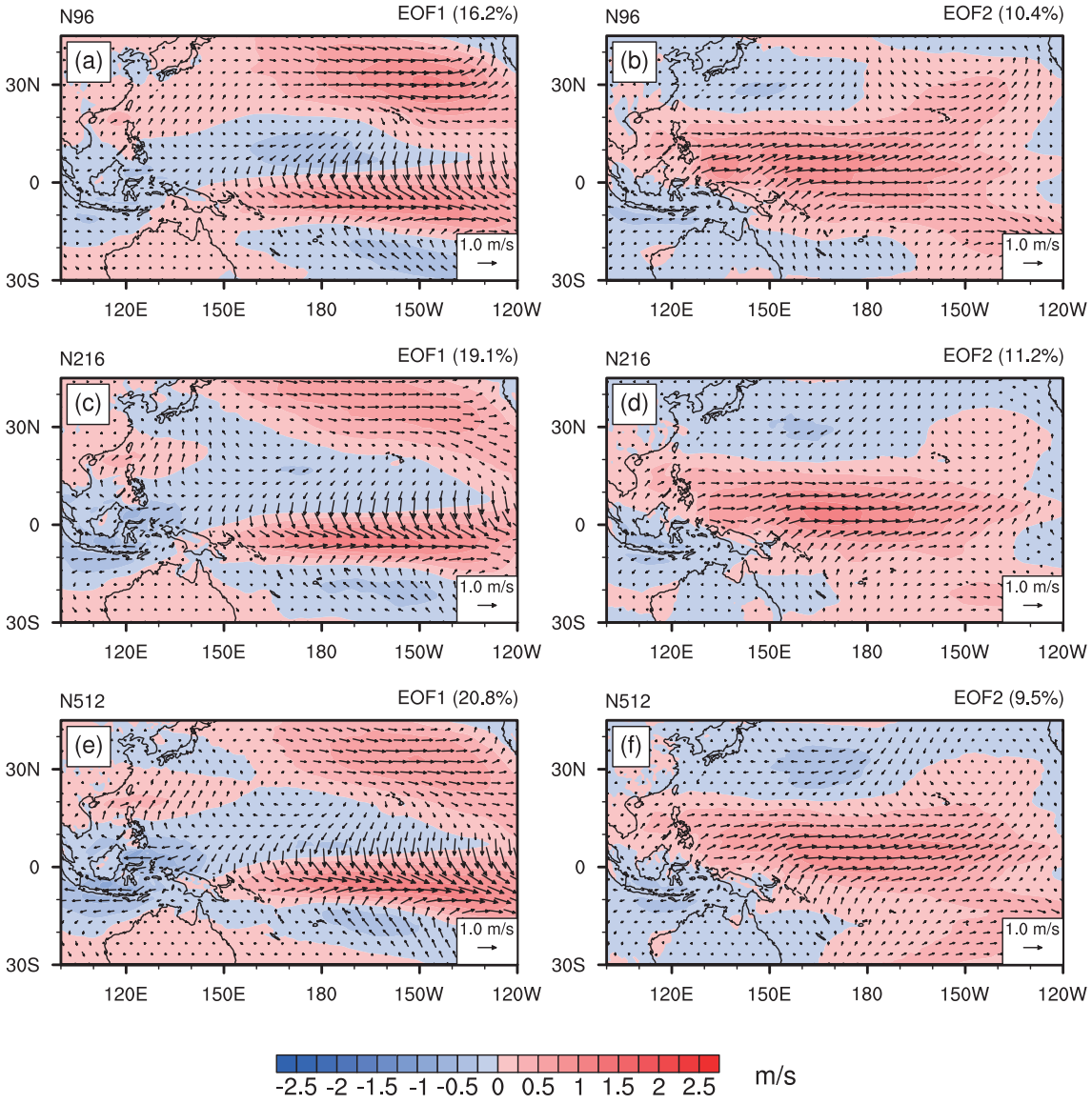

Fig. 8. The leading two EOF spatial patterns of tropical Pacific surface wind anomalies (units: m s^{-1}) for HadleyGEM3 with different resolutions of (a, b) N96, (c, d) N216 and (e, f) N512. Shading indicates the regressed zonal wind anomalies. Percentages of variance explained by the EOF patterns are given in parentheses.

of the model can capture the spatial SST distribution related to the ENSO mode and the C-mode very well, although the C-mode-related warm center over the eastern Pacific is stronger and extends to the central Pacific compared to the observation. The Niño-A index is highly correlated with the PC1s in the model simulations (Figs. 6b–d). The correlation coefficients get higher as the resolution gets higher, which reaches 0.78 in the N512 simulation. This is similar to the relationship between the Niño3.4 index and PC2 in the simulation, as illustrated in the left-hand panel of Fig. 3. This implies that, for both the ENSO mode and C-mode, the atmospheric responses (PCs) are more consistent with the oceanic responses (Niño indices) as the model resolution gets finer.

We also investigate the power spectra of the Niño3.4 and Niño-A indices in the simulations (Figs. 7b–d). In agreement with Fig. 4, the simulated Niño3.4 and Niño-A spectra show a similar performance to PC1 and PC2; the peak frequency bands are overlapped, and therefore they are not easily distinguishable from each other.

3.2.4. *Possible mechanism of the model misrepresentation*

The C-mode emerges from the nonlinear interaction between the ENSO mode and the annual cycle background. It plays an important role in ENSO's phase-lock feature by being responsible for the sudden weakening and southward shift of equatorial westerly anomalies during the termination process of strong El Niño events (Stuecker et al., 2013). We evaluate the phase relationship between PC1 and PC2 by compositing the PCs with respect to the annual cycle evolution for the El Niño events selected by the Niño3.4 indices of

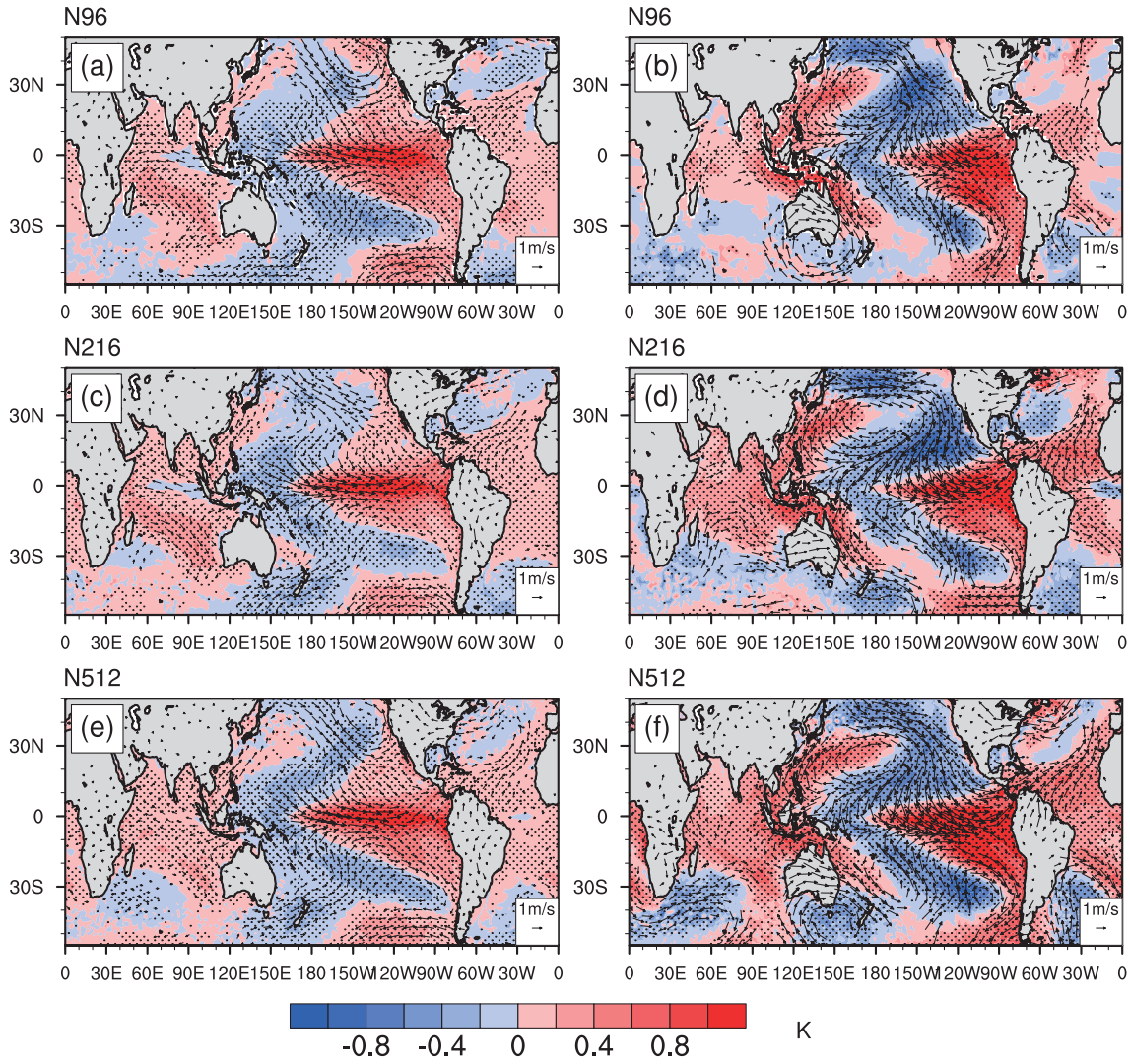

Fig. 9. SST (contours; units: K) and 850-hPa wind (vectors; units: m s^{-1}) anomalies regressed onto the Niño3.4 (left panels) and Niño-A indices (right panels) for the model results at three resolutions. Black dots represent the 99% confidence level of the SST. Only regions with at least either of the two components of wind at the 95% confidence level are shown.

each dataset (Fig. 10). The PC1s of the simulations are able to generally capture the temporal evolution of the C-mode index represented by PC2 in the reanalysis. However, the rapid phase switch around late winter in the reanalysis is not reproduced by the models. As the ENSO mode itself is concerned, the PC2s in the models show a shift in the peak time by about three months compared to the reanalysis. The performance of the middle resolution (N216) model is relatively better, of which the PC1 also matches the theoretical C-mode the best (Fig. 3f). This implies that the unrealistic periodic characteristic of the C-mode in the simulation is partly attributable to the distorted ENSO evolution. Therefore, improving the performance of the ENSO signal period in models is crucial to better simulating the C-mode.

Previous studies have pointed out the southward shift of zonal surface wind anomalies is attributable to the meridional seasonal march of western Pacific background warm SSTs and corresponding intensification of the SPCZ due to the seasonal evolution of solar insolation (Harrison and Vecchi, 1999; Spencer, 2004; Lengaigne et al., 2006; McGregor et al., 2012). The reduced climatological wind speed related to the SPCZ intensification leads to anomalous boundary layer Ekman pumping and a reduced surface momentum damping of the combined boundary layer/lower-troposphere surface wind response to El Niño, which allows the associated zonal wind anomalies to shift south of the equator (McGregor et al., 2012). Besides, Ham and Kug (2014) used CMIP3 and CMIP5 archives to reveal that the climatological mean precipitation over the central/eastern Pacific ITCZ plays an important role in ENSO phase transition by affecting the location of the ENSO-related convection and the wind stress. Figure 11 displays the climatological annual evolution of the precipitation over the central Pacific. The models simulate excessive mean precipitation over the ITCZ through late spring to winter. Also, the SPCZ intensification starts in October in the simulation, while in the observation it occurs in

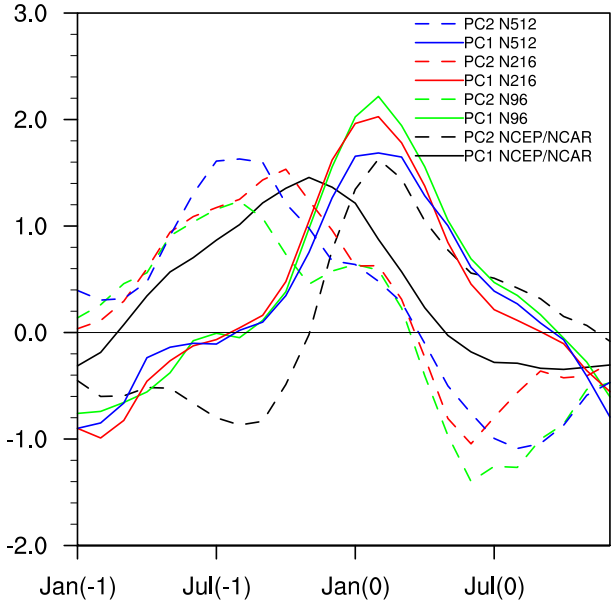

Fig. 10. PC1 (solid) and PC2 (dashed) composites of the El Niño events for the reanalysis and the model results. In the composite, year(0) denotes the developing phase and year(1) the decaying phase.

winter. The unrealistic simulation of the climatological precipitation over the central Pacific could be a factor in the relatively poor representation of the ENSO phase-lock (Fig. 10), and affects the C-mode dynamic process by providing a distorted annual cycle background.

3.3. *Simulated C-mode climate impacts on East Asian rainfall*

Previous studies have indicated the C-mode is essential to the linkage between the East Asian climate and ENSO (Li et al., 2016a; Zhang et al., 2016a, 2016b), especially the Yangtze River summer rainfall (Zhang et al., 2016b). Taking the C-mode signal into consideration could improve the predictability of the summer precipitation in El Niño events. We use the middle resolution (N216) results as an example to check the ability of HadGEM3 to reproduce this connection between the East Asian summer rainfall and ENSO (Fig. 12). Figure 12a demonstrates the average precipitation anomalies in the decaying summer (June–July–August) of the two strongest El Niño events in the N216 simulation, with increased rainfall over the Yangtze River Valley and decreased rainfall over the southeast of China. Using the Niño3.4 index alone can only reconstruct a small fraction of the precipitation anomaly (Fig. 12b). Including the Niño-A index can significantly improve the rainfall reconstruction, especially over the Yangtze River Valley. Therefore, this linkage is reproducible in HadGEM3, which gives us a suggested method to improve the prediction of East Asian summer precipitation associated with ENSO when applying the model outputs.

4. Summary and discussion

In this study, we compare the performance of the UK Met Office Hadley Center's HadGEM3 in representing the ENSO-annual cycle C-mode and the asymmetric SST response with three different resolutions: N96, N216 and N512, respec-

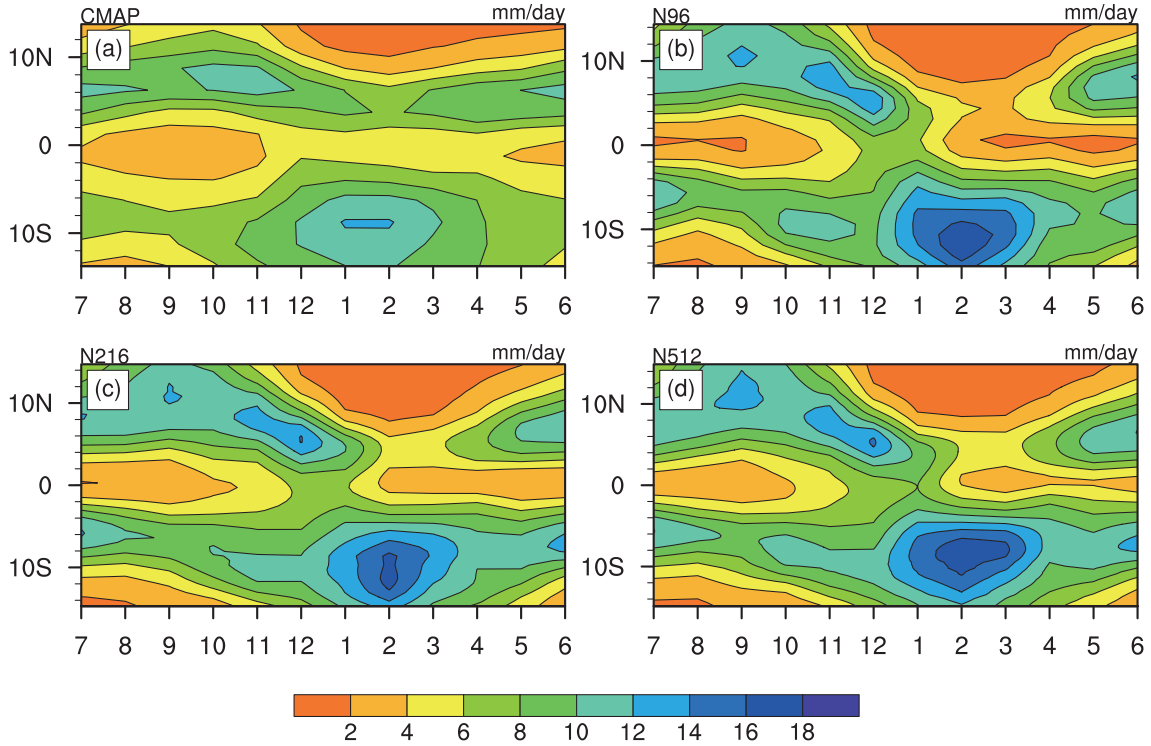

Fig. 11. Climatological annual evolution of the zonal mean (between 160°E and 160°W) precipitation (units: mm d^{-1}) from the CMAP dataset and the model simulation.

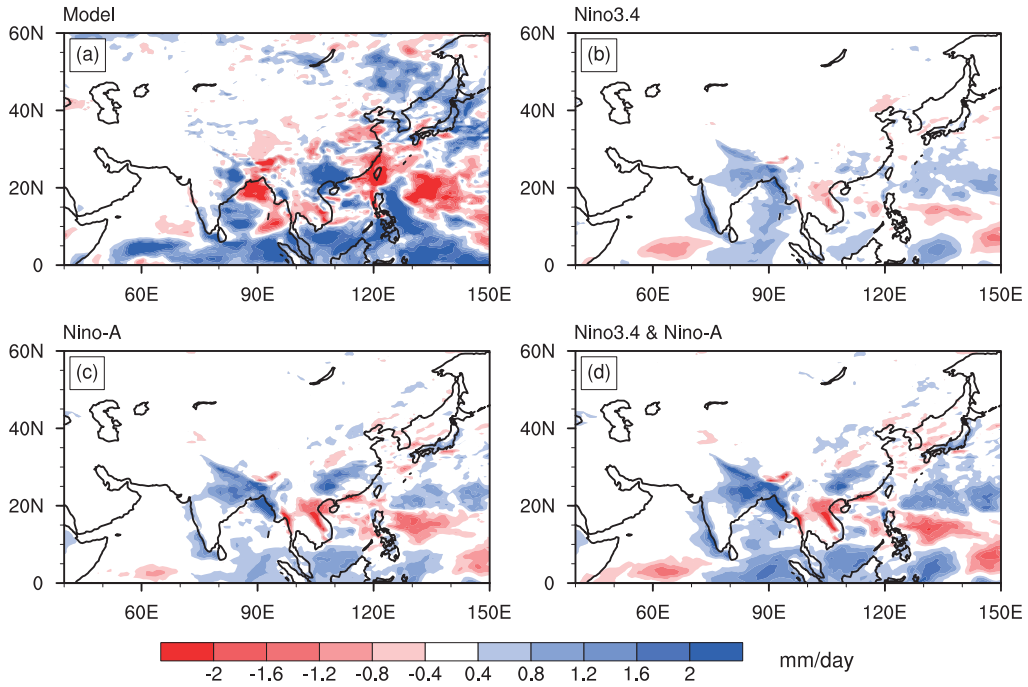

Fig. 12. (a) Precipitation anomalies during the decaying summer of the two strongest El Niño events in the N216 simulation. Reconstruction of precipitation anomalies using linear regression with (b) Niño3.4 index, (c) Niño-A index, and (d) both Niño3.4 and Niño-A indices. Units: mm d^{-1}.

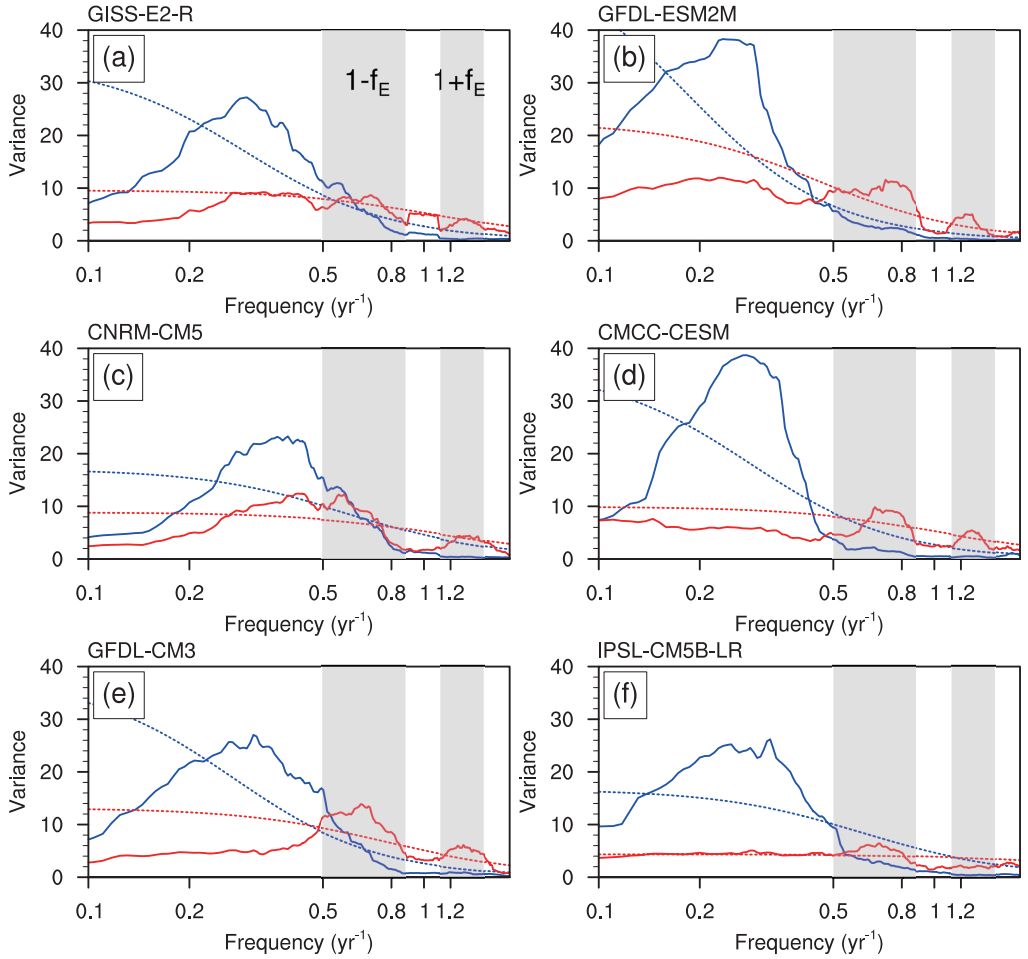

Fig. 13. Spectra curves of PC1 (blue) and PC2 (red) for six models from CMIP5. Dashed lines indicate statistical significance at the 95% confidence level.

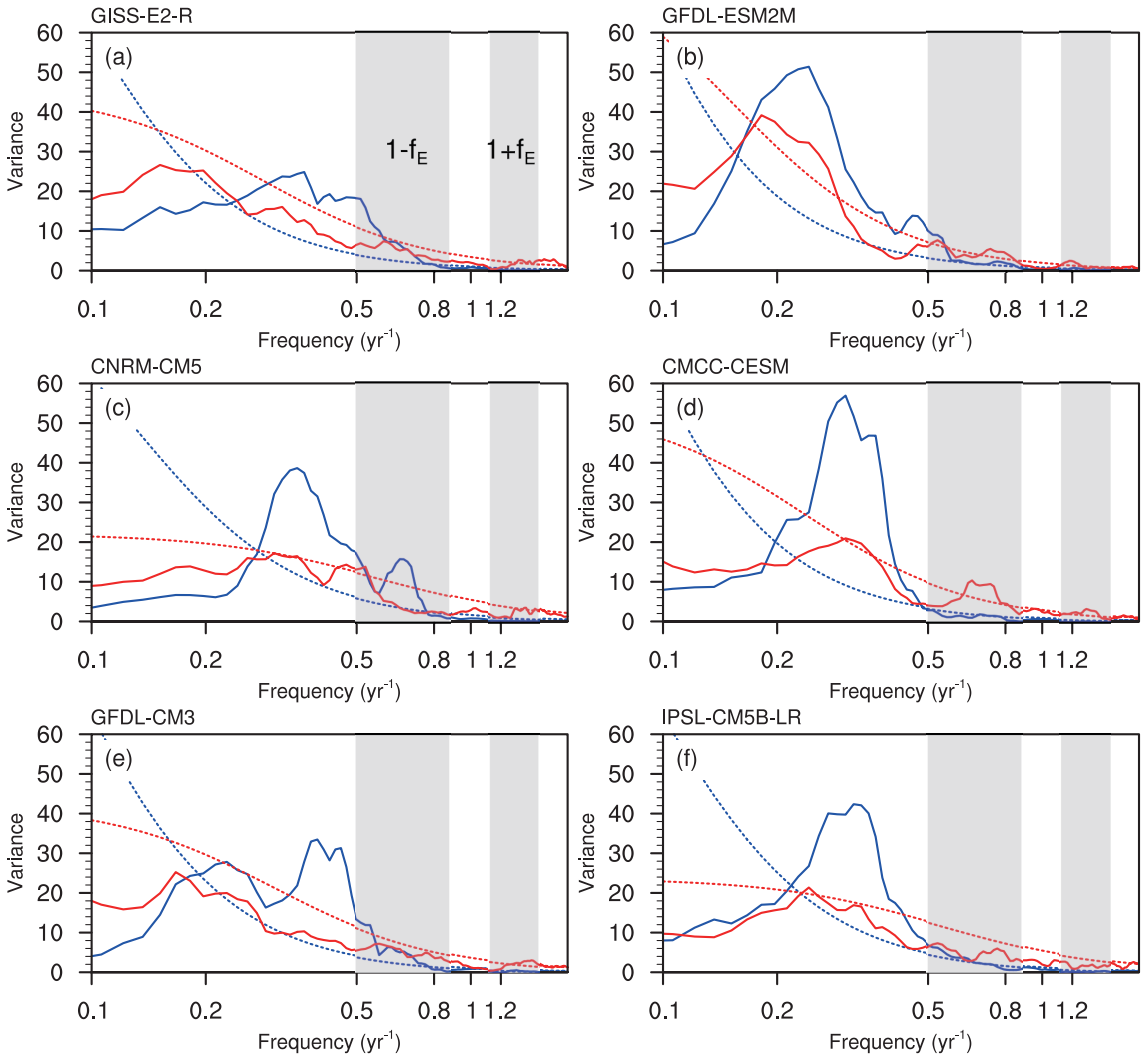

Fig. 14. Spectra curves of standardized Niño3.4 (blue) and Niño-A(red) for six models from CMIP5. Dashed lines indicate statistical significance at the 95% confidence level.

tively. The results indicate that HadGEM3 can capture the spatial characteristics of ENSO and the ENSO-annual cycle C-mode, but it overestimates the C-mode accounted variance such that the C-mode turns into the dominant pattern in the surface wind fields. Meanwhile, the model can reproduce the spectral peaks of the C-mode at periods of about 10 and 15 months, which are the ENSO-annual cycle combined frequency. However, its behavior is not ideal on longer time scales, perhaps due to the relatively unrealistic simulation of the basic ENSO mode with a shorter period and shifted seasonal evolution peak during the El Niño event, which affects the nonlinear coupled process. Also, the model cannot simulate well the rapid PC2 phase transition near late winter. The simulated basic ENSO signal also exhibits a strong signal near the combination frequency both in SST and surface wind variability, implying the model cannot unambiguously tell the difference between the ENSO signal and the C-mode signal.

Ren et al. (2016) compared the atmospheric features of the C-mode simulated by 27 CGCMs from CMIP5, demonstrating that most of them are able to reproduce the spatial pattern of the C-mode well with the correct order of the first two EOFs. Figure 13 illustrates the PC1 and PC2 spectra of the six best performing models in CMIP5, selected according to the correlation coefficients between the observed EOF2 and the simulated EOF2 of the surface wind (Ren et al., 2016). All PC2s show two distinctive combination frequencies without an unrealistic low-frequency peak. The ENSO mode and the C-mode can be distinguished from each other clearly. The circumstances are generaly similar in the oceanic characteristics (Fig. 14), but with relatively weak combination frequency peaks of the Niño-A indices than the PC2s, which is also the case for the observation. These models capture the C-mode better than HadGEM3, possibly because of the more realistic simulation of the ENSO mode.

The C-mode not only plays an important role in the intrinsic dynamical mechanism of ENSO evolution, but also in the process of ENSO affecting climate globally, especially the East Asian summer climate. It is valuable to keep bettering the ability of models in reproducing the C-mode variability,

as well as its influences on global climate. To achieve such progress, it is helpful to improve the simulation of the precipitation climatology as well as the basic ENSO variability, including the spatial pattern, the frequency, the temporal evolution, and other properties.

Acknowledgements. This work and its contributors were jointly supported by the China Meteorological Administration Special Public Welfare Research Fund (Grant No. GYHY201506013), the China National Science Foundation (Grant No. 41606019), and the UK–China Research & Innovation Partnership Fund through the Met Office Climate Science for Service Partnership (CSSP) China as part of the Newton Fund.

REFERENCES

Ham, Y. G., and J. S. Kug, 2014: Effects of Pacific Intertropical Convergence Zone precipitation bias on ENSO phase transition. *Environmental Research Letters*, **9**(6), 064008, https://doi.org/10.1088/1748-9326/9/6/064008.

Harrison, D. E., and G. A. Vecchi, 1999: On the termination of El Niño. *Geophys. Res. Lett.*, **26**(11), 1593–1596, https://doi.org/10.1029/1999GL900316.

Hewitt, H. T., D. Copsey, I. D. Culverwell, C. M. Harris, R. S. R. Hill, A. B. Keen, A. J. McLaren, and E. C. Hunke, 2011: Design and implementation of the infrastructure of HadGEM3: The next-generation Met Office climate modelling system. *Geoscientific Model Development*, **4**(2), 223–253, https://doi.org/10.5194/gmd-4-223-2011.

Jin, F.-F., J. D. Neelin, and M. Ghil, 1994: El Niño on the devil's staircase: Annual subharmonic steps to chaos. *Science*, **264**(5155), 70–72, https://doi.org/10.1126/science.264.5155.70.

Kalnay, E., and Coauthors, 1996: The NCEP/NCAR 40-Year reanalysis project. *Bull. Amer. Meteor. Soc.*, **77**(3), 437–472, https://doi.org/10.1175/1520-0477(1996)077<0437:TNYRP>2.0.CO;2.

Lengaigne, M., J.-P. Boulanger, C. Menkes, and H. Spencer, 2006: Influence of the seasonal cycle on the termination of El Niño Events in a coupled general circulation model. *J. Climate*, **19**(9), 1850–1868, https://doi.org/10.1175/JCLI3706.1.

Li, H., W. J. Zhang, and J. H. He, 2016a: Influences of ENSO and its combination mode on seasonal precipitation over eastern China. *Acta Meteorologica Sinica*, **74**(3), 322–334, https://doi.org/10.11676/qxxb2016.025. (in Chinese with English abstract)

Li, H. Y., W. J. Zhang, J. H. He, and Y. L. Wang, 2016b: Influence of SST annual cycle on local air-sea processes during El Niño events. *Haiyang Xuebao*, **38**(1), 56–58, https://doi.org/10.3969/j.issn.0253-4193.2016.01.006. (in Chinese with English abstract)

McGregor, S., A. Timmermann, N. Schneider, M. F. Stuecker, and M. H. England, 2012: The effect of the South Pacific convergence zone on the termination of El Niño events and the meridional asymmetry of ENSO. *J. Climate*, **25**(16), 5566–5586, https://doi.org/10.1175/JCLI-D-11-00332.1.

Rayner, N. A., D. E. Parker, E. B. Horton, C. K. Folland, L. V. Alexander, D. P. Rowell, E. C. Kent, and A. Kaplan, 2003: Global analyses of sea surface temperature, sea ice, and night marine air temperature since the late nineteenth century. *J. Geophys. Res.*, **108**(D14), 4407, https://doi.org/10.1029/2002JD002670.

Ren, H. L., J. Q. Zuo, F. F. Jin, and M. F. Stuecker, 2016: ENSO and annual cycle interaction: the combination mode representation in CMIP5 models. *Climate Dyn.*, **46**, 3753–3765, https://doi.org/10.1007/s00382-015-2802-z.

Ropelewski, C. F., and M. S. Halpert, 1987: Global and regional scale precipitation patterns associated with the El Niño/Southern oscillation. *Mon. Wea. Rev.*, **115**(8), 1606–1626, https://doi.org/10.1175/1520-0493(1987)115<1606:GARSPP>2.0.CO;2.

Senior, C. A., and Coauthors, 2016: Idealized climate change simulations with a high-resolution physical model: HadGEM3-GC2. *Journal of Advances in Modeling Earth Systems*, **8**, 813–830, https://doi.org/10.1002/2015MS000614.

Spencer, H., 2004: Role of the atmosphere in seasonal phase locking of El Niño. *Geophys. Res. Lett.*, **31**, L24104, https://doi.org/10.1029/2004GL021619.

Stein, K., A. Timmermann, N. Schneider, F. F. Jin, and M. F. Stuecker, 2014: ENSO seasonal synchronization theory. *J. Climate*, **27**(14), 5285–5310, https://doi.org/10.1175/JCLI-D-13-00525.1.

Stuecker, M. F., F. F. Jin, and A. Timmermann, 2015a: El Niño-Southern Oscillation frequency cascade. *Proceedings of the National Academy of Sciences of the United States of America*, **112**(44), 13 490–13 495, https://doi.org/10.1073/pnas.1508622112.

Stuecker, M. F., F. F. Jin, A. Timmermann, and S. McGregor, 2015b: Combination mode dynamics of the anomalous Northwest Pacific anticyclone. *J. Climate*, **28**(3), 1093–1111, https://doi.org/10.1175/JCLI-D-14-00225.1.

Stuecker, M. F., A. Timmermann, F. F. Jin, S. McGregor, and H. L. Ren, 2013: A combination mode of the annual cycle and the El Niño/Southern Oscillation. *Nature Geoscience*, **6**(7), 540–544, https://doi.org/10.1038/ngeo1826.

Trenberth, K. E., and J. M. Caron, 2000: The Southern Oscillation revisited: Sea level pressures, surface temperatures, and precipitation. *J. Climate*, **13**(24), 4358–4365, https://doi.org/10.1175/1520-0442(2000)013<4358:TSORSL>2.0.CO;2.

Trenberth, K. E., G. W. Branstator, D. Karoly, A. Kumar, N. C. Lau, and C. Ropelewski, 1998: Progress during TOGA in understanding and modeling global teleconnections associated with tropical sea surface temperatures. *J. Geophys. Res.*, **103**(C7), 14 291–14 324, https://doi.org/10.1029/97JC01444.

Vecchi, G. A., 2006: The Termination of the 1997–98 El Niño. Part II: Mechanisms of atmospheric change. *J. Climate*, **19**(12), 2647–2664, https://doi.org/10.1175/JCLI3780.1.

Wallace, J. M., E. M. Rasmusson, T. P. Mitchell, V. E. Kousky, E. S. Sarachik, and H. von Storch, 1998: On the structure and evolution of ENSO-related climate variability in the tropical Pacific: Lessons from TOGA. *J. Geophys. Res.*, **103**(C7), 14 241–14 259, https://doi.org/10.1029/97JC02905.

Weisheimer, A., and Coauthors, 2009: ENSEMBLES: A new multi-model ensemble for seasonal-to-annual predictions—Skill and progress beyond DEMETER in forecasting tropical Pacific SSTs. *Geophys. Res. Lett.*, **36**(21), L21711, https://doi.org/10.1029/2009GL040896.

Williams, K. D., and Coauthors, 2015: The Met Office Global Coupled model 2.0 (GC2) configuration. *Geoscientific Model Development*, **8**, 1509–1524, https://doi.org/10.5194/gmd-8-1509-2015.

Zhang, W. J., H. Y. Li, M. F. Stuecker, F. F. Jin, and A. G.

Turner, 2016a: A new understanding of El Niño's Impact over East Asia: Dominance of the ENSO Combination Mode. *J. Climate*, **29**(12), 4347–4359, https://doi.org/10.1175/JCLI-D-15-0104.1.

Zhang, W. J., H. Y. Li, F. F. Jin, M. F. Stuecker, A. G. Turner, and N. P. Klingaman, 2015: The annual-cycle modulation of meridional asymmetry in ENSO's atmospheric response and its dependence on ENSO Zonal Structure. *J. Climate*, **28**(14), 5795–5812, https://doi.org/10.1175/JCLI-D-14-00724.1.

Zhang, W. J., and Coauthors, 2016b: Unraveling El Niño's impact on the East Asian Monsoon and Yangtze River summer flooding. *Geophys. Res. Lett.*, **43**(21), 11 375–11 382, https://doi.org/10.1002/2016GL071190.

doi:10.11676/qxxb2018.027

不同云重叠参数对全球和东亚地区模拟总云量的影响*

王海波[1,2]　张　华[1,2]　荆现文[1]　谢　冰[1,3]

WANG Haibo[1,2]　ZHANG Hua[1,2]　JING Xianwen[1]　XIE Bing[1,3]

1. 南京信息工程大学,气象灾害预报预警与评估协同创新中心,南京,210044
2. 中国气象科学研究院灾害天气国家重点实验室,北京,100081
3. 中国气象局气候研究开放实验室,国家气候中心,北京,100081

1. *Collaborative Innovation Center on Forecast and Evaluation of Meteorological Disasters, Key Laboratory of Meteorological Disaster of Ministry of Education, Nanjing University of Information Science and Technology, Nanjing* 210044, *China*
2. *State Key Laboratory of Severe Weather, Chinese Academy of Meteorological Sciences, Beijing* 100081, *China*
3. *Laboratory for Climate Studies of China Meteorological Administration, National Climate Center, China Meteorological Administration, Beijing* 100081, *China*

2017-12-25 收稿,2018-04-05 改回.

王海波,张华,荆现文,谢冰. 2018. 不同云重叠参数对全球和东亚地区模拟总云量的影响. 气象学报,76(5):767-778

Wang Haibo, Zhang Hua, Jing Xianwen, Xie Bing. 2018. Effects of different cloud overlapping parameters on simulated total cloud fraction over the globe and East Asian region. *Acta Meteorologica Sinica*, 76(5):767-778

Abstract The cloud overlapping parameter (vertical decorrelation length, L_{cf}) from CloudSat/CALIPSO is implemented in Beijing Climate Center's GCM (BCC_AGCM2.0) to reduce the uncertainly in radiation field. Comparing the climate simulation results obtained by using the constant L_{cf} of 2 km with those using the above retrieved L_{cf}, it is found that the total cloud fraction simulation has been obviously improved by using the satellite-based L_{cf}. The error of global mean total cloud fraction between simulations and CERES (Clouds and the Earth's Radiant Energy System) satellite data is decreased by 1.6% in both the winter and summer, of which the positive deviation of total cloud fraction at tropical convection area and the negative deviation in subtropical region both are significantly reduced. These improvements are helpful for better simulation of energy budget differences between different regions. In East Asia, using the satellite-based L_{cf} can decrease the error of average total cloud fraction (compared to the CERES) by 1.8% (1.4%) in the winter (summer). Overall, using L_{cf} from CloudSat/CALIPSO satellite data can improve the simulation of total cloud fraction and thus obtain more accurate simulation of radiation field.

Key words Cloud overlapping parameter, Vertical decorrelation length, Total cloud fraction

摘　要　在国家气候中心全球大气环流模式 BCC_AGCM2.0 中引入一组基于 CloudSat/CALIPSO 卫星观测的、能够体现真实时空变化特征的云垂直重叠参数(抗相关厚度,L_{cf})数据,以减小由云的重叠描述造成的辐射场的不确定性。对比了采用时空变化的云重叠参数和采用恒定云重叠参数的气候模拟结果,发现无论在全球还是东亚区域,采用基于卫星观测的云重叠参

* 资助课题:国家重点研发计划项目(2017YFA0603502)、国家自然科学基金项目(41375080、91644211)和科技部公益性行业(气象)科研专项课题(GYHY201406023)。

作者简介:王海波,主要从事云重叠以及云和辐射相互作用研究。E-mail:haibo_0225@126.com

通讯作者:张华,主要从事大气辐射传输模式、温室气体和气溶胶辐射强迫与气候效应以及云辐射降水相互作用研究。E-mail:huazhang@cma.gov.cn

数对模拟的总云量都有一定程度的改进。采用时空变化的云重叠参数后,冬、夏两季全球平均总云量与云和地球的辐射能量系统(CERES)卫星资料的误差都减少了1.6%,其中热带对流区域总云量的正偏差和副热带地区总云量的负偏差都明显减少,这些有助于正确模拟不同区域间的能量收支差异。在东亚区域,采用时空变化的云重叠参数后,冬、夏两季的东亚区域平均总云量与CERES卫星资料的误差分别减少了1.8%和1.4%。综上所述,基于CloudSat/CALIPSO卫星资料计算得到的L_{cf}有助于改进大气环流模式对总云量的模拟,从而提高模式对辐射场的模拟精度。

关键词 云重叠参数,抗相关厚度,总云量

中图法分类号 P426.5^{+}2

1 引 言

地球表面约60%的面积被云覆盖(Liou,et al,1993)。云通过反射太阳短波辐射和吸收地表与云下大气的长波辐射,对地-气系统的辐射收支平衡产生显著影响。同时,云也影响着地-气系统的水分循环、大气化学和气溶胶相关过程(张华等,2016)。历次政府间气候变化专门委员会(IPCC)评估报告指出,云是迄今为止影响气候变化和气候预测的诸多因子中非常重要但不确定性最大的因子。低云增加4%可抵消二氧化碳浓度倍增引起的2—3℃升温,反之则会扩大相应的升温效应(Randall, et al, 1984)。因此,云的物理和光学性质的准确模拟对提高全球尤其东亚地区气候模拟与预测的准确性具有重要意义。

在目前的大气环流模式中,由于水平分辨率较低(达到百千米尺度),在次网格内对云物理过程的准确描述(例如:云的形成与消散)是一个难题(Wigley, et al, 1990; Wyant, et al, 2006; Jing, et al, 2016),大气环流模式中常采用参数化方法来描述云的宏、微观物理性质(Lu, et al, 2013)。因此,利用观测得到的云的性质来评估模式中云的参数化方案受到了学术界的广泛关注(Hinkelman, et al, 1999; Hogan, et al, 2001; Sengupta, et al, 2004; Bouniol, et al, 2010; Paquin-Ricard, et al, 2010; Song, et al, 2013)。由于全球气候模式中空间分辨率的限制,云参数化需要在每个垂直层上给出云量,即云在该层的覆盖率(Hogan, et al, 2000)。云重叠参数化方案是描述这些单层云量在垂直方向上重叠特征的方法,既影响垂直重叠后的总云量,也间接影响云水路径的水平分布,进而影响云的长、短波反照率和透过率(Barker, 2008; Li, et al, 2005)。因此,云重叠处理方法的评估和改进对模式气象场的模拟效果至关重要。

传统的云垂直重叠模型大多采用固定的重叠假设。常见的云重叠方式有:最大重叠、随机重叠、最大-随机重叠的组合(张华等, 2016)。Hogan等(2000)、Mace等(2002)、Bergman等(2002)发现云层之间的重叠关系随着它们之间的垂直距离的增大而迅速减小,提出了指数衰减重叠,利用云重叠参数——抗相关厚度参数(L_{cf})来表示云层之间的重叠关系。自此,研究人员一直在尝试获取L_{cf}的全球以及季节分布信息并在全球气候模式中加以应用(Barker, 2008; Shonk, et al, 2010; Zhang, et al, 2013; 彭杰等, 2013)。对于抗相关厚度的最简单的描述方法是取全球平均值L_{cf} = 2 km(Barker, 2008)。Oreopoulos等(2012)提出了L_{cf}随纬度和季节变化的方法,但是这种参数化方案在纬度变化上存在缺陷。Zhang等(2014b)提出了不同云类型L_{cf}的计算方法,但这种方法取决于全球气候模式中高度不确定的云分类方案。

云量是云的重要宏观特性,改进全球气候模式对云量的模拟精度具有重要的研究意义。东亚地区是典型的季风区,同时还受到青藏高原地形的影响,其云量的分布具有鲜明的地域和气候特征(吴春强等, 2011)。例如,它是全球唯一的陆地层云区(Klein, et al, 1993),具有同纬度最大的云光学厚度(Yu, et al, 2004; Li, et al, 2004)。抗相关厚度L_{cf}作为描述云重叠参数的因子是影响全球气候模式云量模拟的重要因素。为了更准确地得到云的参数化方案,更全面地了解全球尤其是东亚地区云重叠参数与云量的关系,本研究采用以下两种不同的抗相关厚度的方案来表述全球模式中的典型情况:(1)取全球平均值L_{cf} = 2 km;(2)利用4年(2007—2010年)的CloudSat/CALIPSO卫星观测资料计算得到L_{cf}(下文用L_{cf}^{*}表示)。本研究分别采用了两种方案,利用中国国家气候中心全球大气环流模式BCC_AGCM2.0,比较不同方案对全球以及东亚地

区模拟总云量的影响。将模拟的总云量与卫星资料反演的总云量进行对比,讨论不同的 L_{cf} 取值与总云量的关系。

2 数据和方法

2.1 数 据

本研究采用 CloudSat/CALIPSO 卫星资料,在全球气候模式网格上计算 L_{cf}。CloudSat/CALIPSO 卫星是 A-Trian 中的重要成员,于 2006 年发射成功。CloudSat 是第一颗用主动毫米波雷达在全球范围内观测及研究云量、云分布和垂直结构、辐射特性及降水信息的卫星,搭载的有效载荷是 94 GHz(3 mm 波)云廓线雷达,可以探测云物理属性的垂直廓线。CALIPSO 卫星主要荷载包括正交偏振云-气溶胶偏振雷达(CALIOP)、宽视场相机(WFC)和红外成像辐射计(IIR),可提供全球云和气溶胶观测数据,用于研究云和气溶胶存在的气候效应以及两者间的相互作用。将两颗卫星的资料结合在一起,可以得到更完整的云的资料(Hagihara, et al, 2010; Mace, et al, 2009)。本研究采用 2007—2010 年 2B-GEOPROF 和 2B-GEOPROF-LIDAR 的产品资料。2B-GEOPROF 资料描述的是云的几何廓线,主要包含 CloudSat 轨迹剖面上用来识别云层边界及云顶信息的云判别有效值和相对应的雷达反射率数值,云判别有效值是衡量雷达反射率回波可靠性的重要指标,其值越大表明云的回波信号越强越可靠。2B-GEOPROF-LIDAR 产品是由雷达和激光雷达联合反演得到,其中 94 GHz 毫米波云观测雷达可探测不同云层的光学厚度,而激光雷达对薄云的探测更为敏感,两种仪器联合可以探测到更为权威的云垂直结构信息。该产品提供了垂直方向云层的数目、云量、海平面以上各云层的云顶高度和云底高度。2B-GEOPROF 提供的是经校准的云几何廓线,而 2B-GEOPROF-LIDAR 提供的是联合 94 GHz 毫米波云观测雷达和 CALIOP 的云几何廓线,更为准确。在用此数据进行本研究的计算过程中,2B-GEOPROF 数据中 94 GHz 毫米波云观测雷达的云判别有效值≥20、2B-GEOPROF-LIDAR 数据中的云量≥99%以及雷达反射率≥-30 dBz 三者同时满足时,即判定为该处有云,否则为晴空。具体计算过程请参考 Jing 等(2016)。

采用云和地球的辐射能量系统(CERES)卫星观测资料与不同方案模拟得到的总云量进行对比分析。CERES 是由 NASA 在 1997 年发射的卫星传感器,其数据产品包括各种辐射通量以及云的特性。文中采用 CERES SYN1deg-Month Ed3A 中 2006—2015 年的总云量数据,其分辨率为 1°×1°。

2.2 方 法

2.2.1 抗相关厚度(L_{cf})

假设有上、下两层云分别为 k 和 l 层,两层的云量分别为 C_k 和 C_l。在云重叠的指数衰减重叠模型中,上、下两层(k 和 l 层)的垂直投影总云量为(Jing, et al, 2018)

$$C_{k,l} = \alpha_{k,l} C_{k,l}^{\max} + (1-\alpha_{k,l}) C_{k,l}^{\mathrm{ran}} \tag{1}$$

式中,$C_{k,l}^{\max} = \max(C_k, C_l)$ 和 $C_{k,l}^{\mathrm{ran}} = C_k + C_l - C_k C_l$ 分别表示最大重叠和随机重叠时的总云量。$\alpha_{k,l}$ 表示两层云的重叠系数,$\alpha_{k,l}$ 的值越大则两层云的重叠程度越高。从指数衰减重叠模型中得出:当 $\alpha_{k,l}=0$ 时,指数衰减重叠即为随机重叠;当 $\alpha_{k,l}=1$ 时,指数衰减重叠即为最大重叠。$\alpha_{k,l}$ 由以下公式计算得到(Bergman, et al, 2002)

$$\alpha_{k,l} = \exp\left[-\int_{Z_k}^{Z_l} \frac{\mathrm{d}z}{L_{cf}(z)}\right] \tag{2}$$

式中,L_{cf} 表示云的重叠参数抗相关厚度,物理意义为当重叠系数 $\alpha_{k,l}$ 衰减到 e^{-1} 时两层云(k 和 l 层)之间的距离。Z_k 和 Z_l 分别表示 k 层和 l 层的中间点的高度。从式(2)可以看出,对于给定 Z_k 和 Z_l,随着 L_{cf} 的增大而增大。对于 $C_{k,l}$ 而言,较大的 L_{cf} 对应较小的 $C_{k,l}$;较小的 L_{cf} 对应较大的 $C_{k,l}$。L_{cf} 与云层和大气动力学有关(Naud, et al,2008)。

随着科学技术的发展,人们对 L_{cf} 的认识越来越深入。很多研究者根据不同资料对 L_{cf} 的时、空分布进行了进一步的研究。Barker(2008)利用 1 个月的 CloudSat/CALIPSO 卫星资料计算出 L_{cf} 的纬向平均分布。Zhang 等(2013)同样利用 CloudSat/CALIPSO 卫星资料对东亚地区 L_{cf} 不同地区的季节分布做了研究。Di Giuseppe 等(2015)利用 CloudSat 和 CALIPSO 卫星资料结合 ECMWF 风场分析资料研究了风切变与 L_{cf} 的关系。Jing 等(2016)利用 CloudSat/CALIPSO 卫星资料得到了 L_{cf} 的全球网格的逐月数据。Jing 等(2018)在全球云分析模式中研究 L_{cf} 与热带地区大气对流强度的关系。文中

将此数据应用于国家气候中心的全球气候模式中，以更真实地体现云重叠特征的时、空变化。

2.2.2 模式介绍

为了了解 L_{cf} 时、空分布对所模拟的云量和其他气候场的影响，采用中国气象局国家气候中心大气环流模式 BCC_AGCM2.0 进行模拟研究。BCC_AGCM2.0 是在美国 NCAR 的全球集合大气模式 CAM3 基础上发展的。该模式以欧拉谱动力核为基础，采用 42 波三角截断的水平方案（T42，近似于 2.8°×2.8°），垂直方向采用混合 σ-压力坐标系，共 26 层，模式顶层为 2.9 hPa（Wu, et al, 2010）。Wu 等（2010）在改进动力框架的同时还对部分物理参数化方案进行了更进一步的调整，模式中的对流参数化方案和干绝热调整方案都进行了更新，同时水汽通量、海面感热以及雪覆盖率的计算方法也进一步完善。Wu 等（2010）将模式的模拟结果与观测资料进行比较发现，BCC_AGCM2.0 与 CAM3.0 相比对当前气候平均状态的模拟效果有所提高，尤其是在模拟热带和副热带风场、潜热通量、海洋感热和降水量时，BCC_AGCM2.0 的模拟效果更好。

BCC_AGCM2.0 中采用了 BCC_RAD 辐射传输方案（Zhang, et al, 2003, 2006a, 2006b; 张华, 2016）。该方案将 0.2—1000 μm 的波长区间划分为 17 个带（0.2—3.73 μm 共 9 个短波波段以及 3.73—1000 μm 共 8 个长波波段）。方案中包含了 5 种主要的温室气体（H_2O、CO_2、O_3、N_2O、CH_4）以及 3 种氯氟烃（CFCs），采用改进的相关 k 分布法和 CKD_2.4 方案分别计算以上成分的吸收和连续吸收作用。

为减小模式空间分辨率较低、云次网格描述粗糙所带来的误差，荆现文等（2012）在 BCC_AGCM2.0 中引入了蒙特卡洛独立气柱近似（McICA）来描述次网格云的结构（Pincus, et al, 2003; 荆现文等, 2012; Zhang, et al, 2013, 2014b），通过次网格随机云生成器（Räisänen, et al, 2004a, 2004b）实现云在水平和垂直方向上均更加精细的分布。

2.2.3 试验设计

本研究仅考虑重叠参数的改变对模拟的总云量造成的瞬时影响，而未考虑气候反馈。为诊断这种影响，在全球气候模式的每个时间步长内对总云量进行一次额外的计算：根据表 1 中的试验设计计算得到总云量差异来反映不同 L_{cf} 带来的影响。在模式积分中，模式仅用第 1 次计算得到的总云量结果进行下一步长的计算。因此，以上进行诊断计算的总云量不产生气候反馈。模式运行时间为 10 年。

表 1 诊断 L_{cf} 影响的数值试验设计

Table 1 Experiments conducted to diagnose the effect of L_{cf}

试验名称	参数设置	运行时间(a)
试验 1(EXP1)	L_{cf} = 2 km	10
试验 2(EXP2)	L_{cf}^*	10

3 结果分析

3.1 L_{cf}^* 的分布

3.1.1 全球 L_{cf}^*

图 1 为冬季（12 月—次年 2 月）和夏季（6—8 月）L_{cf}^* 的全球分布。由于卫星在极地附近的观测存在较大的偏差，因此 L_{cf}^* 的有效空间范围为（82°S—82°N，180°W—180°E）。北半球夏季由于大气相对不稳定与对流的存在，云体相对较少（Li, et al, 2015; Zhang, et al, 2014a），L_{cf}^* 相对较小。相反，在北半球冬季大气层稳定、云层厚、L_{cf}^* 相对较大。从全球不同季节 L_{cf}^* 的纬向平均（图 2）可以更直观地看出：北半球冬季的 L_{cf}^* 较夏季大，最大值达到 4.2 km，出现在中高纬度地区，此时大气更加稳定，云的形成与大规模的抬升作用有关，通常可以延伸数千米并具有较大的厚度以及良好的垂直结构；南半球在 30°S—EQ，冬季较夏季大，冬季达到 2.9 km 而夏季为 1.8 km，中纬度地区冬、夏两季的差别小，因为南半球中纬度多为洋面，云层变化小，在高纬度地区则夏季较大，达到 4.8 km。

从图 1 可以很明显看出，无论是冬季还是夏季亚洲大陆都是 L_{cf}^* 的高值区，冬季为 5—6 km，夏季则为 3—4 km，这与 Mace 等（2002）以及 Oreopoulos 等（2011）的地面雷达观测结果一致。印度洋赤道地区 L_{cf}^* 的值普遍大于 2 km，这是由于在印度洋赤道地区经常发生深对流系统，导致云从很低的高度一直发展到对流层上方（Wang, et al, 1998）。在南半球中纬度海洋地区，L_{cf}^* 进一步减小为 1—2 km。这里海温较低，较低的层状云占主导地位（Wood, 2012）。这种云具有不规则的形状，在垂直

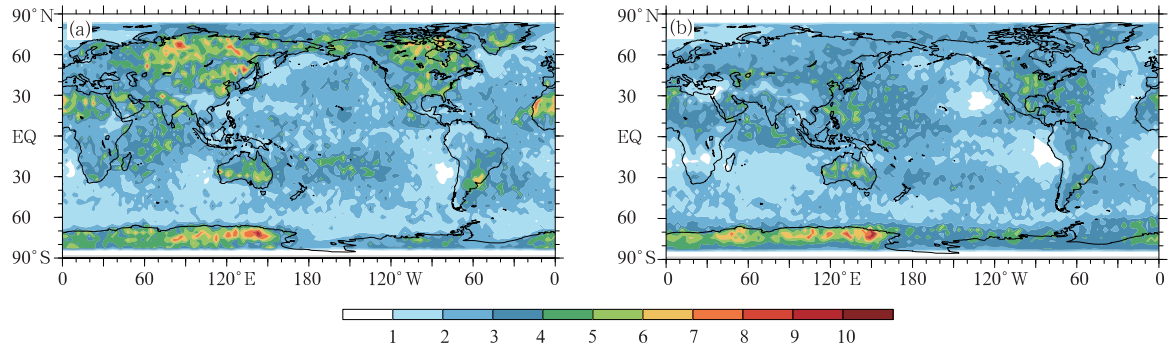

图 1 全球平均 L_{cf}^{*}(单位:km)的季节分布

(a. 冬季, b. 夏季)

Fig. 1 Seasonal distributions of global mean L_{cf}^{*}

(a. winter, b. summer, unit: km)

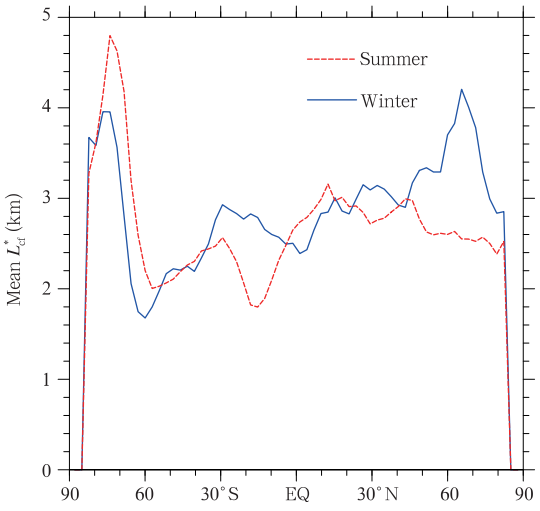

图 2 全球冬、夏两季 L_{cf}^{*}(单位:km)的纬向平均

Fig. 2 Global zonal-mean L_{cf}^{*} (unit: km) in winter and summer

方向上没有发展的动力。在南美洲西部太平洋地区,冬季和夏季都出现了 L_{cf}^{*} 的极小值,出现小于 1 km 的情况。

3.1.2 东亚地区的 L_{cf}^{*}

东亚 L_{cf}^{*} 的季节分布具有明显的区域特点。从整体上看,冬、夏两季东亚 L_{cf}^{*} 在全球分布中处于高值区,平均值(分别为 3.20 和 3.14 km)比全球平均(分别为 2.78 和 2.60 km)高了 15.1%和20.8%。从图 3 可以看出,东亚地区云重叠参数的一个显著特征是海、陆差异明显:冬季,中国的东北部 L_{cf}^{*} 普遍在 5 km 以上甚至出现极大值,约为8 km,而在东亚以东的洋面上 L_{cf}^{*} 的值相对较低,大多在 3 km 以下;夏季,在东亚以东的洋面上 L_{cf}^{*} 达到 4—6 km,而在东亚大陆上 L_{cf}^{*} 的值偏小,大多小于3 km。

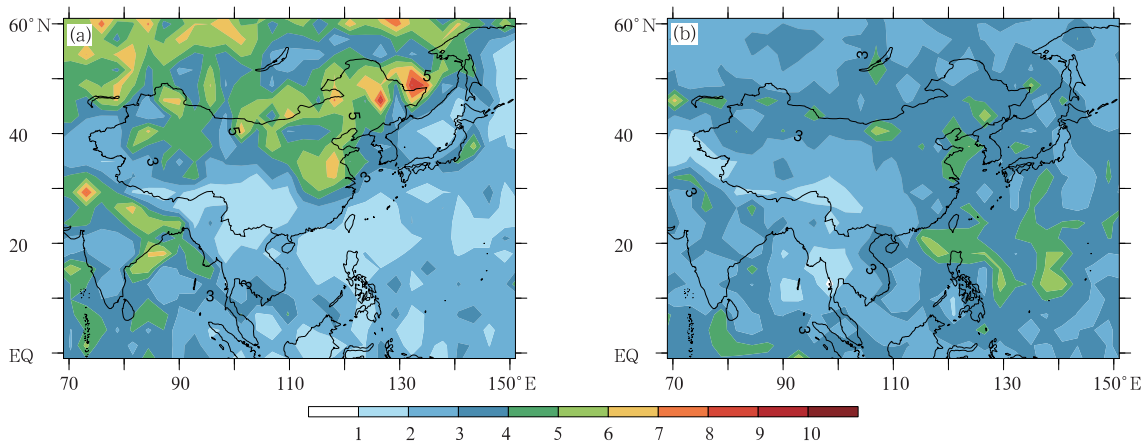

图 3 东亚区域平均 L_{cf}^{*}(单位:km)的季节分布(a. 冬季, b. 夏季)

Fig. 3 Seasonal distributions of East Asian mean L_{cf}^{*}

(a. winter, b. summer, unit: km)

3.2 L_{cf}对模拟总云量的影响

3.2.1 L_{cf}对模拟全球总云量的影响

图4为冬、夏两季CERES的总云量以及本试验模拟得到的总云量的全球平均分布。从CERES卫星观测资料看,总云量在热带对流区域和中纬度海洋较多,而在副热带地区较少。模式基本上模拟出了这种分布特征。CERES卫星资料冬、夏两季的全球平均总云量均为0.61。本试验1、2模拟的全球平均总云量(冬季分别为0.68和0.67;夏季分别为0.65和0.64)均大于卫星资料的值,试验2较试验1更准确。试验2相比于试验1冬、夏两季的全球平均总云量与CERES卫星资料的误差减少了1.6%。

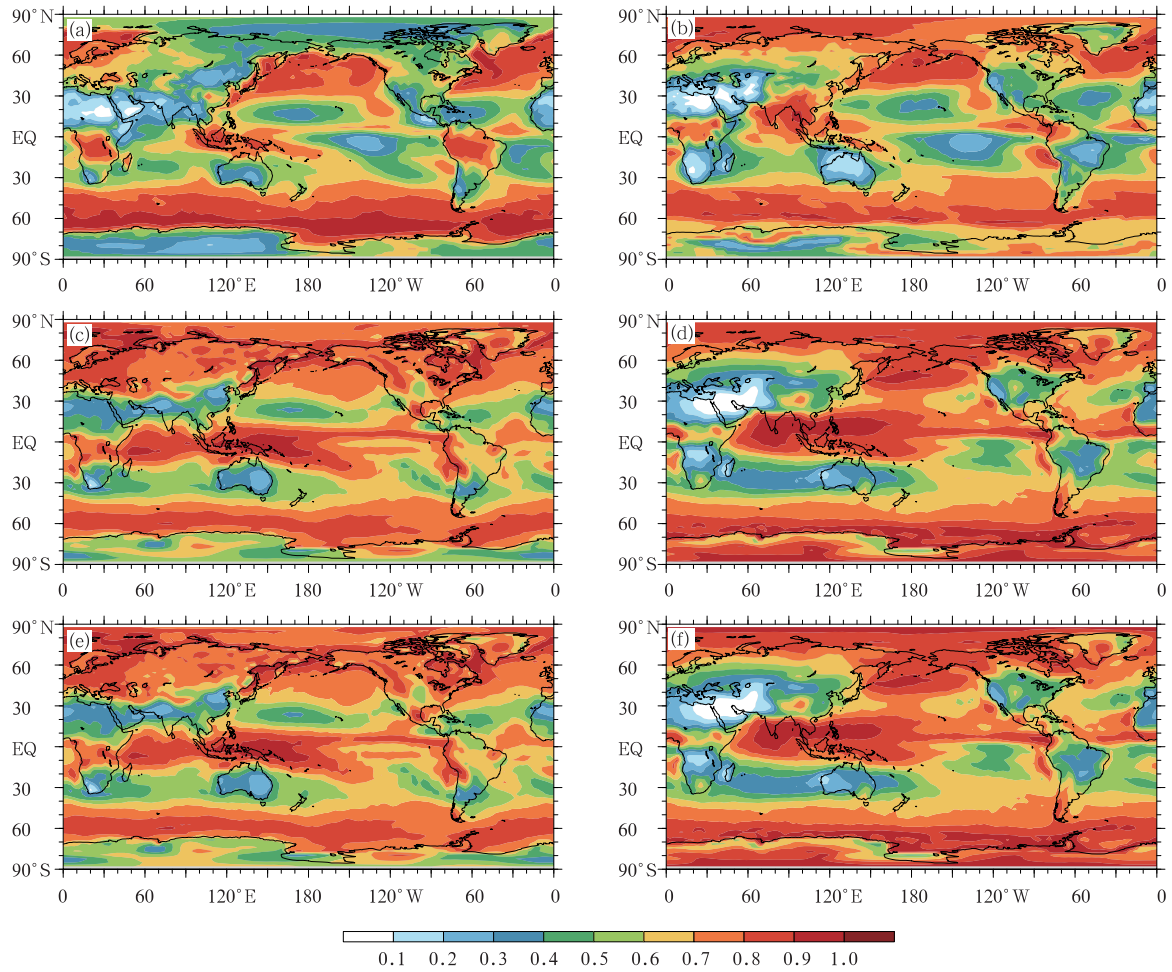

图4 CERES卫星资料(a、b)和试验1(c、d)、试验2(e、f)模拟的冬(a、c、e)、夏(b、d、f)两季全球平均总云量的分布

Fig. 4 Global distributions of total cloud fraction from CERES satellite data (a, b) and from simulation results of EXP1 (c, d) and EXP2 (e, f) averaged in winter (a, c, e) and summer (b, d, f)

图5为试验1、2与CERES卫星资料冬、夏两季总云量差异的全球平均分布。从全球平均分布看,两组试验冬、夏两季与CERES卫星资料总云量差异分布较为一致。冬季,在赤道和中高纬度陆地地区存在明显的正偏差,在中纬度洋面存在明显的负偏差。夏季,在近赤道洋面存在明显的正偏差,在北半球中纬度陆地以及南半球中纬度洋面存在明显的负偏差。从数值上看,冬季的全球平均差值试验2比试验1小5.7%(试验1、2平均差值分别为0.070和0.066),夏季的全球平均差值试验2比试验1小9.5%(试验1、2平均差值分别为0.042和0.038)。

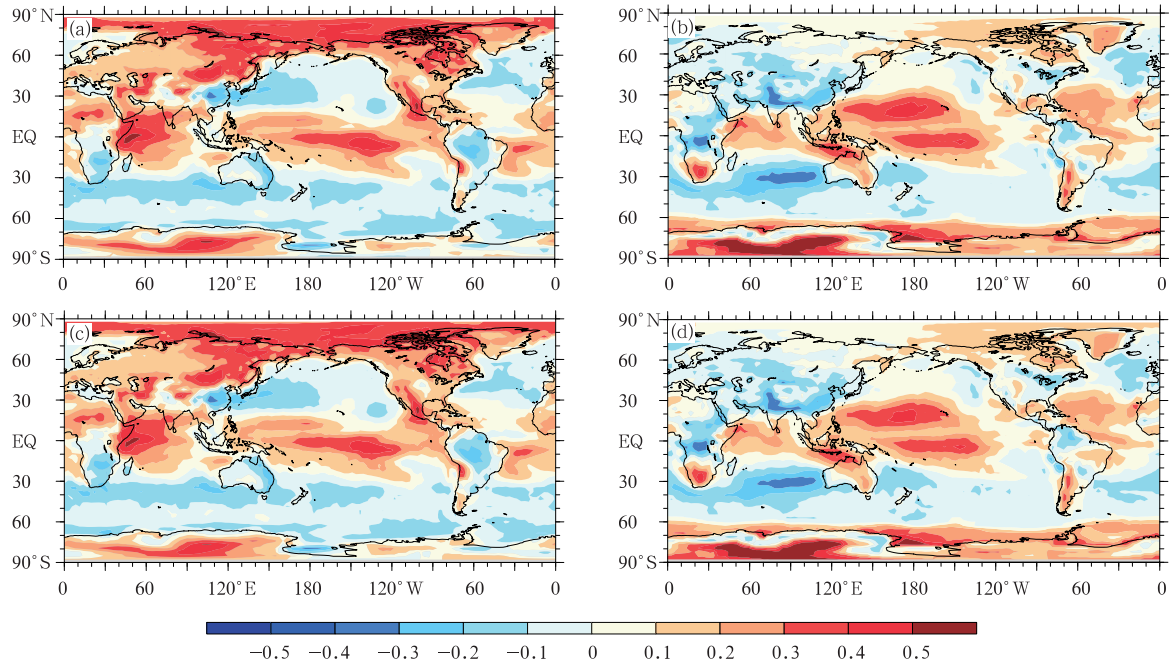

图 5 试验 1(a、b)、试验 2(c、d)与 CERES 卫星资料冬(a、c)、夏(b、d)两季全球平均总云量差值(试验 1(2)减 CERES)分布

Fig. 5 Differences (EXP 1(2) − CERES) between simulations of (a, b) EXP1 and (c, d) EXP2 and the CERES observed global mean total cloud fraction in winter (a, c) and summer (b, d)

从试验 2 与试验 1 模拟得到的冬、夏两季总云量差异的全球平均分布(图 6)可见,与 L_{cf} 取全球平均值 2 km 相比,L_{cf}^{*} 模拟得到的总云量在热带出现负偏差,而在中纬度洋面上呈现正偏差,这是因为 L_{cf}^{*} 在热带大于 2 km 在中纬度洋面上小于 2 km(图 1)。试验 2 与试验 1 模拟得到的冬、夏两季总云量差异的全球纬向平均分布(图 7)表明,冬季在南半球中高纬度存在正偏差,在热带地区存在负偏差;夏季在南半球中低纬度地区存在正偏差,北半球存在负偏差。相对于试验 1,试验 2 总云量在热带地区的减少以及在中纬度洋面的增多分别有助于减少模式在这些区域的总云量的正偏差和负偏差。采用 L_{cf}^{*} 使得模拟结果向正确的方向偏移。

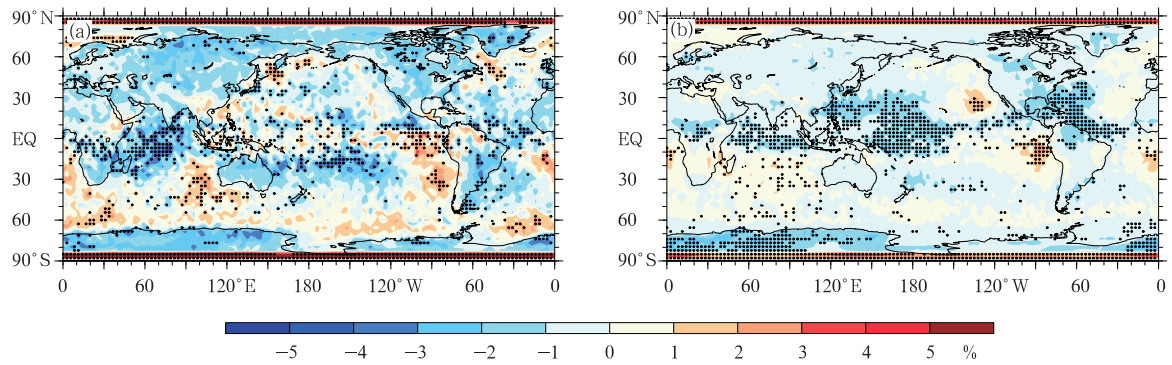

图 6 试验 1、2 冬(a)、夏(b)两季全球平均总云量差值(试验 2 减试验 1)的分布

(黑点标示的地方代表通过了显著性水平为 0.1 的 t 检验)

Fig. 6 Differences (EXP2 − EXP1) in simulated mean total cloud fraction between EXP1 and EXP2 for winter (a) and summer (b) over the globe

(Black dots indicate significance at the level of 0.1 by t-test)

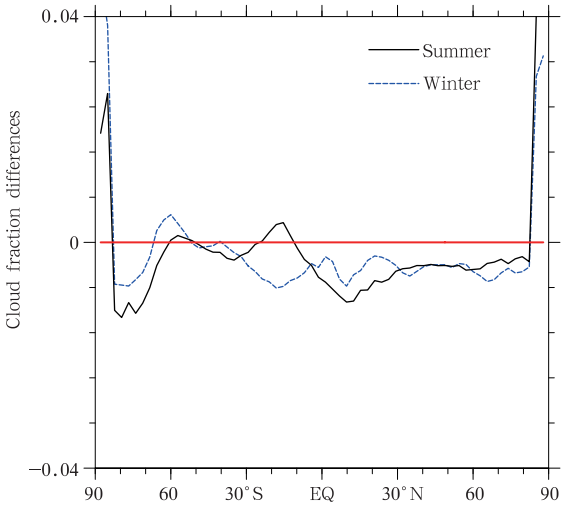

图 7 试验 1、2 冬(a)、夏(b)两季全球平均总云量差值的纬向平均分布

Fig. 7 Differences in simulated zonal mean total cloud fraction between EXP1 and EXP2 for winter (a) and summer (b)

3.2.2 L_{cf}对模拟东亚地区总云量的影响

从 CERES 卫星资料和试验 1、2 东亚地区总云量冬、夏两季的平均分布(图 8)可见,冬季蒙古高原、喜马拉雅山脉两地总云量较低,在东亚东部总云量较高;夏季东亚南部出现较高的总云量。从区域平均看,东亚地区冬、夏两季的平均总云量分别为 0.55、0.67。试验 1、2 模拟的东亚平均总云量(冬季分别为 0.66 和 0.65;夏季分别为 0.70 和 0.69)均大于 CERES 卫星资料的值,试验 2 较试验 1 更准确。试验 2 与试验 1 相比,冬、夏两季的东亚平均总云量与 CERES 的误差分别减少了 1.8%和 1.4%。

从试验 1、2 与 CERES 卫星资料在东亚地区冬、夏两季总云量差异(图 9)的区域分布看,试验 1、2 冬、夏两季与 CERES 卫星资料在总云量差异分布上较为相似。冬季,在蒙古高原、中国东北部存在明显的正偏差;在东亚以东洋面上以及中国东部存在明显的负偏差。夏季,在东亚以东洋面上存在明显

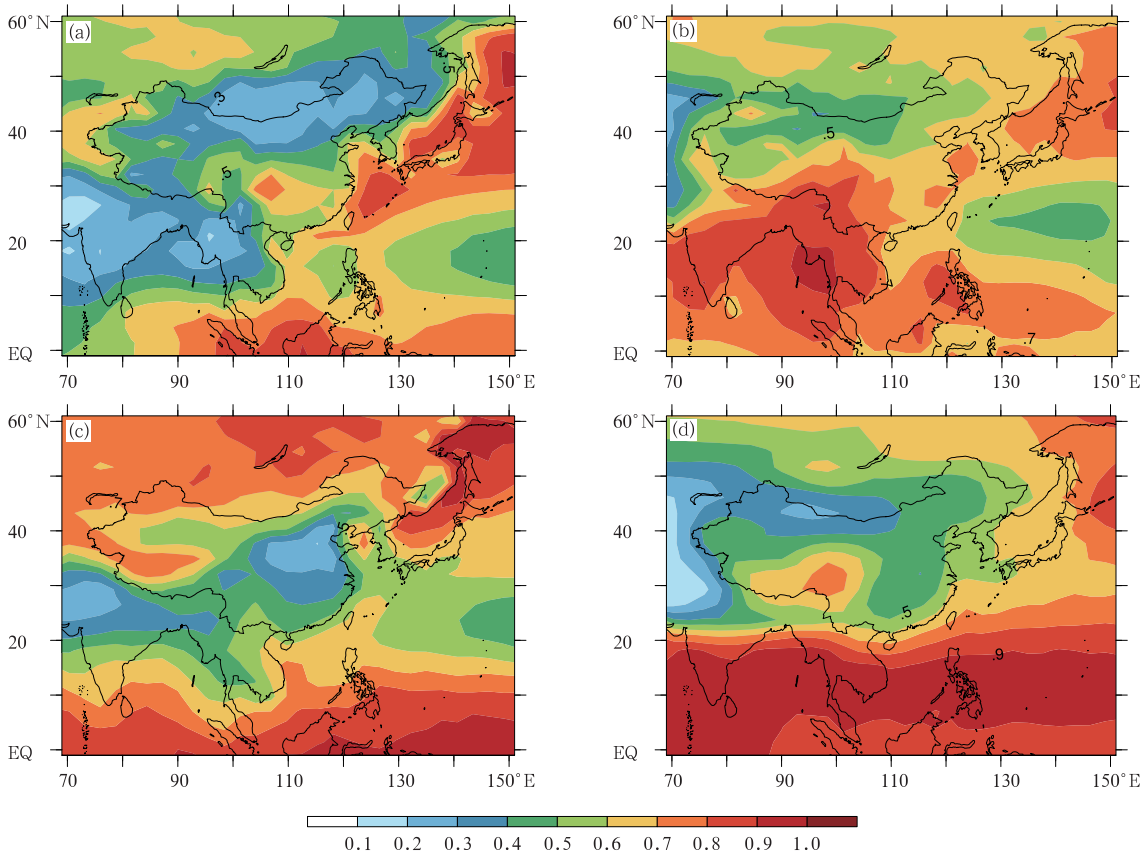

图 8 CERES 卫星资料(a、b)和试验 1(c、d)、试验 2(e、f)模拟的冬(a、c、e)、夏(b、d、f)两季东亚平均总云量的分布

Fig. 8 Total cloud fractions in East Asia from CERES satellite data (a, b) and from simulation results of EXP1 (c, d) and EXP2 (e, f) averaged in winter (a, c, e) and summer (b, d, f)

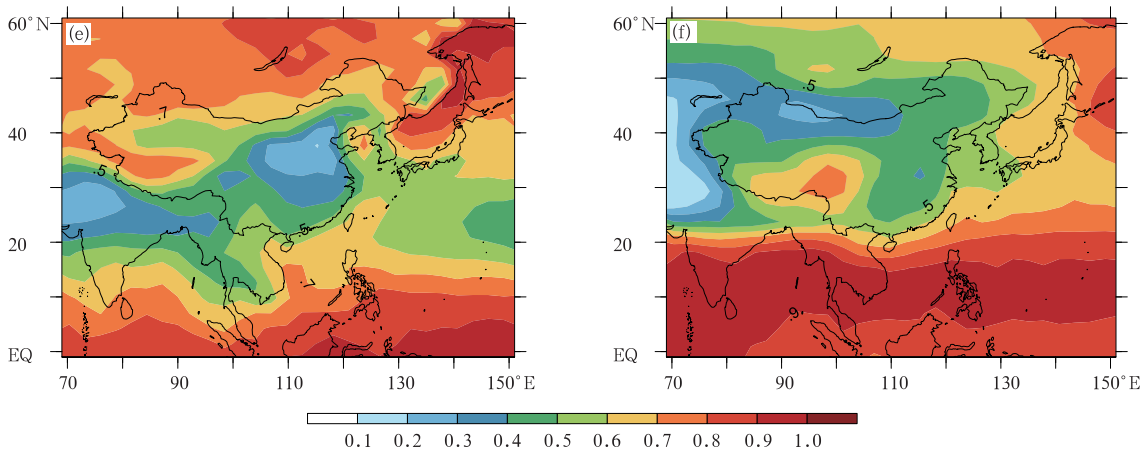

续图 8

Fig. 8 Continued

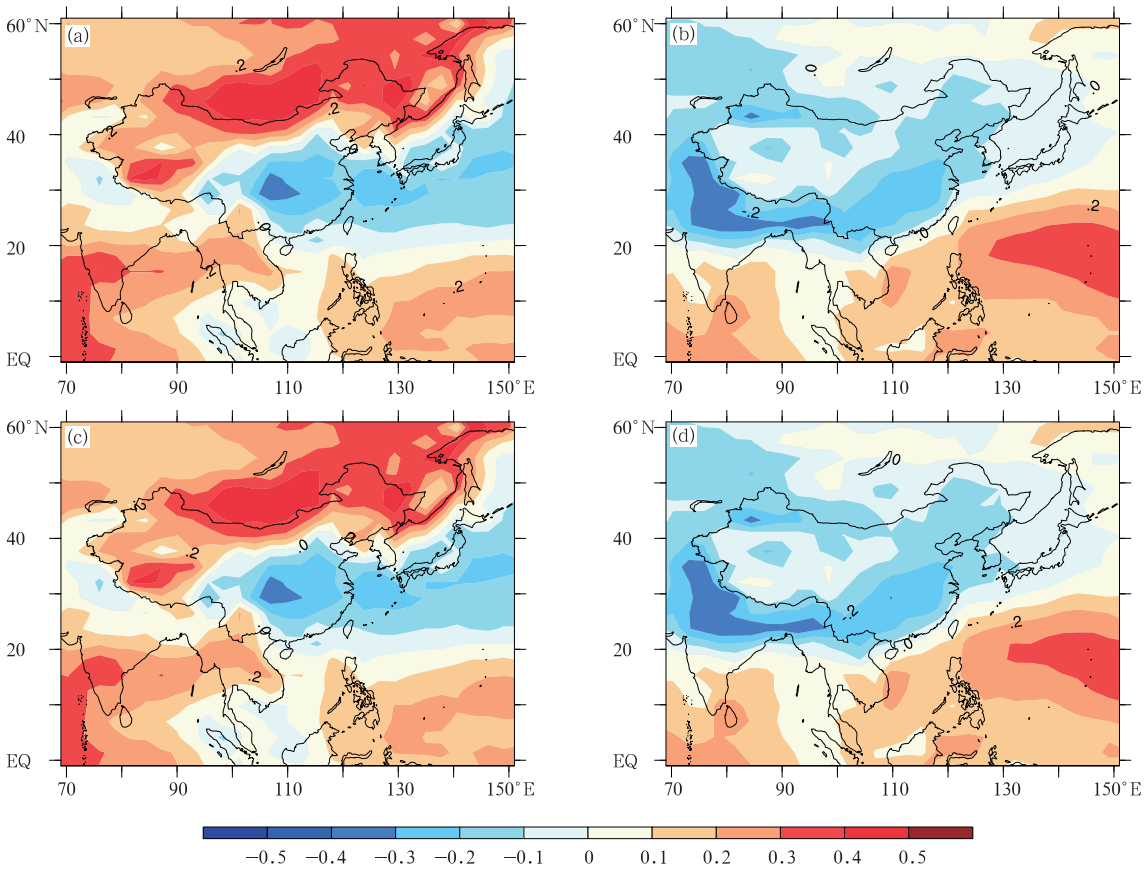

图 9 试验 1(a、b)、试验 2(c、d)与 CERES 卫星资料冬(a、c)、夏(b、d)两季东亚平均总云量的差值(试验 1(2)减 CERES)分布

Fig. 9 Differences (EXP1(2) − CERES) between simulations of (a, b) EXP1, (c, d) EXP2 and the CERES observed total cloud fraction averaged in winter (a, c) and summer (b, d) in East Asia

的正偏差;在陆地上存在明显的负偏差。冬、夏两季云量的差异主要集中在陆地上。从数值上看,冬季的东亚平均差值试验 2 比试验 1 小 3.4%(试验 1、2 平均差值分别为 0.117 和 0.113),夏季的东亚平均

差值试验 2 比试验 1 小 25.9%(试验 1、2 平均差值分别为 0.027 和 0.020)。可见，L_{cf}^{*} 对模拟的东亚总云量有所改进，特别是对夏季总云量的模拟。

从试验 2 与试验 1 模拟得到的东亚冬、夏两季总云量差异(图 10)可见，东亚地区大多呈现负偏差。与 L_{cf} 取全球平均值相比，L_{cf}^{*} 模拟的东亚总云量，冬季在中高纬度大陆区域有所减少，在日本以东和低纬度海洋区域有所增大(图 11)；夏季在西北太平洋有显著减小。这是因为 L_{cf}^{*} 冬季中高纬度大陆大于 2 km，在日本以东和低纬度海洋区域小于 2 km；夏季在西北太平洋大于 2 km。试验 2 相对试验 1 的以上差异，可以抵消模式模拟中相应的正、负偏差(图 8)。可见 L_{cf}^{*} 使得模拟结果向正确的方向偏移。

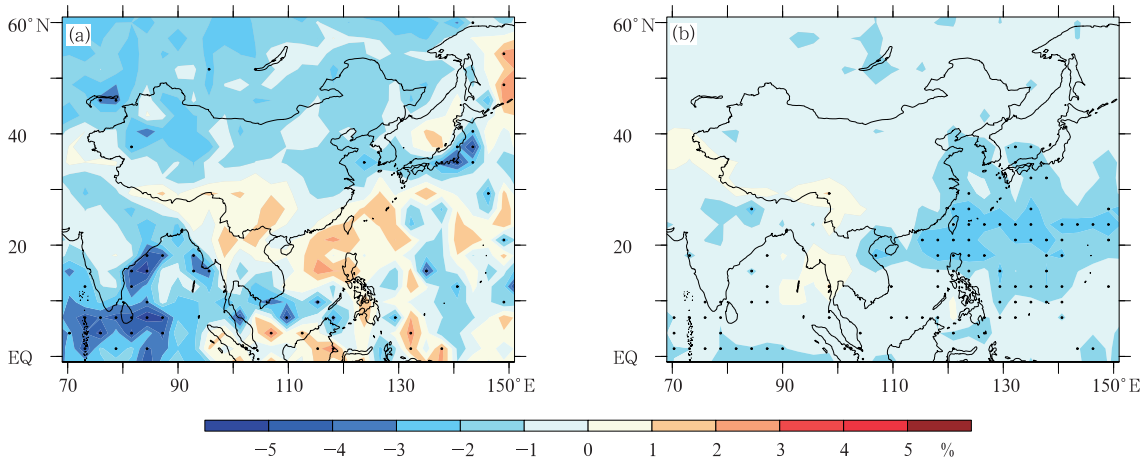

图 10 试验 1、2 冬(a)、夏(b)两季东亚平均总云量差值(试验 2 减试验 1)的分布
(黑色点标示的地方代表通过了显著性水平为 0.1 的 t 检验)

Fig. 10 Differences (EXP2 − EXP1) in total cloud fraction simulation between EXP1 and EXP2 for winter (a) and summer (b) in East Asia
(Black dots indicate significance at the level of 0.1 by t-test)

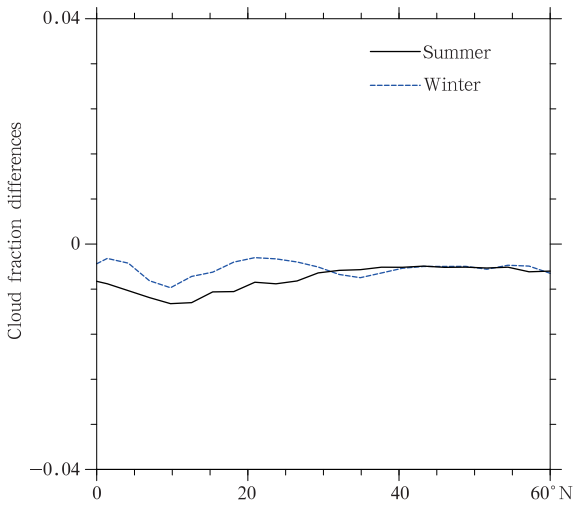

图 11 试验 1、2 冬、夏两季东亚平均总云量差值的纬向平均分布

Fig. 11 Differences in simulated zonal mean total cloud fraction between EXP1 and EXP2 for winter and summer in East Asia

4 结 论

利用中国国家气候中心大气环流模式 BCC_AGCM2.0，研究了在模式中引入基于卫星观测的、时空变化的云重叠参数(即 L_{cf}^{*})对模拟的全球尤其是东亚地区总云量的影响。

对全球总云量的模拟结果与 CERES 卫星资料对比发现，L_{cf}^{*} 比之前固定 L_{cf} 为 2 km 的误差减少了 1.6%。冬季在北半球中高纬度地区以及赤道地区存在正偏差；在南北半球的中纬度洋面存在负偏差。夏季，在赤道两侧的洋面存在正偏差；在北半球中纬度陆地以及南半球中纬度洋面存在负偏差。对比 L_{cf}^{*} 和固定 L_{cf} 为 2 km 模拟的全球总云量与 CERES 卫星资料的差值，冬、夏两季分别减少了 5.7% 和 9.5%。

对于东亚地区，引入 L_{cf}^{*} 后，冬、夏两季的东亚平均总云量与 CERES 卫星资料的误差比目前全球

模式都采用的固定 L_{cf} 为 2 km 的结果分别减少了1.8%和1.4%。冬季在蒙古高原、中国东北部存在正偏差;在东亚以东洋面上以及中国东部存在负偏差。夏季,在东亚以东洋面上存在正偏差;在陆地上存在负偏差。对比两组试验与 CERES 卫星资料的东亚总云量的差值,冬季的东亚平均差值试验 2 比试验 1 小 3.4%,夏季的东亚平均差值试验 2 比试验 1 小 25.9%。引入 L_{cf}^{*} 一定程度上减小了云量偏差,这对提高辐射场的模拟精度具有积极的意义。

综合在全球特别是东亚地区,模拟结果与 CERES 卫星观测结果的差异以及两组模拟试验之间的差异,可以得出:L_{cf}^{*} 使得模拟的总云量向正确的方向偏移,说明具有时空变化特征的 L_{cf}^{*} 比定常不变的 L_{cf} 在描述全球特别是东亚地区次网格云重叠方案时更精确。

最后需要说明的是,提高全球气候模式对总云量的模拟精度涉及到诸多因子。L_{cf} 的改善只是其中的一个因素。相对于模拟与观测总云量之间的误差,云重叠参数的改进对模拟总云量精度的提高要小得多。可见,模式总云量的模拟误差主要来源于全球模式中的云方案本身的误差,不应忽视对云本身参数化过程的改进与提高。

参考文献

荆现文,张华. 2012. McICA 云-辐射方案在国家气候中心全球气候模式中的应用与评估. 大气科学,36(5):945-958. Jing X W, Zhang H. 2012. Application and evaluation of McICA Cloud Radiation framework in the AGCM of the National Climate Center. Chinese J Atmos Sci, 36(5): 945-958 (in Chinese)

彭杰,张华,沈新勇. 2013. 东亚地区云垂直结构的 CloudSat 卫星观测研究. 大气科学,37(1):91-100. Peng J, Zhang H, Shen X Y. 2013. Analysis of vertical structure of clouds in East Asia with CloudSat data. Chinese J Atmos Sci, 37(1): 91-100 (in Chinese)

吴春强,周天军. 2011. CFMIP 大气环流模式模拟的东亚云辐射强迫特征. 气象学报,69(3):381-399. Wu C Q, Zhou T J. 2011. Characteristics of cloud radiative forcings over East Asia as simulated by the AGCMs in the CFMIP. Acta Meteor Sinica, 69(3): 381-399 (in Chinese)

张华. 2016. BCC_RAD 大气辐射传输模式. 北京:气象出版社,44-177. Zhang H. 2016. Atmospheric Radiative Transfer Model of BCC_RAD. Beijing: China Meteorological Press, 44-177 (in Chinese)

张华,荆现文. 2016. 气候模式中云的垂直重叠及其辐射传输问题研究进展. 气象学报,74(1):103-113. Zhang H, Jing X W. 2016. Advances in studies of cloud overlap and its radiative transfer issues in the climate models. Acta Meteor Sinica, 74(1): 103-113 (in Chinese)

Barker H W. 2008. Representing cloud overlap with an effective decorrelation length: An assessment using CloudSat and CALIPSO data. J Geophys Res, 113(D24): D24205

Bergman J W, Rasch P J. 2002. Parameterizing vertically coherent cloud distributions. J Atmos Sci, 59(14): 2165-2182

Bouniol D, Protat A, Delanoë J, et al. 2010. Using continuous ground-based radar and lidar measurements for evaluating the representation of clouds in four operational models. J Appl Meteor Climatol, 49(9): 1971-1991

Di Giuseppe F, Tompkins A M. 2015. Generalizing cloud overlap treatment to include the effect of wind shear. J Atmos Sci, 72(8): 2865-2876

Hagihara Y, Okamoto H, Yoshida R. 2010. Development of a combined CloudSat-CALIPSO cloud mask to show global cloud distribution. J Geophys Res, 115(D4): D00H33

Hinkelman L M, Ackerman T P, Marchand R T. 1999. An evaluation of NCEP Eta model predictions of surface energy budget and cloud properties by comparison with measured ARM data. J Geophys Res, 104(D16): 19535-19549

Hogan R J, Illingworth A J. 2000. Deriving cloud overlap statistics from radar. Quart J Roy Meteor Soc, 126(569): 2903-2909

Hogan R J, Jakob C, Illingworth A J. 2001. Comparison of ECMWF winter-season cloud fraction with radar-derived values. J Appl Meteor, 40(3): 513-525

Jing X W, Zhang H, Peng J, et al. 2016. Cloud overlapping parameter obtained from CloudSat/CALIPSO dataset and its application in AGCM with McICA scheme. Atmos Res, 170: 52-65

Jing X W, Zhang H, Satoh M, et al. 2018. Improving representation of tropical cloud overlap in GCMs based on cloud-resolving model data. J Meteor Res, 32(2): 233-245

Klein S A, Hartmann D L. 1993. The seasonal cycle of low stratiform clouds. J Climate, 6(8): 1587-1606

Li J, Dobbie S, Räisänen P, et al. 2005. Accounting for unresolved clouds in a 1-D solar radiative-transfer model. Quart J Roy Meteor Soc, 131(608): 1607-1629

Li J, Huang J, Stamnes K, et al. 2015. A global survey of cloud overlap based on CALIPSO and CloudSat measurements. Atmos Chem Phys, 15(1): 519-536

Li Y Y, Yu R C, Xu Y P, et al. 2004. Spatial distribution and seasonal variation of cloud over China based on ISCCP data and surface observations. J Meteor Soc Japan, 82(2): 761-773

Liou K N, Davies R. 1993. Radiation and cloud processes in the atmosphere. Phys Today, 46(9): 66

Lu C S, Liu Y G, Niu S J, et al. 2013. Exploring parameterization for turbulent entrainment-mixing processes in clouds. J Geophys Res, 118(1): 185-194

Mace G G, Benson-Troth S. 2002. Cloud-layer overlap characteris-

tics derived from long-term cloud radar data. J Climate, 15(17): 2505-2515

Mace G G, Zhang Q Q, Vaughan M, et al. 2009. A description of hydrometeor layer occurrence statistics derived from the first year of merged Cloudsat and CALIPSO data. J Geophys Res, 114(D8): D00A26

Naud C M, Del Genio A, Mace G G, et al. 2008. Impact of dynamics and atmospheric state on cloud vertical overlap. J Climate, 21(8): 1758-1770

Oreopoulos L, Norris P M. 2011. An analysis of cloud overlap at a midlatitude atmospheric observation facility. Atmos Chem Phys, 11(12): 5557-5567

Oreopoulos L, Lee D, Sud Y C, et al. 2012. Radiative impacts of cloud heterogeneity and overlap in an atmospheric General Circulation Model. Atmos Chem Phys Discuss, 12(19): 12287-12329

Paquin-Ricard D, Jones C, Vaillancourt P A. 2010. Using ARM observations to evaluate cloud and clear-sky radiation processes as simulated by the Canadian regional climate model GEM. Mon Wea Rev, 138(3): 818-838

Pincus R, Barker H W, Morcrette J J. 2003. A fast, flexible, approximate technique for computing radiative transfer in inhomogeneous cloud fields. J Geophys Res, 108(D13): 4376

Räisänen P, Barker H W. 2004a. Evaluation and optimization of sampling errors for the Monte Carlo Independent Column Approximation. Quart J Roy Meteor Soc, 130(601): 2069-2085

Räisänen P, Barker H W, Khairoutdinov M F, et al. 2004b. Stochastic generation of subgrid-scale cloudy columns for large-scale models. Quart J Roy Meteor Soc, 130(601): 2047-2067

Randall D A, Coakley Jr A J, Fairall C W, et al. 1984. Outlook for research on subtropical marine stratiform clouds. Bull Amer Meteor Soc, 65(12): 1290-1301

Sengupta M, Clothiaux E E, Ackerman T P. 2004. Climatology of warm boundary layer clouds at the ARM SGP site and their comparison to models. J Climate, 17(24): 4760-4782

Shonk J K P, Hogan R J, Edwards J M, et al. 2010. Effect of improving representation of horizontal and vertical cloud structure on the Earth's global radiation budget. Part I: Review and parametrization. Quart J Roy Meteor Soc, 136(650): 1191-1204

Song H, Lin WY, Lin Y L, et al. 2013. Evaluation of precipitation simulated by seven SCMs against the ARM observations at the SGP site. J Climate, 26(15): 5467-5492

Wang P H, Minnis P, McCormick M P, et al. 1998. A study of the vertical structure of tropical (20°S－20°N) optically thin clouds from SAGE Ⅱ observations. Atmos Res, 47-48: 599-614

Wigley T M L, Jones P D, Briffa K R, et al. 1990. Obtaining subgrid-scale information from coarse-resolution general circulation model output. J Geophys Res, 95(D2): 1943-1953

Wood R. 2012. Stratocumulus clouds. Mon Wea Rev, 140(8): 2373-2423

Wu T W, Yu R C, Zhang F, et al. 2010. The Beijing Climate Center atmospheric general circulation model: Description and its performance for the present-day climate. Climate Dyn, 34(1): 123-147

Wyant M C, Khairoutdinov M, Bretherton C S. 2006. Climate sensitivity and cloud response of a GCM with a superparameterization. Geophys Res Lett, 33(6): L06714

Yu R C, Wang B, Zhou T J. 2004. Climate effects of the deep continental stratus clouds generated by the Tibetan Plateau. J Climate, 17(13): 2702-2713

Zhang D M, Luo T, Liu D, et al. 2014a. Spatial scales of altocumulus clouds observed with collocated CALIPSO and CloudSat measurements. Atmos Res, 149: 58-69

Zhang H, Nakajima T, Shi G Y, et al. 2003. An optimal approach to overlapping bands with correlated *k* distribution method and its application to radiative calculations. J Geophys Res, 108(D20): 4641

Zhang H, Shi G Y, Nakajima T, et al. 2006a. The effects of the choice of the *k*-interval number on radiative calculations. J Quant Spectrosc Rad Trans, 98(1): 31-43

Zhang H, Suzuki T, Nakajima T, et al. 2006b. Effects of band division on radiative calculations. Opt Eng, 45(1): 016002

Zhang H, Peng J, Jing X W, et al. 2013. The features of cloud overlapping in eastern Asia and their effect on cloud radiative forcing. Sci China Earth Sci, 56(5): 737-747

Zhang H, Jing X, Li J. 2014b. Application and evaluation of a new radiation code under McICA scheme in BCC_AGCM2.0.1. Geosci Model Dev, 7(3): 737-754

吴刚哲,严金哲,任国玉,等. 朝鲜中西部地区春季植被覆盖度与气候因子的关系[J]. 气象与环境学报,2018,34(4):112-118.
WU Gang-zhe, YAN Jin-zhe, REN Guo-yu, et al. Relationship between fractional vegetation and climate factors in spring over the mid-west of DPR Korea [J]. Journal of Meteorology and Environment, 2018, 34(4): 112-118.

朝鲜中西部地区春季植被覆盖度与气候因子的关系

吴刚哲[1,2] 严金哲[1,3] 任国玉[1,4] 索南看卓[1]

(1. 中国地质大学环境学院,湖北 武汉 430074; 2. 元山农业综合大学,朝鲜 元山;
3. 金日成综合大学,朝鲜 平壤; 4. 中国气象局气候研究开放实验室,北京 100081)

摘 要:为了深入了解朝鲜中西部地区春季植被覆盖度(Fractional Vegetation,FV)的变化特征及其与气候因子的关系,利用1992年、2003年和2007年Landsat 5卫星资料及朝鲜中西部地区13个气象站的气温和降水观测资料,对朝鲜中西部地区春季植被的变化特征及其与气候异常的关系进行了分析。结果表明:1992年、2003年和2007年朝鲜中西部地区春季植被覆盖度呈明显增加的趋势,平均增加量为17.5%,平原地区比山地春季植被覆盖度偏高约20.0%。朝鲜中西部地区春季植被覆盖度与春季平均气温呈负相关关系($r=-0.47$),与春季降水量呈正相关关系($r=0.43$);朝鲜中西部地区春季植被覆盖度的变化量与春季平均气温的变化率呈负相关关系($r=-0.53$),与同期降水量的变化率呈正相关关系($r=0.79$),均通过了显著性检验(显著性水平>99%以上,$P<0.05$)。可见,朝鲜中西部地区春季植被覆盖度的变化可能主要受春季气温和春季降水的影响。

关键词:Landsat 5;植被覆盖度;气温;降水;相关分析

中图分类号:TP79 **文献标识码**:A doi:10.3969/j.issn.1673-503X.2018.04.015

引言

由于人类活动的影响及洪水、干旱、森林火灾等灾害性天气气候事件的干扰,全球陆地很多地区,包括朝鲜中西部地区森林植被面积逐渐减少。了解陆地植被的变化,对生态建设和区域经济发展具有重要的指导意义。

植被指数作为陆地植被变化、生态环境现状、土地利用和土地覆盖转换等问题的重要参数,已得到较广泛应用。杨扬等[1]提出了光、温、水等气象因子对植物发育期影响的关键作用。Avissar[2]为了研究植被对城市热环境的潜在影响,在多个模型支持下对城乡热环境和风场进行了对比分析,结果表明植被本质上受风、气温、湿度和降水的影响。Maynard和Levi[3]采用Landsat TM影像、归一化植被指数(Normalized Difference Vegetation Index, NDVI)和支持向量机(Support Vector Machine, SVM)模型分析土壤特征及土壤—气候反馈。孙云鹏[4]利用遥感数据和气候统计资料等,采用湿润指数和植被覆盖指数对2001—2007年河北省及各市的生态质量进行了评价。有研究利用卫星遥感资料及气温、降水量等气候资料,评价了研究区植被指数和植被类型[5-7],表明不同植被类型对气候因素的响应不同,植被指数普遍与气温存在明显或不明显的正相关关系,与降水之间存在较显著的相关性。李菁等[8]分析了1982—2006年宁夏中南部地区植被指数的季节变化特征,指出春季平均植被指数与降水量呈正相关关系(0.401),与气温呈负相关关系(-0.433)。曹磊研究表明[9],江苏省年平均植被指数与气温、降水量和相对湿度的相关系数分别为0.282、-0.142、-0.369。王巧玲等[10]和张晓慧[11]研究了植被指数与气候因子之间的相关特征,发现气温和植被指数之间的相关性与前人研究相同,但降水量不同。也有研究表明[12-15],植被覆盖指数与气候因子之间不同的相关性与地区及季节有关。

植被覆盖度是由NDVI计算的,与植被指数在本质上是相同的。朝鲜地区春季为3—5月,中西部地区春季降水量约占年总降水量的16%。春季,随着植物生长活性越大,水分需求量越多。但每年春季移动性反气旋活动增强,经常控制朝鲜中部地区,降水量较少,并导致严重干旱现象频发。因此,朝鲜春季特殊的环流特征和降水匮乏现象直接影响植被覆盖度(Fractional Vegetation, FV)变化。FV不仅受当年春季气温和降水的直接影响,其变化量也可能与春季气温和降水量的长期变化趋势关系密切。

本文从两个方面分析朝鲜中西部地区春季植被

收稿日期:2017-05-09;**修订日期**:2017-07-03。
资助项目:国家公益性行业(气象)科研专项(GYHY201206012)资助。
作者简介:吴刚哲,男,1978年生,讲师,主要从事遥感气象应用研究,E-mail:okc517@163.com。
通信作者:任国玉,E-mail:guoyoo@cma.gov.cn。

覆盖度 FV 与降水和气温之间的关系,首先分析当年 FV 与春季气温和降水之间的关系;然后分析 1992—2007 年春季 FV 变化与气温和降水量变化率之间的关系,以期了解朝鲜地区陆地植被变化与气候的关系,对朝鲜地区环保部门和国土管理部门的科学决策提供参考。

1　资料与方法

1.1　研究区概况

朝鲜中西部地区(38°36′—39°25′N,125°21′E—126°23′E)总面积为 6990.6 km^2,共包括 2 个市(平壤市和平城市)、11 个郡和区(江东郡、三脊区、祥原郡、胜湖郡、烽火区、大同郡、中和郡、江西区、黄州郡、江南郡和万景台区)。朝鲜中西部地区地势较为平坦,地形主要以平原和低山为主,东部和北部基本为山地(海拔高度为 400 m 以下)。1992—2007 年朝鲜中西部地区年平均气温为 9.7 ℃,1 月平均气温为 −5.7 ℃,8 月平均气温为 24.7 ℃;年平均降水量为 926.6 mm,其中春季降水量比其他季节偏少,干旱多发。朝鲜各市、郡和区均有一个地面气象站,研究区地形和地面气象观测站空间分布见图 1,境界线为在分析过程中用于计算各地区植被覆盖度(FV)平均值的区划界线。

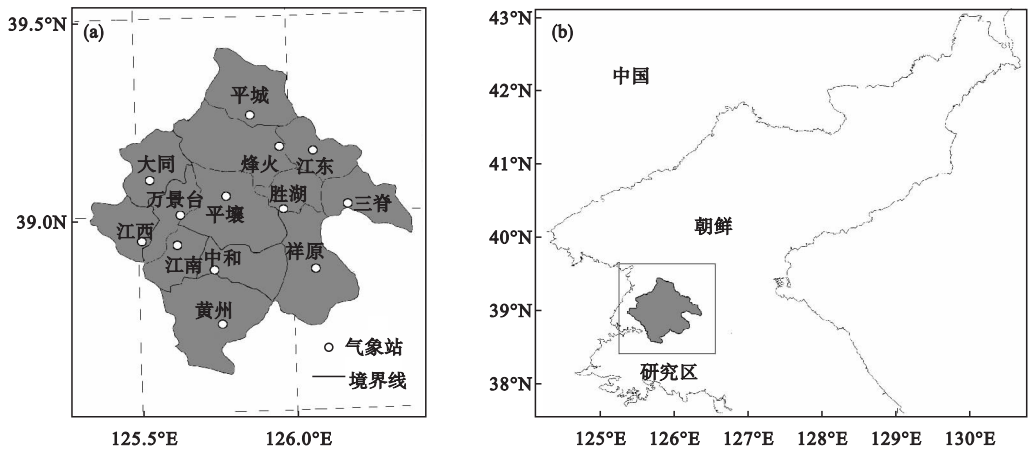

图 1　朝鲜中西部地区地面气象站空间分布(a)和研究区相对位置(b)示意图

Fig. 1　The schematic diagrams of spatial distribution of weather stations over the mid-west of DPR Korea (a) and relative space position of the studied area (b)

1.2　资料来源

本文遥感数据为 Landsat 卫星数据影像(http://www.gscloud.cn/),空间分辨率为 30 m × 30 m,影像日期分别为 1992 年 6 月 1 日、2003 年 5 月 31 日和 2007 年 6 月 3 日,轨道号 path(条带号)为 117,row(行编号)为 33,格林尼治标准时间(Greenwich Mean Time, GMT)分别为 1992 年 6 月 1 日 01:23:24.06、2003 年 5 月 31 日 02:05:32.17 和 2007 年6 月3 日 02:11:06.07,遥感数据均为 1 级产品,经过辐射校正。来源于朝鲜国家地理环境研究中心的 1992—2007 年朝鲜地区地形图、地貌图、行政区划图,气候资料来源于朝鲜中西部地区 13 个气象站(平壤、平城、江东、三脊、祥原、胜湖、烽火、大同、中和、江西、黄州、江南和万景台)1992—2007 年月平均气温和降水量观测资料。

1.3　研究方法

1.3.1　遥感图像预处理

利用遥感图像处理软件 ENVI 5.1(The Environment for Visualizing Images)提供的辐射定标模块(Radiometric Calibration)实现辐射定标;采用 ENVI 5.1中的大气校正模块(FLAASH Atmospheric Correction)进行影像大气校正,消除大气因子和气溶胶的影响。利用 1:5 0000 地形图,以高斯—克吕格(Gauss-Kruger)投影为校正空间,选取 20 个地面控制点(Ground Control Point,GCP),采用控制点校正的方法,首先对 2007 年 6 月 3 日遥感图像进行几何精校正,最终的定位精度控制在 1 个像元之内。在此基础上利用配准模块(Geometric Correction)对 2003 年和 1992 年的遥感图像进行精确配准处理。运用 ENVI 中剪裁模块(Subset Data Via ROIs),基于研究区矢量地理信息对 3 幅 TM 图像进行剪裁,获得研究区遥感图像。

1.3.2　植被覆盖度信息提取

采用对归一化植被指数(NDVI)进行正规化处理的方法获得植被覆盖度,植被覆盖度计算方法[8]将研究区 NDVI 的最大值假定为 100% 覆盖度,而将 NDVI 的最小值假定为 0% 覆盖度,然后将 NDVI 进行标准化处理,公式为:

$$FV = (NDVI_{ind} - NDVI_{min})/(NDVI_{max} - NDVI_{min}) \quad (1)$$

式(1)中,FV 为植被覆盖度,即经正规化的 NDVI;

$NDVI_{ind}$为每个像元对应的 NDVI;$NDVI_{max}$为影像中 NDVI 的最大值;$NDVI_{min}$为影像中 NDVI 的最小值。关于 FV 的定义不同,李得勤等[16]研究表明,FV 为植被覆盖比率。本文利用 ENVI 中的 Basic Tools/Statistics/Compute Statistics 工具,将累积统计值为 90% 和 5% 的 NDVI 值分别作为 $NDVI_{max}$、$NDVI_{min}$,利用 ENVI 中的 band math 工具,依据上式计算的研究区植被覆盖度,然后将植被覆盖度利用归一化模块(Colour mapping/Density slice)进行归一化。在这个过程中,特别注意三个年份的归一化分类范围和颜色保持一致。然后,利用 ArcGIS 10.2 中的剪裁模块(Extract by Mask)和图 1 的研究区边界矢量,计算评价各地区的 NDVI 平均值。

2 结果分析

2.1 *FV* 变化特征

通过对 1992 年、2003 年和 2007 年同期 Landsat TM 遥感影像进行解译,获取朝鲜中西部地区春季植被覆盖度空间分布的基本信息(图 2),为了分析 *FV* 与气候要素之间的相关特征,通过图 1 的地域界线计算各地区的 *FV* 平均值(图 3)。由图 2 和图 3 可见,1992—2007年春季朝鲜中西部地区植被覆盖度增长较明显,东部(江东、三脊、祥原和胜湖)和北部(烽火)山地区域 *FV* 增加量小于西部(大同)和南部(中和、江西和黄州)平原地区,中部地区(平壤市中心部和万景台)*FV* 增加量比山地区域大,但比平原地区小;山地区域 *FV* 的平均增加率约为 6.0%,平原地区 *FV* 的平均增加率约为 26.6%,中部 *FV* 的平均增加率约为 14.9%。由于植被覆盖度可以间接反映气候变化,因此 *FV* 的年际及地区差别表明气候在时间和空间上存在变异性。

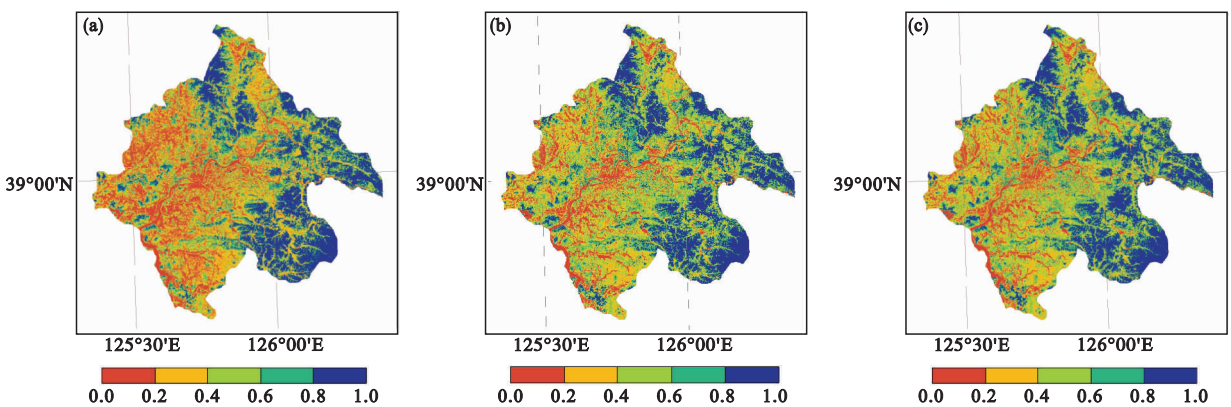

图 2 1992 年 6 月 1 日(a)、2003 年 5 月 31 日(b)和 2007 年 6 月 3 日(c)朝鲜中西部地区植被覆盖度空间分布

Fig. 2 Spatial distributions of *FV* over the mid-west of DPR Korea on June 1,1992 (a), May 31,2003 (b), and June 3,2007 (c)

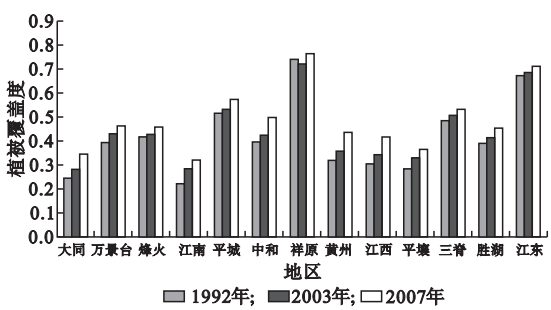

图 3 1992 年、2003 年和 2007 年春季朝鲜中西部地区植被覆盖度平均值的对比

Fig. 3 Comparison among the regionally averaged spring *FV*s in 1992, 2003 and 2007 over the mid-west of DPR Korea

2.2 植被覆盖度与气温和降水的关系

2.2.1 *FV* 变化与气温和降水的关系

图4为1992年、2003年和2007年春季朝鲜中

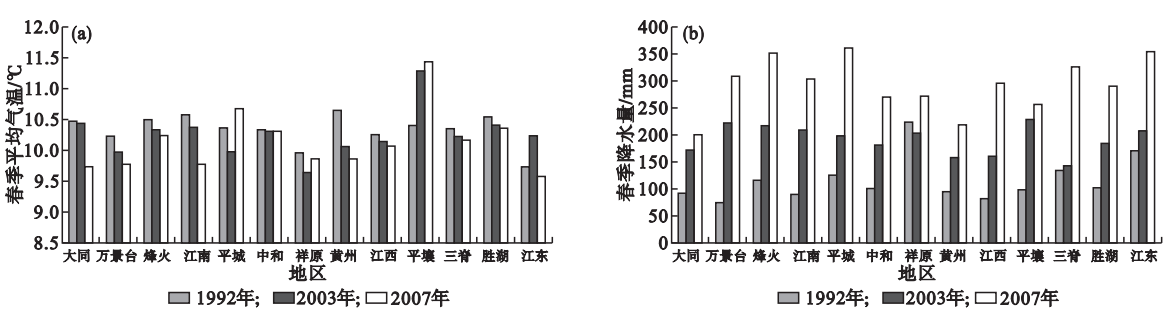

图 4 1992 年、2003 年和 2007 年春季朝鲜中西部地区平均气温(a)与降水量(b)变化

Fig. 4 Variations of the spring mean temperature (a) and precipitation (b) in 1992, 2003 and 2007 over the mid-west of DPR Korea

西部地区 13 个气象站的平均气温和降水量,由图可见,1992—2007 年朝鲜中西部地区春季平均气温基本呈逐渐降低的趋势,但降水量呈明显增加的趋势,大部地区后期降水量均比 20 世纪 90 年代初显著增多。

由图 3 和图 4 对比可见,朝鲜中西部地区春季植被覆盖度 *FV* 与春季降水量存在明显的正向对应关系。祥原地区较特殊,春季降水量自 1992 年以后呈先减少后增加的变化趋势,但与春季 *FV* 的变化也完全一致,进一步证实了降水和 *FV* 之间存在密切正相关。

气温变化幅度虽比降水量小(图 4),但其对 *FV* 的影响也是无法忽略的。各区域气温变化趋势存在差异,但绝大多数地区表现为与 *FV* 增加相反的现象,即呈逐渐减少的变化趋势。平壤市春季平均气温自 1992 年以后逐渐上升,且春季平均气温增长率也为最高,可能和城市发展导致的热岛效应(Urban Heat Island)增强有关。

由图 5 可见,1992 年、2003 年、2007 年朝鲜中西部地区春季平均植被覆盖度 *FV* 与春季气温、降水量

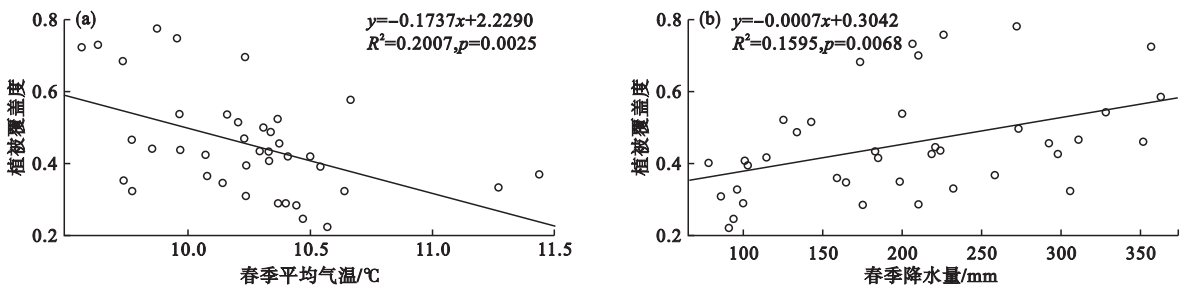

图 5　1992 年、2003 年和 2007 年朝鲜中西部地区春季平均植被覆盖度 *FV* 与春季气温(a)和降水量(b)散点图

Fig. 5　Scatter diagrams of the relationships between spring mean temperature (a), precipitation (b) and mean *FV* in 1992, 2003 and 2007 over the mid-west of DPR Korea

分别呈显著的负相关关系和正相关关系,回归方程的统计检验分别为 $P = 0.0025$(平均气温)、$P = 0.0068$(降水量),显著性水平均为 95.0% 以上,春季气温和春季植被覆盖度 *FV* 呈负相关关系,相关系数为 −0.47。可能与朝鲜中西部地区常年春季降水量一般较少,春旱现象严重,气温下降有利于减少蒸发和蒸腾,土壤保墒条件转好有关。

由图 5b 可见,朝鲜中西部地区春季植被覆盖度 *FV* 和春季降水量存在明显的正相关关系,相关系数为 0.43,主要是由于春季充足的降水有利于减缓研究区春旱现象,保证土壤水分条件处于良好状态,促进后期植被的生长。朝鲜中西部地区春季植被覆盖度与春季降水量的正相关关系也表明 1992 年、2003 年和 2007 年春季降水量可能存在逐渐增加的趋势,有利于降低春季气温,也增加前期土壤水分存储,对植被生长具有正面影响。

本文朝鲜中西部地区春季植被覆盖度 *FV* 与前期气温和降水的相关性与闫新霞和戴翠贤[5]、林德生[7]和李菁等[8]的研究结论基本一致。中国东北地区气温和降水量等气候因子与朝鲜中西部地区较相似,张晓慧[11]和李梦云等[17]研究表明地表气温与植被指数呈负相关关系,降水量与植被指数呈正相关关系,与本文结论一致;但唐晓玲等[18]研究表明地表气温与植被指数呈正相关关系,主要是由于高寒地区气温为植被生长过程中的重要因子之一。

2.2.2　*FV* 与气温和降水变化率之间的关系

进一步分析 1992—2007 年朝鲜中西部地区春季植被覆盖度 *FV* 变化量与春季平均气温和降水量变化速率的相关特征。利用 2007 年与 1992 年春季朝鲜中西部地区春季植被覆盖度 *FV* 的差值得到 1992—2007 年研究区 *FV* 变化的空间分布,由图 6 可见,近 16 a 朝鲜中西部地区东部山地区域的 *FV* 明显减少,而西部和中部地区(平原地区)*FV* 显著增加。

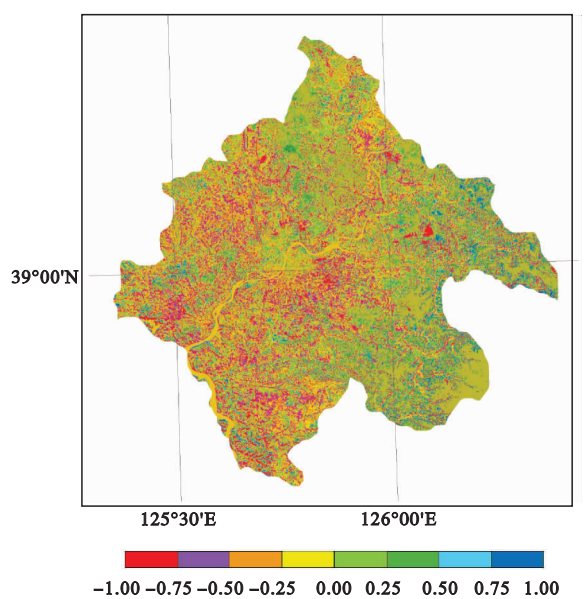

图 6　1992—2007 年春季朝鲜中西部地区植被覆盖度 *FV* 变化量空间分布

Fig. 6　Spatial distribution of the variation of spring *FV* over the mid-west of DPR Korea during 1992-2007

研究期间朝鲜中西部所有地区平均气温增长率统计满足了95.0%以上的显著水平,但对于降水量显著性水平,部分地区(平壤,中和,平城)降水量增长率显著性水平仅为90.0%,因此为了避免这种情况,对这些地区降水数据采用3 a平滑化法将显著性水平达到95.0%以上,然后通过对*FV*与气温、降水量进行趋势分析得到*FV*和春季气候因子的关系。这种分析的理论依据是假设研究地区中所有气象站点均处于同一个地理特征和气候背景下,因此气温和降水的水平与垂直分布差异较小。将朝鲜中西部地区13个气象站的平均气温和降水量的变化率按由小到大的顺序排列后,图7和图8分别为朝鲜中

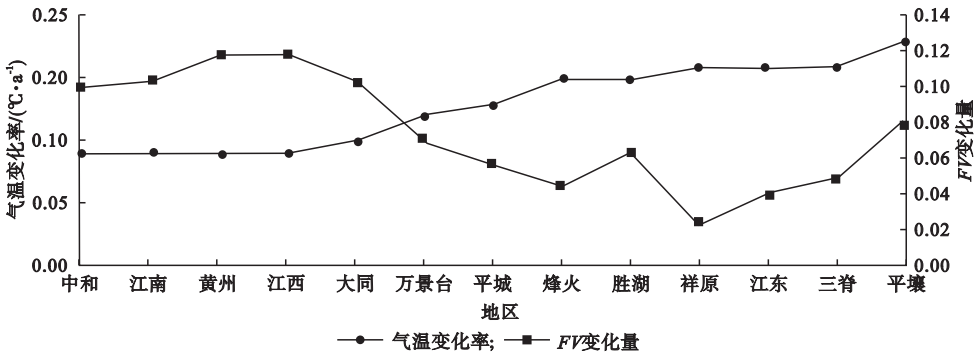

图7 1992—2007年春季朝鲜中西部13个地区气温变化率和1992年与2007年植被覆盖度*FV*变化量

Fig. 7 Change rates of spring mean temperature during 1992-2007 and the variations of spring *FV* between 1992 and 2007 in the 13 subareas over the mid-west of DPR Korea

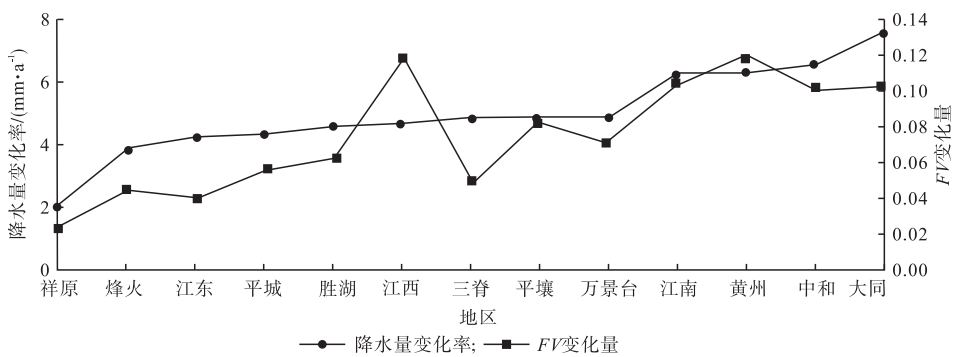

图8 1992—2007年春季朝鲜中西部13个地区降水量变化率和1992年与2007年植被覆盖度*FV*变化量

Fig. 8 Change rate of spring precipitation during 1992-2007 and the variations of spring *FV* between 1992 and 2007 in the 13 subareas over the mid-west of DPR Korea

西部地区春季平均气温变化率、降水变化率与*FV*变化量的变化趋势,其中气温和降水量的变化率是利用1992—2007年观测资料进行线性回归得到,而春季植被覆盖度*FV*变化量则是2007年与1992年的差值。

由图7可见,随着平均气温变化率的增加,*FV*变化量呈逐渐减小的趋势,显著性检验值为$p=0.0050$,显著水平可达99.0%以上,具体来看,烽火、祥原、江东、三脊、胜湖等东部和北部山地区域气温上升率较高,而植被覆盖度*FV*变化量较小。与此相反,黄州、江西、大同等中部和西部平原地区气温上升率较低,植被覆盖度*FV*较高。主要是由于气温的上升率受地域差异的影响,海洋的比热容高于陆地,因此越靠近海岸,气温上升受到的限制越大。

朝鲜中西部地区春季移动性反气旋活动较强,在降水量匮乏和干旱常发生的情况下,较高的气温上升率将抑制植物的生长活动,并限制植被覆盖度的增加,与东亚中纬度地区干旱时期气温上升和植被覆盖度*FV*变化之间呈负相关关系的结论一致[19-20]。但也有一些研究表明气温与*FV*变化之间呈正相关关系[5],可见不同的结果与研究地区的地理位置、年份及季节气候系统和土壤条件的差异有关。

气温增加率和植被覆盖度*FV*变化量之间的相关系数为$r=-0.53$(图7),气温上升率最高的地区为平壤市中心地区,*FV*变化量与气温增加率的关系与多数地区的变化相反,表明平壤市中心地区城市热岛效应非常显著。平壤市植被覆盖度*FV*的增加量,除了自然性增加,城市绿化等人类活动的贡献也较大。

由图8可见,朝鲜中西部各地区春季降水量均呈增加的趋势,由降水增长率的空间分布可知,东部和北部山地区域的降水量变化率(烽火、详原、江东、胜湖和三脊)较低,大部平原地区、西部(大同)和南

部(黄州、中和)地区降水量变化率较高。朝鲜中西部地区大部山地海拔高度较低,因此降水过程中由地形效应降水增加的现象几乎没有发生。

随着降水量变化率的增加,对应植被覆盖度 *FV* 的变化趋势和气温与其的关系不同,呈显著增加的趋势,显著性检验值为 0.0009,达到 99.9% 显著水平。综上可见,在朝鲜中西部地区干旱多发的春季,降水增加量引起植被覆盖度 *FV* 增加,充足的降水有利于改善植物生长所必需的水分条件,同时也抑制了干旱的发生,与之前降水和 *FV* 之间关系的研究结果相同[5,7-8]。

降水量增加率和 *FV* 增加量之间的相关系数较高,为 $r=0.79$。但极端降水事件对季节平均降水量增长率可能具有较大的贡献,而过多的降水量增加也将给植被的生长带来负面影响。

3　结论与讨论

(1)1992 年、2003 年和 2007 年春季朝鲜中西部地区年平均植被覆盖度呈持续性增长的趋势,由植被覆盖的时空变化可知,大部地区植被覆盖度呈增加的趋势,*FV* 平均增加量为 17.5%,山区 *FV* 平均增加量比平原地区偏高约 20.0%。

(2)朝鲜中西部地区春季植被覆盖度与气温之间呈负相关关系(相关系数为 -0.47,显著性检验),但春季植被覆盖度与降水呈正相关关系(相关系数为 0.43,显著性检验)。气温上升率与 *FV* 增加量呈负相关关系,相关系数为 -0.53;但降水上升率与 *FV* 增加量呈正相关关系,相关系数为 -0.79。

(3)朝鲜中西部春季由于移动性高气压的频繁影响为少雨期,此期间由于缺水使植物生物量活性降低,对植被覆盖度的影响较大。因此精确解释春季植被覆盖度与气候因子之间的关系,对生态环境保护和农业部门、城市园林规化等研究具有重要的实际意义。

(4)朝鲜中西部地区植被覆盖度对当年和次年春季气候异常较敏感,降水变化对植被覆盖度的影响比气温大。前期的降水,对后期的土壤水分储蓄具有影响;当前期春季降水偏多时,近期春季土壤水分条件一般较好,有利于植物生长发育,反之亦然;前期气温偏高时,加速土壤水分损失,不利于后期植物生长。

(5)本文研究结果是以每个地区为评价单位得到的地区平均值。虽然结果较客观地反映了植被覆盖度 *FV* 变化与气候之间的相关特征,但是二者资料分布密度存在差异。本文的 Landsat TM 遥感影像资料存在月份的差异,导致计算过程中可能产生一些误差,若采用基于卫星数据反演的地面气温和高分辨率降水数据,可以获得更客观、更定量性的分析结果。

参考文献

[1] 杨扬,罗贤,李荣平,等. 气象要素对植物物候影响及其驱动机制研究进展[J]. 气象与环境学报,2016,32(5):154 - 159.

[2] Avissar R. Potential effects of vegetation on the urban thermal environment [J]. Atmospheric Environment, 1996,30(3):437 - 448.

[3] Maynard J J,Levi M R. Hyper-temporal remote sensing for digital soil mapping: characterizing soil-vegetation response to climatic variability [J]. Geoderma, 2017(285):94 - 109.

[4] 孙云鹏. 基于 RS& GIS 的河北省生态质量气象评价[J]. 唐山师范学院学报,2011,33(5):101 - 103.

[5] 闫新霞,戴翠贤. 天山北麓植被指数变化特征及其与气温和降水的关系[J]. 气象与环境科学,2013,36(2):42 - 46.

[6] 周刊社,袁雷,杨志刚,等. 基于遥感的珠峰地区生态质量气象评价[J]. 草业科学,2014,31(6):1014 - 1021.

[7] 林德生. 三峡库区植被覆盖变化及其气候响应[D]. 武汉:华中农业大学,2011.

[8] 李菁,王连喜,李琪,等. 宁夏中南部近 25 年植被变化特征及其与气候因子的关系[J]. 中国农学通报,2011,27(29):284 - 289.

[9] 曹磊. 江苏省植被 NDVI 动态变化及其与气候因子的关系[D]. 南京:南京农业大学,2014.

[10] 王巧玲,花立民,杨思维. 1982—2006 年祁连山北麓草原植被指数与气候及载畜量的关系[J]. 甘肃农业大学学报,2014,49(4):127 - 135.

[11] 张晓慧. 黑龙江省植被变化特征及其与气候的响应[D]. 哈尔滨:哈尔滨师范大学,2015.

[12] 李晓光. 基于 MODIS - NDVI 的内蒙古植被覆盖变化及其驱动因子分析[D]. 呼和浩特:内蒙古大学,2014.

[13] 杜加强,赵晨曦,贾尔恒·阿哈提,等. 近 30a 新疆月 NDVI 动态变化及其驱动因子分析[J]. 农业工程学报,2016,32(5):172 - 181.

[14] 严晓瑜. 不同时间尺度若尔盖湿地植被变化及其与气候的关系[D]. 北京:中国气象科学研究院,2008.

[15] 张琪,袁秀亮,陈曦,等. 1982—2012 年中亚植被变化及其对气候变化的响应[J]. 植物生态学报,2016,40(1):13 - 23.

[16] 李得勤,文小航,段云霞,等. MODIS 产品反演与 WRF 模式默认植被覆盖度对比研究[J]. 气象与环境学报,2015,31(4):26 - 34.

[17] 李梦云,黄方,陈龙胤. 吉林省西部地区 NDVI 对降水量和土壤湿度的敏感性分析[J]. 东北师大学报:自然

科学版,2013,45(4):141 - 146.
[18] 唐晓玲,任红玲,王杰,等. 吉林省主要产粮区 NDVI 时空变化特征[J]. 气象与环境学报,2015,31(2):103 - 107.
[19] 王琳,景元书. 江西省干旱灾害 MODIS 遥感数据监测分析[C]//中国遥感应用协会. 新世纪以来遥感应用进展交流研讨会论文集. 昆明:中国遥感应用协会,2011.
[20] 张培赢. 基于遥感数据的干旱半干旱地区植被指数及影响因子研究[D]. 哈尔滨:东北林业大学,2016.

Relationship between fractional vegetation and climate factors in spring over the mid-west of DPR Korea

WU Gang-zhe[1,2] YAN Jin-zhe[1,3] REN Guo-yu[1,4] SUONAN Kan-zhuo[1]
(1. School of Environmental Studies, China University of Geosciences, Wuhan 430074, China;
2. Wonsan Agriculture University, Wonsan, DPR Korea; 3. Kim Il Sung University, Pyongyang, DPR Korea; 4. Laboratory for Climate Studies, National Climate Center, China Meteorological Administration, Beijing 100081, China)

Abstract: Based on the Landsat 5 satellite data in 1992, 2003 and 2007 as well as temperature and precipitation data from the 13 weather stations in the mid-west of DPR Korea during 1992-2007, the variation characteristics of fractional vegetation (*FV*) in spring and their relationships with climate abnormality were investigated. The results show that the regionally averaged *FV* in the studied area increases significantly with a rate of about 17.5%. More specifically, the increasing magnitude of *FV* in plain area is about 20.0% higher than that in mountain area. In addition, *FV* has a negative correlation with the spring mean surface temperature ($r = -0.47$) and a positive correlation with the spring precipitation ($r = 0.43$). Moreover, there is a negative and positive correlation between the variations of the spring mean temperature, precipitation and *FV* ($r = -0.53$ and $r = 0.79$), respectively, with a very significant level ($P < 0.05$). So, the variation of spring *FV* in the mid-west of DPR Korea may be mainly affected by spring mean temperature and precipitation.

Keywords: Landsat 5; Fractional Vegetation(*FV*); Temperature; Precipitation; Correlation analysis

吴捷,任宏利,许小峰,等,2018. MJO 对我国降水影响的季节调制和动力-统计降尺度预测[J]. 气象,44(6):737-751.

MJO 对我国降水影响的季节调制和动力-统计降尺度预测*

吴 捷[1,2] 任宏利[2,3] 许小峰[4] 高 丽[5]

1 南京信息工程大学大气科学学院,南京 210044
2 中国气象局国家气候中心气候研究开放实验室,中国气象局-南京大学气候预测研究联合实验室,北京 100081
3 中国地质大学环境学院大气科学系,武汉 430074
4 中国气象局,北京 100081
5 中国气象局数值预报中心,北京 100081

提 要: 利用 1981—2016 年中国区域 CN05.1 格点降水资料和 EAR-Interim 再分析资料,研究了季节循环对于热带大气季节内振荡(MJO)对我国降水影响的调制作用,并基于模式对 MJO 的预报建立了针对延伸期降水的动力-统计降尺度模型。结果表明,MJO 对我国季节内降水异常的影响明显受到季节循环的调制。当 MJO 对流在热带印度洋活跃时,我国降水偏多的区域随季节由南向北推进;当 MJO 对流位于海洋性大陆地区时,在秋、冬季我国东部和高原大部分地区降水异常偏少,而到了春、夏季该关系反转。MJO 对流和基本气流(特别是副热带西风急流)的位置和强度的变化所引起热带外环流响应的不同是造成这种季节性差异的重要原因。模式检验表明,BCC_AGCM2.2 对目标候 MJO 的预报技巧可达 18 d 以上,在此基础上利用模式预报 MJO 信息构建了随季节演变滚动的 MJO 动力-统计降尺度预测模型。独立样本检验表明,该模型在较长时效(10~20 d)下对 MJO 高影响区低频降水异常的预报技巧高于模式的直接预报,特别是在 MJO 活跃时期对降水预报技巧的提升更加明显,这为 MJO 信号释用提供了新的思路。

关键词: MJO,季节调制,BCC 二代大气环流模式(BCC_AGCM2.2),动力-统计降尺度模型,延伸期预报

中图分类号: P461 **文献标志码:** A **DOI:** 10.7519/j.issn.1000-0526.2018.06.002

Seasonal Modulation of MJO's Impact on Precipitation in China and Its Dynamical-Statistical Downscaling Prediction

WU Jie[1,2] REN Hongli[2,3] XU Xiaofeng[4] GAO Li[5]

1 College of Atmospheric Sciences, Nanjing University of Information Science and Technology, Nanjing 210044
2 Laboratory for Climate Studies and CMA-NJU Joint Laboratory for Climate Prediction Studies, National Climate Centre, CMA, Beijing 100081
3 Department of Atmospheric Science, School of Environmental Studies, China University of Geoscience, Wuhan 430074
4 China Meteorological Administration, Beijing 100081
5 CMA Numerical Prediction Centre, Beijing 100081

Abstract: Based on the China regional grid precipitation dataset CN05.1 and EAR-Interim reanalysis data, the seasonal modulation of the impact of Madden-Julian Oscillation (MJO) on China's precipitation anomaly is studied, and a dynamical-statistical downscaling model which focuses on extended-range precipitation

* 国家重点基础研究发展计划(973 计划)(2015CB453203)、国家自然科学基金项目(41505065、41775066、41375062)和公益性行业(气象)科研专项(GYHY201406022)共同资助
2018 年 4 月 8 日收稿; 2018 年 5 月 11 日收修定稿
第一作者:吴捷,主要从事短期气候预测研究. Email:wujie@cma.gov.cn
通信作者:任宏利,主要从事气候动力学与气候预测研究. Email:renhl@cma.gov.cn

forecast is established based on the MJO prediction by numerical model. The results show that the impact of MJO on precipitation anomaly is modulated by seasonal cycle obviously. When the MJO convection is active in tropical Indian Ocean, the above normal precipitation area advance northward along with the changes of seasons. When the MJO convection is active in the maritime continent, precipitation in eastern China and Tibet Plateau is abnormally less in autumn and winter, but this situation is gradually weakened or even reversed in spring and summer. The position and amplitude variation of MJO convection and basic state (especially the subtropical westerly jet) lead to different extra-tropical circulation responses, which are the main causes for these seasonal variations. The model verification suggests that the prediction skill of target pentad RMM index based on BCC_AGCM2.2 can extend to 18 days. In addition, a seasonal rolling MJO dynamical-statistical downscaling precipitation prediction model is established based on the forecasted RMM indices by dynamical model. The independent sample tests show that the dynamical-statistical model achieves higher skills in predicting the low-frequency precipitation anomaly than the direct output of BCC_AGCM2.2 in MJO high impact area during long lead time (10—20 d). The improvement is more obvious in the MJO active period. These findings could provide new thoughts for the MJO interpretation.

Key words: Madden-Julian Oscillation (MJO), seasonal modulation, BCC_AGCM2.2, dynamical-statistical downscaling model, extended-range forecast

引 言

MJO(Madden-Julian Oscillation)是热带大气季节内变率(ISV)的主要模态(Madden and Julian, 1971;1972),也是次季节时间尺度上最具可预报性的模态(Gottschalck et al,2010)。它主要表现为热带地区行星尺度对流和环流相互耦合并向东传播的30～80 d准周期振荡现象(Zhang, 2005),对热带地区的重要天气和气候事件,如台风群发(Fu and Hsu,2011)、南亚地区的极端降水(Xavier et al, 2014)、南海夏季风爆发(林爱兰等,2016)和El Niño事件发展(McPhaden,1999)等起到重要作用。尽管MJO对流异常主要发生在热带地区(15°S～15°N),但其伴随的异常加热能够激发从热带到中高纬的遥相关波列(如太平洋北美型PNA)从而对热带以外地区的环流和降水产生重要影响(Donald et al, 2006;Cassou,2008;李崇银等,2014;2012;Seo and Lee,2017)。因此MJO也被看作联系天气和气候的桥梁(Zhang,2013)。

近年来,针对MJO与我国气候异常联系也开展了一系列研究(林爱兰等,2008;任宏利和沈雨旸, 2016),发现MJO对冬季我国东部地区(Jia et al, 2011;贾小龙和梁潇云,2011;Yao et al,2015)、春季华南(李文锴等,2014)和云南地区(李汀等,2012;吕俊梅等,2012;牛法宝等,2012)、夏季西南(李永华等,2016)和长江流域(Zhang et al,2009)的降水异常均存在不同程度影响,这主要是由于MJO的大尺度对流加热所激发的Rossby波列对副热带高压位置(严欣和琚建华,2016)、东亚地区经向环流(刘冬晴和杨修群,2010;白旭旭等,2012)和副热带急流入口区的上升运动(Jeong et al,2008)进行调制造成的。然而,上述研究主要是针对MJO对某个特定季节和地区的气候异常影响进行研究,还缺乏考虑了气候年循环后MJO对不同地区、不同季节影响的差异对比的综合分析。一方面,MJO自身存在着显著的季节性特征(Adames et al,2016),例如MJO对流中心从冬到夏会从赤道附近移到赤道以北;另一方面,东亚地区作为世界上最为显著的季风区,气候态基本气流也存在显著季节差异,对热带地区热源强迫的响应也会有所不同(Jin and Hoskins, 1995;Henderson et al,2017)。因此,有必要从连续变化的角度来研究MJO对我国降水影响的季节调制,并进一步分析其具体成因。

目前,随着动力模式在初始化方案、集合方法和对流参数化过程等方面的改进,其对MJO的预报性能已有明显提高(任宏利等,2015),国际上的主要业务科研模式,如ECWMF(Vitart,2014)、GFDL(Xiang et al,2015)和CFSv2(Wang et al,2014)对MJO的预报技巧已稳定超过20 d,成为MJO业务预报的主流工具。我国学者也利用气候模式对MJO预测开展了相关研究(Zhao et al,2015;Ren

et al,2016;Liu et al,2017)。然而,由于降水的复杂性,动力模式对延伸期时段降水的直接预报仍然存在着很多问题。我国持续性的强降水事件往往与大气低频信号的活跃存在密切联系(魏雷等,2017;肖莺等,2017);已有研究尝试利用季节内振荡(ISO)信号与降水的关联性建立模型,以期利用 ISO 信息改善延伸期(10～30 d)降水和低温过程的预测(梁萍和丁一汇,2012;Lee et al,2017;陈官军等,2017)。为此,本文将 MJO 作为进行延伸期预报的重要可预报性来源(丁一汇和梁萍,2010),结合模式的动力预测与统计关系建立考虑季节演变的 MJO 对我国降水预报的动力-统计降尺度模型,将 MJO 信号直接释用于延伸期尺度降水预报中。

本文将首先讨论季节循环对 MJO 信号与我国季节内降水变率关系的调制作用,进一步分析与其对应的环流和水汽输送特征,最后建立一个延伸期 MJO 动力-统计相结合的我国降水异常的预报模型,并与模式直接输出的降水预报技巧进行对比。

1　资料和方法

1.1　观测资料

本文使用的降水资料为逐日的中国区域格点化观测数据集 CN05.1,其水平分辨率为 0.25°×0.25°。该数据集基于我国境内 2400 余个台站的观测资料,通过"距平逼近"方法插值建立(吴佳和高学杰,2013),在模式检验和极端事件的分析中得到了广泛应用(田芝平和姜大膀,2013;Hsu et al,2016)。此外,本文使用 ERA-Interim 逐日再分析资料(分辨率为 1.5°×1.5°)描述大尺度环流特征,包括纬向风(u)、经向风(v)、比湿(q)等要素;使用美国国家海洋和大气管理局(NOAA)提供的全球逐日向外长波辐散(outgoing longwave radiation,OLR)场(分辨率为 2.5°×2.5°)表征热带大尺度对流特征。上述所用资料范围为 1980—2016 年,气候态取 1981—2010 年共 30 a 的平均值。

采用 Wheeler and Hendon(2004)定义的一对实时多变量 MJO 指数(real-time multivariate MJO indices,简称 RMM 指数)来表征 MJO 的活动特征。该指数基于热带地区(15°S～15°N)逐日的 850 hPa 纬向风(U850)、200 hPa 纬向风(U200)和 OLR 场的资料,首先减去其多年气候态的 0～3 波以去除季节循环,之后减去前期 120 d 异常值的平均以去除年际变率,最后进行经向平均(15°S～15°N)、除以各自要素的标准差,并投影到多变量联合 EOF 的前两个模态上,即可得到两个 RMM 指数,分别记为 RMM1 和 RMM2。由这两个 RMM 指数构成的空间位相图上较为方便准确地表征 MJO 的对流位置和活动状况,在科研和业务中得到了极为广泛的使用(Gottschalck et al,2010;贾小龙等,2012)。近年来,国家气候中心发展建立了 ISV/MJO 监测预测业务系统(IMPRESS2.0)(任宏利等,2015;吴捷等,2016;Ren et al,2017),实时提供 MJO 监测预测的数据和图形产品,本文所用 RMM 指数的监测预测数据均由该系统提供(http://cmdp.ncc-cma.net/Monitoring/cn_mjo_impress.php)。

1.2　模式资料

本文所用预测资料由国家气候中心第二代大气环流模式(BCC_AGCM2.2)提供。该模式水平分辨率由一代模式的 T42 提升至 T106,垂直方向上分为 26 层(Wu et al,2010),并在此基础上建立了第二代月动力延伸模式业务系统(DERF2.0)(吴统文等,2013)。模式的大气初始场采用 NCEP 1 日 4 次的再分析资料,海表温度初始场采用 NOAA 的最优插值分析资料(OISST),回报试验从 1983 年开始,采用滞后平均法(LAF)每日生成 4 个样本(00、06、12、18 时,世界时),对未来 55 d 进行预报。本文基于 BCC_AGCM2.2 模式输出的 U850、U200 和 OLR 预报场,将每天 4 个起报样本进行平均得到的逐日 RMM 指数预报。采用模式 1991—2010 年共 20 a 的逐日回报资料作为模式自身的气候态,从而剔除模式的系统偏差。具体模式预测的 RMM 指数的计算方法可参考 Wu et al(2016)。

1.3　资料处理与统计方法

为定量表征 MJO 对我国降水的影响,并为建立动力统计客观预报模型打下基础,文中主要采用线性回归方法提取 RMM 指数对我国降水的影响信号(任宏利和沈雨旸,2016)。为了进一步突出季节内变率信号,滤除高频变化部分,本文对资料进行如下处理:(1)将逐日资料进行候平均处理,得到逐候资料(全年共 73 候),去除了天气尺度变率;(2)减去对应候的气候平均值,以去除气候循环;(3)减去之前 24 候的平均值,以去除年际变率。注意对 RMM

指数而言，首先按照 1.1 节所述方法计算逐日指数，之后再做候平均处理，得到逐候 RMM 指数。

2 MJO 对我国降水影响的季节调制

首先，利用传统的二元线性回归方法分析 RMM 指数所表征的 MJO 活动状况对我国同期降水的影响，对回归因子方差贡献的显著性进行 f 检验（施能，2002）（图 1）。需要注意的是，按照 RMM 指数划分的 MJO 位相和对流位置（图 1c，1d），当 RMM1 指数为正时，主要对流区位于海洋性大陆（MC）地区；RMM2 指数则主要反映热带印度洋和西太平洋的对流偶极子分布。为了更加突出印度洋上的 MJO 对流活跃特征，便于与传统合成分析研究的结果（Zhang et al，2009；Jia et al，2011）进行对比和物理解释，对 RMM2×（−1）进行回归。当该指数为正时，热带印度洋对流活跃而西太平洋对流抑制，后文如无特殊说明也进行相应处理。如图 1 所示，我国东部大部分地区的降水与 RMM2×（−1）指数呈正相关，即 MJO 对流位于印度洋（2～3 位相）时，我国南方和长江流域降水偏多；MJO 对流位于西太平洋（6～7 位相）时，我国南方和长江流域降水偏少。而当 MC 对流位于 MC 地区时，仅在高原东部出现零星的少雨区。

然而总体来看，我国降水异常与 MJO 信号的显著相关区偏小，为了充分挖掘 MJO 对我国降水异常的影响信息，下面进一步采用滑动回归的方法提取 MJO 影响的季节演变特征，分析季节循环对 MJO 对我国降水影响的调制作用。为了尽可能获取季节循环的影响信号，同时确保模型的稳定性，以目标候为中心，前后各取 9 候作为窗口进行滑动回归。依此对每个目标候每年可得到 19 候、30 年共得到的 570 候作为回归分析样本。此外，前人的资料分析（任宏利和沈雨旸，2016；李文铠等，2014）和数值试验（白旭旭等，2012）均指出，由于 MJO 的对流信号均在赤道附近，我国降水对 MJO 的响应需要一定时间，滞后时长约为 1～2 候。本文的研究也表明，我国降水对MJO的响应在滞后1候时最为显

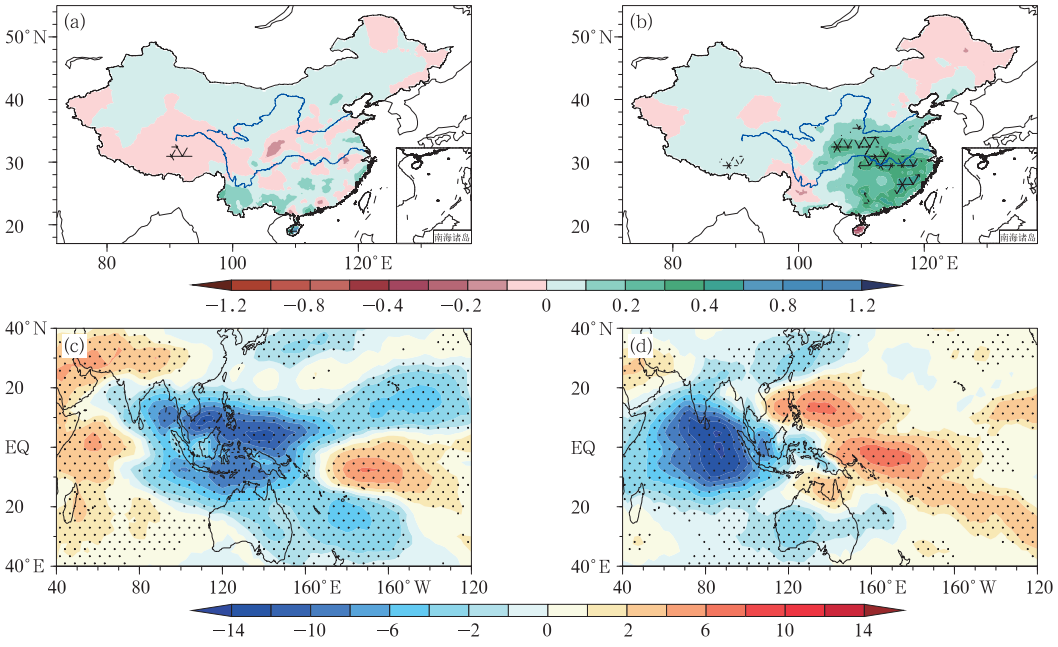

图 1 逐候 RMM1 指数和 RMM2×（−1）指数回归的同期我国降水异常（a，b；单位：mm·d^{-1}）和热带地区 OLR 场异常（c，d；单位：W·m^{-2}）

（a，c）RMM1 指数回归，（b，d）RMM2×（−1）指数回归

（网格和打点覆盖区域表示通过 0.05 显著性水平检验）

Fig. 1 Regression of pentad precipitation anomalies (a, b, unit: mm·d^{-1}) and tropical OLR anomalies (b, d, unit: W·m^{-2}) against RMM1 index and RMM2×(−1) index

(a, c) regression against RMM1 index, (b, d) regression against RMM2×(−1) index

(Results of meshed and stippled areas for precipitation and OLR have passed the 0.05 significance level test)

著,这既符合物理意义,也更具预报价值,因此后文均给出降水滞后 RMM 指数 1 候的响应结果。

图 2 给出四个典型候的滑动回归结果,基本可代表冬、春、夏、秋四个季节的降水响应特征。例如,滑动中心为第 3 候时,分析的范围为前一年第 67 候至当年第 12 候,即前一年 10 月 27 日至当年 3 月 1 日;滑动中心为第 40 候时,分析的范围为第 31 候至第 49 候,即当年 5 月 31 日至 9 月 2 日(以上均不考虑闰年)。由图可见,对 RMM2 指数而言,我国降水异常对MJO信号的响应区域存在明显的季节性北

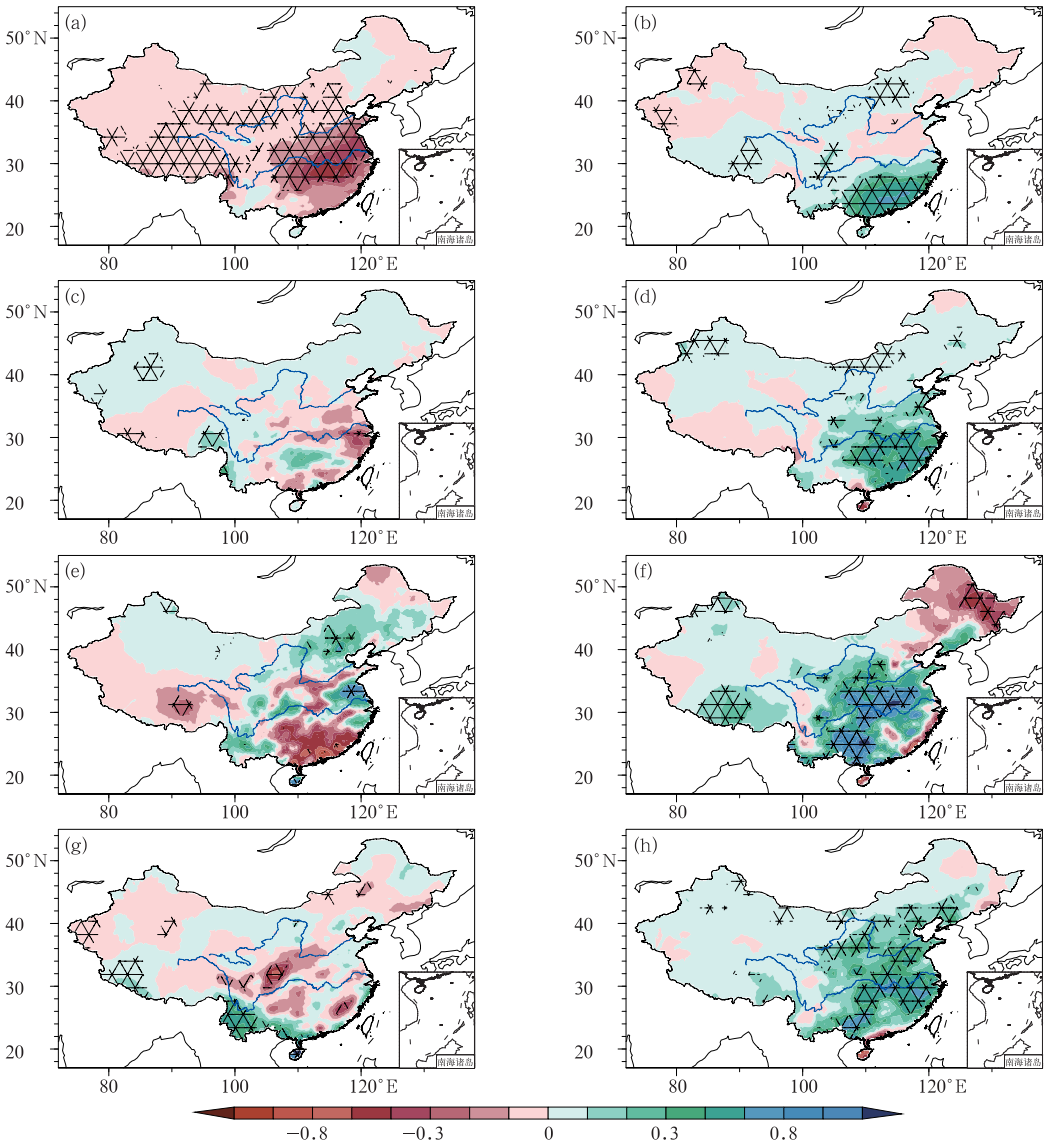

图 2　四个季节典型候 RMM1 指数(a, c, e, g)和 RMM2×(−1)指数(b, d, f, h)滑动回归的滞后 1 候的我国逐候降水异常(单位:mm·d^{-1})

(a, b)滑动中心为第 3 候,(c, d)滑动中心为第 21 候,(e, f)滑动中心为第 40 候,(g, h)滑动中心为第 58 候

(网格覆盖区域表示通过 0.05 显著性水平检验)

Fig. 2　Slide regression of lag-1 pentad precipitation anomalies (unit: mm·d^{-1}) against RMM1 index (a, c, e, g) and RMM2×(−1) index (b, d, f, h) of 4 typical pentads

(a, b) slide center for pentad 3, (c, d) slide center for pentad 21, (e, f) slide center for pentad 40, (g, h) slide center for pentad 58

(Results of meshed and stippled areas have passed the 0.05 significance level test)

进特征，即在冬季主要位于我国华南地区，春季北移到江南和沿江地区，夏季则进一步北移到江汉和黄淮流域，秋季则有所南退。而对 RMM1 指数而言，冬季降水对 MJO 的响应显著区域分布较广，如当指数为正时，我国大部分表现为降水偏少；到了夏季响应显著范围明显收缩，仅在淮河下游和华北地区出现显著偏多区；秋季西南地区易降水偏多。综上所述，MJO 对我国降水的影响确实显著地受到季节循环的调制，在不同的季节，即使 MJO 活动位相一致，我国降水响应的特征、范围和强度也会存在明显差异。

通过对每个 Julian 候进行滑动回归能够得到连续的 MJO 对我国降水影响的季节演变特征，图 3 给出了 105°～125°E 纬向平均的 RMM 指数回归的我国逐候降水异常及其相关系数。由图 3 可见，RMM2 指数所对应的降水异常区域随季节自南向北推进，冬季在 25°N 以南，夏季则向北推进到 35°N 附近，表明 MJO 活动对我国降水主雨带的季节内变率有明显的调制作用；而 RMM1 指数所表征的 MC 地区的对流状况在秋、冬季我国东部大部分地区降水呈负相关，而在春、夏季则呈现出一定的正相关，其对应的环流特征在第 3 节做进一步分析。

3 环流响应的季节演变特征

由前文可知，在不同季节我国降水对 MJO 对流活动的响应表现较大差异，下文将进一步分析大尺度环流变化特征，从而揭示这种季节性差异的物理机制。这里以差异最大的冬、夏两季为例，给出了回归的整层积分水汽通量异常，由此诊断导致我国降水异常差异的水汽输送通道和源地。由图 4 可知，当 RMM1 对应的 MC 地区对流活跃时，从青藏高原以南到我国华南和东部地区均为异常东风和北风水汽输送，表示在冬季我国最重要的来自印度洋的西南水汽通道明显减弱，导致我国东部大部分地区降水偏少，而在高原东部出现异常向北的水汽输送，水汽辐散导致高原地区降水偏少；而夏季的异常水汽输送状况与冬季明显不同，MJO 活动对西南水汽通道的抑制减弱，淮河下游和华北部分地区出现异常西南、偏西水汽输送，从而导致降水偏多。当

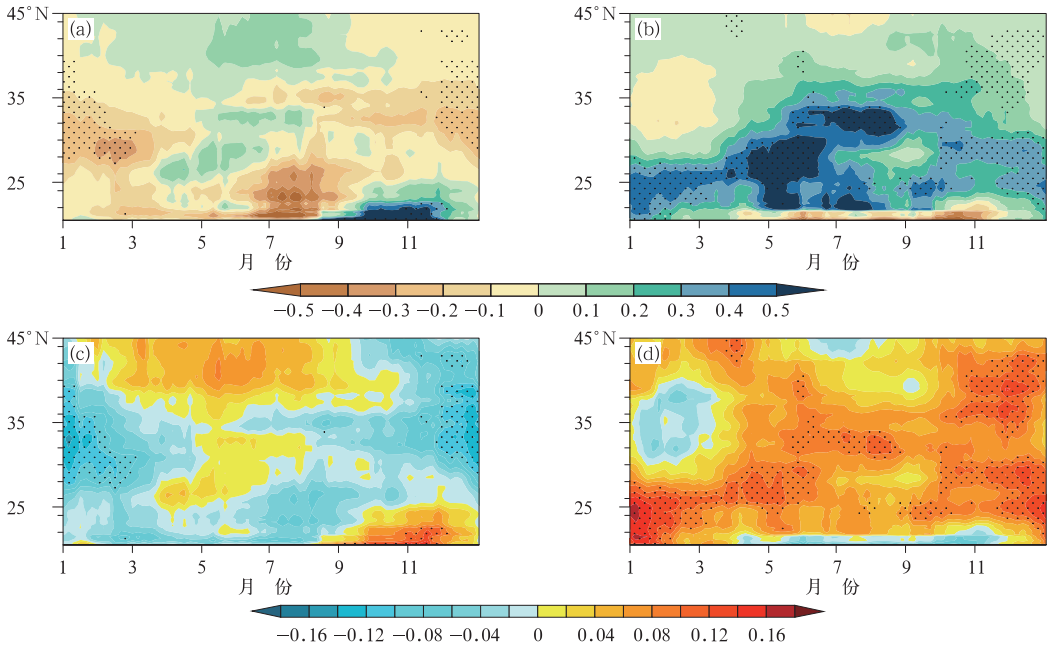

图 3 RMM1 指数(a)和 RMM2×(−1)指数(b)滑动回归的滞后 1 候的 105°～125°E 纬向平均我国逐候降水异常(单位：mm·d^{-1})时间-纬度剖面图；(c，d)同图 3a，3b，但为滑动相关系数

(打点区域表示通过 0.05 显著性水平检验)

Fig. 3 The time-latitude sector of slide regression of lag-1 pentad precipitation anomalies (unit: mm·d^{-1}) against RMM1 index (a) and RMM2×(−1) index (b) averaged between 105°E and 125°E; (c, d) same as Figs. 3a and 3b, but for slide correlation coefficients

(Results of stippled areas have passed the 0.05 significance level test)

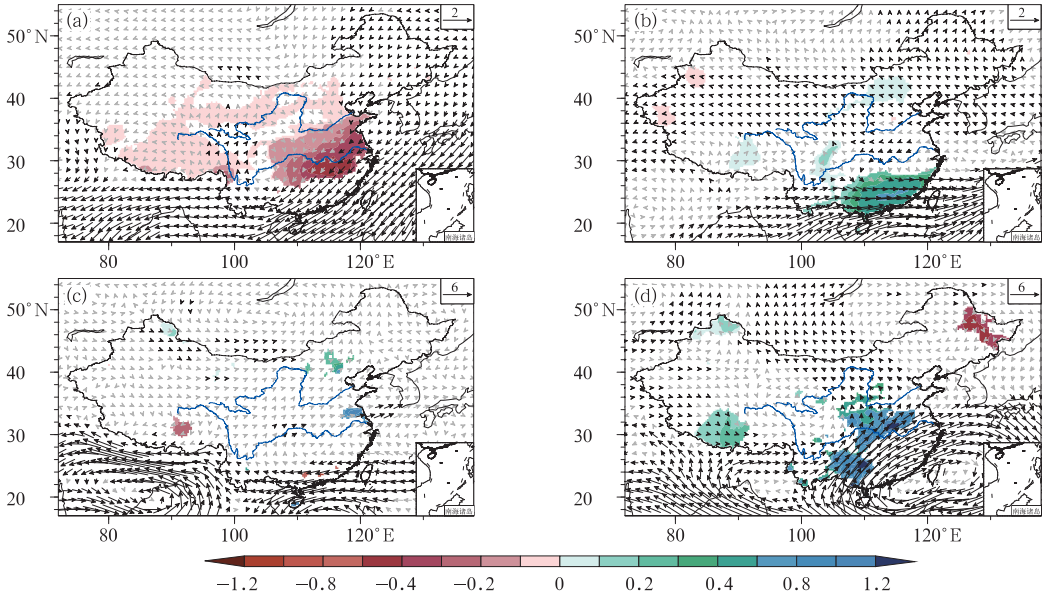

图 4　RMM1 指数(a，c)和 RMM2×(−1)指数(b，d)滑动回归的滞后 1 候的我国逐候降水异常(阴影,单位:mm·d^{-1})和整层积分的水汽通量异常(矢量,单位:g·m^{-1}·s^{-1})

(a，b)滑动中心为第 3 候,(c，d)滑动中心为第 40 候

(阴影和黑色矢量表示通过 0.05 显著性水平检验)

Fig. 4　Slide regression of lag-1 pentad precipitation anomalies (shading, unit: mm·d^{-1}) and water vapor flux anomaly of the whole layer integration (vector, unit: g·m^{-1}·s^{-1}) against RMM1 index (a, c) and RMM2×(−1) index (b, d)

(a, b) slide center for pentad 3, (c, d) slide center for pentad 40

(The shadings for precipitation and thick black vectors for water vapor flux have passed the 0.05 significance level test)

RMM2 指数对应的热带印度洋对流活跃而西太平洋对流抑制时,在冬季异常的西南和西北水汽输送在华南地区辐合,导致华南地区降水增多;而在夏季来自西太平洋的西南水汽输送明显北抬,在水汽通道外围的华南和江南地区西部以及水汽辐合区江汉和黄淮流域降水增多,此外在高原地区受到偏西水汽输送增加的影响同样出现降水增多。

由于大气中的水汽主要集中在低层,整层的异常水汽通量也主要受到低层环流异常的控制,因此我们进一步以 700 hPa 为代表层分析冬、夏两季低层环流对 MJO 对流的响应特征。图 5 给出在两个典型候滑动回归的异常 OLR 场、700 hPa 风场、流函数场和气候平均的 700 hPa 纬向风场(同样经过前后 9 候的滑动)。如图所示,在冬季,MJO 对流中心在赤道附近,响应也类似经典的 Gill 型(Gill,1980),此时气候背景场的副热带西风急流较强,且向西伸展到欧亚大陆边缘,急流附近热带外环流对 MJO 对流的响应较强(Adames and Wallace,2014;Henderson et al,2017)。当对流位于 MC 地区时,我国南方受到异常气旋式环流北侧的偏东风控制,导致来自印度洋的水汽减弱;对流进一步激发北太平洋副热带西风急流附近的气旋环流异常,导致我国北方受到气旋西侧偏北气流控制,东亚冬季风加强,我国东部大部分地区均降水偏少(图 5a);而当对流位于印度洋时,西太平洋地区对流减弱,对应我国南海地区有一西伸脊,副热带高压偏西偏南,其外侧的西南气流输送水汽到我国华南地区,导致降水增多。在夏季,MJO 对应的对流异常整体北移,且呈现出东北—西南走向,而气候场上西风急流向东北方向收缩,强度减弱,导致 MJO 所激发的热带外遥相关波列和环流异常明显减弱。然而,此时 RMM2 指数对应的西北太平洋的对流负异常显著增强,从而在其西北侧激发了一个闭合的反气旋环流,其位置也较冬季的西伸脊明显偏北,使得副热带高压偏西偏强,加强了其西北侧的水汽输送,在 30°N 以北表现出一条暖式切变线,导致我国华南、江南西部和黄淮、江汉地区降水偏多。

图 6 则进一步给出 MJO 对流位置、基本气流和

环流响应的连续变化特征。由图可见，RMM1 指数对应的 MC 地区的对流异常从冬到夏明显北抬，然而由于西风急流的减弱和北抬，热带外环流响应的范围迅速缩小，导致 RMM1 指数所对应的我国降水

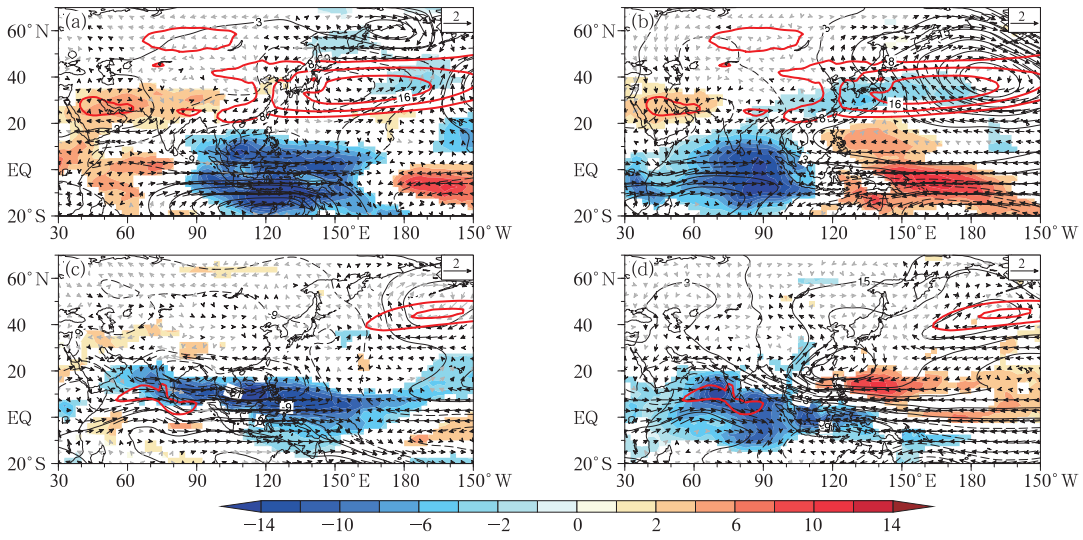

图 5 逐候 RMM1 指数(a，c)和 RMM2×(−1)指数(b，d)滑动回归的同期 OLR 异常场(阴影，单位：W·m^{-2})和滞后 1 候的 700 hPa 风场(矢量，单位：m·s^{-1})和流函数(黑色等值线，单位：10^5 m^2·s^{-1})异常

(a，b)滑动中心为第 3 候，(c，d)滑动中心为第 40 候

(红色等值线代表 700 hPa>8 m·s^{-1}气候平均的纬向风，阴影和黑色矢量表示通过 0.05 显著性水平检验)

Fig. 5 Slide regression of simultaneous OLR anomalies (shading, unit: W·m^{-2}) and lag-1 wind (vector, unit: m·s^{-1}) and stream function (contour, unit: 10^5 m^2·s^{-1}) anomalies at 700 hPa against RMM1 index (a, c) and RMM2×(−1) index (b, d)

(a, b) slide center for pentad 3, (c, d) slide center for pentad 40

(Red contours indicate the climatically averaged zonal wind at 700 hPa which is larger than 8 m·s^{-1}, shadings for OLR and thick black vectors for wind have passed the 0.05 significance level test)

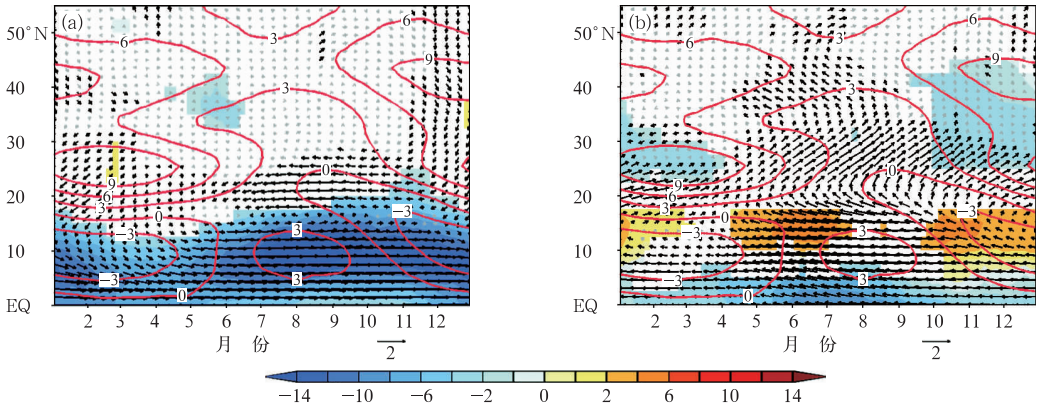

图 6 逐候 RMM1 指数(a)和 RMM2×(−1)指数(b)滑动回归的 105°～125°E 纬向平均的同期 OLR 场(阴影，单位：W·m^{-2})和滞后 1 候的 700 hPa 风场异常(矢量，单位：m·s^{-1})时间-纬度剖面图

(红色等值线代表 700 hPa 气候平均的纬向风，阴影和黑色矢量表示通过 0.05 显著性水平检验)

Fig. 6 The time-latitude sector of slide regression of simultaneous OLR anomalies (shading, unit: W·m^{-2}) and lag-1 wind anomalies (vector, unit: m·s^{-1}) at 700 hPa against RMM1 index (a) and RMM2×(−1) index (b) averaged between 105°E and 125°E

(Red contours indicate the climatically averaged zonal wind at 700 hPa, shadings for OLR and thick black vectors for wind have passed the 0.05 significance level test)

异常响应的范围在冬季较大而夏季缩小;RMM2 指数对应的菲律宾附近的负对流异常从冬到夏位置略有北抬,强度显著增强,激发的其西北侧反气旋式环流的脊线从 15°N 北移到 22.5°N,对应我国异常雨带的北移。值得注意的是,在夏季菲律宾附近的对流异常激发了一个季节内经向波列,其波长约为 20～25 个纬距,即 PJ(太平洋-日本)波列或称为 EAP(东亚-太平洋)遥相关型(Huang and Li,1987; Nitta,1987;吴捷等,2013),可将热带的对流信号带到热带外 50°N 以北的地区。综上所述,由于 MJO 对流和气候态基本气流均表现出明显的季节差异,在两者的共同作用下,热带外环流对 MJO 的响应也明显地受到季节循环的调制,在不同季节展现出有差异的连续变化的特征,改变了水汽输送通道,从而对我国降水异常产生不同的调制作用。

4　基于 MJO 影响季节调制的我国降水预测模型

如前文所述,由于受到基本气流的调制,MJO 对热带外环流和我国降水异常的影响具有显著的季节性差异。在这一部分中,以目前已经业务运行 BCC_AGCM2.2为例,检验模式能否抓住观测中 MJO 活动与我国的降水异常之间的联系,并根据模式对 RMM 指数的动力预报和观测中 MJO 与降水的统计关系,建立一个基于 MJO 信号的我国延伸期降水动力-统计预报模型,定量估计 MJO 信号对延伸期时段我国降水的影响。

首先对BCC_AGCM2.2模式在历史回报和实时预报阶段对 MJO 的预报性能进行检验。Wu et al (2016)指出该模式在历史回报阶段对 MJO 的预报技巧为 16 d 左右。这里根据本文的实际需要,对模式对目标候 RMM 指数的预报技巧进行检验。如图 7 所示,若以相关系数达到 0.5 的天数为参考(Lin et al,2008),在历史回报阶段,模式对目标候 RMM 指数的预报技巧约为 15 d;如果只考虑 MJO 活跃阶段,即 RMM 指数的振幅 RMM_{amp}($RMM_{amp}=\sqrt{RMM1^2+RMM2^2}$)>1 时,模式的预报技巧可达到 18 d;而在独立预报阶段(2011—2016 年),模式对目标候 RMM 指数的预报技巧约为 13 d,这可能与预报初始场替换为 T639 资料有关,若只考虑MJO活跃时,模式的预报技巧仍能超过16 d,说明强 MJO 信号具备更高的可预报性,动力模式对 RMM 指数具备一定的预报能力。

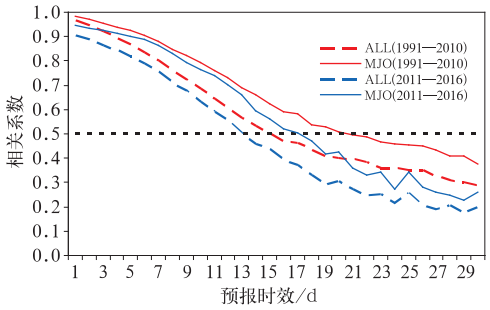

图 7　BCC_AGCM2.2 对目标候 RMM 指数的预报相关技巧
(红线代表 1991—2010 年,蓝线代表 2011—2016 年;虚线代表全部预报个例,实线代表预报候 MJO 活跃的预报个例)

Fig. 7　Correlation skill of target pentad RMM indices forecasted by BCC_AGCM2.2
(Red lines stand for the period 1991－2010, and blue lines stand for the period 2011－2016; dashed lines indicate all forecasting cases, solid lines indicate the events when MJO is active)

为了进一步考察模式能否抓住观测中 MJO 信号与我国降水异常的联系,图 8 给出 BCC_AGCM2.2 模式提前 10 d 预报的候平均 RMM 指数回归的模式降水异常分布。与图 2 对比可知,只有在冬季(图 8a,8b)模式能够在一定程度上描述出观测中 MJO 信号与我国降水异常的对应关系,其空间相关系数(ACC)达到 0.5 左右;而在其他季节,模式中与 MJO 信号对应的降水异常分布与观测均存在着较大差异,特别是在春季和秋季的转换季节,ACC 甚至为负值。这表明,虽然模式对 MJO 信号有着不错的预报性能,但是未能很好地把握 MJO 与我国降水异常之间的联系,进而限制了模式本身对延伸期时段降水的预报技巧(图 10a～10d)。

鉴于上述对动力模式性能的讨论,综合考虑模式对 MJO 预报技巧较高的优点和 MJO 信号与我国季节内降水异常存在着的物理意义明确的对应关系,建立一个基于动力模式预报 MJO 信号和基于统计方法得到 MJO 与我国降水异常关系的动力-统计模型,即 MJO 动力-统计降尺度预报模型(MDSM),从而抓住 MJO 这个季节内变率最显著的可预报性来源,尽可能提取 MJO 对我国降水异常的影响信号,直接对我国延伸期降水异常进行预报。具体公式如下:

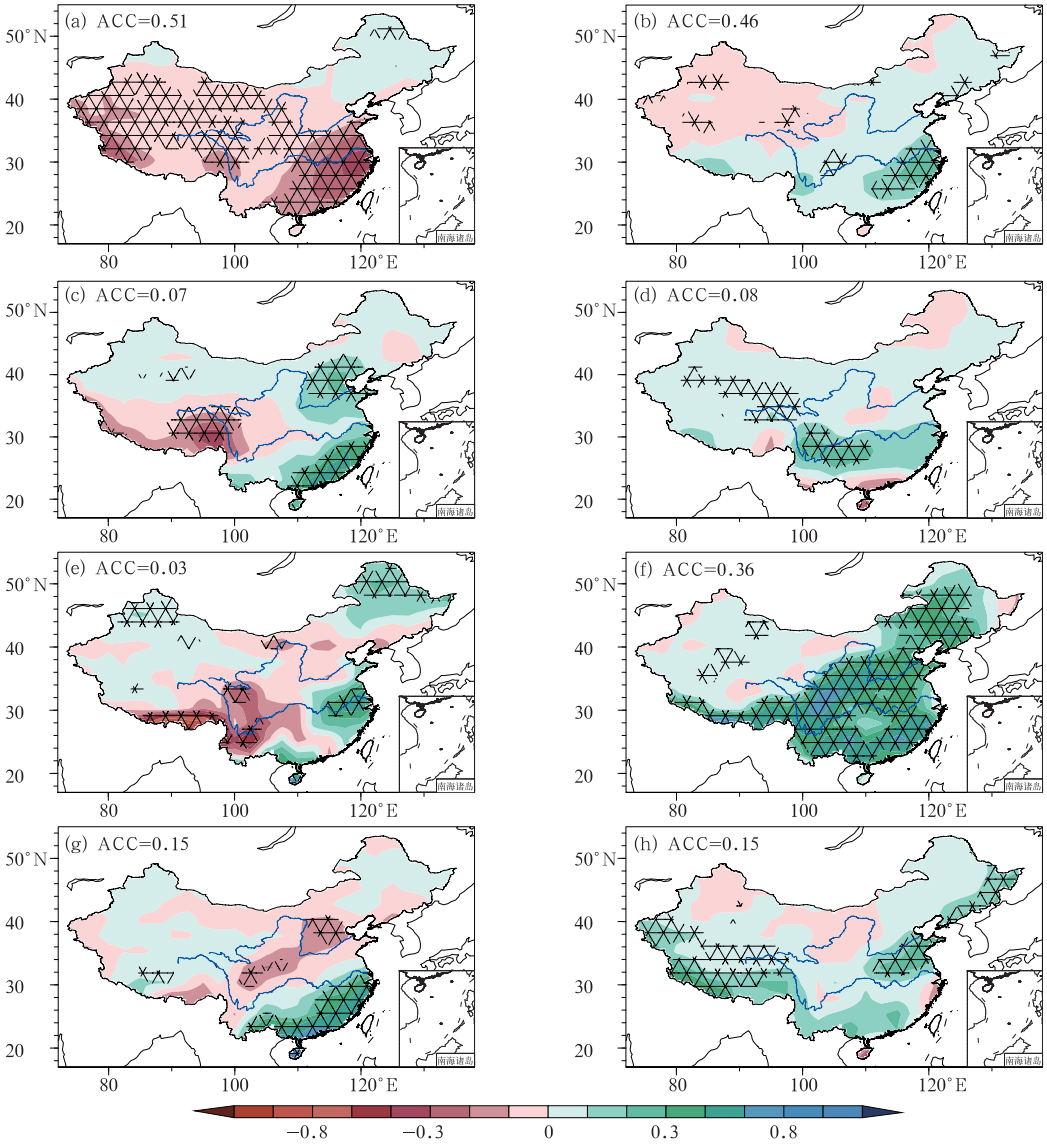

图 8 同图 2,但为 BCC_AGCM2.2 提前 10 d 预报的逐候 RMM 指数与模式降水的回归系数(单位:mm·d^{-1})

(每张图的左上角给出与图 2 中观测型的空间相关系数)

Fig. 8 Same as Fig. 2, but for the slide regression of lag-1 pentad simulated precipitation anomalies (unit: mm·d^{-1}) against RMM indices forecasted 10 d in advance by BCC_AGCM2.2

(The up-left number in each figure is ACC between Fig. 8 and Fig. 2)

$$PREC_ano(itau+5,ipd)=PREC_reg1(ipd)\times RMM1_fcs(itau,ipd-1)+PREC_reg2(ipd)\times RMM2_fcs(itau,ipd-1) \quad (1)$$

式中,$itau$ 代表模式对 RMM 指数的预报时效,取 1~50;ipd 代表预报目标候,取 1~73;$PREC_ano$ 代表预报目标候的降水异常,$PREC_reg1$ 和 $PREC_reg2$ 代表目标候的降水统计回归模型(图 2);$RMM1_fcs$ 和 $RMM2_fcs$ 代表动力模式预报的目标候前 1 候的 RMM 指数。该模型利用数值模式提前较长时段预报的 RMM 指数,乘以前期建立的随季节滑动的二元回归模型,得到目标候的降水异常预报。

图 9 给出了该模型在 2011—2016 年对降水预报的独立样本检验结果。其中图 9a 和 9b 为使用超前 1 候观测的 RMM 指数所得到的降水预报技巧,代表了该动力-统计模式的预报技巧上限,可见在除

东北以外的大部分地区均能得到超过显著性的预报结果,其中在江南、华中和西北的部分地区预报技巧相对较高,这也与前文阐述的 MJO 的高影响范围基本一致;若使用模式超前5 d预报的RMM指数

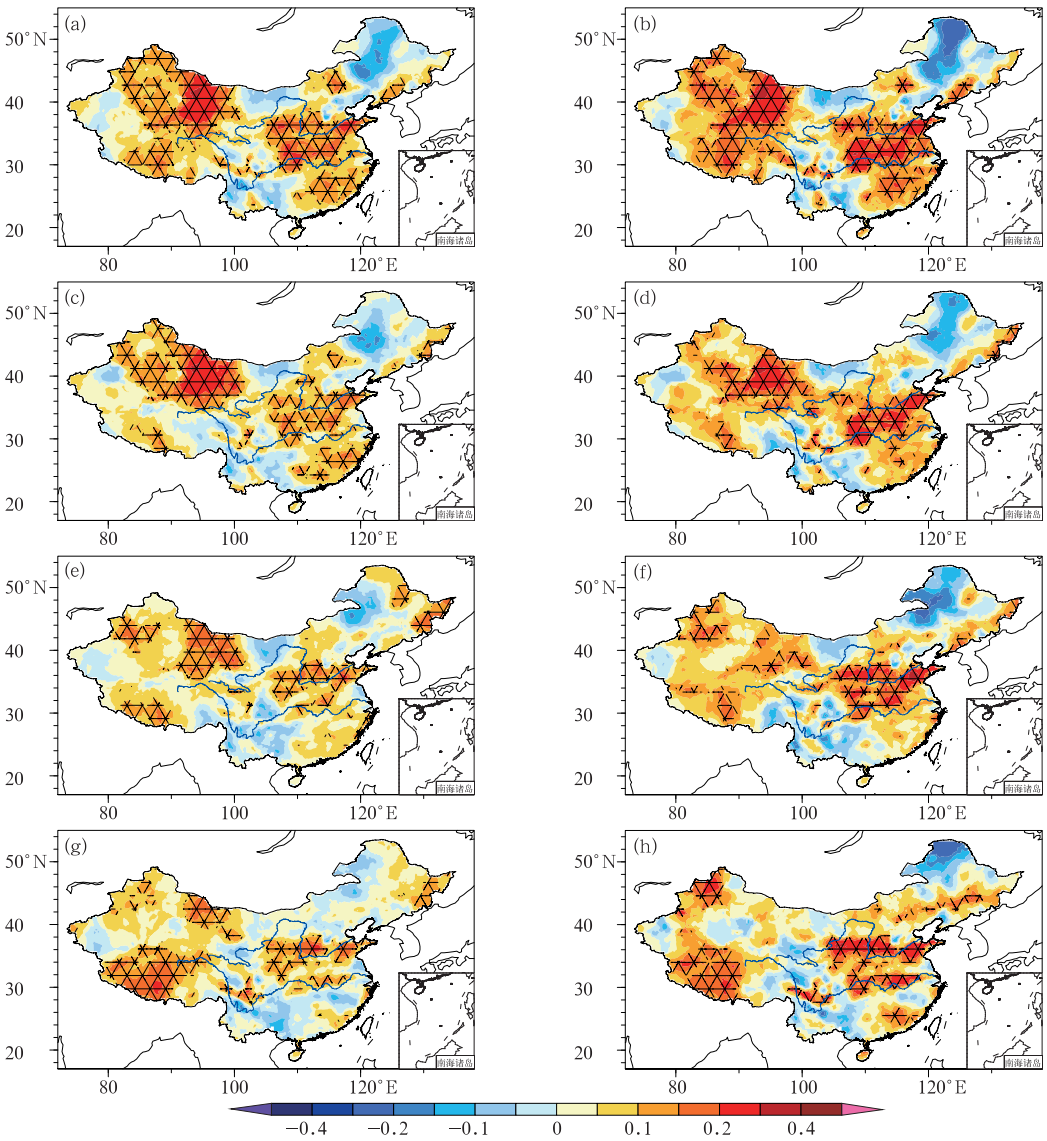

图 9　独立样本检验期间(2011—2016 年)MJO 动力-统计降尺度模型对我国逐候降水距平预报的相关技巧评分:(a, c, e, g)全部样本,(b, d, f, h)MJO 活跃时对应样本
(a, b)超前 0 d 预报(即使用观测的 RMM 指数),(c, d)超前 10 d 预报(即使用模式提前 5 d 预报的 RMM 指数),(e, f)超前 15 天预报(即使用模式提前 10 d 预报的 RMM 指数),(g, h)超前 20 d 预报(即使用模式提前 15 d 预报的 RMM 指数)
(网格覆盖区域表示通过 0.05 显著性水平检验)

Fig. 9　Correlation skill of pentad precipitation anomalies forecasted by the dynamical-statistical model during the independent sample verification: (a, c, e, g) all samples, (b, d, f, h) samples of active MJO
(a, b) forecast 0 d in advance (using observed RMM indices), (c, d) forecast 10 d in advance (using RMM indices 5 d earlier forecasted by BCC_AGCM2.2), (e, f) forecast 15 d in advance (using RMM indices 10 d earlier forecasted by BCC_AGCM2.2), (g, h) forecast 20 d in advance (using RMM indices 15 d earlier forecasted by BCC_AGCM2.2)
(Results of meshed areas have passed the 0.05 significance level test)

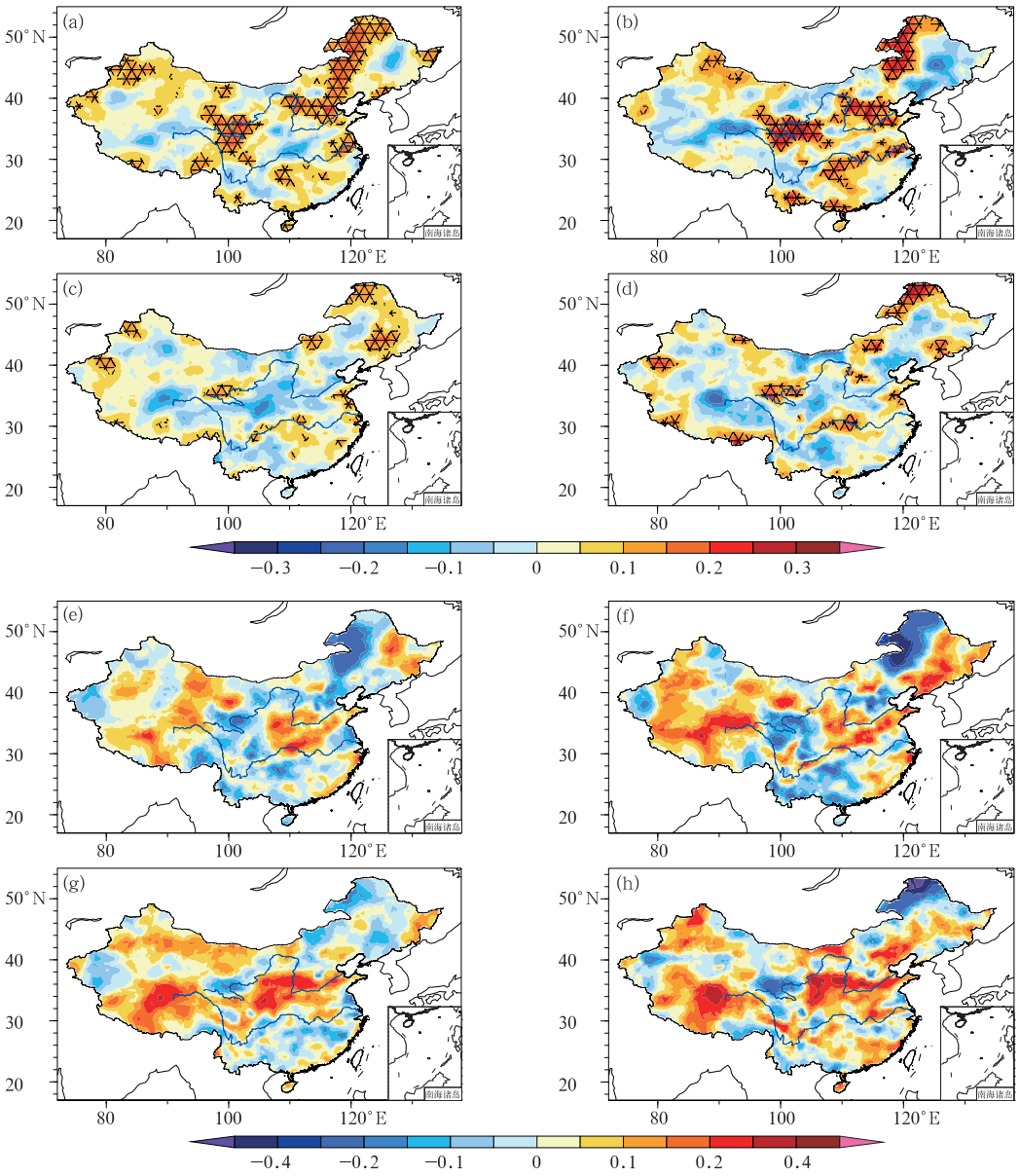

图 10 独立样本检验期间(2011—2016 年)BCC_AGCM2.2 模式直接输出的我国逐候降水距平的相关技巧(a～d)和 MJO 动力-统计降尺度模型(MDSM)与 BCC_AGCM2.2 的技巧之差(e～h);(a, c, e, g)全部样本,(b, d, f, h)MJO 活跃时对应样本

(a, b, e, f)超前 15 d 预报,(c, d, g, h)超前 20 d 预报

(网格覆盖区域表示通过 0.05 显著性水平检验)

Fig. 10 Correlation skill of pentad precipitation anomalies forecasted by the DERF2 model (a−d) and the skill difference between MJO dynamic-statistic model (MDSM) and DERF2 (e−h) during the independent sample verification (2011−2016)

(a, c, e, g) for all samples, (b, d, f, h) for the samples of active MJO

(a, b, e, f) forecast 15 d in advance, (c, d, g, h) forecast 20 d in advance

(Results of meshed areas have passed the 0.05 significance level test)

即在超前 10 d 的情况下,该 MSDM 模型仍然对上述地区具备较高的预报技巧,且随着预报时效的不断延长,该模型的预报技巧下降较为缓慢;在提前 20 d 时,该模型仍然对华中—华北、西北和青藏高原的部分地区有显著的预报技巧。需要注意的是,该模型在华北和西北地区较高的预报技巧主要和

RMM1 指数在初冬与该区域降水的密切联系有关,即在初冬 40°N 附近西风急流首先加强,MC 地区对流偏强时我国北方大部北风气流加强(图 6a),来自南方的水汽输送减弱导致降水偏少。若只考虑 MJO 活跃的情况,上述区域内预报技巧的提升非常明显,华中、江南和西部的部分地区的相关技巧能够超过 0.3,最高可提升至 0.5,这说明该动力-统计模型能在较大程度上提取 MJO 对我国降水异常的影响信息,当 MJO 信号较强时,该模型即使在较长的预报时效下也具备一定的参考意义。

进一步给出 BCC_AGCM2.2 直接输出的逐候降水的预报技巧,并与 MJO 动力-统计降尺度模型(MSDM)的技巧进行对比。如图 10 所示,在延伸期时段,提前 15 d 模式预报的降水仅在华北和东北的部分地区有一定的预报技巧,在提前 20 d 时我国大部分地区的模式预报技巧均较低,参考意义有限。对比 MSDM 模型与 BCC_AGCM2.2 的技巧之差(图 10e～10h)可知,该动力-统计模型能够明显改进我国华中、东南沿海和西部地区的降水预报技巧,这与 MJO 高影响区基本一致,而随着预报时效的延长该动力统计模型的改进更加明显。特别当 MJO 活跃时,MSDM 模型的预报在我国大部分地区明显高于模式的直接输出结果,在华中和西部的部分地区技巧提升超过 0.3,这进一步说明运用该模型可有效提升我国延伸期降水预报水平。

5　结论和讨论

本文利用滑动回归的方法考察了季节循环对 MJO 对我国季节内降水变率影响的调制作用,并分析了典型季节的大尺度环流和水汽输送特征。进一步结合 BCC_AGCM2.2 模式预报结果,研究了 MJO 对我国降水影响的可预报性,在此基础上建立了一个动力-统计降尺度预测模型,将 MJO 信号具体释用到我国延伸期降水预报中,以提升预报技巧。主要结论如下:

(1) 超前的 MJO 对流活动能够对我国大部分地区的季节内低频降水异常产生显著影响,并受到季节循环的调制,呈现出显著的季节性差异。当对流位于 MC 地区(RMM1 指数为正值)时,在秋、冬季我国东部和高原的大部分地区降水异常偏少,在春、夏季这种对应关系减弱甚至反转,在华北和江淮地区降水偏多;当热带印度洋对流活跃而西太平洋对流受到抑制(RMM2 指数为负值)时,我国降水偏多的地区随季节由南向北推移,即在冬季多雨区位于华南,春季位于江南到沿江一带,夏季北进到黄淮流域,秋季则略有南撤。

(2) 在不同季节,MJO 对流和基本气流(特别是副热带西风急流)的位置和强度的变化是造成 MJO 影响季节差异的重要原因。在冬季,MC 地区的对流激发出我国南海和日本东侧的气旋式环流异常,两者共同作用减弱了来自印度洋的水汽输送,加强了东亚冬季风,导致我国大部分地区降水偏弱;在夏季,西风急流减弱北抬,热带外环流响应明显减弱,而西太平洋对流负异常从冬到夏强度加强,所激发的反气旋环流显著地向北推进,增强了副热带高压西北侧的水汽输送,导致所对应的降水偏多范围从华南北推至长江以北地区。

(3) 在 MJO 活跃时 BCC_AGCM2.2 模式对目标候 RMM 指数的预报技巧可超过 18 d,但模式很难抓住观测中 MJO 信号与我国降水异常的关系及其季节变化特征,因此进一步基于动力模式预报的 RMM 指数和观测中 MJO 与我国降水的联系,建立一个针对延伸期时段降水的 MJO 动力-统计降尺度预报模型。独立样本检验表明,该模型能够提前较长时间(10～20 d)对 MJO 高影响区,如华中、江南和西部部分地区的降水异常做出有效的预报,且预报技巧随预报时效的延长下降较缓慢。与模式直接输出的降水预报相比,动力-统计模型在提前 15 d 以上时的预报技巧在我国大部分地区均有提升,特别当存在 MJO 信号时技巧提升更加明显。

本文主要从延伸期预报的角度出发,对 MJO 信号与我国降水异常的线性关系进行讨论。需要注意的是,本文虽然提取了降水的季节内低频变化分量,但一般也是非正态分布的,基于回归方法所建立的动力-统计预报模型只能解释 MJO 和低频降水之间的线性关联部分,主要适用于 MJO 信号较强时的高影响区,如何采用更好的统计手段建立两者的非线性联系,是需要继续探索的方向。此外,如何考虑 MJO 和其他季节内的主要模态,如 BSISO(Hsu et al,2016; Chen and Zhai,2017)、NAO(Cassou,2008)、中高纬 ISO(孔晓宇等,2017)对我国降水的协同影响,则是需要进一步解决的问题。

参考文献

白旭旭,李崇银,李琳,2012. MJO 对中国春季降水影响的数值模拟

研究[J]. 气象学报,70(5):986-1003.

陈官军,魏凤英,姚文清,等,2017. 基于低频振荡信号的中国南方冬半年持续性低温指数延伸期预报试验[J]. 气象学报,75(3):400-414.

丁一汇,梁萍,2010. 基于 MJO 的延伸预报[J]. 气象,36(7):111-122.

贾小龙,梁潇云,2011. 热带 MJO 对 2009 年 11 月我国东部大范围雨雪天气的可能影响[J]. 热带气象学报,27(5):639-648.

贾小龙,袁媛,任福民,等,2012. 热带大气季节内振荡(MJO)实时监测预测业务[J]. 气象,38(4):425-431.

孔晓宇,毛江玉,吴国雄,2017. 2002 年夏季中高纬大气准双周振荡对华南降水的影响[J]. 大气科学,41(6):1204-1220.

李崇银,凌建,宋洁,等,2014. 中国热带大气季节内振荡研究进展[J]. 气象学报,72(5):817-834.

李崇银,潘静,田华,等,2012. 西北太平洋台风活动与大气季节内振荡[J]. 气象,38(1):1-16.

李汀,严欣,琚建华,2012. MJO 活动对云南 5 月降水的影响[J]. 大气科学,36(6):1101-1111.

李文铠,何金海,祁莉,等,2014. MJO 对华南前汛期降水的影响及其可能机制[J]. 热带气象学报,30(5):983-989.

李永华,向波,卢楚翰,等,2016. 热带大气季节内振荡对西南地区东部夏季降水的影响及其可能机制[J]. 大气科学,40(2):437-450.

梁萍,丁一汇,2012. 基于季节内振荡的延伸预报试验[J]. 大气科学,36(1):102-116.

林爱兰,谷德军,李春晖,等,2016. 赤道 MJO 活动对南海夏季风爆发的影响[J]. 地球物理学报,59(1):28-44.

林爱兰,梁建茵,古德军,2008. 热带大气季节内振荡对东亚季风区的影响及不同时间尺度变化研究进展[J]. 热带气象学报,24(1):11-19.

刘冬晴,杨修群,2010. 热带低频振荡影响中国东部冬季降水的机理[J]. 气象科学,30(5):684-693.

吕俊梅,琚建华,任菊章,等,2012. 热带大气 MJO 活动异常对 2009～2010 年云南极端干旱的影响[J]. 中国科学:地球科学,42(4):599-613.

牛法宝,杞明辉,杨素雨,2013. MJO 不同活动中心位置对云南冬半年降水过程的影响[J]. 气象,39(9):1145-1153.

任宏利,沈雨旸,2016. MJO 对我国天气气候影响的新事实[J]. 气象科技进展,6(3):97-105.

任宏利,吴捷,赵崇博,等,2015. MJO 预报研究进展[J]. 应用气象学报,26(6):658-668.

施能,2002. 气象科研与预报中的多元分析方法[M]. 北京:气象出版社:34-37.

田芝平,姜大膀,2013. 不同分辨率 CCSM4 对东亚和中国气候模拟能力分析[J]. 大气科学,37(1):171-186.

魏蕾,房佳蓓,杨修群,2017. 华南夏季 12～30 d 持续性强降水的低频特征分析[J]. 气象学报,75(1):80-97.

吴佳,高学杰,2013. 一套格点化的中国区域逐日观测资料及与其它资料的对比[J]. 地球物理学报,56(4):1102-1111.

吴捷,任宏利,赵崇博,等,2016. 国家气候中心 MJO 监测预测业务产品研发及应用[J]. 应用气象学报,27(6):641-653.

吴捷,许小峰,金飞飞,等,2013. 东亚-太平洋型季节内演变和维持机理研究[J]. 气象学报,71(3):476-491.

吴统文,宋连春,刘向文,等,2013. 国家气候中心短期气候预测模式系统业务化进展[J]. 应用气象学报,24(5):533-543.

肖莺,任永建,杜良敏,2017. 湖北省夏季不同阶段强降水及其大气低频特征[J]. 气象,43(1):77-83.

严欣,琚建华,2016. 夏季 MJO 持续异常的主要特征分析[J]. 大气科学,40(5):1048-1058.

Adames A F, Wallace J M, 2014. Three-dimensional structure and evolution of the MJO and its relation to the mean flow[J]. J Atmos Sci,71:2007-2026.

Adames Á F, Wallace J M, Monteiro J M, 2016. Seasonality of the structure and propagation characteristics of the MJO[J]. J Atmos Sci,73(9):3511-3526.

Cassou C,2008. Intraseasonal interaction between the Madden-Julian Oscillation and the North Atlantic Oscillation[J]. Nature,455(7212):523-527.

Chen Yang,Zhai Panmao,2017. Simultaneous modulations of precipitation and temperature extremes in Southern parts of China by the boreal summer intraseasonal oscillation[J]. Climate Dyn,49(9-10):3363-3381.

Donald A,Meinke H,Power B,et al,2006. Near-global impact of the Madden-Julian oscillation on rainfall[J]. Geophys Res Lett,33(9):L09704,DOI:10.1029/2005GL025155.

Fu Xiaohua,Hsu P C,2011. Extended-range ensemble forecasting of tropical cyclogenesis in the northern Indian Ocean:modulation of Madden-Julian oscillation[J]. Geophys Res Lett,38(15):L15803,DOI:10.1029/2011GL048249.

Gill A E,1980. Some simple solutions for heat-induced tropical circulation[J]. Quart J Roy Meteor Soc,106(449):447-462.

Gottschalck J,Wheeler M,Weickmann K,et al,2010. A framework for assessing operational Madden-Julian oscillation forecasts:A CLIVAR MJO Working Group Project[J]. Bull Amer Meteor Soc,91(9):1247-1258.

Henderson S A,Maloney E D,Son S W,2017. Madden-Julian Oscillation Pacific teleconnections:the impact of the basic state and MJO representation in General Circulation Models[J]. J Climate,30(12):4567-4587.

Hsu P C,Lee J Y,Ha K J,2016. Influence of boreal summer intraseasonal oscillation on rainfall extremes in southern China[J]. Int J Climatol,36(3):1403-1412.

Huang Ronghui,Li Weijing,1987. Influence of the heat source anomaly over the tropical western Pacific on the subtropical high over East Asia[C]// Proceedings of International Conference on the General Circulation of East Asia. Chengdu,China:34(5):40-51.

Jeong J H,Kim B M,Ho C H,et al,2008. Systematic variation in wintertime precipitation in East Asia by MJO-induced extratropical vertical motion[J]. J Climate,21(4):788-801.

Jia Xiaolong,Chen Lijuan,Ren Fumin,et al,2011. Impacts of the MJO on winter rainfall and circulation in China[J]. Adv Atmos Sci,28(3):521-533.

Jin Feifei, Hoskins B J, 1995. The direct response to tropical heating in a baroclinic atmosphere[J]. J Atmos Sci, 52(3): 307-319.

Lee S S, Moon J Y, Wang Bin, et al, 2017. Subseasonal prediction of extreme precipitation over Asia: Boreal summer intraseasonal oscillation perspective[J]. J Climate, 30(8): 2849-2865.

Lin Hai, Brunet G, Derome J, 2008. Forecast skill of the Madden-Julian Oscillation in two Canadian atmospheric models[J]. Mon Wea Rev, 136(11): 4130-4149.

Liu Xiangwen, Wu Tongwen, Yang Song, et al, 2017. MJO prediction using the sub-seasonal to seasonal forecast model of Beijing Climate Center[J]. Climate Dyn, 48(9-10): 3283-3307.

Madden R A, Julian P R, 1971. Detection of a 40－50 day oscillation in the zonal wind in the tropical Pacific[J]. J Atmos Sci, 28(5): 702-708.

Madden R A, Julian P R, 1972. Description of global-scale circulation cells in the tropics with a 40－50 day period[J]. J Atmos Sci, 29(6): 1109-1123.

McPhaden M J, 1999. Genesis and evolution of the 1997－98 El Niño[J]. Science, 283(5404): 950-954.

Nitta T, 1987. Convective activities in the tropical Western Pacific and their impact on the Northern Hemisphere summer circulation[J]. J Meteor Soc Japan, 65(3): 373-390.

Ren Hongli, Jin Feifei, Song Lianchun, et al, 2017. Prediction of primary climate variability modes at the Beijing Climate Center[J]. J Meteor Res, 31(1): 204-223.

Ren Hongli, Wu Jie, Zhao Chongbo, et al, 2016. MJO ensemble prediction in BCC-CSM1. 1 (m) using different initialization schemes[J]. Atmos Ocean Sci Lett, 9(1): 60-65.

Seo K H, Lee H J, 2017. Mechanisms for a PNA-Like teleconnection pattern in response to the MJO[J]. J Atmos Sci, 74(6): 1767-1781.

Vitart F, 2014. Evolution of ECMWF sub-seasonal forecast skill scores[J]. Quart J Roy Meteor Soc, 140(683): 1889-1899.

Wang Wanqiu, Hung M P, Weaver S J, et al, 2014. MJO prediction in the NCEP climate forecast system version 2[J]. Climate Dyn, 42(9-10): 2509-2520.

Wheeler M C, Hendon H H, 2004. An all-season real-time multivariate MJO index: Development of an index for monitoring and prediction[J]. Mon Wea Rev, 132(8): 1917-1932.

Wu Jie, Ren Hongli, Zuo Jinqing, et al, 2016. MJO prediction skill, predictability, and teleconnection impacts in the Beijing Climate Center Atmospheric General Circulation Model[J]. Dyn Atmos Oceans, 75: 78-90.

Wu Tongwen, Yu Rucong, Zhang Fang, et al, 2010. The Beijing Climate Center atmospheric general circulation model: description and its performance for the present-day climate[J]. Climate Dyn, 34: 123.

Xavier P, Rahmat R, Cheong W K, et al, 2014. Influence of Madden-Julian Oscillation on Southeast Asia rainfall extremes: observations and predictability[J]. Geophys Res Lett, 41(12): 4406-4412.

Xiang Baoqing, Zhao Ming, Jiang Xianan, et al, 2015. The 3－4-week MJO prediction skill in a GFDL coupled model[J]. J Climate, 28(13): 5351-5364.

Yao Yonghong, Lin Hai, Wu Qigang, 2015. Subseasonal variability of precipitation in China during boreal winter[J]. J Climate, 28(16): 6548-6559.

Zhang Chidong, 2005. Madden-Julian Oscillation[J]. Rev Geophys, 43(2): RG2003, DOI: 10.1029/2004RG000158.

Zhang Chidong, 2013. Madden-Julian Oscillation: bridging weather and climate[J]. Bull Amer Meteor Soc, 94(12): 1849-1870.

Zhang Lian, Wang Bizheng, Zeng Qingchun, 2009. Impact of the Madden-Julian Oscillation on summer rainfall in southeast China[J]. J Climate, 22(2): 201-216.

Zhao Chongbo, Ren Hongli, Song Lianchun, et al, 2015. Madden-Julian Oscillation simulated in BCC climate models[J]. Dyn Atmos Oceans, 72: 88-101.

KeAi
CHINESE ROOTS
GLOBAL IMPACT

Available online at www.sciencedirect.com

ScienceDirect

Advances in Climate Change Research 9 (2018) 209–217

www.keaipublishing.com/en/journals/accr/

Preliminary assessment on the hindcast skill of the Arctic Oscillation with decadal experiment by the BCC_CSM1.1 climate model

WU Li-Quan[a,b], LI Qing-Quan[a,b,*], DING Yi-Hui[b], WANG Li-Juan[a], XIN Xiao-Ge[b], WEI Min[c]

[a] *Key Laboratory of Meteorological Disaster, Ministry of Education, Joint International Research Laboratory of Climate and Environment Change, Collaborative Innovation Center on Forecast and Evaluation of Meteorological Disasters, Nanjing University of Information Science & Technology, Nanjing 210044, China*
[b] *Laboratory for Climate Studies, National Climate Center, China Meteorological Administration, Beijing 100081, China*
[c] *National Meteorology Information Center, China Meteorological Administration, Beijing 100081, China*

Received 21 August 2018; revised 19 October 2018; accepted 17 December 2018
Available online 20 December 2018

Abstract

The prediction skill of Arctic Oscillation (AO) in the decadal experiments with the Beijing Climate Center Climate System Model version 1.1 (BCC_CSM1.1) is assessed. As compared with the observations and historical experiments, the contribution of initialization for climate model to predict the seasonal scale AO and its interannual variations is estimated. Results show that the spatial correlation coefficient of AO mode simulated by the decadal experiment is higher than that in the historical experiment. The two groups of experiments reasonably reproduce the characteristics that AO indices are the strongest in winter and the weakest in summer. Compared with historical experiments, the correlation coefficient of the monthly and winter AO indices are higher in the decadal experiments. In particular, the correlation coefficient of monthly AO index between decadal hindcast and observation reached 0.1 significant level. Furthermore, the periodicity of the monthly and spring AO indices are achieved only in the decadal experiments. Therefore, the initial state of model is initialized by using sea temperature data may help to improve the prediction skill of AO in the decadal prediction experiments to some extent.

Keywords: BCC_CSM1.1; Climate model; Decadal; Arctic oscillation; Hindcast

1. Introduction

The Arctic mean surface temperature is well known to have increased considerably in recent decades (Cohen et al., 2014). The Arctic Oscillation (AO), which depicts the dominant mode of extra-tropical atmospheric variability, is characterized by a seesaw between the Arctic and the mid-latitude atmospheric mass. AO, which covers the entire polar region and has a strong coupling with the surface temperature of Eurasia (Thompson and Wallace, 1998), has a modulation effect on mid-latitude storm intensity, high latitude blocking, and cold wave outbreak (Thompson and Wallace, 2001). As a strong signal of climate change, AO can exert a substantial influence on winter climate and extreme weather events in China. AO is closely associated with winter temperature in East Asia. With a positive phase of winter AO, cold air in the polar region has little impact on northern China, while most of China is warmer (Gong and Wang, 2003; Liang et al., 2014). When the AO index is abnormal, it might considerably affect the maximum and minimum winter temperatures in China (Suo et al., 2008). Gong and Wang (2003) pointed out that AO has a crucial effect on winter temperature and precipitation on the decadal scale. In addition, AO may have an influence on the climate of other seasons in East Asia (Ju et al., 2006; He et al., 2017). Thus, the impact of AO needs to be considered while studying

* Corresponding author. Laboratory for Climate Studies, National Climate Center, China Meteorological Administration, Beijing 100081, China.
E-mail address: liqq@cma.gov.cn (LI Q.-Q.).
Peer review under responsibility of National Climate Center (China Meteorological Administration).

https://doi.org/10.1016/j.accre.2018.12.001
1674-9278/Copyright © 2018, National Climate Center (China Meteorological Administration). Production and hosting by Elsevier B.V. on behalf of KeAi. This is an open access article under the CC BY-NC-ND license (http://creativecommons.org/licenses/by-nc-nd/4.0/).

the mechanism of climate change in the Northern Hemispheric mid-latitude regions, such as China.

A coupling model is an objective tool for describing the effects of human activities and interactions of various layers in the climate system, and it is also an effective tool for studying AO and predicting its variability. At the same time, AO, which is the dominant mode of atmospheric low-frequency variation during boreal winter, has been taken consideration into the assessment on prediction skill of climate model. Historical simulation from the Coupled Model Intercomparison Project Phase 5 (CMIP5), can reflect the main features of the AO mode, but a significant deviation is observed in the simulation of the AO's intensity, exaggerating the activity center in the North Pacific (Miller et al., 2006; Xin et al., 2008; Cattiaux and Cassou, 2013; Zuo et al., 2013; Gong et al., 2016). Skillful predictions of the temporal and spatial characteristics of winter AO and its climatic anomalies can be obtained by using a seasonal climate prediction system (Stockdale et al., 2015; Sun and Ahn, 2015). Considerable skill in predicting the winter AO has the potential to provide useful regional climate information for Eurasia. However, many government planners usually need predictions further ahead than those provided by seasonal forecasting systems. Dunstone et al. (2016) extended the skillful model prediction of the winter North Atlantic Oscillation (NAO) to more than one year ahead. Some studies showed that NAO, which resembles the AO in many respects, is the local performance of AO in the North Atlantic (Ambaum et al., 2002).

To evaluate and improve climate models, decadal experiments of coupled models have been added to CMIP5. The output results of decadal experiments are favorable for predicting climate change in the future (Taylor et al., 2012). The simulation effects of the AO are mostly evaluated with the outputs of the CMIP5 historical experiments in previous studies (Cattiaux and Cassou, 2013; Zuo et al., 2013; Gong et al., 2016). However, the predictability of AO in the decadal experiments of climate models has been barely explored. In this paper, the seasonal scale AO and its interannual variations in the first year's outputs of the CMIP5 decadal experiments with BCC_CSM1.1 model are analyzed to investigate the AO's interannual predictability. Moreover, through a comparison with the historical hindcasts without initialization, the contribution of climate model initialization to the skill in predicting the seasonal AO is estimated, which can provide a reference for climate prediction and model development.

2. Model, data, and methodology

2.1. BCC_CSM1.1 model

The BCC_CSM1.1 model used in this study is a global climate coupled model that includes four component models. The atmospheric component is BCC_AGCM2.1 model with a horizontal resolution of about 2.8° × 2.8° and 26 levels in the vertical direction (Wu et al., 2010). The oceanic component is the MOM4_L40 model, which has a tripolar grid, 1/3−1° latitude × 1° longitude in the horizontal direction and 40 levels in the vertical direction (Li et al., 2015). The sea ice component is the GFDL Sea Ice Simulator. A layer of snow and two layers of sea ice are present in the vertical direction, with the horizontal resolution being the same as that of the oceanic model. The land model BCC_AVIM1.0 comprises the interaction between atmosphere, vegetation, and soil. A detailed description of the BCC_CSM1.1 model can be found in Wu et al. (2013).

2.2. Data

The outputs of the BCC-CSM1.1 model that is used in the CMIP5 experiments are utilized in this study. The historical runs cover the period of 1850−2012, which has three ensemble members based on the pre-industrial control experiment. The historical experiments did not take account of the model initialization and considered only the impact of external forcing. The decadal prediction experiment is initialized using the global monthly mean sea temperature reanalysis data of Simple Ocean Data Assimilation (SODA) (Carton and Giese, 2008). The initial states of sea temperature come from the consecutively restored run with nudge applied during 1958−2005. The reforecasts, which start every year over the period of 1960−2004, have at least 10-year integration and three ensemble members. The radiation forcing data used in historical and decadal experiments are provided by CMIP5, including greenhouse gases, aerosols, ozone, solar irradiation, and volcanic activity (Xin et al., 2012).

To assess the performances of the model, the observational proxy of the sea level pressure (SLP) are obtained from the monthly mean data of the HadSLP2(r) during 1961−2005, with a 5.0° × 5.0° longitude−latitude resolution (Allan and Ansell, 2006). For convenience, this reanalysis data is referred to as observational data when compared with the model results. To compare the experiment outputs with observations, all data were uniformly interpolated onto 2.5° × 2.5° horizontal grids by using bilinear interpolation before analyses are performed.

2.3. Methods

AO is defined as the first empirical orthogonal function (EOF) mode of the monthly mean SLP anomalies in the circumpolar region of 20°−90° N (Thompson and Wallace, 2000). Before EOF is decomposed, the SLP anomalies are area-weighed by the square root of the cosine of latitude. Following the calculation method of the AO index from the U.S. NOAA's Climate Prediction Center, the AO index is defined as the normalized time series through projecting the monthly SLP onto the AO mode. For convenience in comparing the intensity of the AO mode, the regression coefficients of SLP against the normalized AO index are defined as the AO pattern.

The initialization resulted in systematic errors in the decadal prediction. In other words, the climatic state of the prediction is different from that of the observation, which may

affect the evaluation of the model's prediction skill (García-Serrano and Doblas-Reyes, 2012; Goddard et al., 2013; Wei et al., 2017; Xin et al., 2018). Therefore, we use the method recommended by the World Climate Research Program to calculate the SLP anomalies of the decadal hindcasts so as to reduce the model drift (Wei et al., 2017; Xin et al., 2018). Three ensemble members of decadal predictions were performed by integrating the BCC_CSM1.1 model from September 1, November 1, and January 1 of the following year from 1960 to 2005, respectively. For example, when the experiment begins in 1960, three members start on September 1, 1960, November 1, 1960, and January 1, 1961, respectively, and so on. According to the uniform provisions of the CMIP5, the outputs of the BCC_CSM1.1 model from January 1961 to December 1970 are stored in three samples. To avoid the influence of random initial values, we use the mean of the three ensemble members in both historical and decadal experiments, i.e., the same outputs from January 1961 to December 1970 in three samples starting in 1960. We assess the prediction skill of the model in a set of 12-month hindcasts, that is, the output results of the first year of the model running. For example, when the experiment begins in 1960, the 12-month hindcasts refer to January to December 1961. Thus, the monthly data from January 1961 to December 2005 are generated as the 1-year lead predictions. The mean values in winter (DJF), spring (MAM), summer (JJA), and autumn (SON) are computed. The winter of 1961 was abandoned in this study due to the lack of output in December 1960. Hence, 44 winters spanning from 1962 to 2005 are considered. In addition, statistical methods such as correlation, spectral analysis, EOF decomposition, and moving *t*-test are utilized in this study.

3. Results

3.1. Spatial pattern of AO

The AO pattern is one of the important aspects for evaluating the prediction skill of climate models. The first EOF (EOF1) mode of the monthly mean SLP anomaly over the domain poleward of 20°N is shown in Fig. 1. The observed AO mode has three activity centers (Fig. 1a). Strongly negative SLP anomalies of a dipole structure are observed over the

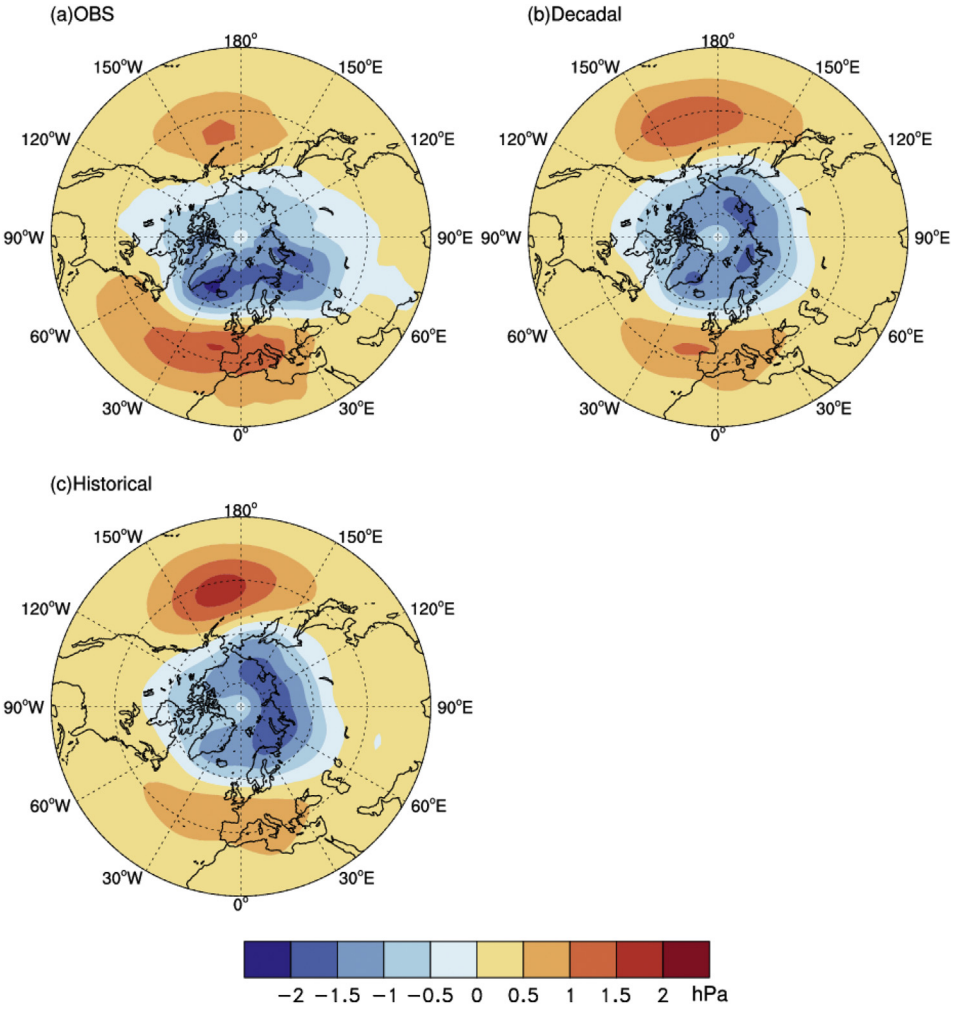

Fig. 1. Leading EOF mode of extra-tropical SLP anomalies in the Northern Hemisphere during 1962–2005 in (a) observation, (b) decadal experiment, and (c) historical experiment.

entire Arctic. One pole is located in the southeast of Greenland, and the other is present over the Ural Mountains, with a strength of −1.5 hPa. A center of observed positive value is located in the North Atlantic Ocean and extends to Europe. Another observed center with the strength of 1.0 hPa is distributed in the middle latitudes of the Pacific, which is weaker than that in the North Atlantic Ocean. Consistent with the results obtained by Thompson and Wallace (1998, 2001), the AO pattern is characterized by an annular mode.

The simulated region of negative values equivalent to the observed range and intensity in the North Pole can be reasonably reproduced in the decadal (Fig. 1b) and historical experiments (Fig. 1c), which also shows a certain prediction skill of the annular mode. In the two groups of experiments, the positive SLP anomalies over the North Pacific are larger than those over the North Atlantic. However, the positive SLP anomalies over the North Pacific/North Atlantic in the interannual prediction are smaller/larger than in the historical simulation. Therefore, the intensity of positive center of AO mode in the Northern Hemispheric mid-latitudes can be improved in the decadal hindcasts with initialization, which is closer to the observation. The biases of AO mode between simulations and observations are not affected by the definition of AO. For instance, differences in the positive anomaly centers still exist in the AO pattern calculated by using the 1000 hPa geopotential height (figure not shown). The positive SLP anomalies over the North Pacific of the winter AO mode are often exaggerated in the climate models and larger than those over the North Atlantic, which is consistent with previous studies (Miller et al., 2006; Xin et al., 2008). The weak linkage between AO and the North Pacific dominant mode (NPM) is exaggerated by the CMIP5 models and may result in the biases of the AO pattern, which can be corrected through a linear regression method to remove the NPM variability from the AO index (Gong et al., 2016). However, this bias correction is only a statistical method and does not improve the climate model.

AO, as the most dominant mode of the extra-tropical atmospheric variability in the Northern Hemisphere, is reflected in both the decadal and historical experiments of the BCC_CSM1.1 model. The spatial pattern of the AO in the decadal and historical experiments explains 23.8% and 25.0% of the total variance, respectively. These values are higher than the observation (20.8%). However, compared with the

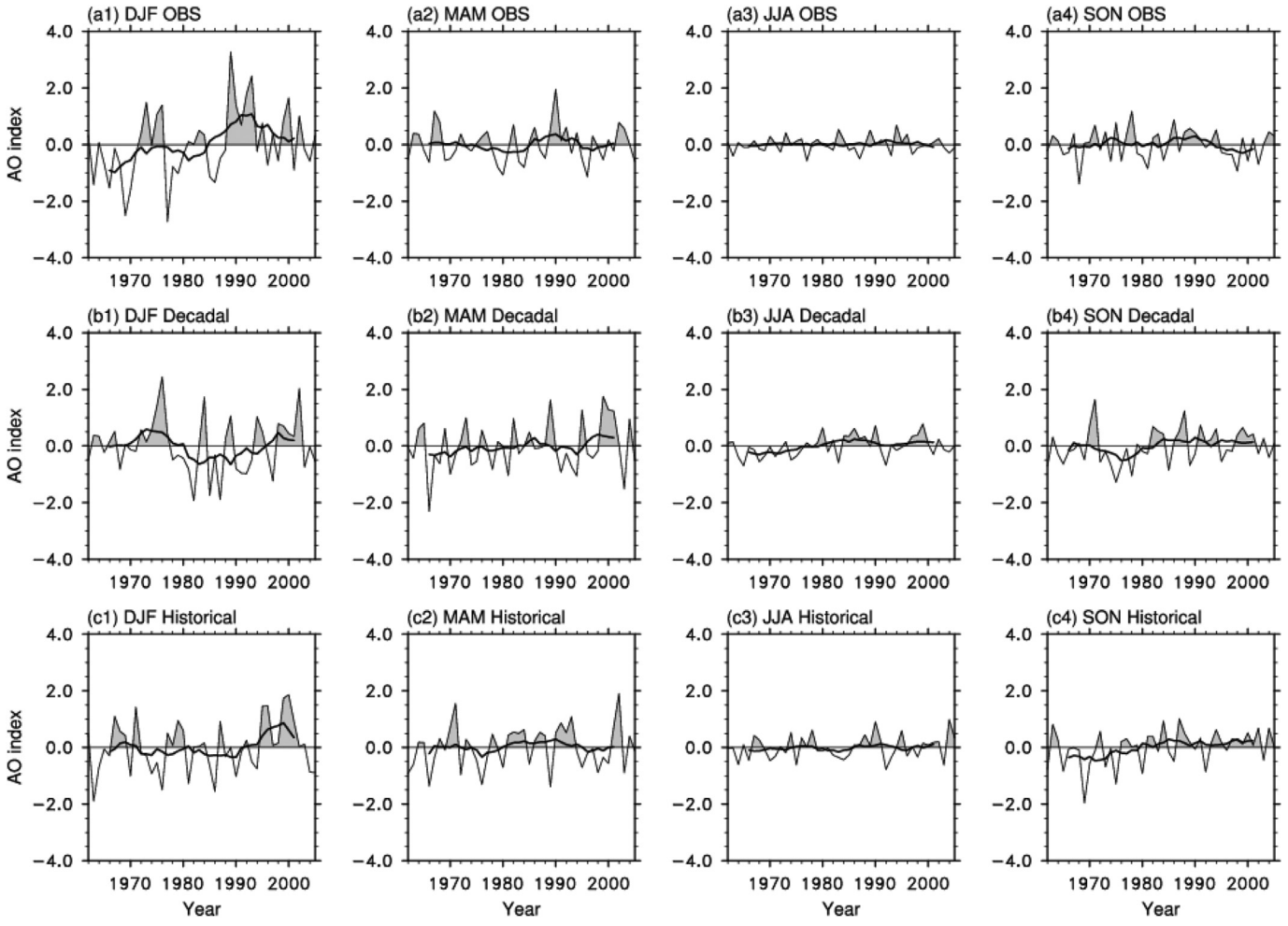

Fig. 2. Seasonal AO indices during 1962−2005 in (a1−a4) observation, (b1−b4) decadal experiment, and (c1−c4) historical experiment (heavy lines indicate 9-year running means).

historical simulation, the decadal hindcast is much closer to the observation. In addition, the spatial correlation coefficient of AO spatial pattern between the observation and the inter-annual prediction is 0.84, which is also slightly higher than that between the historical simulation and the observation (0.81). All these values exceed the 0.05 confidence level.

Overall, the BCC_CSM1.1 model prediction skill of AO pattern in the decadal hindcasts with initialization is higher than that in the historical experiments without initialization.

3.2. Characteristics of AO index

Fig. 2 shows the AO indices of four seasons from observation, decadal, and historical experiments. The simulations agree with the observations, with AO indices being the strongest in winter, the next in spring and autumn, and the weakest in summer. A distinctly positive trend is observed in the winter AO index during 1962–2005, with an interdecadal change from negative to positive phase in the mid-1980s (Fig. 2a1). The results of the moving *t*-test reveal that an abrupt interdecadal change of the observed winter AO index occurs in 1986 (Fig. 3a1), and an abrupt interdecadal change of the observed autumn AO index from positive to negative phase occurs in 1994 (Fig. 3a4). However, both the decadal and historical experiments failed to reproduce the features of the observed winter and autumn AO indices (Figs. 2 and 3). Zhu et al. (2013) also pointed out that the interdecadal transition characteristics of the winter AO index could not be shown in the historical experiments of 28 CMIP5 models.

The linear trend of standardized seasonal AO indices for observation, decadal, and historical simulations during 1962–2005 is calculated (Table 1). The observed AO indices in winter, spring, and summer show an upward trend. However, only the winter AO index is significant at 0.05 confidence level. The winter AO index of historical experiments also shows an upward trend (0.14 per decade), but weaker than the observation. However, the trend of the winter AO index of the decadal experiment is opposite the observation. Consistent with the observation, significant upward trends are observed in the spring and summer AO indices of both decadal and historical experiments, but the strength is overestimated. Differences are more pronounced for the autumn AO index and virtually no trend in observation is found, but a strong positive trend is observed in both decadal and historical experiments.

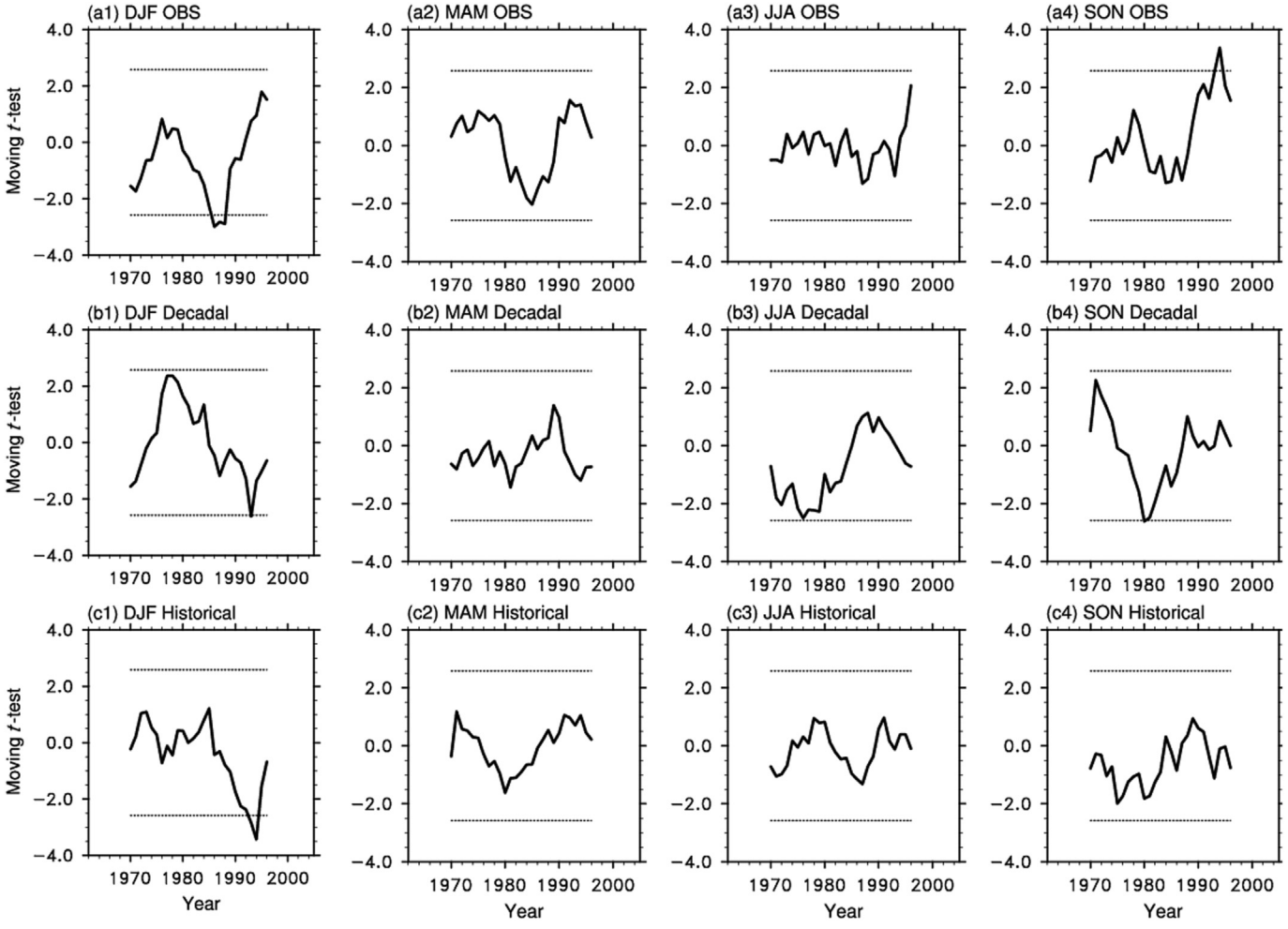

Fig. 3. Moving *t*-test of seasonal AO indices during 1962–2005 in (a1–a4) observation, (b1–b4) decadal experiment, and (c1–c4) historical experiment (dashed lines indicate 0.05 confidence level).

Table 1
Linear trend of seasonal AO indices during 1962−2005 in observation, decadal experiment, and historical experiment (unit: per decade).

Season	Observation	Decadal	Historical
DJF	0.25*	−0.10	0.14
MAM	0.01	0.14	0.12
JJA	0.03	0.25*	0.14
SON	−0.00	0.17	0.25*

Note: * denotes the trend statistically significant at 0.05 confidence level.

Table 2
Correlation coefficients of monthly and seasonal AO indices during 1962−2005 between decadal experiment/historical experiment and observation.

Month/Season	Decadal		Historical	
	Origin	Detrend	Origin	Detrend
Monthly	0.08*	0.08*	−0.01	−0.02
DJF	0.20	0.23	0.03	−0.04
MAM	0.01	0.01	0.07	0.07
JJA	−0.18	−0.20	−0.12	−0.13
SON	0.07	0.08	−0.14	−0.15

Note: * denotes the correlation coefficient statistically significant at 0.1 confidence level.

To further analyze the capability of the model in predicting the interannual variability of the monthly and seasonal AO indices, the correlation coefficients between the simulated and observed AO indices were calculated. As shown in Table 2, correlation coefficients of the undetrended and detrended monthly AO indices are all 0.08 ($p < 0.1$) in decadal hindcasts and higher than those of −0.01 (undetrended) and −0.02 (detrended) in the historical simulations. The AO signal is the strongest in winter and is weak in the other three seasons. For the winter AO index, the correlation coefficients between decadal hindcasts and observations are 0.20 and 0.23 before and after the trend is removed, respectively, which are also higher than those of 0.03 (undetrended) and −0.04 (detrended) in historical simulations. Therefore, the BCC_CSM1.1 model has certain hindcast skills for monthly and winter AO indices in the decadal experiments. However, the simulated spring, summer, and autumn AO indices in both decadal and historical experiments are unreasonable, with a negative correlation between the simulated and observed AO index in summer. Except for those in autumn, the results of decadal hindcasts are better than those of the historical simulations. The autumn AO index of decadal hindcast is positively correlated (0.07) with that of the observation, while the simulated autumn AO index in historical experiment is negatively correlated (−0.14) with the observation. To avoid the influence of the linear trend, we also examined the correlation coefficients of the detrended AO indices between simulations and observations (Table 2). Before and after the trend is removed, only the correlation of the winter AO index changes from positive (0.03) to negative (−0.04) in the historical experiment, and other correlations exhibit no significant changes.

The correlation coefficients between different seasonal AO indices derived from observations and simulations during 1962−2005 are presented in Table 3. The observed AO indices are negatively correlated (−0.10) between spring and summer, whereas they are positively correlated among other different seasons. The observed AO indices have significant correlations between winter and summer as well as between autumn and winter, with the correlation coefficients being 0.36 and 0.33, respectively. The persistence of the AO index in autumn and winter is partly captured by historical experiments, with the correlation coefficient being 0.32 ($p < 0.05$). The positive correlations of the AO indices in winter−spring, autumn−-spring, and summer−autumn can be captured by the interannual predictions, which are obviously better than the results of historical experiments. Sun and Ahn (2015) documented that sea surface temperature (SST), especially the variability of tropical Pacific SST, is a major factor in seasonal climate prediction in current numerical models. Compared with the uninitialized historical experiment, the initial oceanic state in the initialized decadal hindcasts is closer to the observation, which leads to the higher prediction skill of SST. Therefore, the skill in predicting the AO and even the relationship between different seasonal AO can be improved in the decadal experiments of a climate model.

3.3. Variability of AO index

The variances of observed and simulated AO indices in the four seasons are presented in Table 4. Evidently, the variance of observed AO indices is the strongest in winter, the next in spring and autumn, and the weakest in summer. These features can be captured by both decadal and historical experiments.

Table 4
Variance of seasonal AO indices during 1962−2005 from observation, decadal experiment, and historical experiment (Numbers in the brackets denote the variance percentage of simulation to observation).

Season	Observation	Decadal	Historical
DJF	1.44	0.88 (61%)	0.81 (56%)
MAM	0.37	0.71 (192%)	0.54 (146%)
JJA	0.07	0.13 (186%)	0.16 (229%)
SON	0.27	0.36 (134%)	0.36 (134%)

Table 3
Correlation coefficients between seasonal AO indices during 1962−2005 from observation and simulation.

Experiment	DJF−MAM	DJF−JJA	SON−DJF	MAM−JJA	SON−MAM	JJA−SON
Observation	0.23	0.36*	0.33*	−0.10	0.08	0.14
Decadal	0.18	−0.05	−0.06	0.17	0.33*	0.14
Historical	0.01	−0.06	0.32*	0.05	−0.08	0.29*

Note: * denotes the correlation coefficient statistically significant at 0.05 confidence level.

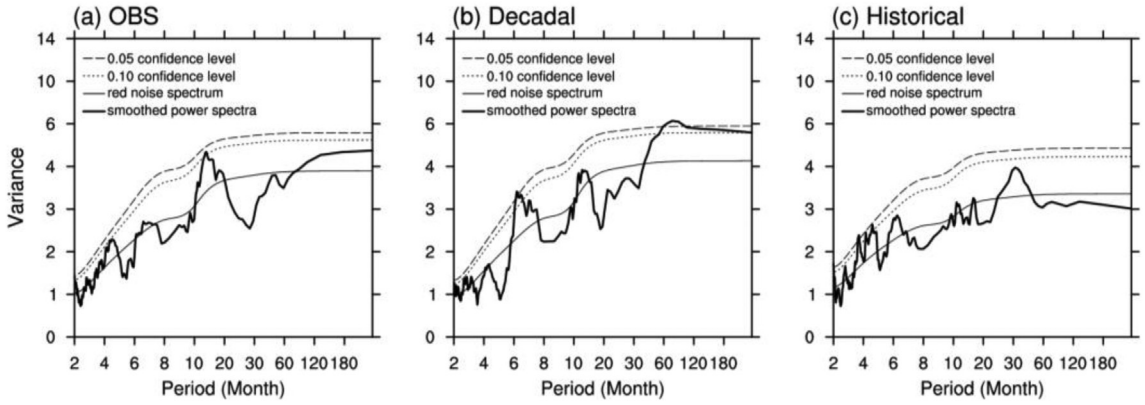

Fig. 4. Smoothed power spectra for monthly AO index during 1962−2005 derived from (a) observation, (b) decadal experiment, and (c) historical experiment.

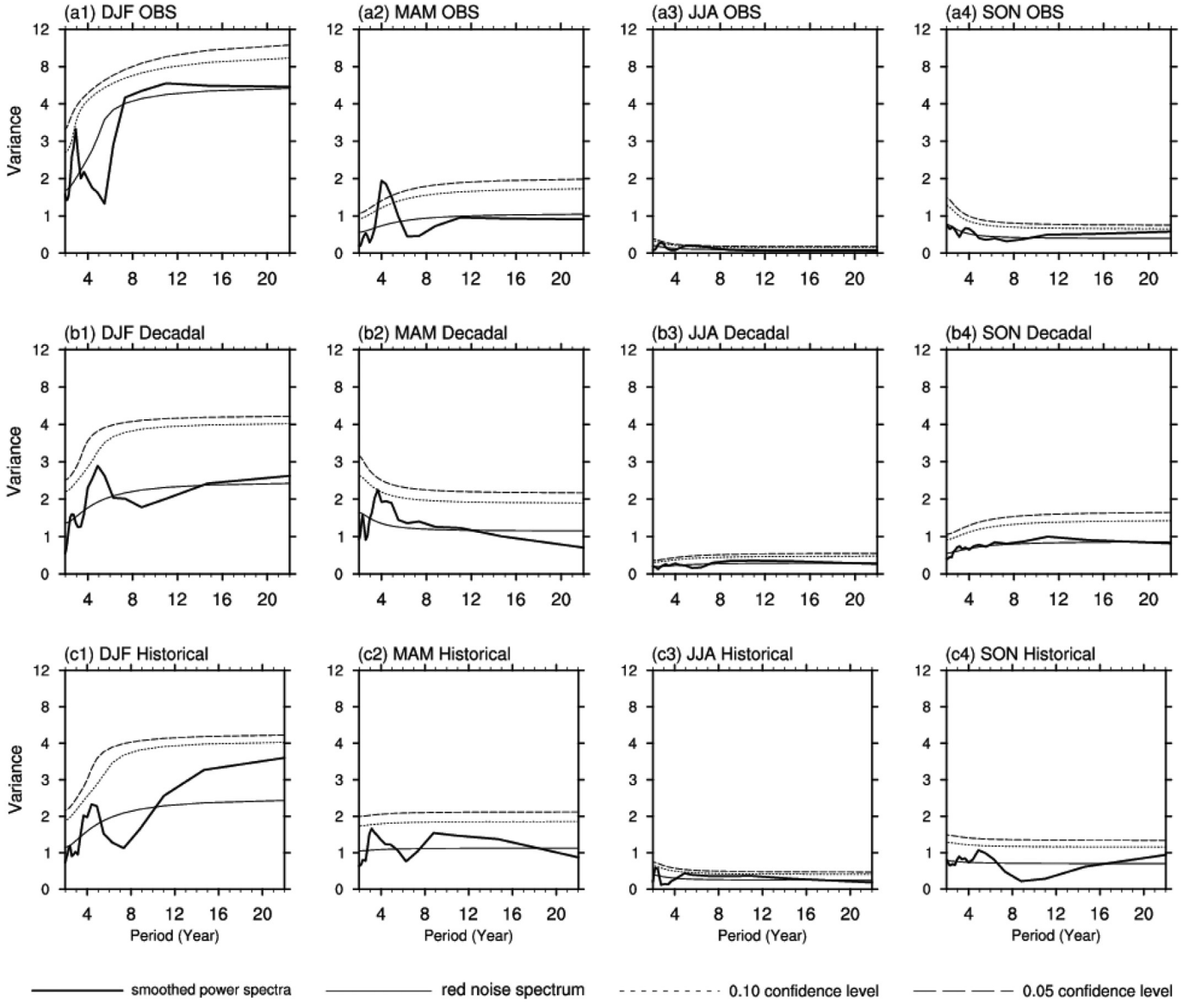

Fig. 5. Smoothed power spectra for seasonal AO indices during 1962−2005 derived from (a1−a4) observation, (b1−b4) decadal experiment, and (c1−c4) historical experiment.

However, the variance of the simulated AO index is weaker than the observation in winter and stronger than the observation in the other three seasons. That is, the BCC_CSM1.1 model underestimates the variance of the winter AO index and overestimates the variance of AO indices in other seasons. Compared with historical experiments, decadal experiments improve the prediction ability of reproducing the variation of winter and summer AO indices. The variance of AO indices between decadal hindcast and observation increases by 5% in winter and decreases 43% in summer, but those in spring and autumn are not improved.

To investigate the abilities in reproducing the periodic variability of AO indices in different experiments, the power spectra of the monthly and seasonal AO indices derived from observation and simulation are calculated (Figs. 4 and 5). Before the power spectra are calculated, the linear trend in AO indices is removed. As shown in Fig. 4, the two notable peak periods of the monthly AO index in the observation are 13 and 5 months ($p < 0.1$), respectively, which means that the AO index has short oscillation periods of half-year and 1-year or so. These features are consistent with previous studies (Zuo et al., 2013). The semiannual periodic change of the observed AO is captured by both decadal and historical experiments, but the annual cycle can be reproduced only by the decadal hindcast. Both the semiannual periodic change and annual cycle exceed the red noise spectrum.

As shown in Fig. 5, the peak periods of 2–3 years and 11 years exist in the power spectrum of the observed winter AO index, thereby passing the confidence test of the red noise spectrum. Unlike the observation, the simulated AO indices exhibit a short period of 4–5 years instead of obvious interdecadal variation. The observed spring AO index has a short period of 4–5 years, which can be captured by both decadal and historical experiments. However, a spurious period of 9–10 years is found in the spring AO of historical simulation. In summer, the observed and simulated AO indices have no periodic oscillation. In autumn, the historical experiment can roughly reflect a short period of about 4 years, while the decadal experiment shows a long period of 11 years. Overall, these results indicate that the decadal experiments better simulate the variability of AO index than the historical experiments.

4. Conclusions and discussion

With the use of the SLP data from HadSLP2(r), decadal and historical experiments of BCC_CSM1.1 model, the prediction skill of the AO pattern and index in initialized decadal experiments as well as the contribution of model initialization to prediction ability are investigated in this paper. The main conclusions are as follows:

(1) The AO pattern is reflected by both decadal and historical experiments. Considering the spatial correlation coefficient of AO pattern and the variance explained by AO mode, the prediction skill of AO pattern in the decadal hindcasts is higher than that in the historical experiments.

(2) That the AO indices are the strongest in winter and the weakest in summer can be reproduced by both decadal and historical experiments. The decadal and historical experiments failed to reproduce abrupt interdecadal change in winter and autumn AO indices, as well as an increasing trend in the winter AO index in the observation. Considering the correlation coefficients, a certain prediction skill of monthly and winter AO indices is found in decadal experiments.

(3) The observed positive correlations of the AO indices between winter and spring, autumn and spring, and summer and autumn are better captured in the interannual predictions compared with the historical simulations. The decadal experiments reproduce the AO index variability in winter and summer better than the historical experiments do.

(4) Decadal and historical experiments both reproduce the observed half-year periodic variation, but the annual cycle can be reproduced only by the decadal hindcasts. The decadal and historical experiments can capture the 4–5-year period in the spring AO index. Historical and decadal experiments can roughly reflect the 4- and 11-year periods in autumn, respectively.

Overall, the hindcast skill of AO pattern and the annual and interdecadal variability of AO index is more robust in the decadal experiments compared with the historical experiment. The BCC_CSM1.1 model is initialized by SODA SST data. A crucial point is that the initialization is not taken into account in historical experiments, which consider only the impact of external forcing. The initial states of SST come from the observed data with the nudging applied, which leads to accurate initial oceanic state in the initialized decadal hindcasts. Jadin (2001) points out that the mechanism for the external generation of the AO can be explained by the effect of interannual SST dipole variations in the North Pacific on a thermal excitation of stationary planetary waves. Given the adoption of the oceanic initialization method, affected by the observed SST forcing, the prediction skill of AO variability is more robust in decadal experiments than in historical experiments.

The BCC_CSM1.1 model is deficient in exaggerating the positive AO centers in the North Pacific, which is stronger than that in the North Atlantic. The initialized decadal simulations improved the skill in predicting AO pattern and variability without contributing to the long-term trend of AO. When the stratosphere and the troposphere are kinetically coupled, the stratospheric polar vortex signal propagates downward, thereby providing an important source of predictability of surface climate variability during winter (Baldwin et al., 2003). Zuo et al. (2016) pointed out that accurate representation of the stratospheric circulation in the initial conditions of the BCC_AGCM2.2 model will improve the predictability of winter surface AO/NAO at sub-seasonal scales. Improving the oceanic initialization scheme and introducing atmospheric initialization in the decadal experiments will enhance the AO prediction skill in the future.

Conflicts of interest

The authors declare no conflict of interest.

Acknowledgments

We thank the Met Office Hadley Centre for the HadSLP2(r) data and the Beijing Climate Center for providing the BCC_CSM1.1 output data. The work is supported by the National Natural Science Foundation of China (41790471, 41175065) and the National Key Research and Development Program of China (2016YFA0602200, 2012CB955203, 2013CB430202).

References

Allan, R., Ansell, T., 2006. A new globally complete monthly historical gridded mean sea level pressure dataset (HadSLP2): 1850-2004. J. Clim. 19, 5816−5842.

Ambaum, M.H.P., Hoskins, B.J., Stephenson, D.B., 2002. Arctic oscillation or North Atlantic oscillation? J. Clim. 14, 3495−3507.

Baldwin, M.P., Stephenson, D.B., Thompson, D.W., et al., 2003. Stratospheric memory and skill of extended-range weather forecasts. Science 301, 636−640.

Carton, J.A., Giese, B.S., 2008. A reanalysis of ocean climate using Simple Ocean Data Assimilation (SODA). Mon. Weather Rev. 138, 2999−3017.

Cattiaux, J., Cassou, C., 2013. Opposite CMIP3/CMIP5 trends in the wintertime Northern Annular Mode explained by combined local sea ice and remote tropical influences. Geophys. Res. Lett. 40, 3682−3687.

Cohen, J., Screen, J.A., Furtado, J.C., et al., 2014. Recent Arctic amplification and extreme mid-latitude weather. Nat. Geosci. 7, 627−637.

Dunstone, N., Smith, D., Scaife, A., et al., 2016. Skilful predictions of the winter North Atlantic Oscillation one year ahead. Nat. Geosci. 9, 809−814.

García-Serrano, J., Doblas-Reyes, F.J., 2012. On the assessment of near-surface global temperature and North Atlantic multi-decadal variability in the ENSEMBLES decadal hindcast. Clim. Dynam. 39, 2025−2040.

Goddard, L., Kumar, A., Solomon, A., et al., 2013. A verification framework for interannual-to-decadal predictions experiments. Clim. Dynam. 40, 245−272.

Gong, D.Y., Wang, S.W., 2003. Influence of arctic oscillation on winter cliamte over China. Acta Geograph. Sin. 58, 559−568.

Gong, H.N., Wang, L., Chen, W., et al., 2016. Biases of the wintertime arctic oscillation in CMIP5 models. Environ. Res. Lett. 12, 014001.

He, S.P., Gao, Y.Q., Li, F., et al., 2017. Impact of arctic oscillation on the East asian climate: a review. Earth Sci. Rev. 164, 48−62.

Jadin, E.A., 2001. Arctic oscillation and interannual variations in sea surface temperature in the Atlantic and Pacific oceans. Russ. Meteorol. Hydrol. 18, 28−40.

Ju, J.H., Lv, J.M., Ren, J.Z., 2006. The effect of interdecadal variations of arctic oscillation on aridization in North China. Plateau Meteorol. 25, 74−81.

Li, Q.Q., Tan, J., Wang, L.N., et al., 2015. Simulation of the natural distribution of carbon and nutrients in the ocean based on the global ocean carbon cycle model MOM4_L40. Chin. J. Geophys. 58, 1−19.

Liang, S.J., Ding, Y.H., Zhao, N., et al., 2014. Analysis of the interdecadal changes of the wintertime surface air temperature over mainland China and regional atmospheric circulation characteristics during 1960-−2013. Chin. J. Atmos. Sci. 38, 974−992.

Miller, R.L., Schmidt, G.A., Shindell, D.T., 2006. Forced annular variations in the 20th century intergovernmental panel on climate change fourth assessment report models. J. Geophys. Res. Atmos. 111, D18101.

Stockdale, T.N., Molteni, F., Ferranti, L., 2015. Atmospheric initial conditions and the predictability of the Arctic Oscillation. Geophys. Res. Lett. 42, 1173−1179.

Sun, J.Q., Ahn, J.B., 2015. Dynamical seasonal predictability of the Arctic Oscillation using a CGCM. Int. J. Climatol. 35, 1342−1353.

Suo, L.L., Huang, J.Y., Tan, B.K., 2008. The Influence of winter Arctic Oscillation on maximum and minimum air temperature over China in winter. J. Trop. Meteorol. 24, 163−168.

Taylor, K.E., Stouffer, R.J., Meehl, G.A., 2012. An overview of cmip5 and the experiment design. Bull. Am. Meteorol. Soc. 93, 485−498.

Thompson, D.W.J., Wallace, J.M., 1998. The Arctic oscillation signature in the wintertime geopotential height and temperature fields. Geophys. Res. Lett. 25, 1297−1300.

Thompson, D.W.J., Wallace, J.M., 2000. Annular modes in the extratropical circulation. Part I: month-to-month variability. J. Clim. 13, 1000−1016.

Thompson, D.W.J., Wallace, J.M., 2001. Regional climate impacts of the Northern Hemisphere annular mode. Science 293, 85−89.

Wei, M., Li, Q.Q., Xin, X.G., et al., 2017. Improved decadal climate prediction in the North Atlantic using EnOI-assimilated initial condition. Sci. Bull. 62, 1142−1147.

Wu, T., Yu, R., Zhang, F., et al., 2010. The Beijing Climate Center atmospheric general circulation model: description and its performance for the present-day climate. Clim. Dynam. 34, 123−147.

Wu, T.W., Li, W.P., Ji, J.J., et al., 2013. Global carbon budgets simulated by the Beijing climate center climate system model for the last century. J. Geophys. Res. Atmos. 118, 4326−4347.

Xin, X.G., Zhou, T.J., Yu, R.C., 2008. The Arctic Oscillation in coupled climate models. Chinese J. Geophys 51, 337−351 (in Chinese).

Xin, X.G., Wu, T.W., Zhang, J., 2012. Introduction of CMIP5 experiments carried out by BCC climate system model. Progressus Inquisitions De Mutatione Climatis 8, 378−382.

Xin, X.G., Gao, F., Wei, M., et al., 2018. Decadal prediction skill of BCC-CSM1.1 climate model in East Asia. Int. J. Climatol. 38, 584−592.

Zhu, X., Dong, W.J., Guo, Y., 2013. Comparison of simulated winter and spring arctic oscillation variability by CMIP5 and CMIP3 coupled models. Progressus Inquisitions De Mutatione Climatis 9, 165−172.

Zuo, J.Q., Li, W.J., Ren, H.L., 2013. Representation of the arctic oscillation in the CMIP5 models. Adv. Clim. Change Res. 4, 242−249.

Zuo, J.Q., Ren, H.L., Wu, J., et al., 2016. Subseasonal variability and predictability of the arctic oscillation/North Atlantic oscillation in BCC_AGCM2.2. Dyn. Atmos. Oceans 75, 33−45.

ADVANCES IN ATMOSPHERIC SCIENCES, VOL. 35, APRIL 2018, 397–409

• **Original Paper** •

Impact of SST Anomaly Events over the Kuroshio–Oyashio Extension on the "Summer Prediction Barrier"

Yujie WU[1,2,3] and Wansuo DUAN*[2,4]

[1]*Laboratory for Climate Studies, National Climate Center, China Meteorological Administration, Beijing* 100081*, China*
[2]*State Key Laboratory of Numerical Modeling for Atmospheric Sciences and Geophysical Fluid Dynamics (LASG), Institute of Atmospheric Physics, Chinese Academy of Sciences, Beijing* 100029*, China*
[3]*CMA-NJU Joint Laboratory for Climate Prediction Studies, Nanjing University, Nanjing* 210023*, China*
[4]*University of Chinese Academy of Sciences, Beijing* 100049*, China*

(Received 21 December 2016; revised 22 June 2017; accepted 21 July 2017)

ABSTRACT

The "summer prediction barrier" (SPB) of SST anomalies (SSTA) over the Kuroshio–Oyashio Extension (KOE) refers to the phenomenon that prediction errors of KOE-SSTA tend to increase rapidly during boreal summer, resulting in large prediction uncertainties. The fast error growth associated with the SPB occurs in the mature-to-decaying transition phase, which is usually during the August–September–October (ASO) season, of the KOE-SSTA events to be predicted. Thus, the role of KOE-SSTA evolutionary characteristics in the transition phase in inducing the SPB is explored by performing perfect model predictability experiments in a coupled model, indicating that the SSTA events with larger mature-to-decaying transition rates (Category-1) favor a greater possibility of yielding a more significant SPB than those events with smaller transition rates (Category-2). The KOE-SSTA events in Category-1 tend to have more significant anomalous Ekman pumping in their transition phase, resulting in larger prediction errors of vertical oceanic temperature advection associated with the SSTA events. Consequently, Category-1 events possess faster error growth and larger prediction errors. In addition, the anomalous Ekman upwelling (downwelling) in the ASO season also causes SSTA cooling (warming), accelerating the transition rates of warm (cold) KOE-SSTA events. Therefore, the SSTA transition rate and error growth rate are both related with the anomalous Ekman pumping of the SSTA events to be predicted in their transition phase. This may explain why the SSTA events transferring more rapidly from the mature to decaying phase tend to have a greater possibility of yielding a more significant SPB.

Key words: Kuroshio–Oyashio Extension, SST, summer prediction barrier, error growth

Citation: Wu., Y. J., and W. S. Duan, 2018: Impact of SST anomaly events over the Kuroshio–Oyashio extension on the "summer prediction barrier". *Adv. Atmos. Sci.*, **35**(4), 397–409, https://doi.org/10.1007/s00376-017-6322-0.

1. Introduction

Better understanding of the climate predictability over areas with significant ocean–atmosphere interaction is of great importance in improving the performance and forecast skill of numerical models. Considerable effort has been invested in exploring the predictability of El Niño–Southern Oscillation (ENSO) events and Indian Ocean Dipole (IOD) events (Webster and Yang, 1992; Lau and Yang, 1996; McPhaden, 2003; Luo et al., 2007; Feng et al., 2014; Yang et al., 2015), both of which have global climatic and social impacts (Cane, 1983; Philander, 1983; Dai and Wigley, 2000; Curtis and Adler, 2003; Yamagata et al., 2004; Chang et al., 2006; Schott et al., 2009). The "spring predictability barrier", which refers to the phenomenon that most ENSO prediction models often experience an apparent drop in prediction skill across boreal spring (Webster and Yang, 1992; Latif et al., 1994), is a well-known characteristic of ENSO forecasts. In numerical forecasts of IOD events, the prediction skill often drops rapidly across boreal winter regardless of the starting month, indicating the existence of a "winter predictability barrier" (Feng et al., 2014). The existence of a "spring predictability barrier" and "winter predictability barrier" often lead to unsuccessful forecasts of ENSO and IOD events, respectively (Webster and Yang, 1992; Latif et al., 1994; Luo et al., 2007), which in turn greatly restricts the prediction skill of climate variability in the tropical Pacific and Indian oceans.

The SST anomalies (SSTA) over the Kuroshio–Oyashio Extension (KOE) play a critical role in the ocean–atmosphere interaction in the North Pacific (Gan and Wu, 2012). However, the forecast skill of SSTA in the KOE region is quite poor (Guemas et al., 2012; Wen et al., 2012), which seriously limits the predictability of North Pacific SSTA. The

* Corresponding author: Wansuo DUAN
Email: duanws@lasg.iap.ac.cn

© Institute of Atmospheric Physics/Chinese Academy of Sciences, and Science Press and Springer-Verlag GmbH Germany, part of Springer Nature 2018

low predictability of SSTA in the KOE region is possibly due to its weakest "memory" being in the boreal summer (Motokawa et al., 2010; Zhao et al., 2012) and the fastest error growth when bestriding the boreal summer in numerical forecasts [i.e., the "summer prediction barrier" described in Duan and Wu (2015)]. The "summer prediction barrier" (SPB) refers to the phenomenon that the prediction errors of SSTA in the central and western North Pacific always increase rapidly in the August–September–October (ASO) season, and ultimately cause large prediction uncertainties at prediction times. Similar to the impact of the "spring predictability barrier" on ENSO forecasts and the "winter predictability barrier" on IOD forecasts, the SPB is considered to be one of the main factors limiting the predictability of North Pacific SSTA (Duan and Wu, 2015; Wu et al., 2016). Therefore, more comprehensive knowledge about the SPB is needed to understand the SSTA predictability in the North Pacific, as well as in the KOE region.

In Duan and Wu (2015), the physical and dynamical mechanisms were explored by primarily focusing on the influence of the climatological mean state and initial errors on the rapid error growth associated with the SPB. However, they did not discuss in depth the impact of the reference states [i.e., the KOE-SSTA events described in Wu et al. (2016)] on the occurrence of the SPB. KOE-SSTA events are defined as SSTA in the KOE region (30°–50°N, 145°E–150°W) larger (smaller) than 0.25 K (−0.25 K) persisting for at least five months (Wu et al., 2016). The SSTA of these events are usually established in boreal spring and reach their peak in boreal summer (Duan and Wu, 2015). The transition from the mature to decaying phase always occurs in the ASO season, which is the period when the error growth associated with the SPB is most significant. That is, the prediction errors associated with the SPB usually increase rapidly during the mature-to-decaying transition phase of the SSTA events to be predicted. It is therefore hypothesized that the evolutionary characteristics in the transition phase of KOE-SSTA events probably have impacts on the SPB. Accordingly, in this paper, we attempt to address the influence of KOE-SSTA events (especially the evolutionary characteristics in the mature-to-decaying transition phase) on the SPB, and further explore the related physical and dynamical mechanisms, which may be helpful in better understanding the SPB and the predictability of North Pacific SSTA. Herein, we investigate these issues by analyzing the results of perfect model predictability experiments in a fully coupled global model. In section 2, we briefly describe the model and approach used in our study. The impact of KOE-SSTA events on the occurrence of the SPB is reported in section 3. In section 4, we investigate the mechanisms responsible for the influence of KOE-SSTA events on the SPB. And finally, a summary of the key findings is presented in section 5.

2. Model and strategy

In this study, the Fast Ocean Atmosphere Model [FOAM; Jacob (1997)] is used to perform perfect model predictability experiments. FOAM is a fully coupled global model: the atmospheric component has a horizontal resolution of 7.2° longitude × 4.75° latitude and 18 levels in the vertical direction; the ocean component has a horizontal resolution of 1.4° latitude × 2.8° longitude and 32 vertical levels. A detailed description of FOAM is available in Wu et al. (2016). FOAM simulates the large-scale sea temperatures and atmospheric circulation of the KOE region well, and the simulation of KOE-SSTA events is also quite reasonable (Duan and Wu, 2015). Thirty 12-month-long KOE-SSTA events, including 15 warm ones and 15 cold ones, are randomly selected from the long-term control run of the fully coupled simulation of FOAM, and regarded as the reference states (i.e., the "true states") to be predicted. Figures 1a and b respectively show the selected warm and cold SSTA events, illustrating that the SSTA of these events are established in boreal spring, reach their peak in boreal summer, and start to transfer to the decaying phase from the ASO season. In addition, some of the KOE-SSTA events rapidly transfer from the mature to decaying phase, with a transition rate (blue bars in Figs. 1a and b) larger than 0.3 K month^{-1} during the ASO season, while other events less so (red bars in Figs. 1a and b). The composite spatial patterns of SSTA and related wind stress anomalies for the warm events of the two categories shown in Fig. 1a are illustrated in Figs. 1c and d. It is apparent that warm SSTA in the KOE region decay very rapidly and almost disappear when leading by six months for Category-1 events (Fig. 1c). However, the warm SSTA of Category-2 events persist for more than six months after the peak phase (Fig. 1d). Therefore, the KOE-SSTA events to be predicted can be classified into two categories based on their mature-to-decaying transition rates: Category-1 (blue lines in Figs. 1a and b) includes SSTA events with transition rates larger than 0.3 K month^{-1} in the ASO season; and Category-2 (red lines in Figs. 1a and b) comprises SSTA events with relatively smaller transition rates. Statistically, there is a total of 56 typical KOE-SSTA warm events and 49 cold events in a 200-year control run of FOAM, and the percentage of warm (cold) events in Category-1 is about 58.9% (51.0%). Similar features of KOE-SSTA events can be found in observations (ERSST.v3b/NOAA during 1950–2014): the percentage of warm (cold) events in Category-1 is about 60.0% (57.1%) events (data not shown), which is similar to the FOAM-simulated results. To investigate which kinds of KOE-SSTA events are more likely to yield a significant SPB, two groups of perfect model predictability experiments are conducted by predicting the SSTA events in Category-1 and Category-2 for 12 months with perturbed initial fields starting from Nov(−1) [i.e., November in Year(−1)], Feb(0) [i.e., February in Year(0)], May(0), and Aug(0). Year(0) denotes the year when the SSTA events attain their peak value, and Year(−1) is the year before Year(0). The difference between these two experiments (referred to as "Exp_Reference" and "Exp_Random") lies in the approaches of constructing initial perturbations (i.e., initial errors).

In Exp_Reference, the approach of constructing initial errors is to calculate the differences between the North Pacific

sea temperature fields (20°–60°N, 120°E–100°W) in the start months of the predictions and other months. As described in Duan and Wu (2015), the warm–cold cycle of the SSTA in the KOE region has a dominant period of three years. It is conceivable that the initial errors also follow a three-year (36-month) oscillation period when the start month of a prediction is given. Therefore, in order to adopt as many initial errors as possible, for every SSTA event we construct 36 initial errors by calculating the differences between the North Pacific sea temperature fields at five levels (surface, 40 m, 60 m, 80 m, and 100 m) in its start month and the successive 36 months before the start month. The initial errors are scaled to the same magnitude, which is about 30%–50% of the initial anomalies, following Duan and Wu (2015). For convenience, we call the initial errors obtained by this method the Ref-type initial errors. Exp_Random is similar to Exp_Reference, except it uses 36 random initial errors. For every random initial error in Exp_Random, the initial error at each grid point is randomly selected from a time series obeying the normal distribution with an average of zero and a standard deviation the same as the Ref-type initial errors. In Exp_Random, all the SSTA events in Category-1 and Category-2 are predicted with the 36 random initial errors. Exp_Random is conducted to confirm the robustness of the results in Exp_Reference. Ultimately, a total of 144 predictions with four start months and 36 Ref-type initial errors (36 random initial errors) can be obtained for every SSTA event in Exp_Reference (Exp_Random). By analyzing the results of these predictions, we investigate the impact of the SSTA events in Category-1 and Category-2 on the SPB.

3. Impact of the SSTA events to be predicted on the SPB

As in Duan and Wu (2015), the monthly error growth rates of the SSTA events at time t ($t = 1, 2, \cdots 12$ months) are roughly estimated by

$$\kappa(t) = \partial\gamma(t)/\partial t \approx [\gamma(t+1) - \gamma(t)]/[(t+1) - t] = \gamma(t+1) - \gamma(t)\,, \quad (1)$$

in which the magnitude of the prediction error is calculated by

$$\gamma(t) = \|T_p(t) - T_r(t)\| = \sqrt{\sum_{(x,y)} (T_{p,(x,y)}(t) - T_{r,(x,y)}(t))^2}\,, \quad (2)$$

(x, y) represent the longitude and latitude in the KOE region, and $T_r(t)$ and $T_p(t)$ are the SSTA of warm or cold events and their predictions, respectively. The large absolute value of $\kappa(t)$ corresponds to the fast error increase or decrease. The seasonal growth rates of prediction errors can be obtained by calculating the sum of the error growth rates during different seasons. To investigate the results of the experiments, the criteria of an SPB in this paper are as follows: (1) the error

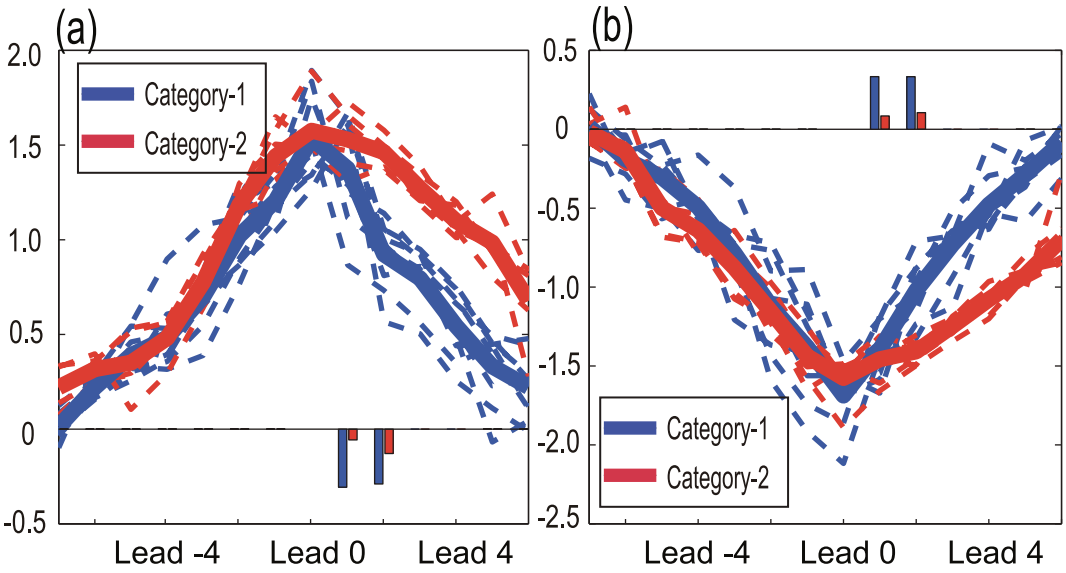

Fig. 1. (a) The warm KOE-SSTA events in Category-1 (dashed blue lines; units: K) and Category-2 (dashed red lines; units: K) and their ensemble means (solid blue line for -Category-1 and solid red line for Category-2). The blue (red) bars represent the mature-to-decaying transition rates (units: K month^{-1}) for Category-1 (Category-2). (b) As in (a) but for cold events. The warm (cold) KOE-SSTA events in (a, b) are randomly selected from the long-term control run of the fully coupled simulation of FOAM according to the definition in section 1. (c) The composite spatial patterns of SSTA (contours; units: K) and sea surface wind stress anomalies (vectors; units: 0.1 N m^{-2}) for the KOE-SSTA warm events in Category-1 shown in (a). (d) As in (c) but for the warm events in Category-2 shown in (a). Color shading in (c, d) represents the 95% confidence level. The lead "0" represents the month when the events attain their peak and the leads "−6(6)", "−4(4)" and "−2(2)" denote the 6th, 4th and 2nd month before (after) the peak month. The black rectangle marks the KOE-SSTA region (30°–50°N, 145°E–150°W) which is the study area in this paper.

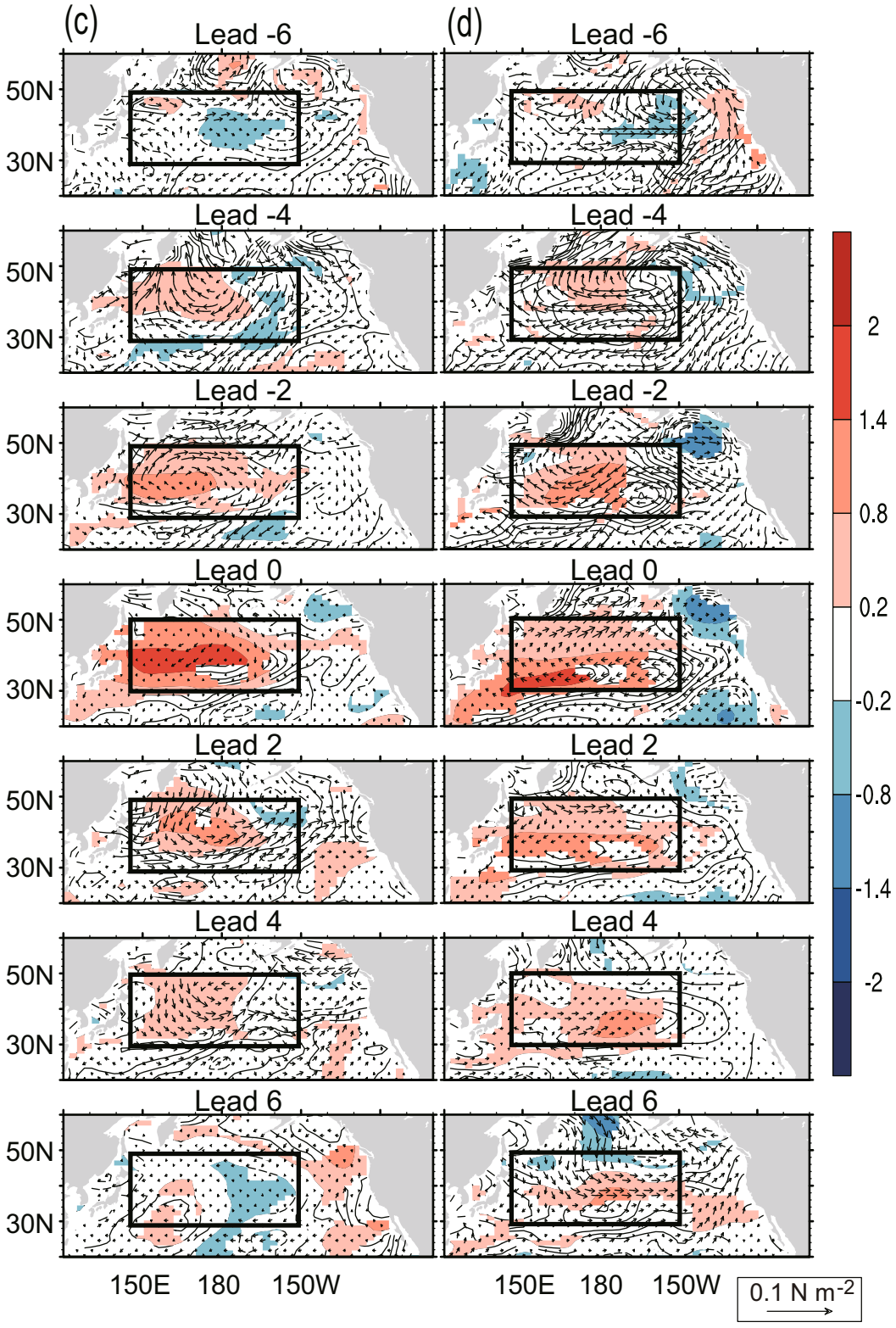

Fig. 1. (Continued)

growth rate in the ASO season (i.e., κ_{ASO}) is larger than the error growth rate in any other season; (2) the prediction error measured by $\gamma(t)$ in the ASO season is five times larger than the magnitude of the initial error (five times the initial error is roughly equivalent to two times the standard deviation of KOE-SSTA). The predictions simultaneously satisfying these two criteria can be regarded as reflecting the occurrence of an SPB.

3.1. *Results from Exp_Reference*

In Exp_Reference, the monthly error growth rates for every KOE-SSTA event are estimated based on their ensemble mean of the 144 predictions reported in section 2. The results show that, regardless of the start month, both of the predictions for Category-1 and Category-2 tend to have the fastest error growth in the ASO season (i.e., the mature-to-decaying transition phase) and exhibit the SPB phenomenon. However, the magnitudes of the error growth rates in the ASO season (referred to as $\kappa_{\rm ASO}$) are different between Category-1 and Category-2. As an example, Fig. 2 shows the seasonal error growth rates measured by $\kappa(t)$ and the seasonal growth rates of regional-mean SSTA errors for the KOE-SSTA events in the two categories starting from Feb(0). The regional-mean KOE-SSTA error at time t ($t = 1, 2, \cdots 12$ months) is calculated by

$$e(t) = |T_p(t)|_{\rm region-mean} - |T_r(t)|_{\rm region-mean} \ . \qquad (3)$$

It is illustrated that although the error growth rates in the ASO season for all the KOE-SSTA events in the two categories are larger than in the other seasons, the magnitudes of $\kappa_{\rm ASO}$ for the SSTA events in Category-1 are significantly larger than those in Category-2. As reported in Duan and Wu (2015), the rapid error growth in the ASO season is the most typical feature of the SPB, and the large prediction uncertainties associated with the SPB are largely contributed by the error growth in the ASO season. That is, the rapid error growth in the ASO season usually implies a significant SPB. So, the magnitude of the error growth rate in the ASO season $\kappa_{\rm ASO}$ can be used to measure the intensity of the SPB, wherein a larger $\kappa_{\rm ASO}$ represents a more significant SPB. Therefore, the results shown in Fig. 2 indicate that SSTA events transferring more rapidly from the mature to decaying phase (i.e., the SSTA events in Category-1) tend to yield a more significant SPB than those events with smaller transition rates (i.e., the SSTA events in Category-2).

Furthermore, as mentioned in section 2, every KOE-SSTA event has 36 predictions initiated with Ref-type perturbations for each start month. Thus, for every SSTA event, the amount among the 36 predictions that have an SPB can be approximately considered as a measurement of the likelihood that an SPB occurs, i.e., the more predictions exhibiting an SPB, the more likely one is to occur. Figure 3 illustrates the amount of predictions with an SPB for every SSTA event in the two categories, initiated from different start months, in Exp_Reference. It is clear that the SSTA events in Category-1 possess many more predictions exhibiting an SPB than those in Category-2, indicating that SSTA events with larger mature-to-decaying transition rates are more likely to yield an SPB than those with smaller rates.

Therefore, the results of Fig. 2 and Fig. 3 allow us to conclude that if the KOE-SSTA events transfer more rapidly from the mature to decaying phase, they tend to have a greater possibility of a more significant SPB. This implies that forecasting KOE-SSTA events in Category-1 may be much less successful, due to the significant SPB, especially when the forecasts are made before and through their transition phase,

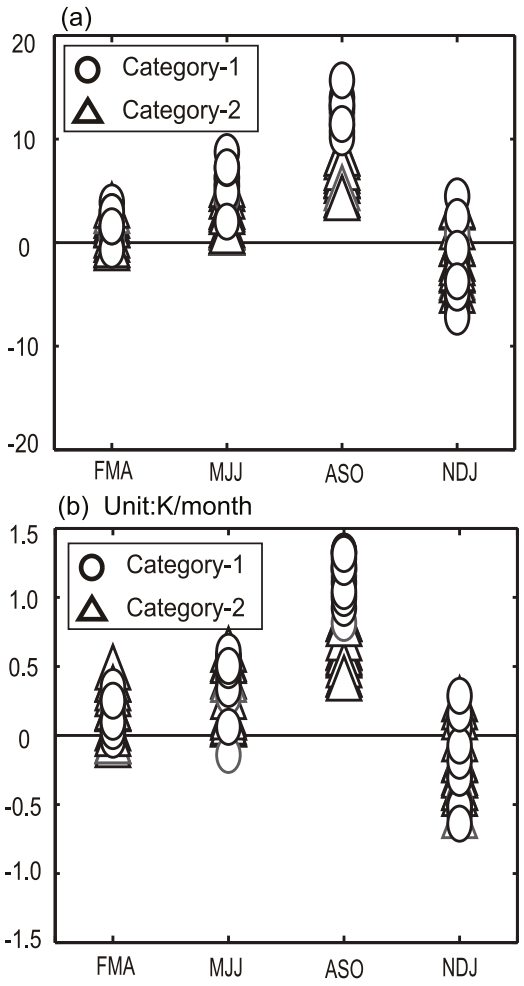

Fig. 2. (a) The seasonal error growth rates measured by $\kappa(t)$ described in section 3 of every KOE-SSTA event in Category-1 and Category-2. (b) As in (a) but for the growth rates of regional-mean KOE-SSTA errors (units: K month^{-1}). The results of every SSTA event are the ensemble mean of the predictions initiated from Feb(0) with 36 Ref-type initial errors in Exp_Reference. It should be noted that the error growth rates for cold events shown in (b) are calculated by $(-1)\times(|T_p(t)|_{\rm region-mean} - |T_r(t)|_{\rm region-mean})$ to visually compare with the result of warm events.

which is usually during the ASO season. In addition, we also predict the SSTA events in Category-1 by perturbing their initial fields with the Ref-type initial errors of the SSTA events in Category-2, or vice versa. The results show that the SSTA events in Category-1 tend to have a greater possibility of a more significant SPB, despite their initial fields being perturbed by the Ref-type initial errors that often fail to cause an SPB for the SSTA events in Category-2. However, the SSTA events in Category-2 have less possibility of yielding an SPB when predicted with the initial errors causing the SPB of the SSTA events in Category-1. These results further demonstrate the robustness of the conclusion reported in this paper.

3.2. *Results from Exp_Random*

In contrast to Exp_Reference, we conduct Exp_Random by predicting the KOE-SSTA events in Category-1 and

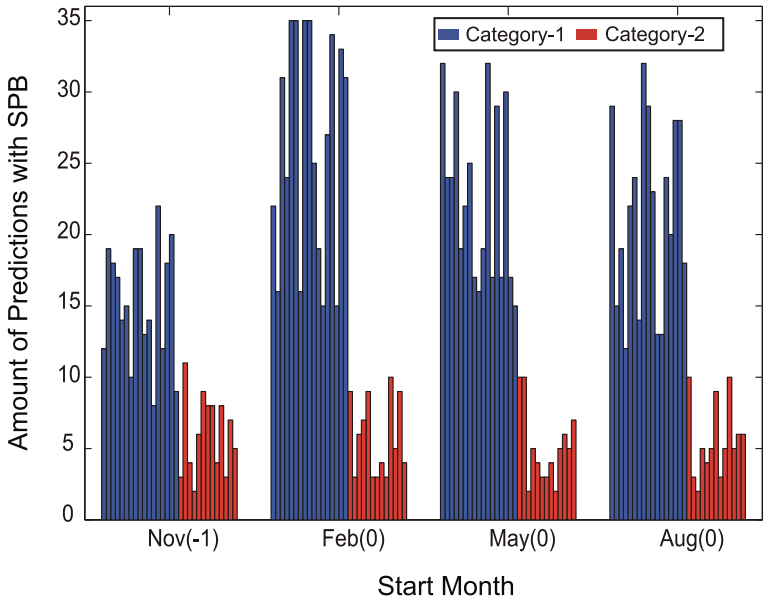

Fig. 3. Each of the bars represents the amount of predictions with an SPB among the 36 predictions for every KOE-SSTA event shown in Figs. 1a and b. The 36 predictions for every SSTA event are obtained by predicting with 36 Ref-type initial errors in Exp_Reference from each of the initial months shown on the horizontal axis. The blue (red) bars represent the results of 17 (13) KOE-SSTA warm and cold events in Category-1 (Category-2) in Figs. 1a and b.

Category-2 with 36 random initial errors (see section 2). The results of the monthly prediction errors are illustrated in Fig. 4. It is shown that when predicted with random initial errors, the SSTA events in Category-1 (blue shaded area) also tend to have a greater possibility of yielding an SPB with large intensity, compared to those events in Category-2 (red shaded area). Therefore, the results of Exp_Random support those of Exp_Reference. As a comparison, the ensemble mean of the monthly prediction errors for Category-1 and Category-2 in Exp_Reference are also shown in Fig. 4. It is apparent that both the predictions with Ref-type initial errors and random initial errors for Category-1 exhibit the rapid error growth in the ASO season and yield the SPB phenomenon. However, the predictions by random initial errors show a slower error growth in the ASO season and a smaller total prediction error than those predictions by Ref-type initial errors, indicating the SPB of the former is relatively weaker. In addition, neither shows a significant SPB when predicting Category-2 events with Ref-type or random initial errors. The results of this experiment suggest two conclusions: The first one is consistent with the main conclusion of this paper, which is that the occurrence of an SPB is dependent on the SSTA events to be predicted, i.e., the KOE-SSTA events with large mature-to-decaying transition rates tend to yield a more significant SPB phenomenon. The second one is that the initial errors with certain spatial patterns, such as the Ref-type initial errors in Exp_Reference, prefer to induce a more significant SPB than the random initial errors. In this paper, we primarily focus on the impact of the KOE-SSTA events on the SPB. Discussion on the role of the initial errors with certain spatial patterns in inducing the SPB is presented in section 5.

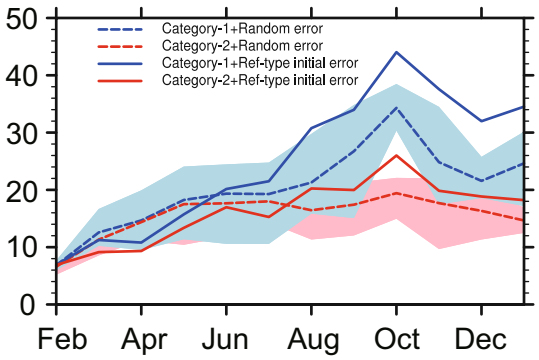

Fig. 4. The ensemble mean of monthly prediction errors by predicting the SSTA events in Category-1 (blue lines) and Category-2 (red lines) with random initial errors (dashed lines) and Ref-type initial errors (solid lines) initiated from Feb(0). The ensemble error evolutions (shaded area) for the predictions with random initial errors are also shown. The measurement of prediction errors is the same as that in section 3.

4. Possible mechanisms

Why do the KOE-SSTA events with larger mature-to-decaying transition rates have a greater possibility of yielding a more significant SPB? What is the relationship between the transition rate of SSTA events and the error growth rate associated with the SPB? To address these issues, we explore which physical processes are responsible for the error growth associated with the SPB and compare their differences between the KOE-SSTA events in the two categories.

Duan and Wu (2015) explored the physical mechanisms responsible for the SPB through mixed-layer heat budget analysis based on the equation governing the mixed-layer temperature, which is a good proxy for SST. The equation can be expressed as:

$$\frac{\partial T}{\partial t} = \frac{Q}{\rho c_p z} - \left(u\frac{\partial T}{\partial x} + v\frac{\partial T}{\partial y}\right) - \Delta T w - \Delta T \frac{\partial z}{\partial t} - \Delta T r + R \ . \quad (4)$$

On the right-hand side of Eq. (4), Q in the first term represents the net sea surface heat flux; ρ, c_p and z are respectively the density of sea water, the specific heat capacity and the mixed-layer depth, which is defined as the layer depth where the sea temperature is 0.5°C less than the SST. The second term, $-[u(\partial T/\partial x) + v(\partial T/\partial y)]$, is the horizontal advection by zonal velocity u and meridional velocity v. In the third term, $-\Delta T w$, $\Delta T = (T - T(-z))/z$ is the entrainment due to the vertical velocity w. The vertical advection induced by the Ekman pumping is one component of this entrainment term because the Ekman pumping is the vertical velocity induced by the wind-stress curl and w implicitly includes the vertical velocity due to the wind stress. On seasonal to annual timescales, the vertical velocity field is usually considered as naturally filtered, and is then approximately equal to the vertical Ekman advection, i.e., $w \approx w_E$ (de Boisséson et al., 2010). The analysis of this study mainly focuses on seasonal timescales. Therefore, this entrainment term in this study is dominated by the vertical advection induced by Ekman pumping. The fourth and fifth terms are respectively the entrainment due to the tendency of the mixed layer depth and the entrainment due to "advection of the mixed layer depth", in which $r = -[u(\partial z)/(\partial x) + v(\partial z)/(\partial y)]$. The last term includes the turbulent mixing and heat diffusion. In the heat budget analysis of KOE-SSTA events (not shown here), it is found that the SSTA tendency of KOE-SSTA events is largely dominated by the net sea surface heat flux, the vertical advection and the horizontal advection. The contributions of the entrainment terms (i.e., $-\Delta T(\partial z/\partial t)$ and $-\Delta T r$) and the turbulent mixing and heat diffusion term R are negligible, which thus can be neglected in our following analysis. Therefore, the equation governing the evolution of KOE-SSTA prediction errors can be expressed as:

$$\begin{aligned}\frac{\partial T'}{\partial t} &= \frac{\partial(\overline{T} + T^* + T')}{\partial t} - \frac{\partial(\overline{T} + T^*)}{\partial t} \\ &= \frac{Q'}{\rho c_p \overline{h}} + (\overline{U}_{\rm adv} + U^*_{\rm adv} + U'_{\rm adv}) + (\overline{V}_{\rm adv} + V^*_{\rm adv} + V'_{\rm adv}) \\ &\quad + (\overline{W}_{\rm adv} + W^*_{\rm adv} + W'_{\rm adv}) \ , \end{aligned} \quad (5)$$

in which,

$$\begin{aligned}&\overline{U}_{\rm adv} = -\overline{u}\frac{\partial T'}{\partial x} - u'\frac{\partial \bar{T}}{\partial x} \ , \quad U^*_{\rm adv} = -u^*\frac{\partial T'}{\partial x} - u'\frac{\partial T^*}{\partial x} \ , \quad U'_{\rm adv} = -u'\frac{\partial T'}{\partial x} \ , \\ &\overline{V}_{\rm adv} = -\bar{v}\frac{\partial T'}{\partial y} - v'\frac{\partial \overline{T}}{\partial y} \ , \quad V^*_{\rm adv} = -v^*\frac{\partial T'}{\partial y} - v'\frac{\partial T^*}{\partial y} \ , \quad V'_{\rm adv} = -v'\frac{\partial T'}{\partial y} \ , \\ &\overline{W}_{\rm adv} = -\overline{w}(\Delta T)' - w'\overline{\Delta T} \ , \quad W^*_{\rm adv} = -w^*(\Delta T)' - w'(\Delta T)^* \ , \quad W'_{\rm adv} == -w'(\Delta T)' \ . \end{aligned} \quad (6)$$

In Eqs. (5)–(6), the climatological mean state, the anomaly and the error are respectively denoted by an overbar, asterisk and prime. Q' represents the sea surface heat flux error and is the sum of the latent heat flux error $Q'_{\rm LH}$, sensible heat flux error $Q'_{\rm SH}$, shortwave radiation flux error $Q'_{\rm SWH}$, and longwave radiation flux error $Q'_{\rm LWH}$. $\overline{h}$ is the climatological monthly mean mixed-layer depth. As in observations (Wang et al., 2012), the simulated $\overline{h}$ in the KOE region is deeper than 150 m in boreal winter and shallower than 30 m in boreal summer. The terms in Eq. (6) indicate the effects of oceanic temperature advection on the SSTA error growth. Duan and Wu (2015) revealed that the latent heat flux errors ($Q'_{\rm LH}$) and the vertical oceanic temperature advection associated with the climatological mean state ($\overline{W}_{\rm adv}$), which are both largely forced by the sea surface wind stress errors, dominate the SSTA error growth associated with the SPB. Clearly, the effects of both $Q'_{\rm LH}$ and $\overline{W}_{\rm adv}$ on the error growth are directly influenced by the climatological annual cycle and prediction errors, but not the SSTA events to be predicted. In Figs. 5a and b, we show the ensemble means of $Q'_{\rm LH}$ and $\overline{W}_{\rm adv}$ averaged over the KOE region in the ASO season for the warm and cold events in Category-1 (black bars) and Category-2 (gray bars), respectively. They both have few differences between the two categories (differences shown in Fig. 5e), indicating that the larger error growth rates of the SSTA events in Category-1 are not due to the physical processes of $Q'_{\rm LH}$ and $\overline{W}_{\rm adv}$. Furthermore, the terms $Q'_{\rm SH}$, $Q'_{\rm SWH}$, $Q'_{\rm LWH}$, $\overline{U}_{\rm adv}$, $U'_{\rm adv}$, $\overline{V}_{\rm adv}$, $V'_{\rm adv}$ and $W'_{\rm adv}$ are not directly influenced by the SSTA events to be predicted and make little contribution to the different error growth rates between Category-1 and Category-2 (not shown here).

Among all terms in Eqs. (5)–(6), only the physical processes of $U^*_{\rm adv} = -u^*(\partial T')/\partial x - u'(\partial T^*)/\partial x$, $V^*_{\rm adv} = -v^*(\partial T')/\partial y - u'(\partial T^*)/\partial y$ and $W^*_{\rm adv} = -w^*(\Delta T)' - w'(\Delta T)^*$ are directly related with the SSTA events to be predicted, and they respectively describe the effect of the prediction errors of the zonal, meridional and vertical oceanic temperature advection associated with the warm or cold events on the SSTA error growth. The u^*, v^*, w^* and T^* are respectively the anomalies of the zonal, meridional, vertical current velocities and SSTA in the North Pacific; and u', v', w' and T' represent their related prediction errors. A larger absolute value of $U^*_{\rm adv}$, $V^*_{\rm adv}$ or $W^*_{\rm adv}$ causes a larger growth tendency (i.e., growth rate) of prediction errors (i.e., $(\partial T')/\partial t$)

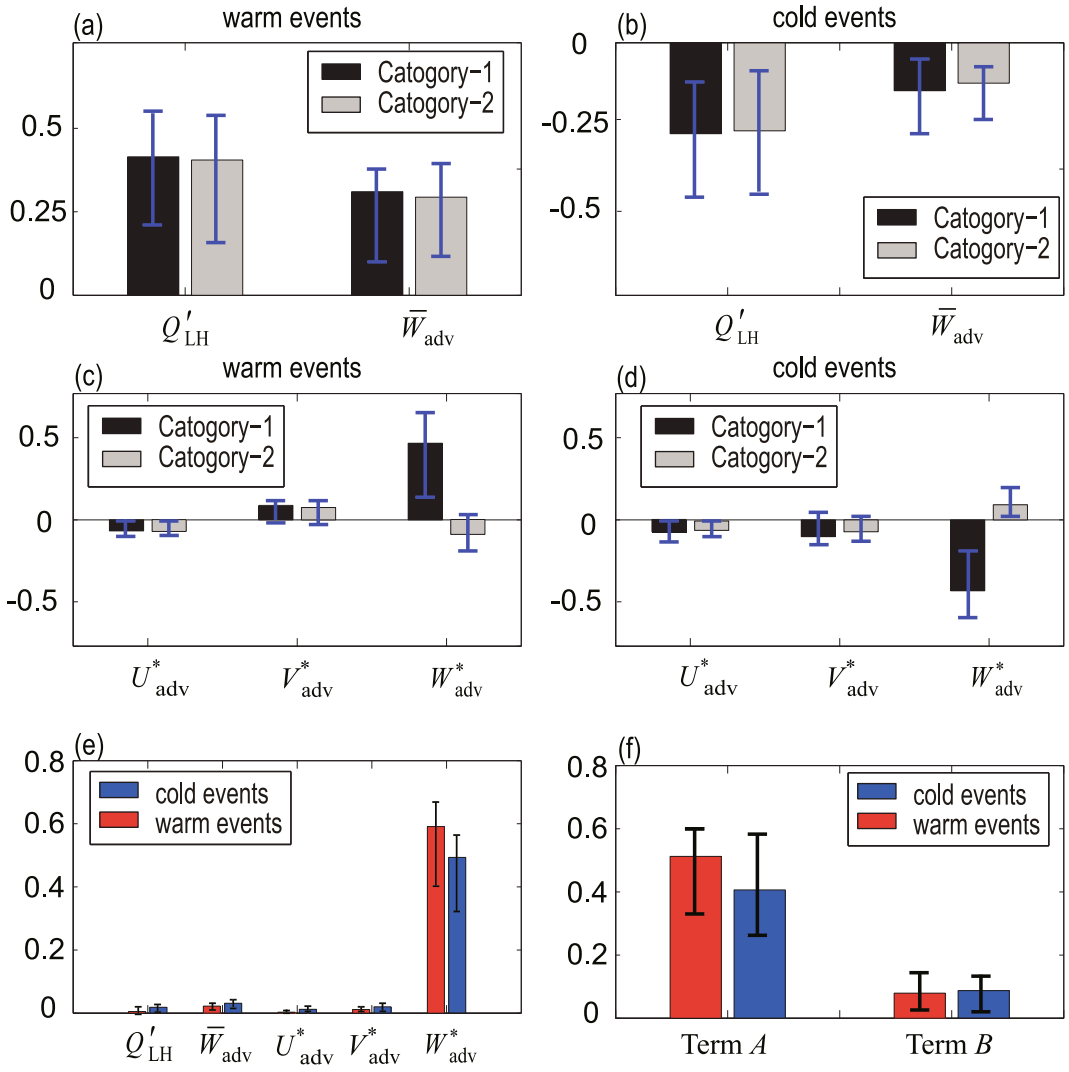

Fig. 5. (a) Ensemble means of Q'_{LH} and $\overline{W}_{adv}$ averaged in the KOE region in the ASO season for the warm events in Category-1 (black bars) and in Category-2 (gray bars). (b) As in (a) but for cold events. (c) Ensemble means of U^*_{adv}, V^*_{adv} and $\overline{W}^*_{adv}$ averaged in the KOE region in the ASO season for the warm events in Category-1 (black bars) and in Category-2 (gray bars). (d) As in (c) but for cold events. (e) The differences in Q'_{LH}, $\overline{W}_{adv}$, U^*_{adv}, V^*_{adv} and W^*_{adv} between the warm (red bars) and cold (blue bars) events in Category-1 and Category-2 shown in (a–d). (f) As in (e) but for the term $A = -w^*(\Delta T)'$ and $B = -w'(\Delta T)^*$. Units: K month^{-1}.

and, as a result, leads to faster error growth. To investigate which of these terms contribute most to the larger error growth rates in the ASO season for the SSTA events in Category-1, the regional-mean U^*_{adv}, V^*_{adv} or W^*_{adv} in the ASO season for the warm and cold events in Category-1 (black bars) and Category-2 (gray bars) are illustrated in Figs. 5c and d. It is shown that only the W^*_{adv}, i.e., the prediction errors of the vertical oceanic temperature advection associated with the SSTA events to be predicted, exhibits a significant difference between the two categories (as shown in Fig. 5e), implying that the difference in W^*_{adv} is the major factor contributing the most to the large difference in error growth rates between the Category-1 and Category-2 events. In addition, a positive (negative) value of the processes on the right-hand side of Eq. (4) indicates the effect of favoring the error growth for warm (cold) events. Therefore, as shown in Figs. 5c and d, a positive (negative) value of W^*_{adv} for the warm (cold) events in Category-1 causes error growth, while a negative (positive) value for the warm (cold) events in Category-2 suppresses error growth, which therefore leads to much larger error growth for the SSTA events in Category-1 than those in Category-2.

$W^*_{adv} = -w^*(\Delta T)' - w'(\Delta T)^*$ is composed of the oceanic temperature advection errors by anomalous vertical currents of KOE-SSTA events [i.e., $A = -w*(\Delta T)' = -w^*(T' - T'_h)/\overline{h}$, T' is the SST error, and T'_h is the temperature error just below the mixed layer base] and the anomalous oceanic temperature advection by vertical current errors [i.e., $B = -w'(\Delta T)^* = -w'(T^* - T^*_h)/\overline{h}$, T^* is the SST anomaly, and T^*_h is the temperature anomaly just below the mixed layer base]. In Fig. 5f, we plot the differences in term A and term B between the two categories for both warm and cold events in the ASO season. It is shown that the dynamical process indicated by

term A plays a more important role in the contribution from W^*_{adv} to the large difference in SSTA error growth between Category-1 and Category-2. Term A, the oceanic temperature advection errors by anomalous vertical currents of KOE-SSTA events, is dominated by the anomalous vertical currents (i.e., the anomalous upwelling or downwelling) and the difference between the SST error and the temperature error just below the mixed layer base [i.e., $(\Delta T)' = (T' - T'_h)/\overline{h}$]. The anomalous upwelling or downwelling can be caused by the Ekman pumping, which is generated by the wind stress curl anomaly. In fact, Ekman pumping can be related to the wind stress by $W_E = \mathrm{curl}_z(\tau/\rho f)$, where τ is the vector wind stress, ρ is the density of sea water and f is the Coriolis parameter (Stewart, 2008, Chapter 9). Obviously, the positive (negative) wind stress curl can cause the upwelling (downwelling). Here, we show the anomalous Ekman pumping and sea surface wind stress anomalies in the ASO season for the warm and cold events in the two categories in Fig. 6, where the positive (negative) shaded values indicate the anomalous upwelling (downwelling). The $(\Delta T)^* = (T^* - T^*_h)/\overline{h}$ and $(\Delta T)' = (T' - T'_h)/\overline{h}$ in the ASO season for both categories are also shown in Fig. 6.

For warm events, the anomalous upwelling induced by the cyclonic wind stress anomalies over the KOE region for Category-1 is much more significant than for Category-2 (Figs. 6a and b). The positive $(\Delta T)^* = (T^* - T^*_h)/\overline{h}$, which also shows a larger value for Category-1 than Category-2

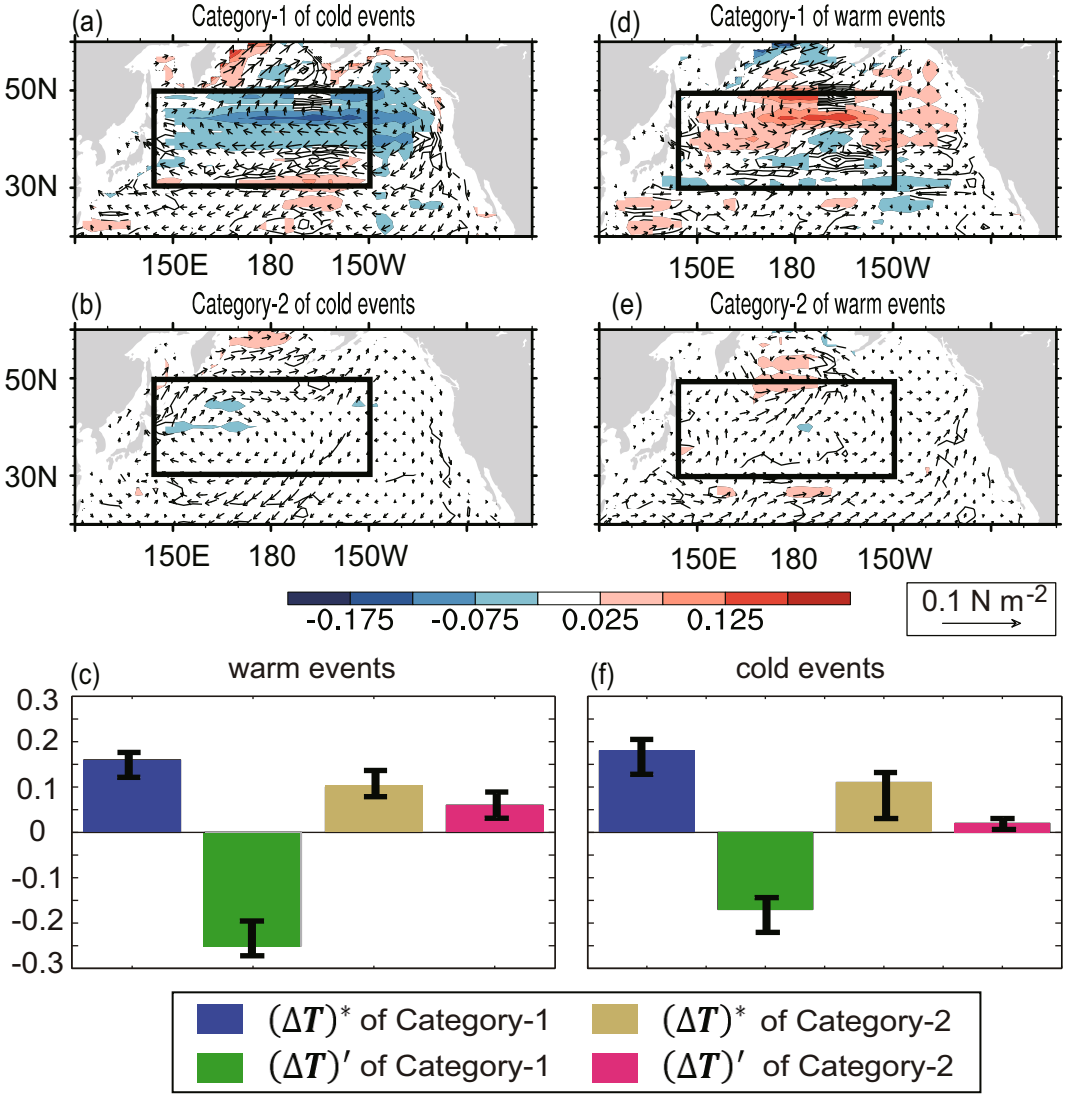

Fig. 6. (a) The anomalous Ekman pumping (i.e. upwelling and downwelling; contours; units: 10^{-5} m s^{-1}) and wind stress anomalies (vectors; units: 0.1 N m^{-2}) in the ASO season for the warm events in Category-1. (b) As in (a) but for the warm events in Category-2. (c) The $(\Delta T)^* = (T^* - T^*_h)/\overline{h}$ and $(\Delta T)' = (T' - T'_h)/\overline{h}$ in the ASO season for warm events (units: K m^{-1}). (d–f) As in (a–c) but for the cold events. Color shading in (a, b) and (d, e) represents the 95% confidence level. The positive (negative) shaded values represent the upwelling (downwelling) of sea waters. The black rectangle marks the KOE-SSTA region (30°–50°N, 145°E–150°W) which is the study area in this paper.

(blue bars and yellow bars in Fig. 6c), implies that the anomalous upwelling brings the cold water to upper ocean layers and leads to the cooling of KOE-SSTA. Therefore, the more significant anomalous upwelling for Category-1 causes much more cooling of KOE-SSTA, which explains why the warm events in Category-1 transfer more rapidly from the mature to decaying phase than those in Category-2. Moreover, Fig. 6c shows that the $(\Delta T)' = (T' - T)/\overline{h}$ is negative with a large absolute value for Category-1 (green bars). Therefore, for the warm events in Category-1, the significant upwelling (i.e., a positive value of vertical velocity w^* in term A) and a negative value of $(\Delta T)' = (T' - T'_h)/\overline{h}$ lead to a positive term A (i.e., positive oceanic temperature advection errors by anomalous vertical currents of the SSTA events), and in turn cause a positive W^*_{adv}, which favors the rapid growth of warm prediction errors according to Eq. (5). Compared with Category-1, the error growth induced by W^*_{adv} is much weaker due to the negligible vertical advection for Category-2 (Fig. 6b). As shown in Fig. 5c, the large difference in W^*_{adv} enhances the difference in error growth rates between the SSTA events in Category-1 and Category-2, and therefore favors a greater possibility of a more significant SPB for the SSTA events in Category-1. The mechanisms are similar for the cold events (see Figs. 6d–f).

Overall, the mature-to-decaying transition of SSTA and the growth of prediction errors in the ASO season are both related with the anomalous upwelling or downwelling in the transition phase of the SSTA events to be predicted. The anomalous upwelling or downwelling in the ASO season for the SSTA events in Category-1 is much more significant than in Category-2, which not only leads to the largest mature-to-decaying transition rate of SSTA but also results in the fastest error growth for the SSTA events in Category-1. Therefore, this explains why the SSTA events transferring more rapidly from the mature to decaying phase tend to yield a greater possibility of a more significant SPB.

5. Summary and discussion

This paper investigates the impact of KOE-SSTA events on the SPB in the North Pacific by analyzing the results from two perfect model predictability experiments (Exp_Reference and Exp_Random). Thirty KOE-SSTA events are randomly selected as the reference states to be predicted, which can be classified into two categories: Category-1 transfers more rapidly from the mature to decaying phase, with a transition rate larger than 0.3 K month^{-1}; and Category-2 has a relatively smaller rate. The KOE-SSTA events in both categories are predicted from different start months with Ref-type initial errors that have certain spatial patterns in Exp_Reference, and with random initial errors in Exp_Random. The results from both experiments show that the SPB usually occurs during the mature-to-decaying transition phase of the SSTA events to be predicted; and the SSTA events in Category-1, which transfer more rapidly from the mature to decaying phase, tend to yield a greater possibility of a more significant SPB than those events in Category-2.

The physical mechanisms responsible for the dependence of the SPB on the mature-to-decaying transition rates of SSTA events are explored. It is found that the SSTA events in Category-1 have larger wind stress curl anomalies over the KOE region during the ASO season than those events in Category-2. For the SSTA events in Category-1, the larger positive (negative) wind stress curl anomalies favor the larger anomalous upwelling (downwelling) of waters dynamically through the Ekman effect for warm (cold) events, which contributes most to the larger oceanic temperature advection errors by anomalous vertical currents of KOE-SSTA events, and in turn leads to the larger prediction errors of vertical oceanic temperature advection associated with SSTA events [i.e., W^*_{adv} in Eq. (4)]. Therefore, the large difference in W^*_{adv} favors the large difference in error growth rates in the ASO season between the Category-1 and Category-2 events. Ultimately, the SSTA events in Category-1 yield a greater possibility of a more significant SPB than those events in Category-2. Furthermore, a more significant anomalous upwelling (downwelling) in the ASO season favors much more SSTA cooling (warming), i.e., the faster SSTA transition from the mature to decaying phase for the warm (cold) events in Category-1. That is, the mature-to-decaying transition rate of SSTA and the error growth rate in the ASO season are both related with the anomalous upwelling (downwelling) induced by wind stress curl anomalies. Therefore, this explains why the SSTA events transferring more rapidly tend to yield a greater possibility of a more significant SPB.

In Fig. 5, it should be noted that the ensemble mean errors associated with latent heat and vertical advection have the same sign as the KOE-SSTA to be predicted, which indicates overestimated SSTA during the mature-to-decaying transition phase in predictions. Duan and Wu (2015) explained that the overestimated SSTA is caused by enhanced anticyclonic (cyclonic) wind stress error for warm (cold) events. Also, the enhanced anticyclonic (cyclonic) wind stress error is probably induced by the perturbed initial sea temperature fields in predictions. The results of Exp_Random are analyzed with the same method as in Exp_Reference, showing that the magnitudes of Q'_{LH} and $\overline{W}_{\text{adv}}$ are much smaller than the results of Exp_Reference (not shown here). This may imply that the Ref-type initial errors can cause more enhanced anticyclonic (cyclonic) wind stress errors and result in larger prediction errors of Q'_{LH} and $\overline{W}_{\text{adv}}$ than the random initial errors. However, how the sea temperature initial errors cause the anticyclonic (cyclonic) wind stress errors for warm (cold) events remains unclear and needs to be explored in future work.

The results presented in this paper suggest that the occurrence of the SPB is dependent on the evolutionary characteristics of the SSTA events to be predicted. The forecast skill may decline dramatically due to the significant error growth when predicting the SSTA events with large mature-to-decaying transition rates. However, it is obvious that the transition rate of an SSTA event is unknown to us before it really happens in real-time forecasts. This matter of what can be considered as the indicator of the transition rate for the KOE-SSTA events should be addressed. It is demonstrated in section 4 that the cyclonic (anticyclonic) wind stresses in

the transition phase are responsible for the SSTA transition for the warm (cold) events. Thus, it is interesting whether the sea surface wind stress is an indicator of the SSTA transition. In Figs. 1c and d, it is shown that the anticyclonic wind stress anomalies favor the development of warm KOE-SSTA for both categories at leads of −4 and −2 months. However, for Category-1, the cyclonic wind stress anomalies appear after the peak, which therefore results in the fast decay of warm SSTA. For Category-2, the wind transformation from anticyclonic to cyclonic is much later, which therefore favors the persistence of warm SSTA. A similar feature of wind evolution also can be seen in observations (not shown here). Furthermore, we show the composite spatial patterns of the seasonal SSTA growth rate and the related growth rate of sea surface wind stress anomalies in the North Pacific for the warm events in the two categories (Fig. 7). The results illustrate that the SSTA transition from mature to decaying phase during the ASO season for the warm events in Category-1 is much more significant than in Category-2 (negative shaded values indicate the SSTA decaying rates for warm events). In addition, the cyclonic wind stress tendency (i.e., wind stress growth rate) in the KOE region appears in the developing phase [the May–June–July (MJJ) season] and becomes much stronger in the transition phase (the ASO season) for Category-1. However, Category-2 does not exhibit this feature. The results for cold events are similar, except for the anticyclonic wind stress tendency in the MJJ season (not shown here). Therefore, the cyclonic (anticyclonic) wind stress appearing in the developing phase may suggest a rapid transition of the warm (cold) KOE-SSTA events. That is, the warm (cold) KOE-SSTA events with cyclonic (anticyclonic) wind stress anomalies in the developing phase may exhibit a significant SPB phenomenon. However, why the evolution of wind stress anomalies between the two categories shows such a large difference is still unclear and further efforts should be addressed to explore this problem.

Furthermore, it is demonstrated that the SPB induced by random initial errors is weaker than the initial errors with spa-

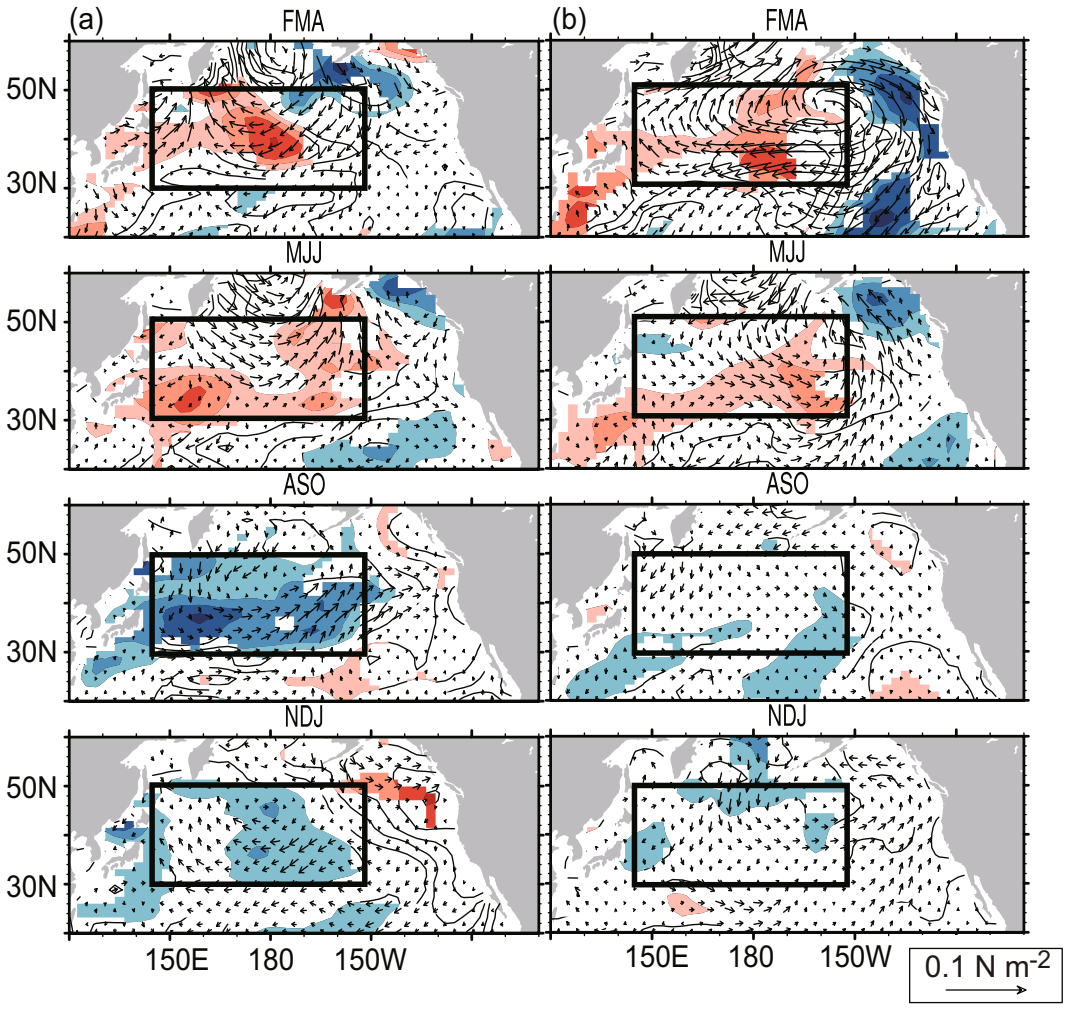

Fig. 7. The seasonal composite of the SSTA growth rate (contours; units: K month^{-1}) and sea surface wind stress growth rate (vectors; units: 0.1 N m^{-2}) of the warm events in (a) Category-1 and (b) Category-2. Color shading represents the 95% confidence level. The black rectangle marks the KOE-SSTA region (30°–50°N, 145°E–150°W) which is the study area in this paper.

tial patterns, such as the Ref-type initial errors in this study. This implies that the initial errors with certain spatial patterns may lead to more prediction uncertainties in the forecasts of North Pacific SSTA. Therefore, it is suggested that removing the initial errors with certain spatial patterns before the predictions may weaken or eliminate the SPB and improve the forecast skill of North Pacific SSTA. In fact, previous studies have demonstrated that the prediction errors caused by the two kinds of initial errors with certain spatial patterns are most likely to induce a spring prediction barrier for ENSO events (Duan et al., 2009; Yu et al., 2009), and removing these kinds of initial errors could reduce the prediction errors in ENSO forecasts (Yu et al., 2012). This encourages us to explore which kinds of initial errors with certain spatial patterns are most likely to induce an SPB of KOE-SSTA and whether the forecast skill can be improved when removing these initial errors in predictions. Furthermore, the initial perturbations in this paper are only superimposed on the North Pacific and there are no perturbations over the equatorial Pacific. The present analyses only consider the local atmosphere–ocean coupling process. It is known that ENSO has a strong influence on the seasonal changes over the extratropical North Pacific. The impact of the tropical Pacific on the predictability of KOE SSTA is also an important issue to be explored. Therefore, further efforts relating to these problems need to be made in our future work.

Acknowledgements. The authors are grateful for the insightful comments and constructive suggestions provided by the anonymous reviewers. This work was jointly sponsored by the National Natural Science Foundation of China (Grant No. 41376018), the Strategic Priority Research Program of the Chinese Academy of Sciences (Grant No. XDA11010303), the China Meteorological Administration Special Public Welfare Research Fund (GYHY201506013), the Project for Development of Key Techniques in Meteorological Forecasting Operation (YBGJXM201705), and the Open Foundation of the LASG/IAP/CAS.

REFERENCES

Cane, M. A., 1983: Oceanographic events during El Niño. *Science*, **222**, 1189–1195, https://doi.org/10.1126/science.222.4629.1189.

Chang, P., and Coauthors, 2006: Climate fluctuations of tropical coupled system-The role of ocean dynamics. *J. Climate*, **19**, 5122–5174, https://doi.org/10.1175/JCLI3903.1.

Curtis, S., and R. F. Adler, 2003: Evolution of El Niño-precipitation relationships from satellites and gauges. *J. Geophys. Res.*, **108**, 4153, https://doi.org/10.1029/2002JD002690.

Dai, A., and T. M. L. Wigley, 2000: Global patterns of ENSO-induced precipitation. *Geophys. Res. Lett.*, **27**, 1283–1286, https://doi.org/10.1029/1999GL011140.

de Boisséson, E., V. Thierry, H. Mercier, and G. Caniaux, 2010: Mixed layer heat budget in the Iceland Basin from Argo. *J. Geophys. Res.*, **115**(18), C10055, https://doi.org/10.1029/2010JC006283.

Duan, W. S., and Y. J. Wu, 2015: Season-dependent predictability and error growth dynamics of Pacific Decadal Oscillation-related sea surface temperature anomalies. *Climate Dyn.*, **44**, 1053–1072, https://doi.org/10.1007/s00382-014-2364-5.

Duan, W. S., X. C. Liu, K. Y. Zhu, and M. Mu, 2009: Exploring the initial errors that cause a significant "spring predictability barrier" for El Niño events. *J. Geophys. Res.*, **114**(C4), https://doi.org/10.1029/2008JC004925.

Feng, R., W. S. Duan, and M. Mu, 2014: The "winter predictability barrier" for IOD events and its error growth dynamics: Results from a fully coupled GCM. *J. Geophys. Res.*, **119**, 8688–8708, https://doi.org/10.1002/2014JC10473.

Gan, B. L., and L. X. Wu, 2012: Modulation of atmospheric response to North Pacific SST anomalies under global warming: A statistical assessment. *J. Climate*, **25**, 6554–6566, https://doi.org/10.1175/JCLI-D-11-00493.1.

Guemas, V., F. J. Doblas-Reyes, F. Lienert, Y. Soufflet, and H. Du, 2012: Identifying the causes of the poor decadal climate prediction skill over the North Pacific. *J. Geophys. Res.*, **117**(D20), D20111, https://doi.org/10.1029/2012JD018004.

Jacob, R. L., 1997: Low frequency variability in a simulated atmosphere-ocean system. PhD dissertation, University of Wisconsin-Madison, 155 pp.

Latif, M., T. P. Barnett, M. A. Cane, M. Flügel, N. E. Graham, H. von Storch, J.-S. Xu, and S. E. Zebiak, 1994: A review of ENSO prediction studies. *Climate Dyn.*, **9**, 167–179, https://doi.org/10.1007/BF00208250.

Lau, K.-M., and S. Yang, 1996: The Asian monsoon and predictability of the tropical ocean-atmosphere system. *Quart. J. Roy. Meteor. Soc.*, **122**, 945–957, https://doi.org/10.1002/qj.49712253208.

Luo, J.-J., S. Masson, S. Behera, and T. Yamagata, 2007: Experimental forecasts of the Indian Ocean dipole using a coupled OAGCM. *J. Climate*, **20**, 2178–2190, https://doi.org/10.1175/JCLI4132.1.

McPhaden, M. J., 2003: Tropical Pacific Ocean heat content variations and ENSO persistence barriers. *Geophys. Res. Lett.*, **3**0, 1480, https://doi.org/10.1029/2003GL016872.

Motokawa, N., N. Matsuo, and N. Iwasaka, 2010: Dominant sea-surface temperature anomaly patterns in summer over the North Pacific Ocean. *Journal of Oceanography*, **66**, 581–590, https://doi.org/10.1007/s10872-010-0048-2.

Philander, S. G. H., 1983: El Niño southern oscillation phenomena. *Nature*, **302**, 295–301, https://doi.org/10.1038/302295a0.

Schott, F. A., S. P. Xie, and J. P. McCreary Jr., 2009: Indian Ocean circulation and climate variability. *Rev. Geophys.*, **47**, RG1002, https://doi.org/10.1029/2007RG000245.

Stewart, R. H, 2008: Introduction to physical oceanography. [Available online at http://oceanworld.tamu.edu/resources/ocng_textbook/PDF_files/book.pdf.]

Wang, H., A. Kumar, W. Q. Wang, and Y. Xue, 2012: Seasonality of the Pacific decadal oscillation. *J. Climate*, **25**(1), 25–38, https://doi.org/10.1175/2011JCLI4092.1.

Webster, P. J., and S. Yang, 1992: Monsoon and ENSO: Selectively interactive systems. *Quart. J. Roy. Meteor. Soc.*, **118**, 877–926, https://doi.org/10.1002/qj.49711850705.

Wen, C. H., Y. Xue, and A. Kumar, 2012: Seasonal Prediction of North Pacific SSTs and PDO in the NCEP CFS Hindcasts. *J. Climate*, **25**, 5689–5710, https://doi.org/10.1175/JCLI-D-11-00556.1.

Wu, Y. J., W. S. Duan, and X. Y. Rong, 2016: Seasonal predictability of sea surface temperature anomalies over the Kuroshio-

Oyashio Extension: Low in summer and high in winter. *J. Geophys. Res.*, **121**, 6862–6873, https://doi.org/10.1002/2016JC011887.

Yamagata, T., S. K. Behera, J.-J. Luo, S. Masson, M. R. Jury, and S. A. Rao, 2004: Coupled ocean-atmosphere variability in the tropical Indian Ocean. *Earth's Climate: The Ocean-Atmosphere Interaction*, C. Wang et al., Eds., American Geophysical Union, **147**, 189–211, https://doi.org/10.1029/147GM12.

Yang, Y., S.-P. Xie, L. X. Wu, Y. Kosaka, N.-C. Lau, and G. A. Vecchi, 2015: Seasonality and predictability of the Indian Ocean dipole mode: ENSO forcing and internal variability. *J. Climate*, **28**, 8021–8036, https://doi.org/10.1175/JCLI-D-15-0078.1.

Yu, Y. S., W. S. Duan, H. Xu, and M. Mu, 2009: Dynamics of nonlinear error growth and season-dependent predictability of El Niño events in the Zebiak-Cane model. *Quart. J. Roy. Meteor. Soc.*, **135**, 2146–2160, https://doi.org/10.1002/qj.526.

Yu, Y. S., M. Mu, W. S. Duan, and T. T. Gong, 2012: Contribution of the location and spatial pattern of initial error to uncertainties in El Niño predictions. *J. Geophys. Res.*, **117**, C06018, https://doi.org/10.1029/2011JC007758.

Zhao, X., J. P. Li, and W. J. Zhang, 2012: Summer persistence barrier of sea surface temperature anomalies in the central western North Pacific. *Adv. Atmos. Sci.*, **29**, 1159–1173, https://doi.org/10.1007/s00376-012-1253-2.

Physica A 494 (2018) 163–168

Contents lists available at ScienceDirect

Physica A

journal homepage: www.elsevier.com/locate/physa

Computing entropy change in synoptic-scale system

Y.P. Wu [a], Y.Y. Hu [a], H.X. Cao [b], C.F. Fu [c], G.L. Feng [a,d,*]

[a] College of Physical Sciences and Technology, Yangzhou University, 22500, Yangzhou, China
[b] Chinese Academy of Meteorological Science, 100081, Beijing, China
[c] Henan Meteorological Institute, Dongminglu, Beiduan, Zhengzhou, Henan, China
[d] Laboratory for Climate Studies, National Climate Center, China Meteorological Administration, Beijing 100081, China

HIGHLIGHTS

- We aim to analyze the entropy change of the synoptic-scale atmosphere as an open system.
- We found that a strong negative entropy flux will appear when the heavy rainfall is coming.
- Our results provide a further evidence for adding the entropy balance equation into the heavy rainfall forecast.

ARTICLE INFO

Article history:
Received 3 September 2017
Received in revised form 9 November 2017
Available online 7 December 2017

Keywords:
Entropy change
Synoptic-scale system
Cyclone development
Heavy rainfall

ABSTRACT

Thermodynamic entropy is of great importance in the atmospheric physics and chemistry process, because it is a non-conserved state function which making a system's tendency towards spontaneous change. But how the entropy forces a synoptic-scale system is still not well known. In this paper, we analyzed the entropy change in atmosphere system, by calculating several examples of extra tropical cyclones over the Yellow River and its adjacent area in summer. The results show that a strong negative entropy flux appears over the north of a stationary front and the thresholds $F_eS \leq -280$ and $\partial s/\partial t \leq -50$ are satisfied. At the same time, the change of total entropy is smaller than zero. Therefore the cyclone developed quickly and daily precipitation reached 371 mm, which is heaviest rain over the Yellows River area in summer. We suggest the dynamical entropy should be developed to improve the forecasting technique of heavy rainfall event in synoptic-scale.
© 2017 Elsevier B.V. All rights reserved.

1. Introduction

Some previous researches show that the most extreme rainfall in most regions of the world will increase in intensity by 3 to 15% [1,2], and the observations are telling us there will be increases in extreme events at almost all latitudes [3,4]. However, it is much more difficult to answer what drives changes in heavy rainfall. Although a great deal of studies on extreme events were carried out, most of them considered atmospheric dynamics instead of thermodynamics. Some researchers realized the important role of thermodynamic entropy in atmospheric physics and chemistry progress. But the studies of entropy change in the climate system are more than that in the weather system [5,6]. Considering extreme events are usually related to weather system (that is synoptic-scale system), we analyzed the entropy change of the atmosphere in synoptic-scale system.

Thermodynamic entropy is a non-conserved state function that is of great importance in the atmospheric physics and chemistry [7]. Entropy can be defined from a classical thermodynamics viewpoint [8], in which the system is viewed

* Corresponding author.
E-mail addresses: ypwu@yzu.edu.cn (Y.P. Wu), fenggl@cma.gov.cn (G.L. Feng).

https://doi.org/10.1016/j.physa.2017.12.010
0378-4371/© 2017 Elsevier B.V. All rights reserved.

from perspective of the gross motion of very large masses of molecules, but it is more generally defined from a statistical thermodynamics viewpoint [9–12], in which the molecular nature of matter is explicitly considered. Historically, the classical thermodynamics definition developed first, and it has more recently been extended in the area of non-equilibrium thermodynamics, the concept of entropy evolved in order to explain why some processes are spontaneous and others are not; systems tend to progress in the direction of increasing entropy, so entropy is the "time's arrow" [13]. Entropy is as such a function of a system's tendency towards spontaneous change [14]. Entropy sometimes increases more rapidly and at other times more slowly; only rarely does it remains constant. The weather is an important example of a non-equilibrium steady state system [15]. The physical quantity which is able to describe both the irreversibility (non-equilibrium) and the steadiness of the weather system at once is the entropy production rate of the system [16].

Many studies on the budgets of momentum, energy and heat of a synoptic-scale system have been made for understanding its motion and structure [17–20]. We focus on thermodynamics of the synoptic-scale system in view of an entropy change, so we first derive a computational scheme of entropy balance equation in the troposphere from thermodynamics, then some computations of the entropy change of extra tropical cyclones over the Yellow River valley were made. The fields of entropy change of them were analyzed in order to diagnose weather of extratropical cyclones and to improve the local weather forecast in the future.

As known in statistical thermodynamics, when a total entropy ds of a system is smaller than zero, i.e. $ds = d_e s + d_i s < 0$, where $d_e s$ is entropy exchange, $d_i s$ inner entropy production, i.e. the system gets a negative entropy flow from its environment, the system will develop. So a fundamental view of this study is to examine the change of negative entropy in the field with the motion of extra tropical cyclone over the Yellow River valley.

2. Models and computational formula

Entropy is a thermodynamic quantity that helps to account for the flow of energy through a thermodynamic process. Originally, entropy was defined as a summation of heat supplied divided by its temperature [21]. If a certain small amount of heat δQ is supplied reversibly to a system with the temperature T, the entropy of the system will increase by an amount [22,23]

$$\Delta S = \int_{\text{is}}^{\text{fs}} \delta Q/T, \tag{1}$$

where ΔS is the incremental entropy of the system between the initial state (is) and the final state (fs) of the process, and δQ is the infinitesimal small change of one path function.

Heat is supplied by radiation, convection, or conduction. When the heat is extracted from the system, the same amount entropy of the system will decrease correspondingly. This is not a violation of the second law of thermodynamics, since the entropy in the surrounding system increases. For an open system which exchanges heat and mass with its surrounding system, the entropy of can either increase or decrease, depending on the direction of the heat transported. Generally speaking, the second law, the law of entropy increase, is valid for a whole isolated system. It remains reasonable for open systems when the system and its environment/reference state are considered as a whole system [24]. So the total change in entropy must be non-negative when we sum up all the entropy changes of interacting subsystems.

Considering that heat can flow from the hot reservoir B to the cold reservoir A which are connected by a small system C, the change rate of entropy of the whole system A+B+C by the heat flow is given by [25].

$$\frac{\partial s_{\text{whole}}}{\partial t} = \frac{\partial s_a}{\partial t} + \frac{\partial s_b}{\partial t} + \frac{\partial s_c}{\partial t} = \frac{F}{T_c} - \frac{F}{T_h} = \frac{T_h - T_c}{T_h T_c} F \geq 0, \tag{2}$$

where $\partial s_{\text{whole}}/\partial t$ is the change rate of the entropy in the whole system, and $\partial s_a/\partial t$, $\partial s_b/\partial t$ and $\partial s_c/\partial t$ are those in the subsystems A, B and C, respectively. F is the flux of heat through the system per unit time. According to Eq. (1), F/T_c is the increased entropy of the cold reservoir A, and $-F/T_h$ are is the decreased entropy of the hot reservoir B since the heat is flowing out from the hot reservoir to the cold. The inequality in Eq. (2) corresponds to the second law of thermodynamics and is a consequence of the fact that heat flows from hot to cold ($F \geq 0$). For a considerably long period of time ($t \to \infty$), the heat of the whole system transport will make the temperature difference negligible, resulting in the entropy of the whole system at a maximum. This final state is called thermodynamic equilibrium.

It is worth mentioning that the maximum work is not attainable generally, because irreversible processes of natural systems are always inevitable. These irreversible conversions of mechanical energy into heat energy (δQ) lead to additional contributions to the entropy production ($\delta Q/T$) in Eq. (1) [26]. In principle, due to some irreversible processes associated with turbulence in a fluid system, the ratio of entropy production can be given by a sum of the change rate of entropy in the system and its surrounding system, which exchanges heat with the system as:

$$\frac{\partial s_{\text{turb}}}{\partial t} = \frac{\partial s_{\text{whole}}}{\partial t} = \int_{\Omega} \frac{1}{T} \left[\frac{\partial(\rho c T)}{\partial t} + \text{div}(\rho c T \vec{V}) + p \, \text{div} \vec{V} \right] d\Omega + \int_A \frac{F_{\text{sur}}}{T} dA, \tag{3}$$

where $\partial s_{\text{turb}}/\partial t$ is the rate of entropy production due to turbulence, ρ is the fluid density, c is the specific heat at constant volume Ω, T is the absolute temperature, $\vec{V}$ is the velocity of the fluid, p is the pressure, Ω is the volume of the fluid system, A is the surface surrounding the system, and F_{sur} is the heat flux at the surface, defined as positive outward. (Material fluxes can also be taken into account by means of chemical potential [27]. The first term represents the change rate of entropy of the fluid system, and the second term represents that of the surrounding system.

3. Calculation scheme for entropy and entropy change

The entropy balance equation of non-equilibrium thermodynamics for an open subsystem is [28]:

$$\frac{\partial s}{\partial t} = -\nabla(s\vec{v}) - \frac{1}{T}\nabla\cdot\vec{J}_q + \sum_k^1 \frac{1}{T}\mu_k\nabla\cdot\vec{J}_k + \sum_k \frac{1}{T}\vec{J}_k\cdot\vec{F}_k - \frac{1}{T}\pi\cdot\nabla\vec{v} - \sum_j \frac{1}{T}J_jA_j, \tag{4}$$

where notations used are as follows: k, component; s, specific entropy; v, barycentric velocity; T, temperature; J_q, heat flux; μ_k, chemical potential; J_k, the diffusive mass flux of the kth chemical species; F_k, external force; π, total pressure tensor; j, chemical reaction; J_j, chemical reaction rate of the reaction j; A_j, chemical affinity potential of the reaction j.

With the p-coordinate the entropy flux divergence due to advection and convection is expressed as

$$-\nabla\cdot(s\vec{v}) = -s\nabla_p\cdot\vec{v} - \vec{v}\cdot\nabla_p s - \frac{\partial}{\partial p}(s\omega), \tag{5}$$

where ω is vertical velocity of air.

The heat flux divergence becomes

$$-\frac{1}{T}\nabla\cdot J_q = g\rho\left(\frac{\partial}{\partial\rho}s_q + \frac{s_q}{T}\frac{\partial T}{\partial p}\right), \tag{6}$$

where ρ is total density, s_q thermal flux entropy by non-adiabatic heating.

The mass diffusion divergence of the third term in (4) is simply expressed as

$$\sum_k \frac{1}{T}\mu_k\nabla\cdot\vec{J}_k = \nabla_p s_d\rho_d\vec{v} + \nabla_p\cdot s_e\rho_e\vec{v} + \nabla_p\cdot s_\omega\rho_\omega\vec{v} + \frac{\partial}{\partial p}\left[\omega\left(s_d\rho_d + s_e\rho_e + \rho\omega s_\omega\right)\right], \tag{7}$$

where s_d, ρ_d, s_e, ρ_e, and s_w, ρ_w are the specific entropy and the density of dry air, vapor, liquid water respectively. Only the gravity is taken into account, so we have approximate relation

$$\sum_k \frac{1}{T}(\vec{J}_k\cdot\vec{F}_k) \approx \frac{\omega}{T}, \tag{8}$$

the fifth term in (4) is smaller than the others and is omitted reasonably.

Considering the chemical reactions of vapor and liquid water, there is a relation

$$-\frac{1}{T}\sum_j A_jJ_j = \frac{\rho_e L}{T}\left[\nabla_p\cdot q\vec{v} + \frac{\partial}{\partial p}(q\omega)\right], \tag{9}$$

where L is latent heat constant, ρ_e density of vapor, with other assumptions, substitute (5)–(9) for (4), the version of entropy balance equation suitable for current weather forecasting is obtained as follows:

$$\begin{aligned}\frac{\partial s}{\partial t} &= -\nabla_p\cdot s\vec{v} + \left\{\nabla_p\cdot s_d\vec{v} + \nabla_p\cdot s_e\rho_e\vec{v} + \nabla\cdot s_\omega\rho_\omega\vec{v}\right\}\\ &\quad + \frac{1}{T}L\rho_e\nabla_p\cdot q\vec{v} - 2\frac{\partial}{\partial p}s\omega + \frac{1}{T}L\rho_e\frac{\partial}{\partial p}(q\omega)\\ &\quad + g\rho\left(\frac{\partial}{\partial p}sq + \frac{sq}{T}\frac{\partial T}{\partial p}\right) + \frac{\omega}{T},\end{aligned} \tag{10}$$

where q is specific humidity.

As the weather phenomena appear mainly in the layer from 1000 to 400 hPa in the troposphere, the total entropy change per unit column of the air approximately is [29]:

$$\begin{aligned}\frac{\partial s}{\partial t} &= \frac{1}{g}\int_{400}^{1000}\frac{\partial s}{\partial t}\frac{dp}{\rho}\\ &= -\frac{1}{g}\int_{400}^{1000}\left(\nabla p\cdot s\vec{v} + \sum_k\nabla_p\cdot\rho_k\vec{v} - \frac{1}{T}L\rho_e\nabla_p\cdot q\vec{v}\right)\frac{dp}{\rho}\\ &\quad - \int_{400}^{1000}\frac{2}{g\rho}(s\omega) + \int_{400}^{1000}\frac{1}{\overline{T}}L\overline{\rho}_e(q\omega) + \int_{400}^{1000}s_q\\ &\quad + \int_{400}^{1000}\overline{s}_q l_n T + \frac{6\times10^4}{\rho g}\frac{\overline{\omega}}{\overline{T}},\end{aligned} \tag{11}$$

where the bar above a letter means averaging the values from 1000 hPa through 400 hPa.

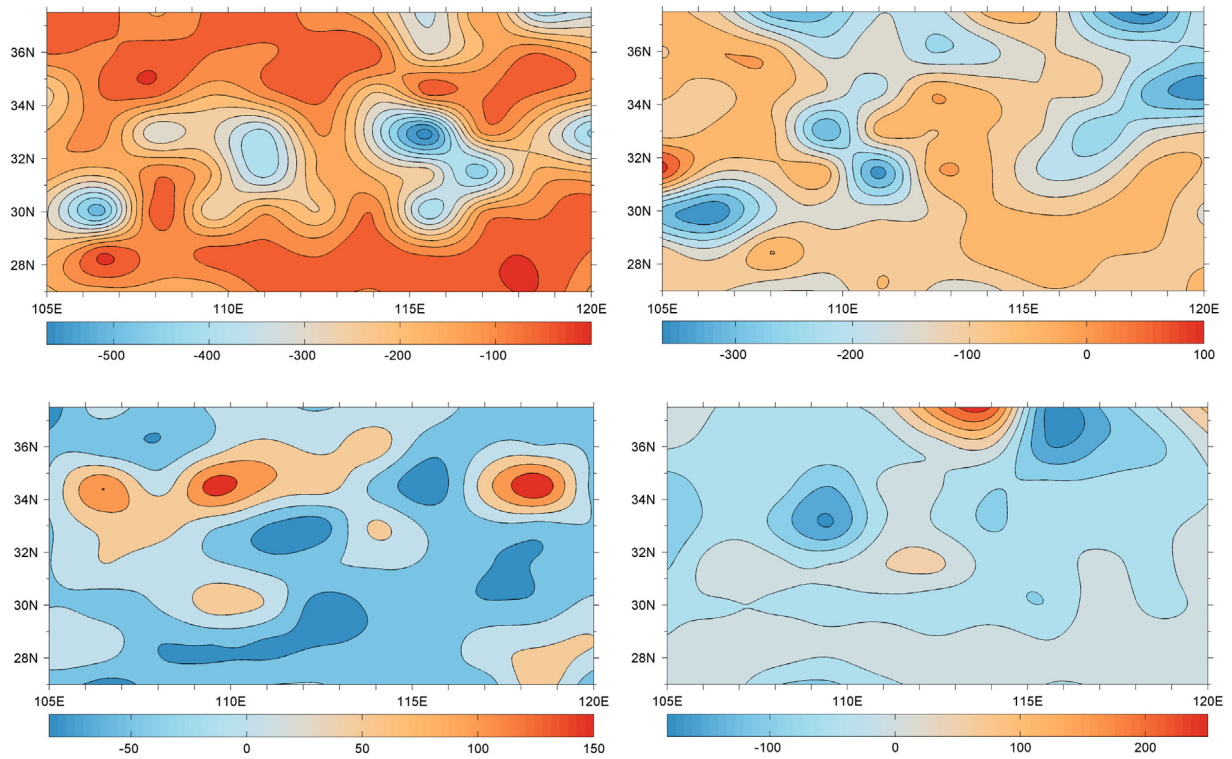

Fig. 1. The entropy flux (upper) and total entropy change (lower) over the area of 27–37.5°N,105–120°E on 00 GMT 21–23 July 1982 (left) on 00 GMT 8–10 July 1985 (right). In the upper left figure, there are two strong negative flux centers at 33N,115.5E and 30N,106.5E, the former is satisfied with the thresholds $F_eS \leq -280$ and $\partial s/\partial t \leq -50$, and the latter just meets the criteria of $\partial s/\partial t \leq -50$.

4. Diagnostic analysis of several cyclones

By using (11) and based on NCEP/NCAR monthly mean reanalysis data ($2.5^\circ \times 2.5^\circ$), we calculate several examples of extra tropical cyclones over the Yellow River and its adjacent area in summer. i.e., 13–15 June and 21–23 July 1982; 30 June–2 July and 18–19 July 1983; 10–12 July and 24–26 July 1984; 15–17 July 1985.

The entropy change fields at the initial stage and the developing stage of them are analyzed, and we obtain the following conclusion about development of the extra tropical cyclones over the Yellows River:

A strong negative entropy flux appears over the north of a stationary front and the change of total entropy is smaller than zero. During 1982–1985 thresholds of strong negative entropy flux (F_eS) and $\partial s/\partial t$ are empirically taken as (unit: $JK^{-1}M^{-2}S^{-1}$)

i. $F_eS \leq -280$

ii. $\partial s/\partial t \leq -50$

In Fig. 1, opposite situations for developing or non-developing of cyclone in a stationary front are given. In the case of 21–23 July 1982 (Fig. 1 left), the strong negative flux appears over the north of the stationary front, at 33N,115.5E, there is a center of strong negative entropy flux and the thresholds $F_eS \leq -280$ and $\partial s/\partial t \leq -50$ are satisfied, at the other center (30N,106.5E) of the negative entropy flux, the condition $\partial s/\partial t \leq -50$ is not satisfied yet. Therefore the cyclone developed quickly and daily precipitation reached 371 mm, which is heaviest rain over the Yellows River area in summer. What is more, both the distribution pattern and its trend in precipitation from 21 to 22 July 1982 were consistent with the entropy change (Fig. 2 left). While in the case of 8–10 July 1985 (Fig. 1 right), although there appear a quite strong negative entropy flux over the north of a stationary front, the conditions i. and ii. are not satisfied, as a result, the cyclone did not appear and the precipitation was not heavy enough, but the distribution pattern was consistent with the entropy on the whole (Fig. 2 right). C. F. Fu got the similar results when he diagnosed and analyzed the atmospheric entropy changing fields of typhoon heavy rain process [28].

In a sense, entropy refers to the disorder degree of the system. The order degree of weather system is high and the entropy of the system is negative the when weather system receives some disturbance. Then the entropy increases as the system makes spontaneous adaptive adjustment to respond to external disturbances. At the same time, the adjustment of the weather system leads to one or more cyclones with heavy rainfall.

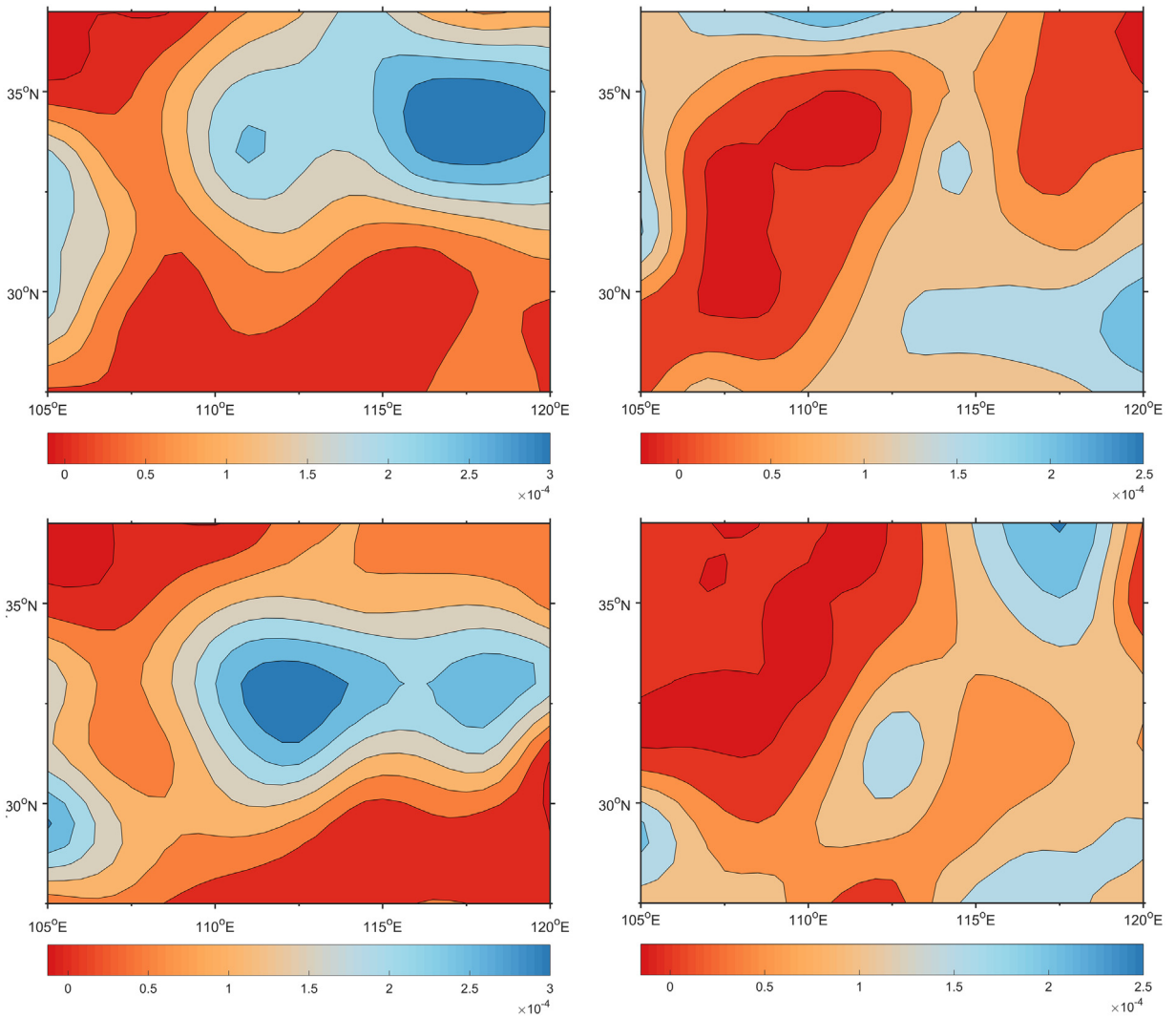

Fig. 2. The precipitation over the area of 27–37.5°N,105–120°E on 21(upper left) and 22 (lower left) July 1982 and 8 (upper right)10 (lower right) July 1985 (unit: kg m^{-2} s^{-1}).

5. Conclusion and discussion

Climate system is an important and typical example of a non-equilibrium steady state system. The theory of non-equilibrium thermodynamics, such as the second law of thermodynamics, entropy increase principle, minimum entropy generation principle and so on, is also very complete. And the effect of entropy and its change on synoptic-scale system has been found. However, the way of entropy forcing a synoptic-scale system like cyclone is still an open question. Here we calculated several examples of extra tropical cyclones and analyzed the related entropy change of the atmosphere, taking Yellow River and its adjacent area in summer as a case. We found that a strong negative entropy flux appears over the north of a stationary front and the thresholds $F_eS \leq -280$ and $\partial s/\partial t \leq -50$ are satisfied. At the same time, the change of total entropy is smaller than zero. Therefore the cyclone developed quickly and daily precipitation reached 371 mm, which is heaviest rain over the Yellows River area in summer. We suggest the dynamical entropy should be developed to improve the forecasting technique of heavy rainfall event in synoptic-scale.

Predecessors have applied the simplified entropy balance equation to the study on weather changes [25,30,31]. Since the simplified equation is obtained under the condition that the temperature and the pressure field are uniform, it deviates greatly the actual atmosphere and may lose many of the information and functions that the original equation would have. In this paper, a more comprehensive local entropy balance equation is used in the analysis of typhoon storm process, and the results show that the strong negative entropy flux likely indicates a heavy rainfall. Fu got the similar results when he diagnosed and analyzed the atmospheric entropy changing fields of typhoon heavy rain process [32]. Scientists were

constantly trying to find new ways to predict precipitation, especially extreme events, but they failed in finding precursors of extreme events [33,34], while the above work on entropy change of synoptic-scale system implied a new direction. It will be prosperous if some new developments, for example, dynamical entropy be included in the entropy equilibrium equation [35]. Through the characteristics of entropy change field, development of cyclones would be revealed to provide useful information for weather stations to forecast the rainstorm or related study [36–39].

Acknowledgments

We are grateful for supports by both the National Science Foundation of China under the Contract (No. 41375079, 41375078) and the Ministry of Science and Technology, P. R. China under the Contract No. GYHY201506001. We also thank to Ms Xuehua Cai for much help in writing this paper.

References

[1] P.R. Grant, Evolution, climate change, and extreme events, Science 357 (2017) 451–452.
[2] R.S. Ajayamohan, J.M. William, V.K. Viatcheslav, Increasing trend of synoptic activity and its relationship with extreme rain events over central India, J. Climate 23 (4) (2010) 1004–1013.
[3] Y.P. Wu, G.L. Feng, B.L. Li, Interactions of multiple atmospheric circulation drive the drought in tarim river basin, Sci. Rep-UK 6 (2016) 26470.
[4] G.L. Feng, Y.P. Wu, Signal of acceleration and physical mechanism of water cycle in xinjiang, China, PloS one 11 (12) (2016) e0167387.
[5] S. Pascale, J.M. Gregory, M. Ambaum, R. Tailleux, Climate entropy budget of the HadCM3 atmosphere–ocean general circulation model and of famous, its low-resolution version, Clim. Dynam. 36 (2011) 1189–1206.
[6] C. Liu, Y. Liu, Negative entropy flow and its effect on the organization of synoptic-scale severe atmospheric systems, Geophys. Res. Lett. 31 (1) (2004) 1–4.
[7] G. Grazzini, R. Borchiellini, U. Lucia, Entropy versus entransy, J. Non-Equil. Thermody. 38 (3) (2013) 259–271.
[8] H.C. Van Ness, Classical Thermodynamics of Non-Electrolyte Solutions, Elsevier, 2015.
[9] T.L. Hill, An Introduction to Statistical Thermodynamics, Courier Corporation, 1960.
[10] J.N. Kapur, H.K. Kesavan, Entropy Optimization Principles and Their Applications Entropy and Energy Dissipation in Water Resources, Springer, Netherlands, 1992, pp. 3–20.
[11] G.Q. Sun, C.H. Wang, Z.Y. Wu, Pattern dynamics of a Gierer–Meinhardt model with spatial effects, Nonlinear Dynam. 88 (2017) 1385–1396.
[12] G.Q. Sun, J.H. Xie, S.H. Huang, Z. Jin, M.T. Li, L. Liu, Transmission dynamics of cholera: Mathematical modeling and control strategies, Commun. Nonlinear Sci. Numer. Simulat. 45 (2017) 235–244.
[13] C. Callender, Thermodynamic Asymmetry in Time. Stanford.library.sydney.edu.au, 2001.
[14] F.L. Lambert, Disorder-A cracked crutch for supporting entropy discussions, J. Chem. Educ. 79 (2) (2002) 187.
[15] R. Stinchcombe, Stochastic non-equilibrium systems, Adv. Phys. 50 (5) (2001) 431–496.
[16] I. Prigogine, D. Kondepudi, Contemporary Thermodynamics: From Heat Engines to Dissipative Structures, 1998.
[17] R.M. Thompson Jr., S.W. Payne, E.E. Recker, R.J. Reed, Structure and properties of synoptic-scale wave disturbances in the intertropical convergence zone of the eastern Atlantic, J. Atmos. Sci. 36 (1) (1979) 53–72.
[18] M.H. Zhang, J.L. Lin, Constrained variational analysis of sounding data based on column-integrated budgets of mass,heat, moisture, and momentum: Approach and application to ARM measurements, J. Atmos. Sci. 54 (11) (1997) 1503–1524.
[19] V. Petoukhov, A. Ganopolski, V. Brovkin, M. Claussen, A. Eliseev, C. Kubatzki, S. Rahmstorf, CLIMBER-2: A climate system model of intermediate complexity. Part I: Model description and performance for present climate, Clim. Dynam. 16 (1) (2000) 1–17.
[20] M.N. Juckes, I.N. James, M. Blackburn, The influence of Antarctica on the momentum budget of the southern extra tropics, Q. J. Roy. Meteor. Soc. 120 (518) (1994) 1017–1044.
[21] R. Clausius, Ueber verschiedene für die Anwendung bequeme Formen der Hauptgleichungen der echanischen Wärmetheorie, Ann. Phys. Chem. 125 (1865) 353–400.
[22] A. Bejan, Advanced Engineering Thermodynamics, John Wiley, New York, 2006.
[23] U. Lucia, Maximum or minimum entropy generation for open systems? Physica A 391 (12) (2012) 3392–3398.
[24] C. Kittel, H. Kroemer, Thermal Physics, W.H. Freeman, New York, 1980.
[25] H. Ozawa, A. Ohmura, R.D. Lorenz, T. Pujol, The second law of thermodynamics and the global climate system: A review of the maximum entropy production principle, Rev. Geophys. 41 (4) (2003).
[26] S.R. De Groot, P. Mazur, Non-equilibrium Thermodynamics, North-Holland, New York, 1962, p. 510.
[27] S. Shimokawa, H. Ozawa, On the thermodynamics of the oceanic general circulation: Entropy increase rates of an open dissipative system and its surroundings, Tellus, Ser. A 53 (2001) 266–277.
[28] S.R. De Groot, P. Mazur, Non-Equilibrium Thermodynamics, North-Holland Publ. Co., Amsterdam, 1969.
[29] C. Fu, Analysis of entropy change field of the atmosphere, derivation and calculation of equation, Technical report, Henan Meteorological Institute, 1986 (in Chinese).
[30] A. Kleidon, Non-equilibrium thermodynamics and maximum entropy production in the Earth system, Naturwissenschaften 96 (2009) 653–667.
[31] Y. Wu, H. Cao, G. Feng, Prospective study on applications of non-equilibrium thermodynamics to climate modeling, J. Coast. Res. 73 (2015) 342–347.
[32] C.F. Fu, Diagnostic and comparative analysis of the atmospheric entropy changing fields of typhoon heavy rain process, Q. J. Appl. Meteorol. 2 (4) (1991) 408–415 (in Chinese).
[33] Y.P. Wu, G.L. Feng, A new algorithm for seasonal precipitation forecast based on global atmospheric hydrological water budget, Appl. Math. Comput. 268 (2015) 478–488.
[34] Z.Q. Gong, C. Hutin, G.L. Feng, Methods for improving the prediction skill of summer precipitation over East Asia–West Pacific, Weather Forecas. 31 (2016) 1381–1392.
[35] Y.Q. Hu, Entropy equilibrium equation and dynamics entropy production in environment liquid, Prog. Nat. Sci. 12 (3) (2002) 180–184.
[36] Z.-K. Zhang, C. Liu, X.-X. Zhan, X. Lu, C.-X. Zhang, Yi-Cheng Zhang, Dynamics of information diffusion and its applications on complex networks, Phys. Rep. 651 (2016) 1–34.
[37] C. Liu, Z.-K. Zhang, Information spreading on dynamic social networks, Commun. Nonlinear Sci. 19 (4) (2014) 896–904.
[38] Z.-K. Zhang, C. Liu, Y.-C. Zhang, T. Zhou, Solving the cold-start problem in recommender systems with social tags, Europhys. Lett. 92 (2010) 28002.
[39] L. Yu, J. Huang, G. Zhou, C. Liu, Z.-K. Zhang, TIIREC: A tensor approach for tag-driven item recommendation with sparse user generated content, Inf. Sci. 411 (2017) 122–135.

Chaos, Solitons and Fractals 107 (2018) 1–4

Contents lists available at ScienceDirect

Chaos, Solitons and Fractals

Nonlinear Science, and Nonequilibrium and Complex Phenomena

journal homepage: www.elsevier.com/locate/chaos

Mathematical modeling of Fog-Haze evolution

Yong-Ping Wu[a,b], Chun-yangzi Zhu[a], Guo-Lin Feng[a,c,*], B. Larry Li[b]

[a] College of Physics Science and Technology, Yangzhou University, Yangzhou, Jiangsu 225002, China
[b] Ecological Complexity and Modeling Laboratory, University of California, Riverside CA 92521–0124, USA
[c] Laboratory for Climate Studies of China Meteorological Administration, National Climate Center, Beijing 100081, China

ARTICLE INFO

Article history:
Received 30 October 2017
Revised 2 December 2017
Accepted 9 December 2017

Keywords:
Fog-Haze
Mathematical modeling
Atmospheric water vapor
Aerosol particles
Diseases

ABSTRACT

Under the global warming, the significant changes in atmospheric water cycle lead to drying in arid region, which is strengthening the effect of aerosol on Fog-Haze generation and accelerating the emergence of infectious diseases. However, the production process of the Fog-Haze is lack of quantitative description based on atmospheric water cycle. In this paper, we modeled the process of Fog-Haze generation, evolution and disappearance fundamentally and theoretically. The budget functions for water vapor and aerosol were coupled by the physical and chemical interaction between water vapor and aerosol. The obtained results may provide new insights on the control of Fog-Haze and the related infectious diseases induced by Fog-Haze.

© 2017 Published by Elsevier Ltd.

1. Introduction

In recent years, many areas, especially China, are suffering a serious impact of Fog-Haze [1–5]. It was reported that no more than one percent of the first 500 largest cities in China reached the air quality standards recommended by World Health Organization [3,6]. The main negative impact of haze on human being includes increasing mortality, chronic diseases exacerbate, respiratory system and worsen heart disease [1], reducing the reproductive ability and changing the structure of the body's immunity. It will also affect the formation of clouds and rainfall, lead to arid region becoming drier, wet zone getting wetter, climate-induced disasters.

Generally, Fog-Haze forces the spread of infectious diseases mainly in three ways: (1) As a result of the weakened Ultraviolet in the near-surface layer, the activity of infectious bacteria in the air is enhanced and infectious diseases are increased; (2) Hazardous substances carried by Fog-Haze damage human respiratory system and reduce human immunity to infectious diseases; (3) Haze particles as carriers of infectious bacteria, spread in the air, increased the probability of transmission through the transmission. Physical processes of the atmosphere decides the generation, Evolution and disappearance of Fog-Haze, through accumulating, transporting and exchanging atmospheric aerosol and water vapor [5]. Atmospheric moisture and condensation nuclei, that is aerosol, are generally the internal factors of the generation of Fog-Haze. There is a complex interaction between water vapor and aerosol. From the monomer to the storm cloud systems, due to the feedback of different scales, water vapor and the aerosol affecting the physical processes of atmosphere, especially the atmospheric water cycle process, through participation in the formation of clouds, fog and haze [7]. For example, condensation nuclei changes will significantly alter the storms of spatial-temporal distribution of precipitation, the frequency distribution of rainfall rate and the height of cloud base and top [8–10]. Air pollution causes an increase in the density of aerosol, and leads to more very small cloud droplets [7,11]. The anthropogenic pollutants emitted from vehicles and unfavorable meteorological conditions exerted a great influence on PM2.5 and black carbon loading and increased the cloud condensation [12]. The continuing role of aerosols leading to reduced precipitation [13] often induces a more stable atmosphere, which is more conducive to the accumulation of air pollutants and contributes to the formation of haze events [14]. Meanwhile, the haze layer will cause thermal diffusion, which occupy the sky lasting moisture, so that rain events decrease during dry season, but intensify during the rainy season [15]. In addition, the pollution of haze droplets may be related to droplet mean volume radius and may depend on the temperature and atmospheric humidity [16,17].

On the contrary, the atmospheric water cycle will also affect the production, Evolution and disappearance of haze. The relative humidity determined by atmospheric water vapor content affects the microstructure of haze, clouds and precipitation [18]. The moisture content tends to produce larger more rain clouds and precipitation in the form of clean air in the atmosphere [2,19], which reduces haze generation to a certain extent. In general, the efficiency of clearing wet aerosol particles is strongly influenced by the rain-

* Corresponding author.
E-mail addresses: ypwu@yzu.edu.cn (Y.-P. Wu), fenggl@cma.gov.cn (G.-L. Feng).

https://doi.org/10.1016/j.chaos.2017.12.006
0960-0779/© 2017 Published by Elsevier Ltd.

fall intensity and depends on the haze particle size [20]. The larger particles is the better rain washes [19]. On the other hand, increasing aerosol can in turn make the precipitation rate decrease [21], which is more conducive to the generation of haze. Aerosol particles mainly consist of biomass combustion, industrial emissions, mine dust, dust and so on. They will diffuse and transfer between adjacent area. The particulate ingredients were different in different regions [22–25]. The influence of water vapor on aerosols depended on the components of aerosol [26,27] and regional characteristics [28]. After complex chemical-physical interaction, such as oxidation, vapor phase nucleation, phase nucleation and growth processes [29–31], the original emission particles and water vapor generate secondary aerosol particles.

Projected changes in the water cycle over the next few decades show similar large-scale patterns to those towards the end of the century, but with smaller magnitude. Changes in the near-term, and at the regional scale will be strongly influenced by natural internal variability and may be affected by anthropogenic aerosol emissions [32].

It can be concluded from above that, water vapor and its condensation nuclei, that is atmospheric aerosol particle, play the leading roles in the formation of Fog-Haze. The circulating of atmospheric water vapor and aerosol particles timely control the dynamic distribution of regional water vapor and aerosol, which directly affects the formation, evolution and disappearance of Fog-Haze. Since global warming, the significant changes in atmospheric water cycle caused reducing precipitation and drying in arid region [33–35], which strengthen the effect of aerosol on haze generation [7,36]. However, the quantitative description and associated prediction mode for the production process of the haze based on water cycle is still unclear. In this paper, to reveal the mechanism of the interaction between atmospheric water vapor and condensation nuclei during atmospheric physical processes from the perspective of hydrological cycle, we model and simulate the process of Fog-Haze generation, evolution and disappearance fundamentally and theoretically.

2. Mathematical modeling of the generation, evolution and disappearing of Fog-Haze

2.1. The function of transformation between water vapor and aerosol

In the atmosphere, many secondary aerosol particles are produced from the complex interactions between any two of aerosol particles and water vapor. In this study, all processes of physical-chemical effects including oxidation, vapor and liquid phases nucleation, and growth, are defined as the material conversion. The related conversion equation is:

$$(j)a_{\Omega i} + (k)H_2O + (l)O_2 = h_{\Omega i}, \tag{1a}$$

where $a_{\Omega i}$is the *i-th* aerosol particles; $h_{\Omega i}$is the corresponding secondary aerosol particles; $(l)O_2$ is optional and only exists in the material oxidation reaction. For example, the interaction among SO_2, H_2O and O_3 can be represented as

$$3SO_2 + 3H_2O + O_3 = 3H_2SO_4 \tag{1b}$$

2.2. The budget functions for water vapor and aerosol

The factors of weather and climate conditions and human activities affecting on the generation of Fog-Haze are very complex. The factors of weather and climate conditions, such as evaporation, precipitation, wind, temperature and so on, and human factors like pollutant emissions, emission type and distribution, as well as physical and chemical reactions between different particles, may lead to changes of water vapor and aerosol concentration in the area. But no matter how change they do, their quality must comply with the law of conservation of matter. Therefore, the dynamic distribution of the water vapor and aerosols within the region and can be calculated and monitored by the balance equations.

We suppose that the atmospheric water vapor content in region Ω at time t is $W_\Omega(t)$, then

$$\frac{\partial W_\Omega(t)}{\partial t} + \frac{\partial [W_\Omega(t)u]}{\partial x} + \frac{\partial [W_\Omega(t)v]}{\partial y} = E_\Omega(t) - P_\Omega(t) + \beta_\Omega(t), \tag{2}$$

where x and y denote the longitude and latitude respectively; $\partial[W_\Omega(t)u]/\partial x$ and $\partial[W_\Omega(t)v]/\partial y$are the divergence term due to atmospheric movement; u and v are macroscopic horizontal velocities of water vapor and particles and mainly related with the meridianal and zonal wind speed; $E_\Omega(t)$ and $P_\Omega(t)$ are evaporation and precipitation respectively; $\beta_\Omega(t)$is the reaction diffusion term, it is namely the additional items generated from the random diffusion of water vapor and aerosols in the unit time and generating substance after material conversion. $\beta_\Omega(t)$ is expressed as:

$$\beta_\Omega(t) = d\left\{\frac{\partial^2 W_\Omega(t)}{\partial x^2} + \frac{\partial^2 W_\Omega(t)}{\partial y^2}\right\} - f_\Omega(t) \tag{3}$$

where $f_\Omega(t)$ is the reaction term obtained by the substance-conversion equation, d is the diffusion coefficient.

Similarly, we assume that there are n kinds of primary aerosol particles in region Ω and the content of the i-th particle at time t is $Q_{\Omega i}(t)$, then

$$\frac{\partial Q_{\Omega i}(t)}{\partial t} + \frac{\partial [Q_{\Omega i}(t)u_i]}{\partial x} + \frac{\partial [Q_{\Omega i}(t)v_i]}{\partial y} = A_{\Omega i}(t) + \alpha_{\Omega i}(t) \tag{4}$$

where $A_{\Omega i}(t)$is the quality of ith aerosol particle generated by natural or human emissions within the region per unit time at time t; $\partial[Q_{\Omega i}(t)u_i]/x$ and $\partial[Q_{\Omega i}(t)v_i]/\partial y$ are divergence term generated from the atmospheric motion; u_i and v_i are the macroscopic meridianal and zonal velocity of ith aerosol particle and are affected by the wind speed and physical properties of the particles; $\alpha_{\Omega i}(t)$ is an additional item resulting in the physical-chemical reaction (material conversion), random diffusion and sedimentation and meets to

$$\alpha_{\Omega i}(t) = d_i\left\{\frac{\partial^2 Q_{\Omega i}(t)}{\partial x^2} + \frac{\partial^2 Q_{\Omega i}(t)}{\partial y^2}\right\} - f_{\Omega i}(t) - s_{\Omega i}(t) \tag{5}$$

where d_i is the diffusion coefficient; $f_{\Omega i}(t)$ is the reaction term, determined by the material conversion equation; $s_{\Omega i}(t)$ is the sedimentation item, aerosols will gradually settle and disappear when their gravity or density is large enough.

2.3. Coupling the matter transformation into the budget equation

Since atmospheric aerosols are composed of variety particles, they have different physical and chemical properties, such as particle size, water-soluble and so on. These different physical and chemical properties of aerosols determine the way and speed they combined with water vapor are not the same. This correspondingly leads to different secondary aerosol particles systems and different influences of climate change on the process of their generating, developing and disappearing. Therefore, a substance conversion-mass balance coupled model need to establish to characterize the formation of aerosol particles system. Here, we add the material conversion equation as coupling terms to balance equations.

Fig. 1 is the framework of the substance converted-balance equation coupled model. Firstly, the amount of n kinds of aerosol particles and water vapor within region Ω at time t are calculated respectively according to the initial conditions, and the water vapor and aerosols net input are computed based on zero-flux

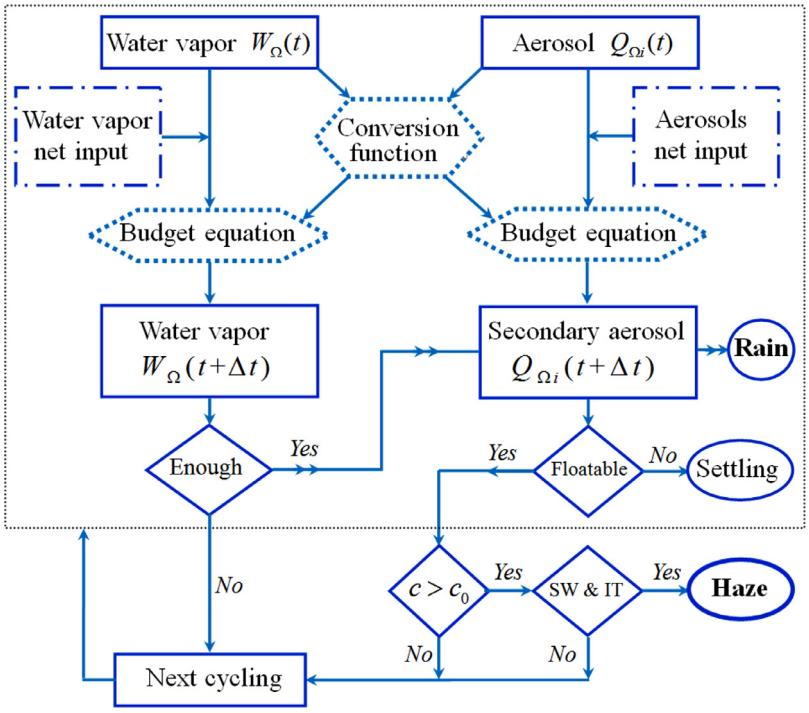

Fig. 1. The framework of matter conversion–balance equation coupled model (SW: Static wind; IT: inversion temperature; Enough: $r_H \geq 90\%$, r_H represents the air relative humidity).

boundary condition which means that no external input is imposed from outside; Secondly, we estimate the secondary aerosol particles generated from material conversion equation and give the additional items of balance equation at time $t + \Delta t$; Thirdly, we couple the additional items to the equilibrium equation to calculate the amount of water vapor and aerosol at $t + \Delta t$ moment; Then we estimate the settling velocity of various secondary particles. If the settling speed is less than a certain value, this kind of particle can be considered as suspended particulate matter and we will statistics its concentration; Finally, we diagnose whether the Fog-Haze occur according to the concentration and static wind and inversion air temperature.

In this process, the total mass of all the suspended aerosol particles at time $t + \Delta t$ also meet the balance equation

$$H_\Omega(t+\Delta t) = H_\Omega(t) + \sum_{i=1}^{n} \Delta H_{\Omega i}(t) - \sum_{i=1}^{n} H^w_{\Omega i}(t+\Delta t) - \sum_{i=1}^{n} H^T_{\Omega i}(t+\Delta t), \quad (6)$$

where $H^w_{\Omega i}(t+\Delta t)$is the additional items when the secondary aerosol particles are blown off by too heavy horizontal wind; $H^T_{\Omega i}(t+\Delta t)$ is the additional items considering the thermal uplift. Given static wind and inversion air temperature, both of them are zero, then

$$H_\Omega(t+\Delta t) = H_\Omega(t) + \sum_{i=1}^{n} \Delta H_{\Omega i}(t). \quad (7)$$

Therefore, under the conditions of calm wind and inversion temperature, scarce water vapor tends to promote the suspended aerosol particles to increase and accelerate the generation and Evolution of Fog-Haze. On the contrary, abundant ($r_H \geq 90\%$, $r_H$represents the air relative humidity) moisture being supported to the aerosol particles enlarges the precipitated particles and makes it to grow up to raindrops falling to the ground as precipitation. Once this situation forms, the haze will gradually dissipate.

3. Conclusion and discussion

In this paper, we present a mathematical model on the evolution of Fog-Haze mainly with respect to atmospheric water vapor content and aerosol particles. Under the framework of our study, one can reveal the intrinsic mechanisms on the formation of Fog-Haze. Our work is a start point on the understanding of Fog-Haze and may provide some useful measures on Fog-Haze control.

It should be noted that Fog-Haze may promote the transmission of infectious diseases, such as cholera [37,38], brucellosis [39,40], hemorrhagic fever with renal syndrome [41] and so on [42]. In this sense, when taking control measures for disease, we need to consider the effects of Fog-Haze. Analyzes of the evolution of Fog-Haze require that data to be highly precise, both in space and time, and also need complex analysis to describe them in detail. When these requirements are met, the approach appears quite useful for targeting Fog-Haze control in space and time. Such collaborations, if successful, would stimulate the further development of this emerging research area.

Acknowledgments

We are grateful for supports by both the National Science Foundation of China under the Contract (No.41375079, 41375078, 41530531) and the Ministry of Science and Technology, P. R. China under the Contract No.GYHY201506001.

References

[1] Szidat S. Sources of Asian haze. Science 2009;323:470–1.
[2] Wang X, Chen J, Sun J, et al. Severe haze episodes and seriously polluted fog water in Ji'nan, China. Sci Total Environ 2014;493:133–7.
[3] Ye B, Ji X, Yang H, Yao X, Chan CK, Cadle SH, et al. Concentration and chemical composition of PM2.5 in Shanghai for a 1-year period. Atmos Environ 2003;37:499–510.
[4] Yu X, Zhu B, Yin Y, et al. A comparative analysis of aerosol properties in dust and haze-fog days in a Chinese urban region. Atmos Res 2011;99:241–7.
[5] Han S, Wu J, Zhang Y, et al. Characteristics and formation mechanism of a winter haze–fog episode in Tianjin, China. Atmos Environ 2014;98:323–30.

[6] Feng Y, Chen Y, Guo H, Zhi G, Xiong S, Li J, et al. Characteristics of organic and elemental carbon in PM2.5 samples in Shanghai, China. Atmos Res 2009;92:434–42.
[7] Thompson G, Eidhammer T. A study of aerosol impacts on clouds and precipitation development in a large winter cyclone. J Atmos Sci 2014;71:3636–58.
[8] Fan J, Leung L R, Li Z, et al. Aerosol impacts on clouds and precipitation in eastern China: results from bin and bulk microphysics. J Geophys Res 2012;117:D16.
[9] Li G, Wang Y, Lee K H, et al. Impacts of aerosols on the development and precipitation of a mesoscale squall line. J Geophys Res 2009;114:D17.
[10] Lee S S, Donner L J, Phillips V T J, et al. The dependence of aerosol effects on clouds and precipitation on cloud-system organization, shear and stability. J Geophys Res 2008;113:D16.
[11] Si-yu C, Jian-ping H, Yun Q, et al. Effects of aerosols on autumn precipitation over mid-eastern China. J Tropical Meteorol 2014;20:242.
[12] Leng C, Zhang Q, Zhang D, et al. Variations of cloud condensation nuclei (CCN) and aerosol activity during fog–haze episode: a case study from Shanghai. Atmos Chem Phys 2014;14:12499–512.
[13] Wang C. Impact of anthropogenic absorbing aerosols on clouds and precipitation: a review of recent progresses. Atmos Res 2013;122:237–49.
[14] Gao Y, Zhang M, Liu Z, et al. Modeling the feedback between aerosol and meteorological variables in the atmospheric boundary layer during a severe fog–haze event over the North China Plain. Atmos Chem Phys 2015;15:4279–95.
[15] Szidat S. Sources of Asian haze. Science 2009;323:470–1.
[16] Podzimek J. Aerosol particle scavenging by fog and haze droplets. Studia Geophysica et Geodaetica 1998;42:540–60.
[17] Ten Brink H M, Schwartz S E, Daum P H. Efficient scavenging of aerosol sulfate by liquid-water clouds. Atmos Environ 1987;21:2035–52.
[18] Lynn B, Khain A, Rosenfeld D, et al. Effects of aerosols on precipitation from orographic clouds. J Geophys Res 2007;112:D10.
[19] Buat-Ménard P, Duce R A. Precipitation scavenging of aerosol particles over remote marine regions. Nature 1986;321:508–10.
[20] He J, Balasubramanian R. Rain-aerosol coupling in the tropical atmosphere of Southeast Asia: distribution and scavenging ratios of major ionic species. J Atmos Chem 2008;60:205–20.
[21] Jiang H, Feingold G, Sorooshian A. Effect of aerosol on the susceptibility and efficiency of precipitation in warm trade cumulus clouds. J Atmos Sci 2010;67:3525–40.
[22] Hu Y, Lin J, Zhang S, et al. Identification of the typical metal particles among haze, fog, and clear episodes in the Beijing atmosphere. Sci Total Environ 2015;511:369–80.
[23] Cheng Z, Wang S, Fu X, et al. Impact of biomass burning on haze pollution in the Yangtze River delta, China: a case study in summer 2011. Atmos Chem Phys 2014;14:4573–85.
[24] Yuan Q, Li W, Zhou S, et al. Integrated evaluation of aerosols during haze–fog episodes at one regional background site in North China Plain. Atmos Res 2015;156:102–10.
[25] Yanqiang D, Changhong C, Cheng H, et al. Anthropogenic emissions and distribution of ammonia over the Yangtze River Delta. Acta Scientiae Circumstantiae 2009;29:611–1617.
[26] Han S, Wu J, Zhang Y, et al. Characteristics and formation mechanism of a winter haze–fog episode in Tianjin, China. Atmos Environ 2014;98:323–30.
[27] Zhang J, Chen J, Yang L, et al. Indoor PM 2.5 and its chemical composition during a heavy haze–fog episode at Jinan, China. Atmos Environ 2014;99:641–9.
[28] Jialei Z, Tijian W, Junjun D, et al. An emission inventory of air pollutants from crop residue burning in Yangtze River Delta Region and its application in simulation of a heavy haze weather process. Acta Scientiae Circumstantiae 2012;32:3045–55.
[29] Xue-jun G, Chang-jin H, Yan-bo G, et al. Experimental evaluation of aerosol formation in SO 2/H 2O/air mixtures. China Environ Sci 2015;35:700–5.
[30] Ying-ying Mu, Sheng-rong Lou, Chang-hong Chen, et al. Aging and mixing state of particulate matter during aerosol pollution episode in autumn shanghai using a single particle aerosol mass spectrometer (SPAMS). Huanjing Kexue 2013;34:2071–80.
[31] Xia WW, Ti R, Zhang Z, et al. Influence factors on particle growth for on-line aerosol matrix-assisted laser desorption/ionization time-of-flight mass spectrometry. Chinese J Chem Phys 2010;23:269–73.
[32] IPCC, 2013, Climate Change 2013, The Physical Science Basis. Contribution of Working Group I to the Fifth Assessment Report of the Intergovernmental Panel on Climate Change. TF Stocker, D Qin, G-K Plattner, M Tignor, SK Allen, J Boschung, A Nauels, Y Xia, V Bex, PM Midgley(Eds), Cambridge University Press, Cambridge, United Kingdom and New York, NY, USA, p.1535.
[33] Kerr RA. The greenhouse is making the water-poor even poorer. Science 2012;336:405.
[34] Sherwood S, Fu Q. A drier future. Science 2014;343:737–9.
[35] Trenberth KE. Changes in precipitation with climate change. Clim Res 2011;47:123.
[36] Khain AP, BenMoshe N, Pokrovsky A. Factors determining the impact of aerosols on surface precipitation from clouds: An attempt at classification. J Atmos Sci 2008;65:1721–48.
[37] Sun GQ, Xie JH, Huang SH, Jin Z, Li MT, Liu L. Transmission dynamics of cholera: mathematical modeling and control strategies. Commun Nonlinear Sci Numer Simul 2017;45:235–44.
[38] Andrews JR, Basu S. Transmission dynamics and control of cholera in haiti: an epidemic model. Lancet 2011;377:1248–55.
[39] Sun GQ, Zhang ZK. Global stability for a sheep brucellosis model with immigration. Appl Math Comput 2014;246:336–45.
[40] Li MT, Sun GQ, Wu YF, Zhang J, Jin Z. Transmission dynamics of a multi-group brucellosis model with mixed cross infection in public farm. Appl Math Comput 2014;237:582–94.
[41] Li L. Monthly periodic outbreak of hemorrhagic fever with renal syndrome in China. J Biol Syst 2016;24:519–33.
[42] Xing Y, Song L, Sun GQ, Jin Z, Zhang Z. Assessing reappearance factors of H7N9 avian influenza in china. Appl Math Comput 2017;309:192–204.

晏红明,李清泉,王东阡.云南雨季的时空特征及与大气环流变化的关系[J]. 热带气象学报,2018,34(1): 12-22.

文章编号: 1004-4965(2018)01-0012-11

云南雨季的时空特征及与大气环流变化的关系

晏红明[1]，李清泉[2,3]，王东阡[2,3]

（1. 云南省气候中心，云南 昆明 650034；2. 国家气候中心 / 中国气象局气候研究开放实验室，北京 100081；
3. 南京信息工程大学气象灾害预报预警与评估协同创新中心，江苏 南京 210044）

摘　　要：为了系统了解和认识云南雨季变化的气候特征、年际特征及其影响因子,利用云南 116 个气象观测站 1961—2015 年 20 时—20 时的逐日降水资料,根据新定义的西南雨季单站标准,系统分析云南雨季变化的时空特征以及相应的大气环流特征。结果表明:(1) 对于 1981—2010 年的气候平均,云南全省平均雨季的开始和结束日期分别为 5 月 22 日和 10 月 15 日,雨季变化的空间差异较大,雨季开始大致表现为从东南向西北推进,结束则从西北和东南逐渐向西南推进，由此导致云南雨季长度和雨季总降水量变化由南至北逐渐减小;(2) 云南雨季变化的年际差异显著,全省平均雨季开始日期最早在 5 月 8 日,最晚在 6 月 8 日,结束日期最早在 9 月 30 日,最晚在 11 月 2 日,早晚相差近 1 个月;(3) 云南雨季开始日期主要受西南季风和中纬度冷空气活动的共同影响,季风建立偏早和中纬度冷空气活动频繁有利于雨季开始早,反之有利于雨季开始晚;而雨季结束日期主要受热带季风环流变化的影响,夏季风向冬季风季节转换早则云南雨季结束早,反之雨季结束晚。

关　键　词：低纬高原;西南雨季标准;雨季开始和结束;西南季风;中高纬度冷空气活动

中图分类号：P426.61.4　　**文献标识码**：A　　**Doi**：10.16032/j.issn.1004-4965.2018.01.002

1 引　　言

云南位于青藏高原向东延伸的低纬高原地区,错综复杂的地形、地貌形成了云南独特的低纬高原季风气候,在南北跨度不足 1 000 km 的范围内,从南到北包含了北热带、南亚热带、中亚热带、北亚热带、南温带、中温带、高原气候区共 7 个气候带[1]。冬季,受来自非洲干旱沙漠地区南支西风气流的影响,晴朗天气较多,气候干燥少雨;夏季,受南亚夏季风和东亚夏季风的交叉影响，气候湿润多雨。由于云南冬夏两季受不同大气环流的控制和影响,干湿季节非常分明。一般而言,11 月—次年 4 月的冬春季节为旱季，降水仅占年降水量的 10%~20%;5—10 月为雨季,80%~90%的年降水量主要集中在这一时段[2]。云南冬春季干旱发生几率较大,所谓的“十年九旱”是对云南冬春季气候最贴切的描述。春末夏初是云南大春作物栽种的关键季节，夏季又是农作物生长发育的关键时段,这时的降水多少对工农业生产有重要影响。因此,云南雨季起迄早晚、雨季长短及雨季降水多少等与工农业生产的关系非常密切，是政府决策部门以及其他相关服务单位十分关注的问题，也是气象部门需要重点研究的关键科学问题。

过去的大多数工作主要集中在对云南 5 月雨量的多少及其大气环流[3-8]、海温变化[9-10]和对流活动[11-12]等特征进行分析,得到的结论对于云南雨季开始期预报有一定指导意义，而对云南雨季变化的气候特征和年际特征，特别是云南雨季结束期的早晚、雨季持续时间以及雨季总降水量等的时空特征还缺乏系统的分析和了解，同时也很少有工作从云南雨季开始期早晚变化的角度去探讨影

收稿日期:2016-10-08;**修订日期**:2017-03-09

资助项目:国家自然科学基金面上项目(4157050542);西南区域重点项目(2014-4);云南省重点基金项目(2016FA041)共同资助

通讯作者:李清泉,女,北京市人,研究员,博士,主要从事气候诊断和模拟研究。E-mail: liqq@cma.gov.cn

响云南雨季变化的因子。近年来,为了进一步满足气象服务的需要，国家气候中心组织相关业务单位对不同区域的季节降水变化和分布特征进行了系统的分析和研究[13-16],对包括西南地区、华南地区和华北地区的雨季，以及长江和江淮地区梅雨的标准重新进行了系统的分析和定义，新定义的标准对原有标准进行了进一步改进和完善。对比分析表明,新的业务标准更合理,并增加了对雨季长度和雨季总降水量等的定义。

本文基于新的《西南雨季业务指标》规定[17],对 1961—2015 年云南地区的雨季起迄日期、雨季长度和雨季降水量等进行回算，利用回算的资料系统分析云南雨季起迄日期、雨季长度和雨季降水量变化的气候特征及年际特征，进一步探讨中高纬度大气环流异常对云南雨季的影响。以期进一步提高云南气候预测的准确率，对做好气象服务具有十分重要的现实意义。

2　资料和云南雨季的定义

2.1　资料和方法

本文所用的资料包括:(1) 国家气象信息中心提供的云南 116 个站 20 时—20 时的逐日降水资料;(2) 美国国家环境预测中心和国家大气研究中心(NCEP/ NCAR)的高、低层经向风和纬向风、高度场、地面气压等月平均再分析资料(Kalnay and Coauthors,1996),网格分辨率为 2.5 °×2.5 °[18];(3) Hadley 中心提供的全球月平均海洋资料，网格分辨率为 1.0 °×1.0 °[19]。上述资料的年限均为 1961—2015 年。气候平均统一采用 1981—2010 年的 30 年气候平均值。

本文分析方法使用了相关分析、合成分析等诊断方法,显著性检验采用 t 检验方法。

2.2　雨季标准的定义

目前对云南雨季判断标准的研究主要集中在雨季开始期[20],因此雨季开始期的判断标准相对较合理。但标准中有些更细致的内容没有具体规定,例如:仅规定了选取 5 d 中的日雨量≥10 mm 的这一天为雨季开始期，并没有考虑雨量没有出现上述情况的处理方法。另外,旧标准规定:若 6 月 30 日雨季还未开始,则人为将雨季开始日期定为 6 月 30 日。以上内容在新标准定义中均作了更细致和客观的规定。对于雨季结束期而言,旧标准是以滑动候平均雨量来定义，判断的结束日期为候,而新标准以 5 d 滑动雨量来判断,得到的结束日期为日,判断结果更为精细和客观合理。雨季长度和雨季总降水量则是新标准中补充完善的新内容。雨季新标准的定义如下。

2.2.1　雨季开始期标准

自 4 月 21 日开始,任意 5 d 滑动累计降水量(R_5)大于等于 5—10 月平均候降水量的气候平均值($\overline{R}_{5-10}/36$)的某一天为止,即:

$$K_b=(R_5/(\overline{R}_{5-10}/36))\geqslant 1 \qquad (1)$$

式中 K_b 为雨季开始日期的判别阈值,$\overline{R}_{5-10}$ 为 5—10 月降水量气候平均值。则有:

(1) 将 $K_b\geqslant 1$ 的 5 d 中降水量首次 >10 mm 的这一天(若日降水量没有出现 >10 mm 时,选降水量最大的一天)确定为雨季开始待定日,在之后的 15 d 内又出现 $K_b\geqslant 1$ 的情况，即将雨季开始待定日确定为雨季开始日，雨季开始日所在的候为雨季开始候;

(2) 若在之后的 15 d 之内仍未出现 $K_b\geqslant 1$ 的情况,则重复步骤(1),重新确定雨季开始待定日和雨季开始日;

(3) 如果计算得到的雨季开始期是 4 月 21 日,则逐日向前按步骤(1)推算符合雨季开始日条件的日期。

2.2.2　雨季结束期标准

自 9 月 21 日开始,任意 5 d 滑动累计降水量(R_5)小于等于 1—12 月平均候降水量的气候平均($\overline{R}_{1-12}/72$)为止,即:

$$K_e=(R_5/(\overline{R}_{1-12}/72))<1 \qquad (2)$$

式中,K_e 为雨季结束日期的判别阈值,$\overline{R}_{1-12}$ 为年降水量气候平均值。则有:

(1) 将 $K_e<1$ 的当天确定为雨季结束待定日,在之后的 15 d 内未再次出现 $K_e\geqslant 1$的情况，即将该雨季结束待定日确定为雨季结束日，雨季结束日所在的候为雨季结束候;

(2) 若在之后的 15 d 之内又出现 $K_e\geqslant 1$的情况,则重复步骤(1),重新确定雨季结束待定日期和雨季结束日期;

(3) 如果计算得到的雨季结束期是 9 月 21 日,则逐日向前按步骤(1)推算符合雨季结束日条件的日期。

2.2.3 雨季长度

单站雨季开始日期至结束日期(含开始日期、不含结束日期)的总天数为该站的雨季长度。

2.2.4 雨季总降水量

在单站雨季开始日期至结束日期(含开始日期、不含结束日期)时段内的降水总量为该站雨季总降水量。

2.3 选站标准

云南共有 128 个气象观测站，本分析仅选取其中的 116 站。云南气候的复杂多样性特征不仅体现在气候带的多样性、降水分布的不均匀性，降水季节变化的特征也呈现出显著差异。在云南西北的部分地区，由于西风气流的季节性南北移动以及高大山系的阻挡作用，高原南侧的部分地区在 2—3 月和 6—8 月呈现出双雨季的现象，有的地区 2—3 月降水甚至比 6—8 月降水还要明显。由于冬夏环流转换的关键季节一般出现在 4—5 月，本文的分析主要关注夏季风活动引起的大范围降水变化，2—3 月的降水并不属于季风降水。因此，为了体现季风降水的特征，我们仅选取 5—10 月降水占年降水量 80%以上的站点(116 个站)进行分析。

3 云南雨季的气候特征

3.1 雨季开始和结束日期

图 1 为云南 116 站 1981—2010 年雨季开始和结束日期的气候平均分布，图中的雨季开始日期中前一位为月份，后两位为日期；结束日期中前两位为月份，后两位为日期。1981—2010 年云南全省平均的雨季开始和结束日期分别为 5 月 22 日和 10 月 15 日。

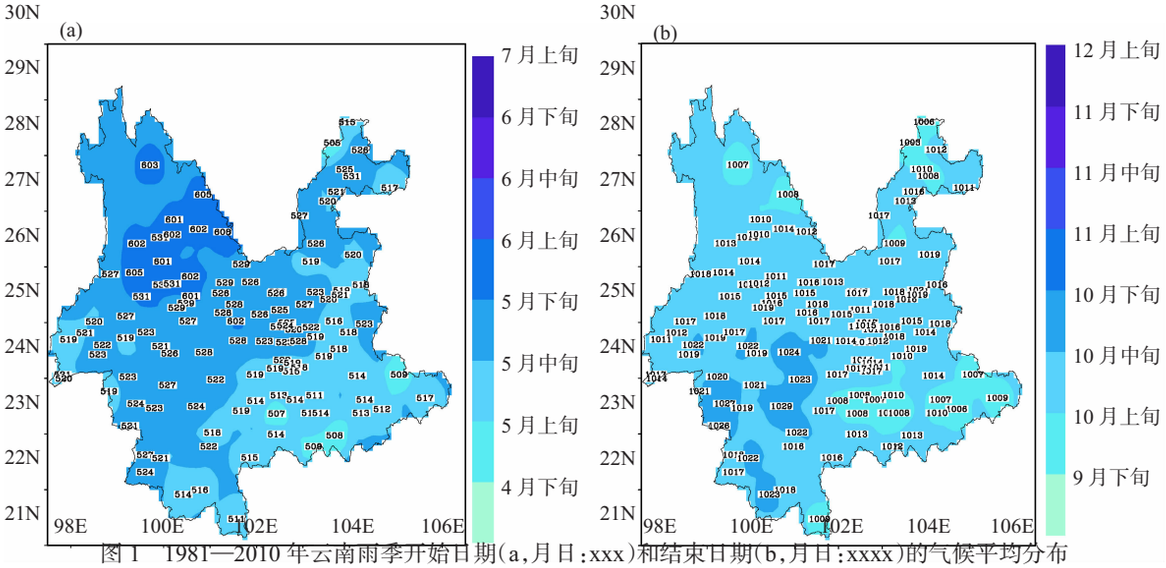

图 1 1981—2010 年云南雨季开始日期(a,月日:xxx)和结束日期(b,月日:xxxx)的气候平均分布

从空间分布来看，云南雨季开始和结束日期的区域差异较显著。图 1a 为云南雨季开始日期的变化，云南雨季开始的过程一直从 5 月上旬持续至 6 月上旬，开始最早日期(5 月 5 日)和最晚日期(6 月 8 日)相差 34 d。云南雨季最早于 5 月上旬在东南部和东北部的部分地区开始，东南部的大部分地区、西南南部和西部边缘的部分地区雨季于 5 月中旬开始，中西部和东北部的大部分地区雨季于 5 月下旬开始，雨季开始最晚的地区在丽江和大理，6 月上旬才开始。就云南雨季开始日期的总体推进过程而言，主要呈现出由东南向西北推进的特征。

云南雨季结束日期的变化(图 1b)同样呈现显著的区域差异，结束最早(10 月 6 日)和最晚(10 月 29 日)的日期相差 23 d。除西南部分地区的雨季于 10 月下旬结束外，其余大部分地区的雨季于 10 月上旬和中旬结束，10 月上旬雨季结束的区域主要分布在东南部、东部和西北部。与云南雨季开始日期的总体推进过程不同，雨季结束日期的推进过程大致呈从西北和东南逐渐向西南推进，西南部分地区的雨季最晚结束。

3.2 雨季长度和总降水量

图 2 分别为 1981—2010 年云南雨季长度和雨季总降水量的 30 年气候平均分布。云南雨季持续时间（图 2a）最长的区域主要分布在南部和东部,大部分地区超过 150 d,部分地区超过 160 d;西北部的丽江和大理的雨季持续时间较短，部分地区不足 130 d;中部大部分地区的雨季持续时间为 140~150 d。全省平均雨季长度为 146 d。

云南雨季总降水量(图 2b)与雨季长度的变化有很好的一致性，雨季持续时间较长的地区降水量多，反之则降水量少。雨季总降水超过 1 000 mm 的区域主要集中在云南南部和西南部，部分地区超过 1 800 mm;最少的区域主要集中在云南中部、西北的南部和东北部地区,雨季总降水量约 600~800 mm，其余大部分地区的降水量为 800~1 000 mm。全省平均雨季总降水量为 883.2 mm。

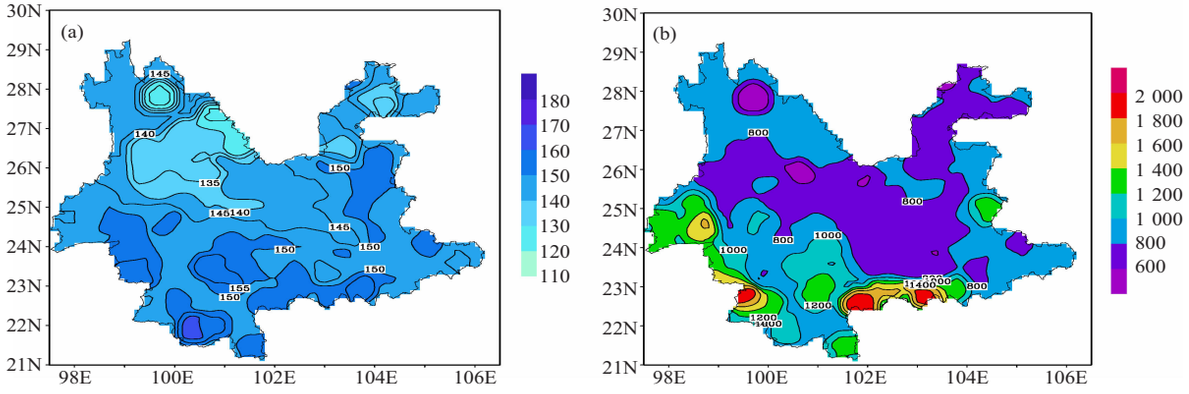

图 2　1981—2010 年云南雨季长度(a,单位:d)和雨季总降水量(b,单位:mm)的气候平均分布

4　云南雨季的年际变化特征

4.1　云南雨季的开始和结束

以上分析表明了云南雨季变化的总体气候特征,下面进一步分析云南雨季的年际变化特征。图 3 为 1961—2015 年全省平均的雨季开始和结束日期距平变化。云南雨季开始和结束日期的年际差异较大。相对全省平均雨季开始日期(5 月 22 日),全省雨季开始最早是 2008 年(图 3a),平均日期为 5 月 8 日,比多年平均雨季开始日期偏早 14 d;全省雨季开始最晚的是 1977 年，平均日期为 6 月 8 日,比多年平均雨季开始日期偏晚 17 d;雨季开始最早和最晚日期相差 1 个月。根据业务规定,本文以大于(小于)5 d 来定义云南雨季开始期偏早(偏晚)，则云南雨季开始偏晚年有 1963、1967、1969、1977、1979、1982、1983、1986、1987、1988、1992、1997、1998、2005、2010、2011、2012、2014、2015 年;偏早年有 1964、1974、1976、1978、1981、1984、1985、1990、1996、1999、2000、2001、2002、2004、2006、2007、2008 年。

雨季结束期的变化同样呈现出显著的年际差异,相对于全省平均雨季结束日期(10 月 15 日),1998 年雨季结束最早(图 3b),全省平均雨季结束日期在 9 月 30 日,比多年平均雨季结束日期偏早 15 d;结束最晚是 1965 年,全省平均雨季结束日期在 11 月 2 日，比多年平均雨季结束日期偏晚 17 d;雨季结束最早和最晚相差 32 d。同样以大于(小于)5 d 来定义云南雨季结束期偏早(偏晚),则云南雨季结束偏早年有 1969、1972、1973、1974、1975、1976、1981、1985、1994、1998、1999、2003、2004、2009、2011、2012、2014 年；偏晚年有 1963、1965、1967、1968、1982、1986、1989、1990、1991、1992、2001、2006、2010 年。

从 1961—2015 年云南省平均雨季开始和结束日期的年际变化来看,尽管年际差异较大,但多数年份雨季的开始日主要集中在 5 月，结束日主要集中在 10 月。分析云南雨季开始和结束日期早晚年份 5 月和 10 月降水距平百分率合成分布(图略)可以看到,云南各地 5 月和 10 月的降水变化与雨季开始和结束早晚的变化密切联系：雨季开始早(晚)年,5 月降水偏多(少);雨季结束早(晚)年,10 月降水偏少(多)。

4.2　云南雨季长度和雨季降水量

图 4 为全省平均雨季长度和雨季总降水量的年际变化。雨季长度变化(图 4a)的年际差异较大,

2001 年雨季最长，为 171 d，比多年气候平均（146 d）偏多 25 d；1998 年雨季最短，仅为 124 d，比多年气候平均偏少 22 d。尽管年代际尺度上雨季长度变化呈弱的增大趋势，但 2009—2015 年雨季长度出现阶段性减小，2009、2011、2012、2014 和2015 年雨季长度均低于 135 d。

雨季总降水量（图 4b）的变化趋势不明显，主要表现为年际差异特征，2001 年雨季降水最多（1114.5 mm），2011 年雨季降水最少（629.3 mm），二者相差近 500 mm。2009—2015 年雨季总降水量均低于气候平均值，其中，2011 和 2009 年云南雨季总降水量不足 700 mm，分别为 1961 年以来雨季降水的最少和次少年份。

对比云南雨季长度和雨季总降水量的变化，虽然在大部分年份两者变化的一致性较好，正相关高达 0.64，即雨季长度长（短），云南大部分地区的降水偏多（少）。但有些年也出现相反的变化趋势，例如 1974 年云南雨季长度偏小，雨季降水量却偏多；2013 年雨季长度偏大，雨季降水量反而偏少。

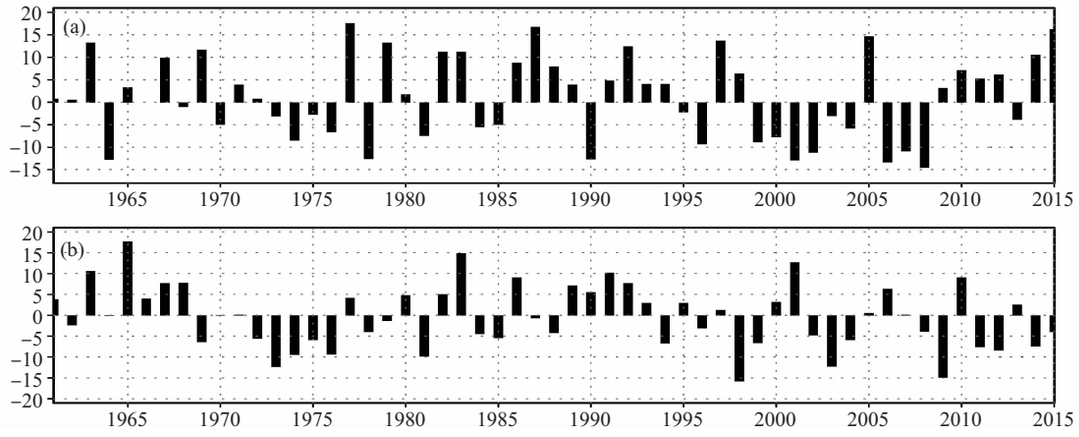

图 3 1961—2015 年云南雨季开始日期（a）和结束日期（b）的距平变化

单位：d。横坐标为年份。负值表示偏早；正值表示偏晚。

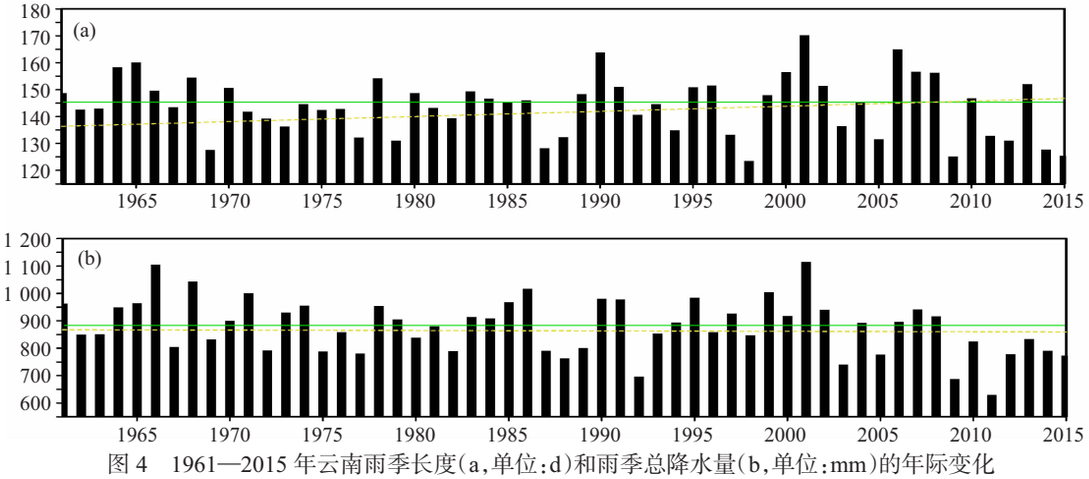

图 4 1961—2015 年云南雨季长度（a，单位：d）和雨季总降水量（b，单位：mm）的年际变化

横坐标为年份。实线为多年平均，虚线为线性趋势。

5 高低层大气环流异常对云南雨季的影响

以上分析表明，云南雨季变化的年际差异较大，下面进一步通过对比分析在雨季异常早、晚年季节转换关键期的 5 月和 10 月大气环流变化的差异，来进一步探讨高低层大气环流异常对云南雨季变化的影响。

5.1 雨季开始期

低纬高原大范围降水与水汽和冷空气的交汇影响密切联系，尤其在干湿转换的关键季节，晏红

明等[4]的分析强调了孟加拉湾季风与中纬度冷空气活动的共同作用对云南 5 月雨量的重要影响。图 5 为雨季开始早、晚年 5 月低层 850 hPa 和高层 200 hPa 距平风场。在雨季开始早年（图 5a），850 hPa 有一支异常气流从南半球经索马里越赤道进入北半球并转向东，经阿拉伯海和孟加拉湾影响云南和中南半岛，孟加拉湾北部为气旋性环流控制，同时在华南沿海有一支异常偏东北气流由中纬度南下至低纬度转向为偏西气流影响云南，云南为异常西南气流和偏东气流的交汇辐合区。而在雨季开始晚年（图 5b），850 hPa 异常气流变化刚好相反，孟加拉湾为异常反气旋性环流控制，云南受异常反气旋环流东北侧的西北气流影响，该异常西北气流在缅甸和云南南部分流为两支，一支转向西经孟加拉湾、阿拉伯海、索马里进入南半球，一支则于中南半岛北部转向北从华南沿海流向中高纬度地区，云南为气流辐散区。另外，雨季开始早、晚年低层环流差异比较显著的区域不仅局限在云南、华南和北印度洋地区，西北太平洋和高纬度乌拉尔山以东地区的环流变化也表现出明显不同的特征：西北太平洋地区，雨季开始早（晚）年，西北太平洋为异常气旋（反气旋），有利于西太平洋副热带高压偏南（偏北）；乌拉尔山以东地区，雨季开始偏早（年）为异常反气旋（气旋）控制（图 5a、5b）。以上两个地区的环流变化与东亚中高纬度地区的冷空气活动联系密切，雨季开始偏晚年这种联系表现得更清楚：自中南半岛北部转向北沿华南至东北的异常偏南气流与贝加尔湖 - 巴尔喀什湖之间的异常气旋性环流的变化有关，西北太平洋地区副热带高压南北位置的变化也与中高纬度地区冷空气活动南北位置的变化密切联系（图 5b）。

在多年气候平均状态下，初夏索马里越赤道气流经阿拉伯海和孟加拉湾进入我国，图 5a、5b 中的雨季开始早、晚年南亚区域异常气流与多年气候平均场的叠加将会进一步加强（减弱）索马里越赤道气流，进而影响孟加拉湾季风活动。晏红明等[21]最近分析孟加拉湾季风爆发的异常特征，得到了孟加拉湾季风爆发的时间系列，发现孟加拉湾季风爆发与本文云南雨季开始日期的相关为 0.33，超过 0.02 的显著性水平检验（r=0.31）。另外，北印度洋地区孟加拉湾季风爆发早、晚年的环流变化与云南雨季开始早、晚年的环流形势非常类似（图略），进一步表明了孟加拉湾季风爆发早、晚对云南雨季开始期变化的重要影响。

南亚高压是亚洲季风系统的重要成员，同时也是影响东亚气候的重要大尺度环流系统，有明显的季节变化特征。在干湿转换季节，南亚高压由西太平洋西移至青藏高原标志着亚洲夏季风的全面建立。晏红明等[13]的分析表明，在气候平均场上，4 月 4—5 候南亚高压突变特征明显，从赤道西太平洋 160 °E 西移至中南半岛 100 °E 附近，之后逐渐向西北移动，6 月上旬移动到青藏高原。云南雨季开始早、晚年的 200 hPa 青藏高原上空环流变化差异最明显，雨季开始偏早年（图 5c），青藏高原为异常反气旋，有利于南亚高压和亚洲夏季风建立偏早。与此相反，雨季开始偏晚年（图 5d），青藏高原为异常气旋，有利于南亚高压和亚洲夏季风建立偏晚。雨季开始早、晚年欧亚中高纬度地区的环流差异也较明显，特别是欧洲区域的环流异常。雨季开始早年欧洲为异常气旋，开始晚年为异常反气旋。欧洲与亚洲区域的环流异常是密切联系的，这种联系在雨季开始晚年表现得尤为明显，从欧洲至东亚沿海为反气旋 - 气旋 - 反气旋（A-C-A）异常波列，这些异常波列的变化与中高纬度冷空气活动有一定联系。

夏季风携带的水汽是中国降水的重要水汽来源，亚洲夏季风爆发早、晚必然会影响季风区的水汽输送异常，进而影响降水变化。图 6a、6b 为云南雨季开始早、晚年 5 月地面至 300 hPa 的整层水汽通量及其散度的距平合成场。雨季开始早、晚年孟加拉湾至云南的水汽通量散度有显著差异：云南及附近区域在雨季开始偏早年为水汽输送辐合区，雨季开始晚年为水汽输送辐散区。其中，水汽输送散度变化最明显的区域位于滇缅之间。表明干湿转换季节季风水汽输送异常对云南雨季开始期早、晚的重要影响。另外，从相应水汽输送距平的方向看到，云南及附近区域水汽输送与来自孟加拉湾区域以及南海区域季风气流的变化有密切联系。

另外，雨季开始早、晚年的高低层环流差异不仅表明低纬度季风环流对云南雨季的影响，中高纬度地区冷空气的活动也起着十分重要的作用。由雨季开始期与海平面气压场和地面气温的相关场（图 7）发现，云南雨季开始期与东亚海平面气压场和温度场的变化关系显著。雨季开始早年（图

7a)，东亚地区大陆冷高压偏强，且活动位置偏南；而雨季开始晚年(图 7b)，大陆冷高压的活动刚好相反。云南雨季开始期的变化与西南、华南及中南半岛地面温度的变化密切联系，雨季开始早年，上述地区的气温偏低，开始晚年则气温偏高，表明了冷空气活动与云南雨季开始早、晚密切联系。

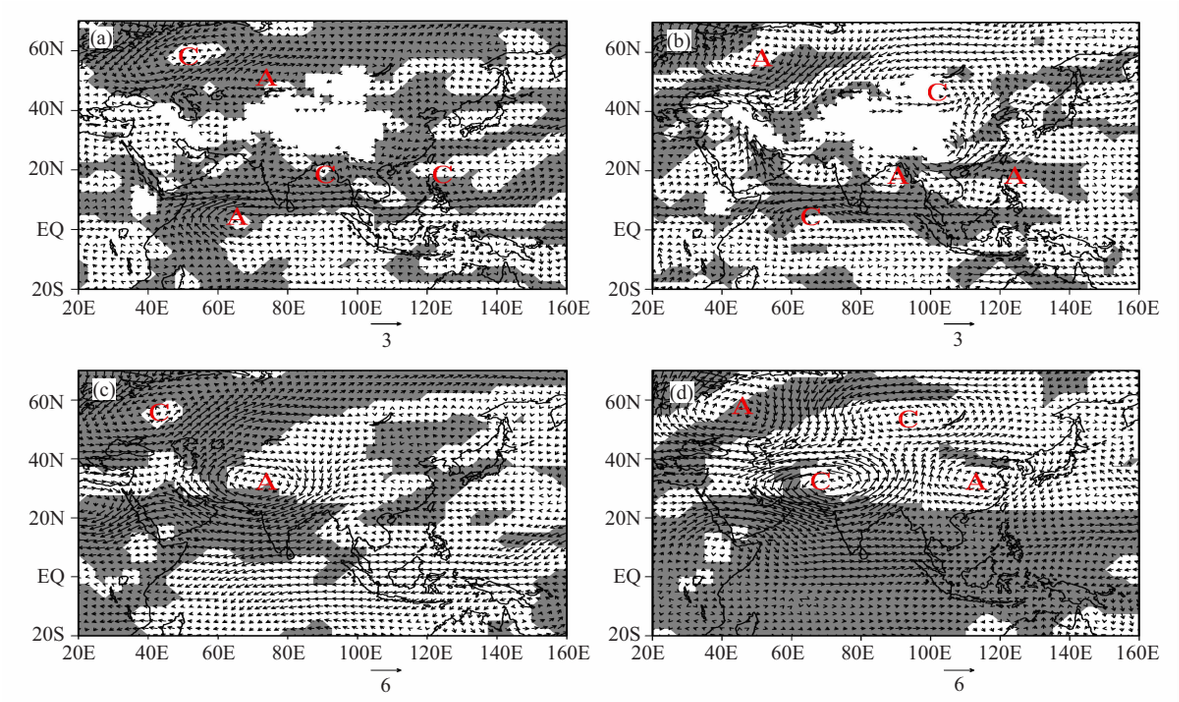

图 5 云南雨季开始早年(a、c)、晚年(b、d)5 月的 850 hPa(a、b)和 200 hPa(c、d)的距平风合成场

单位：m/s。阴影区表示通过 0.05 显著性水平检验的区域。

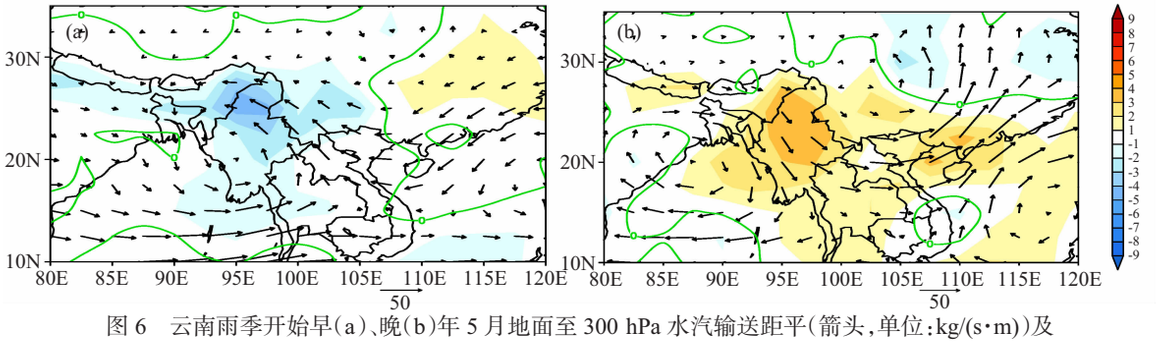

图 6 云南雨季开始早(a)、晚(b)年 5 月地面至 300 hPa 水汽输送距平(箭头，单位：kg/(s·m))及通量散度距平(阴影，单位：10^{-5} kg/(s·m^2))合成场

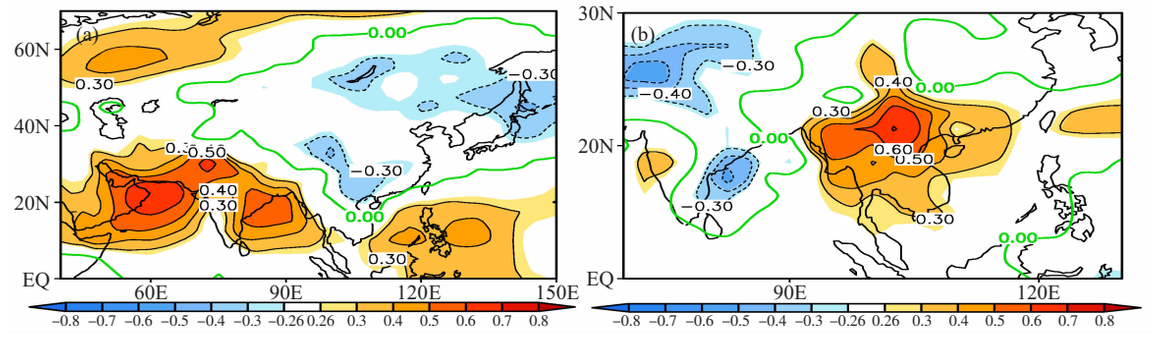

图 7 1961—2015 年云南雨季开始期与 5 月海平面气压场(a)和地面温度场(b)的相关

阴影区表示相关通过 0.05 显著性水平检验的区域。

以上分析表明,低纬度季风爆发早、晚引起的水汽输送异常和中高纬度冷空气的异常活动对云南雨季开始早、晚的重要影响,那么雨季开始早、晚年前期的环流变化是否会表现出类似的前兆信号特征?图 8 为云南雨季开始日期与 3 月和 4 月高、低层风的相关。雨季开始期与前期 850 hPa 赤道印度洋地区的纬向风、孟加拉湾北部和西北太平洋地区的环流变化联系紧密(图 8a、8b)。雨季开始偏晚(早)年前期,赤道印度洋为东风(西风)异常,孟加拉湾为异常反气旋(气旋),西北太平洋为异常反气旋(气旋)环流,赤道西太平洋为异常气旋(反气旋)环流。赤道西太平洋与西北太平洋地区的环流变化刚好相反,其变化有利于雨季开始偏晚(早)年西太平洋副热带高压偏弱(强)。在 200 hPa(图 8c、8d),云南雨季开始偏晚(早)年,前期青藏高原上空的环流也表现出显著的差异,雨季开始晚(早)年青藏高原为异常气旋(反气旋)。雨季开始早、晚年前期 3—4 月的环流异常与 5 月的环流异常有十分类似的特征,特别在印度洋地区。因此,在气候预测中可以通过分析前期印度洋、西太平洋以及青藏高原上空的环流异常特征来预报后期云南雨季开始早晚的变化。

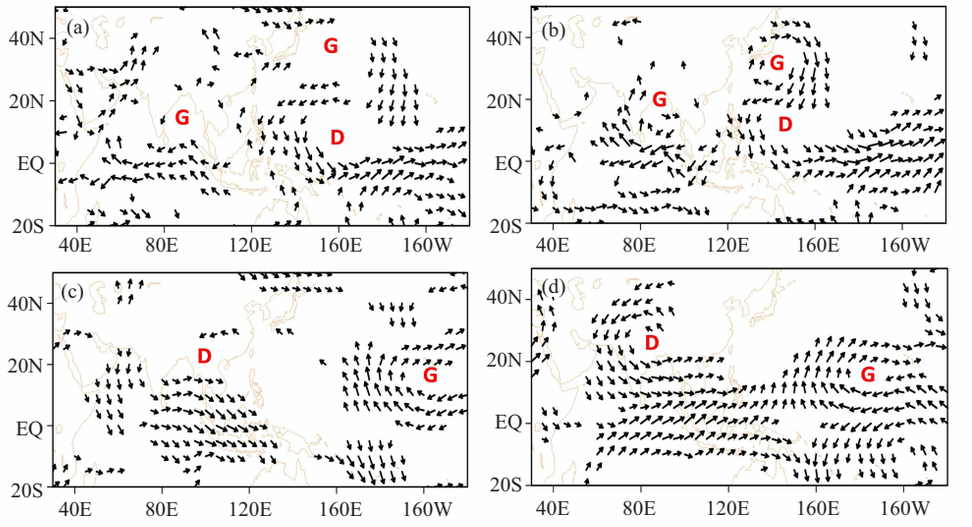

图 8　1961—2015 年云南雨季开始日期与 3 月(a、c)和 4 月(b、d)850 hPa(a、b)和 200 hPa(c、d)风场的相关

矢量表示相关风场通过 0.05 显著性水平检验。

5.2　雨季结束期

雨季结束早、晚年高低层大气环流也表现出明显不同的特征。在低层 850 hPa 异常风场上(图 9a),雨季结束早年南海-阿拉伯海为异常反气旋环流带,其南侧的异常东风气流一直从菲律宾南侧向西延伸至阿拉伯海南部,减弱了热带印度洋向东亚地区的水汽输送,低纬高原地区主要受来自高原南侧的异常西风气流控制;雨季结束偏晚年(图 9b),南海-印度半岛为异常反气旋环流,中心位于南海附近,其南侧的异常东风仅从中南半岛南部向西延伸至孟加拉湾南部,并在孟加拉湾东部转向北从而影响低纬高原地区,该异常气流来自孟加拉湾,携带的水汽含量较大。比较雨季结束早、晚年低层 850 hPa 异常流场(图 9a、9b)及相应的整层水汽通量散度场(图 10),印度半岛-南海地区的环流差异是最明显的,雨季结束偏早年,印度半岛-南海为异常反气旋环流带,影响云南的异常偏西气流来自青藏高原,水汽含量少,云南大部分地区为水汽辐散;而雨季结束偏晚年,云南受来自孟加拉湾东部的异常偏南气流影响,水汽含量大,云南区域为水汽输送辐合。

晏红明等[13]的分析曾指出夏季风的结束主要是由于东亚南部地区的偏东气流逐渐向西推进取代东南亚地区的西风气流。从图 9a、9b 看到,雨季结束偏早年,10 月印度洋赤道附近的异常东风向西扩展至 50 °E 附近,而偏晚年异常东风仅向西扩展至 80 °E 附近。异常场与多年气候平均场叠加,雨季结束偏早年的环流异常有可能使西南季风撤退早,结束晚年则有可能导致西南季风撤退晚。进一步比较雨季结束早、晚年低层 850 hPa 东亚东部地区的环流变化可知,中国中东部地区均为一致的异常南风,环流变化的差异并不十分明

显。表明影响云南雨季结束的因子主要是热带地区的环流异常及由此引起的水汽输送变化，而中高纬度地区冷空气活动并不是主要的影响因子。云南雨季结束日期与 10 月地面温度场的相关也同样表明了雨季结束日期变化与东亚地区冷空气活动的关系很弱(图略)。

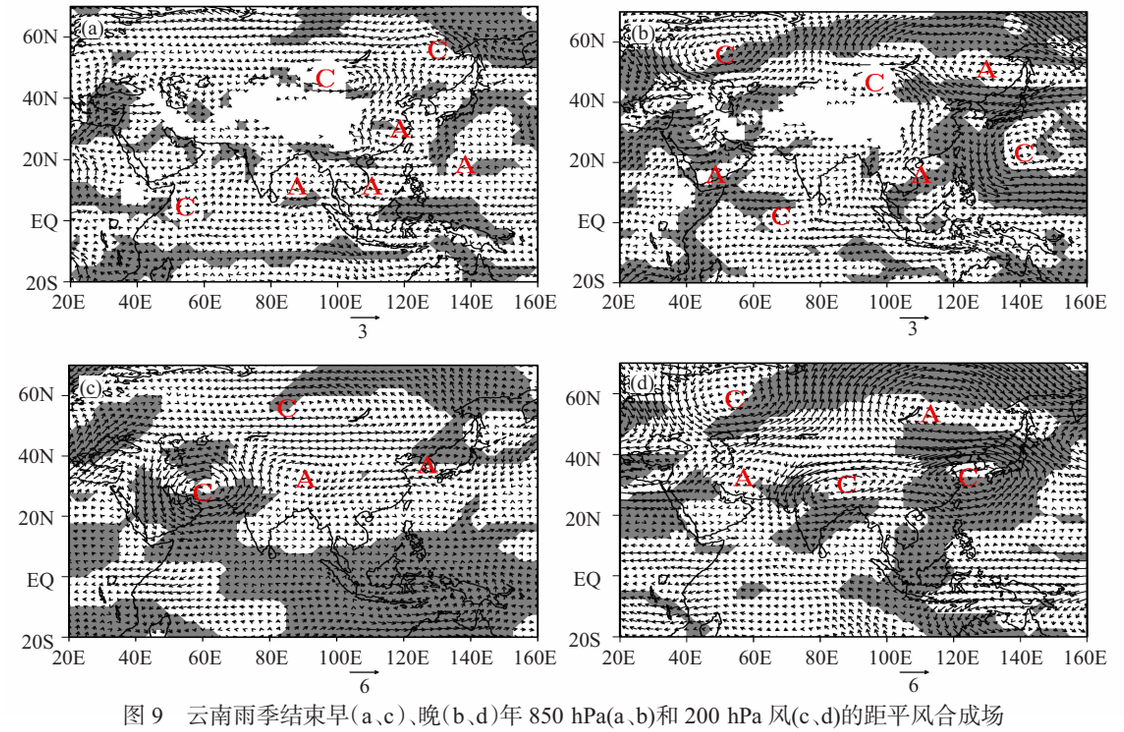

图 9 云南雨季结束早(a、c)、晚(b、d)年 850 hPa(a、b)和 200 hPa 风(c、d)的距平风合成场

阴影区为通过 0.05 显著性水平检验的区域。

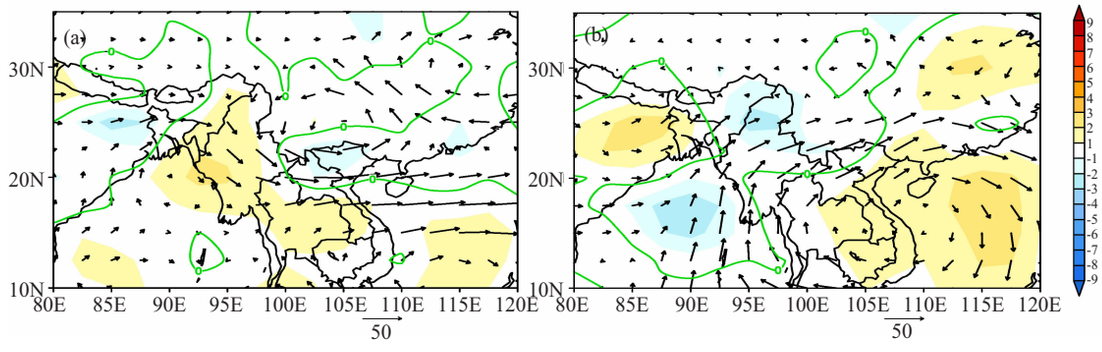

图 10 云南雨季结束早(a)、晚(b)年 10 月整层水汽输送距平(矢量,单位 kg/(s·m))以及通量散度距平合成场(阴影,单位:10^{-5} kg/(s·m^2))

高层 200 hPa 南亚高压季节性变化同样可以反映季风环流的季节转换异常。况雪源等[22]的分析指出夏季风向冬季风转换的季节主要出现 58—60 候(10 月 4—6 候),这期间南亚高压中心从位于 20 °N 以北的青藏高原上空逐渐向东南移至 20 °N 以南的西太平洋上空。对比雨季结束早、晚年 10 月 200 hPa 距平风场(图 9c、9d)可以看到,差异最明显的区域出现青藏高原上空，雨季结束早(晚)年,青藏高原上空为 C-A(A-C)异常环流分布,有利于南亚高压活动位置偏东(西),相应地可能导致夏季风向冬季风转换的季节偏早(晚)。进一步表明了季风活动的异常变化对云南雨季结束期早晚的重要影响。

6 总结与讨论

本文根据新定义的西南雨季标准，回算 1961—2015 年云南雨季开始日期、结束日期、雨季

长度和雨季总降水量，系统分析这些要素的气候特征及年际变化特征，并探讨云南雨季开始和结束日期与关键期的高、低层大气环流变化的关系。

（1）云南全省平均雨季开始日期为 5 月 22 日，雨季开始推进过程总体表现为从东南逐渐向西北推进，东南部地区的雨季一般于 5 月上旬开始,而西北部地区的雨季一般于 6 月上旬开始。云南全省平均雨季结束日期为 10 月 15 日，雨季结束推进过程呈现出由西北和东南逐渐向西南推进的特征,西北和东南地区的雨季一般于 10 月上旬结束,西南地区雨季一般于 10 月下旬结束。

（2）云南雨季开始和结束日期的年际差异非常显著。全省平均雨季开始日期最早在 5 月 8 日,最晚在 6 月 8 日；雨季结束最早在 9 月 30 日,最晚在 11 月 2 日,开始和结束日期的年际差异可高达 1 个月。

（3）云南雨季开始早、晚与西南季风活动和中高纬度冷空气的共同影响密切联系。雨季开始偏早年,西南季风建立早,中纬度地区有冷空气南下配合影响,而雨季开始偏晚年,西南季风建立偏晚,中纬度地区的冷空气活动较弱,对低纬高原地区的影响较小。

（4）季风环流季节转换早、晚是通过影响热带海洋向东亚地区的水汽输送异常进而影响云南雨季结束日期的变化，夏季风向冬季风季节转换早(晚)则云南雨季结束早(晚)。

（5）云南雨季长度变化的南北差异明显,呈现出由南至北逐渐减少的特征，南部大部分区域的雨季持续时间较长,超过 150 d(约 5 个月),北部地区尤其是丽江和大理的雨季持续时间较短,不足 130 d(约 4 个月),中部的大部地区雨季持续时间在 140~150 d 左右(约 4 个半月)。雨季降水与雨季长度变化有较好的一致性，雨季长度较长(短)则相应的雨季总降水量较多(少)。

受亚洲季风活动的影响，我国大部分地区的气候有明显的干湿之分,怎样来定义一个区域干、湿季节转换的关键日期对于气象服务而言是比较关键的。近年来,为了满足气象服务需求,在国家气候中心的技术指导下，不同地理区域相应开展了雨季标准的研究,并取得十分显著的成果,特别是梅雨标准、西南雨季标准、华北雨季标准和华西秋雨标准的建立和不断完善，为于气象服务和气候预测工作提供了很好的指导作用。因此,根据新的雨季标准有必要进一步开展相应区域雨季变化的时空特征及其相应影响因子的研究。云南位于我国西南低纬高原地区，不仅影响系统与我国东部地区差异明显,降水的区域差异也非常明显。虽然本文研究得到热带季风和中高纬度环流异常与云南雨季开始和结束早晚的关系，但是这些环流系统的相互配合及其对低纬高原地区雨季影响的物理过程等比较复杂，很多问题还有待于进一步研究。例如西太平洋副热带高压是亚洲系统的重要成员，季节尺度内其东西位置的异常对云南雨季变化有非常显著的影响,但到目前为止,对西太平洋副热带高压季节内振荡与云南降水变化的关系还不清楚。另外,西南季风是影响低纬高原地区雨季降水的重要因子，但主汛期季风的强弱以及向北推进位置的变化、高低纬度环流相互联系等对低纬高原地区降水异常的影响还缺乏深入研究,有必要进一步加强这方面的工作。

另外，热带海洋温度通过影响热带季风环流异常,对云南雨季也有重要影响,特别是对云南雨季开始期的影响。由于本文篇幅所限,关于热带海温变化的影响还未涉及，将在下一步的工作中重点讨论热带海温异常对云南雨季变化的影响。

参　考　文　献:

[1] 王宇. 云南山地气候[M]. 云南:云南科技出版社, 2005:14-33.
[2] 程建刚, 晏红明, 严华生, 等. 云南重大气候灾害特征和成因分析[M]. 北京: 气象出版社, 2009.
[3] 严华生, 张青, 尤卫红. 大气环流变化对云南 5 月雨量的影响及其预报[J]. 高原气象, 1994, 13(2): 217-222.
[4] 晏红明, 肖子牛, 王灵. 孟加拉湾季风活动与云南 5 月降雨量[J]. 高原气象, 2003, 22(6): 624-630.
[5] 刘瑜, 马振锋, 陶云, 等. 云南 2002 年雨季偏早的环流特征分析[J]. 高原气象, 2003, 22(S1): 102-108.
[6] 琚建华, 李绚丽. 云南初夏降水与前期大气环流的关系[J]. 高原气象, 1999, 18(1): 63-70.
[7] 晏红明, 段旭, 程建刚. 2005 年春季云南异常干旱的成因分析[J]. 热带气象学报, 2007, 23(3): 300-306.
[8] 陈艳, 丁一汇, 陶云, 等. 云南雨季开始期东亚副热带西风急流变化和冷空气活动[J]. 热带气象学报, 2015, 31(5): 577-587.
[9] 谭晶, 王彰贵, 黄荣辉, 等. 云南雨季降水异常的热带海温和大气环流异常分析[J]. 热带海洋学报, 2015, 34(2): 15-23.

[10] 晏红明, 杞明辉, 肖子牛. 云南 5 月雨量与热带海温异常及亚洲季风变化的关系[J]. 应用气象学报, 2001, 12(3): 368-376.
[11] 解明恩, 鲁亚斌, 程建刚, 等. 云南雨季开始期与 5 月雨量的 TBB 特征[J]. 高原气象, 2006, 25(2): 319-324.
[12] 肖子牛, 温敏. 云南 5 月降水量与前期季节内振荡活动相互关系的分析研究[J]. 大气科学, 1999, 23(2): 177-183.
[13] 晏红明, 李清泉, 孙丞虎, 等. 中国西南区域雨季开始和结束日期划分标准的研究[J]. 大气科学, 2013, 37(5): 1111-1128.
[14] 房一禾, 龚志强, 赵连伟, 等. 中国东北区域盛夏雨季的客观识别[J]. 物理学报, 2014, 63(20): 418-429.
[15] 强学民, 杨修群. 华南前汛期开始和结束日期的划分[J]. 地球物理学报, 2008, 51(5): 1333-1345.
[16] 梁萍, 丁一汇, 何金海, 等. 淮区域梅雨的划分指标研究[J]. 大气科学, 2010, 34(2): 418-428.
[17] 国家气候中心. 气象行业标准, QX/T-2014-24[S].
[18] KALNAY E, KANAMITSU M, KISTLER R, et al. The NCEP/NCAR 40-year reanalysis project[J]. Bull Amer Meteor Soc, 1996, 77(3): 437-472.
[19] RAYNER N A, PARKER D E, HORTON E B, et al. Global analyses of SST, sea ice and night air temperature since the late nineteenth century[J]. J Geophys Res, 2003, 108(D14): 4 407-4 437.
[20] 刘瑜, 陶云. 云南雨季开始期标准的再研究[J]. 云南气象, 2004, 2(1): 11-13.
[21] 晏红明, 孙丞虎, 李蕊, 等. 孟加拉湾夏季风爆发的气候特征及其判断指标的研究[J]. 地球物理学报, 待刊.
[22] 况雪源, 张耀存, 刘健. 秋冬季节转换期东亚环流变化特征及机制分析[J]. 高原气象, 2008, 27(1): 17-25.

STUDIES ON SPATIAL–TEMPORAL CHARACTERISTICS OF YUNNAN RAINY SEASON AND ITS RELATIONSHIP WITH ATMOSPHERIC CIRCULATION

YAN Hong-ming[1], LI Qing-quan[2, 3], WANG Dong-qian[2, 3]

(1. Yunnan Climate Center, Kunming 650034, China; 2. Laboratory for Climate Studies, National Climate Center, China Meteorotogical Administration, Beijing 100081, China; 3. Collaborative Innovation Center on Forecast and Evaluation of Meteorological Disasters, NISTN, Nanjing 210044, China)

Abstract: Based on the station standard of southwest rainfall season, the temporal and spatial features of Yunnan rainy seasons were investigated using 116 meteorological observation stations data from 1951-2015. At the same time, the influence of atmospheric circulation on Yunnan rainy seasons were further studied. The results are shown as follows: (1) For the 30-year (1981—2010) climatic mean, the beginning and ending date of Yunnan averaged rainy seasons are respectively on May 22 and October 15. The spatial differences of Yunnan rainy season variation are obvious in different region. The rainy season begins gradually from the southeast to the northwest and ends gradually from the northwest and southeast to the southwest, causing the length and total precipitation of the rainy season to decrease gradually from the south to the north; (2) For the beginning and ending date of annual rainy seasonsin Yunnan for 1961—2015, the earliest beginning date is May 8th and the latest date is June 8th. The endingdate is as early as September 30th and the latest November 2nd; (3) The changes of Yunnan rainy seasons are influenced jointly by the southwest monsoon and mid-latitude cold air. The early (late) establishment of southwest monsoon and frequent influence of cold air coming from the mid-latitude region may result in an early (late) rainy season. Different from the start of the rainy season, the end of a Yunnan rainy season is mainly affected by the tropical monsoon circulation. With early (late) shift of seasonal circulation from summer monsoon to winter monsoon, the Yunnan rainy season ends early (late).

Key words: low-latitude plateau; criterion of Yunnan rainy season; beginning and ending of rainy season; southwest monsoon; cold air activitiesin mid-high latitudes

杨柳，赵俊虎，封国林. 2018. 中国东部季风区夏季四类雨型的水汽输送特征及差异 [J]. 大气科学, 42 (1): 81−95. Yang Liu, Zhao Junhu, Feng Guolin. 2018. Characteristics and differences of summertime moisture transport associated with four rainfall patterns over eastern China monsoon region [J]. Chinese Journal of Atmospheric Sciences (in Chinese), 42 (1): 81−95, doi:10.3878/j.issn.1006-9895.1706.16273.

中国东部季风区夏季四类雨型的水汽输送特征及差异

杨柳[1, 2] 赵俊虎[2] 封国林[1, 2]

1 扬州大学物理科学与技术学院，江苏扬州 225002

2 国家气候中心中国气象局气候研究开放实验室，北京 100081

摘 要 利用 1951～2015 年 NCEP/NCAR 再分析逐日资料和中国 160 站月降水观测资料，及中国东部季风区夏季四类雨型（北方型、中间型、长江型和华南型）的划分结果，分析了东亚水汽输送与中国东部季风区夏季降水的关系，比较了四类雨型的水汽输送、收支特征及其差异，结果表明：（1）夏季影响中国东部季风区的水汽通道主要有以下 6 条：印度洋通道，表征印度季风区偏南的西风水汽输送；高原南侧通道，表征印度季风区偏北的西风水汽输送；太平洋通道，表征由西太平洋副热带高压（副高）带来的西太平洋的水汽；西风带通道，表征西风带的水汽输送；孟加拉湾通道，表征来自孟加拉湾向北的水汽输送；南海通道，表征来自印度洋和孟加拉湾在中南半岛转向及来自南海的水汽；与中国东部不同地区降水异常相联系的水汽通道存在明显的差异，且同一条水汽通道在夏季不同阶段与降水的关系也不尽相同。（2）四类雨型的水汽输送和收支特征有明显的差异，华北盛夏降水主要受亚洲季风水汽输送的影响，其次是西风带水汽输送，北方型年二者往往偏强，尤其是季风水汽输送增加一倍以上，贡献也明显增加，20 世纪 70 年代中期之后，季风水汽输送显著减弱，西风带水汽输送的重要性相对增大；淮河流域夏季降水异常主要受太平洋通道水汽输送异常的主导，其次是高原南侧通道水汽输送，二者偏强并在淮河流域辐合时，淮河流域降水偏多形成中间型年；长江中下游地区夏季降水主要受太平洋通道水汽输送异常的主导，长江型年，副高西北侧的西南水汽输送异常加强，并与北方冷空气异常在长江中下游地区辐合，区域为正的水汽净收支；华南地区夏季降水则受印度洋通道、太平洋通道及南海通道的共同影响，当三条通道异常偏强，水汽与北方冷空气在华南地区辐合，形成华南型年。本研究所得结论加深了我们对四类雨型形成机理的认识，并为汛期主雨带的预测提供了参考。

关键词 中国东部季风区 夏季雨型 水汽输送

文章编号 1006-9895(2018)01-0081-15 **中图分类号** P462 **文献标识码** A

doi:10.3878/j.issn.1006-9895.1706.16273

Characteristics and Differences of Summertime Moisture Transport Associated with Four Rainfall Patterns over Eastern China Monsoon Region

YANG Liu[1, 2], ZHAO Junhu[2], and FENG Guolin[1, 2]

1 *Department of Physical Science and Technology*, *Yangzhou University*, *Jiangshu Province*, *Yangzhou* 225002

收稿日期 2016-11-26；**网络预出版日期** 2017-06-06

作者简介 杨柳，男，硕士，1991 年出生，主要从事短期气候预测研究。E-mail: 917729440@qq.com

通讯作者 赵俊虎，E-mail: zhaojh@cma.gov.cn

资助项目 国家自然科学基金项目 41505061、41530531、41405092，公益性行业（气象）科研专项 GYHY201306021，公益性行业（气象）科硕专项（重大专项）GYHY201506001

Funded by National Natural Science Foundation of China (Grants 41505061, 41530531, 41405092), Special Scientific Research Fund of Meteorological Public Welfare Profession of China (Grant GYHY201306021), Key Special Scientific Research Fund of Meteorological Public Welfare Profession of China (Grant GYHY201506001)

2 *Laboratory for Climate Studies, National Climate Center*, *China Meteorological Administration* (*CMA*), *Beijing* 100081

Abstract Using the reanalysis data from National Centers for Environmental Prediction/ National Center for Atmospheric Research (NCEP/NCAR) and the classification result of FRP (four summer rainfall patterns) (NCP: the northern China rainfall pattern; IRP: the intermediate rainfall pattern; YRP: the Yangtze River rainfall pattern; SCP: the southern China rainfall pattern) over eastern China monsoon region based on monthly rainfall data collected at 160 weather stations in China, climatological characteristics and differences of moisture transport over eastern China monsoon region and their relationships with summer precipitation of the FRP are investigated. The results are as follows. (1) There exist six MTC (Moisture Transport Channel) that affect the summer rainfall over eastern China. The first one is IOMTC (the Indian Ocean Moisture Transport Channel), which represents the northern moisture transport path from Indian monsoon region. The second one is TPMTC (the Tibetan Plateau Southern Side Moisture Transport Channel), which is the southern moisture transport path from Indian monsoon region. The third one is POMTC (the Pacific Ocean Moisture Transport Channel), which is the moisture transport path from the Western Pacific to eastern China under the influence of WPSH (the Western Pacific Subtropical High). The fourth one is WMTC (the Westerly Moisture Transport Channel), which indicates moisture transport from westerly circulations. The fifth one is BBMTC (the Bay of Bengal Moisture Transport Channel), which indicates the northerly moisture transport from the Bay of Bengal. The last one is SCSMTC (the South China Sea Moisture Transport Channel), which is the path of moisture that comes from the Indian Ocean and the Bay of Bengal and turns to the Indo-China Peninsula and the moisture that is originated from the South China Sea and merges into the crossing equator flow. The moisture transport paths associated with precipitation anomalies over different areas in eastern China are obviously different. Furthermore, the relationship between the same moisture transport path and precipitation in different summer stages is not entirely the same. (2) There are obvious differences in moisture transport and budget corresponding to the FRP. The midsummer (July and August) precipitation anomaly in the North China is most influenced by the Asian monsoon moisture transport, followed by that of the westerly moisture transport. In NCP years, the above two types of moisture transport both tend to be much stronger, especially the former whose strength can be more than doubled and its contribution to NCP also increases significantly. However, the moisture transport by Asian monsoon circulation underwent an abrupt weakening at the end of the 1970s, while the contribution of westerly moisture transport to NCP increased. The anomalous summer precipitation over Huaihe River Basin is significantly correlated primarily with the POMTC and secondarily with the TPMTC. The precipitation over the Huaihe River Basin increases when the moisture transport of the two types of MTC enhance and converge over Huaihe River Basin, leading to the formation of the IRP. The summer precipitation over MLYRB (the middle and lower reaches of Yangtze River Basin) is dominated by anomalous moisture transport of POMTC. As for the YRP years, the moisture transport from the northwestern side of the WPSH strengthens and the warm moist air interacts with cold air from the north over the MLYRB. The summer precipitation over South China is affected by the IOMTC, POMTC and SCSMTC. When the moisture transported from the above three MTCs are stronger and converges with cold air from the north over South China, the SCP forms. The results of this study can enhance our understanding of the formation mechanisms of the FRP, and provide a reference for the prediction of the main rain belt during rainy season.

Keyword East China monsoon region, Rainfall pattern in summer, Moisture transport

1 引言

中国地处东亚季风区，受东亚夏季风异常的影响，夏季降水的年际变率非常大，容易发生旱涝灾害（Ding, 1994, 2007; 施能等, 1996; Wu et al., 2010; 封国林等, 2015; 李维京等, 2015），通过揭示中国东部季风区夏季旱涝的形成机制和预测信号，进而做出准确的预测，可以为国家防灾、减灾提供重要的依据（施能等，1999，2001；Wang et al., 2009；丁一汇，2011；赵俊虎等，2012，2014；Feng et al.，2013；封国林等，2013；Gong et al.，2015）。从全国大范围看，夏季主汛期降水主要预报雨带的南北位置，即对雨型的预报（王绍武等，1998；Zhao and Feng，2014；Gong et al., 2016）。正常情况下，夏季雨带从华南向华北推进，但是受多种因素的复杂影响，雨带推进的速度加快或者长时间滞留在某区域，形成了不同的雨型（魏凤英等，2012）。其中，水汽输送的强弱和路径是影响雨带和雨型的重要因素之一，因为水汽是形成降水的必要条件之一。大气中水汽输送和收支是研究全球大气环流持续

和变化的一个重要方面（周天军等，2001；黄荣辉等，2011；江志红等，2011）。早在 20 世纪 30 年代，竺可桢（1934）就提出中国降水与东亚季风水汽输送的关系。涂长望和黄仕松（1944）指出了中国雨带北进和南撤与东亚夏季风水汽输送的进退密切相关。因此研究东亚季风区水汽输送的特征及其与中国夏季降水的关系，对于了解水分循环和预测主雨带的位置有重要的实际意义。

国内外学者们在水汽输送的源和汇、水汽输送路径、水汽输送的年际和年代际变化，及水汽输送与降水的关系等方面开展了大量的研究。谢义炳和戴武杰（1959）指出中国夏季降水的两个水汽来源：一是从太平洋高压南沿以南风及东南风的形式进入中国内陆，二是印度低压的东南方以西南风的形式进入中国西南部。Simmonds et al.（1999）讨论了中国夏季水汽输送和收支，指出东南亚和印度季风环流分别从南海和孟加拉湾为中国东南部提供水汽，而对于东北及华北的部分地区，中纬度的西风水汽输送起主导作用。徐祥德等（2002）分析了南亚季风水汽输送关键区“大三角扇型”区域（以青藏高原地区为顶端，南海季风与印度季风涉及的低纬活动源区为底边）特征，指出夏季青藏高原地区是中国东部地区夏季长江流域梅雨带西边界重要水汽源或“转运站”，大三角区域热源强信号源区域的水分循环时空演变、遥相关特征及其对亚洲季风爆发的综合影响等均是认识中国及东亚旱涝异常成因的重要科学问题。Zhang（2001）指出，当印度季风水汽输送偏强（弱），东亚季风水汽输送偏弱（强）时，对应长江中下游地区降水偏少（多）。谢安等（2002）研究了夏季风期间长江中下游地区水汽输送的气候特征，指出来自孟加拉湾经中南半岛和来自华南的水汽输入是长江中下游地区水汽的主要来源，孟加拉湾地区及南海地区对长江中下游地区水汽输送的长时间维持是造成 1998 年长江流域洪涝的主要原因。黄荣辉和陈际龙（2010）分析了我国东、西部夏季水汽输送特征及其差异，指出两者水汽输送特征明显不同，东部夏季水汽输送经向输送要大于纬向输送，西部则相反。叶敏和封国林（2015）研究了长江中下游地区夏季降水的水汽路径并给出了客观定量化的定义，通过各水汽通量指标与前期海温关系的分析，发现前冬东太平洋发生 El Niño 时，有利于夏季西太平洋水汽输送增强，进而有利于长江中下游地区夏季降水偏多。周晓霞等（2008）研究指出中国大陆的水汽主要经南海北边界输入，水汽输送的北进与雨带的北推相一致，并分析了华北汛期水汽输送的时空特征及其与降水的关系，发现不同水汽通道对华北降水的影响区域不同，华北汛期水汽主要来自亚洲季风区水汽输送，其次是西风带的水汽输送。Sun et al.（2010）利用 NCEP/NCAR 再分析资料研究了东北地区夏季水汽输送与暴雨的关系，结果表明当东北夏季发生大范围的强降水时，东亚夏季风异常活跃，季风向北的水汽输送也明显加强，而局地强降水主要是由西风带的水汽辐合所致。

对于水汽输送和中国雨带关系的研究还不是很多。田红等（2002）分析了夏季水汽输送的特征，并讨论了中国夏季三类雨型与异常水汽输送的关系。Zhou and Yu（2005）分析了长江型降水和淮河型降水的水汽输送差异，发现长江流域的异常降水对应一支东北风和一支西南风水汽输送在该地辐合，而淮河流域的异常降水带为中纬度西风和副热带西南风携带的水汽在此汇合所致。夏季主雨带的分型妥当与否直接影响到预报水平（王绍武，1998）。廖荃荪等（1981）将中国东部夏季降水雨带从北向南划分为三类雨型：I 类，北方型，主要多雨带位于黄河流域及其以北，江淮流域大范围少雨；II 类，中间型，主要多雨带位于黄河至长江之间，雨区中心一般在淮河流域一带；III 类，南方型，主要多雨带位于长江流域或江南，淮河以北大范围地区及东南沿海地区少雨。这种划分雨型类数不多，有利于分析规律和进行预测。但将主要多雨带位于长江流域及其以南地区合为一类范围太广，例如 1954 年长江流域大水为 III 类，1997 年华南至江南多雨也是 III 类，这两年的降水分布和成因差别很大，这显然对寻找每一类的预报指标不利（王绍武等，1998）。孙林海等（2005）利用经验正交函数（EOF）分解、主成分分析等数理统计方法，对 1880～2002 年中国东部季风区夏季降水进行了客观分型，将三类雨型中的南方型细化为长江型和华南—江南南部型，但对 2002 年以后的雨型没有进行划分。王绍武和黄建斌（2006）根据 1951～2005 年每年夏季中国东部最大降水距平百分率所处位置，也将雨带划分为了四类雨型（即北方型、黄淮型、长江型和江南型）。但这两种划分方法，很多年份的雨型不一致。近来，Yang et al.（2016）在前人研究的基础上，利用相似度量法对 1951～2015

年中国东部季风区夏季四类雨型进行了客观划分，并分析了各类雨型与东亚夏季风的关系；Zhao et al.（2017）通过分析四类雨型对应的东亚大气环流系统配置的特点及其差异，研究了不同雨型形成的环流配置特征。那么每一类雨型是由哪一条水汽通道异常主导而形成？对应怎样的水汽输送、收支特征？不同雨型之间有何差异？本文将对这些问题进行讨论，进一步从水汽输送差异的角度认识四类雨型形成的机理。

2 资料和方法

本文所用资料主要包括：1951～2015 年 NCEP/NCAR 全球再分析资料的风场（u、v）、比湿 q 的日平均资料（Kalnay et al.，1996），水平空间分辨率为 2.5°×2.5°，垂直方向从 1000 hPa～300 hPa 共 8 层等压面；中国气象局国家气候中心提供的 160 站月平均降水量资料。气候态为 1981～2010 年 30 年平均值。

（1）水汽输送通量：本文通过计算水汽通量来进行水汽特征分析。其中水汽通量的计算方法参照丁一汇（2005）计算水汽的输送和收支的方法，具体如下：

对于单位面积空气柱而言，总的大气水汽输送通量矢量 $\boldsymbol{Q}$ 可通过如下进行计算：

$$\boldsymbol{Q}=\frac{1}{g}\int_{300}^{p_s} V\cdot q\mathrm{d}p, \tag{1}$$

纬向和经向水汽输送通量分别为

$$Q_\lambda=\frac{1}{g}\int_{300}^{p_s} uq\mathrm{d}p, \tag{2}$$

$$Q_\varphi=\frac{1}{g}\int_{300}^{p_s} vq\mathrm{d}p, \tag{3}$$

边界积分的水汽输送表示为

$$F_u=\int Q_\lambda a\mathrm{d}\varphi, \tag{4}$$

$$F_v=\int Q_\varphi a\cos\varphi\mathrm{d}\lambda, \tag{5}$$

区域的总水汽收支为

$$D_s=\sum(F_u,F_v)=F_\mathrm{I}-F_\mathrm{O}. \tag{6}$$

其中，公式（1）到（6）中，g 是重力加速度，$\boldsymbol{V}$ 是该单位气柱各层大气的风速矢量，u、v 分别为表征纬向风速和经向风速，p_s 表征地表面气压值。F_I 为水汽流入总量，F_O 为水汽流出总量，a 为地球半径。

（2）合成分析及其信度检验：采用合成分析（施能和古文保，1993），对各类雨型及其对应的水汽输送特征进行分析，并进行了信度检验。

$$t=\frac{\overline{x_{1i}}-\overline{x_{2i}}}{\sqrt{\dfrac{n_1\sigma_{1i}+n_2\sigma_{2i}}{n_1+n_2-2}}\sqrt{\dfrac{1}{n_1}+\dfrac{1}{n_2}}}, \tag{7}$$

其中，n_1 和 n_2 为两组样本的时间长度，$\overline{x_{1i}}$ 和 $\overline{x_{2i}}$ 是分别为两组样本第 i 站（格）点的平均值，σ_{1i} 和 σ_{2i} 分别是两组样本第 i 站（格）点的均方差。计算出 $|t|$ 值与自由度为 n_1+n_2-2 的临界值比较，进行信度检验。

3 中国东部季风区夏季雨型划分

Yang et al.（2016）利用相似度量法对 1951～2015 年中国东部季风区夏季四类雨型进行了客观划分。由图 1 可见，北方型年（简称 NCP；图 1a），中国东部主要多雨区位于黄河流域及其以北地区，降水中心一般在河套地区至渤海湾，而淮河流域及其以南大范围少雨，偏少中心在江淮地区；中间型年（简称 IRP；图 1b），主要多雨区位于黄河下游至长江下游之间地区，及东北中、东部，降水中心在淮河流域，而西北至华北西部、及长江以南大部分地区降水偏少，偏少中心在河套地区和江南西部地区；长江型年（简称 YRP；图 1c），主要多雨区位于长江流域，东北西部及内蒙中东部降水也偏多，而西北东部、华北和华南以少雨为主；华南型年（简称 SCP；图 1d），主要多雨区位于华南至江南南部，而长江流域及其以北地区以少雨为主。

由 1951～2015 年的中国东部季风区夏季雨型年份可见（表 1），典型的北方型有 23 年，占总年份的 35.4%，主要发生在 20 世纪 50 年代末至 90 年代初；典型的中间型有 18 年，占总年份的 27.7%，

表 1 1951～2015 年中国东部季风区夏季四类雨型年份表

Table 1 Classification of four typical rainfall patterns in the summer over the East China monsoon region during 1951～2015

雨型类型	年份	年数	频率
北方型（NCP）	1953, 1958, 1959, 1961, 1964, 1966, 1967, 1970, 1973, 1976, 1977, 1978, 1979, 1981, 1985, 1986, 1988, 1990, 1992, 1995, 2004, 2012, 2013	23	35.4%
中间型（IRP）	1951, 1956, 1957, 1960, 1962, 1963, 1965, 1971, 1972, 1974, 1982, 1984, 1989, 2000, 2003, 2005, 2007, 2009	18	27.7%
长江型（YRP）	1954, 1969, 1980, 1983, 1987, 1991, 1993, 1996, 1998, 2010, 2011, 2015	12	18.5%
华南型（SCP）	1952, 1968, 1994, 1997, 1999, 2001, 2002, 2006, 2014	9	13.8%

主要发生在 20 世纪 50 年代末至 70 年代初和 21 世纪 00 年代两个阶段；典型的长江型有 12 年，占总年份的 18.5%，主要发生在 20 世纪 80 年代至 90 年代；典型的华南型有 9 年，占总年份的 13.8%，主要发生在 20 世纪 90 年代中期至 21 世纪初；另外有 3 年雨型不典型（1955 年，1975 年，2008 年），占总年份的 4.6%。由此可见，四类雨型出现的时段具有显著的年代际特征。

4 东亚水汽输送通道及其与中国东部季风区夏季降水的关系

图 2 是东亚季风区 1951～2015 年夏季（6～8 月）平均的整层水汽输送空间分布。图 2a 是夏季东亚季风区多年平均的水汽输送矢量场。总体来

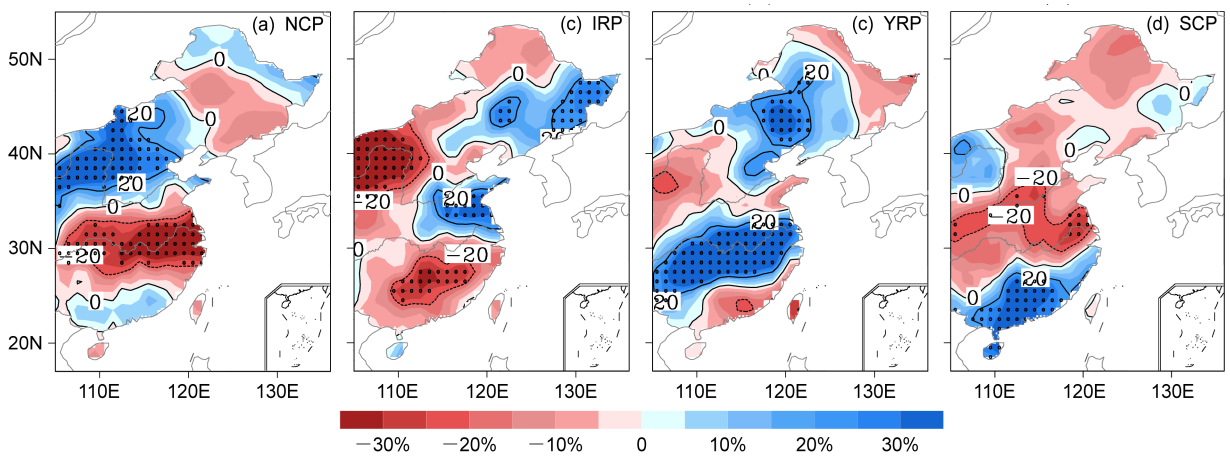

图 1 中国东部季风区四类雨型典型年份降水距平百分率合成

Fig. 1 Composite percentage summer precipitation anomalies in typical years of (a) NCP (the northern China rainfall pattern), (b) IRP (the intermediate rainfall pattern), (c) YRP (the Yangtze River rainfall pattern), and (d) SCP (the southern China rainfall pattern) in East China

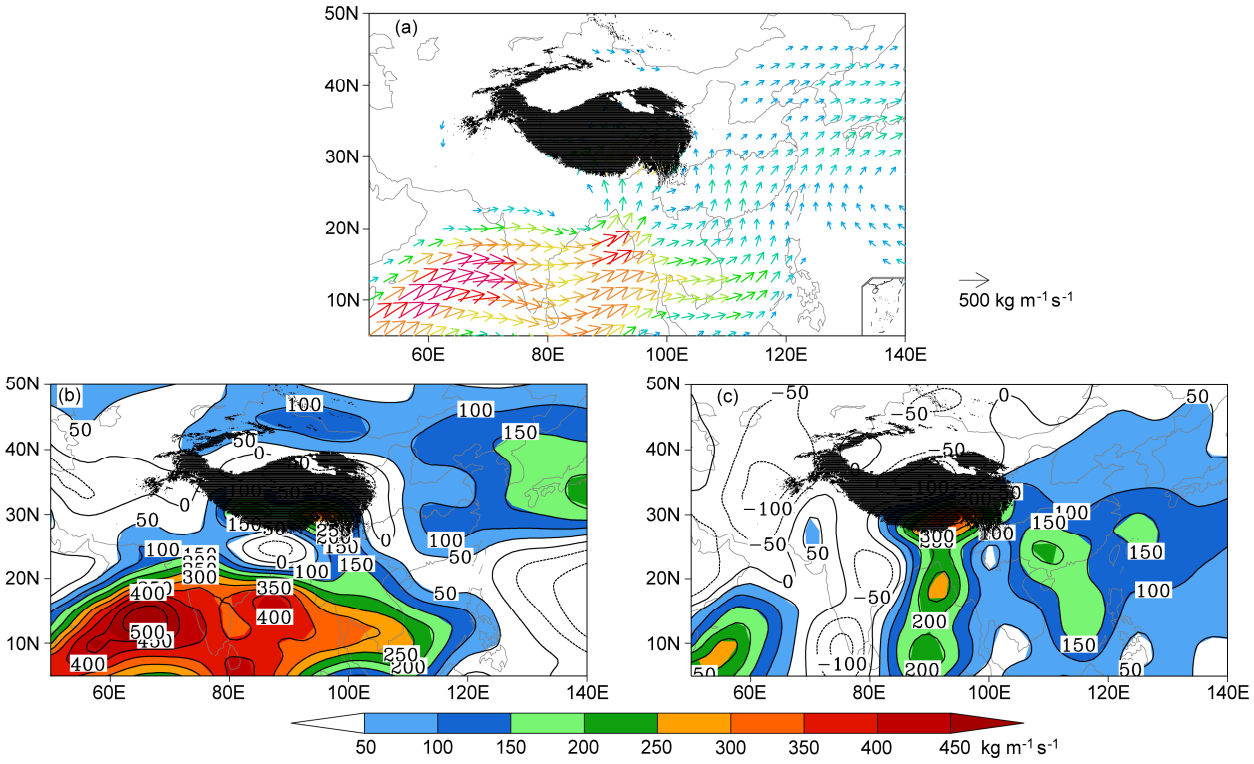

图 2 1951～2015 年夏季平均水汽输送特征（单位：kg m^{-1} s^{-1}）：（a）水汽通量矢量；（b）纬向水汽输送；（c）经向水汽输送。黑色区域表示青藏高原大地形

Fig. 2 Climatological mean distribution of summer (June–July–August) moisture transport during 1951–2015 (units: kg m^{-1} s^{-1}): (a) Zonal moisture transport, (b) meridional moisture transport, and (c) moisture transport flux vectors. Black area represents the Qinghai–Tibet Plateau

看，夏季进入中国大陆的水汽主要有四支：第一支是印度西南季风气流经孟加拉湾和中印半岛进入中国西南边界的水汽；第二支是由 105°E 附近越赤道气流与南亚季风的南支在南海南部汇合，流经南海北部进入中国南边界；第三支是西太平洋水汽沿西太平洋副热带高压（简称副高）西南侧的东南季风输送到达中国东南边界；第四支是中纬度西风气流带来的水汽，从中国西北边境进入并向东输送。由此可见，供给中国东部季风区夏季降水的水汽主要由印度西南季风从孟加拉湾带来的水汽，副热带东南季风从热带西太平洋带来的水汽，越赤道气流从南海带来的水汽以及中纬度西风从北大西洋带来的水汽，这四支水汽基本体现了印度季风、南海季风、副热带季风和中纬度西风带对中国夏季水汽输送和气候的综合影响。从四条水汽输送的量值来看，西北通道要比低纬度三条水汽通道明显偏弱。这与黄荣辉和陈际龙（2010）研究结论相一致。

这四支水汽输送从纬向和经向细分来看，纬向水汽输送可以划分为四条水汽通道（图 2b）：（1）印度洋通道，主要位于（10°～20°N，60°～120°E）范围内，由西向东横贯阿拉伯海经孟加拉湾到达南海南部地区的水汽输送，强度较强，表征印度季风区偏南的西风水汽输送强度，为了体现它对中国东部夏季降水的影响，参照周晓霞等（2008）定义水汽通道的方法，定义 10°～20°N 范围内通过 100°E 截面的纬向通量，表示印度洋通道的水汽输送强度；（2）高原南侧通道，主要位于（20°～30°N，95°～100°E）范围内，是来自印度洋和孟加拉湾转向或经青藏高原转向向东输送的水汽，实际代表印度季风区偏北的西风水汽输送强度，参照李永华等（2010）定义水汽通道的方法，考虑到北部青藏高原的影响，定义 22.5°～27.5°N 范围内通过 100°E 截面的纬向通量，表示高原南侧通道的水汽输送强度；（3）太平洋通道，主要位于（25°～30°N，100°～130°E）范围内，表征来自西太平洋的水汽，经由副高南侧的东风携带并转向为西南水汽输送进入中国东部地区，参照周晓霞等（2008）定义水汽通道的方法，定义 25°～30°N 范围内通过 120°E 截面的纬向通量，表示太平洋通道的水汽输送强度；（4）西风带通道，主要位于（35°～42.5°N，80°～120°E）范围内，表征西风带的水汽输送，定义 35°～42.5°N 范围内通过 110°E 截面的纬向通量，表示西风带通道的水汽输送强度。经向水汽输送主要有两条通道（图 2c）：（1）孟加拉湾通道，主要位于（5°～25°N，85°～100°E）范围内，表征来自孟加拉湾向北的水汽输送，为了体现它对中国东部夏季降水的影响，定义 85°～100°E 范围内通过 20°N 截面的经向通量，表示孟加拉湾通道的水汽输送强度；（2）南海通道，主要位于（10°～25°N，110°～120°E）范围内，表征来自印度洋和孟加拉湾在中南半岛转向以及来自南海的水汽，定义 110°～120°E 范围内通过 20°N 截面的经向通量，表示南海通道的水汽输送强度。

由此可见，图 2a 中的第一支水汽输送可以划分为三条水汽通道：即高原南侧通道、印度洋通道和孟加拉湾通道，这三条水汽通道输送的水汽主要体现印度季风输送水汽的特征，水汽主要来源于印度洋；而太平洋通道水汽主要体现东南季风输送水汽的特征，水汽主要来源于热带太平洋；中南半岛南海水汽通道则比较复杂，它处于印度季风及东南季风的过渡区域，水汽来源比较复杂，既有来自印度洋的，也有来自太平洋的，还有来自南海越赤道气流的；西风带水汽通道，水汽主要来自大西洋和地中海等的蒸发。已有研究也表明，这 6 条水汽输送通道与中国东部夏季降水关系密切（田红等，2002；周晓霞等，2008；李永华等，2010；叶敏和封国林，2015）。

为分析夏季各条水汽通道与中国东部降水的关系，根据图 1 中四类雨型的降水显著区域，选取华北区域（35°～42.5°N，110°～120°E）、淮河流域（32.5°～35°N，115°～120°E）、长江中下游地区（27.5°～32.5°N，110°～120°E）和华南地区（20°～27.5°N，110°～120°E）。将每个区域平均的降水量定义为该区域的降水指数。表 2 详细的给出了 1951～2015 年夏季及逐月各水汽通道与中国东部四个区域降水指数的相关系数。

首先从华北夏季降水与各水汽通道的相关系数可见，华北不同阶段降水与水汽通道的关系差异较大，其中，6～8 月逐月降水与印度洋通道、及 6～7 月降水与高原南侧通道关系均较弱，8 月降水与高原南侧通道呈显著正相关；6～8 月逐月降水与西风带通道均呈正相关，其中 7 月最显著；6～8 月逐月降水与孟加拉湾通道和南海通道均呈正相关，但并不显著；6 月、盛夏（7～8 月）降水与太平洋通道分别呈正、负相关，表明华北夏季降水受副高带来的水汽强弱的影响，但副高的位置是变动的，因此 25°～30°N 范围内通过 120°E 截面的纬向通量仅

表 2　6 条水汽通道与各区域降水指数的相关系数

Table 2　Correlation coefficients between six moisture channels and regional precipitation indexes

区域降水指数	月份	印度洋通道	高原南侧通道	太平洋通道	西风带通道	孟加拉湾通道	南海通道	季风通道
华北	6	−0.14	0.08	0.22	0.08	0.22	0.16	0.04
	7	−0.10	0.10	−0.24	**0.46*****	0.21	0.06	**0.60*****
	8	−0.04	0.26*	−0.05	**0.21**	0.16	0.18	**0.54*****
	7～8	−0.08	0.24	−0.25*	**0.47*****	0.21	0.21	**0.64*****
	6～8	−0.08	0.18	−0.14	**0.48*****	0.21	0.18	**0.54*****
淮河	6	−0.33*	0.23	0.23	−0.04	**0.35****	0.13	
	7	0.04	**0.39****	0.27	−0.05	0.01	0.11	
	8	−0.11	**0.29****	0.22	−0.12	−0.20	0.06	
	7～8	−0.04	**0.34****	0.23	−0.09	−0.16	0.08	
	6～8	−0.13	**0.25***	0.16	−0.08	−0.06	0.07	
长江	6	**−0.26***	**0.20**	**0.65*****	−0.16	0.15	**0.36****	
	7	**−0.17**	**0.32****	**0.54*****	**−0.30****	0.18	**0.25****	
	8	**−0.28***	0.04	**0.54*****	**−0.36****	0.03	0.15	
	6～7	**−0.36****	**0.31****	**0.72*****	**−0.28***	0.09	**0.28***	
	6～8	**−0.42*****	0.21	**0.66*****	**−0.38****	0.07	0.15	
华南	6	−0.06	0.23	**0.27***	−0.18	−0.05	**0.52*****	
	7	**0.50*****	−0.37**	**−0.29***	−0.31**	−0.04	**0.38****	
	8	**0.26***	−0.41***	**0.30***	−0.01	−0.09	**0.41*****	
	6～7	0.23	−0.04	−0.06	−0.19	−0.07	**0.46*****	
	6～8	**0.19**	−0.12	−0.13	−0.22	−0.11	**0.36****	

注：水汽通道的月份与降水指数的月份选取一致。

*表示通过 95%的信度检验。

**表示通过 99%的信度检验。

***表示通过 99.9%的信度检验。

能表示到达长江中下游水汽的强弱，不能很好的反映副高偏北以后的水汽输送强度。事实上，孟加拉湾通道、南海通道及太平洋通道均代表了不同性质的夏季风水汽输送，它们在中国东部汇合以后向华北地区输送。因此将 110°～120°E 范围内通过 35°N 截面的经向通量，定义为季风通道水汽输送强度，它反映了西南季风、南海季风及副热带季风分别从孟加拉湾、南海和太平洋带来的水汽，向北输送后进入华北地区。季风通道与 6～8 月逐月降水的相关系数分别为 0.04、0.64 和 0.54，表明 6 月季风通道的水汽尚未到达华北，盛夏季风水汽输送才影响到华北的降水。综上可见，6 月降水的水汽来源较复杂，没有关系密切的水汽通道，盛夏则主要受季风水汽输送和西风带水汽输送的影响，二者水汽输送偏强时华北降水易偏多。

淮河流域夏季降水与高原南侧通道和太平洋通道水汽输送呈正相关，其中与高原南侧通道的关系较显著，即高原南侧通道和太平洋通道偏强时，有利于水汽向淮河流域输送，进而造成淮河流域降水偏多。此外 6 月降水与印度洋通道和孟加拉湾通道分别呈显著的负、正相关。其中，孟加拉湾水汽通道是经向水汽通道，水汽输送需要经过青藏高原，遇到青藏高原大地形以后水汽部分凝结形成降水，剩余部分转向后到达中国东部地区，它的增强有利于高原南侧通道加强，进而影响淮河流域降水。

长江流域夏季降水与太平洋通道呈显著的正相关，与西风带通道呈显著的负相关，表明长江流域的降水主要受到副高和中高纬度环流的综合影响，副高偏强、偏南时，太平洋水汽通道水汽输送会显著增强，而中高纬西风带水汽输送偏弱则表示经向环流较强，副高携带来的水汽与北方的冷空气在长江中下游地区辐合，容易造成长江中下游地区降水偏多。此外，6～7 月降水与高原南侧通道和南海通道也呈显著的正相关。

从华南夏季降水与各水汽通道的相关系数可见，华南地区夏季逐月降水与南海通道均呈显著的正相关，与孟加拉湾通道关系较弱；其他 4 条水汽通道与各月降水的关系差异则也较大，其中 6 月降水与印度洋通道和高原南侧通道分别呈弱的负、正相关，7～8 月降水则与这两条通道分别呈显著的正、负相关，即反映了华南 7～8 月降水与西南印度季风水汽输送的南支和北支关系的差异，当南支偏强时，北支易偏弱，水汽输送到长江以南地区，造成华南—江南南部降水偏多；6～8 月逐月降水与

太平洋通道分别呈显著的正、负、正相关，反映了夏季副高南北位置的变化对华南降水的影响较大；华南夏季降水与西风带水汽输送呈负相关，其中 7 月最显著，即西风带水汽输送偏弱时中高纬经向环流偏强，北方冷空气南下到华南地区，与南方来的水汽辐合，容易造成华南地区降水偏多。

综上可见，与中国东部不同地区降水异常相联系的水汽通道存在明显的差异，且同一条水汽通道在夏季不同阶段与降水的关系也不尽相同。

5 夏季四类雨型的水汽输送、收支特征及其差异

为进一步分析四类雨型的水汽输送特征及其差异，对每类雨型年的水汽输送通量场、纬向水汽输送距平、经向水汽输送距平、及水汽输送距平分别进行合成分析。

5.1 北方型的水汽输送及收支特征

由于华北夏季降水主要出现在 7～8 月（周晓霞等，2008），两个月降水量占夏季总降水量的 80% 左右，且 6 月华北降水与各水汽通道关系均较弱（表 2），因此这里主要分析北方型年华北盛夏的水汽输送及收支特征（图 3）。由 23 个北方型年盛夏的整层积分的水汽输送的合成（图 3a）可见，中国东部总水汽输送主要来自低纬的水汽输送通道，但中国东部地区中华北（方框区）的水汽输送明显比东部其他地区强。由纬向水汽通量距平合成（图 3b）可见，35°N 以北为西风水汽输送距平，且华北地区较显著，表明北方型年，西风带水汽输送增强；22.5°～35°N 为东风水汽输送距平，且江南地区较显著，表明长江中下游地区的西南水汽输送减弱。由经向水汽通量距平合成（图 3c）可见，30°～40°N 为南风水汽输送距平，表明北方型年，到达北方地区的季风水汽输送增强。由经纬向水汽通量距平合成（图 3d）可见，西太平洋至中国南方地区为气旋距平水汽输送，环渤海地区至日本岛为反气旋距平水汽输送，表明北方型年副高偏北，副高西北侧的西南水汽输送与中纬度西风输送增强，造成北方降水偏多。

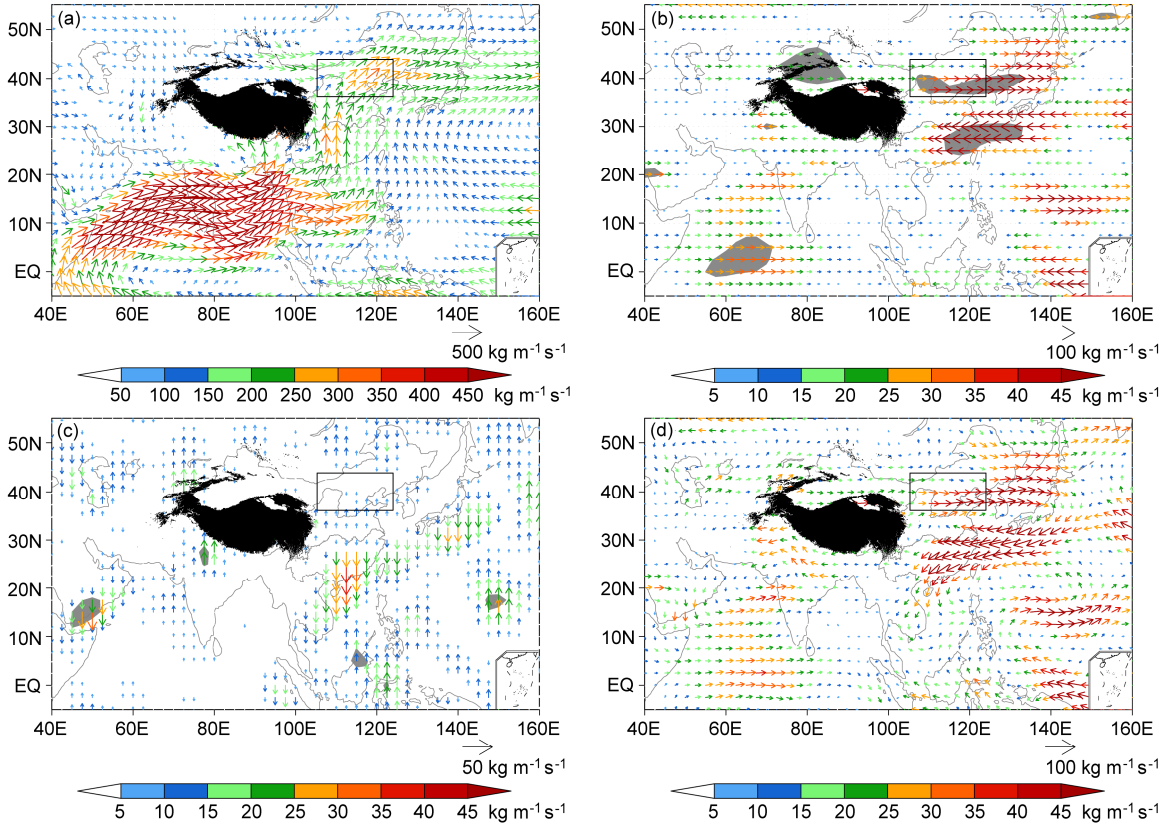

图 3 北方型年盛夏（7～8 月）整层积分的水汽输送通量合成（单位：kg m^{-1} s^{-1}）：（a）原始水汽输送通量；（b）纬向水汽通量距平；（c）经向水汽通量距平；（d）经纬向水汽通量距平。矩形方框表示华北区域，阴影区域表示通过 95%的信度检验

Fig. 3 Composite July and August vertically integrated moisture fluxes in NCP years (units: kg m^{-1} s^{-1}): (a) Moisture fluxes, (b) anomalies of zonal moisture fluxes, (c) anomalies of meridional moisture fluxes, (d) anomalies of zonal and meridional moisture fluxes. The rectangular box indicates North China, shadings indicate the 95% confidence level

分别计算中国东部四个区域四个边界的水汽通量和区域净收支，其中西边界和南边界的水汽通量为正值、东边界和北边界的水汽通量为负值，表示水汽通过边界向区域输入，反之表示水汽通过边界从区域输出；当水汽输入大于水汽输出时，区域净收支为正。从 23 个北方型年华北区域各边界和区域的水汽收支（表 3）可见，华北区域水汽主要从南边界和西边界收入，两条边界气候平均的水汽收入分别为 62.00×10^6 和 44.20×10^6 kg s^{-1}，贡献分别占 58.4%和 41.6%；而北方型年平均的收入分别为 136.75×10^6 和 69.15×10^6 kg s^{-1}，贡献分别占 69.4%和 33.6%，其中正距平分别有 21 年和 20 年，即北方型年季风和西风带水汽输送均增强，尤其是季风水汽输送增加一倍以上，贡献也明显增加。此外，20 世纪 70 年代中后期以来，南边界的水汽输送较之前显著减弱，而西边界的水汽输送没有明显的减弱。从区域水汽净收支可见，华北盛夏多年平均的水汽净收入为 12.43×10^6 kg s^{-1}，而北方型年平均为 26.17×10^6 kg s^{-1}，水汽净收入增加一倍以上，且 23 个北方型年华北区域水汽净收入均为正。

表 3 北方型年盛夏（7～8 月）华北区域各边界和区域水汽收支

Table 3 Moisture budget over North China in July and August in NCP years

	水汽收支（$\times10^6$）/ kg s^{-1}				
	西边界	南边界	东边界	北边界	区域净收支
1953 年	116.70 (+)	198.01 (+)	195.77 (+)	79.05 (+)	39.89
1958 年	87.63 (+)	237.51 (+)	155.81 (+)	160.30 (+)	9.03
1959 年	115.14 (+)	213.27 (+)	186.23 (+)	110.45 (+)	31.73
1961 年	96.05 (+)	487.77 (+)	283.73 (+)	156.80 (+)	143.29
1964 年	63.94 (+)	256.65 (+)	196.56 (+)	55.69 (+)	68.34
1966 年	77.50 (+)	155.53 (+)	183.21 (+)	10.54 (+)	39.28
1967 年	77.59 (+)	185.75 (+)	160.57 (+)	78.37 (+)	24.40
1970 年	30.89 (+)	130.61 (+)	86.74	45.93 (+)	28.83
1973 年	83.99 (+)	204.86 (+)	162.76 (+)	108.18 (+)	17.91
1976 年	82.37 (+)	130.04 (+)	124.59 (+)	68.26 (+)	19.56
1977 年	35.46	64.37 (+)	84.82	14.00 (+)	1.11
1978 年	61.60 (+)	108.35 (+)	128.14 (+)	19.08 (+)	22.73
1979 年	69.84 (+)	65.38 (+)	128.22 (+)	−13.27	20.27
1981 年	68.88 (+)	85.03 (+)	131.78 (+)	8.73 (+)	13.40
1985 年	81.75 (+)	69.73 (+)	133.10 (+)	0.24 (+)	18.14
1986 年	60.30 (+)	18.31	99.85 (+)	−42.32	21.08
1988 年	49.54 (+)	104.59 (+)	96.23	56.58 (+)	1.32
1990 年	95.97 (+)	76.09 (+)	143.90 (+)	7.09 (+)	21.07
1992 年	57.11 (+)	66.72 (+)	105.70 (+)	3.506 (+)	14.62
1995 年	45.96 (+)	79.30 (+)	102.74 (+)	8.05 (+)	14.47
2004 年	10.68	61.71	82.52	−18.52	8.01
2012 年	41.62	64.14 (+)	76.72	16.46 (+)	12.59
2013 年	79.93 (+)	81.46 (+)	158.79 (+)	−10.46	13.06
平均	69.15 (+)	136.75 (+)	139.50 (+)	40.23 (+)	26.17

注：括号内“+”表示相对于气候态的距平符号。

综上可见，华北盛夏水汽主要来自亚洲季风水汽输送，其次是西风带的水汽输送，北方型年二者明显增加，季风水汽输送增加幅度更大，但 1970 年代中后期以来季风水汽输送显著减弱，这与周晓霞等（2008）研究结论相一致。

5.2 中间型的水汽输送及收支特征

图 4 是中间型对应的夏季水汽异常输送。由 18 个中间型年相应的整层积分的水汽输送的合成（图 4a）可见，中国东部总水汽输送主要来自低纬的水汽输送通道，淮河流域（方框区）的水汽输送较强。由纬向水汽通量距平合成（图 4b）可见，30°～34°N 为西风水汽输送距平，表明中间型年，高原南侧水汽输送增强。由经向水汽通量距平合成（图 4c）可见，30°N 以北为南风距平，表明中间型年，到达北方地区的季风水汽输送增强。由经纬向水汽通量距平合成（图 4d）可见，中国北方地区为气旋距平水汽输送，西风异常输送和南风异常水汽输送在淮河流域辐合，造成淮河流域降水偏多。

表 4 给出了中间型年淮河流域各边界和区域的水汽收支情况。由表 4 可见，中间型年，淮河流域水汽主要从南边界和西边界收入，南边界和西边界水汽收入正距平分别有 12 和 15 年，即中间型年季风水汽和高原南侧水汽以偏强为主。从 18 年平均来看，南边界和西边界水汽收入贡献分别占 64.2%

表 4 中间型年夏季淮河流域各边界和区域水汽收支

Table 4 Moisture budget over Huaihe River Basin in summer in IRP years

	水汽收支（$\times10^6$）/ kg s^{-1}				
	西边界	南边界	东边界	北边界	区域净收支
1951 年	29.89 (+)	65.50 (+)	27.34 (+)	59.69 (+)	8.36
1956 年	49.29 (+)	109.91 (+)	46.52 (+)	95.43 (+)	17.26
1957 年	43.58 (+)	68.01 (+)	45.17 (+)	53.90 (+)	15.52
1960 年	59.60 (+)	100.24 (+)	27.51 (+)	126.60 (+)	5.73
1962 年	53.40 (+)	82.97 (+)	33.75 (+)	90.79 (+)	11.82
1963 年	44.61 (+)	87.57 (+)	29.13 (+)	98.68 (+)	4.37
1965 年	38.13 (+)	49.54 (+)	41.92 (+)	34.5 (+)	11.24
1971 年	48.99 (+)	79.45 (+)	55.51 (+)	63.61 (+)	9.32
1972 年	22.92 (+)	40.94 (+)	17.75	41.36 (+)	4.75
1974 年	29.21 (+)	37.42	27.6 (+)	34.44 (+)	4.58
1982 年	15.26	38.60	17.63	27.6	8.63
1984 年	22.16 (+)	37.97	21.28	31.66 (+)	7.19
1989 年	20.0 (+)	19.19	18.92	16.25	4.02
2000 年	6.42	36.03	10.28	26.94	5.23
2003 年	39.86 (+)	42.89 (+)	49.79 (+)	20.84	12.13
2005 年	19.93 (+)	58.81 (+)	29.81 (+)	40.65 (+)	8.28
2007 年	16.79	54.30 (+)	27.16 (+)	36.47 (+)	7.46
2009 年	21.01 (+)	30.93	25.53	19.41	7.0
平均	32.28 (+)	57.79 (+)	30.70 (+)	51.05 (+)	8.33

和 35.8%，由此可见，淮河流域汛期水汽主要来自亚洲季风水汽输送。从区域水汽净收支可见，18 年淮河流域水汽净收入为正。此外，20 世纪 80 年代之后，南边界和西边界的水汽输送较之前显著减弱。

5.3 长江型的水汽输送及收支特征

图 5 给出了长江型年份的水汽输送特征。图 5a 是 12 个长江型年相应的整层积分的水汽输送的合成图，由图可见，中国东部地区中长江中下游地区的水汽输送明显比东部其他地区强。由纬向水汽通量距平合成（图 5b）可见，长江中下游及其以南地区为较显著的西风水汽异常输送，表明长江型年，副高东南侧转向西风水汽输送增强；由经向水汽通量距平合成（图 5c）可见，长江中下游及其以南为显著的南风水汽输送距平，南风距平越过长江，而江北则为北风水汽输送距平，二者在长江中下游地区辐合。由经纬向水汽通量距平合成（图 5d）可见，西太平洋至中国南方地区为反气旋距平水汽输送，表明长江型年副高偏强偏西偏南，副高西北侧的西南异常输送与北方冷空气异常在长江中下游地区辐合，造成该地区降水偏多。

表 5 给出了长江型年长江中下游地区各边界和区域的水汽收支情况。由表 5 可见，12 个长江型年，长江中下游地区水汽主要从南边界和西边界收入（贡献分别占 80.0%和 20.0%），12 年南边界和西边界水汽收入均为正距平，即长江型年副高南侧转向的西风和夏季风水汽输送均偏强。从区域水汽净收支可见，12 个长江型年长江中下游地区水汽净收入均为正。

表 5 长江型年夏季长江中下游地区各边界和区域水汽收

Table 5 Moisture budget over the middle and lower reaches of the Yangtze River Basin in summer in YRP years

	水汽收支（$\times10^6$）/ kg s^{-1}				
	西边界	南边界	东边界	北边界	区域净收支
1954 年	40.28 (+)	273.48 (+)	111.85 (+)	151.83 (+)	50.08
1969 年	66.98 (+)	191.00 (+)	105.82 (+)	110.62 (+)	41.54
1980 年	64.35 (+)	183.29 (+)	143.75 (+)	52.92	50.97
1983 年	71.03 (+)	157.50 (+)	117.89 (+)	69.90 (+)	40.75
1987 年	59.59 (+)	179.92 (+)	122.15 (+)	78.21 (+)	39.14
1991 年	57.31 (+)	182.75 (+)	118.66 (+)	77.70 (+)	43.69
1993 年	49.22 (+)	160.08 (+)	133.51 (+)	34.05	41.74
1996 年	40.47 (+)	186.85 (+)	80.39 (+)	88.47 (+)	58.46
1998 年	65.06 (+)	222.29 (+)	137.31 (+)	79.54 (+)	70.50
2010 年	50.21 (+)	133.58 (+)	66.83 (+)	71.97 (+)	44.99
2011 年	42.84 (+)	133.26 (+)	75.43 (+)	59.85	40.82
2015 年	43.12 (+)	102.93	75.27 (+)	34.53	36.25
平均	54.21 (+)	175.58 (+)	107.41 (+)	75.80 (+)	46.58

5.4 华南型的水汽输送及收支特征

图 6 给出了华南型年的水汽输送特征。由 9 个华南型年相应的整层积分的水汽输送的合成（图 6a）可见，华南地区的水汽输送明显比东部其他地区强。由纬向水汽通量距平合成（图 6b）可见，25°～35°N 为显著的东风水汽输送距平，0～20°N 为显著的西风水汽输送距平。由经向水汽通量距平合成（图 6c）可见，中国东部为北风水汽输送距平，华南南部为南风水汽输送距平，华南至江南南部地区为南北风水汽输送异常交汇地区，即水汽在该地区辐合。由经纬向水汽通量距平合成图（图 6d）可见，长江中下游以南至菲律宾为气旋水汽输送距平控制，华南地区水汽辐合较强，造成华南降水偏多。

表 6 给出了华南型年华南地区各边界和区域的水汽收支情况。从 9 个华南型年各边界平均和气候态的水汽收入来看（表 6），华南地区水汽主要从南边界收入，部分年份西边界也有水汽输入。从区域水汽净收支可见，9 年华南水汽净收入均为正。

表 6 华南型年夏季华南地区各边界和区域水汽收支

Table 6 Moisture budget over South China in summer in SCP years

	水汽收支（$\times10^6$）/ kg s^{-1}				
	西边界	南边界	东边界	北边界	区域净收支
1952 年	−19.35	229.21 (+)	38.85	168.55 (+)	2.47
1968 年	69.96 (+)	154.03 (+)	87.10 (+)	127.29 (+)	9.59
1994 年	−11.22	190.92 (+)	21.22	133.78 (+)	24.69
1997 年	40.88 (+)	186.19 (+)	102.11 (+)	101.37	23.58
1999 年	52.27 (+)	144.37	93.99 (+)	90.6	12.06
2001 年	−5.38	139.4	6.61	96.05	31.36
2002 年	39.85 (+)	152.49 (+)	68.73 (+)	85.99	37.62
2006 年	21.63	169.96 (+)	69.07 (+)	110.28	12.24
2014 年	26.63	147.13	67.93 (+)	80.66	25.17
平均	23.92	168.19 (+)	61.73 (+)	110.51	19.86

综上可见，中国东部季风区夏季四类雨型的水汽输送和收支特征有明显的差异，水汽输送和收支的异常是造成不同雨型的直接原因之一。

6 结论和讨论

本文首先分析了东亚夏季水汽输送的气候特征及其与中国东部季风区夏季降水的关系，在此基础上比较了中国东部季风区夏季四类雨型的水汽输送、收支特征及其差异，发现中国东部夏季不同区域降水异常与不同的水汽通道异常有关，四类雨型的水汽输送和收支特征有明显的差异，具体结论如下：

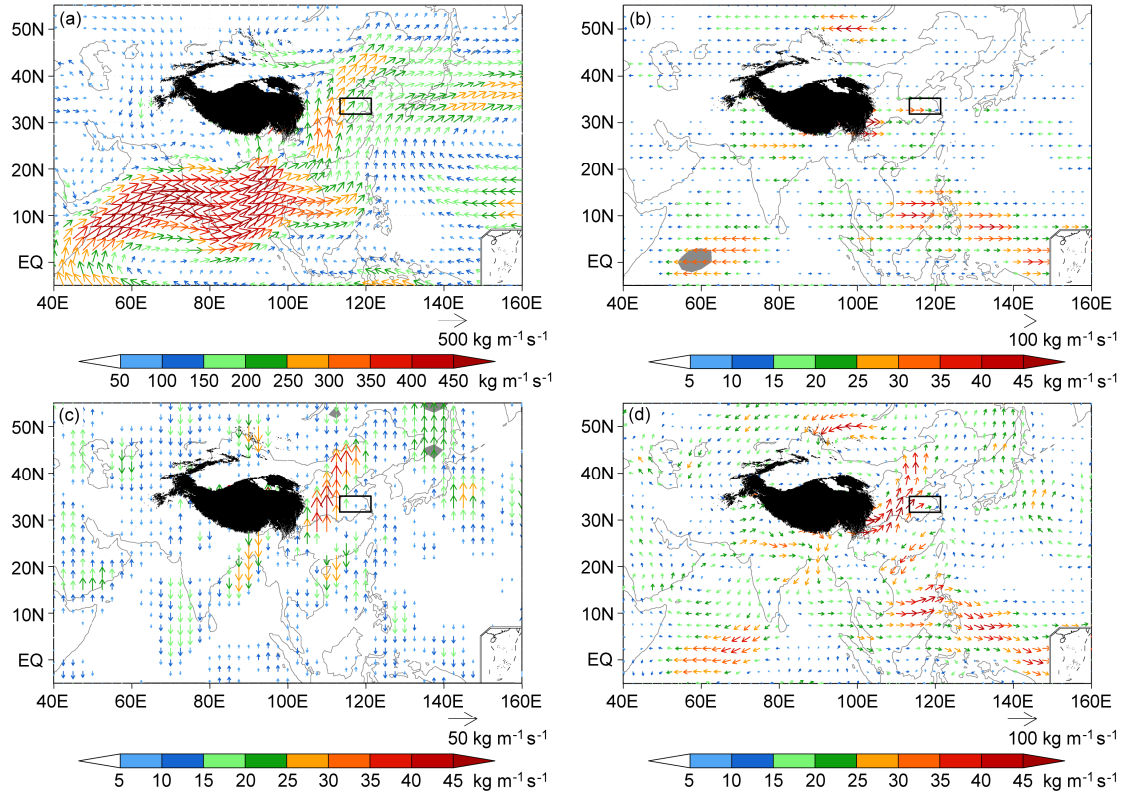

图 4　同图 3，但为夏季中间型年

Fig. 4　Same as Fig. 3, but for IRP years in summer (June–July–August)

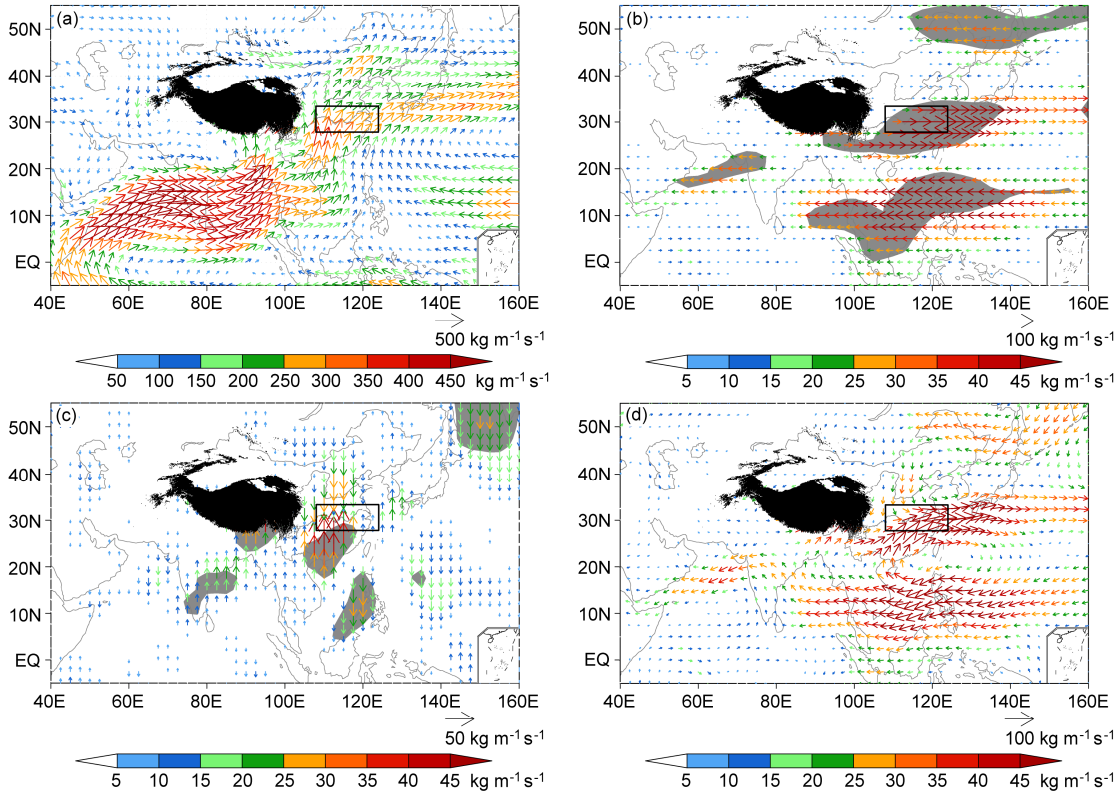

图 5　同图 3，但为夏季长江型年

Fig. 5　Same as Fig 3, but for YRP years in summer (June–July–August)

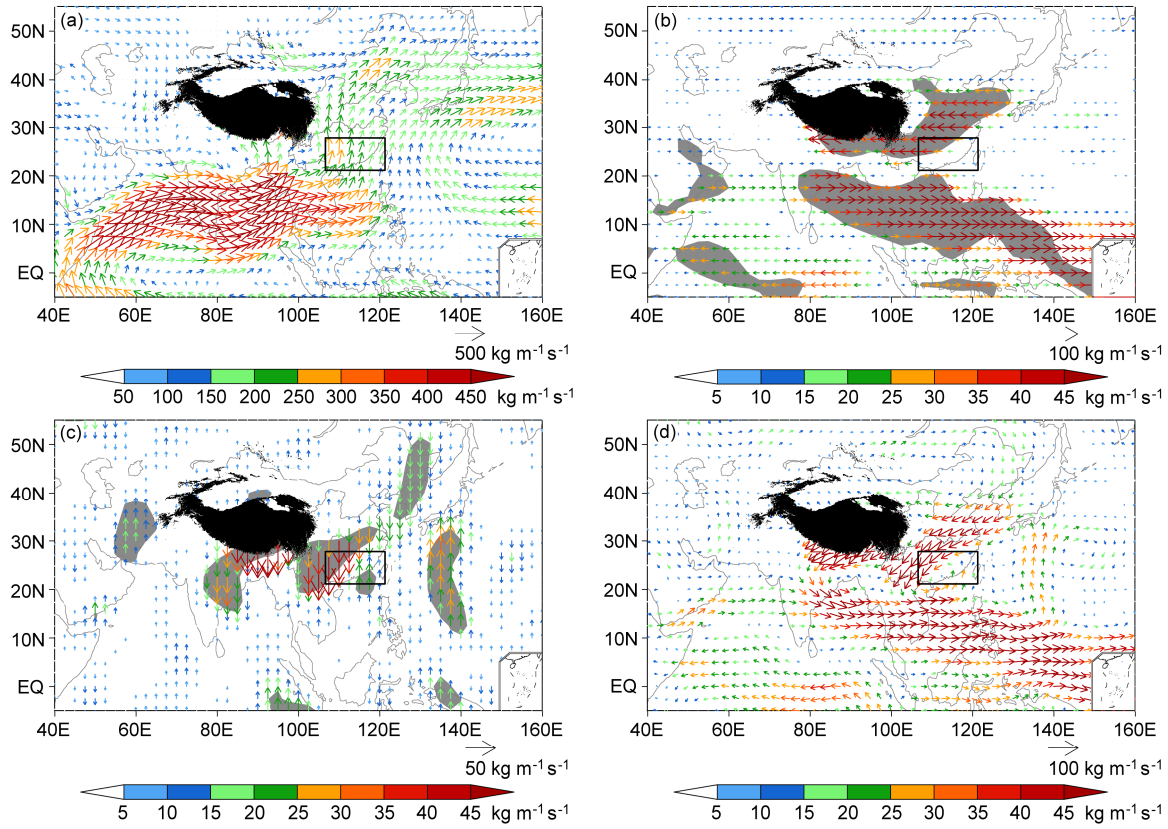

图 6　同图 3，但为夏季华南型年

Fig. 6　Same as Fig 3, but for SCP years in summer (June–July–August)

（1）夏季影响中国东部季风区的水汽通道主要有以下 6 条：印度洋通道，表征印度季风区偏南的西风水汽支输送；高原南侧通道，表征印度季风区偏北的西风水汽支输送；太平洋通道，表征由副高带来的西太平洋的水汽；西风带通道，表征西风带的水汽输送；孟加拉湾通道，表征来自孟加拉湾向北的水汽输送；南海通道，表征来自印度洋和孟加拉湾在中南半岛转向以及来自南海的水汽；中国东部主要为自南向北的季风水汽输送，年际变化较大，这与中国东部季风区夏季旱涝年际变化大相一致；

（2）与中国东部不同地区降水异常相联系的水汽通道存在明显的差异，且同一条水汽通道在夏季不同阶段与降水的关系也不尽相同，华北地区 6 月降水的水汽来源较复杂，没有关系密切的水汽通道，盛夏则主要受季风水汽输送和西风带水汽输送的影响，二者水汽输送偏强时华北降水偏多；淮河流域 6 月降水与印度洋通道和孟加拉湾通道分别呈显著的负、正相关，夏季降水则与高原南侧通道和太平洋通道水汽输送呈正相关，其中与高原南侧通道的关系较显著；长江流域 6～7 月降水与高原南侧通道和南海通道也呈显著的正相关，夏季降水与太平洋通道呈显著的正相关，与印度洋通道和西风带通道呈显著的负相关；华南地区夏季逐月降水与南海通道均呈显著的正相关，与孟加拉湾通道关系较弱，各月降水与其他 4 条水汽通道的关系差异则较大；

（3）四类雨型的水汽输送和收支特征有明显的差异，华北盛夏降水主要受亚洲季风水汽输送的影响，其次是西风带水汽输送，北方型年，二者往往偏强，尤其是季风水汽输送增加一倍以上，贡献也明显增加，20 世纪 70 年代中期之后，季风水汽输送显著减弱，西风带水汽输送的重要性相对增大；淮河流域夏季降水异常主要受太平洋通道水汽输送异常的主导，其次是高原南侧通道水汽输送，二者偏强并在淮河流域辐合时，淮河流域降水偏多形成中间型年；长江中下游地区夏季降水主要受太平洋通道水汽输送异常的主导，长江型年，副高西北

侧的西南水汽异常输送加强，并与北方冷空气异常在长江流域辐合，区域水汽为正的净收支；华南地区夏季降水则受印度洋通道、太平洋通道及南海通道的共同影响，当三条通道异常偏强，水汽与北方冷空气在华南地区辐合，形成华南型年。

本文从水汽输送和收支的角度，研究了中国东部季风区夏季四类雨型水汽输送的差异，得到一些初步的结论，所得结论有助于我们加深对四类雨型形成机理的认识，并为汛期主雨带的预测提供了参考依据。但由于所用资料是再分析资料，它与实际测站所观测到的实际值有一定的误差，在计算过程中对地形的考虑也可能不全面。此外，从 3 个非典型雨型年（1955 年、1975 年和 2008 年）的水汽输送场发现，这 3 年与四类雨型合成的水汽输送场差异很大，中国东部地区有多个水汽辐合中心，导致了这三年多雨中心较多，没有明显的主雨带。这种异常的水汽输送可能与整个夏季低纬度和中高纬度环流系统强烈的季节内振荡有关，需要进一步分析。

致谢 感谢审稿专家提出的宝贵意见，同时也感谢在论文修改过程中陈丽娟研究员的建议和帮助。

参考文献（References）

Ding Y H. 1994. Monsoons over China [J]. London: Kluwer Academic, 419pp.

丁一汇. 2005. 高等天气学 [M]. 2 版. 北京: 气象出版社, 585pp. Ding Yihui. 2005. Advanced Synoptic Meteorology [M]. 2nd ed. Beijing: China Meteorological Press (in Chinese), 585pp.

Ding Y H. 2007. The variability of the Asian summer monsoon [J]. J. Meteor. Soc. Japan, 85B: 21–54, doi:10.2151/jmsj.85B.21.

丁一汇. 2011. 季节气候预测的进展和前景 [J]. 气象科技进展, 1 (3): 14–27. Ding Yihui. 2011. Progress and prospects of seasonal climate prediction [J]. Adv. Meteor. Sci. Technol. (in Chinese), 1 (3): 14–27.

Feng G L, Sun S P, Zhao J H, et al. 2013. Analysis of stable components for extended-range (10–30 days) weather forecast: A case study of continuous overcast-rainy process in early 2009 over the mid–lower reaches of the Yangtze River [J]. Sci. China Earth Sci., 56 (9): 1576–1587, doi:10.1007/s11430-012-4527-8.

封国林, 赵俊虎, 支蓉, 等. 2013. 动力-统计客观定量化汛期降水预测研究新进展 [J]. 应用气象学报, 24 (6): 656–665. Feng Guolin, Zhao Junhu, Zhi Rong, et al. 2013. Recent progress on the objective and quantifiable forecast of summer precipitation based on dynamical-statistical method [J]. Journal of Applied Meteorological Science (in Chinese), 24 (6): 656–665, doi:10.3969/j.issn.1001-7313.2013.06.002.

封国林, 赵俊虎, 杨杰, 等. 2015. 中国汛期降水动力-统计预测研究 [M]. 北京: 科学出版社, 1–330. Feng Guolin, Zhao Junhu, Yang Jie, et al. 2015. The Study on Dynamical and Statistical Prediction on Summer Precipitation over China [M]. Beijing: Science Press, 1–330.

Gong, Z Q, Hutin C, Feng G L. 2016. Methods for improving the prediction skill of summer precipitation over East Asia–West Pacific [J]. Wea. Forecasting, 31 (4): 1381–1392, doi:10.1175/WAF-D-16-0007.1.

Gong Z Q, Zhao J H, Feng G L, et al. 2015. Dynamic-statistics combined forecast scheme based on the abrupt decadal change component of summer precipitation in East Asia [J]. Sci. China: Earth Sci., 58 (3): 404–419, doi:10.1007/s11430-014-4967-4.

黄荣辉, 陈际龙. 2010. 我国东、西部夏季水汽输送特征及其差异 [J]. 大气科学, 34 (6): 1035–1045. Huang Ronghui, Chen Jilong. 2010. Characteristics of the summertime water vapor transports over the eastern part of China and those over the western part of China and their difference [J]. Chinese Journal of Atmospheric Sciences (in Chinese), 34 (6): 1035–1045, doi:10.3878/j.issn.1006-9895.2010.06.01.

黄荣辉, 陈际龙, 刘永. 2011. 我国东部夏季降水异常主模态的年代际变化及其与东亚水汽输送的关系 [J]. 大气科学, 35 (4): 589–606. Huang Ronghui, Chen Jilong, Liu Yong. 2011. Interdecadal variation of the leading modes of summertime precipitation anomalies over eastern China and its association with water vapor transport over East Asia [J]. Chinese Journal of Atmospheric Sciences (in Chinese), 35 (4): 589–606, doi:10.3878/j.issn.1006-9895.2011.04.01.

江志红, 梁卓然, 刘征宇, 等. 2011. 2007 年淮河流域强降水过程的水汽输送特征分析 [J]. 大气科学, 35 (2): 361–372. Jiang Zhihong, Liang Zhuoran, Liu Zhengyu, et al. 2011. A diagnostic study of water vapor transport and budget during heavy precipitation over the Huaihe River Basin in 2007 [J]. Chinese Journal of Atmospheric Sciences (in Chinese), 35 (2): 361–372, doi:10.3878/j.issn.1006-9895.2011.02.14.

Kalnay, Kanamitsu M, Kistler R, et al. 1996. The NCEP/NCAR 40-year reanalysis project [J]. Bull. Amer. Meteor. Soc., 77 (3): 437–471.

李维京, 左金清, 宋艳玲, 等. 2015. 气候变暖背景下我国南方旱涝灾害时空格局变化 [J]. 气象, 41 (3): 261–271. Li Weijing, Zuo Jinqing, Song Yanling, et al. 2015. Changes in spatio–temporal distribution of drought/flood disaster in southern China under global climate warming [J]. Meteor. Mon. (in Chinese), 41 (3): 261–271, doi:10.7519/j.issn.1000-0526.2015.03.001.

李永华, 徐海明, 高阳华, 等. 2010. 西南地区东部夏季旱涝的水汽输送特征 [J]. 气象学报, 68 (6): 932–943. Li Yonghua, Xu Haiming, Gao Yanghua, et al. 2010. The characteristics of moisture transport associated with drought/flood in summer over the East of the southwestern China [J]. Acta Meteor. Sinica (in Chinese), 68 (6): 932–943, doi:10.11676/qxxb2010.088.

廖荃荪, 陈桂英, 陈国珍. 1981. 长期天气预报文集 [M]. 北京: 气象出版社, 103–114. Liao Quansun, Chen Guiying, Chen Guozhen. 1981. Long-Term Weather Forecast Corpus (in Chinese) [M]. Beijing: China Meteorological Press, 103–114.

施能, 古文保. 1993. 大气环流异常分析中使用合成方法的一个问题 [J]. 气象, 19 (9): 32–34. Shi Neng, Gu Wenbao. 1993. A note on composite analysis of atmospheric circulation anomalies [J]. Meteor. Mon. (in Chinese), 19 (9): 32–34.

施能, 朱乾根, 吴彬贵. 1996. 近 40 年东亚夏季风及我国夏季大尺度天气气候异常 [J]. 大气科学, 20 (5): 575–583. Shi Neng, Zhu Qian'gen, Wu Bingui. 1996. The East Asian summer monsoon in relation to summer

large scale weather-climate anomaly in China for last 40 years [J]. Chinese Journal of Atmospheric Sciences (in Chinese), 20 (5): 575–583, doi:10.3878/j.issn.1006-9895.1996.05.08.

施能, 杨永胜, 陈辉. 2001. 我国东部夏季降水百年雨型的多时间尺度变化特征研究 [J]. 气象科学, 21 (3): 316–325. Shi Neng, Yang Yongsheng, Chen Hui. 2001. A study on the features of East-China summer rainfall pattern on the multi-time scale in the past 98 years [J]. Scientia Meteorologica Sinica (in Chinese), 21 (3): 316–325, doi:10.3969/j.issn.1009–0827.2001.03.008.

施能, 陈辉, 冯俊茹, 等. 1999. 我国夏季雨型的前期异常特征及预报方法的初步研究 [J]. 应用气象学报, 10 (S): 70–79. Shi Neng, Chen Hui, Feng Junru, et al. 1999. Study on the preceding anomalous characteristics and forecasting method for summer rainfall patterns in eastern China [J]. Quart. J. Appl. Meteor. (in Chinese), 10 (S): 70–79, doi:10.3969/j.issn.1001–7313.1999.z1.009.

Simmonds I, Bi D H, Hope P. 1999. Atmospheric water vapor flux and its association with rainfall over China in summer [J]. J. Climate, 12 (5): 1353–1367, doi:10.1175/1520-0442(1999)012<1353:AWVFAI>2.0.CO; 2.

Sun L, Shen B Z, Sui B. 2010. A study on water vapor transport and budget of heavy rain in Northeast China [J]. Adv. Atmos. Sci., 27 (6): 1399–1414, doi:10.1007/s00376-010-9087-2.

孙林海, 赵振国, 许力, 等. 2005. 中国东部季风区夏季雨型的划分及其环流成因分析 [J]. 应用气象学报, 16 (S): 56–62. Sun Linhai, Zhao Zhenguo, Xu Li, et al. 2005. Study of summer rain pattern in monsoon region of East China and its circulation cause [J]. Journal of Applied Meteorological Science (in Chinese), 16 (S): 56–62, doi:10.3969/j.issn.1001-7313.2005.z1.007.

田红, 郭品文, 陆维松. 2002. 夏季水汽输送特征及其与中国降水异常的关系 [J]. 南京气象学院学报, 25 (4): 496–502. Tian Hong, Guo Pinwen, Lu Weisong. 2002. Features of water vapor transfer by summer monsoon and their relations to rainfall anomalies over China [J]. Journal of Nanjing Institute of Meteorology (in Chinese), 25 (4): 496–502, doi:10.3969/j.issn.1674-7097.2002.04.009.

涂长望, 黄仕松. 1944. 夏季风进退 [J]. 气象杂志, 18: 1–20. Tu Changwang, Huang Shisong. 1944. The advance and retreat of the summer monsoon [J]. Meteorological Magazing (in Chinese), 18: 1–20.

Wang B, Lee J Y, Kang I S, et al. 2009. Advance and prospectus of seasonal prediction: assessment of the APCC/CliPAS 14-model ensemble retrospective seasonal prediction (1980–2004) [J]. Climate Dyn., 33 (1): 93–117, doi:10.1007/s00382-008-0460-0.

王绍武, 黄建斌. 2006. 近千年中国东部夏季雨带位置的变化 [J]. 气候变化研究进展, 2 (3): 117–121. Wang Shaowu, Huang Jianbin. 2006. The variations of geographical latitude of rain belts in summer over eastern China during the last millennium [J]. Advances in Climate Change Research (in Chinese), 2 (3): 117–121.

王绍武, 叶瑾林, 龚道溢, 等. 1998. 中国东部夏季降水型的研究 [J]. 应用气象学报, 9 (S): 65–74. Wang Shaowu, Ye Jinlin, Gong Daoyi, et al. 1998. Study on the patterns of summer rainfall in eastern China [J]. Quart. J. Appl. Meteor. (in Chinese), 9 (S): 65–74.

魏凤英, 陈官军, 李茜. 2012. 中国东部夏季不同雨带类型的海洋和环流特征差异 [J]. 气象学报, 70 (5): 1004–1020. Wei Fengying, Chen Guanjun, Li Qian. 2012. Differences of oceanic and atmospheric circulation features among the rainfall band patterns in summer in eastern China [J]. Acta Meteor. Sinica (in Chinese), 70 (5): 1004–1020, doi:10.11676/qxxb2012.084.

Wu R G, Wen Z P, Yang S, et al. 2010. An interdecadal change in Southern China summer rainfall around 1992/93 [J]. J. Climate, 23 (9): 2389–2403, doi:10.1175/2009JCLI3336.1.

谢义炳, 戴武杰. 1959. 中国东部地区夏季水汽输送个例计算 [J]. 气象学报, 30 (2): 173–185. Xie Yibing, Dai Wujie. 1959. Certain computational results of water vapour transport over eastern China for a selected synoptic case [J]. Acta Meteor. Sinica (in Chinese), 30 (2): 173–185, doi:doi:10.11676/qxxb1959.021.

谢安, 毛江玉, 宋焱云, 等. 2002. 长江中下游地区水汽输送的气候特征 [J]. 应用气象学报, 13 (1): 67–77. Xie An, Mao Jiangyu, Song Yanyun, et al. 2002. Climatological characteristics of moisture transport over Yangtze River Basin [J]. Journal of Applied Meteorological Science (in Chinese), 13 (1): 67–77, doi:10.3969/j.issn.1001-7313.2002.01.008.

徐祥德, 陶诗言, 王继志, 等. 2002. 青藏高原—季风水汽输送“大三角扇形”影响域特征与中国区域旱涝异常的关系 [J]. 气象学报, 60 (3): 257–266. Xu Xiangde, Tao Shiyan, Wang Jizhi, et al. 2002. The relationship between water vapor transport features of Tibetan Plateau-monsoon “large triangle” affecting region and drought-flood abnormality of China [J]. Acta Meteor. Sinica (in Chinese), 60 (3): 257–266, doi:10.11676/qxxb2002.032.

Yang L, Zhao J H, Feng G L. 2016. Classification of typical summer rainfall patterns in the East China monsoon region and their association with the East Asian summer monsoon [J]. Theor. Appl. Climatol., doi:10.1007/s00704-016-1843-5.

叶敏, 封国林. 2015. 长江中下游地区夏季降水的水汽路径的客观定量化研究 [J]. 大气科学, 39 (4): 777–788. Ye Min, Feng Guolin. 2015. Objective quantification of moisture transport that influences summer rainfall in the middle and lower reaches of the Yangtze River [J]. Chinese Journal of Atmospheric Sciences (in Chinese), 39 (4): 777–788, doi:10.3878/j.issn.1006-9895.1409.14208.

Zhang R H. 2001. Relations of water vapor transport from Indian monsoon with that over East Asia and the summer rainfall in China [J]. Adv. Atmos. Sci., 18 (5): 1005–1017.

Zhao J H, Feng G L. 2014. Reconstruction of conceptual prediction model for the three rainfall patterns in the summer of eastern China under global warming [J]. Sci. China: Earth Sci., 57 (12): 3047–3061, doi:10.1007/s11430-014-4930-4.

Zhao J H, Yang L, Feng G L. 2017. Circulation system configuration characteristics of four rainfall patterns in summer over the East China [J]. Theor. Appl. Climatol., doi:10.1007/s00704-017-2047-3. (in press)

赵俊虎, 封国林, 杨杰, 等. 2012. 夏季西太平洋副热带高压的不同类型与中国汛期大尺度旱涝的分布 [J]. 气象学报, 70 (5): 1021–1031. Zhao Junhu, Feng Guolin, Yang Jie, et al. 2012. Analysis of the distribution of the large scale drought/flood of summer in China under different types of the western Pacific subtropical high [J]. Acta Meteor. Sinica (in Chinese), 70 (5): 1021–1031, doi:10.11676/qxxb2012.085.

赵俊虎, 支蓉, 申茜, 等. 2014. 2012 年我国夏季降水预测与异常成因分析 [J]. 大气科学, 38 (2): 237–250. Zhao Junhu, Zhi Rong, Shen Qian, et al. 2014. Prediction of the distribution of the 2012 summer rainfall in

China and analysis of the cause for anomaly [J]. Chinese Journal of Atmospheric Sciences (in Chinese), 38 (2): 237–250, doi:10.3878/j.issn.1006-9895.2013.12215.

Zhou T J, Yu R C. 2005. Atmospheric water vapor transport associated with typical anomalous summer rainfall patterns in China [J]. J. Geophys. Res., 110 (D8): D08104, doi:10.1029/2004JD005413.

周晓霞, 丁一汇, 王盘兴. 2008. 影响华北汛期降水的水汽输送过程 [J]. 大气科学, 32 (2): 345–357. Zhou Xiaoxia, Ding Yihui, Wang Panxing. 2008. Features of moisture transport associated with the precipitation over North China during July−August [J]. Chinese Journal of Atmospheric Sciences (in Chinese), 32 (2): 345–357, doi:10.3878/j.issn.1006-9895.2008.02.13.

周天军, 宇如聪, 张学洪, 等. 2001. 海气耦合气候模式对大气中水汽输送、辐散辐合与海气间水通量交换的模拟 [J]. 大气科学, 25 (5): 596–608. Zhou Tianjun, Yu Rucong, Zhang Xuehong, et al. 2001. Features of atmospheric moisture transport, convergence and air–sea freshwater flux simulated by the coupled climate models [J]. Chinese Journal of Atmospheric Sciences (in Chinese), 25 (5): 596–608, doi:10.3878/j.issn.1006-9895.2001.05.03.

竺可桢. 1934. 东南季风与中国之雨量 [J]. 地理学报, (1): 1–27. Zhu Kezhen. 1934. The enigma of southeast monsoon in China [J]. Acta Geographica Sinica (in Chinese), (1): 1–27.

Detection of Anthropogenic Influence on Fixed Threshold Indices of Extreme Temperature

HONG YIN

National Climate Center, Laboratory for Climate Studies, China Meteorological Administration, Beijing, China

YING SUN

National Climate Center, Laboratory for Climate Studies, China Meteorological Administration, Beijing, and Collaborative Innovation Center on Forecast and Evaluation of Meteorological Disasters, Nanjing University of Information Science and Technology, Nanjing, China

(Manuscript received 14 December 2017, in final form 4 May 2018)

ABSTRACT

Threshold indices of extreme temperature are defined based on temperature values that fall above or below fixed thresholds and thus have important implications for agriculture, engineering, and human health. Here, we focus on four extreme temperature fixed threshold indices and their detection and attribution at the global and continental scales, as well as within China. These indices include the number of days with daily minimum temperatures below 0°C [frost days (FD)] and above 20°C [tropical nights (TR)] and the number of days with daily maximum temperatures below 0°C [ice days (ID)] and above 25°C [summer days (SU)]. We employ an optimal fingerprinting method to compare the spatial and temporal changes in these fixed threshold indices assessed from observations and simulations performed with multiple models. We find that an anthropogenic signal can be robustly detected in these fixed threshold indices at scales of over the globe, most of the continents, and China. A natural signal cannot be identified in the changes in most of the indices, thus indicating the dominant role of anthropogenic forcing in producing these changes. In North and South America, the models show poor performance in reproducing the fixed threshold indices related to daily maximum temperature. The changes in summer days are not clearly related to their responses to external forcing over these two continents. This study provides a useful complement to other detection studies and sheds light on the importance of anthropogenic forcing in determining most of the fixed threshold indices at the global scale and over most of the continents, compared with internal variability.

1. Introduction

The Fifth Assessment Report (AR5) of Working Group I of the Intergovernmental Panel on Climate Change (IPCC) concludes that "warming of the climate system is unequivocal" (IPCC 2013, p. 4). Climate extremes display clear changes, and all temperature-related indices show significant and widespread warming trends. Since the mid-twentieth century, the numbers of cold days and nights have decreased, whereas the numbers of warm days and nights have increased globally (Alexander et al. 2006; Zhang et al. 2011; Donat et al. 2014). The extreme temperature indices calculated from daily minimum (nighttime) temperatures generally show stronger trends than those calculated from daily maximum (daytime) temperatures. These changes in extreme temperatures have had substantial impacts on society, human health, the economy, and ecosystems. Many authors have investigated different aspects of extreme temperature changes, including their intensity, frequency, and duration. Most studies focus on changes in the intensity and frequency of extreme temperatures because of the high representativeness of these indices. Although the fixed threshold indices are not necessarily meaningful for all climate zones because of the fixed thresholds used in the definitions of the indices, changes in these indices can have profound impacts on particular sectors of society or ecosystems (Alexander et al. 2006).

Denotes content that is immediately available upon publication as open access.

Corresponding author: Ying Sun, sunying@cma.gov.cn

DOI: 10.1175/JCLI-D-17-0853.1

© 2018 American Meteorological Society. For information regarding reuse of this content and general copyright information, consult the AMS Copyright Policy (www.ametsoc.org/PUBSReuseLicenses).

For example, changes in frost days may affect agricultural practices and engineering applications (e.g., Terando et al. 2012). Increases in tropical nights may have serious impacts on human health and are thought to occur primarily in combination with extended heat wave events, particularly in subtropical regions (Sillmann and Roeckner 2008). However, these fixed threshold indices have received less attention than other indices in previous studies, although a few studies indicate that the fixed threshold indices display pronounced changes at the global and regional scales (Donat et al. 2013; Zhou et al. 2016). Sillmann et al. (2013a,b) show that the CMIP5 models are generally able to reproduce the increasing trends in the warm fixed threshold indices (those for summer days and tropical nights) and the decreasing trends in the cold indices (ice days and frost days; these and the preceding indices are defined in section 2) when their anomalies relative to a reference period are considered. These models also project future increases in warm days and decreases in cold days.

There is a clear societal interest in whether changes in extreme events can be linked to anthropogenic forcing or natural climate variability. Many studies have indicated the existence of a human influence on the climate system. Previous studies have shown that the anthropogenic forcing can be identified in long-term changes in extreme temperatures at the global and continental scales, as well as within some countries (Christidis et al. 2005, 2011; Zwiers et al. 2011; Stott et al. 2011; Wen et al. 2013; Kim et al. 2016; Sun et al. 2016; Lu et al. 2016; Yin et al. 2017; Dong et al. 2018). Christidis et al. (2005) applied the optimal fingerprinting method to detect the anthropogenic influence on long-term changes in extreme temperature at the global scale for the first time. Different researchers subsequently used various sets of climate models and methods to identify clear anthropogenic fingerprints in the intensity and frequency of extreme temperatures at the continental and national scales (Min et al. 2013; Wen et al. 2013; Morak et al. 2013; Lu et al. 2016; Yin et al. 2017; Dong et al. 2018). In addition, attribution studies that investigate individual extreme events show that anthropogenic forcing clearly increases the occurrence probability of extreme events associated with high temperatures in different countries (Lewis and Karoly 2013; Sun et al. 2014). Recently, Christidis and Stott (2016) focused on 16 extreme temperature indices and detected anthropogenic forcing signals in these indices in Europe and at the quasi-global scale using HadGEM2-ES Earth system model for the analysis of multidecadal changes and HadGEM3-A atmospheric model for event attribution. This study provides a strong indication that the human influence has significantly influenced the characteristics of temperature extremes in recent decades, and the anthropogenic signal may rise above the internal variability both quasi-globally and on continental scales. However, Christidis and Stott (2016) also note that the effects of the human influence cannot be detected for the frost days and ice days threshold indices. They suggest that the reasons include a high degree of natural variability and the fact that the indices are defined relative to a temperature threshold (0°C) that is not relevant in warmer regions.

These previous studies show clearly that the detection of intensity-based (Min et al. 2013; Wen et al. 2013, Kim et al. 2016; Yin et al.2017) and frequency-based (Morak et al. 2013; Lu et al. 2016) indices of extreme temperature have been widely investigated, whereas other indices, such as fixed threshold indices, have not. The study by Christidis and Stott (2016) is based on only one climate model and focuses on the globe and Europe. The optimal fingerprint method developed by Allen and Stott (2003) was used in this study, and the spatial–temporal evolution of the extreme temperatures were projected to the first few leading empirical orthogonal functions (EOFs) of the model-simulated variability. Whether the changes in these fixed threshold indices in other regions of the world can be detected using the multimodel results is unclear. Here, we focus on four fixed threshold indices, as defined by the Expert Team on Climate Change Detection and Indices (ETCCDI), at the global and continental scales, as well as China. We use the outputs from multiple models that participated in phase 5 of the Coupled Model Intercomparison Project (CMIP5) (Taylor et al. 2012), the HadEX2 observational dataset, and observational data from stations in China. Multimodel ensembles generally provide better estimates of the response of the climate system to external forcings than individual models because the multimodel ensemble has very little influence of internal climate variability. The use of different observational datasets provides an opportunity to test the influence of observational data on the detection results. We also employ an improved detection method that is based on regularized covariance estimation (Ribes and Terray 2013); moreover, we conduct dimension reduction prior to the detection analysis, rather than relying on EOF truncation.

The structure of this paper is as follows. Section 2 describes the observational datasets and the output from the model simulations. The detection methods and data processing procedures are described in section 3. The main results are presented in section 4. The discussion and conclusions are provided in section 5.

2. Data

a. Study region and extreme temperature indices

In this study, detection and attribution are conducted for the globe (GLB) and five continental regions defined

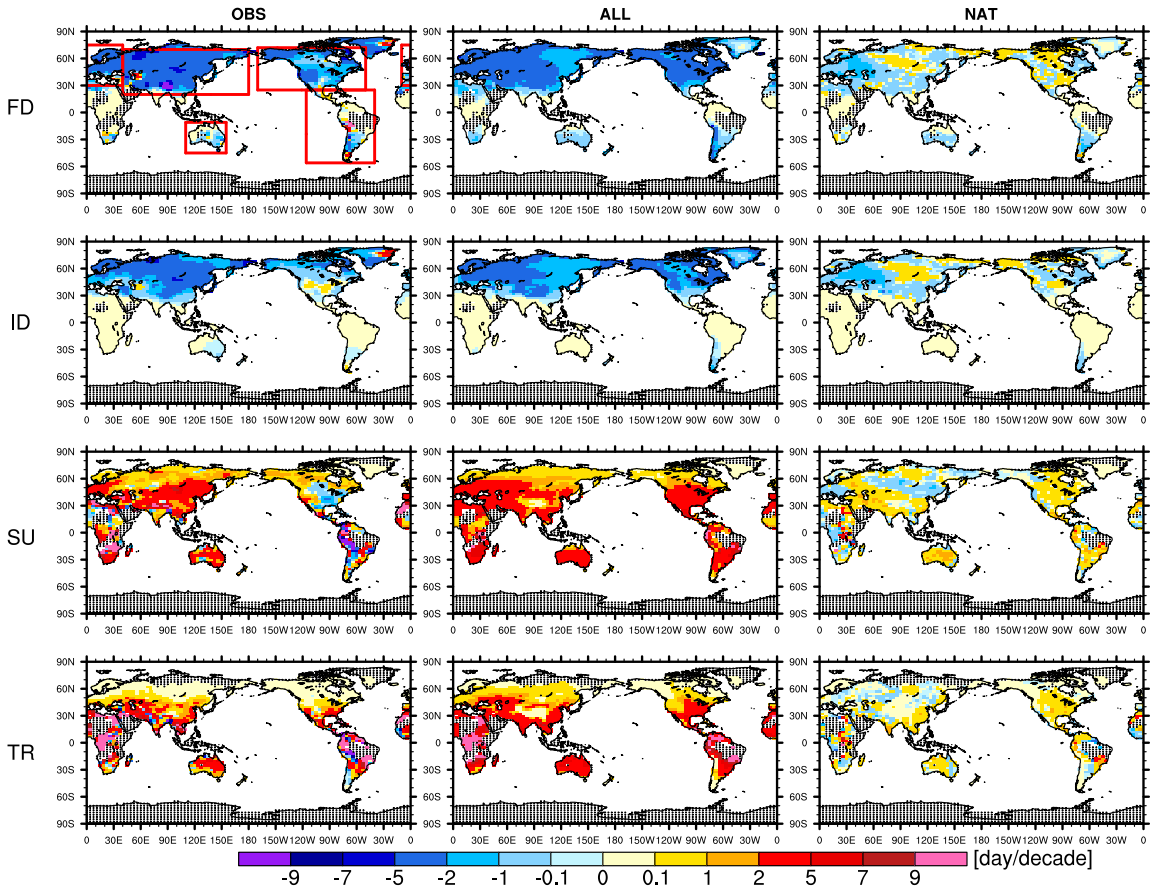

FIG. 1. Geographical distributions of the (left) observed and also the multimodel mean simulated trends under the (middle) ALL and (right) NAT forcings for four extreme temperature indices during 1961–2010. The trends were computed for grid cells with at least 40 years of data available. The black dots in the figure indicate land grid boxes where observations are not available.

by Giorgi and Francisco (2000), specifically Europe (EUR; 30°–75°N, 10°W–40°E), Asia (ASI; 20°–70°N, 40°–180°E), Australia (AUS; 45°–11°S, 110°–155°E), North America (NAM; 25°–72°N, 170°–50°W), and South America (SAM; 56°S–25°N, 116°–40°W) (boxes in Fig. 1). China (CHI) is also used as a study region, since we have a strong interest in changes in extreme temperatures in that country.

The ETCCDI has defined a set of core extreme indices, including percentile-based, absolute, fixed threshold, and duration indices, which can be used to assess different aspects of changes in climate extremes (e.g., Alexander et al. 2006; Zhang et al. 2011). In this study, we focus on the fixed threshold indices of extreme temperature, specifically the annual number of days when the daily maximum temperature is less than 0°C [ice days (ID)], the annual number of days when the daily minimum temperature is less than 0°C [frost days (FD)], the annual number of days when the daily maximum temperature exceeds 25°C [summer days (SU)], and the annual number of days when the daily minimum temperature exceeds 20°C [tropical nights (TR)]. These four fixed threshold indices are calculated for observations and models using the standard code provided by ETCCDI for generating extreme indices (Zhang et al. 2011).

b. *Observations and model simulations*

Daily observational data from HadEX2 and observations made at stations within China are used to calculate the extreme temperature indices. HadEX2 is the second generation of the global land extreme indices dataset developed by Donat et al. (2013) (https://www.climdex.org/gewocs.html). It is based on high-quality observations from over 7000 stations distributed over the global land area with the angular distance weighting interpolation method (Shepard 1968) applied to grid the station data into 3.75° longitude × 2.5° latitude grid box values. The data cover the period of 1901–2010; however, we only use the information after 1961, given the good-quality, better, and more consistent data density/sampling of the data in that period. The extreme indices

calculated from these data within grid boxes are used for the global and continental analyses. For the analyses in China, both the HadEX2 data and the observational data from 2419 stations within China are used for the detection analyses, and the results are compared. The data from stations within China have been homogenized (Cao et al. 2016) using the RHtest V3 software package (Wang and Feng 2010; available at http://etccdi.pacificclimate.org/software.shtml). It is a set of high-quality homogenized data that has undergone strict quality control and has been widely used operationally and in scientific research (e.g., Sun et al. 2016). The values of the extreme indices are first calculated at each station, and the 1961–90 mean is then removed from the individual station series. All of the index data are then averaged onto the 3.75° longitude × 2.5° latitude grid used in HadEX2.

The model data include daily outputs from the CMIP5 model experiments performed under combined historical anthropogenic and natural (ALL) forcings, natural-only (NAT) forcing, greenhouse gas (GHG) forcing, and control experiments. The extreme indices calculated by Sillmann et al. (2013a,b) for the twentieth and the twenty-first centuries—that is, the historical experiments and the representative concentration pathway (RCP) experiments, respectively—are used in this study. The index data that are not available from this earlier study are calculated using the same calculation code for generating extreme indices (Zhang et al. 2011). In total, the ALL forcing experiments include 82 historical simulations performed using 18 climate models for which at least 3 simulations are available. The NAT and GHG forcing experiments include 26 historical simulations from 6 models and 23 simulations from 5 models, respectively. Table 1 lists the number of model simulations that are available for the different forcing experiments used in this study. Because some of the ALL forcing simulations end in 2005, the RCP4.5 simulations for the period of 2006–10 are used to extend the ALL forcing simulations since the differences among the different RCP scenarios during the early twenty-first century are negligible. The response to the anthropogenic forcing (ANT) is estimated from the differences between the model responses to the ALL and NAT forcings. Some studies have shown that temperature responses to different components of external forcings are generally linearly additive at the global and continental scales (Gillett et al. 2004; Shiogama et al. 2013; Marvel et al. 2015). All of the simulations used in this study cover the period from 1961 to 2010.

All of the available model data are regridded using the same 3.75° × 2.5° grid as the HadEX2 dataset. The data are also masked according to the availability of the gridded observed data. Global and regional averages are then calculated to obtain mean time series of the annual temperature indices. The multimodel ensemble mean is computed by first calculating ensemble means from the individual model runs and then averaging over all the available models. The linear trends of observation and multimodel ensemble means are calculated using Kendall's tau method (Sen 1968) because some of the threshold index data in some of the regions are zero.

TABLE 1. List of multimodel simulations used in this study. Numbers represent the sizes (numbers of simulations) of the ALL, GHG, and NAT ensembles or the number of 50-yr chunks for the CTL simulations. (Expansions of acronyms are available online at http://www.ametsoc.org/PubsAcronymList.)

Model name	ALL (18)	GHG (5)	NAT (6)	CTL (28)
BCC-CSM1.1	3			8
BCC-CSM1.1-m	3			6
CanESM2	5	5	5	18
CCSM4	3			2
CESM1-BGC				8
CMCC-CESM				4
CMCC-CM				5
CMCC-CMS				8
CMCC-CM5		6	6	14
CNRM-CM5	10			
CSIRO-Mk3.6.0	10	5	5	8
EC-EARTH				
FGOALS-s2	3			8
GISS-E2-R	3			
GFDL-CM3				13
GFDL-ESM2G				8
GFDL-ESM2M				8
HADCM3	10			
HadGEM2-CC				4
HadGEM2-ES	3	4	4	9
IPSL-CM5A-LR	4	3	3	16
IPSL-CM5A-MR			3	5
IPSL-CM5B-LR				5
MIROC-ESM	3			
MIROC5-ESM-CHEM				4
MIROC5-ESM				10
MIROC4H	3			1
MIROC5	5			11
MPI-ESM-LR	3			16
MPI-ESM-MR	3			16
MPI-ESM-P				19
MRI-CGCM3	5			8
NorESM1-M	3			8
Sum (models)	82 (18)	23 (5)	26 (6)	250 (28)

3. Methods and data processing

a. Detection methods

The observed extreme temperature indices are compared with the model simulations using a standard optimal fingerprinting method (Allen and Stott 2003). The

optimal fingerprinting method expresses the observed changes (Y) as the sum of signals (X) and internal unforced variability (ε); that is, $Y = (X - v)\beta + \varepsilon$. Here, the regression coefficients (or scaling factors) β that provide the best match between the model responses and the observations are determined using the total least squares method (Ribes and Terray 2013). The parameter v indicates the noise in the signal. The regression residual ε represents the internal unforced variability. If the 90% confidence interval of the scaling factor is above zero, the signals of the external forcings are considered to be detected in the observations. If the 90% ranges of the scaling factors also include unity, we conclude that the observed changes are consistent with the response of the model simulations to external forcing.

We conduct both single-signal and two-signal analyses to detect the influence of the different forcings on the changes in extreme temperature. In the single-signal analysis, the observations are regressed onto the multimodel mean responses to the individual forcings (ALL, ANT, GHG, and NAT). In the two-signal analysis, the observations are regressed onto the ALL and NAT responses simultaneously, and linear transformations are applied to the ALL and NAT scaling factors to examine the relative contributions of the NAT and ANT forcings to the observations (Tett et al. 2002; Jones et al. 2013).

b. Data processing

We conduct detection analyses on the four extreme indices, FD, ID, SU, and TR, based on their spatial and temporal evolution. The anomalies of each index are first computed relative to the 1961–90 mean in each grid box. The regional means for the individual model runs are calculated, and the multimodel ensemble mean is subsequently obtained for each region. The detection procedure is applied to the nonoverlapping 3- and 5-yr mean series that cover 1961–2010 for all of the continents and China. The use of 5- and 3-yr mean series reduces the temporal dimension but retains the influence of important natural forcings, such as volcanic eruptions.

To estimate the internal variability, the preindustrial control (CTL) simulations that lack external forcing and performed using 28 models, are split into 50-yr segments. Together with the within-ensemble difference (i.e., the residuals of the ensemble simulations after the ensemble mean has been removed), there are 284 fifty-year chunks in total. These chunks are used to estimate the scaling factor and the 90% confidence interval, as well as to test the consistency of the residuals (Ribes and Terray 2013).

4. Results

a. Observed and modeled trends

Figure 1 displays the linear trends of the four fixed threshold indices determined from the observations and the model simulations under ALL and NAT forcing. The observational data (left column) show that the cold extreme indices (FD and ID) predominantly display decreasing trends, whereas the warm extreme indices (SU and TR) generally display increasing trends. Observed trends in these indices are significant at the 5% level for most of Northern Hemisphere land grids where the indices can be computed. For the cold extreme indices, the largest negative trends are observed over the Eurasian continent at middle to high latitudes. The decreases in FD and ID in North America are smaller than those in other areas at the same latitudes, especially for ID. A positive trend is seen in the Arctic that may be related to the sparsity of data in this region and may not be real. The very small trends in the cold extremes at the low latitudes are related to the small or zero values of these indices in these areas and its trend may not be real. For the warm extreme indices, increasing trends appear almost everywhere over the global land area, except that a cooling trend is seen over the North and South Americas for SU. This warming hole in the warm extremes of North America has also been found by other studies (e.g., Sillmann et al. 2013a; Vose et al. 2017). Large positive trends are generally observed in Europe and Asia, especially in East Asia and the region of Siberia. Tropical nights appear only at middle to low latitudes, and larger trends are seen at the low latitudes than at the middle latitudes.

The multimodel simulations performed using the ALL and NAT forcings (Fig. 1, middle and right columns) show spatially smoothed distributions compared with the observations because a substantial amount of the internal variability has been removed for the model ensemble mean. The ALL results generally exhibit quite good consistency with the observations, whereas the NAT results do not reproduce most of the observed changes. For the cold extreme indices, the model simulations under ALL forcing reproduce the large negative trends in western Europe but underestimate them in Asia. The trends in ID in North America show much larger decrease in the models than in the observations. The models also simulate the small changes seen at low latitudes reasonably well. The NAT results show only very small changes in the cold extremes compared with the observations. For the warm extreme indices, the models largely reproduce the observations in western Europe, South Asia, Africa, and Australia. However, the models underestimate the large positive trends in SU

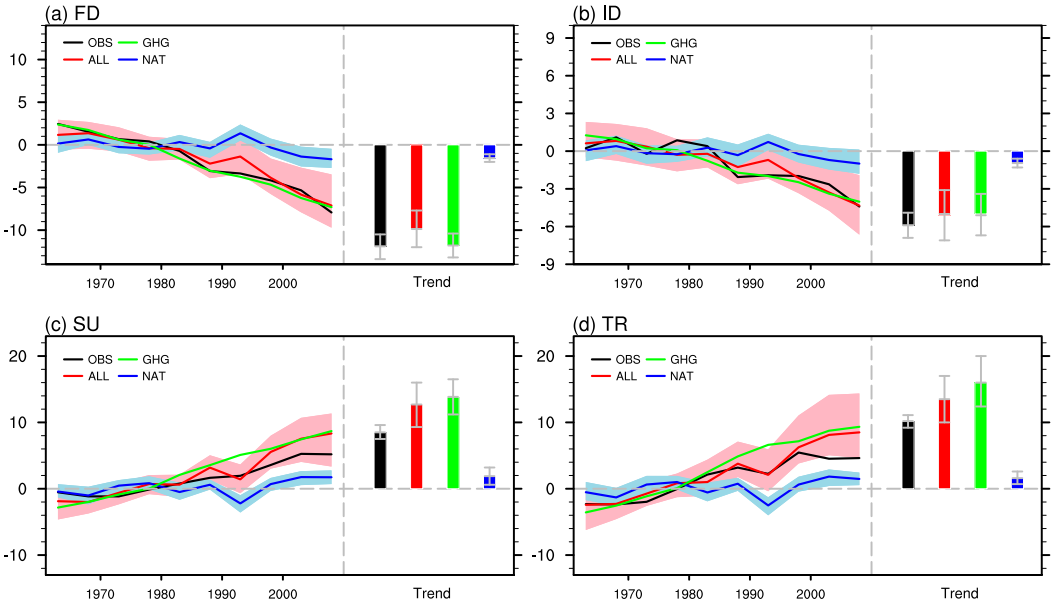

FIG. 2. (left) Global mean 5-yr mean anomalies (relative to the 1961–90 average) and (right) trends of four fixed threshold indices from the HadEX2 observational dataset (black) and the multimodel response to the ALL (red), GHG (green), and NAT (blue) forcings, respectively. Shading indicates the 5%–95% ranges of all of the individual simulations. Gray error bars (right) show the 5%–95% confidence intervals of the linear trends.

in East Asia and Siberia. The models also cannot simulate the observed negative trends in SU in North and South America and overestimate the positive trends in TR in the Americas. The NAT results show much smaller changes compared with the observations in most areas.

Figure 2 shows the global 5-yr mean anomalies of the four fixed threshold indices from observations (HadEX2) and the model simulations under the ALL, GHG, and NAT forcings. The long-term changes in multimodel responses to the ALL forcing generally exhibit good correspondence with the observations. The observations all fall well within the spread of the multimodel ensemble. For the cold extremes (FD and ID), the ALL results evolve similarly to the observations. The simulated increases in the cold extremes around the early 1990s may be related to volcanic eruptions, but this increase is not clearly seen in the 5-yr mean series for observations (although visible in the annual series). The GHG results generally display larger trends, and the NAT simulations show very small trends compared with the observed changes. For the warm extremes (TR and SU), the ALL runs slightly overestimate the observed changes after the 1990s. When compared with the observations, the GHG results show larger changes after the late 1980s but smaller changes before the early 1960s. Although the NAT results exhibit poor agreement with the observed warm extremes, they simulate distinct changes after volcanic eruptions, such as the cooling that followed the Mt. Pinatubo eruption in approximately 1991. Volcanic eruptions appear to have a smaller effect on the cold extremes than the warm extremes in the observations.

For the other continents (not shown), the ALL simulations largely display quite good consistency with the observations for the cold extremes. Very small values can be seen in both the observations and the models at the low latitudes. The GHG results display less severe cold extremes than the ALL results, whereas the NAT results are not consistent with the observations. For the warm extremes, the ALL results reproduce most of the observed changes, except in the Americas. Previous studies (e.g., Knutson et al. 2017) have shown that the observed trends in some extreme temperatures in parts of the Americas are inconsistent with CMIP5 historical runs driven by the ALL forcing; the reason for this discrepancy is unknown, but it may be due to the effects of anthropogenic aerosols, atmospheric circulation, internal climate variability, and changes in land use, among other factors. This study shows that the warming hole also cannot be simulated by the changes in the warm fixed threshold indices. In summary, all of these results confirm and support the findings from Fig. 1. In addition, we compare the 5-yr anomaly time series in China based on HadEX2 and the homogenized within-China station data (Fig. 3) and find that these two different datasets display very similar changes. This result indicates that these two observational datasets are

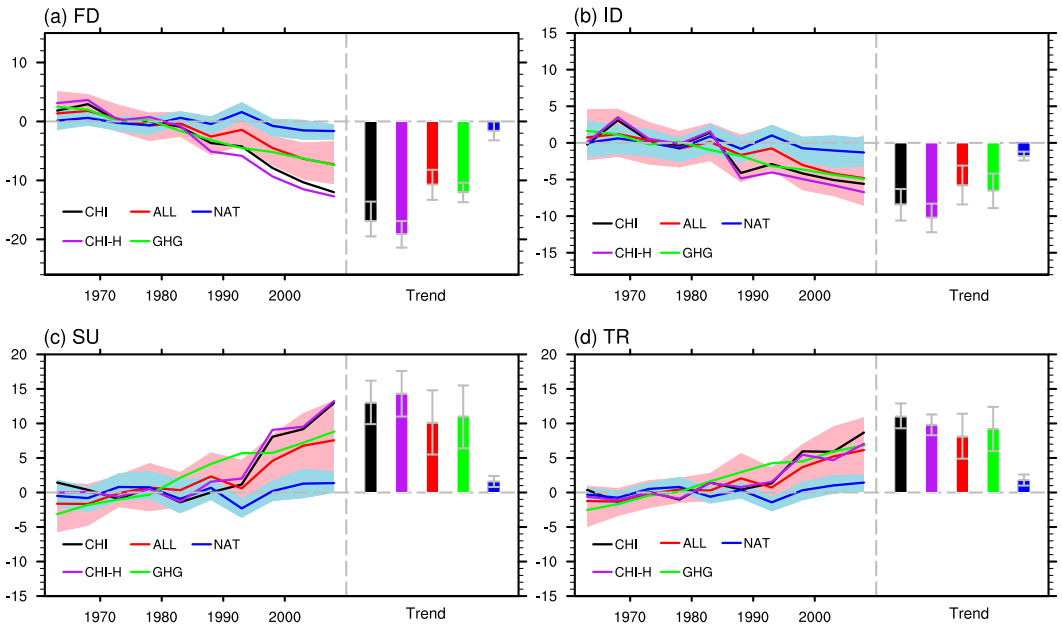

FIG. 3. China mean 5-yr mean anomalies (relative to the 1961–90 average) from two observation datasets CHI (black) and CHI-H (purple) and the multimodel response to the ALL (red), GHG (green), and NAT (blue) forcings, respectively. Shading indicates the 5%–95% ranges of all of the individual simulations. CHI is calculated based on data from more than 2000 stations within China that were obtained from the National Meteorological Information Center (NMIC) of China, whereas CHI-H is based on the HadEX2 dataset.

consistent and are of quite good quality to be used for detection studies.

b. *Detection results*

The spatial–temporal evolution of the observations and model simulations under the ALL, ANT, GHG, and NAT forcings are compared using the optimal fingerprinting method. Figure 4 shows the scaling factors and their 90% confidence intervals obtained using single-signal detection. For the cold extremes, the ALL signal can be clearly detected on the global scale, over all of the continents analyzed, and within China. The residual consistency test is generally passed; however, the models show greater (black downward triangles in Fig. 4) and smaller variability (blue upward triangles) than the observations in NAM and ASI, implying that the uncertainty range of the scaling factors can be conservative or overestimated, respectively. The best estimates of the scaling factors are close to unity over the globe and EUR, suggesting a good consistency between observations and model simulations, while it is greater than unity in Asia and China and smaller than 1 in NAM, indicating an underestimate of model simulations in Asia and an overestimate for the models in NAM when compared with the observations, respectively. The ANT and GHG detection results are similar to those for the ALL signals, although their confidence intervals are slightly larger than ALL. NAT can be detected in most areas, but its scaling factors have large values and confidence intervals compared with other signals, indicating that the modeled NAT response is much smaller than the observed changes. For the warm extremes, the ALL signals cannot be detected in the changes in SU in NAM and SAM. For the other areas, the ALL signals can be detected, and the residual variability is consistent with or larger than the observations. The ANT and GHG results are generally similar to those obtained using ALL, although the residual consistency test shows slightly different results in a few regions. The NAT results show quite large values in most regions and cannot be detected in a few regions.

To simultaneously assess the separate effects of ANT and NAT, we carry out a two-signal analysis; the results are shown in Fig. 5. For the cold extremes, the ANT forcing can be detected, whereas NAT cannot be detected, on the global scale and over all of the continents. This result indicates the dominant role of the ANT forcing in producing changes in the cold extremes. The residual variability of the models is consistent with or larger than that of the observations, reflecting good detectability for the cold extremes. For the warm extremes, the ANT can be detected on the global scale and over all of the continents in TR, but it is not detected in SU over NAM and SAM. NAT cannot be detected in

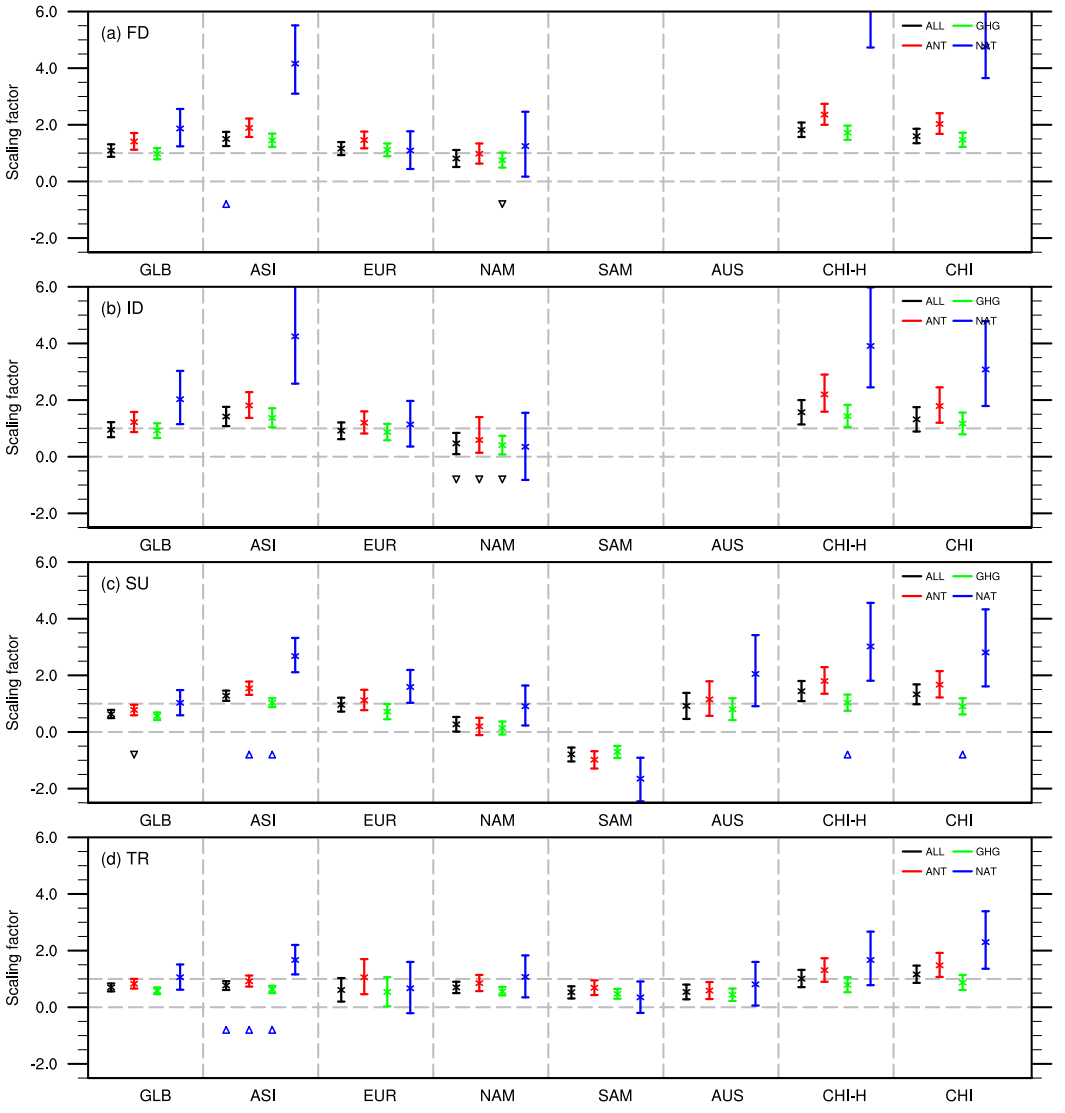

FIG. 4. Best estimates of scaling factors and their 5%–95% confidence intervals from single-signal analyses from 1961 to 2010 for the globe (GLB), Asia (ASI), Europe (EUR), North America (NAM), South America (SAM), Australia (AUS), and China (CHI). See the caption of Fig. 3 for information on CHI and CHI-H data. The black downward triangles indicate that the variability in the model simulations is overestimated, according to the residual consistency test, whereas the blue upward triangles indicate small variability in the model simulations.

most regions. All of these results show the strong effects of the human influence on the fixed threshold indices and confirm the robustness of the detection results obtained using single-signal detection. We also note that very similar detection results are obtained in China using the two different datasets. This result suggests a robust influence of anthropogenic forcing on the fixed threshold indices of extreme temperatures in China.

We further estimate the attributable contributions from the ALL, ANT, and NAT signals to the long-term trends of the observed indices from 1961 to 2010 for the globe, the continents and China (Fig. 6). These are estimated as the linear trends of model-simulated signals multiplied by corresponding scaling factors along with their 90% confidence intervals, which are the part of the observed trend explained by model simulations from different forcings. The best estimates of the ANT contributions to the observed trends in the four temperature indices exceed 90% for most of the regions where the ALL signal can be detected. The ANT attributable contributions for FD, ID, SU, and TR at the global scale are 11.5 days, 5.5 days, 8.0 days, and 9.6 days, and the corresponding 90% ranges are 9.0–14.2 days, 3.5–7.7 days, 5.7–10.4 days, and 7.4–11.9 days, respectively.

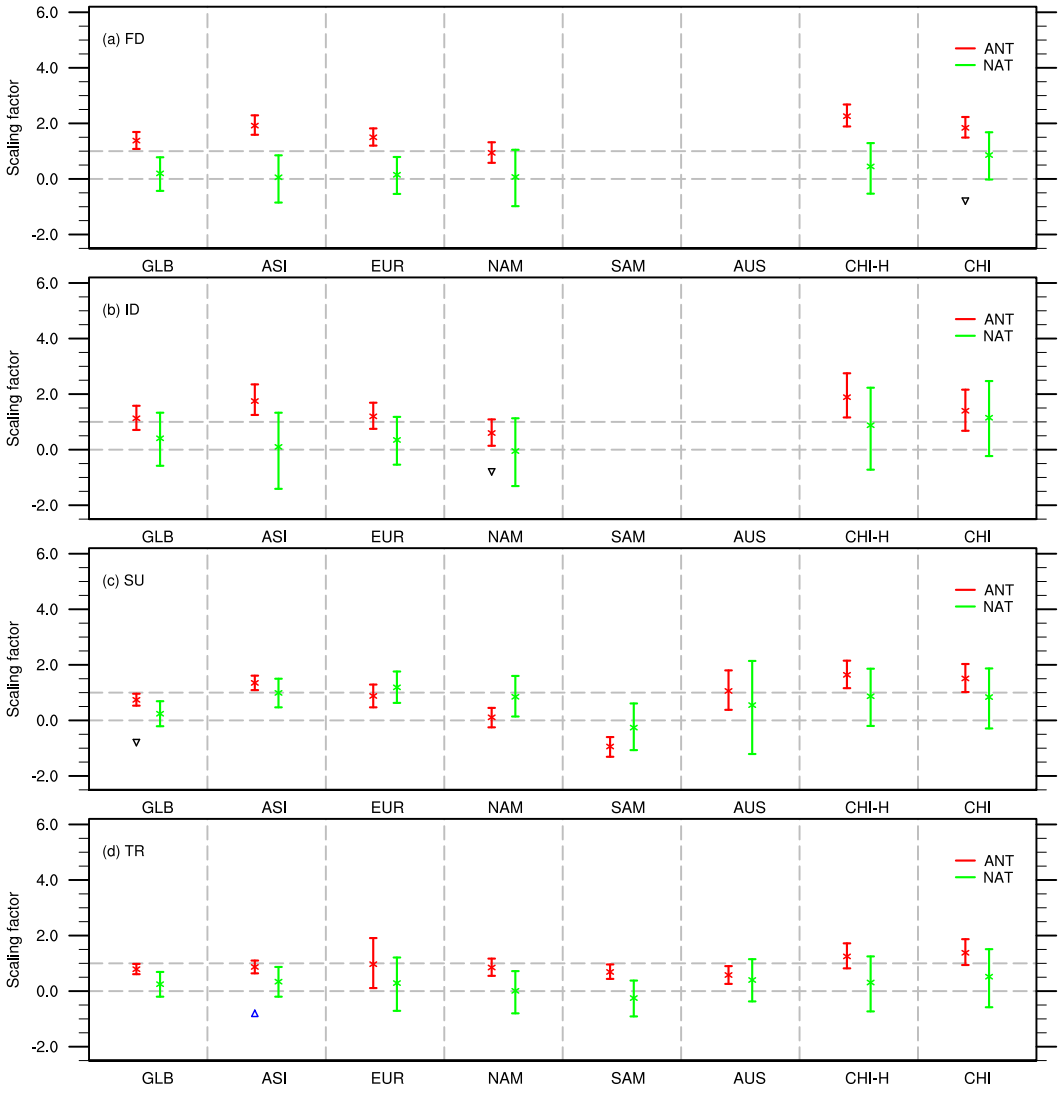

FIG. 5. As in Fig. 4, but for two-signal analyses.

The NAT contribution is less than 10% in most of the regions.

We conduct a series of sensitivity tests to examine the robustness of our detection results. We first evaluate the effects of different methods for reducing the temporal dimension on the detection results, including the use of 3-yr and 5-yr mean nonoverlapping series in the analyses. The scaling factors are quite similar for the two methods, reflecting the robustness of the detection results. We also found the order of operations for estimating trends from multimodel ensembles has little effect: the trend based on multimodel average of the indices is similar to the ensemble mean of trends computed from individual models. We then evaluate the influence of different global averages on the global detection results. Specifically, we consider the global average of the indices over all of the continents and the global average considering only the regions where the fixed threshold indices have observed values; for example, FD and ID are seen only at middle and high latitudes, whereas SU and TR occur only at low latitudes. We find the detection results are similar when different global averages are considered. We also test the influence of the different observational datasets on the detection results in China and obtain robust conclusions about the human influence, as indicated in the previous paragraphs.

5. Discussion and conclusions

Understanding the causes of observed climate changes and the underlying mechanisms provides an

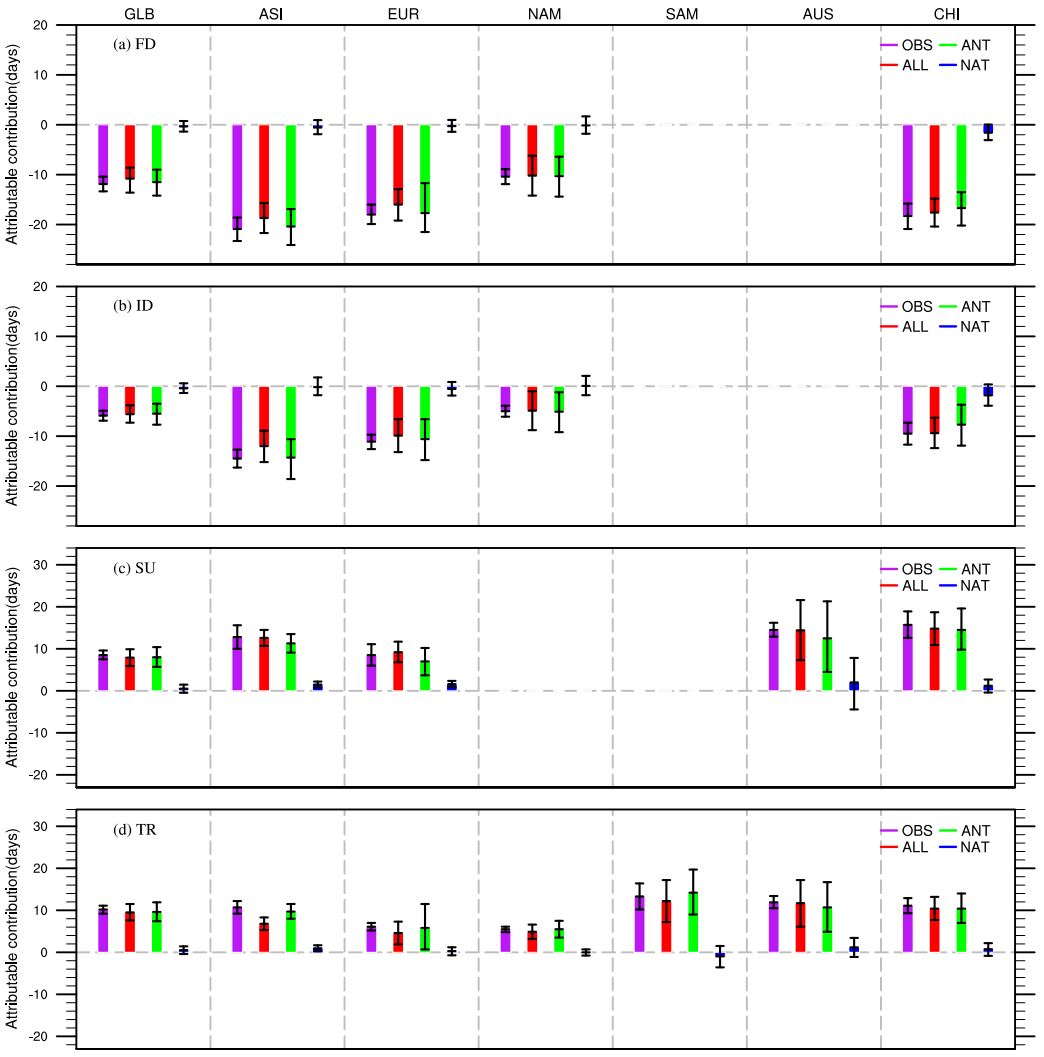

FIG. 6. The warming attributable to the ALL, ANT, and NAT forcings of the observed extreme temperature indices (OBS) and its 5%–95% confidence interval. The attributable contribution is estimated by multiplying the linear least squares trends in the relevant time series by the corresponding scaling factors.

important basis for properly projecting future climate conditions and for making decisions to adapt to climate change. This study focuses on the detection of the fixed threshold indices of extreme temperature at the global scale, as well as over five of the continents and China, using the results of a multimodel ensemble for the first time. The results show that the CMIP5 multimodel simulations generally reproduce the observed changes in the fixed threshold indices of extreme temperature, both at the global scale and over most of the continents. The indices related to the daily maximum temperature in the Americas show some degree of inconsistency with the observations; the reasons for this inconsistency are unknown. The detection analyses show that an anthropogenic signal can be identified for most of the fixed threshold indices, whereas the natural signal cannot be detected. The models generally underestimate the changes in the cold fixed threshold indices but show different features in reproducing the warm fixed threshold indices for different continents. The ANT signal cannot be detected in the changes in summer days in North and South America, which lends additional support to the conclusion from the Fourth National Climate Assessment in the United States (Knutson et al. 2017) that the anthropogenic forcing in temperature extremes in the United States can be detected with only medium confidence. In addition, our study show that the human influence on extreme temperature changes in China is clear and robust based on two different observational datasets. Together with other previous studies

(Lu et al. 2016; Yin et al. 2017), our results indicate that the anthropogenic forcing has affected various aspects of extreme temperatures in China.

Compared with previous findings by Christidis and Stott (2016), this study provides new insights into the anthropogenic influence on the fixed threshold indices at the global scale and continental scales using multimodel results. The human influence is clearly seen in the changes in FD and ID, which may be due to the use of a multimodel ensemble and/or the use of an improved detection method that does not employ EOF truncation and includes a different regional averaging method. The detection over five continents and China provides new evidence of human influence on the fixed threshold indices changes at the continental scale and over China. However, more studies will be conducted in the near future to identify the reasons why the anthropogenic signal is not detected in the changes of summer days over the Americas.

Acknowledgments. We thank three anonymous reviewers for their helpful comments. We thank Xuebin Zhang for his constructive suggestions. We acknowledge the Program for Climate Model Diagnosis and Intercomparison and the Working Group on Coupled Modeling of the World Climate Research Programme (WCRP) for their roles in making the WCRP CMIP multimodel datasets available. This study was supported by the National Key R&D Program of China (2018YFA0605604), the National Science Foundation of China (41675074), and Climate Project (CCSF201805).

REFERENCES

Alexander, L. V., and Coauthors, 2006: Global observed changes in daily climate extremes of temperature and precipitation. *J. Geophys. Res.*, **111**, D05109, https://doi.org/10.1029/2005JD006290.

Allen, M. R., and P. A. Stott, 2003: Estimating signal amplitudes in optimal fingerprinting. Part I: Theory. *Climate Dyn.*, **21**, 477–491, https://doi.org/10.1007/s00382-003-0313-9.

Cao, L., Y. Zhu, G. Tang, F. Yuan, and Z. Yan, 2016: Climatic warming in China according to a homogenized dataset from 2419 stations. *Int. J. Climatol.*, **36**, 4384–4392, https://doi.org/10.1002/joc.4639.

Christidis, N., and P. A. Stott, 2016: Attribution analyses of temperature extremes using a set of 16 indices. *Wea. Climate Extremes*, **14**, 24–35, https://doi.org/10.1016/j.wace.2016.10.003.

——, ——, S. J. Brown, G. C. Hegerl, and J. Caesar, 2005: Detection of changes in temperature extremes during the second half of the 20th century. *Geophys. Res. Lett.*, **32**, L20716, https://doi.org/10.1029/2005GL023885.

——, ——, and ——, 2011: The role of human activity in the recent warming of extremely warm daytime temperatures. *J. Climate*, **24**, 1922–1930, https://doi.org/10.1175/2011JCLI4150.1.

Donat, M. G., L. V. Alexander, H. Yang, I. Durre, R. Vose, and J. Caesar, 2013: Global land-based datasets for monitoring climatic extremes. *Bull. Amer. Meteor. Soc.*, **94**, 997–1006, https://doi.org/10.1175/BAMS-D-12-00109.1.

——, J. Sillmann, S. Wild, L. V. Alexander, T. Lippmann, and F. W. Zwiers, 2014: Consistency of temperature and precipitation extremes across various global gridded in situ and reanalysis data sets. *J. Climate*, **27**, 5019–5035, https://doi.org/10.1175/JCLI-D-13-00405.1.

Dong, S., Y. Sun, E. Aguilar, X. Zhang, T. C. Peterson, L. Song, and Y. Zhang, 2018: Observed changes in temperature extremes over Asia and their attribution. *Climate Dyn.*, **51**, 339–353, https://doi.org/10.1007/s00382-017-3927-z.

Gillett, N. P., M. F. Wehner, S. F. B. Tett, and A. J. Weaver, 2004: Testing the linearity of the response to combined greenhouse gas and sulfate aerosol forcing. *Geophys. Res. Lett.*, **31**, L14201, https://doi.org/10.1029/2004GL020111.

Giorgi, F., and R. Francisco, 2000: Evaluating uncertainties in the prediction of regional climate change. *Geophys. Res. Lett.*, **27**, 1295–1298, https://doi.org/10.1029/1999GL011016.

IPCC, 2013. *Climate Change 2013: The Physical Science Basis*. T. F. Stocker et al., Eds., Cambridge University Press, 1535 pp.

Jones, G. S., P. A. Stott, and N. Christidis, 2013: Attribution of observed historical near-surface temperature variations to anthropogenic and natural causes using CMIP5 simulations. *J. Geophys. Res. Atmos.*, **118**, 4001–4024, https://doi.org/10.1002/jgrd.50239.

Kim, Y.-H., S.-K. Min, X. B. Zhang, F. Zwiers, L. V. Alexander, M. K. Donat, and Y.-S. Tung, 2016: Attribution of extreme temperature changes during 1951–2010. *Climate Dyn.*, **46**, 1769–1782, https://doi.org/10.1007/s00382-015-2674-2.

Knutson, T., J. P. Kossin, C. Mears, J. Perlwitz, and M. F. Wehner, 2017: Detection and attribution of climate change. Climate Science Special Report: Fourth National Climate Assessment, Vol. I, D. J. Wuebbles et al., Eds., U.S. Global Change Research Program, 114–132, https://doi.org/10.7930/J01834ND.

Lewis, S. C., and D. J. Karoly, 2013: Anthropogenic contributions to Australia's record summer temperatures of 2013. *Geophys. Res. Lett.*, **40**, 3705–3709, https://doi.org/10.1002/grl.50673.

Lu, C. H., Y. Sun, H. Wan, X. B. Zhang, and H. Yin, 2016: Anthropogenic influence on the frequency of extreme temperatures in China. *Geophys. Res. Lett.*, **43**, 6511–6518, https://doi.org/10.1002/2016GL069296.

Marvel, K., G. A. Schmidt, D. Shindell, C. Bonfils, A. N. LeGrande, L. Nazarenko, and K. Tsigaridis, 2015: Do responses to different anthropogenic forcings add linearly in climate models? *Environ. Res. Lett.*, **10**, 104010, https://doi.org/10.1088/1748-9326/10/10/104010.

Min, S.-K., X. Zhang, F. W. Zwiers, H. Shiogama, Y.-S. Tung, and M. Wehner, 2013: Multimodel detection and attribution of extreme temperature changes. *J. Climate*, **26**, 7430–7451, https://doi.org/10.1175/JCLI-D-12-00551.1.

Morak, S., G. C. Hegerl, and N. Christidis, 2013: Detectable changes in the frequency of temperature extremes. *J. Climate*, **26**, 1561–1574, https://doi.org/10.1175/JCLI-D-11-00678.1.

Ribes, A., and L. Terray, 2013: Application of regularised optimal fingerprint to attribution. Part II: Application to global near-surface temperature. *Climate Dyn.*, **41**, 2837–2853, https://doi.org/10.1007/s00382-013-1736-6.

Sen, P. K., 1968: Estimates of the regression coefficient based on Kendall's tau. *J. Amer. Stat. Assoc.*, **63**, 1379–1389, https://doi.org/10.1080/01621459.1968.10480934.

Shepard, D., 1968: A two-dimensional interpolation function for irregularly spaced data. *Proc. 23rd ACM Natl. Conf.*, New York, New York, Association for Computing Machines, 517–524.

Shiogama, H., D. Stone, N. Tatsuya, N. Toru, and E. Seita, 2013: On the linear additivity of climate forcing-response relationships at global and continental scales. *Int. J. Climatol.*, **33**, 2542–2550, https://doi.org/10.1002/joc.3607.

Sillmann, J., and E. Roeckner, 2008: Indices for extreme events in projections of anthropogenic climate change. *Climatic Change*, **86**, 83–104, https://doi.org/10.1007/s10584-007-9308-6.

——, V. V. Kharin, X. Zhang, F. W. Zwiers, and D. Bronaugh, 2013a: Climate extremes indices in the CMIP5 multimodel ensemble: Part 1. Model evaluation in the present climate. *J. Geophys. Res. Atmos.*, **118**, 1716–1733, https://doi.org/10.1002/jgrd.50203.

——, ——, F. W. Zwiers, X. Zhang, and D. Bronaugh, 2013b: Climate extremes indices in the CMIP5 multimodel ensemble: Part 2. Future climate projections. *J. Geophys. Res. Atmos.*, **118**, 2473–2493, https://doi.org/10.1002/jgrd.50188.

Stott, P. A., G. S. Jones, N. Christidis, F. W. Zwiers, G. Hegerl, and H. Shiogama, 2011: Single-step attribution of increasing frequencies of very warm regional temperatures to human influence. *Atmos. Sci. Lett.*, **12**, 220–227, https://doi.org/10.1002/asl.315.

Sun, Y., X. B. Zhang, F. W. Zwiers, L. C. Song, H. Wan, T. Hu, H. Yin, and G. Ren, 2014: Rapid increase in the risk of extreme summer heat in eastern China. *Nat. Climate Change*, **4**, 1082–1085, https://doi.org/10.1038/nclimate2410.

——, L. C. Song, H. Yin, B. T. Zhou, T. Hu, X. B. Zhang, and P. Stott, 2016: Human Influence on the 2015 extreme high temperature events in western China. *Bull. Amer. Meteor. Soc.*, **97**, S102–S106, https://doi.org/10.1175/BAMS-D-16-0158.1.

Taylor, K. E., R. J. Stouffer, and G. A. Meehl, 2012: An overview of CMIP5 and the experiment design. *Bull. Amer. Meteor. Soc.*, **93**, 485–498, https://doi.org/10.1175/BAMS-D-11-00094.1.

Terando, A., K. Keller, and W. E. Easterling, 2012: Probabilistic projections of agro-climate indices in North America. *J. Geophys. Res.*, **117**, D08115, https://doi.org/10.1029/2012JD017436.

Tett, S. F. B., and Coauthors, 2002: Estimation of natural and anthropogenic contributions to twentieth century temperature change. *J. Geophys. Res.*, **107**, 4306, https://doi.org/10.1029/2000JD000028.

Vose, R. S., D. R. Easterling, K. E. Kunkel, A. N. LeGrande, and M. F. Wehner, 2017: Temperature changes in the United States. Climate Science Special Report: Fourth National Climate Assessment, Vol. I, D. J. Wuebbles et al., Eds., U.S. Global Change Research Program, 185–206, https://doi.org/10.7930/J0N29V45.

Wang, X. L., and Y. Feng, 2010: RHtestsV3 User Manual. Climate Research Division, Atmospheric Science and Technology Directorate, Science and Technology Branch, Environment Canada, 27 pp.

Wen, H. Q., X. Zhang, Y. Xu, and B. Wang, 2013: Detecting human influence on extreme temperatures in China. *Geophys. Res. Lett.*, **40**, 1171–1176, https://doi.org/10.1002/grl.50285.

Yin, H., Y. Sun, H. Wan, X. Zhang, and C. Lu, 2017: Detection of anthropogenic influences on the intensity of extreme temperatures in China. *Int. J. Climatol.*, **37**, 1229–1237, https://doi.org/10.1002/joc.4771.

Zhang, X. B., L. Alexander, G. Hegerl, P. Jones, A. Klein Tank, T. C. Peterson, B. Trewin, and F. W. Zwiers, 2011: Indices for monitoring changes in extremes based on daily temperature and precipitation data. *Wiley Interdiscip. Rev.: Climate Change*, **2**, 851–870, https://doi.org/10.1002/wcc.147.

Zhou, B. T., Y. Xu, J. Wu, S. Y. Dong, and Y. Shi, 2016: Changes in temperature and precipitation extreme indices over China: Analysis of a high-resolution grid dataset. *Int. J. Climatol.*, **36**, 1051–1066, https://doi.org/10.1002/joc.4400.

Zwiers, F. W., X. B. Zhang, and Y. Feng, 2011: Anthropogenic influence on long return period daily temperature extremes at regional scales. *J. Climate*, **24**, 881–892, https://doi.org/10.1175/2010JCLI3908.1.

atmosphere

MDPI

Article

Diagnosing Changes of Winter NAO in Response to Different Climate Forcings in a Set of Atmosphere-Only Timeslice Experiments

Yu Huang [1,2], Hong-Li Ren [1,2,3,*], Robin Chadwick [4], Zhigang Cheng [1] and Quanliang Chen [1,5]

1 Sichuan Province Key Laboratory of Plateau Atmosphere and Environment, College of Atmospheric Sciences, Chengdu University of Information Technology, Chengdu 610225, China; 1240251365@qq.com (Y.H.); chengzg@cuit.edu.cn (Z.C.); chenql@cuit.edu.cn (Q.C.)
2 Laboratory for Climate Studies &CMA-NJU Joint Laboratory for Climate Prediction Studies, National Climate Center, China Meteorological Administration, Beijing 100081, China
3 Department of Atmospheric Science, School of Environmental Studies, China University of Geoscience, Wuhan 430074, China
4 Met Office Hadley Centre, Exeter EX1 3PB, UK; robin.chadwick@metoffice.gov.uk
5 Center for Plateau Atmospheric and Environmental Research, Chengdu University of Information Technology, Chengdu 610225, China
* Correspondence: renhl@cma.gov.cn

Received: 14 November 2017; Accepted: 2 January 2018; Published: 4 January 2018

Abstract: Changes of the winter North Atlantic Oscillation (NAO) variability in response to different climate forcings, and their possible causes, are decomposed and investigated using a set of atmosphere-only timeslice experiments forced by sea surface temperature (SST) from coupled runs. The results indicate that the effects of uniform SST warming and direct CO_2 radiative forcing could enhance NAO variability, while SST pattern change could lead to large inter-model difference for model simulations. For the influences of uniform SST warming and the direct CO_2 radiative effect, the most significant air temperature increases occur at mid-low latitudes instead of northern polar regions, which produces a greater meridional temperature gradient at mid-high latitudes, thus leading to enhanced westerly winds according to the thermal wind theory. The effects of uniform SST warming and CO_2 direct radiative forcing could lead to intensification of winter NAO variability, although this result does not consider ocean-atmosphere coupling. The meridional temperature gradient decreases in most areas of the northern Atlantic under the forcing of SST pattern change, but with a larger inter-model uncertainty, which makes the change of winter NAO variability in response to SST pattern change an open issue.

Keywords: changes of winter NAO variability; forcing; meridional temperature gradient; response

1. Introduction

The North Atlantic Oscillation (NAO) is a major mode of interannual variability, and manifests as a seesaw in atmospheric mass between the subtropical Azores high and the polar Icelandic low, which is most pronounced during boreal winter [1,2]. The NAO is a focus for researchers as it has a great influence on climate change and variability in the mid-latitudes [3]. For example, the distinct phases of NAO have different impacts on precipitation and atmospheric blocking in Europe [4,5]. Further studies showed that the temperature and precipitation variability over East Asia during the period 1948–2009 are connected to the NAO through its influence on the East Asian monsoon and western Pacific subtropical high [6,7].

The components of the climate system in mid-latitudes are complex and various, which makes the understanding of the NAO a frustrating issue. Dong et al. [8] and Gong et al. [9] indicated that

both the doubled CO_2 concentration compared with 1961–1990 and the increased SST caused by the increased CO_2 could induce NAO pattern change, which is associated with the changes of zonal wind, sea level pressure, and temperature [10], but the causation still seems to be uncertain [3,4]. Kelley et al. [4] found that 19 coupled model simulations from the third phase of the Coupled Model Intercomparison project (CMIP3) have differences in the location of the sea level pressure dipoles compared with the observed NAO, and Davini and Cagnazzo [11] demonstrated that some climate models are unable to correctly simulate the physical processes connected to the NAO, including the frequency of high-latitude blocking over Greenland and the related zonal wind anomalies, which may react differently to distinct scenarios of climate change. The Northern Annular Mode (NAM) has been viewed as having relevance to the NAO, both in space and time [12]. Cattiaux and Cassou [13] investigated the NAM change for the 21st century under the A2 scenario compared with 8.5 W/m^2 Representative Concentration Pathway (RCP), and found that the ensemble mean of CMIP3 generated a positive NAM trend, while the ensemble mean of CMIP5 projections exhibited a negative result, and the discrepancy could be driven by the faster Arctic sea ice loss in early winter as well as the influence of stronger warming in the western tropical Pacific in CMIP5 relative to the projections in CMIP3, which is consistent with the results from Cattiaux et al. [14].

The comprehensive understanding of the mechanisms of NAO change, particularly under future scenarios, is essential for producing more accurate climate model simulations [15]. Besides the lack of research into physical processes, one of the important reasons for imperfect model simulations is the very limited outputs for investigating cloud-radiation interaction and cloud feedback mechanisms [16].

The Cloud Feedback Model Intercomparison Project (CFMIP) aims to understand how the climate will change under future scenarios, using a number of idealized experiments. The improved assessment of cloud feedbacks combined with decomposed forcings can be helpful for better understanding of physical processes as well as mechanisms behind the changes of NAO variability. In this study, a set of timeslice experiments (pilot versions of CFMIP-3 experiments) is applied to investigate (1) the changes of winter NAO variability under different forcings; and (2) the main reasons leading to the NAO variability changes in response to different forcings. The remainder of this paper is organized as follows. Experimental design including data and methods is introduced in Section 2. Section 3 describes the features of NAO pattern changes in each experiment. In Section 4, the possible mechanisms of NAO variability changes in response to different climate forcings are investigated in detail, and finally the summary and discussions are given in Section 5.

2. Models, Experiments, and Methods

2.1. Modelsand Observational Data

In this study, monthly mean outputs from HadGEM2-ES [17], CCSM4 [18], and CNRM-CM5 [19] from the CFMIP-3 pilot experiments are used (Table 1) to estimate the changes of winter NAO variability under different climate forcings. Since the horizontal resolutions of the models are different, all model data were interpolated into a 1.25° × 1.25° grid for comparison with each other.

Table 1. Summary of models used in this study.

Model	Institute	Resolution
HadGEM2-ES (Hadley Centre Global Environmental Model version 2 Earth System model)	Met Office Hadley Centre	1.25° × 1.875°
CCSM4 (Community Climate System Model version 4)	National Center for Atmospheric Research	1.875° × 1.25°
CNRM-CM5 (Centre National de Recherches Meteorologiques global Climate Model)	Centre National de Recherches Meteorologiques/Centre Europeen de Recherche et Formation Avanceesen Calcul Scientifique	1.4° × 1.4°

The observational sea level pressure (SLP) data for the period 1948–2016 are derived from the National Centers for Environmental Prediction/National Center for Atmospheric Research (NCEP/NCAR).

2.2. Experiments

In Coupled General Circulation Models (CGCMs), quadrupled CO_2 will induce SST increases, but this does not show a homogeneous distribution. Instead, the quadrupled CO_2 will induce a patterned SST increase, which can be analyzed as a uniform SST warming, combined with the residual SST pattern change and a direct response to CO_2 forcing. A set of atmosphere-only experiments is applied in this study to diagnose the changes of winter NAO variability as well as the connected causes in response to different aspects of forcing and SST warming. The experiments are piSST, piSST4K, piSST4 $\times$ CO_2, and piSSTFuture. The piSST is an atmosphere-only (AGCM) experiment forced with monthly-varying SSTs and sea-ice from a 30-year climatology from the coupled piControl run using pre-industrial forcing. The other experiments are forced with a uniform SST increase of 4K (piSST4k), quadrupled CO_2 concentrations (piSST4 $\times$ CO_2), which is seen only by the radiation scheme, not by vegetation, a patterned SST anomaly (piSSTFuture-piSST4k), and all-forcings AGCM responses (piSSTTot, includes SST changes and the direct CO_2 effect). For piSSTFuture, a patterned SST anomaly is applied on top of the monthly-varying piSST SSTs. This anomaly is a monthly climatology of the difference between each model's own abrupt4 $\times$ CO_2 and piControl runs (using the mean of years 91–140 of abrupt $\times$ CO_2, and the parallel 50 years section of piControl), then scaled to have a global mean of 4K. Sea ice is unchanged from piSST for all experiments with HadGEM2 and CCSM4, but is allowed to vary in CNRM-CM5 in response to increased SSTs in piSSTFuture and piSST4K. The experimental designs are shown in Table 2. More details can be found in Chadwick et al. [20] and Webb et al. [21].

Table 2. Summary of experiments used in this study.

Experiment	SSTs	CO_2
piControl	Pre-industrial	Pre-industrial
piSST	Forced with Years 101–130 of SSTs taken from piControl	Observation from 1979–2008
piSST4K	As piSST, with uniform +4K anomaly	As piSST
piSST4 $\times$ CO_2	As piSST	The CO_2 is quadrupled compared with piSST, but only seen by the radiation scheme
piSSTFuture	As piSST, with patterned anomaly from abrupt4 $\times$ CO_2-piControl	As piSST
piSSTTot	As piSSTFuture	The CO_2 is quadrupled compared with piSST, and is seen by both the radiation scheme and the plant physiological effect

2.3. Methods

Since the piSST4K experiment is the same as the piSST experiment except for the imposed globally uniform +4K SST anomaly, the net response to the uniform SST +4K can be extracted by subtracting piSST from piSST4K. Similarly, the influence of the direct radiative effect associated with a quadrupling of atmospheric CO_2 can be examined by taking the difference between piSST4 $\times$ CO_2 and piSST. The NAO response to the SST pattern change can be examined by taking the difference between piSSTFuture and piSST4K. Finally, the total response can be investigated by subtracting piSST from piSSTTot. Note that the direct and SST-mediated CO_2 radiative forcings are not tested here and could deserve further analyses given the complex and non-linear atmospheric dynamics of the northern mid-latitudes.

The NAO index (NAOI) is defined as the difference between 35° N and 65° N in the normalized monthly SLP zonal-averaged over the North Atlantic region from 80° W to 30° E [22], for each experiment's climatology. In this study, the boreal winter mean time series of NAOI is used.

3. The Changes of Winter NAO Variability in Response to Different Forcings

The Decomposed Changes of SLP Patterns of Winter NAO

The regression patterns of SLP upon NAOI in the different model experiments are shown in Figure 1 We can see that the three models generally capture the features of winter NAO pattern well in the piSST simulations, though the action centers are relatively shifted eastward in the models compared to the observations for the period 1948–2016 (Figure 2).Averaged across the 3-model ensemble, the standard deviation of the NAOI increases from 5.25 hPa in the piSST simulation to 6.11, 7.15, and 6.62 hPa in response to uniform SST warming (sstPi4K), the direct radiative effects of elevated CO_2 (piSST4 × CO_2), and the SST pattern changes (piSSTFuture-piSST4K), respectively. However, it is clear from Figure 1 that the NAO response to the different climate forcings varies across the three different models.

Figure 3 further depicts the differences of the winter SLP regression pattern between the piSST simulation and the three climate forcing simulations. In response to uniform SST warming, CCSM4 and CNRM show an intensified NAO action center, though the locations of the action centers vary between the models. The centre of the Azores High shifts eastward in CCSM4, while it shifts slightly westward in CNRM. In contrast, in HadGEM2, the NAO action center weakens in response to uniform SST warming. This inconsistency is probably related to the distinct simulation of NAO variability change in HadGEM2 in response to the uniform SST warming. It might be that under the uniform SST warming, the NAO-related pattern as a response in HadGEM2 is preferentially shifted significantly eastward with an enhanced center which appears to be locally weakened over North Atlantic Ocean (Figure 1b), leading to this inter-model difference. It indicates that the influence of uniform SST warming could be complicated and is strongly dependent on the chosen model. The 4 × CO_2 radiative effect enhances the NAO variability in all three models and the result in CNRM also shows the westward shift, while there is a slightly eastward shift in CCSM4, which means the effects of both uniform SST warming and the direct CO_2 radiative effect could cause the intensification of winter NAO variability.

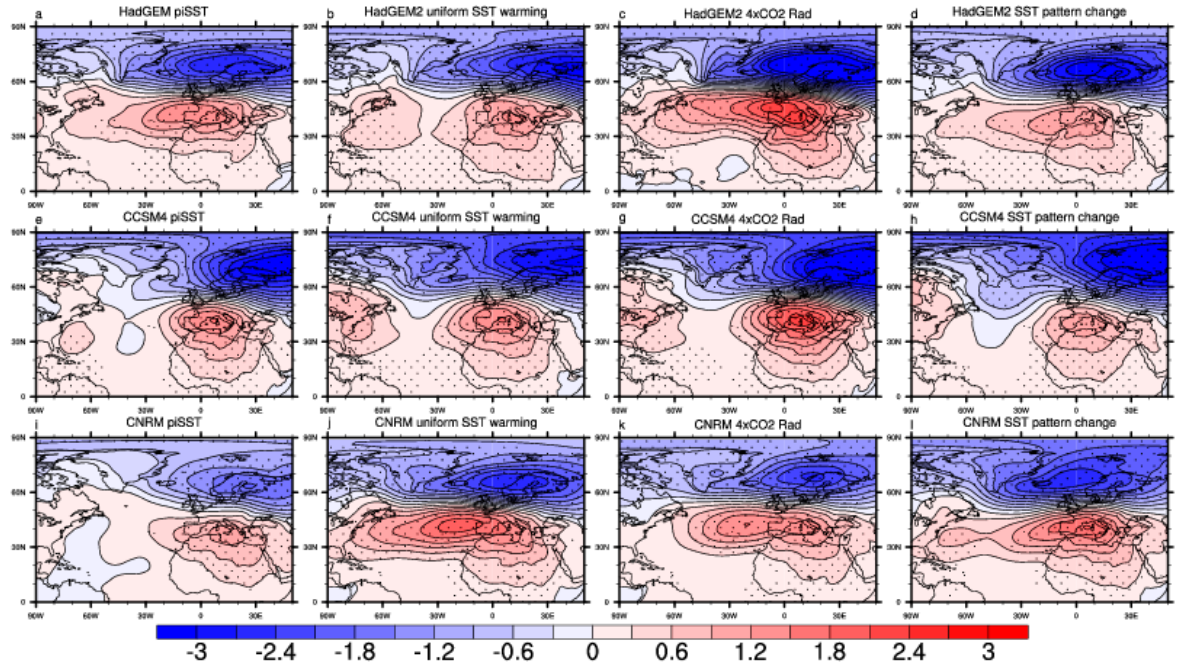

Figure 1. Regression patterns of winter sea level pressure (SLP, hPa) onto the standardized NAO index (NAOI) for the piSST (**a**,**e**,**i**), uniform sea surface temperature (SST) Warming +4K (piSST4K) (**b**,**f**,**j**), 4 × CO_2 (piSST4 × CO_2) (**c**,**g**,**k**), and SST pattern change (piSSTFuture) (**d**,**h**,**l**) experiments. The regressed results at the 95% confidence level are stippled.

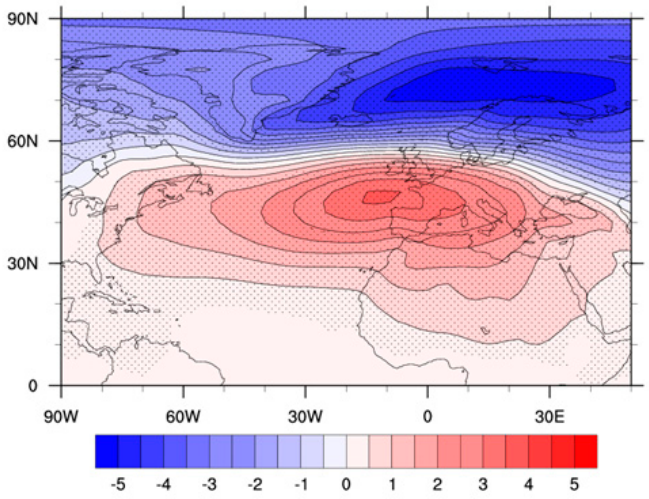

Figure 2. Regression pattern of winter SLP (hPa) onto the standardized NAOI in 1948–2016 for NCEP/NCAR reanalysis. The regressed results at the 95% confidence level are stippled.

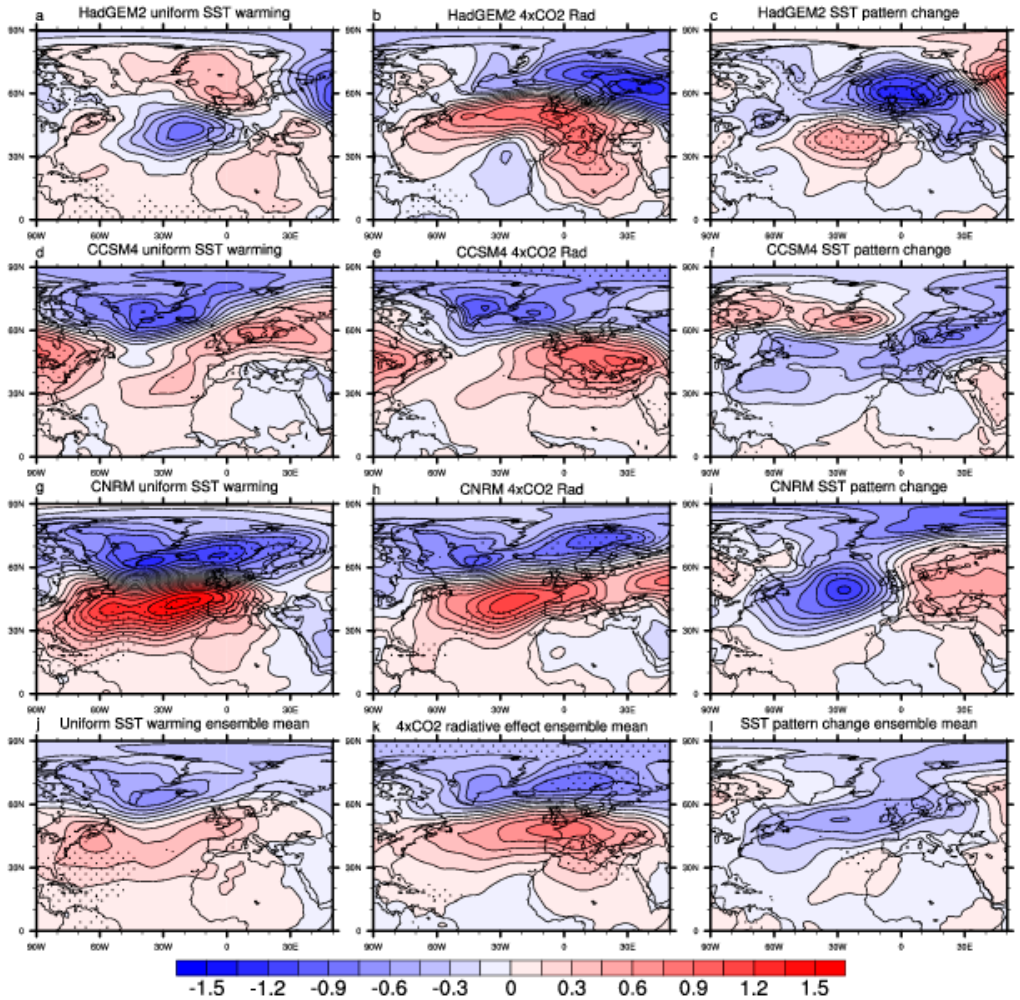

Figure 3. Changes of winter SLP (hPa) patterns regressed onto the standardized NAOI for the uniform SST Warming +4K (**a**,**d**,**g**), 4 × CO_2 (**b**,**e**,**h**), SST pattern change (**c**,**f**,**i**) experiments, and the ensemble mean for each experiment (**j**,**k**,**l**). The changes of regression at the 95% confidence level are stippled using F test.

Chadwick et al. [20] indicated that the SST pattern change is likely to be a major cause of inter-model uncertainty for mean-state circulation changes in the North Atlantic region. In our analysis, we also find that the individual model's projected SST pattern changes drive very different responses in the SLP anomalies associated with the winter NAO. Generally, both uniform SST warming and direct CO_2 radiative heating seem to cause the intensification of the winter NAO (with the exception of uniform warming in HadGEM2), whereas a large uncertainty exists in simulations for the SLP patterns of winter NAO among models in the SST pattern change experiment.

4. Possible Causes of the NAO Variability Changes in Response to Different Climate Forcings

4.1. Observed Changes in NAO Variability and Mean Westerly Wind

Previous studies suggested that the positive NAO phase is associated with the enhanced zonal wind at mid-high latitudes [23,24], but the relationship between the changes of NAO variability and the mean state westerly wind is not quite clear. Dong et al. [8] have found that the interannual NAO variability center intensified and was shifted in 1975–2004, compared with 1948–1974. In order to further investigate such a relationship, we here examine the observations of the NAO variability pattern change and the zonal wind change for these two periods. Figure 4 compares the results of NAO variability for the periods 1948–1974 and 1975–2004, and the intensified NAO variability can be seen in the latter period from their difference. Meanwhile, the mean state change of zonal wind between the two periods (see Figure 5) also clearly shows the enhanced westerly wind appearing around 60° N. These observed results indicate that the intensified NAO variability is probably connected with the enhanced mean state westerly wind at mid-high latitudes. Dong et al. [8] and Lu and Greatbatch [25] pointed out the role of the mean state change on the NAO action center and indicated that the zonal wind changes could have an influence on the NAO variability change by shifting the axis of the North Atlantic storm track, which are probably associated with eddy feedback change. Therefore, the diagnosis of the mean-state zonal wind change in each experiment could be helpful to determine the causes responsible for the changes of NAO variability.

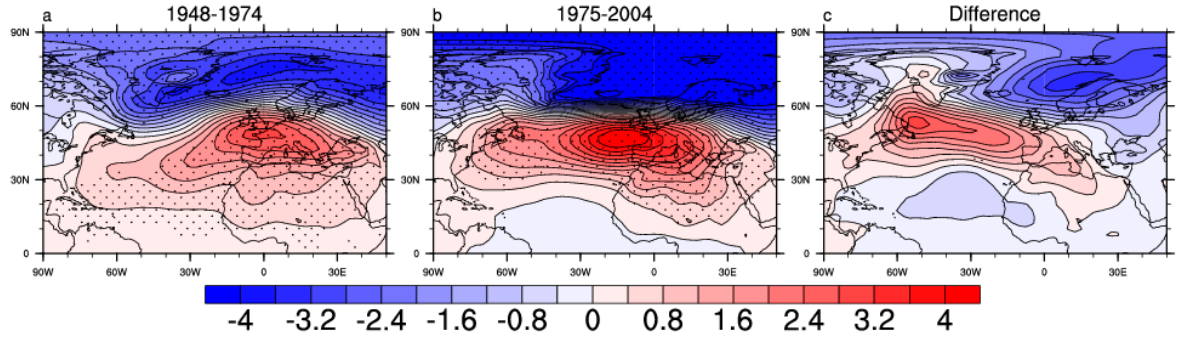

Figure 4. Regression patterns of winter SLP (hPa) onto the standardized NAOI for the periods 1948–1974 (**a**),1975–2004 (**b**), and the difference between **b** and **a** (**c**, **b** minus **a**). The regressed results at the 95% confidence level are stippled.

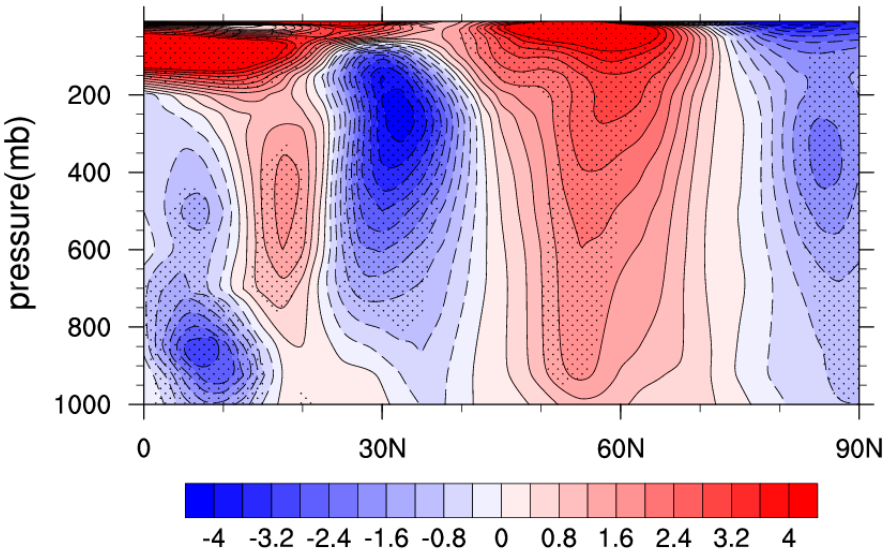

Figure 5. Vertical structure of zonal wind change (m/s) over the North Atlantic region (40° W–30° E) between the periods 1975–2004 and 1948–1974. The zonal wind change at the 95% confidence level are stippled.

4.2. The Mid-Latitude Westerly Jet Changes in Response to Different Climate Forcings

Figure 6 shows the winter SLP changes in response to different forcings over the Atlantic region. Except for the relatively larger difference in response to the uniform SST warming shown in HadGEM2, the intensified Azores high and Icelandic low can be seen in both the uniform SST warming and $4 \times CO_2$ direct radiative effect experiments, and thus it can be inferred that the westerly wind at mid-high latitudes are enhanced in these two experiments. In response to uniform SST warming, the enhanced westerly wind can be seen around 60° N compared to the piSST experiment, though the intensities are not consistent among models (Figure 7a,d,g), which should be conducive to the enhancement of NAO variability. In addition, we can see that the air temperature increases significantly in the whole layer, particularly at mid-low latitudes in the upper atmosphere. This upper atmospheric warming is likely driven by the enhanced tropical convection and the associated latent heat release in the upper tropical troposphere, and it could have an influence on the change of the meridional temperature gradient, which will be discussed later. Similar to the zonal wind response under uniform SST warming, the zonal wind intensifies at mid-high latitudes in the CO_2 direct radiative effect experiments in each model. The CO_2 radiative effect induces a slightly poleward shift of the zonal winds in three models, especially in HadGEM2 (Figure 7b,e,h). Though the rise in air temperature is not as remarkable as that in the uniform SST warming experiments, the increased air temperature also appears in almost the whole troposphere and the most significant increase appears at low latitudes according to the results in CCSM4 and CNRM. Combined with the cooling in mid latitudes, this probably causes meridional temperature gradient anomalies at mid-high latitudes. What's more, the stratospheric cooling in polar regions may enhance the polar vortex and westerly wind at mid-high latitudes. In response to SST pattern change, there is no consistent zonal wind response across models. The air temperature changes show great differences among the three models, especially in CNRM, which could be generated by the slightly different experimental design in CNRM. We note that the data of the air temperature in CCSM4 are missing at low level (close to the surface) in parts of our chosen domain, which could cause the inconsistent results, and we removed these data from the analysis, thus leading to the slightly blank area near the surface in Figure 7d,e,f. The sea-ice was free to change in CNRM-CM5, but not in HadGEM2 or CCSM4, thus inducing the large inter-model spread in simulations for the air temperature change as well as the NAO variability change as a result.

These results suggest that SST pattern change could also be the main source of inter-model uncertainty for NAO variability change in the wider set ofCMIP5 climate projections.

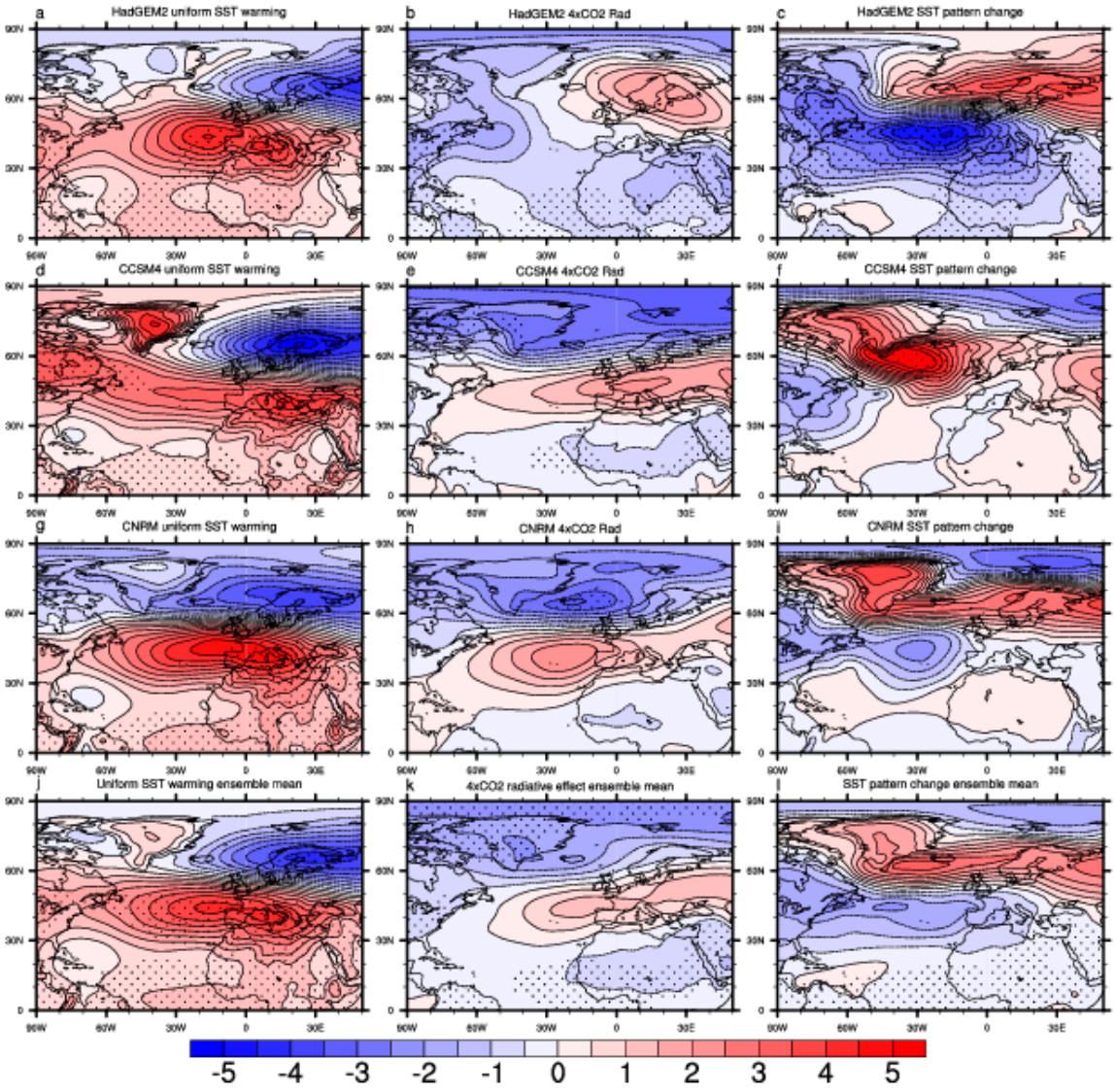

Figure 6. The SLP changes (hPa) for the uniform SST Warming +4K (**a**,**d**,**g**), 4 × CO_2 (**b**,**e**,**h**), SST pattern change (**c**,**f**,**i**) experiments, and the ensemble mean for each experiment (**j**,**k**,**l**). The SLP changes at the 95% confidence level are stippled.

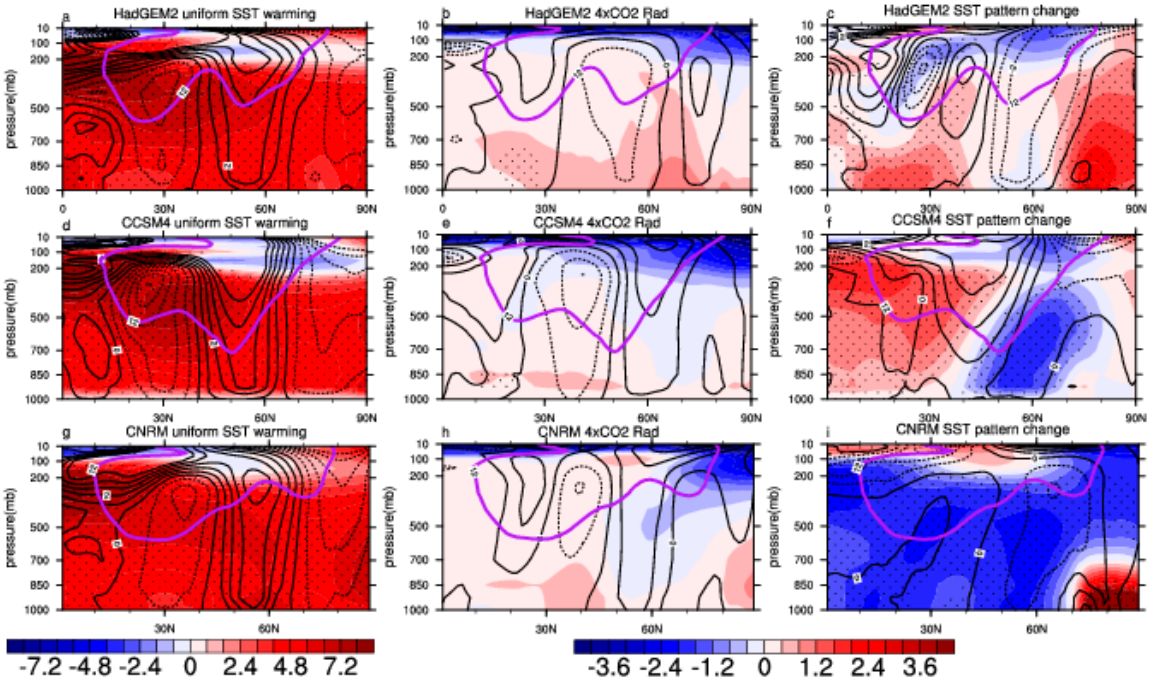

Figure 7. Vertical structure of air temperature changes (°C, shading) and westerly jet changes (m/s, contours), where the black solid lines are enhanced zonal wind and the black dashed lines are the weakened zonal wind for the forced experiments, and the purple solid lines are wind profiles for 12 m/s in the piSST experiment, over the Atlantic region (40° W–30° E) for the uniform SST Warming +4K (**a**,**d**,**g**), 4 × CO_2 (**b**,**e**,**h**), and SST pattern change (**c**,**f**,**i**) experiments. The air temperature changes at the 95% confidence level are stippled.

4.3. The Meridional Temperature Gradient Changes in Response to Different Forcings

It has been shown that the intensified meridional temperature gradient would enhance the mid-latitude zonal wind [8,26,27]. In order to investigate the condition of thermal wind change, we further analyze the meridional temperature gradient changes at 500 hPa as well as the 300 hPa zonal wind changes in different experiments. The results from the uniform SST warming experiment show that the meridional temperature gradient increases at mid-high latitudes to the east of 30° W (Figure 8a,d,g), and it could be driven by the large air temperature increases at mid latitudes, as shown in the previous section. The 300 hPa zonal wind at mid and high latitudes intensifies with a poleward and eastward shift compared to the piSST experiment (Figure 9a,d,g). The circulation change could be connected with the increased meridional temperature gradient according to the thermal wind theory. This westerly wind intensification may be a contributing factor to the strengthening of the NAO in response to uniform SST warming. Similarly, the meridional temperature gradient over mid-high latitudes increases in response to direct CO_2 radiative forcing (Figure 8b,e,h), leading to enhanced westerly wind with the poleward and eastward shift around 60° N in CCSM4 and CNRM, and at higher latitudes for HadGEM2 (Figure 9b,e,h). As for the responses to the SST pattern change, the meridional temperature gradient again does not show a consistent signal across the three models. The inter-model differences in projections for the changes in zonal wind are also large among models. It seems that both the influences of uniform SST warming and CO_2 radiation scheme could induce the enhanced westerly wind at mid-high latitudes, which could be the primary reasons for the intensification of NAO in those two experiments, whereas the meridional temperature gradient and westerly wind changes are not consistent among the models in response to SST pattern change. This indicates that the response of the NAO to SST pattern change is still an open issue, and needs further research.

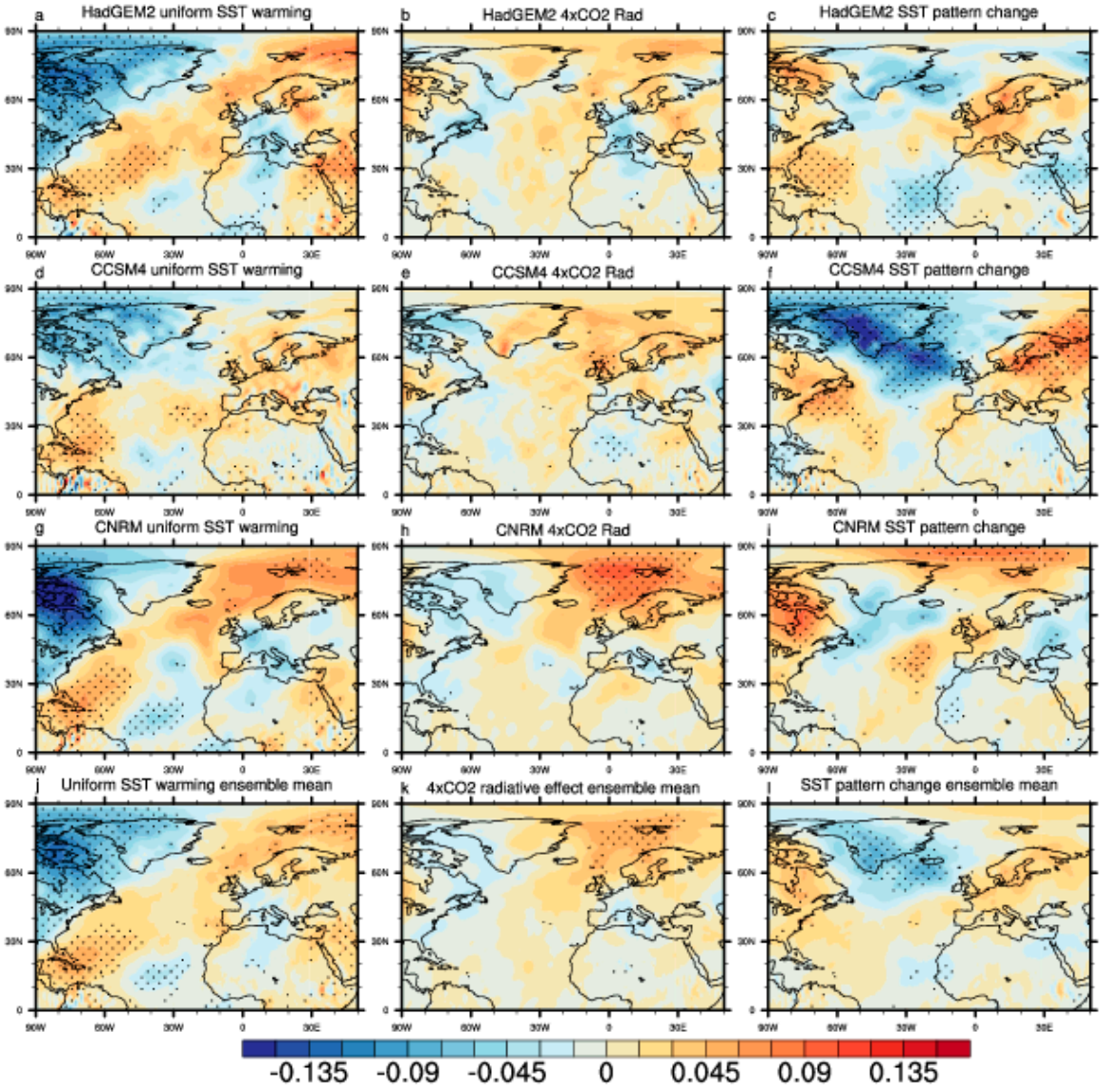

Figure 8. The 500 hPa meridional temperature gradient changes (°C/m, shading) for the uniform SST Warming +4K (**a**,**d**,**g**), 4 × CO_2 (**b**,**e**,**h**), SST pattern change (**c**,**f**,**i**) experiments, and the ensemble mean for each experiment (**j**,**k**,**l**). The meridional temperature changes at the 95% confidence level are stippled.

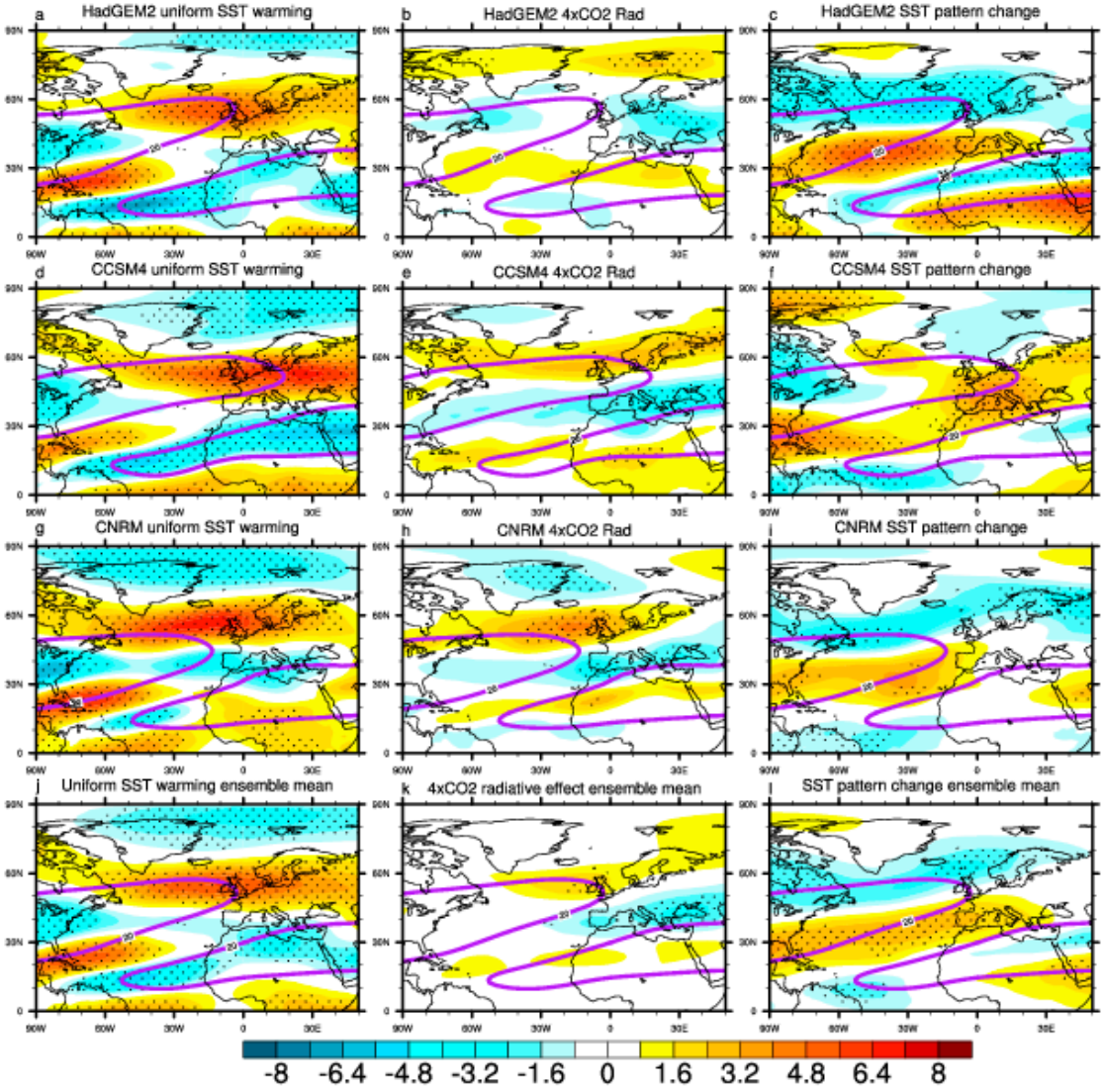

Figure 9. The 300 hPa zonal wind changes (m/s, shading), where the purple solid lines are westerly wind for 20 m/s in the piSST experiment, for the uniform SST Warming +4K (**a**,**d**,**g**), 4 × CO_2 (**b**,**e**,**h**), SST pattern change (**c**,**f**,**i**) experiments, and the ensemble mean for each experiment (**j**,**k**,**l**). The zonal wind changes at the 95% confidence level are stippled.

5. Summary and Discussions

Based on a set of pilot experiments for CFMIP-3, changes in the NAO as well as the possible connected responses under various aspects of forcing and warming are investigated. The main results are summarized as follows.

The influences of uniform SST warming and the direct CO_2 radiative effect are likely to enhance winter NAO variability, except for an inconsistent result in HadGEM2 for the uniform SST warming experiment. In contrast, projected future SST pattern changes in each model drive different responses in the regression pattern of SLP.

To determine the causes responsible for the changes of NAO, we diagnosed the mean changes of zonal wind and air temperature in the different experiments. The results show that in response to uniform SST warming and the direct CO_2 radiative effect, the zonal wind intensifies at mid-high latitudes and shifts poleward and eastward. However, in response to SST pattern change, the zonal wind changes are not consistent among models, which could be connected with the great difference in

simulations of the NAO variability change. The increased meridional temperature gradient over the North Atlantic could strengthen the westerly wind at mid-high latitudes, which leads to the change in baroclinicity and therefore the change in storm track activity that affects the eddy-driven jet and NAO [8]. However, the issue about the correlation between the changes of NAO variability and mean state, as well as the mechanisms behind them is complicated and needs further investigation based on more experiments. This could be investigated as our next step using daily data.

The most significant air temperature increase occurs at mid-low latitudes in uniform SST warming and CO_2 radiation scheme experiments, both leading to the increased meridional temperature gradient at mid-high latitudes, which act to enhance the westerly wind at mid-high latitudes. In contrast, projected changes in SST patterns for each model drive very different responses in tropospheric temperature. These disparate temperature changes contribute to a large spread in zonal wind changes, leaving the understanding of the NAO variability change in response to SST pattern change to be an open issue.

The piSST experiments were designed to analyze regional changes in mean climate, and so caution should be taken when interpreting changes in variability in these experiments. Since these are a set of atmosphere-only experiments, a lack of ocean-atmosphere coupling process could lead to bias compared with coupled simulations. The piSST pilot experiments also do not represent any changes in SST variability that may occur in coupled models. The differences between NAO variability change in the coupled models and this set of atmosphere-only experiments are relatively large, particularly in HadGEM2 and CCSM4 (see Figure 10), which may indicate that the piSST experiments have not captured the coupled response of NAO variability change well. It is also possible that the NAO variability could be influenced by not only the external forcings, but also by the internal forcing (e.g., synoptic eddy forcing [28,29]), and we can see the relatively large inter-model difference in HadGEM2, which could probably be induced by the internal forcing. While the differences are not so remarkable in CCSM4 and CNRM, but with more consistent results compared with CGCM. However, the sea ice change may also play a role, since the sea ice was allowed to change in CNRM, which is different from HadGEM2 and CNRM, probably leading to the large discrepancy among models, and this discrepancy will be investigated in further research on the NAO variability change. The results shown in the current study can be interpreted as showing drivers of NAO variability change (and uncertainty in this change) in the absence of ocean-atmosphere coupling and SST variability change.

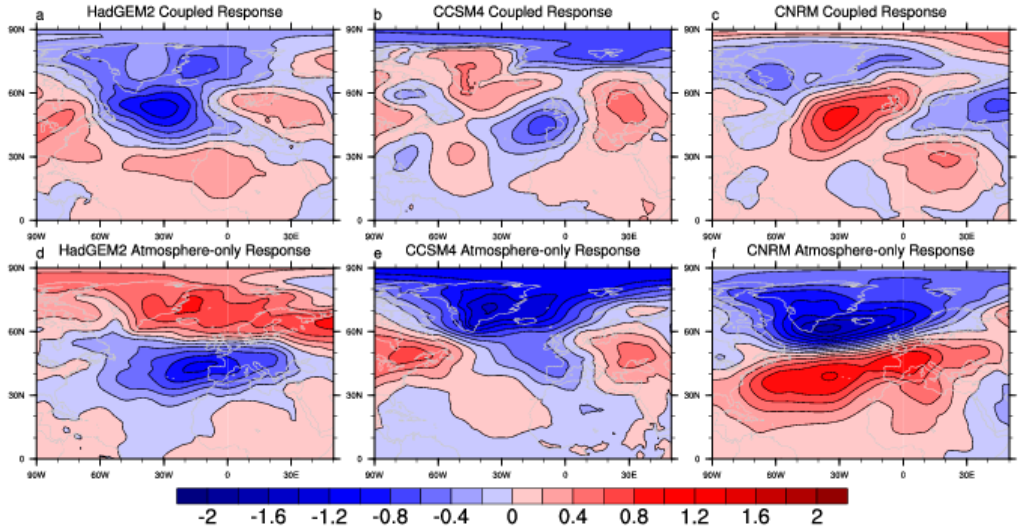

Figure 10. Changes of winter SLP (hPa) patterns regressed onto the standardized NAOI for the abrupt 4 × CO_2 (**a**–**c**) and atmosphere-only experiment (**d**–**f**) across three models.

Acknowledgments: We acknowledge Christopher B. Skinnerfor producing and sharing the CCSM4 simulations, and Hervé Douville and Sophie Tyteca for producing and sharing the CNRM simulations. This work is jointly supported by National Key Research Program and Development of China (2017YFC1502302), China National Science Foundation Projects (41605116, 41705043, 41775066), National Basic Research (973) Program of China under Grant2010CB950404, and the UK-China Research & Innovation Partnership Fund through the Met Office Climate Science for Service Partnership (CSSP) China as part of the Newton Fund.

Author Contributions: Robin Chadwick conceived the experiments; Hong-Li Ren and Yu Huang analyzed the data and wrote this paper; Zhigang Cheng and Quanliang Chen provided the instructions to this article.

Conflicts of Interest: The authors declare no conflict of interest.

References

1. Walker, G.T.; Bliss, E.W. World Weather V. *Mem. R. Meteorol. Soc.* **1932**, *4*, 53–84.
2. Kwok, R. Recent changes in arctic ocean sea ice motion associated with the North Atlantic Oscillation. *Geophys. Res. Lett.* **2000**, *27*, 775–778. [CrossRef]
3. Xu, T.; Shi, Z.; Wang, H.; An, Z. Nonstationary impact of the winter North Atlantic Oscillation and the response of mid-latitude Eurasian climate. *Theor. Appl. Fract. Mec.* **2016**, *124*, 1–14. [CrossRef]
4. Kelley, C.; Ting, M.; Seager, R.; Kushnir, Y. The relative contributions of radiative forcing and internal climate variability to the late 20th century winter drying of the Mediterranean region. *Clim. Dyn.* **2012**, *38*, 2001–2015. [CrossRef]
5. Wan, H.; Luo, D.H. The relationship between wintertime blocking in the north hemisphere and North Atlantic Oscillation. *J. Trop. Meteorol.* **2009**, *25*, 616–620.
6. Beranová, R.; Kysely, J. Relationships between the North Atlantic Oscillation index and temperatures in Europe in global climate models. *Stud. Geophys. Geod.* **2013**, *57*, 138–153. [CrossRef]
7. Zhou, B.T.; Cui, X. Interdecadal change of the linkage between the North Atlantic Oscillation and the tropical cyclone frequency over the western north pacific. *Sci. China Ser. D Earth Sci.* **2014**, *57*, 2148–2155. [CrossRef]
8. Dong, B.; Sutton, R.T.; Woollings, T. Changes of interannual NAO variability in response to greenhouse gases forcing. *Clim. Dyn.* **2011**, *37*, 1621–1641. [CrossRef]
9. Gong, D.; Zhou, T.; Wang, S. Advance in the studies on North Atlantic Oscillation (NAO). *Adv. Earth Sci.* **2001**, *16*, 413–420.
10. Bo, Q.U.; Gabric, A.J.; Zhu, J.N.; Lin, D.R.; Qian, F.; Zhao, F.M. Correlation between sea surface temperature and wind speed in Greenland Sea and their relationships with NAO variability. *Water Sci. Technol.* **2012**, *5*, 304–315.
11. Davini, P.; Cagnazzo, C. On the misinterpretation of the North Atlantic Oscillation in CMIP5 models. *Clim. Dyn.* **2014**, *43*, 1497–1511. [CrossRef]
12. Wallace, J.M. North Atlantic Oscillation/Annular mode: Two paradigms one phenomenon. *Q. J. R. Meteorol. Soc.* **2000**, *126*, 791–805. [CrossRef]
13. Cattiaux, J.; Cassou, C. Opposite CMIP3/CMIP5 trends in the wintertime Northern Annular Mode explained by combined local sea ice and remote tropical influences. *Geophys. Res. Lett.* **2013**, *40*, 3682–3687. [CrossRef]
14. Cattiaux, J.; Douville, H.; Peings, Y. European temperatures in CMIP5: Origins of present-day biasesand future uncertainties. *Clim. Dyn.* **2013**, *41*, 2889–2907. [CrossRef]
15. Jeong, J.H.; Lee, H.; Jin, H.Y.; Kwon, M.H.; Yeh, S.W.; Kug, J.S.; Lee, J.Y.; Lee, J.-Y.; Kim, B.-M.; Son, S.-W.; et al. The status and prospect of seasonal climate prediction of climate over Korea and East Asia: A review. *Asia Pac. J. Atmos. Sci.* **2017**, *53*, 149–173. [CrossRef]
16. Webb, M.J.; Lock, A.P. Coupling between subtropical cloud feedback and the local hydrological cycle in a climate model. *Clim. Dyn.* **2013**, *41*, 1923–1939. [CrossRef]
17. Martin, G.M.; Bellouin, N.; Collins, W.J.; Culverwell, I.D.; Halloran, P.R.; Hardiman, S.C.; Hinton, T.J.; Jones, C.D.; McLaren, A.J.; O'Connor, F.M.; et al. The HadGEM2 family of Met Office united model climate configurations. *Geosci. Model Dev.* **2011**, *4*, 723–757.
18. Meehl, G.; Washington, W.; Arblaster, J.; Hu, A.; Teng, H.; Tebaldi, C.; Sanderson, B.N.; Lamarque, J.-F.; Conley, A.; Strand, W.G.; et al. Climate system response to external forcingsand climate change projections in CCSM4. *J. Clim.* **2012**, *25*, 3661–3683. [CrossRef]

19. Voldoire, A.; Sanchez-Gomez, E.; Mlia, D.S.Y.; Decharme, B.; Cassou, C.; Sénési, S.; Valcke, S.; Beau, I.; Alias, A.; Chevallier, M.; et al. The CNRM-CM5.1 global climate model: Description and basic evaluation. *Clim. Dyn.* **2013**, *40*, 2091–2121. [CrossRef]
20. Chadwick, R.; Douville, H.; Skinner, C.B. Timeslice experiments for understanding regional climate projections: Applications to the tropical hydrological cycle and European winter circulation. *Clim. Dyn.* **2017**, *49*, 3011–3029. [CrossRef]
21. Webb, M.J.; Andrews, T.; Bodassalcedo, A.; Bony, S.; Bretherton, C.S.; Chadwick, R.; Chepfer, H.L.; Douville, H.; Good, P.; Kay, J.E.; et al. The cloud feedback model intercomparison project (CFMIP) contribution to CMIP6. *Geosci. Model Dev.* **2017**, *10*, 1–27. [CrossRef]
22. Li, J.P.; Wang, J.X.L. A modified zonal index and its physical sense. *Geophys. Res. Lett.* **2003**, *30*, 34–35. [CrossRef]
23. Woollings, T.; Franzke, C.; Hodson, D.L.R.; Dong, B.; Barnes, E.A.; Raible, C.C.; Pinto, J.G. Contrasting interannual and multidecadal NAO variability. *Clim. Dyn.* **2015**, *45*, 539–556. [CrossRef]
24. Li, C.; Zhang, Q.Y.; Ji, L.; Peng, J.B. Interannual variations of the blocking high over the Ural Mountains and its association with the AO/NAO in boreal winter. *Acta Meteorol. Sin.* **2012**, *26*, 163–175. [CrossRef]
25. Lu, J.; Greatbatch, R.J. The changing relationship between the NAO and northern hemisphere climate variability. *Geophys. Res. Lett.* **2002**, *29*, 52-1–52-4. [CrossRef]
26. Caian, M.; Koenigk, T.; Döscher, R.; Devasthale, A. Erratum to: An interannual link between Arctic sea-ice cover and the North Atlantic Oscillation. *Clim. Dyn.* **2017**. [CrossRef]
27. Harvey, B.J.; Shaffrey, L.C.; Woollings, T.J. Equator-to-pole temperature differences and the extra-tropical storm track responses of the CMIP5 climate models. *Clim. Dyn.* **2014**, *43*, 1171–1182. [CrossRef]
28. Ren, H.-L.; Jin, F.-F.; Kug, J.-S.; Zhao, J.-X.; Park, J. A kinematic mechanism for positive feedback between synoptic eddies and NAO. *Geophy. Res. Lett.* **2009**, *36*, L11709. [CrossRef]
29. Ren, H.-L.; Jin, F.-F.; Gao, L. Anatomy of synoptic eddy–NAO interaction through eddy-structure decomposition. *J. Atmos. Sci.* **2012**, *69*, 2171–2191. [CrossRef]



© 2018 by the authors. Licensee MDPI, Basel, Switzerland. This article is an open access article distributed under the terms and conditions of the Creative Commons Attribution (CC BY) license (http://creativecommons.org/licenses/by/4.0/).

This authors' personal copy may not be publicly or systematically copied or distributed, or posted on the Open Web, except with written permission of the copyright holder(s). It may be distributed to interested individuals on request.

Vol. 76: 41–57, 2018
https://doi.org/10.3354/cr01523

CLIMATE RESEARCH
Clim Res

Published online September 4

Change in precipitation over the Asian continent from 1901–2016 based on a new multi-source dataset

Y. J. Zhan[1,2,3,4], G. Y. Ren[3,5,*], S. Yang[4]

[1]Chinese Academy of Meteorological Sciences, China Meteorological Administration (CMA), Beijing 100081, PR China
[2]University of Chinese Academy of Sciences, Beijing 100049, PR China
[3]Department of Atmospheric Science, School of Environmental Studies, China University of Geosciences, Wuhan 430074, PR China
[4]National Meteorological Information Center, China Meteorological Administration, Beijing 100081, PR China
[5]Laboratory for Climate Studies, National Climate Center, China Meteorological Administration, Beijing 100081, PR China

ABSTRACT: Asia experiences great regional differences in climatic variations, especially precipitation. Examining changes in precipitation will help us understand large-scale hydro-cycle processes against the background of global climate change. We used a new multi-source dataset of historical global land precipitation records developed by the China Meteorological Administration to analyze long-term change in annual and seasonal precipitation in Asia during 1901–2016. To solve the problem of inhomogeneity, the Russian Bias-corrected Monthly Precipitation dataset was also used for Russia. The normalized precipitation anomaly (NPA) was used to analyze spatial and temporal precipitation trend patterns. Regional average time series for the continent and its 6 subregions were obtained by an area-weighted averaging method. Results show that: (1) regional average annual precipitation increased significantly during this period, and the upward trend was mainly related to a shift in cold areas during the mid-20th century; (2) regional average spring and autumn precipitation amounts had similar characteristics to those of the long-term changes in annual precipitation, and winter precipitation increased slightly for the entire period, with a significant jump occurring from 1945–1955; (3) North and Central Asia experienced a significant upward trend in precipitation for every season except summer during 1901–2016, while South Asia witnessed a significant downward trend in winter during the same period; (4) during 1901–2016, the proportion of summer precipitation declined uniformly in most parts of the continent, with a significant decline in cold areas. Although there are still uncertainties related to the observational data, the analysis results will help in understanding the general pattern of precipitation variation and the possible response of these regions to global climate change.

KEY WORDS: Asia · North Asia · South Asia · Climate change · Precipitation · Trend

Resale or republication not permitted without written consent of the publisher

1. INTRODUCTION

As a major part of Eurasia, Asia is the largest and most populated continent in the world. Asia also features highly complex geomorphological and climatic characteristics known worldwide, including the Qinghai-Tibetan Plateau, which is often called the 'Third Pole' of the earth (Sharma et al. 2016). The Arctic, Indian, and Pacific Oceans surround Asia, leading to the strongest sea–land thermal contrasts in the world and the characteristic Asian monsoon climate. The vast land area, the highest plateau and mountains, and the heterogeneous climate make Asia an ideal continent for investigating large-scale climatology and climate change.

Asia has strong horizontal and vertical gradients in precipitation (Yanai & Li 1994, Qiu 2008, Yao et al. 2012, Sharma et al. 2016). As a result, the distribution of water resources is so uneven that flooding and drought frequently appear simultaneously. The con-

*Corresponding author: guoyoo@cma.gov.cn

© Inter-Research 2018 · www.int-res.com

Author copy

sequences of this effect also make the Asian continent susceptible to climatic change and the effects of human activities. The long-term variation in precipitation plays a vital and significant role in local and regional hydrology, agriculture, ecology, industry, and hydroelectric power generation, features that all rely on the timely and sufficient delivery of water in major river systems. It is also a key indicator in monitoring and detection of large-scale climate change.

It is well documented that the global mean surface temperature has risen significantly during the past century (e.g. Jones et al. 2012, Stocker et al. 2013, Sun et al. 2017). Climate warming is expected to cause change in atmospheric moisture and the intensity and distribution of precipitation at both regional and global scales. Theoretically, the higher global temperature facilitates evaporation, adds more moisture to the atmosphere, and finally causes an increase in precipitation (Trenberth et al. 2003). However, change in the components of the water cycle such as atmospheric vapor content can feedback to the change in temperature. An important issue in the science of climate change is whether or not the total annual precipitation in spatial scales larger than a sub-continent has changed over the past 100 yr in response to the observed global warming. Research related to change in precipitation on the Asian continent can therefore significantly contribute to the understanding of global and regional climate change, and facilitate studies of detection and attribution of climate change and of the response of the global water cycle to the increase in surface temperature. It can also provide useful scientific information for Asian countries in support of attempts to better adapt to climate change in the sectors of agriculture, water sources, ecology, environment, and human society.

The characteristics of global and regional precipitation change are more complex than those of surface air temperature, however. Recent research based on various datasets has found that precipitation experienced an increasing trend at mid- and high latitudes of the Northern Hemisphere, but decreased in subtropical regions, especially the Mediterranean region, during the past century (Dore 2005, Zhang et al. 2007, Trenberth 2011, Donat et al. 2013). Because of the poor data coverage in many areas of the world, especially in most parts of Africa, the estimates of global and continental precipitation change face many uncertainties (Stocker et al. 2013, Wan et al. 2013). Gridded precipitation products based on remote sensing data that are frequently used in studies covering global scales or in the Northern Hemisphere have a relatively short time period of records; the instrumental records are often unable to capture large and abrupt variations in precipitation over short distances because of their coarse resolution and orographic effects in the high-elevation areas (Dahri et al. 2016).

The International Panel on Climate Change (Solomon et al. 2007, Stocker et al. 2013) assessed the long-term trends of precipitation in Asia, and reported that both North and Central Asia showed an increasing precipitation trend during the past century, but the precipitation of South Asia decreased during the same time period. Few publications on change in precipitation for Asia as a whole are available, although many studies have analyzed the decadal variability in precipitation and related mechanisms for regions such as East and South Asia. Choi et al. (2009) found that most countries in the Asian-Pacific region had experienced an insignificant increase in summer precipitation, but their data generally covered the coastal areas of Asia, western Pacific, and Australia, and did not examine the change in precipitation over more than 100 yr. The subcontinental region of mainland China has received much attention with regard to the recent change in precipitation because good data coverage is readily available (e.g. Zhang 1993, Liu et al. 2005, Ren et al. 2005, 2012, 2015, Zhai et al. 2005, Wen et al. 2006, Zhou et al. 2009). Researchers have found that the region-averaged annual precipitation percent anomalies or the annual normalized precipitation anomaly (NPA) experienced a weak upward trend in mainland China over the past half century, but almost no long-term change was detectable for the past century or more (Ding & Ren 2008, Ren et al. 2015, 2016). In West, Central, and North Asia, research covering larger-scale regions using surface observational data are relatively scarce. Tanarhte et al. (2012) found that the annual precipitation rate near the Persian Gulf increased by up to 2% decade^{-1} over the period 1961–2000, but decreased in the northern part of West Asia after 1987. The winter and spring precipitation rate declined at most stations in Iran during 1966–2005 (Tabari & Talaee 2011). Western Asia experienced a decrease in precipitation, which is actually part of a remarkable drying trend witnessed in the entire Mediterranean region during the last 100 yr (Stocker et al. 2013). During 1950–2000, most areas in Central Asia experienced increasing precipitation rates except in western Kazakhstan (Xu et al. 2015). In North Asia, Gruza et al. (1999) found that the annual precipitation rate generally decreased over the period 1951–1995, while the analysis by Groisman et al. (2013) showed that the late 20th cen-

Author copy

tury precipitation rate was larger than that of the early 20th century but both trends were insignificant. Previous work can help understand the large-scale change in precipitation that occurred on the Asian continent. However, some deficiencies exist in revealing the detailed spatial patterns of long-term change in precipitation. Restricted by the quality of the data and the length of records, previous research mostly focused on the change in precipitation over a relatively short period starting after 1950 and ending before 2010, and on a relatively small spatial domain. Continental-scale studies related to long-term precipitation change, or the analysis of the whole of Asia, are lacking.

In this paper, a new monthly dataset was adopted to analyze the change in precipitation over the Asian continent from 1901–2016. We mainly focused on the long-term trends in precipitation on the continent, with special emphasis on the spatiotemporal characteristics of annual and seasonal precipitation trends for various periods and spatial scales.

2. DATA AND METHODS

The source of data for monthly precipitation indices used for the current analysis was the historic global precipitation dataset of the China Meteorological Administration (CMA) V1.1 (CGP; Yang et al. 2016) and the Russian Bias-corrected Monthly Precipitation (RBMP; Bogdanova et al. 2007) dataset of the Voeikov Main Geophysical Observatory (VMGO). The sources of the CGP consist of 4 original global datasets: GHCN-monthly Version 2 (GHCN, Peterson & Vose 1997), European Climate Assessment & Dataset (ECA, Klein Tank et al. 2002), Historical Instrumental Climatological Surface Time Series Of The Greater Alpine Region (HISTALP, Auer et al. 2007), and US Historical Climatology Network Version 1.1 (USHCN, Boden et al. 1990). In addition, some monthly precipitation data were also obtained from 7 national datasets: the Canadian national climate and weather data archive, the Australian high-quality climate change dataset, the Korean exchange dataset, the Vietnamese exchange dataset, the Chinese datasets of the CMA, and the Russian and Japanese meteorological agencies.

The records of GHCN served as the basic data source for building the CGP dataset. When a station was included in both GHCN and other datasets, the station was identified by analyzing the merits of the GHCN and other datasets by comparing the difference and length of monthly records. If the difference was less than 5%, then the stations with longer records were chosen as the data source, and the shorter data series were used to supplement the source records; if the difference was larger than 5%, the data series with the longest records were applied (Yang et al. 2016). The CGP monthly precipitation data has been quality controlled by 2 procedures: detection of abnormal values and a space consistency check (Yang et al. 2016), which is similar to those processes of the GHCN. The CGP dataset contains data from a total of 31 456 observational stations from all over the world, which includes more than half of the stations of the GHCN. Compared to the GHCN dataset, the CGP dataset has a higher station density and a more complete record in mainland China and its neighboring regions (Yang et al. 2016). In mainland China, monthly precipitation records from the national stations of more than 2400 sites were originally used in the new dataset, but we only applied the data of the 800 national reference climate stations and national basic meteorological stations in this work.

However, exploring precipitation changes in Asia is still hampered by a deficiency of the CGP dataset. The monthly precipitation records have not been homogenized except for mainland China. In the region of the former Soviet Union, there were 2 obvious changes in precipitation observational procedure, taking place 1948–1953 and 1966–1967 (Groisman et al. 1991), which resulted in significant inhomogeneities in the observational records. To solve the problem, the RBMP datasets were used in Russia, which encompasses about 76% of the areas belonging to the former Soviet Union. The monthly precipitation data were corrected by using a regression model which considered all known rain gauge measurement biases and metadata about location and environmental conditions over Russia (Bogdanova et al. 2007). There are 457 Russian stations in the RBMP dataset, and these stations can all be found in CGP. However, these stations only contain precipitation data from 1936–2010. To establish the long-term time series of the corrected precipitation data, we blended the CGP data and RBMP data by the methods described below.

If a CGP dataset station was located in Russia, but not included in the RBMP dataset, the station was discarded. In the remaining stations of Russia, the 1936–2010 precipitation data in the RBMP dataset were used. Because the precipitation could be regarded as homogeneous in the period 1901–1947 and 1967–2016, the 1901–1935 and 2011–2016 data in the CGP dataset could be bias-corrected by simply using the average differences between the RBMP

Author copy

and CGP data for the period 1936–1947 and 1967–2010, respectively. For stations with no precipitation record of the same time in the 2 periods, the CGP data were regarded as missing records, and only the RBMP data of 1936–2010 were used (red dots in Fig. 1a). After this step, the issue of the data inhomogeneities in most study areas was largely solved. However, the data were not corrected in the remaining 24% of areas of the former Soviet Union. Some records from Central Asia and Mongolia also had the problem of inhomogeneities; strong winds during the cold season may have resulted in lower catch rates of the gauges before the Tretyakov rain gauges were applied in these regions (Groisman et al. 1991, Zhang et al. 2004).

Stations were further selected for use in this analysis only if 2 conditions were met simultaneously: the World Meteorological Organization (WMO) Station region code was 2, and the stations had to be located within the rectangular region in the range of 40° E to 165° W, 5° to 80° N. In total, 6937 stations were located in this region. The Philippines and Indonesia were not included in the study region because they are considered part of the Oceania sub-region by the WMO, and they are not located on the Eurasian continent. To reduce the influence of missing data, the following steps were applied to select stations and to process the data.

(1) We selected stations that reported at least 10 valid records over all 12 mo of a year during the base period 1961–1990. In this step, a total of 2652 stations were identified (Fig. 1a). These stations were uniformly and densely distributed in the study region except West Asia. The average monthly precipitation in the base period was calculated for every station selected in the previous stage.

(2) For every year with ≥10 valid months of records, the missing monthly precipitation records were filled by the average monthly precipitation obtained in Step 1.

(3) A station had to have records for ≥10 years in 1961–1990, 5 years in 1901–1950, and 5 years in 1991–2016, in order to minimize the impact of missing data in the base period and in the end periods on the analysis results.

(4) A total of 1316 stations were chosen for use in this work (Fig. 1e). These stations were relatively uniformly and densely distributed throughout India, eastern China, Japan, and Thailand, although the coverage was not very good for West Asia, the Arctic region, and western China.

To reduce the biases caused by uneven station density or temporal variations in data coverage, we used the region-average method (Jones & Moberg 2003). Each station was assigned to a regular 5° × 5° latitude–longitude grid box. Each of the total 249 grid boxes of 2652 stations and 220 grid boxes of 1316 stations contained at least 1 station. The temporal variations in the count of grid boxes with stations in the 6 sub-regions are shown in Fig. 1b,f. The total number of grid boxes of 1316 stations in all regions gradually increased before 1936, and increased to an average of more than 180 grid boxes with stations in 1936. After 1940, the number of grid boxes with stations was more than 200 continuously until 2000, but this number fell after 2000. North Asia had the most grid boxes in almost every year, and the number of grid boxes there increased rapidly in 1936 while the number in other regions increased slowly (Fig. 1b,f). The temporal variation of the 249 grid boxes of 2652 stations was similar (Fig. 1b).

The number of stations employed in every grid box is presented in Fig. 1c,g. For the dataset of 1316 stations (Fig. 1g) some grid boxes in West Asia and West China have no stations. There are fewer than 10 stations in Central Asia and Russia. The regions with the best coverage for stations and grid boxes were India, East China, and Japan. For the dataset of 2652 stations (Fig. 1c), nearly all grid boxes in the study region contain stations. However, the years with valid records in West Asia and West China were less than 60 (Fig. 1d) because most stations in these regions had no valid records prior to 1950. To avoid the inconsistency of the coverage of stations, the 1316 long-record station dataset was used for obtaining regional average precipitation series and the spatial pattern of change during the period 1901–2016 in this paper, and the 2652 stations were used to analyze the spatial pattern of change after 1951. Therefore, the records mostly cover more than 60 yr for grid boxes with data except for 7 grid boxes in West Asia, Southeast Asia, and North Asia, meaning that the gridded values provide relatively good coverage for the study period (Fig. 1h).

Above all, the monthly precipitation data for 1316 stations cover most areas of the Asian continent except for West Asia and West China (mostly classified to Central Asia). The other regions have a sufficient temporal and spatial coverage of valid precipitation data records. The grid boxes covered 95, 96, 94, and 88% of the area of North, East, Southeast, and South Asia, respectively, but only covered 64 and 61% of the area of West and Central Asia.

This paper mainly analyzed the annual and seasonal changes in precipitation trends in Asia. The annual total precipitation is the total precipitation

Author copy

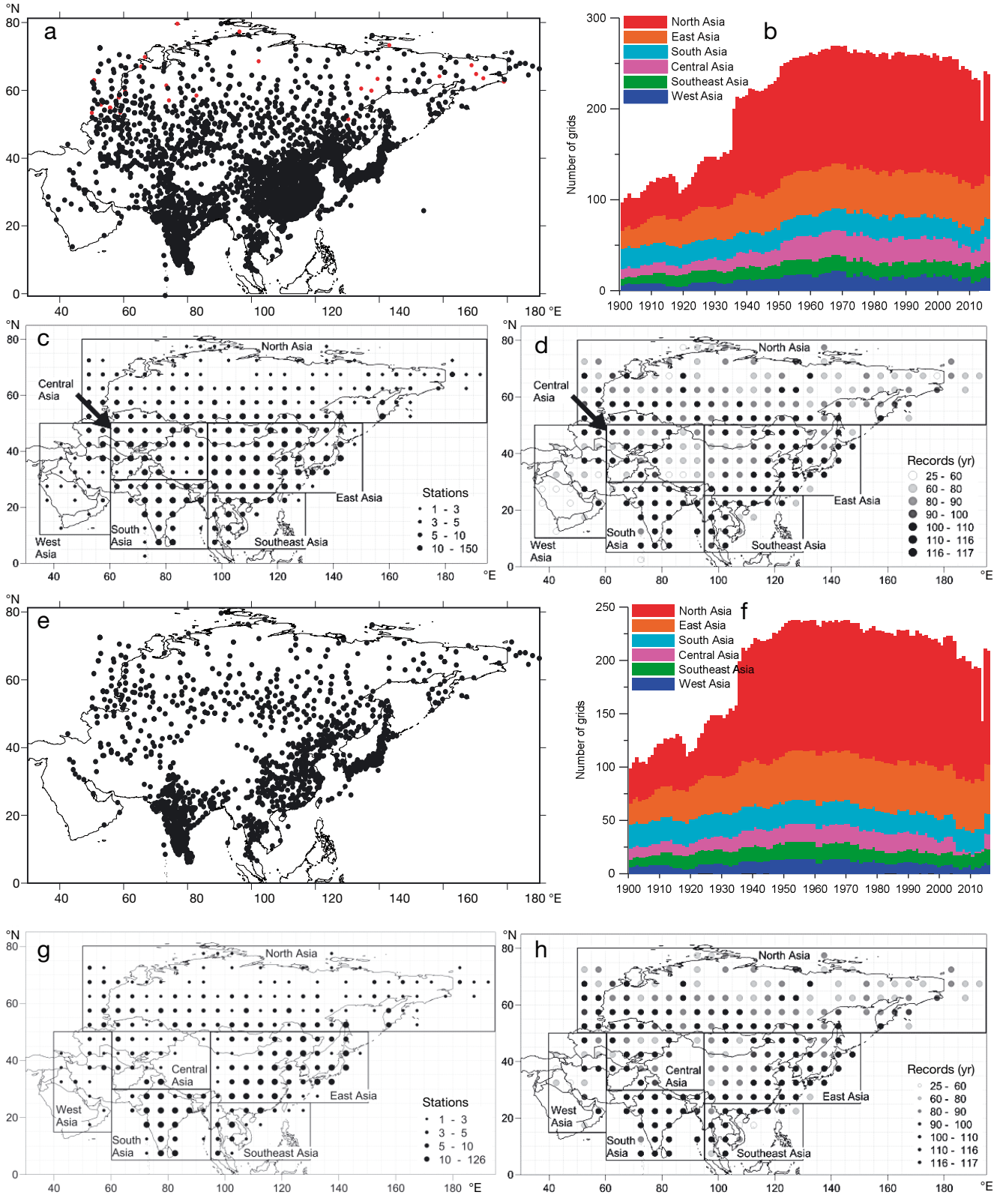

Fig. 1. (a,e) Spatial distribution of precipitation measurement stations in Asia (5–80° N, 40° E–165° W). Red dots in (a) indicate the stations for which RBMP records of 1936–2010 were used. (b,f) Numbers of grid boxes in the 6 sub-regions in 1901–2016; (c,g) number of stations in every grid box, with the bold straight lines showing the boundaries of the 6 sub-regions; (d,h) number of years with valid records in every grid box. (a–d) based on 2652 stations; (e–f) based on 1316 stations

Author copy

received over 12 mo in any given year (mm). The seasonal total precipitation is the sum of 3 mo of precipitation by season as follows: spring represents March, April, and May (MAM); summer is June, July, and August (JJA); autumn is September, October, and November (SON); and winter is December, January, and February (DJF). The proportion of precipitation in every season is the ratio of seasonal total precipitation to annual total precipitation.

The precipitation indices commonly used included the original value, anomaly, percent anomaly (PA), and normalized precipitation anomaly (NPA). All anomalies are the yearly total precipitation minus the average annual total precipitation in the base period. The PA is the annual anomaly divided by the average annual total precipitation in the base period, while NPA is the annual anomaly divided by the standard deviation of the annual total precipitation in the base period.

Previous research has mainly used original precipitation values or anomalies (absolute indices) to analyze long-term changes in precipitation. However, the same amount of precipitation in different areas does not have the same meaning. For example, while a month with 200 mm of precipitation in New Delhi may be a common occurrence, the same amount of precipitation in Riyadh could be rarely seen over several decades. For large regions with wide discrepancies in the distribution of precipitation, such as the Asian continent, the change in precipitation amount in arid areas can hardly be detected during the regional average computing process if absolute values of original indices or anomalies are used.

To solve this problem, the relative values of precipitation indices should be used to examine the change in precipitation in a large-scale analysis. However, the use of PA can sometimes seriously magnify the gain in precipitation in extremely dry areas when computing regional averages. For example, Bahrain Station (26.3° N, 50.7° E) only has 0.012 mm of summer mean precipitation during the base period (1961–1990), but its 1992 percent anomaly was as high as +41 570 % because the summer witnessed a total rainfall event of 5 mm. Such an abnormally high PA will greatly affect any analysis results of regional averages.

As another relative value index, the NPA also faces a similar problem, but the deviation is not as large. In the former example, the 1992 summer NPA of Bahrain Station was +9.5, which does not create too serious of a problem in the regional average time series. Previous studies also considered NPA as a better indicator to analyze the regional average change (Jones & Hulme 1996, Ren et al. 2015). Therefore, NPA was mainly used in the present analysis to calculate the regional average time series.

The grid area-weighted averaging method was applied to establish the Asian and regional average NPA series (Jones & Moberg 2003). NPA values were calculated based on observational station data, and the grid box values were calculated by averaging all of the station values in each of the grid boxes. Finally, the regional average NPA time series was calculated by area-weighted (using the cosines of the mid-grid latitude as weights) average of all grid box values.

The linear trends of the precipitation index series are the linear regression coefficients between the precipitation and ordinal numbers of time (e.g. i = 1, 2, 3, …, 116 for years 1901–2016) obtained by using the least squares method. The 1951–2016 trends, 1981–2016 trends, and the moving linear trends with step lengths of 20, 30, 40, and 50 yr were also calculated to analyze the trend characteristics of varied time periods. In order to calculate the grid trends, the grid boxes had to have at least a 65, 50, or 25 yr record for the 3 periods (1901–2016, 1951–2016, and 1981–2016), respectively; otherwise, the grid boxes were not included in the calculations. The method for calculating moving linear trends was described by Ren et al. (2015). The significance of the linear trends of the NPA series was determined by using a 2-tailed simple t-test. In this assessment, a trend was considered to be statistically significant if it was significant at the 95 % ($p < 0.05$) level.

To analyze the regional change features of Asian precipitation, the entire region was divided into 6 sub-regions as follows: North Asia (50° E–165° W, 50°–80° N, frigid climate), East Asia (95°–150° E, 25°–50° N, temperate and subtropical monsoon climate), Southeast Asia (95°–130° E, 5°–25° N, tropical monsoon climate), South Asia (60°–95° E, 5°–30° N, tropical monsoon climate), West Asia (35°–60° E, 15°–50° N, tropical and subtropical arid climate), and Central Asia (60°–95° E, 30°–50° N, temperate continental climate) (Fig. 1c). The sub-regions were divided based on a combination of climatic (Kottek et al. 2006), geographical, and political boundaries. Areas within the 6 sub-regions have approximately the same climate types, and the boundaries are located near local geographical boundaries. The average values of the 6 sub-regions were also calculated by the area-weighted averaging method. The sub-regions of West, Central, and East Asia may have the problem of data inhomogeneities in the cold seasons. The problem may be more serious in northern parts of West, Central, and East Asia (NWCEA), which was defined as a rectangular region spanning

Author copy

50°–110° E, 40°–50° N, due to the generally stronger wind in winter. In order to understand the influence of the possible inhomogeneities on trend analysis, the average values in these sub-regions and the whole of Asia were also examined with the data of the NWCEA region excluded.

3. RESULTS

3.1. Annual NPA change

The spatial distribution and the zonal mean of linear trends of gridded NPA for the periods of 1901–2016, 1951–2016, and 1981–2016 were all examined (Fig. 2). From 1901–2016, the annual total NPA increased significantly in about half of the grid boxes north of latitude 50° N, while it decreased insignificantly in almost every grid box between 20° and 30° N. In other latitudes, the NPA increased in both Central and Southeast Asia, but decreased in the eastern part of China, although these trends were insignificant (Fig. 2a).

The averaged zonal results show that the NPA decreased in the subtropical zone (20°–30° N) and increased less than 0.040 (decade^{-1}) in the tropical (5°–20° N), temperate (30°–50° N), and polar (75°–80° N) zones. The NPA remarkably increased in the frigid climate zone (50°–80° N), and the rate of increase was more than 0.040 (decade^{-1}).

From 1951–2016, the annual NPA also increased in most grid boxes between latitude 50 and 70° N. The NPA decreased in some grid boxes between 20 and 30° N, such as in the Yunnan-Guizhou Plateau and in the Gangetic and Indus plains. In the temperate (30°–50° N) zone, the NPA decreased slightly in most grid boxes east of 100° E, but increased west of 100° E. The zonal average trends were obviously positive because West China experienced a significant increase in precipitation during the period 1951–2016. The zonal averages showed that the annual NPA decreased slightly in the subtropical (20°–30° N) zone and strongly in the polar (70°–80° N) zone. The NPA increased in most grid boxes of the frigid zone (50°–70° N), but the rate of increase of the zonal mean did not exceed 0.10 decade^{-1} (Fig. 2b).

From 1981–2016, the annual NPA still increased in most grid boxes between latitude 50° and 70° N. Like the trends of 1951–2016, the NPA also decreased in some grid boxes between 20° and 30° N such as in the Yunnan-Guizhou Plateau and in the Gangetic and Indus plains. The Indian and Indo-China peninsulas had an increasing NPA in nearly all grid boxes south of 20° N, but the trends were not significant. The NPA increased with trends more than 0.10 decade^{-1} in most grid boxes of Russia, Japan, West China, and Kazakhstan during this period. The zonal averaged NPA obviously increased in most latitudes except for the subtropical (20°–30° N) and polar (75°–80° N) zones (Fig. 2c). Thus, the annual NPA experienced a significant increase in most parts of North Asia, while it tended to decrease in subtropical zones for every temporal scale. The characteristics of zonal change in averaged precipitation were consistent throughout the past century.

The regional average annual NPA time series for the whole of Asia are presented in Fig. 3. The NPA values were negative for most years before 1952. They changed to positive values suddenly around 1953, and remained positive until 1961. After 1961, the NPA exhibited a rising trend with alternating positive and negative values. Overall, the regional average annual NPA increased over the entire period of 1901–2016, with the rate of change being 0.016 (decade^{-1}), which was significant. The NPA time series without the NWCEA region varied in some years, and the linear trend reduced to 0.012 (decade^{-1}), accounting for a ca. 25% reduction of the trend for the whole of Asia. However, the trend without the NWCEA region was still significant ($p < 0.01$), and the characteristics of the change pattern were not much different, implying that the potential inhomogeneities in the data of the region had an influence on the trend estimate of precipitation over the continent, but they may not have substantially changed the overall characteristics of the annual precipitation change in the time period analyzed.

The running linear trends of the regional average NPA are shown in Fig. 4. Most trends that ended before 1950 were negative. In particular, the 30 and 40 yr trends before 1945 were mostly significant. Every trend beginning before 1940 and ending after 1955 was positive, and most of them were also significant. The 20 yr moving trends after the 1950s were characterized by alternatively positive and negative variations, which were all insignificant, with about a 10 yr cycle. The 30, 40, and 50 yr trends increased slightly after 1950, but the trends were all small and insignificant. The sudden increase in the 1940s and 1950s was a major factor related to the increasing running trends for precipitation from 1901–2016. Before the sudden change in the 1940s and 1950s, the precipitation trends in Asia tended to decrease, while afterward they fluctuated with small running trends.

The regional average annual NPA time series in the 6 sub-regions were examined (Fig. 5). The NPA in

Author copy

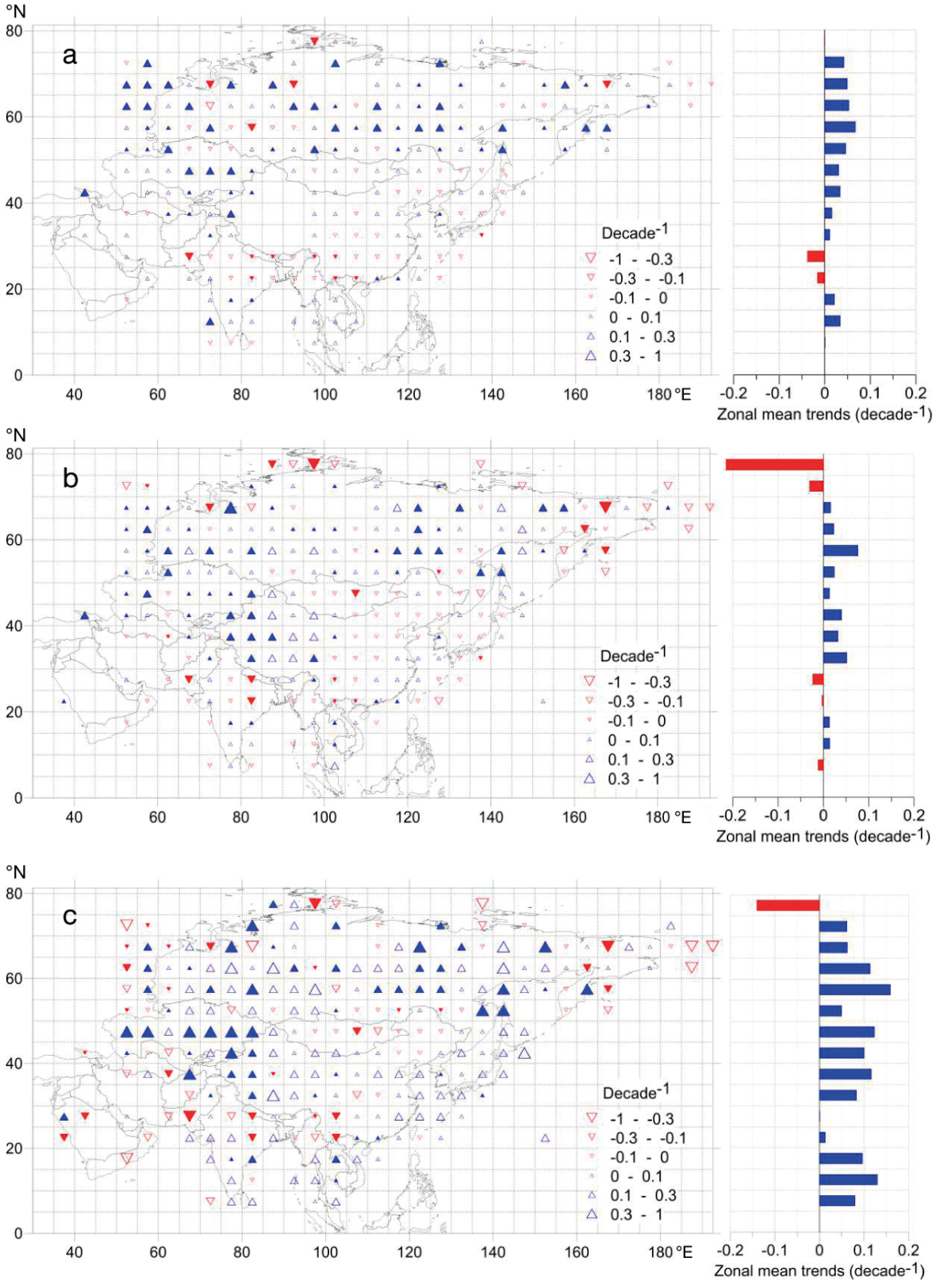

Fig. 2. Spatial distribution and the zonal mean of linear trends of the gridded normalized precipitation anomaly (NPA) for the periods (a) 1901–2016, (b) 1951–2016, and (c) 1981–2016. Data in (a) based on 1316 stations; data in (b) and (c) based on 2652 stations. Red and blue symbols represent negative and positive trends, respectively, and filled symbols represent statistically significant trends

Author copy

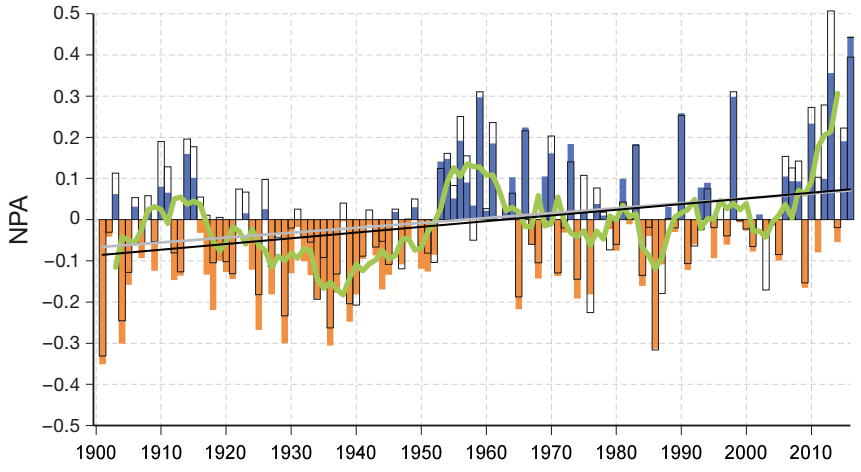

Fig. 3. Regional average normalized precipitation anomaly (NPA) time series in the whole of Asia. Blue and orange bars: positive and negative regional average values of annual NPA, respectively; unfilled portions of the respective bars: regional average values of annual NPA without the northern parts of West Asia, Central Asia, and East Asia (NWCEA region); green line: 5 yr moving average; black and grey lines: linear trends with and without the NWCEA region, respectively

North Asia significantly increased from 1901–2016, especially in the 1930s to 1960s. The change rate was 0.046 (decade^{-1}) for the entire period, about 3 times that of the whole of Asia. The NPA in Central Asia also significantly increased during 1901–2016. A marked decadal increase occurred in the 1950s, and the annual NPA experienced a sudden shift from dry to wet after 2000. Taking out the stations in the NWCEA region, obvious changes appeared in the NPA series of the mid- to high-latitude sub-regions for a few individual years, but the overall linear trends changed little. Specifically, the potential data inhomogeneities of the NWCEA region scarcely affected the NPA series in East Asia, although they may have made the trend slightly smaller in

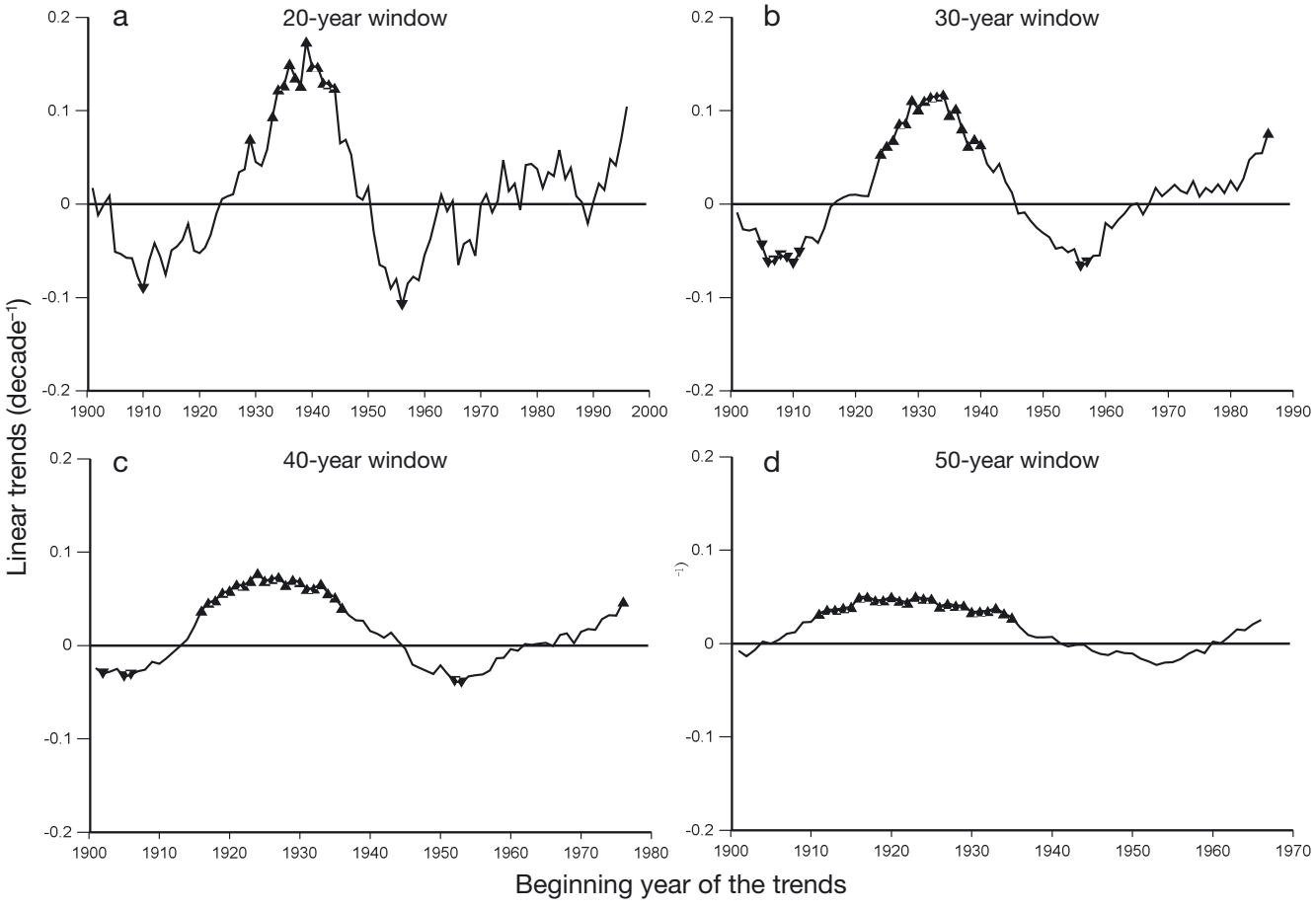

Fig. 4. Annual normalized precipitation anomaly (NPA) running trends for (a) 20 yr, (b) 30 yr, (c) 40 yr, and (d) 50 yr time steps. The solid triangles represent the trends which were significant at the 0.05 confidence level

Author copy

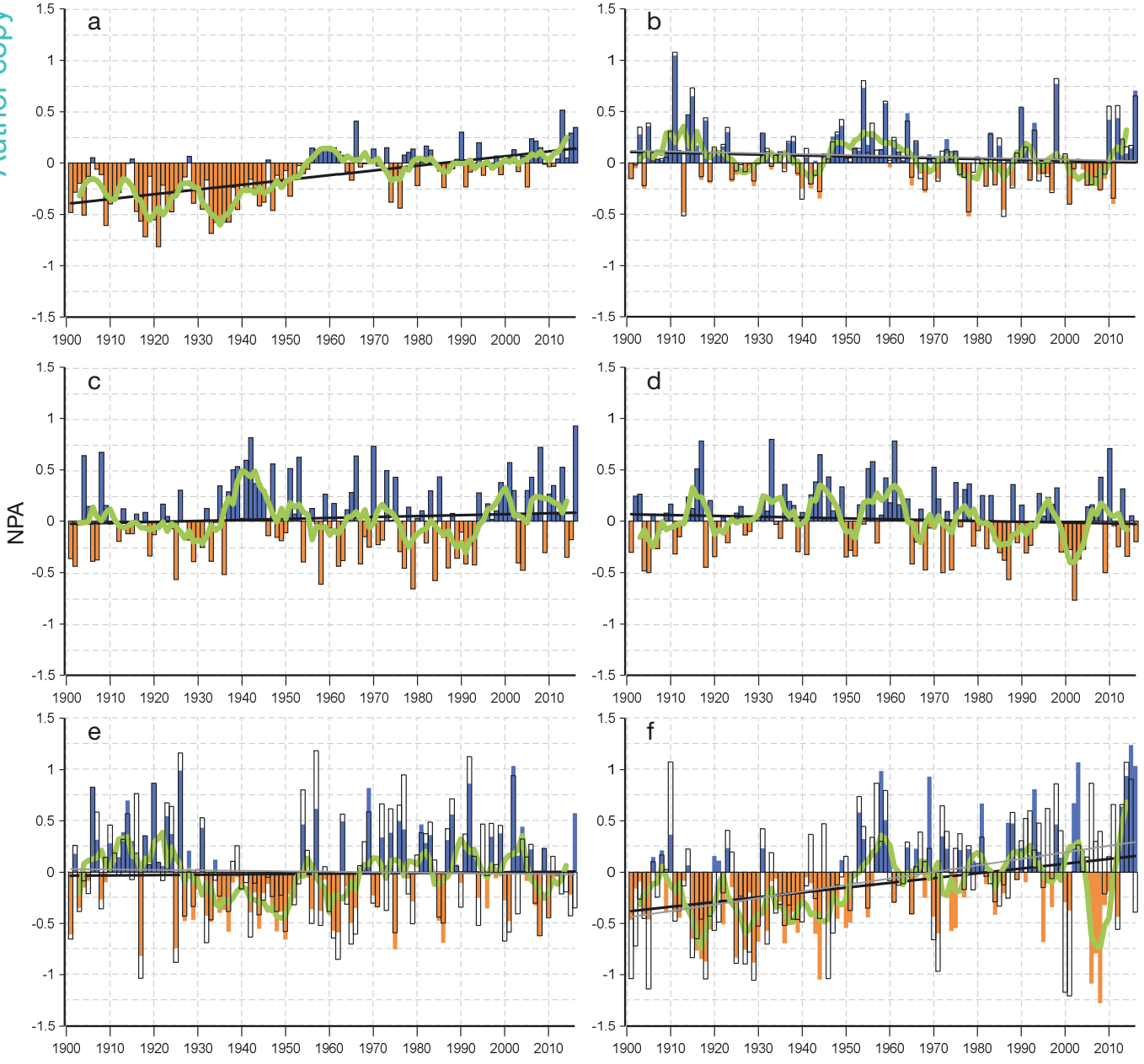

Fig. 5. Regional average annual normalized precipitation anomaly (NPA) time series in (a) North Asia, (b) East Asia, (c) Southeast Asia, (d) South Asia, (e) West Asia, and (f) Central Asia. Blue and orange bars: regional average values of annual NPA; unfilled portions of the respective bars: values without the northern parts of West Asia, Central Asia, and East Asia (NWCEA region) in (b,e,f); green line: 5 yr moving average; black and grey lines (grey line only in b,e,f): linear trends with and without the NWCEA region, respectively

West Asia, with the overall linear trends of these 2 sub-regions unchanged. The NPA in Southeast and West Asia increased slightly, while that in East and South Asia all generally decreased. However, these changes could be better characterized by the decadal and periodic variations rather than linear trends that were all insignificant.

3.2. Seasonal precipitation change

During the period of 1901–2016, the linear trends of the regional average NPA for every season in North Asia and Central Asia all increased, and all are significant except for summer (Fig. 6). The winter NPA in South Asia significantly decreased during

Author copy

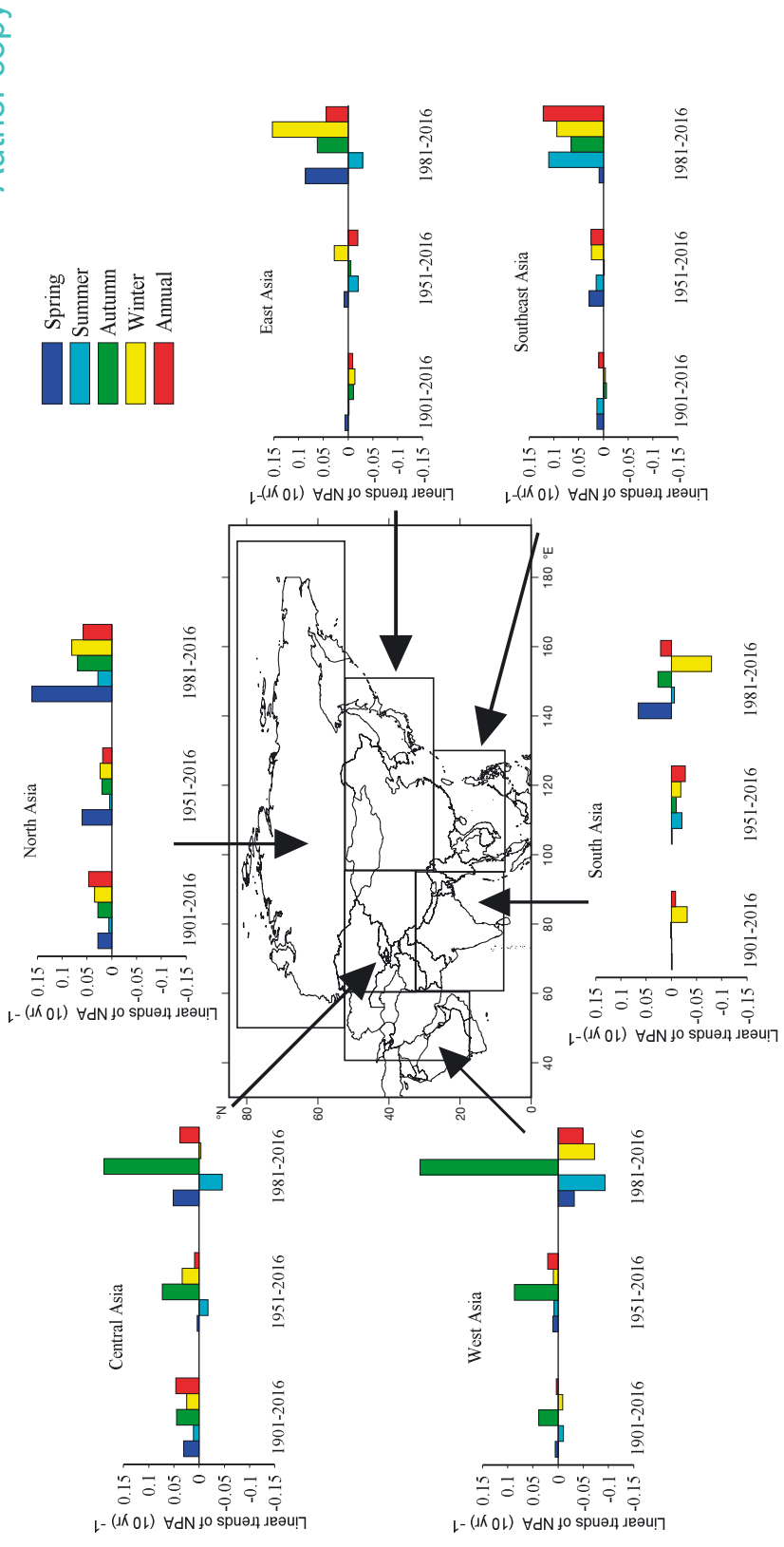

Fig. 6. Linear trends of seasonal and annual normalized precipitation anomaly (NPA) for the periods of 1901–2016, 1951–2016, and 1981–2016 in the 6 sub-regions. Spring: March–May; Summer: June–August; Autumn: September–November; and winter: December–February

1901–2016. The other seasonal changes in NPA from 1901–2016 in every sub-region were all small and insignificant. The seasonal and annual NPA in the whole study region all increased, and the spring, autumn, and annual trends were significant. During the period of 1951–2016, the seasonal and annual NPA in North Asia, West Asia, and the Asian continent all increased, while the NPA in South Asia decreased in every season. However, only the spring NPA in North Asia and in the whole region, the autumn NPA in Central Asia and West Asia registered a significant increase. During the period 1981–2016, the seasonal and annual NPA in North Asia, West Asia, and the whole region had a similar change to that of 1951–2016. The winter NPA in East Asia also increased significantly. No sub-region had a significantly decreasing seasonal or annual NPA during this recent period (Fig. 6).

The spatial distributions of NPA linear trends for the 4 seasons in the period of 1901–2016 were not all the same as those of the entire year (Fig. 7). In spring, precipitation increased in most land areas north of 40° N, and significantly increased in many grid boxes of Russia; in summer, the seasonal precipitation amount did not change much in any continuous area; autumn precipitation increased significantly in most parts of Russia north of 55° N, and also increased in Central Asia, with Northeast China and Japan experiencing a general downward trend; in winter, Russia had the strongest and most significant increase in precipitation except for the grid boxes east of 140° E, and the region with a significant increase extended southward to 45° N, including Kazakhskiy Melkosopochnik (central Kazakhstan), Mongolia, and the northern part of Northeast

Author copy

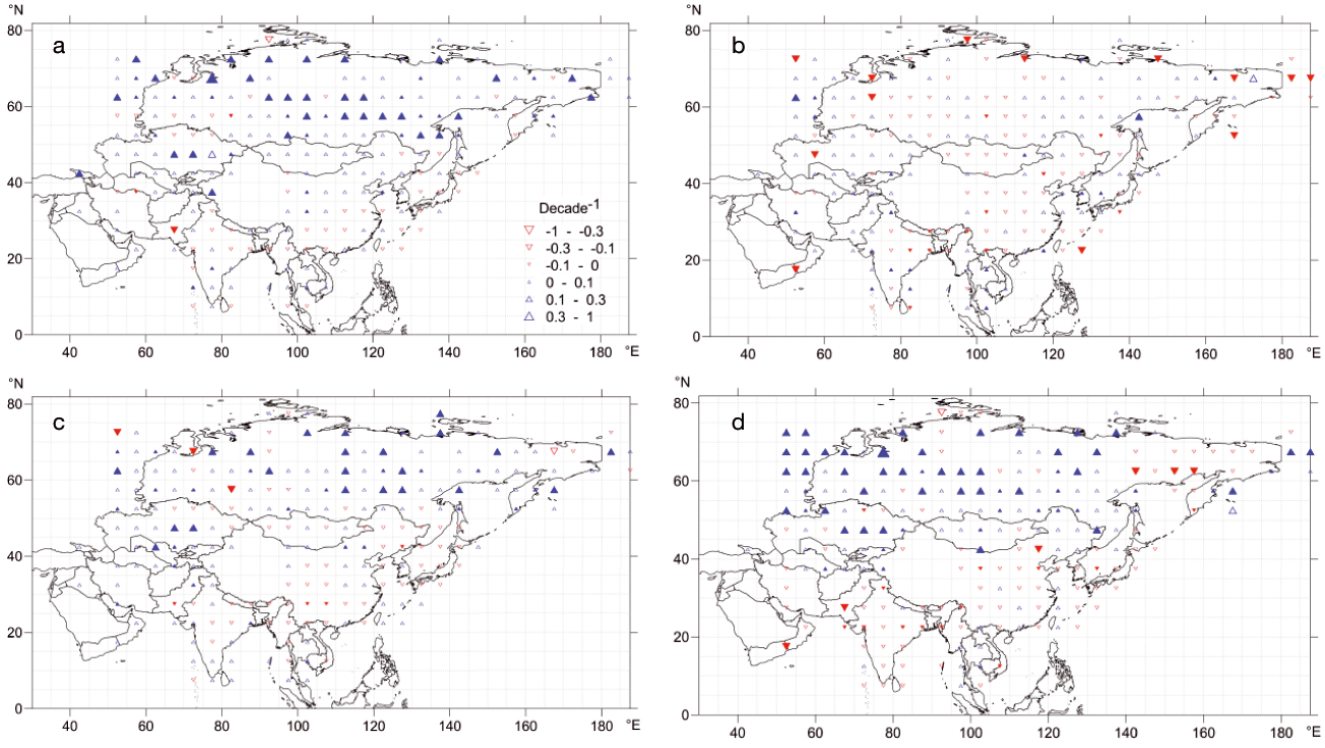

Fig. 7. Spatial distribution of linear trends of gridded seasonal normalized precipitation anomaly (NPA) for the period of 1901–2016 in Asia. (a) Spring, (b) summer, (c) autumn, (d) winter. Filled symbols represent statistically significant trends

China. However, winter precipitation generally decreased in South Asia, with the trend being significant in the northern part of South Asia.

The regional average seasonal NPA time series in the whole region were also not the same (Fig. 8). The spring and autumn NPA significantly increased, with linear trends of 0.016 (decade^{-1}) and 0.011 (decade^{-1}), respectively, during the period 1901–2016. They all declined slightly before 1940 and quickly increased in 1950–1960 and after 2010. The changes in summer were less than those in spring or autumn, with a linear trend of only 0.004 (decade^{-1}) in the period 1901–2016. In winter, the NPA fell dramatically in the 1930s, suddenly rose again in the 1950s, and fluctuated with alternating positive and negative anomalies before 1930 and after 1960. The winter linear trend was 0.001 (decade^{-1}), which did not pass the 0.05 significance test.

The 50 yr running linear trends for seasonal precipitation have shown that the running linear trends in spring and autumn were similar to the annual trend. These trends were significantly negative in several 50 yr periods beginning in the early 20th century. The 50 yr linear trends starting from the mid-1910s and ending to the mid-1990s were all positive, and the trends reached up to 0.020 (decade^{-1}). After this time, the trends fluctuated from negative to positive, and the nearest several 50 yr positive trends were significant. The summer 50 yr running trends all had very small absolute values, with only the 50 yr running linear trends from 1911–1960 to 1921–1970 being significantly positive, while those from 1940–1989 to 1945–1995 were significantly negative. The winter 50 yr running trends were generally negative in the periods starting in the early 20th century, and were all significant when the start year was prior to 1910. However, the 50 yr trends starting later than 1920 became positive, and those with start years from 1930–1945 were mostly significant (Fig. 9).

The proportion of summer precipitation (summer to annual precipitation) declined during 1901–2016 across all of North Asia and most parts of Central Asia and Northwest China. In these areas, the proportions of spring precipitation increased to some extent, and the proportions of autumn precipitation only increased in the Russian Far East. However, in Northeast China, South China, and southern India, the autumn precipitation ratio decreased significantly. In winter, the proportions of precipitation increased significantly in Russia west of 100° E, and decreased in North China, central India, and most parts of West Asia (Fig. 10).

Author copy

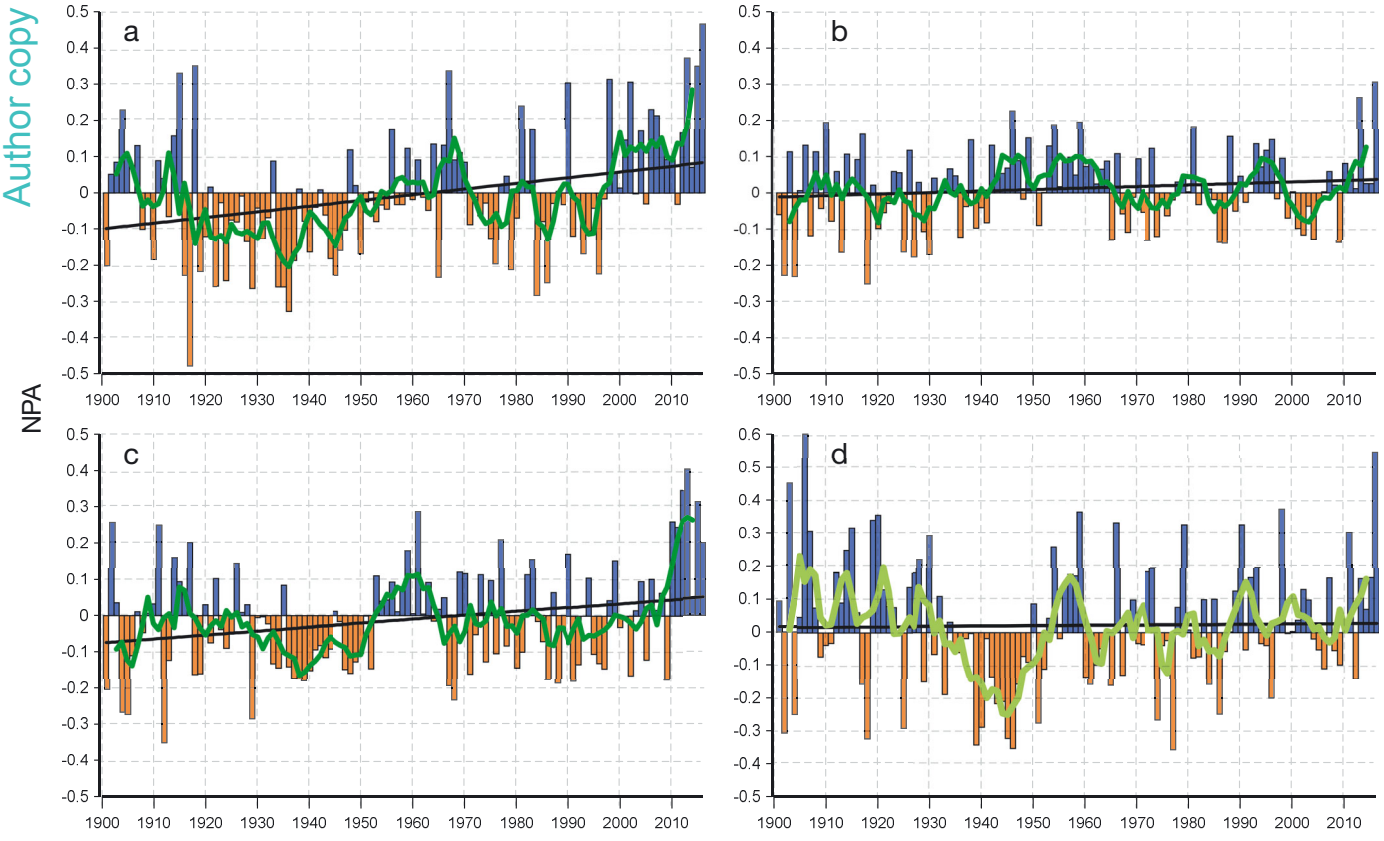

Fig. 8. Regional average seasonal normalized precipitation anomaly (NPA) time series in the whole of Asia. (a) Spring, (b) summer, (c) autumn, (d) winter. Blue and orange bars indicate the regional average values of annual NPA, the green line is a 5 yr moving average, and the black line is the linear trend

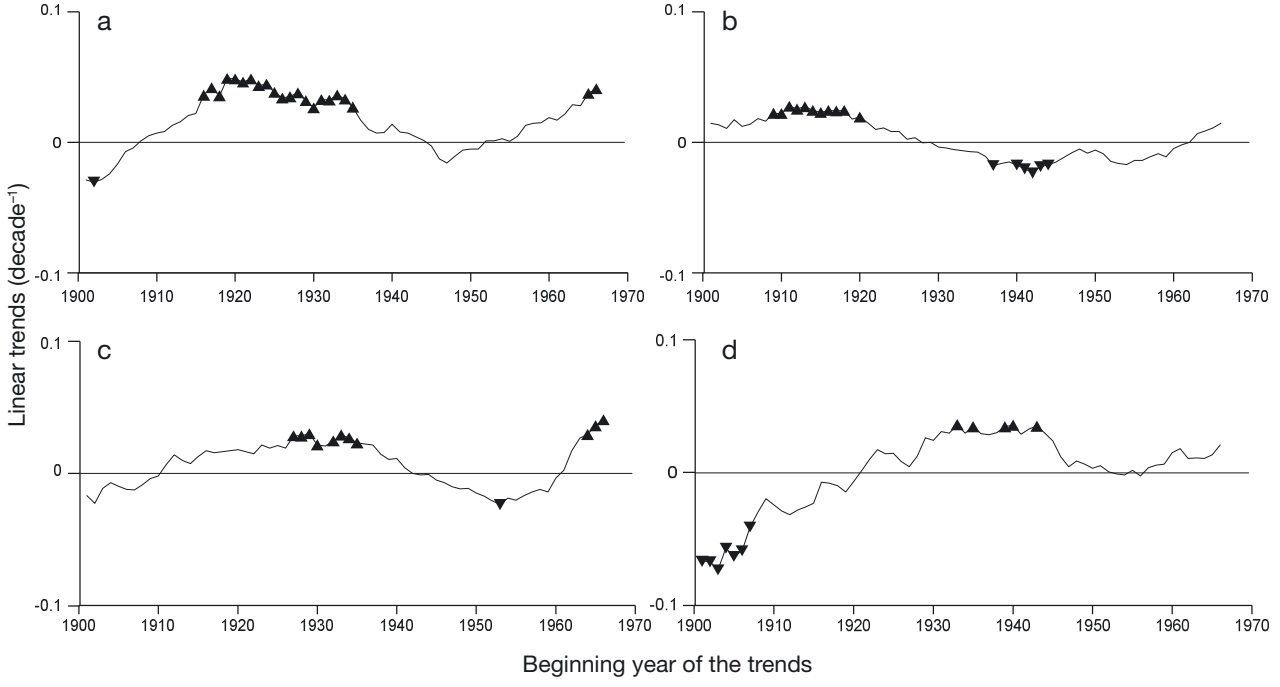

Fig. 9. Seasonal normalized precipitation anomaly (NPA) running trends for a 50 yr step during 1901–2016. (a) Spring, (b) summer, (c) autumn, (d) winter. Solid triangles represent statistically significant trends

Author copy

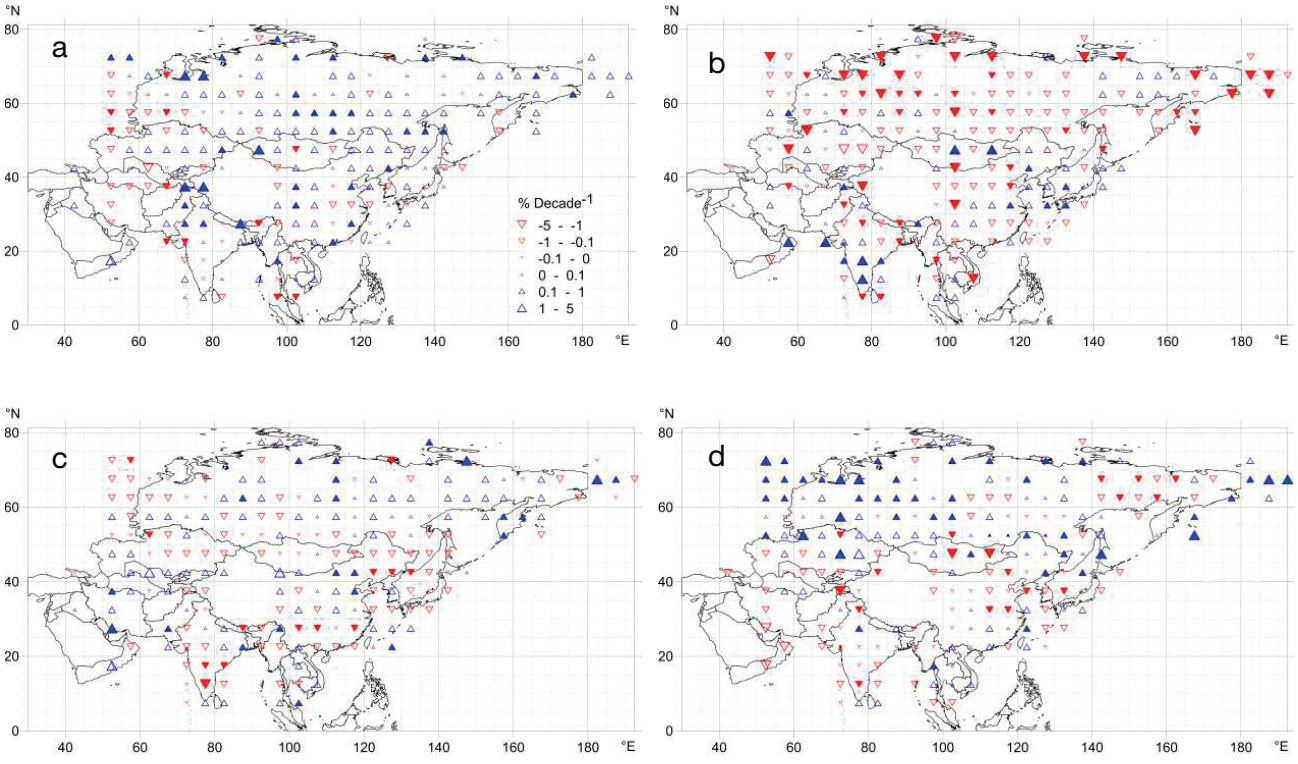

Fig. 10. Spatial distribution of linear trends of gridded seasonal to annual precipitation ratios for the period of 1901–2016 in Asia. (a) Spring, (b) summer, (c) autumn, (d) winter. Filled symbols represent statistically significant trends

4. DISCUSSION

In this study, we analyzed variations in the characteristics of precipitation over the whole of Asia from 1901–2016 by using a new multi-source dataset. This new historical dataset had more valid monthly precipitation data and better data quality than those of single datasets, such as GHCN-D, used in previous works. Our analysis led to some similar conclusions to those of previous studies, but some results reported here are novel and interesting.

The analysis revealed a large and significant change in precipitation in North Asia characterized by a significant increase in annual and seasonal precipitation during 1901–2016. The conclusion was similar to findings that precipitation had increased globally in the mid- and high latitudes based on previous studies (e.g. Trenberth 2011, Stocker et al. 2013). The possible reason for the increasing precipitation might be that as the high-latitude regions became warmer, the moisture levels in the atmosphere increased, thereby increasing the probability of precipitation (Boer 1993, Allen & Ingram 2002).

Nevertheless, we could not eliminate the probability that observation errors produced a false increase in precipitation rates. Most precipitation gauges had difficulty in capturing and measuring precipitation accurately, especially winter snowfall. The influence of the wind makes observations of precipitation smaller than the actual precipitation rate, and this deviation (so-called 'undercatch bias') is much greater in snowfall observations (Groisman & Legates 1995, Yang et al. 2005, Bogdanova et al. 2007, Ren et al. 2016). On the other hand, the near-surface wind speed has declined over the past decades in mid- to high latitudes of Asia (e.g. Ren et al. 2005, Jiang et al. 2010, Vautard et al. 2010, You et al. 2010, Guo et al. 2011). This implies that the catch rates of the rain gauges as applied in most countries and regions experienced an increase. North Asian precipitation mainly arrives as snowfall except in summer, so a decrease in wind speed and the resulting rise in the catch rates of the gauges might be causing a false upward trend in precipitation, especially for winter snowfall.

The bias-corrected precipitation data of the VMGO helped to remove biases over Russia during 1936–2010 to a large extent, and the 1901–1935 and 2011–2016 records were also corrected in this paper. The corrected and uncorrected precipitation in North Asia, however, all showed an increase in annual precipitation from 1933–1956, which was also revealed by global zonal mean analyses based on the Global

Author copy

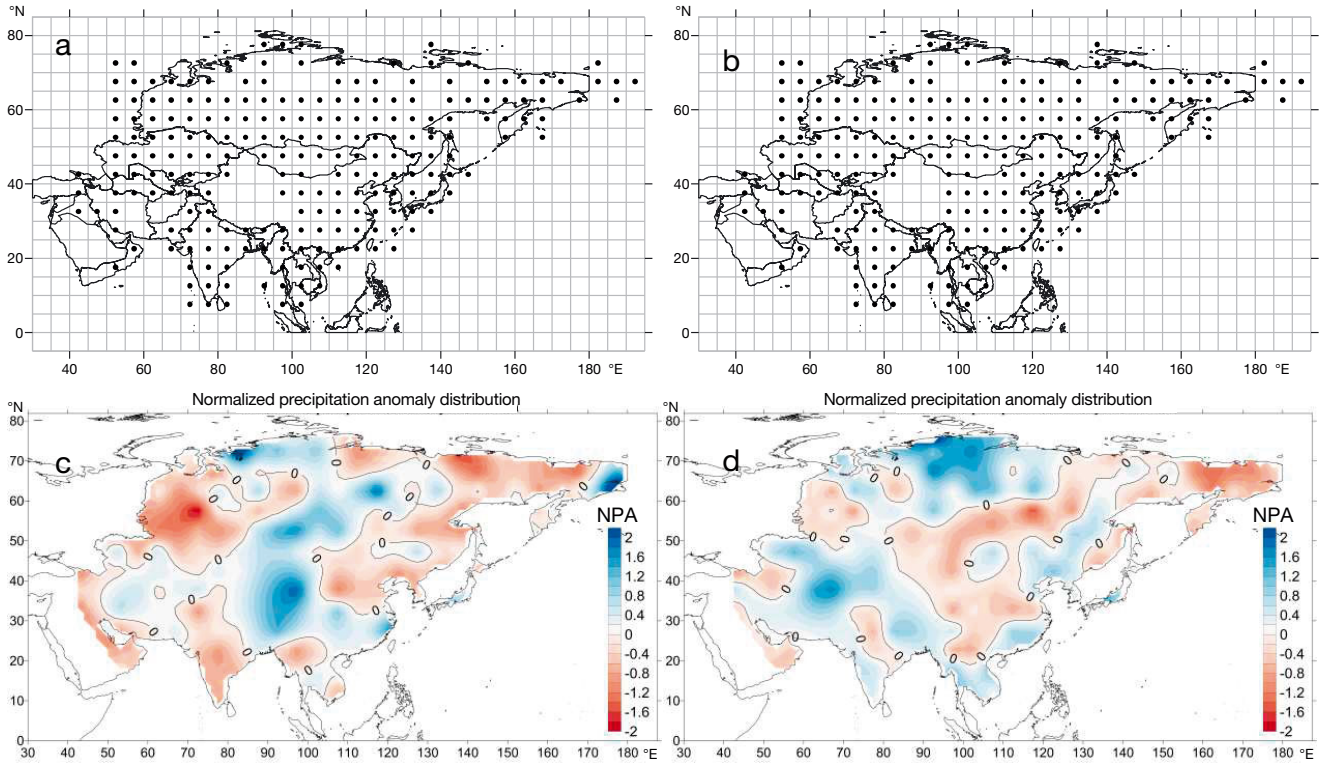

Fig. 11. Grid boxes used to calculate the regional average normalized precipitation anomaly (NPA) values in the whole of Asia for (a) 1952 and (b) 1953, and the spatial distribution of annual NPA in (c) 1952 and (d) 1953

Precipitation Climatology Project (GPCP) dataset (New et al. 2001), indicating that the increase in precipitation in this region may have been a large-scale change. However, the precipitation data in other areas, especially the NWCEA region, were not corrected, although the biases might be relatively small. An examination of the regional series with and without the NWCEA region confirmed that the linear trends of the regional average NPA series in the whole of Asia and the 3 sub-regions containing parts of the NWCEA region were not changed much, although we could not rule out the possibility that the inhomogeneities and systematic errors in the observational data in these cold areas caused false increasing trends of annual and winter precipitation. This problem introduced up to ~25% uncertainties to the estimation of the linear trend of annual NPA in Asia. Further investigation of this issue is needed to reduce the uncertainty.

In addition to the general increase in precipitation over the Asian continent during the past century, a precipitation shift toward a higher level could be found from 1952–1953. This abrupt change was partly in accordance with the analysis by Groisman et al. (2013), but most former studies have not reported an obvious change because of the relatively poor data coverage for the period before 1956 (Gruza et al. 1999). To eliminate the cause of data coverage differences during 1952 and 1953, we examined the grid boxes used to calculate the regional average time series of both of these years (Fig. 11a,b). Clearly, the 1953 grid boxes did not experience a major shift when compared with the 1952 grid boxes, indicating that the sudden change was not derived from variation in data coverage and density. Comparing the NPA spatial distribution of 1952 to that of 1953 (Fig. 11c,d), one can further see that the change in precipitation rate had a strongly negative NPA in the West Siberian Plain and East Siberia in 1952, but the NPA of these areas had a small absolute value in 1953. The datasets (for example, GHCN) used by former studies had very sparse station density in these areas, especially in the plain areas near the Arctic, so that they were less able to detect the precipitation change in the high-latitude areas of Asia (Gruza et al. 1999, Yang et al. 2016). The use of the new multi-source precipitation dataset might have been a reason that we were able to detect the shift and to explain the discrepancies compared to previous studies.

Although the CGP dataset had better station density and record length in China and North Asia, the data coverage was still poor in West Asia, and the

Author copy

early part of the 20th century in western China, which might cause major data uncertainties. Further improvement in processing the spatial and temporal data coverage is underway, but much work is needed to obtain the missing records, and it is almost impossible to fill the data gaps of early years in most parts of western China and West Asia. Uncertainties might also result from the problems with analysis methods. The discrepancies to previous studies could be partly derived from the use of NPA rather than the original precipitation values or anomalies in this analysis. Compared to those absolute-value indices, NPA as used in this paper could better highlight the trends in precipitation change in areas with low precipitation, while the trends might be erased in the process of calculating regional averages using the original precipitation values or their anomalies (Jones & Hulme 1996). The assessment of the applicability of precipitation indices at different spatial and temporal scales, with data that vary in quality, or with different application scenarios, should be part of further quantitative analyses.

5. CONCLUSIONS

A new multi-source dataset was used in this paper to analyze changes in precipitation amounts over the Asian continent during 1901–2016. The main conclusions are as follows:

(1) The regional average annual precipitation in the region has increased significantly. Precipitation prior to the early 1950s was considerably lower than after, however, there were still uncertainties with the data from mid- to high-latitude regions. Large and significant increases mainly occurred in cold areas such as North and Central Asia, with a significant increase occurring in the mid-20th century. The zonal mean annual precipitation of tropical, temperate, and frigid zones tended to increase while that of the sub-tropical zone tended to decrease.

(2) The characteristics of change in the average spring and autumn precipitation over the Asian continent were similar to the annual change. The amount of precipitation in summer increased slightly. The amount of winter precipitation decreased significantly in the 1930s and increased significantly from 1945–1955, and after 2010, with a slight upward trend for the entire period of 1901–2016.

(3) North and Central Asia experienced a significant increase in precipitation for every season except summer during 1901–2016. West Asia showed a significant upward trend in autumn precipitation, and South Asia showed a significant decrease in winter precipitation during the period 1901–2016. No significant changes in seasonal precipitation were observed during 1901–2016 in the other Asian regions.

(4) During 1901–2016, the summer precipitation ratio declined uniformly and significantly in cold areas, and the other 3 seasonal precipitation ratios increased more or less. The autumn precipitation ratio decreased in Northeast China, South China, and southern India.

Acknowledgements. This study was financially supported by the China Natural Science Foundation (CNSF; Grant Number 41575003) and the Ministry of Science and Technology of China (Fund No. GYHY201206012). We thank Dr. Pavel Shabanov for providing the Russian bias-corrected monthly precipitation data from the Voeikov Main Geophysical Observatory.

LITERATURE CITED

Allen MR, Ingram WJ (2002) Constraints on future changes in climate and the hydrologic cycle. Nature 419:224–232

Auer I, Böhm R, Jurkovic A, Lipa W and others (2007) HISTALP historical instrumental climatological surface time series of the Greater Alpine Region. Int J Climatol 27:17–46

Boden TA, Karl TR, Williams CN, Quinlan FT (1990) United States Historical Climatology Network (HCN) serial temperature and precipitation data. Publication 3404. Carbon Dioxide Information and Analysis Center, Environmental Science Division, Oak Ridge, TN

Boer GJ (1993) Climate change and the regulation of the surface moisture and energy budgets. Clim Dyn 8:225–239

Bogdanova EG, Il'in BM, Gavrilova SY (2007) Advanced methods for correcting measured precipitation and results of their application in the polar regions of Russia and North America. Russ Meteorol Hydrol 32:229–244

Choi G, Collins D, Ren G, Trewin B and others (2009) Changes in means and extreme events of temperature and precipitation in the Asia-Pacific Network region, 1955-2007. Int J Climatol 29:1906–1925

Dahri ZH, Ludwig F, Moors E, Ahmad B, Khan A, Kabat P (2016) An appraisal of precipitation distribution in the high-altitude catchments of the Indus basin. Sci Total Environ 548-549:289–306

Ding YH, Ren GY (2008) An introduction to climate change science in China. China Meteorological Press, Beijing (in Chinese)

Donat MG, Alexander LV, Yang H, Durre I and others (2013) Updated analyses of temperature and precipitation extreme indices since the beginning of the twentieth century: the HadEX2 dataset. J Geophys Res D Atmospheres 118:2098–2118

Dore MH (2005) Climate change and changes in global precipitation patterns: What do we know? Environ Int 31: 1167–1181

Groisman PY, Legates DR (1995) Documenting and detecting long-term precipitation trends: Where we are and what should be done. Clim Change 31:601–622

Groisman PY, Koknaeva VV, Belokrylova TA, Karl TR (1991) Overcoming biases of precipitation measurement: a his-

Author copy

tory of the USSR experience. Bull Am Meteorol Soc 72: 1725–1733
Groisman PY, Blyakharchuk TA, Chernokulsky AV, Arzhanov MM and others (2013) Climate changes in Siberia. In: Groisman PY, Gutman G (eds) Regional environmental changes in Siberia and their global consequences. Springer Environmental Science and Engineering Series. Springer, Dordrecht, p 57–109
Gruza G, Rankova E, Razuvaev V, Bulygina O (1999) Indicators of climate change for the Russian Federation. Clim Change 42:219–242
Guo H, Xu M, Hu Q (2011) Changes in near-surface wind speed in China: 1969–2005. Int J Climatol 31:349–358
Jiang Y, Luo Y, Zhao Z, Tao S (2010) Changes in wind speed over China during 1956–2004. Theor Appl Climatol 99: 421–430
Jones PD, Hulme M (1996) calculating regional climatic time series for temperature and precipitation: methods and illustrations. Int J Climatol 16:361–377
Jones PD, Moberg A (2003) Hemispheric and large-scale surface air temperature variations: an extensive revision and an update to 2001. J Clim 16:206–223
Jones PD, Lister DH, Osborn TJ, Harpham C, Salmon M, Morice CP (2012) Hemispheric and large scale land surface air temperature variations: an extensive revision and an update to 2010. J Geophys Res 117:D05127
Klein Tank AMG, Wijngaard JB, Können GP, Böhm R and others (2002) Daily dataset of 20th century surface air temperature and precipitation series for the European Climate Assessment. Int J Climatol 22:1441–1453
Kottek M, Grieser J, Beck C, Rudolf B, Rubel F (2006) World map of the Köppen-Geiger climate classification updated. Meteorol Z 15:259–263
Liu B, Xu M, Henderson M, Qi Y (2005) Observed trends of precipitation amount, frequency, and intensity in China, 1960–2000. J Geophys Res 110:D08103
New M, Todd M, Hulme M, Jones P (2001) Precipitation measurements and trends in the twentieth century. Int J Climatol 21:1889–1922
Peterson TC, Vose RS (1997) An overview of the global historical climatology network temperature database. Bull Am Meteorol Soc 78:2837–2849
Qiu J (2008) The third pole. Nature 454:393–396
Ren G, Guo J, Xu M, Chu Z and others (2005) Climate changes of China's mainland over the past half century. Acta Meteorol Sin 63:942–956 (in Chinese)
Ren G, Ding Y, Zhao Z, Zheng J, Wu T, Tang G, Xu Y (2012) Recent progress in studies of climate change in China. Adv Atmos Sci 29:958–977
Ren G, Ren Y, Zhan Y, Sun X, Liu Y, Chen Y, Wang T (2015) Spatial and temporal patterns of precipitation variability over mainland China. II. Recent trends. Adv Water Sci 26:451–465 (in Chinese with English abstract)
Ren G, Yuan Y, Liu Y, Ren Y, Tao W (2016) Change in precipitation over Northwest China. Ganhanqu Yanjiu 33:1–19 (in Chinese)
Sharma E, Molden D, Wester P, Shrestha RM (2016) The Hindu Kush Himalayan Monitoring and Assessment Programme: action to sustain a global asset. Mt Res Dev 36: 236–239
Solomon S, Qin D, Manning M, Chen Z and others (eds) (2007) Climate change 2007: the physical science basis. Contribution of Working Group I to the Fourth Assessment Report of the Intergovernmental Panel on Climate Change. Cambridge University Press, Cambridge
Stocker TF, Qin D, Plattner GK, Tignor MMB and others (eds) (2013) Climate change 2013: the physical science basis. Contribution of Working Group I to the Fifth Assessment Report of the Intergovernmental Panel on Climate Change. Cambridge University Press, Cambridge
Sun X, Ren G, Xu W, Li Q, Ren Y (2017) Global land-surface air temperature change based on the new CMA GLSAT data set. Sci Bull (Beijing) 62:236–238
Tabari H, Talaee PH (2011) Temporal variability of precipitation over Iran: 1966–2005. J Hydrol (Amst) 396:313–320
Tanarhte M, Hadjinicolaou P, Lelieveld J (2012) Intercomparison of temperature and precipitation data sets based on observations in the Mediterranean and the Middle East. J Geophys Res 117:D12102
Trenberth KE (2011) Changes in precipitation with climate change. Clim Res 47:123–138
Trenberth KE, Dai A, Rasmussen RM, Parsons DB (2003) The changing character of precipitation. Bull Am Meteorol Soc 84:1205–1217
Vautard R, Cattiaux J, Yiou P, Thépaut JN, Ciais P (2010) Northern Hemisphere atmospheric stilling partly attributed to an increase in surface roughness. Nat Geosci 3: 756–761
Wan H, Zhang X, Zwiers FW, Shiogama H (2013) Effect of data coverage on the estimation of mean and variability of precipitation at global and regional scales. J Geophys Res Atmos 118:534–546
Wen XY, Wang SW, Zhu JH, Viner D (2006) An overview of China climate change over the 20th century using UK UEA/CRU high resolution grid data. Chin J Atmos Sci 30: 894–904
Xu L, Zhou H, Du L, Yao H, Wang H (2015) Precipitation trends and variability from 1950 to 2000 in arid lands of Central Asia. J Arid Land 7:514–526
Yanai MH, Li C (1994) Mechanism of heating and the boundary layer over the Tibetan Plateau. Mon Weather Rev 122:305–323
Yang D, Kane D, Zhang Z, Legates D, Goodison B (2005) Bias corrections of long-term (1973-2004) daily precipitation data over the northern regions. Geophys Res Lett 32: L19501
Yang S, Xu W, Xu Y, Li Q (2016) Development of a global historic monthly mean precipitation dataset. J Meteorol Res 30:217–231
Yao T, Thompson LG, Mosbrugger V, Zhang F and others (2012) Third pole environment (TPE). Environ Dev 3: 52–64
You Q, Kang S, Flügel WA, Pepin N, Yan Y, Huang J (2010) Decreasing wind speed and weakening latitudinal surface pressure gradients in the Tibetan Plateau. Clim Res 42:57–64
Zhai P, Zhang X, Wan H, Pan X (2005) Trends in total precipitation and frequency of daily precipitation extremes over China. J Clim 18:1096–1108
Zhang M (1993) Variation of mean annual precipitation in East China during recent hundred years. Sci Atmos Sin 17:451–461 (in Chinese)
Zhang X, Zwiers FW, Hegerl GC, Lambert FH and others (2007) Detection of human influence on twentieth-century precipitation trends. Nature 448:461–465
Zhang Y, Ohata T, Yang D, Davaa G (2004) Bias correction of daily precipitation measurements for Mongolia. Hydrol Processes 18:2991–3005
Zhou T, Gong D, Li J, Li B (2009) Detecting and understanding the multi-decadal variability of the East Asian summer monsoon — recent progress and state of affairs. Meteorol Z 18:455–467

Editorial responsibility: Ricardo Trigo, Lisbon, Portugal

Submitted: June 20, 2017; Accepted: May 17, 2018
Proofs received from author(s): August 10, 2018

章大全,陈丽娟,柳艳菊,等,2018. 2016 年 10 月我国降水预测失败的原因分析[J]. 气象,44(1):189-198.

2016 年 10 月我国降水预测失败的原因分析*

章大全[1] 陈丽娟[1,2] 柳艳菊[1] 柯宗建[1]

1 国家气候中心,中国气象局气候研究开放实验室,北京 100081

2 南京信息工程大学气象灾害预报预警与评估协同创新中心,南京 210044

提 要:本文回顾了 2016 年 10 月降水业务预报中考虑的动力模式预测信息、前兆信号及其影响。2016 年 10 月全国平均降水量为 1951 年以来历史同期最多,且环流形势和要素分布特征在月内均发生明显转折。业务发布预报在华北南部、黄淮、江淮、江汉等地降水异常与实况存在较大差异,同时对月内环流形势调整及降水变率估计不足。数值模式预报和物理因子诊断预测与实况的对比分析表明,环流形势整体分布特征预报与实况较为一致,但对西太平洋副热带高压等环流因子的强度、西伸脊点位置以及月内变率的预报与实况存在较大差异。从大气对热带海温信号的滞后响应以及同期相关分析表明,El Niño 事件次年秋季副热带高压往往持续偏强偏北。10 月赤道太平洋东冷西暖,暖池区对流活跃,东亚上空出现的异常经向环流圈通过低层径向风异常及异常辐合辐散,在日本岛附近形成反气旋式环流距平,也有利于副热带高压加强北抬。9、10 月热带印度洋偶极子负位相有利于印缅槽加强,从而有利于水汽向我国东部地区输送。来自副热带高压外围的异常东南水汽和来自西南的水汽共同输送到我国中东部地区,并与南下冷空气交汇产生异常水汽辐合,造成这些地区降水明显偏多。此外 10 月热带对流活动依然活跃,台风的生成、登陆个数均较常年偏多,是我国东南沿海降水偏多的主要原因。

关键词:月预测,前兆信号,环流因子,海温异常

中图分类号:P461,P466 **文献标志码**:A **DOI**:10.7519/j.issn.1000-0526.2018.01.017

Review on the Failure of Precipitation Prediction in October 2016

ZHANG Daquan[1] CHEN Lijuan[1,2] LIU Yanju[1] KE Zongjian[1]

1 Laboratory for Climate Studies, National Climate Centre, CMA, Beijing 100081

2 Collaborative Innovation Center on Forecast and Evaluation of Meteorological Disasters, Nanjing University of Information Science and Technology, Nanjing 210044

Abstract: This paper reviews the predictive information provided by dynamic models and precursors considered in the operational monthly prediction of precipitation in October 2016. The average amount of precipitation over China in October 2016 is the largest compared to the precipitation in the corresponding period since 1951, and the spatio-temporal characteristics of precipitation distributions and atmospheric circulation changes significantly during the month. There exists considerable difference between operational forecasts of precipitation anomalies issued in late September and observational results in the south of North China, Huanghuai, Jianghuai and Jianghan regions. Meanwhile, the forecasts underestimate the adjustment of general circulation within month and the transition of precipitation anomaly distributions. Analysis of model output and the impact of external forcing signals indicate that the estimation of general atmospheric circulation is basically consistent with observation, while significant difference remains between the forecast and observation results of the intensity, position of ridge line of West Pacific subtropical high (WPSH), etc. Lagged and simultaneous correlation analysis between atmosphere and sea surface temperature

* 国家重点基础研究发展计划(973 计划)(2015CB453203)及国家自然科学基金项目(41605078 和 41675092)共同资助

2017 年 6 月 9 日收稿; 2017 年 9 月 4 日收修定稿

第一作者:章大全,主要从事短期气候预测相关业务及科研工作. Email:zhangdq@cma.gov.cn

(SST) indicates that, the WPSH tends to be intensified and northward in the autumn of decay years of medium and strong El Niño events. In addition, the anomalous meridional circulation induced by active convection in the West Pacific warm pool, which leads to the anticyclonic circulation anomaly around Japan, also contributes the intensification and northward of WPSH. The significant negative phase of tropical Indian Ocean dipole (TIOD) in September and October, which is in favor of strong Indian-Myanmar trough and vapor transport, combined with cold air from north, resulting in more precipitation in east and north China. Moreover, the active convection of tropical West Pacific, and increased number of generated and landed typhoons, is the main reason for heavy rains in the southeast coastal regions of China.

Key words: monthly prediction, precursor, atmospheric circulation factor, sea surface temperature anomaly

引 言

月气候预测介于中期预报和季节预测之间,其中大气初值信息快速衰减,同时海洋异常的影响还没有完全起作用,因此是一个很难预测的时间尺度。分析其可预报性来源,有效提高预报准确率,一直是气候预测领域科研和业务工作的重点和难点(王会军等,2007;陈丽娟等,2008;王绍武,2012)。我国的月气候预测业务自20世纪50年代开始,经历了简单的经验统计分析、数理统计方法的广泛应用、物理统计方法的深入发展以及动力与统计相结合几个阶段,目前已经建立起较为完善的月尺度短期气候预测业务系统(丁一汇,2004)。统计方法在月气候预测业务中的应用由来已久,而动力方法的兴起源自20世纪80年代。受到Miyakoda et al(1983;1986)工作的鼓舞,各国主流数值预报中心相继开展了大量月动力延伸预报试验(Molteni et al,1986;Owen and Palmer,1987;Tracton et al,1989;Déqué and Royer,1992)。对预报结果的检验表明,月平均环流预报技巧主要集中在前两周,两周以上的预报相对于气候预报显示出一定的预报技巧,但还未达到实际业务应用水平(丑纪范,2003a;2003b)。近年来,随着模式性能和资料同化等技术的提高,集合预报技术的广泛应用,数值模式已经逐渐成为月平均大气环流预报的主要手段(郑志海,2013;任宏利等,2014)。

由于影响我国气候变化因素的多重性、相互关系的复杂性和预测方法的多样性,我国月气候预测的基本技术特点是多种因子的综合分析和多种方法的综合应用(贾小龙等,2013),预测集成技术难度非常大。经过不懈努力,目前国家气候中心月平均温度PS预报评分达到79,月平均降水距平百分率PS预报评分达到67(2012年1月至2016年12月平均)。受到月平均气候要素可预报性的年际和季节变化的影响(Jung et al,2011),如不同El Niño位相背景下的可预报性差异(Shukla et al,2000;陈丽娟等,2016),数值模式预报技巧稳定性以及预报对象极端程度等因素的影响,部分月份的预报效果仍然较低。

2016年10月我国东部大部地区降水量异常偏多,为1951年以来历史同期最多,同时环流形势及要素分布特征在月内发生明显转折,该月降水业务预测评分较低。本文从预测的角度对10月降水异常的时空分布特征,预测效果评分以及成因进行总结分析。重点回顾了预测过程中多因子综合分析和多方法综合应用的取舍和得失,总结了预报中的成功与不足,并指出了改善预报技巧的可能途径和思路。

1 资料说明

本文所用资料主要包括:(1)中国气象局国家气象信息中心整编的《中国国家级地面气象站基本气象要素日值数据集(V3.0)》(任芝花等,2012);(2)国家气候中心整编的百项气候系统指数集;(3)美国国家环境预报中心和美国国家大气研究中心(NCEP/NCAR)提供的再分析资料,资料水平分辨率为2.5°×2.5°(Kalnay et al,1996;Kistler et al,2001);(4)美国国家海洋大气管理局(NOAA)提供的最优插值全球海温数据(OISST-v2),分辨率为1°×1°(Reynolds et al,2002)。除海温数据的气候平均场受资料起始时间限制取1982—2010年平均外,其余各要素的气候平均值均为1981—2010年平均。

2　2016 年 10 月我国降水气候特征及预测检验

2016 年 10 月全国大部分地区降水量较常年明显偏多,全国平均降水量 55.4 mm,较常年同期(35.8 mm)偏多 55%,为 1951 年以来历史同期最多(图 1)。从空间分布来看,东北大部、内蒙古中东部、黄淮、江淮、江南东部、华南东部和南部、西北地区东部、新疆大部等地降水偏多,内蒙古中东部、华北中西部、黄淮大部、江淮、江南东部、华南东部和新疆北部等地降水偏多一倍以上,其中部分地区降水量超过气候平均值两倍(图 2)。

10 月降水异常的另一个重要特征是月内变化大。上旬和中旬(图 3)除华北北部、东北中部、内蒙古中东部、新疆以及东南沿海部分地区外,全国大部分地区降水以偏少为主。其中北方地区降水过程主要集中在上旬,此外受台风活动的影响,上中旬东南沿海地区降水持续偏多。进入 10 月下旬(图 3),全国降水分布形势发生较大调整,除东北北部、内蒙古东部和西北西部外,长江以北大部分地区降水异常偏多,异常量级在气候态两倍以上。此外,受 22 号台风海马登陆的影响(21—23 日),江南南部、华南东部降水异常偏多。

2016 年 10 月业务发布降水距平百分率预报(图 4)的趋势异常综合检验 PS 评分为 55.9 分。PS 评分是目前短期气候预测业务检验所采用的主要指标(预报司关于印发《月、季气候预测质量检验业务规定》的通知—气预函〔2013〕98号)。10月降水趋势及异常级预报的评估结果显示(图 5),趋势预报错误的站点主要位于东北南部、华北东部、黄淮、江淮、江汉、西北地区东南部等地。华北中西部、江淮东部、江南东北部和东南沿海部分地区站点均漏报异常级,即对降水偏多的趋势预报虽然正确,但异常级预报显著小于实况。10 月全国异常漏报站数达到 811 个站,占到评分站点总数的 35.5%。

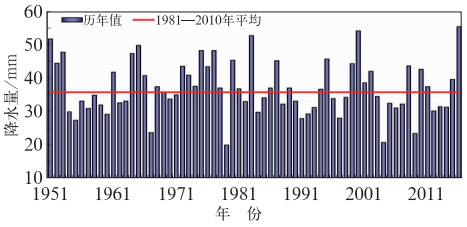

图 1　1951—2016 年 10 月全国平均降水量历年变化

Fig. 1　Time series of total mean precipitation over China in October from 1951 to 2016

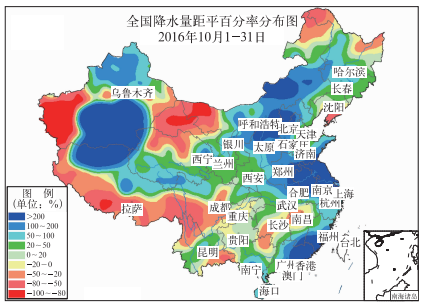

图 2　2016 年 10 月全国降水量距平百分率(单位:%)空间分布

Fig. 2　Distribution of precipitation anomaly percentage over China in October 2016 (unit: %)

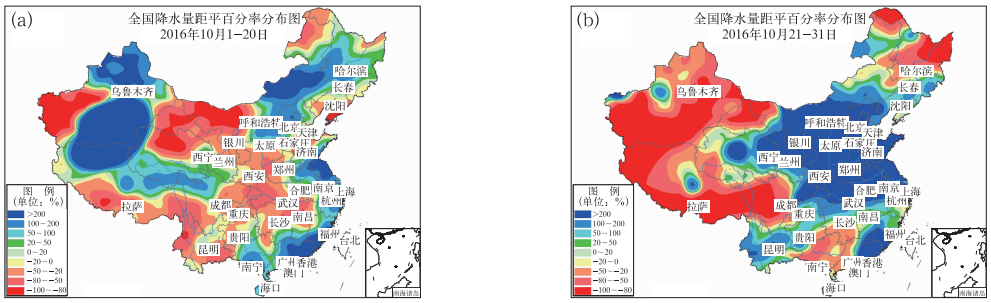

图 3　2016 年 10 月上中旬(a)和下旬(b)降水量距平百分率空间分布(单位:%)

Fig. 3　Distribution of precipitation anomaly percentage over China in the first and second (a) and last dekads (b) of October in 2016 (unit: %)

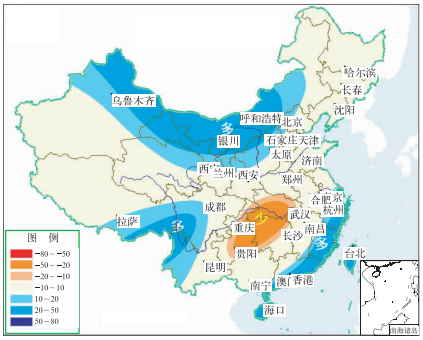

图 4 2016 年 10 月降水量距平百分率预报图(单位:%)

Fig. 4 Prediction of precipitation anomaly percentage (unit: %) over China in October 2016

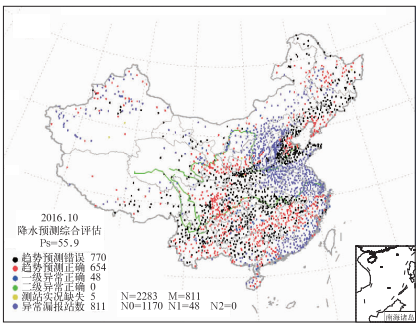

图 5 2016 年 10 月降水预测评估

Fig. 5 Assessment of prediction of precipitation anomaly over China in October 2016

3 10 月降水异常的物理成因分析

10 月我国降水异常偏多的原因主要有两方面(竺夏英和宋文玲,2017;张夏琨等,2017):一方面是北方南下的冷空气与偏强、偏西、偏北的西太平洋副热带高压(以下简称副高)引导的外围暖湿水汽交汇造成的强降水;另一方面是由于西太平洋和南海地区台风生成和登陆造成的强降水。从中高纬度环流形势来看(图 6),10 月北极涛动(AO)持续为负位相,极涡分裂,主体在东半球,有利于极地冷空气扩散并影响亚洲地区。月内中高纬度环流存在阶段性变化,上中旬亚洲中纬度地区环流以纬向为主,冷空气活动路径偏北,主要影响我国新疆北部和东北北部地区。下旬,随着乌拉尔山地区阻塞高压的发展,其东侧高空槽引导冷空气南下,影响我国长江以北的大部分地区。

在低纬度地区,西太平洋副高较常年同期明显偏强、面积偏大、西伸脊点异常偏西、脊线位置偏北,同时索马里和孟加拉湾越赤道气流异常偏强,印缅槽明显偏强。来自副高外围的异常东南水汽和来自西南的水汽共同输送到我国中东部地区,并与南下冷空气交汇产生异常水汽辐合,造成这些地区降水明显偏多。

此外,10 月在西北太平洋和南海地区有 4 个台风生成,并有 2 个登陆我国,均较常年同期偏多。台风活跃也是造成我国东南沿海和华南南部降水明显

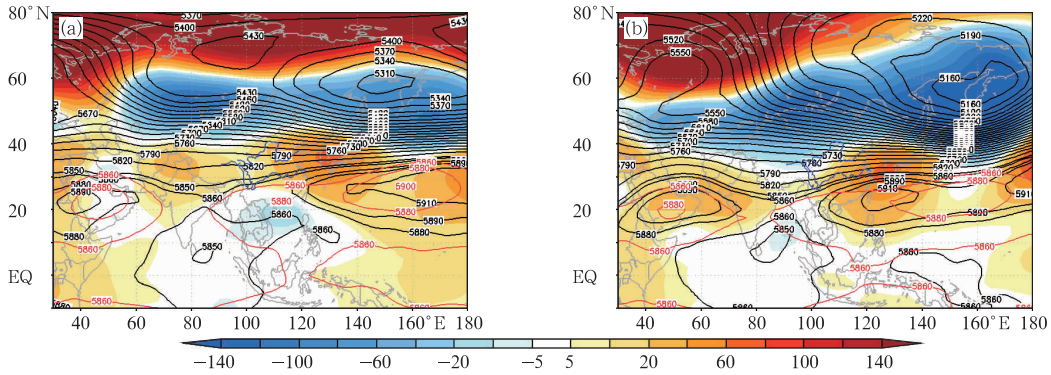

图 6 2016 年 10 月上中旬(a)和下旬(b)500 hPa 位势高度(等值线)及距平场(阴影区)分布

(红色等值线为气候平均态下 5860 和 5880 线,单位:gpm)

Fig. 6 The mean 500 hPa geopotential height (contour) and anomalies (shadow) for the first and second (a), and last (b) dekads in October 2016

(5860 and 5880 of climatology are marked in red, unit: gpm)

偏多的主要原因。而台风活动受到西太平洋有利的热力和动力条件的影响,这是大气对热带海温的显著响应:赤道西太平洋地区海温明显偏暖,沃克(Walker)环流明显偏强,对流活跃,从而有利于台风生成。而副高较常年偏西、偏北,其南侧的偏东气流也有利于引导台风登陆我国,造成沿海地区发生强降水。

4　10 月降水预测失败的原因分析

国家气候中心常规月气候预测业务中主要考虑气候要素的年代际尺度特征、月际变率、国内外动力模式预测、统计方法预报,经预报员综合集成和多模式客观集成给出最终预测结果。随着近年来动力气候模式的发展和预报准确率的提升,模式预报信息在气候预测业务中所占的比重越来越大,从而形成以数值模式客观预报为主,物理统计订正为辅的综合集成预报局面,以下分别从这两个角度进行总结分析。

4.1　数值模式客观预报

动力气候模式高技巧的信息是环流预测,而环流形势的配置关系直接决定了气候要素(降水)的时空分布特征,因此首先需要确定对大尺度环流形势的预测。通过综合考虑国内外动力模式预报以及对海温、海冰等外强迫影响的分析,预测 10 月 AO 正常到弱的负位相,欧亚中高纬度纬向环流形势发展且月内变化较大,东亚高度场北高南低,东亚槽偏弱,西太平洋副高强度正常偏强,脊线偏北,印缅槽偏强。较之实况,预测结论较好地把握了 10 月大尺度环流异常的空间分布特征,但是对环流因子的异常程度和具体的槽脊位置分布上与实况存在较大的差异。这种预测的不确定性也体现在国内外各家动力模式提供的信息上。国内外各主要数值预报中心超前一周时,均预报欧亚中高纬度月平均环流以纬向型为主,但是正负距平及槽脊位置分布存在较大差异。国家气候中心 DERF2.0 和美国 CFSv2 预报欧亚中高纬度位势高度以正距平为主,其中高度场的正异常中心均位于乌拉尔山以东,贝加尔湖以北区域。日本 TCC 预报乌拉尔山高压脊增强、贝加尔湖以北地区为低槽,东亚地区高度场以正距平为主。只有欧洲 ECMWF 预报与实况较为一致,成功预测了巴尔喀什湖至贝加尔湖的低槽,与实况较为一致(图略)。此外,各家动力气候模式均预测北极地区高度场以正距平为主,极涡偏弱,副高加强北抬,这些预测信息与实况也是基本一致的。

在环流形势的月内变化预测方面,DERF2.0 提供了未来 40 天逐旬的平均环流预报,CFSv2 和 ECMWF 均提供了未来 28 天的逐周环流平均预报信息,可以提供一些月内环流形势持续或者转折的预测信息。从模式当时的预报来看,DERF2.0 和 CFSv2 的预测与实况差异较大,均未能对 10 月下旬乌拉尔山阻塞高压加强、副高加强北抬的环流转变特征做出预测。ECMWF 与实况较为接近,但是对后期西太平洋副高加强西伸程度的预测与实况也存在较大的差异,反映出数值模式对于延伸期环流形势转折预报能力的不足。

4.2　物理因子诊断分析

发生在热带太平洋地区的 ENSO 循环现象是年际气候变化中的最强信号(李崇银等,2008;任福民等,2012),也是月气候预测的重要背景和参考因子。2014—2016 年,赤道中东太平洋发生了一次超强 El Niño 事件(图 7),此次事件于 2015 年 11 月达到峰值,12 月开始衰减,并于 2016 年 5 月结束(翟盘茂等,2016;邵勰和周兵,2016;袁媛等,2016;2017;任宏利等,2017)。图 7 给出了 20 世纪 80 年代以来 El Niño 次年 Niño3.4 指数的演变情况,图中实线为中等以上强度的 El Niño 事件次年。从对应的西太平洋副高的强度和脊线位置逐月变化来看,El Niño 事件次年夏、秋季西太平洋副高持续偏强(图 8a),脊线位置以夏季偏南、秋季偏北为主(图 8b)。此外图8还显示,西太平洋副高不仅在季

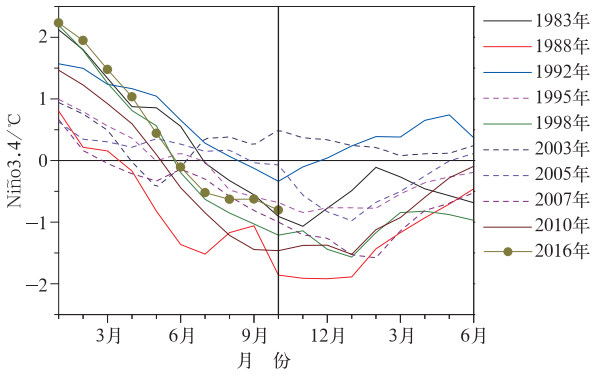

图 7　El Niño 次年 Niño3.4 区海温指数演变
(实线为中等以上强度 El Niño 次年)

Fig. 7　Variation of Niño3.4 in decay years of El Niño
(Solid line denotes decay years of medium and strong El Niño)

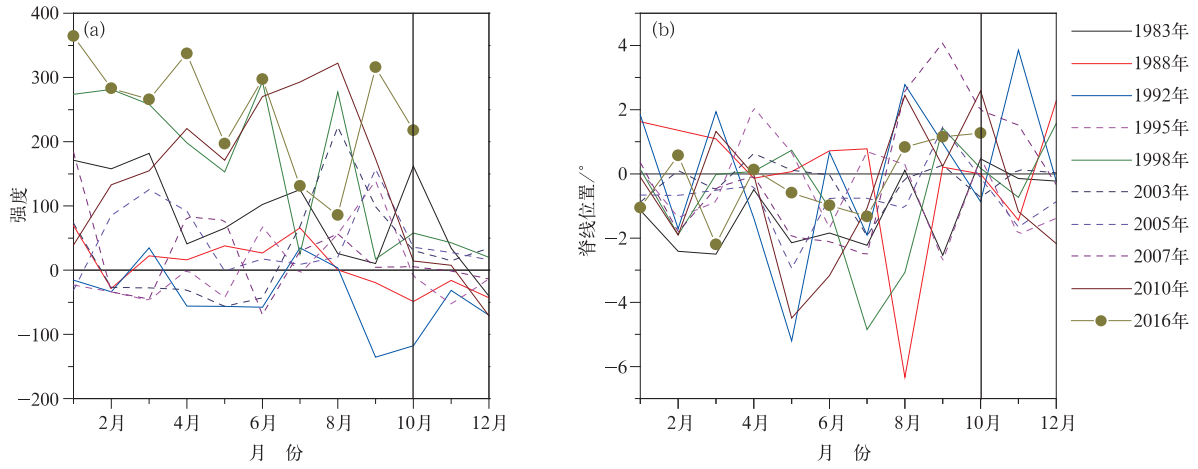

图 8 El Niño 次年西太平洋副高强度(a)和脊线位置(b)演变
(实线为中等以上强度 El Niño 次年)

Fig. 8 Variation of intensity (a) and position of ridge line (b) of WPSH in decay years of El Niño
(Solid line denotes decay years of medium and strong El Niño)

节尺度上受海温外强迫作用的调制,同时具有显著的月际变率,这可能与季节内低频振荡等有关。

对 10 月降水预测与实况出现较大偏差的一个重要原因是对副高强度估计不足。环流预报中认为副高接近正常到偏强,而实况为显著偏强。从大气对赤道中东太平洋海温信号的响应来看,在 El Niño 结束年,大气对海温的响应存在滞后效应。在解释 ENSO 循环与峰值次年夏季东亚环流异常的关系时,Xie et al(2009;2016)提出热带印度洋海温在 El Niño 衰减年的“电容器效应”,认为热带印度洋全区一致海温模态(IOBW)在维持 El Niño 对峰值次年东亚气候异常的影响方面起到了重要的传递作用(图 9a)。正是因为热带印度洋全区一致海温增暖(变冷)在 El Niño(La Niña)衰减时却发展到盛期,因此,通过改变对流活动和 Walker 环流异常以及激发向东传播的 Kelvin 波,印度洋海温像“电容器”一样延续了 El Niño 对大气环流和气候异常的影响。对 IOBW 与北半球 500 hPa 高度场进行相关分析发现(图 10),8、9 月 IOBW 指数与 10 月东亚中纬度高度场呈显著的正相关,我国东部 40°N 以南的大部分地区相关系数通过了 0.05 的显著性水平检验。

从环流对同期热带海温的响应来看,10 月赤道中东太平洋大部为冷海温距平,负距平中心位于 160°W 附近,赤道西太平洋及暖池区为暖海温距平(图 11)。赤道西太平洋及暖池区海温偏高,对流活跃,而中东太平洋下沉运动明显增强,Walker 环流偏强(图 12)。已有研究表明(顾薇等,2012),秋季中东太平洋偏冷,有利于 110°~130°E 范围内径向上出现两个连续的异常环流圈,其中北部的异常环流圈会通过低层径向风异常及异常辐合辐散,在日

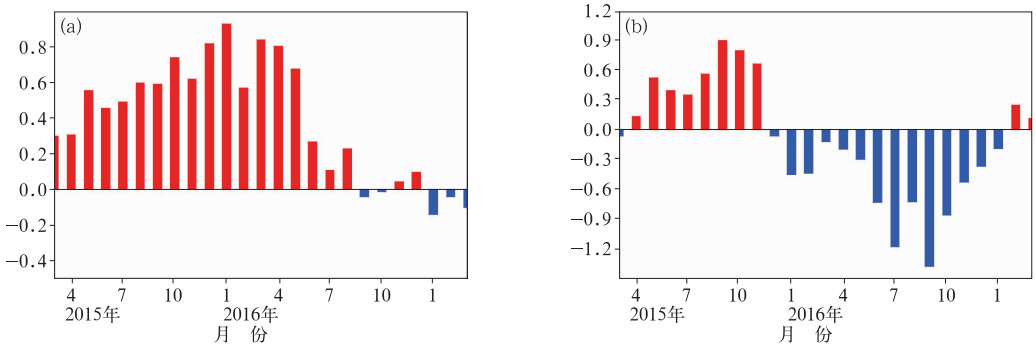

图 9 2015 年 4 月至 2017 年 1 月逐月热带印度洋全区一致模态指数(a,IOBW)和热带印度洋偶极子指数(b,TIOD)变化

Fig. 9 Monthly variation of IOBW index (a) and TIOD index (b) from April 2015 to January 2017

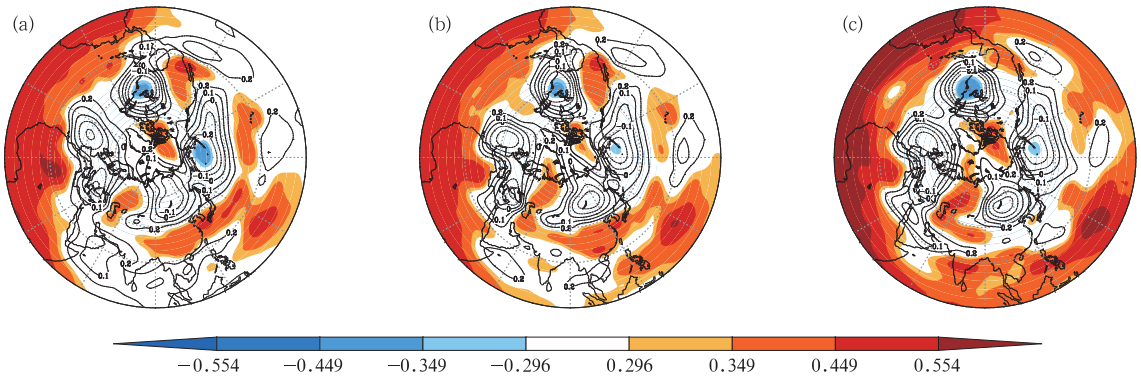

图 10　8 月(a)、9 月(b)、10 月(c)逐月 IOBW 指数与
10 月北半球 500 hPa 高度场距平相关系数分布

Fig. 10　Distribution of correlation coefficient between monthly (a) August, (b) September, (c) October IOBW index and 500 hPa geopotential height in the Northern Hemisphere

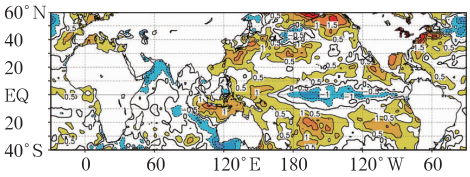

图 11　2016 年 10 月平均海表
温度距平(单位：℃)

Fig. 11　Monthly mean sea surface temperature (SST) anomalies in October 2016 (unit: ℃)

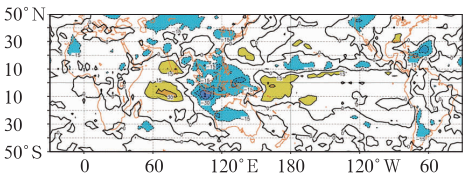

图 12　2016 年 10 月平均向外长波
辐射距平(单位：W·m^{-2})

Fig. 12　Monthly mean anomalies of outgoing longwave radiation (OLR) in October 2016 (unit: W·m^{-2})

本岛附近形成反气旋式环流距平，有利于副高加强北抬。而 10 月热带对流活动活跃，台风生成及登陆我国的个数均偏多，也是造成我国江南南部、华南东部降水异常偏多的主要原因。

对历史上具有相似海温演变特征的 El Niño 结束年 10 月降水及环流场进行分析发现，20 世纪 80 年代以来的 El Niño 结束年，我国 10 月降水的空间分布特征大致可分为两类：一类以 1983 和 1995 年为代表，我国东部大范围地区降水显著偏多；另一类以 1998 和 2010 年为代表，西南至东北降水偏多，同时东南沿海偏多。结合对典型年份的整层积分水汽输送、辐合辐散场以及 850 hPa 风场的合成分析可知(图 13)，在 El Niño 结束典型年份，在 110°～130°E的副热带地区均存在显著的水汽输送路径。1983 和 1995 年副高西伸脊点的位置偏西，以来自南海和西太平洋的东南方向水汽输送充沛，我国东部大部分地区位于水汽辐合区，为降水提供了良好的水汽条件；1998 和 2010 年副高主体位置偏东，水汽输送路径中心位于东部邻海，东南沿海部分地区处于水汽输送路径的边缘。

水汽输送路径和副高西伸脊点位置的正确判断对 10 月降水异常分布预报有着重要影响。西伸脊点位置的判断中重点参考了 El Niño 结束年的副高统计特征以及动力模式对环流形势的预报。统计分析结果显示，20 世纪 80 年代以来 El Niño 结束年的 10 月副高面积偏大、强度偏强、脊线偏北的特征较为明显，而西伸脊点偏西和偏东的年份数相当，并无显著的差异。各家数值模式预报均显示副高西伸脊点接近正常或略偏东，且在延伸期时段副高主体有逐步东移的趋势。因此综合统计和模式环流预报结果，预报认为 10 月副高西伸脊点位置接近常年，即考虑发生类似 1983 和 1995 年水汽输送路径偏西、我国东部大范围降水显著偏多的可能性较低。而实况显示，进入 10 月下旬，副高强度显著加强、西伸脊点在中旬短暂东撤后再度显著偏西(图略)，同时欧亚中高纬度乌拉尔山高压加强，巴尔喀什湖至贝加尔湖低槽加深，南下冷空气与沿副高外围的东南水汽和西南水汽输送汇合，造成我国长江以北大部分地区降水异常偏多。

2016 年秋季海温异常的另一个主要信号是热带印度洋偶极子(TIOD)呈显著的负位相,TIOD 指数于 9 月达到峰值。TIOD 是热带印度洋秋季海温异常最主要模态,空间分布上表现为热带西印度洋和东南印度洋反相的偶极型海温变化特征(Saji et al, 1999)。前期和同期 TIOD 指数与 10 月北半球 500 hPa 高度场距平相关系数分布显示(图 9b,图 14),当9、10月TIOD呈负位相时,印度半岛、孟

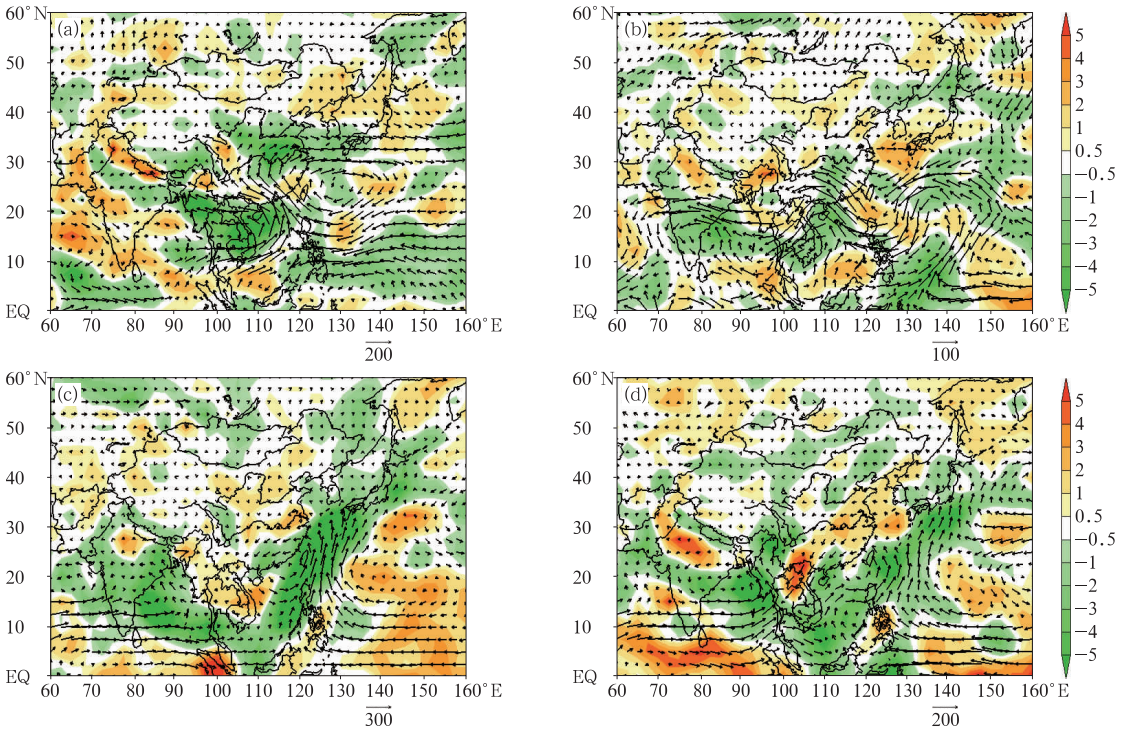

图 13 El Niño 结束年 10 月降水时空分布典型年份对流层整层积分水汽输送(矢量,单位:kg·s^{-1}·m^{-1})及辐合辐散场(阴影,单位:10^{-5} kg·s^{-1}·m^{-2})

(a)1983 年,(b)1995 年,(c)1998 年,(d)2010 年

Fig. 13 Moisture transport anomalies vertically integrated from 1000 hPa to 300 hPa (vector, unit: kg·s^{-1}·m^{-1}), and anomalies of divergence and convergence of moisture transport (shadow, unit: 10^{-5} kg·s^{-1}·m^{-2})

(a) 1983, (b) 1995, (c) 1998, (d) 2010

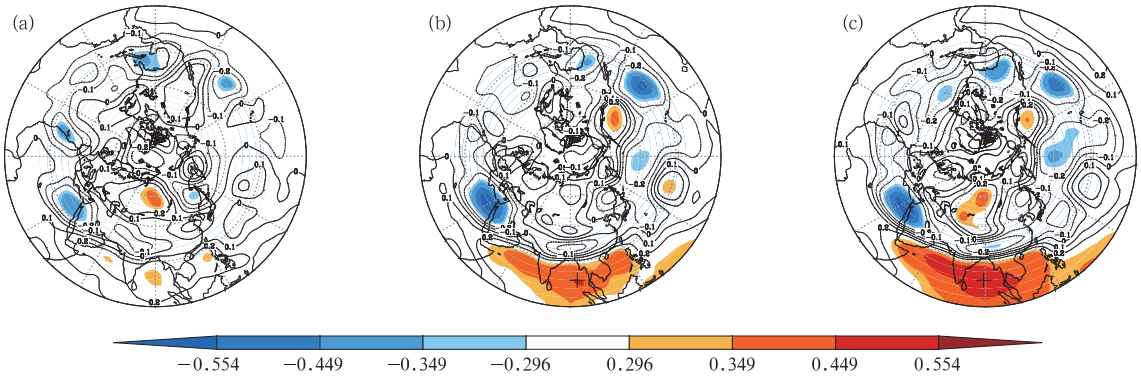

图 14 8 月(a)、9 月(b)、10 月(c)逐月 TIOD 指数与 10 月北半球 500 hPa 高度场距平相关系数分布

Fig. 14 Distribution of correlation coefficient between monthly (a) August, (b) September, (c) October TIOD index and 500 hPa geopotential height in the Northern Hemisphere

加拉湾及中南半岛等地 500 hPa 高度场与 TIOD 呈显著的负相关。即 9、10 月 TIOD 负位相有利于印缅槽加强，从而有利于水汽向我国东部地区输送。

5　结论与讨论

本文从预测回顾的角度对 2016 年 10 月降水的气候特征、异常成因和预报中的成功与不足进行总结分析。对预报发布前能够获取的数值预报和物理因子诊断分析的应用效果进行梳理，结合实况总结各种预测方法和技术的技巧高低，以期加强对我国气候异常成因机理的认识，提高对月尺度气候异常的预测能力。

分析表明，热带太平洋和印度洋海表温度异常对我国秋季气候异常均有显著影响。热带太平洋海温异常集中表现在 ENSO 循环，其峰值次年对我国气候的影响主要通过印度洋海温异常这个“桥梁”实现。从大气对赤道中东太平洋海温信号的滞后响应来看，El Niño 事件次年夏、秋季西太平洋副高持续偏强，脊线位置以夏季偏南、秋季偏北为主。环流与同期热带海温的相关分析表明，10 月赤道太平洋东冷西暖，暖池区海温偏高，对流活跃，Walker 环流偏强，东亚上空出现的异常经向环流圈会通过低层径向风异常及异常辐合辐散，在日本岛附近形成反气旋式环流距平，也有利于副高加强北抬。TIOD 作为热带印度洋秋季海温异常的主导模态，对东亚大气环流和气候有着重要影响。相关分析显示，9、10 月 TIOD 负位相有利于印缅槽加强，从而有利于水汽向我国东部地区输送。来自副高外围的异常东南水汽和来自西南的水汽共同输送到我国中东部地区，并与南下冷空气交汇产生异常水汽辐合，造成这些地区降水明显偏多。

数值模式环流形势预报与实况的对比结果显示，模式对热带和副热带地区的大气月平均环流有一定的预报能力，但对中高纬度环流形势的预报技巧较低。除欧洲 ECMWF 模式外，国内外大部分模式 10 月环流形势预报未能有效预测巴尔喀什湖至贝加尔湖的宽广低槽。此外模式对乌拉尔山阻塞高压加强和西太平洋副高西伸脊点偏西等关键因子的月内变化预测与实况均存在较大差异，反映出数值模式对于延伸期环流形势转折预报能力的不足，也说明了发展多模式集合最优信息提取和解释应用技术对于提高预测水平的重要性。

致谢：感谢中国气象局灾害影响评估系统以及气候与气候变化监测预测系统(CIPAS2.0)为本文提供部分图形。

参考文献

陈丽娟，李维京，刘绿柳，等，2008. 中国区域月气候预测方法和预测能力评估[J]. 高原气象，27(4)：838-843.

陈丽娟，李想，李维京，等，2016. 2015/2016 年超强 El Niño 事件背景下我国月预测技巧差异分析[J]. 大气科学学报，39(6)：756-765.

丑纪范，2003a. 短期气候预测的现状 问题与出路(二)[J]. 新疆气象，26(2)：1-4，11.

丑纪范，2003b. 短期气候预测的现状 问题与出路(一)[J]. 新疆气象，26(1)：1-4.

丁一汇，2004. 我国短期气候预测业务系统[J]. 气象，30(12)：11-17.

顾薇，李维京，陈丽娟，等，2012. 我国秋季降水的年际变化及与热带太平洋海温异常分布的关系[J]. 气候与环境研究，17(4)：467-480.

贾小龙，陈丽娟，高辉，等，2013. 我国短期气候预测技术进展[J]. 应用气象学报，24(6)：641-655.

李崇银，穆穆，周广庆，等，2008. ENSO 机理及其预测研究[J]. 大气科学，32(4)：761-781.

任福民，袁媛，孙丞虎，等，2012. 近 30 年 ENSO 研究进展回顾[J]. 气象科技进展，2(3)：17-24.

任宏利，王润，翟盘茂，等，2017. 超强厄尔尼诺事件海洋学特征分析与预测回顾[J]. 气象学报，75(1)：1-18.

任宏利，张培群，李维京，等，2014. 提高月预报业务水平的动力相似集合方法[J]. 气象学报，72(4)：723-730.

任芝花，余予，邹凤玲，等，2012. 部分地面要素历史基础气象资料质量检测[J]. 应用气象学报，23(6)：739-747.

邵勰，周兵，2016. 2015/2016 年超强厄尔尼诺事件气候监测及诊断分析[J]. 气象，42(5)：540-547.

王会军，陈丽娟，李维京，等，2007. 中国区域月平均温度和降水的模式可预报性分析[J]. 气象学报，65(5)：725-732.

王绍武，2012. 月平均大气环流与短期气候预测[J]. 气象科技进展，2(3)：25-26.

袁媛，高辉，李维京，等，2017. 2016 年和 1998 年汛期降水特征及物理机制对比分析[J]. 气象学报，75(1)：19-38.

袁媛，高辉，贾小龙，等，2016. 2014—2016 年超强厄尔尼诺事件的气候影响[J]. 气象，42(5)：532-539.

翟盘茂，余荣，郭艳君，等，2016. 2015/2016 年强厄尔尼诺过程及其对全球和中国气候的主要影响[J]. 气象学报，74(3)：309-321.

张夏琨，牛若芸，卢晶，2017. 2016 年 10 月大气环流和天气分析[J]. 气象，43(1)：122-128.

郑志海，2013. 月动力延伸预报研究进展回顾[J]. 气象科技进展，3(1)：25-30.

竺夏英，宋文玲，2017. 2016 年秋季中国气候特征及其可能成因[J]. 气象，43(4)：495-500.

Déqué M，Royer J F，1992. The skill of extended-range extratropical winter dynamical forecasts[J]. J Climate，5(11)：1346-1356.

Jung T，Vitart F，Ferranti L，et al，2011. Origin and predictability of

the extreme negative NAO winter of 2009/10[J]. Geophys Res Lett,38(7):L07701. DOI:10.1029/2011GL046786.

Kalnay E,Kanamitsu M,Kistler R,et al,1996. The NCEP/NCAR 40-year reanalysis project[J]. Bull Am Meteor Soc,77(3):437-472.

Kistler R,Kalnay E,Collins W,et al,2001. The NCEP-NCAR 50-year reanalysis: monthly means CD-ROM and documentation [J]. Bull Am Meteor Soc,82(2):247-268.

Miyakoda K,Gordon T,Caverly R,et al,1983. Simulation of a blocking event in January 1977[J]. Mon Wea Rev,111(4):846-869.

Miyakoda K,Sirutis J,Ploshay J,1986. One-month forecast experiments-without anomaly boundary forcings[J]. Mon Wea Rev,114(12):2363-2401.

Molteni F,Cubasch U,Tibaldi S,1986. 30- and 60-day forecast experiments with the ECMWF spectral models[C]// ECMWF Workshop on Predictability in the Medium and Extended Range. UK:ECMWF,Shinfield Park.

Owen J A,Palmer T N,1987. The impact of El Niño on an ensemble of extended-range forecasts[J]. Mon Wea Rev,115(9):2103-2117.

Reynolds R W,Rayner N A,Smith T M,et al,2002. An improved in situ and satellite SST analysis for climate[J]. J Climate,15(13):1609-1625.

Saji N H,Goswami B N,Vinayachandran P N,et al,1999. A dipole mode in the tropical Indian Ocean[J]. Nature,401(6751):360-363.

Shukla J,Anderson J,Baumhefner D,et al,2000. Dynamical seasonal prediction[J]. Bull Am Meteor Soc,81(11):2593-2606.

Tracton M S,Mo K,Chen W,et al,1989. Dynamical extended range forecasting (DERF) at the National Meteorological Center[J]. Mon Wea Rev,117(7):1604-1635.

Xie Shangping,Hu Kaiming,Hafner J,et al,2009. Indian ocean capacitor effect on Indo-Western Pacific climate during the summer following El Niño[J]. J Climate,22(3):730-747.

Xie Shangping,Kosaka Y,Du Yan,et al,2016. Indo-Western pacific ocean capacitor and coherent climate anomalies in Post-ENSO summer: a review[J]. Adv Atmos Sci,33(4):411-432.

Earth's Future

RESEARCH ARTICLE
10.1029/2018EF000832

Key Points:
- The global annual mean ERFs due to changes in SLCPs concentrations, from 2010 to 2050, were 0.1, −0.3, and −0.5 W m^{-2}, under RCP 8.5, 4.5, and 2.6 emission scenarios, respectively
- Under RCP 8.5, changes in SLCP concentrations led global annual mean surface air temperature and precipitation increased by 0.13 K and 0.02 mm d^{-1}, respectively
- Under RCPs 4.5 and 2.6, decreasing SLCP concentrations caused global annual mean temperature decreased by 0.20 and 0.44 K, respectively

Supporting Information:
- Figure S1
- Figure S2
- Figure S3
- Supporting Information S1
- Data Set S1
- Data Set S2
- Data Set S3
- Data Set S4

Correspondence to:
B. Xie,
xieb@cma.cn

Citation:
Zhang, H., Xie, B., & Wang, Z. (2018). Effective radiative forcing and climate response to short-lived climate pollutants under different scenarios. *Earth's Future*, *6*, 857–866. https://doi.org/10.1029/2018EF000832

Received 5 FEB 2018
Accepted 28 MAY 2018
Accepted article online 5 JUN 2018
Published online 19 JUN 2018

©2018. The Authors.
This is an open access article under the terms of the Creative Commons Attribution-NonCommercial-NoDerivs License, which permits use and distribution in any medium, provided the original work is properly cited, the use is non-commercial and no modifications or adaptations are made.

Effective Radiative Forcing and Climate Response to Short-Lived Climate Pollutants Under Different Scenarios

H. Zhang[1,2,3], B. Xie[2,4], and Z. Wang[3]

[1]China University of Geosciences, Department of Atmospheric Science, School of Environmental Studies, Wuhan, China, [2]Nanjing University of Information Science & Technology, Collaborative Innovation Center on Forecast and Evaluation of Meteorological Disasters, Nanjing, China, [3]Chinese Academy of Meteorological Sciences, State Key Laboratory of Severe Weather & Key Laboratory of Atmospheric Chemistry of CMA, Beijing, China, [4]China Meteorological Administration, Laboratory for Climate Studies of China Meteorological Administration, National Climate Center, Beijing, China

Abstract We used an online aerosol-climate model (BCC_AGCM2.0_CUACE/Aero) to simulate effective radiative forcing and climate response to changes in the concentrations of short-lived climatic pollutants (SLCPs), including methane, tropospheric ozone, and black carbon, for the period 2010–2050 under Representative Concentration Pathway scenarios (RCPs) 8.5, 4.5, and 2.6. Under these three scenarios, the global annual mean effective radiative forcing were 0.1, −0.3, and −0.5 W m^{-2}, respectively. Under RCP 8.5, the change in SLCPs caused significant increases in surface air temperature (SAT) in middle and high latitudes of the Northern Hemisphere and significant decreases in precipitation in the Indian Peninsula and equatorial Pacific. Global mean SAT and precipitation increased by 0.13 K and 0.02 mm d^{-1}, respectively. The reduction in SLCPs from 2010 to 2050 under RCPs 4.5 and 2.6 led to significant decreases in SAT at high latitudes in the Northern Hemisphere. Precipitation increased slightly in most continental regions, and the Intertropical Convergence Zone moved southward under both of these mitigation scenarios. Global mean SAT decreased by 0.20 and 0.44 K, and global averaged precipitation decreased by 0.02 and 0.03 mm d^{-1} under RCPs 4.5 and 2.6, respectively.

1. Introduction

Extreme weather and climate events have occurred with increasing frequency during recent decades due to global warming. Observations have shown that near-surface temperature has increased at high latitudes and in Arctic regions (Kaufman, 2009). As a result, melting of alpine tundra, glaciers, and sea ice has been accelerated. Limiting CO_2 emissions cannot reduce the rate of global warming within a short period due to its long lifetime in the atmosphere. Therefore, the United Nations Environment Programme (UNEP) has proposed a reduction in short-lived climate pollutant (SLCP) emissions (UNEP, 2011), including methane (CH_4), tropospheric ozone (O_3), hydro-fluorocarbons (HFCs), and black carbon (BC), which contribute substantially to global warming. BC, tropospheric O_3, CH_4, and HFCs have lifetimes of several days to weeks, a few months, about 12 years, and about 15 years (range, 1–50 years), respectively. They have significant impacts on health and global and regional climate (UNEP, 2011). As important climate-forcing factors, SLCPs contribute to 40–45% of total global warming (UNEP & WMO, 2011). Xie, Zhang, Wang, et al. (2016), Xie, Zhang, Yang, & Wang (2016) used an online aerosol-climate model to simulate the climate response to changes in tropospheric O_3 and CH_4 concentrations. According to their estimate, since the industrial revolution, global mean surface air temperature (SAT) had increased by 0.36 and 0.31°C due to increases in tropospheric O_3 and CH_4 concentrations, respectively, and surface warming was particularly obvious in the middle and high latitudes of the Northern Hemisphere (NH). Chang et al. (2009) simulated impacts of tropospheric O_3 on climate and demonstrated that temperatures over China increased by 0.43°C from 1951 to 2000 due to the change in tropospheric O_3. The impact of SLCPs on regional and global climate will likely diminish rapidly if their emissions are stopped. SLCP mitigation would quickly lead to a less rapidly warming climate compared to scenarios in which SLCPs are not reduced (Myhre et al., 2013). By analyzing nearly 400 air control measures for reducing BC and CH4 emissions using the International Institute for Applied Systems Analysis Greenhouse Gas and Air Pollution Interactions and Synergies model, Shindell et al. (2012) estimated that 2.4 (range, 0.7–4.6) million premature deaths and 52 (30–140) million tons of agricultural annual losses would be avoided from 2030

onward. The same conclusions were obtained by UNEP (2011), which also predicted that a reduction in O_3 would prevent annual agricultural losses of 32 (21–57) million tons. Some studies have estimated that, under full SLCP mitigation, there would be 0.5°C (0.2–0.7) reduction in global warming by 2050 (Shindell et al., 2012) and 0.4°C (0.1–0.6) by 2040 (UNEP, 2011). Ramanathan and Xu (2010) estimated that a temperature increase by 2050 of 0.6°C would be avoided if all four SLCPs were reduced using current technologies and that the 2°C threshold could be delayed by 3–5 decades beyond 2050. Some studies also calculated that full implementation of SLCP mitigation could prevent a sea surface level rise of approximately 25% by 2050 (Hu et al., 2013) and 22–42% by 2100 (Ramanathan & Xu, 2010). However, we lack an evaluation of the radiative forcing and climate response to SLCP changes under different Representative Concentration Pathways (RCPs) for the near future.

Based on the new concept of effective radiative forcing (ERF) provided in the Fifth Assessment Report of Intergovernmental Panel on Climate Change (IPCC, 2013), we used the aerosol-climate model BCC_AGCM2.0_CUACE/Aero, developed by Beijing Climate Center (BCC; Wang et al., 2014; Zhang, Wang, et al., 2012) to simulate ERF and climate responses to changes in SLCPs for the period 2010–2050 under different RCP scenarios. Because the latest ERF of all HFCs was estimated at only 0.02 W m^{-2} (Myhre et al., 2013), which is less than 0.1% of the radiative forcing of total long-lived greenhouse gases (GHGs), we did not consider HFCs in this study. In this work, SLCPs refer only to tropospheric O_3, CH_4, and BC.

Section 2 introduces the model, data sets, and methods used in this study; section 3 describes the ERF and climate response to changes in SLCPs under different scenarios (RCPs 8.5, 4.5, and 2.6); and conclusions are provided in section 4.

2. Data, Model, and Scheme Description

2.1. Model

The BCC_AGCM2.0_CUACE/Aero, an online aerosol-climate model developed by Zhang, Wang, et al. (2012), Zhang et al. (2014) and Wang et al. (2014), was used in this study. The model consists of the atmospheric general circulation model BCC_AGCM2.0, developed by the BCC of the China Meteorological Administration and the CUACE/Aero aerosol model (China Meteorological Administration Unified Atmospheric Chemistry Environment for Aerosols), which was developed by the Chinese Academy of Meteorological Sciences. A detailed description of BCC_AGCM2.0 can be found in Wu et al. (2010). BCC_AGCM2.0 is based on the Eulerian spectral formulation of dynamic equations and has a horizontal T42 spectral resolution (approximately 2.8° × 2.8°) and a terrain-following hybrid vertical coordinate, with 26 levels and a top located at approximately 2.9 hPa. Xin et al. (2013) evaluated the transient climate response of CO_2 in this model is 1.94°C, and the results were consistent with the ensemble mean of 16 climate models in the Coupled Model Intercomparison Project Phase 5. The CUACE/Aero aerosol model is a particle-size-segregated model that includes five typical aerosols (BC, organic carbon [OC], sulfates [SFs], sea salt, and dust). Each aerosol is classified into one of 12 bins as a geometric series for radii between 0.005 and 20.48 μm. We have simulated the ERF of three anthropogenic aerosols (SF, BC, and OC) using this model; the total ERF of these anthropogenic aerosols was −2.49 W m^{-2}, of which the aerosol-radiation interactive ERF (ERFari) and aerosol-cloud interactive ERF (ERFaci) were −0.30 and −2.19 W m^{-2}, respectively (Zhang et al., 2016). The details of this model, including chemical processes and parameter settings, can be found in Zhou et al. (2012).

The radiation scheme BCC_RAD (Zhang, 2016; Zhang et al., 2014) and the McICA cloud vertical overlap scheme (Jing & Zhang, 2012, 2013; Zhang, 2016) were used in BCC_AGCM2.0_CUACE/Aero. These improvements reduce error in the simulated longwave and shortwave radiative fluxes at the top of the atmosphere (TOA) and at the surface compared to the original version. The model also includes physical representations of aerosol direct, semidirect, and indirect effects for liquid-phase clouds (Wang et al., 2014). BCC_AGCM2.0_CUACE/Aero reasonably simulates the atmospheric burden and geographic distribution of aerosols (Zhang, Wang, et al., 2012; Wang et al., 2014). The model has been widely used in studies of aerosol radiative forcing and its impact on climate (Wang, Zhang, Li, et al., 2013; Wang, Zhang, Jing, & Wei, 2013; Wang et al., 2015, 2016; Zhang et al., 2012, 2016; Zhao et al., 2014), and in the comparison between observations and models of aerosols, including an AeroCom phase II comparison of aerosol direct radiative forcing and organic aerosols (Myhre et al., 2012; Tsigaridis et al., 2014).

Table 1
Experimental Design

Test name	year	Emission data	Sea temperature	Running time (years)
ER2010	2010	RCPs	Prescribed SST①	15
ER26	2050	RCP2.6	Prescribed SST	15
ER45	2050	RCP4.5	Prescribed SST	15
ER85	2050	RCP8.5	Prescribed SST	15
CR2010	2010	RCPs	Slab ocean mode②	70
CR26	2050	RCP2.6	Slab ocean mode	70
CR45	2050	RCP4.5	Slab ocean mode	70
CR85	2050	RCP8.5	Slab ocean mode	70

①Observational climatological monthly mean SST (Hurrell et al., 2008). ②A detailed description of this slab ocean mode can be found in Hurrell et al. (2008).

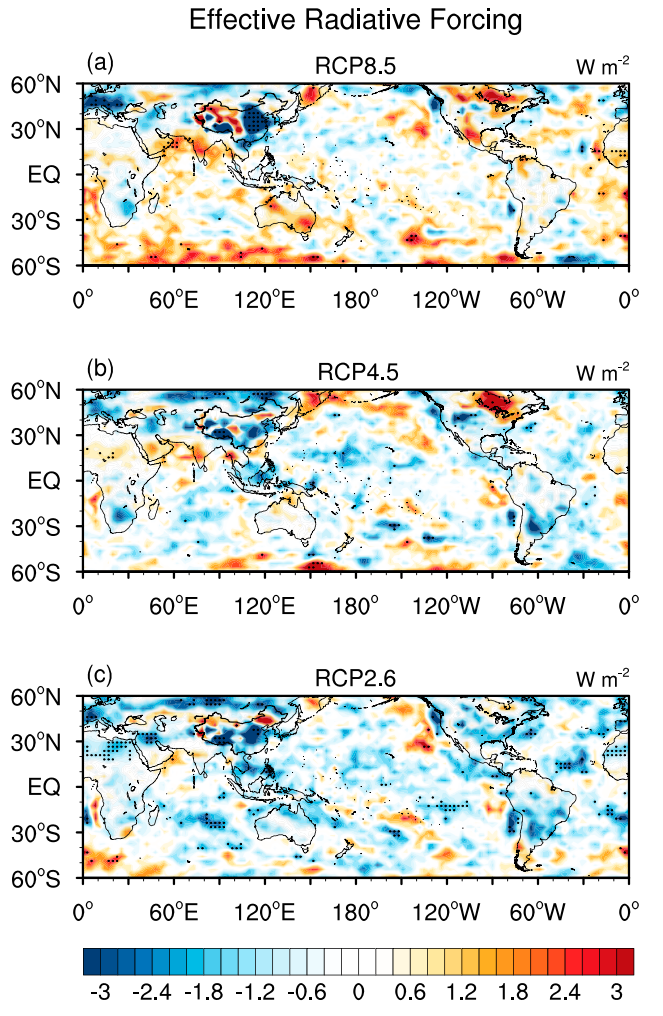

Figure 1. The spatial distribution of effective radiative forcing variations resulting from changes of short-lived climatic pollutants, from 2010 to 2050, in (a) Representative Concentration Pathway 8.5 (RCP8.5), (b) RCP4.5, and (c) RCP2.6. The areas with "·" passed the 95% significance test.

2.2. Data

Four emission scenarios (RCPs) described in Fifth Assessment Report of Intergovernmental Panel on Climate Change were proposed to study the impacts and uncertainties of GHGs and aerosols on climate change. RCPs are divided into four concentration emission paths, RCPs 2.6, 4.5, 6.0, and 8.5, named for their radiation forcing values (unit: W m^{-2}) for 2100. RCPs are representative of plausible alternative scenarios for the future but are not predictions or forecasts of future outcomes (Moss et al., 2008). In this study, we used SLCP concentration and emission data for RCPs 2.6, 4.5, and 8.5 during 2010–2050. SLCP mitigation under RCP 2.6 is very effective for improving future environments and slowing the rate of future climate warming but is every costly economically (Vuuren et al., 2011). Compared to RCP 2.6, the RCP 4.5 scenario reduces the economic pressure of SLCP mitigation and significantly reduces anthropogenic SLCP emissions (Chylek et al., 2014). RCP 8.5 represents the development and utilization of fossil fuels as usual and leads to almost no future reduction in the GHG emissions or contaminants (Riahi et al., 2007). If the emission of BC is reduced, its co-emitted species, SF, and OC would be reduced accordingly. Both SF and OC can cool the climate system by scattering directly solar radiation and increasing the cloud albedo and lifetime by acting as CCN (Boucher et al., 2013). But there are still some control measures targeting BC emission, such as providing modern cooking and heating, clean-burning biomass stoves, brick kilns, and so on (Shindell et al., 2012). Additionally, in SLCP mitigation, the role of BC is regionally important while O_3 and CH_4 contribute mostly to the globe.

2.3. Experiment Design

To calculate ERFs caused by changes in SLCPs under the three emission scenarios from the present to 2050, we performed four sets of experiments, including three numerical experiments (ER26, ER45, and ER85) and one control experiment (ER2010). The experiment configurations are shown in Table 1. According to the definition of ERF, sea surface temperature and sea ice should be kept constant during tests. We ran 15 model-years in each simulation, and the last 10 years of data were averaged to estimate ERFs due to changes in SLCP concentrations. To simulate climate responses to changes in SLCP concentrations from 2010 to 2050 under different scenarios, we performed four separate sets of numerical experiments (CR2010, CR26, CR45, and CR85) using the model coupled with a slab ocean model (Hurrell et al., 2008). Zhao et al. (2014, 2017) had validated the model system with a slab ocean. As suggested by Kristjánsson et al. (2005), to allow global mean SAT to reach a quasi-equilibrium state, the coupled model requires an adjustment of 30 years; therefore, we ran 70 model-years in these four simulation tests, and data sets for the final 40 years were used for analyses in this work. BC and tropospheric O_3 are mainly distributed in middle and low latitudes, and their changes are also significant in middle and low latitudes under RCP8.5, 4.5, and 2.6. Therefore, our analysis is mainly over the area between 60°S and 60°N.

3. Results

3.1. ERF of SLCPs for the Period 2010–2050 Under Different Scenarios

Figure 1 shows the geographical distribution of ERFs under three RCP scenarios for the period 2010–2050. As ERF is the change in net radiation flux after full adjustment of atmospheric temperature, water vapor, and clouds,

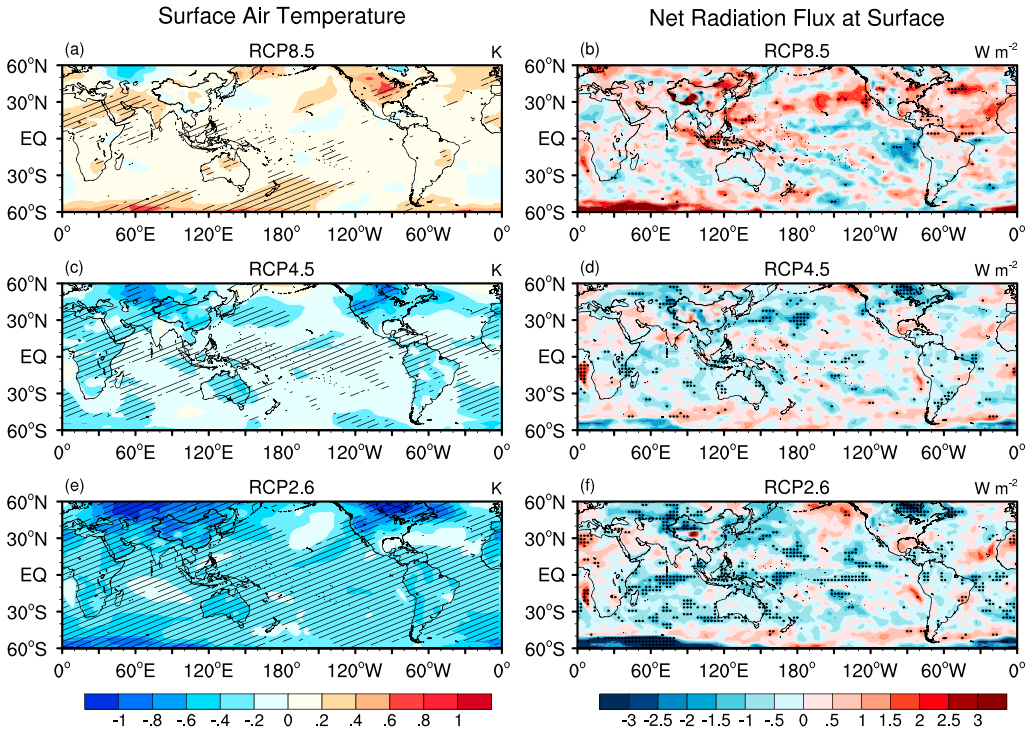

Figure 2. The spatial distribution of (left column) surface air temperature and (right column) surface net radiation flux variations resulting from changes of short-lived climatic pollutants, from 2010 to 2050, in (a and b) Representative Concentration Pathway 8.5 (RCP8.5), (c and d) RCP4.5, and (e and f) RCP2.6. The areas with "·" and "/" passed the 95% significance test.

the geographical distribution of ERFs is not closely correlated with the change in SLCP concentration. Changes in SLCP concentration under the three scenarios all greatly influenced ERF over land but had little effect over ocean. By 2050, CH_4 and tropospheric O_3 concentrations were predicted to continue increasing only under RCP 8.5, which produced notably positive ERFs over most of continental Australia and North America, as well as over the southern Pacific and southern Indian Ocean near 60°S (Figure 1a). The largest positive ERFs occurred over central Asia, reaching 13.8 W m^{-2}. Although positive ERFs were produced over most parts of the globe (between 60°N and 60°S in this study), some negative ERFs remained over North China and Western Europe due to increased low cloud cover (LCC), which reflected more shortwave radiation (Figure 4a). The largest negative ERF was −14.9 W m^{-2}, which occurred over North China. ERFs were weakly negative in South Africa under all three emission scenarios, possibly due to the slight reduction in BC concentration in that region (Yang et al., 2017). The global annual mean ERF was 0.1 W m^{-2} from 2010 to 2050 under RCP 8.5. SLCP concentrations decreased by 2050 under RCPs 4.5 and 2.6; thus, ERFs were notably negative in northern Eurasia, the southern African continent, South America, and most of China, and the United States. Under RCPs 4.5 and 2.6, the largest negative ERFs were located over North China, −15.2 and −16.9 W m^{-2}, respectively. However, under RCP 4.5, some weakly positive ERFs occurred over northern Africa and the Arabian Sea (about 0.4–1.8 W m^{-2}), and a large positive ERF value occurred over eastern Canada (about 7.1 W m^{-2}), where longwave radiation was absorbed by increasingly high cloud cover (HCC, Figure 4d). By 2050, the global annual mean ERFs were −0.3 W m^{-2} under RCP 4.5 and −0.5 W m^{-2} under RCP 2.6.

3.2. Effects of SLCP Changes on Temperature During the Period 2010–2050

According to the above simulation results, changes in SLCP concentration under RCP8.5 produced positive ERFs and warming effects in most parts of the globe from 2010 to 2050 (Figure 2a). Increases in SAT of about 0.4 K (95% significance level) occurred mainly in North America, the Middle East, northern Africa, and the South Pacific. In central North America, the increase was particularly high, 0.78 K. These changes in SAT

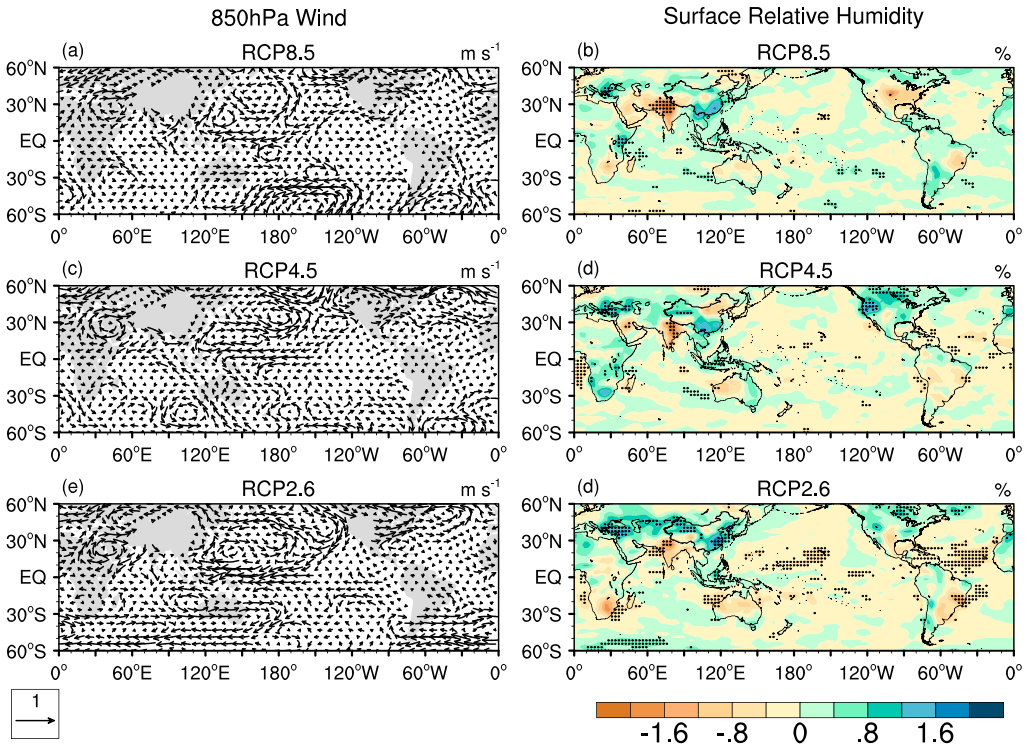

Figure 3. The spatial distribution of (left column) 850-hPa wind field and (right column) surface relative humidity variations resulting from changes of short-lived climatic pollutants, from 2010 to 2050, in (a and b) Representative Concentration Pathway 8.5 (RCP8.5), (c and d) RCP4.5, and (e and f) RCP2.6. The areas with "·" passed the 95% significance test.

may be associated with surface net radiation flux (SNRF). As shown in Figure 2b, in the Middle East, northern Africa, the equatorial Pacific, and northern Atlantic, where SATs increased by varying amounts (about 0.2 to 0.6 K), SNRF was greatly increased, by more than 2.0 W m^{-2}. Decreases in SLCP concentrations under RCPs 4.5 and 2.6 led to no apparent change or slight decreases in SAT in most parts of the ocean but decrease more than 0.4 K in most continental regions (Figures 2c and 2e). At high latitudes in the NH, such as the northern Eurasian continent and western North American, SATs decreased by more than 0.6 K (0.8 K) by 2050 under RCP 4.5 (RCP 2.6), and SNRF (Figures 2d and 2f) decreased by 1.0 W m^{-2} (1.2 W m^{-2}) in these areas, which may have led to a significant cooling effect. Under these two mitigation scenarios, the strongest SAT decreases appeared in eastern Canada, with temperatures decreasing by about 1.0 K under RCP 4.5 and 1.80 K under RCP 2.6. During the period 2010–2050 under RCPs 8.5, 4.5, and 2.6, changes in SLCP concentration led to global average temperature changed by 0.13, −0.2, and −0.44 K, respectively. This means that under full SLCP mitigation, there would be 0.57 K reduction in global warming by 2050 (the difference between CR26 and CR85), which is consistent with the estimations of Shindell et al. (2012) and Ramanathan and Xu (2010).

Comparing the net flux at the TOA and surface (Figure S1 in the supporting information), there was a reduction in atmospheric absorption. The global average atmospheric absorption was 0.0/0.2/0.4 W m^{-2} under RCP8.5/4.5/2.6. Under all three scenarios, the atmospheric absorptions were prominently decreased in eastern China due to the substantial decrease of BC load there. The powerful effects of cloud cover should also be considered. Low clouds (above 680 hPa) can scatter solar radiation, and high clouds (below 440 hPa) can absorb thermal outward radiation. For example, under RCP2.6, the difference of longwave net flux between the TOA and surface was about 1.5 W m^{-2} in the northern and southwestern Pacific (Figure S2, left column), where the HCC increased by more than 3%. Under all three scenarios, LCC increased in eastern China, leading to a difference of shortwave net flux between the TOA and surface of about −1.5 W m^{-2}(Figure S2, right column). LCC and HCC changes have substantial effects on SAT. SNRF decreased significantly in Canada under both mitigation scenarios (RCP4.5 and 2.6), mainly due to the increased LCC (about 1%), which led to apparent decreases of net short-wave flux at the surface (Figure S3, left column). This is why the decreases of SAT

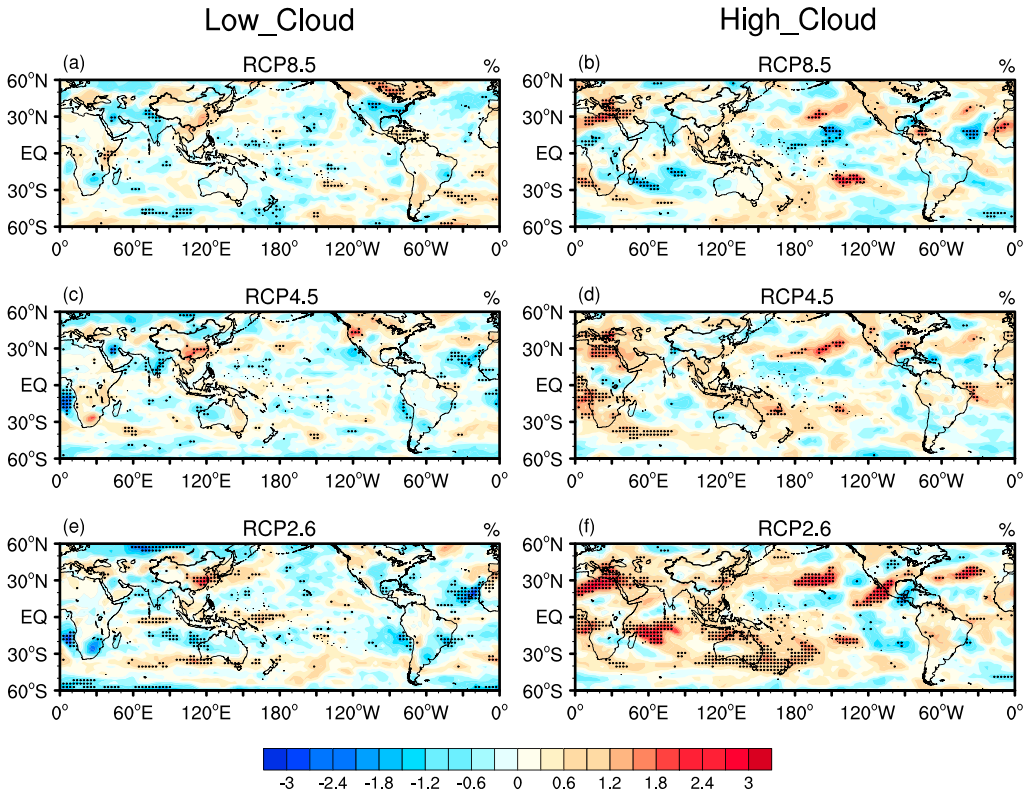

Figure 4. The spatial distribution of (left column) low cloud cover and (right column) high cloud cover variations resulting from changes of short-lived climatic pollutants, from 2010 to 2050, in (a and b) Representative Concentration Pathway 8.5 (RCP8.5), (c and d) RCP4.5, and (e and f) RCP2.6. The areas with "·" passed the 95% significance test.

were obvious over Canada under RCP4.5 and 2.6. Under RCP8.5, HCC increased over northern Africa by about 2%, leading to increases in the net longwave flux at the surface (Figure S3, right column) and SNRF of about 1.5 and 1.0 W m^{-2}, respectively, which is possibly why the SAT increased about 0.4 K over northern Africa.

3.3. Effects of SLCP Changes on Cloud During the Period 2010–2050

Under all three scenarios, changes in SLCP concentrations had little effect on global average cloud cover, but regional effects were apparent. Under RCP 8.5, as shown in Figure 4a, LCC increased at high latitudes of the NH and midlatitudes of the SH, especially over Canada, central Siberia, India, and southeastern China, where the increases were generally greater than 1%. Over the southern African continent, United States, and Eastern Europe, LCC decreased, generally by approximately 1.5%. Under RCPs 4.5 and 2.6, the distributions of LCC change were similar. When SLCP concentrations decreased, LCC decreased by about 0.9% on the both sides of the equatorial Atlantic, the Indian Peninsula, and most parts of South America (Figures 4c and 4e). LCC increased in southeastern China and western North America by more than 1.2%. There may be a link between LCC and surface relative humidity (SRH; Figures 3b, 3d, and 3f). LCC increased where SRH increased, and vice versa. For example, under RCP 8.5, LCC increased by approximately 1.8% in southeastern China, where SRH also increased by about 1.8%. The enhancement of warm and humid air transport from tropical regions (Figure 3a) could be associated with increases in LCC and SRH in those regions. The same phenomena were also observed in southeastern China and western North America under these two mitigation scenarios.

Changes in SLCP concentrations yielded more obvious effects on HCC. Under RCP 8.5, HCC increased by more than 1.2% over the Mediterranean, South Pacific, and North America. Under the two mitigation scenarios, changes in HCC under RCP 2.6 were more prominent than those under RCP 4.5 (Figures 4d and 4f). For example, in northern Africa, the central Indian Ocean, and the northern and southwestern Pacific, HCC increased by around 2% under RCP 4.5 but significantly increased, by more than 3%, under RCP 2.6. In response to the greenhouse effect caused by high clouds, decreases in SAT were weakened in these regions. By 2050, the global average HCC increased by 0.2 and 0.3%, respectively.

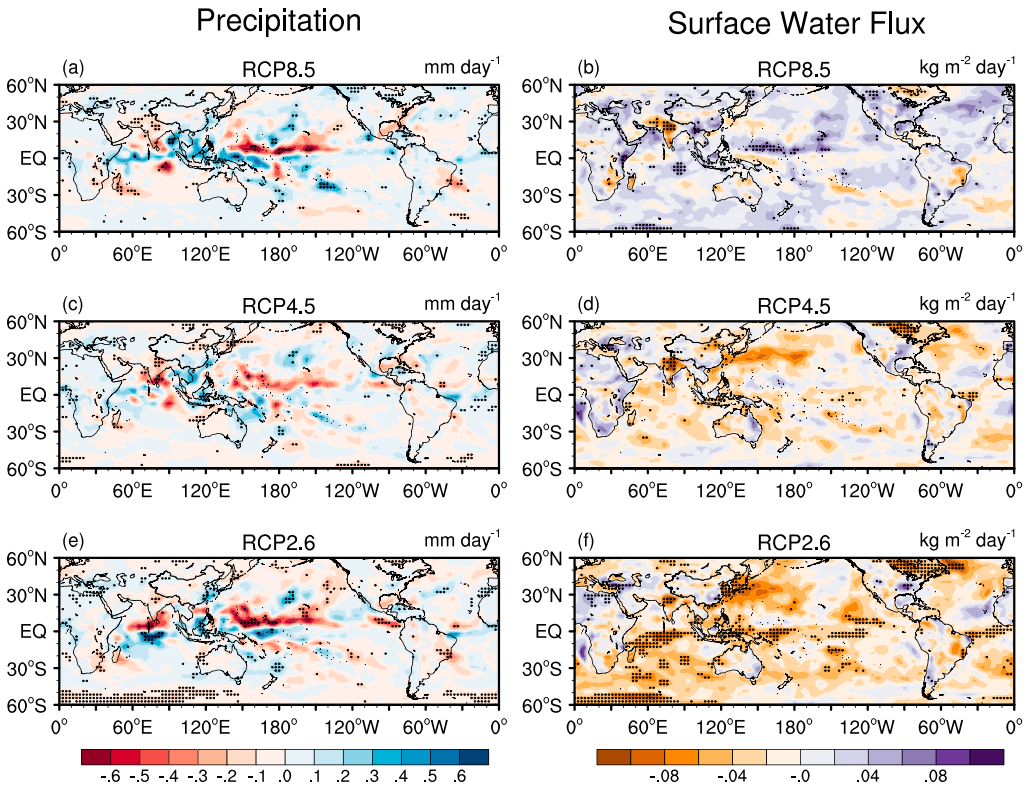

Figure 5. The spatial distribution of (left column) precipitation and (right column) surface water flux variations resulting from changes of short-lived climatic pollutants, from 2010 to 2050, in (a and b) Representative Concentration Pathway 8.5 (RCP8.5), (c and d) RCP4.5, and (e and f) RCP2.6. The areas with "·" passed the 95% significance test.

3.4. Effects of SLCP Changes on Precipitation During the Period 2010–2050

Figure 5 shows changes in precipitation (left column) and surface water vapor flux (SWVF) (right column) caused by SLCP concentration changes during the period 2010–2050 under the three emission scenarios. Under RCP 8.5, increased SLCP concentrations produced a significant increase in SWVF over most parts of the globe (Figure 5b). As the simulation results show, SWVF increased more prominently in the NH than in the SH, especially in the equatorial Pacific, southeastern China, and continental North America, by around 0.05 kg m^{-2} d^{-1}. The most significant increase in SWVF (about 0.08 kg m^{-2} d^{-1}) occurred over the equatorial Pacific. In the SH, SWVF increased over the vast majority of marine areas, except the southern Pacific and Atlantic, where SAT and SNRF decreased slightly (Figures 2a and 2b). Under this scenario, precipitation generally increased over most parts of the globe (Figure 5a). However, with enhanced anticyclonic circulation, precipitation decreased over the Indian Peninsula and equatorial Pacific (about −0.3 to −1.2 mm d^{-1}). Notably, the increase in SLCP concentration led to reductions in precipitation and SWVF over the Indian Peninsula (Figures 5a and 5b), but the decrease in SWVF was less than that in precipitation. This phenomenon may further intensify regional drought in the Indian Peninsula. By 2050, increases in SLCP concentration under RCP 8.5 were predicted to lead to a global average precipitation increase of 0.01 mm d^{-1}. Under mitigation scenarios RCP 4.5 and 2.6 (Figures 5d and 5f), SWVF decreased significantly over the Indian Peninsula, eastern Canada, and most parts of the ocean, by more than −0.04 and −0.06 kg m^{-2} d^{-1}, respectively. The most obvious decreases were both located over the northern Indian Peninsula, reaching −0.21 and −0.21 kg m^{-2} d^{-1}, respectively. Under RCP 2.6, following significant decreases in SAT in the SH, the reduction in SWVF over most oceans in the SH was more prominent than in the NH (Figure 5f). The decreased SNRF might be the main reason for the observed decreases in SWVF; changes in these two climatic factors were very consistent in geographical distribution. In the above-mentioned areas, where SWVF decreased significantly, SNRF also decreased, by about 0.5 to 1.5 W m^{-2}. By 2050, global average SWVFs decreased by 0.02 and 0.03 kg m^{-2} d^{-1} under RCPs 4.5 and 2.6, respectively. As shown in Figures 5c and 5e, there were

slight increases in precipitation over most parts of the continents, for example, by approximately 0.1 mm d^{-1}, over Africa, Australia, and North America. As precipitation is mainly concentrated in the tropics, changes were particularly prominent there. North of the equator, precipitation was generally reduced, and the opposite trend was observed south of the equator. With increasing SLCP mitigation efforts, these opposite trends on either side of the equator intensified. For example, in the tropical Pacific under RCP 4.5, precipitation decreased by about 0.35 mm d^{-1} north of the equator and increased by about 0.25 mm d^{-1} to the south, whereas under RCP 2.6, the decrease in the north was greater than −0.5 mm d^{-1}, and the increase in the south was about 0.5 mm d^{-1}. The same phenomenon was observed over the Indian Ocean. Therefore, a reduction in SLCP concentrations might result in the southward movement of the ITCZ, as was the case for the aerosol effect (Wang, Zhang, Li, et al., 2013; Zhao et al., 2014; Zhou et al., 2017) and CH_4 effect (Xie, Zhang, Yang, & Wang, 2016). By 2050, as SLCP concentrations decreased under RCPs 4.5 and 2.6, global mean precipitation decreased by 0.02 and 0.03 mm d^{-1}, respectively. Salzmann (2016) simulated a robust increase of global mean precipitation of about 1.5 to 2 (6.5 to 7) % K^{-1} in response to GHG (aerosol) forcing. In this study, the precipitation response to SLCPs was 1.5 to 3% K^{-1}, which was consistent with Salzmann (2016).

4. Conclusions

We simulated ERF and climate responses to changes in SLCP concentrations from 2010 to 2050 under different emission scenarios (RCPs 8.5, 4.5, and 2.6) using the aerosol-climate coupled model BCC_AGCM2.0_CUACE/Aero.

The global annual mean ERF of SLCPs due to changes in SLCP concentrations was 0.1 W m^{-2} from 2010 to 2050 if current emissions levels were maintained (RCP 8.5), whereas under the RCP 4.5 and 2.6 emission scenarios, which have different levels of SLCPs mitigation, the global annual mean ERF became −0.3 and −0.5 W m^{-2}, respectively.

Under RCP 8.5, changes in SLCP concentrations led to an increase in SATs over most parts of the globe, and obvious warming in the middle and high latitudes of the NH, with increases reaching 0.50 K. Precipitation decreased by more than 0.3 mm d^{-1} over the Indian Peninsula and equatorial Pacific. Global annual mean SAT and precipitation increased by 0.13 K and 0.02 mm d^{-1}, respectively. Increasing SLCP concentrations had little effect on global average cloud cover but obvious effects on regional cloud cover. LCC increased significantly over high latitudes in the NH and midlatitudes in the SH (by more than 1.0%), whereas HCC increased significantly over the Mediterranean, South Pacific, and North America (by more than 1.2%).

Under RCPs 4.5 and 2.6, decreasing SLCP concentrations caused SAT to drop significantly over northern Eurasia and North America. Global annual mean temperature decreased by 0.20 K under RCP 4.5 and by 0.44 K under RCP 2.6. Precipitation increased slightly over most continental regions; in the tropical Pacific and Indian Oceans, precipitation increased by more than 0.25 mm d^{-1} south of the equator and decreased by about 0.25 mm d^{-1} to the north. These opposite trends due to a reduction in SLCP concentrations resulted in the southward movement of the ITCZ. Decreasing SLCP concentrations caused a reduction in global annual mean precipitation, by 0.02 and 0.03 mm d^{-1} under RCPs 4.5 and 2.6, respectively, but had little effect on global annual mean LCC. However, regional changes in LCC were more significant; over East Asia and areas near 30°S, LCC increased significantly. HCC generally increased as SLCP mitigation efforts increased. Prominent increases in HCC occurred over northern Africa and the southwestern Pacific. Under RCPs 4.5 and 2.6, global annual mean HCC increased, by 0.2 and 0.3%, respectively.

SLCP mitigation is an effective way to reduce short-term warming; however, action on long-lived climate pollutants such as CO_2 is also required. We will examine climate changes resulting from simultaneous reductions in SLCPs and CO_2 under various mitigation scenarios in a subsequent study.

Acknowledgments
This work was financially supported by the (Key) National Natural Science Foundation of China (41575002 and 91644211) and the National Key R&D Program of China (2017YFA0603502). File ERF.nc contains the simulation results of ERF under RCP2.6, 4.5, and 8.5; file CR26-CR2010.nc/CR45-CR2010.nc/CR85-CR2010.nc contains the simulation results of climate response to SLCPs under RCP2.6, 4.5, and 8.5.

References

Boucher, O., Randall, D., Artaxo, P., Bretherton, C., Feingold, G., Forster, P., et al. (2013). Clouds and aerosols. In *Climate change 2013: The physical science basis. Contribution of working group I to the fifth assessment report of the Intergovernmental Panel on Climate Change* (pp. 573–632). Cambridge, UK, New York, NY: Cambridge University Press.

Chang, W., Liao, H., & Wang, H. (2009). Climate responses to direct radiative forcing of anthropogenic aerosols, tropospheric ozone, and long-lived greenhouse gases in eastern China over 1951–2000. *Advances in Atmospheric Sciences*, *26*(4), 748–762.

Chylek, P., Dubey, M. K., Lesins, G., Li, J., & Hengartner, N. (2014). Imprint of the Atlantic multi-decadal oscillation and Pacific decadal oscillation on southwestern US climate: past, present, and future. *Climate Dynamics*, *43*(1–2), 374.
Hu, A., Xu, Y., & Tebaldi, C. (2013). Mitigation of short-lived climate pollutants slows sea-level rise. *Nature Climate Change*, *3*(8), 730–734.
Hurrell, J. W., Hack, J. J., Shea, D., Caron, J. M., & Rosinski, J. (2008). A new sea surface temperature and sea ice boundary dataset for the community atmosphere model. *Journal of Climate*, *21*(19), 5145–5153.
IPCC (2013). Summary for Policymakers. In T. F. Stocker, D. Qin, G.-K. Plattner, M. Tignor, S. K. Allen, J. Boschung, et al. (Eds.). *Climate Change 2013: The Physical Science Basis. Contribution of Working Group I to the Fifth Assessment Report of the Intergovernmental Panel on Climate Change*. Cambridge, United Kingdom and New York, NY: Cambridge University Press.
Jing, X., & Zhang, H. (2012). Application and evaluation of McICA cloud-radiation frame work in the AGCM of the National Climate Center. *Chinese Journal of Atmospheric Sciences*, *36*(5), 945–958.
Jing, X., & Zhang, H. (2013). Application and evaluation of McICA scheme in BCC_AGCM2.0.1. *International Radiation Symposium on Radiation Processes in the American Institute of Physics.*, *1531*, 756–759.
Kaufman, D. S. (2009). Recent warming reverses long-term Arctic cooling (invited). Paper presented at the AGU Fall Meeting.
Kristjánsson, J. E., Iversen, T., Kirkevåg, A., Seland, Ø., & Debernard, J. (2005). Response of the climate system to aerosol direct and indirect forcing: Role of cloud feedbacks. *Journal of Geophysical Research*, *110*, D24206. https://doi.org/10.1029/2005JD006299
Moss, R. H., Babiker, M., Brinkman, S., Calvo, E., Carter, T., Edmonds, J. A., et al. (2008). *Towards new scenarios for analysis of emissions, climate change, impacts, and response strategies* (p. 132). Geneva: Intergovernmental Panel on Climate Change.
Myhre, G., Samset, B. H., Schulz, M., Balkanski, Y., Bauer, S., Berntsen, T. K., et al. (2012). Radiative forcing of the direct aerosol effect from AeroCom Phase II simulations. *Atmospheric Chemistry and Physics Discussions*, *13*(4), 1853–1877.
Myhre, G., Shindell, D., Bréon, F.-M., Collins, W., Fuglestvedt, J., Huang, J., et al. (2013). Anthropogenic and Natural Radiative Forcing. In T. F. Stocker, D. Qin, G.-K. Plattner, M. Tignor, S. K. Allen, J. Boschung, et al. (Eds.), *Climate Change 2013: The Physical Science Basis. Contribution of Working Group I to the Fifth Assessment Report of the Intergovernmental Panel on Climate Change*. Cambridge, United Kingdom and New York, NY: Cambridge University Press.
Ramanathan, V., & Xu, Y. (2010). The Copenhagen accord for limiting global warming: Criteria, constraints, and available avenues. *Proceedings of the National Academy of Sciences of the United States of America*, *107*(18), 8055–8062.
Riahi, K., Gruebler, A., & Nakicenovic, N. (2007). Scenarios of long-term socio-economic and environmental development under climate stabilization. *Technological Forecasting and Social Change*, *74*(7), 887–935.
Salzmann, M. (2016). Global warming without global mean precipitation increase? *Science Advances*, *2*(6), e1501572.
Shindell, D., Kuylenstierna, J. C., Vignati, E., Van, D. R., Amann, M., Klimont, Z., et al. (2012). Simultaneously mitigating near-term climate change and improving human health and food security. *Science*, *335*(6065), 183.
Tsigaridis, K., Daskalakis, N., Kanakidou, M., Adams, P. J., Artaxo, P., Bahadur, R., et al. (2014). The AeroCom evaluation and intercomparison of organic aerosol in global models. *Atmospheric Chemistry and Physics*, *14*(5), 6027–6161.
UNEP (2011). *Near-term climate protection and clean air benefits: Actions for controlling short-lived climate forcers*, (p. 78). Nairobi, Kenya: United Nations Environment Programme (UNEP).
UNEP, & WMO (2011). *Integrated assessment of black carbon and tropospheric ozone*. Nairobi: United Nations Environment Programme.
Vuuren, D. P. V., Edmonds, J., Kainuma, M., Riahi, K., Thomson, A., Hibbard, K., et al. (2011). The Representative Concentration Pathways: An overview. *Climatic Change*, *109*(1), 5.
Wang, Z., Zhang, H., Jing, X., & Wei, X. (2013). Effect of non-spherical dust aerosol on its direct radiative forcing. *Atmospheric Research*, *120*, 112–126.
Wang, Z., Zhang, H., Li, J., Jing, X., & Lu, P. (2013). Radiative forcing and climate response due to the presence of black carbon in cloud droplets. *Journal of Geophysical Research: Atmospheres*, *118*, 3662–3675. https://doi.org/10.1002/jgrd.50312
Wang, Z., Zhang, H., & Lu, P. (2014). Improvement of cloud microphysics in the aerosol-climate model BCC_AGCM2.0.1_CUACE/Aero, evaluation against observations, and updated aerosol indirect effect. *Journal of Geophysical Research: Atmospheres*, *119*, 8400–8417. https://doi.org/10.1002/2014JD021886
Wang, Z., Zhang, H., & Zhang, X. (2015). Simultaneous reductions in emissions of black carbon and co-emitted species will weaken the aerosol net cooling effect. *Atmospheric Chemistry and Physics*, *15*(7), 3671–3685.
Wang, Z., Zhang, H., & Zhang, X. (2016). Projected response of East Asian summer monsoon system to future reductions in emissions of anthropogenic aerosols and their precursors. *Climate Dynamics*, *47*(5), 1455–1468.
Wu, T., Yu, R., Zhang, F., Wang, Z., Dong, M., Wang, L., et al. (2010). The Beijing Climate Center atmospheric general circulation model: Description and its performance for the present-day climate. *Climate Dynamics*, *34*(1), 123–147.
Xie, B., Zhang, H., Wang, Z., Zhao, S., & Qiang, F. (2016). A modeling study of effective radiative forcing and climate response due to tropospheric ozone. *Advances in Atmospheric Sciences*, *33*(7), 819–828.
Xie, B., Zhang, H., Yang, D., & Wang, Z. (2016). A modeling study of effective radiative forcing and climate response due to increased methane concentration. *Advances in Climate Change Research*, *33*(4), 241–246.
Xin, X. G., Tong-Wen, W. U., & Zhang, J. (2013). Introduction of CMIP5 experiments carried out with the climate system models of Beijing Climate Center. *Advances in Climate Change Research*, *4*(1), 41–49.
Yang, D., Zhao, S., Zhang, H., & Shen, X. (2017). Simulation of global distribution of temporal and spatial variation of PM2.5 concentration in the future. *China Environmental Science*, *37*(4), 1201–1212.
Zhang, H. (2016). *BCC_RAD radiative transfer model*. China: China Meteorological Press.
Zhang, H., Jing, X., & Li, J. (2014). Application and evaluation of a new radiation code under McICA scheme in BCC_AGCM2.0.1. *Geoscientific Model Development*, *7*(3), 737–754.
Zhang, H., Shen, Z., Wei, X., Zhang, M., Li, Z., Zhang, H., et al. (2012). Comparison of optical properties of nitrate and sulfate aerosol and the direct radiative forcing due to nitrate in China. *Atmospheric Research*, *113*(37), 113–125.
Zhang, H., Wang, Z., Wang, Z., Liu, Q., Gong, S., Zhang, X., et al. (2012). Simulation of direct radiative forcing of aerosols and their effects on East Asian climate using an interactive AGCM-aerosol coupled system. *Climate Dynamics*, *38*(7–8), 1675–1693.
Zhang, H., Zhao, S., Wang, Z., Zhang, X., & Song, L. (2016). The updated effective radiative forcing of major anthropogenic aerosols and their effects on global climate at present and in the future. *International Journal of Climatology*, *36*(12), 4029–4044. https://doi.org/10.1002/joc.4613
Zhao, S., Zhang, H., & Xie, B. (2017). Simulating the effects of anthropogenic aerosols on terrestrial aridity using an aerosol-climate coupled model. *Journal of Climate*, *30*, 7451–7463. https://doi.org/10.1175/JCLI-D-16-0407.1
Zhao, S., Zhi, X., Zhang, H., Wang, Z., & Wang, Z. (2014). Primary assessment of the simulated climatic state using a coupled aerosol-climate model BCC_AGCM2.0.1_CAM. *Climatic & Environmental Research*, *19*(3), 265–277.

Zhou, C., Zhang, H., & Wang, Z. (2012). Impact of different mixing ways of black carbon and non-absorbing aerosols on the optical properties. *Acta Optica Sinica*, *33*(8), 270–281. https://doi.org/10.3788/AOS201333.0829001

Zhou, C., Zhang, H., Zhao, S., & Li, J. (2017). Simulated effects of internal mixing of anthropogenic aerosols on the aerosol-radiation interactions and global temperature. *International Journal of Climatology*, *37*, 972–986.

Influences of the Internal Mixing of Anthropogenic Aerosols on Global Aridity Change

Hua ZHANG[1,2,3], Chen ZHOU[1,2*], and Shuyun ZHAO[3]

1 *State Key Laboratory of Severe Weather*, *Chinese Academy of Meteorological Sciences*, *Beijing* 100081
2 *Collaborative Innovation Center on Forecast and Evaluation of Meteorological Disasters*, *Nanjing University of Information Science & Technology*, *Nanjing* 210044
3 *Laboratory for Climate Studies*, *National Climate Center*, *China Meteorological Administration*, *Beijing* 100081

(Received November 1, 2017; in final form July 20, 2018)

ABSTRACT

Influences of the mixing treatments of anthropogenic aerosols on their effective radiative forcing (ERF) and global aridity are evaluated by using the BCC_AGCM2.0_CUACE/Aero, an aerosol–climate online coupled model. Simulations show that the negative ERF due to external mixing (EM, a scheme in which all aerosol particles are treated as independent spheres formed by single substance) aerosols is largely reduced by the partial internal mixing (PIM, a scheme in which some of the aerosol particles are formed by one absorptive and one scattering substance) method. Compared to EM, PIM aerosols have much stronger absorptive ability and generally weaker hygroscopicity, which would lead to changes in radiative forcing, hence to climate. For the global mean values, the ERFs due to anthropogenic aerosols since the pre-industrial are –1.02 and –1.68 W m^{-2} for PIM and EM schemes, respectively. The variables related to aridity such as global mean temperature, net radiation flux at the surface, and the potential evaporation capacity are all decreased by 2.18/1.61 K, 5.06/3.90 W m^{-2}, and 0.21/0.14 mm day^{-1} since 1850 for EM and PIM schemes, respectively. According to the changes in aridity index, the anthropogenic aerosols have caused general humidification over central Asia, South America, Africa, and Australia, but great aridification over eastern China and the Tibetan Plateau since the pre-industrial in both mixing schemes. However, the aridification is considerably alleviated in China, but intensified in the Arabian Peninsula and East Africa in the PIM scheme.

Key words: global aridity, internal mixing, anthropogenic aerosols, effective radiative forcing

Citation: Zhang, H., C. Zhou, and S. Y. Zhao, 2018: Influences of the internal mixing of anthropogenic aerosols on global aridity change. *J. Meteor. Res.*, **32**(5), 723–733, doi: 10.1007/s13351-018-7155-1.

1. Introduction

Aerosols are important to the energy budget of earth–atmosphere system and various atmospheric chemical–physical processes. Massive use of fossil fuel has made great contribution to the continuous growth of the anthropogenic aerosols since the pre-industrial era. The anthropogenic aerosols usually consist of four major categories: black carbon (BC), sulfate, organic carbon (OC), and nitrate. BC and OC aerosols are emitted from the combustion of carbon-based materials, e.g., coal, biomass, etc. (Bond et al., 2004, 2007). Sulfate aerosols are usually generated in the uses of petroleum fuel and volcano eruptions (Okada, 1983; Haywood and Boucher, 2000). Nitrate aerosols mainly come from the organic decomposition, fossil fuel combustion, and industrial activities (Ohara et al., 2007). Before 1850, most of aerosols were from natural sources. However, human activities have become a major contributor to BC, OC, and sulfate aerosols in recent decades. Therefore, we define BC, OC, and sulfate as anthropogenic aerosols in this study. Each kind of anthropogenic aerosols has unique impacts on atmospheric thermodynamics, hydrological circulation, and many complex climatic processes (Boucher et al., 2013; Myhre et al., 2013).

The external mixing (EM) scheme of aerosols is commonly used in most model simulations. In EM model, aerosol particles are treated as independent single-component spheres. However, lots of observations have confirmed that internally mixed aerosols are common all

Supported by the (Key) National Natural Science Foundation of China (91644211 and 41575002) and National Key Research and Development Program of China (2017YFA0603502).

*Corresponding author: zhouc@kwantler.com.

©The Chinese Meteorological Society and Springer-Verlag Berlin Heidelberg 2018

over the globe (Andreae et al., 1986; Jacobson, 2000). The description of a particle can be very different according to the selected internal mixing model: homogenous or inhomogeneous, spherical or nonspherical, single particle or cluster. However, one thing in common is that the internally mixed particles are formed by at least two different substances. The differences in particle structure between EM and PIM (partial internal mixing) schemes can bring about significant changes to particle optical properties and thus the direct radiative forcing (DRF) of aerosols. It has been found by many studies that the internal mixing of BC and soluble aerosol substances can largely increase the absorption of BC (Jacobson, 2001; Zhou et al., 2013; Zhang et al., 2015a), since the translucent soluble substances covering the BC core can act as a lens that focuses radiation on the absorptive core (Pósfai et al., 2003), especially when the relative humidity is below deliquescence point of the soluble substance (Lesins et al., 2002). The fact that the internal mixing of BC is beneficial to greater positive DRF and atmospheric warming has been proven in many experiments (Chung et al., 2002; Sato et al., 2003; Li et al., 2010).

Internal mixing can also alter the overall hygroscopic properties as well as the number concentration of aerosol particles, leading to changes in the aerosol–cloud interaction. Bauer et al. (2010) reported that the amount of pure soluble aerosols could be reduced after internally mixed with BC, and thus suppressed the generation of low clouds. However, coated BC aerosol can serve as CCNs (cloud condensation nuclei) under specific conditions, which can increase the brightness of low cloud. The quantitative relationship between coating and the timescale for hydrophobic-to-hydrophilic conversion is poorly constrained, and changes with many environmental variables (McMeeking et al., 2011). Therefore, quantitative evaluation of the impacts of internal mixing on aerosol–cloud interaction is still of large uncertainty.

Until now, the differences in climatic effects of anthropogenic aerosols have not been systematically evaluated between external and internal mixing treatments. Zhao et al. (2017) studied the impact of anthropogenic aerosols on aridity by using EM scheme. In this study, we used the aerosol–climate online coupled model of BCC_AGCM2.0_CUACE/Aero to simulate the effective radiative forcing (ERF) due to PIM anthropogenic aerosols and their effects on surface aridity change since the pre-industrial. In order to simulate aerosol–radiation and aerosol–cloud interactions, we improved the aerosol–cloud interaction module of BCC_AGCM2.0_CUACE/Aero, and included a set of detailed optical properties look-up tables of internally mixed aerosols (Zhang et al., 2015a). Therefore, the influences of internal mixing can be simulated under different volume mixing ratios and relative humidity (RH). Here, we further compare the differences in global aridity due to EM and PIM schemes using the aridity index. Section 2 presents the detailed calculation of aerosol optical properties and aerosol hydrophilism, and then describes the test setup and the aerosol–climate online coupled model, BCC_AGCM2.0_CUACE/Aero. In Section 3, we analyze the influences of the mixing treatments of anthropogenic aerosols on their ERF. Section 4 discusses the changes in global aridity and the related climate factors due to EM and PIM schemes. Finally, Section 5 presents the conclusions.

2. Methods and model

BC, sulfate, and OC are considered as "anthropogenic aerosols" in the BCC_AGCM2.0_CUACE/Aero. Most influences of the nature emissions of BC, OC, and sulfate on radiative forcing, and climate has been excluded by subtracting the results of pre-industrial scene from those of present-day scene. Two mixing schemes, EM and PIM, were evaluated in this study. In EM scheme, all of the aerosol particles were considered independently in both the radiative transfer and hydrophilic processes. In PIM scheme, 30% of the anthropogenic aerosols were internally mixed based on the available observational data (Martins et al., 1998; Abel et al., 2003; Deboudt et al., 2010) into BC–sulfate and BC–OC aerosols, while the rest of the aerosols were externally mixed. The concept of ERF (IPCC, 2013) was applied to describe the influences of aerosols on radiation energy budget.

2.1 *Methods*

Based on the concept of ERF, the calculations can be summarized into two major parts: aerosol–radiation (ERF_{ari}) and aerosol–cloud (ERF_{aci}) interactions. The main part in simulating the ERF_{ari} interaction is detailed calculations of the optical properties of aerosols. In this study, we use "core–shell" model to describe the internally mixed particles. The optical properties were calculated by using Mie theory for externally mixed aerosols, whereas by the coated sphere Mie theory (Bohren and Huffman, 1998) for internally mixed aerosols. Zhang et al. (2015a) have evaluated other internal mixing models (Maxwell–Garnett and Bruggeman equivalent media models) using a single bin radiative transferring model, and found that they had similar impacts on DRF as the core–shell model. The complex refractive indices of dry aerosol substances were adopted from the HITRAN

(High Resolution Transmission) (2004) (Rothma et al., 2005) database. The complex refractive indices corresponding to different RHs were calculated according to Eq. (1) (Bohren and Huffman, 1998). The changes in RH do not influence the refractive indices of BC since BC is treated as insoluble aerosol in BCC_AGCM2.0_CUACE/Aero.

$$m = m_w + (m_d - m_w)\frac{{r_d}^3}{{r_m}^3}, \quad (1)$$

where m is the complex refractive index of a soluble substance after hygroscopic growth; m_w and m_d are the complex refractive indices of water and a dry soluble substance, respectively; r_d and r_m are the equivalent radii of the soluble substance before and after hygroscopic growth, respectively. The hygroscopic growth rates of the soluble substance were obtained by using the κ-Köhler theory (Petters and Kreidenweis, 2007). A set of look-up tables of internal mixing aerosol optical properties were created based on Zhang et al. (2015a). The optical properties between each bin of radius, mixing proportion, and humidity were obtained by using linear interpolation in real-time simulation. In the simulation, anthropogenic aerosols were binarily mixed into BC–sulfate and BC–OC aerosols. Both the volume mixing ratio of each substance and the proportion of each mixture were determined by the mass concentrations of anthropogenic aerosols within each grid box in real-time.

The κ -Köhler theory was used to simulate the aerosol–cloud interaction. In the κ-Köhler theory, the calculations of hygroscopic growth and cloud condensation nucleus activity depend only on a single hygroscopicity parameter, κ. In the classic Köhler theory, the CCN activity is calculated by using several aerosol physicochemical properties, i.e., solute mass, molecular weight, bulk density, dissociable ions, and activity coefficient. However, calculation has been greatly simplified in the κ-Köhler theory. The calculation of κ is based on:

$$\kappa = \frac{4A^3}{27{D_d}^3 \ln^2 S_c}, \quad (2)$$

$$A = \frac{4\sigma_{s/a} M_w}{RT\rho_w}, \quad (3)$$

where κ is the hygroscopicity parameter, D_d is the dry particle diameter, S_c is the critical supersaturation, $\sigma_{s/a}$ is the surface tension of the solution/air interface, M_w is the molecular weight of water, R is the universal gas constant, T is the temperature, and ρ_w is the density of water. After obtaining κ , the hygroscopic diameter growth factor (gf) can be calculated by:

$$\frac{\mathrm{RH}}{\exp\left(\frac{A}{D_d \mathrm{gf}}\right)} = \frac{\mathrm{gf}^3 - 1}{\mathrm{gf}^3 - (1-\kappa)}, \quad (4)$$

where RH is the relative humidity as a fraction. The overall κ value for the internally mixed particles can be calculated by:

$$\kappa = \sum\nolimits_i \varepsilon_i \kappa_i, \quad (5)$$

where ε_i and κ_i are the volume fraction and the hygroscopicity parameter of substance i, respectively. The size distribution spectra of internally mixed anthropogenic aerosols were calculated based on the size distribution and the volume mixing ratio of BC in real-time simulation.

2.2 *Model description*

The general circulation model of BCC_AGCM2.0 (Wu et al., 2010) was developed by the Beijing Climate Center with a T42 horizontal resolution and 26 vertical layers. A new Monte Carlo Independent Column Approximation of McICA (Jing and Zhang, 2012) and a new radiation scheme of BCC_RAD (Zhang et al., 2014) were included in the model with updated aerosol (Wei and Zhang, 2011) and ice cloud (Zhang et al., 2015b) optical properties. BCC_AGCM2.0 was further coupled with the aerosol model of CUACE/Aero (Zhang et al., 2012), to build BCC_AGCM2.0_CUACE/Aero, including five typical aerosol species (BC, OC, sulfate, dust, and sea salt). The concentration of the aerosols was discretized into 12 bins of radii 0.005–20.480 μm. The natural emissions, such as sea salt and soil dust, were calculated online. In this study, the κ -Köhler theory was applied into the aerosol–cloud interaction module of BCC_AGCM2.0_CUACE/Aero.

Wu et al. (2010) evaluated the capability of BCC_AGCM2.0 and CAM 3.0 by comparing to observations, and found that BCC_AGCM2.0 can produce major meteorological fields more accurate than CAM3.0, especially the tropical/subtropical wind field, latent heat flux, oceanic sensible heat flux, and precipitation. BCC_AGCM2.0_CUACE/Aero can simulate sulfate, sea salt, and dust generally consistent with those provided by AEROCOM (Aerosol Comparisons between Observations and Models)–MEDIAN, but the ranges and values of BC and OC were lower (Zhang et al., 2012). However, the simulations of BC and OC distributions, cloud properties, and the net radiative forcing at the top of atmosphere have been notably improved after introducing a new cloud microphysical scheme into the model (Wang et al., 2014). The simulated optical depth, single scattering albedo, and asymmetry parameter of total aerosols at

550 nm were generally consistent with AERONET observations (Zhang et al., 2012; Zhao et al., 2014).

2.3 *Test setup*

Two groups of tests were carried out. Group 1 represented the pre-industrial scene with the emission data of 1850. Tests in group 1 only considered EM due to the low atmospheric burden of anthropogenic aerosols. Group 2 represented the present-day scene with the emission data of 2000. Tests in group 2 considered both PIM and EM. The emissions data of BC, OC, sulfate, and dimethyl sulfide (DMS) were from AeroCom (Nightingale et al., 2000; Bond et al., 2004; van der Werf et al., 2004), and other emissions data were from the Emission Database for Global Atmospheric Research (EDGAR) version 3.2 (Olivier et al., 2001). In each scene, the model was ran for 20 yr (10-yr spin-up), with a prescribed monthly-mean sea surface temperature (SST) and sea ice cover (SI) to calculate the ERF due to anthropogenic aerosols. In addition, the model coupled with the slab ocean model (SOM) was ran for 80 yr (30-yr spin-up) to simulate the climatic features in each scene. A lower bound of cloud droplet number concentration (CDNC) was imposed everywhere as a proxy for natural background aerosols, which were not included in the model (Kirkevåg et al., 2008; Wang et al., 2016).

The results obtained in this study were compared with an earlier study of anthropogenic aerosols conducted by Zhang et al. (2016) using the same model with a similar experimental setup. However, the early study considered neither the lower bound of CDNC (the lack of the lower bound of CDNC would result in a more negative ERF) nor internal mixing, and thus obtained the global annual mean ERF of EM anthropogenic aerosols since 1850 to be –0.30 W m^{-2} as ERF$_{ari}$ and –2.19 W m^{-2} as ERF$_{aci}$, respectively. The major impacts of EM anthropogenic aerosols on the climate and radiative forcing were similar in both studies. More result validation can be found in Zhang et al. (2016).

3. The effective radiative forcing of PIM and EM anthropogenic aerosols

The new concept of ERF has been proposed in IPCC AR5 to describe the change in the energy balance of earth–climate system due to certain factors. ERF allows the adjustment of all physical variables, except those regarding the ocean and sea ice. The inclusion of these adjustments makes ERF a better indicator of the eventual temperature response (Myhre et al., 2013). Compared with earlier concepts of radiative forcing, ERF performs better in predicting climate responses to forcing factors that have multiple feedbacks, especially for short-lifetime components such as aerosols. The change in the energy balance of the earth–atmosphere system due to anthropogenic aerosols will eventually lead to the change in climate field. Therefore, a brief discussion of ERF is needed before exploring the impacts of anthropogenic aerosols on global aridity.

The global annual mean ERFs of anthropogenic aerosols since the pre-industrial are –1.68 and –1.02 W m^{-2} in EM and PIM schemes, respectively. ERF contains various complex feedbacks of the initial changes in radiation flux due to anthropogenic aerosols, and thus shows little corresponding with the geographical distribution of anthropogenic aerosols (compared to early concept of DRF). In both schemes, negative ERF dominates most of the globe and is strongest in the midlatitude Northern Hemisphere due to the high atmospheric burden of sulfate aerosols (Fig. 1). Sulfate aerosol is ideal CCN and is beneficial for generating more clouds, thus causing markedly negative ERF over such areas. The negative ERF is especially strong over Northeast Asia and the North Pacific Ocean where the anthropogenic aerosols emitted from Northeast China are mainly transported to here. Some areas show weak positive ERF, e.g., Sahara Desert, Arabian Peninsula to India, North Alaska, small patches over the oceans, etc., mainly due to the rapid adjustments of the direct radiative effects of BC. The peak of negative ERF appears over the Tibetan Plateau with the peak of positive ERF to the east of it. The negative peak is possibly due to the enhanced water vapor import from northern Indian Ocean (figure omitted, please refer to Zhou et al., 2018), which causes more low cloud as the terrain elevation increases. The positive peak is mostly due to the aerosol–radiation interaction of BC, which is amplified by the rapid change in terrain elevation and high surface albedo of Tibetan Plateau. Compared to EM scheme, the ERF of anthropogenic aerosols has changed obviously in PIM scheme. The negative ERF over the source regions of sulfate and OC aerosols are markedly

Table 1. Test designs

Group	Time node	Emission data	Scheme	Ocean feedback
1	Pre-industrial	Year of 1850	EM	Prescribed coupled SOM
2	Present-day	Year of 2000	EM	Prescribed coupled SOM
			PIM	Prescribed coupled SOM

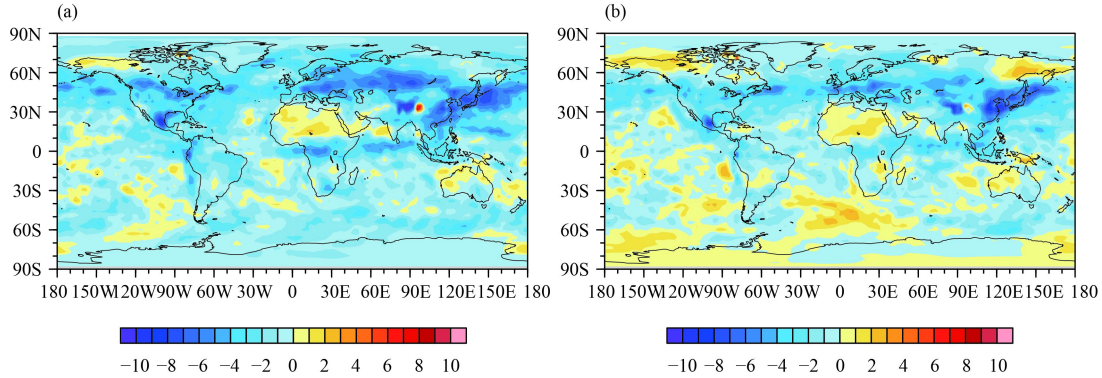

Fig. 1. The annual mean ERF (W m^{-2}) of anthropogenic aerosols since the pre-industrial in (a) EM and (b) PIM.

reduced mainly due to the lower CCN number. The mixture of BC and soluble aerosols is lower in hygroscopicity parameter than the pure soluble aerosols, thus suppresses the generation of clouds, and reduces the cloud albedo. The positive ERF over the oceans and East Siberia are enhanced in PIM scheme as well, which is mostly due to the enhanced rapid adjustments of the direct radiative effects of BC, since the absorption of BC is much stronger in internal mixing than in external mixing. The peaks of both negative and positive ERFs appear over the same regions in two mixing schemes, but are much weaker in PIM scheme. Overall, the PIM scheme can cause positive change in ERF of anthropogenic aerosols over the globe, and reduces the cooling effect of anthropogenic aerosols compared to EM scheme.

Detailed discussion of the impacts of mixing methods on aerosol loading, optical depth as well as the related physical explanations can be found in Zhou et al. (2018).

4. The impacts of anthropogenic aerosols on global aridity

4.1 *Calculation of surface aridity degree*

In this study, we use the Aridity Index (AI) recommended by the United Nations Environment Programme (UNEP) to describe and classify the surface aridity degrees. Compared to the early used classification standards, AI comprehensively considered the influences of precipitation, energy budget, near surface humidity and wind speed, and temperature on surface aridity. Therefore, AI is more accurate in evaluating the impacts of certain factors on surface aridity in climate state (Kottek et al., 2006; Feng and Fu, 2013; Zhao et al., 2015). The calculation of AI is based on Eqs. (6) and (7):

$$\mathrm{ET}_0=\frac{0.408\Delta(R_\mathrm{n}-G)+\gamma\frac{900}{T}\mu_2(e_\mathrm{s}-e_\mathrm{a})}{\Delta+\gamma(1+0.34\mu_2)}, \quad (6)$$

$$\mathrm{AI}=\frac{P}{\mathrm{ET}_0}. \quad (7)$$

In Eq. (6), ET_0 (mm day^{-1}) is the potential evaporation capacity, representing the evaporation demand on the surface. R_n (MJ m^{-2} day^{-1}) is the net radiation flux on the surface; G (MJ m^{-2} day^{-1}) is the soil heat flux density; T (°C), μ_2 (m s^{-1}), e_s (kPa), and e_a (kPa) are the temperature, wind speed, saturated water vapor pressure, and actual water vapor pressure at 2 m above the surface; γ (kPa °C^{-1}) is a psychrometric constant; $\triangle$ (kPa °C^{-1}) is the slope vapor-pressure curve. In Eq. (7), P (mm day^{-1}) is the precipitation rate, and AI represents the water supply–demand ratio, which is proportional to the regional moisture level. According to AI, surface aridity degree can be classified into 6 aridity levels: hyper-arid (AI < 0.05), arid (0.05 ⩽ AI < 0.20), semi-arid (0.2 ⩽ AI < 0.5), dry sub-humid (0.50 ⩽ AI < 0.65), sub-humid (0.65 ⩽ AI < 1), and humid (AI ⩾ 1) (Fig. 2). To reduce the influences of the systemic error of model on outcomes, we use observational data to correct the results corresponding to present-day (Dai, 2011), and reserve the differences in the relative climate factors to analyze the influences of different mixing schemes of anthropogenic aerosols on global aridity since the pre-industrial.

4.2 *Influences of anthropogenic aerosols on AI-related climate factors*

The land annual mean atmospheric temperature at 2 m above the surface (TSA) has decreased by 2.18 and 1.61 K since 1850 in EM and PIM schemes, respectively. The decrease is especially notable over the mid and high latitudes of the Northern Hemisphere due to the strong negative ERF produced by the highly concentrated sulfate aerosol (Fig. 3, upper panels). PIM scheme can largely reduce the negative ERF of anthropogenic aerosols, and suppresses the decrease in TSA compared to EM scheme,

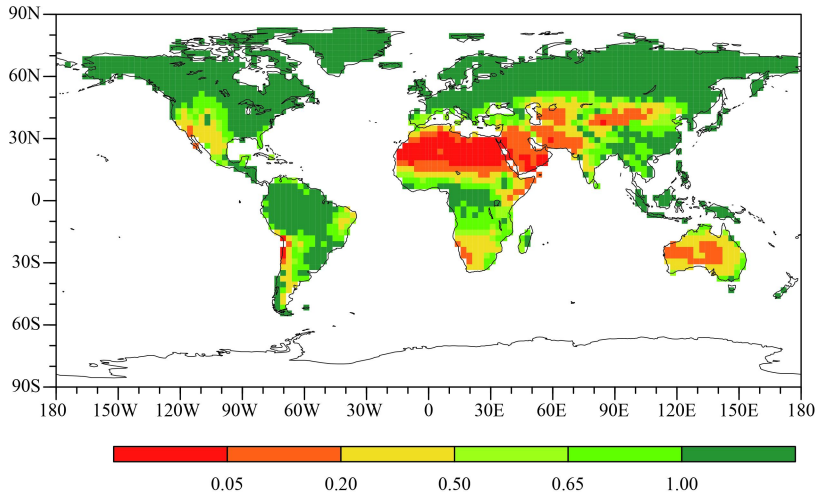

Fig. 2. Global distribution of aridity index, based on EM scheme at present-day.

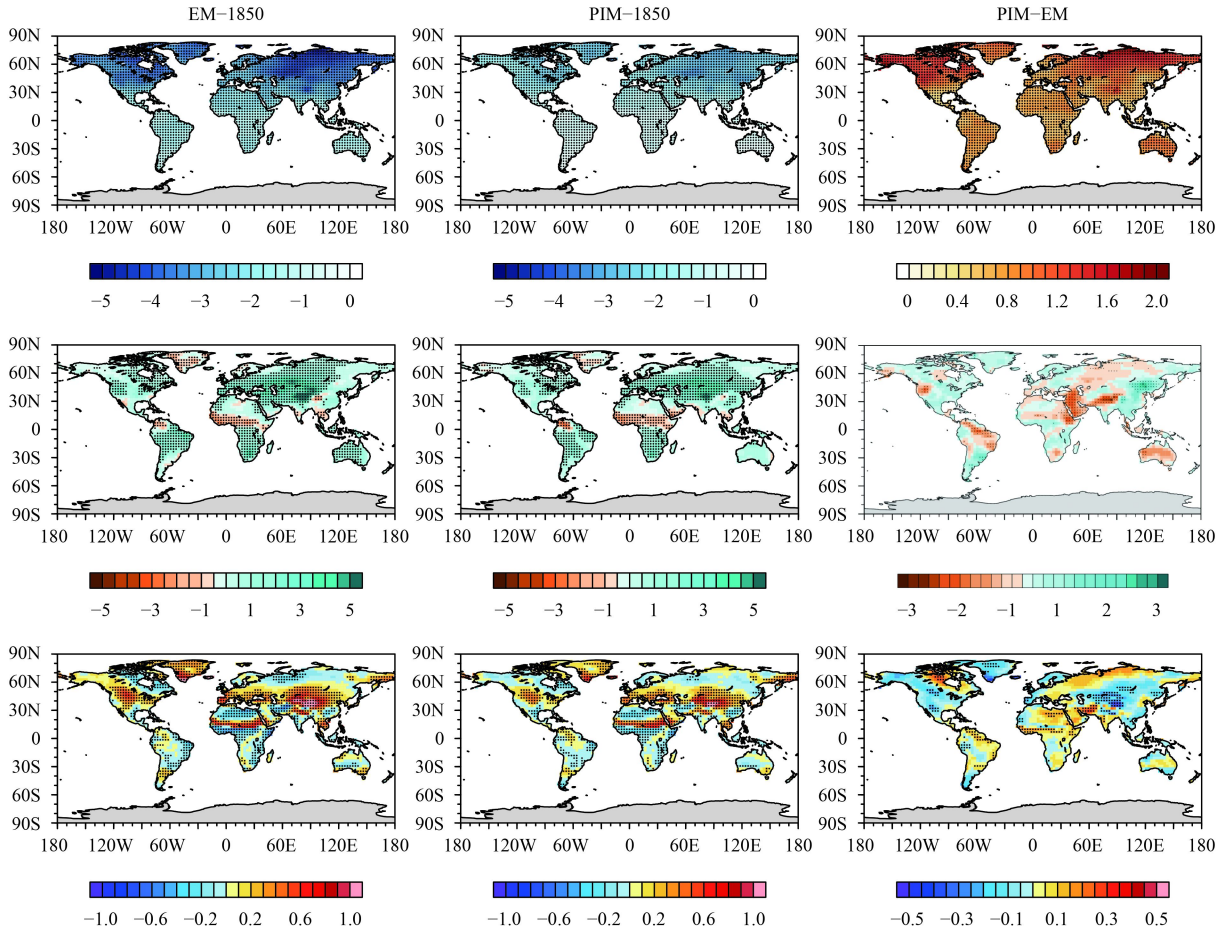

Fig. 3. Changes in TSA (upper; K), RH (middle; %), and μ_2 (bottom panels; m s^{-1}) due to anthropogenic aerosols in different mixing schemes. The left, middle, and right columns represent the differences between EM and 1850, PIM and 1850, and PIM and EM.

especially over the high latitudes of the Northern Hemisphere.

The influences of mixing schemes on RH are complex, since the change in RH is a comprehensive result of the variations of temperature, precipitation, evaporation, circulation, etc. The land annual mean RHs have increased by 1.03% and 0.82% since the pre-industrial in EM and PIM schemes, respectively. The increases in RH

are mainly due to the lower surface temperature. In both mixing schemes, increases in RH are apparent over most of the globe, and are most notable over central Asia and the Tibetan Plateau (Fig. 3, middle panels). Weak decreases in RH are apparent over the narrow region south to the Sahara Desert and northern South America. Compared to EM scheme, PIM anthropogenic aerosols cause increases in RH mainly concentrated over the northeast part of China, whereas causing decreases in RH over the northeast part of the USA, the northwest part of South America, the Arabian Peninsula, and the northeast part of Africa, North India, and Australia. The decreases in RH due to PIM scheme are mostly due to the higher surface temperature, which raises the saturation vapor pressure.

Anthropogenic aerosols can also alter wind speed at 2 m above the surface (μ_2) through various feedbacks (Fig. 3, bottom panels). Throughout the industrial era, land annual mean μ_2 has slightly increased by 0.07 and 0.06 m s^{-2} in EM and PIM schemes, respectively. However, the geographic variations of μ_2 are large. Marked increase in μ_2 can be found over the midlatitudinal Eurasia, and the increase reaches peak over the Tibetan Plateau. Strong increases in μ_2 are also apparent over the narrow region south to the Sahara Desert, central North America, Greenland, and eastern Siberia. Compared to the EM scheme, decreases in μ_2 mostly appear over the midlatitudal Northern Hemisphere and Greenland, while increases in μ_2 mostly appear over northern Canada, Africa, central Europe to central Siberia, Arabian Peninsula, and Iran Plateau in PIM scheme.

Anthropogenic aerosols cause general reduction in precipitation over land mainly due to two reasons: first, the reduction in surface temperature suppresses water evaporation; second, increased anthropogenic aerosol emission provides more CCNs, and thus reduces the cloud droplets radii. Anthropogenic aerosols can also alter the precipitation distribution by changing the large scale circulation, but the influences are obvious only over the oceans (this change cannot be seen in Fig. 4). The land annual mean precipitation rate (P) has decreased by 0.12 and 0.09 mm day^{-1} since the pre-industrial in EM and PIM schemes, respectively. Decreases in precipita-

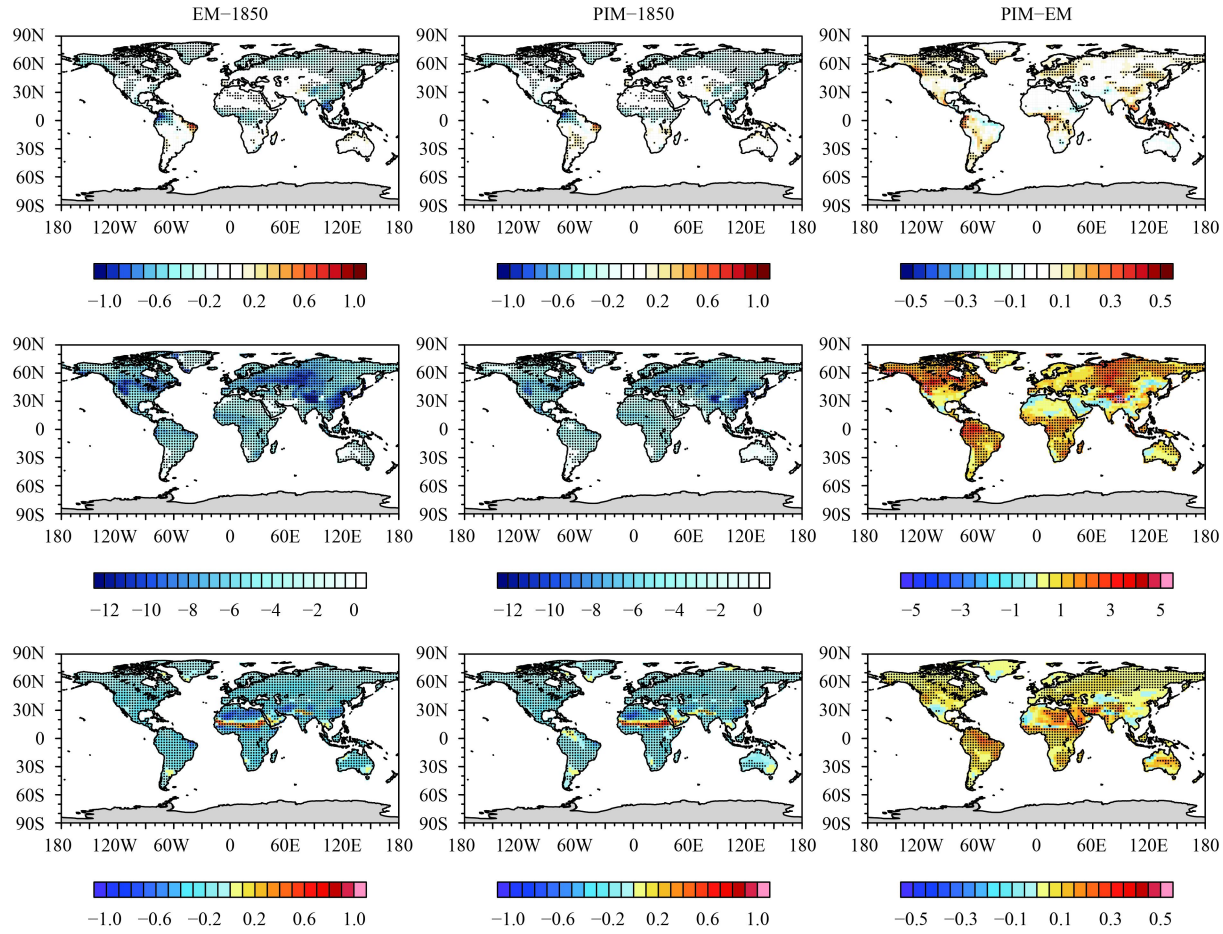

Fig. 4. As in Fig. 3, but for changes in P (upper; mm day^{-1}), R_n (middle; MJ m^{-2} day^{-1}), and ET_0 (bottom panels; mm day^{-1}).

tion are apparent over most land areas in the Northern Hemisphere, and are relatively large over the Tibetan Plateau, central and northern China, central India, and Southeast Asia (Fig. 4, upper panels). The strongest decrease was shown over the Panama region since the water vapor import from the Atlantic Ocean within 0−30°N was considerably reduced. The sole notable increase in precipitation is over northeastern Brazil Plateau, since the enhancement in sea–land breeze provides a better water vapor supply for terrain rainfall. Compared to EM scheme, PIM anthropogenic aerosols show less inhibition on precipitation over most land areas due to higher evaporation. Notable increases can be found over Canada, Europe, northeastern China, and central Africa.

Due to the increase in cloud amount and high scattering capacity of anthropogenic aerosols, the land annual mean net radiation fluxes on the surface (R_n) have decreased by 5.06 and 3.90 W m^{-2} since the pre-industrial in EM and PIM schemes, respectively. The changes in R_n are geographically similar to the change in ERF, and show globally decreases in two mixing schemes (Fig. 4, middle panels). In both mixing schemes, major decreases in R_n are concentrated over the mid and high latitudes of the Northern Hemisphere due to sulfate emission, and relative strong decreases are apparent over South America and central Africa due to OC emission. Compared to EM scheme, R_n is largely increased in PIM scheme due to lower cloud amount/albedo and lower aerosol single scattering albedo. The increase is most obvious over western Siberia, central Asia, southern Canada, and northern South America, and the peak of increase appears over the Tibetan Plateau.

As a comprehensive result of decrease in R_n and TSA and simultaneous increase in RH, the potential evaporation capacity is inhibited over most land areas. The land annual mean potential evaporation capacity (ET_0) has reduced by 0.21 and 0.14 mm day^{-1} since the pre-industrial in EM and PIM schemes, respectively (Fig. 4, bottom panels). In both mixing schemes, most land areas show decreases in ET_0, especially northwestern Africa, Iran Plateau, and southern China. Strong increases in ET_0 are concentrated over the narrow region south to the Sahara Desert, southern Arabian Peninsula, and southern Iran Plateau. Compared to EM scheme, PIM anthropogenic aerosols can cause increases in ET_0 over most land areas, with strong increases concentrated over the Arabian Peninsula, North Africa, and northern South America.

4.3 *Influences of anthropogenic aerosols on AI and surface aridity classification*

The distributions of AIs have markedly changed since the pre-industrial, and the differences in AI between mixing schemes are distinct (Fig. 5). Increases in AIs since the pre-industrial are notable over most land areas in both mixing schemes, especially over the mid and high latitudes of the Northern Hemisphere. The main reason for the global humidification is the decrease in ET_0. The land annual mean AIs have increased by 0.12 and 0.06 since the pre-industrial in EM and PIM schemes, respectively. In both mixing schemes, AI increases markedly over northeastern Canada, western Siberia, and the Tibetan Plateau. Weak decreases in AI are concentrated over northwestern China, Southeast Asia, central Africa, Mexico, and northern South America. Large decreases in AI can be found within the Arctic Circle due to high sensitivity to climate change of the North Pole. However, AI value is very high over this region, and the decreases do not indicate actual aridification.

Decreases in AI are distinctly larger over the mid and high latitudes of the Northern Hemisphere in PIM scheme than in EM scheme, mostly due to the higher R_n and TSA. PIM anthropogenic aerosols can reduce AI over northeastern South America, Sahara Desert, Arabian Peninsula, and Iran Plateau, causing further intensification on the current aridity of these regions. Compared to EM scheme, most areas of China, Southeast Asia, central Africa, and Mexico show AI increases in PIM scheme, which are mostly due to the increases in precip-

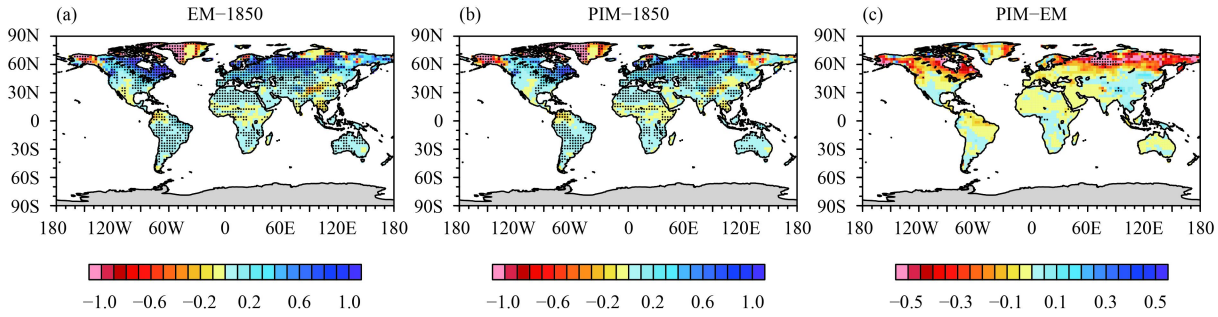

Fig. 5. Differences in AI distribution between (a) EM and 1850, (b) PIM and 1850, and (c) PIM and EM.

itation and RH, also the decreases in near surface wind speed.

The area of humid and sub-humid areas has markedly expanded due to anthropogenic aerosols since the pre-industrial, along with certain expansion of arid areas over some regions (Fig. 6). The influences of EM and PIM schemes on surface aridity are generally similar. Compared to pre-industrial, large expansions in humid and sub-humid areas are apparent over the north shore of Mediterranean, central and West Asia, central Africa, and central South America. Semi-arid area is the transition zone between arid and humid areas, and thus provides a good indication for the change in aridity. According to Huang et al. (2015) and Guan et al. (2016), the semi-arid and semi-wet regions (especially the area with high population density and population change) are also responsible for more than 53% of the anthropogenic dust aerosol emission. Many grid points have changed from arid and semi-arid to sub-humid in Iran Plateau, central Asia, and Australia, which indicates considerable shrink in arid area and possible reduction in local dust aerosol emission. In both mixing schemes, changes from sub-humid to semi-arid are apparent mostly over northern China and the Tibetan Plateau, indicating notable aridification. Similar aridification also appears over western USA and Mexico. In general, throughout the industrial era, anthropogenic aerosols have caused mostly humidification over large part of the globe, but also have caused notable aridification over large part of China.

Compared to EM scheme, PIM scheme can cause notable differences in the surface aridity degrees. Multiple grid points over northeastern China and Tibetan Plateau originally classified as "semi-arid" and "dry sub-humid" in EM scheme show humidification in PIM scheme. Humidification is also apparent over central Asia, northern Mexico, central Africa, and central South America, mainly due to decreased near surface wind speed and increased precipitation. However, PIM scheme can cause great aridification over Arabian Peninsula, East Africa, northern Sahara Desert, and Australia. Weak aridification is apparent over the northern shore of the Mediterranean and western South America. In general, compared to EM scheme, PIM scheme can markedly abbreviate the aridification over northern China, the Tibetan Plateau, and northern Mexico, but intensifies the aridity over Arabian Peninsula and East Africa while weakening the humidification over western Australia.

5. Conclusions

We used the aerosol–climate online coupled model, BCC_AGCM2.0_CUACE/Aero, to simulate the ERF due to PIM anthropogenic aerosols and their impacts on global aridity since the pre-industrial era and compared the results with those of EM ones in detail. The core–shell model and the κ-Köhler theory were used to calculate the optical properties and the hygroscopic capacity of internally mixed aerosols, respectively.

The global annual mean ERFs of EM and PIM anthropogenic aerosols since the pre-industrial are –1.68 and –1.02 W m^{-2}, respectively. PIM scheme causes markedly positive changes in ERF on a global scale due to the higher absorption and lower hygroscopicity parameter. The positive change in ERF due to PIM scheme is the strongest over the mid and high latitudes of the Northern Hemisphere. The changes in the climatic factors related to aridity are also discussed. Since the pre-industrial, the near surface temperature and the net radiation flux have decreased, whereas the near surface wind speed and RH have increased over most land areas in both mixing schemes. These changes lead to a globally decrease in potential evaporation capacity. However, PIM scheme can markedly increase the near surface temperature and net radiation flux on the surface over most land areas compared to EM scheme, resulting in globally increase in potential evaporation capacity, especially over the arid

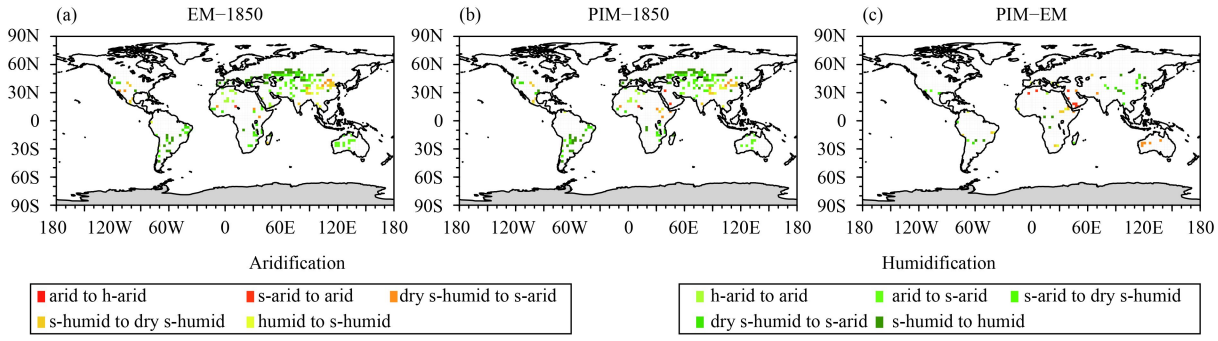

Fig. 6. Differences in surface aridity degrees between (a) EM and 1850, (b) PIM and 1850, and (c) PIM and EM. The references of "h-arid", "s-arid", and "s-humid" stand for "hyper-arid", "semi-arid", and "sub-humid", respectively.

and semi-arid areas (e.g. Sahara Desert, Arabian Peninsula, Iran Plateau, etc.). AI, as a factor representing the regional water supply–demand ratio, has increased over most of the land area since the pre-industrial in both mixing schemes, indicating a general surface humidification due to anthropogenic aerosols. According to surface aridity classification based on AI, large areas in central Asia, East Europe, central South America, and central Africa have changed to more humid climate states since the pre-industrial. However, notable aridification is apparent over northern China and the Tibetan Plateau. Compared to EM scheme, the aridification is notably alleviated over China but greatly intensified over Arabian Peninsula, Iran Plateau, and East Africa in PIM scheme.

REFERENCES

Abel, S. J., J. M. Haywood, E. J. Highwood, et al., 2003: Evolution of biomass burning aerosol properties from an agricultural fire in southern Africa. *Geophys. Res. Lett.*, **30**, 1783, doi: 10.1029/2003GL017342.

Andreae, M. O., R. J. Charlson, F. Bruynseels, et al., 1986: Internal mixture of sea salt, silicates, and excess sulfate in marine aerosols. *Science*, **232**, 1620–1623, doi: 10.1126/science.232.4758.1620.

Bauer, S. E., S. Menon, D. Koch, et al., 2010: A global modeling study on carbonaceous aerosol microphysical characteristics and radiative effects. *Atmos. Chem. Phys.*, **10**, 7439–7456, doi: 10.5194/acp-10-7439-2010.

Bohren, C. F., and D. R. Huffman, 1998: *Absorption and Scattering of Light by Small Particles*. Wiley-VCH, New York, 530 pp.

Bond, T. C., D. G. Streets, K. F. Yarber, et al., 2004: A technology-based global inventory of black and organic carbon emissions from combustion. *J. Geophys. Res. Atmos.*, **109**, D14203, doi: 10.1029/2003JD003697.

Bond, T. C., E. Bhardwaj, R. Dong, et al., 2007: Historical emissions of black and organic carbon aerosol from energy-related combustion, 1850–2000. *Global Biogeochem. Cycles*, **21**, GB2018, doi: 10.1029/2006GB002840.

Boucher, O., D. Randall, P. Artaxo, et al., 2013: Clouds and aerosols. *Climate Change 2013: The Physical Science Basis. Contribution of Working Group I to the Fifth Assessment Report of the Intergovernmental Panel on Climate Change*, T. F. Stocker et al., Eds., Cambridge University Press, Cambridge and New York, 87 pp.

Chung, S. H., and J. H. Seinfeld, 2002: Global distribution and climate forcing of carbonaceous aerosols. *J. Geophys. Res. Atmos.*, **107**, 4407, doi: 10.1029/2001JD001397.

Dai, A. G., 2011: Characteristics and trends in various forms of the Palmer Drought Severity Index during 1900–2008. *J. Geophys. Res. Atmos.*, **116**, D12115, doi: 10.1029/2010JD015541.

Deboudt, K., P. Flament, M. Choël, et al., 2010: Mixing state of aerosols and direct observation of carbonaceous and marine coatings on African dust by individual particle analysis. *J. Geophys. Res. Atmos.*, **115**, D24207, doi: 10.1029/2010JD013921.

Feng, S., and Q. Fu, 2013: Expansion of global drylands under a warming climate. *Atmos. Chem. Phys. Discuss.*, **13**, 14,637–14,665, doi: 10.5194/acpd-13-14637-2013.

Guan, X. D., J. P. Huang, Y. T. Zhang, et al., 2016: The relationship between anthropogenic dust and population over global semi-arid regions. *Atmos. Chem. Phys.*, **16**, 5159–5169, doi: 10.5194/acp-16-5159-2016.

Haywood, J., and O. Boucher, 2000: Estimates of the direct and indirect radiative forcing due to tropospheric aerosols: A review. *Rev. Geophys.*, **38**, 513–543, doi: 10.1029/1999RG000078.

Huang, J. P., J. J. Liu, B. Chen, et al., 2015: Detection of anthropogenic dust using CALIPSO lidar measurements. *Atmos. Chem. Phys.*, **15**, 11653–11665, doi: 10.5194/acp-15-11653-2015.

IPCC, 2013: *Climate Change 2013: The Physical Science Basis. Working Group I Contribution to the Fifth Assessment Report of the Intergovernmental Panel on Climate Change*. Stocker, T. F., et al., Eds. Cambridge University Press, Cambridge, United Kingdom and New York, NY, USA, 1535 pp, doi: 10.1017/CBO9781107415324.

Jacobson, M. Z., 2000: A physically-based treatment of elemental carbon optics: Implications for global direct forcing of aerosols. *Geophys. Res. Lett.*, **27**, 217–220, doi: 10.1029/1999GL010968.

Jacobson, M. Z., 2001: Strong radiative heating due to the mixing state of black carbon in atmospheric aerosols. *Nature*, **409**, 695–697, doi: 10.1038/35055518.

Jing, X. W., and H. Zhang, 2012: Application and evaluation of McICA cloud–radiation framework in the AGCM of the National Climate Center. *Chinese J. Atmos. Sci.*, **36**, 945–958, doi: 10.3878/j.issn.1006-9895.2012.11155. (in Chinese)

Kirkevåg, A., T. Iversen, Ø. Seland, et al., 2008: Aerosol–cloud–climate interactions in the climate model CAM-Oslo. *Tellus A Dyn. Meteor. Oceanogr.*, **60**, 492–512, doi: 10.1111/j.1600-0870.2008.00313.x.

Kottek, M., J. Grieser, C. Beck, et al., 2006: World map of the Koppen–Geiger climate classification updated. *Meteor. Z.*, **15**, 259–263, doi: 10.1127/0941-2948/2006/0130.

Lesins, G., P. Chylek, and U. Lohmann, 2002: A study of internal and external mixing scenarios and its effect on aerosol optical properties and direct radiative forcing. *J. Geophys. Res. Atmos.*, **107**, 4094, doi: 10.1029/2001JD000973.

Li, H., C. Liu, L. Bi, et al., 2010: Numerical accuracy of "equivalent" spherical approximations for computing ensemble-averaged scattering properties of fractal soot aggregates. *J. Quant. Spectrosc. Radiat. Transf.*, **111**, 2127–2132, doi: 10.1016/j.jqsrt.2010.05.009.

Martins, J. V., P. Artaxo, C. Liousse, et al., 1998: Effects of black carbon content, particle size, and mixing on light absorption by aerosols from biomass burning in Brazil. *J. Geophys. Res. Atmos.*, **103**, 32041–32050, doi: 10.1029/98JD02593.

McMeeking, G. R., N. Good, M. D. Petters, et al., 2011: Influences on the fraction of hydrophobic and hydrophilic black carbon in the atmosphere. *Atmos. Chem. Phys.*, **11**, 5099–5112, doi: 10.5194/acp-11-5099-2011.

Myhre, G., D. Shindell, F. M. Bréon, et al., 2013: Anthropogenic and natural radiative forcing. *Climate Change 2013: The*

Physical Science Basis. Contribution of Working Group I to the Fifth Assessment Report of the Intergovernmental Panel on Climate Change, T. F. Stocker et al., Eds., Cambridge University Press, Cambridge, 82 pp.

Nightingale, P. D., G. Malin, C. S. Law, et al., 2000: In situ evaluation of air–sea gas exchange parameterizations using novel conservative and volatile tracers. *Glob. Biogeochem. Cycles*, **14**, 373–387, doi: 10.1029/1999GB900091.

Ohara, T., H. Akimoto, J. Kurokawa, et al., 2007: An Asian emission inventory of anthropogenic emission sources for the period 1980–2020. *Atmos. Chem. Phys.*, **7** , 4419–4444, doi: 10.5194/acp-7-4419-2007.

Okada, K., 1983: Nature of individual hygroscopic particles in the urban atmosphere. *J. Meteor. Soc. Japan*, **61** , 727–736, doi: 10.2151/jmsj1965.61.5_727.

Olivier, J. G. J., J. J. M. Berdowski, J. A. H. W. Peters, et al., 2001: Applications of EDGAR. Including a Description of EDGAR 3.0: Reference Database with Trend Data for 1970–1995. RIVM Report 773301001/NRP Report 410200051, Bilthoven, the Netherlands, RIVM.

Petters, M. D., and S. M. Kreidenweis, 2007: A single parameter representation of hygroscopic growth and cloud condensation nucleus activity. *Atmos. Chem. Phys.*, **7** , 1961–1971, doi: 10.5194/acp-7-1961-2007.

Pósfai, M., R. Simonics, J. Li, et al., 2003: Individual aerosol particles from biomass burning in southern Africa: 1. Compositions and size distributions of carbonaceous particles. *J. Geophys. Res. Atmos.*, **108** , 8483, doi: 10.1029/2002JD002291.

Rothma, L. S., D. Jacquemart, A. Barbe, et al., 2005: The *HITRAN* 2004 molecular spectroscopic database. *J. Quant. Spectrosc. Radiat. Transf.*, **96** , 139–204, doi: 10.1016/j.jqsrt.2004.10.008.

Sato, M., J. Hansen, D. Koch, et al., 2003: Global atmospheric black carbon inferred from AERONET. *Proc. Natl. Acad. Sci. USA*, **100**, 6319–6324, doi: 10.1073/pnas.0731897100.

van der Werf, G. R., J. T. Randerson, G. J. Collatz, et al., 2004: Continental-scale partitioning of fire emissions during the 1997 to 2001 El Niño/La Niña period. *Science*, **303**, 73–76, doi: 10.1126/science.1090753.

Wang, Z. L., H. Zhang, and P. Lu., 2014: Improvement of cloud microphysics in the aerosol–climate model BCC_AGCM2.0.1_CUACE/Aero, evaluation against observations, and updated aerosol indirect effect. *J. Geophys. Res. Atmos.*, **119**, 8400–8417, doi: 10.1002/2014JD021886.

Wang, Z. L., H. Zhang, and X. Y. Zhang, 2016: Projected response of East Asian summer monsoon system to future reductions in emissions of anthropogenic aerosols and their precursors. *Climate Dyn.*, **47**, 1455–1468, doi: 10.1007/s00382-015-2912-7.

Wei, X. D., and H. Zhang, 2011: Analysis of optical properties of nonspherical dust aerosols. *Acta Opt. Sinica*, **31** , 0501002, doi: 10.3788/aos201131.0501002. (in Chinese)

Wu, T. W., R. C. Yu, F. Zhang, et al., 2010: The Beijing Climate Center atmospheric general circulation model: Description and its performance for the present-day climate. *Climate Dyn.*, **34**, 123–147, doi: 10.1007/s00382-008-0487-2.

Zhang, H., Z. L. Wang, Z. Z. Wang, et al., 2012: Simulation of direct radiative forcing of aerosols and their effects on East Asian climate using an interactive AGCM–aerosol coupled system. *Climate Dyn.*, **38** , 1675–1693, doi: 10.1007/s00382-011-1131-0.

Zhang, H., X. Jing, and J. Li, 2014: Application and evaluation of a new radiation code under McICA scheme in BCC_AGCM2.0.1. *Geosci. Model Dev.*, **7**, 737–754, doi: 10.5194/gmd-7-737-2014.

Zhang, H., C. Zhou, Z. L. Wang, et al., 2015a: The influence of different black carbon and sulfate mixing methods on their optical and radiative properties. *J. Quant. Spectrosc. Radiat. Transf.*, **161**, 105–116, doi: 10.1016/j.jqsrt.2015.04.002.

Zhang, H., Q. Chen, and B. Xie, 2015b: A new parameterization for ice cloud optical properties used in BCC-RAD and its radiative impact. *J. Quant. Spectrosc. Radiat. Transf.*, **150**, 76–86, doi: 10.1016/j.jqsrt.2014.08.024.

Zhang, H., S. Y. Zhao, Z. L. Wang, et al., 2016: The updated effective radiative forcing of major anthropogenic aerosols and their effects on global climate at present and in the future. *Int. J. Climatol.*, **36**, 4029–4044, doi: 10.1002/joc.4613.

Zhao, S. Y., X. F. Zhi, H. Zhang, et al., 2014: Primary assessment of the simulated climatic state using a coupled aerosol–climate model BCC_AGCM2.0.1_CAM. *Climatic Environ. Res.*, **19** , 265–277, doi: 10.3878/j.issn.1006-9585.2012.12015. (in Chinese)

Zhao, S. Y., H. Zhang, S. Feng, et al., 2015: Simulating direct effects of dust aerosol on arid and semi-arid regions using an aerosol–climate coupled system. *Int. J. Climatol.*, **35**, 1858–1866, doi: 10.1002/joc.4093.

Zhao, S. Y., H. Zhang, Z. L. Wang, et al., 2017: Simulating the effects of anthropogenic aerosols on terrestrial aridity using an aerosol–climate coupled model. *J. Climate*, **30** , 7451–7463, doi: 10.1175/JCLI-D-16-0407.1.

Zhou, C., H. Zhang, and Z. L. Wang, 2013: Impact of different mixing ways of black carbon and non-absorbing aerosols on the optical properties. *Acta Opt. Sinica*, **33** , 0829001, doi: 10.3788/AOS201333.0829001. (in Chinese)

Zhou, C., H. Zhang, S. Y. Zhao, et al., 2018: On effective radiative forcing of partial internally and externally mixed aerosols and their effects on global climate. *J. Geophys. Res. Atmos.*, **123**, 401–423, doi: 10.1002/2017JD027603.

Tech & Copy Editor: Zhirong CHEN

Theor Appl Climatol (2018) 131:1211–1219
DOI 10.1007/s00704-017-2047-3

ORIGINAL PAPER

Circulation system configuration characteristics of four rainfall patterns in summer over the East China

Junhu Zhao[1] · **Liu Yang**[2] · **Guolin Feng**[1,2]

Received: 13 October 2016 / Accepted: 16 January 2017 / Published online: 26 January 2017
© Springer-Verlag Wien 2017

Abstract In this study, the simultaneous atmospheric circulation system configuration characteristics of the four rainfall patterns (FRP) over the East China during the period 1951–2015 are analyzed in order to investigate their formation mechanisms. The results confirm that the FRP possess obvious differences in the upper-level, middle-level, and lower-level troposphere. In northern China rainfall pattern (NCP) years, the East Asian subtropical westerly jet stream (EAJS) shows a northward trend, with a higher intensity than normal; the blocking high (BH) in the mid-high latitudes is inactive; and the western Pacific subtropical high (WPSH) tends to be stronger, with a location to the north of its normal position. The East Asian summer monsoon (EASM) is stronger, which promotes vapor transport to northern China, and this leads to increased rainfall. In intermediate rainfall pattern (IRP) years, the EAJS position is close to that in normal years; the BH is inactive; the WPSH tends to be weaker, with a location to the east of its normal position; and the EASM is stronger, which is conducive to increased rainfall over the Huaihe River Basin. In Yangtze River rainfall pattern (YRP) years, the circulations are found to be almost opposite in their features to those in NCP years. In South China rainfall pattern (SCP) years, the circulations are found to be almost opposite in their features to those in IRP years. This leads to increased rainfall over South China. Therefore, the different circulation system configuration characteristics lead to the different rainfall patterns.

✉ Junhu Zhao
zhaojh@cma.gov.cn

Liu Yang
huzi348637577@sina.com

Guolin Feng
fenggl@cma.gov.cn

[1] Laboratory for Climate Studies, National Climate Center, China Meteorological Administration, Beijing 100081, People's Republic of China

[2] Department of Physical Science and Technology, Yangzhou University, Yangzhou 225000, People's Republic of China

1 Introduction

As viewed at the national scale, summer rainfall prediction over the East China mainly focuses on the locations of the rain belt (Shi et al. 1999; He et al. 2013; Gong et al. 2015). In other words, predicting the rainfall patterns (Wang et al. 1998; Zhao and Feng 2014). Under normal condition, the rain belt will move from south to north (Ding 1994). And the rain belt is prominently affected by the El Niño-Southern Oscillation (ENSO) (Huang and Wu 1989; Zhang et al. 1999; Chowdary et al. 2011), East Asian summer monsoon (EASM) (Guo 1983; Shi et al. 1999a; Wang et al. 2008; Ding et al. 2008), and other climate factors. Due to the dramatically interannual variability of the ENSO (Chang et al. 2000; Yuan et al. 2012; Feng et al. 2012), EASM (Shi and Zhu 1996b; Ding 2007), and other climate factors, the rain belt may constantly dwell in a fixed area, consequently developing different rainfall patterns (Wei et al. 2012).

However, the classification of summer rainfall patterns over the East China will firsthand influence the forecast accuracy rate (Wang et al. 1998). Liao et al. (1981) had classified the summer rain belt over the East China into three patterns (three rainfall patterns, TRP), which are respectively described as follows: pattern I, the northern pattern; pattern II, the central pattern; and pattern III, the southern pattern. There are both advantages and disadvantages of this classification. The detailed description parallels the previous research (Liao et al. 1981; Wang et al. 1998).

Later, Sun et al. (2005) classified the summer rainfall patterns over the East China during 1880–2002 by using a variety of statistical methods, along with empirical analysis. According to their study, rainfall patterns over the East China can be divided into four patterns (four rainfall patterns, FRP): pattern 1, the northern China rainfall pattern (NCP), the rainfall center is usually in the North China; pattern 2, the intermediate rainfall pattern (IRP),the main rain center is located in the Huaihe River Basin; pattern 3, the Yangtze River rainfall pattern (YRP), the main rain center is located in the Yangtze River Basin; and pattern 4, the South China rainfall pattern (SCP), of which the main rain center is located in the region south of the Yangtze River. However, the classification results after 2002 were not included.

Subsequently, Wang and Huang (2006) divided the rain belt into four patterns during 1951–2005 according to the positions of the maximum summer rainfall anomaly percentage over the East China. However, in many years, the classification results based on the above two classification methods are inconsistent. Therefore, Yang et al. (2016) objectively redivided the summer rainfall patterns over the East China, prolonged the period of coverage to 2015, and analyzed the relationship between the FRP and the EASM. However, the rainfall patterns of East China are not only affected by the EASM but also closely related to other parts of the EASM system, such as the East Asian subtropical westerly jet stream (EAJS) in the upper troposphere (Yang et al. 2002; Zhao et al. 2016), the blocking high (BH) and cold vortices in the mid-high latitudes (Zhao et al. 2013), and the western Pacific subtropical high (WPSH) in the middle troposphere (Zhao et al. 2012; Ye et al. 2014, 2015).

In the above context, it is necessary and meaningful to study the circulation system configuration characteristics of the FRP over the East China. Therefore, in this study, we contrast and analyze the circulation differences in the upper-level, middle-level, and lower-level troposphere for the FRP. The rest of the paper is organized as follows: Section 2 describes the main datasets and methods used in the study. The circulation system configuration characteristics of the FRP are illustrated in Section 3. And lastly, a summary and conclusions are given in Section 4.

2 Data and methodology

The main datasets employed in this study include monthly mean circulation data, gridded at a resolution of 2.5° × 2.5°, from the NCEP–NCAR reanalysis (Kalnay et al. 1996). To avoid the possible influence from global warming, all data were detrended using the linear regression method before analysis.

The summer rainfall pattern classification results are the same as employed in Yang et al. (2016). There are 23 NCP years (1953, 1958, 1959, 1961, 1964, 1966, 1967, 1970, 1973, 1976, 1977, 1978, 1979, 1981, 1985, 1986, 1988, 1990, 1992, 1995, 2004, 2012, 2013), 18 IRP years (1951, 1956, 1957, 1960, 1962, 1963, 1965, 1971, 1972, 1974, 1982, 1984, 1989, 2000, 2003, 2005, 2007, 2009), 12 YRP years (1954, 1969, 1980, 1983, 1987, 1991, 1993, 1996, 1998, 2010, 2011, 2015), and 9 SCP years (1952, 1968, 1994, 1997, 1999, 2001, 2002, 2006, 2014).

Correlation analysis and composite analysis are used to investigate the circulation system configuration characteristics of the FRP. Composite analysis can be used to identify critical areas with significant spatial field differences between two sets of samples, for a certain meteorological variable, and then analyze the various rainfall patterns and corresponding circulation characteristics for reliable testing purposes. The computation formula is as follows (Shi 2009):

$$t = \frac{\overline{x_i(1)} - \overline{x_i(2)}}{\sqrt{\frac{n_1\sigma_{1i} + n_2\sigma_{2i}}{n_1 + n_2 - 2}}\sqrt{\frac{1}{n_1} + \frac{1}{n_2}}} \quad (1)$$

In the equation, n_1 and n_2 are sample time spans; $\overline{x_i(1)}$ and $\overline{x_i(2)}$ are the averages of the i-th station (grid); and σ_{1i} and σ_{2i} are the mean square errors at the i-th station (grid) of the two sets of samples. The calculated $|t|$ value is compared with the critical value, with degrees of freedom of $n_1 + n_2 - 2$, for confidence testing.

3 Circulation system configuration characteristics of the four rainfall patterns

Although the factors affecting the distribution of the summer rainfall anomaly over the East China are varied, the simultaneous atmospheric circulation anomalies represent the most direct and important factor. The 200-hPa U-wind fields, 500-hPa geopotential height fields, and 850-hPa wind fields were selected to analyze the circulation system configuration characteristics and their differences of the FRP.

3.1 Upper-level circulation systems

The upper-level tropospheric westerly jet stream over the subtropical East Asia and the western Pacific—often referred to as the East Asian jet stream (EAJS)—is an important atmospheric circulation system in the Asia–Pacific region (Yang et al. 2002). The enhancement (or weakening) of the summer EAJS intensity, and the position of the EAJS being south (or north), will determine the position of the WPSH being south (or north) (Yang and Zhang 2007). Kuang and Zhang (2006) indicated that when the position of the summer EAJS is

further south (north) than normal, the Yangtze River Basin is prone to flooding (drought).

As representative of the upper atmosphere's circulation, the 200-hPa U-wind fields clearly reflect the anomalies of the EAJS. Figure 1 shows the composites of the 200-hPa U-wind anomalies of the FRP. In NCP years, significant positively anomalous westerly winds exist in North Asia, and the positive anomaly center is located from northern North China to Northeast China. A negative anomaly exists in central and southern Asia, and a significant negative anomaly center is located between the lower reaches of the Yangtze River and the islands of Japan. The 20 m/s contour is north of the climate-average state, indicating that the position of the EAJS presents further north than normal (Fig. 1a). During IRP years, the positively anomalous westerly winds exist between North China and the Yangtze River (Fig. 1b). The 20 m/s contour is consistent with the climate-average state, indicating that the strength and position of the EAJS are close to what they are in normal years. As can be seen in Fig. 1c, the anomaly distribution of the 200-hPa U-wind fields in YRP years is opposite to that in NCP years. Northern Asia presents significant negative anomalies, and the negative anomaly center is located in Northeast China and its surrounding areas. Significant positive anomalies are located between the lower reaches of the Yellow River and the Yangtze River. The 20 m/s contour is south of the climate-average state, indicating that the EAJS is abnormally strong and further south than normal. During SCP years (Fig. 1d), the anomaly distribution of the 200-hPa U-wind fields is basically contrary to that in IRP years. The northern region of the Yangtze River is controlled by significant negative anomalies, indicating an abnormally weak EAJS, while the 20 m/s contour is close to the climate-average state.

Therefore, the main rain belt positions of the FRP correspond well to the strength and location of the EAJS. Considering the occurrence frequency of the westerly wind maximum center, the position index of the EAJS is defined as the regional averaged (80°–140° E) latitude where the 200-hPa U-wind speed is maximum in 80°–140° E. Also, the intensity index of the EAJS is defined as the regional averaged (80°–140° E) U-wind speed in the position of the EAJS. The position index of the EAJS can be used to measure the position of the EAJS axis. In summer, the climate-average position of the EAJS is found to be 40.5° N, with an average intensity of 27.0 m/s. The summer EAJS average position (intensity) indices of the FRP are 41.1° N (27.6 m/s), 40.3° N (27.6 m/s), 39.0° N (28.4 m/s), and 41.0° N (25.1 m/s), respectively (Table 1). That is, the EAJS of NCP years is slightly stronger and further north than in normal years; in IRP years, it is closer to that in normal years; in YRP years, it is abnormally stronger

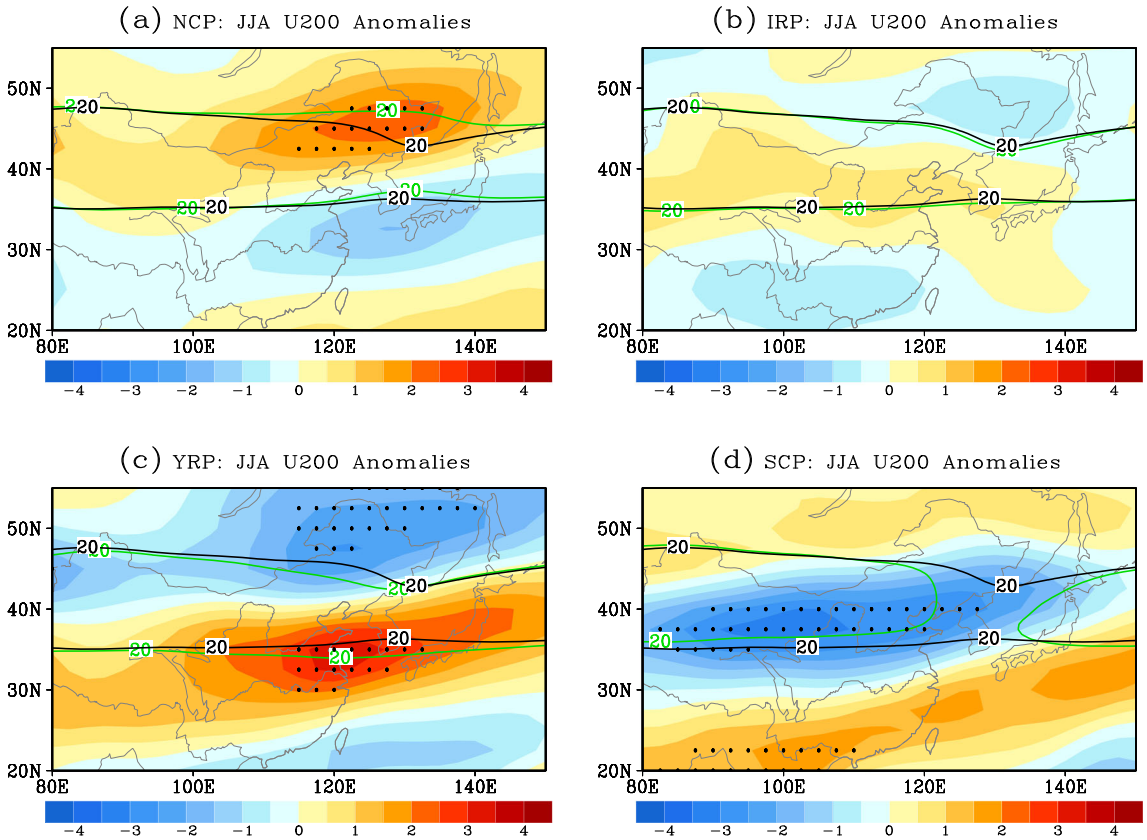

Fig. 1 The summer 200-hPa U-wind anomaly distribution of the four rainfall patterns (units: m/s): **a** NCP, **b** IRP, **c** YRP, and **d** SCP. The *green* (*black*) *line* indicates the velocity of U-wind which is 20 m/s (climate-average state). The *black dots* denote statistical significance at the 95% confidence level

Table 1 The summer circulation indices for the four rainfall patterns during 1951–2015

Index	NCP	IRP	YRP	SCP
Intensity index of the EAJS (m/s)	27.6	27.6	28.4*	25.1*
Position index of the EAJS (° N)	41.1	40.3	39.0*	41.0
UB index	−0.30	−0.28	0.73*	0.37
BB index	−0.33	−0.38	0.72*	0.61*
OB index	−0.35	−0.28	0.74*	0.31
Westward-extending ridge of the WPSH (° E)	0.91	3.22	−9.75*	2.15
Ridge line of the WPSH (° N)	0.57	0.02	−1.03*	0.46
EAP index	−0.29	−0.13	1.03**	−0.23
EASMI_Z	0.30	−0.12	−0.86*	0.72*
EASMI_w	0.02	0.26	−0.18	−0.58*

* and ** indicate the 0.5 and 1 standard deviations, respectively

and abnormally south compared to normal years; and in SCP years, it is slightly weaker and further north than in normal years. These quantitative results are consistent with the conclusions shown in Fig. 1.

3.2 Middle-level circulation systems

As representative of the middle-level atmospheric circulation, the 500-hPa geopotential height fields cannot only clearly reflect the anomaly of the subtropical high system in the mid-low latitudes, as well as the trough and ridge in the mid-high latitudes, but also effectively present the circulation characteristics of the summer rainfall patterns in East China.

As can be seen in Fig. 2a, the circulation configurations of NCP years display the following main characteristics. Firstly, the high latitudes are dominated by positive anomalies, with a positive anomaly center situated in the Barents and Kara seas. The second key characteristic is that vast areas from the Black and Caspian seas to the Okhotsk Sea and Northeast Asia via Lake Baikal are covered by negative anomalies. Meanwhile,

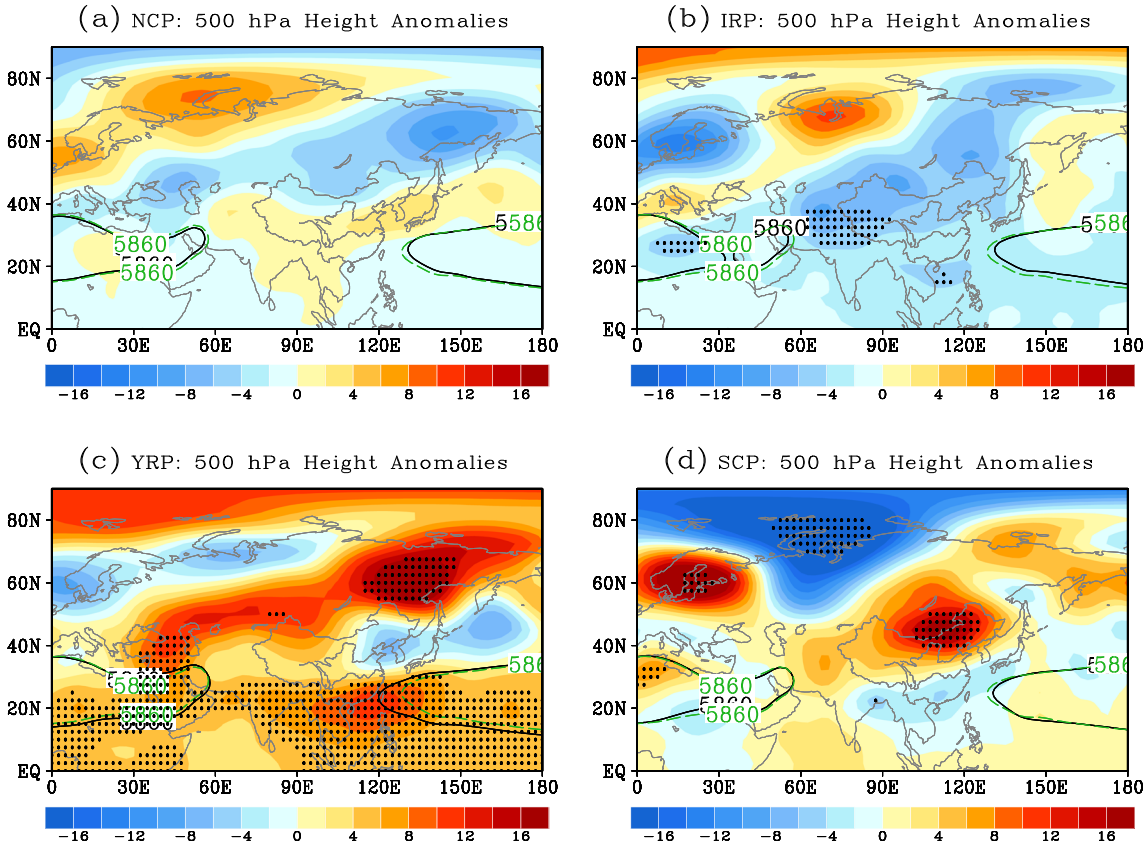

Fig. 2 Same as Fig. 2 but for 500-hPa geopotential height (units: gpm). The *green* (*black*) *lines* indicate 5860 gpm (climate-average state)

the regions between the Yangtze River and Yellow River are covered by positive anomalies, which extend eastward to Japan and its eastern ocean. The third characteristic is that the subtropical and tropical regions to the south of 30° N are controlled by negative anomalies. Such configurations of the anomalous circulation indicate that the Ural Mountains blocking high (UB), Lake Baikal blocking high (BB), and Okhotsk Sea blocking high (OB) are inactive in NCP years (Zhao 1999), and zonal circulation prevails in the mid-high latitudes in the Northern Hemisphere (NH). The WPSH, meanwhile, tends to be weaker and located to the north of its normal position. East Asia shows a "− + −" teleconnection pattern from the low to high latitudes. That is, the East Asia/Pacific teleconnection (EAP) has negative phase characteristics. The cold and warm air converge over the Yellow River Basin and its northern areas, which is conducive to the formation of the NCP.

As can be seen in Fig. 2b, the IRP circulation configurations are similar to those of the NCP. However, there are differences found in the positions of the positive and negative anomaly centers. The positive anomaly center in the high latitudes moves southward to the West Siberian Plain. The Ural Mountains, along with the entire East Asian region, are controlled by negative anomalies. Such configurations of the circulation anomaly fields suggest that the blocking high is weaker in the mid-high latitudes and the mid-high latitudes is dominated by the zonal circulation in IRP years. Also, the WPSH tends to be weaker and located to the east of its normal position.

The circulation configurations of YRP years are almost opposite to those of NCP years (Fig. 2c). The West Siberian Plain shows negative anomalies, while vast areas from the southern Ural Mountains via Baikal Lake to the Okhotsk Sea in the middle latitudes are dominated by significant positive anomalies. The areas from North China via the Korean Peninsula to the eastern ocean of Japan present weak negative anomalies. The areas south of 30° N feature significant positive anomalies. East Asia presents a "+ − +" teleconnection pattern from low to high latitudes. That is, the EAP displays a positive phase. Such configurations of the anomaly fields show that, during YRP years, the mid-high latitude blocking high is abnormally strong, meridional circulation prevails in the mid-high latitudes in the NH, and the WPSH tends to be stronger and located to the south of its normal position. The anomalous water vapor associated with the southwestward extension of the WPSH merges with southward cold air over the middle and lower Yangtze River, which is conducive to the formation of YRP rainfall.

As can be seen in Fig. 2d, the circulation configurations of SCP years are almost opposite to those of IRP years. The North Pole and West Siberian Plain show significant negative anomalies, while the vast areas of the middle latitudes are dominated by significant positive anomalies, with a positive anomaly center situated over the Lake Baikal—northern China region. The regions to the south of 30° N present weak negative anomalies. Such configurations of the anomaly fields indicate that, during SCP years, the BB is abnormally stronger and meridional circulation prevails in the mid-high latitudes in the NH, which is advantageous to cold air moving southwards. The WPSH tends to be stronger and located to the south of its normal position.

Owing to the effects of global warming, tropical and subtropical height fields have been obviously enhanced since the early 1980s (Li et al. 2012). It can be clearly seen from the 500-hPa height difference figures (not shown) that most of the subtropical and mid-latitude regions are significantly higher after the 1980s than before, while they are lower in the polar areas after the 1980s. These results reflect that the subtropical high is inflated, stronger, and located to the south of its normal position under global warming (Zhao et al. 2012; Zhao and Feng 2014). The activities of the blocking highs in the mid-high latitudes are frequent, and the polar vortex spreads southwards with the enhanced meridional circulation and the abating of the EASM (Wang et al. 2008). Such circulation situations are conducive to increased summer YRP and SCP rainfall frequencies.

Figure 2 illustrates that the circulation configurations of NCP years are almost opposite to those of YRP years. Furthermore, the circulation configurations of IRP years are opposite to those of SCP years. Therefore, differences among the 500-hPa height fields during the different rainfall patterns were determined in order to analyze the differences in their circulation systems. The results are shown in Fig. 3.

Firstly, as viewed from the difference in the height fields between NCP and YRP (Fig. 3a), the most significant negative difference occurs in the mid-high latitudes (from the Ural Mountains through Lake Baikal to the Okhotsk Sea), as well as the subtropical regions to the south of 30° N. That is, the critical circulation systems for the two rainfall patterns are the blocking high in the mid-high latitudes, as well as the intensity and position of the subtropical high in the low latitudes. This is consistent with the previous research results (Wei et al. 2012; Zhao and Feng 2014).

Secondly, as viewed from the difference in the height fields between IRP and SCP (Fig. 3b), the most significant positive difference between the two rainfall patterns occurs in the Arctic and West Siberian Plain. The regions to the south of 60° N present negative differences, with a significant center in the Lake Baikal—northern China region. That is, the critical circulation systems between IRP and SCP are the polar vortex and the BB.

In addition, the rain belt of NCP and IRP is to the north of the Yangtze River, while that of YRP and SCP is to the south of the Yangtze River. Between the two groups of rainfall patterns, the rain belt positions are close, and the differences in circulation cause are relatively minor. Therefore, it is necessary to analyze the circulation differences between these two groups.

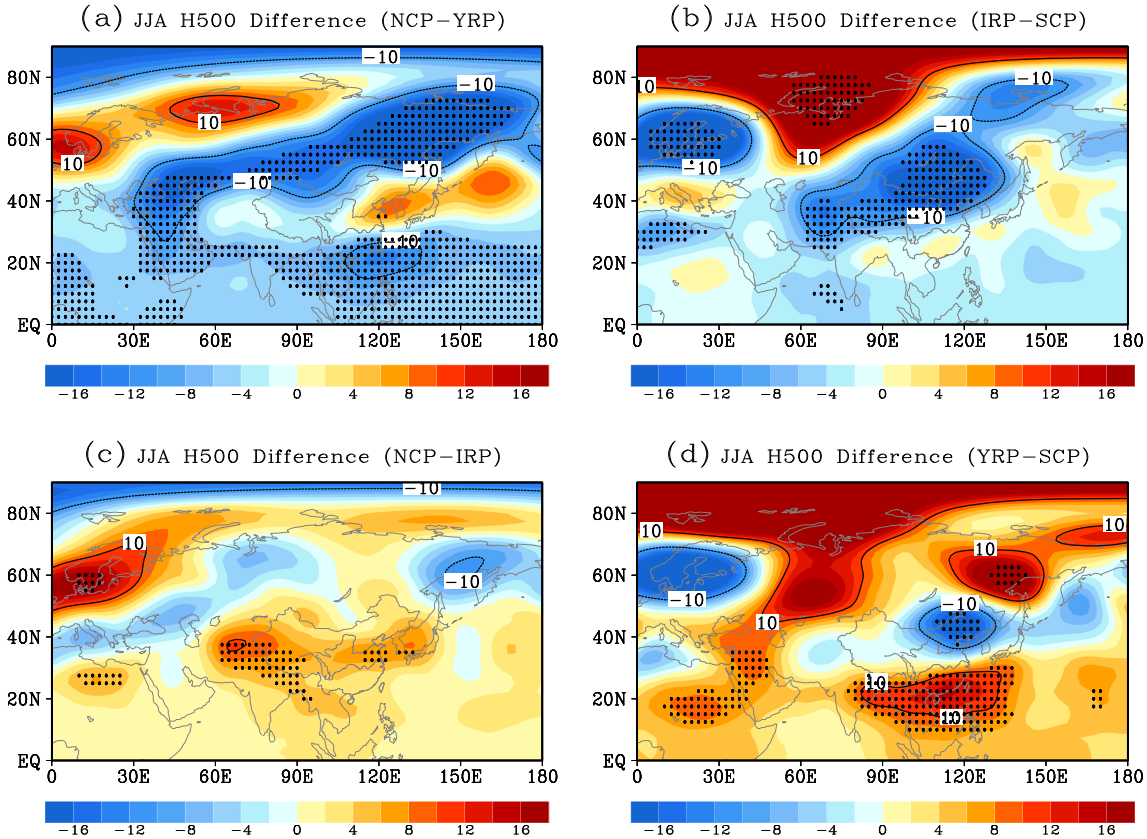

Fig. 3 The difference distributions of summer 500-hPa geopotential height anomaly among the four rainfall patterns (units: gpm): **a** NCP minus YRP, **b** IRP minus SCP, **c** NCP minus IRP, and **d** YRP minus SCP. The *black lines* indicate 10 gpm. The *black dots* denote statistical significance at the 95% confidence level

As viewed from the height difference between NCP and IRP (Fig. 3c), the most significant positive difference of these two patterns occurs from the Yellow River—Yangtze River area to the islands of Japan. This indicates that the WPSH for NCP is stronger and north of that for IRP.

From the height anomaly difference between YRP and SCP (Fig. 3d), the most significant positive difference between these two patterns occurs in the Ural Mountains, Okhotsk Sea, South China, and South China Sea, while a significant negative difference occurs in North China. This indicates that the UB and OB are stronger during YRP years than SCP years. Meanwhile, the WPSH is stronger in YRP years compared to that of IRP years.

In order to quantitatively describe the differences in the circulation systems of the FRP, we use three blocking high indices (UB index, BB index, and OB index) (Zhao 1999), WPSH indices (Liu et al. 2012), and the EAP index (Huang 2004). The blocking high indices indicate the blocking situation, and the greater the index, the stronger the blocking situation. A negative index, meanwhile, indicates an insignificant blocking situation. In addition, the stronger the WPSH, the more west the westward-extending ridge, so that the configuration on the westward-extending ridge index and the ridge line index of the WPSH can be used to reflect the intensity and position of the WPSH (Zhao et al. 2012).

It can be seen from Table 1 that the three blocking high indices during NCP and IRP range from −0.41 to −0.30, which reflect inactive blocking situations in the mid-high latitudes. However, the three blocking high indices of YRP are all above 0.70, and reach 0.5 standard deviations, reflecting abnormally active blocking situations. The three indices of SCP are all above 0.30, especially for the significant BB index, reflecting relatively active blocking situations during SCP years, especially the BB.

As viewed from the two indices of the WPSH, the westward-extending ridge presents an abnormally west position (by 9.42°) than its climatological location during YRP years, and the ridge line is abnormally south (by 1.09°). The westward-extending ridges of the other three rainfall patterns present further east than normal, and the ridge lines are further north. The average EAP index in YRP years is abnormally stronger than the climatology (reaching two standard deviations). Those of the NCP and SCP are weaker, while that of the IRP shows insignificant anomalies. The above analysis indicates that blocking highs, the WPSH, and EAP are important middle-level atmospheric circulation systems that affect the FRP in summer over the East China monsoon region.

3.3 Low-level circulation systems

As representative of the lower atmosphere's circulation, the 850-hPa wind fields clearly reflect the divergence and convergence of the atmospheric circulation and water vapor. Figure 4 shows the 850-hPa wind anomaly fields of the FRP.

The 850-hPa wind anomalies of the NCP (Fig. 4a) have the following main characteristics: The East Asian monsoon trough regions [(10°–20° N, 110°–140° E)] show significant westerly winds, while the Mei-yu frontal area regions [(25°–35° N, 110°–140° E)] present significant easterly winds. The areas south of the Yangtze River to the Philippine Sea are controlled by a cyclonic anomaly, while the middle and lower Yangtze River to the Korean Peninsula show an anticyclonic anomaly. North China presents a southerly wind anomaly. Thus, convection is enhanced in the East Asian monsoon trough regions, but weakened in the Mei-yu frontal areas under this circulation condition. The EASM is stronger, which is conducive to vapor being transported to North China, and in turn leads to more rainfall over the northern region.

In terms of the IRP (Fig. 4b), a large-scale cyclonic anomaly covers the areas from Lake Baikal to northern China, and significant southerly wind anomalies with a stronger EASM cover East China. This is conducive to vapor being transported to North China, causing increased rainfall over the Huaihe River Basin.

For YRP years (Fig. 4c), a large-scale anticyclonic anomaly covers the area from the Yangtze River to the Philippine Sea, while a cyclonic circulation anomaly controls the area north to the middle and lower Yangtze River. North China shows a northerly wind anomaly. Under this circulation condition, the convection is weakened in the East Asian monsoon trough region, but enhanced in the Mei-yu frontal area. The EASM is weaker, which is conducive to the convergence between the northern cold air and the southern vapor in the middle and lower Yangtze River. This leads to increased rainfall over the middle and lower Yangtze River.

As can be seen in (Fig. 4d), the circulation configurations of SCP years at 850 hPa are almost opposite to those of IRP years. A large-scale anticyclonic anomaly controls the area from Lake Baikal to North China. East China has a significant northerly wind anomaly, with a weaker EASM. This is conducive to northern cold air moving southwards to South China. South China is located in a cyclonic anomaly center, which leads to increased rainfall over South China.

Many EASM strength indices have been proposed to measure the intensity of the EASM (Shi et al. 1996a; Wang 2002; Zhang et al. 2003). Zhang et al. (2003) used a vorticity index (EASMI_Z) defined by the U_{850} in (10°–20° N, 100°–150° E) minus the U_{850} in (25°–35° N, 100°–150° E), where U_{850} denotes the zonal wind at 850 hPa. This index can reflect drought and flooding well in the middle and lower reaches

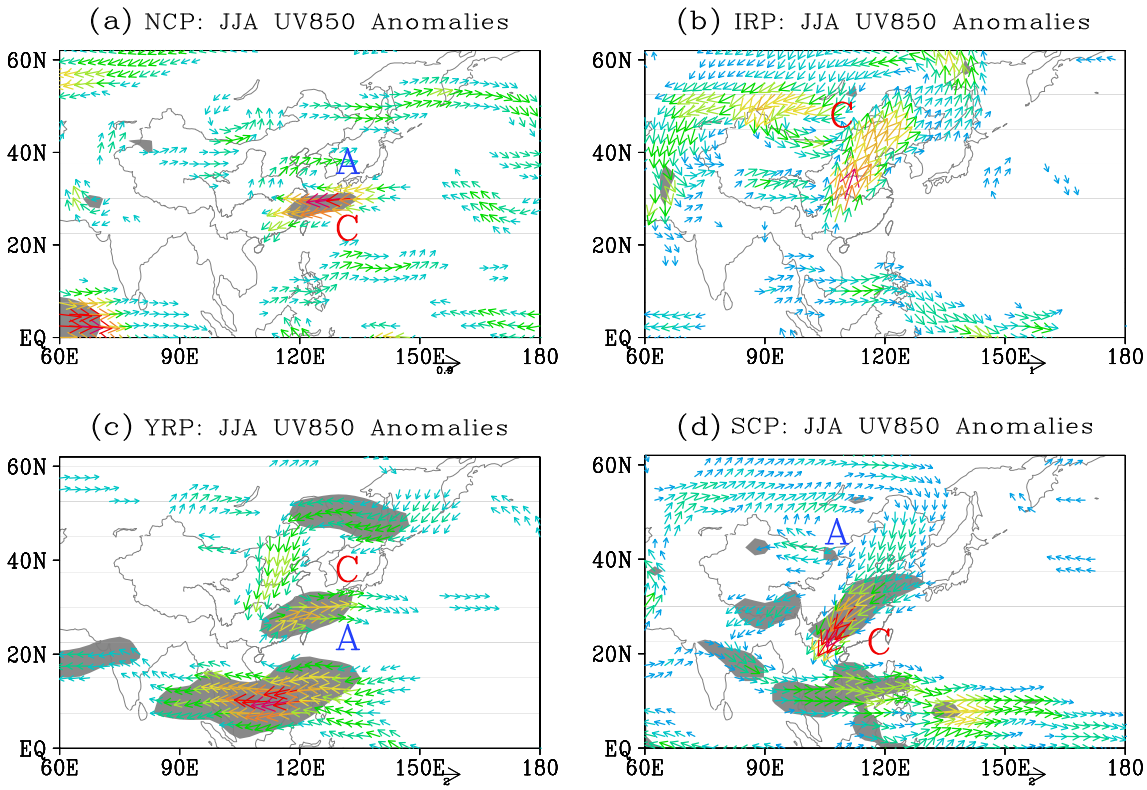

Fig. 4 Same as Fig. 2 but for 850-hPa wind (units: m/s). The *A* (*C*) label represents the anticyclonic (cyclonic) anomaly. The *shaded areas* denote statistical significance at the 95% confidence level

of the Yangtze River. The average EASMI_Z of the FRP is 0.30, −0.12, −0.86, and 0.72, respectively (Table 1). The EASM is significantly weaker during YRP years, mostly weaker in IRP years, and significantly stronger in NCP and SCP years. The EASMI_Z mainly embodies the convection intensity in the Mei-yu frontal area and monsoon trough region, which mainly reflects the intensity of the WPSH and the flood/drought situation of the Yangtze River Basin. The other category directly gauges the strength of the low-level East Asian monsoon winds using the 850-hPa south winds. Wang (2002) defined an index (EASMI_W) using the area-averaged winds within (20°–40° N, 110°–125° E). This index directly reflects the meridional wind intensity over eastern China. The average EASMI_w of the FRP is 0.02, 0.26, −0.18, and −0.58, respectively. The EASM is stronger during NCP and IRP years, while it is weaker during YRP and SCP years (markedly so for the latter). Therefore, the two monsoon indices possess not only similarities but also inconsistencies, within the relationships between the FRP and the EASM. This reflects the complexity of the EASM system and its influences on summer rainfall patterns over East China.

From the above comparative analysis of EASM system index anomalies, the connection between the circulation system anomaly and YRP years is the most significant, followed by SCP and NCP, and is weakest in IRP years. This also reflects the prediction difficulty level of the FRP.

4 Summary

Based on an objective reclassification of the FRP (NCP, IRP, YRP, and SCP) over the East China monsoon region during 1951–2015, we compared and analyzed in this study the circulation system configuration characteristics and differences of the FRP, in order to discuss their formation mechanisms. The key findings of the study can be summarized as follows:

The upper-level circulation characteristics and differences between the FRP were found to be as follows: In NCP years, the East Asian subtropical westerly jet stream (EAJS) shows a northward trend, with a higher intensity than normal. In IRP years, the EAJS position is close to that in normal years. In YRP years, the EAJS is almost opposite to that in NCP years, with the EAJS being stronger and situated abnormally south compared to normal. In SCP years, meanwhile, the EAJS is almost opposite to that in IRP years, being abnormally weak and positioned slightly north.

The middle-level circulation system characteristics and differences of the FRP were found to be as follows: In NCP years, the blocking high is not active in the mid-high latitudes; the WPSH tends to be stronger, with a location to the north of its normal position; and the EAP teleconnection presents a typical negative phase. In IRP years, the blocking high is inactive; the WPSH tends to be weaker, with a location to the east of its normal position; and the EAP anomaly is insignificant. In YRP years, the blocking high is abnormally active, the WPSH is stronger and further west and south than normal, and the EAP is in a significantly positive phase. In SCP years, the blocking high is more active, especially in the area of Lake Baikal; the WPSH shows a slightly east- and northward trend; and the EAP is in a weak negative phase.

The low-level circulation system characteristics and differences of the FRP were found to be as follows: In NCP years, the areas from the Yangtze River Basin to the Philippines are controlled by a cyclonic abnormal circulation, and from the Yangtze River to Northeast China show anticyclonic circulation anomalies. North China presents a southerly wind anomaly with a stronger EASM, conducive to vapor being transported to North China, which in turn leads to increased rainfall over the northern region. In IRP years, Lake Baikal to the North China region is controlled by a cyclonic abnormal circulation, and East China presents a significant southerly wind anomaly with a stronger EASM, which is conducive to vapor being transported to northern China and thereby causing increased rainfall over the Huaihe River Basin. During YRP years, the area south of the Yangtze River to the Philippines is controlled by an anticyclonic abnormal circulation, and North China presents a northerly wind anomaly, with a weaker EASM. When the northern cold air converges with the southern water vapor over the middle and lower reaches of the Yangtze River, it leads to increased rainfall over this region. During SCP years, the area from Lake Baikal to North China is controlled by a significant anticyclonic abnormal circulation, and East China presents a significant northerly wind anomaly with a weaker EASM, conducive to cold air moving southward to South China, which leads to increased rainfall. Generally speaking, the circulation characteristics of the NCP (IRP) are almost opposite to those of the YRP (SCP).

The position of the main summer rain belt over East China is a result of the combined action of different aspects of the EASM circulation system. The areas with a main rain belt are prone to floods. Therefore, objective classification and prediction of rainfall patterns is important not only for short-term climate research but also for climate prediction. The success of climate prediction is directly related to governmental decision-making, as well as disaster prevention and reduction endeavors. In this study, the summer atmospheric circulation system characteristics of the FRP were analyzed in order to discuss their formation mechanisms. The results of the study also provide a reference for improving the accuracy of short-term climate prediction with respect to the main summer rain belts positions of the East China monsoon region.

Acknowledgments This work was jointly supported by the National Natural Science Foundation of China (Grant Nos. 41505061, 41530531, and 41375069), the Special Scientific Research Fund of Public Welfare

Profession of China (Grant No. GYHY201306021), and the Science and Technology Plan Projects in Liaoning Province (Grant No. 2015103038).

References

Chang CP, Zhang Y, Li T (2000) Interannual and interdecadal variations of the East Asian summer monsoon and tropical Pacific SSTs. Part I: roles of the subtropical ridge. J Clim 13:4310–4325

Chowdary JS, Xie SP, Tokinaga H et al (2011) Interdecadal variations in ENSO teleconnection to the Indo–western Pacific for 1870–2007. J Clim 25:1722–1244

Ding YH (1994) Monsoons over China. Kluwer Academic Publishers, Netherlands, pp 419

Ding YH (2007) The variability of the Asian summer monsoon. J Meteorol Soc Japan 85B:21–54

Ding YH, Wang ZY, Sun Y (2008) Inter-decadal variation of the summer precipitation in East China and its association with decreasing Asian summer monsoon. Part I: observed evidences. Int J Climatol 28: 1139–1161

Feng AX, Gong ZQ, Wang QG, Feng GL (2012) Three-dimensional air–sea interactions investigated with bilayer networks. Theor Appl Climatol 109:635–643

Gong ZQ, Zhao JH, Feng GL, Chou JF (2015) Dynamic-statistics combined forecast scheme based on the abrupt decadal change component of summer precipitation in East Asia. Sci China Earth Sci 58: 404–419

Guo QY (1983) The summer monsoon index in East Asia and its variation. Acta Geogr Sin 38:208–217 (in Chinese)

He WP, Wan SQ, Jiang YD, Zhang W, Wu Q, He T (2013) Detecting abrupt change on the basis of skewness: numerical tests and applications. Int J Climatol 33:2713–2727. doi:10.1002/joc.3624

Huang G (2004) An index measuring the interannual variation of the East Asian summer monsoon—the EAP index. Adv Atmos Sci 21:41–52

Huang RH, Wu YF (1989) The influence of ENSO on the summer climate change in China and its mechanism. Adv Atmos Sci 6:21–32

Kalnay E, Kanamitsu M, Kistler R, Collins W, Deaven D, Gandin L, Iredell M, Saha S, White G, Woollen J, Zhu Y, Chelliah M, Ebisuzaki W, Higgins W, Janowiak J, Mo KC, Ropelewski C, Wang J, Leetmaa A, Reynolds A, Jenne R, Joseph D (1996) The NCEP/NCAR 40-year reanalysis project. Bull Am Meteorol Soc 77: 437–471

Kuang XY, Zhang YC (2006) Impact of the position abnormalities of East Asian subtropical westerly jet on summer precipitation in middle-lower reaches of Yangtze River. Plateau Meteorology 25:382–389 (in Chinese)

Li WH, Li LF, Ting MF et al (2012) Intensification of Northern Hemisphere subtropical highs in a warming climate. Nat Geosci 5: 830–834

Liao QS, Chen GY, Chen GZ (1981) Collection of long time weather forecast. Meteorological Press, Beijing, pp 103–114 (in Chinese)

Liu YY, Li WJ, Ai WX et al (2012) Reconstruction and application of the monthly western Pacific subtropical high indices. J Appl Meteor Sci 23:414–423 (in Chinese)

Shi N (2009) Statistical forecast of meteorology. Meteorological Press, Beijing, pp 206–208

Shi N, Zhu QG, Wu BQ (1996a) The East Asian summer monsoon and in relation to summer large scale weather-climate anomaly in China for last 40 years. Chinese Journal of Atmospheric Sciences 20:575–583 (in Chinese)

Shi N, Zhu QG (1996b) An abrupt change in the intensity of the East Asian summer monsoon index and its relationship with temperature and precipitation over East China. Int J Climatol 16:757–764

Shi N, Chen H, Feng JR, Chen SQ (1999) Study on the preceding anomalous characteristics and forecasting method for summer rainfall patterns in eastern China. Q J Appl Meteor 10:70–77 (in Chinese)

Sun LH, Zhao ZG, Xu L et al (2005) Study of summer rain pattern in monsoon region of East China and its circulation cause. Q J Appl Meteor 16:56–62 (in Chinese)

Wang B, Wu ZW, Li JP et al (2008) How to measure the strength of the East Asian summer monsoon. J Clim 21:4449–4462

Wang HJ (2002) Instability of the East Asian summer monsoon-ENSO relations. Adv Atmos Sci 19:1–11

Wang SW, Huang JB (2006) The variations of geographical latitude of rain belts in summer over eastern China during the last millennium. Adv Clim Chang Res 2:117–121 (in Chinese)

Wang SW, Ye JL, Gong DY, Chen ZH (1998) Study on the patterns of summer rainfall in eastern China. Q J Appl Meteor 9:65–73 (in Chinese)

Wei FY, Chen GJ, Li Q (2012) Differences of oceanic and atmospheric circulation features among the rainfall-belt patterns in summer in eastern China. Acta Meteor Sin 70:1004–1020 (in Chinese)

Yang L, Zhao JH, Feng GL (2016) Classification of typical summer rainfall patterns in the East China monsoon region and their association with the East Asian summer monsoon. Theor Appl Climatol. doi:10.1007/s00704-016-1843-5

Yang LM, Zhang QY (2007) Relationships between perturbation kinetic energy anomaly along East Asian westerly jet and subtropical high in summer. J Appl Meteor Sci 18:452–459 (in Chinese)

Yang S, Lau KM, Kim KM (2002) Variations of the East Asian jet stream and Asian–Pacific–American winter climate anomalies. J Clim 15: 306–325

Ye TS, Zhi R, Zhao JH, Gong ZQ (2014) Twice northward jumps of WPSH and its relationship with summer rainfall in eastern China under global warming. Chin Phys B 23:069203

Ye TS, Shen Q, Wang K, Zhang ZS, Zhao JH (2015) Interdecadal change of the northward jump time of the western Pacific subtropical high in association with the Pacific decadal oscillation. J Meteor Res 29:59–71

Yuan Y, Yang S, Zhang ZQ (2012) Different evolutions of the Philippine Sea anticyclone between eastern and central Pacific El Niño: effects of Indian Ocean SST. J Clim 25:7867–7883

Zhang QY, Tao SY, Chen LT (2003) The interannual variability of East Asian summer monsoon indices and its association with the pattern of general circulation over East Asia. Acta Meteor Sin 61:559–568 (in Chinese)

Zhang R, Sumi A, Kimoto M (1999) A diagnostic study of the impact of El Nino on the precipitation in China. Adv Atmos Sci 16:229–241

Zhao JH, Feng GL, Yang J, Zhi R, Wang QG (2012) Analysis of the distribution of the large scale drought/flood of summer in China under different types of the western Pacific subtropical high. Acta Meteor Sinica 70:1021–1031 (in Chinese)

Zhao JH, Feng GL, Gong ZQ, Zhi R (2013) The experiments of transseasonal prediction by combining together the dynamical and statistical methods of the geopotential height fields on the blocking high in the Eurasia mid-high latitudes. Acta Phys Sin 62:099206 (in Chinese)

Zhao JH, Feng GL (2014) Reconstruction of conceptual prediction model for the three rainfall patterns in the summer of eastern China under global warming. Sci China Earth Sci 57:3047–3061

Zhao JH, Yang L, Gu BH, Yang J, Feng GL (2016) On the relationship between the winter Eurasian teleconnection pattern and the following summer precipitation over China. Adv Atmos Sci 33:743–752. doi:10.1007/s00376-015-5195-3

Zhao ZG (1999) Summer droughts and floods and the relative fields circulations in China. China Meteorological Press (in Chinese), Beijing, pp 1–78

Received: 17 August 2017 | Revised: 24 December 2017 | Accepted: 22 January 2018 | Published on: 14 March 2018

DOI: 10.1002/joc.5470

International Journal of Climatology RMetS

RESEARCH ARTICLE

Inter-annual and inter-decadal variability of early- and late-summer precipitation over northeast China and their background circulation

Junhu Zhao[1,2] | Jie Zhou[3] | Liu Yang[4] | Wei Hou[1] | Guolin Feng[2]

[1]Laboratory for Climate Studies, National Climate Center, China Meteorological Administration, Beijing, China

[2]College of Physical Science and Technology, Yangzhou University, Yangzhou, China

[3]Chongqing Climate Center, Chongqing Meteorological Service, Chongqing, China

[4]College of Atmospheric Sciences, Lanzhou University, Lanzhou, China

Correspondence
Guolin Feng, College of Physical Science and Technology, Yangzhou University, Yangzhou 225002, China.
Email: fenggl@cma.gov.cn

Funding information
National Natural Science Foundations of China, Grant/Award Number: 41505061, 41675092, 41375069, 41530531; National Key Research and Development Program of China, Grant/Award Number: 2017YFC1502303

Using precipitation data from weather stations in China and reanalysis data from National Centers for Environmental Prediction/National Center for Atmospheric Research (NCEP/NCAR), the inter-annual and inter-decadal variability of early-summer (May–June) and late-summer (July–August) precipitation (hereinafter referred to as MJP and JAP, respectively) over northeast China (NEC) and their background circulation during 1951–2016 were analysed. The following new findings have been highlighted: (a) There are significantly different inter-annual and inter-decadal variability characteristics between MJP and JAP over NEC. The inter-annual variability of MJP is independent from that of JAP, while the inter-decadal variability of the former is opposite to that of the latter. A significant shift to more MJP (less JAP) occurred in the early 2000s (late 1990s). (b) In terms of the inter-annual timescale, the large-scale atmospheric circulations-associated MJP is notably different from JAP over NEC. The variation in MJP is mainly dominated by the northeast China low (NECL) and the Okhotsk blocking high (OBH), while JAP is mainly influenced by the western Pacific subtropical high (WPSH), the NEC south wind (NESW), and the NECL. (c) On the inter-decadal timescale, MJP is associated with the inter-decadal variation of the East Asia/Pacific (EAP) teleconnection, while JAP is closely related to the inter-decadal variation of the NECL and NESW. When the EAP is in a positive phase, MJP is more than average. Furthermore in late summer, the strong NECL and NESW are both of benefit to the convergence of water vapour from the tropical southwest and East Asian subtropical westerlies over NEC, which contributes to the more JAP than average.

KEYWORDS
circulation, inter-annual, inter-decadal, northeast China, precipitation

1 | INTRODUCTION

The large variability of precipitation in northeast China (NEC) is of great importance to the local agriculture and ecosystems (Sun *et al.,* 2000; Shi and Chen, 2004; Gao *et al.,* 2014). Located in the mid to high latitudes, the summer precipitation in NEC is affected by the atmospheric circulation anomalies both in the tropical and extra-tropical regions, such as blockings in the high latitudes (Yao and Dong, 2000; Feng *et al.,* 2013; He *et al.,* 2013; Zhao *et al.,* 2016), the northeast cold vortex (NHCV) (He *et al.,* 2006; Hu *et al.,* 2010; Zhao *et al.,* 2015), the East Asian summer monsoon (EASM) (Shi and Zhu, 1996; Li and Zeng, 2002; 2003; Wang, 2002; Lian *et al.,* 2003; Sun *et al.,* 2003), and the western Pacific subtropical high (WPSH) (Shen *et al.,* 2011; Ding and Chen, 2015). In addition, numerous studies have indicated that summer precipitation in NEC is also affected by many other external forcing factors, including

soil moisture content in northwest Eurasia (Zhu, 2011), snow cover on the Tibetan Plateau in winter–spring (Shen and Lian, 2004), and the dipole anomaly of summer Arctic atmospheric variability (Wu *et al.,* 2008). Therefore, understanding the main systems that govern the precipitation variability in this region is a big challenge.

Summer precipitation in NEC exhibits significant inter-annual and inter-decadal changes. Sun *et al.* (2000) showed that there were obvious 2–4, 11, 22, and 34-year cycles in the variation of summer precipitation in NEC during 1909–1997. In terms of the inter-decadal variation, the summer precipitation in NEC decreased from the 1960s to the early 1980s, and then began to increase obviously until the end of the 20th century (Ding and Chen, 2015). In addition, a significant shift to less summer (July–August–September) precipitation occurred during 1999–2012, compared with 1984–1998, in NEC (Han *et al.,* 2015). However, the stronger the EASM, the more precipitation there is in NEC, both on inter-decadal and inter-annual timescales (Gong *et al.,* 2005). North China rainfall has been used as a case study for downscaling by the timescale decomposition approach due to its inter-annual and inter-decadal variability in July–August (Guo *et al.,* 2014).

Furthermore, the precipitation over NEC has a crucial sub-seasonal feature in summer (May–August). Precipitation anomalies in different months are affected by the corresponding circulation system. Shen *et al.* (2011) indicated that the inter-annual variation of precipitation over NEC is mainly dominated by a cold vortex in early summer (May and June) and by the EASM in late summer (July and August). In addition, it is also affected by the Northeast Asia blocking high pressure in the mid and high latitudes in August (Shen *et al.,* 2011; Ding and Chen, 2015). The southerly wind anomalies in Northeast Asia in July and August are a good indicator of summer precipitation over NEC (Sun *et al.,* 2003).

Previous studies have primarily focused on either the seasonal evolution characteristics or inter-annual variability of the summer-mean precipitation in NEC. Whether the variation in precipitation in early summer is similar to that in late summer on the inter-annual and inter-decadal timescale? What the difference is in the associated large-scale circulation anomalies? These questions have not yet been investigated. On this basis, the summer precipitation in NEC is divided into two stages in the present study: early summer (May–June) and late summer (July–August). The inter-annual and inter-decadal precipitation characteristics and the associated atmospheric circulation systems in the two stages are compared and analysed. Wish the results will be helpful in understanding the circulation systems and in predicting summer precipitation over NEC.

The article is structured as follows: section 2 introduces the data sets and methods used in the study. The inter-annual and inter-decadal variability of early- and late-summer precipitation over NEC is presented in section 3. The associated atmospheric circulation anomalies associated with inter-annual and inter-decadal early- and late-summer precipitation are presented in sections 4 and 5, respectively. Finally, a brief discussion and conclusions are provided in section 6.

2 | DATA AND METHODS

The data sets employed in this study are as follows:

1. Monthly average precipitation data from 160 weather stations of the National Climate Center (NCC) of China Meteorological Administration (CMA). Twenty-four out of 160 stations are located in NEC (40°–53°N, 118°–132.5°E) (Figure 1a). The time series of the early-summer (May–June) precipitation (MJP) and late-summer (July–August) precipitation (JAP) for 1951–2016 are shown in Figure 1b. The correlation coefficient between MJP and JAP is −.18 during 1951–2016. However, the covariability between MJP and JAP is not highly consistently out-phase during the entire period. We calculated the 11-year-sliding correlations between MJP and JAP (Figure 1c). Negative correlations are detected before the mid-1970s, and weak correlations are found during the late 1970s to the early 1990s. On the contrary, significant positive correlations developed during the mid-1990s to the early 2000s.
2. Monthly mean atmospheric reanalysis data from the National Centers for Environmental Prediction/National Center for Atmospheric Research (NCEP/NCAR) for 1951–2016 (Kalnay *et al.,* 1996), with a horizontal resolution of 2.5 × 2.5°. The variables include monthly geopotential height (h), horizontal wind (u, v), and specific humidity.
3. The definition of East Asia/Pacific (EAP) teleconnection index is as follows: $\mathrm{EAP} = Z_1 - 2 \times Z_2 + Z_3$, where Z_1, Z_2, and Z_3 represent the normalized average 500-hPa geopotential height (H_{500}) within 15°–30°N, 115°–160°E; 55°–65°N, 125°–145°E; and 35°–40°N, 145°–160°E, respectively. Other index data include the Okhotsk blocking high (OBH) index, defined as the area-averaged H_{500} within 55°–65°N, 125°–140°E; the northeast China low (NECL) index, defined as the area-averaged H_{500} within 40°–50°N, 100°–120°E (Zhao *et al.,* 2015); and the northeast south wind (NESW) index, defined as the area-averaged 850-hPa meridional wind (V_{850}) within 35°–45°N, 120°–130°E (Sun *et al.,* 2003).

Power spectrum analysis is primarily used to identify the periodicity of the MJP and JAP. Then, the Fourier decomposition filtering is performed to extract the inter-annual and inter-decadal components. Correlation analysis is used to investigate the relationships between the atmospheric

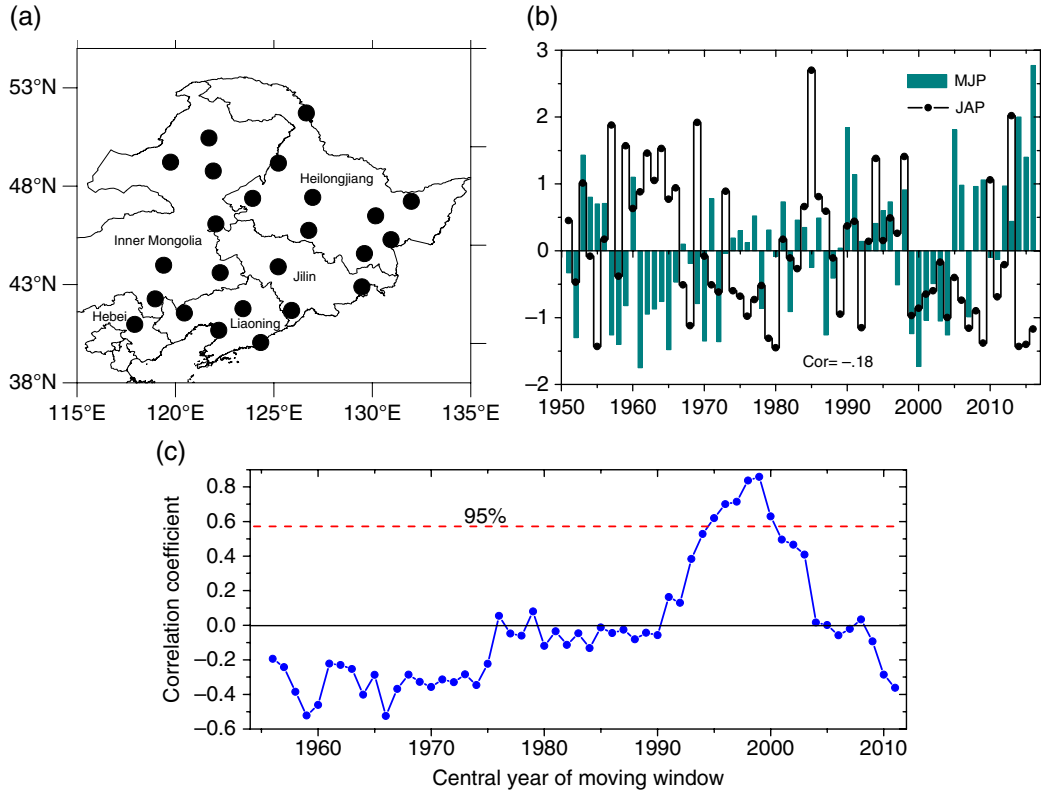

FIGURE 1 (a) Locations of the 24 weather stations in NEC whose data are used in this study. (b) Time series of MJP and JAP in NEC during 1951–2016, which are standardized. (c) The 11-year-sliding correlation coefficients between MJP and JAP. Horizontal red dotted line indicates 95% confidence level estimated using Student's *t* test [Colour figure can be viewed at wileyonlinelibrary.com]

circulation and summer precipitation in NEC. In addition, the linear trends are eliminated before filtering and correlation.

3 | INTER-ANNUAL AND INTER-DECADAL VARIABILITY OF EARLY- AND LATE-SUMMER PRECIPITATION OVER NEC

As shown in Figure 1b, there are significant remarkable inter-annual and inter-decadal variations in MJP and JAP during the past 66 years. Specifically, there are obvious shifts to reduced (increased) MJP in the mid-1950s and late 1990s (mid-1970s and mid-2000s) and to reduced (increased) JAP in the mid-1960s and late 1990s (early 1980s) in NEC. The spectrum analysis shows that there primarily exist two peaks with periods of 2–4 and 20–24 years in MJP and JAP during 1951–2016 (Figure 2a,b), indicating strong inter-annual and inter-decadal variability. To make a distinction between the inter-annual variability of precipitation and the inter-decadal one, observed rainfall data, atmospheric reanalysis data, and climate indexes during 1951–2016 are all decomposed by Fourier decomposition filtering. The data whose variation period is less than 8 years are defined as the inter-annual component. Other data whose variation period is longer than 15 years are defined as the inter-decadal one. The standard deviation of the inter-annual component of MJP (JAP) is

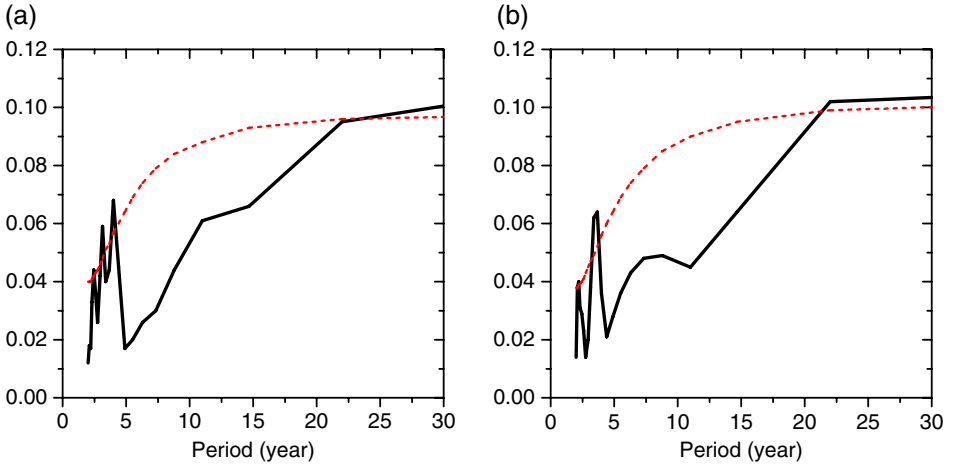

FIGURE 2 Power spectra of the (a) MJP and (b) JAP time series. The red dotted line indicates the confidence level is >80% against a red noise [Colour figure can be viewed at wileyonlinelibrary.com]

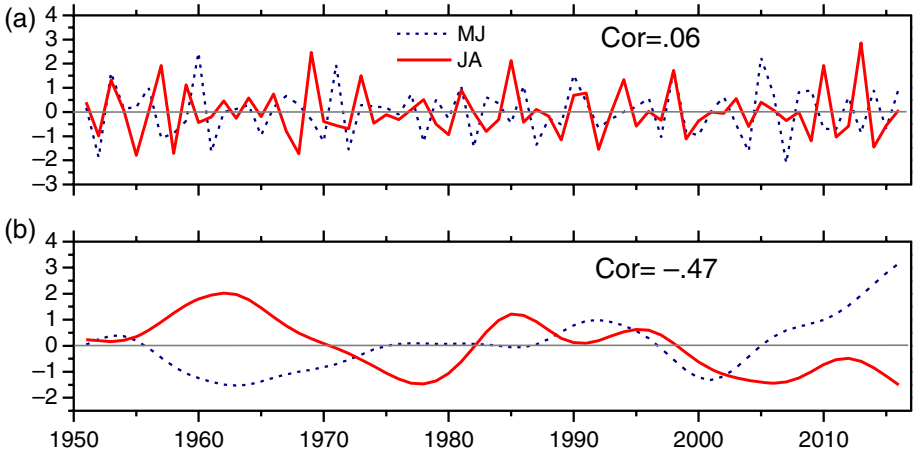

FIGURE 3 The standardized time series of the (a) inter-annual and (b) inter-decadal components of MJP and JAP [Colour figure can be viewed at wileyonlinelibrary.com]

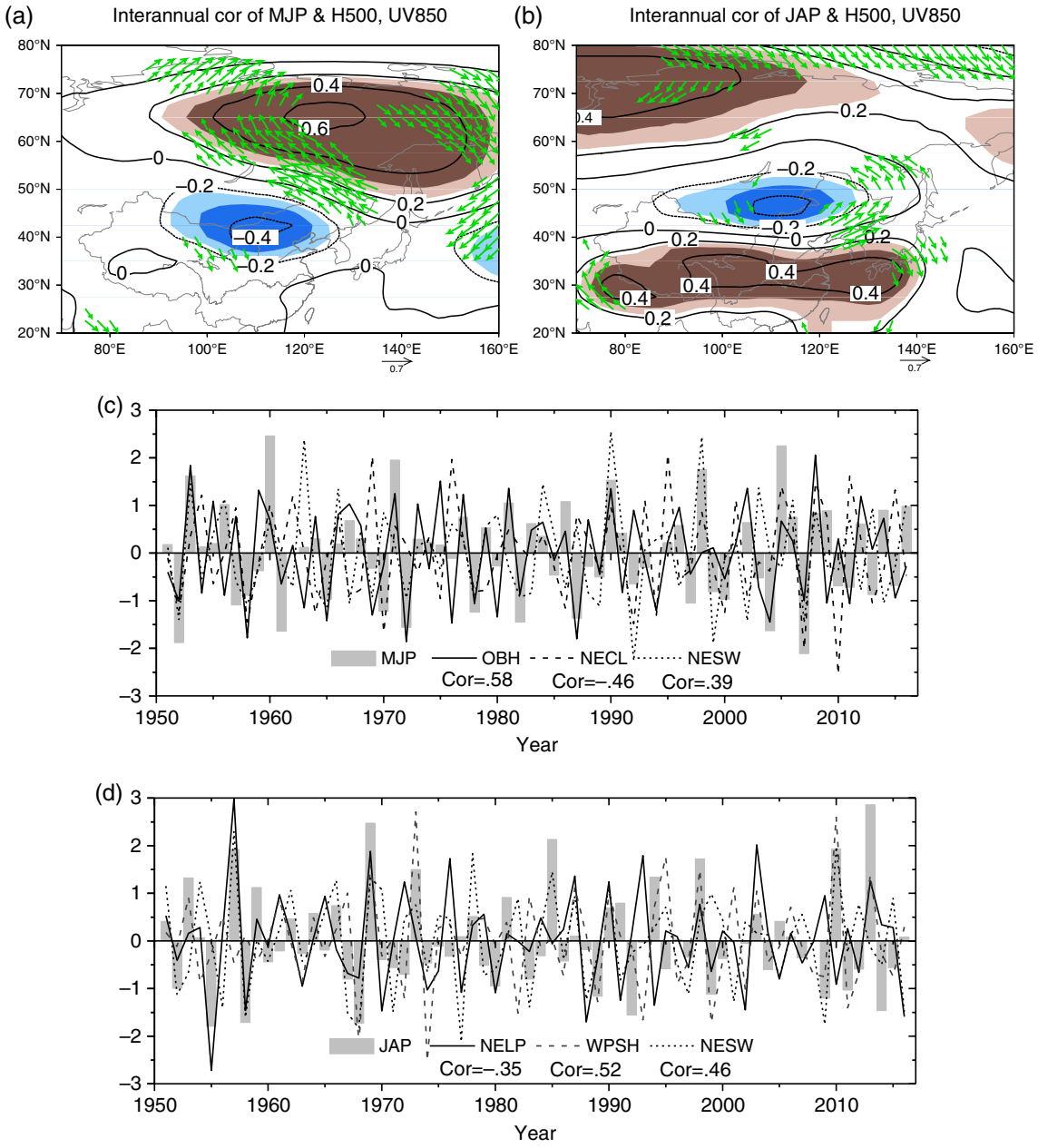

FIGURE 4 Correlation coefficients of detrended time series between inter-annual summer precipitation in NEC and 500-hPa geopotential height (contour) and horizontal winds (vectors) at 850 hPa during 1951–2016: (a) MJP, (b) JAP. The light (dark) shading areas and vectors drawn indicate significance at the .05 (.01) level. (c) The inter-annual time series of the MJP (histogram), OBH, NECL, and NESW. (d) The inter-annual time series of the JAP (histogram), NECL, WPSH, and NESW. The NECL index in (c) and (d) [Colour figure can be viewed at wileyonlinelibrary.com]

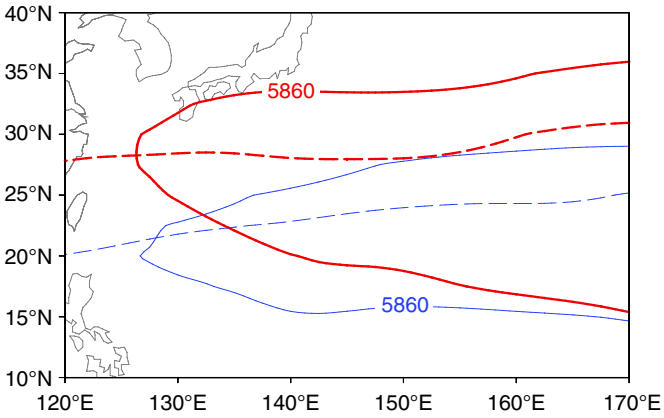

FIGURE 5 The 500-hPa geopotential height and the ridge of WPSH during the early summer (thin line) and late summer (bold lines) [Colour figure can be viewed at wileyonlinelibrary.com]

15.5 mm (31.8 mm), and the standard deviation of the inter-decadal component of MJP (JAP) explains 12.9 mm (23.7 mm). This indicates the necessity for a timescale decomposition of summer precipitation in NEC. Figure 3a,b presents the temporal variations of the inter-annual and inter-decadal components of MJP and JAP, respectively. The correlation coefficient of the inter-annual component between MJP and JAP is .06, indicating that they are independent of each other on the inter-annual timescale. However, there is a negative correlation between the inter-decadal component of MJP and JAP (correlation coefficient is −.47). The inter-decadal variation of MJP in NEC is roughly opposite to that of JAP.

4 | ASSOCIATED ATMOSPHERIC CIRCULATION ANOMALIES WITH INTER-ANNUAL EARLY- AND LATE-SUMMER PRECIPITATION

To explore the possible cause of the mutually independent inter-annual variation between MJP and JAP, the associated atmospheric circulation anomalies are investigated. Figure 4 displays the correlation coefficients of the detrended time series between inter-annual MJP, JAP and 500-hPa geopotential height, and 850-hPa wind, for the period 1951–2016.

In early summer, the correlation between inter-annual MJP and 500-hPa geopotential height (Figure 4a) is significantly positive in most of Northeast Asia and significantly negative from northwest China to NEC. However, in the subtropical region, the main part of the WPSH is located in the upper atmosphere above the ocean. In addition, the ridge line of the WPSH sways between 20°N and 25°N (Figure 5). Therefore, the impacts of the WPSH on precipitation reach only to southern China and do not reach to NEC. That is, the enhanced inter-annual MJP is significantly related to the OBH and the NECL (Liu *et al.,* 2002; Shen *et al.,* 2011; Du *et al.,* 2016). Under the influence of the anomalous OBH and NECL, the low-level atmosphere over NEC is controlled by the anomalous southwesterly winds and easterly winds alike. Influenced by the anomalous low pressure, the southwesterly wind anomaly dominates the low-level atmosphere over NEC. In addition, the abnormal integrated water vapour from the immediate Yellow Sea, Bohai Sea, and Japan Sea converges over NEC, which results in enhanced rainfall. The inter-annual correlation coefficients between the OBH, NECL, NESW, and MJP are .58, −.46, and .39, respectively (Figure 4c). That is, increased inter-annual MJP in NEC mainly covaries with a strong OBH and NECL.

In late summer, the correlation coefficients between inter-annual JAP and 500-hPa geopotential height (Figure 4b) are significantly negative from the southern side of Lake Baikal to northern China, and significantly positive from Tibet to the west of Japan (25°–35°N, 70°–140°E). Compared with the early summer, in late summer, the WPSH gradually moves northwards, and the average ridge line of the WPSH is at 27.5°N (Figure 5). Abnormal high pressure in Japan just appears in the west of the WPSH, which reflects the westwards stretching and northwards

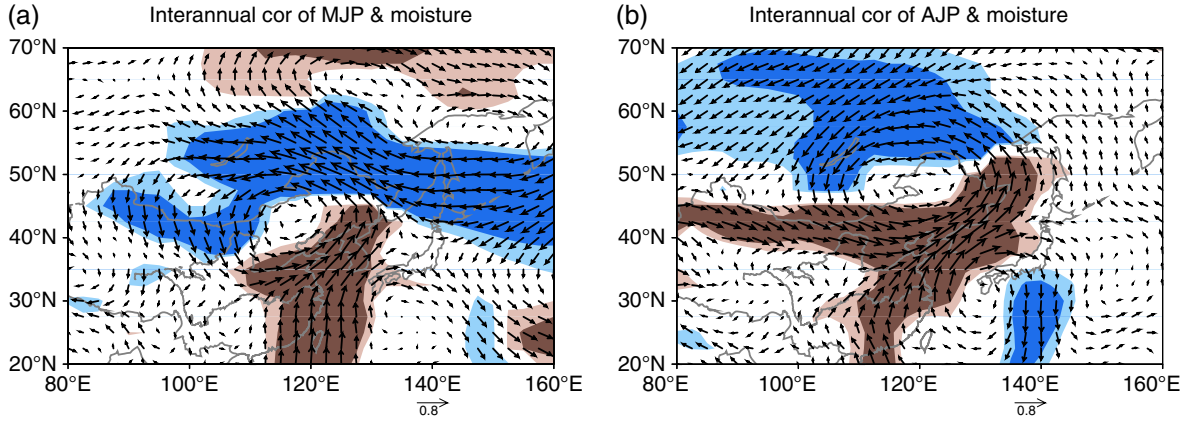

FIGURE 6 Correlation coefficients of detrended time series between inter-annual summer precipitation in NEC and vertically integrated moisture flux during 1951–2016: (a) MJP, (b) JAP. The light (dark) shading areas indicate significance at the .05 (.01) level [Colour figure can be viewed at wileyonlinelibrary.com]

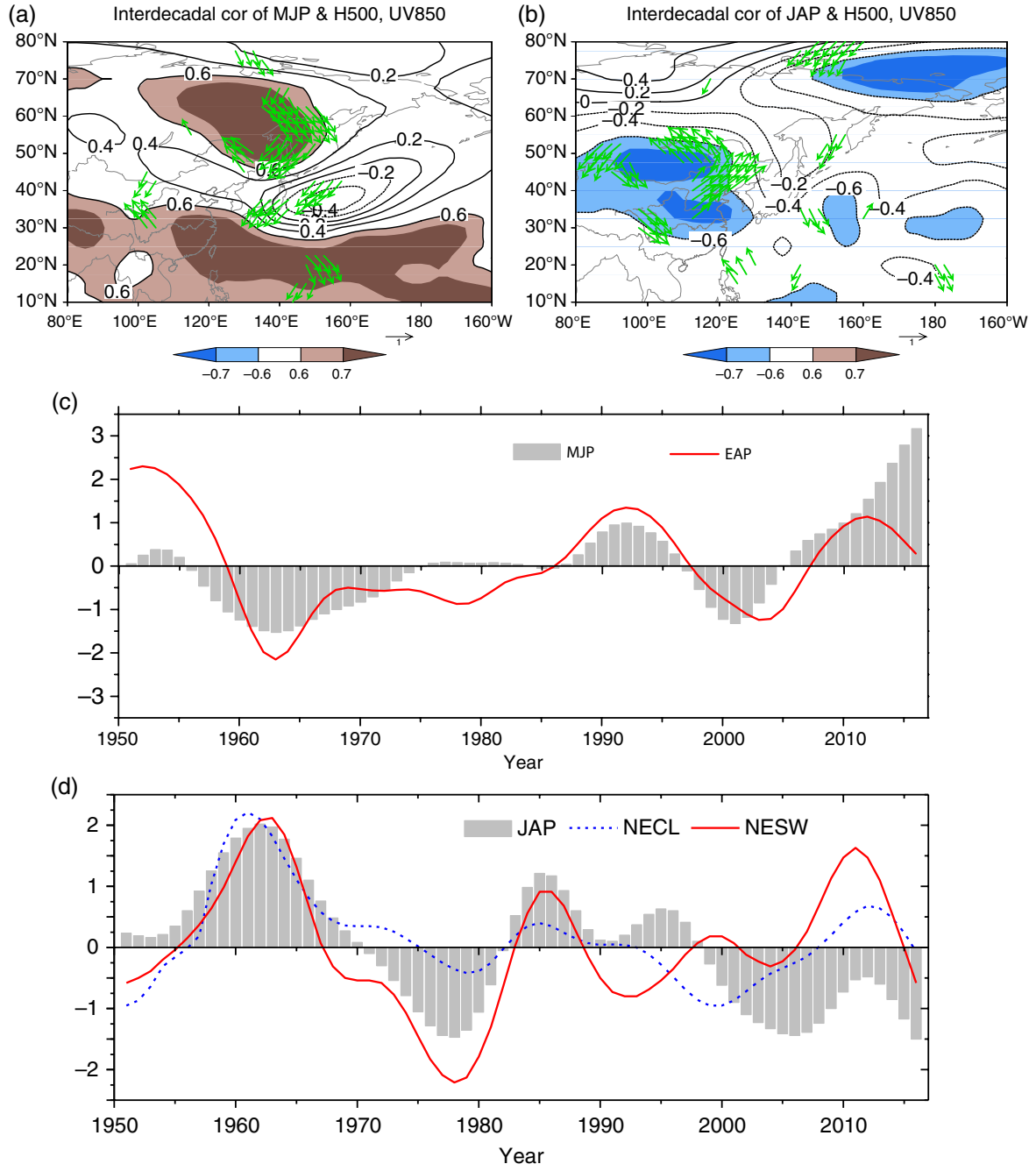

FIGURE 7 Correlation coefficients of detrended time series between inter-decadal summer precipitation in NEC and 500-hPa geopotential height (contour) and horizontal winds (vectors) at 850 hPa during 1951–2016: (a) MJP, (b) JAP. The light (dark) shading areas and vectors drawn indicate significance at the .05 (.01) level. (c) The inter-decadal time series of the MJP (histogram) and EAP index. (d) The inter-decadal time series of the JAP (histogram), NECL, and NESW [Colour figure can be viewed at wileyonlinelibrary.com]

extension of the WPSH. Accordingly, the anomalous geopotential height pattern is linked with a strong southwesterly wind anomaly over NEC in the low-level atmosphere (Figure 4b). That is, when the WPSH is stronger and farther northwards and the NESW is stronger, the abnormal water vapour is transported northwards to the NEC by anomalous southerly winds along the west side of the WPSH (Figure 6b). The inter-annual correlation coefficients between the WPSH, NESW, NECL, and JAP are .52, .46 and −.35, respectively (Figure 4c). Thus, the inter-annual JAP is mainly dominated by the WPSH and NESW. Also, the active NECL is in favour of the more JAP (Sun *et al.*, 2007; 2011).

5 | ASSOCIATED ATMOSPHERIC CIRCULATION ANOMALIES WITH INTER-DECADAL EARLY- AND LATE-SUMMER PRECIPITATION

In this section, the associated atmospheric circulation anomalies with inter-decadal early- and late-summer precipitation

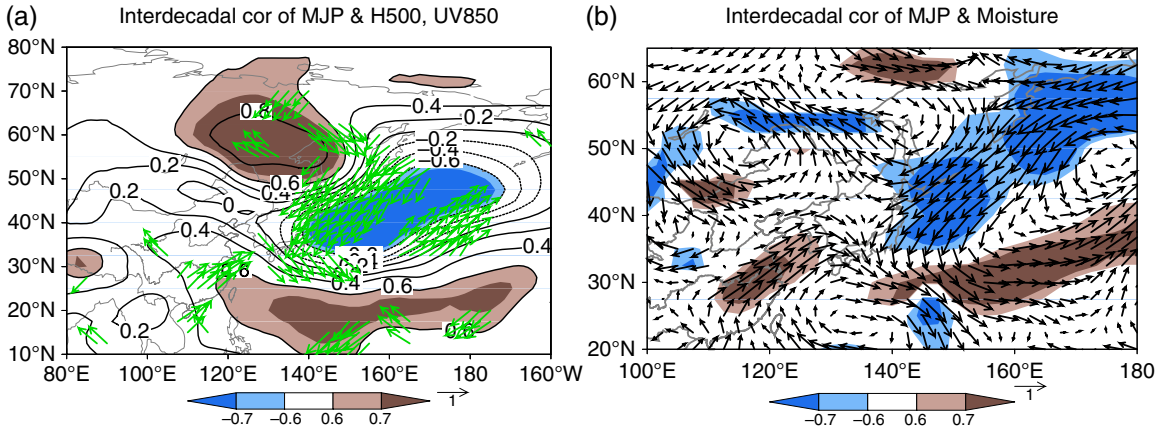

FIGURE 8 Correlation coefficients of detrended time series between inter-decadal EAP and (a) 500-hPa geopotential height (contour) and horizontal winds (vectors) at 850 hPa, and (b) vertically integrated moisture flux during 1951–2016. The light (dark) shading areas and vectors drawn indicate significance at the .05 (.01) level [Colour figure can be viewed at wileyonlinelibrary.com]

are investigated. Figure 7 shows the correlation coefficients between MJP (JAP) and 500-hPa geopotential height, 850-hPa meridional wind on the inter-decadal timescale, respectively.

In early summer, significantly positive correlations between inter-decadal MJP and 500-hPa geopotential height is mainly located over the Okhotsk Sea and the subtropical western Pacific (Figure 7a). A negative correlation is located in the northwest Pacific (35°–45°N, 140°–180°E). The positive and negative correlation centres happen to be the three activity centres of the EAP teleconnection. The positive EAP pattern is accompanied by positive anomaly geopotential height in the Okhotsk Sea and the subtropical western Pacific, and negative anomaly height in northwest Pacific. Huang (2004) indicated that the EAP has an important impact on spring and summer precipitation in Yangtze River basin and NEC. Figure 7c presents the temporal variations of the inter-decadal MJP and EAP. There is a perfect consistency between MJP and EAP during 1951–2016. The correlation coefficient between MJP and the EAP reaches up to .83.

To better understand the relationship between EAP and MJP on the inter-decadal timescale, the atmospheric circulation and vertically integrated moisture flux anomalies associated with the EAP are investigated. The 500-hPa geopotential height and 850-hPa horizontal winds anomalies associated with the EAP are very similar to that associated with the MJP (Figure 8a). The positive phase of the EAP features positive (negative) heights centred over the Okhotsk Sea (northwest Pacific). This large-scale circulation configuration enhances the east winds over the northwest Pacific (35°–50°N, 120°–160°E) and southwest winds over the Yangtze River basin. Meanwhile, a prominent water vapour anticyclone is centred over the west Pacific, a big and prominent water vapour cyclone is centred over the northwest Pacific. The southwest wind in the west flank of the anticyclone and the east wind in the north flank of the cyclone push moisture into NEC together (Figure 8b), which contributes to more MJP.

In late summer, there is a significant negative correlation between inter-decadal JAP and 500-hPa geopotential height from south of Lake Baikal to the middle and lower reaches of the Yangtze River (Figure 7b). This indicates the NECL has an important influence on the inter-decadal JAP. There are significant positive correlations between JAP and 850-hPa wind from the Korean Peninsula to NEC. This demonstrates the NESW in the lower troposphere has an important influence on the inter-decadal JAP. Figure 7d shows the inter-decadal variation of JAP, NECL, and NESW. The correlation coefficient between JAP and NECL (NESW) is −.73 (.83), which indicates that the inter-decadal variation of JAP is closely related to the inter-decadal variability of NECL and NESW. When they are both in a strong phase, the JAP is more than average.

6 | DISCUSSION AND CONCLUSION

Precipitation over NEC shows a remarkable and crucial sub-seasonal feature and significant inter-annual and inter-decadal variations in summer (May–August) during the past 66 years. Based on monthly precipitation data from 24 stations in NEC and NCEP/NCAR reanalysis data during 1951–2016, this study analysed the inter-annual and inter-decadal variability of MJP and JAP in NEC and their associated large-scale monsoon circulation features. The results indicate that there are significantly different inter-annual and inter-decadal variability characteristics and associated notably different atmospheric circulation systems between MJP and JAP. The MJP and JAP have obvious variations in inter-annual and inter-decade scale with clearly quasi 2–4a, 20–24a period. The inter-annual (inter-decadal) variability of MJP is independent from (opposite to) JAP. There are obvious shifts to reduced (increased) MJP in the mid-1950s and late 1990s (mid-1970s and mid-2000s) and to reduced

(increased) JAP in the mid-1960s and late 1990s (early 1980s) in NEC.

The atmospheric circulations that have effects on MJP are different from those influencing the JAP, no matter on the inter-annual timescale or on the inter-decadal one. On one hand, the variation of MJP is mainly affected by the NECL and the OBH, while JAP is mainly controlled by the WPSH, the NESW, and the NECL on the inter-annual timescale. On the other hand, MJP has relationship with the inter-decadal variation of the EAP, while JAP is closely related to the inter-decadal variation of the NECL and NESW on the inter-decadal timescale. When the EAP is in a positive phase, MJP is more than average. In late summer, the strong NECL and NESW are both of benefit to the convergence of water vapour from the tropical southwest and East Asian subtropical westerlies over NEC, which contributes to the more JAP than average.

These results presented in this article will be helpful in understanding the atmospheric circulation systems associated with the summer precipitation in NEC in different stages. In addition, many other factors also need to be analysed, such as the relationship between SST, snow cover, ice density, and summer precipitation in NEC on different timescales and the possible mechanisms involved. Analyses based on observational and reanalysis data and climate model-based studies with numerical simulations are necessary to further investigate these problems, and these will be a focus of our future studies.

ACKNOWLEDGEMENTS

We sincerely acknowledge the two reviewers, whose kind and valuable comments greatly improved the quality of this manuscript.

REFERENCES

Ding, T. and Chen, L.J. (2015) Circulation pattern for summer precipitation in northeast China and application of dynamical climate model information. *Plateau Meteorology*, 34, 1119–1130 (in Chinese).

Du, M.X., Lin, Z.D. and Lu, R.Y. (2016) Inter-decadal change in the summertime northeast Asia low-pressure system in the early 1990s. *Journal of the Atmospheric Sciences*, 40, 805–816 (in Chinese).

Feng, G.L., Sun, S.P., Zhao, J.H. and Zheng, Z.H. (2013) Analysis of stable components for extended-range (10–30 days) weather forecast: a case study of continuous overcast-rainy process in early 2009 over the mid-lower reaches of the Yangtze River. *Science China Earth Sciences*, 56, 1576–1587.

Gao, Z.T., Hu, Z.Z., Zhu, J.S., Yang, S., Zhang, R.H., Xiao, Z.N. and Bhaskar, J.H.A. (2014) Variability of summer rainfall in northeast China and its connection with spring rainfall variability in the Huang-Huai region and Indian Ocean SST. *Journal of Climate*, 27, 7086–7101.

Gong, Q., Wang, P.X., Wang, H.Y. and Li, L.P. (2005) Constitutes and formation cause of inter-decadal and inter-annual variations of summer rainfall anomalies in northeast China. *Journal of Nanjing Institute of Meteorology*, 28, 233–240 (in Chinese).

Guo, Y., Li, J.P. and Li, Y. (2014) Seasonal forecasting of north China summer rainfall using a statistical downscaling model. *Journal of Applied Meteorology and Climatology*, 53, 1739–1749. https://doi.org/10.1175/JAMC-D-13-0207.1.

Han, T.T., Chen, H.P. and Wang, H.J. (2015) Recent changes in summer precipitation in northeast China and the background circulation. *International Journal of Climatology*, 35, 4210–4219. https://doi.org/10.1002/joc.4280.

He, J.H., Wu, Z.W., Qi, L. and Jiang, A.J. (2006) Relationships among the Northern Hemisphere annual mode, the northeast cold vortex and the summer rainfall in northeast China. *Journal of Meteorology and Environment*, 22, 1–5 (in Chinese).

He, W.P., Wan, S.Q., Jiang, Y.D. and He, T. (2013) Detecting abrupt change on the basis of skewness: numerical tests and applications. *International Journal of Climatology*, 33, 2713–2727. https://doi.org/10.1002/joc.3624.

Hu, K.X., Lu, R.Y. and Wang, D.H. (2010) Seasonal climatology of cut-off lows and associated precipitation patterns over northeast China. *Meteorology and Atmospheric Physics*, 106, 37–48.

Huang, G. (2004) An index measuring the interannual variation of the East Asian summer monsoon-the EAP index. *Advances in Atmospheric Sciences*, 21, 41–52.

Kalnay, E., Kanamitsu, M., Kistler, R., Collins, W., Deaven, D., Gandin, L., Jenne, R. and Joseph, D. (1996) The NCEP/NCAR 40-year reanalysis project. *Bulletin of the American Meteorological Society*, 77, 437–471.

Li, J.P. and Zeng, Q.C. (2002) A unified monsoon index. *Geophysical Research Letters*, 29, 1274. https://doi.org/10.1029/2001GL013874.

Li, J.P. and Zeng, Q.C. (2003) A new monsoon index and the geographical distribution of the global monsoons. *Advances in Atmospheric Sciences*, 20, 299–302.

Lian, Y., Shen, B.Z., Gao, Z.T., An, G. and Tang, X.L. (2003) The study of the on-set criterion and the date of East Asian summer monsoon in northeast China and its main characteristic analysis. *Acta Meteorologica Sinica*, 61, 548–558 (in Chinese).

Liu, Z.X., Lian, Y., Gao, Z.T., Sun, L. and Shen, B.Z. (2002) Analyses of the Northern Hemisphere circulation characters during northeast cold vortex persistence. *Chinese Journal of Atmospheric Sciences*, 26, 361–372 (in Chinese).

Shen, B.Z. and Lian, Y. (2004) The preliminary analysis on the relationship between snow cover over the Tibetan Plateau and summer cold vortex precipitation in northeast China. *Journal of Jilin University (Earth Science)*, 34, 112–118.

Shen, B.Z., Lin, Z.D., Lu, R.Y. and Lian, Y. (2011) Circulation anomalies associated with interannual variation of early- and late-summer precipitation in northeast China. *Science China Earth Sciences*, 54, 1095–1104. https://doi.org/10.1007/s11430-011-4173-6.

Shi, N. and Chen, L.W. (2004) Evolution and features of global land June–August dry/wet periods during 1920–2000. *International Journal of Climatology*, 24, 1483–1493.

Shi, N. and Zhu, Q.G. (1996) An abrupt change in the intensity of the East Asian summer monsoon index and its relationship with temperature and precipitation over east China. *International Journal of Climatology*, 16, 757–764.

Sun, B., Zhu, Y.L. and Wang, H.J. (2011) The recent interdecadal and interannual variation of water vapor transport over eastern China. *Advances in Atmospheric Sciences*, 28, 1039–1048.

Sun, L., An, G., Ding, L. and Shen, B.Z. (2000) A climatic analysis of summer precipitation features and anomaly in northeast China. *Acta Meteorologica Sinica*, 58, 70–82 (in Chinese).

Sun, L., An, G. and Tang, X.L. (2003) Relationship between the Northeast Asian summer south wind anomaly and the precipitation in northeast China. *Chinese Journal of Atmospheric Sciences*, 27, 425–434 (in Chinese).

Sun, L., Shen, B.Z., Gao, Z.T., Sui, B., Bai, L.S., Wang, S.H., An, G. and Li, J. (2007) The impacts of moisture transport of East Asian monsoon on summer precipitation in northeast China. *Advances in Atmospheric Sciences*, 24, 606–618.

Wang, H.J. (2002) Instability of the East Asian summer monsoon-ENSO relations. *Advances in Atmospheric Sciences*, 19, 1–11.

Wu, B.Y., Zhang, R.H. and Rosanne, D. (2008) Arctic dipole anomaly and summer rainfall in northeast China. *Chinese Science Bulletin*, 53, 2222–2229.

Yao, X.P. and Dong, M. (2000) Research on the features of summer rainfall in northeast China. *Quarterly Journal of Applied Meteorogy*, 11, 297–303 (in Chinese).

Zhao, J.H., Yang, L., Gu, B.H., Yang, J. and Feng, G.L. (2016) On the relationship between the winter Eurasian teleconnection pattern and the following summer precipitation over China. *Advances in Atmospheric Sciences*, 33, 743–752. https://doi.org/10.1007/s00376-015-5195-3.

Zhao, J.H., Yang, L., Hou, W., Liu, G. and Zeng, Y.X. (2015) Extra-seasonal prediction at summer 500-hPa height field in the area of cold vortices over East Asia with a dynamical–statistical method. *Chinese Physics B*, 24, 059202. https://doi.org/10.1088/1674-1056/24/5/059202.

Zhu, Y.L. (2011) A seasonal prediction model for the summer rainfall in north-east China using the year-to-year increment approach. *Atmospheric Oceanic Science Letters*, 4, 146–150.

How to cite this article: Zhao J, Zhou J, Yang L, Hou W, Feng G. Inter-annual and inter-decadal variability of early- and late-summer precipitation over northeast China and their background circulation. *Int J Climatol*. 2018;38:2880–2888. https://doi.org/10.1002/joc.5470

赵俊虎，陈丽娟，王东阡. 2018. 2016 年我国梅雨异常特征及成因分析 [J]. 大气科学, 42 (5): 1055−1066. Zhao Junhu, Chen Lijuan, Wang Dongqian. 2018. Characteristics and causes analysis of abnormal Meiyu in China in 2016 [J]. Chinese Journal of Atmospheric Sciences (in Chinese), 42 (5): 1055−1066, doi:10.3878/j.issn.1006-9895.1708.17170.

2016 年我国梅雨异常特征及成因分析

赵俊虎[1] 陈丽娟[1, 2] 王东阡[1]

1 中国气象局国家气候中心/中国气象局气候研究开放实验室，北京 100081

2 南京信息工程大学气象灾害预报预警与评估协同创新中心，南京 210044

摘 要 利用国家气候中心梅雨监测资料和 NCEP 再分析资料，对 2016 年我国梅雨异常特征及其大尺度环流成因进行了分析。结果表明：（1）2016 年我国梅雨有明显的区域特征，其中江南区入梅偏早 14 天，与 1995 年并列成为 1951 年以来入梅最早的年份，出梅偏晚 11 天，梅雨期（量）偏长（多），但梅雨期日平均降水量偏少；长江区入梅和出梅均偏晚，梅雨期接近常年，但梅雨量偏多一倍以上，梅雨量和梅雨期日平均降水量分别为 1951 年以来历史同期第三和第二高值；江淮区入梅、出梅及梅雨期接近常年，但梅雨量偏多。（2）对流层高、中、低层环流系统冬夏季节性调整和转变显著提前的共同作用，导致了 2016 年江南区入梅显著偏早；东亚副热带西风急流、西太平洋副热带高压（副高）和东亚夏季风涌在 7 月中旬阶段性地南落导致了江南区和长江区出梅偏晚。（3）受到前冬超强厄尔尼诺衰减和春、夏季热带印度洋全区一致海温模态偏暖的影响，梅雨期副高异常偏强，副高西南侧转向的水汽输送异常偏强，并在长江区和江淮区与北方弱冷空气辐合，造成梅雨量异常偏多。

关键词 入（出）梅 梅雨量 厄尔尼诺 热带印度洋全区一致海温模态 异常成因

文章编号 1006-9895(2018)05-1055-12 **中图分类号** P462 **文献标识码** A

doi:10.3878/j.issn.1006-9895.1708.17170

Characteristics and Causes Analysis of Abnormal Meiyu in China in 2016

ZHAO Junhu[1], CHEN Lijuan[1, 2], and WANG Dongqian[1]

1 *National Climate Center / Laboratory for Climate Studies*, *China Meteorological Administration*, *Beijing* 100081

2 *Collaborative Innovation Center on Forecast and Evaluation of Meteorological Disasters*, *Nanjing University of Information Science & Technology*, *Nanjing* 210044

Abstract Based on the National Climate Center Meiyu monitoring data and NCEP reanalysis dataset, the characteristics of abnormal Meiyu and associated large scale circulation during the Meiyu period of 2016 in China are analyzed. The results are as follows: (1) There were obvious regional characteristics of Meiyu in 2016 in China. The Meiyu onset date over regions to the south of the Yangtze River was 14 days earlier than normal and was the earliest as that in 1995 since 1951. The Meiyu outset date in 2016 was 11 days later than normal with a longer duration and more Meiyu precipitation, whereas daily average precipitation was weaker. The Meiyu onset (outset) date over the Yangtze River valley was later than normal, while the Meiyu duration was close to normal with more than double of normal Meiyu precipitation. The amount of total Meiyu precipitation and average daily precipitation are ranked as the third and the second highest values since 1951, respectively. The Meiyu onset, outset, and duration over the Yangtze–Huaihe valley were close to normal, but

收稿日期 2017-05-21；**网络预出版日期** 2017-08-30

作者简介 赵俊虎，男，1985 年出生，高级工程师，主要从事短期气候预测研究。E-mail: zhaojh@cma.gov.cn

通讯作者 陈丽娟，E-mail: chenlj @cma.gov.cn

资助项目 国家重点基础研究发展计划（973 计划）项目 2015CB453203，国家自然科学基金项目 41875093、41505061、41705074、41275073

Funded by National Basic Research Program of China (Grant 2015CB453203), National Natural Science Foundation of China (NSFC) (Grants 41875093, 41505061, 41705074, 41275073)

the amount of total Meiyu precipitation was more than normal. (2) The significantly early Meiyu onset over regions to the south of the Yangtze River was induced by abnormally early transition of East Asian circulation from winter pattern to summer pattern. The southward shift of East Asian subtropical upper-level westerly jet and the western Pacific subtropical high (WPSH) were combined with the southward displacement of the East Asian summer monsoon surge in middle July, leading to late than normal Meiyu outset. (3) The decay of the extremely strong El Niño event in the previous winter and the persistent warming of the Indian Ocean Basin-Wide mode (IOBW) in spring and summer were the main reasons that caused the WPSH to be extremely strong during the Meiyu period in 2016. The abnormally strong moisture flux from the southwest of the WPSH and weak cold air from the north converged over the Yangtze-Huaihe valley, resulting in higher than normal Meiyu precipitation over this region.

Keywords Meiyu onset (outset), Meiyu precipitation, El Niño, Indian Ocean Basin-Wide mode (IOBW), Abnormal causes

1 引言

梅雨指的是每年 6～7 月在中国长江中下游地区出现的以持续多雨为主要特征的气候现象（Tao and Chen，1987）。梅雨期是东亚夏季风季节性北推过程中的重要阶段，这一时期中国东部雨带主要徘徊在江南至淮河之间，并往往伴随着持续性大暴雨、洪涝灾害的发生，给国家和人民的生命财产等带来巨大损失。因此，揭示梅雨的变化规律及其异常成因，具有重要的科学意义，对防灾、减灾也具有十分重要的指导意义。

国内外学者很早就开展了梅雨的研究工作，并发现了很多有价值的结论和规律（陶诗言等，1958，1988；施能等，1996；丁一汇等，2007；王遵娅和丁一汇，2008；Gu et al., 2009；梁萍等，2010；Sampe and Xie, 2010；赵俊虎等，2011）。例如陶诗言等（1958）指出梅雨的开始和结束与亚洲上空南支西风急流的北跳过程密切相关。丁一汇等（2007）认为，当 6 月中旬东亚夏季风从华南推进到长江流域，同时印度夏季风在印度次大陆爆发时，中国梅雨雨季开始。胡娅敏等（2008）讨论了江淮梅雨丰（弱）梅年的大气环流异常特征。胡娅敏和丁一汇（2009）研究指出西太平洋副热带高压（副高）脊位置的北移、东亚夏季风的加强以及冷空气的减弱，可能是导致 2000～2005 年江淮梅雨带北移的原因。魏凤英和宋巧云（2005）探讨了近百年全球海表温度年代际尺度的空间分布结构与长江中下游梅雨异常变化的联系，发现当北太平洋年代际振荡（Pacific Decadal Oscillation, PDO）暖事件趋势处于较强时期时，长江中下游梅雨为偏多的趋势，反之亦然。梁萍等（2007）进一步总结了中国梅雨的影响因子。此外，梅雨异常年的成因也引起了学者们的关注。李维京（1999）、周兵和文继芬（2007）研究了 1998 年夏季大尺度环流系统对长江流域“二度梅”的影响。汪靖等（2006）分析了 2005 年江淮流域入梅偏晚的环流成因。牛若芸和金荣花（2009）对 2008 年梅雨异常的大尺度环流成因进行了分析，指出对流层高、中、低层多个尺度环流系统都可对江淮梅雨产生直接或者间接影响。封国林等（2012）研究了 2011 年梅雨期长江中下游地区旱涝急转的成因。总之，每年影响梅雨的主导因素不尽相同，导致各年入（出）梅早晚、梅雨期长短、梅雨量的多寡、梅雨型分布等出现不同的组合，给梅雨预报带来很大的难度。

2016 年是一次超强 El Niño 事件的衰减年，本次 El Niño 事件于 2015 年 11 月达到峰值，2016 年 4 月结束，是 1951 年以来峰值强度最强、持续时间最长的一次 El Niño 事件（陈丽娟等，2016；邵勰和周兵，2016；翟盘茂等，2016）。2016 年夏季全国气温较常年同期偏高 0.9°C，是 1961 年以来的最高值；全国平均降水量较常年偏多 5.6%，其中长江流域降水异常偏多，梅雨期间梅雨量较常年偏多一倍以上，南方共发生 11 次区域性暴雨过程，暴雨过程平均综合强度为 1980 年以来最强（曹艳察和张涛，2016；权婉晴和何立富，2016；袁媛等，2017），带来了较大的损失。本文旨在从大尺度环流系统演变及其异常特征入手，分析 2016 年我国梅雨的异常特征及其原因，以提高对梅雨的科学认识和预报水平。

2 资料和方法

本文所用资料主要包括：美国国家环境预报中心和国家大气研究中心（NCEP/NCAR）发布的全球逐日的高度场（H）、风场（u、v 分量）、比湿（q）再分析资料（Kalnay et al., 1996），水平空间分辨率为 2.5°×2.5°，垂直方向从 1000～10 hPa 共 17 层等

压面；亚洲经向环流指数、副高强度指数和脊线指数、Niño3.4 指数及热带印度洋海温全区一致模态（Indian Ocean Basin-Wide，IOBW）指数来自国家气候中心的新百项指数；水汽通量的计算方法参照丁一汇（2005）。为方便表述，这里将梅雨指标达到一倍以上标准差的称为异常。如无特别说明，变量的气候值均为 1981～2010 年的 30 年平均值。

中国气象局预报与网络司于 2014 年发布了梅雨新的监测指标，即《梅雨监测业务规定》[①]。中国梅雨（以下简称梅雨）主要分布在江南至江淮流域，即西自湖北宜昌，东至华东沿海，南端以南岭以北的 28°N 为界，北抵淮河沿线 34°N 一带，其经、纬度范围：（28°～34°N，110°～123°E），涉及的行政区域包含上海、江苏、安徽、浙江、江西、湖北、湖南等 6 省 1 市。按照气候类型可将梅雨监测区域分为江南区（I）、长江区（II）、江淮区（III）（图 1）。确定区域入（出）梅与梅雨期的主要依据是区域内各监测站的降水条件，副高脊线、日平均温度、南海夏季风爆发时间等为辅助条件，关于各区域入梅、出梅和梅雨期、梅雨量的其他业务规范请参考《梅雨监测业务规定》，这里不再赘述。

3 2016 年梅雨异常特征

3.1 入（出）梅特征

表 1 给出了 2016 年梅雨的监测概况。其中江南区 5 月 25 日入梅，较常年平均偏早 14 天，与 1995 年并列成为 1951 年以来入梅最早年份；7 月 19 日出梅，较常年偏晚 11 天，为 2000 年以来第 2 异常偏晚年，仅次于 2015 年（偏晚 18 天）；梅雨期 55 天，与 1998 年并列 1951 年以来梅雨期长度的第 3 位，仅次于 2015 年和 1954 年。长江区 6 月 19 日入梅，较常年同期偏晚 5 天；7 月 21 日出梅，较常年偏晚 8 天；梅雨期 32 天，较常年同期偏多 3 天。江淮区 6 月 20 日入梅，较常年偏早 1 天；7 月 16 日出梅，较常年偏晚 1 天；梅雨期 27 天，较常年同期偏多 2 天。综上可见，江南区入（出）梅显著偏早（晚），梅雨期显著偏长，长江区入（出）梅均偏晚，江淮区接近常年。

3.2 梅雨期降水时空特征

（1）梅雨量和梅雨期日平均降水量。由表 1 可见，2016 年江南区梅雨量为 526.0 mm，较常年平均偏多 44.0%，位列 1951 年以来第 9；梅雨期日平均降水量为 9.6 mm d^{-1}，较常年偏少 2.6 mm d^{-1}，属于强度偏弱年。长江区梅雨量为 584.3 mm，较常年平均偏多 107.9%，位于 1951 年以来的第 3 位，仅次于 1954 年和 1996 年；梅雨期日平均降水量为 18.3 mm d^{-1}，较常年平均偏多 8.6 mm d^{-1}，强度较强，位于 1951 年以来的第 2 位，仅次于 1969 年。江淮区梅雨量为 420.6 mm，较常年偏多 59.1%，梅雨期日平均降水量为 14.9 mm d^{-1}，较常年平均偏多 4.3 mm d^{-1}，强度较强，位于 1951 年以来的第 8 位。

（2）时间演变特征。图 2 是 2016 年 5 月 21 日至 7 月 26 日三个梅雨区平均的逐日降水量演变图。由图可见，三个区域有 3 段相对持续的降水期，分别为 P1：5 月 25 日至 6 月 3 日；P2：6 月 11 日至 7 月 7 日；和 P3：7 月 10～20 日。其中 P2 期降水持续时间长，且降水量较大。长江区 7 月 1～6 日的降水量分别为 60.4、64.3、52.5、45.1、21.8 和 26.3 mm，6 天的总降水量为 270.4 mm，接近长江区整个梅雨期多年平均的降水量（280.4 mm）；江淮区 7 月 1～7 日的降水量分别为 89.9、16.6、19.3、49.5、27.2、8.1 和 19.3 mm，7 天的总降水量为 229.9 mm，接近江淮区整个梅雨期多年平均的降水量（264.4 mm）。而这一时期江南区梅雨量较少。为进一步分析 2016 年三个区域梅雨期内降水量时间演变之间的关系，计算了整个梅雨期（5 月 25 日

表 1 2016 年梅雨监测概况

Table 1 The characteristics of Meiyu in China in 2016

区 域		入梅时间	出梅时间	梅雨期/d	梅雨量/mm	梅雨期日平均降水量/mm d^{-1}
I 型（江南区）	气候平均	6 月 8 日	7 月 8 日	30	365.4	12.2
	2016 年	5 月 25 日(−14 d)	7 月 19 日(+11 d)	55(+25)	526.0(+44.0%)	9.6(−2.6)
II 型（长江区）	气候平均	6 月 14 日	7 月 13 日	29	281.0	9.7
	2016 年	6 月 19 日(+5 d)	7 月 21 日(+8 d)	32(+3)	584.3(+107.9%)	18.3(+8.6)
III 型（江淮区）	气候平均	6 月 21 日	7 月 15 日	25	264.4	10.6
	2016 年	6 月 20 日(−1 d)	7 月 16 日(+1 d)	27(+2)	420.6(+59.1%)	14.9(+4.3)

注：括号中数值为距平或距平百分率，入梅和出梅正（负）值表示偏晚（早）

① 中国气象局预报与网络司. 2014. 关于印发《梅雨监测业务规定》的通知, 气预函（2014）28 号 [R].

至 7 月 20 日）内三个区域的逐日降水量序列相互间的相关系数。其中江南区和长江区、江淮区的相关系数分别为 0.12 和−0.14，呈弱的正、负相关；而长江区和江淮区的相关系数为 0.54，呈显著的正相关。这主要是因为江南区入梅较其他两个区偏早了 20 天以上，梅雨期降水过程相对独立。

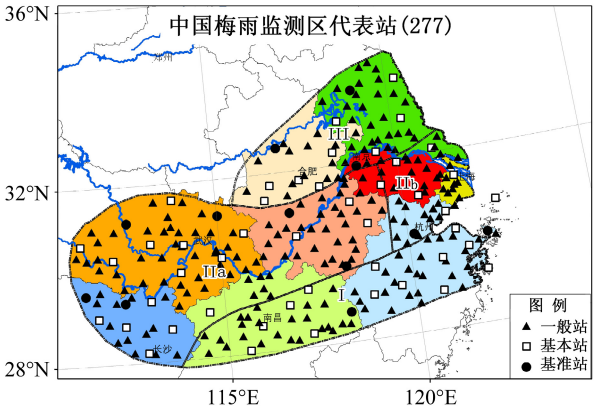

图 1 梅雨监测区域划分及监测站点空间分布示意图（引自《梅雨监测业务规定》）。Ⅰ表示江南区，Ⅱ表示长江区，Ⅲ表示江淮区

Fig. 1 Schematic diagram of the division of the monitoring area and spatial distribution of monitoring stations. Ⅰ indicates regions to the south of the Yangtze River, Ⅱ indicates regions of the Yangtze River valley, Ⅲ indicates the region of Yangtze–Huaihe River basin

（3）空间分布特征。2016 年 6 月 19 日至 7 月 20 日，三个区域基本均处于梅雨期，是梅雨集中期。由图 2 可见，该时期降水中心主要位于长江区，其中湖北东部和南部、湖南北部、江西北部、安徽中部和南部、江苏中部和南部等地降水量在 400 mm 以上（图 3a），较常年同期偏多 5 成以上（图 3b），沿江地区偏多 1 倍以上；湖北东部至安徽南部达到了 600 mm 以上，其中湖北东南部较常年同期偏多 1.5 倍以上；其次是江南北部和淮河下游，降水量有 200～400 mm，偏多 2～5 成；淮河上游降水量有 100～200 mm，偏多 0～2 成。结合表 1 可见：2016 年长江区梅雨量和梅雨期日平均降水量最多，而江南区和江淮区相对偏少。

综上可见，2016 年三个区域梅雨特征有明显差异，其中江南区入梅时间异常早，出梅时间异常晚，梅雨期异常偏长，梅雨量显著偏多，但梅雨期日平均降水量偏小。长江区入梅和出梅均偏晚，梅雨期接近常年，但梅雨量异常偏多，梅雨期日平均降水

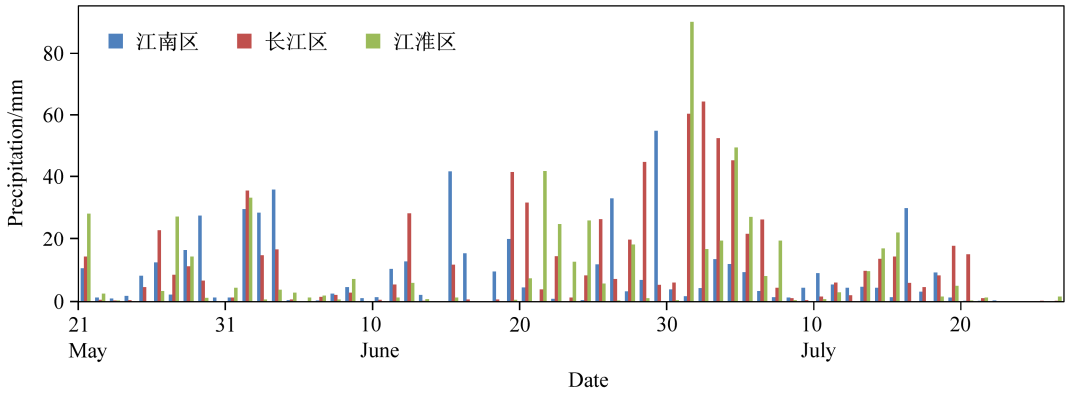

图 2 2016 年 5 月 21 日至 7 月 26 日梅雨区平均降水量逐日演变。横坐标为日期，纵坐标为降水量（单位：mm）

Fig. 2 Regional average percipitation from 21 May to 26 July 2016. The horizontal axis indicates time , and the vertical ordinate shows percipitation (units: mm)

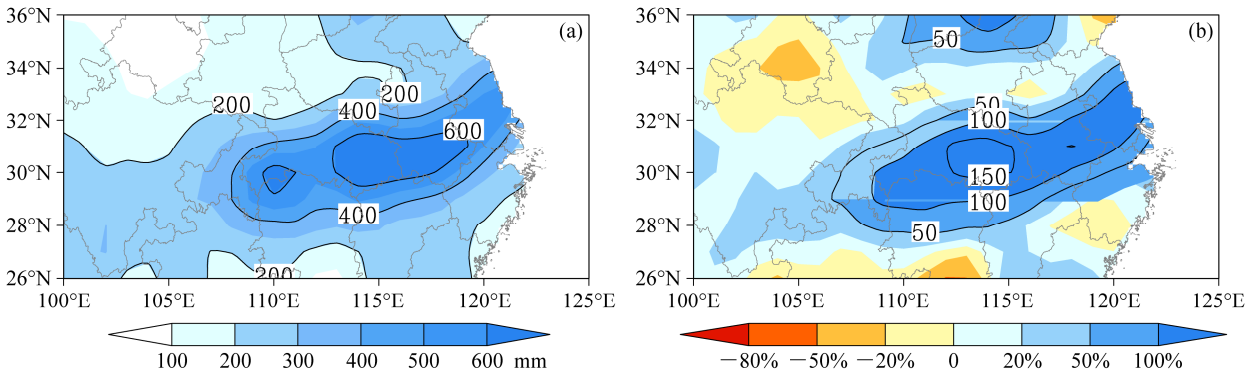

图 3 2016 年 6 月 19 日～7 月 20 日梅雨期（a）总降水量（单位：mm）和（b）总降水量距平百分率

Fig. 3 (a) Accumulated rainfall amount (units: mm) and (b) percentage anomalies during the Meiyu period (from 19 June to 20 July) of 2016

量异常偏多；江淮区入梅、出梅及梅雨期接近常年，但梅雨量偏多，梅雨期日平均降水量偏多。

4 2016 年梅雨异常大尺度环流成因

4.1 江南入梅偏早成因

梅雨是东亚夏季风系统和欧亚中高纬度环流系统相互作用的结果，入梅则体现了东亚大气环流系统完成了从冬季风环流系统向夏季风环流系统的调整。2016 年江南入梅显著偏早，也是这种冬、夏季环流系统季节性调整和转变提前的结果，是对流层高、中、低层环流相互配置、共同作用造成的。

东亚大气环流的季节转换、中国大部分地区雨季的开始和结束都与东亚副热带西风急流位置的南北移动及强度变化有着密切的关系（况雪源和张耀存，2006；杨莲梅和张庆云，2007）。陶诗言等（1958）指出，东亚梅雨的开始和结束与亚洲上空南支西风急流的两次北跳过程密切相关。急流轴位置的变化和副高的变化具有很好的一致性，高层西风急流的北抬有利于中层副高的北跳。

由于 2016 年与 1995 年并列成为 1951 年以来江南区入梅最早年份，因此选取 10 个偏早年（1953、1961、1971、1972、 1973、1990、1995、2000、2006 和 2015 年）进行合成，分析 2016 年与历史偏早年环流的异同。10 个偏早年中，1995 年入梅最早为 5 月 25 日，1953、1961 和 1996 年入梅最迟为 5 月 30 日；10 年平均入梅为 5 月 28 日。图 4 给出了江南区 10 个入梅偏早年和 2016 年的东亚（110°～140°E 平均）上空 200 hPa 西风急流随时间变化的剖面图。从图 4a 可以清楚地看到，江南区入梅偏早年，5 月下旬东亚上空的西风急流加强，急流轴位置北跳至 35°N 以北，此时江南区梅雨开始。此后西风急流稳定维持，直至 6 月中下旬发生第二次北跳。和偏早年合成类似，2016 年 5 月 25 日左右，东亚上空的西风急流风速较常年明显增强，中心风速在 45 m s^{-1} 以上，强度较偏早年合成的更强，急流轴位置第一次北跳较早，急流轴在 38°N 以北（图 4b），较常年同期偏北 5 个纬度，较偏早年更加偏北。这表明 2016 年对流层高层的中高纬度大气环流系统调整和北跳异常偏早，为中层副高的北跳、低层亚洲夏季风向北推进和江南区入梅提供了有利的条件。

研究表明，副高阶段性地北跳与我国东部地区的雨季及多雨带位置直接相关。气候态下，从初夏到盛夏副高有两次明显的季节性北跳，第一次北跳东亚夏季风推进到长江流域，长江中下游地区入梅，第二次北跳东亚夏季风推进到华北，梅雨结束，华北雨季开始（张庆云和陶诗言，1999；陶诗言和卫捷，2006；赵俊虎等，2012；Ye et al., 2014；封国林等，2015）。《梅雨监测业务规定》中也指出了梅雨期副高脊线活动范围，江南区南界≥18°N，北界＜25°N。即脊线≥18°N 时有利于江南区入梅，而脊线在 18°～25°N 这个范围内，有利于江南区梅雨的维持。图 5 给出了江南区 10 个入梅偏早年和 2016 年 500 hPa 高度场沿副高西段（110°～140°E）平均的时间—纬度剖面图。由图 5a 可见，多平均的副高脊线在 6 月 8 日（7 月 8 日）越过 18°N（25°N），江南区平均的入（出）梅时间也正好是 6 月 8 日（7 月 8 日）。入梅偏早年，5 月下旬起副高区域为显著的正高度距平，一直持续到 6 月下旬，副高脊线明显偏北，并维持在 18°N 以北（图 5a），导致江南区入梅偏早。与江南区入梅偏早年合成相比，2016 年副高强度更强，5 月 25 日副高脊线迅速北跳，基本维持在 18°N 以北，维持一周多时间，此时环流条件有利于江南区入梅，直至 6 月 7 日后副高才发生一次明显的南落，6 月 19 日副高北跳至 22°N（图 5b），此时长江区和江淮区陆续入梅，副高的这一次较长时间的南落导致了长江区入梅偏晚。

东亚夏季风的北推，是梅雨区降水水汽来源的动力，入梅的早晚与东亚夏季风的季节进程密切相关。图 6 给出了江南区 10 个入梅偏早年和 2016 年沿 110°～122.5°E 平均的 850 hPa 经向风时间—纬度剖面图。从入梅偏早年的合成可见，5 月下旬起，中国东部的经向风已经加强，大于 4 m s^{-1} 的经向风已经北进至江南区，且逐步向北推进，江南区及其以北为显著的正距平（图 6a），表明东亚夏季风向北推进偏早，强度较常年偏强，导致江南区入梅偏早。与江南区入梅偏早年合成相比，2016 年东亚夏季风于 5 月 25 日迅速加强，并北推至 26°N 以北（图 6b），给江南区带来了充沛的水汽，梅雨开始。6 月 4～10 日，夏季风阶段性减弱，与此同时，梅雨区降水显著减弱（图 3）。6 月 11 之后夏季风再一次增强，6 月 19 日北推至 30°N 以北，长江区和江淮区入梅。

4.2 出梅偏晚成因

2016 年江南区、长江区和江淮区分别在 7 月 19、21 和 16 日出梅，分别偏晚 11 天、8 天和 1 天。

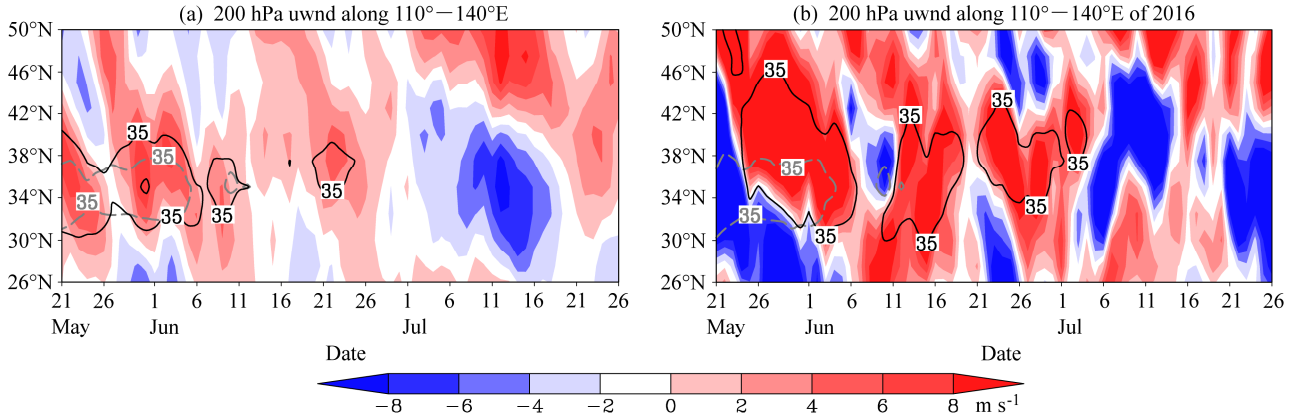

图 4 （a）江南区入梅偏早年和（b）2016 年东亚 110°～140°E 平均的 200 hPa 纬向风时间–纬度剖面图（单位：m s^{-1}）。灰色虚线表示气候平均的 35 m s^{-1} 等值线，黑线表示异常年平均的 35 m s^{-1} 等值线

Fig. 4 Time–latitude cross sections of zonal wind (units: m s^{-1}) at 200 hPa averaged over 110°–140°E in (a) early Meiyu onset years over regions to the South of the Yangtze River and (b) 2016. The gray dotted line represents the climatological mean of 35 m s^{-1} contour, and the black line represents the average of 35 m s^{-1} contour in anomalous years

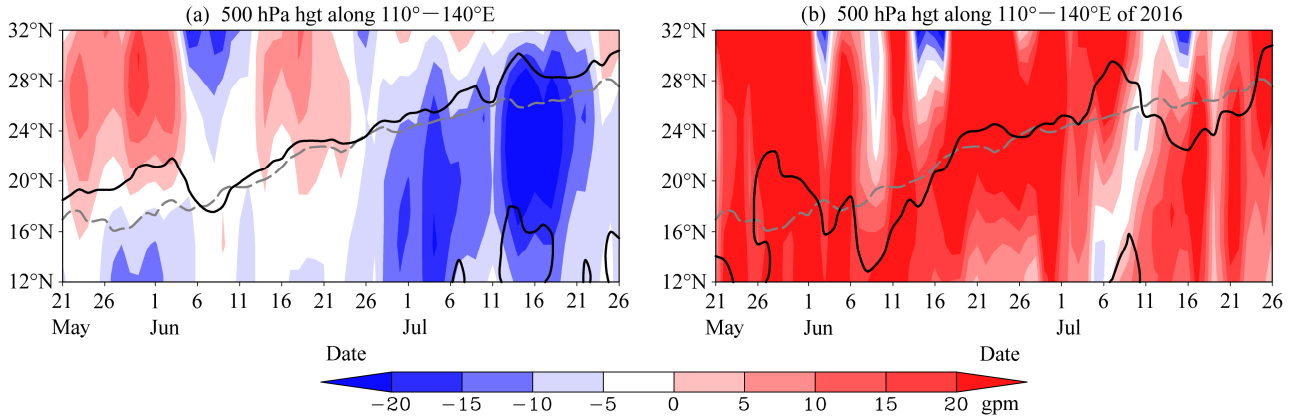

图 5 （a）江南区入梅偏早年和（b）2016 年沿 110°～140°E 平均的 500 hPa 位势高度场时间—纬度剖面图（单位：gpm）。灰色虚线表示气候平均的副高脊线，黑线表示异常年平均的副高脊线

Fig. 5 Time–latitude cross sections of geopotential height at 500 hPa (units: gpm) averaged over 110°–140°E in (a) early Meiyu onset years in regions to the South of the Yangtze River and (b) 2016. The gray dotted line represents the climatological mean subtropical high ridge line, and the black line represents the mean subtropical high ridge line in anomalous years

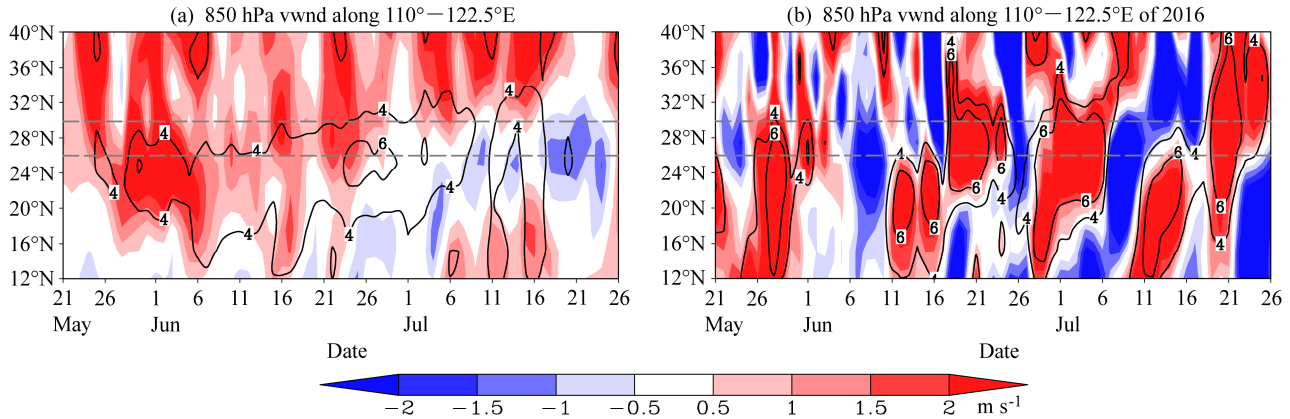

图 6 （a）江南区入梅偏早年和（b）2016 年沿 110°～122.5°E 平均的 850 hPa 经向风时间—纬度剖面图（单位：m s^{-1}）。等值线表示经向风，阴影区表示经向风距平

Fig. 6 Time–latitude cross sections of meridional wind at 850 hPa (units: m s^{-1}) averaged over 110°–122.5°E in (a) early Meiyu onset years in regions to the South of the Yangtze River and (b) 2016. Shaded areas represent meridional wind anomalies, and contours represent the meridional winds

因此，选取江南区和长江区出梅均偏晚 8 天以上的年份（1954、1970、1974、1979、1980、1996、1998、2006、2007 和 2015 年）进行合成，分析 2016 年与历史上出梅偏晚年环流的异同。10 个偏晚年中，1998 年江南区出梅最晚为 8 月 2 日，2006 年和 2007 年出梅最早为 7 月 18 日，江南区和长江区 10 年平均出梅分别为 7 月 23 日和 7 月 26 日。

从出梅偏晚年高层东亚上空西风急流的时间—纬度剖面图（图 7a）可见，7 月 1～23 日期间，26°～40°N 为正距平，中心位于 30°～34°N，40°～50°N 为负距平，表明西风急流轴偏南，强度偏强，有利于江南区和长江区出梅偏晚；7 月 24 日之后，正距平向北发展，急流轴北抬；中层副高和底层夏季风也有类似的北进过程，7 月 1～23 日期间，副高脊线偏南（图 7b），东亚夏季风维持在长江流域及其以南（图 7c），7 月 24 日之后，副高和东亚夏季风逐步北上，江南区和长江区相继出梅。

2016 年 5 月 25 日至 7 月 4 日期间，西风急流主体位置稳定维持在 34°～40°N，有利于梅雨的维持；7 月 8～20 日，急流位置有一次明显的减弱南退过程，急流轴位于 34°N 以南（图 4b），副高在此期间也有一次南落过程，脊线维持在 22°～24°N 之间（图 5b），夏季风北涌也维持在 32°N 以南（图 6b），水汽输送难以北上，有利于江南区和长江区出梅偏晚，7 月 21 日西风急流主体位置迅速北跳至 40°N 以北，副高也发生明显的北跳，夏季风北涌也维持在 32°N 以北，梅雨结束。

此外，2016 年华南前汛期于 3 月 21 日开始，较常年平均的 4 月 2 日明显偏早；江南入梅偏早，三个区域出梅偏晚；华北雨季于 7 月 19 日开始，较常年平均的 7 月 18 日略偏晚。由此可见，2016 年中国东部春、夏季气候季节进程具有前期偏早、后期偏晚的特点。受到海洋外强迫和大气环流季节内振荡的共同作用，东亚大气环流从冬季向夏季转换较常年偏早，体现在对流层高层西风急流北跳偏早、中层副高第一次北跳偏早、低层夏季风加强和北推偏早等多个方面；而 7 月中旬副高和夏季风的阶段性南落，导致了夏季气候季节进程后期偏晚。

4.3 梅雨量异常偏多成因

2016 年梅雨集中期间（6 月 19 日至 7 月 20 日），欧亚中高纬度 500 hPa 环流呈“两槽两脊”型（图 8a），乌拉尔山地区为一个低压槽，阻塞活动明显偏弱，贝加尔湖西北部为较强的高压脊，东北部则为低压槽，鄂霍次克海则为较强的高压脊控制。副高较常年异常偏强，中心位置达到 5910 gpm，偏高 20 gpm 以上，西伸脊点达到 110°E，较常年平均偏西 10 个经度以上，脊线略偏南。菲律宾附近对流层低层为异常反气旋环流控制，长江中下游地区为西风距平，表明梅雨锋偏强；东北地区也为异常反气旋控制，引导冷空气南下到江淮流域（图 8b）。由副高西南侧转向的水汽输送明显偏强，与东路弱冷空气配合，造成长江中下游地区水汽通量异常辐合（图略），造成梅雨期降水异常偏多。

此外，需要说明的是 1951 年以来梅雨量最多的 1954、1996 和 1998 年，梅雨期间欧亚中高纬度为典型的“两脊一槽”型环流，乌拉尔山和鄂霍次克海为较强的高压脊，贝加尔湖为低压槽（图略），中高纬度冷空气活动较强。而 2016 年梅雨期中高纬度冷空气势力相对较弱，6～7 月东亚经向环流指数的监测结果（图 9a）也表明这一点，这是一个不同之处。监测结果也表明 2016 年 6～7 月副高较气候平均明显偏强，其强度为历史第二，仅次于 2010 年同期（图 9b）；梅雨集中期间（6 月 19 日至 7 月 20 日）经过长江中下游地区南边界的水汽通量强度明显偏强（图 9c），整个长江中下游地区（27.5°～32.5°N，110°～120°E）水汽净收支为历史第一（图 9d）。由此可见，充沛的水汽条件是 2016 年长江区梅雨量异常偏多的主要成因之一，而这样强盛的水汽主要来自异常偏强的副高西南侧的转向气流。

2014 年秋季赤道中、东太平洋暖海温开始迅速发展，但由于受到南太平洋中纬度海温异常偏低的影响，2014 年 El Niño 事件并没有形成（Min et al., 2015），但赤道中、东太平洋暖海温仍然维持。图 10 给出了 2015 年 1 月至 2016 年 8 月 Niño3.4 指数和 IOBW 指数的演变。Niño3.4 于 2015 年 4 月大于 0.5°C，并持续 6 个月以上大于 0.5°C，形成了一次 El Niño 事件，于 2015 年 11 月达到 2.5°C，达到峰值，此后逐步衰减，于 2016 年 5 月低于 0.5°C，El Niño 事件结束。这是 1951 年以来峰值强度最强、持续时间最长的一次 El Niño 事件（陈丽娟等，2016；邵勰和周兵，2016；翟盘茂等，2016）。2016 年夏季处于超强 El Niño 事件的衰减年，受 El Niño 事件影响，副高在 2015 年秋、冬季持续偏强，并在 2015/2016 年冬季达到历史最强，IOBW 也表现出持续偏暖的特征（图 10），并在 2015/2016 年冬季和 2016 年春季均达到 1951 年以来最暖（袁媛等，

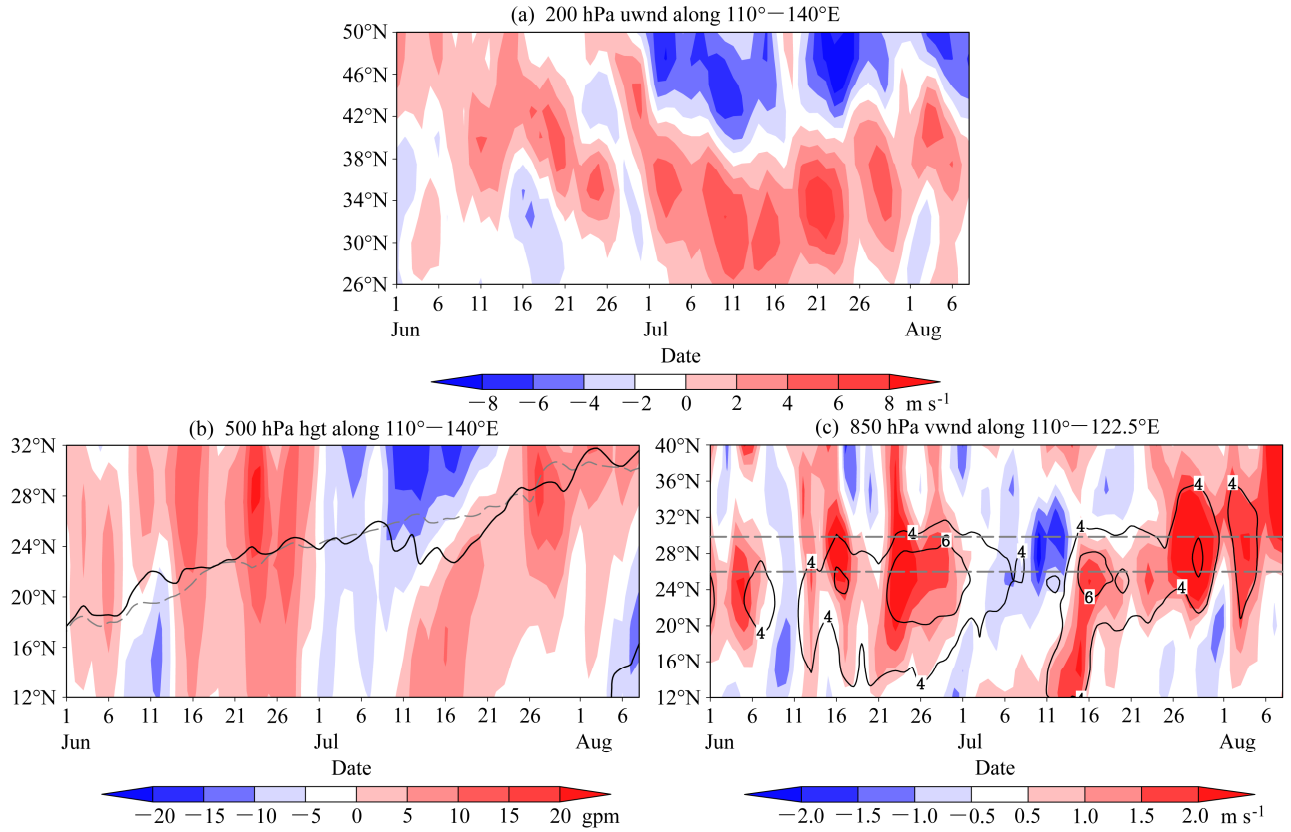

图 7 江南区和长江区出梅偏晚年（a）沿 110°～140°E 平均的 200 hPa 纬向风距平时间—纬度剖面（单位：m s^{-1}），（b）沿 110°～140°E 平均的 500 hPa 位势高度距平场时间—纬度剖面（单位：gpm），（c）沿 110°～122.5°E 平均的 850 hPa 经向风距平时间—纬度剖面（单位：m s^{-1}）。（b）中灰色虚线表示气候平均的副高脊线，黑色实线表示异常年平均的副高脊线。（c）中阴影区表示经向风距平，黑色实线表示经向风大小

Fig. 7 Time–latitude cross sections of (a) zonal wind (units: m s^{-1}) at 200 hPa averaged over 110°–140°E, (b) geopotential height anomalies at 500 hPa (units: gpm) averaged over 110°–140°E, and (c) meridional wind at 850 hPa (units: m s^{-1}) averaged over 110°–122.5°E in late Meiyu outset years in regions to the South of the Yangtze River and the Yangtze River valley. The gray dotted line in (b) represents the climatological mean subtropical high ridge line, and the black line represents the mean subtropical high ridge line in anomalous years. Shaded areas in (c) represent meridional wind anomalies, and the black lines represent the meridional winds

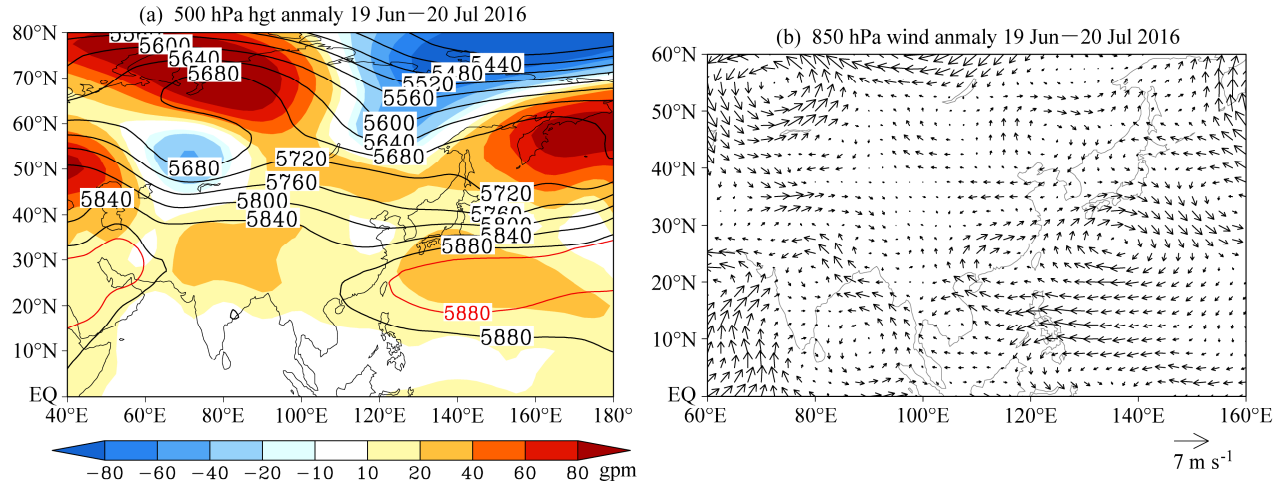

图 8 2016 年梅雨期间平均大气环流距平场：（a）500 hPa 位势高度场（等值线，单位：gpm）及其距平场（阴影区），红色等值线表示气候平均的 5860 和 5880gpm 等值线；（b）850 hPa 距平风场（单位：m s^{-1}）

Fig. 8 Averaged atmospheric circulation anomalies during Meiyu period of 2016: (a) 500 hPa geopotential height (contours, units: gpm) and its anomalies (shading), red contours stand for the climatological 5860 and 5880 gpm contours; (b) 850 hPa wind anomalies (units: m s^{-1})

2016）。

El Niño 事件一般在秋、冬季达到峰值，春季衰减，到了夏季发生位相转换，而 IOBW 常在冬季开始发展，第二年春季达到最强。El Niño 发展年的秋、冬季，东亚副热带地区会通过 Rossby 波遥相关作用在菲律宾附近激发异常反气旋环流，它是 El Niño 影响东亚天气、气候的重要因素。但在 El Niño 衰减年的夏季，由于赤道中东太平洋异常暖水已经减弱，此时菲律宾附近异常反气旋环流和副高偏强的维持主要是 IOBW 持续正位相滞后响应的结果。众多研究也表明，IOBW 是对 El Niño 事件的滞后响应，它在维持 El Niño 对东亚天气、气候的影响中起到重要的“接力”作用（Yang et al, 2007；Xie et al，2009；陈丽娟等，2013；黄刚等，2016；袁媛等，2017）。由图 10 可见，2016 年 6 月 Niño3.4 指数已经转为负值，并在 7～8 月负指数持续扩大，赤道中、东太平洋已经转为冷海温；而 IOBW 在春、夏季一直维持较强的正位相。

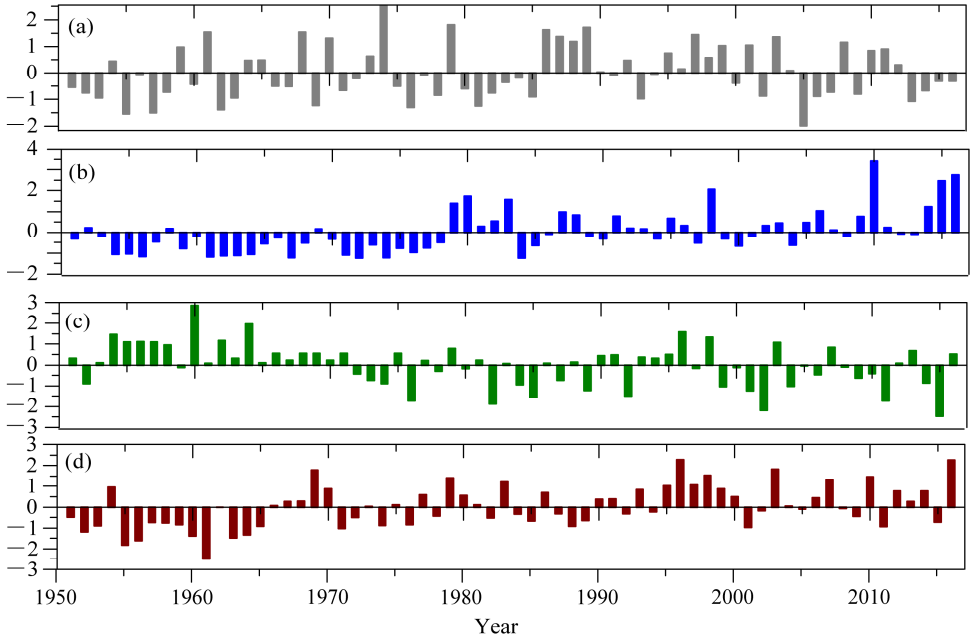

图 9　1951～2016 年环流和水汽输送指数标准化时间序列：（a） 6～7 月东亚经向环流指数；（b）6～7 月西太平洋副热带高压强度指数；（c）6 月 19 日至 7 月 20 日经过长江中下游地区南边界的水汽通量；（d）6 月 19 日至 7 月 20 日长江中下游地区水汽净收支

Fig. 9　Time series of atmospheric circulation and moisture transport index anomalies from 1951 to 2016: (a) Asian meridional circulation index in June–July; (b) intensity index of the western Pacific subtropical high (WPSH) in June–July; (c) moisture budget along the southern boundary of the middle and lower reaches of the Yangtze River (MLYR) from 19 June to 20 July; (d) moisture budget over the MLYRB from 19 June to 20 July

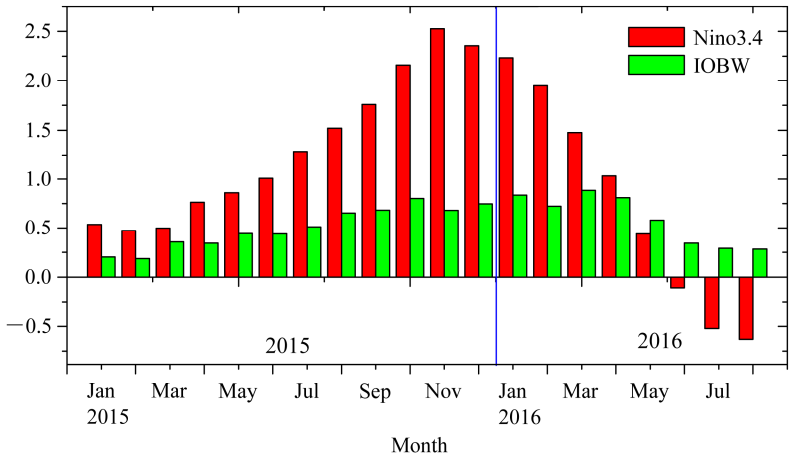

图 10　2015 年 1 月至 2016 年 8 月 Niño3.4 指数和 IOBW 指数

Fig. 10　Time series of Niño3.4 index and the Indian Ocean Basin-Wide mode (IOBW) index from January 2015 to August 2016

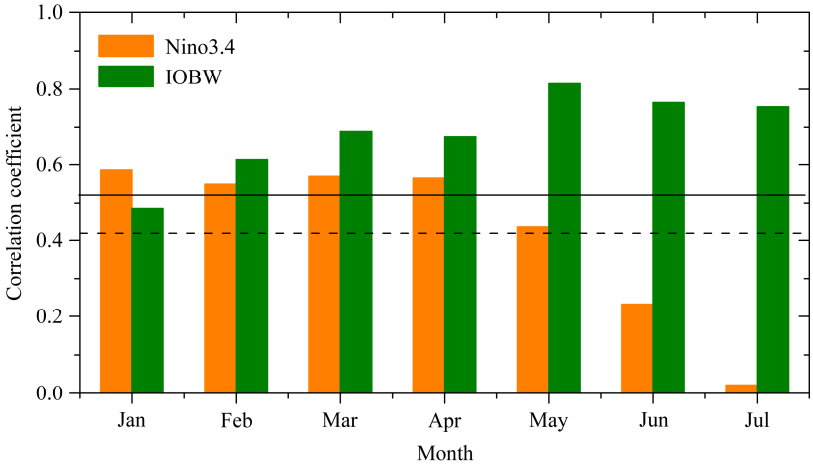

图 11　1981～2015 年 1～7 月逐月 Niño3.4 指数和 IOBW 指数与 6～7 月平均的副高强度指数的相关系数（实线和虚线分别表示置信水平达到 99.9% 和 99%）

Fig. 11　Correlation coefficients of intensity index of WPSH averaged in June–July with monthly (from January to July) Niño3.4 index and IOBW index during 1981–2015, respectively (the solid line and dotted line indicate values at the 99.9% and 99% confidence levels, respectively)

从 1～7 月各月 Niño3.4 指数和 IOBW 指数与 6～7 月平均的副高强度指数的相关系数变化（图 11）可以清楚地看出，1～4 月逐月 Niño3.4 指数与 6～7 月平均的副高强度指数呈显著的正相关，置信水平达到 99.9%，6 月的相关系数小于 0.01 信度的临界值，7 月的相关系数接近 0，表明赤道中东太平洋海温对副高强度的影响是逐步减弱的。2～7 月 IOBW 指数与 6～7 月平均的副高强度指数呈显著的正相关，置信水平均达到 99.9%，其中 5～7 月的相关系数分别高达 0.82、0.77 和 0.75，表明印度洋海温对于副高强度的影响是显著且持续加强的。这也进一步证明了，2016 年夏季梅雨期副高的异常偏强在很大程度上是 IOBW 暖海温持续造成的。

此外，除 2016 年外，1983 年和 1998 年夏季也处于超强 El Niño 事件的衰减年，这两年春季印度洋也异常偏暖，IOBW 指数分别位列 1951 年以来的第 11 位和第 2 位；6～7 月副高强度也异常偏强，分别位列第 6 位和第 4 位；导致这两年长江区梅雨期异常偏长，梅雨量异常偏多。

5　结论和讨论

梅雨是中国东部雨季进程中最重要的一个过程，梅雨的异常会给我国长江中下游地区带来严重的旱涝灾害。本文利用国家气候中心 2014 年发布的新的梅雨监测资料和 NCEP 再分析资料，对 2016 年我国梅雨异常特征及其大尺度环流成因进行了分析。具体结论如下：

（1）2016 年我国梅雨有明显的区域特征，其中江南区入梅异常偏早，出梅异常偏晚，梅雨期异常偏长；梅雨量偏多，但由于梅雨期偏长，导致梅雨期日平均降水量偏小；长江区入梅和出梅均偏晚，梅雨期接近常年，但梅雨量偏多一倍多，梅雨期日平均降水量异常偏多；江淮区入梅、出梅及梅雨期接近常年，但梅雨量偏多。2016 年梅雨期降水时空分布不均匀，长江区梅雨最强，江南区和江淮区相对偏弱一些，属于长江区型梅雨；7 月 1～7 日长江区和江淮区梅雨量持续偏多，累积雨量接近常年梅雨期平均的总梅雨量。

（2）对流层高、中、低层环流系统冬夏季节性调整和转变显著提前的共同作用，导致了 2016 年江南区入梅显著偏早，即 5 月 25 日，对流层高层的西风急流加强北跳、中层西太平洋副热带高压也加强北跳过 18°N。同时，低层东亚夏季风开始明显加强和北推，北推至 26°N 以北，给江南地区带来了充沛的水汽；西风急流、副高和东亚夏季风涌在 7 月中旬阶段性地南落导致了江南区和长江区出梅偏晚。

（3）受到前冬超强 El Niño 衰减和春、夏季 IOBW 暖海温持续偏暖的共同影响，梅雨期副高异常偏强，副高西南侧转向的水汽输送异常偏强；欧亚中高纬度呈“两槽两脊”型，鄂霍次克海为较强的高压脊控制，冷空气路径偏东，北方弱冷空气与南方充沛的水汽输送于长江区和江淮区辐合，造成梅雨量异常偏多。

综上可见，入梅早晚与东亚大气环流系统由冬季向夏季转换的早晚和快慢密切相关，在入梅的中期预报中，需要密切关注东亚副热带西风急流和副高第一次北跳，及越赤道气流爆发和东亚夏季风推进的早晚，并从历史资料和模式预报中提取影响以上环流系统的外强迫信号。梅雨量的多寡则主要与中高纬度环流和低纬副热带环流系统是否能达到较好的配置及稳定维持有关，来自中高纬度的冷空气强度和路径、来自副热带系统携带的水汽输送的强弱，直接影响到梅雨量的多寡和强度，而副热带环流系统的异常则主要受到前期至同期赤道中、东太平洋和印度洋等关键区域海温外强迫异常的调控。本文从大尺度环流系统异常演变、及前期至同期海温外强迫作用的角度入手，分析了 2016 年我国梅雨的异常特征及其原因，以提高对梅雨的科学认识和预报水平。

参考文献（References）

曹艳察, 张涛. 2016. 2016 年 6 月大气环流和天气分析 [J]. 气象, 42 (9): 1154–1160. Cao Yancha, Zhang Tao. 2016. Analysis of the June 2016 atmospheric circulation and weather [J]. Meteor. Mon. (in Chinese), 42 (9): 1154–1160, doi:10.7519/j.issn.1000-0526.2016.09.013.

陈丽娟, 袁媛, 杨明珠, 等. 2013. 海温异常对东亚夏季风影响机理的研究进展 [J]. 应用气象学报, 24 (5): 521–532. Chen Lijuan, Yuan Yuan, Yang Mingzhu, et al. 2013. A review of physical mechanisms of the global SSTA impact on EASM [J]. J. Appl. Meteor. Sci. (in Chinese), 24 (5): 521–532, doi:10.3969/j.issn.1001-7313.2013.05.002.

陈丽娟, 顾薇, 丁婷, 等. 2016. 2015 年汛期气候预测先兆信号的综合分析 [J]. 气象, 42 (4): 496–506. Chen Lijuan, Gu Wei, Ding Ting, et al. 2016. Overview of the precursory signals of seasonal climate prediction in summer 2015 [J]. Meteor. Mon. (in Chinese), 42 (4): 496–506, doi:10.7519/j.issn.1000-0526.2016.04.014.

翟盘茂, 余荣, 郭艳君, 等. 2016. 2015/2016 年强厄尔尼诺过程及其对全球和中国气候的主要影响 [J]. 气象学报, 74 (3): 309–321. Zhai Panmao, Yu Rong, Guo Yanjun, et al. 2016. The strong El Niño in 2015/2016 and its dominant impacts on global and China's climate [J]. Acta Meteor. Sinica (in Chinese), 74 (3): 309–321, doi:10.11676/qxxb2016.049.

丁一汇. 2005. 高等天气学 [M]. 2 版. 北京: 气象出版社, 585pp. Ding Yihui. 2005. Advanced Synoptic Meteorology (in Chinese) [M]. 2nd ed. Beijing: China Meteorological Press, 585pp.

丁一汇, 柳俊杰, 孙颖, 等. 2007. 东亚梅雨系统的天气—气候学研究 [J]. 大气科学, 31 (6): 1082–1101. Ding Yihui, Liu Junjie, Sun Ying, et al. 2007. A study of the synoptic–climatology of the Meiyu system in East Asia [J]. Chinese Journal of Atmospheric Sciences (in Chinese), 31 (6): 1082–1101, doi:10.3878/j.issn.1006-9895.2007.06.05.

封国林, 杨涵洧, 张世轩, 等. 2012. 2011 年春末夏初长江中下游地区旱涝急转成因初探 [J]. 大气科学, 36 (5): 1009–1026. Feng Guolin, Yang Hanwei, Zhang Shixuan, et al. 2012. A preliminary research on the reason of a sharp turn from drought to flood in the middle and lower reaches of the Yangtze River in late spring and early summer of 2011 [J]. Chinese Journal of Atmospheric Sciences (in Chinese), 36 (5): 1009–1026, doi:10.3878/j.issn.1006-9895.2012.11220.

封国林, 赵俊虎, 杨杰, 等. 2015. 中国汛期降水动力—统计预测研究 [M]. 北京: 科学出版社, 1–330. Feng Guolin, Zhao Junhu, Yang Jie, et al. 2015. The Study on Dynamical and Statistical Prediction on Summer Precipitation over China (in Chinese) [M]. Beijing: Science Press, 1–330.

Gu W, Li C Y, Wang X, et al. 2009. Linkage between Mei-yu precipitation and North Atlantic SST on the decadal timescale [J]. Adv. Atmos. Sci., 26 (1): 101–108, doi:10.1007/s00376-009-0101-5.

胡娅敏, 丁一汇. 2009. 2000 年以来江淮梅雨带北移的可能成因分析 [J]. 气象, 35 (12): 37–43. Hu Yamin, Ding Yihui. 2009. Possible reasons for northward shift of Meiyu belt in Yangtze Huaihe River region during 2000–2005 [J]. Meteor. Mon. (in Chinese), 35 (12): 37–43, doi:10.7519/j.issn.1000-0526.2009.12.005.

胡娅敏, 丁一汇, 廖菲. 2008. 江淮地区梅雨的新定义及其气候特征 [J]. 大气科学, 32 (1): 101–112. Hu Yamin, Ding Yihui, Liao Fei. 2008. A study of updated definition and climatological characters of Meiyu season in the Yangtze–Huaihe region [J]. Chinese Journal of Atmospheric Sciences (in Chinese), 32 (1): 101–112, doi:10.3878/j.issn.1006-9895.2008.01.09.

黄刚, 胡开明, 屈侠, 等. 2016. 热带印度洋海温海盆一致模的变化规律及其对东亚夏季气候影响的回顾 [J]. 大气科学, 40 (1): 121–130. Huang Gang, Hu Kaiming, Qu Xia, et al. 2016. A review about Indian Ocean basin mode and its impacts on East Asian summer climate [J]. Chinese Journal of Atmospheric Sciences (in Chinese), 40(1): 121–130, doi:10.3878/j.issn.1006-9895.1505.15143.

Kalnay E, Kanamitsu M, Kistler R, et al. 1996. The NCEP/NCAR 40-year reanalysis project [J]. Bull. Amer. Meteor. Soc., 77 (3): 437–471, doi:10.1175/1520-0477(1996)077<0437:TNYRP>2.0.CO;2.

况雪源, 张耀存. 2006. 东亚副热带西风急流位置异常对长江中下游夏季降水的影响 [J]. 高原气象, 25 (3): 382–389. Kuang Xueyuan, Zhang Yaocun. 2006. Impact of the position abnormalities of East Asian subtropical westerly jet on summer precipitation in middle–lower reaches of Yangtze River [J]. Plateau Meteor. (in Chinese), 25 (3): 382–389, doi:10.3321/j.issn:1000-0534.2006.03.004.

李维京. 1999. 1998 年大气环流异常及其对中国气候异常的影响 [J]. 气象, 25 (4): 20–25. Li Weijing. 1999. General atmospheric circulation anomaly in 1998 and their impact on climate anomaly in China [J]. Meteor. Mon. (in Chinese), 25 (4): 20–25, doi:10.3969/j.issn.1000-0526.1999.04.004.

梁萍, 汤绪, 柯晓新, 等. 2007. 中国梅雨影响因子的研究综述 [J]. 气象科学, 27 (4): 464–471. Liang Ping, Tang Xu, Ke Xiaoxin, et al. 2007. Review of study on influencing factors of China Meiyu [J]. Scientia Meteorologica Sinica (in Chinese), 27 (4): 464–471, doi:10.3969/j.issn.1009-0827.2007.04.018.

梁萍, 丁一汇, 何金海, 等. 2010. 江淮区域梅雨的划分指标研究 [J]. 大气科学, 34 (2): 418–428. Liang Ping, Ding Yihui, He Jinhai, et al. 2010. A study of determination index of regional Meiyu over the Yangtze–Huaihe basin [J]. Chinese Journal of Atmospheric Sciences (in Chinese), 34 (2): 418–428, doi:10.3878/j.issn.1006-9895.2010.02.15.

Min Q Y, Su J Z, Zhang R H, et al. 2015. What hindered the El Niño pattern

in 2014 [J]. Geophys. Res. Lett., 42 (16): 6762–6770, doi:10.1002/2015GL064899.

牛若芸, 金荣花. 2009. 2008 年梅雨异常大尺度环流成因分析 [J]. 高原气象, 28 (6): 1326–1334. Niu Ruoyun, Jin Ronghua. 2009. Causes analysis of large scale circulation of abnormal characteristic in Meiyu period of 2008 [J]. Plateau Meteor. (in Chinese), 28 (6): 1326–1334.

权婉晴, 何立富. 2016. 2016 年 7 月大气环流和天气分析 [J]. 气象, 42 (10): 1283–1288. Quan Wanqing, He Lifu. 2016. Analysis of the July 2016 atmospheric circulation and weather [J]. Meteor. Mon. (in Chinese), 42 (10): 1283–1288, doi:10.7519/j.issn.1000-0526.2016.10.014.

Sampe T, Xie S P. 2010. Large-scale dynamics of the Meiyu-Baiu rainband: Environmental forcing by the westerly jet [J]. J. Climate, 23 (1): 113–134, doi:10.1175/2009JCLI3128.1.

邵勰, 周兵. 2016. 2015/2016 年超强厄尔尼诺事件气候监测及诊断分析 [J]. 气象, 42 (5): 540–547. Shao Xie, Zhou Bing. 2016. Monitoring and diagnosis of the 2015/2016 super El Niño event [J]. Meteor. Mon. (in Chinese), 42 (5): 540–547, doi:10.7519/j.issn.1000-0526.2016.05.003.

施能, 朱乾根, 吴彬贵. 1996. 近 40 年东亚夏季风及我国夏季大尺度天气气候异常 [J]. 大气科学, 20 (5): 575–583. Shi Neng, Zhu Qian'gen, Wu Bingui. 1996. The East Asian summer monsoon in relation to summer large scale weather–climate anomaly in China for last 40 years [J]. Chinese Journal of Atmospheric Sciences (Scientia Atmospherica Sinica) (in Chinese), 20 (5): 575–583, doi:10.3878/j.issn.1006-9895.1996.05.08.

陶诗言, 赵煜佳, 陈晓敏. 1958. 东亚的梅雨期与亚洲上空大气环流季节变化的关系 [J]. 气象学报, 29 (2): 119–134. Tao Shiyan, Zhao Yujia, Chen Xiaomin. 1958. The relationship between May-Yü in Far East and the behaviour of circulation over Asia [J]. Acta Meteor. Sinica (in Chinese), 29 (2): 110–134, doi:10.11676/qxxb1958.014.

陶诗言, 卫捷. 2006. 再论夏季西太平洋副热带高压的西伸北跳 [J]. 应用气象学报, 17 (5): 513–525. Tao Shiyan, Wei Jie. 2006. The westward, northward advance of the subtropical high over the West Pacific in summer [J]. J. Appl. Meteor. Sci. (in Chinese), 17 (5): 513–525, doi:10.3969/j.issn.1001-7313.2006.05.001.

陶诗言, 朱文妹, 赵卫. 1988. 论梅雨的年际变异 [J]. 大气科学, 12 (S): 13–21. Tao Shiyan, Zhu Wenmei, Zhao Wei. 1988. Interannual variability of Meiyu rainfalls [J]. Chinese Journal of Atmospheric Sciences (Scientia Atmospherica Sinica) (in Chinese), 12 (S): 13–21, doi:10.3878/j.issn.1006-9895.1988.t1.02.

Tao S Y, Chen L X. 1987. A review of recent research on the East Asian summer monsoon in China [M]//Chang C P, Krishnamurti T N. Monsoon Meteorology. New York: Oxford University Press, 60–92.

汪靖, 刘宣飞, 韩桂荣, 等. 2006. 2005 年江淮流域入梅偏晚的成因分析 [J]. 气象, 32 (12): 76–81. Wang Jing, Liu Xuanfei, Han Guirong, et al. 2006. Causality analysis of late Meiyu over the Changjiang and Huaihe River basins in 2005 [J]. Meteor. Mon. (in Chinese), 32 (12): 76–81, doi:10.3969/j.issn.1000-0526.2006.12.013.

王遵娅, 丁一汇. 2008. 中国雨季的气候学特征 [J]. 大气科学, 32 (1): 1–13. Wang Zunya, Ding Yihui. 2008. Climatic characteristics of rainy seasons in China [J]. Chinese Journal of Atmospheric Sciences (in Chinese), 32 (1): 1–13, doi:10.3878/j.issn.1006-9895.2008.01.01.

魏凤英, 宋巧云. 2005. 全球海表温度年代际尺度的空间分布及其对长江中下游梅雨的影响 [J]. 气象学报, 63 (4): 477–484. Wei Fengying, Song Qiaoyun. 2005. Spatial distribution of the global sea surface temperature with interdecadal scale and their potential influence on Meiyu in middle and lower reaches of Yangtze River [J]. Acta Meteor. Sinica (in Chinese), 63 (4): 477–484, doi:10.11676/qxxb2005.047.

Xie S P, Hu K M, Hafner J, et al. 2009. Indian Ocean capacitor effect on Indo-western Pacific climate during the summer following El Niño [J]. J. Climate, 22 (3): 730–747, doi:10.1175/2008JCLI2544.1.

Yang J L, Liu Q Y, Xie S P, et al. 2007. Impact of the Indian Ocean SST basin mode on the Asian summer monsoon [J]. Geophys. Res. Lett., 34 (2): L02708, doi:10.1029/2006GL028571.

杨莲梅, 张庆云. 2007. 夏季东亚西风急流 Rossby 波扰动异常与中国降水 [J]. 大气科学, 31 (4): 586–595. Yang Lianmei, Zhang Qingyun. 2007. Anomalous perturbation kinetic energy of Rossby wave along East Asian westerly jet and its association with summer rainfall in China [J]. Chinese Journal of Atmospheric Sciences (in Chinese), 31 (4): 586–595, doi:10.3878/j.issn.1006-9895.2007.04.04.

Ye T S, Zhi R, Zhao J H, et al. 2014. The two annual northward jumps of the West Pacific subtropical high and their relationship with summer rainfall in eastern China under global warming [J]. Chin. Phys. B, 23 (6): 069203, doi:10.1088/1674-1056/23/6/069203.

袁媛, 高辉, 贾小龙, 等. 2016. 2014～2016 年超强厄尔尼诺事件的气候影响 [J]. 气象, 42 (5): 532–539. Yuan Yuan, Gao Hui, Jia Xiaolong, et al. 2016. Influences of the 2014–2016 super El Niño event on climate [J]. Meteor. Mon. (in Chinese), 42 (5): 532–539, doi:10.7519/j.issn.1000-0526.2016.05.002.

袁媛, 高辉, 柳艳菊. 2017. 2016 年夏季我国东部降水异常特征及成因简析 [J]. 气象, 43 (1): 115–121. Yuan Yuan, Gao Hui, Liu Yanju. 2017. Analysis of the characteristics and causes of precipitation anomalies over eastern China in the summer of 2016 [J]. Meteor. Mon. (in Chinese), 43 (1): 115–121, doi:10.7519/j.issn.1000-0526.2017.01.013.

张庆云, 陶诗言. 1999. 夏季西太平洋副热带高压北跳及异常的研究 [J]. 气象学报, 57 (5): 539–548. Zhang Qingyun, Tao Shiyan. 1999. The study of the sudden northward jump of the subtropical high over the western Pacific [J]. Acta Meteor. Sinica (in Chinese), 57 (5): 539–548, doi:10.11676/qxxb1999.052.

赵俊虎, 封国林, 王启光, 等. 2011. 2010 年我国夏季降水异常气候成因分析及预测 [J]. 大气科学, 35 (6): 1069–1078. Zhao Junhu, Feng Guolin, Wang Qiguang, et al. 2011. Cause and prediction of summer rainfall anomaly distribution in China in 2010 [J]. Chinese Journal of Atmospheric Sciences (in Chinese), 35 (6): 1069–1078, doi:10.3878/j.issn.1006-9895.2011.06.07.

赵俊虎, 封国林, 杨杰, 等. 2012. 夏季西太平洋副热带高压的不同类型与中国汛期大尺度旱涝的分布 [J]. 气象学报, 70 (5): 1021–1031. Zhao Junhu, Feng Guolin, Yang Jie, et al. 2012. Analysis of the distribution of large-scale drought/flood of summer in China under different types of western Pacific subtropical high [J]. Acta Meteor. Sinica (in Chinese), 70 (5): 1021–1031, doi:10.11676/qxxb2012.085.

周兵, 文继芬. 2007. 1998 年夏季我国东部降水与大气环流异常及其低频特征 [J]. 应用气象学报, 18 (2): 129–136. Zhou Bing, Wen Jifen. 2007. Abnormality of summertime precipitation of eastern China and general circulation with LFO in 1998 [J]. J. Appl. Meteor. Sci. (in Chinese), 18(2): 129–136, doi:10.3969/j.issn.1001-7313.2007.02.001.

doi:10.11676/qxxb2018.025 气象学报

基于新监测指标的江南入梅早晚的气候特征及影响系统分析*

赵俊虎[1] 陈丽娟[1,2] 熊开国[3]
ZHAO Junhu[1] CHEN Lijuan[1,2] XIONG Kaiguo[3]

1. 中国气象局国家气候中心,中国气象局气候研究开放实验室,北京,100081
2. 南京信息工程大学气象灾害预报预警与评估协同创新中心,南京,210044
3. 武汉区域气候中心,武汉,430074
1. *Laboratory for Climate Studies, National Climate Center, CMA, Beijing* 100081, *China*
2. *Collaborative Innovation Center on Forecast and Evaluation of Meteorological Disasters, Nanjing University of Information Science & Technology, Nanjing* 210044, *China*
3. *Wuhan Regional Climate Center, Wuhan* 430074, *China*

2017-12-28 收稿,2018-03-30 改回.

赵俊虎,陈丽娟,熊开国. 2018. 基于新监测指标的江南入梅早晚的气候特征及影响系统分析. 气象学报,76(5):680-698
Zhao Junhu, Chen Lijuan, Xiong Kaiguo. 2018. Climate characteristics and influential systems of Meiyu to the south of the Yangtze River based on the new monitoring rules. *Acta Meteorologica Sinica*, 76(5):680-698

Abstract Using the NCEP/NCAR reanalysis data, NOAA Sea Surface Temperature (SST) data, the Chinese Meiyu onset dates determined based on "Meiyu Monitoring Business Rules" released by China Meteorological Administration in 2014, and other data from 1951-2015, anomalous climate characteristics of the Meiyu onset date in three regions of South China are analyzed. The relationships between the Meiyu onset date to the south of the Yangtze River (MODSYR) with variations of atmospheric circulation in May-June and preceding SST are analyzed using the correlation and composition analysis methods. The results show that MODSYR has significant interannual variability in the recent 65 years. The mean MODSYR during 1951-2015 was on 8 June. The difference between the earliest and the latest MODSYR was 47 days. The MODSYR was usually in June (accounting for 80.0%). There exist significant differences in the large-scale circulation from the upper troposphere to the lower troposphere during the same period (May to June) between the earlier and later MODSYR years. In the early MODSYR years, the South Asia high (SAH) and East Asia subtropical westerly jet stream (SWJS) establish earlier and are stronger compared with their climatological means in the upper troposphere, the SAH moves northward to the Tibetan Plateau earlier than normal, and the SWJS also moves northward earlier. The mid- and high-latitudes is dominated by strong meridional circulation, and the first northward jump of the western Pacific subtropical high (WPSH) occurs earlier than normal. The cross-equatorial flow in the lower troposphere establishes earlier, and the onset of the South China Sea summer monsoon is earlier, too. However, the opposite is true for late MODSYR years. SST anomalies (SSTA) in the preceding winter and spring are important forcing factors that affect the MODSYR, and they are also critical early predictive signals. When the eastern Pacific SSTA is abnormally cold in the preceding winter, the SST gradient index to the East Australia (ASI) is in positive phase to the East of Australia and the spring North Atlantic Triassic (NAT) is in the positive phase, the MODSYR is earlier than normal.

* 资助课题:国家重点基础研究发展计划(2015CB453203)、国家自然科学基金项目(41875093、41505061、41705074、41275073)与公益性行业(气象)科研重大专项(GYHY201506001)。
作者简介:赵俊虎,主要从事短期气候预测研究。E-mail: zhaojh@cma.gov.cn
通讯作者:陈丽娟,主要从事短期气候预测研究。E-mail: chenlj@cma.gov.cn

The relationship between the December ASI, the March NAT and MODSYR are the closest. When the December ASI is in positive phase, the first northward jump of the WPSH occurs earlier than normal. When the NAT is on positive phase in March, the SWJS will be stronger and located more northward in June, which is favorable for earlier MODSYR.

Key words Meiyu, Meiyu onset date, Climatic characteristics, Atmospheric circulation, SSTA

摘 要 利用中国气象局2014年发布的《梅雨监测业务规定》中的入梅日期资料、NCEP/NCAR再分析资料及NOAA海温资料等,重点研究了1951—2015年江南入梅早、晚的气候特征,及其与同期(5—6月)大气环流及前期海表温度变化的关系。结果表明,近65年来江南入梅日具有显著的年际变化特征,入梅平均日期为6月8日,最早和最晚相差47 d。入梅日主要出现在6月,占80.0%。江南入梅偏早和偏晚年,对流层高层至低层的同期大尺度环流存在明显的差异。入梅偏早年,高层南亚高压和东亚副热带西风急流(西风急流)的建立较早,强度较强,南亚高压北移到青藏高原上空亦偏早,西风急流北跳偏早;中层中高纬度经向环流较强,而西北太平洋副热带高压(副高)第1次北跳偏早;低层索马里越赤道气流建立较早,强度较强,西太平洋为反气旋式距平环流;入梅偏晚年上述环流系统演变特征则基本相反。冬、春季海表温度的异常是影响入梅早、晚的重要的外部强迫因子,也是重要的前期预测信号:当冬季东太平洋海表温度为负距平、澳大利亚东部海表温度偶极子为正位相及春季北大西洋三极子处于正位相时,江南入梅偏早;上一年12月澳大利亚东侧海表温度偶极子和当年3月北大西洋三极子与江南入梅早、晚关系最为密切,当12月澳大利亚东部海表温度偶极子为正位相时,副高第1次北跳偏早,当3月北大西洋三极子为正位相时,6月西风急流偏强、偏北,有利于江南入梅偏早。

关键词 梅雨,入梅,气候特征,大气环流,海温异常

中图法分类号 P461

1 引 言

传统梅雨指的是每年6—7月在中国长江中下游地区、朝鲜半岛最南部(称为Changma)和日本中南部(称为Baiu)出现的以持续多雨为主要特征的气候现象(竺可桢,1934;Tao, et al,1987;魏凤英等,2004;丁一汇等,2007;周兵等,2007;闵屾等,2008)。它是一种季风气候现象,且为东亚地区所特有,其出现的早晚和强度与东亚大气环流的季节变化,特别是夏季风的变化特征紧密关联(陶诗言等,1958;Ding,1992;徐海明等,2001a;2001b;张庆云等,2003;葛全胜等,2007)。梅雨期(6—7月)是东亚夏季风季节性北推过程中的重要阶段,这一时期中国东部雨带主要徘徊在江南至淮河之间,梅雨对这一地区夏季旱涝有重要的影响(施能等,1996;鲍名,2009;梁萍等,2010;刘屹岷等,2013)。梅雨期的强降水与梅雨区洪涝灾害密切相关,如1998年夏季,长江中下游梅雨期降水强度大,7月下旬还出现二度梅,导致该地区出现严重涝灾(李维京,1999)。因此,揭示梅雨的变化规律及其与东亚季风气候系统的关系,具有重要的科学意义;在此基础上准确预测梅雨趋势,对当地的工农业生产及防灾、减灾具有十分重要的指导意义。

有关梅雨的定义、年际变化及其影响机制已有许多研究成果。20世纪80年代初,中国气象界开展了关于梅雨问题尤其是入、出梅标准的讨论。讨论的分歧主要在于:是以天气(降水)实况为主或是以环流调整为主或二者兼顾来划分入、出梅日期(林春育,1979;上海气象局预报组,1980;李小泉,1981)。总体来说,目前中国各个省(市)主要通过西北太平洋副热带高压(副高)位置、气温、雨日或雨量来确定入、出梅日期。由于划分标准因地、因人而异,因而所得结果的可比性较差(周后福,2005;胡娅敏等,2008;李勇等,2017)。此外,各省(市)台站主要关心本地的梅雨开始、结束,迟迟未开展整个区域梅雨的开始、结束时间的划定业务。从整个长江中下游地区层面出发,亟待有一种统一的认定梅雨的思路和方法。为了进一步做好梅雨监测工作,建立适用于中国国家级和省级业务相对统一的指标体系,在中国国家气候中心和相关省、市业务试运行的效果检验评估基础上,2014年5月,中国气象局发布了中国《梅雨监测业务规定》[①],作为中国国家级和相关省(市)级气象部门开展梅雨监测预测业务的重要依据。

[①] 中国气象局预报与网络司. 2014. 关于印发《梅雨监测业务规定》的通知(气预函(2014)28号)。

由于东亚夏季风活动年际变率大,直接影响梅雨的年际变化。叶笃正等(1958)指出,印度西南季风爆发后深入中国大陆东南部,与北方冷空气交汇形成梅雨锋。陶诗言等(1958)指出印度西南季风爆发与东亚入梅之间相互关联,两者在日期上存在一致性。Tao 等(1987)、陶诗言等(1988)对东亚夏季风系统的成员进行了详细分析,认为东亚夏季风的异常活动导致东亚季风系统成员的偏北或偏南会影响到江淮流域的入梅时间及梅雨持续天数。已有的诸多研究往往是将长江和淮河流域作为一个整体,研究时段多选定为整个梅汛期来探讨梅雨形成的大气环流特征及其影响机制。而《梅雨监测业务规定》对梅雨进行了气候分区:按照气候类型可将梅雨监测区域分为江南区、长江中下游区、江淮区。由于各区梅雨均受到外强迫信号和季风系统的影响,使得它们具有一定的共性,但各区梅雨受季风季节内变率的作用以及天气系统的影响不同,使得不同区域梅雨异常对应的对流层高、中、低层多个大尺度环流系统有明显差异(吴志伟等,2006;牛若芸等,2009)。因此,需要对不同区域进行有针对性的分析。江南地区位于华南地区和江淮地区之间,是中国梅雨监测定义的最南区域。江南梅雨是春末夏初华南前汛期(平均 4 月第 2 候入汛)向江淮梅雨过渡季节中的重要天气、气候现象,每年梅雨的开始与结束、梅雨期的长短、梅雨量的多寡,不仅反映了该年从春季过渡到盛夏期间,亚洲上空大气环流季节变化与调整的各种演变特征,而且直接与江南地区旱涝灾害的形成与持续有关。因此揭示江南入梅早、晚的变化特征及其成因对于深入认识东亚季风气候系统的演变具有重要意义。那么基于新的监测结果,江南入梅早、晚有何特征?与长江和江淮入梅之间有何联系?影响入梅早、晚的高、低层环流系统有哪些?前期预测信号是什么?对这些问题的回答是开展江南梅雨预测的基础和依据。

基于此,利用《梅雨监测业务规定》中提供的 1951—2015 年中国三个区域入梅的监测结果,分析了三个区域入梅早、晚的气候特征,在此基础上重点分析了与江南入梅异常相联系的东亚夏季风系统及其演变,以及与前冬、春季关键区域海表温度异常的关系,所得研究结论对准确预测江南梅雨的特征具有重要意义。

2 资料和方法

所用资料主要包括:美国国家环境预报中心和国家大气研究中心(NCEP/NCAR)再分析资料(Kalnay, et al,1996),水平分辨率为 2.5°×2.5°;美国国家海洋和大气管理局(NOAA)的全球 2°×2°月平均海温重建资料(Reynolds, et al,2002),时段均为 1948 年 1 月—2015 年 12 月。Nino4 指数和北大西洋海表温度三极子(NAT)指数来自中国国家气候中心(获取网址为:http://cmdp.ncc-cma.net/Monitoring/cn_index_130.php)。其中,Nino4 指数定义为(5°S—5°N,160°E—150°W)内海表温度距平(SSTA)的区域平均值;北大西洋海表温度三极子指数定义为北大西洋中纬度(34°—44°N,62°—72°W)海表温度距平与高纬度(44°—56°N,24°—44°W)和低纬度(0°—18°N,24°—46°W)平均的海表温度距平之差。气候平均值均采用 1981—2010 年平均。

梅雨新的监测指标是按照《梅雨监测业务规定》来确定,中国梅雨主要分布在江南至江淮流域,即西自湖北宜昌,东至华东沿海,南端以南岭以北的 28°N 为界,北抵淮河沿线 34°N 一带,其范围为(28°—34°N,110°—123°E);涉及的行政区域包含上海、江苏、安徽、浙江、江西、湖北、湖南等 6 省 1 市。按照气候类型可将梅雨监测区域分为江南区(Ⅰ)、长江中下游区(Ⅱ,以下简称长江区)、江淮区(Ⅲ)(图 1)。确定区域入(出)梅与梅雨期的主要依据是区域内各监测站的降水条件,副高脊线、日平均温度、中国南海夏季风爆发时间等为辅助条件,其中入梅日定义方法如下:

(1) 雨日的确定:某日区域中有 1/3 以上气象监测站出现≥0.1 mm 的降水,且区域内日平均降水量≥R_d,该日为一个雨日。其中,安徽江淮之间、江苏(长江区)、湖南和上海等地 R_d 取为 1.0 mm,其他区域 R_d 均为2.0 mm。

(2) 雨期开始日的确定:从第 1 个雨日算起,往后 2,3,…,10 日中的雨日数占相应时段内总日数的比例≥50%,则第 1 个雨日为雨期开始日。

(3) 入梅时间的确定:第 1 个雨期的开始日即为入梅日。

关于梅雨的其他业务规范可参考《梅雨监测业务规定》。

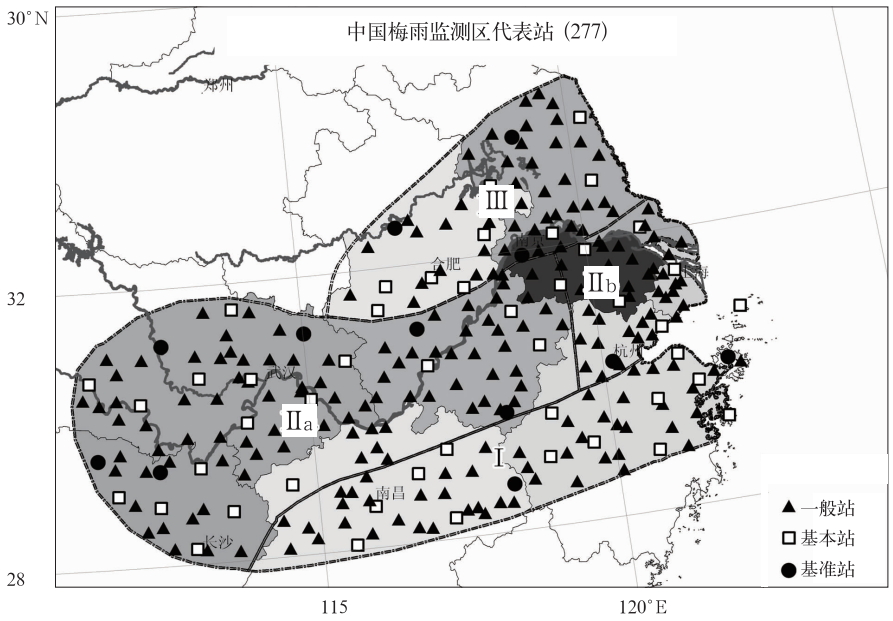

图 1 梅雨监测区域划分及监测站点空间分布(引自《梅雨监测业务规定》;
Ⅰ表示江南区,Ⅱ表示长江区,Ⅲ表示江淮区)

Fig. 1 Schematic diagram of the division of the Meiyu monitoring area and spatial distribution of monitoring stations (Ⅰ indicates the region to the south of the Yangtze River, Ⅱ indicates the region of the Yangtze River basin, Ⅲ indicates the regions of the Yangtze-Huaihe basin)

3 中国梅雨入梅日的气候特征

图 2 为 1951—2015 年 3 个区域梅雨入梅日的年际变化、线性趋势及其 9 年滑动平均曲线。可见 3 个区域入梅日均存在显著的年际变化。1951—2015 年江南区入梅平均日期为 6 月 8 日,标准差为 8 d(表 1);入梅最早的为 1995 年(5 月 25 日),入梅最晚为 2005 年(7 月 11 日),最早和最晚相差 47 d。入梅日主要出现在 6 月(52 年,占 80.0%),其次是 5 月(10 年,占 15.6%),只有 2 年出现在 7 月(占 3.1%)。长江区入梅平均日期为 6 月 14 日,标准差为 11 d;江淮区入梅平均日期为 6 月 21 日,标准差为11 d(表 1)。年际尺度上,3 个区域入梅时间较一致,江南区和长江(江淮)区的相关系数为 0.48 (0.45),长江区和江淮区的相关系数为 0.57。从入梅日的 9 年平滑曲线看其存在显著的年代际变化:江南区入梅从 20 世纪 50 年代直至 60 年代末主要以偏晚为主,70 年代初期以偏早为主,70 年代中后期至 80 年代末以偏晚为主,90 年代以偏早为主,21 世纪初以偏晚为主。由功率谱分析可见(图略),江南区入梅日存在显著的 6 年周期。线性趋势显示近 65 年来江南、长江和江淮区的入梅日无明显长期变化趋势(图 2)。

旧的梅雨监测主要利用上海、南京、芜湖、九江、汉口 5 个站的逐日降水量和副高在 110°—125°E 范围内的脊线位置作为基本资料,来划分长江中下游地区的梅雨期,平均入梅日在 6 月 17 日前后(陶诗言等,1958;徐群,1965;杨义文等,2001;竺夏英等,2008)。而新的梅雨监测则主要考虑了中国梅雨的区域性特征,江南区至江淮区南北跨度 6 个纬度,入、出梅的早晚、梅雨期的长短及梅雨量的多寡,均具有明显的区域差异。新的监测指标正是考虑到这种区域差异,对梅雨区进行了客观的划分,将旧的梅雨监测区域拓展并细化为江南区、长江中下游区和江淮区 3 个区域,从表 1 也可见,3 个区域平均入梅日具有先后差异,江南区较长江中下游区偏早一周,而长江中下游区较江淮区偏早一周。从梅雨量来看,3个区域也具有明显的年际差异。由此可见,新

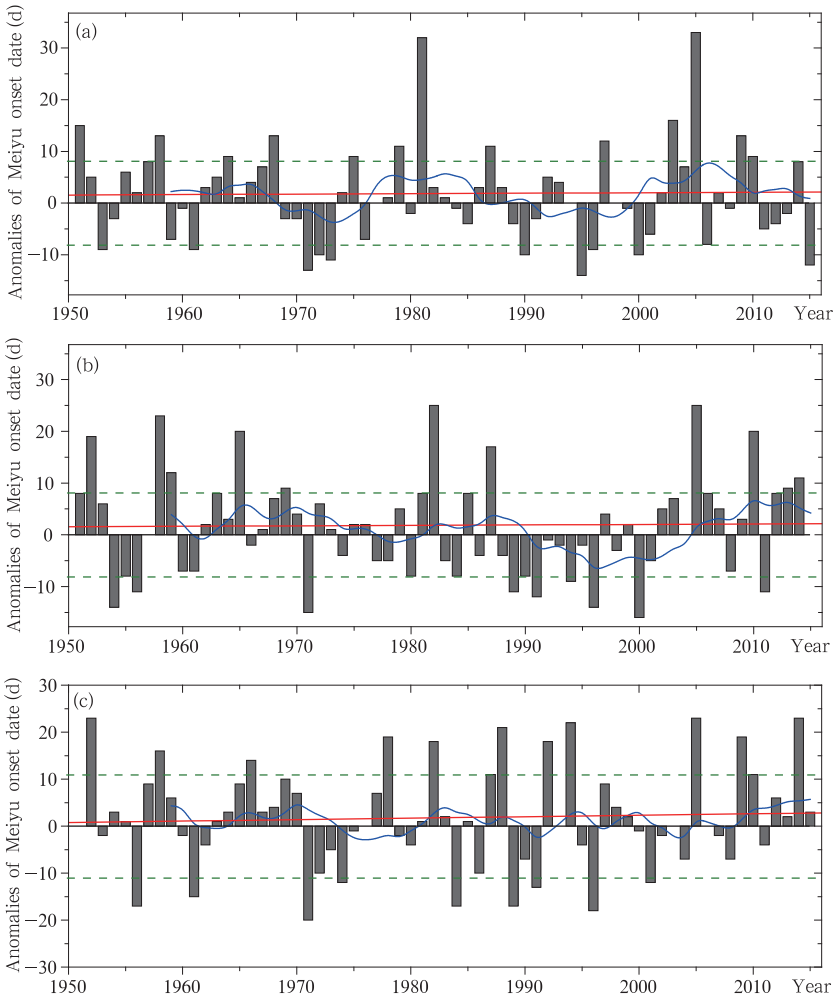

图 2 1951—2015 年 3 个区域入梅日距平

(a. 江南区, b. 长江区, c. 江淮区; 红色直线表示线性趋势,
蓝色曲线表示 9 年滑动平均, 虚线表示 1 倍标准差)

Fig. 2 Anomalies of Meiyu onset date from 1951 to 2015

(a. in the region to the south of the Yangtze River, b. in the region of the Yangtze River basin, c. in the region of the Yangtze-Huaihe basin; The red straight line in each panel represents the linear trend, the blue curve represents the 9-year running average, and the dotted line represents the 1-fold standard deviation)

的梅雨监测更加客观和合理,有利于细致刻画东亚夏季风的季节内进程,并使得监测和预测业务更有针对性。

此外,3 个区域的入梅日与各自的梅雨期日数的相关系数分别为 −0.55、−0.57 和 −0.70,3 个区域的入梅日与各自的梅雨量的相关系数分别为 −0.49、−0.45 和 −0.49,6 个相关系数均通过了 99.9%的置信度 t 检验。表明入梅早、晚与梅雨期的长短及梅雨量的多寡均有密切的关系,入梅偏早,通常梅雨期就容易偏长、同时梅雨量偏多;入梅偏晚,通常梅雨期就容易偏短、同时梅雨量偏少。这也从侧面反映了研究入梅早、晚的影响系统和预测信号的重要意义,即通过预测入梅早晚,可以预判梅雨期的长短和梅雨量的多寡,进而预测梅雨异常是否会导致某一区域发生旱涝灾害。由于中国雨季开始后一般从南向北推进,3 个梅雨区中,江南入梅最早,是东亚夏季风系统影响中国的最早体现之一。因此,选取江南区,研究影响其入梅早晚的系统。

表 1 1951—2015 年 3 个区域入梅日的特征

Table 1 Climatic characteristics of the Meiyu onset date from 1951 to 2015

	江南	长江	江淮
平均	6 月 8 日	6 月 14 日	6 月 21 日
标准差(d)	8	11	11
最早	5 月 25 日(1995 年)	5 月 29 日(2000 年)	6 月 1 日(1971 年)
最晚	7 月 11 日(2005 年)	7 月 9 日(1982 年)	7 月 14 日(1952 年)
异常偏早 10 年	1953,1961,1971,1972,1973,1990,1995,2000,2006,2015	1954,1955,1956,1971,1989,1991,1994,1996,2000,2011	1956,1961,1971,1972,1974,1984,1989,1991,1996,2001
异常偏晚 10 年	1951,1958,1964,1968,1979,1987,1997,2003,2005,2010	1952,1958,1959,1965,1969,1982,1987,2005,2010,2014	1952,1958,1978,1982,1988,1992,1994,2005,2009,2014

4 江南区入梅早晚与东亚夏季风环流系统的关系

由于梅雨是东亚夏季风环流系统季节性调整的产物,入梅前后环流系统发生明显的变化。因此,首先从环流形势的角度出发,分析江南区入梅早、晚与高层到低层大气环流系统的关系。

4.1 高层环流系统对入梅早、晚的影响

南亚高压是亚洲夏季风系统的主要成员之一,也是梅雨天气系统的重要组成部分(王黎娟等,2013)。选取江南区入梅异常偏早和偏晚各 10 年(表 1)进行典型年份合成分析,5 月 28 日为平均偏早日,平均偏早 11 d;6 月 8 日为入梅平均日;6 月 25 日为平均偏晚日,平均偏晚17 d。图 3 给出了江南区入梅偏早年和偏晚年分别在平均偏早日、平均日、平均偏晚日对应的 200 hPa 高度场的差值及南亚高压的位置。5 月 28 日,江南区入梅偏早与偏晚年的差值场上(图 3a),伊朗高原至日本岛及其东南洋面这一纬度带为正距平差值,两个正距平中心分别位于伊朗高原和日本岛东北洋面上,而西太平洋为负距平,中心位于菲律宾群岛及其以东洋面;且偏早年 12500 gpm 等值线较偏晚年偏西、偏北,表明入梅偏早年南亚高压建立和北移至青藏高原上空较早,而偏晚年相反。6 月 8 日与 5 月 28 日的空间分布类似,偏早年 12500 gpm 等值线区域较偏晚年明显偏大和偏北(图 3b)。表明入梅偏早年南亚高压建立后,强度较强,北跳较早,而偏晚年相反。6 月 25 日,西太平洋为正距平,而其余大部分地区为负距平(图 3c)。由于此时偏晚年份也已入梅,偏早年份已处于梅雨期,二者环流系统差异不大,但是偏早年南亚高压仍呈偏东的特征。

在南亚高压的北侧,有一条纬向风速较大的西风气流,即东亚副热带西风急流(西风急流),它通常与高空锋区相对应,东亚大气环流的季节转换、中国大部分地区雨季的开始和结束都与西风急流的南北位置及强度变化有密切关系(况雪源等,2006;杨莲梅等,2007;刘芸芸等,2008)。陶诗言等(1958)指出,东亚梅雨的开始和结束与亚洲上空南支西风急流的两次北跳过程密切相关。从多年平均来看,5 月西风急流主要位于东亚东部上空,中心位于江淮流域至日本岛,急流轴位置位于 35°N 附近(图略);6 月西风急流强度减弱,主体位置发生北抬,中心向西伸展至中国西北地区上空,急流轴位置北抬至 40°N 附近;7 月西风急流强度进一步减弱,主体位置进一步北抬,中心位于新疆上空,急流轴位置北抬至 40°N 以北。图 4 分别给出了江南区入梅偏早和偏晚年东亚(110°—140°E 平均)上空 200 hPa 西风急流随时间变化的剖面。从图 4a 可见,入梅偏早年,5 月第 4 候西风急流中心风速增至 35 m/s 以上,急流轴位置第 1 次北跳至 37°N 以北,此时江南区梅雨开始。此后西风急流稳定维持,直至 6 月中下旬发生第 2 次北跳。入梅偏晚年,5 月第 5 候之后,西风急流风速较常年明显弱,中心风速在 35 m/s 以下,急流轴位置第 1 次北跳较晚,急流轴在 35°N 以南(图 4b),导致入梅明显偏晚。

以上分析表明,江南区入梅之前,高层的大气环流发生快速的调整,南亚高压不断北推,中心强度逐渐加强,范围增大,其北侧的西风急流随之加强北跳。总体来看,入梅偏早年,南亚高压和西风急流调整较常年偏早,南亚高压偏强、偏东,西风急流偏强、偏北,且稳定维持,有利于梅雨的维持,而偏晚年调整较常年偏晚。

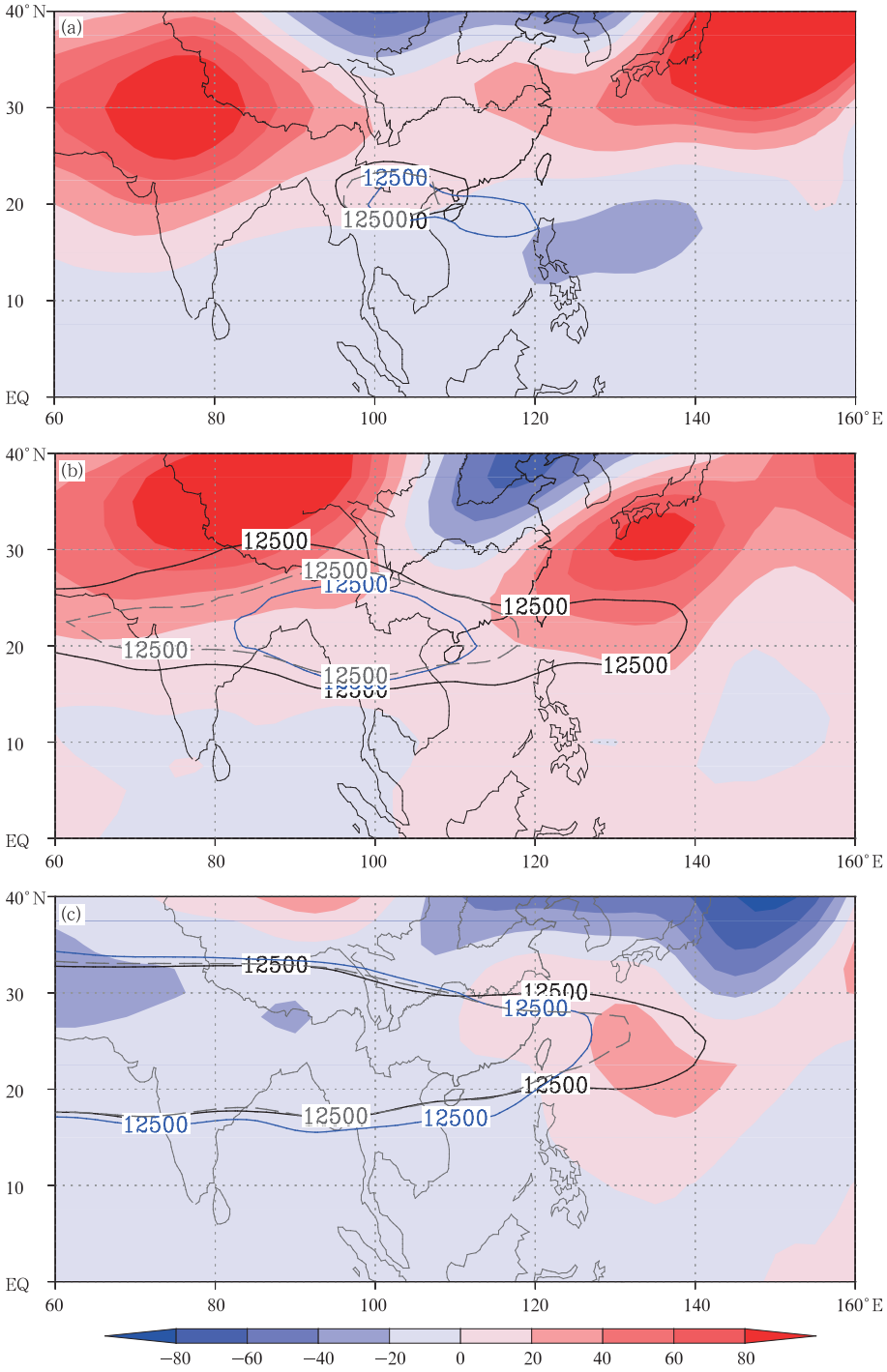

图 3 江南区入梅偏早与偏晚年不同阶段 200 hPa 高度场的差异(单位:gpm)
(a. 平均偏早日(5 月 28 日),b. 平均日(6 月 8 日),c. 平均偏晚日(6 月 25 日);
阴影区表示偏早年与偏晚年的差值,等值线为 12500 gpm,黑色等值线表示偏早年,
蓝色等值线表示偏晚年,灰色虚线表示多年平均)

Fig. 3 Differences in 200 hPa geopotential height at different time between the early and late Meiyu onset years in the region to the south of the Yangtze River (unit: gpm)
(a. On 28 May, b. on 8 June, c. on 25 June; The black and blue contours in each panel are the isolines of 12500 gpm in early and late Meiyu onset years;
the gray dashed line represents the multi-year average)

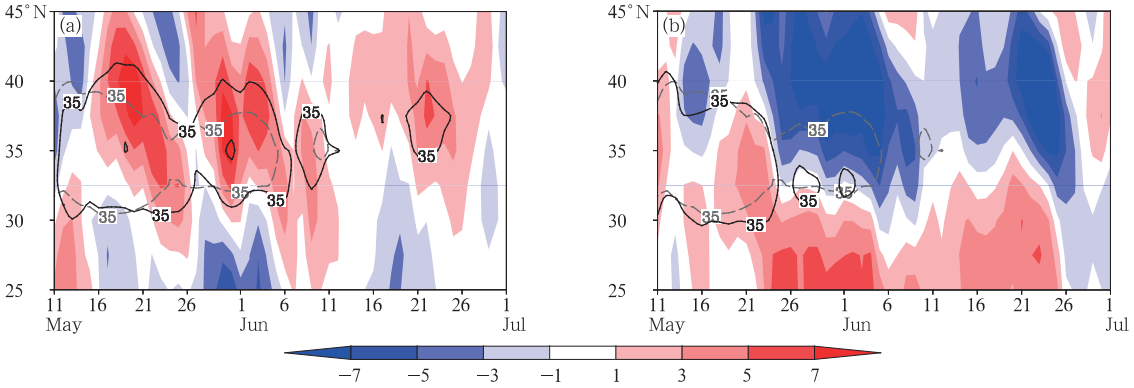

图 4 江南区入梅偏早年(a)和偏晚年(b)东亚 110°—140°E 平均的
200 hPa 纬向风距平(单位:m/s)时间-纬度剖面
(虚线表示气候平均的 35 m/s 等值线,实线表示异常年平均的 35 m/s 等值线)

Fig. 4 Time-latitude cross sections of zonal wind anomaly (unit: m/s) at 200 hPa averaged over 110° − 140°E in (a) early Meiyu onset years to the south of the Yangtze River and in (b) late years
(The dotted line represents the climatological mean of 35 m/s, and the solid line represents the average of 35 m/s in anomalous years)

4.2 中层环流系统对入梅早、晚的影响

500 hPa 高度场作为对流层中层大气环流的代表,可以较清晰地反映东亚气候异常所对应的大气环流特征(Feng, et al, 2013;赵俊虎等,2014)。这一层环流中,低纬度的副高和中、高纬度的环流对中国的天气、气候有重要的影响。图 5 给出了 5 月 28 日、6 月 8 日和 25 日 3 个阶段的江南区入梅偏早和偏晚年合成的 500 hPa 高度场及其距平场。

入梅偏早年 500 hPa 高度距平场上,5 月 28 日,乌拉尔山为显著的正高度距平,阻塞明显,蒙古高原至日本岛为显著的负高度距平,欧亚中、高纬度西高东低,以经向型环流为主;副高偏强、偏西、偏北(图 5a),这样的环流配置有利于冷、暖空气在江南至长江中下游地区交汇,导致江南区入梅偏早;6 月 8 日,欧亚中、高纬度仍维持较强的经向环流,副高维持偏强、偏西(图 5b);6 月 25 日,乌拉尔山和鄂霍次克海西部均为负高度距平,欧亚中、高纬度呈弱的经向环流,副高强度和位置接近常年(图 5c),这种中、高纬度和副热带环流的配置及演变,有利于梅雨较长时间的维持。

入梅偏晚年中高纬度和副热带环流的配置及演变与偏早年相反:5 月 28 日,乌拉尔山及其以东为负高度距平,贝加尔湖至中国东北为正高度距平,欧亚中、高纬度以纬向环流为主,副高偏弱、偏东(图 5d),这种环流形势不利于入梅;6 月 8 日,欧亚中、高纬度仍维持纬向环流,不利于冷空气南下,而副高偏弱、偏东(图 5e),整体环流条件不利于梅雨的形成;6 月 25 日,乌拉尔山和鄂霍次克海南部均转为正高度距平,欧亚中高纬度调整为经向型环流,有利于冷空气南下,副高强度和位置也接近常年(图 5f),环流配置利于梅雨的形成。

由此可见,中、高纬度环流和副高的配置对梅雨的开始和维持起到了关键性的作用。研究表明,副高的季节性变异对短期气候异常有重要影响(张庆云等,1999;赵俊虎等,2012),其阶段性地北跳与中国东部地区的雨季及位置直接相关,从初夏至盛夏副高有两次明显的季节性北跳,第 1 次北跳东亚夏季风推进到长江流域,江淮流域入梅,第 2 次北跳东亚夏季风推进到华北,江淮流域梅雨结束,华北雨季开始(张庆云等,1999;陶诗言等,2006;Ye, et al, 2014)。《梅雨监测业务规定》中也指出了梅雨期副高脊线活动范围,江南区南界≥18°N,北界<25°N。即脊线≥18°N 时有利于江南入梅,而脊线在 18°—25°N 这个范围内,有利于江南区梅雨的维持。图 6 给出了江南区入梅异常年 500 hPa 高度场沿副高区域(110°—140°E)平均的时间-纬度剖面。由图 6a 可见,入梅偏早年,5 月中旬起副高区域为显著的正高度距平,一直持续到6月下旬初,副高脊线总体

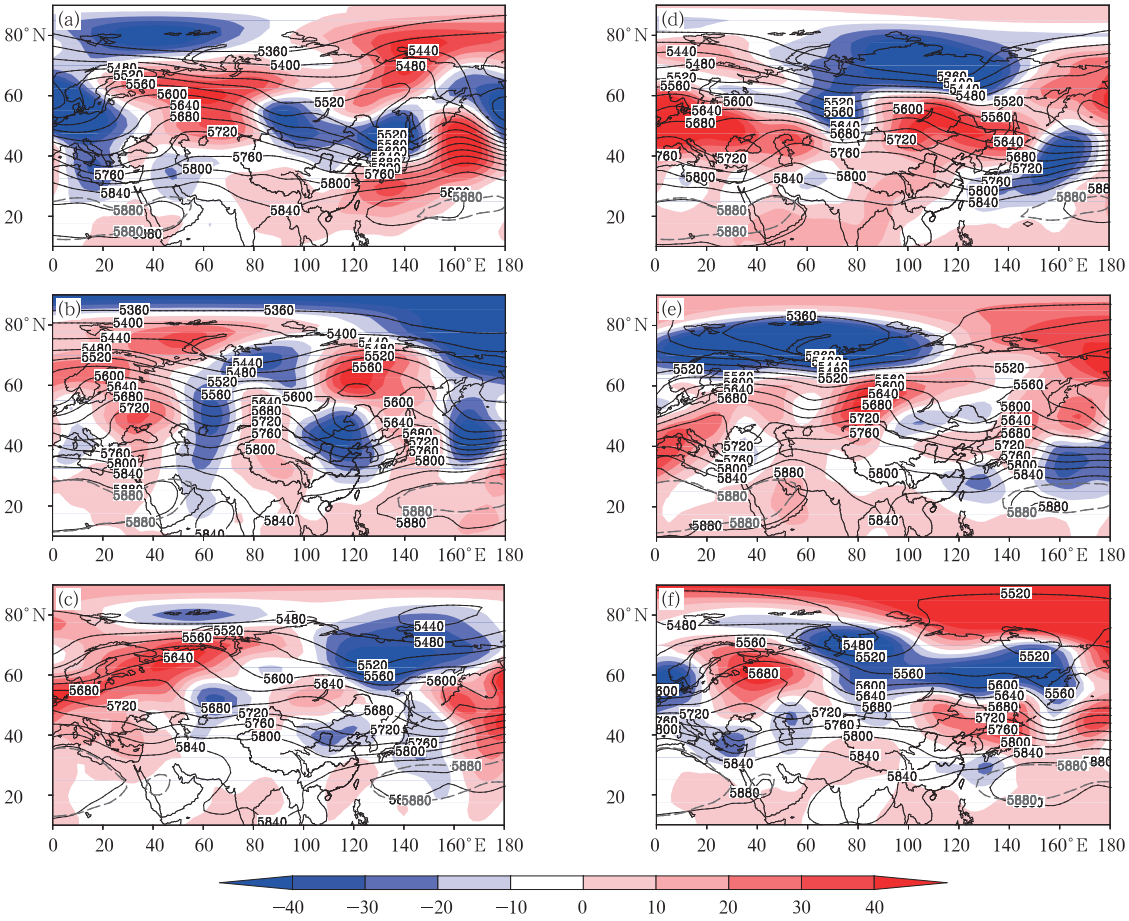

图 5 江南区入梅偏早年(a、b、c)和偏晚年(d、e、f)不同阶段 500 hPa 高度场(单位:gpm)的特征
(阴影区为距平,黑色等值线为合成的高度场,灰色虚线为气候态;a、d. 平均偏早日(5 月 28 日),
b、e. 平均日(6 月 8 日),c、f. 平均偏晚日(6 月 25 日))

Fig. 5 Characteristics of 500 hPa geopotential height (unit: gpm) at different stages in (a, b, c) early Meiyu onset years and (d, e, f) late Meiyu onset years to the south of the Yangtze River
(shaded areas indicate the anomaly field, black contours show the composite geopotential height, gray dotted lines indicate the climatological mean; a and d. 28 May, b and e. 8 June, c and f. 25 June)

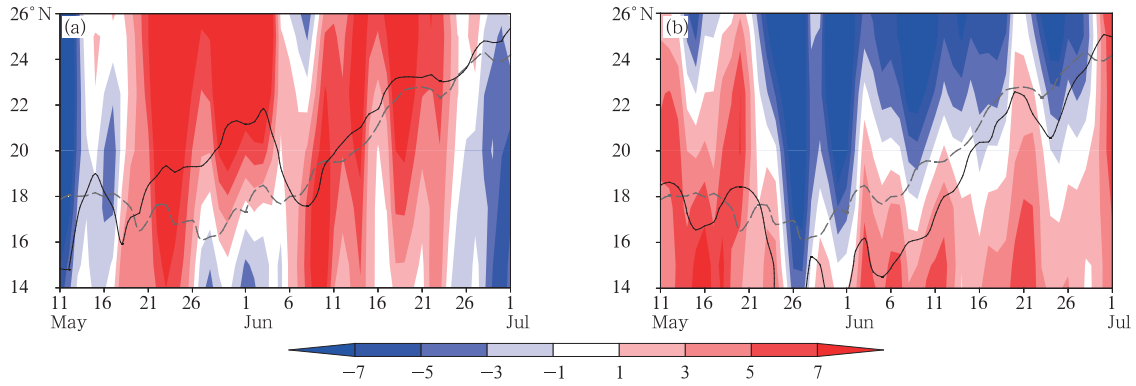

图 6 江南区入梅异常年 500 hPa 高度场(单位:gpm)沿 110°—140°E 平均的时间-纬度剖面
(a. 偏早年,b. 偏晚年;阴影区为距平,虚线表示气候平均副高脊线,实线表示异常年平均副高脊线)

Fig. 6 Time-latitude cross sections (unit: gpm) of 500 hPa geopotential height averaged over 110°—140°E
(a. early Meiyu onset years , b. late onset years to the south of the Yangtze River; shaded areas indicate the anomaly field, the dotted line represents the climatological subtropical high ridge line, and the solid line represents the mean subtropical high ridge line in anomalous years)

偏北,并维持在 20°N 以北;入梅偏晚年,5 月下旬起副高区域北部(副高多年平均的脊线北部)为明显的负高度距平,副高区域南部为正高度距平,这一特点一直持续到 6 月下旬;5 月下旬至 6 月中旬副高脊线明显偏南,维持在 20°N 以南(图 6b)。

Ye 等(2014)研究了副高两次北跳的定义及定量化计算方法,利用其定义,计算出 1951—2015 年副高脊线第 1 次北跳的时间,多年平均为 6 月第 2 候,与张庆云等(1999)的研究结论一致。江南区入梅的平均时间也为 6 月第 2 候,与副高第 1 次北跳时间相对应。图 7 给出了江南区入梅时间与副高第 1 次北跳时间距平的年际变化及二者的 21 年滑动相关。由图 7a 可见,二者的年际变化具有较好的一致性,江南区入梅极端早(晚)年,副高第 1 次北跳也偏早(晚),如 1953、1961、1971、1990、1995 和 1996 年(1967、1968、1987、1992、1997、2003、2004、2005、2009 和 2014 年)。65 年中二者距平符号一致的有 48 年,占 74%。其中,1951—1980 年距平符号一致的有 17 年,占 57%,二者的相关系数也仅为 0.15;但 1986—2015 年距平符号一致的有 26 年,占 87%,二者的相关系数为 0.55。从二者的 21 年滑动相关系数(图 7b)也可以清楚地看出,1986 年之前为弱的正相关,1986 年之后为显著的正相关。以上分析表明,副高第 1 次北跳对江南区入梅有重要的作用,副高第 1 次北跳偏早,有利于水汽向江南输送,有利于梅雨的开始,但这种关系存在年代际的变化,20 世纪 80 年代之前关系不显著,80 年代之后关系显著。这可能与变暖后副高膨胀有关系,20世纪

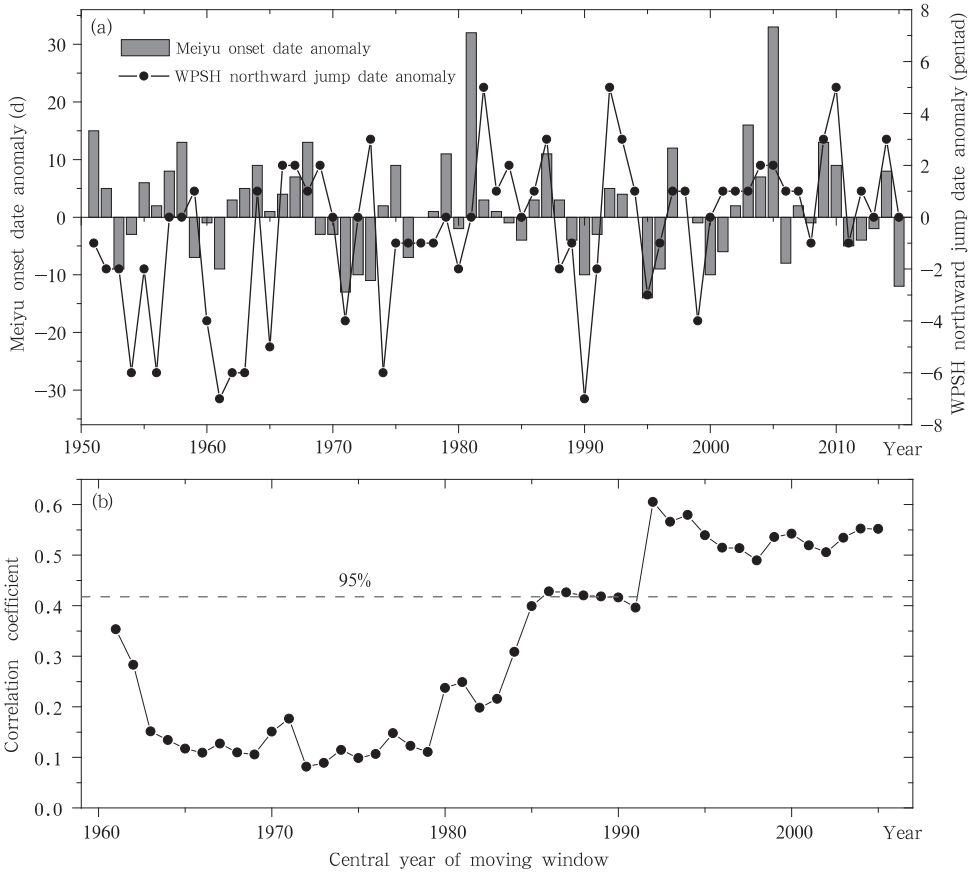

图 7 江南区入梅时间与副高第 1 次北跳时间距平的(a)年际变化及(b)二者 21 年滑动相关(虚线表示通过 95%的置信度 t 检验)

Fig. 7 Time series of anomalies of the first northward jump of the western Pacific subtropical high and the Meiyu onset date to the south of the Yangtze River (a. interannual variability, b. 21-year sliding correlations; The dashed line indicates significance at/above the 95% confidence level)

80年代之后副高偏强、偏西(Li, et al,2012;赵俊虎等,2012;Zhao, et al,2014),北跳偏晚(Ye, et al,2014),江南区入梅也处于偏晚的年代际特征。在年代际变化一致的背景下,副高第1次北跳对江南区入梅的作用在加强,二者的年际关系也更密切。

4.3 低层环流系统对入梅早、晚的影响

低层环流系统可直接反映越赤道气流、东亚夏季风爆发早晚及其强弱及水汽的辐合、辐散等。图8分别给出了江南区入梅偏早和偏晚年5月28日、6月8日、25日3个时期的850 hPa风场距平。

入梅偏早年850 hPa风距平场上,5月28日(图8a),热带印度洋西部为南风距平,并在阿拉伯海转为西风距平,表明索马里急流爆发偏早;同时,西太平洋为较强的反气旋式距平环流,中心在台湾以东地区,表明菲律宾反气旋显著。越赤道气流加强、菲律宾反气旋显著均有利于水汽向中国南方地区输送,而中国西北地区为偏西北风距平,有利于冷空气南下。低层环流系统的这种配置有利于冷暖空气在中国江南地区交汇,进而有利于梅雨的开始。6月8日(图8b),孟加拉湾至中南半岛西南风距平明

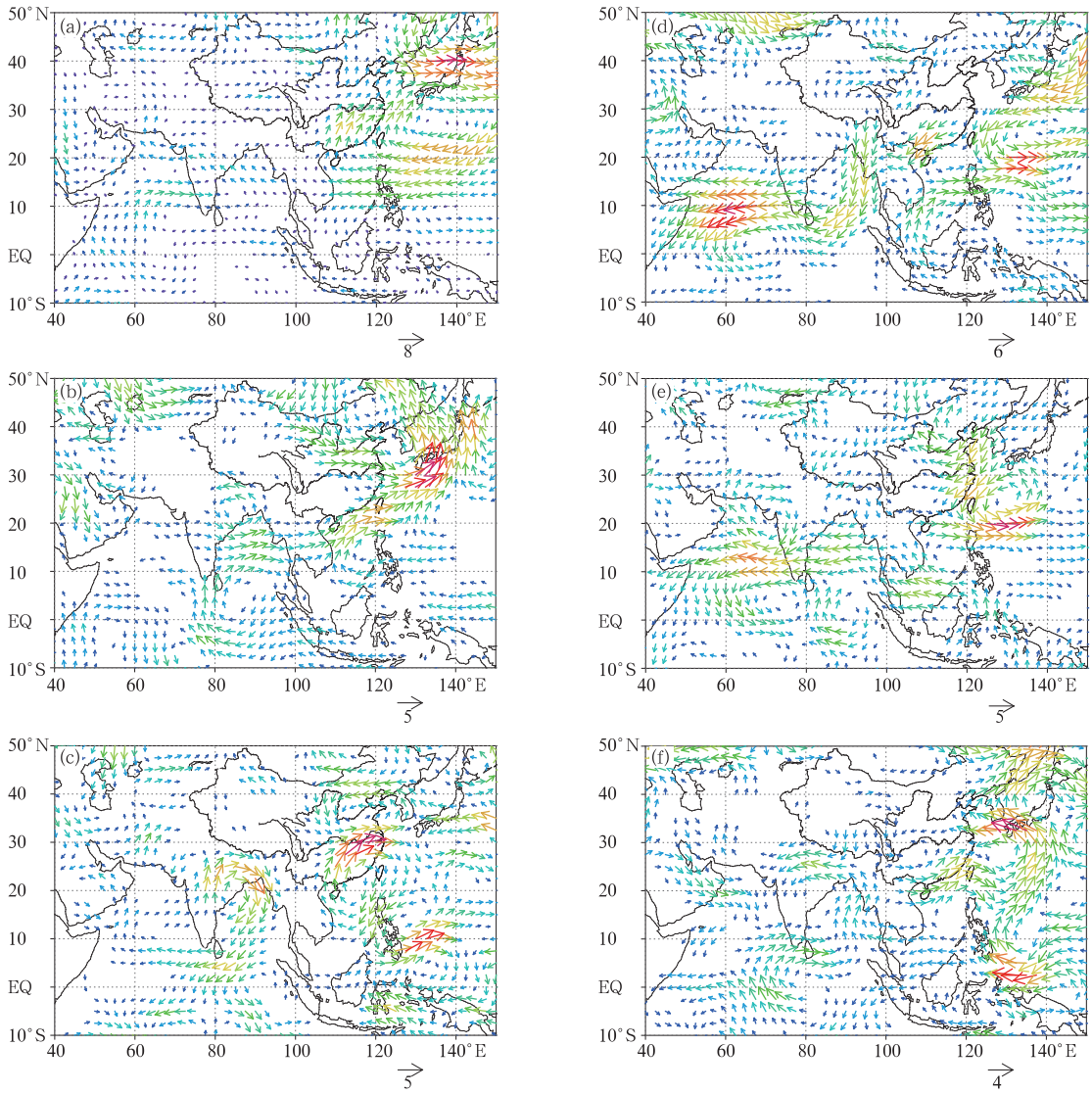

图8 江南区入梅偏早年(a、b、c)和偏晚年(d、e、f)不同阶段850 hPa风场(单位:m/s)的特征

(a、d.平均偏早日(5月28日),b、e.平均日(6月8日),c、f.平均偏晚日(6月25日))

Fig. 8 Characteristics of 850 hPa wind field at different stages in (a, b, c) early Meiyu onset years and (d, e, f) late onset years to the south of the Yangtze River (unit: m/s)

(a and d. 28 May, b and e. 8 June, c and f. 25 June)

显加强,表明南海夏季风已爆发,同时,中国南海至菲律宾为反气旋式距平环流,中心西移至菲律宾附近,加强了印度洋至中国南海的水汽向中国南方地区输送;中国西北至长江流域为强盛的西北风距平,有利于冷空气南下,这样的低层环流系统配置有利于梅雨形势的维持。6月25日(图8c),孟加拉湾为反气旋式距平环流,西太平洋仍为反气旋式距平环流,中心北移至中国南海北部,中国西北地区东部至长江流域为西北风距平,有利于冷空气南下,冷、暖空气在长江流域辐合,这样的低层环流系统配置有利于梅雨较长时间的维持,且此时梅雨从江南扩大至江淮的广大区域。

偏晚年则相反,5月28日(图8d),热带印度洋西部为北风距平,阿拉伯海至孟加拉湾地区为东风距平,表明索马里急流爆发偏晚,越赤道气流较弱,西太平洋为气旋式距平环流,中国西北地区为偏东风距平,这样的环流系统配置不利于冷空气南下和水汽向中国南方地区输送,不利于入梅;6月8日(图8e),中南半岛经孟加拉湾至阿拉伯海仍为东风距平,表明越赤道气流仍较弱,西太平洋仍维持气旋式距平环流,这样的低层环流系统演变不利于中国南海夏季风爆发和水汽向中国南方地区输送,不利于入梅;6月25日(图8f),索马里急流不显著,澳大利亚西部的越赤道气流增强,孟加拉湾地区转为南风距平,并经中南半岛转为西南风进入中国南方地区,西太平洋反气旋距平环流较弱,且中心位于菲律宾以东地区,造成水汽输送路径偏东。由此可见江南入梅偏晚年,入梅时的环流型与偏早年入梅时的环流型有明显的差异,即越赤道气流不同,菲律宾反气旋的位置也不同。

索马里越赤道气流具有季风性质且为夏季低层最强的越赤道急流,对东亚季风活动和气候都具有重要作用。在中国南海夏季风爆发前两候,索马里急流会有一次迅速地增强(高辉等,2006),多年平均的建立时间是5月第3候(代玮等,2014),急流年际尺度上的强弱对中国南海季风爆发迟早起重要作用(施宁,2001)。图9给出了江南区入梅异常年925 hPa高度场沿赤道的时间-经度剖面。入梅偏早年,5月上旬开始60°E附近为显著的南风距平,表明索马里越赤道气流爆发偏早,强度明显偏强,尤其是5月下旬,风速大于1 m/s(图9a),有利于中国南海夏季风的爆发和入梅;而入梅偏晚年相反,5月上

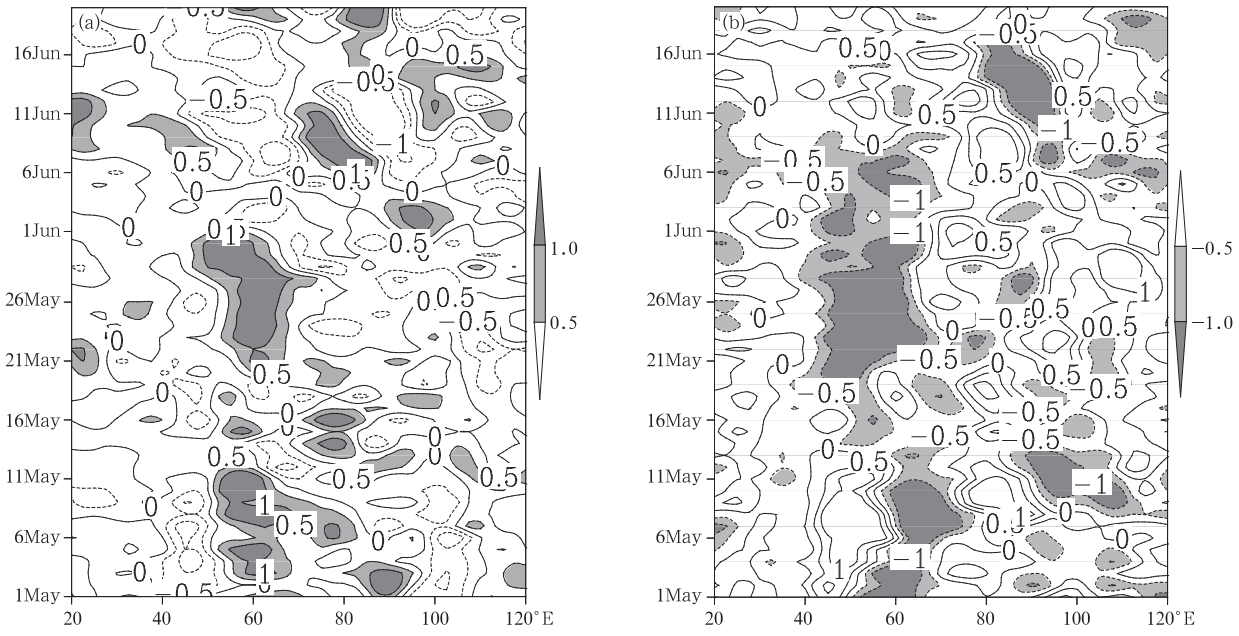

图9 江南区入梅异常年925 hPa越赤道经向风(单位:m/s)的时间-经度剖面

(a. 偏早年,b. 偏晚年)

Fig. 9 Time-longitude cross sections of meridional cross-equator wind at 925 hPa (unit: m/s) in (a) early Meiyu onset years and (b) late onset years to the south of the Yangtze River

旬—6月上旬,60°E附近为显著的负距平,表明索马里越赤道气流爆发偏晚,强度明显偏弱(图9b),不利于中国南海夏季风的爆发和入梅。李崇银等(2002)研究指出,索马里越赤道气流的稳定建立是中国南海夏季风爆发的重要物理机制之一,可导致赤道印度洋地区西风的持续加强和向东扩展,并最终在中国南海地区形成西南气流。索马里越赤道气流建立偏早,有利于中国南海夏季风爆发偏早和江南区入梅。

5 江南区梅雨入梅早、晚的前兆信号

大气环流异常除了内部的动力过程外,还受到外强迫的作用,海表温度异常是影响环流异常的关键因子,也是短期气候预测重要的前兆信号(魏凤英等,2005;封国林等,2012;陈丽娟等,2013)。图10为1951—2015年江南区入梅日与前冬、春季海表温度的相关系数分布。由图10a可见,入梅日与前冬中东太平洋海表温度成正相关,与西太平洋及澳大利亚周边海表温度成负相关,与北大西洋海表温度从北向南呈"+ - +"的相关分布,上述相关分布型类似中部型厄尔尼诺;其中,赤道中太平洋海表温度的正相关、澳大利亚西南部及东南部海表温度的负相关及澳大利亚以东150°W附近海表温度的正相关均通过95%的置信度t检验。入梅日与春季海表温度的相关分布大体上与冬季类似,但除赤道中太平洋外,其余通过置信度检验的区域有明显的改变,其中与北大西洋从北至南"+ - +"的相关分布更显著,而与澳大利亚周边海表温度的相关性减弱(图10b)。由此可见,江南区入梅日主要与冬季的中太平洋和澳大利亚东南部海表温度及春季北大西洋海表温度三极子关系较密切。

选取Nino4指数、北大西洋海表温度三极子指数和澳大利亚东部海表温度偶极子指数(ASI,50°—40°S,150°—170°E区域平均海表温度减去46°—36°S,200°—220°E区域平均海表温度),分析逐月3个海表温度指数与江南入梅日的关系。图11给出了上一年1月至当年12月逐月的3个海表温度指数与入梅日相关系数演变情况。其中上一年4月至当年12月的Nino4指数与入梅日维持了弱的正相关;上一年1月至当年12月的澳大利亚东部海表温度偶极子指数与江南入梅日维持了负相关,其中上一年11月至当年2月的关系通过了99%的置信度t检验,尤其是上一年12月的相关系数高达-0.42;而上一年9月至当年12月的北大西洋海表温度三极子指数与入梅日维持了负相关,其中,当年3月的关系通过了99%的置信度t检验。

由此可见,冬季澳大利亚东部海表温度偶极子和春季北大西洋海表温度三极子对入梅早、晚的影响较显著,选取入梅当年3月的北大西洋海表温度三极子指数和上一年12月澳大利亚东部海表温度偶极子指数与入梅年6月东亚大气环流进行回归分析。从3月的北大西洋海表温度三极子指数回归的6月200 hPa纬向风场(图12a)可见,中国黄河流域至日本岛为显著的正值区,表明3月北大西洋海表温度三极子正位相时,6月西风急流偏强偏北,有利于江南入梅偏早和梅雨的维持;从上一年12月的澳大利亚东部海表温度偶极子指数回归的6月500 hPa高度场(图12b)可见,20°N以南为显著的负值区,而西太平洋西部22°—30°N区域为正值区,且12月澳大利亚东部海表温度偶极子指数与副高第1次北跳的相关系数高达0.39,表明12月的澳大利亚东部海表温度偶极子指数为正值时,副高第

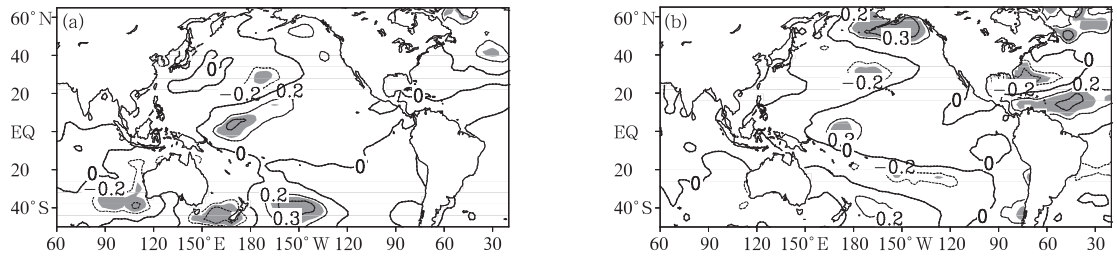

图10 1951—2015年江南区梅雨入梅日与冬季(a)和春季(b)海表温度的相关系数分布
(阴影区表示通过95%的置信度t检验)

Fig. 10 Correlation coefficients of the Meiyu onset date to the south of the Yangtze River with (a) winter SST and (b) spring SST during 1951-2015
(Shaded areas indicate significance at/above the 95% confidence level)

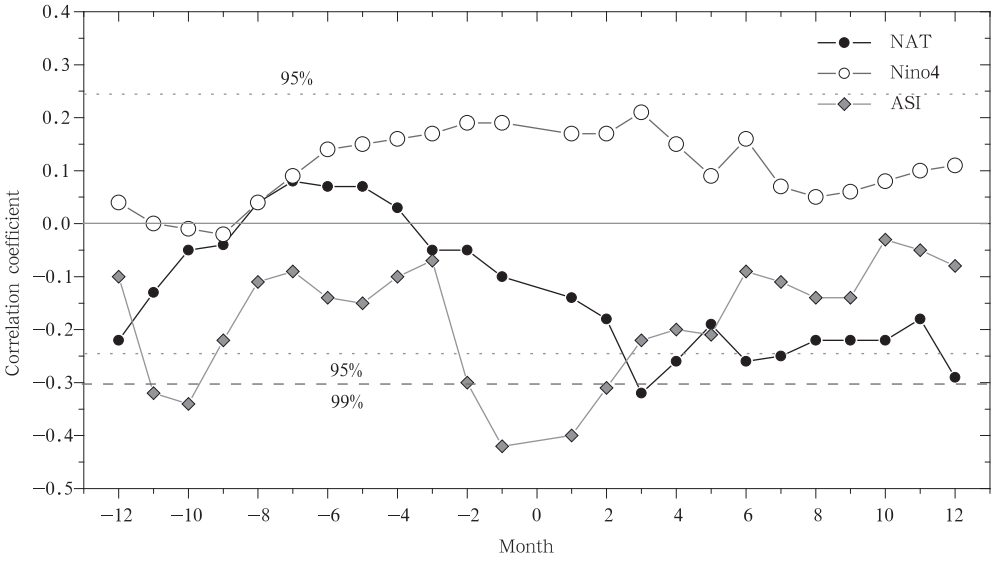

图 11 1951—2015 年江南区入梅日与关键区域海表温度指数的时滞相关
(点(虚)线表示通过 95%(99%)的置信度 t 检验)
Fig. 11 Time-lag correlations of the SST index in critical area with the Meiyu onset date to the south of the Yangtze River between 1951 and 2015
(The dot (dashed) line indicates significance at the 95% (99%) confidence level)

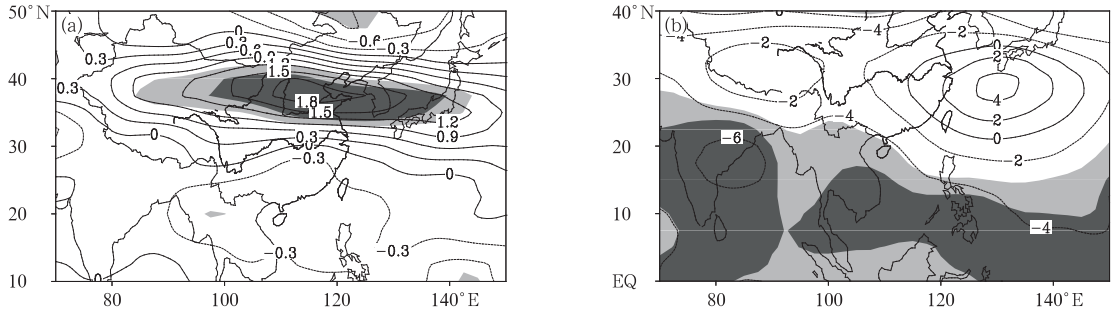

图 12 入梅当年 3 月的北大西洋海表温度三极子指数回归的 6 月 200 hPa 纬向风(a),入梅上一年 12 月的澳大利亚东部海表温度偶极子指数回归的 6 月 500 hPa 高度场(b)(浅(深)阴影表示通过 95%(99%)的置信度 t 检验)
Fig. 12 Linear regression of 200 hPa zonal wind in June onto the NAT index in March (a), linear regression of 500 hPa geopotential height in June onto the ASI index in the preceding December (b)
(Light (deep) shadings indicate significance at/above the 95% (99%) confidence level)

1 次北跳偏早,6 月副高偏北(多年平均的 6 月副高脊线为 21.8°N),有利于江南入梅偏早。众多研究也表明,北大西洋海表温度异常对中国夏季的气候有重要的影响。徐海明等(2001a,2001b)研究发现,江淮入梅的年际变化与前期冬春北大西洋海表温度异常有密切的联系,入梅偏早年,北大西洋海表温度较常年偏暖(25°—40°N,90°—40°W),偏晚年则海表温度偏冷。此外,前冬澳大利亚东侧局地海域海表温度异常对中国夏季降水具有重要的影响,当海表温度偏暖时,随后夏季副高和东亚西风急流位置往往偏南,中国大陆沿岸低层盛行异常的西南风,有利于长江流域降水增多(刘舸等,2008;周波涛,2011)。这些研究结论也佐证了文中揭示的江南入梅早、晚的前兆信号:前期冬春澳大利亚东部海表温度偶极子和北大西洋海表温度三极子。不同之处是,过去这些研究主要针对季节尺度旱涝的前兆信号及影响途径,而文中则主要针对江南入梅早晚这一季节内尺度的气候现象。

6 结论和讨论

中国地处东亚季风区,雨季的开始与东亚夏季风环流系统的建立和推进密切相关。其中入梅早晚

一直是短期气候预测的重点和难点。基于中国气象局2014年发布的中国《梅雨监测业务规定》及其相关资料,重点研究了江南入梅早、晚年的同期(5—6月)大尺度大气环流和前期海表温度的异常特征,主要结论如下:

(1) 从多年平均的情况来看,中国雨季最早从华南开始(伍红雨等,2015),4月第2候华南进入前汛期,持续1个多月之后,在5月第3候索马里越赤道气流建立,5月第5候中国南海夏季风爆发,此后高层环流也开始快速调整,6月第1候副热带西风急流北抬,6月第2候副高第1次北跳,与此同时中国江南梅雨开始,长江流域滞后1候左右入梅(图13a);以上是从气候态的角度给出了中国梅雨开始前的环流调整,而实际上东亚大气环流具有较强的

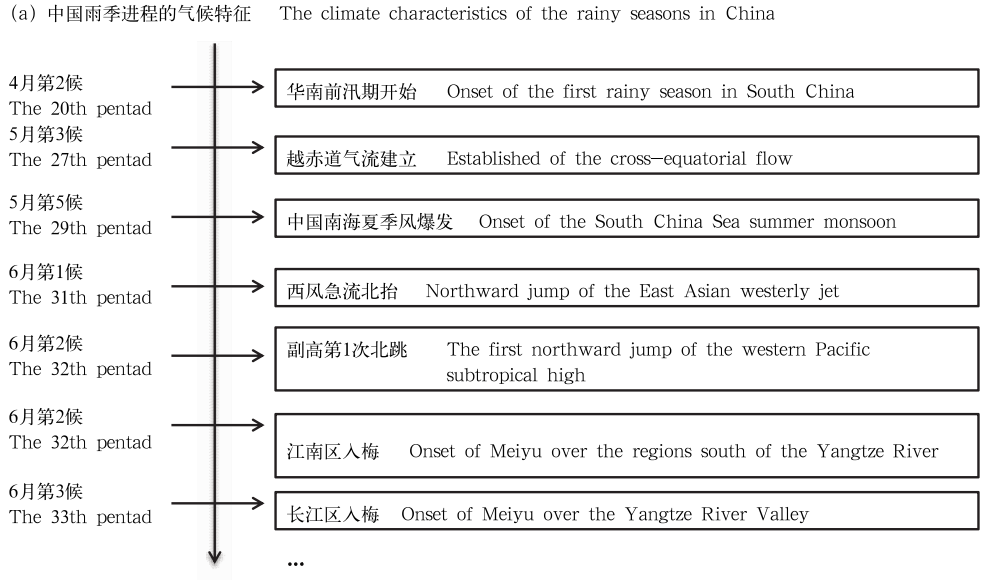

图13 中国雨季进程的气候特征(a)和江南入梅早晚影响系统概念(b)

Fig. 13 The climatic characteristics of the Chinese rainy season (a) and The impact system concept map of early and late Meiyu onset of regions south of the Yangtze River (b)

年际变化,导致入梅早晚也存在较大的年际差异。

(2) 江南区入梅早、晚年对流层高层到低层的大尺度大气环流具有明显的差异(图 13b),入梅偏早年,南亚高压和东亚副热带西风急流的建立较早,强度较强,南亚高压北移到青藏高原上空也偏早,西风急流北跳偏早;中高纬度经向环流较强,有利于冷空气南下,而副高第 1 次北跳偏早,越赤道气流建立较早,中国南海夏季风爆发偏早,有利于水汽向中国南方地区输送,冷空气与暖湿水汽较早在江南对峙,导致江南区入梅偏早;入梅偏晚年上述环流系统演变特征则基本相反。

(3) 冬春季海表温度异常是影响入梅早晚的重要外强迫因子,也是重要的前期预测信号:当冬季中东太平洋海表温度为负距平、澳大利亚东部海表温度偶极子为正位相、春季北大西洋海表温度三极子为正位相时,江南区入梅偏早;其中入梅上一年 12 月澳大利亚东部海表温度偶极子和当年 3 月北大西洋海表温度三极子与入梅关系最为密切,当 12 月澳大利亚东部海表温度偶极子为正位相时,副高第 1 次北跳偏早,而 3 月北大西洋海表温度三极子为正位相时,6 月西风急流偏强、偏北,有利于入梅偏早(图 13b)。

以上这些结论为江南入梅的短期气候预测提供了参考依据,但是仍有一些问题需要继续开展研究:文中提到的副高第 1 次北跳时间与江南区入梅时间的年际关系在 20 世纪 80 年代存在年代际转变,这种转变的内在原因是什么? 同时,从现在的分析结果来看,前冬澳大利亚东部海表温度偶极子可以影响后期初夏副高北跳早晚,这可能是前者通过影响澳大利亚高压的强弱和位置进而影响到西太副高北跳的早晚;而春季北大西洋三极子可以影响初夏副热带西风急流的位置,进而影响入梅的早晚。上述影响的内在物理过程还有待于做进一步的诊断分析和数值试验来验证。此外,研究表明中国长江中下游梅雨异常与全球范围内大尺度环流相联系,入梅的早晚和梅雨量的多寡,不仅与东亚环流异常有关,还与春季北大西洋涛动(NAO)、南半球春夏季环流的异常密切相关。例如,Tian 等(2012)研究发现,5 月北大西洋涛动与长江中下游夏季极端降水频次呈现显著的负相关;范可(2006)研究指出,春季南极涛动正异常、南半球副热带高压在春夏季持续加强有利于长江中下游夏季降水偏多。但南北半球相互作用及其对东亚夏季气候、尤其是梅雨的影响机理是一个复杂的问题,尚有待进一步深入研究。

参考文献

鲍名. 2009. 从中期天气过程看近几年长江中下游梅雨偏少的原因. 大气科学, 33(4): 708-718. Bao M. 2009. Causes of deficit Meiyu over the middle and lower reaches of the Yangtze river in the last several years viewed from medium range weather process. Chinese J Atmos Sci, 33(4): 708-718 (in Chinese)

陈丽娟, 袁媛, 杨明珠等. 2013. 海温异常对东亚夏季风影响机理的研究进展. 应用气象学报, 24(5): 521-532. Chen L J, Yuan Y, Yang M Z, et al. 2013. A review of physical mechanisms of the global SSTA impact on EASM. J Appl Meteor Sci, 24(5): 521-532 (in Chinese)

代玮, 肖子牛. 2014. 索马里急流多时间尺度的变化特征及其与中国降水的联系. 热带气象学报, 30(2): 368-376. Dai W, Xiao Z N. 2014. Multi-time scale variation characteristics of Somali jet and its contact with precipitation in China. J Trop Meteor, 30(2): 368-376 (in Chinese)

丁一汇, 柳俊杰, 孙颖等. 2007. 东亚梅雨系统的天气-气候学研究. 大气科学, 31(6): 1082-1101. Ding Y H, Liu J J, Sun Y, et al. 2007. A study of the synoptic-climatology of the Meiyu system in East Asia. Chinese J Atmos Sci, 31(6): 1082-1101 (in Chinese)

范可. 2006. 南半球环流异常与长江中下游夏季旱涝的关系. 地球物理学报, 49(3): 672-679. Fan K. 2006. Atmospheric circulation anomalies in the Southern Hemisphere and summer rainfall over Yangtze River Valley. Chinese J Geophys, 49(3): 672-679 (in Chinese)

封国林, 杨涵洧, 张世轩等. 2012. 2011 年春末夏初长江中下游地区旱涝急转成因初探. 大气科学, 36(5): 1009-1026. Feng G L, Yang H W, Zhang S X, et al. 2012. A preliminary research on the reason of a sharp turn from drought to flood in the middle and lower reaches of the Yangtze River in late spring and early summer of 2011. Chinese J Atmos Sci, 36(5): 1009-1026 (in Chinese)

葛全胜, 郭熙凤, 郑景云等. 2007. 1736 年以来长江中下游梅雨变化. 科学通报, 52(23): 2792-2797. Ge Q S, Guo X F, Zheng J Y, et al. 2008. Meiyu in the middle and lower reaches of the Yangtze River since 1736. Chinese Sci Bull, 53(1): 107-114

胡娅敏, 丁一汇, 廖菲. 2008. 江淮地区梅雨的新定义及其气候特征. 大气科学, 32(1): 101-112. Hu Y M, Ding Y H, Liao F. 2008. A study of updated definition and climatological characters of Meiyu season in the Yangtze-Huaihe region. Chinese J Atmos Sci, 32(1): 101-112 (in Chinese)

况雪源，张耀存. 2006. 东亚副热带西风急流位置异常对长江中下游夏季降水的影响. 高原气象，25(3)：382-389. Kuang X Y，Zhang Y C. 2006. Impact of the position abnormalities of East Asian subtropical westerly jet on summer precipitation in middle-lower reaches of Yangtze River. Plateau Meteor，25(3)：382-389 (in Chinese)

李崇银，吴静波. 2002. 索马里跨赤道气流对南海夏季风爆发的重要作用. 大气科学，26(2)：185-192. Li C Y，Wu J B. 2002. Important role of the somalian cross-equator flow in the onset of the South China Sea summer monsoon. Chinese J Atmos Sci，26(2)：185-192 (in Chinese)

李维京. 1999. 1998 年大气环流异常及其对中国气候异常的影响. 气象，25(4)：20-25，57. Li W J. 1999. General atmospheric circulation anomaly in 1998 and their impact on climate anomaly in China. Meteor Mon，25(4)：20-25，57 (in Chinese)

李小泉. 1981. 从整体上研究梅雨期的划分. 气象，7(6)：9-10. Li X Q. 1981. Study on division of Meiyu from regional viewpoint. Meteor Mon，7(6)：9-10 (in Chinese)

李勇，金荣花，周宁芳等. 2017. 江淮梅雨季节强降雨过程特征分析. 气象学报，75(5)：717-728. Li Y，Jin R H，Zhou N F，et al. 2017. An analysis on characteristics of heavy rainfall processes during the Meiyu season in Jianghuai region. Acta Meteor Sinica，75(5)：717-728 (in Chinese)

梁萍，丁一汇，何金海等. 2010. 江淮区域梅雨的划分指标研究. 大气科学，34(2)：418-428. Liang P，Ding Y H，He J H，et al. 2010. A Study of determination index of regional Meiyu over the Yangtze-Huaihe basin. Chinese J Atmos Sci，34(2)：418-428 (in Chinese)

林春育. 1979. 长江中下游的梅雨和预报. 气象，5(5)：2-8. Lin C Y. 1979. The Meiyu and its forecasting in the middle and lower reaches of the Yangtze River. Meteor Mon，5(5)：2-8 (in Chinese)

刘舸，张庆云，孙淑清. 2008. 澳大利亚东侧环流及海温异常与长江中下游夏季旱涝的关系. 大气科学，32(2)：231-241. Liu G，Zhang Q Y，Sun S Q. 2008. The Relationship between circulation and SST anomaly East of Australia and the summer rainfall in the middle and lower reaches of the Yangtze River. Chinese J Atmos Sci，32(2)：231-241 (in Chinese)

刘屹岷，洪洁莉，刘超等. 2013. 淮河梅雨洪涝与西太平洋副热带高压季节推进异常. 大气科学，37(2)：439-450. Liu Y M，Hong J L，Liu C，et al. 2013. Meiyu flooding of Huaihe River Valley and anomaly of seasonal variation of subtropical anticyclone over the Western Pacific. Chinese J Atmos Sci，37(2)：439-450 (in Chinese)

刘芸芸，丁一汇. 2008. 印度夏季风的爆发与中国长江流域梅雨的遥相关分析. 中国科学 D 辑：地球科学，38(6)：763-775. Liu Y Y，Ding Y H. 2008. Teleconnection between the Indian summer monsoon onset and the Meiyu over the Yangtze River Valley. Science in China Series D：Earth Sciences，51(7)：1021-1035

牛若芸，金荣花. 2009. 2008 年梅雨异常大尺度环流成因分析. 高原气象，28(6)：1326-1334. Niu R Y，Jin R H. 2009. Causes analysis of large scale circulation of abnormal characteristic in Meiyu period of 2008. Plateau Meteor，28(6)：1326-1334 (in Chinese)

闵屾，钱永甫. 2008. 江淮梅雨分区特征的比较研究. 应用气象学报，19(1)：19-27. Min S，Qian Y F. 2008. Comparative investigation on Meiyu parameters in different subregions of the Changjiang-Huaihe Valley. J Appl Meteor Sci，19(1)：19-27 (in Chinese)

上海气象局预报组. 1980. 梅雨中期预报方法的研究. 大气科学，4(1)：1-11. Forecasting Group，Shanghai Meteorological Bureau. 1980. A study on the methods of mid-range forecast for "plum rains". Chinese J Atmos Sci，4(1)：1-11 (in Chinese)

施能，朱乾根，吴彬贵. 1996. 近 40 年东亚夏季风及我国夏季大尺度天气气候异常. 大气科学，20(5)：575-583. Shi N，Zhu Q G，Wu B G. 1996. The East Asian summer monsoon in relation to summer large scale weather-climate anomaly in China for last 40 years. Chinese J Atmos Sci，20(5)：575-583 (in Chinese)

施宁，施丹平，严明良. 2001. 夏季越赤道气流对南海季风及华东旱涝的影响. 热带气象学报，17(4)：405-414. Shi N，Shi D P，Yan M L. 2001. The effects of cross-equatorial current on South China Sea monsoon onset and drought/flood in East China. J Trop Meteor，17(4)：405-414 (in Chinese)

陶诗言，赵煜佳，陈晓敏. 1958. 东亚的梅雨期与亚洲上空大气环流季节变化的关系. 气象学报，29(2)：119-134. Tao S Y，Zhao Y J，Chen X M. 1958. The relationship between May-Yü in far east and the behaviour of circulation over Asia. Acta Meteor Sinica，29(2)：119-134 (in Chinese)

陶诗言，朱文妹，赵卫. 1988. 论梅雨的年际变异. 大气科学，12(S1)：13-21. Tao S Y，Zhu W M，Zhao W. 1988. Interannual variability of Meiyu rainfalls. Chinese J Atmos Sci，12(S1)：13-21 (in Chinese)

陶诗言，卫捷. 2006. 再论夏季西太平洋副热带高压的西伸北跳. 应用气象学报，17(5)：513-525. Tao S Y，Wei J. 2006. The westward，northward advance of the subtropical high over the West Pacific in summer. J Appl Meteor Sci，17(5)：513-525 (in Chinese)

王黎娟，郭帅宏，何金海等. 2013. 4～5 月南亚高压建立早晚年份环流差异及其可能成因. 大气科学，37(6)：1165-1178. Wang L J，Guo S H，He J H，et al. 2013. Circulation differences and possible mechanism underlying the South Asia high establishment from April to May in the early or delayed establishment years. Chinese J Atmos Sci，37(6)：1165-1178 (in Chinese)

魏凤英，张京江. 2004. 1885～2000 年长江中下游梅雨特征量的统计分析. 应用气象学报，15(3)：313-321. Wei F Y，Zhang J J.

2004. Climatic variation of Meiyu in the middle-lower reaches of Changjiang River during 1885～2000. J Appl Meteor Sci, 15(3): 313-321 (in Chinese)

魏凤英, 宋巧云. 2005. 全球海表温度年代际尺度的空间分布及其对长江中下游梅雨的影响. 气象学报, 63(4): 477-484. Wei F Y, Song Q Y. 2005. Spatial distribution of the global sea surface temperature with interdecadal scale and their potential influence on Meiyu in middle and lower reaches of Yangtze River. Acta Meteor Sinica, 63(4): 477-484 (in Chinese)

伍红雨, 杨崧, 蒋兴文. 2015. 华南前汛期开始日期异常与大气环流和海温变化的关系. 气象学报, 73(2): 319-330. Wu H Y, Yang S, Jiang X W. 2015. Anomalous onset date of the first rainy season in South China and its relationship with the variation of the atmospheric circulation and SST. Acta Meteor Sinica, 73(2): 319-330 (in Chinese)

吴志伟, 江志红, 何金海. 2006. 近50年华南前汛期降水、江淮梅雨和华北雨季旱涝特征对比分析. 大气科学, 30(3): 391-401. Wu Z W, Jiang Z H, He J H. 2006. The comparison analysis of flood and drought features among the first flood period in South China, Meiyu period in the Yangtze River and the Huaihe River valleys and rainy season in North China in the last 50 years. Chinese J Atmos Sci, 30(3): 391-401(in Chinese)

徐海明, 何金海, 周兵. 2001a. 江淮入梅前后大气环流的演变特征和西太平洋副高北跳西伸的可能机制. 应用气象学报, 12(2): 150-158. Xu H M, He J H, Zhou B. 2001. The features of atmospheric circulation during Meiyu onset and possible mehanisms for westward extension (northward shift) of Pacific subtropical high. J Appl Meteor Sci, 12(2): 150-158 (in Chinese)

徐海明, 何金海, 董敏. 2001b. 江淮入梅的年际变化及其与北大西洋涛动和海温异常的联系. 气象学报, 59(6): 694-706. Xu H M, He J H, Dong M. 2001. Interannual variability of the Meiyu onset and its association with North Atlantic oscillation and SSTA over North Atlatic. Acta Meteor Sinica, 59(6): 694-706 (in Chinese)

徐群. 1965. 近八十年长江中、下游的梅雨. 气象学报, 35(4): 507-518. Xu Q. 1965. The Meiyu in the middle and lower reaches of the Yangtze River in recent 80 years. Acta Meteor Sinica, 35(4): 507-518 (in Chinese)

杨莲梅, 张庆云. 2007. 夏季东亚西风急流Rossby波扰动异常与中国降水. 大气科学, 31(4): 586-595. Yang L M, Zhang Q Y. 2007. Anomalous perturbation kinetic energy of Rossby wave along East Asian westerly jet and its association with summer rainfall in China. Chinese J Atmos Sci, 31(4): 586-595 (in Chinese)

杨义文, 徐群, 杨秋明. 2001. 近116年长江中下游的梅雨(二)//刘志澄. 暴雨·灾害(五). 北京: 气象出版社, 54-65. Yang Y W, Xu Q, Yang Q M. 2001. The Meiyu in middle-lower reaches of Yangtze River during 116 recent years (Ⅱ)//Liu Z C. Rainstorm and Disaster. Beijing: Meteorology Press, 54-65 (in Chinese)

叶笃正, 陶诗言, 李麦村. 1958. 在六月和十月大气环流的突变现象. 气象学报, 16(4): 249-263. Ye D Z, Tao S Y, Li M C. 1958. The abrupt change of circulation over the northern hemisphere during June and October. Acta Meteor Sinica, 16(4): 249-263 (in Chinese)

张庆云, 陶诗言. 1999. 夏季西太平洋副热带高压北跳及异常的研究. 气象学报, 57(5): 539-548. Zhang Q Y, Tao S Y. 1999. The study of the sudden northward jump of the subtropical high over the western Pacific. Acta Meteor Sinica, 57(5): 539-548 (in Chinese)

张庆云, 陶诗言, 陈烈庭. 2003. 东亚夏季风指数的年际变化与东亚大气环流. 气象学报, 61(5): 559-568. Zhang Q Y, Tao S Y, Chen L T. 2003. The inter-annual variability of East Asian summer monsoon indices and its association with the pattern of general circulation over East Asia. Acta Meteor Sinica, 61(5): 559-568 (in Chinese)

赵俊虎, 封国林, 杨杰等. 2012. 夏季西太平洋副热带高压的不同类型与中国汛期大尺度旱涝的分布. 气象学报, 70(5): 1021-1031. Zhao J H, Feng G L, Yang J, et al. 2012. Analysis of the distribution of the large-scale drought/flood of summer in China under different types of the western Pacific subtropical high. Acta Meteor Sinica, 70(5): 1021-1031 (in Chinese)

赵俊虎, 支蓉, 申茜等. 2014. 2012年我国夏季降水预测与异常成因分析. 大气科学, 38(2): 237-250. Zhao J H, Zhi R, Shen Q, et al. 2014. Prediction of the distribution of the 2012 summer rainfall in China and analysis of the cause for anomaly. Chinese J Atmos Sci, 38(2): 237-250 (in Chinese)

周兵, 文继芬. 2007. 1998年夏季我国东部降水与大气环流异常及其低频特征. 应用气象学报, 18(2): 129-136. Zhou B, Wen J F. 2007. Abnormality of summertime precipitation of eastern China and general circulation with LFO in 1998. J Appl Meteor Sci, 18(2): 129-136 (in Chinese)

周波涛. 2011. 冬季澳大利亚东侧海温与长江流域夏季降水的联系及可能物理机制. 科学通报, 56(16): 1301-1307. Zhou B T. 2011. Linkage between winter sea surface temperature east of Australia and summer precipitation in the Yangtze River valley and a possible physical mechanism. Chinese Sci Bull, 56(17): 1821-1827

周后福. 2005. 梅雨期划分方法的再提出. 成都信息工程学院学报, 20(4): 483-487. Zhou H F. 2005. Representation of demarcation method of Meiyu period. J Chengdu Univ Inf Technol, 20(4): 483-487 (in Chinese)

竺可桢. 1934. 东南季风与中国之雨量. 地理学报, 1(1): 1-27. Chu C. 1934. The enigma of southeast monsoon in China. Acta Geograph Sin, 1(1): 1-27 (in Chinese)

竺夏英，何金海，吴志伟. 2008. 长江中下游入梅指数及早晚梅年的海气背景特征. 大气科学，32(1)：113-122. Zhu X Y，He J H，Wu Z W. 2008. Regional Meiyu onset index over the middle and lower reaches of the Yangtze River and the associated ocean-atmospheric features for the early/late Meiyu onset years. Chinese J Atmos Sci，32(1)：113-122 (in Chinese)

Ding Y H. 1992. Summer monsoon rainfalls in China. J Meteor Soc Japan，70(1B)：373-396

Feng G L，Sun S P，Zhao J H，et al. 2013. Analysis of stable components for extended-range (10－30 days) weather forecast：A case study of continuous overcast-rainy process in early 2009 over the mid-lower reaches of the Yangtze River. Sci China Earth Sci，56(9)：1576-1587

Kalnay E，Kanamitsu M，Kistler R，et al. 1996. The NCEP/NCAR 40-year reanalysis project. Bull Amer Meteor Soc，77(3)：437-472

Li W H，Li L F，Ting M F，et al. 2012. Intensification of Northern Hemisphere subtropical highs in a warming climate. Nat Geosci，5(11)：830-834

Reynolds R W，Rayner N A，Smith T M，et al. 2002. An improved in situ and satellite SST analysis for climate. J Climate，15(13)：1609-1625

Tao S Y，Chen L X. 1987. A review of recent research on the East Asian summer monsoon in China//Chang C P，Krishnamurti T N. Monsoon Meteorology. Oxford，UK：Oxford University Press，60-92

Tian B Q，Fan K. 2012. Relationship between the late spring NAO and summer extreme precipitation frequency in the middle and lower reaches of the Yangtze River. Atmos Oceanic Sci Lett，5(6)：445-460

Ye T S，Zhi R，Zhao J H，et al. 2014. The two annual northward jumps of the West Pacific subtropical high and their relationship with summer rainfall in eastern China under global warming. Chin Phys B，23(6)：069203

Zhao J H，Feng G L. 2014. Reconstruction of conceptual prediction model for the three rainfall patterns in the summer of eastern China under global warming. Sci China Earth Sci，57(12)：3047-3061

欢迎订阅 2019 年度《气象学报》

《气象学报》中文版创刊于 1925 年，是由中国气象局主管，中国气象学会主办的全国性大气科学学术期刊，主要刊载有关大气科学及其交叉科学研究的具有创新性的论文；国内外大气科学发展动态的综合评述；新观点、新理论、新技术、新方法的介绍；研究工作简报及重要学术活动报道；优秀大气科学专著的评介以及有关本刊论文的学术讨论等。

《气象学报》中文版 2003 年和 2005 年连续两次荣获中华人民共和国新闻出版总署颁发的第二届、第三届“国家期刊奖百种重点学术期刊”奖；2013、2015、2017 年入选国家新闻出版广电总局“百强报刊”；2007—2011 年和 2015—2017 年获得中国科学技术协会精品科技期刊工程项目的资助，2008、2011、2014、2017 年被评为“中国精品科技期刊”；2003—2007、2009、2016 年被中国科学技术信息研究所评为“百种中国杰出学术期刊”；2012、2013、2014、2015 年获评“中国最具国际影响力学术期刊”；2016、2017 年获评“中国国际影响力优秀学术期刊”。

《气象学报》为大气科学研究提供了学术交流平台，一直致力于推动中国大气科学基础研究和理论研究的发展，服务于中国气象现代化建设事业。作者和读者对象主要为从事气象、海洋、地理、环境、地球物理、天文、空间及生态等学科的科研人员、高校师生。

《气象学报》中文版为双月刊，国内外发行。

2019 年全年共 6 期，定价 240 元/年。

邮发代号：2-368(国内)　　BM329(国际)

通讯地址：北京市中关村南大街 46 号　中国气象学会《气象学报》编辑部

邮政编码：100081

联系电话：010-68406942，68408571（传真）

邮　　箱：cmsqxxb@263.net；qxxb@cms1924.org

期刊主页：http://www.cmsjournal.net/qxxb_cn

开户银行：北京建行白石桥支行

户　　名：中国气象学会

帐　　号：11001028600059261046

Atmos. Chem. Phys., 18, 1863–1877, 2018
https://doi.org/10.5194/acp-18-1863-2018
© Author(s) 2018. This work is distributed under
the Creative Commons Attribution 3.0 License.

Atmospheric Chemistry and Physics
Open Access
EGU

The effects of El Niño–Southern Oscillation on the winter haze pollution of China

Shuyun Zhao[2,3], **Hua Zhang**[1,2,3], **and Bing Xie**[2,3]

[1]Department of Atmospheric Science, School of Environmental Studies, China University of Geosciences, Wuhan, China
[2]Collaborative Innovation Center on Forecast and Evaluation of Meteorological Disasters, Nanjing University of Information Science and Technology, Nanjing, China
[3]Laboratory for Climate Studies, National Climate Center, China Meteorological Administration, Beijing, China

Correspondence: Hua Zhang (huazhang@cma.cn)

Received: 31 May 2017 – Discussion started: 22 June 2017
Revised: 7 December 2017 – Accepted: 11 December 2017 – Published: 8 February 2018

Abstract. It has been reported in previous studies that El Niño–Southern Oscillation (ENSO) influenced not only the summer monsoon, but also the winter monsoon over East Asia. This contains some clues that ENSO may affect the winter haze pollution of China, which has become a serious problem in recent decades, through influencing the winter climate of East Asia. In this work, we explored the effects of ENSO on the winter (from December to February) haze pollution of China statistically and numerically. Statistical results revealed that the haze days of southern China tended to be fewer (more) than normal in El Niño (La Niña) winter, whereas the relationships between the winter haze days of northern and eastern China and ENSO were not significant. Results from numerical simulations also showed that ENSO influenced the winter atmospheric anthropogenic aerosol content over southern China more obviously than it did over northern and eastern China. Under the emission level of aerosols for the year 2010, winter atmospheric anthropogenic aerosol content over southern China was generally greater (less) than normal in El Niño (La Niña) winter. This was because the transport of aerosols from South and Southeast Asia to southern China was enhanced (weakened), which masked the better (worse) scavenging conditions for aerosols in El Niño (La Niña) winter. The frequency distribution of the simulated daily surface concentrations of aerosols over southern China indicated that the region tended to have fewer clean and moderate (heavy) haze days, but more heavy (moderate) haze days in El Niño (La Niña) winter.

1 Introduction

Haze pollution, especially in winter, has become a very serious problem for China in recent decades (Ding and Liu, 2014; Tao et al., 2016). For example, in January 2013, most parts of central and eastern China experienced extremely heavy and persistent haze pollution (Tao et al., 2014; Mu and Zhang, 2014; Zhang et al., 2014b; Wang et al., 2014a, b; Zou et al., 2017). In the last decade, haze pollution in winter has received wide concern from the scientific community, the government of China, and the public.

Haze pollution is a phenomenon mainly caused by human-emitted pollutants under stagnant meteorological conditions. The increase in anthropogenic emissions of aerosols and their precursors in recent decades has been the main reason for the worsening air quality in China (Cao et al., 2007; Zhang et al., 2012a; Zhu et al., 2012). In addition to the increase in anthropogenic emissions of aerosols and their precursors, climate change caused by anthropogenic and/or natural forcings also exerted great influence on the haze pollution in China, especially through changing the strength of the East Asian monsoon (Zhang et al., 2010, 2014b; Liu et al., 2011; Yan et al., 2011; Chin, 2012; Zhu et al., 2012; Mu and Zhang, 2014; Chen and Wang, 2015; Li et al., 2016a, b; Cai et al., 2017). Studies generally showed that the wintertime haze days across central and eastern China had a close negative relationship with the strength of the East Asian winter monsoon (EAWM; Zhang et al., 2014b; Mu and Zhang, 2014; Chen and Wang, 2015; Li et al., 2016a; Cai et al., 2017). In summer, the increase in surface aerosol concentration and optical depth over eastern and northern China correlated with

the weakening of the East Asian summer monsoon (EASM; Zhang et al., 2010; Yan et al., 2011; Zhu et al., 2012), whereas Yang et al. (2014) found that the gaseous pollutant of surface O_3 over China had a positive relationship with the EASM.

Wang et al. (2015a) and Zou et al. (2017) revealed that the increasing winter haze pollution in eastern China in recent years was related to the decreasing Arctic sea ice in preceding autumn. Many studies suggested that under global warming, the future climate will be more stagnant and the weather conditions conducive to severe haze in eastern China will be more frequent (Jacob and Winner, 2009; Wang et al., 2015a; Cai et al., 2017). However, Jacob and Winner (2009) also pointed out that the effects of future climate change on particulate matter (PM) were complicated, as the projection of precipitation, wildfires, atmospheric chemistry, and natural emissions of aerosols by models is still in need of improvement.

El Niño–Southern Oscillation (ENSO) is the dominant changing mode of the tropical sea surface temperature (SST) on interannual scale (Rasmusson and Carpenter, 1982), of which the climatic effects are global (Bjerknes, 1972; Huang and Wu, 1989; Zhang et al., 1999; Lau and Nath, 2003; Zhai et al., 2016, etc.). ENSO influences not only the EASM (Chang et al., 2000; Li et al., 2007; Zhao et al., 2017, etc.) but also the EAWM, especially over low latitudes (Chen et al., 2013; He and Wang, 2013; Kim et al., 2016, etc.), which indicates that ENSO may affect the haze pollution over East Asia through influencing the monsoon circulation. Wu et al. (2013) found that the aerosol variations over the Maritime Continent and western North Pacific presented a biennial feature, which could be attributed to the impacts of ENSO. From the results of Wu et al. (2013), it seemed that ENSO only influenced the aerosols over eastern China (30–40° N, 110–120° E) around October in El Niño or La Niña developing years and July in El Niño or La Niña decaying years. Gao and Li (2015) revealed statistically and through case analyses that El Niño (La Niña) events were more likely to bring about more (fewer) haze days in eastern China (25–35° N, 105–122.5° E). Feng et al. (2016) simulated the influence of the 1994/1995 El Niño Modoki event on the aerosol concentrations over southern China (20–35° N, 105–120° E), and found that the aerosol concentrations increased during the mature phase (in boreal winter) of the event. Feng et al. (2017) simulated the influence of the 1998/1999 and 2000/2001 La Niña Modoki events on the aerosol concentrations over eastern China (105–120° E), and found that the geographical distributions of aerosols over eastern China during the winters of the two events were opposite with each other. Most previous studies discussed the effects of ENSO on the winter haze pollution of China based on observation or case simulation separately. In this study, we try to explore the effects of ENSO on the winter haze pollution of China statistically and numerically. ENSO is a recurring climate pattern, and many climate centers around the world monitor it systematically and use it in climate prediction extensively. Therefore, exploring the effects of ENSO on the winter haze pollution in China may provide useful information for the prediction of haze for the country.

The article is organized as follows: methodology is given in Sect. 2, including data and model introduction; results including statistical and model results are presented in Sect. 3, followed by conclusions and discussions in Sect. 4.

2 Methodology

2.1 Data used in statistical analysis

We first analyzed the relationship between the winter haze days of China and global SST in Sect. 3. The monthly haze days from the data set for haze project version 1.0 of the National Meteorological Information Center, China Meteorological Administration (CMA) were used. The CMA defines haze using visibility (< 10 km) and relative humidity ($< 80\,\%$; Tao et al., 2014). The time span of the data set is January 1954–July 2014, but only the data after 1960 were actually used in this study, as the data set has steadily included more than 2000 stations since 1960. A merged monthly SST data set (Hurrell et al., 2008) formed by the SST data of the Hadley Centre and the National Oceanic and Atmospheric Administration (NOAA) was used in the correlation analysis. The SST data together with a merged sea ice (SI) data set of the same sources were used in the following numerical simulation. The SST and SI data are both from 1870 to 2012, with a horizontal resolution of $1° \times 1°$.

2.2 Model description and experimental setup

The aerosol–climate coupled model BCC_AGCM2.0_CUACE/Aero (Zhang et al., 2012b) of the National Climate Center (NCC), CMA, was used in the numerical study of the effects of ENSO on atmospheric aerosol content. The coupled model comprises the NCC/CMA climate model (BCC_AGCM2.0; Wu et al., 2010) and the CMA Unified Atmospheric Chemistry Environment/Aerosol model (CUACE/Aero; Gong et al., 2002, 2003). The coupled model employs a horizontal T42 spectral resolution (about $2.8° \times 2.8°$) and a hybrid vertical coordinate with 26 levels, the top of which is located at about 2.9 hPa. Five types of aerosol (including emission, gaseous chemistry, transport, coagulation, and removal) are considered in the model: sulfate (SF), black carbon (BC), organic carbon (OC), dust, and sea salt. The emissions of the first three types of aerosol and/or their precursors are prescribed, and the last two types of aerosol are emitted online (Gong et al., 2002). The particle radii of each type of aerosol are divided into 12 size bins from 0.005 to 20.48 μm. Each type of aerosol is assumed to be externally mixed with the others. Sulfate, organic carbon, and sea salt are considered to be hygroscopic, and the other two types are

Table 1. Simulation setup.

Group name	SST	Running time	Output frequency
CLI	Climatologic SST	Oct^0–Aug^1	Monthly and daily
EL	Climatologic SST + $\Delta SST_{El\ Niño}$	Oct^0–Feb^1	Monthly and daily
LA	Climatologic SST + $\Delta SST_{La\ Niña}$	Oct^0–Feb^1	Monthly and daily

The superscripts of the third column of 0 and 1 represent the first and second model year, respectively.

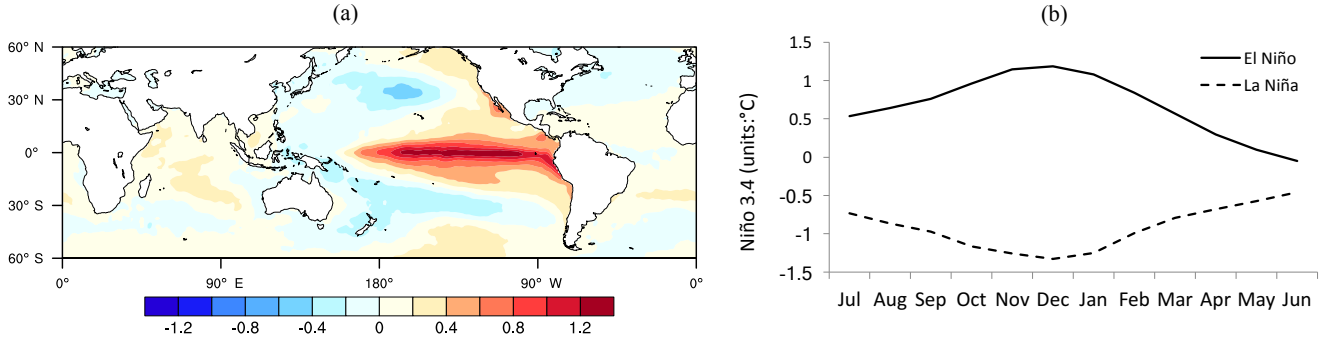

Figure 1. (a) Typical ENSO mode (units: °C/°C) and **(b)** average monthly Niño3.4 (units: °C) of 21 El Niño and 18 La Niña events from 1951 to 2015.

considered to be non-hygroscopic. The coupled model has been introduced, evaluated, and used in many studies of the radiative forcings and climatic effects of aerosols (e.g., Zhang et al., 2014a, 2016; Wang et al., 2015b; Zhao et al., 2014).

Three groups of experiments were conducted (Table 1), named CLI, EL, and LA (climatological means, El Niño and La Niña), with each group including 20 members by altering initial conditions. To get different initial conditions, a preparation experiment was run first with the model's default setting (Zhao et al., 2014). Three types of files (initial, restart, and history files) of the preparation experiment were output, and the output frequency was set to daily. Twenty initial files output from the preparation experiment were then used as the different initial conditions for different ensemble members. The group of CLI used the climatological mean (from 1981 to 2010) monthly SST and SI, which was introduced in Sect. 2.1 but interpolated to the model's resolution, as boundary conditions. In the groups of EL and LA, the climatological-mean monthly SST was superposed by El Niño and La Niña SST perturbations, respectively, and the SI was identical to that in CLI. The El Niño and La Niña SST perturbations were obtained by scaling a typical ENSO mode (Fig. 1a) with the average monthly Niño3.4 indices of 21 El Niño and 18 La Niña events (selected from 1951 to 2015, Fig. 1b), respectively. The Niño3.4 indices from January 1951 to the present can be downloaded from the website of NCC/CMA (cmdp.ncc-cma.net/download/Monitoring/Index/M_Oce_Er.txt). The typical ENSO mode was obtained through the regression between the monthly Niño3.4 index and the SST field after removing their linear trends. The running period of the group of CLI was from October to the following August, in order to confirm if the model can capture the general features of the circulations of the East Asian winter and summer monsoons. In the confirmation process, the geopotential height and wind from the National Centers for Environmental Prediction (NCEP) reanalysis data were used. The running periods of EL and LA were both from October to the following February. The results in boreal winter (December, January, and February: DJF) of the three groups were used in the analysis, using the two previous months for the atmosphere to respond to SST perturbations.

The emission data of SF, BC, OC, and/or their precursors used in all experiments were from the Representative Concentration Pathway 4.5 (RCP 4.5) of the Intergovernmental Panel on Climate Change (IPCC) for year 2010. In this study, only the changes in the atmospheric contents of SF, BC, and OC caused by different SST perturbations were analyzed, as the three types of aerosol were mainly emitted by anthropogenic activities and the important components of haze pollutants. In the analyzing process, the median instead of the average of the changes of a specific variable between different groups of experiments (e.g., EL–CLI) was used, as median is more robust and resistant to extreme large or small values that may happen in some ensemble members. In addition, we also marked the grids where the differences of a specific variable between more than 70 % of ensemble member pairs had the same sign as the median differences, as a reflection of significance.

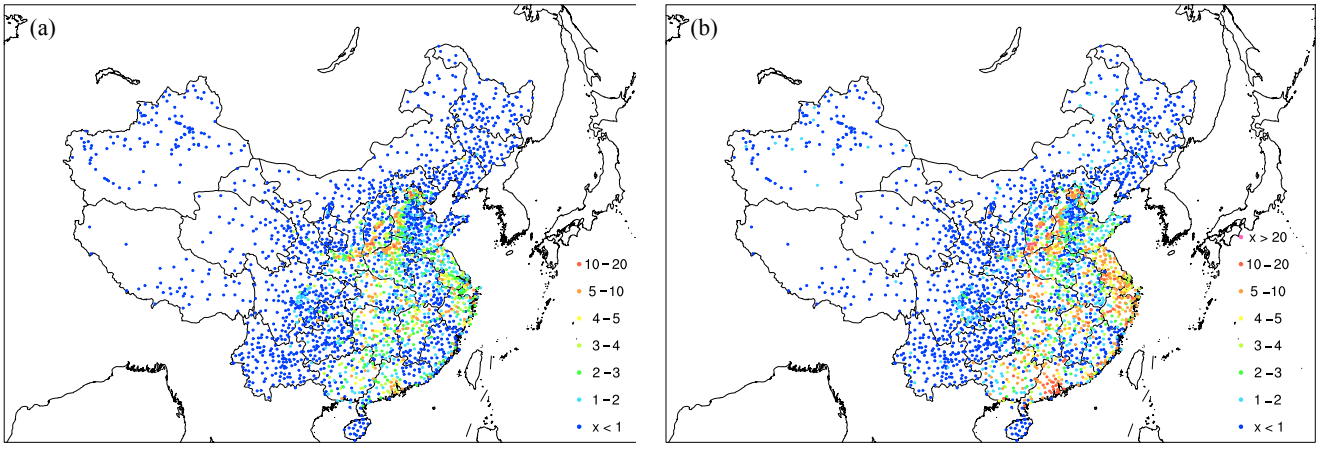

Figure 2. The winter-average monthly haze days (units: days month^{-1}) during years **(a)** 1960–2013 and **(b)** 2000–2013 over mainland China.

3 Results

3.1 Statistical results

In this section, we first present the geographical distribution of the winter haze days in mainland China over the past approximately 50 years and since year 2000. Then, three typical polluted regions are selected, and the correlations between their respective winter haze days and global SST are analyzed.

It can be seen from Fig. 2a that Beijing, southwestern Hebei, central and southern Shanxi, central Shaanxi, and northern Henan suffered from winter haze pollution more frequently than elsewhere in China during 1960–2013, with 10–20 days being the most common DJF mean monthly haze day ranges. The diffusive conditions of these areas are not good because of the influence of the Taihang and Qinling mountains. Besides the above areas, stations with more than 5–10 DJF mean monthly haze days during 1960–2013 were distributed densely in the provinces of Hubei, Hunan, Jiangxi, Zhejiang, Guangxi, and Guangdong. Compared with 1960–2013, winter haze pollution in mainland China generally became more frequent during 2000–2013 (Fig. 2b). For example, in the Yangtze River delta and Pearl River delta, there were many more stations with 5–10 and 10–20 DJF mean monthly haze days during 2000–2013 than during 1960–2013. At some stations of Shanxi Province, the DJF mean monthly haze days during 2000–2013 were even more than 20 (Fig. 2b). The locations of the Chinese provinces mentioned above and in the following can be found in Fig. S1 in the Supplement.

Three representative regions – JJJ (Beijing, Tianjin, and Hebei province; accounting for 179 stations), JZH (Jiangsu and Zhejiang provinces, and Shanghai; accounting for 164 stations), and GG (Guangdong and Guangxi provinces; accounting for 178 stations) – were selected to represent northern, eastern, and southern China, respectively. From

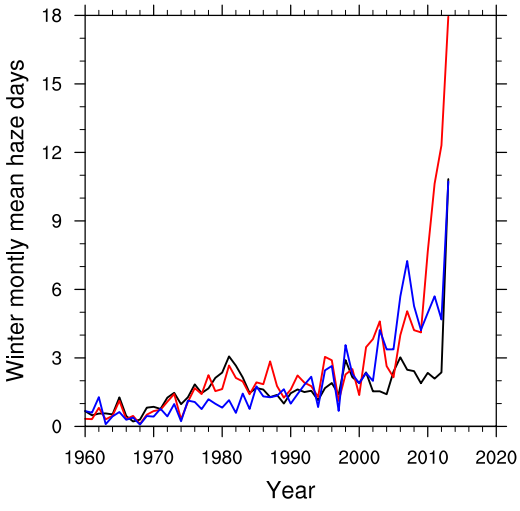

Figure 3. Time series of the winter-average monthly haze days (units: days month^{-1}) of JJJ (black), JZH (red), and GG (blue).

Fig. 3 we see that there were generally fewer than 3 DJF mean monthly haze days in these three regions before year 2000, with a small peak around 1980 in northern and eastern China. After year 2000, the number of DJF mean monthly haze days over eastern and southern China grew rapidly. The DJF mean monthly haze days of northern China increased much later than the other two regions after year 2000. Actually, the DJF mean monthly haze days over northern China were relatively few until 2012, which was consistent with the result of Chen and Wang (2015).

Considering that the increases in the DJF mean monthly haze days over eastern and southern China increased very abruptly after year 2010, only the winter haze days of the three regions from 1960 to 2010 were used in analyzing their relationships with winter SST. In order to remove the interdecadal variabilities, we applied 2–8-year band-pass filter-

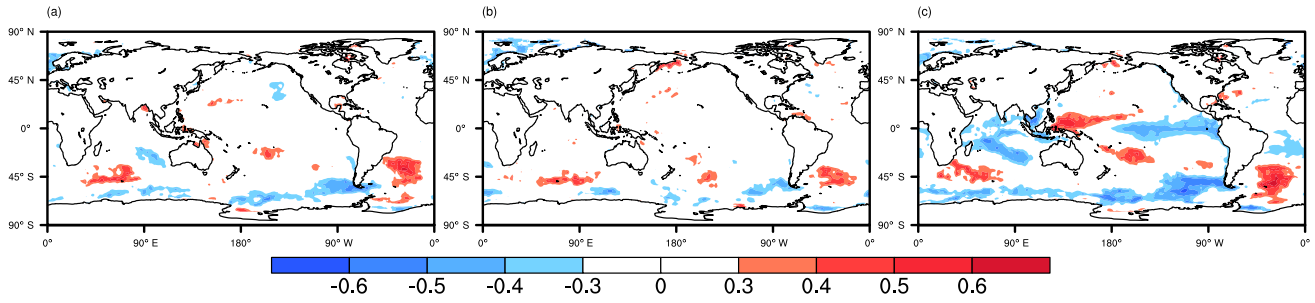

Figure 4. Correlation coefficients (unitless) of the monthly haze days of **(a)** JJJ, **(b)** JZH, and **(c)** GG with SST in winter, after applying band-pass filtering of 2–8 years to both the data of haze days and SST. Shade denotes that results pass 95 % significance level.

ing to both the data of haze days and SST. It can be seen from Fig. 4 that only the winter haze days of southern China had significant negative relationships with the equatorial SST over the central and eastern Pacific and central Indian Ocean, and positive relationships with the equatorial SST over the western Pacific. The geographical distribution of the correlation coefficients between the winter haze days over southern China and SST was generally an opposite phase of the typical ENSO mode shown in Fig. 1a, indicating that southern China tended to suffer from more (fewer) haze days than normal in La Niña (El Niño) winter. This could also be seen from the comparison of the DJF mean monthly haze days between several selected pairs of La Niña and El Niño winters over southern China (Fig. S2). In order to avoid the influence of the variations in the emissions of haze particles and their precursors, each pair of La Niña and El Niño winters were selected with intervals of no longer than 2 years.

The relationships between the winter haze days of northern and eastern China and equatorial SST were not significant (Fig. 4a and b), indicating that ENSO did not influence the winter haze days of these two regions significantly. This is probably because, as a tropical phenomenon, ENSO affects the climate over southern China more directly than over northern and eastern China, especially in winter when the western Pacific subtropical high (WPSH) is generally weaker and located further south than in other seasons. Zou et al. (2017) linked the extreme winter haze events over east China plains (112–122° E, 30–41° N, including JJJ and most parts of JZH) to Arctic sea ice loss in the preceding autumn and extensive Eurasia snowfall in early winter. Gao and Li (2015) found that the winter haze days of eastern China had positive relationship with the SST over the eastern equatorial Pacific. However, "eastern China" in Gao and Li (2015) included most regions between the Yangtze and Yellow rivers east of 105° E, which was much larger and further west than the representative region of eastern China in this work, and further south and west than the concerned region in Zou et al. (2017).

3.2 Model results

3.2.1 Winter and summer circulations, and atmospheric aerosol content

First, the simulated winter and summer circulations over East Asia in the group of CLI were checked by comparing with NCEP reanalysis data (Fig. 5). The model was able to capture the general features of the winter and summer circulations over East Asia. For example, in winter, the deepening of East Asian trough (EAT), the overwhelming of northwesterly over eastern China, and the strengthening of the easterly north of the Equator were all depicted by model results (Fig. 5a); in summer, the northward shift of WPSH and the strengthening of the cross-equatorial westerly over the Indian Ocean and Maritime Continent were also generally captured by the model (Fig. 5b). However, the EAT simulated by the model in winter was weaker and narrower, and located further west than NCEP reanalysis data. In summer, the simulated WPSH was weaker and located further east than NCEP reanalysis data. It seemed that the simulated cross-equatorial flow was stronger than reanalysis data both in winter and summer, which was probably the reason for the weakness of the simulated EAT in winter and WPSH in summer. In the model results of the group of CLI, the stronger cross-equatorial westerly over the Indian Ocean and Maritime Continent obstructed the westward stretch of the WPSH in summer, resulting in positive precipitation biases over South Asia and Southeast Asia, and negative precipitation biases over southern China (Zhao et al., 2014).

The simulated winter surface concentration (CONCsur) values and loadings of aerosols in the group of CLI (Fig. 6) showed that central and eastern China (east of about 105° E) were the most haze-polluted regions of the country, in line with the observational distribution of winter haze days shown in Fig. 2. The maximum of the winter CONCsur of aerosols was centered in Henan Province at about 20 $\mu g\,m^{-3}$. Compared with other observational studies (e.g., Cao et al., 2007; Zhang and Cao, 2015; Cai et al., 2017), the simulated CONCsur values of aerosols shown in Fig. 6a were underestimated by about 1–2 orders of magnitude. It should be noted

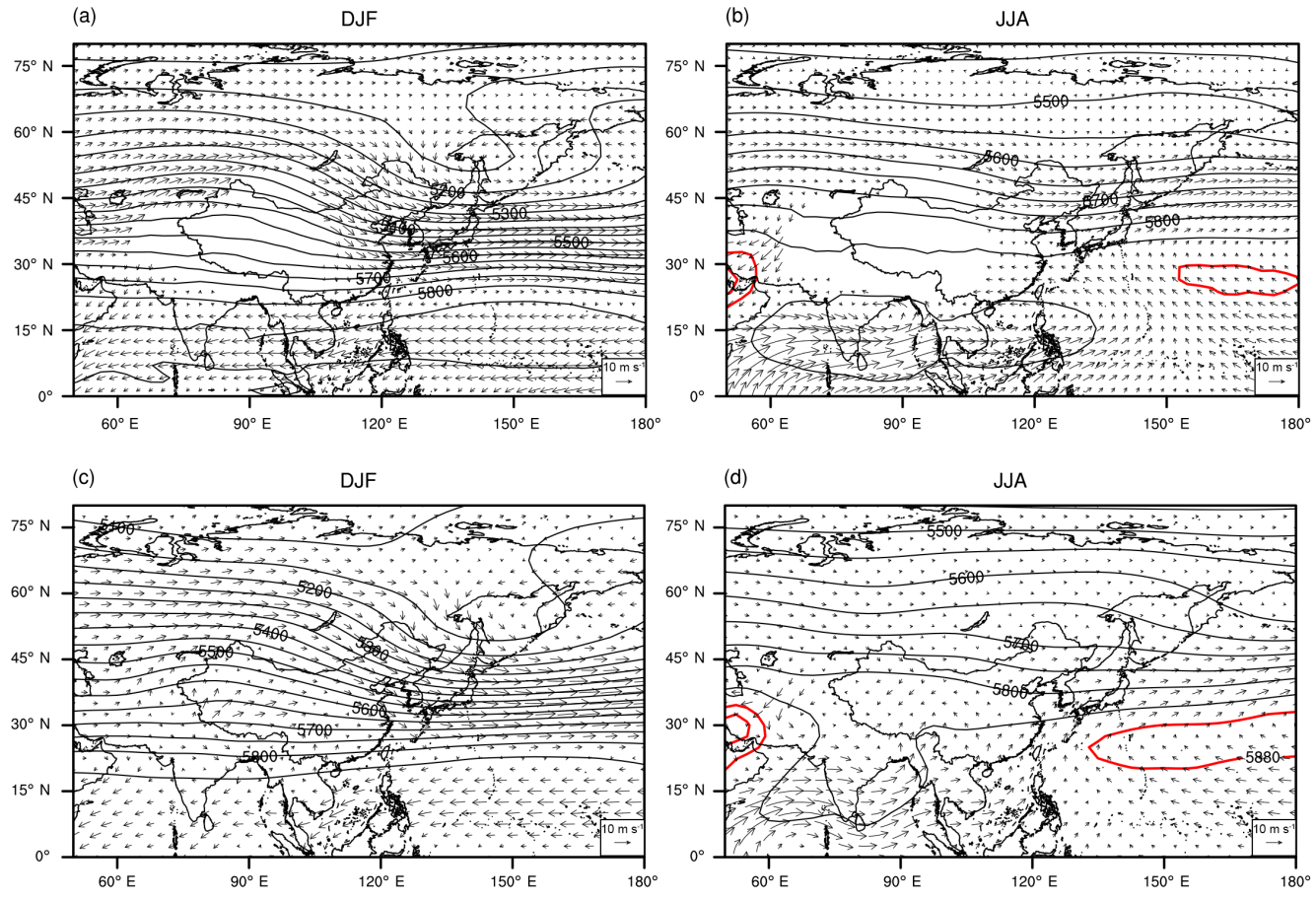

Figure 5. Comparisons between **(a, b)** the simulated and **(c, d)** reanalysis winter and summer geopotential height at 500 hPa (contour; units: geopotential meters, gpm) and wind at 850 hPa (vector; units: $\mathrm{m\,s^{-1}}$), with the blank places in **(a)** and **(b)** are due to the influence of the Tibetan Plateau. Model results are from the group of CLI, and reanalysis data are from NCEP.

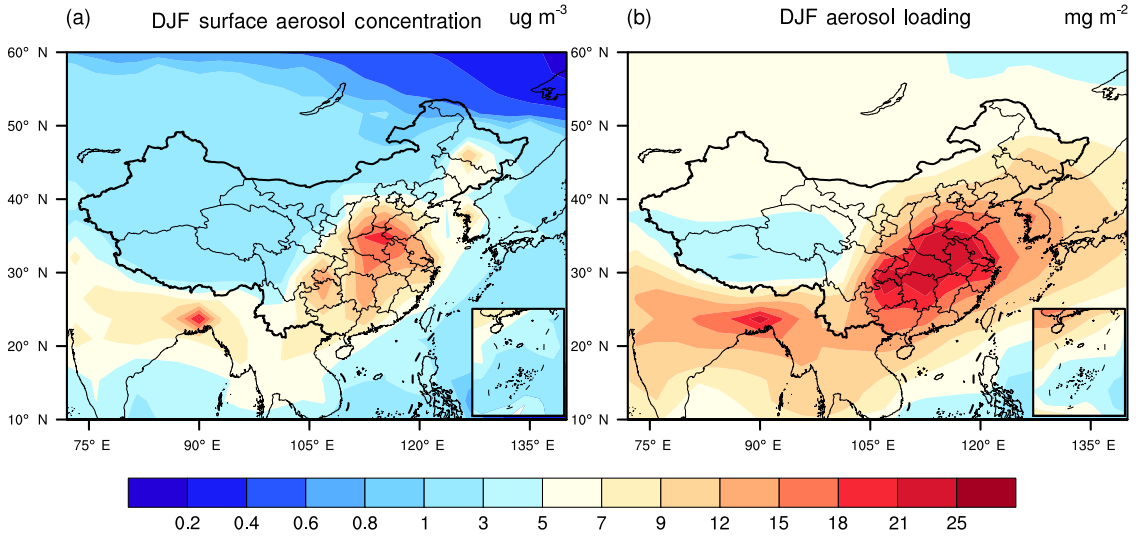

Figure 6. The simulated winter-average **(a)** surface aerosol concentrations (units: $\mu\mathrm{g\,m^{-3}}$) and **(b)** aerosol loadings (units: $\mathrm{mg\,m^{-2}}$) in the group of CLI.

that aerosol CONCsur values in this study were the lowest-level aerosol concentrations in the model. As introduced in Sect. 2.2, the model used in this study has 26 levels in the vertical hybrid σ–pressure axis, and the middle height of the lowest level is about 50–70 m above the surface in China (not shown). Therefore, the aerosol concentrations at the lowest level of the model actually reflect the mean of the aerosol concentrations from the surface to a height of about 100–140 m (or maybe even higher) above the surface. This certainly brought about underestimation as to aerosol CONCsur. Another reason for the underestimation was that we excluded all naturally emitted aerosols (dust and sea salt), in order to focus our attention on haze, as another meteorological phenomenon occurring frequently in late winter and spring over northern China – sandstorms – have quite different weather conditions than haze. The exclusion of naturally emitted aerosols was also the reason why the northwestern China was much cleaner than it was expected to be.

The maximum of the simulated winter aerosol loadings in China was 21–25 mg m^{-2}, and heavy aerosol loadings ($\geq$ 18 mg m^{-2}) in China were located east of 105° E, and between the Yellow and Yangtze rivers (Fig. 6b). The median of the 10 models that participated in the Aerosol Comparisons between Observations and Models (AeroCom; http://aerocom.met.no/cgi-bin/aerocom/surfobs_annualrs.pl) showed that the maximums of the loadings of SF, BC, and OC in January 2000 in China were 15–30, 2.5–5, and more than 10 mg m^{-2}, respectively. The model used in this study is also a member of AeroCom. Zhao et al. (2014) compared the simulated loadings of five kinds of aerosols (SF, BC, OC, sea salt, and dust) with the model using AeroCom median, and found that the model generally simulated the distributions and magnitudes of aerosol loadings well, though with some underestimations in BC and OC loadings.

3.2.2 The effects of ENSO on winter circulation and precipitation

The effects of ENSO on the winter circulation and precipitation over East Asia were discussed first, as these meteorological fields determine the transport, diffusion, and removal of aerosols, and consequently influence atmospheric aerosol content.

Two important features were apparent in the winter anomalous circulation field caused by El Niño (Fig. 7a). First, negative and positive anomalous geopotential heights at 500 hPa were seen near the Ural Mountains and Lake Baikal, respectively. Secondly, two anomalous anticyclones at 850 hPa were seen over the western North Pacific, with one in the Philippine Sea and the other one at the mid-latitudes. It was expected that the anomalous southwesterly in the northwest of the Philippine Sea anticyclone would bring more water vapor and also more aerosols to southern China, as Southeast Asia and South Asia were both areas with heavy aerosol loadings (Fig. 6b), whereas the anomalous geopotential heights at 500 hPa caused by La Niña were positive and negative near Ural Mountains and Lake Baikal, respectively, and two anomalous cyclones were caused by La Niña over the western North Pacific (Fig. 7b).

The differences in circulation between El Niño and La Niña winters were shown in Fig. 7c. It can be seen in Fig. 7c that the negative and positive anomalies in 500 hPa geopotential heights caused by El Niño were more obvious than that in Fig. 7a over the Ural Mountains and Lake Baikal, respectively. In addition, the anomalous anticyclones in the western North Pacific were also more obvious than that in Fig. 7a. Wang et al. (2000) found that the anomalous anticyclones over the western North Pacific formed in the boreal autumn of a developing El Niño, attained its peak in winter, and persisted into the following spring and early summer. In the sea level pressure field, the land–sea gradient in winter was decreased by El Niño (not shown), indicating that El Niño caused the weakness of the EAWM. The weakness of the EAWM caused by El Niño could also be seen from the weakness of East Asian jet stream and the decrease in EAWM index caused by El Niño (Fig. S3). The EAWM index used in Fig. S3 was the one defined by Li and Yang (2010). It has been suggested in previous studies that the weakness of East Asian jet stream and the Philippine Sea anticyclonic anomalies in winter caused by El Niño connected with each other by local Hadley circulation over East Asia (Kang and Lee, 2017).

Previous studies have also found that the EAWM tended to be weak in El Niño winter (e.g., Chen et al., 2000; Huang et al., 2012; Wang and Chen, 2014; Kang and Lee, 2017). Wang et al. (2000) has explored how ENSO influenced its upstream climate in East Asia and found that the Pacific–East Asian teleconnection (PEAT) was the key bridge. PEAT is a vorticity wave pattern that starts from the central Pacific and extends poleward and westward to East Asia. In Fig. 7c, PEAT could be recognized from the 850 hPa wind anomalies with a cyclonic vorticity over the central Pacific, the anticyclonic vorticities over the western North Pacific, and a cyclonic vorticity over northeast Asia. The PEAT could be seen more clearly from the differences in the stream function at 500 hPa between El Niño and La Niña winters (Fig. S4), which had the opposite sign of vorticity.

Corresponding to the anomalous anticyclones at 850 hPa over the western North Pacific caused by El Niño, winter precipitation decreased over Southeast Asia and the northwestern Pacific, and increased over southern China (Fig. 8a). In contrast, precipitation increased over Southeast Asia and the northwestern Pacific, and decreased over southern China during La Niña winter (Fig. 8b). The opposite effects of El Niño and La Niña on the winter precipitation over southern China can be seen more clearly in Fig. 8c, which was in accordance with the observational relationship between ENSO index and China precipitation in winter (http://cmdp.ncc-cma.net/pred/cn_enso.php?product=cn_enso_corr&season=DJF#corr). The decrease in

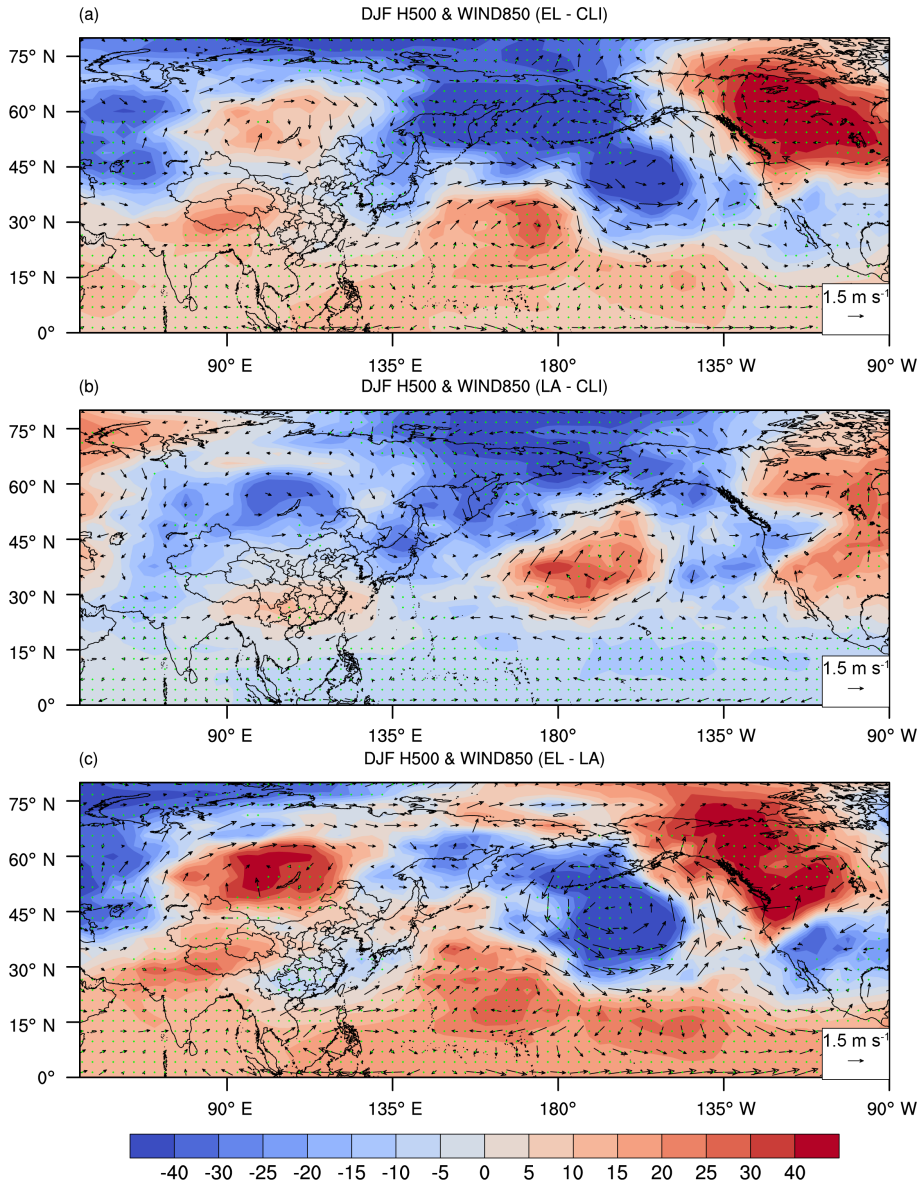

Figure 7. Medians of the simulated differences in winter-average geopotential height at 500 hPa (H500, shaded; units: gpm) and wind at 850 hPa (WIND850, vector; units: $m\,s^{-1}$) between **(a)** EL and CLI, **(b)** LA and CLI, and **(c)** EL and LA, with green dots indicating that the differences of H500 between more than 70 % of ensemble member pairs have the same sign as the median differences.

winter precipitation over southern China caused by La Niña was very likely the reason for the higher-than-normal number of haze days over the region during La Niña winter (Fig. 4c), as less precipitation meant slower cleaning of particles out of the atmosphere, which will be discussed in the next section (Fig. 11b and c). Another reason which should probably not be neglected is that drier conditions over southern China during La Niña winter could not allow for the confusion of haze days for fog days.

3.2.3 The effects of ENSO on winter atmospheric aerosol content

In this section, the changes in the winter aerosol CONCsur values and loadings over China caused by ENSO are presented, and then the mechanism by which ENSO affected winter atmospheric aerosol content is analyzed from the perspective of wet and dry depositions and interregional transport of aerosols.

It can be seen from Fig. 9a that the winter CONCsur values of aerosols were decreased by El Niño over northeastern China and eastern China. The winter aerosol CONCsur val-

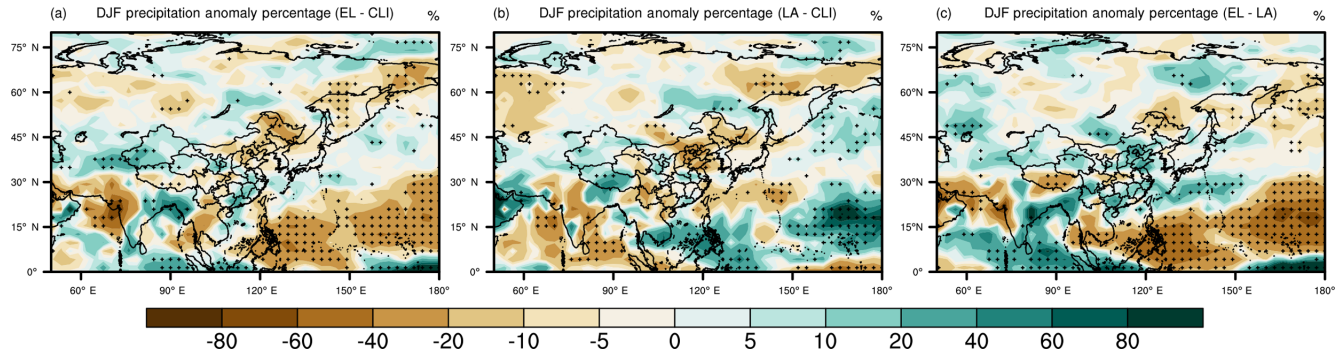

Figure 8. Medians of the simulated differences in winter-average precipitation in percentage (%) between **(a)** EL and CLI, **(b)** LA and CLI, and **(c)** EL and LA, with black dots indicating that the differences between more than 70 % of ensemble member pairs have the same sign as the median differences.

ues were also decreased by La Niña over northeastern China and eastern China, as well as part of northern China and most areas south of the Yangtze River (Fig. 9b). Over southern China, although the increases in the winter CONCsur values of aerosols caused by El Niño were not very clear in Fig. 9a, they were obvious by comparing with La Niña winter (Fig. 9c), which was generally in line with the simulation result of Feng et al. (2016). It can be seen in Fig. 9d that the winter aerosol loadings were increased by El Niño over most areas east of 105° E and south of 40° N, and decreased over northeastern China and part of northern China. In Fig. 9e, it can be seen that the anomalous winter aerosol loadings caused by La Niña presented a meridional "$-+-$" pattern over eastern China. The different influences of El Niño and La Niña on the winter aerosol loadings were the most obvious over large areas south of the Yangtze River (Fig. 9f).

From Fig. 9c and f, it was found that the differences in atmospheric aerosol content between El Niño and La Niña winters were more obvious over southern China than other areas of the country. To obtain more information, Fig. 9c and f were plotted in another way with different significance levels (Fig. S5), which also showed that ENSO affected winter atmospheric aerosol content over southern China more obviously than it did over other areas of the country. This was to some extent in line with the results in Fig. 4 that only the winter haze days over southern China had significant relationship with ENSO. Therefore, in the following analysis, we focused on the mechanism how ENSO affected winter atmospheric aerosol content over southern China.

In Sect. 3.1, we discussed that the haze days over southern China tended to be fewer (more) than normal in El Niño (La Niña) winter, which was to some extent contradictory to the increase (decrease) in winter atmospheric aerosol content over southern China caused by El Niño (La Niña). In the following, we first explain why the changes in the winter haze days and atmospheric aerosol content caused by ENSO over southern China were not consistent with each other. Then, we explore the reasons for the increase (decrease) in winter atmospheric aerosol content caused by El Niño (La Niña) over southern China.

Figure 4c showed statistically that southern China tended to suffer from more (fewer) haze days than normal in La Niña (El Niño) winter, which was also seen in the four selected pairs of El Niño and La Niña winters (Fig. S2) with one of them near 2010 (in numerical simulations, the aerosol emissions were fixed in 2010). However, numerical results showed that La Niña (El Niño) caused a decrease (increase) in winter atmospheric aerosol content over southern China (Fig. 9). Is it possible for southern China to have more (fewer) haze days but less (greater) atmospheric aerosol content than normal in La Niña (El Niño) winter? To answer this question, the frequency distributions of the simulated winter daily aerosol CONCsur values averaged over southern China (21–27° N, 104–118° E; see Fig. S1) in the groups of CLI, EL, and LA were plotted in Fig. 10. Section 3.2.1 demonstrated that the simulated aerosol CONCsur values in this study were smaller than observational studies by 1–2 orders of magnitude. Therefore, for calibration, the simulated winter daily aerosol CONCsur values over southern China were amplified by 10 before plotting the frequency distributions.

It can be seen from Fig. 10 that the frequency distribution of the simulated winter daily aerosol CONCsur over southern China was a little right-skewed in the group of CLI, reaching peak at around 65 $\mu g\,m^{-3}$. The frequency distribution of the simulated winter daily aerosol CONCsur over southern China in the group of LA was a little left-shifting compared with that in CLI when aerosol CONCsur was larger than 40 $\mu g\,m^{-3}$. The frequency distribution of the simulated winter daily aerosol CONCsur over southern China in EL was a little right-shifting compared with that in CLI. The average numbers of days in winter with aerosol CONCsur values below 40, between 40 and 80, and above 80 $\mu g\,m^{-3}$ in CLI, EL, and LA were also given in the top right corner of Fig. 10. It was found that the number of days in winter with aerosol CONCsur values between 40 and 80 $\mu g\,m^{-3}$ was the largest in LA and smallest in EL, whereas the number of days in

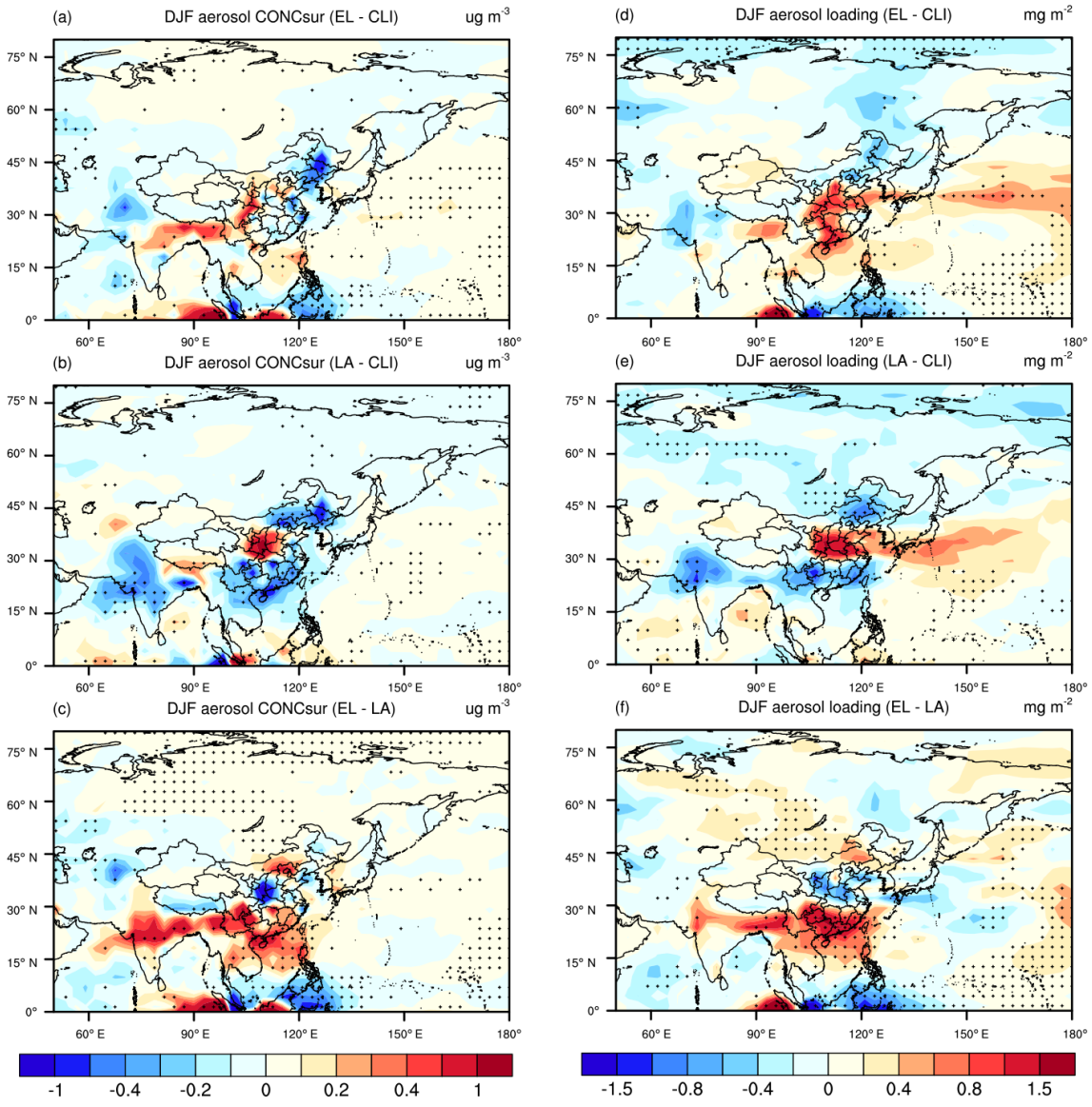

Figure 9. Medians of the simulated differences in winter-average aerosol surface concentrations (left panel; units: $\mu g\,m^{-3}$) and aerosol loadings (right panel; units: $mg\,m^{-2}$) between EL and CLI **(a, d)**, LA and CLI **(b, e)**, and EL and LA **(c, f)**, with black dots indicating that the differences between more than 70 % of ensemble member pairs have the same sign as the median differences.

winter with aerosol CONCsur values above $80\,\mu g\,m^{-3}$ was the largest in EL and smallest in LA. Figure 10 indicated that southern China tended to have a smaller number of clean and heavy haze days but a greater number of moderate haze days than normal in La Niña winter, whereas in El Niño winter, southern China tended to have a greater number of heavy haze days but fewer clean and moderate haze days than normal. This explained why southern China had fewer (more) haze days but greater (less) atmospheric aerosol content than normal in El Niño (La Niña) winter. It should be noted that here we used regional mean aerosol CONCsur values over southern China subjected to the low model spatial resolution, which was the reason why the curves in Fig. 10 were close to each other. In practice, however, haze days and their severities are judged station by station (e.g., Fig. 2), and the thresholds are not necessarily the same as those used in Fig. 10. Therefore, we can get some rough information about the effects of ENSO on the winter haze days over southern China from the shifts of curves in Fig. 10, but cannot compare it with observational data directly.

As the emissions of aerosols were kept the same in all experiments (Sect. 2.2), the speed at which aerosols were removed from the atmosphere, especially through wet deposition, could affect atmospheric aerosol content greatly (Zhang et al., 2016). It was found that ENSO influenced the winter wet depositions more obviously than the winter dry deposi-

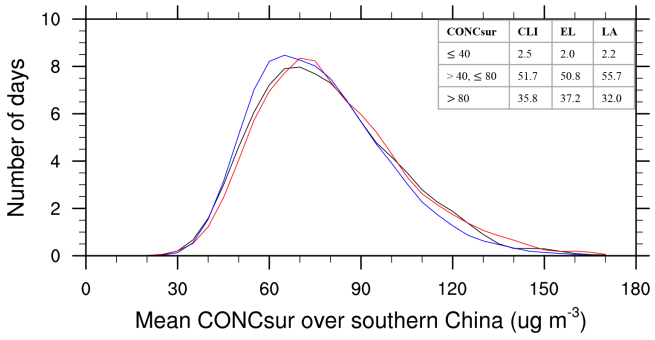

Figure 10. Frequency distributions of the simulated winter daily surface aerosol concentrations (CONCsur; units: $\mu g\,m^{-3}$) averaged over southern China (after being amplified by 10), with black, red, and blue lines representing the results from CLI, EL, and LA, respectively. The average numbers of days in winter with CONCsur ≤ 40, $40 <$ CONCsur ≤ 80, and CONCsur > 80 in CLI, EL, and LA are given in the table at the top right corner.

tions of aerosols over China (Fig. 11). The winter dry depositions of aerosols were decreased both by El Niño and La Niña over southern China (Fig. 11c–f). Compared with dry deposition, wet deposition is a faster process. The winter wet depositions of aerosols over southern China were increased (decreased) by El Niño (La Niña; Fig. 11a–c), corresponding to the changes in winter precipitation (Fig. 8). Comparing Figs. 9 and 11, it was found that the winter atmospheric contents and wet depositions of aerosols were both increased (decreased) by El Niño (La Niña) over southern China. It seemed that the changes in the winter wet depositions of aerosols were the result rather than the reason for the changes in winter atmospheric aerosol content over southern China.

Besides local emission and removal, the interregional transport of aerosols could also influence atmospheric aerosol content over a specific region. It was mentioned in Zhang et al. (2016) that South and Southeast Asia had become important source areas of anthropogenic aerosols in 2010, which was also seen in the simulated aerosol CONCsur values and loadings over these regions (Fig. 6). A low-level anomalous anticyclone (cyclone) was caused by El Niño (La Niña) over the Philippine Sea in winter (Fig. 7). The southwesterly (northeasterly) at the northwest of the anomalous anticyclone (cyclone) led to enhanced (weakened) transport of aerosols from South and Southeast Asia to southern China in El Niño (La Niña) winter (Fig. 12). As the changes in winter atmospheric aerosol content over southern China caused by ENSO could not be explained by local emission or removal, it could only be attributed to the changes in the transport of aerosols from South and Southeast Asia to southern China. Zhu et al. (2012) has also pointed out that in determining aerosol concentrations, the changes in monsoon circulation were more dominant than that in precipitation (or wet deposition of particles) in East Asia. It is expected that when the emissions of aerosols over South and Southeast Asia diminish in the future, the contradiction between the influence of ENSO on winter haze days and on atmospheric aerosol content over southern China will also disappear.

4 Conclusions and discussions

The effects of ENSO on winter haze days and atmospheric aerosol content over China were discussed statistically and numerically. Statistical results showed that southern China tended to have fewer (more) haze days than normal in El Niño (La Niña) winter, which was in line with the simulated greater (less) winter precipitation over southern China caused by El Niño (La Niña). Statistical results indicated that the relationships between the winter haze days over northern and eastern China and ENSO were not significant. Numerical results also revealed that the influence of ENSO on winter atmospheric aerosol content over northern and eastern China was not as obvious as over southern China. As a tropical phenomenon, it seemed that ENSO affected the winter haze pollution over southern China more significantly than it did over northern and eastern China.

Numerical results indicated that atmospheric aerosol content over southern China was greater (less) than normal in El Niño (La Niña) winter, which was to some extent not in line with the effects of ENSO on the winter haze days of the region. In 2010, South and Southeast Asia became important source areas of anthropogenic aerosols (Zhang et al., 2016). The enhanced southwesterly (northeasterly) at the northwest of the winter anomalous anticyclone (cyclone) over the Philippine Sea caused by El Niño (La Niña) enhanced (weakened) the transport of aerosols from South and Southeast Asia to southern China. The frequency distributions of the simulated daily surface concentrations of aerosols in winter over southern China indicated that the region tended to have a greater number of heavy (moderate) haze days, but fewer clean and moderate (heavy) haze days than normal in El Niño (La Niña) winter. However, it should be noted again that the emission data of aerosols used in our study were fixed in 2010, and if the emissions of aerosols change the effects may be different.

Many studies have found that the haze pollution over northern and eastern China was influenced by the EAWM, as cited in Sect. 1. In addition, previous studies also found that ENSO could influence the strength of the EAWM, as discussed in Sect. 3.2.2 that El Niño could weaken the EAWM. It was expected that there would be some connection between ENSO and the winter haze pollution over northern and eastern China. However, the connection between ENSO and the winter haze pollution over northern and eastern China was not strong; i.e., the correlations between the winter haze days of the two regions and ENSO were not significant. This made us consider how haze pollutants over northern China were cleared away in winter. Usually, a few clean days in

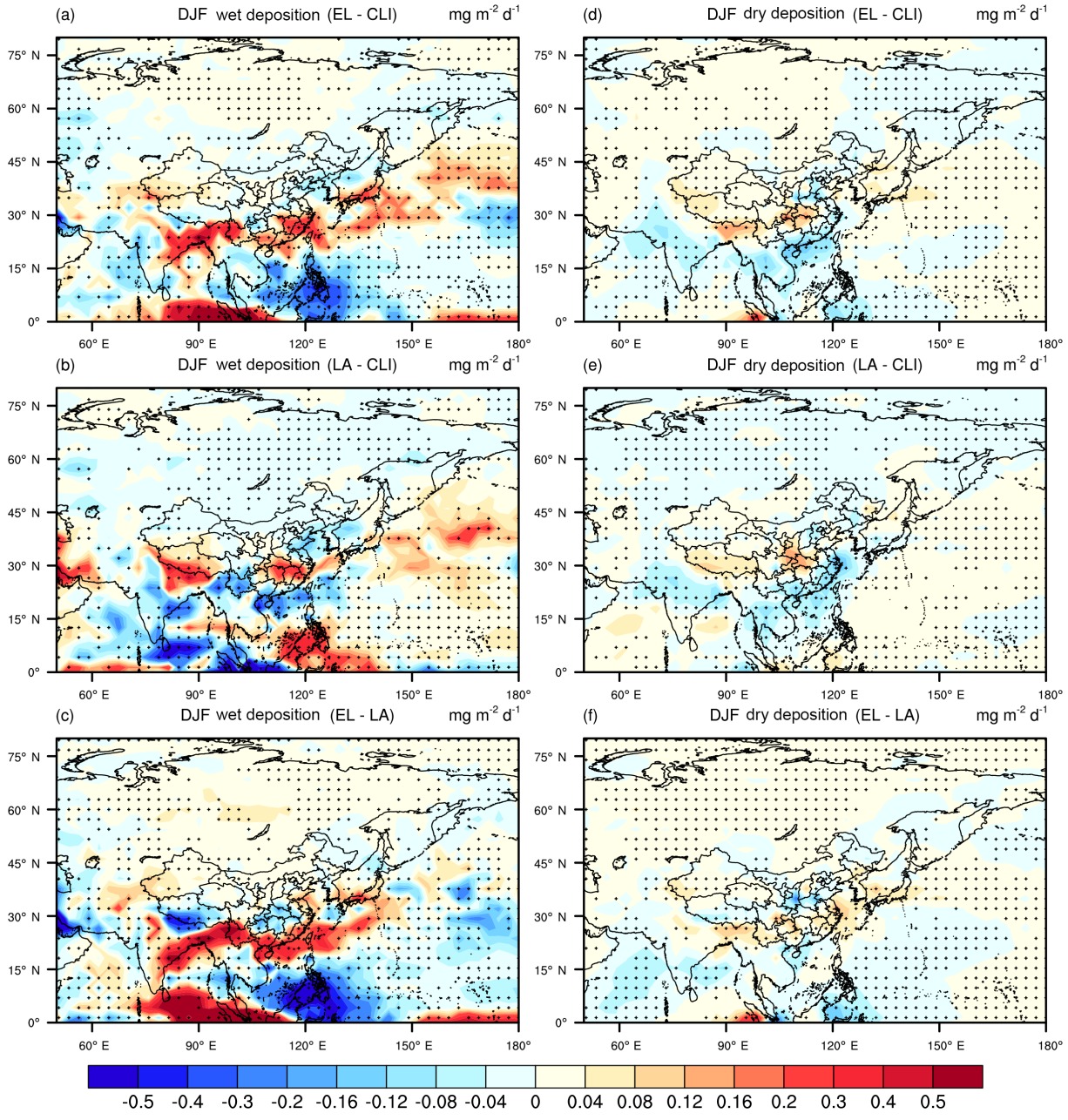

Figure 11. Medians of the simulated differences in winter-average wet depositions (left panel) and dry depositions (right panel) of aerosols (units: $\mathrm{mg\,m^{-2}\,d^{-1}}$) between EL and CLI **(a, d)**, LA and CLI **(b, e)**, and EL and LA **(c, f)**, with black dots indicating that the differences between more than 70 % of ensemble member pairs have the same sign as the median differences.

northern China followed a breakout of an atmospheric blocking over high-latitude Asia, during which a stream of cold air swept southwardly and rapidly from Siberia or Mongolia. Therefore, we obtained some information about the influence of ENSO on the winter haze pollution over northern China from the frequency of cold air recorded in China in El Niño and La Niña winters. In both December 1986 (during the 1986/1987 El Niño event) and December 2010 (during the 2010/2011 La Niña event), cold air appeared in China 7 times, equaling the maximum frequency of cold air days in December during 1960–2011 (Fig. S6). This indicated that El Niño (La Niña) did not necessarily reduce (increase) the cold air frequency of China in winter, even though it could weaken (strengthen) the EAWM. To the contrary, it seemed that El Niño (La Niña) conditions were favorable for (not favorable for) the appearance of cold air in China in winter (Fig. S7). The relationship between ENSO and the cold air frequency of China in winter made the connection be-

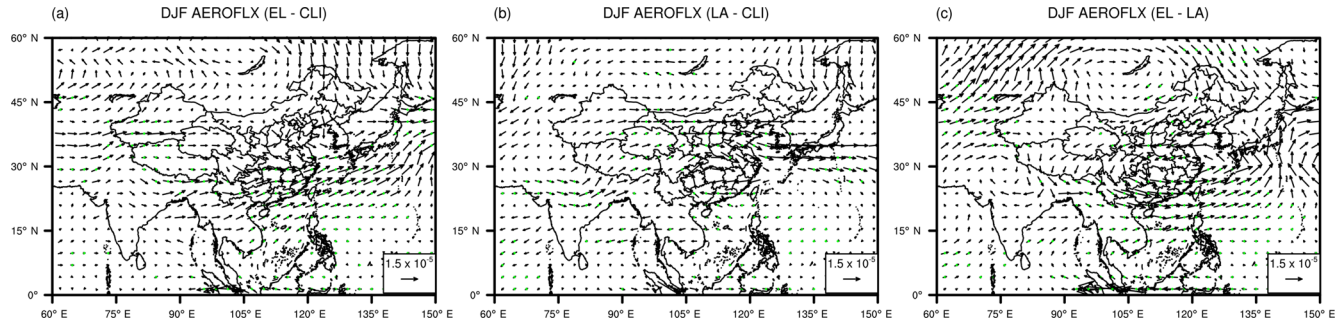

Figure 12. Medians of the simulated differences in the winter-average vertical integral of aerosol horizontal fluxes (AEROFLX; units: $\mathrm{kg\,m^{-1}\,s^{-1}}$) between **(a)** EL and CLI, **(b)** LA and CLI, and **(c)** EL and LA, with green dots indicating that the differences of the zonal components of AEROFLX between more than 70 % of ensemble member pairs have the same sign as the median differences.

tween ENSO and the winter haze pollution over the northern China more complicated than expected simply from the perspective of the EAWM. The cold air frequency of China in winter is also influenced by the upstream conditions in the Atlantic Ocean, the Arctic ice, and the Eurasian snow cover (not shown). This emphasizes the importance of exploring the comprehensive effects of ENSO and the extratropical systems on the haze pollution of China.

Haze pollution is a very sophisticated problem because it is the comprehensive result of human activities and weather conditions. Weather conditions determine the dispersion and removal of haze particles over a specific region, influence the complex chemistry reactions among different components, and also connect the haze pollution of a specific region with the emissions of neighboring regions. Complicating matters further, haze pollution and weather conditions interact with each other closely over some areas. This work explores the effects of ENSO on the winter haze pollution over China under relatively simple experimental settings, with prescribed SST and fixed aerosol emissions, which means that SST does not response to aerosols. Additionally, the chemistry reactions in the model we used are also simplified, especially without the complex reactions related to nitrate aerosols. Therefore, studies with more sophisticated experimental designs (e.g., with atmosphere–ocean coupled models) and chemistry schemes are still needed for related future research on this topic.

Data availability. The data set for haze project version 1.0 of the National Meteorological Information Center, China Meteorological Administration, is not yet available for the public to download. The merged SST and SI data set of the Hadley Centre and the National Oceanic and Atmospheric Administration is available at https://climatedataguide.ucar.edu/climate-data/. The National Centers for Environmental Prediction (NCEP) reanalysis data are available at ftp://ftp.cdc.noaa.gov/Datasets//ncep.reanalysis/surface. Model simulation results are available at http://doi.org/10.5281/zenodo.1167952.

The Supplement related to this article is available online at https://doi.org/10.5194/acp-18-1863-2018-supplement.

Author contributions. The work was done under the guidance of Hua Zhang. Shuyun Zhao and Hua Zhang designed the experiment and prepared the manuscript. Bing Xie conducted model simulations. The analysis of results and preparation of all figures and tables were done by Shuyun Zhao.

Competing interests. The authors declare that they have no conflict of interest.

Acknowledgements. This work was financially supported by the (Key) National Natural Science Foundation of China (91644211 & 41575002). In addition, we would like to thank Shao Sun of the National Climate Center, Chinese Meteorological Administration, for his kind help in plotting figures.

Edited by: Toshihiko Takemura
Reviewed by: three anonymous referees

References

Bjerknes, J.: Large-scale atmospheric response to the 1964–65 Pacific equatorial warming, J. Phys. Oceanogr., 2, 212–217, https://doi.org/10.1175/1520-0485(1972)002<0212:LSARTT>2.0.CO;2, 1972.

Cai, W.-J., Li, K., Liao, H., Wang, H.-J., and Wu, L.-X.: Weather conditions conducive to Beijing severe haze more frequent under climate change, Nat. Clim. Change, 7, 257–262, https://doi.org/10.1038/nclimate3249, 2017.

Cao, J.-J., Lee, S.-C., Chow, J.-C., Watson, J. G., Ho, K.-F., Zhang, R.-J., Jin, Z.-D., Shen, Z.-X., Chen, G.-C., Kang, Y.-M., Zou, S.-C., Zhang, L.-Z., Qi, S.-H., Dai, M.-H., Cheng, Y., and Hu, K.: Spatial and seasonal distributions of carbonaceous aerosols over China, J. Geophys. Res., 112, D22S11, https://doi.org/10.1029/2006JD008205, 2007.

Chang, C.-P., Zhang, Y.-S., and Li, T.: Interannual and interdecadal variations of the East Asian summer monsoon and tropical Pacific SSTs. Part I: Roles of the subtropical ridge, J. Climate, 13, 4310–4325, https://doi.org/10.1175/1520-0442(2000)013<4310:IAIVOT>2.0.CO;2, 2000.

Chen, H.-P. and Wang, H.-J.: Haze days in North China and the associated atmospheric circulations based on daily visibility data from 1960 to 2012, J. Geophys. Res.-Atmos., 120, 5895–5909, https://doi.org/10.1002/2015JD023225, 2015.

Chen, W., Graf, H. F., and Huang, R.-H.: The interannual variability of East Asian winter monsoon and its relation to the summer monsoon, Adv. Atmos. Sci., 17, 48–60, https://doi.org/10.1007/s00376-000-0042-5, 2000.

Chen, W., Lan, X.-Q., Wang, L., and Ma, Y.: The combined effects of the ENSO and the Arctic Oscillation on the winter climate anomalies in East Asia, Chinese Sci. Bull., 58, 1355–1362, https://doi.org/10.1007/s11434-012-5654-5, 2013.

Chin, M.: Dirtier air from a weaker monsoon, Nat. Geosci., 5, 449–450, https://doi.org/10.1038/ngeo1513, 2012.

Dawson, J. P., Adams, P. J., and Pandis, S. N.: Sensitivity of $PM_{2.5}$ to climate in the Eastern US: a modeling case study, Atmos. Chem. Phys., 7, 4295–4309, https://doi.org/10.5194/acp-7-4295-2007, 2007.

Ding, Y.-H. and Liu, Y.-J.: Analysis of long-term variations of fog and haze in China in recent 50 years and their relations with atmospheric humidity, Sci. China Earth Sci., 57, 36–46, https://doi.org/10.1007/s11430-013-4792-1, 2014.

Feng, J., Li, J.-P., Zhu, J.-L., and Liao, H.: Influences of El Nino Modoki event 1994/1995 on aerosol concentrations over southern China, J. Geophys. Res.- Atmos., 121, 1637–1651, https://doi.org/10.1002/2015JD023659, 2016.

Feng, J., Li, J.-P., Zhu, J.-L., Liao, H., and Yang, Y.: Simulated contrasting influences of two La Niña Modoki events on aerosol concentrations over eastern China, J. Geophys. Res.- Atmos., 122, 2734–2749, https://doi.org/10.1002/2016JD026175, 2017.

Gao, H. and Li, X.: Influences of El Nino Southern Oscillation events on haze frequency in eastern China during boreal winters, Int. J. Climatol., 35, 2682–2688, https://doi.org/10.1002/joc.4133, 2015.

Gong, S.-L., Barrie, L. A., and Lazare, M.: Canadian Aerosol Module (CAM): a size-segregated simulation of atmospheric aerosol processes for climate and air quality models 2. Global sea-salt aerosol and its budgets, J. Geophys. Res., 107, D244779, https://doi.org/10.1029/2001JD002004, 2002.

Gong, S.-L., Barrie, L. A., Blanchet, J.-P., von Salzen, K., Lohmann, U., Lesins, G., Spacek, L., Zhang, L.-M., Girard, E., Lin, H., Leaitch, R., Leighton, H., Chylek, P., and Huang, P.: Canadian aerosol module: a size-segregated simulation of atmospheric aerosol processes for climate and air quality models 1. Module development, J. Geophys. Res., 108, D14007, https://doi.org/10.1029/2001JD002002, 2003.

He, S.-P. and Wang, H.-J.: Oscillating relationship between the East Asia winter monsoon and ENSO, J. Climate, 26, 9819–9838, https://doi.org/10.1175/JCLI-D-13-00174.1, 2013.

Huang, R.-H. and Wu, Y.-F.: The influence of ENSO on the summer climate change in China and its mechanism, Adv. Atmos. Sci., 6, 21–32, https://doi.org/10.1007/BF02656915, 1989.

Huang, R.-H., Chen, J.-L., Wang, L., and Lin, Z.-D.: Characteristics, processes, and causes of the spatio-temporal variabilities of the East Asian monsoon system, Adv. Atmos. Sci., 29, 910–942, https://doi.org/10.1007/s00376-012-2015-x, 2012.

Hurrell, J. W., Hack, J. J., Shea, D., Caron, J. M., and Rosinski, J.: A new sea surface temperature and sea ice boundary data set for the Community Atmosphere Model, J. Climate, 21, 5145–5153, https://doi.org/10.1175/2008JCLI2292.1, 2008.

Jacob, D. J. and Winner, D. A.: Effects of climate change on air quality, Atmos. Environ., 43, 51–63, https://doi.org/10.1016/j.atmosenv.2008.09.051, 2009.

Kang, D. and Lee, M.-I.: ENSO influence on the dynamical seasonal prediction of the East Asian Winter Monsoon, Clim. Dynam., https://doi.org/10.1007/s00382-017-3574-4, 2017.

Kim, J.-W., An, S.-I., Jun, S.-Y., Park, H.-J., and Yeh, S.-W.: ENSO and East Asian Winter Monsoon relationship modulation associated with the anomalous northwest Pacific anticyclone, Clim. Dynam., 4, 1157–1179, https://doi.org/10.1007/s00382-016-3371-5, 2016.

Lau, N.-C. and Nath, M. J.: Atmosphere–ocean variations in the Indo–Pacific sector during ENSO episodes, J. Climate, 16, 3–20, https://doi.org/10.1175/1520-0442(2003)016<0003:AOVITI>2.0.CO;2, 2003.

Li, Y. and Yang, S.: A dynamical index for the East Asian Winter Monsoon, J. Climate, 23, 4255–4262, https://doi.org/10.1175/2010JCLI3375.1, 2010.

Li, Y., Lu, R.-Y., and Dong, B.-W.: The ENSO–Asian monsoon interaction in a coupled ocean–atmosphere GCM, J. Climate, 20, 5164–5177, https://doi.org/10.1175/JCLI4289.1, 2007.

Li, Q., Zhang, R.-H., and Wang, Y.: Interannual variation of the wintertime fog-haze days across central and eastern China and its relation with East Asian Winter Monsoon, Int. J. Climatol., 36, 346–354, https://doi.org/10.1002/joc.4350, 2016a.

Li, Z.-Q., Lau, W. K.-M., Ramanathan, V., Wu, G., Ding, Y., Manoj, M.-G., Liu, J., Qian, Y., Li, J., Zhou, T., Fan, J., Rosenfeld, D., Ming, Y., Wang, Y., Huang, J., Wang, B., Xu, X., Lee, S.-S., Cribb, M., Zhang, F., Yang, X., Zhao, C., Takemura, T., Wang, K., Xia, X., Yin, Y., Zhang, H., Guo, J., Zhai, P.-M., Sugimoto, N., Babu, S.-S., and Brasseur, G.-P.: Aerosol and monsoon climate interactions over Asia, Rev. Geophys., 54, 866–929, https://doi.org/10.1002/2015RG000500, 2016b.

Liu, X.-D., Yan, L.-B., Yang, P., Yin, Z.-Y., and North, G. R.: Influence of Indian Summer Monsoon on aerosol loading in East Asia, J. Appl. Meteorol. Clim., 50, 523–533, https://doi.org/10.1175/2010JAMC2414.1, 2011.

Mu, M. and Zhang, R.-H.: Addressing the issue of fog and haze: a promising perspective from meteorological science and technology, Sci. China Earth Sci., 57, 1–2, https://doi.org/10.1007/s11430-013-4791-2, 2014.

Rasmusson, E. M. and Carpenter, T. H.: Variations in tropical sea surface temperature and surface wind fields associated with the Southern Oscillation/El Niño, Mon. Weather Rev., 110, 354–384, https://doi.org/10.1175/1520-0493(1982)110<0354:VITSST>2.0.CO;2, 1982.

Tao, M.-H., Chen, L.-F., Xiong, X.-Z., Zhang, M.-G., Ma, P.-F., Tao, J.-H., and Wang, Z.-F.: Formation process of the widespread extreme haze pollution over northern China in January 2013: implications for regional air quality and climate, Atmos. Environ., 98, 417–425, https://doi.org/10.1016/j.atmosenv.2014.09.026, 2014.

Tao, M.-H., Chen, L.-F., Wang, Z.-F., Wang, J., Tao, J.-H., and Wang, X.-H.: Did the widespread haze pollution over China increase during the last decade? A satellite view from space, Environ. Res. Lett., 11, 054019, https://doi.org/10.1088/1748-9326/11/5/054019, 2016.

Wang. L. and Chen, W.: An intensity index for the East Asian Winter Monsoon, J. Climate, 27, 2361–2374, https://doi.org/10.1175/JCLI-D-13-00086.1, 2014.

Wang, B., Wu, R.-G., and Fu, X.-H.: Pacific–East Asian teleconnection: how does ENSO affect East Asian climate?, J. Climate, 13, 1517–1536, https://doi.org/10.1175/1520-0442(2000)013<1517:PEATHD>2.0.CO;2, 2000.

Wang, Y.-S., Yao, L., Wang, L.-L., Liu, Z.-R., Ji, D.-S., Tang, G.-Q., Zhang, J.-K., Sun, Y., Hu, B., and Xin, J.-Y.: Mechanism for the formation of the January 2013 heavy haze pollution episode over central and eastern China, Sci. China Earth Sci., 57, 14–25, https://doi.org/10.1007/s11430-013-4773-4, 2014a.

Wang, Z.-F., Li, J., Wang, Z., Yang, W.-Y., Tang, X., Ge, B.-Z., Yan, P.-Z., Zhu, L.-L., Chen, X.-S., Chen, H.-S., Wand, W., Li, J.-J., Liu, B., Wang, X.-Y., Wand, W., Zhao, Y.-L., Lu, N., and Su, D.-B.: Modeling study of regional severe hazes over mid-eastern China in January 2013 and its implications on pollution prevention and control, Sci. China Earth Sci., 57, 3–13, https://doi.org/10.1007/s11430-013-4793-0, 2014b.

Wang, H.-J., Chen, H.-P., and Liu, J.-P.: Arctic sea ice decline intensified haze pollution in eastern China, Atmos. Ocean. Sci. Lett., 8, 1–9, https://doi.org/10.3878/AOSL20140081, 2015a.

Wang, Z.-L., Zhang, H., and Zhang, X.-Y.: Projected responses of East Asian Summer Monsoon system to future reductions in emissions of anthropogenic aerosols and their precursors, Clim. Dynam., 47, 1455–1468, https://doi.org/10.1007/s00382-015-2912-7, 2015b.

Wu, T.-W., Yu, R.-C., Zhang, F., Wang, Z.-Z., Dong, M., Wang, L.-N., Jin, X., Chen, D.-L., and Li, L.: The Beijing Climate Center atmospheric general circulation model: description and its performance for the present-day climate, Clim. Dynam., 34, 123–147, https://doi.org/10.1007/s00382-008-0487-2, 2010.

Wu, R.-G., Wen, Z.-P., and He, Z.-Q.: ENSO contribution to aerosol variations over the Maritime Continent and the Western North Pacific during 2000–10, J. Climate, 26, 6541–6560, https://doi.org/10.1175/JCLI-D-12-00253.1, 2013.

Yan, L.-P., Liu, X.-D., Yang, P., Yin, Z.-Y., and North, G. R.: Study of the impact of summer monsoon circulation on spatial distribution of aerosols in East Asia based on numerical simulation, J. Appl. Meteorol. Clim., 50, 2270–2282, https://doi.org/10.1175/2011JAMC-D-11-06.1, 2011.

Yang, Y., Liao, H., and Li, J.: Impacts of the East Asian summer monsoon on interannual variations of summertime surface-layer ozone concentrations over China, Atmos. Chem. Phys., 14, 6867–6879, https://doi.org/10.5194/acp-14-6867-2014, 2014.

Zhai, P.-M., Yu, R., Guo, Y.-J., Li, Q.-X., Ren, X.-J., Wang, Y.-Q., Xu, W.-H., Liu, Y.-J., and Ding, Y.-H.: The strong El Niño of 2015/16 and its dominant impacts on global and China's climate, J. Meteorol. Res.-P.R.C., 30, 283–297, https://doi.org/10.1007/s13351-016-6101-3, 2016.

Zhang, Y.-L. and Cao, F.: Fine particulate matter ($PM_{2.5}$) in China at a city level, Sci. Rep., 5, 14884, https://doi.org/10.1038/srep14884, 2015.

Zhang, R.-H., Sumi, A., and Kimoto, M.: A diagnostic study of the impact of El Niño on the precipitation in China, Adv. Atmos. Sci., 16, 229–241, https://doi.org/10.1007/BF02973084, 1999.

Zhang, L., Liao, H., and Li, J.-P.: Impacts of Asian Summer Monsoon on seasonal and interannual variations of aerosols over eastern China, J. Geophys. Res., 115, D716, https://doi.org/10.1029/2009JD012299, 2010.

Zhang, H., Wang, Z.-L., Wang, Z.-Z., Liu, Q.-X., Gong, S.-L., Zhang, X.-Y., Shen, Z.-P., Lu, P., Wei, X.-D., Che, H.-Z., and Li, L.: Simulation of direct radiative forcing of aerosols and their effects on East Asia climate using an interactive AGCM-aerosol coupled system, Clim. Dynam., 38, 1675–1693, https://doi.org/10.1007/s00382-011-1131-0, 2012a.

Zhang, X. Y., Wang, Y. Q., Niu, T., Zhang, X. C., Gong, S. L., Zhang, Y. M., and Sun, J. Y.: Atmospheric aerosol compositions in China: spatial/temporal variability, chemical signature, regional haze distribution and comparisons with global aerosols, Atmos. Chem. Phys., 12, 779–799, https://doi.org/10.5194/acp-12-779-2012, 2012b.

Zhang, H., Xie, B., Zhao, S.-Y., and Chen, Q.: $PM_{2.5}$ and tropospheric O_3 in China and an analysis of the impact of pollutant emission control, Adv. Clim. Change Res., 5, 136–141, https://doi.org/10.1016/j.accre.2014.11.005, 2014a.

Zhang, R.-H., Li, Q., and Zhang, R.-N.: Meteorological conditions for the persistent severe fog and haze event over eastern China in January 2013, Sci. China Earth Sci., 57, 26–35, https://doi.org/10.1007/s11430-013-4774-3, 2014b.

Zhang, H., Zhao, S.-Y., Wang, Z.-L., Zhang, X.-Y., and Song, L.-C.: The updated effective radiative forcing of major anthropogenic aerosols and their effects on global climate at present and in the future, Int. J. Climatol., 36, 4029–4044, https://doi.org/10.1002/joc.4613, 2016.

Zhao, S.-Y., Zhi, X.-F., Zhang, H., Wang, Z.-L., and Wang, Z.-Z.: Primary assessment of the simulated climatic state using a coupled aerosol-climate model BCC_AGCM2.0.1_CAM, Clim. Environ. Res., 19, 265–277, https://doi.org/10.3878/j.issn.1006-9585.2012.12015, 2014 (in Chinese).

Zhao, S.-Y., Chen, L.-J., and Cui, T.: Effects of ENSO phase-switching on rainy-season precipitation in north China, Chinese J. Atmos. Sci., 41, 857–868, https://doi.org/10.3878/j.issn.1006-9895.1701.16226, 2017 (in Chinese).

Zhu, J.-L., Liao, H., and Li, J.-P.: Increases in aerosol concentrations over eastern China due to the decadal-scale weakening of the East Asian Summer Monsoon, Geophys. Res. Lett., 39, L09809, https://doi.org/10.1029/2012GL051428, 2012.

Zou, Y.-F., Wang, Y.-H., Zhang, Y.-Z., and Koo, J.-H.: Arctic sea ice, Eurasia snow, and extreme winter haze in China, Sci. Adv., 3, e1602751, https://doi.org/10.1126/sciadv.1602751, 2017.

郑祚芳，任国玉，2018. 北京地区大气湿度变化及城市化影响分析[J]. 气象，44(11)：1471-1478.

北京地区大气湿度变化及城市化影响分析*

郑祚芳[1,3] 任国玉[2,3]

1 中国气象局北京城市气象研究所，北京 100089

2 国家气候中心，中国气象局气候研究开放实验室，北京 100081

3 中国地质大学环境学院大气科学系，武汉 430074

提 要：应用北京 20 个常规气象站 1976—2015 年逐日观测及同期北京城市发展数据，并借鉴一个新的城、郊区代表站点分类方法，分析了北京地区相对湿度的分布、变化特征及其对城市化的响应。结果表明：(1)北京地区相对湿度的空间分布不均匀，城市化发展早期相对湿度的分布主要受地形影响，城市化程度较高的年代城市效应的影响更为明显；(2)近 40 年来北京地区平均相对湿度呈现下降趋势，线性倾向率为－0.9%·(10 a)$^{-1}$。城区相对湿度的下降速率比郊区大，城、郊差异主要表现在 20 世纪 90 年代以后；(3)近 40 年来北京城市干岛强度呈上升趋势，线性倾向率为 1.3%·(10 a)$^{-1}$，城市干岛效应在季节分布上以冬季为最强，秋、春季次之，夏季较弱。检验表明自 1995 年以来北京干岛效应呈现出更为明显的增强趋势；(4)北京城市干岛效应与城市化进程有密切联系，其与北京城市化率及城市热岛强度之间具有显著的高相关性，相关系数分别高达 0.87和 0.86。

关键词：城市化，相对湿度，气候变化，干岛效应，北京

中图分类号：P463，X16 **文献标志码**：A **DOI**：10.7519/j.issn.1000-0526.2018.11.010

Analysis on Atmospheric Humidity Change and Its Response to Urbanization in Beijing Area

ZHENG Zuofang[1,3] REN Guoyu[2,3]

1 Institute of Urban Meteorology, CMA, Beijing 100089

2 Laboratory for Climate Studies, National Climate Centre, CMA, Beijing 100081

3 Department of Atmospheric Science, School of Environmental Studies, China University of Geosciences, Wuhan 430074

Abstract: Based on the daily observations of Beijing's 20 conventional meteorological stations from 1976 to 2015 and the urban development data of Beijing in the same period, the distribution and variation characteristics of relative humidity in Beijing and its response to urbanization are analyzed by using a new classification method of representative stations in urban and suburban areas. The results show that the spatial distribution of relative humidity in Beijing is uneven, in which the spatial distribution of relative humidity is mainly affected by topography in the early stage of urbanization and by urbanization in the stage of higher urbanization. In recent 40 years, the average relative humidity in Beijing presents a downward trend with a linear tendency rate of －0.9%·10 a^{-1}, and the decline rate of urban relative humidity is larger than that of suburbs especially after 1990s. Moreover, the intensity of urban dry islands in Beijing shows an upward trend in the past 40 years, with a linear tendency rate of 1.3%·10 a^{-1}. The urban dry island effect is the strongest in winter, followed by autumn and spring, and weaker in summer. Note that the dry island effect of Beijing has shown a more obvious trend of enhancement since 1995. Additionally, the urban

* 国家重点研发计划(2017YFC1502104)、国家自然科学基金项目(41575010)和北京市自然科学基金重点项目(8171002)共同资助
2017 年 6 月 14 日收稿； 2018 年 2 月 28 日收修定稿

第一作者：郑祚芳，主要从事区域气候及精细天气预报相关研究. Email：zfzheng@ium.cn

dry island effect of Beijing is closely related to the urbanization process, and has a significant high correlation with the urbanization rate and the intensity of urban heat island, with the correlation coefficients as high as 0.87 and 0.86 respectively.

Key words: urbanization, relative humidity, climate change, dry island effect, Beijing

引 言

近年来,有关城市化对区域气候的影响开始引起人们越来越多的关注。城市化带来生产、生活活动的集中化,使得气象灾害和大气环境污染造成的影响更为集中且严重。同时城市大范围不透水下垫面也对大气结构和水热交换过程造成了明显的影响,这些结构导致城市区域局地气候的显著变化(徐祥德等,2004;王迎春等,2012)。以往有关城市化对局地气候的影响大多针对城市热岛效应展开(徐兆生等,1987;周淑贞,1983;沈滢洁等,2017),结果表明城市化对城市地区气温具有明显正效应,在不同季节均表现为增温趋势。相对于城市热岛效应而言,有关大气湿度影响的研究还不多见。城市下垫面对低层大气的影响不仅包括热力方面,也包括动力影响。当地表气温增加以后,近地表大气露点温度上升,饱和水汽压增加,如果实际水汽压不变,则会使相对湿度减少(丁一汇和柳艳菊,2014)。大气湿度对远距离能源输送(常蕊等,2016)、降水(王宇虹等,2015)、大气能见度(白永清等,2016;樊高峰等,2016)、及环境空气质量(潘玮等,2017)、城市气候承载力(闫胜军等,2016)都有很明显的影响。大气湿度其不仅会影响人体舒适度,而且在边界层雾-霾转变中亦起着重要的作用,探讨区域和局地尺度大气湿度变化的特征,对于深入认识雾、霾长期变化的原因与雾-霾转换宏观气象条件的变化也是十分有益的(丁一汇和柳艳菊,2014)。

国外针对大气湿度的研究开展较早,Hage(1975)利用城区及郊区机场地面观测资料对美国芝加哥市大气湿度进行的研究发现,芝加哥城、郊相对湿度差具有明显的季节差异。在冬季,芝加哥市区相对湿度要高于乡村;其他季节,市区相对湿度则要低于乡村。Fortuniak et al(2006)分析了波兰 Lodz 地区 1997—2002 年相对湿度的城、乡差异,亦发现城市地区的相对湿度要明显低于乡村,在某些时段内城、郊相对湿度差值甚至可达到 40%。Ahmed(2003)进一步研究了不同相对湿度下人体体感舒适气温的分布特征,发现在气温较高时,人体体感舒适性对局地相对湿度具有高敏感性。Willett et al(2008)的分析还发现,1973—2003 年全球比湿整体具有增加的趋势,并且这种增湿趋势在热带地区和北半球尤为显著。国内有关区域大气湿度及其与城市化影响的相关研究开展较晚,姜江等(2017)研究发现,中国区域年干湿指数总体上呈现下降趋势,空间上表现为西部湿润化和东部干旱化共存的特征;Liu et al(2009)分析表明,大规模的城市效应会使得城区的相对湿度和水汽压减小。窦晶晶等(2014)应用近 5 年自动气象站观测资料,分析了北京区域平均大气湿度的日变化及季节差异,得到和 Hage(1975)类似的结论。由于城市化本身是一个较长时间的发展过程,为了更好地探讨城市化的区域气候效应,需要考虑更长时间气象要素的变化情况。王晓默等(2014)分析了近 30 年来山东省济宁市城市化过程对本地相对湿度的影响,发现济宁城市干岛效应呈增加趋势,并具有明显的季节性变化特征,表现为春季干岛效应最强,秋、冬季次之,夏季最弱。

近几十年来北京城市化进程加快,城市规模迅速扩大,但目前对于这种快速、大规模城市化过程对大气湿度产生的影响,还缺少足够的了解。本文应用 20 个常规气象站较长时间的逐日观测资料,分析讨论北京地区相对湿度的分布、变化特征及其对城市化的响应,以期增进对相关科学问题的认识。

1 资料及处理方法

本文所用的资料主要为 1976—2015 年北京地区 20 个常规站逐日观测序列,以及同期北京城市化率数据(城市人口占总人口数比率),分别来源于北京市气象信息中心及北京统计信息网。有研究表明(Li and Yan, 2009; 薛筝筝等,2017),历史观测期间气象观测站点的迁站及观测手段、时次的变化,容易导致观测数据出现不连续现象(或称“断点”),这种资料的非均一性会直接影响气候统计结果的代表性及准确性。朱亚妮等(2015)的研究亦指出,中国

地面相对湿度资料存在较严重的非均一性问题,其中高达 68%的台站数据存在断点。因而,对历史观测资料进行非均一性检测和修订正,对于提高气象预报预测服务水平和气候变化研究水平,都具有重要的意义(任国玉等,2010)。最近,赵煜飞和朱亚妮(2017)采用薄盘样条法进行空间内插,建立了中国地面均一化相对湿度月值 0.5°×0.5°格点资料集,这套数据为相关研究提供了较好的数据基础,但针对精细化的分析,分辨率仍显不足。Reeves et al (2007)曾经对标准正态检验、双相回归及威尔科克森非参数检验等几种主要的断点检测和订正方法进行了比较评估,结果表明在不使用参考序列时,标准正态检验方法效果最好。本文即采用标准正态检验方法,并借鉴 Wang and Gaffen(2001)的做法,首先对北京 20 站 1—12 月的年数据序列进行检验。对于被确认的资料断点,用断点年前后各 5 年的平均值的差值作为补偿值,来进行订正处理。例如,经检测发现北京站(54511 站)在 1981、1997 年存在数据断点,经查证历史沿革资料证实,这两个数据断点是由迁站引起的。订正时先对 1997 年的断点进行处理,即用 1998—2002 年各月平均值,减去 1992—1996 年相应月平均值,得到 12 个月的补偿值;然后把过去的序列订正到现在的站址记录上,即把断点前直至再早一个断点所有年的各个月,均加上那个月的补偿值,得到月订正值。之后再对前一个断点,依次进行订正。

作为一个样例,图 1 给出的是北京站订正前、后的年平均相对湿度序列。原序列中 1981、1997 年前后湿度分布具有较大的跃变,经过订正处理后的序列较好地修复了这种记录中的不连续性。订正前、后北京站近 40 年来的变率分别为−1.8%·(10 a)$^{-1}$和−2.2%·(10 a)$^{-1}$。经过断点订正后,相对湿度的下降趋势更为明显。

在讨论城市化影响的时候,其中一个关键的问题在于不同站点类型(如城市站和乡村站)的划分方法。过去的研究大多采用人口或经济规模,夜晚灯光指数以及遥感观测的土地覆盖信息,或者直接依据站点地理位置进行城乡站点划分(Ren et al, 2008;Peterson, 2003;Gallo et al, 1993;窦晶晶等, 2014)。不同的方法得到的分类结果很不一致,导致最后得到的气候趋势分析结果也不一致。最近,王君等(2013)采用聚类分析等方法,将北京地区 20 个常规观测站点分为 4 类(城市站、近郊站、乡村站和山地站)。其分类结果虽与前人略有不同,但能通过遥感夜间灯光数据的合理性验证和 *t*-test 显著性检验,被认为综合了前述几种站点分类方法的优点。本文借鉴该方法,从北京 20 站中挑出 7 个城区代表站(北京、昌平、丰台、门头沟、通州、海淀、石景山)和 3 个郊县参考站(怀柔、平谷、密云),分别计算其平均值用来代表城、郊区的相对湿度值,以避免应用单一站点可能导致代表性不足的缺陷。

参考城市热岛强度的定义,文中定义城市干岛强度为:

$$\Delta RH_{u-r} = -(\overline{RH_u} - \overline{RH_r}) \tag{1}$$

式中,ΔRH_{u-r}为干岛强度,$\overline{RH_u}$为城区站点的平均相对湿度,$\overline{RH_r}$为郊区站点的平均相对湿度。当$\Delta RH_{u-r}>0$时,称为城市干岛;反之,当$\Delta RH_{u-r}<0$时,则称为城市湿岛。

本文通过计算距平百分率方法来分离相对湿度记录中的大尺度气候背景和局地变化(于淑秋,

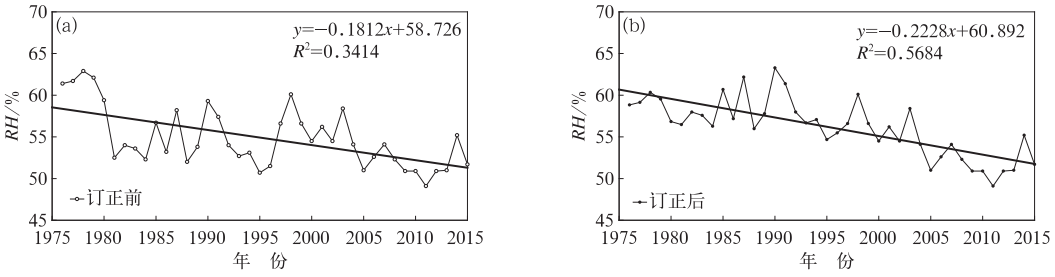

图 1　北京站(a)订正前,(b)订正后相对湿度序列

Fig. 1　Time series of annual relative humidity at Beijing Station

(a) before homogenization, (b) after homogenization

2007)。具体做法是用北京20个站40年相对湿度(记为RH_{ij})资料,先对20个站年相对湿度作平均,得到北京地区年相对湿度序列(记为RH_j)代表大尺度相对湿度,将它的多年平均记为RH_m,则局地相对湿度距平百分率可定义为$DRH_{ij}=(RH_{ij}-RH_j)/RH_m$其中$i=1,2,\cdots,20$,$j=1,2,\cdots,40$。它反映的是各站点间相对湿度的局地差异。

此外,本文中还应用到线性趋势分析及Mann-Kendall统计方法用来检验序列的变化趋势及突变特征。

2 北京地区相对湿度的时间与空间分布特征

图2给出的是北京地区相对湿度的空间分布。从近40年的平均状况来看(图1a),各站点间相对湿度分布不均匀,大部分站点的相对湿度位于54%~60%。其中,西部高海拔山区为相对湿度低值区,西南部及东北部平原地带为相对湿度高值区,房山站、平谷站的值甚至超过了60%。郑祚芳等(2013)通过检验发现,近40年北京的城市化进程可分为两个阶段,分别为城市化发展初期和成熟期,这两个阶段分界点约在1990年前后。在城市化发展较早时期(图2b),相对湿度的分布主要受地形影响,等值线基本沿地形梯度分布,这一时期北京城区站点的相对湿度平均值为55.6%,郊区站点的相对湿度平均值为58.6%,城、郊相对湿度相差约3%。在城市化集中度较高的年代(图2c),城市效应的影响变得更为明显,等值线基本上以城区站点为中心向外呈现发散性分布。同期内城区站点的相对湿度平均值为52.7%,郊区站点的相对湿度平均值为57.6%,城、郊相对湿度差扩大到4.9%。同时我们注意到,在图2c中(下文图4b类似),海淀站与其他城区站点表现不太一致,在所有城区站点中相对湿度的值最高,形成"孤岛",可能与海淀站所处位置有关,海淀站毗邻海淀公园,对相对湿度的测量影响较大。

从相对湿度的年际分布看出(图3a,3b),近40 a来北京地区相对湿度呈波动性减少趋势,年际差异较大,20站相对湿度的平均递减率约为0.9%·(10 a)$^{-1}$。其中城区、郊区相对湿度的递减率分别为1.7%·(10 a)$^{-1}$和0.4%·(10 a)$^{-1}$,城区站点相对湿度的下降速率约是郊区站点的4倍,其下降趋势超过$\alpha=0.001$的显著性水平检验。此外可见,在20世纪90年代中期(1995年)之前,城区、郊区间相对湿度差异较为稳定,自1995年以来,城区相对湿度显著减少,下降趋势要明显大于郊区,这与近年来北京城市化进一步加快,城市建筑密度的进一步增强有很大关系。图3c给出的是北京城区、郊区近40年平均相对湿度的月际分布。在不同的月份,城区相对湿度均低于郊区,且均为单峰型结构。表现在夏、秋季平均湿度较高,其中7月最大(分别为88.1%和90.7%)。冬、春季相对湿度较小,其中4月最小(分别为45.3%和49.3%)。

本文对北京城区、郊区平均相对湿度差值即城市干岛强度进行了Mann-Kendall检验。检验结果发现,在$\alpha=0.01$显著性水平检验的标准下,城区、郊区间相对湿度差值的上升趋势在1995年超过了临界线(图3d),表明北京城区干岛效应自1995年以来呈现出更为明显的增强趋势,与图3b中对应良好。这一时间点略滞后于年北京地区平均气温的增暖性突变年份(1993年)。

表1给出的是北京城区、郊区各季节相对湿度的线性变化趋势。可见无论在城区还是在郊区,其春、夏、秋、冬四季相对湿度的年变化与年平均相对湿度的变化趋势一致,均表现为下降趋势,但季节间差异较大。相对湿度在春季下降趋势最为明显:城区下降速率为2.75%·(10 a)$^{-1}$,郊区为1.48%·(10 a)$^{-1}$,表明北京地区大气湿度的减少主要是由于春季的变干所导致。其次为秋季:城区为1.66%·(10 a)$^{-1}$,郊区为0.61%·(10 a)$^{-1}$,夏季和冬季相对湿度的下降趋势相对较弱。

表1 北京城、郊区不同季节和年平均相对湿度线性趋势

Table 1 Seasonal changes of mean relative humidity in Beijing Area

	春季	夏季	秋季	冬季	年
城区	−2.75%·(10 a)$^{-1}$	−0.57%·(10 a)$^{-1}$	−1.66%·(10 a)$^{-1}$	−0.82%·(10 a)$^{-1}$	−1.68%·(10 a)$^{-1}$
郊区	−1.48%·(10 a)$^{-1}$	−0.16%·(10 a)$^{-1}$	−0.61%·(10 a)$^{-1}$	−0.12%·(10 a)$^{-1}$	−0.41%·(10 a)$^{-1}$

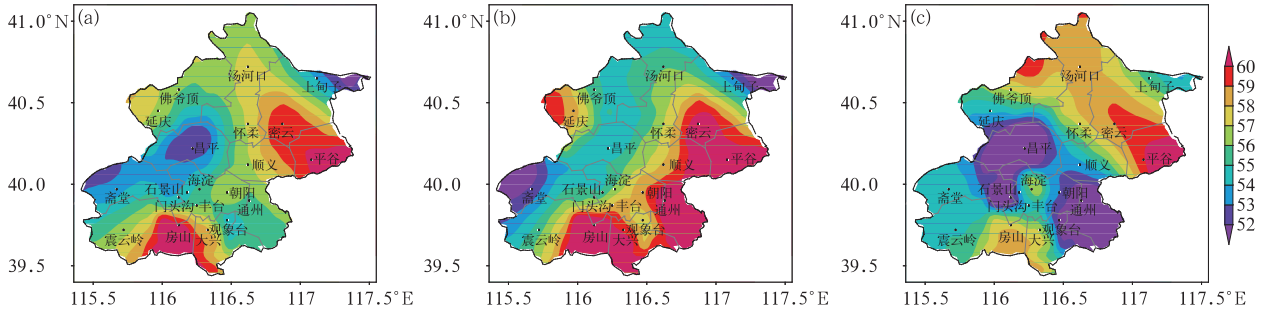

图 2　北京地区(a) 1976—2015 年,(b) 1976—1985 年,(c) 2006—2015 年平均相对湿度分布(单位:%)

Fig. 2　Spatial distributions of annual mean relative humidity in Beijing Area (unit: %) (a) 1976－2015, (b) 1976－1985, (c) 2006－2015

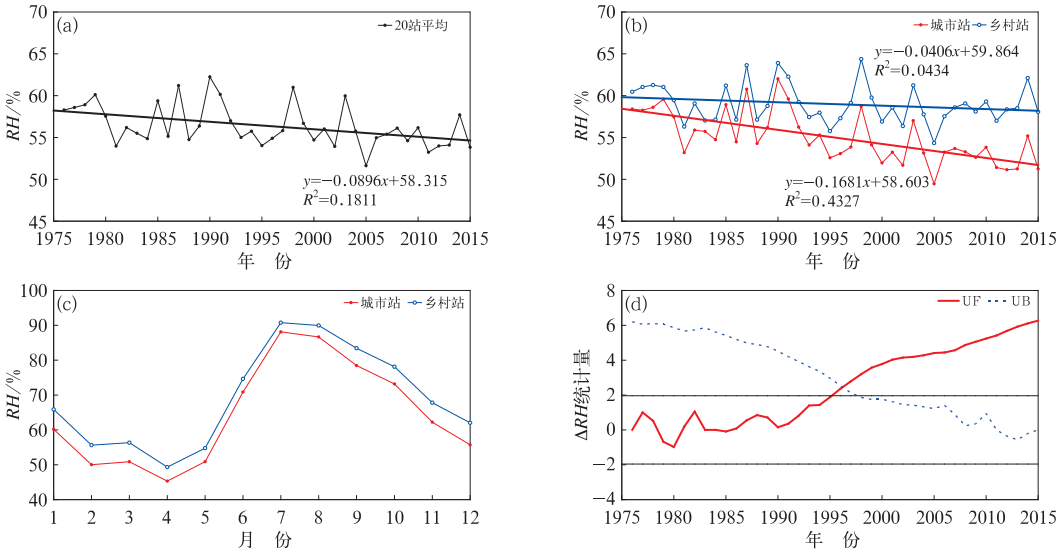

图 3　北京地区相对湿度年际变化(a,b)、月际变化(c)及城、郊差值的 Mann-Kendall 检验结果(d)

Fig. 3　Variations of interannual mean relative humidity (a, b), monthly mean relative humidity (c) and Mann-Kendall abrupt change test of annual mean relative humidity series (d) in Beijing Area

3　北京城市干岛效应

为了讨论相对湿度的局地变化特征,按前文方法计算并绘制了北京城市化发展不同时期相对湿度的空间距平百分率(图 4)。这种计算变换消除了原始观测序列中的大尺度气候背景,反映的是各站点间局地湿度的变化差异(于淑秋,2007)。在城市化发展早期(图 4a),北京相对湿度空间距平百分率的分布与图 2b 类似,主要受地形梯度影响较大,西部、北部高海拔山区以负距平为主,山前平原地带主要为正距平区。城区、郊区站点间相对湿度的局地变化差异不明显。这与期间北京城市化发展较缓慢,城、郊代表站点间下垫面差异没有本质的不同有关(赵娜等,2011)。在城市化集中度较高的时期(图 4b),情况则有很大的不同,表现在等值线以城区站点为中心向外呈现发散性分布。在城区站点所在的区域,大多为负距平区(如昌平站的中心强度可达－6%以上),而包括乡村站、近郊站和山地站的其他地方均为正距平区,这种分布形态表现出明显的城市干岛效应特征,城市化发展使得相对湿度下降。这种现象与郑祚芳等(2013)关于北京地区降水量的分析结果是类似的。表明在这一时期,城市化效应已成为影响局地大气湿度分布的主要因子。

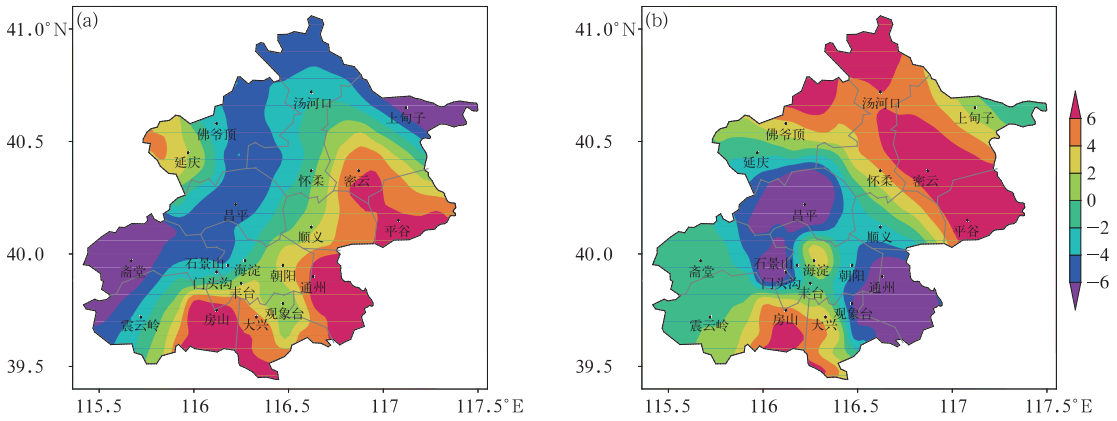

图 4 北京地区(a) 1976—1985 年,(b) 2006—2015 年平均
相对湿度空间距平百分率(单位:%)

Fig. 4 Distribution of annual mean relative humidity anomaly porcentages (unit: %) over Beijing Area in 1976−1985 (a) and 2006−2015 (b)

图 5a 给出的是北京城市干岛强度的年际、月际分布。可以很清楚地看到,近 40 年来北京城市干岛强度呈现波动上升趋势,特别是 20 世纪 90 年代中期以来,干岛强度快速增加。统计表明,1976—1985 年期间干岛强度的均值为 2.3%,而最近 10 年(2006—2015)这个值已经达到 6.0%,提高了 2.6 倍。北京地区近 40 年干岛强度的线性倾向率为 1.3%·(10 a)$^{-1}$,上升趋势远超过 $\alpha=0.001$ 的显著性水平检验($R^2=0.803$)。这一数值亦远大于王晓默等(2014)统计得到的山东省济宁城市干岛强度倾向率[0.2%·(10 a)$^{-1}$],可见城市干岛现象在不同城市之间的差异是很明显的,城市规模越大,其对区域大气湿度的影响也越明显。

季节变化统计表明,北京城市干岛效应以冬季为最强(5.9%),秋季(5.1%)、春季(4.5%)次之,夏季干岛强度最弱(3.2%)。线性倾向率则以春季[1.2%·(10 a)$^{-1}$]为最大,秋季[1.0%·(10 a)$^{-1}$]、冬季[0.6%·(10 a)$^{-1}$]次之,夏季[0.4%·(10 a)$^{-1}$]最小。图 5b 是近 40 年平均的干岛强度的月际分布。可见,北京地区干岛在 12 月最强(达 6.3%),7 月最弱(仅为 2.6%)。

由前文分析表明,在城市化发展不同时期,北京城、郊区间的相对湿度的分布具有很大的不同。北京的城、郊相对湿度差与城市化进程之间相关性如何?是值得关注的问题。为此,本文统计了近 40 年来北京城市化率(即城镇人口占总人口的比例)与城市干岛(ΔRH)间的对应分布(图 6a)。可见,北京城市干岛强度与城市化率之间有着良好的协同关系,城市化率越高,对应的城市干岛强度越大。近 40 年来,北京城市化率每提升 10%,城市干岛强度就会相应地增加约 2.8%,二者间的线性相关系数达到 0.87,超过 0.001 的信度标准。

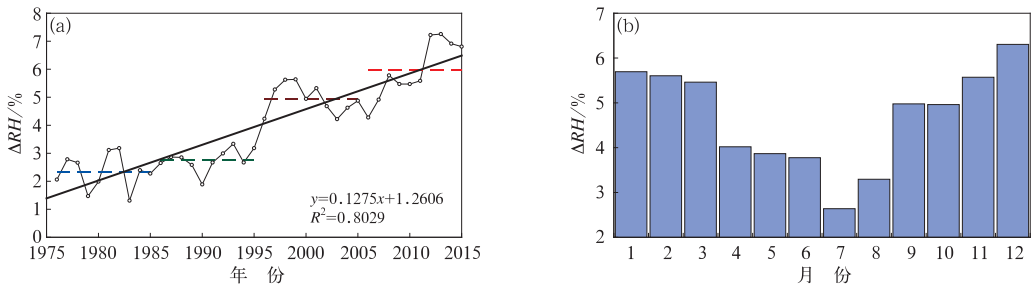

图 5 北京地区干岛强度的年际(a)及月际(b)分布
(图 5a 中虚线为每 10 年干岛强度的平均值)

Fig. 5 Variation of dry island intensity in Beijing Area
(a) interannual variation, (b) monthly mean dry island intensity
(dotted line for mean of decadal variation in Fig. 5a)

此外,还有研究表明,大气中的水汽存储能力随着气温升高具有增加的趋势(Boer, 1993)。当地表温度增加后,地表饱和水汽压将会增加,如果实际水汽压不变,则会导致相对湿度的减少。Allen and Ingram(2002)通过数值模拟发现,全球平均气温每增加 1℃,平均相对湿度会减少约 3.4%。这一关系也为探讨城市热岛与城市干岛效应的关系提供了基础。理论上,城市热岛与城市干岛强度之间应该具有正相关关系。图 6b 给出的是近 40 年北京城市干岛强度(ΔRH)随城市热岛强度(ΔT)的分布。可见清楚地看到,在城市热岛较强的年份,城市干岛也相对较强,城市热岛较弱的年份,城市干岛也相对较弱。计算得到北京城市干岛强度与热岛强度间的相关系数为 0.86,亦超过 $\alpha=0.001$ 显著性水平检验标准,具有显著的高相关性。近 40 年来北京城市干岛强度随热岛强度的增加速率约为 4.7%·℃$^{-1}$,这意味着随着北京城市化集中度的不断提高,城市暖、干化趋势将会变得越来越明显。

4　结　论

应用北京 20 个常规气象站 1976—2015 年逐日观测及同期北京城市发展数据,在对历史观测数据进行订正处理的基础上,借鉴一个新的站点分类方法,分析了北京地区相对湿度的分布、变化特征及其对城市化的响应,主要结论如下:

(1) 数据均一化订正能够较好地修复记录中的不连续性。订正前、后北京站近 40 年来相对湿度的线性倾向率分别为 −1.8%·(10 a)$^{-1}$ 和 −2.2%·(10 a)$^{-1}$。经过订正处理后,相对湿度的下降趋势更为明显。

(2) 北京地区相对湿度的空间分布不均匀,城市化发展早期相对湿度的分布主要受地形影响,城市化程度较高的年代城市效应的影响更为明显。

(3) 近 40 年来北京地区平均相对湿度呈下降趋势,线性倾向率约为 −0.9%·(10 a)$^{-1}$。城区相对湿度的下降速率比郊区大,且自 1990 年代以来下降趋势要明显大于郊区。

(4) 近 40 年来北京城市干岛强度的上升趋势约为 1.3%·(10 a)$^{-1}$,季节分布上以冬季为最强,秋、春季次之,夏季较弱。检验表明北京城区干岛效应自 1995 年以来呈现出更为明显的增强趋势。

(5) 北京城市干岛效应与城市化进程有密切联系,其与北京城市化率及城市热岛强度之间具有显著的高相关性,相关系数分别高达 0.87 和 0.86。

5　讨　论

相较于城市热岛效应的高关注度而言,有关城市干岛现象的研究还不是很多见。本文统计发现,北京地区干岛强度具有显著的上升趋势,最近 10 年的干岛强度较 30 年前已经提高了一倍多。得到的北京城市干岛强度要远大于王晓默等(2014)统计得到的山东省济宁市的城市干岛强度,可见城市规模越大,其对区域大气湿度的影响也越明显。在讨论城市化影响的时候,城、郊区代表站点的选取是很重要的,不同的站点划分方案往往会导致不同的分析结果。本文在分析时参考了王君等(2013)新提出的方案,虽然考虑了诸多因素,但应该注意到该分类方案中的郊区代表站(怀柔、平谷、密云)还是都位于县城附近,这些站点本身都正在经历着或强或弱的城市化过程,因而他们还不能称之为严格意义上的“乡村站”。此外,文中海淀站近 10 年来相对湿度的变化与其他城市站点相比明显偏高,这很可能与海淀

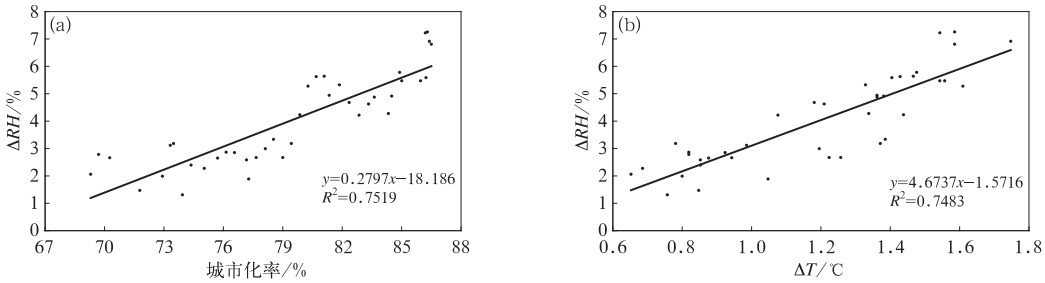

图 6　北京城市干岛与城市化率(a)及城市热岛(b)的相关性

Fig. 6　The correlations between urban dry island and urbanization rate (a), and heat island (b) in Beijing City

站的具体位置有关(毗邻海淀公园)。因此,文中由此得到的干岛强度及其变化速率,应该说也是保守的,真正的值要比这更大。今后,仍有必要进一步研究更合理的站点划分及代表站点的遴选方法。

由于大气湿度变化不仅会影响人体舒适度、对降水产生影响,其在雾-霾转变中亦起着重要的作用,因而其对区域大气环境也会产生影响(丁一汇和柳艳菊,2014)。北京地区近40年来相对湿度的持续下降表明,发生在本地的霾向雾转换会变得更加不容易,这意味着在污染源排放保持不变的情况下,北京地区的霾日将可能持续更长的时间或更容易发生。其次,北京城市热岛强度的不断增强及其与城市干岛强度之间存在的显著高相关性表明,发生于城区的霾污染将可能比郊区更为严重。因而,进一步采取措施减缓城市干岛效应,对于改善城市空气质量也是有益的。

参考文献

白永清,祁海霞,刘琳,等,2016.武汉大气能见度与$PM_{2.5}$浓度及相对湿度关系的非线性分析及能见度预报[J].气象学报,74(2):189-199.

常蕊,周宁,王欣雯,等,2016.河南电网"污闪"故障的综合气象因素分析[J].气象,42(11):1387-1394.

丁一汇,柳艳菊,2014.近50年我国雾和霾的长期变化特征及其与大气湿度的关系[J].中国科学:地球科学,44(1):37-48.

窦晶晶,王迎春,苗世光,2014.北京城区近地面比湿和风场时空分布特征[J].应用气象学报,25(5):559-569.

樊高峰,马浩,张小伟,等,2016.相对湿度和$PM_{2.5}$浓度对大气能见度的影响研究:基于小时资料的多站对比分析[J].气象学报,74(6):959-973.

姜江,姜大膀,林一骅,2017.中国干湿区变化与预估[J].大气科学,41(1):43-56.

潘玮,左志燕,肖栋,等,2017.近50年中国霾年代际特征及气象成因[J].应用气象学报,28(3):257-269.

任国玉,张爱英,初子莹,等,2010.我国地面气温参考站点遴选的依据、原则和方法[J].气象科技,38(1):78-85.

沈滢洁,王成刚,曹乐,等,2017.屋顶绿化对城市降温效应的模拟分析——以南京市为例[J].气象,43(5):610-619.

王君,严中伟,李珍,等,2013.近30年城市化对北京极端温度的影响[J].科学通报,58(33):3464-3470.

王晓默,谷山青,董宁,2014.城市化发展对相对湿度的影响——以济宁市为例[J].中国农学通报,30(26):242-247.

王迎春,梁旭东,苗世光,等,2012.城市气象研究动向的思考[J].气象,38(10):1232-1237.

王宇虹,徐国强,贾丽红,等,2015.太行山对北京"7.21"特大暴雨的影响及水汽敏感性分析的数值研究[J].气象,41(4):389-400.

徐祥德,丁国安,卞林根,等,2004.BECAPEX科学试验城市建筑群落边界层大气环境特征及其影响[J].气象学报,62(5):663-671.

徐兆生,沈建桂,王德辉,1987.北京城市热状况及热岛形成原因的探讨[J].地理研究,6(3):17-25.

薛筝筝,高英育,郭建侠,等,2017.探测环境变化对密云气象站地面风观测的影响[J].气象,43(1):84-90.

闫胜军,何霄嘉,王烜,等,2016.城市气候承载力定量化评价方法初探[J].气候变化研究进展,12(6):476-483.

于淑秋,2007.北京地区降水年际变化及其城市效应的研究[J].自然科學進展,17(5):632-638.

赵娜,刘树华,虞海燕,2011.近48年城市化发展对北京区域气候的影响分析[J].大气科学,35(2):373-385.

赵煜飞,朱亚妮,2017.中国地面均一化相对湿度月值格点数据集的建立[J].气象,43(3):333-340.

郑祚芳,王在文,高华,2013.北京地区夏季极端降水变化特征及城市化的影响[J].气象,39(12):1635-1641.

周淑贞,1983.上海城市发展对气温的影响[J].地理学报,38(4):397-405.

朱亚妮,曹丽娟,唐国利,等,2015.中国地面相对湿度非均一性检验及订正[J].气候变化研究进展,11(6):379-386.

Ahmed K S,2003. Comfort in urban spaces:defining the boundaries of outdoor thermal comfort for the tropical urban environments[J]. Energy and Buildings,35(1):103-110.

Allen M R,Ingram W J,2002. Constraints on future changes in climate and the hydrologic cycle[J]. Nature,419(6903):224-232.

Boer G J,1993. Climate change and the regulation of the surface moisture and energy budgets[J]. Climate Dyn,8(5):225-239.

Fortuniak K,Klysik K,Wibig J,2006. Urban-rural contrasts of meteorological parameters in Lódz[J]. Theor Appl Climatol,84(1-3):91-101.

Gallo K P,McNab A L,Karl T R,et al,1993. The use of NOAA AVHRR data for assessment of the urban heat island effect[J]. J Appl Meteor,32(5):899-908.

Hage K D,1975. Urban-rural humidity difference[J]. J Appl Meteor,14(7):1277-1283.

Li Zhen,Yan Zhongwei,2009. Homogenized daily mean/maximum/minimum temperature series for China from 1960-2008[J]. Atmos Oceanic Sci Lett,2(4):237-243.

Liu Weidong,You Huanling,Dou Junxia,2009. Urban-rural humidity and temperature differences in the Beijing area[J]. Theor Appl Climatol,96(3-4):201-207.

Peterson T C,2003. Assessment of urban versus rural in situ surface temperatures in the contiguous United States:no difference found[J]. J Climate,16(18):2941-2959.

Reeves J,Chen Jien,Wang X L,et al,2007. A review and comparison of changepoint detection techniques for climate data[J]. J Appl Meteor Climatol,46(6):900-915.

Ren Guoyu,Zhou Yaqing,Chu Ziying,et al,2008. Urbanization effects on observed surface air temperature trends in North China[J]. J Climate,21(6):1333-1348.

Wang J X L,Gaffen D J,2001. Late-twentieth-century climatology and trends of surface humidity and temperature in China[J]. J Climate,14(13):2833-2845.

Willett K M,Jones P D,Gillett N P,et al,2008. Recent changes in surface humidity:development of the HadCRUH dataset[J]. J Climate,21(20):5364-5383.

支蓉,陈丽娟,竺夏英,2018. 2017 年秋季我国北方地区降水异常偏多成因分析[J]. 气象,44(4):572-581.

2017 年秋季我国北方地区降水异常偏多成因分析*

支 蓉[1] 陈丽娟[1,2] 竺夏英[1]

1 国家气候中心,中国气象局气候研究开放实验室,北京 100081

2 南京信息工程大学气象灾害预报预警与评估协同创新中心,南京 210044

提 要:根据国家气象信息中心提供的中国台站气温、降水资料,NCEP/NCAR 逐日大气环流再分析资料和 NOAA 提供的月平均海温资料,分析了 2017 年秋季我国北方地区降水异常偏多的成因。结果表明 2017 年秋季我国降水阶段性特征明显,9—10 月北方地区降水异常偏多主要受东亚环流型组合异常的影响。东亚 500 hPa 高度距平场从高纬至低纬呈"+−+"的异常分布,极区高度场偏高,极涡分裂偏向东北亚地区,贝加尔湖-巴尔喀什湖地区为显著低槽区,西太平洋副热带高压较常年偏强偏西偏北,有利于华西秋雨偏强。此外,850 hPa 距平风场上朝鲜半岛的反气旋式环流异常有利于引导偏东路径的冷湿气流输送至黄河与长江之间的地区,与来自孟加拉湾和南海的暖湿气流交汇,形成水汽通量异常辐合区,造成黄淮及江淮等地降水异常偏多。进一步诊断表明热带中东太平洋海温秋季转为偏冷状态,热带太平洋地区 Walker 环流明显增强,有利于西太平洋副热带高压偏强西伸偏北;9—10 月热带印度洋偶极子维持正位相有利于在孟加拉湾形成反气旋式环流异常,并同样有利于副热带高压西伸偏北。因此,海温外强迫信号的影响加上中高纬环流异常的共同作用造成 9—10 月东亚环流型异常特征,并进一步导致我国北方地区降水异常偏多。

关键词:秋季降水,北方地区,西太平洋副热带高压,海温异常

中图分类号:P461 **文献标志码**:A **DOI**:10.7519/j.issn.1000-0526.2018.04.011

Analysis of Characteristics and Causes of Precipitation Anomalies over Northern China in Autumn 2017

ZHI Rong[1] CHEN Lijuan[1,2] ZHU Xiaying[1]

1 Laboratory of Climate Studies, National Climate Centre, CMA, Beijing 100081

2 Collaborative Innovation Center on Forecast and Evaluation of Meteorological Disasters, Nanjing University of Information Science and Technology, Nanjing 210044

Abstract: The stage characteristics of precipitation over China in the autumn of 2017 is obvious, and the significantly above-normal precipitation over northern China from September to October was mainly influenced by the East Asia circulation pattern anomaly. The distribution of 500 hPa height anomaly field in East Asia was "+−+" from high to low latitude. The polar height field was higher than normal, the polar vortex split and inclined to Northeast Asia, the area between Baikal Lake and Balkhash Lake was under a significantly low trough, and the West Pacific subtropical high was stronger, stretching more westward and northward than normal, which is favorable to the intensive autumn rainfall in West China. In addition, anticyclonic circulation anomaly over Korean Peninsula was conducive to guiding the cold and wet airflow

* 国家自然科学基金面上项目(41575074)、国家重点基础研究发展计划(973 计划)(2015CB453203)和国家自然科学基金重点项目(41730964)共同资助

2018 年 2 月 11 日收稿; 2018 年 3 月 19 日收修定稿

第一作者:支蓉,主要从事短期气候预测研究. Email: zhirong@cma.gov.cn

通信作者:陈丽娟,主要从事短期气候预测研究. Email: chenlj@cma.gov.cn

along the easterly path to the area between the Yellow River and the Yangtze River, and to converging with the warm and wet airflow from the Bay of Bengal and the South China Sea. The water vapor flux convergence resulted in precipitation anomalies in the Huanghuai and Jianghuai regions. Further diagnosis shows that the tropical Middle East Pacific sea surface temperature turned cold in autumn, and the Walker circulation in the tropical Pacific increased obviously, which is beneficial to the westward and northward extension of the stronger West Pacific subtropical high. The positive phase of the tropical Indian Ocean dipole in September—October was favorable for the formation of anticyclonic circulation anomalies in the Bay of Bengal, and also beneficial to the westward and northward extension of the West Pacific subtropical high. Therefore, the influence of the external forcing signal of sea surface temperature and the circulation anomaly in the middle and high latitudes over East Asia led to more precipitation over northern China.

Key words: autumn precipitation, northern China, West Pacific subtropical high, sea surface temperature anomalies

引　言

中国地处东亚季风区,季风气候显著。秋季是夏季风环流向冬季风环流转变的过渡时期,随着东亚夏季风系统的南撤,季风槽南移,西太平洋副热带高压(以下简称副高)东撤南退,中国东部地区雨季结束。但此时来自孟加拉湾的西南季风和水汽输送仍然较强,同时中高纬冷空气活动开始活跃,在有利的形势下,往往造成冷暖空气交汇,从而使得某些地区降水出现异常。这其中华西地区由于特殊的地理位置,秋雨特征显著,很早就引起气象学家的重视(高由禧,1958;高由禧和郭其蕴,1958)。同时由于秋季是我国秋收秋种的重要季节,秋季的天气气候异常将对我国粮食生产和人民生活安全造成严重的影响。因此做好秋季气候异常的诊断分析和预测(鲍媛媛等,2003;贾小龙等,2008;王朋岭等,2014;司东等,2015;聂羽等,2016;竺夏英和宋文玲,2017)将有利于认识秋雨发生的科学规律,有助于防灾减灾。

自 20 世纪 90 年代以来,我国秋季气温总体处于偏暖的年代际背景下;而秋季降水自 21 世纪以来进入偏多的时段。此外秋季气候受到海温等多种外强迫因子的影响(谌芸和施能,2003;韩晋平等,2013;王春学等,2015b),还有显著的年际变化特征。2017 年,我国秋季气候总体表现为"暖湿"的特征,全国大部分地区气温偏高,但降水偏多区域主要集中在长江以北地区。本文从 2017 年秋季我国主要气候特点出发,通过诊断分析造成气候异常的大气环流特征和外强迫信号,探讨造成 2017 年秋季气候异常的可能成因,为今后的气候预测和服务提供参考。

1　资料和方法

本文使用的资料主要有:中国气象局国家气象信息中心整编的 1961—2017 年中国地面基本气象要素日值数据集(V3.0)逐日气温和降水观测资料、国家气候中心提供的 160 站月降水观测资料、NCEP/NCAR 逐日再分析大气环流资料(Kalnay et al,1996)以及 NOAA 提供的逐月海温资料(Reynolds et al,2007)。文中部分图形出自国家气候中心开发的"气象灾害影响评估系统"及"大气环流交互诊断系统"(http://cmdp.ncc-cma.net/Monitoring/cn_stratosphere.php#seasonal)。文中气候态取 1981—2010 年平均。使用的统计方法主要有相关、合成等。

2　2017 年秋季我国主要气候异常特征

2017 年秋季,全国平均气温为 10.8℃,较常年同期(9.9℃)偏高 0.9℃(图 1a)。从空间分布看,全国大部分地区气温接近常年同期至偏高,其中内蒙古西部、西北地区西南部和中部、西藏、西南地区西部、江南地区南部和东部等地气温较常年同期偏高 1～2℃,局部偏高 2℃以上;而内蒙古东部、东北地区北部和东部、江淮地区西部和江汉地区东部等地气温较常年同期偏低,其中内蒙古东部局部和东北地区北部局部偏低 0.5～1℃(图 1b)。

2017 年秋季,全国平均降水量为 123.2 mm,较常年同期(119.8 mm)偏多2.8%(图2a),但空间分

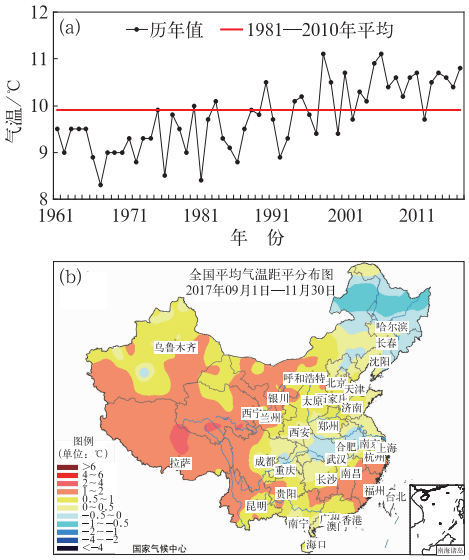

图 1 1961—2017 年秋季全国平均气温历年变化(a)及 2017 年秋季全国气温距平分布(b)

Fig. 1 Time series of autumn mean temperature over China during 1961－2017 (a) and distribution of temperature anomalies in autumn 2017 (b)

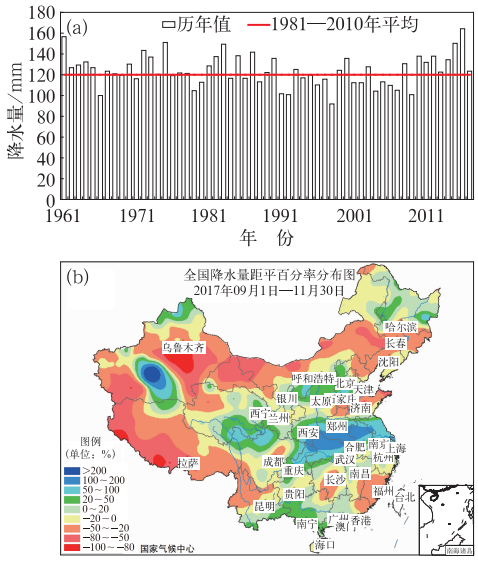

图 2 1961—2017 年秋季全国平均降水量历年变化(a)及 2017 年秋季全国降水量距平百分率分布(b)

Fig. 2 Time series of autumn rainfall over China during 1961－2017 (a) and distribution of precipitation anomaly percentage in autumn 2017 (b)

布非常不均匀，其中长江以北的大部分地区降水较常年明显偏多。新疆北部、西南北部和东部局部、东北北部、华北大部、黄淮南部、江汉、江淮大部、江南东北部及华南西部等地较常年偏多 2～5 成，尤其是西南北部、江汉、黄淮南部至江淮大部等黄河与长江之间的大部分地区降水偏多 1 倍以上，汉水流域发生洪涝灾害；内蒙古中东部和西部、新疆东部、西藏大部、东北南部、黄淮北部及江南东南部等地降水较常年明显偏少，部分地区偏少 8 成至 1 倍(图 2b)。

根据国家气候中心华西秋雨监测业务规定(2015 年试行)，2017 年华西秋雨监测区(图 3)降水总体较常年偏多 48.6%。其中北区华西秋雨开始日期较气候平均值偏早 14 d，结束日期偏晚 5 d，秋雨期偏长 19 d，累积降水量偏多 71.5%。南区华西秋雨开始日期偏早 16 d，结束日期偏早 5 d，秋雨期偏长 11 d，累积降水量偏多 74.7%，居 1961 年以来第三位(表 1)。

2017 年秋季我国气候总体呈现“暖湿”特征，但季节内降水的空间分布具有明显的阶段性变化特征：9—10 月的主要降水异常落区为华西、黄淮大部及江淮等地，同时决定了季节尺度主要多雨带的

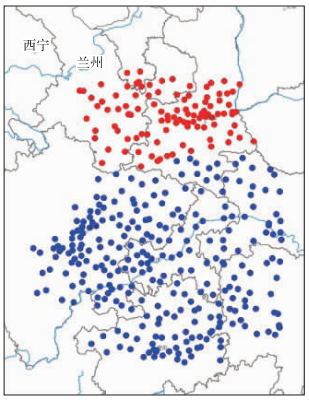

图 3 华西秋雨监测站点
(红点：北区，蓝点：南区)

Fig. 3 West China autumn rain monitoring stations
(red dot: northern area, blue dot: southern area)

表 1 2017 年华西秋雨指数特征

Table 1 Indexes of autumn rainfall in West China in 2017

	开始时间(气候值)	结束时间(气候值)	持续时间/d(气候值)	秋雨量/mm(气候值)
北区	8 月 25 日(9 月 8 日)	10 月 18 日(10 月 13 日)	54(35)	234.1(136.5)
南区	8 月 24 日(9 月 9 日)	10 月 26 日(10 月 31 日)	63(52)	322.2(184.4)
总体	8 月 24 日(8 月 31 日)	10 月 26 日(11 月 1 日)	63(62)	301.4(202.8)

特征(图 4a);而 11 月降水异常的空间特征则发生了显著变化,主要多雨区位于江南中东部到华南地区(图 4b)。降水异常空间型的变化伴随着大气环流的调整和次季节尺度大气演变特征。为了突出气候异常特征并使降水成因分析更有针对性,下面将重点分析 9—10 月我国北方地区降水异常偏多的原因,该时段是华西秋雨发生的典型阶段,同时也是黄淮及江淮出现异常降水的集中时段。

在何敏(1984)的研究中将我国秋雨区分成一般秋雨区和明显秋雨区,华西属于明显秋雨区,而黄淮和长江中下游的大部分地区属于一般秋雨区。2017 年秋季降水不仅表现为华西地区降水较常年偏强,

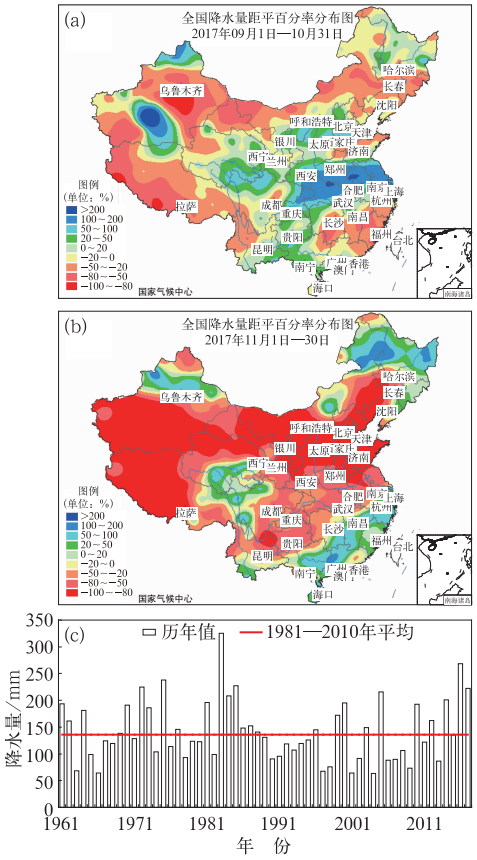

图 4　2017 年 9—10 月平均(a)和 11 月(b)全国降水量距平百分率分布,1961—2017 年 9—10 月黄淮和江淮平均降水量历年变化(c)

Fig. 4　The distribution of precipitation anomaly percentage in China in September—October (a) and November (b) 2017; (c) time series of autumn rainfall over Huanghuai and Jianghuai regions during 1961－2017

黄淮和江淮的秋雨强度也不弱于华西地区。统计显示(图 4c),2017 年黄淮和江淮地区 9—10 月平均降水量较常年同期偏多 63.9%,居 1961 年以来第六位。黄淮和江淮地区出现的明显秋汛对当地秋收秋种产生显著的不利影响,因而更值得探讨该地区降水异常偏多的成因。

3　2017 年 9—10 月我国北方降水异常偏多成因分析

3.1　造成 9—10 月北方降水偏多的大气环流异常特征

2017 年 9—10 月,东亚地区 500 hPa 高度距平场(图 5a)自高纬至低纬呈“＋－＋”的异常分布特征,极区高度场偏高,有利于冷空气扩散,且极涡分裂偏向东北亚地区导致该地区高度场偏低,中纬度贝加尔湖-巴尔喀什湖地区为显著的低槽区,低纬度副高偏强并异常西伸至 100°E 以西,脊线位置偏北,且我国东部黄河以南的区域上空高度场偏高。值得注意的是在850 hPa 高度距平场(图 5b)上,朝鲜半岛附近为高度场正距平中心,850 hPa 距平风场(图 5c)上东北南部到朝鲜半岛地区为异常反气旋式环流,有利于引导偏东路径的冷空气南下。影响我国的冷空气活动一般分为西路、中路、东路等路径,其中偏东路径的冷空气活动一般与极涡分裂及形态有密切关系。从图 5c 可以看出,来自新疆、蒙古国等西路和中路的冷空气并不强,长江以北地区没有偏北风距平,但是通过朝鲜半岛地区异常反气旋式环流引导的冷空气沿半岛南部的偏东风分量很强,将来自东北亚和日本海的冷湿气流向我国黄淮和江淮等区域输送。此外,图 5c 还显示菲律宾附近为异常气旋式环流,南海北部为偏东风距平;孟加拉湾东部到中南半岛为异常反气旋式环流,中南半岛北部为偏西风距平,两支暖湿气流在华南交汇后北上。该气流与来自东北亚和日本海的冷湿气流在我国长江与黄河的区域交汇,在该区域形成水汽通量异常辐合区(图 5d),造成西南地区北部、江汉、黄淮及江淮等地降水明显偏多。

根据前人的研究,贝加尔湖-巴尔喀什湖地区低槽偏强和副高偏强偏西的环流配置非常有利于华西秋雨偏强,2017 年 9—10 月的环流型及华西地区降水偏强的特征与已有研究结论相符合(冯丽文和郭

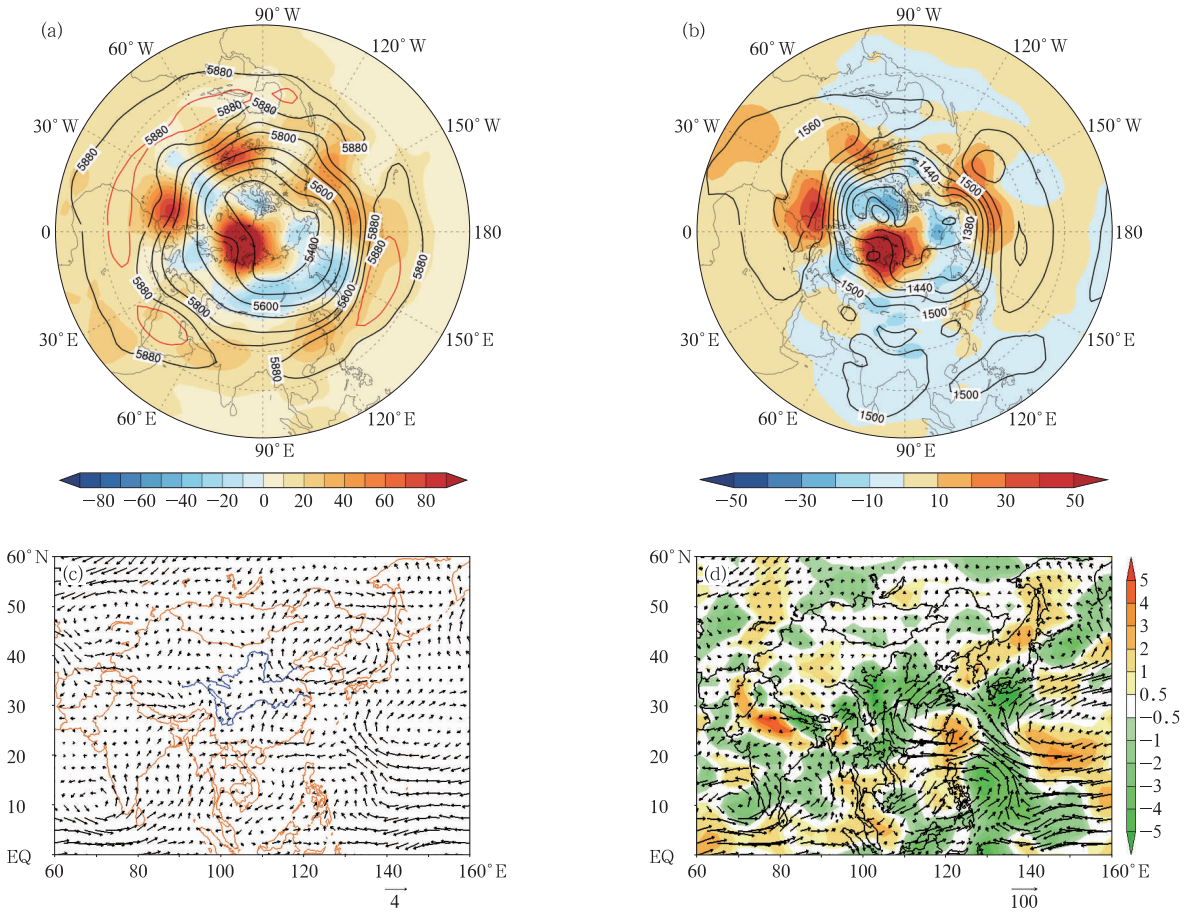

图 5 2017 年 9—10 月平均大气环流距平场

(a)500 hPa 和(b)850 hPa 位势高度(等值线)及距平场(填色)(红色线为气候平均的 5880 gpm 等值线)(单位:gpm);(c)850 hPa 距平风场(单位:$m \cdot s^{-1}$);(d)对流层整层积分水汽通量距平(矢量,单位:$kg \cdot s^{-1} \cdot m^{-1}$)及水汽通量散度距平场(填色,单位:$10^{-5}\ kg \cdot s^{-1} \cdot m^{-2}$)

Fig. 5 Averaged atmospheric circulation anomalies in September—October 2017

(a) 500 hPa and (b) 850 hPa geopotential height (contours) and anomalies (colored areas) (Red contours stand for the climatological 5880 gpm contours) (unit: gpm); (c) 850 hPa wind anomalies (unit: $m \cdot s^{-1}$); (d) anomalies of moisture flux integrated from 100 hPa to 300 hPa (vectors, unit: $kg \cdot s^{-1} \cdot m^{-1}$) and divergence (colored areas, unit: $10^{-5}\ kg \cdot s^{-1} \cdot m^{-2}$)

其蕴,1983;何敏,1984;白虎志和董文杰,2004;王遵娅和丁一汇,2008)。而黄淮和江淮等地的秋雨偏强显然与两个关键环流因素有关,一是副高偏北偏西,使得江南东部为对流层中低层的反气旋式环流中心,对暖湿水汽自南向北的输送和多雨区在北方的位置起到关键作用;二是朝鲜半岛的反气旋式环流异常有利于引导偏东路径的冷湿气流沿朝鲜半岛南部西进到黄河与长江之间的地区,从而与北上的暖湿水汽汇合,形成异常辐合,由于水汽条件充足,形成强降水和秋汛。

3.2 造成 9—10 月大气环流异常的关键海温外强迫因子

西太平洋副高特征是决定我国水汽输送条件的关键因子,而副高又受到太平洋和印度洋等海温外强迫信号的影响。继 2014—2016 年的超强厄尔尼诺事件(邵勰和周兵,2016;袁媛等,2016;翟盘茂等,2016)于 2016 年春季结束后,赤道中东太平洋转入近中性状态(图 6),其中 2016 年 7—11 月 Niño 3.4 指数≤−0.5℃,2017 年 5—7 月维持在 0.5℃附近,

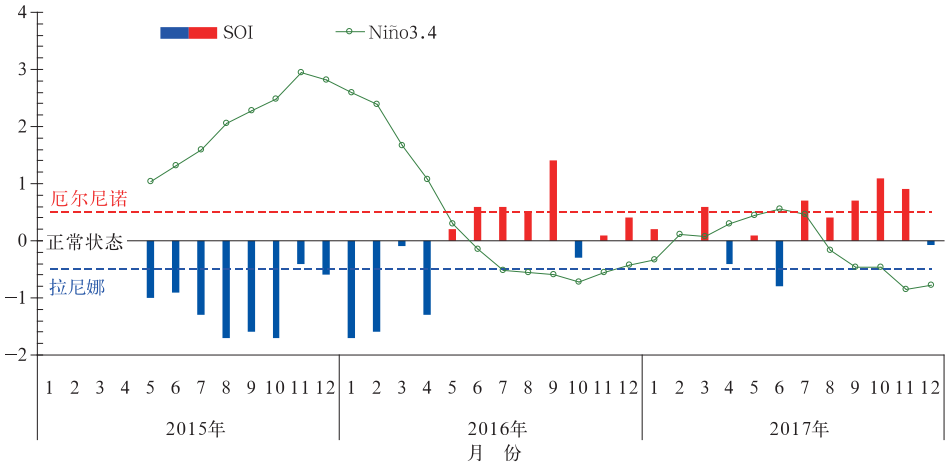

图 6　2015—2017 年 Niño3.4 指数(单位:℃)和 SOI 指数

Fig. 6　Monthly Niño3.4 (unit: ℃) and SOI index during 2015－2017

随后于 9 月开始再次≤－0.5℃。值得注意的是 SOI 指数在 2017 年 7—11 月持续维持正位相,赤道中东太平洋冷水状态与热带太平洋上空大气的耦合度较高,这一特征显著不同于 2016 年秋季的弱冷水阶段。同时通过 9—10 月 Walker 环流距平图(图 7)可以看到,赤道西太平洋上升气流和中东太平洋下沉气流的整体性很强,显示 Walker 环流明显增强的特征,是典型的 La Niña 状态特点。

有大量研究探讨了热带太平洋海温特征与我国秋季降水的关系(李耀辉等,2001;谌芸和施能,2003;贾小龙等,2008;顾薇等,2012;韩晋平等,2013;Gu et al,2015;何珊珊等,2015),多数观点认为,热带中东太平洋处于拉尼娜状态或偏冷位相时,抑制了该地区上空大气的对流活动,而在热带西太平洋上空对流旺盛,从而导致西北太平洋出现异常反气旋,引起西太平洋副高偏强西伸,我国北方秋雨偏多而南方偏少。其中顾薇等(2012)的研究考虑到热带中东太平洋的海温变化与西太平洋海温变化的差异,能更好地反映海温东西变率差异与我国秋季降水的关系。尤其是从春季开始逐步发展并维持至冬季的赤道中东太平洋(Niño3 区＋Niño4 区,下同)一致偏暖/冷,有利于秋季长江以北的黄淮、江淮、华北及河套等地区降水偏少/多。根据国家气候中心 ENSO 监测业务标准及顾薇等(2012)的定义计算了 1982—2017 年赤道中东太平洋夏季和秋季季节平均海温指数(图 8),可以看出,夏、秋季赤道中东太平洋海温持续性非常好,同号率达到88.9%;仅 1983、1992、2005 和 2017 年出现了夏、秋季海温指数不同号的情况,均由夏季的正海温异常转为秋季的负海温异常。2017 年夏季赤道中东太平洋总体为中性偏暖状态,秋季则迅速转为较显著的偏冷状态。

分夏、秋季赤道中东太平洋持续偏暖且秋季海温指数≥0.5℃(1982、1986、1987、1991、1994、1997、2002、2004、2006、2009、2014 和 2015 年)和夏、秋季赤道中东太平洋海温持续偏冷且秋季海温指数≤－0.5℃(1984、1988、1995、1998、1999、2000、2007、2010 和 2011 年)两种情况,选取典型年进行 9—10 月平均 500 hPa 高度距平场合成分析(图 9)。可以看出,在赤道中东太平洋夏、秋季持续偏暖的年份,东亚地区 500 hPa 环流场自北向南呈“－＋－＋”的异常分布,极地高度场负异常,45°N 以北为高度场正异常,中国中东部20°～45°N范围内为高度场负

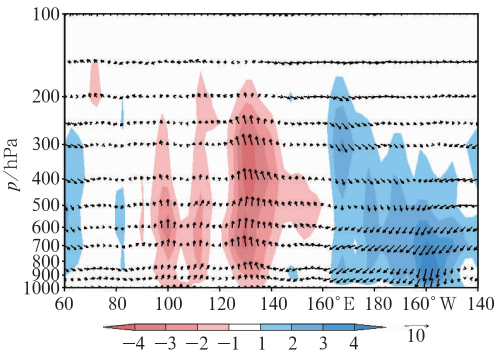

图 7　2017 年 9—10 月平均 Walker 环流距平图

(阴影,单位:0.01 Pa·s^{-1})

Fig. 7　Walker circulation anomalies in September－October 2017

(shaded area, unit: 0.01 Pa·s^{-1})

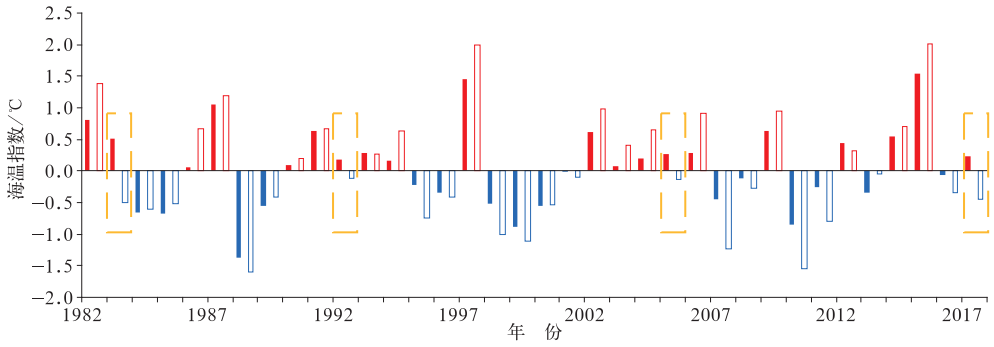

图 8 1982—2017 年赤道中东太平洋夏季(实心柱)和秋季(空心柱)海温指数演变

(黄色方框表示夏、秋季赤道中东太平洋海温指数由正转负的年份)

Fig. 8 Sea surface temperature index of equatorial middle−east Pacific in summer (solid column) and autumn (hollow column) during 1982−2017

(Yellow boxes indicate the years when sea surface temperature index of equatorial middle−east Pacific changed from positive in summer to negative in autumn)

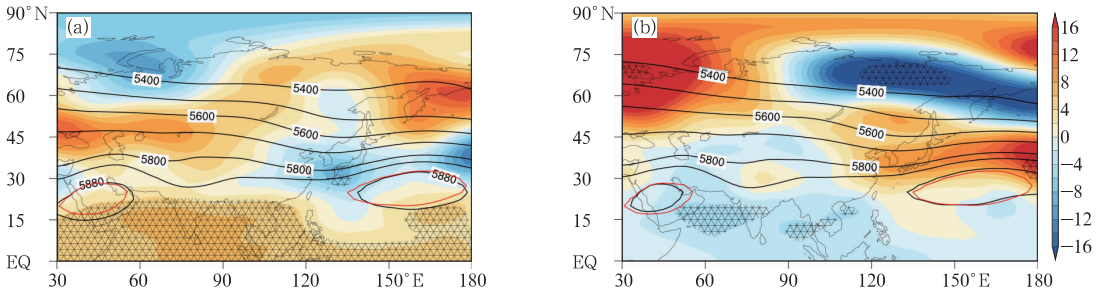

图 9 2017 年 9—10 月 500 hPa 位势高度距平场合成分析

(a)夏、秋季赤道中东太平洋持续偏暖且秋季海温指数≥0.5℃的年份,

(b)夏、秋季赤道中东太平洋持续偏冷且秋季海温指数≤−0.5℃的年份

(红色线为气候平均的 5880 gpm 等值线,阴影区为通过 0.10 显著性水平检验区域,单位:gpm)

Fig. 9 Composite anomalies of 500 hPa geopotential height in September−October 2017 (a) years when sea surface temperature index of equatorial middle−east Pacific in summer is positive and the index ≥0.5℃ in autumn; (b) years when sea surface temperature index of equatorial middle−east Pacific in summer is negative and the index ≤−0.5℃ in autumn

(Red contours stand for the climatological 5880 gpm contours, shading indicates the area has passed the 0.10 significance level test, unit: gpm)

距平,西太平洋副高偏东偏南(图 9a)。在赤道中东太平洋夏秋季持续偏冷的年份,东亚地区 500 hPa 高度距平场的特征与偏暖年份恰好相反,自北向南呈“+−+−”的异常分布,中国中东部 28°~55°N 为正高度距平,西太平洋副高偏西偏北(图 9b)。对比图 5a 与图 9b 可以发现,两者在中高纬度的特征非常相似。

ENSO 循环对中国秋季降水有重要影响,考虑到海温的慢变特性及大气对海温变化的响应往往有滞后效应存在,在以往的研究和预测应用中,通常将前期夏季的海温状况作为最重要的前兆信号来考虑,但回顾 2017 年 9—10 月的降水实况及类似的 1983、1992 和 2005 年环流、降水特征,热带太平洋海温夏、秋季的持续性在统计上显著但也有例外年份。这说明除了考虑大气对热带太平洋海温冷暖转换的响应程度和响应速度外,还需要同时考虑其他海温因素的影响。

除热带太平洋外,热带印度洋是影响东亚环流的另一个重要因素。已有研究探讨过印度洋海温异常尤其是热带印度洋偶极子(TIOD)与中国秋季降水的关系(刘宣飞和袁慧珍,2006a;2006b;肖莺等,2013;刘佳等,2015)。一般认为夏、秋季印度洋偶极

子均与中国南方秋季降水有很好的正相关关系,同时 ENSO 事件的发生对 TIOD 与中国秋季降水的关系有调制作用,导致 TIOD 与 ENSO 事件联合作用和独立作用时对秋季气候的影响不同。

根据国家气候中心的监测,TIOD 指数自 2017 年 2 月由负位相转为正位相之后,一直持续加强,至 9—10 月有所减弱,但依然维持正位相特征(图 10a)。从 1982—2017 年 9—10 月平均 TIOD 指数与赤道中东太平洋海温逐月指数的超前滞后相关可以看出(图 10b),TIOD 对赤道中东太平洋海温变化存在 3 个月左右的显著滞后响应。虽然赤道中东太平洋在 2017 年 9 月进入显著冷水状态,但 TIOD 一直维持正位相,仍然表现为对前期春、夏季赤道中东太平洋中性偏暖状态的滞后响应。

根据刘宣飞和袁慧珍(2006b)的研究,我们首先计算了 1982 年以来 9—10 月赤道中东太平洋海温指数与同期 TIOD 指数的相关,相关系数达到 0.68,通过了 0.01 的显著性水平检验,表明在全球变暖的背景下,当前 TIOD 与 ENSO 之间的关系依然显著。对 1982 年以来 TIOD 正位相与 El Niño 联合发生年(1982、1991、1994、1997、2002、2006 和 2015 年)及 TIOD 正位相独立发生年(2007、2011 和 2012 年)分别进行了典型年降水量距平百分率的合成。可见 TIOD 正位相与 El Niño 联合发生年秋季降水的主要区域集中在长江以南地区(图 11a),而 TIOD 正位相独立发生年秋季降水主要落区明显偏北(图 11b)。图 11c 给出了 TIOD 正位相独立发生年 9—10 月平均 500 hPa 高度场减去 TIOD 正位相与 El Niño 联合发生年 9—10 月平均 500 hPa 高度场的差值场,结果表明 TIOD 正位相独立发生年西太平洋副高偏强偏西偏北的特征更为显著,从而有利于暖湿水汽输送至我国更偏北的地区。此外,两组典型年份 9—10 月平均 850 hPa 风场的差值场(图 11d)显示,TIOD 正位相独立发生年更有利于在孟加拉湾地区形成反气旋式环流异常,从而进一步加强了自南向北输送向我国的暖湿气流。

上述分析显示,2017 年 9—10 月东亚环流特征受到多种环流异常配置及海温外强迫因子的影响,极涡分裂偏向东北亚地区及 850 hPa 距平风场上朝鲜半岛的异常反气旋式环流为偏东路径的冷空气活动提供了条件,而赤道中东太平洋冷水状态和热带印度洋偶极子正位相的组合影响有利于西太平洋副高偏强偏西偏北,从而为暖湿气流向北输送奠定了基础。正是在这样的环流异常组合影响下,有利于 2017 年秋季北方降水异常偏多。

4　结论和讨论

本文利用国家气象信息中心提供的中国台站气温降水资料、NCEP/NCAR 逐日大气环流再分析资料和 NOAA 提供的月平均海温资料,首先揭示了 2017年秋季中国气候异常的主要特征,然后分析了

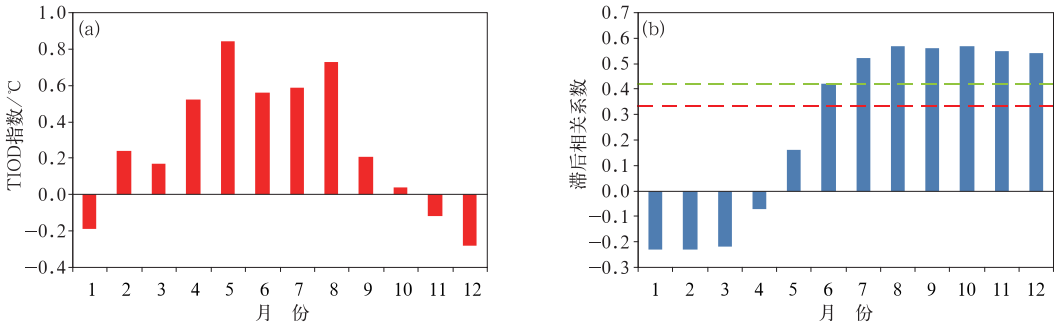

图 10　(a)2017 年 TIOD 指数逐月演变;(b)1982—2017 年 9—10 月平均 TIOD 指数与逐月赤道中东太平洋海温指数的超前滞后相关

(红色虚线和绿色虚线分别表示通过 0.05 和 0.01 显著性水平检验)

Fig. 10　(a) Monthly TIOD index in 2017; (b) lag correlation between TIOD index of September−October and monthly sea surface temperature index of equatorial middle−east Pacific for the period 1982−2017

(Dashed lines of red and green indicate the areas have passed the significance test at levels of 0.05 and 0.01, respectively)

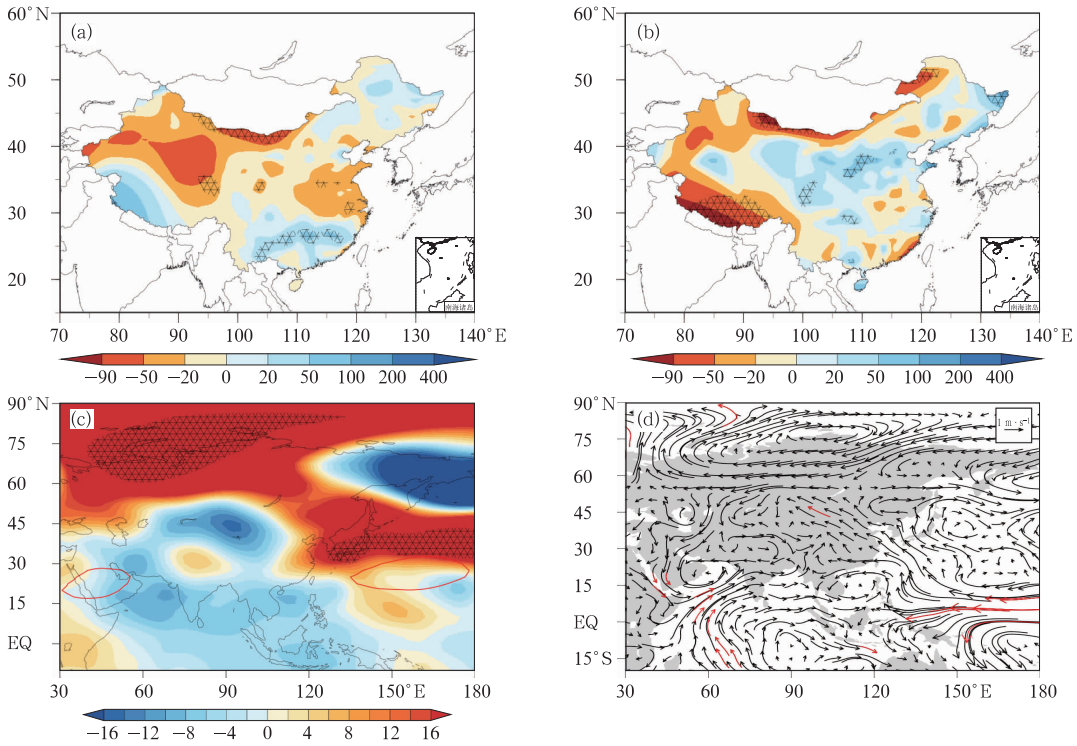

图 11 TIOD 正位相与 El Niño 联合发生年(a)及 TIOD 正位相独立发生年(b)9—10 月平均降水量距平百分率合成分析(阴影区为通过 0.10 显著性水平检验的区域,单位:%);TIOD 正位相独立发生年减去 TIOD 正位相与 El Niño 联合发生年 9—10 月平均 500 hPa 高度场(红色线为气候平均的 5880 gpm 等值线,阴影区为通过 0.10 显著性水平检验区域,单位:gpm)(c)及 850 hPa 风场(红色箭头为通过 0.10 显著性水平检验区域)(d)的差值场

Fig. 11 Composite precipitation anomaly percentage of September−October over years of (a) TIOD positive phase and El Niño concurrence and (b) TIOD positive phase only (Shading indicates the area has passed the 0.10 significance level test, unit: %); differences of (c) 500 hPa geopotential height (colored areas) (Red contours stand for the climatological 5880 gpm contours, unit: gpm) and (d) 850 hPa wind (Red arrows indicate the areas have passed the 0.10 significance level test) between the years of TIOD positive phase only and the years of TIOD positive phase and El Niño concurrence in September−October (the years of TIOD positive phase only minus the years of TIOD positive phase and El Niño concurrence)

造成该异常的环流特征和外强迫信号,主要结论如下:

(1) 2017 年秋季我国总体呈现“暖湿”的气候特征。全国大部分地区气温接近常年同期到偏高,全国平均气温为 10.8℃,较常年同期偏高 0.9℃。全国平均降水量为 123.2 mm,较常年同期偏多 2.8%,但空间分布不均,其中长江以北的大部分地区降水较常年明显偏多,不仅华西秋雨偏强,黄淮及江淮等地降水更是较常年同期偏多 5 成至 1 倍以上,且降水时段主要集中在 9—10 月份,阶段性特征明显。

(2) 2017 年 9—10 月北方地区降水异常偏多主要受到东亚环流型的影响。东亚 500 hPa 高度距平场从高纬至低纬呈“＋－＋”的异常分布,极区高度场偏高,极涡分裂偏向东北亚地区,中纬度在贝加尔湖-巴尔喀什湖地区为显著的低槽区,低纬度西太平洋副高偏强,异常西伸,脊线位置偏北。一方面,极涡分裂偏向东北亚地区有利于极地冷空气沿鄂霍茨克海向南扩散,对流层低层的 850 hPa 距平风场上朝鲜半岛的反气旋式环流异常有利于引导偏东路径的冷湿气流沿朝鲜半岛南部西进到黄河与长江之间的地区;另一方面,850 hPa 距平风场上孟加拉湾东部到中南半岛为异常反气旋式环流,中南半岛北部为偏西风距平,菲律宾附近为异常气旋式环流,南海

北部为偏东风距平,两支暖湿气流在我国华南交汇后北上。冷湿气流与暖湿气流在我国长江与黄河之间的区域交汇,使得该区域成为水汽通量异常辐合区,进而造成西南地区北部、江汉、黄淮及江淮等地降水明显偏多,秋汛显著。

(3) 2017 年秋季赤道中东太平洋海表温度由夏季的中性偏暖迅速转为秋季的显著偏冷,同时 TIOD 在 2—10 月持续正位相。随着赤道中东太平洋海温的转冷,热带太平洋地区大气显示出对冷海温的清晰响应,Walker 环流明显增强,有利于西太平洋副高偏强偏西偏北;此外 9—10 月受 TIOD 正位相(且没有 El Niño 发生)的独立影响,有利于在孟加拉湾形成反气旋式环流异常,同时有利于副高西伸偏北。赤道中太平洋冷海温和 TIOD 的共同作用是导致西太平洋副高较常年异常偏强偏西偏北的重要外强迫信号。

本文主要针对造成我国秋季降水异常的环流型以及热带太平洋和热带印度洋海温异常对环流的影响进行了初步的诊断分析。实际上,造成我国秋季气候异常的因素还有很多,包括多种大气涛动(刘晓云等,2016;徐金霞等,2017)、其他海域海温异常的影响(韩晋平等,2013)、多时间尺度特征(王春学等,2015a)等,都值得做更进一步的参考和分析。

参考文献

白虎志,董文杰,2004. 华西秋雨的气候特征及成因分析[J]. 高原气象,23(6):884-889.

鲍媛媛,阿布力米提,李峰,等,2003. 2001 年华西秋雨时空分布特点及其成因分析[J]. 应用气象学报,14(2):215-222.

谌芸,施能,2003. 厄尔尼诺/南方涛动与我国秋季气候异常[J]. 热带气象学报,19(2):137-146.

冯丽文,郭其蕴,1983. 华西秋雨的多年变化[J]. 地理研究,2(1):74-84.

高由禧,1958. 东亚的秋高气爽[J]. 气象学报,29(2):83-92.

高由禧,郭其蕴,1958. 我国的秋雨现象[J]. 气象学报,29(4):264-273.

顾薇,李维京,陈丽娟,等,2012. 我国秋季降水的年际变化及与热带太平洋海温异常分布的关系[J]. 气候与环境研究,17(4):467-480.

韩晋平,张人禾,苏京志,2013. 中国北方秋雨与热带中太平洋海表冷却的关系[J]. 大气科学,37(5):1059-1071.

何敏,1984. 我国主要秋雨区的分布及长期预报[J]. 气象,10(9):10-13.

何珊珊,张文君,祁莉,等,2015. 两类厄尔尼诺事件发展年秋季印度洋海温异常特征对比[J]. 气象学报,73(3):515-528.

贾小龙,张培群,陈丽娟,等,2008. 2007 年我国秋季降水异常的成因分析[J]. 气象,34(4):86-94.

李耀辉,李栋梁,赵庆云,2001. 中国西北地区秋季降水异常的特征分析[J]. 高原气象,20(2):158-164.

刘佳,马振峰,杨淑群,等,2015. 印度洋偶极子和华西秋雨的关系[J]. 高原气象,34(4):950-962.

刘晓云,王劲松,杨金虎,等,2016. APO 异常对我国西北地区东部秋季干湿变化影响[J]. 应用气象学报,27(4):454-462.

刘宣飞,袁慧珍,2006a. 印度洋偶极子与中国秋季降水的关系[J]. 南京气象学院学报,29(5):644-649.

刘宣飞,袁慧珍,2006b. ENSO 对印度洋偶极子与中国秋季降水关系的影响[J]. 南京气象学院学报,29(6):762-768.

聂羽,孙冷,李清泉,等,2016. 2015 年秋季我国气候异常及暖湿成因分析[J]. 气象,42(4):507-513.

邵勰,周兵,2016. 2015/2016 年超强厄尔尼诺事件气候监测及诊断分析[J]. 气象,42(5):540-547.

司东,邵勰,孙冷,等,2015. 2014 年秋季我国华西地区降水异常的成因分析[J]. 气象,41(4):508-513.

王春学,马振峰,邵鹏程,等,2015a. 我国华西秋雨的气候变化规律及其影响因子[J]. 干旱区研究,32(6):1113-1121.

王春学,马振峰,王佳津,等,2015b. 华西秋雨准 4 年周期特征及其与赤道太平洋海表温度的关系[J]. 大气科学,39(3):643-652.

王朋岭,李多,柳艳菊,等,2014. 2013 年秋季东北地区气候异常及成因分析[J]. 气象,40(4):510-514.

王遵娅,丁一汇,2008. 中国雨季的气候学特征[J]. 大气科学,32(1):1-13.

肖莺,杜良敏,任永建,2013. 汉江流域秋汛期典型旱涝年与前期海温的关系研究[J]. 暴雨灾害,32(2):182-187.

徐金霞,闫彩霞,钟燕川,等,2017. 北半球秋季欧亚遥相关与华西秋雨的关系[J]. 气象科技,45(3):492-498.

袁媛,高辉,贾小龙,等,2016. 2014－2016 年超强厄尔尼诺事件的气候影响[J]. 气象,42(5):532-539.

翟盘茂,余荣,郭艳君,等,2016. 2015/2016 年强厄尔尼诺过程及其对全球和中国气候的主要影响[J]. 气象学报,74(3):309-321.

竺夏英,宋文玲,2017. 2016 年秋季中国气候特征及其可能成因[J]. 气象,43(4):495-500.

Gu Wei, Wang Lin, Li Weijing, et al, 2015. Influence of the tropical Pacific east-west thermal contrast on the autumn precipitation in South China[J]. Int J Climatol, 35(7): 1543-1555. DOI: 10.1002/JOC.4075.

Kalnay E, Kanamitsu M, Kistler R, et al, 1996. The NCEP/NCAR 40-Year Reanalysis Project[J]. Bull Amer Meteor Soc, 77(3): 437-471.

Reynolds R W, Smith T M, Liu Chunying, et al, 2007. Daily high-resolution-blended analyses for sea surface temperature[J]. J Climate, 20(22): 5473-5496.

AGU PUBLICATIONS

JGR

Journal of Geophysical Research: Atmospheres

RESEARCH ARTICLE
10.1002/2017JD027603

Key Points:
- An updated effective radiative forcing (ERF) due to aerosols was obtained; ERF_{ari} and ERF_{aci} were given separately
- The influences of partial internal mixing (PIM) on aerosol optical properties, hygroscopicity, and particle numbers were considered
- Compared to external mixing (EM), PIM brought about apparent surface warming, less southward shifted ITCZ, and weaker Hadley circulation

Correspondence to:
H. Zhang,
huazhang@cma.gov.cn

Citation:
Zhou, C., Zhang, H., Zhao, S., & Li, J. (2018). On effective radiative forcing of partial internally and externally mixed aerosols and their effects on global climate. *Journal of Geophysical Research: Atmospheres*, *123*, 401–423. https://doi.org/10.1002/2017JD027603

Received 15 AUG 2017
Accepted 4 DEC 2017
Accepted article online 12 DEC 2017
Published online 4 JAN 2018

©2017. American Geophysical Union. All Rights Reserved.

On Effective Radiative Forcing of Partial Internally and Externally Mixed Aerosols and Their Effects on Global Climate

Chen Zhou[1,2,3], Hua Zhang[1,3], Shuyun Zhao[1,3], and Jiangnan Li[4]

[1]Collaborative Innovation Center on Forecast and Evaluation of Meteorological Disaster, Nanjing University of Information Science and Technology, Nanjing, China, [2]Graduate School of Chinese Academy of Meteorological Sciences, Beijing, China, [3]Laboratory for Climate Studies, National Climate Center, China Meteorological Administration, Beijing, China, [4]Canadian Center for Climate Modeling and Analysis, University of Victoria, Victoria, British Columbia, Canada

Abstract The total effective radiative forcing (ERF) due to partial internally mixed (PIM) and externally mixed (EM) anthropogenic aerosols, as well as their climatic effects since the year of 1850, was evaluated and compared using the aerosol-climate online coupled model of BCC_AGCM2.0_CUACE/Aero. The influences of internal mixing (IM) on aerosol hygroscopicity parameter, optical properties, and concentration were considered. Generally, IM could markedly weaken the negative ERF and cooling effects of anthropogenic aerosols. The global annual mean ERF of EM anthropogenic aerosols from 1850 to 2010 was -1.87 W m^{-2}, of which the aerosol-radiation interactive ERF (ERF_{ari}) and aerosol-cloud interactive ERF (ERF_{aci}) were -0.49 and -1.38 W m^{-2}, respectively. The global annual mean ERF due to PIM anthropogenic aerosols from 1850 to 2010 was -1.23 W m^{-2}, with ERF_{ari} and ERF_{aci} of -0.23 and -1.01 W m^{-2}, respectively. The global annual mean surface temperature and water evaporation and precipitation were reduced by 1.74 K and 0.14 mm d^{-1} for EM scheme and 1.28 K and 0.11 mm d^{-1} for PIM scheme, respectively. However, the relative humidity near the surface was slightly increased for both mixing cases. The Intertropical Convergence Zone was southwardly shifted for both EM and PIM cases but was less southwardly shifted in PIM scheme due to the less reduction in atmospheric temperature in the midlatitude and low latitude of the Northern Hemisphere.

Plain Language Summary The internal mixing of aerosols is common in atmosphere. Different aerosol species merged together and become inhomogeneous particles with complex interior structures. Compared to the individual pure particles of external mixing, the treatment of internal mixing is much more complex and can bring about large changes in the optical and hygroscopic properties to the aerosol particles. In this paper, we discussed the impacts of anthropogenic aerosol mixing state on effective radiative forcing and some major climate factors since preindustrial era by introducing two mixing schemes of external mixing and partial internal mixing (PIM) to the BCC's Atmospheric General Circulation Model (BCC_AGCM2.0_CUACE/Aero). The results show that the cooling effect of anthropogenic aerosols is greatly reduced, the southward shift of ITCZ is alleviated, and the Hadley circulation is further inhibited due to PIM. However, to obtain the mixing properties (volume ratio, mixing rate, and material composition) of aerosols in a global scale is very difficult. The quantitative evaluation of aerosol internal mixing is still of large uncertainty.

1. Introduction

In many studies, aerosols are treated as externally mixed (EM), which means they form into independent single-component spherical particles, with no geometric contact and multiphase scattering between each other. However, accumulated observations have confirmed that internal mixing (IM) aerosols are common all over the globe (Andreae et al., 1986; Jacobson, 2000). The components of the IM aerosol particles, as well as their mixing ratios, change largely according to time and location (Abel et al., 2003; Shiraiwa et al., 2008; Vanderlei et al., 1998). The IM black carbon (BC) particles are even more common in urban areas and are commonly coated with sulfate and organic matter (Adachi & Buseck, 2008). The structure of IM particles is complex and inhomogeneous, and thus causes differences in various particle physical properties compared to EM particle.

The IM scheme can bring about large changes in particle optical properties compared to the EM scheme (Bohren & Huffman, 1998; Garnett, 1904; Niklasson et al., 1981). Early studies suggested that translucent

soluble substances covering the BC core can act as a lens that focuses radiation on the absorptive core, increasing the radiation flux on the core surface and thus increasing the total particle absorption (Pósfai et al., 2003). The lensing effect is stronger when relative humidity is low, producing even higher absorption (Lesins et al., 2002). Jacobson (2001) compared the direct radiative forcing (DRF) of BC using the coated IM and EM treatments and found 1.9 times of increase in the positive DRF of BC by using the IM scheme. Under the typical atmospheric conditions of East Asia, the complete IM BC-sulfate mixture can cause double of the negative DRF at the surface, but half of negative DRF at the top of the troposphere compared to EM one (Zhang, Zhou, et al., 2015). Saleh et al. (2015) simulated the DRF of BC-OA (organic aerosols) mixture and found that IM can markedly increase the DRF of BC, especially when OA is considered as "scattering aerosol."

IM also has notable impacts on aerosol condensation and activation, and consequently on aerosol-cloud interactions. The role of BC in determining cloud droplet number concentrations (CDNC) is strongly dependent on the mixing state of BC with soluble species (Adams & Seinfeld, 2003). Bauer et al. (2010) reported that the IM scheme would reduce the amount of pure soluble aerosols, and thus reduce the amount of low clouds, but the coated BC particles can serve as CCN under specific conditions and change the lifetime of clouds and increase the brightness of low clouds. In recent years, several modeling groups have developed sophisticated aerosol microphysical schemes to simulate the IM of BC (e.g., Goddard Institute for Space Studies, Goddard Chemistry Aerosol Radiation and Transport, and Max-Planck-Institut-Hamburg Aerosol Model), which include the physical processes of nucleation, evolving particle size distribution, particle coagulation, and mixing by condensation of gases onto particles.

However, there are still some deficiencies in the existing studies of aerosol IM. Validating the sophisticated aerosol microphysical schemes with observations is still a challenging work, and these schemes are not apparent in improving BC simulations (Koch et al., 2009). Many models predict the occurrence of IM particles based on the time scale for hydrophobic-to-hydrophilic conversion of BC. However, the aging timescale of BC is not well constrained. The assumption of the aging timescale as a single parameter is oversimplified and can bring about errors in estimating the BC burden (Riemer et al., 2009). The quantitative relationship between coating and hygroscopicity of ambient BC particles is still not clear (McMeeking et al., 2011). As it has been reported in Bauer et al. (2010), the aging of BC could cause the reduction in pure soluble aerosols. However, some model studies changed the hygroscopicity of BC when it was IM, but did not correspondingly reducing the pure soluble aerosol concentrations. Most of the models evaluated by Koch et al. (2009) did not consider the impacts of IM on the optical properties of BC. In conclusion, to evaluate the impacts of aerosol IM on climate requires the consideration of the changes in aerosol optical properties, hygroscopicity, and the effects of BC aging on other soluble aerosol concentrations.

In the Fifth Assessment Report of the Intergovernmental Panel on Climate Change (IPCC, 2013), a newly defined effective radiative forcing (ERF) was used to describe the impacts of aerosols on radiation and climate. ERF consists of two parts, i.e., the effective radiative forcing due to aerosol-radiation interactions (ERF_{ari}) and the effective radiative forcing due to aerosol-cloud interactions (ERF_{aci}). ERF_{ari} accounts for the initial changes in radiation due to the scattering and absorption of aerosols (direct effect) and the rapid adjustments to the initial changes in radiation (also known as the "semidirect effect"). ERF_{aci} accounts for aerosol-related microphysical modifications to the cloud albedo, as well as any secondary effects that result from clouds adjusting rapidly to changes in their environment. ERF allows for the adjustments to all physical variables except those regarding the ocean and sea ice. The inclusion of these adjustments makes ERF a better indicator of the eventual temperature response (Boucher et al., 2013; Myhre et al., 2013; Sherwood et al., 2015). In our early work, we simulated the aerosol-radiation interaction of anthropogenic aerosols (Zhou et al., 2017). The RF_{ari}/ERF_{ari} of anthropogenic aerosol since 1850 to 2000 was $-0.34/-0.42$ W m^{-2} in external mixing case and was $-0.23/-0.34$ W m^{-2} in partial internal mixing case, respectively. In this work, we systematically investigated the influences of IM on aerosol radiative forcing and climate considering both the aerosol-radiation and aerosol-cloud interactions.

The ERF due to PIM and EM anthropogenic aerosols was estimated using an aerosol-climate coupled model of BCC_AGCM2.0_CUACE/Aero (Gong et al., 2002; Wu et al., 2010). This study was performed to explore the physics of aerosol IM by taking the influences of IM on aerosol optical properties, hygroscopicity, and the concentration of pure soluble aerosols into account. At present day, the BC, sulfate, and organic carbon (OC)

Table 1
The Complex Refractive Indices at 550 nm Wavelength and the Density of Substances

Substance	Complex refractive index	Density (kg m^{-3})
Black carbon	1.75–0.44 i	1,500.0 (dry)
Sulfate	1.43–1 × 10^{-8} i	1,769.0 (dry)
Organic carbon	1.53–0.0059 i	1,300.0 (dry)
Soil dust	1.53–0.008 i	2,650.0 (dry)
Sea salt	1.50–9.7 × 10^{-9} i	2,170.0 (dry)
Water	1.33–3 × 10^{-9} i	1,000.0

aerosols are produced mostly by anthropogenic emissions; thus, we defined these aerosols in this work as "anthropogenic aerosols" for short. The radiative forcing and climatic effects due to the changes of anthropogenic aerosols since 1850 were derived by subtracting the results of 1850 from those of 2010 simulations to exclude the most influences of natural emissions. Section 2 presents the calculation methods of aerosol optical properties and hygroscopicity, the numerical test setup, and the model in detail. Section 3 discusses the influences of different mixing schemes on the optical depth and ERF of total anthropogenic aerosols. Section 4 compares the climatic effects of EM and PIM anthropogenic aerosols. Section 5 discusses the influences of IM rate on ERF and surface temperature. Finally, section 6 gives the conclusions and discussions.

2. Methods and Model

Two mixing schemes of EM and PIM were examined in this study. In EM scheme, all aerosol particles were considered independently in both the radiative transfer and hydrophilic processes. In PIM scheme, 30% (observational data suggested 10 to 50%; Abel et al., 2003; Deboudt et al., 2010; Vanderlei et al., 1998) of the anthropogenic aerosols were internally mixed into BC-sulfate and BC-OC aerosols, while the rest of the anthropogenic aerosols was EM. Actually, the occurrence rate of IM aerosol particles is very difficult to obtain on a global scale as it changes rapidly with various environmental factors, and the observational data are far from sufficient. Thus, the value (30%) used in this study as a sensitivity test represents the mean of available observational data. There might be some overestimations or underestimations according to location and time.

In the real atmosphere, a considerable part of BC particles is IM with other aerosols, e.g., sea salt and soil dust. The optical properties of IM aerosols show a strong dependence on the aerosol species that form the shell (Bond et al., 2006). However, as it has been depicted in many studies, to fully explore the impacts of IM aerosol is a complex task. Therefore, in this study, BC was assumed to only internally mix with sulfate and OC under a prescribed IM rate to give probable ranges and patterns for the ERF and climatic effects of anthropogenic aerosols.

2.1. Calculation of the Physical Properties of Aerosols

The key factor in simulating the aerosol-radiation interactions is the optical properties of aerosols. The optical properties of EM aerosols were calculated using Mie theory. The core-shell model was used to represent IM in this study due to its capability of simulating the multiphase scattering within two-layer spherical particles. Other IM models, such as the Maxwell and the Bruggeman equivalent media models, were evaluated in the previous work and shown to have similar impacts on aerosol optical properties as the core-shell model (Zhang, Zhou, et al., 2015). The optical properties of the IM aerosols were calculated using Bohren and Hoffman's coated sphere Mie theory (Bohren & Huffman, 1998), in which the electric and magnetic multipole coefficients were calculated based on the refractive indices of both substances and the radius of core and shell. The rest of the calculations were similar to the classic Mie theory. The complex refractive indices of dry aerosol substances were adopted from the HITRAN (2004) database (Rothman et al., 2005). OC aerosol was considered as "scattering aerosol" in this study (Table 1).

The effects of relative humidity on the complex refractive indices of sulfate and OC aerosols were calculated according to equation (1) (Bohren & Huffman, 1998). BC was considered to be insoluble, so its complex refractive indices did not change with the relative humidity.

$$m = m_w + (m_d - m_w)\frac{{r_d}^3}{{r_m}^3}. \quad (1)$$

Here m is the complex refractive index of a specific soluble particle after hygroscopic growth; m_w and m_d are the complex refractive indices of water and the dry particle, respectively; and r_d and r_m are the equivalent radii of the soluble particle before and after hygroscopic growth (can be calculated based on the growth factor, refer to equation (6)), respectively. The hygroscopic growth rates of the soluble particle were obtained using the κ-Köhler theory (Köhler, 1936; Petters & Kreidenweis, 2007). In addition to relative humidity, the

volume mixing ratios of different substances in IM aerosols are also crucial to determine the optical properties of the IM aerosols, and the volume mixing ratios of different substances change markedly with both time and location. In this study, the proportions of BC-sulfate and BC-OC aerosols, as well as the volume mixing ratios of BC, sulfate, and OC in the two kinds of IM aerosols, were determined by the real-time concentrations of the three aerosols within each model grid box:

$$P_{\mathrm{BC-OC}} = \frac{1}{1 + \left(\frac{M_{\mathrm{SF}}/\rho_{\mathrm{SF}}}{M_{\mathrm{OC}}/\rho_{\mathrm{OC}}}\right)}. \tag{2}$$

$$VF_{\mathrm{BC-OC}} = 1 - \frac{(M_{\mathrm{OC}}/\rho_{\mathrm{OC}})}{(M_{\mathrm{BC}}/\rho_{\mathrm{BC}}) \times P_{\mathrm{BC-OC}} + (M_{\mathrm{OC}}/\rho_{\mathrm{OC}})}. \tag{3}$$

where $P_{\mathrm{BC\text{-}OC}}$ is the proportion of BC that becomes the core of BC-OC aerosol in the IM BC; M_{OC}, M_{SF}, and M_{BC} are the real-time mass concentrations of OC, sulfate, and BC (kg m^{-3}); ρ_{OC}, ρ_{SF}, and ρ_{BC} are the real-time densities of OC, sulfate, and BC (kg m^{-3}); and $VF_{\mathrm{BC\text{-}OC}}$ is the volume fraction of BC in BC-OC aerosol. $P_{\mathrm{BC\text{-}SF}}$ and $VF_{\mathrm{BC\text{-}SF}}$ can be calculated similarly. The size of BC-sulfate and BC-OC aerosols were calculated based on the size of BC core and the real-time volume mixing ratios. In the simulation, the part of pure aerosols that forms IM aerosols was removed from original catalogs.

The κ-Köhler theory was used in the simulation of aerosol-cloud interactions. In the κ-Köhler theory, the hygroscopic growth and cloud condensation nucleus activation depend only on a single parameter κ, known as the "hygroscopicity parameter." In the classic Köhler theory (Köhler, 1936), the CCN activation is calculated using several aerosol physicochemical properties, i.e., solute mass, molecular weight, bulk density, dissociable ions, and activity coefficient. Comparing with classic Köhler theory, the calculation has been greatly simplified in the κ-Köhler theory:

$$\kappa = \frac{4A^3}{27{D_d}^3 \ln^2 S_c}. \tag{4}$$

$$A = \frac{4\sigma_{s/a} M_w}{RT\rho_w}. \tag{5}$$

where κ is the hygroscopicity parameter, D_d is the dry particle diameter, S_c is the critical supersaturation, $\sigma_{s/a}$ is the surface tension of the solution/air interface, M_w is the molecular weight of water, R is the universal gas constant, T is the temperature, and ρ_w is the density of water. The hygroscopic diameter growth factor (gf) can be calculated by

$$\frac{RH}{\exp\left(\frac{A}{D_d gf}\right)} = \frac{gf^3 - 1}{gf^3 - (1 - \kappa)}. \tag{6}$$

where RH is the relative humidity and gf is used to calculate the growth in particle sizes corresponding to different RH (e.g., "r_m" in equation (1)), which is closely related to aerosol optical properties and activation. The total κ value for the IM particles can be calculated by

$$\kappa = \sum_i \varepsilon_i \kappa_i. \tag{7}$$

where ε_i and κ_i are the volume fraction and the hygroscopicity parameter of substance i, respectively. According to Ghan et al. (2001), the values of κ for sulfate, hydrophilic OC, and BC and hydrophobic OC aerosols were assumed to be 0.51, 0.14, and 1×10^{-10}, respectively.

A look-up table including the optical properties of the IM aerosols (in 17 wavelength bands, 12 radius bins, 10 volume mixing ratio bins, and 6 relative humidity intervals) was made according to the above calculations. Then the optical properties of the IM aerosols in a real-time simulation could be calculated using linear interpolation. By prescribing the optical properties in a look-up table, computations can be considerably simplified in real-time simulations. In other studies, the amplification factor of BC absorption constrained from observations and laboratory experiments (Peng et al., 2016; etc.) is often used to calculate the optical properties of IM BC. Some models (e.g., the standard GC-RT model; Wang et al., 2014) calculate the mass absorption coefficients (MAC) of IM BC by multiplying the MAC of EM BC with a single amplification factor. However, the amplification factor changes little only when the shell is thick enough and may not hold constant under other circumstances according to Bond et al. (2006). First, the

amplification factor needs nonlinear fits, even using an exponential fit can cause an error up to 40% in some cases (Bond et al., 2006). Second, the amplification factor changes largely with core/shell mass ratio and the shell substance (Bond et al., 2006; Liu et al., 2017). Therefore, the amplification factor can be used to calculate the MAC of IM BC fast and approximately, but the accuracy is lower compared to coated Mie theory.

2.2. Model Description

The BCC's Atmospheric General Circulation Model version 2.0 was developed by the Beijing Climate Center (BCC) of Chinese Meteorological Administration (Wu et al., 2010). The BCC model has been participated in the IPCC (IPCC-13) Coupled Model Intercomparison Project Phase 5 and has been validated to be state-of-the-art against satellite observations (e.g., Jiang et al., 2012, 2015). BCC_AGCM2.0 was further coupled with the aerosol model CUACE/Aero (Zhang et al., 2012; Zhou et al., 2012). CUACE/Aero is a size-segregated multicomponent aerosol module (including BC, OC, sulfate, dust, and sea salt) incorporating processes such as emission, nucleation, condensation, coagulation, dry deposition, hygroscopic growth, and wet removal. The radius of the aerosols was discretized into 12 bins from 0.005 to 20.48 μm. The emissions and/or the precursors' emissions of BC, OC, and sulfate were prescribed. The emissions of sea salt and soil dust were calculated online (Gong et al., 2003) based on a surface emission rate function depending on particle size and surface wind speed. Internal mixing was considered in the wet deposition process of BC in CUACE/Aero. A new scheme of Monte Carlo Independent Column Approximation (Pincus et al., 2003; Jing & Zhang, 2012) to treat vertical cloud overlapping and a new radiation scheme (BCC_RAD, Zhang et al., 2014; Zhang, Wang, et al., 2015), with new aerosol and ice cloud optical properties (Wei & Zhang, 2011; Zhang, Chen, et al., 2015) were introduced in the model. In BCC_RAD, the optical properties of aerosols were divided into 17 spectral bands from 0.204 to 1,000 μm. The horizontal resolution of BCC_AGCM2.0_CUACE/Aero was set to T42 (~2.8° × 2.8°) with a hybrid σ-pressure vertical coordinate with 26 layers. The κ-Köhler theory (Köhler, 1936; Petters & Kreidenweis, 2007) was used in the aerosol-cloud interaction module of BCC_AGCM2.0_CUACE/Aero. Originally, the model treated aerosols as EM in radiation transferring and cloud droplet condensation processes. The schemes of internal mixing were introduced into the aerosol-radiation interaction by a previous work (Zhou et al., 2017) and aerosol-cloud interaction by this work, respectively.

The capacity of BCC_AGCM2.0_CUACE/Aero in reproducing meteorological fields and major aerosols had been evaluated by Zhang et al. (2012), Wang, Zhang, Li, et al. (2013), Wang, Zhang, Jing, et al. (2013), and Zhao et al. (2014, 2015).

2.3. Numerical Test Setup

The tests were carried out in two groups. Group 1 used the emission data of aerosols (BC, sulfate, and OC) and/or their precursors in the year of 1850, and all aerosols were considered to be EM due to their low concentrations at that time. Group 2 used the emission data in the year of 2010, and aerosols were considered both PIM and EM. The 2010 and 1850 emission data were from Representative Concentration Pathway (RCP) database version 2.0 (Richard et al., 2010), and the emissions in 2010 were based on RCP4.5. Under each time node, the model was run for 20 years (10 years for spin-up) with prescribed monthly mean climatology sea surface temperature (SST) and sea ice (SI) to calculate the ERF (Hansen et al., 2005; Myhre et al., 2013). Meanwhile, to simulate the climatic effects of anthropogenic aerosols, model was run for 80 years (30 years for spin-up) with a slab ocean model (SOM) coupled, distinguish from the ERF simulations. A lower limitation (15 cm^{-3}) of CDNC was introduced in every grid box as a proxy for background aerosols, which can act as CCNs but were not included in the model (e.g., nitrate and biological particles; Kirkevåg et al., 2008; Wang, Zhang, & Zhang, 2015). All the experimental setups were the same in each time node, except the emissions related to BC, OC, and sulfate aerosol, to ensure that the radiative forcing and changes in climate were due to anthropogenic aerosols. In the following discussion, we use the terms "EM_rad," "EM_clm," "PIM_rad," and "PIM_clm" to refer to the tests in group 2 (Table 2).

The two parts that compose ERF, ERF_{ari} and ERF_{aci}, have clear physical definitions, but to isolate them in the model simulations is difficult because of the interactions between ERF_{ari} and ERF_{aci}. We followed the method proposed by Ghan et al. (2012) to derive ERF_{aci} from ERF_{ari}.

Table 2
Numerical Test Designs

Group	Time node	Emission data	Scheme	Test setup	Abbreviation
1	1850	BC, OC, and sulfate of 1850	External	Prescribed SST and SI	–
				Coupled SOM	–
2	2010	BC, OC, and sulfate of 2010	External	Prescribed SST and SI	EM_rad
				Coupled SOM	EM_clm
			Partial internal	Fixed SST and SI	PIM_rad
				Coupled SOM	PIM_clm

3. Radiative Forcing Due to PIM and EM Anthropogenic Aerosols

3.1. Aerosol Column Burden

The atmospheric column burden of aerosols was determined by both the emission and climatic conditions. PIM can change the column burden of aerosols through various feedback, such as wet deposition and circulation. Compared to EM, the 2010 simulations (abbreviated as "2010" in the following) show that PIM generally caused a lower burden of anthropogenic aerosols in the midlatitude and high latitude of the Northern Hemisphere (NH) but higher burdens over many areas, such as the North Atlantic Ocean and Mediterranean (Figure 1a). The maximal increase in column burden was found over East Asia, and the maximal decrease was found over northeast India. The southwest wind at 850 hPa over south China and the westerly wind over eastern China were suppressed (Figure 11b) due to PIM, which weakened the diffusion of aerosols over East Asia and caused the increase in the column burden of aerosols. Figure 1b shows that PIM could cause an increase in precipitation about 0.3 to 0.4 mm d^{-1} over northern India. This resulted in a more efficient aerosol wet deposition.

3.2. Aerosol Optical Depth

Aerosol optical depth (AOD) consists of scattering aerosol optical depth (SAOD) and absorption aerosol optical depth (AAOD). The 1850 simulation (abbreviated as "1850" in the following) showed that the global annual mean AOD of anthropogenic aerosols at the wavelength of 550 nm was 0.012. A large AOD can be seen in the eastern part of North America, Europe, eastern Siberia, and the high latitudes of the Southern Hemisphere (SH). Naturally emitted sulfate aerosol made a great contribution to total AOD in 1850. In 2010, the global annual mean AOD of anthropogenic aerosols has increased to 0.0344 and 0.0337 in EM_rad and PIM_rad, respectively.

In 2010, most of the large AOD was concentrated in the latitudes above 30°N, mainly due to the high atmospheric burden of sulfate aerosols (Figure 2a). The maximum in AOD was seen in East Asia where both BC and

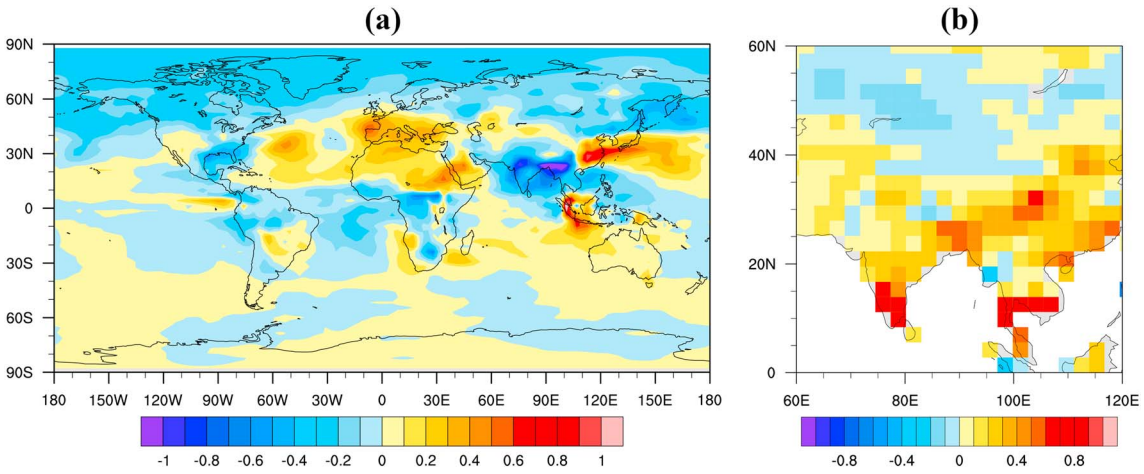

Figure 1. Differences in the column burden of anthropogenic aerosols (mg m^{-2}) and precipitation (mm d^{-1}) between PIM_rad and EM_rad: (a) column burden and (b) precipitation.

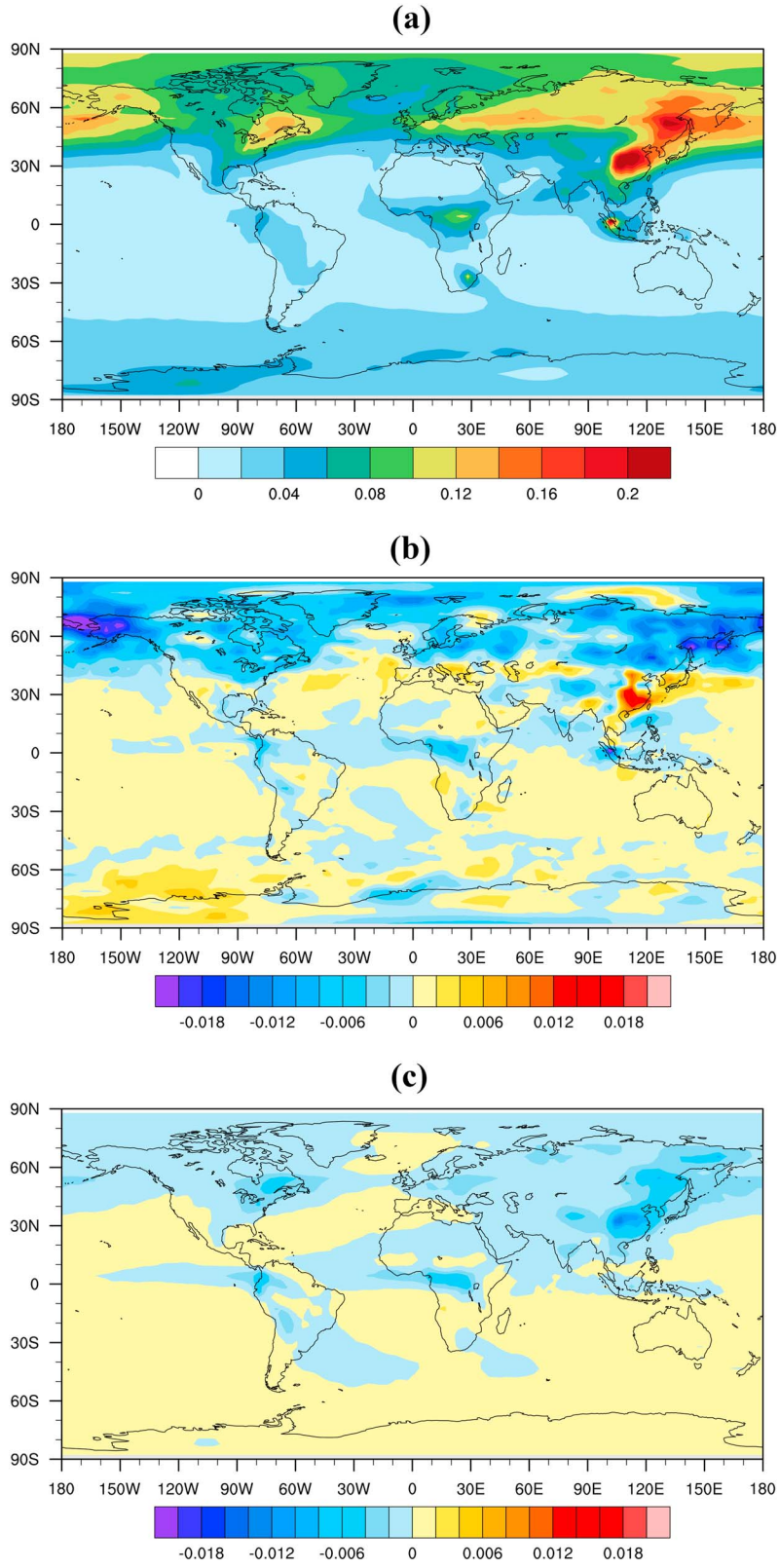

Figure 2. The simulated AOD of anthropogenic aerosols and the difference in AOD between mixing schemes: (a) the simulated AOD of anthropogenic aerosols at present day in EM_rad, (b) the difference in AOD simulated in PIM_rad and EM_rad, and (c) the difference in AOD between PIM and EM aerosols caused only by their difference in optical properties, without response of aerosol column burden.

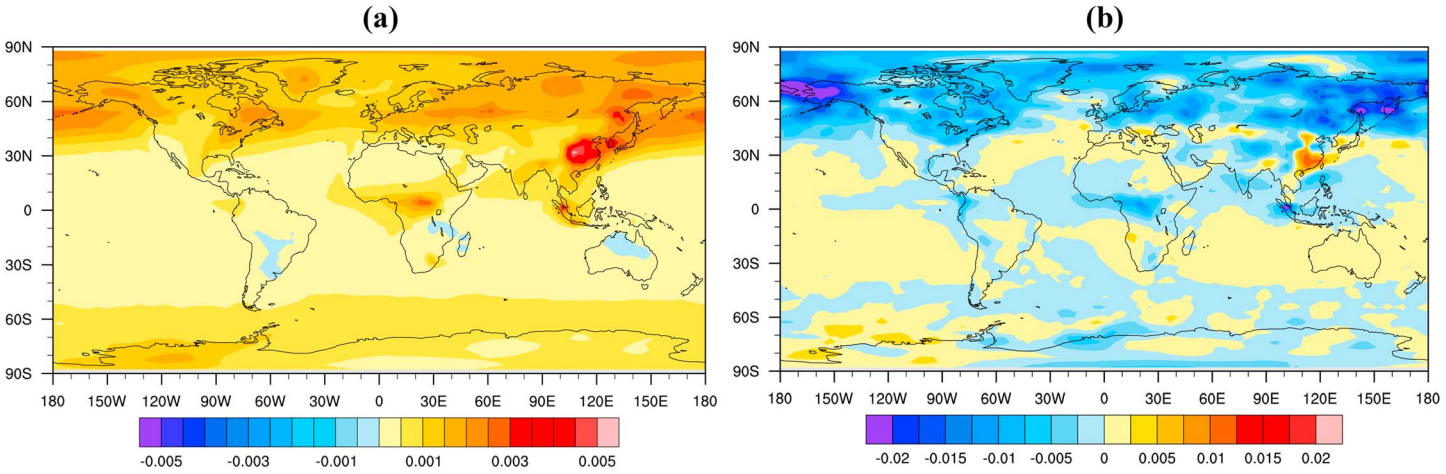

Figure 3. Differences in absorptive aerosol optical depth (AAOD) and scattering aerosol optical depth (SAOD) between PIM_rad and EM_rad: (a) AAOD and (b) SAOD.

sulfate were highly concentrated. A relatively high AOD was located in central Africa and Singapore. The global annual mean AOD was higher in EM_rad than PIM_rad by 0.0007 (Figure 2b). A large decrease in AOD due to PIM was found in most midlatitude and high latitude of the NH and other anthropogenic aerosol source areas. But, there was a large increase in AOD simulated in PIM_rad over East Asia, compared to that in EM_rad.

To evaluate the impact on AOD of the difference in optical properties between PIM and EM aerosols, we ran a diagnostic calculation based on EM_rad, which did not affect the whole simulation process. In this diagnostic calculation, the radiative transfer module was called twice at every time step: one using PIM scheme, and the other using EM scheme. The results showed that the changes in optical properties of aerosols due to PIM caused a decrease in global annual mean AOD by 0.0002. From Figure 2c, the decreases in AOD caused by the differences in optical properties were apparent over most of the anthropogenic aerosol concentrated areas, especially over East Asia (of value 0.006 to 0.01). Compared to the simulated difference in AOD between PIM_rad and EM_rad (Figure 2b), the changes in AOD due to the difference in optical properties (Figure 2c) were relatively small over most of the midlatitude and high latitude of the NH. Over East Asia, the changes in AOD shown in Figures 2b and 2c even had different signs. As indicated by Seinfeld and Pandis (2012), the decreased scattering effect in the IM aerosol is generally balanced by the increased absorption. So it can be inferred that the changes in aerosol column burden might be the major reason for the differences in AOD between PIM_rad and EM_rad. A well positive correlation was found between the changes in aerosol column burden and the changes in AOD over the NH (Figures 1a and 2b).

The global annual mean AAOD in PIM_rad was increased by about 0.0006 compared to EM_rad. Increases in AAOD appeared over most of the midlatitude and high latitude (Figure 3a) in PIM_rad due to the higher aerosol absorption. A large increase in AAOD can be seen over East Asia due to both a higher column burden and the stronger absorption of IM aerosols. Despite the large reduction in aerosol column burden over northeastern India, increases in AAOD were still found due to the marked increase in the absorptive ability of IM aerosol particles. Compared to EM_rad, the annual mean SAOD was markedly decreased by about 0.0014 in PIM_rad. Decreases in SAOD can be seen over most of the globe (Figure 3b), with the only large increase in East Asia due to the higher aerosol burden. The decreases in SAOD were 2 to 3 times higher in magnitude than the increases in AAOD over the NH. Through the changes in SAOD and AAOD, it can be inferred that the proportion of AAOD in the total AOD was largely increased in PIM_rad, and this could lead to an enhancement of atmospheric solar absorption and a positive change in ERF on a global scale.

3.3. Effective Radiative Forcing

The ERF due to anthropogenic aerosols since 1850 was −1.87 and −1.23 W m^{-2} in EM_rad and PIM_rad (Figures 4a and 4b), respectively. ERF_{ari} and ERF_{aci} due to anthropogenic aerosols since 1850 were −0.49 and −1.38 W m^{-2} in EM_rad, respectively, and were −0.23 and −1.01 W m^{-2} in PIM_rad, respectively. ERF changed markedly with latitude and was much larger in the NH than in the SH (Figure 4d). As ERF

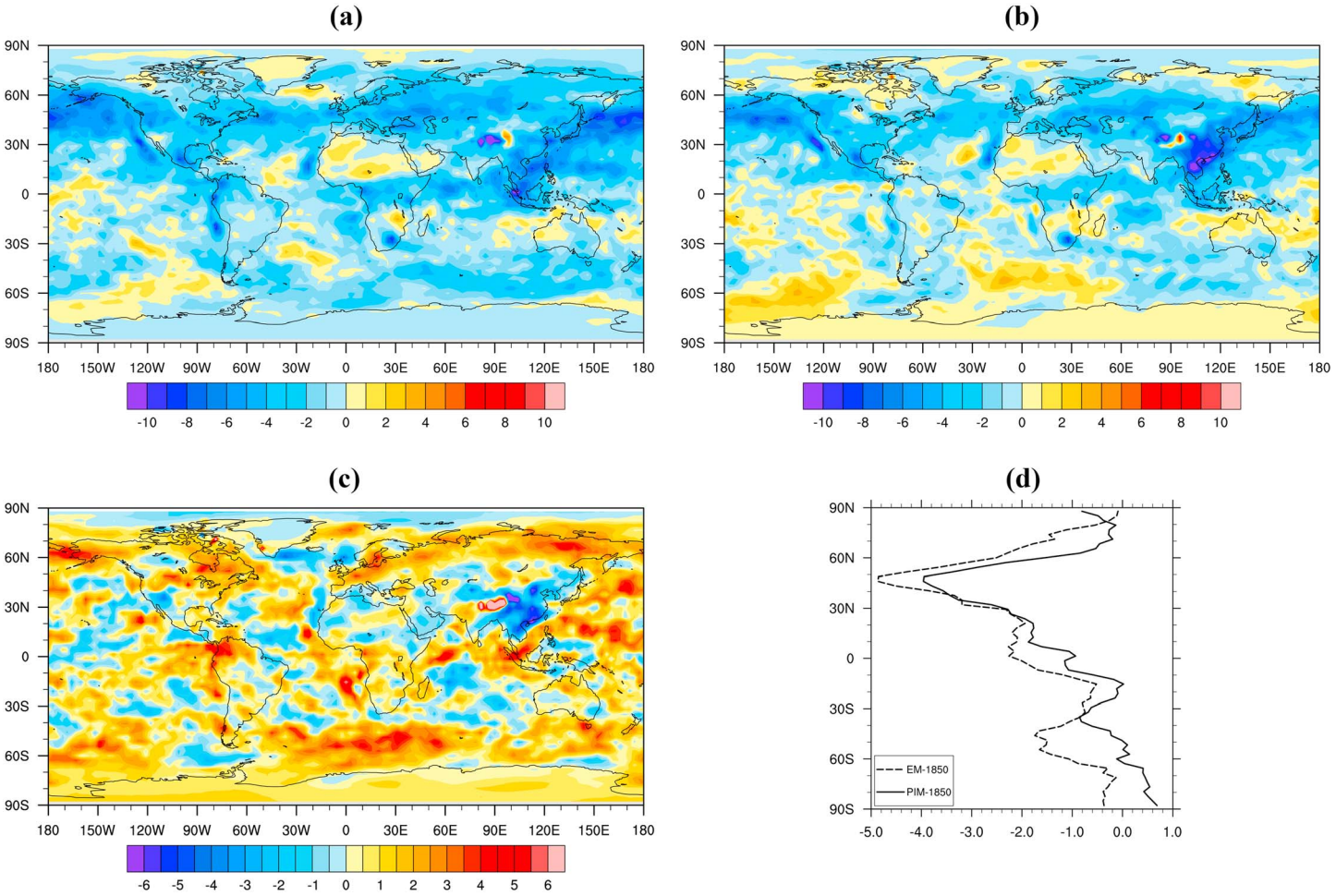

Figure 4. Annual mean effective radiative forcing (ERF) (W m^{-2}) of anthropogenic aerosols since 1850: (a) ERF in EM_rad, (b) ERF in PIM_rad, (c) the differences in ERF between PIM_clm and EM_clm, and (d) the latitudinal mean value of Figures 4a and 4b.

contained complicated feedback from clouds, the distribution of ERF showed low geographic consistency with the distribution of aerosols. However, a strong negative ERF was still concentrated in the source areas of anthropogenic aerosols, because many of the anthropogenic aerosols were ideal cloud condensation nuclei. In EM_rad, a negative ERF dominated most of the globe, with a weak positive ERF over the Sahara Desert and small patches in the SH. Strong negative ERFs can be seen over 40°S to 60°S (about -1.7 W m^{-2}), the equator (about -2.3 W m^{-2}), and 30°N to 60°N (about -2.6 to -4.9 W m^{-2}). The strongest negative ERF appeared over the Tibetan Plateau, with the strongest positive ERF to the east of it. This was likely due to the high surface albedo and rapid changes in terrain elevation of the Tibetan Plateau that enlarged the cloud feedback. Another strong negative ERF was located over the northwest Pacific Ocean, which was the area to which the aerosols from East Asia were mainly transported.

Compared to EM_rad, globally positive changes in ERF were apparent in PIM_rad (Figure 4c). On one hand, the proportion of AAOD in total AOD was increased and resulted in a stronger absorption. On the other hand, although BC particles were much easier to activate after being covered by soluble substances, but part of the pure soluble substances were formed into smaller IM particles, which was harder to activate compared to the external mixing case (the IM particle was generally smaller in size than the pure soluble particles). Therefore, the number of activated condensation nuclei was generally decreased in PIM_rad (Figure 5), which could reduce the cloud generation and the cloud albedo, and thus weakened the negative ERF. The negative ERF was also weakened over the northern Pacific Ocean mainly due to the lower aerosol burden. However, a large increase in negative ERF appeared over East Asia due to the enhanced low cloud. There were three

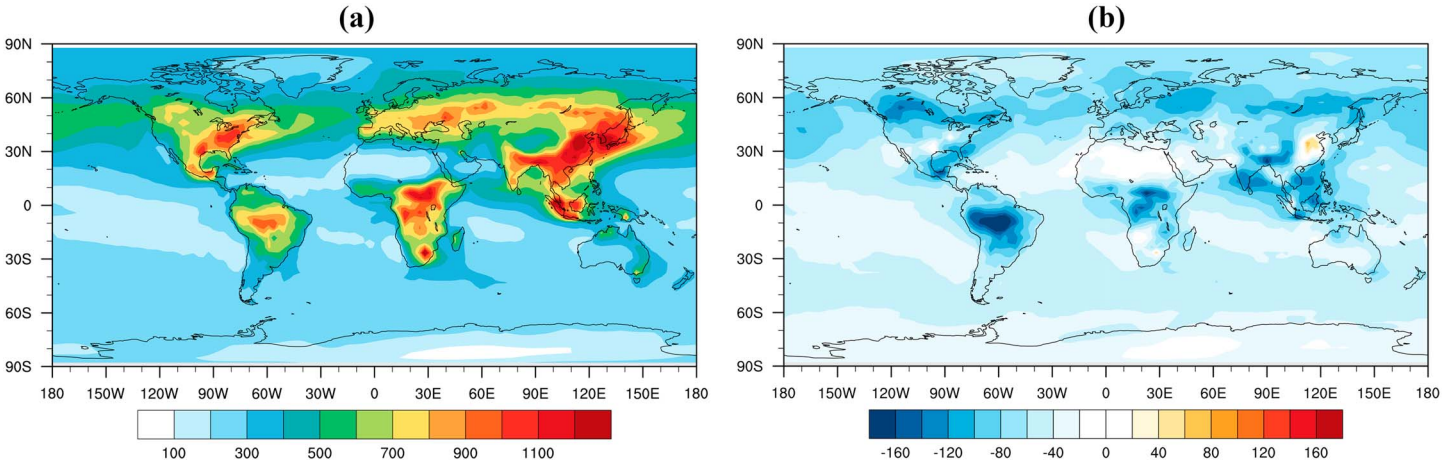

Figure 5. Annual mean vertically integrated number concentration of activated anthropogenic aerosol particles of each layer (m^{-3}): (a) in EM_rad and (b) the differences between PIM_rad and EM_rad.

explanations for the enhancement in low cloud. First, the CCN number was increased due to the higher column burden of anthropogenic aerosols. Second, the water vapor conditions were improved, as evaporation was increased due to PIM, and the water vapor imported from Southeast Asia and the midlatitudinal Pacific Ocean was increased (see sections 4.2 and 4.3). Third, as explained by Bond et al. (2013, section 7.3.1), the absorptive aerosols below clouds can promote convective activity, which was beneficial for generating more convective cloud. While over East Asia, most of BC was concentrated in the lower troposphere. Comparing PIM_rad to EM_rad, the areas of positive ERF over the oceans in the SH were clearly expanded and the values were increased, and thus greatly weakened the negative ERF near 60°S.

The results obtained in this study were compared with an earlier study of anthropogenic aerosols conducted by Zhang et al. (2016) using the same model with the same emission data and a similar experimental setup. However, the early study considered neither the lower bound of CDNC (the lack of the lower bound of CDNC would result in a more negative ERF) nor IM, and thus determined the global annual mean ERF of EM anthropogenic aerosols since 1850 to be -0.30 W m^{-2} as ERF_{ari} and -2.19 W m^{-2} as ERF_{aci}, respectively. The major impacts of EM anthropogenic aerosols on climate and radiative forcing were similar in both studies. More result validation can be found in Zhang et al. (2016).

4. Climatic Effects of Anthropogenic Aerosols

As discussed in section 3, the ERF of anthropogenic aerosols was less negative in magnitude when anthropogenic aerosols were IM compared to EM. The differences in the energy budget between mixing schemes would probably bring about notable differences between the climate states. The changes in temperature, evaporation, relative humidity, circulations, cloudiness, and precipitation since 1850 based on the EM and PIM schemes are discussed in this section.

4.1. Temperature

Surface temperature is an important factor for evaluating the climatic impacts and is closely related to the change in ERF. In EM_clm, the simulated global annual mean surface temperature has decreased by 1.74 K due to anthropogenic aerosols increase since 1850 (Figure 6a). Changes in temperature since 1850 were statistically significant over all the grids. Anthropogenic aerosols caused surface cooling over most areas, especially over the North Pole. Previous studies suggested that the temperature change over the Arctic region was much larger than the rest part of the globe due to the snow cover and sea ice amplification (Cohen et al., 2012; Screen & Simmonds, 2010). Strong cooling (>3.0 K) was apparent in the midlatitude and high latitude of the NH where sulfate aerosol was highly concentrated (Figure 6d) and caused a strong negative ERF due to increases in low-cloud amount and brightness. The temperature decrease was large (5.0 to 6.0 K) over the northern Pacific Ocean because a large amount of sulfate aerosol was transported to this region from

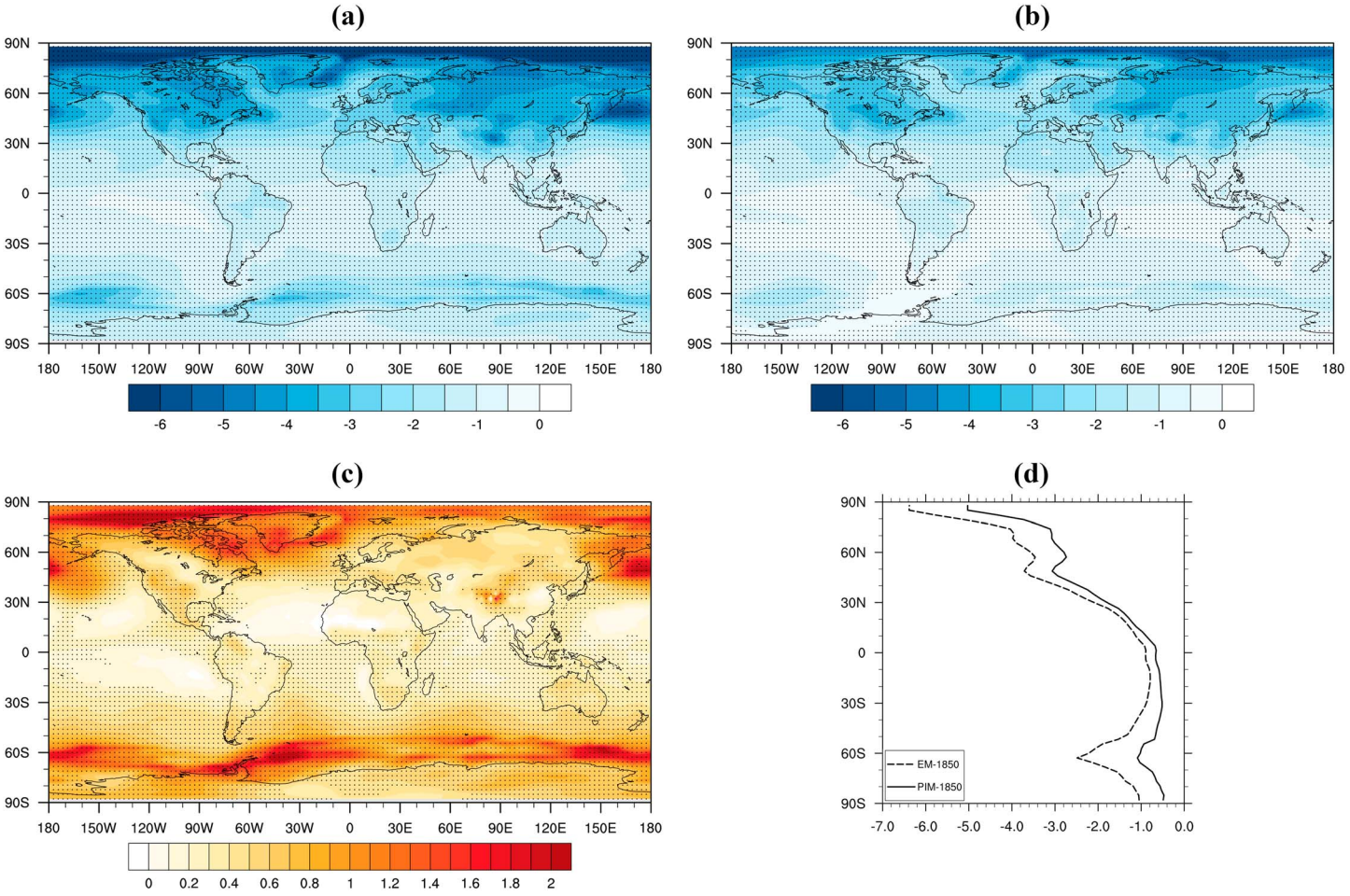

Figure 6. Changes in surface temperature (K) since 1850: (a) in EM_clm, (b) in PIM_clm, (c) the differences between PIM_clm and EM_clm, and (d) the latitudinal mean value of Figures 6a and 6b. The dots indicate the results above a significance level of 0.95 (same as below).

eastern China and enhanced the low-level cloud. No notable changes in surface temperature were found over central Africa or South America, where relatively large carbonaceous aerosol burdens can be found. The climate response was generally smaller in the SH than in the NH due to the larger ocean coverage in the SH, which weakened the aerosol cooling effect over center Africa and South America. Another strong reduction (about 2.0 K) in surface temperature can be seen near 60°S, mainly due to the change in circulation that brought colder air from the South Pole (see section 4.3).

In PIM_clm, the simulated global annual mean surface temperature has decreased by about 1.28 K due to anthropogenic aerosols increase since 1850 (Figure 6b). Changes in temperature since 1850 were statistically significant over most of the globe. Strong cooling was found in 30°N to 60°N (Figure 7d). However, compared to EM_clm, the cooling was generally weakened all over the globe in PIM_clm (Figure 6c). Compared to EM_clm, increases in surface temperature by 0.2 to 1.8 K can be found in the midlatitude to high latitude of the NH, since the CCN concentration was generally lower over this region and suppressed the low-cloud. The increase in surface temperature was especially strong over the Arctic regions mainly due to the snow cover and sea ice effects. Large increases (0.5 to 1.8 K) also occurred near 60°S, since the change in circulation reduced the amount of cold air imported from the South Pole (see section 4.3). No notable change in surface temperature was found over East Asia with high BC aerosol concentration since the warming produced by BC absorption increase was canceled by the simultaneous cooling produced by the low-cloud enhancement. In summary, PIM could considerably reduce the cooling effect of anthropogenic aerosols on the surface compared to EM, especially in the midlatitude to high latitude of both hemispheres.

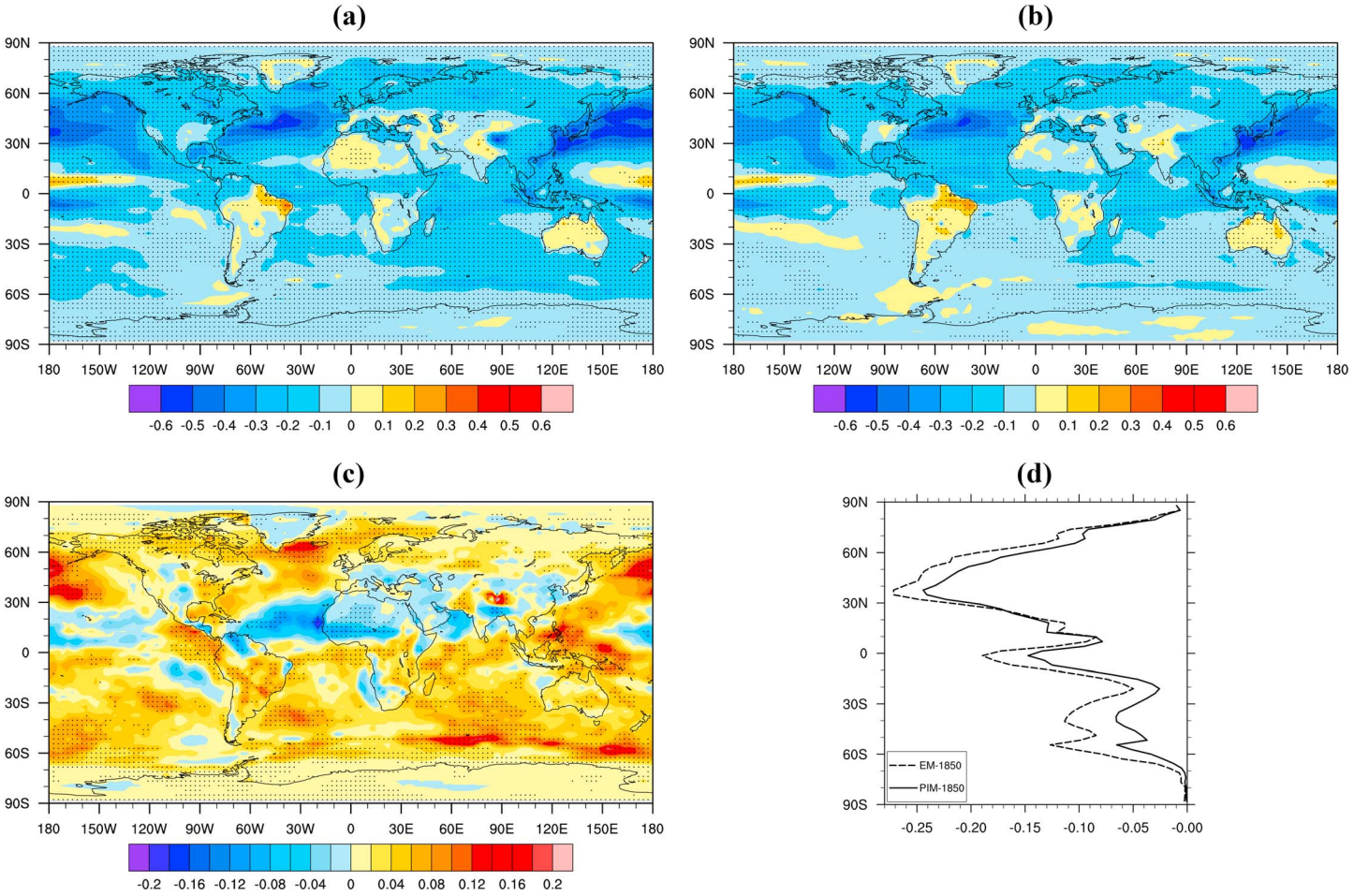

Figure 7. Changes in water evaporation (mm d^{-1}) since 1850: (a) in EM_clm, (b) in PIM_clm, (c) the differences between PIM_clm and EM_clm, and (d) the latitudinal mean value of Figures 7a and 7b.

4.2. Evaporation and Relative Humidity

In 1850, the simulated global annual mean surface water evaporation rate was 2.78 mm d^{-1}. Most of the evaporation was concentrated over the oceans in the low and midlatitudes and decreased rapidly at higher latitudes.

In EM_clm, a reduction in water evaporation was seen over most of the globe (Figure 7a) and the global annual mean water evaporation decreased by 0.14 mm d^{-1} due to anthropogenic aerosols increase since 1850. Changes in evaporation since 1850 were statistically significant over most of the globe. The decrease was particularly apparent over the northern Pacific Ocean, northern Atlantic Ocean, and the Tibetan Plateau (0.3 to 0.6 mm d^{-1}) due to strong surface cooling (Figure 6a). Mild increases in evaporation were seen in the Sahara Desert, Australia, and northern India. Relatively large increases in evaporation appeared in the northeast Brazil Plateau and the Pacific Ocean in the northern tropics (0.2 to 0.3 mm d^{-1}). In terms of a zonal mean, evaporation decreased larger in the NH than in the SH. The peak of the decrease in evaporation was between 30°N and 60°N (Figure 8d).

In PIM_clm, a general decrease in evaporation happened over the globe since 1850 (Figure 7b), like in EM_clm. The global annual mean evaporation has decreased by 0.11 mm d^{-1} since 1850. Changes in evaporation since 1850 were statistically significant over most of the globe. The strongest reduction in evaporation occurred over the midlatitudes of the NH but was less intense compared to EM_clm (Figure 7c). The stronger evaporation in PIM_clm than in EM_clm was mainly due to two reasons. First, the net radiative flux at the surface as well as the temperature was less reduced in PIM_clm than in EM_clm. Second, the wind

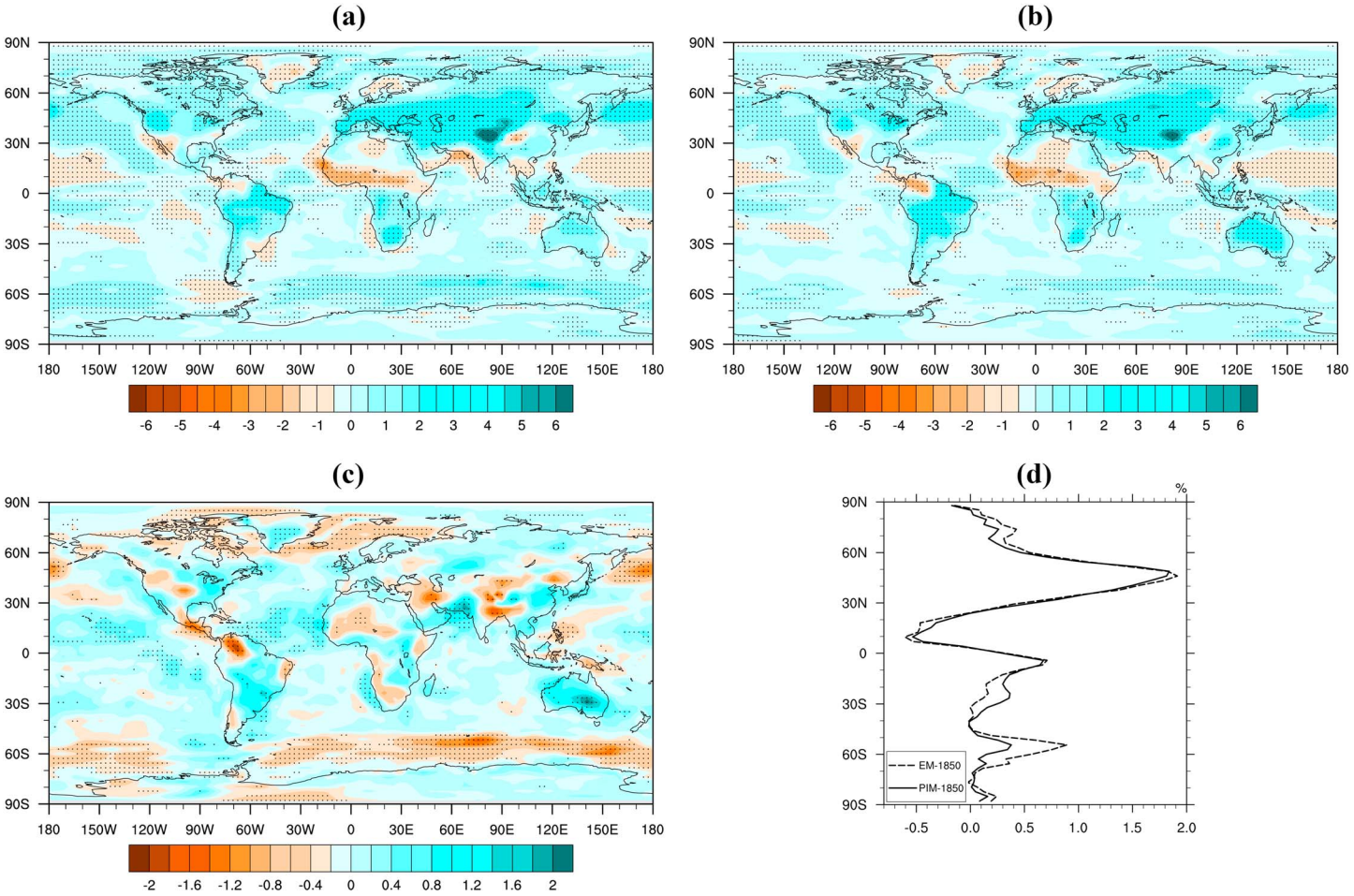

Figure 8. Changes in near surface relative humidity (%) since 1850: (a) in EM_clm, (b) in PIM_clm, (c) the differences between PIM_clm and EM_clm, and (d) the latitudinal mean value of Figures 8a and 8b.

speed near the surface was also increased in PIM_clm compared to EM_clm over some regions (e.g., the northern Atlantic Ocean, figure ignored), resulting in a more efficient water exchange between the surface and atmosphere. The evaporation in the SH in PIM_clm was much higher than that in EM_clm, corresponding to the expansion of positive forcing area in the SH.

Despite the reduction in water evaporation, the global annual mean relative humidity near the surface has increased by 3.4% and 3.5% since 1850 in EM_clm and PIM_clm, respectively.

In EM_clm, large increases in relative humidity occurred in the midlatitudes of the NH and in 50°S to 70°S (Figures 8a and 8d). Changes in relative humidity since 1850 were statistically significant over most part of the midlatitude and low latitude, especially over land areas. There were marked increases in relative humidity (about 2.0%) in most areas from Europe to central Asia, South America, and South Africa. The largest increase (>6.0%) occurred over the Tibetan Plateau. Strong decreases in relative humidity (2.0 to 3.0%) mainly appeared in the narrow region to the south of the Sahara Desert, possibly due to less precipitation and enhanced sinking air (see sections 4.3 and 4.4). Slight decreases can be found over the Pacific Ocean in the northern tropic. Relative humidity is the ratio of actual water vapor pressure to saturated vapor pressure. Although the actual water vapor pressure was reduced due to less evaporation, the decreased temperature lowered the saturated vapor pressure simultaneously and still caused an overall increase in relative humidity.

In PIM_clm, the changes in relative humidity near the surface since 1850 were similar to those in EM_clm, and increases occurred over most of the land surface (Figures 8b and 8d). Changes in relative humidity since 1850 were statistically significant over most part of the midlatitude and low latitude in the NH and most land areas

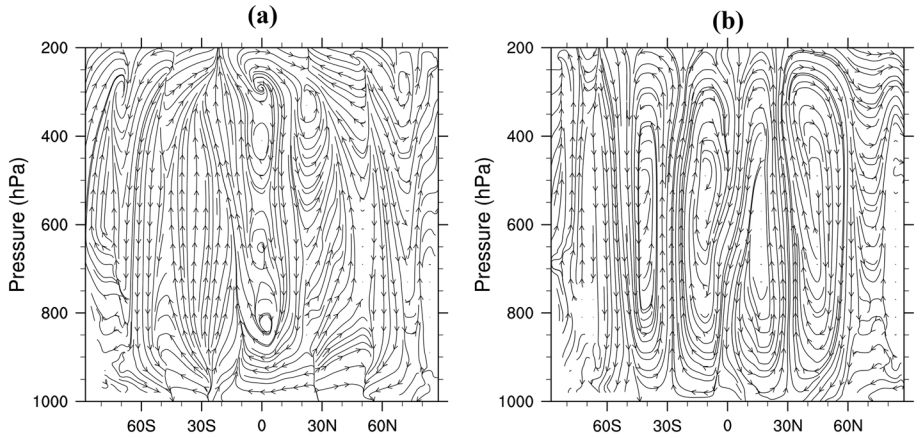

Figure 9. Changes in meridional circulation since 1850: (a) in EM_clm and (b) the difference between PIM_clm and EM_clm.

in the SH (except the South Pole). Compared PIM_clm to EM_clm, relative humidity changed at many land areas (Figure 8c), and these changes well corresponded to those in precipitation rate (Figure 14). The latitudinal variation in relative humidity was mostly similar to that in EM_clm. However, no notable increases in relative humidity were found at 50°S to 70°S in PIM_clm, because the evaporation and surface temperature were much less reduced compared to EM_clm.

4.3. Atmospheric Circulation

In EM_clm, a strong descending trend was appearing in the tropical region of the NH since 1850. In contrast, a relatively strong ascending trend was apparent in the tropical region of the SH (Figure 9a). Correspondingly northerly wind across the equator and southerly wind across the equator were found in the upper and lower troposphere, respectively. This suggested that the anthropogenic aerosols could cause the Intertropical Convergence Zone (ITCZ) to shift southwardly. As has been discussed in Broccoli et al. (2006) and Hwang et al. (2013), the southward shift of the ITCZ was closely related to the cooling in the NH. Anthropogenic aerosols produced enhanced surface cooling over the midlatitude and high latitude of the NH (Figure 6a) and led to a southward shift of the maximum SST (Rotstayn & Lohmann, 2002). The anomalous Hadley circulation, which caused the southward shift of the ITCZ, was then induced to keep the tropospheric temperature gradients relatively flat over the tropics by transporting energy from the SH to the NH in the upper troposphere and water vapor in the opposite direction in the lower troposphere (Hwang et al., 2013). The southward shift of the Hadley convergence center over the equator also caused an inhabitation on Hadley circulation, and inverse movement of Hadley circulation can be seen over the midlatitude and high latitude of both hemispheres (Figure 9a). The northerly wind over the NH high latitudes and the southerly wind over the NH midlatitudes were strengthened in the lower troposphere. This could slow down the meridional diffusion of aerosols and intensify the cooling in the midlatitude and high latitude of the NH. The ascending near 30°N and the descending near 60°N caused by EM anthropogenic aerosols could cause an increase and decrease of cloud fraction near 30°N and 60°N, respectively (Figure 12d). The enhancement of the southerly wind in the lower troposphere over the high latitudes of the SH indicated that more cold air was transported from the South Pole to the oceans around Antarctic, where a strong surface cooling could be seen (Figure 6a). The descending near 60°S could result in a decrease in cloud and precipitation (Figures 12d and 13d).

In PIM_clm, the changes in meridional circulation since 1850 were similar to those in EM_clm but were more intense (Figure 9b). Compared to EM_clm, ascending was apparent over 30°N and 30°S due to the increase in surface temperature. Weak descending can be found over 60°N and 60°S, while strong descending was found over the equator. These differences suggested that the Hadley circulation was further inhibited in PIM_clm. Ming and Ramaswamy (2011) and Wang, Jiang, and Su (2015) indicated that the modern-day aerosol can cause a weakening in Hadley circulation mainly though the redistribution of radiation. By altering the large scale of radiation budget, the modern-day aerosols caused an increase in atmospheric temperature above 200 hPa over the tropics and the associated reduction in tropopause height was attributed to the weakened tropical convections (Wang, Jiang, & Su, 2015). Increase in temperature can be found around 200 hPa over

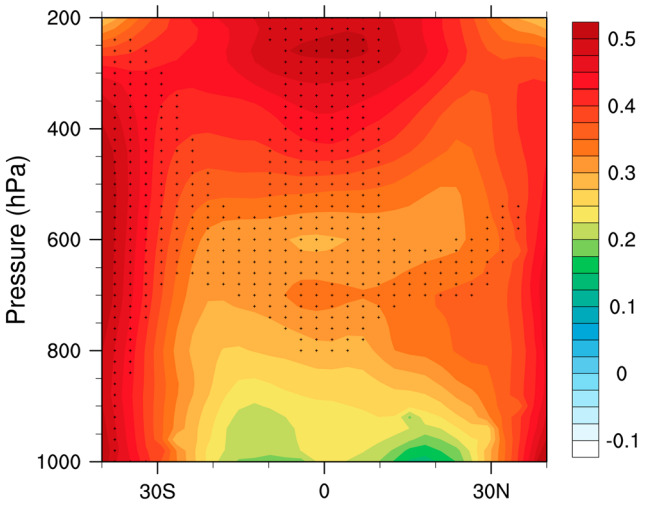

Figure 10. The differences in atmospheric temperature between PIM_clm and EM_clm.

tropics compared PIM_clm to EM_clm (Figure 10), which caused the descending enhancement over tropics and was an important reason for the inhabitation on Hadley circulation. The cross-equator wind in both the upper and lower troposphere was suppressed in PIM_clm, which indicated the weakening in the southward shift of the ITCZ. Compared to EM_clm, the increase in atmospheric temperature in PIM_clm was generally larger over the northern tropic than over the southern tropic (Figure 10). This resulted in a smaller tropical temperature gradient, and thus weakened the cross-equator transportation of energy and water vapor. Compared to EM_clm, the stronger descending over 60°S in PIM_clm could also suppress the cold air transportation from the South Pole to the oceans around the Antarctic, increasing the surface temperature near 60°S. A large scale of airflow convergence was apparent in the lower troposphere over 15°N to 60°N, indicating that the latitudinal diffusion of aerosols in the midlatitudes of the NH was further suppressed than that in EM_clm. This could associate with the increase in aerosol column burden over the midlatitude and low latitude of the NH (Figure 1a).

The low-level jet stream between 850 and 700 hPa is important to water vapor transportation. Since 1850, a strong enhancement of the westerly wind at 850 hPa appeared at 30°N to 45°N in EM_clm (Figure 11a), which favored water vapor transportation from the Atlantic Ocean to Western Europe and the transportation of anthropogenic aerosols from North America and East Asia to remote ocean areas. A strong enhancement of the easterly wind was apparent near 60°S and over the northern Atlantic Ocean at 50°N to 75°N. Enhancement of the easterly wind was also found over the Pacific Ocean to the north of the equator.

The differences in the wind field at 850 hPa between PIM_clm and EM_clm were most notable over midlatitude and high latitude (Figure 11b). Easterly enhancement of wind was found over Canada, the Atlantic Ocean in the midlatitude and high latitude of the NH, and the northern Pacific Ocean. The enhancement of easterly wind helped to transport more water vapor from the oceans to North America and northeast Asia, and thus caused a small increase in precipitation (Figure 14). However, the enhancement led to an inhibitory effect on the diffusion of anthropogenic aerosols and amplified their regional climate effects over North America and East Asia. In PIM_clm, the northeast wind was enhanced over the northern India and the water vapor imported from the Indian Ocean was reduced. In addition, only few water vapor could be transported from China to India due to the high terrain elevation of the Tibetan Plateau. As a result, a reduction in precipitation was apparent over the northern India (Figure 14). In PIM_clm, the cyclonic circulation over the North Pacific Ocean was considerably strengthened in winter compared to EM_clm and could influence the large-scale transportation of heat and water vapor over the northern Pacific Ocean and the western coast of North America.

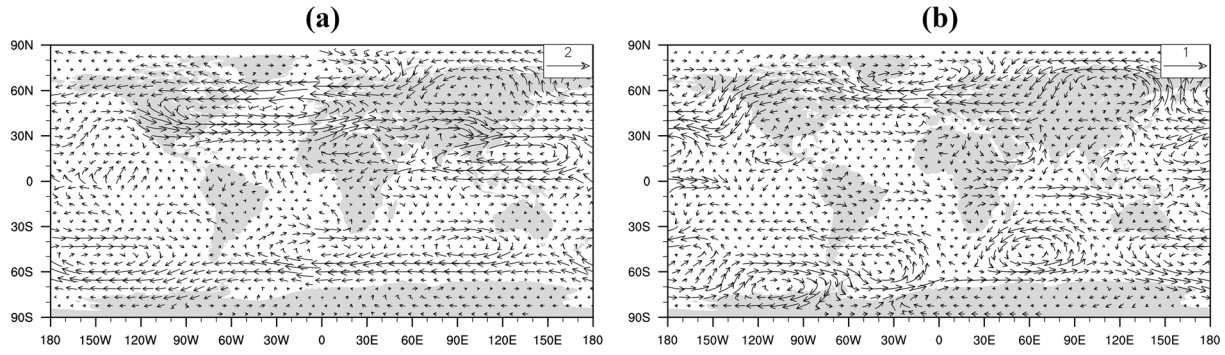

Figure 11. Differences in the wind field (m s^{-1}) at 850 hPa: (a) the differences since 1850 in EM_clm and (b) the differences between PIM_clm and EM_clm at present day.

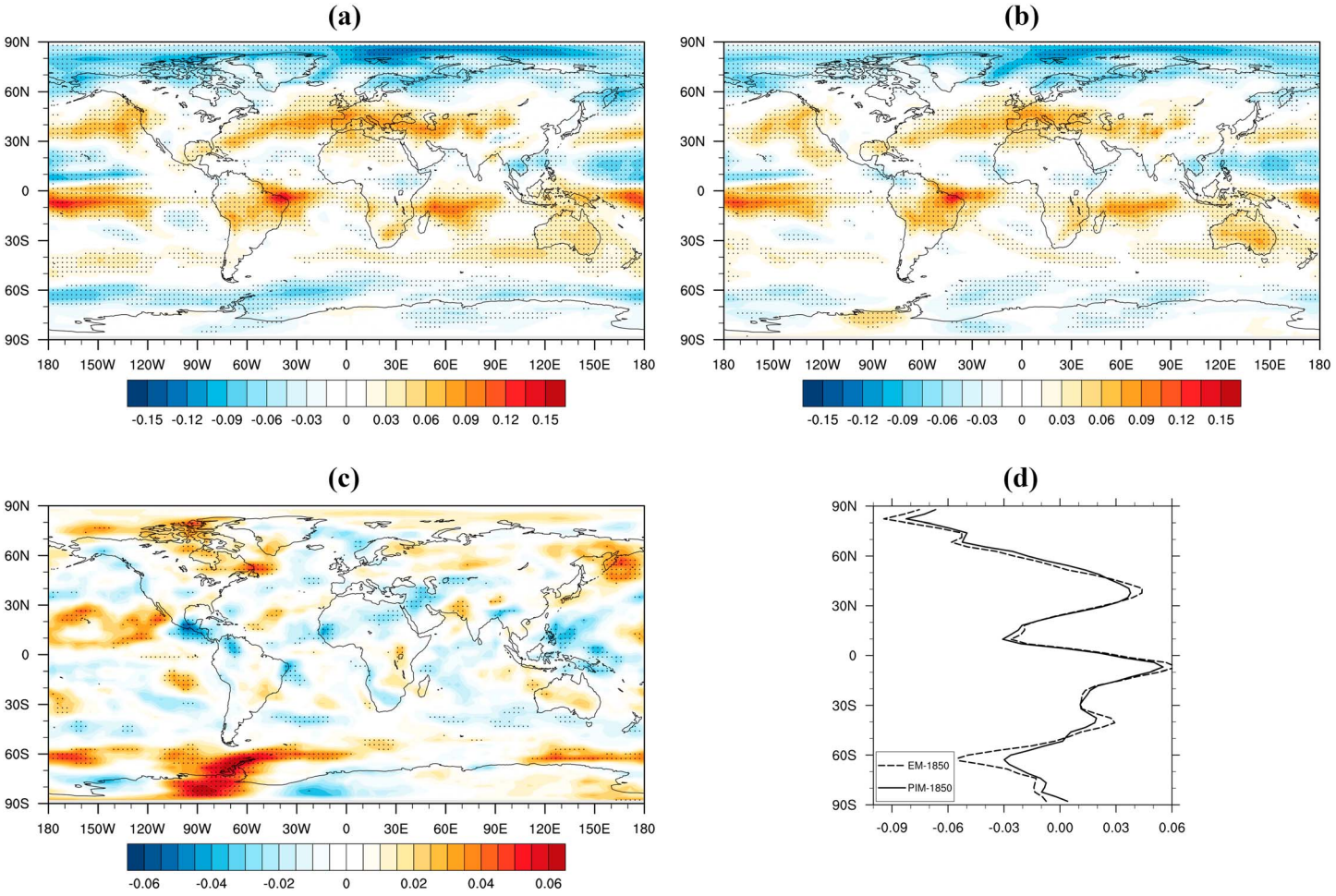

Figure 12. Changes in the amount of vertical accumulated cloud (fraction) due to anthropogenic aerosols since 1850: (a) in EM_clm, (b) in PIM_clm, (c) the differences between PIM_clm and EM_clm, and (d) the latitudinal mean value of Figures 12a and 12b.

4.4. Cloud and Precipitation

Cloudiness is an important indicator of moisture budget and the water balance between the atmosphere and surface. The simulated global annual mean vertical accumulated cloud cover (sum of low, middle, and high clouds as fractions) in 1850 was 0.613 and increased by about 0.01 in both mixing schemes at the present day.

In EM_clm, notable increases in cloud amount since 1850 appeared in 0 to 30°S and 30°N to 60°N, while decreases appeared in 0 to 30°N, near 60°S, and over the North Pole (Figure 13c). Most of the grids that showed a change in cloudiness above 0.015 have passed the significance test. Large increases in cloud amount were apparent from the northern Atlantic Ocean to central Asia, South America, South Africa, Australia, and the central Pacific Ocean (Figure 13a). Since 1850, anthropogenic aerosols have provided much more effective CCNs in the midlatitudes of the NH, South America, and central Africa, thus helped to generate more cloud in these areas. However, no notable increase in cloud amount was found in East Asia due to the simultaneous increase in the low-cloud amount (due to more CCNs) and decrease in the amount of the higher cloud (due to the decreased temperature in the lower atmosphere that increased the atmospheric stability). The change in the low-level jet stream (Figure 12a) strengthened the sea-land breeze and offshore wind over South America, South Africa, and the Sahara Desert and caused more cloud over the land areas and slightly less cloud over the offshore wind-affected areas. A large increase in cloud amount was seen in the low latitudes of the SH, while a smaller decrease was seen on the other side of the equator. This was mainly due to the southward shift of the ITCZ. Large reductions in the cloud amount (mainly low cloud) were apparent over the North Pole and the oceans around the Antarctic, which were due to the decrease in surface temperature (Figure 6a) and enhanced descending (Figure 9a).

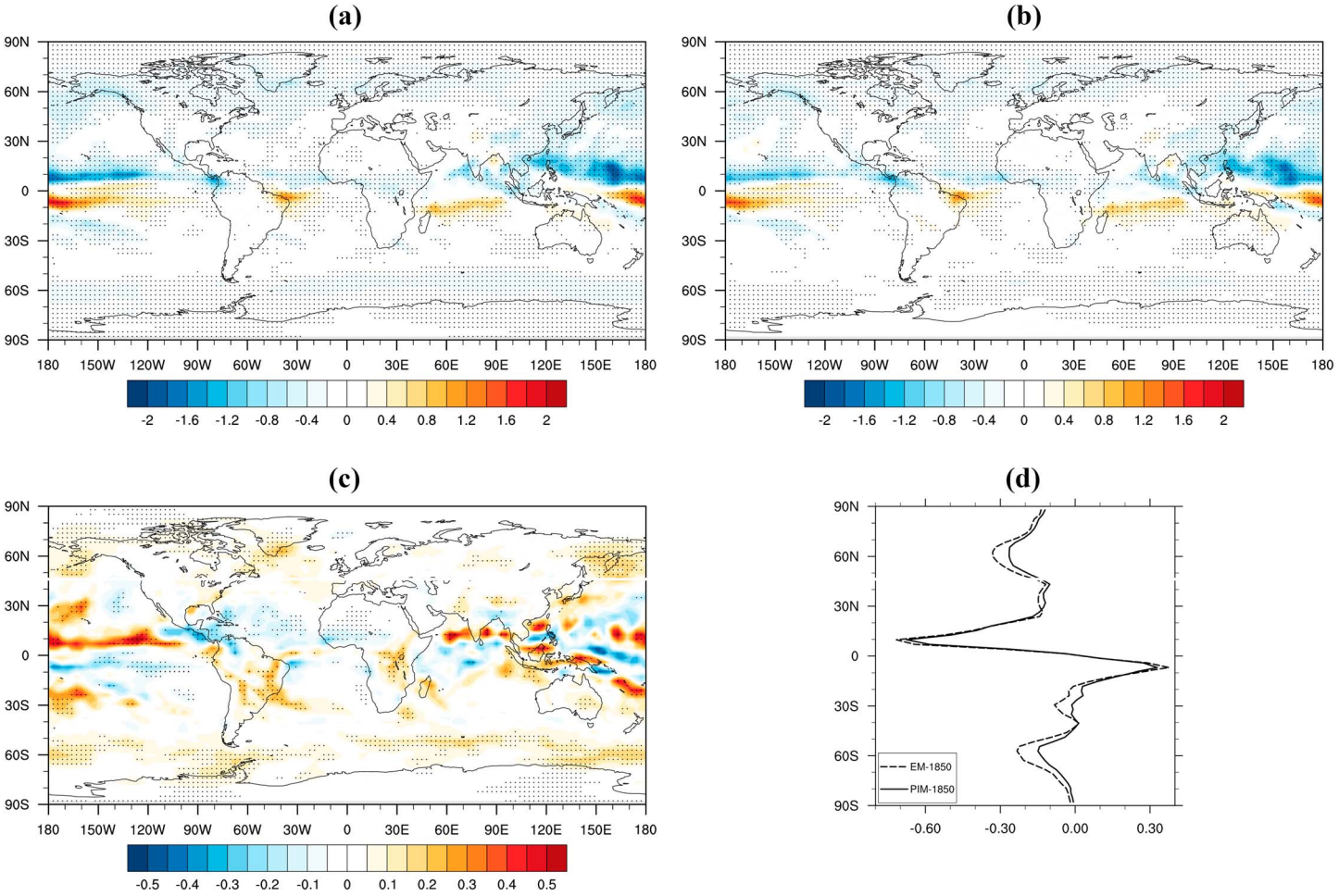

Figure 13. Changes in precipitation (mm d^{-1}) due to anthropogenic aerosols since 1850: (a) in EM_clm, (b) in PIM_clm, (c) the differences between PIM_clm and EM_clm, and (d) the latitudinal mean value of Figures 13a and 13b.

In PIM_clm, major changes in the cloud amount since 1850 were similar to those in EM_clm, but usually with a smaller magnitude (Figures 12b and 12d). Most of the grids that showed a change in cloudiness above 0.015 have passed the significance test. Compared to 1850, increases in cloud amount were concentrated in 0 to 30°S and 30°N to 60°N, while decreases were concentrated in the low latitudes of the NH and the North Pole. The activated particle number was reduced in PIM_clm compared to EM_clm, but the water vapor supply was simultaneously increased due to more evaporation. Therefore, no notable change in cloud amount was apparent over the anthropogenic aerosol concentrated areas (Figure 12c). Most of the differences in cloud amount between PIM_clm and EM_clm matched well with the changes in water vapor transportation, and the meridional circulation showed in section 4.3. The strongest decrease was shown over the Panama region since the evaporation over the Atlantic Ocean in 0 to 30°N was considerably reduced compared to EM_clm. The strongest increase was seen near 60°S due to the higher surface temperature and evaporation compared to EM_clm.

Since 1850, the global annual mean precipitation has decreased by about 0.14 and 0.11 mm d^{-1} in EM_clm and PIM_clm, respectively. Most areas in the tropics and high latitudes showed statistical significance in changes, while most of the grids in the midlatitudes of the SH did not show statistical significance. In both EM_clm and PIM_clm, the major changes in precipitation occurred in the tropics of both hemispheres (Figures 13a and 13b). Strong decreases of about 0.8 to 2+ mm d^{-1} occurred over the Pacific Ocean north of the equator, while strong increases of about 0.6 to 2+ mm d^{-1} occurred over the tropics of the SH. The changes in tropical precipitation clearly indicated the southward shift of the ITCZ. The larger decreases in

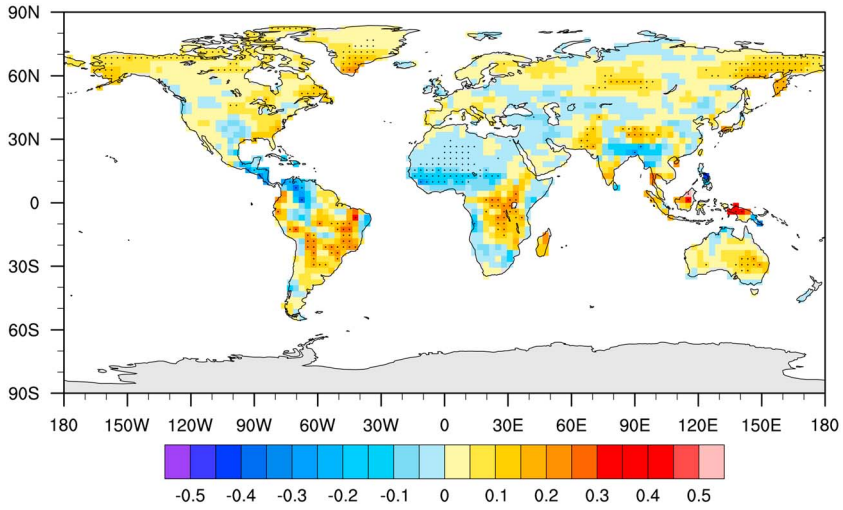

Figure 14. Differences in precipitation (mm d^{-1}) over land areas between PIM_clm and EM_clm.

precipitation happened near 60°S and 60°N due to the decreases in cloud amount and evaporation. Compared to EM_clm, the changes in precipitation over tropics were reduced in PIM_clm (Figure 13c), since the ITCZ was less southward shifted. The precipitation was increased compared to EM_clm near the 60°S, corresponding to the increased cloud amount and evaporation. Guo et al. (2015) examined 24 historical experiments from CMIP5 and found a reduction in monsoon precipitation over South and East Asia since preindustrial due to the combined aerosol-radiation and aerosol-cloud interactions. Our simulation results suggested the same trend.

Compared to EM_clm, most of the land areas showed increases in precipitation in PIM_clm, and the annual mean value was 0.024 mm d^{-1} higher (Figure 14). Notable decreases in precipitation were mainly found over south of the Sahara Desert, northeast India, and northern South America. Although the southward shift of the ITCZ was weakened in PIM_clm, the decrease in precipitation can still be found in the south of the Sahara Desert, possibly due to the strong descending motion. A large decrease (about 0.2 mm d^{-1}) in precipitation was shown over northeast India (different from Figure 1b due to the inclusion of sea temperature and ice feedback). Guo et al. (2015) explained that the decrease over northeast India was due to the decrease in evaporation, because the increase in sulfate aerosol burden since preindustrial has provided more CCNs and thus caused stronger cloud reflection to solar radiation. However, our results suggested that the decrease was mainly due to the suppressed moisture import from the Indian Ocean (Figure 11b), since aerosol column burden and cloud amount were both lower over northeast India in PIM_clm than those in EM_clm. As the evaporation was lower over the equatorial Atlantic Ocean and the north of the Amazon Basin, a large decrease (0.2 to 0.3 mm d^{-1}) in precipitation was appearing over the northern South America and Panama region. Increase in precipitation was mainly found over central South America, central Africa, and Australia, as evaporation and ascending motion were enhanced over the midlatitude and low latitude of the SH. Weak increases were apparent over most part of the midlatitude and high latitude of the NH as a result of enhancement of evaporation. Enhanced sea-land breeze caused more precipitation over eastern Siberia, Iran Plateau, Greenland, and South Asia. No notable change in precipitation was seen over East Asia, where both the evaporation and water vapor import was enhanced. Possibly due to the increased activated particle number (Figure 5b) reduced the sizes of cloud droplets, and thus suppressed precipitation.

5. Cases With Other IM Rates

Another set of tests were carried to study the impacts of aerosol IM on a full IM rate spectrum. In these tests, 50%, 70%, 90%, and 100% of IM rates were considered, and changes in ERF and surface temperature were given correspondingly (Figure 15).

The ERFs of anthropogenic aerosols and the changes in surface temperature since 1850 were −0.82/−0.35/0.40/1.04 W m^{-2} and −0.69/−0.19/0.52/1.30 K corresponding to 50/70/90/100% of IM rates. The increase in

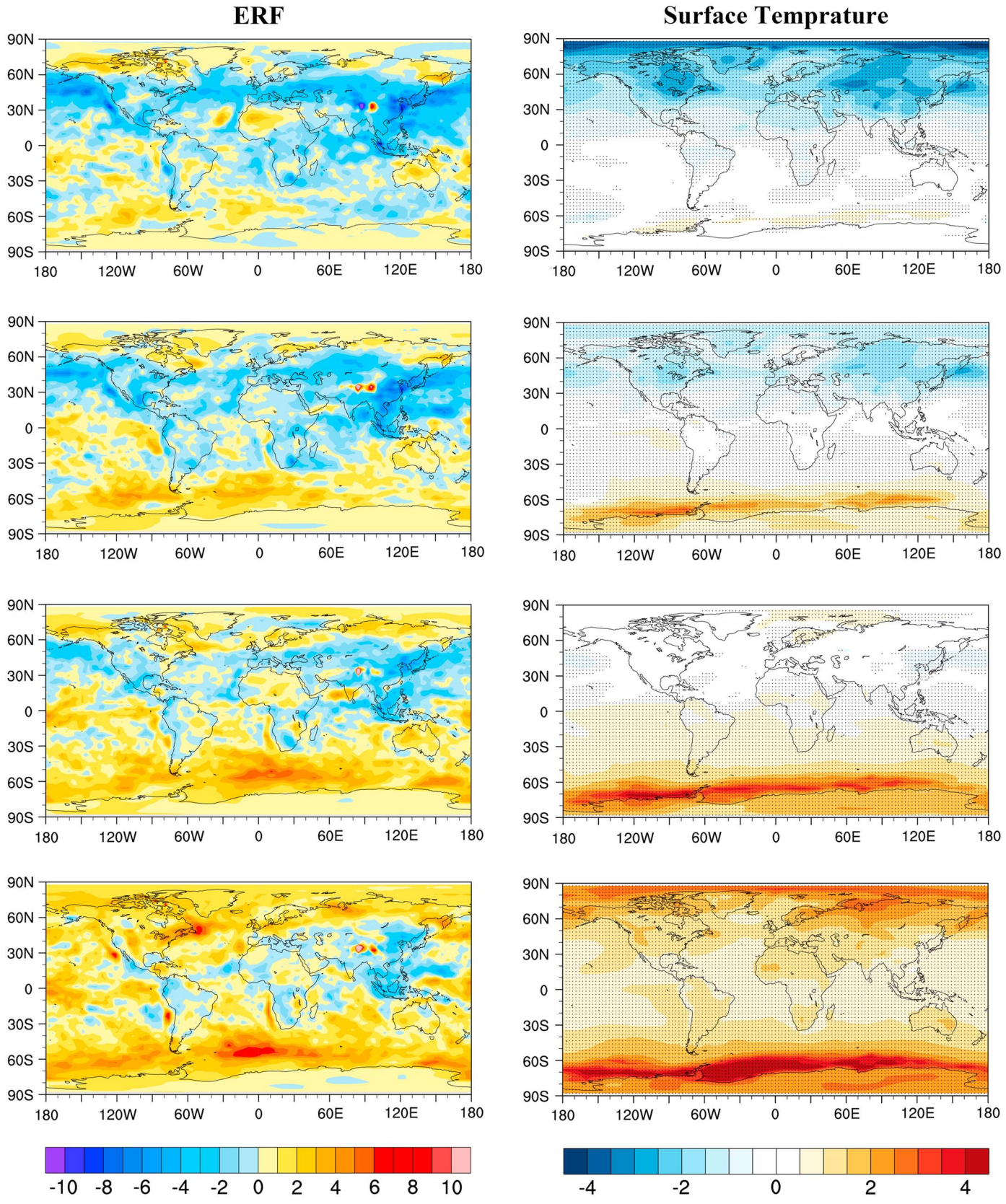

Figure 15. Annual mean ERF (W m^{-2}) of anthropogenic aerosols and changes in surface temperature (K) since 1850 corresponding to 50/70/90/100% (from top to bottom line) of IM rate.

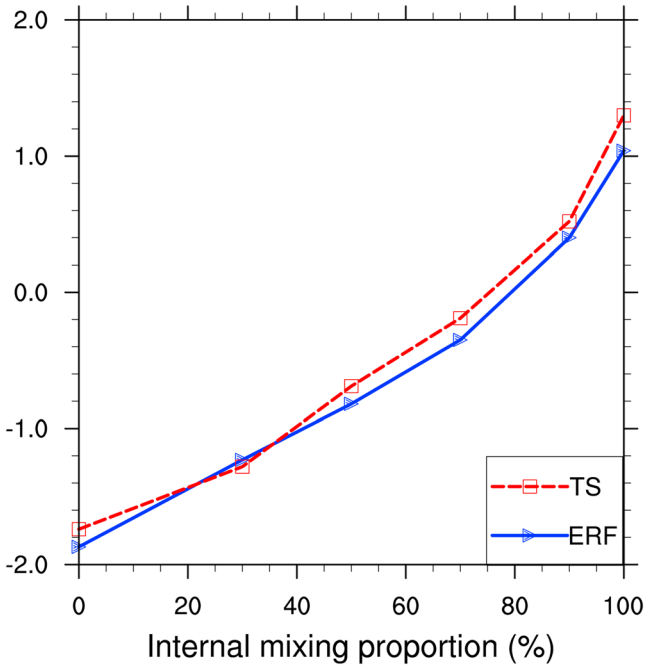

Figure 16. Change in annual mean ERF and surface temperature with IM rate. The English in this document has been checked by at least two professional editors, both native speakers of English. For a certificate, please see http://www.textcheck.com/certificate/0hdi2D

IM rate can cause globally positive changes in ERF, especially over the SH mainly due to the decrease in cloud. Most areas of the SH and high latitudes of the NH showed positive ERF when IM rate reaches 70%. The increase in IM rate can also strengthen the positive changes in surface temperature globally, especially over areas around Antarctica and over the North Pole mainly due to the amplification of sea ice. Combined with the differences between EM and PIM cases discussed earlier, the patterns of the changes in ERF and surface temperature remain similar in different ranges of IM rate compared to EM case.

Both ERF and surface temperature change approximately linearly with IM rate, but the slopes increase as IM rate grows (Figure 16). The ratios of global mean ERF (W m^{-2}) to IM rate (%) are 0.022, 0.038, and 0.064 (W m^{-2} for per percentage of IM rate) in IM rate ranges of 0 to 70%, 70% to 90%, and 90% to 100%. The ratios of the change in global mean surface temperature (K) to IM rate (%) are about 0.023, 0.036, and 0.078 (K for per percentage of IM rate) in the corresponding IM rate ranges stated above.

6. Conclusions

Two mixing schemes of external mixing (EM) and partial internal mixing (PIM) of BC, sulfate, and OC were examined in this study. The aerosol-climate coupled model, BCC_AGCM_2.0_CUACE/Aero, was used to simulate the ERF and climatic impacts of anthropogenic aerosols since 1850. The influences of IM on the optical properties, hygroscopicity, and concentration of the aerosol particles were considered. Comparisons were made between the two mixing schemes in terms of changes in AOD, ERF, surface temperature, evaporation, relative humidity, atmospheric circulation, cloud amount, and precipitation.

The increase in global mean AOD of anthropogenic aerosols at the wavelength of 550 nm since 1850 was 0.022 and 0.021 due to EM and PIM, respectively. However, the proportion of AAOD in AOD was much higher in PIM, especially in areas with high concentrations of both BC and sulfate, e.g., East Asia and India. The difference in AOD was mainly due to the change in the column burden of anthropogenic aerosols other than the differences in optical properties. The global annual mean ERF since 1850 was −1.87 W m^{-2} (with −0.49 and −1.38 W m^{-2} as ERF_{ari} and ERF_{aci}, respectively) and −1.23 W m^{-2} (with −0.23 and −1.01 W m^{-2} as ERF_{ari} and ERF_{aci}, respectively) in the EM and PIM schemes, respectively. In the simulations, part of the pure soluble aerosols was formed into smaller IM particles in the PIM scheme. These particles were harder to activate than the pure ones mainly due to smaller sizes. The reduction in the number of activated aerosol particles suppressed the cloud generation and lowers the cloud albedo simultaneously in the PIM scheme. This change in cloud properties was responsible for the positive change in ERF over many areas. However, a much stronger negative ERF was seen over East Asia in PIM scheme due to enhanced lower clouds, since the evaporation, water vapor import, and convective motion were enhanced.

The global mean surface temperature has decreased by 1.74 and 1.28 K since 1850 in the EM and PIM schemes, respectively. PIM can weaken the cooling effect of anthropogenic aerosols on the surface by higher absorption and lower cloud scattering (fewer CCNs would result in larger cloud droplets). The global annual mean evaporation has decreased by 0.14 and 0.11 mm d^{-1}, but the relative humidity near the surface has increased by 3.4% and 3.5% in EM and PIM, respectively, mainly due to the marked cooling on the surface. In both mixing schemes, anthropogenic aerosols suppressed the Hadley circulation and caused the ITCZ to shift southward. However, the Hadley circulation was more suppressed and the ITCZ was less southward shifted in PIM scheme. The global annual mean precipitation has decreased by 0.14 and 0.11 mm d^{-1} since 1850 based on the EM and PIM schemes, respectively. Due to the southward shift of the ITCZ, precipitation increased markedly in the low latitudes of the SH but decreased even more largely in the low latitudes of the NH in both mixing schemes. The precipitation over land areas was generally higher in the PIM scheme than in EM scheme.

Both ERF and surface temperature change positively with IM rate in approximately linear correlations on the full IM rate spectrum, and the slopes increase as IM rate grows. Compared to EM case, the changing patterns of ERF and surface temperature remain similar regardless of the difference in IM rate. This might imply a relatively high certainty in the climatic effects of aerosol IM despite the low certainty in the physical properties of IM particle. To accurately simulate aerosol IM, a lot more observation and experiment are needed to obtain three-dimensional IM information on a global scale.

Acknowledgments
This work was financially supported by the (Key) National Natural Science Foundation of China (91644211 and 41575002), the National Key R&D Program of China (2017YFA0603502), and Colleges and Universities in Jiangsu Province Plans to Graduate Research and Innovation (KYLX_0845). All data for this paper are properly cited and referred to in the reference list.

References

Abel, S. J., Haywood, J. M., Highwood, E. J., Li, J., & Buseck, P. R. (2003). Evolution of biomass burning aerosol properties from an agricultural fire in southern Africa. *Geophysical Research Letters*, *30*(15), 1783. https://doi.org/10.1029/2003GL017342

Adachi, K., & Buseck, P. R. (2008). Internally mixed soot, sulfates, and organic matter in aerosol particles from Mexico Coty. *Atmospheric Chemistry and Physics*, *8*, 6464–6481. https://doi.org/10.5194/acpd-8-9179-2008

Adams, P. J., & Seinfeld, J. H. (2003). Disproportionate impact of particulate emissions on global cloud condensation nuclei concentrations. *Geophysical Research Letters*, *30*(5), 1239. https://doi.org/10.1029/2002GL016303

Andreae, M. O., Charlson, R. J., Bruynseels, F., Storms, H., Van Grieken, R., & Maenhaut, W. (1986). Internal mixture of sea salt, silicates, and excess sulfate in marine aerosols. *Science*, *232*(4758), 1620–1623. https://doi.org/10.1126/science.232.4758.1620

Bauer, S. E., Menon, S., Koch, D., Bond, T. C., & Tsigaridis, K. (2010). A global modeling study on carbonaceous aerosol microphysical characteristics and radiative forcing. *Atmospheric Chemistry and Physics*, *10*(15), 7439–7456. https://doi.org/10.5194/acp-10-7439-2010

Bohren, C. F., & Huffman, D. R. (1998). *Absorption and scattering of light by small particles*. New York: Wiley-Interscience Publication.

Bond, T. C., Doherty, S. J., Fahey, D. W., Forster, P. M., Berntsen, T., DeAngelo, B. J., … Zender, C. S. (2013). Bounding the role of black carbon in the climate system: A scientific assessment. *Journal of Geophysical Research: Atmospheres*, *118*, 5380–5552. https://doi.org/10.1002/jgrd.50171

Bond, T. C., Habib, G., & Bergstrom, R. W. (2006). Limitations in the enhancement of visible light absorption due to mixing state. *Journal of Geophysical Research*, *111*, D20211. https://doi.org/10.1029/2006JD00731

Boucher, O., Randall, D., Artaxo, P., Bretherton, C., Feingold, G., Forster, P., … Zhang, X. Y. (2013). Clouds and aerosols. In T. F. Stocker, et al. (Eds.), *Climate change 2013: The Physical Science Basis. Contribution of working group I to the Fifth Assessment Report of the Intergovernmental Panel on: Climate Change* (pp. 571–658). Cambridge University Press.

Broccoli, A. J., Dahl, K. A., & Stouffer, R. J. (2006). Respond of the ITCZ to Northern Hemisphere cooling. *Geophysical Research Letters*, *33*, L01702. https://doi.org/10.1029/2005GL024546

Cohen, J. L., Furtado, J. C., Barlow, M. A., Alexeev, V. A., & Cherry, J. E. (2012). Arctic warming, increasing snow cover and winter cooling. *Environmental Research Letters*, *7*(1), 014007. https://doi.org/10.1088/1748-9326/7/1/014007

Deboudt, K., Flament, P., Choël, M., Gloter, A., Sobanska, S., & Colliex, C. (2010). Mixing state of aerosols and direct observation of carbonaceous and marine coatings on African dust by individual particle analysis. *Journal of Geophysical Research*, *115*, D24207. https://doi.org/10.1029/2010JD013921

Garnett, J. C. M. (1904). Colors in metal glasses and in metallic films. *Philosophical Transactions of the Royal Society*, *203*, 385–420. https://doi.org/10.1098/rsta.1904.0024

Ghan, S. J., Easter, R. C., Hudson, J. G., & Bréon, F.-M. (2001). Evaluation of aerosol indirect radiative forcing in MIRAGE. *Journal of Geophysical Research*, *106*, 5317–5334. https://doi.org/10.1029/2000JD900501

Ghan, S. J., Liu, X., Easter, R. C., Zaveri, R., Rasch, P., & Shi, X. (2012). Toward a minimal representation of aerosols in climate: Description and evaluation in the community atmosphere model CAM5. *Geoscientific Model Development*, *5*(3), 709–739. https://doi.org/10.5194/gmd-5-709-2012

Gong, S. L., Barrie, L. A., & Lazare, M. (2002). Canadian Aerosol Module (CAM): A size-segregated simulation of atmospheric aerosol processes for climate and air quality models 2. Global sea-salt aerosol and its budgets. *Journal of Geophysical Research*, *107*(D24), 4779. https://doi.org/10.1029/2001JD002004

Gong, S. L., Barrie, L. A., Blanchet, J. P., Von Salzen, K., Lohmann, U., Lesins, G., … Huang, P. (2003). Canadian Aerosol Module: A size-segregated simulation of atmospheric aerosol processes for climate and air quality models 1. Module development. *Journal of Geophysical Research*, *108*(D1), 4007. https://doi.org/10.1029/2001JD002002

Guo, L., Turner, A. G., & Highwood, E. J. (2015). Impacts of 20th century aerosol emissions on the South Asian monsoon in the CMIP5 models. *Atmospheric Chemistry and Physics*, *15*, 6367–6378. https://doi.org/10.5194/acp-15-6367-2015

Hansen, J., Sato, M., Ruedy, R., Nazarenko, L., Lacis, A., Schmidt, G. A., … Zhang, S. (2005). Efficacy of climate forcings. *Journal of Geophysical Research*, *110*, D18104. https://doi.org/10.1029/2005JD005776

Hwang, Y. T., Frierson, M. W., & Kang, S. M. (2013). Anthropogenic sulfate aerosol and the southward shift of tropical precipitation in the late 20th century. *Geophysical Research Letters*, *40*, 1–6. https://doi.org/10.1002/grl.50502

IPCC (2013). *Climate change 2013: The physical science basis. Contribution of Working Group I to the Fifth Assessment Report of the Intergovernmental Panel on Climate Change*. Cambridge, United Kingdom and New York: Cambridge University Press.

Jacobson, M. Z. (2000). A physically-based treatment of elemental carbon optics: Implications for global direct forcing of aerosols. *Geophysical Research Letters*, *27*, 217–220. https://doi.org/10.1029/1999GL010968

Jacobson, M. Z. (2001). Strong radiative heating due to the mixing state of black carbon in atmospheric aerosols. *Nature*, *409*(6821), 695–697. https://doi.org/10.1038/35055518

Jiang, J. H., Su, H., Zhai, C., Janice Shen, T., Wu, T., Zhang, J., … Shiotani, M. (2015). Evaluating the diurnal cycle of upper tropospheric ice clouds in climate models using SMILES observations. *Journal of the Atmospheric Sciences*, *72*(3), 1022–1044. https://doi.org/10.1175/JAS-D-14-0124.1

Jiang, J. H., Su, H., Zhai, C., Su, H., Zhai, C., Perun, V. S., … Del Genio, A. (2012). Evaluation of cloud and water vapor simulations in CMIP5 climate models using NASA A-Train satellite observations. *Journal of Geophysical Research*, *117*, D1410. https://doi.org/10.1029/2011JD017237

Jing, X. W., & Zhang, H. (2012). Application and evaluation of McICA cloud-radiation framework in the AGCM of the National Climate Center. *Chinese Journal of Atmospheric Sciencesi. (in Chinese)*, *36*(5), 945–958. https://doi.org/10.3878/j.issn.1006-9895.2012.11155

Kirkevåg, A., Iversen, T., Seland, Ø., Debernard, J. B., Storelvmo, T., & Kristjánsson, J. E. (2008). Aerosol-cloud-climate interactions in the climate model CAM-Oslo. *Tellus A*, *60*(3), 492–512. https://doi.org/10.1111/j.1600-0870.2008.00313.x

Koch, D., Schulz, M., Kinne, S., McNaughton, C., Spackman, J. R., Balkanski, Y., … Zhao, Y. (2009). Evaluation of black carbon estimations in global aerosol models. *Atmospheric Chemistry and Physics*, *9*(22), 9001–9026. https://doi.org/10.5194/acp-9-9001-2009

Köhler, H. (1936). The nucleus in and the growth of hygroscopic droplets. *Transactions of the Faraday Society*, *32*(0), 1152–1161. https://doi.org/10.1039/TF9363201152

Lesins, G., Chylek, P., & Lohmann, U. (2002). A study of internal and external mixing scenarios and its effect on aerosol optical properties and direct radiative forcing. *Journal of Geophysical Research*, *107*(D10), 4094. https://doi.org/10.1029/2001JD000973

Liu, D. T., Whitehead, J., Alfarra, M. R., Reyes-Villegas, E., Spracklen, D. V., Reddington, C. L., … Allan, J. D. (2017). Black-carbon absorption enhancement in the atmosphere determined by particle mixing state. *Nature Geoscience*, *10*(3), 184–188. https://doi.org/10.1038/ngeo2901

McMeeking, G. R., Good, N., Petters, M. D., McFiggans, G., & Coe, H. (2011). Influences on the fraction of hydrophobic and hydrophilic black carbon in the atmosphere. *Atmospheric Chemistry and Physics*, *11*(10), 5099–5112. https://doi.org/10.5194/acp-11-5099-2011

Ming, Y., & Ramaswamy, V. (2011). A model investigation of aerosol-induced changes in tropical circulation. *Journal of Climate*, *24*(19), 5125–5133. https://doi.org/10.1175/2011JCLI4108.1

Myhre, G., Shindell, D., Bréon, F. M., Collins, W., Fuglestvedt, J., Huang, J., … Zhang, H. (2013). Anthropogenic and natural radiative forcing. In T. F. Stocker, et al. (Eds.), *Climate change 2013: The physical science basis. Contribution of Working Group I to the Fifth Assessment Report of the Intergovernmental Panel on Climate Change* (pp. 659–740). Cambridge: Cambridge University Press.

Niklasson, G. A., Granqvist, C. G., & Hunderi, O. (1981). Effective medium models for the optical properties of inhomogeneous materials. *Applied Optics*, *20*(1), 26–30. https://doi.org/10.1364/AO.20.000026

Peng, J. F., Hu, M., Guo, S., Du, Z., Zheng, J., Shang, D., … Zhang, R. (2016). Markedly enhanced absorption and direct radiative forcing of black carbon under polluted urban environments. *Proceedings of the National Academy of Sciences*, *113*(16), 4266–4271. https://doi.org/10.1073/pnas.1602310113

Petters, M. D., & Kreidenweis, S. M. (2007). A single parameter representation of hygroscopic growth and cloud condensation nucleus activity. *Atmospheric Chemistry and Physics*, *7*(8), 1961–1971. https://doi.org/10.5194/acp-7-1961-2007

Pincus, R., Barker, H. W., & Morcrette, J. J. (2003). A fast, flexible, approximate technique for computing radiative transfer in inhomogeneous cloud fields. *Journal of Geophysical Research*, *108*(D13), 4376. https://doi.org/10.1029/2002JD003322

Pósfai, M., Simonics, R., Li, J., Hobbs, P. V., & Buseck, P. R. (2003). Individual aerosol particles from biomass burning in southern Africa: 1. Compositions and size distributions of carbonaceous particles. *Journal of Geophysical Research*, *108*(D13), 8483. https://doi.org/10.1029/2002JD002291

Richard, H. M., Jae, A. E., Kathy, A. H., Manning, M. R., Rose, S. K., van Vuuren, D. P., … Wilbanks, T. J. (2010). The next generation of scenarios for climate change research and assessment. *Nature*, *463*(7282), 747–756. https://doi.org/10.1038/nature08823

Riemer, N., West, M., Zaveri, R., & Easter, R. (2009). Estimating black carbon aging time-scales with a particle-resolved aerosol model, *J. Aerosol Science*, *41*(1), 143–158. https://doi.org/10.1016/j.jaerosci.2009.08.009

Rothman, L. S., Gordon, I. E., Babikov, Y., Barbe, A., Benner, D. C., Bernath, P. F., … Wagner, G. (2005). The HITRAN 2004 molecular spectroscopic database. *Journal of Quantitative Spectroscopy and Radiation Transfer*, *96*(2), 139–204. https://doi.org/10.1016/j.jqsrt.2013.07.002

Rotstayn, L. D., & Lohmann, U. (2002). Tropical rainfall trends and the indirect aerosol effect. *Journal of Climate*, *15*, 2103–2116. https://doi.org/10.1175/1520-0442(2002)015%3C2103:TRTATI%3E2.0.CO;2

Saleh, R., Marks, M., Heo, J., Adams, P. J., Donahue, N. M., & Robinson, A. L. (2015). Contribution of brown carbon and lensing to the direct radiative effect of carbonaceous aerosols from biomass and biofuel burning emissions. *Journal of Geophysical Research: Atmospheres*, *120*, 19. https://doi.org/10.1002/2015JD023697-T

Screen, J. A., & Simmonds, I. (2010). The central role of diminishing sea ice in recent Arctic temperature amplification. *Nature*, *464*(7293), 1334–1337. https://doi.org/10.1038/nature09051

Seinfeld, J. H., & Pandis, S. N. (2012). *Atmospheric chemistry and physics: From air pollution to climate change*. New York: John Wiley & Sons.

Sherwood, S. C., Bony, S., Boucher, O., Bretherton, C., Forster, P. M., Gregory, J. M., & Stevens, B. (2015). Adjustments in the forcing-feedback framework for understanding climate change. *Bulletin of the American Meteorological Society*, *96*(2), 217–228. https://doi.org/10.1175/BAMS-D-13-00167.1

Shiraiwa, M., Kondo, Y., Moteki, N., Takegawa, N., Sahu, L. K., Takami, A., … Blake, D. R. (2008). Radiative impact of mixing state of black carbon aerosol in Asian outflow. *Journal of Geophysical Research*, *113*, D24210. https://doi.org/10.1029/2008JD010546

Vanderlei, M. J., Artaxo, P., Liousse, C., Reid, J. S., Hobbs, P. V., & Kaufman, Y. J. (1998). Effects of black carbon content, particle size, and mixing on light absorption by aerosols from biomass burning in Brazil. *Journal of Geophysical Research*, *103*, 32,041–32,050. https://doi.org/10.1029/98JD02593

Wang, X., Heald, C. L., Ridley, D. A., Schwarz, J. P., Spackman, J. R., Perring, A. E., … Clarke, A. D. (2014). Exploiting simultaneous observational constraints on mass and absorption to estimate the global direct radiative forcing of blackcarbon and brown carbon. *Atmospheric Chemistry and Physics*, *14*(20), 10,989–11,010. https://doi.org/10.5194/acp-14-10989-2014

Wang, Y., Jiang, J. H., & Su, H. (2015). Atmospheric responses to the redistribution of anthropogenic aerosols. *Journal of Geophysical Research: Atmospheres*, *120*, 9625–9641. https://doi.org/10.1002/2015JD023665

Wang, Z. L., Zhang, H., Jing, X. W., & Wei, X. (2013). Effect of non-spherical dust aerosol on its direct radiative forcing. *Atmospheric Research*, *120-121*, 112–126. https://doi.org/10.1016/j.atmosres.2012.08.006

Wang, Z. L., Zhang, H., Li, J. N., Jing, X., & Lu, P. (2013). Radiative forcing and climate response due to the presence of black carbon in cloud droplets. *Journal of Geophysical Research: Atmospheres*, *118*, 3662–3675. https://doi.org/10.1002/jgrd.50312

Wang, Z. L., Zhang, H., & Zhang, X. Y. (2015). Projected response of East Asian summer monsoon system to future reductions in emissions of anthropogenic aerosols and their precursors. *Climate Dynamics*, *47*, 1455–1468. https://doi.org/10.1007/s00382-015-2912-7

Wei, X. D., & Zhang, H. (2011). Analysis of optical properties of non-spherical dust aerosols. *Acta Optica Sinica (in Chinese)*, *31*(5), 0501002. https://doi.org/10.3788/aos201131.0501002

Wu, T., Yu, R., & Zhang, F. (2010). The Beijing Climate Center atmospheric general circulation model: Description and its performance for the present-day climate. *Climate Dynamics*, *34*, 123–147. https://doi.org/10.1007/s00382-008-0487-2

Zhang, H., Chen, Q., & Xie, B. (2015). A new parameterization for ice cloud optical properties used in BCC_RAD and its radiative impact. *Journal of Quantitative Spectroscopy and Radiation Transfer*, *150*, 76–86. https://doi.org/10.1016/j.jqsrt.2014.08.02

Zhang, H., Jing, X. W., & Li, J. N. (2014). Application and evaluation of a new radiation code under McICA scheme in BCC_AGCM2.0.1. *Geoscientific Model Development*, *7*, 737–754. https://doi.org/10.5194/gmd-7-737-2014

Zhang, H., Wang, Z. L., Wang, Z. Z., Liu, Q., Gong, S., Zhang, X., … Li, L. (2012). Simulation of direct radiative forcing of aerosols and their effects on East Asian climate using an interactive AGCM-aerosol coupled system. *Climate Dynamics*, *38*(7-8), 1675–1693. https://doi.org/10.1007/s00382-011-1121-0

Zhang, H., Wang, Z. L., Zhang, F., & Xianwen, J. (2015). Impact of four-stream radiative transfer algorithm on aerosol direct radiative effect and forcing. *International Journal of Climatology*, *35*(14), 4318–4328. https://doi.org/10.1002/joc.4289

Zhang, H., Zhao, S. Y., Wang, Z. L., Zhang, X., & Song, L. (2016). The updated effective radiative forcing of major anthropogenic aerosols and their effects on global climate at present and in the future. *International Journal of Climatology*, *36*(12), 4029–4044. https://doi.org/10.1002/joc.4613

Zhang, H., Zhou, C., Wang, Z. L., Zhao, S., & Li, J. (2015). The influence of different black carbon and sulfate mixing methods on their optical and radiative properties. *Journal of Quantitative Spectroscopy and Radiation Transfer*, *161*, 105–116. https://doi.org/10.1016/j.jqsrt.2015.04.002

Zhao, S. Y., Zhang, H., Feng, S., & Fu, Q. (2015). Simulating direct effects of dust aerosol on arid and semi-arid regions using an aerosol-climate coupled system. *International Journal of Climatology*, *35*(8), 1858–1866. https://doi.org/10.1002/joc.4093

Zhao, S. Y., Zhang, H., Zhi, X., Wang, Z., & Wang, Z. (2014). A primary assessment of the simulated climatic state by a coupled aerosol-climate model BCC_AGCM2.0.1_CAM. *Climate of Environmental Research (in Chinese)*, *19*(3), 265–277. https://doi.org/10.3878/j.issn.1006-9585.2012.12015

Zhou, C., Zhang, H., Zhao, S. Y., & Li, J. (2017). Simulated effects of internal mixing of anthropogenic aerosols on the aerosol-radiation interaction and global temperature. *International Journal of Climatology*, *37*, 972–986. https://doi.org/10.1002/joc.5050

Zhou, C. H., Gong, S., Zhang, X. Y., Liu, H. L., Xue, M., Cao, G. L., … Niu, T. (2012). Toward the improvements of simulating the chemical and optical properties of Chinese aerosols using an online coupled model-CUACE/Aero. *Tellus B*, *64*(1). https://doi.org/10.3402/tellusb.v64i0.18965

论文编目索引

1. Bao, B., G. Y. Ren. 2018: Sea-Effect Precipitation over the Shandong Peninsula, Northern China. *Journal of Applied Meteorology and Climatology*, 57: 1291-1308. doi:10.1175/JAMC-D-17-0200.1.
2. 卞　韬，任国玉，张立霞. 2018：城市化对石家庄站近地面风速趋势的影响. *气候变化研究进展*，14(1)：21-30.
3. 陈　琪，张　华. 2018：Henye-Greenstein 近似对冰云短波辐射计算的影响. *光学学报*，38(8)：doi:10.3788/AOS201838.0801001.
4. Chao Qingchen, Feng Aiqing. 2018: Scientifc basis of climate change and its response. *Global Energy Interconnection*, 1(4): 420-427. doi:10.14171/j.2096-5117.gei.2018.04.002.
5. Dong S Y, Sun Y. 2018: Comparisons of observational data sets for evaluating the CMIP5 precipitation extreme simulations over Asia. *Climate Research*, 76(2): 161-176.
6. Feng G, Zou M, Qiao S, Zhi R, Gong Z. 2018: The changing relationship between the December North Atlantic Oscillation and the following February East Asian trough before and after the late 1980s. *Climate Dynamics*, doi:10.1007/s00382-018-4165-8.
7. Samantha Ferrett and Matthew Collins, Hongli Ren. 2018: Diagnosing Relationships between Mean State Biases and El Niño Shortwave Feedback in CMIP5 Models. *Journal of Climate*, 1315-1335, doi:10.1175/JCLI-D-17-0331.1.
8. Feng Taichen, Tao Su, Fei Ji, Rong Zhi, Zixuan Han. 2018: Temporal Characteristics of Actual Evapotranspiration Over China Under Global Warming. *Journal of Geophysical Research: Atmospheres*, 123, 5845-5858.
9. 胡　泊，申红艳，王晓娟，封国林. 2018：东北亚地区初夏、盛夏和传统夏季降水特征及环流型的异同性研究. *大气科学*，42(1)：109-123.
10. Li Chengcheng, Hongli Ren, Fang Zhou, Shuanglin Li, et al. 2018: Multi-pentad prediction of precipitation variability over Southeast Asia during boreal summer using BCC_CSM1.2. *Dynamics of Atmospheres and Oceans*, 82, 20-36.
11. Weijing Li, Hongchang Ren, Jinqing Zuo, Hongli Ren. 2018: Early summer southern China rainfall variability and its oceanic drivers. *Clim Dyn*, 50: 4691-4705. doi:10.1007/s00382-017-3898-0.
12. 李维京，刘景鹏，任宏利，左金清. 2018：中国南方夏季降水的年代际变率主模态特征及机理分析. *大气科学*，42(4)：859-876.
13. Li Xin, Qinglong You, Guoyu Ren, Suyan Wang, Yuqing Zhang, et al. 2018: Concurrent droughts and hot extremes in Northwest China from 1961 to 2017. *International Journal of Climatology*, 1-11.
14. Li Yan, Li Qingquan, Wang Qingyuan, et al. 2018: A Comparison and Evaluation of Two Centennial-scale Sea Surface Temperature Datasets in the China Seas and Their Adjacent Sea Areas. *Journal of Tropical Meteorology*, 24(4): 448-456.
15. Liu Jingpeng, Hong Li Ren, Weijing Li and Jinqing Zuo. 2018: Remarkable impacts of Indian Ocean sea surface temperature on interdecadal variability of summer rainfall in Southwestern China. *Atmosphere*, 9(103): doi:10.3390/atmos9030103.
16. Liu Jingpeng, Hongli Ren, Weijing Li and Jinqing Zuo. 2018: Diagnosing the leading mode of interdecadal covariability between the Indian Ocean sea surface temperature and summer precipitation in Southern Chi-

na. *Theoretical and Applied Climatology*, doi:10.1007/s00704-018-2430-8.

17. 刘明竑，任宏利，张文君，任鹏飞. 2018：超强厄尔尼诺事件对中国东部春夏季极端降水频率的影响. 气象学报，76(4)：539-553.
18. Liu Ying, Ren Hongli, et al. 2018: Evaluation and statistical downscaling of East Asian summer monsoon forecasting in BCC and MOHC seasonal prediction systems. *Quarterly Journal of the Royal Meteorological Society*, 144:2798-2811, doi:10.1002/qj.3405.
19. 刘玉莲，任国玉. 2018：基于度-时法的哈尔滨冬季采暖强度评价. *自然资源学报*，33(1)：139-148.
20. 刘玉莲，任国玉，张广英，等. 2018：地面气温对微环境空间差异的响应—以漠河站为例. 气象科技，46(2)：215-223.
21. 刘玉莲，任国玉，孙秀宝. 2018：降水相态分离单临界气温模型建立和检验. *应用气象学报*，29(4)：449-459. doi:10.11898/1001-7313.20180406.
22. Lu B, Jin F F, Ren H L. 2018: A Coupled Dynamic Index for ENSO Periodicity. *Journal of Climate*, 31: 2361-2376.
23. Lu B, Ren H L, Scaife A A, et al. 2018: An extreme negative Indian Ocean Dipole event in 2016: dynamics and predictability. *Climate Dynamics*, 51: 89-100.
24. Lu B, Ren H L, Eade R. 2018: Indian Ocean SST modes and Their Impacts as Simulated in BCC_CSM1.1(m) and HadGEM3. *Advances in Atmospheric Sciences*, 35: 1035-1048.
25. Lu C H, Y Sun, X B Zhang. 2018: Multimodel detection and attribution of changes in warm and cold spell durations. *Environmental Research Letters*, 13: 074013, doi:org/10.1088/1748-9326/aacb3e.
26. Xianwen JING, Hua ZHANG, Masaki SATOH and Shuyun Zhao. 2018: Improving representation of tropical cloud overlap in GCMs based on cloud-resolving model data. *Journal of Meteorological Research*, 32(2): 233-245, doi:10.10.1007/s13351-018-7095-9.
27. Om Kum-Chol, Guoyu Ren, Shuanglin Li, Kang-Chol O. 2018: Climatological characteristics and long-term variation of rainy season and torrential rain over DPR Korea. *Weather and Climate Extremes*, doi: org/10.1016/j.wace.2018.09.003.
28. Yun Qin, Guoyu Ren, Tianlin Zhai, Panfeng Zhang and Kangmin Wen. 2018: A new Methodology for Estimating the Surface Temperature Lapse Rate Based on Grid Data and Its Application in China. *Remote Sensing*, 10.1617; doi:10.3390/rs10101617.
29. Hongli Ren, Bo Lu, Jianghua Wan, Ben Tian and Peiqun Zhang. 2018: Identification Standard for ENSO Events and Its Application to Climate Monitoring and Prediction in China. *Journal of Meteorological Research*, 32(6): 923-936, doi:10.1007/s13351-018-8078-6.
30. Ren Pengfei, Hongli Ren, Joshua Xiouhua Fu, Jie Wu and Liangmin Du. 2018: Impact of boreal summer intraseasonal oscillation on rainfall extremes in southeastern China and its predictability in CFSv2. *Journal of Geophysical Research: Atmospheres*, 123, 4423-4442.
31. Rim C B, K C Om, G Y Ren, Su Song Kim, Hyok Chol Kim, Kang Chol O. 2018: Establishment of a wildfire forecasting system based on coupled weather-wildfire modeling. *Applied Geography*, 90: 224-228.
32. Shen Yuyang, Ren Hongli, Li Weijing, et al. 2018: Relationship Between Summer Low-Frequency Rainfall Over Southern China and Propagation of Tropical Intraseasonal Oscillation. *Journal of Tropical Meteorology*, 24(1): 92-101, doi:10.16555/j.1006-8775.2018.01.009.
33. 孙　劭，王东仟，尹宜舟，等. 2018：2017年全球重大天气气候事件及其成因. 气象，44(4)：556-564.

34. Sun X B, Guoyu Ren, Qinglong You, Yuyu Ren, Wenhui Xu, et al. 2018: Global diurnal temperature range (DTR) changes since 1901. *Climate Dynamics*, doi:org/10.1007/s00382-018-4329-6.
35. Sun Ying, Hu Ting, Zhang Xuebin. 2018: Substantial Increase in Heat Wave Risks in China in a Future Warmer World. *Earth's Future*, 6, 1528-1538, doi.org/10.1029/2018EF000963.
36. 索南看卓，任国玉，贾文茜，孙秀宝. 2018：武汉城市相对湿度气候学特征与长期变化趋势. *气候与环境研究*，23(6)：715-724，doi:10.3878/j.issn.1006-9585.2017.17122.
37. Wang F and Yang S. 2018: Can CFMIP2 models reproduce the leading modes of cloud vertical structure in the CALIPSO-GOCCP observations? *Theoretical and Applied Climatology*, 131: 1465-1477. https://doi.org/10.1007/s00704-017-2051-7.
38. Wan Jianghua, Ren Hongli. 2018: Representation of the ENSO Combination Mode and its Asymmetric SST Response in Different Resolutions of HadGEM3. *Advances in Atmospheric Sciences*. 35(8): 1063-1076.
39. 王海波，张　华，荆现文，谢　冰. 2018：不同云重叠参数对全球和东亚地区模拟总云量的影响. *气象学报*，76(5)：767-778，doi:10.11676/qxxb2018.027.
40. 吴刚哲，严金哲，任国玉，等. 2018：朝鲜中西部地区春季植被覆盖度与气候因子的关系. *气象与环境学报*，34(4)：112-118.
41. 吴　捷，任宏利，许小峰，等. 2018：MJO 对我国降水影响的季节调制和动力-统计降尺度预测. *气象*，44(6)：737-751.
42. Wu Liquan, Li Qingquan, et al. 2018: Preliminary Assessment on the Hindcast Skill of the Arctic Oscillation with Decadal Experiment by the BCC_CSM1.1 Climate. *Model. Advance in Climate change Research*, 9(4): 209-217.
43. Yujie Wu, Wansuo Duan. 2018: Impact of SST Anomaly Events over the Kuroshio-Oyashio Extension on the "Summer Prediction Barrier". *Advances in Atmospheric Sciences*, 35(4): 397-409.
44. Wu Y P, Hu Y Y, Cao H X, Fu C F, Feng G L. 2018: Computing entropy change in synoptic-scale system. *Physica A*, 494, 163-168.
45. Wu Yongping, Zhu Chunyangzi, Feng Guolin, Li B Larry. 2018: Mathematical modeling of fog-Haze evolution. *Chaos, Solitons and Fractals*, 107(2018)1-4.
46. 晏红明，李清泉，王东阡. 2018：云南雨季的时空特征及与大气环流变化的关系. *热带气象学报*，34(1)：12-22.
47. 杨　柳，赵俊虎，封国林. 2018：中国东部季风区夏季四类雨型的水汽输送特征及差异. *大气科学*，42(1)：81-95，doi:10.3878/j.issn.1006-9895.1706.16273.
48. Yin H and Y Sun. 2018: Detection of Anthropogenic Influence on Fixed Threshold Indices of Extreme Temperature. *Journal of Climate*, 31: 6341-6352, doi:10.1175/JCLI-D-17-0853.1.
49. Huang Yu, Hong Li Ren, Robin Chadwick, Zhigang Cheng, Quanliang Chen. 2018: Diagnosing changes of winter NAO in response to different climate forcings in a set of atmosphere-only timeslice experiments. *Atmosphere*, 9(1): 10. doi:10.3390/atmos9010010.
50. Zhan Y J, Ren G Y, Yang S. 2018: Change in precipitation over the Asian continent from 1901－2016 based on a new multi-source dataset. *Climate Research*, 76:41-57. https://doi.org/10.3354/cr01523.
51. 章大全，陈丽娟，柳艳菊，等. 2018：2016 年 10 月我国将水预测失败的原因分析. *气象*，44(1)：189-198.
52. H Zhang, B Xie and Z Wang. 2018: Effective radiative forcing and climate response to short-lived climate pollutants under different scenarios. *Earth's Future*, 6, 857-866.

53. Hua Zhang, Chen Zhou and Shuyun Zhao. 2018: Influences of the internal mixing of anthropogenic aerosols on global aridity change. *Journal of Meteorological Research*, 32(5): 723-733.
54. Junhu Zhao, Liu Yang, Guolin Feng. 2018: Circulation System Configuration Characteristics of Four Rainfall Patterns in Summer over the East China. *Theor Appl Climatol*, 131:1211-1219. doi: 10.1007/s00704-017-2047-3.
55. Zhao J H, Zhou J, Yang L, Hou W, Feng G L. 2018: Inter-annual and inter-decadal variability of early- and late-summer precipitation over Northeast China and their background circulation. *International Journal of Climatology*, 38: 2880-2888. doi:10.1002/joc.5470.
56. 赵俊虎，陈丽娟，王东阡. 2018：2016 年我国梅雨异常特征及成因分析. 大气科学. 42(5)：1055-1066，doi：10.3878/j.issn.1006-9895.1708.17170.
57. 赵俊虎，陈丽娟，熊开国. 2018：基于新监测指标的江南入梅早晚的气候特征及影响系统分析. 气象学报，76(5)：680-698，doi:10.11676/qxxb2018.025.
58. Zhao Shuyun, Zhang Hua, Xie Bing. 2018: The Effects of El Niño-Southern Oscillation on the Winter Haze Pollution of China. *Atmospheric Chemistry and Physics*, 18, 1863-1877.
59. 郑祚芳，任国玉. 2018：北京地区大气湿度变化及城市化影响分析. 气象，44(11)：1471-1478.
60. 支　蓉，陈丽娟，竺夏英. 2018：2017 年秋季我国北方地区降水异常偏多成因分析. 气象，44(4)：572-581.
61. Chen Zhou, Hua Zhang, Shuyun Zhao, Jiangnan Li. 2018: On effective radiative forcing of partial internally and externally mixed aerosols and their effects on global climate. *Journal of Geophysical Research: Atmoshpheres*, 123, 401-423.



LCS

气候研究开放实验室